(31)

VOLUME 30 NUMBER

JANUARY 1969

THE JOURNAL OF PHYSICS AND CHEMISTRY OF SOLIDS

AN
INTERNATIONAL
JOURNAL

Editor-in-Chief
HARVEY BROOKS
Cambridge, Mass.

Associate Editors

H. B. G. CASIMIR
Eindhoven

B. CHALMERS FRAZER
Brookhaven

JACQUES FRIEDEL
Paris

I. M. LIFSHITZ
Kharkov

PERGAMON PRESS NEW YORK · OXFORD · LONDON · PARIS

THE JOURNAL OF PHYSICS AND CHEMISTRY OF SOLIDS

Editors

Prof. Harvey Brooks (*Editor-in-Chief*), 217 *Pierce Hall, Harvard University, Cambridge* 38, *Mass., U.S.A.*

Prof. Dr. H. B. G. Casimir, *N.V. Philips' Gloeilampenfabrieken, Eindhoven, The Netherlands*

Dr. B. Chalmers Frazer, *Brookhaven National Laboratory, Upton, Long Island, New York, U.S.A.*

Prof. Jacques Friedel, *Service de Physique des Solides, Faculté des Sciences* (*Group II*), *B.P. No.* 11, *Orsay*, (*S. & O.*), *France*

Prof. I. M. Lifshitz, *Physico-Technical Institute, Academy of Science, Yumorskii tupik, Khar'kov, U.S.S.R.*

Editorial Advisory Board

U.S.A.

E. N. Adams, White Plains, N.Y.
D. Alpert, Urbana, Ill.
L. Apker, Schenectady, N.Y.
J. Bardeen, Urbana, Ill.
D. S. Billington, Oak Ridge, Tenn.
R. G. Breckenridge, Canoga Park, Calif.
Leo Brewer, Berkeley, Calif.
E. Burstein, Philadelphia, Penn.
J. A. Burton, Murray Hill, N.J.
N. Cabrera, Charlottesville, Va.
G. C. Danielson, Ames, Iowa
G. J. Dienes, Long Island, N.Y.
J. C. Fisher, Schenectady, N.Y.
F. G. Fumi, Chicago, Ill.
H. K. Henisch, University Park, Penn.
F. Herman, Palo Alto, Calif.
C. Herring, Murray Hill, N.J.
A. R. von Hippel, Cambridge, Mass.
J. H. Hollomon, Washington, D.C.
W. V. Houston, Houston, Texas
H. B. Huntington, Troy, N.Y.
H. M. James, Lafayette, Ind.
C. Kittel, Berkeley, Calif.
W. Kohn, La Jolla, Calif.
J. A. Krumhansl, Ithaca, N.Y.
A. W. Lawson, Riverside, Calif.
H. W. Leverenz, Princeton, N.J.
O. T. Marzke, Pittsburgh, Penn.
B. T. Matthias, La Jolla, Calif.
L. R. Maxwell, Silver Spring, Md.
J. E. Mayer, La Jolla, Calif.
J. W. Mitchell, Charlottesville, Va.
E. W. Montroll, Rochester, N.Y.
D. Pines, Urbana, Ill.
M. H. L. Pryce, Los Angeles, Calif.
G. T. Rado, Washington, D.C.
H. Reiss, Thousand Oaks, Calif.
J. R. Reitz, Dearborn, Mich.
A. Rose, Princeton, N.J.
R. A. Smith, Cambridge, Mass.
R. Smoluchowski, Princeton, N.J.
F. H. Spedding, Ames, Iowa
D. Turnbull, Cambridge, Mass.
J. H. Van Vleck, Cambridge, Mass
B. E. Warren, Cambridge, Mass.
E. P. Wigner, Princeton, N.J.
B. H. Zimm, La Jolla, Calif.

Canada

R. E. Burgess, Vancouver
W. B. Pearson, Ottawa

United Kingdom

M. Born, Bad Pyrmont
A. Charlesby, Shrivenham, Berks.
W. J. Dunning, Bristol
F. C. Frank, Bristol
H. Jones, London
A. B. Pippard, Cambridge
O. C. Simpson, Baldock, Herts.
K. W. H. Stevens, Nottingham
F. C. Tompkins, London

Czechoslovakia

J. Tauc, Praha

France

E. F. Bertaut, Grenoble
A. Guinier, Orsay
Louis Néel, Grenoble
Louis Weil, Grenoble

Germany

Ulrich Dehlinger, Stuttgart
R. Hilsch, Gottingen
G. Leibfried, Aachen
E. Mollwo, Erlangen
H. Pick, Stuttgart
W. Welker, Erlangen

Israel

I. Estermann, Haifa

Italy

F. G. Fumi, Palermo

Japan

Toshinosuke Muto, Tokyo

The Netherlands

A. Michels, Amsterdam
G. W. Rathenau, Eindhoven

Sweden

J. O. Linde, Stockholm
Per-Olov Löwdin, Uppsala

Switzerland

G. Busch, Zurich
P. Scherrer, Zurich

U.S.S.R.

G. S. Zhdanov, Moscow

Publishing Offices

American Continent: Pergamon Press Inc., 44–01 21*st Street, Long Island City, N. Y.* 11101.
Rest of the World: Pergamon Press Ltd, 84–86 *Malahide Road, Coolock, Dublin* 5.

Published monthly. *Annual subscription for libraries, research establishments and all other multiple-reader institutions,* $1 *private individuals, whose Departmental Libraries subscribe, may obtain this Journal for their personal use at a reduced price of* *per annum, including postage. All subscription enquiries are to be addressed to The Manager, Subscriptions Department, Pergamon Press, Headington Hill Hall, Oxford, England. Back issues are available, write for Back Issues Price Lists.*

Copyright © 1969 Pergamon Press Ltd.

PERGAMON PRESS, INC.
44-01 21st STREET, LONG ISLAND CITY, N.Y. 11101 HEADINGTON HILL HALL, OXFORD

THE JOURNAL OF PHYSICS AND CHEMISTRY OF SOLIDS

AN INTERNATIONAL JOURNAL

VOLUME 30 1969

EDITORS

Editor-in-Chief: **HARVEY BROOKS** *Cambridge, Mass.*

Associate Editors:

H. B. G. CASIMIR
Eindhoven

B. CHALMERS FRAZER
and
DAVID E. COX
Brookhaven

JACQUES FRIEDEL
Paris

I. M. LIFSHITZ
Khar'kov

Supported by an International Editorial Advisory Board

Copyright © 1969
Pergamon

PERGAMON PRESS

OXFORD . NEW YORK . LONDON . PARIS

THE JOURNAL OF PHYSICS AND CHEMISTRY OF SOLIDS

Editors

PROF. HARVEY BROOKS (*Editor-in-Chief*), 217 *Pierce Hall, Harvard University, Cambridge* 38, *Mass., U.S.A.*

PROF. DR. H. B. G. CASIMIR, *N. V. Philips' Gloeilampenfabrieken, Eindhoven, The Netherlands*

DR. B. CHALMERS FRAZER and DR. DAVID E. COX (*Assistant Editor*) *Brookhaven National Laboratory, Upton, Long Island, New York, U.S.A.*

PROF. JACQUES FRIEDEL, *Laboratoire de Physique des Solides, Bâtiment* 210, *Faculté des Sciences*, 91-*Orsay, France*

PROF. I. M. LIFSHITZ, *Physico-Technical Institute, Academy of Science, Yumorskii [illegible]k, Khar'kov, U.S.S.R.*

Editorial Advisory Board

U.S.A.
F. N. ADAMS, White Plains, N.Y.
D. ALPERT, Urbana, Ill.
L. APKER, Schenectady, N.Y.
J. BARDEEN, Urbana, Ill.
D. S. BILLINGTON, Oak Ridge, Tenn.
R. G. BRECKENRIDGE, Canoga Pk., Calif.
LEO BREWER, Berkeley, Calif.
E. BURSTEIN, Philadelphia, Penn.
J. A. BURTON, Murray Hill, N.J.
N. CABRERA, Charlottesville, Va.
G. C. DANIELSON, Ames, Iowa
G. J. DIENES, Long Island, N.Y.
J. C. FISHER, Schenectady, N.Y.
F. G. FUMI, Chicago, Ill.
H. K. HENISCH, University Park, Penn.
F. HERMAN, San Jose, Calif.
C. HERRING, Murray Hill, N.J.
A. R. VON HIPPEL, Cambridge, Mass.
J. H. HOLLOMON, Washington, D.C.
W. V. HOUSTON, Houston, Texas
H. B. HUNTINGTON, Troy, N.Y.
H. M. JAMES, Lafayette, Ind.
C. KITTEL, Berkeley, Calif.
W. KOHN, La Jolla, Calif.
J. A. KRUMHANSL, Ithaca, N.Y.
A. W. LAWSON, Riverside, Calif.
H. W. LEVERENZ, Princeton, N.J.
O. T. MARZKE, Pittsburgh, Penn.
B. T. MATTHIAS, La Jolla, Calif.
L. R. MAXWELL, Silver Spring, Md.
J. E. MAYER, La Jolla, Calif.
J. W. MITCHELL, Charlottesville, Va.
E. W. MONTROLL, Rochester, N.Y.
D. PINES, Urbana, Ill.
M. H. L. PRYCE, Los Angeles, Calif.
G. T. RADO, Washington, D.C.
H. REISS, Thousand Oaks, Calif.
J. R. REITZ, Dearborn, Mich.
A. ROSE, Princeton, N.J.
R. A. SMITH, Cambridge, Mass.
R. SMOLUCHOWSKI, Princeton, N.J.
F. H. SPEDDING, Ames, Iowa
D. TURNBULL, Cambridge, Mass.
J. H. VAN VLECK, Cambridge, Mass.
B. E. WARREN, Cambridge, Mass.
E. P. WIGNER, Princeton, N.J.
B. H. ZIMM, La Jolla, Calif.

Canada
R. F. BURGESS, Vancouver
W. B. PEARSON, Ottawa

United Kingdom
M. BORN, Bad Pyrmont
A. CHARLESBY, Shrivenham, Berks
W. J. DUNNING, Bristol
F. C. FRANK, Bristol
H. JONES, London
A. B. PIPPARD, Cambridge
O. C. SIMPSON, Baldock, Herts.
K. W. H. STEVENS, Nottingham
F. C. TOMPKINS, London

Czechoslovakia
J. TAUC, Praha

France
E. F. BERTAUT, Grenoble
J. BOK, Paris
B. DREYFUS, Grenoble
A. GUINIER, Orsay
A. HERPIN, Gif-sur-Yvette
B. JACROT, Grenoble
LOUIS NÉEL, Grenoble

Germany
ULRICH DEHLINGER, Stuttgart
R. HILSCH, Gottingen
G. LEIBFRIED, Aachen
E. MOLLWO, Erlangen
H. PICK, Stuttgart
W. WELKER, Erlangen

Israel
I. ESTERMANN, Haifa

Italy
F. G. FUMI, Palermo

Japan
TOSHINOSUKE MUTO, Tokyo

The Netherlands
A. MICHELS, Amsterdam
G. W. RATHENAU, Eindhoven

Sweden
J. O. LINDE, Stockholm
PER-OLOV LÖWDIN, Uppsala

Switzerland
G. BUSCH, Zurich
P. SCHERRER, Zurich

U.S.S.R.
G. S. ZHDANOV, Moscow

Publishing Offices

American Continent: Pergamon Press Inc., Maxwell House, Fairview Park, Elmsford, N.Y. 10523

Rest of the World: Pergamon Press Ltd., 84–86 Malahide Road, Coolock, Dublin 5.

Published monthly. Annual subscription for libraries, research establishments and all other multiple-reader institutions, £60 ($150.00); private individuals, whose departmental libraries subscribe, may obtain this Journal for their personal use at a reduced price of £6 ($15.00) per annum, including postage. All subscription enquiries are to be addressed to The Manager, Subscriptions Department, Pergamon Press, Headington Hill Hall, Oxford OX3 0BW, England. Back issues are available, write for Back Issues Price Lists.

Copyright © 1969 Pergamon Press Ltd.

PERGAMON PRESS
MAXWELL HOUSE, FAIRVIEW PARK, ELMSFORD, N.Y. 10523
HEADINGTON HILL HALL, OXFORD OX3 0BW

LIST OF CONTENTS

JANUARY

K. H. Mader, E. Segal and W. E. Wallace: Magnetic and crystallographic characteristics of $(Pr,La)Al_3$, $(Pr,Y)Al_3$, $(Pr,La)Al_2$ and $(Pr,Y)Al_2$ 1
W. E. Wallace, F. Kissell, E. Segal and R. S. Craig: On the magnetic characteristics of Pr–La and Pr–Y alloys and the nature of elemental praseodymium at low temperatures 13
H. B. Johnson, N. J. Tolar, G. R. Miller and I. B. Cutler. Electrical and mechanical relaxation in CaF_2 doped with NaF 31
R. W. T. Wilkins, E. F. Farrell and C. S. Naiman: The crystal field spectra and dichroism of tourmaline . 43
L. A. Shuvalov, N. R. Ivanov, L. F. Kirpichnikova and N. M. Schagina. On the nature of the low-temperature phase of $NaD_3(SeO_3)_2$ 57
R. M Yu Photoconductivity in cadmium iodide 63
W. T. Berg: The low temperature heat capacity of platinum 69
B. Morris: A dielectric study of the synthetic Linde type-*A* zeolite – I. Experimental methods and the Linde 5-*A*-water system 73
B. Morris A dielectric study of the synthetic Linde type-*A* zeolite – II. Dielectric properties of 5-*A* with adsorbed ammonia, sulphur dioxide, carbon dioxide and *N*-pentane 89
B Morris: A dielectric study of the synthetic Linde type-*A* zeolite – III. Dielectric properties of 3-*A*, 4-*A* and Ag-*A* with adsorbed water 103
D W Hafemeister: Calculation of the ion–ion repulsive interaction in the rare gas solids and in the noble metals 117
M B. Panish and S. Sumski: Ga–Al–As phase, thermodynamic and optical properties 129
R. A. Reynolds and D. A. Stevenson. Self-diffusion of zinc and tellurium in zinc telluride . . 139
Z. Ogorelec and B. Čelustka: On the relation between electrical conductivity and phase transition of non-stoichiometric cuprous selenides 149
D. M. Roessler, W. C. Walker and E. Loh: Electronic spectrum of crystalline beryllium oxide . . 157
J. C. Ho and R. Viswanathan: Low temperature specific heat of h c p. Mo–Ru and Mo–Rh alloys . . 169
E. F. Young and R. I. Gayley: Magnetic field enhancement in superconducting tubes . . 175
R. C Wayne and F. A. Smith: The pressure induced metamagnetic transition in Au_2Mn and the pressure dependence of the ferromagnetic Curie temperature 183
A Ruşi: Processus de transfert d'activité du Fe(III) dans le trioxalatoferrate de potassium 187
C. W. F. T. Pistorius and E. Rapoport: Polymorphism of potassium sulphate, selenate and chromate to 40 kbar 195
H. A. Brown: Mixed magnetic systems: a model with application to $(1-x)CdCr_2S_4 \times xCdCr_2Se_4$. 203
B. Felton: The mobilities of holes and electrons in iodine single crystals 211
G Giuliani. Migration of anion vacancies and formation of complex colour centres in KCl . 217

FEBRUARY

J B MacChesney and H J Guggenheim: Growth and electrical properties of vanadium dioxide single crystals containing selected impurity ions . . . 225
G Hutton and B. Pedersen: Proton and deuteron magnetic resonance in partly deuterated crystals – III. Gypsum 235
G A. Antcliffe and H. Kraus. Preparation and transport properties of epitaxial HgTe films . . . 243
A. P. Young and C. M. Schwartz. Electrical conductivity and thermoelectric power of Cu_2O 249
B Tuck: Diffusion of zinc in GaAs 253
J. B. Goodenough. Descriptions of outer *d* electrons in thiospinels 261
S R. Butler, J. E. Hanlon and R. J. Wasilewski Electric and magnetic properties of TiCo and related compositions 281
G. A. N. Connell, J. A. Wilson and A. D. Yoffe Effects of pressure and temperature on exciton absorption and band structure of layer crystals, molybdenum disulphide 287
P. R. Moran. Phase modulation in magnetic resonance experiments 297
J Ruvalds: Rigorous magnetic susceptibility for a magnetic breakdown model 305
L. D. Kandel, M. C. G. Passeggi and T. Buch Gyromagnetic factors and covalency in tetrahedral d^5-complexes 321
H. Nagasaki, I. Wakabayashi and S. Minomura: The pressure dependence of the lattice parameters of MnSb and MnTe 329
R. A. Oriani: Thermomigration in solid metals 339
E. A Hauschild and C R. Kannewurf: Optical transmission in single crystal silicon diselenide . 353

A. Rosencwaig, M. Ron, A. Kidron and H. Shechter: Polarization and opacity effects on Mössbauer spectral area . . . 359
J. L. Feldman: The Debye–Waller factor Debye temperature for nickel . . . 367
M. J. Dignam and D. B. Gibbs: The electric field dependence of the net activation energy for migration of ionic species across an activation barrier . . . 375
G. Lehmann: Interstitial incorporation of di- and trivalent cobalt in quartz . . . 395
R. Lindström. Chemical diffusion in alkali halides . . . 401
M. D. Weber and R. J. Friauf: Interstitialcy motion in the silver halides . . . 407
J. P. Gracey and R. J. Friauf: Experimental verification of the correlation factor for vacancy diffusion in silver chloride . . . 421
R. J. Friauf: Comments on diffusion by divalent ions in alkali and silver halides . . . 429
W. Kinase, Y. Uemura and M. Kikuchi: Correction of dipole field due to lattice deformation of a Perovskite-type crystal . . . 441
D. K. Steinman and G. C. Summerfield: Neutron incoherent scattering from KDP . . . 449

Technical Notes

L. Heaton, M. H. Mueller, K. D. Anderson and D. D. Zauberis. Neutron diffraction study of the low temperature transition in UP . . . 453
B. K. Chakraverty: On the excess entropy of fusion of semiconducting and semimetallic elements . 454
R. G. Fuller and M. H. Reilly: Possible trivacancy contribution to ionic conductivity . . . 457
R. L. Gayley: Coalescence in an enclosed superconductor . . . 459
H. A. Papazian: On the irradiation of alkali metal azides . . . 462

Erratum . . . 464

MARCH

Č. Jech and R. Kelly. A gas-release study of the annealing of bombardment-induced disorder (studies on bombardment-induced disorder—I) . . . 465
H. Wiedersich and W. V. Johnston: On the thermodynamic properties of the solid electrolyte $RbAg_4I_5$. 475
F. Brewig, W. Kierspe, U. Schotte and D. Wagner: Effects of transition metal solutes on the thermoelectric power of copper . . . 483
J. Sworakowski and K. Pigoń. Trap distribution and space-charge limited currents in organic crystals. Anthracene . . . 491
M. Jaroš and P. Kostecký: Pseudopotential impurity theory and covalent bonding in semiconductors . . 497
W. J. Bitler, Indradev and F. Williams: Experimental and theoretical studies of low-voltage electroluminescence of ZnS single crystals . . . 503
G. Deutscher, J. P. Hurault and P. A. van Dalen: Electrodynamical properties of superconducting contacts . . . 509
L. M. Amzel and L. N. Becka: A model for the evaluation of thermodynamic properties for the solid–solid and melting transitions of molecular crystals . . . 521
C. M. Hurd. Some magnetic properties of Mn dissolved in Cu, Ag and Au . . . 539
A. G. Revesz and R. J. Evans: Kinetics and mechanism of thermal oxidation of silicon with special emphasis on impurity effects . . . 551
J. E. Bauerle and J. Hrizo. Interpretation of the resistivity temperature dependence of high purity $(ZrO_2)_{0.90}$-$(Y_2O_3)_{0.10}$ . . . 565
L. H. Ngai: High temperature NMR studies of bromine and iodine chemical shifts in alkali bromides and iodides and in thallium bromide . . . 571
G. A. Castellion, L. A. Siegel and H. Burkhard: The preparation and semiconducting properties of hexagonal $Zn_{1-x}Mn_xAs_2$ . . . 585
R. A. Miller and D. E. Schuele: The pressure derivatives of the elastic constants of lead . . . 589
G. Stephan, Y. Le Calvez, J. C. Lemonnier et Mme S. Robin: Propriétés optiques et spectre électronique du MgF_2 et du CaF_2 de 10 à 48 eV . . . 601
R. J. Jelitto: The density of states of some simple excitations in solids . . . 609
U. Merten, K. D. Vos and A. P. Hatcher: Distribution coefficient studies in indium antimonide . . . 627
H. D. Rees: Calculation of distribution functions by exploiting the stability of the steady state . . . 643
S. Ogawa and J. Smit. Nuclear magnetic resonance and relaxation of the Heusler alloy . . . 657
J. E. Kettler, W. L. Shanholtzer and W. E. Vehse: Conduction electron spin susceptibility of metallic lithium . . . 665
S. M. Horszowski: Thermal annealing of natural semiconducting diamond . . . 669
V. Kumar and Y. P. Gupta. Cation self-diffusion in single crystal CaO . . . 677
F. Abel, G. Amsel, M. Bruneaux et E. d'Artemare: Canalisation des deutons dans le quartz . . . 687

R. Szwarc: The defect contribution to the excess enthalpy of uranium dioxide-calculation of the Frenkel energy 705
G. B. Bacskay, P. J. Fensham, I. M. Ritchie and R. N. Ruff: The EPR spectra of Gd^{3+} and Eu^{2+} in lead chalcogenides 713
R. F. Brebrick: Homogeneity ranges and Te_2-pressure along the three-phase curves for $Bi_2Te_3(c)$ and a 55–58 at.% Te. peritectic phase 719
G. H. Lander, L. Heaton, M. H. Mueller and K. D. Anderson: Neutron diffraction study of NpC 733
Y. Nishina and B. Lax: Interband Faraday rotation and Voigt effect in Ge 739
K. Suzuki and E. Hanamura: Effective mass theoretical approach to optical and microwave phenomena in semiconductors – II. Theory of the Faraday and Voigt effects due to excitons in germanium 749
E. F. Bertaut: Classical effective spin Hamiltonian and symmetry groups of the multispin-axis model of CoO 763

Technical Notes:

T. G. Campbell and A. W. Lawson: The dielectric constant of EuS 775
E. Adachi: Energy band parameters of gallium antimonide 776
N. Hariharan and J. Sobhanadri: E.S.R. studies of paramagnetic centres in irradiated Li_2So_4. H_2O 778
H. Claus: The electronic specific heat of h.c.p. Fe–Ru alloys 782

Notice 783

Erratum 784

APRIL

Y. S. Tyan, L. E. Toth and Y. A. Chang: Low temperature specific heat study of the electron transfer theory in refractory metal borides 785
B. E. F. Fender and F. D. Riley: Thermodynamic properties of $Fe_{1-x}O$. Transitions in the single phase region 793
F. K. Lotgering, R. P. Van Stapele, G. H. A. M. Van Der Steen and J. S. Van Wieringen: Magnetic properties, conductivity and ionic ordering in $Fe_{1-x}Cu_xCr_2S_4$ 799
R. Buhl: Manganites spinelles purs d'éléments de transition préparations et structures cristallographiques 805
R. A. Kashnow and K. A. McCarthy: Phonon scattering in magnesium fluoride 813
W. Kündig, M. Kobelt, H. Appel, G. Constabaris and R. H. Lindquist: Mössbauer studies of Co_3O_4; bulk material and ultrafine particles 819
M. F. Striefler and S. S. Jaswal: An H^- impurity in KBr 827
G. G. Roberts, E. L. Lind and E. A. Davis: Photoelectronic properties of synthetic mercury sulphide crystals 833
C. Laj and P. Bergé: On the enhancement of γ-ray coloration by Mn^{2+} and Mg^{2+} in lithium fluoride 845
P. Burlet et E. F. Bertaut: Signe et grandeur des intégrales d'échange dans les solutions solides $Mn_xCr_{1-x}S$ 851
T. Matsuda: Hall coefficient of dilute copper alloys 859
A. Ikushima and T. Mizusaki: Superconductivity in niobium and niobium–tantalum alloys 873
W. L. George and R. E. Grace: Formation of point defects in calcium titanate 881
W. L. George and R. E. Grace: Diffusion of point defects in calcium titanate 889
W. Schilz: Magneto-acoustic investigation of the Fermi surface and spin splitting of the Landau levels in p-type and n-type PbTe 893
F. Franceschi and G. L. Olcese: Structural and magnetic properties of nonstoichiometric praseodymium monophosphide 903
C. Greskovich and V. S. Stubican: Interdiffusion studies in the system MgO–Cr_2O_3 909
C. R. Hall: On the scattering of X-rays by structures containing a random distribution of defects 919
L. R. Walker, B. B. Cetlin and D. Hone: The spin wave Green's function for a body-centered two sublattice antiferromagnet 923
N. S. Satya Murthy, R. J. Begum, C. S. Somanathan, B. S. Srinivasan and M. R. L. N. Murthy: Ferrimagnetic structure of Mn_2Co_2C 939
I. N. Frantsevich, D. F. Kalinovich, I. I. Kovenskii and M. D. Smolin: Electrotransport and diffusion in molybdenum–tungsten and iron–nickel alloys over wide ranges of temperatures 947
H. Buttner and E. Gerlach: Optical conductivity in alkali metals 959
W. C. Holton, M. De Wit, R. K. Watts, T. L. Estle and J. Schneider: Paramagnetic copper centers in ZnS 963
H. Le Gall, B. Desormière and E. Milot: Transient processes in spin-wave systems with magnetic dipole radiation – I. Theory 979
M. J. Mindel and S. R. Pollack: The effect of metal vacancies on the oxidation kinetics of metals 993
M. Baker and A. Taylor: Cation diffusion in fluorite single crystals 1003

Technical Notes:

Z. Smetana: Ferromagnetic resonance linewidth and relaxation in the system $Mn_xFe_{1-x}O_{1-\gamma}$ 1009

P. C. Mehendru and G. D. Sootha: Effect of impurities on the growth of *F* and *M* bands in KCl . . 1012
V. Hari Babu and K. G. Bansigir: The role of poison and undersaturation of the solvent in the etching mechanism 1015
V. V. Goldman: Some comments on the Lindemann melting formula 1019
P. C. Mehendru and V. Mitra: *F* centers growth and thermoluminescence in Mn doped KCl crystals 1021

MAY

J. B. Lightstone and G. G. Libowitz: Interaction between point defects in nonstoichiometric compounds . 1025
E. Laredo: Etude par rayons X de la dilatation de NaCl à haute température 1037
L. Dobrzynski and D. L. Mills: Vibrational properties of an adsorbed surface layer on a simple model crystal 1043
L. W. Rupp, Jr and P. H. Schmidt: Conduction-electron spin resonance in alkaline-earth hexaborides . 1059
M. Rosen, G. Erez and S. Shtrikman: Elastic and anelastic behavior of several delta-stabilized plutonium alloys at low temperatures 1063
D. S. Perloff, M. Vlasse and A. Wold: Anisotropic electrical behavior of the blue potassium molybdenum bronze, $K_{0.30}MoO_3$ 1071
P. N. Adler: Pressure-induced transformation behavior of some quasi-binary alloys of InSb 1077
M. B. Panish: The Ga–GaAs–GaP system: phase chemistry and solution growth of $GaAs_xP_{1-x}$ . . 1083
M. J. P. Musgrave: An interpretation of the *P–T* diagram for tin 1091
H. E. Cook: The influence of static atomic displacements on the diffuse intensity scattered by solid solutions 1097
L. G. Ferreira: A local approximation for exchange and correlation in band structure calculations . 1113
J. A. Roberson and R. A. Rapp: Electrical properties of NbO and NbO_2 1119
B. E. Cook and W. E. Spear: The optical properties of orthorhombic sulphur crystals in the vacuum ultra-violet 1125
B. Desormière, E. Milot and H. Le Gall: Transient processes in spin-wave systems with magnetic dipole radiation—II. Experimental investigations 1135
J. C. Lemonnier, G. Stephan, Y. Le Calvez et Mme S. Robin: Propriétés optiques de couches minces d'indium dans l'ultra violet extrême 1147
A. J. Bosman and C. Crevecoeur: Electrical conduction in Li-doped CoO 1151
W. N. Lawless: Thermodynamics of electrocaloric phenomena in KCl: OH. Paraelectric cooling . . 1161
Ya. E. Geguzin, Yu. S. Kaganovsky and V. V. Slyozov: Determination of the surface heterodiffusion coefficient by the method of mass transfer 1173
E. D. Thompson: Density of states and the electronic specific heat: palladium 1181
J. F. Ullrich and D. H. Vincent: Te^{125} Mossbauer effect study of neutron capture effects in PbTe, Te and TeO_2 1189
D. Gerlich and E. S. Fisher: The high temperature elastic moduli of aluminum 1197
I. Shidlovsky and I. Mayer: Mossbauer spectra of rare earth silicides and germanides . . . 1207
V. V. Boldyrev: Mechanism of thermal decomposition of potassium permanganate in the solid phase . 1215
K. Nassau, P. B. Jamieson and J. W. Shiever: The neodymium molybdate–tungstate system . . . 1225
L. Marshall Libby and F. J. Thomas: New melting law at high pressures 1237
D. Miliotis and D. N. Yoon: Existence of air-gaps in specimen-electrode contacts and their effect on dielectric relaxation phenomena in KCl and NaCl 1241
C. O. Pollard, Jr: Second-rank tensor anion polarizabilities in some rutile group crystals . . . 1251
H. Jacobi, B. Vassos and H.-J. Engell: Electrical properties of β-phase NiAl 1261

Technical Notes:

C. F. Buhrer: Magnetic properties of U_3P_4 and U_3As_4 single crystals 1273
F. Slotwinski and J. Trivisonno: Temperature dependence of the elastic constants of single crystal lithium 1276
S. C. Jain, V. K. Jain and G. D. Sootha: Some ESR studies of *F* centers in highly pure and doped KCl crystals 1279
M. Certier, C. Wecker and S. Nikitine: Zeeman effect of bound excitons in CuCl 1281
A. E. Austin: High pressure transformations of transition metal difluorides 1282
T. Lukes: A variational method for anisotropic effective mass theory 1285
S. Lee and H. K. Henisch: Photocapacitive effects in ZnS 1286
E. W. Williams and H. B. Bebb: Photoluminescence in lightly doped epitaxial GaAs:Cd and GaAs:Si . 1289
J. A. W. van der Does de Bye: Comment on the application of configuration coordinates to the red emission of gallium phosphide 1293
W. T. Brydges: Some observations on dislocation etching in copper 1294

JUNE

D. B. HOLT: Antiphase boundaries in semiconducting compounds 1297
W. K. CHEN and R. A. JACKSON: Oxygen self-diffusion in undoped and doped cobaltous oxide . . . 1309
A. P. BATRA and L. SLIFKIN: Impurity halide diffusion in silver chloride and silver bromide 1315
J. TATENO: On the phase transition in mixed valence type oxides 1321
Y. P. GUPTA and U. D. MISHRA: Electrical conduction and electron microscopy of vitreous solids in the K_2O–SiO_2 system 1327
P. R. ELLISTON, J. G. GREER and G. J. TROUP: Antiferromagnetic resonance in $LiMnPO_4$ 1335
A. CASALOT et P. HAGENMULLER: Sur l'evolution en fonction de la composition de propriétés semi-conductrices a des propriétés metalliques au sein d'une phase de type 'bronzes oxygénes de vanadium'. . . . 1341
P DURAND, Y. FARGE and M. LAMBERT: The creation of *F* centers in lithium fluoride between 77° and 600°K and their interpretation by a recombination model of insterstitial-vacancies 1353
Y. FARGE: Interpretation of the creation of *F* centers by ionizing radiation above 77°K by a recombination model of interstitials and vacancies 1375
I. ROSENMAN: Effet Shubnikov de Haas dans Cd_3As_2: forme de la surface de Fermi et modèle non parabolique de la bande de conduction 1385
J. D AXE: Infrared dielectric dispersion in divalent europium chalcogenides 1403
J WITTIG: A study of the superconductivity of antimony under pressure and a search for super-conductivity in arsenic 1407
S. N. VAIDYA, J. AKELLA and G. C. KENNEDY: Melting of germanium to 65 kbar 1411
J. C. HAYGARTH, H. D. LUEDMANN, I. C. GETTING and G C. KENNEDY: Determination of portions of the bismuth III–V and IV–V equilibrium boundaries in single-stage piston–cylinder apparatus 1417
H. ZETSCHE and R. FISCHER: Photoluminescence of trigonal selenium single crystals 1425
F. K. LOTGERING: Magnetic and electrical properties of $Co_{1-x}Cu_xRh_2S_4$ 1429
P B. P. PHIPPS and F. A. KRÖGER: Long wavelength optical absorption of brominated silver bromide . . 1435
P. J. LIN-CHUNG and R. F. WALLIS: Zeeman perturbations on shallow acceptor states in germanium . . 1453
J. S. PRENER, W. W. PIPER and R. M. CHRENKO: Hydroxide and oxide impurities in calcium halophosphates . 1465
A. L. HARMER, A. LINZ and D. R. GABBE: Fluorescence of Nd^{3+} in lithium yttrium fluoride 1483
R. C. NEWMAN and R. S. SMITH: Vibrational absorption of carbon and carbon–oxygen complexes in silicon . 1493
B LEBECH and K. MIKKE: On the coexistence of the magnetic phases in chromium alloys . . 1507
F. C. SCHWERER, J. W. CONROY and S. ARAJS: Matthiessen's rule and the electrical resistivity of iron–silicon solid solutions 1513
R. N. SCHOCK and J. C. JAMIESON: Pressure-induced phase transformations in the B1 Ag-halides . . 1527
C. M. BOWDEN, H. C. MEYER, P. F. McDONALD and J. D STETTLER: Superhyperfine interactions in the EPR and UPR spectra of $CaF_2:U^{4+}$ 1535
S. BLOW A Mössbauer effect study of the metallic compounds U_6Fe and Pu_6Fe, and the relevance of the results to theories of the behaviour of actinide metals 1549
J. M. DANIELS and A ROSENCWAIG: Mössbauer spectroscopy of stoichiometric and non-stoichiometric magnetite 1561
J M. CAYWOOD and J. D. TAYNAI: Optical absorption of selenium in the α-monoclinic crystal and some solvents 1573
H. BAESSLER, G. HERRMANN, N. RIEHL and G. VAUBEL: Space-charge-limited currents in tetracene single-crystals 1579
M. S. ANDERSON, E. J GUTMAN, J. R. PACKARD and C. A. SWENSON. Equation of state for cesium metal to 23 kbar 1587
T. ITAMI, H. HOSHINO and M SHIMOJI: Thermoelectric power of ionic crystals – IV. Thermoelectric power and ionic conductivity of potassium iodide containing cadmium iodide 1603
H. KATZMAN, T. DONOHUE, W. F. LIBBY, H. L. LUO and J. G. HUBER: A high-pressure super-conducting polymorph of cadmium tin diarsenide 1609
F CATALANO, R. G. BEDFORD, V. G. SILVEIRA and H. H. WICKMAN: Nonstoichiometry in rare-earth fluorides 1613

Technical Notes:

J. B VAN TRICHT and B. A. M. VAN DER KRAAY: Activation energy from thermoluminescence and phosphorescence of α-Al_2O_3 1629
G. GESCHWIND: Anion reduced ionic conductivity in LiF 1631
R E. PIAZZA: ESR study of simultaneous optical bleaching and X-irradiation of KCl . . . 1635
J. M. NOOTHOVEN VAN GOOR and H. M. G. J. TRUM: Distribution coefficient and acceptor valency of tin in bismuth 1636
D GERLICH: Elastic Grüneisen parameters in crystals of low symmetry 1638
M. KUZNIETZ, G. H. LANDER and F. P. CAMPOS: Antiferromagnetic structures of USb and UBi . . 1642

S. Chandra, G. K. Pandey and V. K. Agrawal: Rotational barrier height for OH^- ion trapped in KCl, KBr, NaCl and RbCl matrices . . . 1644

Erratum . . . 1647

JULY

H. L. Arora and S. Wang. Application of the polaron model to the *F′* center . . . 1649
C. M. Bowden and J. E. Miller: Spin-lattice coefficients for substitutional Gd^{3+} in CaF_2 . . . 1661
Y. Syono, S. Akimoto, Y. Ishikawa and Y. Endoh: A new high pressure phase of $MnTiO_3$ and its magnetic property . . . 1665
T. Staflin: I.R. absorption corresponding to transitions of holes from impurity levels to the valence band in silicon and germanium . . . 1673
P. L. Land: New methods for determining electron trap parameters from thermoluminescent or conductivity 'glow curves' . . . 1681
P. L. Land: Equations for thermoluminescence and thermally stimulated current as derived from simple models . . . 1693
D. J. Newman: Second quantized formalism for non-orthogonal states . . . 1709
H. M. O'Bryan, Jr. and H. J. Levinstein: The structure of $Mn_{1.88}Fe_{1.12}O_4$ . . . 1719
J. E. Epperson and J. E. Spruiell: An X-ray single crystal investigation of iron-rich alloys of iron and aluminum—I. Phase relations in alloys containing between 14 and 23 at.% aluminum . . . 1721
J. E. Epperson and J. E. Spruiell: An X-ray single crystal investigation of iron-rich alloys of iron and aluminum—II. Diffuse scattering measurements of short-range order in alloys containing 14·0 and 18·3 at.% aluminum . . . 1733
G. Gorodetsky. Exchange constants in orthoferrites $YFeO_3$ and $LuFeO_3$ . . . 1745
R. Kewley: Electron paramagnetic resonance spectra from gamma-irradiated potassium thiocyanate . . . 1751
O. Berkooz: Isomer shifts of ^{151}Eu in divalent europium compounds . . . 1763
A. M. Stoneham and M. Lannoo: The Jahn–Teller instability with accidental degeneracy . . . 1769
G. B. Springfellow and P. F. Green. Calculation of III–V ternary phase diagrams: In–Ga–As and In–As–Sb . . . 1779
A. C. Tomlinson and B. Henderson: Some studies of defects in calcium oxide—I. Impurity effects . . . 1793
B. Henderson and A. C. Tomlinson: Some studies of defects in calcium oxide—II. Intrinsic lattice defects . . . 1801
P. Rai-Choudhury: Doping of epitaxial silicon—behavior of solid solutions . . . 1811
M. Robbins, G. K. Wertheim, A. Menth and R. C. Sherwood: Preparation and properties of polycrystalline cerium orthoferrite ($CeFeO_3$) . . . 1823
G. Williams and J. W. Loram: Low temperature electrical resistivities of some dilute *Pd* Fe alloys . . . 1827
L. Ramqvist, K. Hamrin, G. Johansson, A. Fahlman and C. Nordling. Charge transfer in transition metal carbides and related compounds studied by ESCA . . . 1835
L. Ramqvist, B. Ekstig, Elisabeth Källne, E. Noreland and R. Manne: X-ray study of inner level shifts and band structure of TiC and related compounds . . . 1849
A. Taroni and G. Zanarini: Space charge limited currents in *P–N* junctions . . . 1861
S. P. Morris: Bloch electrons in a magnetic field perturbation approach . . . 1873
C. R. Fritzsche: Anodic growth, dielectric breakdown and carrier transport in amorphous SiO_2 films . . . 1885

Technical Notes.

K. J. Siemsen and H. D. Riccius. Multiphonon processes in amorphous selenium . . . 1897
J. D. Graham, C. W. Spangler, S. K. Lott and M. J. Joncich: Exploding wire phenomena in the coinage metals . . . 1900

Errata . . . 1903

AUGUST

B. J. Marshall and C. R. Cleavelin: Elastic constants of LiBr from 300° to 4·2°K . . . 1905
D. W. Wood and N. W. Dalton: Some transition properties of the Ising model super-exchange antiferromagnet . . . 1909
C. M. Wu and B. Roessler: The energy of ordering in the alloy CuPt . . . 1917
R. M. Barrer and J. A. Davies: Heat of exchange between gaseous ions and ions in anhydrous zeolites . . . 1921
S. R. Butler, J. E. Hanlon and R. J. Wasilewski: Electric and magnetic properties of B2 structure compounds: NiAl, CoAl . . . 1929
W. N. Honeyman: Preparation and properties of single crystal $CuAlS_2$ and $CuAlSe_2$ . . . 1935
S. I. Youssef, M. G. Natera, R. J. Begum, B. S. Srinivasan and N. S. Satya Murthy. Polarised neutron diffraction study of nickel ferrite . . . 1941

J. H. WERNICK, A. MENTH, T. H. GEBALLE, G. HULL and J. P. MAITA: Superconducting, thermal and magnetic susceptibility behavior of some intermetallic compounds with the fluorite structure 1949
Y. YAFET: Effective spin-orbit coupling of impurity states in metals 1957
C. A. COULSON and F. P. LARKINS: Electronic structure of the neutral isolated divacancy in diamond . . 1963
B. J. H. JACKSON and D. A. YOUNG: Ionic conduction in pure and doped single-crystalline lithium iodide . 1973
C. K. SCHILLER and H. BULOW: The effect of preferred crystal growth on the angular dependence of the magnetic-transition field in quenched thin In films 1977
A. A. SHULTIN and S. V. KARPOV: Intermolecular interaction and infra-red spectra of the three crystalline phases of potassium nitrate—II. Internal-lattice combination band region 1981
M. W. SHAFER and T. R. MCGUIRE: Preparation and properties of ferrimagnets in the $RbMgF_3$–$RbCoF_3$ system 1989
A. K. VIJH: Correlation between bond energies and forbidden gaps of inorganic binary compounds . . 1999
S. KURTIN and C. A. MEAD: Surface barriers on layer semiconductors: GaS, GaSe, GaTe 2007
M. BRUNEL et F. DE BERGEVIN: Ordre à courte distance, déplacements locaux des ions et énergie électrostatique dans $FeLiO_2$ 2011
F. J. DUDEK and L. I. GROSSWEINER: The optical conversion of F centers to M centers in KCl with repetitive light pulses 2023
R. K. CROUCH and T. E. GILMER, JR.: Thermal ionization energy of lithium and lithium–oxygen complexes in single-crystal silicon 2037
J. SKALYO, JR., B. C. FRAZER, G. SHIRANE and W. B. DANIELS: The pressure dependence of the transition in KDP and ADP 2045
A. P. BATRA, A. L. LASKAR and L. SLIFKIN: Low temperature suppression by chlorine of diffusion of gold in silver chloride 2053
A. L. LASKAR, A. P. BATRA and L. SLIFKIN: Diffusion of strontium ion in silver chloride 2061
J. C. SWARTZ: Stress relaxations in internally oxidized Ag(Cu) 2065
U. SCHERZ: Cubic fields with tetragonal and trigonal distortions in crystal field theory of transition metal ions 2077
R. GROVER, R. N. KEELER, F. J. ROGERS and G. C. KENNEDY: On the compressibility of the alkali metals . 2091

Technical Notes:

R. G. FULLER and H. B. ROSENSTOCK: Equilibrium concentration of impurity-vacancy complexes . . 2105
C. L. HERZENBERG and D. L. RILEY: Mössbauer resonant absorption in the garnet-type compound ferric molybdate 2108

SEPTEMBER

Y. ISHIBASHI and H. L. STADLER: Ferroelectric electroreflectance of gold films 2113
G. AMSEL, C. CHERKI, G. FEUILLADE and J. P. NADAI: The influence of the electrolyte on the composition of 'anodic oxide films' on tantalum 2117
M. CERTIER, C. WECKER and S. NIKITINE: Zeeman effect of free and bound excitons in CuCl 2135
T. M. SEARLE: Optical studies of the thermal dissociation of OH^- ion aggregates in MgO 2143
B. OKAI, Y. ONODA, S. MINOMURA and S. NAKAMURA: Effect of pressure on the Knight shift in V^{51} and β-Mn^{55} metals 2153
T. P. ABELES, W. G. BOS and P. J. OUSEPH: ^{161}Dy isomer shifts in dysprosium compounds . . 2159
P. LEONARD, M. C. CADEVILLE, J. DURAND and F. GAUTIER: Experimental proof for a two-band conduction in nickel alloys 2169
F. LÖFFLER and H. RAUCH: A neutron depolarization study on dysprosium and terbium 2175
A. R. ALLNATT and L. A. ROWLEY: The statistical mechanics of imperfect molecular crystals . . . 2187
P. WYNBLATT: On the formation and migration entropies of vacancies in metals 2201
R. KLEIM and F. RAGA: Exciton luminescence in lead iodide lifetime, intensity and spectral position dependence on temperature 2213
W. SCHAIRER and W. GRAMAN: Photoluminescence of Ge-doped GaAs grown by vapor-phase epitaxy . . 2225
R. POLÁK and K. KLIER: Spectra of synthetic zeolites containing transition metal ions—III A simple model calculation of the system adsorbed molecule-NiA zeolite 2231
A. N. THORPE, F. E. SENFTLE and G. DONNAY: Magnetic susceptibility and exchange coupling in the mineral ardennite 2235
M. H. MANGHNANI and W. M. BENZING: Pressure derivatives of elastic moduli of Vycor glass to 8 kbar . . 2241
D. A. RIGNEY and J. A. BLODGETT: The Knight shift in metals: liquid arsenic 2247
R. TAYLOR, B. T. KELLY and K. E. GILCHRIST: The thermal conductivity of fast neutron irradiated graphite . 2251
M. WUTTIG and E. T. YEN: Isotope effect of carbon diffusion in an Fe–Si alloy 2269
R. ALEONARD, P. BOUTRON et D. BLOCH: Anisotropie de la susceptibilité paramagnétique des monocristaux de terres rares: Gd, Tb, Dy, Ho et Er 2277
D. F. WINTERSTEIN and E. F. SIECKMANN: Electrical conductivity and optical absorption changes related to the 3800 Å band of CaO:Ca 2287

C. E. Rossi and W. Paul: The preparation of NiO thin films and their use in optical measurements in the visible and ultraviolet 2295

J. W. Gadzuk: Theory of dielectric screening of an impurity at the surface of an electron gas 2307

Technical Notes:

C. W. Frank, G. de Pasquali and H. G. Drickamer: The effect of pressure on the isomer shift of ^{57}Fe(^{57}Co) as an impurity in ZnSe, ZnTe and CdTe 2321

M. R. Tubbs: Dispersion effects in interference methods for the measurement of refractive index . . 2323

M. W. Shafer and J. D. Kuptsis: On the nature of the magnetic inclusions in EuF_2 2325

K. Ždánský and F. Kubec: Temperature dependence of the hyperfine coupling of Mn^{2+} in Cds . . 2327

M. C. Naik and R. P. Agarwala: Anomalous diffusion in beta zirconium, beta titanium and vanadium . 2330

C. Borghese: Compositional compensation points in magnetic garnets 2334

OCTOBER

M. I. Valic and D. Llewelyn Williams: A nuclear magnetic resonance study of gallium single crystals—I. Low field spectra 2337

R. Ruppin: Size effects on plasmon–phonon modes in polar semiconductors 2349

P. Novák: Interactions between octahedrally co-ordinated E_g Jahn–Teller ions 2357

R. F. Bingham and C. R. Brooks: The effect of magnetic and configurational disordering on the high temperature heat capacity of a Ni-50 at.% Pd alloy 2365

D. J. Sellmyer: High-field and quantum oscillatory effects in the magnetoresistance of AuSn . 2371

A. K. Ghosh: Optical properties of electron and hole traps in Ag-doped aluminoborate glass 2385

L. Dobrzynski: Calculation of the entropies of lattice vacancies 2395

A. Mookherji and S. P. Chachra: Magnetic studies on dysprosium ethyl sulphate single crystals . . 2399

H. Nagasaki, I. Wakabayashi and S. Minomura: The pressure dependence of the lattice parameters of CrTe and CrSb 2405

M. Lannoo and P. Lenglart: Study of the neutral vacancy in semi-conductors 2409

S. Haraldson and C.-G. Ribbing: ESR-resonances in doped GaAs and GaP 2419

H. E. Cook: The kinetics of clustering and short-range order in stable solid solutions . . 2427

C. F. Lee: On the solution of the equation of diffusion processes during the uptake of excess calcium by calcium fluoride 2439

G. A. Saum, R. H. Glaenzer and J. F. Dueker: Low temperature electroluminescence of ZnSe:Cu:Br 2447

M. Bernasson, P. Descouts, P. Donzé and A. Treyvaud: Magnetic susceptibilities and NMR properties of V–Ru alloys 2453

T. D. George and J. B. Wagner, Jr.: Diffusion of nickel into lead telluride between 200° and 400°C . . 2459

B. Boucher, R. Buhl et M. Perrin: Structure magnétique a trois sous-réseaux dans l'approximation du champ moleculaire 2467

Technical Notes

R. L. Odle, G. Becker and S. Sotier: Knight shift measurements in liquid alloys of Al, Cu and Mn 2479

A. R. Patel and K. J. Mathai: Dislocation pits in α-silicon carbide by heating 2482

V. T. Deshpande and S. V. Suryanarayana: X-ray determination of the thermal expansion of calcium molybdate 2484

K. L. Van der Lugt, J. Comas and F. A. Wolicki: Coloration of LiF produced by 3.0 MeV ^{40}Ar ions . 2486

M. S. Abrahams and J. J. Tietjen: Stacking faults in $GaAs_{1-x}P_x$ alloys 2491

S. K. Datta: Some comments on "On the magnetic anisotropy and susceptibility of $CoF_2 5HF \cdot 6H_2O$ and $NiF_2 5HF \cdot 6H_2O$" 2493

Errata 2495

NOVEMBER

H. U. Rahman: A linear interpolation of the electronic levels of f^2-system in octahedral coordination . . 2497

D. L. Fancher and G. R. Barsch: Lattice theory of alkali halide solid solutions—I. Heat of formation . . 2503

D. L. Fancher and G. R. Barsch: Lattice theory of alkali halide solid solutions—II. Entropy of mixing and solid solubility 2517

G. J. Edwards, M. Springford and Y. Saito: The Fermi surface of AuSn 2527

K. C. Rustagi: Model band structures in nonlinear optics 2547

H. D. Fair, Jr. and A. C. Forsyth: Optical and electrical properties of thin films of α-lead azide . . . 2559

M. Schoijet: Theory of the kinetics of short range order 2571

P. C. Clapp: Theoretical determination of n-site configuration probabilities from pair correlations in binary lattices 2589

G. Villela, Y. Saïkali, A. Louat, J. Pâris et F. Gaume-Mahn: Le métatitanate de magnésium, nouvelle matrice pour l'étude de la fluorescence de l'ion Mn^{4+}. Préparation et propriétés de luminescence . . 2599
J. F. D'Amico and H. B. Huntington: Electromigration and thermomigration in gamma-uranium . . 2607
H. L. Arora, C. K. Mahutte and S. Wang: On shoulder bands of the *U* band 2623
R. B. McLellan and W. W. Dunn: A quasi-chemical treatment of interstitial solid solutions: its application to carbon austenite 2631

DECEMBER

P. J. Jorgensen and R. W. Bartlett: High temperature transport processes in lithium niobate . . . 2639
P. C. Souers, T. S. Blake, R. M Penpraze and C. Cline: Pulsed nuclear magnetic resonance of gamma-irradiated lithium hydride 2649
J. E. Bauerle: Study of solid electrolyte polarization by a complex admittance method 2657
T. Nishino, M. Okuyama and Y. Hamakawa: Electroreflectance of *p*-type GaAs 2671
J. Rossat-Mignod, R. Ballestracci, G. Quezel, C. Linares et F. Tcheou: Interprétation de la susceptibilité magnétique de l'oxysulfure de samarium par un modèle de champ cristallin 2679
S. M. Myers, H. Meyer and J. P. Remeika: Spin-lattice relaxation of ^{57}Fe nuclei in yttrium iron garnet . . 2687
L. I. Amstutz, H. Meyer, S. M. Myers and R. L. Mills: Longitudinal nuclear relaxation measurements in hcp H_2 2693
R. L. Gilbert and J. J. Markham: A self-consistent *F*-center calculation for the optical absorption and emission 2699
P. A. Lee, G. Said, R. Davis and T. H. Lim: On the optical properties of some layer compounds . . . 2719
D. J. Newman and M. M. Curtis: Crystal field in rare-earth fluorides—I. Molecular orbital calculation of PrF_3 parameters 2731
W. R. Hunter and S. A. Malo: The temperature dependence of the short wavelength transmittance limit of vacuum ultraviolet window materials—I. Experiment 2739
B. V. R. Chowdari: Electron paramagnetic resonance of Mn^{2+} in $(NH_4)_2Co_2(SO_4)_3$ and $(NH_4)_2Ni_2(SO_4)_3$ single crystals 2747
V. G. Manzhelii, A. M. Tolkachev and V. G. Gavrilko: Thermal expansion of solid CH_4 and CD_4 . . 2759
C.-Y. Young: The frequency and temperature dependence of the optical effective mass of conduction electrons in simple metals 2765
E. R. Fitzgerald: Detonation in crystalline solids 2771

Technical Notes:

E. Gmelin: Anomalies in the low temperature heat capacities of BeO and MgO, containing Fe^{3+} . . 2789
W. J. Potvin, Jr. and S. Greenblatt: Mössbauer study of the disintegration products of a high surface area iron oxide gel 2792
H. Katzman, T. Donohue, W. F. Libby and H. L. Luo: A high-pressure superconducting polymorph of cadmium germanium diarsenide 2794

Errata 2797

NOTES FOR CONTRIBUTORS

I. GENERAL

1. Submission of a paper to *The Journal of Physics and Chemistry of Solids* will be taken to imply that it represents original research not previously published (except in the form of an abstract or preliminary report), that it is not being considered for publication elsewhere, and that if accepted it will not be published elsewhere in the same form, in any language, without the consent of the editor-in-chief. It should deal with original research work in the field of the physics and chemistry of solids.

2. Papers should be submitted to the appropriate regional editor (all English-language papers to be sent to the U.S. editor).

3. Short communications may be published as "Technical Notes" and will receive somewhat more rapid handling than full length articles. Short communications requiring the maximum speed of publication should be submitted to one of the editors of "Solid State Communications".

II. SCRIPT REQUIREMENTS

1. **Papers** submitted should be concise and written in a readily understandable style. Scripts should be typed and double spaced with good margins on one side of the paper only and submitted in duplicate to facilitate refereeing.

It will be appreciated if authors clearly indicate any special characters used. An abstract not exceeding 200 words, should be provided in the language of the paper. French and German papers should be submitted with English abstract and titles, but if this is not possible the abstract will be translated by the publishers. To conserve space **authors are requested to mark less important parts of the paper,** such as details of experimental technique, methods, mathematical derivations, etc. **for printing in small type.** The technical description of methods should be given in detail only when such methods are new. Authors will receive proofs for correction when their papers are first set, and **alterations must be restricted to printer's errors.** Other than these, any substantial changes may be charged to the authors.

2. **Illustrations** should not be included in the typescript of the paper, and legends should be typed on a separate sheet. Line drawings which require redrawing should include all relevant details and clear instructions for the draughtsman. If figures are already well drawn it may be possible to reproduce them direct from the originals, or from good photo-prints if these can be provided. It is not possible to reproduce from prints with weak lines. Illustrations for reproduction should normally be about twice the final size required. The lettering should be sufficiently large and bold to permit this reduction. Photographs should only be included where they are essential.

3. **Tables and figures** should be so constructed as to be intelligible without reference to the text. Every table and column should be provided with an explanatory heading. Units of measure must always be clearly indicated. The same data should not be published in both tables and figures. The following standard symbols should be used on line drawings since they are easily available to the printers: ○, ●, +, ×, □, ■, △, ▲, ◊, ⧫, ▽, ▼.

4. **References** are indicated in the text by *numbers on the line in brackets, and the full* reference should be given in a list at the end of *the paper in the following form:*

1. BARNES R. G., BORSA F. and PETERSON D., *J. appl. Phys.* **36**, 940 (1965).
2. KNIGHT W. D., In *Solid State Physics* (Edited by F. Seitz and D. Turnbull), Vol. 2, p. 93. Academic Press, New York (1957).

Abbreviations of journal titles should follow those given in *World List of Scientific Periodicals* (4th Edn.). It is particularly requested that authors' initials, and appropriate volume and page numbers, should be given in every case.

Footnotes, as distinct from literature references should be indicated by the following symbols—*, †, ‡, §, commencing anew on each page; they should *not* be included in the numbered reference system.

5. Due to the international character of the journal no rigid rules concerning notation and spelling will be observed, but each paper should be consistent within itself as to symbols and units.

infrared physics

Board of Editors

P. Goerlich *Jena* **S. Passman** *Washington DC*
T.S. Moss *Camberley* **W.K. Weihe** *Fort Belvoir*

Papers published in this journal concern infrared physics and its applications. The theory, experiment, techniques and instrumentation of all aspects of infrared generation, transmission and detection in the fields of meteorology, geophysics, aeronautics, space and industry are fully covered.

Topics included are all types of detectors, together with associated data processing or cooling problems; optical materials and systems; transmission, emission and reflection; sources and modulation problems, with particular interest in all types of lasers; electronic and electro-optical instrumentation with infrared applications.

Review articles are occasionally published on optical infrared properties of semi-conductor materials: to date these have dealt with germanium and silicon.

Relevant conference or symposia proceedings are also published, the most recent being that of the *Symposium on Infrared Components, Techniques and Systems* held at the Royal Radar Establishment, Malvern in April 1967.

Papers appearing in Volume 8 (1968) include

G. Baker and D. Charlton: Low frequency noise in copper doped germanium infrared detectors caused by thermal impedance fluctuations

J. Lytollis, C.K. Kao and G.I. Turner: Infrared optical communication systems

J.R. Thomas, E.E. Jones and R.E. Peterson: Two promising empirical techniques for closed form functional representation of 14-16 micron radiance profiles

P. Coufova and J. Novak: Preparing of powder samples for transmission infrared spectroscopy

E. Feldner, P. Goerlich, A. Krohs and G. Wagner: Some aspects of the influence of temperature on the photoconductive properties of PbS layers

Published quarterly

Write for full details and an inspection copy. Details of other journals in this field can also be sent to you.

PERGAMON PRESS

OXFORD NEW YORK

Journal of Inorganic and Nuclear Chemistry

Editors
C.B. Amphlett Harwell **J.J. Katz** Argonne
A.G. Maddock Cambridge **J.H. van Santen** Eindhoven

The broad areas of inorganic and nuclear chemistry are covered in this Journal which provides an international medium of communication among research workers. Contributions deal with structural inorganic chemistry, coordination chemistry, the kinetics and mechanisms of inorganic reactions, and nuclear properties and reactions.

Papers published in Volume 30 (1968) include
T.N. Srivastava and **S.K. Tandon:** Triarylgermanium pseudohalides
E. Paletta und **H. Muller-Buschbaum:** Zur Kristallstruktur von $SrTb_2O_4$
A. Clearfield, R.H. Blessing and **J.A. Stynes:** New crystalline phases of zirconium phosphate possessing ion-exchange properties
M.M. Faktor, R. Hanks and **T.H. Lemon:** Thermal analysis of proustite
D.C. Jackman and **C.W. Keenan:** Alkali metal ammonia reaction as catalyzed by glass
R.E. Stone and **E.K. Hulet:** Radiochemical determination of the alpha half-life of ^{241}Am
M.J. Cabell and **M. Wilkins:** Mass spectrometric measurements of the neutron capture cross sections of ^{142}Nd, ^{143}Nd, ^{144}Nd and ^{145}Nd for Maxwellian and reactor neutrons
C.H. Ke, P.C. Kong, H.S. Cheng and **N.C. Li:** The stability of some lanthanide complexes with bimalonate and bisuccinate

Published monthly
Please write for full details and an inspection copy. Details of other journals in this field can also be sent to you.

PERGAMON PRESS
OXFORD · NEW YORK

an international journal reporting research on crystal growth and materials preparation and characterization

Materials Research Bulletin

Joint Editors-in-Chief:
Heinz K. Henisch and Rustum Roy
The Pennsylvania State University

Materials Research Bulletin is a focal point for research on materials in relation to the fields of physics, chemistry, engineering and earth sciences.
Papers are published within six weeks after acceptance, and cover the structure and properties of electronically, optically or mechanically interesting solids, which are considered and discussed as a function of preparational parameters. Other subjects include the synthesis of new phases, high pressure and high temperature phase changes, crystal growth mechanism and techniques, defect structure analysis, the preparation and structure of noncrystalline solids, and the development of new characterizing criteria and experimental methods.

Papers appearing during 1968 include
A. Madeysk and W. W. Smeltzer: Oxygen diffusion in monoclinic zirconia
S. A. Levy and R. Gashler: On the origin of lamellae in high resistivity KTN
B. G. Bagley, H. S. Chen and D. Turnbull: Characterization of amorphous alloy films
A. Roger et R. Fruchart: Etude magnétique et structurale de la solution solide MnP - MnAs
A. Vasko: Examination of internal defects in chalcogenide glasses by infrared defectoscopy methods

Published monthly
Write for full details and an inspection copy

PERGAMON PRESS LTD
OXFORD · NEW YORK

ARMS CONTROL AND DISARMAMENT annual review

an International Journal published under the joint auspices of the Hudson Institute and Pergamon Press

Edited by *Donald G. Brennan* Hudson Institute and *Robert Maxwell* Pergamon Press

Arms Control and Disarmament is concerned with the broad field of this subject as it is generally understood, publishing articles, reviews, factual and bibliographic material on aspects ranging from political, technical, economic, legal and theoretical viewpoints. Articles are written by those who have substantial responsibilities for the arms control policies of their respective countries and by experts who provide intellectual contributions, such as improved understanding of arms control issues, and illuminating summaries of recent events.

Other material published in the Review includes lists of selected books and papers and factual details such as military budgets and force levels.

The Editors may also provide opinion in the form of signed or unsigned editorials, or special articles, or comments on the articles in the Review, with the purpose of stimulating discussion and controversy.

Papers from the first issue include

O Bassir Arms control and the developing nations
A Beaufre Some reflections on the problem of arms control
K E Boulding Accomplishments and prospects of the peace research movement
D G Brennan The risks of spreading weapons: A historical case
L W Martin Ballistic missile defense and arms control
M Singer A non utopian [illegible] for future world
L B Sohn Enforcement of disarmament controls with respect to states which have not ratified a disarmament or arms control treaty
J J Stone Arms control: where is it?

Arms Control and Disarmament is published on a non profit basis; should revenues exceed expenses, the balance will be used to support studies on arms control.

Write for full details and subscription rates

PERGAMON PRESS LTD
OXFORD NEW YORK

J. Phys. Chem. Solids Pergamon Press 1969. Vol. 30, pp. 1-12. Printed in Great Britain.

MAGNETIC AND CRYSTALLOGRAPHIC CHARACTERISTICS OF $(Pr,La)Al_3$, $(Pr,Y)Al_3$, $(Pr,La)Al_2$ AND $(Pr,Y)Al_2$*

K. H. MADER, E. SEGAL and W. E. WALLACE
Department of Chemistry, University of Pittsburgh, Pittsburgh, Pa. 15213, U.S.A.

(*Received* 8 *April* 1968; *in revised form* 10 *June* 1968)

Abstract – Magnetization data are reported for $PrAl_2$ (cubic) and $PrAl_3$ (hexagonal) and ternary alloys in which Pr is partially replaced by Y and La. Between 50 and 300°K Curie–Weiss behavior is observed with slopes as expected for tripositive Pr. The cubic alloys exhibit Curie temperatures ranging from 38·5°K for $PrAl_2$ to 5°K for $Pr_{0.05}La_{0.95}Al_2$. $Pr_{0.05}Y_{0.95}Al_2$ is the single exception; it remains paramagnetic to 4°K. The hexagonal alloys all develop Van Vleck paramagnetism at low temperatures. The operator equivalent method is employed to obtain eigenfunctions, eigenvalues and magnetic moments for the crystal field states for Pr^{+3} in both the cubic and hexagonal environments Fourth and sixth order interactions are included in both instances and the second order term is also included for $PrAl_3$ since its axial ratio is not ideal. Susceptibility-temperature behavior of $PrAl_3$ and the hexagonal ternaries can be accounted for with two sets of parameters which concern the relative importance of the second, fourth and sixth order interactions; in each case the overall splitting is about 120°K The maximal value of the overall splitting for the cubic alloys is established to be 25°K. Using a molecular field approach it is possible to understand the development of ferromagnetism in $PrAl_2$ which occurs despite the lack of a permanent moment for Pr in its ground state With this approach T_c is calculated to be 39°K, which is in excellent agreement with experiment, 38·5°K. The same approach gives a reasonably satisfactory accounting for the composition dependence of T_c and the saturation moment.

1. INTRODUCTION

THE MAGNETIC characteristics of intermetallic compounds containing the lanthanide elements have been extensively studied in recent years[1]. In a number of cases, e.g. $GdAl_2$ and $GdNi_2$, the lanthanide moment observed is in good agreement with that of the free tripositive ion. In others, e.g. $TbIr_2$[2], the observed moment is substantially lower. The reduced moment in a number of instances has been related[1] to the quenching effect of the crystalline field on the orbital contribution to the moment. In this respect PrBi and PrSb are of special interest[3] in that their crystal field is so strong compared to exchange that they fail to order at low temperatures; they become instead Van Vleck paramagnets. In them the Γ_1 non-magnetic state splits off as the ground state and upon cooling the ions settle into it before ordering has a chance to occur.

Most praseodymium compounds show more complex behavior than PrBi and PrSb undoubtedly because in them exchange and the crystal field interaction are more nearly comparable in magnitude. The cubic Laves phase $PrNi_2$, which has been extensively studied in this Laboratory[4–6], is a typical example of this. To date it has not been possible to establish whether at 4·2°K it is more proper to regard $PrNi_2$ as a ferromagnet with a strongly quenched moment or a Van Vleck paramagnet that is experiencing appreciable exchange.

The hexagonal compound $PrAl_3$ has recently been studied by Buschow and Fast[7]. The magnetic behavior reported for it resembles that observed for $PrNi_2$; susceptibility measured at 4°K is field dependent in each case and in addition both compounds exhibit negative deviations from Curie–Weiss behavior in the temperature region just above the point at which the onset of temperature-independent susceptibility, associated with their presumed Van Vleck paramagnetism, begins. Moreover, the ground state of Pr in both compounds is a singlet; that is, it does not carry a permanent moment.

---

*This work was assisted by a contract with the U.S. Atomic Energy Commission.

The present work was undertaken in an effort to obtain a clearer view of the influence of the crystal field on the low temperature magnetic behavior of hexagonal materials such as $PrAl_3$, to complement the earlier work on the cubic compounds PrSb and PrBi. For this purpose it is convenient to suppress exchange, while leaving the strength of the crystal field essentially unchanged. This may be accomplished by the substitution of non-magnetic Y or La into the Pr sublattice, a procedure which is similar in concept to that used earlier on the $(Ce,La)Al_2$ system by White *et al.*[8]. Analysis of the data has required the development of an appropriate calculational framework. This has entailed theoretical treatments generally similar to those made earlier by Penney and Schlapp[9] and Lea, Leask and Wolf[10] for cubic systems. The work was later extended to $PrAl_2$ based systems. Williams *et al.*[11] observed that $PrAl_2$ orders ferromagnetically with a Curie temperature of about 35°K. It was hoped that in the $(Pr,La)Al_2$ and $(Pr,Y)Al_2$ ternaries exchange could be suppressed to a point that Van Vleck paramagnetism rather than ferromagnetic ordering would develop at low temperatures; if so, analysis similar to that used earlier for PrSb and PrBi could be employed to estimate the magnitude of the crystal field splitting. To anticipate that which is described more fully below, this hope was not realized; the cubic Laves phases samples, with a single exception, continued to order ferromagnetically at the highest Pr dilutions. Furthermore, as regards $PrAl_3$ results differing slightly from those of Buschow and Fast were obtained. $PrAl_3$, as well as several ternary alloys which were studied, behaved as essentially ideal Van Vleck paramagnets, in the sense that the negative deviations from Curie–Weiss behavior referred to above were not observed.

2. EXPERIMENTAL DETAILS

The Y-, La- and Pr-metals used were obtained from the Research Chemical Division of Nuclear Corporation of America, Phoenix, Arizona. They were rated at 99·9 per cent purity. The Al(99·999 per cent) was a gift of Alcoa. Two typical Pr analyses are:

Pr major, $Y < 0{\cdot}01\%$,
$Si < 0{\cdot}01\%$, $Mg < 0{\cdot}01\%$

Pr major, $Y < 0{\cdot}005\%$,
$Si < 0{\cdot}01\%$, $Mg < 0{\cdot}01\%$, $Fe < 0{\cdot}01\%$.

The impurities in the Y- and La-metals used are similar.

Samples were prepared by levitation melting under an argon atmosphere of 600 mm. After melting and X-raying, a portion of each sample was annealed in a high putity MgO-crucible sealed in a vycor tube under low argon atmosphere. All samples were annealed[12] at 850°C for more than 400 hrs, after which X-ray patterns for the determination of the lattice constants were obtained.

For the X-ray work a GE XRD 5 unit was used (with Ni-filtered Cu K_α radiation). All samples showed excellent X-ray patterns with good resolution of the K_α-doublet. The lattice constants have errors of ±0·003 and ±0·005 Å for the cubic and hexagonal forms, respectively.

Magnetic measurements were made using the Faraday method. The technique employed has been described[3–5]. Saturation moments were obtained by extrapolating magnetization (σ) vs. $1/H_{eff}$ plots to $1/H_{eff} = 0$. Curie temperatures were established by extrapolating σ^2 vs. temperature plots to $\sigma^2 = 0$.

3. RESULTS

(A) The $(Pr,La)Al_2$ and $(Pr,Y)Al_2$ systems

Results are largely summarized in Tables 1 and 2 and Figs. 1 and 2. As noted above the $PrAl_2$-based systems showed magnetic ordering at all Pr dilutions. The ternary

Table 1. *Magnetic and crystallographic characteristics of* (Pr,La)Al_2 *and* (Pr,Y)Al_2 *alloys**

	a_0 (Å)	μ_S mole Pr at 4·2°K	T_c (°K)	μ_{eff} mole Pr (μ_B)	θ (°K)
$LaAl_2$	8·140				
$Pr_{0.05}La_{0.95}Al_2$	8·136	1·73†	5	3·72†	−11†
$Pr_{0.2}La_{0.8}Al_2$	8·118	2·34	8	3·64	−8
$Pr_{0.4}La_{0.6}Al_2$	8·093	2·47	13	3·59	3
$Pr_{0.6}La_{0.4}Al_2$	8·073	2·59	19	3·50	11
$Pr_{0.8}La_{0.2}Al_2$	8·050	2·50	30	3·55	18
$PrAl_2$	8·029	2·52	39	3·46	31
$PrAl_2$	8·028	2·57	38	3·56	28
$Pr_{0.8}Y_{0.2}Al_2$	7·990	2·36	32	3·53	22
$Pr_{0.6}Y_{0.4}Al_2$	7·959	2·09	25	3·60	17
$Pr_{0.4}Y_{0.6}Al_2$	7·933	1·83	20	3·70	10
$Pr_{0.2}Y_{0.8}Al_2$	7·898	1·44	15	3·70	3
$Pr_{0.1}Y_{0.9}Al_2$	7·878	0·83†	13	3·68†	−9†
$Pr_{0.05}Y_{0.95}Al_2$	7·862			3·58†	-5†
YAl_2	7 858				

*a_0 is the lattice parameter. T_c and θ are the Curie temperature and Weiss constant, respectively.

†corrected for YAl_2 or $LaAl_2$ respectively.

$Pr_{0.05}Y_{0.95}Al_2$ is the single exception to this, exhibiting Curie–Weiss behavior for temperatures down to 4°K. Curie temperatures (T_c) for the others are listed in Table 1. A decline in T_c as the Pr concentration is reduced, as is expected from the weakened exchange, is

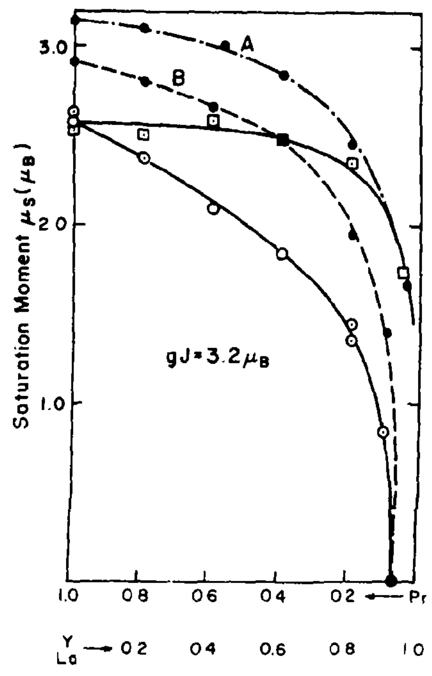

Fig. 1. Saturation moments vs. compositions for $Pr_xM_{1-x}Al_2$ alloys with M = Y(○) and La (□). The filled circles are values computed from equation (1) using values of λ, the molecular field coefficient, 30 (Curve A) and 18·2 (Curve B).

Table 2. *Magnetic and crystallographic characteristics of* (Pa,La)Al_3 *and* (Pr,Y)Al_3 *alloys**

	a_0 (Å)	c_0 (Å)	$\frac{c_0}{a_0}$	$\frac{\mu_{eff}}{\text{mole Pr}}$ (μ_B)	θ (°K)	$10^3\chi_m$ 4·2°	$\left(\frac{\text{emu}}{\text{mole Pr}}\right)$ 300°K
$Pr_{0.2}La_{0.8}Al_3$	6·63	4·61	$0{\cdot}69_5$	3·66	−6	85 9	5 45
$Pr_{0.4}La_{0.6}Al_3$	6·61	4·61	$0{\cdot}69_7$	3·61	−6	83·9	5·30
$Pr_{0.6}La_{0.4}Al_3$	6·57	4·61	$0{\cdot}70_2$	3·67	−6	74·4	5·34
$Pr_{0.8}La_{0.2}Al_3$	6·54	4·60	$0{\cdot}70_3$	3·65	−6	74·1	5·40
$PrAl_3$	6·51	4·60	$0{\cdot}70_7$	3·67	−7	71·0	5·38
$PrAl_3$	6·51	4·60	$0{\cdot}70_6$	3·68	−9	68 8	5·44
$Pr_{0.8}Y_{0.2}Al_3$	6·47	4·60	$0{\cdot}71_1$	3·64	−10	62·1	5·41
$Pr_{0.6}Y_{0.4}Al_3$	6·42	4·60	$0{\cdot}71_6$	3·70	−12	62·0	5·48
$Pr_{0.4}Y_{0.6}Al_3$	6·38	4·60	$0{\cdot}72_1$	3·67	−9	60·5	5·35
$Pr_{0.2}Y_{0.8}Al_3$	6·33	4·60	$0{\cdot}72_7$	3·64	−14	52·3	5·20

*a_0 and c_0 are the lattice parameters. The other symbols have the same significance as in Table 1.

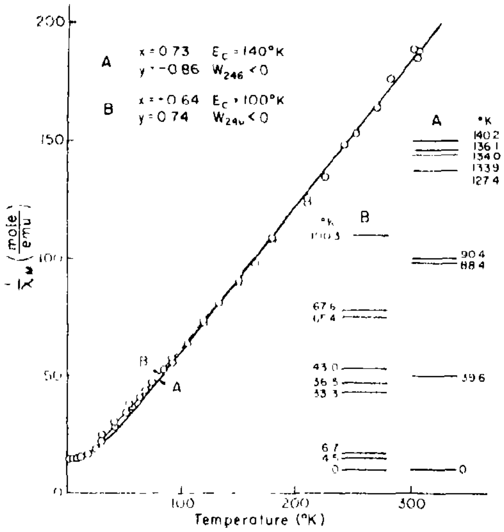

Fig. 2. $1/\chi$ vs. temperature for $PrAl_3$. Points are experimental. The curves are computed as indicated in the text using the two sets of energy levels shown to the right (see also Table 4).

readily apparent. The average saturation moment observed for $PrAl_2$, 2·55 μ_B per formula unit, is in good agreement with the value reported by Williams *et al.*[11], 2·62 μ_B. These values are lower than the free Pr ion value, 3·2 μ_B, and are also lower than the moment for Pr in $PrAl_2$, 2·9 μ_B, obtained by Olsen *et al.*[13] using neutron diffraction work. The critical temperatures obtained for $PrAl_2$ in this study are in close agreement with that observed by Olsen *et al.*[13], namely 38°K.

Results obtained for the paramagnetic region for $PrAl_2$ and the several ternaries give an average effective moment of 3·60 μ_B per Pr ion, which is in good agreement with the value calculated by Van Vleck for the free tripositive ion[14]. Saturation moments for the several ternaries at 4°K are listed in Table 1 and plotted in Fig. 1. Results are significantly different depending upon whether Pr is diluted with Y or La.

(*B*) *The* $(Pr,La)Al_3$ *and* $(Pr,Y)Al_3$ *systems*

In contrast with the behavior of the Laves phase systems described above these two groups of ternaries remain paramagnetic to the lowest temperatures studied, 4°K. The data for $PrAl_3$ plotted in Fig. 2 are typical of the results obtained for the eight ternaries listed in Table 2. In all cases Curie–Weiss behavior is exhibited for temperatures above 25°K but at lower temperatures the $1/\chi$ vs. temperature plots flatten off to give a susceptibility which is essentially independent of temperature below 10°K. Thus these materials become Van Vleck paramagnets at reduced temperatures instead of developing a magnetically ordered strucutre, indicating the predominance of the crystal field interaction over exchange. As noted above the contrary situation obtains in the cubic ternaries.

The present results for $PrAl_3$ and the several hexagonal ternaries differ from the results obtained by Buschow and Fast in that there is no negative deviation from Curie–Weiss behavior at temperatures just above the point at which Van Vleck paramagnetism begins to be clearly shown. Buschow and Fast report field dependent susceptibility at 4°K, suggesting a ferromagnetic contaminant (probably $PrAl_2$) in their sample, which could account for the negative deviation from Curie–Weiss behavior. The present samples were carefully annealed in an effort to produce the pure single phase hexagonal material. The X-ray patterns gave no indication of the presence of the cubic Laves phase $PrAl_2$ or orthorhombic $PrAl_4$ in the samples used for magnetic studies. Moreover, χ measured at 4·2°K was independent of the field strength used. These features together with the absence of the negative deviation reported by Buschow and Fast all confirm that the preparative procedure produced a material free of ferromagnetic phases and suggest that the present results are more nearly characteristic of the pure hexagonal phases than those obtained by Buschow and Fast.

The effective moments obtained for the 10 samples listed in Table 2 in the Curie–Weiss region averaged 3·65 μ_B per Pr ion, which is in good agreement with that of the free tripositive ion[14].

4. DISCUSSION OF RESULTS

(*A*) *The* (Pr, La)Al$_2$ *and* (Pr, Y)Al$_2$ *systems*

As set forth in the Introduction the motivation for studying these alloys was to obtain an estimate of the crystal field splitting for the Pr^{+3} ion. Dilution of Pr^{+3} to suppress exchange failed to convert these into Van Vleck paramagnets. Hence the classical method used by Penney and Schlapp[9] to estimate the splitting could not be employed. However, from the fact that the tendency toward Van Vleck paramagnetism must develop only below 4°K, if at all, it is possible to set an upper limit to the splitting.

The 9-fold degenerate ground state of the Pr^{+3} ion in PrAl$_2$ is decomposed into Γ_1, Γ_4, Γ_3 and Γ_5 states, with the ground state being either Γ_1 (singlet) or Γ_5 (triplet). For a tetrahedron of positive ligands or an octahedron of negative ligands, Γ_1 is the ground state. White *et al.*[8] have examinated the crystal field potential in CeAl$_2$ and concluded that the lowest lying state is a doublet. This has recently been confirmed experimentally by Swift and Wallace[15]. It seems reasonable that the interaction is similar in PrAl$_2$ and for the ternaries containing La and Y, in which case Γ_1 is the ground state. Therefore in the analysis which follows, the Γ_1 state is regarded as lowest lying. However, the possibility that Γ_5 is the ground state was also considered. This possibility was rejected since the results obtained on this basis are not in accord with experiment.

Noticeable deviations from Curie–Weiss behavior (toward Van Vleck paramagnetism) become evident at temperatures which correspond to the energy difference (expressed as temperature) between the Γ_4 and Γ_1 states. This energy difference, Δ, is roughly one fourth[9, 16] of E_c, the overall splitting by the crystal field. Since Curie–Weiss behavior extends to about 5°K, we conclude that E_c cannot exceed about 25°K. This is less by a factor of 8 than the value found [8, 15] for CeAl$_2$. However, the doublet ground state for Ce in CeAl$_2$ requires[8] a negative formal charge for Al. This negative formal charge is undoubtedly a consequence of the field supplied by conduction electrons, which are lumped up along lines joining the central ion to its ligands. These lumped up conduction electrons apparently contribute enough to change the sign of the potential at the site of the central ion. Since the contribution of the ion cores and the conduction electrons are opposite in sign, a modest decrease in the latter can substantially alter E_c. We believe this to be responsible for the small E_c for PrAl$_2$.

Since the PrAl$_2$ based ternaries failed to develop Van Vleck paramagnetism upon dilution with La and Y, it became necessary to extend the theoretical treatments to provide an appropriate basis for analyzing the data obtained. Eigenfunctions and eigenvalues were obtained using the operator equivalent method for the Hamiltonian $\mathscr{H} = g\mu_B(J\cdot H) + W_{46}\ [x(O_4/F_4) + (1-|x|)(O_6/F_6)]$. The nomenclature corresponds to that used by Lea, Leask and Wolf[10], except that their W is represented here as W_{46}. $F_4 = 60$ and $F_6 = 1260$. x is the parameter which established the relative importance of the fourth and sixth order contributions to the crystal field. Results are developed in terms of the quantity C. $C = E_M/E_c$, where E_M is the energy of the magnetic perturbation alone, $2gJ\mu_BH$. Calculations were made for a wide range of the x and C parameters. In our analysis we have considered values of x ranging from unity to 0·80. The latter is the value of x used in the successful treatment of elemental Pr[17] and its alloys with La and Y and corresponds closely with Bleaney's estimate[18] of the sixth order contribution. $x = 0{\cdot}80$ is favored since calculations based on this value of the parameter are in best agreement with experiment.

We can understand the development of order in PrAl$_2$ by considerations very similar to those used in the treatment[17] of Pr and the Pr–Y and Pr–La systems. We use a molecular field approach with λ, the molecular field constant, estimated from Θ, the observed Weiss constant.

$$M = \alpha \frac{\sum_i \mu_i \exp(-T_i/T)}{Q}. \qquad (1)$$

Here M is the magnetization expressed in erg/Oe. mole, μ_i is the moment of the i^{th} state, Q is the partition function, and α is a constant, $1{\cdot}786 \times 10^4$ erg/(Oe. mole). With $E_c = 25°K$ and for fields up to 10 kOe μ_i is linear with field strength. Values of the constants in the expression $\mu_i = a_i + b_i H$ are listed in Table 3. H, the total field acting on the ion, is made up of H_0, the applied field, and H_M the molecular field. Thus

Table 3. Magnetic moment data for cubic* Pr^{+3} *with* x = 0·80, $E_{c.f.}$ = 25°*K*

	a_i	$10^6 b_i$	Energy (°K)
Γ_5	−0·625	−6·20	25
	0·000	−3·98	
	0·625	−7·18	
Γ_3	0·000	−13·44	15·5
	0·000	−13·56	
Γ_4	−0·125	+19·90	9·0
	0·000	−15·38	
	0·125	+19·78	
Γ_1	0·000	+19·40	0

*a_i and b_i are constants in the equation for the magnetic moments $\mu_i = a_i + b_i H$. This gives moments in units of $gJ\mu_B$

$$\mu_i = a_i + b_i(H_0 + \lambda M). \qquad (2)$$

We obtain from equations (1) and (2)

$$M = \frac{A + BH_0}{Q - \alpha B\lambda} \qquad (3)$$

where

$$A = \sum_i a_i \exp(-T_i T),\ B = \sum_i b_i \exp(-T_i/T)$$

and T_i represents the energy of the i^{th} state in °K. Since A, Q and B are functions of M, the solution of equation (3) for M is not straightforward. The procedure entailed is discussed at some length elsewhere[17]. At higher temperatures (e.g. $T > 50°K$ in the present case), the solution for $H_0 = 0$ is always $M = 0$. As T is reduced, the denominator D in equation (3) decreases toward zero. The second term in the denominator relates to the enhancement of M over that produced by H_0 and it follows that as this term approaches Q in size, a vanishingly small value of H_0 can produce a sizeable value of M. In other words a spontaneous moment appears with reduced temperature and it seems from qualitative considerations that this should occur at the temperature where D vanishes, or at very nearly this temperature. In the treatment of Pr it is shown[17] that T_c, the temperature at which spontaneous magnetization appears, is given by the expression

$$T_c = \frac{\alpha\lambda g J \mu_B}{k} \frac{\sum_i a_i^2 \exp(-T_i/T_c)}{Q^0 - \alpha\lambda B}. \qquad (4)$$

The superscripts on Q^0 and B^0 indicated that they are to be evaluated for M (or H) = 0. It is furthermore shown[17] that T_c differs from T_c', the temperature at which D vanishes, by less than one °K and hence in practice we merely seek the temperature for $D = 0$. This condition implies an infinite value of M for $T = T_c$. We shall consider this 'infinity catastrophe' and how it is avoided below.

To evaluate T_c from equation (4) a value for the molecular field constant λ is needed. We estimate it from the observed Weiss Constant (Table 1). Using the simple Weiss molecular field theory,

$$\lambda = 18{\cdot}2 \frac{(\mathrm{Oe.})^2\,\mathrm{mole}}{\mathrm{erg}}.$$

(Throughout this paper λ will be given in these units which are omitted for brevity.) More comprehensive molecular field treatments[19] indicate that the simple approach seriously underestimates exchange. Following Rushbrooke and Wood[20] we estimate $\lambda = 30$ and use this value in treating $PrAl_2$. Using equation (3) together with $\lambda = 30$ we calculate $T_c = 39°K$, which is in excellent agreement with the observed ordering temperature. Equation (3) thus provides a basis for understanding the development of order in a substance in which the ground state lacks a permanent moment. It furthermore suggests that order develops on cooling with atypical rapidity. The data of Swift[21] shown in Fig. 3 clearly support this idea. Interestingly the calculated value for T_c is quite insensitive to the choice for E_c, differing by less than 2°K for crystal field splittings in the range from 10 to 150°K.

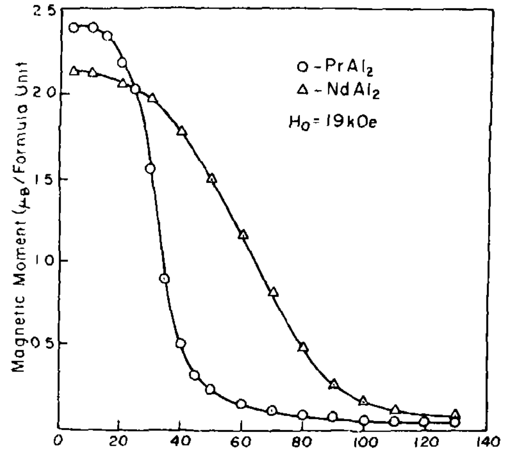

Fig. 3. Magnetization vs. temperature for $PrAl_2$ and $NdAl_2$ taken from Swift (reference [21]).

The decline in T_c with decreasing Pr content is made clear through equation (3). λ clearly decreases as Pr is diluted with Y or La. We can estimate the reduction for $Pr_{0.05}La_{0.95}Al_2$ from observations made on Ln–Y and Ln–Lu alloy systems, in which Ln is a heavy lanthanide. Néel temperatures have been found to vary with $N_{Ln}^{2/3}$, where N_{Ln} is the Ln concentration. This was first observed from susceptibility measurements by Weinstein, Craig and Wallace[22] and later confirmed through neutron diffraction measurements by Koehler and his associates[23]. We thus regard λ as linear with $N_{Pr}^{2/3}$ from which we estimate λ for $Pr_{0.05}La_{0.95}Al_2$ to be 4·1. From this we compute $T_c = 4.6°K$, which is in extraordinarily good agreement with the experimental value, 5°K. Calculations for the other ternaries listed in Table 1 are shown in Fig. 5 together with results obtained assuming a linear variation of λ with N_{Pr}. We see that the dependence of T_c on composition is generally in line with expectations based on equation (3) and the $N_{Pr}^{2/3}$ dependence for the Y but not the La ternaries. This parallels the findings of Koehler[23], who found that the dependence of T_N on $N_{Ln}^{2/3}$ did not hold for Ln–La alloys.

Examination of equation (3) shows that there is a critical value of λ, λ_c, below which ordering cannot occur. For $E_c = 25°K$ this is 2·84. Alloys in which 90 per cent or more of the Pr ions have been replaced have λ values approaching λ_c. They are thus in a critical stage in that further dilution and/or an increase in E_c will prevent the development of order. The behavior of $Pr_{0.05}Y_{0.95}Al_2$ in not ordering provides suggestive evidence for an increase in E_c with inclusion of Y in the lattice.

We now turn attention to the behavior of the Laves phase system for $T < T_c$. As noted above the denominator in equation (3) vanishes for T just below T_c and hence an infinite M would result. Clearly this does not happen. The reason for this is that equation (3) ceases to be valid at large M. It is a form of equation (1) which is valid for low M values and is very useful for determining T_c. Below the critical temperature, M rises very rapidly, as noted above, so that very quickly a large effective field (λM) is developed. The expression $\mu_i = a_i + b_i H$ is valid only for H less than about 50 kOe.; for larger fields μ_i begins to saturate. Saturation can be formally recog-

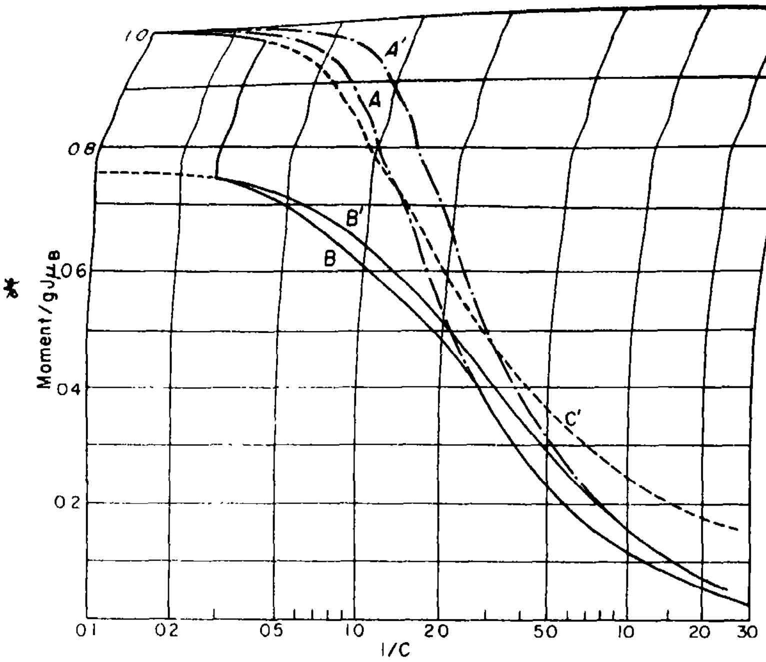

Fig. 4. Moment vs. $1/C$ for the two lowest lying energy states. Curves A and B refer to the singlet state (Γ_1). A and B are for $x = 0{\cdot}8$ and with H in the 111 and 100 directions respectively. A' and B' are corresponding curves for $x = 1{\cdot}0$. The lowest lying state is indicated by the full line; thus for the 111 direction the energy states cross over at $1/C = 0{\cdot}27$. C' in the figure represents the lowest lying member of the Γ_4 triplet.

nized by a decrease in b_i with increasing H. Thus, for large H (or M) values, the b_i's decrease and hence the term involving B in equation (3) is correspondingly reduced. It is readily shown that B at large values of H is reduced so that the denominator never vanishes, although it does become quite small.

Equation (3) is inconvenient for use in the evaluation of M below T_c. We use instead equation (1) and find the ionic moment from the value of M which satisfies this equation. For $PrAl_2$ at 4·2°K we find a saturation moment of 3·1 or 2·9 μ_B per Pr^{+3} ion for $\lambda = 30$ or 18·2, respectively. Assuming λ to vary as the 2/3 power of the Pr concentration, we obtain the values plotted in Fig. 1 for the ternaries in which Pr is diluted with Y or La. The value obtained for $PrAl_2$ with $\lambda = 18{\cdot}2$ is in exact agreement with the neutron diffraction result[13] and the Pr moment in $PrAl_2$ estimated from heat capacity measurements below 1°K[24]. The measured saturation moments obtained in this work and elsewhere[11, 15, 21] are somewhat lower. The reason for the smaller moment estimated from bulk magnetic measurements is not clear. One possibility is that saturation was not achieved; higher fields are needed to assess this possibility. Another possibility, which seems more likely, is that the lower moment results from conduction electron polarization effects. The trend of the computed moment (Fig. 1) agrees with experiment for the ternaries containing Y but not those in which Pr has been replaced by La. The situation resembles the above calculations of the dependence of T_c on composition; there also results for the Y-containing alloys were more nearly in accord with expectations.

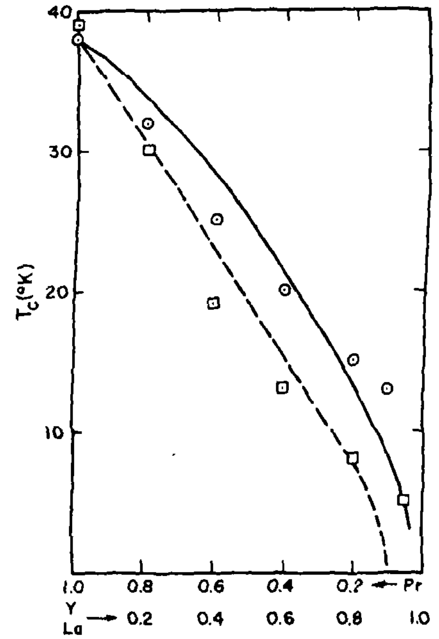

Fig. 5. T_c vs. composition for $\mathrm{Pr}_x\mathrm{M}_{1-x}\mathrm{Al}_2$ ternaries with $M = \mathrm{Y}$(○) or La (□). Points are experimental, the full line is calculated assuming λ varies as $x^{2/3}$. The dashed line is computed assuming λ varies linearly with x.

The calculations referred to above were made using results obtained for E_i and μ_i with H applied in the 111 direction. T_c and μ_i at values computed were insignificantly different using the E_i and μ_i obtained with H along the 100 direction. The set of data involved in computing the PrAl_2 moment is given in the Appendix. This is illustrative of the several thousand similar sets of data obtained and made use of in computing results for the ternary alloys.

Since both Y and La are tripositive non-magnetic ions, the difference in behavior, referred to above and shown in Fig. 1, is at the outset surprising. After more careful scrutiny, however, their differing behaviors become less mysterious. At low temperatures metals show[25] an intrinsic resistivity which varies as T^3 or T^5. The fifth power dependence arises from the normal scattering of conduction electrons by phonons. When the dominant feature as regards transport processes is electron scattering into (real or virtual) f or d-states, resistivity varies as T^3. La shows cubic dependence, implying dominance of s–f scattering, and Hamilton and Jensen[26] have in fact found it necessary to invoke the involvement of virtual f-states to account for the superconducting behavior of La. In contrast, Y exhibits fifth power dependence.

In view of the contrasting conductivity behavior of La and Y it does not seem unreasonable to suppose that they would affect the exchange interaction differently when they replace Pr on the Pr sublattice, since this interaction is transmitted via the conduction electrons. It is also possible that the conduction electron polarization contribution to the measured moment would also be different. The difference in Y and La behavior shows not only in the results cited in Fig. 1 but also in the fact that LaAl_2 becomes[27] a superconductor in the liquid helium range whereas YAl_2 does not. (This shows that the differences between La and Y as elements carry over into its Laves phase compounds.) Furthermore La and Y behave very differently when alloyed with a heavy lanthanide such as Tb. Replacement of Tb by Y favors [28] the antiferromagnetic, i.e. noncollinear, structure, whereas insertion of La into the Tb lattice results in enhanced stability[29] of the ferromagnetic, i.e. collinear, structure. Viewed in this light the different behavior of the ternaries seems not too surprising.

(*B*) *The* (Pr, La)Al_3 *and* (Pr, Y)Al_3 *systems*

As in the case of the cubic phases, the appropriate theoretical framework did not exist for treating the magnetic measurements. It was developed using the Hamiltonian

$$\mathscr{H} = g\mu_B(J \cdot H) + W_{246} \times \left\{(1-|y|)\frac{O_2}{F_2} + y\left[x\frac{O_4}{F_4} + (1-|x|)\frac{O_6}{F_6}\right]\right\}.$$

Taking the c axis as the z axis, the operators O_n are:

$$O_2 = O_2^0,\ O_4 = O_4^0 \quad \text{and} \quad O_6 = O_6^0 + \frac{77}{8} O_6^6.$$

For Pr $F_2 = 1$, $F_4 = 60$ and $F_6 = 1260$. In this case since the axial ratio is 13·5 per cent less than ideal, the second order term must be included[30]. The parameter x has the same significance as in the cubic Hamiltonian whereas y relates to the importance of the second order contribution. Both $|x|$ and $|y| \leq 1$. The coefficients B'_n associated with the equivalent operators are given by: $B'_2F_2 = (1-|y|)W_{246}$, $B'_4F_4 = xyW_{246}$ and $B'_6F_6 = (1-|x|)yW_{246}$. The following relations hold

$$\frac{B'_4F_4}{B'_6B_6} = \frac{x}{1-|x|} \quad \text{and} \quad \frac{B'_4F_4}{B'_2F_2} = \frac{y}{1-|y|}x.$$

The Hamiltonian was solved for the eigenvalues to obtain the energy levels, E_i, of the system $H|i\rangle = E_i|i\rangle$. The eigenfunctions $|i\rangle$ were formed as linear combinations of the functions $|M\rangle$

$$|i\rangle = \sum_{M=-J}^{J} a_{iM}|M\rangle. \tag{4}$$

The magnetic moment associated with each level is given by

$$\mu_i = g\mu_B\langle i|J_z|i\rangle = g\mu_B \sum_{M=-J}^{J} a_{iM}^2 M. \tag{5}$$

Susceptibility (χ) is obtained from the fundamental expression

$$\chi = \frac{N}{HQ}\sum_i \mu_i \exp(-T_i/T). \tag{6}$$

Calculations were made for a wide range of the x and y parameters and for various values of the overall crystal field splitting. The data were used in equation (6) to determine the dependence of χ on temperature. A reasonable fit (Fig. 2) was obtained for two sets of the parameters:

(A) $x = 0{\cdot}73 \pm 0{\cdot}03$, $y = -0{\cdot}86 \pm 0{\cdot}03$,
$E_c = 140 \pm 20°\text{K}$, $W_{246} < 0$.

(B) $x = -0{\cdot}64 \pm 0{\cdot}06$, $y = 0{\cdot}74 \pm 0{\cdot}02$,
$E_c = 100 \pm 20°\text{K}$, $W_{246} < 0$.

Further details pertaining to these two possibilities are given in Table 4. In each case the fit achieved is satisfactory. Case (B) is experimentally preferable but case (A) cannot be excluded. However, it is to be noted that the point charge model gives results more nearly in agreement with alternative (B).

Point charge model calculations, using the twelve nearest neighbor aluminum ions, taking into account the departure from the ideal c/a ratio, gives for B'_n – the crystal field parameters – the following expressions:

$$B'_2 = \left\{\frac{3}{2} + R^{-5}\left[\frac{1}{2} - 3\left(\frac{c}{a}\right)^2\right]\right\}\alpha\langle r^2\rangle\frac{e^2}{a^3}Z_{\text{Al}}$$

$$B'_4 = -\frac{1}{32}\left\{9 + R^{-9}\left[24\left(\frac{c}{a}\right)^4 - 24\left(\frac{c}{a}\right)^2 + 1\right]\right\}$$
$$\times\ \beta\langle r^4\rangle\frac{e^2}{a^5}Z_{\text{Al}}$$

$$B'_6 = \frac{1}{128}\left\{15 - R^{-13}\left[48\left(\frac{c}{a}\right)^6 - 120\left(\frac{c}{a}\right)^4\right.\right.$$
$$\left.\left. + 30\left(\frac{c}{a}\right)^2 - \frac{5}{9}\right]\right\}\gamma\langle r^6\rangle\frac{e^2}{a^7}Z_{\text{Al}}.$$

Here

$$R = \left[\frac{1}{3} + \left(\frac{c}{a}\right)^2\right]$$

$a = \frac{1}{2}a_0$ = the distance between two neighboring ions in the same layer, $c = \frac{1}{2}c_0$ = the distance between two adjacent layers. (a_0, c_0 are the lattice parameters for PrAl_3.) $e^2 = 1{\cdot}67097(4) \times 10^4\,°\text{KÅ}$.

When taking for c/a the ideal ratio, i.e. $(c/a)^2 = 2/3$, B'_2 vanishes, B'_4 and B'_6 reduce the expressions given by Bleaney[30] for the ideal case.

Table 4. Energy levels, eigenfunctions and parameters used for interpreting the experimental results of $PrAl_3$

(A): $x = 0{\cdot}73 \quad y = -0{\cdot}86 \quad E_c = 140°K \quad 1/C = 16 \quad W_{246} < 0$

$\frac{B'_4F_4}{B'_6F_6} = 2{\cdot}7 \quad \frac{B'_4}{B'_6} = 57 \quad \frac{B'_4F_4}{B'_2F_2} = -4{\cdot}5 \quad \frac{B'_4}{B'_2} = -0{\cdot}075$

(B): $x = -0{\cdot}64 \quad y = 0{\cdot}74 \quad E_c = 100°K \quad 1/C = 12 \quad W_{246} < 0$

$\frac{B'_4F}{B'_6F} = -1{\cdot}8 \quad \frac{B'_4}{B'_6} = -58 \quad \frac{B'_4F_4}{B'_2F_2} = -1{\cdot}8 \quad \frac{B'_4}{B'_2} = -0{\cdot}030$

(A) eigenfunction	$\mu_i/gJ\mu_B$	energy (°K)	(B) eigenfunction	$\mu_i/gJ\mu_B$	energy (°K)
$\vert 0\rangle$	0	140·2	$\vert 0\rangle$	0	100·3
$\vert -1\rangle$	−0·250	136·1	$\vert -1\rangle$	−0·250	67·6
$0{\cdot}9386\vert -4\rangle + 0{\cdot}3450\vert 2\rangle$	−0·822	134·0	$\vert 1\rangle$	0·250	65·4
$\vert 1\rangle$	0·250	133·9	$0{\cdot}9403\vert -4\rangle - 0{\cdot}3405\vert 2\rangle$	−0·826	43·0
$0{\cdot}4501\vert -2\rangle + 0{\cdot}8930\vert 4\rangle$	0·696	127·4	$-0{\cdot}4687\vert -2\rangle + 0{\cdot}8833\vert 4\rangle$	0 671	36·5
$0{\cdot}8930\vert -2\rangle - 0{\cdot}4501\vert 4\rangle$	−0·196	90·4	$0{\cdot}7726\vert -3\rangle - 0{\cdot}6349\vert 3\rangle$	−0·145	33·3
$-0{\cdot}3450\vert -4\rangle + 0{\cdot}9386\vert 2\rangle$	0·322	88·4	$0{\cdot}8833\vert -2\rangle + 0{\cdot}4687\vert 4\rangle$	−0·171	6·7
$0{\cdot}7625\vert -3\rangle + 0{\cdot}6470\vert 3\rangle$	−0·122	39·6	$0{\cdot}3405\vert -4\rangle + 0{\cdot}9403\vert 2\rangle$	0·326	4·5
$-0{\cdot}6470\vert -3\rangle + 0{\cdot}7625\vert 3\rangle$	0·122	0	$0\ 6349\vert -3\rangle + 0{\cdot}7726\vert 3\rangle$	0·145	0

For Pr:

$$\alpha = -0{\cdot}02101010 \qquad \beta = -7{\cdot}346189 \times 10^{-4}$$
$$\langle r^2\rangle = 0{\cdot}304 Å^2 \qquad \langle r^4\rangle = 0{\cdot}221 Å^4$$
$$\gamma = 0{\cdot}6099400 \times 10^{-4}$$
$$\langle r^6\rangle = 0{\cdot}345 Å^6.$$

The values of x and y derived from these parameters do not depend on Z_{VI}. One obtains $x = -0{\cdot}45$, $y = 0{\cdot}25$. We see that case (B) is preferable by the point charge model as the signs of the parameters agree with the values obtained from experiment. The discrepancy for y is considerable; however, greater error is expected for y than for x as the influence of the other ions is greater on B'_2 than on B'_4 or B'_6. On the basis of magnetic measurements alone it is not possible to decide between the two alternatives. Heat capacity measurements, which will be initiated shortly in this Laboratory, should enable us to eliminate one of the possibilities.

5. CONCLUSIONS

The susceptibility measurements on $PrAl_2$ and the ternaries based on it indicate that the crystal field splitting for this compound cannot be greater than about 25°K. If we accept this value, we can account for the development of order in $PrAl_2$ and can elucidate the main features of the composition dependence of T_c and the saturation moment. The magnetic polarizability of the Γ_1 state is the crux of the matter.

$PrAl_3$ and the ternaries based on it become Van Vleck paramagnets at low temperature. The formalism has been developed to enable the susceptibility of an assemblage of Pr ions in a hexagonal environment to be calculated. In this case second, fourth and sixth order contributions to the crystal field must be included. Two sets of the parameters (and hence two distributions of energy levels) have been found, which permit an accounting for the observed dependence of susceptibility on temperature. In each case the crystal field splitting required is about 120°K.

Acknowledgements – The authors are pleased to acknowledge the assistance of Professor J. B. Muskat of the Computer Center for assistance in providing programs for use in the calculations. Assistance of the National Science Foundation through general support of the Computer Center is gratefully acknowledged.

REFERENCES

1. WALLACE W. E., In *Rare Earth Science and Technology* (Edited by L. Eyring), Vol. 3. To appear. This article gives a comprehensive review of the magnetic work and the influence of crystal field on the bulk magnetic characteristics of lanthanide intermetallics.
2. FELCHER G. P. and KOEHLER W. C., *Phys. Rev.* **131**, 1518 (1963).
3. TSUCHIDA T. and WALLACE W. E., *J. chem. Phys.* **43**, 2087 and 2885 (1965).
4. SKRABEK E. A. and WALLACE W. E., *J. appl. Phys.* **34**, 1356 (1963)
5. FARRELL J. J. and WALLACE W. E., *Inorg Chem.* **5**, 105 (1966).
6. AOYAGI M., *Low Temperature Thermal Characteristics of Some Intermetallics Containing Lanthanides*. Ph D Dissertation. University of Pittsburgh (1967)
7. BUSCHOW K. H. J. and FAST J. F., *Z. phys. Chem* **50**, 1 (1966)
8. WHITE J A., WILLIAMS H J., WERNICK J H. and SHERWOOD R C., *Phys. Rev.* **131**, 1039 (1963)
9. PENNEY W G. and SCHLAPP R., *Phys. Rev.* **41**, 194 (1932)
10. LEA K. R., LEASK M. J M. and WOLF W P., *J. Phys. Chem Solids* **23**, 1381 (1962)
11. WILLIAMS H J, WERNICK J H., NESBITT F A and SHERWOOD R. C, *J. phys. Soc. Japan* **17**, Suppl. B-1, 91 (1962).
12. BUSCHOW K. H. J and VAN VUCHT J H N., *Z Metallk.* **57**, 162 (1966)
13. OLSEN C F, ARNOLD G. and NERESON H, *J appl. Phys.* **38**, 1395 (1967).
14. VAN VLECK J H *The Theory of Electric and Magnetic Susceptibilities*, p. 243. Oxford University Press, Oxford (1932).
15. SWIFT W. and WALLACE W. E., Unpublished work.
16. SCHUMACHER D. P. and HOLLINGSWORTH C. A., *J. Phys. Chem. Solids* **27**, 749 (1966).
17. WALLACE W. E., KISSELL F., SEGAL E. and CRAIG R. S., *J. Phys. Chem. Solids* **30**, 13 (1969).
18. BLEANEY B., *Proc. R. Soc.* **A276**, 28 (1963).
19. SMART J S., *Effective Field Theories of Magnetism*, p. 43. Saunders, Philadelphia (1966).
20. RUSHBROOKE G. S. and WOOD P. J., *Mol. Phys.* **1**, 257 (1958).
21. SWIFT W. M. Ph.D. Thesis. University of Pittsburgh (1967).
22. WEINSTEIN S., CRAIG R. S. and WALLACE W. E., *J. chem. Phys.* **39**, 1449 (1963); *J. appl. Phys.* **34**, 1354 (1963).
23. KOEHLER W C., *J. appl. Phys.* **36**, 1078 (1965).
24. McDERMOTT M J., Private Communication pertaining to work done at the Clarendon Laboratory, Oxford University.
25. ENGELHARDT L. L. WEBB G. W. and MATTHIAS B. T, *Science* **155**, 191 (1967)
26. HAMILTON D. C. and JENSEN M. A, *Phys. Rev. Lett.* **11**, 205 (1963).
27. HAMILTON D. C., RAUB Ch J., MATTHIAS B. T, CORENZWIT E. and HULL G. W. Jr., *J. Phys. Chem. Solids* **26**, 665 (1965).
28. KOEHLER W. C, CHILD H. R., WOLLAN E O. and CABLE J. W., *J. appl. Phys.* **34**, 1335 (1963).
29. KOEHLER W. C, CHILD H. R. and WOLLAN E O., Magnetic Properties of Rare Earth-Lanthanum Alloys, paper presented at the *International Congress on Magnetism*. Boston-Cambridge, Sept. 11-15, 1967
30. BLEANEY B., *Proc. R Soc.* **A276**, 39 (1963).

APPENDIX

Eigenvalues, eigenfunctions and magnetic moments for $C = 9$ *and* $x = 0{\cdot}8$*

					a_i					
E_i(°K)	μ_i	$M = -4$	$M = -3$	$M = -2$	$M = -1$	$M = 0$	$M = 1$	$M = 2$	$M = 3$	$M = 4$
226	0·9958	0·000000	0·000000	0·004346	0·000000	0·000000	0·074457	0·000000	0·000000	0·997215
187	0·7420	0·000000	0·003180	0·000000	0·000000	0·103112	0·000000	0·000000	0·994665	0·000000
165	0·4986	0·004562	0·000000	0·000000	0·041967	0·000000	0·000000	0·999109	0·000000	0·000000
140	0·2530	0·000000	0·000000	−0·039366	0·000000	0·000000	0·996464	0·000000	0·000000	−0·074229
112	0·0028	0·000000	−0·082368	0·000000	0·000000	0·991317	0·000000	0·000000	−0·102502	0·000000
84	−0·2533	−0·078043	0·000000	0·000000	0·996087	0·000000	0·000000	−0·041484	0·000000	0·000000
51	−0·4988	0·000000	0·000000	0·999215	0·000000	0·000000	0·038934	0·000000	0·000000	−0·007262
16·5	−0·7448	0·000000	0·996597	0·000000	0·000000	0·081602	0·000000	0·000000	−0·011646	0·000000
0	−0·9954	0·996940	0·000000	0·000000	0·077784	0·000000	0·000000	−0·007820	0·000000	0·000000

***Nomenclature is as follows:* $C = E_H/E_c$ where $E_H = 2gJ\mu_B H$ and E_c represents the overall crystal field splitting. x is a parameter defining the relative importance of the sixth and fourth order interactions; μ_i is the moment in units of $gJ\mu_B$, the a_i's are the coefficient in the linear combinations which represent the eigenfunctions and E_i is the eigenvalue in °K $\overline{\mu}$ is computed from this expression: $\overline{\mu} = \sum_i \mu_i \exp(-T_i/T)/Q$. Above results apply to the case in which H is in the 111 direction.

J. Phys. Chem. Solids Pergamon Press 1969. Vol. 30, pp. 13–29. Printed in Great Britain.

ON THE MAGNETIC CHARACTERISTICS OF Pr–La AND Pr–Y ALLOYS AND THE NATURE OF ELEMENTAL PRASEODYMIUM AT LOW TEMPERATURES*

W. E. WALLACE, F. KISSELL, E. SEGAL and R. S. CRAIG
Department of Chemistry, University of Pittsburgh, Pittsburgh, Pa. 15213, U.S.A.

(*Received* 8 *April* 1968; *in revised form* 10 *June* 1968)

Abstract—Magnetic susceptibilities of Pr and Pr–Y alloys are reported for the temperature range 2–300°K and for field strengths (H) up to 21 kOe. The alloys show deviations from Curie–Weiss behavior and a tendency toward temperature-independent susceptibility similar to that exhibited by elemental Pr. χ at 4·2°K for Pr decreases sharply with alloying, its Weiss constant changes sign with as little as 10 per cent La or Y. χ at 4·2°K is observed to decrease with increasing H above 10 kOe; the decrease is progressively eliminated by alloying with Y or La, and also is not observed at 300°K.

The operator equivalent method is used to calculate the energy level structure and associated magnetic moments for cubic and hexagonal Pr^{+3} ions. Influence of the sixth order term and H is included. *Using standard formulae it is possible to account for the* χ *vs.* T *behavior for* $Pr_{0.5}La_{0.5}$; *the* overall splittings at the cubic and hexagonal sites are the same as those found by Bleaney for Pr. Extension of the analysis to Pr enables most of its unusual characteristics to be understood. Appearance of spontaneous magnetization is predicted at T_c, where T_c is calculated to be in the range 24·4 to 32°K, depending on the choice of the molecular field coefficient. This compares favorably with 25°K observed by neutron diffraction techniques. From the analysis it is also clear why (a) the magnetic ordering in Pr is only a weakly cooperative process and (b) order is confined to the hexagonal sites. the new concept of Pr represents a way of harmonizing the two seemingly contradictory models used earlier in describing its low temperature magnetic behavior.

1. INTRODUCTION

PRASEODYMIUM in many respects is the most unusual of all the lanthanide elements. Among those with an incomplete $4f$ shell it is unique in that bulk susceptibility and heat capacity work on it give no indication of the formation of a cooperative phase at low temperatures. There is a thermal anomaly in the heat capacity [1] but instead of the relatively sharp λ-type excess associated with the break-up of an ordered structure it is very broad, extending from about 5 to 200°K. The associated entropy is close to R ln 9, which is R ln $(2J+1)$ for Pr, and hence this thermal anomaly has been associated with thermal excitation of the electronic states produced by crystal field splitting of the $4f$ levels.

Several workers have shown[2–4] that below 20°K the susceptibility (χ) of Pr deviates from that expected from the Curie–Weiss law and becomes virtually temperature invariant in the liquid helium range. This behavior has led investigators to regard it as a Van Vleck paramagnet, a point of view which has been elaborated upon in some detail by Bleaney[5]. Penney and Schlapp[6] pointed out many years ago that an assemblage of Pr^{+3} ions which interact only with the crystal field should behave in this way if the ground state of the Pr ion is non-degenerate. This is the case for Pr^{+3} in a cubic[6] or hexagonal[5] environment of positively charged ligands.

Elemental Pr has the A3′ structure[7], which contains two crystallographically distinguishable types of ions—c and h (for those in positions of local hexagonal and cubic symmetry, respectively) types. Bleaney [5] by analysis of the temperature dependency of χ and C_p provided an estimate of the magnitude of the crystal field splittings in ions at the c and h sites. The lowest energy degenerate levels (i.e. for electronic configurations

---

*This work was assisted by the U.S. Atomic Energy Commission.

with permanent moments) were located at 87 and 63°K, for the *c* and *h* sites, respectively. The viewpoint held by many and made explicit by Bleaney (hereafter called the VVP viewpoint) is that exchange is so weak that the excited states depopulate on cooling before ordering sets in. According to this point of view, the material remains a paramagnet (of the Van Vleck type) down to the lowest attainable temperatures, and in this respect differs from the other (magnetic) lanthanide elements, which order in some way on cooling into the liquid helium range.

Bleaney[5] has drawn attention to two troublesome features of Pr when considered from the VVP viewpoint—(a) its limiting susceptibility (χ_0) is threefold larger than expected and (b) Pr has a detectable heat capacity associated with its hyperfine structure, $(c_p)_{\text{hfs}}$[8, 9]. The observed $(c_p)_{\text{hfs}}$ is only about $\frac{1}{30}$ of that expected for ordered Pr^{+3} ions carrying the full free ion moment but is very large for a pure Van Vleck paramagnet, whose $(c_p)_{\text{hfs}}$ should vanish. Bleaney attributed the awkwardly intermediate value of $(c_p)_{\text{hfs}}$ and the enhanced limiting susceptibility to exchange, and suggested that this interaction is so large that Pr avoids becoming ferromagnetic at low temperatures by a rather narrow margin.

In 1964 Cable *et al.*[10] published results obtained in a study of Pr at low temperatures by neutron diffraction techniques. They found that at least some of the ions (1) carry a moment in the liquid helium range and (2) are ordered antiferromagnetically below 25°K. They also showed that the magnitude of $(c_p)_{\text{hfs}}$ for Pr is consistent with their observed moment, which is reduced well below the free ion value presumably due to crystal field quenching effects.

There are thus two contradictory viewpoints in regard to the magnetic nature of Pr in the liquid helium range represented by what we term the VVP and AF models. As an outgrowth of work involving Pr compounds, primarily intermetallics, we have noted another unusual feature of this element which appears to have escaped observation heretofore and which seemed to be of considerable importance in regard to the acceptability of the two competitive models. At 4·2°K, the susceptibility of Pr varies appreciably with field strength above 10 kOe, decreasing monotonically as H, the strength of the applied field, is increased. This behavior is not expected from either model—at least if viewed in a conventional fashion. A Van Vleck paramagnet is ordinarily thought of as having a susceptibility which is invariant with H; however, χ for it must decrease at high fields where saturation effects become important. On the basis of the AF model χ might be expected to increase with H due to disruption of the magnetic structure by the applied field. Thus the observed field dependency of χ clearly favors the VVP model over the AF model. The latter is, however, unambiguously supported by the neutron diffraction data.

We have studied the influence of field strength on χ in some detail, including the effect of diluting Pr with non-magnetic La and Y. In the course of analyzing these results we have been led to a better understanding of elemental Pr at low temperatures. One of us (E.S.) has been engaged in a very extensive series of calculations, dealing with crystal field interactions of the lanthanides. In this paper we use the eigenvalues developed in this work for $J = 4$ to treat the thermal and magnetic behavior of Pr and Pr-based alloys. Our concept, which is closely related to that put forth by Bleaney, represents a method for harmonizing the seemingly contradictory VVP and AF models. The treatment makes it clear why the magnetic order develops in a weakly cooperative fashion. It also permits us to account for the temperature at which order begins to be observed in Pr. Our analysis, moreover, enables us to confirm that the ordering is confined to half of the sites, as has been suggested by neutron diffraction observations and especially by the conductivity behavior of Pr in the liquid helium range (*vide infra*). The general features of the Pr ordering process which emerge as a result of this analysis differ substantially from those for the other lanthanide elements.

2. EXPERIMENTAL

The technique used in the experimental work is essentially identical with that employed in this Laboratory in numerous studies involving intermetallic compounds containing lanthanides[11–14]. Susceptibilities were measured at temperatures extending from 2 to 300°K and at field strengths ranging from 2 to 20 kOe. Alloys were prepared by levitation melting. The praseodymium used in the work was obtained from two independent suppliers. Deviations between the magnetic behavior of metal obtained from different sources were insignificant at room temperature but χ measured at 4°K varied by about 10 per cent. Other samples of nominally pure metal (not used in this work) gave a 4·2° susceptibility as much as 25 per cent lower—indicative of a strong impurity dependence.

3. RESULTS

The observations are largely summarized in Tables 1 and 2 and Figs. 1–6. All the alloys listed in Table 2 except $Pr_{0\cdot5}Y_{0\cdot5}$ showed essentially the same powder X-ray diffraction pattern as that observed for pure Pr, indicating a common structure. At $Pr_{0\cdot5}La_{0\cdot5}$ the Pr lattice was expanded slightly over 1 per cent and at $Pr_{0\cdot8}Y_{0\cdot2}$ the lattice was contracted by 1 per cent. In keeping with the findings of Spedding, Valetta and Daane[15], $Pr_{0\cdot5}Y_{0\cdot5}$ was found to occur in the Sm structure.

Table 1. Magnetic susceptibilities of praseodymium

	χ(erg/G mole) 2 and 5 kOe (4·2°K)	20 kOe (4·2°K)	67 kOe (1·3°K)
Lock*	0·218		
This work (Sample *A*)	0·235	0·191	
This work (Sample *B*)	0·241	0·197	
This work (Sample *C*)	0·241	0·197	
Henry†			0·087

*Reference[2].

†Computed from the moment measured for Pr by W. E. Henry, reference[16].

The results obtained for pure Pr in the present study at fields of 10 kOe or less were in agreement in most respects—effective moments, Weiss constant and onset of temperature independent susceptibility at low temperatures—with those obtained earlier by Lock[2], Graf[3] and Kubota and Wallace[4]. These earlier investigators employed fields under 10 kOe and hence did not observe the diminished χ at higher field strengths revealed in Table 1 and Fig. 2.

Table 2. Magnetic characteristics of Pr–La *and* Pr–Y *alloys*

At. % Pr	χ(erg/G mole) 300°K	4·2°K 11 kOe	Effective moment (μ_B/Pr ion)	Θ (°K)
		Pr–La system		
100	$5\cdot68 \times 10^{-3}$	approx. 0·20	3·61	6°
99	5·30	0·178	3·62	4
95	5·02	0·155	3·59	2
90	4·78	0·123	3·57	0°
80	4·30	0·093	3·59	−4°
50	2·70	0·045	3·63	−9
		Pr–Y system		
90	$4\cdot85 \times 10^{-3}$	0·107	3·61	−1°
80	4·32	0·088	3·65	−4
50	2·66	0·022	3·52	+3

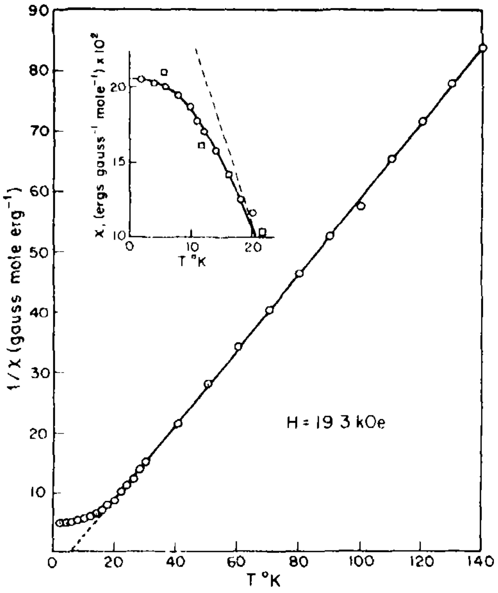

Fig. 1. Susceptibility-temperature behavior for Pr. Experimental data are given by -○- and results calculated from equation (6) (inset) are given by □. The Curie-Weiss dependence is shown by the dashed line in the inset.

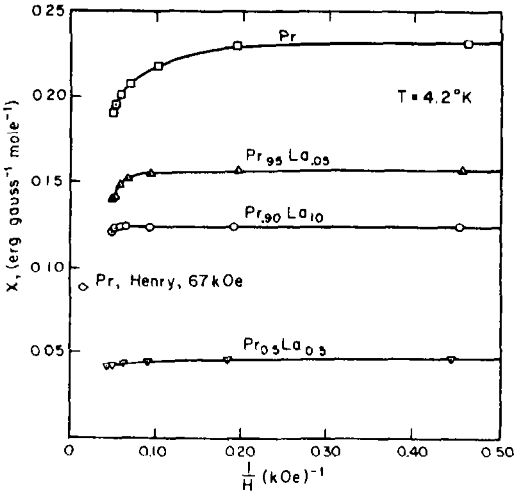

Fig. 2. χ vs 1/*H* for Pr and levitated Pr–La alloys at 4·2°K.

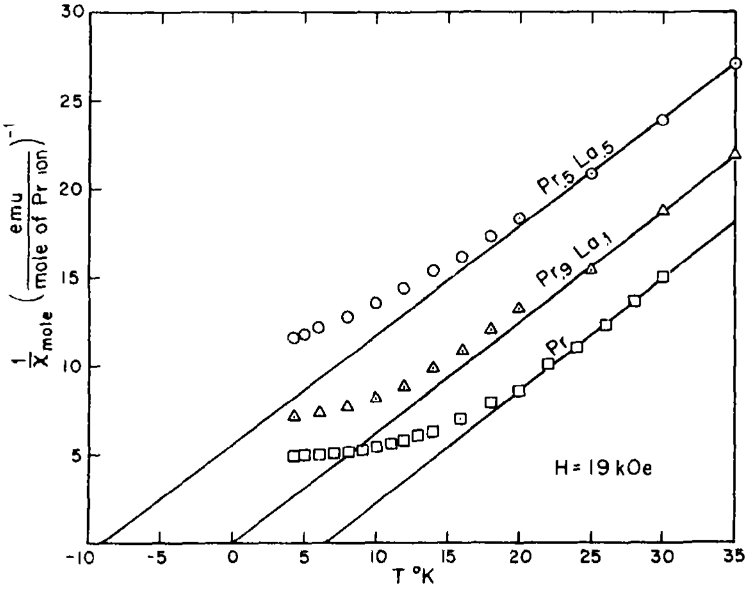

Fig. 3. 1/χ vs. *T* for Pr and Pr–La alloys at 19 kOe.

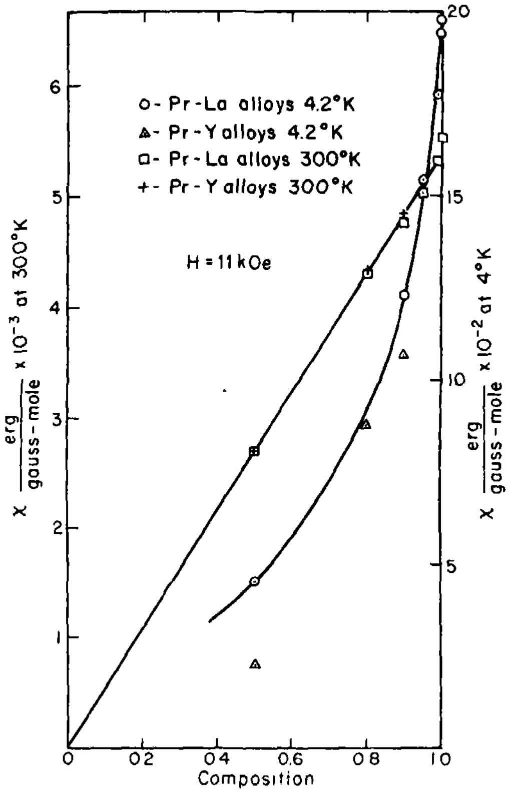

Fig. 4 χ vs composition for Pr–La and Pr–Y alloys at 11 kOe Scale at left applies to measurements at 300°K, that at right to measurements at 4·2°K.

From the results presented in the tables and figures we note the following:

1. Above 10 kOe χ decreases monotonically with increasing field strength at 4·2°K. χ is independent of field strength between 0 and 20 kOe at 300°K.

2. Insertion of La or Y into the Pr lattice reduces χ at 4·2°K and also its dependence on field strength (Fig. 2). χ at 300°K varies linearly with the Pr content of the alloy. The decrease of χ with dilution for alloys rich in Pr is much more pronounced at 4·2 than at 300°K.

3. The inverse susceptibility-temperature behavior of Pr and the various alloys are generally similar. Results for only two alloys are shown (Fig. 3) but these are representative of all the binary systems studied.

4. The effective moment per Pr atom in the alloys is independent of composition in the paramagnetic region.

5. The Weiss constant changes sign on dilution.

6. Since the results are essentially the same whether La or Y is used, it appears that the magnetic behavior of Pr is not highly sensitive to the distance between near neighbors.

7. Results for $Pr_{0\cdot5}Y_{0\cdot5}$, in particular its susceptibility and Weiss constant, are not in accord with those obtained for the other alloys studied. This is undoubtedly due to its different structure.

4. DISCUSSION OF RESULTS

(*A*) *Calculation of energy level structure and magnetic moments*

Interpretation of the magnetic behavior of Pr and its alloys requires knowledge of the sets of energy levels and the associated magnetic moments, and the dependence of these on the strength of the magnetic field, *H*. Prior to the present study the necessary information was unavailable. Penney and Schlapp[6] provided the information needed for cubic Pr^{+3} but neglected the sixth order contribution to the crystal field potential. Others included the sixth order term but confined attention to the case in which $H = 0$. Bleaney[5] treated the case of hexagonal Pr^{+3} but only for the zero magnetic field case.

Following Lea, Leask and Wolf[17] the Hamiltonian used was of the form

$$\mathscr{H} = g\mu_B(J\cdot H) + W\left[x\frac{O_4}{F_4} + (1-|x|)\frac{O_6}{F_6}\right].$$

Eigenfunctions and eigenvalues of this Hamiltonian were obtained. The magnetic field *H* was assumed to be along the hexagonal *c* axis for the ions in the *B* and *C* layers (hexagonal sites), or along the cubic [111] direction for the ions in the *A* layers (cubic sites).

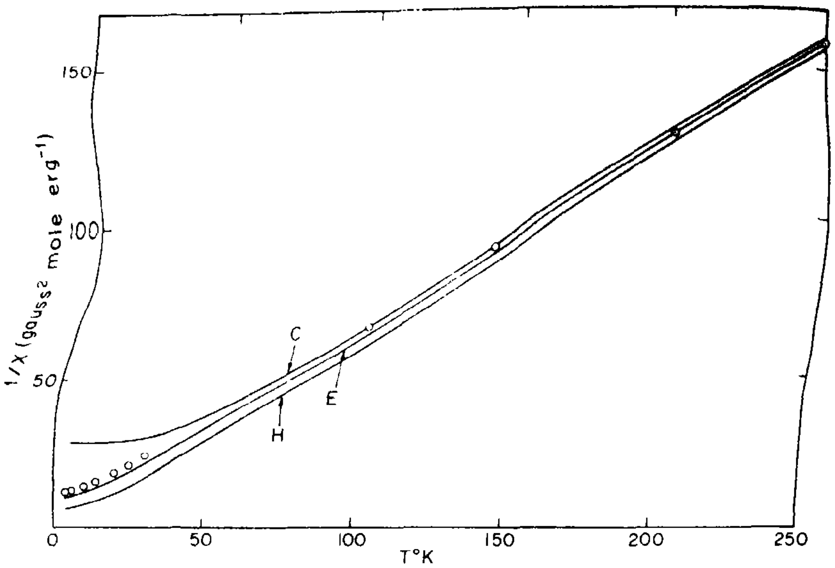

Fig. 5. Inverse susceptibility-temperature behavior for an assemblange of Pr^{+3} ions. Curves C and H pertain to one mole of Pr^{+3} ions in sites of cubic and hexagonal symmetry, respectively. Curve E is calculated for 1 mole of Pr^{+3} ions with equal numbers on cubic and hexagonal sites. Experimental results for 1 mole of Pr^{+3} ions in $Pr_{0.5}La_{0.5}$ are given by the circles.

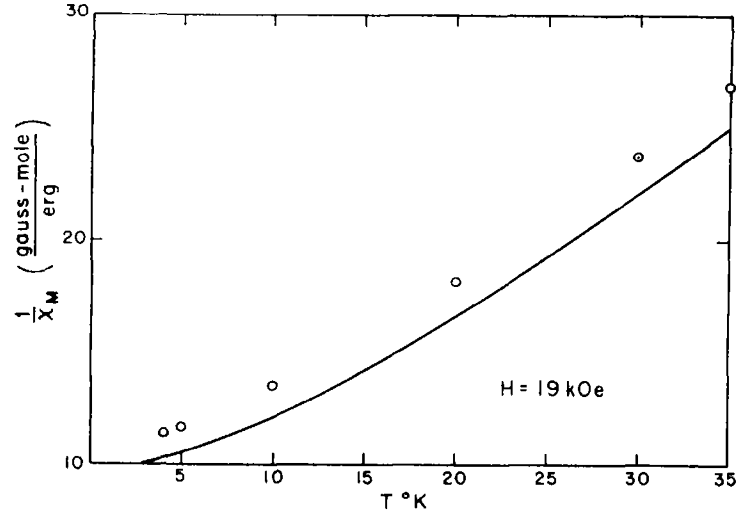

Fig. 6. Data corresponding to Curve E in Fig. 5. The circles give the experimental data and the line gives the calculated result.

When we take the z axis as the hexagonal c axis we have for the ions in the A layers:

$$O_4 = O_4^0 + 20\sqrt{2}\, O_4^3$$

$$O_6 = O_6^0 - \frac{35}{\sqrt{8}} O_6^3 + \frac{77}{8} O_6^6$$

and for the ions in the B and C layers:

$$O_4 = O_4^0$$

$$O_6 = O_6^0 + \frac{77}{8} O_6^6$$

O_n^m are the equivalent operators. For Pr $F_4 = 60$ and $F_6 = 1260$. (It is to be noted that our x differs from that used by Lea, Leask and Wolf.) x and W are related to the point charge quantities[5] B_4' and B_6' as follows: $B_4' F_4 = xW$ and $B_6' F_6' = (1-|x|)W$.

For $x = 0{\cdot}8$ the overall splitting, E_c, produced by the crystal field is given by $E_c = 36{\cdot}55\, W$. The magnetic moment of each energy level, $E_i (i = 1,9)$ is given by the expectation value of the operator $\mu_B (L + 2S) = g\mu_B J$.

$$\mu_i = g\langle i | J | i \rangle \mu_B$$

or

$$\mu_i = g\mu_B \sum_{M=-J}^{J} a_{iM}^2 M,$$

where

$$|i\rangle = \sum_{M=-J}^{J} a_{iM} |M\rangle.$$

The coefficients a_{iM} were calculated by diagonalizing the above Hamiltonian. Some coefficients a_{iM} with magnetic moment, and energy levels associated with them, are listed in the appendix. Further details of the calculation are given elsewhere[18]. Results were obtained for various values of two parameters, c and x. c is defined as $8g\mu_B H/E_c$, where E_c is the overall splitting produced by the crystal field; it is therefore a direct measure of the magnetic field, H. x pertains to the relative importance of the fourth to sixth order interactions. Calculations were made for a wide variety of values of these parameters and for the Pr^{+3} ion in sites of cubic and hexagonal symmetry. The several sets of data shown in the appendix are illustrative of the several hundred sets that have been obtained.

(*B*) *Susceptibility behavior of* $Pr_{0.5}La_{0.5}$

Experimental results for this alloy are shown in Figs. 5 and 6. Calculated susceptibilities for the cubic and hexagonal sublattices are shown in Figs. 5 and for one mole of Pr composed equally of cubic and hexagonal sites in Figs. 5 and 6. Calculations were made using the fundamental Van Vleck[20] equation

$$\chi = \frac{N\Sigma\mu_i \exp(-T_i/T)}{H \qquad Q} \tag{1}$$

where μ_i is the moment of the i^{th} crystal field state, T_i is its energy in °K (Table 3), Q is the partition function and N is the number of

Table 3. *Energy spectrum and ionic moments for* $Pr_{0.5}La_{0.5}$ *for* H = 20 *kOe and* x = 0·80

Energy (°K)	Moment (μ_B/gJ)
Hexagonal sites	
122	−0·9648
114	+0·9459
111	0·0000
102	−0·2500
100	+0·2500
64	−0·4459
60	+0·4648
26	−0·1814
0	+0·1814
Cubic sites	
246	−0·6383
243	−0·0081
241	+0·6109
152	−0·0274
152	−0·0268
90	−0·0841
89	−0·0316
89	+0·1658
0	+0·0397

atoms. Calculations were made for $H \leq 20$ kOe in which range χ of $Pr_{0.5}La_{0.5}$ is independent of H. E_c was taken to be 122° and 246°K for the hexagonal and cubic sites respectively, the values found by Bleaney in treating the thermal anomaly in Pr. These values lead to excellent agreement with experiment for Pr (*vide infra*) and should apply to the alloy as well. x, the parameter which represents the sixth order contribution, is taken throughout this and the following section to be 0·80. This is very close to 0·82, the value for x which corresponds to the value chosen by Bleaney for his z parameter. μ_i and T_i used in equation are listed in Table 3. Agreement between calculated and observed χ values is excellent. Some additional comments about this alloy are merited but these are postponed until after the discussion of the element Pr.

Table 4. *Energy spectrum and ionic moments for* Pr^{+3} *ions for* $x = 0{\cdot}80$

Energy This work $H=0$	Energy This work $H = 37$ kOe	Energy Bleaney* (for $x = 0{\cdot}82$)	Magnetic moments a†	Magnetic moments $10^7 b$†
		Hexagonal sites		
122(2)	122	122(2)	−0·957	−3·97
	110		+0·957	−5·57
114	110	118	0	0
105(2)	102	106	−0·250	0
	99		+0·250	0
63(2)	65	63(2)	−0·457	+5·57
	56·5		+0·457	+3·97
26	27	23	0	−91·1
0	0	0	0	+91·1
		Cubic sites		
246(3)	246	246(3)	−0·625	−6·65
	241		0	−4·05
	236		+0·625	−7·05
154(2)	152	150(2)	0	−13·8
	152		0	−13·4
90(3)	90	87(3)	−0·125	+20·5
	87		0	−15·8
	87		0·125	+20·5
0	0	0	0	+19·9

*Reference [5]

†Constants in the equation $\mu = a + bH$. μ is the moment of the state in units of gJ H is in G.

(*C*) *Elemental praseodymium* [20]

1. *The Weiss field and the overall splittings.* In Table 4 we show the energy spectrum for Pr^{+3} ions in a site of hexagonal symmetry for $H = 0$ and $H = 37$ kOe. Our choice of 37 kOe is a consequence of the neutron diffraction measurements. These have been interpreted by assuming a moment of $1\mu_B$ if only half the sites are ordered or of $0{\cdot}7\mu_B$ if all sites are involved in the ordered structure. Later we shall show that moment exists only on the hexagonal sites, as has been suggested by the resistance minimum observed [21] for Pr, and hence we accept $1\ \mu_B$ as the proper Pr moment. Moreover, since essentially all ions are in the ground state at 4°K, we can evaluate the effective field at the hexagonal site from the variation of ground state moment vs. field strength shown in Fig. 7. This requires that $c = 0{\cdot}13$, or $H = 37$ kOe, if E_c is taken to be 122°K. We thus obtain $H = 37$ kOe for the hexagonal sites. We regard the field to be identical at the cubic sites, with $E_c = 246$°K, but note that the results are essentially unaffected by the choice of the cubic field. Our choice of the overall crystal field splitting is identical with that of Bleaney. In the ensuing discussion we shall show that this choice provides an excellent accounting for most of the characteristics of Pr.

2. *The excess heat capacity.* The crystal field contribution to the heat capacity has been calculated using the energy levels given in Table 4 for $H = 37$ kOe. Results are given in Fig. 9 along with the corresponding calculation by Bleaney, which is for $H = 0$. Both calculations give a good general accounting for the excess heat capacity. However, the present energy level assignment is clearly superior near the maximum.

3. *Magnetic properties and the weakly cooperative development of a spontaneous moment.* We now consider the magnetic properties of Pr. Its positive Weiss constant suggests predominance of ferromagnetic exchange even though neutron diffraction work indicates antiferromagnetism. It is to be noted, however, that the structure proposed for Pr involves ferromagnetic coupling of

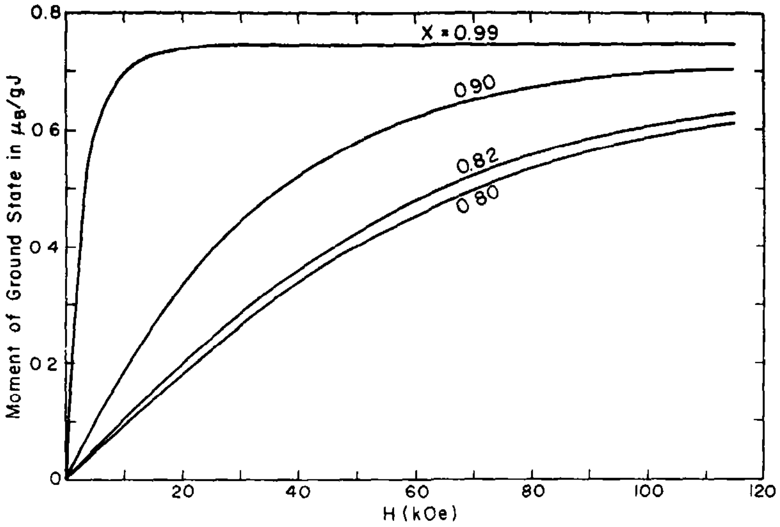

Fig. 7. Ground state moment vs. field strength for hexagonal Pr^{+3} ions for several values of x. The parameter x specifies the relative importance of the sixth and fourth order crystal field interactions. For $x = 1$ it is pure fourth order. The overall crystal field interaction (E_c) is 122°K

first neighbors. In discussing the magnetic behavior of elemental Pr cognizance must be taken of exchange. We do this by making use of the molecular field approach.

Θ for Pr is +6°K. Penney and Schlapp[6] pointed out many years ago that there are two contributions to Θ—exchange and interactions with the crystal field. Calculations for the 'exchange free' $Pr_{0.5}La_{0.5}$ alloy show that the crystal field contributes −9°K to Θ (see Fig. 5). Hence the exchange component alone would lead to a Weiss constant of + 15°K. The Weiss constant may be used to evaluate the molecular field coefficient λ. If the simple Weiss theory is used,

$$\lambda = 9{\cdot}3\frac{(\mathrm{Oe})^2\,\mathrm{mole}}{\mathrm{erg}}.$$

If more sophisticated approaches are used, as for example, Rushbrooke and Wood[22],

$$\lambda = 13{\cdot}1\frac{(\mathrm{Oe})^2\,\mathrm{mole}}{\mathrm{erg}}.$$

We can regard λ as composed of a cubic and hexagonal contribution so that

$$\lambda = \frac{\lambda_c + \lambda_h}{2}.$$

The relative size of λ_c and λ_h can be estimated from the ordering temperatures of Nd. It is isostructural with Pr and develops an ordered magnetic structure resembling that in Pr. The Néel temperatures for the cubic and hexagonal Nd sites are 7·4 and 19·5°K[23]. We assume that λ_c and λ_h are in this ratio for Pr, from which we calculate

$$\lambda_h = 13{\cdot}5 \quad \text{or} \quad 19{\cdot}1\frac{(\mathrm{Oe})^2\,\mathrm{mole}}{\mathrm{erg}}$$

depending upon whether λ is taken to be 9·3 or 13·1. The lower value of λ is favored in the remainder of this paper since there is doubt as to the applicability of the more sophisticated treatment to a metal of the structural complexity of Pr.

The magnetization per mole of hexagonal sites, M_h is given by the expression

$$M_h = \frac{1{\cdot}786 \times 10^4 \sum_i \mu_i \exp(-T_i/T)}{Q} \qquad (2')$$

or

$$M_h = \frac{1{\cdot}786 \times 10^4 [A + B(H_0 + \lambda_h M_h)]}{Q}. \qquad (2)$$

Here M_h is in ergs/Oe mole, A and B represent the sums

$$\sum_i a_i \exp(-T_i/T) \quad \text{and} \quad \sum_i b_i \exp(-T_i/T)$$

respectively, and H_0 is the applied field. The moment of the i^{th} state in equation (2) is expressed as a linear function of H

$$\mu_i = a_i + b_i H. \qquad (3)$$

Values of a and b are listed in Table 4. The numerical constant in equation (2) is the product of $3{\cdot}2\,\mu_B$, the free Pr^{+3} ion moment and 0·5581, the molar magnetization corresponding to an atomic moment of 1 μ_B. The data plotted in Figs. 7 and 8 show that equation (3) is not accurate at large values of H but it is adequate for the present argument up to about 50 kOe. Deviation from linearity at 40 kOe is not more than 5 per cent.

Equation (2′) may be looked upon as the counterpart of the equation

$$M = Ng\mu J B_J(x) \qquad (4')$$

which occurs in the familiar Weiss Theory of ferromagnetism. The quantity x in equation (4′) represents $g\mu_B HJ/kT$. M in the Weiss Theory is evaluated by noting the value of M at the intersection of the curve M vs. x from equation (4) and the linear relationship $M = xkT/\lambda g\mu_B J$. For $T > T_c$ the intersection occurs at the origin and $M = 0$. With reduced temperature the slope of the linear plot decreases and below T_c the intersection occurs for $M > 0$. The condition for T_c is that the slopes of the linear plot and of equation (4′) be equal at $M = 0$.

Equation (2′) is solved by procedures analagous to those summarized for the Weiss Theory in the preceding paragraph. We

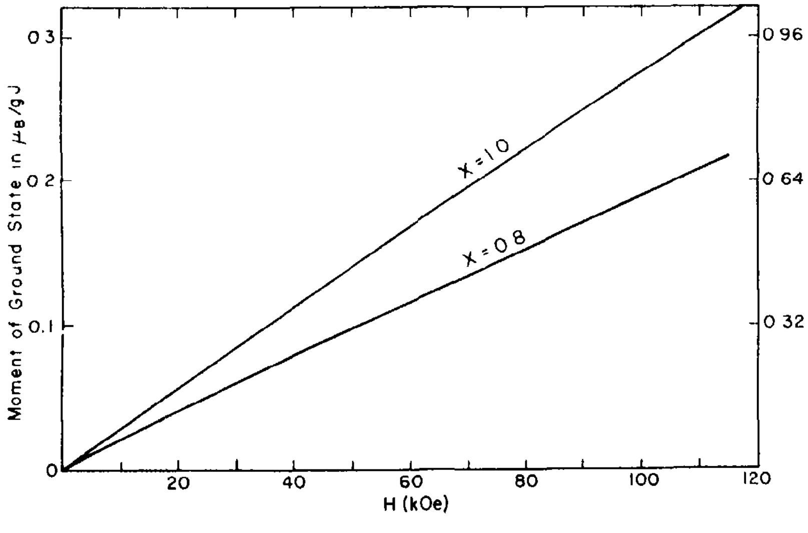

Fig. 8. Results for cubic Pr^{+3} ions. Nomenclature is the same as in Fig. 7. $E_c = 246°$. The scale to the right gives moments in μ_B.

designate the left hand side of equation (2′) as F. The quantities μ_i are determined as functions of H (and hence M) by the methods outlined in Section 4(A) and the quantity F is evaluated as a function of M. A series of plots of F vs. M are then made, allowing T to vary as a parameter. Typical curves of F vs. M are shown in Fig. 10. The solutions of this equation are the values of M corresponding to the intersection of the curves of F vs. M with the straight line of unit slope $F = M$. It is noted that at higher temperatures this intersection occurs only at $M = 0$. As the temperature is reduced the slope increases until at T_c the limiting slopes of the two lines become equal and at this point the system can sustain a permanent moment.

Equation (2) may be solved explicitly for M to yield

$$M_h = \frac{1{\cdot}786 \times 10^4 (A + BH_o)}{Q - 1{\cdot}786 \times 10^4 B\lambda_h} \tag{4}$$

and this equation may be employed conveniently to evaluate T_c. Following the procedure described above, we equate the right hand side of (4′) to F and note that T_c is the temperature at which $(\mathrm{d}F/\mathrm{d}M) = 1$ for $M = 0$. This leads to the condition

$$T_c = \frac{1{\cdot}786 \times 10^4 \times (gJ\mu_B)}{k} \frac{\sum_i a_i^2 \exp(-E_i/kT_c)}{Q^0 - 1{\cdot}786 \times 10^4 B^0} \tag{5}$$

where the superscripts on Q and B indicate that they are to be evaluated for M (or H) $= 0$. From equation (5) it is found that T_c is 24·4°K if $\lambda_h = 13{\cdot}5$ or 32°K if $\lambda_h = 19{\cdot}1$ (Oe)^{2}mole/erg.

It is instructive to note that the appearance of a spontaneous moment follows directly from the properties of equation (4). The second term in the denominator in the latter equation leads to an enhancement of M by the applied field H_0 and it follows that as this term approaches Q in size a vanishingly small value of H_0 can produce a sizeable value of M. The rapid decrease of the value of the denominator in equation (4) (and also (5)) as the temperature decreases toward T_c provides another convenient way of estimating T_c. Actually at T_c the value of the denominator in equation (5) is about 0·14. Moreover, since D is a strong function of temperature, T_c can be conveniently established (and with as great reliability as needed) as the temperature at which D vanishes. This is only about 1 deg lower than the temperature obtained from equation (5). The temperature at which spontaneous magnetization appears, according to equation (5), is in very good agreement with that observed[10], namely 25°K. We believe that the considerations set forth represent the essential features leading to the development of order in Pr at low temperatures.

The argument just presented indicates that the spontaneous magnetization according to equation (4) can be calculated only over a very narrow temperature range—from T_c obtained by use of equation (5) down to the temperature at which D vanishes—that is about 1°K lower. The question arises: what happens when D vanishes? The μ_i's (and M) increase very rapidly (assuming λ remains constant) through the action of the molecular field and very quickly equation (3) ceases to be valid. μ becomes a constant independent of field and the second term in both the numerator and denominator of equation (4) vanishes. It (equation (4)) then tends toward equation (4′) and the usual Weiss approach is required. It is obvious that equation (4) cannot be used at temperatures below T_c to calculate curves of F vs. M, such as those shown in Fig. 10, because of the failure of equation (3) and the vanishing of the denominator. The quantities plotted in Fig. 10 were calculated directly from equation (2′).

In the absence of susceptibility information and the neutron diffraction measurements we should expect ferromagnetism to develop in Pr for $T < T_c$. Clearly this does not happen and we shall return to this point later. As T is decreased below T_c, the system can lower its

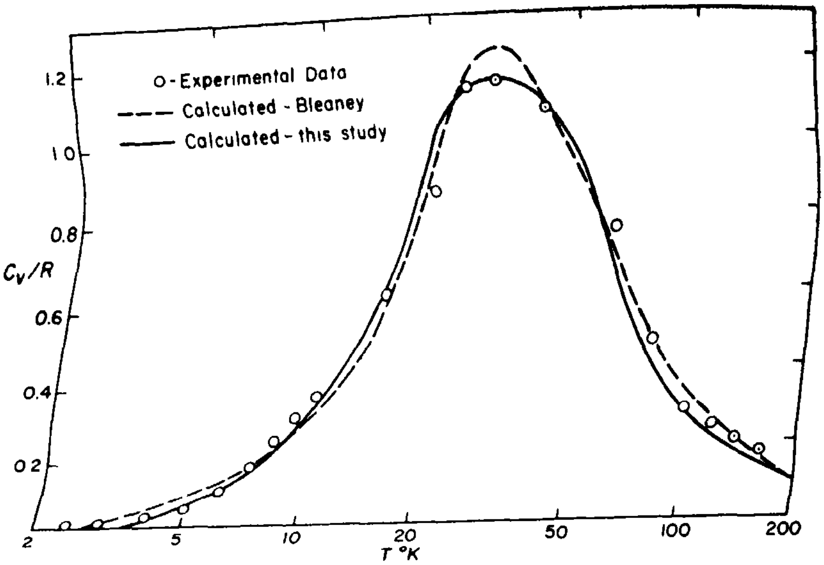

Fig. 9. Crystal field capacity for Pr. Points are data taken from reference [1]. The dashed line gives the results of the calculation by Bleaney (reference [5]) The solid line represents results computed in the present work using the energy levels given in Table 4

energy by developing a spontaneous magnetization. This is made clear by reference to Fig. 11. Repopulation of the doublets *a*, *b* and *c* which are split by the developing magnetic field results in a lowering of the energy of the system as does the repopulation of the two singlet levels S_1 and S_2, which act like a Kramer's doublet except that the splitting remains for $H = 0$. This process does not occur for $T > T_c$.

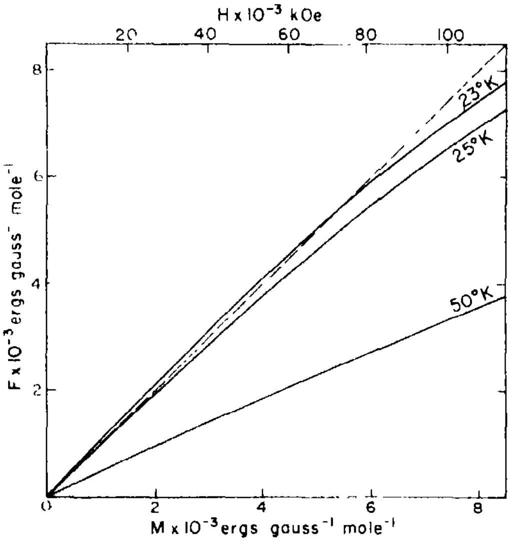

Fig. 10. Plot of *F* (the right hand side of equation (2')) vs. *M*. Solutions correspond to intersections of the curve with the dashed line $F = M$.

The situation involved in equation (4) resembles the conventional molecular field description of the development of ferromagnetism. There are, however, three differences, two of which underlie the strange behavior of Pr. First and least important is that the development of M_h involves as stated the 3 doublets and the two singlet states instead of the $2J+1$ equally spaced states in the conventional ferromagnet. Second, the moment of each state is not constant but increases with *M*. Third, the spacing between the two singlet states is weakly dependent on *H* and does not vanish for $H = 0$, whereas in the usual development of ferromagnetism the spacing between states is linearly dependent on *H* (or *M*) producing the avalanching effect and leading to the cooperative nature of the process. It is this

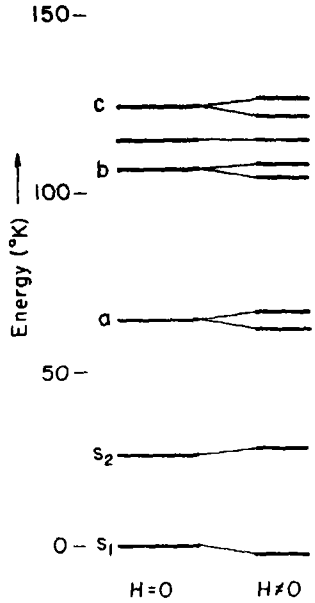

Fig. 11. Schematic representation of the alteration of the energy levels of hexagonal Pr^{+3} ions by a magnetic field.

third feature which is responsible for the weakly cooperative nature of the ordering in Pr. The data in Table 4 show that the energy separation of the two singlet states is only trivially altered by the development of the Weiss field. Hence the avalanching effect is absent. Thus the thermal anomaly is of the Schottky type with only a minor perturbation associated with the development of order.

As noted above we expect a spontaneous moment to appear in Pr when it is cooled below T_c, where $T_c \approx 25$°K. T_c is fixed by λ_h, the polarizability of the two singlet states S_1 and S_2, and their separation. The original problem was to account for the fact that the Pr^{+3} ions do not fall into two singlet ground states at low temperatures and the assemblage of ions act as a simple Van Vleck paramagnet.

The problem now is not one of producing M which is non-vanishing; it is instead one of accounting for the fact that M remains finite at $T \leqslant T_c$. The value of λ for Pr is such that cooperative ordering would occur somewhere around 15°K if it behaved as a conventional paramagnet. Thus below T_c exchange is strong and ordering of the moments is not unanticipated. If the ordering were simple ferromagnetism, as implied by the sign of λ, the third term in equation (2) would produce an increase in M_h up to the limiting value of the ground state. Bulk magnetic measurements and the neutron diffraction results show that the order which develops is a complicated variety of antiferromagnetism, with first neighbors coupled essentially ferromagnetically. The development of antiferromagnetic order corresponds to a decrease in λ_h and the situation for $T < T_c$ can be formally described as a decrease in λ_h at such a rate that D does not vanish. On this basis it is necessary that

$$\lambda_h \leqslant 6{\cdot}1 \frac{(\mathrm{Oe})^2\,\mathrm{mole}}{\mathrm{erg}} \quad \text{at} \quad 4{\cdot}2\text{°K}.$$

Since $A \approx 0{\cdot}02$ at this temperature, $\lambda_h = 6{\cdot}1\text{-}\delta$. In order that the moment be 1 μ_B per atom δ must be on the order of 10^{-6}. λ_c, from the earlier considerations, is given by $0{\cdot}38\,\lambda_h$, where $\lambda_h = 13{\cdot}5$, the value for the paramagnetic region. Thus λ at 4·2°K is 5·6. $1/\chi = 1/\chi_0 - \lambda$, where $1/\chi_0$ represents the exchange-free value. Taking $1/\chi_0$ at 4·2°K to be 10·1 from the calculations used to produce Fig. 6, we compute $1/\chi$ at 4·2°K to be

$$4{\cdot}5 \frac{(\mathrm{Oe})^2\,\mathrm{mole}}{\mathrm{erg}}$$

which compares very favorably with 4·3, the average of the values in Table 1. If λ_h is taken to be 19·1, the computed 4·2°K value is

$$3{\cdot}7 \frac{(\mathrm{Oe})^2\,\mathrm{mole}}{\mathrm{erg}}.$$

Thus in a formal sense we can account for the trend toward temperature independence of χ below 20°K and the limiting value of $1/\chi$ in the liquid helium range through the use of equation (4). In general then λ can be expressed as follows:

$$\lambda = \frac{1}{2}\left(\lambda_c + \frac{Q}{1{\cdot}786 \times 10^4 B}\right). \qquad (6)$$

With equation (6) and the data in Fig. 6, χ vs. T can be computed. The agreement with experiment, especially considering that the measured χ's vary by 10 per cent, shown in Fig. 1, can be regarded as entirely satisfactory.

The field dependency of χ, which was largely responsible for initiating the considerations presented in this paper, can also be rationalized through equations (4) and (6). When the field acting on the assemblage of Pr ions is increased by applying an external field, H_0, Q is reduced and B is increased. To prevent the infinity catastrophe for M_h, λ must decrease. Thus $1/\chi$ is increased and χ decreases with increased H_0. This is, however, only part of the effect. We believe that the trend toward saturation for heaxgonal Pr^{+3} ions shown in Fig. 7 is also involved, although the details are not clear. If the magnetic structure can be ignored except for the existence of a non-vanishing λ_h, it can readily be shown that the variation of magnetization with field strength at 4·2°K can be obtained from the plots in Figs. 7 and 8 using as an effective field $H_0/(1-\gamma\lambda)$ where $\gamma = 0{\cdot}163$ and $0{\cdot}036$ for hexagonal and cubic sites, respectively. Taking $\lambda_c = 5{\cdot}1$ it is found that $\lambda_h = 3{\cdot}2$ to account for the low field susceptibility. Using this value of λ_h, the expression $H_{\text{eff}} = H_0/(1-\gamma\lambda)$ and the variation of moment with field given in Figs. 7 and 8, we obtain the calculated χ values shown in Fig. 2. The agreement is excellent but may be fortuitous since λ_h required for the field dependency is significantly different from 6·1, the value used above to account for χ at 4·2°K. This discrepancy indicates the representation of the properties of antiferromagnetic Pr by a single molecular field parameter is at best a crude approximation.

From the foregoing remarks it is clear that the 'excess' susceptibility is due to predominantly ferromagnetic exchange. We note (Fig. 4) that the susceptibility falls rapidly with dilution. This can be regarded as due to the rapid decrease of λ as Y or La replaces Pr in the lattice.

The observation that antiferromagnetic instead of ferromagnetic order develops merits comment. The general features of the structure are consistent with the nature of the exchange in the lanthanide metals. It is accepted that exchange is indirect—of the Ruderman–Kittel type. Polarization of the conduction electrons provides the coupling mechanism. This polarization is oscillatory so that the interaction changes sign as distance from the central ion is increased. All the evidence from the lanthanide elements indicates that first neighbor interactions are ferromagnetic. It seems likely that the interactions involving second neighbors are of opposite sign for Pr and Nd. In this way we can understand the sinusoidal variation of moments in the basal plane and the antiferromagnetic coupling of adjacent hexagonal layers in Nd and Pr. Thus as moments develop below T_c in the Pr ions which are in the two singlet states, they couple antiferromagnetically leading to the reduced λ_h referred to above. At 25°K 86 per cent of the ions are in the two lowest energy states. For higher temperatures these states are without moment and for magnetic order to develop the higher energy doublet states would have to be involved. Their dilution is such that ordering is not expected; it must await the development of moment on the singlet states whose ions occupy the bulk of the hexagonal sites.

4. *Lack of order at the cubic sites.* We now turn attention to the question of whether spontaneous moments develop and order at the cubic sites. From equation (4) we conclude that this does not happen. The condition is that D, the denominator, must vanish. For the cubic sites $D_c = Q_c - 1{\cdot}786 \times 10^4 \lambda_c B_c$. $\lambda_c = 5{\cdot}1$ and the maximal value of B (see Table 4) is $19{\cdot}9 \times 10^{-7}$. Hence $D_c = Q_c - 0{\cdot}181$. Since $Q_c \geqslant 1$, D_c can never vanish.

Thus we conclude that spontaneous moments do not exist at the cubic sites.

At this point it is appropriate to return to the alloy $Pr_{0\cdot5}La_{0\cdot5}$ and consider the importance of exchange in regard to its properties. The treatment accorded it tacitly assumed that all interactions except with the crystal field are negligible. It should now be re-examined in the light of equation (4). The limit of D_h as T approaches zero is $Q_h - 0\cdot163\,\lambda_h = 1 - 0\cdot163\lambda_h$. Hence for a spontaneous moment to appear

$$\lambda_h \leq \frac{1}{0\cdot163} = 6\cdot1.$$

λ_h for Pr is, as noted earlier, 13·5. Dilution with La will reduce λ_h. The rate of reduction is unknown but if linearity with composition is assumed λ_h for the alloy is 6·8, which is close to the minimal value for a spontaneous moment to appear. We thus regard $Pr_{0\cdot5}La_{0\cdot5}$ as having interactions so weak that the conditions for a spontaneous moment can hardly be met, if at all. This and the chemical dilution of Pr makes it unlikely that the conditions which lead to magnetic structure in the element can be met in the alloy. It is for these reasons that the exchangefree susceptibility applies to the alloy.

5. CONCLUDING REMARKS

To summarize the foregoing remarks, out analysis shows that spontaneous moments will develop at the hexagonal sites in Pr for a critical temperature, T_c. T_c is established to lie in the range 24·4 to 32°K depending on the value of the molecular field parameter. The calculated value is in good agreement with experiment, 25°K. The general features of the interactions involving lanthanide are such that we expect the moments to couple so that near neighbors couple ferromagnetically. Modulation of the structure is expected, however, so that more distant neighbors are not collinear. Conditions for the appearance of a spontaneous moment cubic sites are not favorable so that they remain non-magnetic at the lowest accessible temperatures. These moments and structure involve ions in singlet states. The difference between Pr in cubic and hexagonal sites stems from the fact that the polarizability of the latter is larger by a factor of 4·5.

Using overall splittings of 122 and 246°K for the hexagonal and cubic sites, the values found earlier by Bleaney, we are able to give an excellent accounting for the χ vs. T behavior of $Pr_{0\cdot5}La_{0\cdot5}$ alloy, for which exchange effects are insignificant, and the thermal anomaly of Pr. The molecular field approached is employed in the prediction of T_c and the variation of χ for Pr with temperature, field strength and composition. It provides an excellent accounting for T_c and a fair accounting for the other properties.

The ordering is primarily between the singlet ground states that are split 26° by the crystal field. Since this splitting is only trivially altered by the field which develops during ordering, the ordering process is very weakly cooperative. It is for this reason that Pr exhibits no λ-type thermal anomaly [24] and no abberation in χ at T_c. Splitting of the two ground state singlet states is produced by the sixth order contribution, as Bleaney pointed out earlier. Hence this interaction is of crucial importance in respect to the low temperature behavior of Pr. The various considerations set forth make it clear that while Pr is antiferromagnetic its structure is an incidental feature and for most purposes it can be treated as a Van Vleck paramagnet which is experiencing appreciable exchange.

Acknowledgements—We wish to express our appreciation to Professors R. A. Butera and D. P. Schumacher and to Dr. K. H. Mader for the benefit of many helpful discussions. We are also pleased to acknowledge the assistance of Professor J. B. Muskat of the Computer Center for assistance in programming the calculation. Assistance of the National Science Foundation through general support of the Computer Center is gratefully acknowledged.

REFERENCES

1. PARKINSON D. H., SIMON F. E. and SPEDDING F. H., *Proc. R. Soc.* **A207**, 137 (1951).
2. LOCK J. M., *Proc. phys. Soc.* **B70**, 566 (1957).
3. GRAF P., *Z. angew. Phys.* **13**, 534 (1961)

4. KUBOTA Y. and WALLACE W. E., *J. appl. Phys.* **34**, 1348 (1963).
5. BLEANEY B., *Proc. R. Soc* **A276**, 39 (1963).
6. PENNEY W. G. and SCHLAPP R., *Phys. Rev.* **41**, 194 (1932).
7. SPEDDING F. H., DAANE A. H. and HERMANN K. W., *Acta crystallogr.* **9**, 599 (1956).
8. DREYFUS B., GOODMAN B. B., TROLLIET G. and WEIL L., *C.r. hebd. séanc. Acad. Sci., Paris* **253**, 1764 (1961).
9. DEMPSEY C. W., GORDON J. F. and WOLLER, T., *Bull. Am. phys. Soc.* **7**, 309 (1962).
10. CABLE J. W., MOON R. M., KOEHLER W. C. and WOLLAN E. O., *Phys. Rev. Lett.* **12**, 553 (1964).
11. SKRABEK E. A. and WALLACE W. E., *J. appl. Phys* **34**, 1356 (1963).
12. SCHUMACHER D. P. and WALLACE W. E., *J. appl. Phys.* **36**, 984 (1965)
13. TSUCHIDA T. and WALLACE W. E., *J. chem. Phys.* **43**, 2087 and 2885 (1965).
14. FARRELL J. J. and WALLACE W. E., *Inorg. Chem.* **5**, 105 (1966).
15. SPEDDING F. H., VALLETA R. M. and DAANE A. H., *Trans. Am. Soc. metals.* **55**, 483 (1962).
16. HENRY W. E. In *Rare Earth Research*, (Edited by E. V. Kleber), p. 169. MacMillan, New York (1961).
17. LEA K. R., LEASK M. J. M. and WOLF W. P., *J. Phys. Chem. Solids* **23**, 1381 (1962).
18. MADER K. H., SEGAL E. and WALLACE W. E., *J. Phys. Chem. Solids* **30**, 1 (1969).
19. VAN VLECK J. H., *The Theory of Electric and Magnetic Susceptibilities*, p. 182. Oxford University Press, London (1932).
20. *The present discussion is confined to the temperature region 4°K and above. Unpublished measurements by BUTERA R. A. and his associates and by CRAIG R. S. and DIXON M. in this Laboratory have disclosed a number of anomalous effects in Pr between 1 and 4°K, the origin of which is as yet unclear.*
21. NAGASAWA H. and SUGAWARA T., *J. phys. Soc. Japan* **23**, 701 (1967).
22. RUSHBROOKE G. S. and WOOD P. J., *Mol. Phys.* **1**, 257 (1958).
23. MOON R. M., CABLE J. W. and KOEHLER W. C., *J. appl Phys.* **35**, 1041 (1964).
24. The region around 25°K has been carefully examined recently by LOUNASMAA and SUNDSTROM (Private communication from Professor LOUNASMAA) and by DIXON AND CRAIG (Unpublished measurements in this Laboratory). The new work is in agreement with that of Parkinson *et al.*[1] in that no λ type thermal anomaly is detectable at the temperature at which the antiferromagentic structure develops.

APPENDIX

Table A1. *Eigenfunctions*, $|i\rangle$. *Values of* a_{iM} *in the expression* $|i\rangle = \sum_{M=-J}^{J} a_{iM}|M\rangle$ *hexagonal* Pr^{+3}

$M = -4$	$M = -3$	$M = -2$	$M = -1$	$M = 0$	$M = 1$	$M = 2$	$M = 3$	$M = 4$
$x = 0{\cdot}80$, $c = 0{\cdot}1$								
0·000000	0·000000	0·147066	0·000000	0·000000	0·000000	0·000000	0·000000	0·989127
0·979783	0·000000	0·000000	0·000000	0·000000	0·000000	0·200063	0·000000	0·000000
0·000000	0·000000	0·000000	0·000000	1·000000	0·000000	0·000000	0·000000	0·000000
0·000000	0·000000	0·000000	0·000000	0·000000	1·000000	0·000000	0·000000	0·000000
0·000000	0·000000	0·000000	1·000000	0·000000	0·000000	0·000000	0·000000	0·000000
−0·200063	0·000000	0·000000	0·000000	0·000000	0·000000	0·979783	0·000000	0·000000
−0·000000	−0·000000	0·989127	−0·000000	−0·000000	−0·000000	−0·000000	−0·000000	−0·147066
0·000000	0·576457	0·000000	0·000000	0·000000	0·000000	0·000000	0·817128	0·000000
−0·000000	0·817128	−0·000000	−0·000000	−0·000000	−0·000000	−0·000000	−0·576457	−0·000000
$x = 0{\cdot}80$, $c = 0{\cdot}2$								
0·000000	0·000000	0·129621	0·000000	0·000000	0·000000	0·000000	0·000000	0·991564
0·000000	0·000000	0·000000	0·000000	1·000000	0·000000	0·000000	0·000000	0·000000
0·970159	0·000000	0·000000	0·000000	0·000000	0·000000	0·242469	0·000000	0·000000
0·000000	0·000000	0·000000	0·000000	0·000000	1·000000	0·000000	0·000000	0·000000
0·000000	0·000000	0·000000	1·000000	0·000000	0·000000	0·000000	0·000000	0·000000
−0·242469	0·000000	0·000000	0·000000	0·000000	0·000000	0·970159	0·000000	0·000000
−0·000000	−0·000000	0·991564	−0·000000	−0·000000	−0·000000	−0·000000	−0·000000	−0·129621
0·000000	0·458245	0·000000	0·000000	0·000000	0·000000	0·000000	0·888826	0·000000
−0·000000	0·888826	−0·000000	−0·000000	−0·000000	−0·000000	−0·000000	−0·458245	−0·000000

Table AII. *Eigenfunctions,* $|i\rangle$. *Values of* a_{iM} *in the expression* $|i\rangle = \sum_{M=-J}^{J} a_{iM}|M\rangle$ *Cubic* Pr^{+3}

$M=-4$	$M=-3$	$M=-2$	$M=-1$	$M=0$	$M=1$	$M=2$	$M=3$	$M=4$
$x = 0·8, c = 0·1$								
0·000000	0·000000	−0·111550	0·000000	0·000000	0·652195	0·000000	0·000000	0·749799
0·000000	−0·339138	0·000000	0·000000	0·859775	0·000000	0·000000	0·381801	0·000000
0·686941	−0·000000	−0·000000	−0·707361	−0·000000	−0·000000	−0·166590	−0·000000	−0·000000
−0·000000	−0·000000	−0·707382	−0·000000	−0·000000	0·477822	−0·000000	−0·000000	−0·520861
0·493689	0·000000	0·000000	0·286024	0·000000	0·000000	0·821256	0·000000	0·000000
−0·000000	−0·000000	0·697974	−0·000000	−0·000000	0·588497	−0·000000	−0·000000	−0·408050
0·000000	0·661963	0·000000	0·000000	−0·070269	0·000000	0·000000	0·746235	0·000000
0·533275	0·000000	0·000000	0·646399	0·000000	0·000000	−0·545698	0·000000	0·000000
−0·000000	0·668423	−0·000000	−0·000000	0·505815	−0·000000	−0·000000	−0·545309	−0·000000
$x = 0·8, c = 0·2$								
0·000000	0·000000	−0·091682	0·000000	0·000000	0·623514	0·000000	0·000000	0·776417
−0·000000	−0·319051	−0·000000	−0·000000	0·857106	−0·000000	0·000000	0·404445	−0·000000
−0·649902	0·000000	0·000000	0·731902	0·000000	0·000000	0·204809	0·000000	0·000000
−0·000000	−0·000000	−0·639970	−0·000000	−0·000000	0·560464	−0·000000	−0·000000	−0·525660
0·478840	0·000000	0·000000	0·185047	0·000000	0·000000	0·858178	0·000000	0·000000
0·000000	0·614411	0·000000	0·000000	−0·137864	0·000000	0·000000	0·776848	0·000000
−0·000000	−0·000000	0·762910	−0·000000	−0·000000	0·545078	−0·000000	−0·000000	−0·347646
0·590203	0·000000	0·000000	0·655802	0·000000	0·000000	−0·470727	0·000000	0·000000
−0·000000	0·721600	−0·000000	−0·000000	0·496350	−0·000000	−0·000000	−0·482629	−0·000000

Table B. *Energies** (E_i) *and moments** (μ_i) *corresponding to the eigenfunctions in Table* A *hexagonal* Pr^{+3}

E_i	μ_i	E_i	μ_i
$x = 0·80, c = 0·1$		$x = 0·80, c = 0·2$	
0·142603E 02	0·9676	0·160356E 02	0·9748
0·107667E 02	−0·9400	0·104000E 02	−0·0000
0·104000E 02	−0·0000	0·907226E 01	−0·9118
0·785689E 01	0·2500	0·831378E 01	−0·2500
0·694311E 01	−0·2500	0·648622E 01	−0·2500
0·408049E 01	0·4400	−0·329981E 01	0·4118
0·574649E 01	−0·4676	−0·660800E 01	−0·4748
0·161133E 02	0·2515	−0·154738E 02	0·4350
0·242867E 02	−0·2515	−0·249262F 02	−0·4350

* E_i is in units of W. μ_i is the ionic moment in units of $gJ\mu_B$.

J. Phys. Chem. Solids **Pergamon Press 1969. Vol. 30, pp. 31–42. Printed in Great Britain.**

ELECTRICAL AND MECHANICAL RELAXATION IN CaF_2 DOPED WITH NaF

H. B. JOHNSON*, N. J. TOLAR†, G. R. MILLER and I. B. CUTLER
Division of Materials Science and Engineering, University of Utah,
Salt Lake City, Utah 84112, U.S.A.

(*Received* 1 *March* 1968; *in revised form* 6 *June* 1968)

Abstract—A loss peak caused by addition of NaF to CaF_2 was studied by dielectric loss and internal friction methods. The observed relaxation times of the sodium ion-fluorine vacancy dipole in electrical and mechanical fields are given by equations (1) and (2).

$$T_{\text{elec}} = 7{\cdot}25 \times 10^{-15} \exp\left(\frac{0{\cdot}53}{kT}\right) \tag{1}$$

$$T_{\text{mech}} = 3{\cdot}29 \times 10^{-15} \exp\left(\frac{0{\cdot}53}{kT}\right). \tag{2}$$

It is proposed that the dipole relaxation occurs by fluorine vacancy jumps in the $\langle 100\rangle$ direction of the first coordination shell of the sodium impurity. A possible explanation of the observed peak broadening as a function of dipole concentration is offered.

1. INTRODUCTION

THE CaF_2 structure allows considerable solid solution of impurities as well as a high degree of mobility of F^- interstitials and F^- vacancies at relatively low temperatures. These features have made CaF_2 a useful material for the study of dipole relaxation in solids.

Recently Chen[1] and McDonnough[2] have reported dielectric loss peaks in CaF_2 doped with Sm^{+3}, U^{+3} and Y^{+3}. They postulate a relaxation mechanism for rotation of dipoles made up of M^{+3} substitutional impurity and its F^- charge compensator at the nearest interstitial site. They reported activation energies of 1·7, 1·4 and 1·2 eV for U^{+3}, Sm^{+3} and Y^{+3} respectively. Southgate has also studied[3] the relaxation of CaF_2 doped with Y^{+3} where the conclusion is drawn that the interstitial F^- ion is associated with Y^{+3} and occupies NN and NNN sites.

The above dielectric loss studies involve relaxation of a substitutional +3 impurity—fluorine interstitual dipoles in CaF_2. In this research the effect of a substitutional +1 impurity in CaF_2 is reported, the dipole produced by solution of NaF in CaF_2. The structure of CaF_2 and CaF_2 doped with NaF are shown in Fig. 1. Tressler has determined the CaF_2 rich side of the CaF_2–NaF phase diagram and reports[4] a maximum solubility of about 2 mole per cent NaF at 820°C. This is in contrast with a solubility[5] of 45 mole per cent trivalent yttrium in CaF_2. Sodium fluoride is reported[5, 6] to go into solid solution in CaF_2 by forming a substitutional Na^+ and a F^- vacancy which can associate to create (Na^+–V_F) dipoles. The relaxation of these dipoles was first reported[7] by the present authors in a previous note. This paper gives additional experimental observations on the (Na^+–V_F) dipole in CaF_2 and interprets these results in terms of the theoretical treatments by Wachtman[8] and Chang[9] who have

---

Based on a portion of the Ph.D. Theses of H. B. Johnson and N. J. Tolar of the Department of Ceramic Engineering, University of Utah, Salt Lake City, Utah.

*Present address: Pittsburgh-Corning Research and Engineering Center, Pittsburgh, Pennsylvania.

†Present address: Texas Instruments Corporation, Semiconductor Laboratory, Dallas, Texas.

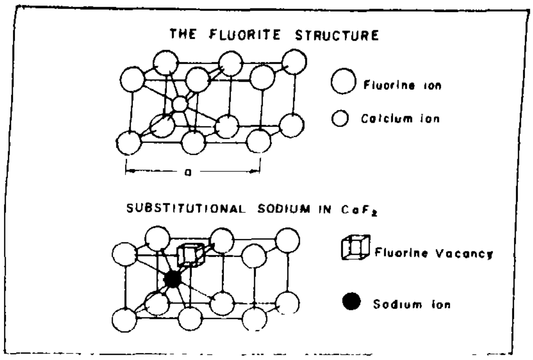

Fig. 1. Structure of CaF_2 and (Na^+-V_F) dipole

considered the modes of dipole relaxation in the fluorite lattice.

2. EXPERIMENTAL PROCEDURE

(1) *Specimens*

The polycrystalline specimens used in this investigation were prepared from J. T. Baker and Mallinkrodt reagent grade CaF_2 powder and J. T. Baker reagent grade NaF powder. Powder mixtures were pressed into disc and rod shaped specimens and fired at 750–1000°C, depending on the extent of doping. High purity CaF_2 single crystals in ⟨100⟩, ⟨110⟩ and ⟨111⟩ orientations in the form of rods 6·4 mm in dia. by 100 mm in length and discs 40 mm in dia. by 8 mm thick were obtained from the Optivac Company. The polycrystalline samples were approximately the same size. The single crystal rods were doped by diffusing NaF into them.

Gold was evaporated onto the faces of the discs to form electrodes. This method of electrode application was found to be free from space charge effects which can cause serious errors.

(2) *Apparatus*

Dielectric loss data were measured with a General Radio Type 716–C capacitance bridge. Both the specimen and the lead wires were electrically shielded. The specimen was surrounded by a copper ring which made thermal contact with two thermoelectric elements. This assembly could function both as a low temperature furnace or a refrigerator depending on the desired sample temperature. Tap water was used as a heat sink for the thermoelectric elements. A bell jar enclosed the entire assembly. Argon gas, which had been dried over Drierite, $(CaSO_4)$, then Anhydrone, $Mg(ClO_4)_2$, was passed over the sample and exited through a vacuum oil bubbler, which kept a positive pressure inside the sample chamber.

The Förster technique[10] was used for internal friction measurements. An Atlas model PD 50–T loudspeaker driver connected to a Hewlett–Packard Model 200CD wide band oscillator was used to drive the samples while an Astatic Model 64TS phonograph pickup was used to measure the amplitude of the sample vibrations. The output from the phonograph pickup was connected to a Tektronix type 2A61 differential amplifier which served as the vertical section of a Tektronix 564 storage oscilloscope. The horizontal section of the oscilloscope consisted of a Tektronix type 2B67 time base plug-in unit. Vertical signals could then be observed at any desired sweep rate. The vertical plates of the oscilloscope cathode ray tube were connected to the inputs of a Hewlett–Packard 400H vacuum tube AC voltmeter and an Atec Model 7A86 frequency counter. The voltage on the vertical plates of the oscilloscope CRT, and consequently the voltage displayed on the VTVM, served as a measure of the amplitude of the sample's vibrations.

Sample rods were suspended near the nodes by 40 ml dia. chromel wire in a chamber in which the sample was surrounded by a split copper tube assembly. The copper tube was connected at each end to thermoelectric elements which could be used to heat or cool the sample relative to the heat sink. (An ethanol-dry ice bath proved to be a convenient heat sink for the temperature range desired.) Helium gas was passed through the sample chamber to prevent moisture from the air from condensing on the sample. The gas was first dried over Drierite, ($CaSO_4$), followed by Anhydrone, ($Mg(ClO_4)_2$), and then cooled to the chamber temperature before passing over the sample and out of the chamber near the sample support wires.

(3) *Procedure*

In the case of dielectric loss measurements, the capacitance and dissipation factor were measured as a function of frequency so that the loss spectra could be plotted at each temperature.

The internal friction data were obtained from the amplitude decay curve displayed on the oscilloscope screen and recorded with a Polaroid camera. Anelastic loss was measured at a number of different temperatures to find the loss peak for each frequency studied. The fundamental frequency of the rod was increased by decreasing the sample length.

Figure 2 shows the theoretical curve of tan δ for a crystal containing free vacancies and dipoles. The dielectric losses are composed of ohmic losses due to free vacancies and dipole orientation losses due to bound vacancies. The ohmic losses are given by the first term of the equation in Fig. 2. Note that the ohmic losses depend on f^{-1}; this produces a straight line with a 45° slope on a log tan δ vs. log f plot. This feature allows one to graphically subtract the ohmic losses from the total losses to give the dipole losses. It is important to have low frequency data so the ohmic loss line can be subtracted accurately.

The shape of the dipole losses shown in Fig. 2 is that given by the Debye equation which assumes the dipoles have one relaxation time and that there is no interaction between dipoles. Perfect Debye losses give a peak which has a half height frequency ratio (peak width) of $f_2/f_1 = 13{\cdot}8$.

In the case of internal friction the losses are plotted vs. $1/T$, thus the peak widths are measured in electron volts instead of a frequency ratio.

3. RESULTS AND DISCUSSION

(1) *Effect of temperature and concentration on loss peaks*

The dipole relaxation in CaF_2 doped with NaF was studied as a function of concentra-

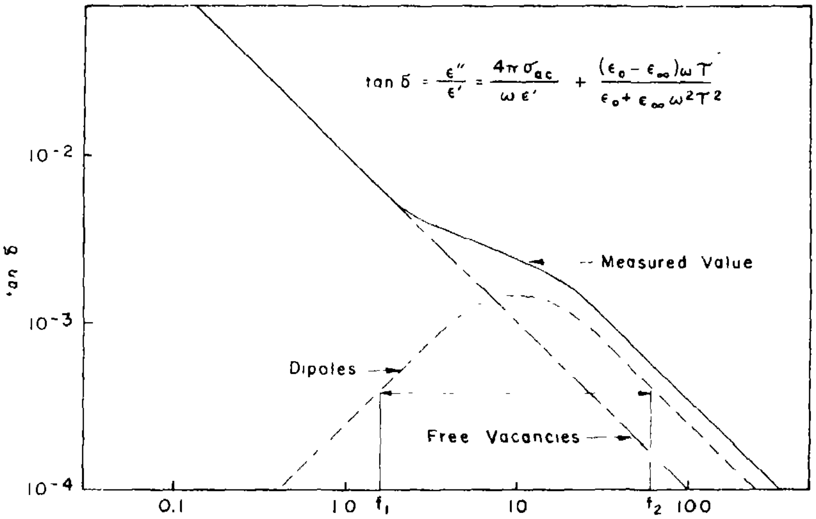

Fig. 2. Theoretical curve of tan δ for a crystal containing free vacancies and dipoles.

tion and temperature. Figure 3 shows the effect of NaF concentration on the dielectric loss spectra of polycrystalline CaF_2.

The relaxation time, T_{elec}, appeared to be independent of concentration. Similarly internal friction measurements showed that the mechanical relaxation frequency was also independent of dipole concentration. Figure 4 shows a typical mechanical loss vs. reciprocal temperature plot for CaF_2 doped with NaF.

The dependence of the frequency of the loss peaks on temperature is shown in Fig. 5. The

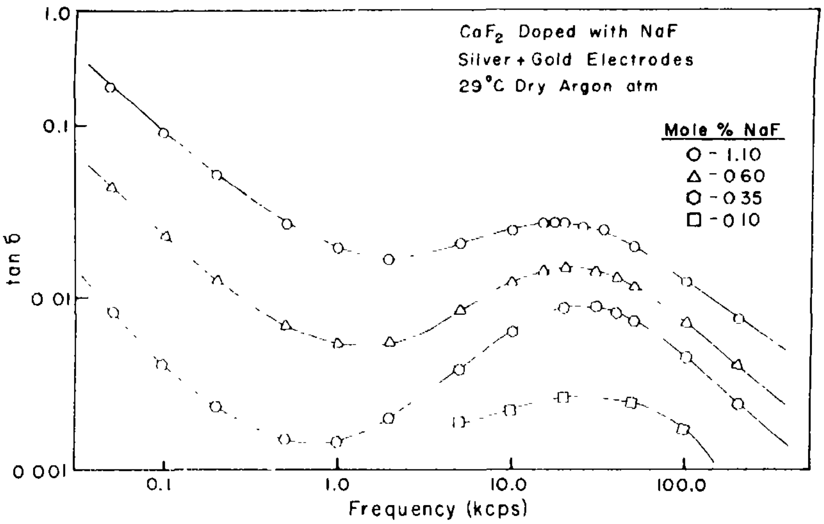

Fig. 3 Effect of NaF addition on observed dipole relaxation in CaF_2.

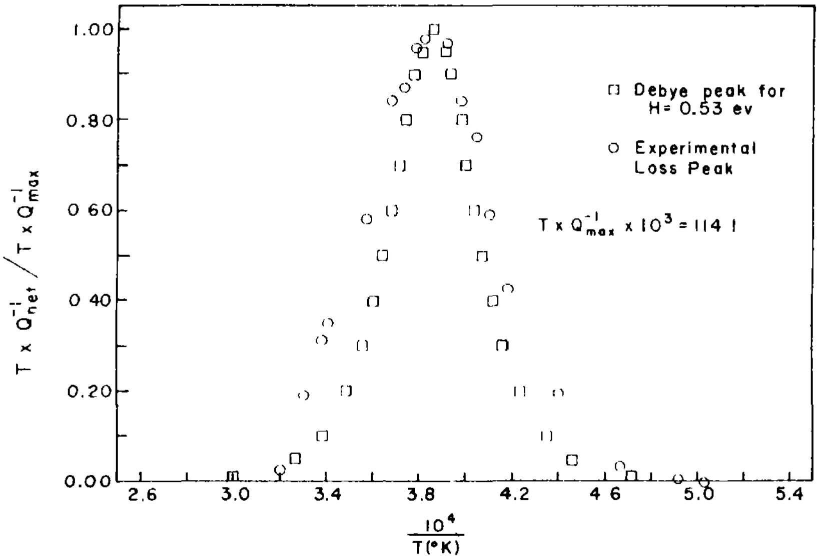

Fig. 4 Internal friction loss peak for polycrystalline CaF_2 with 1 per cent NaF.

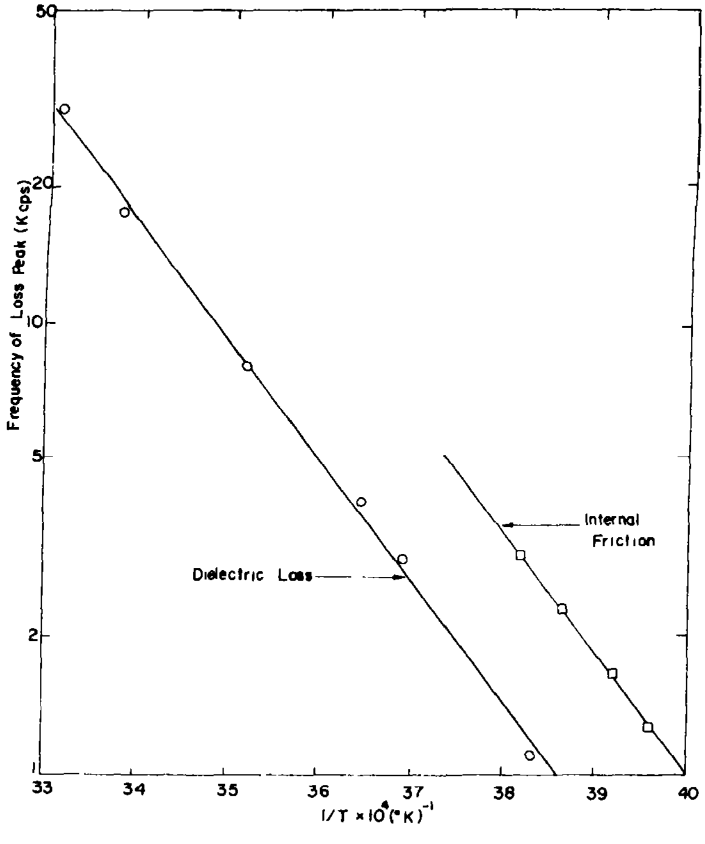

Fig. 5 Temperature dependence of loss peaks of CaF$_2$ doped with NaF

method of least squares with 95 per cent confidence limits was used to calculate T and $\Delta H\ddagger$ from the frequency of the loss peak at each temperature. The activation energy for dipole relaxation is 0·53 + 0·05 eV from dielectric loss data and 0·53 ± 0·03 eV from internal friction data. Observed relaxation times for dipole relaxation in an electric field are given by equation (1); mechanical dipole relaxation times are given by equation (2).

$$T_{\text{elec}} = (7{\cdot}25 \times 10^{-15}\,\text{sec}) \exp\left(\frac{0{\cdot}53}{kT}\right) \quad (1)$$

$$T_{\text{mech}} = (3{\cdot}29 \times 10^{-15}\,\text{sec}) \exp\left(\frac{0{\cdot}53}{kT}\right). \quad (2)$$

These observed activation energies agree well with that required for V_{F^-} diffusion which is reported[5, 11] to be 0·55 ± 0·03 eV.

The dielectric loss peak width appeared virtually independent of temperature and the internal friction peaks were not broadened on one side any more than the other. This would support the idea of a single activation enthalpy for the relaxation process, since if more than one relaxation enthalpy were involved, the dielectric loss peak width should decrease with increasing temperature and the internal friction peaks should be broadened on the low temperature side. It is possible that the activation enthalpy is the energy required to create an activated state from which different types of jumps could occur. If this were the case, the different relaxation times would result purely from different activation entropies and the loss peak width would be independent of temperature. Inspection of scale size solid models of the Na^+–V_F dipole in CaF_2 indicate that the ⟨100⟩ jump should occur with much less lattice strain than either the ⟨110⟩ or the ⟨111⟩ jump.

It is interesting to compare the electric dipole relaxation time of the (Na^+–V_F) dipole to that recently reported[12] for the (O –V_F) dipole in CaF_2.

$$T_{\mathrm{elec}}(Na^+-V_F) = 7{\cdot}25 \times 10^{-15} \exp\left(\frac{0{\cdot}53}{kT}\right)$$

$$T_{\mathrm{elec}}(O\;\;-V_F) = 10{\cdot}00 \times 10^{-15} \exp\left(\frac{0{\cdot}42}{kT}\right).$$

The (O^{--}–V_F) dipole is expected to relax by the O^{--} jumping into the V_F in a ⟨100⟩ direction. The (Na^+–V_F) dipole can relax by ⟨100⟩ jumps of the V_F into any one of 3 F^- ion positions, but only the F^- in the original V_F site can reverse the (Na^+–V_F) dipole. Since O and F^- have virtually the same mass, one would expect that the (Na^+–V_F) dipole can reorientate in 1/3 the time of the (O^{--}–V_F) dipole in one direction, but will require equal time to return to its original orientation. Thus, the pre-exponential of the relaxation time for (O^{--}–V_F) should be 1·5 times longer than that for (Na^+–V_F) because of the relative number of jump sites. Comparison of the (Na^+–V_F) and the (O^{--}–V_F) pre-exponential terms shows that the (O^{--}–V_F) pre-exponential is on the order of 1·5 times greater. Ideally, one should compare microscopic relaxation times of the dipoles instead of macroscopic relaxation times as is done here. The relaxation between macroscopic and microscopic relaxation times will be discussed later in the appendix.

When the ohmic losses were subtracted from the loss spectra, the height of the dielectric loss peak due to dipole relaxation was found to be directly proportional to the NaF concentration. However, the internal friction peak height of polycrystalline samples was not strictly proportional to the initial NaF concentration. The high vapor pressure of NaF can result in heterogenous samples because the NaF is expected to concentrate in the neck regions which are formed during the initial stages of sintering. The rod shaped samples were not fired to theoretical density; therefore, most of the flexing of the sample is expected to occur in the neck region since this area has a smaller cross sectional area than the grains. Thus one can expect both the dipole concentration and the stress concentration to the greater in the neck regions unless the samples are sintered to theoretical density to remove necks and distribute the NaF uniformly. Another problem which affected the preparation of the NaF doped rods resulted because of the necessity that the rods hang free while they were sintered. The hanging rods were subject to NaF vaporization during the sintering process. This NaF loss during sintering would be expected to be greatest at the outside surfaces of the rod shaped samples where internal friction measurements are particularly sensitive to changes in the number mechanical dipoles. Thus the loss peak height is a function of the initial NaF concentration and the sample preparation conditions.

(2) *Dipole–dipole interaction of* (Na^+–V_F) *dipoles*

When one studies the shape of the loss curves for both dielectric loss and internal friction, it can be seen that the experimentally observed loss peaks are broader than those predicted by the Debye equations. This alone is not surprising since the Debye equations are based on a single relaxation time and the correct internal field leads to a distribution of relaxation times.

In the case of dielectric loss, the loss peaks show some evidence of a slightly enhanced low frequency broadening. It is most obvious low losses. Internal friction measurements do not detect enhanced low frequency broadening; thus, if the low frequency dielectric loss peak is due to dipole relaxation, the relaxation would have to correspond to a $\langle 111 \rangle$ V_F jump through the Na^+ ion or a jump involving one of the 24 next nearest neighbor sites which are active in electric fields and not mechanical fields. It appears more likely that small electrode problems are the cause of the observed dielectric broadening since the effect was most obvious at low losses where slight electrode effects would cause the greatest error.

The slight electrode effects or possible second loss peak do not account for the *symmetrical* broadening of the loss peaks observed by both dielectric loss and internal friction. This broadening could be caused by dipole–dipole interaction or additional modes of relaxation associated with second nearest or more distant sites.

The observed relation between the dielectric loss peak broadening and the NaF concentration can be expressed empirically by equation(3)

$$\ln (f_2/f_1) = KC_{NaF} \tag{3}$$

where K = constant and C_{NaF} = NaF concentration.

Increasing the NaF concentration should cause more dipole interaction as is observed in Fig. 6. When the $\ln f_2/f_1$ vs. concentration is extrapolated to the hypothetical perfect Debye peak f_2/f_1 ratio, (13·8), it is seen that a separation of 14·6 Å is predicted as the approximate separation between the (Na^+–V_F) dipoles in order to avoid noticeable dipole–dipole interaction assuming that this explanation is indeed operating.

Because of the previously discussed problems in controlling the NaF concentration in the internal friction specimens, the relation-

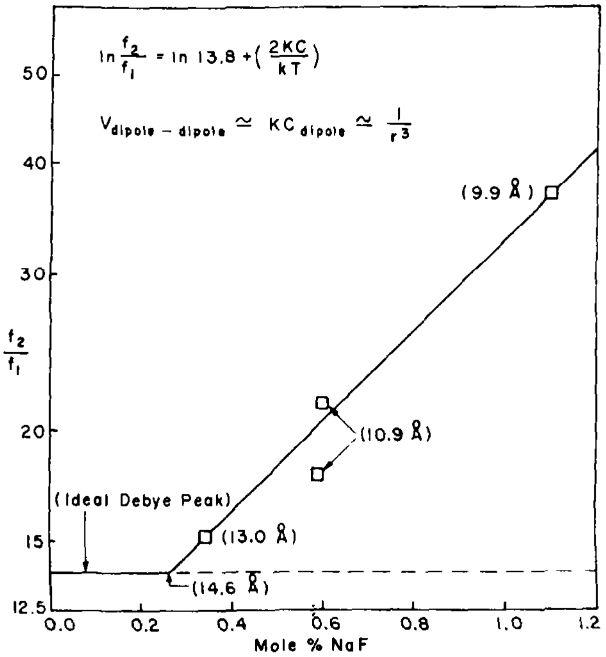

Fig. 6. Dipole broadening in NaF doped CaF_2.

ship between the internal friction loss peak width and the dipole concentration is less clear. However, it was found that the area of the internal friction peaks appears to have the same relationship to the peak width as the NaF concentration in the dielectric loss case. This would be the case if the 'effective' dipole concentration was proportional to the loss peak area.

(3) *Possible mechanisms of* (Na^+–V_F) *dipole relaxation*

The dipole relaxation of NaF doped CaF_2 has the same activation energy as that for V_F motion, thus indicating that the (Na^+–V_F) dipole relaxes by a fluorine vacancy jump from one site to another while the substitutional Na^+ remains fixed for all intensive purposes. Wachtman[8] and Chang[9] have considered the modes of relaxation of dipoles with the structure of (Na^+–V_F). Wachtman's 8-position model applies to the possible sites of a V_F neighboring a Na^+ ion. This model has been confirmed by measuring the dipole length and comparing it with the expected dipole length for a V_F in the first coordination shell of Na^+. The change in dielectric constant from the relaxed side of the loss peak to the unrelaxed side was used with equation (4) to calculate the dipole length.

$$(\epsilon_0' - \epsilon_\infty') = \frac{Ne^2a^2}{3kT} \tag{4}$$

where a is the dipole length and where N, the dipole concentration, is assumed equal to the NaF concentration times the fraction of theoretical density (0·88).

The calculated dipole length of 2·38 Å agrees well with the (Na^+–V_F), (Ca^{+2}–F^-) distance of 2·36 Å as given by Pauling[13] for F^- in the first coordination shell of Ca^{+2} in the CaF_2 lattice.

Further evidence that the V_F can be considered in one of the 8 positions in the first coordination shell of the Na^+ is given by internal friction measurements on NaF doped CaF_2 single crystal rods. If the V_F is in the first coordination shell, the rods with the ⟨111⟩ and ⟨110⟩ directions parallel to their axes should exhibit the polycrystalline loss peak whereas the ⟨100⟩ rod should be inactive under mechanical stress.

Figure 7 shows the internal friction of CaF_2 single crystal rods of different orientations both before and after NaF was diffused into the surface regions. The ⟨110⟩ and ⟨111⟩ rods had loss peaks which agreed with the relaxation times, (equation (2)), of the NaF doped polycrystalline CaF_2. A similar ⟨100⟩ specimen showed no corresponding relaxation peak. The agreement of the ⟨110⟩ and ⟨111⟩ orientations and the absence of a similar ⟨110⟩ loss peak support the theoretical predictions of the 8-position model discussed by Wachtman.

The nature of the low temperature peak in the ⟨100⟩ orientation was not identified; it is possible it could be due to O^{--} contamination or suspension problems.

Both dielectric loss measurement of dipole length and internal friction measurements on single crystal relaxations confirm the dipole structure of Na^+ surrounded by a V_F in one of the eight nearest neighbor sites. When one considers the V_F to be in the first coordination shell, there are three different types of jumps that the vacancy can make. These are shown in Fig. 8. When the vacancy jumps to relieve the stress imposed on the dipole, the number of possible jumps depends on the type of jump which occurs and the nature of the stress imposed, (i.e. whether electrical or mechanical).

When the normal modes of a dipole are known, it is possible to write the equations relating the jump frequency to the type of stress field imposed. The normal modes for the 8-position model have been worked out by Wachtman[8] and Chang[9], and Wachtman derived equations (5) and (6) which relate the relaxation modes to the types of jumps and the nature of the applied stress.

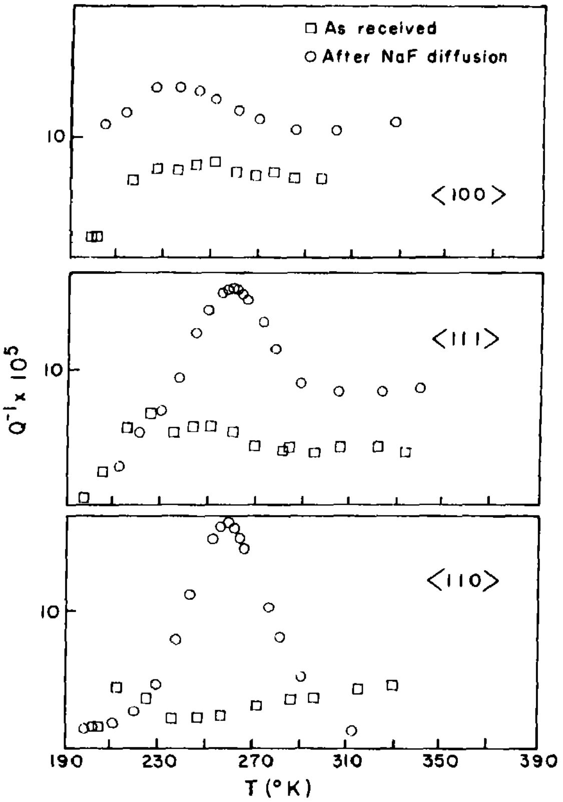

Fig. 7. Internal friction of CaF_2 single crystals.

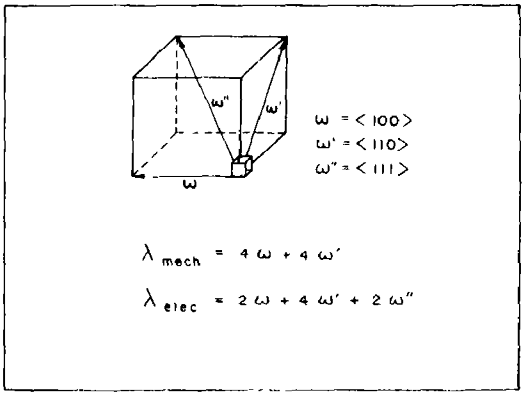
ω″
ω′
ω
ω = <100>
ω′ = <110>
ω″ = <111>
$\lambda_{mech} = 4\omega + 4\omega'$
$\lambda_{elec} = 2\omega + 4\omega' + 2\omega''$

Fig. 8. Types of V_k jumps in 1st coordination shell of Na in CaF_2.

$$\lambda_{\text{mech}} = 4(\omega+\omega') \tag{5}$$

$$\lambda_{\text{elec}} = 2(\omega+2\omega'+\omega''). \tag{6}$$

It is interesting to note that the ω'' jump which corresponds to the jump along the body diagonal does not appear in the mechanical modes. Also, the nearest neighbor jump, ω, corresponding to the $\langle 100\rangle$ direction, should occur twice as often in the mechanical case as the electrical case because there are always two ω jumps to relieve mechanical stress whereas there is only one electrical ω jump which can relieve stress. If the $\langle 100\rangle$ jump were the only important jump, the electrical relaxation time should be exactly twice the mechanical relaxation time, giving

$$\frac{T_{\text{elec}}}{T_{\text{mech}}} = \frac{2{\cdot}00}{1{\cdot}00}. \tag{7}$$

If the $\langle 110\rangle$ jump were the only type of important jump, the $T_{\text{elec}}/T_{\text{mech}}$ ratio should be 1·00. Thus the ratio of $T_{\text{elec}}/T_{\text{mech}}$ enables one to learn the relative importance of the various mechanisms of relaxation. Of course, the relaxation times reported earlier must be corrected for internal field effects; these are discussed in the appendix. None of the corrections change the value of $T_{\text{elec}}/T_{\text{mech}}$ significantly.

4. SUMMARY

It appears that the relaxation time was unaffected by changing dipole concentration. The results of dielectric loss and internal friction measurements show that the V_F is located in one of the 8 nearest neighbor positions around Na^+. The ratio of the mechanical and electrical relaxation times agree with Wachtman's theoretical prediction of the ratio which would result if dipole relaxation occurs by $\langle 100\rangle$ jumps of the V_F in the first coordination shell of the Na^+.

Both dielectric loss and internal friction loss peaks were broader than Debye loss peaks. The effect of dipole concentration on dielectric loss peak broadening followed a linear relationship with dipole concentration which could result from classical dipole-dipole interaction.

Acknowledgements—The authors gratefully acknowledge the financial support of the Office of Naval Research Contract Nonr-1288 (06). Dr. Tolar was recipient of the General Electric Foundation Scholarship.

REFERENCES

1. CHEN J. H. and McDONNOUGH M. S., *Bull Am. phys. Soc.* **11**, 195 (1966).
2. CHEN J. H. and McDONNOUGH M. S., *Bull Am. phys. Soc.* **9**, 647 (1964).
3. SOUTHGATE P. D., *J. phys. Chem.* **27**, 1623 (1966).
4. TRESSLER R. E., Unreported S. M. *Thesis*, Department of Metallurgy, M.I.T. (1964).
5. URE R. W., Jr., *J. chem. Phys.* **26**, 1363 (1957).
6. SCOULER W. J. and SAMKULA A., *Phys Rev* **120**, 1154 (1960).
7. JOHNSON H. B., TOLAR N. J., MILLER G. R. and CUTLER I. B., *J. Am. Ceram. Soc.* **49**, 458 (1966).
8. WACHTMAN J. B., Jr., *Phys. Rev.* **131**, 517 (1963)
9. CHANG R., *J. Phys. Chem. Solids* **25**, 1081 (1964)
10. FORSTER F., *Z. Metallk.* **29**, 109 (1937).
11. BONTINCK W., *Physica* **24**, 650 (1958).
12. ROSSING B. R. and COBLE R. L., *Electrical Conductivity and Defect Structure of* CaF_2. Joint Session I. Electric Phenomena. Annual meeting American Ceramic Society (1967).
13. PAULING L., *Nature of the Chemical Bond*, p. 536 Cornell University Press, Ithaca, N.Y. (1936)
14. DEBYE P., *Polar Molecules*, p. 36 Dover, New York (1945).
15. ONSAGER L., *J. Am. chem. Soc.* **58**, 1486 (1936).
16. FROOD D. G. and DEKKER A. J., *J. chem. Phys.* 1030 (1952).
17. COLE R. H., *J. chem. Phys.* **6**, 385 (1938).
18. POWLES J. G., *J. chem. Phys.* **21**, 633 (1953).
19. COLE R. H., *J. chem. Phys* **42**, 637 (1966)
20. SCAIFE B. K. P., *Proc. phys. Soc.* **86**, 15 (1966)

APPENDIX

Relaxation time corrections

It is often necessary to apply a correction to the macroscopic relaxation times derived from tan δ measurements in order to obtain the microscopic relaxation times of the dipoles.

In the case of internal friction, the relaxation time correction depends on $(Y_0/Y_\infty)^{1/2}$, where Y_0 is Young's modulus on the low frequency side of the loss peak and Y_∞ is Young's modulus on the high frequency side. For CaF_2 doped with NaF the difference between the relaxed and unrelaxed values of Young's modulus was less than 1 part in 1000. Thus the value of the macromechanical relaxation time, T, is essentially the as the microscopic relaxation time, τ.

macroscopic relaxation time derived from dielec- ss data is subject to the following corrections. When ipole concentration is large, the dielectric constant, ill change significantly on passing from the relaxed e unrelaxed side of the dielectric loss peak. This e in the dielectric constant causes the relaxation derived from tan δ measurements to differ from the ation time derived from loss factor, ϵ'' peak. The onship between the two is given by equation (8).

$$T_{\epsilon''} = \left(\frac{\epsilon_0}{\epsilon_\infty}\right)^{1/2} T \tan \delta \,. \tag{8}$$

e effect of the internal field on dipole relaxation time ften neglected. However, the tendency for the ization to maintain itself is always active to some t so that macroscopic relaxation time, T, is always er than the microscopic relaxation time, τ. The t to which the polarization maintains itself depends he internal field; thus any equations relating the oscopic dielectric relaxation time to the microscopic xation time must consider the internal field.

ebye in his original theory of dielectric relaxation d[14] the Lorentz internal field, $E_i = [(\epsilon_0'+2)/3]E$. s leads to the following relation:

$$\tau_{\text{Debye}} = \left[\frac{\epsilon_\infty + 2}{\epsilon_0 + 2}\right] T_{\epsilon''}. \tag{9}$$

s fairly well agreed that both the Lorentz field and the ulting correction factor are in error and lead to essive corrections.

nsager[15] proposed that the part of the internal field ich can orientate a dipole is given by an empty cavity around the dipole. The Onsager internal field is $E_i = (3\epsilon_0/2\epsilon_0 + 1)E$. Onsager pointed out that the remaining part of the internal field, the reaction field, is parallel to the dipole moment and therefore cannot orient the dipole. Cole modified[17] the Debye theory using the Onsager internal field; unfortunately his result cannot be given in terms of the Debye equations because the Onsager internal field leads to a distribution of relaxation times. However, if the macroscopic relaxation is represented by a single relaxation time, T*, it is found that T* can be related to τ by equation (10).

$$\tau_{\text{Cole}} = \left(\frac{2\epsilon_\infty + 1}{2\epsilon_0 + 1}\right) T^* \tag{10}$$

Powles[18] used a time dependent Onsager type internal field in an *ad hoc* manner to obtain equation (11). This correction has more fundamental support from Cole's recent paper[19] which uses correlation function theory.

$$\tau_{\text{Powles}} = \left[\frac{2\epsilon_0 + \epsilon_\infty}{3\epsilon_0}\right] T^* \tag{11}$$

It can be noted that the macroscopic and microscopic relaxation times obtained from Powles equation are close, the maximum ratio being 1·5 for very large differences between ϵ_0 and ϵ_∞.

Scaife[20] has used an Onsager internal field, but also included an additional term in his equation to attempt to take into account any additional torque on the dipole due to fluctuating polarization of the surroundings. He concluded that there is a distribution of relaxation times as found earlier by Cole[17] and Powles[18] due to the use of the cavity field. However, the dipole coupling term resulted in a shift in the single relaxation time used to represent the

Table 1. *Effect of correction factors on electric relaxation time of* 1 *per cent solution of* (Na$^+$–V$_F$) *dipoles in* CaF$_2^*$

Microscopic relaxation τ_0	Dielectric loss correction factor applied to $T_0 \tan \delta$	$\tau_0 \times 10^{-15}$ sec^{-1}	$\frac{T_{0\text{elec}}}{T_{0\text{mech}}}$
$\tau_0 \tan \delta$	—	7·25	2·21
$\tau_0 \epsilon''$	$\left[\frac{\epsilon_0}{\epsilon_\infty'}\right]^{1/2} \tau_0 \tan \delta$	7·97	2·43
$\tau_{0\text{Debye}}$	$\left[\frac{\epsilon_0}{\epsilon_\infty'}\right]^{1/2} \left[\frac{\epsilon_\infty' + 1}{\epsilon_0' + 2}\right]$	6·33	1·93
$\tau_{0\text{Cole}}$	$\left[\frac{\epsilon_0}{\epsilon_\infty}\right]^{1/2} \left[\frac{2\epsilon_\infty' + 1}{2\epsilon_0' + 1}\right]$	6·12	1·87
$\tau_{0\text{Powles}}$	$\left[\frac{\epsilon_0}{\epsilon_\infty}\right]^{1/2} \left[\frac{2\epsilon_0' + \epsilon_\infty'}{3\epsilon_0'}\right]$	7·34	2·25

$\tau_{0\text{mech}} = 3{\cdot}28 \times 10^{-15}$ sec^{-1}
$\epsilon_0' = 9{\cdot}92$
$\epsilon_\infty' = 7{\cdot}50$

*1·1 per cent NaF added to CaF$_2$.

distribution of microscopic relaxation times. This shift would apply to both the electrical and mechanical relaxation times since the dipole interaction occurs regardless of the type of stress field applied. Thus, this correction factor does not change the $\tau_{0elec}/\tau_{0mech}$ ratio.

The Scaife correction factor is given by

$$\tau_{Scaife} = \left[\frac{1+(\epsilon_0-1)^2}{\tau_0(\tau_0+2)}\right]^{-1} T^*. \tag{12}$$

When the factor is applied to CaF_2 doped with 1·1 per cent NaF, it predicts that the observed mechanical and electrical relaxation times are reduced by the factor 0·607.

A summary of the various correction factors for electrical relaxation times is given in Table 1. The corrections are applied to the observed relaxation of a CaF_2 sample doped with 1·1 per cent NaF so the effect of the corrections on the electrical relaxation time and the ratio of the electrical to mechanical relaxation time can be seen. The correction factor of Powles currently appears to be the most acceptable. Regardless which correction factor is used, the $\tau_{0elec}/\tau_{0mech}$ ratio is near 2·0/1·0 which means the principal mechanism of dipole reorientation is by ⟨100⟩ jumps of V_F in the first coordination shell of Na^+. This agrees with the hard sphere models made to scale and shows that the ⟨100⟩ vacancy jump can occur in the CaF_2 lattice with much less lattice strain than either the ⟨110⟩ or the ⟨111⟩ jumps.

J. Phys. Chem. Solids Pergamon Press 1969. Vol. 30, pp. 43–56. Printed in Great Britain.

THE CRYSTAL FIELD SPECTRA AND DICHROISM OF TOURMALINE

R. W. T. WILKINS
Department of Geological Sciences, Harvard University, Cambridge, Mass. 02138, U.S.A.

E. F. FARRELL
Center for Materials Science and Engineering and Department of Electrical Engineering, M.I.T., Cambridge, Massachusetts, U.S.A.

C. S. NAIMAN
MITHRAS, a Division of Sanders Associates, Cambridge, Massachusetts, U.S.A.

(*Received* 27 *March* 1968; *in revised form* 20 *May* 1968)

Abstract—Optical absorption spectra of colorless, pink, green, blue, brown and black tourmaline have been taken to determine the origin of the colors and to explain the color changes which occur on heating. Absorption data were taken with polarized radiation parallel and perpendicular to the *c* axis at 77 and 300°K. Cell dimensions supported by partial chemical analyses were used to characterize the specimens.

The data combined to show that generally speaking the color is due to electronic transitions in and the amount of Fe^{2+}, Fe^{3+} and Mn^{2+} in the crystal. Specimens on the dravite-schorl join are characteristically colored shades of brown. With small to moderate concentrations of transition metal ions, colors on the elbaite-schorl join are clear pinks, greens and blues according to the $Fe^{2+}/(Fe^{2+}+Fe^{3+}+Mn^{2+})$ ratio in the tourmaline.

Intensity changes of absorption peaks and shifts in the absorption edges, correlated with removal of hydrogen and consequent oxidation of Fe^{2+} to Fe^{3+} in the structure, account for color changes observed when tourmaline is heated in air. Blue tourmaline becomes green on short-term heating and redish-brown on further heating.

Assignments of absorption peaks from 0·3 to 2·0 μ to specific transitions in the appropriate cations have been made and the origin of the characteristic dichroism is discussed.

INTRODUCTION

TOURMALINE is the name given to members of a complex compositional series. The basic members of the series are dravite, $NaMg_3Al_6B_3Si_6O_{27}(OH, F)_4$; schorl, $Na(Fe, Mn)_3Al_6B_3Si_6O_{27}(OH, F)_4$ and elbaite, $Na(Li, Al)_3Al_6B_3Si_6O_{27}(OH, F)_4$. The series is continuous between schorl and elbaite and between dravite and schorl, but a gap is thought to exist between dravite and elbaite.

Tourmaline has a hardness of 7 on the Mohs scale, it is very dichroic, its color is variable depending on composition, the space group is R3m and cell dimensions vary from *a* 15·84–16·03 Å and *c* 7·10–7·25 Å. Tourmaline is commonly associated with granites and granite pegmatites and has long been used as a gem stone.

The structure consists of linked layered islands. A tetrahedral layer is formed by a ring of six nearly regular Si tetrahedra pointing in the same direction along the *c* axis. It is bonded to an octahedral layer which may contain Mg, Al, Li, Fe and other cations in smaller amounts. According to the refinement of dravite[1] the three central octahedra contain Mg ((b) position) and the six smaller peripheral octahedra contain aluminum ((c) position). Boron triangles are attached to oxygen ion vertices of the octahedral layer. An additional cation site, filled typically by Na or Ca is situated near a central hydroxyl on the 3-fold axis inside the silicate ring. Three other hydroxyl ions in the octahedral layer occupy a position such that each is shared by one inner and one outer octahedron.

Epprecht[2] has compiled a useful set of chemical analyses. X-ray structure determinations have been reported by Donnay and Buerger[3] (dravite) and Ito and Sadanaga[4]. on what was supposed to be an elbaite[5]. Recent structural refinements of dravite and buergerite have been reported by Buerger *et al.*[1] and Barton[5].

Bradley and Bradley[6] studied the spectra of pink and green tourmaline in zoned material. Their data do not extend far enough into the infrared or ultraviolet to make specific assignments of transitions in the $3d$ level electrons, although they were partly correct in indicating that the color of pink tourmaline is due to Mn^{2+} and green to Fe^{2+}. They also noted color and cell dimension changes which occur on heating.

Grum-Grzhimailo[7] studied three green and one blue tourmaline but did not include the ultraviolet nor extend the spectra beyond $1{\cdot}2\,\mu$ in the near infrared. He correctly related the color to Fe^{2+}, but attributed some peaks to Mn^{3+}. No specific assignments to d–d transitions were made.

It is the purpose of this paper to extend the previous optical work, to correlate the X-ray and chemical analyses with absorption data, to assign d–d transitions to appropriate cations and to explain the color in normal and heated tourmaline, and to clarify the origin of the strong dichroism found in all spectra.

EXPERIMENTAL

Absorption spectra between $0{\cdot}3$ and $2{\cdot}0\,\mu$ were recorded on a Cary 14 spectrophotometer using calcite air gap prisms for polarizers. Crystal face development, extinction directions and back reflection Laue photographs were used to orient samples which were then cut into plates with a diamond saw and polished with Linde A powder and diamond paste. Absorption spectra were run at 300 and 77°K, the latter using a liquid nitrogen cryostat. The data have been plotted in terms of the absorption coefficient α and wavelength in microns; wavenumbers are given for reference. Heating experiments were carried out in a resistance furnace in air. The reduction was done in a sealed tube furnace in a hydrogen atmosphere.

Precision unit cell parameters were obtained from X-ray powder diffractometer data with silicon internal standard using the Burnham[8] least squares computer program. Twenty resolved peaks between 20° and 50° $2\,\theta$ were used and each specimen was run in duplicate. Partial chemical analyses were made on representative specimens. Total Fe and Mn determinations offered little difficulty and were done by conventional colorimetric and volumetric methods. Total iron was checked by atomic absorption flame photometry. The results are given in Table 1. Ferrous ion determinations were attempted by Ingamels[9] method, but in many cases the results were unsatisfactory and they are not quoted here.

DISCUSSION

The optical absorption spectra of the specimens measured at 77°K are shown in Figs. 2–7. Room temperature measurements which are essentially identical are not shown. Specimens were selected for their range in color. The spectra include two black tourmalines, one schorl and one low alumina tourmaline[10], two brown tourmalines, one blue tourmaline heated and unheated, one light green tourmaline heated and unheated, two darker green tourmalines for comparison and one pink, and one colorless sample.

X-ray determination of the unit cell parameters (Fig. 1) indicates that the composition of most samples falls close to the join between schorl and elbaite. The two brown specimens are dravites, the black specimen, No. 7, is schorl, and the low alumina tourmaline, No. 10, has anomalous parameters. After heating at 800°C for 18 hr, the cell dimensions of the blue tourmaline. No. 5, underwent considerable change, a decreasing from $15{\cdot}908$ to $15{\cdot}838$ Å and c increasing from $7{\cdot}123$ to $7{\cdot}135$ Å. This is consistent with increase in the buergerite type structure unit of this

Table 1. Unit cell dimensions and chemical analyses of tourmaline

No.	Sample	a	c	c/a	Total Fe (Wt. %)	Total Mn (Wt. %)
1	Pink (Mt. Mica, Maine) 108916*	15·845	7·103	0·4483	0·19	0·26
2	Colorless (Mt. Mica, Maine) 108917*	15·840	7·108	0·4484		
3	Pale green (Mt. Mica, Maine) 108913*	15·871	7·112	0·4481	1·82	1·22
4	Green (locality unknown) 108915*	15·896	7·123	0·4481	4·03	0·61
5	Pale Blue (Mt. Mica, Maine) 108912*	15·908	7·122	0·4477	4·85	0·76
6	Green (Governador, Minas Geras, Brazil) 97723*	15·914	7·128	0·4479	5·60	0·04
7	Black (locality unknown) 108914*	15·965	7·198	0·4509	7·35	0·088
8	Brown (Gouverneur, N. York) 86312*	15·956	7·208	0·4517		
9	Brown (Brazil) 86330*	15·946	7·213	0·4523	1·38	
10	Black (Madagascar, low aluminum, 108796*	16·045	7·238	0·4511	$Fe^{2+} = 3{\cdot}65$ $Fe^{3+} = 7{\cdot}43$	
11	Pale blue No. 5 heated in air 800°C, 18 hr.	15·838	7·135	0·4505		

* Harvard Museum number.

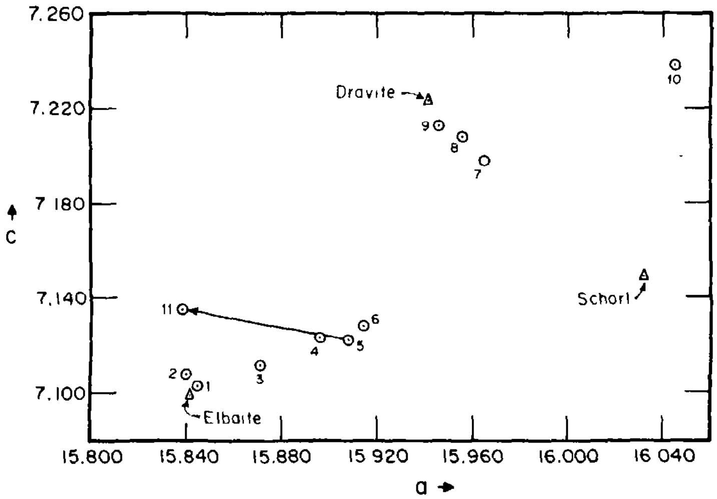

Fig. 1. *a* vs. *c* lattice parameters of the tourmaline samples discussed in this paper.

specimen due to oxidation of ferrous ion and release of hydrogen [11].

Electronic transitions in the transition metal ions contained in tourmaline give rise to the optical absorption bands, while the sharper infrared bands are due to vibrational transitions in OH and possibly some H_2O molecules. The transition metals which are nearly always present[2] in varying amounts are $Fe^{2+}(d^6)$, $Fe^{3+}(d^5)$, $Mn^{2+}(d^5)$, possibly $Mn^{3+}(d^4)$ and Ti of uncertain oxidation state. Ti is usually only present in minor amounts.

Of the two octahedral cation sites, one has symmetry m and the other symmetry 1. Of the three end-members only dravite has a structure determination of high refinement[1], but the structure of the oxy-tourmaline buergerite has also been carefully refined[5]. Although preliminary work has been done on a schorl[3], no final data have been published.

With this in mind the Buerger structural refinement of dravite will be accepted as the most relevant information available. In this structure the central octahedral (b) position is filled with Mg. The major distortion of the octahedron is a tetragonal elongation along the $O_1 - O_3(OH_1 - OH_{II})$ axis. The Mg ion is displaced from the center of the octahedron. The $O_1 - O_3$ axis makes an angle of about 63° with the crystallographic c axis. The average metal-oxygen distance is about 2·05 Å. The general position (c) is mainly filled with Al and is much more irregular. The mean metal-oxygen distance is 1·93 Å.

In buergerite the Fe-O_3 distance is shortened rather than lengthened as in dravite, but the pseudosymmetry of position (b) may still be taken as 4 mm.

When allowance is made for the two positions of differing symmetry, magnetic susceptibility measurements are consistent with a ^5T ground state for Fe^{2+} and a ^6A ground state for Fe^{3+}[12, 13].

PINK TOURMALINE

Both colorless and pink tourmalines show some weak but definite absorption in the visible (Fig. 2 and Table 2). The colorless sample shows only a faint pink color on close examination and came from the clear termination of a pink rubellite crystal. Even though there are weak absorption peaks, they are broad and nearly flat, permitting all wavelengths to be transmitted, thus appearing colorless.

Table 2 Crystal field spectra of various colored tourmalines, showing absorption peak positions in angstroms and wavenumbers*

$E \parallel c$		$E \perp c$	
(λA)	(νcm^{-1})	(λA)	(νcm^{-1})
		4,400	22,730
		4,600	21,740
5,200	19,230	5,200	19,230
		5,800	17,240
7,200	13,890	7,200	13,890
		8,200	12,195
Green tourmaline (Fig. 3(a))			
4,100	24,400		
		5,500	18,000
7,200	13,890	7,200	13,890
11,100	9,000	11,100	9,000
Blue tourmaline (Fig. 5(a))			
4,900	20,410	4,900	20,410
5,500	18,180	5,900	16,950
7,200	13,890	7,200	13,890
12,500	8,000	11,000	9,090
Brown tourmaline (Fig. 6(a) and (b))			
4,400	22,730	4,400	22,730
7,200	13,890	7,000	14,300
10,800	9,260	10,800	9,260
Black tourmaline (Fig. 7(a))			
4,400	22,730		
4,600	21,740		
5,000	20,000	5,000	20, 00
5,400	18,520	5,600	17,860
7,200	13,890	7,500	13,330
10,800	9,260	11,000	9,090
Black, low aluminum tourmaline (Fig 7(b))			
4,400	22,730		
5,000	20,000		
		5,800	17,240
7,500	13,330	8,000	12,500
11,300	8,849	11,300	8,849

*Excludes (OH) vibrational peaks.

Rubellite, on the other hand, has a peak at 5200 Å, absorbing in the blue-green and transmitting in the red. Chemical analysis gives 0·26% Mn and 0·19% Fe in the crystal, indicating that transitions in Mn^{2+} and Fe^{3+} can account for this peak. Both ions have a d^5 configuration. The divalent Mn and trivalent Fe spectra are due to spin forbidden

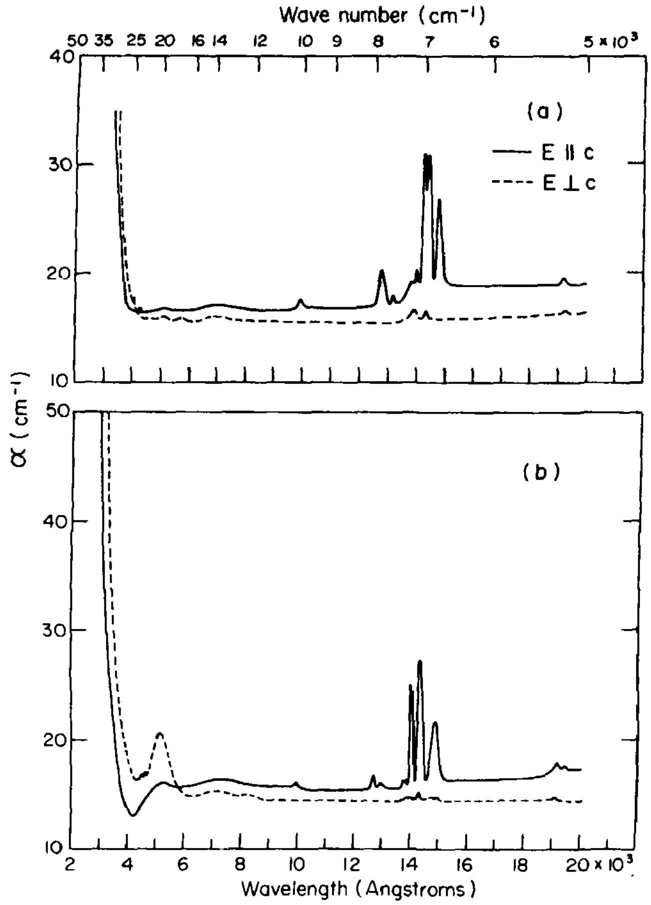

Fig 2 (a)The absorption spectra of a visually colorless termination of an otherwise pink tourmaline from Mt. Mica, Maine, (No. 2, Table 1). (b)The absorption spectra of the pink portion of the same crystal (No. 1, Table 1).

transitions from the $^6A_1$ ground state to excited quartet states. There is little evidence on the distribution of available cations between the (b) and (c) positions in tourmaline. Analyses[2] indicate that there is nearly always sufficient Al to fill the (c) position, but it cannot be assumed that this will always occur. Indeed, the structure determination on buergerite[5] indicates that more than 8 per cent of the (c) position is filled with Fe, although the chemical analysis shows sufficient Al to completely fill this position. Mn^{2+}, because of its size and valence, most reasonably occupies the (b) position and, although other interpretations are possible, the spectra can be interpreted most simply by assuming that Fe^{3+} occupies the (b) position as well.

In a site of 4 mm symmetry each degenerate quartet level is split[14], giving rise to additional peaks in the absorption spectrum. The transition $^4T_2(G) \leftarrow {}^6A_1$ is resolved into two peaks and accounts for absorptions at 5200 and 5800 Å in the E⊥c spectrum of the colorless sample. $^4T_2 \leftarrow {}^6A_1$ is the strong peak at 5200 Å in rubellite, while the $^4T_2 \leftarrow {}^6A_1$ lower energy transition is represented by a shoulder at 5800 Å. The sharp peaks between 4600 and 4000 Å are probably due to one or more of the following: $^4A_1$(G), ^4E(G), $^4T_2$(D) and ^4E(D). Burns and Strens[14] have assigned ^4E, $^4A_1 \leftarrow {}^6A_1$ to the peaks at 4700 and 4500 Å in epidote and it seems correct to assign these to the tourmaline peaks at 4600 and 4400 Å. The sharpness of these peaks is consistent with the fact that the energies of the ^4E and $^4A_1$ terms do not change much relative to the $^6A_1$ ground state term with changes in the crystal field splitting parameter. The weak peak at 7200 and 8200 Å are asigned to a split $^4T_1 \leftarrow {}^6A_1$ transition. Since the analysis indicates both Fe and Mn, an alternative explanation which is also possible would argue that the doubling of the peaks in this region is due to the difference in the Orgel diagrams of Mn^{2+} and Fe^{3+}, and that each transition is seen twice, one peak originating from Mn^{2+}, the other from Fe^{3+}. The field independent transition ^4E, $^4A_1 \leftarrow {}^6A_1$ for Mn^{2+} would not be observed since it would occur on the absorption edge, where instrumental resolution is low.

Heating a deep pink rubellite for as short a period as two hours at 650°C has the effect of flattening out the absorption peaks, giving the sample the appearance of being only slightly colored. This presumably is due to disorder of Fe^{3+} and Mn^{2+} between the (b) and (c) positions, overlap between the absorptions of the two ions distributed over two sites producing a smeared spectrum; however, this is a point that will require further investigation.

GREEN AND BLUE TOURMALINE

Fe^{2+} is by far the most common transition element ion in most analysed tourmalines and of Fe^{2+}, Fe^{3+} and Mn^{2+} is the only ion having a spin-allowed transition ($^5E \leftarrow {}^5T_2$) in an octahedral environment. In green tourmaline there are two broad absorption peaks at 7200 and about 11,000 Å. Although there can be no doubt that the 11,000 · peak is due to Fe^{2+}, the origin of the 7200 Å peak requires some discussion.

The ionic radius of Fe^{+2} being larger than that of Al^{3+}, most Fe^{2+} ions are expected to be situated in the (b) position. Since the crystal field splitting parameter Δ is approximately proportional to the inverse fifth power of the mean metal-oxygen distance, if the 11,000 Å peak is associated with Fe^{2+} in the (b) position, Fe^{2+} in the (c) position would absorb at about 9200 Å. This maximum value is based on dravite metal-oxygen distances. Clearly the 7200 Å band is not due to distribution of Fe^{2+} among the (b) and (c) positions.

Grum Grzhimailo[7] has assigned the 7200 Å absorption to Mn^{3+}, but this band always has approximately the same ratio of intensity to the Fe^{2+} band at about 11,000 Å, which is inconsistent with the widely varying ratio of Mn to Fe^{2+} in analyzed tourmalines. The spectrum of tourmaline, No. 6 (Fig. 4(b) for example, shows a large absorption at 7200 Å, but the analysis is very low in Mn; also in rubellite, when the Mn content may be high, none of several specimens examined shows a band of any intensity in this region.

Recently Hush[15] and Allen[16], studying vivianite and crocidolite respectively, have ascribed bands around 7000 Å to intervalence transfer between Fe^{2+} and Fe^{3+}. Since tourmaline commonly contains iron in both valence states, it may be asked if the band at 7200 Å in tourmaline is due to the same cause.

One would expect the intensity of the band to be related to the concentration ratio of Fe^{3+} to Fe^{2+}, but in blue tourmaline (to be discussed in more detail later) where the 7200 Å band is very well developed, both our spectra and chemical analysis[2] show very low concentrations of Fe^{3+}. Certainly the 7200 Å band is no better developed in green tourmaline, where the Fe^{3+}/Fe^{2+} ratio is much higher. In fact, whether the Fe^{3+} concentration is high or low, the 7200 Å band correlates in intensity with the 11,000 Å band; consequently we feel that intervalence transfer is not a valid explanation for tourmaline. Hence the two peaks at 7200 Å and 11,000 Å are most readily explained by crystal field tran-

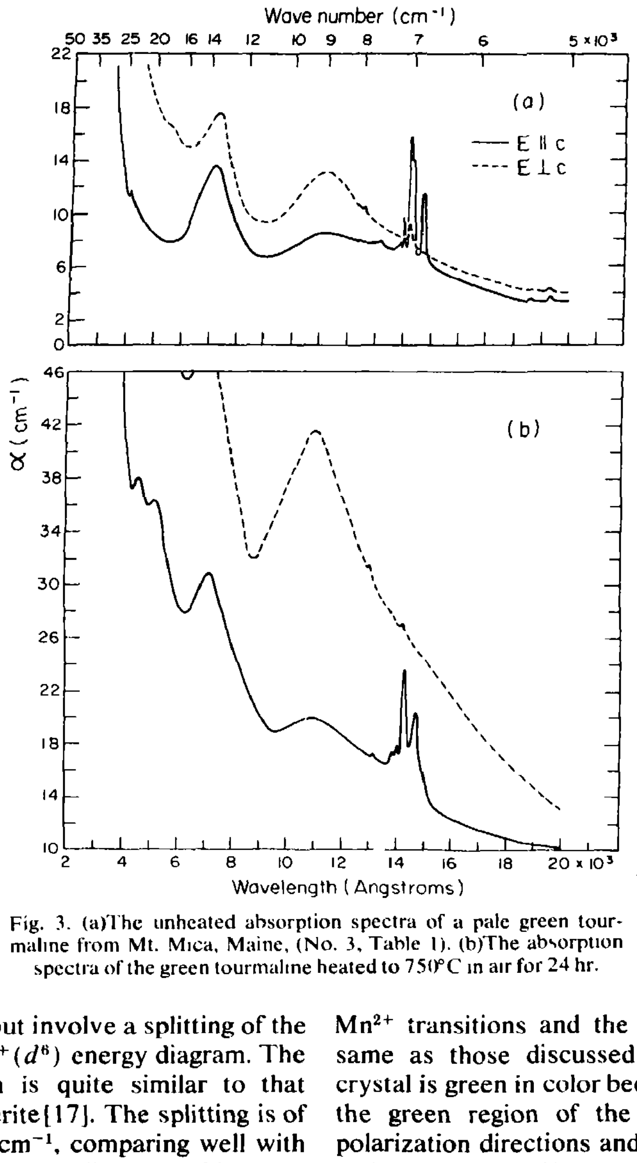

Fig. 3. (a)The unheated absorption spectra of a pale green tourmaline from Mt. Mica, Maine, (No. 3, Table 1). (b)The absorption spectra of the green tourmaline heated to 750°C in air for 24 hr.

sitions $^5E \leftarrow {}^5T_2$, but involve a splitting of the ^5E state in the $Fe^{2+}(d^6)$ energy diagram. The resulting spectrum is quite similar to that reported for cordierite[17]. The splitting is of the order of 5000 cm^{-1}, comparing well with the maximum cordierite splitting of 6000 cm^{-1}, As in cordierite is felt that the splitting can be accounted for by distortions of the octahedra occupied by Fe^{2+}, although the possibility of splitting due to the dynamic Jahn–Teller effect cannot be dismissed.

The other peaks in the green tourmaline region 6000–3500 Å are due to Fe^{3+} and Mn^{2+} transitions and the transitions are the same as those discussed for rubellite. The crystal is green in color because it transmits in the green region of the spectrum in both polarization directions and absorbs in the red and blue regions. Two other spectra of green specimens are given for comparison, Figures 4(a) and 4(b), and show that green tourmalines have essentially the same spectra. A difference of some significance is that in both the comparative specimens there is about 1300 Å difference between peak positions in the two optical directions. The strongly asymmetric

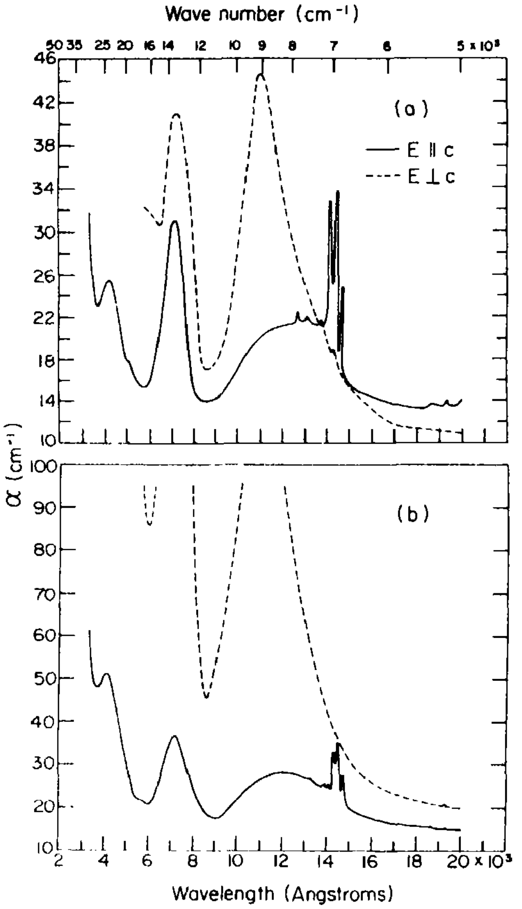

Fig. 4. (a,b) The unheated absorption spectra of two green tourmalines given here for comparison with Fig. 3(a). (a)No 4, Table 1), locality unknown; (b)(No 6, Table 1), Governador, Minas Geras, Brazil

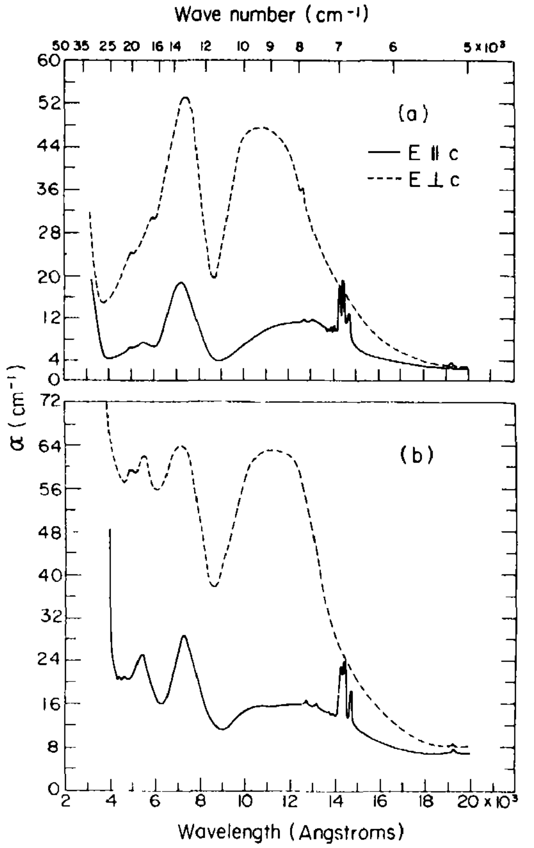

Fig 5 (a)The absorption spectra of an unheated pale blue tourmaline from Mt. Mica, Maine, (No. 5, Table 1). (b)The same blue sample heated to 800°C in air, (No. 11, Table 1)

absorption at 10,800 Å in the $E \perp c$ spectrum of Fig. 4(a) must be interpreted as two overlapping bands of differing intensity about 1300 Å apart. They could possibly represent distribution of Fe^{2+} between the two available sites, or the effect of an additional lower symmetry crystal field component.

The spectrum of blue tourmaline, Fig. 5, is again dominated by two peaks at 7200 and 10,800 ($E \perp C$) and 12,300 ($E \parallel c$). These peaks have the same origin as in the green crystals, that is, $^5E \leftarrow {}^5T_2$ transitions with the ^5E state split by structural distortions. The interesting feature of the spectra is low absorption in the blue region, indicating a low amount of Fe^{3+} and Mn^{2+}. The crystal is blue, not only because of this transmission, but also because of absorption in the green region.

The band at 10,800 ($E \perp c$) is again clearly composite and the development of the peak in the $E \parallel c$ spectrum at 10,300 Å after the specimen has been heated to 800°C for 18 hr is due to the $Fe^{+3}\,{}^4T_1 \leftarrow {}^6A_1$ transition, since it is not present in the spectrum of the sample after the oxy-tourmaline layer is removed.

BROWN TOURMALINE

The two brown tourmalines (Figs. 6(a) and 6(b)) studied fall close to the dravite-schorl join. The spectra are characterized by strong absorption in the blue region, indicating Fe^{3+} or Mn^{2+} transitions, but partly due to overlap from the tail of the charge transfer band in the ultraviolet. Despite the low percentage of Fe^{3+} in these samples (total Fe 1·38% Brazilian) the $^4E, ^4A_1 \leftarrow ^6A_1$, 4400 Å, and the $^4T_2 \leftarrow ^6A_1$, 5600 Å, are without splitting and quite intense. The Fe^{3+} spectra do not compare well with those observed in rubellite and oxidized blue tourmaline where Fe^{3+} and Mn^{2+} are probably in the pseudo-tetragonally distorted (b) position, and it is suggested that Fe^{3+} may be characteristically present in the (c) position of dravites. The color is due to absorption in the blue-green and some of the red region and transmission in the yellow-orange region of the spectrum. The actual color of the samples is a yellow-brown for (b) and an orange for (a) in Fig. 4.

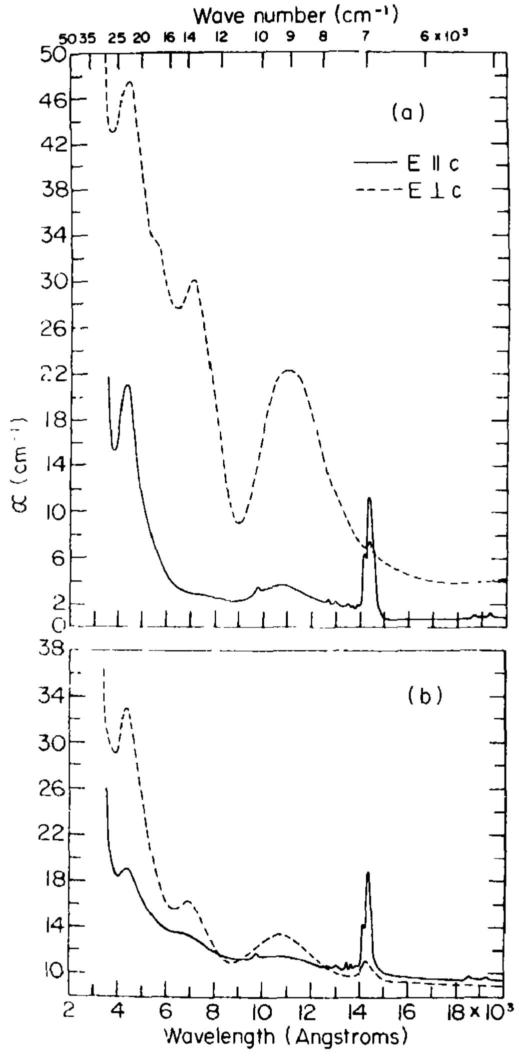

ıg 6 (a)The absorption spectra of a brownish dravite rom Brazil, (No 9, Table 1). (b)The absorption spectra f a brown-orange dravite from New York (No. 8, Table 1).

The low absorption in the near infrared at 7200 and 11,000 Å would suggest that only a small proportion of the iron is present as Fe^{2+} in these specimens. The dravite absorption spectrum is quite characteristic and distinct from other tourmalines examined as a consequence of the more intense absorption in the blue (Fe^{3+}) region of the spectrum as compared with Fe^{2+} absorption in the near infrared due to greater concentration of Fe^{3+} in the highly distorted general site. Analyses [2] indicate Ti in dravite, consequently Ti^{3+} may also contribute to the u.v. spectrum.

BLACK TOURMALINE

The absorption spectrum in Fig. 7(a) is of a schorl whose lattice parameters locate the sample on the dravite-schorl join. Although quite opaque in hand specimen, the sample was translucent in thin section. The crystal analyzed at 7·35 per cent total Fe.

Peaks at about 7500 and 11,000 Å occur on the absorption spectrum and are due to the transitions $^5E \leftarrow ^5T_2$ in ferrous iron with the ^5E level split by structural distortions as previously discussed. The peaks around 5000 Å are due to Fe^{3+} and if previous assignments are correct must be interpreted as due to Fe^{3+} in both (b) and (c) positions. The dichroism is quite marked in this specimen.

The spectrum of the low aluminum tour-

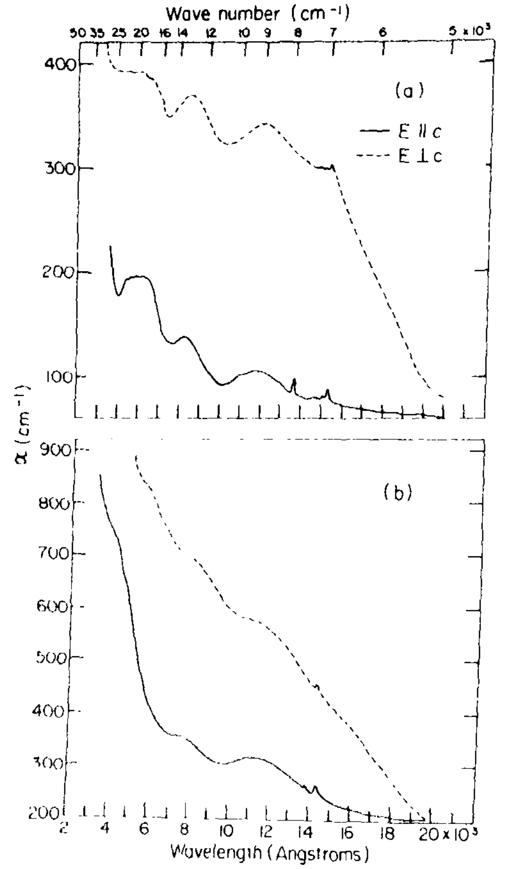

Fig. 7 (a) The absorption spectra of a black tourmaline (locality unknown) (No. 7, Table 1) (b) The absorption spectra of the low aluminum tourmaline (black), (No. 10, Table 1).

maline[10], Fig. 7(b) shows an almost featureless rise from the near infrared to the blue region of the spectrum. The sharp rise in absorption in the visible reflects the high amount, 7·43 per cent of ferric iron. Peaks on the spectrum are quite broad and nearly masked by the high blue absorption, but maxima at 7200 and 11,000 Å are easily discernible, especially in the $E \perp c$ direction. The spectrum is, therefore, in accord with the chemical analysis which shows some ferrous iron. The largely featureless Fe^{3+} region is also what would be expected from the distribution of a large amount of ferric iron over both (b) and (c) positions as suggested by Frondel *et al.*[10]. The high absorption throughout the visible, falling off towards the red, results in a brownish color in thin section.

HEATING EXPERIMENTS

The nature of the oxidation is the same as that recorded for amphiboles[18, 19] and biotite micas[20, 21], and involves the oxidation of Fe^{2+} by OH^- and consequent loss of hydrogen. The same reaction may be expected to occur in any silicate which has OH^- adjacent to Fe^{2+} in its structure. The uneven thickness of the surface oxidation layer shows that removal of hydrogen parallel to the layer structure is faster than normal to the layers. No visible change occurred when an oxidized thick section of blue tourmaline was reduced in hydrogen at 800°C for 8 hr. The effect of heating on the spectra of green and blue tourmaline is to be seen in Figs. 3(b) and 5(b) respectively. The rise in intensity in the blue-green region of the spectrum in both cases results from the oxy-tourmaline layer. This gives rise to a reddish-brown color in the oxidized sample. The original color may be restored by removal of the oxy-tourmaline layer.

Interpretation of the dichroism of the optical absorption spectra of tourmaline

The characteristic dichroism of all the tourmaline spectra has been noted early in the literature[22, 23]. Examination of the absorption spectra in Figs. 2–7 shows that except for the sharp peaks in the 14,000 Å region assigned to the OH and/or H_2O molecular vibrations, *all* the optical spectra are much stronger for $E \perp c$ than $E \parallel c$. Additionally, the spectra generally appear to be residing upon strong charge transfer bands polarized similarly. Within each polarization, the intensity of the optical bands appears to increase with proximity to the ultraviolet charge transfer band. This suggests that the mechanism invoked by Englman[24] is the main source of their intensity. Namely, the odd crystal field mixes a small amount of the charge transfer state into the d^n states, making the $d^n \rightarrow d^n$ forbidden states slightly allowed. The relationship to the charge transfer band appears stronger, affecting the polarization too. To further investigate this, sample 3 (see Table 1) was cut down and its absorption spectrum was run in the near ultraviolet. As suspected, an intense band appeared at about 24,000 cm^{-1}, also strongly polarized in the $E \perp c$ direction. We tentatively identified this band as due to an Fe^{3+} transition. This band itself resides upon stronger bands in the further ultraviolet, having the same polarization properties. This is further evidence for Englman mixing.

Thus we see that though the local point symmetry of the 3*d* ion is quite low, the strong polarization dependence of the absorption spectra suggests that the mechanism that is responsible for making these forbidden transitions allowed is quite symmetric. The different states' energies will still reflect the distorted environment by showing considerable splittings. It is important to note that this is not inconsistent. This is because the crystal field can always be expanded in a set of decreasing terms, some of which are odd and some of which are even in their symmetry properties. The detailed splittings will be due to the even *and* odd terms of the lowest symmetry. However, the intensities are only due to the odd symmetry terms with the major portion due to the *largest* odd terms. This is what allows us to talk of one symmetry for assigning energy levels and another for intensities.

An important criterion exists, however, experimentally in order to see the effect of this odd field symmetry. It must be related in a simple way to the crystal symmetry axes. Analyzing the coordination of the metal ions, we find that the *largest odd* field term is a trigonal field in the main diagonal direction of the octahedral field. This direction almost coincides with the *c* axis of the tourmaline host, so we may take our main contribution to the intensity as due to a pseudotrigonal field in this direction.

Based on this approach, we believe that the dichroism can be completely explained by the combination of the d^n states mixing with the nearby charge transfer states and the trigonal component of the local crystal site that effects this mixing field. Furthermore, this interpretation is quite general, and is quite independent of the assignment of the particular state in the visible. Qualitatively, the approach goes as follows:

This strong dichroism in the near ultraviolet in a trigonal crystal field allows us to assign the symmetry of the two states involved in this transition. It was found that two possible choices only exist. We then assume that all optical transitions borrow their intensity from this allowed band, mixing due to the trigonal field. The leading odd term in this field has been shown to be of the same symmetry as that of the electric dipole operator, so that except for a proportionality constant, the same selection rules apply in calculating the perturbation matrix element.

We then consider the $E \parallel c$ and $E \perp c$ polarization terms, using the electric dipole selection rules, for optical d^n states of either of the two possible state symmetries in the trigonal field. This means we consider four cases in all. For two of these the $E \parallel c$ terms vanish altogether, certainly suggesting that the $E \perp c$ absorption spectrum will be greater than for $E \parallel c$. For the other two cases, where neither $E \parallel c$ nor $E \perp c$ vanish, the $E \perp c$ term is expected to be larger than $E \parallel c$ because of the much smaller perturbation energy denominator in the latter. This forces the optical intensity states to take on the polarization character of the allowed band, yielding the strong dichroism even in the optical.

Trigonal field selection rules and assignment of symmetry of the "allowed" ultraviolet band

We now focus on the dichroism of the strong ultraviolet bands. We assume C_3 symmetry, where the trigonal states arising from octahedral states A_1, A_2, E, T_1, T_2 all may be grouped into either A or E in terms of their symmetry properties with respect to the trigonal c axis. The selection rules are then

$$\text{for } E \parallel c\text{:}\quad A \leftrightarrow A,\ E \leftrightarrow E,\ A \nleftrightarrow E$$

$$\text{for } E \perp c\text{:}\quad A \leftrightarrow E,\ E \leftrightarrow E,\ A \nleftrightarrow A$$

This implies that if we see a transition in $E \perp c$ and not $E \parallel c$ it must be $A \leftrightarrow E$ in character, though it does not specify which is the ground state. We will carry along this ambiguity in our calculations.

Perturbation properties of Laporte forbidden transitions in a trigonal field

Laporte's rule forbids electric dipole transitions between d^n configurations, because both the initial and final state are even functions. If the crystal field lacks a center of symmetry, the d^n states can have mixed into them higher states of odd symmetry, which will then make the transitions 'slightly allowed'. Let the three states under consideration be called ψ_1, ψ_2 and ψ_3 with their respective energies in ascending values E_1, E_2 and E_3. Then perturbation theory tells us[25] that

$$\psi_1' = \psi_1 - C_{13}\psi_3, \quad \psi_2' = \psi_2 - C_{23}\psi_3$$

$$C_{13} = \frac{\langle\psi_1|V^{\text{odd}}|\psi_3\rangle}{E_3 - E_1}, \quad C_{23} = \frac{\langle\psi_2|V^{\text{odd}}|\psi_3\rangle}{E_3 - E_2}$$

where ψ_1' and ψ_2' are the new wave functions for the d^n states that consist most of the 'old' even part, ψ_1 and ψ_2, and a small amount of the odd ψ_3 state. V^{odd} is the odd part of the crystal field and the bracket notation is used to denote integrals over all space, e.g.

$$\langle\psi_i|V^{\text{odd}}|\psi_j\rangle = \int \psi_i V^{\text{odd}} \psi_j \, \mathrm{d}\tau.$$

We have also assumed that ψ_3 is the main odd state that is effective in the mixing process, due to its proximity, and neglect higher states.

V^{odd} must reflect the C_3 symmetry and, as shown by Sugano and Tanabe[26] the leading term in the expansion in powers of the electronic coordinates will be linear, and this of the same symmetry as the electric dipole moment operator itself. This allows us to express the V^{odd} matrix elements in terms of the electric dipole moment elements. Letting $\mathbf{r}$ denote the electric dipole operator with components $\mathbf{r}_\parallel$ and $\mathbf{r}_\perp$ for ∥ and ⊥ to the c axis, respectively, we may then define

$$\langle\psi_i|V^{\text{odd}}|\psi_j\rangle = \langle\psi_i|V\mathbf{r}_\parallel + V\mathbf{r}_\perp|\psi_j\rangle$$
$$= V\langle\psi_i|\mathbf{r}_\parallel|\psi_j\rangle + V\langle\psi_i|\mathbf{r}_\perp|\psi_j\rangle.$$

Applying this to our case we make use of the experimental fact

$$\langle\psi_1|\mathbf{r}_\parallel|\psi_3\rangle = 0$$

and get

$$\psi_1' = \psi_1 - \left\{\frac{V\langle\psi_1|\mathbf{r}_\parallel|\psi_3\rangle + V\langle\psi_1|\mathbf{r}_\perp|\psi_3\rangle}{E_3 - E_1}\right\}\psi_3$$
$$= \psi_1 - \frac{V\langle\psi_1|\mathbf{r}_\perp|\psi_3\rangle}{E_3 - E_1}\psi_3.$$

(*In general we may consider V to include all additional normalizing constants.*)

POLARIZATION FORMULAE FOR TRIGONAL SYMMETRY

The general expression for the electric dipole matrix element $\mathbf{r}_\parallel$ or $\mathbf{r}_\perp$ between the two new states ψ_1 and ψ_2' is

$$\langle\psi_1'|\mathbf{r}_{\parallel,\perp}|\psi_2'\rangle = \langle\psi_1|\mathbf{r}_{\parallel,\perp}|\psi_2\rangle$$
$$+ C_{13}C_{23}\langle\psi_1|\mathbf{r}_{\parallel,\perp}|\psi_3\rangle$$
$$- C_{13}\langle\psi_3|\mathbf{r}_{\parallel,\perp}|\psi_2\rangle$$
$$- C_{23}\langle\psi_1|\mathbf{r}_{\parallel,\perp}|\psi_3\rangle.$$

The first two terms of the right-hand side of the equation will vanish due to Laporte forbiddeness.

Using the previously derived expression along with $\langle\psi_3|\mathbf{r}_\parallel|\psi_1\rangle = 0$ again, we get

$$\langle\psi_1'|\mathbf{r}_\parallel|\psi_2' = -V\langle\psi_1|\mathbf{r}_\perp|\psi_3\rangle$$
$$\times \langle\psi_3|\mathbf{r}_\parallel|\psi_2\rangle(E_3 - E_1)^{-1} + 0$$

$$\langle\psi_1'|\mathbf{r}_\perp|\psi_2'\rangle = -V\langle\psi_1|\mathbf{r}_\perp|\psi_3\rangle\langle\psi_3|\mathbf{r}_\perp|\psi_2\rangle$$
$$\times\left[\frac{1}{E_3 - E_1} + \frac{1}{E_3 - E_2}\right]$$
$$- V\frac{\langle\psi_2|\mathbf{r}_\parallel|\psi_3\rangle\langle\psi_3|\mathbf{r}_\perp|\psi_1\rangle}{E_3 - E_2}$$

Let us now consider the four possible combinations of states ψ_1, ψ_2, ψ_3 and calculate the electric dipole matrix element for $E\|c$ and $E \perp c$ for all of them. These are given in Table 3. The two cases where $\langle \psi_1'|\mathbf{r}_\||\psi_2'\rangle$ vanishes, of course, immediately show why we should expect the absorption for $E \perp c \gg E\|c$. For the case where ψ_1, ψ_2, ψ_3 are respectively E, A, A, we note that the two differ in only that $\langle \psi_1'\mathbf{r}_\|\psi_2'\rangle$ $(E_3 - E_1)^{-1}$ and $\langle \psi_1'\mathbf{r}_\perp \psi_2'\rangle$ $(E_3 - E_2)^{-1}$. However, $E_3 - E_2$ is always less than $E_3 - E_1$ (and for states ψ_2 that are near the blue, considerably less), so again $E \perp c > E\|c$. For the final case, where ψ_1, ψ_2, ψ_3 are A, E, E respectively, these comments apply, over and above two *additional* terms that contribute to the $E \perp c$ matrix element.

In conclusion, we wish to point out a useful result of these last mathematical arguments. Namely, the ratio

$$\left(\frac{E_3 - E_1}{E_3 - E_2}\right)^2$$

provides a measure of the minimum dichroism of intensity to be expected on this simple model. This also implies that in general the dichroism will increase as we approach the ultraviolet.

SUMMARY

In conclusion, we have seen that tourmaline, a complex solid solution of composition $(\mathrm{Na, Ca})[\mathrm{Mg, FeAl, Li}]_9 \cdot \mathrm{B_3Si_6O_{27}(OH, F)_4}$, has colors and dichroism which are a function of the amount of iron, particularly $\mathrm{Fe^{2+}}$, and manganese substituting in (b) and (c) positions *of the crystal structure. The dichroism has* been explained by the combination of two mechanisms. The d^n states mixing with the charge transfer states provide the basic mechanism for making the optical transitions allowed, while the trigonal component of the local point symmetry in the crystal then provides the mechanism for the dichroism. Consideration of the selection rules of the trigonal field shows that the $E \| c$ terms are weak, while the $E \perp c$ terms are strong, thus producing the particular dichroism so characteristic of tourmaline. The splittings of bands, however, have been explained on the basis of all the components of the low local point symmetries, especially the (b) position.

Experiments have demonstrated that color

Table 3. Electric dipole matrix elements for E‖c *and* E ⊥ c

ψ_1	ψ_2	ψ_3	$-\langle \psi_1' \lvert \mathbf{r}_\| \rvert \psi_2' \rangle$*	$-\langle \psi_1' \lvert \mathbf{r}_\perp \rvert \psi_2' \rangle$*
A	A	E	0	$V\langle \psi_1 \lvert \mathbf{r}_\perp \rvert \psi_3\rangle\langle \psi_3 \lvert \mathbf{r}_\perp \rvert \psi_2\rangle$ $\times\left[\frac{1}{E_3 - E_1} + \frac{1}{E_3 - E_2}\right]$
A	E	E	$\frac{V}{E_3 - E_1}\langle \psi_1 \lvert \mathbf{r} \rvert \psi_3\rangle\langle \psi_3 \lvert \mathbf{r} \rvert \psi_2\rangle$	$\frac{V}{E_3 - E_2}\langle \psi_1 \lvert \mathbf{r} \rvert \psi_3\rangle\langle \psi_3 \lvert \mathbf{r} \rvert \psi_2\rangle$ $+ V'\langle \psi_1 \lvert \mathbf{r} \rvert \psi_3\rangle\langle \psi_3 \lvert \mathbf{r} \rvert \psi_2\rangle$ $\times\left[\frac{1}{E_3 - E_1} + \frac{1}{E_3 - E_2}\right]$
E	A	A	$\frac{V}{E_3 - E_1}\langle \psi_1 \lvert \mathbf{r}_\perp \rvert \psi_3\rangle\langle \psi_3 \lvert \mathbf{r}_\| \rvert \psi_2\rangle$	$\frac{V}{E_3 - E_2}\langle \psi_1 \lvert \mathbf{r} \rvert \psi_3\rangle\langle \psi_3 \lvert \mathbf{r} \rvert \psi_2\rangle$
E	E	A	0	$V'\langle \psi_1 \lvert \mathbf{r}_\perp \rvert \psi_3\rangle\langle \psi_3 \lvert \mathbf{r}_\perp \rvert \psi_2\rangle$ $\times\left[\frac{1}{E_3 - E_1} + \frac{1}{E_3 - E_2}\right]$

*Note: For convenience we have considered the negative of the matrix element. In practice the intensity is proportional to the square, anyway changes induced by heating are largely surface effects and can be explained by oxidation of Fe^{2+} to Fe^{3+} and are attendant on the removal of hydrogen during heating.

Acknowledgements—We wish to extend our thanks to A. Vetrovs for preparing our samples, to D. Guernsey for some of the chemical analyses, and to D. R. Waldbaum for use of his modified Burnham least square cell dimension program. Particular thanks to C. Frondel for use of tourmaline samples from the Harvard Museum. To A. Linz and to T. R. Davidson we are grateful for clarification of certain experimental points on spectra and chemical analysis respectively.

This research was sponsored by the Advanced Research Projects Agency (ARPA) under Contract No. SD-90, by MITHRAS, Inc., a Division of Sanders, and by the Committee on Experimental Geology and Geophysics, Harvard University.

REFERENCES

1. BUERGER M. J., BURNHAM C. W. and PEACOR D. R., *Acta crystallogr.* **15**, 583 (1962).
2. EPPRECHT W., *Schweiz. Min. Petr. Mitt.* **33**, 481 (1953).
3. DONNAY G. and BUERGER M. J., *Acta crystallogr.* **3**, 379 (1950).
4. ITO T. and SADANAGA R., *Acta crystallogr.* **4**, 385 (1951).
5. BARTON R., *Acta crystallogr.* In press (1968).
6. BRADLEY J. E. S. and BRADLEY O., *Min. Mag.* **30**, 26 (1953).
7. GRUM-GRZHIMAILO S. V., *Trudy Inst. Krist., Akad. Nauk. SSSR* **12**, 79 (1956).
8. BURNHAM C. W., *Carnegie Inst., Washington, Year Book*, **61**, 132 (1962).
9. INGAMELLS C. O., *Talanta* **4**, 268 (1960).
10. FRONDEL C., BIEDL A. and ITO T., *J. Am. Mineral.* **51**, 1501 (1966).
11. MASON B., DONNAY G. and HARDIE L. A., *Science* **144**, 71 (1964).
12. KRUGLYAKOVA G. I., *Aspects of Theoretical Mineralogy in the U.S.S.R.* Macmillan, New York (1964).
13. DONNAY Gabrielle, SENFTLE F. E., THORPE A. and WHITE, S., *Carnegie Inst., Washington, Year Book*, **65**, 295 (1966).
14. BURNS R. G. and STRENS R. G. J., *Min. Mag.* **36**, 204 (1967).
15. HUSH N. S., *Progress in Inorganic Chemistry*, Vol. 8, pp. 391–444. Interscience, New York.
16. ALLEN G. C., *Thesis*. Bristol University, England (1965).
17. FARRELL E. F., NEWNHAM R. E., *Am. Mineral.* **52**, 380 (1967).
18. BARNES V. E., *Am. Mineral.* **15**, 393 (1930).
19. ADDISON W. E. and SHARP J. H., *Clays Clay Minerals*. 11th Conf., pp. 95–104 (1963).
20. WONES D. R. and EUGSTER, H. P., *Am. Mineral* **50**, 1228, (1965).
21. VEDDER W. and WILKINS R. W. T., *Am. Mineral.* In press (1968).
22. HAUY ABBE, *Traite de Mineralogie*, Vol. 3. Bachelier, Paris (1822).
23. MOHS F., *Treatise on Mineralogy*, Vol. 1 (Translated by W. Haidinger). Constable, Edinburgh (1825).
24. ENGLMAN R., *Mol. Phys.* **3**, 48 (1960).
25. BALLHAUSEN C. J., *An Introduction to Ligand Field Theory*, Chap. 8. McGraw Hill, New York (1962).
26. SUGANO S. and TANABE Y., *J. phys. Soc. Japan* **13**, 880 (1958).

J. Phys. Chem. Solids Pergamon Press 1969. Vol. 30, pp. 57–62. Printed in Great Britain.

ON THE NATURE OF THE LOW-TEMPERATURE PHASE OF $NaD_3(SeO_3)_2$

L. A. SHUVALOV, N. R. IVANOV, L. F. KIRPICHNIKOVA and N. M. SCHAGINA
Institute of Crystallography of the Academy of Sciences of the USSR, Moscow, USSR

(*Received* 14 *December* 1967; *in revised form* 3 *May* 1968)

Abstract – Dielectric and optical properties of $NaD_3(SeO_3)_2$ single crystals were studied. From the results obtained the low-temperature phase of $NaD_3(SeO_3)_2$ is considered to be ferroelectric. It is shown that the phase transition is attended with $2/m \rightarrow m$ symmetry change associated with disappearance on strong deuteration of the interstitial triclinic ferroelectric phase which was found to exist for $NaH_3(SeO_3)_2$.

INTRODUCTION

THE LARGE isotopic shift of the Curie point in $NaH_3(SeO_3)_2$ crystals upon substitution of *D* for *H* was discovered by Blinc and co-workers[1] and independently by Gavrilova-Podolskaya *et al.*[2]. Such an isotope effect is entirely consistent with similar effects found in many other ferroelectrics. In addition to the shift of Curie temperature with deuteration, it was concluded that the character of the lower phase changed and that $NaD_3(SeO_3)_2$ was antiferroelectric [1, 3–6]. As a similar isotope effect of a change in character of the lower phase has not yet been observed in any other system, one might question the conclusion that $NaD_3(SeO_3)_2$ is antiferroelectric. In this connection a detailed analysis of the nature of the low-temperature phase of $NaD_3(SeO_3)_2$ was made.

PREPARATION OF CRYSTALS AND EXPERIMENTAL PROCEDURE

The synthesis of $NaD_3(SeO_3)_2$ was carried out as follows. D_2SeO_3 was obtained by dissolving SeO_2 in D_2O; on interaction of D_2SeO_3 with Na_2CO_3 solution in heavy water $NaD_3(SeO_3)_2$ material was obtained. The crystals were grown in the temperature range 40–30° by the temperature decreasing method. During a month's time colourless transparent crystals were grown, their weight reaching 50 g. The orientation of the orthogonal crystallophysic axes adopted by us coincides with the system of coordinates which we had used previously for $NaH_3(SeO_3)_2$ crystals[7]. This orientation differs from that developed by Blinc *et al.*[4] so that our *x*-, *y*- and *z*-axes, being parallel to the main axes of the optical indicatrix, coincide with the directions $-X \cos 36°$, Y, $-Z \cos 36°$ reported in[4].

Measurements were carried out using plates 0·5–1 mm thick and 1 cm² in area. Low-frequency (800 Hz) dielectric constant measurements were performed for a field strength of 10 v/cm with a RFT 1007 bridge. A nitrogen cryostat was used for sample thermal stabilization which is believed to be accurate to 0·01°. The temperature was measured to within 0·05° with the help of a copper-constantan thermocouple. The polarimetrical measurements employed the techniques and apparatus described in[8, 9]. Dielectric hysteresis loops were obtained in the usual manner. For these measurements both fresh and one year old crystals were used.

EXPERIMENTAL RESULTS

Figure 1 shows the results of dielectric measurements on crystals for which the amount of deuteration was 60 and 98 per cent (deuteration per cent was determined in accordance with[3]). As one can see from the graph, the temperature of maximum dielectric constant, ϵ_x, (which is considered for $E_\sim = 0$ as the transition temperature)

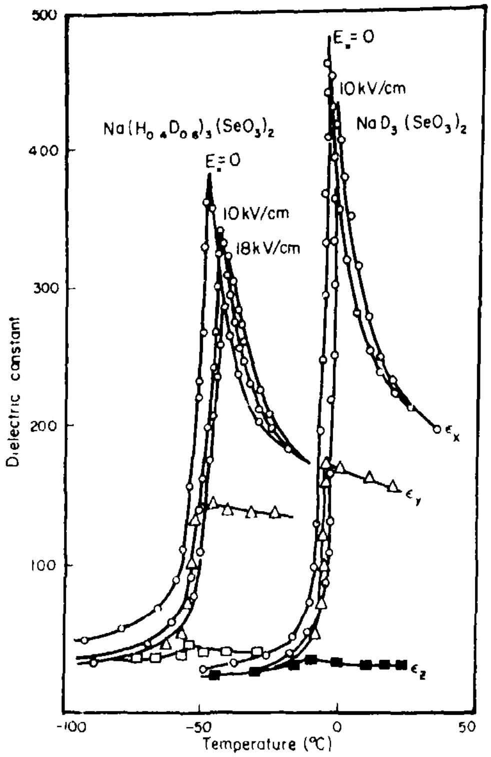

Fig. 1. Temperature dependence of dielectric constant components of $Na(H_{0.4}D_{0.6})_3(SeO_3)_2$ and $NaD_3(SeO_3)_2$ crystals at various biasing field strengths ($E = E_x$). y- and z-component are shown for zero biasing field. Note that maximum of ϵ_y shifts in the field E_x in the same direction as maximum of ϵ_x does.

shifts towards a higher temperature region with applied d.c. electric field, $E = E_x$. The character of the shift is nonlinear, it is closer to an $E^{2/3}$ law than to the linear one (Fig. 2.). Figure 2 also shows the dielectric constant, ϵ_x, vs. d.c. biasing field for different temperatures in the low temperature phase.

The behaviour of ϵ_x follows a Curie–Weiss law both for $E = 0$ and $E \neq 0$: for $E = 0$, $C = (0{\cdot}8 \pm 0{\cdot}5) \times 10^3$ deg and $T_0 = -1{\cdot}1 \pm 0{\cdot}5$°C, at $T < T_{tr} = -5{\cdot}6 \pm 0{\cdot}1$°C; $C = (7{\cdot}9 \pm 1) \times 10^3$ deg and $T_0 = -34 \pm 4$°C at $T > T_{tr}$ for $NaD_3(SeO_3)_2$ (Fig. 3). These values satisfactorily agree with the results obtained by Blinc *et al.*[1]. It should be mentioned that the Curie–Weiss constant, $C_{T<T_{tr}}$, has a tendency to decrease with a d.c. biasing field increase. At the same time the characteristic slope change in the dependencies $(\epsilon_x - 1)^{-1}$ (T) in the vicinity of the phase transition has a tendency to disappear with the d.c. field increase. But neither temperature hysteresis, nor discontinuity in dielectric constant change (as well as in other properties investigated) were observed within experimental error.

To establish the symmetry of the low-temperature phase of $NaD_3(SeO_3)_2$ we used a polarimetrical method of measuring the rotation angle of the optical indicatrix, as was also the case with $NaH_3(SeO_3)_2$[7].

In $NaD_3(SeO_3)_2$ crystal the indicatrix, at temperatures both above and below T_{tr}, rotates about the y-axis only (Fig. 4). This can be described in terms of the thermooptic effect. It is of interest to note that due to the phase transition the thermooptic coefficient changes its sign. The same phenomenon was observed in the case of $NaH_3(SeO_3)_2$, although the existence of an interstitial phase makes the rotation curve more complicated[6].

We have found that it is impossible to observe domain structure by means of polarizing microscope method, while the domains in $NaH_3(SeO_3)_2$ crystals are visible[7]. This fact is important for further discussion of the crystal symmetry.

From the data reported by Blinc[1, 3] one could expect that double hysteresis loops reflect the nature of $NaD_3(SeO_3)_2$ itself. However our observations show that double loops take place only for aged specimens, while as-grown crystals show normal hysteresis loops. Double loops of our aged crystals have a low critical field comparable with the value of a coercive one which is about 2 kv/cm for −20°C. Cycling in the a.c. filed gradually decreases the critical field strength and leads to its complete disappearance, which is also in accordance with the behaviour of loops discussed in[1].

Temperature dependence of spontaneous polarization determined from dielectric hysteresis loops measurements is shown in Fig. 5. The dependence P_s (T) is much

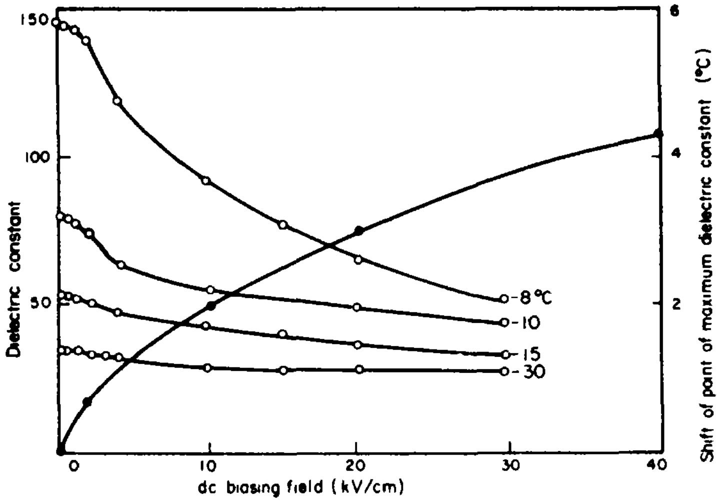

Fig. 2 Shift of point of maximum of ϵ_r of $NaD_3(SeO_3)_2$ crystal under the action of an electric field and $\epsilon_r(E\ )$ dependence for different temperatures in the low-temperature phase.

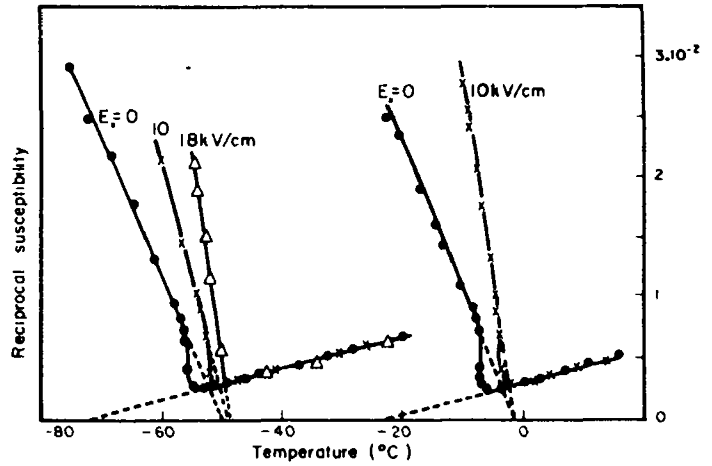

Fig. 3. X-component of the reciprocal susceptibility vs. temperature for various biasing field strengths $(E_{-} = E_{r})$.

smoother than that given by Blinc *et al.*[1]. The measurements of hysteresis loops were carried out at an a.c. field strength about two or three times the value of the coercive field.

DISCUSSION

The questions under discussion are the character of transition, the nature of low-temperature phase (i.e. the choice between ferroelectric and antiferroelectric states), the symmetry of the phase and a comparison with $NaH_3(SeO_3)_2$ (i.e. the peculiarity of isotopic effect).

(1) As one can see from the results of the experiment described above the phase transition in $NaD_3(SeO_3)_2$ has the features of both first and second order. This can be seen on the one hand, in the behaviour of the shift of

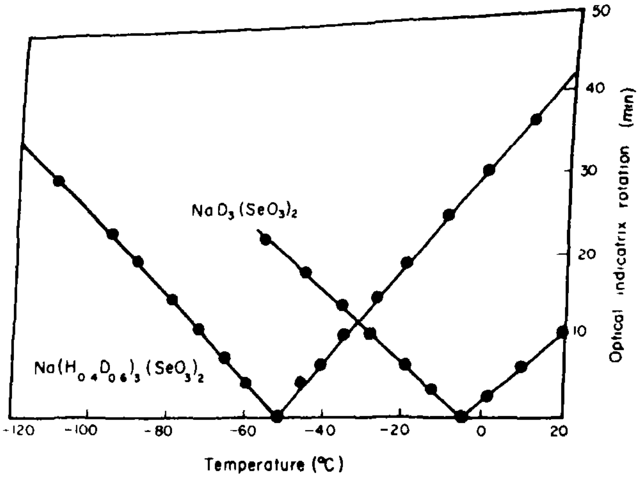

Fig. 4. Thermal rotation of the optical indicatrix about the x-axis. Indicatrix rotation about y and z axes does not take place

dielectric constant maximum with the d.c. field, in the continuity of the physical properties during transition, in the absence within experimental error limits of thermal hysteresis of dielectric and optical properties and, on the other hand, in the change of slope of reciprocal susceptibility near the phase transition as well as in the difference between the extrapolated Curie–Weiss temperatures, T_0, in the two phases. Thus one can conclude that we deal with either transition of second order, close to first order, or that of first order, close

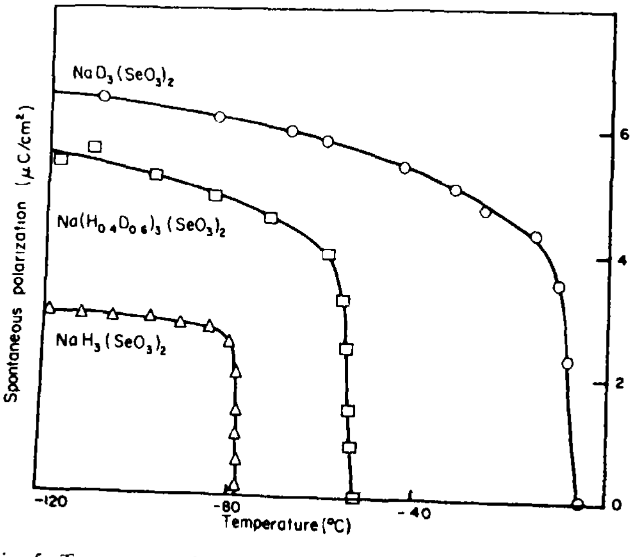

Fig. 5. Temperature dependence of spontaneous polarization for $NaD_3(SeO_3)_2$ and $Na(H_{0.4}D_{0.6})_3(SeO_3)_2$ crystals. $P_{sx}(T)$ curve for $NaH_3(SeO_3)_2$ crystal according to[7].

to second order. The choice between these two possibilities can be made only on the basis of more precise experiments.

(2) Nevertheless the nature of the low-temperature phase of $NaD_3(SeO_3)_2$ can be determined whatever the order of transition may be. Thermodynamic theory predicts and experimental results confirm the shift of the point of maximum of $\epsilon(T)$ with applied d.c. field towards the higher temperatures for ferroelectrics. So far there is no theoretically well-grounded answer to the question of the direction of shift of transition temperature for antiferroelectrics, however experiments show that the temperature of the maximum dielectric constant lowers under the external field[10]. Therefore from our experiments on the shift of the temperature of the maximum dielectric constant one can suppose that $NaD_3(SeO_3)_2$ is ferroelectric. This becomes all the more evident if one takes into account the fact that young crystals and crystals to which a field treatment has been given have normal hysteresis loops.

The explanation of the fact that double hysteresis loops are observable should be based on consideration of the influence of impurities and ageing-rejuvenating effects rather than on the assumption that the antiferroelectric and field induced ferroelectric phase coexist.

(3) The thermooptic measurements clearly demonstrate that $NaD_3(SeO_3)_2$ exhibits a transition from the monoclinic phase $2/m$ to the monoclinic one. The impossibility to observe the domain structure by means of a polarizing microscope method also strongly confirms the fact that the crystal in the low-temperature phase has a monoclinic symmetry. In addition, the electric measurements show that the P_s vector lies in the mirror plane of the paraelectric phase ($P_s = P_{sx}$) whereas the y-component of P_s is zero. All these measurements, as compared to the data reported in [7], clearly show that an interstitial triclinic ferroelectric phase of $NaH_3(SeO_3)_2$ disappears upon a high degree of deuteration and $NaD_3(SeO_3)_2$ undergoes a transition with $2/m \rightarrow m$ symmetry change.

From the analysis of previously known results and our own results obtained for $NaD_3(SeO_3)_2$ crystals we can make the following conclusions.

i. The phase transition in $NaD_3(SeO_3)_2$ has the features of both first and second order. More precise experiments are necessary to define transition order.

ii. The transition is attended with the change of symmetry $2/m \rightarrow m$. An interstitial triclinic ferroelectric phase of $NaH_3(SeO_3)_2$ crystals disappears upon a high degree of deuteration.

iii. The low-temperature phase of $NaD_3(SeO_3)_2$ crystals is ferroelectric not antiferroelectric as it has been considered up to the present.

Acknowledgements – For $Na(H_{0.4}D_{0.6})_3(SeO_3)_2$ crystal the authors are indebted to K. S. Aleksandrov. We are very grateful to Dr. W. Reese for the useful criticism made upon reading the manuscript.

REFERENCES

1. BLINC R., JOVANOVIC A., LEVSTIC A. and PRELFSNIK A., *J. phys. Chem. Solids* **26**, 1359 (1965).
2. GAVRILOVA-PODOLSKAYA G. V., LUNDIN A. G. and YUDIN A. I., *Zh. Eksper. Teoret. Fiz. Pis'ma i redaktziyu* **1**, 36 (1965).
3. BLINC R. and VOVK D., *Phys. Lett.* **19**, 177 (1965).
4. BLINC R., POBERAJ S., SCHARA M. and STEPISNIK J., *J. Phys. Chem. Solids* **27**, 1391 (1966).
5. GAVRILOVA-PODOLSKAYA G. V., GABUDA S. P. and LUNDIN A. G., *Fiz. Tverd. Tela* **9**, 1166 (1967).
6. ZHEREBTZOVA L. I. and ROSTUNTZEVA A. I., *Kristallografiya* **13**, 536 (1968).
7. SHUVALOV L. A. and IVANOV N. R., *Phys. Status Solidi* **22**, 279 (1967).
8. IVANOV N. R. and SHUVALOV L. A., *Kristallografiya* **11**, 614 (1966).
9. IVANOV N. R., SCHUVALOV L. A., MIRENSKY A. V. and SHNYREV G. D., *Kristallografiya* **12**, 307 (1967).
10. MAKITA Y., *J. phys. Soc. Japan* **20**, 1567 (1965).
11. BLINC R. *et al.*, *Phys. Lett.* **26A**, 290 (1968).

APPENDIX

The paper was presented at the 5th Annual Solid State Physics Conference 3-6 January, 1968 held at the University of Manchester Institute of Science and Technology, England. Some of the conclusions made in this paper are in agreement with the recent NMR data obtained by R. Blinc and co-workers[11], which became available to us after manuscript had been sent to the editorial board

The results of our recent studies of the phase diagram of the system $Na(H_{1-x}D_x)_3(SeO_3)_2$ show in addition to our previously obtained data that the interstitial triclinic ferroelectric phase exists in crystals at $0 \leq x \leq 0.5$. The upper phase transition curve is found to split into two curves, i.e. the sequence of transitions $2m \rightarrow m \rightarrow 1 \rightarrow m$ occurs on lowering the temperature. (*Zh. Eksper. Teoret. Fiz. Pis'ma v redaktziyu* **8**, 235 (1968)). Moreover, the more precise $\mathscr{E}(T)$ measurements show a small hysteresis on transition from paraelectric phase for all $Na(H_{1-x}D_x)_3(SeO_3)_2$ crystals which supports the suggestion on first order of the transition.

,. Chem. Solids Pergamon Press 1969. Vol. 30, pp. 63–68. Printed in Great Britain.

reco
volt
the

PHOTOCONDUCTIVITY IN CADMIUM IODIDE

R. M. YU*
H. H. Wills Physics Laboratory, University of Bristol, England

(*Received* 2 *May* 1968)

Abstract—Experimental measurements of the spectral distribution of photoconductivity in single crystals of cadmium iodide have been compared with the distribution calculated from De Vore's theory to estimate the phenomenological parameters governing the photosensitivity of this material. For solution grown cadmium iodide crystals subjected to an excitation rate of 5×10^{16} photons $sec^{-1} m^{-2}$ the lifetime of photo-electrons is of the order of 1·5 nsec and the surface recombination velocity is estimated to be of the order of 400 km sec^{-1}. The photon energy corresponding to peak photoconductivity is 3·2 eV at 290°K. It decreases linearly with temperature at the rate of $-1{\cdot}5 \times 10^{-3}$ $eV °K^{-1}$, which is similar to the temperature shift of the optical absorption edge. At peak photosensitivity, the photocurrent is proportional to the 0·7th power of the light intensity over two orders of magnitude of illumination intensity. The photocurrent-light intensity variation also depends on the photon energy. For the same value of photocurrent the rise and decay times are shorter for photocurrents excited by photons of higher energy.

1. INTRODUCTION

CADMIUM IODIDE is a typical layer-structure ionic solid. The basic structural unit is a sandwich consisting of two layers of close-packed iodide ions and one layer of Cd^{++} ions lying in the octahedral interstices between the iodide ions. The cleavage plane is the plane which separates two iodide layers containing no Cd^{++} ions[1]. Fotland[2] first reported that photocurrents could be observed in cadmium iodide single crystals illuminated with photons in the energy range between 3·0 and 3·3 eV. In the present work photoconductivity in cadmium iodide is studied quantitatively and in much greater detail. In particular, the variation of photosensitivity with photon energy is reported and a well-defined photosensitivity peak is found at about 3·2 eV (3874 Å): the exact photon energy of the peak is slightly dependent on the thickness of the crystal. To interpret the nature and shape of the photoconductivity spectral curve it is necessary to know the spectral distribution of optical absorption for this material. Although photocurrents in most photoconductors are attributed to free charge carriers generated by band-to-band transitions, in some photoconductors the dominant process may involve the dissociation of excitons. Recent optical absorption studies on cadmium iodide have revealed many interesting exciton features in the high energy part of the absorption spectrum[3–5]; but no exciton lines have been observed near 3·2 eV by any of these workers although Gross and Kaplyanskii[6] did report one line in a much earlier paper. Absorption near 3·2 eV is now attributed to indirect band-to-band transitions and the present photoconductivity results are interpreted on this model.

2. EXPERIMENTAL TECHNIQUES

Photoconductivity measurements are made on cadmium iodide single crystals grown by allowing aqueous solutions of 5*N*-pure cadmium iodide (principal impurity being Si, 5 ppm) to evaporate in a light-tight desiccator. The crystallization process takes place in about 2 weeks. It is important to keep the solution in complete darkness, as cadmium iodide slowly decomposes when exposed to sun-light. Cadmium iodide forms

---

*[*Present address*. Physics Department, University of Hong Kong, Hong Kong.

colourless, transparent, hexagonal crystal platelets with areas up to 1 cm^2 and thicknesses between 10 and 1000 μm.

The cadmium iodide crystal is mounted on a P.T.F.E. holder. Electrical contacts to the crystal are obtained by cementing two corners of the crystal onto nickel electrodes with colloidal silver solution. These nickel-silver contacts are ohmic since the photocurrent and ionic current are both found to vary linearly with the electric field over a wide range of electric field strength (from 1 kV m^{-1} up to at least 100 kV m^{-1}).

A quartz lens focusses the light beam from a 2kW xenon discharge lamp onto the input slit of a double quartz-prism monochromator. The bandwidth of the monochromator is 40 Å at the cadmium iodide photoconductivity peak at 3900 Å (at 3600 and 4300 the bandwidths are 30 and 55 Å respectively). The light beam coming out of the monochromator is focussed by a second quartz lens onto the crystal surface. A piece of optically flat quartz plate is interposed at an angle of 45 deg between the monochromator and the second condensing lens to reflect 4·6 per cent (at 4000 Å) of the light intensity onto a Mullard type 150 u.v. photocell, so that the light intensity incident on the crystal can be monitored. The absolute and spectral sensitivities of the photocell have been calibrated by the National Physical Laboratory. To determine the true spectral variation of photosensitivity, one has to ensure that the number of photons incident on the crystal per sec per unit area remains unchanged while the photon energy is varied. This is achieved by monitoring the photocell current and adjusting a neutral density filter interposed between the light source and the monochromator. This method is preferable to altering the slit width as a means of changing the light intensity, since it has the advantage of keeping the bandwidth and the cross-sectional area of the outgoing light beam constant. The same technique is also used to study the variation of photocurrent with light intensity.

3. SPECTRAL DEPENDENCE OF PHOTOCONDUCTIVITY

3.1 *Theory*

De Vore[7] has presented a theoretical analysis of photoconductivity spectral response curves taking into account the optical absorption coefficient, the surface and volume recombination processes and the diffusion of photo-electrons due to a concentration gradient. He considers the case in which a light beam of intensity I photons per sec per unit area is incident perpendicularly on the surface of a photoconductor of unit area and thickness d. Assuming the photons have unit quantum efficiency in producing free electron-hole pairs and neglecting any reflection from the back surface of the photoconductor, he finds that the number of conduction electrons produced in the photoconductor is given by

$$N = \frac{I'\tau(1-e^{-Z})}{1+\xi\coth(\frac{1}{2}\lambda)} \times \left\{1+\frac{\xi\lambda[\lambda\coth(\frac{1}{2}\lambda)-Z\coth(\frac{1}{2}Z)]}{\lambda^2-Z^2}\right\} \quad (1)$$

where $I' = I(1-R)$

R = reflectivity of the surface

τ = electron lifetime

$Z = d\alpha = \lambda\zeta$

α = absorption coefficient of the photoconducting material

$\lambda = d/(D\tau)^{1/2}$

$\zeta = \alpha(D\tau)^{1/2}$

D = diffusion constant of conduction electrons, related to mobility by Einstein relation

$\xi = S(\tau/D)^{1/2}$

S = surface recombination velocity

$$= \frac{\text{recombination rate per unit area at the surface}}{\text{excess concentration just below the surface}}$$

De Vore has computed $N/(I'\tau)$ for a wide range of parameters and plotted the corresponding photosensitivity spectral response curves. The following limiting cases of equation (1) are of interest:- (A) if surface recombination is negligible compared with volume recombination, i.e. if $S \ll (D/\tau)^{1/2}$ then

$$N \to I'\tau(1-e^{-Z})$$

$$\doteqdot (\text{total number of absorbed photons}) \times (\text{electron lifetime}). \qquad (2)$$

In this case N increases monotonically from zero for small values of Z to $I'\tau$ for large values of Z. There is no peak in the photosensitivity spectral curve; (B) if surface recombination is large compared with volume recombination, i.e. if $S \gg (D/\tau)^{1/2}$, then

$$N \to 0 \quad \text{as} \quad Z \to 0$$

$$N \to \frac{I'\tau}{\xi \coth(\frac{1}{2}\lambda)} \text{ for large } Z. \qquad (3)$$

N has a maximum value for intermediate values of Z, the Z-value corresponding to maximum N depends on λ and ξ.

3.2 *Experimental results and discussion*

The experimentally observed spectral variation of photocurrent in a 400 μm-thick cadmium iodide single crystal at room temperature is shown in Fig. 1. In order to compare the experimental results with De Vore's theoretical prediction, it is necessary to plot the photocurrent as a function of the parameter $Z = \alpha d$, rather than the photon energy. Using Greenaway and Nitsche's[3] values of absorption coefficient the photoconductivity results on the 400 μm-thick crystal are replotted as a function of Z in Fig. 2. The fairly sharp photosensitivity peak observed suggests that ξ is of the order of 1000. Assigning a value of 1000 to ξ, it is found from equation (1) that when $\lambda = 4$, the position of the theoretical photosensitivity peak will coincide with that of the experimental peak at $Z = 2$. Figure 2 shows that the theoretical curve fits the experimental curve only approximately, this is because:- (1) De Vore's theoretical analysis does not take all the relevant factors into consideration. For example, the effect of direct recombination of charge carriers at high densities is neglected; (2) the absorption coefficient α is difficult to determine accurately when it is smaller than 10 cm^{-1} and larger than 2000 cm^{-1}. Any inaccuracy in the absorption coefficient data will change the shape of the experimental curve; (3) the flat shoulder located at $Z = 10$ to 20 in the experimental curve is a genuine feature of cadmium iodide photoconductivity spectral distribution curves. It cannot be explained satisfactorily by the simple De Vore theory. The nature of this shoulder and the photoconductive behaviour of cadmium iodide at higher excitation energies are being investigated by Wright (Private communication) at the University of Warwick.

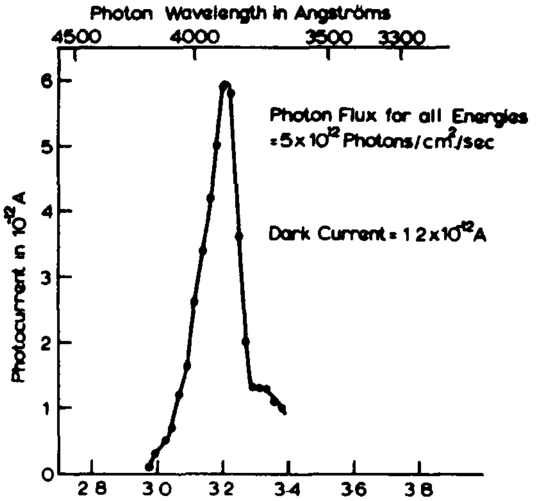

Fig. 1. Spectral distribution of photocurrent in a 400 μm-thick cadmium iodide single crystal.

The quantitative measurements of photoconductivity as a function of incident photon energy and intensity enables the carrier lifetime and surface recombination velocity to be calculated. For a photoconductor of area $a \times b$ and thickness d, the resultant photocurrent J due to N free electrons in an electric field E along b direction is

$$J = aN\mu eE \qquad (4)$$

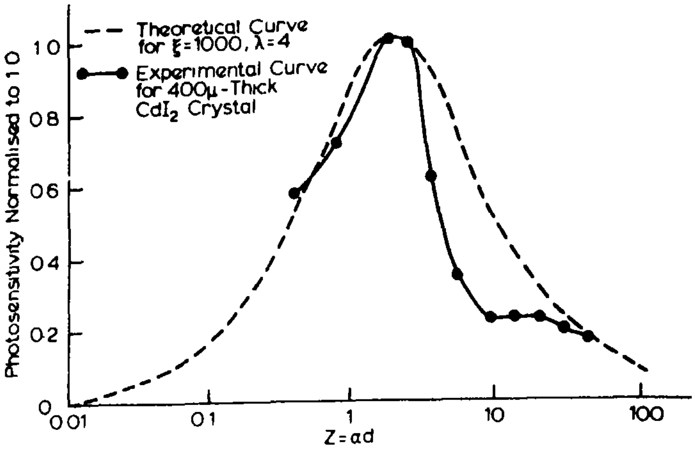

Fig. 2. Comparison of experimental and theoretical photosensitivity curves.

where e = electronic charge = $1{\cdot}6\times10^{-19}$C: μ = mobility of conduction electrons. The data for the 400 μm-thick cadmium iodide crystal are as follows:

$$a = 0{\cdot}55\ \text{cm}$$
$$b = 0{\cdot}35\ \text{cm}$$
$$d = 400\ \mu\text{m}$$
$$R = 0{\cdot}25$$
$$I = 5\times10^{16}\ \text{photons sec}^{-1}\ \text{m}^{-2}$$
$$Z_{\text{max}} = 2$$
$$\xi = 1000$$
$$\lambda = 4$$
$$J_{\text{max}} = 6\times10^{-12}\ \text{A}$$
$$E = \frac{100\ \text{V}}{0{\cdot}35\ \text{cm}} = 286\ \text{V cm}^{-1}.$$

From a survey of photoconductive properties of ionic solids in general, it is reasonable to assume that in cadmium iodide, as in other ionic solids, the dominant charge carriers liberated by photo-excitation are conduction electrons with a mobility of the order of 100 cm^2 V^{-1} sec^{-1} (the electron mobilities of CdS, ZnO and AgBr are 200, 180 and 240 cm^2 V^{-1} sec^{-1} respectively). The electron mobilities of all known photoconducting ionic solids do not differ from 100 cm^2 V^{-1} sec^{-1} by more than one order of magnitude[8]. Equation (4) gives the number of photoelectrons in one square metre of the 400 μm-thick crystal as

$$N = \frac{J_{\text{max}}}{ea\mu E} = 2{\cdot}4\times10^7. \tag{5}$$

By substituting this value of N and the other experimental data into equation (1) the electron lifetime τ is found to be 1·5 nsec. Since the quantity $N/(I'\tau)$ varies only slightly with the parameters λ, ξ and μ, uncertainties in these parameters do not change the value of τ by more than one order of magnitude. The surface recombination velocity is found from the definition of ξ to be of the order of 400 km sec^{-1}.

The variation with temperature of the photon energy corresponding to peak photoconductivity in cadmium iodide has been studied in the temperature range 287° to 420°K. The results show that in the temperature range studied the photon energy of the photoconductivity peak decreases approximately linearly with temperature at a rate of $-(1{\cdot}5\pm0{\cdot}2)\times10^{-3}$ eV°K^{-1}. This is similar to the temperature shift of the optical absorption edge[3].

4. DEPENDENCE OF PHOTOCURRENT ON ILLUMINATION INTENSITY

Moss[9] has shown that for a model similar to the one considered in Section 3, the photocurrent increases linearly with light intensity at low levels of illumination, but only increases as the cube root at high light intensities. For a photoconductor with a large surface recombination velocity, there is an intermediate region in which the photocurrent varies as the square root of light intensity, but ultimately it increases as the cube root at high illumination intensities.

In this work the dependence of cadmium iodide photocurrents on the excitation energy as well as the illumination intensity has been studied. Figure 3 shows the relation between photocurrent and light intensity (on a log–log plot) at three different excitation energies for a 954 μm-thick crystal. For 3 eV(4130 Å) photons on the low energy side of the photosensitivity peak, the slope β in the photocurrent–light intensity plot is equal to 0·8. For 3·12 eV (3950 Å) photons corresponding to peak photosensitivity, β is equal to 0·7. For 3·23 eV(3820 Å) photons on the high energy side of the photosensitivity peak, β changes from 0·5 to 0·3 as the illumination intensity increases. Thus β is a function of the energy (i.e. the absorption coefficient of the crystal) as well as the intensity of the incident photons. The cause of this variation in the value of β as a function of excitation energy is attributed to variations in the carrier lifetime at different excitation energies. Even for the same illumination intensity, a higher concentration of charge carrier is generated by the high energy photons than the low energy photons, since the former are strongly absorbed in a thin layer near the crystal surface. The carrier lifetime is consequently shortened by the increased surface recombination and direct recombination. This accounts for the observed decreases in the value of β from 0·8 to 0·7, 0·5 and 0·3 for the three excitation energies. The general behaviour of photocurrent–light intensity relations in cadmium iodide is thus quite well accounted for by the theory developed by Moss[9]. The fact that photocurrents excited by photons of different energies have different values of β implies that the photoconductivity spectral curve is a function of the intensity of illumination as well as the other crystal parameters such as thickness and absorption coefficient.

5. TRANSIENT RESPONSE OF PHOTOCURRENTS

Investigations on transient behaviour of photocurrents in cadmium iodide at room

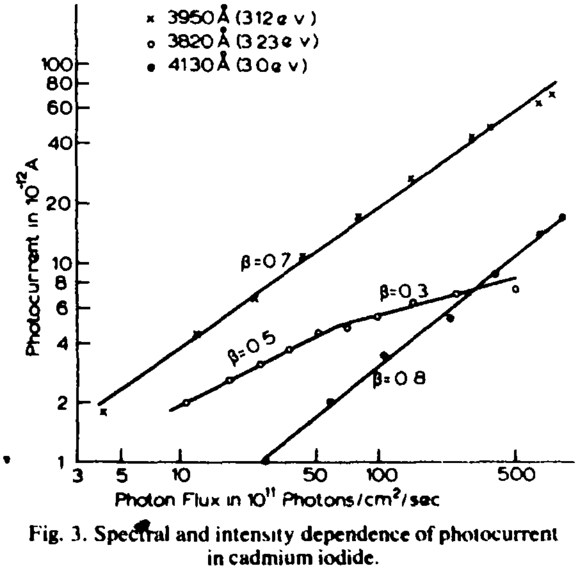

Fig. 3. Spectral and intensity dependence of photocurrent in cadmium iodide.

temperature show that the response times (rise and decay times) are of the order of one minute (electrometer response time less than one second) as compared to the calculated electron lifetime of 1·5 nsec. This shows that the loss of conduction electrons by recombination is replenished by electrons thermally liberated from trapping centres so that the observed decay time is much longer than the electron lifetime. For the same magnitude of photocurrent, the response times are shorter for photocurrents excited by photons of higher energy, that is, by photons which are most strongly absorbed by the cadmium iodide crystal (see Fig. 4). This observation supports the view that the recombination rate at the surface is higher than that in the volume of the photoconductor (refer Section 3).

Acknowledgements—I should like to thank Professor A. J. Forty for encouragement and general supervision of this work, Professor F. C. Frank, F.R.S., Mr. D. F. Gibbs and Dr. M. R. Tubbs for their interest and valuable discussion. Dr. Tubbs has also kindly read the manusscript in detail and made many constructive suggestions. I am grateful to the staff of the H. H. Wills Physics Laboratory for their hospitality and the Sir Robert Black Trust Fund Committee of Hong Kong for the award of a grant.

REFERENCES

1. WELLS A. F., *Structural Inorganic Chemistry*, 3rd Edn Oxford University Press, London (1962).
2. FOTLAND R. A., *J. chem. Phys.* **33**, 956 (1960).
3. GREENAWAY D. L. and NITSCHE R., *J. Phys. Chem. Solids*, **26**, 1445 (1965).
4. BRAHMS S., *Phys. Lett.* **19**, 272 (1965).
5. TUBBS M. R., *J. Phys. Chem. Solids* **29**, 1191 (1968).
6. GROSS E. F. and KAPLYANSKII A. A., *Zh. tekh. Fiz.* **25**, 2061 (1955).
7. De VORE H. B., *Phys. Rev.* **102**, 86 (1956).
8. BUBE R. H., *Photoconductivity of Solids*, Wiley New York (1960).
9. MOSS T. S., *Optical Properties of Semiconductors*. Butterworths, New York (1961).

Postscript. The Editor kindly draws my attention to the fact that Dr. D. L. Greenaway of RCA Laboratories, Zurich, has recently observed an exciton absorption peak at 3·24 eV in cadmium iodide at 77°K. The temperature coefficient of the exciton is $-2{\cdot}1 \times 10^{-4}$ eV°K^{-1} compared to $-1{\cdot}26 \times 10^{-3}$ eV°K^{-1} for the absorption edge. As the temperature is raised the absorption edge at 3·48 eV smoothly approaches the 3·24 eV peak and completely covers it at 300°K. In the light of this new information the observed photocurrent in cadmium iodide at room temperature can arise from both band-to-band transitions and dissociation of excitons. Low temperature photoconductivity measurements are being undertaken by Wright (Private communication) to separate these contributions. Since the observed temperature coefficient of the photoconductivity peak agrees with that of the absorption edge and is one order of magnitude larger than that of the exciton, the room temperature photoconductivity peak should be essentially band-to-band transition in origin. The shoulder located at $Z = 10$ to 20 in Fig. 2 could be due to room temperature broadened exciton. I am most grateful to Dr. D. L. Greenaway for making available to me his unpublished new results on optical absorption of cadmium iodide and for his helpful comments on this paper.

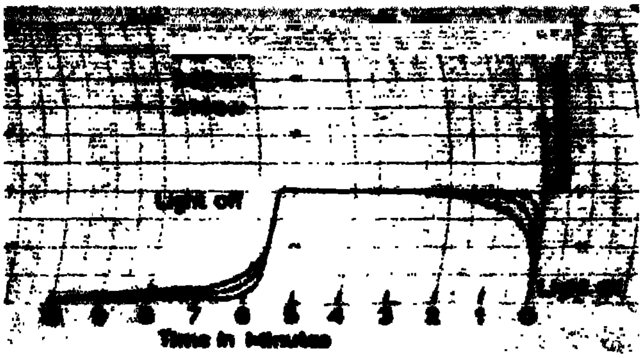

Fig. 4. Transient responses of cadmium iodide photocurrents excited by photons of various energies.

J. Phys. Chem. Solids **Pergamon Press 1969. Vol. 30, pp. 69–72. Printed in Great Britain.**

THE LOW TEMPERATURE HEAT CAPACITY OF PLATINUM*

W. T. BERG
Solid State Division, Oak Ridge National Laboratory, Oak Ridge, Tenn. 37830, U S.A.

(*Received* 31 *January* 1968; *in revised form* 11 *April* 1968)

Abstract – The heat capacity of platinum has been measured between 2·6° and 20°K. Analysis of the results gave $\gamma = 6{\cdot}59 \times 10^{-3}$ J/g-atom deg^2 and 240·1°K for the Debye temperature at 0°K.

1. INTRODUCTION

THE HEAT capacity of platinum at low temperatures has been the subject of several investigations[1–5]. There are, however, significant differences in the value of γ, the electronic coefficient of the heat capacity, and the value of the Debye temperature at 0°K. While the results of this research were being prepared for publication, Shoemake and Rayne[6] published the results of their measurements on platinum between 1·4° and 100°K. As will be seen later there is reasonable agreement between the two values of γ; however, there remains some uncertainty as to $\theta_0{}^c$.

2. SAMPLE

The calorimetric sample consisted of eight rods, ¼ in. dia. and 1 in. long, supplied by Materials Research Corporation, Orangeburg, New York. The rods had been subjected to a three-pass electron-beam zone-refining procedure by the supplier. Table 1 gives the results of the spectrographic analysis performed by the Spectrochemical Laboratory of ORNL.

The platinum sample was treated with warm concentrated HCl, thoroughly washed with distilled water, and dried in an air stream. The rods were then vacuum annealed (1×10^{-5} Torr.) at 1000°C for 24 hr. After cooling, the rods were placed in the calorimeter vessel and the vessel evacuated to 1×10^{-6} Torr. and then sealed off with $1{\cdot}6 \times 10^{-6}$ g-atom of helium gas for heat conduction. The sample weight was 135·982 g.

Table 1. *Spectrographic analysis of the platinum sample* (*Values given are in ppm by weight*)

Al	15	Fe	30	Ru	0·5
Au	<10	Ir	<2	Si	90
Ca	2	Mg	1	Sn	0·2
Nb	1	Mn	1	V	1
Co	0·1	Ni	4	W	1
Cr	3	Pd	2	Zr	1
Cu	1	Rh	15		

3. EXPERIMENTAL

The adiabatic calorimeter assembly is similar to the one described by Morrison *et al.*[7] except that a copper can is used as a helium reservoir in place of a Simon bomb and the adiabatic shield is automatically controlled[8]. The working thermometer is an Allen Bradley nominal 10 Ω, ¼ watt carbon resistor. The derivation of the temperature scale has been previously described[9].

4. RESULTS AND DISCUSSION

The experimental results are collected in Table 2. Below 4°K the inaccuracy of the data is thought to be no worse than ±2 per cent, decreasing to ±0·5 per cent above 10°K. In the region 10–20°K the results of Clusius

---

*Research sponsored by the U.S. Atomic Energy Commission under contract with Union Carbide Corporation.

Table 2. The heat capacity of platinum in J/g-atom deg θ_D (Calculated from the experimental data using $\gamma = 6{\cdot}59 \times 10^{-3}$ J/g-atom deg^2)

T°K	Cp	θ_D	T°K	Cp	θ_D
2·637	0·02005	237·2	9·763	0·2151	228·9
2·962	0·02322	238·9	10·178	0·2394	228·3
3·147	0·02520	238·4	10·959	0·2902	227·2
3·438	0·02844	239·1	11·290	0·3142	226·8
3·700	0·03171	237·8	12·137	0·3817	225·8
3·884	0·03400	238·5	12·346	0·4003	225·5
4·286	0·03971	237·2	13·268	0·4877	224·7
4·348	0·04054	237·8	13·436	0·5052	224·5
4·824	0·04812	237·3	14·342	0·6058	223·8
4·885	0·04929	236·6	14·452	0·6187	223·7
5·304	0·05688	236·5	15·358	0·7342	223·1
5·496	0·06070	236·3	15·440	0·7454	223·1
5·813	0·06765	235·2	16·299	0·8697	222·5
6·150	0·07546	234·8	16·579	0·9117	222·3
6·327	0·07971	234·8	17·259	1·020	222·3
6·815	0·09294	234·0	17·694	1·094	222·1
7·040	0·09984	233·2	18·239	1·195	221·8
7·675	0·1209	232·0	18·786	1·296	221·7
7·969	0·1315	231·8	19·247	1·388	221·6
8·689	0·1612	230·6	19·900	1·523	221·5
9·025	0·1769	230·0	20·300	1·609	221·4

and co-workers[10] are about 7 per cent higher at 10°K, and at 20°K they are 2 per cent lower than the results reported here. The earlier data of Kok and Keesom[5] are 1–3 per cent higher below 9°K, and above 9°K they are 2–5 per cent lower than the present results. Direct comparison with the results of other investigators[1–4, 6] can only be made on the basis of derived parameters.

At low temperatures the heat capacity of a simple metal can be written as

$$C_v = \gamma T + aT^3 + bT^5 + cT^7 + \dots \qquad (1)$$

where γT is the electronic contribution to the total heat capacity. The remaining terms in the series give the lattice contribution. The coefficients a, b and c are related to the coefficients of the series expansion for the lattice frequency spectrum at low frequencies. In particular, a gives the Debye temperature at 0°K by means of the relation

$$\theta_0^c = \left(\frac{1943{\cdot}7}{a}\right)^{1/3} \qquad (2)$$

where a is in units of J/g-atom deg^4.

The usual practice in analyzing calorimetric data on metals is to plot C_v/T vs. T^2 and then fit a straight line to the graph. The intercept at $T^2 = 0$ gives γ and the slope of the line gives a. This method gives good results if the data extend to very low temperatures where the effects of the dispersive coefficients, b and c, are small. Barron and Morrison[11] have shown the importance of including terms beyond T^3 in order to obtain accurate estimates of θ_0^c. This is fairly straightforward for insulators; however, in the case of metals there is the added complication of the electronic term. A more sensitive method of treating the data is to plot $(C_v - \gamma T)/T^3$ against T^2. This type of plot is shown in Fig. 1 using the experimental results of this investigation with the γ values given by Dixon and coworkers[1] and by Ramanathan and Srinivasan[3] from measurements in the range $1 < T < 4{\cdot}2$. The results below 5°K show large changes in slope, indicating that in one case γ has been underestimated and the lattice

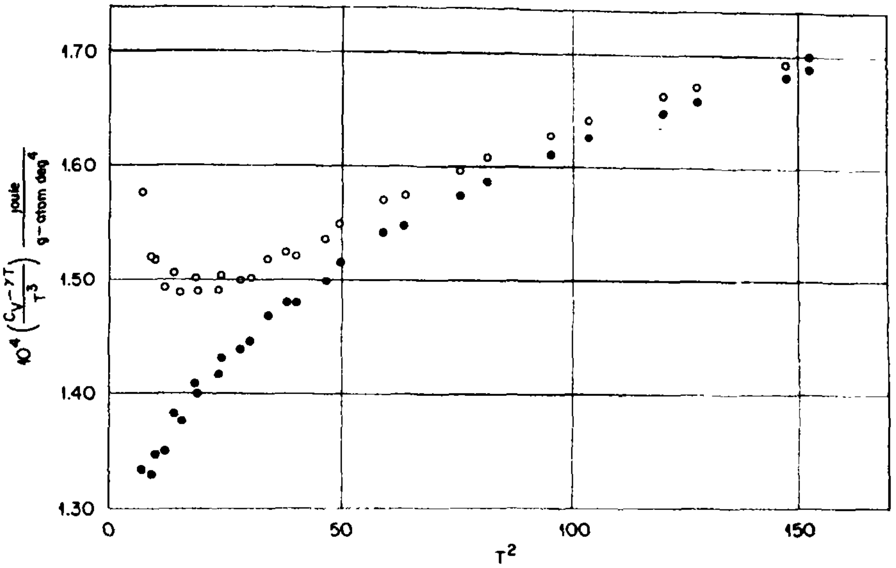

Fig. 1. Graph of $(C_v-\gamma T)/T^3$ vs. T^2. Open circles $\gamma = 6{\cdot}507 \times 10^{-3}$ J/g-atom deg^2 from Dixon *et al.*[1]. Filled circles $\gamma = 6{\cdot}676 \times 10^{-3}$ J/g-atom deg^2 from Ramanathan and Srinivasan[2].

heat capacity is too large while in the other case γ is too large.

Although the present experiments extended to only 2·6°K, an attempt was made to extract γ from the data. The parameters in equation (1) were determined by a least-squares analysis of the data below 7°K. Numerical values of the coefficients are given with the values of other investigators in Table 3. The value for c is not included because the

Table 3. Parameters derived from heat capacity and elastic constant measurements

	$\gamma \times 10^3$ (J/g-atom deg^2)	$a \times 10^4$ (J/g-atom deg^4)	θ_0^c (°K)	$b \times 10^7$ (J/g-atom deg^6)	θ_0 (elastic)
This work	6·59 ± 0·03	1·404 ± 0·040	240·1 ± 2·3	2·3 ± 1·5	
Shoemake and Rayne[a]	6·56 ± 0·03		234·4 ± 2·5	1·8 ± 2	
Dixon *et al.*[b]	6·507 ± 0·006		234·9 ± 0·4		
Budworth *et al.*[c]	6·41 ± 0·026		235·3 ± 1·3		
Ramanathan and Srinivasan[d]	6·676 ± 0·042	1·410 ± 0·058	239·7 ± 3·1		
Rayne[e]	6·90 ± 0·33				
Kok and Keesom[f]	6·74				
MacFarlane *et al.*[g]					237·8 ± 1·5

[a] Reference [6].
[b] Reference [1].
[c] Reference [2].
[d] Reference [3].
[e] Reference [4].
[f] Reference [5].
[g] Reference [12].

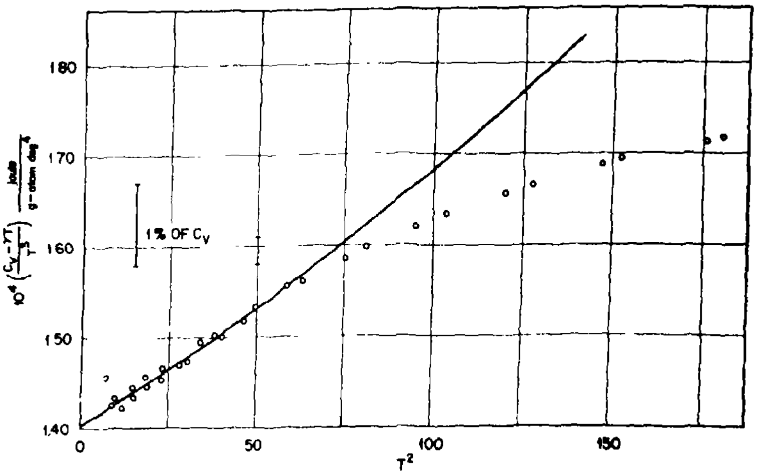

Fig. 2. Graph of $(C_v-\gamma T)/T^3$ vs. T^2 with $\gamma = 6{\cdot}59\times10^{-3}$ J/g-atom deg^2 The vertical bars show the effect of a 1 per cent change in C_v, keeping the electronic contribution constant The smooth curve shows the fit of a least-squares analysis to the experimental points below 7°K.

error limits make its value, $5(\pm10)\times10^{-10}$ J/g-atom deg^8, uncertain. The agreement with $\theta_0{}^C$ obtained by Ramanathan and Srinivasan must be fortuitous in view of the different values deduced for γ.

Figure 2 again shows $(C_v-\gamma T)/T^3$ vs. T^2 using the γ calculated from the data ($\gamma = 6{\cdot}59\times10^{-3}$ J/g-atom deg^2), and the smooth curve shows the resulting fit of the least-squares analysis. The large change in slope has been removed and the extrapolation goes smoothly to $T^2 = 0$. Included in Table 2 are Debye temperatures calculated from the experimental heat capacities using the same value of γ as in Fig. 2.

As seen from Table 3 the agreement with the recently published work of Shoemake and Rayne[6] is almost satisfactory. They carried out experiments between 1·4° and 100°K and analyzed their data with the same method used in this work. The values of γ agree within the uncertainties shown; however, the values of $\theta_0{}^C$ differ by over 2 per cent. Also listed in Table 3 is θ_0(elastic) determined by MacFarlane *et al.*[12] from low temperature elastic constant measurements. $\theta_0{}^C$ derived from the present measurements agrees with this value of θ_0 (elastic) within 1 per cent.

Acknowledgements—The author wishes to thank L. C. Templeton for his valuable assistance in all of the experiments and the Spectrochemical Laboratory of ORNL for carrying out the analysis of the platinum sample.

REFERENCES

1. DIXON M., HOARE F. E., HOLDEN T. M. and MOODY D. E., *Proc. R. Soc.* **A285**, 561 (1965).
2. BUDWORTH D. W., HOARE F. E. and PRESTON J., *Proc. R. Soc.* **A257**, 250 (1960).
3. RAMANATHAN K. G and SRINIVASAN T. M., *Proc. Indian Acad. Sci.* **A49**, 55 (1959).
4. RAYNE J. A., *Phys. Rev.* **95**, 1428 (1954).
5. KOK J. A. and KEESOM W. H., *Physica* **3**, 1035 (1936).
6. SHOEMAKE G. E. and RAYNE J. A., *Phys. Lett.* **26A**, 222 (1968).
7. MORRISON J. A., PATTERSON D. and DUGDALE J. S., *Can. J. Chem.* **33**, 375 (1955).
8. GAYLE T. M. and BERG W. T., *Rev. scient. Instrum.* **37**, 1740 (1966).
9. BERG W. T., *Phys. Rev.* **167**, 583 (1968).
10. CLUSIUS K., LOSA C. G. and FRANZOSINI P., *Z. Naturf.* **12**, 34 (1957).
11. BARRON T. H. K. and MORRISON J. A., *Can. J. Phys.* **35**, 799 (1957).
12. MacFARLANE R. E., RAYNE J. A. and JONES C. K., *Phys. Lett.* **18**, 91 (1965).

Phys. Chem. Solids Pergamon Press 1969. Vol. 30, pp. 73–88. Printed in Great Britain.

A DIELECTRIC STUDY OF THE SYNTHETIC LINDE TYPE-*A* ZEOLITE–I. EXPERIMENTAL METHODS AND THE LINDE 5-*A*-WATER SYSTEM

BRIAN MORRIS*

Edward Davies Chemical Laboratory, University College of Wales, Aberystwyth, U. K.

(*Received* 10 *April* 1968)

Abstract–A system, designed particularly for the study of the dielectric properties of zeolites on the adsorption of vapours, is described. It enables compacted disc samples to be dehydrated at 450°C and 10^{-5} Torr., and then measured, in the frequency range 5 Hz–148 kHz, with any equilibrium pressure, up to 760 Torr., of most gaseous adsorbates.

Measurements of the permittivity and dielectric loss factor have been made for the Linde Molecular Sieve zeolite type 5-*A* in the dehydrated state and with adsorbed water at all water contents up to saturation. By the use of conventional dielectric measuring techniques the water saturated material has been measured in the frequency range 5 Hz–8·5 GHz.

A well defined region of dielectric absorption, occurring in the low frequency (< 148 kHz) range, has been ascribed to movement, within the zeolite cavities, of the interstitial cations. The behaviour of this absorption with variation of water content and temperature has been investigated. A further low frequency absorption, attributed to the adsorbed water, has been observed and its behaviour with water content and temperature studied. The results suggest that the total dipole polarisation due to the water relaxes in two stages: one is of a low frequency ice-like character, the other, relatively much smaller dispersion, gives absorption(s) throughout the MHz region.

The permittivity increment shows a sequence of linear increases with water content which have been interpreted as indicating coverage of the first and second most active adsorption sites in the zeolite cavities.

Possible mechanisms of these processes are discussed.

INTRODUCTION

THE ZEOLITES offer unusually interesting models of molecular and ionic behaviour with their essentially rigid anionic aluminosilicate framework regularly incorporating molecularly large cavities and channels in which different cations can be introduced and where they can move between preferred positions. A great variety of molecules, limited in size by the channels, can be adsorbed and their mobility in these systems has been studied by a number of methods in recent years: n.m.r. [1], infra-red [2], neutron scattering [3], etc.

In the absence of adsorbates, dielectric studies might well establish aspects of cation movements. Non-polar adsorbates should influence such movements–and the strong ionic fields might detectably polarise the adsorbates. With polar adsorbates a wide spectrum of interactions might be revealed by dielectric studies. Perhaps experimental difficulties have limited such studies, especially over significant frequency ranges. Lebrun[4] found that the type-*A* zeolites gave complex dielectric spectra, but there was little control of the adsorbate content in that study and few conclusions are established by the results. Recently Dubinin *et al.*[5] have published accounts of systematic dielectric studies of the type-*A* zeolite where the adsorbate content has been well controlled. Relevant aspects of these results will be referred to later. One special feature of the zeolites is their remarkable avidity for water. So pronounced an aspect of their behaviour is this that the present studies almost necessarily commenced

---

*[*] *Present address:* Division of Applied Chemistry, National Research Council of Canada, Ottawa 7, Ontario, Canada.

with a survey of the dielectric properties of a typical zeolite-water system. In suitable instances the permittivity (ϵ') and dielectric loss (ϵ'') have been measured from 5 Hz to 8·5 GHz.

EXPERIMENTAL

Several experimental difficulties are encountered in a dielectric study of zeolites, the two major problems being the form of the sample and the adsorbate content control. Dubinin used powder samples, as have many other workers in dielectric studies of adsorbent-adsorbate systems. While this method simplifies the measuring cells required and facilitates the achievement of the high vacua and temperatures required for activation of adsorbents, it greatly increases the possible occurrence of interfacial polarisation and the method requires the use of equations, such as the Böttcher relation[6], to approximate to the permittivity and loss factor of the bulk crystal.

In the particular case of the type-*A* zeolite it is impossible to obtain single crystals of the size required for dielectric studies and in the present work compacted discs of the crystalline powder have been used. It has been well established that compacted discs give dielectric parameters quantitatively comparable (±2 to ±5 per cent) with the bulk material solidified from the melt for organic materials including polymers. Such materials are generally relatively soft and tend to flow under applied pressures. The hardness of the zeolites reduces the degree of compacting in a pressed disc and so the attainment of a density matching that of the bulk crystal. No data are available in the literature comparing the permittivity and loss of single crystals with those of compacted discs of hard crystalline inorganic materials. However Ducros[7] showed that compacted discs of the natural zeolite chabazite gave dielectric parameters comparable with the bulk crystal (to within ±2 per cent).

Heterogeneity in compacted discs can occur at the surface of the disc and at particle-particle interfaces due to local distortion (or destruction) of the lattice by the high applied pressures[8]. Freeman and Stamires investigated the difficult problem of compacting zeolite specimens[9] and, using more severe conditions than those of the present work, did not find any structural damage when the powder was pressed with only small amounts of adsorbed water present; large amounts of adsorbed water did lead to structural damage. They have patented[10] a technique which presses the zeolite powder at a temperature of 150°–200°C under a vacuum of 10^{-2} Torr. for 15 mins at a pressure greater than 10,000 p.s.i.; using this method they achieved densities close to 90 per cent of the single crystal value. No structural damage occurred until pressures above 50,000 p.s.i. were used[9].

In the present work the crystalline powder, after dehydrating at 450°C for 24 hr, was pressed in an accurately machined die of 50 mm dia. with an applied pressure of approximately 15,000 p.s.i. This gave discs which had densities of about 75 per cent of the X-ray crystal density. Large amounts of adsorbed water reduced the density of the discs obtained; samples almost saturated with water gave densities only 50 per cent of the X-ray value. Compacted co-axial samples of external dia. 14·10 mm and internal dia. 6·10 mm were also prepared. The smaller surface area enabled greater pressures to be applied and with pressures of 40,000–45,000 p.s.i. compacts of density 85 per cent of the X-ray crystal density were obtained. Vacuum pressing was not tried. Heating the die did not result in denser compacts and all pressing was carried out at room temperature.

Pressing the zeolite powder to the maximum extent (i.e. for co-axial line samples) did not affect the adsorptive properties. The samples were allowed to saturate by standing over distilled water: determination of the amount sorbed, by ignition at 1000°C, showed that the total intracrystalline volume was available to the water. This also indicated that structural damage was minimal. In view of the lower pressures used in compacting the 50 mm disc samples it was unlikely that structural damage occurred and this source of heterogeneity has been assumed to be absent.

The presence of 15–25 per cent air in the compacted samples could also give rise to spurious effects in the dielectric properties. Good reproducibility was obtained between samples of less than 70 per cent density and samples of more than 80 per cent density suggesting that the presence of air, presumably in the form of voids and fissures in the compacted disc, had little effect on the dielectric properties. A Maxwell–Wagner loss process arising from this source would probably be small and its detection in the presence of the large reproducible losses of the zeolite/adsorbate system was unlikely. The major effect of the voids or air gaps is to reduce the permittivity and loss relative to those for the ideal zeolite lattice in essentially the same ratio as the density. As, however, experimental evidence for the validity of a density correction is not immediately available in these systems, no such correction has been applied to the data.

A further source of heterogeneity in synthetic zeolites arises from the possible occlusion of sodium aluminate in the sodalite cages of the type-*A* structure. It is well established that $NaAlO_2$ can be occluded in varying degrees up to a maximum of one molecule of $NaAlO_2$ per unit cell[11, 12]. While the first two causes of heterogeneity occur during the preparation of the sample for measurement and can, to some extent, be eliminated, the occluded sodium aluminate presents a difficult problem in that it cannot be removed. The presence of such an ion-pair can affect the dielectric properties considerably since, although it is unable to escape from the sodalite cage, it is conceivably free to rotate within the cage and can be expected to give rise to dielectric dispersion.

The second experimental problem, that of adsorbate content control, varies considerably with the measuring procedure used. In the present work measurements have been made over the frequency range 5·25 Hz to 8·5 GHz using the following equipment.

(i) Thompson Bridge[13]; 5·25 Hz to 148 kHz
(ii) Boonton R-X Meter[14]: 0·5 to 140 MHz
(iii) General Radio Slotted Line[15]: 250 to 900 MHz
(iv) Microwave Dielectrometer[16]: 1·0, 3·0 and 8·5 GHz.

With the Slotted Line and Dielectrometer co-axial lines and waveguides are used: these are normally open to the atmosphere and consequently variations of adsorbate content are difficult to eliminate. The use of such lines has currently been limited to the water-saturated material. No significant loss of adsorbed water occurred from these samples in the measuring cells over a period of 48 hr.

For the Boonton Bridge a co-axial cell is used which may be completely enclosed. The water content may be varied in this system by starting with a saturated sample and 'drying' it at a particular temperature, then weighing the water lost from saturation. Samples were 'dried' at various temperatures for at least 24 hr which ensured equilibrium at each stage. Many samples were ignited at 1000°C after measurement to check on the water content; in all cases the agreement was excellent. Water contents down to about 30 per cent of saturation may be measured in this way without significant pick-up of water.

The large majority of measurements have been made on the Thompson Bridge, i.e. at 5·25 Hz–148 kHz. In this case three different methods of measurement and two methods of water content variation were used. In the first instance a conventional two terminal parallel plate capacitor, the plate gap being adjustable by the use of a micrometer screw, was used and the sample measured by a direct substitution method. The water content was varied as for the co-axial line. Aluminium foil electrodes were attached to the sample to reduce electrode and surface conductivity effects. Colloidal silver electrodes were also tried but they gave little improvement over aluminium foil and had the disadvantage of considerably impairing the adsorptive properties of the sample.

Temperature variation with a parallel plate capacitor is difficult and a 30 cm length of co-axial air-line may be conveniently sealed at one end to form a cell which can be immersed in suitable thermostat baths. The water content was controlled as already described: that no moisture pick-up occurred during measurement was adequately checked by finally returning the specimen to its original temperature and remeasuring it. At water contents close to saturation, temperatures above room temperature cannot be employed as loss of water occurs. At other water contents the maximum temperature used was taken as 10°C less than that used to equilibriate the sample when establishing the water content; this prevented further loss of water.

To investigate the zeolites at low water contents, and also with other adsorbates, required the design and construction of a dielectric cell capable of being heated to 450°C and evacuated to 10^{-4}–10^{-5} Torr. A parallel plate capacitor was used to accommodate thin disc samples offering a large surface area to adsorbate vapours. The use of a three terminal cell gave greater accuracy and eliminated the effect of the long leads necessary in the cell. Figure 1 shows the main cell compartment. The glass body is a standard 'Q.V.F. Unequal Tee Piece' of minimum internal dia. 15 cm and height 30 cm; the side arm has an internal dia. 5 cm. The top and the base are of 2 cm Duralumin plate with the surface machined over the area mating with the ground glass ends of the cell body. The seal between the two is effected by 'Q.V.F. Hycar' rubber gaskets 3 mm thick. Exit to the vacuum line is through the side arm via a standard 'Q.V.F. Hose Connector' welded on to the vacuum line. The seal between the main cell side arm and the hose connector ground faces again being affected by a 'Hycar' rubber gasket.

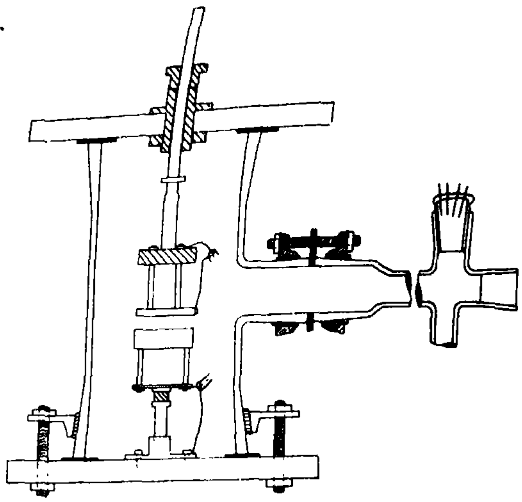

Fig. 1. Section of the vacuum dielectric cell showing exit to vacuum line, electrical lead outlets and general arrangement of the electrodes.

Movement of the top electrode is allowed by a double 'O' ring shaft seal; this, together with the electrode assembly is shown in detail in Fig. 2. The electrode is insulated from the shaft by being suspended from a teflon plate 1·5 cm thick by means of three pillars, the electrode connection being made to one of these pillars. The electrode is 40 mm in dia. and surrounded by a guard ring 8 mm wide, both of stainless steel, the mica insulated gap being 1 mm wide.

The base electrode is 5·75 cm in dia. and is supported from the baseplate as shown in Fig. 1, insulation being provided by the teflon insulator shown in Fig. 2. The cavity in the base electrode, shown in Fig. 2, contains a heater capable of heating the 6·5 mm thick plate forming the electrode surface to about 600°C. The heater can also be used for temperature variation. Since only the base electrode is heated, equilibration depends solely on conduction and consequently takes some considerable time. When the cell is evacuated a considerable temperature gradient develops across the sample but in the presence of a gas temperature equilibration is more readily achieved.

The thermocouple, electrode and heater leads are taken out of the main cell com-

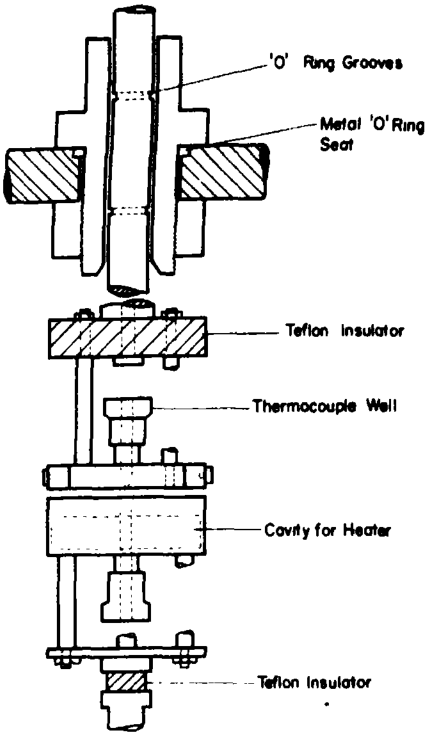

Fig. 2. Electrode assembly and 'O' ring shaft seal which allows movement of the top electrode inside the cell compartment.

partment via the side arm and out of the system through the two B34 cone 'pinch' seals shown in Fig. 1. All leads are insulated with aluminous porcelain insulators. The electrode leads are screened, the earthed screens being attached as shown in Fig. 1.

The whole system can be evacuated to a pressure of 10^{-5} Torr. by a 4-stage oil diffusion pump. A gas handling system permits any required pressure of adsorbate vapour to be established over the sample. The system does not contain an adsorption balance and available isotherms were used to determine the adsorbate contents from the known equilibrium pressures.

Whilst initially desorbing from high adsorbate contents the disc became very mobile, moving about the base electrode surface on a cushion of desorbing vapour. A thin annular ring of aluminium ensured the samples remained on the electrode. The ring, 0·5 mm thick and 3 mm wide, did not affect the capacitance measurements at electrode gaps above 1·5 mm. This was the lower limit of sample thicknesses used.

The sample thickness determines the electrode separation and the two electrodes have no common support for alignment. Accordingly it was important to check the reproducibility of the capacitances of standard samples after repeated movement of the upper electrode and after dismantling of the cell. Measurements of capacitance to 1 in 10^3 showed them reproducible for sample thicknesses from 0·75 to 4·0 mm to ±0·5 per cent. By clamping a micrometer screw to the shaft seal the electrode gap (t) was controlled. Good linear plots were obtained for the measured capacitance ($C_{\text{meas.}}$) against $1/t$ for both air and teflon specimens. Then from the relation,

$$C_{\text{meas.}} = \epsilon' C_0 + C_a$$

where ϵ' is the known permittivity of the teflon (2·08) or air, the cell constants (C_0 and C_a) were obtained. Both C_0 and C_a vs. $1/t$ plots were linear in the thickness range 1·0–3·5 mm. The optimum zeolite sample thickness for the Thompson Bridge range was 2·0 mm. Further checks of the measuring system showed; (i) the known permittivities of discs of various materials were reproduced; (ii) no loss was measurable for loss-less samples; (iii) the losses measured for materials otherwise characterized dielectrically in this laboratory showed good agreement; there was good agreement for identical zeolite specimens measured in the vacuum cell and in standard conventional capacitors.

MATERIALS

The zeolites studied in the present work are various cation forms of the type-*A* zeolite. The mixed ion forms available commercially as Linde Molecular Sieves Types 3*A*, 4*A* and 5-*A* were used. The present paper reports the results for the 5-*A*/H_2O system. The composition of 5-*A* is quoted as $Ca_{4\cdot5}Na_3[(AlO_2)_{12}(SiO_2)_{12}]30H_2O$ for the hydrated material[17]. The pure powdered material with no clay binder as supplied by B.D.H. Ltd. was used. In the vacuum cell distilled deionised water, to provide the vapour, was first degassed by repeated freezing and evacuation to remove dissolved air.

RESULTS

All results refer to a temperature of 22 ± 1°C unless otherwise stated. The dielectric methods will be referred to as: Method I for the conventional method using parallel plate and co-axial capacitors as described above, and Method II for those obtained using the vacuum cell. The state of the sample in all cases was a compacted disc with a density of 75 ± 5 per cent of the X-ray crystal density, or a compacted co-axial sample with a density of 80 ± 5 per cent of the X-ray value. The accuracy in determining the dielectric parameters is ±2 per cent both ϵ' and ϵ''. The water contents for Method I are quoted as molecules of water per unit cell of zeolite, checks on which gave agreement to $\pm 0\cdot2\,H_2O$ p.u.c. The water contents quoted for Method II are obtained from isotherms provided by the Linde Division of Union Carbide Corporation and have been described elsewhere[18]. No quantitative data for the uncertainties in these data are available but the agreement obtained between the dielectric parameters obtained by Methods I and II suggest that the values are accurate to about $\pm 0\cdot2\ H_2O$ p.u.c. The equilibrium water vapour pressures at the various water contents are given in the tables where applicable. Dielectric reproducibility between samples was generally better than ±4 per cent, but varied somewhat with water content, i.e. increasing from ±2 per cent at dehydration to about ± 5 per cent at saturation. Some comments on the procedure accompany the presentation of the results: these should clarify their significance before attempting their interpretation.

Table 1. *Dielectric parameters of anhydrous* 5-A

Frequency (Hz)	ϵ'	$10^3\epsilon''$
5·25	2·40 ± 0·05	45 ± 5
18·0	2·39 ± 0·05	30 ± 3
54·0	2·38 ± 0·05	25 ± 3
179	2·37 ± 0·05	17 ± 3
525	2·36 ± 0·05	17 ± 3
1586	2·35 ± 0·05	15 ± 3
5269	2·34 ± 0·05	15 ± 3
$15\cdot9 \times 10^3$	2·33 ± 0·05	15 ± 3
$51\cdot9 \times 10^3$	2·32 ± 0·05	15 ± 3
148×10^3	2·32 ± 0·05	15 ± 3

Table 1 gives the dielectric parameters by Method II for the dehydrated 5-*A* zeolite after desorption, at 400–450°C and 10^{-4}–10^{-5} Torr., of not only H_2O but also for CO_2, SO_2 and NH_3. Under the above conditions desorption times for water exceeded 24 hr; for other adsorbates 12 hr sufficed. The values in Table 1 are mean values obtained from three different samples after firstly desorbing water and then the subsequent adsorption/desorption of one or more of the other adsorbates. After desorption of water at 350°C the values obtained were larger by about 5 per cent Desorption at 500°C reproduced Table 1.

The increase in both ϵ' and ϵ'' at low frequencies probably shows conductivity together with some electrode polarisation (foil electrodes were avoided in Method II). From values of $\epsilon'' \times f = 1\cdot8 \times 10^{12} k$, a maximum conductivity, k, may be estimated. As is usual with solid samples $\epsilon''f$ still varies at low frequencies and the value of ϵ'' at $f = 5\cdot25$ Hz suggests $k = 1\cdot31 \pm 0\cdot15 \times 10^{-13}\ \Omega^{-1}\ cm^{-1}$. Topchieva[19] reported that the conductivity of anhydrous Ca-*A* was less than $10^{-12}\,\Omega^{-1}\ cm^{-1}$. Values of conductivity obtained from dielectric measurements are maximum possible values since ϵ'' (measured) contains dielectric loss and loss due to electrode polarisation or Maxwell–Wagner effects. Provided $\epsilon''_{max.}$ and $f_{max.}$ of a dielectric loss peak are known the value of ϵ'' (dielectric) may be calculated at any frequency from the Fuoss–Kirkwood relation. Thus ϵ'' at 5·25 Hz can be corrected for the dielectric loss to estimate the conductivity.

Figure 3 shows the permittivity, ϵ', and loss factor, ϵ'', of completely hydrated 5-*A* (5-*A* 30 H_2O p.u.c.) over the frequency range 5·25 Hz–3 GHz. The region above 100 MHz has not been investigated at water contents other than 30 H_2O p.u.c., and over a range of temperature below 22°C to −50°C. The loss and permittivity values decrease as the large absorption at 16 kHz moves to lower frequencies. The absorption at 400 MHz moves very little, if at all, with temperature indicating an extremely low activation energy. This suggests this feature is not due to adsorbed water as the liquid has an activation energy, for dipole reorientation, of about 5 kcal. mole^{-1} and an increased value would be expected for absorbed water. The 10 GHz absorption does move to lower frequencies and appears either to broaden or to fall in peak height as the temperature falls and it merges with the 400 MHz feature. The results do show that major absorptions due to the adsorbed water are below 100 MHz and the value $\epsilon' = 4{\cdot}0$ at 8·5 GHz emphasizes that virtually no dipolar dispersion occurs above that frequency.

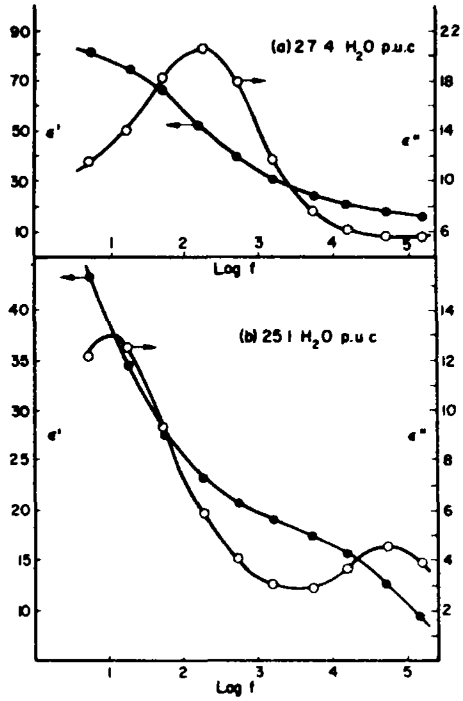

Fig. 4. Absorption I in 5-A/H_2O at two water contents (a) 27·4 H_2O p.u.c. (b) 25·1 H_2O p.u.c.

The frequency range 5·25 Hz–100 MHz has been fully investigated with variation of water content. Figure 4 shows some typical loss curves at various water contents obtained by Method I. As water is removed from 5-*A* the large absorption at 16 kHz moves rapidly to lower frequencies, the peak height (ϵ''_{max}) also

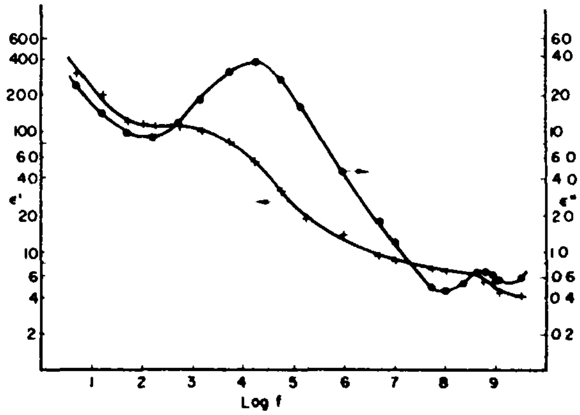

Fig. 3. Permittivity (+) and dielectric loss (●) in 5-A 30H_2O p.u.c.

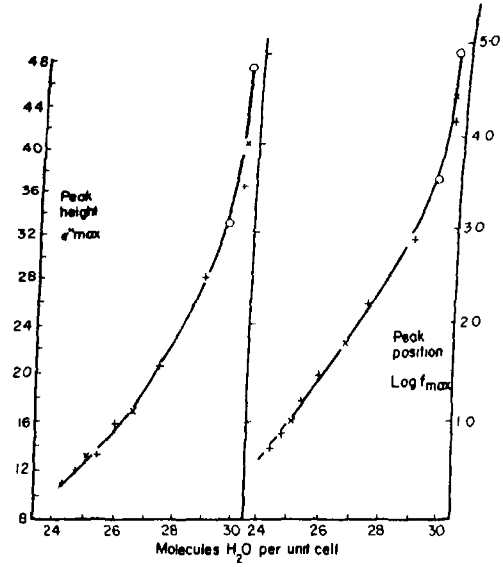

Fig 5. Variation of peak position, $\log f_{max}$, and peak height, ϵ''_{max}, for absorption I in 5-A/H_2O, with water content. Different specimens indicated by × ○ +.

falling rapidly. Figure 5 shows the variation of peak position and peak height with water content. The curves in Fig. 5 include results from various samples and show their resproducibility. Table 2 lists the dielectric parameters for this absorption (which will be referred to as absorption I) obtained by Method I. ϵ''_{max}, ϵ_0 and ϵ_∞ are obtained from Cole-Cole circular arc plots [20], $\log f_{max.}$ is obtained from Fuoss-Kirkwood plots [21] i.e.

$$\cosh^{-1}(\epsilon''_{max.}/\epsilon'') = 2{\cdot}303\,\beta(\log_{10} f_{max.} - \log_{10} f)$$

where β is the Fuoss-Kirkwood distribution parameter. Such a plot allows an assessment of relaxation time and its distribution on the basis of loss factors only and also gives a measure of the total dispersion involved from

$$\int_0^\infty \epsilon''\, d\ln f = \frac{\epsilon''_{max.}}{\beta} = \frac{(\epsilon_0 - \epsilon_\infty)}{2}.$$

The relaxation time, τ, is obtained from the relation $\tau = 1/\omega = 1/2\pi f_{max.}$.

The variation in β values and ϵ_∞ at water contents close to saturation is readily understood as the effect of removal of more water is observed. When absorption I has moved to low frequencies a second smaller peak (absorption II) is revealed. The increase in ϵ'' values on the high frequency side of absorption I due to absorption II overlapping causes β to vary. A similar effect appears on the low frequency side of absorption I by an increase in ϵ'' values from conductivity. At water contents below 26 H_2O p.u.c. the ϵ_∞ and β values for absorption I become constant. Figure 4(b), for a water content of 25·1 H_2O p.u.c., clearly shows the presence of two peaks. Absorption II follows the first to lower frequencies, the curve of its movement with water content being shown in Fig. 6. The various points on Fig. 6 show the good agreement obtained between the two methods of measurement in which the water contents were controlled in

Table 2. Dielectric absorption parameters for absorption I in 5-A at various water contents

H_2O *p.u.c.*	ϵ_0	ϵ_∞	ϵ''_{max}	$\log f_{max}$ ±0·03	β ±0·1	τ (sec)
30	108	10·5	36·4	4·20	0·62	$1{\cdot}0 \times 10^{-5}$
28·8	102	22·7	27·5	2·90	0·49	$2{\cdot}0 \times 10^{-4}$
27·4	89·4	18·6	21·9	2·20	0·53	$1{\cdot}0 \times 10^{-3}$
26·5	79·0	17·3	16·9	1·83	0·46	$2{\cdot}4 \times 10^{-3}$
25·9	69·0	20·8	16·0	1·45	0·56	$5{\cdot}7 \times 10^{-3}$
25·4	57·0	21·0	13·5	1·13	0·52	$1{\cdot}2 \times 10^{-2}$
25·1	55·6	20·8	12·9	1·02	0·53	$1{\cdot}5 \times 10^{-2}$
24·7	52·5	20·2	12·3	0·85	0·53	$2{\cdot}3 \times 10^{-2}$
24·3	51·2	20·1	11·2	0·65	0·52	$3{\cdot}6 \times 10^{-2}$

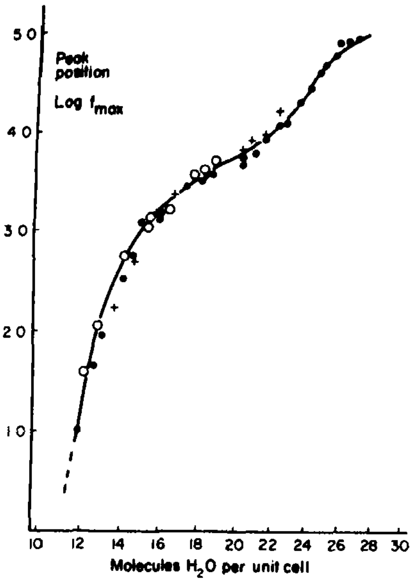

Fig. 6. Variation of peak position, $\log f_{max}$, for absorption II in 5-A/H_2O with water content; different specimens, Method I ● +, Method II ○.

quite different ways and entirely different capacitance cells used. The amplitude of absorption II remains essentially constant at all water contents. Table 3 lists some typical values of the dielectric absorption parameters obtained by Method II. Table 4 gives the permittivity and loss values at water contents below those for which absorption II is in this frequency range. The loss values at 11·0 and 9·5 H_2O p.u.c. do not permit estimation of the peak position assuming a constant ϵ''_{max}, since the low frequency values are increased by conductivity and electrode polarisation effects and do not give circular arcs in Cole–Cole plots. This difficulty is inherent in Method II measurements and the water content pick up during measurement forbids the use of Method I.

Figure 7 shows the temperature variation of absorption I in 5-*A* 30 H_2O p.u.c. at various temperatures. An Arrhenius plot of $\log f_{max}$ vs. $10^3/T$°K gives an activation energy of 16·7 ± 1·0 kcal. mole^{-1}. The large temperature coefficient limited the range over which these data could be collected: the almost water saturated samples could be studied only below room temperatures. Temperature variation for absorption II was studied in a cell consisting of a modified 30 cm co-axial air line. The results have been evaluated on the basis of Eyring's rate equation:

$$\tau = \frac{h}{kT}\exp\left(\frac{\Delta H_E^*}{RT}\right)\exp\left(\frac{-\Delta S_E^*}{R}\right)$$

This gives $\Delta H_E^* = \Delta H^*$ (Arrhenius)$-RT$, and from its best values ΔS_E^* is evaluated. Table 5 shows the variation of activation enthalpy and entropy at various water contents for absorption II.

Table 3. Dielectric absorption parameters for absorption II in 5-A at various water contents obtained by Method II

H_2O p.u.c.	H_2O vap. press. Torr.	ϵ_0 ±0·1	ϵ_∞ ±0·1	ϵ''_{max} ±0·1	β ±0·1	$\log f_{max}$ ±0·03	τ (sec)
20·3	1·0	17·80	4·45	4·60	—	3·90	$2·0 \times 10^{-5}$
19·7	$6·0 \times 10^{-1}$	17·70	4·40	4·40	—	3·76	$2·8 \times 10^{-5}$
19·4	$4·5 \times 10^{-1}$	17·75	4·30	4·30	—	3·70	$3·2 \times 10^{-5}$
18·4	$2·2 \times 10^{-1}$	16·40	4·10	4·10	0·50	3·67	$3·4 \times 10^{-5}$
18·1	$1·8 \times 10^{-1}$	15·50	4·05	4·05	0·49	3·63	$3·7 \times 10^{-5}$
17·6	$1·4 \times 10^{-1}$	15·50	4·10	4·10	0·52	3·56	$4·4 \times 10^{-5}$
16·4	$8·0 \times 10^{-2}$	15·25	3·85	3·85	0·52	3·18	$1·1 \times 10^{-4}$
15·4	$5·5 \times 10^{-2}$	14·60	3·75	3·75	0·54	3·13	$1·2 \times 10^{-4}$
15·1	$5·0 \times 10^{-2}$	15·40	3·80	3·80	0·55	3·06	$1·4 \times 10^{-4}$
14·0	$3·5 \times 10^{-2}$	15·50	3·75	3·75	0·49	2·74	$2·9 \times 10^{-3}$
12·8	$2·45 \times 10^{-2}$	15·60	3·65	3·65	0·47	2·01	$1·6 \times 10^{-3}$
12·1	$2·0 \times 10^{-2}$	15·40	3·60	3·60	0·48	1·71	$3·1 \times 10^{-2}$

Table 4. Dielectric parameters in 5-A at various water contents

H_2O vapour pressure Torr.	$1\cdot5 \times 10^{-2}$		$1\cdot1 \times 10^{-2}$		$8\cdot0 \times 10^{-3}$		$4\cdot5 \times 10^{-3}$		$1\cdot5 \times 10^{-4}$	
H_2O p.u.c.	11·0		9·5		8·0		6		2	
Freq. Hz	ϵ'	ϵ''	ϵ'	ϵ''	ϵ'	ϵ''	ϵ'	ϵ''	ϵ'	ϵ''
5·25	11·93	5·04	10·12	4·84	7·46	3·65	4·86	1·82	2·94	0·21
18·0	9·16	3·89	7·39	3·37	5·65	2·01	4·24	0·94	2·88	0·18
54·0	6·77	2·85	5·77	2·30	4·75	1·22	3·98	0·57	2·79	0·16
179	5·26	1·67	4·81	1·37	4·24	0·78	3·79	0·34	2·68	$0\cdot10_1$
525	4·58	1·14	4·30	0·84	3·98	0·51	3·69	0·26	2·62	$0\cdot07_1$
1586	4·18	0·68	3·98	0·53	3·77	0·34	3·54	0·22	2·59	$0\cdot05_4$
5269	3·90	0·43	3·77	0·35	3·64	0·26	3·45	0·19	2·56	$0\cdot04_3$
15·9k	3·71	0·31	3·62	0·27	3·47	0·20	3·30	0·16	2·55	$0\cdot03_1$
51·9k	3·58	0·22	3·52	0·19	3·41	0·15	3·22	0·11	2·54	$0\cdot02_3$
148k	3·47	0·15	3·41	0·13	3·34	0·10	3·15	0·07	2·54	$0\cdot01_9$

Values of the apparent conductivity, obtained as already indicated, at various water contents, together with the activation energy of conductivity, are given in Table 6. ΔH^{*}_{1} (cond) increases approximately linearly with increase in water content in the above range.

DISCUSSION

It is appropriate firstly to recall the salient features of the zeolite lattice structure[11, 17, 22]. The crystal structure of type-*A* consists of large cavities (α-cages) of 11·4 Å dia. separated, in a cubic array, by 4·2 Å dia. windows formed by 8-membered oxygen rings. The structure also contains smaller cavities (β-cages) of 6·6 Å dia. separated from the large α-cage by 2·2 Å dia. windows, formed by 6-membered oxygen rings. The mobile interstitial cations (K^+ in 3-*A*, Na^+ in 4-*A* and Ca^{2+} in 5-*A*) occupy preferred positions in the lattice. There are eight type-I ion sites[23, 24] close to the 6-membered oxygen ring windows. This is the preferred cation site and the cations remain close to this position in the presence of an adsorbate. The type-II cation sites are close to the 8-membered oxygen ring windows in the dehydrated material but in the presence of an adsorbate the cations from these positions are

Table 5. Variation of activation energy and entropy for absorption II in 5-A with water content

H_2O p.u.c.	ΔH^{*}_{F} kcal.mole^{-1}	ΔS^{*}_{E} e.u.
12·2	12·1 ± 0·2	−7·9
14·1	12·7 ± 0·1	0·4
16·5	13·9 ± 0·1	7·9
20·4	14·9 ± 0·1	13·0
22·4	14·3 ± 0·5	14·2
23·3	14·5 ± 0·2	14·5

Table 6. Apparent conductives of 5-A at 22°C and various water contents and their activation energies

H_2O p.u.c	k. Ω^{-1} cm^{-1} at 5·25 Hz	ΔH°_{1}(cond) kcal. mole^{-1}
30·0	68×10^{-12}	10·5 ± 1·2
27·4	14×10^{-12}	
25·9	$4\cdot4 \times 10^{-12}$	
22·4	$3\cdot5 \times 10^{-12}$	6·7 ± 0·9
20·4	$3\cdot0 \times 10^{-12}$	5·8 ± 0·8
19·8	$2\cdot9 \times 10^{-12}$	5·9 ± 0·5
15·0	$2\cdot6 \times 10^{-12}$	5·0 ± 0·2
0	$1\cdot31 \pm 0\cdot15 \times 10^{-13}$	

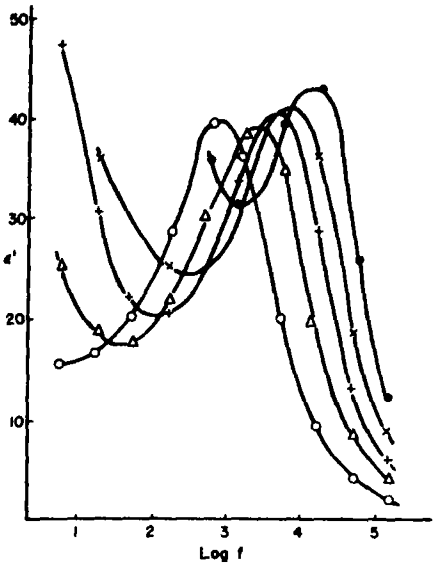

Fig. 7. Temperature variation of absorption I in 5-A $30H_2O$ p.u.c. O −20°C; Δ −10·5°C; + −5°C; × −1°C; ● +3·5°C.

believed to move into the centre of the cavity to form a cluster with the adsorbate[24]. The type 5-*A* zeolite, to which this paper refers, has only the type-I cation sites occupied.

FREQUENCIES ABOVE 100 MHz

Whilst the results obtained at frequencies above 100 MHz are very limited they do provide the important conclusion that most of the adsorbed water, even near saturation, does not behave as bulk water. The permittivity at 3 GHz, i.e. before the dispersion indicated at higher frequencies (see Fig. 3) is 4·37 at 20°C. An estimate of the permittivity after the dispersion may be obtained using Lichteneckers logarithmic mixing rule[25]

$$\log \epsilon'_{\mathrm{mix.}} = \theta_1 \log \epsilon'_1 + \theta_2 \log \epsilon'_2$$

where θ_1 and ϵ'_1 are the volume ratio and permittivity of the zeolite lattice and θ_2 and ϵ'_1 are those for water. Taking ϵ'_1 as the dehydrated 5-*A* permittivity, 2·32, and ϵ'_2 as ϵ_∞ for water, 4·5, and θ_1 and θ_2 as 0·68 and 0·32[22] a value of ϵ_∞ for the 5-A/H_2O system of 2·87 is obtained. Hence $(\epsilon_0 - \epsilon_\infty)$ for the highest frequency absorption is about 1·50: in liquid water this is 76 and in ice at 0°C, 88. A dispersion of this size could not possibly account for more than about 2 per cent of the water present. The permittivity at liquid air temperature is 2·96 and the loss 90×10^{-3}. This permittivity is in reasonable agreement with the above estimated value of 2·87.

ABSORPTION II

The striking feature of the results from 5·25 Hz to 100 MHz is the constancy of peak height, $\epsilon''_{\mathrm{max.}}$, of absorption II. This suggests that the absorption is not due to the adsorbed water. If it were due say to that water bound to the most energetic adsorption sites (which would be a constant amount and the last to be removed on dehydration thus accounting for the peak height constancy) then it is difficult to envisage why the activation energy for the process should vary in the way it does. Further, a similar peak is observed with adsorbates other than water[26] (CO_2, SO_2 and NH_3). This peak is accordingly ascribed to an ionic jumping process.

For a cation jumping process the variation of activation energy with water content is understandable. As the water content increases the water molecules will impede the movement of a cation (or cations) either by simple steric hindrance, or by becoming attached to the cation and increasing its effective volume. In the region beyond 20 H_2O p.u.c. the cavities are about two thirds full of water and the latter is approaching a state similar to that in the liquid. The cation movement could then be considered as taking place 'in solution', the activation energy decreasing as the 'solution' becomes more dilute. The increasing entropy of activation is also consistent with this interpretation. As the water content increases the cation has to push more water aside in jumping from one site to another, causing greater disorder in its environment. The negative entropy of activation is difficult to interpret. However, it should be realised that there is much doubt as to the quantitative correctness of the Eyring absolute rate expression for dielectric relaxation [27] and that the ΔS terms are arbitrary and only their increasing positive trend is significant. It may have been anticipated that the Eyring model would be applicable to the present process, i.e. a cation effectively loosening a bond at one site and forming a bond to another; were it strictly applicable the negative ΔS^* would imply that the activated state is one of more order than the initial one. This is difficult to envisage.

DIELECTRIC ISOTHERMS

Dielectric isotherms are plots of the permittivity increase, at a fixed frequency, as a function of amount sorbed. Care must be taken in obtaining such plots to ensure that the frequency is sufficiently high so that no interference from movable peaks passing through the measuring frequency is observed in the permittivity. Such a dielectric isotherm may be obtained for the 5-*A*/H_2O system by plotting ϵ_∞ for absorption II against water content. An isotherm obtained in this way is shown in Fig. 8. Values of ϵ_∞ used are those from Table 3 and, at water contents below 12 H_2O p.u.c., the values are the 148 kHz values of ϵ' from Table 4. The initial slope, which extends up to 6 H_2O p.u.c., implies that over this range the addition of water has had a smoothly continuous influence, i.e. that they are all of the same (most strongly adsorbed) type and that this type is 'saturated' at 6 H_2O p.u.c. The second change in slope at about 17 H_2O p.u.c. could then indicate the start of capillary condensation after the full occupation of the second most active sites. N.m.r. studies [1(b)] indicate the existence of two types of active centre in type-*A* zeolites.

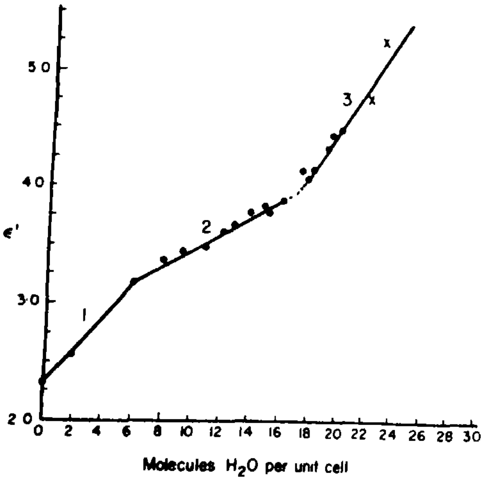

Fig. 8. Dielectric isotherm for water on 5-A, (●) Method II, (×) Method I.

The figure of 6 H_2O p.u.c. for completion of occupation of the most active sites is supported by the indications from the vapour isotherms [18]: for both 4-*A* and 5-*A* zeolites a definite 'kink' in the isotherms occurs at about 6 H_2O p.u.c. The value of 6 H_2O p.u.c. also matches a discontinuity in Dubinin's dielectric isotherm for 4-*A* [5]. A similar discontinuity was observed in the increase of conductivity with water content at 6 H_2O p.u.c [28]. The agreement for 4-*A* and 5-*A* from four different sources merits some consideration as to exactly which are the most active sites in these two ion forms. Accepting that these sites are the same in 4-*A* and 5-*A*, as it is difficult to envisage otherwise with the same value for full occupation in both, the type-II cations can be ruled out as they are not present in 5-*A*. If the type-I cations form the most active sites for initial water adsorption then a figure of 8 H_2O p.u.c., or some multiple of this, would be defined for their full occupation in 4-*A*.

Plausible sites in the type-*A* cavity which could give a figure of 6 H_2O p.u.c. for the most active centres would be the six 8-membered oxygen ring windows. Good general reasons can be advanced for choosing this anionic rather than cationic site for the first adsorption. The interaction energies will be principally of ion-dipole character. The local charge (and hence field) is much stronger at the (H^+) sites in the water molecule and so, for ions of equal size, interaction with an anion will be preferred. Further, polarisability is much higher for anions than cations, giving an enhanced dipole-induced dipole energy. This would mean that each window had to offer two such sites since each is shared by two cavities. It does this naturally by holding one water molecule on each side of its plane. It is precisely this position that a water molecule first encounters on entering the cavity and in such a position it can hydrogen-bond to the oxygens of the windows in alternative orientations, i.e. it has a favourable entropy term. In the case of monovalent ion types a water molecule could at the same time be associated through its oxygen to the type-II cation, which in the dehydrated material lies just inside the cavity from the 8-membered ring window. This would increase the interaction in monovalent ion types and stabilize the position of a water molecule in the ring. Such a mechanism for adsorption is supported by the X-ray work of Lewis[29] who showed that the sites in which adsorbed water molecules have a relatively long residence time are these sites in the 8-membered ring windows in both 4-*A* and 5-*A*.

Some further information can be obtained from the dielectric isotherm. It is reasonable to suppose that the dielectric increment, $\Delta\epsilon'$, above that of the value of 2·32 for anhydrous 5-*A* is entirely due to water. The high frequency results showed that the large amount of water could not be accounted for by the intensity of the high frequency (above 3 GHz) loss. That the contribution of water to the permittivity increment, in the form of orientation polarisation, varies is obvious from the form of the dielectric isotherm. In order to attempt to estimate the amount of water contributing to the loss above 100 MHz the apparent dipole moment of water at various concentrations has been calculated. For an order of magnitude calculation the Onsager equation[30] appropriate for a polar solute in a non-polar medium has been used.

$$\epsilon_0-\epsilon_\infty=\Delta\epsilon'=\frac{4\pi n\mu^2}{3kT}\left[\frac{\epsilon_1(\epsilon_{\infty 2}+2)}{2\epsilon_1+\epsilon_{\infty 2}}\right]^2$$

n is the number of polar molecules per cm^3: ϵ_∞, the high frequency permittivity of the pure solute species and ϵ_1 the solvent permittivity. Regarding the system as water ($\epsilon_{\infty 2}=4{\cdot}5$) dissolved in the zeolite ($\epsilon_1=2{\cdot}32$) *apparent* molecular moments for the adsorbed water can be obtained from the permittivity increments. ϵ_∞ for the system has been estimated by Lichteneckers rule.

Over the range of the initial linear portion of the isotherm a mean dipole moment of 0·84 D may be obtained from the slope, i.e. $\Delta\epsilon'/H_2O$. In the second and third regions of the isotherm no useful information can be obtained from the slopes since the extrapolated lines do not pass through the anhydrous zeolite permittivity. Over these regions of water content the dipole moments must be obtained on an incremental basis. The values are given in Table 7.

Table 7. Apparent dipole moment of adsorbed water in 5-A *obtained from the permittivity increments given by the dielectric isotherm*

H_2O p.u.c.	μ_{Onsager} D
6·0	0·79
8·0	0·74
10·0	0·71
12·0	0·69
14·0	0·67
16·0	0·66
18·0	0·67
20·0	0·72
22·0	0·75
24·0	0·79

The form of the dielectric isotherm and these reduced dipole moment values could be interpreted by considering a possible model for adsorption. Maintaining the most active sites already suggested, a molecule held by hydrogen bonds to the lattice oxygens would be able to contribute to the total polarisation by a rocking movement about the hydrogen bonds. In this case the observed dipole moment would be $\mu(1-\cos\theta)$ where θ is the angle through which the dipole could move and μ is the total dipole moment for water. In the first region θ would be 57°. As more water is adsorbed the rocking movement would be reduced by the presence of neighbouring molecules, i.e. if those molecules, adsorbed at water contents above the monolayer, also become attached to the cavity walls. In the third region, the molecules adsorbed at these water contents could be expected to fill the cavity centre and thus behave more like liquid water.

If it is supposed that the third region of the dielectric isotherm is due to water in a state similar to the liquid, the data for this region extrapolated to a water content of 30 H_2O p.u.c., i.e. assuming linearity up to this water content, gives a dielectric increment of 3·29. Assuming the normal (and liquid phase) value $\mu(H_2O) = 1{\cdot}82$ D[32] an apparent concentration for water behaving as liquid water of 5·9 g.mole.l.$^{-1}$ is obtained from the Onsager equation. This amounts to 5 or 6 molecules per unit cell, or about 17–20 per cent of the total water at saturation. However, perhaps what is more likely is that the water molecules in this region are hydrogen bonded to those molecules attached to the cavity walls and reorientate at most about one (O–H) bond.

ABSORPTION I

Since the permittivities and losses at frequencies above 100 MHz are too small to account for more than 20 per cent of the adsorbed water at saturation it seems in every way reasonable to suggest that absorption I is due to adsorbed water. The reproducibility of peak position and height from sample to sample would not be expected of a Maxwell–Wagner process which may be considered to be an alternative cause of absorption I. Some support for attributing absorption I to adsorbed water can be obtained from a consideration of the relaxation time observed and a comparison with those from other techniques. N.m.r.[1(b)] gives relaxation times for water in type-*A* zeolites of the order of 10^{-8} sec, whilst slow neutron scattering studies[3] leads to a diffusion coefficient for water with a time constant of 10^{-5} sec. These values are close to that obtained here for 5-*A* 30 H_2O p.u.c. i.e. $1{\cdot}0\times 10^{-5}$ sec. This value is also close to the relaxation time of water molecules in ice at $-0{\cdot}1$°C ($2{\cdot}2\times 10^{-5}$ sec). This is in agreement with Barrer's conclusion[33] from measurements of diffusion coefficients of water in zeolites that such water is intermediate in state between supercooled water at -2°C and ice at -2°C.

From the peak height in saturated 5-*A* it is possible to estimate the contributing amount of water assuming the full dipole moment of 1·82 D. Insufficient data are available to use the Onsager equation and the Böttcher approximation of the Debye equation[34] has been used;

$$\epsilon_0 - \epsilon_\infty = \frac{2\epsilon''_{\text{max.}}}{\beta} = (\epsilon'+2)^2\frac{4\pi n\mu^2}{27kT}$$

where ϵ' is the permittivity after the dispersion under consideration $= 15{\cdot}0$, $\epsilon''_{\text{max.}} = 36{\cdot}4$ and $\beta = 0{\cdot}62$. This gives a value of the concentration of water contributing to the loss peak of 19·2 g. mole.l.$^{-1}$, which is equivalent to about 75 per cent of the total water. Even though this is very approximate, due to the inadequacy of the Debye equation, it does suggest that absorption I could account for the bulk of the adsorbed water.

CONDUCTIVITIES

The apparent conductivities of the 5-*A* zeolite with adsorbed water also merit consideration in view of the comparatively low values obtained. In all the dielectric studies made on type-*A* zeolites low values of conductivity have been derived, i.e. Dubinin concluded that the conductivity of 4-*A* decreased as the amount of water increased and gave values of conductivity of the order of $10^{-12}\ \Omega^{-1}\text{cm}^{-1}$. A very different conductivity was reported by Stamires[9, 28] for the

4-A/H_2O system. His values, based on resistance measurements, increased from about $10^{-8}\Omega^{-1}cm^{-1}$, in the dehydrated material, to about $10^{-3}\Omega^{-1}cm^{-1}$ at saturation. If these values were correct then the dehydrated zeolite would be difficult to measure dielectrically at frequencies less than 1 kHz and quite impossible to measure in the hydrated state. The fact that dielectric measurements have been made casts considerable doubt on Stamires' values, particularly since the state of the sample in the present work colsely reproduces his. In view of the agreement between the values obtained here and those of Dubinin and Topchieva, it must be concluded that Stamires' values are unreliable.

The increase in ΔH^* (conductivity) with increasing water content in the 5-*A* zeolite (also reported by Dubinin for 4-*A*) can be accepted as further evidence of the hindering effect of water on cation movement: this has already been deduced from the absorption II behaviour.

CONCLUSION

The observed dielectric properties of the 5-*A* zeolite-adsorbed water system have been interpreted in terms of possible processes in the zeolite cavity. One well defined region of dielectric loss has been attributed to movement, within the cavity, of the interstitial cations. Regions of dielectric loss in type-*A* zeolites were attributed to similar processes by Lebrun and Dubinin.

While a direct analysis of the data suggests that the major bulk of adsorbed water has an ice-like character and the remainder behaves more as in liquid water this interpretation is probably over simplified. The absence of a high frequency absorption due to liquid-like water shows that the amount of water not contributing to the ice-like process has a wide spectrum of relaxation times. Also the fact that the ice-like absorption process falls in intensity immediately water is removed indicates the over simplification. Probably the best interpretation that can be given is that the whole amount of water can contribute to the high frequency polarisation by relaxing some small part of its dipole moment whereas the major part of the dipole moment relaxes as in ice. Here again the picture may be oversimplified but to allow greater definition of the exact nature of adsorbed water in zeolites requires further insight from other techniques over wide variations of water content and temperature.

Acknowledgements – I am indebted to Dr Mansel Davies for much interest and discussion during the progress of this work. I also wish to thank Professor R. M. Barrer for helpful discussion; and The Linde Division of Union Carbide Corporation for making their isotherm data available. I also acknowledge the receipt of an S.R.C. Research Studentship.

REFERENCES

1. (a) KIRIYAMA R. *et al.*, *J. chem. Soc. Japan* **68**, 1488 (1965); (b) MACKEY J.H., Thesis, Princeton (1962); (c) COHEN ADDAD J. P., *Brit. Radiospec. Grp. Conf.* England (1966).
2. KISELEV A. V. and LYGIN V. I., In *Infra-Red Spectra of Adsorbed Species* (Edited by L. H. Little). Chap. 14. Academic Press, New York (1966).
3. EGELSTAFF P. A., STRETTON DOWNES J. and WHITE J. W., *Proc. S.C.I. Conf. Mol. Sieves.* London (1967).
4. LEBRUN A., *Revue Gen. Elec.* **74**, 948 (1965)
5. GLAZUN B. A. DUBININ M. M., FEDOROV V. M. and ZHILENKOV I. V. *Izv A.N.S.S.S.R. Ser Khim.* 1930 (1964), 393, 1129, 1249, 1253, 1668 (1966); 977, 982, 987 (1967).
6. BOTTCHER C. J. F., *Rec. Trav. Chim* **64**, 47 (1945).
7. DUCROS P., Thesis, Paris (1960).
8. BARRER R. M., Private communication.
9. FREEMAN D. C. and STAMIRES D. W., *J. chem. Phys.* **35**, 799 (1961).
10. FREEMAN D. C. and STAMIRES D. N., U.S. Patent No 3,213,164.
11. BARRER R. M. and MEIER W. M., *Trans. Faraday Soc.* **54**, 1074 (1958).
12. BARRER R. M. and DENNY A. F., *J. chem. Soc.* 4684 (1964).
13. THOMPSON A. M., *Proc. Inst. Elec. Engng* **B103**, 704 (1956).
14. Boonton Radio Co., Rockaway N.J., U.S.A.
15. WILLIAMS G., *J. phys. Chem* **63**, 534 (1959).
16. ROBERTS S. and VON HIPPEL A. *J. appl. Physics* **17**, 610 (1946); Central research Laboratories Inc., Redwing, Minnesota.
17. REED T. B. and BRECK D. W., *J. Am. chem. Soc.* **78**, 5972 (1956).
18. MORRIS B., Thesis, Wales (1967).

19. TOPCHIEVA K. V., MOSKOVSKAYA I. F. and STETSENKO V. YA., *Russ. J. Phys. Chem.* **37**, 1020 (1963).
20. COLE K. S. and COLE R. H., *J. chem. Phys.* **9**, 341 (1941).
21. FUOSS R. M. and KIRKWOOD J. G., *J. Am. chem. Soc.* **63**, 385 (1941).
22. BRECK D. W., EVERSOLE W. G., MILTON R. M., REED T. B. and THOMAS T. L., *J. Am. chem. Soc.* **78**, 5963 (1956).
23. SEFF K. and SHOEMAKER D. P., *Acta crystallogr.* **22**, 162 (1967).
24. SMITH J. V., *Proc. S.C.I. Conf Mol Sieves.* London (1967).
25. LICHTENECKER K., *Phys. Z.* **10**, 1005 (1909).
26. MORRIS B., *J. Phys. Chem. Solids* **30**, 89 (1968).
27. CLEMETT C. J. and DAVIES M. M., *J. Phys. Chem. Solids* **18**, 80 (1961).
28. STAMIRES D. N., *J. chem. Phys.* **36**, 3174 (1962).
29. LEWIS P. H., *J. phys. Chem.* **63**, 527 (1959).
30. ONSAGER L., *J. Am. chem. Soc.* **58**, 1486(1936).
31. McINTOSH R. L., *Dielectric Behaviour of Physically Adsorbed Gases.* Butterworths, London (1962).
32. HILL N. E., *Trans. Faraday Soc.* **59**, 344 (1963).
33. BARRER R. M., *Proc. Brit. Ceram. Soc.* **1** 145 (1964).
34. BOTTCHER C. J. F., *Theory of Electric Polarisation.* Elsevier, Amsterdam (1952).

J. Phys. Chem. Solids Pergamon Press 1969. Vol. 30, pp. 89–101. Printed in Great Britain.

A DIELECTRIC STUDY OF THE SYNTHETIC LINDE TYPE-*A* ZEOLITE—II. DIELECTRIC PROPERTIES OF 5-*A* WITH ADSORBED AMMONIA, SULPHUR DIOXIDE, CARBON DIOXIDE AND *N*-PENTANE

BRIAN MORRIS
Edward Davies Chemical Laboratory, University College of Wales, Aberystwyth, U.K.

(*Received* 10 *April* 1968)

Abstract—The dielectric properties of the Linde Molecular Sieve Zeolite Type 5-*A* with a series of polar and non-polar adsorbates (NH_3, SO_2, CO_2 and n–C_5H_{12}) have been investigated in the frequency range 5 Hz to 148 kHz. A region of dielectric absorption is observed which has been assigned to a jumping process involving the interstitial cations. A possible mechanism for the process is discussed and the results analysed on the basis of the apparent dipole moment, associated with the cation jump, which is obtained from the dielectric absorption parameters. The theoretical basis of the analysis is given in an appendix.

Plots of the permittivity increment against adsorbate content for polar adsorbates are discussed in terms of the rotational mobility of the sorbed phase.

INTRODUCTION

IN PART I[1] the dielectric properties of the synthetic zeolite Linde 5-*A* with water as the adsorbed phase were discussed. A region of dielectric absorption was attributed to movement, within the cavities, of the interstitial cations. Further support for this assignment will be given in the present paper which reports the results, obtained in the frequency range 5 Hz to 148 kHz, for 5-*A* with some typical adsorbates, both polar and non-polar.

EXPERIMENTAL

All the results given in this paper were obtained using the vacuum cell described in Part I. As in the case of water it was not possible to determine the adsorption isotherms for the various adsorbates and available isotherms [2] have been used to obtain the adsorbate contents quoted. In some cases, particularly with sulphur dioxide as the adsorbed phase, these are only approximate and in all cases the equilibrium adsorbate pressure is given with the results. As before all results refer to a temperature of 22° ± 1°C unless stated otherwise.

The adsorbates used were purified as follows.

(I) Ammonia: liquid ammonia, obtained from a cylinder, was distilled and degassed, by repeated freezing and evacuation, before use.
(II) Sulphur dioxide: liquid sulphur dioxide, from a cylinder, was distilled and degassed before use.
(II) Carbon dioxide: carbon dioxide was vacuum sublimed from solid carbon dioxide.
(IV) *n*-Pentane: laboratory reagent grade *n*-Pentane was degassed before use.

All adsorbates were passed through a zeolite trap into the cell, which served the dual purpose of removing traces of water and, by loading the trap with the adsorbate, allowed easy manipulation of low adsorbate pressures. Samples were measured every 15 min after the pressure had become steady, following the admission of adsorbate vapour, and equilibrium was assumed to be attained when the dielectric parameters became constant: this generally took 60–90 min. All samples were allowed at least 120–150 min equilibration before the final measurements were taken. In some cases when up to 12 hr were allowed for equilibration no change in the dielectric parameters occurred after 2 hr.

RESULTS

The conditions pertaining to the individual systems are briefly considered before a discussion of the general conclusions. The remarks in Part I concerning the accuracy of measurements also apply to the present data.

(A) Ammonia on 5-A zeolite

The results obtained on the first adsorption of ammonia were irreproducible but all subsequent adsorption/desorption runs gave reproducible results. Figure 1 shows the effect of various ammonia pressures on the dielectric loss in 5-*A*. The appearance of a dielectric loss peak, moving to high frequencies as the ammonia content increases, is clearly shown. Figure 2 shows the movement of the loss peak with ammonia content, including the first adsorption. The experimental points for the second adsorption/desorption show some evidence of slight hysteresis between 4 and 14 NH_3 per unit cell. Table 1 gives the dielectric parameters for one adsorption/desorption run. ϵ_0, ϵ_∞ and $\epsilon''_{max.}$ were obtained from Cole–Cole circular arc plots[3] of the data and the $\log f_{max.}$ values were obtained from Fuoss–Kirkwood plots[4]; β is the Fuoss–Kirkwood distribution parameter.

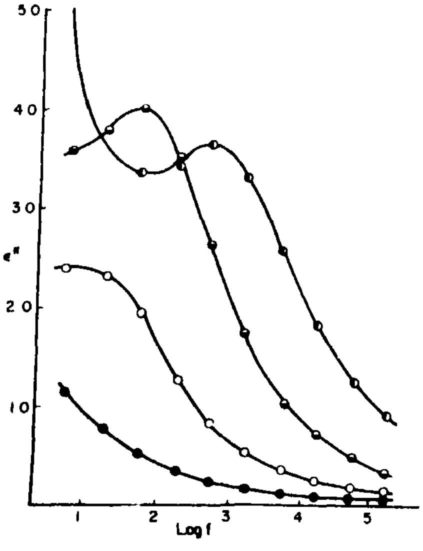

Fig. 1. Effect of adsorbed ammonia on dielectric loss in 5-*A*. (●) 0·031 Torr.; (○) 0·090 Torr.; (◒) 1·00 Torr.; (◐) 160 Torr.

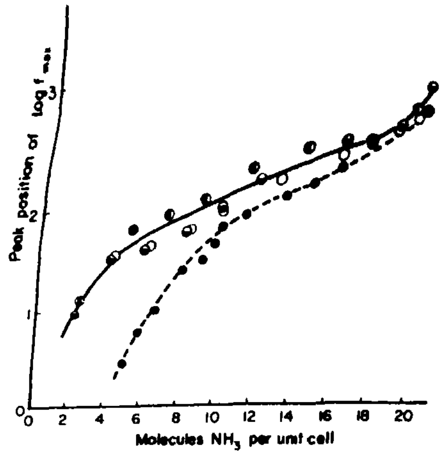

Fig. 2. Movement of the dielectric absorption in 5-*A*/NH_3 with ammonia content. (●) 1st adsorption; (○) 1st desorption; (◒) 2nd adsorption; (◐) 2nd desorption; (⊕) 3rd adsorption.

The $\epsilon''_{max.}$ values are reasonably constant over all values of ammonia content, except 2·0 NH_3 p.u.c., and show no tendency to increase or decrease with ammonia content above 3 NH_3 p.u.c. The β values, however, show a considerable fall as adsorption progresses reaching a minimum at saturation. From the indication in Fig. 1 (i.e. curve 2) and the peak height at 2·0 NH_3 p.u.c., there is a suggestion that the peak height falls at low ammonia contents. Table 2 gives the absorption parameters obtained in investigating this change and Fig. 3 shows the variation in $\epsilon''_{max.}$ with ammonia pressure.

Temperature variation gave little information since no adsorption isosteres were available to enable constant ammonia

Table 1. Dielectric absorption parameters in 5-A at various ammonia contents (adsorption/desorption)

NH_3 pressure Torr.	NH_3 p.u.c.	ϵ''_{max} ±0·1	ϵ_0 ±0·1	ϵ_∞ ±0·1	log. $f_{max.}$ ±0·03	β ±0·01
0·09	2·0	2·46	11·60	2·90	0·950	0·43
0·22	3·8	4·00	16·00	3·30	1·500	0·46
0·45	5·7	4·08	16·25	3·40	1·580	0·44
1·00	7·9	4·02	16·35	3·65	1·725	0·44
3·60	9·9	3·90	16·30	3·70	1·950	0·42
8·20	11·7	4·03	16·55	3·80	2·175	0·41
39·0	15·8	3·50	15·35	3·85	2·500	0·39
160·0	18·3	3·75	16·10	4·25	2·600	0·37
760	19·7	3·25	17·10	3·50	3·040	0·35
301·0	19·1	3·55	17·40	4·25	2·825	0·35
77·0	17·0	3·70	17·60	4·00	2·550	0·36
17·0	13·9	3·58	16·25	3·75	2·460	0·38
7·0	11·2	3·78	16·30	3·75	2·280	0·38
1·75	8·9	3·65	16·10	3·50	2·025	0·40
0·65	6·8	3·88	16·05	3·60	1·920	0·43
0·35	5·0	3·92	16·30	3·45	1·790	0·43

Table 2. Dielectric absorption parameters in 5-A at low ammonia pressures

NH_3 pressure Torr.	ϵ''_{max}	ϵ_0	ϵ_∞	log. f_{max}	β
$3{\cdot}1 \times 10^{-2}$	1·59	8·50	2·55	−0·20	0·41
$4{\cdot}1 \times 10^{-2}$	1·58	8·55	2·60	0·20	0·41
$4{\cdot}7 \times 10^{-2}$	1·81	8·55	2·70	0·29	0·41
$5{\cdot}2 \times 10^{-2}$	2·88	12·20	2·85	0·33	0·43
$7{\cdot}0 \times 10^{-2}$	3·18	12·60	2·95	0·45	0·45
$7{\cdot}7 \times 10^{-2}$	3·58	14·75	3·00	0·525	0·46
$1{\cdot}1 \times 10^{-1}$	4·11	16·75	3·00	1·10	0·46

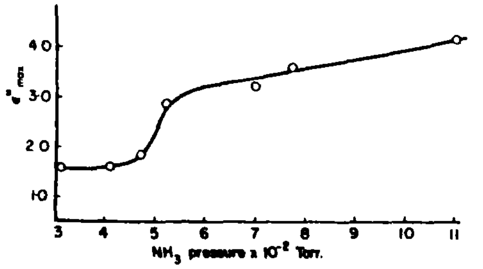

Fig. 3. Variation of the amplitude of the dielectric absorption in 5-*A*/NH_3 at low ammonia pressures.

content to be maintained. The apparent activation energies obtained are therefore minimum possible values, since increase in log $f_{max.}$ due to increase in temperature will be compensated for, to some extent, by reduction of log f_{max} due to adsorbate loss. Examination of Fig. 2 shows that small losses of adsorbate at saturation lead to large shifts in log. $f_{max.}$. Temperature variation was thus carried out at an ammonia content of 18 NH_3 p.u.c. (NH_3 pressure 170 Torr.), i.e. at the top of the flatter portion of the curve in Fig. 2. The results obtained gave a reasonably good linear Arrhenius plot, Fig. 4, with an activation energy of 11·0 ± 1·0 kcal. mole^{-1}.

(*B*) *Sulphur dioxide*

The effect of sulphur dioxide on dielectric loss in 5-*A* is somewhat similar to that of

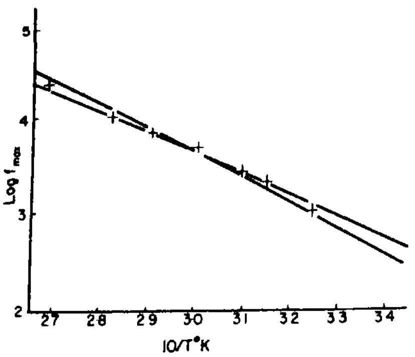

Fig. 4. Arrhenius plot for the dielectric absorption in 5-*A*/NH_3 at approximately 170 Torr NH_3 pressure.

ammonia in that a dielectric loss peak appears and moves to higher frequencies with increase in sulphur dioxide content. As with ammonia the first adsorption gave anomalous results.

Figure 5 shows the effect of various equilibrium sulphur dioxide pressures on the dielectric loss. Curves 5 and 6 show some indication of a dielectric loss peak. At higher sulphur dioxide pressures than those shown in Fig. 5 the loss curve remains similar in shape to curve 6 but moves to higher frequencies. The conductivity loss increases and the dielectric loss peak is not then completely resolved. The Cole–Cole circular arc plot proves very successful in separating the loss process from the conductivity. For a conductivity process the loss factor generally increases at a much greater rate than the permittivity as the frequency falls so that the Cole–Cole plot usually distinguishes between the two, but the procedure is effective only when the dielectric loss process is not too small relative to the conduction process over a significant frequency range. In Fig. 6(a) the loss factor and permittivity is shown for a sulphur dioxide pressure of 50 Torr. Figure 6(b) shows the Cole–Cole plot for the data. It is the interdependence of ϵ' and ϵ'' in the Debye function which makes the Cole–Cole plot a discriminating one for such cases. Once a value of ϵ''_{max} is estimated by the Cole–Cole plot log. f_{max}.

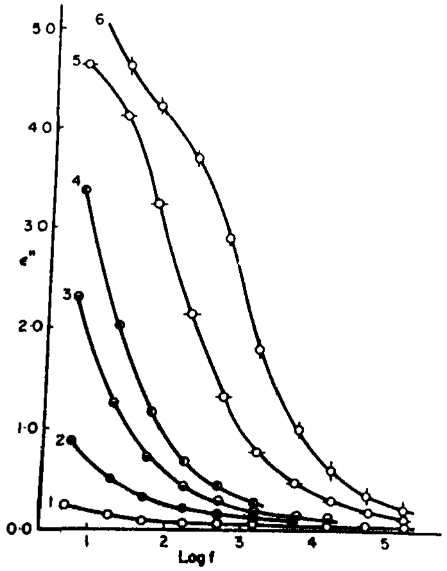

Fig. 5. Effect of adsorbed SO_2 on dielectric loss in 5-*A*, (○) 0·07 Torr.; (●) 0·26 Torr.; (◒) 0·70 Torr.; (◐) 0·85 Torr.; (-○-) 2·20 Torr.; (ϕ) 4·00 Torr.

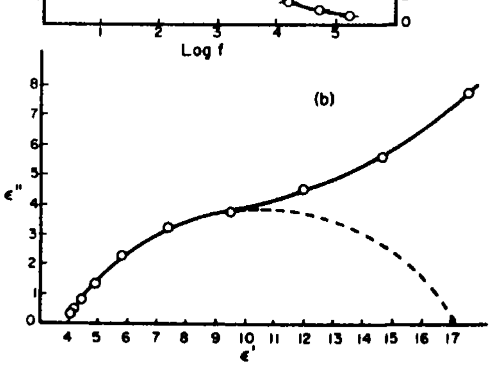

Fig. 6. (a) Permittivity (ϕ) and loss (-○-) in 5-*A* with 50 Torr. SO_2 pressure; (b) Cole–Cole plot of the data showing the dielectric absorption resolved from the conductivity.

is obtained from the Fuoss–Kirkwood plot. The major uncertainty in such an analysis is in obtaining the appropriate value of $\epsilon''_{max.}$. The value given by the Cole–Cole plot is only approximate since generally several circular arcs fit the experimental points, $\epsilon''_{max.}$ typically varying by about ±0·2. Adjustment of the value of $\epsilon''_{max.}$ obtained from the Cole–Cole plot, when used in the Fuoss–Kirkwood plot shows that the Cole–Cole values tend to be the maximum possible values in most cases since on increasing these values the Fuoss–Kirkwood plot deviates from linearity. On decreasing the $\epsilon''_{max.}$ values the Fuoss–Kirkwood plot remains linear for $\epsilon''_{max.}$ values 0·2 to 0·3 less than the Cole–Cole values so that a mean $\epsilon''_{max.}$ may be obtained with an uncertainty of ±0·15 (i.e. 5 per cent). Log $f_{max.}$ varies with this range of $\epsilon''_{max.}$ values by about 0·1, so that the uncertainty in log $f_{max.}$ is ±0·05 and in β it is ±0·01. The values of $\epsilon''_{max.}$ given here are those obtained directly from the Cole–Cole plot and the log. $f_{max.}$ values are obtained from these. Table 3 gives the dielectric absorption parameters for one typical absorption/desorption run, and Fig. 7 shows the movement of the loss peak with sulphur dioxide content. The values of SO_2 p.u.c. are only approximate due to the inadequacy of the available isotherm.

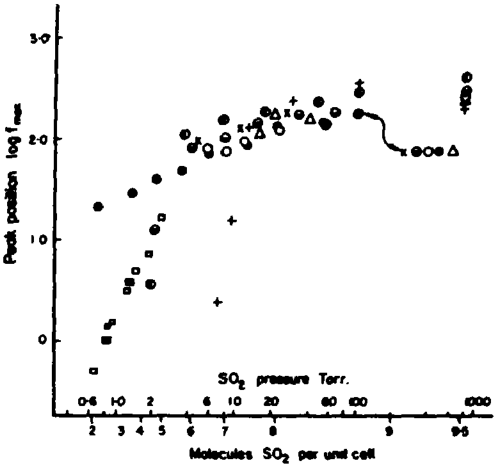

Fig. 7. Movement of the dielectric loss peak in 5-*A*/SO_2 with SO_2 content, (+) 1st adsorption; (×) 1st desorption; (◐) 2nd adsorption; (◒) 3rd adsorption; (△) 4th adsorption/desorption; (○) 5th adsorption; (●) 5th desorption; (□) 6th adsorption; (■) 7th adsorption, after ammonia desorption.

In Fig. 7 there is no evidence of dielectric hysteresis on adsorption and desorption above 3 Torr. SO_2 pressure. Below 3 Torr. there is some evidence that dielectric hystere-

Table 3. Dielectric absorption parameters in 5-A at various sulphur dioxide contents (5th adsorption/desorption)

SO_2 Pressure Torr.	SO_2 p.u.c.	ϵ''_{max}	ϵ_0	ϵ_∞	log. f_{max}	β
6·0	6·6	3·60	15·95	4·00	1·875	0·49
7·6	6·9	3·74	16·00	3·95	1·850	0·47
11·0	7·4	3·52	15·70	3·87	2·000	0·48
21·0	8·0	3·62	16·00	4·00	2·070	0·47
50·0	8·5	3·85	17·30	3·85	2·150	0·47
100	8·8	3·80	16·30	4·10	2·250	0·47
760	9·5	3·60	16·70	4·12	2·400	0·44
100	8·8	3·73	16·10	4·07	2·275	0·48
51·0	8·5	3·79	16·20	4·02	2·150	0·48
21·0	8·0	3·55	15·60	3·98	2·100	0·47
11·0	7·4	3·52	15·40	3·80	1·970	0·48
5·8	6·5	3·54	15·40	3·78	1·875	0·49
3·3	5·6	3·63	15·50	3·80	1·675	0·46
2·0	4·6	3·73	15·75	3·70	1·580	0·47
1·3	3·4	3·60	15·50	3·78	1·460	0·46
0·7	2·2	3·60	15·50	3·70	1·310	0·47

sis occurs. The specimen was allowed over 12 hr for equilibration at each pressure on the fifth desorption below 3 Torr. hence the deviation shown by these points is perhaps less an expression of non-stoichiometric equilibrium in the adsorption than of non-uniformity within the adsorbent.

There is no indication that $\epsilon''_{\text{max.}}$ falls at low SO_2 pressures as was the case with ammonia. To ascertain if the anomalous results obtained on the first adsorption were peculiar to adsorptions following water desorptions, one sulphur dioxide adsorption was made on a sample after desorption of ammonia. The points are shown in Fig. 7. It can be seen that this did not give anomalous results.

Temperature variation is subject to the same limitations as for ammonia, since no sulphur dioxide isosteres are available, thus activation energies obtained are minimum values. Reasonably good linear Arrhenius plots were obtained giving the activation energies in Table 4. The equilibrium pressure variation is also given in the table. Above room temperature the dielectric loss peak moved out of the conductivity loss and the peak was clearly distinguishable. This confirms the dielectric loss indicated by the Cole-Cole plots and shows the loss process has a higher activation energy than the conductivity process.

(C) Carbon dioxide

As in the two previous cases the first adsorption gave irreproducible results, subsequent adsorption/desorptions gave reproducibility. Figure 8 shows the effect of various equilibrium carbon dioxide pressures on the observed dielectric loss in 5-*A*. The curve for 760 Torr. carbon dioxide indicated the possible presence of a dielectric loss peak. Cole–Cole and Fuoss–Kirkwood analysis confirmed this. Table 5 gives the dielectric absorption parameters thus obtained: it can be seen that some variation of $\epsilon'_{\text{max.}}$ occurs on adsorption/desorption but no variation occurs in $\log f_{\text{max.}}$.

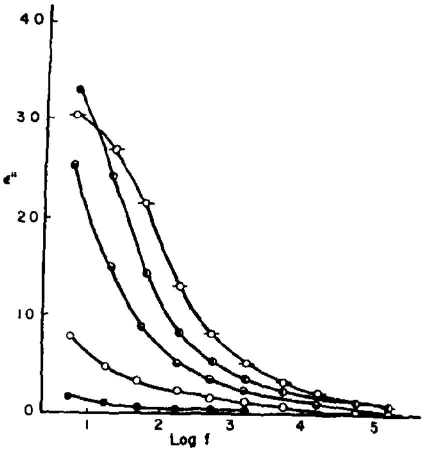

Fig. 8 Effect of adsorbed CO_2 on dielectric loss in 5-*A*, (●) 1·0 Torr.; (○) 10 Torr.; (◒) 50 Torr.; (◐) 150 Torr.; (-○-) 760 Torr.

Table 4. Activation energy of the observed dielectric loss process in 5-A/SO_2 at various SO_2 contents, with the equilibrium pressure variation corresponding to the extremes of temperature used

Temp. °C max.	Temp. °C min.	Pressure Torr. max.	Pressure Torr. min.	ΔH^{*} kcal. mole^{-1}
73·0	25·0	760	760	14·5 ± 1·5
61·0	22·5	37·0	28·0	9·6 ± 1·0
110	35·5	19·0	8·1	6·8 ± 1·0

Temperature variation is made difficult since the peak only moves into the measurable frequency range at saturation and, although isosteres for carbon dioxide adsorption are available, pressures above 760 Torr. are required to maintain constant carbon dioxide content and the apparatus is not suitable for this purpose. The Arrhenius plot obtained by temperature variation with a carbon dioxide atmosphere of 760 Torr. is shown in Fig. 9. The activation energy obtained, i.e. $8{\cdot}5 \pm 1{\cdot}0$ kcal.mole^{-1}, is again a minimum possible value.

(D) n-pentane

The effect of various *n*-pentane pressures on the dielectric properties of 5-*A* is given

Table 5. Dielectric absorption parameters in 5-A at various carbon dioxide contents (adsorption/desorption)

CO_2 Pressure Torr.	CO_2 p.u.c.	ϵ''_{max} $\pm 0{\cdot}1$	log. $f_{max.}$ $\pm 0{\cdot}05$	β
50	6·5	3·84 ± 0·3	−0·20	0·50
150	7·8	3·94	0·20	0·46
300	8·2	3·40	0·55	0·47
760	9·0	3·02	0·98	0·48
300	8·2	3·17	0·55	0·46
150	7·8	3·32	0·30	0·47
50	6·5	3·66 ± 0·2	−0·23	0·47

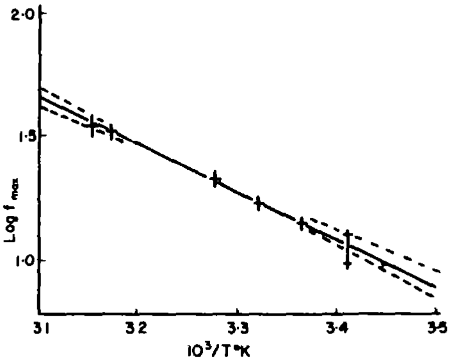

Fig. 9. Arrhenius plot of 5-*A*/CO_2 loss peak at 760 Torr. CO_2 pressure.

in Table 6. There is a considerable increase in both permittivity and loss on *n*-pentane adsorption, although variation of the amount adsorbed has little effect on the loss after the first amount adsorbed.

DISCUSSION

The most striking feature of the above results is the similarity of the dielectric loss peak observed with ammonia, sulphur dioxide and carbon dioxide as the adsorbed phases. There is also a striking similarity to the dielectric loss peak, absorption II, observed in the 5-*A*/H_2O system[1]. The appearance of an absorption having very similar characteristics in the presence of four very different adsorbates indicates that the process is not due to the adsorbate itself, particularly in the case of the non-polar carbon dioxide. The present data indicate that the process is ionic in character and supports the assignment of absorption II in Part I to such a process. Other authors have favoured ionic mechanisms for similar processes observed in silica gel, e.g. Heukelon[5] showed that a region

Table 6. Permittivity and loss factor of 5-A at various n-C_5H_{12} *pressures*

C_3H_{12} Pressure Torr.	11		39		230		230 after 24 hr	
Freq. Hz	ϵ'	$10^2\epsilon''$	ϵ'	$10^2\epsilon''$	ϵ'	$10^2\epsilon''$	ϵ'	$10^2\epsilon''$
5·25	3·09	37·8	3·21	41·5	3·23	40·7	3·21	39·0
18·0	2·96	24·9	3·02	26·3	3·04	28·4	3·02	28·1
54·0	2·90	17·5	2·90	18·3	2·96	20·1	2·96	17·6
179	2·84	11·7	2·84	12·3	2·88	13·5	2·88	11·9
525	2·82	8·6	2·82	9·0	2·84	9·8	2·84	8·7
1586	2·78	6·1	2·78	6·1	2·82	6·5	2·82	6·0
5269	2·76	4·5	2·78	4·7	2·78	4·9	2·78	4·7
15·9k	2·76	4·2	2·76	4·2	2·78	4·4	2·78	4·2
51·9k	2·72	4·0	2·76	4·0	2·78	4·1	2·78	4·0
148k	2·70	3·8	2·72	3·8	2·76	3·8	2·76	3·6

of loss in silica gel was independent of the nature of the adsorbate and Zhilenkov[6] favoured this mechanism on the basis of movement to higher frequencies of the loss process with increasing amount adsorbed.

To suggest a specific mechanism for the cation process is hazardous but a consideration of the possibilities is worthwhile. Firstly some other relevant data should be mentioned; a similar process has been observed in the K^+(3-*A*), Na^+(4-*A*) and Ag^+ ion forms of type-*A*[7], the frequency of occurrence, and value of $\epsilon''_{max.}$ varying with the cation. It is reasonable to assume that the process is due to the same type of cation in all these ion forms and that the most probable cations involved are those which lie close to the 6-membered oxygen-ring windows in the type-*A* cavity, i.e. the type-I cations. The basis of this assumption is, firstly, that in 5-*A* these are the only cations present and secondly, in 3-*A*, 4-*A* and Ag-*A* the type-II cations will be moved away from their sites to form a cluster with the adsorbate[8]. They are thus unlikely to jump between well defined sites and hence give rise to such a constant value of $\epsilon''_{max.}$, whereas the type-I cations move only slightly, if at all, from their sites in response to an adsorbate[8–10]. The process in 5-*A* is believed not to be due to the sodium ions present since in 4-*A* the cation process occurs at a very much higher frequency than that observed in 5-*A*.

The immediately obvious possibilities for a cation jump between well defined sites for the type-I cations are: (I) If the cation does not lie in the plane of the 6-membered oxygen ring: a jump through the 6-membered ring window to an electrostatically equivalent site on the opposite side; (II) A jump from one type-I site to another type-I site; (III) A jump from a type-I site to a position close to the 8-membered oxygen-ring window, i.e. the type-II ion site in the anhydrous material.

While jump (I) is possible for unhydrated cations it is unlikely that a hydrated cation, particularly the K^+ ion, would pass through a 2·66 Å dia. window. Further, it is difficult to envisage how the presence of an adsorbate would have the effect on the activation energy observed if the cation remains unhydrated for this jump. Jump (II) is even less likely since this would necessitate a type-I ion site being vacant for the ion to jump to. Whilst this may be possible in 5-*A*, in the univalent ion types all the type-I sites are occupied and for the process to occur it would require a type-I ion first jumping to another position to create a vacancy.

Jump (III) is thus the most likely since it could occur in all the ion forms. A cation jump of this nature can explain the observed experimental facts. In the dehydrated state, the type-I cations would be so tightly bound in their sites that the jump would occur at a very low frequency or practically not at all at room temperatures. As an adsorbate fills the cavities the type-I ions move away slightly from the oxygen-anion-ring in response to the adsorbate, hence weakening the bond between the cation and the lattice. That the activation energy for the process increases as the cation becomes more mobile, i.e. see Part I and SO_2 data this paper, can be accounted for, as in Part I, by either simple steric hindrance or by the adsorbate becoming attached to the cation.

To estimate the actual effective polarisation and hence dielectric absorption to be associated with a cation jump is a distinctly arbitrary process. The closeness of approach of the ions to the lattice makes polarisation (induced moments) of major significance and it is difficult to assess this quantitatively. Because of the large negative charge associated with the zeolite lattice a simple cation jump giving rise to an effective dipole moment $\mu = 1/2\ ed$, where e is ionic charge and d the distance it moves, as used by Volger *et al.*[11] for dielectric loss due to cation jumping in glass, cannot be used. In the present case it is more realistic to consider the effective dipole formed by the cation and the lattice in each of these two sites and relate these to the observed moment. A treatment of a case such as this is given in the appendix, the particular result immediately applicable is that of the special case (III) in which the energy difference between the two potential minima must be zero, so that the observed dielectric loss maxima, $\epsilon''_{\text{max.}}$, and thus μ_{eff} is independent of temperature as is here observed. Such a situation can arise in the zeolites since Barrer[12] has shown that translation of certain ions between 6- and 8-membered rings may not involve large energy changes, e.g. when a sodium ion approaches a 6- or 8-membered ring along the axis normal to the plane of the ring the minimum electrostatic energies are 154 and 155 kcal.g.ion^{-1} respectively. Since in the present situation the proposed mechanism involves sites close to 6- and 8-membered rings then special case (III) in the appendix can apply. Thus the observed dipole moment for the process, μ_{eff}, is given by

$$\mu^2_{\text{eff}} = \frac{(\mu_1 - \mu_2)^2}{4}$$

where μ_1 and μ_2 are vector quantities representing the dipoles formed between the ion and the lattice in each of the two sites. The observed dipole, and hence $\epsilon''_{\text{max.}}$ is merely a function of the steric positioning of the cation in the two sites relative to the lattice.

The dipole moment associated with the cation process has been evaluated using the Onsager equation[13] for a solution of a polar solute, i.e.

$$\frac{2\epsilon''_{\text{max}}}{\beta} = \epsilon_0 - \epsilon_\infty = \frac{4\pi N_1 u^2}{3kT}\left[\frac{\epsilon_1(\epsilon_{\infty 2}+2)}{2\epsilon_1 + \epsilon_{\infty 2}}\right]^2$$

and treating the system as a solution of cations in the zeolite. In the above equation N_1 is the number of dipoles per cm^3 of solution. With the assumption that only one cation per unit cell jumps during the process and taking a constant density of 2·0 for 5-*A* the Ca^{2+} concentration is 1·2 g ions.l.$^{-1}$. $\epsilon''_{\text{max.}}$ has a mean value for all adsorbates of 3·70 and β has a mean value of 0·48. The terms ϵ_1, the solvent permittivity, and $\epsilon_{\infty 2}$, the solute high frequency permittivity, may both be given the value 2·32, i.e. the anhydrous zeolite permittivity, since the cation process is independent of the adsorbate. With these values the effective dipole moment for the cation process in 5-*A* is 10·0 D independent of adsorbate or content.

In 5-*A* the cation lies close to the plane of the 6-membered oxygen ring so that μ_1 for the cation in site I will be small, i.e. the induced dipoles in the ring oxygens will tend to cancel each other and the effective positive and negative centres will tend to coincide, so that to a first approximation we may take $\mu_1 = 0$. μ_{eff} then becomes $\mu_2/2$, i.e. $\mu_2 =$ 20·0 D. From $\mu = e.d$, $d = 20{\cdot}0/9{\cdot}6 = 2{\cdot}1$ Å. This means that in site II the cation lies about 2·1 Å away from the plane of the 8-membered ring. In Na-A the type-II cation position is about 2·5 Å away from the 8-membered ring [10]. It is quite probable that for a Ca^{2+} ion this distance would be smaller because of the double charge on the calcium ion, and a value of 2·1 is not unreasonable. This distance will increase if μ_1 is not zero, i.e. if the Ca^{2+} ion moves from the plane of the 6-membered ring in response to the adsorbate.

The fact that the absorption appears to fall in intensity at low ammonia contents indicates that possibly a certain amount of adsorbate is required before the process can take place; possibly the amount corresponding to coverage of the most active sites. Alternatively an equilibrium distribution of the ammonia throughout the disc may not have been achieved, although if this were the case some increased distribution of relaxation times (i.e. a smaller value of β) would have been expected.

DIELECTRIC ISOTHERMS

In Part I a dielectric isotherm was obtained for the 5-*A*/H_2O system. In a similar manner, i.e. by plotting ϵ_∞ for the cation process against adsorbate content, dielectric isotherms can be obtained for ammonia and sulphur dioxide on 5-*A*. These are shown in Fig. 10(a) and (*b*). The adsorbate contents quoted for SO_2 are only approximate due to the inadequacy of the available isotherm, as has been indicated.

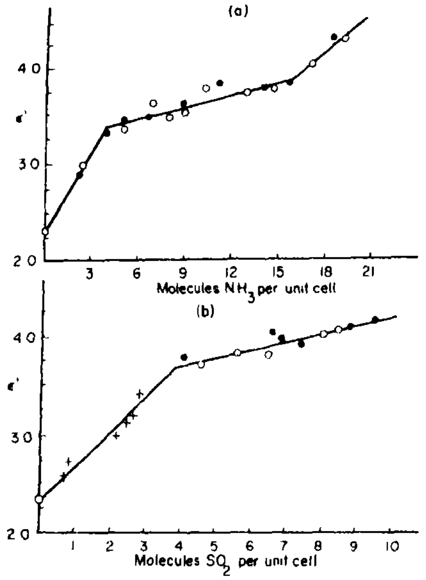

Fig. 10. Dielectric isotherms for (a) ammonia on 5-*A*, (●) adsorption (○) desorption, (b) sulphur dioxide on 5-*A* (●) adsorption; (○) desorption; (+) low pressure run.

Therefore little reliance can be placed on the adsorbate content required for coverage of the most active sites.

From the ammonia isotherm, Fig. 10(a), coverage of the most active sites occurs between 3 and 4 molecules per unit cell. Ammonia is capable of hydrogen bonding and may be expected to have similar most active sites in the zeolite cavity to those of water. If this is the case, i.e. that the 8-membered oxygen ring windows form these sites as suggested for water in Part I, then a figure of 3 or 4 molecules would indicate that the presence of one ammonia molecule in the window prevents a second also being there. The X-ray work of Lewis[10] showed that the 8-membered ring windows were the sites where ammonia molecules had the longest residence time.

The form of the ammonia isotherm is similar to that of water, again showing three linear regions, except that for ammonia the slope of the third region is less than that of the first; this is unexpected. Because of the hydrogen bonding capabilities of ammonia the same interpretation of the isotherm as for water can be given (Part I), i.e. the contribution to the high frequency permittivity by relaxation of part of the dipole being suppressed by neighbouring adsorbate molecules as the cavity fills up. This would indicate that the final ammonia molecules adsorbed are hydrogen bonded to those on the cavity walls by at least two hydrogen bonds thus reducing the dipole contribution to the high frequency permittivity.

Evaluation of the dipole moment of adsorbed ammonia over the range of the isotherm by the Onsager equation is prevented by the absence of an ϵ_∞ value for ammonia. An estimate can be obtained using the Böttcher approximation of the Debye equation[14],

$$\Delta\epsilon' = (\epsilon_0+2)^2\,\frac{4\pi N_1\mu^2}{27kT}$$

where ϵ_0 is the zeolite permittivity (2·32) and N_1 is the number of dipoles per cm^3. Evaluation of $\mu(H_2O)$ by this equation when compared with the values obtained from the Onsager equation (Part I) showed the Debye dipole moment values to be increased by about 30 per cent. The values obtained for ammonia are given in Table 7. Comparing these with $\mu(NH_3) = 1{\cdot}42$ D[15] shows that in no region does the ammonia molecule contribute its full dipole moment to the high frequency polarisation (i.e. allowing for the increase due to the Debye equation). This result is, however, a normal one for adsorbed molecules; if they are rigidly held then, as in most polar molecule crystal lattices, μ(obs) becomes zero. The significantly large μ(obs) measures the residual mobility of the ammonia molecular moment.

Table 7. Apparent dipole moment of adsorbed ammonia at various ammonia contents, obtained from the dielectric isotherm

NH_3 p.u.c.	Debye D
1·5	1·36
3·0	1·37
4·5	1·28
6·0	1·14
7·5	1·06
9·0	1·00
10·5	0·95
12·0	0·92
13·5	0·90
15·0	0·87
16·5	0·86
18·0	0·88
19·5	0·90

In the case of sulphur dioxide the lower slope in the second region of the dielectric isotherm is particularly unexpected. The adsorbed molecules are unable to hydrogen bond to the lattice and once the most active sites have been covered, in this case probably the cations, then the full dipole should be able to contribute. The dipole moments of adsorbed SO_2, again from the Debye equation, are given in Table 8. Comparing these with $\mu(SO_2) =$ 1·61 D[15] and again allowing for up to 30 per cent increase due to the use of the Debye equation shows that the reverse of the expected behaviour is the case. Several causes of lower slopes in the second region of dielectric isotherms have been suggested in the literature. Petrie and McIntosh[16] suggested a different electric field may exist within the pores from that within the solid, Chapman and McIntosh[17] suggested that interaction between the material in the first layer and subsequent adsorbed layers could be the explanation and Zhilenkov[18] suggested that as further layers form the dipoles in the first layer become localised. The explanation of Chapman and McIntosh is essentially that given here for water and ammonia on 5-*A*, the interaction between molecules on the most active sites and their neighbours on the cavity walls possibly becoming so great as to meet Zhilenkov's condition. These conclusions seem less applicable to sulphur dioxide except in the more general sense that steric restriction to the reorientation of the adsorbed molecules is enhanced as the cavities are filled: the first molecules have a partial mobility which is lost.

Table 8. Apparent dipole moment of adsorbed sulphur dioxide at various SO_2 contents, obtained from the dielectric isotherm

SO_2 p.u.c.	Debye D
1·0	1·51
2·0	1·57
3·0	1·61
4·0	1·61
5·0	1·49
6·0	1·42
7·0	1·37
8·0	1·33
9·0	1·30

Acknowledgements—I am grateful to Dr Mansel Davies for his interest and much discussion during the course of this work, and to Dr Graham Williams for helpful discussion and for providing the appendix to this paper. I also acknowledge the receipt of an S.R.C. Research Studentship

REFERENCES

1. MORRIS B., *J. Phys. Chem. Solids* **30**, 73 (1969).
2. Linde Molecular Sieves Adsorption Data Sheets
3. COLE K. S. and COLE R. H., *J. chem. Phys.* **9**, 341 (1941).
4. FUOSS R. M. and KIRKWOOD J. G., *J. Am. chem. Soc.* **63**, 385 (1941).
5. HEUKELON W. and VAN REIJEN I. L., *J. Chim. Phys.* **51**, 632 (1954).
6. ZHILENKOV I. V., *Zh. fiz. Khim* **30**, 2519 (1956).
7. MORRIS B., *J. phys. Chem. Solids* **30**, 103 (1969).
8. SMITH J. V., *Proc. S.C.I. Conf. Mol. Sieves.* London (1967).
9. MEIER W. M. and SHOEMAKER D. P., *Z. kristallogr.* **123**, 357 (1966).
10. LEWIS P. H., *J. phys. Chem.* **63**, 527 (1959).
11. VOLGER J., STEVELS J. M. and VAN AMERONGEN C., *Phillips Res. Rep.* **8**, 452 (1953).
12. BARRER R. M. and BRATT G. C., *J. Phys. Chem. Solids* **12**, 154 (1959).
13. ONSAGER L., *J. Am. chem. Soc.* **58**, 1486 (1936).
14. BÖTTCHER C. J. F., *Theory of Electric Polarisation*. Elsevier, Amsterdam (1952).

15. McCLELLAN A. L., *Tables of Experimental Dipole Moments*, Freeman, London (1963).
16. PETRIE E. and McINTOSH R. L., *Can. J. Chem.* **35**, 183 (1957)
17. CHAPMAN I. and McINTOSH R. L., *Can. J. Chem.* **40**, 92 (1962).
18. ZHILENKOV I. V., *Izv. Akad Nauk. SSSR Otd Khim Nauk.* 282 (1957)
19. HOFFMAN J. D and PFEIFFER H G., *J. chem. Phys.* **22**, 132 (1954).
20. COLE R. H., *J. chem Phys.* **42**, 637 (1965)

APPENDIX

by G. WILLIAMS and B. MORRIS

We wish to evaluate the dielectric behaviour for the two site model shown in Figure A 1 We consider the case where the dipole moment of a unit in site 1 is given by $\boldsymbol{\mu}_1 = \mu_1\rho_1\mathbf{x}$ and the dipole moment for a unit in site 2 is $\boldsymbol{\mu}_2 = \mu_2\rho_2\mathbf{x}$ Here μ_1 and μ_2 are the magnitudes of the dipole moments, $\rho_1 = \pm 1$ and $\rho_2 = \pm 1$, and $\mathbf{x}$ is the unit vector in the positive x direction as indicated in the figure. The units move between sites 1 and 2 in the absence of an applied electric field according to the elementary transition probabilities k_{12} and k_{21}, and the energy difference between the sites is denoted as V so that $k_{12}/k_{21} = \exp - V/k = S$, say.

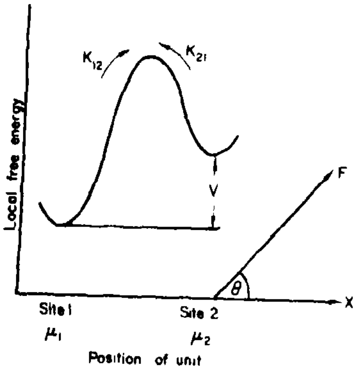

Fig. A1 Local free energy diagram for the assumed two site model. Occupation by the unit of sites 1 and 2 leads to resultant dipole moments of μ_1 and μ_2 respectively

The occupational probabilities of sites 1 and 2 at time t are given by [19]

$$P_1(t) = \frac{1}{1+S} + m\psi(t)$$
$$P_2(t) = \frac{S}{1+S} - m\psi(t). \qquad (A.1)$$

Here $\psi(t) = \exp - (k_{12} + k_{21})t$, and m is to be determined from the initial conditions.

We may now evaluate the dielectric behaviour for a polycrystalline sample (coordinates fixed with respect to time, but randomly oriented in space). Two methods will be used. (A) The perturbation of the barrier system by an applied electric field, as outlined by Hoffman and Pfeiffer [19] and (B) a correlation function method similar to that outlined by Cole[20].

(*A*) *Relaxation due to the withdrawal of a steady electric field*

If a steady electric field F is applied to the system (see Fig. A.1) then the occupational probabilities of the sites at equilibrium will be given by

$$\frac{{}^\circ P_1{}^F}{{}^\circ P_2{}^F} = \frac{\exp^{\boldsymbol{\mu}_1\cdot F/kT}}{S\exp^{\boldsymbol{\mu}_2\cdot F/kT}} \qquad (A.2)$$

${}^\circ P_1{}^F$ and ${}^\circ P_2{}^F$ represent the equilibrium occupational probabilities of sites 1 and 2 respectively in the presence of the field. For low field densities, equation (A.2) may be expanded, and with the aid of the relation ${}^\circ P_1{}^F + {}^\circ P_2{}^F = 1$, we have

$$\left.\begin{aligned} {}^\circ P_1{}^F &= {}^\circ P_1 + {}^\circ P_1{}^\circ P_2\frac{(\boldsymbol{\mu}_1\cdot F - \boldsymbol{\mu}_2\cdot F)}{kT} \\ {}^\circ P_2{}^F &= {}^\circ P_2 - {}^\circ P_1{}^\circ P_2\frac{(\boldsymbol{\mu}_1\cdot F - \boldsymbol{\mu}_2\cdot F)}{kT}. \end{aligned}\right\} \qquad (A.3)$$

Here, ${}^\circ P_1 = 1/(1+S)$, ${}^\circ P_2 = S/(1+S)$, correspond to the equilibrium occupational probabilities of sites 1 and 2 respectively in the absence of an electric field. A comparison of (A.1) and (A.3) shows that if the steady electric field is withdrawn at $t = 0$, then $P_1(t)$ decays to ${}^\circ P_1$, according to equation (A.1) with $m = {}^\circ P_1{}^\circ P_2(\boldsymbol{\mu}_1\cdot F - \boldsymbol{\mu}_2\cdot F)/kT$. The relaxation time for this process is obtained via $\psi(t)$, so that

$$\tau = (k_{12} + k_{21})^{-1}. \qquad (A.4)$$

The magnitude of the dielectric relaxation process is obtained by evaluating the averaged polarization in the presence of the field. Since $\boldsymbol{\mu}_1$ and $\boldsymbol{\mu}_2$ lie along the x axis, the polarization arises from the component of the polarization along this axis so the polarization per unit is given by

$$\mathscr{P}_x = [{}^\circ P_1{}^F \mu_1 + {}^\circ P_2{}^F \mu_2].\cos\theta \qquad (A.5)$$

The averaged value of $\mathscr{P}_x$ is obtained by averaging over all directions of F, so a combination of equations (A 2) and (A 5), with $\langle\cos^2\theta\rangle = \frac{1}{3}$ gives

$$\begin{aligned} \langle\mathscr{P}_x\rangle &= {}^\circ P_1{}^\circ P_2\frac{(\mu_1\rho_1 - \mu_2\rho_2)^2 F}{3kT} \\ &= {}^\circ P_1{}^\circ P_2\frac{(\boldsymbol{\mu}_1 - \boldsymbol{\mu}_2)^2 F}{3kT}. \end{aligned} \qquad (A.6)$$

The dipole polarizability per unit is given by

$$\alpha_\mu = \frac{\langle\mathscr{P}_x\rangle}{F} = {}^\circ P_1{}^\circ P_2\frac{(\boldsymbol{\mu}_1 - \boldsymbol{\mu}_2)^2}{3kT}. \qquad (A.7)$$

Thus the system behaves as if it had an effective dipole moment μ_{eff} per unit, where

$$\begin{aligned} \mu_{\text{eff}}^2 &= {}^\circ P_1{}^\circ P_2(\boldsymbol{\mu}_1 - \boldsymbol{\mu}_2)^2 \\ &= \frac{S}{(1+S)^2}(\boldsymbol{\mu}_1 - \boldsymbol{\mu}_2)^2. \end{aligned} \qquad (A.8)$$

The result is that the system yields a single relaxation time as given by equation (A.4), and appears to have an effective dipole moment per unit of μ_{eff}.

We note for the special case $\boldsymbol{\mu}_1 = -\boldsymbol{\mu}_2$, which was the case considered by Hoffman and Pfeiffer, that $\mu_{eff}^2 = 4°P_1°P_2\,\mu^2$, in agreement with the result of these authors.

(*B*) *Correlation function method*

Cole has derived the relations[20]

$$\frac{\epsilon^* - \epsilon_\infty}{\epsilon_0 - \epsilon_\infty} = \left[1 + \frac{3\epsilon_0}{2\epsilon_0 + \epsilon_\infty}\{\mathscr{L}(-\gamma(t)) - 1\}\right]^{-1} \quad (A.9)$$

$$\gamma(t) = \frac{\langle \boldsymbol{\mu}(0)\cdot\boldsymbol{\mu}(t)\rangle}{\langle \boldsymbol{\mu}(0)\cdot\boldsymbol{\mu}(0)\rangle}. \quad (A.10)$$

$\mathscr{L}$ indicates the LaPlace transform and $\gamma(t)$ is the dipole moment correlation function. The theory was derived for N units, each having the same dipole moment μ. In the present case the dipole moment in sites 1 and 2 are different. It seems reasonable to suppose that the dipole decay function may be expressed as the weighted sum of the individual decay functions so that

$$\langle \boldsymbol{\mu}(0)\cdot\boldsymbol{\mu}(t)\rangle = \sum_{i=1}^{2} [\boldsymbol{\mu}(0)\cdot\boldsymbol{\mu}(t)]_i\cdot°P_i. \quad (A.11)$$

Here $[\boldsymbol{\mu}(0)\cdot\boldsymbol{\mu}(t)]_i$ is the decay function for units initially in site i at $t = 0$, and the summation is taken in this case over the two available sites.

For units in site 1 at $t = 0$, then $P_1(0) = 1$ so equations (A 1) read

$$P_1(t) = \frac{1}{1+S}[1 + S\psi(t)]$$

$$P_2(t) = \frac{S}{1+S}[1 - \psi(t)] \quad (A.12)$$

Now $[\boldsymbol{\mu}(0)]_1 = \boldsymbol{\mu}_1$ and

$$[\boldsymbol{\mu}(t)]_1 = P_1(t)\cdot\boldsymbol{\mu}_1 + P_2(t)\cdot\boldsymbol{\mu}_2. \quad (A.13)$$

Thus a combination of (A.12) and (A.13) yields

$$[\boldsymbol{\mu}(0)\cdot\boldsymbol{\mu}(t)]_1 = \frac{1}{1+S}[\boldsymbol{\mu}_1\cdot(\boldsymbol{\mu}_1 + S\boldsymbol{\mu}_2) + S\boldsymbol{\mu}_1\cdot(\boldsymbol{\mu}_1 - \boldsymbol{\mu}_2)\psi(t)] \quad (A.14)$$

In a similar manner we obtain for units in site 2 at $t = 0$

$$[\boldsymbol{\mu}(0)\cdot\boldsymbol{\mu}(t)]_2 = \frac{1}{1+S}[\boldsymbol{\mu}_2\cdot(\boldsymbol{\mu}_1 + S\boldsymbol{\mu}_2) - \boldsymbol{\mu}_2\cdot(\boldsymbol{\mu}_1 - \boldsymbol{\mu}_2)\psi(t)] \quad (A.15)$$

From equations (A.11), (A.14) and (A.15) we have

$$\langle \boldsymbol{\mu}(0)\cdot\boldsymbol{\mu}(t)\rangle = \frac{1}{(1+S)^2}[(\boldsymbol{\mu}_1 + S\boldsymbol{\mu}_2)^2 + S(\boldsymbol{\mu}_1 - \boldsymbol{\mu}_2)^2\psi(t)] \quad (A.16)$$

For a polycrystalline sample the time independent term in equation (A.16) will not contribute to the dielectric relaxation so we may write

$$[\langle \boldsymbol{\mu}(0)\cdot\boldsymbol{\mu}(t)\rangle]_{\text{polycrystalline}} = \frac{S}{(1+S)^2}(\boldsymbol{\mu}_1 - \boldsymbol{\mu}_2)^2\psi(t). \quad (A.17)$$

From equations (A.10) and (A.17) we have

$$\gamma(t) = \psi(t) \quad (A.18)$$

so from equation (A.9)

$$\frac{\epsilon^* - \epsilon_\infty}{\epsilon_0 - \epsilon_\infty} = \frac{1}{1 + \dfrac{3\epsilon_0}{2\epsilon_0 + \epsilon_\infty}\cdot j\omega\tau}. \quad (A.19)$$

Here τ is given by equation (A.4).

The magnitude of the process is proportional to $\langle \boldsymbol{\mu}(0)\cdot\boldsymbol{\mu}(0)\rangle$ so equation (A.17) gives

$$\mu_{eff}^2 = [\langle \boldsymbol{\mu}(0)\cdot\boldsymbol{\mu}(0)\rangle]_{\text{polycrystalline}} = \frac{S}{(1+S)^2}\cdot(\boldsymbol{\mu}_1 - \boldsymbol{\mu}_2)^2. \quad (A.20)$$

Thus the system behaves according to equations (A 19) and (A.20), and we see that the correlation function method yields the same result as method (A) above.

This is the general solution for a two site model and μ_{eff} increases with increasing temperature through S. Considering the special cases of variables $\boldsymbol{\mu}_1$, $\boldsymbol{\mu}_2$ and S.

$$\boldsymbol{\mu}_1 = -\boldsymbol{\mu}_2; \quad \mu_{eff}^2 = 4\mu^2\frac{S}{(1+S)^2} \quad (I)$$

$\boldsymbol{\mu}_1 = -\boldsymbol{\mu}_2$ and if in Fig. A 1, $V = 0$ i.e. $S = 1$

$$\mu_{eff} = \frac{4\mu^2}{4} = \mu^2 \quad (II)$$

and μ_{eff} is independent of temperature.

With $V = 0$ and $\boldsymbol{\mu}_1 \neq \boldsymbol{\mu}_2$

$$\mu_{eff}^2 = \frac{(\boldsymbol{\mu}_1 - \boldsymbol{\mu}_2)^2}{4}. \quad (III)$$

μ_{eff} is again independent of temperature.

J. Phys. Chem. Solids **Pergamon Press 1969. Vol. 30, pp. 103–115. Printed in Great Britain.**

A DIELECTRIC STUDY OF THE SYNTHETIC LINDE TYPE-*A* ZEOLITE–III. DIELECTRIC PROPERTIES OF 3-*A*, 4-*A* AND Ag-*A* WITH ADSORBED WATER

BRIAN MORRIS
Edward Davies Chemical Laboratory, University College of Wales, Aberystwyth, U.K

(*Received* 10 *April* 1968)

Abstract—The permittivity and dielectric loss factor for the Molecular Sieve Zeolites type 3-*A* and 4-*A* and a silver exchange form of type-*A* have been measured in the frequency range 5 Hz to 140 MHz with various amounts of adsorbed water present.

A region of dielectric loss in all three may be attributed to movement, within the cavities, of the interstitial cations. The activation energy for the process varies with water content and at any one water content a linear relationship exists between the activation energies and the size of the cations concerned. The behaviour of the activation energy with temperature suggests some change of phase of the adsorbed water takes place, equivalent to freezing, at a temperature well below 0°C.

A further region of dielectric absorption has been observed which has been attributed to relaxation, with an ice-like character, of the major part of the adsorbed water dipole moment. The remainder of the water dipole relaxing by motions, other than complete reorientation, at higher frequencies than those available in the present study.

INTRODUCTION

In Parts I and II[1] the dielectric properties of the Linde Molecular Sieve Zeolite type 5-*A* with various polar and non-polar molecules constituting the adsorbed phase are reported. In the present paper the dielectric study of the type-*A* zeolite is extended to the K^+(3-*A*), Na^+(4-*A*) and Ag^+ ion forms. In these cases the number of cations per cavity is increased from the 7·5 in 5-*A* (i.e. $Ca_{4.5}$ Na_3) to 12 in the monovalent ion forms. This may be expected to have some influence on the dielectric properties of these types. The only adsorbate studied in these ion forms so far is water.

EXPERIMENTAL

The majority of results reported in the present work were obtained using the conventional techniques, i.e. Method I, described in Part I, and cover the frequency range 5·25 Hz to 140 MHz. The materials used were the commercially available Molecular Sieve Zeolites type 3-*A* ($K_9Na_3[(AlO_2)_{12}(SiO_2)_{12}]$ $27H_2O$) and type 4-*A* ($Na_{12}[(AlO_2)_{12}(SiO_2)_{12}]$ $27H_2O$). The pure powder material was used, containing no clay binder, as supplied by B.D.H. Ltd.

A silver form of type-*A* was prepared by ion-exchange. The 4-*A* or 5-*A* material was shaken for 24 hr at room temperature with each of four portions of $AgNO_3$ solution containing an excess of $AgNO_3$ above that required for complete exchange of the starting material in any one exchange. Analysis of the product showed 100 per cent exchange to the silver form to have taken place. A sample of Ag-*A* containing 80 per cent silver was also prepared. Several batches of Ag-*A* were prepared:

From 5-*A*	100% exchange $Ag_{12}[(AlO_2)_{12}(SiO_2)_{12}]24\,H_2O$
From 4-*A*	80% exchange $Ag_{10}Na_2[A]24\,H_2O$
From 4-*A*	100% exchange $Ag_{12}[A]24\,H_2O$.

The saturation water contents quoted are those given by Breck[2].

RESULTS

(*A*) *Type* 3-*A*

Only one sample of 3-*A* has so far been measured in the vacuum cell after dehydrating

Table 1. *Dielectric parameters for anhydrous* 3-A *zeolite*

Frequency (Hz)	ϵ'	ϵ''
5·25	4·60	1·690
18·0	3·87	0·903
54·0	3·60	0·529
179	3·36	0·291
525	3·23	0·181
1586	3·15	0·106
5269	3·10	0·070
$15{\cdot}9 \times 10^3$	3·08	0·049
$51{\cdot}9 \times 10^4$	3·04	0·038
148×10^3	3 04	0·029

at 450°C and 10^{-4} Torr.; it gives the values in Table 1. The value of ϵ' at 148 kHz (3·04) is somewhat higher than the value for 5-*A* in the anhydrous state (2·32). This, together with the increase in both ϵ' and ϵ'' in moving to low frequencies, could be due to a greater conductivity arising from the presence of the more mobile type-II K^+ ions. From ϵ'' at 5·2 Hz, using the relation $\epsilon'' \times f = 1{\cdot}8 \times 10^{12}$ k, a maximum possible value of the d.c. conductivity is obtained of $5 \times 10^{-12}\ \Omega^{-1}\text{cm}^{-1}$.

The effect of adsorbed water on the dielectric properties of 3-*A* is similar to its effect in 5-*A*. Figure 1 shows the permittivity, ϵ', and loss factor, ϵ'', of 3-*A* completely saturated with water, i.e. 3-*A* 27 H_2O p.u.c. in the frequency range 1 kHz to 140 MHz. Below 1 kHz ϵ'' continues to rise, presumably due to conductivity, and at frequencies below 100 Hz becomes too great to measure on the Thompson Bridge. As water is removed the large peak at 200 kHz moves rapidly to lower frequencies, the peak height also falling rapidly. Figure 2 shows the peak movement, and its variation in height, ϵ''_{max}, with water content. The agreement between two different specimens is indicated on the figure. Table 2 lists the dielectric absorption parameters for this absorption (absorption I).

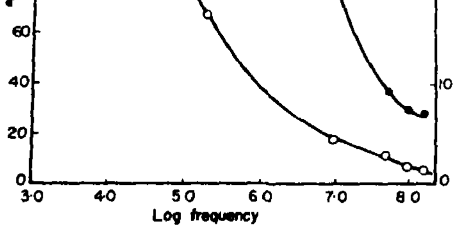

Fig. 1. Permittivity (○) and dielectric loss (●) in 3-*A* 27H_2O p.u.c.

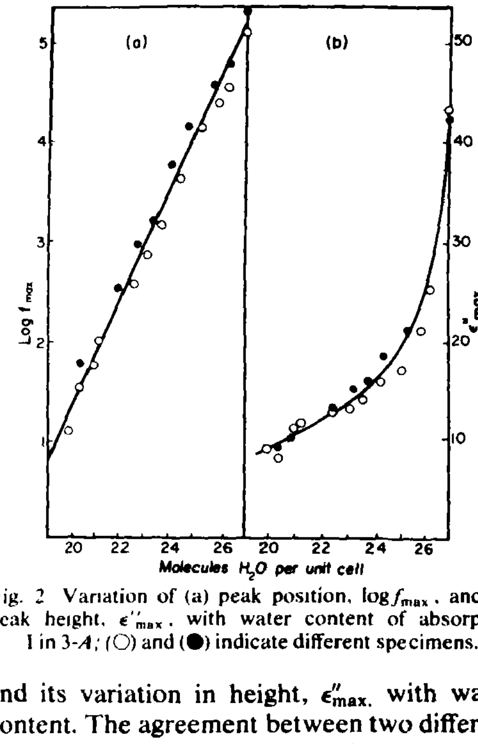

Fig. 2 Variation of (a) peak position, $\log f_{\text{max}}$, and (b) peak height, ϵ''_{max}, with water content of absorption I in 3-*A*; (○) and (●) indicate different specimens.

As absorption I moves to low frequencies it is followed by a second dielectric loss peak, (absorption II). As was the case with 5-*A* the peak height for absorption II is constant, but in 3-*A* the frequency separation between the two absorptions is greater. Figure 3 shows the movement of absorption II with water content and Table 3 lists the dielectric absorption parameters. In Table 3 values of ϵ_0 and ϵ_∞ are not given at high water contents since good

Table 2. Dielectric absorption parameters for absorption I *in* 3-A *at various water contents*

H_2O p.u.c.	$\epsilon''_{max.}$	ϵ_0	ϵ_∞	$\log f_{max.}$ $\pm 0{\cdot}05$	β $\pm 0{\cdot}01$	τ (sec)
27·0	42·0 ± 1·0	125 ± 2	8·0 ± 2·0	5·30	0·68	$7{\cdot}9 \times 10^{-7}$
26·2	31·0 ± 0·5	113 ± 2	11·0 ± 2·0	4·73	0·60	$3{\cdot}0 \times 10^{-6}$
25·5	22·1 ± 0·3	95 ± 2	10·0 ± 2·0	4·55	0·50	$4{\cdot}5 \times 10^{-6}$
24·4	18·3 ± 0·2	86·5 ± 1·0	12·0 ± 1·0	4·12	0·51	$1{\cdot}2 \times 10^{-5}$
23·3	15·6 ± 0·2	79·0 ± 1·0	15·5 ± 1·0	3·40	0·50	$6{\cdot}3 \times 10^{-5}$
22·5	13·0 ± 0·2	72·0 ± 1·0	15·5 ± 1·0	3·00	0·49	$1{\cdot}6 \times 10^{-4}$
20·8	10·3 ± 0·2	57·0 ± 1·0	16·5 ± 1·0	1·75	0·52	$2{\cdot}8 \times 10^{-2}$
20·3	9·4 ± 0·2	55·0 ± 1·0	17·0 ± 1·0	1·60	0·53	$4{\cdot}0 \times 10^{-2}$

Table 3. Dielectric absorption parameters for absorption II *in* 3-A *at various water contents*

H_2O p.u.c.	$\epsilon''_{max.}$ $\pm 0{\cdot}05$	ϵ_0 $\pm 0{\cdot}2$	ϵ_∞ $\pm 0{\cdot}2$	$\log f_{max.}$ $\pm 0{\cdot}03$	β $\pm 0{\cdot}01$	τ (sec)
22·5	3·15			6·27	0·33 ± 0·03	$8{\cdot}5 \times 10^{-8}$
21·1	3·15			5·98	0·39 ± 0·02	$1{\cdot}7 \times 10^{-7}$
19·9	3·20			5·76	0·42	$2{\cdot}8 \times 10^{-7}$
19·0	3·25			5·63	0·42	$3{\cdot}7 \times 10^{-7}$
17·7	3·20			5·40	0·47	$6{\cdot}3 \times 10^{-7}$
16·4	3·20			5·10	0·53	$1{\cdot}3 \times 10^{-6}$
15·4	3·05	14·7	5·5	4·95	0·54	$1{\cdot}8 \times 10^{-6}$
13·6	3·25	14·6	5·2	4·70	0·55	$3{\cdot}2 \times 10^{-6}$
12·4	3·30	14·4	5·0	4·48	0·60	$5{\cdot}3 \times 10^{-6}$
11·3	2·95	12·8	4·4	4·27	0·60	$8{\cdot}5 \times 10^{-6}$
10·9	3·05	12·8	4·4	4·23	0·60	$9{\cdot}3 \times 10^{-6}$

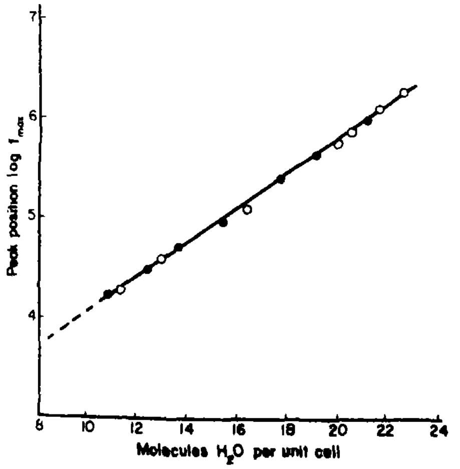

Fig. 3. Position of absorption II in 3-*A* at various water contents. (○) and (●) indicate different specimens.

Cole–Cole arc plots were not obtainable; the low frequency points, used to define ϵ_0, are increased due to the tail of absorption I and the high frequency values required to define ϵ_∞ are above 140 MHz.

Temperature variation of absorption I has not been investigated for the same reasons as in the case of the 5-*A* specimens. Temperature variation of absorption II showed the change of activation energy with water content to be more marked than for absorption II in 5-*A*. Arrhenius plots were obtained for four water contents, 11·1, 12·2, 15·4 and 18·0 H_2O p.u.c. For 11·1 and 12·2 H_2O p.u.c. good linear plots were obtained but for 15·4 and 18·0 H_2O the presence of two lines was clearly indicated, as can be seen in Fig. 4. Figure 5 shows the ϵ'' vs. log f plots at various temperatures for 18·0 H_2O p.u.c. These indicate the reason for the large uncertainty in log f_{max} at −25° and

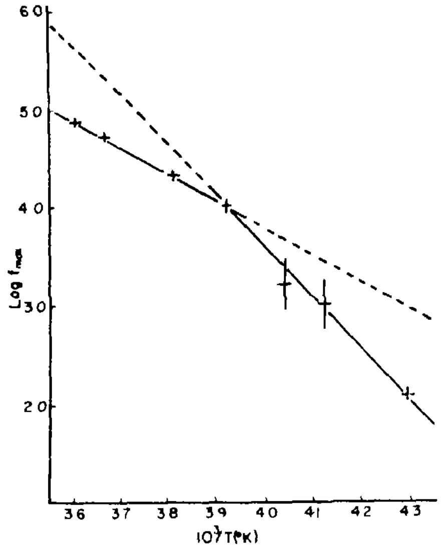

Fig. 4. Arrhenius plot for absorption II in 3-*A* 18 H_2O p.u.c.

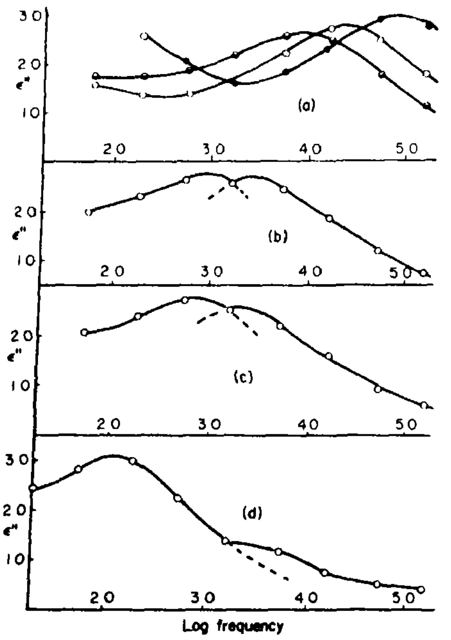

Fig. 5. Dielectric loss in 3-*A* 18·0 H_2O p.u.c. (a) ● 5°C, ○ – 10°C, ◒ – 19°C; (b) – 25°C; (c) – 30°C; (d) – 40°C.

–30°C shown in Fig. 4. A similar apparent change in activation energy occurs for 15·4 H_2O p.u.c. Figure 6 shows the variation of activation energy with water content.

The apparent conductivities, as evaluated from the relation $\epsilon''f = 1{\cdot}8 \times 10^{12}$ k, at some water contents where the dielectric loss and conductivity loss can be separated are given in Table 4.

(*B*) *Type* 4-*A*

The adsorbed water results repeat those of 3-*A* and 5-*A* in that a large dielectric loss peak (absorption I), situated at between 10^5 and 10^6 Hz in the saturated material, moves to lower frequencies and diminishes in peak height as water is removed. Instead of moving out of the frequency range, as occurred with 3-*A* and 5-*A* after removal of 8 or 10 molecules of water per cavity, the peak subsequently moves more slowly and assumes an approximately constant peak height. Figure 7 shows the movement of the peak and Fig. 8 the variation of $\epsilon''_{\text{max.}}$ with water content. The dielectric absorption parameters for absorption I are given in Table 5. Temperature variation has been studied in absorption I

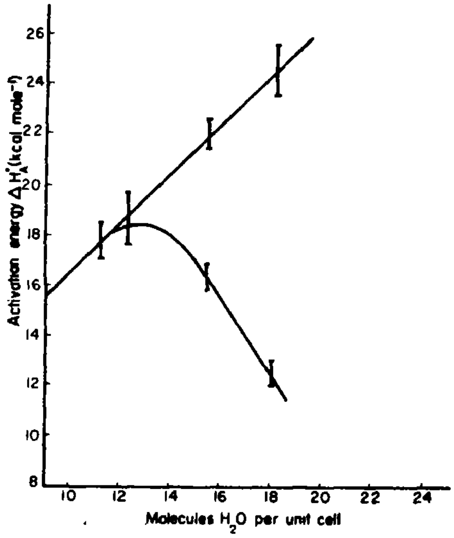

Fig. 6. Variation of activation energy for absorption II in 3-*A* with water content.

Table 4. Apparent conductivity of 3-A at various water contents

H_2O p.u.c.	k.Ω^{-1} cm^{-1} at 5·25 (Hz)
27·0	$6{\cdot}34 \times 10^{-9}$ at 179 Hz
26·2	$1{\cdot}58 \times 10^{-10}$
25·5	$9{\cdot}13 \times 10^{-11}$
24·5	$5{\cdot}95 \times 10^{-11}$
23·8	$3{\cdot}21 \times 10^{-11}$
23·3	$2{\cdot}20 \times 10^{-11}$
22·5	$1{\cdot}40 \times 10^{-11}$

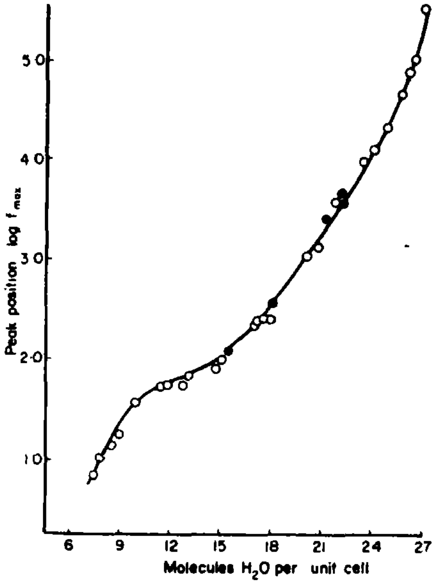

Fig. 7. Movement of absorption I in 4-*A* with water content. (○) and (●) indicates different specimens.

at three water contents over the range where the peak height has ceased falling rapidly, i.e. 22·0, 18·0 and 15·5 H_2O p.u.c. Good Arrhenius plots were obtained showing the activation energy to be constant over this range of water contents i.e. 16·0 ± 0·8, 16·8 ± 0·8 and 16·4 ± 1·0 kcal. mole^{-1} respectively.

Figure 9 shows the permittivity and loss for a water content of 7·4 H_2O p.u.c. in the frequency range 5·25 Hz to 148 kHz. There is a clear indication of a second peak following absorption I to low frequencies. This could not be fully investigated by Method I due to water pick up at the low water contents at which the peak moves into the available frequency range. The peak has been fully observed at low temperatures as shown in Fig. 10. The activation energies obtained at 14·4 and 11·5 H_2O p.u.c. were 13·5 ± 0·9 and 8·0 ± 0·4 kcal.mole^{-1} respectively. Over the temperature range used there was no positive indication of a change in activation energy at low temperatures, as occurred in 3-*A*, although

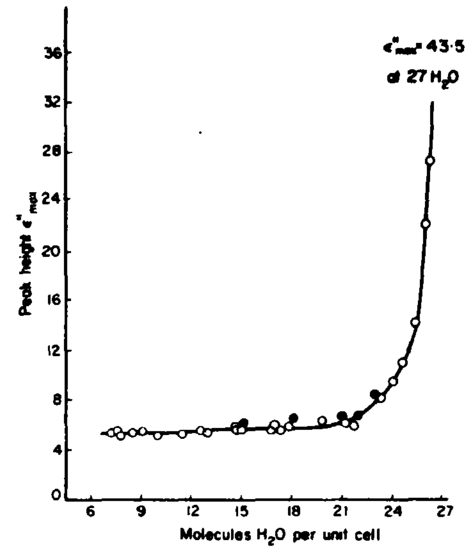

Fig. 8. Variation of amplitude of absorption I in 4-*A* with water content.

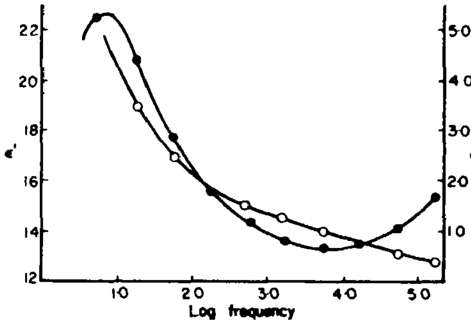

Fig. 9. Permittivity (○) and dielectric loss (●) in 4-*A* 7·4H_2O p.u.c.

Table 5. Dielectric absorption parameters for absorption I *in* 4-A *at various water contents*

H_2O p.u.c.	$\epsilon''_{max.}$	ϵ_0	ϵ_0	$\log f_{max.}$ $\pm 0\cdot03$	β $\pm 0\cdot01$	τ (sec)
27·0	43·5 ± 0·5	123 ± 1·0	34 ± 1·0	5·51	0·71	$4\cdot9 \times 10^{-7}$
25·9	21·7 ± 0·5	79·5 ± 1·0	21·0 ± 1·0	4·85	0·63	$2\cdot3 \times 10^{-6}$
24·8	11·0 ± 0·2	46·1 ± 0·5	17·3 ± 0·5	4·32	0·61	$7\cdot6 \times 10^{-6}$
23·4	8·0 ± 0·2	37·0 ± 0·5	16·3 ± 0·5	3·95	0·65	$1\cdot8 \times 10^{-5}$
21·2	6·2 ± 0·1	32·8 ± 0·3	16·3 ± 0·3	3·41	0·61	$6\cdot2 \times 10^{-5}$
19·9	6·0 ± 0·1	31·6 ± 0·3	15·9 ± 0·3	3·00	0·62	$1\cdot6 \times 10^{-4}$
17·9	5·5 ± 0·1	29·5 ± 0·3	15·3 ± 0·3	2·38	0·60	$6\cdot6 \times 10^{-4}$
16·8	5·2 ± 0·1	29·2 ± 0·3	15·2 ± 0·3	2·34	0·60	$9\cdot2 \times 10^{-4}$
14·9	5·5 ± 0·1	29·5 ± 0·3	15·4 ± 0·3	1·98	0·62	$1\cdot7 \times 10^{-3}$
13·0	5·2 ± 0·1	28·2 ± 0·3	15·7 ± 0·3	1·90	0·65	$2\cdot0 \times 10^{-3}$
11·4	4·9 ± 0·1	29·5 ± 0·3	14·8 ± 0·3	1·78	0·65	$2\cdot6 \times 10^{-3}$
9·9	4·9 ± 0·1	27 1 ± 0·3	14·8 ± 0·3	1·56	0·66	$4\cdot4 \times 10^{-3}$
8·5	5·2 ± 0·1	—	—	1·15	0·72	$1\cdot1 \times 10^{-2}$
7·8	4·9 ± 0·1	—	—	1·00	0·73	$1\cdot6 \times 10^{-2}$
7·3	5·3 ± 0·1	—	—	0·70	—	$3\cdot2 \times 10^{-2}$

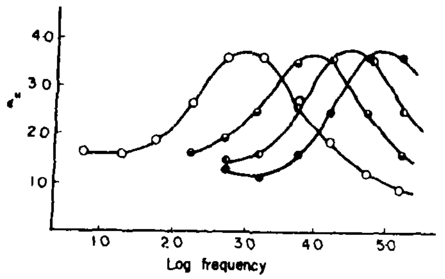

Fig. 10. Absorption II in 4-*A* 14 4 H_2O. ○ −63°C. ◒ −50°C; ◐ −40°C; ● −30°C.

Table 6. Apparent conductivity of 4-A *at various water contents*

H_2O p.u.c.	k $\Omega^{-1}cm^{-1}$ at 5·25 (Hz)
27·0	$1\cdot19 \times 10^{-10}$
25·9	$1\cdot54 \times 10^{-11}$
24·8	$8\cdot31 \times 10^{-12}$
23·4	$4\cdot26 \times 10^{-12}$
21·2	$1\cdot75 \times 10^{-12}$
7·0	$1\cdot75 \times 10^{-12}$

for 11·5 H_2O p.u.c. the lowest temperature point (−73·5°C) deviated considerably from the good linear Arrhenius plot obtained from the other points. The loss peak at this temperature also broadened; β falling from a mean of 0·47 for temperatures from −19·0°C to −60·0°C to 0·39 at −73·5°C. This suggests that a similar change to that observed in 3-*A* may occur, but at a much lower temperature. ϵ_∞ for this second loss peak, absorption II, in 4-*A* fell from 6·9 ± 0·2 at 14·4 H_2O p.u.c. to 3·70 ± 0·1 at 11·5 H_2O p.u.c. At liquid air temperature ϵ' was constant at 3·01 from 5·25 Hz to 148 kHz for 11·5 H_2O p.u.c.

Apparent conductivity values for 4-*A* at high water contents are given in Table 6. Below 21·2 H_2O p.u.c. the conductivity remains almost constant at $1\cdot75 \pm 0\cdot6 \times 10^{-12}$ Ω^{-1} cm^{-1} down to 7·0 H_2O p.u.c.

(C) Type Ag-*A*

No difference in results were observed between the silver forms obtained from the 4-*A* or 5-*A* material. The results obtained were similar to those for 4-*A*. A large peak, absorption I, moves to lower frequencies as water is removed, $\epsilon''_{max.}$ also falling. Figures 11 and 12 show the variation of peak position and peak height with water content. Little difference was observed between the 80 and 100 per cent exchanged samples at any stage; the two being indicated in the figure. Table 7 summarises the dielectric absorption para-

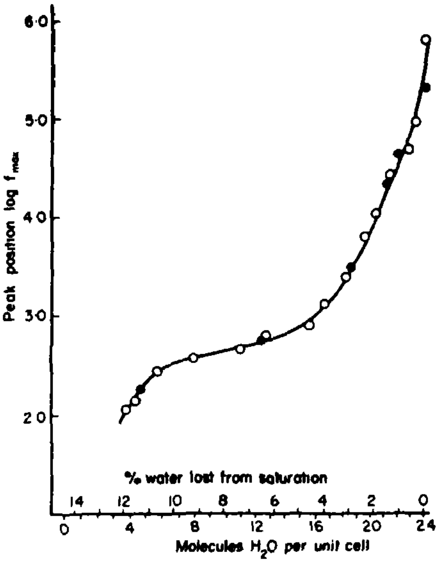

ig. 11. Movement of absorption I in Ag-*A* with water content, (○) 100% silver; (●) 80% silver.

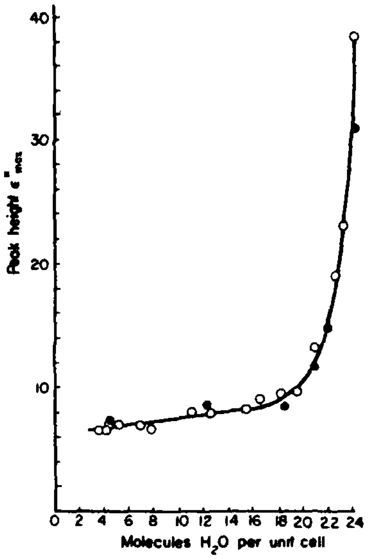

Fig. 12. Variation of amplitude of absorption I in Ag-*A* with water content, (○) 100% silver; (●) 80% silver.

Table 7. Dielectric absorption parameters for absorption I *in* Ag-A *at various water contents*

H_2O p.u.c.	ϵ''_{max}	$\log f_{max}$	β	τ (sec)
24·0	38·5	5·80	0·61	$2{\cdot}5 \times 10^{-7}$
23·1	23·0	4·92	0·50	$1{\cdot}9 \times 10^{-6}$
22·6	19·1	4·77	0·54	$2{\cdot}6 \times 10^{-6}$
21·1	13·2	4·45	0·61	$5{\cdot}6 \times 10^{-6}$
20·2	10·5	4·04	0·61	$1{\cdot}5 \times 10^{-5}$
19·4	9·7	3·80	0·60	$2{\cdot}5 \times 10^{-5}$
18·2	9·5	3·38	0·61	$6{\cdot}6 \times 10^{-5}$
16·5	9·1	3·20	0·59	$1{\cdot}0 \times 10^{-4}$
15·5	8·4	2·92	0·62	$1{\cdot}9 \times 10^{-4}$
12·5	8·0	2·80	0·63	$2{\cdot}5 \times 10^{-4}$
11·0	8·0	2·65	0·62	$3{\cdot}6 \times 10^{-4}$
7·8	6·6	2·63	0·62	$3{\cdot}3 \times 10^{-4}$
6·9	7·0	2·45	0·59	$5{\cdot}7 \times 10^{-4}$
5·2	7·1	2·40	0·58	$6{\cdot}3 \times 10^{-4}$
4·4	7·0	2·20	0·53	$1{\cdot}0 \times 10^{-3}$
4·2	6·6	2·15	0·53	$1{\cdot}1 \times 10^{-3}$
3·6	6·5	2·05	0·51	$1{\cdot}4 \times 10^{-3}$

meters for absorption I in the 100 per cent exchanged material. The silver form of type-*A* is more readily dehydrated and less susceptible to water pick-up than the other ion forms [3], this enabled the low water contents to be measured by Method I.

A second absorption, absorption II, followed the first to low frequencies, its movement with water content is shown in Fig. 13. The dielectric absorption parameters for absorption II are summarised in Table 8. In contrast to the results for the other ion forms ϵ''_{max}, for absorption II in Ag-*A* increases with decrease in water content. Good estimates of ϵ_0 and ϵ_∞ could be obtained for neither absorption from Cole-Cole plots due to the close proximity of the two peaks. For both absorptions the peaks are clearly defined from ϵ'' vs. log f plots. Fuoss Kirkwood plots were obtained from ϵ'' values close to the peaks.

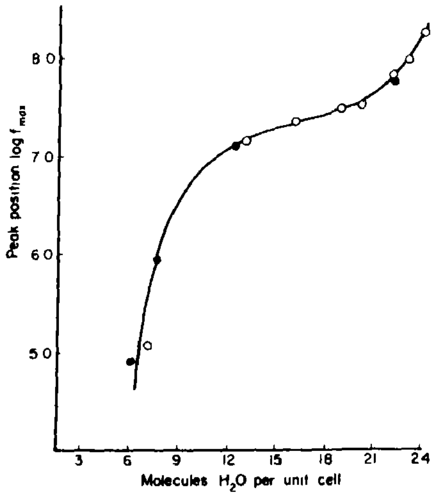

Fig. 13. Movement of absorption II in Ag-*A* with water content. (○) and (●) indicates different specimens.

Enhanced polarisation effects, due to the higher conductivity of Ag-*A*, vitiated temperature variation studies of absorption I. For absorption II the variation of activation energy with water content was similar to that in 3-*A*. Again an apparent change in activation energy was observed. Figure 14 shows the Arrhenius plot obtained at a water content of 22·0 H_2O p.u.c. In this case the change occurs at a much lower temperature than in 3-*A*. Figure 15 shows the variation of activation energy with water content. For water contents of 20·4 and 22·0 H_2O p.u.c. the intercept of the two lines in the Arrhenius plots occured at temperatures of −68′ ± 2°C and −65 ± 1°C respectively, the higher activation energies occurring below these temperatures. At 6·0 H_2O p.u.c. ϵ' was constant at 4·51 over the frequency range 5 Hz–148 kHz at liquid air temperature.

The apparent conductivity of Ag-*A* considerably exceeds that of the other ion forms. Table 9 summarises the variation of conductivity with water content.

Table 8. Dielectric absorption parameters for absorption II *in* Ag-A *at various water contents*

H_2O p.u.c.	ϵ''_{max}	log f_{max} ± 0·03	β ± 0·01	τ (sec)
24·0	6·5	8·20	0·59	$1{\cdot}0 \times 10^{-9}$
23·1	6·2	7·93	0·62	$1{\cdot}9 \times 10^{-9}$
22·0	6·8	7·70	0·53	$3{\cdot}2 \times 10^{-9}$
19·6	6·7	7·58	0·50	$4{\cdot}2 \times 10^{-9}$
18·8	6·4	7·45	0·48	$5{\cdot}6 \times 10^{-9}$
15·9	6·9	7·32	0·60	$7{\cdot}6 \times 10^{-9}$
12·8	7·6	7·13	0·56	$1{\cdot}2 \times 10^{-8}$
12·2	8·1	7·07	0·62	$1{\cdot}4 \times 10^{-8}$
7·9	8·0	6·20	0·57	$1{\cdot}0 \times 10^{-7}$
7·6	8·0	5·93	0·61	$1{\cdot}9 \times 10^{-7}$
6·0	8·6	4·92	0·60	$1{\cdot}9 \times 10^{-6}$

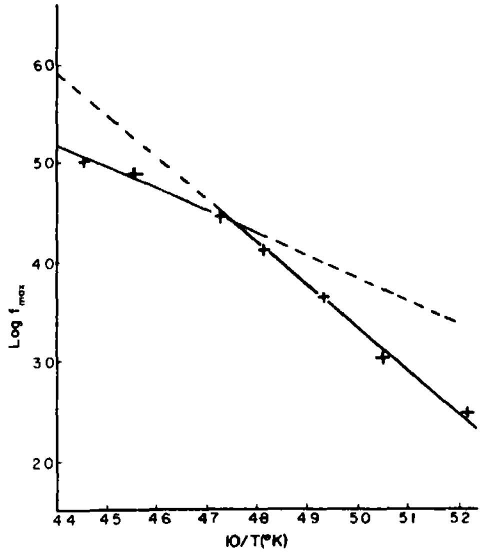

Fig 14. Arrhenius plot for absorption II in Ag-*A* 22·0 H_2O p.u.c.

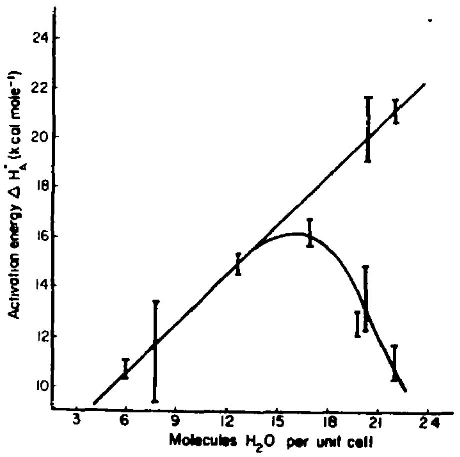

Fig 15 Variation of activation energy for absorption II in Ag-*A* with water content.

Table 9. Apparent conductivity of Ag-A *at various water contents*

H_2O p.u.c.	k. Ω^{-1}cm^{-1}
24·0	$3{\cdot}6\times10^{-8}$ at 1·5 kHz
23·1	$1{\cdot}8\times10^{-9}$ at 54 Hz
22·6	$9{\cdot}0\times10^{-10}$ at 54 Hz
21·9	$3{\cdot}6\times10^{-10}$ at 5 Hz
20·9	$8{\cdot}8\times10^{-11}$ at 5 Hz
19·4	$4{\cdot}0\times10^{-11}$ at 5 Hz
18·4	$3{\cdot}5\times10^{-11}$ at 5 Hz
16·0	$1{\cdot}3\times10^{-11}$ at 5 Hz
12·5	$8{\cdot}8\times10^{-12}$ at 5 Hz
11·0	$4{\cdot}3\times10^{-12}$ at 5 Hz
4·5	$4{\cdot}0\times10^{-12}$ at 5 Hz

DISCUSSION

Absorption II

It was suggested in Parts I and II that the region of dielectric loss, absorption II, in 5-*A*/H_2O and the absorption observed in 5-*A* with SO_2, NH_3 and CO_2 as adsorbates was probably due to a cation-jumping process. The region of loss, absorption II, observed in the 3-*A*, 4-*A* and Ag-*A* water systems behaves similarly to absorption II in 5-*A*/H_2O, and is probably due to the same cause. For a cation process some correlation between the properties of the ion and the dielectric absorption might be expected. Figure 16 shows the activation energies of absorption II as a function of ionic radius for the two water contents at which ΔH^*_A is known for 4-*A*, i.e. 11·5 and 14·4 H_2O p.u.c. The corres-

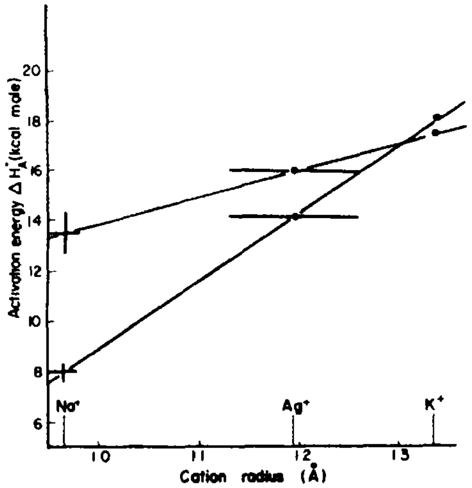

Fig. 16. Activation energy of absorption II in monovalent ion forms of type-*A* zeolite as a function of cation radius (Cation radii are mean of Goldschmidt and Pauling values).

ponding values of ΔH_A^* for 3-*A* and Ag-*A* are obtained from Figs 6 and 15 respectively. Both the Pauling and Goldschmidt values of ionic radius[4] are shown on the figure because of the large difference between these values for the Ag^+ ion. The correlation in Fig. 16 supports the proposal that absorption II is due to a cation process in 3-*A*, 4-*A* and Ag-*A*. It was also suggested in Part II that this cation jump, as in 5-*A*, is a jump involving the type-I cations. The type-II cations would not be expected to undergo jumps between well defined sites, to give rise to a constant ϵ''_{max} as they are moved from their sites in the presence of an adsorbate to form a cluster in the cavity with the adsorbate molecules[5]. These cations are so mobile that they would be expected to give rise to conductivity rather than a dielectric loss process. The linear relationship in Fig. 16 suggests that the ions behave as though they were unsolvated. Thus, although the hydration numbers of Na^+ and K^+ are similar (5 ± 1 and 4 ± 2 respectively)[6] the Ag^+ ion is considerably less susceptible to hydration and would not be expected to give a linear plot with the two hydrated ions. For the type-II ions to behave as unhydrated ions is extremely unlikely and this again indicates that the process concerns the type-I cations in the monovalent ion forms.

It thus appears that the mechanism proposed for the cation process in 5-*A* in Part II also applies to these monovalent ion types. If this is correct it also implies that the variation of activation energy is due to steric hindrance, by the adsorbate molecules, of unhydrated ion migration, at least in that adsorbate content region where the activation energy increases. The fall in activation energy observed in 5-*A*, 3-*A* and Ag-*A* at high water contents, attributed in Part I to cation movement in conditions approaching 'solution', does imply hydration to some extent. Alternatively the fall in activation energy could be due to a general fall in the binding energy of the water molecules to the zeolite surface as more water becomes adsorbed, thus reducing the impedance of the ion jumping by such molecules. The apparent change in activation energy which occurs at low temperatures in 3-*A* and Ag-*A*, and probably also in 4-*A*, can be interpreted as an effective 'freezing' of the zeolite water, perhaps its rigidification into a glassy form. The cation jump would then revert to the fully hindered condition as is indicated by the linearity in Figs 6 and 15 between ΔH_A^* values at low water contents and the higher activation energies at high water contents.

The suggestion that some change of state of the water molecules, or at least a change in mobility, at low temperatures is supported by n.m.r. studies[7], where line shape transitions at about $-75°C$ were observed in Na-*A* and Na-*X* zeolites: on cooling the signal changes from a narrow line, characteristic of liquid water, to a broad line, characteristic of ice. The temperature at which the change occurs depending on the water content; increasing as the water content increases. Kiselev[8] has recently confirmed that phase transitions (melting) occur when adsorbed molecules are present at concentrations higher than those corresponding to monolayer coverages. From the results given here it appears that the temperature at which the transition occurs is also dependent upon the cation, since in 3-*A* $18H_2O$ p.u.c. the change in ΔH_A^* occurs at about $-20°C$ (or, more likely, over the range $-20°$ to $-30°C$) whereas in Ag-*A*, $20H_2O$ p.u.c. the change occurs in the region $-60°$ to $-70°C$.

That the activation energy for absorption II in 5-*A* is slightly less than that for 4-*A* at the same water content i.e. at 14·4 H_2O p.u.c. $\Delta H_A^*(4\text{-}A) = 13{\cdot}5\ \text{kcal.mole}^{-1}$ and $\Delta H_A^*(5\text{-}A) = 12{\cdot}9\ \text{kcal.mole}^{-1}$ is unexpected. As the ionic radii of Na^+ and Ca^{2+} are similar, 0·96 and 0·99 Å respectively, an activation energy of about twice that for 4-*A* could have been expected for 5-*A* because of the double charge on Ca^{2+}. That is, of course, on the assumption that absorption II in 5-*A*/H_2O is due to Ca^{2+} jumping and not to a process involving the small amount of Na^+ present. The latter possibility is unlikely since a process involving Na^+ would have been anticipated to occur at a much higher frequency, i.e. similar to that for absorption II in 4-*A*. The similarity in activation energy is reasonable if the main contribution to ΔH_A^* comes from the hindering effect of the water rather than from the binding energy of the cation to its site in the lattice, so that the activation energy depends mainly on the ion size and not on the charge. Further work with divalent ions is required to clarify this point.

We can apply the analysis of the apparent dipole moment associated with the cation dielectric process given in Part II, i.e.

$$\mu_{\text{eff}}^2 = \frac{(\mu_1 - \mu_2)^2}{4}$$

where μ_1 and μ_2 are the dipoles formed by the cation in sites I and II, to the present data. For the 4-*A* zeolite an estimate can be based on the Onsager equation,

$$\frac{2\epsilon''_{\text{max}}}{\beta} = \epsilon_0 - \epsilon_\infty = \frac{4\pi N_1 \mu^2}{3kT}\left[\frac{\epsilon_1(\epsilon_{\infty 2} + 2)}{2\epsilon_1 + \epsilon_{\infty 2}}\right]^2$$

by taking the zeolite lattice permittivity as 3·01, i.e. the value of ϵ' at liquid air temperature. The concentration of one sodium ion per cavity is 1·05 gm.ion.l.$^{-1}$ $\epsilon''_{\text{max.}}$ has a mean value of 3·40 and $\beta = 0·47$ over the temperature range $-20°$ to $-70°$C. These values give an apparent dipole moment of 7·8 D. The position of a type-I sodium ion is a position 0·4 Å from the plane of the 6-membered oxygen ring window, this gives μ_1 = e.d. = 1·9 so that μ_2 is 13·7 D. This gives a value for the distance of the Na^+ ion from the plane of the 8-membered ring window of 2·9 Å. In dehydrated 4-*A* the type-II cation position is about 2·5 Å away from the plane of this window[9]. The similarity between the value obtained here and the observed cation position indicates that the suggested cation jump is reasonable.

No data are available for the cation positions in 3-*A* and Ag-*A*. If the analysis is applied to the data for absorption II in 3-*A* an apparent dipole moment of 7·7 D is obtained. This is similar to the value for 4-*A* and indicates that the cation positions are similar to those in 4-*A*. A smaller value may have been anticipated since in site I the cation would be expected to lie further than 0·4 Å from the 6-membered ring for steric reasons thus increasing μ_1. In the case of Ag-*A*, taking the lattice permittivity as 4·51, i.e. the liquid air value at 6·0 H_2O p.u.c., gives an apparent dipole moment of 8·9 D. The fact that $\epsilon''_{\text{max.}}$ increases in moving to lower water contents (i.e. see Table 8) probably indicates that the Ag^+ ion moves towards the cavity centre as the adsorbate content increases thus causing μ_1 to increase and hence μ_{eff} to decrease. The cation ring distances obtained by this analysis will be maximum values since contributions to μ_1 and μ_2 by induced dipoles in the ring oxygens have been neglected. However the model suggested appears at least qualitatively consistent with the variety of data reported.

Absorption I

As in the case of 5-*A*, absorption I in 3-*A*, 4-*A* and Ag-*A* is most probably due to relaxation of water molecules. Although ϵ_∞ for the cation process is not so well defined for the monovalent ion types to enable a dielectric isotherm to be drawn, the indications are that a similar behaviour occurs and that the large amount of water present cannot be accounted for by the permittivity increment at frequencies above 100 MHz. The observed relaxation times at 22°C in the various ion forms saturated with water are:

3-*A*	4-*A*
$7·9 \times 10^{-7}$ sec.	$4·9 \times 10^{-7}$ sec.
Ag-*A*	5-*A*
$2·5 \times 10^{-7}$ sec.	$1·0 \times 10^{-5}$ sec.

N.m.r. studies give similar relaxation times for water in type-*A* zeolites. Mackey[10] concluded that the bulk of the adsorbed water relaxes by a variety of processes having correlation times of the order of $10^{-7}-10^{-7}$ sec, the actual time depending on the cation. Cohen–Addad[11] gives correlation times for nuclear relaxation of water in 4-*A* of about 10^{-6} sec. This time was associated with jumps of molecules from one lattice site to another. A shorter correlation time was also found (10^{-8} sec) and ascribed to molecular rotation for molecules not attached to the cage walls.

The similarity between the n.m.r. values and dielectric relaxation times given here supports the suggestion that absorption I is due to adsorbed water. The smaller relaxation times observed in the monovalent ion types from that in 5-*A* are reasonable since in liquid water the effect of ions is to reduce the relaxation time of water[12] e.q. $\tau(H_2O)$ at $25°C = 9{\cdot}4\times10^{-12}$ sec; $\tau(H_2O)$ in 1·0 molar NaCl solution $= 8{\cdot}6\times10^{-12}$ sec. The very much higher concentrations of cations in the zeolites would be expected to give a greater shift of the relaxation time, thus reducing the relaxation time from that in 5-*A*, which has no type-II cations present, to that in the monovalent ion forms which have these ions.

The closeness of these relaxation times to that of water in ice[13] ($2{\cdot}2\times10^{-5}$ sec at $-0{\cdot}1°C$) and the fact that absorption I begins to fall in intensity on removal of the first amounts of water from saturation indicates that all the adsorbed water relaxes the major part of its dipole moment in a manner similar to that in ice and only contributes some small part of its dipole to the polarisation at high frequencies by some other process such as a rotation about one (OH) bond or the flapping of a molecule attached to the cavity walls. The absence of a well-defined dielectric absorption at frequencies between 100 MHz and 8·5 GHz in 5-*A* 30 H_2O p.u.c. indicates that the partial contribution to the high frequency loss occurs by a variety of processes having a wide spectrum of relaxation times.

The analogy to ice is perhaps a poor one since, as the effect of low temperatures on the cation process suggests, the adsorbed water undergoes a further rigidification at low temperatures. In the zeolite cavity at these lower temperatures the water must be as tightly bound as is water of crystallisation. It would be interesting to observe the effect of low temperature on absorption I: this would, however, occur at frequencies lower than those used in the present work.

The levelling off in $\epsilon''_{\mathrm{max.}}$ observed as the water content decreases in 4-*A* and Ag-*A* could be due to some process involving the type-II ions which only becomes possible at low water contents, such as a jump from one water molecule to another. Figure 2 shows some indication that a similar levelling off may occur in 3-*A*, as would be expected for a monovalent ion form. That the relaxation process is a complex one involving both the water molecules and the type-II cations is expected from the clustering of these species at high water contents.

The activation energy of absorption I appears to be constant at about 16 kcal. mole^{-1} in both 5-*A* 30H_2O p.u.c. and 4-*A* at various water contents. This is significantly greater than the activation energy for dipole reorientation in ice (13·4 kcal.mole^{-1}) and again reflects the rigidity of the adsorbed water molecules.

Acknowledgements—I wish to thank Dr Mansel Davies for his interest and much helpful discussion during the course of this work, and S.R.C. for a Research Studentship.

REFERENCES

1. MORRIS B., *J. Phys. Chem. Solids* **30**, 73 (1969). **30**, 89 (1969)
2. REED T. B. and BRECK D. W., *J. Am. chem. Soc.* **78**, 5972 (1956).
3. TSITSISHVILI G. V., *Akad. Nauk. SSSR Otd Khim. Nauk.* p. 41 (1962).
4. PAULING L., *The Nature of the Chemical Bond.* O.U.P. London (1960).
5. SMITH J. V., *Proc. S. C. I. Conf. Mol. Sieves.* London (1967).

6. CONWAY B. E. and O'M. BOCKRIS J., In *Modern Aspects of Electrochemistry* (Edited by Bockris), Chap. 2. Butterworth, London (1954).
7. KIRIYAMA R., KIRIYAMA H., KAWAI S., WADA T. and MURAYAMA W., *J. chem. Soc. Japan* **68**, 1488 (1965).
8. KISELEV A. V., *C. S. Symposium – The Gas Solid Interface* (1967).
9. LEWIS P. H., *J. phys. Chem.* **63**, 527 (1959).
10. MACKEY J. H., Thesis, Princeton (1962).
11. COHEN ADDAD J. P., *Brit. Radiospec. Grp. Conf.* England (1966).
12. HASTED J. B., RITSON R. M. and COLLIE C. H., *J. chem. Phys.* **16**, 1 (1948).
13. AUTY R. P. and COLE R. H., *J. chem. Phys.* **20**, 1309 (1952).

J. Phys. Chem. Solids Pergamon Press 1969. Vol. 30, pp. 117-128. Printed in Great Britain.

CALCULATION OF THE ION-ION REPULSIVE INTERACTION IN THE RARE GAS SOLIDS AND IN THE NOBLE METALS

D. W. HAFEMEISTER*

Department of Physics, Carnegie-Mellon University, Pittsburgh, Pa. 15213, U.S.A.

(*Received* 7 *March* 1968)

Abstract—An exchange charge model technique which was fairly successful for the ionic alkali halides is now extended to the rare gas solids and the noble metals. The radial dependence of the repulsive Born-Mayer potential which is caused by overlapping core states is obtained. Exchange charges are calculated in terms of overlap integrals and the resulting repulsive potentials are obtained by a summation of the exchange charge potentials. The calculated radial dependences of this interaction for the rare gas solids are in quite good agreement (2·5 per cent) with the experimental data. For the noble metals, the outer *d* free ion functions are certainly an approximation to the actual case with the result that the agreement (25 per cent) is less satisfactory. For the noble metal series the magnitude of the exchange charges, the fractional closure failures for the elastic constants, and the ratio C_{12}/C_{44} all display the same behavior. This implies that the overlap mechanism can account for the non central contribution to the elastic constants. The rare gas and noble metal overlap integrals and their radial dependence are tabulated.

1. INTRODUCTION

IT IS WELL known that the Pauli exclusion principle prevents atomic matter from collapsing and that is is the primary cause of the classical Born-Mayer (BM) repulsive potential,

$$U_{\text{rep}} = A\exp(-r/\rho). \tag{1}$$

However, since valid quantum mechanical calculations of this potential can be quite difficult to perform, it is desirable to resort to some approximate method. Simplified calculations are often useful in that they add to the physical insight and enable us to treat more complex systems and phenomena.

Certainly the rare gas molecules and solids, on the one hand, and the noble metals on the other, form two distinctly different types of materials, and thus one might consider a separate discussion for each. However, since the simple model which we shall use appears to approximately describe the repulsive potentials of both materials, we shall treat them both here. The Born-Mayer interaction is the main cause of the interionic repulsive interaction for the rare gases, but it is only a partial cause of the repulsive interaction of the noble metals. However, Fuchs [1] has shown that, for the noble metals, the Born-Mayer interaction is the main cause of the elastic constants C_{44} and $(C_{11}-C_{12})$, and that it gives the main contribution to compressibility of copper. Succeeding experiments in the noble metals have shown that a many-body, non-central force is needed in order to understand the data.

In our calculations we will use some of the approximations which Dick and Overhauser [2] used for their work with the Exchange Charge Model (ECM). This model has been successful in explaining the many diverse properties of the alkali halides such as the dielectric constants[2], the failure of the Cauchy relation $C_{12}=C_{44}$[3], and the Born-Mayer repulsive potential[4]. It is the purpose of this paper to extend the ECM to two other systems, the rare gas solids and the

---

*Supported by the National Science Foundation and the Office of Naval Research.

noble metals. The ECM considers the deformation of the free ion wave function which is caused by the overlapping of the outer atomic shells, and which results in a decrease of the electronic density in the region between the ions. It represents this lack of negative electric charge as a 'point-like' positive charge which resides at the point of tangency between an ionic shell and its neighbor. The magnitude of an exchange charge is simply related to its overlap integrals. As a solid is compressed the overlap integrals increase, resulting in enhanced exchange charge effects.

A few first-order[5, 6] perturbation calculations have been performed on the repulsive interaction of rare gases, as well as calculations of the non central many-body component[7] of this force. However, similar calculations for the noble metals have not been performed. Since the free ion *d*-wave functions which we have used for the noble metals are only an approximation of the actual wave functions, our results on the noble metals will be only approximate. However, because our results on the metals agree fairly well with the experimental data, we can hope that some of the ECM ideas might be applicable for the calculation of many-body effects in the noble metals.

The Exchange Charge Model will be discussed further in Section 2 and the results for the rare gases and the noble metals will be discussed and compared with experimental data in Sections 4 and 5, respectively.

2. THEORETICAL CONSIDERATIONS

(*A*) *The Exchange Charge Model*

The nature of exchange charges can be seen by considering[2, 8] the Heitler–London wave function of the triplet state of the hydrogen molecule

$$\psi(1,2) = N(\phi_A(1)\phi_B(2) - \phi_A(2)\phi_B(1)). \tag{2}$$

The electron density of the (1) electron can be obtained by calculating

$$\begin{aligned} -|e| \int \psi^*(1,2)\psi(1,2)\, d\tau_2 &= -|e| N^2 [\phi_A{}^2(1) + \phi_B{}^2(1) \\ &\quad - 2S_{AB}\phi_A(1)\,\phi_B(1)] \end{aligned} \tag{3}$$

where the overlap integral $S_{AB} = \langle\phi_A(2)|\phi_B(2)\rangle - \delta_{AB}$ and the normalization constant $N = [2(1 - S_{AB}^2)]^{-1/2}$. By considering $S_{AB} \ll 1$, equation (3) can be rewritten in terms of an enhanced negative electron density

$$\begin{aligned} \rho^{el}(1) \cong -\frac{|e|}{2}[(1 + S_{AB}^2)\,\phi_A{}^2(1) \\ + (1 + S_{AB}^2)\phi_B^2(1) \end{aligned} \tag{4}$$

and a positive exchange charge density

$$\rho^{ex}(1) \cong + |e| S_{AB}\ \phi_A(1)\phi_B(1). \tag{5}$$

The electron densities given by equations (4) and (5) can also be obtained by a consideration[4] of the leading terms in the charge densities given by Lowdin's[9] technique of symmetrical orthogonalization. By integrating equations (4) and (5), it follows that the total electronic charge, q^{el}, and the total exchange charge, q^{ex}, are given by

$$q^{el} = -|e|\ (1 + S_{AB}^2) \tag{6}$$

and

$$q^{ex} = +|e| S_{AB}^2 \tag{7}$$

thus conserving the total electronic charge. For the interaction of atoms with configurations more complex than the $(ls)_A(ls)_B$ H–H configuration, S_{AB}^2 should be considered to be a summation over the outer orbitals of its neighbors, $\sum_\nu |S_{AB}^\nu|^2$.

By evaluating the He–He interaction integrals[8] which were obtained within the Heitler–London framework, Dick and Overhauser[2] have shown that all the interactions are proportional to S_{AB}^2/r, and that the interaction between exchange charges and effect nuclear charges is the main part of the repulsive potential. They found that it is

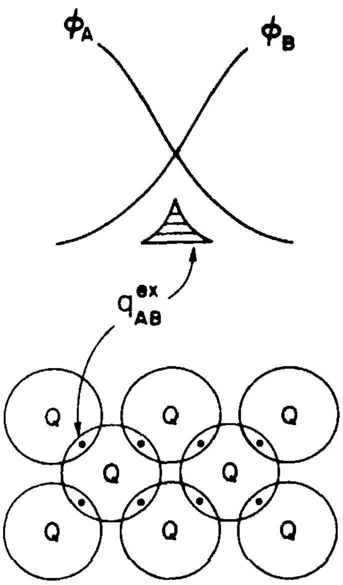

Fig. 1. The exchange charge model for the f.c.c. phase of the rare gas solids and the noble metals. The nuclear effective charge is represented by Q and the exchange charge which is created by the overlap of ϕ_A and ϕ_B is represented by q^{ex}_{AB}.

given by

$$U_{\text{rep}} = 2\,S^2_{AB}\,e^2/r = 2|e|q^{ex}/r \qquad (8)$$

where the separation of the two helium nuclei is denoted by r. Equation (8) implies that the repulsive interaction in solids which stems from orthogonality considerations can be considered to be merely the repulsive coulombic interaction of 'point-like' positive exchange charges, q^{ex}, and positive nuclear effective charges, Q. Figure 1 represents the exchange model of a rare gas solid or noble metal in the f.c.c. phase. This same approximation has been applied[4] to more complex closed-shell systems such as the alkali halides and the agreement with the experimental data was quite satisfactory (~ 10 per cent). In this previous work the radial dependence of equation (8) was fitted near the equilibrium position r_0 to the Born–Mayer exponential

$$2\sum_{\nu} |S^{\nu}_{AB}(r)|^2\, e^2/r \approx B\exp(-r/\rho) \qquad (9)$$

where the summation was carried out for both nearest neighbors and next nearest neighbors. Since the ionic cores of the rare gases and the noble metals are also closed-shell ions, it is not too unreasonable that this same approximation can also be applied to these systems. Because there is only one type of ion for the rare gases and the noble metals, and because the next nearest neighbor overlaps are considerably less than the nearest neighbor overlaps, the summation must be carried for nearest neighbors only. In considering the region from $(r_0 - 0{\cdot}2\,\text{Å})$ to $(r_0 + 0{\cdot}2\,\text{Å})$, we have found that equation (9) can be described by an exponential to within about 0·2 per cent. In Section 3 the summation $\sum_{\nu} |S^{\nu}_{AB}|^2$ is explicitly written out in terms of the s-, p- and d-orbitals.

In order to obtain the electrostatic energy between exchange charges and nuclear effective charges, as well as between the exchange charges themselves, it is necessary to show that the effective charges are reasonably well-localized in space. To investigate this we have performed integrations of the type $\langle\phi_A|1/r_A|\phi_B\rangle$ for several interatomic distances r. Our results show that to within 10 per cent the following relation is correct near r_0:

$$\langle\phi_A|1/r_A|\phi_B\rangle \cong \frac{S_{AB}}{r/2}\,. \qquad (10)$$

This indicates that the exchange charges are quite well localized in space and that their positions remain at the points of tangency of the intersecting ionic spheres, $r/2$.

(B) *Many-body forces*

Since the magnitude of the exchange charge depends on the overlap of two ions, it is obvious that the description above only pertains to central forces, However, when one considers the interaction between an effective charge and a distant nuclear effective charge, the force becomes many-body and noncentral in its nature. This type of force can possibly be thought of as being similar to the many-body interactions which have been discussed in detail by Löwdin[9] and by Lombardi and Jansen[7]. These authors have indicated that the magnitude of the three-body potential is about 10 per cent or less of the total cohesive energy for an ionic crystal. In a more recent work, Lombardi and Jansen[10] have indicated that, for the rare gas solids, the contribution to the cohesive energy from the four-body force is considerably smaller than the contribution from the three-body force. These authors feel that it is the many-body force which causes the rare gases to solidify in the f.c.c. structure, but because of the small magnitude of its contribution we shall ignore this force in our calculations. Even is such an interaction had been included, our results would not have been greatly modified because only one value of the nuclear effective charge is used here and because of the rapid decrease of S_{AB}^2 as the separation distance is increased.

It is also possible to construct a four-body force from the interaction of two exchange charges, but since this involves terms proportional to the fourth power of the overlap integral

$$q_{ij}^{er}\, q_{kl}^{er}\; \alpha |S_{ij}|^2\, |S_{kl}|^2\, \alpha\, S^4 \leqslant S^2 Q \qquad (11)$$

we can neglect this interaction.

3. OVERLAP INTEGRALS

Numerical Hartree–Fock (HF), analytical Hartree–Fock, and numerical Hartree–Fock–Slater (HFS) wave functions with the full Slater exchange approximation were used for the calculations. Since the overlap integrals are extremely sensitive to the extremities of the wave functions at large radii, we felt the necessity of employing several types of SCF wave functions.

The overlaps which involved just s- and p-wave functions were evaluated by the same techniques that are described in reference[11] and with the coordinate system shown in Fig. 2. For the overlaps which involved d-orbitals, the two center integrals can be expressed solely in terms of the coordinates of center A*. This is done by using the following geomtrical relations

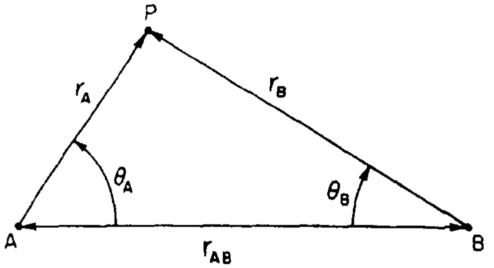

Fig. 2. The coordinate system used to compute the two center integrals.

$$r_B = (r_{AB}^2 + r_A{}^2 - 2r_A r_{AB}\cos\theta_A)^{1/2} \qquad (12)$$

$$\cos\theta_B = (r_{AB} - r_A\cos\theta_A)/(r_{AB}^2 + r_A{}^2 - 2r_{AB}r_A\cos\theta_A)^{1/2} \qquad (13)$$

$$\sin\theta_B = r_A\sin\theta_A/(r_{AB}^2 + r_A{}^2 - 2r_{AB}r_A\cos\theta_A)^{1/2} \qquad (14)$$

and we obtain

$$s_A|d_{\sigma_B}\rangle = \frac{\sqrt{5}}{4}\int_0^\infty\int_0^\pi \left[\frac{P_s(r_A)P_d(r_B)\sin\theta_A r_A[2(r_{AB}-r_A\cos\theta_A)^2 - r_A{}^2\sin^2\theta_A]}{(r_{1B}^2 + r_A{}^2 - 2r_{AB}r_A\cos\theta_A)^{3/2}}\right] \mathrm{d}r_A \mathrm{d}\theta_A \qquad (15)$$

$$\langle d_{\sigma_A}|s_B\rangle = \frac{\sqrt{5}}{4}\int_0^\infty\int_0^\pi \left[\frac{P_d(r_A)P_s(r_B)(2\cos^2\theta_A - \sin^2\theta_A)\sin\theta_A r_A}{(r_{1B}^2 + r_A{}^2 - 2r_{AB}r_A\cos\theta_A)^{1/2}}\right] \mathrm{d}r_A \mathrm{d}\theta_A \qquad (16)$$

---

*If the coordinate system had been picked so as to have $\theta' = \pi - \theta_B$, then the $\langle p_{\sigma A}|p_{\sigma B}\rangle$, $\langle s_A|p_{\sigma B}\rangle$, $\langle p_{\pi A}|d_{\pi B}\rangle$, $\langle d_{\sigma_A}|p_{\sigma_B}\rangle$ and $\langle d_{\pi_A}|d_{\pi_B}\rangle$ integrals would have had the opposite sign.

$$p_{\sigma_A}|d_{\sigma_B}\rangle = \frac{\sqrt{15}}{4}\int\limits_0^\infty\int\limits_0^\pi \left[\frac{P_p(r_A)P_d(r_B)\cos\theta_A\sin\theta_A r_A[2(r_{AB}-r_A\cos\theta_A)^2-r_A{}^2\sin^2\theta_A]}{(r_{AB}^2+r_A{}^2-2r_{AB}r_A\cos\theta_A)^{3/2}}\right]\mathrm{d}r_A\mathrm{d}\theta_A \tag{17}$$

$$\langle d_{\sigma_A}|p_{\sigma_B}\rangle = \frac{\sqrt{15}}{4}\int\limits_0^\infty\int\limits_0^\pi \left[\frac{P_d(r_A)P_p(r_B)(2\cos^2\theta_A-\sin^2\theta_A)(r_{AB}-r_A\cos\theta_A)\sin\theta_A r_A}{(r_{AB}^2+r_A{}^2-2r_{AB}r_A\cos\theta_A)}\right]\mathrm{d}r_A\mathrm{d}\theta_A \tag{18}$$

$$\langle p_{\pi_A}|d_{\pi_B}\rangle = \frac{\sqrt{45}}{4}\int\limits_0^\infty\int\limits_0^\pi \left[\frac{P_p(r_A)P_d(r_B)\sin^3\theta_A r_A{}^2(r_{AB}-r_A\cos\theta_A)}{(r_{AB}^2+r_A{}^2-2r_{AB}r_A\cos\theta_A)^{3/2}}\right]\mathrm{d}r_A\mathrm{d}\theta_A \tag{19}$$

$$\langle d_{\pi_A}|p_{\pi_B}\rangle = \frac{\sqrt{45}}{4}\int\limits_0^\infty\int\limits_0^\pi \left[\frac{P_d(r_A)P_p(r_B)\cos\theta_A\sin^3\theta_A r_A{}^2}{(r_{AB}^2+r_A{}^2-2r_{AB}r_A\cos\theta_A)}\right]\mathrm{d}r_A\mathrm{d}\theta_A \tag{20}$$

$$\langle d_{\sigma_A}|d_{\sigma_B}\rangle = \frac{5}{8}\int\limits_0^\infty\int\limits_0^\pi \Bigg[\frac{P_d(r_A)P_d(r_B)\sin\theta_A r_A(2\cos^2\theta_A-\sin^2\theta_A)}{(r_{AB}^2+r_A{}^2-2r_{AB}r_A\cos\theta_A)^{3/2}}$$
$$\times[2(r_{AB}-r_A\cos\theta_A)^2-r_A{}^2\sin^2\theta_A]\Bigg]\mathrm{d}r_A\mathrm{d}\theta_A \tag{21}$$

$$\langle d_{\pi_A}|d_{\pi_B}\rangle = \frac{15}{4}\int\limits_0^\infty\int\limits_0^\pi \left[\frac{P_d(r_A)P_d(r_B)\cos\theta_A\sin^3\theta_A r_A{}^2(r_{AB}-r_A\cos\theta_A)}{(r_{AB}^2+r_A{}^2-2r_{AB}r_A\cos\theta_A)^{3/2}}\right]\mathrm{d}r_A\mathrm{d}\theta_A \tag{22}$$

$$\langle d_{\delta_A}|d_{\delta_B}\rangle = \frac{15}{16}\int\limits_0^\infty\int\limits_0^\pi \left[\frac{P_d(r_A)P_d(r_B)\sin^5\theta_A r_A{}^3}{(r_{AB}^2+r_A{}^2-2r_{AB}r_A\cos\theta_A)^{3/2}}\right]\mathrm{d}r_A\mathrm{d}\theta_A \tag{23}$$

where $P_d(r_A) = r_A\phi_d(r_A)$, etc.

The results were tested by performing overlap integrals between similar ions with $r_{AB} = 0$ and noting that the orthogonality between the spherical harmonics was obeyed to within two parts in 10^4, i.e.

$$\langle s_A|d_{\sigma_A}\rangle = 0,\quad \langle p_{i_A}|d_{i_B}\rangle = 0,\quad \langle d_{i_A}|d_{j_B}\rangle = 0,$$
$$\text{and}\quad \langle d_{i_A}|d_{i_B}\rangle = 1.$$

In addition it was noted that for finite separations

$$\langle d_{\sigma_A}|s_B\rangle = \langle s_A|d_{\sigma_B}\rangle,\quad \langle d_{\sigma_A}|p_{\sigma_B}\rangle = \langle p_{\sigma_A}|d_{\sigma_B}\rangle$$
and
$$\langle d_{\pi_A}|p_{\pi_B}\rangle = \langle p_{\pi_A}|d_{\pi_B}\rangle$$

to within two parts in 10^4.

For the numerical Hartree-Fock functions we have used Hartree's Ar[12] and Cu$^+$[13], and Mayer's Xe[14], Worsley's Ag$^+$[15] and Mann's Ne, Ar, Kr and Xe functions[16]. In addition we have used Watson's Kr and Xe analytical Hartree-Fock functions[17] and Cowan's Hartree-Fock-Slater functions[18] for Cu$^+$, Ag$^+$ and Au$^+$. Because the numerical Hartree-Fock functions are not required to fit a limited basis set, we shall consider the results from these functions to the the closest to the actual free ions. Excellent agreement (~0·4 per cent) was obtained when comparing the overlaps calculated from Mann's HF functions to the overlaps calculated from Hartree's HF Ar functions. Similarly, the results obtained with Mann's HF Xe functions agreed to within 0·2 per cent when compared with Mayer's HF Xe functions. The results obtained from the analytical HF functions deviated by about 10 per cent from the HF numerical results. We shall not use the analytical results because we feel that they are obtained with a restricted basis set.

Since the HF functions for the Au^+ ion were not available, we have extrapolated the HF value for Au^+ from the HFS results for Au^+. The extrapolation procedure also used the results for K^+, Cs^+, Cu^+ and Ag^+ which were obtained[19] from both the HF and HFS functions. Since the full Slater exchange overestimates the exchange interaction, the calculated HFS ions are smaller than the HF ions. However, because this compression[19] is a slowly varying function of Z, we feel confident that we have been able to extrapolate to the HF Au^+ case to within about 3 per cent.

Calculations[19] of overlap integrals with the relativistic Dirac–Slater functions and with the nonrelativistic Hartree–Fock and Hartree–Fock–Slater functions indicate that the integrals between the heavier ions (i.e. $I^- - I^-$) are reduced by relativistic effects by about 10 per cent. Because these results are strongly dependent on the amount of Slater exchange used, we ignore this correction here.

The sums of the squares of the overlap integrals can be defined using the above integrals. For the rare gases

$$\Sigma\ |S^{\nu}_{AB}|^2 = 2\langle s|s\rangle^2 + 4\langle s|p_\sigma\rangle^2 + 4\langle p_\pi|p_\pi\rangle^2 + 2\langle p_\sigma/p_\sigma\rangle \quad (24)$$

whereas for the noble metals the following terms must be added to equation (24)

$$2\langle d_\sigma|d_\sigma\rangle^2 + 4\langle d_\pi|d_\pi\rangle^2 + 4\langle d_\delta|d_\delta\rangle^2 + 4\langle d_\sigma|s\rangle^2 + 4\langle d_\sigma|p_\sigma\rangle^2 + 8\langle d_\pi/p_\pi\rangle^2. \quad (25)$$

Because these overlap integrals may be useful to other workers, we have decided to list them for the crystalline equilibrium spacing r_0. Their radial dependence about r_0 can be obtained from the equation

$$S(r) = S(r_0)\exp\left[-(r-r_0)/\rho\right] \quad (26)$$

where the parameter ρ is also listed. We have used our results for the rare gases in Table 1 to recalculate* the pressure dependence of the Xe NMR chemical shift[20] in gaseous Xe. For the noble metals we have listed in Table 2 only the overlaps which involved the d-orbitals since they are considerably larger than the overlaps involving the s- and p-orbitals.

4. RARE GAS SOLIDS

The interaction energy of two rare gas atoms consists mainly of the attractive Van der Waals force and the repulsive Born–Mayer interaction. The most common form for this interaction is the Lennard–Jones

---

*The values of the Xe overlaps which we have calculated from the HF wave functions are about 15 per cent larger than those calculated by Adrian[20] from the HFS wave functions. This amount of contraction of the HFS ions caused by the overestimate of the Slater exchange agrees with previous comparisons[19]. Adrian has used his overlaps in a discussion of the effect of exchange interactions on the pressure dependence of the NMR chemical shift of Xe in Xe gas. By using our values

$$(S_{\sigma\sigma} + S_{\pi\pi})^2 = 0{\cdot}01060\exp\left[-(r-r_0)/0{\cdot}38006\right]$$

where $r_0 = 3{\cdot}39$ Å. Adrian has calculated $\langle\sigma_\rho\rangle = -4{\cdot}0\times 10^{-7}\rho'$ for the density dependence of the chemical shift of Xe in xenon gas. The density ρ' is in amagats where one amagat is the density of an ideal gas at 273°K and 760 mm Hg pressure. This new value of $\langle\sigma_\rho\rangle$ is closer to the experimental value of $\langle\sigma_\rho\rangle = -4{\cdot}3\times 10^{-7}\rho'$ than the previously calculated value of $-2{\cdot}85\times 10^{-7}\rho'$.

We have also calculated the volume dependence of the chemical shift of Xe in solid xenon and we obtain

$$\frac{\partial\sigma}{\partial\rho} = -\frac{64\alpha^2 r}{3\Delta\rho}\langle r^{-3}\rangle_{5p}\left[\frac{S^2_{\sigma\sigma}}{\rho_{\sigma\sigma}} + \frac{S^2_{\pi\pi}}{\rho_{\pi\pi}} + \frac{S^2_{\sigma\pi}}{\rho_{\sigma\pi}} - S_{\sigma\sigma}S_{\pi\pi}\left(\frac{1}{\rho_{\sigma\sigma}} + \frac{1}{\rho_{\pi\pi}}\right)\right]$$

where α is the fine structure constant and Δ is the average excitation energy. Using the values $\langle r^{-3}\rangle = 17{\cdot}8a_0^{-3}$ and $\Delta = 9{\cdot}6$ eV, we obtain $\partial\sigma/\partial\rho' = -8{\cdot}3\times 10^{-7}$ amagat^{-1}. Although we did not consider the temperature dependent effects, this value agrees with experimental data within a factor of two.

Table 1. Overlap integrals for the rare gases obtained from Mann's Hartree–Fock wave functions. The values of the integrals have been fit to within* 0·2 *per cent to the expression* S = C exp(−r/ρ). *The first row refers to the values of* ρ *(in Angstroms) and the second row refers to the values of the overlap integrals at the crystalline equilibrium separation. The sum of the overlaps* $\sum_\nu |S^\nu_{AB}|^2$ *is defined by equation* (24)

	$\langle s\|s\rangle$	$\langle s\|p_\sigma\rangle$	$\langle p_\sigma\|p_\sigma\rangle$	$\langle p_\pi\|p_\pi\rangle$	$\sum_\nu \|S^\nu_{AB}\|^2$
Ne ρ	0·3234	0·4208	0·5046	0·4232	0·2393
3·130 Å	0·0005941	−0·003626	0·009268	0·001450	0·0002335
Ar ρ	0·4237	0·5360	0·6455	0·5139	0·3056
3·815 Å	0·002065	−0·009787	0·02502	0·004054	0·001709
Kr ρ	0·4607	0·5827	0·7087	0·5777	0·3347
4·074 Å	0·002699	−0·01281	0·03345	0·005527	0·003031
Xe ρ	0·5228	0·6503	0·7901	0·6349	0·3706
4·435 Å	0·004790	−0·01870	0·04550	0·007598	0·005816

*Reference [16]

Table 2. Overlap integrals for the noble metals obtained from Hartreee–Fock wave functions. The values of the integrals have been fit to within* 0·2 *per cent to the expression* S = C exp(−r/ρ). *The first row refers to the values of* ρ *(in Angstroms) and the second row refers to the values of the integrals at the crystalline equilibrium. The contribution by the* d-*overlaps equation* (25) *accounts for* 99·5 *per cent of* $\sum_\nu |S^\nu_{AB}|^2$

	$\langle d_\pi\|p_\pi\rangle$	$\langle d_\sigma\|p_\sigma\rangle$	$\langle d_\sigma\|s\rangle$	$\langle d_\delta\|d_\delta\rangle$	$\langle d_\pi\|d_\pi\rangle$	$\langle d_\sigma\|d_\sigma\rangle$	$\sum_\nu \|S^\nu_{AB}\|^2$
Cu^+ ρ	0·3849	0·4663	0·4487	0·4355	0·5449	0·7561	0·2777
2·55 Å	−0·003394	−0·01099	0·01124	0·003545	0·01720	0·02343	0·003413
Ag^+ ρ	0·3848	0·4736	0·4344	0·4185	0·5198	0·6949	0·2727
2·88 Å	−0·00390	−0·01460	0·01111	0·003188	0·01875	0·03054	0·004788
Au^+ ρ	0·38	0·48	0·44	0·43	0·53	0·72	0·27
2·88 Å	−0·00633	−0·0288	0·0166	0·00505	0·0293	0·0457	0·012

*For Cu^+, Reference [13]; for Ag^+, Reference [15]; For Au^+, Reference [18] and Section 3.

(6,*n*) potential where the Van der Waals terms is proportaional to r^{-6} and the repulsive part is proportional to r^{-n} where *n* is usually 12. However, the r^{-12} repulsion term is not well founded theoretically from quantum mechanics, and thus a more realistic repulsive potential is desired. Calculations[5, 6] of the interaction of rare gas atoms have indicated that the usual Born–Mayer exponential $e^{-r/\rho}$ is preferable, and because of this, we will only compare our results to the more realistic Buckingham (6, exp) potential.

The parameter ρ for the rare gases has been determined by Mason and Rice[21] and others[22] from the experimental data of the equilibrium properties (L_0, the heat of sublimation at 0°K; r_0, the crystal lattice spacing; and $B(t)$ the temperature dependence of the second virial coefficient) as well as the transport properties such as the viscosity coefficient. The potentials derived from the equilibrium properties agree only fairly well with the potentials derived from the non-equilibrium transport properties (thermal conductivity, diffusion). Reviews of the rare gas potentials have been published by Jones and Dobbs[23] and by Pollack[24]. Recently Munn and Smith[25] have shown that the low temperature viscosities calculated from Mason and Rice's potential are somewhat too small.

The values of ρ which we have calculated for the rare gases are compared to Mason and Rice's values in Table 3 and in Fig. 3. We have not calculated solid helium because its zero point kinetic energy is approximately equal to the potential energy. The agreement (2·5 per cent) is very good, in fact, surprisingly good in view of the approximations of our work as well as the approximations of Mason and Rice. In addition our result for Ar ($\rho = 0{\cdot}282$ Å) is also in good agreement with Kunimune's[6] first-order perturbation calculation ($\rho = 0{\cdot}273$ Å). Certainly the neglect of many-body forces and the use of a point exchange charge, coulombic potential are our greatest approximations. Nevertheless, we interpret the agreement in magnitude and trend as a clear indication that the exchange charge model is valid for the rare gas solids. Thus, it appears that many additional parameters for the rare gases, such as the elastic constants, the dielectric constants, and phonon dispersion curves might be calculated within the framework of the exchange charge model.

Table 3. The calculated and experimental value of the repulsive parameter ρ (in Angstroms) for the rare gas solids and the noble metals

	ρ calculated	ρ experimental
Ne	0·222	0·217$^{(a)}$
Ar	0·282	0·278$^{(a)}$
Kr	0·309	0·330$^{(a)}$
Xe	0·342	0·342$^{(a)}$
Cu	0·250	0·219$^{(b)}$, 0·191$^{(c)}$, 0·201$^{(d)}$, 0·200$^{(e)}$, 0·188$^{(f)}$, 0·183$^{(g)}$, 0·159$^{(h)}$,
Ag	0·249	0·203$^{(f)}$, 0·182$^{(d)}$, 0·168$^{(h)}$
Au	0·25	0·177$^{(i)}$, 0·168$^{(h)}$

(a) Reference[21].
(b) Reference[36], with $m^* = m$.
(c) Reference[36], with $m^* = 1{\cdot}38$ m.
(d) Reference[37].
(e) Reference [30].
(f) Reference[32].
(g) Reference[29].
(h) Reference[31].
(i) Reference[38].

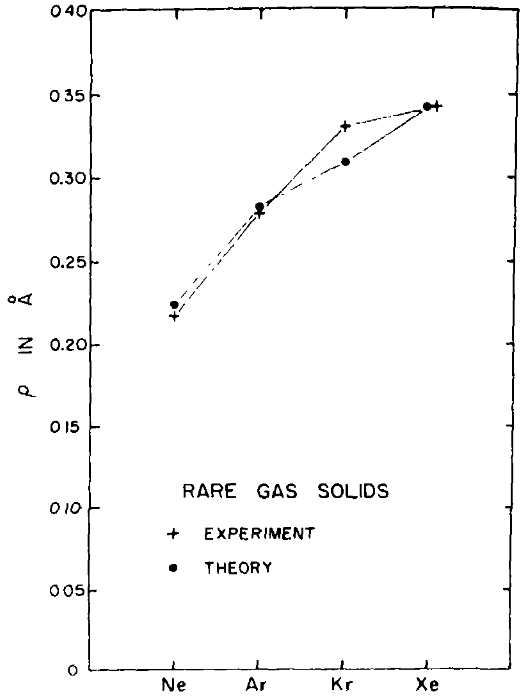

Fig. 3. Comparison on the calculated and experimentally determined values of the repulsive parameter ρ for the rare gas solids.

Recently, Barron and Klein[26] have

calculated the elastic constants and Debye temperatures at 0°K for the rare gas solids using the (6, 12) potential. It might well be useful to apply the (6, exp) potential to calculate these quantities and compare them with recent compressibility data[27, 28].

5. THE NOBLE METALS

The BM potential is most strongly felt in metals where there is a considerable overlapping of the ionic cores. Thus we shall consider only the noble metals, which have rather extensive outer *d*-wave functions, and not the alkali metals. Historically, it was Fuchs[1] who first recognized the importance of the repulsive potential in the noble metal copper. While carrying out a Wigner–Seitz calculation of copper, he pointed out that such a potential was needed to explain its compressibility and sheer constants. Fuchs made corrections to the shear constants for electrostatic effects and he indicated that these corrections were about 1/4 to 1/10 smaller than the contributions caused by the ion–ion overlap. By considering a two-body, central, repulsive force such as equation (1), Fuchs obtained the elastic constants of a f.c.c. metal,

$$\tfrac{1}{2}(C_{11}-C_{12}) = \frac{1}{4v_a}\left[r_0^2 U''_{\mathrm{rep}} + 7r_0 U'_{\mathrm{rep}}\right] \qquad (27)$$

and

$$C_{44} = \frac{1}{2v_a}\left[r_0^2 U''_{\mathrm{rep}} + 3r_0 U'_{\mathrm{rep}}\right] \qquad (28)$$

where v_a is the atomic volume, r_0 is the nearest neighbor separation. $U'_{\mathrm{rep}} = \mathrm{d}U_{\mathrm{rep}}/\mathrm{d}r]_{r0}$ and $U''_{\mathrm{rep}} = \mathrm{d}^2U_{\mathrm{rep}}/\mathrm{d}r^2]_{r_0}$. Fuchs did not directly calculate the BM potential, but used an approximate result from a Fermi–Thomas method. The BM potential has also been shown to be of importance for other problems in the noble metals such as self-diffusion[29] and radiation damage[30]. In all of these calculations it has been necessary to use potentials which have been obtained from experimental data rather than to calculate them from an interaction.

In addition, it should be pointed out that measurements of the pressure dependence of the elastic constants (C_{44}, $C_{11}-C_{12}$, $C_{11}+2C_{12}$) of the noble metals by Daniels and Smith[31] have indicated that equation (1) does not adequately describe the repulsive potential. Because these workers have measured the elastic constants at one atmosphere as well as their pressure dependence, they have obtained six experimental values which more than overdetermines the parameters A and ρ of the BM potential. Their results show that it is necessary to add closure factors, ΔC to equation (27) and (28). We have plotted these factors in Fig. 4 and it should be noted that ΔC is strongly dependent on the atomic number of the noble metal. It is quite small for Cu, and it becomes progressively larger for Ag and Au. These results indicate that equation (27) and (28) are not valid and that a many-body force is needed.

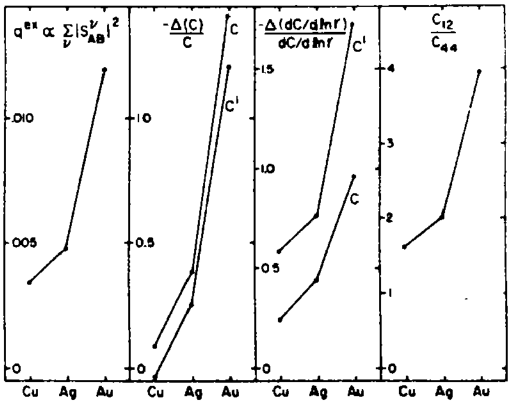

Fig. 4. Values of the exchange charges for the noble metals, fractional closure failures for the elastic constants, fractional closure failures for the hydrostatic strain derivative of the elastic constants, and the ratio C_{12}/C_{44} indicating the failure of the Cauchy relation $C_{12} = C_{44}$. Deviations from 0, 0 and 1 for the 2nd, 3rd and 4th graphs are caused by noncentral many-body forces or by contributions from the distortion of the Fermi surface. On this graph $C = C_{44}$ and $C' = (C_{11}-C_{12})/2$.

Part of the closure failure is certainly dependent on some aspects of band theory.

we have calculated U_{rep} directly from overlaps, it would seem reasonable to calculate U_{rep}^{AB} directly from the overlap integrals S_{AB}.

Acknowledgements – We are grateful to R. D. Cowan, J. B. Mann, R. E. Watson and D. F. Mayers for the Hartree–Fock functions; to F. J. Adrian for the calculation for the pressure dependence of the NMR chemical shift of Xe in Xenon gas; to J. A. Rayne for fruitful discussions; to S. M. Wolfson for computational aid, and to S. DeBenedetti and A. S. Klotz for a critical reading of the manuscript.

REFERENCES

1. FUCHS K., *Proc. R. Soc.* **A151**, 585 (1935); **153**, 622 (1936).
2. DICK B. G. and OVERHAUSER A. W., *Phys. Rev.* **112**, 90 (1958).
3. DICK B. G., *Phys. Rev.* **129**, 1583 (1963).
4. HAFEMEISTER D. W. and ZAHRT J. D., *J. chem. Phys.* **47**, 1428 (1967).
5. BLEICK W. E. and MAYER J. E., *J. chem. Phys.* **2**, 252 (1934).
6. KUNIMUME M., *J. chem. Phys.* **18**, 754 (1950).
7. LOMBARDI E. and JANSEN L., *Phys. Rev.* **136**, A1011 (1964).
8. ROSEN N., *Phys. Rev.* **38**, 255 (1931).
9. LÖWDIN P. O., *Adv. Phys.* **5**, 1 (1956).
10. LOMBARDI E. and JANSEN L., *Phys. Rev.* **167**, 822 (1968).
11. HAFEMEISTER D. W. and FLYGARE W. H., *J. chem. Phys.* **43**, 795 (1965)
12. HARTREE D. R. and HARTREE W. H., *Proc. R. Soc.* **A166**, 450 (1938)
13. HARTREE D. R. and HARTREE W. H., *Proc. R. Soc.* **A157**, 490 (1936).
14. MAYERS D. F. and O'BRIAN F., *Phys. Soc. London, J. phys. B (Atomic Mol.)* 1, 145 (1968)
15. WORSLEY B. H., *Proc. R. Soc.* **A247**, 390 (1958).
16. MANN J. B., Rep. Nos. LA-3690 and LA-3691. Los Alamos Scientific Laboratory.
17. WATSON R. E. and FREEMAN A. J., *Phys. Rev.* **124**, 1117 (1961).
18. COWAN R. D., LARSON A., LIBERMAN D., MANN J. B. and WABER J. T., *Phys. Rev.* **144**, 5 (1966).
19. HAFEMEISTER D. W., *J. chem. Phys.* **46**, 1929 (1967).
20. ADRIAN F. J., *Phys. Rev.* **136**, A980 (1964).
21. MASON E. A. and RICE W. E., *J. chem. Phys.* **22**, 843 (1954).
22. HIRSCHFELDER J. O., CURTISS C. F. and BIRD R. B., *Molecular Theory of Gases and Liquids*, p. 178. Wiley, New York (1954).
23. DOBBS E. R. and JONES G. O., *Rep. Prog. Phys.* **20**, 516 (1957).
24. POLLACK G. L., *Rev. mod. Phys.* **36**, 748 (1964).
25. MUNN R. J. and SMITH F. J., *J. chem. Phys.* **43**, 3998 (1965)
26. BARRON T. H. K. and KLEIN M. L., *Proc. phys. Soc.* **85**, 533 (1965).
27. BATCHELDER D. N., LOSEE D. L. and SIMMONS R. O., *Phys. Rev.* **162**, 767 (1967).
28. URVAS A. O., LOSEE D. L. and SIMMONS R. O., *J. Phys. Chem. Solids* **28**, 2269 (1967).
29. HUNTINGTON H. B., *Phys. Rev.* **91**, 1092 (1953).
30. DIENES G. J., *Phys. Rev.* **86**, 228 (1952).
31. DANIELS W. B. and SMITH C. S., *Phys. Rev.* **111**, 713 (1958).
32. COLLINS J. G., *Phys. Rev.* **155**, 663 (1967).
33. LEIGH R. S., *Phil. Mag.* **42**, 139 (1951).
34. SCHMUNK R. E. and SMITH C. S., *J. Phys. Chem. Solids* **9**, 100 (1959).
35. JAN J. P. and TEMPLETON I. M., *Phys. Rev.* **161**, 556 (1967).
36. JASWAL S. S. and GIRIFALCO L. A., *J. Phys. Chem. Solids* **28**, 457 (1967).
37. HIKI Y., THOMAS J. F. and GRANATO A. V., *Phys. Rev.* **153**, 764 (1967).
38. GOULDING B., MOSS S. C. and AVERBACH B. L., *Phys. Rev.* **158**, 637 (1967).

J. Phys. Chem. Solids Pergamon Press 1969. Vol. 30, pp. 129–137. Printed in Great Britain.

Ga–Al–As:PHASE, THERMODYNAMIC AND OPTICAL PROPERTIES

M. B. PANISH and S. SUMSKI
Bell Telephone Laboratories Incorporated, Murray Hill, N.J. 07974, U.S.A.

(*Received* 31 *May* 1968; *in revised form* 10 *July* 1968)

Abstract—The liquidus isotherms in the Ga rich corner of the Ga–Al–As phase diagram have been determined from 800 to 1100°C and at 1000°C the corresponding solidus isotherm was obtained. A simple thermodynamic treatment which permits calculation of the solid and liquid isotherms is described. Approximate values of the change in the absorption edge of $Ga_xAl_{1-x}As$ as a function of composition are given and the implications of the phase data for solution epitaxy are discussed.

INTRODUCTION

THE GaAs–AlAs mixed crystal system is one in which there exists the possibility of obtaining crystals with selected energy gaps, within the limits imposed by the energy gaps of GaAs and AlAs. Such crystals are of considerable interest because of their potential value for optoelectronic and other solid state devices. Furthermore, it has been amply demonstrated for GaAs [1–6] that device, or bulk materials grown from Ga solution generally have more efficient radiative recombination than materials prepared in other ways. This is presumably due to the lower Ga vacancy concentration in such material [6].

Black and Ku [7] have prepared $Ga_xAl_{1-x}As$ crystals by iodide vapor transport and from the melt, and have studied diodes prepared by iodide transport [8]. Ruprecht, Woodall and Pettit [9] have prepared *p–n* junctions in $Ga_xAl_{1-x}As$ by solution epitaxy. The latter junctions had high external quantum efficiencies. As is to be expected, the relative intensity of the low energy to the near gap electroluminescence is smaller for solution grown diodes of Ruprecht *et al.* than for the vapor grown material of Black and Ku.

In this paper we present the ternary liquidus–solidus phase diagram of the Ga–Al–As system in the region of primary interest for solution epitaxy, and discuss the thermodynamic implications of that phase diagram with particular reference to the 1000°C liquidus and solidus isotherms. The approximate band gap relationship with Al content of the solid is also presented, and the implications of the optical and phase properties of the system toward solution epitaxy are discussed.

EXPERIMENTAL

Differential thermal analysis studies

Ga, GaAs and Al with purities better than 99·99 per cent were used in this work. The required amounts of Ga, GaAs and Al were weighed and placed into boron nitride crucibles which were sealed under vacuum into fused silica capsules in the manner shown in Fig. 1. The volume of melt used in a run ranged from 5 to 8 cc. The differential thermal analysis cell was placed in a large steel block inside a resistance furnace. Ceramic fiber was packed around and over the cell in order to provide a poor heat transfer path between the cell and the steel block.

The furnace, and thus the steel block and the DTA cell were heated to 100–200°C above the expected temperature for the first appearance of solid. When the cell had reached the desired temperature, the furnace power was either reduced or turned off. Thermal effects were noted by continuously

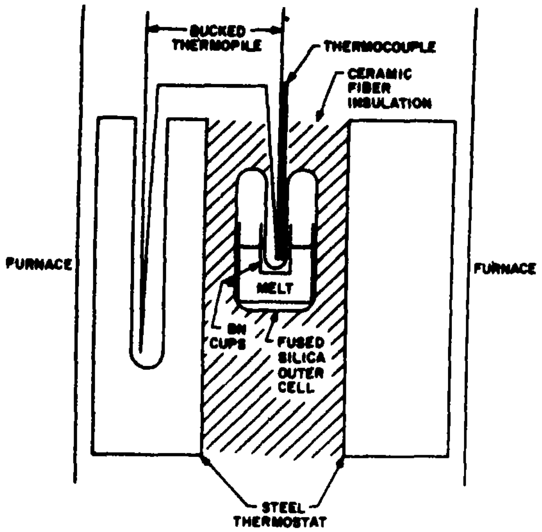

Fig. 1. The differential thermal analysis apparatus.

recording the output of a thermopile consisting of four Cr–Al thermocouples in the cell thermocouple well, bucked against four thermocouples placed in the well in the steel block. Temperature was measured with an additional thermocouple in the DTA cell thermocouple well. Further details of DTA studies with similar cells were presented earlier[10].

Liquid epitaxy

For most of the work reported here it was convenient to use a tipping technique which permitted the growth of epitaxial layers of $Ga_xAl_{1-x}As$ quickly, with a small amount of source solution. For some of the work, however, a dipping technique similar to that reported by Ruprecht[9] was employed.

The tipping technique reported by Nelson [1] for GaAs could not be used, particularly for solutions containing appreciable amounts of Al, because of the formation of an Al_2O_3 scum on the liquid surface. A system was therefore designed, which would effectively remove the oxides so that uniform wetting and crystal growth could occur. In this tipping technique the solution is held stationary in a recess in the bottom of a graphite boat (Fig. 2). The substrate crystal is carried by a sliding holder which simultaneously wipes away the oxide scum from the surface of the gallium solution and deposits the substrate seed on a clean oxide free solution. Growth is achieved by cooling the solution with a programmed furnace control system between 0·5 to 5°C/min. In this range with Al above 1 at. % in the liquid, the cooling rate did not appear to affect the amount of Al in the solid. The growth could be stopped at any time by tipping the furnace and sliding the seed away from the source solution while simultaneously wiping its surface. All epitaxial layers were grown on the 111 As surface of boat grown GaAs purchased from the Monsanto Corporation. Semiconductor grade Ga and Al were used for this work. All layers were grown under pure H_2 produced by a Mathieson Corporation Model 8315 generator.

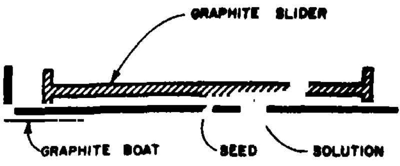

Fig. 2. The tipping apparatus.

The best control over the composition of the regrown layer was obtained, either with dipping or tipping techniques, where the dipping or tipping was done at a temperature which corresponded to the temperature of first formation of solid for the solution being used. Generally, therefore, a solution was prepared by adding the amounts of Ga, GaAs and Al required to yield a solution which would be completely liquid above the dipping or tipping temperature with solid precipitating below that temperature. For most of the work reported here, the 1000°C isotherm of the ternary was used. It was generally necessary to heat the solution to 50–100°C above the tipping temperature to dissolve all of the GaAs in a reasonable length of time.

The epitaxially grown layers were used both for optical transmission measurements to aid in the estimation of the way in which the absorption edge changes with Al concentration, and were analyzed with an electron beam microprobe to provide data for the determination of the solid solubility isotherm.

Optical measurements

In order to determine, approximately, the change of the absorption edge, E_Δ, as a function of aluminum concentration in the $Ga_xAl_{1-x}As$ mixed crystals, the optical absorption of the layers and the substrate GaAs was measured as a function of wavelength. This was done by focusing an illuminated source slit on a thin polished bar of the substrate plus epitaxial layer and projecting the image of the slit (as transmitted through either the epitaxial layer or the substrate) upon the entrance slit of a 0·5 m grating spectrometer. We were not able to obtain precise enough data for absolute transmittance values for the samples; but an estimate of the way E_Δ varied with composition was obtained by comparing the relative transmittance of GaAs and the layer on the same bar as a function of wavelength. The selection of a transmission value for comparison was arbitrary. The energy difference at the highest transmission of which the curves for both GaAs and the mixed crystal were exponential was taken as E_Δ. It is understood that this is not a precise way of obtaining E_Δ and thus the band gap energy as a function of Al concentration. It does, however, provide data of sufficient accuracy that we can show the gross behaviour E_Δ with increasing aluminum concentration and show approximately at what composition the transition from direct to indirect gap material occurs.

RESULTS AND DISCUSSION

Liquidus isotherms in the Ga–Al–As *ternary phase diagram: thermodynamic properties of the system*

The only thermal effect studied in this work was that for the first formation of solid upon slowly cooling the liquid. The data for the various compositions studied are given in Table 1. The Ga–As binary diagram of Thurmond[11] was the only binary boundary used in the construction of the ternary phase diagram. Since this work was done only in the Ga-rich corner of the ternary system the As–Al boundary was not needed. As will be shown below, part of the liquidus for that phase diagram may be estimated from the work presented here. For all compositions considered, the formation of the first solid in the ternary occurred above the liquid temperature for any composition in the Ga–Al system, that binary was therefore not used for the drawing of isotherms in the ternary.

Table 1. *Temperature for the formation of first solid when cooling* Ga–Al–As *liquid solutions*

Ga	At % Al	As	T°C
96·5	1·0	2·5	898
94·0	1·0	5·0	952
89·0	1·0	10·0	1037
84·0	1·0	15·0	1082
92·5	5·0	2·5	1002
90·0	5·0	5·0	1067
85·0	5·0	10·0	1140
82·5	15·0	2·5	1074

In order to obtain the liquidus isotherms for the Ga–Al–As ternary, the data of Table 1 were plotted in two ways. First, with isoarsenic curves for the transition temperature T, as a function of Al concentration, Fig. 3, and second with isoaluminum curves for the As concentration as a function of $1/T$, Fig. 4. Interpolation and extrapolation of these curves yields data points for the Ga rich corner of the ternary diagram of Ga–Al–As, Fig. 5. The isotherms shown in Fig. 5 were drawn through points thus obtained.

The shapes of the isotherms of Fig. 5 are

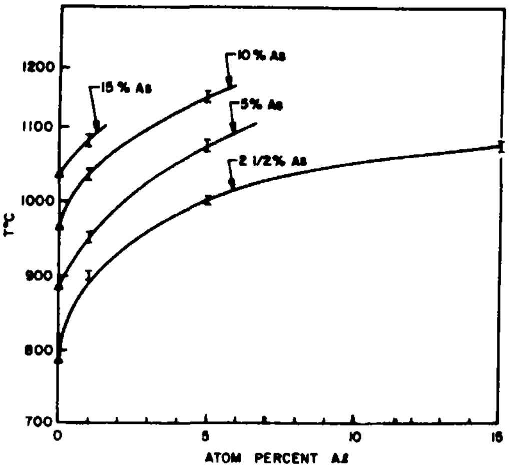

Fig. 3. Isoarsenic curves of the liquidus temperature (T) as a function of aluminum concentration in the liquid. Data on the zero % Al axis is from Thurmond[11].

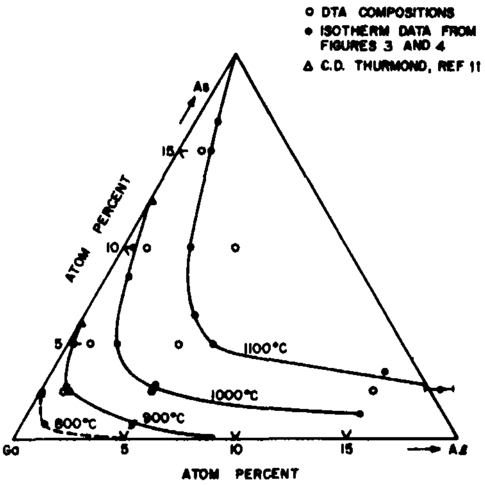

Fig. 5 The Ga-rich corner of the Ga–Al–As ternary phase diagram.

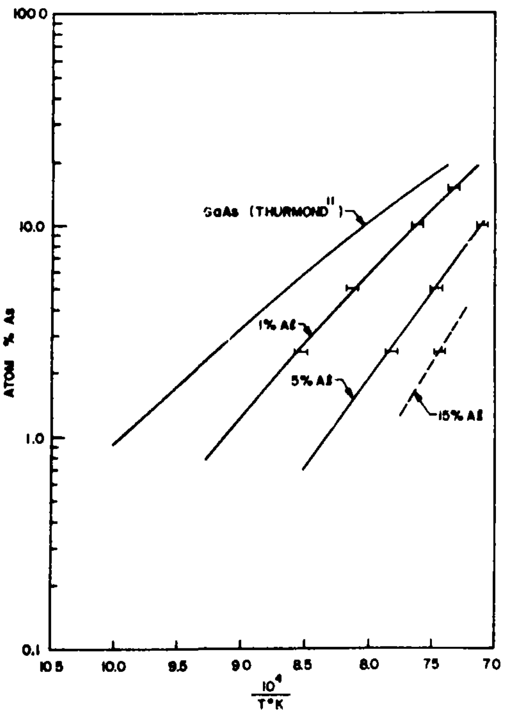

Fig. 4. Isoaluminum curves of arsenic concentration as a function of $1/T$.

quite interesting. The addition of Al to a solution of Ga and As severely depresses the arsenic solubility. Since the liquidus isotherm shapes depend upon interactions among the components in the liquid and in the solid as well as upon the stability of the pure solid components, it is of interest to understand how these factors contribute to the isotherm shape in the Ga–Al–As system.

For the equilibrium of the mixed $Ga_xAl_{1-x}As$ solid with the ternary liquid we may write:

$$GaAs_{(s)} \rightleftarrows Ga_{(l)} + As_{(l)} \tag{1}$$

$$K_{GaAs} = \frac{\gamma_{Ga_l}X_{Ga_l}\gamma_{As_l}X_{As_l}}{\gamma_{GaAs_s}X_{GaAs_s}} \tag{2}$$

and

$$AlAs_{(s)} = Al_{(l)} + As_{(l)} \tag{3}$$

$$K_{AlAs} = \frac{\gamma_{Al_l}X_{Al_l}\gamma_{As_l}X_{As_l}}{\gamma_{AlAs_s}X_{AlAs_s}} \tag{4}$$

with the restrictions

$$\chi_{Ga_l} + \chi_{Al_l} + \chi_{As_l} = 1 \tag{5}$$

and

$$\chi_{GaAs_s} + \chi_{AlAs_s} = 1. \tag{6}$$

Reactions (1) and (3) show formally, the equilibrium between the components of the mixed crystal solid and the liquid, K_{GaAs} and K_{AlAs} are the equilibrium constants for equations (1) and (3), and the γ's and χ's are activity coefficients and atom or mole fractions for the components in the liquid (l) and the solid (s).

In this work we are dealing only with the Ga and Al rich part of the system so far as the liquid is concerned. Since the Ga–Al binary phase diagram[12] is nearly that which would be expected for an ideal mixture, we expect that in the liquid solution at higher temperature with a small amount of As present, the system might reasonably be treated as one in which the Al and Ga atoms were indistinguishable from each other. Furthermore, the lattice constants for GaAs and AlAs are almost identical (AlAs; $a = 5{\cdot}639$ to $5{\cdot}662$[13–16], GaAs; $a = 5{\cdot}6532$[17]). It therefore does not seem to be unreasonable to expect that the solid might behave like an ideal solution.

It is illustrative to estimate liquidus and solidus isotherms on the basis of several simple models for the liquid and solid.

(A) *The liquid and solid are ideal*: in this case all the activity coefficients of equations (2) and (4) are unity and equations (2), (4), (5) and (6) may be combined to yield

$$K'_{AlAs}(\chi_{Ga_l} - \chi^2_{Ga_l} - \chi_{Ga_l}\chi_{Al_l}) + K'_{GaAs} \times (\chi_{Al_l} - \chi^2_{Al_l} - \chi_{Ga_l}\chi_{Al_l}) - K'_{GaAs}K'_{AlAs} = 0 \quad (7)$$

where $'$ indicates the ideal equilibrium constants for reactions 1 and 3.

From Thurmonds Ga–As binary[11] at 1000°C, $K'_{GaAs} = 0{\cdot}1095$. We have evaluated K'_{AlAs} by obtaining the best fit of equation (7) to the experimental data in the Al concentration range from 4 to 15 at. % Al in the liquid. This was found to be $K'_{AlAs} = 1{\cdot}74 \times 10^{-3}$, and the resulting liquidus isotherm from equation (7) is shown in Fig. 6. Considering the scale of Figs. 5 and 6, the ideal curve is in excellent agreement with the experimental curve. For the ideal case the experimental liquidus isotherm can be used to obtain the corresponding solid solubility isotherm from equation (2) with all activity coefficients equal to unity and $K'_{GaAs} = 0{\cdot}1095$ at 1000°C. The ideal solidus obtained in this manner is shown in Fig. 7.

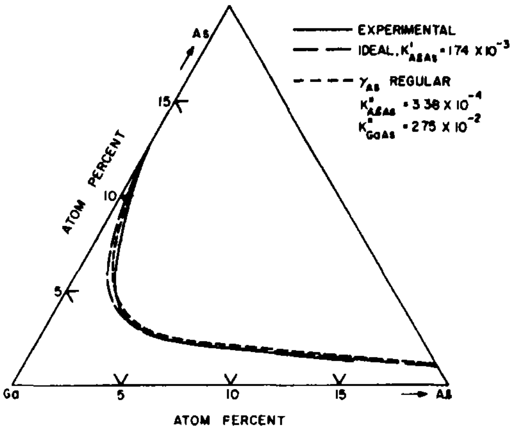

Fig. 6. The 1000°C liquidus isotherm – experimental and calculated.

(B) *The solid and Ga and Al in the liquid are taken to be ideal, but γ_{As_l} varies with concentration at a given temperature according to the binary regular solution relation:*

$$\log \gamma_{As_l} = a(1 - \chi_{As_l})^2 \quad (8)$$

where a is constant*. For convenience we will refer to this solution as 'binary-regular'.

From equations (1–6) with the conditions above imposed

$$K''_{AlAs}(\chi_{Ga_l} - \chi^2_{Ga_l} - \chi_{Ga_l}\chi_{Al_l}) + K''_{GaAs} \times$$

$$(\chi_{Al_l} - \chi^2_{Al_l} - \chi_{Ga_l}\chi_{Al_l}) - \frac{K''_{AlAs}K''_{GaAs}}{\gamma_{As\ l}} = 0 \quad (9)$$

---

*These assumptions cannot be rigorously true. γ_{Al} and γ_{Ga} must differ from unity and vary in accordance with the Gibbs–Duhem relation. For this work the assumptions are sufficient because effects ascribable to nonconstant γ_{Ga} and γ_{Al} are not observed within the experimental accuracy of the data.

where

$$K''_{\mathrm{GaAs}} = \frac{\chi_{\mathrm{Ga}_l}\chi_{\mathrm{As}_l}\gamma_{\mathrm{As}_l}}{\chi_{\mathrm{GaAs}_s}} \tag{10}$$

and

$$K''_{\mathrm{AlAs}} = \frac{\chi_{\mathrm{Al}_l}\chi_{\mathrm{As}_l}\gamma_{\mathrm{As}_l}}{\chi_{\mathrm{AlAs}_s}} \tag{11}$$

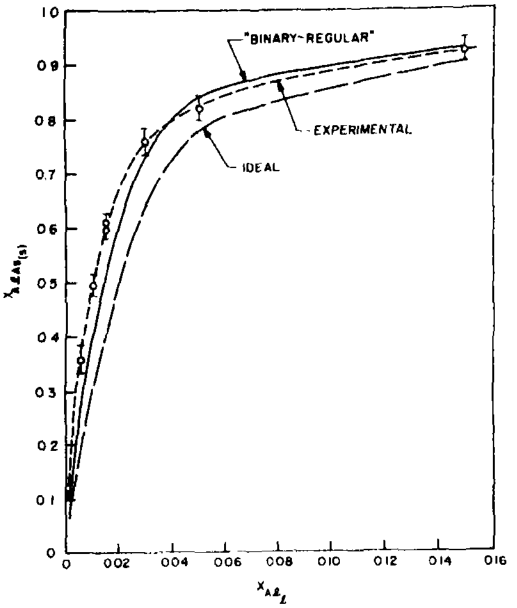

Fig. 7. The 1000 solid solubility isotherm for Al in gallium aluminum arsenide, experimental and calculated.

From the Ga–As binary phase data of Thurmond[11] and the Ga–As binary activity coefficient data of Arthur[18], at 1000°C, $K''_{\mathrm{GaAs}} = 2{\cdot}745 \times 10^{-2}$. K''_{GaAs} and equations (8) and (9) have been used to determine the liquidus isotherm at 1000°C by fitting the curve at one experimental point ($\chi_{\mathrm{Ga}_l} = 0{\cdot}900$, $X_{\mathrm{As}_l} = 0{\cdot}021$). Where this is done we obtain $K''_{\mathrm{AlAs}} = 3{\cdot}38 \times 10^{-4}$ and the 'binary-regular' curve shown in Fig. 6. The 'binary-regular' 1000°C isotherm is in excellent agreement (probably within the limits of experimental error) with the experimental isotherm over the entire experimentally determined composition range.

The 1000°C solid solubility isotherm for the 'binary-regular' solution model was obtained with equations (8) and (10) and is shown in Fig. 7. The experimental solid solubility data are also plotted on Fig. 7.

The 'binary-regular' solid solubility isotherm of Fig. 7 is in excellent agreement with the experimental isotherm over most of the concentration range studied. There is a small difference between these curves in the lower Al concentration range which can probably be attributed to a small degree of non-ideality in the solid.

The system Al–As *and the heat of formation of* AlAs

The degree of agreement between the calculated and experimental 1000°C solidus and liquidus isotherms lends support to the idea that the solid solutions are, in this case, almost ideal and that the liquid does have the properties described above for case (*B*) above. Equations (8) and (9) may then be used with Arthur's[18] activity coefficient data and Thurmonds binary phase diagram, to obtain K''_{AlAs} for each experimental point. These may be used with equation (8) and (11) and the $\gamma_{\mathrm{As}l}$ data of Arthur[18] to estimate the Al rich liquidus of the Al–As binary as is shown in Fig. 8. The AlAs melting point is taken as 1740°C from Kischio[19]. The scatter of the points is an indication of the precision of the data of Table 1.

For any reaction the standard free energy change, $\Delta F° = RT \ln \mathrm{Keq}$. $\Delta F_3° - \Delta F_1°$ may then be obtained at any T from $K''_{\mathrm{GaAs}}/K''_{\mathrm{AlAs}}$ (with the understanding that $\gamma_{\mathrm{Al}l} \approx \gamma_{\mathrm{Ga}_l} \approx 1$). On this basis, from the ternary data, at 1000°C $\Delta F_3° - \Delta F_1° = 10{\cdot}6$ kcal/mole. This value may be used, with thermodynamic data for GaAs[11, 18], As[18, 20], Al[20] and Ga[20], to obtain a value of $-26{\cdot}6$ kcal/mole for the 298°K heat of formation, ΔH_f^{298}, of AlAs. Since no heat capacity data are available for AlAs, the corresponding data for GaP (in the form of free energy functions [11]) were used since GaP and AlAs are isoelectronic with closely matching molecular weights. ΔH_f^{298} thus determined is in excellent

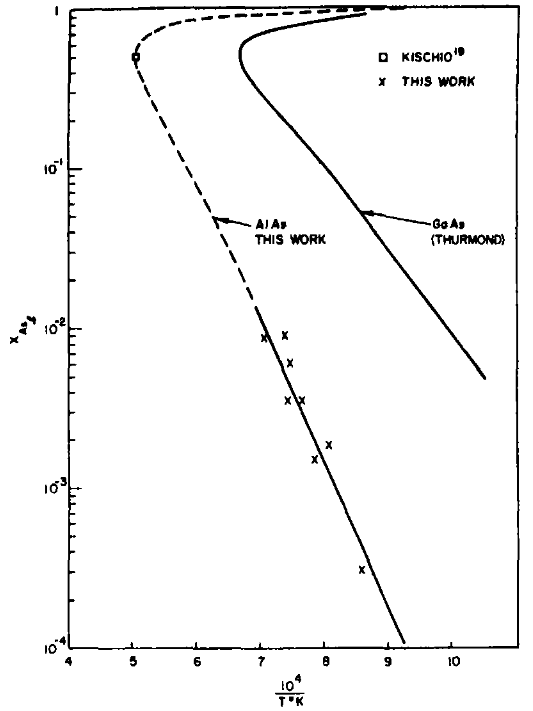

Fig. 8. The estimated Al-As binary. The Ga-As binary is shown for comparison.

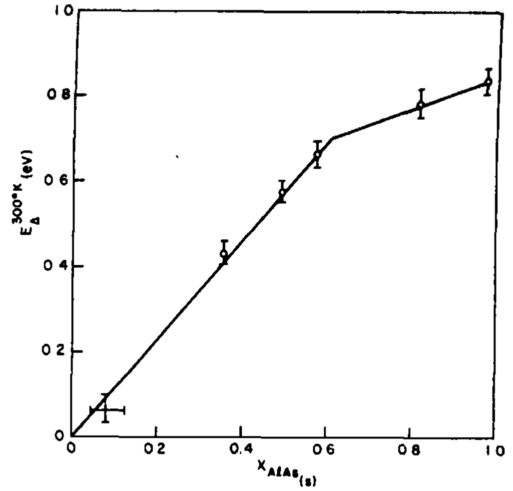

Fig. 9. $E_{\Delta}^{300°K}$ as a function of composition in gallium aluminum arsenide mixed crystals. Note: We have not attempted to compare E_{Δ} to the band gap shift because the method of evaluation of the absorption data could lead to systematic errors of as much as 0·1 eV.

agreement with that reported by Kischio[19] (−27·8 ± 0·5 kcal/mole). Hoch and Hinge[21] have determined ΔH_f^{298} as −35·4 ± 3·1 kcal/mole by a third law calculation and ∼ −28·5 kcal/mole by a second law calculation with the same data. For their third law calculation they assumed that heat capacity data for AlN could be used for AlAs. If instead we use their experimental data with the GaP heat capacity data, their third law ΔH_f^{298} is −29 ± 3 kcal/mole.

Implications of the phase and optical data for liquid epitaxy

The approximate change of the absorption edge (E_{Δ}) with aluminum concentration in the GaAs-AlAs system is given in Fig. 9. The characteristic shape of the curve is in agreement with previously reported data[7, 9] in which the band gap (Eg) vs. composition curve is broken down to two straight lines which intersect at the composition (in this case, approximately $\chi_{AlAs} = 0·6$) at which the transition between direct gap and indirect gap material occurs. Such a transition is to be expected because GaAs is a direct gap material with $Eg^{300°K} = 1·43$ eV[22] while AlAs is an indirect gap material with $Eg^{300°K} \approx 2·2$ eV[19, 23]. Perhaps of equal significance, for its implications towards device fabrication by solution epitaxy, is the E_{Δ} vs. 1000°C liquidus Al concentration curve of Fig. 10.

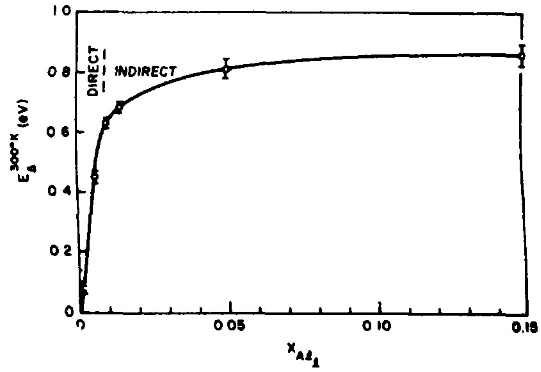

Fig. 10. $E_{\Delta}^{300°K}$ as a function of liquidus composition from which crystals are grown on the 1000°C isotherm.

This curve shows that direct gap material, which is most interesting for devices, can only be obtained from solutions containing approximately 0·8 at. % Al or less. In this region the distribution coefficient for aluminum in the solid and liquid (Fig. 11) is high and changing rapidly with Al composition. This is also the region where the arsenic solubility is highest and therefore where the thickest liquid epitaxy layers will be obtained. All of these factors combine to make reproducible aluminum concentration in the growth of epitaxial Ga–Al–As layers in the direct gap region most difficult. The optimum conditions for the growth of layers with uniform composition in the direct gap region will be attained by using the largest volume of Ga possible to grow a layer over the shortest temperature range possible, starting with a liquid which contains no solid. The liquid composition should be precisely at the composition of the liquidus isotherm at the temperature at which the solution touches the seed and growth starts.

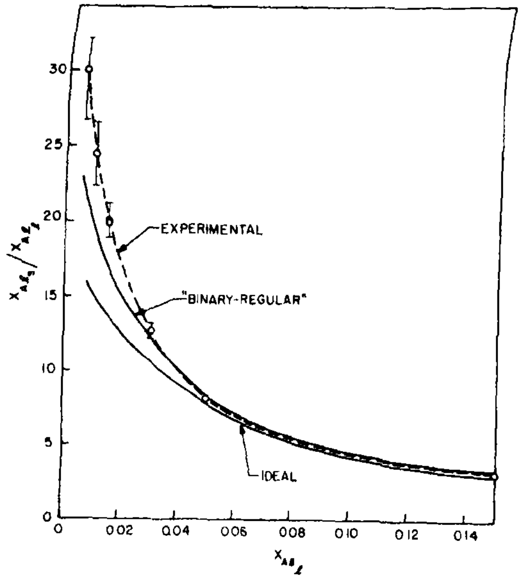

Fig. 11. The distribution coefficient as a function of Al concentration in the liquid on the 1000°C isotherm. Note: The units here are atom fraction Al in the solid and in the liquid.

CONCLUSIONS

The 800, 900, 1000 and 1100°C liquidus isotherms in the Ga rich corner of the Ga–Al–As ternary phase diagram have been determined experimentally along with the 1000°C solid solubility isotherm. When a single experimental liquidus point is used, along with data for the GaAs binary, it is possible to obtain calculated liquidus and solidus isotherms (for the 1000° case) which are in excellent agreement with the experimental data, by the use of a very simple model. In this model the solid is taken to be ideal and the liquid non-ideal. In the liquid, Ga and Al atoms are assumed to be indistinguishable from each other and have activity coefficients which do not change with As concentration, while the arsenic atoms in the liquid are taken to behave as though the solution were regular. Since γ_{As_l} changes only slightly in the composition region studied, this means that the shapes of the liquidus and solidus isotherms are primarily determined by the difference in the free energy of formation of pure solid GaAs and AlAs. This is substantiated by the excellent agreement between the heat of formation of AlAs at 298°K obtained in this work from the ternary Ga–Al–As liquidus surface (−26·6 kcal/mole) and that obtained directly for AlAs (−27·8 kcal/mole) by Kischio[19].

Transmission measurements reveal that the transition from direct to indirect gap material occurs at approximately $\chi_{AlAs} = 0{\cdot}6$ in the GaAs–AlAs mixed crystals and that direct gap material is obtained (at 1000°C) only from solutions containing less than approximately 0·8 atom % Al. The distribution coefficient for Al in $Ga_xAl_{1-x}As$ was shown to be high and changing rapidly with Al concentration in the liquid in this composition region. It is to be expected that this will result in composition control problems for solution epitaxy of gallium aluminum arsenide in the direct gap composition range.

Acknowledgements—We would like to acknowledge the help of C. D. Thurmond in a number of useful discussions, and of D. R. Wonsidler and J. W. Colby who did the electron beam microprobe analyses needed for this study.

REFERENCES

1. NELSON H., *RCA Rev.* **24**, 603 (1963).
2. DOUSMANIS G. C., NELSON H. and STAEBLER D. L., *Appl. Phys. Lett.* **5**, 174 (1964).
3. PILKUHN M. H., RUPRECHT H. and WOODALL J., *IEEE J. Quant. Electron.* **1**, 184 (1965).
4. PANISH M. B., QUEISSER H. J. DERICK L. and SUMSKI S., *Solid State Electron.* **9**, 311 (1966).
5. QUEISSER H. J. and PANISH M. B., *J. Phys. Chem. Solids* **28**, 1177 (1967).
6. PANISH M. B., *J. Phys. Chem. Solids* **29**, 409 (1968).
7. BLACK J. F. and KU S. M., *J. Electrochem. Soc.* **113**, 249 (1966).
8. KU S. M. and BLACK J. F., *J. appl. Phys.* **37**, 3733 (1966).
9. RUPRECHT H., WOODALL J. M. and PETTIT G. D., *Appl. Phys. Lett.* **11**, 81 (1967).
10. PANISH M. B., *J. Phys. Chem. Solids* **27**, 291 (1966).
11. THURMOND C. D., *J. Phys. Chem. Solids* **26**, 785 (1965).
12. ELLIOT R. P., *Constitution of Binary Alloys*, First Supplement. McGraw Hill, New York (1965).
13. GOLDSCHMIDT V. M., *Skrifter Norski Videnskaps Akad. Oslo, I: Mat. Naturv.* Kl VIII (1926), as reported in [17].
14. NATTA G. and PASSERINI L., *Gazz Chim. Ital.* **58**, 458 (1928).
15. SHMARTSEV YU V., VOLOV YU A., BORSHCHEVSKII A. S., *Refractory Semiconductor Materials* (Edited by N. A. Goryinova and D. N. Nasledov). Consultants Bureau Translation (1966).
16. KALYUNZHNAYA G. A., TRET'YAKOV D. N. BORSHCHEVSKII A. S. and VAEPOLIN A. A., *Soviet Research in New Semiconductor Materials* (Edited by D. N. Nosledov and N. A. Goryunova). Consultants Bureau Translation (1965).
17. GIESECKE G., *Semiconductors and Semimetals; Physics of III–V Compounds* (Edited by R. K. Willardson and A. C. Beer). Vol. 2. Academic Press, New York (1966).
18. ARTHUR J., *J. Phys. Chem. Solids* **28**, 2257 (1967).
19. KISCHIO W., *Z. anorg. allg. Chem.* **328**, 187 (1964).
20. STULL D. R. and SINKE G. C., *Thermodynamic Properties of the Elements.* American Chemical Society, Washington (1956).
21. HOCH M. and HINGE K., *J. chem. Phys.* **35**, 451 (1961).
22. STURGE M. D., *Phys. Rev.* **127**, 768 (1962).
23. RUEHRWEIN R. A., Deutsche Auslegeschrift DAS 1132098.

Phys. Chem. Solids **Pergamon Press 1969. Vol. 30, pp. 139–147. Printed in Great Britain.**

SELF-DIFFUSION OF ZINC AND TELLURIUM IN ZINC TELLURIDE

R. A. REYNOLDS* and D. A. STEVENSON
Department of Materials Science, Stanford University, Stanford, Calif. 94305, U.S.A.

(*Received* 20 *May* 1968; *in revised form* 26 *June* 1968)

Abstract—The high temperature defect equilibria of ZnTe were investigated by measuring the tracer self-diffusion coefficients of Zn^{65} and Te^{123} as functions of temperature, component pressure, and added impurity content. The experimental results reveal that the self-diffusion coefficient of Zn in undoped ZnTe is independent of component partial pressure and is described as

$$D = 14\exp\left(\frac{-2{\cdot}69 \pm 0{\cdot}08\ \text{eV}}{kT}\right)\ \text{cm}^2/\text{sec}.$$

The self-diffusion coefficient of Te increases with increasing partial pressure of Te, and in ZnTe saturated with Te is described by

$$D = 2\times 10^4 \exp\left(\frac{-3{\cdot}8 \pm 0{\cdot}4\ \text{eV}}{kT}\right)\ \text{cm}^2/\text{sec}.$$

The addition of $10^{19}/\text{cm}^3$ Al to ZnTe enhances the self-diffusion coefficient of Zn at temperatures below about 950°C. The addition of $5\times 10^{19}/\text{cm}^3$ Ag to ZnTe does not influence the self-diffusion coefficient of Zn at 782°C.

The results may be explained assuming that the self-diffusion of Zn in undoped ZnTe is controlled by native defect concentrations which depend only on thermal disorder, rather than deviation from stoichiometry. Either Frenkel disorder on the Zn sublattice or Schottky disorder dominates the charge neutrality condition at high temperatures. The enhanced Zn diffusion in the Al doped crystals below 950°C is interpreted as extrinsic diffusion with charged zinc vacancies compensating the impurity donor. The dominant mobile defect proposed for the Te sublattice is an interstitial Te species of undetermined electrical activity.

INTRODUCTION

Native defects play an important role in controlling the physical properties of the II–VI compounds. In order to improve our knowledge of the native defect equilibria in ZnTe, we have determined the radiotracer self-diffusion coefficients of Zn and Te as functions of temperature and component partial pressure. Studies of the defect equilibria in ZnTe have been made through measurements of the electron transport, optical and electron spin resonance behavior; hence, the present self-diffusion data provide new information concerning the character of the native defects in this compound. The advantage of using self-diffusion measurements to characterize the high temperature defect equilibria is that the results are not affected by changes occurring in a sample during cooling from high temperatures. Since the II–VI compounds have a pronounced tendency for defects to agglomerate in the form of associates or precipitates during cooling from high temperatures[1–3], one must use care in interpreting properties measured at room temperature or below in terms of the high temperature defect equilibria.

The interpretation of the self-diffusion data leads to the hypothesis that the defect important in the self-diffusion of Zn arises from thermal disorder rather than from deviation from stoichiometry, and that the defect important in the self-diffusion of Te is an interstitial Te acceptor defect. This model of the high temperature defect equilibria in ZnTe differs from the model based on the interpretation of electrical property measurements[4–6] which postulates that Zn vacancies are the principal lattice defects at high temperatures.

**Present address*: Texas Instruments, Dallas, Texas.

EXPERIMENTAL PROCEDURES

Crystal growth

Elemental Zn and Te were reacted to form ZnTe by encapsulating approximately 100 g of stoichiometric charge in a graphite coated quartz capsule, and then slowly heating the capsule to about 940°C over a period of about 48 hr. The reacted material was sublimed in a dynamic vacuum (background pressure $\leq 10^{-5}$ Torr.) by heating the charge to about 750°C. The sublimed ZnTe was free of unreacted Zn, Te, precipitates, or voids, and was used to prepare crystals by the Bridgman method or by the vapor transport method of Piper and Polich[7]. Mass and emission spectrographic analyses of these ingots showed an impurity content of about $1-5\times10^{17}/\text{cm}^3$, with the principal impurities being Cu, Si, and the transition metals (Fe, Ni, and Cr). Both single and polycrystalline samples from melt-grown and vapor transport-grown ingots were used in the diffusion studies with no detectable difference in the bulk diffusion behavior.

*Choice of boundary conditions for the diffusion measurements**

The self-diffusion coefficients of the component elements in II–VI compounds can be functions of the equilibrium component pressure as well as the temperature. It is therefore necessary to measure D as a function of both temperature and component pressure, in order to achieve the maximum amount of information. Experimentally, it is convenient to introduce the radioactive tracer in a liquid reservoir, since this obviates the time consuming operation of applying a nonreplenished source. In the mathematical analysis of the diffusion problem, one may assume that isotopic exchange occurs between the sample and the liquid phase. The vapor serves as a transfer medium liquid and solid.

From the standpoint of experimental and analytical convenience, the diffusion source was chosen so that $L \ll k_d/Dt$, where L represents an equivalent width of the liquid phase, k_d the solid-liquid distribution coefficient for the diffusing element, D the bulk diffusion coefficient in cm²/sec and t the time in seconds. For this limiting case*, the diffusion equation becomes

$$C^*(x,t)=\frac{C_0^*L}{\sqrt{(\pi Dt)}}\exp\frac{-X^2}{4Dt} \qquad (1)$$

where x is the penetration depth in cm, C_0^* is the initial surface concentration of tracer, and $C^*(x,t)$ is the tracer concentration at time t and depth x.

The experimental method described above was found satisfactory for measuring the self-diffusion coefficient of Zn in ZnTe in equilibrium with liquid Zn, and the self-diffusion coefficinets of Zn and Te in ZnTe in equilibrium with Te. The self-diffusion of Te in ZnTe in equilibrium with liquid Zn, however, could not be measured in this manner. The vapor pressure of Te in the presence of excess Zn is suppressed to such low values that a uniform distribution of the Te radioisotope in the liquid and vapor phases is not achieved. The diffusion of Te in ZnTe in equilibrium with liquid Zn, therefore, was done using the nonreplenished source method by evaporating a thin layer (≤500 Å thick) of radioactive Te onto the surface.

The diffusion of Zn and Te in ZnTe having the congruently subliming composition was also performed using the nonreplenished source method. Capsules were filled with an inert gas to minimize effects of thermal etching and bulk transport on the sample surface. However, the temperature range for experimental measurements was limited to 675–750°C. The congruently subliming composition was established by annealing crystals in large evacuated capsules prior to the diffusion anneal and the tracer was an evaporated layer of radioactive ZnTe, since additions of the pure elements would alter the sample composition.

---

*A detailed discussion of experimental problems concerning the selection of boundary conditions for diffusion studies in II–VI compounds is given in reference[1].

*The boundary conditions for the diffusion equation are discussed in more detail in the Appendix.

Sample preparation, diffusion and counting procedures

The ZnTe ingots were sliced into wafers approximately 2 mm thick and 8–12 mm in dia. Samples were then polished and encapsulated with the desired tracer source and excess component. The tracers used were Zn^{65} and enriched Te^{123}. In the case of excess Zn or Te additions, enough was added to maintain the three-phase equilibrium solid-liquid-vapor at the diffusion temperature, so that the self-diffusion data in these instances correspond to either diffusion in Zn-saturated or Te-saturated ZnTe. When no Zn or Te was added to the crystal, the sample composition corresponded to the congruently subliming composition.

During the diffusion anneal, the capsule was contained in a heavy walled inconel tube to minimize temperature gradients and to prevent temperature oscillations during the control cycle. In all cases the maximum possible temperature error due to thermocouple calibration, controller drift, etc., was no more than ±2·5°C. At the end of the diffusion anneal the capsules were withdrawn from the furnace and quenched in water. In all instances, the heating and cooling times were very short compared to the time for the diffusion anneal. Sample edges were removed to a depth of about 1/2 mm, so that tracer which diffused in from the edges would not affect the penetration profile. The tracer concentration profiles were determined by conventional sectioning and counting methods[1]. Typical profiles for a single crystal sample and a polycrystalline sample are shown in Fig. 1. In the early stages of the investigation each sample was first annealed under conditions identical to the diffusion anneal, so that any compositional changes which might occur during the diffusion anneal would be minimized. As results were accumulated, it was found that the pre-diffusion anneal had no effect on the measured value of the self-diffusion coefficients; any compositional changes which occurred upon heating the sample to the diffusion temperature occurred in times short compared to the diffusion anneal*. The self-diffusion co-efficients also were independent of the diffusion

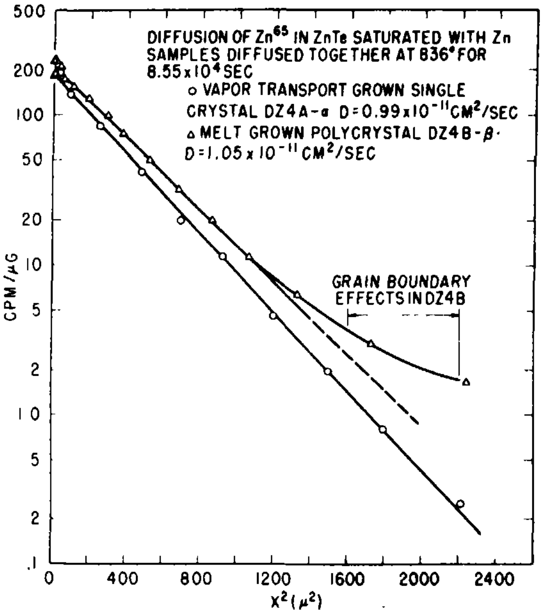

Fig. 1. Penetration profile of Zn^{65} in single and polycrystalline ZnTe.

---

*This result is to be expected since the compositional changes are the result of diffusion in a large activity gradient, and the chemical diffusion coefficients which control these changes are much larger than the self-diffusion coefficients[1, 8, 9].

time, further verifying that composition changes during the diffusion anneal did not influence the self-diffusion measurements.

In order to determine whether or not the boundary conditions assumed were fulfilled, the surface activity of several samples, as determined from the concentration profile, was compared with that calculated from the activity of the liquid reservoir after the diffusion anneal, using equation (1) with $x = 0$. In all cases the two values differed by 5 per cent or less, confirming that the assumption of surface equilibrium is valid.

In order to insure that inhomogeneous tracer distributions did not influence the results, autoradiographs were taken of all samples after diffusion, and with some samples, at various stages in the determination of the concentration profile. Typical results showing the distribution of Zn^{65} appear in Fig. 2; similar observations were made with samples containing Te^{123}. Figure 2(a) shows a uniform distribution of Zn^{65} in samples diffused under conditions of Zn or Te saturation. Figure 2(b) shows a uniform isotope distribution near the surface of a polycrystalline sample, while Fig. 2(c) shows the predominance of grain boundary diffusion deep in the crystal. Some of the radioactive isotope revealed in Fig. 2(c) is not associated with grain boundary diffusion. Apparently some other 'short circuit' path also is important, presumably subgrain boundaries or dislocations. All concentration profiles which were not described by the proper solution to the diffusion equation were obtained on samples exhibiting nonuniform isotope distributions and were discarded.

EXPERIMENTAL RESULTS

Self-diffusion of Zn *in* ZnTe

The data for the self-diffusion of Zn^{65} in ZnTe are shown in Fig. 3. It is apparent that in undoped crystals there is no dependence of D^T_{Zn} on Zn partial pressure. The data in undoped crystals for all temperatures and at Zn saturation, Te saturation, and in the congruently subliming composition are well represented by

$$D^T_{Zn} = 14 \exp\left(\frac{-2{\cdot}69 \pm 0{\cdot}08\,\text{eV}}{kT}\right)\frac{\text{cm}^2}{\text{sec}}. \quad (2)$$

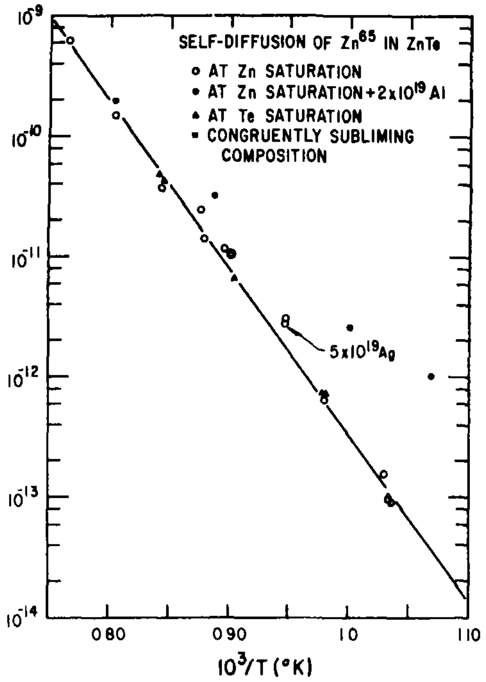

Fig. 3. Data for the self-diffusion of Zn in ZnTe.

An approximate representation of the self-diffusion coefficient of Zn in Zn saturated, Al doped ZnTe is given by:

$$D^T_{Zn} \approx 10^{-4} \exp\left(\frac{-1{\cdot}7\,\text{eV}}{kT}\right) \text{cm}^2/\text{sec}. \quad (3)$$

Self-diffusion of Te *in* ZnTe

The results for the self-diffusion of Te^{123} in ZnTe are shown in Fig. 4. This system was more difficult experimentally because D^T_{Te} was small and surface deterioration occurred to depths of $x \approx 2\sqrt{Dt}$. As a consequence, there is a larger uncertainty in the data for the self-diffusion of Te^{123} due to the uncertainty in defining the position $x = 0$.

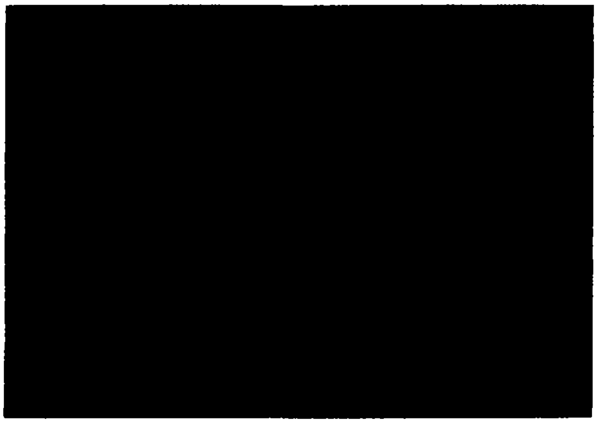

Fig. 2(a). Uniform distribution of Zn^{65} in samples diffused under conditions of Zn or Te saturation.

Fig. 2(b). Uniform isotope distribution near the surface of a polycrystalline sample.

Fig. 2(c). Evidence of grain boundary diffusion deeper in the crystal.

Fig. 2(a–c). Autoradiographs revealing Zn^{65} distribution in ZnTe.

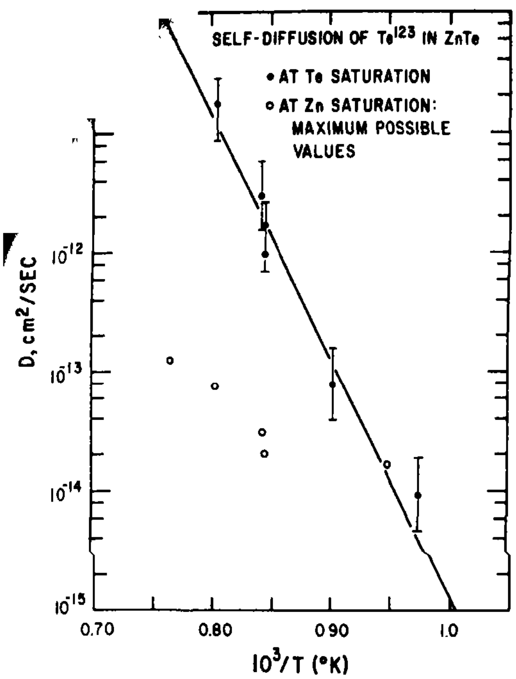

Fig. 4. Data for the self-diffusion of Te in ZnTe.

The maximum and minimum values of D^T_{Te} for each sample were calculated by defining $x = 0$ at first the outer surface and then at the greatest depth of the surface attack respectively. The two values of D^T_{Te} thus calculated never differed by more than a factor of three to four, and the averages of the two values are plotted in Fig. 4. The solid line was determined on the basis of all six data points, and the least squares equation of this line is

$$D^T_{Te} = 2\times10^4 \exp\left[\frac{-3\cdot8\pm0\cdot4\text{ eV}}{kT}\right]. \qquad (4)$$

The maximum resolution of the lapping technique corresponded to $D \approx 10^{-14}$ cm²/sec; therefore, the lowest temperature point may represent a maximum value only.

The self-diffusion of Te^{123} in ZnTe saturated with Zn was so small that in all experiments bulk diffusion dominated only to depths of 1–4 μ. Autoradiographs revealed that at greater depths the only diffusion of Te proceeded down short circuit paths (subgrain boundaries, etc.). The tracer concentration profiles were rather erratic in the region where bulk diffusion dominated due to surface deterioration to depths of 2–3 μ during the long diffusion times used. Nevertheless, the profiles could be used to estimate upper limits on the magnitude of D^T_{Te} in Zn saturated ZnTe. These upper limits are plotted as circles in Fig. 4.

In a sample having the minimum vapor pressure composition, the value of D^T_{Te} was determined to be less than 10^{-14} cm²/sec at 695°C.

These data for the self-diffusion of Zn^{65} and Te^{123} in ZnTe are summarized in Fig. 5. It is seen that the Zn self-diffusion coefficient in undoped samples is independent of Zn partial pressure. The Zn self-diffusion coefficient is not affected by doping with Ag at 782°C, but it is increased by the presence of 10^{19}/cm³ Al at temperatures below 950°C. The self-diffusion coefficient of Te is seen to decrease with decreasing Te_2 pressure, values of D^T_{Te} being too small to measure on the Zn side of the phase field. In the temperature range investigated the Te self-diffusion coefficient is always much smaller than that of Zn.

DISCUSSION

The independence of D^T_{Zn} from P_{Zn} implies that the concentration of defects responsible for the self-diffusion of Zn is independent of component pressure. This behavior is explained by thermal disorder rather than deviation from stoichiometry controlling the concentration of native defects and the charge neutrality condition at high temperatures. For singly ionized Schottky or Frenkel disorder, the charge neutrality condition can be

$$[V^-_{Zn}] = [V^+_{Te}] = \sqrt{K_S}, \qquad (5)$$

or

$$[Zn_i^+] = [V^-_{Zn}] = \sqrt{K_F}. \qquad (6)$$

Here V^+_{Te} is a singly ionized Te donor vacancy, V^-_{Zn} a singly ionized Zn acceptor vacancy,

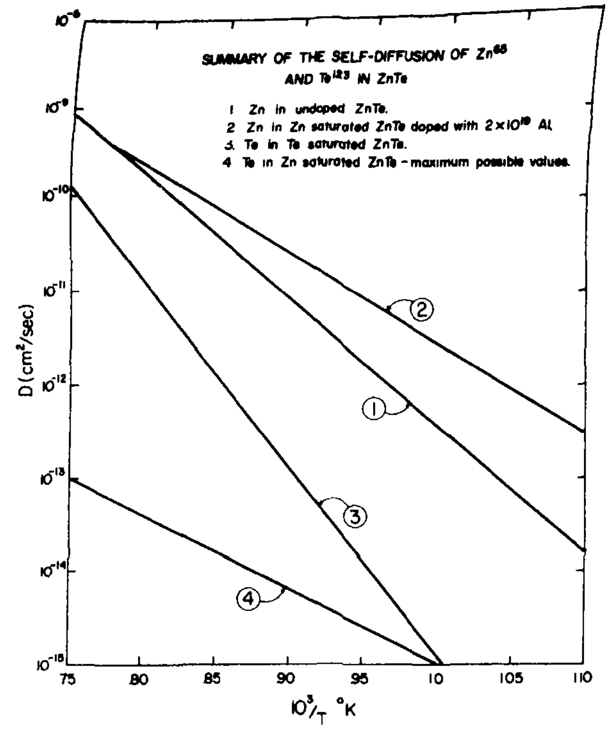

Fig 5. Summary of data for the self-diffusion of Zn and Te in ZnTe.

$K_{S'}$ is the Schottky constant relating the concentration of V_{Zn}^- and V_{Te}^+, Zn_i^+ a singly ionized Zn interstitial donor, and $K_{F'}$ is the Frenkel constant relating the concentrations of Zn_i^+ and V_{Zn}^-. The defects in (5) and (6) could be doubly ionized rather than singly ionized. The constants $K_{S'}$ and $K_{F'}$ depend only on temperature[10], so that the self-diffusion coefficient of Zn depends only on temperature. For Schottky disorder, diffusion would proceed via a vacancy mechanism in contrast to a vacancy and/or interstitial mechanism in the case of Frenkel disorder. If Schottky disorder were predominant, one would have to assume that the jump probability of V_{Te} in its appropriate charge state is so low that another native defect of the Te sublattice is responsible for the self-diffusion of Te because D_{Te}^T is much smaller than D_{Zn}^T and is dependent on component partial pressure. The concentration of this defect would have to decrease as P_{Te_2} is decreased. An interstitial Te defect would meet this requirement. If Frenkel disorder on the Zn sublattice is predominant at high temperatures, then the defect which dominates the self-diffusion of Te could be any species whose concentration decreases as the equilibrium partial pressure of Te_2 over the crystal is decreased. Again, an interstitial Te defect is the simplest sort of disorder which could fulfill the criterion.

If Schottky disorder dominates the defect equilibria at high temperatures, then the enhanced self-diffusion of Zn in Al-doped ZnTe at lower temperatures is explained by a new charge neutrality condition, i.e.

$$[V_{Zn}^-] = [Al^+]. \qquad (7)$$

The limiting slope ($<1{\cdot}7$ eV) of the data in Al doped ZnTe in Fig. 3 would then represent the activation energy of motion for V_{Zn}, ΔH^*, in its appropriate charge state. The data also suggest that the concentration of Schottky defects in ZnTe is of the order $10^{19}/\mathrm{cm}^3$ at 950°C. The lack of any effect of Ag doping in $D^{\mathrm{T}}_{\mathrm{Zn}}$ could be due to Ag possessing a deep acceptor level, which prevents it from affecting the charge neutrality condition at 782°C or higher temperatures.

If Frenkel disorder dominates the high temperature defect equilibria then the influence of Al on $D^{\mathrm{T}}_{\mathrm{Zn}}$ can be explained only if it is assumed that $\mathrm{V}^{-}_{\mathrm{Zn}}$ and Zn^{+}_{i} have comparable mobilities. If Zn^{+}_{i} were more mobile than $\mathrm{V}^{-}_{\mathrm{Zn}}$ it would dominate the diffusion behavior in the Al doped crystal at high temperatures (intrinsic region), when the charge neutrality is given by equation (6). However, in the extrinsic region when the charge neutrality condition is expressed by equation (7), the concentration of Zn^{+}_{i} is given by

$$[\mathrm{Zn}_i{}^{+}] = \frac{K_{F'}}{[\mathrm{V}^{-}_{\mathrm{Zn}}]} = \frac{K_{F'}}{[\mathrm{Al}^{+}]} \tag{8}$$

so that

$$D^{\mathrm{T}}_{\mathrm{Zn}} = (D_{\mathrm{Zn}_i{}^{+}})[\mathrm{Zn}_i{}^{+}] = (D_{\mathrm{Zn}_i{}^{+}})\frac{K_F}{[\mathrm{Al}]} \tag{9}$$

where $D_{\mathrm{Zn}_i{}^{+}}$ is the diffusion coefficient of singly ionized Zn interstitials. In the intrinsic crystal, however,

$$D^{\mathrm{T}}_{\mathrm{Zn}} = (D_{\mathrm{Zn}_i{}^{+}})[\mathrm{Zn}_i{}^{+}] = (D_{\mathrm{Zn}_i{}^{+}})K_F{}^{1/2}. \tag{10}$$

The activation energy for diffusion in equation (9) is larger than that in (10) by an amount $\frac{1}{2}\Delta H_F$ (the enthalpy of formation of the Frenkel disorder), so that as T is decreased and the charge neutrality changes from that in equation (6) to that in (7), ΔH for Zn self-diffusion should increase, contrary to experimental observations. The larger value of ΔH would persist until the diffusion became dominated by the large concentration of vacancies, at which point the activation energy for diffusion would decrease to ΔH^*, the enthalpy of motion of V^{-}_{Zn}.

It is reasonable to expect that the mobilities of Zn^{+} and $\mathrm{V}^{-}_{\mathrm{Zn}}$ could be of comparable magnitude if the interstitial Zn resides in the Te coordinated interstitial sites. In this case the atomic jump distance and the geometric barrier encountered by the interstitial Zn are nearly identical to the jump distance and geometric barrier encountered by a Zn atom of the Zn sublattice exchanging with a vacancy on a neighboring Zn lattice site.

A bound Schottky pair (a Zn vacancy and a Te vacancy on neighboring lattice sites) could also account for the pressure independence of the self-diffusion of Zn in undoped ZnTe. In this case the defect would have to be electrically neutral in undoped ZnTe so that its concentration would be dependent on temperature only. The Schottky pair, however, is considered unlikely because its movement through the lattice would require that the Te self-diffusion coefficient be much more comparable to that of Zn than is observed experimentally. Other complex defects could also be postulated to account for the Zn diffusion data. It is only required that the defect not introduce a deviation from stoichiometry and that it be electrically neutral.

An alternative explanation of the lack of a pressure dependence of $D^{\mathrm{T}}_{\mathrm{Zn}}$ could be that the concentration of the native defect taking part in the Zn self-diffusion is controlled at all temperatures by an unknown impurity. This is believed unlikely for three reasons. First, no impurity was consistently detected in a high enough concentration in the analyses of the ZnTe crystals. Second, the concentration of the impurity would have to be identical in all samples in order to produce the consistent values of $D^{\mathrm{T}}_{\mathrm{Zn}}$ observed. This is not likely since a large number of crystals from two different growth methods were used in the experiments. Third, the samples that were purposely doped with Al donors show the same intrinsic high temperature behavior.

The self-diffusion behavior of Zn and Te in ZnTe is similar to that observed for components in other II–VI compounds. The self-diffusion of Cd in CdTe[11, 12] is independent of Cd partial pressure due to Frenkel disorder dominating the defect equilibria on the metal sublattice at high temperature[11]. In CdS[13] and CdSe[2] the self-diffusion of Cd increases with increasing Cd partial pressure apparently due to interstitial Cd donors dominating the charge equilibria at high temperatures. Hence self-diffusion measurements suggest that interstitial metal atom defects are of great importance in these compounds at high temperature.

The self-diffusion of the chalcogen components in ZnO[14], ZnSe[15], ZnTe, CdSe[16] and CdTe[11] all increase with increasing partial pressure of the chalcogen. In all cases the diffusion behavior of the chalcogen is best accounted for by an interstitial defect. In ZnO, CdTe and CdSe the self-diffusion coefficients of the chalcogens were found to be proportional to the square root of the partial pressure of the chalcogen dimer, suggesting that the interstitial defect is electrically neutral.

Since there is no evidence of chalcogen vacancies taking part in chalcogen self-diffusion it appears that Schottky disorder is not dominant in self-diffusion in the II–VI compounds investigated thus far. Thus charge neutrality at high temperatures in undoped crystals is most likely determined by either Frenkel disorder (ZnTe and CdTe) or by an interstitial metal donor—electron disorder (CdS and CdSe).

CONCLUSIONS

The self-diffusion behavior of Zn and Te in ZnTe suggest that thermal disorder dominates the high temperature defect equilibria. On the basis of the present results for ZnTe, it is not possible to distinguish unambiguously whether Frenkel disorder on the Zn sublattice, or Schottky dosorder, which involves both sublattices, is dominant. However, Frenkel disorder appears to be the more likely. The self-diffusion of Te in ZnTe suggests that the principal defect associated with the Te sublattice is an interstitial Te atom of unknown electrical activity. The high temperature defect equilibria in ZnTe are qualitatively the same as those in other II–VI compounds as deduced from self-diffusion measurements.

Acknowledgements—The authors are grateful to Dr. Robert A. Burmeister, Hewlett Packard Laboratories, and Dr. Paul M. Borsenberger, Eastman Kodak Laboratories, for helpful discussions, and to Dr. Lou Bailey, Texas Instruments Incorporated, for assistance with mass and emission spectrometric analysis. This research was supported by the U.S. Atomic Energy Commission under Contract AT(04-3)283 and equipment and facilities partially furnished by the Advanced Research Projects Agency through the Center for Materials Research at Stanford University.

REFERENCES

1. REYNOLDS R. A., Ph.D. Thesis. Stanford University, Department of Materials Science (1965).
2. BORSENBERGER P. M., STEVENSON D. A. and BURMEISTER R. A., In *Proc. Int. Conf. II–VI Semiconducting Compounds*, p. 439. Benjamin, New York (1967).
3. LYNCH R. T., THOMAS D. G. and DIETZ R. E., *J. appl. Phys.* **34**, 706 (1963).
4. AVEN M. and SEGALL B., *Phys. Rev.* **130**, 81 (1963).
5. THOMAS D. G. and SADOWSKY E. A., *J. Phys. Chem. Solids* **25**, 395 (1964).
6. MANDEL G., *Phys. Rev.* **134**, 1073 (1964).
7. PIPER W. W. and POLICH S., *J. appl. Phys.* **32**, 1278 (1961).
8. WAGNER C., *J. chem. Phys.* **21**, 1819 (1953).
9. BREBRICK R. F., *J. appl. Phys.* **30**, 811 (1959).
10. KROGER F. A., *The Chemistry of Imperfect Crystals*, Chap. 13 Wiley, New York (1964).
11. BORSENBERGER P. M. and STEVENSON D. A., *J. Phys. Chem. Solids* **29**, 2677 (1968).
12. WHELAN R. C. and SHAW D., *Proc. Int. Conf. II–VI Semiconducting Compounds*, p. 451. Benjamin, New York (1967).
13. WOODBURY H. H., *Phys. Rev.* **134**, A492 (1963).
14. MOORE W. J. and WILLIAMS E., *Disc. Faraday Soc.* **28**, 86 (1959).
15. WOODBURY H. H. and HALL R. B., *Phys. Rev.* **157**, 3, 641 (1967).
16. WOODBURY H. H., *Phys. Rev. Lett.* **17**, 1093 (1966).
17. CARSLAW H. S. and JAEGER J. C., *Conduction of Heat in Solids*, p. 304. Clarendon Press, Oxford (1959).

APPENDIX A

The boundary conditions for the solution to the diffusion equation are demonstrated in Fig. 1A for a sample of unit area. The amount of liquid is considered finite, and the sample semi-infinite (i.e. sample dimensions $\gg \sqrt{Dt}$). The initial conditions are

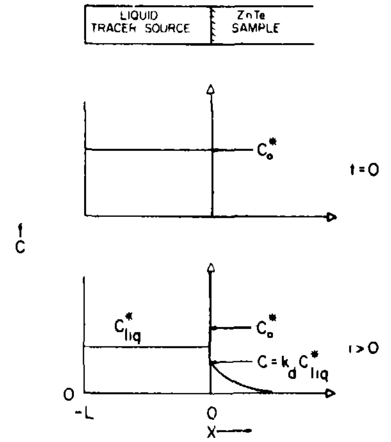

Fig. 1A. Illustration of boundary conditions for solution of the diffusion equation.

$$\left.\begin{aligned} C^* &= C_0^*, -L < x < 0 \\ C^* &= 0, x > 0 \end{aligned}\right\} \tag{1}$$

and the boundary conditions are

$$(C^*)_{\text{ZnTe}} = k_d (C^*)_{\text{fluid}}, \quad \text{at} \quad x = 0 \tag{2}$$

and

$$\left(\frac{-L}{k_d}\right) \frac{\partial (C^*)_{\text{fluid}}}{\partial t} = -D \left(\frac{\partial (C^*)_{\text{ZnTe}}}{\partial x}\right)_{x=0}. \tag{3}$$

In these equations, C^* is the concentration of radioactive tracer in counts per min/cm³, D is the self-diffusion coefficient in cm²/sec for the diffusing element, t is the time in seconds, and k_d and L are the equilibrium distribution coefficient for the diffusing element and the width of the liquid phase (in cm) respectively and given by:

$$L = \frac{\text{(weight of liquid source)}}{\text{(density of liquid)} \times \text{(area of sample)}} \tag{4}$$

and

$$k_d = \frac{(\text{number/cm}^3 \text{ in ZnTe})}{(\text{number/cm}^3 \text{ in liquid source})}. \tag{5}$$

The solution to the diffusion equation for these boundary conditions is not available in the literature but may be derived from one given by Carslaw and Jaeger[17] for the equivalent heat flow problem. The result is

$$C^*(x, t) = k_d C_0^* \exp\left(\frac{k_d x}{L} + \frac{k_d^2 Dt}{L^2}\right) \times \operatorname{erfc}\left(\frac{x}{2\sqrt{Dt}} + \frac{k_d \sqrt{Dt}}{L}\right). \tag{6}$$

There are two limiting cases for this solution. If $L \gg k_d\sqrt{Dt}$, equation (6) simplifies to the error function complement solution to the diffusion equation for a constant surface composition:

$$C^* = k_d C_0^* \operatorname{erfc}\left(\frac{x}{2\sqrt{Dt}}\right). \tag{7}$$

If $L \leqslant \frac{1}{2} k_d \sqrt{Dt}$, the argument of the error function complement is always $\geqslant 2$, so that the error function complement in equation (6) can be approximated by the first term in its expansion[17] giving

$$C^* = \frac{C_0^* L}{\sqrt{(\pi Dt)}} \exp\left(\frac{-x^2}{4Dt}\right) \tag{8}$$

which is the nonreplenished source solution to the diffusion equation. The essence of this result is that for large sample areas and small liquid volumes (small L), nearly all of the radioactive tracer is exchanged from liquid to solid in times short compared to the diffusion time, so that the liquid acts as a nonreplenished source of the radioactive tracer.

J. Phys. Chem. Solids Pergamon Press 1969. Vol. 30, pp. 149–155. Printed in Great Britain.

ON THE RELATION BETWEEN ELECTRICAL CONDUCTIVITY AND PHASE TRANSITION OF NON-STOICHIOMETRIC CUPROUS SELENIDES

Z. OGORELEC* and B. ČELUSTKA†
Institute 'Rudjer Boskovic', Zagreb, Yugoslavia

(*Received* 28 *December* 1967; *in revised form* 3 *June* 1968)

Abstract – The electrical conductivity of non-stoichiometric cuprous selenide samples having various compositions was examined. Measurements were performed over the temperature interval where the phase transformation appears. Conductivity variations are explained considering non-stoichiometric cuprous selenide as the binary system ($Cu_2Se + Se$), in which alpha and beta phases in mutual equilibrium have different compositions, i.e. different concentrations of holes. The equations derived on the basis of an equilibrium process of phase transition describe the experimental curves with satisfactory agreement. Further consequences of such an approach to non-stoichiometric compounds are also discussed.

INTRODUCTION

SEMICONDUCTING cuprous selenide exists in a composition range which does not include the ideal stoichiometric composition Cu_2Se. Lorenz and Wagner[1] have concluded by coulometric titration that x in Cu_xSe extends from 1·9975 to less than 1·86 at 400°C without the creation of any other phase, e.g. precipitation of copper or another compound richer in selenium. Such a compound exhibits mixed ionic and electronic conductivity, but the ionic component is less than 1 per cent below 300°C [2–4] and may be neglected. The electronic conductivity is always of p-type with a concentration of holes depending on the copper deficit in the lattice [4, 5].

The high temperature or β-phase of Cu_xSe is cubic with the space group Fm3m found by Rahlfs[6], Borchert[7] and Boettcher[8]. These authors give different results for the symmetry of the low temperature or α-phase, so that structural examinations are required.

Cuprous selenide is a semiconductor with a theoretically predicted and experimentally demonstrated energy gap greater than 1eV [4, 9, 10] but the temperature dependence of its conductivity exhibits an extrinsic behaviour from −192°C up to 600–700°C depending on the deviation from stoichiometry. Moreover, this behaviour is characteristic of an exhaustion range of conductivity where all acceptors, i.e. copper defects in Cu_xSe [4, 5] are ionized.

An exception to the monotonic change of conductivity occurs at the temperature of the phase transformation [2, 3, 11]. The thermoelectric power [2, 3, 11, 12] and coefficient of thermal expansion [13] show a similar behaviour. One can observe that all these properties of cuprous selenide behave unusually at its phase transition.

Our interest in the anomalous change of conductivity arose from the fact that it occurs over a range of temperature, similarly to the changes of thermoelectric power and coefficient of thermal expansion. Our unpublished measurements of DTA show that the latent heat of transformation is liberated also in an interval of temperature with an unsymmetrical maximum. Therefore, the present

---

Permanent address: Institute of Physics, Faculty of Science, University of Zagreb, Zagreb, Yugoslavia.

†*Permanent address:* Institute of Physics, Faculty of Medicine, University of Zagreb, Zagreb, Yugoslavia.

work is intended to give the results of more extensive measurements of conductivity and the corresponding explanation of its changes at the phase transition.

CONDUCTIVITY IN THE TWO PHASE REGION OF Cu_xSe

Our explanation of the conductivity behaviour at the phase transition of Cu_xSe is based on the following suppositions:

1. Cu_xSe can be considered as a solid solution of Se in stoichiometric Cu_2Se, i.e. as the binary system ($Cu_2Se + Se$). The justifications for assuming this are Lorenz and Wagner's[1] examinations on homogeneity range of β-Cu_xSe, the dependence of the transition temperature on the selenium content[14] and the continual dependence of electrical properties in both phases upon the selenium concentration[2, 3, 12].
2. Two phases of solid Cu_xSe, being in mutual equilibrium have not the same composition. This supposition is supported by recent examinations of Heyding[14]. In his paper the composition of the α-phase was referred to as a stoichiometric one, but a possibility that this phase is only richer in copper than the β-phase was also allowed. Besides, the α-phase behaves like the β-phase, i.e. as a strongly doped semiconductor.
3. All conditions for an equilibrium process of the phase transition can be fulfilled choosing a proper heating or cooling rate. In spite of the fact that solid state changes are generally extraordinarily slow in the case of Cu_xSe an equilibrium transition is easily established. The fast diffusion of copper ions[2, 3, 5] cancels any concentration gradients in a short time. In order to examine the the conditions for an equilibrium process of transformation, the conductivity was measured with different rates of heating and cooling. It has been found that good reproducibility is obtained with a rate of 2°C/min, or less. The quenching of the sample from 150°C to room temperature shows that the phase transition is retarded for less than one second.

If the concentration of excess Se in Cu_2Se is denoted by C (at. %), then the statement of unequal compositions of both phases can be expressed as $C_\alpha \neq C_\beta$. Because of the fact that an addition of Se lowers the transition temperature, the ratio of concentrations C_α/C_β or the coefficient of distribution is less than unity. The equilibrium diagram of the ($Cu_2Se + Se$) system is shown in Fig. 1. It means that the β-phase with the initial concentration C_0 separates during an equilibrium process of cooling into β- and α-phases with the concentrations C_β and C_α, respectively. The separation starts at the temperature T_β and ends at T_α. Below the temperature T_α only the α-phase exists again with the concentration C_0. In the temperature range between T_β and T_α the concentration of the β-phase varies from C_0 to $C_{\beta 0}$, while the concentration of the α-phase changes from $C_{\alpha 0}$ to C_0. The relative quantities of both phases in this range are governed by the 'lever' rule.

In the next paragraph we shall mention a few experimental facts which enable us to conclude that in Cu_xSe there is a very simple relation between the concentration of excess selenium and that of holes. Like in cuprous sulphide[15] every defect copper atom gives a hole, or in other words, every excess selenium atom gives two holes taking part in the conductance of the sample. Then below T_α and above T_β the sample has a constant concentration of holes which may be written as

$$p_{\alpha 0} = \frac{2Ad_{\alpha 0}}{M_0} C_0, \quad p_{\beta 0} = \frac{2Ad_{\beta 0}}{M_0} C_0 \qquad (1)$$

where A is Avogadro's number, $d_{\alpha 0}$ and $d_{\beta 0}$ are the densities of the phases, and M_0 is

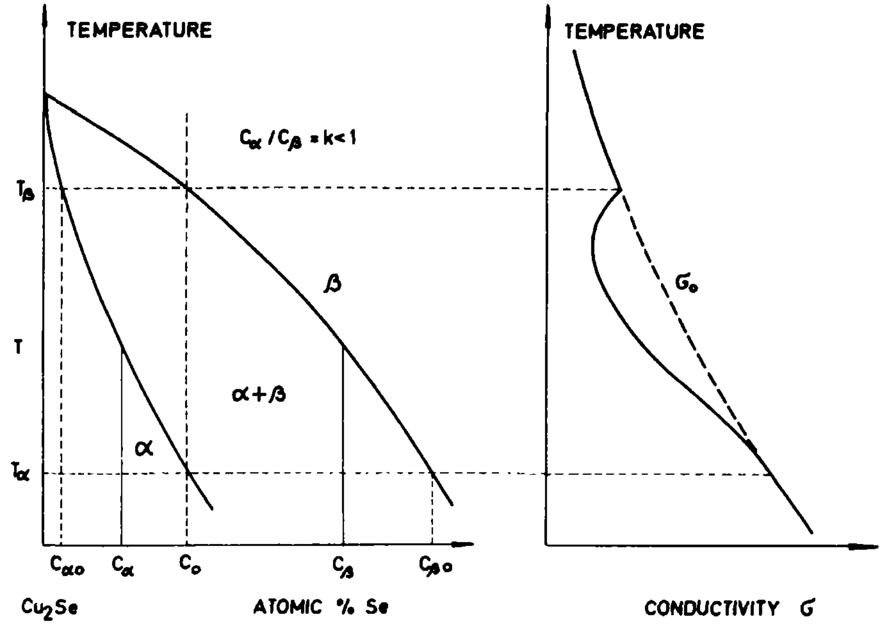

Fig. 1. Equilibrium diagram of non-stoichiometric cuprous selenide and the corresponding conductivity variation.

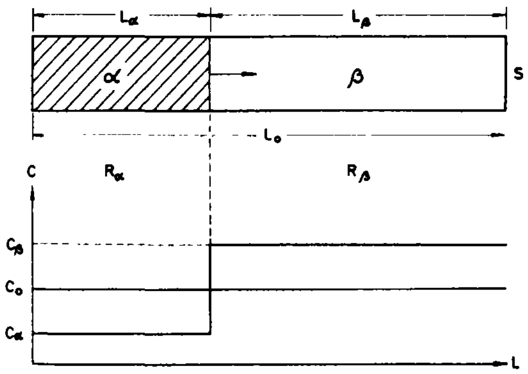

Fig. 2. Idealized distribution of selenium during the phase transition of non-stoichiometric cuprous selenide.

the molecular weight of the sample. Consequently, the conductivities of both phases, $\sigma_{\alpha 0} = e p_{\alpha 0} \mu_{\alpha 0}$ and $\sigma_{\beta 0} = e p_{\beta 0} \mu_{\beta 0}$, change with temperature only due to the temperature variations of hole mobilities μ_0. The variation of conductivity in the range between T_α and T_β is evidently not so simple and requires a further discussion.

Let us imagine that a sample of cuprous selenide has a bar shape and that the phase transition starts at one end of it. As the temperature decreases we shall consider two possibilities. In the first case the phase boundary moves along the sample remaining perpendicular to its length. In an equilibrium cooling process the α- and β-phases are homogeneous and have the concentrations of dissolved excess selenium C_α and C_β, respectively. As the concentrations of holes (twice that of excess selenium) are unequal, the conductivities of both phases are different. Now the sample may be considered as a serial connection of two resistors with resistances R_α and R_β, and the total resistance of the sample is then

$$R = R_\alpha + R_\beta = \frac{1}{\sigma_\alpha}\frac{L_\alpha}{S} + \frac{1}{\sigma_\beta}\frac{L_0 - L_\alpha}{S}. \qquad (2)$$

If we introduce the formal conductivity of the sample σ by the formula $R = L_0/\sigma S$ we can write equation (2) in the form

$$\frac{1}{\sigma}=\frac{1}{e}\left(\frac{1}{p_\alpha\mu_\alpha}-\frac{1}{p_\beta\mu_\beta}\right)\frac{L_\alpha}{L_0}+\frac{1}{ep_\beta\mu_\beta} \tag{3}$$

where p_α, μ_α and p_β, μ_β are concentrations and mobilities of holes in the α- and β-phases, respectively. In the second possible case, where the phase boundary moves parallel to the length of the sample, the distribution of holes between the phases has no influence on the conductivity. When considering a bar with a small temperature gradient along it, the first case is more probable than the second. Further analysis will therefore be based on the first case, assuming that the parallel moving may introduce some deviation in comparison with experiments.

Thus, from the condition that the total quantity of dissolved selenium must be conserved in the sample we obtain the equation

$$\frac{L_\alpha}{L_0}=\frac{M_\alpha d_0 C_\beta-C_0}{M_0 d_\alpha C_\beta-C_\alpha} \tag{4}$$

which combined with (1) and (3) gives

$$\frac{1}{\sigma}=\frac{M_\alpha d_0}{2eAM_0 d_\alpha}\left(\frac{M_\alpha}{\mu_\alpha d_\alpha C_\alpha}-\frac{M_\beta}{\mu_\beta d_\beta C_\beta}\right)\times\frac{C_\beta-C_0}{C_\beta-C_\alpha}+\frac{M_\beta}{2eA\mu_\beta d_\beta C_\beta}. \tag{5}$$

This equation enables us to calculate the conductivity of Cu_xSe samples in the temperature range $T_\alpha < T < T_\beta$, if the equilibrium diagram of the ($Cu_2Se + Se$) system is known.

EXPERIMENTAL RESULTS AND DISCUSSION

1. *Determination of compositions*

In order to determine the equilibrium diagram of the ($Cu_2Se + Se$) system, i.e. the temperatures T_α and T_β for Cu_xSe with various x, a series of samples having fixed compositions is necessary. Another possibility is to change the initial composition of a sample by some procedure. We chose the second way.

The sample with the initial composition $Cu_{1\cdot820}Se$ (9 at. % of Se in Cu_2Se) was prepared from precisely weighed pure components in an evacuated and sealed quartz tube. The composition was determined from the masses of copper and selenium used in the synthesis. After the temperatures T_α and T_β were fixed on this sample (see below), it was placed into another evacuated quartz tube and heated at about 450°C. At this temperature the evaporation of selenium from the sample was remarkable and the initial composition shifted to greater x. After properly chosen time of heating the sample was cooled to room temperature and precisely weighed. The new composition was determined from the initial composition and the mass of the sample, assuming that only selenium was evaporated from it. This procedure was repeated several times giving a sample with different and known compositions which cover the whole homogeneity range of Cu_xSe. The last measurements of T_α and T_β were performed on the sample $Cu_{1\cdot962}Se$ (1·9 at. % of Se) obtained after heating for 36 hrs.

2. *Determination of the equilibrium diagram*

The temperatures T_α and T_β may be determined from any physical parameter which is influenced by the separation of selenium between the two phases. The parameters may be electrical conductivity, thermoelectric power, DTA or thermal expansion. All these properties show a beginning and an end, or an interval of phase transformation in Cu_xSe. We chose conductivity measurements as a detecting method owing to its higher accuracy in determining T_α and T_β and the possibility of their measurements far below room temperature.

T_α and T_β were determined observing the temperatures at which the measured σ branches off from σ_0 (see Fig. 1). This procedure was performed after each composition change described above. The results of some conductivity measurements are pre-

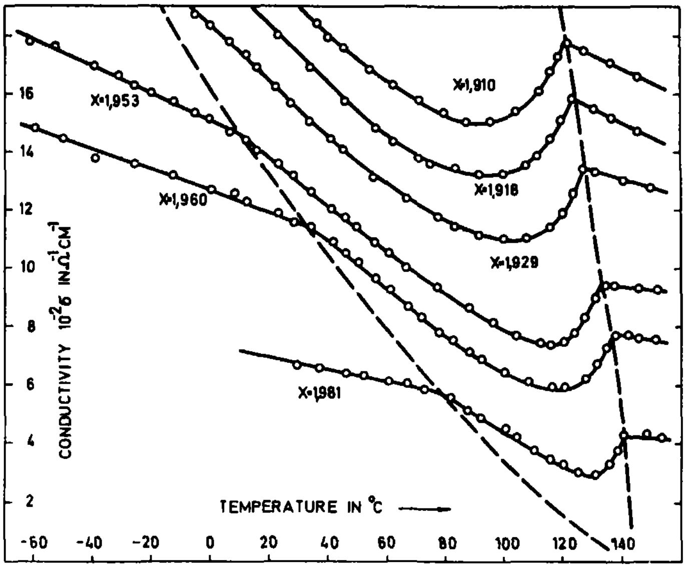

Fig. 3. Conductivity of Cu_xSe having various compositions and phase lines in the σ-T representation.

sented in Fig. 3. Each curve has a characteristic shape with an unsymmetrically placed minimum nearer to the temperature T_β. Thus the determination of T_α is less reliable than T_β. The repetition of conductivity measurements on the same sample shows T_α to be accurate up to ±7°C or better, depending on T_α. The absolute error in T_β is less than ±1°C. T_α and T_β were always found in the heating cycles, but similar results were also obtained in the cooling cycles. These cycles showed a hysteresis from about 6° to 8°C with a small dependence on the stoichiometric deviation.

The two dashed curves in Fig. 3, connecting all points $\sigma(T_\alpha)$ and $\sigma(T_\beta)$, respectively, are the equilibrium diagram of the ($Cu_2Se + Se$) system in a σ, T, representation. Knowing the composition of samples and the corresponding temperatures T_α and T_β this diagram can be represented in its usual form. It is shown in Fig. 4. Both curves extrapolated to zero percent of selenium touch the ordinate axis at 142°C. This temperature would be the transition point of Cu_2Se existing as a stoichiometric compound. It is interesting to mention that the values for T_α and T_β determined by measurements of thermal expansion are very close to those obtained by conductivity measurements. Heyding's curve of DTA signals[14] determined in the cooling cycles is also shown in Fig. 4.

3. *Measurement and evaluation of conductivity*

Measurements of conductivity and its dependence on temperature were carried out by means of the standard two-probe method. The low thermoelectric voltage due to the temperature gradient along the sample was eliminated reading only the voltage drop caused by the current impulse through the sample.

Conductivity measurements could be compared directly with the calculations according to equation (5). However, the properties of Cu_xSe enable us to simplify this equation, taking into account the following facts. Firstly, cuprous selenide in both phases is an extrinsic semiconductor in the exhaustion range of conductivity, where all

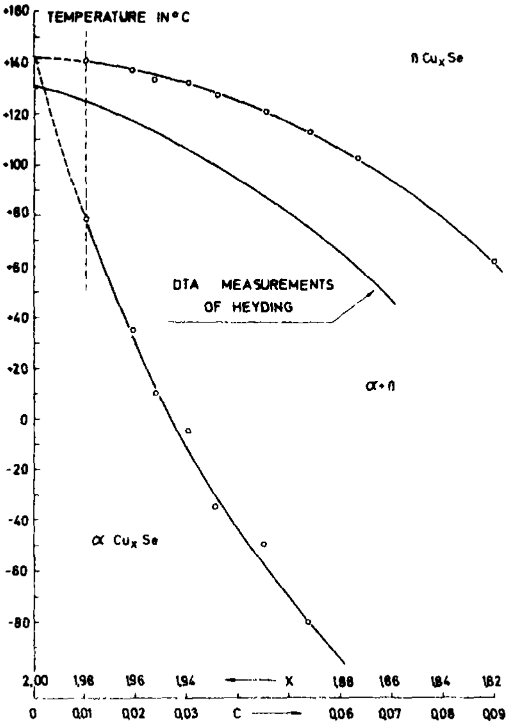

Fig. 4. Equilibrium diagram of the ($Cu_2Se + Se$) system.

acceptors are ionized. So it has a constant, i.e. a temperature independent concentration of holes. Secondly, acceptor states in Cu_xSe are caused by copper deficit. Since the linear dependence of the conductivity upon the composition, together with Hall effect measurements[9] show that every defect copper atom gives a hole, equations (1) are correct. Making a reasonable approximation $d_\alpha = d_\beta = d_{\alpha 0} = d_{\beta 0} = d$, from (1) we obtain $p_{\alpha 0} = p_{\beta 0} = p_0$. As the curve $\sigma = \sigma(T)$ above T_β is always a continuation of this curve below T_α, and both are parts of a unique monotonic curve $\sigma = \sigma_0(T)$, there is no discontinuity in hole mobility at the phase transition. We can therefore put $\mu_\alpha = \mu_\beta = \mu_{\alpha 0} = \mu_{\beta 0} = \mu$ and equation (5) reduces to

$$\sigma = \frac{\sigma_0}{P\frac{C_\beta - C_0}{C_\beta C_\alpha} - Q\frac{C_\beta - C_0}{C_\beta} + U\frac{1}{C_\beta} - W} \qquad (6)$$

where $\sigma_0 = \sigma_{\alpha 0} = \sigma_{\beta 0} = 2eA\mu_0 d_0/M_0 = ep_0\mu_0$ is the conductivity of a hypothetical sample without the phase transformation. Below T_α and above T_β, σ_0 is the real conductivity. Other symbols have the following meaning

$$P = M^2_{Cu_2Se}C_0/M_0^2 \quad Q = 2M_{Cu_2Se}M_{Cu}C_0/M_0^2$$

$$U = M_{Cu_2Se}C_0/M_0 \quad W = 2M_{Cu}C_0/M_0. \quad (7)$$

In rearranging equation (5) to (6) the expressions $M_\alpha = M_{Cu_2Se} - 2M_0C_\alpha$ and $M_\beta = M_{Cu_2Se} - 2M_0C_\beta$ are used.

Let us now discuss equation (6). At temperatures above T_β and below T_α the conductivity changes are due to $\mu_0(\mu_0 \sim T^{-a}$ only, where a is same constant). Inside the interval $T_\alpha < T < T_\beta$ an additional change occurs due to the temperature variations of C_α and C_β, causing a decreasing $\Delta\sigma = \sigma_0 - \sigma$. For $T = T_\alpha$, i.e. $C_\alpha = C_0$, and for $T = T_\beta$, i.e. $C_\beta = C_0$, the formal conductivity σ equals σ_0.

Figure 5 shows the experimental conductivity of $Cu_{1\cdot953}Se$ and the comparison with the calculations according to equation (6). The shapes of both curves are very similar, indicating a two-phase region at the phase transition of Cu_xSe. It can be seen that the decrease in conductivity is much smaller than predicted by theory. The approximations made here had some influence, especially the assumption that the phase boundary moves perpendicular to the length of the sample. However, we believe that the main reason for this disagreement lies in the fact that the calculations do not take into account the limited homogeneity range of the (Cu_2Se+ Se) system. For example, calculating the conductivity of an $Cu_{1\cdot953}Se$ specimen (Fig. 5) at temperatures between 78° and 136°C, the necessary concentrations C_α were taken from the extrapolated (dashed) α-phase line, not taking into account the probable copper precipitation. Similarly for the same specimen at temperatures below 60°C the concentrations C_β exceed 9 at. %

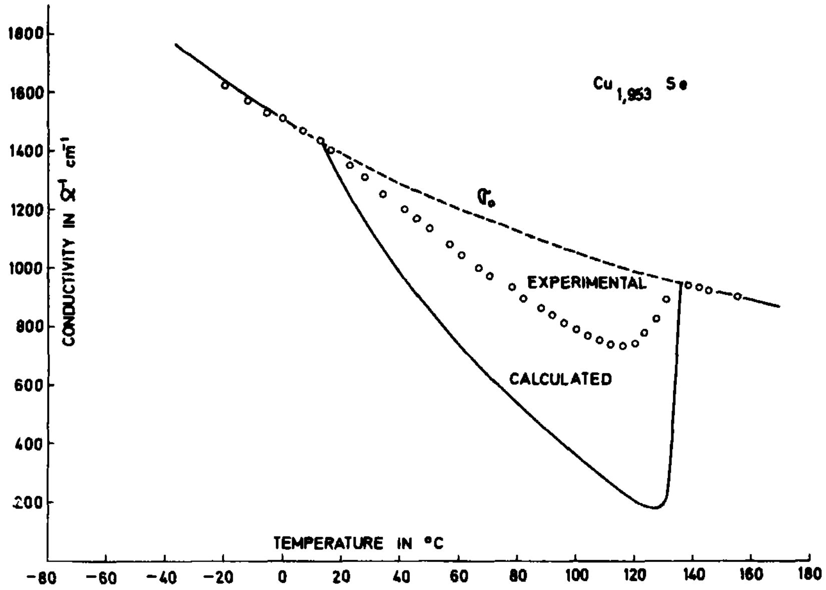

Fig. 5. Conductivity of $Cu_{1.953}$ at the phase transition.

of Se and belong to the range where homogeneity is very doubtful. Such effects change C_α and C_β proposed by the extrapolated equilibrium diagram and, according to [6], cause a variation of $\Delta\sigma$ and the temperature of the minimal σ.

In spite of this disagreement, it seems that in such a case it is possible to make a direct correlation between the conductivity measurements and the phase change. We believe that our considerations and calculations can be applied to other non-stoichiometric systems which will allow a similar equilibrium treatment.

REFERENCES

1. LORENZ G. and WAGNER C., *J. chem. Phys.* **26**, 1607 (1957).
2. REINHOLD H. and MÖHRING H., *Z. phys. Chem.* **B38**, 221 (1938).
3. REINHOLD H. and SEIDEL H., *Z. phys. Chem.* **B38**, 245 (1938).
4. OGORELEC Z., *Thesis*, Faculty of Science, University of Zagreb, Zagreb (1966).
5. ČELUSTKA B. and OGORELEC Z., *J. Phys. Chem. Solids* **27**, 957 (1966).
6. RAHLFS P., *Z. phys. Chem.* **B31**, 157 (1935).
7. BORCHERT W., *Z. Cristallgr.* **106**, 5 (1945).
8. BOETTCHER A., HAASE G. and TREUPEL H., *Z. angew. Phys.* **7**, 478 (1955).
9. ABDULAEV G. B., ALIAROVA Z. A. and ASADOV G. A., *Phys. Status Solid*, **21**, 461 (1967).
10. SUCHET J. P., *Chimie Physique des Semiconducteurs*. Dunod, Paris (1962).
11. OGORELEC Z. and ČELUSTKA B, *J. Phys. Chem. Solids* **27**, 615 (1966).
12. JUNOD P., *Helv. Phys. Acta* **32**, 567 (1959).
13. OGORELEC Z. and ČELUSTKA B., *Acta Metall.* **14**, 687 (1966).
14. HEYDING R. D., *Can. J. Chem.* **44**, 1233 (1966).
15. MIYATANI S. and SUZUKI Y., *J. phys. Soc. Japan* **8**, 680 (1953).

J. Phys. Chem. Solids Pergamon Press 1969. Vol. 30, pp. 157–167. Printed in Great Britain.

ELECTRONIC SPECTRUM OF CRYSTALLINE BERYLLIUM OXIDE

D. M. ROESSLER[*] **and W. C. WALKER**[†]
Department of Physics, University of California, Santa Barbara, Calif. 93106, U. S. A.

and

EUGENE LOH
McDonnell Douglas Corporation, Santa Monica, California, U.S.A.

(*Received* 11 *April* 1968; *in revised form* 27 *May* 1968)

Abstract — The normal-incidence reflectance of BeO single crystals has been measured in the range 5–28 eV at room temperature, and from 5–12 eV at 77°K. The data have been analyzed by means of the Kramers–Kronig inversion to yield the dielectric function, $\hat{\epsilon} = \epsilon_1 + i\epsilon_2$, and the energy loss function, $\text{Im}(1/\epsilon^{\wedge})$. Exciton features near Γ may be clearly distinguished from broader interband structure at higher energies and consist of two peaks, at 10·455 and 10·585 eV (77°K). The stronger, low energy peak represents the $\Gamma_{5,1}$ exciton and it is possible that an exciton phonon complex produces the second peak. There are two very broad structures in the interband spectrum above 11 eV, centered near 12·5 and 17·3 eV (in ϵ_2). Although BeO is hexagonal rather than cubic, its band structure is probably not greatly different from that of MgO and the spectrum shows certain analogies. There may also be analogies with corresponding spectral features seen in other wurtzite materials such as CdS. A detailed interpretation is not possible from the present data, which do not exhibit readily identifiable critical point structure, and must await band structure calculations.

The energy loss function is dominated by a very large, broad peak near 26 eV, caused by a bulk plasma resonance. This peak also appears in other similar metal oxides such as MgO and Al_2O_3

1. INTRODUCTION

RECENT experimental and theoretical work on magnesium oxide[1–3] and sodium chloride[4] emphasized analogies in the u.v. optical spectra of the single crystals which arose from similarities in their electronic band structure. The experimental reflectance data, together with the dielectric parameters computed via Kramers–Kronig dispersion relations, exhibit sharp, temperature dependent structure typical of excitons and higher energy structure associated with interband transitions. Examination of the energy-loss function, derived from the optical data, for both magnesium oxide and sodium chloride, leads to unambiguous identification of plasma resonance phenomena within these materials.

It is only recently that theoretical band structure calculations have been made for these large band-gap, ionic materials: many features in existing u.v. data, on the alkali halides for example, remain unidentified, particularly where the transitions involved occur probably at regions of the Brillouin zone other then Γ, and reach conduction band levels other than the lowest. The success of the empirical pseudopotential method (EPM) in describing the spectrum of MgO[1, 3] is strong encouragement to examine analogous materials in the hope that the appearance of familiar features in the optical data arises from a similar band structure. This was certainly the case[4] for MgO and NaCl: it seemed worthwhile to examine beryllium oxide on the assumption that the presence of beryllium rather than magnesium would not greatly alter the electronic spectrum. One might also expect similarities between the data from BeO and those from lithium fluoride[5] as indeed had already been pointed out by Loh[6].

---

[*] *Present address:* Bell Telephone Laboratories, Murray Hill, New Jersey 07971, U.S.A.

[†] Work supported by NASA.

The only known previous measurements [6] of the far u.v. spectrum of single crystal BeO revealed a sharp reflectance peak at 10·3 eV with broader structure at higher energies. In the present work we present more extensive measurements, together with a Kramers-Kronig transform of these data and analysis of the spectra.

2. EXPERIMENTAL PROCEDURE

The samples available were in the form of two single crystals of beryllium oxide, furnished by S. B. Austerman, North American Aviation. Ideally only freshly cleaved crystals should be examined whereas the reflectances measured here refer to as-grown or polished surfaces. Only two crystals were measured, so that the present data should be regarded as preliminary. It will be shown below, however, that internal features of the data obtained indicate that within the above limitations we obtained a useful picture of the intrinsic optical properties and electronic spectra of BeO.

Reflectance measurements were made at near-normal incidence (7½°) and at 300°K (5–28 eV) and 77°K (5–12 eV). The limit of 12 eV imposed on the low temperature data arose from the necessity of sealing the vacuum chamber of the reflectometer from the main chamber of the monochromator by means of a lithium fluoride window. The light source consisted of an electric discharge in the carrier gas contained in a 3 mm diameter capillary bored in boron nitride. The brass anode and cathode assemblies were water cooled with additional cooling being provided by a fan. During operation, the source gas was allowed to flow into the main chamber of the monochromator before being pumped away. The pressure in this chamber was about 10^{-5}–10^{-6} Torr., depending upon the gas used. For measurements below 14 eV, a d.c. glow discharge in hydrogen furnishes intense radiation, including a continuum below about 7·5 eV. At higher energies, a pulsed spark discharge in argon provided dense line emission useful to about 28 eV, beyond which the inefficiency of the normal-incidence reflection grating in the monochromator limits the useful intensity at the exit slit.

The stainless steel reflectometer was bolted onto the exit turret of the monochromator and housed a glass light pipe, which had its face coated with sodium salicylate to monitor the u.v. radiation. The resulting signal from an EMI 6256 photomultiplier was fed directly to a picoammeter and recorder. To prevent contamination of the samples at low temperatures, a Vacion-titanium sublimation pumping system, which maintained a pressure of better than 10^{-7} Torr. was used. A detailed description of the instrumentation has been given elsewhere[7].

3. EXPERIMENTAL RESULTS

Figures 1–3 show the room temperature and 77°K reflectance, at normal incidence, from two single crystals. Sample 1 was grown with the *c*-axis perpendicular to the surface examined, whereas sample 2 represents data from an unoriented crystal. The relative accuracy of the measurements is about 5 per cent below 14 eV, but about 8 per cent above, owing to the use of the spark discharge source. The density of line emission in the radiation source is by no means uniform, and there are some gaps of about 0·4–0·5 eV between certain lines above 14 eV. It is possible that sharp structure in such regions may therefore have been missed: however, there is no evidence of such structure in the data obtained and the curves in Fig. 1 were drawn smoothly through the data points. Rinsing the crystal surfaces with acetone followed by alcohol caused no differences in the measured spectra, and repeated data runs over a period of several months did not differ significantly. The spectra of Fig. 1

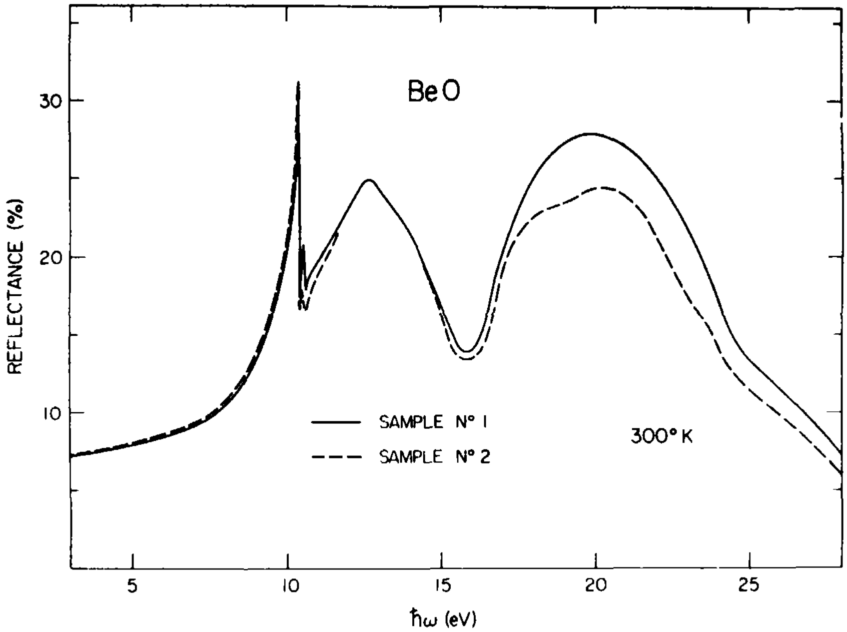

Fig. 1. Room temperature normal incidence reflectance of two BeO crystals. The full curve (sample No. 1) corresponds to a reflecting surface grown perpendicular to the c-axis.

broadly resembles the lithium fluoride spectrum[5], but more closely resembles that of MgO[2].

The fundamental parameter, which best describes the spectrum in terms of interband transitions, and which is the most fruitful for purposes of comparison with theoretical work, is ϵ_2, the imaginary part of the complex dielectric response.

The approximation technique used to obtain ϵ_2 from R through the Kramers-Kronig relation when only a portion of the reflectance spectrum is known has been described in detail elsewhere[8, 9], together with a discussion of the errors introduced by the approximation. The dielectric parameters were computed from the original reflectance data, and are shown for sample No. 1 at 77°K in Fig. 4. A portion of the ϵ_1 curve near the sharp structure at 10·5 eV has been omitted to preserve the clarity of the diagram: for completeness it is shown again in Fig. 5. The parameter, ϵ_1, is essentially a measure of the polarization and because it is not relevant to the remainder of this paper will not be discussed further.

It is readily seen that the basic features in Fig. 1 are preserved in Fig. 4; in particular there are only small shifts in the energies of the main features, both in decreasing the temperature and in going from reflectance to the dielectric response. The importance of deriving ϵ_2 becomes more apparent when one attempts to account for the relative intensities of transitions and the details of line-shapes. The broad feature above 15 eV in the reflectance, for example, changes quite markedly in ϵ_2 compared to the feature at 12·5 eV. It must be pointed out, of course, that the low temperature reflectance data extend only as far as 12 eV, and that the higher energy data are assumed to be not strongly temperature dependent in the range 77–300°K. Indeed it was found that only the exciton region was significantly temperature dependent; data above 10·9 eV showed no noticeable temperature dependence. This is in accord with the

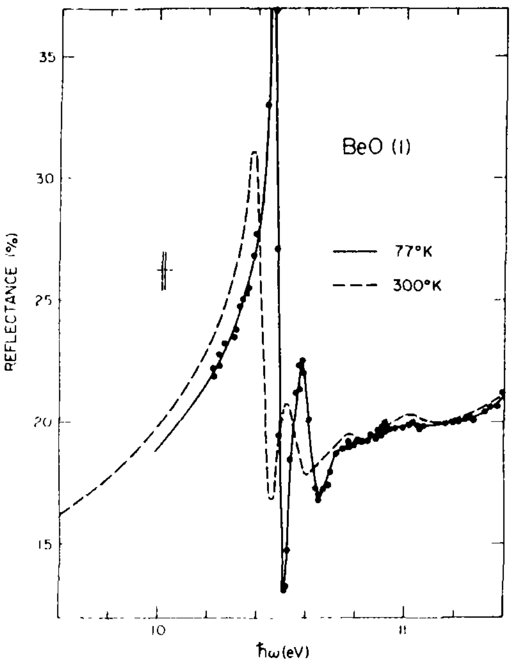

Fig. 2. Temperature-dependence of reflectance near the exciton structure in BeO for a crystal grown with the reflecting surface perpendicular to the c-axis (sample No. 1).

expectation that the structure above 12 eV is due mainly to direct interband transitions, which are not strongly dependent on temperature.

The errors in the dielectric parameters of Fig. 4 stem primarily from errors in the experimental determination reflectance. The nature of the approximation technique used in the Kramers–Kronig analysis leads to computational errors only at the end-points of the experimental data range. At the low energies, the raw reflectance data were smoothly extrapolated into the visible using known values of the refractive index[10]. The only significant computational error therefore occurs at the high-energy limit of 28 eV. The magnitude of the error is strongly peaked at the end-point and rapidly decreases with energy. The data in Fig. 4 are truncated at 27 eV and comparison with the original reflectance data shows no reason to suspect significant error.

The remaining uncertainty arises from the availability of only two samples. It is possible that freshly cleaved surfaces examined from a large number of crystals will show that the intrinsic optical properties of BeO exhibit sharper and stronger features than shown here. On the other hand, the observed magnitudes and form of the structure is consistent with those of the analogous materials MgO and LiF. We believe that any future measurements will reveal only small discrepancies, and will not seriously affect the analysis given below.

In discussing the spectra it is convenient to treat the exciton structure separately from the interband features. The third section of the analysis will deal with the energy loss spectrum.

4. EXCITON FEATURES

The sharp, temperature-dependent structure near 10·5 eV in the spectra of Figs. 1–4 is so reminiscent of that in MgO and alkali halides such as NaCl, that one has little hesitation in associating it with a Γ-exciton. Unlike MgO, which has a f.c.c. lattice with a corresponding truncated octahedron for the first Brillouin zone, BeO has a wurtzite structure with a hexagonal prismatic Brillouin zone. We assume that the exciton originates from the Γ_5, Γ_1 levels of the valence band (corresponding to the Γ_{15} valence band level in MgO and NaCl). The exciton structure is shown in more detail in Figs. 2 and 3 which refer to samples 1 and 2 respectively. In both cases one notes the sharpening and the shift to higher energies as the temperature is decreased. For sample 1 (surface perpendicular to c-axis) the room temperature peak lies at 10·39 ± 0·01 eV and moves to 10·455 ± 0·01 eV at 77°K – a shift of about 3×10^{-4} eV/°K. The first sharp peak in sample 2 (unoriented specimen) exhibits a similar shift, moving from 10·32 ± 0·02 eV at 300°K to 10·39 ± 0·02 eV at 77°K. These shifts with temperature are therefore less than those associated with similar structure in the alkali halides[5, 11] where the values are over 8×10^{-4} eV/°K as is also the case in MgO[2]. The first peak is truncated in Fig. 2, but increases to about

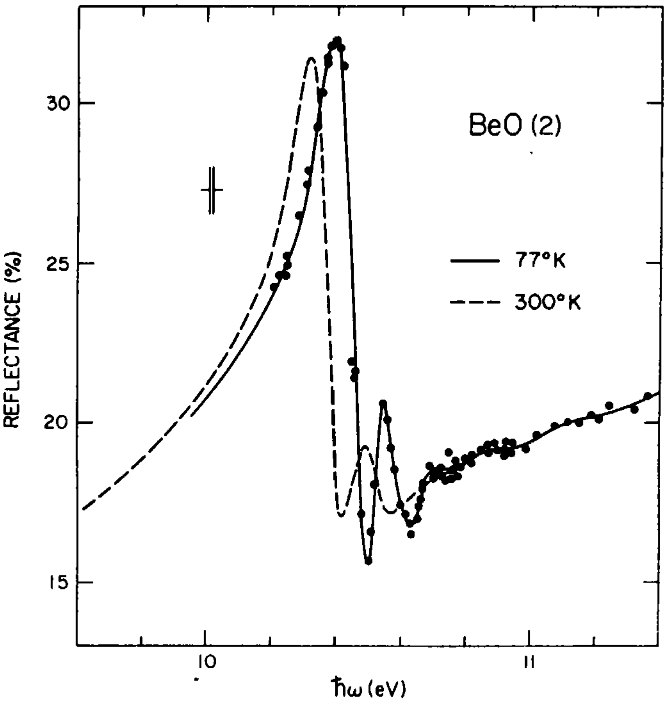

Fig. 3. Temperature dependence of exciton reflectance for an unoriented BeO single crystal (sample No. 2).

38 per cent reflectance at 77°K from its room-temperature value of 31 per cent. It is not clear why the corresponding peak in Fig. 3 does not indicate a similar increase although both orientation and crystal surface quality may be factors.

A smaller peak occurs at higher energies in both crystals and exhibits strong temperature dependence similar to the first peak. The splitting between these peaks is about 0·13 eV in the first sample and 0·16 eV for the second. The difference in these values is of the order of the uncertainty of peak locations and may not be significant. The instrumental resolution was about 0·01 eV in the range 10–11 eV, but the radiation source emits lines rather than a continuum in this region, rendering precise location of peaks and minima difficult. The spectral shift to higher energies as one goes from the unoriented specimen to that in which the electric vector is perpendicular to the c-axis is not surprising in view of the slightly longer Be–O internuclear distance in the c-axis direction[12].

For convenience we shall confine our remaining remarks to the spectrum from the first sample ($E \perp c$). In Fig. 5, the dielectric parameters for this specimen are shown in detail at 77°K. While, as expected, no strong changes occur in structure through the Kramers–Kronig inversion of the reflectance data, the ϵ_2 spectrum provides a better basis for analysis. The shape of the low energy tail of the first band, below 10·4 eV, is uncertain in practice, and depends on the way in which the original reflectance tail is extrapolated into the near u.v. visible region. In the raw reflectance data there is considerable scatter in this region, due to additional contributions from reflectance at the back surface of the crystal

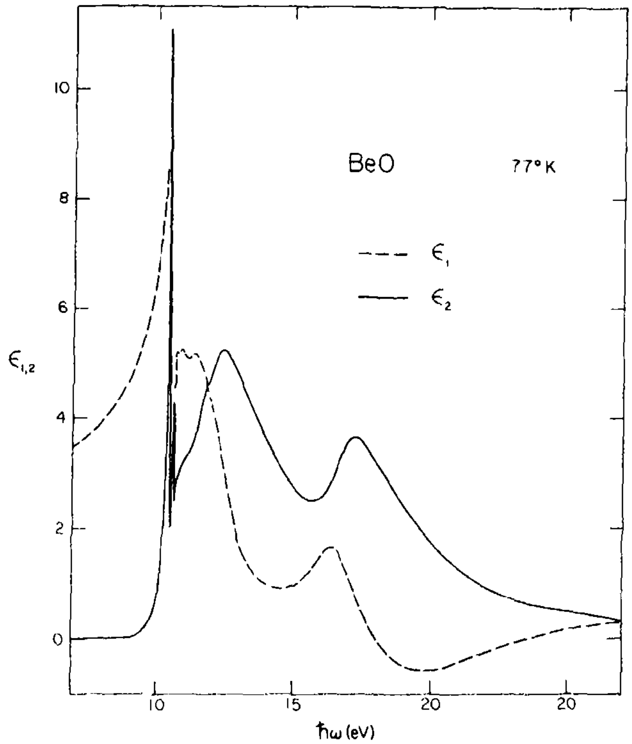

Fig. 4. Dielectric parameters of BeO at 77°K, derived from a Kramers–Kronig analysis of the reflectance data in Fig. 1 (sample No. 1). The portion of ϵ_1 near the exciton peak has been removed to preserve clarity.

in regions of transparency. It is difficult to estimate the error from this cause owing to a lack of sufficient refractive index data in this spectral region. For this reason our estimate of 0·05 eV for the half-width of the first peak is tentative. At 77°K the sharp structure has peaks at 10·455 ± 0·01 eV and 10·585 ± 0·01 eV, giving a separation of 0·13 ± 0·02 eV.

The correct interpretation of this structure is not yet clear although a possible explanation has been given elsewhere[13] and will be reviewed below. While the highest valence band is p-like, as in MgO and NaCl, the degeneracy at Γ occurring for these cubic crystals is lifted for hexagonal materials such as BeO. The three fold Γ_{15} levels are replaced by the doubly degenerate Γ_5 and non-degenerate Γ_1 levels, split by the non-isotropic crystal field. Further, the inclusion of spin-orbit interaction (giving Γ_8- and Γ_6- levels in the f.c.c. crystals and consequently a $j = \frac{3}{2}, \frac{1}{2}$ splitting in the observed transitions) replaces the Γ_5 level by Γ_9 and Γ_7 levels, and Γ_1 by an additional lower Γ_7 level. Transitions at Γ from the valence band to the lowest conductor band (s-like) are allowed and give rise to much of the initial strong structure in the spectra considered. The separations between these levels can be estimated from the free oxygen ion splitting to be of the order of a few hundreths of an electron volt and cannot account for the second peak near 10·6 eV. Even if there is considerable mixing of d-states from the beryllium ion with the p-states of the oxide in the valence band, spin-orbit splitting effects are still too small by a factor of at

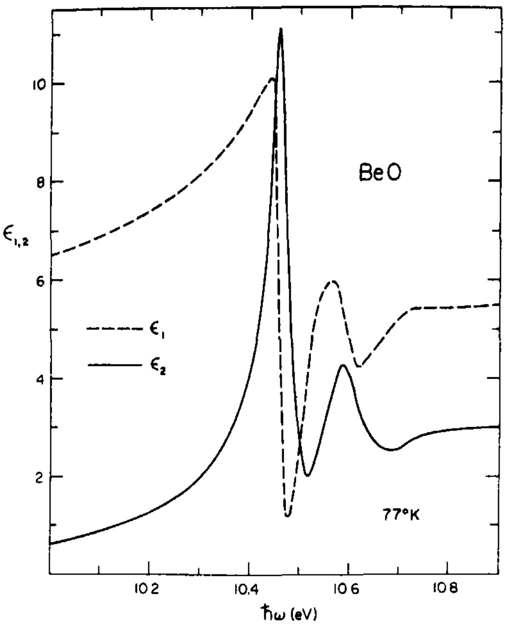

Fig. 5. Dielectric parameters of BeO (sample No. 1) at 77°K, in the region of the Γ exciton structure.

least three (the observed separation from Fig. 5 is 0·13 ± 0·02 eV). A similar situation occurs in MgO[14] where one, however, could argue that the exciton was not highly localized and that, further, the hole saw additional splitting from the neighboring cations. This interpretation, given by Krumhans[15] for barium oxide, would be particularly weak in the case of beryllium oxide because of the small size of the cation.

It is interesting to note that near Γ there may be additional critical point structure along $\Gamma_1 - \Sigma_1$ in the conduction band structure of MgO[3] which could possibly account for the form of the exciton structure. Until similar calculations are carried out for BeO it is fruitful to consider alternative models.

If one assumes a Wannier model for the exciton the nth member of the hydrogenic-like series will then be related to the band-gap, E_G, by the expression:

$$E_n = E_G - B/n^2.$$

There is some evidence[16] that BeO is considerably more like the alkali halides in ionicity than other wurtzite materials such as hexagonal CdS and ZnO. Although the applicability of the above expression, particularly for the $n = 1$ member of the series, is questionable for such ionic materials, its use can at least provide and estimate for the exciton parameters. If we use values of $E_1 = 10{\cdot}455$ eV and a band-gap of 10·63 eV, as derived in Section 5, the binding energy of the exciton, B, is about 0·17 eV. The reduced mass ratio μ/m is determined from the expression[17]

$$B = \frac{\mu e^4}{2\hbar^2\epsilon^2} = \frac{13{\cdot}6\,\mu(\mathrm{eV})}{\epsilon^2 \quad m}$$

to be about 0·04, where we have used an optical value of about 1·72 for the dielectric parameter ϵ. On the same model, the effective radius for the nth excited state is given by the formula

$$a_n = \frac{\hbar^2\epsilon n^2}{\mu e^2} = \frac{0{\cdot}529}{\mu/m}\epsilon.$$

The radius of the $n = 1$ state is therefore about 25 A, nearly ten times greater than the lattice constant, a(~2·69 Å). Obviously the above values of effective mass and radius should not be taken too seriously in view of the extreme approximation used. The effective mass in particular seems much too small.

Liang and Yoffe[18] recently measured the transmission spectra of ZnO and invoked the concept of a bound exciton–phonon complex (EPC) to interpret part of the structure. EPC peaks are expected to occur at energy intervals slightly less than longitudinal optic (L.O.) phonon energy at Γ and be favoured in crystals of increasing ionicity. A similar explanation would account for the exciton structure in BeO and MgO since the separation in MgO is 0·07 eV, with a L.O. phonon energy of 0·09 eV, while in BeO the separation is 0·13 eV, and the L.O. phonon energy[12] is 0·135 eV. The second peak shows somewhat less temperature sensitivity than expected for purely excitonic transitions, but at the present time little is known theoretically concerning the nature of such peaks.

The 10·585 eV peak is probably too strong and of the wrong shape to be regarded as a simple L.O. phonon emission although the energy separation from the zero-phonon line is reasonable. If phonon emission together with some strong coupling effects were responsible for the large intensity, one would also expect a phonon absorption line to appear near 10·3 eV. In the original reflectance data, this energy lies near the increased scatter due to back-surface reflection and no evidence of such a line can be seen at roomtemperature (where it should be stronger than at 77°K). The problem may be one of intensity, since the absorption line will be considerably weaker than the emission line.

At the present time the EPC concept is attractive as a model for the observed structure, but more data are required for a detailed analysis.

5. INTERBAND TRANSITIONS

There is some evidence of structure below 11·5 eV in addition to that mentioned above. It appears only weakly, however (Figs. 1 and 2) and is not easily distinguishable from the data scatter. The major features of the remaining spectrum consist of two very broad bands centered near 12·5 eV and 17 eV respectively. As in the case of MgO we assume that the lack of structure beyond about 22 eV implies that the oscillator strength available for interband transitions involving the higher valence bands is essentially exhausted. Contributions from the tightly bound core electrons are not expected at energies within the spectral range examined here. If an analogy with MgO is used as a guide, then only the first two conduction bands are involved in the transitions occurring below 22 eV.

Where transitions are direct and reasonably well isolated, the appearance of single Van Hove singularities[19] or critical points provides great help in identification. This is not the case here as Fig. 4 indicates. It is probable that the marked change in absorption near 10·7, 11·2 and 16 eV are due to M_0 edges, but the bulk of the structure almost certainly arises from near-degenerate clusters of transitions where the resultant line shape is due to combinations of edges.

We expect to find an M_0 edge lying under the initial exciton structure (Fig. 5), giving a value for the $\Gamma_{5,1} \rightarrow \Gamma_1$ transition of about $10{\cdot}63 \pm 0{\cdot}10$ eV. The uncertainty (0·10 eV) is large primarily because the identification of the 10·58 eV peak is not clear, and it is difficult to separate this from the underlying structure. As expected, the band-gap of BeO is therefore less than that of the isoelectronic LiF[5] and greater than that of MgO. In the latter case, transitions at L and Λ produced the next higher energy structure. In the Brillouin zone for BeO the zone center Γ' replaces the L point of the [111] face in the MgO zone. Along the c-axis, corresponding to the Γ-Γ' line (mid-point A) in the double-zone[20] scheme for wurtzite materials, we therefore expect to see structure arising from transitions at Δ and A. There is a rough correspondence between the spectrum of BeO and that of hexagonal CdS[21] if one considers the E_1 and E_2, E_1' features in the latter to correspond to the two broad bands in BeO. In this case the 12·5 eV peak would be analogous to the E_1 structure and be interpreted as due to transitions at Δ (forbidden for $E \| c$) and along the Σ line to the zone edge at $M(M_4 \rightarrow M_1)$. It should be noted that M_1 critical points near the U line have recently been used by Cohen to explain part of the E_1 structure: transitions near U may also be involved in the present case.

A characteristic feature of both the MgO and NaCl spectra is the strong peak arising from near degeneracies of M_1 and M_2 edges produced by transitions along Δ and Σ respectively. This particular combination does not appear to be preserved in going from the f.c.c. structures to the hexagonal structure of BeO. There is no evidence for such a feature in Fig. 4. It should be noted however that the reflectance data show considerable scatter in the region of overlap of the u.v. radiation sources (14–15 eV) and several sharp structures here may have been missed.

The structure near 17 eV commences with a strong increase in absorption characteristic at an M_0 edge near 16 eV. In the case of MgO similar feature marked the onset of transitions to conduction bands above the lowest. The E_2 peak[22] in hexagonal CdS, however, has been assigned to transitions at K ($K_{3,2} \rightarrow K_2$) with transitions to the Γ_6 conduction band level giving the E_1' peak at higher energies. In neither case are the transitions strongly localized and no easily identifiable, single critical point can be seen in the spectra at these higher energies. Detailed analysis is not possible until band-structure calculations are available for BeO. Measurements using polarized light may be useful in identifying some of the transitions.

6. ENERGY LOSS SPECTRUM

The energy losses suffered by electrons transmitted through thin films can be described[23] by the function Im($1/\hat{\epsilon}$), where the dielectric response function $\hat{\epsilon}$ relates to the electron–electron interaction. There is considerable evidence[24] that in regions where the random phase approximation is valid the longitudinal and transverse dielectric functions are equal and the loss function Im($1/\hat{\epsilon}$) derived from optical parameters identifies electron loss structure. The loss function is useful in revealing plasma resonance phenomena as distinct from normal interband transitions. Figure 6 shows this function, Im($1/\hat{\epsilon}$), computed via the Kramers-Kronig inversion of reflectance. Whereas the exciton and interband absorption shown in Fig. 4 also appears in Fig. 6, the latter is dominated by

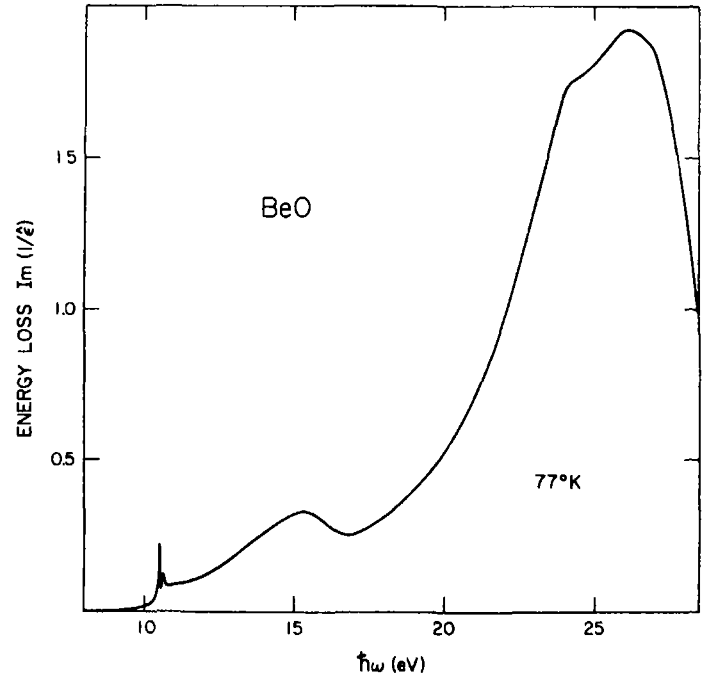

Fig. 6. The energy loss function, Im($1/\hat{\epsilon}$), for BeO, computed from the optical reflectance data of Fig. 1.

a very large energy loss centered near 26 eV. The magnitude of this loss is rather uncertain as it depends critically on the accuracy of the reflectance data in this region. The reflectance is small near 26 eV and further, this region is near the end-point of the energy range where errors from the Kramers–Kronig approximation become important. There is no corresponding structure above 20 eV in the ϵ_2 data and the 26 eV loss is probably directly analogous to that at 22·2 eV in MgO[2]. The valence electrons in BeO are able to undergo collective rather than one-particle excitation at this energy, resulting in the bulk plasma resonance band. In BeO there are effectively $7{\cdot}32\times10^{22}$ molecules/cc and the free electron model predicts a plasma frequency, ω_p, given by

$$\omega p^2 = \frac{4\pi N e^2}{m}$$

where N is the density of absorbing electrons. An assumption of 6 valence electrons per molecule therefore gives a plasma energy of about 24·4 eV, remarkably close to the observed loss in view of the simplicity of this model. There is a striking similarity between the loss function of BeO and those of similar metal oxides, in particular MgO[2] and Al_2O_3[25]. It is interesting to note that these metallic oxides all possess small cations, are large band-gap insulators and exhibit very distinct and broad plasma loss peaks near 25 eV, although representing three different crystal structures (wurtzite, f.c.c., and α-corundum respectively). It would be rather interesting to see if Li_2O (fluorite structure) was in the same category; electron energy loss measurements on thin films would give this information more easily than optical data unless single crystals can be readily obtained. The optical energy loss function corresponds roughly with available electron loss data. Jull[26] measured energy losses in oxidized Be films and found a large peak near 23 eV. A similar loss peak near 28 eV was observed earlier by Watanabe[27].

The three plasma peaks mentioned (BeO, MgO and Al_2O_3) have not only similar energies, but also similar half-widths and absolute intensities, these parameters being very roughly about 25 eV, 5 eV and 1·5 respectively. In considering plasma oscillations in metals Kanazawa[28] derived an expression governing the half-width for the resonance which may be written

$$2\hbar\Gamma/\hbar\omega_p = \epsilon_2.$$

For BeO the left hand side of this expression is about 0·4, which is very close to the value of ϵ_2 near the resonance energy (Fig. 4). Although, as mentioned above, the validity of applying a free electron model is questionable, it is interesting that in practice it can provide a rough guide to the observed loss structure.

REFERENCES

1. COHEN M. L., LIN P. J., ROESSLER D. M. and WALKER W. C., *Phys. Rev.* **155**, 992 (1967).
2. ROESSLER D. M. and WALKER W. C., *Phys. Rev.* **159**, 733 (1967).
3. FONG C. Y., SASLOW W. and COHEN M. L., *Phys. Rev.* In press (1968).
4. ROESSLER D. M. and WALKER W. C., *Phys. Rev.* **166**, 599 (1968).
5. ROESSLER D. M. and WALKER W. C., *J. Phys. Chem. Solids* **28**, 1507 (1967).
6. LOH E., *Solid State Commun.* **2**, 269 (1964).
7. ROBERTS R. A., *Ph.D. dissertation.* University of California (1966).
8. ROESSLER D. M. *Br. J. appl. Phys.* **16**, 1119 (1965).
9. ROESSLER D. M., *Br. J. appl. Phys.* **17**, 1313 (1966).
10. University of California, Lawrence Radiation Laboratory, Rep. No. UCRL-12403 (1965).
11. ROESSLER D. M. and WALKER W. C., *J. opt. Soc. Amer.* **57**, 677 (1967).
12. LOH E., *Phys. Rev.* **166**, 673 (1968).
13. WALKER W. C., ROESSLER D. M. and LOH E., *Phys. Rev. Lett.* **20**, 847 (1968).
14. ROESSLER D. M. and WALKER W. C., *Phys. Rev. Lett.* **17**, 319 (1966).
15. KRUMHANSL J. A., In *Proc. Conf. Photoconductivity, Atlantic City, 4–6 November 1954* (Edited by R. G. Breckenridge *et al.*). Wiley, New York (1956).

16. SIRDESHMUKH D. B., *J. appl. Phys.* **39**, 349 (1968).
17. KNOX R. S., *Theory of Excitons*. Academic Press, New York (1963).
18. LIANG W. Y. and YOFFE A. D., *Phys. Rev. Lett.* **20**, 59 (1968).
19. PHILLIPS J. C., *Phys. Rev.* **104**, 1263 (1956).
20. BIRMAN J. L., *Phys. Rev.* **115**, 1493 (1959).
21. CARDONA M. and HARBEKE G., *Phys. Rev.* **137**, A1467 (1965).
22. COHEN M. L., *Proc. Int. Conf. on II–VI Semiconducting Compounds, September* 6–8, *1967, Brown University, Providence, Rhode Island* (Edited by D. G. Thomas). Benjamin, New York (1967).
23. FRÖHLICH H. and PELZER H., *Proc. phys. Soc.* **A68**, 525 (1965).
24. CREUZBURG M., *Z. Phys.* **196**, 433 (1966).
25. SWANSON N., *Phys. Rev.* **165**, 1067 (1968).
26. JULL G. W., *Proc. phys. Soc.* **B69**, 1237 (1956).
27. WATANABE H., *J. phys. Soc. Japan* **9**, 920 (1954).
28. KANAZAWA H., *Prog. theor. Phys.* **13**, 227 (1955).

Note added in proof: It should be noted that the 10·585 eV peak in Fig. 5 (ϵ_2 at 77°K) occurs at about the energy at which one might expect to see the second member of a hydrogenic-like exciton series (the 10·455 eV peak at Γ being the first member). The enhanced strength of the peak may then result from interference with the L.O. phonon.

J. Phys. Chem. Solids **Pergamon Press 1969. Vol. 30, pp. 169–173. Printed in Great Britain.**

LOW TEMPERATURE SPECIFIC HEAT OF H.C.P. Mo–Ru AND Mo–Rh ALLOYS*

JAMES C. HO and R. VISWANATHAN†
Metal Science Group, Battelle Memorial Institute, Columbus, Ohio, U.S.A.

(*Received* 25 *March* 1968; *in revised form* 27 *May* 1968)

Abstract – Low temperature calorimetric measurements were made on some h.c.p. Mo–Ru and Mo–Rh alloys. By plotting the electronic specific heat coefficient (γ) as a function of the average number of valence electrons to atom ratio (e/a), a common curve was obtained to approximate the $4d$ band shape in the e/a range of 7·0–8·4. This curve has a minimum at $e/a \sim 8{\cdot}1$. The variation of Debye temperature with e/a is inversely correlated to that of γ.

Superconducting properties of some of the alloys are discussed.

INTRODUCTION

THE LOW temperature calorimetry is one of the most important techniques for determining the electronic density of states $N(E_F)$ at the Fermi level of metals. Recently, extensive studies have been carried out on various alloys of transition elements[1]. For the $3d$ series, Cheng *et al.*[2] first pointed out that $N(E_F)$ can usually be related to a single parameter e/a, the average number of valence electrons to atom ratio, suggesting that the well known rigid band model is a good approximation in describing the $3d$ band structure. For the $4d$ series, similar results[1] have been reported for b.c.c. alloys with $e/a < 6{\cdot}5$ and f.c.c. alloys with $e/a > 9$, but leaving a large open gap in the intermediate region, where alloys have mainly h.c.p. structure[3].

In this work, calorimetric measurements on some h.c.p. Mo–Ru ($e/a = 7{\cdot}0$–$8{\cdot}0$)[4] and Mo–Rh ($e/a = 7{\cdot}5$–$8{\cdot}4$)[5] alloys were undertaken to complete the whole picture of the $4d$ band shape. The validity of the rigid band model can be tested in the overlapping region of the two systems. These measurements are also useful in obtaining the values of Debye temperature θ_D for these alloys and, in some cases, information on the occurrence of superconductivity.

EXPERIMENTS AND RESULTS

The specimens, weighing about 100 g each, were prepared from high purity material (Mo of nominal purity 99·9 per cent from Climax Molybdenum Company; Ru and Rh of nominal purity 99·98 per cent from Engelhard Industries) by repeated arc-melting followed by drop-casting into a cylindrical mold. Weight loss of these specimens during melting was in all cases negligible so that alloy composition could be adequately described by the nominal values.

A He^4 cryostat was set up for calorimetric measurements. The fairly standard technique was used by thermally isolating the specimen from the helium bath, applying a known amount of electrical heat input, and measuring the temperature increase of the specimen. The test run on a high purity copper specimen gave results $[C(\text{mJ/mole-°K}) = 0{\cdot}707\,T + 0{\cdot}050\,T^3]$ in reasonable agreement with those reported previously by other investigators. A 1/10W–56 Ω Allen-Bradley resistor thermometer calibrated against the He^4 vapor pressure (1958 scale) was initially used for temperature measurements between 1·5 and 4·0°K. It was later replaced by a precalibrated germanium thermometer[7], which enabled measurements to be extended to

---

*Research sponsored jointly by the Columbus Laboratories of the Battelle Memorial Institute and the Office of Naval Research (Contract Nonr-3589-(00)).

†*Present address:* University of Cincinnati, Cincinnati, Ohio.

higher temperatures. The specific heat of the as-cast specimens was first measured. Several alloys were found to undergo a broad superconducting transition, and were therefore remeasured after being annealed for 48 hrs at 1850°C in a vacuum furnace. The transition temperature, T_c, became well defined ($\Delta T_c \sim 0{\cdot}2$°K) after annealing, which, however, had so significant effect on the normal state ($T > T_c$) specific heat. The same heat treatment was given to $Mo_{0{\cdot}40}Rh_{0{\cdot}60}$, which is not superconducting above 1·5°K, and there was also no change observed in the results.

The experimental data are shown as C/T vs. T^2 in Figs 1 and 2 for the Mo–Rh and Mo–Ru system, respectively. For each specimen except $Mo_{0{\cdot}50}Ru_{0{\cdot}50}$, which will be discussed later, but including all other superconducting alloys at $T > T_c$, the data fit a straight line represented by the equation

$$C = \gamma T + \beta T^3. \tag{1}$$

The intercept of this straight line on the C/T axis gives the electronic specific heat coefficient γ proportional to $N(E_f)$; the slope β relates to θ_D.

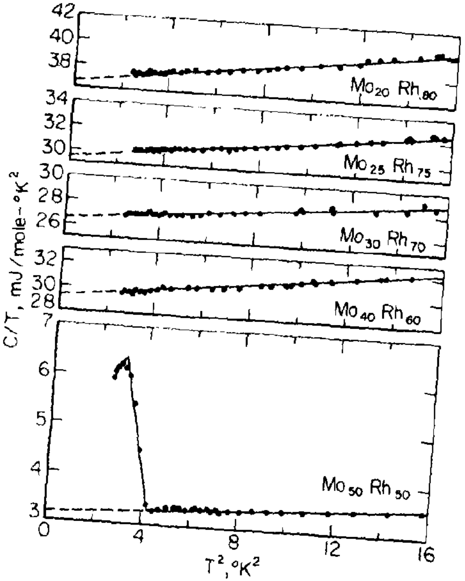

Fig. 1. Specific heat of h.c.p. Mo–Rh alloys.

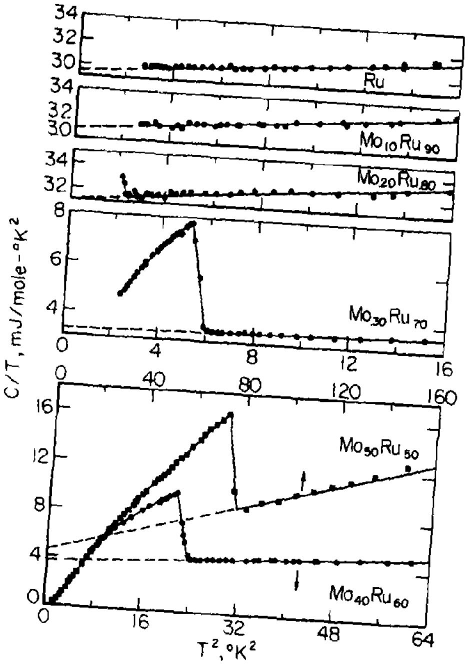

Fig. 2. Specific heat of h.c.p. Ru and Mo–Ru alloys.

For $Mo_{0{\cdot}50}Ru_{0{\cdot}50}$ with a high $T_c = 8{\cdot}7$°K and a low $\theta_D \sim 330$°K, the lattice specific heat just starts to deviate from the T^3 dependence at $T \gtrsim T_c$. In this case, the γ and β values are determined by the electronic entropy considerations for superconducting transition. That is,

$$\int_0^{T_c} \frac{(\gamma T)}{T} \mathrm{d}T = \int_0^{T_c} \frac{C_{es}}{T} \mathrm{d}T \tag{2}$$

as shown in Fig. 3, with the superconducting state ($T < T_c$) electronic specific heat calculated from

$$C_{es} = C - \beta T^3. \tag{3}$$

All the values of γ, β, θ_D, and T_c thus obtained are listed in Table 1. The estimated accuracies are about 2 and 3 per cent in γ and θ_D, respectively.

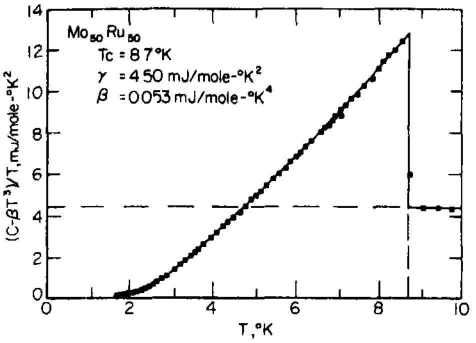

Fig. 3. The electronic entropy balance at T_c for $Mo_{0.50}Ru_{0.50}$. The area under the data curve ($0 \leq T \leq T_c$) is equal to the area under the horizontal line $(C-\beta T^3)/T = \gamma(0 \leq T \leq T_c)$.

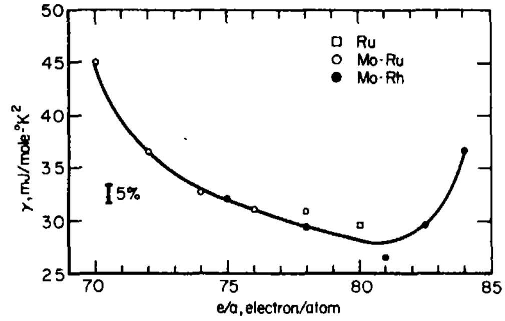

Fig. 4. Electronic specific heat coefficient as a function of the average number of valence electrons to atom ratio for all specimens.

Table 1. *Results of low temperature specific heat measurements on h.c.p.* Mo–Ru *and* Mo–Rh *alloys*

Specimen	e/a (electrons/atom)	γ (mJ/Mole-°K²)	β (mJ/Mole-°K⁴)	θ_D (°k)	T_c (°K)
Ru	8·0	2·95	0·013	530	0·47*
$Mo_{0.10}Ru_{0.90}$	7·8	3·08	0·015	505	
$Mo_{0.20}Ru_{0.80}$	7·6	3·10	0·015	505	1·45
$Mo_{0.30}Ru_{0.70}$	7·4	3·27	0·017	485	2·35
$Mo_{0.40}Ru_{0.60}$	7·2	3·65	0·025	425	4·7
$Mo_{0.50}Ru_{0.50}$	7·0	4·50	0·053	330	8·7
$Mo_{0.20}Rh_{0.80}$	8·4	3·66	0·023	440	
$Mo_{0.25}Rh_{0.75}$	8·25	2·95	0·019	465	
$Mo_{0.30}Rh_{0.70}$	8·1	2·65	0·015	505	
$Mo_{0.40}Rh_{0.60}$	7·8	2·93	0·019	465	
$Mo_{0.50}Rh_{0.50}$	7·5	3·20	0·023	440	1·9

*BATT R. H., *Ph. D. Thesis*. University of California, Berkeley (1964).

DISCUSSION

The results of earlier low temperature calorimetric measurements on pure Ru contained large discrepancies (Table 2). The γ value obtained in this work is in good agreement with that given by Batt. Figure 4 shows the measured γ values as a function of e/a. One common curve can fit quite well the data for specimens from the two different systems. Beyond its ends, this curve, with a minimum at $e/a \sim 8 \cdot 1$, can be connected smoothly to the previously determined branches for b.c.c. and f.c.c. alloys, respectively [1]. For various h.c.p. alloys of the 4*d* series. Booth[7] has found a similar e/a dependence of their magnetic susceptibility, which is another property closely related to $N(E_F)$. There is also a minimum at $e/a \sim 8 \cdot 1$. These results strongly indicate that the rigid band model is valid in this region, and the calorimetric measurement data can be taken as approximating the band shape. The θ_D values are plotted against e/a in Fig. 5. Even with a relatively large uncertainty in the θ_D values thus obtained, due to the fact that the lattice term is only a small fraction of the total measured specific heat, it is obvious that the variation of θ_D is opposite to that of γ. This effect is indicative of the influence of conduction electrons on the lattice vibrations (1),

Table 2. Low temperature specific heat of h.c.p. ruthenium

	Purity	γ (mJ/mole-°K^2)	θ_D (°K)
Wolcott[(a)]	99·98	3·35	600
Clusius and Piesbergen[(b)]		2·6	505
Batt[(c)]	99·99	2·98	
This work	99·98	2·95	530

[(a)] WOLCOTT N. M., *Conference de Physique des Basses Temperatures, Paris, 1955*, p. 286. Centre de National de la Recherche Scientifique and UNESCO, Paris (1956).

[(b)] CLUSIUS K. and PIESBERGEN U., *Z. Naturforsch.* **14a**, 23 (1959).

[(c)] Batt R. H., *Ph D. thesis*. University of California, Berkeley (1964).

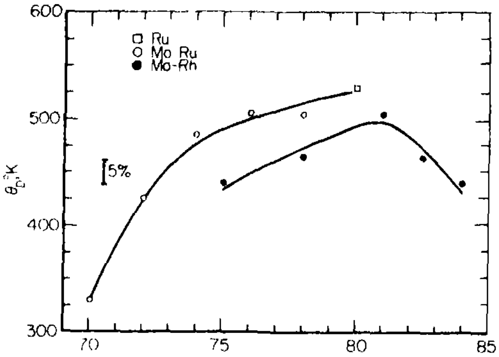

Fig. 5. Debye temperature as a function of the average number of valence electrons to atom ratio for all specimens.

and should be most apparent in transition metals and alloys in which $N(E_F)$ is large. Similar observations have been found in b.c.c. V–Fe and V–Ru alloys[8], and in f.c.c. Ni–Co alloys[9].

Calorimetric investigations of superconductivity are particularly interesting since, because the entire volume of the specimen is involved, it is possible to distinguish between homogeneous and non-homogeneous transitions. As shown in Figs. 1 and 2, for each annealed superconducting specimen, there is a sharp discontinuity in its specific heat at T_c. The jump $(c_{es}/\gamma T)_{Tc}$ is close to the BCS[10] value of 2·43. C_{es} is expected to drop exponentially with decreasing temperature at $T < T_c/1{\cdot}5$, such that,

$$C_{es}/\gamma T_c = a\,\exp(-bT_c/T). \tag{4}$$

This is well illustrated in Fig. 6 for $Mo_{0{\cdot}50}Ru_{0{\cdot}50}$ with a highest transition temperature. The parameters a and b are 10·3 and 1·59, respectively.

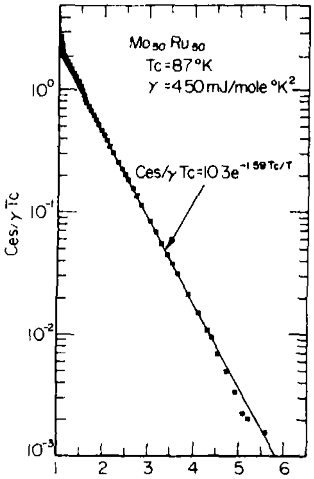

Fig. 6 Superconducting state electronic specific heat of $Mo_{0\,50}Ru_{0\,50}$.

According to the BCS expression[10]

$$T_c \approx 0{\cdot}85\,\theta_D \exp(-1/N(E_F)V) \tag{5}$$

one can calculate the electron interaction parameter V associated with the superconducting state by using the calorimetrically determined values of T_c, θ_D and γ and taking $N(E_F) = 3\gamma/2\pi^2k^2$ (k: Boltzmann's constant). For the Mo–Ru system, V ranges from 0·23 eV for $Mo_{0\cdot50}Ru_{0\cdot50}$ to 0·30 eV for pure Ru. The fact that the variations in both V and θ_D are relatively small for a particular system leads to the resemblance between the variation of T_c and that of γ often observed in transition metal alloys.

Acknowledgement – We wish to thank Dr. E. W. Collings of the Metal Science Group of Battelle for helpful discussion.

REFERENCES

1. For a recent coverage see HEINIGER F., BUCHER E. and MULLER J., *Phys. Kondens. Materie* **5**, 243 (1966).
2. CHENG C. H., WEI C. T. and BECK P. A., *Phys. Rev.* **120**, 426 (1960).
3. RUDMAN P., *Trans. Metall. Soc. A.I.M.E.* **239**, 64 (1967).
4. ANDERSON E. and HUME-ROTHERY W., *J. Less-Common Metals* **2**, 443 (1960).
5. ANDERSON E. and HUME-ROTHERY W., *J. Less-Common Metals* **2**, 19 (1960).
6. Supplied by CryoCal Inc., Riviera Beach, Florida, with calibration traceable to the NBS Provisional Scale of 1965.
7. BOOTH J. G., *Phil. Mag.* **17**, 205 (1968).
8. BUCHER E., HEINIGER F. and MULLER J., *Proceedings of the IXth International Conference on Low Temperature Physics, Columbus, Ohio, 1964*, p. 1059. Plenum Press, New York (1965).
9. HO J. C. and VISWANATHAN R. *Phys. Rev.* In press (1968).
10. BARDEEN J., COOPER L. N. and SCHRIEFFER J. R., *Phys. Rev.* **108**, 1175 (1957).

J. Phys. Chem. Solids Pergamon Press 1969. Vol. 30, pp. 175–181. Printed in Great Britain.

MAGNETIC FIELD ENHANCEMENT IN SUPERCONDUCTING TUBES*†

E. F. YOUNG‡ and R. I. GAYLEY
State University of New York at Buffalo, Buffalo, N.Y. 14214, U.S.A.

(*Received* 14 *March* 1968; *in revised form* 27 *May* 1968)

Abstract—The magnetic behavior of tubes of superconducting material cooled in an axial magnetic field has been studied in an attempt to understand the increase in field strength that occurs in the holes of these tubes. It was found that the magnitude of this effect is determined largely by the shape and size of the tube and that it is qualitatively the same for a variety of materials. The results show that what is characteristic of a given tube is the amount of flux that will move into the hole rather than the field increase that will occur.

INTRODUCTION

MAGNETIC field strength can be enhanced in a superconducting tube by cooling the tube in a constant field[1,2] or by causing the field to break into the tube from the outside[3]. The investigation reported in this paper was undertaken in order to learn the cause of the former effect. When this work was begun, there was no theory of field enhancement, but it was not hard to think of a variety of possible explanations. This made a variety of experiments necessary in order to obtain clues as to the cause of the effect as well as to rule out as many competing explanations as possible. Only the most pertinent results are given here[4], and they show that the enhancement effect is caused by the fact that in the early stages of the transition the phase boundaries coalesce so as to trap flux in the tube, and they show further that what fraction of this trapped flux will be able subsequently to move into the hole is determined largely by the shape of the tube.

Most of the measurements involved cooling a tube in constant axial field and monitoring the field strength in the hole, but some auxiliary studies of flux expulsion are also reported.

EXPERIMENTAL DETAILS

Most of the tubes studied were machined from polycrystalline rods of pure tin that had been cast in glass tubes and cooled very slowly under forepump vacuum. After machining, the tubes normally were etched. A tin-indium alloy and a pure indium tube were prepared in similar fashion. A pure single crystal tin tube was made by Semi-Elements Inc. with as-grown inner and outer surfaces. A mercury tube was made by filling a glass mold and allowing it to freeze. This mercury tube had rounded ends and also had mercury guard rings, of diameter roughly the same as the o.d. of the tube, at each end. None of the other specimens had guard rings.

A uniform magnetic field was provided by a solenoid, with Helmholtz coils used to cancel out the horizontal component of the earth's field.

The axial field in the hole of the tube normally was measured with a commercial Hall probe, but in a few cases, in which the hole was very small, a fine-wire superconducting probe of a type that has been described elsewhere[5] was used.

---

[*] Supported in part by the Research Corporation and the National Science Foundation.

[†] Based in part on the Ph.D. thesis by E. F. Young, State University of New York at Buffalo, 1966 (Unpublished).

[‡] *Present address:* Xerox Corp., Rochester, N.Y.

The temperature was monitored with a carbon resistance thermometer that was calibrated against the vapor pressure of the helium bath. An X–Y recorder and a strip chart recorder were used to record field vs. temperature as well as temperature vs. time. A pressure regulator manufactured by the Cryonetic Corporation was used to achieve controlled, steady, cooling rates.

RESULTS AND DISCUSSION

All of the tubes studied were Type I superconductors, but a variety of materials were employed, as can be seen from Tables 1 and 2. Field enhancement has been observed for every tube on every cooling, showing that the effect is quite general. Also, the magnitude of the effect does not appear to depend on the material used.

The enhancement factor f is defined as the ratio of the final field achieved on cooling to the applied field. Because some specimens showed some dependence on field and cooling rate, f_{av}, the average of all of the values of f obtained for a given specimen, was computed. Normally fields of 5, 10 and 25 G and cooling

Table 1. *Standard, flat-ended tubes (polycrystalline tin unless otherwise specified)*

Specimen No.	o.d. (cm)	i.d. (cm)	Length (cm)	f_{av}	Comments
1.	1·8	1·5	12	1·2	Smith and Rorschach*
3.	1·9	0·4	6·2	2·8	
	1·82	0·41	4·0	2·1	
	1·8	0·80	4·0	1·5	
	1·8	0·8	2·8	1·3	
4.	2·38	0·40	7·4	2·9	
	1·83	0·40	2·0	1·4	
5.	2·38	0·39	7·4	2·8	
6.	2·47	0·40	7·4	2·8	Tin+0·1 per cent indium
12.	2·52	0·39	10·6	1·9	Indium
13.	2·47	0·45	7·4	2·9	
	2·42	1·01	7·4	1·6	
14.	2·46	0·46	7·4	3·8	
15.	2·50	0·17	7·5	7·6	
16.	2·46	0·17	6·7	3·5	light etch
17.	2·47	0·40	7·4	3·7	
18.	2·48	0·40	7·2	3·6	
19.	2·44	0·39	7·6	5·1	
	2·43	0·39	4·7	3·3	
	2·43	0·40	2·7	2·8	
	2·43	0·40	1·9	2·7	
	2·42	0·40	1·26	2·0	
20.	2·45	0·4	7·2	4·6	
	1·88	0·4	7·2	5·4	
	1·24	0·4	7·1	3·6	
	0·88	0·4	7·1	1·9	
21.	2·45	0·42	15·4	4·1	
	2·40	0·4	9·8	2·7	
	2·40	0·44	4·7	2·0	
22.	2·5	0·40	10·2	3·2	Single crystal

*SMITH T. I., Unpublished data.

Table 2. Other tubes (polycrystalline tin unless otherwise specified)

Specimen No.	o.d. (cm)	i.d. (cm)	Length (cm)	Ends	f_{av}	Comments
2	1·7	0·95	10	rounded	1·4	mercury, as cast, with guard rings at ends
3.	1·90	0·41	8·9	60° inward	10·2	
	*1·9	0·4	6·2	flat	2·8	
	1·8	0·41	6·2	30° inward	10·6	
	*1·82	0·41	4·0	flat	2·1	
	*1·8	0·80	4·0	flat	1·5	
	1·8	0·8	4·0	45° outward	1·4	
	*1·8	0·8	2·8	flat	1·3	
7.	2·60	0·42	8·1	15° outward	2·8	
	2·60	0·42	8·1	30° outward	2·9	
8.	2·40	0·42	7·9	45° outward	3·0	
	2·45	0·42	7·4	60° outward	2·2	
9.	2·04	0·39	7·8	75° outward	1·5	
10.	2·38	0·41	7·4	5° inward	1·8	
	2·37	0·40	7·4	10° inward	2·1	
11.	2·46	0·39	15·2	60° outward	2·0	
13.	2·52	0·40	7·6	flat	2·1	light etch
	*2·47	0·45	7·4	flat	2·9	normal etch
	2·46	0·47	7·4	flat	2·7	heavy etch
14.	2·48	0·39	7·4	flat	2·0	unetched
	2·48	0·39	7·4	flat	2·2	light etch
	*2·46	0·46	7·4	flat	3·8	normal etch
	2·46	0·46	7·4	30° inward	5·9	
	2·42	0·46	7·4	60° inward	9·3	
17.	2·49	0·39	7·4	flat	3·8	not machined, unetched
	*2·47	0·40	7·4	flat	3·7	light etch
	2·46	0·44	7·4	flat	3·5	heavy etch
18.	2·52		7·3	flat		solid rod, light etch
	*2·48	0·40	7·2	flat	3·6	
	2·48	0·40	7·2	30° outward	3·3	
	2·48	0·4	7·2	60° outward	3·1	
	2·44	0·41	4·9	round	3·7	
21.	*2·45	0·42	15·4	flat	4·1	
	2·4	0·4	15	60° outward	2·4	
	2·4	0·4	15	rounded	2·4	approx. ellipsoidal
	*2·40	0·4	9·8	flat	2·7	
	*2·40	0·44	4·7	flat	2·0	
23.	1·3	0·4	10·0	rounded	1·6	indium, approx. ellipsoidal

*Also listed in Table 1.

rates of roughly 0·1 and 1°K per min were employed. (It should be pointed out that some tubes showed no dependence on field or cooling rate.) Table 1 lists the results obtained with standard flat-ended tubes, and other specimens are listed in Table 2.

First consider the flat-ended tubes. In an earlier publication[2], a regular variation of f_{av} with o.d./i.d. was reported. This regularity has not been continued by specimens studied more recently, perhaps because the newer tubes were made in a slightly different way, using a slower cooling of the casting. By carefully classifying the tubes according to the details of their manufacture, it is possible to find systematic groupings, but the most clear-cut way to study shape and size dependence seems to be to repeatedly machine the same specimen.

Figure 1 shows how f_{av} for a given tube varies as either the o.d. or i.d. is changed, and Fig. 2 shows the dependence on length. While different tubes of the same material and size may have quite different values of f_{av}, the variation of f_{av} with machining is remarkably regular. Note that changing either the o.d. or the i.d. is equally effective in changing f_{av}.

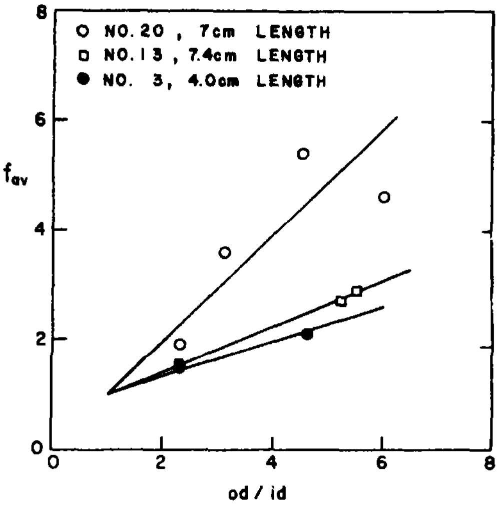

Fig 1. Variation of average enhancement f_{av} with o.d./i.d. as either o.d. or i.d. is changed without changing length. For tube No. 20, the o.d. was varied, while for No.'s 3 and 13, the i.d. was changed. The straight lines are intended to be merely suggestive.

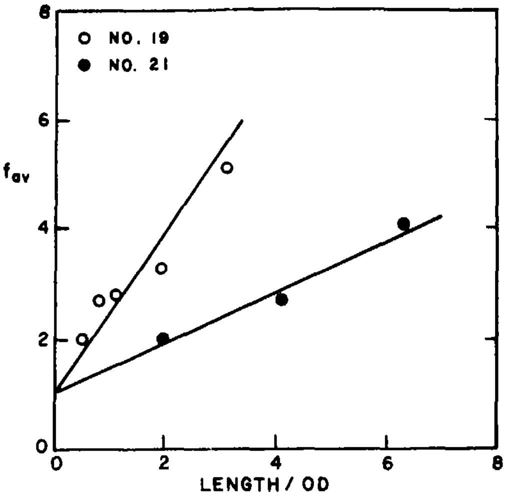

Fig 2. Variation of f_{av} with length/o.d. as the length of a tube is varied. The straight lines are intended to be merely suggestive

A natural question is whether the enhancement is basically an end effect or a bulk effect. By an end effect is meant one which arises because of the non-uniform fields that occur near the ends of the specimen and which becomes weaker as the length to diameter ratio increases. Figure 2 shows that the reverse is true; f_{av} is larger for longer specimens. However, the ends play some role, as can be seen from Fig. 3, which shows the effect of tapering the ends in either concave or convex fashion. One interpretation that can be put on Figs. 2 and 3 is that the reduction

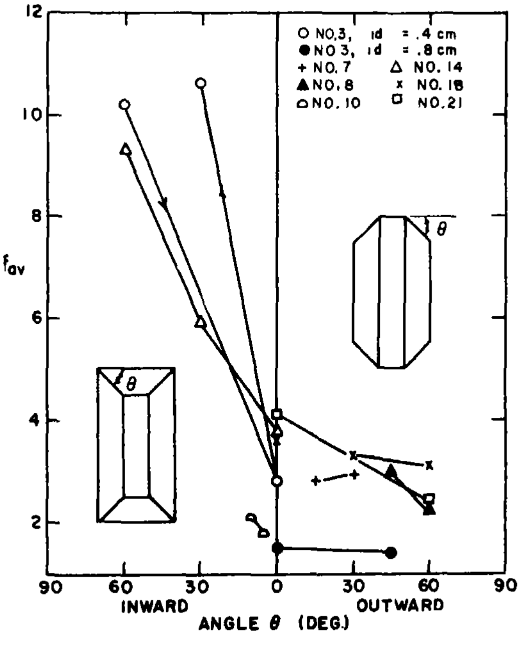

Fig. 3. Variation of f_{av} with angle of taper of the ends. The definition of θ for inward and outward tapers is illustrated in the longitudinal sections shown. The angle was varied without changing the overall length, except for No. 3 with i.d. = 0·4 cm, for which the arrows indicate the order in which the points were obtained.

in f_{av} caused by having a finite length can be counteracted in part by making the ends concave.

In addition to the tapered specimen, four rounded-end tubes are listed in Table 2. No.'s 2 and 18 were rounded so as to have no sharp edges. No.'s 21 and 23 were rounded so as to closely approximate an ellipsoid with a hole, and they had sharp edges at the ends of the holes. Shoenberg's work[6] suggests that an ellipsoidal tube would exhibit a very good Meissner effect, and this might lead one to expect that such a tube would give very little enhancement, but in fact only a moderate reduction in f_{av} was produced by rounding.

Other aspects of the tubes that might influence the degree of completeness of the Meissner effect are the perfection of the bulk and the smoothness of the surface. It is therefore interesting to note that the single-crystal tube with as-grown surfaces had an f_{av} that was similar to those of polycrystalline tubes. However surface condition can play a small role, as is shown by the effect successive etches produced on specimens 13, 14 and 17 (see Table 2).

In considering field expulsion on cooling it is necessary to examine the role that might be played by thermal gradients within a tube. If the surface cools faster than the bulk, the surface may enter the superconducting state before the bulk, and this would surely influence the Meissner effect and probably would affect the enhancement as well. Such an effect would depend strongly on the cooling rate near the start of the transition and would disappear for sufficiently slow cooling. From this argument it can be seen that thermal gradients are not the fundamental cause of enhancement, since some tubes show no dependence whatever on cooling rate, and since attempts to reduce enhancement by cooling quasistatically were not successful.

In some coolings, a ballistic galvanometer was used in conjunction with a coil fitted around the tube to observe flux expulsion. It was found that there was an expulsion of typically 10–30 per cent of the flux, which began before the field in the hole started to increase. (A solid tin rod made in the same way as the tubes expelled 20–30 per cent of the flux.) Within a rather narrow temperature interval this flux expulsion ceased, meaning that a closed superconducting loop formed around the outer surface of the tube. The flux then trapped did not come out on further cooling or on holding the temperature constant. (However, curiously, some of it would begin to come out any time the specimen started to warm.) Generally, the amount of flux that moved into the hole was a few percent of the flux originally in the walls, and the majority of the flux was permanently trapped in the walls. The largest fraction of the flux in the walls ever observed to move into the hole was 68 per cent. This occurred on one trial with tube No. 3 with concave ends and gave an f of 15·3.

Since there is a large amount of flux remaining in the walls, a natural question is, what limits f? Why is f not much larger? Two possible kinds of answers that come to mind are: (1) Enhancement ceases when the difference between the inside and outside fields becomes too large. (Perhaps the walls cannot support a greater field difference.) (2) Enhancement stops when a given amount of flux moves into the hole. (It might be that only some of the trapped flux has an easy path to the hole.)

That possibility (1) is certainly wrong and that (2) is at least close to the truth is shown by measurements made on a tube in which the effective area of the hole could be varied. In these experiments, a lead rod, somewhat longer than the specimen and cut so as to fill part of the cross-sectional area of the hole, was inserted into the hole. This rod was superconducting throughout the measurements, and so the magnetic field was excluded from the region occupied by the rod. (The amount of flux penetrating into the surface of the rod was negligible.) The effective area of the hole was then the area inside the tube but outside the rod. When enhancement occurred, a given amount of flux was compressed into this smaller area, giving a larger increase in field. In other words, if a given tube drove a given fraction of its flux into the hole, regardless of the area of that hole, then the smaller the effective area the greater would be the enhancement.

Three different lead rods were used with tube No. 13, giving four values of the effective area. f_{av} was 1·6 with no rod, and increased to 3·0 when the effective area had been reduced to one-fourth of its original value. The detailed results are presented in Fig. 4. $\Delta\phi$ is the amount of flux that moved from the walls into the hole during enhancement, and H_I is the initial, applied field. $\Delta\phi/H_A$ has units of area and may be regarded as the apparent area of the walls from which the flux is expelled into the hole. The figure shows that this apparent area is roughly 0·4 cm² for all cases, although it may decrease somewhat for the smaller effective areas. It is perhaps interesting to note that 0·4 cm² is the area of a 0·12 cm strip around the hole, and that the cross-sectional area of the wall was 3·74 cm².

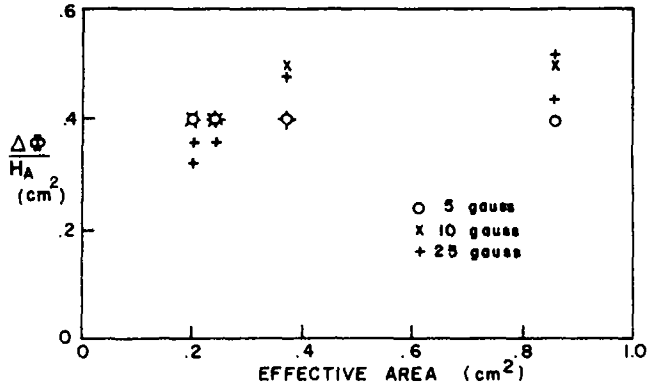

Fig. 4. Results obtained by inserting various lead rods into the hole of tube No 13, so as to vary the effective area of the hole The amount of flux that moved into the hole on a given cooling, $\Delta\phi$, is calculated from f, and H_I is the applied field.

Having established that what is characteristic of a given cooling is the flux that will move into the hole rather than the enhancement produced, the next question is what determines this characteristic amount of flux? That this amount of flux has been fixed soon after the initial flux expulsion is completed is shown by the following experiment.

On several occasions, a specimen was cooled quasistatically while the field was modulated in steps of ±5 per cent. The output of the Hall probe in the hole followed this modulation. At some temperature, the probe ceased to follow the field changes, showing that a closed superconducting loop had been formed around it. At this point, which was before field enhancement had begun, the external field was slowly brought to zero. Subsequent cooling led to an f of 1·5, whereas a more typical value for this tube was 2·2. A second tube, which normally had $f = 2·6$, gave a value of 2·2 under these conditions. The effect of turning the field off is surprisingly small. In cases in which the cooling proceeded somewhat further before the field was turned off, f was the same as if the field were still on.

These experiments lead to the conclusion that flux is trapped in such a way that only a certain fraction of it has an easy path to the hole. In other words, the way that the phase boundaries propagate during the initial flux expulsion and the way that they coalesce to give trapping is what ultimately determines the field enhancement. It seems most natural to suppose that the flux that is able to move into the hole is that which lies in normal regions which make contact with the hole.

Acknowledgements—We are indebted to Dr. T. I. Smith for permission to use his unpublished results, to Dr. S. Mrozowski for the loan of some equipment, and to Drs. R. D. Parks, H. E. Roschach, Jr., and B. Serin for helpful discussions. Mr. J. Mooney and Mr. E. Pruuli helped construct the equipment and perform the experiments. We are particularly grateful to Mr. J. Langan, who made some of the specimens and some of the measurements.

REFERENCES

1. SMITH T. I. and RORSCHACH H. E., Jr., *Rev. Mod. Phys.* **36**, 277 (1964).
2. GAYLEY R. I. and YOUNG E. F., *Phys. Lett* **20**, 104 (1966).
3. YOUNG E. F. and GAYLEY R. I., *Phys. Lett.* **23**, 15 (1966).
4. Further details may be found in YOUNG E. F., Ph.D. Thesis, State University of New York at Buffalo, unpublished (1966).
5. GAYLEY R. I., *Cryogenics* 7, 215 (1967).
6. SHOENBERG D., *Proc. Phil. Soc.* **33**, 260 (1937).

Note added in proof: After this manuscript was written, a rounded electropolished indium tube (No. 23) was studied. The results are preliminary, particularly since one end of the hole was damaged during polishing, and it is not clear what effect this might have had. On cooling, the field in the hole rose in the usual manner, but, beginning at a point which depended on cooling rate, the field subsequently decreased again. The value of f_{avg} was about 1·2, instead of the value of 1·6 that was found before polishing. In one case, a rapid cooling in a field of 10 G, the field in the hole rose to a maximum of 19 G and then fell to 14 G, corresponding to f values of 1·9 and 1·4 respectively. In a slow cooling, the values of 1·5 and 1·07 were obtained from the maximum and the final field values. These results are tentatively interpreted as showing that the explanations referred to in the text as possibilities (1) and (2) are both relevant to this specimen. These findings are also significant in that they provide the first evidence that it may be possible, with proper specimen preparation, to eliminate enhancement.

J. Phys. Chem. Solids Pergamon Press 1969. Vol. 30, pp. 183–185. Printed in Great Britain.

THE PRESSURE INDUCED METAMAGNETIC TRANSITION IN Au_2Mn AND THE PRESSURE DEPENDENCE OF THE FERROMAGNETIC CURIE TEMPERATURE*

R. C. WAYNE
Sandia Laboratory, Albuquerque, N.M. 87115, U.S.A.

and

F. A. SMITH
Argonne National Laboratory, Argonne, Ill. 60439, U.S A.

(*Received* 24 *May* 1968)

Abstract—The AFM-FM transition in Au_2Mn has been induced at zero field by the application of hydrostatic pressure. The transition pressure is independent of temperature. The ferromagnetic Curie temperature increases linearly with a slope of $3{\cdot}0 \pm 0{\cdot}3°C\ kbar^{-1}$ between 18 and 24 kbar.

THE INTERMETALLIC compound Au_2Mn is known to exhibit a metamagnetic transition from a helicoidal antiferromagnetic (AFM) state to a ferromagnetic (FM) state when placed in a magnetic field of about 10 kOe [1, 2]. Several investigations have been made to determine the dependence of the critical field H_c on pressure and on temperature [3–5]. In the work of Grazhdankina and Rodionov[3], measurements of H_c at pressures up to 10·6 kbar showed a pressure dependence of $(dH_c/dP) = -0{\cdot}68$ kOe/kbar [3]. There is no simple relation of this to the temperature effect since H_c increases slightly with decreasing temperature[3, 4]. Extrapolation of the data of reference[3] to zero field indicates that Au_2Mn should become ferromagnetic at a critical pressure P_c of 15 ± 3 kbar.

Our sample was prepared by holding the mixture of Mn and Au in the melt for 20 min and then allowing it to furnace cool. Part of the ingot was annealed for four days at 680°C and water quenched; no detectable difference in bulk magnetic behavior was noted due to the annealing process. Analysis showed the sample contained $34{\cdot}3 \pm 0{\cdot}1$ at. % Mn and X-ray data indicated a trace of antiferromagnetic AuMn was present.

The experiment was performed under hydrostatic conditions using pentane as pressure fluid. An inductance measurement technique (described in reference[6], was employed to detect the FM-nonFM transitions. Both the critical pressure P_c and the Curie temperature θ were measured in the pressure range of 0–25 kbar and in the temperature range 20°–150°C.

The data in Fig. 1 show the appearance of ferromagnetic character in Au_2Mn as pressure is increased through the 10–20 kbar region. This transition is broad and is centered at 16·1 kbar, a value which is in reasonable agreement with the extrapolated value of reference[3]. The data of $P_c(T)$ and $\theta(P)$ are plotted in Fig. 2. The data show that, within experimental error, P_c is independent of temperature between 20 and 90°C. Tentative evidence that P_c has only a small temperature dependence down to 4·2°K is provided by neutron diffraction[7] and Mössbauer [8] measurements. It is interesting to note at this point that the *field* induced transition

---

*This work was supported by the U.S. Atomic Energy Commission.

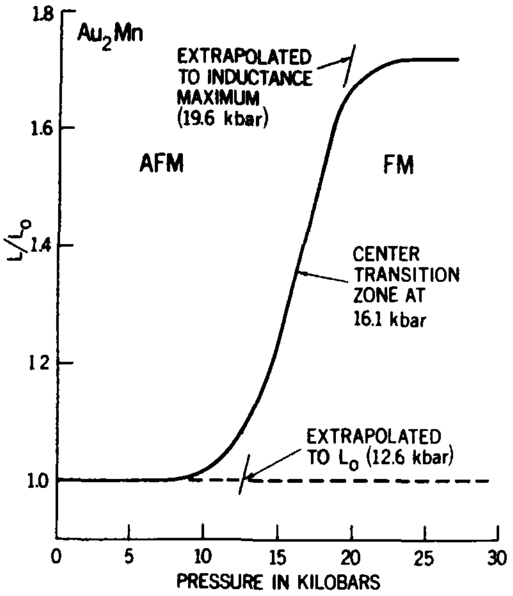

Fig. 1. Pressure induced AFM-FM transition in Au_2Mn (T = 22°C). The inductance of a coil containing a sample is seen to increase from its air core value L_0 as a net magnetic moment appears in the sample.

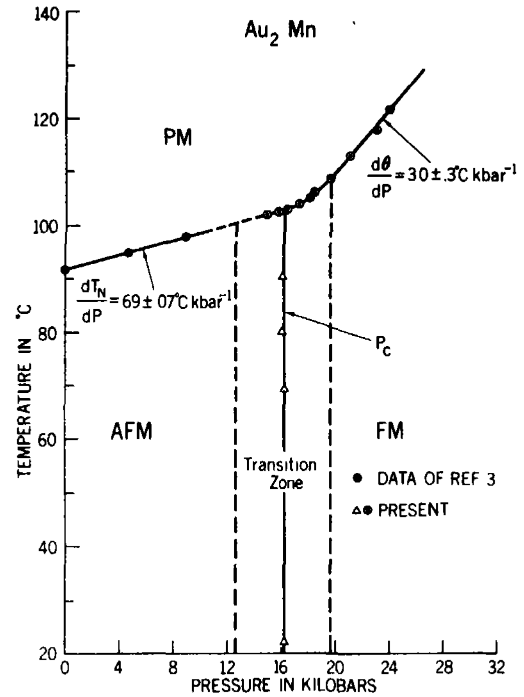

Fig. 2. *P*-*T* phase diagram for Au_2Mn showing the AFM-FM transition line and the pressure dependence of the Néel and Curie temperatures.

from the AFM to the FM state observed by Grazhdankina and Rodionov[3] was also a very weak function of temperature between room temperature and 77°K.

The pressure dependence of θ is also shown in Fig. 2. At the lowest pressures for which measurements were possible viz, the pressure at which an appreciable net moment appears in the sample, $(d\theta/dP)$ is about 0·7°C kbar^{-1}. This is in good agreement with the measured pressure dependence of the Néel temperature, $(dT_N/dP) = 0{\cdot}69 \pm 0{\cdot}07$°C kbar^{-1} given in reference[3]. The value for $(d\theta/dP)$ increases as the pressure is increased until at pressures greater than 19–20 kbar a constant value of $(d\theta/dP) = 3{\cdot}0 \pm 0{\cdot}3$°C kbar^{-1} is observed.

Several of our experimental observations suggest that the AFM-FM transition is second order. First, as has just been mentioned, $(d\theta/dP)$ changes continuously and by a large amount (a factor of 4) in only a few kilobars. It is difficult to envision a mechanism for such a change in the FM phase if the transition is first order (even if a mixed phase region exists). Conversely, this behavior of θ is compatible with a second order transition. Second, from the Clausius-Clapeyron equation and the fact that we find P_c to be temperature independent, it is required that the entropy change $\Delta S = 0$ (within the accuracy of the P_c measurement). Further indications suggesting that the transition is second order arise from both the lack of observable hysteresis and the appreciable width of the transition. It is recognized that first order transitions may be spread over a broad region by mixed phases, composition inhomogenieties, pressure and temperature gradients; however in this case, the last two clearly cannot contribute. Measurements made on a second sample, which was prepared differently and is of slightly different composition (33 per cent Mn) showed behavior identical to that in Figs. 1 and 2, but with a 12 per cent higher value of P_c. This effect of composition is not enough to account for the transition breadth. The above arguments strongly suggest, although do not prove, that the AFM-FM transition is second order.

These observations are consistent with behavior which might be expected from the model suggested by Herpin and Meriel that the spiral spin structure collapses to a fan structure with field (or pressure in this instance). On the basis of this model, previous[7] and present results suggest the following as characteristic of the microscopic magnetic behavior of Au_2Mn under pressure. As pressure is applied to Au_2Mn the spin angle decreases linearly from 51° at 0 kbar to ≈ 42° at 9 kbar[7]. When the pressure is ≈12 kbar, the spiral structure of the Mn moments in the basal plane starts to distort until a fan structure is reached at about 16 kbar. Additional pressure closes the fan until saturation is reached for pressures greater than 20 kbar.

To establish the compositional and preparation tolerances on the alloy, and to determine the magnetic structure through the AFM-FM transition at low temperatures, further experiments employing neutron diffraction are in progress by one of the authors (FAS).

REFERENCES

1. MEYER A. J. P. and TAGLANG P., *J. Phys. Radium* **17**, 457 (1956).
2. HERPIN A. and MERIEL P., *J. Phys. Radium* **22**, 337 (1961).
3. GRAZHDANKINA N. P. and RODIONOV K. P., *Soviet Phys. J.E.T.P.* **16**, 1429 (1963).
4. RODBELL D. S., *Progress in Very High Pressure Research* (Edited by Bundy, Hibbard and Strong), p. 283. Wiley, New York (1968).
5. KANEKO T., MATSUMOTO M. and KAZAMA N., *J. Phys. Soc. Japan* **24**, 647 (1968).
6. WAYNE R. C., *Phys. Rev.* **170**, 523 (1968).
7. SMITH F. A., BRADLEY C. C. and BACON G. E., *J. Phys. Chem. Solids* **27**, 925 (1966).
8. ROBERTS L. D., *Bull. Am. phys. Soc.* **12**, 24 (1967).

J. Phys. Chem. Solids Pergamon Press 1969. Vol. 30, pp. 187–193. Printed in Great Britain.

PROCESSUS DE TRANSFERT D'ACTIVITÉ DU Fe(III) DANS LE TRIOXALATOFERRATE DE POTASSIUM

A. RUŞI
Institut de physique atomique, Bucarest, Roumanie

(*Received* 26 *February* 1968; *in revised form* 10 *May* 1968)

Résumé—Le processus de transfert d'activité du Fe(III) de $Fe(OH)_3$ à $K_3[Fe(C_2O_4)_3]3H_2O$ et à $K_3[Fe(C_2O_4)_3]$ a lieu selon une cinétique où chaque isotherme correspond à un palier caractéristique d'une façon analogue au recuit du produit irradié.

La présance de l'eau de cristallisation a la même influence sur le processus de transfert que dans le cas de cristaux irradiés par neutrons.

Les petites valeures des énergies d'activation calculées pour le processus de transfert montrent que celui-ci peut intervenir préferentiellement dans le processus de recuit.

Les spectres des énergies d'activation en présence de l'eau de cristallisation indiquent un seul groupe de pics dans la cas de la substance dopée tandis que dans le cas de la substance irradiée on observe nettement deux groupes de pics.

En conformité avec ces observations on peut considérer que dans le processus de recuit thérmique du fer de recul, la dernière étape c'est à dire le passage du Fe(III) de la forme simple dans la forme complexe, peut être représentée par un processus de transfert.

DANS LE cas du trioxalatoferrate de potassium irradié par neutrons on a montré la présence du fer sous deux états de valence[1], comme suite des processus de recul. Les études concernant le processus de recuit on misent en évidence la fait que dans ces processus participe le Fe(III) seulement. L'oxydation du Fe(II) à Fe(III) précède la réaction de guérison thermique qui se produi selon une cinétique spécifique. L'oxydation du Fe(II) a lieu à des températures auxquelles la guérison ne peut pas commencer.

Des recherches récentes sur la cinétique de recuit thermique en certaines cristaux ont misent en évidence l'existence de processus de transfert d'activité entre les formes différentes du même élement[3–5].

Les processus de transfert étudiés dans le cupferate de fer[6] ont montré la possibilité d'un transfert d'activité dans le cas du Fe(III). Le transfert d'activité du Fe(II) dans le cupferrate de fer se produi seulement en présence du Fe(III)[7]. Dans le cupferrate de fer irradié par neutrons l'oxydation du Fe(II) de recul à Fe(III) précède le processus de recuit de la même manière que dans le trioxalatoferrate de potassium. Mais dans ce cas la réaction d'oxydation, ainsi que la réaction de guérison thermique se produisent à la même température.

Si on compare les processus qui précedent la réaction de recuit aux processus de transfert on peut mettre en évidence la différence suivante: dans le cas de la substance irradiée la réaction précedente est une réaction d'oxydation du Fe(II) à Fe(III)[2] tandis que dans le cas des processus de transfert la réaction précedente semble être une réaction de transfert du Fe(II) à Fe(III).

L'état de valence du fer est une condition nécessaire, mais le transfert du fer de l'état non complexée dans une combinaison complexe est conditionné par la forme chimique de l'agent employé pour le dopage. L'étude du système sulfate ferreux-hydroxyde ferrique a demontré que le processus de transfert est accompagné par une transformation de phase; seulement le fer qui se trouve dans la duexième phase (probablement γ-Fe_2O_3) peut transférer ensuite dans la forme complexe.

Dans le présent mémoire nous étudions la cinétique du processus de transfert d'activité du Fe(III) dans le trioxalatoferrate de potassium. Par différence au cupferrate de fer où les isothermes de recuit thermique se reunissent dans un palier unique, dans le cas du trioxalatoferrate de potassium le processus de transfert correspond à une cinétique dont les isothermes de recuit ont des paliers différents. Nous étudions également l'influence de l'eau de cristallisation sur le processus de transfert.

PARTIE EXPÉRIMENTALE

Le trioxalatoferrate de potassium a été préparé en suivant la méthode décrite dans la littérature[8] qui emploie comme substances de départ le sulfate ferrique, l'oxalate de baryum et l'oxalate de potassium. La purification a été réalisée par plusieurs recristallisation répétées dans l'eau bidistillée. Le produit anhydre a été obtenu par le chauffage de la substance hydratée à 160°C pendant 10 hr. Le mélange des cristaux de trioxalatoferrate de potassium avec d'hydroxyde ferrique marqué avec du Fe^{59} a été comprimé sous vide à environ 50 atm.

La séparation du fer à l'état simple du fer à l'état complexée, ainsi que la détermination du fer ont été effectuées à l'aide des résines échangeuses d'ions en utilisant la méthode publiée en[9]. Les traitements thermiques ont été effectués dans un thermostate. De cette manière il a été possible de maintenir la stabilité de la température avec une précision d'environ ±1°C.

L'hydroxyde ferrique a été préparé par la précipitation des ions ferriques, marqués avec du Fe^{59}, au moyen d'une solution d'hydroxyde d'ammonium. Le précipité a été filtré et l'eau évaporée à la température ambiante; l'hydroxyde a été ensuite maintenu dans un dessicateur avec de chlorure de calcium.

RÉSULTATS EXPÉRIMENTAUX

Le trioxalatoferrate de potassium présente une grande stabilité thermique, ce qui a rendu possible l'étude du transfert d'activité à des températures élevèes.

Nous avons étudié deux systèmes: Fe(III)-$K_3[Fe(C_2O_4)_3]\,3H_2O$ et Fe(III)-$K_3[Fe(C_2O_4)_3]$. La variation du transfert (Tf) en fonction du temps (t) à plusieurs températures (120–220°C) est montrée sur la Fig. 1 pour le produit qui contient de l'eau de cristallisation. On peut constater qu'à chaque isotherme correspond un palier spécifique, d'une manière analogue au produit irradié. Mais le transfert commence à une température d'environ 10°C plus élevée. Sur la Fig. 2 nous avons représenté les isothermes de transfert à différentes températures pour les cristaux anhydres.

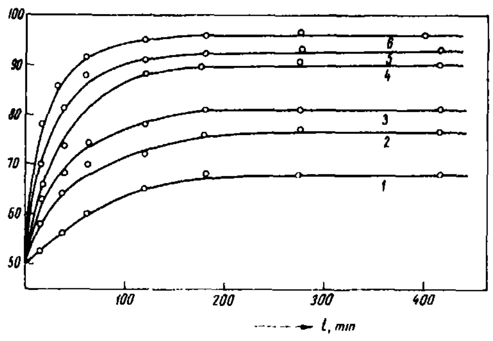

Fig. 1. Isothermes de transfert dans le $K_3[Fe(C_2O_4)_3]\,3H_2O$-$Fe(OH)_3$; 1–120°; 2–130°; 3–150°; 4–180°; 5–200°; 6–220°C.

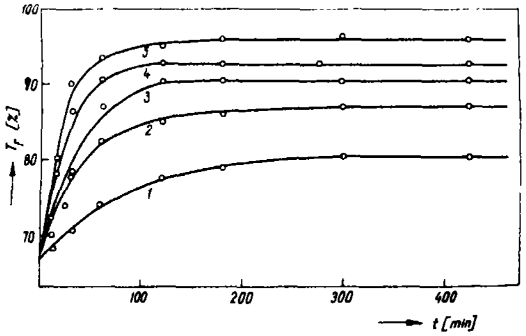

Fig. 2. Isothermes de transfert dans le $K_3[Fe(C_2O_4)_3]$-$Fe(OH)_3$; 1–175°; 2–180°; 3–200°; 4–210°; 5–220°C.

Le processus de transfert est plus rapide pour les cristaux avec de l'eau de cristallisation par rapport aux cristaux anhydres, d'une manière analogue à la substance irradiée par neutrons. Le transfert d'activité du Fe(III) dans le $K_3[Fe(C_2O_4)_3]$ commence également à des températures plus élevées. Le domaine de température dans lequel le processus a été étudié est situé entre 175 et 220°C.

Il est intéressant de remarquer qu'à partir de la température de 180°C les paliers sont assez rapprochés pour les deux systèmes, par différence aux basse température où ils restent visiblement écartés.

Le calcul de la quantité transférée a été éffectué selon la formule suivante:

$$Tf = \frac{\text{Fe(IIIc)}}{\text{Fe(III)} + \text{Fe(IIIc)}}$$

ou Fe(III) représente l'activité du fer trivalent et Fe(IIIc) représente l'activité du fer dans le complexe.

INTERPRÉTATION DES RÉSULTATS

Les Figs. 1 et 2 montrent que le processus de transfert d'activité du Fe(III) dans le trioxalatoferrate de potassium est caractérisé par un group d'isothermes ayant des paliers caractéristiques. Le processus de transfert pour les deux systèmes peut être représenté par le schemà suivant:

$$\text{Fe(III)} \xrightarrow{\ominus} K_3[Fe(C_2O_4)_3]\,3H_2O$$

et

$$\text{Fe(III)} \xrightarrow{\ominus} K_3[Fe(C_2O_4)_3]$$

où le symbol $\xrightarrow{\ominus}$ est employé pour désigner une réaction de transfert [6].

L'énergie d'activation du processus peut être calculée à partir des isothermes de transfert. Pour éffectuer ce calcul nous avons représenté la fraction transférée en fonction du logarithme du temps. Les courbes composées de transfert (Figs. 3 et 4) ont été tracées par le déplacement de l'échelle du temps correspondant à ces isothermes, $\Delta \log t$, par rapport à une courbe de référence (180°C pour la courbe Fig. 3 et 180°C pour la courbe Fig. 4).

Par la représentation des valeures $\Delta \log t$ en fonction de l'inverse de la température absolue ($1/T$) nous avons obtenu les droites montrées sur les Figs. 5 et 6; les pentes de ces droites déterminent les températures

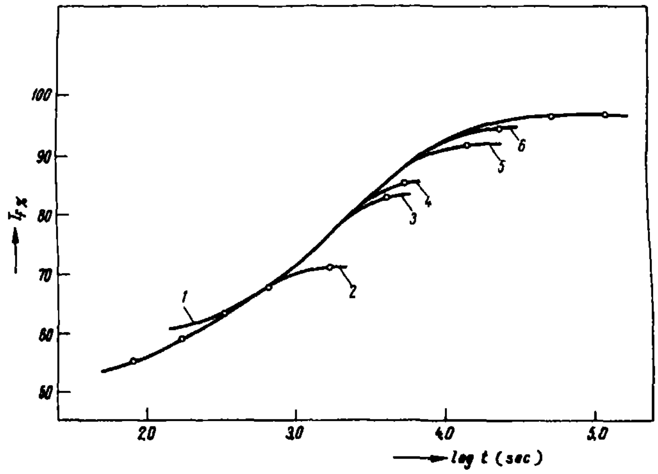

Fig. 3. Courbe composée de transfert correspondant aux isothermes de la Fig. 1; 1-120°; 2-130°; 3-150°; 4-180°; 5-220°C.

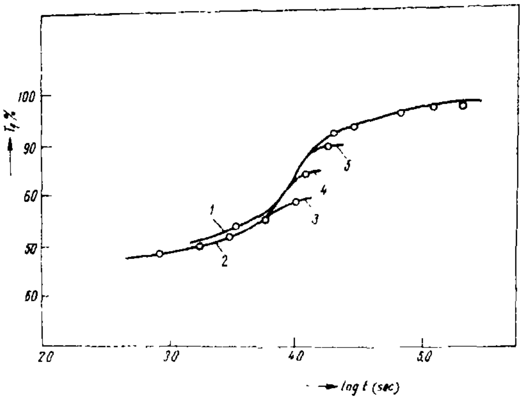

Fig. 4. Courbe composée de transfert correspondant aux isothermes de la Fig. 2; 1–175°; 2–180°, 3–200°; 4–210°; 5–220°C.

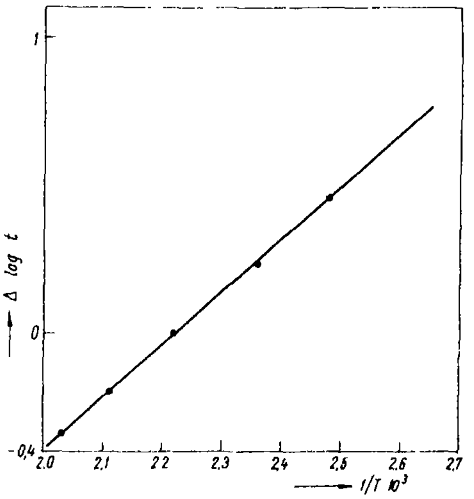

Fig. 5. Température d'activation du processus de transfert, correspondant au système $K_3[Fe(C_2O_4)_3]$ $3H_2O$–$Fe(OH)_3$.

d'activation du processus de transfert du Fe(III) dans le $K_3[Fe(C_2O_4)_3]$ $3H_2O$ de 1780°K (0,14 eV) et du même transfert dans le $K_3[Fe(C_2O_4)_3]$ de 5000°K (0,4 eV).

On remarque que la présence de l'eau de cristallisation diminue la valeur de la température d'activation.

Pour comparer les résultats obtenues lors du recuit thermique en $K_3[Fe(C_2O_4)_3]$ $3H_2O$ et en $K_3[Fe(C_2O_4)_3]$ irradiés par neutrons et dopés avec d'hydroxyde ferrique, nous avons calculé les spectres de distribution dans les énergies d'activation selon la méthode de Vand et de Primak. Nous avons premierement représenté la valeur:

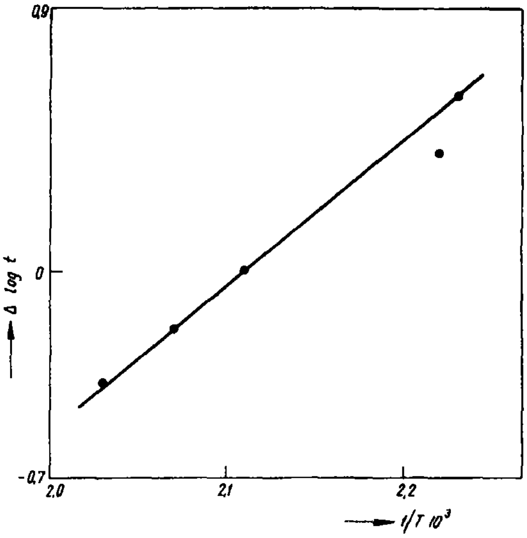

Fig. 6. Température d'activation du processus de transfert, correspondant au système $K_3[Fe(C_2O_4)_3]$–$Fe(OH)_3$.

$$p_0 = \frac{1}{kT} \cdot \frac{\mathrm{d}\,Tf}{\mathrm{d}(\ln t)} \tag{1}$$

en fonction de l'énergie d'activation donnée par la relation:

$$E_0 = kT \ln (Bt) \tag{2}$$

ou Tf représente le transfert d'activité, k la constante de Boltzmann, T la température absolue, t le temps et B un facteur de fréquence.

Sur la Fig. 7 est représenté le spectre de distribution des énergies d'activation qui correspond au produit qui contient d'eau de cristallisation et sur la Fig. 8 le méme spectre pour le produit anhydre. Les valeurs caractéristiques des énergies d'activation sont 0,325 eV (Fig. 7) pour le produit avec d'eau de cristallisation et 0,32 eV (Fig. 8) pour le produit anhydre.

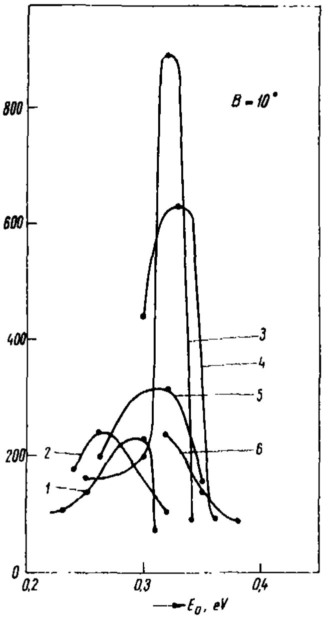

Fig. 7. Spectre de distribution des énergies d'activation pour le produit cristallisé avec de l'eau de cristallisation.

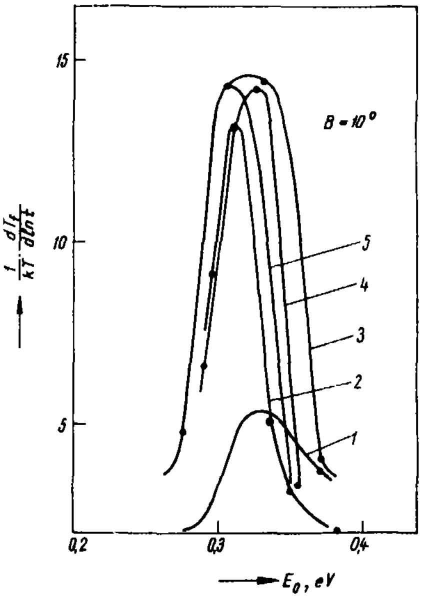

Fig. 8. Spectre de distribution des énergies d'activation pour le produit anhydre.

Il est à remarquer les valeurs très petites des facteurs de fréquence *B*. Nous avons calculé ces facteurs en essayant successivement plusieurs valeurs différents et nous avons finalement choisi les facteurs correspondant à une meilleure superposition des courbes. On peur expliquer les petites valeurs de ces facteurs, et donc les petites valeurs des énergies d'activation, par l'éventualité d'une réactivité chimique entre le ligand et la forme dans laquelle se trouvent la substance dopante dans le cas du transfert ou les atomes de recul dans le cas de la guérison.

En ce qui concerne les différences entres les valeurs des énergies d'activation calculées au moyen de la représentation du $\Delta \log t$ en fonction de $1/T$ et les mêmes valeurs calculées au moyen de la méthode de Vand et de Primak on peut faire la remarque suivante: une erreur égale à un ordre de grandeur dans le choix du facteur de fréquence correspond à une erreur égale à 0,1 eV pour l'énergie d'activation. D'une part la précision des résultats expérimentaux ne permêt pas en général de se situer au-dessous de ces erreurs, d'autre part il est bien connu qu'on obtient une différence des valeurs calculées au moyen de ces méthodes.

DISCUSSION DES RÉSULTATS

Il faut premierement préciser que l'hydroxyde ferrique, utilisé comme substance de dopage, n'est lui-même pas stable pendant le chauffage. Selon les données bibliographiques [10, 11] ses poduits de transformation sont γ-FeOOH et surtout γ-Fe_2O_3. Ce problème sera étudié en détail dans un autre memoire [7]. Pour le travail présent il a été important d'employer un composé simple du fer trivalent qui n'est pas hygroscopique.

Les valeurs initiales du *Tf* (Figs. 1 et 2) sont relativement grandes. Dans le cas du cupferrate de fer le *Tf* initial est appréciablement influencé par la présence des traces d'eau ou d'autre solvent. A cet egard il faut également prendre en considération l'effet de la compression qui peut produire le transfert dans le cas du trioxalatoferrate de potassium. Pour l'étude de la cinétique de recuit les quelques dizaines de pour cent disponibles pour l'étude du transfert représentent un domaine comparable au domaine disponible dans le cas de la guérison du même produit irradié.

Si on compare les isothermes de transfert d'activité dans les cristaux dopés avec d'hydroxyde ferrique (Figs. 1 et 2) aux isothermes de recuit thermique de mêmes cristaux irradiés par neutrons (Figs. 1 et 4[1]) on constate une analogie remarquable entre ces deux processus. Dans le cas du chromate de potassium[4], ainsi que dans le cas du cupferrate de fer[6] la vitesse du processus de transfert est plus petite par rapport à la vitesse de recuit dans les cristaux irradiés par neutrons. Par contre dans le trioxalatoferrate de potassium le transfert est plus rapide pour le produit dopé par rapport au produit irradié. Le calcul des énergies d'activation indique des valeurs comparables pour les processus de transfert d'activité et les processus de recuit. Il résulte donc que dans le trioxalatoferrate de potassium le recuit peut se produire préferentiellement par un mécanisme de transfert.

Un autre élement de comparaison entre le transfert et le recuit est représenté par les spectres de distribution dans les énergies d'activation. Dans le cas des cristaux hydratés, irradiés par neutrons, le spectre montre l'existence de deux familles de pics (Fig. 8[1]), tandis que dans le cas des cristaux anhydres le même spectre montre une seule famille (Fig. 10[1]). Pour les processus de transfert les spectres mettent en évidence dans les deux cases une seule famille de pics (Figs. 7 et 8) seulement.

Les différences que l'on constate entre le recuit et le transfert sont explicables par le fait que l'éspèce qui transfère dans ce cas (l'hydroxyde ferrique ou son produit de transformation) est différente de l'éspèce de recul. L'influence de la forme chimique dans laquelle se trouve le Fe(III) utilisé comme dopant a un important rôle dans certains systèmes[7]. C'est la raison pour laquelle la comparaison entre le recuit et le transfert doit prendre en considération certaines circonstances spéciales. À cet égard on peur remarquer que le cas le plus frequent, correspond à la situation lorsque la présence de la substance de dopage fréine le processus de recuit dans les cristaux irradiés par neutrons. Dans le cas d'autres substances, comme c'est le trioxalatoferrate de potassium, la forme chimique dans laquelle se trouve la substance de dopage accélère le transfert qui se produi plus rapidement par rapport au recuit des éspèces de recul. La différence qu'on observe lors du recuit entre les éspèces formées par recul et les éspèces de dopage est également augmentée par l'action des radiations gamma qui agissent dans le réacteur, produissant des défauts dans le réseau des cristaux.

L'influence de l'eau de cristallisation sur le processus de transfert dans le système $Co(dipy)_3(ClO_4)_3 3H_2O$ a été expliquée par Nath[12, 13] prenant en considération la constante diélectrique du réseau. Le commencement du recuit du complexe hydraté à une température plus petite que le complexe anhydre est expliqué par la valeur plus grande de la constante diélectrique des cristaux hydratés. Ces observations ont été interprétées conformément au modèle du "variable-depth-electron-donors-isotropic-exchange" qui est fondé sur le fait que la vitesse de recuit est proportionelle à la densité des électrons libres. La vitesse de recuit dans le complexe hydraté est plus grande que dans le complexe anhydre, parce que dans le premier, pour les mêmes conditions de recuit, est disponible une plus grande quantité d'électrons libres. Si on accepte cette hypothèse du rôle de la densité des électrons libres, la présence de l'eau de cristallisation explique l'analogie dans le comportement du produit irradié et du produit dopé.

Nous pouvons tirer la conclusion que la comparaison des résultats expérimentaux obtenues dans le présent mémoire, concernant le processus de transfert dans les cristaux de trioxalatoferrate de potassium avec les résultats obtenues auparavant dans les mêmes cristaux irradiés par neutrons[1], confirme l'hypothèse antérieurement émise sur le rôle du transfert dans les processus de recuit. En se basant sur ces considérations on peut accepter que dans le processus de recuit thermique du fer de recul, la derniere étape c'est à dire le passage du Fe(III) simple dans la forme complexe peut être représentée par un processus de transfert.

REFERENCES

1. RUŞI A. et CĂLUŞARU A., *Radiochim. Acta* **4**, 206 (1965).
2. CĂLUSARU A. et RUŞI A., *Radiochim. Acta* **6**, 147 (1966).
3. KAUCIC S. et VLATCOVIC M., *Croatica Chem. Acta* **35**, 365 (1963).
4. APERS D. J., COLLINS K. E., GHOOS Y. F. et CAPRON P. C., *Radiochim. Acta* **3**, 18 (1964).
5. COLLINS C. H., COLLINS K. E., GHOOS Y. F. et APERS D. J., *Radiochim. Acta* **3**. 18 (1964).
6. CĂLUŞARU A. et RUŞI A., *Radiochim. Acta* **9**, 1 (1968).
7. RUŞI A., Serra publié.
8. YOST DON M., *Inorganic Synthesis* (Edited by H. S. Booth), Vol. I, p. 36. McGraw-Hill, New York (1963).
9. RUŞI A. et IONESCO S., *Studii şi Cercetări de Fizică* **2**, 127 (1963).
10. WELLS F., *Structural Inorganic Chemistry* 3rd Edn, Clarendon Press, Oxford (1962).
11. MELLOR J. W., *Inorganic and Theoretical Chemistry*, Vol. XIII, p. 859–860. Longmans, London (1957).
12. NATH A. et VAISH S. P., *J. chem. Phys.* **46**, 12 (1967).
13. NATH A., KHORANA S., MATHUR P. K. et SARUP S., *Ind. J. Chem.* **4**, 51 (1966).

J. Phys. Chem. Solids Pergamon Press 1969. Vol. 30, pp. 195–201. Printed in Great Britain.

POLYMORPHISM OF POTASSIUM SULPHATE, SELENATE AND CHROMATE TO 40 KBAR

CARL W. F. T. PISTORIUS and ELIEZER RAPOPORT

Chemical Physics Group of the National Physical and National Chemical Research Laboratories,
South African Council for Scientific and Industrial Research, P.O. Box 395, Pretoria, South Africa

(*Received* 7 *May* 1968)

Abstract – Phase transitions of K_2SO_4, K_2SeO_4 and K_2CrO_4 have been studied to 30–40 kbar by means of differential thermal analysis. The first-order transition temperatures increase with pressure from room-pressure values of 584°, 476° and 688·5°C with initial slopes of 18·3, 22·7 and 22·1 deg/kbar, respectively. The transition lines of K_2SO_4 and K_2CrO_4 appear to have triple points at 22·6 kbar, 996° and 16·6 kbar, 994°, respectively, with the appearance of new high-temperature phases. The analysis of earlier high-temperature X-ray results on the thermal expansion of K_2CrO_4 suggests strongly that the inversion at 668·5°C is preceded by second-order changes in the range 300–550° as in the case of K_2SO_4.

INTRODUCTION

THE CRYSTAL chemistry of X_2YO_4 substances has been fairly thoroughly studied and correlated at atmospheric pressure[1]. At elevated pressures a single extended phase diagram appears to be sufficient to describe the polymorphism of Na_2SO_4, Na_2CrO_4[2] and Na_2SeO_4[3], and the polymorphism of the corresponding silver salts[4] is closely related to that of the sodium salts. The lithium salts[5], on the other hand, have phase diagrams without any obvious relationship to the other salts studied, and there is comparatively little resemblance even among the phase diagrams of the lithium salts themselves. The corresponding potassium salts have not yet been studied under pressure, except for brief reports on the polymorphism of K_2SO_4 to 1000 bar[6] in hydrostatic apparatus, and the polymorphism of K_2CrO_4 using uniaxial apparatus[7]. However, it is now recognized that results obtained in uniaxial apparatus are not reliable unless quite elaborate calibration procedures are carried out[8, 9].

The orthorhombic pseudohexagonal room-temperature modification of K_2SO_4 has been studied by Robinson[10]. It belongs to the space group D_{2h}^{16}-Pnma, with a unit cell of $a_0 = 7{\cdot}46$, $b_0 = 5{\cdot}773$, $c_0 = 10{\cdot}07$ Å[11]. The atomic arrangement is not close-packed, and bears no relationship to the superficially similar chrysoberyl structure[12, 13]. At 583–586°[6, 14–17] a transition occurs to hexagonal K_2SO_4 I. The space group of K_2SO_4 I had been the subject of some controversy, but recently[18] was shown to be D_{3d}^3-P3m1, with $a_0 = 5{\cdot}788$, $c_0 = 7{\cdot}93$ Å at 615°C. In addition to this major structural transformation, recent thermal and dilatometric studies on orthorhombic K_2SO_4 II have provided evidence for higher-order transitions at ~ 300°C, ~ 350°C, ~ 450°C and possibly at ~ 390°[6, 15–17]. These changes are observable as irregularities in the thermal expansion, but are also suggested in DTA studies[6]. Their exact nature is unknown at present, but it would appear possible that K_2SO_4 II just below the 584°C transition is not orthorhombic any more[6].

K_2SeO_4 II at room temperature belongs to the same space group as K_2SO_4 II, but with a unit cell of $a_0 = 7{\cdot}66$, $b_0 = 6{\cdot}00$, $c_0 = 10{\cdot}47$ Å [19]. The transition to probably hexagonal K_2SeO_4 I occurs at 472°C[19].

K_2CrO_4 II at room temperature also belongs to the space group D_{2h}^{16}-Pnma, with $a_0 = 7{\cdot}663$, $b_0 = 5{\cdot}919$, $c_0 = 10{\cdot}391$ Å[7]. The transition to K_2CrO_4 I occurs at 665–671°C[20, 21].

K_2CrO_4 I is hexagonal with $a_0 = 6{\cdot}125$, $c_0 = 8{\cdot}245$ Å at 705°C[7]. The space group is probably the same[7] as for K_2SO_4 I, i.e. D^3_{3d}-$P\bar{3}m1$. Three further forms in the pressure range to 100 kbar were suggested on the basis of resistance studies in uniaxial apparatus[7], but the observed effects were more probably due to recrystallization[22] or to the effect of impurities.

EXPERIMENTAL PROCEDURES

Analytical reagent grade K_2SO_4 and K_2CrO_4 with a certified purity of 99·8 per cent were obtained from Merck. K_2SeO_4 was obtained from Hopkin and Williams Ltd. with reported purity of 99 per cent.

Pressures up to 40 kbar were generated in a piston-cylinder device[23]. The furnace assembly was similar to that used by Klement *et al.*[24]. Phase changes were detected by means of differential thermal analysis (DTA) using Chromel/Alumel (for K_2SeO_4) or platinum/platinum-10 per cent rhodium-thermocouples (for K_2SO_4 and K_2CrO_4). Corrections were made for the effect of pressure on the thermocouples[25]. The salts were contained in nickel or stainless steel capsules which incorporated thermocouple wells[26]. Typical DTA signals obtained are shown in Fig. 1. In the case of K_2SeO_4 some reaction with the capsule material occurred. Post-mortem examination showed that it was limited to the edge of the sample touching the capsule. This slightly broadened the beginning of the DTA signals, but when the uncontaminated bulk of the sample subsequently transformed, a sharp reversal of the DTA curve still occurred. K_2CrO_4 became greenish in colour after lengthy exposure to temperatures above ~ 1000°C in nickel capsules, but not in stainless steel. This effect is apparently due to reduction of Cr^{6+} to Cr^{4+} or Cr^{3+}[27]. Most of the points were therefore discarded, and only the first few points above 1000°C obtained in any run were used. Each phase diagram was based on 3–6 separate runs, the results of which were consistent. The heating rate was in the range 1–3°C/second. Sliding friction was determined by comparing results obtained on increasing and on decreasing pressure. At the temperatures of this study there were no non-symmetrical pressure losses[28]. The pressures are believed accurate to better than ±0·5–1·0 kbar. The points plotted represent the mean of heating and cooling cycles.

RESULTS AND DISCUSSION

Potassium sulphate

The phase diagram of K_2SO_4 is shown in Fig. 2. The II/I transition yielded sharp but small DTA signals (Fig. 1(i)), with 2–7°C thermal hysteresis. The present results are in excellent agreement with the points of Majumdar and Roy[6] to 1000 bar. The transition line rises linearly with pressure to 22·6 kbar, 996°C, where the slope changes sharply from 18·35°C/kbar to 13·5°C/kbar. There is no marked change in the nature of the DTA signals at this point, but we nevertheless suggest that the change of slope indicates a splitting of the II/I phase boundary and appearance of K_2SO_4 III as indicated in Fig. 2. No DTA signals corresponding to the postulated I/III phase transition could be observed. The phase relations of K_2SO_4 are summarized in Table 1. The transition lines were fitted by means of least-squares.

The heat of transition corresponding to K_2SO_4 II → I is 2140 cal/mole[29]. This transition is among the very few for which the thermochemical heat data are most dependable. Using the observed slope of $18{\cdot}35 \pm 1\ 1$ deg/kbar, and applying the Clapeyron relation, the volume change is found to be

$$\Delta v_{II/I} = 1{\cdot}92 \pm 0{\cdot}12 \ \text{cm}^3/\text{mole}$$

in gross disagreement with the value of 1·01 cm³/mole obtained from high-temperature X-ray measurements on the basis of a uniform orthorhombic indexing from 30–580°C. The present results therefore confirm

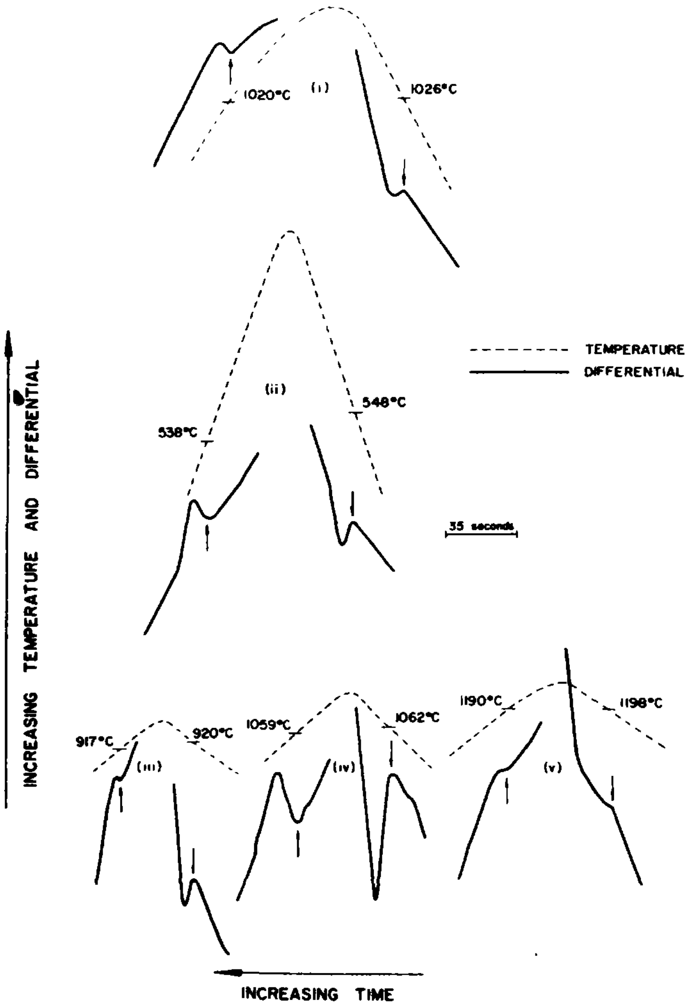

Fig. 1. Typical DTA signals obtained. (i) K_2SO_4 II/III at 24·8 kbar. (ii) K_2SeO_4 II/I at 3·1 kbar. (III) K_2CrO_4 II/I at 12·7 kbar. (iv) K_2CrO_4 II/III at 20·9 kbar. (v) K_2CrO_4 III/I at ~ 18·7 kbar.

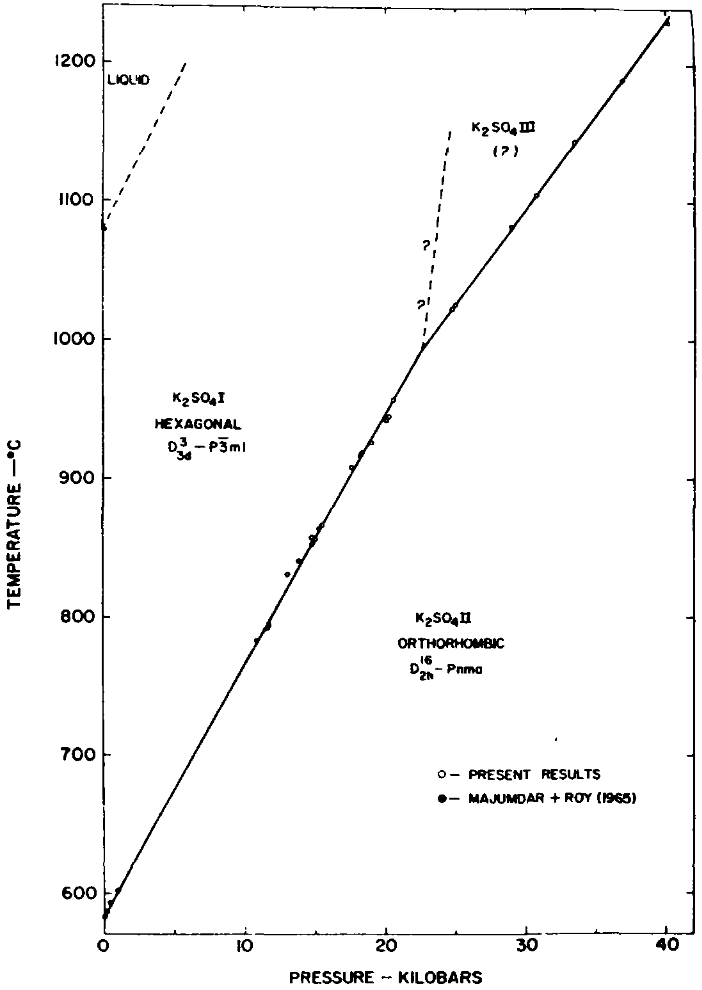

Fig. 2. Phase diagram of K_2SO_4 to 40 kbar.

Table 1. *Phase behaviour of* K_2SO_4, K_2SeO_4 *and* K_2CrO_4

Transition line	Fit	Standard deviation
K_2SO_4 II/I	$t(°C) = 584 + 18{\cdot}25P$	3·3°C
K_2SO_4 II/III	$t(°C) = 996 + 13{\cdot}5(P - 22{\cdot}6)$	1·4°C
K_2SeO_4 II/I	$t(°C) = 476 + 22{\cdot}65P - 0{\cdot}150P^2$	2·8°C
K_2CrO_4 II/I	$t(°C) = 668{\cdot}5 + 22{\cdot}14P - 0{\cdot}170P^2$	3·2°C
K_2CrO_4 II/III	$t(°C) = 994 + 15{\cdot}5(P - 16{\cdot}6)$	3·2°C
K_2CrO_4 I/III	$P = 16{\cdot}6 + 0{\cdot}0083(t - 994)$	0·48 kbar

Majumdar and Roy's[6] conclusion that K_2SO_4 II at ~ 580°C differs crystallographically from the phase stable at room temperature. We did not succeed in observing the second-order changes at ~ 300°C, ~ 350°C and ~ 450°C by means of high-pressure DTA.

Potassium selenate

The phase boundary of K_2SeO_4 is shown in Fig. 3. The II/I transition also yielded sharp but small DTA signals (Fig. 1(ii)), with 1–9°C thermal hysteresis. Our present room-pressure point is 476 ± 2°C, being the mean of 12 determinations, as compared to the literature value of 472°C[19]. The transition line rises with pressure with an initial slope of 22·65 ± 0·8 deg/kbar, but shows some curvature at higher pressures. It could not be followed beyond 30·7 kbar, 1026°C due to reaction of the sample with all the capsule materials tried. Up to this point there is no evidence of a sudden slope change as in the case of K_2SO_4. The analytical expression of the phase boundary is given in Table 1.

Potassium chromate

The phase diagram of K_2CrO_4 is shown in Fig. 4. The II/I transition (Fig. 1(iii)) had a thermal hysteresis varying between 1–6°C. Our present room-pressure point is 668·5 ± 3°C, being the average of 6 determinations. The II/I transition line rises with almost exactly the same initial slope and curvature as the K_2SeO_4 II/I transition line (Table 1) up to 16·6 kbar, 994°C, where the slope of the transition line as well as the signals change markedly (Fig. 1(iv)). A search of the high-temperature region near this pressure revealed smeared-out DTA signals of poor quality (Fig. 1(v)) which were nevertheless reproducible and consistent, and could be ascribed to a transition K_2CrO_4 I/III which is the counterpart of the K_2SO_4 I/III transition postulated above. The K_2CrO_4 I/III transition temperature increases very rapidly with pressure. The II/III transition has a thermal hysteresis of only 1–3°C, and is linear in the present pressure range.

The thermal expansion coefficients of K_2CrO_4 II[7] are closely similar to the corresponding coefficients for K_2SO_4 II[6]. In particular, the irregularities in the thermal expansion of the b_0 parameter (in Pnma orientation) found for K_2SO_4 II are also present in the case of K_2CrO_4 II, although they were not originally recognized as such. This shows that there is at least one, and possibly more, second-order changes below the K_2CrO_4 II/I transition at room pressure. As in the case of K_2SO_4, the volume change of the K_2CrO_4 II/I transition determined from an orthorhombic indexing of the high-temperature diffraction patterns can therefore not be correct. However, the heat of transition has not been determined very well. The two values in the literature, viz. 1·7[21] and 2·44[20] kcal/mole, respectively, are in bad agreement. Using these values together with the observed initial slope of 22·14 ± 1·2 deg/kbar, we find

$$\Delta v_{II/I} = 1{\cdot}68 \text{ or } 2{\cdot}4\ \mathrm{cm^3/mole}$$

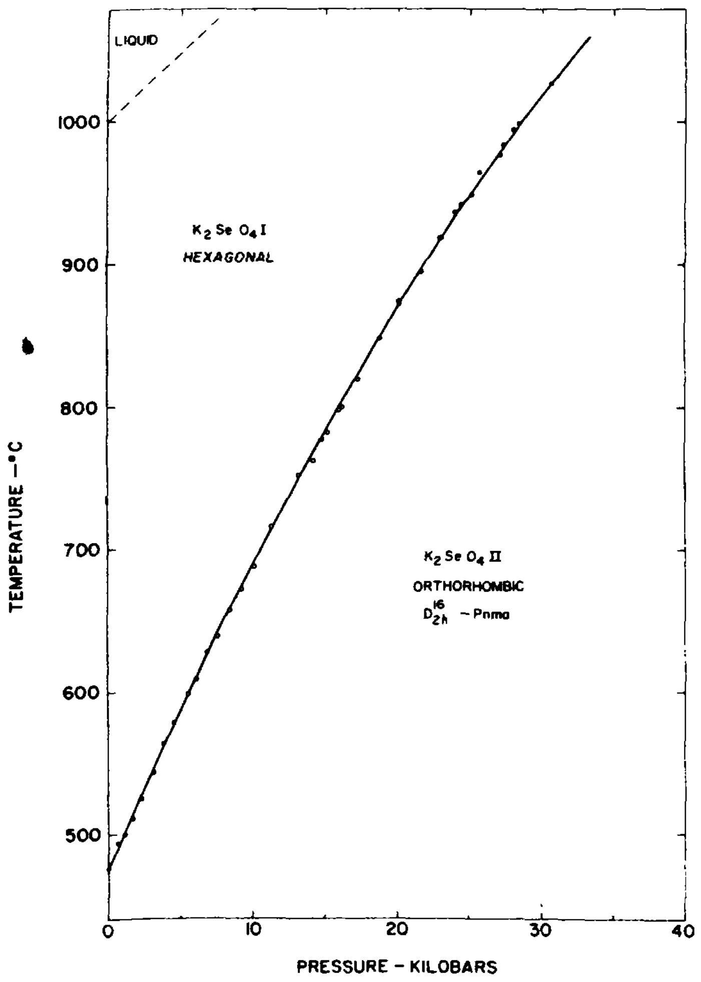

Fig. 3. Transition line of K_2SeO_4 to 32 kbar.

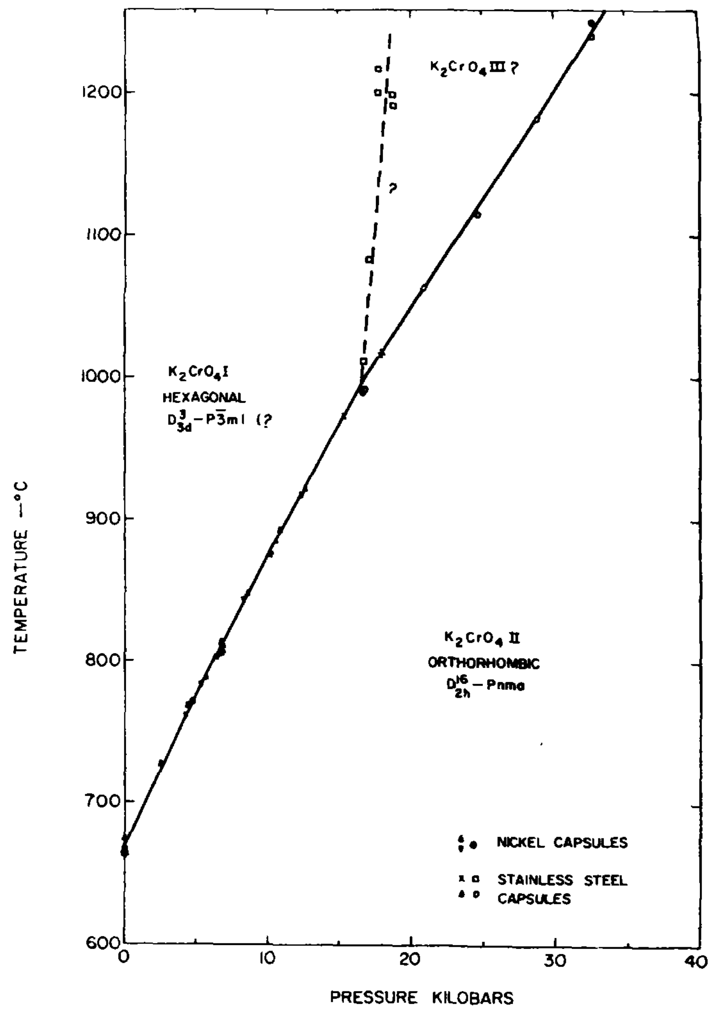

Fig. 4. Phase diagram of K_2CrO_4 to 32 kbar.

respectively. The probably unreliable diffractometric value is 1·9 cm^3/mole.

The initial slope of the II/I transition observed in the uniaxial apparatus[7] was ~ 8 deg/kbar. This low value can be ascribed partly to overestimation of pressure, and partly to contamination of the very small samples during the experiments.

CONCLUSION

The phase diagrams of K_2SO_4, K_2SeO_4 and K_2CrO_4 are very similar. A phase corresponding to K_2SO_4 III and K_2CrO_4 III may be expected in the phase diagram of K_2SeO_4 at higher pressures. The structures of these new phases are not known at present, but in view of the similarity in behaviour of the II/I and II/III transition lines in every case it is probable that the phases III are structurally not very different from the phases I. $LiKSO_4$[30, 31] has a structure closely related to those of glaserite or K_2SO_4 I. It is hexagonal, space group C_6^6-$P6_3$, and has a unit cell of the same shape as that of K_2SO_4 I. In fact, the positions of half the cations and of the sulphur atoms would be the same in the two structures if $u(S)$ were 0·25 instead of 0·17 in the $LiKSO_4$ structure. It is therefore entirely possible that K_2SO_4 III and K_2CrO_4 III may also be hexagonal, but with the $LiKSO_4$ structure instead of a glaserite-like structure.

A comparison of the phase diagrams of K_2SO_4 and K_2CrO_4 with those of Na_2SO_4 and Na_2CrO_4[2] is instructive. The high-temperature phases Na_2SO_4 I and Na_2CrO_4 I are hexagonal, and probably isostructural[18] with K_2SO_4 I and K_2CrO_4 I. Na_2SO_4 III and Na_2CrO_4 II are orthorhombic, space group D_{2h}^{17}-Cmcm[32] and have structures somewhat similar to that of K_2SO_4 II. At higher pressures the Na_2SO_4 III/I and Na_2CrO_4 II/I transition lines each splits into two with the appearance of Na_2SO_4 VII and Na_2CrO_4 IV, which were suggested to be isostructural. The Na_2SO_4 VII/I and Na_2CrO_4 IV/I transition lines behave in a somewhat similar fashion as the K_2SO_4 II/I and K_2CrO_4 II/I lines in that there are slope changes at higher pressures with the appearance of new, possibly hexagonal, hightemperature phases Na_2SO_4 VIII and Na_2CrO_4 V. If such a similarity is real, it would imply that Na_2SO_4 VII and Na_2CrO_4 IV may have the K_2SO_4 II structure. Gattow [1] has shown that, for the ionic radii of Na_2SO_4, the K_2SO_4 II structure is slightly denser than the Na_2SO_4 III(V) structures, and can therefore be expected to occur as a high-pressure form.

Acknowledgements—The least-squares calculations were carried out on the IBM System 360 of the National Research Institute for Mathematical Sciences. The authors would like to thank Mrs Martha C. Pistorius for writing the computer programs and Mr J. B. Clark for assistance with some of the experimental work. Mr J. Erasmus and his staff and Mr G. O'Grady and his staff kept the equipment in good repair, and were responsible for the manufacture of the furnace parts. A portion of this work was carried out in Professor George C Kennedy's high-pressure laboratory and the authors are grateful for the use of laboratory equipment.

REFERENCES

1. GATTOW G., *Z. anorg. allg. Chem.* **333**, 134 (1964).
2. PISTORIUS C. W. F. T., *J. chem. Phys.* **43**, 2895 (1965).
3. PISTORIUS C. W. F. T., *J. Phys. Chem. Solids* **28**, 449 (1967).
4. PISTORIUS C. W. F. T., *J. chem. Phys.* **46**, 2167 (1967).
5. PISTORIUS C. W. F. T., *J. Phys. Chem. Solids* **28**, 1811 (1967).
6. MAJUMDAR A. J. and ROY R., *J. phys. Chem.* **69**, 1684 (1965).
7. PISTORIUS C. W. F. T., *Z. phys. Chem.* **35**, 109 (1962).
8. KITAHARA S., TAKENOUCHI S. and KENNEDY G. C., *Am. J. Sci.* **264**, 223 (1966).
9. KLEMENT W. and JAYARAMAN A., *Prog. solid State Chem.* **3**, 289 (1966).
10. ROBINSON M. T., *J. phys. Chem.* **62**, 925 (1958).
11. BERNARD M. and HOCART R., *Bull. Soc. fr. Miner. Cristallogr.* **84**, 306 (1961).
12. BRAGG W. L. and BROWN G. B., *Proc. R. Soc.* **110A**, 34 (1926); *Z. Kristallogr.* **63**, 122 (1926).
13. FARRELL E. F., FANG J. H. and NEWNHAM R. E., *Am. Miner.* **48**, 804 (1963).
14. BREDIG M. A., *J. phys. Chem.* **46**, 747 (1942).
15. BERNARD M. and JAFFRAY J., *C. r. hebd. séanc. Acad. Sci. (Paris)* **240**, 1078 (1955).
16. MOREAU R., *Bull. Soc. Roy. Sci. Liège* **32**, 252 (1963).

17. PANNETIER G. and GAULTIER M., *Bull. Soc. chim. Fr.* 1069 (1966).
18. PANNETIER G. and GAULTIER M., *Bull. Soc. chim. Fr.* 188 (1966).
19. GATTOW G., *Acta crystallogr.* **15**, 419 (1962).
20. HARE A., *Phil. Mag.* **48**, 412 (1924).
21. RICCARDI R. and SINISTRI C., *Ricerca Sci.* **8**, 1026 (1965).
22. PISTORIUS C. W. F. T., *Z. Kristallogr.* **116**, 220 (1961).
23. KENNEDY G. C. and LAMORI P. N., In *Progress in Very High Pressure Research* (Edited by F. P. Bundy, W. R. Hibbard and H. M. Strong). Wiley, New York (1961).
24. KLEMENT W. Jr., COHEN L. H. and KENNEDY G. C., *J. Phys. Chem. Solids* **27**, 171 (1966).
25. HANNEMAN R. E. and STRONG H. M., *J. appl. Phys.* **36**, 523 (1965); *idem. ibid.* **37**, 612 (1966).
26. PISTORIUS C. W. F. T., *J. Phys. Chem. Solids* **26**, 1543 (1965).
27. KAWAI N., SAWAOKA A., KIKUCHI S. and TAMAGAWA N., *Jap. J. appl. Phys.* **6**, 1397 (1967).
28. PISTORIUS C. W. F. T., RAPOPORT E. and CLARK J. B., *Rev. Sci. Instrum.* **38**, 1741 (1967).
29. SHOMATE C. H. and NAYLOR B. F., *J. Am. chem. Soc.* **67**, 72 (1945).
30. BRADLEY A. J., *Phil. Mag.* **49**, 1225 (1925).
31. FISCHMEISTER H. F., *Monatsh. Chem.* **93**, 420 (1962).
32. NIGGLI A., *Acta crystallogr.* **7**, 776 (1954).

J. Phys. Chem. Solids Pergamon Press 1969. Vol. 30, pp. 203–209. Printed in Great Britain.

MIXED MAGNETIC SYSTEMS: A MODEL WITH APPLICATION TO $(1-x)\text{CdCr}_2\text{S}_4 \cdot x\text{CdCr}_2\text{Se}_4$

H. A. BROWN
Physics Department, University of Missouri at Rolla, Rolla, Missouri, U.S.A.

(*Received* 6 *May* 1968)

Abstract—The Curie temperatures and asymptotic Curie temperatures are calculated for mixed magnetic systems by a semi-classical Bethe–Peierls–Weiss cluster approach. The systems are typified by $(1-x)\text{CdCr}_2\text{S}_4 \cdot x\text{CdCr}_2\text{Se}_4$ in which the substitution changes the anions but not the magnetic cations. It is found that next-nearest-neighbor interactions are needed to match the data but that, with them, excellent agreement can be obtained for a reasonably unique choice of the exchange integrals.

1. INTRODUCTION

THERE ARE many substances in which there is an exchange interaction between magnetic ions which takes place by way of some intervening ions whose type can be varied. In these cases, there is an interaction between a fixed number of magnetic ions, but the strength (and possibly the sign) of the interaction can change with the composition of the intervening ions which are responsible for transmitting the interaction. It is the purpose of this paper to suggest a simple model which may be of use in interpreting the behavior of these substances. Application of the model is made to the ferromagnetic chromium chalcogenide spinel system[1]:

$$(1-x)\text{CdCr}_2\text{S}_4 \cdot x\text{CdCr}_2\text{Se}_4.$$

2. THE MODEL

Let our system consist of only one kind of magnetic ion, but let there be two exchange integrals between neighboring pairs, J_1 and J_2. These two represent the pertinent exchange integrals for the two pure substances of which our system is a mixture.

A plausible Hamiltonian for the Bethe[2] cluster will then include the interaction of the central atom (spin S_0) with its n nearest neighbors (NNs) of which n_1 are reached by way of ions that produce an interaction J_1 and n_2 that produce J_2. Then, with applied field H_0 and internal field H_1, the cluster Hamiltonian can be written:

$$H = -2J_1 S_0 \cdot \sum_1^{n_1} S_i - 2J_2 S_0 \cdot \sum_1^{n_2} S_i - g\beta H_0 \cdot S_0 - g\beta H_1 \cdot \sum_1^{n} S_i \qquad (1)$$

where $n_1 + n_2 = n$ is the coordination number. In this Hamiltonian, interactions between the NNs themselves are supposed not to exist.

If we now make the classical spin approximation[3], the partition function can be written as

$$Z = \int P_1{}^{n_1} P_2{}^{n_2} \, e^{cz} \, d\Omega_0 \qquad (2)$$

where

$$P_i = \int e^{b_i \eta_i + a\nu_i} \, d\Omega_i \qquad (3)$$

$$b_i = \frac{2J_i S^2}{kT} \qquad (4)$$

$$a = \frac{g\beta H_1 S}{kT} \qquad (5)$$

$$c = \frac{g\beta H_0 S}{kT} \qquad (6)$$

$$\begin{aligned} \eta_i &= \cos(S_0, S_i) \\ \nu_i &= \cos(S_i, H_1) \\ \nu_0 &= \cos(S_0, H_0) \end{aligned} \qquad (7)$$

with H_0 and H_1 chosen to be along the z-axis and $d\Omega_i$ an element of solid angle in the direction S_i. We then find

$$\begin{aligned}\ln Z &= n_1 \ln\alpha_1 + n_2 \ln\alpha_2 \\ &\quad + \frac{c^2}{6} + (n_1L_1 + n_2L_2)\frac{ac}{3} \\ &\quad + (n_1Q_1 + n_2Q_2 + 2n_1n_2L_1L_2)\frac{a^2}{6} \qquad (8)\end{aligned}$$

to second order in the fields. Here

$$\alpha_i = \frac{\sinh b_i}{b_i} \qquad (9)$$

$$L_i = \frac{\alpha_i'}{\alpha_i} = \coth b_i - \frac{1}{b_i} \qquad (10)$$

$$Q_i = (n_i - 1)L_i^2 + 1. \qquad (11)$$

From (8), the magnetizations of the central atom, m_0, and one of its neighbors, m_1, are obtained from

$$\frac{\partial \ln Z}{\partial c} \quad \text{and} \quad \frac{1}{n}\frac{\partial \ln Z}{\partial a}.$$

Equating these two for consistency gives the equation which locates the Curie temperature, T_c, for zero applied field:

$$n_1Q_1 + n_2Q_2 + 2n_1n_2L_1L_2 - n(n_1L_1 + n_2L_2) = 0. \qquad (12)$$

(For an antiferromagnetic, the consistency condition is $m_0 = -m_1$. Since L is an odd function of J, this results in the same equation for T_c.)

The susceptibility is obtained from m_0/c and turns out to be (for both ferro- and antiferromagnetics):

$$\chi = \frac{(g\beta S)^2}{3kT} \cdot \frac{n_1Q_1 + n_2Q_2 + 2n_1n_2L_1L_2 - (n_1L_1 + n_2L_2)^2}{n_1Q_1 + n_2Q_2 + 2n_1n_1L_1L_2 - n(n_1L_1 + n_2L_2)}. \qquad (13)$$

For temperatures well above T_c, this approaches the Curie–Weiss law:

$$\chi = \frac{C}{T - \theta} \qquad (14)$$

$$\theta = \frac{2S^2}{3k}(n_1J_1 + n_2J_2). \qquad (15)$$

If $n_1 = nx$ and $n_2 = n(1-x)$, we have a linear relation between the asymptotic Curie temperature and the composition variable, x. This high-temperature limit is known to be well described by the cluster approximation from the agreement of the first few terms of the series expansion method and the cluster method when expanded in powers of J/kT. In this limit the results of the molecular field theory are obtained, i.e. the asymptotic Curie temperatures of the cluster model are the Curie temperatures of the molecular field theory applied to the same model.

If, for $x = 1$, we call the asymptotic Curie temperature $\theta(1)$, and for $x=0$, $\theta(0)$, we see that

$$\frac{\theta(1)}{\theta(0)} = \frac{J_1}{J_2}. \qquad (16)$$

In these two limiting cases of pure substances we find that (12) reduces to:

$$L(b_c) = \frac{1}{n-1} \qquad (17)$$

so that the two roots for b_c are the same, which means

$$\frac{T_c(1)}{T_c(0)} = \frac{J_1}{J_2}. \qquad (18)$$

We also find, on solving (12) for T_c as a function of x, a nearly linear relation between them, essentially the same as $\theta(x)$ in (15).

2.1 To make the model a little more general and to remove the requirement that

$$\frac{\theta(1)}{\theta(0)} = \frac{T_c(1)}{T_c(0)} \qquad (19)$$

imposed by (16) and (18), we consider the following extension: Suppose that the interaction between two magnetic ions goes by way of *two* of the ions whose composition we are varying. This apparently is the case, e.g. in the ferrospinel system

$$(1-x)\mathrm{CdCr_2S_4} \cdot x\mathrm{CdCr_2Se_4}$$

each Cr ion (on the B-sites) interacts with its NN Cr through two anions (S or Se). There are then three possible effective exchange integrals; J_1 when both anions are Se, J_2 when one is Se and one S, and J_3 when both are S. Our Hamiltonian (1) is now modified by the addition of the term

$$-2J_3S_0\cdot\sum_1^{n_3}S_i$$

where

$$\begin{aligned} n_1 &= nx^2 \\ n_2 &= 2nx(1-x) \\ n_3 &= n(1-x)^2 \end{aligned} \qquad (20)$$

and

$$n_1+n_2+n_3=n,$$

assuming the anions are distributed randomly. The partition function is then

$$Z=\int P_1^{n_1}P_2^{n_2}P_3^{n_3}\,\mathrm{e}^{c\nu_0}\,\mathrm{d}\Omega_0 \qquad (21)$$

from which we find the equation for T_c to be

$$\sum n_iQ_i+\sum_{i>j}2n_in_jL_iL_j-n\sum n_iL_i=0$$
$$(i,\ j=1,\ 2,\ 3) \qquad (22)$$

and the asymptotic Curie temperature is

$$\theta=\frac{2S^2}{3k}(n_1J_1+n_2J_2+n_3J_3). \qquad (23)$$

To investigate these equations we must make some assumptions about the J's. It seems most reasonable to assume that

$$J_2=\tfrac{1}{2}(J_1+J_3). \qquad (24)$$

If we do this, we find that (23) reduces to a linear equation identical with (15):

$$\theta=\frac{2nS^2}{3k}(J_1x+J_3(1-x)). \qquad (25)$$

Also, in the region of small b, when L is linear, (24) implies that $L_2=\tfrac{1}{2}(L_1+L_3)$. In that case (22), which is a quartic in x, reduces to a quadratic, the coefficients of x^4 and x^3 vanishing identically, and the behavior of T_c with x is again almost linear, much like that of θ in (25), except that $\theta/T_c\simeq 1{\cdot}25$. Unless the variation of J_2 with x is left arbitrary, the theory will be inadequate to explain anything but linear results for $T_c(x)$, and nearly constant values of θ/T_c. As we shall see, the necessary generalization of the theory is to include more distant exchange interactions.

2.2 It has been suggested[1] that next-nearest-neighbor (NNN) interactions are present and that these might be weakly antiferromagnetic. We can roughly include these by adding to the Hamiltonian the terms:

$$-2J_4S_0\cdot\sum_1^{n_4}S_i-g\beta H_2\cdot\sum S_i \qquad (26)$$

when J_4 is the NNN exchange integral and H_2 is the internal field acting on the NNN atoms of which there are n_4. The partition function is now:

$$Z=\int P_1^{n_1}P_2^{n_2}P_3^{n_3}P_4^{n_4}\,\mathrm{e}^{c\nu_0}\,\mathrm{d}\Omega_0, \qquad (27)$$

and there are two consistency conditions:

$$m_0=m_1=m_2 \qquad (28)$$

to eliminate the two internal fields. The Curie temperature equation that results from this is

$$\left[\sum_i n_i(n_i-1)L_i^2+\sum_{i>j}2n_in_jL_iL_j-n\sum n_iL_i+n\right]$$
$$\times(1+L_4)+(\sum n_iL_i^2-n)n_4L_4$$
$$=0\ i,j=1,2,3 \qquad (29)$$

while the asymptotic Curie temperatures are

$$\theta=\frac{2S^2}{3k}(n_1J_1+n_2J_2+n_3J_3+n_4J_4). \qquad (30)$$

Before calculating T_c from (29), values must be chosen for n_4, and the ratio of J_4 to, say, J_3. If the substitution proceeds without affecting the atoms producing the NNN exchange, n_4 and J_4 will be constants, independent of x. If not, we will have to know how many exchange paths there are to each NNN, and how many of the substitution sites are in each path. We would then know how many different types of exchange interactions are needed to replace J_4 and how their relative numbers depend on x. Now, the NNN exchange mechanism is apparently not known with certainty so the required information is lacking. In view of this, and because of the probable relative smallness of J_4, we simplify the problem by replacing J_4 by $\bar{J}(x)$ which depends on x in some reasonable way (linear, quadratic, etc.), once the details of the NNN exchange paths are assumed. The coordination number, n_4, is then a constant.

The solution of (29) is then effected by assigning the ratios $J_1:J_3:J_4$, (J_2 is fixed by (24)), evaluating the n_i for a given x and finding a compatible solution for $L_{1,2,3,4}$.

The end points of the curves are considerably simpler to find. For $x = 0$ and 1, we find from (29)

$$L_4 = \frac{1-(n-1)L_i}{(n_4-1)+(n_4+n-1)L_i} \tag{31}$$

where $L_i = L_3$ and L_1, respectively.

3. APPLICATIONS AND CONCLUSIONS

We let

$$J_1 = J_0(1+\alpha x+\beta x^2) \tag{32}$$

and employ equations (20) and (24) in solving (29) and (30) for T_c and θ. The results obtained using arbitrarily chosen parameters are shown in Figs. 1–6. In all cases we have taken $n = 6$ and $n_4 = 30$ and $J_1:J_2:J_3 = 1{\cdot}4:1{\cdot}2:1{\cdot}0$. In Figs. 1 and 2, J_3/J_0 is −20; in Figs. 3 and 4 it is −40; and in Figs. 5 and 6 it is +20. For the negative ratios, the magnitude must be greater than about 18·5 or there is no transition. (Near this critical value, T_c falls rapidly because of the competing NN and NNN interactions.) Increasing the magnitude of J_1/J_3 increases the value of $T_c(1)/T_c(0)$, but rather slowly for positive ratios J_3/J_0. For fixed $\alpha+\beta$, the end points of the curves are the same, but not their shapes, and we see that the end points are rather sensitive to the value of the sum.

The variety of curves obtained by varying only J_3/J_0, α and β make it seem hopeful that a variety of experimental data can be matched and that, if all the parameters are not totally unknown, this match may be for a restricted set – or even a unique choice – of parameters.

We have attempted to match the experimental data[4] for

$$(1-x)\mathrm{CdCr_2S_4}\cdot x\mathrm{CdCr_2Se_4}$$

assuming $n = 6$ and $n_4 = 30$. This leaves four parameters to adjust; the three just mentioned and J_1/J_3. The measured value of θ/T_c at $x = 0$ fixes J_3/J_0 and at $x = 1$ provides a relation between J_1/J_0 and $\alpha+\beta$. The value of $T_c(0)/T_c(1)$ leads to another relation between these same two quantities. The two are adjusted to provide a satisfactory match to the end-points of the curves while α and β are varied, their sum constant, to obtain the correct shapes of the curves. In this way, we obtain the results shown in Fig. 7. Here we have plotted the solutions of equations (29) and (30) for the parameters that gave an optimal fit, viz.,

$$J_1 = 16{\cdot}96°\mathrm{K}$$
$$J_3 = 13{\cdot}94°\mathrm{K}$$
$$J_0 = -0{\cdot}691°\mathrm{K}$$
$$\alpha = 0{\cdot}520$$
$$\beta = -0{\cdot}520$$

and

$$J_2 = \tfrac{1}{2}(J_1+J_3) = 15{\cdot}45°\mathrm{K}.$$

The agreement of these curves and the data is seen to be excellent. In view of the inadequacies of our model, the precise numerical values here may be of less significance than their relative values and, as mentioned below, the x-dependence of the effective exchange integrals. That is, the ratios of these J's will give $T_c(x)$ and $\theta(x)$ curves of the correct shape, the actual values of the J's will properly normalize these curves to the data.

Also shown in the figure are the curves that result if the parameters are changed (the dashed curves). It is seen that a 3 or 4 per cent change in J_1 or J_3 produces a noticeable change in the result for $T_c(x)$ or θ/T_c. Although not shown, a similar change in J_0 has a similar effect. On the other hand, $\theta(x)$ is not nearly so sensitive as this, as one would infer from (30). Changing the value of $\alpha+\beta$ is also not very critical, although it too affects T_c more than θ. The effect on the latter of a

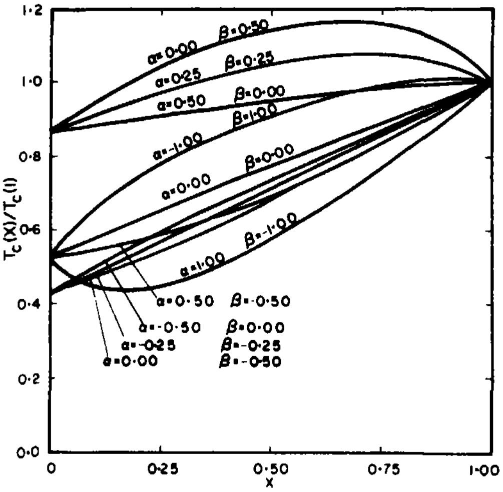

Fig. 1.

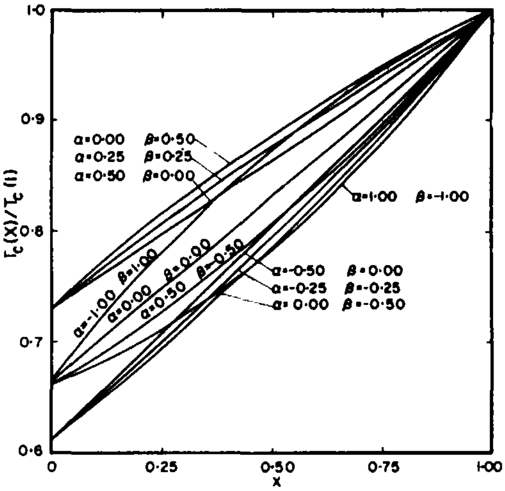

Fig. 3.

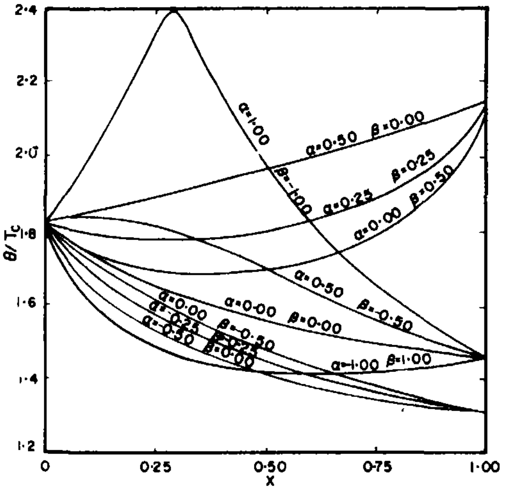

Fig. 2.

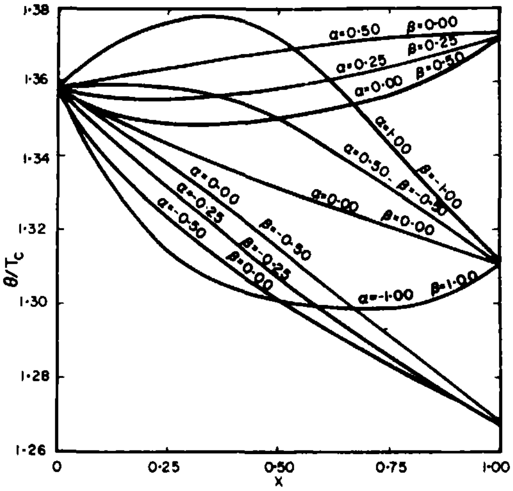

Fig. 4.

change of about 20 per cent in α and β is shown in the figure.

Finally the effect of changing the NNN coordination number, n_4, from 30 to 24 or 36 was investigated. It was found that the major change was in J_0, but that n_4J_0 stayed constant to within about 3 per cent. This is gratifying because J_0 is really an average of the several different types of NNN interaction whose total number is n_4. It is fortunate, therefore, that the theory is not sensitive to the value of n_4J_0.

In matching the θ and T_c data at $x = 0$ and 1, we found the following four sets of parameters were satisfactory:

J_1	J_3	J_0	$\alpha+\beta$	$\theta(\frac{1}{2})$
−11	−8·7	3·8	0·3	53
−11	14	−0·7	−8·5	96
17	−8·7	3·8	−1·2	45
17	14	−0·7	0	170

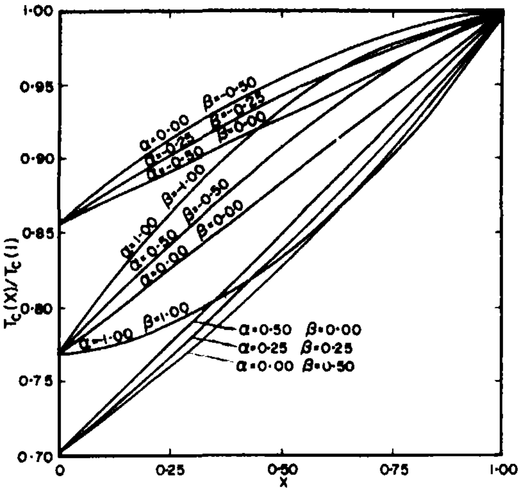

Fig. 5.

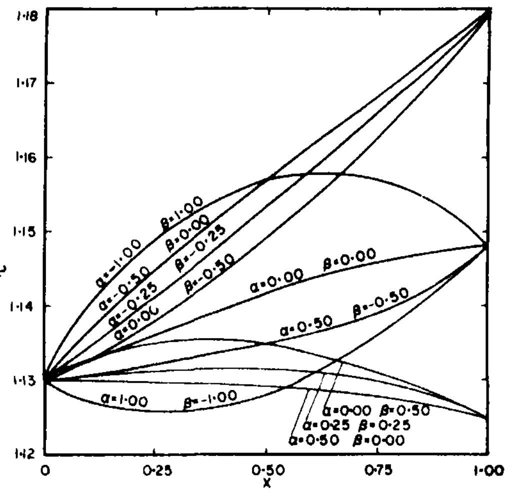

Fig. 6.

Fig. 1–6. Calculated values of the reduced transition temperatures, $T_c(x)/T_c(1)$, and the ratio of the asymptotic to the actual transition temperatures, $\theta(x)/T_c(x)$, vs. the composition, x. The curves were calculated from equations (29) and (30) and are meant to apply to no particular substance. The choice of the parameters is discussed in the text. In Fig. 1 and 2, J_3/J_0 is −20, in 3 and 4 it is −40 and in 5 and 6, +20.

However, only the last set gave a reasonable fit elsewhere as shown, for example, by the value of θ at $x = \frac{1}{2}$ given in the last column. The measured value is 180°K.

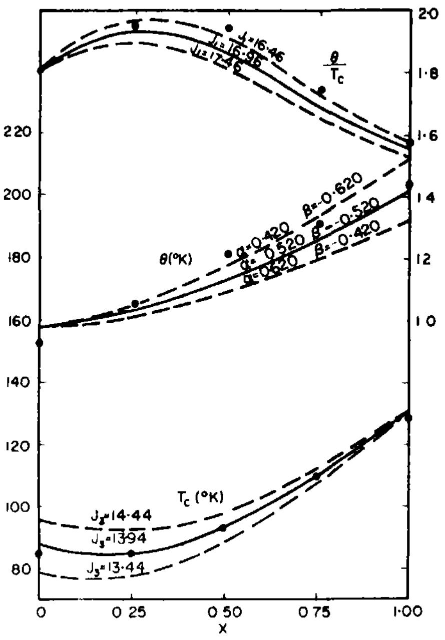

Fig. 7. Calculated values of T_c, θ and θ/T_c vs. x. The isolated points refer to the data on $(1-x)\mathrm{CdCr_2S_4}\cdot x\mathrm{CdCr_2Se_4}$ from reference [4]. The parameters for the theoretical curves are discussed in the text.

It thus appears possible to choose the parameters in our theory to match the observed behavior of T_c and θ as functions of composition. Moreover, if the NN and NNN coordination numbers are assumed known and the manner in which the NN exchange effects vary with x is postulated, the proper choice of parameters is apparently unique.

Another theoretical interpretation of the data has been made[1, 4]. In this work, both high-temperature series expansions and a two-particle cluster theory were employed and the x-dependences of the effective NN and NNN exchange integrals were fixed to match the $T_c(x)$ and $\theta(x)$ data. In Fig. 8 we compare these functions with ours. Our effective *NN* exchange integral is of course a linear function of x:

$$J = \frac{1}{n}[n_1J_1 + n_2J_2 + n_3J_3] = J_3 + (J_1 - J_3)x$$

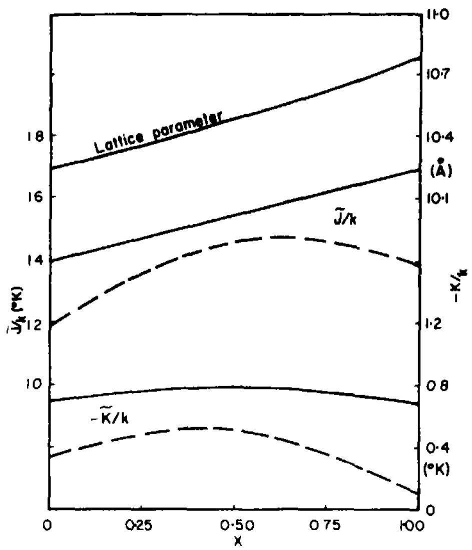

Fig. 8. The effective nearest-and next-nearest-neighbor exchange integrals on the basis of the present theory (solid lines) and an alternate interpretation from reference [4](dashed lines). Also shown is the lattice parameter as a function of composition.

and the NNN exchange integral is a weak quadratic function,

$$K_4 = J_4 \simeq J_0(1+\tfrac{1}{2}x-\tfrac{1}{2}x^2).$$

Considerably greater variation with x is required by the analysis of Wojtowicz *et al.*

Also shown in the figure are the experimental data[4] for the lattice constant. It is seen to vary almost linearly with x with a total change of about 5 per cent between $x = 0$ and 1.

The principal defects in the model we have employed are probably the following:

1. Interactions between NN's and NNN's of the cluster are ignored, even though some of the NNN's are NN's to each other.
2. The several different types of NNN sites and their exchange integrals are lumped together and their effect approximated by some total effective number of equal exchange integrals. (See reference [5] for a criticism.)
3. The NNN interaction itself was treated in its composition dependence in a different manner from the NN exchange integrals. The assumed quadratic dependence on x is, moreover, probably too simple considering the complexity of the possible NNN exchange paths.

Despite these shortcomings, more than just reasonable agreement with experiment has been obtained. We plan an extension of these calculations with a model that should improve the situation.

Acknowledgements—I wish to thank the University of Missouri for a summer research grant under which this research was begun and Mr. W. E. Holland for his assistance with the calculations.

REFERENCES

1. BALTZER P. K., ROBBINS M. and WOJTOWICZ P. J. *J. appl. Phys.* **38**, 953 (1967); BALTZER P. K., ROBBINS M., WOJTOWICZ P. J. and LOPATIN E., *Phys. Rev.* **151** 367 (1966).
2. BETHE H. A., *Proc. R. Soc.* **150**, 552 (1935).
3. BROWN H. A., *J. Phys. Chem. Solids* **26**, 1369 (1965).
4. WOJTOWICZ P. J., BALTZER P. K. and ROBBINS M., *J. Phys. Chem. Solids* **28**, 2423 (1967).
5. DWIGHT K. and MENYUK N., *J. appl. Phys.* **39**, 660 (1968).

J. Phys. Chem. Solids Pergamon Press 1969. Vol. 30, pp. 211–215. Printed in Great Britain.

THE MOBILITIES OF HOLES AND ELECTRONS IN IODINE SINGLE CRYSTALS

BRIAN FITTON*
Department of Natural Philosophy, Glasgow University, Glasgow, Scotland

(*Received* 6 *May* 1968)

Abstract – The mobilities were measured by the observation of the transit times of optically generated current pulses moving across the crystal under space-charge limited conditions. The majority carriers were holes at room temperature. These had a mobility, measured in the b-direction, which varied as exp $-\Delta E/kT$ *with* $\Delta E = 0{\cdot}08$ eV over the temperature range 190–280°K. The mobility was 0·66 cm²/Vsec at 293°K. The transit of electrons was also observed in the temperature range 140–260°K. The electron mobility varied as $T^{-0{\cdot}8}$ over this range, with $\mu_e = 0{\cdot}6$ cm²/Vsec at 250°K. The holes created by light absorption in either of the two main iodine absorption bands have essentially the same mobility, indicating hole transport in a common valence band.

1. INTRODUCTION

THEORIES of the processes occurring within an insulator during the initial stages of space charge limited current flow have been developed independently by Many and Rakavy[1] and by Helfrich and Mark[2]. The oscillatory decay of this current pulse towards the steady state condition described by Mott and Gurney[3] has been considered by Schilling and Schachter[4]. Many *et al.*[5] confirmed the main features of the transient S.C.L.P.C. theory in experiments on iodine single crystals. In this paper the hole mobility deduced from the S.C.L.P.C. pulse transit time as a function of temperature is re-examined, and in addition data on the electron mobility is provided. The mobility of holes originating from blue light and from red light absorption, corresponding to the two main absorption regions, was examined to check whether a difference existed sufficient to indicate separate valence bands.

According to Many and Rakavy, in the absence of a space charge control, the transit time of a sheet of charge moving across a crystal of width L is $t_0 = L^2/\mu V$, where μ is the mobility and V the voltage applied.

At higher voltages and with an appropriate *density of carriers in the charge reservoir* at one face the transit time is

$$t_1 = 2(1-e^{-1/2})\frac{L^2}{\mu V} \approx 0{\cdot}8t_0. \qquad (1)$$

They also showed that the instantaneous current j_0 immediately after the generation of the charge layer by a highly absorbed light flash is given by

$$j_0 = 4{\cdot}4\times10^{-14}\frac{\mu V^2}{L^3}(\text{Amps/cm}^2). \qquad (2)$$

Thereafter the current increases up to a maximum at time t_y corresponding to the sheet of carriers at the opposite electrode.

The treatment by Schilling and Schachter of the behaviour of this current beyond t_1 predicts a strongly damped oscillatory decay to the steady state value j_{t_∞}.

$$j_{t_\infty} = \frac{9}{8}\frac{\mu\epsilon V^2}{L^3} \qquad (3)$$

according to

$$J(t) = j\exp(-\lambda t) \qquad (4)$$

with the dominant mode

$$\lambda_0 = \frac{3}{4}\left(\frac{\mu V_A}{L^2}\right)[3{\cdot}82+j(8{\cdot}36)]. \qquad (5)$$

The carrier mobility can, at least in principle, be determined using either equation (1), (2) or (5). In practice however j_0 is strongly influenced by other factors which are not well understood at the moment[6]. The oscillatory decay is found to be very strongly damped and the determination of the current maxima grossly inaccurate, so that equation (5) is not of use for mobility determinations. The most accurate method is undoubtedly the measurement of carrier transit times by observing the cusp in the current pulse corresponding to the arrival of the front of the charge sheet at the opposite electrode. This method is therefore used here, measuring the transit time as a function of applied voltage for a known crystal thickness.

**Present address:* Noranda Research Centre, Pointe Claire, Quebec, Canada.

2. EXPERIMENTAL

The iodine single crystals were grown by sublimation from 99·998 per cent purity iodine supplied by the Koch-Light Laboratories. This iodine was heated to about 60°C and condensation allowed at 18°C in a closed tube containing nitrogen at a pressure of 65 cm of mercury.

The iodine single crystals selected were provided with electrodes of transparent tin oxide coated onto a silica disc for one face and a platinum guard ring and centre electrode on the opposite face. The growth habit of these wafer crystals is such that the current is directed along the *b*-axis in these experiments.

The transparent electrode was biased by a d.c. arrangement over the range 0–1,000 V, whilst the back electrode was connected to earth via a 22K ohm load resistor. The guard ring was maintained at earth potential. Pulse amplification used a pre-amplifier and type L plug-in unit of a Tektronix type 541 Oscilloscope. The rise time overall was 0·4 μ sec, with a current sensitivity extending down to 10^{-8} A.

A pulsed argon arc generated a light flash of about 0·2 μ sec duration which was focussed down onto the iodine through the transparent electrode to provide the charge reservoir at that electrode.

The specimen and its electrodes were sealed within a vacuum tight copper container with provision for electrical connections. This was fastened to the end of a 'cold finger' type liquid nitrogen dewar. Temperature measurement was by a thermocouple attached to the platinum guard ring.

3. RESULTS

Figure 1 shows a current pulse for hole transit obtained with this system. In this case the temperature was 243°K with +400 V on the illuminated face of a 0·25 mm thick crystal. The shape is that anticipated for transit through a crystal exhibiting bulk trapping and recombination[1]. The cusp corresponding to the arrival of the carriers at the back electrode after the transit time t_1 is followed by a series of maxima in the oscillatory decay. The first such maximum occurs 0·75 t_1 after the cusp, in agreement with the theory of Schilling and Schachter. A detailed comparison with that theory, however, was not possible due to the very strong damping to which these oscillations are subjected in most of the pulses observed.

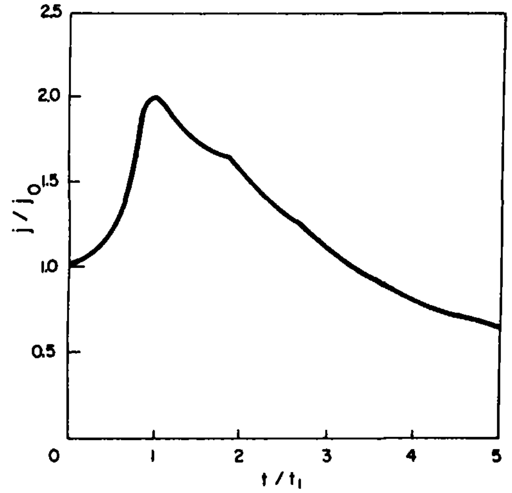

Fig. 1. The time dependence of the hole current, represented in dimensionless form, with t_1 the transit time of the holes across the crystal and j_0 the initial current amplitude.

For both hole and electron transit the initial photocurrent was found to vary linearly with voltage at very low fields changing to the V^2 dependence expected for a space charge limited current, and finally saturating at fields above 10^4 V/cm, particularly at low light levels.

In the regime of space charge limited current flow a plot of the transit time versus reciprocal voltage should yield a slope of $2L^2/\mu \times (1-e^{-1/2})$. Figure 2 shows typical results obtained, in this case at 243° and 293°K.

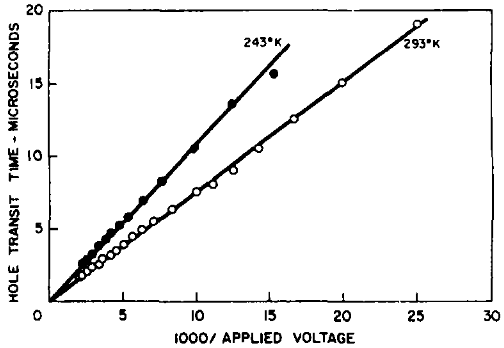

Fig. 2. Dependence of the hole transit time on the applied voltage for 293° and 243°K.

Similar curves were constructed at temperatures down to approximately 170°K to provide the data for the mobility-temperature relationship. In order to reduce the effects of internal polarization fields [7], consequent upon charge localization in traps, only the first pulse was recorded for each voltage chosen at temperatures below 250°K. Reheating and discharging was used to try to clear these polarization fields after each measurement.

The logarithm of the hole mobility obtained from a series of such measurements is shown as a function of reciprocal temperature in Fig. 3. The activation energy associated with this curve is 0·08 eV. The mean curve obtained by Many *et al.* [8] for the hole mobility in iodine single crystals is included in the same figure. Although the hole mobility for the two sets possibly tend towards a common curve above 280°K, at lower temperatures the results are quite different.

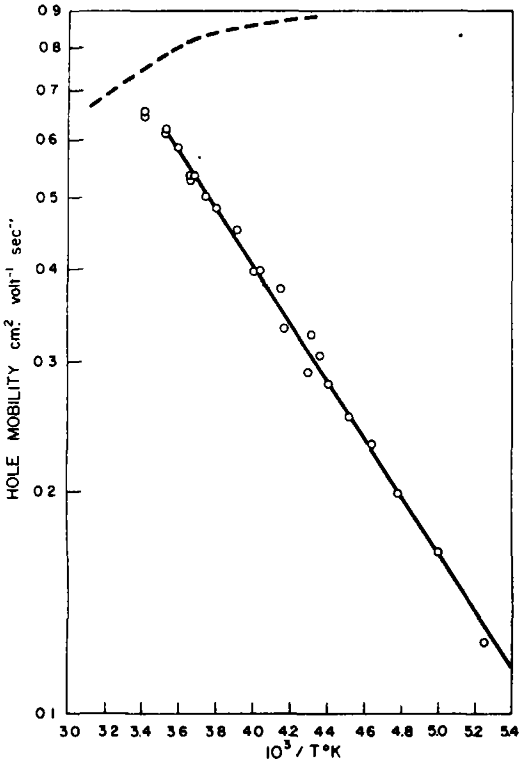

Fig. 3. Temperature dependence of the hole drift mobility along the *b*-axis. The dashed curve is the mean of the mobility results of Many *et al.*[8] for drift parallel to the *b*-axis.

Under normal conditions the transit of electrons cannot be observed. However, if several transits of holes are allowed and then the field suddenly reversed, pulses are obtained showing the cusp indicative of a normal transit of charge across the crystal (Fig. 4). Such pulses could be sustained over periods up to 30 min after such a field reversal at temperatures below 250°K. The effect of the field reversal does not seem to lie in an increased effective internal field since the transit times remain almost constant, independent of the gradual decay of final pulse height in successive pulses. Rather the main effect must be to produce conditions giving an

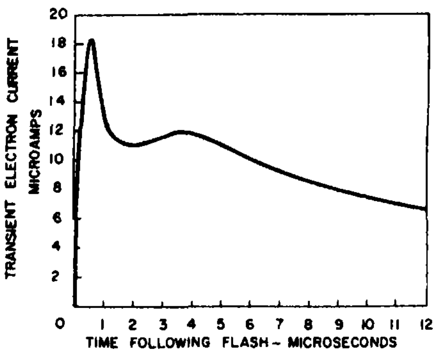

Fig. 4. Electron current through a 0·25 mm thick crystal with 160 V applied and the temperature 178°K. The overshoot of the initial photocurrent is observable also in some circumstances during hole transit.

increased lifetime for the electrons. The possibility of a back transfer of holes was ruled out because the blue light used for stimulation would have a penetration depth of only ~0·5 μ. A linear variation of transit time with reciprocal voltage was obtained as expected for space charge limited current flow. From a series of such curves the electron mobility as a function of temperature was found and is shown in Fig. 5. The mobility is seen to vary as $T^{-0\cdot 8}$ over the range 140–260°K.

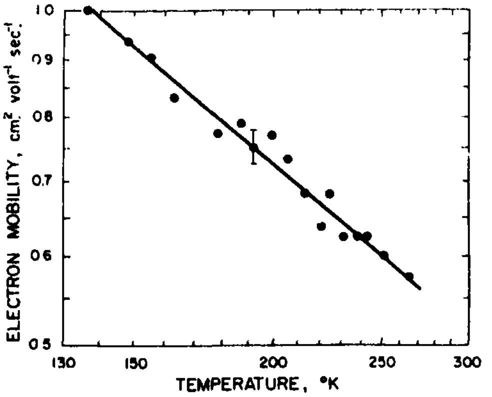

Fig. 5. The temperature dependence of the electron drift mobility along the b-axis of an iodine singly crystal.

The possibility of two separate valence bands was checked by using blue and then red light to create the charge reservoir with biasing as for hole transit. The transit time as a function of reciprocal voltage is shown in Fig. 6. The slopes, which are proportional to the mobilities, are different, the ratio being 0·85. The maximum intensity of output from the light source used lies in the blue region of the spectrum. The ratio of the slopes for weak and strong illumination should be 0·8, corresponding to space charge free and space charge limited current flow respectively[5]. The transit times for the weak red light excitation are increased as anticipated so that the small difference in the mobilities is probably an apparent one due to the differing illumination conditions. A common valence band therefore seems very probable.

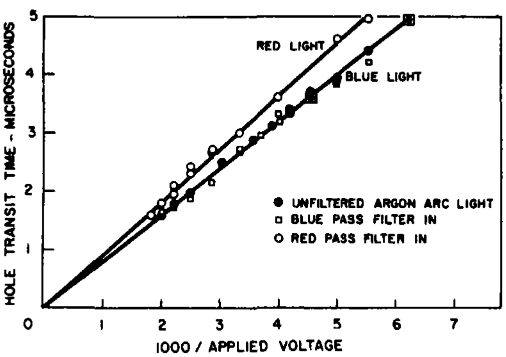

Fig. 6. The voltage dependence of the hole transit time for stimulation by red and blue light.

4. DISCUSSION

The activated transport process for holes in the b-direction of these iodine single crystals is considered to be the result of a trap controlled drift mobility[9] rather than the result of a 'hopping' motion[10]. The former interpretation is favoured largely because a process fundamental to the iodine lattice, as in the case of a hopping motion, would be expected to manifest itself in a regular manner and be relatively independent of specimen history. The considerable divergence between the results of Many *et al.* and those presented here suggests that the mobility below room temperature is in fact quite sensitive to specimen treatment. Thus the mobility in this batch of crystals is thought to have been controlled, below 280°K, by a set of traps of density N_t lying about 0·08 eV above the valence band.

In the absence of higher temperature results for these samples it is assumed that the departure from the exponential curve around 280°K is the beginning of the transition to a lattice scattering controlled mobility as found by Many *et al.* The consistent results obtained in this region by this group would seem to justify such an assumption. Using this data above 300°K for the lattice scattering mobility $\mu_L = \alpha T^{-3/2}$, gives $\alpha = 3{\cdot}8\times 10^4\,\mathrm{cm}^2\mathrm{sec}^{-1}V^{-1}\,{}^{\circ}\mathrm{K}^{3/2}$. Below 280°K the hole mobility can be written

$$\mu_h \approx \mu_L\left(\frac{N_v}{N_t}\right)\exp\left(-\frac{\Delta E}{kT}\right). \qquad (6)$$

The effective density of states is estimated on the basis of $m_h^* \approx m$. Substituting then for N_v in (6) gives a trap density of $10^{18}\,\mathrm{cm}^{-3}$.

Thermoluminescence measurements by Braner and Chen[11] have shown the existence of traps 0·11 and 0·13 eV above the valence band. The identiy of these traps however was not discussed.

The main impurity in iodine is water[12], which can be as much as 0·1 per cent in ordinary laboratory material. Following vacuum treatment Reid and Mills[13], using tritiated water for labelling, found that the concentration is reduced to about 100 ppm. It is known [14] that drying iodine further by sublimation in the presence of P_2O_5 removes the trapping levels situated about 0·3 eV above the valence band. The question whether water is also responsible for the presence of these very shallow levels must await an extension of such measurements. It would appear however to be a likely explanation for the difference in these two sets of results obtained on samples having different storage conditions. It would be very interesting to have mobility measurements on iodine which has been subjected to the molecular sieve drying process, used by Reid and Mills, which reduced the water content to less than 1 ppm.

The electrons appear to be subjected mainly to strong trapping in deep levels, with no appreciable release during a transit time. The observed temperature dependence of the electron mobility must therefore arise from a combination of normal acoustic mode scattering, with a $T^{-3/2}$ dependence, and the positive temperature dependence of a screened Coulomb scattering process. The Coulomb scattering may be the result of the presence of more than 10^{18} hole traps/cm³ in these crystals, since those trapping sites having an energy of 0·3 eV are known to be ionized[14].

Acknowledgements—The author would like to thank Dr. G. A. P. Wyllie and Dr. P. M. Dryburgh for their helpful discussions during the course of this work. The financial assistance given by Glasgow University and the Plessey Company is gratefully acknowledged.

REFERENCES

1. MANY A. and RAKAVY G., *Phys. Rev.* **126**, 1980 (1962).
2. HELFRICH W. and MARK P., *J. appl. Phys.* **33**, 205 (1962).
3. MOTT N. F. and GURNEY R. W., *Electronic Processes in Ionic Crystals*, p. 172. Oxford University Press (1940).
4. SCHILLING R. B. and SCHACHTER H., *J. appl. Phys.* **38**, 1643 (1962).
5. MANY A., WEISZ S. Z. and SIMHONY M., *Phys. Rev.* **126**, 1989 (1962).
6. LEMKE H. and MÜLLER G. O., *Phys. Status Solidi* **24**, 127 (1967).
7. FREEMAN J. R., KALLMAN H. P. and SILVER M., *Rev. mod. Phys.* **33**, 553 (1961).
8. MANY A., SIMHONY M., WEISZ S. Z. and TEUCHER Y., *J. Phys. Chem. Solids* **25**, 721 (1964).
9. ADAMS A. R. and SPEAR W. E., *J. Phys. Chem. Solids* **25**, 1113 (1964).
10. GIBBONS D. J. and SPEAR W. E., *J. Phys. Chem. Solids* **27**, 1917 (1966).
11. BRANER A. A. and CHEN R., *J. Phys. Chem. Solids* **24**, 135 (1963).
12. WASHINGTON R. A. and WALDRETT S. N., *J. Am. chem. Soc.* **77**, 4232 (1955).
13. REID A. F. and MILLS R., *J. inorg. nucl. Chem.* **26**, 892 (1964).
14. FITTON B., *Solid State Commun.* In press (1968).

J. Phys. Chem. Solids Pergamon Press 1969. Vol. 30, pp. 217–223. Printed in Great Britain.

MIGRATION OF ANION VACANCIES AND FORMATION OF COMPLEX COLOUR CENTRES IN KCl

G. GIULIANI
Istituto di Fisica dell'Università di Pavia, Italy, Gruppo Nazionale di Struttura della Materia del C.N.R.

(*Received* 3 *May* 1968)

Abstract—A new technique is presented, which allows to send anion vacancies and electrons separately through an alkali halide crystal. This technique can, in principle, be applied to the production of any complex colour centre involving anion vacancies and electrons. In this paper we report the results obtained by applying this new technique to the production of F_A- and Z_1-centres.

1. INTRODUCTION

IT IS WELL known that F-light absorbed by an alkali halide crystal containing F-centres and kept near room temperature (RT) leads to the formation of F-aggregate centres (M, R- and N-centres). However, if the sample contains divalent impurities such as Ca, Sr or Ba or suitable monovalent impurities (for instance Li or Na in KCl), the main product of the F-light illumination is given by Z_1-centres and F_A-centres respectively. The process of formation of F-aggregate centres as well as that of F_A- and Z_1-centres has recently received renewed attention by several authors[1–6]. All these studies have been done by carefully investigating the processes set up by the simultaneous migration of ionic defects and electrons.

In this paper results are reported which show how it is possible to produce complex colour centres in two steps by sending anion vacancies and electrons separately through the crystal. The efficacy of this new procedure has been checked by producing F_A-centres (whose structure is known and consists of an F-centre with a monovalent impurity ion as a nearest neighbour[7]) in lithium doped KCl samples; on the other hand the use of this procedure in Z_1-centre production shows how it can give useful information about both the intermediate products of the process of formation of complex colour centres and the structure of the colour centres themselves*.

2. EXPERIMENTAL PROCEDURE

The colour centres' transformations produced in KCl samples by various treatments have been studied by observing the corresponding changes in the absorption spectrum of the samples. A Hilger type E-791 monochromator and a Beckmann DU spectrophotometer have been used in the 170–200 mμ and in the visible range respectively. The crystals have been grown in our laboratory in nitrogen atmosphere by the Kyropoulos method. The reported amounts of impurities refer always to the quantities added to the melt. All the results reported in this paper have been obtained with X-rayed samples.

3. RESULTS AND DISCUSSION

3.1 *Production and migration of anion vacancies. Formation of* F_A*-centres*

To send anion vacancies through the crystal requires: (*a*) to produce isolated anion vacancies (α-centres) and (*b*) to allow the anion vacancies to migrate by, for instance, warming up the crystal to an appropriate temperature. Condition (*a*) can be easily met by X-raying a KCl sample at a low enough temperature or by shining F-light on a sample containing F-centres (produced by additive colouration or by X-rays) and kept at a suitable temperature. However, when a KCl sample X-rayed at low temperatures is warmed up to higher temperatures, the disappearence of α-centres is mainly due to their recombination with mobile interstitial negative ions[9]. Also the warming up of an additively coloured KCl sample in which a fraction of the F-centres has been transformed into an equal number of α- and F'-centres, does not produce a detectable migration of anion vacancies. In fact, in this case, the main effects of the warming are the thermal ionization of F'-centres and the capture of the thermally released electrons by empty anion vacancies [10]. Therefore, it is clear that, in order to observe the migration of anion vacancies, one should warm up a sample containing α-centres but no F'-centres or interstitials which could become mobile during the warming. This may be done as follows. A KCl sample is X-rayed at liquid nitrogen temperature (LNT), warmed up to RT ($\simeq 290°$K) and kept at this temperature for about 12 hrs*. The sample is then illuminated with F-light and subsequently with F'-light at 150°K. The net result of the $(F+F')$-illumination consists in a decrease of the F band and in the growth of the α band†. After the $(F+F')$-illumination no F' band is present. In this way one obtains a sample containing isolated anion vacancies but no F'-centres. However, it is to be stressed that the electrons released by the $(F+F')$-illumination may change the structure of the hole centres giving rise to some kind of interstitial not present before the illumination. Therefore, the decay of the α band which occurs when the sample is warmed up, may be due to the migration of these interstitials. Though we can not definitely rule out this possibility, we shall see below that the decay of the α band produced as described above is due, at least partially, to the migration of anion vacancies.

---

*Preliminary results on the Z_1-centre production have been presented to the 'Colloque sur les centres colorés', Saclay, March 1967. The text of the communication has been published as from reference [8].

The thermal decay of the α band has been studied by a pulse annealing method: the sample was warmed up to a temperature higher than 150°K, kept at this temperature for 15 min and then cooled down to LNT for the optical measurement. The results obtained are reported in Fig. 1 and show that anion vacancies produced by ionization of F-centres in X-rayed samples are stable up to 200°K and are totally destroyed if the sample is warmed up to 250°K. From Fig. 1 it appears also that the presence of monovalent (Li^+) or divalent (Sr^{++}) impurities does not affect the thermal decay of α-centres.

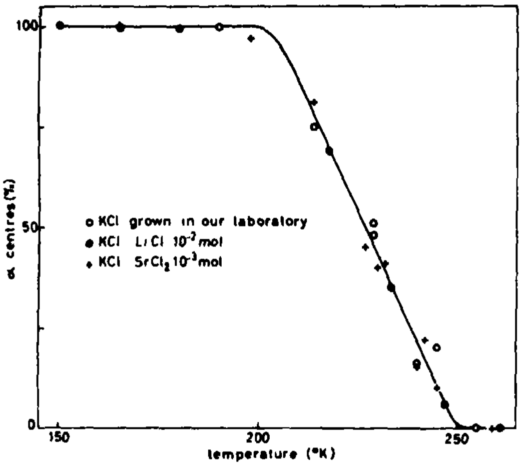

Fig. 1. Thermal decay of α-centres produced by optical bleaching of F-centres in X-rayed KCl samples.

The proof that the thermal decay of α-centres produced by ionization of F-centres in X-rayed samples is due, at least partially, to their own migration, is given by the following experiment. α-centres are produced as described above in a lithium doped KCl sample. In Fig. 2(a) we have reported the changes in the visible region of the absorption spectrum due to the $(F+F')$-illumination at 150°K: the only observed change is a decrease of the F band. The changes due to the warming up which follows the $(F+F')$-illumination at 150°K are shown in Fig. 2(b): here again the only observed change is due to a decrease of the F band. At this point the sample is illuminated again at 150°K with F-light and subsequently with F'-light*: the corresponding changes of the absorption spectrum are shown in Fig. 2(c). From this figure it appears that this illumination, unlike the first one (cf. Fig. 2(a)), not only decreases the F band but causes also the F_A bands to grow.

---

*The sample could be X-rayed directly at RT. However, the RT irradiation of strontium doped KCl samples results in a large increase of the absorption in the tail of the fundamental edge, making it difficult to observe further changes of the absorption spectrum in this region.

†The α band is due to exciton transitions localized near isolated anion vacancies and peaks, in KCl, at 177 mμ[11, 12].

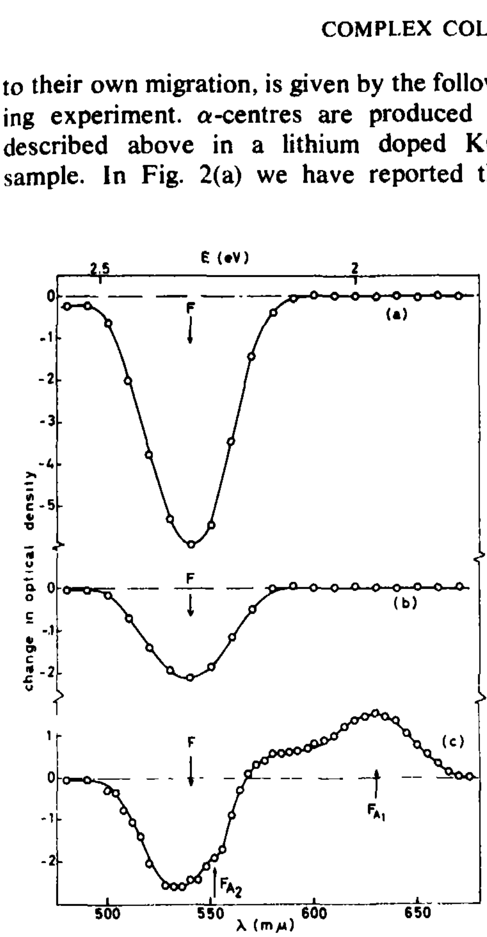

Fig. 2. (a) change in the visible region of the absorption spectrum produced by an $(F+F')$-illumination carried out at 150°K on a lithium doped (10^{-2} mol) KCl sample X-rayed at LNT and warmed up to RT. (b) changes in the visible region of the absorption spectrum due to the warming to 250°K of the sample of Fig. 2(a). (c) changes in the visible region of the absorption spectrum produced by an $(F+F')$-illumination carried out at 150°K on the sample of Fig. 2(b).

In order to explain the above results, we shall begin by emphasizing that the primary effect of the two illuminations is the same and consists in the production of free electrons. However, the final products of each illumination depend on the distribution of the free electrons among the available electron traps. The fact that the F_A bands grow only under the second illumination (cf. Figs. 2(a) and 2(c)) shows that during the second illumination electron traps not present during the first one transform into F_A-centres by capturing an electron. These electron traps must have been formed during the warming up which follows the first illumination and must be α_A-centres (i.e. α-centres with a lithium ion as a nearest neighbour). The formation of α_A-centres is possible only if anion vacancies migrate and join lithium ions. Therefore, we can conclude that the decay of the α band which takes place during the warming up of the sample to 250°K (cf. Fig. 1) is due, at least partially, to the migration of anion vacancies.

Before leaving this subject, it is worth stressing that: (*a*) the optical ionization of F-centres at 150°K is not accompanied by the migration of anion vacancies; (*b*) the migration of anion vacancies is not accompanied, in the experimental conditions described above, by a detectable production of free electrons. In fact, if points (*a*) and (*b*) were not true, the F_A bands should have grown both during the first $(F+F')$-illumination and during the subsequent warming up of the sample. However, no detectable growth of F_A bands is observed in either case (cf. Figs. 2(a) and 2(b)).

---

*In this case the F'-illumination is not essential. However, since the F' band produced by the F-illumination decreases under the action of the light used for the optical measurement, it is convenient to destroy all the F'-centres before the measurement.

3.2 *Formation of Z_1-centres*

In this section we shall see how Z_1-centres can be formed in a strontium doped KCl sample by sending anion vacancies and electrons separately through the crystal (cf. the end of Section 3.1). The procedure is the same as the one described in Section 3.1 for the production of F_A-centres. Nevertheless, in order to make the exposition and the explanation of the results easier, the main steps of the procedure will be recalled here. A strontium doped KCl sample is: (I) X-rayed at LNT and warmed up to RT; (II) illuminated with F-light and subsequently with F'-light at 150°K: as reported in Section 3.1 this illumination causes the F band to decrease and the α band to grow. Furthermore, as in the case of the lithium doped sample (cf. Fig. 2(a)), the decrease of the F band is the only change produced in the visible region of the spectrum by the $(F+F')$-illumination (cf. Fig. 3(a)); (III) warmed up to 250°K; as shown in Section 3.1, the warming causes the α band produced in step II to disappear. Furthermore, the disappearance of the α band is due, at least partially, to the migration of anion vacancies (cf. Section 3.1); (IV) illuminated with F-light and subsequently with F'-light at 150°K. This illumination causes the F band to decrease and the Z_1 band to grow (cf. Fig. 3(b)).

As in the case of F_A-centre formation (cf. Section 3.1), we must draw our attention to the $(F+F')$-illuminations carried out in steps II and IV. The illumination performed in step II does not give rise to the Z_1 band (cf. Fig. 3(a)), while the one carried out in step IV does (cf. Fig. 3(b)). This implies that during the illumination carried out in step IV, electron traps not present during the illumination

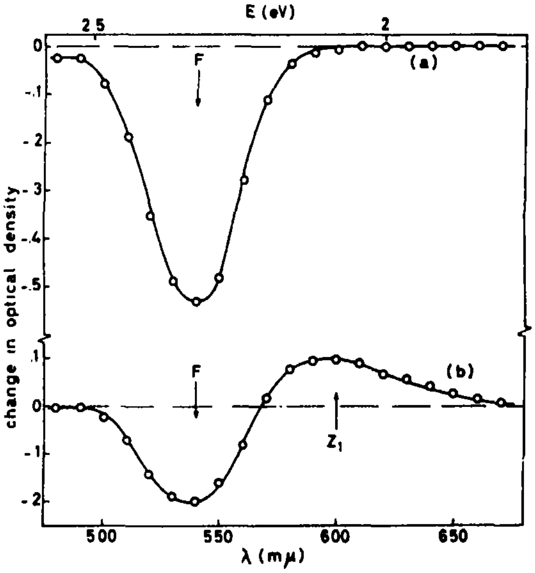

Fig. 3. (a) changes in the visible region of the absorption spectrum produced by an $(F+F')$-illumination carried out at 150°K on a strontium doped (10^{-3} mol) KCl sample X-rayed at LNT and warmed up to RT. (b) changes in the visible region of the absorption spectrum produced by an $(F+F')$-illumination carried out at 150°K on the sample of Fig. 3(a) after its warming up to 250°K.

performed in step II, transform into Z_1-centres by capturing an electron. These electron traps can be referred to as ionized Z_1-centres or Z_1^+-centres and must have been formed during the migration of anion vacancies which occurs in step III. Therefore, since Z_1^+-centres form during the migration of anion vacancies (just in the same way as α_A-centres do; cf. Section 3.1), it is quite reasonable to conclude that Z_1^+-centres contain an anion vacancy as a component. As far as the entire structure of the Z_1^+-centres is concerned, we can observe that two configurations are possible: (i) a vacancy pair and, (ii) a divalent impurity with an associated vacancy pair*. Accordingly, the Z_1-centre will consist of a vacancy pair with a trapped electron or of a divalent impurity-cation vacancy complex with an associated F-centre. Possibility (i) seems unlikely since the capture of an electron by a vacancy pair is expected to end up in the formation of an F-centre and an isolated cation vacancy. On the other hand possibility (ii) is supported by the Z_1-centre ENDOR spectrum obtained by Bushnell[13]. In any case, it is worth emphasizing that the results reported in this section clearly show that the Z_1-centre *contains an F-centre as a component*†.

3.3 *The* Z_1^+*-centre*

According to what has been said in Section 3.2, the Z_1^+-centre is very likely made up by a divalent impurity-cation vacancy complex with an associated anion vacancy. Therefore, it is expected to give rise to a localized exciton band. In this connection, let us consider the following results: (i) the thermal decay of the α band which occurs in step III of section 3.2 is accompanied by the growth of a band peaking at about 173 mμ (cf. Fig. 4); ii) the F-illumination carried out in step IV of Section 3.2 causes not only the Z_1 band to grow (cf. Fig. 3(b)) but also the 173 mμ band to decrease (cf. Fig. 5); (iii) Z_1-centres can be bleached by Z_1-light at 200°K; the product of the bleaching is given by Z_1^+-centres as it is proved by the fact that Z_1-centres can be reformed by a subsequent F-light illumination carried out at 150°K. Figure 6 shows that the $Z_1 \rightarrow Z_1^+$ conversion is accompanied by the growth of the 173 mμ band; (iv) the Z_1 band does not appear in step IVof Section 3.2 if the sample, in step III, is warmed up to 300°K

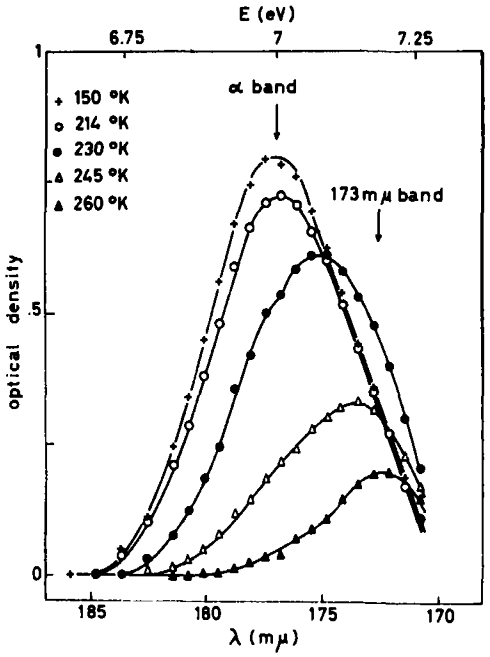

Fig. 4. Thermal decay of the α band produced by optical bleaching of the F band at 150°K in a strontium doped (10^{-3} mol) KCl sample. All these curves have been obtained by subtracting the absorption curve measured before the $F \rightarrow \alpha$ conversion to the absorption curve measured after the warming up of the sample to the reported temperature. As evident from this figure, the decay of the α band is accompanied by the growth of a band peaking at about 173 mμ.

---

*That these are indeed the only two possible configurations for the Z_1^+-centre can easily be accounted for on the basis that Z_1^+-centres contain an anion vacancy as a component and form only in samples doped with divalent impurities.

†Very recently, further evidence for a model of the Z_1-centre including an F-centre has been obtained from Faraday rotation (14) and circular dichroism[15] measurements.

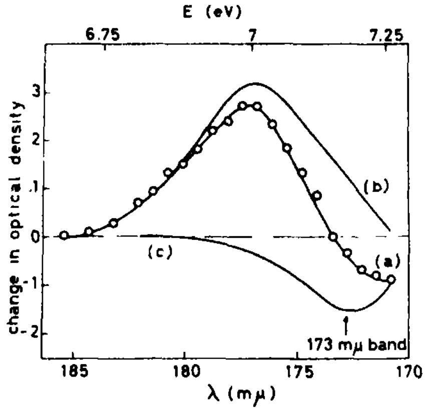

Fig. 5 (a) change of the absorption spectrum near the fundamental edge produced by an $(F+F')$-illumination carried out at 150°K on a strontium doped (10^{-4} mol) KCl sample containing Z_1^+-centres; (b) change that would have been observed if the growth of the α band were the only effect of the illumination. This curve has been drawn by making use of the known shape of the α band and of the fact that the contribution to the absorption of the 173 mμ band above 180 mμ is negligible (cf. Fig. 4), (c) difference between (a) and (b) showing that the 173 mμ band decreases under the $(F+F')$-illumination.

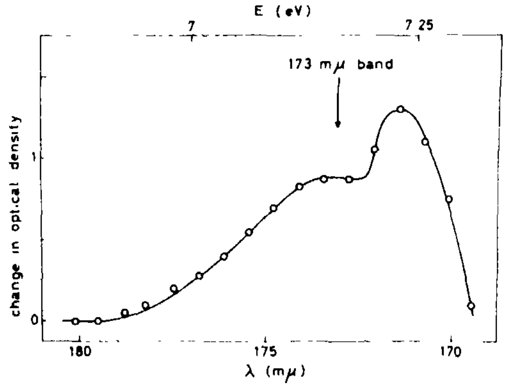

Fig. 6. Change of the absorption spectrum near the fundamental edge produced by a Z_1-light illumination carried out at 200°K on a strontium doped (10^{-3} mol) KCl sample containing Z_1-centres (light source: white light from a 500 W lamp filtered through a Kodak 89B wratten filter). The narrow band on the short wavelength side of the 173 mμ band is of unknown origin. However, it is worth reporting that it has been observed also in some lithium or strontium doped KCl sample X-rayed at LNT, warmed up to RT and subjected to an $(F+F')$-illumination (KCl:LiCl) or to a white light illumination (KCl:$SrCl_2$) at 150°K.

for 30 min in order to destroy the 173 mμ band.

It is clear that the above data, though only qualitative in nature, allows one to reasonably assign the 173 mμ band to Z_1^+-centres.

4. FINAL COMMENTS

The results reported in this paper prove that the processes of formation of F_A- and Z_1-centres take place through the migration of anion vacancies and the formation of α_A- and Z_1^+-centres respectively. There is experimental evidence that anion vacancies play the same role in the M-centre formation[1–4]. Therefore, it should be possible to produce M-centres by the same procedure used here for the F_A- and the Z_1-centre production. However, it must be stressed that a necessary condition for this method to be applied to the production of M-centres (or other F-aggregate centres) is that the intermediate product of the process (i. e. the F_2^+-centre in the case of the M-centre formation) must be stable at least at temperatures just higher than the temperature (200°K; cf. Fig. 1) at which the anion vacancies begin to migrate.

As reported in Section 3.3, Z_1^+-centres are unstable near RT*. In this connection it is worth emphasizing that, since Z_2-centres seem to be the product of the thermal decomposition of Z_1-centres[16], ionized Z_2-centres may be one of the products of the thermal destruction of Z_1^+-centres. If this hypothesis is correct, it should be possible to produce Z_2-centres in two steps by producing ionized Z_2-centres which will then transform into Z_2-centres through electron capture. Measurements to check this possibility (which may give useful information about Z_2-centre production and structure) are now in progress.

Acknowledgements—The author would like to thank Mr. G. Guala for having performed some of the measurements.

---

*Preliminary results on the thermal stability of Z_1^+-centres have already been obtained[8]. More detailed measurements are now in progress in connection with the study of the Z_2-centre production (see below).

REFERENCES

1. FARGE Y., LAMBERT M. and SMOLUCHOWSKI R., *Solid State Commun.* **4**, 333 (1966).
2. ASAI K. and OKUDA A., *J. phys. Soc. Japan* **21**, 2197 (1966).
3. NAHUM J., *Phys. Rev.* **158**, 814 (1967).
4. HIRAI M. and SCOTT A. B., *J. chem. Phys.* **46**, 2896 (1967).
5. HÄRTEL H. and LÜTY F., *Z. Phys.* **177**, 369 (1964).
6. HÄRTEL H. and LÜTY F., *Z. Phys.* **182**, 111 (1964).
7. MIEHER R. L., *Phys. Rev. Lett.* **8**, 362 (1962).
8. GIULIANI G., *J. Phys. Radium, Paris* **28**, Suppl., C4-175 (1967).
9. GIULIANI G. and REGUZZONI E., *Phys. Status solidi* **25**, 437 (1968).
10. ONAKA R., FUJITA I. and FUKUDA A., *J. phys. Soc. Japan* **18**, Suppl. 11, 263 (1963).
11. ONAKA R. and FUJITA J., *Phys. Rev.* **119**, 1597 (1960).
12. CHIAROTTI G., GIULIANI G. and LYNCH D. W., *Il Nuovo Cim.* **17**, 989 (1960).
13. BUSHNELL J. C., *Thesis.* Urbana (1964).
14. PAUS H. and LÜTY F., *Phys. Rev. Lett.* **20**, 57 (1968).
15. GEHRER G. and LANGER H., *Phys. Lett.* **26A**, 232 (1968).
16. KLEEFSTRA M., *J. Phys. Chem. Solids* **24**, 1567 (1963).

vacuum

Vacuum is the international journal and abstracting service for vacuum science and technology

This monthly publication is devoted to the exchange of information in the field of vacuum science, a medium for expression of new ideas and a means whereby new techniques in vacuum technology may be revealed. A classified international abstracts section forms an important part of the journal. This section deals with classified abstracts of the world's vacuum literature, including the U.S.S.R. and Japan. The section 'Vacuum News' reports on the latest developments in vacuum equipment and products in addition to articles on commercial developments, news of personalities and reports from the various national and international vacuum organizations. Vacuum also covers biographies of authors, news from the Vacuum Societies and Short Communications.

Articles from recent issues include:

Thermal degradation of polythylene and polytetrafluoroethylene during vacuum evaporation: P. P. Luff and M. White
Leak detection in sealed-off devices: D. J. Thorpe
A perforation hollow cathode electron beamgun: G. D. S. Ward
Ion pumping effects in inert gas mixtures in an ionization tube: R. Konjevic, W. A. Grant and G. Carter
Some possible consequences of electrical breakdown within vacuum insulated power cables: D. A. Swift
Monomolecular contamination of optical surfaces: H. Shapiro and J. Hanyok

A. S. D. Barrett is the Co-ordinating Editor of a distinguished Board of Editors

Subscription rate: £20.0.0 U.S. $50.00

Enter your subscription with:

Training & Technical Publications
Division (T. & T.P.D.)
PERGAMON PRESS LTD.
Headington Hill Hall
Oxford OX3 OBW, England

or

PERGAMON PRESS INC.
Maxwell House, Fairfield Park
Elmsford, New York 1053, U.S.A.

an international journal reporting research on crystal growth and materials preparation and characterization

Materials Research Bulletin

Joint Editors-in-Chief:
Heinz K. Henisch and Rustum Roy
The Pennsylvania State University

Materials Research Bulletin is a focal point for research on materials in relation to the fields of physics, chemistry, engineering and earth sciences.
Papers are published within six weeks after acceptance, and cover the structure and properties of electronically, optically or mechanically interesting solids, which are considered and discussed as a function of preparational parameters. Other subjects include the synthesis of new phases, high pressure and high temperature phase changes, crystal growth mechanism and techniques, defect structure analysis, the preparation and structure of noncrystalline solids, and the development of new characterizing criteria and experimental methods.

Papers appearing during 1968 include
A. Madeysk and W. W. Smeltzer: Oxygen diffusion in monoclinic zirconia
S. A. Levy and R. Gashler: On the origin of lamellae in high resistivity KTN
B. G. Bagley, H. S. Chen and D. Turnbull: Characterization of amorphous alloy films
A. Roger et R. Fruchart: Etude magnétique et structurale de la solution solide MnP - MnAs
A. Vasko: Examination of internal defects in chalcogenide glasses by infrared defectoscopy methods

Published monthly
Write for full details and an inspection copy

PERGAMON PRESS LTD
OXFORD · NEW YORK

ARMS CONTROL AND DISARMAMENT annual review

an International Journal published under the joint auspices of the Hudson Institute and Pergamon Press

Edited by *Donald G. Brennan* Hudson Institute and *Robert Maxwell* Pergamon Press

Arms Control and Disarmament is concerned with the broad field of this subject as it is generally understood, publishing articles reviews, factual and bibliographic material on aspects ranging from political technical, economic legal or theoretical viewpoints Articles are written by those who have substantial responsibilities for the arms control policies of their respective countries and by experts who provide intellectual contributions, such as improved understanding of arms control issues and illuminating summaries of recent events

Other material published in the Review includes lists of selected books and papers and factual details such as military budgets and force levels.

The Editors may also provide opinion in the form of signed or unsigned editorials, or special articles, or comments on the articles in the Review, with the purpose of stimulating discussion and controversy

Papers from the first issue include

O Bassir : Arms control and the developing nations
A Beaufre : Some reflections on the problem of arms control
K E Boulding Accomplishments and prospects of the peace research movement
D G. Brennan The risks of spreading weapons A historical case
L W Martin Ballistic missile defense and arms control
M. Singer : A non-utopian, non-nuclear future world
L B Sohn Enforcement of disarmament controls with respect to states which have not ratified a disarmament or arms control treaty
J J Stone . Arms control where is it ?

Arms Control and Disarmament is published on a non profit basis should revenues exceed expenses the balance will be used to support studies on arms control

Write for full details and subscription rates

PERGAMON PRESS LTD
OXFORD · NEW YORK

Scripta Metallurgica

Editor **Bruce Chalmers** Harvard University

This is a new journal providing the most rapid publication for short communications dealing with the science of metallic and nonmetallic solids from theoretical and experimental studies which contribute to the understanding of the properties and behaviour of solids in terms of fundamental particles, forces and energies.
Papers are in the form of letters or short reports of new work or discussions of work already published. Summaries of reports, theses and manuscripts which are too lengthy for publication are published on the understanding that the completed paper will be available from the author or publisher.

PAPERS RECENTLY PUBLISHED INCLUDE:

D. Mills, J.T. McGrath and W.J. Bratina: Deformation paramets of an iron-0.2 % zirconium alloy and iron-carbon alloys.

G. Brebec, N. van Doan and M. Gerl: Relation entre chaleur de transport et valence efficace.

G. Wobser and W. Frank: Graphical determination of G, H, and S from an arrhenius plot.

P. Pietrokowsky: Phase relationships in the system Ti_3AU-Ti_3Pt.

G.G. Bentini, C. Donolato and P.M. Strocchi: Influence of hydrogen content on the relaxation spectrum of *a* titanium.

Monthly. Write for full details and an inspection copy.

PERGAMON PRESS LTD.
OXFORD · NEW YORK

Spectrochimica Acta

This international journal for the [illegible]
[illegible] part

Part A Molecular Spectroscopy *monthly*

Editors: H. W. Thompson and M. Kent Wilson

This deals particularly with qualitative and quantitative analysis, the determination of molecular parameters and general theory. Also included are papers on nuclear magnetic resonance spectra, electron spin resonance spectra, optical rotary dispersion, and the design and performance of instruments and components.

Papers recently published include:

P. J. N. Brown and E. F. Mooney: The infra-red spectra of fluorinated aromatic compounds—I. Methyl substituted 2, 3, 4, 5, 6 – pentafluorodiphenyls

P. R. Griffiths and H. W. Thompson: Far infra-red spectra of prolate and oblate symmetric tops

M. Hori, K. Kimura and H. Tusbomura: The electronic spectrum and the chemiluminescence of tetrakis-(dimethylamino)-ethylene (TDAE)

L. Lunazzi and F. Taddei: Proton magnetic resonance study of molecular interactions—II. Association shifts of chloroform with a number of organic bases

Part B Atomic Spectroscopy *monthly*

Editors: M. Margoshes and K. Laqua

Presents research papers on all regions of the electromagnetic spectrum, in-so-far as they have direct physicochemical interest. The main subjects include the determination of fundamental atomic data, new experimental procedures, and measurements or calculations of the properties of radiation sources or detectors

Papers recently published include:

J. Bril: Contribution a l'etude des phenomenes thermochimiques accompagnant la volatilisation des substances mises en oeuvre l'arc spectrographique-Cas des melanges oxydes-graphite

W. Snelleman: An a.c. scanning method with increased sensitivity in atomic absorption analysis using a continuum primary source

J. A. Fiorino, R. N. Kniseley and V. A. Fassel: A versatile long-path, slot burner for atomic and molecular absorption spectroscopy with oxyacetylene and nitrous oxide-acetylene flames

Write for full details and an inspection [illegible]
[illegible]

PERGAMON PRESS LTD
OXFORD [illegible]

INTERNATIONAL JOURNAL FOR

radiation physics & chemistry

EDITOR-IN-CHIEF:
H. Hering Centre d'Etudes Nucléaires de Saclay, France
EDITORS:
N. Bach Akademiya Nauk SSSR, Institut Elektrokhimii, USSR
A. Chapiro Laboratoire de Chimie des Radiations, France
A. Charlesby Royal Military College of Science, England
A. J. Dyne Atomic Energy of Canada Ltd., Canada
A. Henglein Hahn-Meitner Institut fur Kernforschung, Germany
S. Okamura Kyoto University, Japan

The International Journal for Radiation Physics and Chemistry is a new journal providing a specialized medium for papers dealing with the physical and chemical effects of ionising radiation

It surveys the whole range of phenomena from the physical step of energy deposition to the chemical reactions of resulting products, and includes techniques primarily intended to investigate such effects.

Papers are published in English, French, German or Russian and are selected on the merit of their contribution to the further understanding of radiation physics and radiation chemistry.

Papers from Volume 1 Number 1 include

J. H. Baxendale and A. A. Khan: The pulse radiolysis of p-nitrosodimethylaniline in aqueous solution

C. von Sonntag und W. Brüning: Strahlenchemie von Alkoholen-V, Die Methanbildung bei der γ-Radiolyse von Hepta-deutero-isopropanol

T. Iwamoto, K. Hayashi, S. Okamura, K. Hayashi and H. Yoshida: Ion radicals of styrene in irradiated organic glasses studied by electron spin resonance

D. I. Baasov, J. A. Kolbanovsky and L. S. Polak: Radiation defects and adsorption as studied by the exo-electron method

J. B. Briggs and P. G. Clay: Evidence for the participation of oxygen atoms in CO_2 formation during gamma radioloysis of carbon monoxide gas

Quarterly
Write for full details and an inspection copy

PERGAMON PRESS LTD
OXFORD NEW YORK

11/68

INDIA Council of Scientific and Industrial Research

Pergamon Press are the sole distributors outside India for journals published by the Council of Scientific and Industrial Research, New Delhi. These publications deal with all fields of interest at all levels of research, encouraging scientific growth in India and the rest of the world.

Journal of Scientific and Industrial Research *monthly*	*Official Organ of the Council of Scientific and Industrial Research* Publishes critical comments and technical and progress reports on the activities and achievements of the major scientific organizations in India and elsewhere.
Indian Journal of Chemistry *monthly*	This journal contains original research work in the various branches of chemistry—physical, organic, inorganic, analytical and nuclear.
Research and Industry *quarterly*	Communications from research workers cover all aspects of developmental work leading to new processes, services and products, and the utilization of by-products and industrial waste.
Indian Journal of Experimental Biology *quarterly*	This is the first journal from India to embrace all fields of experimental biology, including animal and plant physiology, radiobiology, immunology, pharmacology, bacteriology, virology and cancer research.
Science Reporter *monthly*	Designed to be readily understood by laymen, this journal publishes articles of wide interest dealing with recent developments in science and technology.
Indian Journal of Pure and Applied Physics *monthly*	Presents original research in pure and applied physics emanating from national laboratories and university research departments.
Salt Research and Industry *quarterly*	*Journal of the Central Salt and Marine Chemicals Research Institute* Publishes work on the production of salt, recovery of by-products, manufacture of potassium fertilisers from sea-water bitterns, cultivation and utilization of marine algae, chemical engineering studies, and plant development and design.
Indian Journal of Biochemistry *quarterly*	This journal is published in collaboration with the Society of Biological Chemists, India, and contains advanced research in biochemistry. Papers receive wide and prompt noticing in international abstracting and indexing periodicals.
Vigyan Pragati *monthly*	This is a popular scientific periodical which is published in Hindi and other Indian languages. Articles are concerned with all scientific disciplines, including defence science, and attention is given to relevant literature and special reading matter for students.
Indian Journal of Technology *monthly*	Covers research of an applied nature which is of value in areas of chemical technology and engineering, unit operations, metallurgy, mining and mineralogy, food and textile technology, illumination engineering, glass and ceramics.

Enquiries about any of these journals are welcome and should be addressed to

Pergamon Press
Headington Hill Hall Oxford England
Maxwell House Fairview Park Elmsford New York 10523 USA

Journal of the Mechanics and Physics of Solids

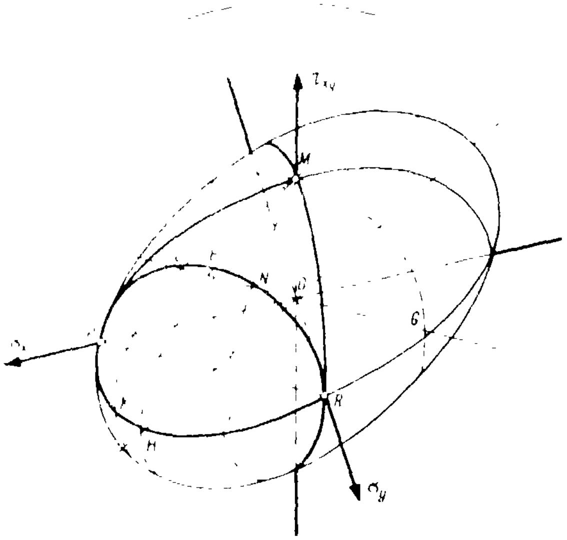

Editor-in-Chief: H G HOPKINS
Editorial Advisors: A H Cottrell, V V Sokolovsky and R Hill

The Journal of the Mechanics and Physics of Solids, an international journal of the theoretical and applied mechanics and the physics of solids. Brings together and relates research by mathematicians, engineers, metallurgists and physicists on the properties of constructional materials. Gives equal coverage to theory and experiment. Particularly concerned with the development and application of fundamental ideas bearing on the connections between continuum and micro-structural properties of materials and on the solution of materials and on the solution of practically significant problems.

Papers published recently
J F Bell: Large deformation dynamic plasticity at an elastic-plastic interface
R Hill: On constitutive inequalities for simple materials—II
U Lindborg: Creep cracks and the concept of damage
E Smith: Crack bifurcation in brittle solids
J W Hutchinson: Plastic stress and strain fields at a crack tip
J L Sackman and **I Kaya**: On the propagation of transient pluses in linearly viscoelastic media

Published bi-monthly
Write for further information and an inspection copy.
Details of other journals in this field can also be supplied.

Pergamon Press
Headington Hill Hall Oxford OX3 0BW England
Maxwell House Fairview Park Elmsford New York 10523 USA

11/68

J. Phys. Chem. Solids Pergamon Press 1969. Vol. 30, pp. 225–234. Printed in Great Britain.

GROWTH AND ELECTRICAL PROPERTIES OF VANADIUM DIOXIDE SINGLE CRYSTALS CONTAINING SELECTED IMPURITY IONS

J.B. MacCHESNEY and H. J. GUGGENHEIM
Bell Telephone Laboratories Incorporated, Murray Hill, N. J. 07971, U.S.A.

(*Received* 18 *July* 1968; *in revised form* 5 *September* 1968)

Abstract—A series of vanadium dioxide single crystals containing small concentrations of different impurity ions were grown by a thermal decomposition technique. The impurity ions were chosen to have different electronic structure from the V^{4+} ion they replace. It was expected that these ions would produce a systematic change in the semiconductor-metallic transition exhibited by the VO_2 phase. Contrary to expectations, no correlation with the electronic configuration of the substitutent ions could be recognized. However, this study leads to three qualitative conclusions relating the effect of impurities to the transition in conductivity: (1) The transition temperature is unaffected by the conductivity, i.e. carrier concentration, of the crystal. (2) Significant changes in the transition temperature are produced only by high doping levels—on the order of 1 mol %. (3) The direction of the change in transition temperature can be correlated with the relative size of the impurity ion compared to that of the V^{4+} ion.

INTRODUCTION

IT HAS been eight years since Morin[1] first reported a semiconductor-metallic transition in vanadium dioxide single crystals. This discovery sparked considerable interest and led to an effort both to understand the chemistry of VO_2 and to explain the transition between the semiconducting and metallic states. Phase equilibria studies[2–6] have resulted in a reasonably complete phase diagram for the vanadium–oxygen system, and during this period of time, techniques for the growth of single crystals have also been developed. Frequently the latter preceded knowledge of the phase equilibria. In addition to the hydrothermal method[7] used to prepare the crystals measured by Morin, crystals have been prepared by decomposition of V_2O_5[8] and by vapor transport[9].

Paralleling this effort numerous explanations of the transition in conductivity have been advanced. The phenomenon was first explained by Morin[1] who proposed that the conduction band of this substance was split by antiferromagnetic ordering at temperatures below that of the transition, resulting in a semiconducting state. Collapse of this bandgap at the Néel temperature produced a transition to the metallic state. However, it was soon learned that accompanying this transition in conductivity there was a crystallographic transition[10]. Much later[11, 12] evidence became available that VO_2 was not magnetically ordered below the transition temperature.

Taking account of this crystallographic change, Goodenough[13] explained that in the monoclinic phase below the transition temperature vanadium ions were paired along the *b*-axis. Here potential carriers (conduction electrons) were trapped in homopolar bonds extending between these paired ions. Upon transition to the tetragonal (rutile) structure, the positions of these ions were shifted to equidistant spacings along the *c*-tetragonal axis. In this configuration, separation of vanadium ions is less than the critical distance necessary for the onset of the metallic state.

Quite recently Adler and Brooks[14] have described a general model for the semiconductor to metallic transition. Here it is proposed that an energy gap between the conduction and valence bands exists when the material is in the semiconducting state. With rising temperature this gap is decreased by excitation of carriers across it. Rapid disappearance of the gap occurs via a first or second order transition depending on the change in gap with the number of excited carriers. The model treats two possible cases: one in which the gap results from antiferromagnetic ordering and the other where it results from crystallographic distortion.

These models imply that the semiconductor to metallic transition of VO_2 is related to the band structure of this phase and should be sensitive to changes in it. Thus we might expect that substituent impurity ions of different electronic structure from that of the tetravalent vanadium ion would affect the parameters determining the transition and cause a systematic variation, dependent on the electronic structure of the substituted impurity ions.

To investigate this expectancy we have measured numerous single crystals into which different impurity ions, some in more than one concentration, have been incorporated during growth. Although the chemical equilibria governing the incorporation of these ions is complex and the valence state of these ions in the VO_2 lattice is not unequivocal, qualitative assessment of the effects produced by impurities on the electrical properties of this phase is attempted.

In this investigation single crystals of VO_2 were grown by the thermal decomposition of V_2O_5. Here, advantage was taken of the temperature dependence of the decomposition of the V_2O_5 melt to produce stoichiometric single crystals of VO_2 by heating in an inert atmosphere. This same procedure was used to prepare crystals doped with various 3*d* and 4*d* transition metal cations as well as selected second and fourth series cations. Data obtained from four probe resistivity measurements are interpreted in light of prevailing theories relating to this material.

EXPERIMENTAL PROCEDURE AND RESULTS

Crystals of VO_2 can be grown by heating V_2O_5 for several days in a nitrogen atmoshpere at about 1000°C. However, the crystals are usually small needles which are most difficult to remove either chemically or mechanically from the V_2O_5 matrix.

In this paper we report the preparation of large single crystals by a modified decomposition method. This can be characterized as programmed decomposition of V_2O_5. When this phase is melted and held at a high temperature in a reducing or neutral atmosphere, oxygen is continuously removed from the melt in response to the lowered oxygen partial pressure of the atmosphere. When a limiting composition of the melt is reached, VO_2 starts to crystallize at a rate controlled by the temperature and the gaseous atmosphere used. Large crystals are grown by using a crucible with a conical shaped bottom to restrict the area of nucleation and thus minimize the number of nuclei. The rate of crystallization is comparable to that of the Stockbarger–Bridgman method, i.e. on the order of 1–10 mm of axial growth per hour.

A typical run was made as follows: a platinum crucible with a conical shaped bottom, Fig. 1, was filled with approximately 700 g of reagent grade V_2O_5 and positioned in a vertical tubular furnace to give a temperature gradient of 100°C with the cooler end at the bottom. The furnace temperature was raised to 1250°C and held for 12 hr in air to attain equilibrium. Then a nitrogen atmosphere was provided by the flow of nitrogen through the inlet tube of the platinum crucible, Fig. 1. At this point, heating at a rate of one degree per hour was started and continued for 100 hr. Cooling from 1350°C to room temperature was carried out over a 24 hr period. The VO_2 crystals grown by this procedure consisted of an intergrowth which completely filled the bottom of the crucible as shown in Fig. 2. These were easily removed from the V_2O_5

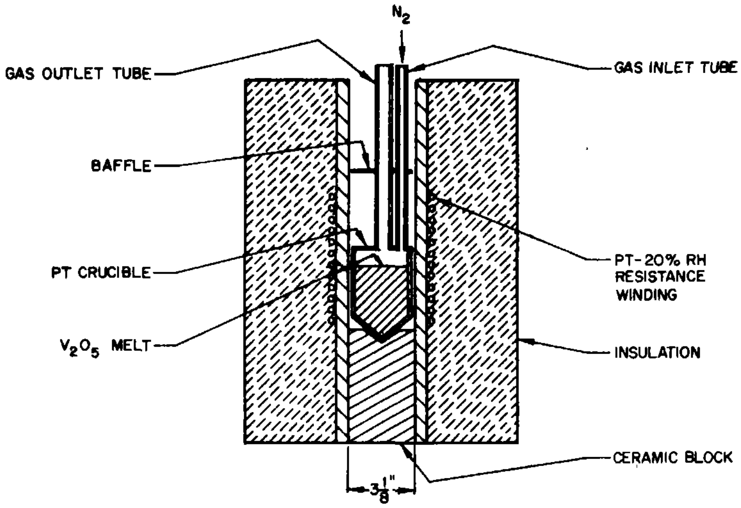

Fig. 1. Crystal growing assembly showing platinum crucible provided with tubes for gas flow over surface of melt.

interface, and as shown in Fig. 3 were easily separated along the (011) plane.

Doping was accomplished by incorporating known concentrations of impurity ions in the melt. During crystallization these were distributed between the liquid and the crystalline phases. The concentration of impurities in the crystals were determined by semiquantitative spectrographic analysis and, where possible, by atomic absorption analysis.

Some of these crystals were X-rayed using CuKα radiation to see if a second phase was present. This proved not to be the case. Resistivity measurements were found to be a better means of characterizing these crystals. Four-probe measurements of resistance were made in the range from approximately 25 to 100°C using a Leeds and Northrup Speedomax Recorder arranged so that the current, voltage, and specimen temperature could be simultaneously recorded. The heating and cooling rates were maintained at approximately 0·25°C/min. Indium-gallium alloy was used as electrodes.

It will be appreciated that the method of growth described is a very different situation than that normally employed in single crystal growth. Usually growth proceeds by cooling from the liquid through the two phase-liquid + crystal-region. In the present method it takes place by gradual decomposition of the liquid phase, which occurs when inert gas (nitrogen in the present case) is passed over the surface of the V_2O_5 melt. Oxygen is removed from the melt as it attempts to establish an equilibrium partial pressure. The composition of the melt is thus shifted toward VO_2 and initiates precipitation of the crystalline phase. Since the rate at which oxygen is removed by the inert gas stream is low, the rate of precipitation is low and controlled. Single crystal growth results.

This method of crystal growth has a further implication. Although homogeneous equilibria, i.e. equilibria between condensed phases and the gas phase is probably not established throughout the system, equilibrium conditions between the condensed phases are approached. To the first approximation, then, VO_2 crystals will be in equilibrium with the liquid phase, and their composition will be fixed by the phase boundary between the liquid and the VO_2 phase. Chemical analysis of representative undoped single crystals grown in this manner showed them to be stoichiometric.

With confidence then that this method of growth yields nominally stoichiometric crystals, we attempted to study the effects produced by foreign ions upon the electrical properties of VO_2. Table 1 lists the single crystals investigated along with the conditions of their growth and impurity concentrations. The electrical characteristics of these crystals are shown by resistivity vs. reciprocal temperature diagrams of Figs. 4–7.

The diagram of Fig. 4 represents data for the undoped specimen. Here comparatively high resistivity (10^2 Ωcm) is observed at room temperature. The transition temperature is clearly marked by a precipitous drop in the

Table 1

Run No	Impurity	Conc added to melt (Mol %)	Conc. of impurity metal found in VO_2 (At. %)
1044	SiO_2	0·05	Not found
623	Al_2O_3	0·8	0·247
1317	Al_2O_3	5·0	0·49
1052	Cr_2O_3	1·0	2·38
1305	Cr_2O_3	5·0	5·17
1045	TiO_2	1·0	0·816
814	MnO_2	1·0	0·015
816	Fe_2O_3	2·0	0·145
817	Co_3O_4	1·0	0·035
815	Nb_2O_5	0·5	1·10

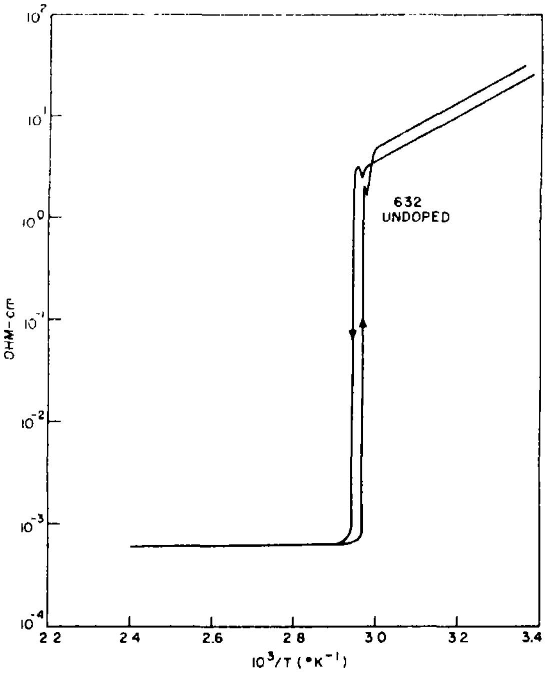

Fig. 4. Resistivity vs. reciprocal temperature ($10^3/T°K^{-1}$) for undoped specimen.

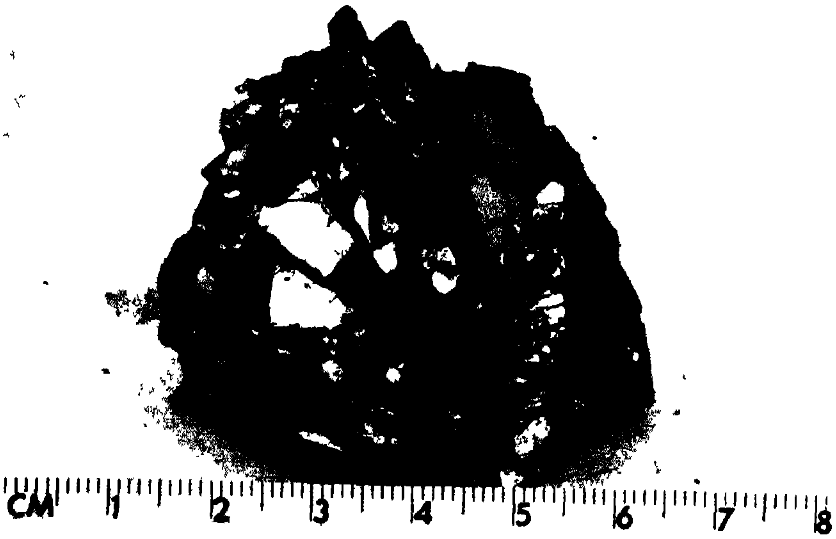

Fig 2 VO_2 crystals as grown, before separation into individual crystals

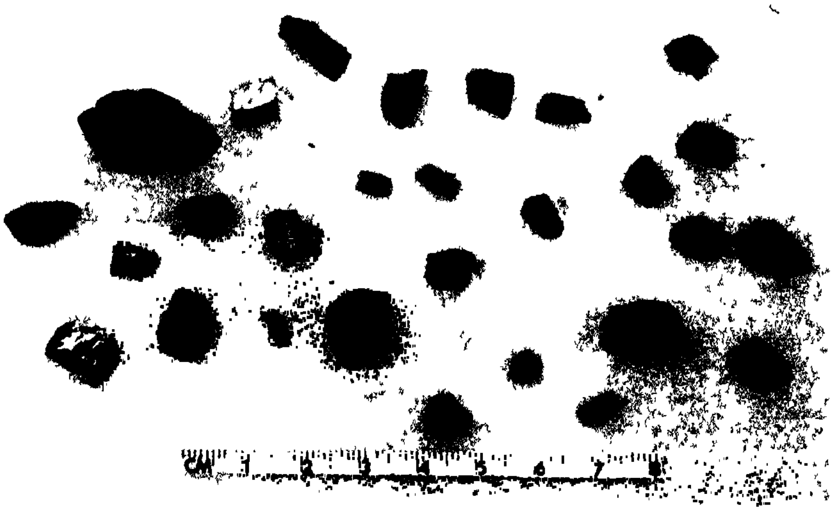

Fig. 3 Typical assortment of single crystals after separation from crystallized mass

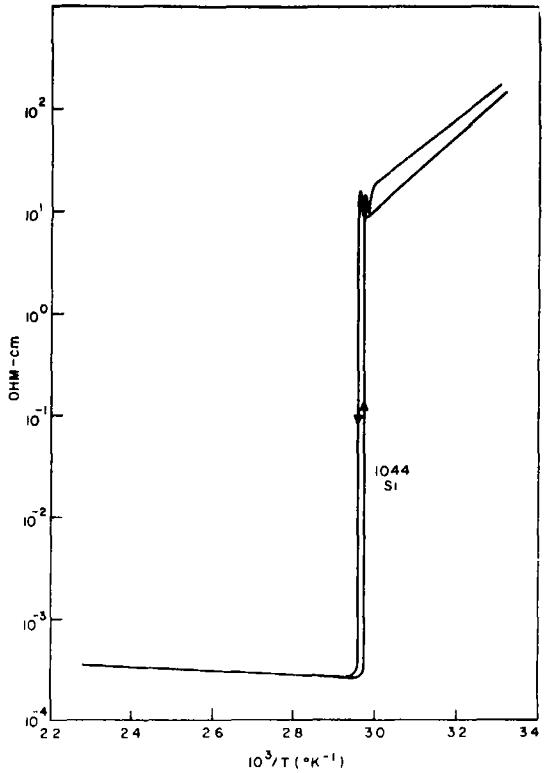

Fig. 5. Resistivity vs. reciprocal temperature for specimen grown from a melt containing 0·05 mole % SiO_2.

resistivity at a temperature of 67°C (2·94 on the reciprocal temperature scale). Above this temperature the conductivity is metallic and the value of resistivity is 6×10^{-4} Ωcm. Upon cooling, a small hysteresis of approximately 2°C is seen before the resistivity returns to the higher values of the semiconducting state. It is to be noted here that the resistivity values for this state are slightly higher than those initially observed. This effect is quite common and may be due to development of micro-fractures in the crystals during cooling through the transition. Another feature of the curve is the small dip in resistivity just below the transition upon cooling. We assume this to be associated with changes of the twining patterns that have been reported, by Fillingham[15], to occur in the immediate vicinity of the transition. Since the anisotropy in the conductivity[9, 16] along the *a*-parallel and *a*-perpendicular monoclinic direction can be greater than one order of magnitude, this effect can easily be accounted for.

Figure 5 shows the results for a specimen grown from a melt containing 0·5 per cent silicon, even though no silicon was detected in the crystal by spectrographic analysis. Atomic absorption analysis is insensitive to this element and was not attempted. The electrical characteristics here are very similar to those observed for the preceding figure, i.e. resistivities in the semiconducting state are high and a very large drop (greater than four orders of magnitude) is observed at the transition. In the high temperature state the conductivity is metallic and the resistance exhibits a positive

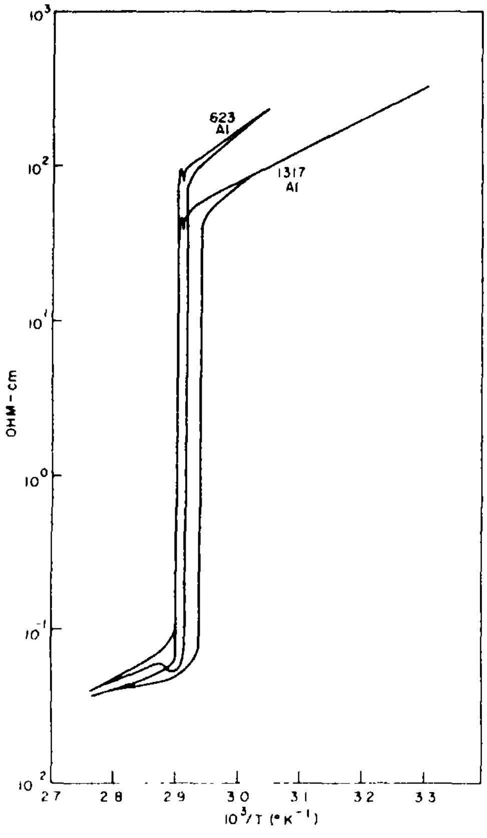

Fig. 6. Resistivity vs reciprocal temperature for specimens containing respectively 0·247 at % Al (#623) and 0·49% Al (#1817)

temperature coefficient. The transition temperature is not significantly altered from that observed for the undoped specimen.

In Fig. 6 results for two aluminum dopings are shown. Here again, comparatively high room temperature resistivities are preserved but the transition is observed to take place between two semiconducting states. It will be noted that the transition temperatures are raised slightly to 72°C.

In Fig. 7 the results of doping with chromium and titanium are shown. Again the reasonably high resistivity levels in the semiconducting state are maintained. The transition appears to take place between two semiconducting states in the case of titanium and between the semiconducting and metallic states in the case of chromium. Two different chromium containing specimens were prepared; the transition temperatures of these are 70° and 72°C. This represents a small increase over that of the titanium doped specimen as well as those undoped and silicon containing specimens shown previously. It will be observed that the cooling curves for the crystals containing chromium are indicated by dashed lines. In both cases the crystals fractured upon passing through the

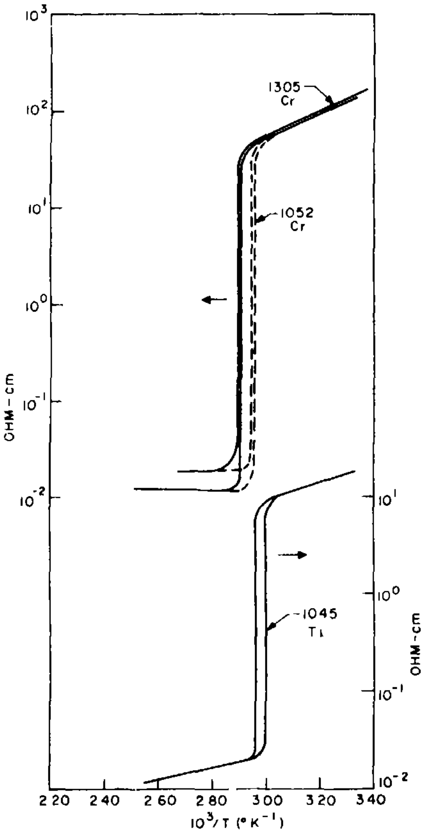

Fig. 7. Comparison of resistivity data for chromium containing crystals. #1052-2·38 at.% and #1305-5·17%, with a titanium doped specimen containing 0·816%. Dashed lines are used to represent the cooling curves of the chromium containing crystals. In each case the crystal fractured after an initial rise in resistivity, presumably the transition, and subsequent measurements were erratic.

transition and erratic resistivity values were recorded below this point.

Measurements for cobalt, manganese and iron doped specimens are compared in Fig. 8.

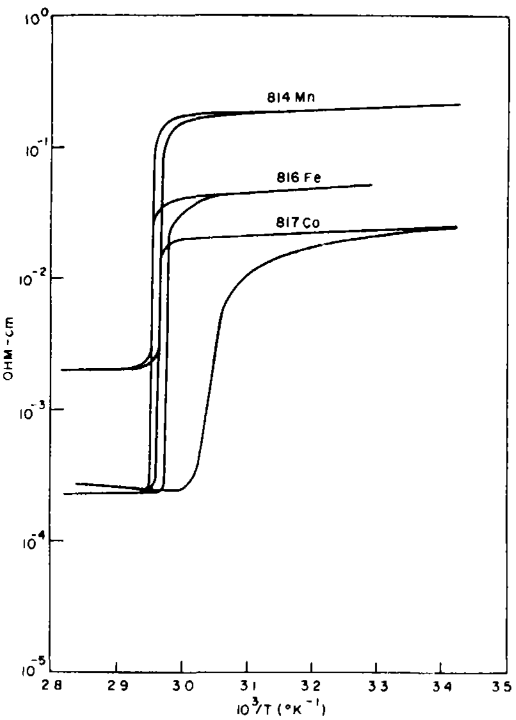

Fig. 8. Comparison of resistivity data for manganese (0·015 at. %), iron (0·145%), and cobalt (0·035 at. %).

These results are qualitatively different from those of the preceding figures. Here the transition appears to take place between semiconducting and metallic states. The resistivity values of these specimens in the higher resistance state are approximately two orders of magnitude below those of the specimens described previously. The transition temperature for the manganese doped specimen is very close to that observed for the undoped while that of the cobalt and iron containing specimens are if anything, slightly raised. The transition magnitude of the resistance changes are not as great as those observed in the previous figures.

In the last of these figures (Fig. 9) we observe the effects of doping with niobium. This shows a decidedly lowered transition temperature, and reduced resistivity in the semiconducting state relative to the undoped specimen.

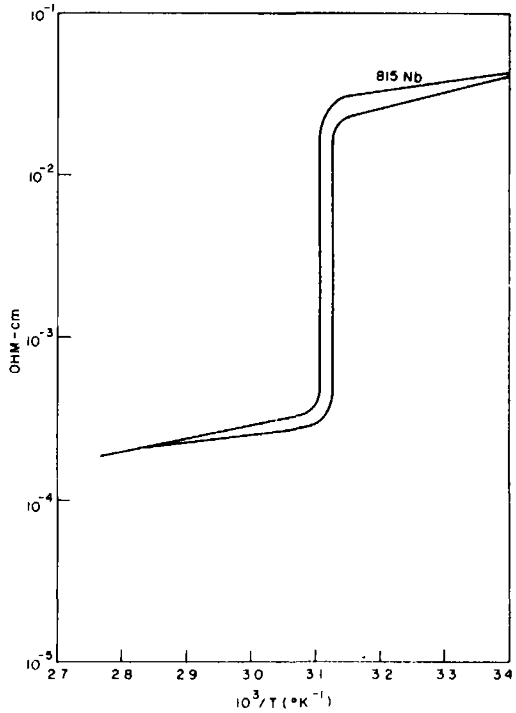

Fig. 9. Resistivity vs. reciprocal temperature for niobium doped specimen containing 1·1 at. % Nb.

DISCUSSION

In the preceding section the term 'decomposition' was used to describe the method of crystal growth. This serves to distinguish the present method from one employing a reducing atmosphere to attain equilibrium within the system during crystal growth. The reason for making this distinction can be appreciated if one considers for the moment the phase rule as applied to the present system. This can be stated as: $P+F=C+2$. The number of components, C, is two: vanadium and oxygen.

Thus, the number of degrees of freedom plus the number of phases is 4. Now if the total pressure is fixed at one atmosphere and the temperature is arbitrarily chosen, only two phases can exist at equilibrium. One of these must be a gaseous phase containing oxygen at some oxygen pressure and the other a condensed vanadium oxide phase. Let's then consider the situation when a liquid phase is present. There exists two degrees of freedom such that temperature and the composition of the gaseous phase can be varied independently (within restricted limits) without changing the phase assemblage. If, however, these limits are exceeded so that a crystalline phase begins to separate, it must proceed at a fixed temperature and oxygen partial pressure until all the liquid disappears.

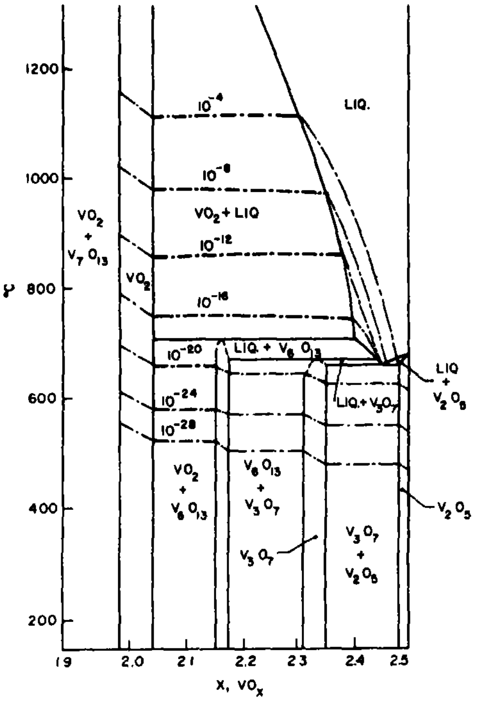

Fig. 10 Phase diagram for vanadium-oxygen system constructed after Kosage[4], MacChesney *et al.*[6] and modified on the basis of recent data. Heavy dash-dot lines are oxygen isobars which denote oxygen partial pressures in atmospheres. Estimates of the position of these in adjoining areas of the diagram are shown by light dash-dot lines.

The implications of this situation to crystal growth of VO_2 can be better appreciated by reference to the phase diagram of Fig. 10. Here dashed curves known as oxygen isobars overlay the diagram. Their significance is that, in a system at equilibrium with an atmosphere of fixed oxygen partial pressure, the total composition of the system will change in response to changing temperature along one of the family of these lines. It is apparent then, that under such conditions, there is only one temperature at which VO_2 and liquid are in equilibrium with an atmosphere of reduced oxygen partial pressure. By maintaining the melt in an atmosphere having an oxygen partial pressure lower than that of its equilibrium partial pressure, oxygen escapes as the liquid phase attempts to establish equilibrium. The rate at which oxygen is removed depends upon the temperature of the melt, the oxygen partial pressure of the atmosphere and the flow rate of the atmosphere. In the present case, oxygen present as an impurity produced an oxygen partial pressure of approximately 10^{-6} atm. At 1250°C the difference between the equilibrium oxygen partial pressure of the melt and that present in the nitrogen atmosphere is small. Controlled nucleation of the VO_2 phase results. Rapid crystal growth was achieved by gradually increasing the temperature while providing a constant flow of nitrogen over the surface of the melt.

Turning our attention now to the effects of impurity ions on the electrical properties of VO_2, it is to be noted that there is an increasing body of information describing the effects of these ions on the semiconduction-metallic transition exhibited by this phase. For some time it has been known, on the basis of the sharp decrease in magnetic susceptibility at this transition, that Nb[17] and Ti [18] lower the transition temperature. It has recently been reported that Ga[19, 20] raises this temperature. Where comparisons can be made, our results are in agreement with these data. In addition we show that Cr and Al also increase the transition temperature.

When trying to apply these results to the models of the semiconductor to metallic transition described earlier, one is surprised that ions of such diverse nature can produce similar effects. For instance, consider those ions that contribute to lowering the transition temperature. Niobium in the tetravalent state would have a $(5d)^1$ configuration, while titanium, in the same valence state is $(3d)^0$. When these are compared to the ions that serve to raise the transition temperature $Cr^{4-}-(3d)^2$ and Al^{3+} and Ga^{3+}, which have noble gas configurations, no consistent variation arises. There is no distinction to be made between diamagnetic and paramagnetic ions. Neither is there any relation to be discerned between the effect of incorporation of these ions on the resistivity—i.e. carrier concentration—of the specimen and its transition temperature. This disparity between the ion-types and their effect on electrical properties leads to the question: can one find a common property between those ions which lower the transition temperature and between those which raise the transition temperature? Certainly it is not obvious that their electronic structures have anything in common.

Here, however, one had better go a bit slow. First, it must be admitted that not much is known about the valence state of these ions when incorporated into the VO_2 lattice, or about the anion stoichiometry of these substituted crystals. To illustrate this point consider the effects produced when vanadium dioxide crystals are doped with iron. Here it is anticipated that Fe^{4+} will substitute for V^{4+}. However, at the temperatures from which these crystals are grown the tetravalent iron ion is not stable, and iron is found in VO_2 as the trivalent ion. Charge compensation is accomplished, according to the interpretation of the Mössbauer spectra of these crystals, Kosage[11] and Wertheim[12], by creation of anion vacancies. The similarities of the resistivity vs. reciprocal temperature behavior exhibited by manganese and cobalt specimens lead us to believe that these behave in a like manner. Gallium and aluminum must also be incorporated in the VO_2 lattice as trivalent ions. However, here different characteristics are observed. The low resistivity and degenerate behavior associated with the oxygen-vacancy defect type does not occur. Instead resistivities remain high and comparable to the values for the undoped specimens. The supposition here is that charge compensation is accomplished by creation of pentavalent vanadium ions. These ions would probably not serve as donors, and the electron concentration would not be appreciably altered by their presence.

The effects of nonstoichiometry is another problem which experimentalists, including ourselves, have not really fully determined. Although a procedure was developed for determining the valence state of vanadium in these crystals, we applied it only to the undoped crystals. These were found to have the composition $VO_{2\cdot01\pm0\cdot01}$. This method used a redox titration which is difficult to apply where other altervalent ions are present and thus was not attempted. However, the reported range of oxygen content exhibited by this phase is large and its possible effect on transition temperatures should not be neglected.

These uncertainties are especially relevant to a discussion of impurity affects on transition temperatures in light of recent studies by Umeda *et al.*[21] and Mitsuishi[22]. These authors report the existence of a third phase at temperatures in the vicinity of the transition. It is characterized by triclinic symmetry and exists, apparently metastably, over varying ranges of temperature. Its occurrence is promoted by the presence of trivalent impurity-cations or oxygen deficiency and where present results in erratic transition temperatures upon repeated cycling through the transition. Although we have not observed this behavior, we were not in every case able to make repeated measurements. The latter mentioned authors 'potted' their specimens to prevent breaking upon cycling through the transition temperature. Mechanical strain introduced in this manner could be responsible for the erratic behavior.

With these considerations in mind it is apparent that no definitive statements can be made concerning the mechanism by which impurities alter the semiconductive-metallic transition temperature. The role these ions play in determining properties is still vague. However, we would like to point out that the ionic radii of those ions which cause an increase in transition temperature, are smaller than that of V^{4+}, or, as in the case of Al^{3+} and Ga^{3+}, are thought to create V^{5+} defects which would be smaller than V^{4+}. All of the ions that cause a decrease in the transition temperature are larger than V^{4+}. It is apparent that transition temperatures are significantly changed only when large concentrations of impurities can be incorporated into the crystal.

Thus it would seem that regardless of the origin of this transition, the effects of incorporation of impurity ions on the transition temperature are not readily explained by invoking changes in the band structure. Rather it appears that if the transition is of electronic origin, then the band structure giving rise to this transitions must be sensitive to changes in the lattice produce by incorporation of impurity ions into VO_2 crystals.

Acknowledgements – It is a pleasure to acknowledge experimental assistance by J. F. Potter and W. J. Ordille. We also appreciate useful discussions with R. H. Walden, C. N. Berglund, and G. A. Rozgonyi.

REFERENCES

1. MORIN F. J., *Phys. Rev. Lett.* **3**, 34 (1959).
2. ANDERSON G., *Acta chem. scand.* **8**, 1599 (1954).
3. AEBI F., *Helv. Chim. Acta* **31**, 8 (1948).
4. KOSUGE K., *J. Phys. Chem. Solids* **28**, 1613 (1967).
5. TUDO J. and TRIDOT A., *C. r. hebd. Séanc. Acad. Sci., Paris* **261**, 2911 (1965).
6. MacCHESNEY J. B., POTTER J. F. and GUGGENHEIM H. J., *J. electrochem. Soc.* **115**, 52 (1968)
7. LAUDISE R. A. and NIELSON J. W., In *Solid State Physics* (Edited by F. Seitz and D. Turnbull), Vol. 12, p. 209. Academic Press, New York (1961).
8. SASAKI H. and WATANABE A., *J. phys. Soc. Japan* **19**, 1748 (1964)
9. BONGERS P. F. *Solid State Commun.* **3**, 275 (1965).
10. WESTMAN S., *Acta chem. scand.* **15**, 217 (1961).
11. KOSUGE K., *J. phys. Soc. Japan* **22**, 551 (1962).
12. WERTHEIM G. K., GUGGENHEIM H. J., and BACHANEN O. N. E., *Bull. Am. Phys. Soc.* **12**, 23 (1967)
13. GOODENOUGH J. B., *Phys. Rev.* **117**, 1442 (1960).
14. ADLER O. and BROOKS H., *Phys. Rev.* **155**, 826 (1967).
15. FILLINGHAM P. J., *J. appl. Phys.* **38**, 4823 (1967).
16. EVERHART C. R. and MacCHESNEY J. B., *J. appl. Phys.* **39**, 2872 (1968).
17. RÜDORFF W. and MARKLIN J., *Z. anorg. allg. Chem.* **334**, 142 (1964).
18. RÜDORFF W., WALTER G. and STADLER J., *Z. anorg. allg. Chem.* **297**, 1 (1958)
19. ARIYA S. M. and GROSSMAN G., *Soviet Phys. solid St.* **2**, 1166 (1960).
20. KITAHIRO I. and WATANABE S., *Jap. J. appl. Phys.* **6**, 1023 (1967).
21. UMEDA J., ASHIDA S., KUSUMOTO H. and NARITA K., *J. phys. Soc. Japan* **21**, 1461 (1966).
22. MITSUISHI T., *Jap. J. appl. Phys.* **6**, 1060 (1967).

J. Phys. Chem. Solids Pergamon Press 1969. Vol. 30, pp. 235–242. Printed in Great Britain.

PROTON AND DEUTERON MAGNETIC RESONANCE IN PARTLY DEUTERATED CRYSTALS–III. GYPSUM†

GARY HUTTON
Fysisk institutt, Universitetet i Oslo, Oslo 3, Norway
and
BJØRN PEDERSEN
Sentralinstitutt for industriell forskning, Oslo 3, Norway

(*Received* 24 *June* 1968; *in revised form* 12 *August* 1968)

Abstract—Single crystals of gypsum containing approximately 50 per cent deuterium have been made by heating natural gypsum crystals in heavy water at 110°C for 24 hr. The room temperature D(euteron)MR- and P(roton)MR-spectra of these partly deuterated crystals have been analyzed in detail. The water molecules are flipping fast at room temperature making the two deuterons in each molecule magnetically equivalent. The quadrupole coupling constant has been found to be 118·3 ± 0·7 kHz and the asymmetry factor 0·877 ± 0·009 The directions of the principal axes are closely related to the orientation of the water molecule as given by neutron diffraction.

From the hyperfine structure in the DMR-spectra and the second moments of the PMR-spectra the mole fractions of H_2O, HDO and D_2O molecules in the crystal are derived. The deuteron distribution in the crystal is found to be different from a random distribution on the available sites. The data indicate that the molecular distribution within the crystal is random, but intermolecular proton–deuteron exchange does not seem to take place inside the crystal to a measurable extent.

LARGE SINGLE crystals of gypsum are easily available from natural sources[1], and the physical and chemical properties of gypsum are well known[2]. The crystal structure was determined as early as 1936 from X-ray diffraction data[3] and the structure was refined from neutron diffraction data in 1958 [4]. Gypsum was the first hydrate to be studied with proton magnetic resonance (PMR) methods by Pake[5] who analyzed the fairly well resolved fine structure by PMR-spectra. Later, investigations of the asymmetry of the individual line components in the PMR-spectra[6], the second moment of the spectra [7] and the spin-lattice relaxation time[8, 9] of gypsum have been carried out.

We will in this paper report on the exchange of protons with deuterons in single crystals of gypsum, and discuss the information obtained from the deuteron- and proton-magnetic resonance spectra of these partly deuterated crystals. The knowledge of the crystal structure permits a detailed discussion of the obtained results. As in the earlier studies of partly deuterated hydrates in our laboratory [10] we have discussed the orientation of the principal axes of the electric field gradient relative to the orientation of the water molecule. Furthermore, we will show that the spectra contain useful information on the deuteron distribution in the crystals. Natural single crystals have been used where a fraction of the protons has been exchanged with deuterons at 110°C, and the deuteron distribution will depend on the diffusion processes operative in gypsum at this temperature.

EXPERIMENTAL DETAILS

The deuterated crystals were prepared directly from natural crystals‡ by the simple method of proton-deuteron exchange. The exchange was accomplished by immersing

---

†This work was supported by The Royal Norwegian Council for Scientific and Industrial Research

‡Selenite crystals from Kansas through Filer's and crystals of unknown source from Ward's Natural Science Establishment.

the natural crystals in 99·7 per cent D_2O at 110°C in a closed pyrex glass tube for 24 hr. The crystals were sanded to the form of a cylinder and the amount of D_2O in the tube was approximately 5 times the water content in the crystal. The extent of exchange was measured by measuring the concentration of protons in the liquid with high-resolution NMR-technique. In the crystal used in the recording of the PMR-spectrum in Fig. 1, 35 per cent of the protons were exchanged, which means that the concentration of D_2O in the liquid only dropped from 99·7 per cent to about 93 per cent.

This method of producing deuteron containing single crystals is quite reliable, but temperature control must be within ±2° in order to give reproducible results. To give examples of the temperature sensitivity of the exchange of protons with deuterons: there are only a few per cent proton-deuteron exchange if a crystal is treated at 105°C for 2 to 3 weeks (about 400 hr), but about 50 per cent exchange for crystals treated at 110°C for 24 hr. Also one crystal which was treated at 125°C for 24 hr was completely deuterated, but was polycrystalline even though its shape was unchanged.

On the crystals treated at 110°C a polycrystalline surface was formed on all faces except (010) making the crystal difficult to orient optically. Only in the case of the *b*-axis rotation was it possible to use fully the precision inherent in the optical goniometer. The reason for this was that the proton-deuteron exchange seemed to be highly anisotropic and only left the (010) face relatively clean. This is understandable from the crystal structure as the crystal is built up of layers of cations and anions normal to the *b*-axis, and these layers are interconnected with a water layer[3, 4]. It is therefore probably much easier for the water molecule to diffuse within one layer than to get through the ionic layer separating one water layer from the next. The internal appearance of the crystals after treatment (110°C for 24 hr) was marked by white translucent striations in the [101] direction. This process of proton-deuteron exchange should be studied further, but, for the present investigation it was adequate to insure that the resulting crystals were free from distortions and were still good gypsum single crystals. This was shown to be the case by the appearance of the PMR- and the DMR-spectra.

The DMR- and PMR-spectra were recorded using a Varian Associates (Mod. V-4200B) wide line spectrometer and the (mod. V-4012A) 12 in. electromagnet system with the 'Fieldial' control. The frequency for the DMR-spectra was approximately 9·2 MHz and for the PMR-spectra approximately 16·0 MHz, which allowed the use of only one probe (V-4230B 8–16 MHz) and prevented an accidental misalignment of the crystal during a probe change. The crystal was rotated about an axis oriented perpendicular to the magnetic field and the spectra recorded every 10° covering a range of 180°. The DMR- and PMR-spectra were recorded for exactly the same crystal orientations making it possible to accurately relate them to each other. The field was calibrated using a liquid sample and the sweep was found to be linear within the accuracy of measurement. The limiting factor in the accuracy of the line splittings was the uncertainty of the absolute orientation of the crystal in the magnetic field. This uncertainty was estimated to be ±1·5°.

EXPERIMENTAL RESULTS

The gypsum structure is monoclinic with one water molecule in the asymmetric unit [4]. The two H-atoms in each water molecule are therefore crystallographic non-equivalent. The water molecules can be divided in two symmetry related sets with each member of each set oriented parallel to all the other members of its own set. This means that, with regard to *proton* magnetic resonance, only when the magnetic field is normal to or along the *b*-axis, are all the proton positions magnetically equivalent. In all other orientations we have two sets of magnetically equivalent protons[5, 6]. From the standpoint of *deuteron* magnetic resonance however, there will be *four* magnetically different deuteron sites in the crystal in the general orientation and *two* magnetically different deuteron sites when the magnetic field is orthogonal to or parallel to the *b*-axis as the two deuterons within each molecule are not related by symmetry. This is true if the water molecules are static, however, if they are flipping sufficiently fast, then, on the average, the two deuterons in each water molecule will be magnetically equivalent[8]. In this fast-flipping case, the number of line components in the DMR-spectra will be the same as in the PMR-spectra; if they are static the number of lines in the DMR-spectra will be twice the number of lines in the PMR-spectra.

We have recorded the PMR- and the DMR-spectra of the gypsum crystals at room temperature rotating the crystal in steps of 10°C about the axes *a*, *b* and c^* (the Atoji and Rundle[4] axes). The number of quadrupole split lines in the DMR-spectra, maximum four, is the same as observed in the PMR-spectra which immediately tells us that the water molecules are flipping fast[8]. This is as expected because the activation energy hindering the flip motion in gypsum is about the same as in barium chlorate monohydrate where Chiba[11] has found that the water molecules are flipping fast enough above −40°C†. Some examples of the DMR-spectra are given in Fig. 1. PMR-spectra of gypsum have earlier been published by Pake[5].

The line components in the DMR-spectra show a partly resolved fine structure due to the dipole–dipole coupling in some orientations. The shapes of the PMR-spectra are about the same as found for the undeuterated crystals[7, 8]. We will first discuss the quadrupole coupling and deduce the quadrupole coupling tensor from the main splitting in the DMR-spectra. We will then discuss the dipole–dipole fine structure in the DMR- and the PMR-spectra and the information obtained from this coupling.

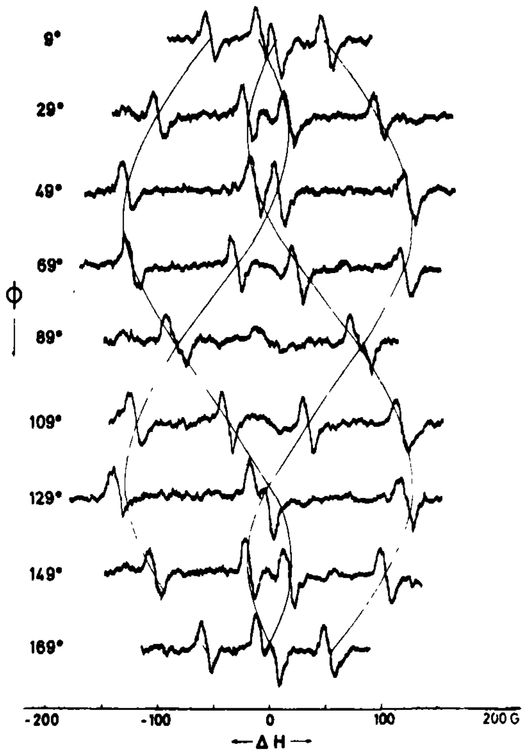

Fig. 1. Some experimental DMR-spectra of gypsum obtained by turning the crystal about the c^*-axis. ϕ is the angle between the magnetic field and the *a*-axis. The drawn curve is calculated from equation (2) with the coefficients given in Table 1.

THE QUADRUPOLE COUPLING

The coupling between the electric quadrupole moment of the deuteron and the electric field gradient at the deuteron site splits the DMR-spectrum in two line components separated by ΔH. ΔH is directly proportional to the component of the electric field gradient $\mathcal{V}$ along the magnetic field e_H and can always be written[12]:

---

†The temperature dependence of the gypsum spectra is presently being studied in our laboratory, and the results will be presented later.

$$\Delta H = \frac{2\pi}{\gamma}\frac{e^2qQ}{h} e_H \cdot V' \cdot e_H \qquad (1)$$

$$\Delta H = A + B \cdot \cos 2\phi + C \sin 2\phi. \qquad (2)$$

Here e^2qQ/h is the quadrupole coupling constant, ϕ is the angle between the magnetic field and a reference line in the plane normal to the axis of rotation. We have measured ΔH as a function of ϕ for three different orthogonal axes. The coefficients in equation (1) have been determined by least squares methods as discussed earlier[10], and the obtained values are given in Table 1. Some representative DMR-spectra are given in Fig. 1.

Table 1. Experimental coefficients (equation (1)) (Standard deviations in parenthesis)

Axis of rotation	Reference axis	A (G)	B (G)	C (G)
a	b	−27·7 (0·4)	192·2 (0·6)	±27·7 (1·0)
b	c^*	−82·2 (0·4)	−137·6 (0·5)	−102·8 (0·5)
c^*	a	109·9 (0·4)	−54·6 (0·5)	±137·5 (0·5)

* The coefficients given in Table 1 have been corrected for small misalignments of the rotation axes by requiring that they satisfy the interrelationships given by Volkoff, Petch and Smellie[13], and also shifted so that the ϕ rotations are referred to the proper crystal axes[10]

From the experimental values of the coefficients in equation (1) we have calculated the quadrupole coupling constant, the asymmetry factor and the directions of the principal axes using the method of Volkoff *et al.*[13]. The obtained values of the quadrupole coupling constant and the asymmetry factor η at room temperature are:

$$\frac{e^2qQ}{h} = 118{\cdot}3 \pm 0{\cdot}7\,\text{kHz};\ \eta = 0{\cdot}8772 \pm 0{\cdot}0086.$$

The direction cosines of the principal axes are given in Table 2 together with the direction cosines of some specific directions connected to the orientation of the water molecule as calculated from the atomic positions determined by Atoji and Rundle[4]. We see that the uncertainty in the direction cosines of the principal axes are smaller than the uncertainty of the direction cosines from the neutron diffraction study. The data in Table 2 strongly indicate that the orientation of the principal axes is closely connected to the orientation of the water molecule as generally found[10, 14]. The angle between each of the principal axes and the direction it is compared to is about 10°, but due to the fairly large uncertainty this angle is not significantly different from zero. However, we will return to the relative orientation of R and Z-axis at the end of this paper.

Table 2. Direction cosines of the principal axes X, Y and Z of the electric field gradient and direction cosines of some directions connected to the water molecule (standard deviation in parenthesis)

	a	b	c^*
X	−0·740(0·016)	0·606(0·011)	0·292(0·017)
normal from O to R	−0·704(0·030)	0·567(0·032)	0·428(0·030)
Y	0·332(0·004)	−0·047(0·003)	0·942(0·014)
normal to the H_2O plane	0·333(0·030)	−0·268(0·030)	0·904(0·030)
Z	0·585(0·010)	0·794(0·010)	−0·167(0·023)
R	0·627(0·028)	0·779(0·023)	0·004(0·030)

THE DIPOLE COUPLING

The shape of the dipole broadened line components in the NMR-spectra of a partly deuterated crystal depends both on the deuteron distribution and on the positions of the H and D atoms in the crystal. In the first partly deuterated crystal we investigated, the fine structure in the spectra, determined by the *intra*-molecular dipole–dipole coupling, was well resolved making it possible to obtain separate spectra from each of the molecular species present: D_2O, DHO and H_2O[10, 15]. The relative intensity of each of these spectra gave us directly the mole fractions of each of the molecular species. In the spectra of gypsum, however, the fine structure is less resolved, due to the much stronger *inter*-molecular coupling, and the spectra from each of the molecular species strongly overlap. We are then confronted with the task of extracting information on the deuteron distribution and the atomic positions simultaneously. To simplify the discussion, however, we will first discuss the deuteron distribution and then the atomic positions derived.

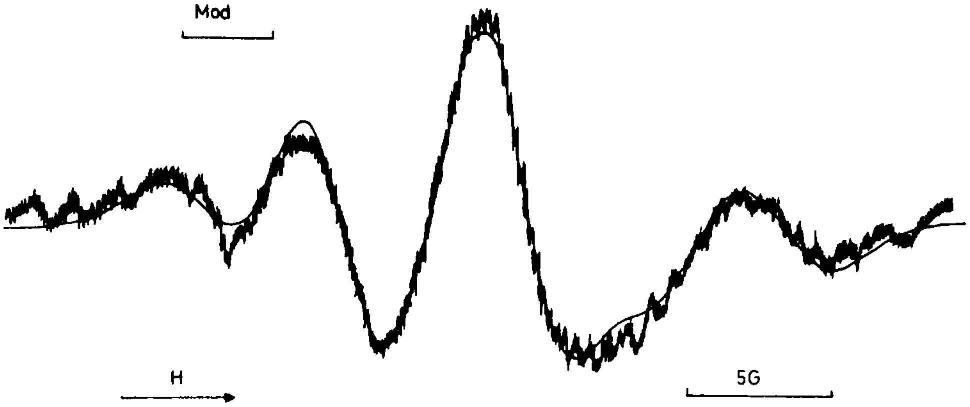

Fig. 2. The high-field line component in the DMR-spectrum of gypsum at room temperature showing the dipolar hyperfine structure. The crystal was oriented with the magnetic field in the (001)-plane making an angle of 119° with the *a*-axis.

THE DEUTERON DISTRIBUTION

The most direct information on the deuteron distribution is obtained from the analysis of the hyperfine structure in the DMR-spectra. Figure 2 shows one of the line components in the DMR-spectrum where the hyperfine structure is most resolved. A theoretical spectrum has been fitted to the experimental spectrum by least squares methods[16]. This curve fitting gives us directly the ratio $[HDO]/[D_2O]$ as the intensity of the two outermost peaks compared to the innermost D_2O-triplet is a measure of the number of HDO-molecules to D_2O-molecules in the crystal[15].

We have earlier determined the fraction of protons substituted by deuterons in the crystal and for the crystal under investigation we found

$$g = \frac{2[D_2O]+[HDO]}{2[D_2O]+2[HDO]+2[H_2O]}$$

$$= x_{DD}+\tfrac{1}{2}x_{HD} = 0{\cdot}35\pm 0{\cdot}05$$

$$[HDO]/[D_2O] = x_{HD}/x_{DD} = 0{\cdot}21\pm 0{\cdot}04$$

where [ABO] = number of ABO-molecules per unit volume and x_{AB} = mole fraction of ABO-molecules.

From these two ratios we can calculate the mole fraction of each of the molecular species, and we obtain:

$$x_{DD} = 0{\cdot}32 \pm 0{\cdot}05;\ x_{HD} = 0{\cdot}07 \pm 0{\cdot}02;$$
$$x_{HH} = 0{\cdot}61 \pm 0{\cdot}05.$$

The mole fraction of the different molecular species can also be obtained from the PMR-spectra. We have recorded the PMR-spectra for the orientations when the magnetic field is normal to the b-axis. Due to the fairly large intermolecular coupling the fine structure is not completely resolved in this orientation, and the analysis must therefore be based on the total second moments[7]. For a partially deuterated crystal the theoretical total second moment is given as:

$$M_2 = [k_H{}^2(1-z) + k_D{}^2 z]M_{2p} + [k_H{}^2 x_{HH} + \tfrac{1}{4}(k_H + k_D)^2 x_{HD} + k_X{}^2 x_{DD}]M_{2q} \qquad (1)$$

where

$$k_H{}^2 = (3\mu_H/2)^2;\ k_D{}^2 = 2\mu_D{}^2/3$$
$$M_{2p} = (R^{-3}[3\cos^2\delta\cos^2(\phi-\phi_0) - 1])^2 \qquad \text{(Intrapair)}$$
$$M_{2q} = \frac{1}{8}\sum_{j=2}^{N}(b_{11,j1} + b_{11,j2} + b_{12,j1} + b_{12,j2})^2 \qquad \text{(Interpair)}$$

R = intrapair distance; δ = angle between R and plane of rotation of magnetic field vector; ϕ_0 = rotation angle reference to a crystal axis.

$$b_{1i,j1} = (3\cos^2\theta_{1i\,j1} - 1)r^{-3}_{1i\,j1}$$

$r_{1i,j1}$ = distance between atom 1 of pair i to atom 1 of pair j; $\theta_{1i,j1}$ = angle between field and $r_{1i,j1}$; $z = x_{HD}/(2x_{HH} + x_{HD})$.

As $k_D{}^2$ is only 3 per cent of $k_H{}^2$ the equation can be simplified to

$$M_2 = (1-z)k_H{}^2M_{2p} + (x_{HH} + 0{\cdot}25x_{HD})k_H{}^2M_{2q}. \qquad (2)$$

Table 3. Experimental and calculated second moments of gypsum

ϕ	$k_H{}^2M_{2p}$	$k_H{}^2M_{2q}$	M_{2t}	M_{2x}
0	0·59	5·89	4·8	4·6
10	0·50	5·43	4·5	4·4
20	0·09	4·14	3·4	3·3
30	0·15	2·61	2·6	2·7
40	1·64	1·61	3·4	3·4
50	5·19	1·67	6·5	6·3
60	10·60	2·84	11·9	11·1
70	16·77	4·68	18·4	18·6
80	22·03	6·43	24·0	23·3
90	24·81	7·34	27·0	27·6
100	24·22	7·06	26·3	26·7
110	20·35	5·75	22·1	22·0
120	14·68	4·01	16·2	16·4
130	8·60	2·63	10·0	9·8
140	3·74	2·18	5·5	6·2
150	0·92	2·79	2·4	3·9
160	0·01	4·07	2·3	3·5
170	0·23	5·33	4·1	4·0

$k_H{}^2M_{2p}$: *intra*-molecular part of the second moment.

$k_H{}^2M_{2q}$: *inter*-molecular part of the second moment.

M_{2t}: calculated total second moment, equation (2).

M_{2x}: experimental second moment.

M_{2p} has been calculated from the value $3\mu_H R^{-3} = 10{\cdot}0$ G found earlier[7] and $\phi_0 = 3{\cdot}3°$ and $= 51{\cdot}6°$. (The choice of these values for the angles ϕ_0 and will be discussed below). M_{2q} has been calculated using the H-coordinates of Atoji and Rundle[4] taking into account the eight nearest neighbour water molecules. The calculated values of $k_H{}^2M_{2p}$ and $k_H{}^2M_{2q}$ together with the experimental second moments are given in Table 3. The experimental second moments have been analyzed by fitting the observed values to an equation of the following form by least squares methods:

$$M_{2t} = A + Bk_H{}^2M_{2p} + Ck_H{}^2M_{2q}. \qquad (3)$$

We find $A = 1{\cdot}03$ G^2, $B = 0{\cdot}882$; $C = 0{\cdot}552$.

The constant A has been included to take into account the coupling of the next nearest neighbours not included in the calculation of

M_{2q}. From equation (2) we can now calculate the values of the mole fractions from the values of B and C, and we get:

$$x_{DD} = 0{\cdot}34; \quad x_{HD} = 0{\cdot}14; \quad x_{HH} = 0{\cdot}52.$$

It is difficult to estimate uncertainty limits in these values, but these values are in fair agreement with the values found from the analysis of the DMR-spectrum given above. The mole fraction of HDO-molecules is larger by a factor of two from the value found above. However, x_{HD} is still much smaller than expected if the deuterons in the crystals were distributed randomly on the available sites because then $\chi_{DD} = g^2 = 0{\cdot}12$, $x_{HD} = 2g(1-g) = 0{\cdot}46$ and $x_{HH} = (1-g)^2 = 0{\cdot}42$. As the crystal was made by proton–deuteron exchange from a reservoir of between 93–100 per cent D_2O this result can be interpreted on the basis of two different models for the diffusion process: (1) The proton-deuteron exchange is a molecular process where molecules from the surroundings are exchanged with molecules in the crystal and no inter-molecular proton-deuteron exchange takes place within the crystal. The distribution of all the molecular species is uniform in the crystal. (2) The partly deuterated crystal consists of a shell of mainly D_2O-molecules and an unperturbed core of H_2O-molecules and the HDO-molecules are found at the interface between these two phases.

We will now show that the spectrum in Fig. 1 also contains information making it possible to distinguish between these two models.

The theoretical spectrum in Fig. 2 is calculated on the basis of gaussian line components, $\exp(-h^2/2\beta^2)$, and the broadening parameter for the HDO-fine structure, β_H, is found to be approximately equal to the broadening parameter for the D_2O-fine structure, β_D: $\beta_H = 1{\cdot}11$ G and $\beta_D = 1{\cdot}06$ G. This tells us that on the average the HDO and the D_2O-molecules experience the same local surroundings. Hence, the different molecular species, HDO and D_2O, are uniformly distributed inside the crystal. As a proton neighbour gives about 3 times the contribution from a deuteron to the local dipole field at a deuteron site, β should be a susceptible measure of the average total field. If, therefore, the crystal had contained regions with a high concentration of D_2O molecules β_D would have been much smaller than β_H. The data therefore support the deuteron distribution (1): A random distribution of the different molecular species and with the concentration of each species equal to the number diffusing into the crystal.

In equation (1) above for the second moment it has been assumed that the model (1) applies. If we assume that model (2) applies the value of C in equation (3) should have been found approximately equal to 1, as then the H_2O-molecules will be surrounded by H_2O-molecules. The experimental value is 0·55 which is far from 1, and we reject model (2) for this reason.

To check this conclusion made on the basis of an analysis of only one single crystal we have also prepared another. A crystal was prepared by heating in a 1 : 1 mixture of D_2O and H_2O in the same manner as before, and a fraction $g = 0{\cdot}23$ of the protons was substituted with deuterons. The crystal was oriented similarly to the crystal used when recording the DMR-spectrum shown in Fig. 1, and a similar spectrum was recorded. The signal/noise was not as good but the analysis gave $[HDO]/[D_2O] = 1{\cdot}9 \pm 0{\cdot}2$. If proton-deuteron exchange takes place inside the crystal the ratio $[HDO]/[D_2O]$ should have been 6·70. however, the found value $1{\cdot}9 \pm 0{\cdot}2$ shows that this ratio is equal to the ratio in the liquid. This supports the conclusion drawn above that the number of HDO and D_2O-molecules in the crystal are equal to the number diffusing into the crystal.

THE ATOMIC POSITIONS

The orientation dependence of the *intra*-molecular dipole coupling is determined by the orientation and length of the intra-molecular H–H line. The angular variation of the *inter*-molecular dipole coupling is in addition determined by the location of this H–H line in the unit cell. It is a general experience from the analysis of second moment data that it is difficult to locate with any precision the position of the H–H line in the unit cell. We will therefore limit this discussion of the angular dependence of the dipole-coupling to the information we can get on the orientation of the H–H line, R. In Table 4 the angles R make with the crystallographic axes a, b and c^+ are given. These values are derived from the values of ϕ_0 and δ chosen in the equation for the intra-molecular part of the second moment given above. The values of ϕ_0 and δ have been determined from a first moment least squares fit, and we estimate the uncertainty to be: $\phi_0 = 3·3° \pm 2·0°$ and $\delta = 51·6° \pm 1·0°$.

Table 4. The angles R *and the Z-axis make with the crystallographic axes (in degrees)*

	a	b	c^+
Z-axis	52·2 ± 0·7	37·4 ± 1·0	99·6 ± 1·4
R (neutron dif), reference [4]	51·1 ± 2·0	38·8 ± 1·3	89·8 ± 1·8
R (dipole-coupling)	51·4 ± 1·0	38·4 + 1·0	87·4 ± 2·0

From the data in Table 4 it can be concluded that the orientation of R as determined from the second moment data within the experimental uncertainty is equal to the direction of R as determined from neutron diffraction data. However, the direction of the Z-axis seems to deviate significantly from R. R seems to be located in the a–b plane, but the Z-axis is making an angle of about 10° with this plane. As the principal axes determined in this study are the averages of two non-equivalent principal axes systems the physical basis for this deviation is probably easier to discuss when the low temperature study of gypsum, now in progress, has been completed.

Acknowledgement – We would like to thank Mrs. Merete Jørve for technical assistance.

REFERENCES

1. *Dana's System of Mineralogy*, 7th Edn, p. 481. Wiley, New York (1952).
2. *Gmelins Handb Anorg. Chem.* **28**, 725 (1961).
3. WOOSTER W. A., *Z. Kristallogr.* **94**, 375 (1936).
4. ATOJI M. and RUNDLE R. F., *J. chem. Phys.* **29**, 1306 (1958).
5. PAKE G. E., *J. chem. Phys.* **16**, 327 (1948).
6. PEDERSEN B. and HOLCOMB D. F., *J. chem. Phys.* **38**, 61 (1963).
7. PEDERSEN B., *J. chem. Phys.* **39**, 720 (1963)
8. HOLCOMB D. F. and PEDERSEN B., *J. chem. Phys.* **36**, 3270 (1962).
9. LOOK D. C. and LOWE I. J., *J. chem. Phys.* **44**, 2995 (1966)
10. PEDERSEN B., *Acta chem. scand.* **22**, 453 (1968); HÄLAND K. and PEDERSEN B., Submitted to XVth Colloque Ampere, Grenoble (1968).
11. CHIBA T., *J. chem. Phys.* **39**, 947 (1963).
12. COHEN M. H. and REIF F., *Solid St. Phys.* **5**, 333 (1957)
13. VOLKOFF G. M., PETCH H. E. and SMELLIE D. W. J., *Can. J. Phys.* **30**, 270 (1952).
14. CHIBA T. and SODA G., *Proceedings of the XIVth Colloque Ampere, Ljubljana*, p. 721. North–Holland, Amsterdam (1967)
15. PEDERSEN B. and HALAND K., *Chem. Phys. Lett.* **2**, 61 (1968)
16. HÅLAND K. and PEDERSEN B., *J. chem. Phys.* **49**, in press (1968).
17. PEDERSEN B., *J. chem. Phys.* **41**, 122 (1964).

J. Phys. Chem. Solids Pergamon Press 1969. Vol. 30, pp. 243–248. Printed in Great Britain.

PREPARATION AND TRANSPORT PROPERTIES OF EPITAXIAL HgTe FILMS

G. A. ANTCLIFFE and H. KRAUS
Texas Instruments Incorporated, Dallas, Texas 75222, U.S.A.

(*Received* 18 *April* 1968; *in revised form* 22 *July* 1968)

Abstract – Highly perfect, epitaxial HgTe films have been successfully deposited on semi-insulating CdTe substrates using vapor phase epitaxial techniques. This report describes the preparation of these films and also a number of electrical measurements which were performed over the temperature range 4·2–300°K in order to characterize these thin semimetal layers. It was found that the electrical properties were considerably complicated by the presence of cadmium which diffused from the substrate during film growth. Nevertheless, apparent electron mobilities greater than 10^5 cm^2/V sec and apparent electron densities about 2×10^{15} cm^{-3} were encountered. Strong quantum oscillations were observed in the magnetoresistance at 4·2°K which represents the first observation of the Shubnikov–de Haas effect in a thin film of any material. Also at 4·2°K, nonohmic conduction was observed at electric field strengths greater than about 5 V/cm. Evidence was obtained to suggest that this behavior was due to a warm electron distribution and therefore a field dependent electron mobility.

1. INTRODUCTION

EPITAXIAL growth of the semimetal HgTe on a CdTe substrate in an isothermal environment has been reported[1]. However, such a method offers little control over the kinetics of the film growth and we have therefore, considered the application of the more usual techniques of vapor phase epitaxy to the deposition of epitaxial HgTe layers. While CdTe is an ideal substrate material in many respects, any diffusion of Cd into the HgTe during film growth will play an important role in determining the electrical characteristics of the film since it is well known that the electron effective mass varies rapidly with composition in the HgCdTe alloy system[2, 3]. Thus the presence of Cd in the HgTe layer will drastically modify the band structure and lead to complications in the film characteristics which would not be expected to occur in pure HgTe.

The present paper describes the preparation of highly perfect epitaxial HgTe films on semi-insulating CdTe substrates together with some measurements of their electrical transport properties in the temperature range 4·3–300°K. One of the most interesting results to come from these measurements was the observation that the carrier mobility was not badly degraded by the presence of the spatially non-uniform Cd distribution resulting from diffusion from the CdTe substrate. In fact, the mobility was sufficiently high so that strong magnetoresistance oscillations could be observed, which, to the best of our knowledge, represents the first observation of magnetic quantum effects in an epitaxial layer. It was also observed that the electrical conductivity of the films investigated increased significantly at electric fields greater than about 5 V/cm while the carrier concentration remained constant. This behavior has been interpreted as resulting from a mobility increase induced by moderate heating of the electron distribution by the electric field.

It should be pointed out that a detailed analysis of most of the transport data to be described below will not be attempted in this paper. The reason for this is that the presence of diffused Cd will most certainly lead to gradients in mobility and carrier concentration which cannot be described in a straightforward way. The presence of a magnetic field will complicate the issue still further[4]. The following sections therefore, contain only sufficient qualitative discussion to illustrate what we consider to be the most striking features of these epitaxial HgTe films. Nevertheless, it is our opinion that these results demonstrate very clearly the important and often unique properties which are peculiar to a thin epitaxial layer.

2. EXPERIMENTAL

Single crystal layers of HgTe were prepared by the following vaporphase reaction:

$$Hg_{(g)} + \tfrac{1}{2}Te_{2(g)} \rightleftharpoons HgTe_{(c)}.$$

The epitaxial deposition took place in an open tube reactor system shown schematically in Fig. 1. The reactor had four temperature zones which were independently controlled to within ±1°C with proportional control equipment. Ultra-pure mercury (Hg-9, E. H. Sargent Co.) and six-nines tellurium (ASARCO) were used as the source materials. The respective vapor species were transported by passing a palladium catalyzed hydrogen stream over the heated reservoirs during the entire deposition cycle. Single crystal CdTe substrates approximately 1 mm thick and 8 mm in dia. were used and the films were deposited on [211], [111]*A* or *B*, [110] and [100] surfaces. After polishing to a surface finish of 0·3 μ with wet alumina powder, the substrates were etched with a bromine/methanol mixture to remove surface damage incurred during polishing. In addition, some thermal etching took place during the heating period of the reactor. Before heating, the entire system was flushed with He followed by H_2. The vapor sources, the reaction zone, and the substrate zone were then brought up to operating temperature as quickly as possible (15–30 min) during which time the hydrogen flow through the reservoirs was kept to a minimum (2–5 ml/hr). Once the temperature zones had been stabilized, the hydrogen flows were increased to the desired levels. After deposition had been completed, the run was terminated by rapidly cooling the outer walls of the entire reactor via a high velocity stream of compressed air. At 96 mm of Hg and 0·1 mm of Te_2, the optimum H_2 flow rate was 20 ml/min and 50 ml/min, respectively. The flow through the reactor, excluding reservoirs, was 80 ml/min. Under those conditions and with a reaction zone temperature of 480°C and a substrate temperature of 470°C, highly perfect HgTe films were obtained. Electron diffraction studies of these films revealed in most cases the presence of strong Kikuchi lines (Fig. 2). Under the optimized conditions given above, the growth rate of the films was found to depend on the crystallographic orientation of the substrate. A rate of 2 μ/hr was observed on [110] and [111]A surfaces which increased to 3 μ/hr for [211] and [100] and to 4·5 μ/hr for [111]*B* surfaces. The following remarks may be made concerning the effects of small deviations from the optimum operating conditions. Increasing the vapor pressure or flow rate of Hg did not lead to any improvement but decreasing this flow gave Te-rich layers. The film growth could be accelerated by increasing the Te_2 vapor pressure by 50 per cent but this tended to produce Te-rich films. Lowering the substrate temperature was found to reduce crystal perfection initially and eventually to create Te-rich deposits while an increase in temperature led to excessive thermal etching and

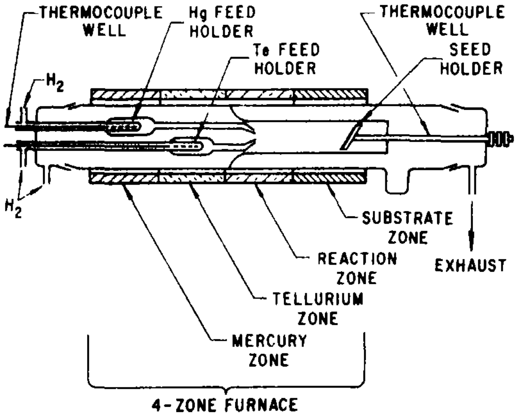

Fig. 1. Schematic diagram of the expitaxial reactor system.

Fig. 2. Electron diffraction transmission pattern for a typical epitaxial HgTe film showing Kikuchi lines.

finally no deposits above 550°C. Changing the temperature of the intermediate reactor zone resulted in moving the deposit relative to the ends of the vapor ducts (Fig. 1). Only meager deposits were formed below 440°C. Non-critical factors were found to be the flow rate over the Te-reservoir and the total reactor flow rate.

The presence of Cd in the HgTe layers was confirmed by scanning with an electron beam microprobe across an edge of the film which had been lapped at a shallow angle. This Cd concentration results from diffusion from the substrate during growth. From the diffusion profiles, the diffusion coefficient of Cd in HgTe was determined to be approximately 1×10^{-11} cm^2/sec. Most of the experimental results described below were taken on films labeled H88 and H90. The thickness of these films was 13 and 7 μ respectively and the microprobe indicated essentially zero Cd on the surface of H88 but about 6 per cent for H90. For H90 the Cd concentration increased almost linearly toward the substrate. Film H88 was deposited at a slightly lower temperature than H90 and was therefore, expected to be the more homogeneous although of slightly lower crystal perfection. Electrical measurements were made using conventional methods. The Van de Pauw technique[5] was used to determine the resistivity and Hall coefficient. The measurements of conductivity vs. electric field were performed on films deposited on substrates about 1·5 cm long and 3 mm wide so that the current pattern would be undistorted. Electrical contacts were made by first plating a small area with rhodium and then soldering lead wires to these dots with indium. No evidence was found to indicate that these contacts were not ohmic. Measurements over the range 4·2–300°K were made using an Andonian Associates variable temperature dewar. A Texas Instruments Model 304 calibrated germanium resistance thermometer was used to measure the temperature between 4·2 and 40°K. From 40 to 300°K a calibrated platinum resistance thermometer was used. The Shubnikov–de Haas magnetoresistance oscillations were studied using a sensitive derivative recording technique which has been described elsewhere[6]. Electric fields up to about 20 V/cm were obtained using square voltage pulses of width 5 μsec, applied at a rate of 30 per sec from a Rutherford B7B pulse generator. The current through the film was monitored by a Tetronix P 6019 current probe with 1 per cent linearity over the range of interest, while voltages were measured either across two potential contacts or between the two large area current electrodes. Both measurements led to identical current versus electric field curves suggesting that the contacts were ohmic. Voltages were measured using a Tetronix 536 oscilloscope and a Type W or Type Z calibrated differential comparator. In all cases the voltage and current pulses were identical in shape and no distortion was observed to suggest that the contacts were injecting or that sample heating was occurring during the pulse.

3. RESULTS AND DISCUSSION

The electrical characteristics of several films are given in Table 1 where the resistivity ρ and the low field Hall coefficient R_0 at 4·2, 77 and 300°K are tabulated. For comparison, data for bulk HgTe is also shown.

Table 1. Values of Hall coefficient R *and resistivity* ρ *at* 42, 77 *and* 300°K *for two epitaxial* HgTe *films. Also given are typical data for bulk* HgTe (*reference*[7])

	(°K)	R (cm^3/C)	ρ (Ω cm)
HeTe	4·2	−3000	$8{\cdot}4 \times 10^{-3}$
	78	−98	$1{\cdot}2 \times 10^{-3}$
	300	−15	
H88	4·2	−3500	$6{\cdot}31 \times 10^{-1}$
	77	−240	$1{\cdot}85 \times 10^{-3}$
	300	−25·6	$1{\cdot}30 \times 10^{-3}$
H90	4·2	−920	$7{\cdot}52 \times 10^{-2}$
	77	−322	$1{\cdot}90 \times 10^{-3}$
	300	−36·8	$1{\cdot}75 \times 10^{-3}$

The low field plateau for the Hall coefficient was obtained for all films below 100 Oe. Since HgTe is a semimetal[7] with an electron to hole mobility ratio about 300, the electron density is given to within about 5–10 per cent by $n = (R_0ec)^{-1}$. An attempt was made to estimate the two band corrections for the films by fitting the magnetic field variation of the Hall coefficient at 4·2°K between 100 Oe and 20 kOe. The classical two band formula was found to give an unsatisfactory fit to the data for any reasonable values of the parameters involved. The variation of $\mu_{\text{eff}} = R_0\rho^{-1}$ (Fig. 3) above 4·2°K is unique to the films but whether or not it is completely due to the film inhomogenity we cannot ascertain at present. Above about 100°K $\mu_{\text{eff}} \propto T^{-n}$ where $n = 1{\cdot}5$–$2{\cdot}0$.

Of particular interest was the observation of strong quantum oscillations in the magnetoresistance of both H88 and H90 at 4·2°K. That these effects can occur at all in the presence of an inhomogeneous Cd distribution suggests that the films have a layer-like structure in which carrier transport in the film plane can occur without appreciable interlayer scattering which would reduce the mobility. The actual data from H90 is shown in Fig. 4 which is taken directly from an x–y recorder trace of $\partial^2R/\partial H^2$ vs. H (R is the

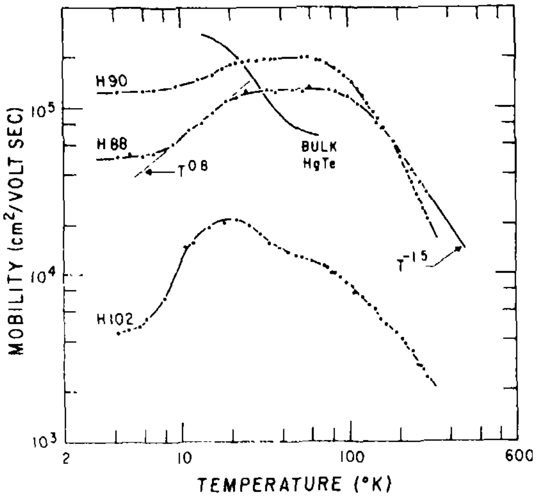

Fig. 3. Variation of the effective mobility $\mu_{\text{eff}} = R_0\rho^{-1}$ between 4·2 and 300°K. Also shown is the variation of μ for pure bulk HgTe (reference [8])

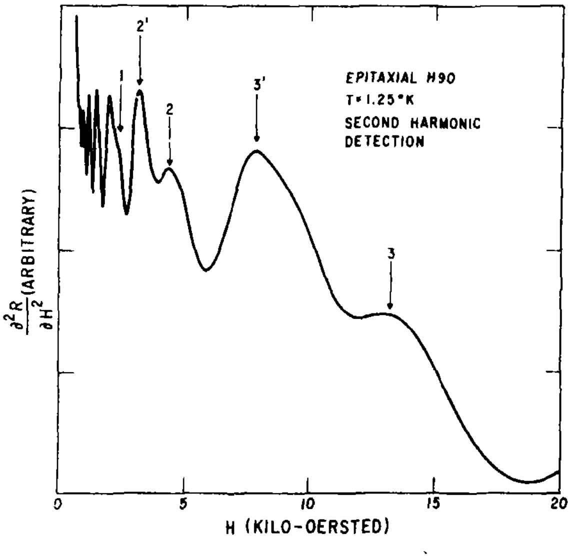

Fig. 4. Data for HgTe H90 showing $\partial^2R/\partial H^2$ vs. H where R is the sample resistance. The temperature is 1·25°K and the magnetic field is parallel to ⟨211⟩.

sample resistance). The magnetic field H, was parallel to $\langle 211\rangle$ and perpendicular to the plane of the film. In the low field region there appears to be a single period, $\Delta_1 = 1{\cdot}78 \times 0^{-4}\,\mathrm{Oe}^{-1}$. The Fermi level passes through the last Landau level of this series at 7·75 kOe so that the additional oscillations shown in Fig. 4 (positions 1, 2, 3) appear to form a second series with an apparent periodicity Δ_2 equal to that of the Δ_1 series. The oscillatory patterns for both H90 and H88 were observed to be essentially independent of the direction of H thus confirming that the Fermi surface was spherical as in bulk HgTe. A detailed study was not made, however, since for some apparently arbitrary directions of H, the oscillations could not be detected. This behavior was considered to reflect the sample inhomogeneity rather than any property of the electron Fermi surface. For a spherical Fermi surface the electron density may be simply calculated from the (single) Shubnikov–de Haas period Δ since

$$n^{2/3} = \frac{3{\cdot}16\times 10^{6}}{\Delta}.$$

Δ_1 corresponds to $n = 2{\cdot}40\times 10^{15}\,\mathrm{cm}^{-3}$ which is very poor agreement with the value of $n = 6{\cdot}72\times 10^{15}\,\mathrm{cm}^{-3}$ which is calculated from the measured low field Hall coefficient using the overall film thickness. For H88 only oscillations due to the passage of the $N = 1$, 2 and 3 quantum levels through the Fermi level were detected because of the lower electron mobility in this film. A single period of $2{\cdot}70\times 10^{-4}\,\mathrm{Oe}^{-1}$ was observed corresponding to $n = 1{\cdot}30\times 10^{15}\,\mathrm{cm}^{-3}$. For this more homogeneous film, improved agreement with the value calculated from R_0 of $1{\cdot}82\times 10^{15}\times\mathrm{cm}^{-3}$ was obtained indicating a more uniform electron concentration. No additional oscillations were observed at higher fields as for H90. Recent data[9] taken on bulk HgTe has also indicated a second period as in H90 above. Although we have no conclusive evidence concerning the origin of this series, it may be noted that no oscillations were observed for the more homogeneous film H88. For H90 the effective mass of the carriers contributing to the Δ_1 series was determined by observing the temperature variation of the amplitude of the four low field oscillations between 4·2 and 1·25°K. The theoretical expression[10] for this amplitude contains the temperature dependent term $u\,\mathrm{Sinh}\,u$ where $u = 2\pi^2kT/\hbar\omega_c$, where $\omega_c = eH/m^*c$. For $H\|\langle 211\rangle$, $m^* = 0{\cdot}011\pm 0{\cdot}0015\,m_0$, which may be compared to $m^* = 0{\cdot}029\,m_0$ for pure bulk HgTe[7] with $n = 2{\cdot}0\times 10^{15}\,\mathrm{cm}^{-3}$. The lighter mass observed shows that oscillations do arise from the Cd rich regions of the film.

Nonohmic conductivity was observed at 4·2°K for both H88 and H90. The current vs. electric field strength curves are given in Fig. 5. The resistivity decreased at a lower electric field for the higher mobility film, H90. The low field Hall coefficient R_0 was observed

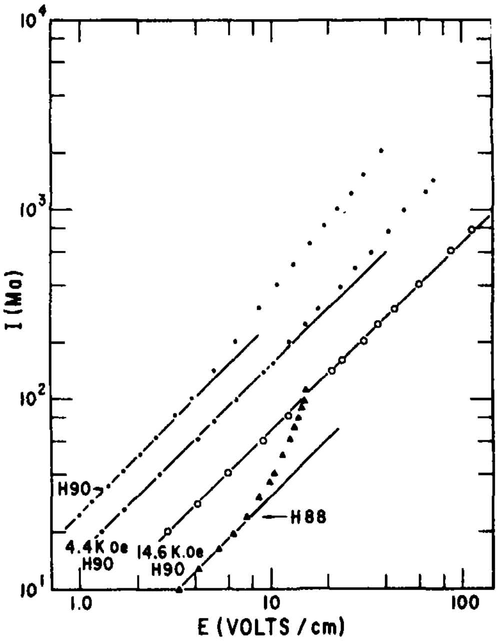

Fig. 5. Current vs. electric field strength E for two epitaxial films H88 and H90 at 4·2°K. Also shown is the effect of an external magnetic field on the characteristic of film H90.

to be essentially independent of the electric field in the nonohmic region implying a constant electron concentration. Therefore, the observed decrease in resistance most probably results from an increase in carrier mobility. A small (5 per cent) decrease in R_0 occurs at the highest fields which can however probably be explained in terms of a current redistribution in the film brought about by the change in resistance. The effect of an increasing external magnetic field normal to the plane of the film is to extend the ohmic region progressively to higher electric fields (Fig. 5). Below about 6 V/cm the change in resistivity $\Delta R/R$ was observed to increase quadratically with E. Since R_0 is independent of E, we may therefore write $\Delta\mu/\mu_0 = \beta E^2$. The field dependence and sign of this mobility change are both consistent with the presence of a warm electron distribution for which the momentum loss rate is determined by ionized impurity scattering[11, 12]. Such effects are well documented for InSb[12] where for an electron concentration of 2×10^{15} cm^{-3}, the value of β is 3 cm^2/V^2. For H88 and H90, $\beta =$ 0·0025 and 0·0048 cm^2/V^2 respectively. The values of β give a lattice scattering mobility [12, 13] of 1×10^6 cm^2/V sec which may be compared with theoretical estimates of 3×10^9 cm^2/V sec and $1{\cdot}2\times 10^7$ cm^2/V sec for predominate acoustic or polar scattering respectively. The effect of an external magnetic field (Fig. 5) is also in qualitative agreement with the behavior of a warm electron distribution since the power input to the carriers is progressively reduced by the field.

Acknowledgements—We wish to thank C. A. Dearman for the film preparation and D. W. Attaway for technical assistance. The bulk HgTe data was kindly supplied prior to publication by T. C. Harman of MIT Lincoln Laboratory. We also acknowledge the assistance of E. L. Jones and J. C. Hooper and the many discussions held with R. T. Bate and M. A. Kinch.

REFERENCES

1. COHEN-SOLAL G., MARFAING Y., BAILY F. and RODOT M., *C. r. hebd. Séanc. Acad. Sci. Paris* **261**, 931 (1956).
2. HARMAN T. C., KLEINER W. H., STRAUSS A. J., WRIGHT G. B., MAVROIDES J. G., HONIG J. M. and DICKEY D. H., *Solid State Commun.* **2**, 305 (1964).
3. HARMAN T. C., STRAUSS A. J., DICKEY D. H., DRESSELHAUS M. S., WRIGHT G. B. and MAVROIDES J. G., *Phys. Rev. Lett.* **7**, 403 (1961).
4. BATE R. T., *Semiconductors and Semimetals* (Edited by R. K. Willardson and A. C. Beer), Vol. IV, p. 459. Academic Press, New York (1968).
5. VAN DER PAUW L. J., *Philips Res. Rep.* **13**, 1 (1958).
6. BATE R. T. and EINSPRUCH N. G., *Phys. Rev.* **153**, 796 (1967).
7. See for example HARMAN T. C., *Physics and Chemistry of II-VI Compounds* (Edited by M. Aven and J. S. Prener), p. 769. Wiley, New York (1967).
8. GROVES S. H., SMITH F. T. and STRAUSS A. J., *MIT Lincoln Laboratory Quart. Rep.* **4**, 29 (1967).
9. YAMAMOTO M., *J. phys. Soc. Japan* **24**, 73 (1968).
10. ADAMS E. N. and HOLSTEIN T. D., *J. Phys. Chem. Solids* **10**, 254 (1959).
11. See for example the recent review by CONWELL E. M., *High Field Transport in Semiconductors*. Academic Press, New York (1967).
12. SLADEK R. J., *Phys. Rev.* **120**, 1589 (1960).
13. GUNN J. B., *Progress in Semiconductors* (Edited by A. F. Gibson), Vol. 2, p. 213. Heywood, London (1957).

J. Phys. Chem. Solids Pergamon Press 1969. Vol. 30, pp. 249–252. Printed in Great Britain.

ELECTRICAL CONDUCTIVITY AND THERMOELECTRIC POWER OF Cu_2O*

A. P. YOUNG and C. M. SCHWARTZ
Battelle Memorial Institute, Columbus Laboratories, Columbus, Ohio 43201, U.S.A.

(*Received* 11 *July* 1968)

Abstract—Measurements of electrical conductivity and Seebeck coefficient have been made on *p*-type cuprous oxide single crystals in the temperature range from 300° to 500°K. The thermoelectric power decreased only slightly with temperature. Conductivity increased with temperature, with an activation energy of 0·26 eV. Cu_2O may be nearly ionic and extrinsic conductivity could occur by thermally activated hopping, with electron exchange between Cu^{2+} and Cu^+ ions. However, this interpretation is in disagreement with data on the Hall effect which indicate that hole mobility in the 300–500°K range decreases with increasing temperature.

INTRODUCTION

BECAUSE of the technical importance of cuprous oxide, its electrical properties have been the object of many investigations. Conductivity and Hall measurements have been made on polycrystalline Cu_2O in the extrinsic conductivity temperature range from 300° to 500°K. Brattain summarized the data from several investigators and concluded that conductivity in Cu_2O could be explained by the usual band picture[1]. However, the Hall and conductivity data were almost invariably from samples which had been aged to give low resistance. To determine the mechanism of charge transport in semiconductors, high resistance samples with low defect concentrations should be examined. Generally, measurements of at least two electrical properties such as Hall effect and conductivity or thermoelectric power and conductivity are required. Single crystals should be used if possible.

In this work, measurements were made of electrical conductivity and thermoelectric power of high-resistance cuprous-oxide single crystals.

EXPERIMENTAL DETAILS

Cu_2O single crystals were grown by the Trivich method[2]. After abrading off more than half the thickness from one side, to eliminate the center-voids layer, disks 0·07 cm dia. by 0·03 cm thick were cut out ultrasonically. To insure good thermal contact to the sample surfaces, electrical measurements were made in a Bridgman-anvil high pressure apparatus. The method for measuring conductivity and Seebeck voltage was similar to one previously described[3]. However, in the present work, an Isomica ring was used in place of paper to contain the sample. Also each anvil was furnace heated separately so that the temperature gradient could be controlled. The press load was such that the average pressure over the ½ in. Isomica ring-sample assembly was about 5 kb.

To measure the sample surface temperatures, the junctions of 0·002 in. thick chromel and alumel strips were in contact with the piston faces close to the sample. This was assured by inserting 0·002 in. mica strips between the thermocouple strips and the pistons. Only the tips of the thermocouple strips close to the sample were exposed, and in direct contact.

Seebeck voltages were determined by measuring the voltage across like thermocouple leads. Temperature differences of about 25°C were maintained throughout 300–500°K range. Possible errors in reading the piston-face temperatures due to shorting of a thermocouple lead to the outer edge of a piston or due to some other cause were checked periodically during a run by adjusting the separate heater inputs so that the measured piston temperatures were equal. If at the same time the Seebeck voltage across the sample was zero, the temperature readings were assumed to be correct.

RESULTS AND DISCUSSION

The thermoelectric power of Cu_2O single crystals was positive, indicating *p*-type material. The magnitude of the Seebeck coefficient Q and the electrical conductivity of typical Cu_2O single crystals at 5 kb pressure and temperatures from 300 to 500°K are shown in Figs. 1 and 2. There is a close resemblance between our results and those of Greenwood and Anderson[4] on high resistance polycrystalline Cu_2O in the same temperature range. In both instances, the Seebeck coefficient was nearly constant with temperature from 300° to 500°K. The activation energy for conductivity was 0·30 eV in the Greenwood and Anderson samples compared with 0·26 eV in our single crystals.

---

*This work was supported in part by Air Force Office Scientific Research, Office of Aerospace Research, United States Air Force under AFOSR Grant Number AF-AFOSR-262-65.

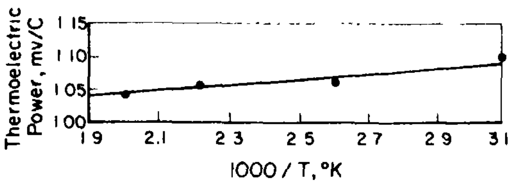

Fig. 1. Thermoelectric power of cuprous oxide single crystal vs 1/T

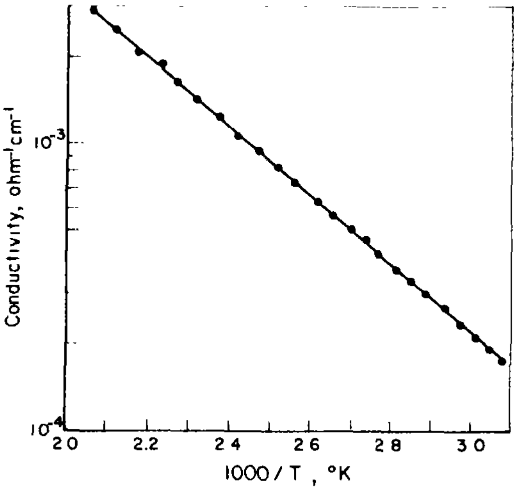

Fig. 2. Conductivity of cuprous oxide single crystal vs 1/T

If the increase in conductivity with temperature were due to an increase in hole concentration, then according to any of the accepted formulas for thermoelectric power in semiconductors, the Seebeck coefficient should decrease with temperature. Inasmuch as the near constancy of the Seebeck coefficient is indicative of changes in hole concentration too small to account for the effect of temperature on conductivity, it would appear that hole transport in Cu_2O is a thermally activated process.

O'Keefe and Moore[5] have also concluded from electrical conductivity measurements on Cu_2O single crystals at low oxygen pressure and low temperature that $\epsilon_3 = 0{\cdot}295$ eV represents the activation energy required to dissociate holes from traps, the nature of which was left open. The activation energy $\epsilon_3 = 0{\cdot}295$ eV is close to the activation energy for conductivity in our samples and those of Greenwood and Anderson.

Any theory of conduction in Cu_2O should presumably account for electrical properties above 500°K. However, interpretation of electrical measurements above 500°K is complicated by the fact that Cu_2O is thermodynamically unstable in air at temperatures below 1000°K. O'Keefe and Moore have postulated that the conductivity at temperatures above 500°K will depend in part at least, on the heat of the reaction

$$4CuO \rightleftarrows 2Cu_2O + O_2. \qquad (1)$$

At temperatures where Cu_2O decomposition occurs, the expected activation energy for conductivity should be about 0·96 eV[5]. This is in good agreement with the reported high temperature activation energy reported by Greenwood and Anderson on polycrystalline samples and by Kotsyumakha, Kushnir and Perelygin[6] on single crystal Cu_2O. Because of the instability of Cu_2O, it appears that the mechanism of hole transport in Cu_2O can best be determined at temperatures below 500°K where the decomposition of Cu_2O is slow enough to have little effect on electrical properties.

Our data and those of others cited above indicate that holes in Cu_2O are trapped. The work on single crystals rules out the possibility of trapping at grain boundaries. Trapping at dislocations might be possible. Andrievskii and Mocharnyuk[7] have observed dislocation densities of 10^6 to 10^8 per cm^2 in Cu_2O. The average distances between dislocations would be several orders of magnitude larger than the hole mean free path, and it seems unlikely that trapping at dislocations is important. The usual equations relating hole concentration to Seebeck coefficient would refer to holes freed from both defect sites and dislocations.

An apparent thermally activated hole mobility in *p*-type NiO has been explained by assuming that short range self polarization of the lattice traps holes at local ion sites[8]. Hole transport occurs by electron exchange between Ni^{3+} ions and adjacent Ni^{2+}. For this type of trapping and hopping transport, a material must be nearly ionic and the cation should have the possibility of more than one valence, since hole trapping as in NiO presupposes a localized Ni^{3+} ion. Hole trapping in MgO, for instance, would be unlikely since the Mg^{3+} ion would be in too high an energy state. Copper ions can of course be found as both Cu^{1+} and Cu^{2+} ions.

There is both theoretical and experimental evidence for the ionicity of Cu_2O. In calculating energy bands in Cu_2O Dahl and Switendeck[9] assumed initially a crystal potential obtained by placing Cu^{1+} and O^{2-} ions at the crystal sites. The resulting calculation was reasonably consistent with the ionic picture of Cu_2O in that the oxygen 2*s*- and 2*p*-bands were found to lie well below the copper 3*d*- and 4*s*-bands. Experimental investigation of the pressure effect on the quadrupole resonance frequency of the Cu^{63} nucleus in Cu_2O, appeared to confirm its ionic nature[10]. Self trapping was proposed for NiO as a possible explanation for the nonmetallic conductivity in the unfilled *d*-band. Such an explanation is not required for Cu_2O where the *d*-band is filled. The filled *d*-band does not preclude, however, the possibility of charge transport in nonstoichiometric Cu_2O by localized electron exchange between Cu^{2+} and Cu^{1+} ions.

The principal evidence for band conduction in Cu_2O is from Hall and electrical conductivity data. Kotsyumakha *et al.*[6] have determined the temperature dependence of the electrical conductivity and Hall effect in Cu_2O single crystals. If the usual equation,

$$R_H = -1/\text{pec} \tag{2}$$

relating the Hall coefficient R_H to the hole density *p*, is used, the Kotsyumakha data indicate that the hole mobility at temperatures from 300° to 500°K decreases with increasing temperature. However, if extrinsic conductivity in Cu_2O is of the hopping type, equation (2) may no longer hold[12]. The relationship between the Hall coefficient and hole density will depend on the crystal structure of the material.

According to Friedman and Holstein[11], jump processes involving the occupation of at least three sites must be taken into account in treating the Hall effect. The case where three mutually near neighbor sites lie at the vertices of an equilateral triangle has been considered in detail. This analysis applies to Cu_2O where nearest neighbors lie along [110] directions. The equilateral triangle connecting nearest neighbor sites lies in a (111) plane.

According to the Friedman analysis the activation energy for hole mobility enters into the relation between R_H and *p*. Denoting the activation energy for hole mobility by ϵ, then

$$R_H = \frac{AT \exp(2\epsilon/3kt)}{\text{pec}}. \tag{3}$$

On applying equation(3) to the Kotsyumakha-Hall data, the hole mobility still decreases with increasing temperature. Thus, the direction of the temperature dependence of hole mobility is opposite in the interpretations from Hall and thermoelectric data. If the hopping model is assumed there is also a difference of several orders of magnitude in the calculated hole density and mobility in the two interpretations. Values of unbound hole concentration in Kotsyumakha single crystals at room temperature calculated from Hall measurements were 1×10^{12} and $6{\cdot}8 \times 10^{12}$ per cm^3. Some flattening of the conductivity and Hall coefficient slopes at about 500°K indicated the total hole concentration, bound and unbound, at low temperatures was about 5×10^{14} per cm^3 in the Kotsyumakha crystals. The hole concentration in our samples calculated from Seebeck coefficients varied from about $8{\cdot}5 \times 10^{16}$ at 300°K to $2{\cdot}5 \times 10^{17}$ per cm^3 at at 500°K. Hole mobility varied from about 0·08 cm^2/V sec at 300°K to 1 cm^2/V sec at 500°K.

If the hole concentration in the Kotsymakha crystals were due to nonstoichiometry or to some impurity, the calculated value of 5×10^{11} represents a departure from stoichiometry or an impurity content of 1 part in 10^8. This is low impurity level for copper compounds, and it would have to be assumed that impurities present in concentrations of parts per million must be at least 100 times less effective on the electrical properties than the defects responsible for the holes. From this viewpoint, the hole concentrations of 10^{16} to 10^{17} obtained from thermoelectric power data seem more reasonable.

If the conductivity and thermoelectric power measurements were the only existing data on Cu_2O, hole transport by hopping might be assumed. There is however, the evidence from Hall measurements and other experiments such as those on photoconductivity[12], which indicate a hole mobility 1 or 2 orders of magnitude larger than from the hopping transport model. However, some of the experiments, such as those on photoconductivity, may not refer to low energy holes in the 300–500°K range. Higher energy holes may be in valence bands while low energy holes may transport charge by a different mechanism. Other types of experiments to measure the drift mobility of low energy holes in Cu_2O may be required to explain the discrepancy between the interpretations from Hall and Seebeck data.

REFERENCES

1. BRATTAIN W. H., *Rev. mod. Phys.* **23**, 1 (1951).
2. TOTH R. S., KILKSON R and TRIVISH D., *Phys. Rev.* **122**, 482 (1961).
3. YOUNG A. P., ROBBINS P. B., WILSON W. B. and SCHWARTZ C. M., *Rev. scient. Instrum.* **31**, 70 (1960).
4. GREENWOOD N N. and ANDERSON J. S., *Nature* **164**, 346 (1949).
5. O'KEEFE M and MOORE W. J., *J. chem. Phys.* **35**, 1324 (1961).
6. KOTSYUMAKHA P. A., KUSHNIR YA J. and PERELYGIN A. V., *Izv. Akad. Nauk SSSR Ser. Fiz.* **28**, 1328 (1964).
7. ANDRIEVSKII A I. and MOCHARNYUK G. F., *Kristallografiva* **8**, 120 (1963).
8. YAMASHITA J and KUROSAWA T., *J Phys. Chem. Solids* **5**, 34 (1958).
9. DAHL J P. and SWITENDECK A. G, *J Phys. Chem. Solids* **27**, 931 (1966).
10. BENEDEK G. B., In *Magnetic Resonance at High Pressure in Solids*, p. 34. Interscience, New York (1963).
11. FRIEDMAN L. and HOLSTEIN T., *Ann. Phys.* **21**, 494 (1963).
12. APFEL J. H. and PORTIS A. M., *J. Phys. Chem. Solids* **15**, 33 (1960).

J. Phys. Chem. Solids **Pergamon Press 1969. Vol. 30, pp. 253–260. Printed in Great Britain.**

DIFFUSION OF ZINC IN GaAs

BRIAN TUCK*
Mullard Research Laboratories, Redhill, Surrey, England

(*Received* 27 *February* 1968; *in revised form* 24 *June* 1968)

Abstract—The diffusion of zinc into GaAs at 1000°C, at dissociation pressure and under excess arsenic pressure is described. A technique using very small amounts of radio-active zinc was developed and the Boltzman–Matano method for analysis of diffusion profiles was extended to low zinc concentrations. The diffusion coefficient was generally found to vary in the extrinsic region as the square of the zinc concentration, as predicted by the substitutional-interstitial mechanism for diffusion. At high concentrations a maximum was reached for the diffusion coefficient. This can be attributed to a breakdown in the vacancy equilibrium. In the intrinsic region the coefficient tended to a constant value which was larger in the case of the dissociation pressure diffusions than in that of the excess arsenic diffusions by a factor of about three. This suggests that the substitutional-interstitial mechanism continues to operate at least down to a concentration of 10^{17}/cc.

1. INTRODUCTION

THE DIFFUSION of an element into a solid from the vapour phase can often be described by a simple diffusion coefficient, D. In this case the solution of Fick's law for the distribution of the element at a distance x from the solid surface at time t is given by an error function complement curve. It was first shown by Cunnell and Gooch[1] that when zinc is diffused into GaAs from the vapour at 1000°C a simple error function complement diffusion profile is not in general obtained. This can be explained by assuming that D falls with decreasing zinc concentration. Two techniques have been used to follow this variation of D with concentration.

(1) *The isoconcentration technique*[2]. In this method non-radio-active zinc is diffused into a slice of GaAs until it is distributed homogeneously, with concentration c_0. The experiment is then repeated on the same slice using, this time, radio-active zinc. The total amount of zinc in the specimen is constant throughout this second experiment and an error function complement profile is obtained for the radio-active tracer.

The great difficulty with this technique is the prohibitively long time required to diffuse a specimen to give a constant doping of less than about 10^{19}/cc.

(2) *A graphical technique, used in references* [1] *and* [5]. The diffusion curve is analysed according to the Boltzman–Matano method[3] wherebye D may be calculated by measuring the slope and area under the profile at various points.

In principle this method can give the variation of D with c, at a given temperature, from a single diffusion profile. The difficulty here is in the very sharp fall in the diffusion profile below 3×10^{19}/cc if the usual amounts of zinc are used in the diffusion tube. This makes any accurate determination of slope impossible at low concentrations, so that the variation can only be plotted in the rather small range between $c_0(1-2\times10^{20}/\text{cc})$ and 3×10^{19}/cc. If profiles with $c_0 < 3\times10^{19}$/cc are plotted, however, this difficulty can be overcome. In order to do this it is necessary to use very low pressures of zinc in the diffusion ampoule. In the work to be described zinc was diffused into GaAs at 1000°C. Amounts of zinc in a standard 10 cc ampoule between 1 mg and a few μg were used. Each profile contributed a different range in which the Boltzman-Matano analysis could be carried out accurately. The variation of diffusion coefficient with zinc concentration was followed over the range 10^{17}–10^{20}/cc. Each experiment was carried out both with and without an excess pressure of arsenic in the diffusion tube.

---

*Present address: Department of Electrical and Electronic Engineering, University of Nottingham, Nottingham, England.

2. EXPERIMENTAL

Diffusion profiles were plotted using radiotracer Zn^{65} with a ½ life of 245 days. In order to achieve the low surface concentrations required, very small amounts of highly active material were needed. A simple preparation technique was used. Thin layers of non-radioactive zinc were evaporated on to a number of silica dice, about 5 mm square. The dice were packed in an ampoule and irradiated in the A.E.R.E. reactor PLUTO for seven days in a flux of 2×10^{14} neutrons/cm²/sec. An atmosphere of helium was used in the ampoule to improve the heat exchange and keep the silica dice as cool as possible. They were then set aside for three weeks for short-lived isotopes to decay, after which spectrometric measurements confimed that the only isotope present was Zn^{65}. Using this technique amounts of radio-active zinc as small as a few microgram could be prepared and easily handled.

A slice of n-type GaAs weighing about 0·2 g was polished in bromine-methanol solution and soaked in KCN. It was sealed in an evacuated 10 cc ampoule with the radioactive zinc and heat treated at 1000°C. Diffusions were carried out with amounts of zinc in the tube of 6 μg, 80 μg, 1 mg. Each diffusion was carried out twice, once without excess arsenic in the tube and once with 1 mg arsenic in the tube, giving an arsenic pressure of 4×10^{-2} atm. Full details are given in Table 1.

In Fig. 1 are shown the profiles resulting from the diffusions at dissociation pressure. Surface concentrations vary between 5×10^{18}/

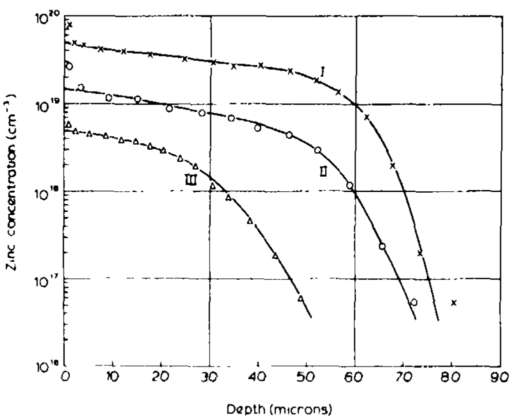

Fig. 1. Diffusion profiles for zinc in GaAs at 1000°C at dissociation pressure of arsenic. See Table for diffusion conditions.

Table 1. *Diffusion conditions. Because the zinc atmosphere is different in different experiments, dissociation pressure varies between* $1{\cdot}5 \times 10^{-4}$ atm *for curve* I *and* 1×10^{-1} atm *for curve* III [10]. *The variation in arsenic pressure for the diffusions with added arsenic is negligable*

Curve	c_0	Arsenic pressure	Heat treatment at 1000°C
I	5×10^{19}	dissociation	3 hr
II	$1{\cdot}5 \times 10^{19}$	dissociation	80 hr
III	5×10^{18}	dissociation	320 hr
IA	2×10^{20}	4×10^{-2} atm	3 hr
IIA	6×10^{19}	4×10^{-2} atm	80 hr
IIIA	7×10^{18}	4×10^{-2} atm	320 hr
IB	(1) –	4×10^{-2} atm	(1) 320 hr in arsenic atmosphere
	(2) $1{\cdot}5 \times 10^{20}$	4×10^{-2} atm	(2) 3 hr in arsenic and zinc
isoconcentration	$1{\cdot}4 \times 10^{18}$	dissociation	320 hr

cc and 5×10^{19}/cc. Each of these profiles contributes a range in which the Boltzman–Matano analysis may be used with reasonable accuracy, and the diffusion coefficient may be plotted as a function of zinc concentration over a range 10^{17}–5×10^{19}/cc. This is shown in Fig. 2. In the range over which they can be compared, these results agree very well with the isoconcentration data of Chang and Pearson, D varying approximately as the square of concentration. Below about 10^{18}/cc D begins to level out to a constant value of 10^{-12} cm^{2}sec^{-1}.

A check was carried out on these results by performing an isoconcentration experiment on material doped with zinc to a level of $1{\cdot}4 \times 10^{18}$/cc. The profile is shown in Fig. 3: it is an error function complement and the diffusion coefficient is plotted as a special point on Fig. 2. It agrees well with the Boltzman curve.

In Fig. 4 are shown the diffusion profiles obtained from experiments in which there was arsenic in the tube. The excess arsenic pressure has the effect of increasing solubility of zinc[4], so the surface concentrations are higher. The shapes of the profiles IA, IIA are quite different from I, II, even though the same amounts of zinc and the same diffusion times were used. Curves similar to IA have been found at 1000°C by Cunnell and Gooch, using excess arsenic and by Casey *et al.* [5] at dissociation pressure, although in both cases the surface concentrations were higher than the 2×10^{20} of IA.

The effect of heating GaAs in 0·1 atm of arsenic is to change the stiochiometry of the crystal, increasing the number of gallium vacancies by a factor 3–4 and decreasing the arsenic vacancies so as to keep the product of their concentrations constant[1]. (This is why the zinc solubility changes.) This change can only progress into the crystal as fast as the vacancies diffuse. Profile IA represents a diffusion anneal of only 3 hr. It seems possible, therefore, that its rather strange shape could be due to a variation in stoichiometry in the crystal, the 'correct'

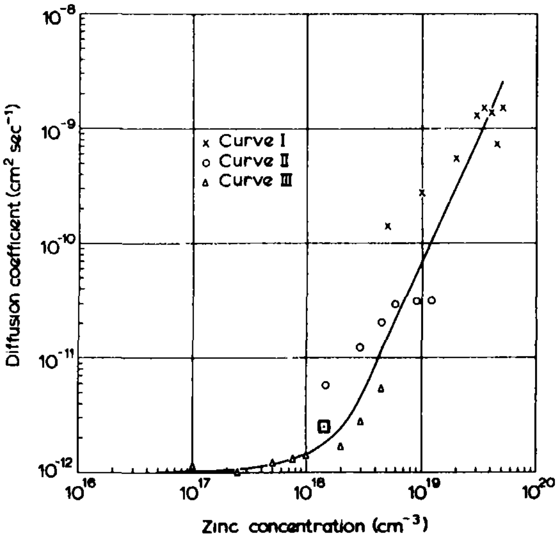

Fig. 2. Diffusion coefficient vs. zinc concentration using Boltzman–Matano method, from profiles of Fig. 1. The diffusion coefficient from the isoconcentration curve of Fig. 3 is plotted as a special point.

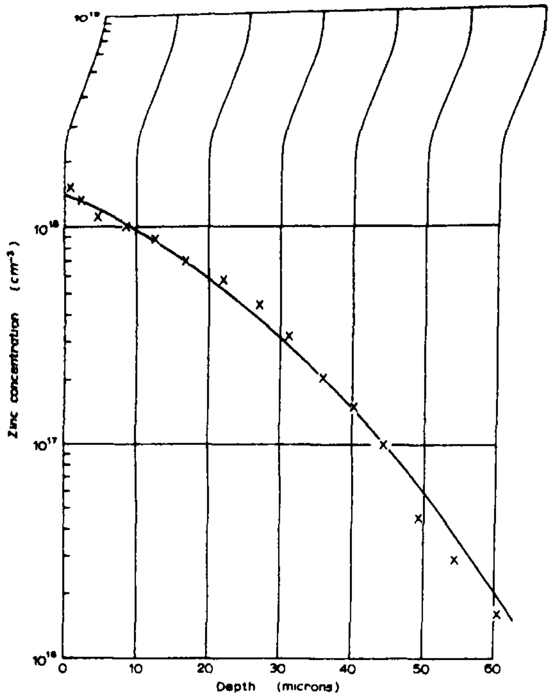

Fig. 3. Profile obtained from an isoconcentration diffusion on a sample homogeneously doped with zinc to a level of $1 \cdot 4 \times 10^{18}$/cc. The curve is an error function complement.

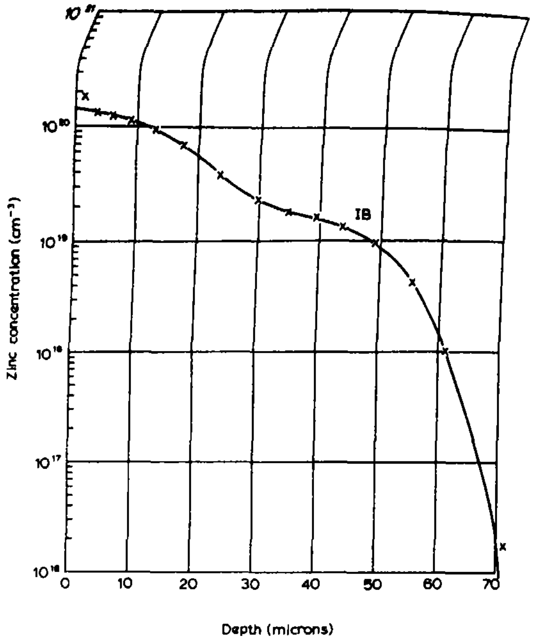

Fig. 5. Diffusion profile for zinc in GaAs at 1000°C under excess arsenic pressure, after pre-anneal in arsenic.

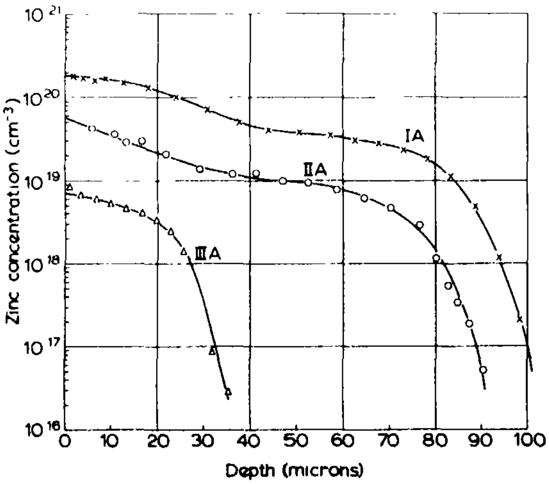

Fig. 4. Diffusion profiles for zinc in GaAs at 1000°C under excess arsenic pressure. See Table for diffusion conditions.

stoichiometry occurring only just below the surface. In order to check this, a GaAs slice was annealed in an arsenic atmosphere for 320 hr before repeating the zinc diffusion experiment. This produced profile IB, shown in Fig. 5. The curve shows the same features as IA, but is not identical.

The Boltzman plots of diffusion coefficient against zinc concentration, from profiles IA, IB, IIA, IIIA are shown in Fig. 6. The lack of agreement between the curves in the concentrations for which they overlap is much greater than experimental error. Curves IA, IB, IIA all show a maximum in D, but not at the same concentration of diffusion coefficient. Curve IIIA has no maximum and shows similar behaviour to Curve III in Fig. 2, although it tends to a lower constant value below 10^{18}/cc.

Finally the technique was checked by twice repeating the diffusion experiment giving rise to profile IIA. A high degree of reproducibility was shown in the diffusion profiles.

3. THE SUBSTITUTIONAL-INTERSTITIAL DIFFUSION MECHANISM

This mechanism was suggested by Frank and Turnbull[6] to account for the anomalous diffusion behaviour of copper in germanium. It has since been generalised by Sturge[7] and adapted by Chang and Pearson[2] to explain their isoconcentration results for zinc in GaAs. It is assumed that a small proportion of the diffusing zinc exists interstitially, c_i, and that the diffusion coefficient for the interstitial species, D_i, is much greater than that of the substitutional species, D_s. The interstitial and substitutional zinc concentrations are related by an equation involving the gallium vacancies:

$$Zn_i^+ + V \rightleftharpoons Zn_s^- + 2e^+ \qquad (1)$$

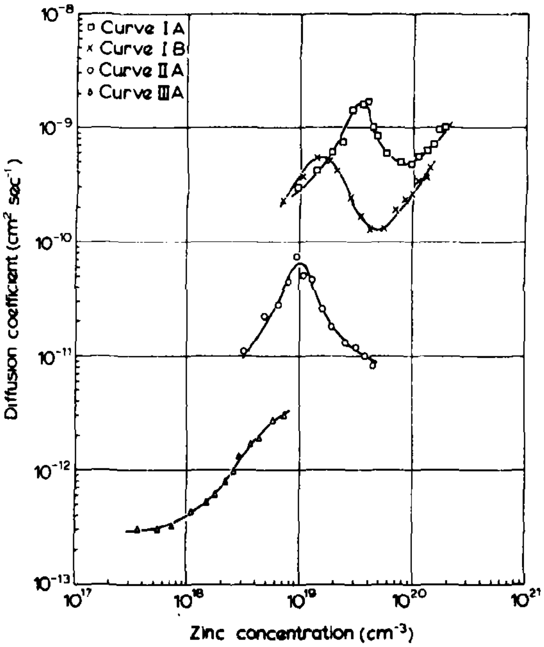

Fig. 6. Diffusion coefficient vs. zinc concentration using Boltzmann–Matano method, from profiles of Figs. 4 and 5.

where it is assumed that the interstitial species exists as a singly ionised donor. If it is assumed that there is instantaneous local equilibrium then:

$$c_i = \frac{Kc_s(\gamma p)^2}{c_v} \qquad (2)$$

where c_s is the substitutional concentration; γ is the activity coefficient for holes, approximately unity for concentrations less than 10^{20}/cc,[8]; p is the hole concentration; c_v is the gallium vacancy concentration. For high concentrations, $c_s \simeq p$, and we have $K = c_i'c_v'/c_s'^3$, the primes denoting equilibrium values.

The conservation equations for zinc atoms and vacancies give:

$$\frac{\partial c_v}{\partial t} = D_v \cdot \frac{\partial^2 c_v}{\partial x^2} - \frac{\partial c_s}{\partial t} + k(c_v - c_v') \qquad (3)$$

and

$$\frac{\partial c_i}{\partial t} + \frac{\partial c_s}{\partial t} = D_i \cdot \frac{\partial^2 c_i}{\partial x^2} \qquad (4)$$

D_v is the diffusion coefficient for vacancies; k is the rate of production of vacancies in the bulk. It is assumed that the rate of creation or removal of vacancies by dislocations is proportional to the deviation of c_v from its equilibrium value.

D_s is assumed negligible small.

Equations (5–7) can be solved only for limiting cases; the two simplest are

(i) Vacancy equilibrium is maintained, i.e. $c_v = c_v'$. This assumption is the one usually made[2, 4]. An effective diffusion coefficient is obtained:

$$D_1 \simeq \left(\frac{3c_i'D_i}{c_s'^3}\right) \cdot c_s^2. \qquad (5)$$

This is similar to the expression derived by Chang and Pearson. Their equation shows a cubic dependence of diffusion coefficient on concentration because they assumed interstitial zinc to be a double ionised donor. In this work interstitial zinc is taken to be a singly ionised donor because this fits the results rather better and seems on physical grounds to be the more reasonable assumption.

(ii) No production of vacancies in the bulk, i.e. $k = 0$. In this case the mechanism for the diffusion of the substitutional zinc atoms will be that they dissociate into vacancies and interstitial zinc, which diffuse independently. The high interstitial diffusivity then maintains c_i close to c_i' since the diffusion coefficient for interstitials is much greater than that for vacancies. Equations (5–7) then give an effective diffusion coefficient:

$$D_2 \simeq \left(\frac{3c_i'}{c_s'^3} \cdot Dv\right)c_s^2. \qquad (6)$$

It will be shown below that $D_1 \gg D_2$.

Assuming case (i) holds at low concentrations then $c_v = c_v'$, $\gamma = 1$ $p = n_i$ and

$$D_1 \simeq \frac{Kn_i^2}{c_v'} \qquad (7)$$

a constant value (a result also derived by Chang and Pearson).

4. DISCUSSION

The first set of diffusions, taken at dissociation arsenic pressure, obeys the (zinc concentration)^2 law up to a concentration of 5×10^{19}/cc. (Fig. 2). The results obtained using excess arsenic show the law to be approximately obeyed until a maximum is reached. This maximum appears at different concentrations on different curves. The occurrence of a maximum D is not confined to diffusions carried out under an excess pressure of arsenic, however. Casey *et al.* using high zinc atmospheres in their diffusion ampoules plotted diffusion profiles at dissociation pressure with surface concentrations as high as 4×10^{20}/cc. Their Boltzman plots at 1000°C showed curves similar to 1A, Fig.

with a maximum for D at 1×10^{20}/cc. No maximum is shown in Fig. 3, therefore, presumably because this concentration was not reached by any of the first set of diffusions.

The disagreement between the curves in Fig. 6 is greater than experimental error. The reason may be sought in a consideration of the validity of the Boltzman analysis. This analysis replaces the two variables x, t, with a single variable $x/t^{1/2}$. If the diffusion constant is dependant on time, then it follows that Boltzman–Matano plots of D vs. c will be different for different diffusion times. This is the probable reason for the discrepancy between curves IA, IIA, of Fig. 6 for instance. The first of these profiles is plotted from a 3 hr diffusion, the second took 80 hr. The concentration at which the maximum D occurs can also be varied by varying the arsenic overpressure. Profiles I, IA, IB, for instance, all represent 3 hr diffusions in the same zinc atmosphere but show respectively no maximum, a maximum at 4×10^{19}/cc and one at $1{\cdot}5 \times 10^{19}$/cc. The maximum for curve IIA occurs at 1×10^{19}/cc (Fig. 2, Fig. 6).

Casey *et al.*[5] also observed a maximum in the D vs. c curve and explain the deviation from the (concentration)^2 law in the following way. They point out that the activity coefficient for holes γ (see equation (2)) may be accurately put equal to unity only at low acceptor concentrations. At concentrations high enough for the zinc acceptor levels to broaden and merge with the valence band, they suggest that γ becomes less than one. They use this effect to explain the shape of their Boltzman curves and show that if γ drops quite sharply below one at a zinc concentration of 10^{20}/cc then a maximum D is reached at about the same concentration. The value of γ should depend only on Fermi level position at constant temperature. The fall in the value of γ should therefore occur at a unique zinc concentration and so should the maximum in the D vs. c curve. It does not seem possible, therefore, to reconcile this theory with the results presented above, in which the maximum appears at different zinc concentrations for different experimental conditions.

In calculations of the diffusion coefficient of zinc in GaAs it is usual to assume that vacancy equilibrium is maintained, i.e. $c_v = c_v'$. The measured diffusion coefficient is then D_1, as given by equation (5). If in some region of the crystal vacancies cannot be replaced as fast as they are used up, then the diffusion coefficient will be some compromise between D_1 and D_2. It is fairly easy to show $D_1 \gg D_2$: from equations (5, 6),

$$\frac{D_1}{D_2} = \frac{c_i' D_i}{c_v' D_v} = \frac{c_i' D_i}{D_{\mathrm{Ga}}} \tag{8}$$

where D_{Ga} is the self diffusion coefficient of gallium in GaAs, which is $< 10^{-15}\,\mathrm{cm^2 sec^{-1}}$ at 1000°C[9], and c_i' is written as a fractional concentration. D_i has been estimated at 10^{-4} by Chang and Pearson on the basis of their isoconcentration work. Using the data of Fig. 2 and equation (8), c_i' can be calculated for a given zinc concentration. Taking a concentration of 10^{19}, $c_i' \simeq 3 \times 10^{-7}$ and $c_i' D_i \simeq 3 \times 10^{-11}\,\mathrm{cm^2 sec^{-1}}$. Hence $D_1 \gg D_2$ and any breakdown in the vacancy equilibrium will be accompanied by a fall in the measured diffusion coefficient. It seems reasonable to suggest that the maximum in D shown in Fig. 6 represents such a breakdown at high zinc concentrations.

From this explanation it is entirely reasonable that a change in arsenic overpressure should change the position of the maximum in D. The concentration at which the maximum occurs depends on the vacancy equilibrium and this in turn depends on the arsenic overpressure. The position of the maximum should also be expected to depend on time.

If it is assumed that for very low concentrations $c_v = c_v'$, then one more interesting piece of information may be extracted from the results. At concentrations below about 10^{18}/cc, GaAs is intrinsic at 1000°C. It has been shown in Section 3 that in this case D_i becomes constant at approximately $K.n_i^2/c_v'$. As pointed out by Chang and Pearson, however, it is quite likely that the substitutional-interstitial mechanism no longer operates at these low concentrations and a straightforward substitutional diffusion takes over. A simple substitutional diffusion coefficient is proportional to the vacancy concentration, i.e. $D_{sub} \propto c_v'$. So by changing the concentration of gallium vacancies it should be possible to determine which of the two possible mechanisms operates at low concentrations of zinc.

In the work described above, experiments were carried out at dissociation arsenic pressure ($\sim 10^{-4}$ atm at 1000°C[10]) and at an arsenic pressure of approximately 4×10^{-2} atmospheres. Assuming the species in the vapour to be As_4, the gallium vacancy concentration varies as (arsenic pressure)$^{1/4}$, i.e. by a factor of about 4 in these experiments. Comparison of Fig. 2 and Fig. 6 shows that the effect of increasing the gallium vacancy concentration is to decrease the constant value of D by a factor just over 3. This is consistent with the substitutional-interstitial mechanism continuing to operate down to the lowest zinc concentrations measured in this work.

Acknowledgement—I should like to thank Mr. M. R. Burgess who carried out the radio-active counting work.

REFERENCES

1. CUNNELL F. A. and GOOCH C. H., *J. Phys. Chem. Solids* **15**, 127 (1960).
2. CHANG L. L. and PEARSON G. L., *J. appl. Phys.* **35**, 1960 (1964).
3. SHEWMON P. G., *Diffusion in Solids*, p. 29. McGraw-Hill, New York (1963).
4. McCALDIN J. O., *J. appl. Phys.* **34**, 1748 (1963).
5. CASEY H. C., PARISH M. B. and CHANG L. L., *Phys. Rev.* **162**, 660 (1967).
6. FRANK F. C. and TURNBULL D., *Phys. Rev.* **104**, 617 (1956).
7. STURGE M. D., *Proc. phys. Soc.* **73**, 297 (1959).
8. ROSENBERG A. J., *J. chem. Phys.* **33**, 665 (1960).
9. GOLDSTEIN B., *Phys. Rev.* **121**, 1305 (1961).
10. SHIH K. K., ALLEN J. W. and PEARSON G. L., *J. Phys. Chem. Solids* **29**, 367 (1968).

s. Chem. Solids Pergamon Press 1969. Vol. 30, 261–280. Printed in Great Britain.

DESCRIPTIONS OF OUTER *d* ELECTRONS IN THIOSPINELS

JOHN B. GOODENOUGH
Lincoln Laboratory,* Massachusetts Institute of Technology, Lexington, Mass. 02173, U.S.A.

(*Received* 7 *May* 1968; *in revised form* 17 *June* 1968)

Abstract—The constraints [1] of symmetry imposed by the spinel structure and [2] of internal consistency within the periodic table are used to construct phenomenological energy diagrams for the transition-metal thiospinels. It is found that band narrowing via intra-atomic exchange is sufficient to localize the *d* electrons to a cation only if there are at least three unpaired spins at the cation. *A*-site Co^{2+} ions may have collective *d* electrons, but exhibit a spontaneous atomic moment in Co $[Cr_2]S_4$. The compounds $A[Cr_2]S_4$, where $A =$ Zn, Cd, Mn and Fe, contain localized *d* electrons, although the antiparalled-spin electron per Fe^{2+} ion is just localized. It is argued that the compounds $Cu[B_2]S_4$, $B =$ V, Cr, Rh and 1/2(Rh + Cr), have one hole per molecule in primarily *d*-like, collective orbitals that are primarily Cu–S in character. Where the *B* cations have no spontaneous atomic moment ($B \neq$ Cr), the compounds are superconducting at lowest temperatures. $Cu[Ti_2]S_4$ and $Cu[Co_2]S_4$, though metallic and without spontaneous magnetism, exhibit no superconducting transition above 0·05°K. $Cu[Ti_2]S_4$ and probably $Cu[Co_2]S_4$ are distinguished by a lack of (or less than one per molecule) holes in the *d*-like, collective Cu–S states. $Cu^{2+} + Cr^{3+}$ is argued to be more stable than $Cu^{+} + Cr^{4+}$ in the chalcogenide spinels, as it is known to be in $Cu[Cr_2]O_4$. The low Curie constant of $CuCrRhSe_4$, as compared with $CuCrTiS_4$, is attributed to a temperature-dependent molecular field, which is primarily due to mobile charge carriers in the selenide, rather than to Cr^{4+} excited states at high temperatures. The decrease in optical energy gap below T_c in $CdCr_2Se_4$, in contrast to its increase in $CdCr_2S_4$, is attributed to high-spin and low-spin Cr^{2+} ions of approximately the same energy.

1. INTRODUCTION

THE FERROMAGNETIC, metallic spinels $Cu[Cr_2]X_4$, where $X =$ S, Se, or Te, illustrate well two fundamental difficulties encountered in any first-principles description of the transition-metal chalcogenides: (1) The outer *d* electrons may be either localized and spontaneously magnetic, collective without spontaneous magnetization (other than superconducting diamagnetism), or transitional between these two extremes. In the spinels $Cu[Cr_2]X_4$, the chromium *d* electrons exhibit a spontaneous magnetism; any copper *d* holes are collective and exhibit only an induced magnetism due to the internal fields created by the chromium moments. (2) Covalent mixing between anionic *s*, *p* orbitals and cationic orbitals, *d* as well as *s* and *p*, influences sensitively not only the one-electron periodic potential in which collective electrons move, but also the cationic potential in which any localized *d* electrons are trapped. Therefore positioning of the *d*-electron energies relative to themselves and, even more, relative to the *s*, *p*-electron band edges is not quantitatively reliable with present-day computing techniques. This situation forces reliance on phenomenological approaches. This paper provides a semiempirical description of the transition-metal thiospinels that conforms to the symmetry constraints of the spinel structure and to variations of the phenomenological parameters of theory that are qualitatively consistent with the constraints of the periodic table.

Application of the constraints of the periodic table is well illustrated by the variation in energy gap E_g of the equiatomic II–VI compounds *MX*. Figure 1 schemat-

---

*Operated with support from the U.S. Air Force.

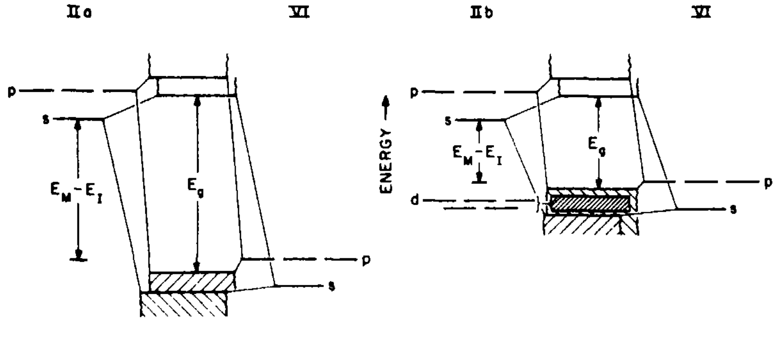

(a) (b)

Fig. 1 Schematic band structures for equiatomic II–VI compounds.

ically illustrates how E_g varies sensitively with E_M-E_I, the difference in the Madelung and ionization energies for the effective charges on the ions. The smaller the covalent mixing, the larger the effective charges and hence the larger the energy E_M-E_I. Since the lighter cations of any row of the periodic table are more electropositive, a II(a)–VI compound should have a larger E_g than the corresponding II(b)–VI compound (e.g. CaS vs. ZnS). Similarly, lighter anions of any column of the periodic table are more electronegative, so that E_g should decrease on going from the oxide to the sulfide to the selenide to the telluride. Thus the fact that ZnO has a smaller energy gap than ZnS is an anomaly that requires explanation. The other members of the series Zn*X* have energy gaps E_g that vary regularly.

The transition-metal atoms *T* are located between II(a) and II(b) in the periodic table. Thus for *TX* compounds, especially if they have the same structure, traversal from II(a) to II(b) of any of the three long periods, while keeping *X* the same, should be accompanied by a continuous decrease in E_M-E_I, and hence in E_g. Simultaneously, the relative stability of the *d* electrons increases with increasing atomic number *Z* on traversing any long period, so that the energy difference ϵ_g between the filled *s*, *p* bands and the lowest unoccupied *d* level decreases even more rapidly than E_M-E_I. The variation in stability of the *d* bands is also influenced by intra-atomic exchange and crystal-field splittings. Whether the *d* electrons are localized or collective, the formal cationic valences indicate the number of *d*-like electrons per cation so long as $\epsilon_g > 0$. However, if the Fermi energy E_F falls within overlapping *d* and *s*, *p* bands, so that $\epsilon_g = 0$, then formal ionic valencies have no physical meaning and are only misleading.

In the case of Zn*X*, the cationic *d* and the bonding *s*, *p* states are all filled, and the essential ambiguity is only the relative energies of the top of the valence *s*, *p* bands and the top of the *d* bands. In ZnS, ZnSe and ZnTe, where E_g decreases regularly on going down column VI of the periodic table, the *d* bands are below the top of the valence bands. In ZnO this is probably not the case, which would account for the anomalously small $E_g \approx 3{\cdot}3$ eV. The fact that CuO clearly has empty *d* states above the top of the valence band ($\epsilon_g > 0$) is consistent with *d*-like states at the top of the valence bands in ZnO. Any *d* levels above the top of the valence band are antibonding and hence destabilized by covalent mixing, thereby reducing E_g.

Similar reasoning from the periodic table is used in this paper to extrapolate from a measured parameter in one compound to its approximate value in another.

2. ENERGY BANDS FOR THE NORMAL SPINEL Cd[In$_2$]S$_4$

The structure of a normal spinel $A[B_2]X_4$ belongs to the same space group O_h^7 = Fd3m as the diamond structure. The primitive rhombohedral unit cell of Fig. 2 contains two formula units; the coordinates of the atoms are given in Table 1, where the u parameter is $u \gtrsim 3/8$. The A cations are in tetrahedral anionic interstices and the B cations in octahedral interstices. Each of the four B cations has a trigonal-field axis along a different ⟨111⟩ direction.

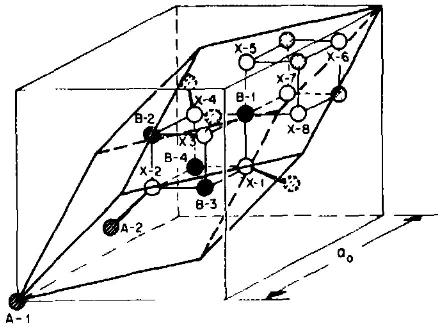

◌ = A-2 AND ○ = B-2, B-3, B-4 OUTSIDE OF PRIMITIVE CELL

Fig. 2. Primitive unit cell of face-centered-cubic spinel structure. Ionic numbering corresponds to Table 1.

Symmetrized combinations of atomic orbitals for the Γ point in the Brillouin zone can be constructed. The corresponding irreducible representations are indicated in Table 2 for the different ionic orbitals $p(A)$, ..., $s(X)$. According to group theory, orbitals having the same representation interact with one another. It follows from Table 2 that, if the cationic d orbitals are neglected, 24 orbitals (48 states, including spin degeneracy) per unit cell interact to form antibonding, cationic σ^* orbitals and bonding, anionic σ orbitals. This leaves 8 nonbonding anionic orbitals. Of these, the primarily $s(X)$ Γ^+_{25} orbitals are the most stable. The resulting energy levels at the center of the Brillouin zone (Γ point) are shown schematically in Fig. 3. In Mg[Al$_2$]O$_4$ there is a large electronegativity difference between the cations and the anions, giving a large E_g; in Cd[In$_2$]S$_4$ any E_M-E_I is much smaller, and the energy gap is reduced to $E_g \approx 2{\cdot}2$ eV[1]. There is no appreciable reduction in E_g due to the presence of stable, cationic 4d core orbitals, since the d orbitals lie below the top of the

Table 1. Coordinates of the atoms in an $A[B_2]X_4$ spinel

Number of site	Coordinates, relative to a_0, of A	B	X
1	(0, 0, 0)	$(\frac{5}{8}, \frac{5}{8}, \frac{5}{8})$	$(\bar{u}, \bar{u}, u)$
2	$(\frac{1}{4}, \frac{1}{4}, \frac{1}{4})$	$(\frac{7}{8}, \frac{7}{8}, \frac{5}{8})$	(u, u, u)
3		$(\frac{5}{8}, \frac{7}{8}, \frac{7}{8})$	$(\bar{u}, \bar{u}, \bar{u})$
4		$(\frac{7}{8}, \frac{5}{8}, \frac{7}{8})$	$(u, \bar{u}, \bar{u})$
5			$(\frac{1}{4}+u, \frac{1}{4}+u, \frac{1}{4}-u)$
6			$(\frac{1}{4}-u, \frac{1}{4}-u, \frac{1}{4}-u)$
7			$(\frac{1}{4}+u, \frac{1}{4}-u, \frac{1}{4}+u)$
8			$(\frac{1}{4}-u, \frac{1}{4}+u, \frac{1}{4}+u)$

Table 2. Irreducible representations for atomic orbitals symmetrized for the Γ points. Unit cell contains $A_2B_4X_8$

Atomic orbitals	Representations	Atomic orbitals	Representations	Atomic orbitals	Representations
$p(A)$	$\Gamma^-_{15}, \Gamma^+_{25}$	$p(B)$	$\Gamma_2^-, \Gamma_{12}^-, 2\Gamma_{15}^-, \Gamma^-_{25}$	$p(X)$	$\Gamma_1^+, \Gamma_2, \Gamma^+_{12}, \Gamma^-_{12}$ $\Gamma^+_{15}, 2\Gamma^-_{15}, 2\Gamma^+_{25}, \Gamma^-_{25}$
$s(A)$	Γ_1^+, Γ_2^-	$s(B)$	$\Gamma_1^+, \Gamma^+_{25}$		
				$s(X)$	$\Gamma_1^+, \Gamma_2^-, \Gamma^-_{15}, \Gamma^+_{25}$

Supersctipts + and − refer to symmetric and antisymmetric states under an inversion. Dimensionalities: Γ_1, Γ_2 are [1], Γ_{12} is [2], and Γ_{15}, Γ_{25} are [3].

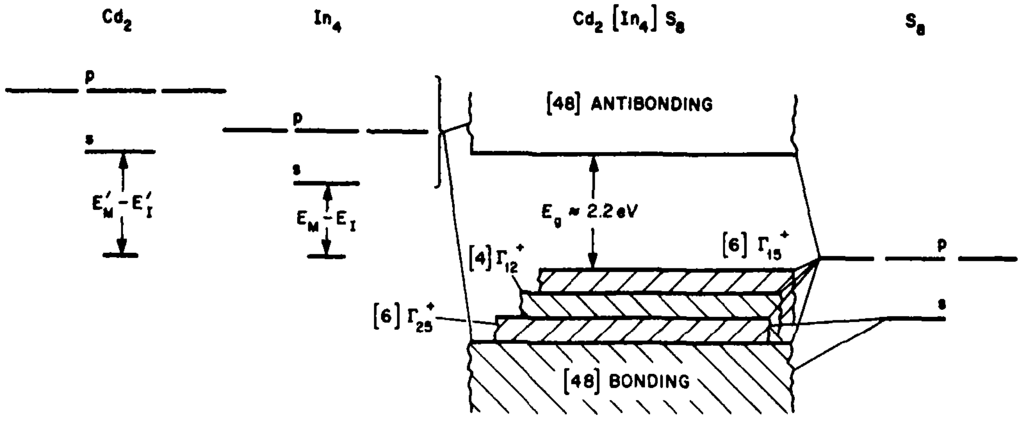

Fig. 3. Schematic ordering of energy levels at the Γ point (center of Brillouin zone) for the normal spinel $Cd_2[In_4]S_8$. Ordering of individual cation-anion bonding and antibonding levels not shown, but the irreducible representations are listed in Table 2. [n] indicates orbital degeneracy of a representation.

Γ_{15}^+ valence band and do not mix with it. Rehwald[2] neglects the d orbitals in estimating from tight-binding theory the $E(\mathbf{k})$ vs. $\mathbf{k}$ plot of Fig. 4 for the highest valence band. $Cd[In_2]S_4$ undergoes an order $\rightleftarrows$ disorder transition at $T_t = 130°C$[3], but no studies have been made of the effect of cationic order on E_g.

Since the cationic d orbitals do not mix with the Γ_{15}^+ orbitals, transition-metal thiospinels would have an $E_g > 2{\cdot}2$ eV whatever the state of the d electrons. In the discussions that follow, the top of the Γ_{15}^+ valence band, E_v, is used as a reference energy, since placement of the d-electron energies relative to E_v should vary regularly with changing atomic number.

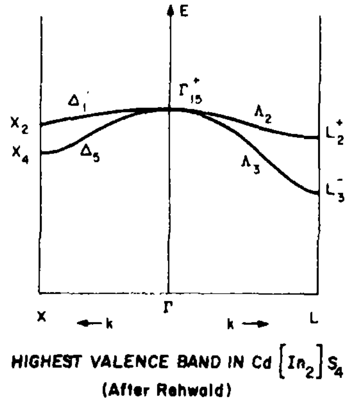

Fig. 4. The $E_{\mathbf{k}}$ vs. $\mathbf{k}$ plot for highest valence band of $Cd[In_2]S_4$ from tight-binding theory (after Rehwald). X and L points are intersections of [100] and [111] lines in reciprocal space with the surface of the first Brillouin zone.

Although the Zn and Cd d^{10} core electrons do not appear to influence the considerations of this paper, let me emphasize here that they may mix strongly with the anionic orbitals and therefore be perturbed by any spontaneous atomic moment on the B sites, as occurs in $Cd[Cr_2]X_4$. This fact may have important consequences for the nuclear magnetic resonance of the A-site Cd^{2+} ion.

3. DESCRIPTIONS OF d ORBITALS

(A) *Localized orbitals*

In spinels containing oxygen, the outer $3d$ electrons of first-row transition-metal ions are generally localized, since their orbitals overlap near-neighbor atomic orbitals to a much smaller extent than do the outer s and p orbitals. The Schroedinger equation $\mathscr{H}\Psi = E\Psi$ describing localized, crystal-field orbitals contains the Hamiltonian

$$\mathscr{H} = \mathscr{H}_o + V_{el} + V_{cf} + \mathscr{H}_{ex} \qquad (1)$$

where $\mathcal{H}_0$ corresponds to the energy of a single localized electron moving in the spherical potential of its atomic nucleus and the average position of all the other atomic electrons. This gives *d* wave functions of the form $R(r)Y_{l=2}^{(m)}(\theta,\phi)$. The angular-dependent part of the wave functions have the form

$$f_A \sim (3z^2-1)/r^2 = 3\cos^2\theta - 1$$

$$f_D \pm if_E \sim 2(yz \pm izx)/r^2 = \sin 2\theta \exp(\pm i\phi) \qquad (2)$$

$$f_B \pm if_C \sim (x^2-y^2 \pm ixy)/r^2 = \sin^2\theta \exp(\pm i2\phi).$$

V_{el} is an interatomic exchange energy that vanishes for only one outer *d* electron or hole; and V_{cf} is the crystal-field energy, including cation–anion covalent mixing. The intra-atomic exchange energy $\mathcal{H}_{ex}$ includes the covalent contribution from interactions between localized electrons on neighboring atoms. In the examples to be considered, spin-orbit coupling and Jahn–Teller distortions do not occur in first-order theory. Therefore these energies have been omitted from equation (1).

Figure 5 shows a cation in an octahedral anionic interstice. With one outer *d* electron ($V_{el} = 0$) and *x*, *y*, *z* axes defined by the principal axes of the interstice, the orbitally fivefold-degenerate ^2D level is split into a threefold-degenerate $T_{2g}(\Gamma'_{25})$ level and a twofold-degenerate $E_g(\Gamma_{12})$ level, where the three t_{2g} orbitals are linear combinations of f_C, f_D, f_E and the two e_g orbitals are linear combinations of f_A, f_B. (The Mullikan notation E_g and T_{2g} is used to designate the *d* orbitals.) With a point-charge electrostatic model for the anions, the E_g level is less stable than the T_{2g} level. A more realistic electrostatic model leaves the electrostatic splitting Δ_M small and of uncertain sign[4]. On the other hand, the e_g orbitals overlap the anionic *s* and p_σ orbitals, but are orthogonal to the p_π orbitals; conversely the t_{2g} orbitals overlap only the p_π orbitals. Since localized cationic orbitals are less stable than the anionic *p* orbitals, cation-anion covalent mixing destabilizes the *d* orbitals, unambiguously raising the E_g energy relative to the T_{2g} energy since σ bonding is stronger than π bonding. The total cubic-field splitting is

$$10Dq = \Delta_M + (\lambda_\sigma^2 - \lambda_\pi^2)(E_M - E_l) \qquad (3)$$

where the covalent mixing parameters $\lambda_\sigma, \lambda_\pi \sim (E_M - E_l)^{-1}$ are defined by

$$\Psi_e = N_\sigma(f_e + \lambda_\sigma\phi_\sigma), \quad \Psi_t = N_\pi(f_t + \lambda_\pi\phi_\pi). \qquad (4)$$

Here ϕ_σ, ϕ_π are site-symmetrized *s*, p_σ and p_π orbitals. Note that covalent mixing destroys conservation of energy of the *d*-state manifold.

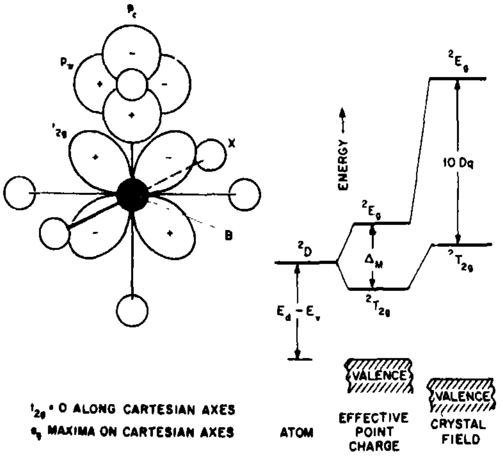

Fig. 5. Cubic-field splitting of a *B*-cation ^2D level.

The order of the tetrahedral-site *d* levels is inverted (Fig. 6), as can be readily obtained from similar arguments: Linear combinations of the t_{2g} orbitals are directed along the ⟨111⟩ axes toward near-neighbor anions of a tetrahedral interstice.

With more than one outer *d* electron (or hole), the Pauli exclusion principle prevents electrons of the same spin from occupying the same orbital. Consequently electrons of parallel spin screen one another less from the atomic nucleus and are therefore more tightly bound than electrons of antiparallel spin. This provides the perturbation V_{el}, which stabilizes the highest spin state relative to

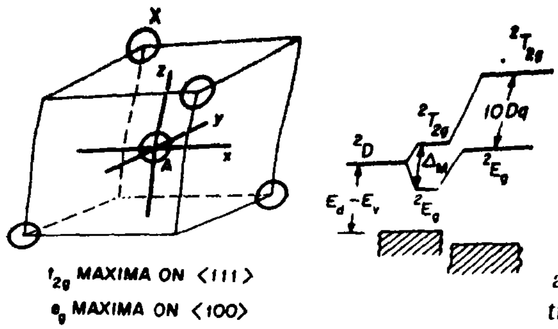

Fig. 6. Cubic-field splitting of an A-cation ^2D level.

a lower-spin state by an energy J. So long as J is $J > 10Dq$, the cation is in a high-spin state. Where $J < 10Dq$ occurs, octahedral-site (or tetrahedral-site) cations are in a low-spin state if the number n_d of d electrons per cation is $4 \leq n_d \leq 7$(or $3 \leq n_d \leq 6$). For example, octahedral-site Co^{3+} and Rh^{3+} ions, having outer-electron configurations d^6, always occur in the spinel structure with $J < 10\,Dq$. They are therefore diamagnetic with outer-electron configuration $t_{2g}^6\ e_g^0$. On the other hand, octahedral-site Cr^{3+} is in a high-spin state $t_{2g,\alpha}^3\ t_{2g,\beta}^0\ e_{g,\alpha}^0\ e_{g,\beta}^0$ for any J, so long as the d electrons are localized. Here the subscripts α,β refer to spin states, and the multielectron symmetry notation is $^4A_{2g}$. An octahedral-site Cr^{2+} ion, on the other hand, may have either a high-spin $^5E_g(t_{2g}^3\ e_g^1)$ or a low-spin $^3T_{1g}(t_{2g}^4\ e_g^0)$ ground state, depending upon the relative magnitudes of J and $10\,Dq$.

In the spinel structure, the u parameter is $u > 3/8$. This leaves the tetrahedral A sites with cubic symmetry, but it produces a negative trigonal component to the crystalline field at the octahedral B sites. This trigonal component is opposed by a positive trigonal field from the near-neighbor B-cation configuration. The net trigonal component introduces a small splitting of the T_{2g} level into E_g and A_{1g} levels. Mixing occurs between the two E_g levels, and the atomic orbitals become

$$a^T \sim 3\cos^2\theta' - 1$$

$$e^T \sim c_1\sqrt{2}\sin^2\theta'\exp(\mp i2\phi') \pm c_2 \sin 2\theta' \exp(\pm i\phi') \quad (5)$$

$$\bar{e}^T \sim c_1\sqrt{2}\sin 2\theta'\exp(\mp i\phi') \pm c_2 \sin^2\theta' \exp(\pm i2\phi')$$

where θ' and ϕ' are referred to the trigonal axis. In a cubic field $c_1 = c_2$. Since $c_1 \approx c_2$ in cubic spinels and since we shall consider only those cases where the $a^T + e^T$ orbitals are either empty, half-filled, or full, the trigonal component to the B-site field is neglected in the remainder of this paper. Only cubic-field splittings into t_{2g} and e_g orbitals will be used for both the A and the B cations.

(B) *Magnetic interactions*

The interaction between localized electrons on neighboring cations has the form[5]

$$\mathscr{H}_{ex} = -\sum_{ij}\{J_{ij}(\mathbf{S}_i\,.\,\mathbf{S}_j)+\ldots\} \quad (6)$$

where the higher-order and anisotropic contributions may be neglected in the present discussion and, for an integral number of d electrons per like cation,

$$J_{ij} = (C\text{-}D\text{-}E)/4S^2, \quad |D|>|E| \gg C. \quad (7)$$

The term D of particular interest arises from mixing electron-transfer excited states into the crystal-field ground state. Three interactions between electrons on neighboring atoms can arise: (1) between electrons in half-filled orbitals, (2) between two electrons in a filled orbital of a cation having a net spin and one electron in a half-filled orbital, (3) between an electron in a half-filled orbital and an empty orbital of a cation having a net spin. From the Pauli exclusion principle, an electron can jump without change of spin (conservation of spin angular momentum) from a half-filled orbital on one atom to a half-filled orbital on a neighboring atom only if the two spins are antiparallel. Further, the matrix element connecting the two states is a transfer energy $b_{ij} = (\Psi_i,\ h\Psi_j) \approx \epsilon\Delta_{ij}$, where $\Delta_{ij} = (\Psi_i,\ \Psi_j)$ is the overlap integral, and the energy h represents the change in the local potential energy as a result of the presence of the other cation. The energy required to move an electron from a half-filled orbital into an occupied orbital is U, and from second-order perturbation theory,

$$D_{h\text{-}h} = +2b^2/U \qquad (8)$$

where the subscripts h-h refer to interactions between half-filled orbitals. The plus sign corresponds to antiferromagnetic coupling. Where the electron transfer is from a full to a half-filled orbital, $D_{f\text{-}h}$, or from a half-filled to an empty orbital, $D_{h\text{-}e}$, then the Pauli exclusion principle allows electron transfer whatever the spin, but the maximum-spin excited states are stabilized by the intral atomic exchange energy J. This gives ferromagnetic coupling with

$$D_{f\text{-}h} = D_{h\text{-}e} = 2b^2\Delta(1/U') = -2b^2J/U'^2. \qquad (9)$$

For the sake of discussion, consider D_{h-h}. The Coulomb energy U is $U = (|\psi_j|^2, V|\psi_j|^2)$, where $V = (e^2/r_{12} \exp(-\xi\rho_{12})$ contains a screening parameter $\xi(b)$ that increases with increasing b. Therefore U decreases with increasing b, and the magnitude of D_{h-h} increases with increasing b. Hence there must be a critical parameter b_c such that the assumption of localized d electrons breaks down for $b \geqslant b_c$. Since b/U may be expected to change rapidly with b via $\xi(b)$ in the neighborhood of b_c, this critical parameter should be quite sharply defined. Thus a localized description of the d electrons is only valid in the domain $b < b_c$. Further, the magnetic-ordering temperature is proportional to D_{h-h} and therefore increases with b according to equation (8) throughout the domain $b < b_c$. Although the d orbitals of the known transition-metal oxyspinels fall in the localized-electron domain ($b < b_c$), this is not generally true for the thiospinels and selenospinels.

(C) *Collective* d *electrons*

In the domain $b > b_c$, a collective-electron description of the d electrons is required. Where $U < b$, a conventional tight-binding, Hartree–Fock theory for a single electron in a periodic potential may be used. In this theory it is assumed that $U = 0$. The periodic Wannier functions are the crystal-field orbitals of equation (4), and the bandwidths are $w_b \sim b$. In this domain, a partially filled d band gives metallic conductivity and a temperature-independent Pauli paramagnetism at normal temperatures. At lowest temperatures there may be a transition to a superconducting, diamagnetic state for $T < T_{cs}$. With smaller values of b/U, where $b \gtrsim b_c$, a transitional description is required. The important correlation-energy parameter to be introduced into the collective-electron Hamiltonian is the Coulomb energy U. In the localized-electron limit, the d-electrons are outside closed shells, provided the Fermi energy falls within E_g, and have multielectron, one-ion energies corresponding to their formal valence state. The ${}^4A_{2g}$ level of octahedral-site Cr^{3+} ions is such a d-electron energy. Thus for $b < b_c$, the ground-state d level corresponding to the formal cationic valence state M^{m+} is separated from that for $M^{(m-1)+}$ by the energy U if the interacting orbitals are half-filled; by the energy U' if half-filled orbitals interact with empty orbitals. This is consistent with our earlier assertion that excitation of an electron from one cation to a neighbor requires the energy U (or U'). It is equivalent to saying that there is an energy gap U between filled valence states and empty conducting states, as illustrated schematically in Fig. 7(a). In the broad-band limit the partially filled d band is illustrated schematically by Fig. 7(d). In the intermediate region, the M^{m+} and $M^{(m-1)+}$ levels are broadened into energy bands of width w'_b, and the energy gap[6]

$$E_g{}^d = (U^2 + \tfrac{1}{4}w_b{}^2)^{1/2} - \tfrac{1}{2}w'_b \qquad (10)$$

decreases with increasing b, falling to zero at a $b = b_m$. Again the ratio b/U enters the definition, so that b_m should be quite sharply defined. Since antiferromagnetic order increases the

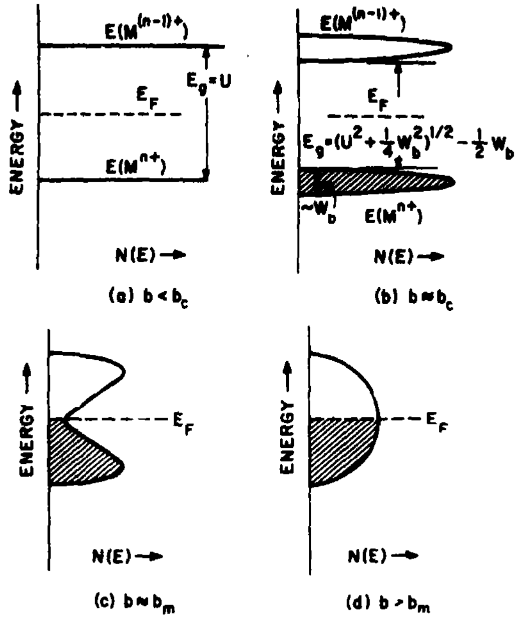

(a) $b < b_c$ (b) $b \approx b_c$ (c) $b \approx b_m$ (d) $b > b_m$

Fig. 7. Schematic d-orbital energies for different transfer energies b.

potential difference at the two interacting sites, it introduces an increase in $E_g{}^d$ that stabilizes the occupied states at the expense of the empty states. Such a stabilization is decreased by thermal excitation of electrons into the conducting states, so that the Néel temperature T_N decreases with decreasing E_g, and hence with increasing b. These considerations lead to the electronic phase diagram of Fig. 8. Empirical considerations confirm a $b_c < b < b_m$, but the width of this transitional region is apparently quite small[7].

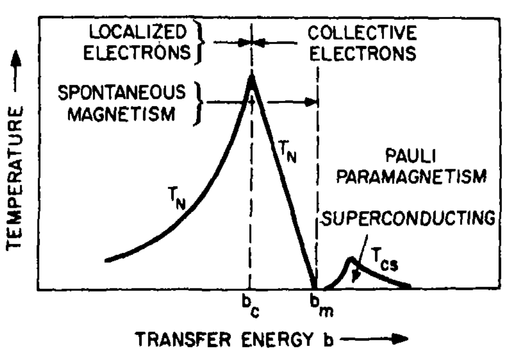

Fig. 8. Schematic, electronic T-b diagram for one electron per interacting d orbital.

A similar argument is available for D_{f-h} or for D_{h-e}. The Stoner[8] criterion for spontaneous, band ferromagnetism is

$$U_w \cdot N(E_F) \geq 1, \quad N(E_F) \sim w_b^{-1} \sim b^{-1} \qquad (11)$$

which again defines a b_m, determined by a b/U_w, such that spontaneous band ferromagnetism only occurs for $b < b_m$. (The Weiss molecular-field energy is $U_w \approx U/(1+UG)$, where G is a density of states function $\sim w_b{}^{-1}$.)

4. APPLICATION TO SOME SPINELS

(A) Cd[Cr$_2$]S$_4$ *vs.* Cd[Cr$_2$]Se$_4$

The normal spinels Cd[Cr$_2$]S$_4$ and Cd[Cr$_2$]Se$_4$ are ferromagnetic ($T_c = 85$°K, 130°K, respectively) and semiconducting [9–12]. The magnitude of the atomic moment approaches 6 μ_B/molecule, corresponding to a ${}^4A_{2g}(t_{2g}^3 e_g^0)$ ground state for localized 3 d-electrons at the Cr^{3+} ion. Near-neighbor B cations share common octahedral-site edges, and any other interactions are via at least two intermediary anions (see Fig. 2). From Fig. 9, there are two components to each near-neighbor Cr^{3+}–Cr^{3+} interaction, an antiferro-

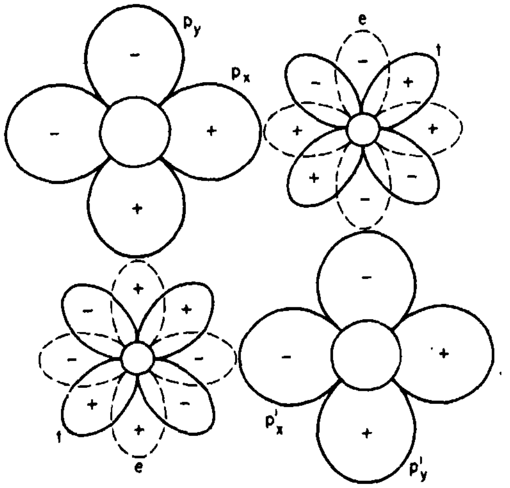

Fig. 9. B cations sharing a common octahedral-site edge.

magnetic cation–cation interaction $-J_{cc}$ due to overlapping, half-filled t_{2g} orbitals on neighboring atoms and a ferromagnetic 90° cation–anion–cation interaction J_{cac} due to half-filled t_{2g} orbitals overlapping empty e_g orbitals on neighboring atoms. The antiferromagnetic interaction $-J_{cc}$ couples a $^4A_{2g}(Cr^{3+})$ ground state to a $^3T_{1g}(Cr^{2+})$ excited state, the ferromagnetic interaction J_{cac} couples the $^4A_{2g}(Cr^{3+})$ ground state to a $^5E_g(Cr^{2+})$ state, where $^3T_{1g}(Cr^{2+}) \approx {}^5E_g$ (Cr^{2+}), since octahedral-site Cr^{3+} ions have a $10\,Dq \approx J$. The intermediary-anion p orbital simultaneously π-bonds with a t_{2g} orbital of one cation and σ bonds with the e_g orbital of the other. Thus whereas the cation–cation transfer energy is $b_{cc} = b_{cc}(R)$, where R is the cation–cation separation, the cation–anion–cation transfer energy is $b_{cac} \sim \lambda_\pi\lambda_\sigma$. On going from oxygen to sulfur to selenium, R increases and the transfer energy $b_{cc}(R)$ decreases. Simultaneously E_M–E_l decreases, so that $b_{cac} \sim \lambda_\pi\lambda_\sigma \sim (E_M - E_l)^{-2}$ increases. In oxides the net Cr^{3+}–Cr^{3+} interaction is negative $(J_{cc} > J_{cac})$, whereas $-J_{cc} + J_{cac} > 0$ increases on going from sulfur to selenium to tellurium, as predicted from the localized-electron model. The effect of more-distant-neighbor interactions, which induce a spiral-spin configuration in $Zn[Cr_2]Se_4$, has been discussed by several authors, but most adequately by Dwight and Menyuk[13].

Given a $^4A_{2g}(Cr^{3+})$ ground state and $^3T_{1g}$ $(Cr^{2+}) \approx {}^5E_g(Cr^{2+})$ electron-transfer excited states, the d levels are placed in the s,p band structure of Fig. 3 as shown in Fig. 10(a). Significantly, Ag-doped p-type $Cd[Cr_2]Se_4$ has a hole Hall mobility $\mu_H{}^+ = 32\ cm^2/V$-sec at room temperature, whereas In-doped n-type $Cd[Cr_2]Se$ has an electron Hall mobility $\mu_H{}^-$ more than two orders of magnitude smaller[12]. Since Hall mobilities $\mu_H < 1\ cm^2/$ V-sec are characteristic of localized electrons and $\mu_H > 100\ cm^2/V$-sec are characteristic of broad-band electrons[7], the electrons appear to be narrow-band electrons or small polarons, as expected for the Cr^{2+} level, and the holes to be collective charge carriers, as expected for the valence band Γ_{15}^+.

From Fig. 4, the top of the valence band E_v occurs at the center of the Brillouin zone in $Cd[In_2]S_4$. Substitution of In by Cr would not change this, since the octahedral-site d orbitals have Γ_{12} and Γ_{25}^- symmetry and do not interact with the Γ_{15}^+ orbitals at the top of the valence band. Therefore optical data as a function of temperature provide the magnitude of the energy ϵ_g of Fig. 10. They also give information about the relative stabilities of the high-spin $^5E_g(Cr^{2+})$ and low-spin $^3T_{1g}(Cr^{2+})$ levels. Harbeke and Pinch[14] observed a room-temperature $\epsilon_g \approx 1{\cdot}6\ eV$ and $1{\cdot}3\ eV$ in $Cd[Cr_2]S_4$ and $Cd[Cr_2]Se_4$, respectively, which are compatible with a smaller E_g (or less stable E_v) in the more covalent selenide. Surprisingly, they found that on lowering

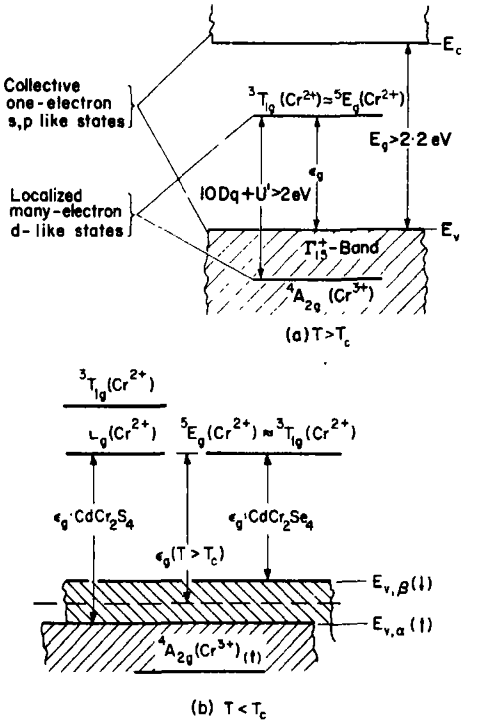
Collective one-electron s,p like states
Localized many-electron d-like states
E_c
$^3T_{1g}(Cr^{2+}) \approx {}^5E_g(Cr^{2+})$
$E_g > 2{\cdot}2$ eV
ϵ_g
$10Dq + U' > 2$ eV
E_v
Γ_{15}^+-Band
$^4A_{2g}(Cr^{3+})$
(a) $T > T_c$
$^3T_{1g}(Cr^{2+})$
$L_g(Cr^{2+})$
$^5E_g(Cr^{2+}) \approx {}^3T_{1g}(Cr^{2+})$
$\epsilon_g \cdot CdCr_2S_4$
$\epsilon_g \cdot CdCr_2Se_4$
$\epsilon_g(T > T_c)$
$E_{v,\beta}(\downarrow)$
$E_{v,\alpha}(\uparrow)$
$^4A_{2g}(Cr^{3+})_{(\uparrow)}$
(b) $T < T_c$

Fig. 10. Band structure for $Cd[Cr_2]X_4$ spinels. $^3T_{1g}(Cr^{2+}) \approx {}^5E_g(Cr^{2+})$ because $J \approx 10Dq$. At room temperature, $^5E_g < {}^3T_{1g}$ and $\epsilon_g \approx 1{\cdot}6$ eV in $Cd[Cr_2]S_4$; $^3T_{1g} \approx {}^5E_g$ and $\epsilon_g \approx 1{\cdot}3$ eV in $Cd[Cr_2]Se_4$.

the temperature through the Curie temperature T_c, there is an anomalous increase of over 0·2 eV in the optical ϵ_g of Cd[Cr$_2$]S$_4$ and an anomalous decrease of over 0·2 eV in the optical ϵ_g of Cd[Cr$_2$]Se$_4$. This observation suggests the following interpretation: Ferromagnetic correlations, especially long-range magnetic order, among the Cr^{3+} *d*-electrons of a multiatomic crystalline volume, must induce within that volume a stabilization of the parallel-spin valence-band electrons and a corresponding destabilization of the antiparallel-spin electrons, as shown in Fig. 10(b). The magnitude of the band-edge shifts would be proportional to the molecular field $J\langle S_z\rangle/S$. Although the long-range molecular field vanishes above the Curie temperature, a short-range molecular field persists within the domains of short-range order. The duration of such a transient field would be long compared to the time required for an optical transition. Therefore optical excitation from the valence band to a localized-electron state within a domain of short-range order should reflect polarizations of the valence-band orbitals by the short-range molecular field. Further, if the high-spin $^5E_g(\mathrm{Cr}^{2+})$ level is lower than the low-spin $^3T_{1g}(\mathrm{Cr}^{2+})$ level by $^3T_{1g}-{}^5E_g > E_{v,\beta}-E_{v,\alpha}$, then $\epsilon_g = {}^5E_g - E_{v,\alpha}$ where $E_{v,\alpha}$ and $E_{v,\beta}$ are the top of the Γ^+_{15} valence band having spins parallel and antiparallel to the spins on the Cr^{3+} ions. This follows from conservation of spin angular momentum. On the other hand, if $^3T_{1g}-{}^5E_g < E_{v,\beta}-E_{v,\alpha}$, then $\epsilon_g = {}^3T_{1g}-E_{v,\beta}$. Since $E_{v,\alpha}$ becomes more stable and $E_{v,\beta}$ becomes less stable as ferromagnetic order sets in, the energy $^5E_g - E_{v,\alpha}$ increases and the energy $^3T_{1g}-E_{v,\beta}$ decreases with increasing $\langle S_z\rangle$ as the temperature is lowered through T_c. The two localized-electron Cr^{2+} levels, which experience the full intra-atomic-exchange stabilization at all temperatures, would be shifted only by interatomic exchange interactions. Figure 10(b) can unambiguously account qualitatively for the reversal in sign of the optical shifts on passing from Cd[Cr$_2$]S$_4$ to Cd[Cr$_2$]Se$_4$ if the $^5E_g(\mathrm{Cr}^{2+})$ level is destabilized by ferromagnetic order and the $^3T_{1g}(\mathrm{Cr}^{2+})$ level is stabilized by ferromagnetic order.

Cr^{2+}–Cr^{3+} interactions are dominated by transfer of a Cr^{2+} electron to a Cr^{3+} ion, since this occurs in first-order rather than second-order theory. The electron transferred from a Cr$^{2+}(^5E_g)$ ion is an e_g electron with spin parallel to the Cr^{2+}-ion spin. It transfers to a half-filled Cr$^{3+}t_{2g}$ orbital, so that the interaction is antiferromagnetic. This conclusion has been confirmed by experiments[15] on Cr^{2+}-doped Cd[Cr$_2$]X_4 spinels. It follows that the unoccupied $^5E_g(\mathrm{Cr}^{2+})$ level at a Cr^{3+} ion is destabilized by ferromagnetic coupling of the Cr^{3+} ions. In the case of low-spin Cr$^{2+}(^3T_{1g})$ ions, on the other hand, a t_{2g} electron antiparallel to the net Cr^{2+} spin is transferred. Because the antiparallel-spin electrons have larger radial extension, since intra-atomic exchange does not reduce the electron screening from the nuclear charge for these electrons, transfer to a half-filled Cr$^{3+}t_{2g}$ orbital is stronger for Cr^{2+}–Cr^{3+} than for Cr^{3+}–Cr^{3+} interactions and is ferromagnetic via equation (9). Transfer from a filled Cr$^{2+}t_{2g}$ orbital to an empty Cr$^{3+}e_g$ orbital contributes to the coupling only in higher order. Therefore it is reasonable to anticipate ferromagnetic coupling of low-spin Cr^{2+} ions to the Cr^{3+} ions and hence a stabilization of the $^3T_{1g}$ level as a result of ferromagnetic order.

This model for the optical data requires that in the sulfide high-spin Cr^{2+} is more stable than low-spin Cr^{2+}; that in the selenide, where the optical energy gap starts to decrease in the region of short-range order above T_c, $^3T_{1g}-{}^5E_g \leqslant 0$. Magnetic data on doped and reduced sulfides and selenides indicate high-spin Cr^{2+} ions (coupled antiparallel to the Cr^{3+} array, as anticipated if Cr^{2+} → Cr^{3+} transfer dominates the 90° cation–anion–cation superexchange interaction) in both cases[15], which requires either $^3T_{1g} \approx {}^5E_g$ in the selenide or another model for the optical data. Since $10\,Dq$ is larger in the selenide, according to quation (3), a ${}^3T_{1g} \approx {}^5E_g$ in the selenide is ntirely plausible, the ${}^5E_g$ level being stabilized elative to the ${}^3T_{1g}$ level in the doped and reuced selenides by lattice relaxation and local ahn–Teller deformations.

Callen[16] has argued that the optical shifts elow the Curie temperature are due to change striction. Magnetic-electron bands ould shift by an energy $\Xi_1\epsilon_1$, where Ξ_1 is a mmetrized deformation potential and ϵ_1 is a mmetry strain induced by exchange stricon:

$$\epsilon_1(T, H) = \sum_{ij} D_{ij}\langle \mathbf{S}_i\cdot\mathbf{S}_j\rangle (T, H)/(c_{11}+2c_{12})$$

where c_{11}, c_{12} are the usual elastic constants and the D_{ij} are the derivatives of the exchange parameters J_{ij} with respect to volume strain. Without a detailed model, Callen is forced to make the *ad hoc* assumption that other states are in thermal equilibrium with the magnetic-electron band states. In our model, such an assumption is not required because excitation is from the valence s-p bands. Although Callen claims that the magnitude of $\epsilon_1\Xi_1$ could alone account for the observed shifts of about 0·2 eV, nevertheless he provides no mechanism for a change in the sign of Ξ_1 on going from Cd[Cr]S$_4$ to Cd[Cr$_2$]Se$_4$. Furthermore, the component of the exchange interaction that is most sensitive to the lattice parameter is the cation–cation interaction. It is for this reason that exchange striction gives an anomalous *expansion* of the lattice parameter with ferromagnetic ordering below T_c, signaling the antiferromagnetic character of the cation–cation components of the superexchange interaction between Cr^{3+} ions. Thus exchange striction only reduces the magnitude of the destablization of the ${}^5E_g$ (Cr^{2+}) level with ferromagnetic ordering. The exchange striction would also reduce stabilization of the ${}^3T_{1g}$ levels, since the Cr^{3+}–Cr^{3+} interactions produce an anomalous expansion. It can, of course, never produce an energy shift greater than that due to the interatomic interactions themselves. If Callen's estimate of the magnitude of the exchange-strictive shift is correct, the shift of the Cr^{2+} levels due to interatomic exchange interactions would alone be of sufficient magnitude to account for the observations.

Note added in proof: MARTIN G. W., KELLOGG A. T., WHITE R. L. and WHITE R. M., *J. appl. Phys.* Issue on *New York Magnetism Conference*, In press (1969); report changes in lattice parameter between 4·2°K and T_c of $\Delta a/a \approx 10^{-3}$ for Cd[Cr$_2$]Se$_4$ and Cd[Cr$_2$]S$_4$, which would require a deformation potential of the order of 100 eV. This is at least an order of magnitude larger than can be anticipated, which appears to confirm our conclusion that Callen's exchange-striction mechanism is not responsible for the large absorption-edge shifts in these materials.

(*B*) *The ferromagnetic spinels* Cu[Cr$_2$]X_4

The chalcogenide spinels containing copper exhibit many interesting properties, and their interpretation has been the subject of controversy. The controversy centers about the proper interpretation of the ferromagnetic, metallic spinels Cu[Cr$_2$]X_4, X = S, Se or Te, having a saturation moment at 0°K approaching 5μ_B/molecule. These materials were first reported by Lotgering[17], who interpreted his data on an ionic model with the formal valency assignments Cu$^+$[Cr^{3+}Cr^{4+}]X_4. Ferromagnetism and high electrical conductivity were believed to be due to the Zener–deGennes[18] double-exchange mechanism between Cr^{3+} and Cr^{4+} ions. In this mechanism, electron transfer without change of spin, Cr^{3+} + Cr^{4+} = Cr^{4+} + Cr^{3+}, couples neighboring spins ferromagnetically, since the transfer is from a half-filled to an empty t_{2g} orbital. Further, charge transfer does not require an activated mobility in the limit $b \approx b_c$.

Goodenough[19] rejected the Lotgering model for two reasons: (1) In the oxyspinel Cu^{2+}[Cr$_2^{3+}$]O$_4$, it is known that Cu$^+$ cannot be stable in the presence of Cr^{4+}. It is unreasonable to postulate a reversal of this ordering of energy levels on passing from an oxide to a sulfide. (2) An alternate model for the Cu-[Cr$_2$]X_4 spinels is available. This alternative emerged from my study of isostructural series of compounds, including the thiospinels, to determine where the transition from $b < b_c$ to $b > b_m$ occurred. It is based on the conclusion that any holes in the d-like Cu–X bands must be collective and without spontaneous magnetism ($b > b_m$). This conclusion was derived, in turn, from the requirement of consistency over the periodic table together with the observation that the spinel Co_3S_4 is metallic and without spontaneous magnetism. The argument proceeds as follows:

In the spinel structure, cationic A–A and A–B interactions occur via an anion intermediary, so that a $b > b_c$ for A-site d orbitals requires large covalent mixing between cationic d and anionic s,p orbitals. Covalent mixing with the d orbitals increases with atomic number in any long period of the periodic table both because the d orbitals are relatively more stable and because the cations are less ionic. That these two influences outweigh any contraction of the atomic, d-orbital radial extension is made evident by the increasing Néel temperatures in the oxides with rocksalt structure: MnO, FeO, CoO, NiO have respective Néel temperatures $T_N = 122$, 198, 291, and 520°K. Covalent mixing also increases with decreasing intra-atomic-exchange stabilization, such stabilization sharply reducing the radial extension of the d orbitals. It follows that the transfer energy $b \sim \lambda_\sigma^2$ increases with atomic number from Mn^{2+} to Cu^{2+} and that the b_β for the antiparallel-spin electrons in high-spin ions is larger than the b_α for five parallel-spin electrons comprising the half-filled d shell, especially in Fe^{2+} where there is only one antiparallel-spin electron. For later reference, we summarize this latter conclusion as

$$b_\beta > b_\alpha, \text{ especially in } Fe^{2+} \text{ ions.} \qquad (12)$$

The trivalent ions Co^{3+}, Ni^{3+}, Rh^{3+} are in a low-spin state in the spinel structure, where $(\lambda_\sigma - \lambda_\pi)$ is relatively large. The diamagnetic Co^{3+} and Rh^{3+} ions have a ${}^1A_{1g}(t_{2g}^6 e_g^0)$ ground state, the Ni^{3+} ion a ${}^2E_g(t_{2g}^6 e_g^1)$ ground state if the d electrons are localized. However, the fact that the perovskite $LaNiO_3$ is metallic, Pauli paramagnetic, and exhibits no Jahn-Teller distortion to lowest temperatures indicates that the 180° cation-anion-cation interactions $\sim \lambda_\sigma^4$ are strong enough to make $b > b_m$, even in the oxide[20]. Similarly high-temperature $LaCoO_3$, with a mixture of high-spin and low-spin Co^{3+}, exhibits a first-order electronic transition that indicates a $b \approx b_c$[21]. Therefore in the more covalent sulfides it is necessary to anticipate a $b > b_m$ for the σ-bonding d orbitals of the low-spin, trivalent cations Co^{3+}, Rh^{3+}, Ni^{3+}. In the octahedral B sites, this leads to the one-electron configurations

$$t_{2g}^{B*6}\sigma^{*0} \quad \text{for} \quad Co^{3+}, Rh^{3+} \qquad (13)$$

$$t_{2g}^{B*6}\sigma^{*1} \quad \text{for} \quad Ni^{3+} \qquad (14)$$

where collective-electron, antibonding σ^* orbitals replace the localized $e_g{}^{B*}$ orbitals. In the spinel structure, a strong 130° A–anion–B interaction ($b_{ij} \sim \lambda_\sigma{}^A\lambda_\sigma{}^B$) is implied by (13) and (14). The pyrite CoS_2 contains low-spin Co^{2+} ions and is metallic and ferromagnetic [22], indicating that the Co^{2+}–S–Co^{2+} interactions are strong enough to give $b_c < b_{ij} < b_m$. Since $b_{ij} \sim \lambda_{\sigma i}\lambda_{\sigma j}$ and λ_σ increases with formal cationic valence, this result implies that the Co^{2+}–S–Co^{3+} interactions in Co_3S_4 would be enough stronger to make $b_{ij} > b_m$ in this compound. It is reassuring, therefore, to find that the spinels Co_3S_4, $NiCo_2S_4$ are all metallic and without spontaneous magnetism [23], characteristic of a $b > b_m$. Thus A-site Co^{2+} and Ni^{2+} ions would have the one-electron configurations

$$e_g^{A*4}\sigma^{*4} \quad \text{for} \quad Co^{2+}, \quad e_g^{A*4}\sigma^{*5} \quad \text{for} \quad Ni^{2+}. \qquad (15)$$

However, assignment of formal valences is meaningless in these metals, even though the smaller crystal-field splitting $10\,Dq$ at the A sites would make the bottom of the σ^* band more σ_A^* than σ_B^* in character. This situation is illustrated schematically in Fig. 11. The σ^* bands should not overlap the $e_g{}^{A*}$ and $t_{2g}{}^{B*}$ bands, since they are antibonding with

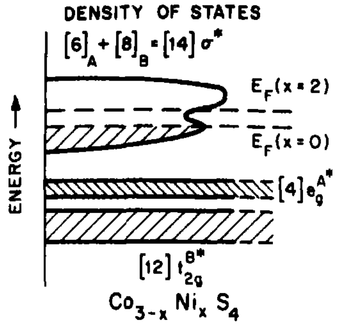

Fig. 11. Schematic *d*-band structure of $Co_{3-x}Ni_xS_4$, where the Fermi energy E_F increases with x, $[n]$ is number of states per AB_2X_4 formula unit.

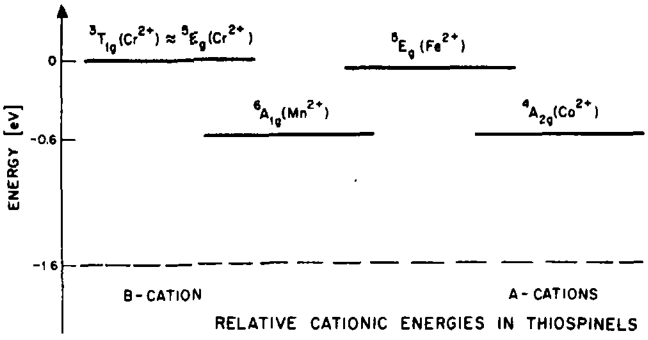

Fig. 12. Relative cationic stabilities in $A[B_2]S_4$ spinels. The $^3T_{1g}(Cr^{2+})$ level dominates *A–B* interactions, but the $^5E_g(Cr^{2+})$ level the Cr–Cr interactions.

respect to the anionic array, therefore becoming less stable with increasing λ_σ. The magnetic susceptibility of Co_3S_4 shows some temperature dependence, suggesting that the σ^* band is very narrow and $b_{ij} \approx b_m$. The number of electrons per $Co_{3-x}Ni_xS_4$ molecule in the σ^* band is $n_e = 3+x$, and the band contains 14 states per molecule. The top of the *s,p* valence band, which is not shown, is nearly 1 eV below the Fermi energy E_F. (E_F is close to the $^4A_{2g}(Co^{2+})$ level in Fig. 12.)

Consistency with the periodic table requires a $b_{ij} > b_m$ in $NiCo_2S_4$ and $CuCo_2S_4$ if $b_{ij} > b_m$ occurs in Co_3S_4. However, it does not necessarily follow that $b_{ij} > b_m$ in $Cu[Cr_2]S_4$, since λ_σ for *B*-site Cr^{3+} is smaller than λ_σ for the heavier *B*-site ion Co^{3+}. In fact the Co^{2+} ion exhibits a spontaneous magnetic moment in the ferrimagnetic spinel $Co[Cr_2]S_4$ discussed below. Nevertheless a $b_{ij} > b_m$ for the copper *d* orbitals of t_{2g} symmetry is anticipated from the periodic table, since the Co^{2+} ions appear to have $b_c < b_{ij} < b_m$ in $Co[Cr_2]S_4$ (see below). The fact that $Cu[Cr_2]S_4$ is a metallic ferromagnet led me to postulate the formal valences $Cu^{2+}[Cr_2{}^{3+}]S_4$ having a metallic conductivity due to one *d* hole per molecule in a σ_A^* band, where the subscript *A* is used to signify a deeper electron potential at the *A* vs. the *B* site. This postulate was based on the assumption that E_v is below the Fermi energy E_F in the sulfide. Four testable predictions follow from this postulate: (1) There should be only one type of chromium ion present, and this should carry a moment of 3 μ_B. (2) The observed saturation moment of 5 μ_B per molecule is due to an antiparallel-spin polarization of the σ_A^* band that increases to -1 μ_B per molecule with increasing correlation function $\langle \mathbf{S}_i \cdot \mathbf{S}_j \rangle$ among Cr^{3+} ions, the antiferromagnetic coupling being similar to the 130° *A–S–B* coupling found in the ferrimagnetic spinels $A[Cr_2]S_4$, A = Mn, Fe, Co. Further, the spin density of the polarized σ_A^* band may be distributed over the crystal rather than localized at the copper atoms. (3) The Seebeck voltage should be positive, corresponding to σ_A^* holes. (4) The ferromagnetic Cr^{3+}–Cr^{3+} interactions are enhanced by indirect coupling via the mobile holes. The Weiss molecular field parameter

$$W = W_0 + \alpha_W T + \dots \tag{16}$$

enters the Curie–Weiss law as

$$\chi = C/(T-CW) = C_{\rm eff}/(T-C_{\rm eff}W_0) \tag{17}$$

$$C_{\rm eff} = C/(1-C\alpha_W). \tag{18}$$

Well above T_c, where $\langle \mathbf{S}_i \cdot \mathbf{S}_j \rangle \approx 0$, there is no σ_A^* moment to contribute to $C_{\rm eff}$ and $C_{\rm eff}W_0 = \theta_p \geqslant T_c$. The indirect coupling via mobile holes decreases with decreasing mobility, and hence with increasing temperature, so that its contribution to α_W is negative, thereby decreasing the measured C_{eff} relative to a theoretical C. On the other hand, the antiferromagnetic cation–cation interaction $-J_{cc}$ also decreases with increasing lattice parameter, and hence with temperature, which gives a positive contribution to α_{ii}. A low C_{eff} could reflect a stronger contribution to $\alpha_{ii'}$ from the indirect ferromagnetic interaction via the mobile σ_A^* holes.

The third prediction was known ($\alpha \approx 10\,\mu V/\text{deg}$), as was a $\theta_p \approx T_c$ and a low C_{eff} [17]. Subsequent neutron-diffraction investigations [24, 25] confirmed the first of these predictions, 3 μ_B per chromium ion, and found no measurable atomic moment on the copper sites. Nuclear magnetic resonance [26] on $\text{Cu}[\text{Cr}_2]\text{Se}_4$ and $\text{Cu}[\text{Cr}_2]\text{Te}_4$ also indicated only one type of chromium atom. This rules out the Lotgering ionic model and, together with the magnetization data, implies an antiparallel polarization of 1 μ_B/molecule having a distributed spin density. However, whether the polarized hole is in the Γ_{15}^+ valence band or in the σ_A^* band remains an open question. If it is a σ_A^* band that is polarized, the induced spin density is not localized at the copper atoms.

Lotgering and Van Stapele [27], influenced by a suggestion from Haas, argued that the hole responsible for the metallic conductivity was in the s, p valence band. Insisting on Cu^+ ions, they placed the ${}^4A_{2g}(\text{Cr}^{3+})$ level just below E_F and well above the copper d bands. In a modified and improved discussion of their argument [28], they assumed that at low temperatures ($T < T_c$) the interatomic exchange stabilization of the ${}^4A_{2g}(\text{Cr}^{3+})$ level placed it below the Fermi level E_F, leaving one antiparallel-spin electron in a polarized, valence p band (the Γ_{15}^+ band of Fig. 4). This gives consistency with neutron data, but begs the question why polarization of the valence band gives an antiparallel spin. (My interpretation in Fig. 10(b) of the optical data for $\text{Cd}[\text{Cr}_2]X_4$, $X = \text{S}$ or Se, requires a normal parallel-spin polarization of this band.) However, it permits them to account for the high-temperature Curie constant $C_{\text{eff}} = 1{\cdot}1_5$ (vs. $C_{\text{calc}} = 1{\cdot}87$, $1{\cdot}0$ for Cr^{3+}, Cr^{4+}) that they obtained for metallic, ferromagnetic CuCrRhSe_4 by postulating the high-temperature configuration $\text{Cu}^+[\text{Cr}^{4+}\text{Rh}^{3+}]\text{Se}_4$. My model calls for the configuration $\text{Cu}^{2+}[\text{Cr}^{3+}Rh^{3+}]\text{Se}_4$, the metallic conductivity and saturation moment reflecting one hole per molecule in a σ_A^* band that has an antiparallel spin below T_c. Their entire argument for Cr^{4+} in the presence of Cu^+ hinges on the $C_{\text{eff}} = 1{\cdot}1_5$ in this compound compared with a $C_{\text{eff}} = 1{\cdot}84$ in the semiconducting compound CuCrTiS_4 ($\theta_p = 4°\text{K}$), where the formal valences Cu^+, Cr^{3+}, Ti^{4+} may be assumed. However, the low C_{eff} is also compatible with prediction (4) above, since a $\theta_p = 4°\text{K}$ in CuCrTiS_4 reveals that the strong ferromagnetic coupling in CuCrRhSe_4 is due almost entirely to the indirect interaction via the mobile holes. (There are no mobile holes in CuCrTiS_4, and $C_{\text{eff}} \approx C$.) A $C_{\text{eff}} = 1{\cdot}1_5$ vs. a $C = 1{\cdot}87$ could be produced by $\alpha_{ii'} = -1/3$, corresponding to an $|\alpha_{ii'}|/W_0 \sim 10^{-3}$. Thus the low C_{eff} does not require the fortuitous placing of a ${}^4A_{2g}(\text{Cr}^{3+})$ level just below E_F or the reversal both in the sign of the polarization of the valence band and in the ordering of the Cu^+, Cr^{4+} energies.

Finally, Sleight [29], using X-ray and neutron-diffraction data in the literature, compared the observed Cu–X distances with those calculated on the basis of Pauling's tetrahedral covalent radii. His comparisons, together with the observed Cr–X separations, are listed in Table 3. Clearly the $\text{Cu}[\text{Cr}_2]X_4$ compounds having $X = \text{S}$, Se, Te all have Cu–X separations consistent with Cu^{2+} and inconsistent with Cu^+. This finding indicates

Table 3. Interatomic distances in some $\text{Cu}[\text{Cr}_2]X_4$ *spinels*

Compound	Cu–X (obs)	Cu^{+1}–X (calc)	Cu^{+2}–X (calc)	Cr–X (obs)
$\text{Cu}[\text{Cr}_2]\text{S}_4$	2·28	2·39	2·28	2·37
$\text{Cu}[\text{Cr}_2]\text{Se}_4$	2·38	2·49	2·38	2·50
$\text{Cu}[\text{Cr}_2]\text{Se}_3\text{Br}$	2·51	2·48	2·37	2·47
$\text{Cu}[\text{Cr}_2]\text{Te}_4$	2·53	2·67	2·56	2·72

that the holes responsible for the metallic conductivity in these compounds are the Cu–X d-like holes in the σ_A^* band, not holes in the Γ_{15} anionic p band. An objection may be raised about the validity of the Pauling radii. However, even more convincing are the data for $Cu[Cr_2]Se_3Br$. Substitution of one Se^{2-} by Br^- fills up the hole in the conducting band, whether it be a σ_A^* band or an anionic p band or both overlapping. Thus this compound has the formal valence configuration $Cu^+ \cdot [Cr_2^{3+}]Se_3Br$ and is a semiconductor with either model. If the result of bromine substitution is to fill up holes in the σ_A^* band (formally reducing Cu^{2+} to Cu^+), the Cu–X distances must increase while the Cr–X distances decrease slightly to accommodate the smaller Br^- ions. On the other hand, if bromine substitution fills up holes in the anionic p band, the Cr–X distance should increase at least as much as the Cu–X distance—and much more so if there is any reduction of Cr^{4+} ions to Cr^{3+} ions. As can be seen from Table 3, the changes in interatomic distance are those expected for holes in a σ_A^* band and appear to rule out the Lotgering–van Stapele hypothesis that the copper d^{10} core electrons are far below E_v.

Note added in proof: LOTGERING F. K. and VAN STAPELE R. P., *Mat. Res. Bull.* **3**, 507 (1968), have questioned the reliability of the structural data for $Cu[Cr_2]Se_3Br$ used in Table 3, which were taken from ROBBINS M., BALTZER P. K. and LOPATIN E., *J. appl. Phys.* **39**, 662 (1968) and WHITE J G. and ROBBINS M., *J. appl. Phys.* **39**, 664 (1968). SLEIGHT A. W. and JARRETT H. S., *J. Phys. Chem. Solids* **29**, 868 (1968) have reported structural data for carefully characterized compounds in the system $Cu[Cr_2]Se_{4-x}Br_x$ and $Cu[Cr_2]S_{4-y}Cl_y$. In the first system they were able to prepare solid solutions in the range $0 \leqslant x \leqslant 0{\cdot}8$ and in the second for $0 \leqslant y \leqslant 1$. The first system showed an increase in cell volume with x that extrapolated to a value near that reported by Robbins *et al.* A similar increase in cell volume with y was observed in the second system. MIYATANI K., WADA Y. and OKAMOTO F., *J. phys. Soc. Japan* **25**, 369 (1968) have grown single crystals of $Cu[Cr_2]Se_3Br$ that have a lattice parameter essentially in agreement with that of Robbins *et al.* Therefore unless the u parameter obtained by White and Robbins is in error, the Sleight argument must stand. LOTGERING F. K., *J. Phys. Chem. Solids* **29**, 699 (1968), has also shown that whereas $A[Cr_2]Se_4$, A = Zn, Cd, Hg, are semiconductors with fairly large activation energies $Cd_{0{\cdot}998}Cu_{0{\cdot}002}[Cr_2]Se_4$, $Zn_{0{\cdot}98}Cu_{0{\cdot}02}[Cr_2]Se_4$, and $Hg_{0{\cdot}95}Cu_{0{\cdot}05}[Cr_2]Se_4$ are much better conductors, the activation energies decreasing sharply with copper content. Although he argues for valence-band holes in these p-type semiconductors, there is no reason to exclude, from his data, Cu^{2+} acceptor levels that approach the formation of impurity bands as the copper concentration exceeds 5 per cent.

Although these arguments appear to be sufficient to establish the essential features of the band structure in the metallic, ferromagnetic chalcogenides $Cu[Cr_2]X_4$, it would be helpful to have some estimate of the energy separation $E_F - E_v$, even though E_v loses its physical definition when the σ_A^* band overlaps the Γ_{15}^+ band. Such an estimate will now be made, and it will be shown to be consistent with an $(E_F - E_v) \gtrsim 0$ in the sulfides and selenides and with a $Cu^{2+} + Cr^{3+}$ configuration more stable than the $Cu^+ + Cr^{4+}$ configuration.

(*C*) $A[Cr_2]S_4$, A = Mn, Fe, Co

The three chromium thiospinels $A[Cr_2]S_4$, A = Mn, Fe, or Co, form Néel-type ferrimagnetic spinels with collinear spins, the Curie temperatures T_c = 95, 195, 240 ± 10°K increasing regularly with atomic number. Above T_c, the magnetic susceptibility exhibits a Curie–Weiss law[30]. Superficially, these observations are consistent with localized d electrons at the A cations and a superexchange parameter $b_{ij} \sim \lambda_\sigma{}^A \lambda_\sigma{}^B \sim (E_M - E_l)_A{}^{-1} \lambda_\sigma{}^B$. However, there are anomalies. $Mn[Cr_2]S_4$ either has a slightly reduced Mn^{2+}-ion moment [31] or slightly canted A-site spins at lowest ($T < 5°K$) temperatures[32], $Fe[Cr_2]S_4$ exhibits no known Jahn–Teller distortion even though a localized-electron Fe^{2+}-ion ground state would be a ^5E_g state (there is a Jahn–Teller distortion from cubic symmetry in $Fe[Cr_2]O_4$), and neutron-diffraction data for $Co[Cr_2]S_4$ indicate reduced atomic moments[33].

The fact that $b_{ij} > b_m$ in Co_3S_4 indicates that the anomalously low moments in Co$[Cr_2]S_4$ suggested by neutron-diffraction data probably reflect a $b_c < b_{ij} < b_m$ for the A–B interactions in this compound. If $b_{ij} < b_c$ in Co$[Cr_2]S_4$, then the transition region $b_c < b_{ij} < b_m$ must be extremely small. Given a $b_c < b_{ij} < b_m$ in Co$[Cr_2]S_4$, it leaves open the possibility that $b_c \leqslant b_{ij,\beta} < b_m$ in Fe$[Cr_2]S_4$, where from (12) $b_\beta > b_\alpha$ is the transfer integral for the antiparallel-spin electron at the Fe^{2+} ion. (It is parallel to the Cr^{3+}-ion spin.) A Jahn–Teller distortion would signal a $b_{ij,\beta} < b_c$[34].

High-temperature susceptibility data is not a sensitive measure of whether $b_c < b_{ij} < b_m$. Lotgering[30] reports average atomic Curie constants per magnetic cation of $C_{at} = 2{\cdot}54$, $2{\cdot}22$, $2{\cdot}08$, $1{\cdot}67 \pm 0{\cdot}07$ for $A =$ Mn, Fe, Co, and Zn. These are to be compared with the spin-only calculated Curie constants $C_{calc} = 2{\cdot}71$, $2{\cdot}25$, $1{\cdot}87$ and $1{\cdot}87$. The low C_{at} of Zn$[Cr_2]S_4$ cannot be attributed to a temperature-dependent Weiss constant W, since α_W of equation (18) is dominated by $-J_{cc}$, there being few mobile charge carriers in this semiconductor. Therefore $\alpha_W > 0$. Hence the small C_{at} observed for Zn$[Cr_2]S_4$ must reflect either a reduced atomic moment on the Cr^{3+} ions, which is difficult to accept where there is ferromagnetic coupling, or difficulties with sample characterization. Since the preparation of stoichiometric samples is extremely difficult, it is reasonable to assume that chemical problems are responsible, and these may introduce a measured $C_{at}(Cr^{3+}) \leqslant 1{\cdot}87$ in all the compounds $A[Cr_2]S_4$. This makes too large the Co^{2+} contribution to the measured $C_{at} = 2{\cdot}08 \pm 0{\cdot}07$ for Co$[Cr_2]S_4$, which is consistent with $b_c < b_{ij} < b_m$. In the range of transfer integrals $b_c < b_{ij} < b_m$, there should be a continuous transition from the localized-electron Curie–Weiss law to a nearly temperature-independent Pauli paramagnetism, so that in this range the apparent C_{at} would be larger than any C_{calc} based on spin-only, localized-electron atomic moments. The discrepancy would increase as b_{ij} approached b_m, C_{at} probably increasing continuously with b_{ij} through b_m, but most rapidly at $b_{ij} \approx b_m$.

Note added in proof: BLASSE G., *Phys. Lett.* **19**, 110 (1965), reported that Co$[Rh_2]S_4$ is antiferromagnetic with a Neél temperature $T_N = 400°K$, which is high compared to the oxide Co$[Rh_2]O_4$ where $T_N = 27°K$. Since A-site Co^{2+} has the configuration $e_g^4 t_{2g}^3$, the σ-bonding orbitals are half-filled and Fig. 8 is applicable. The high T_N suggests $b_{ij} \approx b_c$. The difference in the energies of the Rh^{3+}. σ_B^* orbitals and the $Co^{2+}\sigma_A^*$ orbitals is much larger than that between $Co^{3+}\sigma_B^*$ orbitals and $Co^{2+}\sigma_A^*$ orbitals, which makes consistent the fact that Co_3S_4 is metallic and Co$[Rh_2]S_4$ is antiferromagnetic. Interactions between like atoms are always stronger than those between unlike atoms.

Although this reasoning indicates that the t_{2g}^{A*} electrons of the Co^{2+} ions are collective σ^{A*} electrons, nevertheless so long as the Coulomb energy $U \neq 0$ is large enough to split this band into occupied α-spin and unoccupied β-spin states ($b_{ij} < b_m$), it is meaningful to consider the ionic energies corresponding to the crystal-field configurations ${}^6A_{1g}$, ${}^5E_g$, ${}^4A_{2g}$ for A-site Mn^{2+}, Fe^{2+} and Co^{2+}. Further, the positions of these ionic energies relative to the ${}^5E_g(Cr^{4+})$ level can be obtained from transport measurements. Resistivity vs. temperature measurements[23] have the form $\rho = \rho_0 \exp(-\epsilon_l/kT)$, where $\epsilon_l = 0{\cdot}30$, $0{\cdot}04$ and $0{\cdot}32$ eV, respectively, above T_c. Since the chromium e_g^{B*} orbitals would participate in a σ^* band in Co$[Cr_2]S_4$, any activation energy in the mobility of the chromium e_g^{B*} electrons would be negligible, except in the vicinity of T_c where magnetic polarons are confined to regions of short-range order[12]. Therefore a $2\epsilon_l < \epsilon_g$, where ϵ_g is defined by Fig. 10(a), should give the positions of the ionic d-state manifold relative to the ${}^5E_g(Cr^{2+})$ level at $\sim 1{\cdot}6$ eV above E_v. This is shown diagrammatically in Fig. 12.

Consistency with the periodic table is argued as follows: Since a high-spin Mn^{2+} ion has a greater intra-atomic exchange stabilization J and a larger atomic number than a Cr^{2+} ion, the Mn^{2+} ${}^6A_{1g}$ ground state should lie below the Cr^{2+} ${}^5E_g$ ground state. An energy separation

$$ {}^5E_g(Cr^{2+}) - {}^6A_{1g}(Mn^{2+}) \approx 0{\cdot}6\,\text{eV} \quad (19) $$

is quite reasonable. On passing from Mn^{2+} to Fe^{2+}, there is a sharp loss (~1 eV) in the exchange stabilization due to the extra electron of β spin. It is reasonable to anticipate that about half of this energy is compensated by the larger atomic number, giving

$$^5E_g(\mathrm{Cr}^{2+}) - {}^5E_g(\mathrm{Fe}^{2+}) \approx 0{\cdot}08\,\mathrm{eV}. \tag{20}$$

However, on passing to the Co^{2+} ion the increase in atomic number plus the exchange stabilization between the two β-spin electrons makes $^5E_g(\mathrm{Fe}^{2+}) - {}^4A_{2g}(\mathrm{Co}^{2+})$ approach the 0·6 eV of equation (19), which is consistent with a

$$^5E_g(\mathrm{Cr}^{2+}) - {}^4A_{2g}(\mathrm{Co}^{2+}) \approx 0{\cdot}64\,\mathrm{eV}. \tag{21}$$

Unfortunately $NiCr_2S_4$ crystallizes in the monoclinic, vacancy-ordered NiAs structure, since both Ni^{2+} and Cr^{3+} ions have strong octahedral-site preference energies. However, a simple extrapolation of the interpretations of equations (19–21) would give

$$^5E_g(\mathrm{Cr}^{2+}) - {}^2T_{1g}(\mathrm{Cu}^{2+}) \approx 1{\cdot}3\,\mathrm{eV} \tag{22}$$

after allowance was made for an A-site crystal-field splitting of about 0·5 eV. It has already been argued that, because the Cu^{2+} ion is heavier than the Co^{2+} ion, consistency with the periodic table is satisfied with collective $(b_{ij} > b_m)\sigma_A^*$ copper d holes. However, with only one collective σ_A^* hole per copper atom, the Fermi energy E_F would fall roughly at the energy $^2T_{1g}(\mathrm{Cu}^{2+})$, so that equation (22) may be modified—within the crude accuracy of the extrapolation—to read

$$^5E_g(\mathrm{Cr}^{2+}) - E_F(\mathrm{Cu}^{2+}) \approx 1{\cdot}3\,\mathrm{eV} \tag{23}$$

$$E_F - E_v \approx 0{\cdot}3\,\mathrm{eV\ in\ Cu[Cr_2]S_4} \tag{24}$$

$$E_F \approx E_v\,\mathrm{in\ Cu[Cr_2]Se_4} \tag{25}$$

$$E_F < E_v \quad \mathrm{in\ Cu[Cr_2]Te_4} \tag{26}$$

This placement of $E_F > E_v$ in the sulfide and selenide is consistent with the conclusions derived from Table 3. However, for the telluride, where an $E_F < E_v$ is anticipated, the formal-valence designation Cu^{2+} becomes physically misleading. Also worthy of re-emphasis is the fact that with overlapping σ_A^* and Γ_{15}^+ bands, the definition of an E_v becomes blurred even though the anionic p states that mix strongly with the e_g^{A*} orbitals to form σ_A^* band orbitals come from lower p bands. Further, with overlapping σ_A^* and anionic p bands, a distributed spin density for the induced magnetization of the σ_A^* band is not unreasonable. Figure 13 summarizes schematically the band structure of the selenides at $T < T_c$ that emerges from these various considerations. (Polarization of the Γ_{15}^+ band, though presumably present as in Fig. 10(b), is not indicated.)

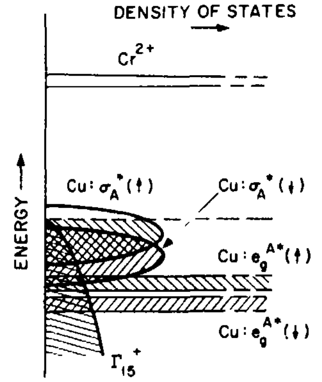

Fig. 13. Schematic band structure of Cu[Cr$_2$]Se$_4$ at $T < T_c$, where polarization of the Γ_{15}^+ band is not shown. The $^4A_{2g}(\mathrm{Cr}^{3+})$ ↑ level is below the Cu d bands.

The relative position of the $^4A_{2g}(\mathrm{Cr}^{3+})$ level is yet to be discussed. From optical data for octahedral-site Cr^{3+} ions in oxides, a crystal-field splitting parameter $10\,Dq \approx 2$ eV is anticipated for the B-site Cr^{3+} ions. This is considerably larger than the estimate of about 0·5 eV for the A-site Cu^{2+} cations because (1) the Cr^{3+} carries a larger formal charge, (2) by geometry octahedral-site splitting is over twice as large as tetrahedral-site splitting, and (3) the fact that the t_{2g} orbitals are half-filled and the e_g orbitals empty in Cr^{3+} is conducive to a maximum difference in the covalent-mixing parameters λ_σ and λ_π. This places the $^4A_{2g}(\mathrm{Cr}^{3+})$ level at least 0·4 eV below E_F in the thiospinels, which means that Cr^{4+} ions should not exist in these compounds[35]. Further, this gives

$$^{2}T_{1g}(Cu^{2+}) - {}^{4}A_{2g}(Cr^{3+}) \approx 0{\cdot}7\,\mathrm{eV} \quad (27)$$

which conforms with the known ordering of the levels existing in the oxyspinel $Cu^{2+}[Cr_2^{3+}]O_4$.

(D) *Other thiospinels containing copper*

1. *The system* $Fe_{1-x}Cu_x[Cr_2]S_4$. Electrical, magnetic, and Mossbauer studies[36, 37] of compositions in the system $Fe_{1-x}Cu_x[Cr_2]S_4$ indicate two distinct regions: $0 \leq x \leq 0{\cdot}5$ and $0{\cdot}5 \leq x \leq 1$. In the first region the copper d orbitals are filled (formal valence Cu^+), in accordance with Fig. 12, and the ferrimagnetic spinels contain two types of iron atoms below T_c, Fe^{2+} and Fe^{3+}. However, small isomer shifts with respect to metallic iron indicate considerable covalence, which increases with copper concentration, and at temperatures $T > T_c$ only one, narrow Mossbauer line is found. Haacke and Nozik[37] interpret their data as indicating a fast electronic exchange between the divalent and trivalent cations above T_c. Such a fast exchange implies that the iron d electrons outside half-filled shells (the single antiparallel-spin d electron per Fe^{2+} ion) occupy orbitals having a $b_{ij} \approx b_c$, which is consistent with our interpretation of $b_c < b_{ij} < b_m$ in $Co[Cr_2]S_4$ and the lack of a Jahn–Teller distortion in $Fe[Cr_2]S_4$.

The sign of the Seebeck voltage is dominated by the Fe^{2+}–Fe^{3+} exchange in the interval $0 < x < 0{\cdot}5$, and it changes from positive to negative with increasing x before $x = 0{\cdot}25$, the composition with equal numbers of Fe^{2+} and Fe^{3+} ions. In the compositional range $0{\cdot}5 < x \leq 1$, Mossbauer data indicate a single type of iron atom, presumably Fe^{3+}. From Fig. 12, $(2x-1)$ Cu^{2+} ions are created, and the Seebeck voltage, which is positive, is dominated by Cu^+–Cu^{2+} exchange. For $x \leq 0{\cdot}59$, the temperature dependence of the resistivity is semiconducting, but changes to metallic by $x = 1$. This implies that a σ_A^* band is not formed until nearly all of the A-site atoms become copper atoms, which is quite reasonable. Were the mobile holes in the anionic Γ_{15}^+ band in the range $0{\cdot}5 < x < 1$, metallic conductivity should be present for all $x > 0{\cdot}5$. This provides one more piece of indirect evidence favoring σ_A^* d-like holes in $Cu[Cr_2]S_4$.

2. *Superconducting spinels* $Cu[B_2]S_4$. As has already been mentioned, the intra-atomic exchange energy J determines critically where a $b_{ij} < b_c$ or a $b_{ij} > b_m$ occurs[38]. Where $J \gg w_b$, $w_b \sim b_{ij}$ being the bandwidth, localized electrons stabilized by J are more stable than collective electrons stabilized by a reduced kinetic energy. Conversely, where J is small, the conditions for a $b_{ij} > b_m$ are more easily satisfied. Since Co^{2+} ions, with $S = 3/2$, have been found to contribute a $b_{ij} < b_m$ in $Co[Cr_2]S_4$ and a $b_{ij} > b_m$ in Co_3S_4, where $b_{ij} \sim \lambda_\sigma{}^A\lambda_\sigma{}^B$, it is consistent with the periodic table to anticipate that B cations having a net spin $S \leq 1$ will have collective d electrons in $Cu[B_2]S_4$ spinels even if the B cation is lighter than chromium (i.e. V^{3+} or Ti^{3+}). Therefore it is gratifying to find that $Cu[Ti_2]S_4$, $Cu[V_2]S_4$, $Cu[Co_2]S_4$ and $Cu[Rh_2]S_4$ are metallic and Pauli paramagnetic[23]. However, it seems significant that $Cu[V_2]S_4$, $Cu[Rh_2]S_4$ and $Cu[Rh_2]Se_4$ are superconducting ($T_{cs} \approx 4{\cdot}45$, $4{\cdot}8$, $3{\cdot}5$°K) whereas $Cu[Ti_2]S_4$ and $Cu[Co_2]S_4$ are not superconducting above 0·05°K[39].

Although it is difficult to estimate the relative positions of the various d bands, extrapolation from Fig. 12 would place a $^{2}T_{1g}(Ti^{3+}: t_{2g}^{1}e_g{}^0)$ level above a $^{3}T_{1g}(V^{3+}: t_g{}^2e_g{}^0)$ level by about 0·6 eV and above the $^{4}A_{2g}(Cr^{3+}: t_{2g}^{3}e_g{}^0)$ level by about 1·2 eV, greater stabilization occurring for larger atomic number and intra-atomic exchange stabilization. Where the t_{2g}^{B*} orbitals are collective ($b_m < b_{ij} \sim \lambda_\pi{}^B\lambda_\sigma{}^B$) B-site orbitals, $E_F(B^{3+}) \approx T_{1g}(B^{3+})$. Since $E_F(Cu^{2+})$ was estimated to be about 0·7 eV above the $^{4}A_{2g}(Cr^{3+})$ level, this puts the Fermi energy E_F above the top of the σ_A^* copper band in $Cu[Ti_2]S_4$, but below it in $Cu[V_2]S_4$, as shown schematically in Fig. 14. This reasoning suggests that superconductivity appears where there are holes in the Cu–σ_A^* band and no localized electrons present at the *B* cations. Since consistency with the periodic table would make the Cu–σ_A^* band the broadest of the possible 3*d* bands, this result is compatible with Fig. 8 and does not necessarily depend upon special features of the σ_A^* band that are distinguishable from *B*-sublattice t_{2g}^{B*} bands.

The low saturation moment of $2{\cdot}1_5\mu_B$/CuCrRhSe$_4$ molecule appears to be only compatible with $Cu^{2+}[Cr^{3+}Rh^{3+}]Se_4$, corresponding to filled Rh–t_{2g}^{B*} orbitals and one Cu–σ^*_A hole per molecule giving a moment antiparallel to the $3\,\mu_B/Cr^{3+}$ ion. Therefore there must be one hole per molecule in the Cu–σ_A^* band of $Cu[Rh_2]X_4$, $X = S$ or Se, and no spontaneous moment on the Rh^{3+} ions. The fact that these compounds are superconductors is therefore satisfying.

The Fermi energy in Co_3S_4 should be close to the $^4A_{2g}$ level for *A*-site Co^{2+} ions, which is about 1 eV above E_v (see Fig. 12). Therefore a crystal-field stabilization would probably place the center of the Co^{3+}–t_{2g}^{B*} band over 0·4 eV below $E_F(Cu^{2+})$. However, if the bandwidth is $w_b \sim 1$ eV for the Co^{3+}–t_{2g}^{B*} band, this would place the top of this band at or just above the top of the Cu^{2+}–σ_A^* band. Therefore it is possible that the single hole per $Cu[Co_2]S_4$ formula unit is at least partially, if not wholly, in the Co–t_{2g}^{B*} band. This would be compatible with a superconductivity requirement of $n_e > f$ holes per formula unit in σ_A^* bands, where *f* is a large fraction, and no localized electrons present at the *B* cations.

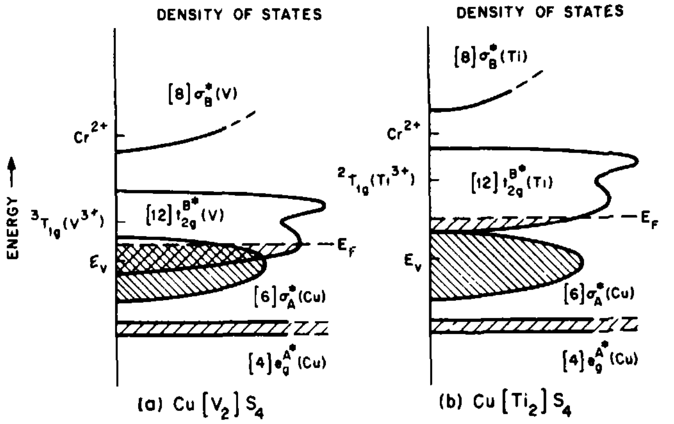

Fig. 14. Schematic *d*-band structures of $Cu[V_2]S_4$ and $Cu[Ti_2]S_4$. Relative positions of F_f and $^5E_g(Cr^{2+})$ levels in $A[Cr_2]S_4$ spinels indicated on energy scale for reference. [*n*] is number of states per formula unit.

5. CONCLUDING COMMENTS

Although much work must yet be done to clarify our descriptions of the outer electrons in transition-metal chalcogenide spinels, the necessary conceptual basis for interpreting the many striking properties of these compounds appears to be at hand. The development given here follows closely that given earlier[19], but the considerable amount of new data has permitted a sharpening of the argument. The relationship of the anionic valence bands to the *d*-orbital energies has been emphasized, whereas it was neglected in the earlier discussion of the thiospinels. The controversy over $Cu^+ + Cr^{4+}$ vs. $Cu^{2+} + Cr^{3+}$ in $Cu[Cr_2]X_4$ spinels seems to be resolved in favor of the latter alternative. Optical absorption vs temperature in $Cd[Cr_2]X_4$ spinels shows a strong energy shift with increasing magnetization. This appears to be due to Cr^{2+}-level shifting plus a spin polarization of the valence band. Reversal in the sign of the shift on going from $Cd[Cr_2]S_4$ to $Cd[Cr_2]Se_4$ can be consistently interpreted as a change from a high-spin toward a low-spin state for the most stable Cr^{2+} level. Mention has also been made of band narrowing as a result of the intra-atomic exchange stabilization J. In fact the chalcogenide spinels discussed illustrate this effect, a $b_{ij} < b_c$ occurring only where there can be three or more unpaired spins: $Cr^{3+}(3\ \mu_B)$, $Cr^{2+}(4\ \mu_B)$, $Mn^{2+}(5\ \mu_B)$, $Fe^{2+}(4\ \mu_B)$, and marginally $Co^{2+}(3\ \mu_B)$. Where the number of possible unpaired spins is less than three, as in $V^{3+}(S = 1)$; $Cu^{2+}V^{4+}$, Ti^{3+}, low-spin Ni^{3+} $(S = 1/2)$; low spin Co^{3+} and Rh^{3+} $(S = 0)$, there a $b_{ij} > b_m$ is found. Exchange narrowing can also induce narrow-band, itinerant electrons to become trapped in regions of short-range order. Finite regions of short-range order are most pronounced near a Curie temperature T_c, and giant magnetoresistance effects may be encountered at temperatures near T_c[12].

REFERENCES

1. KOELMANS M. and GRIMMEISS H. G., *Physica* **25**, 1287 (1959).
2. REHWALD W., *Phys. Rev.* **155**, 861 (1967)
3. CZAJA W., *Helv. Phys. Acta* **40**, 352 (1967)
4. KLEINER W. H., *J. chem. Phys.* **20**, 1784 (1952)
5. GOODENOUGH J. B., *Magnetism and the Chemical Bond*, p 184. Interscience, Wiley, New York (1963).
6. HUBBARD J., *Proc. R. Soc.* **A276**, 238 (1963); **A281**, 401 (1964).
7. GOODENOUGH J B., *J. appl. Phys.* **39**, 403 (1968).
8. STONER E. C., *Proc. R. Soc.* **A165**, 372 (1938); *ibid.* **A169**, 339 (1939).
9. MENYUK N, DWIGHT K., ARNOTT R. J. and WOLD A., *J. appl Phys.* **37**, 1387 (1966).
10. BALTZER P. K., WOJTOWICZ P. J., ROBBINS M. and LOPATIN E., *Phys. Rev.* **151**, 367 (1966).
11. LEHMANN H. W. and ROBBINS M., *J. appl. Phys.* **37**, 1389 (1966).
12. LEHMANN H. W., *Phys. Rev.* **163**, 488 (1967).
13. DWIGHT K. and MENYUK N., *Phys. Rev.* **163**, 435 (1967); *J. appl. Phys.* **38**, 660 (1968).
14. HARBEKE G. and PINCH H., *Phys. Rev. Lett.* **17**, 1090 (1966).
15. BERGER S. B. and PINCH H. L., presented at *Second International Conference on Solid Compounds of Transition Elements at Enschede (Holland)*, Unpublished (1967).
16. CALLEN E., *Phys. Rev. Lett.* **20**, 1045 (1968).
17. LOTGERING F. K., *J. Phys. Chem. Solids* **23**, 1153 (1962); *Proc. Int. Conf. on Magnetism, Nottingham, September 1964*, p. 533.
18. DE GENNES P-A., *Phys. Rev.* **118**, 141 (1960).
19. GOODENOUGH J. B., Colloques Internationaux du CNRS No. 157, Propriétés Thermodynamiques, Physiques, et Structurales des Dérives Semi-Métalliques, Orsay, September 28 to October 1, 1965 (Editions du CNRS, 1967).
20. GOODENOUGH J. B. and RACCAH P. M., *J. appl. Phys.* **36**, 1031 (1965).
21. RACCAH P. M. and GOODENOUGH J. B., *Phys. Rev.* **155**, 932 (1967).
22. BITHER T., Brown Univ. Solid State Chemistry Conf (Summary by J. B. Goodenough), *Mat. Res. Bull.* **2**, 741 (1967).
23. BOUCHARD R. J., RUSSO P. A. and WOLD A., *Inorg. Chem.* **4**, 685 (1965).
24. COLOMINAS C., *Phys. Rev.* **153**, 558 (1967).
25. ROBBINS M., LEHMANN H. W. and WHITE J. G., *J. Phys. Chem. Solids* **28**, 897 (1967).
26. YOKOYAMA H., WATANABE R. and CHIBA S., *J. phys. Soc. Japan* **23**, 450 (1967).
27. LOTGERING F. K. and VAN STAPELE R. P., *Solid State Commun.* **5**, 143 (1967).
28. VAN STAPELE R. P. and LOTGERING F. K., *J. appl. Phys.* **38**, 403 (1968).
29. SLEIGHT A. W., *Mat. Res. Bull.* **2**, 1107 (1967).
30. LOTGERING F. K., *Philips Res. Rep.* **11**, 190 (1956).
31. MENYUK N., DWIGHT K. and WOLD A., *J. appl. Phys.* **36**, 1088 (1965).
32. LOTGERING F. K., *J. Phys. Chem. Solids* **29**, 2193 (1968).
33. DWIGHT K., MENYUK N. and WOLD A., Unpublished research.
34. GOODENOUGH J. B., *Mat. Res. Bull.* **2**, 37, 165 (1967).
35. Addition of an electron to Cr^{3+} to make Cr^{2+} also requires an intra-atomic election–electron Coulombic energy V'. The apparent d-to-d transition at about 1·6 eV observed by HARBEKE G. and PINCH H., *Phys. Rev. Lett.* **17**, 1090 (1967) in $Cd[Cr_2]S_4$ could be a transition from the ground state $^4A_{2g}(Cr^{3+})$ to an excited Cr^{3+} level.
36. HAACKE G. and BEEGLE L. C., *J. Phys. Chem. Solids* **28**, 1699 (1967); *J. appl. Phys.* **39**, 656 (1968).
37. HAACKE G. and NOZIK A. J., Personal communication.
38. GOODENOUGH J. B., *J. appl. Phys.* **37**, 1415 (1966).
39. VAN MAAREN N. H., SCHAEFFER G. M. and LOTGERING F. K., *Phys. Lett.* **25A**, 238 (1967).

J. Phys. Chem. Solids Pergamon Press 1969. Vol. 30, pp. 281–286. Printed in Great Britain.

ELECTRIC AND MAGNETIC PROPERTIES OF TiCo AND RELATED COMPOSITIONS

S. R. BUTLER, J. E. HANLON and R. J. WASILEWSKI*
Central Research Department†, E. I. du Pont de Nemours and Company,
Wilmington, Del. 19898, U.S.A.

(*Received* 17 *June* 1968)

Abstract—A series of compositions surrounding TiCo, from 48 to 52 at. per cent cobalt, have been investigated. Microstructural and X-ray powder diffraction studies of several heat treatments indicate the stoichiometric TiCo is not congruently melting. High-temperature X-ray measurements show these compositions to be in the ordered B2 structure up to at least 1100°K. Electrical resistivity, magnetic susceptibility, and thermoelectric power were measured. Residual resistivity ratio shows a maximum at about 49·50 per cent for all heat-treating conditions. The largest value obtained was 58. The magnetic susceptibility follows a Curie–Weiss relation with a large negative Weiss constant (−499°K for 50·0 per cent). All compositions had *n*-type thermoelectric power of about 20 μV/°C. The results are discussed in terms of the effect of atomic ordering on the properties of transition metal compounds using the concept of the average valence electron number. It is suggested that the energy bands responsible for the properties of these materials may be constructed according to the procedures of Goodenough.

INTRODUCTION

THE STUDY of transition-metal intermetallic compounds forms an interesting addition to the investigation of these elements and their alloys. In particular, compounds with the ordered B2 structure should be closely related to b.c.c. metal alloys[1, 2]. If the 'average valence electron number'[3] is regarded as an important parameter in determining physical properties, a direct relation between the properties of these compounds and certain alloys should exist. Several recent studies [1, 2] of intermetallic compounds with ordered B2 structures have followed this point of view. In general, a single composition from within the stability range of each of a series of compounds was investigated to give a broad view of property variations.

Because of the lack of detailed metallurgical information[4], it is often difficult to prepare a widely varying series of compounds in a well-defined condition. The investigation of only one composition from within the stability field ignores an important characteristic of these compounds, namely, that they are not 'line compounds' but exhibit a range of compositions[4]. Also the physical properties often vary greatly within this stability field[5–8]. Therefore, we have investigated a series of more closely spaced compositions surrounding the equiatomic compound TiCo. We report here microstructural information (optical metallography and X-ray crystal structure) in addition to electrical resistivity, magnetic susceptibility, and some thermoelectric power data on this series of materials.

EXPERIMENTAL PROCEDURE

Compositions in the range 48–52 per cent‡ Co were prepared by repeated non-consumable arc melting in purified argon. The starting materials were iodide titanium (Foote Mineral Co., purity > 99·7 per cent) and zone-melted§ cobalt (United Min. & Chem. Co., purity > 99·9 per cent). Balance of materials was checked on the samples, and all those studied had weight changes of less than ±0·02 per cent (for 100 g ingots). The specimens for

---

*R. J. Wasilewski is now at Battelle Memorial Institute, Columbus, Ohio.

†Contribution No. 1468.

‡All compositions are given in atomic per cent Co.

§Zone melting carried out in this laboratory by D. Worden.

study were cut from these ingots and heat treated in sealed silica capsules (Ta foil lined). X-ray diffractometer scans (XRD-5) were carried out on polished metallographic surfaces and on ground and annealed powders.

The electrical resistivity and thermoelectric power measurement techniques have been described previously[5]. The precision of the resistivity measurement is ±0·1 per cent but the accuracy is decreased to ±2 per cent mainly because of uncertainty in voltage probe separation. The thermoelectric power measurements are only accurate to ±10 per cent. The magnetic susceptibility was measured by the vibrating sample method. The accuracy is ±1 per cent. The temperatures (77 and 298°K) for the majority of the measurements are uncertain to < 1 per cent. The fixed temperature measurements were made as a function of magnetic field to 16 kOe In all cases (except for 48·5 per cent sample) the magnetic moment was linear in the field and the data could be extrapolated through zero indicating no significant ferromagnetic contamination.

RESULTS

Each ingot was analyzed for oxygen and nitrogen and in all cases the oxygen was < 300 ppm (weight) and nitrogen ≤ 30 ppm. Emission spectrographic analysis showed that all ingots had about the same metallic impurity content (Table 1). Representative photomicrographs are presented in Figs. 1 and 2. In no case was it possible to obtain a completely single-phase sample.

The hardness (1 kg load D.P.N.) was measured on the metallographic samples, and a minimum value of 190±3 (900°C heat treatment) was found at 49·75 per cent Co with an increase of 10 to 15 points at 49·50 and 50·00 per cent. X-ray diffraction confirms the matrix to be the ordered B2 structure, as indicated by the presence of the (100) superlattice reflection. The lattice parameter of *alloys containing less than 50·0 per cent Co at 25°C is constant,* $a_0 = 2{\cdot}996_0 \pm 0{\cdot}0003$ Å. For higher Co compositions the parameter decreases slightly, to $a_0 = 2{\cdot}9877$ Å at 52 per cent Co, in good agreement with the observations of Stüwe and Shimomura[9]. All compositions showed weak reflections corresponding to Ti_2Co (or $Ti_4Co_2O_x$, $0 \leq x \leq 1$). Since this structure is known to be stabilized by very low oxygen contents[10], it is likely that most of the oxygen (and possibly, also nitrogen) is combined in this phase. Samples with Co content greater than 50 per cent also showed weak reflections from the (cubic) Co_2Ti.

Table 1. Nominal impurity content of TiCo *samples determined by emission spectrographic analysis* (ppm)

Mg	< 10
Al	< 20
Cr	≤ 100
Mn	≤ 200
Fe	≤ 100
Ni	≤ 500
Cu	≤ 50

To check the possibility of structural transformation X-ray diffractometer scans were made on a 50 per cent composition from 5 to 1100°K. Throughout the entire temperature range the matrix remained in the ordered B2 structure. The lattice expansion shows no discontinuity, and the expansion coefficient between 298 and 1000°K is $11{\cdot}7 \times 10^{-6}$/°K. Since the X-ray and metallographic observations suggested that equiatomic TiCo may not melt congruently, the melting behavior was checked directly on a 50 per cent composition. This showed partial melting at 1500°C, the liquid phase being Ti-rich. It seems probable, therefore, that a maximum melting temperature may occur at a Co-rich composition.

Electrical resistivity determined below room temperature is shown in Fig. 3. Residual resistivity ratios are shown in Fig. 4. Several resistivity measurements were also made above room temperature (Fig. 5). The thermoelectric power of all the samples was n-type and ranged between 16 and 24 μV/°C which is consistent with Goff[11]. However, the details of the composition dependence were very sensitive to the thermal history of the samples (heat-treatment temperature and cooling procedure). Since this measurement is only accurate to 10 per cent and could be sensitive to the amount and distribution of the second phase, it was not pursued in detail.

The magnetic susceptibilities determined at

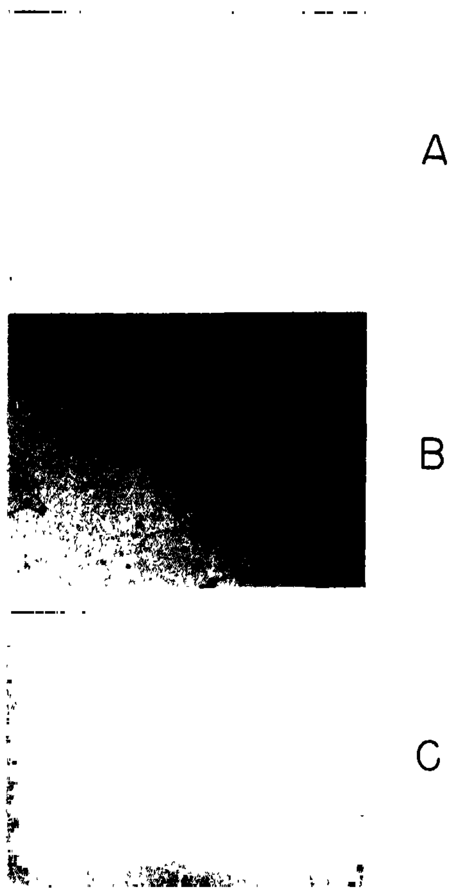

Fig. 1. Photomicrographs of TiCo compositions in the as arc-melted condition (original magnification 125X). (*a*) 49·25 per cent cobalt; (*b*) 50·00 per cent cobalt; (*c*) 51·00 per cent cobalt.

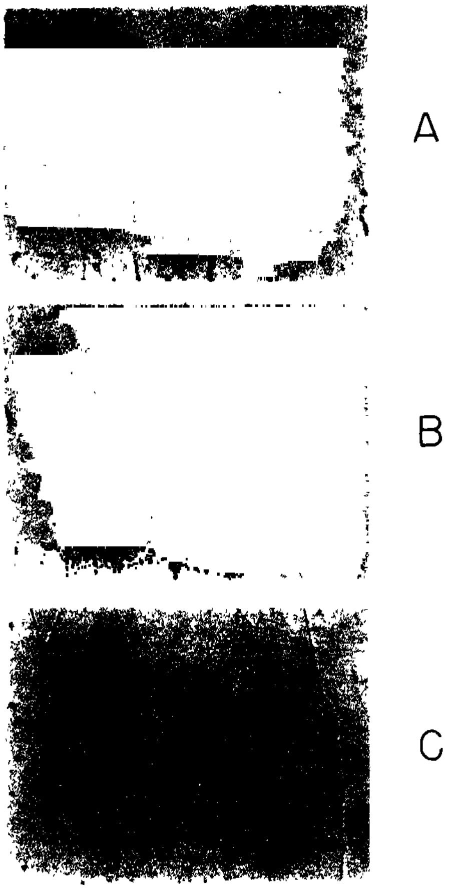

Fig. 2. Photomicrographs of TiCo compositions after heat treatment at 1050°C for 90 hr and rapidly cooled (original magnification 125X). (*a*) 49·50 per cent cobalt; (*b*) 50·00 per cent cobalt; (*c*) 50·50 per cent cobalt.

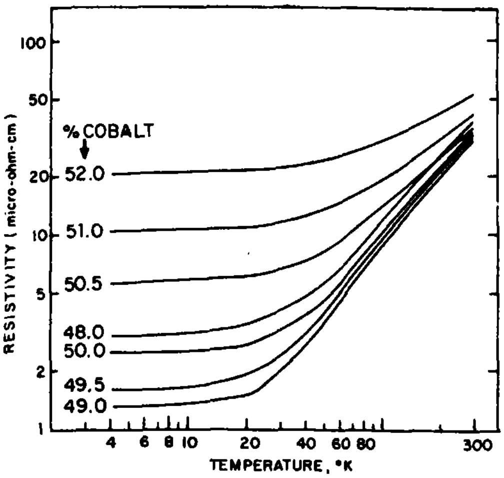

Fig. 3. Electrical resistivity of TiCo samples of various compositions from 4 to 300°K. Samples in an arc-melted condition.

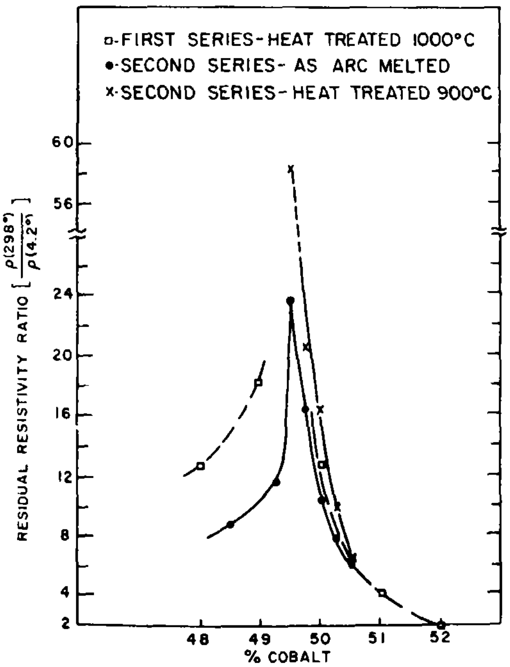

Fig 4. Residual resistivity ratio of TiCo samples for several heat treatment conditions.

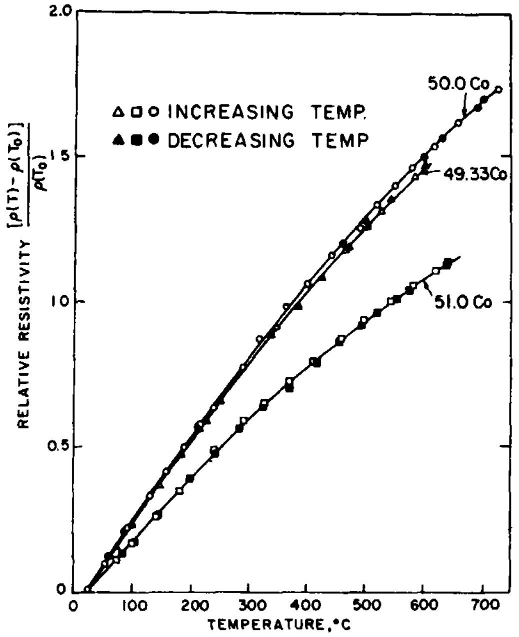

Fig. 5. Relative resistivity of TiCo samples above room temperature. All samples previously heat treated 1050°C for 90 hr

298 and 77°K are presented in Fig. 6. Figure 7 gives the complete temperature run from 4 to 400°K on a 50·0 per cent sample. The deviation from the straight line between 300 and 400° is due to thermal lag of the thermocouple with respect to the sample temperature. The Curie-Weiss constants for the straight line are $C = 7{\cdot}08 \times 10^{-3}$ (e.m.u. °K/g Oe) and $\theta = -499$°K.

DISCUSSION

The presence of phases other than TiCo is, at least in part, due to the non-congruent melting of the equiatomic composition. Heat treatments at 1050°C and below (900°) either decrease slightly or leave unchanged the amount of second phase. However, at higher temperatures (1200°C) the microstructure definitely degenerates in most of the compositions studied. Detailed phase relationships have not been established. The metallography

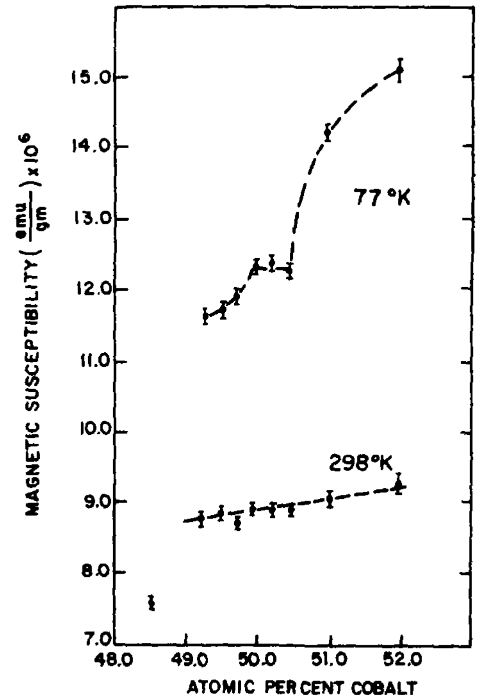

Fig. 6. Magnetic susceptibility of TiCo samples at 77 and 298°K

indicates the most nearly single-phase sample to be at ~50·50 per cent Co. This deviation from 50·00 per cent cannot be accounted for by the presence of the $Ti_4Co_2O_x$ phase. The formation of this phase would tend to drive the matrix composition to a higher Co content than the nominal values given. The low-temperature electrical resistivity results (Figs. 3 and 4) show an interesting contrast to the metallography since the 'most perfect' conductor appears to be the 49·50 per cent Co composition. With the measured oxygen content (~300 ppm) this deviation from 50·00 per cent could be ascribed to the formation of 0·5 per cent (Mole) of $Ti_4Co_2O_{0\cdot2}$ since this would shift the matrix back from 49·50 to 50·00 per cent. This speculation has not been verified experimentally. At present the experimental results are consistent with a single-phase region extending from 49·0 to ~51·0 per cent for temperatures ≤ 1000°C.

The electrical resistivity plots (Fig. 3) show a very similar temperature dependence for all samples with Co content above 49·25 per cent. The residual resistivity increases faster than linearly with composition. If the temperature dependence of $\rho(T) - \rho(4{\cdot}2°)$ for this series of compositions is approximated as T^n, the value of n would decrease from $n \sim 2$ for $20° \leq T \leq 80°$ to $n = 0{\cdot}6$ for $700° \leq T \leq 1000°K$. This decrease in the temperature dependence is consistent with the X-ray results which show no significant disordering of the B2 structure below 1000°K. The results compare satisfactorily with DeSavage and Goff[8] for their nominal 50·0 per cent

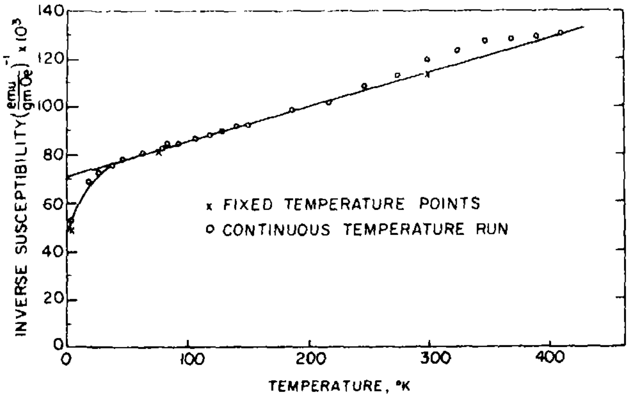

Fig. 7. Inverse susceptibility as a function of temperature for a 50·00 per cent cobalt sample as heat treated 1050°C, 90 hr.

composition. However, their residual resistivity is about like our 50·5 per cent sample. In addition our inverse susceptibility plot (Fig. 7) shows slightly larger values.

As Allgaier[2] has pointed out, the electrical properties of TiCo do not seem to fit with his attempt to extend Lomer's[12, 13] work on Cr. He suggested a magnetic effect may be important in this case. Chandross and Shoemaker[14] have briefly remarked that no magnetic order is seen in TiCo at 4·2°K by neutron diffraction. We might speculate on this point by considering several materials with $N_{ve}^{*} = 6·5$, i.e. MnCr and FeV. MnCr is b.c.c. and antiferromagnetic[15], and the experimental results[16] have been interpreted in terms of a spin-density wave[17]. FeV is weakly ferromagnetic[18, 14] with $T_c \sim 280°K$ in the partially ordered state obtained by annealing at 625°C. This ordering process has an associated contraction in the lattice parameter and decrease in magnetization of $\sim \frac{1}{2}\mu_B$[19]. The similarity of the χ vs. T data for MnCr below 500°C and TiCo (Fig. 7) is suggestive but the high-temperature resistivity for TiCo does not have the cusp found in MnCr at its Neél point. The Ti–Co distance in the TiCo lattice is 2 per cent less than expected from the metallic radii (corrected for 8 coordination). This discrepancy may be interpreted as an 'ordering contraction,' as occurs in FeV, suggesting electron transfer.

In a discussion of electrical properties of TiFe through TiNi[20] Goff noted the importance of ordering (as have several authors considering Cr[12, 13, 21]). He suggested 3 bands as important to this system: (1) a hole-like band of moderate mobility and rather large carrier concentration that exists throughout the series; (2) a highly mobile hole-like band of smaller carrier concentration which fills by $N_{ve} = 6·2$; and (3) a high mobility, small carrier concentration electron-like band for the higher electron concentration after band 2 fills. The origin of these bands can be suggested from Goodenough's[22] discussion of b.c.c. transition metals. The high mobility bands would be formed if the Brillouin zone boundary due to the B2 structure ordering caused a cusp in the $N(E)$ curves for the s–p band at about the position of the 'localized' e_g level. The high-density hole-like band would be the t_{2g} bonding band. The ferromagnetism observed by DeSavage and Goff [8] fits this, as would the thermoelectric power data if we assume the s–p band to be 'divided,' the lower part filling at $N_{ve} = 6·2$. However, in order to explain the lack of ferromagnetism above 6·3 a rigid band model cannot be used[22], i.e. the position and energy separations of the 'd-bands' depend on the strength of the atomic ordering. Thus the ferromagnetism of VFe ($N_{e_g} = 1$) is destroyed in TiCo by the lowering of the s–p band and raising of the e_g levels because of the larger ordering energy shifts. Further work in the systems composed of these elements, e.g., VFe–TiFe, should enable a more complete description to be evolved. The appearance of superconductivity for a *very* narrow range at $N_{ve} = 6·25$ ($TiFe_{0·5}Co_{0·5}$)[8] shows the sensitive nature of the interaction between band structure and ordering in these systems.

Acknowledgements – The authors wish to thank D. Worden and J. Bailey for assistance in the experimental portion of this work. We also wish to thank J. Goff for communicating his results prior to publication. The authors express their appreciation to C. G. Fredericks for the magnetic measurements.

REFERENCES

1. GOFF J. F., *J. appl. Phys.* **35**, 2919 (1964).
2. ALLGAIER R., *J. Phys. Chem. Solids* **28**, 1293 (1967).
3. CHENG C. H. *et al.*, *Phys. Rev.* **120**, 426 (1960).
4. ELLIOTT R. D., *Constitution of Binary Alloys*, Suppl. 1, p. 339. McGraw-Hill, New York (1965).
5. HANLON J. E. *et al.*, *Trans. Am. Inst. Min. Engrs* **239**, 1323 (1967).
6. WEST G. W., *Phil. Mag.* **9**, 979 (1964).

---

*The average valence electron number is defined as the total number of electrons outside of closed shells per formula unit divided by the number of atoms per formula unit.

7. WEST G. W., *Phil. Mag.* **12**, 1061 (1965).
8. DESAVAGE F. B. and GOFF J. F., *J. appl. Phys.* **38**, 1337 (1967).
9. STÜWE H. P. and SHIMOMURA Y. Z., *Z. Metallk.* **51**, 180 (1960).
10. NEVITT M. V., *Trans. Am. Inst. Min. Engrs* **218**, 327 (1960)
11. GOFF J. F., *Bull. Am. phys Soc.* **10**, 451, 1104 (1965).
12. LOMER W. M., *Proc. phys. Soc.* **84**, 327 (1964).
13. LOMER W. M., *Proc. Intern. Conf. Magnetism, Nottingham*, p. 127 (1964).
14. CHANDROSS R. J. and SHOEMAKER D. P., *J. phys. Soc. Japan* **17**, Suppl. B-III, 16 (1962).
15. KASPER J. S. and WATERSTRAT R. M., *Phys. Rev.* **109**, 1551 (1958).
16. HAMAGUCHI Y. and KINITOMI N., *J. phys. Soc. Japan* **19**, 1849 (1964).
17. OVERHAUSER A. W., *Phys. Rev.* **128**, 1437 (1962).
18. NEVITT M. V., *J. appl. Phys.* **34**, 463 (1963).
19. NEVITT M. V. *et al.*, *Phys. Rev.* **131**, 1428 (1963).
20. GOFF J. F., *J. appl. Phys.* **39**, 2208 (1968).
21. ASANO S. and YAMACHITA J., *J. phys. Soc. Japan* **23**, 714 (1967).
22. GOODENOUGH J. B., *Magnetism and the Chemical Bond*, Chap. 3, Sect. 3. Interscience, New York (1963)

J. Phys. Chem. Solids Pergamon Press 1969. Vol. 30, pp. 287–296. Printed in Great Britain.

EFFECTS OF PRESSURE AND TEMPERATURE ON EXCITON ABSORPTION AND BAND STRUCTURE OF LAYER CRYSTALS: MOLYBDENUM DISULPHIDE

G. A. N. CONNELL, J. A. WILSON and A. D. YOFFE
Cavendish Laboratory, University of Cambridge, England

(*Received* 4 *June* 1968)

Abstract – The effect of pressures of up to 60 kbars on the exciton series in the spectral region of 2 eV in molybdenum disulphide has been investigated at room and liquid nitrogen temperatures, using a diamond anvil device. An electronic band model, suggested by the crystallography of the layered material and the optical spectra of the various polytypes, is made the basis for the discussion of the experimental results. An indirect energy gap of 0·25 eV determines the electrical properties of the intrinsic material, but transitions from a lower, spin-orbit split valence band produce the exciton series and fundamental absorption edge It is shown that under these circumstances the pressure coefficient of an exciton peak can be separated into two parts; the pressure coefficient of the direct gap and the pressure dependence of the exciton binding energy which is a result of changes in the free carrier density that are necessarily related to the pressure variation of the indirect gap.

1. INTRODUCTION

MOLYBDENUM disulphide is a layer-type material in which, within a layer, there is trigonal prism type co-ordination between each metal atom and six sulphur atoms. The resultant sandwiches are loosely stacked into hexagonal (2H) or rhombohedral (3R) plate-like polytypes[1], weakly bound together by van der Waal's forces, so that perfect cleavage occurs in (0001) planes. This allows the preparation of thin crystals which are eminently suitable for optical transmission measurements using light with the electric vector E perpendicular to the crystal c-axis. The initial optical work by Frindt and Yoffe[2] indicated that the fundamental absorption edge was characterized by two series of exciton absorption bands, which later proved to be hydrogenic[3, 4], in spite of the extreme anisotropy of the crystal structure. This unlikely result led Ralph[5] to the conclusion that in molybdenum disulphide the ratio of the longitudinal and transverse exciton masses was equal to the ratio of the transverse and longitudinal dielectric constants, since under these circumstances, the excitons are much flattened in the c-direction, but their energies correspond to the isotropic case.

This paper describes an experimental investigation of the effect of 'quasi-hydrostatic' pressure at various temperatures on the two exciton series, using experimental techniques described in Section 2. A simple, zero pressure band model, developed in Section 3, in which there is full mixing between molybdenum s, p and d-orbitals and sulphur orbitals, is made the basis for the discussion of the experimental results, presented in Sections 4 and 5. In Section 4, we describe the effect of pressure on the exciton absorption bands, and indicate how the shape and position of the first exciton peak (A_1) are influenced by the presence of an indirect forbidden energy gap. Further evidence for this interpretation is presented in Section 5, where the variation in the binding energies of the A-series excitons is accounted for by a change in electron density in the conduction band.

2. EXPERIMENTAL TECHNIQUES

2.1 *Apparatus*

A Barr and Stroud V. L. 2 monochromator with a glass prism giving a spectral resolution of 0·004 eV in conjunction with a quartz iodine lamp was used to provide monochromatic radiation. The light incident upon and transmitted through the crystals was monitored with an E.M.I. 9558Q photomultiplier tube, the signal from which was amplified and phase detected at a chopping frequency of 225 cps. The rectified signal was finally recorded in chart form as a function of photon energy over the region of interest.

Optical measurements were performed at high pressure and low temperature in a unit that was based upon the high pressure cell devised by van Valkenburg[6]. The specimen was cooled by heat conduction along the brass body of the apparatus and good thermal connection was ensured by intimate contact with the diamond anvils. It should be noted that at liquid nitrogen temperature the thermal conductivity of diamond is 25 times greater than that of copper. In this way, temperatures of 80°K were obtained with pressures in excess of 100 kbars.

The apparatus is shown in Fig. 1. Two gem-cut type II diamonds comprise the anvils. They are ground into square-based truncated tetrahedra, and mounted over holes in stainless steel pistons.

The pistons are free to slide in a stainless steel bearing, that sits in a brass block carrying the pressure generating equipment. One piston, which rests in a cavity in the face plate, can be tilted by levelling screws, while at the other end, a stainless steel transmission plate bears against the second piston. The force transmission lever is activated at its upper end by helium gas pressure inside a flexible stainless steel bellows.

The specimen is cooled by liquid nitrogen in the stainless steel dewar that constitutes the upper part of the apparatus. A copper radiation shield surrounds the high pressure region and the whole is encapsulated in a stainless steel tail-piece. Light enters the apparatus through spectrosil windows, mounted on O-ring seals for easy replacement.

Exciton absorption is characterized by a high absorption coefficient in the region of 10^5 cm^{-1}, so that a crystal having a thickness of 2000 Å or less must be used. However, as the thickness of the specimen is reduced, it becomes impossible for a single crystal to fill the space between the diamond anvils arising from their concavitation under compression. The result is that the concavitation is reduced by an increase in pressure at the edges and a reduction near the centre, leading to a limit in the hydrostatic pressure attainable[7]. This problem was surmounted by incorporating a pressure transmitting medium of standard thickness between the anvils.

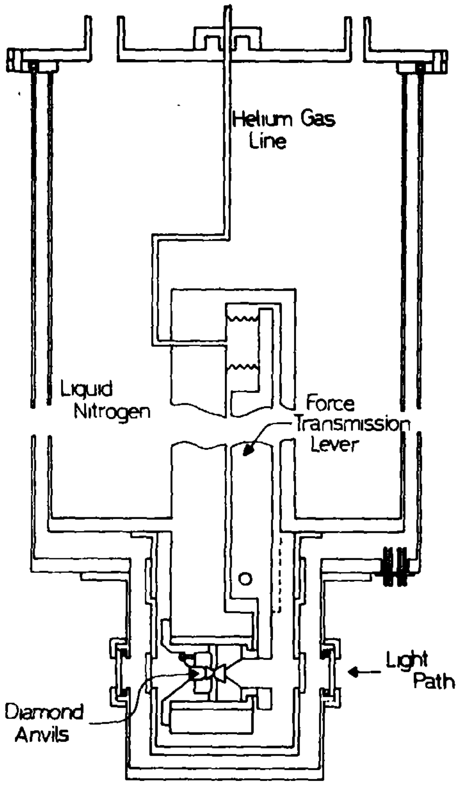

Fig. 1. Liquid nitrogen cryostat for optical transmission measurements at high pressures.

ZnS single crystals were chosen for several reasons. Firstly, the absorption edge occurs at about 29,000 cm^{-1} and moves to even higher energies under pressure, until a phase change occurs at 240 kbars[8]. Consequently, its optical properties do not interfere with our work. Secondly, for a thickness of 20 μ, our standard, a centrally peaked pressure distribution is obtained, and thirdly, its refractive index is very similar to that of diamond, thereby avoiding any problems caused by interference fringes, produced by multiple reflections in the ZnS layer.

The cell arrangement is shown schematically in Fig. 2. An evaporated layer of luminescent grade ZnS, 5000 Å thick, effectively protects the specimen against disintegration, which would otherwise occur on account of the microscopic uneveness of ZnS single crystal surfaces. Calibration was effected by using as a specimen, an evporated layer of nickel dimethylglyoxime, in which an absorption peak shifts at a known rate under pressure[9].

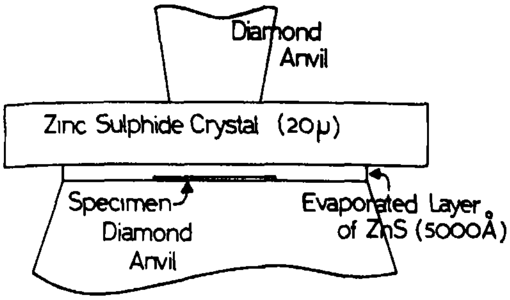

Fig. 2. Schematic representation of the pressure cell. The diagram is not to scale.

The light path was restricted to a small area near the centre of the specimen across which the pressure is essentially constant.

By reducing the area of the crystal under examination the pressure variation can, in principle, be made as small as required. However, signal to noise considerations in the detection system put a lower bound on the area that could be selected. Nevertheless it was shown that in a typical experiment for which $r_s = 0{\cdot}1\, r_0$, where r_s and r_0 are the sampling and anvil radii respectively, the variation in pressure across the specimen was no greater than 1 per cent of the measured pressure. Moreover, the equations of Jackson and Waxman[10] suggest that whenever

$$\frac{2fr_0}{t} \gg 1$$

where f is the coefficient of friction between ZnS and diamond, and t is the ZnS thickness, the pressure at the centre of the anvils is hydrostatic for all types of centrally peaked pressure distributions. Therefore, although we are aware that a solid pressure transmitting medium may produce non-uniform strains, the experimental observations are most probably described by changes in the 'quasi-hydrostatic' pressure experienced by the specimen.

2.2 *Material*

The samples were cleaved from a large natural single crystal of MoS_2 using 'Sellotape'. Suitable specimens can then be transferred to an anvil, by dissolving away the glue with trichloroethylene, and at the same time allowing surface forces to pull the crystal down into intimate contact [11(a)]. The crystals are relatively impure, but there is no observable effect due to these impurities in the region of the excition absorption bands. This has been verified in the case of the analogous material WS_2 by comparing natural and synthetic crystals.

The electrical and photoelectrical properties of these natural crystals, perpendicular to the *c*-direction, have been investigated by Wieting[12], and the carrier density at room temperature of about $10^{17}\,cm^{-3}$ is similar to the value ($5 \times 10^{16}\,cm^{-3}$) obtained by Fivaz and Mooser[13], for crystals grown by vapour phase transport. Therefore, the major impurities, Al and Si, in the natural crystals make little or no contribution to the electrical properties. Inspection of the effective potential in which excess carriers in a layer lattice move, reveals the explanation of this effect. Within each layer but outside the atomic cores the potential is low and varies slowly. Between the layers, however, the contributions of the different atoms add up to high and fairly wide potential barriers. The carriers therefore become localized within individual layers and thus behave as if moving through a stack of independent lamellae. Moreover, this tendency is accompanied by a strong interaction between the free carriers and the homopolar phonons, polarized at right angles to the layers, which leads to an anomalously strong temperature dependence of mobility[14]. Furthermore, impurities lying within the van der Waal's gap, cannot influence either the concentration or scattering behaviour of the charge carriers, although the existence of electrical polarization in the natural crystals and the absence of this polarization in grown crystals[12] indicates that these impurities are present as polarizable molecules, such as Al_2O_3, SiO_2, or possibly aluminium silicate. However, substitutional impurities within a layer produce n-type material, in which impurity scattering and extrinsic conduction occur below about 250°K (see Sections 4.3 and 5).

3. BAND STRUCTURE AND EXCITON ASSIGNMENT

3.1 *Bonding considerations*

In the following discussions a single layer model is used for the deduction of the relative positions of the energy bands, since interlayer interactions must produce only small perturbations on the interlayer potential [15].

The hybridisation of the atomic wavefunctions, which is required to give the MoS_2 layer structure has been described by Hultgren [16]. The $4d$, $5s$ and $5p$ orbitals, outside the core of the Mo atom, are combined to make six equivalent cylindrical bond functions with a trigonal prism configuration, together with two degenerate (d/p hybridisation) and one non-degenerate (d_{z^2}) non-bonding orbitals. The sulphur atoms at the corners of the prisms, on the other hand, use $3p$ orbitals in the bonding, so that the orbitals perpendicular to the layers, which are then responsible for the interlayer van der Waal's forces, are saturated $3s$ subshells. It is now necessary to consider how such hybridised orbitals give rise to a band structure.

It appears that the overlap integral between the atomic levels in the molybdenum and sulphur atoms in MoS_2 is so large that in the solid the outer s, p and d orbitals form filled valence bands and empty conduction bands which are separated by a large energy. Indeed, the energy of formation of MoS_2 is comparable to CdI_2, so that the basic bonding gap is of order 5 eV. This implies that the electronic properties are imparted by electrons in bands formed from the non-bonding orbitals, which have energies that lie within the basic gap. Direct evidence for the existence of such bands comes from electron energy loss experiments in the energy range 0–60 eV, which have recently been made by Liang and Cundy [17].

In Fig. 3 are shown the relative positions of the bands, which follow directly from such considerations. The lower valence bands, labelled X_1, and the upper conduction bands X_1^* correspond to σ and σ^*-bonds between the hybridised s, p and d orbitals of molybdenum, and the p orbitals of sulphur respectively. The location of the Fermi level depends on the number of outer electrons per molecule, and in MoS_2 lies between the narrow non-bonding bands, X_2 and X_3. The formation of bands from d-functions in this way, is not surprising as the metal–metal distance is only 3·16 Å. Furthermore, the large conductivity in NbS_2, 10^6 times greater than in

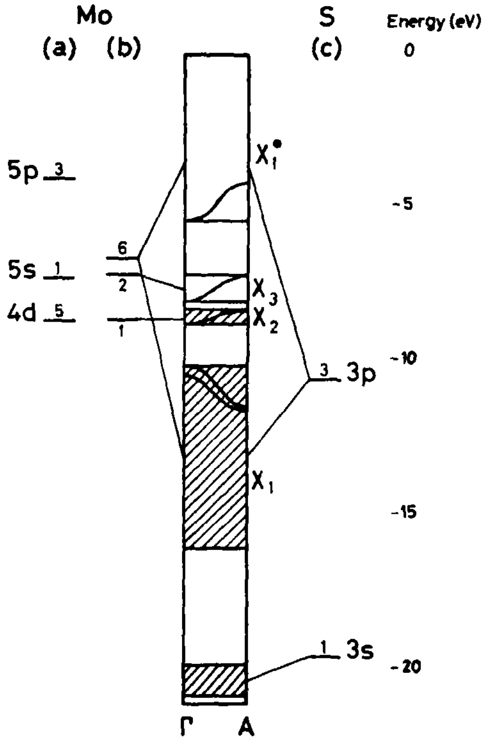

Fig. 3. Suggested electronic band structure of $2H$-MoS_2. The energies and degeneracies of the levels in the Mo and S atoms, and in the hybridised Mo atom are shown in columns (a), (c) and (b) respectively. The absolute energy scale is subject to considerable error, but the relative positions of the bands, X_1, X_2, X_3 and X_1^* are correct to a few tenths of an eV.

MoS_2[18], is explained by a half-filled X_2 bands, since NbS_2 is crystallographically similar to MoS_2. No separation of bonding and antibonding states occurs in X_2 since the band is essentially equivalent to the ground state in 2-D metallic hydrogen. A separation in X_3, however, may occur, but is probably too small to be observed. Finally, an inspection of the band structure of GaS[19], in which the sulphur atoms occupy similar crystallographic positions, suggests that the sulphur $3s$ subshells form a narrow valence band that lies below the other valence bands in X_1.

3.2 *Comparison with optical data*

More comprehensive optical measurements have been made by Wilson on MoS_2 and the related transition metal dichalcogenides [11(b)]. A weak absorption was observed at room temperature at about 0·25 eV, showing that the direct transition between the non-bonding bands is forbidden and that the curvature of one band at $k = 0$ is not related to the other through the $k.p$ perturbation. In addition, the existence of a weak shoulder at the bottom of the fundamental absorption edge in NbS_2, in which band X_2 is half empty, suggests that an indirect Burstein transition is involved, and the minimum gap between bands X_2 and X_3 is not at the Γ-point.

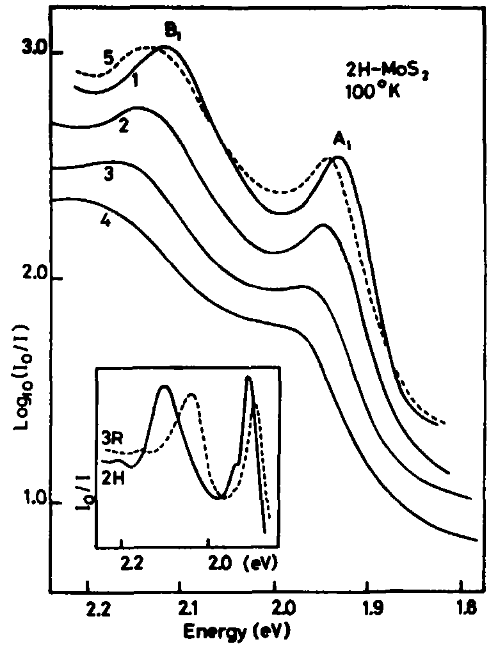

Fig. 4. Some experimental absorption spectra for 2H-MoS_2 at 100°K and at different pressures. Curves numbered in the order in which the data were taken: (1) 0·5 kbars (2) 15·8 kbars; (3) 30·0 kbars; (4) 45·0 kbars; (5) 3·0 kbars. Intermediate and higher pressure curves were consistent with those shown. The curves have been shifted vertically for clarity from the zero pressure absorption curve. The inset shows the absorption spectra in the region of the fundamental absorption edge of 2H-MoS_2 and 3R-MoS_2.

The optical spectra of the different stacking polytypes of MoS_2 are basically the same. The majority of transitions occur in pairs that are characteristic of a spin-orbit split valence band, although the magnitude of the splitting differs in 2H- and 3R- material as shown by the inset in Fig. 4. Group theoretic arguments, however, suggest that spin-orbit split bands can occur only along the ΓZ axis of the rhombohedral Brillouin zone corresponding to point group C_{3v}[20], and therefore the majority of transitions in 3R-MoS_2 occur on this axis, at critical points required by the symmetry of the zone. These are situated at Γ and Z, but, as already emphasized, the band structure is largely determined by a single layer, so that as a first approximation, we suggest that the transitions in 2H-MoS_2 occur at the analogous critical points Γ and A, in the hexagonal Brillouin zone corresponding to point group D_{6h}.

If the exciton series are now associated with the direct gap at Γ between the spin-orbit split valence band in X_1 and the conduction band in X_3, the remaining absorption peaks in the whole family of materials may be consistently assigned to transitions allowed by the model [11(a), 21]. Furthermore, the widths of bands X_2 and X_3, the splitting of the valence band edge in X_1, and the widths of the forbidden energy gaps, all shown in Fig. 3, are determined with an accuracy of a few tenths of an eV.

However, the work function of the material has not been measured, but it is possible to assign absolute energies to the system, by the examination of the relevant valence states in the sulphur atom and the hybridised molybdenum atom. In this approximation the work function is 8 eV, although an error of the order of an eV must be expected.

The rest of the paper describes an experimental investigation of the band model. The approach taken is to measure the effect of pressure on the exciton series and to relate the results to shifts in the various band edges.

4. EFFECT OF PRESSURE ON EXCITON FORMATION

4.1 *Introduction*

Measurements on the shape and position of the A_1 and B_1 peaks have been made at both room and liquid nitrogen temperatures. The main features in both cases are the shift of the peak positions to higher energies and a considerable weakening and eventual disappearance of the peaks themselves at the highest pressures. However, with the reduction of pressure, the peaks reappear and return to their zero pressure positions. Figure 4 summarizes these statements for a typical run at 100°K. Intermediate and higher pressure curves were consistent with those shown, but have been omitted for clarity. The second order exciton was not observed at pressures above 5 kbars, nor after the reduction of pressure, although the resolution of the system was better than 0·005 eV in this spectral range. It will also be noticed that the absorption coefficient at the minimum the A_1 and B_1 peaks has increased on returning to zero pressure. Similar effects were observed previously by Evans and Young[4] when MoS_2 crystals were subjected to mechanical working. We suggest, therefore, that changes in the dislocation density occur during the initial application of pressure to the cell, owing to very high, though localized, stress concentrations that temporarily exist around non-uniformities in the surface of the ZnS crystal. The reversible region is reached when plastic flow has produced intimate contact throughout the cell.

4.2 *Pressure coefficient of the* A_1*-peak*

The shift of the A_1-peak is shown at both room and liquid nitrogen temperatures in Fig. 5. In both cases a linear change occurs at lower pressures, but at higher energies, the shift becomes non-linear. The error in positioning the exciton peak increases at these higher pressures, but is insufficient to explain the deviation from linear behaviour.

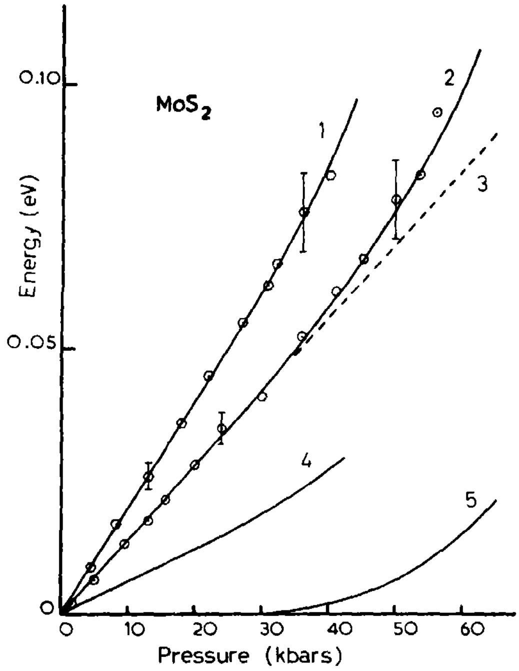

Fig. 5. The effect of pressure on the A_1-peak at 300° (1) and 100°K (2). Curve (3) indicates the relative shift of the band edges in X_1 and X_3 at the Γ-point, so that curves (4) and (5) represent the change in binding energy of the exciton with increase in pressure at 300° and 100°K respectively.

Apart from these similarities in shape, a most striking difference in pressure coefficient exists for the two temperatures. The values obtained in the linear regions are

$$\left(\frac{\partial E_{A_1}}{\partial p}\right)_{300} = (2{\cdot}0 \pm 0{\cdot}1) \times 10^{-6}\,\text{eV/bar}$$

$$\left(\frac{\partial E_{A_1}}{\partial p}\right)_{100} = (1{\cdot}4 \pm 0{\cdot}2) \times 10^{-6}\,\text{eV/bar}.$$

It is now shown that these differences may be explained by a reduction in binding energy of an exciton at high pressures and that the linear region at 100°K corresponds to the relative shift of the band edges of X_1 and X_3 at $k = 0$.

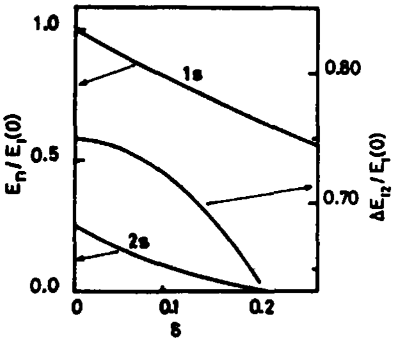

Fig. 6. The variation in the binding energy, E_n, of an n^{th} order exciton with the screening parameter δ (after Harris[25]).

4.3 *Changes in electron-hole interaction caused by increased screening*

Minomura and Drickamer[22] observed that the resistance of MoS_2 decreased under pressure. However, the mobility and effective mass of the electrons are expected to be relatively constant[21], so that an increase in carrier concentration is responsible for the decrease in resistance. As a result, the magnitude of the electron-hole interaction at a particular temperature will be reduced at high pressure, until at some critical free carrier density, exciton formation will no longer be possible.

The conditions for the existence of an exciton in such a Yukawa potential have been discussed by Casella[23] and Rawls and Schultz[24]. However, the most comprehensive treatment has been given by Harris[25], who shows that at a particular temperature T, the binding energies of $1\,S$ and $2\,S$ excitons are reduced by an increase in free carrier density in the way shown in Fig. 6. The screening parameter $\delta(T, p)$ is related to the free carrier density $N(T, p)$ by

$$\delta^2(T,p) = \left(\frac{a_\perp}{a_0}\right)^2 \frac{N(T,p)}{10^{23}kT\epsilon_\perp} = \left(\frac{a_\parallel}{a_0}\right)^2 \frac{N(T,p)}{10^{23}kT\epsilon_\parallel} \quad (1)$$

where a_0 is the Bohr radius, $\epsilon_\parallel$ and $\epsilon_\perp$ are the dielectric constants parallel and perpendicular to c, $a_\parallel$ and $a_\perp$ are the exciton radii parallel and perpendicular to c in a coulombic potential and kT is measured in electron-volts. With this model, it is apparent that the non-linear behaviour of the exciton position at high pressures and low temperatures is to be attributed to a reduction in binding energy, caused by an increase in free carrier density. At room temperature, more electrons are excited for a given energy gap between X_2 and X_3, so that the exciton binding energy is already reduced at zero pressure. The magnitude of the reduction relative to the binding energy at zero pressure at both room and liquid nitrogen temperature is obtained from the difference between the experimental curves and the line corresponding to the relative shift of the band edges in X_1 and X_2 at $k = 0$. These are shown as curves 4 and 5 in Fig. 5. It may be shown that at low temperatures, the changes in effective mass of the exciton and the dielectric constant of the crystal with pressure tend to cancel, and together make a negligible contribution to the change in peak position.

The density of free carriers in a non-degenerate semi-conductor can be written as

$$N(T,p) = \text{const}\; T^{3/2} \exp\left[-E(T,p)/kT\right] \quad (2)$$

where for extrinsic conduction in a compensated material, E is the donor ionisation energy

$$E(T,p) = E_d; \quad T \leqslant 250°\text{K} \quad (3)$$

and for intrinsic conduction, E depends upon the indirect gap between bands X_2 and X_3.

$$E(T,p) = E_{x_1x_3}(T,p)/2; \quad T \geqslant 250°\mathrm{K} \quad (4)$$

The transition from extrinsic to intrinsic behaviour occurs at approximately 250°K, as indicated later in Section 5. This is consistent with the mobility behaviour of the less pure crystals grown by Fivaz and Mooser[13].

Using equations (1), (2) and (4), it follows that for a given temperature in the intrinsic region, the pressure coefficient of $E_{x_1x_3}$ is

$$\left(\frac{\partial E_{x_1x_3}}{\partial p}\right)_T = -\frac{4kT}{p}\log_e\frac{\delta(T,p)}{\delta(T,0)}. \quad (5)$$

With values of $(\partial E_{x_1x_3}/\partial p)_{300}$ ranging from $-2{\cdot}0\times10^{-6}$ eV/bar to $-3{\cdot}0\times10^{-6}$ eV/bar, in steps of $0{\cdot}1\times10^{-6}$ eV/bar, the binding energy was calculated by computer as a function of pressure for a series of values of δ(300, 0) ranging from 0 to 0·35 in steps of 0·01. The best fit was obtained with

$$\left(\frac{\partial E_{x_1x_3}}{\partial p}\right)_{300} = (-2{\cdot}5\pm0{\cdot}5)\times10^{-6}\,\mathrm{eV/bar}$$

and

$$\delta(300,0) = 0{\cdot}22\pm0{\cdot}02$$

or

$$N(300,0) = (2{\cdot}0\pm0{\cdot}5)\times10^{17}\,\mathrm{cm}^{-3}$$

giving a value for N(300, 0) in agreement with the electrical measurements of Wieting[12]. The pressure coefficient of $E_{x_1x_3}$ may also be calculated from the measurements of Minomura and Drickamer[22], since to a good approximation it may be shown that

$$\left(\frac{\partial E_{x_1x_3}}{\partial p}\right)_{300} = 2kT\frac{\partial \log_e R}{\partial p}$$

$$= (-2{\cdot}0\pm0{\cdot}5)\times10^{-6}\,\mathrm{eV/bar}$$

in the low pressure region. ($p < 50$ kbars), further confirming our analysis.

4.4 *Pressure coefficient in the* B₁*-peak*

The general behaviour of the B_1-peak is very similar to that of the A_1-peak. The pressure coefficients at 300° and 100°K in the linear regions are

$$\left(\frac{\partial E_{B_1}}{\partial p}\right)_{300} = (2{\cdot}2\pm0{\cdot}1)\times10^{-6}\,\mathrm{eV/bar}$$

$$\left(\frac{\partial E_{B_1}}{\partial p}\right)_{100} = (1{\cdot}4\pm0{\cdot}2)\times10^{-6}\,\mathrm{eV/bar}.$$

Now it has already been assumed that the separation of the A_1 and B_1 peaks is related to the spin-orbit splitting of the band edge in X_1 at Γ. Moreover, the spin-orbit interaction term in the Hamiltonian is

$$H_{so} = \frac{\hbar}{4m^2c^2}\boldsymbol{\sigma}\cdot(\nabla V\times \boldsymbol{p})$$

where $\boldsymbol{\sigma}$ are Pauli matrices, V is the electrical potential between an electron and the nuclei and $\boldsymbol{p}$ is the momentum operator. Consequently, ∇V, and therefore H_{so} will only be large near nuclear sites, so that little change is expected in the magnitude of spin-orbit splitting with pressure.

The experimental evidence is strongly in favour of this interpretation. The pressure coefficient of the B_1-peak at low temperatures is equal to that of the A_1-peak, while the difference that exists at room temperature is attributed to a greater reduction in binding energy of the B_1-peak for an increment of pressure.

5. TEMPERATURE DEPENDENCE OF EXCITON BINDING ENERGY

It follows from 1 that the binding energy of an exciton is a function of temperature at a given pressure. Owing to changes in the electron-phonon interaction with temperature, it is difficult to test this theory directly by an investigation of the A_1-peak alone. The second order exciton A_2, however, is also subject to changes in the screening parameter δ(T, p) so that measurements on the relative positions of the two peaks as a function of temperature would be sufficient to test the theory, as indicated in Fig. 6. The temperature range over which the experiment may be carried out is unfortunately relatively narrow, since below liquid nitrogen temperatures only small changes in binding energy are expected from from the nature of the exponent in the expression for $N(T, p)$, while above liquid nitrogen temperature, it becomes increasingly difficult to locate the position of peak A_2.

Figure 7 shows the separation of exciton peaks A_1 and A_2 at temperatures between 4° and 200°K. The separation at 300°K was that deduced from the pressure measurements. As expected, the separation is reduced as the temperature is increased, but by using (1) and (2), a more quantitative analysis is possible. We can write

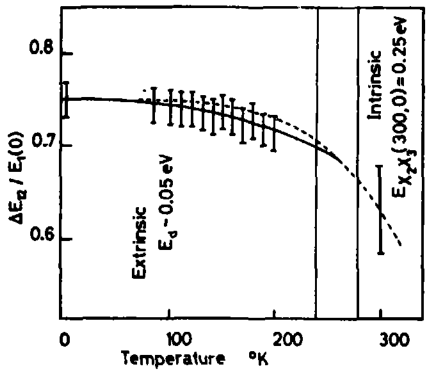

Fig. 7 The variation in the separation of the A_1 and A_2 exciton peaks with temperature. The transition from extrinsic to intrinsic behaviour occurs at about 250°K.

$$\delta(T, 0) = \delta(T_s, 0)\left(\frac{T}{T_s}\right)^{1/4} \times \exp\left[\frac{E(T_s, 0)}{2k}\left\{\frac{1}{T_s} - \frac{1}{T}\frac{E(T, 0)}{E(T_s, 0)}\right\}\right] \quad (6)$$

in which T_s is a specified, fixed temperature in either the extrinsic or intrinsic region and $E(T_s, 0)$ is the activation energy, defined in Section 4, in the conduction region containing T_s. If the temperature variation of $E_{x_2x_3}$ and E_d are neglected, then (6) may be expressed as

$$\delta(T, 0) = \delta(T_s, 0)\left(\frac{T}{T_s}\right)^{1/4} \times \exp\left[\frac{E(T_s, 0)}{2k}\left\{\frac{1}{T_s} - \frac{1}{T}\right\}\right] \quad (7)$$

to a good degree of accuracy.

The variation $\delta(T, 0)$, and, accordingly in the separation of peaks A_1 and A_2, owing to changes in the intrinsic carrier concentration, is shown as the dotted line in Fig. 7. In this calculation, the value of $\delta(300, 0)$ is taken from the pressure measurements. We see that at low temperatures, the reduction in separation is underestimated, owing to the dominance of extrinsic effects. The electrical measurements available suggest that E_d is $(0{\cdot}05 \pm 0{\cdot}03)$ eV, so that, with the value of $\delta(250, 0)$ taken from the intrinsic curve, the change in binding energy, owing to an extrinsic carrier concentration, can be calculated. The calculation, however, is relatively insensitive at low temperatures to the exact value of E_d within this range, and therefore the result for E_d equal to 0·05 eV, shown as the solid curve, brings the theoretical calculations in line with the experimental observations.

6. CONCLUSION

The excitonic doublet below the fundamental absorption edge of MoS_2 has been explained in terms of transitions from a spin-orbit split valence band X_1 to a doubly degenerate conduction band X_3, lying on each side of a full narrow d-band X_2, (Fig. 3). The effect of pressure on the intensity and width of each absorption peak is well described by an increase in electron-hole screening, caused by a reduction of $E_{x_2x_3}$ with pressure, and it is evident that $E_{x_2x_3}$ is always greater than the exciton binding energy. However, at liquid helium temperatures, the free carrier density is sufficiently reduced for the binding energy of the B_1 exciton to be equal to $E_{x_2x_3}$ at about

60 kbars. Under these conditions, the original ground state is expected to become unstable against exciton formation, and a new ground state is formed[26–29]. This might be observed as a crystallographic phase change.

The pressure coefficients of the excitonic doublets in the related family of materials have also been measured, but these will be published later, together with the pressure coefficients of the absorption peaks at higher energies.

Acknowledgements – The authors are grateful to Professor F. P. Bowden and Professor Sir Nevil Mott for helpful discussions, and to the Science Research Council for a grant to the laboratory.

REFERENCES

1. JELLINEK F., BRAUER G. and MULLER H., *Nature, Lond.* **185**, 376 (1960).
2. FRINDT R F. and YOFFE A D., *Proc. R. Soc.* **273A**, 69 (1963).
3. EVANS B. L. and YOUNG P. A., *Proc. R. Soc.* **284A**, 402 (1965).
4. EVANS B L and YOUNG P. A., *Proc. R. Soc.* **298A**, 74 (1967).
5. RALPH H. I., *Solid State Commun.* **3**, 303 (1965).
6. VAN VALKENBURG A., ASME Rep. No. 62-WA-269 (1962).
7. CONNELL G. A. N., *Br. J. appl. Phys.* **17**, 399 (1966).
8. SAMARA G. and DRICKAMER H. G., *J. Phys Chem. Solids* **23**, 457 (1962).
9. ZAHNER J. C. and DRICKAMER H. G., *J chem. Phys.* **33**, 1625 (1960).
10. JACKSON J. W. and WAXMAN M., *High Pressure Measurement*, p. 39, Butterworths, Washington (1963).
11. (a) WILSON J. A., Ph.D. Dissertation, Cambridge (1968). (b) CONNELL G. A. N., WIETING T. J., WILSON J. A. and YAFFE A. D. *IX Int. Conf. Phys. of Semiconductors*. Moscow (1968).
12. WIETING T. J., Ph.D. Dissertation, Cambridge (1968).
13. FIVAZ R. and MOOSER E., *Phys. Rev.* **163**, 743 (1967).
14. FIVAZ R. and MOOSER E., *Phys. Rev.* **136A**, 833 (1964).
15. FIVAZ R., *J. Phys. Chem. Solids* **28**, 839 (1967).
16. HULTGREN R., *Phys. Rev.* **40**, 891 (1932).
17. LIANG W. Y. and CUNDY S. L., *Phil. Mag.* To be published.
18. KERSHAW R., VLASSE M. and WOLD A., *J. inorg. Chem.* **6**, 1599 (1967).
19. BASSANI R. and PARRAVICINI G. P., *Nuovo Cim.* **50B**, 4259 (1967).
20. DIMMOCK J. O. and WHEELER R. G. Properties of 32 Point Groups, Rep. No. AFOSR TN 61-830, Yale (1961).
21. CONNELL G. A. N., Ph.D. Dissertation, Cambridge (1968).
22. MINOMURA S. and DRICKAMER H. G., *J. appl. Phys.* **34**, 3043 (1963).
23. CASELLA R. C., *J. appl. Phys.* **34**, 1703 (1962).
24. RAWLS J. M. and SCHULTZ M., *Am. J. Phys.* **33**, 444 (1965).
25. HARRIS G. M., *Phys. Rev.* **125**, 1131 (1962).
26. DES CLOIZEAUX J., *J. Phys. Chem. Solids* **26**, 259 (1965).
27. KOHN W., JEROME D. and RICE T. M., *Phys. Rev.* **158**, 462 (1967).
28. KOHN W., *Phys. Rev. Lett.* **19**, 439 (1967).
29. ZITTARTZ J., *Phys. Rev.* **162**, 752 (1967).

J. Phys. Chem. Solids **Pergamon Press 1969. Vol. 30, pp. 297–304. Printed in Great Britain.**

PHASE MODULATION IN MAGNETIC RESONANCE EXPERIMENTS*

P. R. MORAN
Physics Department, University of Wisconsin, Madison, Wisc. 53706, U.S.A.

(*Received* 27 *May* 1968)

Abstract—This paper investigates the general relations that exist in resonance experiments between phase modulation of the exciting fields and energy level modulation. When the response of the system to excitation is described so that it is properly phase-reference to the phase of the exciting fields, one obtains directly that there is a complete equivalence between the total time rate of change of the phase of the exciting fields and, in the case of magnetic resonance experiments, the instantaneous magnetic field strength. The role played by line-broadening and relaxation mechanisms is considered, and some of the applications and implications of these results are discussed.

INTRODUCTION

IN EXPERIMENTAL resonance spectroscopy there has been continuing interest in the relation between techniques in which the transition frequencies of the sample are modulated and techniques in which the phase (or frequency) of the exciting radiation field is modulated. Specific applications range from the early work of Karplus[1] on absorption lineshapes and sideband structure in frequency modulated microwave molecular spectroscopy of collision broadened systems, through fast-passage NMR and rotary saturation[2] in ferromagnetic systems, through f.m. spin disordering of pure quadrupole levels in the double nuclear resonance experiments of Slusher and Hahn[3], to our interest in spin-locking effects of transient phase shifts in short pulse NMR on organic crystals.

The basic ideas involved in the general relations between phase modulation of exciting fields and energy modulation of the levels of the excited system are relatively simple and widely recognized; they have been implicitly stated in the work of a large number of investigators. Nevertheless, a detailed description of how these relations may be understood in specific cases is apparently unavailable and, consequently, it seemed worthwhile to offer an explicit examination of these considerations.

The following treatment is carried out specifically for a nuclear resonance spin system whose static interactions are dominated by large Zeeman splittings; the obvious extensions of this description to other resonant systems is outlined in a subsequent section.

DYNAMICAL RESPONSE OF THE SPIN SYSTEM

Description of observed signals

In NMR experiments the observed signals are generated by the induced nuclear magnetization which causes a time dependent flux-linkage of the turns of an inductor. One is therefore concerned with the time dependence of a particular component of the nuclear magnetization, say M_y. The description of the characteristic response of a resonant system to a driving force is simplified by expressing the time development in terms of the amplitude and phase of the induced response. It is, for example, the phase response relative to the phase of the exciting fields that distinguishes resistive from reactive components, or absorption from dispersion.

Thus in the NMR system, one wishes to describe the component of nuclear magnetiza-

---

*This work supported by the Air Force Office of Scientific Research under Grant AF-AFOSR-1065-66.

tion, M_y, by specifying its phase components with respect to the phase of the exciting field. If the exciting field is applied at a single frequency, ω, the behavior of the spin system is most easily described in a rotating reference frame[4] whose rotation angle increases linearly in time,

$$\phi = \omega t \qquad (1)$$

that is, the equations of motion are transformed to a frame of reference rotating in-phase with the exciting field. When the exciting field is frequency modulated, its accumulated phase is

$$\phi(t) = \omega t + \Delta(t) \qquad (2)$$

where $\Delta(t)$ is the phase modulation term; the instantaneous frequency of the exciting field is the time derivative of the total phase,

$$\omega_{\text{inst}} = \partial_t\phi(t) = \omega + \partial_t\Delta. \qquad (3)$$

It is important to note that, in this case, the most convenient reference frame for describing the spin dynamics is not one which rotates uniformly at frequency ω, but rather one which is phase-locked to the accumulated phase of the exciting field as given in equation (2). In this reference frame the components of induced magnetization are directly phase-referenced to the exciting field.

Equations of motion

The system we are specifically considering is a spin system of identical nuclei dominated by a large Zeeman interaction, $\mathscr{H}_0$. The system has a variety of weaker linebroadening and relaxation interactions described by a Hamiltonian term $\mathscr{H}_B$, and it is subjected to excitation by an r.f. magnetic field interaction $\mathscr{H}_{rf}$. We can temporarily assume that the Zeeman interaction is produced by a large external magnetic field, H_0, directed along the z axis of a fixed Cartesian coordinate system,

$$\mathscr{H}_0 = -\gamma\hbar H_0 \textstyle\sum_j I_{jz}. \qquad (4)$$

The summation index 'j' refers to the j^{th} nucleus in the system and γ is the gyromagnetic ratio of the nuclear species. One can simplify the notation by letting the spin-operator without a summation index refer to the summation, e.g.

$$\mathscr{H}_0 = -\gamma\hbar H_0 \textstyle\sum_j I_{jz} = -\gamma\hbar H_0 I_z. \qquad (5)$$

The r.f. field is taken along the y axis and has a field strength $2H_1$; the interaction with the spins is

$$\mathscr{H}_{rf} = -\gamma\hbar 2H_1 \cos(\phi(t)) I_y \qquad (6)$$

where the phase factor $\phi(t)$ is of the form given in equation (2). The total Hamiltonian for the system is then

$$\mathscr{H} = -\gamma\hbar H_0(t) I_z - \gamma\hbar 2H_1 \cos(\phi(t)) I_y + \mathscr{H}_B \qquad (7)$$

where the external field may be an explicit function of time, $H_0(t)$, and the various roles played by the interactions gathered into the term $\mathscr{H}_B$ will be considered later.

To find the time evolution of any component of magnetization M_k one can employ the density matrix description,

$$M_k(t) = \langle\gamma I_k\rangle = Tr\{\rho(t)\gamma I_k\} \qquad (8)$$

where the equation of motion for the density matrix is

$$\partial_t\rho(t) = -(i/\hbar)[\mathscr{H}, \rho]. \qquad (9)$$

The question of the effect of phase modulation of the r.f. field relative to energy level modulation, modulation of H_0, is now reduced to the question of how the phase and field modulation enter relatively into the commutator of equation (9). The trace operation of equation (8) is independent of the representation used to describe the system; thus the simplest description for our purposes is to express the equations of motion, equation (9), in a representation corresponding to a reference frame rotating in the Larmor sense about the z axis phase-locked to the exciting r.f. fields. An operator Q transforms into the rotating representation operator Q according to

$$Q' = UQU^{-1} \tag{10}$$

where U is the unitary operator

$$U = \exp\{-i\phi(t)I_z\}. \tag{11}$$

One can then rewrite equation (9) as

$$\partial_t(U^{-1}\rho' U) = -(i/\hbar)U^{-1}[\mathscr{H}', \rho']U \tag{12}$$

and by carrying out the time differentiation and collecting terms one finds that the phase-locked reference frame equations of motion are

$$\partial_t\rho' = -(i/\hbar)[\mathscr{H}' + \hbar\partial_t\phi(t)I_z, \rho']. \tag{13}$$

The transformed Hamiltonian has a Zeeman term from equation (5) which is unaltered by the transformation,

$$\mathscr{H}'_0(t) = -\gamma\hbar H_0(t)I_z. \tag{14}$$

The r.f. interaction of equation (6) has two terms: the first is a component rotating in the Larmor sense which appears static when transformed into the rotating frame, and the second is an anti-Larmor sense rotating component which, when transformed to the rotating frame, appears as a field rotating with twice the phase accumulation rate,

$$\mathscr{H}'_{rf} = -\gamma\hbar H_1 I_y - \gamma\hbar H_1(I_y\cos(2\phi(t)) + I_x\sin(2\phi(t))). \tag{15}$$

The phase derivative term in the commutator of equation (13) can be combined with the Zeeman term of equation (14) to give the effective Zeeman interaction in the rotating frame,

$$\begin{aligned}(\mathscr{H}'_0)_{\text{eff}} &= \mathscr{H}'_0(t) + \hbar\partial_t\phi(t)I_z \\ &= -\gamma\hbar(H_0(t) - \partial_t\phi(t)/\gamma)I_z. \end{aligned} \tag{16}$$

The system is presumed to be a resonant system where $\mathscr{H}_{rf}$ and $\mathscr{H}_B$ give a line broadening small compared with the resonant frequency γH_0. The external field modulations and the phase modulation factor of equation (3) are also presumed to be free of such severe modulation rates as would produce instantaneous effective frequencies of negative algebraic sign according to equation (3) and approaching the Larmor frequency in absolute magnitude. In this case, the time dependent terms in equation (15) remain highly non-secular and will consequently exert a negligible influence on the spin system. These anti-Larmor sense rotating components† of the exciting field are therefore ignored, and equation (13) can then be written

$$\partial_t\rho' = -i[-\gamma(H_0(t) - \partial_t\phi(t)/\gamma)I_z - \gamma H_1 I_y + \mathscr{H}'_B, \rho']. \tag{17}$$

The essential feature in equation (17) concerning the relation between energy level modulation and phase modulation of the exciting field is that the effective field along the z axis, $H_0(t) - \partial_t\phi(t)/\gamma$, depends only on the difference between externally applied magnetic field and the instantaneous frequency of the excitation. In general, the interactions which are collected together in the $\mathscr{H}_B$ term will have components which transform with different time dependences according to whether the phase-locked reference frame corresponds to a single frequency, as in equation (1), or to a frequency modulated experiment as indicated in equation (2). Nevertheless, as is discussed later, there is a very wide variety of conditions under which the effects of $\mathscr{H}'_B$ are quite independent of the character of the modulation. When such is the case, one may express the field strength modulation as

$$H_0(t) = H_0^{\circ} + H_M(t) \tag{18}$$

and the excitation phase modulation according to equation (2). Then the dynamical behavior of the spin system as expressed in equation (17) depends only on the static effective magnetic field,

---

†These anti-Larmor components do cause a second order energy level shift whose time average is not zero. This is the Bloch-Siegert shift, and produces a fractional resonance shift of $\frac{1}{4}(H_1/H_0)^2$, which might be typically 10^{-7}.

$$\mathbf{H}_e = (H_0^\circ - \omega/\gamma)z + H_1 y \tag{19}$$

an effective field modulation term, $h(t)z$, where

$$h(t) = H_M(t) - \partial_t\Delta(t)/\gamma \tag{20}$$

and finally upon the line-broadening and relaxation effects contributed by $\mathscr{H}_B$. Figure 1 shows these effective fields as they appear in the phase-locked reference frame.

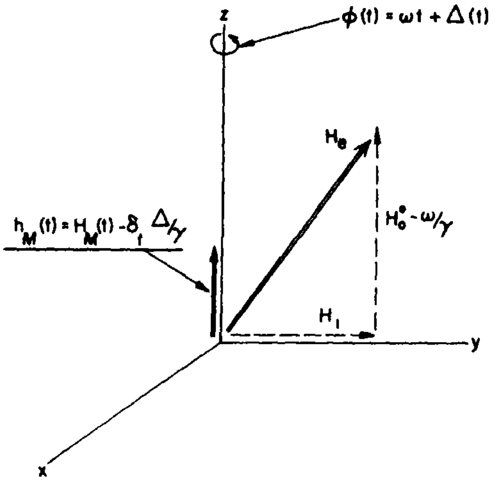
z
$\phi(t) = \omega t + \Delta(t)$
H_e
$H_0^\circ - \omega/\gamma$
$h_M(t) = H_M(t) - \delta_t \Delta/\gamma$
H_1
y
x

Fig. 1. Diagram of the effective magnetic fields as they appear in the phase-locked reference frame

Thus the basic relation which exists between field and frequency modulation is that of equivalence between an external field modulation $H_M(t)$ and the negative of the time derivative of the exciting field phase modulation factor $\Delta(t)$. There seem to be two common points of confusion regarding these notions, and it would be worthwhile to comment upon them. The first point concerns an alternative notation sometimes used to express the frequency of an r.f. field under the conditions of very wide-band non-sinusoidal frequency modulation; this involves what may be called the 'f.m. frequency'.

$$\omega_{fm} = \omega + \delta\omega(t) \tag{21}$$

where the oscillation of the r.f. field is expressed as

$$H_1(t) = H_1 \cos(\omega_{fm} t)\ . \tag{22}$$

Only in certain limits is there an equivalence between the field modulation, $H_M(t)$, and the *fm* term, $-\delta\omega(t)$; the true equivalence exists between $H_M(t)$ and the time rate of change of the phase modulation as indicated in equation (20).

The second point of confusion arises when one describes the spin behavior in a frame of reference which is rotating at the average frequency ω. In this reference frame any phase modulation appears as an amplitude modulation of H_1 along the y axis combined with an effective oscillating field proportional to H_1, but directed along the x axis. It would *appear, at first consideration, that only* severe limiting conditions would result in an equivalence between an external field modulation in the z direction and the transverse modulation components resulting from the phase modulation. This is resolved by the fact that the magnetization components described in this uniformly rotating frame are not phase referenced to the phase of the exciting field. A subsequent transformation is necessary to accomplish this, and the result, of course, is the same as if the original transformation had been made to the phase-locked rotating frame.

Before going on to a discussion of some of the specific applications resulting from the equivalence of field and phase modulation, a more careful consideration of the effects associated with the perturbing terms in $\mathscr{H}'_B$ is in order.

EFFECTS OF PERTURBING TERMS

Relaxation effects

One may group the contributions to $\mathscr{H}_B$ into an average static set of interactions, $\mathscr{H}_{B0}$, and a set of interactions which fluctuate in time, $\mathscr{H}_B(t)$. We consider first the time dependent set which causes the spin-relaxation effects.

One can further distinguish among the terms within $\mathscr{H}_B(t)$ according to whether the operators involved do, or do not, commute with I_z. One may define the sum of all the commuting terms as $\mathscr{H}_{Bz}(t)$ and the sum of all non-commuting terms as $\mathscr{H}_{Bn}(t)$, that is,

$$\mathscr{H}_B(t) = \mathscr{H}_{Bz}(t) + \mathscr{H}_{Bn}(t)\,, \qquad (23)$$

where

$$[\mathscr{H}_{Bz}(t), I_z] = 0 \qquad (24)$$

and

$$[\mathscr{H}_{Bn}(t), I_z] \neq 0. \qquad (25)$$

Because of the commutation relation of equation (24), the rotating frame transformation of equation (10) leaves $\mathscr{H}_{Bz}$ unchanged; $\mathscr{H}'_{Bz}$ therefore enters the equation of motion in equation (17) in a manner independent of the presence or absence of phase modulation of the exciting field. Its role is therefore defined exclusively in relation to the other quantities in equation (19) and, since these are specified in terms of the effective field of equation (19) and the modulation field of equation (20), the relaxation effects of $\mathscr{H}_{Bz}(t)$ are independent of any distinction between phase and field modulation.

In the case of the non-commuting terms of equation (25), the spin-relaxation effects do, in principle, depend upon whether phase modulation or external field modulation is employed. Transitions between spin levels produced by $\mathscr{H}_{Bn}(t)$ will be normally characterized as $\Delta M_I = 1$ or $\Delta M_I = 2$; the former arise from modulation of such interactions as the C and D terms[6] in the nuclear dipole-dipole coupling, the hyperfine interaction with paramagnetic electron states, and in the case of nuclei with a quadrupole moment, the V_{+1} terms† of the quadrupole coupling. The $\Delta M_I = 2$ transitions can be produced from modulation of the dipole-dipole E and F terms† or the $V_{\pm 2}$ terms† of the quadrupole interaction.

From the point of view concerned with relaxation effects on the spin system, the only essential difference between the $\Delta M_I = 1$ and $\Delta M_I = 2$ terms is that the former must have a time dependence producing Fourier components at the spin transition resonant frequency and the latter's time dependence must produce Fourier components at twice the resonant transition frequency. Consequently, only the $\Delta M_I = 1$ terms are discussed in detail here. One can view the $\Delta M_I = 1$ interactions as a time-dependent internal magnetic field, and thereby express $\mathscr{H}_{Bn}(t)$ as

$$\mathscr{H}_{Bn}(t) = -\gamma\hbar\Sigma_j(H_j(t)I_{jx} + H_{jy}(t)I_{jy}). \quad (26)$$

When this interaction is transformed to the rotating frame appropriate to the equation of motion expressed in equation (17), one finds

$$\mathscr{H}'_{Bn}(t) = \tfrac{1}{2}(H_j(t)\mathrm{e}^{-i\phi(t)} + \text{c.c.})I_{jx}$$
$$+\tfrac{1}{2}(iH_j(t)\mathrm{e}^{-i\phi(t)} + \text{c.c.})I_{jy}\,, \quad (27)$$

where $H_j(t)$ is related to the field components in equation (28) by

$$H_j(t) = H_{jx}(t) - iH_{jy}(t). \qquad (28)$$

One can gain some insight into the relaxation effects produced by $\mathscr{H}'_{Bn}(t)$ by considering the behavior of equation (17) in two limits. First, consider the limit in which the effective z component of field is very small compared with the characteristic local fields specified by the time independent term $\mathscr{H}_{B0}$ or with H_1 or both. That is, the experiment is performed on-resonance with $\gamma H_0(t) \cong \partial_t\phi(t)$; in this limit, the phase factors entering equation (27) can be written as

$$\exp\{-i\phi(t)\} = \exp\left\{i\int_0^t H_0(t')\mathscr{H}'\right\}. \quad (29)$$

The matrix elements of $\mathscr{H}'_{Bn}(t)$ have an additional time dependence coming from the difference in energy between the states involved, but this is related to the magnitude of H_1 and the local field strength associated with $\mathscr{H}_{B0}$. Consequently, the effects generated by $\mathscr{H}'_{Bn}(t)$ are, according to equation

---

†The notation used here and effects produced by these interactions are presented in detail in the book by C. P. Slichter cited in reference[4].

29, independent of whether phase or field modulation is employed.

The second limit is the off-resonance limit in which the spin system's behavior is dominated by the z component field, $(H_0(t) - \gamma_t\phi(t)/\gamma)$. In the perturbation theory calculation† of the spin relaxation rate, W, caused by $\mathscr{H}'_{Bn}(t)$, the time dependences of the perturbation and those of the frequency difference between the levels involved in the transition are combined in a Fourier integral,

$$W = K\int_{-\infty}^{\infty} \mathrm{d}t\langle H_j(0)H_j^*(t) + \text{c.c}_{\text{av}}\rangle \exp\left\{-i\phi(t) - i\int_0^t (H_0(t') - \partial_t\phi(t'))\,\mathrm{d}t'\right\}. \tag{30}$$

In equation (30), the two terms involving $\phi(t)$ cancel each other; this happens because these phase factors appear only through transformation of the interaction and the wavefunctions into the rotating frame. The resulting expression for the spin-transition rate,

$$W = K\int_{-\infty}^{\infty} \mathrm{d}t\langle H_j(0)H_j^*(t) + \text{c.c.}\rangle_{\text{av}} \exp\left(-i\int_0^t H_0(t')\mathrm{d}t'\right) \tag{31}$$

indicates, as expected, that in the off-resonance limit the spin relaxation processes are entirely insensitive to the r.f. exciting field. The integral in equation (31) can be rewritten by standard theorems for Fourier integrals as the convolution of the spectral density of the fluctuating interaction $\langle H_u(0)H_j^*(t) + \text{c.c.}\rangle_{\text{av}}$ with the frequency spectrum of the modulated spin energy levels, $\exp\left(-i\int_0^t H_0(t')\mathrm{d}t'\right)$.

Terms in $\mathscr{H}'_{Bn}(t)$ which cause $\Delta M_I = 2$ transitions may be carried through in a completely analogous manner; the only difference from the treatment above is that all the phase terms are multiplied by a factor of two.

The preponderance of NMR spin-lattice relaxation processes are dominated by fluctuating interactions having short correlation times. In this case, the spectral density associated with the correlation function in equation (31) will be broad compared with spin-level spectrum generated by $H_0(t)$, i.e. T_1 is essentially independent of H_0, and the experimentally observed behavior of the NMR system will be independent of whether frequency modulation or external field modulation is used. One can, however, imagine a case in which the nuclear spin relaxation processes are dominated by a long correlation time interaction. In this case, external field modulation which shifts the spin levels over a range of frequencies large compared with the inverse of the interaction correlation time can produce experimentally observed T_1 effects which will not occur if only the frequency of the exciting r.f. field is swept over the same range with H_0 remaining fixed.

Line broadening and shifting

The average, time independent, parts of $\mathscr{H}_B$, which have been referred to as $\mathscr{H}_{B0}$, can be examined in a manner similar to that for the fluctuating terms. The sub-terms in $\mathscr{H}_{B0}$ which do not commute with I_z are highly non-secular for a resonance system and, for our considerations, they can be neglected. The terms in $\mathscr{H}_{B0}$ which do commute with I_z will be referred to as $\mathscr{H}_{B0z}$, and consist of such interactions as the chemical shift and Knight shift terms in the nuclear spin coupling to electrons, the secular parts of the nuclear dipole-dipole interaction, and the secular parts of static quadrupole interactions. These terms are invariant under the rotating frame transformation and, consequently, enter the equations of motion in equation (17) as $\mathscr{H}'_{B0z} = \mathscr{H}_{B0z}$. Therefore, all the observed effects which arise from these interactions are independent of the distinction between phase and field modulation of the experimental system. This might seem inconsistent with the fact that the chemical shift and Knight shift interactions depend linearly upon $H_0(t)$

---

†Thorough treatments of relaxation processes and calculations can be found in the books cited in reference [4].

and not upon $\partial_t\phi(t)$, but these field shift terms can be accounted for by including them in the applied field, $H_0(t)$, appearing in equation (17). These effects are thus exhibited only as a small change in the effective gyromagnetic ratio which appears in equation (20).

APPLICATIONS AND IMPLICATIONS

When an NMR system is subjected to r.f. excitation and the external field, H_0, is appropriately modulated, one observes additional resonance effects due to the phenomenon of rotary saturation[5]. Rotary saturation effects due to both single and multiple quanta transitions at the modulation frequency have been observed and analyzed by J. Franz[6, 7]. For off-resonance excitation, the spin transitions involve one or more photons at the modulation frequency absorbed simultaneously with a photon at the excitation frequency. For excitation on resonance, there is no net absorption of resonant frequency quanta. In experiments where the exciting source is phase modulated, one observes[1] resonance signals when an f.m. sideband passes through the resonant frequency. In addition, the on-resonance signals in a phase modulated experiment can display altered behavior due to the interference between the carrier and sideband frequencies. The results of the previous sections show that the rotary saturation effects and the f.m. sideband effects are actually equivalent phenomena in all respects. One viewpoint or the other might happen to be preferable under particular circumstances; for example, in off-resonance rotary saturation it is a complex calculation to find the intensity of the three-photon transitions, but it is relatively simple to find the intensity of the equivalent phase-modulation third sideband. On the other hand, the frequency shift generated by a strong off-resonance field is difficult to calculate from the f.m. viewpoint, but is immediately given in the rotary saturation picture from the effective field of equation (19).

It is also evident that these notions are not confined to the specific case of nuclear magnetic resonance. Further consideration of the derivation of the phase-locked representation of the equations of motion given in equation (17) shows that the general result requires only a system of relatively sharp energy levels and an exciting field that induces resonant transitions among the levels. A general transformation to the representation in which the transition-inducing field components are time independent is readily carried out. The result is that the resonant transition frequency and the instantaneous frequency of the excitation appear on equivalent footings in the difference term, $(\omega_{\text{res}}-\partial_t\phi(t))$. Thus, it is a basic feature of all such systems that phase modulation of the excitation is equivalent, in all essential detail, to modulation of the energy level spacing. This behavior is treated in detail for pure quadrupole nuclear spin interactions by Slusher and Hahn [3] who wish to describe spin-disordering achieved by f.m. techniques.

Other systems where the resonant frequency is not under the full control of external experimental conditions are, for example, nuclei in ferromagnets or those nuclei in diamagnetic solids which neighbor paramagnetic defects and for which the dominant interaction is the hyperfine interaction with electronic moments. In these systems, phase modulation of the excitation can produce the same detailed effects as would modulation of the effective static field at the nucleus.

Another useful application of these equivalences is found in double resonance experiments where two different resonances are simultaneously excited. One frequently wishes to field modulate or perform rotary saturation on one resonance while leaving the other unaffected; phase modulation of the appropriate source produces an effective field modulation only for those spins whose transition frequencies are nearly resonant with that source.

The complement may also be useful; for

example, in some multiple-pulse NMR techniques, several fast, accurate phase-shifts might be required. It might prove much easier experimentally to introduce equivalent magnetic field pulses than multiple phase-shifts of the r.f. source.

One can also readily understand from these ideas how the presence of spurious phase shifts can produce experimentally undesirable results. For example, in short pulse, high power NMR experiments, we have observed that transient changes in driver and transmitter stage bias levels during the pulse turn-on can produce phase shifts of as much as 10 deg/μsec for periods of several microseconds. For pulse lengths short compared with the transient times this produces a pulse effectively off resonance by 15KHz, and for longer pulses it generates a degree of spin-locking otherwise unanticipated.

We have carried out many simple NMR experiments relating both to field modulation and phase-shifting and have found detailed experimental verification, in all cases, of the equivalence expressed in equation (20).

Acknowledgements – The author wishes to acknowledge many fruitful discussions with Professor L. W. Anderson as well as Mr. David Lang, who performed most of the NMR experiments.

REFERENCES

1. KARPLUS R., *Phys. Rev.* **73**, 1027 (1948).
2. COWAN D. L. and ANDERSON L. W., *Phys. Rev.* **135**, A1046 (1964); *ibid.* **139**, A424 (1965).
3. SLUSHER R. E. and HAHN E. L., *Phys. Rev.* **166**, 332 (1968).
4. Excellent discussions of the rotating frame representation are given by ABRAGAM A., In *Principles of Nuclear Magnetism.* Oxford University Press, London (1961); SLICHTER C. P., In *Principles of Magnetic Resonance.* Harper and Row, London (1963).
5. REDFIELD A. G., *Phys. Rev.* **98**, 1787 (1955).
6. FRANZ J., Thesis, Univ. of Illinois, 1965 (unpublished).
7. FRANZ J. R. and SLICHTER C. P., *Phys. Rev.* **148**, 287 (1966).

J. Phys. Chem. Solids Pergamon Press 1969. Vol. 30, pp. 305–320 Printed in Great Britain.

RIGOROUS MAGNETIC SUSCEPTIBILITY FOR A MAGNETIC BREAKDOWN MODEL*†

J. RUVALDS‡
Department of Physics, University of Oregon, Eugene, Oregon 97403, U.S.A.

(*Received* 20 *May* 1968)

Abstract—The exact diamagnetic susceptibility is calculated as a function of the magnetic field for a magnetic breakdown model which has been previously presented. The susceptibility is obtained by numerically evaluating the appropriate derivative of the Helmholtz free energy using the exact eigenvalues of the model Hamiltonian. The susceptibility calculated by this method includes the contributions from both the zero-field diamagnetism and the de Haas–van Alphen effect. The periodicities in the susceptibility are related to the semiclassical electron orbits corresponding to this model: for low magnetic fields the periods are determined by two closed orbits, one within the other; for high fields a single period is observed corresponding to the broken down case of two identical intersecting elliptical orbits. The behavior in the transition region is compatible with the expression for the breakdown probability derived by several authors. An approximate calculation of the oscillatory part of the diamagnetism is also carried out using the semiclassical method of Falicov and Stachowiak. When the influence of the energy gap on the orbit geometry is taken into account, their method yields results which are in good agreement with the exact susceptibility. Evaluation of the steady diamagnetism for the model using the expression for the susceptibility derived by Wannier and Upadhyaya yields results which are in agreement with the numerical calculations and, in addition, exhibits anomalous features of the zero-field diamagnetism in the neighborhood of critical points of the Fermi surface.

1. INTRODUCTION

SINCE the proposal of the concept of magnetic breakdown by Cohen and Falicov[1], several authors have investigated the phenomena of magnetic breakdown both theoretically and experimentally[2]. Various means have been employed to derive an expression for the breakdown probability[3–7]. In addition, Pippard[5, 8] has developed a semiclassical theory to treat coupled orbits in strong magnetic fields which permits an approximate investigation of the energy level structure in the presence of magnetic breakdown. Falicov and Stachowiak[9] have proposed a semiclassical method for calculating the oscillatory free energy of an electron system taking into account magnetic breakdown effects. The Falicov and Stachowiak theory thus provides a straightforward technique for studying the de Haas–van Alphen effect in a system of coupled orbits. The problem of calculating the free energy for coupled orbits has also been treated by Chambers[10] and Glasser[11]. Their results are consistent with the Falicov and Stachowiak theory within the framework of the approximations involved.

Recently a model Hamiltonian has been presented which exhibits magnetic breakdown effects and which can be solved exactly[12]. Exact eigensolutions for the model in the presence of a magnetic field have been obtained and a comparison has been made with the model eigenvalues calculated using Pippard's method, thus providing a test of the validity of Pippard's approximations[12].

The purpose of the present work is to calculate the rigorous diamagnetic susceptibility for the above model and study the effects of magnetic breakdown on the de Haas–van Alphen effect as well as the zero-field susceptibility. Application of the Falicov and Stachowiak method to the model then provides a direct check on the validity of their theory

---

*Work supported by the National Science Foundation.

†Based on a thesis submitted to the University of Oregon in partial fulfillment of the requirements for the Ph.D. degree.

‡*Present address:* James Franck Institute, University of Chicago, Chicago, Illinois 60637, U.S.A.

and suggests modifications in their approximations which improve substantially the agreement with the exact results.

A description of the model, as well as a brief discussion of the corresponding eigensolutions, is presented in Section 2. In Section 3(*A*) the exact eigenvalues of the Hamiltonian are used to evaluate numerically the appropriate derivative of the Helmholtz free energy, thus yielding the rigorous susceptibility as a function of the magnetic field. The susceptibility calculated in this fashion includes the contributions from both the steady diamagnetism and the de Haas–van Alphen effect. An approximate calculation of the oscillatory susceptibility is carried out in Section 3(*B*) using the semiclassical method of Falicov and Stachowiak[9]. The results obtained by their method are compared with the exact case and, in Section 3(*C*), the magnetic field dependence of the dHvA amplitudes is studied using both methods. In the exact calculation, the field dependence of the oscillation amplitudes is investigated by Fourier analyzing the susceptibility.

Section 4 contains an independent calculation of the zero-field diamagnetism for the model using the result derived by Wannier and Upadhyaya[13]. The steady susceptibility is obtained as a function of the Fermi energy and is found to exhibit interesting features in the vicinity of singular points of the Fermi surface. Finally, the results of the present work are summarized in Section 5.

2. MODEL AND EIGENSOLUTIONS

The model[12] is based on the **k**·**p** method [14] in which the Hamiltonian is expanded about a symmetry point in *k*-space. Use of the **k**·**p** representation requires that the two degenerate energy bands which exhibit magnetic breakdown must be isolated in energy from all other bands. However, the model differs from most previous work in that it is not restricted to weak lattice potentials.

We construct the Hamiltonian in the presence of a magnetic field using the method of Luttinger and Kohn[15]; thus we replace the quantity k_y by k_y by $k_y - iS\,\partial/\partial k_x$, where $S = eH/\hbar c$, e is the electronic charge, H is the magnetic field (parallel to the z axis), $\hbar$ is Planck's constant divided by 2π, c the velocity of light, and the vector potential is given by $A = (0, Hx, 0)$. The model Hamiltonian is then chosen to be of the form

$$\mathscr{H} = \mathscr{H}_0 + Rk_z^2 \tag{2.1}$$

where

$$\mathscr{H}_0 = \begin{vmatrix} Ak_x^2 + B(k_y - iS\,\partial/\partial k_x)^2 + \Delta & Dk_x \\ Dk_x & Ak_x^2 + B(k_y - iS\,\partial/\partial k_x)^2 - \Delta \end{vmatrix}. \tag{2.2}$$

In equations (2.1) and (2.2), the vector **k** denotes a point in *k*-space measured from a symmetry point; *A*, *B*, *R* and *D* are momentum matrix elements which appear in the **k**·**p** formalism, and Δ is a constant energy gap. Curves of constant energy corresponding to the Hamiltonian (2.1) are obtained by setting $S = 0$ and diagonalizing $\mathscr{H}$ to obtain

$$E(\mathbf{k}) = Ak_x^2 + Bk_y^2 + Rk_z^2 \pm (D^2k_x^2 + \Delta^2)^{1/2}. \tag{2.3}$$

The energy is plotted as a function of k_x in Fig. 1, with the origin taken to be at a Brillouin zone boundary. For a fixed value of k_z, say $k_z = 0$, the semiclassical electron trajectories corresponding to the model are displayed in Fig. 2. The solid lines indicate the electron oribts for low magnetic fields. For high enough fields (state of complete breakdown) the trajectories are obtained by ignoring the energy gap, i.e. $\Delta = 0$. In the region of positive energies the electron, upon approaching the Brillouin zone boundary, can tunnel through and complete the elliptical orbits indicated by the dotted lines in Fig. 2(a). For negative energies the broken-down trajectories are the nonintersecting elliptical orbits shown in Fig. 2(b). In order for the present treatment to be valid the electron orbits must be confined to a small region of the Brillouin zone.

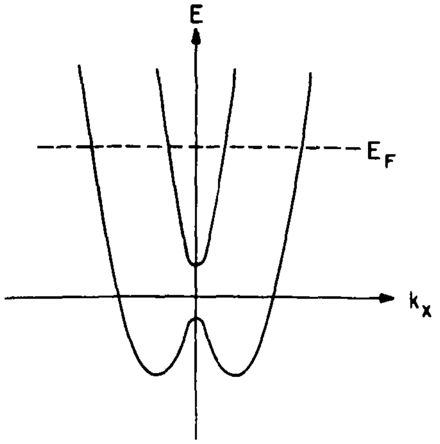

Fig. 1. Energy vs. k_x curves for the Hamiltonian (2.1) in the absence of a magnetic field.

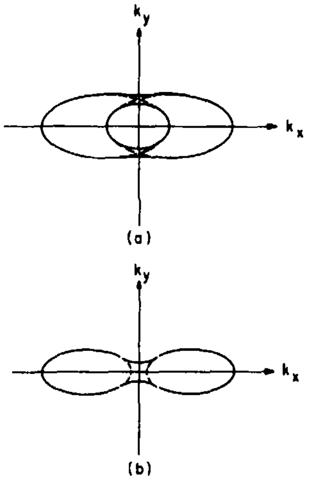

Fig 2. Constant energy curves in $k_x - k_y$ plane for the Hamiltonian (2.1) with the magnetic field parallel to the k_z axis. The $k_y - k_z$ plane is a Brillouin zone boundary. (a) Electron orbits for positive energies. (b) orbits corresponding to negative energies.

The electron motion in the k_z direction is not affected by the magnetic field. Consequently, to find the discrete magnetic eigenvalues we need to consider the Schrödinger equation corresponding to $\mathscr{H}_0$. It is shown in reference [12] that the Schrödinger equation can be reduced to a pair of coupled difference equations which in turn, can be solved numerically. For convenience we introduce the following set of dimensionless variables: $\gamma = 4\Delta A/D^2$ is a dimensionless energy gap, $\epsilon = 4EA/D^2$ is the dimensionless energy, $\tau = 4Ak_BT/D^2$ is a dimensionless temperature (k_B is Boltzmann's constant and T the temperature), and the dimensionless magnetic field is defined by $\beta = 8SA^{3/2}B^{1/2}/D^2$. It is possible to obtain exact solutions for the magnetic energy eigenvalues ϵ at fixed values of the energy gap γ and the field β or, alternately, solve for the inverse magnetic field spectrum holding the energy gap γ and the energy ϵ constant[12]. For a detailed discussion of the eigenvalue spectrum, as well as a comparison of these results with eigensolutions obtained by Pippard's method, we refer the reader to reference [12]. In the limit of complete breakdown the eigenvalue spectrum is given by the relation

$$\epsilon = (l+\tfrac{1}{2})\beta - 1 \qquad (2.4)$$

where l is a positive integer. As the possibility of breakdown decreases these levels split apart and, in the limit of negligible breakdown, evolve into the eigenvalues predicted by the Onsager rule[12-16]. Pippard's method, applied to the present model, yields eigenvalues which are in generally good agreement with the exact results in cases where the effect of the energy gap on the geometry of the orbits may be neglected.

3. MAGNETIC SUSCEPTIBILITY

(*A*) *Exact calculation*

The results of Section 2 are now used to calculate the rigorous diamagnetic susceptibility for the present model. We begin with the expression for the Helmholtz free energy

$$F = N\mu - 2k_BT \int \rho(E,H) \times ln\{1+\exp[(\mu - E)/k_BT]\}\, dE, \qquad (3.1)$$

where N is the total number of electrons, μ

the Fermi energy, k_B is Boltzmann's constant, T is the temperature, and the field-dependent density of states (apart from spin, which is included explicitly in (3.1)) is denoted by $\rho(E,H)$. In terms of F, the magnetic susceptibility per unit volume is given by the standard formula

$$\chi = -\frac{1}{\Omega H}\frac{\partial F}{\partial H}, \tag{3.2}$$

where Ω is the volume of the sample. In the following discussion all energies will be measured from the bottom of the energy band. Integrating (3.1) by parts we obtain

$$\begin{aligned} F = N\mu - 2k_BTZ(E,H) \\ \times ln\{1+\exp[(\mu-E)/k_BT]\}\Big|_0^\infty \\ -2\int f(E)Z(E,H)\mathrm{d}E \end{aligned} \tag{3.3}$$

where $f(E)$ is the Fermi–Dirac distribution function and $Z(E,H)$ is defined by

$$Z(E,H) = \int_0^E \rho(E',H)\,\mathrm{d}E'. \tag{3.4}$$

The function $Z(E,H)$ gives the number of states (apart from spin) below an energy E. The second term in (3.3) vanishes at both limits, and consequently we are left with an equivalent expression for the free energy

$$F = N\mu - 2\int Z(E,H)f(E)\mathrm{d}E. \tag{3.5}$$

In the presence of a magnetic field the energy levels of an electron are given by

$$E(l,k_z) = E_l(H) + Rk_z^2 \tag{3.6}$$

where the levels $E_l(H)$ are the exact magnetic energy eigenvalues discussed in Section 2. The degeneracy of the levels can be derived following the procedure for free electrons [17]. If the normalization volume is taken as a cube of side length L, then $\Omega = L^3$ and the degeneracy d of the levels (3.6), for a fixed value of k_z, is given by

$$d = (eHL^2/2\pi\hbar c). \tag{3.7}$$

Including the k_z degeneracy, $L/2\pi$, for these states and summing over allowed k_z values, we find the number of states of energy below E to be

$$Z(E,H) = (Ld/\pi R^{1/2}) \sum_l [E-E_l(H)]^{1/2}, \tag{3.8}$$

where the sum is understood to extend over those integers l for which the integrand is real.

To find the magnetic susceptibility we differentiate the free energy (3.5) with respect to the field, holding the number of particles constant. Substituting (3.8) into the expression for the free energy, differentiating with respect to the field and noting that the terms containing $\partial\mu/\partial H$ cancel, we obtain for the susceptibility

$$\begin{aligned} \chi = \frac{e}{\pi^2\hbar cR^{1/2}}\int \mathrm{d}E \sum_l f(E)\Big\{\frac{1}{H}[E-E_l(H)]^{1/2} \\ -\frac{1}{2}[E-E_l(H)]^{-1/2}\partial E_l/\partial H\Big\}. \end{aligned} \tag{3.9}$$

The exact energy eigenvalues $E_l(H)$ were used to calculate $\partial E_l/\partial H$ numerically. For convenience in computation the expression for χ in equation (3.9) was integrated by parts to eliminate the troublesome terms $[E-E_l(H)]^{-1/2}$. The resulting integral, which contains $\partial f/\partial E$ in the integrand, was evaluated numerically using Simpson's rule. The susceptibility calculated by the above method includes the contributions from both the zero-field diamagnetism and the de Haas–van Alphen effect.

The magnetic susceptibility for a low value of the temperature is plotted as a function of the inverse magnetic field in Fig. 3. Also shown in Fig. 3 are the exact inverse magnetic field eigenvalues for the same values of energy and energy gap which were used in the susceptibility calculation. Several features of the susceptibility can be explained directly by examining the inverse field spectrum and the electron orbits corresponding to the model. Note that the peaks in the susceptibility coin-

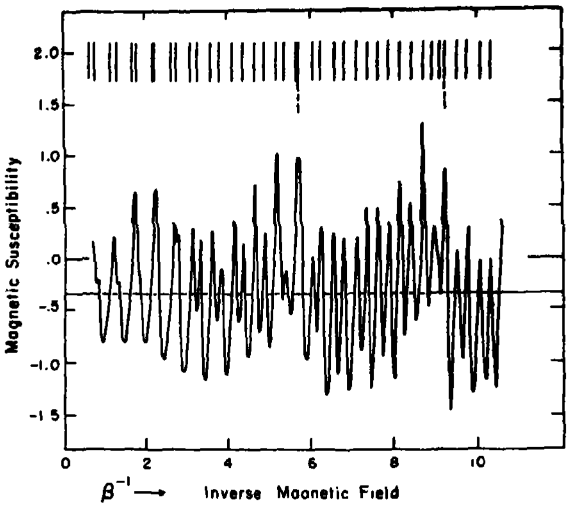

Fig. 3. Exact magnetic susceptibility as a function of the inverse magnetic field for dimensionless energy gap $\gamma = 0{\cdot}4$, dimensionless energy $\epsilon = 1{\cdot}0$ and a dimensionless temperature $\tau = 0{\cdot}005$. The vertical lines indicate the inverse field eigenvalues for the same energy and energy gap.

cide with the inverse field eigenvalues. The β^{-1} eigenvalues corresponding to the small orbit depicted in Fig. 2 have a marked effect on the susceptibility in the low field region due to the small effective mass of this orbit. These eigenvalues modulate the oscillations with a large period ($\delta\beta^{-1} = 3{\cdot}54$) and, in addition, distort the structure of various peaks in the susceptibility, e.g. note the structure in the vicinity of $\beta^{-1} = 5{\cdot}7$ and $\beta^{-1} = 9{\cdot}2$. For high fields, the influence of the small orbit is diminished by magnetic breakdown effects. The periodicities in the susceptibility are related to the semiclassical electron trajectories shown in Fig. 2. For low fields the small period ($\delta\beta^{-1} = 0{\cdot}27$) corresponds to the area of the dumbbell-shaped orbit and the large period ($\delta\beta^{-1} = 3{\cdot}54$) is due to the small orbit. For high fields a single period ($\delta\beta^{-1} = 0{\cdot}5$) is observed corresponding to the broken down case of two identical intersecting elliptical orbits. Fourier analysis of the susceptibility, which is discussed in detail in Section 3(*C*), reveals that other periodicities, due to harmonic frequencies and sums of the three basic frequencies, are also present and contribute substantially to the detailed structure of the susceptibility. The breakdown field, $\beta_0^{-1} = 4{\cdot}0$, obtained from Upadhyaya's[7] result appears to be compatible with the behavior of the oscillations in the transition region. The solid line drawn through the oscillations at $\chi = -0{\cdot}35$ is the value of the steady susceptibility taken from the high temperature results.

The role of the steady diamagnetism is more explicit in the results for the susceptibility at higher temperatures. Oscillations in the susceptibility are due to energy eigenvalues passing through the Fermi level as the magnetic field is varied and consequently are very sensitive to the shape of the Fermi-Dirac distribution function $f(E)$ in the neighborhood of the Fermi energy. For high temperatures the distribution function is spread out in this region and, as a result, the oscillations are damped. Thus, the remaining contribution to the susceptibility in the high temperature limit is due to the steady diamagnetism. Figure 4 shows the susceptibility as a function of inverse magnetic field for the same energy and energy gap ($\epsilon = 1{\cdot}0, \gamma = 0{\cdot}4$) used in the above calculation, but with a dimensionless temperature $\tau = 0{\cdot}05$. For this value of the temperature the high frequency oscillatory components are damped out in the region of low magnetic fields. The dotted line in Fig. 4 corresponds to the zero-field susceptibility obtained by calculating the average value of the susceptibility in the low field region. It is interesting to note that the steady diamagnetism is in the neighborhood of the average susceptibility even in the high field region, thus indicating that magnetic breakdown does not appreciably affect the zero-field susceptibility for the model.

The zero-field diamagnetism is calculated independently in Section 4 using the expression for the susceptibility derived by Wannier and Upadhyaya[13]. The constant susceptibility obtained from their result is in agreement with the value obtained by the high-temperature calculation which was described above.

(*B*) *Falicov and Stachowiak method*

Falicov and Stachowiak[9] have recently proposed a semiclassical method for calculating the oscillatory part of the magnetic susceptibility. Their method is based on Pippard's network model for coupled orbits, which includes the possibility of magnetic breakdown by assuming that at each orbit junction the electron is Bragg-reflected with probability amplitude q or transmitted with probability amplitude p. The breakdown probability is taken as $P^2 = \exp(-H_0/H)$, where H_0 is the breakdown field which can be calculated from the results of Upadhyaya and others[2].

Remembering that the electron orbits in k-space are similar to the orbits in real space but rotated by $\pi/2$ in the plane normal to the magnetic field, we can apply the method of

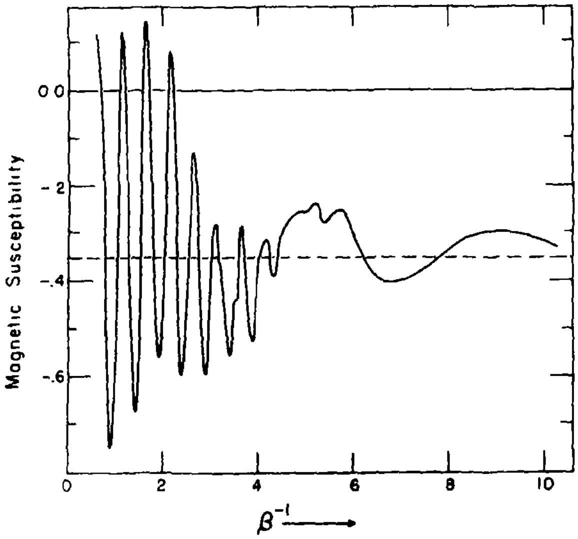

Fig. 4. Exact susceptibility as a function of the inverse magnetic field for a dimensionless energy gap $\gamma = 0{\cdot}4$, dimensionless energy $\epsilon = 1{\cdot}0$, and a dimensionless temperature $\tau = 0{\cdot}05$. The dotted line is the average value of the susceptibility in the low field region.

Falicov and Stachowiak in either real space or in k-space. In describing their method, we follow Falicov and Stachowiak and consider the electron motion in real space. Their result for the magnetic susceptibility is then applied to the present model in k-space.

The major task in their treatment is the determination of the field-dependent density of states $\rho(E,H)$ which appears in the expression for the free energy (3.1). Falicov and Stachowiak develop a Green's function formulation to calculate the density of states $\rho(E,H)$ which, in turn, is used to evaluate the oscillatory part of the free energy of the system. They introduce a propagator $G(\mathbf{r},\mathbf{r}_0,t)$ for a wave packet initially localized at $\mathbf{r}=\mathbf{r}_0$, which, as time evolves, spreads out along the network. The density of states is obtained by Fourier transforming the part of the propagator which corresponds to those portions of the wave packet which return to $\mathbf{r}_0$ after a given interval of time t. The Green's function $G(\mathbf{r},\mathbf{r}_0,t)$ is approximated by a superposition of wave packets that follow the semiclassical electron trajectories with phases determined by the Onsager rule[9, 16]. The wave packets are formed by electron wave functions in the neighborhood of the Fermi surface and consequently yield the oscillatory components of the density of states. These states give rise to the de Haas–van Alphen effect but do not include the contribution to the steady diamagnetism.

For systems with orbits coupled by magnetic breakdown, Falicov and Stachowiak find that the z component of the Green's function $G(\mathbf{r}_0,\mathbf{r}_0,t)$ is given by

$$G_z(r_0,r_0,t)=\frac{2m}{\hbar}\sum_j C_j M_j R_j \exp(i\varphi_j)\delta(t-t_j), \tag{3.10}$$

where the symbols used here are defined below. The label j refers to all equivalent wave packets which return to $\mathbf{r}_0$ at the same time t_j with the phase φ_j after having followed similar trajectories in the network. The phases φ_j are determined by the Onsager rule in the form $\varphi_j=A_j(k_z)/\beta-\varphi_{j0}$, where A_j is the dimensionless extremal area in k-space of the jth orbit, β is the dimensionless magnetic field in our notation, and φ_{j0} is a constant phase. The weight factor C_j includes the sum of the amplitudes of all equivalent packets j and is defined as the product of the effective mass of the fundamental frequency, m_j, and the number of equivalent non-identical orbits which contribute to j. In the present calculation we neglect the influence of impurity scattering and therefore choose the Dingle scattering factor M to be equal to unity. The influence of magnetic breakdown is taken into account by the factor R_j which is defined as

$$R_j=(ip)^{n_{1j}}\,q^{n_{2j}} \tag{3.11}$$

where n_{1j} is the number of junctions where the broken down path is followed and n_{2j} is the number of junctions where the Bragg-reflected path is followed. Although there is some arbitrariness in the choice of phases [2, 5, 12] for the breakdown probability amplitudes, we follow Falicov and Stachowiak and use Pippard's[5] phase choice:

$$\arg(p)=\frac{\pi}{2},\quad \arg(q)=0. \tag{3.12}$$

The breakdown probability function p can be calculated from Upadhyaya's result and, for the present model, is given by $p^2=\exp(-\pi\gamma^2/2\beta\sqrt{\epsilon})$. The reflection probability function q is defined by $q=(1-|p|^2)^{1/2}$. Finally, the t_j which appears in the argument of the δ-function is given by $t_j=m_jt_1$, where m_j is the effective mass of the jth orbit and $t_1=2\pi m^*c/eH$ is the cyclotron period corresponding to the elliptical orbits.

The field-dependent density of states $\rho(E,H)$ can now be obtained by taking the Fourier transform of $G_z(\mathbf{r}_0,\mathbf{r}_0,t)$ with respect to $\mathbf{r}_0$ and time, and integrating the resulting expression over all values of k_z. The resulting density of states is then used to calculate the free energy using (3.1).

On the basis of the above considerations, Falicov and Stachowiak obtain the following expression for the oscillatory part of the free energy[9]

$$F_{osc}=\pi^{-2}L^3m\sum_j C_jS^{1/2}m_j^{-5/2}t_1^{-2}(ip)^{n_{1j}}q^{n_{2j}}$$

$$\times\frac{X_j}{\sinh(X_j)}\cos\left[a_j(0)/\beta-\varphi_{j0}-\pi/4\right], \quad (3.13)$$

where $S=eH/\hbar c$ and $X_j=2\pi^2k_BTm_j/\hbar\omega_c$. The cyclotron frequency ω_c is given by eH/m^*c, where m^* is the effective mass corresponding to the elliptical orbits for the present model. The expression for the oscillatory free energy (3.13) is equal to the result (equation (3.15)) in reference [9] divided by 2. The extra factor of 2 in reference [9] appears to be due to an error in including the spin degeneracy twice in the calculation of the free energy.

The summation in (3.13) was evaluated numerically to an accuracy of one part in 10^3. For the present calculation the summation included roughly 10 harmonics. The magnetic susceptibility obtained by the method of Falicov and Stachowiak, using the same parameters as in the exact calculation in the preceding section, is shown in Fig. 5. The susceptibility scale is in the same dimensionless units which were used in the exact calculation. The periodicities in the susceptibility in the low field region are related to the approximate electron orbits indicated by the dotted lines in Fig. 2(A), i.e. orbits obtained by neglecting the influence of the energy gap. For high fields the period which is observed corresponds to the identical broken-down elliptical orbits. The transition region is determined by the choice of the breakdown field, $\beta_0^{-1}=4{\cdot}0$ for the present case, in the expression for the breakdown probability. The breakdown field was calculated from Upadhyaya's[7] result which is well suited to our model.

The behavior of the susceptibility obtained by the method of Falicov and Stachowiak is generally in good agreement with the exact

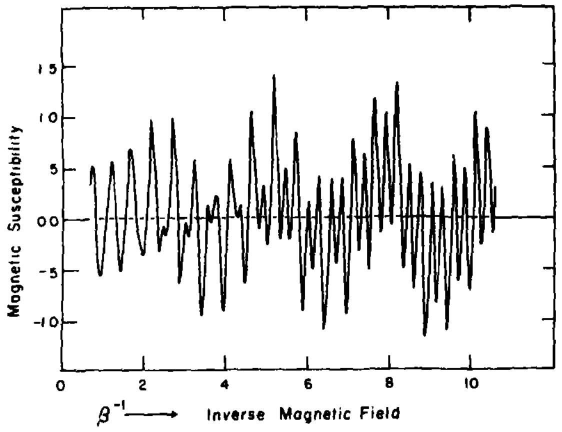

Fig. 5 Magnetic susceptibility calculated by the method of Falicov and Stachowiak for dimensionless energy gap $\gamma=0{\cdot}4$, dimensionless energy $\epsilon=1{\cdot}0$, and a dimensionless temperature $\tau=0{\cdot}005$. The susceptibility is plotted against dimensionless magnetic field. The vertical scale is in the same dimensionless units which were used for the exact results (Fig. 3).

results. Although there are discrepancies in the structure of various peaks, the overall amplitude of the oscillations is in accord with the exact results. In the region of high magnetic fields the semiclassical result displays the correct periods corresponding to the areas of the elliptical orbits and, in addition, the amplitudes of the oscillations are in agreement with the exact results in this limit. The structure of the semiclassical susceptibility in the transition region, ($\beta^{-1} \approx 4{\cdot}0$) differs in detail from the exact results, but exhibits a similar transition from the high field periodicity ($\delta\beta^{-1} = 0{\cdot}5$ for complete breakdown) to the periodicities determined by the areas of the low field orbits.

Aside from differences in details of structure, the major discrepancies in the susceptibility appear in the low field limit. In this region the amplitude and period of the oscillations due to the large dumbbell-shaped orbit compare favorably with the exact case. However, the period associated with the small orbit is overestimated, by 30 per cent for the choice of energy and energy gaps used in the present calculation, due to neglecting the effect of the energy gap on the geometry of the orbit. Also, the amplitude of the small orbit oscillations is larger than the exact value due, in part, to the influence of the energy gap on the effective masses. It is interesting to note that although the effect of the energy gap on the small orbit area is large, the influence of the energy gap on the effective mass is considerably smaller; the effective mass of the small orbit is changed by 5 per cent for the present choice of energy and energy gap. The oscillation amplitudes and their magnetic-field dependence are considered in detail in the following section.

(*C*) *Field-dependence of* dHvA *amplitudes*

The magnetic-field dependence of the amplitudes of the susceptibility oscillations is of considerable interest in regard to the de Haas-van Alphen effect in the presence of magnetic breakdown. In order to study this dependence for the exact calculation, we treat the susceptibility as experimental data and Fourier analyze finite sections of the susceptibility. The present calculation is greatly simplified by the fact that the frequencies of the various oscillatory components are known a priori. Thus we use the method of least squares to fit the exact susceptibility data to a function of the form

$$f(\beta) = \sum_{i} \{A_i \cos(\omega_i/\beta) + B_i \sin(\omega_i/\beta)\} \tag{3.14}$$

where the ω_i are constant dimensionless areas of the various orbits shown in Fig. 2, and β is the dimensionless magnetic field. Fourier analyzing consecutive inverse field intervals in this manner enables us to determine approximate values of the amplitudes $([A_i^2 + B_i^2])^{1/2}$, corresponding to the frequencies ω_i, as a function of inverse magnetic field. The results of this calculation, which was carried out including nine areas ω_i, are exhibited in Fig. 6. The solid lines are the amplitudes of oscillations in the exact susceptibility corresponding to the three basic orbits for the

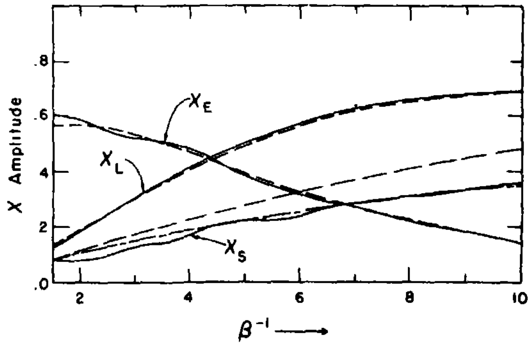

Fig. 6. Magnetic-field dependence of amplitudes of fundamental oscillations in the susceptibility. Solid lines indicate amplitudes obtained from the exact calculation of the susceptibility. Amplitudes predicted by the method of Falicov and Stachowiak are represented by the dotted lines: their result using the correct effective-masses and areas is indicated by the dot-dash line. Amplitudes corresponding to the large dumbbell-shaped orbit, the small orbit, and the elliptical orbits are designated by χ_L, χ_S and χ_E respectively.

model. Harmonic frequencies have a reasonably large influence on the oscillation amplitudes for the value of the temperature considered here and, together with the effects due to analyzing finite sections of the susceptibility, cause some of the small fluctuations of the amplitudes.

Falicov and Stachowiak's method provides a straightforward method for calculating the magnetic-field dependence of amplitudes of various oscillatory components. We differentiate the oscillatory free energy (3.13) with respect to the magnetic field and obtain the following analytic expression for the amplitude A_j of oscillations corresponding to the jth basic orbit

$$\begin{aligned} A_j = {} & C_j m_j^{-3/2} k_B T (e/\hbar c)^{3/2} \\ & \times [H^{1/2}]/[2\pi^2 \sinh (X_j)] \\ & \left\{\left[H^{-1}(1{\cdot}5 + X_j \coth (X_j))(ip)^{n_U} q^{n_D} \right.\right. \\ & \left. + \frac{\partial}{\partial H}(ip)^{n_U} q^{n_D}\right]^2 + \frac{a_j^2}{H^4}\frac{\hbar^2 C^2 D^2}{64 e^2 A^3 B} \\ & \left. \times (ip)^{2n_U} q^{2n_D}\right\}^{1/2} \qquad (3.15) \end{aligned}$$

where the various terms are the same as those defined in the previous section.

The Falicov and Stachowiak amplitudes (3.15) of oscillations corresponding to the basic orbits are indicated by the dotted lines in Fig. 6. It is apparent that their semiclassical method yields amplitudes which are in good agreement with the exact results for the large dumbbell-shaped orbit and the elliptical orbits. In the case of the small orbit, however, the semiclassical treatment predicts a substantially larger amplitude, especially in the low-field region. This discrepancy is primarily due to neglecting the effects of the energy gap on the geometry of the orbits. Much better agreement with the exact results is obtained when the correct values for the effective mass *and* the orbit area, i.e. including the distortion due to the energy gap, are substituted in the expression for the dHvA amplitudes in equation (3.15). The result is illustrated by the dot-dash line in Fig. 6. The agreement is especially good in the low-field region, even though the oscillations due to the small orbit are associated with energy levels of small quantum numbers ($l = 2$ for $\beta^{-1} \approx 9$).

The Falicov and Stachowiak theory predicts a somewhat larger amplitude for the small orbit oscillations in the high-field region. In this quantum limit the choice of phases for the breakdown probability functions p and q, and the consequent shift of the zero-point energy, should have an appreciable effect on the oscillation amplitude. Although the Falicov and Stachowiak amplitudes are independent of the probability amplitude phase choice, the effect of the phases on the dHvA amplitudes calculated in the semiclassical network approximation can be studied independently by Fourier analyzing the inverse magnetic field spectrum obtained by Pippard's method[5]. The above calculation was carried out in reference [12] and yields a lower Fourier amplitude for the exact β^{-1} eigenvalue spectrum than for the case of the semiclassical spectra calculated using three different phase choices. The latter conclusions are consistent with the highfield results shown in Fig. 6.

Amplitudes of the basic oscillations were also obtained by both of the exact calculation and Falicov and Stachowiak's method for the same energy and energy gap used in the above calculation, but with a dimensionless temperature $\tau = 0{\cdot}01$. The agreement between the results obtained by the two methods is in accord with the case considered above. In addition, the Falicov and Stachowiak theory predicts the correct temperature dependence of the de Hass–van Alphen amplitudes.

4. ZERO-FIELD SUSCEPTIBILITY

We now calculate the zero-field magnetic susceptibility for the present model using the result derived by Wannier and Upadhyaya[13]. Their result is equivalent with that of Hebborn and Sondheimer[18] and others[19–22]. The present calculation provides an independent check on the value of the steady susceptibility obtained from the high-temperature results of Section 3. In addition, the behavior of the susceptibility is investigated for various values of the Fermi energy and energy gap, and a comparison is made of the relative magnitudes of the contributions to the zero-field susceptibility.

The calculation of the steady susceptibility is carried out in two steps:

(a) Transforming the model Hamiltonian in the absence of a magnetic field to diagonal form by means of a unitary transformation.

(b) Evaluating matrix elements which appear in Wannier and Upadhyaya's result using the transformed wave functions, which are now in the Bloch representation, and subsequently calculating the zero-field diamagnetism for the model.

To diagonalize the Hamiltonian (2.1) with $S = 0$ we seek a unitary transformation $T(\mathbf{k})$ such that

$$\hat{\mathscr{H}} = T(\mathbf{k})\mathscr{H}T(\mathbf{k})^{-1} \qquad (4.1)$$

where $\hat{\mathscr{H}}$ is in the diagonal form

$$\hat{\mathscr{H}} = \begin{pmatrix} Ak_x^2+(D^2k_x^2+\Delta^2)^{1/2}+Bk_y^2+Rk_z^2 & 0 \\ 0 & Ak_x^2-(D^2k_x^2+\Delta^2)^{1/2}+Bk_y^2+Rk_z^2 \end{pmatrix} \qquad (4.2)$$

It is readily shown that the transformation $T(\mathbf{k})$ is given by

$$T(\mathbf{k}) = \begin{pmatrix} \dfrac{1}{N} & \dfrac{\alpha}{N} \\ -\dfrac{\alpha}{N} & \dfrac{1}{N} \end{pmatrix} \qquad (4.3)$$

where

$$\alpha = [(D^2k_x^2+\Delta^2)^{1/2}-\Delta]/Dk_x \qquad (4.4)$$

and $N = (1+\alpha^2)^{1/2}$. The Hamiltonian (4.2) is written in the Bloch representation with wave functions $\Psi_{n\mathbf{k}}(\mathbf{r}) = u_{n\mathbf{k}}(\mathbf{r})e^{i\mathbf{k}\cdot\mathbf{r}}$. The periodic parts of the Bloch functions are related to the "$\mathbf{k}\cdot\mathbf{p}$" functions

$$\chi_{n\mathbf{k}}(\mathbf{r}) = u_{n0}(\mathbf{r})e^{i\mathbf{k}\cdot\mathbf{r}} \qquad (4.5)$$

by the transformation

$$u_{n\mathbf{k}}(\mathbf{r}) = \sum_m T_{nm}(\mathbf{k})u_{m0}(\mathbf{r}). \qquad (4.6)$$

We are now able to calculate the matrix elements between Bloch functions which appear in Wannier and Upadhyaya's result for the susceptibility. In particular, we need to evaluate the Adams operators[23, 24] X_{qs} and Y_{qs} which are defined by

$$X_{qs} = i\int u^*_{q\mathbf{k}}(\mathbf{r})\frac{\partial u_{s\mathbf{k}}(\mathbf{r})}{\partial k_x}\,\mathrm{d}\tau \qquad (4.7)$$

and

$$Y_{qs} = i\int u^*_{q\mathbf{k}}(\mathbf{r})\frac{\partial u_{s\mathbf{k}}(\mathbf{r})}{\partial k_y}\,\mathrm{d}\tau \qquad (4.8)$$

where the integration is over the unit cell. The $\mathbf{k}\cdot\mathbf{p}$ functions $u_{n0}(\mathbf{r})$ are independent of $\mathbf{k}$ and hence the $\mathbf{k}$-dependence of the functions $u_{n\mathbf{k}}(\mathbf{r})$ is entirely in the transformation $T(\mathbf{k})$. Substituting the functions (4.6) into the definition (4.8) of the Adams operator Y_{qs} and noting that $T(\mathbf{k})$ is a function of k_x only, it follows that $Y_{qs} = 0$. In order to calculate the operator X_{qs} we have to take the k-dependence of $T(\mathbf{k})$ into account explicitly. We consider first the diagonal elements X_{qq}. Substituting the $u_{n\mathbf{k}}(\mathbf{r})$ into equation (4.7), performing the integration over $\mathbf{r}$, and using the orthonormality of the $u_{n0}(\mathbf{r})$ functions, we obtain

$$X_{11} = i\left\{T_{11}\frac{\partial T_{11}}{\partial k_x}+T_{12}\frac{\partial T_{12}}{\partial k_x}\right\} \qquad (4.9)$$

and, substituting the matrix elements from equation (4.3),

$$X_{11} = i\left\{\frac{1}{N}\frac{\partial}{\partial k_x}\left(\frac{1}{N}\right)+\frac{\alpha}{N}\frac{\partial}{\partial k_x}\left(\frac{\alpha}{N}\right)\right\} = 0. \qquad (4.10)$$

Similarly, it is easy to show that $X_{22} = 0$.

In calculating the off-diagonal elements of the Adams operator X_{qs} we make use of the same procedure which was employed above. Thus,

$$X_{12} = i\left\{T_{11}\frac{\partial T_{21}}{\partial k_x} + T_{12}\frac{\partial T_{22}}{\partial k_x}\right\} \quad (4.11)$$

becomes, using the elements of $T(\mathbf{k})$ from (4.3),

$$X_{12} = X_{21}^{*} = \frac{-i}{N^2}\frac{\partial \alpha}{\partial k_x} \quad (4.12)$$

where α is defined in equation (4.4). We now have the necessary matrix elements to compute the steady diamagnetism from Wannier and Upadhyaya's result.

The total steady susceptibility for the model is the sum of the contributions from each of the two energy bands. Wannier and Upadhyaya[13] find the zero-field susceptibility of a single Bloch band to be, in the form of an integral over the first Brillouin zone,

$$\begin{aligned}\chi_q = -\frac{1}{2\pi^3}\int \mathrm{d}\mathbf{k}\Bigg\{&\frac{-e^2}{24\hbar^2c^2}\left[\frac{\partial^2 W_q^{(0)}}{\partial k_x^2}\frac{\partial^2 W_q^{(0)}}{\partial k_y^2} - \left(\frac{\partial^2 W_q^{(0)}}{\partial k_x \partial k_y}\right)^2\right]\frac{\mathrm{d}f(W_q^{(0)}-\mu)}{\mathrm{d}W_q^{(0)}}\\ &+ \tfrac{1}{2}(W_q^{(1)}(\mathbf{k}))^2\frac{\mathrm{d}f(W_q^{(0)}-\mu)}{\mathrm{d}W_q^{(0)}}\\ &+ W_q^{(2)}(\mathbf{k})f(W_q^{(0)}-\mu)\Bigg\}\end{aligned} \quad (4.13)$$

where the functions used here will be defined in turn. The function f is the Fermi–Dirac distribution function, μ is the Fermi energy, and $W_q^{(0)}$ is either of the field-free energy band functions defined in equation (4.2). The energy functions $W_q^{(1)}$ and $W_q^{(2)}$ are defined in terms of the zero-field bands in reference [13], and will be calculated below. We consider each of the terms in (4.13) separately and retain only those contributions which are non-vanishing for the present model.

Before proceeding with the calculation of the susceptibility, it is worthwhile to examine the physical origin of the terms in equation (4.13). The first term is known as the Landau–Peierls term and arises due to the breakup of the band continuum into discrete states. It is the only term present if the electrons are free or, for the present case, if the electrons follow the completely broken down elliptical trajectories.

The second term in (4.13) is a paramagnetic contribution. Due to the fact that the diagonal Adams operators X_{qq} are zero and all the Y_{qs} vanish for the present model, $W_q^{(1)} = 0$; and consequently there is no paramagnetic contribution to the susceptibility for the case considered here.

The last and most complex term in equation (4.13) is due to the induced magnetic moment. This term contains the contribution of the atomic diamagnetism and other terms whose origin is not clearly understood. The contribution of the atomic diamagnetism is zero for the present case due to the fact that the model Hamiltonian does not contain terms in $\mathbf{k}$ higher than second order.

At this point it is convenient to recall the form of the field-free energy band functions for the present model. From equation (4.2) we have

$$W_{\pm}^{(0)} = Ak_x^2 \pm (D^2k_x^2 + \Delta^2)^{1/2} + Bk_y^2 + Rk_z^2. \quad (4.14)$$

In terms of these $W_q^{(0)}$ the part of $W_q^{(2)}$ which is non-zero for the present model is given by[13]

$$W_q^{(2)} = \sum_{s\neq q}\frac{-1}{W_s^{(0)} - W_q^{(0)}}\left|\left\langle s\left|\frac{\partial W_q^{(0)}}{\partial k_y}X\right|q\right\rangle\right|^2 + \tfrac{1}{2}\frac{\partial^2 W_q^{(0)}}{\partial k_y^2}\langle q|X^2|q\rangle. \quad (4.15)$$

Also, from the form of $W_{\pm}^{(0)}$, we see that the cross derivatives $\partial^2 W/\partial k_x \partial k_y$ vanish. Thus we are left with a tractable expression for the steady susceptibility for a single band

$$\chi_q = \frac{-1}{2\pi^3}\int \mathrm{d}\mathbf{k}\left\{\frac{-e^2B}{12\hbar^2c^2}\frac{\mathrm{d}f(W_q^{(0)}-\mu)}{\mathrm{d}W_q^{(0)}}\frac{\partial^2 W_q^{(0)}}{\partial k_x^2} + W_q^{(2)}(\mathbf{k})f(W_q^{(0)}-\mu)\right\} \quad (4.16)$$

where $W_q^{(2)}$ is defined in equation (4.15). Since the temperature dependence of the steady diamagnetism is expected to be small, we pass to the limit of zero temperature and replace the derivative of the Fermi function by a Dirac δ-function. The first term, hereafter referred to as $\chi_{LP}(\pm)$ may then be written in the form

$$\chi_{LP}(\pm)=\frac{-e^2B}{24\pi^3\hbar^2c^2}\int \mathrm{d}\mathbf{k}\left\{2A\pm\frac{D^2}{\omega}\mp\frac{D^4k_x^2}{\omega}\right\}$$
$$\times\,\delta[Ak_x^2\pm\omega+Bk_y^2+Rk_z^2] \qquad (4.17)$$

where $\omega=(D^2k_x^2+\Delta^2)^{1/2}$.

The integral may be conveniently evaluated using cylinhrical coordinates as follows

$$k_x\surd A=z \qquad (4.18a)$$
$$k_y\surd B=\rho\cos\theta \qquad (4.18b)$$
$$k_z\surd C=\rho\sin\theta. \qquad (4.18c)$$

Performing the trivial integration over θ we obtain

$$\chi_{LP}(\pm)=\frac{-e^2BA}{24\pi^2\hbar^2c^2}\int_{-\infty}^{\infty}\mathrm{d}z\,\frac{\partial^2W_\pm^{(0)}}{\partial z^2}$$
$$\times\int_0^{\infty}\delta(z^2\pm\omega+\rho^2-\mu)\,\mathrm{d}(\rho^2). \qquad (4.19)$$

Utilizing the properties of the δ-function and noting that $\partial^2W_\pm^{(0)}/\partial z^2$ is a function of z only, the Landau–Peierls term becomes

$$\chi_{LP}(\pm)=\frac{-\Gamma A^{1/2}}{16D}\frac{\partial W_\pm^{(0)}}{\partial z}\Bigg|_{-z_0}^{z_0} \qquad (4.20)$$

where z_0 is determined by the condition

$$\mu=z_0^2\pm\left(\frac{D^2z_0^2}{A}+\Delta^2\right)^{1/2} \qquad (4.21)$$

and Γ is defined by $\Gamma=2e^2DB^{1/2}/3\pi^2\hbar^2c^2\surd R$. Transforming to the dimensionless variable $\hat{z}=2A^{1/2}z/D$, and evaluating the derivative of the energy band function which appears in equation (4.20), we obtain the following result for the Landau–Peierls term:

$$\chi_{LP}(\pm)=\frac{-\Gamma\hat{z}}{8}\{1\pm(\hat{z}^2+\gamma^2/4)^{-1/2}\}\Bigg|_{\eta_1(\pm)}^{\eta_2(\pm)} \qquad (4.22)$$

where the upper band limiting values of $\hat{z}$ are

$$\eta_2(+)=[\epsilon-2-2(\epsilon+1+\gamma^2/4)^{1/2}]^{1/2} \qquad (4.23a)$$
$$\eta_1(+)=0 \qquad (4.23b)$$

for $\gamma\leqslant\epsilon$ and, in the case of the lower band,

$$\eta_2(-)=[\epsilon+2+2(\epsilon+1+\gamma^2/4)^{1/2}]^{1/2} \qquad (4.24a)$$

for all values of ϵ while

$$\eta_1(-)=0,\quad -\gamma\leqslant\epsilon \qquad (4.24b)$$

or

$$\eta_1(-)=[\epsilon+2-2(\epsilon+1+\gamma^2/4)^{1/2}]^{1/2},\quad -\gamma>\epsilon \qquad (4.24c)$$

where we recall that γ is the dimensionless energy gap and ϵ is the dimensionless Fermi energy defined in Section 2.

Turning now to the induced magnetism term

$$\chi^{(2)}(\pm)=-\frac{1}{2\pi^3}\int \mathrm{d}\mathbf{k}\,W_\pm^{(2)}(\mathbf{k})f(W_\pm^{(0)}-\mu) \qquad (4.25)$$

we substitute the Adams operators from equation (4.12) into the definition of $W_\pm^{(2)}$ in equation (4.15) to obtain, again in dimensionless units,

$$\chi^{(2)}(\pm)=\frac{-3\Gamma}{8\pi}\int_{-\infty}^{\infty}\mathrm{d}z\frac{1}{N^4}\left(\frac{\partial\alpha}{\partial\hat{z}}\right)^2\int_0^{\pi}\mathrm{d}\theta$$
$$\times\int_0^{\infty}\mathrm{d}\left(\frac{\hat{\rho}}{2}\right)^2\left\{1\pm\frac{\hat{\rho}^2\cos^2\theta}{\sigma}\right\}f(W_\pm^{(0)}-\mu) \qquad (4.26)$$

where $\sigma\equiv(\hat{z}^2+\gamma^2/4)^{1/2}$ and $\hat{\rho}^2=4A\rho^2/D^2$. The integration over θ and $\hat{\rho}^2$ can be done in a straightforward manner by noting that $f(W_\pm^{(0)}-\mu)$ is a Heaviside step function in the limit of zero temperature. The result is

$$\chi^{(2)}(\pm) = \frac{-3\Gamma}{8}\int_{\eta_1(\pm)}^{\eta_2(\pm)} \mathrm{d}\hat{z}\,\frac{1}{N^4}\left(\frac{\partial\alpha}{\partial z}\right)^2 \hat{\rho}_0{}^2(\pm) \times\left[1 \pm \frac{\hat{\rho}_0{}^2(\pm)}{4\sigma}\right] \tag{4.27}$$

where η_1 and η_2 are defined in equations (4.23–4.24), and $\hat{\rho}_0{}^2(\pm)$ is given by

$$\hat{\rho}_0{}^2(\pm) = \epsilon - \hat{z}^2 \mp 2(\hat{z}^2 + \gamma^2/4)^{1/2}. \tag{4.28}$$

Finally, the remaining integration over z can be carried out by using the definitions of α and N from equation (4.4). The result is conveniently expressed as the sum of two terms

$$\chi^{(2)}(\pm) = A_1(\pm) + A_2(\pm) \tag{4.29}$$

where, defining $\lambda = \gamma/2$ for convenience,

$$A_1(\pm) = \frac{-3\Gamma}{16}\left\{\frac{(\epsilon-\lambda^2)\hat{z}}{2\sigma^2} + \frac{(\epsilon-\lambda^2)}{2\lambda} \times \tan^{-1}\left(\frac{\hat{z}}{\lambda}\right) \pm \frac{2\hat{z}}{\sigma}\right\}\Bigg|_{\eta_1(\pm)}^{\eta_2(\pm)} \tag{4.30}$$

and

$$A_2(\pm) = \frac{\pm 3\Gamma}{64}\left\{-\hat{z}(4-\lambda^2+\epsilon^2/\lambda^2) - \lambda^2\log(\hat{z}+\sigma) + \hat{z}^3(\lambda^2+2\epsilon+\epsilon^2/\lambda^2) \pm 2\hat{z}(\epsilon+\lambda^2)/\sigma^2 \pm \frac{2(\epsilon-\lambda^2)}{\lambda}\tan^{-1}\left(\frac{\hat{z}}{\lambda}\right)\right\}\Bigg|_{\eta_1(\pm)}^{\eta_2(\pm)} \tag{4.31}$$

The results for the zero-field susceptibility obtained by the above method are exhibited in Fig. 7. The total steady susceptibility given by equations (4.30) and (4.31) is indicated by the solid line. For the case of completely broken down elliptical orbits the only contribution to the constant diamagnetism is due to the Landau-Peierls terms χ_{LP}. The resulting susceptibility for this limiting case is indicated by the dashed line in Fig. 7. The two dotted lines represent the individual Landau-Peierls contributions for the small orbit and the large dumbbell-shaped orbit.

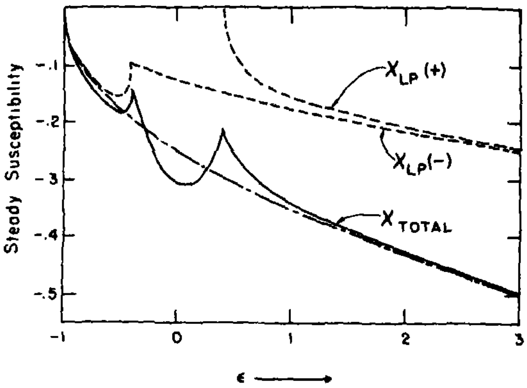

Fig. 7. The zero-field susceptibility obtained using the result derived by Wannier and Upadhyaya plotted as a function of the Fermi energy for a dimensionless energy gap $\gamma = 0{\cdot}4$. The total steady susceptibility is indicated by the solid line. The dashed line corresponds to the steady susceptibility for the limiting case $\tau = 0$. The two dotted lines are the Landau-Peierls contributions from the individual bands.

The present calculation yields a steady diamagnetism $\chi_0 = -0{\cdot}34$ for the choice of energy $\epsilon = 1{\cdot}0$ and energy gap $\gamma = 0{\cdot}4$, which is in agreement with the result of the high-temperature calculation of Section 3(*A*) ($\chi_0 = -0{\cdot}35$) within the accuracy of the latter calculation.

In the limit of large Fermi energies the total steady susceptibility is approximately equal to the sum of the individual Landau-Peierls contribution as shown in Fig. 7. For these energies the distortion of the orbits due to the energy gap is diminished and the induced magnetism terms $\chi^{(2)}(\pm)$ become quite large (~ 10 for $\epsilon = 4{\cdot}0$). However, the $\chi^{(2)}(\pm)$ contributions from the two bands are opposite in sign and cancel in the limit that γ/ϵ becomes very small.

As we decrease the Fermi energy the small orbit decreases in size and, in the limit $\epsilon = 0{\cdot}4$, vanishes. The character of the orbits as a function of the energy can be observed from the energy vs. k curves in Fig. 1. Thus, as we approach this limit the Landau-Peierls and the $\chi^{(2)}(+)$ contributions from the small orbit become small and are identically zero for $\epsilon = 0\cdot4$. By decreasing the energy further, we can study the relative magnitudes of the terms in the susceptibility due to the large orbit and, for energies less than $\epsilon = -0\cdot4$, observe the effects on the diamagnetism as the dumbbell-shaped orbit is truncated into two non-intersecting orbits. In the absence of $\chi^{(2)}(-)$ the total steady susceptibility in the region $\epsilon > 0\cdot4$ would be given by the Landau–Peierls term (dotted line). Thus, it is apparent from Fig. 7 that in this region of energy the contribution from the induced diamagnetism $\chi^{(2)}(-)$ is of the same order of magnitude as the Landau–Peierls term. The latter result is consistent with the work of Adams[23].

It is interesting to note that the cusps in the susceptibility near singular points in the Fermi surface, i.e. $\epsilon = \pm 0\cdot4$, are sharply accentuated. In the vicinity of $\epsilon = -0\cdot4$ the peak in the diamagnetism is strongly enhanced by the Landau-Peierls term due to the discontinuous change in the Fermi surface topology, while in the case of $\epsilon \approx 0\cdot4$ the $\chi^{(2)}(-)$ term accentuates the cusp in the steady susceptibility.

5. SUMMARY AND CONCLUSIONS

The effects of magnetic breakdown on the diamagnetic susceptibility have been investigated for a model Hamiltonian which yields exact solutions. It was demonstrated that the periodicities in the suceptbility are related to the semiclassical electron orbits corresponding to the model and that the oscillatory behavior is compatible with the breakdown field derived from Upadhyaya's[7] result. The steady susceptibility obtained from a high-temperature calculation of the rigorous susceptibility was found to be relatively insensitive to magnetic breakdown effects.

An approximate calculation of the oscillatory susceptibility for the model was also carried out using the semiclassical method of Falicov and Stachowiak. Their theory yields results which are in good agreement with the exact case for both the large dumbbell shaped orbit and the broken down elliptical orbits. Although the semiclassical theory predicts a large amplitude for the oscillations due to the small orbit, most of the discrepancies can be removed by using the correct effective masses *and* the correct areas in the Falicov and Stachowiak expression for the susceptibility. Thus, with the above modifications, their theory may be applied to situations where the distortion of the Fermi surface topology due to the energy gap is not negligible.

An independent calculation of the zero-field susceptibility was carried out using the result derived by Wannier and Upadhyaya. The results were compatible with the high-temperature calculation of the total susceptibility and, in addition, exhibited anomalous peaks in the steady susceptibility near singular points of the Fermi surface. In the case of two nearly degenerate bands separated by very small energy gaps, i.e. a case favorable for magnetic breakdown to occur, the contributions to the steady diamagnetism from each band were quite large but opposite in sign. This cancellation suggests that for the case considered here the total steady susceptibility is largely unaffected by magnetic breakdown. However, by decreasing the Fermi energy and passing to the case where only one band contributes to the Fermi surface, the steady susceptibility displays a marked cusp which is accentuated by the induced magnetism contributions. The latter effect can be observed experimentally in cases where alloying or high pressures distort the Fermi surface topology in the manner described above[25].

There is no system known to the author which is as simple as the present model and which can be investigated experimentally. The model is actually a fair approximation to the case of graphite when the magnetic field is perpendicular to the c-axis[26]. However, the breakdown field for graphite is much too small for one to be able to observe

Table 1. *Experimental values of* g *in tetrahedral* Fe^{3+} *complexes*

X	ζ_L (cm^{-1})	h	Δg	$(\Delta g/\zeta_L h).10^5$	Reference*
O	140	1·2	0·004	2·4	*a*
S	384	2·7	0·016	1·6	*b*
Cl	590	2·0	0·017	1·45	*c, d*
Se	1650	3·0	0·044	0·88	*e, f*
Br	2500	2·3	0·052	0·9	*c*
Te	4200	(3·3)	0·095	0·7	*g*

*a: WALSH W. M., Jr. and RUPP L. W., Jr., *Phys. Rev.* **126**, 952 (1962).
b: RAUBER A., SCHNEIDER J. and MOTOSSI F., *Z. Naturf.* **17a**, 654 (1962).
c: This work
d: SWANSON T. and LAURIE V., *J. phys. Chem.* **69**, 244 (1965).
e: HOSHINA T., *J. phys. Soc. Japan* **22**, 1049 (1967).
f: ESTLE T. L. and HOLTON W. C., *Phys. Rev.* **150**, 159 (1966).
g: HANSEL J. C., *Bull. Am. phys. Soc.* **9**, 244 (1964).

plex, B_0 its free-ion value, and k_c a numerical constant characteristic of the metal ion. It is easy to see that there exists a very close, almost linear relation between $\Delta g = g - 2{\cdot}0023$ and $\zeta_L h_L$. This correlation enables us to propose as a working hypothesis, that the g-shift in these compounds can be essentially adscribed to the combined effects of covalency and LSO coupling. The correlation is displayed in Fig. 1.

As we shall show on the example $[Cl_4Fe]^-$, an effective detailed calculation bears out the essential validity of the hypothesis.

3. SPIN-ORBIT COUPLING

Consider a Fe(III) ion tetrahedrally surrounded by four ligands, X. We shall not consider zero-field splitting; in the case $X = Cl$ the resonance signal is perfectly symmetrical indicating negligible zero-field splitting, and furthermore, crystallographic studies indicate tetrahedral coordination in the complex[21]. We choose central and ligand ('local') coordinate systems as shown in Fig. 2.

The spin-orbit coupling operator can be written as[5]:

$$H_{SO} = \sum_i \sum_\alpha \zeta_\alpha(r_{i\alpha})\mathbf{l}_\alpha . \mathbf{s}_i \qquad (3.1)$$

where $\zeta_\alpha(r_{i\alpha})$ is the spin-orbit coupling function of electron i on nucleus α, $\mathbf{l}_\alpha$ is the angular momentum of electron i relative to nucleus α, s_i the i-electron spin, α runs over all atoms and i over all electrons in the complex.

The wavefunctions describing the electronic motion will be antisymmetrized products of molecular orbitals, which we take to

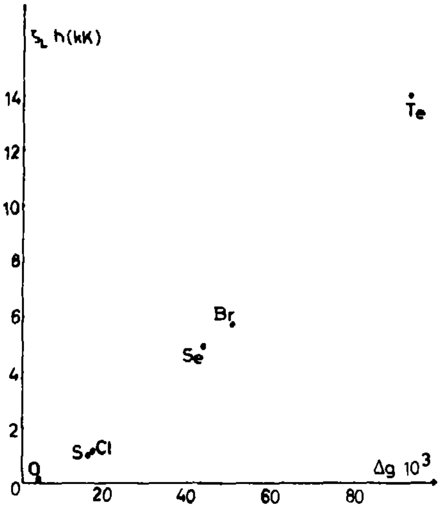

Fig. 1. Empirical correlation between g-shift, covalency and LSO coupling.

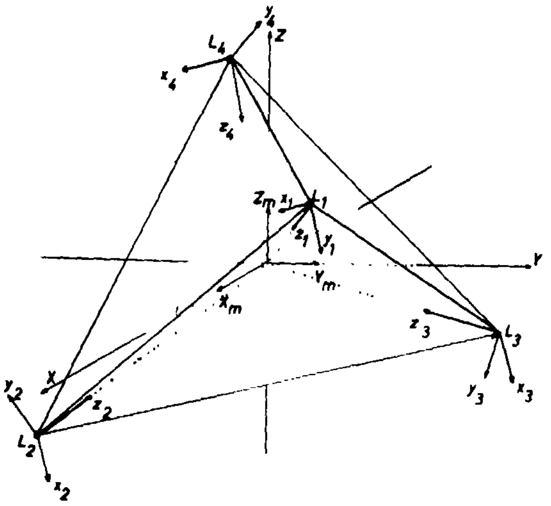

Fig. 2. Geometry and choice of central (subscript M) and ligand (subscript 1, 2, 3, 4) coordinate systems.

be linear combinations of atomic orbitals. Since H_{SO} is a one-electron operator, its matrix elements with such wavefunctions will reduce to one-electron matrix elements. We shall further make the usual approximation, that when calculating matrix elements of (3.1) with MO-LCAO functions only one center terms must be considered, that is

$$\langle \sum_{\alpha} c_{\alpha}^{*}\alpha | \sum_{\alpha'} H_{\text{SO}}(\alpha') | \sum_{\alpha''} c'_{\alpha''}\alpha'' \rangle = \sum_{\alpha} c_{\alpha}^{*}c'_{\alpha}\langle \alpha | H_{\text{SO}} | \alpha \rangle. \quad (3.2)$$

This is justified by the strong radial dependence of $\zeta_{\alpha}(r_{\alpha})$, which makes two or three center terms completely negligible[9].

If all ligands are equal, equation (3.1) can be written (for one electron)

$$H_{\text{SO}} = \zeta_c(r_c)\mathbf{l}.\mathbf{s} + \zeta_L(r_L)\boldsymbol{\Omega}.\mathbf{s} = \boldsymbol{\tau}_i.\mathbf{s}_i \quad (3.3)$$

where

$$\boldsymbol{\Omega} = \sum_{LJj_l} \cos(j,j_L)\mathbf{l}_{jL}.\boldsymbol{\epsilon}_i \quad (3.4)$$

and

$$\boldsymbol{\tau}_i = \zeta_{ci}(r_{ci})\mathbf{l}_i + \zeta_L(r_{Li})\boldsymbol{\Omega}_i. \quad (3.5)$$

$\mathbf{l}_{jL}$ is the j_L-th (x_L, y_L, z_L) component of $\mathbf{l}_L$ in the 'local' system of atom L, (j, j_L) is the angle between the 'local' axis j_L and the central axis j, $\boldsymbol{\epsilon}_j$ is a unit vector in the direction j and i refers to the i-th electron.

With our definitions and orientations (see Fig. 2) the components of the vector operator $\boldsymbol{\Omega}$ are

$$\begin{aligned}
\Omega_z &= -1/\sqrt{3}(\mathrm{l}_{z1} - \mathrm{l}_{z2} - \mathrm{l}_{z3} + \mathrm{l}_{z4}) \\
&\quad -2/\sqrt{6}(\mathrm{l}_{y1} - \mathrm{l}_{y2} + \mathrm{l}_{y3} - \mathrm{l}_{y4}) \\
\Omega_x &= 1/\sqrt{2}(\mathrm{l}_{x1} + \mathrm{l}_{x2} + \mathrm{l}_{x3} + \mathrm{l}_{x4}) \\
&\quad +1/\sqrt{6}(\mathrm{l}_{y1} + \mathrm{l}_{y2} + \mathrm{l}_{y3} + \mathrm{l}_{y4}) \\
&\quad -1/\sqrt{3}(\mathrm{l}_{z1} + \mathrm{l}_{z2} - \mathrm{l}_{z3} - \mathrm{l}_{z4}) \quad (3.6) \\
\Omega_y &= -1/\sqrt{2}(\mathrm{l}_{x1} - \mathrm{l}_{x2} - \mathrm{l}_{x3} + \mathrm{l}_{x4}) \\
&\quad +1/\sqrt{6}(\mathrm{l}_{y1} - \mathrm{l}_{y2} - \mathrm{l}_{y3} + \mathrm{l}_{y4}) \\
&\quad -1/\sqrt{3}(\mathrm{l}_{z1} - \mathrm{l}_{z2} + \mathrm{l}_{z3} - \mathrm{l}_{z4}).
\end{aligned}$$

Table 2 lists the atomic functions and their linear combinations forming bases for the various irreducible representations of the symmetry group T_d. Appendix 1 gives the effect of the operators Ω_i upon the ligand functions.

The molecular orbital functions describing the approximate eigenstates of our system are best classified according to the spatial symmetry group T_d. In order to calculate the effect

Table 2. Central and ligand atomic orbitals forming MO's *in* T_d

Symmetry	Central atom orbitals	Ligand orbitals σ	Ligand orbitals π	Non-ligand orbitals
A_1	s	$A_{1s} = (1/2)(s_1+s_2+s_3+s_4)$ $A_{1z} = (1/2)(z_1+z_2+z_3+z_4)$		
E_u	$d_{x^2-y^2}$		$D_{x^2-y^2} = (1/2)(x_1+x_2-x_3-x_4)$	
E_v	d_{z^2}		$D_{z^2} = -(1/2)(y_1+y_2-y_3-y_4)$	
$T_{2\xi}$	$\begin{cases} p_x \\ d_{yz} \end{cases}$	$s_L{}^{yz} = (1/2)(s_1+s_2-s_3-s_4)$ $D^{\sigma}_{yz} = (1/2)(z_1+z_2-z_3-z_4)$	$D^{\pi}_{yz} = -(\sqrt{3}/4)(x_1+x_2+x_3+x_4)$ $-(1/4)(y_1+y_2+y_3+y_4)$	
$T_{2\eta}$	$\begin{cases} p_y \\ d_{xz} \end{cases}$	$s_L{}^{xz} = (1/2)(s_1-s_2+s_3-s_4)$ $D^{\sigma}_{xz} = (1/2)(z_1-z_2+z_3-z_4)$	$D^{\pi}_{xz} = (\sqrt{3}/4)(x_1-x_2-x_3+x_4)$ $-(1/4)(y_1-y_2-y_3+y_4)$	
$T_{2\zeta}$	$\begin{cases} p_z \\ d_{xy} \end{cases}$	$s_L{}^{xy} = (1/2)(s_1-s_2-s_3+s_1)$ $D^{\sigma}_{xy} = (1/2)(z_1-z_2-z_3+z_4)$	$D^{\pi}_{yz} = (1/2)(y_1-y_2+y_3-y_4)$	
T_{1a}				$a = (1/4)(x_1+x_2+x_3+x_4)$ $-(\sqrt{3}/4)(y_1+y_2+y_3+y_4)$
T_{1c}				$c = (1/4)(x_1-x_2-x_3+x_4)$ $+(\sqrt{3}/4)(y_1-y_2-y_3+y_4)$
T_{1b}				$b = -(1/2)(x_1-x_2+x_3-x_4)$

of spin-orbit coupling between the MO's we should redifine these in terms of the correct zero-order functions, transforming according to the irreducible representations of the spinor group, $T_d \times D_{5/2} = T_d^*$:

$$|\Gamma^*\gamma(\Gamma)\rangle = \sum_{M_\Gamma, M_S, S} \langle \Gamma M_\Gamma S M_s | \Gamma^*\gamma(\Gamma)\rangle \; |\Gamma M_\Gamma S M_S\rangle. \quad (3.7)$$

In this expression, $\Gamma^*\gamma$ is component γ of the irreducible representation Γ^* of T_d^*, reducing to Γ when spin is neglected: $\Gamma^* \subset \Gamma \times D_S$. In this basis the non-zero matrix elements of spin-orbit coupling are

$$\begin{aligned} &\langle \Gamma^*\gamma(\Gamma)| \sum_i \boldsymbol{\tau}_i.\mathbf{s}_i |\Gamma^*\gamma(\Gamma')\rangle \\ &= \sum_{\substack{M_\Gamma, M_S, S \\ M'_\Gamma, M'_S, S'}} \langle \Gamma' M'_\Gamma S' M'_S | \Gamma^*\gamma(\Gamma')\rangle \\ &\times \{\Gamma^*_\gamma(\Gamma)\,|\Gamma M_\Gamma S M_S\rangle \\ &\qquad \times \langle \Gamma M_\Gamma S M_S | \sum_i \boldsymbol{\tau}_i.\mathbf{s}_i |\Gamma' M'_\Gamma S' M'_S\rangle \quad (3.8) \end{aligned}$$

$$\begin{aligned} &\langle \Gamma M_\Gamma S M_S | \sum_i \tau_i.s_i |\Gamma' M'_\Gamma S' M'_S\rangle \\ &= \lambda \langle \Gamma M_\Gamma S M_S | \boldsymbol{\pi}.\boldsymbol{s} |\Gamma' M'_\Gamma S' M'_S\rangle \\ &= f(S,S',M_S,M'_S)\langle \Gamma M_\Gamma |\boldsymbol{\tau}|\Gamma' M'_\Gamma\rangle \quad (3.9) \end{aligned}$$

where the components of the vector **f** are numerical functions of the arguments written [10].

The orbital matrix element vanishes unless $\Gamma_\tau \subset \Gamma \times \Gamma'$. To see what levels may interact with the ground state via spin-orbit coupling, it is therefore sufficient to consider the transformation of the orbital term of spin-orbit coupling, and it is therefore not necessary to project the wavefunction into the irreducible representations of the spinor group. In the tetrahedron, τ transforms as T_1. Since the ground state has $\Gamma' = A_1$, the only excited states able to interact will have the spatial symmetry T_1. These states are the following, in a strong field classification:

Ground state: ${}^6A_1((4t_2)^3(2e)^2)$
Sextuplets: ${}^6T_1((4t_2)^3(2e)^3(t_1)^5)$
${}^6T_1((4t_2)^4(2e)^2(t_1)^5)$
${}^6T_1((4t_2)^3(2e)^3(3t_2)^5)$
${}^6T_1((4t_2)^4(2e)^2(3t_2)^5)$
${}^6T_1((4t_2)^3(2e)^3(2t_2)^5)$
${}^6T_1((4t_2)^4(2e)^2(2t_2)^5)$
${}^6T_1((4t_2)^4(2e)^2(1e)^3)$
${}^6T_1((4t_2)^3(2e)^3(1t_2)^5)$
${}^6T_1((4t_2)^4(2e)^2(1t_2)^5)$
Quadruplets: ${}^4T_1((4t_2)^3(2e)^2)$

$${}^4T_1((4t_2)^4(2e)^1)$$
$${}^4T_1((4t_2)^2(2e)^3)$$

The one-electron functions refer to Fig. 3 and Section 4.

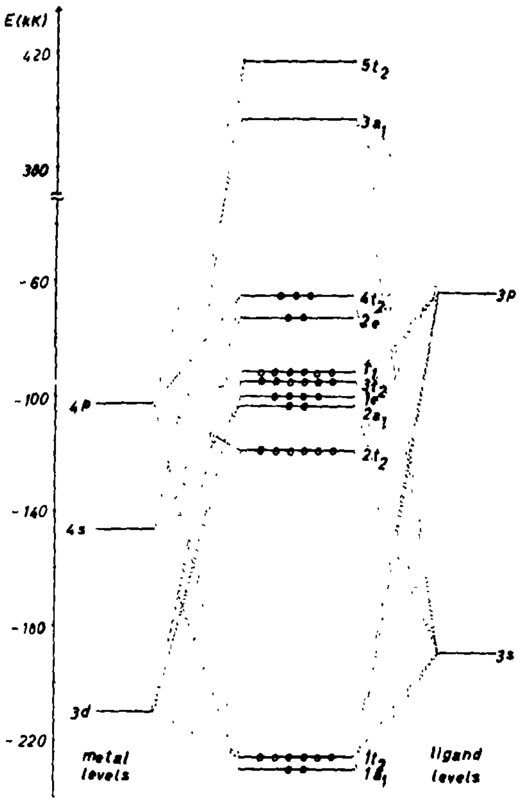

Fig 3. One-elctron molecular energy levels in $[FeCl_4]^-$.

Most of these excited levels have been neglected in earlier papers. Watanabe[4] considered only those terms arising from excitation of $3t_2$ electrons. But the energy level diagram (Fig. 3) shows that there are several one-electron levels fairly closed spaced, so that none can be neglected among them. Especially the terms coming from the charge-transfer states obtained by excitation of a t_1 (non-bonding) electron into antibonding $(4t_2)$ and $(2e)$ orbitals are entirely new, since they are strictly zero if LSO is not included, since t_1 electrons are entirely on the ligands. For completeness we also include the three quadruplets ${}^4T_1$ of the ground configuration [2].

In Appendix 2 we give the wavefunctions corresponding to all these states. The sextuplet functions were obtained by the projection operator method. The quadruplet functions and energies were obtained solving the electrostatic interaction matrix[11], using the experimental values, $10Dq = 5{\cdot}0$ Kk, $B = 625$ cm^{-1} and $C = 4B$[12].

4. MOLECULAR ORBITALS

To perform a numerical calculation of the spin-orbit coupling energies and of g we require a detailed knowledge of the coefficients of the atomic orbitals in the MO's. We have obtained these coefficients by one of the 'modern' semiempirical approximation based on the Wolfsberg–Helmholz method[13]. This type of calculation is a currently very active field[14–19]. Our calculation was based on the following points: (a) Valence State Ionization Energies (VSIE's) with the semiempirical parameters given by Basch *et al.* [14]; (b) Electrostatic correction (crystal-field effect) on the diagonal matrix elements [17] of the Hamiltonian; (c) Wolfsberg–Helmholz approximation of the off-diagonal matrix elements using the K-factors given by Radtke and Fenske[16]; (d) Hartree–Fock atomic wavefunctions[20]; (e) Self-Consistent charges and configurations.

Since the Radtke and Fenske K_{ij}-values are obtained by approximation to the exact Coulomb and Exchange integrals, and not by fitting the energies, the method is no doubt the best possible at the present stage. Calculations were performed with Fortran programs written for the IBM/360 computer of the University of Chile.

Appendix 3 gives the most important results of this calculation. The resulting self-consistent charges are $+1{\cdot}418$ for Fe and $-0{\cdot}605$ for Cl for a Fe–Cl distance of $4{\cdot}15$ a.u. $(2{\cdot}19$ Å$)$[21]. Fig. 3 shows the one electron energy levels, their relative positions and nomenclature.

5. RESULTS

(a) Spin-orbit parameters: Consequently with the semiempirical method used, the atomic spin-orbit coupling parameters ζ_{Fe} and ζ_{Cl} corresponding to the self-consistent charges were obtained by a quadratic interpolation between the values corresponding to the free ions, Fe^+, Fe^{2+}, Fe^{3+}; Cl^+, Cl^0, Cl^-[7]. The values thus obtained are: $\zeta^{Cl} = 566\ cm^{-1}$, $\zeta_{Fe} = 374\ cm^{-1}$.

(b) With these values, the formulas of Appendix 3, the Appendix 1 and the data of Appendix 3, the perturbed ground state function was obtained as:

$$|{}^6A_1 5/2\rangle = |{}^6A_1 5/2\rangle_0 + \sum_j B_j |{}^6T_1 j5/2\rangle + \sum_k C_k |{}^4T_1 k3/2\rangle. \tag{5.1}$$

The values of the mixing coefficients (matrix elements of spin-orbit coupling divided by the energies of the excited states) are listed in column 3 of Table 3.

(c) Next we calculate the expectation value of the Zeeman Effect in the perturbed ground state, equation (5.1) by means of the operator

$$H_Z = \beta H_z \sum_i (l_{zi} + 2{\cdot}0023\, s_{zi}) \tag{5.2}$$

where the external magnetic field H can be placed along the z-axis, since g is isotropic. When operating with $\mathbf{l}_z$ on the ligand functions it is important to compute the terms originating in the transport of $\mathbf{l}_z$ onto the ligands:

$$\mathbf{l}_z = \mathbf{l}_z^{\alpha} + (R^{\alpha} \times p)_z \tag{5.3}$$

where R^{α} is the position vector of ligand α and all vectors are expressed in the central system of coordinates[9, 22].

In the absence of zero-field splitting, the six levels of the ground state are symmetrical spread out, and allowed transitions have $\Delta M_s = \pm 1$ and a g-factor.

$$g = \Delta E/(\beta H) = (1/M_S)\langle {}^6A_1 M_S| \sum_i (l_{zi} + 2{\cdot}0023\, s_{zi}) |{}^6A_1 M_S\rangle. \tag{5.4}$$

With the values mentioned above, for the MO coefficients of the various one-electron functions, the g-value for $[FeCl_4]^-$ is

$$g = 2{\cdot}0186$$

in excellent agreement with the experimental value of $2{\cdot}0193 \pm 0{\cdot}0004$.

To ascertain what part of the calculated value is due to LSO coupling, we performed the calculation of the g-factor a second time putting $\zeta_L = 0$. One obtains the value 2·0110, so that half the g-shift stems from LSO.

Table 3. Spin orbit coupling and g-factor contributions of excited levels

Level	Energy (kK)	SO coef. × 10^3	*id.* with $\zeta_L = 0 \times 10^3$	Contribution to g	Contribution to g with $\zeta_L = 0$
${}^6T_1(4t_2)^3(2e)^3(t_1)^5$	19·6	5·05	0·0	0·00222	0·0
${}^6T_1(4t_2)^4(2e)^2(t_1)^5$	25·4	0·473	0·0	0·00173	0·0
${}^6T_1(4t_2)^3(2e)^3(3t_2)^5$	22·6	−10·9	−4·3	0·00694	0·00272
${}^6T_1(4t_2)^4(2e)^2(3t_2)^5$	28·4	3·51	−2·2	0·00230	−0·00118
${}^6T_1(4t_2)^3(2e)^3(2t_2)^5$	46·0	−0·82	−3·0	0·00100	0·00365
${}^6T_1(4t_2)^4(2e)^2(2t_2)^5$	51·8	0·74	−1·96	−0·00035	0·00092
${}^6T_1(4t_2)^4(2e)^2(1e)^3$	32·8	−4·69	−5·0	0·00227	0·00379
${}^6T_1(4t_2)^4(2e)^2(1t_2)^5$	159·0	−0·09	−0·11	0·00002	0·00002
${}^6T_1(4t_2)^4(2e)^3(1t_2)^5$	153·0	−0·15	−0·13	0·00002	0·00002
${}^4T_1(4t_2)^3(2e)^2$	26·0		−17·0		
${}^4T_1(4t_2)^4(2e)^1$	31·0	−8·15	−11·1	0·00016	0·0
${}^4T_1(4t_2)^2(2e)^3$	15·0	−6·3	−7·6		

6. DISCUSSION

In Table 3 we have collected the results of the calculation of spin-orbit coupling and g-factor. For each contributing excited level we show the mixing coefficient with and without LSO (columns 3 and 4).

In the first place, we observe that the non-bonding electron transfer from the ligands to central ion d-orbitals is quite important for the spin-orbit energy. This effect vanishes in the absence of LSO.

The most important contributions to g originates in electron transfer from $p\pi$ ligand orbitals to mainly d-antibonding orbitals. Here also, neglect of LSO leads to assign preference to $p\sigma$ to d transfer.

It is at any rate evident that calculations neglecting LSO are unable to explain the g-shift in $[FeCl_4]^-$ and the empirical correlation expressed in Table 1 and Fig. 1 of g-shift, covalency and LSO coupling.

Unfortunately it is impossible to give a compact, easy to use expression for the g-shift. This is due to the relatively large number of excited states giving significant contributions to the g-shift, and to the fact that each of these excited levels needs several MO coefficients for its characterization, leading to very unwieldy expressions.

For the same reason it is impossible to generalize the results of one compound to another in a more than qualitative manner, and thus the detailed interpretation of the correlation of Δg with $h_L\zeta_L$ is not possible without a complete MO calculation.

REFERENCES

1. GABRIEL J. R., JOHNSTON D. F. and POWELL M. J. D., *Proc. R. Soc.* **A264**, 503 (1961).
2. WATANABE H., *Prog. theor. Phys.* **18**, 405 (1957).
3. FIDONE I. and STEVENS K. W. H., *Proc. R. Soc.* **73**, 116 (1959).
4. WATANABE H., *J. Phys. Chem. Solids* **25**, 1471 (1964).
5. MISETICH A. A. and BUCH T., *J. chem. Phys.* **41**, 2524 (1964).
6. BLUME M. and WATSON R. E., *Proc. R. Soc.* **A271**, 565 (1963).
7. MOORE C. E., Atomic Energy Levels, *Natn. Bur. Stand. Circ.* 467 (1952).
8. JØRGENSEN C. K., *Structure and Bonding* **1**, 3 (1966).
9. MISETICH A. A. and WATSON R. E., *Phys. Rev.* **143**, 335 (1966).
10. GRIFFITH J. S., *The Theory of Transition Metal Ions*. Cambridge University Press, Cambridge (1964).
11. TANABE Y. and SUGANO S., *J. phys. Soc. Japan* **9**, 753 (1953).
12. JØRGENSEN C. K., *Absorption Spectra and Chemical Binding in Complexes*. Pergamon Press, Oxford (1962).
13. WOLFSBERG M. and HELMHOLZ L., *J. chem. Phys.* **20**, 837 (1952).
14. BASCH H., VISTE A. and GRAY H. B., *Theorie Chim. Acta* **3**, 458 (1965).
15. BALLHAUSEN C. J. and GRAY H. B., *Molecular Orbital Theory*. Benjamin, New York (1965).
16. RADTKE D. D. and FENSKE R. F., *J. Am. chem. Soc.* **89**, 2297 (1967).
17. ROS P., *Molecular Orbital Calculations on Copper Chloride Complexes*. Thesis, Eindhoven (1964).
18. NIEUWPOORT W. C., *Philips Res. Rep.* Suppl. No. 6 (1965).
19. CUSACHS L. C., *J. chem. Phys.* **43**, 5157 (1965).
20. WATSON R. E., *Tech. Rep.* 12, M.I.T. (1959); WATSON R. E. and FREEMAN A. J., *Phys. Rev.* **123**, 521 (1961).
21. RICHARDS R. R. and GREGORY N. W., *J. phys. Chem.* **69**, 239 (1965).
22. MAKI A. H. and McGARVEY B. R., *J. chem. Phys.* **29**, 31 (1958).

APPENDIX 1. EFFECT OF THE LIGAND ANGULAR MOMENTUM OPERATOR ON LIGAND FUNCTIONS

$$\Omega_z D_{x^2-y^2} = -(i/\sqrt{3})D_{xy}^{\pi} + (i\sqrt{2}/\sqrt{3})D_{xy}^{\sigma}$$

$$\Omega_z D_{z^2} = -(i/\sqrt{3})b$$

$$\Omega_z D_{yz}^{\sigma} = -(i/\sqrt{6})c - (i/\sqrt{2})D_{xz}^{\pi}$$

$$\Omega_z D_{yz}^{\pi} = (i/2\sqrt{3})c - (i/2)D_{xz}^{\pi} - (i/\sqrt{2})D_{xz}^{\sigma}$$

$$\Omega_z D_{xz}^{\sigma} = -(i/\sqrt{6})a + (i/\sqrt{2})D_{yz}^{\pi}$$

$$\Omega_z D_{xz}^{\pi} = (i/2)D_{yz}^{\pi} + (i/\sqrt{2})D_{yz}^{\sigma} + (i/2\sqrt{3})a$$

$$\Omega_z D_{xy}^{\sigma} = -(i\sqrt{2}/\sqrt{3})D_{x^2-y^2}$$

$$\Omega_z D_{xy}^{\pi} = (i/\sqrt{3})D_{x^2-y^2}$$

$$\Omega_{\pm} D_{x^2-y^2} = -(i/\sqrt{6})D_{yz}^{\sigma} \pm (1/\sqrt{6})D_{xz}^{\sigma} + (i/2)a + (i/2\sqrt{3})D_{yz}^{\pi} \pm (1/2)c \mp (1/2\sqrt{3})D_{xz}^{\pi}$$

$$\Omega_{\pm} D_{z^2} = -(i/\sqrt{2})D_{yz}^{\sigma} \mp (1/\sqrt{2})D_{xz}^{\sigma} - (i/2\sqrt{3})a + (i/2)D_{yz}^{\pi} \pm (1/2\sqrt{3})c \pm (1/2)D_{xz}^{\pi}$$

$$\Omega_{\pm} D_{yz}^{\sigma} = (i/\sqrt{2})D_{z^2} + (i/\sqrt{6})D_{x^2-y^2} \mp (1/\sqrt{2})D_{xy}^{\pi} \pm (1/\sqrt{6})b$$

$$\Omega_{\pm} D_{yz}^{\pi} = -(i/2)D_{z^2} - (i/2\sqrt{3})D_{x^2-y^2} \mp (1/\sqrt{2})D_{xy}^{\sigma} \pm (1/2)D_{xy}^{\pi} \pm (1/2\sqrt{3})b$$

$$\Omega_{\pm} D_{xz}^{\sigma} = -(i/\sqrt{2})D_{xy}^{\pi} - (i/\sqrt{6})b \pm (1/\sqrt{2})D_{z^2} \mp (1/\sqrt{6})D_{x^2-y^2}$$

$$\Omega_{\pm} D_{xz}^{\pi} = -(i/\sqrt{2})D_{xy}^{\sigma} - (i/2)D_{xy}^{\pi} + (i/2\sqrt{3})b \mp (1/2)D_{z^2} \pm (1/2\sqrt{3})D_{x^2-y^2}$$

$$\Omega_\pm D^\sigma_{xy} = -(i/\sqrt{6})c + (i/\sqrt{2})D^\pi_{xz} \pm (1/\sqrt{6})a \pm (1/\sqrt{2})D^\pi_{yz}$$

$$\Omega_\pm D^\pi_{xy} = (i/\sqrt{2})D^\sigma_{xz} + (i/2\sqrt{3})c + (i/2)D^\pi_{xz} \pm (1/\sqrt{2})D^\sigma_{yz} \mp (1/2\sqrt{3})a \pm (1/2)D^\pi_{yz}$$

$$\Omega_z a = (i/\sqrt{6})D^\sigma_{xz} - (i/2)c - (i/2\sqrt{3})D^\pi_{xz}$$

$$\Omega_z b = -(i/\sqrt{3})D_{t_1} - (i\sqrt{2}/\sqrt{3})A_{t_1}$$

$$\Omega_z c = (i/\sqrt{6})D^\sigma_{yz} - (i/2\sqrt{3})D^\pi_{yz} + (i/2)a$$

APPENDIX 2. T_1 LEVELS' WAVEFUNCTIONS FOR TETRAHEDRAL d^5-SYSTEMS

Nomenclature: Each function is a Slater determinant of [illegible] *Each one-electron orbital is a molecular orbital, linear combination of central and ligand functions* transforming according to the adequate irreducible representation and component, as displayed in Table 2, with coefficients given in Appendix 3. The MO function of the ground state $(4t_2)$ and $(2e)$ are written without a subscript. Those of the other levels $(1e, nt_2$ with $n = 2,3)$ are written with n as a subscript. They differ from the ground state MO's only in the coefficients. As usual, a bar above a symbol means β spin and no bar means α spin. Only open subshells are indicated.

Only the z component of the sextuplets and x and y components of quadruplets are given. The other components are obtained by the adequate symmetry operations.

Only the maximal spin projection is given in each case. Other components of the spin multiplets are obtained by action of operator S_-.

$$|^6T_1(z)(4t_2)^4(2e)^2(nt_2)^5 5/2\rangle =$$
$$(1/\sqrt{2})[|\xi\bar{\xi}\eta\zeta uv;\ \xi_n\bar{\xi}_n\eta_n\zeta_n\bar{\zeta}_n\rangle + |\xi\eta\bar{\eta}\zeta uv;\ \xi_n\eta_n\bar{\eta}_n\zeta_n\bar{\zeta}_n\rangle]$$
$$|^6T_1(z)(4t_2)^3(2e)^3(nt_2)^5 5/2\rangle = |\xi\eta\zeta u\bar{u}v;\ \xi_n\bar{\xi}_n\eta_n\bar{\eta}_n\zeta_n\rangle$$
$$|^6T_1(z)(4t_2)^4(2e)^2(1e)^3 5/2\rangle = |\xi\eta\zeta\bar{\zeta}uv;\ u_nv_n\bar{v}_n\rangle$$
$$|^6T_1(z)(4t_2)^4(2e)^2(t_1)^5 5/2\rangle =$$
$$(1/\sqrt{2})[|\xi\bar{\xi}\eta\zeta uv;\ a\bar{a}b\bar{b}c\rangle - |\xi\eta\bar{\eta}\zeta uv;\ ab\bar{b}c\bar{c}\rangle]$$
$$|^6T_1(z)(4t_2)^3(2e)^3(t_1)^5 5/2\rangle = |\xi\eta\zeta uv\bar{v};\ a\bar{a}bc\bar{c}\rangle$$
$$|^4T_1(x)3/2\rangle = a_1[(\sqrt{3}/2)|\xi\bar{\xi}\eta\zeta u\rangle -$$
$$(1/2)|\xi\bar{\xi}\eta\zeta v\rangle] + (a_2/\sqrt{2})[|\xi\zeta\bar{\zeta}uv\rangle + |\xi\eta\bar{\eta}uv\rangle] +$$
$$a_3[1/2|\eta\zeta u\bar{u}v\rangle - (\sqrt{3}/2)|\eta\zeta uv\bar{v}\rangle]$$
$$|^4T_1(y)3/2\rangle = a_1[(\sqrt{3}/2)|\xi\eta\bar{\eta}\zeta u\rangle +$$
$$(1/2)|\xi\eta\bar{\eta}\zeta v\rangle] + (a_2/\sqrt{2})[|\eta\zeta\bar{\zeta}uv\rangle + |\xi\bar{\xi}\eta uv\rangle] +$$
$$a_3[(1/2)|\xi\zeta u\bar{u}v\rangle + (\sqrt{3}/2)|\xi\zeta uv\bar{v}\rangle]$$

Table [illegible] of the [illegible]

	[illegible]	a_1	a_2	a_3
$^4T_1(4t_2)^4(2e)^1$	31·40	0·832	−0·405	0·331
$^4T_1(4t_2)^3(2e)^2$	25·98	0·454	0·888	−0·083
$^4T_1(4t_2)^2(2e)^3$	14·96	0·259	−0·220	−0·938

APPENDIX 3. MOLECULAR ORBITALS IN $[FeCl_4]^-$

The one-electron functions of symmetries t_2 and e are (see Table 2)

$$|nt_2, \gamma\rangle = a_d{}^n d_\gamma + a_p{}^n p_\gamma + a_s{}^n s_L{}^\gamma + a_\sigma{}^n D_\gamma{}^\sigma + a_\pi{}^n D_\gamma{}^\pi$$
$$|me, \delta\rangle = b_d{}^m d_\delta + b_\pi{}^m D_\delta{}^\pi$$

where $\gamma = \xi, \eta, \zeta$ and $\delta = u, v$ indicate components of the respective irreducible representation; $m = 1, 2$; $n = 1, 2, 3, 4, 5$. The coefficiets a and b are:

	a_d	a_p	a_s	a_σ	a_π
$n = 1$	0·065	0·086	0·944	−0·004	0·019
2	0·432	0·107	−0·109	0·824	0·107
3	0·304	−0·080	0·061	−0·193	0·873
4	0·850	−0·160	−0·067	−0·425	−0·497
5	0·158	0·150	−0·897	−0·561	0·589
	b_d	b_π			
$m = 1$	0·527	0·801			
2	0·855	−0·606			

Other results:

Overlap matrix

t_2	d	p	s_L	σ	π
d		0	0·084	0·106	0·054
p			0·557	0·283	−0·444
s_L				−0·042	−0·056
σ					−0·053

e Overlap $(d, \pi) = 0{\cdot}095$

Energies (kK): $2e - 4t_2 = 5{\cdot}80$; $t_1 - 4t_2 = 25{\cdot}40$; $3t_2 - 4t_2 = 28{\cdot}40$; $3t_2 - 2e = 22{\cdot}60$; $t_1 - 2e = 19{\cdot}60$; $1e - 2e = 27{\cdot}04$.

J. Chem. Solids Pergamon Press 1969. Vol. 30, pp. 329–337. Printed in Great Britain.

THE PRESSURE DEPENDENCE OF THE LATTICE PARAMETERS OF MnSb AND MnTe

HIROSHI NAGASAKI, IPPEI WAKABAYASHI and SHIGERU MINOMURA
The Institute for Solid State Physics, The University of Tokyo, Roppongi, Minato-ku, Tokyo, Japan

(*Received* 22 *July* 1968)

Abstract—The effect of pressure up to 170 kbar has been measured on the lattice parameters of MnSb and MnTe at room temperature. MnSb exhibits an anomalous compression in a axis below 65 kbar, at which the Curie temperature falls to room temperature; $-\Delta a/a_0 = 1{\cdot}32\times10^{-4}P + 4{\cdot}64\times10^{-6}P^2$ (below 65 kbar, ferromagnetic state), $-\Delta a/a_0 = 2{\cdot}7\times10^{-3} + 4{\cdot}64\times10^{-4}P - 1{\cdot}21\times10^{-6}P^2$ (above 65 kbar, paramagnetic state), $-\Delta c/c_0 = 9{\cdot}42\times10^{-4}P - 2{\cdot}50\times10^{-6}P^2$ (through pressure range). This anomaly in the low-pressure range has been explained by the pressure dependence of the volume magnetostriction. MnTe exhibits the compression in a and c axes through pressure range, $-\Delta a/a_0 = 5{\cdot}52\times10^{-4}P - 1{\cdot}18\times10^{-6}P^2$, $-\Delta c/c_0 = 10{\cdot}6\times10^{-4}P - 2{\cdot}79\times10^{-6}P^2$. The pressure dependence of the Néel temperature has been discussed by the c/a ratio.

INTRODUCTION

IT IS KNOWN that the magnetic properties of ferromagnetic or antiferromagnetic materials of NiAs-type crystals depend largely on the hydrostatic pressure, and especially, the magnetic transition temperatures mostly decrease with pressure in the rate of 3–12 deg per kbar. MnSb is a ferromagnet with the Curie temperature 313°C which decreases with pressure by the rate $-3{\cdot}2\times10^{-3}$ deg bar^{-1}[1]. MnTe is, on the other hand, an antiferromagnet with the Néel temperature 34°C, which increases with pressure by $+2{\cdot}6\times10^{-3}$ deg bar^{-1}[3]. The large change in the transition temperature with pressure can be understood mainly by the high compressibilities of NiAs-type crystals, but the negative pressure dependence would be difficult to explain by a simple localized model. While, Hirone *et al.*[1] measured the change of spontaneous magnetization with pressure at several temperatures for MnSb, and concluded that the negative dependence of the Curie temperature is understood by the large decrease of magnetization with pressure at absolute zero temperature.

Lynch[2] have measured the lattice parameters of MnSb as function of pressure to 100 kbar, using diamond anvil X-ray cell. The negative pressure dependence of the Curie temperature has been discussed qualitatively by three shortest Mn-Mn distances; $c/2$, a and $(c^2/4+a^2)^{1/2}$.

In this work, we measured the lattice parameters of MnSb and MnTe up to 170 kbar, and discussed the pressure dependences of their transition temperatures in relation to the volume magnetostriction.

EXPERIMENTAL

Powder photographs of MnSb and MnTe were taken at quasihydrostatic pressure and at room temperature using a Drickamer-type high pressure X-ray cell[4,5]. The materials were diluted 5 times of weight by boron powder for reduction of X-ray absorption, and small amount of NaCl was used as internal markers. Pressure was determined by NaCl compressibility data[6,7]. Maximum pressure was 170 kbar for MnSb and 130 kbar for MnTe.

Powder samples of MnSb and MnTe were obtained from Dr. T. Kaneko of Tohoku University and Dr. S. Anzai of Keio University, respectively. The X-ray diffraction patterns taken at atmospheric pressure show that they are both in single phase, and the lattice parameters are as follows; $a = 4{\cdot}13$ Å.

$c = 5{\cdot}78$ Å, $c/a = 1{\cdot}400$ for MnSb and $a = 4{\cdot}15$ Å, $c = 6{\cdot}71$ Å, $c/a = 1{\cdot}617$ for MnTe.

The lattice parameters at high pressure were calculated by least square method using the following diffraction lines; (101)(102)(110)(103) and, in some cases, (202)(004)(211)(212)(114)(213) for MnSb: (101)(102)(110)(201) and, sometimes, (202)(203) for MnTe. The errors of the parameters at each pressure are within 0·02 A for a, 0·04 A for c and 0·01 for c/a both in MnSb and MnTe.

RESULTS

(*a*) *MnSb*

Figure 1 is a plot of lattice parameters a and c of hexagonal MnSb vs. pressure. The a axis shows an anomalous compression in the lower pressure range; a vs. P curve is convex upward to about 65 kbar, while it is normally concave above 65 kbar. We can not trace, therefore, all measured points with single smooth curve in the whole range of pressure. Two different curves which intersect at 65 kbar are drawn. It is difficult to determine the exact point of the intersection by the measured points, but 65 kbar was determined by an interpretation of the anomaly in a axis. The c axis, on the contrary, shows normal compression within the experimental errors.

As a result of the anomaly of a axis, c/a vs. P curve also shows a kink point at 65 kbar. In Fig. 2, smoothed curve of c/a vs. pressure is shown. In Table 1, the smoothed data of $-\Delta a/a_0$, $-\Delta c/c_0$, $-\Delta v/v_0$ and c/a for MnSb are given. They are written in the following form; $-\Delta a/a_0 = 1{\cdot}32 \times 10^{-4} P + 4{\cdot}64 \times 10^{-6} P^2$ (below 65 kbar); $-\Delta a/a_0 = 2{\cdot}7 \times 10^{-3} + 4{\cdot}64 \times 10^{-4} P - 1{\cdot}21 \times 10^{-6} P^2$ (above 65 kbar); $-\Delta c/c_0 = 9{\cdot}42 \times 10^{-4} P - 2{\cdot}50 \times 10^{-6} P^2$ (through pressure range).

Lynch's data[2] exhibit no anomalous compressions in a axis, contrary to our results. This discrepancy would be caused by the fact that the anomaly is clearly recognized when a is pursued to the pressure above 100 kbar, whereas his measurements were practiced under lower pressure than 100 kbar.

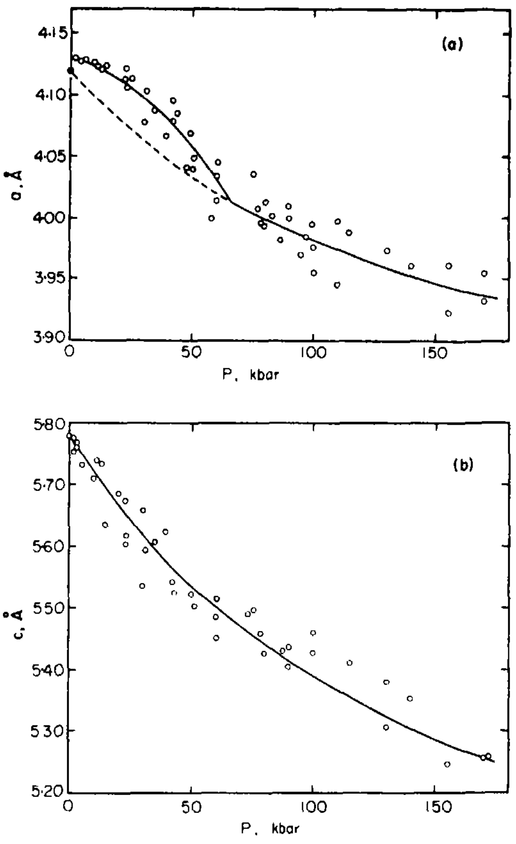

Fig. 1. (a) a vs. pressure for MnSb. Dotted line shows the compression curve of a for fictions nonmagnetic state of MnSb. (b) c vs. pressure for MnSb.

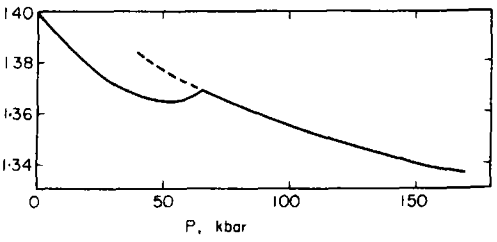

Fig. 2. c/a *vs.* pressure for hexagonal MnSb.

(*b*) *MnTe*

Figure 3 is a plot of lattice parameters a and c of hexagonal MnTe vs. pressure. No anomalous compressions are found both for a and

Table 1. *The smoothed date of* $-\Delta a/a$ and c/a *for* MnSb

P (kb)	$-\Delta a/a_0 (\times 10^3)$	$-\Delta c/c_0 (\times 10^3)$	$-\Delta V/V_0 (\times 10^2)$	c/a
0	0	0	0	1·400
10	1·9	10·9	1·48	1·388
20	4·6	20·1	2·91	1·378
30	8·2	28·9	4·47	1·371
40	12·6	36·0	6·02	1·367
50	18·2	42·6	7·71	1·365
60	24·5	48·6	9·47	1·366
65	28·4	51·2	10·48	1·367
70	29·8	53·8	10·95	1·366
80	32·3	58·5	11·83	1·362
90	34·4	63·3	12·68	1·358
100	36·4	67·8	13·44	1·354
110	38·3	71·6	14·14	1·352
120	40·0	75·4	14·79	1·349
130	41·7	79·1	15·44	1·346
140	43·4	82·4	16·04	1·343
150	44·9	85·6	16·59	1·340
160	46·3	88·6	17·12	1·338
170	47·5	90·8	17·52	1·337

c axes, but the rate of change of a and c axes with pressure is different and c/a decreases monotonously with increasing pressure, as shown in Fig. 4. In Table 2, smoothed values of $-\Delta a/a_0$, $-\Delta c/c_0$, $-\Delta v/v_0$ and c/a are given. They are written as,

$$-\Delta a/a_0 = 5{\cdot}52\times 10^{-4}P - 1{\cdot}18\times 10^{-6}P^2$$

$$-\Delta c/c_0 = 10{\cdot}6\times 10^{-4}P - 2{\cdot}79\times 10^{-6}P^2.$$

DISCUSSIONS

(i) *Exchange interaction curve*

Empirical exchange interaction curves relating magnetic transition temperatures to interatomic distances have been frequently discussed in NiAs-type compounds. Curie temperatures of MnAs, MnSb and MnBi, and Néel temperature of MnTe are plotted versus the shortest Mn–Mn distances ($c/2$) in Fig. 5, and versus the bonding angles of nearest neighboring atoms (c/a) in Fig. 6. The solid curves show the atmospheric pressure values and the dotted curves shown the corresponding change with pressure.

The dependence of magnetic transition temperatures on the lattice parameters of $c/2$ and c/a, which are given by implicit parameters of pressure and composition, indicates the same sign of slope in the former, but the opposite sign of slope in the latter.

The negative pressure dependence of magnetic transition temperature in MnSb would expect the contribution by the negative term with pressure. The fact may mean the negative change in the exchange interaction or that in the intrinsic magnetic moment with pressure, the latter of which is caused by the change in the band structure or the redistribution of electrons between the spin orientations.

(ii) *Volume magnetostriction*

(a) MnSb. According to the measurements [8] of temperature variation of lattice parameters in MnSb at the atmospheric pressure, an anomaly of a axis is predicted in ferromagnetic state and it disappears at the Curie temperature, while there is no such anomaly in c axis through the temperature range. The anomaly is a positive dilatation of a axis (about

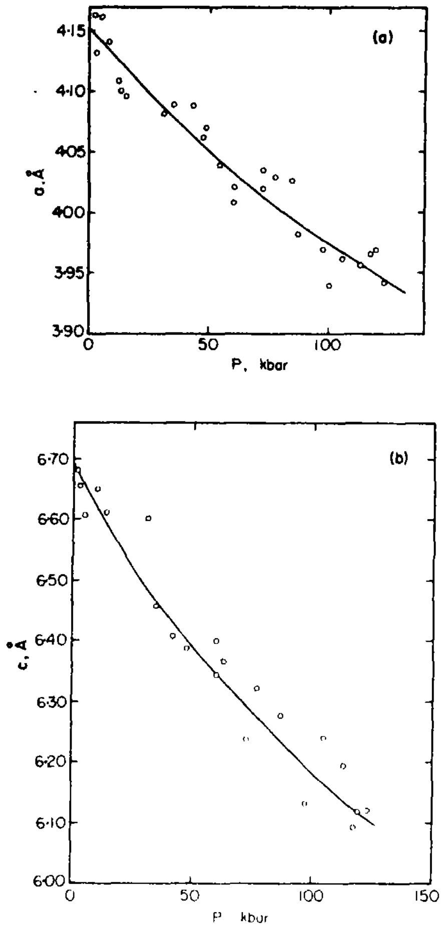

Fig. 3. (a) a (b) c vs. pressure for MnTe.

$2{\cdot}7\times 10^{-3}$ at room temperature) and it would be due to the spontaneous exchange magnetostriction of ferromagnetic MnSb.

On the other hand, the pressure dependence of the Curie temperature in MnSb was measured by Samara and Giardini [9] up to 60 kbar. One would expect that the Curie temperature descends to room temperature at about 65 kbar. Magnetostriction should naturally vanish at this pressure. In Fig. 1, one finds that the anomaly of the compression curve of a axis in the lower pressure range also disappears at about 65 kbar. Therefore, the anomaly could be interpreted as the result of pressure effect on the exchange magnetostriction. In Fig. 1, atmospheric and room temperature value of a axis for fictitious paramagnetic MnSb is shown, and a dotted curve is drawn continuously from this point to the compression curve of paramagnetic state above 65 kbar. The dotted curve would show the compression curve of fictitious paramagnetic MnSb at the pressure range from zero to 65 kbar. Therefore, we can get the magnetostriction at pressure P by subtracting this values from the corresponding measured points of a axis. In Fig. 7, the relative values of the magnetostriction vs. pressure are plotted. Although the scattering of the points is large, it is obvious that the magnetostriction at first increases with pressure and shows a maximum at about 30 kbar.

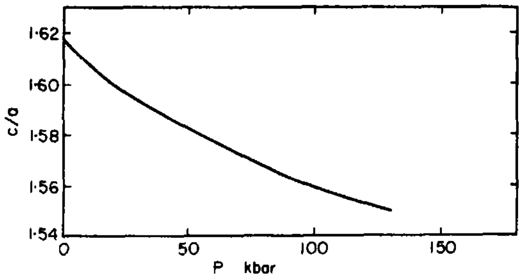

Fig. 4. c/a vs. pressure for hexagonal MnTe.

The change of the volume magnetostriction of MnSb with pressure is discussed by the molecular field approximation. The magnetostriction at absolute zero temperature is first considered.

The energy of ferromagnetic MnSb is expressed as

$$E = E_{ex} + E_{el} \tag{1}$$

where E_{ex} is the magnetic interaction energy and E_{el} is the elastic energy. E_{el} is written as

$$E_{el} = \frac{(\Delta V)^2}{2KV}$$

Table 2. The smoothed date of $-\Delta a/a_0$, $\Delta c/c_0$, $\Delta V/V_0$ *and* c/a *for* MnTe

P (kb)	$-\Delta a/a_0(\times 10^3)$	$-\Delta c/c_0(\times 10^3)$	$-\Delta V/V_0(\times 10^3)$	c/a
0	0	0	0	1·617
10	5·55	11·94	2·35	1·607
20	10·86	22·39	4·43	1·598
30	15·69	30·60	6·17	1·593
40	20·52	38·36	7·65	1·588
50	24·86	45·52	9·30	1·583
60	28·72	52·98	10·70	1·577
70	32·58	58·95	11·91	1·573
80	36·45	65·07	13·22	1·569
90	40·06	71·34	14·43	1·564
100	43·21	77·61	15·57	1·559
110	46·34	82·68	16·52	1·556
120	49·48	87·31	17·39	1·553
130	52·14	91·34	18·35	1·550

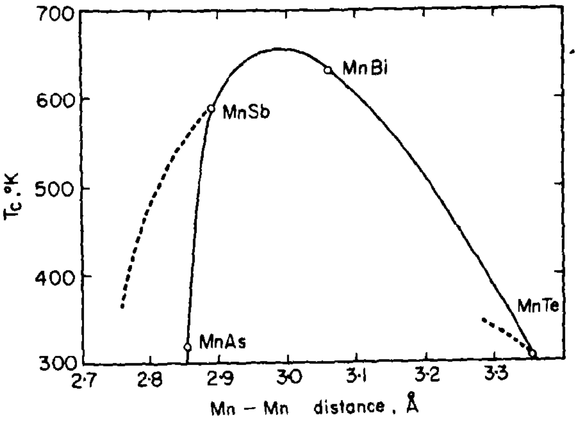

Fig. 5. Magnetic transition temperature Tc vs. the shortest Mn–Mn distance ($c/2$) for MnAs, MnSb, MnBi and MnTe. Dotted lines show the corresponding change of Tc and $c/2$ with pressure for MnSb and MnTe.

where ΔV is the volume distortion, $K = -(1/V) \cdot (\mathrm{d}V/\mathrm{d}P)$ the compressibility and V the volume at pressure P. Minimizing equation (1) as regards ΔV, one can get the general equation of the volume magnetostriction,

$$\Delta V = -K_{\text{para}}V_{\text{para}}\frac{\partial E_{\text{ex}}}{\partial V} = \frac{K_{\text{para}}V_{\text{para}}}{K_{\text{ferro}}V_{\text{ferro}}} \times \frac{\partial E_{\text{ex}}}{\partial P} \simeq \frac{\partial E_{\text{ex}}}{\partial P} \tag{2}$$

where the differences of the compressibilities and volumes between ferromagnetic and fictitious paramagnetic state are neglected.

According to molecular field approximation, E_{ex} is expressed as follows,

$$E_{\text{ex}} = -\frac{1}{2}n\sigma^2 = -\frac{3k}{2}T_c \tag{3}$$

where n the coefficient of molecular field, σ the magnetization per unit mass at absolute

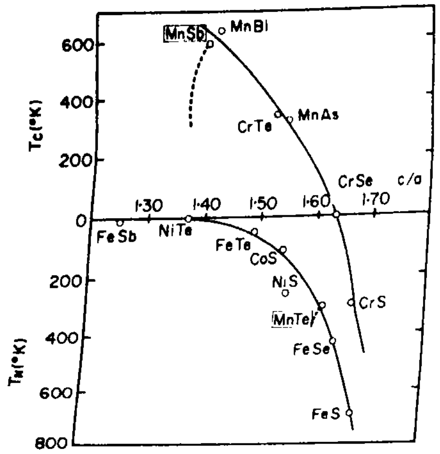

Fig. 6. Magnetic transition temperature *vs c/a* for NiAs-type compounds. *Dotted lines show the corresponding* changes with pressure for MnSb and MnTe.

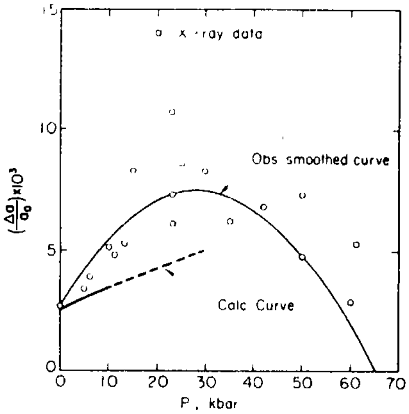

Fig. 7. Exchange magnetostriction $\Delta a/a_0$ vs. pressure for MnSb at room temperature. O: observed values; solid line: calculated from equation (12).

zero temperature, k the Boltzman constant and T_c the Curie temperature. From equation (2) and (3), the volume magnetostriction is written as,

$$\frac{\Delta V}{V_0} = -\frac{1}{2V_0}\frac{\partial n\sigma^2}{\partial P} = -\frac{3k}{2V_0}\frac{\partial T_c}{\partial P}. \qquad (4)$$

In the case of MnSb, the magnetostriction is observed only in a axis,

$\Delta V/V_0$ is replaced by $\Delta a/a_0$

$$\frac{\Delta V}{V_0} = 2\frac{\Delta a}{a_0}. \qquad (5)$$

Considering the measurements by Hirone *et al.*[1] we approximate the pressure dependence of n and σ by the following equations,

$$n \propto J = J_0\left(1 + \alpha\frac{P}{P_c}\right)$$
$$\sigma = \sigma_0\left(1 - \frac{P}{P_c}\right) \qquad (6)$$

where, J is the exchange interaction, P_c the critical pressure supposed to transform from ferromagnetic state to paramagnetic state at 0°K, and α a positive constant. The assumption of equation (6) that σ decreases linearly with pressure would be rather a crude approximation, especially at the pressure near P_c, and it is necessary to consider higher order pressure dependence of σ for rigorous discussions. Owing to the deficiency of experiments, however, we can not predict at present an exact function between magnetization and pressure.

Equation (6) means that the Curie temperature has the following pressure dependence in the limit of molecular field theory,

$$T_c = T_c^0\left(1 - \frac{P}{P_c}\right)^2\left(1 + \alpha\frac{P}{P_c}\right) \qquad (7)$$

where, T_c^0 is the atmospheric value of the Curie temperature. Figure 8 shows that this expression fits farely well to the measured values of Samara and Giardini, and that $P_c = 150$ kbar, $\alpha = 1{\cdot}52$.

Going back to the expressions of equation (6), initial pressure dependence of J_0 and σ_0 at zero pressure can be get numerically;

$$\frac{1}{J_0}\frac{\partial J_0}{\partial P} = \frac{\alpha}{P_c} = 10 \times 10^{-6}\,\text{bar}^{-1}$$

$$\frac{1}{\sigma_0}\frac{\partial \sigma_0}{\partial P} = -\frac{1}{P_c} = -6{\cdot}7 \times 10^{-6}\,\text{bar}^{-1}.$$

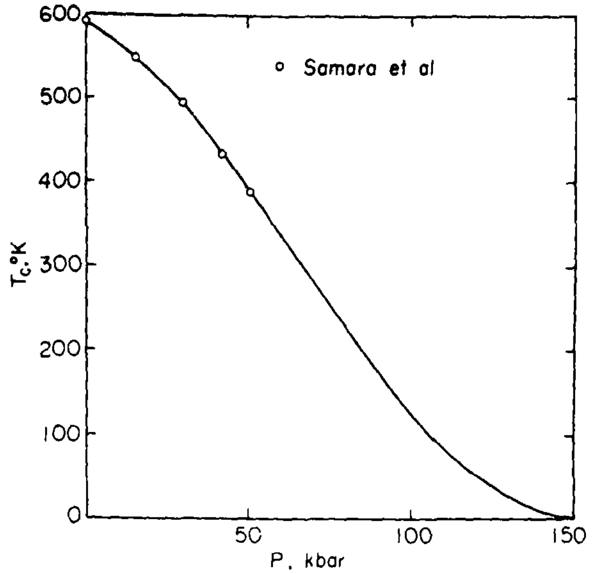

Fig. 8. The Curie temperature vs. pressure for MnSb. ○: after the measurements of Samara and Giardini; solid line: after equation (7).

These values are to be compared to the experimentally determined ones[1], $1/\sigma_0(\partial\sigma_0/\partial P) = -5{\cdot}9\times10^{-6}\,\mathrm{bar}^{-1}$ and $1/J_0(\partial J_0/\partial P) = 1/T/_c^0\ (\partial T_c^0/\partial P) - 2/\sigma_0\ (\partial\sigma_0/\partial P) = 6{\cdot}0\times10^{-6}\,\mathrm{bar}^{-1}$. Considering rather large errors of P_c and α, the agreements of the above values are seen satisfactory and give the expressions of equation (6) an another support. In accordance with the experimental results of Hirone *et al.*, we would also like to emphasize the fact that the exchange interaction J increases with pressure and the more rapid decrease of σ with pressure does cover the increase of J and, as the result, the Curie temperature falls by compression.

Now, from equations (4), (6) and (7), the magnetostriction at pressure P and temperature zero for MnSb is obtained as,

$$\frac{\Delta a}{a_0} = \left(\frac{\Delta a}{a_0}\right)\left(1-\frac{P}{P_c}\right)\left(1+9{\cdot}4\frac{P}{P_c}\right) \quad (8)$$

where,

$$\left(\frac{\Delta a}{a_0}\right)_0 = -\frac{3k}{4V_0}\left(\frac{\partial T_c}{\partial P}\right)_{P=0} = 7{\cdot}8\times10^{-3}$$

is the magnetostriction at absolute zero temperature and zero pressure, and to be compared with experimentally estimated value[8] 3×10^{-3}.

In Fig. 9, $\Delta a/a_0$ vs. P/P_c curve is drawn according to the equation (8). As mentioned above, the equation is limited in the pressure range except for $P \simeq P_c$. The magnetostriction at absolute zero temperature increases about

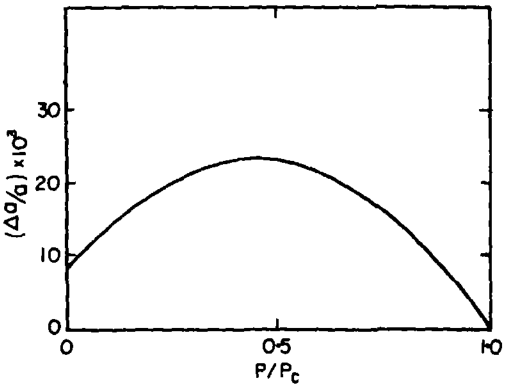

Fig. 9. Exchange magnetostriction $\Delta a/a_0$ vs. normalized pressure P/Pc (P_c = 150 kbar) for MnSb at 0°K, calculated from equation (8).

3 times near $P = 0{\cdot}5\,P_c$ and falls to zero at $P = P_c$.

At room temperature, volume magnetostriction would be given approximately by

$$\Delta V = \frac{\partial E_{ex}}{\partial P} = -\frac{\partial n\sigma_s^2}{2\partial P} \qquad (9)$$

where σ_s is spontaneous magnetization per unit mass at room temperature. Using the experimental results of Hirone *et al.*[1] $\sigma_s(P)$ and $J(P)$ are written as follows near $P = 0$,

$$\sigma_s(P) = \sigma_s(0)\,(1 - 4{\cdot}0 \times 10^{-6}\,P)$$
$$J(P) = J(0)\,(1 + 6{\cdot}0 \times 10^{-6}\,P) \qquad (10)$$

where $1/J(\partial J/\partial P)$ is assumed temperature independent. From equation (10),

$$\frac{1}{E_{ex}}\frac{\partial E_{ex}}{\partial P} = \frac{1}{J}\frac{\partial J}{\partial P} + \frac{2}{\sigma_s}\frac{\partial \sigma_s}{\partial P} = -2{\cdot}0 \times 10^{-6}\,\mathrm{bar}^{-1}.$$

Assuming a Brillouin function[10], $\sigma_s(300°\mathrm{K}) \simeq 0{\cdot}95\,\sigma_s(0°\mathrm{K})$, and exchange energy at room temperature would be,

$$E_{ex}(300°\mathrm{K}) = E_{ex}(0°\mathrm{K}) \times 0{\cdot}95^2$$
$$= \left(-\frac{3K}{2}T_c\right) \times 0{\cdot}95^2.$$

According to the above estimation, the volume magnetostriction at room temperature and zero pressure is, $\Delta V = \partial E_{ex}/\partial P = 2{\cdot}19 \times 10^{-25}\,\mathrm{cm}^3$ (per Mn atom) $= 4{\cdot}38 \times 10^{-25}\,\mathrm{cm}^3$ (per unit cell). Then,

$$\frac{\Delta a}{a_0} = \frac{1}{2}\frac{\Delta V}{V_0} = 2{\cdot}6 \times 10^{-3} \qquad (11)$$

This value is to be compared with experimental one $2{\cdot}7 \times 10^{-3}$[8].

Now, from equations (9–11), the equation

$$\Delta a/a_0 = 2{\cdot}6 \times 10^{-3}(1 + 3{\cdot}2 \times 10^{-5}\,P - 1{\cdot}44 \times 10^{-10}\,P^2) \qquad (12)$$

is get for magnetostriction near zero pressure and drawn in Fig. 7. Calculated and observed initial slopes are $0{\cdot}83 \times 10^{-7}$ and $3{\cdot}3 \times 10^{-7}$ bar^{-1}, respectively. Calculated curve qualitatively explains observed values in the low pressure range. At higher pressure, equation (12) is not to be used, but $\sigma_s(T/T_c)$ rapidly decreases and diminishes at 65 kbar according to a Brillouin function, as T_c decreases with pressure and T/T_c approaches to unity. Therefore, the magnetostriction at room temperature, which increases in the lower pressure range, would disappear at the Curie point 65 kbar through a maximum point.

(*b*) MnTe. The temperature dependence of lattice parameters in MnTe at atmospheric pressure exhibits an anomaly in *c* axis accompanying magnetic ordering, but no anomaly in *a* axis[11]. This anomaly would be caused by exchange magnetostriction. The volume magnetostriction at absolute zero temperature and zero pressure is

$$\Delta V/V_0 = -\frac{3k}{2V_0}\frac{\partial T_N}{\partial P} = -10{\cdot}5 \times 10^{-3},$$

while experimental value is about -8×10^{-3}. The agreement is found both in their signs and values. In this case, however, we can not discuss the pressure dependence of the magnetostriction; it is impossible to separate the contribution due to the magnetostriction from our compression curve of *c* axis, as the Néel temperature increases with pressure and MnTe would remain in antifferomagnetic state through the pressure range.

It may also suppose in the positive pressure dependence of the Néel temperature that the exchange interaction $-J$ increases with pressure and σ_0 decrease more slowly.

Acknowledgements—We wish to thank Dr. T. Kaneko of Tohoku University and Dr. S. Anzai of Keio University for providing us the materials of our experiments. We also like to thank Dr. S. Anzai for useful discussions.

REFERENCES

1. HIRONE T. KANEKO T. and KONDO K., In *Physics of Solid at High Pressure* (Edited by C. T. Timizuka and R. M. Emrick), p. 298. Academic Press New York (1965).
2. LYNCH R. W., *J. chem. Phys.* **47**, 5180 (1967).
3. OZAWA K., ANZAI S. and HAMAGUCHI Y., *Phys. Lett.* **20**, 132 (1966).
4. PEREZ-ALBUERNE E. A., FORSGREN K. F. and DRICKAMER H. G., *Rev. scient. Instrum.* **35**, 29 (1964).
5. NAGASAKI H. and MINOMURA S., *J. phys. Soc. Japan* **19**, 1496 (1964).
6. BRIDGMAN P. W., *Proc. Am. Acad. Arts Sci.* **76**, 1 (1945).
7. PEREZ-ALBUERNE E. A. and DRICKAMER H. G., *J. chem. Phys.* **43**, 1381 (1963).
8. WILLIS B. T. M. and ROOKSBY H. P., *Proc. phys. Soc.* **67**, 290 (1954).
9. SAMARA G. A. and GIARDINI A. A., In *Physics of Solids at High Pressure* (Edited by C. T. Tomizuka and R. M. Emrick), p. 308. Academic Press, New York (1961).
10. KITTEL C., *Introduction to Solid State Physics*, p. 164. Wiley, New York (1953).
11. GREENWALD S., *Acta crystallogr.* **6**, 396 (1953).

J. Phys. Chem. Solids Pergamon Press 1969. Vol. 30, pp. 339–351. Printed in Great Britain.

THERMOMIGRATION IN SOLID METALS

R. A. ORIANI
Edgar C. Bain Laboratory For Fundamental Research, United States Steel Corporation, Research Center, Monroeville, Pa. 15146, U.S.A.

(*Received* 29 *March* 1968; *in revised form* 15 *July* 1968)

Abstract—Thermomigration, the flux of mass induced by an applied temperature gradient, is analyzed phenomenologically in a variety of alternate ways to demonstrate that the experimentally determined heat of transport does not contain contributions from equilibrium-thermodynamic quantities. Hence, the experimental quantity is to be compared directly with atomistic kinetic models. The experimental data are briefly reviewed. A class of atomistic models, those based on the Wirtz theory, is shown to be incompatible with the requirements of the thermodynamics of irreversible processes. Such compatibility is demonstrated for the zero-field model involving phonon and electron scattering by the activated complex, and the ideas underlying this model are reviewed.

THE FLUX of a component of a solution induced by an impressed temperature gradient may be termed thermomigration. This phenomenon has also been called thermal diffusion, a name better reserved for the flow of heat. The establishment of a concentration gradient due to the impressed temperature gradient is also known as the Ludwig–Soret effect.

Thermomigration is a manifestation of details of the dynamics of the diffusion process which are in no other way made evident, and hence is of great theoretical interest. It may in addition have technological importance where alloys, particularly those containing interstitial solutes, are employed for long periods of time under large temperature gradients. Indeed the generalized force upon an atom arising from a temperature gradient may be larger than that due to a concentration gradient in isothermal diffusion. For example we may consider hydrogen dissolved in α-iron at room temperature. The force generated by a concentration gradient is $F_c = kT\,\nabla\ln c$, and that by a temperature gradient is $F_A = Q\,\nabla\ln T$, where Q is the head of transport of dissolved hydrogen (to be discussed below). Taking $\nabla\ln c = 1\ \mathrm{cm}^{-1}$, $Q = -10{,}000$ cal/g atom (extrapolated from reference[1], and $\nabla\ln T = 3{\cdot}33\ \mathrm{cm}^{-1}$ one finds $F_c = 4{\cdot}2\times 10^{-14}$ dyn/atom, and $F_T = 2{\cdot}3\times 10^{-12}$ dyn/atom.

This paper summarizes the experimental information currently available on thermomigration in one- and two-component solid metals. Various ways of describing the phenomena in terms of irreversible thermodynamics are developed and compared. The phenomenological heat of transport defined for isothermal conditions is given an atomistic interpretation.

EXPERIMENTAL SITUATION

It is not our purpose to examine in detail the experimental methods that have been used in this field, but it is necessary to point out the main characteristics of the two types of measurements that are made. In the case of two-component alloys one generally measures a property associated with concentration, or concentration itself, as a function of position in a specimen held for a long time in a measured temperature gradient, ∇T. If the concentration gradient ∇c becomes independent of time during the anneal, then the quantity Q_m in

$$-kT\,\nabla\ln c_1 = Q_m\,\nabla\ln T \qquad (1)$$

is a measure of the thermomigration. We will call Q_m the *measured heat of transport* to distinguish it from other possible heats of transport to be discussed subsequently. The significance of Q_m will also be discussed below.

In the case of a pure metal one attempts to measure the time-independent flux of matter, J_1, produced by the impressed temperature gradient upon an unconstrained specimen. The flux of matter, when the vacancy mechanism operates, is the negative of the flux of vacancies, J_v, and since J_v is a function of temperature one may expect that the separation between two surface scratches or between two inert markers embedded at different points in the specimen held in a temperature gradient will change with time. This furnishes the generally employed principle for the measurement of J_1. We note in passing that the rate of separation of two inert markers disposed along grad T measures $J_V = -J_1$ only if there is no change in the lateral dimensions of the specimen in the region between the two markers. If vacancy generation and annihilation occur only by dislocation climb perpendicular to grad T there will be no change in lateral dimensions and then J_1 will be given by the rate of separation of markers. Any tendency toward isotropy of dislocation climb would mean that J_1 is larger than that calculated from the marker motion, so that suitable correction must be made by the aid of concurrent measurements of changes of the dimensions normal to grad T. Assuming that a correct time-independent J_1 has been measured, the quantity Q'_m in

$$\frac{-kT\gamma}{c_1D_1}J_1 = Q'_m \nabla \ln T \qquad (2)$$

measures the thermomigration of the material component. In this relation D_1 and c_1 are, respectively the tracer diffusivity and number of atoms per unit volume of the pure component 1, and γ is the correlation coefficient, which is 0·78 in f.c.c. and 0·73 in b.c.c. lattices[2]. We note that phenomenologically the Q_m's of equations (1) and (2) are different.

In Tables 1–3 are collected the best data for thermomigration in pure solid metals, in interstitial solid solutions, and in binary substitutional solid solutions. In every case the measured heat of transport as defined by equation (1) or (2) is given, and it always is that of the material component(s) not that of the vacancy. In comparing these tabulated values with those in the original references it must be kept in mind that the original authors may not have accounted for the correlation coefficient, may be presenting a heat of transport of the vacancy, or may have added the heat of formation of a vacancy, h_v, to the measured heat of transport.

Inspection of the present tables reveals the paucity of well studied systems and the variability of results obtained by various investigators for the same system. Very few general statements can be made about this collection of data. One of these is that the various interstitial solutes in one solvent metal have the same sign for Q_m. Another weak statement that may be made is that there is a trend to large $|Q_m|$ for the transition metals. For the moment we may regard Q_m simply as a measure of the magnitude and sense of the thermomigration. We proceed now to develop the basis for its atomistic interpretation.

PHENOMENOLOGICAL RELATIONS

In order to attempt an atomistic interpretation of thermomigration it is necessary first to develop the phenomenological equations from irreversible thermodynamics[3]. This is important because there exists in the literature much confusion as to the significance of the heat of transport even at the phenomenological level. We begin with the case of a pure metal in a temperature gradient.

(A) One-component solid metal

Knowing that thermomigration experiments have been successfully carried out on pure metals where the distance between successive markers changes with time, and knowing that

Table 1. Heats of transport in self-thermomigration in solid metals*

Metal	Q'_m (kcal/g atom)	Reference
Li	+12	LODDING A. and THERNQVIST P., *Z. Naturf.* **21a**, 857 (1966).
Li	$(Q'_m)_{Li}7 > (Q'_m)_{Li}6$	THERNQVIST P. T. and LODDING A., *Z. Naturf.* **22a**, 837 (1967).
Na	−1·5	SULLIVAN G. A., *Phys. Rev.* **154**, 605 (1967).
Al	−1·5	SWALIN R. A. and YIN C. A., *Acta Metall.* **15**, 245 (1967).
Cu	+4	MEECHAN C. J. and LEHMAN G. W., *J. appl. Phys.* **33**, 634 (1962).
	−5·4	JAFFEE D. and SHEWMON P. G., *Acta Metall.* **12**, 515 (1964).
	0	ADDA Y., BREBEC G., DOAN N. V., GERL M. and PHILIBERT J., *Proceedings of a Symposium (July 1965, Vienna) on Thermodynamics*. International Atomic Energy Agency (1966).
Ag	0	ADDA Y., BREBEC G., DOAN N. V., GERL M. and PHILIBERT, *Proceedings of a Symposium (July 1965, Vienna) on Thermodynamics*. International Atomic Energy Agency (1966).
	0	SHEWMON P. G., *J. chem. Phys.* **29**, 1032 (1958).
Au	−5	MEECHAN C. J. and LEHMAN G. W., *J. appl. Phys.* **33**, 634 (1962).
	−6·5	JAFFEE D. and SHEWMON P. G., *Acta Metall* **12**, 515 (1964).
	0	ADDA Y., BREBEC G., DOAN N. V., GERL M. and PHILIBERT J., *Proceedings of a Symposium (July, 1965, Vienna) on Thermodynamics*. International Atomic Energy Agency (1966).
	−5·5 ± 0·9	MOCK W. and LAZARUS D., Private communication.
Pb	+2·1 ± 4	THERNQVIST P. and LODDING A., *Z. Naturf.* **21a**, 1310 (1966).
Zn	0	SHEWMON P. G., *J. chem. Phys.* **29** 1032 (1958).
	0	FELLER H. G. and WEVER H., *J. Phys. Chem. Solids* **24**, 969 (1963).
	−2·3	SWALIN R. A., OLANDER W. C. and LIN P., *Acta Metall.* **13**, 1063 (1965).
	+3·5	ARCHBOLD T. F. and McCORMICK P. G., *Trans. metall. Soc. A.I.M.E.* **236** 713 (1966).
	−0·2 ± 1·5	THERNQVIST P. and LODDING A., *Z. Naturf.* **21a**, 1310 (1966).
α-Fe	0	BRAMMER W. G., *Acta Metall.* **8**, 630 (1960).
	+9·2	ADDA Y., BREBEC G., DOAN N. V., GERL M. and PHILIBERT J., *Proceedings of a Symposium (July 1965, VIENNA) on Thermodynamics*. International Atomic Energy Agency (1966).
γ-Fe	neg.	FELLER H. G., *Arch. Eisenhuttenwes.* **11**, 859 (1963).
	+18 to +75	HERING H. and WEVER H., *Acta Metall* **15**, 377 (1967).
Co	+130 to +330†	HO P. S., reference [21].
Ni	neg.	KLEMENS D. and WEVER H., Unpublished work.
Pt	+9 to 14†	HO, P. S., HEHENKAMP Th. and HUNTINGTON H. B., *J. Phys. Chem. Solids* **26**, 251 (1965).
β-Ti	+185	Est'd. by P. S. HO, reference [21] from FELLER H. G. and WEVER H., *J. Phys. Chem. Solids* **24**, 969 (1963).
	neg.	DUBLER H. and WEVER H., *Symposium*. Munster (1965).
β-Zr	−120	FELLER H. G. and WEVER H., *J. Phys. Chem. Solids* **24**, 969 (1963).
	−6·8 ± 2·2	CAMPBELL D. R. and HUNTINGTON H. B., To be published. (using $\gamma = 0·2$)

*The heat of transport tabulated is that for the atom, and is defined by Eq. (2).
†Well characterized temperature dependence.

Table 2. Heats of transport for interstitial solutes*

Solute	Matrix	Q'_m (kcal/g atom)	Reference
H, D	αFe	−8 to −5·5†	Reference [1].
C	αFe	−24	Reference [15] and SHEWMON P. G., *Acta Metall.* **8**, 605 (1960).
C	dFe	−17·5	SHAW J. G. and OATES W. A., Private communication
N	αFe	−18	Reference [15].
C	γFe	−2	SHEWMON P. G., *Acta Metall.* **8**, 605 (1960).
H, D	Ni	−1·5 to −0·2†	Reference [1].
H	$\gamma\mathrm{Fe}_{0\cdot 6}\mathrm{Ni}_{0\cdot 4}$	−1·7 to −1·2†	Reference [1].
H	β-Zr	+3·5 to +6†	Reference [20].
H	$\mathrm{ZrH}_{1\cdot 6}$	+0·5	MERTEN U., BOCKROS J. C., GUGGISBERG D. G. and HATCHER A. P., *J. nucl. Mater.* **10**, 201 (1963).
H	$\mathrm{ZrH}_{1\cdot 69}$	+1·3	SOMMER A. W. and DENNISON W. F., U.S.A.E.C. Rep. NAA-SR-5066 (1960).
0	β-Zr	+20	RIECK G. D. and VOGEL D. L., *Acta Metall.* In press (1968).
N	β-Zr	pos.	RIECK G. D. and VOGEL D. L., *Acta Metall.* In press (1968).
H	αZr Zircalloy Zircally + 0·6 % Y αZr + 2·6 % Nb	+5·7 ± 0·5	SAWATSKY A., *J. nucl. Mater.* **9**, 364 (1963).
D	α-Zr	+6·5	SAWATSKY A., *J. nucl. Mater.* **2**, 321 (1960).
H	αTi	+5·3	MARSHALL R. P., *Trans. metall. Soc. A.I.M.E.* **233**, 1449 (1965).
Ag	$\mathrm{Bi_2Te_3}$	+6·1 ± 0·9	DIBBS H. P. and TREMBLAY J. R., *J. appl. Phys.* **39**, 2976 (1968).

*The heat of transport tabulated is for the interstitial solute, and is defined by equation (1).

†Well characterized temperature dependence.

vacancy exchange is the prevalent mechanism for volume diffusion, it is natural to consider explicitly the flux of vacancies. In order to establish an appropriate set of conjugate forces and fluxes, we write the Gibbs equation for a unary system in which the vacancy concentration can be independently varied as

$$dU = TdS - PdV + \mu_v dn_v$$

in which μ_v is the chemical potential of the vacancies referred to some arbitrary reference state. The Onsager formulation[3] of irreversible thermodynamics is that the fluxes are the time derivatives of the conservative state variables, so that

$$J_v = \mathrm{d}n_v/\mathrm{d}t; \quad J_u = \mathrm{d}U/\mathrm{d}t.$$

The conjugate forces, X_i, are given by gradients of the rate of change of the entropy with the corresponding state variable. Thus, neglecting the PdV term,

$$X_u = \nabla(\partial S/\partial U)_{n_v} = \nabla(1/T)$$

$$X_v = \nabla(\partial S/\partial n_v)_U = -\nabla(\mu_v/T).$$

The sum of the products of conjugate fluxes and forces, $\sum_i J_i \cdot X_i$, is the rate of entropy production,

In the domain of small forces, one may consider that the forces and fluxes are linearly related through phenomenological coefficients,

Table 3. Heats of transport in dilute substitutional alloys*

Solvent	Solute	Q_m (kcal/g atom)	Reference
Zn	Ag	+1 (∥ c-axis)	WINTER F. R. and DRICKAMER H. G., *J. chem. Phys.* **24**, 492 (1956).
	Ag	+0·9 (⊥ *c*-axis)	*J. chem. Phys.* **24**, 492 (1956).
	Tl	−3 (∥ *c*-axis)	*J. chem. Phys.* **24**, 492 (1956).
	Tl	−5 (⊥ *c*-axis)	*J. chem. Phys.* **24**, 492 (1956).
	In	−6 (⊥ *c*-axis)	*J. chem. Phys.* **24**, 492 (1956).
Cu	Ag	−5	JAFFE D. and SHEWMON P. G., *Acta Metall.* **12**, 515 (1964).
	Au	−5	JAFFEE D. and SHEWMON P. G., *Acta Metall.* **12**, 515 (1964).
	Co	+4	JAFFEE D. and SHEWMON P. G., *Acta Metall.* **12**, 515 (1964).
	Ge	−8	JAFFEE D. and SHEWMON P. G., *Acta Metall.* **12**, 515 (1964).
	26% Au	pos.	Reference[15].
Ag	Au	0	JAFFE D. and SHEWMON P. G., *Acta Metall.* **12**, 515 (1964).
	Sb	−29	BIERMAN W., HEITKAMP D. and LUNDY T. S. *Acta Metall.* **13**, 71 (1965).
	Ru	pos.	JAFFEE D. and SHEWMON P. G., *Acta Metall.* **12**, 515 (1964).
Au	Ag	−4	JAFFEE D. and SHEWMON P. G., *Acta Metall.* **12**, 515 (1964).
	Tl	−8	

*The tabulated values are defined as per equation (1) in which the concentration term refers to the solute.

L'_{ij}, which are functions of the state variables,

$$J_v = -L'_{vv}\nabla(\mu_v/T) + L'_{vu}\nabla(1/T)$$

$$J_u = -L'_{uv}\nabla(\mu_v/T) + L'_{uu}\nabla(1/T)$$

and the Onsager reciprocity relation insures that $L'_{vu} = L'_{uv}$. In order to facilitate comparison with de Groot[3] (Chap. VII) and with other references, we will rewrite these equations in the form

$$J_v = -L_{vv}T\nabla(\mu_v/T) - L_{vu}T\left[\frac{1}{T}\nabla\ln T\right]$$

$$= -L_{vv}T\nabla(\mu_v/T) - L_{vu}\nabla\ln T \qquad (3)$$

$$J_u = -L_{vu}T\nabla(\mu_v/T) - L_{uu}T\left[\frac{1}{T}\nabla\ln T\right]$$

$$= -L_{vu}T\nabla(\mu_v/T) - L_{uu}\nabla\ln T \qquad (4)$$

where $TL_{ij} = L'_{ij}$, and we take cognizance of the fact that the generalized forces still remain $X_v = -\nabla(\mu_v/T)$ and $X_u = \nabla(1/T) \equiv -(1/T)\nabla\ln T$.

Defining

$$Q_v \equiv \frac{L_{vu}}{L_{vv}}, \qquad (5)$$

we may rewrite (3) and (4) as

$$J_v = -L_{vv}[T\nabla(\mu_v/T) + Q_v\nabla\ln T] \qquad (6)$$

$$J_u = -L_{vv}Q_vT\nabla(\mu_v/T) - L_{uu}\nabla\ln T \qquad (7)$$

To see the physical significance of Q_v, multiply (6) by Q_v and subtract the resulting equation from (7), obtaining

$$J_u - Q_vJ_v = (L_{vv}Q_v^2 - L_{uu})\nabla\ln T.$$

Hence in an isothermal system

$$J_u = Q_vJ_v \qquad (8)$$

so that Q_v is the quantity that relates the flux of energy to the flux of vacancies in an isothermal situation.

Dimensionally Q_v is expressible as cal/unit of mass and has for this reason been called the heat of transport. We will continue to use this name which has the force of tradition, but we point out that the basic significance of Q_v is that of a flux of energy produced by a unit flux of vacancies in an isothermal system, and that any atomistic model for Q_v must be based on a mechanism that operates in an isothermal system, or at least it must be reducible to that basis.

Equations (6) and (7) are general in that one does not inquire into how a $\nabla(\mu_v/T)$ arises. The usual assumption that has been made is that the vacancies are in local equilibrium, that is, that the local concentration is that demanded by

$$x_v^\circ(T) = \exp(-h_v/kT) \tag{9}$$

at the local temperature, where x_v° is the atomic fraction of vacancies at thermal equilibrium and h_v is the enthalpy of formation of one vacancy. That the assumption of local vacancy equilibrium is generally a good one is shown by the work of Seidman and Balluffi[4] on the efficiency of dislocation climb. Making this assumption then, and taking the chemical potential of vacancies relative to that of the vacancy concentration, x_v°, at thermal equilibrium, i.e.

$$\mu_v = kT \ln(x_v/x_v^\circ) \tag{10}$$

one finds* that $\nabla(\mu_v/T) = 0$, so that equations (6) and (7) become

$$J_v = -L_{vv}Q_v \nabla \ln T = -\frac{D_v c_v}{kT} Q_v \nabla \ln T \tag{11}$$

$$J_u = -L_{uu} \nabla \ln T \tag{12}$$

where D_v and c_v are respectively the diffusivity and the volume concentration of vacancies. Remembering that $J_v = -J_1$ and therefore $Q_v = -Q_1$, and that $D_v c_v = D_1 c_1/\gamma$, where 1 represents the pure component and D_1 is the tracer self diffusion coefficient of 1, (γ is the correlation coefficient) equation (11) becomes

$$J_1 = -\frac{D_1 c_1}{kT\gamma} Q_1 \nabla \ln T, \tag{13}$$

where Q_1 has the significance given by (see equation (8))

$$J_u = Q_1 J_1 \, (\nabla T = 0). \tag{14}$$

Comparing equation (13) with equation (2) we see that $Q_1 = Q'_m$. We note in passing that if sources and sinks for vacancies are not perfectly efficient, $\nabla(\mu_v/T)$ would acquire a nonzero value such that J_v would be smaller than that given by equation (11); consequently the calculated $|Q_1|$ would be smaller than if vacancies were everywhere in local equilibrium.

We need not have chosen $x_v^\circ(T)$ as the reference state for μ_v; it is just as reasonable to refer the μ_v to some constant, temperature-independent vacancy concentration, x'_v. With this choice, $\mu_v = kT \ln(x_v/x'_v)$, and $\nabla(\mu_v/T) = k \nabla \ln x_v$. Under the assumption, as before, that the vacancies are everywhere in local thermal equilibrium, $x_v = x^\circ$,

$$(\mu_v/T) = k \nabla \ln x_v^\circ$$

and by equation (9),

$$(\mu_v/T) = \frac{h_v \nabla T}{T^2} = \frac{h_v}{T} \nabla \ln T$$

Substituting in relations (3) and (4) and proceeding as before, we obtain

$$J_v = -L_{vv}(Q_v + h_v) \nabla \ln T \tag{15}$$

$$J_u = -(L_{vv}Q_v h_v + L_{uu}) \nabla \ln T \tag{16}$$

where the J_u of equation (16) is different from that of equation (12). To see the relation between these two energy fluxes, we make use of the invariance[3] of the rate of entropy production with respect to choice of forces and fluxes. Using the superscripts to signify the equation, and hence the development

---

*Since by hypothesis, $x_v = x_v^\circ$ everywhere,

$$(\mu_v/T) = k \nabla \ln(x_v/x_v^\circ) = k \nabla \ln(x_v^\circ/x_v^\circ) = 0.$$

For an alternative proof see Appendix to Chap. XV of reference [5].

to which the quantities refer, we can write the rate of entropy production, $\Delta\dot{S}$, as

$$\Delta\dot{S} = J_v^{(11)}\cdot[-\nabla(\mu_v/T)]^{(11)} + J_u^{(12)}\cdot\left[-\frac{\nabla \ln T}{T}\right]$$

$$= J_v^{(15)}\cdot[-\nabla(\mu_v/T)]^{(15)} + J_u^{(16)}\cdot\left[-\frac{\nabla \ln T}{T}\right]$$

Substituting $J_v^{(11)} = J_v^{(15)} = J_v$, $[\nabla(\mu_v/T)]^{(11)} = 0$, and $[\nabla(\mu_v/T)]^{(15)} = (h_v/T)\nabla \ln T$, one obtains

$$J_u^{(16)} = J_u^{(12)} - h_v J_v \tag{17}$$

or since $J_v = -J_1$,

$$J_u^{(12)} = J_u^{(16)} - h_v J_1. \tag{18}$$

To see the relation between the heats of transport we first rewrite equation (15) in the equivalent fashion

$$J_1 = -\frac{D_1 c_1}{kT\gamma}(Q_1 - h_v)\nabla \ln T \tag{19}$$

and comparing with equation (13) we see that

$$Q_1^{(13)} = Q_1^{(19)} - h_v = Q'_m. \tag{20}$$

Thus we see by comparing equations that whereas $Q_1^{(13)}$ relates $J_u^{(12)}$ to J_1, $Q_1^{(19)}$ relates $(J_u^{(12)} + h_v J_1)$ to J_1, all in isothermal systems, and since $Q_1^{(19)} = Q_1^{(13)} + h_v$ (equation (20)) in the formulation stemming from the choice of a constant vacancy concentration as the reference state for μ_v both the heat of transport $Q^{(19)}$ and the energy flux $J_u^{(16)}$ have corresponding contributions from h_v. Such contributions are absent in both $Q_1^{(13)}$ and $J_u^{(12)}$. Q_m^1 remains independent of h_v in both formalisms (equation 20).

It is instructive now to choose another generalized force, $(-\nabla\mu_v)_T$, in terms of which to express the fluxes:

$$J_v = -L_{vv}(\nabla\mu_v)_T - L_{vu}\nabla \ln T \tag{21}$$

$$J_u = -L_{vu}(\nabla\mu_v)_T - L_{uu}\nabla \ln T \tag{22}$$

in which J_u and the coefficients need not have the same values as in the foregoing relations. We will again assume local thermal equilibrium of the vacancy concentration, and use equation (10) to express μ_v. Then

$$(\nabla\mu_v)_T = kT\nabla(\ln x_v - \ln x_v^\circ) = kT\nabla \ln x_v \tag{23a}$$

where $\nabla \ln x_v$ corresponds to the actual distribution of concentration that obtained in the temperature gradient, and since we require local thermal equilibrium of vacancies,

$$\nabla \ln x_v = \nabla \ln x_v^\circ(T) = \frac{\mathrm{d}\ln x_v^\circ}{\mathrm{d}T}\nabla T$$
$$= \frac{h_v}{kT^2}\nabla T. \tag{23b}$$

Substituting into equations (21) and (22), and defining $Q_v \equiv L_{vu}/L_{vv}$ one obtains equations identical with equations (15) and (16) and all the subsequent relations follow.

It is also possible to develop a formalism on the basis of considering the vacancies as a chemical component. This is justifiable since, in principle at least, the ratio between the vacancies and the atoms can be varied at will at any one temperature, for example by quenching from a higher temperature in circumstances where sources and sinks for vacancies are absent or ineffectual. If the vacancies are to be considered as independent entities, then

$$J_1 + J_v = 0 \tag{24}$$

$$x_1 \mathrm{d}\mu_1 + x_v \mathrm{d}\mu_v = 0 \tag{25}$$

where (25) is the Gibbs–Duhem equation, valid in an isothermal system. Because of equation (24), and using $-\nabla(\mu/T)$ as the generalized force, the phenomenological equations are

$$J_1 = -L_{11}T[\nabla(\mu_1/T) - \nabla(\mu_v/T)] - L_{1u}\nabla \ln T \tag{26}$$

$$J_u = -L_{u1}T[\nabla(\mu_1/T) - \nabla(\mu_v/T)] - L_{uu}\nabla \ln T. \tag{27}$$

We recall the thermodynamic relation,

$$\nabla(\mu/T) = \frac{1}{T}(\nabla\mu)_T + (\nabla T)[\partial(\mu/T)/\partial T]_x \tag{28}$$

and we apply it both to component 1 and to the vacancies. Defining $Q_1 \equiv L_{1u}/L_{11}$, we obtain

$$J_1 = -L_{11}\left\{-\frac{x_v}{x_1}(\nabla\mu_v)_T - (\nabla\mu_v)_T + (h_v - h_1 + Q_1)\nabla \ln T\right\}$$

$$J_u = -L_{11}Q_1\left[-\frac{x_v}{x_1}(\nabla\mu_v)_T - (\nabla\mu_v)_T + (h_v - h_1)\nabla \ln T\right] - L_{uu}\nabla \ln T.$$

These equations are quite general and may be used for any vacancy concentration gradient existing in the specimen; we note that $(\nabla\mu_v)_T$ is evaluated at constant temperature for the concentration distribution actually existing in the specimen under the temperature gradient. h_1 is the specific, partial enthalpy of component 1 and arises from the term $\partial(\mu_1/T)/\partial T$ of equation (28). If now we again consider that the vacancies in the specimen in a temperature gradient are everywhere at local thermal equilibrium, and use equation (10) to express μ_v, equations (23) apply. Then neglecting x_v/x_1 in comparison with unity one obtains

$$J_1 = -L_{11}(Q_1 - h_1)\nabla \ln T = -\frac{D_1c_1}{kT\gamma} \times (Q_1 - h_1)\nabla \ln T \quad (29)$$

$$J_u = (L_{11}Q_1h_1 - L_{uu})\nabla \ln T. \quad (30)$$

Comparing equations (13) and (29) one sees that

$$Q_1^{(29)} = Q_1^{(13)} + h_1 \quad (31)$$

and by comparing the expressions for the rate of entropy production,

$$J_u^{(30)} = J_u^{(12)} + h_1J_1. \quad (32)$$

Thus, both Q_1 and J_u of this formalism have a contribution from h_1, but it is not necessary to know the magnitude of h_1 since it cancels out, for the measurable quantity, Q'_m, is

$$Q'_m = Q_1^{(29)} - h_1. \quad (33)$$

The fifth and last formalism[5, 6] that we shall discuss is that using $-(\nabla\mu)_T$ as the generalized force in the context of vacancies as an independent component. The general equations are subsequently (as in the foregoing section) reduced to the case of local thermal equilibrium concentration of vacancies, obtaining

$$J_1 = -L_{11}(Q_1 - h_v)\nabla \ln T = -\frac{D_1c_1}{kT\gamma} \times (Q_1 - h_v)\nabla \ln T \quad (34)$$

$$J_u = (L_{11}Q_1h_v - L_{uu})\nabla \ln T. \quad (35)$$

As with equations (15) and (16),

$$Q_1^{(34)} = Q_1^{(13)} + h_v$$
$$J_u^{(35)} = J_u^{(12)} + h_vJ_1$$
$$Q'_m = Q_1^{(34)} - h_v.$$

We may summarize this section as follows:

$$Q'_m = Q_1^{(13)} = Q_1^{(19)} - h_v = Q_1^{(29)} - h_1 = Q_1^{(34)} - h_v. \quad (36)$$

The lesson to be drawn from these comparisons is that the phenomenological quantity which is to be interpreted atomistically is Q'_m, a quantity free of equilibrium-thermodynamic parameters h_1 and h_v. In particular, for the atomistic interpretation of thermomigration one need not add h_v to, or subtract h_v from, the measured heat of transport, Q'_m.

(*B*) *Two-component solid solutions*

The same variety of formalisms can be applied to systems of two material components. To avoid repetition we will only outline the procedures and give the results.

We consider first the interstitial solid solution in which only the interstitial solute diffuses at the temperatures of interest and the lattice of host atoms provides a convenient frame of reference for the diffusive flux. If 1 represents the mobile component and we employ $-\nabla(\mu_1/T)$ and $-(1/T)\nabla \ln T$ as the generalized forces, the resulting phenomenological equations are

$$J_1 = -\frac{D_1c_1}{kT}[(\nabla\mu_1)_T + (Q_1 - h_1)\nabla \ln T] \quad (37)$$

$$J_u = -\frac{D_1c_1}{kT}Q_1[(\nabla\mu_1)_T - h_1\nabla\ln T] - L_{uu}\ \ln T \qquad (38)$$

where $Q_1 \equiv L_{1u}/L_{11}$, and equation (28) has been used. If the experiment is continued to the steady state of $J_1 = 0$, and if the activity coefficient is constant in the composition range of interest, the above equations become

$$-kT\frac{\mathrm{d}\ln c_1}{\mathrm{d}\ln T} = (Q_1 - h_1) \qquad (39)$$

$$J_u(J_1 = 0) = \left(\frac{D_1c_1}{kT}Q_1^2 - L_{uu}\right)\nabla\ln T. \qquad (40)$$

Comparing equations (39) and (1) we see that

$$Q_m = Q_1 - h_1. \qquad (41)$$

If on the other hand, the generalized forces are taken as $-(\nabla\mu_1)_T$ and $-(1/T)\nabla\ln T$, the corresponding relations for the interstitial solute are

$$-kT\frac{\mathrm{d}\ln c_1}{\mathrm{d}\ln T} = Q_1 \qquad (42)$$

$$J_u(J_1 = 0) = \left(\frac{D_1c_1}{kT}Q_1^2 - L_{uu}\right)\nabla\ln T \qquad (43)$$

and

$$Q_m = Q_1. \qquad (44)$$

The interrelations between the two Q_1's and the two heat fluxes are

$$Q_1^{(42)} = Q_1^{(39)} - h_1 \qquad (45)$$

$$J_u^{(43)} = J_u^{(40)} - h_1J_1 \qquad (46)$$

so that both $Q_1^{(39)}$ and $J_u^{(40)}$ (in the $\nabla\ (\mu_1/T)$ formalism) have contributions from h_1. It follows that Q_m is independent of h_1, irrespective of formalism.

For the case of two mobile components in a two-component system, each one moving by the vacancy exchange mechanism we shall only present the equations developed in a particularly general way by Lidiard[6]. Taking vacancies as a third independent component, the generalized forces as $(\nabla\mu_v)_T - (\nabla\mu_i)_T$ (where $i = 1, 2$) since $J_1 + J_2 + J_v = 0$, and using the Gibbs–Duhem equation $x_1\mathrm{d}\mu_1 + x_2\mathrm{d}\mu_2 + x_v\mathrm{d}\mu_v = 0$, he obtains for the flux with respect to the fixed parts of the specimen (i.e. where there are negligible concentration and temperature gradients)

$$J_2 = \mathbf{D}\nabla c_2 - \frac{c_1c_2}{kT} \times \frac{[D_2(Q_2 - h_v) - D_1(Q_1 - h_v)]}{\left(1 + \frac{\partial\ln\gamma_1}{\partial\ln c_1}\right)}\nabla\ln T \qquad (47)$$

where $\mathbf{D} = c_2D_1 + c_1D_2$ and γ_1 is the activity coefficient of component 1. This equation was derived on the supposition of local thermal equilibrium vacancy concentration, and represents exactly the same formalism underlying equation (34). It will be noted that (47) reduces to (34) when component 2 is the sole chemical component.

At steady state (i.e. $J_2 = 0$), equation (47) becomes

$$kT\frac{\nabla\ln c_2}{\nabla\ln T} = \frac{c_1[D_1(Q_1 - h_v) - D_2(Q_2 - h_v)]}{\mathbf{D}\left(1 + \frac{\partial\ln\gamma_1}{\partial\ln c_1}\right)}. \qquad (48)$$

Comparison with equation (1) shows that for the case of a substitutional alloy

$$-Q_m = \frac{c_1[D_1(Q_1 - h_v) - D_2(Q_2 - h_v)]}{\mathbf{D}\left(1 + \frac{\partial\ln\gamma_1}{\partial\ln c_1}\right)}. \qquad (49)$$

Lidiard[6] has shown that for a substitutional alloy dilute in component 2, equation (48) reduces to

$$-kT\frac{\nabla\ln c_2}{\nabla\ln T} = (Q_2 - h_v) - \frac{D_1^{(c)}}{D_2} \times (Q^\circ_1 - h_v) = Q_m \qquad (50)$$

where

$$D_1^{(c)} = D_1\left(1 + \frac{\partial\ln\gamma_1}{\partial\ln c_1}\right),$$

D_1 and D_2 are the tracer diffusion coefficients of 1 and 2 respectively, and Q_1° is the heat of transport for the pure solvent species 1. In general then, Q_m for a binary substitutional alloy is a complex quantity, but since $Q_t^{(49)}$ contains h_c (see equation (34) *et seq.*) one does not need to consider h_v in an atomistic interpretation of Q_m.

All the equations presented in this section and relevant to a vacancy exchange mechanism have been obtained on the assumption of local equilibrium concentration of vacancies. Blackburn[7] has considered possible supersaturations of vacancies produced by temperature gradients, and these are generally negligible. It should be remarked that accounting for actual vacancy supersaturations would in effect correct the observed J_1, but would not improve the phenomenology as a basis for the atomistic description of the heat of transport.

ATOMISTIC INTERPRETATION OF HEAT OF TRANSPORT

The central problem in thermomigration is the formulation of an atomistic model for the mechanism underlying the heat of transport. This may be done either on the basis of the mass flux produced by an impressed temperature gradient (represented by relations of the type of equation (13)), or on the basis of the energy flux produced by a flux of mass under isothermal conditions (represented by relations of the type of equation (14)). Indeed, one of the virtues of irreversible thermodynamics is that the underlying identity between the finite-field effect (e.g. equation (13)) and the zero-field effect (e.g. equation (14)) is clearly evident. It follows that an atomistic model that purports to represent the mechanism of the finite-field effect must also represent that of the zero-field phenomenon. In fact it can be asserted that a model that is able to represent one process but not the other must be incorrect.

There is a group of models[8–13] that explicitly depend upon a temperature gradient for their mechanism, the most general of which is that of Wirtz[8]. One considers that a portion of the activation energy is utilized at one temperature, T_1, to shake the jumping atom loose from its environing neighbors, another portion is used at T_2 to move aside the atoms situated between the original and the final position of the jumping atom, and still another portion of the activation energy is utilized at T_3 to prepare the arrival site. In the case of a vacancy mechanism, the last portion is interpreted as the energy of vacancy formation, h_v. Depending upon the details of the model, one obtains $Q_m = E$, the activation energy for migration, or $Q_m = E - h_v$, but in any case $|Q_m| \leq E$. Such models have been criticized [5, 14], unjustifiably we believe, on account of the difficulty of specifying a difference of temperature between two atomic planes. A more serious criticism is that experimental values of $|Q_m|$ are often larger than E. In addition, it appears impossible to infer from the Wirtz-type mechanism a flux of energy due to an isothermal flux of mass (e.g., equation (14)) driven, for example, by a concentration gradient. The only feature of the Wirtz model that persists in the domain of $\nabla T = 0$ is the spatially inhomogeneous distribution of activation energy. Since nothing is said about the decay of this distribution nothing is specified about the flux of energy accompanying the atom jump. Hence the Wirtz model does not touch upon the crux of the problem of thermomigration as embodied in equation (14). For these reasons this writer concludes that the Wirtz-type of model does not correctly represent the physics of thermomigration.

This writer[15–17] has reasoned from the point of view of the isothermal effect (equation (14)) and has stressed that the kernel of the problem is the difference between the spatial distribution of the dissipation of E after the jump of the atom and the spatial distribution of E as it collects about the atom prior to its jump. The original thinking led to the conclusion that $|Q_m| \leq E$. Haga[18, 6] has also reasoned along the same lines and obtained $0 < Q_m \leq E$. More recently it has been recognized[1] that there has been a basic misconception in considering Q_m to signify a quantity of energy, as the ratio of J_u to J_1

would indicate (equation (14)). Adhering closely to the physical meaning given by equation (14) to $Q_1 (= Q_m)$, that of heat flux per unit mass flux at $\nabla T = 0$, and recalling from equation (36) that Q_m is a quantity free of equilibrium-thermodynamic parameters, one can utilize transition-state reaction theory to develop an expression* for Q_m.

Consider a one-dimensional, isothermal crystal in which the diffusive displacement of the atom is λ. The number of successful (i.e. completed) jumps by one vacancy (or by one interstitial solute atom) per second will be given by $(kT/h)\exp(-E/kT)$. If c is the number density of vacancies (or of interstitial solute atoms), the number of vacancy (or interstitial atom) jumps per second per unit volume in just *one* sense will be

$$N_j = \frac{c}{2}\frac{kT}{h}\exp(-E/kT).$$

Of course in this isothermal system there will be an equal number of jumps in the opposite sense. Since the displacement per jump is $\lambda_v (= -\lambda_1)$ the vacancy flux in one sense will be

$$j_v = N_j\lambda_v. \quad (53)$$

Now, the thermal energy involved per jump is E, the activation energy for the change of place. Since the jump of the vacancy (or interstitial atom) represents an intrinsic asymmetry in the process one must expect an asymmetry due to the jump between how E is gathered in before the jump and how it is dissipated into the surrounding lattice after the jump. Let λ_E represent the displacement of the fraction, f, of E that is dissipated asymmetrically. f is a function of the scattering cross-section of the jumping entity for the energy carriers, and λ_E is a function of the energy dissipation mechanisms in the environing lattice. In these terms, $2N_jE$ is the amount of thermal energy per second per unit volume that would be subject to asymmetric dissipation. Hence, the flux of energy in *one* sense is

$$j_u = N_j f E\lambda_E. \quad (54)$$

One can now use equations (53) and (54) in equation (8) to obtain

$$fE\lambda_E = -Q_v\lambda_1 = Q_1\lambda_1$$

and since λ_E and λ_1 are colinear vectors one can write

$$Q_1 = \frac{\lambda_E}{\lambda_1} fE. \quad (55)$$

Thus, Q_1 (and hence Q_m) can be larger or smaller in magnitude than E, and may be a positive or a negative quantity depending on whether λ_E is parallel or antiparallel with λ_1. It may be remarked that there is no change in this formalism when going to a three-dimensional system with diffusion in only one dimension.

This kinetic model for the heat of transport was developed for the zero-field effect (equation (14)). That it is also consistent with the finite-field phenomenon (equation (13)) can be seen with the help of the le Chatelier principle. An externally impressed temperature gradient will favor a j_u (associated with the mass flux) directed towards lower temperatures since a j_u in that direction tends to moderate the applied generalized force (i.e. the grad T). Hence, of the opposite and equal j_1's in the isothermal case, the j_1 that produces the j_u directed toward lower temperatures will be favored in the presence of grad T. Thus, for j_1 parallel to j_u (positive Q_1) the applied grad T will favor j_1 towards the lower temperatures, and for j_1 antiparallel to j_u (negative Q_1) a net mass flux, J_1, towards the higher temperatures will be produced. This is of course in keeping with equation (13).

Our argument based on the zero-field effect has led us to focus on the asymmetric dissipation of the activation energy for the jump of the atom and to relate this to the asymmetry inherent in the atomic displacement. Clearly what is involved is energy transfer between the dynamic entity called the activated complex and the energy carriers of the lattice, the phonons and electrons. The moving phonon packet, in terms of which the activation complex may be regarded, interacts dynamically with the phonon field of the atomic lattice, and in the case of a metal, with the field of conduction electrons, producing an asymmetric phonon flux and an asymmetric electron (including electron holes) flux. The electron flux thus produced gives rise to the phenomenon of electromigration[19], and both the electron flux and the phonon flux contribute to J_u (see equation (14)) in proportion to the scattering cross-sections for electrons and for phonons, respectively, and to the electron and phonon mean free paths.

---

*This is a simplification and clarification of the argument in reference[1].

Because in a metal the primary energy carrier is the electron, one would expect that the chief mechanism of Q would be electron scattering[1], and indeed in simple metals, where the only charge carriers are the electrons (i.e. absence of electron holes), a simple correlation may be adduced[1] between the sign of the electromigration charge of transport and the sign of the heat of transport in thermomigration. In general such a correlation is not to be expected, however. Because collision cross-sections and mean free paths in general have finite temperature coefficients one would expect Q_m to be temperature dependent; in contrast, the Wirtz-type models predict temperature independence. It is interesting that whenever sufficiently accurate data for Q_m have been obtained[1, 20, 21], a large temperature dependence has been found.

In the foregoing we used the le Chatelier principle of moderation to show the equivalence at the phenomenological level of the interpretation of Q_m from the zero-field effect and from the finite-field effect. Similarly, at the mechanistic level of collision cross-sections we can utilize Newton's Third Law to demonstrate that equivalence. The mechanism that we have proposed, based on equation (14), is that the moving activated complex transfers momentum and energy to the phonon and electron fields, but since action equals reaction, it is equally valid to consider that electrons and phonons moving in response to an applied temperature gradient can transfer momentum and energy to the activated complex, thereby biasing the otherwise random atomic jumps to produce a net mass flux. This is in fact the point of view taken by Fiks with respect to phonons[22], and subsequently with respect to electrons[23]. Fiks, as well as Gerl[14], has made quantitative estimates of the contribution to the heat of transport arising from the momentum transfer between moving conduction electrons and the jumping atom. Huntington and Grone[24] and Bosvieux and Friedel[25] have attempted similar calculations for the closely allied problem of electromigration.

These calculations are very difficult to do accurately since what is required is the scattering cross-section, and its variation with electron energy, of the activated complex for electrons and for electron holes. This requires a knowledge of the electron screening of the jumping atom as the environing atoms change their positions. In addition, it is not enough to consider the exchange of momentum between the phonon and electron fields and the jumping atom itself, but the entire disturbed region as a whole must be considered. In particular, for $Q_1 < 0$, so that at $\nabla T = 0$, j_1 and j_u are antiparallel, the only way to understand how energy can be moved backwards relative to the displacement of the jumping atom is to consider that the sphincter atoms (i.e. those most impeding passage of the jumping atom) themselves have a backward component of motion, thereby imparting momentum and energy to the phonon and electron fields in the sense opposite to that of the jumping atom. The problem of momentum transfer between a phonon current and a jumping vacancy in a linear chain of atoms, has been treated by Schottky[26], and for three-dimensional lattices by Gerl[14]. The same difficulties arise here as discussed above.

In a bar of metal having only electrons as charge carriers and supporting a temperature gradient, there exist two countercurrent fluxes of electrons. The more energetic electrons carry energy from the higher- to the lower-temperature end of the bar, and the zero net electrical current is accomplished by an equal flux of 'cold' electrons toward the hotter end of the specimen. Hence, any contribution from the electron-phonon interaction to the heat of transport must, in such one-band metals, be due only to the variation of electron–phonon scattering cross-section with electron energy. However a metal that has both electrons and electron holes as charge carriers can satisfy the requirement of zero net electrical current by co-directional fluxes of electrons and holes towards the lower-temperature part of the specimen. Hence as Huntington[27] has suggested, one would expect in such a metal a larger Q_m, since the electron and the electron hole interactions with the activation complex both would have the same sense. It is perhaps for this reason that there appears the trend, noted earlier, for larger heats of transport in the transition metals.

SUMMARY AND CONCLUDING REMARKS

By comparing the results of carrying out the formalism of irreversible thermodynamics we have shown that the experimentally observable quantities always lead to a heat of transport, Q_m, that has no contribution from equilibrium-thermodynamic quantities h_v or h_1. The basic reason for this is that both the phenomenologically defined J_u and Q_1 have the same contributions from such quantities. The Q_m is to be interpreted completely kinetically as the flux of energy produced in an isothermal system by a unit flux of mass. Because of this the Wirtz-type of model is rejected as not at all representing the basic mechanism of thermomigration.

Based upon the physical significance of Q_m in an isothermal system, a qualitative model is developed for the asymmetric dissipation of the activation energy of the atomic jump; energy dissipation via both electrons and phonons is stressed and the close connection is pointed out between thermomigration and electromigration in metals. This model is shown to be equivalent to that independently developed by Fiks for the non-isothermal situation. The quantitative evaluation of these models will necessarily be very difficult.

Acknowledgements—The Author is grateful for helpful critical comments by Drs. J. C. M. Li, Charles A. Johnson, and N. P. Louat, all of the E.C. Bain Laboratory.

REFERENCES

1. GONZALEZ O. D. and ORIANI R. A., *Trans. metall. Soc. A.I.M.E.* **233** 1878, (1965).
2. COMPAAN K. and HAVEN Y., *Trans. Faraday Soc.* **52**, 786 (1956); **54**, 1498 (1958).
3. DE GROOT S. R., *Thermodynamics of Irreversible Processes*, Chap. 1. Interscience, New York (1951).
4. SEIDMAN D. N. and BALLUFFI R. W., *Phys. Status Solidi* **17**, 531 (1966).
5. ADDA Y. and PHILIBERT J., *La Diffusion dans les Solides*, Vol. II. Institut National des Sciences et Techniques Nucleaires, Saclay (1966).
6. LIDIARD A. B., *Proceedings of a Symposium (July 1965, Vienna) on Thermodynamics*, Vol. II, pp. 3–22. International Atomic Energy Agency (1966).
7. BLACKBURN D. A., *J. Phys. Chem. Solids* **27**, 1653 (1966).
8. WIRTZ K., *Phys. Z.* **44**, 221 (1943).
9. LeCLAIRE A. D., *Phys. Rev.* **93**, 344 (1954).
10. BRINKMAN J. A., *Phys. Rev.* **93**, 345 (1954).
11. KEYES R. W., *Phys. Rev.* **94**, 1389 (1954).
12. GIRIFALCO L. A., *Phys. Rev.* **128**, 2630 (1962).
13. ALLNATT A. R. and RICE S. A., *J. chem. Phys.* **33**, 573 (1960).
14. GERL M., *J. Phys. Chem. Solids* **28**, 725 (1967).
15. DARKEN L. S. and ORIANI R. A., *Acta Metall.* **2**, 608 (1954).
16. ORIANI R. A., *Proceedings Symposium on Thermophysical Properties, ASME*, p. 123. Purdue University (1959).
17. ORIANI R. A., *J. chem. Phys.* **34**, 1773 (1961).
18. HAGA E., *Proc. phys. Soc.* **15**, 1949 (1960).
19. ORIANI R. A. and GONZALEZ O. D., *Trans. metall. Soc. A.I.M.E.* **239**, 1041 (1967).
20. DROEGE J. W., USAEC Report, Battelle Memorial Institute 1502.
21. HO P. S., *J. Phys. Chem. Solids* **27**, 1331 (1966).
22. FIKS V. B., *Soviet Phys. solid St.* **3**, 724 (1961).
23. FIKS V. B., *Soviet Phys. solid St.* **5**, 2549 (1964).
24. HUNTINGTON H. B. and GRONE A. R., *J. Phys. Chem. Solids* **20**, 76 (1961).
25. BOSVIEUX C. and FRIEDEL J., *J. Phys. Chem. Solids* **23**, 123 (1962).
26. SCHOTTKY G., *Phys. Status Solidi* **8**, 357 (1965).
27. HUNTINGTON H. B., *Bull. Am. phys. Soc.* **11**, 265 (1966).

J. Phys. Chem. Solids **Pergamon Press 1969. Vol. 30, pp. 353–357. Printed in Great Britain.**

OPTICAL TRANSMISSION IN SINGLE CRYSTAL SILICON DISELENIDE*

E. A. HAUSCHILD† and C. R. KANNEWURF
Department of Electrical Engineering, Northwestern University, Evanston, Ill. 60201, U.S.A.

(*Received* 7 *March* 1968; *in revised form* 11 *July* 1968)

Abstract—Single crystal filament type samples of silicon diselenide, $SiSe_2$, have been prepared by vapor deposition. The crystal system is body-centered orthorhombic belonging to the C42 structure type. Optical absorption measurements over the wavelength range 0·45 to 2·2 μ were made with the incident radiation polarized both parallel and perpendicular to the crystallographic *c* axis, the direction of length in the growth habit of the single crystals. Analysis of the absorption curves indicates the material to be an indirect band gap semiconductor with $E_g \leq 1{\cdot}73 \pm 0{\cdot}05$ eV. Semiconductor behavior has been predicted for materials belonging to the C42 structure type.

INTRODUCTION

In a recent report from this laboratory some optical properties of silicon ditelluride were discussed[1]. Similar measurements have been completed for silicon diselenide, $SiSe_2$, and are presented in this paper. Silicon diselenide was first synthesized by Sabatier [2]. Weiss and Weiss[3] prepared crystalline material and determined the crystal structure to be body-centered orthorhombic. The structure is isotypic with that of silicon disulfide, the prototype for the C42 class of structure types. The compounds SiS_2, $SiSe_2$, and one form of SiO_2 are the only known members of the C42 class. A general summary of this structure type is given by Parthé[4].

In a survey of materials Mooser and Pearson[5] predicted semiconductor behavior for a number of crystalline solids including SiS_2. This conclusion is based principally upon identifying in the various structure types the presence of predominantly covalent bonds. In the case of the SiS_2 structure they noted the tetrahedral coordination of the silicon atoms in conjunction with the two-coordinated sulfur atoms. Since $SiSe_2$ is isotypic to SiS_2, their prediction should extend to the diselenide as well. In view of this prediction and the fact that physical properties other than crystal structure have not been reported for any of the three C42 type materials it seemed desirable to extend the silicon chalcogenide work to the Si–Se system. The choice of the selenide for this investigation was due to the fact that better quality single crystal material could be prepared of $SiSe_2$ than for either the oxide or sulfide.

CRYSTAL PREPARATION AND GROWTH ORIENTATION

Polycrystalline ingots of $SiSe_2$ were obtained by direct synthesis of stoichiometric proportions of the elements* in quartz tubes evacuated to 10^{-3} Torr. Synthesis tubes were placed in a furnace that was maintained at a temperature of 1000°C for periods of 4–7 days. Variation in cooling rates had no appreciable effect on the homogeneity of the ingot. Single crystal sections large enough for physical measurements could not be obtained from the ingots. The most successful method employed to obtain single crystal material was

---

*This research was supported in part by the Advanced Research Projects Agency of the Department of Defense through the Northwestern University Materials Research Center.

†*Present address:* Bell Telephone Laboratories Inc., Naperville, Illinois, U.S.A.

*Silicon was obtained from the A. D. MacKay Co., purity: 5-nines; selenium from the American Smelting and Refining Co., purity: 5-nines.

vapor transport of ingot material in evacuated tubes using iodine as the transporting agent. Optimum results were obtained in a two stage oven with the high temperature zone at 810°C and the low temperature zone at 730°C. Single crystal growth on the tube walls is in the form of dark red rods 1 to 1·5 cm long, typical cross section dimensions: 1 by 0·1 mm. Larger crystals were found to be generally inhomogeneous. The crystals tend to split along the length of the rods but show no identifiable pattern of geometrical cleavage.

As long as the crystals are stored in vacuum of 10^{-3} Torr. or better no appreciable amount of chemical decomposition takes place. Freshly prepared material, when exposed to laboratory atmosphere, reacts in a matter of minutes with water vapor in the air causing the surface to decompose and form a region composed of selenium and silicon oxide. The decomposed surface forms a semi-protective shield which tends to retard the rate of decomposition of the inner volume of the crystals. Most measurements were made with freshly prepared material in vacuum or immersed in carbon tetrachloride. Evidence of decomposition with crystals immersed in CCl_4 could not be found for periods of time less than 2 weeks. From chemical analysis of crystals stored in CCl_4 the iodine content was found to be 0·18 per cent. As a result of the chemical instability of the material, it was not possible by using a radioactive iodine tracer method to accurately determine whether the majority of this rather high level of iodine content was contained primarily in the surface layers and not the interior of the crystals. Since iodine is readily soluble in CCl_4, any residual iodine vapor that condensed on the crystal surface during the growth tube cooling period has already been dissolved. An analysis for silicon content showed a deficiency of only 0·04 per cent from stoichiometric composition.

To confirm the crystal structure assignment, Debye–Scherer photographs were prepared. Weiss and Weiss[3] reported the crystal system to be body-centered orthorhombic with lattice values $a = 6{\cdot}03$, $b = 9{\cdot}76$ and $c = 5{\cdot}76$ Å; the space group is D_{2h}^{26} – Ibam. Each unit cell contains 4 molecules of $SiSe_2$. To the extent of the crystal structure information presented by Weiss and Weiss[3,6], agreement with their work was obtained in the present investigation. Also a general correspondence was obtained with the more complete structure details reported for SiS_2[7] and SiO_2[6]. In all X-ray powder photographs the presence of selenium could be identified, indicating various degrees of decomposition in the powder samples. After a 2½ hr X-ray exposure the amount of elemental selenium found in the $SiSe_2$ powder samples varied from 1 to 5 per cent. A measured density of $3{\cdot}63 \pm 0{\cdot}03$ gm/cm^3 was found for single crystal material which is in good agreement with the calculated value of 3·64 gm/cm^3 using the lattice values given by Weiss and Weiss[3].

From an analysis of Laué photographs the growth orientation of the single crystals was determined. Figure 1 shows the typical growth orientation with respect to the principal crystallographic directions. The direction of length in the rods is along the c axis. The major parallel surfaces of the rods were found to be (110) type planes; thus the direction of the width of the rods is along a [110] direction. The location of the atoms with respect to the lattice is in a fibrous type arrangement along the direction of the c axis. The silicon–selenium bonding can be symbolically represented by the following pattern:

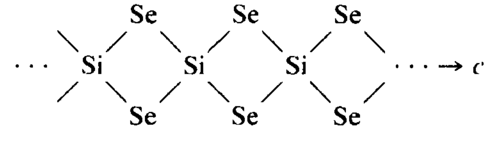

This is essentially a one-dimensional chain with the minimum interatomic Si–Se distance being 2·23 Å. Such a scheme was proposed by Zintl and Loosen[7] in their structure analysis of SiS_2. Three-dimensional representations of

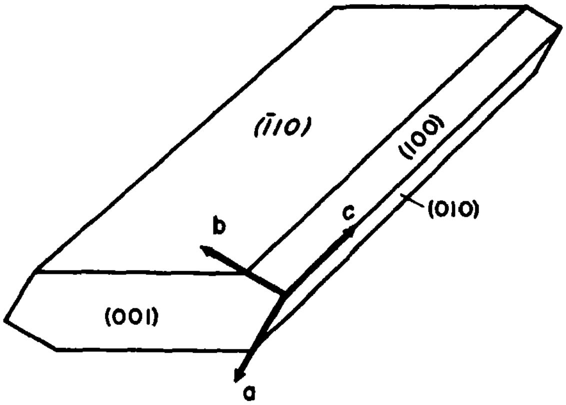

Fig. 1. Single crystal growth orientation with respect to principal crystallographic directions.

the C42 structure type are available in the literature[4,7].

OPTICAL ABSORPTION

The sample-in sample-out technique was employed to obtain the percent transmission through single crystal material. A brief description with spectral resolution values for the optical system employed has been given in previous papers from this laboratory (See e.g. reference [1]). Samples were placed over precision apertures and the entire sample holder immersed in GC-spectrophotometric grade CCl_4. The reference aperture was also positioned in the light beam while immersed in CCl_4. The carbon tetrachloride environment was found necessary for reproducible transmission measurements. The effect of chemical decomposition was readily observed in transmission data for samples mounted in inert gases or vacuum due primarily in the latter case to the time delay in positioning the sample on the aperture plate and evacuating the transmission chamber. Without any protective care as the selenium layer increases in the deteriorating surface, the optical transmission through crystals on the long wavelength side of the absorption edge at 1·0 μ was found after a three hour exposure to laboratory atmosphere to be only 1/4 to 1/12 of the transmission through crystals of comparable thickness in a CCl_4 environment. With aperture plates to be immersed in CCl_4 for the actual transmission measurements, sample handling and mounting operations could be performed with the crystals immersed immediately after a growth tube was opened. Throughout the spectral range of interest CCl_4 has no major absorption bands.

The incident radiation was normal to the (110) type planes of the crystal, polarized either parallel or perpendicular to the crystallographic *c* axis. Absorption coefficients were calculated using the numerical tables prepared by Kahan[8,9] for the analysis of optical transmission measurements in semiconductor materials. Figure 2 shows the absorption coefficient versus wavelength over the wavelength range of 0·45 to 2·2 μ. These curves represent data from a number of samples over a range in thickness of 75–400 μ. In the vicinity of the absorption edge the curves are clearly separated at all wavelengths except at the onset of the edge in the neighborhood of $\lambda = 0{\cdot}64\ \mu$ where as shown in the insert section of Fig. 2 the separation is of the same order of magnitude as the spectral resolution of the optical system. The general growth habit of the single crystals was unfavorable for absorption measurements to

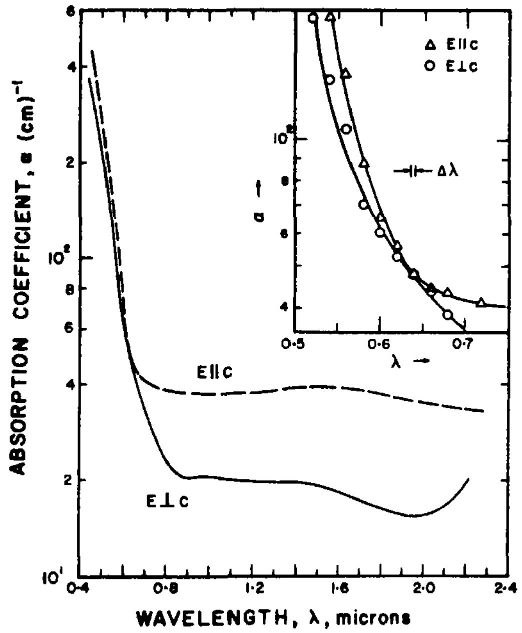

Fig. 2. Absorption coefficient vs. wavelength at 300°K for the incident radiation polarized both parallel and perpendicular to the c axis. The insert figure expands the scale in the vicinity of the onset of the absorption edge; a few representative data points are shown for comparison.

be made for the incident radiation directed along either of the other two principal crystallographic axes. As the temperature of the crystal is decreased to 77°K the absorption edge shifts toward shorter wavelengths, and toward longer wavelengths as the temperature increases above 300°K. If a crystal growth tube is removed from the furnace at 730–750°C and immediately examined in white light, the crystalline shapes are a transparent yellow in color. As the tube cools below approximately 700°C, there is an abrupt change to an opaque gray metallic appearance which indicates a possible major phase change taking place in the structure. Weiss and Weiss[10] reported the formation of a yellow vitreous form of $SiSe_2$ above 1060°C which upon slow cooling devitrified and the crystalline structure reformed.

Although transmission data were reproducible to better than ± 1 per cent, surface decomposition and other surface irregularities made it impossible to extract refractive index values from direct reflectivity measurements especially since reliable reflectivity values could not be obtained with the sample surfaces immersed in CCl_4.

The average dark resistivity of the single crystal material at 300°K is $2\times 10^7\,\Omega$-cm, about two orders of magnitude greater than that of intrinsic silicon. A small decrease in resistivity (about 13 per cent) was observed with the samples illuminated by white light. It was not satisfactorily determined whether this effect is a result of surface decomposition or bulk $SiSe_2$ behavior.

DISCUSSION

The absorption curves of Fig. 2 were examined for evidence of any indirect type transitions. For such transitions the absorption coefficient, α, should vary as $(h\nu - E_g \pm E_p)^m/h\nu$ where m is 2 for allowed and 3 for forbidden transitions; E_g is the minimum forbidden energy gap and E_p is the energy for the phonon being absorbed (+) or emitted (−) in the transition[11]. The best agreement was found for both curves with the energy dependence for allowed indirect transitions. A slightly better fit is obtained for the $E \parallel c$ curve. Neither curve shows any agreement with the energy dependence for an indirect forbidden type transition. Figure 3 shows the extrapolated value for the indirect energy gap. For $E \parallel$ to the c axis $E_g \leq 1{\cdot}72$ eV; for $E \parallel$ to to the (110) type planes, i.e. ($E \perp c$), $E_g \leq 1{\cdot}74$ eV. Thus to within experimental error the indirect energy gap is essentially the same for both curves: $E_g \leq 1{\cdot}73 \pm 0{\cdot}05$ eV. Since transmission data were obtained only in the low absorption region, it was not possible to attempt to identify the presence of other types of absorption mechanisms. Neither curve follows an exponential dependence on wavelength or energy.

In view of the results of primarily the optical absorption measurements silicon diselenide should be classified as a semiconductor

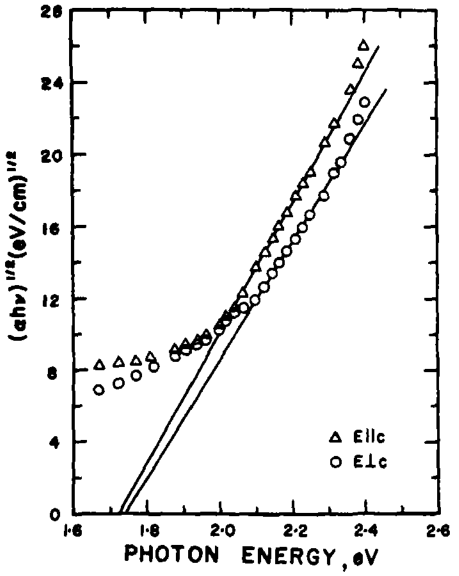

Fig. 3. $(\alpha h\nu)^{1/2}$ vs. photon energy extrapolated to the threshold energy for indirect phonon assisted transitions.

which appears to be of the indirect band gap type. Thus the Mooser and Pearson[5] prediction of semiconductor behavior for the SiS_2 type structure has been verified for the isotypic $SiSe_2$. The chemical instability in ordinary laboratory atmosphere of materials belonging to this crystal class has prevented reliable measurements to be made for properties other than optical transmission.

Acknowledgements – The authors would like to thank Mr. John W. Rau for many helpful discussions during the course of this work and Mr. Craig E. Miller who assisted in the X-ray diffraction measurements.

REFERENCES

1. RAU J. W. and KANNEWURF C. R., *J. Phys. Chem. Solids* **27**, 1097 (1966).
2. SABATIER P., *C.r. hebd. Séanc. Acad. Sci., Paris* **113**, 132 (1891).
3. WEISS A. and WEISS A., *Z. Naturf.* **7b**, 483 (1952).
4. PARTHÉ E., *Crystal Chemistry of Tetrahedral Structures*. Gordon and Breach, New York (1964).
5. MOOSER E. and PEARSON W. B., *J. Electron.* **1**, 629 (1956).
6. WEISS A. and WEISS A., *Z. anorg. allg. Chem.* **276**, 95 (1954).
7. ZINTL E. and LOOSEN K., *Z. phys. Chem.* **174**, 301 (1935).
8. KAHAN A., *Appl. Optics* **3**, 314 (1964); KAHAN A., AFCRL-63-325 (II) (1963).
9. KAHAN A. and LIPSON H. G., AFCRL-63-325 (I) (1963).
10. WEISS A. and WEISS A., *Z. Naturf.* **8b**, 104 (1953).
11. BARDEEN J., BLATT F. J. and HALL L. H., *Photoconductivity Conference* (Edited by Breckenridge, Russell and Hahn), p. 146. Wiley, New York (1956).

J. Phys. Chem. Solids Pergamon Press 1969. Vol. 30, pp. 359–365. Printed in Great Britain.

POLARIZATION AND OPACITY EFFECTS ON MÖSSBAUER SPECTRAL AREA

A. ROSENCWAIG*, M. RON and A. KIDRON
Technion, Israel Institute of Technology, Haifa
and
HANAN SHECHTER†
University of Washington, Seattle, Wash. 98105, U.S.A.

(*Received* 18 *April* 1968; *in revised form* 8 *July* 1968)

Abstract—The alignment of domains in ferromagnets has produced changes in the observed Mössbauer spectral area. The variation in the spectral area with the externally applied magnetic field exhibits close similarity to the corresponding magnetization curves. The results reflect the relative phase quantities in ferromagnets.

1. INTRODUCTION

THE MÖSSBAUER effect has been used for quantitative studies of multiphase properties of iron, iron compounds and alloys[1, 2]. Difficulties have been found in the analysis of the relative quantities of precipitated ferromagnetic phases particularly in cold worked samples and thin films. The discrepancies in the results could be corrected mainly by applying the correct polarization relations between the total spectral area of the ferromagnetic phase and the effective absorber thickness for non-magnetized and magnetized samples. The relation between the spectral area and the opacity of a ferromagnet to a recoiless incident radiation has been discussed by Nussbaum and Housley[3] and Hanna[4]. The consequences of the changes in the spectral area caused by the magnetic polarization of the sample are discussed in this note.

2. EXPERIMENT AND RESULTS

Mössbauer studies reported here have been carried out on various metallic irons and iron compounds when weak magnetic fields (up to 3000 G) were applied. Constant ALNICO magnets were used.

The Mössbauer spectrometer was of a constant velocity type: the constant velocity drive had in this case the advantage of a more careful evaluation of the spectral background, by counting relatively high (constant) velocities. The source used throughout was a single-line source of Co^{57} diffused into a 0·5 ml copper foil.

Special precautions were taken to insure that the photomultiplier and the transducer were not affected by the applied magnetic field. Also, the total number of counts per channel and the percentage of counts due to resonant 14·4 keV gammas were known and preserved to within 2 per cent from spectrum to spectrum. The source was shielded to prevent fringing fields at the source (this field was found to be less than 10 G for a 3000 G field at the absorber). The ambient temperature was kept $(19 \pm 0\cdot 1)°C$.

The total spectral area determined by the absorption lines was computed, considering background and broadening corrections and percentage of 14·4 keV in each case. n, the number of resonant nuclei per square cm was determined by weight and composition.

---

*[*] *Present address:* Department of Physics, University of Toronto, Toronto, Canada.

[†] On leave from Technion, Israel Institute of Technology, Haifa, Israel.

Values for σ_0, the on-resonance cross-section of Fe^{57}, ($2{\cdot}32\times10^{-18}$cm^2) and f_a(the Mössbauer fraction of the absorber) at room temperature were obtained from the literature (the *change* in the spectral area does not require the accurate value of σ_0 and f_a).

When a paramagnetic material, such as 310 stainless steel foil, or an antiferromagnet, like α-Fe_2O_3, was used as the absorber, no changes in the Mössbauer spectrum were observed when a weak external magnetic field was applied. There were no polarization effects (such as changes in the relative intensity of the absorption lines or changes in the total spectral intensity). The precautions were applied to verify in each case the decrease in the spectral area. When ferromagnetic materials were used as absorbers, some very marked results were obtained. When an enriched iron foil (1·9 mg of Fe-57 per cm^2) was subjected to a magnetic field at right angle to the beam of the detected gamma rays, the spectra obtained (Figs. 1 (a–c) clearly illustrated that besides the (usual) change in the relative intensities [5] and reduced h.f.s. the total spectral area decreased with the increase of the intensity of the applied magnetic field. The *net* decrease in the total area was

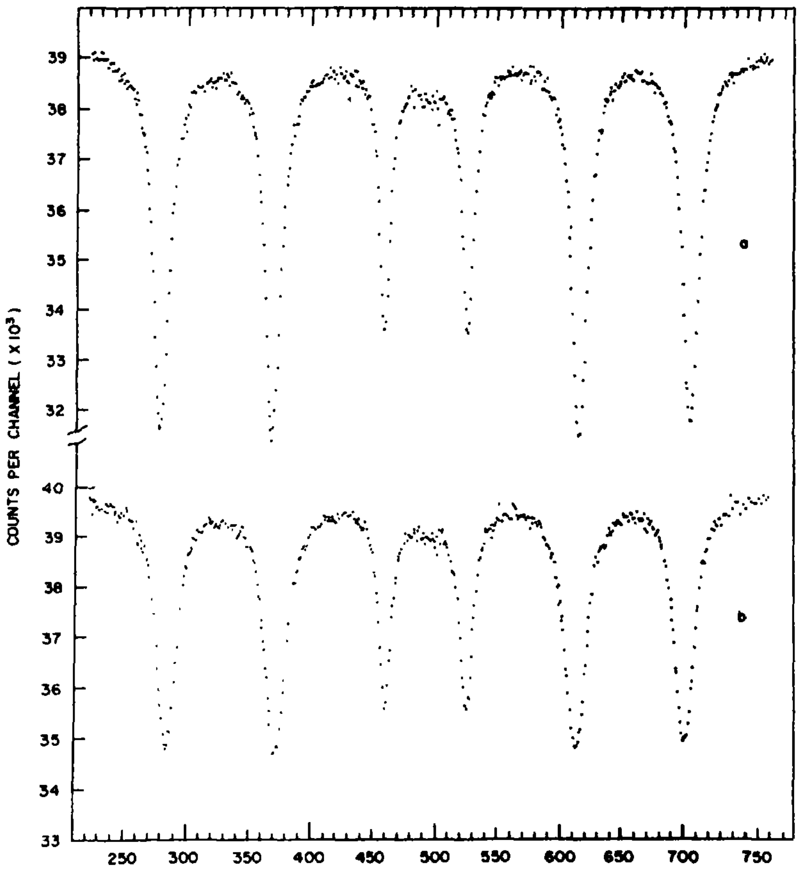

Fig. 1. (a) Enriched Fe-57 sample with no applied external magnetic field. (b) Same sample with an external transverse field of 3500 G. 91 per cent 14·4 keV obtained for both spectra. 1 channel ≈ 0·0024$_8$mm/sec.

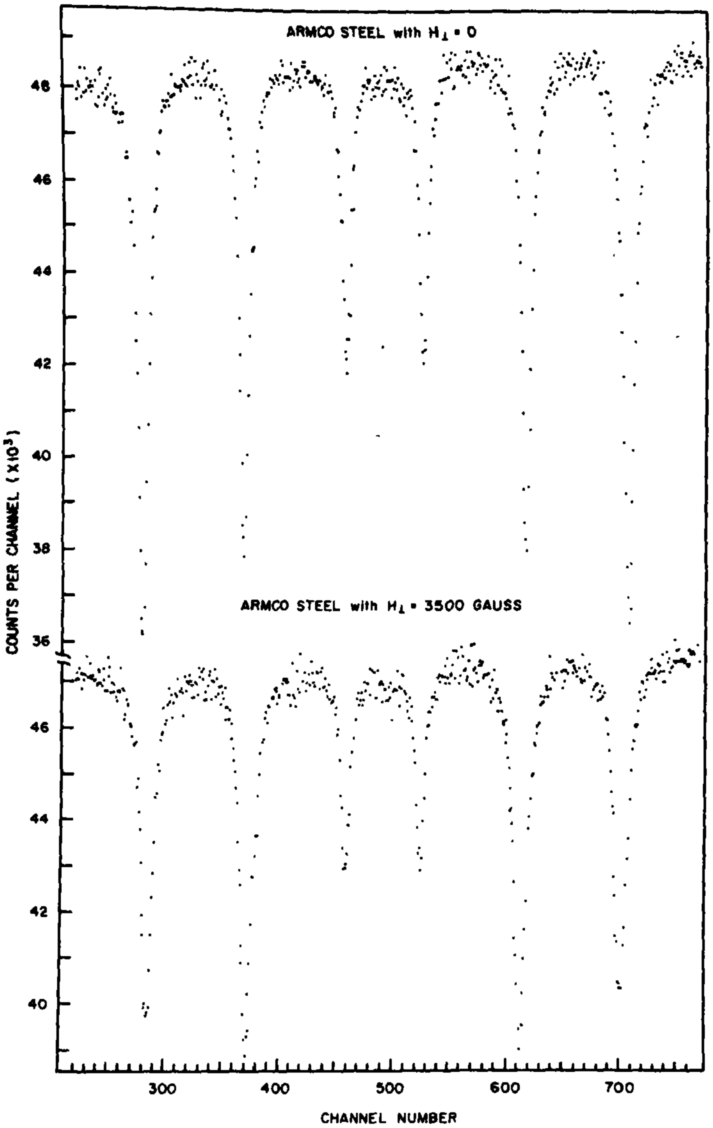

Fig. 1. (c) The change in the spectrum of Armco steel under an external magnetic field (1 channel = $0{\cdot}024_8$mm/sec).

found to reach a saturation value of about 20 percent in the region of 2000 G (Fig. 2) and to remain constant at this value up to the highest field value (3500 G) used through these experiments. The decrease in the spectral area was followed by a broadening of *all* six components (taken care of for the area measurements).

An investigation of the magnetization curve for this sample under these field conditions showed that the magnetization also reached saturation in the region of 2000 G (in general, the variation in the values of $\Delta A/A$ – the fractional change in the total spectral area –

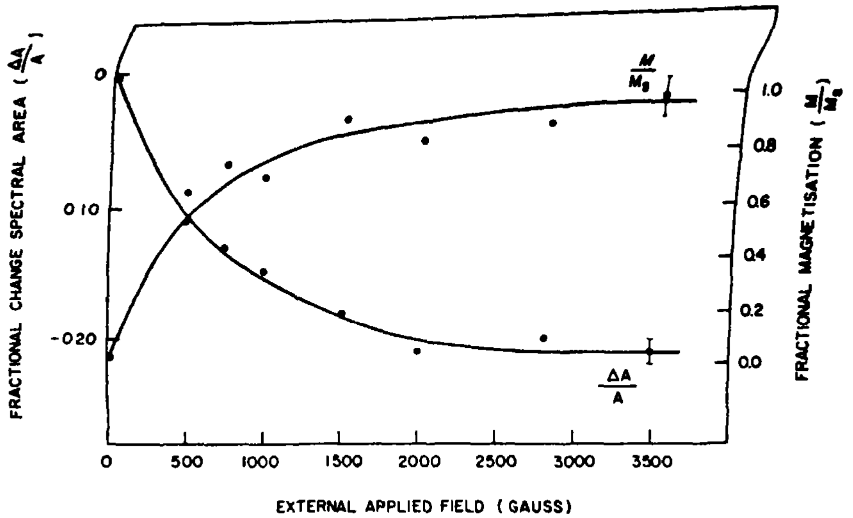

Fig. 2. The relative decrease ($\Delta A/A$) of the spectral area with externally applied transverse magnetic field (H) for an enriched (92·8 per cent Fe-57) foil, $t = 36{\cdot}8$.

obtained at the same values of H_{ext}, agreed with the expected variation in the relative magnetization M/M_s for the different substances at the particular value of H_{ext}; that is, the smaller the quantity M/M_s, the smaller was the observed $\Delta A/A$ for a given effective thickness.

This effect was also observed during recent work on 'thin' CuFe alloys[6] where the Mössbauer spectrum consisted of both paramagnetic and ferromagnetic phases. The absorber thickness giving rise to the ferromagnetic component was 0·2 mg of Fe-57 per cm². The application of a transverse magnetic field resulted in a decrease of ~13 percent in the spectral area of the ferromagnetic component but no change whatsoever occurred in the paramagnetic component of the spectrum.

3. DISCUSSION

The non-polarized incident radiation in the absence of an external field at the absorber is resonantly scattered equally in all directions on the absorber plane; the directions of the domain fields in this case are randomly distributed and the on-resonance spectral area is thickness dependent. (The dependence of the *relative* intensities of the transition on the direction of the domain field has been discussed elsewhere[7]). The relation between the total spectral area, A, and the effective absorber thickness, t, for this case is given by[4]

$$A(t) = f_s \int_0^\infty (1\text{-}e^{-t\Sigma(E)})\,dE \qquad (1)$$

where $t = n\sigma_0 f_a$; n = number of resonant nuclei per cm² of absorber σ_0–on resonance cross-section, f_a and f_s are the Mössbauer fractions for the absorber and source, respectively. $\Sigma(E)$ is used here to denote the sum over six lines in such a way that the total cross-section, $\sigma(E)$, will be represented by:

$$\sigma(E) = \sigma_0 \Sigma(E) = \sum_{i=1}^{6} q_i \chi_i(E,E_i) \qquad (1a)$$

where $\chi_i(E,E_i) = \Gamma_a^2/4(E-E_i)^2 + \Gamma_a^2$. $\chi(E,E_i)$ is the line shape, E_i the energy of the i-th transition, q_i are the normalized ratios of the six absorption lines of the iron, given by: 1/4: 1/6: 1/12: 1/12: 1/6: 1/4; Γ_a the natural line width of the transition in the absorber.

When a transverse $H_{\rm ext}$ is applied (in a direction lying in the absorber plane) the domain fields become polarized in the direction of the field (the field at the Fe-57 nuclei is opposite to the $H_{\rm ext}$). In this case, at most *half* of the incident radiation can be absorbed on-resonance, the transmitted part will be linearly polarized and not absorbed resonantly. (Experiments with two magnetized iron foils show that the transmitted intensity decreases when the two magnetization axes tend to be perpendicular). The expected decrease in the spectral area is compensated by the increase of the effective thickness in the direction of $H_{\rm ext}$. For thin absorbers, where $A(t)$ is practically linear, no net decrease in the area is expected. For thicker absorbers the compensation is not complete (due to saturation effects) and a net decrease in the total spectral area is observed.

When the domain fields are aligned by an external field, the q_i's are given[3, 4, 7] by two normalized parts $q_i^{\parallel}(\Delta m = \pm 1)$ which are in the ratio $\frac{3}{8}:0:\frac{1}{8}:\frac{1}{8}:0:\frac{3}{8}$ and $q_i^{\perp}(\Delta m = 0)$, in the ratio $0:\frac{1}{2}:0:0:\frac{1}{2}:0$. In this case, the total spectral area will be

$$A'(t) = f_a \int_0^{\infty} \left[1 - \tfrac{1}{2} e^{-t\Sigma^{\parallel}(E)} - \tfrac{1}{2} e^{-t\Sigma^{\perp}(E)}\right] \quad (2)$$

where

$$\left.\begin{aligned} \Sigma^{\parallel}(E) &= \sum_{i=1}^{6} q_i^{\parallel}\chi_i(E,E_i); \quad \Big(\sum_{i=1}^{6} q_i^{\parallel} = 1\Big). \\ \Sigma^{\perp}(E) &= \sum_{i=1}^{6} q_i^{\perp}\chi_i(E,E_i); \quad \Big(\sum_{i=1}^{6} q_i^{\perp} = 1\Big). \end{aligned}\right\} \text{(2a)}$$

A computer was used to calculate $A(t)$ and $A'(t)$ for various thicknesses t for Lorentzian lines, the results are shown in Fig. 3. The expected difference in the spectral area can be obtained, for the absorber of a thickness t, from this curve.

The difference in the spectral area obtained for the absorber of a thickness t with random magnetic orientation and the area for an absorber with transverse orientation becomes significant for higher thicknesses when equations (1) and (2) begin to diverge.

The line broadening observed in a polarized sample is a straightforward result[8] of the increase of the effective thickness in the direction of $H_{\rm ext}$. If $t_i = q_i n\sigma_0 f_a$ is the effective thickness for the i-th transition in a random oriented sample, $t_i' = q_i n\sigma_0 f_a$ is the thickness in the presence of a transversal $H_{\rm ext}$, then $t_1 \propto \frac{1}{4}$, $t_1' \propto \frac{3}{8}$; $t_2 \propto \frac{1}{6}$, $t_2' \propto \frac{1}{2}$; $t_3 \propto \frac{1}{12}$; $t_3' \propto \frac{1}{8}$, etc. The effective thickness for each transition increases, resulting in line broadening of *all* the transitions. The line broadening is apparent in thick absorbers; sample No. 1 (Table 1, Fig. 1a) shows an increase of ~10 per cent in the line width of lines 1, 6, ~20 per cent in lines 2, 5. Sample No. 2 shows ~8 and ~15 per cent in lines 1, 6 and 2, 5, respectively. The broadening in lines 3, 4, was within the experimental error.

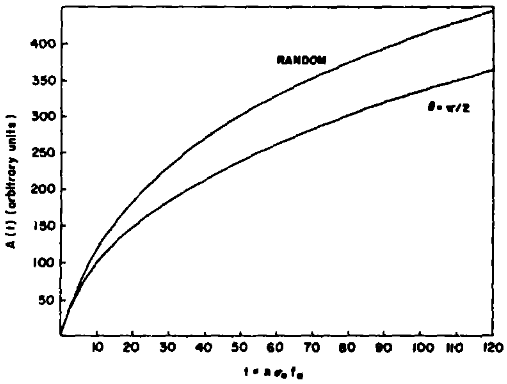

Fig. 3. The dependence of the total spectral area on the effective absorber thickness t, for the case of random orientation (equation (1)) of the magnetic domains, and for alignment by a transverse magnetic field (equation (2)).

As can be seen from Table 1, the effect of opacity on the total spectral area can be considerable even for relatively thin absorbers. This is a fact which is often not fully appreciated in works dealing with measurements of either the total spectral area or of the relative areas and line shapes of individual lines in the spectrum. Even when unmagnetized samples are concerned, ferromagnetic foils often exhibit partial domain polarization

Table 1. Changes in the total spectral area of Fe^{-57} *nuclei in ferromagnetic absorbers due to application of an external magnetic field* (3500 G)

Sample	mg/cm^2 of Fe^{-57}	t	$\Delta A/A$(%) measured	$\Delta A/A$(%) calculated (Fig. 3)
1. Iron foil (enriched)	1·90	36·8	20 ± 2	21
2. Armco iron foil (natural)	0·38	7·3	15	17
3. Cu–Fe alloy (foil)	0·20	3·8	13	10
4. Fe_3O_4 (powder)	0·14	2·6	9	8

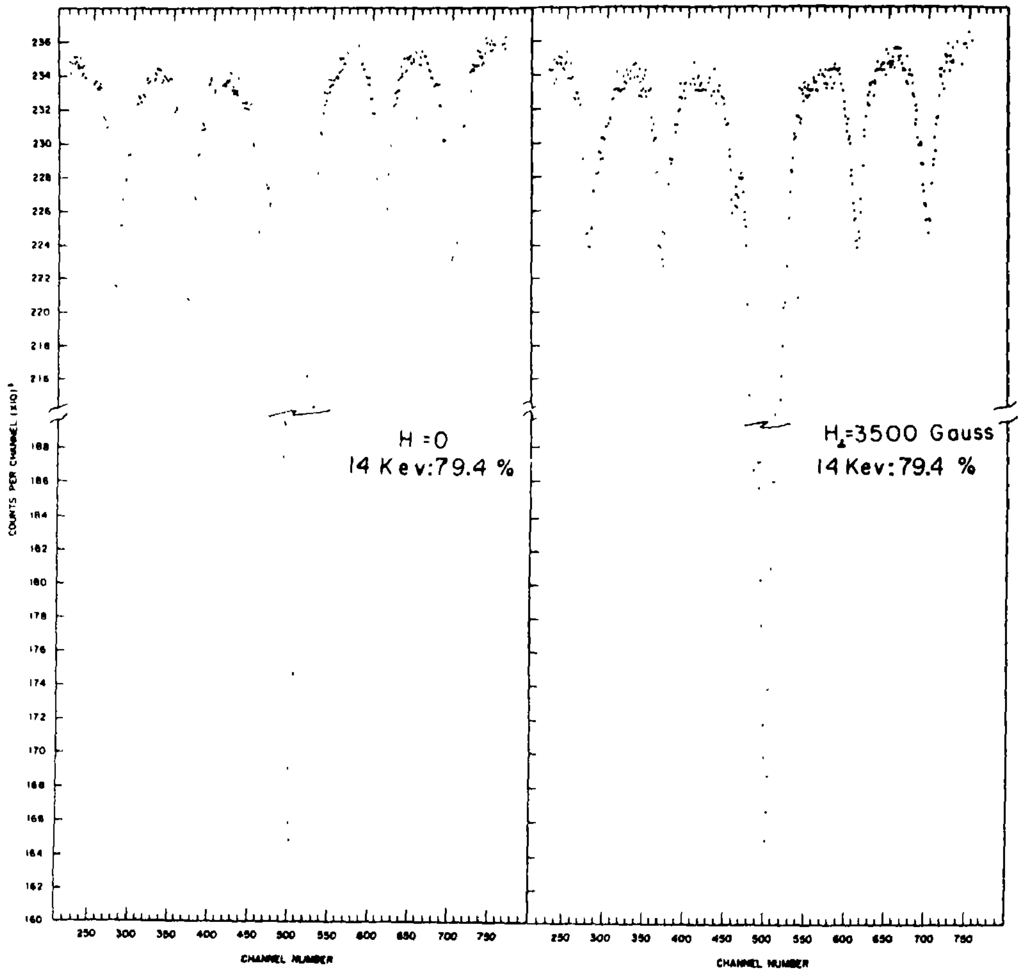

Fig. 4. The relative decrease of the spectral area with externally applied transverse magnetic field (H) for Cu–Fe alloy ($t = 3·8$).

in the plane of the foil as a consequence of a cold working. These treatments result not only in that the iron lines are not only in the random ratios 3:2:1:1:2:3, but also the total spectral area may be considerably different than for the pure random case. The chemical analysis of the rolled Cu–Fe alloy, for instance, (Fig. 4) show higher relative amounts of iron content than the figures obtained by relative area measurements: the ratio of the lines in the ferromagnetic phase, however, is not 3:2:1:1:2:3 and a partial polarization is obviously observed. A better fit was obtained by using the area corrections (Fig. 3).

Acknowledgements—The authors are indebted to Dr. R. M. Housley and Professor J. G. Dash for their valuable remarks.

REFERENCES

1. HILLMAN P., SHECHTER H. and RON M., *J. appl. Phys.* **37**, 3043 (1966).
2. RON M., SHECHTER H. and NIEDZWIEDZ S., *J. appl. Phys.* **39**, 265 (1968).
3. NUSSBAUM R. H. and HOUSLEY R. M., *Nucl. Phys.* **68**, 145 (1965).
4. HANNA S. S. and PRESTON R. S., *Phys. Rev.* **139**, A722 (1965).
5. HANNA S. S., HEBERLE J., LITTLEJOHN C., PERLOW G. J., PRESTON K. S. and VINCENT D. H., *Phys. Rev. Lett.* **4**, 177 (1969).
6. RON M., ROSENCWAIG A., SHECHTER H. and KIDRON A., *Phys. Lett.* **22**, 44 (1966).
7. FRAUENFELDER H., NAGLE D. E., COCHRAN F. and W. M. VISSCHER, *Phys. Rev.* **126**, 1065 (1962).
8. HOUSLEY R. M., Private communication.

J. Phys. Chem. Solids Pergamon Press 1969. Vol. 30, pp. 367–373. Printed in Great Britain.

THE DEBYE–WALLER FACTOR. DEBYE TEMPERATURE FOR NICKEL*

JOSEPH L. FELDMAN
Laboratory for Crystallographic Research, Department of Physics and Astronomy,
Rensselaer Polytechnic Institute, Troy, N.Y. 12181, U.S.A.

(*Received* 17 *May* 1968; *in revised form* 28 *June* 1968)

Abstract – Three Born–von Kármán lattice dynamical models obtained from neutron measurements and elastic constant measurements on Ni have been considered chiefly to calculate the Debye–Waller factor Debye temperature, $\theta^M(T)$. The results are compared with X-ray experimental data in the region $100°\text{K} \leq T \leq 520°\text{K}$. Also considered are the dispersion curves, the moments of the frequency spectrum and the dependence of these moments upon the temperature. It is seen that for $\theta^M(T = 296°\text{K})$, the models based on the neutron data yield 403° and 406°K, the model based on the elastic constant data yields 425°K, and the X-ray experimental value is 410°K. It appears that at high temperatures the temperature dependence of $\theta^M(T)$ determined using the model based on the elastic constant data agrees closely with experiment whereas the temperature dependence of $\theta^M(T)$ determined from thermal expansion effects alone is too small by a factor of two. However, due to experimental scatter, it is possible that only volume expansion effects are important in determining the temperature dependence of $\theta^M(T)$ at high temperatures.

1. INTRODUCTION

THE Debye–Waller factor Debye temperature, $\theta^M(T)$, for Ni, has been determined[1] by X-ray relative intensity measurements in the region $100°\text{K} \leq T \leq 520°\text{K}$. Wilson[1] interpreted the data with the use of a continuum model based on the measured elastic constants [2]. In this paper[3] results of calculations of $\theta^M(T)$ for Ni based on simple Born–von Kármán lattice dynamical models are presented and the comparison between theory and experiment is shown. Several studies of $\theta^M(T)$, based on the use of force models or on analyses of thermodynamic data have appeared in the literature for other substances [4, 5]. We used a fourth nearest neighbor Begbie–Born model, a fifth nearest neighbor axially symmetrical model, and a first nearest neighbor Begbie–Born model. The force constants of the latter model were determined from available elastic constant data[2] in the usual way[6–8]. Hopefully, anharmonic or electron–phonon interaction effects in the Debye–Waller factor are accounted for in an approximate way by the inclusion of the temperature dependences of the elastic constants and equilibrium volume[9] in determining the harmonic force constants. It should also be pointed out that the elastic constant measurements were performed in the presence of a magnetic field. The force constants given by Birgeneau *et al.*[10] were used for the remaining models, which are based on the neutron data of Birgeneau *et al.* at $T = 296°\text{K}$[10]. Birgeneau *et al.* presented results of calculations of the frequency spectrum, the specific heat Debye temperature and several moments of the frequency spectrum for the fourth neighbor model.

A recent calculation[11], on the basis of the Birgeneau *et al.* fourth neighbor model, of the Debye–Waller factor for nickel at $T = 300°\text{K}$ has been brought to the author's attention by the referee. In their calculation Barron and Smith use 1000 phonons in the Brillouin zone and an integration over 1/1000th of the Brillouin zone with an approximation for the long wavelength modes.

---

*This work was supported in part by the National Aeronautics and Space Administration through the Rensselaer Polytechnic Institute Interdisciplinary Materials Research Center, and the Army Research Office (Durham).

In addition, Gleiss[12] has calculated the Mössabuer fraction for nickel at temperatures less than 200°K. Most of Gleiss's calculations are based on the moments of the frequency spectrum with the use of high and low temperature expansions. He used moments for the Birgeneau *et al.* fourth nearest neighbor model and moments which he obtained from an analysis of the thermodynamic data. Gleiss also considered a second nearest neighbor model based on elastic constant data and he compared his results with Mössbauer measurements[13]. We believe that our calculations constitute a significant improvement over previous work on the Debye–Waller factor for nickel because our method of calculation (to be discussed) appears to be more exact than the methods used by Barron and Smith and by Gleiss, and because our calculations involve a few models, including the Birgeneau *et al.* fifth neighbor model (not considered in previous studies) and a wide range of temperatures.

In the harmonic or quasi-harmonic approximation $\theta^M(T)$ for a cubic monatomic crystal is given by

$$\sum_{\vec{f},j}\frac{e_{vib}(\omega,T)}{\omega^2}=\frac{9N\hbar^2}{kTx}\left[\frac{1}{4}+\frac{1}{x^2}\int_0^x\frac{x'\mathrm{d}x'}{e^{x'}-1}\right] \quad (1)$$

where $x=\theta^M/T$ and where $e_{vib}(\omega,T)$ is the contribution to the vibrational energy of the mode of frequency ω and of wave vector and polarization index $\vec{f}$ and j, respectively. Although the left hand side of (1) can be evaluated with the use of a calculated frequency distribution[14], the normal mode sums discussed in this paper were performed directly over a cubic grid of 2992 points in the irreducible element of the Brillouin zone.

In order to make further comparison among the various models, the dispersion curves and the moments of the frequency distribution at $T=296$°K were also considered. The moments of the frequency distribution are expressed in terms of an effective Debye frequency[15] or, equivalently, an effective Debye temperature,

$$\theta_D(n)=\frac{\hbar}{k}\{\tfrac{1}{3}(n+3)\langle\omega^n\rangle\}^{1/n} \quad (2)$$

where $\langle\omega^n\rangle$ is the n'th moment of the frequency distribution and where the limit of the right hand side of (2) is taken for $n=-3$ and for $n=0$. We note that for values of n of -3, 2, -1, -2, and 0, $\theta_D(n)=\theta_0{}^c$, $\theta_\infty{}^c$, $\theta_0{}^M$, $\theta_\infty{}^M$, and $\theta_\infty{}^s$, respectively. The superscripts c and s denote specific heat and entropy, respectively, and the subscripts refer to limiting temperatures.

2. RESULTS

The dispersion curves for the symmetry directions are shown in Fig. 1 for the first neighbor Begbie–Born model. The elastic constants at $T=300$°K were used. The small disagreement between theory and experiment in the long wavelength region represents a discrepancy between elastic constant measurements and neutron measurements which has been noted previously[10, 16] and which is of theoretical interest[16]. Results for the Birgeneau *et al.* models, which were fitted to the experimental data points to within about 2 per cent, are not shown in the figure.

In Fig. 2 the comparison between the Barron Plots, i.e. $\theta_D(n)$ vs. n, is shown for the three models considered in this paper at room temperature. The values of $\theta_D(-3)$ were obtained with the use of de Launay's tables.* The calculations were performed at intervals of n of 0·5 and 1 depending on the range of n. The deviations of the values of $\theta_D(-2\cdot5)$ from the respective $\theta_D(n)$ curves are believed to be due to the crudeness of the grid size for calculating $\theta_D(n)$ near $n=-3$. The estimated errors in $\Theta_D(n\geqslant -z)$ and $\Theta^M(T)$, due to the grid size, are less than 2°K.

The calculated values of $\theta^M(T)$ for the fourth and first neighbor models are compared with experiment in Fig. 3. The minimum temperature interval for which the calculations

---

*We agree with the elastic constant value of Alers *et al.* of $\theta_0{}^c=476$°K given in their *Bull. Am. Phys. Soc.* paper.

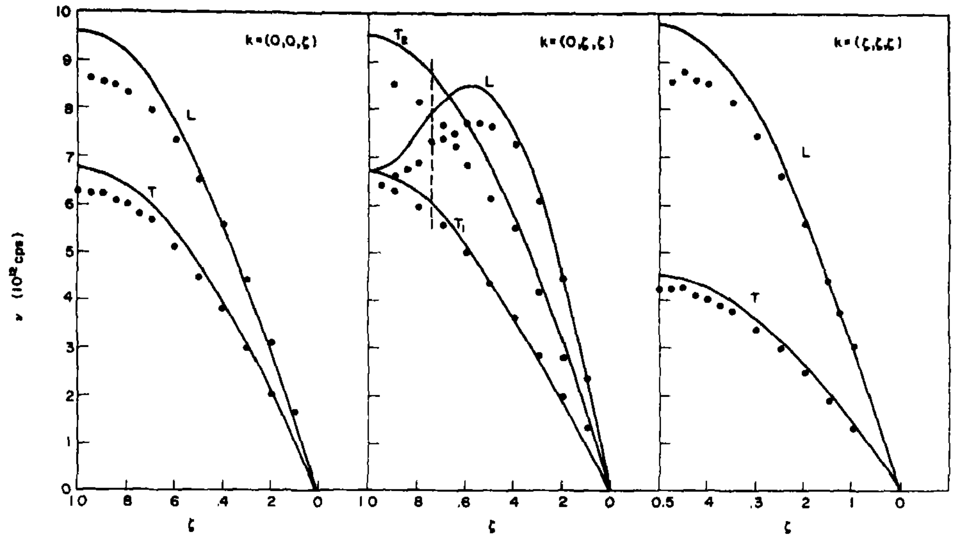

Fig. 1. Dispersion curves for Ni at $T = 296$°K. L and T refer to the longitudinal and transverse branches. The circles correspond to the neutron measurements of Birgeneau *et al.* (reference [10]), the solid lines correspond to the Begbie–Born first nearest neighbor model and the dashed vertical line corresponds to the Brillouin zone boundary.

were performed was 20°K and was in the region $0 \leqslant T \leqslant 100$°K. The effect of thermal expansion on $\theta^M(T)$, as shown in the figure, was obtained with the use of the approximate relation[18].

$$\frac{\Delta\theta^M}{\theta^M} = -\gamma\frac{\Delta V}{V} \tag{3}$$

where γ is the Gruneisen parameter and where $\Delta\theta^M$ and ΔV are the shifts in the Debye-Waller factor Debye temperature and equilibrium volume from their values at $T = 296$°K. It was assumed that $\gamma = 2$ at all temperatures and the thermal expansion data of Nix and McNair[9] for $\Delta V/V$ was used. It should also be noted that the $\theta^M(T)$ curve for the fifth neighbor model lies less than 1 per cent above the $\theta^M(T)$ curve for the fourth neighbor model.

3. DISCUSSION

Three Born–von Kármán force models for nickel have been considered chiefly to calculate $\theta^M(T)$, the effective Debye-Waller factor Debye temperature, and the results have been compared with experiment. Two of these models were proposed by Birgeneau *et al.* on the basis of their neutron data at $T = 296$°K[10]. The other model is the Begbie–Born first neighbor model which has been considered on the basis of the elastic constant data of Alers *et al.*[2]. The model which yields results in best agreement (less than 1 per cent) with the quoted experimental value of $\theta^M = (410 \pm 10)$°K at room temperature is the fifth neighbor axially symmetrical model considered by Birgeneau *et al.* However, the difference in $\theta^M(T)$ between the two Birgeneau *et al.* models is less than 1 per cent which may be of the order of the error in $\theta^M(T)$ for either model due to uncertainties in the neutron data. The first neighbor model yields a result for θ^M at room temperature which is about 5 per cent above the respective Birgeneau *et al.* models and the quoted experimental value. It should be pointed out that all three models agree with the quoted experimental value for θ^M at room temperature to within the accuracy of the

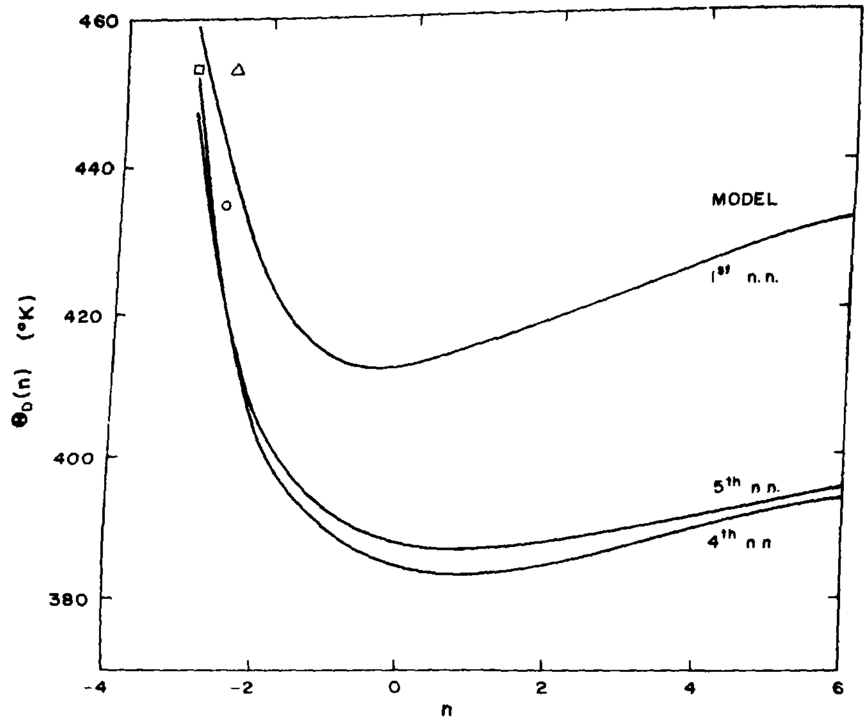

Fig. 2. Barron plots for Ni at $T = 296$°K calculated from the three force models considered in the text $\theta_D(-3)$ was calculated using de Launay's tables whereas other values of $\theta_D(n)$ were calculated using a cubic grid of 2,992 points in 1/48 of the Brillouin zone. The square refers to $\theta_D(-3)$ calculated from Bozorth *et al.*'s elastic constant measurements (reference [17]) and the circle and triangle refer to $\theta_D(-2{\cdot}5)$ calculated for the fourth and first nearest neighbour models, respectively. The fourth and fifth *n.n.* models cross between $n = -2$ and $n = -3$.

latter value which is limited by experimental error and by the method[1] of determining $\theta^M(T)$ from the data. However, as suggested by the investigation of Birgeneau *et al.*, it is seen that the first neighbor model is inadequate for representing the measured dispersion curves.

Our results can easily be compared with the calculation of Barron and Smith[11] and with the experimental results of Inkinen and Suortti (see Barron and Smith for reference) at $T = 300$°K. Barron and Smith considered the coefficient B of $\sin^2\theta/\lambda^2$ in the Debye–Waller factor. They report $B = 0{\cdot}381 \pm 0{\cdot}008$ Å^2 for the calculated value and $B = 0{\cdot}37 \pm 0{\cdot}02$ Å^2 for the experimental value. The value $\pm 0{\cdot}008$ Å^2 is due to uncertainties in the neutron data. We obtain $B = 0{\cdot}377$ Å^2 for the fourth neighbor model, which is in good agreement with Barron and Smith's value, and $B = 0{\cdot}372$ Å^2 for the fifth neighbor model.

The effect of thermal expansion on $\theta^M(T)$ has been treated approximately. The justification of this treatment is suggested by the experimental information on the temperature dependence of the Gruneisen parameter for Ni[19] and reference is made to previous papers[5, 20, 21] for a more detailed discussion of thermal expansion effects. It is hoped that the first neighbor Begbie–Born model provides an estimate of the full anharmonic effect in $\theta^M(T)$ although the theory may not be justifiable. A more exact treatment of the anharmonic effect is avail-

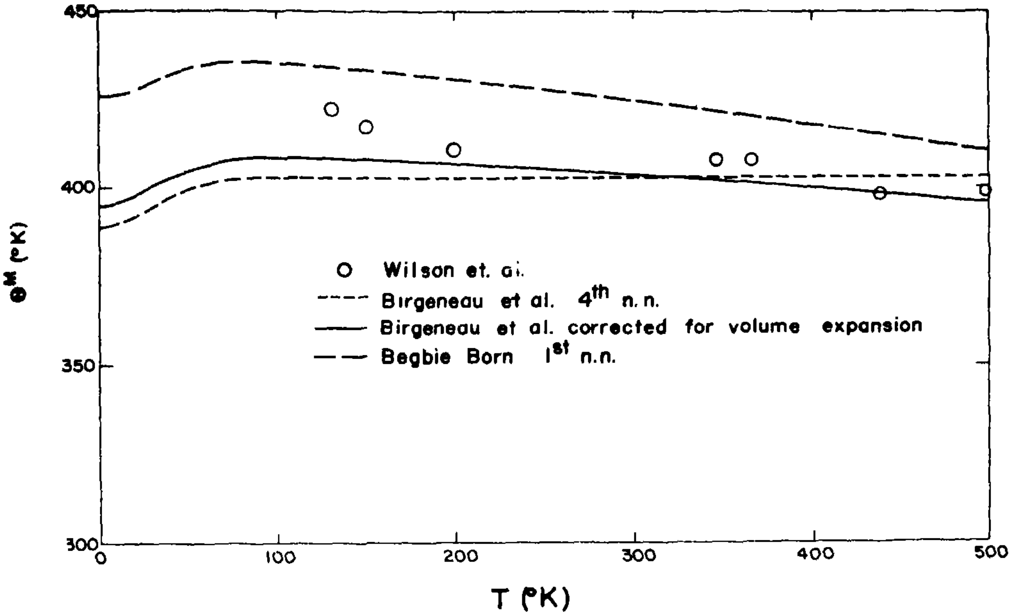

Fig. 3. Effective Debye temperature for the Debye-Waller factor of Ni as a function of temperature. The effect of thermal expansion on the Birgeneau *et al.* fourth nearest neighbor model was obtained from the approximate relation $\Delta\theta^M/\theta^M = -\gamma\Delta V/V$ with $\gamma = 2$. The circles represent the experimental values.

able for a mathematically simplified force model[22]. It is of interest that at high temperature the temperature dependence of $\theta^M(T)$ as given by the first neighbor Begbie-Born model is in close agreement with experiment, as seen in Fig. 3. However, due to experimental scatter, the temperature dependence of $\theta^M(T)$ given by the thermal expansion effect alone cannot be ruled out.

Recently, Gilat and Nicklow[23] have introduced the parameter

$$\bar{\gamma}_n = -\frac{V}{\theta_D(n)}\frac{\Delta\theta_D(n)^*}{\Delta V}$$

where the Δ operator takes the difference in the quantity between two temperatures (we used 100° and 500°K). The plot of $\bar{\gamma}_n$ vs. n for Ni is shown in Fig. 4. The results are similar to those of Gilat and Nicklow who studied force models based on neutron data quantity $\bar{\gamma}_n$ is a monatonically decreasing for aluminum at different temperatures. The function of n and has values close to the value of the thermodynamic Gruneisen parameter for large n. As noted for aluminum[23] the relatively large fractional changes of the transverse mode frequencies as compared to the fractional changes of the longitudinal mode frequencies appears to be important in determining the shape of the γ_n vs. n curve. However, we have found that in some directions the fractional change in frequency for a particular polarization depends strongly on the wave length, and we intend to study the model dependence of the $\bar{\gamma}_n$ vs. n curve. Finally it is pointed out that experimental and theoretical studies of the lattice dynamics of Ni at various temperatures are being carried out for temperatures greater than those considered in this paper[24]*.

---

*Analogous to the parameter $\gamma_D(n) \equiv \dfrac{-\partial \ln \theta_D(n)}{\partial \ln V}$

*I am grateful to Dr. Earl F. Skelton for bringing this work to my attention.

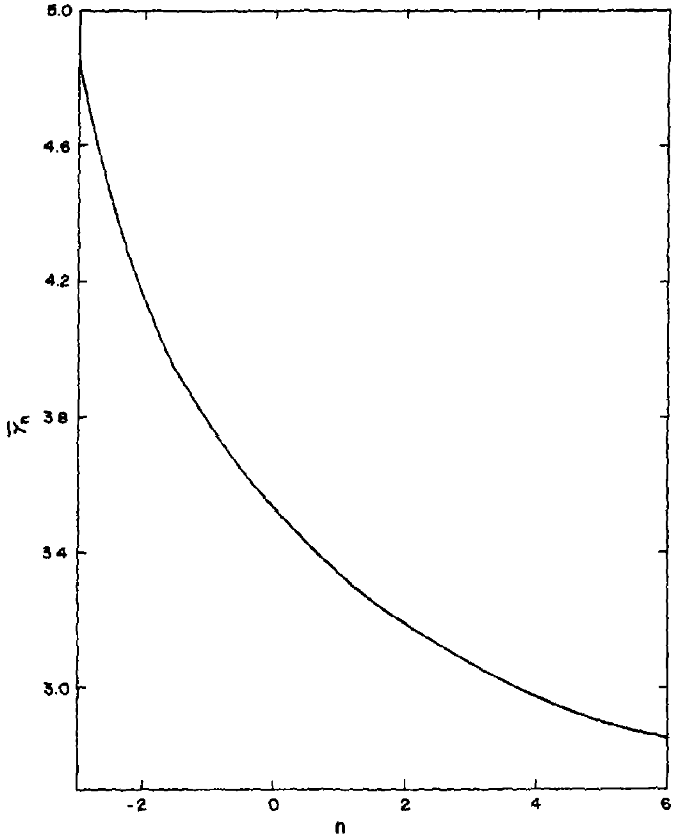

Fig. 4. A plot of $\gamma_n = -\frac{\Delta\theta_D(n)}{\theta_D(n)}\frac{V}{\Delta V}$ vs. n, where the Δ operator takes the difference in the quantity between $T = 100°$ and $T \approx 500°K$.

Acknowledgements—I wish to thank Anita Skelton and Dr. Earl F. Skelton for writing some of the computer programs. I also wish to thank Professor J. L. Katz and Dr. M. L. Klein for helpful conversations.

REFERENCES

1. WILSON R. H., SKELTON E. F. and KATZ J. L., *Acta crystallogr.* 21, 635 (1966); WILSON R. H., Ph.D. Thesis, Rensselaer Polytechnic Institute, Troy, New York (1964).
2. ALERS G. A., NEIGHBOURS J. R. and SATO H. J., *J. Phys. Chem. Solids* 13, 40 (1958); *Bull. Am. phys. Soc.* **4**, 131 (1959).
3. FELDMAN J. L., *Bull. Am. phys. Soc.* **12**, 80 (1967).
4. BARRON T. H. K. and MUNN R. W., *Acta crystallogr.* **22**, 170 (1967).
5. See review articles: SALTER L. S., *Adv. Phys.* **14**, 1 (1965); BARRON T. H. K., LEADBETTER A. J., MORRISON J. A. and SALTER L. S., *Acta crystallogr.* **20**, 125 (1966).
6. BEGBIE G. H. and BORN M., *Proc. R. Soc.* **A188**, 179 (1947).
7. HORTON G. K. and SCHIFF H., *Proc. R. Soc.* **A250**, 248 (1959).
8. HUNTINGTON H. B., *The Elastic Constants of Crystals*. Academic Press, New York (1958).
9. NIX F. C. and MacNAIR D., *Phys. Rev.* **60**, 597 (1941).
10. BIRGENEAU R. J., CORDES J., DOLLING G. and WOODS A. D. B., *Phys. Rev.* **136**, A1359 (1966).
11. BARRON T. H. K. and SMITH T., *J. Phys. Chem. Solids* **27**, 1951 (1966).

12. GLEISS R., *Phys. Status Solidi* **17**, 761 (1966).
13. OBENSHAIN F. E. and WEZENER H. H. F., *Phys. Rev.* **121**, 1344 (1961).
14. GILAT G. and DOLLING G., *Phys. Lett.* **8**, 304 (1964).
15. BARRON T. H. K., BERG W. T. and MORRISON J. A., *Proc. R. Soc.* **A242**, 478 (1957).
16. COWLEY R. A., *Proc. phys. Soc.* **90**, 1127 (1967).
17. BOZORTH R. M., MASON W. P. and McSKIMMIN H. J., *Bell Syst. tech. J.* **30**, 970 (1951).
18. PASKIN A., *Acta crystallogr.* **10**, 667 (1957).
19. COLLINS J. G. and WHITE G. K., *Prog. Low Temp. Phys.* **4**, 450 (1964).
20. BARRON T. H. K., LEADBETTER A. J., MORRISON J. A. and SALTER L. S., *Inelastic Scattering of Neutrons in Solids and Liquids*, Vol. 1, p. 49. International Atomic Energy Agency, Vienna (1963).
21. FELDMAN J. L. and HORTON G. K., *Phys. Rev.* **132**, 644 (1963).
22. MARADUDIN A. A. and FLINN P. A., *Phys. Rev.* **129**, 2529 (1963).
23. GILAT G. and NICKLOW R. M., *Phys. Rev.* **143**, 487 (1966).
24. DeWIT G. A. and BROCKHOUSE B. N., *J. appl. Phys.* **39**, 451 (1968).

J. Phys. Chem. Solids Pergamon Press 1969. Vol. 30, pp. 375–393. Printed in Great Britain.

THE ELECTRIC FIELD DEPENDENCE OF THE NET ACTIVATION ENERGY FOR MIGRATION OF IONIC SPECIES ACROSS AN ACTIVATION BARRIER

M. J. DIGNAM and D. B. GIBBS
Department of Chemistry, University of Toronto, Toronto, Canada

(*Received* 20 *May* 1968; *in revised form* 27 *June* 1968)

Abstract—The question of the functional form of the net activation energy, $W(E)$, for the field assisted migration of ionic defects across an activation barrier is examined particularly with regard to the representation of $W(E)$ as a power series in the field strength, E. The contribution to the coefficient of E^2 in such a series made by each of four different effects, was estimated and the estimates compared with empirical values obtained from an analysis of L. Young's data for the anodic oxidation of Ta and Nb. All four effects examined could conceivably make a significant contribution to the empirical coefficient, although the dominant effect is probably that arising from a shift of the positions of maximum and minimum energy for the mobile defect brought about by the field.

The influence of the choice of the form of $W(E)$ on the empirical values for the zero field activation energy and activation dipole is also examined.

INTRODUCTION

THE MIGRATION of charged species across an activation barrier can play a major role in the kinetic behaviour of a number of systems [1, 2]. In a recent paper, one of us (M.J.D.) has examined the case of ion transport in solids under conditions which include large electric fields[3]. In this paper it was assumed that the net activation energy, $W(E)$, for the migration of ionic species across an activation barrier could be represented as a power series in the field strength, E. The present paper is concerned with the functional form of the net activation energy particularly with regard to its representation as a power series. The data for the anodic oxidation of tantalum and niobium are then examined against the theory.

Defining the net activation energy for high field ionic conduction through equation (1.1);

$$i = i_0 \exp[-W(E)/kT] \qquad (1.1)$$

where i is the current density and i_0 is a constant, the form of $W(E)$ which has until recently been favoured is given in (1.2)

$$W(E) = W_0 - qaE \qquad (1.2)$$

where W_0 is the activation energy at zero applied field, a the activation distance and q the magnitude of the charge on the ion (both a and q assumed constant). Equation (1.2) is obtained on treating the problem in an approximate manner[2]. A more general treatment of the problem has been presented recently by one of us (M.J.D.)[2], a further development of which follows.

2. FUNCTIONAL FORM OF *W(E)*

Focussing attention on a particular ion, displacement of its nucleus in the absence of any external field by an amount x from its local equilibrium position will bring about a charge displacement, u, and an increase in potential energy for the system, U_1. In the presence of a superimposed external field, E, directed in the $+x$ direction, there will be an additional potential energy term arising from the interaction of the various charged species with the field, which is clearly given by $-uE$. Thus

$$U(u, E) = U_1 - uE. \qquad (2.1)$$

We may proceed from (2.1) in a straightforward manner[2] provided that

$$(\mathrm{d}U_1/\mathrm{d}E)_u = 0. \qquad (2.2)$$

It is almost certain that (2.2) is at best only approximately correct. We proceed nevertheless on the basis of (2.2) returning to the question of the field dependence of U_1 in Section 4.

If in the absence of a field, adjacent positions of minimum and maximum potential energy correspond to $u = 0$ and $u = q\mathrm{d}/2$ (where q is the charge carried by the mobile defect and d the distance separating minima) then in the presence of a homogeneous external field, E, the relevant positions of minimum and maximum potential energy will no longer lie at $u = 0$ and $u = q\mathrm{d}/2$ respectively, but will be positioned instead at $u = u_0$ and $u = u_m$ respectively, where u_0 and u_m are solutions to the equation $\mathrm{d}U(u, E)/\mathrm{d}u = 0$ or using (2.1), to the equation

$$\mathrm{d}U_1/\mathrm{d}u = E. \tag{2.3}$$

$W(E)$, the net activation energy in the presence of the field, is clearly given by

$$W(E) = U(u_m, E) - U(u_0, E) \tag{2.4}$$

or using equation (2.1), by

$$W(E) = U_1(u_m) - U_1(u_0) - (u_m - u_0)E. \tag{2.5}$$

In the previous publication[2] the form of $W(E)$ was evaluated in the above manner for each of three assumed functional forms for $U_1(u)$, namely clipped parabolic, cosine and Morse functions respectively. Before summarizing these, we turn briefly to the model proposed by Young and Zobel[4] and the form of $W(E)$ predicted by it.

According to this model, ions are assumed to "move fairly freely in channels through the labyrinthine open structure of these films, but may become trapped by coulombic attraction at pockets of excess negative charge which will be present, due to the random nature of the glassy structure, at infrequent places along the channels.... The obvious and simplest way to treat the above model is in fact ...... *to assume that except very near to the* traps the attraction between the mobile ions and the trapping centres is coulombic." Young and Zobel point out that such a model gives rise to conduction according to the Schottky law, viz.

$$W(E) = \phi - \gamma E^{1/2}. \tag{2.6}$$

An analysis of the model in the above manner, however, gives:

$$W(E) = \phi[1 - 2(bE)^{1/2} + bE] \tag{2.7}$$

$$\phi = q_1 q_2/4\pi K \epsilon_0 x_0 \tag{2.8}$$

$$b = x_0 q_1/\phi \tag{2.9}$$

where q_1 and q_2 are the charges on the mobile ion and trapping site respectively, x_0 the distance of closest approach of the charges, K the dielectric constant of the medium and ϵ_0 the permittivity of free space. Only for $2(bE)^{1/2} \gg bE$ does (2.7) reduce to (2.6), in which case γ is given by:

$$\gamma = 2b^{1/2}\phi = (q_1^2 q_2/\pi K \epsilon_0)^{1/2}. \tag{2.10}$$

It appears to us that (2.7) will represent the behaviour of this model rather poorly as no account is taken of the short range interaction between the ion on one hand and the trapping site and channel walls on the other. We retain the equation nevertheless for comparison purposes.

The form of $W(E)$ arising from various forms of U_1 are summarized below for future reference where in all cases u^* and ϕ are the activation dipole (charge-activation distance product in previous terminology) and activation energy respectively in the limit of low field strength.

1. Infinitely sharp positions of extrema in U_1

$$W(E) = \phi(1 - bE) \tag{2.11}$$

where $b = u^*/\phi$.

2. Exact Schottky law $-U_1$ calculated from charge pair interaction

$$W(E) = \phi[1-2(bE)^{1/2}-bE]$$

$$b = x_0q_1/\phi,\ \phi = q_1q_2/4\pi K\epsilon_0x_0. \quad (2.12)$$

3. Approximate Schottky law, $bE \ll 1$

$$W(E) = \phi[1-2(bE)^{1/2}]. \quad (2.13)$$

4. Cosine potential energy function, i.e.

$$U_1(u) = (\phi/2)[1-\cos(\pi u/u^*)] \quad (2.14)$$

$$W(E) = \phi\left\{\left[1-\left(\frac{2bE}{\pi}\right)^2\right]^{1/2} - bE + \frac{2}{\pi}bE\sin^{-1}\left(\frac{2bE}{\pi}\right)\right\} \quad (2.15)$$

where $b = u^*/\phi$.

5. Clipped parabolic potential energy function, i.e.

$$U_1(u) = \phi(u/u^*)^2,\ u^* \geqslant u \geqslant 0 \quad (2.16)$$
$$= \phi,\ u \geqslant u^*$$
$$W(E) = \phi[1-bE+(bE)^2/4] \quad (2.17)$$

where $b = \omega^*/\phi$.

6. Morse function potential energy curve, i.e.

$$U_1(u) = \phi[1-\exp(-u/\omega^*)]^2 \quad (2.18)$$

$$W(E) = \phi\left\{[1-2bE]^{1/2} - bE\ln\left[\frac{1+(1-2bE)^{1/2}}{1-(1-2bE)^{1/2}}\right]\right\} \quad (2.19)$$

where $b = \omega^*/\phi$.

7. Expansion of $W(E)$ as a power series in E

$$W(E) = \phi[1-bE+(bE)^2/C_2 + (bE)^3/C_3 + \ldots] \quad (2.20)$$

where $b = u^*/\phi$; and C_2, $C_3 \ldots$ are dimensionless constants characteristic of the shape of the potential energy function, $U_1(u)$, with ϕ and u^* being the activation energy and activation dipole respectively in the limit as $E \to 0$.

3. POWER SERIES REPRESENTATION OF $W(E)$

The purpose of this section is to develop a power series representation of $W(E)$ given $U_1(u)$ in the form of a power series.

We begin by choosing the adjacent positions of minimum and maximum in the relevant potential energy barrier, $U_1(u)$, to coincide with $u = 0$ and $u = u^*$ respectively. u^* thus becomes the zero field activation dipole. The zero field activation energy is then defined through the equation

$$\phi = U_1(u^*) - U_1(0). \quad (3.1)$$

We may now represent $U_1(u)$ over the range of interest (i.e. $u^* \geqslant u \geqslant 0$) in the following manner:

$$U_1(u) = \phi f_1[u/u^*], \quad u_c \geqslant u \geqslant 0$$
$$= \phi(1-f_2[1-u/u^*]), \quad u^* \geqslant u \geqslant u_c \quad (3.2)$$

where the functions $f_1(Z)$ and $f_2(Z)$ determine the 'shape' of the function U_1, whereas ϕ and u^* determine its dimensions. In order that U_1 be continuous and have a continuous first derivative, $f_1(Z)$ and $1-f_2(1-Z)$ and their first derivatives respectively should be equal at $Z = u_c/u^*$. Since U_1 has a minimum at $u = 0$ and a maximum at $u = u^*$, it must contain at least one inflection point between these limits. u_c is chosen to coincide with the position of the principal inflection point, that is the inflection point at which dU_1/du is a maximum. The reason for defining $U_1(u)$ in terms of two functions of (u/u^*) will be clear shortly, but is merely one of convenience. It is worth noting at this point, however, that if the inflection point represents a centre of symmetry for U_1 then $f_1(Z) = f_2(Z)$ provided that the zero of potential energy is chosen so that $U_1(0) = 0$. Adopting this latter convention it is apparent that $f_1(0) = 0 = f_2(0)$ in the general case. Furthermore, since both $f_1(Z)$ and $f_2(Z)$ have a minimum at $Z = 0$, $f_1'(0) = 0 = f_2'(0)$ in the general case, where $f_j'(0)$ is the first derivative of $f_j(Z)$ evaluated at $Z = 0$.

Substituting (3.2) into (2.3) to obtain expressions for the positions of minimum and maximum potential energy (u_0 and u_m respectively) in the presence of a homogeneous field, E, and noting that u_0 must lie in the interval $(0, u_c)$ and u_m in the interval (u_c, u^*), the following equations are obtained

$$\begin{aligned} f_1'[u_0/u^*] &= bE \\ f_2'[1 - u_m/u^*] &= bE \end{aligned} \tag{3.3}$$

where $b = u^*/\phi$.

Representing the inverse of the functions f_j' by g_j, i.e.

$$g_j(f_j'[Z]) \equiv Z, \quad j = 1, 2 \tag{3.4}$$

(3.3) becomes

$$\begin{aligned} u_0 &= u^* g_1(bE) \\ u_m &= u^*[1 - g_2(bE)] \end{aligned} \tag{3.5}$$

Substituting (3.5) in (2.5) we obtain an expression for the net activation energy, $W(E)$, viz.:

$$W(E) = \phi[1 - bE + F_1(bE) + F_2(bE)] \tag{3.6}$$

where

$$F_j(Z) \equiv Z g_j(Z) - f_j[g_j(Z)], \quad j = 1, 2. \tag{3.7}$$

An alternative expression for $W(E)$ may be derived by noting that the first derivative of $F_j(Z)$ is given by:

$$F_j'(Z) = g_j(Z). \tag{3.8}$$

To show this we differentiate (3.7) to obtain

$$F_j'(Z) = Z g_j'(Z) + g_j(Z) - f_j'[g_j(Z)] \,.\, g_j'(Z)$$

which reduces to (3.8) above since $f_j'[g_j(Z)] \equiv Z$, f_j' and g_j being inverse functions. Integration of (3.8) for the boundary condition $F_j(0) = 0$ gives:

$$F_j(bE) = \int_0^{bE} g_j(Z)\, \mathrm{d}Z. \tag{3.9}$$

That this is the correct boundary condition follows from the conditions stated previously, namely $f_j(0) = 0 = f_j'(0)$ from which by (3.4), $g_j(0) = 0$ and hence from (3.7), $F_j(0) = 0$. Substituting (3.9) in (3.6), the following expression for $W(E)$ is obtained in terms of the functions g_j

$$W(E) = \phi\Big[1 - bE + \int_0^{bE} [g_1(Z) + g_2(Z)]\, \mathrm{d}Z\Big]. \tag{3.10}$$

We now show that expanding $f_1(Z)$ and $f_2(Z)$ about $Z = 0$ as power series in Z, permits (3.10) to be written in the form:

$$W(E) = \phi[1 - (bE) + (bE)^2/C_2 + (bE)^3/C_3 \ldots.] \tag{3.11}$$

where the dimensionless constants C_2, C_3 etc. are related to the coefficients in the expansions of $f_1(Z)$ and $f_2(Z)$. To find the relationships we begin by expressing $f_1(Z)$ and $f_2(Z)$ as follows:

$$f_j(Z) = \sum_{k=2}^{\infty} k^{-1} a_{jk} Z^k \tag{3.12}$$

from which

$$f_j'(Z) = \sum_{k=2}^{\infty} a_{jk} Z^{k-1}. \tag{3.13}$$

That the first term in the expansion of $f_j(Z)$ is a term in Z^2 follows from the properties of $f_j(Z)$ stated previously i.e. $f_j(0) = 0 = f_j'(0)$. Reversion of (3.13) gives:

$$g_j(Z) = \sum_{k=2}^{\infty} A_{jk} Z^{k-1} \tag{3.14}$$

and hence

$$\int_0^y g_j(Z)\, \mathrm{d}Z = \sum_{k=2}^{\infty} k^{-1} A_{jk} y^k \tag{3.15}$$

where the coefficients A_{jk} can be evaluated in terms of the coefficients a_{jk} by a successive approximations procedure or from tables,[5].

Comparing (3.10) and (3.11), from (3.15) the coefficients C_k are given by:

$$\frac{1}{C_k} = \frac{1}{k}(A_{1k}+A_{2k}), \quad k = 2 \text{ to } \infty. \quad (3.16)$$

4. CONSEQUENCES OF ALLOWING FOR A FIELD DEPENDENCE OF U_1

Assuming the function U_1 may be represented as a power series in u for constant E (i.e. defining U_1 through (3.2), (3.12) and (3.13)) then we may presumably take account of the probable field dependence of U_1 by expanding ϕ, u^* and the coefficients a_{jk} as power series in the field E. It is immediately apparent that this procedure will still lead to a power series form for $W(E)$, a result which is hardly surprising. We pursue the matter further, however, in order to ascertain to what extent the new coefficients in the power series can be related to the form of the potential energy function at zero field strength. We shall concern ourselves only with terms which make a contribution to $W(E)$ which is of order 2 or less in the field strength. It is clear that the field dependent terms in the expansions of the coefficients a_{jk} will contribute only to terms of order 3 and higher. For present purposes, therefore, the field dependence of these coefficients is unimportant.

We examine now the possible field dependence of the parameter ϕ. In the present analysis we are concerned with the first three terms in the field expansion of ϕ.

$$\phi = \phi_0 + \phi_1 E + \phi_2 E^2. \quad (4.1)$$

The term which is first order in E is identically zero if we define the activation dipole u^* according to equation (4.2)

$$u^* = \operatorname*{Limit}_{E\to 0} \frac{\mathrm{d}[W(E)]}{\mathrm{d}E}. \quad (4.2)$$

The question then arises, however, as to whether this definition of u^* coincides with the previous definition. That is, is u^* as defined by (4.2) necessarily the charge displacement required to go from the position of minimum to that of maximum potential energy in the absence of a field? If the potential barrier in question is symmetrical and separates positions of minimum potential energy which are also symmetrical (such as might be found to transport within a crystalline solid) then one can show by a fairly simple argument that the two definitions of u^* are indeed equivalent. Defining u^* in terms of the potential energy function at zero field strength, the adjacent positions of minimum potential energy lie at $u = 0$ and $u = 2u^*$ respectively for $E = 0$. By symmetry $U_1(0) = U_1(2u^*)$ for all values of field strength E including $E = 0$. It therefore follows that $U_1(u^*) - U_1(0) = U_1(u^*) - U_1(2u^*)$ for all values of E, or in other words if ϕ depends on the field strength it is independent of the field direction. ϕ must therefore be an even function of the field strength which requires that the coefficient ϕ_1 be zero.

Essentially this same result has been proven using a different argument in an earlier publication[3], where it has also been shown that for this case $u^* = q\mathrm{d}/2$ where q is the valence charge and d the distance between adjacent minima. It is apparent, however, that the above symmetry conditions will not be satisfied for a potential barrier situated at an interface. In this case $u^* \neq q\mathrm{d}/2$ in general, and furthermore the two definitions of u^* will not be equivalent. It seems probable, however, that u^* as defined in (4.2) will not differ greatly from the charge displacement required to go from the position of minimum to that of maximum potential energy in the absence of a field.

It is consistent with the above argument that ϕ be an even function of field strength, so that the coefficient ϕ_2 in (4.1) may not be dropped. As two different physical phenomena can be identified which will contribute to ϕ_2, we divide ϕ_2 into two terms

$$\phi_2 = \phi_2^{(e)} + \phi_2^{(\alpha)} \quad (4.3)$$

where $\phi_2^{(e)}$ arises from electrostriction effects and $\phi_2^{(\alpha)}$ from the interaction of induced dipole moments with the electric field. We shall consider the term $\phi_2^{(e)}$ first.

Young was the first to propose a quadratic field variation of the activation energy, ϕ, arising from electrostriction[6]. The following treatment of the effect is essentially the same as that given by Young, though differing from it in detail. The effect may be regarded as arising from a volume change brought about by electrostriction. As ϕ would be expected to change with volume, then a change in E will lead to a change in ϕ. Accordingly we write:

$$\frac{\phi_2^{(e)}}{\phi_0} \simeq -\frac{\mathrm{d}(\ln \phi)}{\mathrm{d}(\ln V)} \cdot \beta \cdot \frac{\mathrm{d}p}{\mathrm{d}E^2} \qquad (4.4)$$

where V is the specific volume of the relevant phase or interphase, p is the hydrostatic pressure, and $\beta = -\mathrm{d}(\ln V)/\mathrm{d}p$ is the coefficient of compressibility. Evaluating $\mathrm{d}p/\mathrm{d}E^2$ from the relationship $p = \frac{1}{2}\epsilon_0 K E^2$, where K is the dielectric constant, and assuming $\phi \propto V^{-n}$, (4.4) becomes

$$\phi_2^{(e)}/\phi_0 \simeq \beta\epsilon_0 K n/2. \qquad (4.5)$$

Mott and Gurney estimate that for crystals such as rock-salt, $n \sim 2$[7]. Although it is difficult to justify this particular estimate, it seems unlikely that n would be as large as 10, say.

We turn out attention to considering the term $\phi_e^{(\alpha)}$. Assigning a polarizability, α, to the mobile defect, there will be a contribution $-\frac{1}{2}\alpha E_L^2$ to the potential energy of the defect arising from the field induced-dipole interaction, where E_L is the local electrostatic field strength. In general, both α and E_L will vary with position in the solid or interface so that we may write:

$$\phi_2^{(\alpha)} E^2 = -\tfrac{1}{2}\alpha^* E_L^{*2} + \tfrac{1}{2}\alpha^{(0)} E_L^{(0)2} \qquad (4.6)$$

where * and $^{(0)}$ refer to the positions $u = u^*$ and $u = 0$ respectively. Setting $E_L = (1 + \frac{1}{3}\gamma\chi)E$ where χ is the electric susceptibility of the medium and γ a structural factor (equal to 1 if E_L is equal to the Lorentz field), (4.6) becomes:

$$\phi_2^{(\alpha)} = \tfrac{1}{2}\alpha^{(0)}(1 + \tfrac{1}{3}\gamma^{(0)}\chi)^2 - \tfrac{1}{2}\alpha^*(1 + \tfrac{1}{3}\gamma^*\chi)^2 \qquad (4.7)$$

An equation similar to (4.7) was first proposed by Ibl[8] employing a rather different approach to the problem. The above equation is somewhat more general than that due to Ibl in that it allows not only for the variation of α with position but also for the variation of E_L (or γ) with position.

In order to obtain an equation from which $\phi_2^{(\alpha)}$ may be estimated, we shall attempt to determine the magnitude of the terms in (4.7). If the bonding in question can be regarded as essentially 100 per cent ionic then $\alpha^{(0)}$ and α^* should be essentially identical, and equal to the atomic polarizability of the mobile ion. Inertial contributions can be ignored to a first approximation as the relaxation time for these are too long to allow them to make a significant contribution to $\phi_2^{(\alpha)}$. This follows from the fact that the time available for relaxation will be only about one quarter of the period of vibration of the mobile defect in the direction which corresponds to surmounting the potential barrier.

We now attempt to show that for crystalline solids $\gamma^{(0)}$ and γ^* will probably have opposite signs. For simplicity we shall examine the case of a symmetrical barrier. We note first of all that:

$$E = \frac{1}{2u^*}\int_{-\frac{1}{2}u^*}^{\frac{3}{2}u^*} E_L\,\mathrm{d}u = \frac{1}{2}\left[\frac{1}{u^*}\int_{-\frac{1}{2}u^*}^{+\frac{1}{2}u^*} E_L\,\mathrm{d}u + \frac{1}{u^*}\int_{\frac{1}{2}u^*}^{\frac{3}{2}u^*} E_L\,\mathrm{d}u\right] \qquad (4.8)$$

a result which follows from simple symmetry considerations[3]. Setting

$$E_L^{(0)} \simeq \frac{1}{u^*}\int_{-\frac{1}{2}u^*}^{+\frac{1}{2}u^*} E_L\,\mathrm{d}u \text{ and } E_L^* \simeq \frac{1}{u^*}\int_{+\frac{1}{2}u^*}^{+\frac{3}{2}u^*} E_L\,\mathrm{d}u$$

[4.8] becomes

$$(E_L^{(0)}+E_L^*)/2 \simeq E \qquad (4.9)$$

or setting $E_L = (1+\frac{1}{3}\gamma\chi)E$

$$\gamma^{(0)}+\gamma^* \simeq 0. \qquad (4.10)$$

Provided that (4.8) can be regarded as defining the mean external field strength for a symmetrical barrier situated at an interface, (4.10) can be considered to apply to an interfacial potential barrier as well. For lack of a better approximation we shall proceed on this basis.

If the defects in question are vacancies, then for crystalline solids $\gamma^{(0)}$ should be of the same order, though perhaps a little smaller, than the value of γ(γ' say) used to obtain agreement between measured values of the high frequency dielectric constant, K_0, and values calculated from ionic polarizabilities [9]. For interstitial ions, the situation is less clear, but it seems likely that in this case, $\gamma^{(0)} \lesssim \gamma'$. Mott and Gurney conclude that for all the alkali halide, γ' lies between zero and 0·25[9]. Setting $-\gamma^* \simeq \gamma^{(0)} \simeq \gamma'$ and $\alpha^{(0)} \simeq \alpha^* = \alpha'$, the ionic polarizability of the mobile species,

$$\phi_2^{(\alpha)} \sim \tfrac{1}{3}\gamma'\chi\alpha'. \qquad (4.11)$$

Although the situation for an interfacial barrier is far less clear, (4.11) will presumably represent the correct order of magnitude of the effect with the one difference that χ will be the electric susceptibility of the interphase rather than of a bulk phase.

If the bonding in question involves an appreciable covalent component, then we would no longer expect $\alpha^{(0)}$ and α^* to be the same. In fact α^* should be considerably larger than $\alpha^{(0)}$. Thus when an interstitial ion is situated at the position corresponding to $u = 0$, the molecular orbitals associated with the defect will be centered roughly on this same position. The same is true of the position corresponding to $u = 2u^*$. In the transition state (i.e. $u = u^*$) however, the molecular orbitals will be delocalized over both regions, and should accordingly lead to a higher polarizability in this state. Setting $\frac{1}{2}\alpha^* \sim \alpha^{(0)} \sim \epsilon_0\chi_0 N$, where χ_0 is the electric susceptibility at optical frequencies and N the volume concentration of atoms of the type which are involved in the rate process, and setting $-\gamma^* \sim \gamma^{(0)} \sim \gamma'$ as before, Equation (4.7) becomes

$$\phi_2^{(\alpha)} \sim \left(\frac{\epsilon_0\chi_0}{2N}\right)(2\gamma'\chi - 1 - \tfrac{1}{9}\gamma'^2\chi^2). \qquad (4.12)$$

Since α', appearing in (4.11), will be of the order of or less than $\epsilon_0\chi_0/N$, we can compare the estimates of $\phi_2^{(\alpha)}$ given by (4.11) and (4.12). We note that (4.11) always predicts the larger value of $\phi_2^{(\alpha)}$ except for a certain range of values of $\gamma'\chi$. Within this range the maximum ratio of values occurs when $\gamma'\chi = 3$, for which case (4.12) predicts a value of $\phi_2^{(\alpha)}$ twice that predicted by (4.11). We may thus summarize the results of (4.11) and (4.12) by writing

$$\phi_2^{(\alpha)} \leqslant \left(\frac{2\epsilon_0\chi_0}{3N}\right)\gamma'\chi \qquad (4.13)$$

where $0 \leqslant \gamma' \leqslant 1$.

We conclude now by considering the possibility of a linear field term in the field expansion of the parameter u^*. Presumably such a term could arise due to displacement of positively charged species relative to negatively charged ones in the environment which constitutes the potential energy barrier, which would lead to an asymmetric distortion of the barrier. We may estimate the magnitude of such an effect for a barrier within a solid from a knowledge of the magnitude of the contribution of lattice ion displacement to electrical polarization (i.e. to the dielectric constant). For this purpose we shall use a simple model consisting of alternately positioned ions of charge ± Ze, separated from one another by a distance a_0 (e.g. the sodium chloride structure). In the presence of a field, E, this distance will change to $a = a_0+\Delta$ and $a = a_0-\Delta$, resulting therefore in a displacement polarization per ion pair of magnitude ΔZe, and hence to a displacement polarization per unit volume, P_d, given by

$$P_d = \Delta Ze/2a_0^3. \qquad (4.14)$$

However, P_d is also given by:

$$P_d \doteqdot \epsilon_0(K-K_0)E\dagger \qquad (4.15)$$

where K and K_0 are the static and high (optical) frequency dielectric constants respectively for the solid. Elimination of P_d therefore gives:

$$|a_0-a| = \Delta = 2(a_0^3/Ze)\epsilon_0(K-K_0)E. \qquad (4.16)$$

Assuming, now, that $u^* \propto a$, (4.16) becomes

$$u^* = u_0^* + u_1^* E \qquad (4.17)$$

where u_0^* is the value of u^* at $E = 0$, and u_1^* is given by:

$$|u_1^*/u_0^*| = 2(a_0^2/Ze)\epsilon_0(K-K_0). \qquad (4.18)$$

On substituting $\Omega = 2a_0^3/Z$, (4.18) becomes

$$|u_1^*/u_0^*| = (\Omega^{2/3}/e)(2/Z)^{1/3}\epsilon_0(K-K_0) \qquad (4.19)$$

which upon setting $(2/Z)^{1/3} \simeq 1$ gives

$$|u_1^*/u_0^*| \simeq (\Omega^{2/3}/e)\epsilon_0(K-K_0) \qquad (4.20)$$

where Ω is the volume occupied by an atom equivalent in the solid (i.e. Ω = equivalent weight/density X Avogadro's number). Three minor points are perhaps worth mentioning: First, equation (4.19) should apply equally well to ionic crystals consisting of ions of different charge. Second, the effect of charge delocalization or covalent bonding on the estimate represented by (4.20) is not clear. Finally, if relatively long range movement of defects contributes to the static dielectric constant, which appears to be likely for anodically formed oxides and glasses, then a smaller value for K should be used to estimate u_1^*/u_0^*, perhaps the dielectric constant for the bulk crystalline form.

It seems almost certain that u_1^*/u_0^* is positive, that is to say, u^* increases with increasing field. Thus, for example if we consider the case of a positively charged defect surmounting a potential energy barrier, in all probability the position of maximum potential energy will reside at a region of local excess positive charge, with the adjacent positions of minimum potential energy residing at regions of local excess negative charge. For such a case, u^* for transport in the direction assisted by the field would clearly increase with increasing field. The same conclusion is reached if a negatively charged defect is considered. We suggest therefore that u_1^* may be estimated from the relation

$$u_1^*/u_0^* \sim (\Omega^{2/3}/e)\epsilon_0(K-K_0). \qquad (4.21)$$

Again, it appears likely that (4.21) will represent the correct order of magnitude of the effect for a barrier situated at an interface, K and K_0 in this case referring however to the interphase.

On substituting $\phi = \phi_0 + \phi_2^{(e)}E^2 + \phi_2^{(\alpha)}E^2$ and $u^* = u_0^* + u_1^* E$ into (3.11) and dropping terms of order 3 or higher in E, the following result is obtained:

$$W(E) = \phi_0[1-(bE)+(bE)^2/C_2' + \cdots] \qquad (4.22)$$

where

$$b = u_0/\phi_0 \qquad (4.23)$$

and

$$\frac{1}{C_2'} = \frac{1}{C_2} + \frac{\phi_0\phi_2^{(e)}}{u_0^{*2}} + \frac{\phi_0\phi_2^{(\alpha)}}{u_0^{*2}} - \frac{\phi_0 u_1^*}{u_0^{*2}}. \qquad (4.24)$$

Furthermore, from (4.5), (4.13) and (4.21) respectively, we have

---

†This result may be obtained from the equations derived by Mott and Gurney[9] upon setting their overlap parameter, γ', equal to zero. It appears that $\gamma' \simeq 0$ for the alkali halides[9].

$$\frac{\phi_0\phi_2{}^{(e)}}{u_0^{*2}} \simeq \frac{\beta\epsilon_0 Kn}{2b^2} \tag{4.25}$$

$$\frac{\phi_0\phi_2{}^{(\alpha)}}{u_0^{*2}} \leqslant \left(\frac{2\epsilon_0\chi_0}{3Nb^2\phi_0}\right)\chi \tag{4.26}$$

and

$$\frac{\phi_0 u_1^*}{u_0^{*2}} \sim \frac{\Omega^{2/3}\epsilon_0(K-K_0)}{be}. \tag{4.27}$$

A discussion of the expected numerical magnitudes of the terms contributing to C_2' will be left to Section 6 of the paper.

5. EXAMINATION OF DATA OBTAINED DURING STEADY-STATE ANODIC OXIDATION STUDIES ON TANTALUM AND NIOBIUM

In order to provide results for the examination of the foregoing theory, Young's data for tantalum and niobium[10, 11, 4] were fitted to equation (1.1) using least squares procedures with the net activation energy $W(E)$ being represented in turn by the various functions listed in Section 2. The data processed in this way include two sets, (one for tantalum and one for niobium) in which film thicknesses were determined using the minimum reflectance technique[10, 11], and two sets (again one for tantalum and one for niobium) in which the film thicknesses were determined using an ellipsometer[4]. All four sets cover a fairly large range of current density and temperature. One set of data for tantalum[10] excels particularly in this regard and was therefore most suitable for judging the relative merits of the various functional forms for $W(E)$.

The method of analysis was as follows. The data in the form log i as a function of T and E were processed by a 7094 IBM computer using a non-linear least squares program which chose the parameters to minimize the variance in log i. In addition, the RMS deviation of the experimental log i values from those calculated using the least squares parameters, and the standard deviations of the parameters themselves were determined. The calculations were carried out in both single and double precision in order to be certain that the results were indeed reliable.

In order to compare the relative ability of the various forms of $W(E)$ to represent the data in Table 1 the RMS deviations of log i for the four sets of data have been tabulated against the assumed functional form of $W(E)$. A fifth set of data has been included which was obtained by a smoothing procedure from one of the sets of tantalum data. The data (log i vs. E) were smoothed independently at each temperature using a polynomial fit procedure. The purposes of analyzing the smoothed data was to ascertain the relative importance of systematic vs. random errors in determining the RMS deviation of log i.

It is apparent that the RMS deviation for the tantalum-A data is markedly dependent upon the form assumed for $W(E)$, varying from a maximum of 0·136 for case 1 to 0·034 for case 7. The tantalum-B data does not display quite as sensitive a dependence on the functional form of $W(E)$ as does the tantalum-A data, due primarily to the fact that the B data cover a range of field strengths which is significantly narrower than that covered by the A data. The niobium data, both A and B sets, show an even weaker dependence upon the form of $W(E)$, due again to the even narrower range of field strengths covered by the data. In every case, however, the quadratic and cubic expansions give the best fit to the data, and a fit which is very substantially better than that obtained for the sharp extreme case (linear expansion of $W(E)$). Furthermore, the general trend with respect to the RMS deviations is much the same in all four sets of data with the exception of the sensitivity feature already discussed. We shall therefore focus our attention on the tantalum-A data.

Young has postulated that the Schottky Law represents the anodic oxidation data for tantalum and niobium quite well[4]. It is apparent, however, from the tantalum-A data, that the improvement in going from

Table 1. Root-mean-square deviation of log i *from curves calculated using least squares parameters, assuming various forms for* W(E). *The numbers in brackets represent the standard deviations of the RMS deviations of log* i

	RMS deviations of log (i, a/cm^2) for Young's data for Ta and Nb				
Functional form of $W(E)$	Smoothed data Ta-A[10]	Ta-A[10]	Ta-B[4]	Nb-A [11]	Nb-B[4]
1. Sharp	0·1325	0·1358	0·1071	0·0868	0·0875
extrema	(0·0121)	(0·0124)	(0·0174)	(0·0091)	(0·0196)
2. Exact	0·0943	0·0987	0·0888	0·0700	0·0727
Schottky	(0·0086)	(0·0090)	(0·0144)	(0·0073)	(0·0163)
3. Approx.	0·0829	0·0880	0·0831	0·0663	0·0693
Schottky	(0·0076)	(0·0080)	(0·0135)	(0·0069)	(0·0155)
4. Cosine	0·0880	0·0928	0·0763	0·0705	0·0722
potential	(0·0080)	(0·0085)	(0·0124)	(0·0073)	(0·0161)
5. Parabolic	0·0717	0·0775	0·0655	0·0659	0·0680
potential	(0·0065)	(0·0071)	(0·0106)	(0·0069)	(0·0152)
6. Morse	0·0676	0·0737	0·0676	0·0638	0·0665
potential	(0·0062)	(0·0067)	(0·0110)	(0·0067)	(0·0149)
7(a) Quadratic	0·0197	0·0353	0·0435	0·0585	0·0626
expansion	(0·0018)	(0·0032)	(0·0073)	(0·0062)	(0·0148)
7(b) Cubic	0·0172	0·0339	0·0434	0·0585	0·0614
expansion	(0·0016)	(0·0032)	(0·0074)	(0·0062)	(0·0154)

the simple linear expansion of $W(E)$ (i.e. case 1) to either the exact or approximate Schottky Law, although significant, is small compared to the improvement obtained using the quadratic or cubic expansion. Likewise the Morse potential, which was proposed by one of us[2], although representing a better fit than the Schottky Law, still leads to a much poorer fit than does either the quadratic or cubic expansion. Thus, on going from the sharp extrema to the Morse potential, the RMS deviation is dropped in half, with a further reduction by one half occurring on going from the Morse potential to the quadratic expansion. It is clear that of the functional forms tested, only the quadratic and cubic expansions can be considered to represent the data well.

On comparing the raw and smoothed tantalum-A data, it is apparent that the smoothing process has led to only a small reduction in the RMS deviation values for all the functional forms of $W(E)$ except the quadratic and cubic expansions, where the influence of smoothing is quite dramatic, the RMS deviation being reduced by close to 50 per cent. The implication of this result is that in the case of the quadratic and cubic expansions, the RMS deviation arises mainly as a result of random errors, systematic deviation between the data and the functional form making only a minor contribution.

On comparing the RMS deviations for the quadratic and cubic expansions, it is clear that the cubic expansion represents a very minor improvement over the quadratic expansion. In fact, the improvement is barely statistically significant even in the case of the smoothed data. We conclude, therefore, that the quadratic expansion represents the data extremely well, far better than any other functional form proposed to date, and that the inclusion of a cubic term leads to a negligible improvement.

In Table 2 the kinetic parameters, log i_0, ϕ and b_g for the tantalum-A data, are tabulated against the various assumed functional forms for $W(E)$. It is apparent that although the

Table 2. Values for the parameters log i_0, ϕ *and* b_s *calculated from Young's* Ta *data (set* A [10]*) assuming various forms for* W(E). *The numbers in brackets represent the standard deviations of the calculated parameters*

Functional form of $W(E)$	Log (i_0, a/cm^2)	ϕ (eV)	b_s (Å/V)	$u_s^* = b_s\phi$ (eÅ)
1. Sharp extrema	8·19 (0·22)	1·62 (0·02)	9·50 (0·16)	15·4 (0·3)
2. Exact Schottky	8·26 (0·16)	2·31 (0·02)	1·53 (0·01)	
3. Approx. Schottky	8·27 (0·14)	2·51 (0·02)	2·18 (0·06)	
4. Cosine potential	8·24 (0·15)	1·81 (0·02)	12·09 (0·07)	21·9 (0·3)
5. Parabolic potential	8·25 (0·12)	1·90 (0·01)	13·18 (0·07)	25·0 (0·2)
6. Morse potential	8·27 (0·12)	2·13 (0·02)	3·63 (0·02)	
7(a). Quadratic expansion	8·33 (0·06)	2·21 (0·02)	16·14 (0·36)	35·7 (0·8)
7(b). Cubic expansion	8·33 (0·06)	2·57 (0·17)	21·20 (3·70)	54 (10)

values of log i_0 are essentially independent of the form chosen for $W(E)$, the values of ϕ and b_s show no such constancy. Thus the activation energy, ϕ, is seen to vary from a low of 1·62 to 2·57 eV. It is interesting to note the large difference in the parameters ϕ and b_s calculated for the exact and approximate Schottky Laws. This emphasizes a result which was apparent from Table 1, namely, that the approximate Schottky Law does not represent a satisfactory approximation to the exact Schottky Law at the high field strengths encountered. The parameter b_s may not be compared for all the potential energy functions, as it represents in different instances different physical quantities. An additional column has therefore been added in which $u_s^* = b_s\phi$ has been calculated for those potential functions in which u_s^*, the steady-state activation dipole, appears. Again, a large range of values for this parameter is evident. We favour the parameters calculated on the basis of the quadratic expansion of $W(E)$ since this form represents the data extremely well, and furthermore all the relevant parameters can be calculated with a fairly small standard deviation. The addition of a cubic term in the expansion of $W(E)$, although improving the fit very slightly, introduces a large standard deviation in the calculated parameters, particularly b_s and μ_s^*. The lesson to be learned from the results of Table 2, however, is that the zero field activation energy, ϕ, can probably not be determined more accurately than to within about 0·3 eV because of the uncertainty as to the correct form for $W(E)$ to use. Likewise, there is probably an uncertainty in the steady-state activation dipole μ_s^*, of perhaps as much as 10 eÅ. These uncertainties could be reduced somewhat by increasing the range of field strengths over which measurements are made. The only practical way of accomplishing this is to make measurements over a wide temperature range.

In Table 3, the kinetic parameters for all four sets of data are presented in which $W(E)$ is represented in turn as a linear, quadratic and cubic function of the field strength. It is

Table 3. Values for the parameters calculated from Young's data for Ta *and* Nb *assuming* W(E) *to be represented by a linear, quadratic and cubic function of* E *respectively. The numbers in brackets represent the standard deviations of the calculated parameters*

		Log (i_0, a/cm^2)	ϕ (eV)	b_s (A/V)	C_2'	C_3'
Ta Data – *A*	1. Linear	8·189	1·616	9·505		
		(0·217)	(0·023)	(0·163)		
	7(a). Quadratic	8·329	2·210	16·134	3·313	
		(0·057)	(0·022)	(0·357)	(0·179)	
	7(b). Cubic	8·334	2·570	21·203	2·314	−13·180
		(0·055)	(0·167)	(3·705)	(1·022)	(8·888)
Ta Data – *B*	1. Linear	4·155	1·482	11·708		
		(0·540)	(0·050)	(0·370)		
	7(a). Quadratic	4·473	2·365	20·659	3·535	
		(0·228)	(0·095)	(1·636)	(0·622)	
	7(b). Cubic	4·459	1·949	13·379	−2·694	1·860
		(0·237)	(1·221)	(34·996)	(28·867)	(15·476)
Nb Data – *A*	1. Linear	7·728	1·433	11·607		
		(0·235)	(0·025)	(0·226)		
	7(a). Quadratic	7·844	1·802	18 411	3·262	
		(0·161)	(0·053)	(1·324)	(0·636)	
	7(b). Cubic	7·844	1·900	21·058	2·444	−14·778
		(0·163)	(0·431)	(16·214)	(6·112)	(72·722)
Nb Data – *B*	1. Linear	7·025	1·500	13·547		
		(0·442)	(0·045)	(0·460)		
	7(a). Quadratic	7·177	1·913	21·393	3·358	
		(0·337)	(0·145)	(3·918)	(1·646)	
	7(b) Cubic	7·195	2·720	38·044	2·107	−10·940
		(0·352)	(1·451)	(47·667)	(5·709)	(42·213)

apparent that there is a discrepancy between the results calculated from the A and B sets of data, the discrepancy being particularly large in the case of the tantalum data. We can think of no reason why such a large discrepancy should occur, but are inclined to favour the *A*-sets of data because of the extreme care and precision apparently involved in these measurements.

It is apparent from the standard deviations of the coefficients that only in the case of the tantalum-*A* data are the experimental results sufficiently precise and extensive to permit an evaluation of the parameters in the cubic expansion of $W(E)$, and even here the standard deviation of the coefficient C_3 is almost as large as the coefficient itself. In the quadratic expansion, on the other hand, the parameters are determined with reasonable precision for all four sets of data, with the coefficient C_2 being essentially identical for all sets. It seems safe to conclude, therefore, that a value of C_2 equal to 3·31 is characteristic of the behaviour of both tantalum and niobium, and indeed aluminum as well[2]. We have, accordingly, calculated a family of effective potential energy functions, U_{eff}, setting $C_2 = 3{\cdot}31$ and using equation (A14) in the manner outlined in Appendix A. (The parameter '*a*' is calculated from (A11).) Representative members of the family are presented in Fig. 1, any one of which in conjunction with equations (2.5) and (1.1) and the appropriate values for i_0, ϕ and b_s will reproduce any one of the sets of data within experimental error. As shown in Appendix A, the kinetic data are unable to select from among these potential energy functions, as they are precisely equivalent in

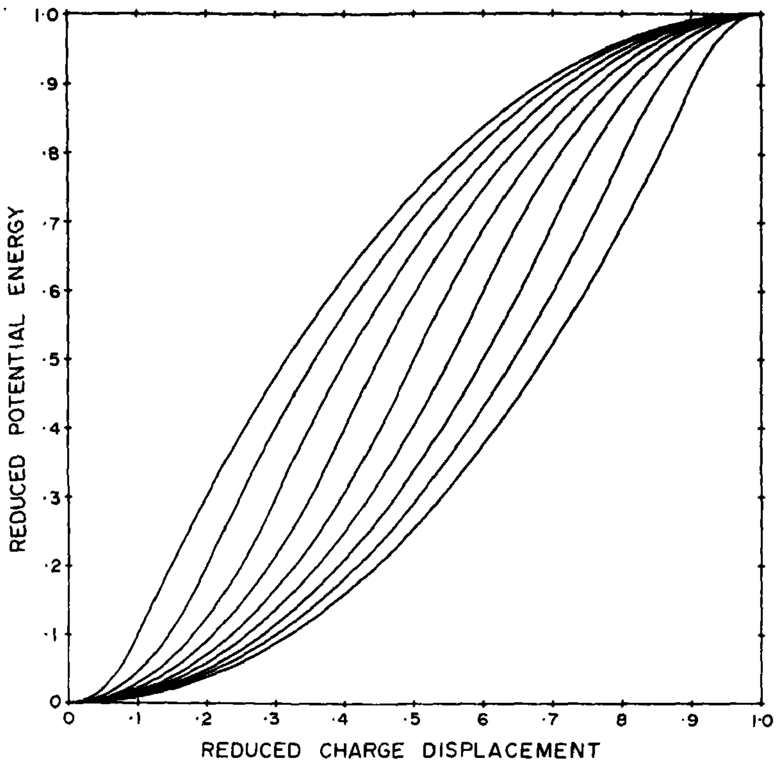

Fig. 1. Reduced potential energy function for the mobile defect, V_{eff}/ϕ, vs. its reduced charge displacement, $2u/de$, for α_1 equal to 0·1, 0·2, ... 0·9 respectively, proceeding from the left to right. The curves were calculated using (A.14) and Young's data for Ta[10].

terms of kinetic behaviour. Whether or not any member of the family represents the 'true' potential energy function at zero field strength depends upon the relative magnitudes of the various terms contributing to C_2' (see equation (4.24)) and upon the precise mechanism operative during the anodic oxidation of the valve metals. If, for example, the high field Frenkel defect theory[12] is correct in describing the behaviour of these systems, then one needs not one but two potential energy functions to represent their behaviour. If, on the other hand, transient ionic conduction phenomena are correctly explained in terms of dielectric polarization phenomena [13, 14], then only one potential energy function is required. In this latter case, the potential energy function would be that for ion transport across one or more interfaces [13, 15]. In Appendix B, we show that a single potential energy function in conjunction with the latter theory[13, 15] is sufficient to account for transient phenomena, and hence proceed on this basis. It must be admitted, however, that this need not be the case, even if the basic postulates of the dielectric polarization theory are accepted.

6. ESTIMATE OF THE MAGNITUDE OF THE TERMS CONTRIBUTING TO THE QUADRATIC FIELD COEFFICIENT C_2'

The relevant equations of Section 4 (equations (4.2–4.27) are summarized as follows

$$W(E) = \phi_0[1 - bE + (bE)^2/C_2'] \quad (6.1)$$

$$\frac{1}{C_2'} = \frac{1}{C_2} + T_e + T_\alpha + T_a \quad (6.2)$$

$$T_e \simeq \beta\epsilon_0 Kn/2b^2 \quad (6.3)$$

$$T_\alpha \leqslant (2\epsilon_0\chi_0/3Nb^2\phi_0)\chi \quad (6.4)$$

$$T_a \sim \Omega^{2/3}\epsilon_0(K - K_0)/be \quad (6.5)$$

$$b = u_0/\phi_0 \quad (6.6)$$

where the terms T_e, T_α and T_a are the contributions to the quadratic field coefficient made by the electrostriction effect, the field-induced dipole interaction, and the asymmetric barrier distortion respectively. It is important to point out that although the empirical values for b obtained using equation (8.1) will depend on whether or not E is taken to be the Maxwell field, the empirical value of C_2' is independent of this choice. Thus we may substitute for C_2' the empirical value obtained from the tantalum data say (i.e. $C_2' = 3{\cdot}31$; see Table 3). Similarly, the value of ϕ_0 is independent of the scale factor chosen for E and can accordingly be deduced from the experimental data ($\phi_0 = 2{\cdot}21$ eV; see Table 3). If it is assumed that the appropriate field to use is indeed the Maxwell field then $b = b_s = 16{\cdot}1$ Å/V (see Table 3). Present results, however, militate against this assumption. Thus from Table 3 we see that the empirical steady-state activation dipole, $b_s\phi$, obtained from the quadratic expansions is about 40 eÅ for all four sets of data. From the point of view of energetics it is highly improbable that the mobile defect in these oxides will bear a charge of +5(15). Nevertheless, even if we assume such is the case, the zero field activation distance is calculated to be about 8 Å. It is inconceivable that the activation barrier could have such a large half width. We are led to the conclusion, therefore, that the rate controlling process or processes *must* occur within one or more interphases, the fields within which are much greater than the Maxwell field or mean field within the oxide film. We may estimate an effective low frequency dielectric constant of the interphase, K_i, from the continuity condition of the normal component of the electric displacement at the boundary between the oxide and the interphase and the relationship between the steady-state and transient field coefficients. Accordingly from $K_1/K_i = E_e/E = b_1\phi_0 u_0^*$ (see Appendix B) and setting $b_s/b_1 = 3{\cdot}21$ (Table 4), $b_s = 16{\cdot}1$ Å/V, $\phi_0 = 2{\cdot}21$, $K_1 = 27{\cdot}6$[18] and estimating $u_0^* \simeq 3$ eÅ, we obtain $K_i \simeq 7$. Essentially the same estimate for K_i is obtained if the relevant data for Nb_2O_5 are used. It is interesting to note that the above estimate of K_i is close to the value for the dielectric constant usually assigned to the electrode-aqueous electrolyte double layer, namely 6. For the purposes of the following calculations, we shall assume that the high frequency dielectric constant of the interphase, K_{i0}, is about 3. Note that a larger estimate for u_0^* will lead to a larger estimate of K_i. Since a larger estimate of u_0^* will also lead to a larger estimate of $b = u_0^*/\phi_0$, the net effect of increasing the estimate of u_0^* is to reduce the estimates of T_e and T_α, leaving the estimate of T_a essentially unchanged. Since u_0^* is unlikely to be significantly smaller than 3 eÅ, the estimates of the T terms obtained with this value will be upper limit estimates.

We estimate the term T_e first, setting $K = K_i = 7$ and $b = u_0^*/\phi_0 = 3/2{\cdot}21 = 1{\cdot}36$ A/V. Mott and Gurney estimate that n for the alkali halides is of the order of 2. Although there appears to be no justification for such a postulate it appears probable that for almost any system n will be of the order of magnitude of unity. The compressibility coefficient, β, is of the order of 10^2 cm²/erg for most solids. A similar value would presumably apply to the highly structured oxide-electrolyte double layer. Substituting these values into (6.3) we obtain $T_e \sim 0{\cdot}03$ which is an order of magnitude smaller than $1/C_2' = 0{\cdot}30$. This conclusion is consistent with that reached by one of us in a previous publication[2] in which it was stated that the electrostriction effect or condenser pressure effect probably made an insignificant contribution to the quadratic field term. The agreement between the results of the present and the previous calculation is, however, largely accidental as the bases of the two calculations are quite different. In the previous calculations, a value for b equal to b_i was used, which from present considerations would appear to be incorrect. The effect of pressure on ϕ was also estimated in a different manner in the two cases, leading to fortuitous agreement.

Estimating the magnitude of the term T_α arising from the interaction of the induced dipole moment of the mobile defect with the local field, we obtain on setting $\chi_0 \sim 2$, $\chi \sim 6$, $N \sim 10^{23}\,\text{cm}^{-3}$ and $b = 1{\cdot}36$ ÅV the result $T_\alpha \leqslant 0{\cdot}1$. In this case we see that the contribution of this term to the empirical coefficient C_2' could be significant. However, if instead of $b = 1{\cdot}36$ Å/V, $\chi = 6$ and $\chi_0 = 2$ we set $b = b_s = 16{\cdot}1$ Å/V and set $\chi = 26{\cdot}7$, $\chi_0 = 7$ (the values appropriate for Ta_2O_5) then the term T_α becomes negligible compared with $1/C_2'$. Indeed, in discussing the contribution of the field-induced dipole interaction to the quadratic field term Ibl[8] concludes initially that the contribution would be negligible. He then goes on to say that if the polarizable units in the oxide film are microcrystallites, as postulated in a theory by one of us[13], one can arrive at a proper magnitude for the quadratic field coefficient. This argument is fallacious, however, as the relevant polarizability term is that for the mobile ionic species and can have nothing to do with any larger polarizable configuration. The larger estimate arrived at here arises from the fact that local field effects have been taken into consideration in the present treatment, whereas they were not taken into account in Ibl's treatment.

We proceed now to calculate the term T_a. Setting $\Omega^{2/3} \sim 10^{15}\ \text{cm}^{-3}$, $K - K_0 \simeq 4$ and $b = 1{\cdot}36$ Å/V, we obtain $T_a \sim 0{\cdot}01$, which is an order of magnitude smaller than $1/C_2'$.

Finally, assuming that the potential energy barrier at zero field strength is similar to a cosine function, $1/C_2 \sim 2/\pi^2 = 0{\cdot}20$[2], which agrees quite well with the empirical value of $1/C_2'$, 0·30.

Since our estimate of the magnitudes of the terms T_e, T_a and T_a could be in error by an order of magnitude, it is conceivable that all four terms on the right hand side of (6.2) are of the same order of magnitude as $1/C_2'$. Thus we must conclude in general that all four effects can contribute significantly to the quadratic field coefficient. It appears almost certain, however, that C_2, the coefficient relating to the shape of the zero field potential energy function, makes a major contribution to the empirical quadratic field coefficient, and quite possibly the dominant contribution. Of the remaining effects, the field-induced dipole interaction is probably the most important. In any event, it is clear that we are not at a loss to account for the existence and the magnitude of the quadratic field coefficient.

7. SUMMARY AND CONCLUSIONS

The extremely large values for the activation dipole calculated from the data of Table 3 assuming the local field to be the mean field or Maxwell field, combined with the success of the dielectric polarization theory in accounting for both ionic transients and the field dependence of the steady-state and transient differential field coefficients, lends strong support to the postulate that the local field assisting the rate controlling process or processes for the anodic oxidation of tantalum, niobium and aluminum is substantially larger than the mean field. In estimating the magnitude of the various terms contributing to the quadratic field coefficient, the local field effect must be taken into account. This is most easily done by employing an estimate of the activation dipole u^* rather than the steady-state empirical value u_s^*. The chief uncertainty in estimating u^* concerns the magnitude of the charge on the species involved in the rate controlling step. In the foregoing analysis this has been set at about 1 or 2 e with the activation distance given a value of around 1 to 2 Å leading to $u^* \sim 3$ eÅ.

Estimates of the magnitudes of the contributions to the quadratic field coefficient in the field expansion of $W(E)$, the net activation energy, have been made based on the above value for u^* in conjunction with numerous assumptions with respect to a detailed model for the matrix containing the barrier. Four different effects have been examined with respect to their contribution to the quadratic field term and, surprisingly, all four could conceivably make a significant contribution. The four different effects may be described as follows. The first, giving rise to the term $1/C_2$, arises from the fact that upon superimposing the linear potential energy function, arising from the field-charge interaction, upon the zero field potential energy function for the barrier, the positions of minimum and maximum in the composite potential energy function differ from those for the zero field potential energy function. This gives rise to higher order field terms in the expansion of the net activation energy. For reasonably shaped potential energy functions, however, the cubic and higher order terms are of little significance. The entire quadratic field coefficient can be accounted for on this basis alone. Although it is possible to derive a unique net activation energy function, $W(E)$, given the functional form of the potential energy barrier and assuming no other contribution to the higher order field terms, the inverse process does not lead to a unique function for the barrier but rather to a family of potential energy functions such as those illustrated in Fig. 1.

A second effect contributing to a quadratic field term arises from electrostriction (condenser pressure effect using Young's terminology). That is, compression of the phase containing the barrier will lead to an increase in the zero field activation energy. Such an effect can occur whether or not the rate controlling process resides within the oxide film. For example, if the rate controlling process were to take place at the oxide-electrolyte interface, electrostriction effects would occur within the oxide-electrolyte double layer. It is clear, however, that in such a case the local field rather than mean or Maxwell field must be employed in order to estimate the magnitude of the effect. Proceeding in this way we conclude that this effect contributes a term T_p which is about an order of magnitude smaller than the empirical quadratic field coefficient.

The third contributing effect arises from the fact that the ionic species associated with the process of field-assisted migration over the activation barrier will be subjected to different local fields at the positions of minimum and maximum potential energy, and furthermore will in general have different polarizabilities in these two regions. The latter of these two effects has been discussed previously by Ibl[8] whose development led to the conclusion that the effect would make a negligible contribution to the quadratic field coefficient. Allowing for local field effects we find, however, that the term could be of the same order of magnitude as the empirical field coefficient, our upper limit estimate giving a value of about 1/3 of the latter.

Finally, an estimate was made of the contribution to the quadratic field term arising from asymmetric distortion of the potential energy barrier brought about by inertial polarization of the matrix containing the barrier. The estimated magnitude of this contribution is about a factor of 30 smaller than the empirical value of the quadratic field coefficient. On the basis of these calculations, therefore, we are obliged to conclude that all four effects could conceivably make significant contributions to the quadratic field term. This conclusion, however, should be tempered by the following considerations. The leading and most obvious term, $1/C_2$, may be readily calculated given the shape of the potential energy barrier. Furthermore, almost any reasonable assumption concerning the shape of the potential energy barrier leads to a quadratic field coefficient which is in agreement with the empirical coefficient to better than a factor of 2. It seems likely that this term does dominate. The situation is, however, by no means certain. The magnitude of the electrostriction term might be determined more accurately by carrying out kinetic measurements over a range of hydrostatic pressures. It would be extremely difficult, however, to obtain improved estimates of the terms, T_α and T_n.

In conclusion, there is ample theoretical justification for the inclusion of a quadratic field term in the field expansion of the net activation energy $W(E)$. Furthermore, the existence of such a term is borne out by the experimental data pertaining to the anodic oxidation of aluminum, niobium and tantalum. Such an effect should also be present, however, for all electrode reactions occurring either at high overpotentials if the reactions do not involve film formation, or at high field strengths if film formation is involved. This means that the symmetry factor which appears in the theory of electrode reactions (and is frequently given the symbol α or β) should be a decreasing function of electrode potential, or more correctly, a decreasing function of the charge on the electrode. We are currently testing this hypothesis.

Acknowledgements—The authors are grateful to the National Research Council of Canada for supporting this research and for a scholarship (D.B.G.).

REFERENCES

1. YOUNG L., *Anodic Oxide Films*. Academic Press New York (1961).
2. DIGNAM M. J., *Can. J. Chem.* **42**, 1155 (1964).
3. DIGNAM M. J., *J. Phys. Chem Solids* **29**, 249 (1968).
4. YOUNG L. and ZOBEL F. G. R., *J. electrochem. Soc.* **113**, 277 (1966).
5. JOLLEY L. B. W., *Summation of Series*, 2nd Edn, p. 30. Dover Publications, New York (1960).
6. YOUNG L., *J. electrochem Soc.* **110**, 589 (1963).
7. MOTT N. F. and GURNEY R. W., *Electronic Processes in Ionic Crystals*, 2nd Edn, p. 31. Oxford University Press, London (1957).
8. IBL N., *Electrochim. Acta* **14**, 1043 (1967).
9. MOTT N. F. and GURNEY R. W., *Electronic Processes in Ionic Crystals*, 2nd Edn, Chap. I, Sect. 5. Oxford University Press, London (1957).
10. YOUNG L., *Proc. R. Soc.*, **258**, 496 (1960).
11. YOUNG L., *Trans. Faraday Soc.* **52**, 502 (1956).
12. BEAN C. P., FISHER J. C. and VERMILYEA D. A., *Phys. Rev.* **101**, 551 (1956).
13. DIGNAM M. J., *J. electrochem. Soc.* **112**, 722 (1965).
14. DIGNAM M. J., *J. electrochem. Soc.* **112**, 729 (1965).
15. DIGNAM M. J. In Preparation. Presented at Meeting of Electrochem. Soc., Dallas, Texas, May 1967.
16. YOUNG L., *Proc. R. Soc., Ser. A*, **244**, 41 (1958).
17. YOUNG L., *Proc. R. Soc., Ser. A*, **263**, 395 (1961).
18. DIGNAM M. J. and RYAN P. J., *Can. J. Chem.* **46**, 536 and **46**, 549 (1967).

APPENDIX A

Calculation of effective potential energy function from knowledge of W(E)

Returning to the approximation that the periodic potential energy function U_1, is independent of field strength, it is clear from (3.10) that given U_1 as a function of u (and hence g_1 and g_2 as functions of u), $W(E)$ can be determined as a function of E. On the other hand if $W(E)$ is known as a function of E (from empirical fit to data say) it is impossible to determine the form of $U_1(u)$ uniquely. In fact it will always be possible to construct an infinite number of potential energy functions all of which will lead to identically the same function for $W(E)$. Thus choosing f_1 (and hence g_1) arbitrarily within certain limits (i.e. the form of $f_1(Z)$ must have certain general properties, such as a minimum at $Z = 0$ etc.) we can always find a function f_2 (and hence g_2) which will satisfy (3.10) for any given function. $W(E)$. A potential energy function which generates the correct form for $W(E)$ we shall call an effective potential energy function and designate it U_{eff}. Allowing for the field dependence of U_1 does not alter the situation materially in that $W(E)$ defines through (3.10) an infinite set of functions. U_{eff}. The only difference between the cases $dU_1/dE = 0$ and $dU_1/dE \neq 0$ is that in the former case, U_1 is contained in $\{U_{\text{eff}}\}$ whereas in the latter case it is not.

We develop now a procedure for generating an infinite set of functions U_{eff} given $W(E)$ as a power series in E in which the cubic and higher order terms are very small. We make no attempt to generate the entire set $\{U_{\text{eff}}\}$ but instead limit consideration to functions containing one inflection point between adjacent extrema and for which the regions around the extrema in U_{eff} can be well represented by parabolae. The subset $\{U_{\text{eff}}\}'$ which we shall attempt to generate in this way will consist of functions made up essentially from a pair of parabolae (one inverted relative to the other) a cubic term being introduced into each in order to effect the necessary continuity at their junction. Even with the restrictions imposed so far, we are still left with a family of functions involving two parameters, of which one distributes $1/C_2$ between A_{12} and A_{22} and the other distributes $1/C_3$ between A_{13} and A_{23} (see equation (3.16)). Since we have postulated that the cubic term in the field (i.e. the term involving $1/C_3$) is very small, the parameter relating to the distribution of $1/C_3$ will be of little importance so that we define a single parameter set of functions $\{U_{\text{eff}}\}'$ through the following equations.†

We begin by defining $f_j(Z)$ as follows:

$$f_j(Z) = \alpha_j f(Z/\alpha_j), \quad \alpha_j \geq Z \geq 0, \quad j = 1, 2 \qquad \text{(A1)}$$

where α_j are constants such that

$$\alpha_1 + \alpha_2 = 1 \qquad \text{(A2)}$$

and $f(Z)$ has the following properties

$$f(1) = 1, \quad f(0) = 0, \quad f'(0) = 0 \qquad \text{(A3)}$$

From (A1) to (A3) it is easily shown that $f_1(Z)$ and $1 - f_2(1-Z)$ join at $Z = \alpha_1$ and have a common first derivative at this point. From (5.1) we now have:

$$f_j'(Z) = f'(Z/a_j) \qquad \text{(A4)}$$

and hence

$$g_j(Z) = \alpha_j g(Z) \qquad \text{(A5)}$$

where $g(Z)$ and $f'(Z)$ are inverse functions. The integral appearing in (3.10) is therefore given by

$$\int_0^{bE} [g_1(Z) + g_2(Z)]\,\mathrm{d}Z = \int_0^{bE} g(Z)\,\mathrm{d}Z. \qquad \text{(A6)}$$

We see that having chosen $g(Z)$ and hence $f(Z)$ consistent with the empirical form for $W(E)$ and with (A3), we may choose any value for α_1 in the interval (0, 1), so that the empirical data in this case generate a single parameter family of potential energy curves.

Assuming $f(Z)$ may be represented satisfactorily by two terms of a power series expansion, we have

$$f(Z) = aZ^2 + (1-a)Z^3 \qquad \text{(A7)}$$

$$f'(Z) = 2aZ + 3(1-a)Z^2 \qquad \text{(A8)}$$

$$g(Z) = [1/2a]Z - [3(1-a)/8a^3]Z^2 \qquad \text{(A9)}$$

correct to terms in Z^2. Hence

$$\int_0^{bE} g(Z)\mathrm{d}Z = [1/4a](bE)^2 - [(1-a)/8a^3](bE)^3. \qquad \text{(A10)}$$

Comparing (3.10) and (3.11), using the relations (A6) and (A10), we have

$$C_2 = 4a, \quad C_3 = -8a^3/(1-a) \qquad \text{(A11)}$$

and hence

$$C_3 = -C_2^3/2(4-C_2) \qquad \text{(A12)}$$

The net activation energy is therefore given by.

$$W(E) = \phi\left[1 - bE + \frac{(bE)^2}{C_2} - \frac{2(4-C_2)(bE)^3}{C_2^3}\right]. \qquad \text{(A13)}$$

For the anodic oxidation of the valve metals, $bE \simeq 0{\cdot}9$ and $C_2 = 3$ so that the cubic term in (A13) is $\sim 0{\cdot}05$, which is small compared with the linear term, as postulated at the outset of this development. Employing equation (A13), the constants ϕ, $b = u^*/\phi$ and C_2 may be determined from a fit to empirical data, and hence 'a' calculated from (A11). Substituting into (3.2) the expressions for f_j given by (A1) and (A7) and replacing U_1 by U_{eff} we obtain:

$$U_{\text{eff}}/\phi = \alpha_1[a(u/u^*\alpha_1)^2 + (1-a)(u/u^*\alpha_1)^3, \quad 0 \leq u/u^* \leq \alpha_1$$

$$= 1 - (1-\alpha_1)\left[a\left(\frac{1-u/u^*}{1-\alpha_1}\right)^2 + (1-a)\left(\frac{1-u/u^*}{1-\alpha_1}\right)^3\right],$$

$$\alpha_1 \leq u/u^* \leq 1. \qquad \text{(A14)}$$

Allowing α_1 to take values in the interval (0, 1), (A14) in conjunction with empirical values for ϕ, u^* and a, generate a family of effective potential energy functions. Such a family of functions consistent with Young's data for Ta[10], has been calculated using (A14) and is illustrated in Fig. 1. Details of the calculations of the parameters ϕ, b^* and C_2 are given in Section 5.

APPENDIX B

Transient differential field coefficient for tantalum, and its relationship to W(E)

The purpose of this Appendix is to examine certain transient data obtained by L. Young for tantalum [17], to see whether or not the dielectric polarization theory[13, 14] (a theory which need involve only a single potential energy function) will account for the data. Before doing this, however, we outline very briefly the salient features of the polarization theory[13, 15] as they relate to the question at hand.

The ion current density is assumed to be given by an equation of the form of (1.1) with E, the Maxwell field strength within the film, replaced by E_e, the field strength within the interphase or interphases at which the rate is controlled. Thus:

$$i_0 = i_0 \exp(-W(E_e)/KT). \qquad \text{(B1)}$$

Accordingly, from the continuity condition for the normal component of the electric displacement at an interface between dielectrics, the dielectric polarization of the oxide film will make a contribution to E_e given by

$$K_i E_e = E + P/\epsilon_0 \qquad \text{(B2)}$$

where K_i is the effective dielectric constant of the interphase. It is then assumed that there are both fast and slow processes contributing to P so that for steady-state conditions we may write

$$P_{s.s.} = \epsilon_0(K_s - 1)E \qquad \text{(B3)}$$

whereas for conditions of very rapidly changing field we have

$$\underset{\dot{E}\ \text{large}}{\text{Limit}} \frac{\mathrm{d}P}{\mathrm{d}E} = \epsilon_0(K_1 - 1) \qquad \text{(B4)}$$

---

†The same symbols used in Section 3 will be used here, even though they refer now to U_{eff} rather than U_1. This avoids the necessity of defining new symbols and should not lead to any confusion.

Table 4. Comparison of one parameter fit of Young's transient differential field coefficient values for Ta *assuming various forms for* W(E)*, with an independent three parameter fit*

Functional form of $W(E)$	RMS deviation for B_1 (Å/V)	Std. deviation of RMS value (Å/V)	$b_s/b_1 = K_s/K_1$
1. Sharp extrema	9·61	1·16	4·48
2. Exact Schottky	6·91	1·15	3·12
3. Approx. Schottky	6·13	1·02	2·87
4. Cosine potential	6·41	1·61	3·98
5. Parabolic potential	5·31	0·89	3·77
6. Morse potential	7·57	1·26	4·62
7(a). Quadratic expansion	3·91	0·65	3·21
7(b). Cubic expansion	3·64	0·61	2·33
Independent three parameter fit	3·51	0·62	

where K_s and K_i are the static and dynamic dielectric constants of the oxide respectively. For steady-state conditions, therefore, we obtain from (B1) to (B3)

$$i_{s.s.} = i_0 \exp(-W([K_s/K_i]E)/kT). \qquad \text{(B5)}$$

Hence for any of the functional forms chosen for $W(E)$, since E always occurs multiplied by b, (B5) may be written

$$i_{s.s} = i_0 \exp(-W_s(E)/kT) \qquad \text{(B6)}$$

where $W_s(E)$ is obtained from $W(E)$ on replacing b by $b_s = (K_s/K_i)b$. Accepting this theory we see from (B6) that the values labelled b_s in Tables 2 and 3, are related to b as above. We now define the transient differential field coefficient, B_1, through the following equation:

$$B_1 = \underset{\dot{E}\text{ large}}{\text{Limit}} \frac{\mathrm{d}\ln i}{\mathrm{d}E} = \underset{\substack{\Delta E\to 0\\ \Delta t\to 0}}{\text{Limit}} \frac{\Delta \ln i}{\Delta E}. \qquad \text{(B7)}$$

Substituting (B1), (B2) and (B4) in (B7) now gives

$$B_1 = -\frac{1}{kT}(K_1/K_i)\frac{\mathrm{d}\,W(E_e)}{\mathrm{d}E_e}. \qquad \text{(B8)}$$

The data to be analyzed were obtained commencing from steady-state conditions so that $\mathrm{d}W(E_e)/\mathrm{d}E_e$ may be evaluated at steady-state giving:

$$B_1 = -\frac{1}{kT}(b_1/b_s)\frac{\mathrm{d}\,W_s(E)}{\mathrm{d}E}. \qquad \text{(B9)}$$

where $b_1 = (K_1/K_i)b$. The important result expressed in equation (B9) *is that once we have obtained the form of* $W_s(E)$ from steady-state data, only one additional constant, $b_1/b_s = K_1/K_s$, is required in order to obtain B_1 as a function of temperature and field strength.

Young's transient data for tantalum[16] were obtained by first establishing steady-state formation conditions, then changing the current suddenly by a factor of 2 and, after correcting for capacitance effects, noting the instantaneous change in field strength. Measurements of this kind were made over a fairly wide range of temperature and initial field strength. The change in field strength arising from such measurements is sufficiently small that the limiting conditions imposed upon equation (B7) are satisfied to a very good approximation so that B_1 may be calculated directly from the ratio of $\Delta \ln i$ to ΔE.

To test the validity of equation [B9] the experimental values of B_1, tabulated as a function of E and T, were fitted to equation [B9] using an IBM 7094 digital computer, substituting in turn for $W_s(E)$ the various functional forms listed in Tables 1–3 and using the values for the coefficients appearing in the tables. In these analyses, the only unknown parameter is the ratio b_1/b_s, which was chosen to minimize the RMS deviation of the experimental from the calculated values of B_1. In Table 4 the results of these calculations are given along with the results obtained on representing B_1 as a cubic function in the field strength, the fit in this case involving three independent parameters. As was the case for the steady-state data, we see that the best fit (i.e. least RMS deviation for B_1) is obtained for the quadratic and cubic expansions. Furthermore the fit obtained using three independent parameters is not significantly better than the single parameter fit obtained using the quadratic and cubic expansion forms for $W_s(E)$. There is no doubt, therefore, that equation (B9) accounts for the transient data well within experimental error, the degree of accord achieved, in fact, being quite remarkable. A similar result has been shown in respect to the anodic oxidation of aluminum[18]. The uncertainty in the values of the parameters arising from the aluminum data however was considerably greater than that associated with the data analysed here, due to the narrow range in field strengths employed (all the measurements were made at 25°C).

It is clear that other theories can also account for the transient data but at the cost of introducing additional independent parameters[14].

J. Phys. Chem. Solids **Pergamon Press 1969. Vol. 30, pp. 395–399. Printed in Great Britain.**

INTERSTITIAL INCORPORATION OF DI- AND TRIVALENT COBALT IN QUARTZ

GERHARD LEHMANN

Institut für physikalische Chemie der Universität Münster, 44 Münster, Germany

(*Received* 17 *June* 1968)

Abstract – Trivalent cobalt in synthetic quartz shows absorption bands of a distorted octahedral complex indicating interstitial incorporation of this ion. Upon heating the cobalt is reduced to the divalent state. The absorption spectrum is now identical to that of synthetic quartz doped with divalent cobalt. It is compatible with a tetrahedral or cubic site symmetry and has been attributed to Co^{2+} substituting Si^{4+} in the lattice. From kinetic considerations and the experimental Dq value as well as the similarity of the spectrum of Co^{2+} in high alkali glasses it is concluded that the divalent cobalt occupies an interstitial position of distorted tetrahedral symmetry arising from the octahedral site by a displacement of $c/6$ along the c axis channels of the quartz structure.

INTRODUCTION

LIGAND field bands of transition metal ions have been extensively used to determine the site symmetry of these ions in different host lattices[1–6]. Difficulties in interpretation arise for host lattices with open structure and low symmetry for several reasons:

(a) A lower than cubic symmetry can shift and split degenerate levels,
(b) there may be more than one site leading to the same type of spectrum,
(c) weak bands in addition to assigned strong ones may be due to spin forbidden transitions arising from the same configuration or to low concentrations of the same ion in a different site (or a different ion in the same site) and
(d) tetrahedral and cubic (hexahedral) symmetry lead to nearly the same band positions.

This latter effect is very surprising and requires some explanation. According to electrostatic calculations Dq for a cube should be twice that for a tetrahedron if the distances between ion and ligands remain unchanged. Dq has been shown theoretically and experimentally[7–9] to vary with the inverse of the fifth power of this distance:

$$Dq \propto R^{-5}$$

Thus an increase of about 15 per cent in R is needed to bring Dq for a cubic symmetry back to the value for a tetrahedron while one expects only about 10 per cent elongation. Only cations larger than those of the first row transition metals form structures with coordination number eight resulting in an additional elongation for an impurity ion. The only case reported so far is Co^{2+} in CaF_2 [10] with a Dq value of 350 cm^{-1}[1], even smaller than expected for tetrahedral symmetry.*

Cations can be incorporated in the α-quartz structure in four different positions as seen in Fig. 1:

(a) substitutionally for Si^{4+} into an almost regular tetrahedral site. Only Fe^{3+} of all transition metal ions has been shown to occupy these sites under certain conditions[11, 12, 6].

---

*It is interesting to look at the Dq ratio for octahedral and tetrahedral symmetry: One would expect a ratio of $-0{\cdot}6$ instead of the value $-4/9$ following from point charge calculation if the distance change is taken to be about 6 per cent. The experimental ratio is close to or below $-0{\cdot}5$.

(b) into a distorted tetrahedral interstitial position I_4 midway between two silicon on the twofold axes,

(c) a distorted octahedral interstitial position I_6 arising from I_4 by a displacement of $c/6$ along the c axis channels. Fe^{2+} has been shown to occupy this site in synthetic quartz[6] and Cr^{3+} also prefers it in the isostructural $AlPO_4$[5],

(d) a third interstitial position with eight oxygens as nearest neighbors I_8 in a distorted cubic symmetry. This site lies midway between two silicon on the c axis.

The sites I_4 and I_8 are expected to lead to the same type of spectrum and to very similar band positions.

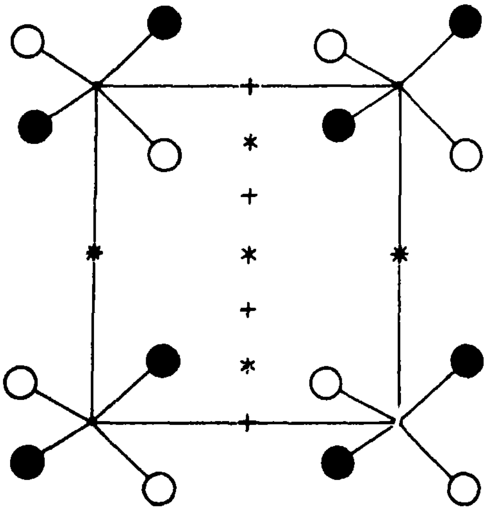

Fig. 1. Possible sites for cations in α-quartz. A prism plane of the unit cell is shown. Small circles: silicon large circles: oxygen (full: before, open: behind plane of paper). The asterisks mark the positions of the interstitial sites in this plane, the number of prongs indicating its coordination number.

EXPERIMENTAL

Two crystals of synthetic quartz were used in this study: a yellow one doped with trivalent cobalt and a slightly blue one doped with divalent cobalt. They were kindly supplied by Mr. B. Sawyer of Sawyer Research Products, Eastlake, Ohio, USA. The yellow crystal was analyzed spectroscopically and chemically and contained 0·033 per cent Co and 0·012 per cent Fe (as Fe^{3+}). The cobalt content of the other crystal was determined from the known molar extinction coefficient of the strong band to be 14·6 ppm. The Fe content was very low (estimated from the charge transfer band at 227 nm to be 1·6 ppm taking its oscillator strength to be 0·5). A dark blue Na_2O–CaO–SiO_2 glass was also used for comparison. Its cobalt content was determined by chemical analysis to be 0·20 per cent.

Absorption spectra of cut and polished specimens (basal sections in the case of quartz) were taken using a Zeiss PMQII single beam spectrophotometer.

A plate cut from the yellow crystal was heated to 500°C in air for several hours.

RESULTS AND DISCUSSION

Absorption bands of the yellow crystal before heating are shown in Fig. 2. Maxima are seen at 15·8; 25·5 and 30·3 kK and an additional very broad band at about 19·6 kK. Molar extinction coefficients ε and halfwidths δ are given in Table 1. These values are

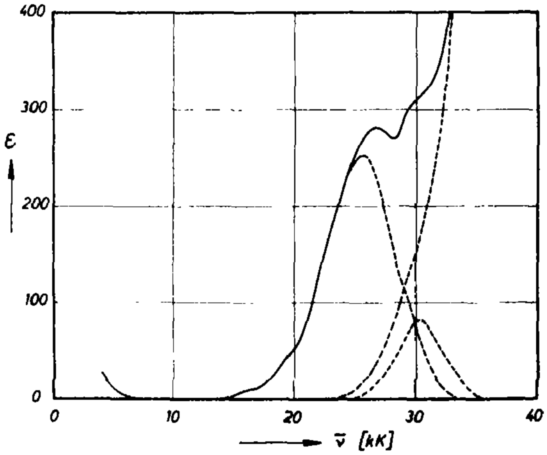

Fig. 2. Absorption bands of Co^{3+} in quartz (1 kK equals $1000 cm^{-1}$).

rather uncertain since an unarbitrary separation is impossible due to the unusually large halfwidths. As seen from Table 1 only an octahedral site symmetry can explain this spectrum since a tetrahedral complex should give a single band near 9 kK. The large halfwidths and high intensities of the two strong bands can be taken as evidence for a considerable distortion of the octahedral symmetry. The broad band near 19·6 kK could be one of the split components of the $^1T_1$ term.

Table 1. Absorption bands of Co^{3+} *in quartz*

		Postulated		
(a) *Tetrahedral:* $Dq = 900\ cm^{-1}$				
Transition	$\bar{\nu}$(kK)	ϵ	$\delta(cm^{-1})$	f
$^5E \rightarrow {}^5T_2$	9·0	100	3000	10^{-3}
(b) *Octahedral:* $Dq = 1800\ cm^{-1}; C = 3000\ cm^{-1}; C/B = 4{\cdot}8$				
$^1A_{1g} \rightarrow {}^1T_{1g}$	15·0	100	3000	10^{-3}
$^1T_{2g}$	25·0	200	3000	2×10^{-3}
$^1T_{2g}$	31·6	100	3000	10^{-3}
		Observed		
	15·8	8	4000	10^{-4}
	25·5	252	6700	8×10^{-3}
	30·3	84	4500	2×10^{-3}

After heating to 500°C this crystal shows a completely different spectrum seen as curve 1 in Fig. 3. It consists of two triplets, the second one showing some additional structure. The spectrum of Co^{2+} in a Na_2O–CaO–SiO_2 glass is shown for comparison as curve 2. Band positions, relative heights and halfwidths are nearly identical, but molar extinction coefficients are slightly more than half of those in quartz. The same difference between glass and quartz was noticed for a borate glass by Wood and Ballman[2]. They only observed the band in the visible region in a synthetic quartz doped with about 6 ppm of divalent cobalt. Their molar extinction coefficient agrees with our value to within a few percent.

In Table 2 postulated and observed band positions and oscillator strengths are given together with Dq value and term difference between P and F taken from the band positions.

Since this spectrum cannot be explained with an octahedral site symmetry of the ion a migration must have occured in addition to the reduction. Wood and Ballman[2] tentatively ascribed the spectrum to a substitutional Co^{2+}. This would mean diffusion of the ion from an interstitial to a substitutional site in our heating experiment. This process certainly requires a high activation energy and has never been observed in this temperature range. In addition the compression of the ion in the constricted silicon site should lead to a higher Dq value near 600 cm^{-1} assuming the already mentioned variation of Dq with R^{-5} (R taken as the mean value between normal Si–O distance (1·62 Å) and calculated Co–O distance for a tetrahedral complex (1·91 Å). Finally the lower intensity in glass compared to quartz can be taken as evidence for a higher distortion of the CoO_4 tetrahedra in quartz again consistent with an interstitial environment only.

Since octahedral and tetrahedral interstitial sites are very close together in the c axis channels a rapid conversion can be expected if one of the oxidation states has a site preference for the position nearby. The possibility of incorporation of the ion into the distorted

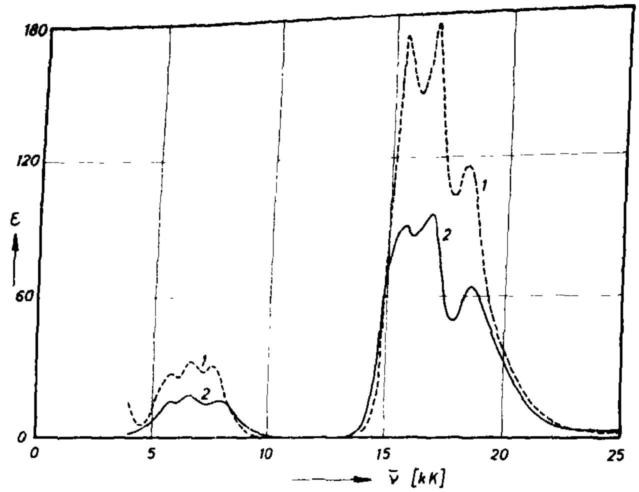

Fig. 3 Absorption bands of Co^{2+} in quartz and glass. Curve 1: quartz, curve 2. Na_2O–CaO–SiO_2 glass.

cubic site cannot be excluded with certainty. But the close resemblance of the spectra in glass and quartz makes this possibility unlikely especially since Co^{2+} does not normally occupy a site of hexahedral symmetry. Furthermore, diffusion from octahedral to cubic interstitial position should require a higher activation energy then the small displacement in the *c* axis channel that can almost be regarded a large amplitude vibration.

This example shows that a valence change in the solid state can well be accompanied by migration of the reacting ion. However, several conditions must be satisfied:

1. The final state of the ion must prefer a site symmetry different from the one originally occupied,

Table 2. Absorption bands of Co^{2+} *in quartz*

		Postulated		
(a) *Octahedral:* $Dq = 850$ cm^{-1}; $E(P-F) = 12{,}500$ cm^{-1}				
Transition	$\bar{\nu}$(kK)	ϵ	δ(cm^{-1})	f
$^4T_{1g} \rightarrow {}^4T_{2g}$	8·5	10	3000	10^{-4}
$^4A_{2g}$	17·5	1	3000	10^{-5}
$^4T_{1g}$	20·0	20	3000	2×10^{-4}
(b) *Tetrahedral:* $Dq = 400$ cm^{-1}, $E(P-F) = 12{,}000$ cm^{-1}				
$^4A_2 \rightarrow {}^4T_2$	4·0	30	3000	4×10^{-4}
$^4T_1$	7·0	(triplet)		5×10^{-4}
$^4T_1$	17·0	(triplet)		5×10^{-3}
		Observed		
	(< 4·0)			
	6·7	(triplet)		$8{\cdot}3 \times 10^{-4}$
	16·9	(triplet)		$5{\cdot}7 \times 10^{-3}$

$Dq = 380$ cm^{-1}; $E(P-F) = 12{,}100$ cm^{-1}.

2. such a site must be available in the structure and
3. mobility must be high enough to allow rapid diffusion in the temperature range of the conversion.

While condition 1 can be easily met by a number of transition metal ions (especially by one originally occupying sites of tetrahedral symmetry), conditions 2 and 3 are more severe. The high mobility of interstitial ions in the *c* axis channels must be regarded an exception possible only in network structures with small coordination numbers.

Acknowledgements – I am indebted to Mr. B. Sawyer of Sawyer Research Products, Eastlake, Ohio, USA for supplying the quartz samples used in this study. My thanks are also due to Professor F. Umland, Institut fur Anorganische Chemie der Universität Münster, Germany for carrying out the chemical analyses.

REFERENCES

1. see LIEHR A. D., *J. phys. Chem.* **67**, 1314 (1963).
2. WOOD D. L. and BALLMAN A. A., *Am. Miner.* **51**, 216 (1966).
3. WOOD D. L. and REMEIKA J. P., *J. chem. Phys.* **46**, 3595 (1967).
4. BANCROFT G. M. and BURNS R. G., *Am. Miner.* **52**, 1278 (1967); WHITE W. B. and KEESTER K. L. *Am. Miner.* **52**, 1508 (1967).
5. HENNIG J. C. M., LIEBERTZ J. and VAN STAPELE R. R., *J. Phys. Chem. Solids* **28**, 1109 (1967).
6. LEHMANN G., *Z. Naturf.* **22a**, 2080 (1967).
7. ORGEL L. E., *Nature* **179**, 1348 (1957).
8. PARSONS R. W. and DRICKAMER H. G., *J. chem. Phys.* **29**, 930 (1958); STEPHENS D. R. and DRICKAMER H. G., *J. chem. Phys.* **34**, 937 (1961); MINOMURA S. and DRICKAMER H. G., *J. chem. Phys.* **35**, 903 (1961); DRICKAMER H. G., *J. chem. Phys.* **47**, 1880 (1967).
9. HARDER H. and LEHMANN G., Fe^{2+} and Fe^{3+} in sapphire. To be published (1969).
10. STAHL-BRADA R. and LOW W., *Phys. Rev.* **113**, 775 (1959).
11. BARRY T. I., McNAMARA P. and MOORE W. J., *J. chem. Phys.* **42**, 2599 (1965).
12. LEHMANN G. and MOORE W. J., *J. chem. Phys.* **44**, 1741 (1966).

J. Phys. Chem. Solids **Pergamon Press 1969. Vol. 30, pp. 401–405. Printed in Great Britain.**

CHEMICAL DIFFUSION IN ALKALI HALIDES

R. LINDSTRÖM
Department of Physics, University of Turku, Turku, Finland

(*Received* 7 *March* 1968; *in revised form* 17 *June* 1968)

Abstract – Chemical diffusion in AY–BY type alkali halide couples has been discussed from phenomenological and atomistic viewpoints. Equations for the chemical interdiffusion coefficient, Kirkendall shift velocity and diffusion potential gradient have been derived.

PHENOMENOLOGICAL THEORY

WE SHALL discuss the interdiffusion in AY–BY type alkali halide couples. The fluxes relative to local lattice are then

$$
\begin{aligned}
J_a &= L_{aa}X_a + L_{ab}X_b + L_{av}X_v \\
J_b &= L_{ba}X_a + L_{bb}X_b + L_{bv}X_v \\
J_v &= L_{va}X_a + L_{vb}X_b + L_{vv}X_v. \qquad (1)
\end{aligned}
$$

Here the L_{ij} are coefficients relating the fluxes J_i to the thermodynamic forces X_j. We shall derive the expressions for the L_{ij} coefficients with the aid of Manning's kinetic theory[1] and as it is seen below (from equations (27)) in this approximation the cross-coefficients L_{av} and L_{bv} vanish. If we suppose that Onsager reciprocity relations $L_{av} = L_{va}$ and $L_{bv} = L_{vb}$ are valid, equations (1) simplify to

$$
\begin{aligned}
J_a &= L_{aa}X_a + L_{ab}X_b \\
J_b &= L_{ba}X_a + L_{bb}X_b \\
J_v &= L_{vv}X_v. \qquad (2)
\end{aligned}
$$

We suppose that there are equal numbers of cation and anion vacancies and that the vacancies are everywhere in thermal equilibrium. In the case A and B are cations and Y is anion, X_j are given by

$$
\begin{aligned}
X_a &= -\nabla\mu_a - e\nabla\phi \\
X_b &= -\nabla\mu_b - e\nabla\phi \\
X_v &= e\nabla\phi \qquad (3)
\end{aligned}
$$

where μ_a and μ_b are the chemical potentials of species A and B; ϕ is the diffusion potential and e the electric charge of a cation. The chemical potentials are written as follows:

$$
\begin{aligned}
\mu_a &= \mu_{0a}(T, P) + kT \ln c_a\gamma_a \\
\mu_b &= \mu_{0b}(T, P) + kT \ln c_b\gamma_b \qquad (4)
\end{aligned}
$$

where γ_a and γ_b are the activity coefficients of species A and B, c_a and c_b are the mole fractions of A and B ions. The numbers of A, B and Y ions per unit volume are N_a, N_b and $N_y = N = N_a + N_b$ respectively.

The thermodynamic forces are restricted by Prigogine's theorem

$$N_aX_a + N_bX_b + NX_v = 0. \qquad (5)$$

Equations (3), (4) and (5) give then

$$\frac{\partial \ln \gamma_a}{\partial \ln c_a} = \frac{\partial \ln \gamma_b}{\partial \ln c_b} = \frac{\partial \ln \gamma}{\partial \ln c}. \qquad (6)$$

The local lattice moves during diffusion relative to one end of specimen with velocity v where

$$v = \frac{J_a + J_b}{N} = \frac{J_v}{N}. \qquad (7)$$

To determine the interdiffusion coefficient we must know the fluxes relative to the end of specimen. These fluxes are

$$
\begin{aligned}
J_a' &= J_a - Nc_av \\
J_b' &= J_b - Nc_bv \\
J_v' &= J_v - Nv = 0. \qquad (8)
\end{aligned}
$$

With the aid of equations (2) and (7) we obtain in 1-dimensional case for the diffusion potential gradient

$$e\frac{\partial\phi}{\partial x}=-kT\left(1+\frac{\partial\ln\gamma}{\partial\ln c}\right)\times\frac{\dfrac{L_{aa}}{c_a}-\dfrac{L_{ab}}{c_b}-\dfrac{L_{bb}}{c_b}-\dfrac{L_{ba}}{c_a}}{L_{aa}+L_{ab}+L_{bb}+L_{ba}+L_{yy}}\frac{\partial c_a}{\partial x} \tag{9}$$

and for the Kirkendall shift velocity

$$v=\frac{L_{yy}}{N}e\frac{\partial\phi}{\partial x}. \tag{10}$$

Now with the aid of equations (10) and (9) J_a' may be given by

$$J_a'=-\tilde{D}N\frac{\partial c_a}{\partial x} \tag{11}$$

where the chemical interdiffusion coefficient $\tilde{D}$ is

$$\tilde{D}=\frac{kT}{N}\left(1+\frac{\partial\ln\gamma}{\partial\ln c}\right)\left\{\frac{c_b}{c_a}L_{aa}-L_{ab}+\frac{c_a}{c_b}L_{bb}-L_{ba}-\frac{[c_b(L_{aa}+L_{ab})-c_a(L_{bb}+L_{ba})]\left[\dfrac{L_{aa}}{c_a}-\dfrac{L_{ab}}{c_b}-\dfrac{L_{bb}}{c_b}+\dfrac{L_{ba}}{c_a}\right]}{L_{aa}+L_{ab}+L_{bb}+L_{ba}+L_{yy}}\right\}. \tag{12}$$

KINETIC THEORY

To find the equations of the L_{ij} coefficients we shall use the same method as Manning[1] when he treated chemical diffusion in an A–B alloy. Manning has shown that the fluxes in a binary alloy may be written as follows:

$$J_i=Nc_iD_i^*2d^{-1}(A_i+B_i)-ND_i^*\frac{\partial c_i}{\partial x}-Nc_iD_i^*\frac{\partial\ln\nu_i}{\partial x}\quad(i=a,b). \tag{13}$$

Here D_i^* is the tracer diffusion coefficient of species i in a homogeneous alloy having the concentration c_i. It can be written in the form

$$D_i^*=\tfrac{1}{6}\lambda^2z\nu_if_i=\tfrac{1}{6}\lambda^2zc_vw_if_i\quad(i=a,b) \tag{14}$$

where ν_i is the basic jump frequency for an atom jump between two neighbor sites in a homogeneous alloy; λ is the distance between these sites; d is the distance between neighboring planes perpendicular to the direction of diffusion; w_i is the basic jump frequency for a vacancy to exchange with an atom i in a homogeneous alloy; c_v is the mole fraction of vacancies; z is the number of nearest neighbors; and f_i is the correlation factor of species i in a homogeneous alloy which arises from that a given vacancy may exchange with the same atom more than once. A_i and B_i are proportional to the driving force and are discussed below.

A chemical concentration gradient or some other driving force may cause the jump frequencies to deviate from the basic values ν_i and w_i. Let the direction of the driving force be $+x$ direction and ν_{i+} the jump frequency from a site on plane 0 to one of the neighboring sites on plane +1 immediately on the right of plane 0 and ν_{i-} respectively. Then

$$\nu_{i\pm}=\nu_i(1\pm A_i) \tag{15}$$

where A_i is a small quantity. Now the jump frequency w_{igh} for exchange of a vacancy on site g (on plane g) with an atom of species i on site h (on plane h) is given by

$$w_{igh}=w_{ighm}(1+\epsilon_i)$$
$$w_{ighm}=w_{ighG}(1+\delta_i) \tag{16}$$

where w_{ighm} is the value of w_{igh} in a homogeneous alloy having the composition associated with the plane midway between planes g and h; w_{ighG} is that in a homogeneous alloy having the composition associated with the plane G; and ϵ_i and δ_i are small quantities.

Manning[1, 2] has shown that for tracer atoms in a chemical concentration gradient

$$A_i = \delta_i - \epsilon_i + d\frac{\partial \ln c_v}{\partial x} \qquad (17)$$

where

$$\delta_i = \frac{d}{2}\frac{\partial \ln w_i}{\partial x} \qquad (18)$$

and

$$\epsilon_i = \frac{d}{2}\left(\frac{\partial \ln \gamma_i}{\partial x} + \frac{\partial \ln c_v}{\partial x}\right). \qquad (19)$$

If there is a diffusion potential in an AY–BY couple where A and B are cations, it decreases the jump frequency of the faster moving cation to the direction of its concentration gradient with a factor

$$\exp\left(\frac{de}{2kT}\frac{\partial \phi}{\partial x}\right).$$

Then in equation (17) we have to replace ϵ_i by $\epsilon_i + \epsilon_d$, where

$$\epsilon_d = \frac{de}{2kT}\frac{\partial \phi}{\partial x}.$$

Taking into account that $\nu_i = c_v w_i$ we obtain

$$A_i = \frac{d}{2}\left(\frac{\partial \ln \nu_i}{\partial x} - \frac{\partial \ln \gamma_i}{\partial x} - \frac{e}{kT}\frac{\partial \phi}{\partial x}\right). \qquad (20)$$

When a vacancy flow goes to $-x$ direction, the individual vacancies are more likely to approach the tracer atom on plane 0 from $+x$ direction than from $-x$ direction. This changes the effective jump frequency of the tracer by a factor

$$G_{i\pm} = 1 \pm B_i \qquad (21)$$

where B_i is a small quantity. Manning[1] has shown that in a f.c.c. binary alloy B_i may be written in the form

$$B_i = \frac{1}{7{\cdot}15}\left(d\frac{\partial \ln c_v}{\partial x} - 2\epsilon\right). \qquad (22)$$

ϵ is defined by

$$W_{gh} = W_{ghm}(1+\epsilon) \qquad (23)$$

where $W_{gh} = c_{ah}w_{agh} + c_{bh}w_{bgh}$ is in a binary alloy the average frequency for exchange of a vacancy on site g with an atom on site h; and W_{ghm} is the value of W_{gh} in a homogeneous alloy having the composition associated with the plane midway between planes g and h. Taking into account that

$$c_{ih} = c_{im}\left(1 + \frac{d}{2}\frac{\partial \ln c_i}{\partial x}\right) \qquad (24)$$

we obtain by substituting the equation of $\epsilon_i + \epsilon_d$ into equation (16) and it into equation (23) for cations in chemical concentration gradient and diffusion potential gradient

$$\epsilon = \frac{d}{2}\left[\frac{w_a - w_b}{W}\left(1 + \frac{\partial \ln \gamma}{\partial \ln c}\right)\frac{\partial c_a}{\partial x} + \frac{\partial \ln c_v}{\partial x} + \frac{e}{kT}\frac{\partial \phi}{\partial x}\right]. \qquad (25)$$

Here $W = c_a w_a + c_b w_b$. Then

$$B_i = -\frac{d}{7{\cdot}15}\left[\frac{w_a - w_b}{W}\left(1 + \frac{\partial \ln \gamma}{\partial \ln c}\right)\frac{\partial c_a}{\partial x} + \frac{e}{kT}\frac{\partial \phi}{\partial x}\right]. \qquad (26)$$

Equations (13) may now be written in the form

$$J_a = -D_a^*\left(1 + \frac{\partial \ln \gamma}{\partial \ln c}\right)N\frac{\partial c_a}{\partial x} \times\left(1 + \frac{2}{7{\cdot}15}\frac{w_a - w_b}{W}c_a\right) - Nc_a D_a^* \times\left(1 + \frac{2}{7{\cdot}15}\right)\frac{e}{kT}\frac{\partial \phi}{\partial x} \qquad (27)$$

$$J_b = -D_b^*\left(1+\frac{\partial \ln \gamma}{\partial \ln c}\right)N\frac{\partial c_b}{\partial x}$$
$$\times\left(1-\frac{2}{7{\cdot}15}\frac{w_a-w_b}{W}c_b\right)-Nc_bD_b^*$$
$$\times\left(1+\frac{2}{7{\cdot}15}\right)\frac{e}{kT}\frac{\partial \phi}{\partial x}.$$

Comparing the equation (27) of J_a to the corresponding equation (1) we find that there must be

$$\frac{L_{aa}}{c_a}-\frac{L_{ab}}{c_b}=\frac{ND_a^*}{kT}\left(1+\frac{2}{7{\cdot}15}\frac{w_a-w_b}{W}c_a\right)$$

$$L_{aa}+L_{ab}-L_{av}=\frac{Nc_aD_a^*}{kT}\left(1+\frac{2}{7{\cdot}15}\right). \quad (28)$$

The former equation gives

$$L_{aa}=\frac{Nc_aD_a^*}{kT}\left(1+\frac{2}{7{\cdot}15}\frac{c_aw_a}{W}\right)$$
$$L_{ab}=\frac{Nc_aD_a^*}{kT}\frac{2}{7{\cdot}15}\frac{c_bw_b}{W} \quad (29a)$$

and then the latter equation yields $L_{av}=0$. Respectively we obtain

$$L_{bb}=\frac{Nc_bD_b^*}{kT}\left(1+\frac{2}{7{\cdot}15}\frac{c_bw_b}{W}\right)$$
$$L_{ba}=\frac{Nc_bD_b^*}{kT}\frac{2}{7{\cdot}15}\frac{c_aw_a}{W} \quad (29b)$$

and $L_{bv}=0$. If we suppose that Onsager reciprocity relations are valid, $L_{va}=0=L_{vb}$ and the fluxes in the system are represented by equations (2). From equations (29) we see that the relation $L_{ab}=L_{ba}$ yields

$$\frac{D_a^*}{D_b^*}=\frac{w_a}{w_b} \quad (30)$$

or that the correlation factors of A and B ions f_a and f_b are equal. This does not hold in strict sense. Manning[5] has shown that taking into account the difference between f_a and f_b the deviations of the equations of interdiffusion coefficient and Kirkendall shift velocity from Darken's equations in a binary alloy are smaller than in the case $f_a=f_b$.

Next we shall consider the diffusion of anions. Now the only driving force is the diffusion potential gradient. Also in this case we make use of Manning's equation (13). Instead of equations (20) and (26) we obtain

$$A_v=\frac{d}{2}\left(\frac{\partial \ln \nu}{\partial x}+\frac{e}{kT}\frac{\partial \phi}{\partial x}\right) \quad (31)$$

and

$$B_v=\frac{de}{7{\cdot}15\,kT}\frac{\partial \phi}{\partial x}. \quad (32)$$

Then from equation (13) follows

$$J_v=ND_v^*\left(1+\frac{2}{7{\cdot}15}\right)\frac{e}{kT}\frac{\partial \phi}{\partial x}. \quad (33)$$

Comparing equation (33) to the corresponding equation (2) one finds

$$L_{vv}=\frac{ND_v^*}{kT}\left(1+\frac{2}{7{\cdot}15}\right). \quad (34)$$

When the equations of L_{ij} coefficients (29) and (34) are substituted into equations (12), (9) and (10) we obtain taking into account equation (30) for the chemical interdiffusion coefficient

$$\tilde{D}=\left(1+\frac{\partial \ln \gamma}{\partial \ln c}\right)$$
$$\times\left\{c_bD_a^*+c_aD_b^*+0{\cdot}28c_ac_b\frac{(D_a^*-D_b^*)^2}{c_aD_a^*+c_bD_b^*}\right.$$
$$\left.-1{\cdot}28c_ac_b\frac{(D_a^*-D_b^*)^2}{c_aD_a^*+c_bD_b^*+D_v^*}\right\} \quad (35)$$

for the diffusion potential gradient

$$\frac{e}{kT}\frac{\partial \phi}{\partial x}=-\frac{D_a^*-D_b^*}{c_aD_a^*+c_bD_b^*+D_v^*}$$
$$\times\left(1+\frac{\partial \ln \gamma}{\partial \ln c}\right)\frac{\partial c_a}{\partial x} \quad (36)$$

and for the Kirkendall shift velocity

$$v = -1{\cdot}28\,\frac{(D_a^* - D_b^*)\,D_v^*}{c_a D_a^* + c_b D_b^* + D_v^*}\left(1 + \frac{\partial \ln \gamma}{\partial \ln c}\right)\frac{\partial c_a}{\partial x}. \qquad (37)$$

The limiting values of $\tilde{D}$, $\partial\phi/\partial x$ and v are found when (i) $D_v^* \gg D_a^*$ and D_b^* and (ii) $D_v^* \ll D_a^*$ and D_b^*. In the case (i) $\partial\phi/\partial x \approx 0$ and equations (35) and (37) yield the equations of a binary alloy A–B. In the case (ii) the diffusion potential gradient is strongest and the Kirkendall shift velocity is essentially dominated by D_v^*. The author has not found any experimental data of D_a^* and D_b^*. So to get an idea of the deviations of $\tilde{D}$ given by (35) from Darken's formula

$$\left(1 + \frac{\partial \ln \gamma}{\partial \ln c}\right)(c_b D_a^* + c_a D_b^*)$$

we have to suppose some value for the ratio D_a^*/D_b^*. When $D_a^* = 3D_b^*$ and $c_a = 0{\cdot}5$, the deviations are in the case (i) +7 per cent and (ii) −25 per cent which are rather remarkable.

DISCUSSION

In the derivation of the preceding equations for the chemical interdiffusion coefficient, Kirkendall shift velocity and diffusion potential gradient we have neglected the effects of porosity and aliovalent impurities which may be appreciable in the measured results. Somewhat different equations may be obtained if the correlation effects are more strictly taken into account. However we think the above equations to describe the chemical diffusion in alkali halide diffusion couples so well that experimental verifications may be planned on this base.

Acknowledgements—The author wishes to thank Professor M. Kantola for his continuous interest in this work. The author is also indebted to Leo and Regina Wainstein's Foundation for financial support.

REFERENCES

1. MANNING J. R., *Phys. Rev.* **124**, 470 (1961).
2. MANNING J. R., *Phys. Rev.* **139**, A 126 (1965).
3. MANNING J. R., *Acta Metall.* **15**, 817 (1967).

J. Phys. Chem. Solids Pergamon Press 1969. Vol. 30, pp. 407–419. Printed in Great Britain.

INTERSTITIALCY MOTION IN THE SILVER HALIDES*†

MAX D. WEBER‡ and ROBERT J. FRIAUF
University of Kansas, Lawrence, Kansas 66044, U.S.A.

(*Received* 13 *June* 1969)

Abstract – Results are reported for the diffusion of Ag in single crystals of AgCl between 300 and 435°C. Diffusion coefficients are measured with radioactive tracers by the sectioning method. The correlation factor f_{Ag} is obtained by comparison to the ionic conductivity with the Einstein relation. An analysis of f_{Ag} shows that the interstitial silver ion moves by a combination of two kinds of interstitialcy jumps, with an activation energy of 0·008 eV for the collinear jump and 0·13 eV for the non-collinear jump. Earlier diffusion measurements for AgBr are also re-analyzed with more recent correlation factors and mobility data to give revised activation energies of 0·058 eV and 0·27 eV, respectively.

1. INTRODUCTION

FOR MANY years it has been realized that AgCl and AgBr contain Frenkel defects, namely, silver ion vacancies and interstitial ions[1]. Both of these defects are mobile and contribute to the ionic conductivity in pure crystals at elevated temperatures. Subsequent investigators have measured the conductivity of crystals containing divalent ions in order to determine the concentration of Frenkel defects and the mobilities of the vacancies and interstitials. Diffusion measurements have also shown that ionic transport by negative ions is three to four orders of magnitude smaller[2, 3], in confirmation of earlier transport measurements in which the transport number of silver was found to be unity[4].

The mechanism for motion of a vacancy seems to be clear enough: one of the neighboring silver ions simply jumps into the vacancy. At first glance it might be thought that an interstitial ion would move by direct jumps between neighboring interstitial positions. But even a brief examination of the distortions involved in such a jump suggests that this is energetically unfavorable[5], and this idea is substantiated by more extensive calculations [6]. A much more favorable process is one in which the interstitial ion jumps toward a silver ion on an adjacent lattice site, knocks the lattice ion into an interstitial position, and occupies the vacated lattice site. This combination of events is called indirect interstitial or *interstitialcy* motion[7].

Comparison of tracer diffusion coefficients with the ionic conductivity has shown that interstitialcy motion does, indeed, occur in these substances. For AgBr, in fact, two kinds of interstitialcy jumps have been identified, and it has been possible to evaluate the individual jump frequencies[8]; for AgCl the presence of the two kinds of jumps has been indicated qualitatively[2, 9]. In this paper new diffusion measurements are reported for Ag in AgCl, and the results are analyzed to give estimated values for the individual jump frequencies. In addition the previous results for diffusion of Ag in AgBr are re-analyzed in view of more recent information about correlation factors and vacancy mobilities.

2. DIFFUSION AND IONIC CONDUCTIVITY

(*A*) *Correlation factors*

We consider a pure crystal containing equal mole fractions $x_v = x_i = x_0$ of vacancies and interstitials. The *microscopic* diffusion coefficient and the mobility for the vacancy are given by

---

*Work supported by the U.S. Atomic Energy Commission. This is Technical Report COO-1197-22.

†Based in part on a thesis submitted to the University of Kansas in partial fulfillment of the requirements for an M.S. degree for MDW.

‡*Present address:* U.S. Navy Mine Defense Laboratory, Panama City, Florida.

$$d_v = \tfrac{1}{6}\nu_v\lambda_v^2, \quad \mu_v = e\nu_v\lambda_v^2/6\,kT. \tag{1}$$

The jump distance λ_v is defined in Fig. 1; the jump frequency ν_v represents the total probability per second of a vacancy jump. For the moment we use similar expressions for the interstitial (the different kinds of interstitialcy jumps are considered in detail below) and find the microscopic Einstein relation to be

$$\frac{d_v}{\mu_v} = \frac{d_i}{\mu_i} = \frac{kT}{e}. \tag{2}$$

In terms of the mobility ratio

$$\phi = \frac{\mu_i}{\mu_v} = \frac{d_i}{d_v} \tag{3}$$

the conductivity for the pure crystal is

$$\sigma_0 = N_0 e x_0 \mu_v (1+\phi) \tag{4}$$

where N_0 is the total number of silver ions per unit volume.

The diffusion of silver ions would be given by $D_{Ag} = x_v d_v + x_i d_i$ if the successive jumps of a particular ion formed a genuine random walk sequence. Combination of this relation with equations (2) and (4) yields the normal macroscopic Einstein relation

$$D_\sigma/\sigma_0 = kT/N_0 e^2 \tag{5}$$

which we shall use to calculate D_σ from the measured value of the conductivity. In actuality the sequence of jumps for a radioactive tracer ion is not a completely random walk, and it is therefore necessary to introduce correlation coefficients in the expression for the tracer diffusion coefficient.

$$D^*_{Ag} = f_v x_v d_v + f_i x_i d_i. \tag{6}$$

The comparison of experimental measurements of D^*_{Ag} and σ_0 is conveniently expressed as a ratio of D^*_{Ag} to D_σ,

$$f_{Ag} = \frac{D^*_{Ag}}{D_\sigma} = \frac{f_v + \phi f_i}{1+\phi} \tag{7}$$

where the last expression follows from equations (4–6). Thus the observed results involve contributions from both vacancies and interstitials. In order to separate out the correlation factor f for interstitials, it is necessary to have independent knowledge of ϕ from conductivity measurements on crystals with divalent impurities. Then f_i can be obtained from equation (7) as

$$f_i = f_{Ag} - (f_v - f_{Ag})/\phi. \tag{8}$$

When the details of a jump mechanism are specified, it is possible to obtain a theoretical value for the correlation factor by considering diffusion of probability on an appropriate lattice[10]. By this means an accurate value has been obtained for vacancy motion on a face centered cubic lattice, namely, $f_v = 0{\cdot}78146$[11]. An experimental check of this value has also been made in AgCl and AgBr containing enough Cd so that interstitials are completely suppressed and only vacancies contribute to diffusion and conductivity [12,13]. The various possibilities for interstitial motion are illustrated in Fig. 1, and the theoretical correlation factors are listed in Table 1 [8,9,14]. In the subsequent treatment we shall consider only the collinear interstitialcy λ_1 and the non-collinear interstitialcy λ_2. The direct interstitial jump λ_0 appears to be excluded by energetic considerations (see Table 5), and the experimental results show no evidence of its presence. The partially backwards interstitialcy jump λ_3 also appears to be energetically unfavorable, and the analysis of the experimental results is not sufficiently detailed to reveal its presence.

It is also necessary to consider the simultaneous occurrence of (at least) two kinds of interstitialcy jumps, with a relative frequency $\kappa \equiv \nu_1/\nu_2$. The microscopic *diffusion coefficient for an interstitial is then*

$$d_i = \tfrac{1}{6}(\nu_1\lambda_1^2 + \nu_2\lambda_2^2) = \tfrac{1}{3}\nu_2 a^2(\tfrac{3}{2}\kappa + 1). \tag{9}$$

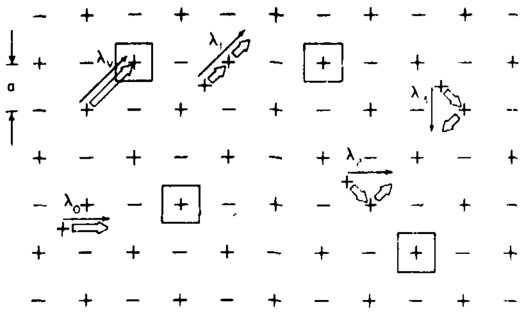

Fig. 1. Silver ion jump processes. The figure is projected onto a plane of the NaCl type structure. Thus if each interstitial ion is initially located a distance $\frac{1}{2}$ *a above* the plane, the final position is $\frac{1}{2}$ *a below* the plane for the collinear interstitialcy with $\lambda_1 = \sqrt{3}a$, $\frac{1}{2}$ *a below* the plane for the non-collinear interstitialcy with $\lambda_2 = \sqrt{2}\,a$, but $\frac{1}{2}$ *a above* the plane for the partly backwards interstitialcy with $\lambda_3 = a$. The vacancy jump with $\lambda_v = \sqrt{2}\,a$ and the direct interstitial jump with $\lambda_0 = a$ are parallel to the plane.

The corresponding tracer diffusion coefficient is related to d_i by the factor f_i as defined in equation (6), where [8, 14]

$$f_i = f_i' f_i'' = \left\{\frac{1}{2}\frac{\kappa+1}{\kappa+\frac{2}{3}}\right\}\left\{1-\left(\frac{\kappa+\frac{1}{3}}{\kappa+1}\right)^2\right\}P(\kappa). \tag{10}$$

The first factor in braces gives the effect of the difference in displacement between the interstitial and the tracer in an interstitialcy jump, and the second factor shows the effect of correlations between successive jumps of the tracer. The quantity $P(\kappa)$ is a slowly varying function involving the probabilities of return of the interstitial ion to the tracer from various directions; a detailed calculation shows that a fairly good interpolation formula is given by [14]

$$P(\kappa) = (\kappa+1)/3(\kappa+11/9). \tag{11}$$

Insertion of equation (11) into equation (10) yields

$$f_i = \frac{9\kappa^2+27\kappa+16}{27\kappa^2+51\kappa+22}, \tag{12}$$

which can be solved to give

$$\kappa = \frac{(25f_i^2-26f_i+17)^{1/2}-(17f_i-9)}{6(3f_i-1)}. \tag{13}$$

The mobility of the interstitial defect is obtained by use of the microscopic Einstein relation of equation (2).

$$\mu_i = (e/kT)\,d_i = \mu_1+\mu_2. \tag{14}$$

With d_i from equation (9) we find

$$\mu_1 = ea^2\nu_1/2kT, \quad \mu_2 = ea^2\nu_2/3kT. \tag{15}$$

Hence $\mu_1 T$ and $\mu_2 T$ are proportional to the corresponding jump frequencies. After κ is obtained from equation (13), μ_1 and μ_2 can be calculated from

$$\mu_2 = \mu_i/(\tfrac{3}{2}\kappa+1), \quad \mu_1 = \tfrac{3}{2}\kappa\mu_2. \tag{16}$$

(*B*) *Analysis of conductivity measurements*

The analysis of the diffusion results to determine κ, μ_1, and μ_2 depends vitally on knowledge of the mobility ratio ϕ, which enters into the separation of the vacancy contribution in equation (8). The values of ϕ are obtained, in turn, from an analysis of conductivity measurements made on crystals containing divalent ions. Hence it is important

Table 1. *Jump mechanisms and correlation factors. The length* a *is defined in Fig. 1. The displacement effect is given by* f′, *the correlation effect by* f″, *and the overall correlation factor by* f = f′f″

Mechanism	ν	λ	f'	f''	f
Vacancy	ν_v	$\sqrt{2}\,a$	1	0·78146	0·78146[(a)]
Direct interstitial	ν_0	a	1	1	1
Collinear interstitialcy	ν_1	$\sqrt{3}\,a$	$\frac{1}{2}$	2/3	0·3333[(b)]
Non-collinear interstitialcy	ν_2	$\sqrt{2}\,a$	$\frac{3}{4}$	32/33	0·7273[(b)]
Mixed interstitialcy	$\nu_1 = \nu_2$		3/5	0·8782	0·5269[(b, c)]
Backwards interstitialcy	ν_3	a	$\frac{3}{2}$	0·9643	1·4464[(b)]

[(a)] From reference [11].
[(b)] From reference [14].
[(c)] The interpolated result obtained with equation (12) is 0·5200.

to consider the three methods of analysis that have been used for the silver halides[15].

(i) The simplest assumption is that a divalent ion such as Cd^{++} exerts an influence only by virtue of its excess charge. Then the vacancy concentration is increased, the interstitial concentration is decreased because of the mass action law for Frenkel defects,

$$x_v x_i = x_0^2 \tag{17}$$

and the conductivity of the doped crystal is expressed by

$$\frac{\sigma}{\sigma_0} = \left[\left(\frac{c}{2x_0}\right)^2 + 1\right]^{1/2} - \left(\frac{c}{2x_0}\right)\frac{\phi - 1}{\phi + 1} \tag{18}$$

where c is the mole fraction of divalent impurity. Since $\phi > 1$ the conductivity isotherm has a minimum, for which

$$\left(\frac{\sigma}{\sigma_0}\right) = \frac{2\phi^{1/2}}{\phi + 1}. \tag{19}$$

After ϕ is obtained from this result, x_0 is found from the slope of the conductivity isotherm at $c = 0$, and the mobilities are then calculated from equations (3) and (4). Methods based on equation (18) are common because of the simplicity of the analysis, and it appears possible to obtain a good fit to the observed isotherms up to an impurity concentration of perhaps 0·1 per cent.

(ii) The next assumption supposes that a fraction of the divalent ions is associated with vacancies at nearest neighbor positions. The association removes some vacancies from those which are free according to a mass action law that is usually written as

$$x_k[x_v(c - x_k)]^{-1} = K_2(T) \tag{20}$$

where x_k is the mole fraction of complexes. Equations (17) and (20) are combined with the condition of electric neutrality to give a cubic equation for x_v.

$$\frac{c}{x_0} = \left(\frac{x_v}{x_0} - \frac{x_0}{x_v}\right)(1 + x_v K_2) \tag{21}$$

The conductivity isotherm is expressed by

$$\frac{\sigma}{\sigma_0} = \frac{(x_v/x_0) + (x_0/x_v)\phi}{1 + \phi}. \tag{22}$$

By using implicit differentiation it can be shown that $(\sigma/\sigma_0)_{\min}$ is given by equation (19) for this case also, hence inclusion of association does not affect the values obtained for ϕ. Because of the availability of an additional parameter, it is possible to fit the observed results to somewhat larger values of c, but the method has never really been entirely satisfactory over a wide range of temperature and impurity concentration.

(iii) One of the deficiencies of method (ii) is the neglect of long range Coulomb interactions among the vacancies, interstitials, and unassociated divalent impurities. These can be included in a formal way by introducing activity coefficients γ into equations (17) and (20) as multiplicative factors for x_v, x_i, and $(c - x_k)$. The concentration of charged defects appears in the Debye–Hückel screening constant

$$b = [8\pi e^2 N x_0/\epsilon kT]^{1/2} \tag{23}$$

and the activity coefficient is

$$\log \gamma = -(e^2/2\epsilon kT)b(1 + bR)^{-1} \tag{24}$$

where ϵ is the dielectric constant and R is a distance of closest approach of defects. Since x_0 appears in equation (23), as well as in the modified form of equation (21), it is necessary to solve by iteration to obtain a consistent solution. A detailed calculation has shown that these effects are of some quantitative importance even for the pure crystal[21]: $\gamma = 0{\cdot}88$ for $x_0 = 0{\cdot}001$ per cent and $\gamma = 0{\cdot}76$ for $x_0 = 0{\cdot}01$ per cent in AgCl. Of especial importance for our purposes is the fact that values of ϕ calculated by this method are at least 50 per cent larger than values obtained from method (i) or (ii).

3. EXPERIMENTAL RESULTS FOR AgCl

Experimental techniques were generally similar to those previously used for AgBr[8, 16]. The pure material was precipitated from 0·5 M solutions of analytical reagent grade $AgNO_3$ and HCl. Single crystals were grown by the Bridgman technique in a sealed quartz tube. The powder was outgassed in vacuum for 12 hr at 350°C before sealing off, and the melt was held for 8 hr at 500°C (45°C above the melting point) before withdrawal in order to eliminate voids. Cylindrical samples approximately 1 cm in all dimensions were machined on a lathe; smooth end faces were obtained by microtoming.

All samples were provided with silver electrodes, first a 2000 Å layer by vacuum evaporation, followed by a thick layer of silver conducting paint. For diffusion samples about 1 μc of $Ag^{110}Cl$ was evaporated onto one end before the silver evaporation; after a diffusion run all silver was removed in heated 6 M nitric acid. Conductivity measurements were made at a frequency of 1 to 10 kc with an a.c. bridge.

During diffusion and conductivity measurements the sample was kept in an atmosphere of nitrogen. The furnace temperature was controlled to ±½°C, but variations at the sample were much smaller because of the large thermal inertia of the furnace. Temperature was measured with the same chromel–alumel thermocouple for the entire series of measurements, and the effect of possible calibration errors was minimized by measuring conductivity during the diffusion run.

After diffusion a microtome was used to take 10 μ slices parallel to the original surface. The slices were collected in planchets and weighed with a semi-micro balance (sensitivity 0·01 mg) to determine the amount of material. In order to obtain a uniform distribution on the bottom of the planchet, the AgCl was dissolved in 6 M NH_4OH, which was then slowly evaporated at 50°C. A minimum of 10,000 counts was obtained with a Geiger tube. The diffusion profiles gave the expected straight line for a plot of log (activity) vs. (penetration depth)² in all cases; the diffusion coefficients were obtained from a least squares fit of this line.

The largest source of error for conductivity comes from the sample dimensions; repeatability for different samples showed an error of 0·2 to 0·7 per cent. Errors in the diffusion coefficients were approximately 0·2 per cent from the area, 0·2 per cent from finite slice thickness and misalignment, 0·6 per cent from the correction for finite heating and cooling times, and 0·8 per cent for the slope of the diffusion profile, giving a total error in D of about 1·0 per cent.

The measured diffusion coefficients are shown in Fig. 2. There is good agreement between our results and those of Compton [2, 17]. Also shown are values of D_σ calculated from the measured conductivity with the normal Einstein relation of equation (5). The general agreement of all workers is reasonably good, but there are several minor discrepancies. The reason for the deviation and scatter of Compton's conductivities[17] at the higher temperatures is not known, but this has made it infeasible to use his results for a quantitative analysis of the type presented in the next section. The deviation of Ebert and Teltow's values[18] at the lower temperatures is probably due to impurities; an impurity content of 20 to 30 ppm has been estimated by Müller[19]. The D_σ points for this work are calculated from the conductivity actually measured during the diffusion runs; the line is the average of all conductivity measurements. The points for Compton[17], Ebert and Teltow[18] and Abbink[20, 21] have also been calculated from quoted values of the conductivity. For Müller's results[19], however, the conductivity has been calculated from the published values of activation energies and pre-exponential factors for x_0, μ_v, and μ_i because no numerical values are given and the graphs are too small to yield useful numbers. The rather large discrepancy for these results at the higher temperatures occurs because the fit is based on a different temperature range (50 to 250°C) in order to avoid the complications caused by large defect concentrations above 250°C.

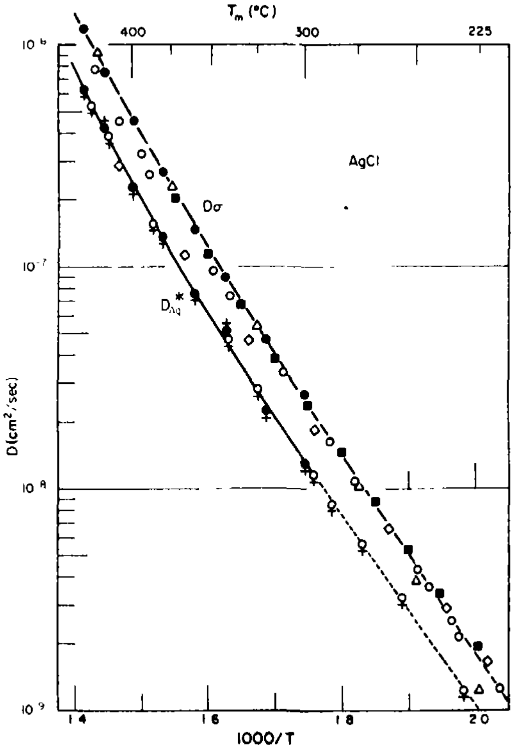

Fig. 2. Diffusion coefficients for AgCl. Measured by radioactive tracers: ♀ —— this work, ♀ ---- Compton (reference [17]). Calculated from the ionic conductivity with the normal Einstein relation: ● —— this work, ○ Compton (reference [17]), ■ Abbink (reference [20]), △ Ebert and Teltow (reference [18]), ◇ Müller (reference [19]).

The observed values of D^*_{Ag} and σ are listed in Table 2; these are based on sample dimensions measured at room temperature. When values of f_{Ag} are calculated from equation (7), a room temperature value of the lattice constant is also used to obtain the number of silver ions per unit volume in equation (5); by this procedure the effect of thermal expansion is cancelled, and correct values are obtained for f_{Ag}. The combined errors for f_{Ag} are obtained from the individual errors for D^*_{Ag} and σ and are quoted as standard deviations.

4. ANALYSIS OF RESULTS FOR AgCl

The experimental values of f_{Ag} are calculated from measured values of D^*_{Ag} and σ_0 with equations (5) and (7) and are shown in Fig. 3. Also shown by the dotted lines are the results to be expected for f_{Ag} if a single type of

Table 2. Conductivity and diffusion data for AgCl. *The correlation factor is* $f_{Ag} = D^*_{Ag}/D_\sigma$ *where* D_σ *is obtained from* σ_0 *with equation* (5)

T (°C)	σ_0 $(\Omega\ \text{cm})^{-1}$	D^*_{Ag} (cm²sec)	f_{Ag}
300·25	$2{\cdot}05 \times 10^{-3}$	$1{\cdot}304 \times 10^{-8}$	0·487 ± 0·011
320·0	3·46	2·228	0·476 ± 0·006
342·0	6·32	5·159	0·582 ± 0·007
358·0	10·05	7·481	0·517 ± 0·006
380·0	17·7	13·52	0·513 ± 0·006
400·0	29·6	22·76	0·501 ± 0·005
420·0	47·7	42·30	0·562 ± 0·008
435·0	72·4	63·02	0·540 ± 0·007

interstitial jump mechanism were present. It is evident that a mixture of two types of interstitialcy jumps will be required to account for the observed results.

In order to proceed with the analysis it is necessary to know the mobility ratio $\phi = \mu_i/\mu_v$. Published values of this ratio are shown in Fig. 4. In most cases the conductivity isotherms have been analyzed by the simple theory according to equation (19), in which all interactions between defects are ignored; in this case the same result is obtained for ϕ even if the formation of complexes is included with equation (20). The results obtained with this simple analysis by Abbink[21] and by Ebert and Teltow[18] agree quite well. (The re-analysis of Ebert and Teltow's data with Kurnick's method was done in an earlier attempt to interpret the diffusion measurements reported here[16].) When Debye–Hückel interactions are included in the analysis with equations (23) and (24), however, considerably larger values of ϕ are obtained, and this has an important influence on the analysis of the diffusion data. Müller[19] has employed only the simple analysis of equation (18), but by working with lower temperatures (50–250°C) and impurity concentrations (less than 150 ppm) he has apparently avoided some of the deficiencies of neglecting the Deybe–Hückel interactions for the larger defect concentrations. Since Abbink's analysis appears to be more thorough and since his data correspond more nearly to the temperature range of the diffusion measurements, his mobilities will be used for the subsequent analysis.

With ϕ and f_v known, the vacancy contribution to f_{Ag} is removed with equation (8). Then $\kappa = \nu_1/\nu_2$ is calculated from f_i with equation (13). Finally μ_1 and μ_2 are obtained from μ_i

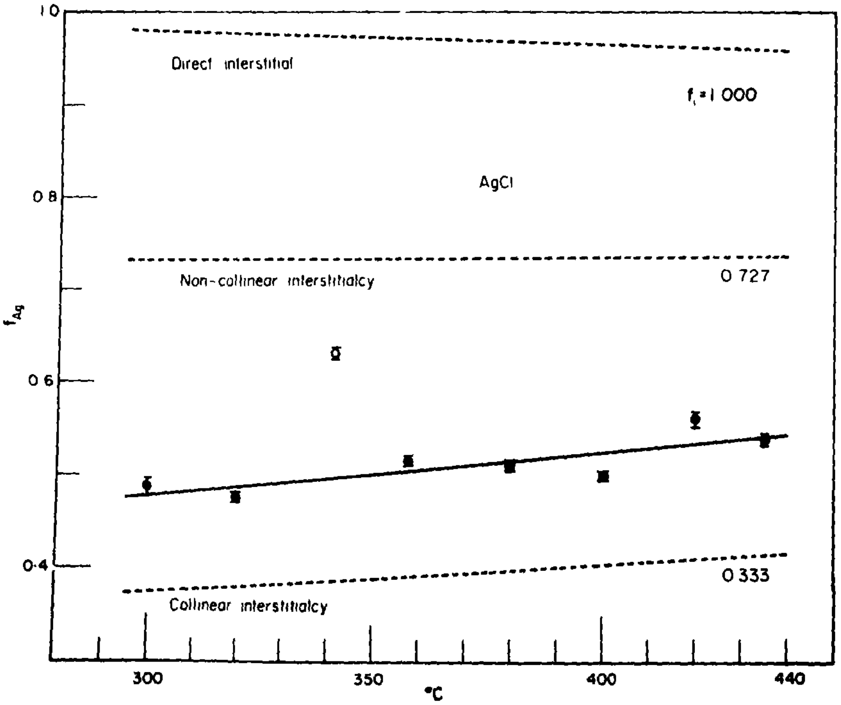

Fig. 3. The correlation factor f_{Ag} for AgCl. The bars on the experimental points show the estimated errors. The vacancy contribution to the dotted lines is calculated with Abbink's mobilities with Debye–Hückel interactions. (See Fig. 4). The solid line is calculated with the smoothed values of κ from Fig. 5.

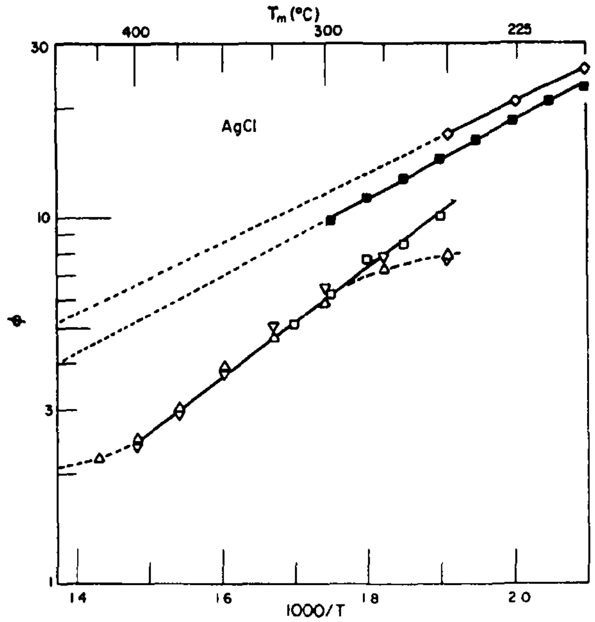

Fig. 4. Values of $\phi = \mu_i/\mu_r$ for AgCl. Conductivity analyzed according to simple theory: □ Abbink (reference [21]), △ Ebert and Teltow (reference [18]), ▽ Ebert and Teltow's results analyzed by Kurnick's method (reference [22]), ◇ Müller (reference [19]). Conductivity analyzed with Debye–Hückel interactions: ■ Abbink (reference [21]). The dotted lines indicate the extent of extrapolations.

and κ with equation (16). The results for κ, μ_1, and μ_2 are shown in Figs. 5 and 6. Even though there is appreciable scatter, which is due primarily to inaccuracies in the diffusion measurements, the overall trend is clear, and reasonable values for the activation energy are obtained for both μ_1 and μ_2. The smoothed values of κ from the line in Fig. 5 are then used to calculate the solid line for f_{Ag} in Fig. 3; a fairly good fit is obtained.

The dotted line in Fig. 4 shows the fitted values of κ which are obtained when the analysis of f_{Ag} is carried through with Müller's mobilities. The individual points (not shown) also lie slightly below those obtained with Abbink's mobilities, and the general result is practically unchanged. An earlier attempt was made to use the mobility ratio obtained from Ebert and Teltow's data with the simple theory[16]; in this case considerably larger

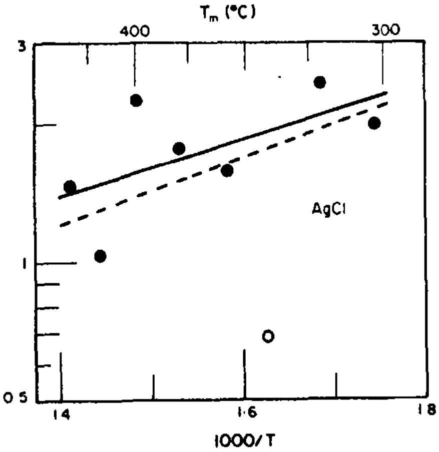

Fig. 5. Values of $\kappa = \nu_1/\nu_2$ for AgCl obtained by using Abbink's mobilities with Debye–Hückel interactions. The solid line is a least squares fit of the solid circles. The dashed line is a least squares fit of the corresponding points obtained from Müller's mobilities.

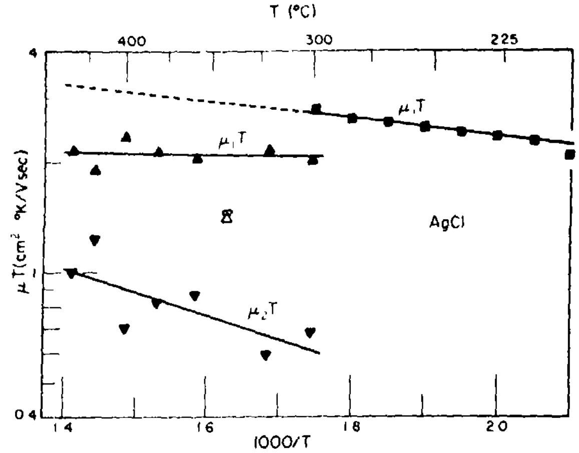

Fig. 6. Interstitialcy mobilities for AgCl. The solid squares are Abbink's values for μ_i with Debye-Hückel interactions; the line is a least squares fit of the six interior points and corresponds to the stated activation energy. The lines for μ_1 and μ_2 are least squares fits of the solid triangles in each case.

values of κ were obtained (up to 7·0), and the slope of κ had the opposite sign, which led to a negative activation energy for μ_2. This completely untenable result indicates the importance of having proper values for ϕ.

For each of the jump frequencies associated with defect motion the temperature dependence can be written with expressions of the form[15]

$$\nu_1 = \nu_0 \exp\left(-\Delta g_1/kT\right) = \nu_{10}\exp(-\Delta h_1/kT). \tag{25}$$

With

$$\Delta g_1 = \Delta h_1 - T\Delta s_1$$

we find

$$\nu_{10} = \nu_0 \exp\left(\Delta s_1/k\right).$$

The mobilities are related to the frequencies by equations such as equation (15); the different numerical constants arise from the different values of λ in Table 1. The activation energies for the two interstitialcy jumps have been obtained from least squares fits to the points in Fig. 6, with the point at 342°C excluded in all cases because of its large deviation. The values obtained in this fashion are listed in Table 3.

The frequency factors such as ν_{10} have been evaluated from the corresponding pre-exponential terms of μT according to equation (15). (For the 'interstitial' this process does not have any direct physical meaning, but the frequency factor has been obtained with $\lambda_i = a$ for comparison purposes.) If we suppose that ν_0 in equation (25) is the same for both collinear and noncollinear interstitialcy jumps, the ratio of the frequency factors is

$$\nu_{10}/\nu_{20} = \exp\left[-(\Delta s_1 - \Delta s_2)/k\right] \tag{26}$$

where Δs_1 and Δs_2 are the appropriate entropies of activation.

5. RE-ANALYSIS OF RESULTS FOR AgBr

There are two reasons for a re-analysis at this time. In the first place somewhat more accurate values are known for the correlation factors. Secondly, the importance of considering Debye-Hückel interactions in obtaining the mobility ratio ϕ also indicates the desirability of re-examining the values of ϕ to be used. The possibilities are shown in Fig. 7, which should be compared with Fig. 4 for AgCl. Again there is fairly good agreement for the results obtained from the simple theory between 200 and 300°C by Teltow[5] and

Table 3. Activation energies and frequency factors for AgCl

Process	Abbink[a]	Müller[b]	Ebert and Teltow[c]
Activation energies			
Formation of Frenkel pair			
Simple theory	1·6 eV	1·25 eV	1·69 eV
Simple association			1·43
Debye-Hückel interactions	1·55		
Defect mobility			
Vacancy	0·26	0·35	0·334
Interstitial (average)	0·045	0·16	0·149
Interstitialcy mobility			
Collinear	0·008 ± 0·021	0·114 ± 0·022	
Non-collinear	0·132 ± 0·050	0·260 ± 0·046	
Frequency factors			
Defect frequencies			
Vacancy	$176 \times 10^{11}\,\mathrm{sec}^{-1}$	$890 \times 10^{11}\,\mathrm{sec}^{-1}$	
Interstitial	44·7	444	
Interstitialcy frequencies			
Collinear	5·41	45·2	
Non-collinear	29·4	403	

[a] Reference [17]. Mobility values are calculated with Debye-Huckel interactions.
[b] Reference [19]. Mobility values are calculated from the simple theory.
[c] Reference [18]. Mobility values are calculated from the simple theory.

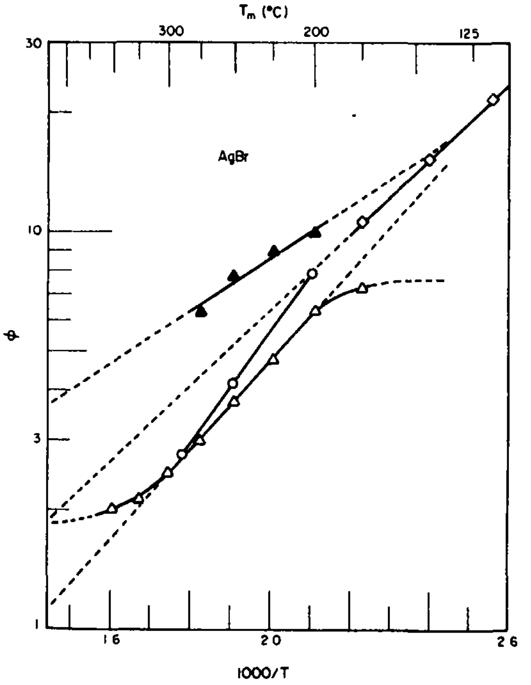

Fig. 7. Values of $\phi = \mu_i/\mu_v$ for AgBr. Conductivity analyzed with simple theory: △ Teltow (reference [5]). ◇ Müller (reference [19]), ○ Kurnick (reference [22]). Conductivity analyzed with Debye-Hückel interactions: ▲ Teltow (reference [5]). The dotted lines indicate the extent of extrapolations.

by Kurnick[22]. But when Debye-Hückel interactions are considered[5], much larger values are again obtained. As for AgCl Müller[19] has considered lower temperatures (15–175°C) and impurity concentrations (less than 150 ppm) in an attempt to make the analysis with the simple theory more appropriate; again he has been only partially successful according to the figure. For these reasons the re-analysis will be carried through primarily with Teltow's results including Debye-Hückel interactions.

The analysis proceeds in the same manner as for AgCl, and the results are shown in Figs. 8 and 9. Only the more reliable diffusion data have been used, but it is apparent that the peculiar behavior above 350°C is still present [8]. Since the crystals at the two lower temperatures may have been contaminated with sulfur, the activation energies in Table 4 are determined from the four intermediate points between 200 and 325°C. The diffusion data of Miller[12] for high purity AgBr are in good agreement with those used here but are limited to temperatures below 210°C; the more extensive data for reagent grade

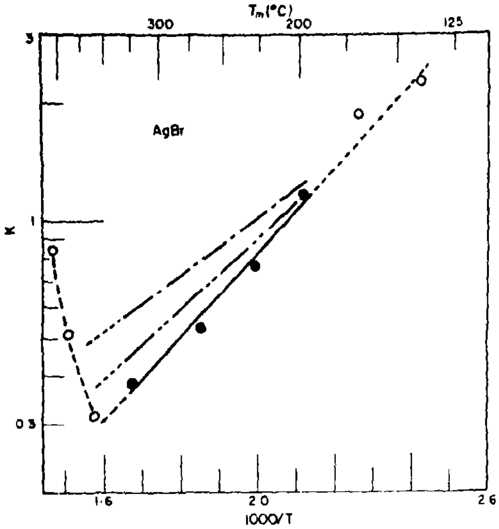

Fig. 8. Values of $\kappa = \nu_1/\nu_2$ for AgBr obtained by using Teltow's *mobilities with* Debye–Huckel interactions. The solid line is a least squares fit of the solid circles. The other lines are least squares fits with mobility data obtained by using the simple theory to analyze the conductivity. —·—Teltow, —··— Muller.

AgBr show considerable deviations and do not appear to be suitable for a quantitative analysis.

In the previous analysis values of ϕ were taken from Teltow's results with the simple theory, including the extrapolations along the curved lines in Fig. 7, and activation energies of 0·078 and 0·23 eV were reported for the collinear and non-collinear interstitialcies[8]. When the same mobilities are used in the present analysis, values of 0·121 and 0·27 eV are obtained. The difference comes from the different values used here for f_v in equation (8) and for $P(\kappa)$ in f_i in equation (10). It is now considered, however, that the results listed in Table 4 are more reliable, for the reasons stated above.

6. DISCUSSION

A good qualitative picture of the diffusion results is given in Fig. 3 for AgCl, and a similar picture is obtained for AgBr[8]. The fact that f_{Ag} is considerably smaller than $f_v = 0·781$ shows that interstitialcy processes must be prominent for the motion of interstitial ions, and the intermediate values of f_{Ag} also make it clear that at least two kinds of interstitialcy jumps must be present. In particular the

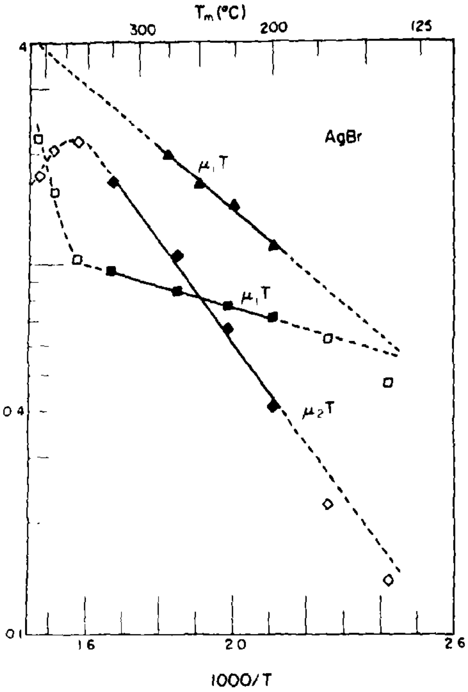

Fig. 9 Interstitialcy mobilities for AgBr. The solid triangles are Teltow's values for μ_i with Debye–Hückel interactions. The straight lines are least squares fits of the solid points in each case.

absolute calibration of the comparison of diffusion and conductivity measurements[12, 13] makes it unlikely that there are any appreciable systematic errors that might affect the general interpretation.

For the quantitative evaluation of μ_1 and μ_2, however, it is necessary to separate out the vacancy contribution, and thus a good knowledge of $\phi = \mu_v/\mu_i$ becomes necessary The discussion for both AgCl and AgBr emphasizes the importance of considering Debye–Hückel interactions in treating the conductivity. Even in cases where the simple theory appears to be self-consistent up to moderate impurity concentrations, the values obtained for ϕ may not really be correct, as illustrated especially by the inability to use the results of the simple theory for AgCl. Furthermore in both materials it would be desirable to have a

Table 4. Activation energies and frequency factors for AgBr

Process	Teltow[a]	Müller[b]
Activation energies		
Formation of Frenkel pair		
Simple theory	1·27(eV)	1·06(eV)
Debye–Hückel interactions	1·13	
Defect mobility		
Vacancy	0·30	0·34
Interstitial (average)	0·17	0·15
Interstitialcy mobility		
Collinear	0·058 ± 0·003	0·064 ± 0·006
Non-collinear	0·274 ± 0·017	0·245 ± 0·018
Frequency factors		
Defect frequencies		
Vacancy	527×10^{11} sec^{-1}	1930×10^{11} sec^{-1}
Interstitial	435	301
Interstitialcy frequencies		
Collinear	6·10	7·86
Non-collinear	1090	581

[a] Reference [5]. Mobility values are calculated from the conductivity with stated values of x_0 and ϕ obtained with Debye–Hückel interactions. The activation energies and frequency factors are obtained by plotting $\ln(\mu_r T)$ and $\ln(\mu_i T)$ vs. $1/T$. Teltow quotes different values for the activation energies because he plotted $\ln\mu_r$ and $\ln\mu_i$.

[b] Reference [19]. Mobility values are calculated from the simple theory.

better match for the temperature ranges for the analysis of ϕ and of f_{Ag}. The problems of long range Coulomb interactions are particularly important in the silver halides because of the rather large concentration of Frenkel defects ($x_0 = 0{\cdot}01\% = 100$ ppm at 300° in AgCl and 210° in AgBr), and it is evident that a complete quantitative understanding of these interactions is not yet available.

A notable feature of the results is the very small activation energy for the collinear interstitialcy, especially for AgCl. This is associated, of course, with the relatively small observed value for μ_i, which represents the average interstitial contribution to the conductivity. The method of obtaining μ_I from equation (16), in fact, forces Δh_I for μ_I to be approximately proportional to, but somewhat smaller than, Δh_i for μ_i. For AgCl Abbink [21] states that $\Delta h_i = 0{\cdot}045$ eV, which is obtained from the six inner points in Fig. 6. If the two outer points are also included, it is found that $\Delta h_i = 0{\cdot}061$ eV. Abbink also points out that the value of R used to correct for the Debye–Hückel interactions in equation (24) affects this result: when he uses $R = 2{\cdot}9$ Å instead of $\sqrt{2}a = 3{\cdot}9$ Å, he obtains $\Delta h_i = 0{\cdot}08$ eV [20]. This is another illustration of the influence of the method of handling defect interactions on the results obtained here.

The values obtained for the activation energies are somewhat smaller for AgCl than for AgBr. This is caused partly by a smaller temperature dependence of f_{Ag} for AgCl but also partly by the lower value of Δh_i given by Abbink; the values obtained in Table 3 with Müller's mobilities are appreciably larger. Since both Teltow and Müller obtain comparable values for Δh_i for AgBr in Table 4, the activation energies may also be somewhat too large for AgBr.

The frequency factors in Tables 3 and 4 appear to be reasonable, with perhaps somewhat small values for the collinear interstitialcy. The ratio of frequency factors for the two interstitialcy jumps is $\nu_{20}/\nu_{10} = 5{\cdot}43$ for AgCl and 179 for AgBr. Since there are three equivalent non-collinear jumps but only one possible collinear jump, this leaves factors of $5 \cdot 43/3 = 1 \cdot 81$ and $179/3 = 60$ to be accounted for by the entropies of activation in equation (26). The possibility seems quite reasonable for AgCl but a bit farfetched for AgBr. (The previous analysis gave $38/3 = 13$ for AgBr[8].)

Activation energies for interstitialcy motion are compared to some theoretical calculations in Table 5. The very small values for the collinear interstitialcy fall well within the predicted range. The appearance of a negative value in the theory simply means that an interstitial ion at the center of a small cube may not be in a position of minimum energy; a dumbbell configuration, in which two ions share equally in the distortion at a lattice site, may have lower energy. In contrast the observed values for the non-collinear interstitialcy are noticeably smaller than the prediction. The theoretical value is, however, only an upper limit since only one path through the saddle point was considered[6]; if the dumbbell is indeed the equilibrium configuration, this might well account for the lower activation energy. Some support for the dumbbell configuration is suggested by preliminary results of isotope effects for diffusion in the silver halides by Barr[23]. He finds a much smaller mass dependence of the diffusion coefficient than for other ionic crystals where vacancy mechanisms predominate. This indicates that the diffusion jump of the interstitial involves a considerable number of ions, thereby supporting the interstitialcy or perhaps even the dumbbell mechanism. There are also two possible ways of motion for the dumbbell, corresponding to the collinear and non-collinear interstitialcies, and it can be shown that the corresponding correlation factors are identical to those for the interstitialcy mechanisms[24]. Hence this analysis is unable to distinguish between the interstitialcy and dumbbell mechanisms.

The very small activation energy for the collinear interstitialcy should cause this mechanism to dominate the interstitial motion at lower temperatures, as is especially evident from Fig. 9 for AgBr. The presence of two contributions to interstitial motion should, in fact, produce a curvature in the plot of $\mu_i T$, in much the same way as a curvature is observed for the total conductivity. The present determinations of μ_i, however, are not sufficiently accurate and do not extend over a large enough temperature range to display any curvature[20]. In any case the ability of interstitial ions to move easily even at room temperatures certainly plays an important part in making the silver halides outstandingly suitable for the photographic process[25], and this ease is clearly made possible largely by the operation of the interstitialcy mechanism.

Table 5. Activation energies for interstitial mobility

Process	AgCl[(a)] theory	AgCl[(b)] experiment	AgBr[(c)] experiment
Collinear interstitialcy	−0·1 to 0·4 eV	0·008 eV	0·058 eV
Non-collinear interstitialcy	< 0·8	0·132	0·274
Direct interstitial	> 3·0		

[(a)] Hove (reference [6]).
[(b)] With Abbink's mobilities with Debye–Hückel interactions. See Table 3.
[(c)] With Teltow's mobilities with Debye–Hückel interactions. See Table 4.

Acknowledgements—The authors would like to express their appreciation to D. W. Lynch for sending the thesis of H. C. Abbink, to R. J. Maurer for sending the theses of W. D. Compton and A. Miller, and to L. W. Barr for the communication of his results prior to publication. We have also enjoyed the privilege of many stimulating discussions with these persons. The data analysis and least squares fits were made possible by the cooperation of the Computation Center at The University of Kansas.

REFERENCES

1. KOCH E. and WAGNER C., *Z. phys. Chem.* **B38**, 295 (1937).
2. COMPTON W. D. and MAURER R. J., *J. Phys. Chem. Solids* **1**, 191 (1956) for Cl in AgCl.
3. TANNHAUSER D., *J. Phys. Chem. Solids* **5**, 224 (1958) for Br in AgBr.
4. TUBANDT C. and REINHOLD H., *Z. Elektrochem.* **29**, 313 (1923); **31**, 84 (1925).
5. TELTOW J., *Ann. Phys.* **5**, 63, 71 (1949).
6. HOVE J. E., *Phys. Rev.* **102**, 915 (1956).
7. SEITZ F., *Acta crystallogr.* **3**, 355 (1950).
8. FRIAUF R. J., *Phys. Rev.* **105**, 843 (1957).
9. McCOMBIE C. W. and LIDIARD A. B., *Phys. Rev.* **101**, 1210 (1956).
10. BARDEEN J. and HERRING C., In *Imperfections in Nearly Perfect Crystals*, (Edited by W. Shockley) p. 281. Wiley, New York (1952).
11. COMPAAN K. and HAVEN Y., *Trans. Faraday Soc.* **52**, 786 (1956).
12. MILLER A. S. and MAURER R. J., *J. Phys. Chem Solids* **4**, 196 (1958).
13. GRACEY J. and FRIAUF R. J., *J. Phys. Chem.* Solids **30**, 421 (1969).
14. COMPAAN K. and HAVEN Y., *Trans. Faraday Soc.* **54**, 1498 (1958).
15. LIDIARD A. B., *Handb. Phys.* **20**, 246 (1956) presents a comprehensive review.
16. WEBER M. D., U.S. Atomic Energy Commission Tech. Rep. No. COO-1197-12 (1964) contains detailed information.
17. COMPTON W. D., Thesis, University of Illinois (1955).
18. EBERT I. and TELTOW J., *Ann. Phys.* **15**, 268 (1955).
19. MÜLLER P., *Phys. Status Solidi* **9**, K193 (1965); **12**, 775 (1965).
20. ABBINK H. C. and MARTIN D. S. Jr., *J. Phys. Chem. Solids* **27**, 205 (1966).
21. ABBINK H. C., Thesis, Iowa State University (1964).
22. KURNICK S. W., *J. chem. Phys.* **20**, 218 (1952).
23. BARR L. W., Private communication.
24. LIDIARD A. B., *Nuovo Cim.* **7**, Suppl. No. 2, 620 (1958).
25. FRIAUF R. J., *J. phys. Chem.* **66**, 2380 (1962).

J. Phys. Chem. Solids Pergamon Press 1969. Vol. 30, pp. 421–427. Printed in Great Britain.

EXPERIMENTAL VERIFICATION OF THE CORRELATION FACTOR FOR VACANCY DIFFUSION IN SILVER CHLORIDE*†

JOSEPH P. GRACEY‡ and ROBERT J. FRIAUF
University of Kansas, Lawrence, Kansas 66044, U.S.A.

(*Received* 13 *June* 1968)

Abstract – Diffusion coefficients for Ag tracers and ionic conductivity have been measured in AgCl containing 100 to 250 mole ppm Cd at temperatures of 125–225°C. Under these circumstances cation vacancies should be dominant, thereby allowing an unambiguous comparison of the measured correlation factor to the theoretical value for vacancies on a f.c.c. lattice. In practice it is found necessary to correct for a finite concentration gradient of Cd along the length of the samples and for a small contribution of residual interstitial Ag ions at the higher temperatures. The possible contribution to diffusion of Ag by cation vacancies associated with divalent Cd ions to form complexes is shown to be negligible at all temperatures because of the very small jump frequency of the Cd ion in the complex. With these corrections complete agreement is found between experimental and theoretical correlation factors within the experimental error of 1·0 to 1·5 per cent, thus demonstrating the absence of any systematic error in either diffusion or conductivity measurements.

1. INTRODUCTION[1]

IN IONIC crystals the motion of point defects – vacancies, interstitial ions, and complexes – gives rise to both ionic conductivity and diffusion. On the microscopic scale these are related by the Einstein relation for each type of defect, but on the macroscopic scale it is necessary to introduce a correlation factor for diffusion by tracers[2]. This effect was first pointed out by Bardeen and Herring[3], and theoretical values of the correlation factor have now been calculated for many types of defects and crystal structures by Compaan and Haven[4, 5], Manning[6], Howard[7] and others. Thus by comparing experimentally measured correlation factors to a table of theoretical values, it is often possible to obtain rather detailed information about the diffusion mechanism in particular substances[8].

The experimental correlation factor is obtained by measuring the total ionic conductivity σ, calculating $D_\sigma = (kT/N_0e^2)\sigma$ with the 'normal' Einstein relation, and comparing to the diffusion coefficient D_T^* measured with radioactive tracers. For silver ions, for instance,

$$f_{\mathrm{Ag}} = D^*_{\mathrm{Ag}}/D_\sigma. \qquad (1)$$

Thus the determination of f_{Ag} involves the absolute comparison of two quantities – σ and D^*_{Ag} – obtained by rather different kinds of experimental techniques. Since even a variation of a few per cent may lead to considerable differences in the interpretation of the results, a small systematic error in either measurement might well be significant. In this laboratory, for instance, results have been obtained giving a correlation factor 10 to 15 per cent larger than expected for single vacancies for both Na in NaCl[9, 10] and Cl in TlCl[8, 11, 12], thus strongly suggesting some additional diffusion mechanism, such as vacancy pairs, if the correlation factors can be relied upon to this accuracy. For this reason it is desirable to have a measurement of the correlation factor for some system where there can be no ambiguity about the theoretically expected result.

---

*Work supported by the U.S. Atomic Energy Commission. This is Technical Report COO-1197-24.

†Based in part on a thesis submitted to The University of Kansas in partial fulfillment of the requirements for an M.S. degree for JPG.

‡*Present address:* Western Electric Co., Lee's Summit, Missouri.

The principal requirement is that one, and only one, type of defect mechanism contribute to both ionic conductivity and diffusion. The alkali halides are not very suitable for two reasons, even though the diffusion of cation and anion vacancies can be immediately distinguished by using chemically distinct tracers. In the first place there is usually a non-negligible contribution of anion vacancies to the total ionic conductivity in pure crystals; recent work suggests 10 to 50 per cent in many cases[13–15]. Doping with divalent positive ions can eliminate this problem by suppressing the anion vacancies but will not influence the concentration of neutral vacancy pairs, which appear to make noticeable contributions to the diffusion of both anions[16–18] and cations[10]. The situation in the silver halides, in contrast, is more favorable. Both transport and diffusion measurements show that only Ag ions contribute to the conductivity in both pure and doped crystals, doping with divalent positive ions suppresses the interstitial Ag ions and leaves Ag ion vacancies predominant, and any possible contribution of vacancy pairs to diffusion of Ag ions is shown to be negligible by the exceedingly small values of the anion diffusion[19].

The system selected for these experiments is AgCl:Cd. AgCl is slightly preferable to AgBr since the somewhat smaller intrinsic defect concentrations in AgCl allow suppression of interstitial defects at more moderate doping concentrations. Cd is a convenient doping agent, and a detailed analysis of the defect interactions for this case is available in Abbink's work[20, 21]. For Cd concentrations of several hundred ppm[*] and temperatures of 100–200°C, then, the crystal should contain exclusively Ag ion vacancies, and the correlation factor for vacancies on a f.c.c. lattice is well known to be $f_v = 0{\cdot}78146$[4, 5]. Similar results for AgBr:Cd have been given by Miller[22, 23]. For 280 ppm Cd he finds $f^*_{Ag} = 0{\cdot}80$ between 90° and 150°C; at higher temperatures f^*_{Ag} decreases because of the increasing contribution of interstitial ions, which have $f_i = 0{\cdot}33$ to $0{\cdot}73$[5], and at lower temperatures f^*_{Ag} increases towards 1·0, possibly because of a contribution of divalent positive ion-cation vacancy complexes (but see the discussion in Section 4). We have initiated the experiments on AgCl:Cd both to increase the accuracy of the comparison and to provide a direct test of the procedures used in this laboratory.

2. EXPERIMENTAL PROCEDURE AND RESULTS

The experimental procedures have been described previously[2, 24], and only an outline indicating modifications will be given here[25]. The AgCl for this work was prepared according to the procedures of Nail, Moser, Goddard and Urbach[26] from distilled reagent grade hydrochloric acid and recrystallized silver nitrate[27]. Doping was done by mixing approximately 200 ppm analytical reagent grade $CdCl_2$ powder with the AgCl powder before melting, and crystals were grown by the Bridgman technique in a sealed quartz tube with 0·8 atm He to limit volatilization. During conductivity and diffusion the sample was held between silver electrodes in a He atmosphere in a sample holder containing only quartz, silver, and a chromel-alumel thermocouple in the high temperature region. In order to eliminate thermocouple calibration errors the same thermocouple was used for all measurements, and conductivity was observed during diffusion for each sample. Conductivity was measured with an ac bridge at 1 to 10 kHz, and diffusion coefficients were determined by taking 10 to 20 μ sections with a microtome and plotting the diffusion profile.

Since there is always some finite heating and cooling time, as well as small fluctuations in the temperature during the diffusion anneal, an effective time at the diffusion temperature T_0 must be calculated by

$$t_{eff} = D_0^{-1} \int_0^\infty D(T)\,dt \qquad (2)$$

where $D_0 = D(T_0)$. As long as most of the correction comes from temperatures near T_0, as is usually the case, it is quite satisfactory to use $D(T) = D_0\exp(-W_0/kT)$ for this purpose. For the doped samples used in this work, however, it was eventually realized that a noticeable amount of diffusion occurs even at room temperature. The additional correction for this time is calculated from

---

[*] All concentrations are given as the mole fraction in parts per million; i.e. a mole fraction of 0·1 per cent is 1000 ppm.

$$t'_{\text{eff}} = (f_0^* T_0 \sigma_0)^{-1} \int_0^\infty f^*(T) T \sigma(T) \, \mathrm{d}t \qquad (3)$$

where D has been expressed in terms of σ with the Einstein relation and equation (1). For lack of more precise information the ratio $f^*(T)/f_0$ is set equal to one; Miller's results[22] indicate that the value should lie between 0·8 and 1·0. The value of $\sigma(T)$ at room temperature is obtained by extrapolating from the measured conductivity at about 100°C according to the slope taken from Abbink's data[21] for a sample of comparable impurity concentration. Since an appreciable time elapsed in some cases between evaporation of the radioactive tracer and slicing of the sample, t'_{eff} ranged from 2·5 per cent of t_{eff} for sample 14 D1 to 13·3 per cent for 13 B; no correction was required for the pure sample or for 14 D2, which was stored at liquid nitrogen temperature.

Conductivity measurements for 3 conductivity samples and 4 diffusion samples from the doped crystals are compared to Abbink's results in Fig. 1, and the values of the conductivities and diffusion coefficients for the diffusion samples are summarized in Table 1 [25]. The errors for f_{Ag} are comprised of 0·2 to 0·5 per cent from σ with the balance from D^*_{Ag} and are given as standard deviations. The diffusion measurement on the pure sample at 250°C compares reasonably well to the value of $f_{\text{Ag}} = 0{\cdot}451$ extrapolated from Weber's results for 300–440°C[28].

3. ANALYSIS OF RESULTS

The values of f_{Ag} for the doped samples in Table 1 are in the general neighborhood of the theoretically expected value of $f_v = 0{\cdot}78146$ for diffusion by isolated vacancies on a f.c.c. lattice. Before a detailed comparison can be made, however, two other factors that lead to small corrections of the experimental values must be considered. The first is the existence of a gradient of the Cd concentration along the length of the samples, and the second is the possible contribution of other defect mechanisms, in particular interstitial ions and complexes, to the conductivity and diffusion of Ag tracers.

(*A*) *Influence of concentration gradient*

The conductivity curves in Fig. 1 show good agreement with Abbink's results[20, 21] and we may utilize this feature to determine the Cd concentration of our samples. When a plot of Abbink's concentration isotherms is made in the form of log σ vs. log c, straight lines are obtained for the temperatures and concentrations of interest here. These lines provide a convenient means of graphical interpolation, and the concentrations stated in Fig. 1 and Table 1 have been determined in this fashion. The straight lines also show that an *empirical* formula of the form

$$\sigma = Ac^n \qquad (4)$$

is a good respresentation of the data, with $n = 0{\cdot}85$ to $0{\cdot}90$. If there were no association, a value of $n = 1$ would be expected; the observed values of n slightly less than 1

Table 1. *Conductivity and diffusion data*

Sample	Conc. (ppm)	T (°C)	x_{rms} (μ)	D^*_{Ag} (cm²/sec)	σ (Ω-cm)$^{-1}$	f_{Ag}
14 D2 *a*†	216	125·2	93	$2{\cdot}31 \times 10^{-10}$	$3{\cdot}08 \times 10^{-5}$	0·827† ± 0·012
14 D2 *b*†			88	2·05		0·734‡ ± 0·011
13 B	135	150·0	105	2·27	3·64	0·646 ± 0·006
14 E	190	175·3	121	5·65	7·81	0·707 ± 0·012
14 D1 *a*†	216	199·9	123	$1{\cdot}11 \times 10^{-9}$	$1{\cdot}31 \times 10^{-4}$	0·787 ± 0·008
14 C	232	225·0	155	1·80	2·03	0·779 ± 0·008
12 C	pure	249·8	117	1·96	3·54	0·465 ± 0·007

†Sample 14 D was first used at 199·9° for diffusion into end *a*. After removal of all residual radioactivity it was used a second time at 125·2°C for diffusion into both ends *a* and *b*.

‡The average of these two values is 0·780 ± 0·012.

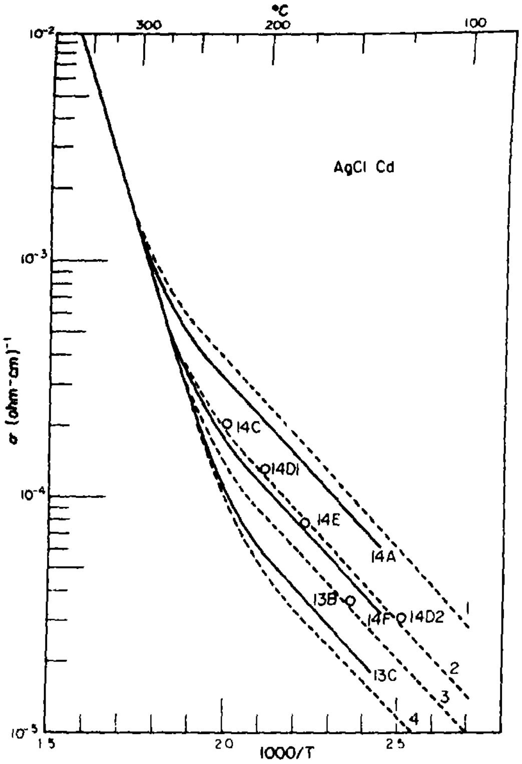

Fig. 1. Conductivity in AgCl:Cd. Points are shown for the conductivity of diffusion samples measured during the diffusion anneal. The concentrations of Cd, in mole ppm, are for conductivity samples: 14 A (354), 14 F (175), 13 C (77); and for Abbink's samples from reference [21]: 1 (441), 2 (198), 3 (128), 4 (64).

apparently represent a first order correction for association in some average sense.

The observed concentrations for our samples show a monotonic decrease along the length of the ingot (13 and 14 are two different ingots, and samples are labeled A, B, C,... in order, with A freezing first), indicating a segregation coefficient somewhat greater than 1 as found by others[21]. This shows that there must also be a concentration gradient along the length of each sample, and the very small diffusion coefficients for Cd at the temperatures of concern[29] do not allow any appreciable redistribution during the course of our experiments. With upper limits of $D = 3 \times 10^{-10}$ cm²/sec[30] and $t = 10^5$ sec, for instance, we find $x_{rms} = \sqrt{2Dt} \leq 0{\cdot}01$ cm, which is still small compared to the sample lengths of 0·47 to 0·68 cm. For lack of more specific information a linear concentration gradient is assumed, and therefore the change in concentration between the center and the end of a particular sample is taken as one-half the change in average concentration between this sample and the immediately adjacent one.

The concentration gradient influences the results because the measured diffusion coefficient refers to a small region at one end of the sample ($x_{rms} = 90$ to $150\,\mu$) whereas the observed conductivity reflects an average over the entire length of the sample. In order to estimate the required correction let us consider a sample of length $2l$ and write a linear concentration gradient as

$$c(z) = c_0[1 + q(z/l)] \tag{5}$$

where c_0 is the concentration at the middle of the sample ($z = 0$) and q measures the size of the concentration gradient. By relating $\sigma(z)$ to $c(z)$ with equation (4) the conductivity for the sample is found to be

$$\sigma_{\text{obs}} = 2(1-n)q\,[(1+q)^{1-n} - (1-q)^{1-n}]^{-1}\sigma_0 \tag{6}$$

where $\sigma_0 = \sigma(c_0)$. With use of the Einstein relation and equation (1), the correlation factor calculated from diffusion at end $a(z = l)$ is then

$$f_a = \frac{D^*_{\text{Ag}}(c_a)}{D_\sigma(\sigma_{\text{obs}})} = f_{\text{Ag}}\frac{\sigma(c_a)}{\sigma_{\text{obs}}} = f_{\text{Ag}}\frac{(1+q)^n}{\sigma_{\text{obs}}/\sigma_0} \tag{7}$$

and a similar expression is found for end $b(z = -l)$ with $(1+q)^n$ replaced by $(1-q)^n$. The first order effect of the concentration gradient can be eliminated by averaging f_a and f_b, and the second order effect is obtained by combining equations (6) and (7) and expanding.

$$f_{\text{avg}} = \tfrac{1}{2}(f_a + f_b) = f_{\text{Ag}}[1 + \tfrac{1}{8}n(2n-1)q^2]. \tag{8}$$

With typical values of $n = 0{\cdot}9$ and $q = 0{\cdot}1$ (20 per cent change in c from one end of the sample to the other) the error amounts to only 0·24 per cent.

(*B*) *Contribution of other defects*

Since the doped samples of AgCl contain a large amount of Cd ($c \gg x_0$, where c = mole fraction of Cd and x_0 = mole fraction of Frenkel defects in the pure crystal at the same temperature), we expect silver ion vacancies to be dominant and therefore $f_{\text{Ag}} \approx f_v$. There may still be a small concentration of interstitial silver ions, however, and the contribution of these is enhanced by their large mobility at low temperatures[31]. There are also a large number of complexes formed by the association of a divalent Cd ion and a silver ion vacancy, and the associated vacancy may make a contribution to the diffusion of Ag tracers[30].

Hence we must consider a crystal containing mole fractions x_v, x_i, and x_k of vacancies, interstitial ions, and complexes, respectively. The contribution of vacancies is $eN_0\mu_v x_v$ to conductivity and $f_v d_v x_v$ to diffusion, where the mobility μ_v and vacancy diffusion coefficient d_v are related by the microscopic Einstein relation $\mu_v/d_v = e/kT$, and similar expressions apply for interstitial ions. The complexes contribute only to diffusion by an amount $f_1 d_0' x_k$, where $d_0' = (4/3)w_1 a_0^2$ in the notation of the following paper[32]. It is convenient to introduce relative mole fractions $y_i = x_i/x_v$ and $y_k = x_k/x_v$ and mobility ratios $\phi_i = \mu_i/\mu_v = d_i/d_v$ and $\phi_k = d_0'/d_v$. From the conductivity, then, we find

$$D_\sigma = d_v x_v(1+\phi_i y_i) \tag{9}$$

and the total diffusion coefficient is

$$D^*_{\text{Ag}} = d_v x_v(f_v + f_i \phi_i y_i + f_1 \phi_k y_k). \tag{10}$$

By combining these equations according to equation (1) and rearranging terms slightly, we obtain

$$f_{\text{Ag}} = f_v - (f_v - f_i)\frac{\phi_i y_i}{1+\phi_i y_i} + f_1 \frac{\phi_k y_k}{1+\phi_i y_i}, \tag{11}$$

in which the three terms show the contributions of isolated vacancies, interstitial ions, and vacancies in complexes, respectively.

The evaluation of f_{Ag} for a sample at a specified temperature and impurity concentration involves three calculations. First, the mole fractions x_v, x_i and x_k must be determined from x_0, c and K_2, the mass action constant for association. For this purpose Abbink's results and procedures[20, 21] for 200° to 300°C have been used, with partial extrapolation, for our temperature range of 125° to 225°C. Second, the value of f_i may be calculated from Weber's results for the pure crystal[2] since the ratio $\kappa = \nu_1/\nu_2$ of the frequency of collinear to non-collinear interstitialcy jumps should not be affected by the presence of Cd. For this purpose we have extrapolated κ down from 300° according to Fig. 5 and have then calculated f_i from equation (12)[2]. Third, the contribution of vacancies in complexes may be evaluated from the observed diffusion D_0 of Cd by these complexes according to the following paper, where it is shown in equation (33) that

$$f_1 \phi_k = f_1 d_0'/d_v = 17{\cdot}6\, D_0/d_v \tag{12}$$

when $\kappa_1 = w_2/w_1 \ll 1$[30]. D_0 is obtained from the corrected results of Reade and Martin[29] in Fig. 3[30].

4. DISCUSSION

The effects of the two corrections described in the preceding section are summarized in Fig. 2. First the contribution of other defects is calculated from equation (11). The relative fraction of complexes y_k ranges from 0·80 at 125° to 0·16 at 225°C, but the contribution of these to diffusion of Ag is less than 0·0001 in f_{Ag} even at 225°C and hence is negligible at all temperatures. The reason is that D_0 for Cd is very much smaller than d_v in equation (12), presumably because the diffusion of the complex is limited by the very small jump frequency of the Cd^{2+} ion[30]. The interstitial ions, on the other hand, have a relative fraction y_i of only 0·0042 even at 225°C, but their contribution lowers f_{Ag} by 1·1 and 3·3 per cent, respectively, at the two highest temperatures, because of the large values of ϕ_i, namely, 24 and 19.

Next the correction for the concentration gradient is calculated with equation (7)[*]. For samples 13 B and 14 C it was possible to estimate q from the adjacent sample only for the end with the lower concentration; in these cases the same value of q was assumed for the other end. The high and low concentration ends of the samples were not initially distinguished, but the assignment in Fig. 2 appears to be unique. With the exception of 14 E the observed and calculated values of f_{Ag} agree to better than 1·4 per cent, which is somewhat remarkable in view of the uncertainties in estimating the concentration gradients.

By far the most reliable comparison, however, is afforded by the results for sample 14 D2. In the first place this sample was stored in liquid nitrogen so that none of the possibly doubtful room temperature correction from equation (3) was needed. Secondly the diffusion coefficients were measured at both ends of the sample for the same diffusion anneal; according to equation (8) the average should agree with f_{Ag} to well within the experimental error even without any knowledge of the actual size of the concentration gradient. Thirdly the end a of sample 14 D was marked between runs 1 and 2, and the results of the two runs on end a suggest the necessity of including the effect of interstitial ions at the higher temperatures, but

---

[*] Strictly speaking it is not quite correct to assume that f_{Ag} is independent of c, as implied in equations (7) and (8). Since both corrections are fairly small, however, this additional dependence has been neglected in the present treatment.

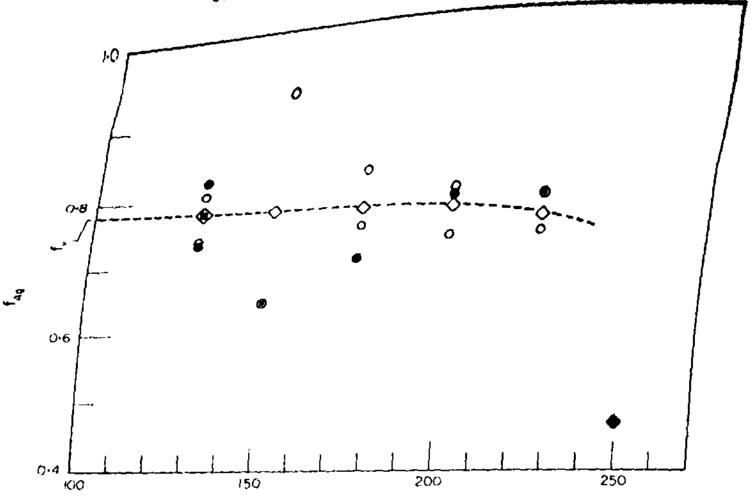

Fig. 2. Correlation factors for Ag diffusion in AgCl:Cd. Experimental: ● diffusion coefficient measured at one end of the sample, ■ average of diffusion coefficients for two ends, ◆ diffusion coefficient for pure sample. Theoretical: $f_v = 0{\cdot}78146$ for vacancies from reference [5], f_{Ag} including contributions of interstitial ions and complexes from equation (11), ○ f_{Ag} corrected for estimated concentration gradient according to equation (17). The dashed curve does not represent any particular function of temperature since different samples have different concentrations, it merely helps to show the general influence of the appearance of a few interstitial ions at the higher temperatures.

the correction for this effect is negligible at 125°C. The average for the two ends is $f_{\mathrm{Ag}} = 0{\cdot}780 \pm 0{\cdot}012$ from Table 1, and this agrees very well with the theoretical value of $f_v = 0{\cdot}78146$.

The very good agreement for sample 14 D2, along with the general consistency in Fig. 2, shows that there is no detectable systematic error within the experimental error of 1·0 to 1·5 per cent. The decrease of f_{Ag} at higher temperatures can definitely be ascribed to the influence of interstitial ions, in agreement with the suggestion for Miller's results in AgBr:Cd [22, 23]. The negligibly small contribution of complexes to diffusion of Ag, however, suggests that a different explanation may be required for the rise in f_{Ag} above f_v observed by Miller at lower temperatures.

Acknowledgements—The authors would like to express their appreciation to D. W. Lynch, L. W. Barr, and especially R. J. Maurer for helpful discussions and correspondence. The data analysis and least squares fits were done at the University of Kansas Computation Center.

REFERENCES

1. FRIAUF R. J. and GRACEY J., *Bull. Am. phys. Soc.* **12**, 326 (1967) contains a preliminary account of this work.
2. WEBER M. D. and FRIAUF R. J., *J. Phys. Chem. Solids* **30**, 407 (1969) gives, for instance, an analysis for pure AgCl.
3. BARDEEN J. and HERRING C., In *Imperfections in Nearly Perfect Crystals* (Edited by W. Shockley), p. 281. Wiley, New York (1952).
4. COMPAAN K. and HAVEN Y., *Trans. Faraday Soc.* **52**, 786 (1956).
5. COMPAAN K. and HAVEN Y., *Trans. Faraday Soc.* **54**, 1498 (1958).
6. MANNING J., *Phys. Rev.* **139**, A2027 (1965) and earlier papers.
7. HOWARD R. E., *Phys. Rev.* **144**, 650 (1966).
8. FRIAUF R. J., *J. appl. Phys.* **33**, 494 (1962).
9. DOWNING H. and FRIAUF R. J., To be published.
10. NELSON V. C. and FRIAUF R. J., In *Mass Transport in Oxides*, (Edited by J. B. Wachtman, Jr. and A. D. Franklin), p. 9. Natl Bur. Stand. Special Publication 296, Wash. (1968).
11. FRIAUF R. J., *J. Chem. Phys. Solids* **18**, 203 (1961).
12. FRIAUF R. J., To be published.
13. GRÜNDIG H., *Z. Phys.* **182**, 477 (1965).

14. BEAUMONT J. H. and JACOBS P. W. M., *J. chem. Phys.* **45**, 1496 (1966).
15. FULLER R. G. and REILLY M. H., *Phys. Rev. Lett.* **19**, 113 (1967).
16. LAURANCE N., *Phys. Rev.* **120**, 57 (1960).
17. BARR L. W., MORRISON J. A. and SCHROEDER P. A., *J. appl. Phys.* **36**, 624 (1965).
18. FULLER R. G., *Phys. Rev* **142**, 524 (1966).
19. More extensive discussion and references are given in WEBER M. D. and FRIAUF R. J., *J. phys. Chem. Solids* **30**, 407 (1969).
20. ABBINK H. C. and MARTIN D. S., Jr., *J. Phys. Chem. Solids* **27**, 205 (1966).
21. ABBINK H. C., Thesis, Iowa State University (1964).
22. MILLER A. S. and MAURER R. J., *J. Phys. Chem. Solids* **4**, 196 (1958).
23. A presentation similar to Fig. 2 of this paper is given in FRIAUF R. J. *J. appl. Phys.* **33**, 494 (1962).
24. FRIAUF R. J., *Phys. Rev.* **105**, 843 (1957).
25. GRACEY J. P., U.S. Atomic Energy Commission Technical Rep. No. COO-1197-21 (1967) contains detailed information.
26. NAIL N., MOSER F., GODDARD P. and URBACH F., *Rev. scient. Instrum.* **28** 4, 275 (1957).
27. Special Product X491, Eastman Organic Chemical Sales Division, Rochester, New York.
28. See Fig. 3 of WEBER M. D. and FRIAUF R. J., *J. Phys. Chem. Solids* **30**, 407 (1969)
29. READE R. F. and MARTIN D. S., *J. appl. Phys.* **31**, 1965 (1960).
30. FRIAUF R. J., *J. Phys. Chem. Solids* **30**, 429 (1969). See Fig. 3.
31. See Fig. 4 of WEBER M. D. and FRIAUF R. J., *J. Phys. Chem. Solids* **30**, 407 (1969).
32. See equation (31) of FRIAUF R. J., *J. Phys. Chem. Solids* **30**, 429 (1969).

J. Phys. Chem. Solids Pergamon Press 1969. Vol. 30, pp. 429–439. Printed in Great Britain.

COMMENTS ON DIFFUSION BY DIVALENT IONS IN ALKALI AND SILVER HALIDES*

ROBERT J. FRIAUF
University of Kansas, Lawrence, Kansas 66044, U.S.A.

(*Received* 13 *June* 1968)

Abstract – The theory of diffusion by complexes of divalent cations and cation vacancies is reviewed. First the microscopic diffusion coefficients for both the divalent ion and the host ion are expressed in terms of appropriate jump frequencies and correlation factors. Next the concentration dependence of the macroscopic diffusion coefficient for divalent ions is expressed in terms of the degree of association of the complexes and their distribution in the sample. A number of experimental arrangements are considered, involving chemical diffusion and tracer diffusion with and without carrier, and a number of examples are given of both correct and incorrect application of the analysis for experiments in the alkali halides. The results for diffusion of Cd in AgCl are re-examined, and it is suggested that inclusion of the concentration dependence indicates that Cd diffusion occurs by means of complexes at all temperatures. For Cd in AgBr it appears that proper treatment of the concentration dependence introduced by the complexes may remove the need for most or all of the previously proposed increase of mobility with concentration. Finally the relative contribution of complexes to diffusion of Ag and Cd in AgCl:Cd is obtained for use in interpreting experiments on tracer diffusion of Ag in this system.

1. INTRODUCTION

IT IS GENERALLY agreed that positive divalent ions Me^{2+} are usually incorporated into a monovalent ionic crystal of the type MX by substitution for M^+ ions on regular lattice sites. The condition of electric neutrality then requires an equal number of positive ion vacancies, which may be present either as isolated vacancies throughout the crystal or in association with divalent ions to form complexes. Since the divalent ions may diffuse by jumping into the associated vacancies, the extent of complexing is an important factor in determining the rate of diffusion by this mechanism.

The theory of diffusion of divalent ions by means of vacancy complexes has been treated by Lidiard[1,2] and Howard[3]. A number of experimental investigations have shown a dependence of diffusion coefficient on concentration in general agreement with the theory – Cd in AgCl[4] and AgBr[5], Ca[6] and Mn[7] in NaCl, Pb in KCl[8–11] and NaCl[12], Cd in NaCl[13] and KCl[14], and Zn in NaCl[15] – and thus have supported this model for diffusion. There have been numerous misinterpretations of the theory, however, some relatively minor but others appreciably influencing the interpretation of the results, and this is one reason for the present discussion. Particular attention will also be given to the diffusion of Cd in the silver halides because of its relevance to the preceding paper[16]; this arises because the vacancy attached to a Cd^{2+} ion in a complex can also make jumps involving Ag^+ ions and thus provide an additional contribution to the diffusion of Ag.

Once the cation vacancy-divalent ion complex is accepted as the model for the diffusion process, there are two separate aspects of the diffusion problem. The first is to express the microscopic diffusion coefficient for a divalent ion in a complex in terms of the appropriate jump lengths and frequencies. This aspect has not been of much concern in most of the experiments listed above, but it is of vital importance for estimating the contribution of the complexes

---

*Work supported by the U.S. Atomic Energy Commission. This is Technical Report COO-1197-25.

to diffusion of the host ion in the silver halides and hence will be reviewed in Section 2. The second problem is to relate the observable macroscopic diffusion coefficient for divalent ions to the number of complexes and their distribution in the sample, and this may again be subdivided into two parts. One concerns determination of the amount of complexing through application of appropriate mass action laws or statistical mechanics, taking into account all vacancies and impurity ions that may be present in a particular situation. The other concerns the influence of the spatial distribution of the amount of complexing, whenever this exists, on the macroscopic diffusion coefficients. Both of these parts contribute to the concentration dependence of the diffusion coefficient, and it is in this area that misinterpretation has most frequently occurred. In Section 3 a simple formulation of the general problem is first presented, and then a number of special cases are discussed to illustrate the treatment of different experimental conditions. Finally the results for the silver halides are examined in Section 4, both for their intrinsic interest and for their application to the preceding paper[16].

2. DIFFUSION COEFFICIENTS AND CORRELATION FACTORS

Let us consider a cation vacancy-divalent cation complex in a f.c.c. lattice, which is appropriate for all of the alkali and silver halides considered in this paper. The anion-cation separation is a_0, which is half the lattice parameter, and the jump distance for the vacancy is $a = \sqrt{2}a_0$. For the pertinent jump frequencies we follow the notation of Lidiard[1]: w_2 is the frequency for a jump of the divalent ion into the vacancy, w_1 is for any one of the four jumps of an M$^+$ ion that leaves the complex bound, and k_1 is for any other jump of the M$^+$ ion that leads to dissociation.

A divalent impurity atom in a complex can diffuse by jumping into the associated vacancy. A random walk treatment neglecting correlation gives the usual result.

$$D_0 = \tfrac{1}{6}w_2a^2 = \tfrac{1}{3}w_2a_0^2. \tag{1}$$

More correctly a correlation factor f_2 should be included to take account of the correlation that exists between the directions of successive jumps of the divalent ion.

$$D_0 = \tfrac{1}{3}w_2a_0^2f_2. \tag{2}$$

An exact expression for f_2 can be obtained if dissociation jumps are neglected completely ($k_1 = 0$) as shown by Lidiard[1, 2] and by Compaan and Haven[17].

$$f_2 = w_1/(w_1 + w_2). \tag{3}$$

A commonly used expression for rather tightly bound complexes ($k_1 < w_1$) has been obtained by kinetic methods[1, 3].

$$f_2 = (w_1 + 3{\cdot}5\,k_1)/(w_1 + w_2 + 3{\cdot}5\,k_1). \tag{4}$$

More general expressions have also been given for weakly bound complexes by Howard and Lidiard[3] and by Manning[18]. An important limiting case occurs when the divalent ion jumps into the vacancy much less frequently than the M$^+$ ions neighboring the complex. Then $w_2 \ll w_1$, all expressions for the correlation factor reduce to $f_2 = 1$ (even for weakly bound complexes[1]), and determination of D_0 gives a direct measure for w_2 from equation (1).

The vacancy associated with a complex provides jumps not only for the divalent ion but also for near-by M$^+$ ions. These jumps afford a second means for diffusion of M$^+$ ions, in addition to jumps into isolated vacancies. The contribution to diffusion *for a single complex* is

$$D_0' = 4 \times \tfrac{1}{6}w_1a^2f_1(\kappa_1) = (4/3)w_1a_0^2f_1(\kappa_1). \tag{5}$$

The factor 4 appears because there are 4 jumps of the M$^+$ ion that leave the complex bound, each with frequency w_1. The correlation factor f_1 depends on the ratio of jump frequencies $\kappa_1 = w_2/w_1$; values have been obtained for tightly bound complexes ($k_1 = 0$) by Compaan and Haven[17] and by Howard[19], whose results are shown in Fig. 1. In the limit as w_2 goes to zero f_1 must also go to zero since there can then be no *macroscopic* displacement of an M$^+$ ion. In the limit as w_2 goes to infinity f_1 approaches an asymptotic value of 0·4862; this is a typical value for situations where only 4 jumps are possible (compare to 0·5000 for a diamond lattice and 0·4669 for a plane square lattice)[17]. An important feature of the behavior shown in Fig. 1 occurs when $w_2 \ll w_1$; then f_1 becomes proportional to κ_1, as expected on general grounds.

$$f_1 = 4{\cdot}4\,\kappa_1 = 4{\cdot}4\,w_2/w_1, \quad \kappa_1 < 0{\cdot}01. \tag{6}$$

3. CONCENTRATION DEPENDENCE

(*A*) *Diffusion coefficient for divalent ions*

Consider a crystal that contains a non-uniform distribution of divalent ions. We denote the total number of ions per unit

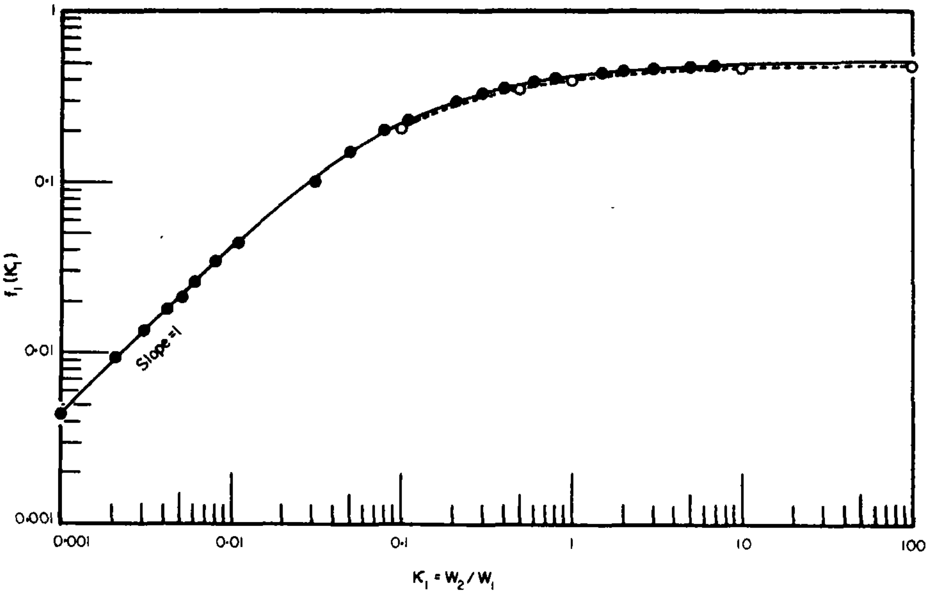

Fig. 1. Correlation factor vs. frequency ratio for host ion diffusion by means of associated vacancies on a f.c.c. lattice. ●—● Howard, reference [19]; O---O Compaan and Haven, reference [17].

volume by N_0, the number of divalent ions per unit volume by n_c, and the mole fraction of these by $c = n_c/N_0$. Of the divalent ions a certain number n_k per unit volume will be associated with positive ion vacancies to form complexes, with a corresponding mole fraction $x_k = n_k/N_0$. The fraction of the divalent ions in complexes is then

$$\beta = \frac{x_k}{c} = \frac{n_k}{n_c}. \tag{7}$$

Since diffusion lengths in actual experiments are of the order of 1 to 1000 μ, which is a very large distance compared to interatomic spacings, we shall assume that β is determined at each location in the crystal by the local concentrations of divalent ions and vacancies.

Let us first use a very simple kinetic picture of diffusion in order to show how the concentration dependence arises[1]. We may suppose the concentration gradient to be along a [100] axis of the crystal with no loss in generality since the diffusion coefficient must be isotropic in a cubic crystal. The diffusion coefficient for divalent ions is then defined by Fick's law.

$$J = -D(c)(\mathrm{d}n_c/\mathrm{d}x) = -N_0D(c)(\mathrm{d}c/\mathrm{d}x). \tag{8}$$

A unit area of the plane at $x = 0$ perpendicular to the [100] axis contains $a_0n_k(0)$ divalent ions in complexes, and in a f.c.c. lattice one third of these, on the average, have the associated vacancy located on the plane at $x = a_0$. The current to the right across the plane at $x = \frac{1}{2}a_0$ is then

$$J_{\text{right}} = \tfrac{1}{3}a_0n_k(0)w_2,$$

if we neglect correlation effects for the moment. The net current across this plane is readily found with the customary Taylor's expansion of $n_k(x)$.

$$J_{\text{net}} = J_{\text{right}} - J_{\text{left}} = -\tfrac{1}{3}w_2a_0^2(\mathrm{d}n_k/\mathrm{d}x).$$

In order to compare this result to equation (8), we must introduce the dependence of c on x. This is done by using $n_k = \beta cN_0$ and realizing that n_k depends on x only through c (and β).

$$\frac{dn_k}{dx} = N_0\frac{d(\beta c)}{dx} = N_0\frac{d(\beta c)}{dc}\frac{dc}{dx}.$$

Thus we find

$$D(c) = \tfrac{1}{6}w_2a_0^2[d(\beta c)/dc]. \qquad (9)$$

The previous result was obtained by neglecting correlation effects, in which case $\frac{1}{6}w_2a_0^2 = D_0$ according to equation (1), and we obtain

$$D(c) = D_0[d(\beta c)/dc]. \qquad (10)$$

This equation actually has more general validity provided D_0 is obtained from equation (2) with an appropriate expression for the correlation factor. The only requirement is that the complexes be rather tightly bound, i.e. their lifetime is reasonably long compared to the time $1/w_2$ for a single jump of the divalent ion. Then the complexes may be regarded as diffusing particles with a microscopic diffusion coefficient D_0. The only new feature of the present considerations is the spatial dependence of the concentration of complexed divalent ions, and this introduces the factor $d(\beta c)/dc$ in the expression for $D(c)$.

The result in equation (10) contains the concentration dependence of $D(c)$ for all circumstances if the dependence of β on c is treated properly, and this will be illustrated for a number of situations in Section 3(C). The form of equation (10), however, is directly applicable only when there is an actual concentration gradient of the divalent ion, as in chemical diffusion for which the result was originally obtained[1]. In diffusion experiments with radioactive tracers, rather different circumstances often occur, and we wish to consider one of these now. Suppose we have a carrier-free tracer of the divalent ion with a half life of one year, that we desire to use an activity of 1 μc on a sample face with area 1 cm^2, and that we have a penetration length of 1 μ into a crystal containing approximately 2×10^{22} molecules/cm^3. Then the average mole fraction of tracers is of the order of $10^{-6} = 1$ ppm, which is usually smaller than the concentration of residual divalent impurities in the crystal. If the half life is shorter or the penetration length longer, the mole fraction of tracers is even smaller. Furthermore diffusion experiments are often performed in crystals deliberately doped with a *uniform* concentration of divalent ions up to several hundred ppm. The important point is that in these circumstances the amount of complexing β is not appreciably influenced by the concentration gradient of radioactive tracers and is therefore independent of x. Indicating radioactive tracers by an asterisk, we have for Fick's law

$$\begin{aligned} J^* &= -N_0D^*(c)(dc^*/dx) \\ &= -N_0D_0[d(\beta c^*)/dx], \end{aligned}$$

and when β depends on x only through c^* this gives

$$D^*(c) = D_0[d(\beta c^*)/dc^*]. \qquad (11)$$

In particular when β is independent of x, as in the situations considered above, we find

$$D^*(c) = D_0\beta. \qquad (12)$$

The different forms for the concentration dependence of the diffusion coefficient in equations (10) and (12) arise from the different conditions for performing the experiments. This has been pointed out several times [2, 3] but has not always been considered properly in interpreting experimental results, as we shall see in some of the examples below. In order to obtain the explicit variation of $D(c)$ on c in either case, however, we must now review briefly the method of determining β as a function of c.

(B) *Treatment of association*

For convenience we shall consider explicitly the simple association theory of Teltow and Stasiw[20]. Inclusion of Debye–Hückel interactions can be accomplished when desired without introducing any qualitatively new features[2]. We denote mole fractions by x (except for $c \equiv x_c$) and use the following subscripts: v for positive ion vacancies, s for the other kind of intrinsic defect (negative ion vacancies in the alkali halides or interstitial silver ions in the silver halides), c for divalent ions, and k for complexes. The basic equations are electric neutrality, mass action for intrinsic defects, and mass action for association of complexes.

$$
\begin{aligned}
x_v &= x_s + c - x_k \\
x_v x_s &= x_0^2(T) = \exp(-g_s/kT) \qquad (13)\\
x_k[x_v(c-x_k)]^{-1} &= K_2(T) = 12\exp(\Delta g_k/kT).
\end{aligned}
$$

When c, x_0, and K_2 are specified these three equations can be solved for x_v, x_s and $\beta = x_k/c$. The following cases can be distinguished.

(1) *Predominance of intrinsic defects* ($c \ll x_0$). It is convenient to rewrite the general form of the mass action law from equation (13) in terms of β.

$$\beta_0(1-\beta)^{-1} = x_v K_2. \qquad (14)$$

When $c \ll x_0$ we have $x_v \approx x_0$ and find

$$\beta = x_0 K_2 (1 + x_0 K_2)^{-1}. \qquad (15)$$

In this case the value of β_0 is determined by the intrinsic defect concentration and is therefore characteristic of the pure crystal. Since β_0 is independent of c and hence also of x, either equation (10) or (12) gives

$$D(c \to 0) = D_0 \beta_0 \qquad (16)$$

which may be called 'the self-diffusion coefficient of the divalent impurity in the pure crystal.' As the temperature increases K_2 decreases but x_0 increases according to equation (13), and it is not uncommon for the product $x_0 K_2$ to increase. Usually, however, $x_0 K_2 \ll 1$, whence $\beta_0 \ll 1$ from equation (15).

A similar analysis is also appropriate when a large concentration x_1 of positive ion vacancies already exists in the crystal because of the presence of other divalent impurities (not necessarily the same as the diffusing species). Since x_1 may be much larger than x_0, it is quite possible in this case to have

$$x_1 K_2 \gg 1, \quad \beta \approx 1, \quad D(c) \approx D_0. \qquad (17)$$

(2) *Predominance of impurity controlled defects* ($c \ll x_0$). In this case we have $x_v = c(1-\beta)$ and equation (14) becomes

$$\beta(1-\beta)^{-2} = cK_2. \qquad (18)$$

For use in equation (10) we also find

$$\frac{\mathrm{d}(\beta c)}{\mathrm{d}c} = \frac{2\beta}{1+\beta} = 1 - \frac{1}{(1+4cK_2)^{1/2}}. \qquad (19)$$

These are the forms given explicitly by Lidiard[1,2]. They are usually appropriate for the alkali halides but may not be valid for the silver halides because of the larger values of x_0. As c becomes very large, however, both β and $\mathrm{d}(\beta c)/\mathrm{d}c$ approach unity, and for any experimental situation

$$D(c \to \infty) = D_0 \qquad (20)$$

from either equation (10) or equation (12).

(3) *Intermediate concentrations* ($c \sim x_0$). In this case a cubic equation is obtained for x_v from equations (13)[21]. By further substitution and implicit differentiation we find[22]

$$\beta = \frac{x_v K_2}{1 + x_v K_2}, \quad \frac{\mathrm{d}(\beta c)}{\mathrm{d}c} = \frac{2\beta}{1+\beta}\,\frac{1 + 2x_v K_2}{1 + 2x_v K_2 + (x_0/x_v)^2}. \qquad (21)$$

For small concentrations ($c \ll x_0$) we have $x_v K_2 \ll 1$, $\beta \ll 1$, and $x_0 \approx x_v$, whereby equation (21) reduces to $\mathrm{d}(\beta c)/\mathrm{d}c = \beta$ in agreement with equation (16). For large concentrations ($c \gg x_0$) we have $x_v \gg x_0$ and equation (21) gives $\mathrm{d}(\beta c)/\mathrm{d}\beta = 2\beta/(1+\beta)$ in agreement with equation (19).

The general behavior of the factors governing the concentration dependence of the diffusion coefficient is shown in Fig. 2 for typical values of $x_0 = 10^{-5} = 10$ ppm and $K_2 = 10^3$, corresponding to $\Delta g_k = 4{\cdot}4\,\mathrm{k}T$ in equation (13). Similar curves for the large concentration region have been shown by Lidiard[1, 2], but this figure also illustrates the behavior at intermediate and small concentrations. For small concentrations $D(C \to 0)$ is given by equation (16) with $\beta_0 < 10^{-2}$ in many cases, for intermediate concentrations $\mathrm{d}(\beta c)/\mathrm{d}c \approx 2\beta$ and both quantities are approximately proportional to c, and for large concentrations both curves approach saturation and $D(c)$ becomes equal to D_0 as in equation (20). The calculations for the figure indicate that equation (16) is a good approximation (error less than 1 per cent) when $c < 10^{-1}x_0$ and equation (19) is a good approximation when $c > 10x_0$.

(C) *Examples for alkali halides*

(1) *Chemical diffusion*. In this case there must be an actual concentration gradient of the diffusing impurity, and by combining equations (10) and (19) we find

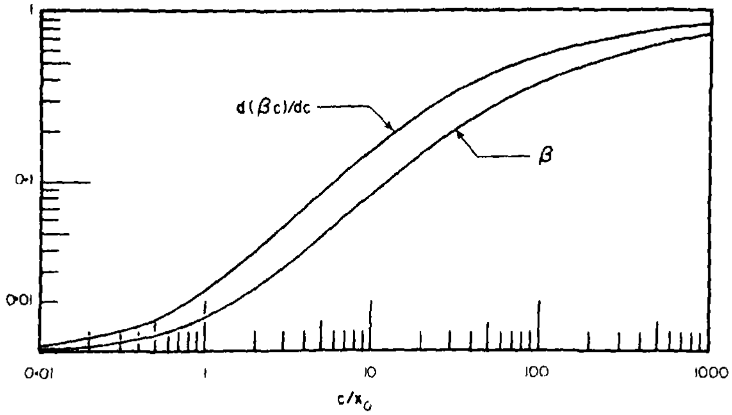

Fig 2. Concentration dependence of the degree of association calculated from equation (21) for $x_0 = 10^{-5}$ and $K_2 = 10^3$. The limiting values are the same for both curves: $\beta_0 = 0{\cdot}0099$ for $c = 0$ and $\beta_{max} = 1$ for $c = \infty$.

$$D(c) = D_0[2\beta/(1-\beta)] \qquad (22)$$

since usually $c \gg x_0$ in these circumstances. This result was originally applied[1] to diffusion of Cd and Pb in AgBr by Schöne, Stasiw and Teltow[23]; the general approach to saturation at high concentration was suggested, but the data were not accurate enough for a detailed analysis[1]. More recently Ikeda[13] has diffused Cd from the vapor into NaCl and has also applied equation (22). He expands equation (19), however, with the assumption that $\beta \ll 1$ in order to obtain $D(c) = D_1c$; this corresponds to the behavior for $c/x_0 = 1$–10 in Fig. 2. Since the larger concentrations make $cK_2 \sim 1$ at the surface, this assumption may introduce some uncertainty in his analysis.

(2) *Diffusion of tracer with carrier.* In many diffusion experiments a radioactive tracer is used with an appreciable amount of carrier of non-radioactive atoms of the same element. Sometimes a carrier free tracer is not available, and in other cases it may be necessary to add a carrier to suppress evaporation of a volatile halide at high temperatures. In these circumstances we assume that $c(x) = Mc^*(x)$, with M independent of c and x. Application of equation (11) then gives the result of equation (10)

$$D^*(c) = D_0\frac{d(\beta c^*)}{dc}\frac{dc}{dc^*} = D_0\frac{d(\beta c)}{dc}; \qquad (23)$$

the concentration gradient has the same influence on both tracer and carrier atoms. This procedure has been used by Fredericks and coworkers for diffusion from the vapor of Pb into KCl[8, 9] and NaCl[12] and Cd into KCl[14], and the curvature in their diffusion profiles shows clearly the concentration dependence of $D^*(c)$. Since $c \gg x_0$ (intrinsic defects) and $c > x_1$ (defects introduced by doping or background impurities) in most cases, they have correctly used equation (19) to evaluate $d(\beta c)/d\beta$ and to obtain equation (22) for analysis of their results. On the other hand Reade and Martin[4] did not consider any concentration dependence for the diffusion of Cd in AgCl (see Section 4(A)).

(3) *Carrier free tracer in doped crystal.* It is often advantageous to carry out diffusion of a divalent impurity into a crystal already doped with a uniform concentration of the impurity. When the uniform concentration c_1 is much larger than the concentration c^* of tracers, the amount of complexing is not influenced by the tracers, β is therefore independent of x, and the results of Section 3(A) apply,

$$D^*(c_1) = D_0\beta(c_1) \qquad (24)$$

as in equation (12). The curves in Fig. 2 show that $D^*(c)$ saturates less rapidly in this case than in cases (1) and (2) above where the limiting form of the concentration dependence is given by $2\beta/(1+\beta)$. With large doping concentrations it is possible to have $c_1 \gg Mc^*$ even if carrier free tracers are not available. This was the situation for Zn in NaCl studied by Rothman, Barr, Rowe, and Selwood[15]. Their diffusion profiles showed that D^* was independent of x for heavily doped crystals; for pure and lightly doped crystals at lower temperatures the situation was more nearly $c_1 \sim Mc^*$, and the concentration dependence of D^* was revealed by some curvature in their diffusion profiles. For Cd in AgBr Hanlon[5] also realized the importance of using carrier free tracers in order to obtain straight diffusion profiles (see further disucssion in Section 4(B)). For Ca and Mn in NaCl Murin and co-workers[6, 7] have similarly used heavily doped crystals, for which c_1 should be greater than Mc^*. But their activation energies are probably unreliable because they have introduced an expansion for equation (18) assuming $\beta = 1$ ($cK_2 \gg 1$) although values for β range down to less than 0·5. Furthermore they have applied *both* equation (23) and equation (24) in their first treatment, despite the fact that the experimental conditions indicate that *only* equation (24) is correct.

(4) *Carrier free tracer in pure crystal.* In the ideal situation we hope to have $c^* \ll x_0$. Then β_0 is determined by equation (15) and $D(c \to 0) = D_0\beta_0$ by equation (16). This situation was undoubtedly realized for Cd in pure

AgBr[5] and perhaps for Zn in pure NaCl above 700°C [15]. For Pb in pure KCl between 230° and 340°C[8], however, the diffusion coefficients were approximately equal for carrier free tracers and for tracers with enough carrier to make the surface concentration ~ 6000 ppm! In each case the diffusion profile shows no dependence of D^* on x. The most likely explanation is that $\beta \approx 1$ even in the 'pure' crystals because of the presence of other divalent impurities[10]; then even a large additional concentration cannot produce a further change in β or lead to a dependence of D^* on x. If this explanation is correct, these values of D^* should be compared to values of D_0 obtained by a different technique at higher temperatures, rather than to $D^*(c \rightarrow 0)$ as done by the authors. In the next paper[9], however, activation energies are indeed obtained from a plot of D_0 vs. T^{-1}.

(5) *Carrier free tracers in general.* The analysis in the last two paragraphs has assumed $c^* \ll x_0$ or c_1. When this is not the case, we may proceed as follows. We let

$$c(x) = c_1 + c^*(x)$$

and proceed with equation (21) to find

$$\frac{\mathrm{d}(\beta c^*)}{\mathrm{d}c^*} = \beta + c^* \frac{\mathrm{d}\beta}{\mathrm{d}c} = \beta\left[1 + \frac{c^*}{c}\frac{1-(x_0/x_v)^2}{1+(x_0/x_v)^2+2x_vK_2}\right] \quad (25)$$

for use in equation (11)[24]. For $c^* \ll c_1$ this reduces immediately to equation (12) or (24), and for $c^* \gg c_1$ this goes to equation (21). For large concentrations $x_0 \ll x_v$ and the result simplifies to

$$\frac{\mathrm{d}(\beta c^*)}{\mathrm{d}c^*} = \beta\left[1 + \frac{c^*}{c}\frac{1-\beta}{1+\beta}\right]. \quad (26)$$

Use of the latter form has been suggested by Reisfeld, Glasner and Honigbaum[10] for Pb in KCl, but there may have been some confusion about the proper use of the mass action law for complexing[11].

(*D*) *Summary*

There are two points to be made concerning the general application of these results. (1) The proper form to be used for the concentration dependence of the diffusion coefficient is determined by the experimental conditions. There are two important limiting cases: (a) diffusion with a concentration gradient of the impurity, equation (22) or (23), and (b) diffusion of a carrier free tracer, equation (16) or (24). Intermediate cases must be handled by equation (25) or (26). (2) The basic information about the jump frequencies in the complex is contained in D_0 according to equation (2). If it is desired to obtain activation energies for w_2, for instance, it is necessary to obtain D_0 for $c \rightarrow \infty$ and not $D(c \rightarrow 0)$, but this distinction has not always been made properly[8, 10].

4. ANALYSIS FOR SILVER HALIDES

(*A*) AgCl

The only published data for diffusion of divalent ions in AgCl is for Cd in AgCl by Reade and Martin[4]. Since diffusion coefficients were measured with a surface counting technique, there was no direct evidence for a dependence of $D^*(c)$ on c, and any possibility of a concentration dependence was explicitly ignored by these authors. They observed a change in slope of the Arrhenius plot for $D^*(c)$ as indicated in Fig. 3, made an approximate fit with the sum of two activated processes, and then attributed the behavior at low temperatures to diffusion of Cd^{2+} ions in complexes and at high temperatures to diffusion of unassociated Cd^{2+} ions (mechanism unspecified). More recently it has been suggested that the change in slope or 'break' in the Arrhenius plot near 320°C indicates diffusion by interstitial Cd^{2+} at low temperatures and by Cd^{2+} ions in complexes at high temperatures[25]. The estimates given below will show that it is just as reasonable to suppose that diffusion occurs at all temperatures by means of Cd^{2+} ions associated with vacancies, with the break in the Arrhenius plot caused simply by a change in the association process from domination by impurity controlled defects at low temperatures to domination by intrinsic defects at high temperatures.

The first problem is to estimate the concentration of Cd in the crystal during diffusion. The Cd^{115} tracer used in the experiments contained a considerable amount of carrier (at the specific activity of 100 mc/g for the 53 hr half-life Cd^{115m}, only 2 Cd atoms in 10^7 are radioactive). The two statements that a maximum amount $Q = 10^{-8}$ mole of Cd was used and that this would give a mole fraction $c < 1/500$ if distributed uniformly over a layer of thickness 1 micron combine to give an effective area $A = 1{\cdot}3\ \mathrm{cm}^2$ (the quoted sample dimensions give $1{\cdot}39\ \mathrm{cm}^2$). The standard solution of the diffusion equation for diffusion from a plane source into a semi-infinite medium for a *constant* diffusion coefficient[26] gives

$$c_0 = c(x=0, t) = \frac{Q/A}{N_0(\pi D t)^{1/2}} = \left(\frac{2}{\pi}\right)^{1/2} \frac{Q/A}{N_0 x_{rms}} \quad (27)$$

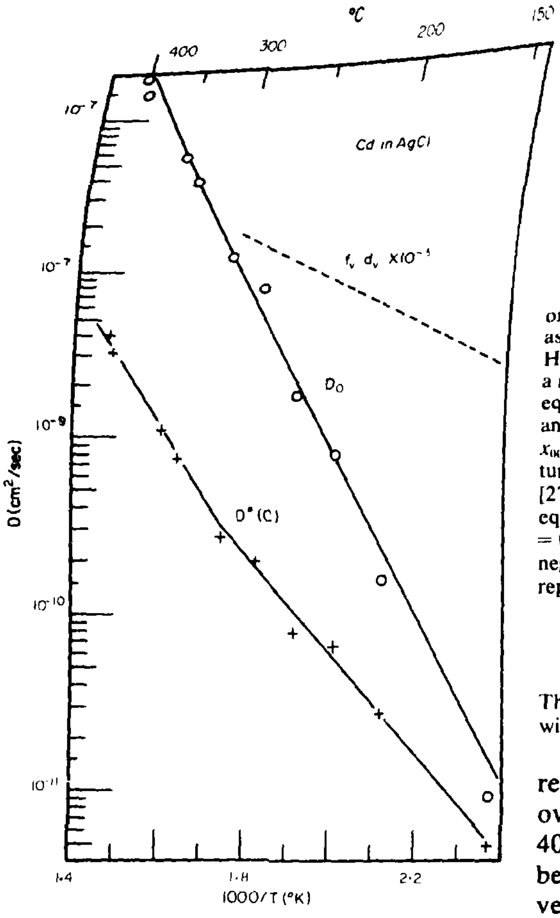

Fig. 3. Diffusion of Cd and Ag in AgCl. $D^*(c)$ was measured with Cd^{115} tracers containing an appreciable amount of carrier (reference [4]). D_0 is calculated from $D^*(c)$ as described in the text. d_v for isolated Ag vacancies is obtained from the mobility in reference [27] by means of the Einstein relation $d_v = (kT/e)\mu_v$; $f_v = 0{\cdot}781$ for vacancies on a f.c.c. lattice from reference [17].

where $x_{rms} = \sqrt{2Dt}$. The stated values of D and t at each temperature were used to calculate x_{rms}, and then c_0 was obtained from equation (27) with the values of Q and A indicated above. c_0 represents the maximum concentration at any given time, but larger concentrations occur at shorter times; hence c_0 may serve as some sort of representative average. The values of x_{rms} range from 12 μ at 149°C to 260 μ at 398°C and give corresponding values of c_0 from 133 to 6 ppm.

The next problem is to determine the degree of association β, and from this the relationship between $D^*(c)$ and D_0. For this purpose we may use the method of analysis and the results of Abbink for conductivity measurements

Table 1. Diffusion parameters for divalent ions in AgCl

Ion	R (Å)	Δh_2 (eV)	D_{00} (cm²/sec)
Zn^{2+}	0·74^(a)	1·07^(b)	12^(b)
Cd^{2+}	0·97^(a)	0·93^(c)	2·0^(c)
Sr^{2+}	1·13^(a)	0·96^(b)	0·30^(b)

(a) From reference [32].
(b) From reference [25].
(c) From Fig. 3 of this paper.

on AgCl containing Cd[27, 28]. Instead of the simple association theory of Stasiw and Teltow he used a Debye–Hückel analysis by introducing an activity coefficient γ as a multiplicative factor for x_v, x_s and $c - x_k$ in the last two of equation (13)[29] and obtained reliable values for x_0 and K_2 between 200° and 300°C. We have extrapolated $x_{00} = \gamma_0 x_0$ and $x_{00}K_2$ to both lower and higher temperatures according to the activation energies given by Abbink [27] and have also cheerfully used the Debye–Hückel equations at all temperatures (even though $x_v \sim 1000$ ppm $= 0{\cdot}1$ per cent at the highest temperature)[30]. If we neglect the small dependence of γ on c, equation (21) is replaced by

$$\frac{d(\beta c)}{dc} = \frac{2\beta}{1+\beta}\,\frac{1+2\gamma^2 x_v K_2}{1+2\gamma^2 x_v K_2 + \gamma^{-2}(x_{00}/x_v)^2}. \qquad (28)$$

Then D_0 is calculated from the observed values of $D^*(c)$ with equation (23), which is appropriate for this situation.

The results in Fig. 3 show that D_0 can be fit reasonably well by a single activated process over the entire temperature range of 150° to 400°C. Before discussing this result, it should be re-emphasized that the calculations are very tentative because of the many approximations involved both in estimating the impurity concentration and in extrapolating Abbink's results and procedures. The difference between the plots for $D^*(c)$ and D_0 is nonetheless striking, and typical values are obtained (see Table 1) for the diffusion parameters defined by

$$D_0(T) = D_{00} \exp(-\Delta h_2/kT). \qquad (29)$$

It is probably not sheer coincidence that the break in $D^*(c)$ occurs near the temperature where $c_0 \sim x_{00}$ ($c_0/x_{00} = 0{\cdot}93$ at 275° and 0·46 at 300°C). At lower temperatures $c_0/x_{00} \gg 1$ for the most part, β decreases noticeably from 0·36 at 149° to 0·028 at 249°C, and $d(\beta c)/dc$ decreases from 0·53 to 0·046. At higher temperatures $c_0/x_{00} \ll 1$, β changes only slightly from 0·019 at 300° to 0·022 at 400°, and $d(\beta c)/dc$ changes slowly from 0·022 down to a broad minimum at 0·0195 and back to 0·022. The high temperature region gives a slope for $D^*(c)$ approximating that of D_0, whereas the decrease of $d(\beta c)/dc$ with increasing T diminishes the apparent slope of $D^*(c)$ at lower temperatures. Thus we obtain no inconsistencies if we assume that the diffusion of Cd^{2+} ions occurs by means of associated vacancies at all temperatures, and this is perhaps the most likely hypothesis on the basis of the present somewhat meagre evidence.

(*B*) AgBr

The available data for divalent ions in AgBr are those of Hanlon for the diffusion of Cd[5]. The diffusion coefficients were determined by the sectioning technique with carrier free Cd^{109} tracers; an early experiment with Cd^{115} showed an appreciable curvature of the diffusion profile because of the concentration dependence of $D^*(c)$. Results were obtained for both pure and doped crystals and were interpreted in all cases in terms of diffusion by complexes as considered here. For diffusion of Cd^{109} tracers into pure AgBr, intrinsic defects should be predominant (the 'pure' crystals contained ~20 ppm of Mg and Fe[5], but $x_0 > 50$ ppm even at the lowest temperature of 192°C[33, 34]), and the results were analyzed correctly with equation (15) and (16).

A number of experiments were also performed in which Cd^{109} tracers were diffused into crystals doped with large and essentially uniform concentrations of non-radioactive Cd (0·23–3·30 per cent). In this situation the considerations of Section 3(C3) should apply, and the concentration dependence should be given by equation (24). The results in the original paper, however, were analyzed by means of equation (22), with the factor $2\beta/(1+\beta)$ expressed in the equivalent form of equation (19). In order to fit the observed values of $D^*(c)$ to this equation, especially at large concentrations, it was then necessary to introduce an *additional* dependence of D_0 on c, in the form $D_0(c) = D_0(0)\ (1+\alpha c)$ with $\alpha \sim +1{\cdot}0$ per cent. Presumably this additional dependence must arise from the frequency factors in equation (2) and would therefore also affect the mobility of ions in the crystal; it seems difficult to imagine a physical process for causing this much *increase* in mobility with increasing concentration of impurity. The suggestion here is that at least some of the apparent increase in $D^*(c)$ at large concentrations is due to the incorrect application of equation (22). It is seen in Fig. 2 that the factor $d(\beta c)/dc \approx 2\beta/(1+\beta)$ in equation (22) approaches saturation for smaller values of c then does the factor β in equation (24). (With Hanlon's value of K_2 at 186°C and $c = 3{\cdot}3$ per cent, for instance, $2\beta/(1+\beta) = 0{\cdot}73$ whereas $\beta = 0{\cdot}57$.) Hence a re-analysis with equation (24) would certainly reduce the required value of α. A graphical estimate indicates that perhaps it would be possible to obtain a fairly good fit with $\alpha = 0$ if K_2 were reduced so that $\beta_{max} \sim 0{\cdot}3$ at 3·3 per cent, but this is by no means certain and would probably introduce some further discrepancy between the values of Δg_k estimated for pure and doped crystals[35]. In any case the importance of correct treatment of the concentration dependence arising from complexing is indicated.

(*C*) Jump frequencies

For the positive ion vacancy associated with a complex we have distinguished two jump frequencies, w_2 for the jump of the divalent ion into the vacancy and w_1 for any of the four silver ion jumps that leave the complex bound, and in the next section we shall need the ratio of these frequencies. Since we shall find that $w_2 \ll w_1$ we may calculate w_2 directly from D_0 with equation (1). We may obtain an order of magnitude estimate for w_1 by calculating the jump frequency w_0 for an isolated silver ion vacancy from the vacancy mobility μ_v.

$$w_0 = (3kT/ea_0^2)\mu_v. \tag{30}$$

By taking D_0 for AgCl from Fig. 3 and for AgBr from Hanlon's estimates[5], along with values of μ_v from conductivity experiments[27, 33], we obtain the frequencies shown in Table 2. It is seen that the ratio $\kappa_0 = w_2/w_0$ is less than 3×10^{-3} for AgCl and 4×10^{-4} for AgBr.

The frequency w_1 can also be measured directly by dielectric loss measurements at low temperatures[36]. Even though the comparison involves a rather long extrapolation from the measuring temperatures of 150–200°K, the results in Table 2 do not appear unreasonable. w_1 is less than w_0 by a factor of about 10 for AgCl and 40 for AgBr, making $\kappa_1 = w_2/w_1$ less than 10^{-2} for most temperatures in both substances.

Table 2. Jump frequencies for vacancies in AgCl *and* AgBr

Frequency	AgCl 149°	AgCl 275°	AgCl 402°C	AgBr 186°	AgBr 361°C
$w_2^{(a)}$	0·04	30	600	2·5	80×10^6 (Hz)
$w_1^{(b)}$	9	90	420	7	60×10^8 (Hz)
$w_0^{(c)}$	14	80	220	26	230×10^9 (Hz)

[a] Obtained from D_0 with equation (1).

[b] Obtained from dielectric loss measurements by extrapolation.

[c] Obtained from μ_v with equation (30).

(D) Contribution of complexes to diffusion of silver

We have already seen in Section 2 that the jumps of the vacancy in a complex make a contribution to the diffusion of the host ions as well as of the divalent ions. In connection with the preceding paper[16] we need an estimate of the amount of this diffusion for Ag ions in crystals of AgCl doped with Cd. The situation in the experiments described there is that there is a concentration gradient of Ag^{110} radioactive tracers diffusing through a crystal with an essentially uniform concentration of Cd^{2+} ions. The contribution of a single complex is given by equation (5), and the probability that a particular Ag ion will be involved with a complex is simply the mole fraction of complexes $x_k = \beta c$[17].

$$D'_{Ag} = D'_0\beta c = (4/3)w_1 a_0^2 f_1(\kappa_1)\beta c. \quad (31)$$

In order to evaluate this expression directly we should need an independent measurement of w_1, but we can circumvent this problem by comparing to the observed diffusion of Cd^{2+} ions as measured by D_0. From equation (2) we obtain

$$D'_{Ag}/D_0 = (4f_1/\kappa_1 f_2)\beta c. \quad (32)$$

In particular when $\kappa_1 \ll 1$ we have $f_2 = 1$ from equation (3) and $f_1 = 4{\cdot}4\kappa_1$ from equation (6).

$$D'_{Ag}/D_0 = 17{\cdot}6\,\beta c, \quad \kappa_1 \ll 1. \quad (33)$$

The results of the previous section show that κ_1 is indeed small compared to unity in AgCl and AgBr. This is not surprising since it would be expected that the double charge on the divalent ion should give a considerably larger activation energy for the jump of this ion into the vacancy. This expectation is confirmed by the observed activation energies in AgCl: $\Delta h_2 = 0{\cdot}93$ eV from D_0 in Fig. 3, $\Delta h_1 = 0{\cdot}38$ eV from dielectric loss measurements[36], and $\Delta h_0 = 0{\cdot}26$ eV from the mobility of Ag vacancies[27]. A similar situation usually occurs in the alkali halides, namely, Δh_2 is appreciably larger than Δh_0; the only exception appears to be Cd in KCl, where $\Delta h_2 = 0{\cdot}54$ eV compared to $\Delta h_0 = 0{\cdot}76$ eV[14]. The fact that $w_2 \ll w_1$ or w_0 is illustrated vividly for AgCl in Fig. 3, which shows that below 300°C the diffusion of a single complex represented by D_0 is considerably more than three orders of magnitude smaller than the diffusion of a single isolated vacancy represented by $f_v d_v$. Since the macroscopic diffusion coefficients for Ag ions are found by multiplying D_0 by $17{\cdot}6\,x_k$ from equation (33) and $f_v d_v$ by x_v, respectively, it is clear that the contribution of defects will be small even when x_k is comparable to x_v. The reason, of course, is that the diffusion of silver ions by complexes is limited by the very small values of w_2, which enter through the correlation factor f_1.

REFERENCES

1. LIDIARD A. B., *Phil. Mag.* **46**, 815, 1218 (1955).
2. LIDIARD A. B., *Handbuch der Physik*, Vol. XX, pp. 246–349. Springer–Verlag, Berlin (1957).
3. HOWARD R. E. and LIDIARD A. B., *Rep. Prog. Phys.* **27**, 161 (1964).
4. READE R. F. and MARTIN D. S., *J. appl. Phys.* **31**, 1965 (1960).
5. HANLON J. E., *J. chem. Phys.* **32**, 1492 (1960).
6. MURIN A. N., BANASEVICH S. N. and GRUSKO Yu. S., *Fiz. Tverd. Tela* **3**, 2427 (1961); *Soviet Phys. solid St.* **3**, 1762 (1962).
7. LUR'E B. G., MURIN A. N. and BRIGEVICH R. F., *Fiz. Tverd. Tela* **4**, 1957 (1962); *Soviet Phys. solid St.* **4**, 1432 (1963).
8. KENESHA F. J. and FREDERICKS W. J., *J. chem. Phys.* **38**, 1952 (1963).
9. KENESHA F. J. and FREDERICKS W. J., *J. chem. Phys.* **41**, 3271 (1964).
10. REISFELD R., GLASNER A. and HONIGBAUM A., *J. chem. Phys.* **43**, 2923 (1965).
11. KENESHA F. J. and FREDERICKS W. J., *J. chem. Phys.* **43**, 2925 (1965).
12. ALLEN C. A., IRELAND D. T. and FREDERICKS W. J., *J. chem. Phys.* **46**, 2000 (1967).
13. IKEDA T., *J. phys. Soc. Japan* **19**, 858 (1964).
14. KENESHA F. J. and FREDERICKS W. J., *J. Phys. Chem. Solids* **26**, 501 (1965).
15. ROTHMAN S. J., BARR L. W., ROWE A. H. and SELWOOD P. G., *Phil. Mag.* **14**, 501 (1966).
16. GRACEY J. P. and FRIAUF R. J., *J. Phys. Chem. Solids* **30**, 421 (1969).
17. COMPAAN K. and HAVEN Y., *Trans. Faraday Soc.* **52**, 786 (1956).

18. MANNING J. R., *Phys. Rev.* **116**, 819 (1959); *ibid.* **128**, 2169 (1962).
19. HOWARD R. E., *Phys. Rev.* **144**, 650 (1966).
20 STASIW O. and TELTOW J., *Ann. Phys.* **1**, 261 (1947).
21. WEBER M. D. and FRIAUF R. J., *J. Phys. Chem. Solids* **30**, 407 (1969), see equation (21).
22. The expression for d(βc)/dβ corresponds exactly to the concentration dependence in equations (5.2.11) of HOWARD R. E. and LIDIARD A. B., *Rep. Prog. Phys.* **27**, 161 (1964).
23. SCHÖNE E., STASIW O. and TELTOW J., *Z. phys. Chem.* **197**, 145 (1951).
24. After sufficient transcription of notation and manipulation it can be shown that this is the exact counterpart of equation (5.2.14) of HOWARD R. E. and LIDIARD A. B., *Rep. Prog. Phys.* **27**, 161 (1964).
25. SLIFKIN L. M., LASKAR A. L., and BATRA A. P., *Bull. Am. phys. Soc.* **13**, 488 (1968).
26. CRANK J., *The Mathematics of Diffusion*, equation (2.7). Oxford University Press, Oxford (1956).
27. ABBINK H. C. and MARTIN D. S., Jr., *J. Phys. Chem. Solids* **27**, 205 (1966).
28. ABBINK H. C., Thesis, Iowa State University (1964).
29. The activity coefficient γ is defined by equations (23) and (24) of WEBER M. D. and FRIAUF R. J. *J. Phys. Chem. Solids* **30**, 407 (1969). In the next sentence γ_0 is the value of γ in the pure crystal.
30. The peculiar behavior of K_2 above 250°C is also ignored in the extrapolation procedure. See ABBINK H. C., Thesis, Iowa State University (1964).
31. Values of the dielectric constant at high temperatures were obtained from SMITH G. C., Thesis, Cornell University (1962).
32. PAULING L., *Nature of the Chemical Bond*, p. 346. Cornell University Press, Ithaca, N.Y. (1945).
33. TELTOW J., *Ann. Phys.* **5**, 63, 71 (1949).
34. MÜLLER P., *Phys. Status Solidi* **9**, K193 (1965); *ibid.* **12**, 775 (1965).
35. See the discussion following equation (13) of HANLON J. E., *J. chem. Phys.* **32**, 1492 (1960).
36. BÖTTGER H., *Phys. Status Solidi* **4**, 669 (1964).

J. Phys. Chem. Solids **Pergamon Press 1969. Vol. 30, pp. 441–447. Printed in Great Britain.**

CORRECTION OF DIPOLE FIELD DUE TO LATTICE DEFORMATION OF A PEROVSKITE-TYPE CRYSTAL

WATARU KINASE
Department of Physics, School of Science and Engineering, Waseda University, Nishiokubo, Shinjuku, Tokyo, Japan

YOICHIRO UEMURA* and MASATAKA KIKUCHI
Department of Applied Physics, School of Science and Engineering, Waseda University, Nishiokubo, Shinjuku, Tokyo, Japan

(*Received* 9 *November* 1967; *in revised form* 3 *June* 1968)

Abstract – Correction of Lorentz field coefficients in a Perovskite-type crystal is discussed by considering orthorhombic deformation of a simple cubic lattice. If one considers the deformation of crystal structure from the simple cubic lattice a^3 to the orthorhombic lattice $a(1+\Delta_1)\times a(1+\Delta_2)\times a(1+\Delta_3)$, a change of the internal field at some respective points caused by the dipole interaction is calculated as follows. The internal electric fields at $(0\ 0\ 0)$, $(\frac{1}{2}\frac{1}{2}\frac{1}{2})$ etc. are given by the equations

$$E_n(000) = \{\tfrac{4}{3}\pi + S_n(000) + 2{\cdot}1563\,(\Delta_1+\Delta_2) - 16{\cdot}8793\Delta_3\}p/a^3$$
$$E_n(\tfrac{1}{2}\tfrac{1}{2}\tfrac{1}{2}) = \{\tfrac{4}{3}\pi + S_n(\tfrac{1}{2}\tfrac{1}{2}\tfrac{1}{2}) - 10{\cdot}0622\,(\Delta_1+\Delta_2) + 7{\cdot}5578\Delta_3\}p/a^3 \text{ etc.}$$

where S_n' s represent the Lorentz correction terms and p is the dipole moment placed at the lattice points. By applying the results the quantitative discussions are possible for many phenomena accompanied by the lattice deformation, namely, ferroelectricity, piezoelectricity, photoelasticity and so on. As an example calculations are made to estimate the birefringences of the $BaTiO_3$ and WO_3 crystals.

1. INTRODUCTION

VARIOUS quantitative problems in the theory of ferroelectricity have been treated by considering the interaction among the dipoles of the crystal lattice[1–5]. In such treatment several numerical values of Lorentz field coefficients[6] have been calculated only for the simple cubic lattice. But crystal structure is generally deformed from the simple cubic shape to the tetragonal and orthorhombic ones etc. by the polarization.

The correction of the dipole field, however, has been done by considering only the nearest neighbour lattice points[2–4] and has not yet been calculated accurately. This calculation is quite indispensable for the discussion of many sorts of the problems regarding the polarization in ferroelectricity or antiferroelectricity, namely, spontaneous polarization, piezoelectric effect, photoeleasticity and so forth.

The purpose of this paper is to calculate a change of Lorentz field due to the orthorhombic deformation of the cubic lattice accurately by taking the whole lattice sum in order to advance the quantitative discussion about the various problems of the polarization.

In this paper the method of calculation is explained in Section 2, and the results are listed in Section 3, and the application of the results to the theory of double refraction is shown in Section 4. The further discussion about the results is made in Section 5.

2. CALCULATION

We take a simple cubic dipole array which is obtained by placing a dipole of moment p in the definite direction n at every lattice point of a single cubic lattice. The dipoles are placed at the point $li+mj+nk$, where l, m, and n are integers, i, j and k are unit vectors and their magnitudes are equal to the lattice constant a, and each dipole is arranged in the k direction (conveniently called as the n direction).

**Present address:* National Institute for Researches in Inorganic Materials.

The dipole field in the n direction at the location (ξ, η, ζ) is given as

$$E_n(\xi,\eta,\zeta) = \sum_{lmn} \frac{3\cos^2\theta_{lmn}-1}{r_{lmn}^3} p \qquad (1)$$

where

$$r_{lmn} = a\{(l-\xi)^2+(m-\eta)^2+(n-\zeta)^2\}^{1/2}$$

and

$$\cos\theta_{lmn} = \frac{(n-\zeta)a}{r_{lmn}}.$$

Then we get the equation

$$E_n(\xi,\eta,\zeta) = \sum_{lmn} \times \frac{2(n-\zeta)^2-(l-\xi)^2-(m-\eta)^2}{\{(l-\xi)^2+(m-\eta)^2+(n-\zeta)^2\}^{5/2}} \frac{p}{a^3}. \qquad (2)$$

Now we consider a change of the dipole field due to the lattice deformation. If the lattice constants in the l, m and n directions change from a to $a(1+\Delta_1)$, $a(1+\Delta_2)$ and $a(1+\Delta_3)$ respectively, r_{lmn} and $\cos\theta_{lmn}$ are expressed as

$$r_{lmn} = a\{(l-\xi)^2(1+\Delta_1)^2+(m-\eta)^2(1+\Delta_2)^2 + (n-\zeta)^2(1+\Delta_3)^2\}^{1/2}$$

$$\cos\theta_{lmn} = \frac{(n-\zeta)(1+\Delta_3)a}{r_{lmn}}.$$

Therefore, if we take account of only the first order terms of Δ's on the condition that the Δ's are much smaller than unity, the field in the n direction at the point (ξ, η, ζ) is given as

$$\begin{aligned} E_n(\xi,\eta,\zeta) = & \sum_{lmn} \frac{2(n-\zeta)^2-(l-\xi)^2-(m-\eta)^2}{\{(l-\xi)^2+(m-\eta)^2+(n-\zeta)^2\}^{5/2}} \frac{p}{a^3} \\ & + \sum_{lmn} \frac{3(l-\xi)^2\{(l-\xi)^2+(m-\eta)^2-4(n-\zeta)^2\}}{\{(l-\xi)^2+(m-\eta)^2+(n-\zeta)^2\}^{7/2}} \Delta_1 \frac{p}{a^3} \\ & + \sum_{lmn} \frac{3(m-\eta)^2\{(l-\xi)+(m-\eta)^2-4(n-\zeta)^2\}}{\{(l-\xi)^2+(m-\eta)^2+(n-\zeta)^2\}^{7/2}} \Delta_2 \frac{p}{a^3} \\ & + \sum_{lmn} \frac{3(n-\zeta)^2\{3(l-\xi)^2+3(m-\eta)^2-2(n-\zeta)^2\}}{\{(l-\xi)^2+(m-\eta)^2+(n-\zeta)^2\}^{7/2}} \Delta_3 \frac{p}{a^3} \end{aligned} \qquad (3)$$

where the first term corresponds to so to speak Lorentz correction $S_n(\xi, \eta, \zeta)$ and the following three terms are the further correction terms due to the orthorhombic deformation, the calculation of which is the main project of this article. If we express the lattice sums of the three terms concerning Δ_1, Δ_2 and Δ_3 as γ_1, γ_2 and γ_3 respectively, equation (3) can be simplified as

$$E_n(\xi,\eta,\zeta) = \{\tfrac{4}{3}\pi + S_n(\xi,\eta,\zeta) + \gamma_1\Delta_1 + \gamma_2\Delta_2 + \gamma_3\Delta_3\} p/a^3. \qquad (4)$$

Numerical values of γ_1, γ_2 and γ_3 at the lattice are calculated by taking the whole lattice summation. The results of calculation are listed in the next section.

3. RESULTS

The numerical results are listed in Table 1.

In the columns of γ_1, γ_2 and γ_3 of Table 1, the numerical results are shown for the representative lattice points, and the values in the parentheses are those previously obtained by the nearest neighbour approximation[3].

4. APPLICATION TO THE THEORY OF DOUBLE REFRACTION

We apply our results obtained in this article to the actual physical phenomena. As an example we now correct our previous results of the birefringences in the $BaTiO_3$ and WO_3 crystals[4].

By the results in this article, therefore, we can rewrite the relations between the local fields acting on the respective ions of the crystal and the electric dipole moments of

Table 1

Lattice points (ξ, η, ζ)	γ_1	γ_2	γ_3
(0 0 0)	2·1563 (6)	2·1563 (6)	−16·8793 (−12)
$(\frac{1}{2}\,\frac{1}{2}\,\frac{1}{2})$	−10·0622 $(-128/9\sqrt{3})$	−10·0622 $(-128/9\sqrt{3})$	7·5578 $(256/9\sqrt{3})$
$(0\,\frac{1}{2}\,\frac{1}{2})$	−1·5792 (0)	−27·1726 $(-18\sqrt{2})$	3·1835 $(6\sqrt{2})$
$(\frac{1}{2}\,0\,\frac{1}{2})$	−27·1726 $(-18\sqrt{2})$	−1·5792 (0)	3·1835 $(6\sqrt{2})$
$(\frac{1}{2}\,\frac{1}{2}\,0)$	11·4225 $(12\sqrt{2})$	11·4225 $(12\sqrt{2})$	−9·4084 (0)
$(0\,0\,\frac{1}{2})$	−2·1158 (0)	−2·1158 (0)	−98·5810 (−96)
$(0\,\frac{1}{2}\,0)$	1·5947 (0)	43·0072 (48)	−12·0452 (0)
$(\frac{1}{2}\,0\,0)$	43·0072 (48)	1·5947 (0)	−12·0452 (0)

the electron clouds of the respective ions as follows.*

$$\begin{aligned}E_{\mathrm{Ti}} = \frac{p_{\mathrm{Ti}}}{\alpha_{\mathrm{Ti}}} = E + \frac{1}{v}\,[\{&\tfrac{4}{3}\pi + 2{\cdot}1563(\Delta_1 + \Delta_2)\\ &- 16{\cdot}8793\Delta_3\}P_{\mathrm{Ti}}\\ &+ \{\tfrac{4}{3}\pi - 10{\cdot}0622(\Delta_1 + \Delta_2)\\ &+ 7{\cdot}5578\Delta_3\}P_{\mathrm{Ba}}\\ &+ \{\tfrac{4}{3}\pi + q - 2{\cdot}1158(\Delta_1 + \Delta_2)\\ &- 98{\cdot}5810\Delta_3\}P_{\mathrm{O}_1}\\ &+ \{\tfrac{4}{3}\pi - \frac{q}{2} + 1{\cdot}5947\Delta_1 + 43{\cdot}0072\\ &\times \Delta_2 - 12{\cdot}0452\Delta_3\}P_{\mathrm{O}_2}\\ &+ \{\tfrac{4}{3}\pi - \frac{q}{2} + 43{\cdot}0072\Delta_1 + 1{\cdot}5947\\ &\times \Delta_2 - 12{\cdot}0452\Delta_3\}P_{\mathrm{O}_3}]\end{aligned}$$

$$\begin{aligned}E_{\mathrm{Ba}} = \frac{p_{\mathrm{Ba}}}{\alpha_{\mathrm{Ba}}} = E + \frac{1}{v}[\{&\tfrac{4}{3}\pi - 10{\cdot}0622(\Delta_1 + \Delta_2)\\ &+ 7{\cdot}5578\Delta_3\}P_{\mathrm{Ti}}\\ &+ \{\tfrac{4}{3}\pi + 2{\cdot}1563(\Delta_1 + \Delta_2)\\ &- 16{\cdot}8793\Delta_3\}P_{\mathrm{Ba}}\\ &+ \{\tfrac{4}{3}\pi - p + 11{\cdot}4225(\Delta_1 - \Delta_2)\\ &- 9{\cdot}4084\Delta_3\}P_{\mathrm{O}_1}\\ &+ \{\tfrac{4}{3}\pi + \frac{p}{2} - 27{\cdot}1726\Delta_1 - 1{\cdot}5792\\ &\times \Delta_2 + 3{\cdot}1835\Delta_3\}P_{\mathrm{O}_2}\\ &+ \{\tfrac{4}{3}\pi + \frac{p}{2} - 1{\cdot}5792\Delta_1\\ &- 27{\cdot}1726\Delta_2 + 3{\cdot}1835\Delta_3\}P_{\mathrm{O}_3}]\end{aligned}$$

$$\begin{aligned}E_{\mathrm{O}_1} = \frac{p_{\mathrm{O}_1}}{\alpha_{\mathrm{O}}} = E + \frac{1}{v}[\{&\tfrac{4}{3}\pi + q - 2{\cdot}1158(\Delta_1 + \Delta_2)\\ &+ 98{\cdot}5810\Delta_3\}P_{\mathrm{Ti}}\\ &+ \{\tfrac{4}{3}\pi - p + 11{\cdot}4225(\Delta_1 + \Delta_2)\\ &- 9{\cdot}4084\Delta_3\}P_{\mathrm{Ba}}\\ &+ \{\tfrac{4}{3}\pi + 2{\cdot}1563(\Delta_1 + \Delta_2)\\ &- 16{\cdot}8793\Delta_3\}P_{\mathrm{O}_1}\\ &+ \{\tfrac{4}{3}\pi + \frac{p}{2} - 1{\cdot}5792\Delta_1 - 27{\cdot}1726\\ &\times \Delta_2 + 3{\cdot}1835\Delta_3\}P_{\mathrm{O}_2}\\ &+ \{\tfrac{4}{3}\pi + \frac{p}{2} - 27{\cdot}1726\Delta_1\\ &- 1{\cdot}5792\Delta_2 + 3{\cdot}1835\Delta_3\}P_{\mathrm{O}_3}]\end{aligned}$$

$$\begin{aligned}E_{\mathrm{O}_2} = \frac{p_{\mathrm{O}_2}}{\alpha_{\mathrm{O}}} = E + \frac{1}{v}[\{&\tfrac{4}{3}\pi - \frac{q}{2} + 1{\cdot}5947\Delta_1\\ &+ 43{\cdot}0072\Delta_2 - 12{\cdot}0452\Delta_3\}P_{\mathrm{Ti}}\\ &+ \{\tfrac{4}{3}\pi + \frac{p}{2} - 27{\cdot}1726\Delta_1\\ &- 1{\cdot}5792\Delta_2 + 3{\cdot}1835\Delta_3\}P_{\mathrm{Ba}}\\ &+ \{\tfrac{4}{3}\pi + \frac{p}{2} - 1{\cdot}5792\Delta_1\\ &- 27{\cdot}1726\Delta_2 + 3{\cdot}1835\Delta_3\}P_{\mathrm{O}_1}\\ &+ \{\tfrac{4}{3}\pi + 2{\cdot}1563(\Delta_1 + \Delta_2)\\ &- 16{\cdot}8793\Delta_3\}P_{\mathrm{O}_2}\\ &+ \{\tfrac{4}{3}\pi - p + 11{\cdot}4225(\Delta_1 + \Delta_2)\\ &- 9{\cdot}4084\Delta_3\}P_{\mathrm{O}_3}]\end{aligned}$$

---

*In the previous paper[4] the direction of the external field E is considered as the l-direction, whereas we take here as the n-direction. Therefore the subscripts 1 and 3 of the elongation factors Δ's and the oxygen O's have been exchanged for each other.

$$
\begin{aligned}
E_{O_3} = \frac{P_{O_3}}{\alpha_0} = E + \frac{1}{v}[\{ & \tfrac{4}{3}\pi - \frac{q}{2} + 43\cdot0072\Delta_1 \\
& + 1\cdot5947\Delta_2 - 12\cdot0452\Delta_3\}P_{Ti} \\
& + \{\tfrac{4}{3}\pi + \frac{p}{2} - 1\cdot5792\Delta_1 \\
& - 27\cdot1726\Delta_2 + 3\cdot1835\Delta_3\}P_{Ba} \\
& + \{\tfrac{4}{3}\pi + \frac{p}{2} - 27\cdot1726\Delta_1 \\
& - 1\cdot5792\Delta_2 + 3\cdot1835\Delta_3\}P_{O_1} \\
& + \{\tfrac{4}{3}\pi - p + 11\cdot4225(\Delta_1 + \Delta_2) \\
& - 9\cdot4084\Delta_3\}P_{O_2} \\
& + \{\tfrac{4}{3}\pi + 2\cdot1563(\Delta_1 + \Delta_2) \\
& - 16\cdot8793\Delta_3\}P_{O_3} \qquad (5)
\end{aligned}
$$

where E_{Ti}, E_{Ba}, E_{O_1}, E_{O_2} and E_{O_3} denote the local fields acting on the respective ions shown by the subscripts, which are caused by the electric field E of the incident light: P_{Ti}, P_{Ba}, P_{O_1}, P_{O_2} and P_{O_3} are electric dipole moments of the electron clouds of the respective ions; α_{Ti}, α_{Ba}, and α_0, are the electronic polarizabilities of the respective ions; v is the volume of the standard unit cell; p and q are the Lorentz correction factor of the local field, that is, $p = 8\cdot668$, $q = 30\cdot082$[6]. Here the direction of the external electric field E corresponds to the line connecting the Ti and O_1 ions.

By solving the set of the above simultaneous equations, the values of P_{Ti}, P_{Ba}, P_{O_1}, P_{O_2} and P_{O_3} can be obtained as the function of E, Δ_1, Δ_2 and Δ_3, while the total polarization P can be obtained as

$$
P = (P_{Ti} + P_{Ba} + P_{O_1} + P_{O_2} + P_{O_3})/v^* \qquad (6)
$$

where the notation v^* means the true volume of the unit cell, that is, $v(1+\Delta_1)(1+\Delta_2)(1+\Delta_3)$.

Thus we can calculate the optical index n by the relation given as

$$
n^2 = \epsilon = 1 + \frac{4\pi P}{E} \qquad (7)
$$

where ϵ is the optical dielectric constant and E is the electric field of an incident light wave.

We calculate the birefringence $\delta_n = n_c - n_a$ by taking the parameter α_0.

Here n_a, n_b and n_c are the optical indices concerning the respective axes a, b and c which correspond to the l, m and n directions respectively. The index n_a for the polarized light, whose electric field is applied in the direction to the a-axis, is obtained by putting

$$
\Delta_3 = \Delta_a, \quad \Delta_1 = \Delta_b, \quad \Delta_2 = \Delta_c
$$

Similarly for n_b and n_c we substitute

$$
\Delta_3 = \Delta_b, \quad \Delta_1 = \Delta_c, \quad \Delta_2 = \Delta_a
$$

and

$$
\Delta_3 = \Delta_c, \quad \Delta_1 = \Delta_a, \quad \Delta_2 = \Delta_b
$$

respectively. Here the observed values of the tetragonal phase at room temperature $\Delta_a = -0\cdot0016$, $\Delta_b = -0\cdot0016$ and $\Delta_c = 0\cdot0087$ are used[7].

For the sake of comparison to the previous results we draw Fig. 1 which shows the value of the birefringence $\delta_n = n_c - n_a$ vs. α_0, where the refractive index n of the standard cube is regarded to keep the constant value 2·398[8]. The relation between α_0 and α_{Ba} is shown in Fig. 2, where α_{Ti} keeps the constant value 0·186 Å^3.

As for the WO_3 crystal, the similar method mentioned above can be used in a more simple way, that is, the role of the Ba-site ion can be entirely neglected. The birefringences obtained for the WO_3 crystal with the deformation ratio $\Delta_a = -0\cdot0266$, $\Delta_b = 0\cdot00378$ and $\Delta_c = 0\cdot0235$[9] (the standard cubic lattice is taken to have the lattice parameter 3·737 Å) are shown in Fig. 3.

5. DISCUSSION

In this paper, by the direct summation method we have calculated the lattice sum with regard to the neighbouring dipole chains

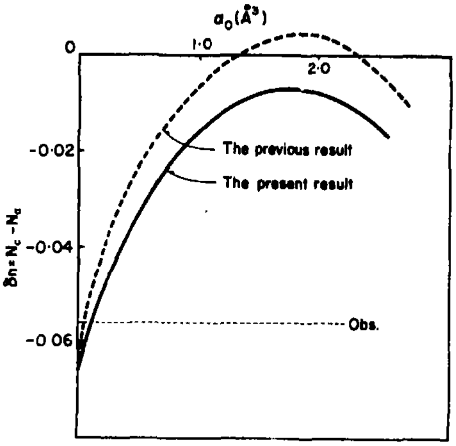

Fig. 1. Birefringence $\delta n = n_c - n_a$ of BaTiO$_3$ vs. electronic polarizability of oxygen α_0.

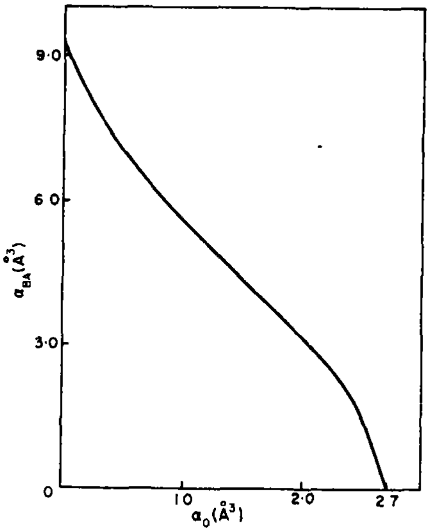

Fig. 2. The relation between α_0 and α_{Ba} of BaTiO$_3$, where the refractive index keeps the constant value 2·398.

one by one with the electronic computer TOSBAC 3121.*

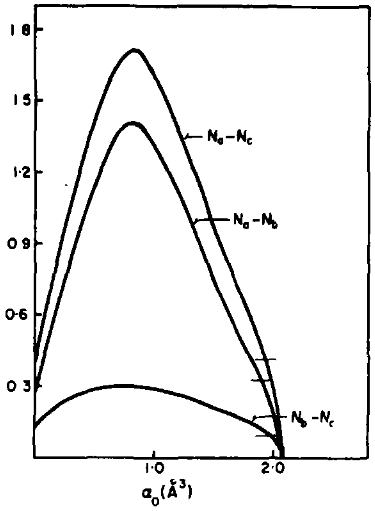

Fig. 3. Birefringences of WO$_3$ vs. α_0, where the crossed short bars show the observed values.

Now we consider the relation between γ_1, γ_2 and γ_3, which were calculated in the previous sections. Summing up the three coefficients γ_1, γ_2 and γ_3 of equation (4), we can get the following relation by simplifying the sum after resolving the numerator into factors, that is,

$$\sum_{i=1}^{3} \gamma_i = -3 \sum_{lmn} \frac{2(n-\zeta)^2 - (l-\xi)^2 - (m-\eta)^2}{\{(l-\xi)^2 + (m-\eta)^2 + (n-\zeta)^2\}^{5/2}}. \tag{8}$$

It can be readily found that this sum is nothing but the usual lattice sum of the dipole field. So the relation

$$\sum_{i=1}^{3} \gamma_i = -3\{\tfrac{4}{3}\pi + S_n(\xi, \eta, \zeta)\} \tag{9}$$

can be obtained.

This relation can be verified by the consideration as follows. Assuming a cubic lattice, which is obtained by expanding the original cubic lattice uniformly by an amount Δ in every direction, we get a unit cell whose volume is increased by the factor $(1+\Delta)^3$

---

*Here we take for one dipole chain the summation of fifty lattice points up and down from the lattice point considered, and then substitute the further lattice sum by the integration. Such lattice sums are accumulated in the region of the cylinder, whose radius is equal to the thirty lattice constants.

from the original one. Since the dipole interaction is in inverse proportion to the volume of the unit cell, the dipole field must be weakened by the factor $(1+\Delta)^{-3}$.

If Δ is small, this factor can be regarded as $1-3\Delta$. In equation (4), on the other hand, replacing every Δ_i by Δ, we can readily find the dipole field

$$E_n = \left\{\tfrac{4}{3}\pi + S_n(\xi, \eta, \zeta) + \sum_{i=1}^{3} \gamma_i \Delta\right\} p/a^3 \qquad (10)$$

which is also equal to

$$\{\tfrac{4}{3}\pi + S_n(\xi, \eta, \zeta)\}(1-3\Delta)p/a^3 \qquad (11)$$

by the above consideration. The equation (9) can be easily verified by equation (10) and (11).

By using the relation of equation (9) we can check our results. Then it is found that our results are accurate in significant five figures.

Now in Table 1 when we compare the values calculated here with the values previously calculated by the nearest neighbour approximation[3], we see that some ones are close to each other while some ones are rather different. For example, the values γ_1 at $(\frac{1}{2}00)$ are very close to each other, which means that the correction is almost achieved only by considering the nearest lattice points. Then it will be concluded that the nearest neighbour approximation gives rather good values when the effect of the nearest lattice point is large. But it is not always the case. For example in the column (0 0 0) we see that we cannot neglect the effect of the long range correction and that we cannot get the good values without such correction.

Generally the theoretical and quantitative treatments of ferroelectricity of the perovskite structure have been performed on the assumption of the cubic symmetry. One of the authors[2, 3] and Lawless[5] discussed considering the lattice deformation in $BaTiO_3$. The discussions were made, however, by taking account of the correction of the dipole interaction due to lattice deformation of only some of the nearest neighbour lattice points. So the previous treatments should be more fully investigated.

By applying our results in this paper we can now consider the correction of the long range part of the dipole interaction accurately. In such treatment the effects of the correction given in this paper seem remarkable especially in the discussion of the birefrigences (WO_3 and perovskite type). Because in calculating the birefrigences theoretically, we consider the differences between the refractive indices of the *l*, *m* and *n* directions respectively by taking account of the effect of the lattice deformation of the crystal. In this case these refractive indices are very close to each other and their differences are very small, so even the effect of a small correction is considered as remarkable.

As shown in Section 4, where we compare the present results with the previous ones in the $BaTiO_3$ crystal, the calculated birefringence in this paper is optical negative, which corresponds to the observed one qualitatively Therefore it is found that the theory of the previous paper is improved considerably by the correction in this paper. The correction cannot, however, interprete the observed one quantitatively enough. It is considered that in order to explain the observed one more accurately we must take account of not only the effect of the lattice deformation but also the electro-optic effect and the anisotropy of electronic polarizability and so on, of which we are now making a study. Furthermore in the WO_3 crystal the electronic polarizabilities of the oxygen ion are given as 1·90(1·62)Å^3, 1·94(1·80)Å^3 and 1·98(2·02)Å^3 respectively, where we determine the oxygen electronic polarizability which satisfies the observed data for the birefringence $n_a - n_b$, $n_a - n_c$ and $n_b - n_c$ (the values in the parentheses are the results of the previous paper[4]). In the present results the respective values of electronic polarizabilities of the oxygen ion are found to be nearly equal to each other, while it is not the case in the previous results. Therefore in the case of the WO_3 crystal, we can explain the observed data more accurately than in the $BaTiO_3$ crystal on the assumption that the electronic polarizabilities of the constituted ions are isotropic.

The numerical values calculated in this paper are essential to the quantitative discussion of the electrical properties of materials accompanied by the lattice deformation, for example, photoelasticity, which is a change of refractive indices due to the lattice deformation, and piezoelectricity, which is a change of polarization due to the lattice deformations and so on.

Furthermore either in spontaneous or induced polarization, the polarization in ferroelectricity is necessarily accompanied by the lattice deformation, so it is essentially important to consider the polarization taking account of the lattice deformation. Strictly speaking the discussions in ferroelectricity, which do not take account of the lattice deformation, are not correct quantitatively.

By applying the numerical values in this paper we shall advance the theoretical treatment of ferroelectricity later.

REFERENCES

1. SLATER J. C., *Phys. Rev.* **78**, 748 (1950).
2. KINASE W., *Prog. theor. Phys.* **13**, 529 (1955).
3. KINASE W. and TAKAHASI H., *J. phys. Soc. Japan* **10**, 942 (1955).
4. KINASE W., ISHIBASHI Y., and HYAKUBU S., *J. phys. Soc. Japan* **20**, 1438 (1965).
5. LAWLESS W. N., *Phys. Rev.* **138**, 6A, 1751 (1965).
6. TAKAHASI H., *J. phys. Soc. Japan* **19**, 499 (1963).
7. JOHO P., *Z. Kristallogr.* **120**, 329 (1964).
8. LAWLESS W. N. and DeVRIES R. C., *J. appl. Phys.* **35**, 2638 (1964).
9. MERZ W., *Phys. Rev.* **76**, 1221 (1949).

J. Phys. Chem. Solids Pergamon Press 1969. Vol. 30, pp. 449–451. Printed in Great Britain.

NEUTRON INCOHERENT SCATTERING FROM KDP*

D. K. STEINMAN† and G. C. SUMMERFIELD‡
Department of Nuclear Engineering, The University of Michigan, Ann Arbor,
Mich. 48104 U.S.A.

(*Received* 4 *March* 1968)

Abstract – The incoherent, inelastic neutron cross section is derived for KH_2PO_4 following the model discussed by Tokunaga and Matsubara. This expression should give the dominant contribution of the proton tunneling motion to the cross section. Matsubara has given the coherent cross section for KDP. However the scattering in hydrogen is primarily incoherent.

INTRODUCTION

In a recent paper Tokunaga[1] derived the coherent, neutron cross section for the proton tunneling motion in KH_2PO_4 (KDP). Neutron scattering from hydrogen is primarily incoherent (98 per cent). Since the dominant contribution in neutron scattering in this case is incoherent, we extend Tokunaga's calculations to include the incoherent cross section.

Several papers[2–5] describe KDP as having the hydrogens occupying sites in a double minimum potential well on the hydrogen bonds which connect adjacent PO_4 groups. For a more detailed description the reader is refered to references [2–5]. Our calculations indicate that the proton tunneling between the two possible sites on the hydrogen bonds should be observed most easily in the incoherent cross section for a single crystal of KDP.

CALCULATIONS

In the model proposed in reference [2], the proton field operators are taken to be

$$\psi(r) = \sum_{v,l} b_{vl}\phi_{vl}(r) \tag{1}$$

where

$$b_{vl} = \begin{pmatrix} b_{vl1} \\ b_{vl2} \end{pmatrix} \tag{2}$$

and 'v' labels the hydrogen bonds, l labels the two minima in the potential. The ϕ's are taken to be orthonormal wave functions, localized at the potential minima. (We will later choose these to be harmonic oscilator wave functions.)

$b^{\dagger}_{vlj}$ is a fermion creation operator and the b's satisfy the anticommutation relations

$$[b_{vlj}, b^{\dagger}_{v'l'j'}]_{+} = \delta_{vv'}\delta_{ll'}\delta_{jj'}. \tag{3}$$

The condition that there is one proton on each bond is

$$\sum_{l,j} b^{\dagger}_{vlj}b_{vlj} = 1. \tag{4}$$

Using these relations the Hamiltonian is[2]

$$\begin{aligned} H = {} & -2\Omega \sum_{vj} (b^{\dagger}_{v1j}b^{\dagger}_{v2j} + b^{\dagger}_{v2j}b_{v1j}) \\ & -\tfrac{1}{2} \sum_{\substack{vj \\ v'j'}} J_{v'v}(b^{\dagger}_{v1j}b_{v1j} - b^{\dagger}_{v2j}b_{v2j}) \\ & \times (b^{\dagger}_{v'1j'}b_{v'1j'} + b^{\dagger}_{v'2j'}b_{v'2j'}). \end{aligned} \tag{5}$$

In the molecular field approximation[4], we can write H as

$$\begin{aligned} H = -\sum_{vj} [& 2\Omega(b^{\dagger}_{v1j}b_{v2j} + b^{\dagger}_{v2j}b_{v1j}) \\ & + J\langle Z\rangle (b^{\dagger}_{v1j}b_{v1j} - b^{\dagger}_{v2j}b_{v2j})] \end{aligned} \tag{6}$$

---

*Work supported in part by the U.S. National Science Foundation.

†U.S. Atomic Energy Commission Predoctoral Fellow.

‡Physics Department, Virginia Polytechnic Institute, Blacksburg, Virginia, U.S.A.

where

$$\langle Z\rangle = \Big\langle \sum_{j} (b^{\dagger}_{v1j}b_{v1j} - b^{\dagger}_{v2j}b_{v2j})\Big\rangle_{T}. \qquad (7)$$

Equation (6) is easily transformed into

$$H = \sum_{vj} \lambda_{+}\alpha^{\dagger}_{vj+}\alpha_{vj+} + \sum_{vj} \lambda_{-}\alpha^{\dagger}_{vj-}\alpha_{vj-} \qquad (8)$$

where

$$\lambda_{\pm} = \pm\sqrt{((2\Omega)^2 + (J\langle Z\rangle)^2} \qquad (9)$$

and

$$\alpha_{v\pm} = c_{1\pm}b_{v1} - c_{2\pm}b_{v2} \qquad (10)$$

$$c_{1\pm} = \frac{(J\langle Z\rangle \pm \sqrt{(J^2\langle Z\rangle^2 + (2\Omega)^2)}}{\sqrt{(2(J^2\langle Z\rangle^2 + (2\Omega)^2 \pm J\langle Z\rangle\sqrt{(J^2\langle Z\rangle^2 + (2\Omega)^2))}}}$$

$$c_{2\pm} = \frac{2\Omega}{\sqrt{(2(J^2\langle Z\rangle^2 + (2\Omega)^2 \mp J\langle Z\rangle\sqrt{(J^2\langle Z\rangle^2 + (2\Omega)^2))}}} \qquad (11)$$

For unpolarized neutrons, the cross section is

$$\frac{d^2\sigma}{d\Omega d\epsilon} = \frac{k'}{2\pi\hbar k}\int_{-\infty}^{\infty} dt$$

$$\times e^{i\epsilon t/\hbar}\{|a_{inc}|^2\langle \boldsymbol{\rho}(-\boldsymbol{\kappa})\cdot\boldsymbol{\rho}(\boldsymbol{\kappa},t)\rangle_T$$

$$+ |a_{coh}|^2\langle \rho_0(-\boldsymbol{\kappa})\rho_0(\boldsymbol{\kappa},t)\rangle_T\} \qquad (12)$$

where

$$a_{inc} = a_{+} - a_{-}.$$

$$\boldsymbol{\rho}(\boldsymbol{\kappa}) = \int d^3r\psi^{\dagger}(\boldsymbol{r})e^{-i\boldsymbol{\kappa}\cdot\boldsymbol{r}}\mathbf{J}\psi(\boldsymbol{r}) \qquad (13)$$

J is the spin of the target nuclei. The components of **J** are the Pauli matrices, and

$$\rho_0(\boldsymbol{\kappa}) = \int d^3r\psi^{\dagger}(\boldsymbol{r})e^{-i\boldsymbol{\kappa}\cdot\boldsymbol{r}}\psi(\boldsymbol{r}). \qquad (14)$$

The second term on the right-hand side of (12) is discussed in some detail by Matsubara[1]. Consequently, we will concern ourselves exclusively with the first term, the incoherent part.

Using (1) we see that

$$\boldsymbol{\rho}(\boldsymbol{\kappa}) = \sum_{\substack{vv'\\ ll'}} F_{ll'vv'}(\boldsymbol{\kappa})b^{\dagger}_{l'v'}\mathbf{J}b_{lv}. \qquad (15)$$

Noting that $F_{ll'vv'}(\boldsymbol{\kappa}) = F_{lv}(\boldsymbol{\kappa})$ due to the orthonormality of the ϕ_{lv} we get

$$\frac{d^2\sigma^{inc}}{d\Omega d\epsilon} = \frac{k'}{k}|a_{inc}|^2\sum_{\substack{v\\ ll'}} F_{lv}(-\boldsymbol{\kappa})F_{l'v}(\boldsymbol{\kappa})q_l^2 q_{l'}^2\frac{1}{\mathscr{F}}$$

$$\times\{\delta(\epsilon)(e^{-\beta\lambda_+}p_l^2p_{l'}^2 + e^{\beta\lambda_+})$$

$$+ (e^{-\beta\lambda_+}\delta(\epsilon - 2\lambda_+) + e^{\beta\lambda_+}\delta(\epsilon + 2\lambda_+))$$

$$\times p_lp_{l'}\} \qquad (16)$$

where

$$F_{lv} = \int d^3r e^{-i\boldsymbol{\kappa}\cdot\boldsymbol{r}}|\phi_{lv}|^2$$

$$p_1 = -\frac{J\langle Z\rangle + \lambda_+}{2\Omega}$$

$$p_2 = -\frac{J\langle Z\rangle - \lambda_+}{2\Omega}$$

$$q_1 = \frac{2\Omega}{[2(\lambda_+^2 - J\langle Z\rangle\lambda_+)]^{1/2}}$$

$$q_2 = -\frac{(J\langle Z\rangle - \lambda_+)}{[2(\lambda_+^2 - J\langle Z\rangle\lambda_+)]^{1/2}}. \qquad (17)$$

$\mathscr{F} = 2\cosh\beta\lambda_+$ is the partition function per proton[2].

DISCUSSION

We can see the properties of neutron scattering from the hydrogen tunneling motions more clearly by taking an explicit model for the proton wave functions. First we define $\mathbf{d}_v$ with magnitude d and direction $\boldsymbol{\Omega}_v$ to be the vector distance between the potential minima on the vth bond.

We now take the ϕ's to be harmonic oscillator ground state wave functions with characteristic frequencies ω_d for motions along the bond and ω_r for motions perpendicular to the bond. With this model we have

$$F_{1v} = \mathrm{e}(-(\boldsymbol{\kappa} \cdot \boldsymbol{\Omega}_v)^2/4\,a^2 - (\boldsymbol{\kappa} \times \boldsymbol{\Omega}_v)^2/4\,b^2)$$

$$F_{2v} = e^{i\boldsymbol{\kappa}\cdot\mathbf{d}_v} F_{1v} \tag{18}$$

where

$$a^2 = m\omega_d/\hbar$$

$$b^2 = m\omega_r/\hbar.$$

These F's give the inelastic part of (16) as

$$\frac{\mathrm{d}^2\sigma_{inc}}{\mathrm{d}\Omega\,\mathrm{d}\epsilon} = \frac{k'}{k}|a_{inc}|^2 \frac{1}{\mathscr{F}}\{\mathrm{e}^{-\beta\lambda_+}\delta(\epsilon - 2\lambda_+) + \mathrm{e}^{\beta\lambda_+}\delta(\epsilon + 2\lambda_+)\}$$

$$(x) \sum_v |F_{1v}|^2 \frac{2\Omega^2}{\lambda_+^2}(1 - \cos \boldsymbol{\kappa}\cdot\mathbf{d}_v). \tag{19}$$

We can see from (19) that the inelastic cross section vanishes for $\boldsymbol{\kappa}$ oriented perpendicularly to $\mathbf{d}_v$. Such an orientation can be made to within 3° by keeping $\boldsymbol{\kappa}$ along the c axis of the crystal. This effect along with the diffraction effect from the factor$(1 - \cos \boldsymbol{\kappa} . \mathbf{d}_v)$ should serve to distinguish the contribution of the tunneling motion from the other motions in the crystal.

Acknowledgements—We wish to thank Professor G. Venkataraman and Professor J. M. Carpenter for bringing this problem to our attention and for many valuable conversations.

REFERENCES

1. TOKUNAGA M., *Prog. theor. Phys.* **36**, 857 (1966).
2. TOKUNAGA M. and MATSUBARA T., *Prog. theor. Phys.* **36**, 581 (1966).
3. DE GENNES P. G., *Solid St. Commun.* **1**, 132 (1963).
4. BLINC R., *J. Phys. Chem. Solids* **13**, 204 (1960).
5. BLINC R. and RIBARIC M., *Phys. Rev.* **130**, 1816 (1963).

J. Phys. Chem. Solids Pergamon Press 1969. Vol. 30, p. 453. Printed in Great Britain.

TECHNICAL NOTES

Neutron diffraction study of the low temperature transition in UP*

(*Received* 3 *June* 1968; *in revised form* 25 *July* 1968)

As a result of our increased effort to study the magnetic structures of actinide materials, we have reinvestigated UP at lower temperatures with neutron diffraction. Sidhu *et al.*[1] at this Laboratory, investigated antiferromagnetism in UP by neutron diffraction to liquid nitrogen temperatures only. Curry[2], at Harwell, carried out a concurrent study to near liquid helium temperatures and noted an increase in the intensity of the magnetic reflections at 33°K with a width of about 7K deg. Our original UP sample was recooled to liquid helium temperatures and an increase in the intensities of the magnetic reflections of this Type-I magnetic structure was likewise noted. Measurements of the integrated intensity of the magnetic (1 10) reflection were made during both heating and cooling, as shown in Fig. 1.

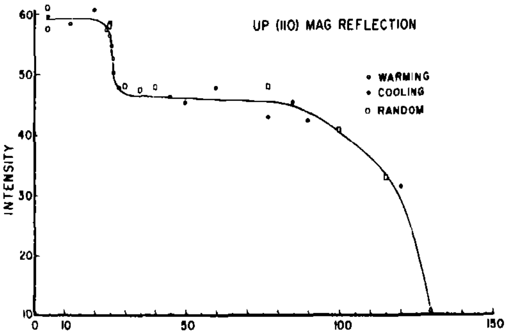

Fig. 1. Neutron diffraction integrated intensity of UP (1 10) reflection vs. temperature.

The transition, which was considerably sharper than that found by Curry, occurred over an interval of less than 2 K deg at a temperature of 25 ± 1·0°K. Although the sample was rather large (7/16 in. dia. by 1–1/2 in. length), temperature variation was held to less than 0·5 K deg over the length of the sample by means of an exchange gas cryostat. Temperature control was well within 0·2 K deg. The observation of the transition at 25°K is in close agreement with the value reported by Counsell *et al.*[3] who described an exceedingly sharp transition at 22·5°K from heat capacity studies. An abrupt decrease in magnetic susceptibility also was observed below 20°K by Gardner[4].

Our low-temperature investigations and the results from Curry, both with powdered samples, indicate a general increase in all of the magnetic reflections; however, all except the (1 10) reflection are very weak. Single crystals of sufficient size are needed in order to determine possible changes in the magnetic form factor due to electronic changes. A few single crystals that weigh 4–5 mg. have been produced[5]; however, the neutron diffraction intensities may still be too weak.

Recent neutron diffraction results on $U(P_{0 \cdot 95}S_{0 \cdot 05})$ obtained by Lander, Kuznietz and Baskin[6], at this Laboratory, showed that a broader and higher temperature transition is observed as a result of sulfur addition to the sample.

Argonne National Laboratory,
Metallurgy Division,
Argonne, Ill. 60439,
U.S.A.

L. HEATON
M. H. MÜELLER
K. D. ANDERSON
D. D. ZAUBERIS

REFERENCES

1. SIDHU S. S., VOGELSANG W. and ANDERSON K. D., *J. Phys. Chem. Solids* **27**, 1197 (1966).
2. CURRY N. A., *Proc. phys. Soc.* **89**, 427 (1966).
3. COUNSELL J. F., DELL R. M., JUNKISON A. R. and MARTIN J. F., *Trans. Faraday Soc.* **63**, No. 529, 72 (1967).
4. GARDNER W. E., Private communication cited in reference [3].
5. WILLIAMS JACK M., BASKIN Y. and CAMPOS F. P., Private communication.
6. LANDER G. H., KUZNIETZ MOSHE and BASKIN Y., *Sold State Commun.* To be published (1969).

---

*Work performed under the auspices of the U.S. Atomic Energy Commission.

J. Phys. Chem. Solids Vol. 30, pp. 454–457.

On the excess entropy of fusion of semiconducting and semimetallic elements

(*Received* 5 *July* 1968)

ENTROPY of fusion of semiconductors and semimetals are abnormally higher than that for most closepacked metallic elements[1] e.g. about 6 e.u for germanium or silicon, about 4 e.u for bismuth or gallium to be compared with about 2 e.u for most closepacked metals. It is the object of the present note to point out that the excess of the entropy of fusion of these elements over the common metals can be considered as entirely due to the configuration of the bonding electrons.

Since in metals the cohesion between atoms is due to metallic bonding and that in semiconductors due to co-valent bonding, a result essentially of two rather extreme behaviors of the bonding electrons*, we can hope to express in general the entropy of fusion ΔS_m as

$$\Delta S_m = \alpha f + (1-f)\beta \tag{1}$$

where f is the fraction of valence (or bonding) electrons non-localised in the solid at the melting point i.e. behaving as free electrons giving rise to metallic bonding; β–α is the excess entropy of fusion of a perfectly co-valent element over a purely metallic solid.

Equation (1) implies that for these solids at the melting point, the electronic wave functions are mixed in character and can be considered simply as linear superposition of a metallic and co-valent wave function. If equation (1) is general, it will suffice to plot it for a few known values of ΔS_m and f, both of which are available precisely for elemental semiconductors. The fraction of valence electrons in these elements that are free are those which are thermally excited into the conduction band from the valence band and is given by the standard relation[2]

$$f = \exp\frac{-E_g}{2RT_m} \tag{2}$$

where E_g is the band gap at the melting temperature T_m; R is the gas-constant.

The data for Ge, Si and Te are shown in Table 1 and are plotted in Fig. 1.

A fourth point (rather a cluster of points) is used with ΔS_m for alkali metals for which f is taken to be 1. The resultant curve is indeed quite linear and thus justifies equation (1). We have also indicated on the curve, the possible positions of the semi-metals [10] (from their known entropies of fusion) as well as that of the semiconductor selenium. The interesting feature embodied in the selenium anomaly will be discussed.

The excess entropy of fusion for a perfectly co-valent solid over a perfectly metallic one is $(\beta-\alpha)$ and is seen to be 5·4 e.u. from Fig. 1. We propose that this entropy contribution is purely a configurational entropy for the co-valently bounded electrons in the valence band. It arises from liberating these electrons completely on melting, from their initially localised positions, and thus is a process of randomisation and entropy gain. Considering a solid that has 4 N electrons per unit volume in the valence band, co-valently paired by opposite spins, the entropy gained if its melting is accompanied by decoupling the spins of the 2 N pairs and freeing them in the liquid state completely (i.e. we assume $f = 1$, in the liquid semiconductors at the melting point), is given by

$$\Delta S_{\text{Config}} = k \log_e \left[\frac{4N!}{(2N!)^2}\right] \tag{3}$$

---

*The rare earth metals are not considered here at all, as they have significant amount of ionic bonds.

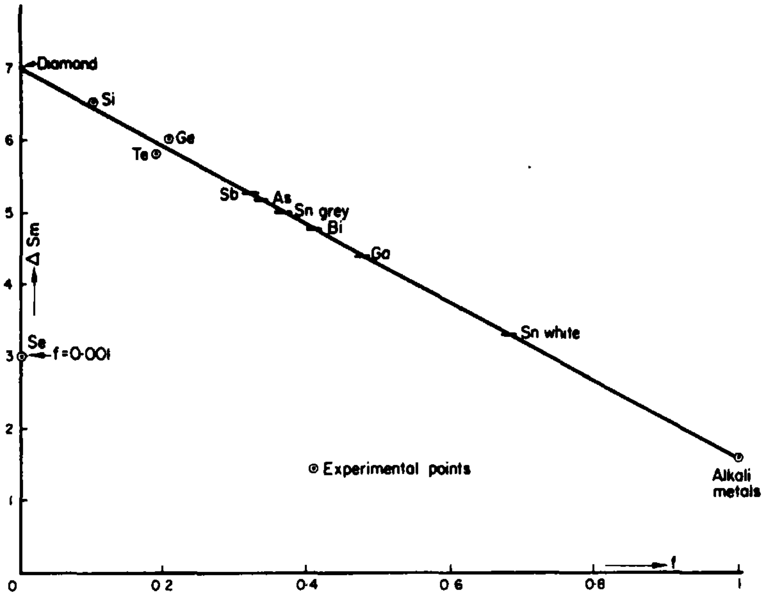

Fig. 1

Table 1

Element	Melting temp. T_m (°K)	Band gap at 0°K (eV)	$\frac{dE_g}{dT}$ (eV/°K)	$E_g(T_m)$ (eV)	$f(T_m)$	Entropy of melting e.u.-
Si	1690	1·153(a)	−2·3(a)10^{-4}	0·786	$7{\cdot}8 \times 10^{-2}$	6·5(b)
Ge	1210	0·744(a)	−3·7(a)10^{-4}	0·33	$2{\cdot}06 \times 10^{-1}$	6·0(b)
Te	723	0·33(a)	−1·7(a)10^{-4}	0·206	$1{\cdot}91 \times 10^{-1}$	5·8(c)
Alkali metals K, Li, Na,					1	1·6(d)
Se	493·5(a)	1·74(a) at 300°K			~0·001	3(a)

(a) See reference [7].
(b) See reference [8].
(c) See reference [9].
(d) See reference [10].

where k is the Boltzmann constant; N is the number of atoms/unit vol. This gives

$$\Delta S_{\text{Config}} = 4\times 1\cdot 38\,(\text{Cals/}^{\circ}\text{K-gr atom}) = 5\cdot 52\ \text{e.u.} \tag{3a}$$

and is in almost complete agreement with the excess entropy (β–α) obtained experimentally from Fig. 1.

The following important features can be deduced from Fig. 1.

(a) $(1-f)$ is the fraction of valence electrons available as free electrons on melting. For most closepacked metals and alkali metals in particular, this is seen to be zero, a fact also borne out by the experimentally observed constancy of knight shift[3] on melting of these metals. On the other hand for the semimetals, like Sb or Ga or Bi, it can be seen from the Fig. 1 that about 50 per cent more electrons are liberated on melting and this could explain the well-known 'anomalous' electrical conductivity increase[4] on melting of these metals – the experimentally observed ratio of the electrical conductivity increase on melting is typically about 50 per cent.

(b) The curve extrapolated to the other extreme for $f = 0$, gives an entropy of fusion of 7 e.u, which can be considered as that of the most ideal co-valent element. Diamond fills the recipe, with a band gap larger than 5 eV (giving $f \approx 0$) and an entropy of fusion of 6·8 e.u, calculated from the data of Seitz[5].

(c) The fact that Ge, Si and Te have the excess entropy of fusion very close to the ideal value indicates that melting is associated in these elements with the complete liberation of the bound valence electrons. These semiconductors are indeed quite metallic in their liquid state, the melting being accompanied with large electrical conductivity increase. Selenium on the other hand occupies an anomalous position on the Fig. 1, with its excess entropy of fusion rather low. This would unambiguously indicate that in case of selenium, melting is not accompanied by the decoupling of the electron-spin pairs in its valence band, while the element transforms from solid to liquid. This would indicate that right after melting selenium still keeps the band structure. The electrical conductivity of liquid Se[6] is 10^{12} times lower than that for liquid Ge or Si ($10^{-8}\,\Omega\,\text{cm}^{-1}$ for liquid Se against $2\times 10^{4}\,\Omega\,\text{cm}^{-1}$ for liquid Ge) substantially confirms the conclusion that electrons remain tightly bound to the atoms as co-valent pairs and are not free for electrical conduction. Further the positive temperature coefficient of the electrical conductivity of Se and the X-ray evidence of the[6] persistence of the chain structure in the liquid state would indicate persistence of the semiconducting behavior and hence the low excess extropy of fusion. The selenium anomaly actually helps to establish that excess entropy of fusion is indeed the configurational entropy of the co-valently bounded electron pairs. Looking from the other direction, the liquid semiconductors on passing through the freezing point, compensates the loss of the excess entropy by gaining in the cohesive energy due to co-valent pairing of the electrons.

Acknowledgements – The author wishes to acknowledge helpful discussions with Dr. C. Kooi of Lockhead Research Laboratory, Palo Alto, California and with Mr. A. Deneuville of this Laboratory.

B. K. CHAKRAVERTY

Section Physique des Couches Minces,
Laboratorie d'Electrostatique et de Physique du Métal,
B.P. 319, Grenoble,
France

REFERENCES

1. SWALIN R., *Thermodynamics of Solids*, p. 61. Wiley, New York (1962).
2. HANNAY N. B., (Editor), *Semiconductors*, p. 30. Reinhold, New York (1960).
3. KNIGHT W. D. *et al. Annls Phys.* **8**, 173 (1959).
4. MOTT N. F. and JONES H., *Theory of the properties of Metals and alloys*, p. 278. Dover, New York (1958).
5. SEITZ F., *Modern Theory of Solids*, McGraw Hill, New York (1940).
6. MOTT N. F., *Adv. Phys.* **16**, 49 (1967).
7. AIGRAIN P. and BALKANSKI M., *Selected Constants relative to semiconductors*. Pergamon Press, Oxford (1961).
8. THURMOND C. D., *J. Phys. Chem. Solids* **26**, 785 (1965).
9. KUBASCHEWSKI O. and EVANS E., *Metallurgical Thermochemistry*. Pergamon Press, Oxford (1958).
10. HULTGREN, ORR, ANDERSON and KELLEY, *Selected values of Thermodynamic properties of metals and Alloys*. Wiley, New York (1963).

J. Phys. Chem. Solids Vol. 30, pp. 457–459.

Possible trivacancy contribution to ionic conductivity

(*Received* 13 *June* 1968)

FULLER and Reilly[1], Fuller, Reilly, Marquardt and Wells[2], and Allnatt and Pantelis[3] have recently reported the results of measurements of the intrinsic electrical conductivity σ of RbCl, KCl and NaCl, respectively. All of these results showed an anomalous behavior of the log (σT) vs. T^{-1} plot at temperatures near the melting points of the various crystals. It is the purpose of this note to discuss the suggestion[4] that the anomaly may be due to a trivacancy mechanism.

The plots of the log (σT) vs. T^{-1} were found to have too great a positive curvature in the intrinsic region to be described by the usual conductivity equations[5], even when the corrections for Coulomb interactions[6] were used in the analyses[7]. To explain the 6 per cent deviation between their theoretical and experimental results for NaCl at 794°C Allnatt and Pantelis[3] suggested the presence of cationic Frenkel disorder. In their subsequent least squares analysis the interstitial Na ions were found to carry about 61 per cent of the electrical current in NaCl at 794°C. According to the Nernst–Einstein relation the mobile interstitial Na ions would also make a large contribution to the cation diffusion in NaCl. A large interstitial contribution to Na diffusion in NaCl has never been reported[8]. It therefore seems important to point out the characteristics of trivacancy contributions to conductivity.

Trivacancies could exist in the crystal in two types, the cation type (+−+) or the anion type (−+−). Each type of trivacancy could exist in a collinear form (part a, Fig. 1) or an elbow form (part b, Fig. 1). Our simple point ion calculations for a rigid, unpolarizable lattice indicate that, because the repulsive interaction between vacancies of similar charge is larger in the elbow form of trivacancy, the collinear trivacancy is the favored form by about 1.1 eV in NaCl and 0·9 eV in KCl and RbCl.

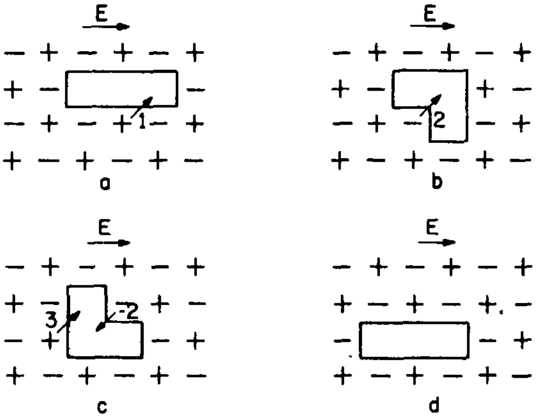

Fig. 1. A typical series of jumps by which a trivacancy could move through the lattice in the presence of an electric field E.

The equations for determining the concentration of trivacancies can be written as functions of temperature and divalent cation impurity concentration n_i as follows:

$$n_a n_c = \exp(-g/kT) = n_0^2(T) \qquad (1)$$

$$t_c = 3n_an_c^2 \exp(g_c/kT) = 3n_cn_0^2(T) \exp(g_c/kT) \qquad (2)$$

$$t_a = 3n_a^2n_c \exp(g_a/kT) = 3n_an_0^2(T) \exp(g_a/kT) \qquad (3)$$

$$n_c + t_c = n_a + t_a + n_i - n_k \qquad (4)$$

$$n_k/(n_c(n_i - n_k)) = 12 \exp(\delta/kT) \qquad (5)$$

where the symbols are defined as follows.

n_a	mole fraction of isolated anion vacancies.
n_c	mole fraction of isolated cation vacancies,
n_i	mole fraction of divalent impurity cations.
n_k	mole fraction of divalent impurity cation-cation vacancy complexes,
n_0	mole fraction of intrinsic Schottky defects,
t_a	mole fraction of anion type trivacancies.
t_c	mole fraction of cation type trivacancies,
g	free energy of Schottky defect formation,
g_a	free energy of binding for an anion type trivacancy,
g_c	free energy of binding for a cation type trivacancy.
δ	free energy of binding for an impurity-vacancy complex.

The factor of 12 in equation (5) results from the twelve equivalent orientations of the impurity-vacancy complex The factor of 3 appears in equations (2) and (3) as a result of the assumption that the trivacancies exist in the collinear form which has three equivalent orientations.

Unfortunately, theoretical calculations of the formation and migration energies of trivacancies have not yet been reported; so we have crudely extended the theoretical calculations for vacancy pairs[9] and Schottky-defects[10]. We have used a rigid unpolarizable lattice approximation which includes point ion Coulomb interactions and nearest neighbor repulsion[10] to compute the work done to take an isolated vacancy and put it next to a vacancy pair. It is predicted that the cation type of trivacancy is favored over the anion type in NaCl (by 0·6 eV), KCl (by 0·3 eV) and RbCl (by 0·2 eV). Hence, the ratio of the concentration of trivacancies, essentially all of the cation type, to the concentration of cation vacancies is independent of the impurity concentration, but dependent on the temperature, and has the form

$$t_c/n_c = A \exp(B/kT) \qquad (6)$$

where A and B are temperature independent constants. It follows that the ratio of the amount of electrical current carried via a trivacancy mechanism to that carried by a single cation vacancy mechanism is also independent of the impurity concentration and has a form similar to equation (6). Therefore, in the high temperature extrinsic regions of conductivity (i.e. $n_i > 5n_0(T)$), the presence of trivacancies might be detectable.

For example, the results for the conductivity of KCl and KCl:$SrCl_2$[7] may be used to estimate the trivacancy contribution to the ionic conductivity of KCl:$SrCl_2$ crystals. If the 10 per cent discrepancy between the theoretical and experimental results at 750°C for pure KCl[7] is assumed to be the result of a trivacancy contribution to the conductivity, the results from reference [7] (Table 2, Column 2) for the formation entropies and enthalpies of vacancies can be used to compute the trivacancy contribution to the conductivity of KCl:Sr Cl_2 crystals. The results of these computations (Table 1) show that when the impurity concentration is relatively large, i.e. $n_i > 5n_0(T)$, the anion vacancy contribution to the conductivity becomes negligible. It can also be shown that in KCl:$SrCl_2$ crystals any possible interstitial cation contribution to the conductivity would be similarly reduced. Therefore, it can be concluded that a slight 'knee' in the log (σT) vs. T^{-1} plot at high temperatures for alkali halide crystals containing relatively large amounts of a divalent cation impurity would be evidence for the presence of a trivacancy contribution to the conductivity. Such a 'knee' is suggested by the present experimental results for KCl:$SrCl_2$ [11] and KBr:$CaBr_2$[12]. It is hoped that future work will furnish evidence of a more definitive nature.

A typical series of jumps by which a trivacancy can move through the lattice in the presence of an electric field is shown in Fig. 1. After jump (1) the collinear trivacancy (part a, Fig. 1) has the elbow form shown in part b of Fig. 1. The second jump (2) requires that a negative ion move against the force of the electric field, but the potential barrier to such a jump is probably quite low since both of the gate ions are missing from the lattice. However, after jump (2) has occurred the field would increase the probability that the negative ion would jump back across the low barrier into its original site as shown by the -2 labelled jump in part c of Fig. 1. The trivacancy would remain in a fluctuating elbow form, shown in parts b and c, Fig. 1. Then the trivacancy will either return to its original position by a reverse of jump (1) or make a contribution to the conductivity by the occurence of jump (3).

Table 1. *The contributions of vacancy mechanisms to the electrical conductivity of* KCl : $SrCl_2$ *crystals at* 750°C *as a function of* Sr *concentration*

Sr mole fraction	Per cent contribution* Anion vacancy	Cation vacancy	Cationic trivacancy
0	56%	34%	10%
100 ppm	18%	63%	18%
200 ppm	6%	73%	21%
500 ppm	1 %	76½%	22½%
1000 ppm	—	77%	23%

*Computed using the simple theory including association results reported in reference[7], Table 2, column 2. The intrinsic vacancy concentration was computed to be about 40 ppm at 750°C.

In summary, these considerations indicate that the anomalous curvature in the intrinsic region of conductivity for RbCl, KCl and NaCl may be the result of a trivacancy contribution. The presence of the cation type of trivacancy might be verified by high temperature conductivity measurements in alkali halide crystals containing large ($n_i > 5n_0$) amounts of a divalent cation impurity. The calculation of the formation and migration energies for trivacancies would seem to be a potentially fruitful theoretical endeavor.

Acknowledgements—We would like to acknowledge the benefit received from discussions with Professor L. M. Slifkin, Dr. M. N. Kabler and Mr. C. L. Marquardt.

U.S. Naval Research Laboratory,
Washington, D.C. 20390,
U.S.A.

R. G. FULLER
M. H. REILLY*

---

*NRC-NRL postdoctoral research associate.

REFERENCES

1. FULLER R. G. and REILLY M. H., *Phys. Rev. Lett.* **19**, 113 (1967).
2. FULLER R. G., REILLY M. H., MARQUARDT C. L. and WELLS Jr., J. C., *Phys. Rev. Lett.* **20**, 662 (1968).
3. ALLNATT A. R. and PANTELIS P., *Solid State Commun* **6**, 309 (1968).
4. LIDIARD A. B., *Symposium on Mass Transport in Oxides*, oral comments. National Bureau of Standards (1967).
5. BEAUMONT J. H. and JACOBS P. W. M., *J. chem. Phys.* **45**, 1496 (1966).
6. LIDIARD A. B., *Phys. Rev.* **94**, 29 (1954).
7. FULLER R. G., MARQUARDT C. L., REILLY M. H. and WELLS Jr., J. C., To be published.
8. SÜPTITZ P. and TELTOW J., *Phys. Status Solidi* **23**, 9 (1967).
9. TOSI M. P. and FUMI F. G., *Nuovo Cim.* **8**, 95 (1958).
10. TOSI M. P. and DOYAMA M., *Phys. Rev.* **151**, 642 (1966).
11. See, for example, the four highest temperature data points in Fig. 4, reference [7].
12. BARR L. W., Private communication.

J. Phys. Chem. Solids Vol. 30, pp. 459–462.

Coalescence in an enclosed superconductor*

(*Received* 15 *April* 1968)

THE ENCLOSED superconductor arrangement [1], in which the specimen, a long thin rod, is enclosed in a cylindrical shell of another superconductor, allows the transition from the normal to the superconducting state to be studied under conditions which are not found in most geometries. On the one hand, the applied magnetic field is parallel to the surface of the specimen everywhere except at the ends. On the other hand, the enclosing shell gives to the specimen an effective demagnetizing coefficient[1], so that the specimen can be put into a stable intermediate state.

---

*This work was supported in part by the Research Corporation and by the National Science Foundation.

In the experiments reported here, an impure indium rod, enclosed in a tin shell, was cooled in the presence of a constant, axial magnetic field. It was observed that superconducting regions in the indium rod coalesced before the transition was complete. This coalescence led to the formation of a closed superconducting surface which inhibited flux expulsion from the rod.

Faber and Pippard[2] have given reasons for expecting coalescence to be unlikely, but they also point out the importance of surface condition. Further experiments with electropolished specimens should help to clarify the role of surface roughness.

Figure 1 shows a cross-sectional view of the specimen and shell. The specimen was a rod with rounded ends cast and machined from an alloy of indium plus 0·2 per cent bismuth. It was 10 cm long and had a diameter of 1·3 cm. After machining, the rod was etched. The tin shell was made by melting pure tin into a copper tube and then machining a 1·9 cm hole.

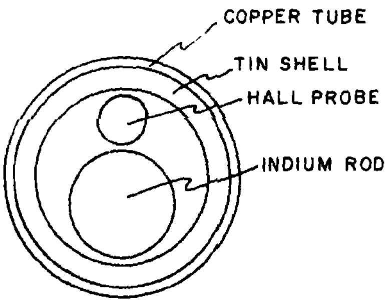

Fig. 1. A cross-sectional view of the specimen showing the enclosing tin shell and the Hall probe.

The axial field between the two superconductors was measured with a commercial Hall probe, and the temperature was monitored with a carbon resistor.

Figure 2 shows a typical result for the enclosed field vs. temperature for a cooling and warming cycle. Proceeding from the right hand side in that figure, and following the cooling curve, we see that the tin shell began its superconducting transition at point A. The small increase of field that occured there was due to flux expelled inward from the tin [3]. At point B, the transition of the indium rod began, and as the cooling went on more and more flux was expelled. At point D the transition of the rod was apparently complete. The warming curve is very similar, but there is a significant difference in the vicinity of point C. This is interpreted as showing that coalescence occurred during cooling, at least in the vicinity of C.

That a closed superconducting surface existed at C is clear because comparison with the warming curve shows that the field there was less than the critical value. Other measurements have shown that if the cooling had been stopped at C, the field would not have increased with time, at least over a period of many minutes. If a closed superconducting ring had not been present, flux would have moved out of the specimen until the enclosed field reached the critical value, and a stable point such as C would not have been possible.

Coalescence also shows clearly in Fig. 3, which shows a study of temperature hysteresis in the neighborhood of a point like C of Fig. 2. The dashed lines show typical cooling and warming curves. The solid line was obtained by cooling, then warming to point A, and then cooling slowly. From A to B, the slope of the curve is not too different from that of the warming curve. At B, a closed superconducting loop formed (or at least became stronger if it already existed), and then at C the system began to follow a typical cooling path. This suggests that this typical cooling path represents a definite equilibrium

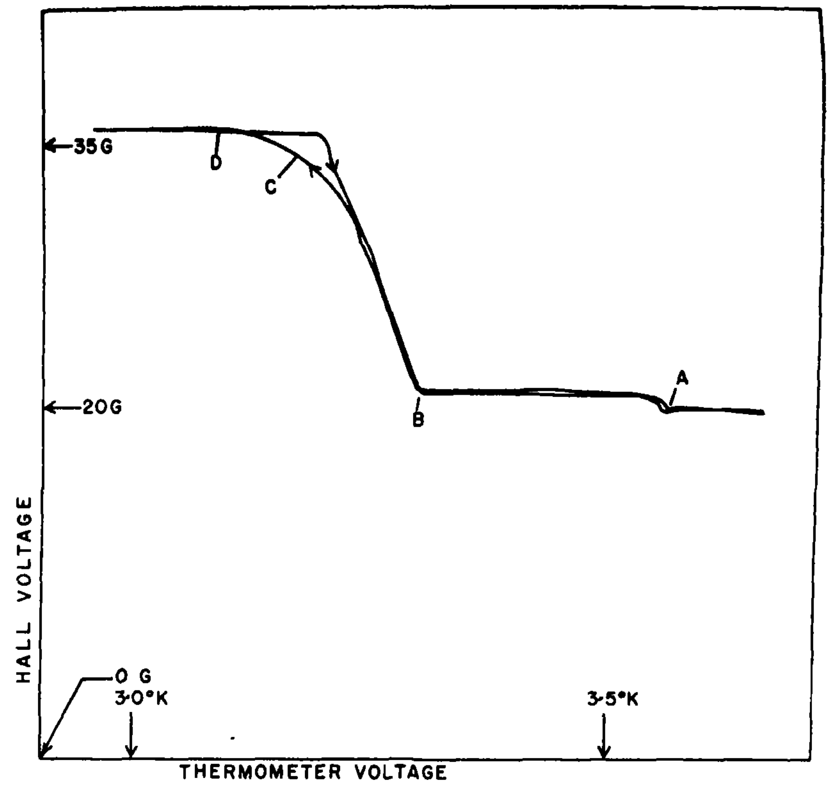

Fig. 2. A typical cooling and warming curve for an initial applied field of 20 G. Approximate field and temperature calibrations are indicated. To the right of point *A*, the entire system is normal and the field measured is just the applied field. Between *A* and *B* the tin shell is superconducting with a certain trapped field. From *B* to *D*, as more and more of the indium rod becomes superconducting, more and more flux is expelled from the rod. Since the tin shell keeps the total enclosed flux constant, as flux is expelled from the rod the field strength increases.

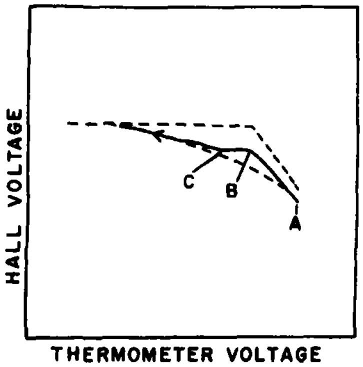

Fig. 3. A portion of a temperature hysteresis loop. Beyond *B*, no more flux leaves the indium rod until the cooling curve meets the typical curve at *C*.

curve of field versus temperature for this specimen.

The occurence of coalescence is not restricted to the alloy rod described above. Very similar behavior was observed with a pure indium rod. Coalescence has also been observed repeatedly in studies of field enhancement in tubes of pure tin and indium[4].

It is to be noted that the coalescence leads to the formation of a superconducting skin, over at least part of the surface. Experimentally, this phenomenon might easily be confused with the 'surface superconductivity' that has been discussed by Saint-James and deGennes[5], but in this specimen and in the pure indium specimen the value of the Ginzburg–Landau parameter κ is too low to permit surface superconductivity.

An investigation of the role played by surface defects would seem to be most desirable, and we plan to extend the measurements to electropolished specimens.

Acknowledgements – It is a pleasure to acknowledge the assistance of A. I. Rothman, J. D. Langan, and E. F. Young.

Department of Physics,
State University of New York,
Buffalo, New York 14214,
U.S.A.
R. I. GAYLEY

REFERENCES

1. GAYLEY R. I., *Cryogenics* **5**, 89 (1965).
2. FABER T. E. and PIPPARD A. P., In *Progress in Low Temperature Physics* (Edited by C. J. Gorter), Vol. 1, p. 159, Interscience, New York (1957).
3. SMITH T. I. and RORSCHACH H. E., Jr., *Rev Mod Phys.* **36**, 277 (1964); GAYLEY R. I and YOUNG E. F., *Phys. Lett.* **23**, 15 (1966).
4. YOUNG E. F. and GAYLEY R. I., **30**, 175 (1969).
5. SAINT-JAMES D. and DeGENNES P. G., *Phys Lett.* **7**, 306 (1963).

J. Phys. Chem. Solids Vol. 30, pp. 462–463

On the irradiation of alkali metal azides

(*Received* 10 *January* 1968)

RECENTLY it has been shown[1] by a vibrational frequency calculation and group theoretical considerations that upon irradiation of NaN_3 at low temperature some of the normally linear $D_{\infty h}$ azide ions of the crystal assume the equilateral triangle D_{3h} symmetry. Since the experimental observations on the several alkali metal azides after irradiation are quite similar, it is of considerable interest to consider the consequences of this symmetry and to note how it may be used to explain the observations.

Experimentally it is observed[2] that upon irradiation of an alkali-metal azide at liquid nitrogen temperature, one new infrared band is produced and intimately associated with it is one new electronic absorption in the visible region. The infrared band is the doubly degenerate fundamental of the D_{3h} ion[1] and is the only infrared active fundamental. Consideration of the electronic symmetry[3] shows the ground state of the ion to be A_1'. In the excited electronic state symmetry properties yield[3] three accessible states A_1'', A_2'' and E''. (These states are easily correlated with the one electron excitation of the linear ion.) The general selection rule[3] yields only one permitted electronic transition $A_2'' \leftarrow A_1'$. Thus the experimental observation of one new electronic band and one new infrared band can be explained by the D_{3h} symmetry for the azide ion as the 'color center'.

During the warm-up from liquid nitrogen temperature other new bands appear[2] in Kn_3 and RbN_3. The single i.r. band splits into two bands of approximately equal intensity; simultaneously the electronic band develops a side band[2], of considerably weaker intensity[2, 4, 5], on the long wavelength side. These observations may be explained by assuming the equilateral D_{3h} ion to undergo a slight distortion which takes it into the C_{2v} symmetry of an isoceles triangle; the distortion being caused by some (unspecified) relaxation mechanism in the crystal during warm-up. The infrared splitting[2] is 12 cm^{-1} in KN_3 and 29 cm^{-1} in RbN_3 and is almost exactly the same magnitude as the splitting caused by isotopic substitution in NaN_3 which also takes the D_{3h} ion into the C_{2v} symmetry[1]. The similarity of the magnitude of the splitting suggests only a slight distortion when the D_{3h} ion goes into the C_{2v} symmetry for the mechanism presented here.

In the C_{2v} symmetry all three ($3n$-6) fundamental vibrations are i.r. active, i.e. the doubly degenerate active vibration of the D_{3h} ion splits and the inactive fundamental becomes i.r. active. Experimentally only two bands were observed[2]; however, a frequency calculation shows that the third band lies in a fundamental of the crystal itself and therefore cannot be observed. In the frequency calculations[1] for the NaN_3, central forces were assumed, and the force constants were found to be $a_{11} = 16{\cdot}3 \times 10^5$ dyn cm^{-1} and $a_{33} = 11{\cdot}1 \times 10^5$ dyn cm^{-1}. With the available data only a_{11} can be calculated for KN_3 and RbN_3, and a_{11} is 14·7 and $14{\cdot}5 \times 10^5$ dyn cm^{-1}, respectively. As a reasonable approximation a_{33} is taken to be in the same ratio to a_{11} as is found in NaN_3. Then the required third band, ν_1, for the C_{2v} ion is calculated to be about 2350 cm^{-1}. This is in the strongly absorbing fundamental, ν_3, of the crystal[6, 7] and therefore cannot be observed.

In the electronic ground state the C_{2v} ion is of A_1 symmetry, and the two lowest excited states are A_2 and B_2, of which A_2 lies lower than B_2. Only the $B_2 \leftarrow A_1$ transition is permitted by the general selection rule[3]. However, forbidden transitions may become active when the Bohn–Oppenheimer approximation is not used for the eigenfunctions, i.e. when interaction with a vibrational level is considered[3]. The forbidden transition $A_2 \leftarrow A_1$ therefore can become active by interaction with the $\nu_3(B_1)$ vibration of the ion. This transition should be of weaker intensity and lie on the long wavelength side of the permitted transition. This is in agreement with experimental observation that a weak electronic band lies on the long wavelength side of a strong electronic adsorption band.

The experimental observations during warmup therefore may be accounted for in a reasonable manner by assuming a slight distortion in the D_{3h} ion.

One might expect a wavelength shift in the strong electronic absorption after the postulated distortion of the D_{3h} ion to the C_{2v} symmetry, but no wavelength shift has been reported[2]. The observed bands are quite broad (~0·5eV) and small wavelength shifts in the peak maximum could very well have been overlooked.

It would be of considerable interest to compare the strong electronic band maxima at liquid helium temperature before and after the postulated distortion. A search for any possible alteration, such as a shoulder, in the ν_3 fundamental vibration of the crystal after the splitting of the degenerate vibration of the 'color center' would be of value for, if observed, it could establish the C_{2v} azide ion with a high degree of certainty as a thermally produced 'color center.'

Martin Marietta Corp.,
Denver, Colorado,
U.S.A.

HAROLD A. PAPAZIAN

REFERENCES

1. PAPAZIAN H. A., *J. Phys. Chem. Solids* **27**, 906 (1966).
2. PAPAZIAN H. A., *J. Phys. Chem. Solids* **21**, 81 (1961).
3. HERZBERG G., *Electronic Spectra of Polyatomic Molecules*. Van Nostrand, New Jersey (1966).
4. TOMPKINS F. C. and YOUNG D. A., *Proc. R. Soc.* **236A**, 10 (1956).
5. CUNNINGHAM J. and TOMPKINS F. C., *Proc. R. Soc.* **251A**, 27 (1959).
6. PAPAZIAN H. A., *J. chem. Phys.* **34**, 1614 (1961).
7. BRYANT J. I., *J. chem. Phys.* **38**, 2845 (1963).

J. Phys. Chem. Solids Pergamon Press 1969. Vol. 30, p. 464. Printed in Great Britain.

ERRATUM

O. F. SCHIRMER: The Structure of the Paramagnetic Lithium Center in Zinc Oxide and Beryllium Oxide. *J. Phys. Chem. Solids* **29**, 1407 (1968).

The printer regrets that equation (2) on page 1411 should read:

$$\mathscr{H} = \beta \mathbf{S}\mathbf{g}\mathbf{H} + \mathbf{I}\mathbf{A}\mathbf{S} + \mathbf{I}\mathbf{P}\mathbf{I} - g_n\beta_n\mathbf{I}\mathbf{H} \tag{2}$$

with $S = \frac{1}{2}$, $I = \frac{3}{2}$, ...

The sentence containing equation (14) on page 1422 should read:

For the p-character of the axial hybrid, γ^2, for instance, one calculates

$$\gamma^2 = \frac{1 - 3\cos^2\tau}{\sin^2\tau} \tag{14}$$

from the orthonormality of the O^- hybrids.

Equation (22) on page 1425 should read:

$$V = \tfrac{1}{2}(3z^2 - \rho^2)\left(\frac{e\rho_{\mathrm{Li}^+}}{l^3} + 3\,\frac{e\rho_{\mathrm{me}^{2+}}}{v^3}\left(1 - \tfrac{3}{2}\sin^2\tau\right)\right) \tag{22}$$

The sentence preceding eq. (23) on page 1425 should read:

Thus the negative second derivative of (20) or, more detailed, of (22) is the field gradient *eq* occuring in the relation which defines the quadrupole coupling constant P[30] used in (2):

The sentence following equation (24) on page 1426 should read:

(k' force constant of the axial bond, k force constant of the non-axial bonds), if valence forces are considered only.

carbon

Editor-in-Chief: S. Mrozowski

'Carbon' is a journal devoted to the physics, chemistry and to scientific aspects of the technology of a class of materials ranging from organic crystals and polymers, through chars and carbons, to graphite. It provides a source of information on important research on these materials, and occasional reviews of limited problems. A special reference section to research published elsewhere is also included.

Papers published recently
R N Katz: Effect of post deposition heat treatment on the flexural strength of pyrolytic graphite
Y Tamai, Y Nishiyama and M Takahashi: Carbon deposition on iron and nickel sheets from light hydrocarbons
R E Woodley: The oxidation of boronated graphite
E S Golovina and L L Kotova: The role of sublimation and self-diffusion of carbon in interaction with carbon dioxide
P D Zavitsanos: Mass spectrometric analysis of carbon species generated by laser evaporation

Published bi-monthly
Please write for further information and inspection copy
Details of other journals in this field can also be sent to you

Pergamon Press
Headington Hill Hall Oxford OX3 OBW England
Maxwell House Fairview Park Elmsford New York 10523 USA

11/68

CORROSION SCIENCE

Editor-in-Chief: L L SHREIR

'Corrosion Science' is the official journal of the Corrosion and Protection Society, and is associated with Centre Belge d'Etude de la Corrosion.
Its primary purpose is to publish original research in the fields of corrosion science and technology, which makes an important contribution to an understanding of the phenomena of corrosion and its control in practice.
The scope covers high temperature oxidation, passivity, anodic oxidation, aqueous and fused salt corrosion, bio-chemical corrosion, stress-corrosion cracking, and mechanisms and methods of corrosion control.
Papers range from the highly theoretical to the essentially practical, with the intention of producing a publication in which there is an appropriate balance between corrosion science and technology.

Papers published recently
J S Armijo and B E Wilde: Influence of Si content on the corrosion resistance of austenitic Fe-Cr-Ni alloys in oxidizing liquid
A B Ijzermans and A J van der Krogt: Pitting corrosion of an austenitic Cr-Ni stainless steel in H_2SO_4 containing H_2S
Z Zembura: Relationship between metallic corrosion and limiting current using the rotating disk method
J E Antill, K A Peakall and J B Warburton: Oxidation of mild and low-alloy steels in CO_2 based atmospheres

Monthly
Write for further details and an inspection copy of this journal, and information on other journals in the field.

Pergamon Press
Headington Hill Hall Oxford OX3 OBW England
Maxwell House Fairview Park Elmsford New York 10523 USA

11/68

ELECTROCHIMICA
Acta

Editor-in-Chief T P Hoar Cambridge

is an international journal of pure and applied electrochemistry, published under the auspices of the International Committee for Electrochemical Thermodynamics and Kinetics (CITCE).

Executive Editorial Board
T P Hoar, University of Cambridge
J O'M Bockris, University of Pennsylvania
N Ibl, Swiss Federal Institute of Technology
P Van Rysselberghe, Stanford University
G Valensi, Faculté des Sciences de Poitiers

It publishes papers on every branch of this field, and, since its inception in 1959, has included contributions from nearly every electrochemical laboratory of importance. Over 200 papers are presented each year, either as original reports or as serious critical reviews. In this way, it is possible to keep electrochemists up-to-date with modern work in the whole of the fast-growing field of electrochemistry.

Recently published papers include
N A Pangarov, L A Uvarov and A T Vagranyan:
Preferred orientation of electrodeposited nickel crystallites at high temperatures
E Gileadi, L Duic and J O'M Bockris:
A comparison of radiotracer and electrochemical methods for the measurement of the electrosorption of organic molecules
A Sanfeld, C Devillez and M Lubelski:
Influence of molar volumes, polarization and activity coefficients on the repulsion between two plane layers
W E Triaca, C Solomons and J O'M Bockris:
The mechanism of the electrolytic evolution and dissolution of chlorine on graphite

Published monthly
For further information and an inspection copy write to

11/68

Pergamon Press
Headington Hill Hall Oxford OX3 0BW England
Maxwell House Fairview Park Elmsford New York 10523 USA

Journal
of the
Mechanics
and
Physics
of Solids

Editor-in-Chief: H G HOPKINS
Editorial Advisors: A H Cottrell, V V Sokolovsky and R Hill

The Journal of the Mechanics and Physics of Solids, an international journal of the theoretical and applied mechanics and the physics of solids. Brings together and relates research by mathematicians, engineers, metallurgists and physicists on the properties of constructional materials. Gives equal coverage to theory and experiment. Particularly concerned with the development and application of fundamental ideas bearing on the connections between continuum and micro-structural properties of materials and on the solution of materials and on the solution of practically significant problems.

Papers published recently
J F Bell: Large deformation dynamic plasticity at an elastic-plastic interface
R Hill: On constitutive inequalities for simple materials—II
U Lindborg: Creep cracks and the concept of damage
E Smith: Crack bifurcation in brittle solids
J W Hutchinson: Plastic stress and strain fields at a crack tip
J L Sackman and **I Kaya**: On the propagation of transient pluses in linearly viscoelastic media

Published bi-monthly
Write for further information and an inspection copy.
Details of other journals in this field can also be supplied.

11/68

Pergamon Press
Headington Hill Hall Oxford OX3 OBW England
Maxwell House Fairview Park Elmsford New York 10523 USA

J. Phys. Chem. Solids Pergamon Press 1969. Vol. 30, pp. 465–474. Printed in Great Britain.

A GAS-RELEASE STUDY OF THE ANNEALING OF BOMBARDMENT-INDUCED DISORDER*

(STUDIES ON BOMBARDMENT-INDUCED DISORDER – I)

ČESTMIR JECH
Institute of Physical Chemistry, Czechoslovak Academy of Sciences, Prague

and

ROGER KELLY
Institute for Materials Research, McMaster University, Hamilton, Ontario, Canada

(*Received* 17 *June* 1968; *in revised form* 16 *September* 1968)

Abstract – Many oxides and diamond-type materials become disordered, e g. amorphous, when bombarded with heavy ions at doses greater than 10^{14}–10^{16} ions/cm^2. Though the most direct evidence for such disorder is probably electron diffraction, much information can also be gained by studying the motion of the ions used to produce the disorder. We have in this way established the following temperatures for disorder annealing (all in °C and for a time scale of 25°C/min): 730 with α-Al_2O_3, 445 with Cr_2O_3, 535 with α-Fe_2O_3, 480 with rutile, 325 with MgO, 285 with NiO, 470 with Ge, and 720 with Si. A significant point is that the ratios of the disorder-annealing temperatures to those for atomic-scale cation self-diffusion are similar for most of the materials studied. The temperature widths of the annealing were also measured, and it could be shown that they were, except for MgO and NiO, compatible with single-jump kinetics, namely 45–70°C. It is concluded that the annealing process probably involves the growth of crystalline material towards the bombarded surface, such that the bombarding ions are swept out as the disorder-crystal interface reaches the surface. This model is of interest in implying that the activation enthalpies of the annealing, e.g. 52 ± 3 kcal/mole with rutile, are similar to those for self-diffusion in the disordered phase.

1. INTRODUCTION

THE USE OF inert-gas motion as a marker or probe for studying the annealing of radiation damage has been recently discussed in a number of papers, including work by the present authors and by Matzke and Whitton [1–3]. A particular case of such damage annealing concerns *bombardment-induced disorder*, of which bombardment-induced amorphousness is the most common example.

A relation between inert-gas motion and the annealing of bombardment-induced disorder appears to have been initially noted with diamond-type materials (MacRae and Gobeli [4], Jacobson and Wehner[5]), though was first studied in detail with oxides (Matzke and Whitton[3]). Altogether, it has now been described with some 7 substances: 3–5 compounds[4], Ge[5], α-Al_2O_3[3, 6–8], MgO, rutile, and U_3O_8[3], and quartz[9], while in the present work the further examples Cr_2O_3, α-Fe_2O_3, NiO and Si will be added to the list.

Previous work on the relation between inert-gas motion and disorder annealing has been concerned mainly with identifying the existence of the annealing, the main theoretical excursion being that of references[7, 8], where activation enthalpies were derived for α-Al_2O_3. The calculation depended on the observation that the temperature width of the disorder annealing was similar to that of a process with a single rate-controlling jump. Single-jump kinetics was therefore assumed and the range of values 69–79 kcal/mole was obtained.

We will in what follows give new high-

---

*This paper includes material which was presented at the conference "The applications of ion beams to semiconductor technology", Grenoble, 1967.

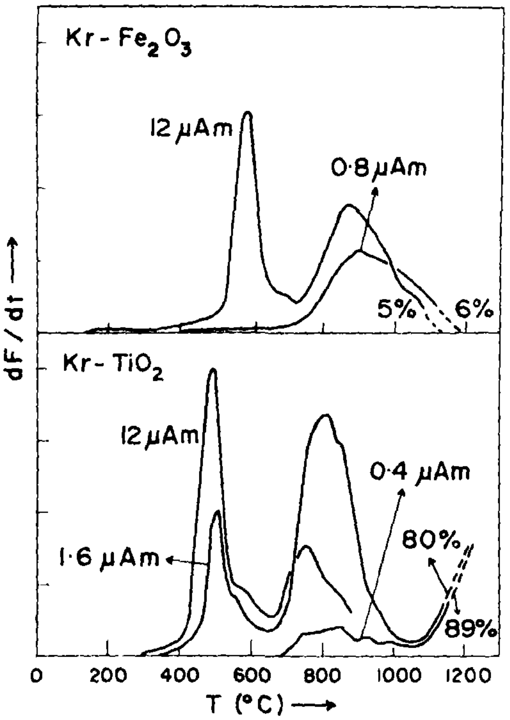

Fig. 3. dF/dt vs. T curves for α-Fe_2O_3 and rutile which have been ion-bombardment labeled with 10 keV Kr. The volume of the counting chamber was always 100 cm^3. Only the first part of the 12 μAmin/cm^2 curve for rutile is shown, the curve in reality extending to 1150°C *and accounting for the release of all but 12 per cent of the* Kr.

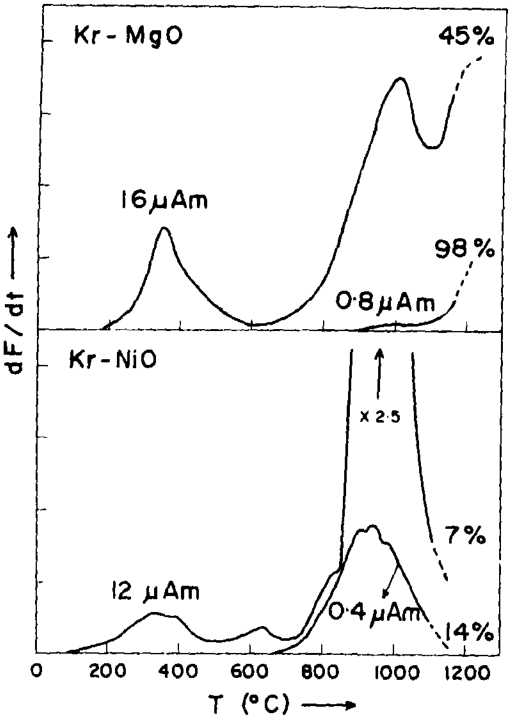

Fig. 4. dF/dt vs. T curves for MgO and NiO which have been ion-bombardment labeled with 10 keV Kr The volume of the counting chamber was always 100 cm^3.

4.1 α-Al_2O_3, Cr_2O_3, α-Fe_2O_3 *and rutile (Figs. 2 and 3)*

These four oxides show closely similar gas-release behaviour, the main features of which, for 10 keV bombardments, are the occurrence of either two or three peaks. As seen in Table 1 and with the help of equation (4), the lowest-temperature peaks, which are favoured by high doses, have widths suggestive of single-jump motion. With α-Al_2O_3 bombarded at 40 keV, the corresponding feature was identified by Matzke and Whitton [3] as representing the amorphous-crystalline transition on the basis of the fact that its temperature, 600–700°C in 5 min, was similar to that determined by electron diffraction for the annealing of bombardment-induced amorphousness, 650–710°C in 5 min; we would also point out that Hass[13] has observed *stripped* anodic Al_2O_3 to crystallize at 650–700°C in 1 hr. Similar arguments can now be made also for rutile, it being previously [3] difficult due to lack of resolution in the gas-release spectra: thus the gas-release temperature is 480°C, bombardment-induced amorphousness heals at 425–500°C in 5 min [3], while evaporated TiO_2 on a glass substrate crystallizes at 450–500°C in 1 hr[14]. With Cr_2O_3 and α-Fe_2O_3, the lowest-temperature gas-release peaks can be attributed to amorphous-crystalline transitions by analogy with α-Al_2O_3, since these materials have a similar crystal structure to α-Al_2O_3 and bombardment-induced amorphousness is known to exist[15]. With α-Fe_2O_3 there is the additional information that natural amorphousness heals at < 650°C in an unspecified time[16].

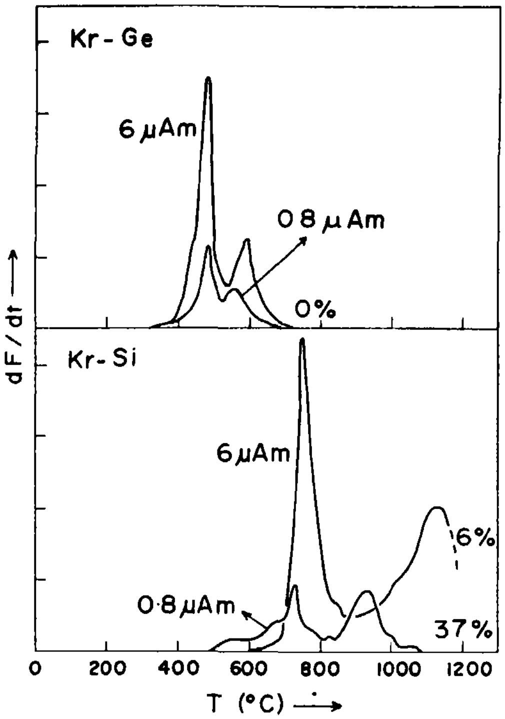

Fig. 5. dF/dt vs. T curves for Ge and Si which have been ion-bombardment labeled with 10 keV Kr. The volume of the counting chamber was always 10 cm^3.

Intermediate-temperature peaks are well-defined with Cr_2O_3 and rutile, where they are seen to be favoured by intermediate doses and to be relatively wide (Table 1). The peaks appear to be *related* to self-diffusion: with rutile, atomic-scale self-diffusion has been shown[17] to set in at 685 ± 20°C, hence just at the beginning of the peak, while with Cr_2O_3 the temperatures at which cation and anion self-diffusion should begin, 530–905°C (Table 1 of reference [2]), roughly bracket the peak. Possibly one is dealing with the healing of polycrystallinity left from the amorphous-crystalline transitions. See, for example the work of Krikorian and Sneed[18], where a well-defined polycrystalline–crystalline transition was identified in the annealing of amorphous Ge, and the work of Matzke and Whitton[3], where polycrystallinity in rutile consequent to the disappearance of amorphousness annealed in the interval 750–900°C in 5 min.

The final gas-release peaks are favored by low doses, and in the two cases where the temperatures are accessible, Cr_2O_3 and α-Fe_2O_3, the peaks are seen to have the widths for diffusion of e^{-x}-type distributions (Table 1), to lead to nearly complete release, and to agree fairly well with ultra-low dose data of Matzke[19]. The peaks thus have the general properties to be expected for normal, unperturbed gas motion and are of no interest in the present context.

4.2 MgO *and* NiO *(Fig. 4)*

MgO and NiO show sufficient similarity in their gas-release behaviour to be discussed together. The lowest-temperature peaks, though they are favored by high doses, have widths much greater than the corresponding features found with such oxides as α-Al_2O_3 (Table 1). Notwithstanding this fact, the peak has, in the case of MgO, been convincingly associated by Matzke and Whitton[3] with a disorder-crystalline transition of an untypical kind: thus single-crystal MgO becomes partially polycrystalline after high-dose bombardment but recovers somewhere *below* 500°C in 5 min. With NiO, it is more difficult to reach a conclusion on the nature of the peak. Nevertheless, the following four features are suggestive of disorder annealing: (a) the peak is favored by high doses yet it is distinct from that at 400°C attributed elsewhere[17] to nickel self-diffusion, (b) there is some evidence for partial polycrystallinity setting in at very high doses[15], (c) NiO exhibits bombardment-enhanced solubility which anneals *below* 500°C in 1 min[20], and (d) the ratio $T_{\text{gas-release}}/T_{\text{self-diffusion}}$ is, as will be shown in Section 4.4, similar to what is found with known disorder annealing.

The peak at 965°C with MgO, which is most prominent at intermediate doses, was suggested elsewhere[2] to be related to self-diffusion and we have nothing further to add. The final peaks, which with MgO is just

Table 1. *The principle gas-release processes**

Material	T_m (°C)	$\Delta T_{1/2}$	$\Delta T_{1/2}/T_m$† (T_m in °K)	Cause‡
α-Al_2O_3	730	60§	0·060	amorphousness
Cr_2O_3	445	65	0·091	amorphousness
	875	undefined		*not* stage IIA
	~1090	~220	~0·161	stage IIA
α-Fe_2O_3	535	60	0·074	amorphousness
	855	~235	~0·208	stage IIA
rutile	480	70	0·093	amorphousness
	775	165	0·157	*not* stage IIA
MgO	325	120	0·201	disorder
	965	undefined		*not* stage IIA
NiO	285	~190	~0·341	possibly disorder
	935	220	0·182	stage IIA
Ge	470	45	0·061	probably amorphousness
Si	720	70	0·071	probably amorphousness

*The various peak temperatures (T_m) and temperature widths ($\Delta T_{1/2}$) are based not only on the data displayed in the figures, but also on duplicate runs. They have in all cases been corrected for the 24 or 12°C temperature error discussed in Section 2.

†See equation (4) for the expected temperature widths.

‡The term 'stage IIA' is used, as discussed in reference[2], to refer to normal, unperturbed gas diffusion.

§Based on present data plus those of reference[7, 8].

beginning at ~ 1100°C but with NiO goes to completion, are most prominent at low doses; moreover, with NiO it has the width expected for diffusion of an e^{-x}-type distribution (Table 1) and leads to essentially complete gas release. We attribute these latter peaks to normal, unperturbed gas motion.

4.3 Ge *and* Si (*Fig.* 5)

Ge and Si are still in a preliminary stage of study, though enough is known to estimate the temperatures and temperature widths for disorder annealing. Both substances are characterized, for the particular doses used, by dominant gas-release peaks having widths suggestive of single-jump motion. With Ge, the peak lies at 470°C, and, by way of comparison, we note that Mayer *et al.*[21], in a study of helium scattering from Ge single crystals rendered amorphous by bombardment with 40 keV In, found that channeling was restored at 350–450°C in 10 min, while Parsons and Balluffi[22] observed evaporated films of Ge to crystallize at 450–500°C in 15 min. There is thus good reason to believe that the gas-release peak represents the amorphous-crystalline transition.*

With Si, the dominant release peak occurs at 720°C. It can again be inferred to represent an amorphous-crystalline transition on the basis of (a) helium scattering from P, Sb, Ga and As bombarded Si[21], where channeling was restored at 550–650°C in 10 min, (b) an electron-microscope study of bombardment-induced amorphousness[24], where annealing took place at ~ 650°C in 1 hr, and (c) the fact that evaporated films of Si crystallize at ~ 700°C in 1 hr[25].

---

*Jacobson and Wehner[5] reported a substantially lower temperature for gas-release due to disorder annealing in Ge, namely ~ 250°C. The difference may lie in the fact either that they were concerned with the extreme outer surface (cf. Fig. 6 of[23]) or else that disordering was incomplete (cf. Fig. 8 of[21]).

4.4 *Correlations involving disorder annealing*

Additional insite into the annealing of bombardment-induced disorder can be gained by making comparisons with melting and cation self-diffusion. Values of the ratio $T_{\text{annealing}}/T_{\text{melting}}$ are given in Table 2. They are seen to scatter rather widely, though, with the exception of Cr_2O_3, are similar for a given type of compound.

*Table 2. Correlations involving disorder annealing**

Material	$(T_{\text{annealing}})/(T_{\text{melting}})$ (°K/°K)	$T_{\text{self-diffusion}}$ (°K)	$(T_{\text{annealing}})/(T_{\text{self-diffusion}})$ (°K/°K)
α-Al_2O_3	0·43	1350†	0·74
Cr_2O_3	0·27	1060† 825†	0·68 0·87
α-Fe_2O_3	0·44	1080†	0·75
rutile	0·35	960[17]	0·78
MgO	0·19	~1045†	~0·57
NiO	0·25	800[33]	0·70
Ge	0·61	850[34]	0·87
Si	0·59	1185[35]	0·84

*$T_{\text{annealing}}$ is taken from Table 1. $T_{\text{self diffusion}}$ is derived by substituting cation self-diffusion parameters into equation (2a), which for $T_m = 1100$°K (logarithmic term only) and $\beta_{\min} = 25$°C/min can be written $\Delta H/T_m = 75{\cdot}6 + 4{\cdot}58 \log_{10}(D_0/0{\cdot}3)$.

†Diffusion parameters summarized in reference [2].

Table 2 also contains a summary of cation self-diffusion temperatures, generally derived from self-diffusion parameters using equation (2a), together with values of the ratio $T_{\text{annealing}}/T_{\text{self-diffusion}}$. We now find a rather good correlation even for different types of compounds, with the temperature ratios lying, except for MgO, between 0·68 and 0·87. Such a correlation should be of use for predicting annealing temperatures with unstudied materials; in addition, however, it suggests that disorder annealing is in some way related to self-diffusion.

5. DISCUSSION

5.1 *General features of disorder annealing*

Any model for the annealing of bombardment-induced disorder must take into account the following general features: (a) Except with MgO and NiO, the temperature width for gas-release coinciding with disorder annealing is similar to that for a single rate-controlling jump (Table 1). Thus it is much greater than that for *pure* sequential motion yet much less than that for diffusion of an e^{-x}-type distribution. (b) Disorder annealing correlates in general with cation self-diffusion, and, for a particular type of compound, also with melting (Table 2). (c) Bombardment-induced disorder would for *very high doses* be expected to take the form of an approximately uniform skin resting on crystalline material. The disorder is believed to develop due to the overlapping of small, spherical, disordered regions, as demonstrated by electron microscopy[24, 26], and this suggests that for *moderate doses* a disordered layer will be bounded both by a macroscopic disorder-crystal interface and also by remnants of the original crystalline material. (d) The annealing of amorphous layers on Ge and Si was demonstrated by Mayer *et al.* [21] to begin mainly at the disorder-crystal interface. In addition, however, one must consider, as discussed by Primak[27] for quartz, the possibility that annealing begins also from any remnant crystalline regions present. (e) With α-Al_2O_3, rutile, Ge and Si, bombardment-induced and natural amorphousness anneal at similar temperatures, while with α-Fe_2O_3 the temperatures agree to within roughly 100°C.

5.2 *Model based on crystal growth*

Perhaps the most straightforward mechanism for disorder annealing follows from the correlation with cation self-diffusion, namely that it is similar to the growth of a finite crystal into an undercooled liquid, the growth proceeding both from the macroscopic disorder-crystal interface and from any remnant crystalline regions. This phenomenon has been discussed in detail by Hartshorne[28] and by Turnbull and Cohen[29], who showed that the velocity of growth should be

$$v = (fD/\lambda)(1-\exp(-\Delta G/RT)) \qquad (5)$$

where f is the fraction of crystal surface sites to which molecules can be attached, D is *related* to the diffusion coefficient for self-diffusion in the undercooled liquid, λ is the mean atomic spacing, and ΔG is the free energy of fusion at the temperature of interest. This equation expresses the condition that the velocity of growth is given by the difference between the rate of jumps leading to extension of the crystal and the rate of jumps leading to recession. In the case of bombardment-induced disorder, the disorder-crystal interface would be expected to sweep along the bombarding ions, e.g. inert gas, and finally cause their release at the surface.

It is readily shown that, for the materials dealt with here, $\Delta G/RT$ is large and positive, while f is believed[29] to be in general similar to unity for large undercoolings. If, moreover, the undercooled liquid has the form of a plane sheet and we replace v by thickness/time, equation (5) yields the following condition for *complete* crystallization, thence for *complete* gas release:

$$\alpha R_m/t = (D_0/\lambda^2)\exp(-\Delta H/RT) \qquad (6)$$

where ΔH is the activation enthalpy of the rate-controlling jump and α is a numerical factor such that αR_m is the thickness of the disordered layer in units of mean atomic spacings. α is apparently near unity, being ~ 2 with mica[20], ~ 1 with Si[24], and ~ 1 with α-Al_2O_3[30]. The condition for the *beginning* of crystallization, thence for the *beginning* of gas-release, follows by noting that, for remnant crystalline regions near the surface, equation (6) will still hold but with $\alpha R_m \approx 1$. Altogether, gas-release would thus be described by a mixture of sequential kinetics ([6] as is) and single-jump kinetics ([6] with $\alpha R_m \approx 1$), thence by a combination of equations (1) and (2).

This model has the advantage of being consistent with all the general features of disorder annealing outlined in Section 5.1, though the temperature width presents difficulty at first sight. We would propose that the similarity of $\Delta T_{1/2}$ to what is expected for single-jump motion is misleading. In fact, if the beginning of gas-release is described by equation (2a) and the completion by (1a) with $R = \alpha R_m$, it is readily shown that the temperature width should be roughly as follows:

$$\Delta T/T_m \approx 0{\cdot}066 \log_{10}\alpha R_m$$

or for $\alpha R_m = 22$ mean atomic spacings,

$$\Delta T/T_m \approx 0{\cdot}089.$$

This is very similar to what is observed in Table 1 for gas-release associated with disorder annealing, except with MgO and NiO, and there is thus no need to assume single-jump motion.

Table 3 contains the implied ΔH's, as derived from the disorder annealing temperatures of Table 1, for those materials where the temperature widths suggest that the crystal-growth model is valid. As in similar calculations elsewhere[6-9] the main uncertainty probably lies not in parameters such as α or R_m but in the use of an idealized

Table 3. Activation enthalpies for disorder annealing (tentative values dependent on the assumption $D_0 = 3 \times 10^{-1\pm1}$ cm²/sec)

Material	ΔH* (kcal/mole)
α-Al_2O_3	69 ± 4†
Cr_2O_3	49 ± 3
α-Fe_2O_3	56 ± 4
rutile	52 ± 3
Ge	51 ± 3
Si	68 ± 5

*Derived with equation (1a), which for $T_m = 800°K$ (logarithmic term only), $D_0 = 3 \times 10^{-1\pm1}$ cm²/sec, $R = \alpha R_m \approx 22$ mean atomic spacings, and $\beta_{min} = 25°$ C/min can be written $\Delta H/T_m = 68{\cdot}8$.

†The value would be 75 kcal/mole, similar to what was reported in references[7, 8], if single-jump kinetics were assumed. The 40 keV data of reference[3] yield 65 kcal/mole for sequential kinetics with $R = \alpha R_m \approx 60$ mean atomic spacings.

range of values for D_0, namely $3 \times 10^{-1\pm1}$ cm²/sec; for, while there is good reason to accept an idealized D_0 for normal, unperturbed gas motion, it still remains to be demonstrated whether D_0 is ideal for the annealing of disorder. According to Turnbull and Cohen[29] these ΔH's should be interpreted as those for self-diffusion in the disorder phase, though it would be necessary before accepting this conclusion in full to make a comparison with ΔH's obtained in other types of experiments.

5.3 *Model based on a single rate-controlling jump*

We have seen that the temperature width of gas-release due to disorder annealing is often similar to what would be expected for single-jump kinetics. Such kinetics might possibly arise, for example, if nucleation of the crystalline phase were rate controlling. It is, however, difficult to envisage why nucleation would play a role when the disordered regions are bordered by intact crystal, and in any case Matzke[9, 31] has shown that F vs. $\sqrt{t}$ curves for Xe release from amorphous SiO_2 do not have the shape expected for slow nucleation. A more plausible situation is that, as discussed by Childs[32] in connection with stored-energy release from U_3O_8, the initial jump causes heat to be liberated such that subsequent jumps are enhanced; i.e. the annealing is autocatalytic. A possible argument against autocatalysis is that we are dealing here with very thin disordered surface layers from which heat could readily escape, whereas Childs' specimens were disordered on a macroscopic scale.

5.4 *Model based on gas diffusion*

Still a further model for disorder annealing can be developed on the non-unreasonable assumption that the rate-controlling step involves gas diffusion in the disordered layer. The geometry for such diffusion would be essentially that for a linearly decreasing distribution in a plane sheet of thickness αR_m, and it is readily shown that the predicted temperature widths are similar to those observed. A possible argument against this model is that the annealing temperatures for Ge and Si are essentially the same whether the bombarding ion is an inert gas or a species such as Ga or In, while those for α-Al_2O_3, rutile, Ge and Si are similar whether natural or bombardment-induced amorphousness is considered.

6. SUMMARY

(a) The object of this work is to use gas-release techniques to characterize the annealing of bombardment-induced disorder. (b) α-Al_2O_3, Cr_2O_3, α-Fe_2O_3, rutile, Ge and Si all show prominent gas-release components at high doses which coincide with known or inferred amorphous-crystalline transitions and which have temperature widths of 45–70°C. With MgO and NiO there is evidence for disorder annealings which do *not* involve amorphousness and which have temperature widths of 120–190°C.

(c) The various examples of disorder annealing correlate in general with cation self-diffusion and, for a particular type of compound, also with melting. For example, the ratio $T_{\text{annealing}}/T_{\text{self-diffusion}}$ generally lies between 0·68 and 0·87.

(d) Three different models for disorder annealing can be envisaged. If crystal growth into the disordered phase is rate-controlling, then a mixture of sequential and single-jump kinetics would be expected. A single jump would be rate-controlling if nucleation were slow or if the annealing were autocatalytic. Gas-diffusion in the disordered phase might also be important.

(e) The balance of the evidence seems to be in favor of the model based on crystal growth. To the extent that this model is valid, and provided D_0 is similar to 0·3 cm²/sec, it is possible to derive ΔH's as in Table 3.

Acknowledgements—The authors are particularly grateful to Dr. Hj Matzke (Euratom, Ispra, Varese, Italy) for communicating experimental results in advance of publication and for discussing this manuscript.

REFERENCES

1. JECH Č., *Phys. Status Solidi* **4**, 499 (1964)
2. KELLY R. and JECH Č., *Proc. Brit. Ceram. Soc.* **9**, 243 (1967).
3. MATZKE Hj. and WHITTON J. L., *Can. J. Phys.* **44**, 995 (1966).
4. MACRAE A. U. and GOBELI G. W., *J. appl Phys.* **35**, 1629 (1964).
5. JACOBSON R. L. and WEHNER G. K., *J. appl. Phys.* **36**, 2674 (1965).
6. KELLY R. and MATZKE H., *J. Nucl. Mat.* **17**, 179 (1965)
7. JECH Č. and KELLY R., *J. Nucl. Mat.* **20**, 269 (1966).
8. JECH Č. and KELLY R., *Proc. Brit. Ceram. Soc.* **9**, 259 (1967).
9. MATZKE Hj., *Phys. Status Solidi* **18**, 285 (1966).
10. KELLY R. and MATZKE Hj., *J. Nucl. Mat.* **20**, 171 (1966).
11. KELLY R. and JECH Č., To be published.
12. KELLY R., *J. appl. Phys.* In press.
13. HASS G., *Optik* **1**, 134 (1946).
14. HASS G. and BRADFORD A. P., *J. Opt. Soc. Am.* **44**, 810 (1954).
15. MATZKE Hj., *Proc. Intern. Conf. Applic. of Ion Beams to Semiconductor Technology*, p. 369, Grenoble (1967).
16. FINCH G. I., *J. Chem. Soc.* **1938**, 1137 (1938).
17. KELLY R. and JECH Č., To be published.
18. KRIKORIAN E. and SNEED R. J., *Trans. Nat. Symp. Vacuum Technol.* **10**, 368 (1963).
19. MATZKE Hj., *J. Mat. Sci.* **2**, 444 (1967).
20. JECH Č., *Phys. Status Solidi* **21**, 481 (1967).
21. MAYER J. W., ERIKSSON L., PICRAUX S. T. and DAVIES J. A., *Can. J. Phys.* **46**, 663 (1968).
22. PARSONS J. R. and BALLUFFI R. W., *J. Phys. Chem. Solids* **25**, 263 (1964).
23. JECH Č. and KELLY R., *Proc. Intern. Conf. Applic. of Ion Beams to Semi-Conductor Technology*, p. 305, Grenoble (1967).
24. MAZEY D. J., NELSON R. S. and BARNES R. S., *Phil Mag.* **17**, 1145 (1968).
25. HASS G. and SCOTT N. W., *J. Phys. Radium* **11**, 394 (1950).
26. PARSONS J. R., *Phil. Mag.* **12**, 1159 (1965).
27. PRIMAK W., *Phys. Rev.* **110**, 1240 (1958).
28. HARTSHORNE N. H., *Disc. Faraday Soc.* **5**, 149 (1949).
29. TURNBULL D. and COHEN M. H., In *Modern Aspects of the Vitreous State*, p. 38. Butterworth, London (1960).
30. JECH Č., To be published.
31. MATZKE Hj., Personal communication.
32. CHILDS B. G., *J. Nucl. Mat.* **5**, 128 (1962).
33. LINDNER R. and ÅKERSTRÖM Å., *Disc. Faraday Soc.* **23**, 133 (1957).
34. WIDMER H. and GUNTHER-MOHR G. R., *Helv. Phys. Acta* **34**, 635 (1961).
35. PEART R. F., *Phys. Status Solidi* **15**, K119 (1966).

J. Phys. Chem. Solids Pergamon Press 1969. Vol. 30, pp. 475–482. Printed in Great Britain.

ON THE THERMODYNAMIC PROPERTIES OF THE SOLID ELECTROLYTE $RbAg_4I_5$

H. WIEDERSICH and W. V. JOHNSTON

Science Center, North American Rockwell Corporation, Thousand Oaks, Calif. 91360, U.S.A.

(*Received* 4 *September* 1968)

Abstract – The non-random distribution of Ag^+ ions on three crystallographically nonequivalent sets of tetrahedral sites in $RbAg_4I_5$ is a consequence of both site energy differences and mutual repulsion of silver ions on nearest neighbor sites. A method similar to the quasichemical approximation, used in the theory of order-disorder transformations, has been applied to obtain the configurational entropy and excess specific heat associated with the disorder of the silver ions. Site energy differences of ~ 0·027 and ~ 0·042 eV between the different types of silver sites and a mutual repulsion energy between silver ions on nearest neighbor sites of ~ 0·035 eV accounts well for the experimentally observed quantities. The configurational entropy is an appreciable fraction (~ 10 per cent at 300°K) of the total entropy content.

INTRODUCTION

THE RECENTLY discovered high conductivity solid electrolytes of the composition $M\,Ag_4I_5$ with $M =$ Rb, K, or NH_4 are isostructural [1,2]. Unlike all other known solid electrolytes, they remain highly conducting to low temperatures[2]. Although the compounds are unstable thermodynamically below 27, 36 and 32°C, for $M =$ Rb, K and HN_4[3], with respect to the decomposition reaction

$$M\,Ag_4I_5 \rightarrow \tfrac{1}{2}M_2AgI_3 + \tfrac{7}{2}AgI \qquad (1)$$

they can be retained at room temperature and below for indefinite periods of time in a dry atmosphere.

Since the discovery of this family of solid electrolytes their conductivity[1,2] has been measured, the crystal structure has been determined[4], and the change in free energy, enthalpy and entropy connected with the decomposition reaction (1) has been measured [3]. Further, the self diffusion coefficient for Ag[5] and the specific heat of $RbAg_4I_5$ have been obtained.

The purpose of the present paper is to relate the thermodynamic properties qualitatively and, where possible, semiquantitatively to the crystal structure. As some of the quantities have been measured only for $RbAg_4I_5$ the discussion will be restricted to the latter compound, even though it is expected that much of what is said will apply to the other members of this family as well.

CRYSTAL STRUCTURE

The crystal structure of $RbAg_4I_5$ has been solved by Geller[4]. It is cubic ($a = 11·24$ Å) with four formula units per unit cell. The iodide ions provide 56 tetrahedra per unit cell which serve as sites for the silver ions. The four Rb ions are surrounded by distorted I^- octahedra. In common with other high ionic conductivity solids, as for instance the high temperature modifications of AgI[7] and Ag_2HgI_4[8], the crystal structure provides more than one site per cation, here 3·5 (= 56/16) for each silver ion. The cubic structure of $RbAg_4I_5$ exists between 209°K and its incongruent melting point at 505°K. Two low temperature modifications exist both of which exhibit birefringence (and hence are not cubic). The transitions between the phases is marked by peaks in the specific heat at 209° and 122°K[6]. No discontinuity in the electric conductivity is observed at the higher temperature transition whereas a sharp drop in conductivity accompanies the transition to the lowest temperature phase[2]. Both transitions appear to be connected with only minor distortions of the iodide–rubidium lattice because the diffraction lines of the cubic phase persist with little change as the dominant lines of the powder patterns of both low temperature phases[9]. The space groups of the low temperature modifications have not yet been determined.

In the cubic phase, which will be the main concern here, three distinct sets of Ag$^+$ sites exist, one 8-fold (c) and two 24-fold (e) sets. Some pertinent features of the types of sites are summarized in Table 1. The types are identified by Roman numerals. As pointed out previously, all Ag$^+$ sites are within iodide tetrahedra. However, only the II-sites are surrounded by silver sites across all four tetrahedron faces as indicated in the third column of Table 1. For the I- and III-sites the remaining face(s) of the tetrahedron are directed towards Rb$^+$ ions. The II-sites and at least one of the other types of sites must be involved in the Ag$^+$ ion transport[4]. Alternating II- and III-sites form channels parallel to the cube directions. These channels are linked directly by II-sites and indirectly by I-sites. However, the crystal is also penetrated by a network of sites with the sequence I-II-II-I-II- with the I-sites as branching points.

Table 1

Type	Number of sites per unit cell	No. and type of nearest neighbor sites	Fractional occupation
I	8	3 II	0·111
II	24	1 I, 1 II, 2 III	0·391
III	24	2 II	0·229

The fractional occupations or concentrations (number of Ag$^+$ ions on a given type of site divided by the number of sites of this type) measured[4] at room temperature is given in the last column of Table 1. The values deviate appreciably from randomness ($16/56 = 0{\cdot}286$ for all types). The distances between adjacent silver sites are rather short (1·76 Å average) and a coulomb repulsion between Ag$^+$ ions should make simultaneous occupation of nearest neighbor sites unfavorable. However, inspection of Table 1 shows that this repulsion cannot be the sole reason for the observed fractional occupations of the sites since then the concentrations should decrease in the sequence III → I → II as the number of nearest neighbor sites increases. Thus, it can be concluded that the energy of a silver ion depends on the site which it occupies.

The non-random occupations of the sites implies immediately a temperature dependence of the fractional occupations which in turn lead to a temperature dependent configurational entropy of the Ag$^+$ ions and to an excess specific heat.

CONFIGURATIONAL ENTROPY AND ENERGY

The configurational entropy and energy contributions of the silver ions will be evaluated on the basis of site energies and nearest neighbor pair interactions. The treatment follows essentially the quasi-chemical method of Fowler and Guggenheim used in the theory of order–disorder transformations [10, 11]. This method has been chosen rather than the simpler Bragg–Williams approximation because the latter does not provide for any short range order above the ordering temperature. The Takagi method[11] leads to the same results as the quasi-chemical approximation.

The outline of the procedure is as follows: We will obtain an expression for the free energy* (F) of the system as a function of the number of Ag$^+$-ions (n_i) on the different sites and the number of Ag$^+$-pairs (m_j) on neighboring sites using as parameters the site energies (e_i) and the pair interaction energies (u_j). Minimization of the free energy should then yield the relations between the equilibrium values of the variables and the various energies.

---

*Since the system is condensed and no high pressures are considered, the Gibbs and the Helmholtz free energies are essentially the same.

We consider a crystal containing a total of $n(= n_I + n_{II} + n_{III})$ silver ions. Inspection of Table 1 shows that with 16 Ag^+ ions per unit cell there are $N_I = 0{\cdot}5\,n$ and $N_{II} = N_{III} = 1{\cdot}5\,n$ sites of the indicated type in the crystal. Table 2 summarizes relevant numbers relating to the pairs. Column 1 gives the types of site-pairs. It should be noted that all pairs include at least one site of type II; further, the pairs which can be formed between a II-site and the two neighboring III-sites are distinct and, therefore, listed separately. The number of site-pairs, column 2, is equal to the number of II-sites ($N \equiv N_{II}$) with the exception of the number of pairs II-II which, of course, contains a factor ½. The third column defines the symbols for the numbers of nearest neighbor silver–silver pairs which will be used as variables. The last three columns give the number of site-pairs containing vacant sites (V) in a disposition as indicated in the column headings. These entries follow from the quantities defined already; e.g. row 1, column 5: n_I silver ions are part of $3n_I$ site pairs (II-I) of which m_I are $(Ag_{II}{}^+ - Ag_I{}^+)$-pairs, the remainder can be $(V_{II}\text{-}Ag_I{}^+)$-pairs only. The other entries are obtained in a similar fashion.

Table 2

Type of site-pairs	Number of site-pairs	No. of site-pairs with the occupations:			
		Ag–Ag	Ag–V	V–Ag	V–V
$II-I$	$M_I = N$	m_I	$n_{II} - m_I$	$3n_I - m_I$	$N - n_{II} - 3n_I + m_I$
$II-II$	$M_{III} = \frac{1}{2}N$	m_{II}	$\frac{1}{2}n_{II} - m_{II}$	$\frac{1}{2}n_{II} - m_{II}$	$\frac{1}{2}N - n_{II} + m_{II}$
$(II-III)_1$	$M_{III1} = N$	m_{III1}	$n_{II} - m_{III1}$	$n_{III} - m_{III1}$	$N - n_{II} - n_{III} + m_{III1}$
$(II-III)_2$	$M_{III2} = N$	m_{III2}	$n_{II} - m_{III2}$	$n_{III} - m_{III2}$	$N - n_{II} - n_{III} + m_{III2}$

With the assumption that the energy of the system can be written as the sum of the individual site energies and pair interaction energies we obtain the free energy as

$$\begin{aligned} F = {} & n_I e_I + n_{II} e_{II} + n_{III} e_{III} + m_I u_I + m_{II} u_{II} \\ & + m_{III1} u_{III1} + m_{III2} u_{III2} - T S_c\ (n_I, n_{II}, n_{III}, \\ & m_I, m_{II}, m_{III1}, m_{III2}) \end{aligned} \tag{2}$$

where S_c is the configurational entropy of the silver ions as a function of the site occupations and number of Ag^+–Ag^+ pairs. Implicit in equation (2) is the assumption that the lattice vibrations can be considered as independent of the distribution of Ag^+ ions.

The entropy, S_c, is given by

$$S_c = k \ln W_c \tag{3}$$

where k is the Boltzmann constant and W_c the total number of distinguishable arrangements of Ag^+ ions which yield the specified occupations, n_i, *and* number of pairs, m_j.† Of the total number of arrangements in which the silver ions can be distributed for a given set of n_2 only a fraction, f, will have the prescribed number of pairs, m_j. Hence,

$$W_c = f \times \frac{N_I!}{(N_I - n_I)!\,n_I!} \cdot \frac{N_{II}!}{(N_{II} - n_{II})!\,n_{II}!} \times \frac{N_{III}!}{(N_{III} - n_{III})!\,n_{III}!}. \tag{4}$$

As in the quasi chemical approximation, we assume this fraction to be proportional to the number of ways in which the pair occupations given in Table 2, columns 3–6, can be distributed over the number of the corresponding site pairs (neglecting correlations). Thus, we write

$$f = h(n_I, n_{II}, n_{III}) \cdot g_I \cdot g_{II} \cdot g_{III1} \cdot g_{III2} \tag{5}$$

with

$$g_I = \frac{N!}{m_I!(n_{II} - m_I)!(3n_I - m_I)!(N - n_{II} - N - n_{II} - 3n_I + m_I n_I + m_I)!} \tag{5a}$$

---

†The subscript i assumes the values I, II, III, and the subscript j the values I, II, III1, III2 here and in the following.

and the corresponding expressions for the other g's. The sum of the f's over all possible combinations of m_j, but fixed n_i, must be unity from which the proportionality factor, h, is obtained. For sufficiently large assemblies, the sum can be replaced by its maximum term which leads to

$$1=\sum_{m_i} f \simeq f^* = h g_{\text{I}}^* \cdot g_{\text{II}}^* \cdot g_{\text{III1}}^* \cdot g_{\text{III2}}^* \qquad (6)$$

where the asterisks indicate the maxima with respect to the m_j's. Combining equations (4–6) we have

$$W_c = \frac{N_{\text{I}}!}{(N_{\text{I}}-n_{\text{I}})!n_{\text{I}}!}\cdot\frac{N_{\text{II}}!}{(N_{\text{II}}-n_{\text{II}})!n_{\text{II}}!} \times \frac{N_{\text{III}}!}{(N_{\text{III}}-n_{\text{III}})!n_{\text{III}}!} \times \frac{g_{\text{I}}}{g_{\text{I}}^*}\cdot\frac{g_{\text{II}}}{g_{\text{II}}^*}\cdot\frac{g_{\text{III1}}}{g_{\text{III1}}^*}\cdot\frac{g_{\text{III2}}}{g_{\text{III2}}^*}. \qquad (7)$$

Here

$$\frac{g_I}{g_{\text{I}}^*} = \frac{m_{\text{I}}^*!(n_{\text{II}}-m_{\text{I}}^*)!(3n_{\text{I}}-m_{\text{I}}^*)!(N-n_{\text{II}}-3n_{\text{I}}+m_{\text{I}}^*)!}{m_{\text{I}}!(n_{\text{II}}-m_{\text{I}})!(3n_{\text{I}}-m_{\text{I}})!(N-n_{\text{II}}-3n_{\text{I}}+m_{\text{I}})!} \qquad (7a)$$

with

$$m_{\text{I}}^* = \frac{n_{\text{II}}\cdot 3n_{\text{I}}}{N} \qquad (7b)$$

which is the m_{I} at which g_{I} has its maximum. m_{I}^* is, of course, the number of Ag_{II}–Ag_{I} pairs which results from random distribution of n_{II} Ag^+ ions on the II-sites and n_{I} on the I-sites. Expressions entirely corresponding to (7a) and (7b) result for the remaining factors in equation (7). Using Stirling's approximation and converting to fractional site and pair concentrations, $c_i \equiv n_i/N_i$ and $p_j \equiv m_j/M_j$, the entropy per formula unit (RbAg_4I_5) can be written as

$$\begin{aligned} s_c(c_i,p_j) = k\{&4A(c_{\text{I}})+18A(c_{\text{II}})+6A(c_{\text{III}})\\ &-6B(c_{\text{I}},p_{\text{I}})-3B(c_{\text{II}},p_{\text{II}})\\ &-6B(c_{\text{III}},p_{\text{III1}})-6B(c_{\text{III}},p_{\text{III2}})\} \end{aligned} \qquad (8)$$

The functions $A(c_i)$ and $B(c_i,p_j)$ are defined by

$$A(c_i) = c_i\ln c_i + (1-c_i)\ln(1-c_i) \qquad (8a)$$

and

$$\begin{aligned} B(c_i,p_j) = {}& p_j\ln p_j + (c_{\text{II}}-p_j)\ln(c_{\text{II}}-p_j)\\ &+(c_i-p_j)\ln(c_i-p_j)\\ &+(1-c_{\text{II}}-c_i+p_j)\ln(1-c_{\text{II}}-c_i+p_j). \end{aligned} \qquad (8b)$$

Finally, the configurational free energy per formula unit is

$$\begin{aligned} f_c(c_i,p_j) = {}& 2c_{\text{I}}e_{\text{I}}+6c_{\text{II}}e_{\text{II}}+6c_{\text{III}}e_{\text{III}}\\ &+6p_{\text{I}}u_{\text{I}}+3p_{\text{II}}u_{\text{II}}\\ &+6p_{\text{III1}}u_{\text{III1}}+6p_{\text{III2}}u_{\text{III2}}-Ts_c(c_i,p_j). \end{aligned} \qquad (9)$$

Because there are, per formula unit, 4 Ag^+ ions and 2, 6 and 6 sites of the types I, II and III, respectively, we have the relation

$$4 = 2c_{\text{I}}+6c_{\text{II}}+6c_{\text{III}}. \qquad (10)$$

Minimization of f_c with respect to the c_i's and p_j's subject to the condition (10) yields

$$\boxed{\begin{aligned} \frac{e_{\text{I}}-e_{\text{II}}}{kT} &= \ln\frac{c_{\text{I}}^2(1-c_{\text{II}})^3(1-c_{\text{II}}-c_{\text{I}}+p_{\text{I}})^2(c_{\text{II}}-p_{\text{I}})(c_{\text{II}}-p_{\text{II}})(c_{\text{II}}-p_{\text{III1}})(c_{\text{II}}-p_{\text{III2}})}{(1-c_{\text{I}})^2c_{\text{II}}^3(c_{\text{I}}-p_{\text{I}})^3(1-2c_{\text{II}}+p_{\text{II}})(1-c_{\text{II}}-c_{\text{III}}+p_{\text{III1}})(1-c_{\text{II}}-c_{\text{III}}+p_{\text{III2}})} && (11\text{a})\\ \frac{e_{\text{III}}-e_{\text{II}}}{kT} &= \ln\frac{c_{\text{III}}(1-c_{\text{II}})^3(c_{\text{II}}-p_{\text{I}})(c_{\text{II}}-p_{\text{II}})(c_{\text{II}}-p_{\text{III1}})(c_{\text{II}}-p_{\text{III2}})}{(1-c_{\text{III}})c_{\text{II}}^3(1-c_{\text{II}}-c_{\text{I}}+p_{\text{I}})(1-2c_{\text{II}}+p_{\text{II}})(c_{\text{III}}-p_{\text{III1}})(c_{\text{III}}-p_{\text{III2}})} && (11\text{b}) \end{aligned}}$$

and four relations of the form

$$\frac{u_j}{kT} = \ln\frac{(c_j-p_j)(c_{\text{II}}-p_j)}{p_j(1-c_{\text{II}}-c_j+p_j)} \qquad (11\text{c–f})$$

with $j = \mathrm{I, II, III1, III2}$. The last two indices convert to III when subscripts of c. The equations (10) and (11) determine the equilibrium values of c_i and p_j as function of temperature in terms of the site energy differences, $e_{\mathrm{I}} - e_{\mathrm{II}}$ and $e_{\mathrm{III}} - e_{\mathrm{II}}$, and the pair interaction energies, u_j.

EVALUATION AND COMPARISON WITH EXPERIMENT

The equations (11) could be used directly to obtain the two site energy differences, Δe_k, and the four pair interaction energies, u_j, if the site occupations, c_i, *and* the pair concentrations, p_j, were known. However, values of the p_j's are not available and we will make, therefore, some simplifying assumptions about the pair interaction energies. The small Ag^+ ions are surrounded by large, highly polarizable I^- ions.* As a crude approximation, the interaction energy between pairs of Ag^+ ions is assumed to be inversely proportional to the distance, r_j[4], between the different site-pairs, i.e. the Ag^+ ions are considered point charges in a dielectric continuum:

$$u_j = a/r_j. \tag{12}$$

With this assumption, the site energy differences which are required to yield the experimental site occupations[4] at room temperature can be obtained as functions of a single pair interaction energy by the use of equations (10) and (11). Values for $e_{\mathrm{I}} - e_{\mathrm{II}}$ and $e_{\mathrm{III}} - e_{\mathrm{II}}$ are shown as functions of u_{II} in Fig. 1. We note that except for $u_{\mathrm{II}} \lesssim 0{\cdot}15$ eV the site energies are essentially independent of the chosen u_{II}. The reason for this is, of course, that only few nearest neighbor Ag–Ag exist at room temperature for $u_{\mathrm{II}} \gtrsim 0{\cdot}15$ eV (the other pair interaction energies are slightly larger than u_{II}).

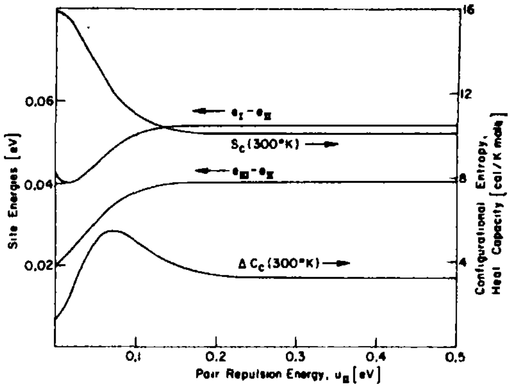

Fig. 1. Site energy differences, configurational entropy, s_c, and excess heat capacity, ΔC_c, as function of the pair repulsion energy, u_{II}.

The configurational entropy associated with the Ag^+ ions is also shown in Fig. 1. It decreases from 15·8 cal/°K mole at $u_{\mathrm{II}} = 0$ (no pair repulsion) to 10·1 cal/°K mole for $u_{\mathrm{II}} \gtrsim 0{\cdot}15$ eV. This configurational entropy should be released during the decomposition reaction given in equation (1) since the reaction products, AgI and Rb_2AgI_3, have normal types of crystal structure, i.e. the ions occupy their respective sublattices essentially completely.* Topol and Owens have derived an entropy release of 9·9 cal/°K mole for $RbAg_4I_5$ from the measured temperature dependence of the free energy of reaction 1 [3]. The closeness of the calculated s_c for large u_{II} to the experimental value of Δs would indicate rather strong pair repulsion. However, this would presuppose that the vibrational entropy contents of the reaction partners are nearly the same.

The calculated results may also be compared with the configurational entropy obtained from heat capacity measurements on $RbAg_4I_5$ starting at a temperature below the configurational changes. The total heat capacity can be divided into a vibrational and a configurational part. The method often used to approximate the vibrational part by the sum of the heat capacities of the components (here $4AgI + RbI = RbAg_4I_5$) was inapplicable because of the anomalous heat capacity of AgI. Therefore, the vibrational heat capacity (at constant volume) was approximated by a Debye specific heat function as follows. The specific heat[6] measured at constant pressure, C_p, was converted to the specific heat at constant volume, C_v, with the relation[10]

---

*If one assumes an iodide ionic radius of 2·16 Å (obtained for 6-coordination, an Ag^+ radius of only ≈ 0·70 Å results.

*AgI shows an anomalous high heat capacity above ≈ 180°K (PITZER K. S., *J. Am. Chem. Soc.* **63**, 516 (1941)) which may be associated with some disorder. The excess entropy remaining in the decomposition product AgI is estimated to be ~ 0·9 cal/°K per mole $RbAg_4I_5$.

$$C_v = C_p - \beta^2 VT/K_T. \qquad (13)$$

Here β is the cubic expansion coefficient (obtained from X-ray powder diffraction patterns taken at several temperatures)* V the molar volume, and K_T the compressibility (obtained from the single crystal elastic constants[12]).†

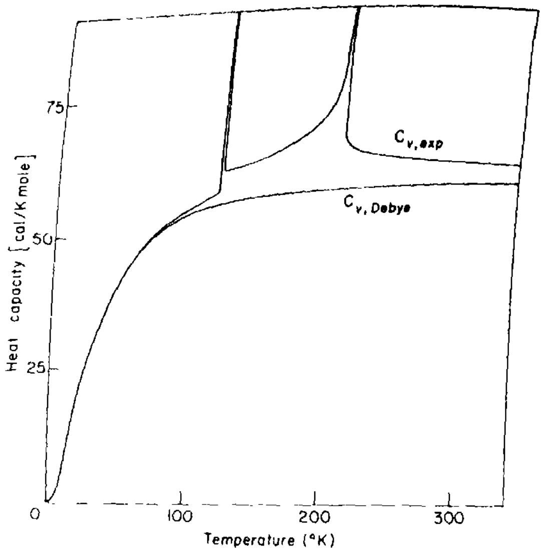

Fig. 2. Heat capacity of $RbAg_4I_5$ at constant volume, $C_{v,exp}$, and estimated vibrational contribution to the heat capacity, $C_{v,Debye}$.

In the temperature range from 20 to 100°K the Debye temperature, θ, was determined formally as function of temperature from $C_v(T)$. θ reaches a maximum of 140° at 55°K and then diminishes, presumably on account of the beginning of the 122°K transition. The vibrational heat capacity above 55°K was obtained from the tabulated Debye function taking ten ions per formula unit and, somewhat arbitrarily, the maximum of θ, 140°K. This estimated vibrational specific heat is shown in Fig. 2 together with the experimental C_v. The difference, ΔC, is taken as the configurational heat capacity. By integration of $\Delta C/T$ the entropy associated with the excess heat capacity is obtained as 9·6 cal/°K mole at 300°K. This includes the entropies of the transitions at 122° and 209°K with 1·53 and 1·0 cal/°K mole, respectively. Of course, it is uncertain what fractions of the transition entropies are associated with the configurational entropy. The experimental excess entropy is somewhat smaller than the range of configurational entropies obtained as function of the pair repulsion energies in Fig. 1.

For any given set of site energy differences, Δe_k, and pair repulsion energies, u_j, the equilibrium values of the site occupations and pair concentrations can be determined as a function of temperature by solving equations (10) and (11). The internal energy (see equation (9)) is then readily obtained as a function of temperature and, therefrom, the excess specific heat associated with the change of the silver ion distribution. The calculated excess specific heat ΔC_v at 300°K is shown in Fig. 1 as a function of u_{11}. The experimental ΔC_v at this temperature is 4 cal/°K mole which corresponds to a pair repulsion energy of either ~ 0·035 or 0·15 eV.

The excess specific heats, ΔC, for a number of different pair repulsion energies are shown in Fig. 3 as function of temperature. The assumption has been made that the energies Δe_k and u_j are independent of temperature and the phase transitions have been ignored. The

---

*As mentioned previously, the lines present in the pattern of the cubic phase persist in the patterns of the other two phases and, hence, can be used to determine the expansion coefficient to a good approximation (see also [4]).

†The values for β and K_T of the intermediate phase were used also for the low temperature phase because of insufficient data; this should not result in serious errors because $C_p - C_v$ is small at these temperatures.

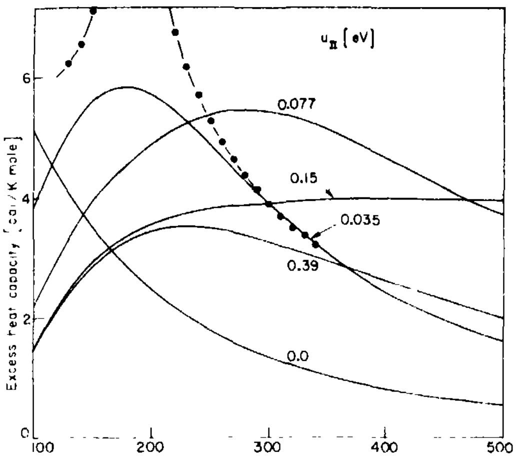

Fig. 3. Calculated (solid lines) and experimental (with points) excess heat capacity. The parameter indicates the assumed pair repulsion energy, u_{II}, in eV.

qualitative trend of these curves with increase in pair repulsion energy is easily understood. At $u_{II} = 0$ the site energy differences are small and therefore, the major contribution to ΔC occurs at low temperatures and ΔC is decreasing rapidly towards higher temperatures. With increasing u_{II} not only the increasing site energy differences (see Fig. 1) but, more important, contributions from pair interactions result in a large excess specific heat at intermediate and higher temperatures. Finally, when the pair repulsion energy becomes large few Ag–Ag pairs form and ΔC at the higher temperatures diminishes. The experimental values of the specific heat agree quite well with the calculated curve for $u_{II} = 0{\cdot}035$ eV sufficiently above the 209°K transition. Even though little reliance can be placed on the accuracy of this value a reasonably low pair repulsion energy is indicated rather than a value $\sim 0{\cdot}15$ eV which would lead to an essentially constant excess specific heat over a large temperature range. The transition at 209°K which is very probably a second order transformation is not an order-disorder reaction of the Ag^+ ions; this follows from the continuity of the conductivity[2] through the transition. It may be a result of the interplay between changes in site energy differences, in site occupations, and the concurrent lattice distortion. For example, the I-sites may be depleted below the transition. As mentioned before, the Ag^+ ion transport on the II-III-network of sites would be little affected by the depletion of the I-sites.*

The configurational entropy at 300°K corresponding to the pair repulsion energy $u_{II} = 0{\cdot}035$ eV is 14·4 cal/°K mole which amounts to $\approx$ 10 per cent of the total entropy content[6]. It is higher than the experimental values of 9·9 and 9·6 cal/°K mole obtained from the decomposition reaction and the excess specific heat respectively. In the case of the decomposition reaction and the remaining entropy difference (4·5 cal/°K mole) may be the difference in vibrational entropy content of the reaction partners and, perhaps, some disorder entropy in AgI. For the other case, one might speculate that some of the cation disorder freezes in and does not show in the measured specific heat.† However, in view of the uncertainties in the values derived from the measurements as well as from the calculations the values of these entropy differences must not be taken too seriously.

SUMMARY

The high conductivity solid electrolyte $RbAg_4I_5$ exhibits a large degree of cation (Ag^+) disorder within an essentially rigid iodine–rubidium framework. A method akin to the quasi-chemical approximation has been used to calculate the configurational entropy and excess heat capacity associated with the disorder of the silver ions. Site energy differences ($\approx 0{\cdot}027$ and $\approx 0{\cdot}042$ eV) between the different types of silver sites and the mutual repulsion between silver ions on nearest neighbor sites ($\approx 0{\cdot}035$ eV) have been taken into account. The configurational entropy is an appreciable fraction ($\approx$ 10 per cent) of the total entropy content. The high heat capacity of $RbAg_4I_5$ is a consequence of changes in site occupations and Ag^+–Ag^+ pair concentrations. The model used for the calculation accounts quite well for the experimentally observed quantities.

---

*Below the transition at least some of the site types must be differentiated in sub-types.

†*Note added in proof*: We have derived a residual entropy of $2{\cdot}3 \pm 1{\cdot}4$ cal/°K mole for $RbAg_4I_5$ from new and existing thermodynamic measurements.

The method described could be applied not only to the other members of the isostructural compounds MAg_4I_5 but also to other crystals with high disorder by taking the specific topology of their structures into account.

Acknowledgements—We appreciate fruitful discussions with S. Geller, A. Sosin, H. B. Levine and D. A. McQuarrie. We thank P. B Crandall for X-ray powder diffraction patterns of $RbAg_4I_5$ at various temperatures.

REFERENCES

1. BRADLEY J. N. and GREEN P. D., *Trans. Faraday Soc.* **62**, 2069 (1966) and **63**, 424 (1967).
2. OWENS B. B. and ARGUE G. R., *Science* **157**, 308 (1967).
3. TOPOL L. E. and OWENS B. B., *J. phys. Chem.* **72**, 2106 (1968).
4. GELLER S., *Science* **157**, 310 (1967).
5. BENTLE G. G., *J. appl. Phys.* **39**, 4036 (1968).
6. JOHNSTON W. V., WIEDERSICH H. and LINDBERG G., To be published.
7. STROCK L. W., *Z. Phys. Chem.* **B 25**, 441 (1934) and **B 31**, 132 (1935).
8. KETELAAR J. A. A., *Z. Kristallogr.* **87**, 436 (1934).
9. GELLER S., Private communication.
10. see e.g. FOWLER R. H. and GUGGENHEIM E. A., *Statistical Thermodynamics*, University Press, Cambridge (1960).
11. see e.g. MUTO T. and TAKAGI Y., In *Solid State Physics* (Edited by F. Seitz and D. Turnbull), Vol. 1, p. 193. Academic Press, New York (1955).
12. CHANG R. and GRAHAM L. J., To be published.

J. Phys. Chem. Solids Pergamon Press 1969. Vol. 30, pp. 483–490. Printed in Great Britain.

EFFECTS OF TRANSITION METAL SOLUTES ON THE THERMOELECTRIC POWER OF COPPER

E. BREWIG and W. KIERSPE
Institut für Theoretische Physik, Abtlg. für Metallphysik, Köln

and

U. SCHOTTE and D. WAGNER
Institut für Theoretische Physik, Köln

(*Received* 2 *May* 1968; *in revised form* 26 *August* 1968)

Abstract—The thermoelectric power (TEP) of dilute copper alloys containing transition metals of the first great period have been measured with reference to pure copper in the temperature range from 4·2 to 273°K. In the first part the description of the experimental procedure and the results are given. In the second part an interpretation is made according to the Anderson model. By combining the TEP data with previous results on the resistivity and susceptibility of the same alloys, one is able to give numerical estimates of the position and width of the virtual impurity levels.

1. INTRODUCTION

ACCORDING to the Friedel–Anderson model [1, 2], when an iron-group atom is dissolved in a simple metal, the electrons which formerly occupied 4 *s* and 3 *d* bound states on the free atom are lost to the conduction band. Due to the uncompensated charge on the impurity atom, the conduction band electrons can undergo resonant scattering, being trapped in 3 *d*-like orbits about the impurity; one talks about a virtual bound state or resonant level. This scattering mechanism considerably affects the transport properties and magnetic behaviour of these dilute alloys.

This paper reports work done on the thermoelectric power (TEP) of dilute alloys of Ti, V, Cr, Mn, Fe, Co and Ni in copper. Measurements of the resistivity and susceptibility of these alloys using the same samples have been reported earlier[4–6]. These results will be used here in connection with the discussion of the TEP. A more complete description of the virtual levels is achieved, but on the other hand some limitations of the Friedel–Anderson model are shown up.

2. EXPERIMENTAL PROCEDURE AND RESULTS

Detailed description of alloy preparation and material sources has been given elsewhere [3]. We give here a brief description only. The samples were prepared using 99·9997 per cent copper obtained from the Unterharzer Berg- und Hüttenwerke. The solute elements were also supplied by the Unterharzer Berg- und Hüttenwerke. Table 1 shows the concentrations given in atomic percent calculated from the constituent weights. The constituents were placed in crucibles of Al_2O_3 and ZrO_2 and melted in an argon atmosphere by induction heating.

Measurements of the electrical resistivity [5] and the magnetic susceptibility [6] have shown that the transition elements are dissolved to a large extent in the copper lattice. The authors did not anneal the samples to prevent precipitation of the constituents with a small solubility in copper. The samples were drawn into wires of 0·2 mm dia.

The arrangement for the measurements of the thermal electromotive force (e.m.f.) is shown in Fig. 1. Five different samples, a copper wire and a chromel-constantan thermo-

Table 1. The composition of the copper alloys

Alloy	at. %			Used for alloying
Cu–Ti	0·1	0·15	0·2	Ti: 99·9 weight-%
Cu–V	0·06	0·08	0·1	V: 99·5 weight-%
Cu–Cr	0·04	0·08	0·12	Cr: Electrolyte.-Cr 99·99 weight-%
Cu–Mn	0·5	1	3	Mn: Electrolyt.-Mn 99·9 weight-%
Cu–Fe	0·05	0·075	0·1	Fe: Armco-Fe
Cu–Co	0·1	0·15	0·2	Co: 99·95 weight-%
Cu–Ni	0·5	1	2	Ni: reduced from Nickeloxide p. a.

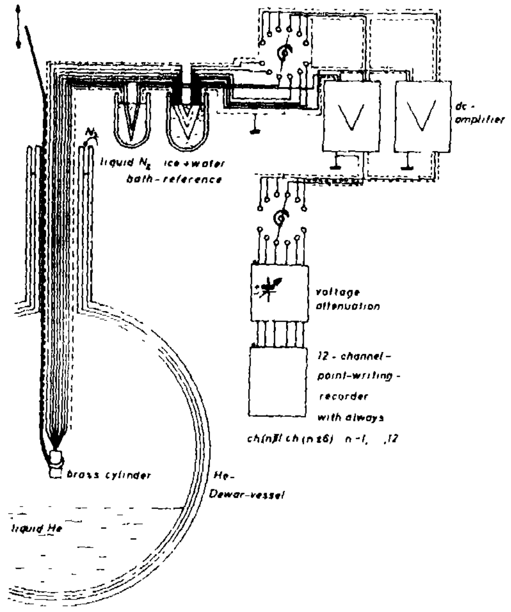
dc - amplifier
N_2
liquid N_2
ice + water bath - reference
voltage attenuation
12 - channel - point-writing - recorder with always
ch(n)//ch(n±6) n - 1, ,12
brass cylinder
He - Dewar-vessel
liquid He

Fig. 1. Low-temperature thermo-e.m.f. experimental arrangement The sample wires are insulated by plastic sleeves and drawn in the following succession from the left: 1–5. different alloys; 6. pure Cu; 7–8. chromel and constantan.

couple were soldered to the face center of a brass cylinder of 5 mm dia. and 20 mm length.

The chromel-constantan thermocouple, used to measure the temperature of the connection described above was calibrated in liquid He, liquid N_2 and ice water each time before use. Thus, the differences of the thermo-e.m.f. caused by changing the samples and soldering them were eliminated. For all temperature measurements the reference junction of the chromel-constantan thermocouple was immersed in liquid N_2. For the thermo-e.m.f. measurements of the copper alloys with respect to copper an ice water bath reference was used. The thermo-e.m.f. values were amplified by d.c.-amplifiers 860–4300 of Hewlett and Packard and registrated by a 12 channel point writing recorder of Hartmann and Braun.

The temperature variation was achieved by first immersing the brass cylinder with its sample wires into the liquid He and into liquid N_2 respectively and then pulling it out step by step to the top of the Dewar vessel. In this way the e.m.f. and the temperature could be measured in the two ranges from 4·2 to 77°K and from 77 to 273°K in a continuous and reproducible way.

Figure 2 shows the thermo-e.m.f. of the different alloys with respect to that of copper.

The absolute TEP of the alloys was determined from the slope of the e.m.f. vs. temperature curve to which the absolute TEP values of pure copper as given by Gold *et al.*[7] (specimen Cu2) were added. While in the temperature range above 100°K the values given in [7] are comparable with those of other authors[8,9] there are discrepancies below 100°K (presumably due to impurities). As the TEP will be discussed for temperatures above 100°K only, it is given in Fig. 3 in the appropriate temperature range.

Previous work on dilute Cu-alloys in this temperature range was done by Christenson [10]. He measured the TEP of Cr, Mn, Fe, Co and Ni in Cu on samples annealed at high

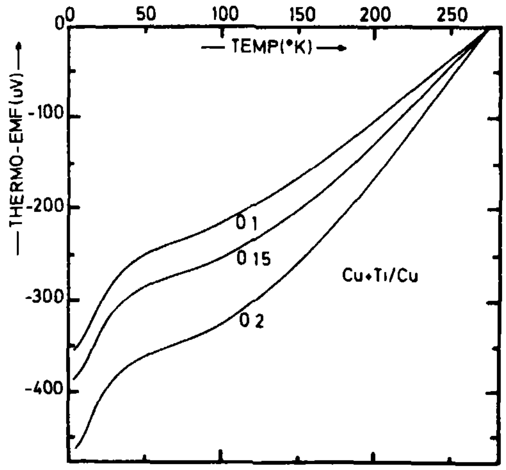

Fig. 2(a).

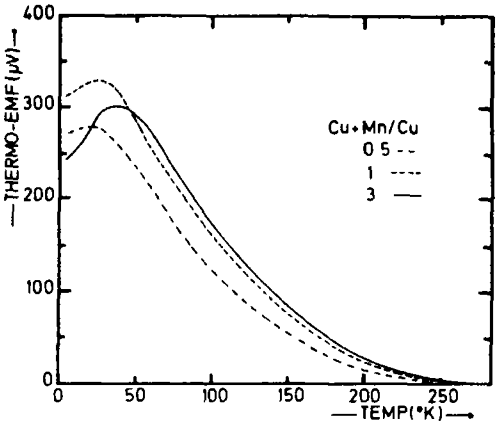

Fig. 2(d).

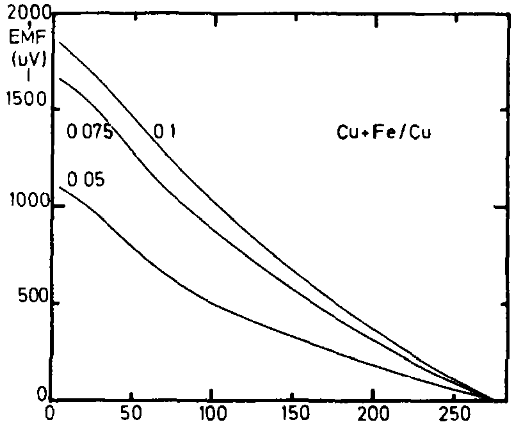

Fig. 2(e).

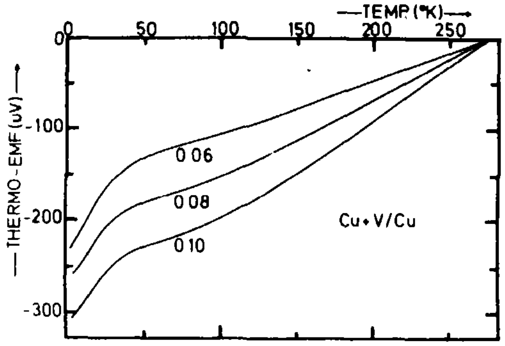

Fig. 2(b).

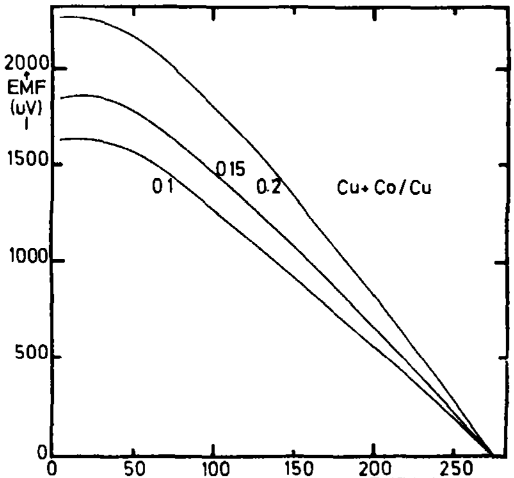

Fig. 2(f).

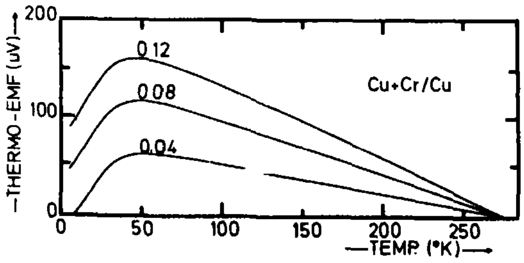

Fig. 2(c).

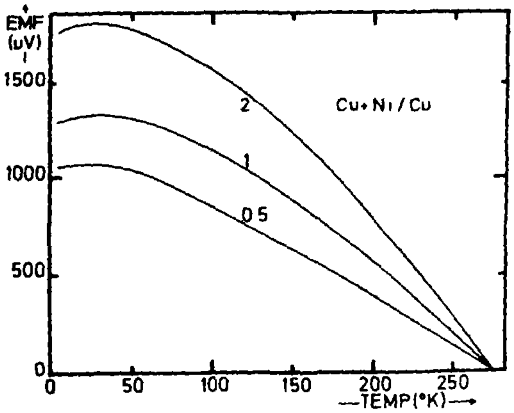

Fig. 2(g).

Fig. 2. Thermo-e.m.f. of the copper alloys with respect to pure copper as a function of temperature. The numbers refer to the concentration in atomic per cent of the transition element dissolved in copper.

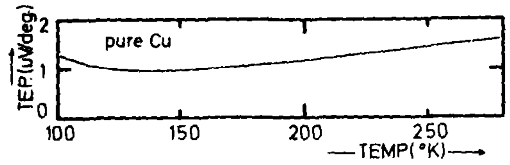

Fig. 3(a).

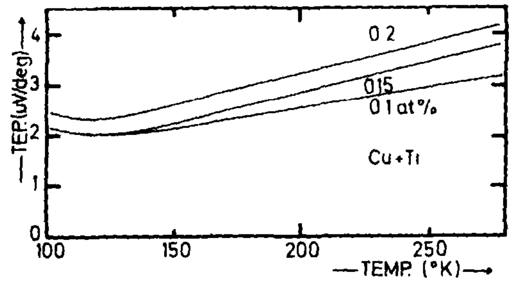

Fig. 3(b).

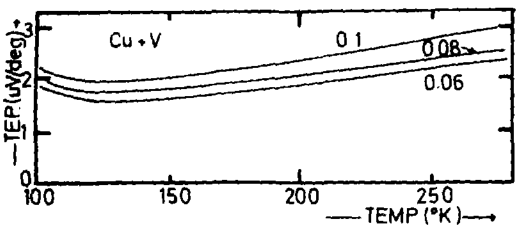

Fig. 3(c).

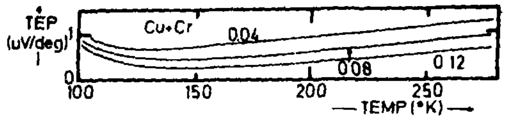

Fig. 3(d).

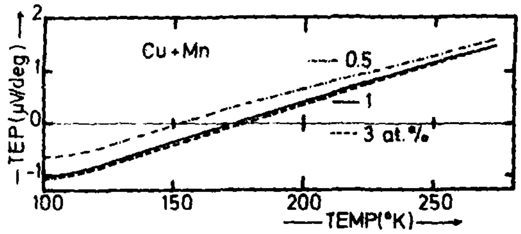

Fig 3(e).

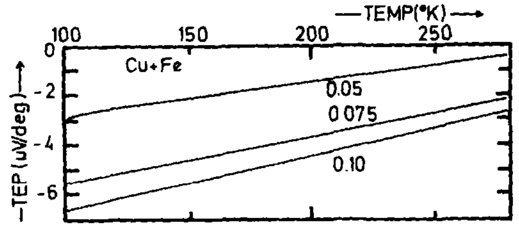

Fig. 3(f).

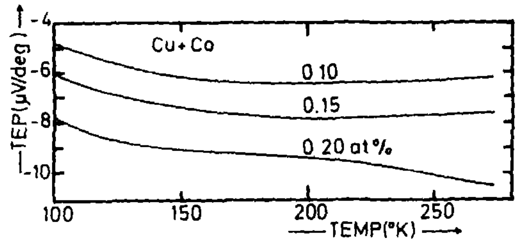

Fig. 3(g).

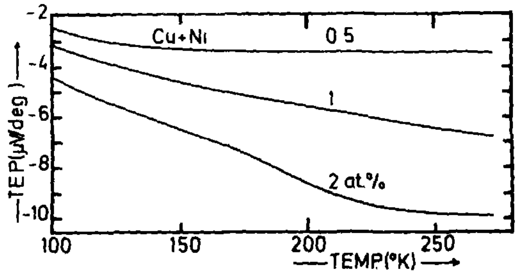

Fig. 3(h).

Fig. 3. Absolute TEP of pure copper and copper alloys as a function of temperature. The numbers refer to the concentration in atomic per cent of the transition elements dissolved in copper.

temperatures. We believe that the disagreement between his and our results in the cases of the alloys containing Fe and Co respectively is due to annealing which probably caused precipitations. Rather good agreement (within 1 $\mu V/°K$) was found in the cases of the Cr-, Mn- and Ni-alloys.

More recent data on Cu–Ni by Schroeder *et al.*[11] agree with ours and Christenson's in the same range.

We will not go into the rather difficult question to what extent other impurities introduced into the alloys by the transition element partner influence the results. We are sure that our samples contain less than 10 ppm of additional impurities having a magnetic moment in the alloy. This can be concluded from the susceptibility measurements by Weiss[6]. Above 100°K their influence seems negligible.

3. THEORY

We discuss the experimental results on the basis of the Anderson model, the parameters of which can be determined by combining the TEP data with those on the resistivity[5] and the susceptibility[6] of the same alloys as follows: The absolute TEP of the alloys is derived from the total resistivity $\rho = \rho_{\text{Cu}} + \delta\rho$

$$Q_{\text{alloy}} = \frac{\pi^2 k_B{}^2 T}{3|e|} \frac{\partial \ln(\rho_{\text{Cu}} + \delta\rho)}{\partial\epsilon}\bigg|_{\epsilon=\epsilon_F} = \frac{Q_{\text{Cu}}\rho_{\text{Cu}} + \dfrac{\pi^2 k_B{}^2 T}{3|e|}\dfrac{\partial(\delta\rho)}{\partial\epsilon}\bigg|_{\epsilon=\epsilon_F}}{\rho_{\text{Cu}} + \delta\rho} \tag{1}$$

where ρ_{Cu} and Q_{Cu} are the resistivity and the TEP of pure copper respectively, the values of which are taken from experiment[3,7]. $\delta\rho$ is the additional resistivity caused by the impurities. According to the Anderson model the high temperature expression for $\delta\rho$ is given in [12] (equation (48)):

$$\delta\rho = \frac{m^*}{ne^2}\sum_\sigma \frac{N_i\langle V_{dk}{}^2\rangle\Delta}{E_\sigma{}^2 + \Delta^2} \times\left(1 - \frac{k_B T}{\Delta}\frac{E_\sigma{}^2 + 2E_\sigma\Delta\dfrac{U}{D}n_{-\sigma}\delta_{-\sigma} - \Delta^2}{E_\sigma{}^2 + \Delta^2}\right) \tag{2}$$

where m^* and n are the mass and the density of the s-electrons in Cu respectively, N_i is the number of impurities, σ denotes the spin of the two virtual levels, the energy E_σ of which is measured from the fermi level. U is the Coulomb interaction of the d-electrons on the impurity atom, $2D$ is the conduction band width and Δ the width of the virtual level. Δ is related to Anderson's s–d mixing potential V_{dk} by

$$\Delta = \pi\rho_0\langle V_{dk}{}^2\rangle \tag{3}$$

ρ_0 being the density of states per spin taken as constant for simplicity. The derivation and discussion of the T dependent term in equation (2) is given in [12]. It describes the influence of phonons on the additional resistivity via s-electron–phonon interaction. δ_σ is proportional to the displacement of the virtual levels with temperature (cf. equation (46) of [12]). In deriving equation (2) only one orbital has been considered. Actually one has to consider the contributions of the five orbitals of the $3d$-electrons. Assuming complete orbital degeneracy we find a factor 5. For the same reason U has to be replaced by an effective U_{eff}, we will come back to this later.

Taking the fermi energy $\epsilon_F = 7\,\text{eV}$ and $m^* = 1{\cdot}5\, m_0$ one finds:

$$\delta\rho = 7{\cdot}8\sum_\sigma \frac{\Delta^2}{E_\sigma{}^2 + \Delta^2}(1 + C_\sigma\cdot T) \quad [\mu\Omega\text{cm/At.\%}]. \tag{4}$$

Inserting this expression into (1) and neglecting a small term due to the variation of n with ϵ, one has:

$$Q_{\text{alloy}} = \frac{Q_{\text{Cu}}\rho_{\text{Cu}} + \dfrac{\pi^2 k_B{}^2 T}{3|e|}\delta\rho\cdot 2x}{\rho_{\text{Cu}} + \delta\rho}. \tag{5}$$

If one neglects the T dependent term in $\delta\rho$ for the calculation of $\partial(\delta\rho)/\partial\epsilon$ one has

$$x = \frac{E_+(E_-^2+\Delta^2)+E_-(E_+^2+\Delta^2)}{(E_+^2+E_-^2+2\Delta^2)(E_-^2+\Delta^2)(E_+^2+\Delta^2)} \tag{6}$$

In general x has a rather complicated T dependence. In deriving (5) the influence of potential scattering (Linde's rule) has been neglected because it has been shown to be small relative to resonant scattering[13].

The parameters x and

$$y \equiv \frac{\delta\rho}{7{\cdot}8} \approx \sum_\sigma \frac{\Delta^2}{E_\sigma^2+\Delta^2}$$

$$\text{(for small } T \text{ dependence)} \tag{7}$$

have been calculated for different temperatures from the experimental values of $Q_{\mathrm{Cu}}^{(7)}$, $\rho_{\mathrm{Cu}}^{(3)}$, $\delta\rho^{(5)}$ and Q_{alloy} from Fig. 3. In Table 2, y is listed for 250°K and x for 100° and 250°K. We found that in the case of the non-magnetic impurities (Ti, V, Co, Ni; Co is treated as non-magnetic though it may have a small moment[13]) the T dependence of x is negligible, while for Cr, Mn and Fe, x varies appreciably. The small values of x for Mn and Cr indicate that $E_+ \approx -E_-$, i.e. the two magnetic levels lie nearly symmetrical about the fermi level, therefore the temperature effects seem relatively large for Cr and Mn.

Table 2. Numerical values of y *(equation (7)) and* x *(equation (6)),* y *is calculated from the resistivity,* x *from the TEP of the alloys*

	y (at 250°K)	$x\,(\mathrm{eV})^{-1}$ (at 100°K)	(at 250°K)
Ti	1·3	0·45	0·42
V	0·92	0·44	0·47
Cr	0·7	−0·06	−0·1
Mn	0·36	−0·3	+0·1
Fe	0·85	−2·4	−1
Co	0·55	−2·1	−2·1
Ni	0·15	−1·2	−1·4

For the non-magnetic impurities the parameters $E_+ = E_- \equiv E, \Delta$ and N, the occupation number of 3 d-electrons on the impurity can be determined from x and y. N is given by [2, 13]-

$$N = \frac{5}{\pi}\operatorname{arccot}\frac{E}{\Delta}. \tag{8}$$

The calculated parameters at 150°K are given in Table 3.

For Ti, Co and Ni, N and E are qualitatively as expected[14], the position of the virtual level moving from above to below the fermi level. The case of V will be discussed below. The width Δ, however, depends strongly on the position of the level, decreasing with decreasing distance from the bottom of the conduction band in a non-linear manner. This may be due to the variation of the density of states in the conduction band and or the dependence of V_{dk} on the energy of the s-electrons. Apparently it is a bad approximation to treat Δ as constant.

We also estimated the temperature dependent part of the residual resistivity from the

Table 3. The parameters of the Anderson model for the nonmagnetic impurities ($N = N_+ + N_-$, $\eta = (1 - U_{\mathrm{eff}}\rho_d/10)^{-1}$. *Energies are taken relative to the Fermi level of copper*

	E/Δ	Δ (eV)	E (eV)	N	U_{eff}/Δ	U_{eff} (eV)	η^{-1}
Ti	0·75	1·1	0·8	3	4	4·5	0·17
V	1·1	1·2	1·3	2·3	6·5	7·5	0·05
Co	−1·6	0·2	−0·3	8·2			
Ni	−3·5	0·2	−0·7	9·1	35	7	0·16

calculated values of E and Δ and found $\rho^{-1}|\partial(\delta\rho)/\partial T| \approx 10^{-4}$ which is the right order of magnitude[5]. We compare our results on Ni with those of Foiles[15] and Klein and Heeger[14]. Foiles included potential scattering and used low temperature TEP data. Our value of Δ for Ni in Cu agrees with his and is not far from that for Ni in Beryllium as found by Klein and Heeger. If one wants to calculate the intraatomic Coulomb interaction U, one needs further information. U appears only in E, which contains the atomic level E_d as well as a further unknown parameter.

$$E = E_d + UN. \tag{9}$$

We determine U from the additional Pauli susceptibility due to the impurities[14]:

$$\chi_{\text{Pauli}} = \frac{N_i \mu_B^2 \rho_d}{1-(U+4J)\rho_d/10} \equiv \eta \cdot N_i \mu_B^2 \rho_d \tag{10}$$

η is the enhancement factor, $U+4J$ contains the intraatomic exchange energy and can be understood as an effective U_{eff} replacing Anderson's U. μ_B is the magnetic moment of a d-electron (= 1 magneton) and ρ_d is the density of d-states at the fermi level:

$$\rho_d = \frac{10\Delta}{\pi(E^2+\Delta^2)}. \tag{11}$$

Equating (10) with the measured values of χ_{Pauli} for Ti, V and Ni[6, 18] one can calculate U_{eff} and the enhancement factors, listed in Table 3. For Co the values for χ_{Pauli} were not available.

While Ti and Ni turn out to behave as expected according to the Friedel–Anderson model, V does not seem to fit into the picture. The resonant levels are expected to move from above to below the fermi level when passing from Ti to Ni, so that for V one should find a non-magnetic level below that of Ti. We find however $E_{\text{Ti}} = 0{\cdot}8$ eV $< E_v = 1{\cdot}3$ eV. We also find a large enhancement factor for V $\eta \approx 25$ which means $U_{\text{eff}}\rho_d/10 \approx 1$, so that according to the stability condition for Anderson's magnetic solution, analagous to the Stoner criterion, $U_{\text{eff}}\rho_d/10 > 1$, V lies on the verge of forming a local moment. This assumption is confirmed by the fact that V has a local moment in the dilute *Au*–V alloy[17]. We conclude that V is a complicated case for which the H.F. approximation does not work and the parameters for V in Table 3 are not reliable.

The discussion of alloys with impurities having local moments is complicated by the fact that Δ is strongly energy dependent. One should distinguish between $\Delta(E_+)$ and $\Delta(E_-)$ which is not consistent with the model.

Assuming still a constant Δ, one can only try to find approximate values which fit into the values of x, y and the magnetic moment m[6]. m is given by [2]

$$m = N_+ - N_- = \frac{5}{\pi}\left(\operatorname{arccot}\frac{E_+}{\Delta} - \operatorname{arccot}\frac{E_-}{\Delta}\right). \tag{12}$$

U_{eff} can then be calculated from m and $E_\pm$. As this has not been done explicitly before, we give the simple derivation. The Hamiltonian for the d-electrons is [2, 13]:

$$H_d = \left(E_d - \frac{U-J}{2}\right)\sum_\sigma N_\sigma + \frac{U}{2}\sum_{\sigma,\sigma'} N_\sigma N_{\sigma'} - \frac{J}{2}\sum_\sigma N_\sigma^2 \tag{13}$$

where N_σ is the number operator for d-electrons with spin σ.

Assuming five fold orbital degeneracy, the energy in *H*-*F*-approximation is given by:

$$E_\sigma = E_d + UN_{-\sigma} + \tfrac{4}{5}(U-J)N_\sigma \tag{14}$$

(in (14) the N_σ are c-numbers) from which one has:

$$E_- - E_+ = \frac{U_{\text{eff}}}{5}(N_+ - N_-); U_{\text{eff}} \equiv U + 4J. \tag{15}$$

As far as Mn and Cr are concerned, x is relatively small, indeed for Mn, $x = 0$ at about 200°K, indicating $E_- \approx -E_+$. Then for Mn, taking $E_+ = -E_-$, $|E_\pm|/\Delta = 2{\cdot}1$ from y, one finds $N \equiv N_+ + N_- = 5$, $m = 3{\cdot}6$, which is close to the experimental value $m = 3{\cdot}96$[6], and $U_{\text{eff}}/\Delta = 5{\cdot}8$ from (15). We saw no way of finding the parameters independently. For Cr the values of x and y agree with $E_+ = -1{\cdot}2\,\Delta$, $E_- = 1{\cdot}4\,\Delta$, $\Delta = 0{\cdot}34$ eV. From these one calculates $N = 4{\cdot}5$; $m = 2{\cdot}8$. The experimental value is $m = 2{\cdot}46$[6]. From (15) one has $U_{\text{eff}}/\Delta = 5$ and $U_{\text{eff}} = 2$ eV which seems rather small.

It is very difficult to say anything about the parameters of Fe. The relatively large x indicates a non-symmetrical position of the virtual levels relative to the fermi level. We found no values for $E_\pm$ and Δ fitting into the experimental results for x, y and $m = 3{\cdot}8$[6].

One concludes from the interpretation of the experimental results in terms of the Friedel–Anderson model, that the model in *H-F*-approximation together with the simplifications ($\rho_0 =$ const, $\Delta =$ const) gives a good description of the nonmagnetic impurities Ti, Co and Ni and of the magnetic impurities Cr, Mn with nearly symmetric levels about the fermi level. The *H-F*-approximation seems not appropriate for *Cu*–V. A weak point of the model is the assumed constancy of Δ which leads to difficulties in the analysis of magnetic alloys especially of *Cu*–Fe. Temperature effects, presumably due to *s*-electron-phonon interaction, are important in the case of magnetic alloys and should not be neglected.

REFERENCES

1. FRIEDEL J., In *Metallic Solid Solutions* (Edited by J. Friedel and A. Guiner). New York (1963).
2. ANDERSON P. W., *Phys. Rev.* **124**, 41 (1961).
3. DOMENICALI C. A. an CHRISTENSON E. L., *J. appl. Phys.* **32**, 2450 (1961).
4. RICHTER F. and KIERSPE W., *Z. Naturf.* **20a**, 1371 (1965).
5. KIERSPE W., *Z. Metallk.* **58**, 895 (1967).
6. WEISS W. D., *Z. Metallk.* **58**, 909 (1967).
7. GOLD A. V., Mc DONALD D. K. C., PEARSON W. P. and TEMPLETON I. M., *Phil. Mag.* **5**, 765 (1960).
8. NYSTRÖM J., *Ark. Mat. Astr. Fys.* **34A**, No. 27.
9. WILSON A. H., *The Theory of Metals*. Cambridge (1965).
10. CHRISTENSON E. L., *J. appl Phys.* **34**, 1485 (1963).
11. SCHRÖDER P. A., *Phys. Rev.* **138**, 105 (1965).
12. HERBST U. and WAGNER D., *Z. Phys.* **208**, 490 (1968).
13. KLEIN A. P. and HEEGER A. J., *Phys. Rev.* **144**, 458 (1966).
14. DANIEL E., *J. Phys. Chem. Solids* **23**, 975 (1962).
15. FOILES C. L., *Phys. Rev.* **169**, 472 (1968).
16. SCHRIEFFER J. R., *J. appl. Phys.* **38**, 1143 (1967).
17. VOGT E. and GERSTENBERG D., *Ann. Phys.* (7) **4**, 145 (1959).
18. PUGH E. and RYAN F. M. *Phys. Rev.* **111**, 1038 (1958).

J. Phys. Chem. Solids Pergamon Press 1969. Vol. 30, pp. 491–496. Printed in Great Britain.

TRAP DISTRIBUTION AND SPACE-CHARGE LIMITED CURRENTS IN ORGANIC CRYSTALS. ANTHRACENE

J. SWORAKOWSKI and K. PIGOŃ
Department of Physical Chemistry, Wroclaw Technical University, Wybrzeze Wyspiańskiego 27, Wrocław, Poland

(*Received* 29 *May* 1968; *in revised form* 15 *August* 1968)

Abstract—A simplified theory of space-charge limited currents in a crystal with the 'diffuse trap level' has been discussed. The equations derived have been applied to experimental current-voltage and current-temperature characteristics in anthracene crystals. The hole trap band having the bottom at −0·76 eV approximately has been found.

INTRODUCTION

STEADY-STATE space-charge limited currents /SCLCs/ in organic crystals have been reported by many authors. The current-voltage characteristics have usually been interpreted according to the equations given by Lampert[1] for the crystal with a shallow trap level, and by Rose[2] and Mark and Helfrich[3] for the crystal with traps distributed exponentially within the whole forbidden gap. Although general features of the characteristics are correctly described under these assumptions, in some cases only qualitative agreement was achieved.

In the present paper the current-voltage dependence has been discussed following the simple treatment applied by Lampert, and Mark and Helfrich. Unlike those authors, however, the crystal with a 'diffuse trap level' (trap band) has been considered. Hence a unified approach has been achieved to the both cases discussed by previous authors.

The theory has been compared with the experimental results obtained for the system: anthracene-liquid redox electrode. The temperature dependence of SCLC has also been investigated. From the above measurements the position of the bottom of the trap band as well as that of the maximum of the trap distribution have been estimated.

THEORY

In the present paper the following assumptions have been made:

1. The band model is applied to describe the current carrier behaviour in the crystal*.
2. One of the electrodes forms an 'ohmic contact', i.e. is capable to inject the carriers into the crystal at a sufficiently high rate.
3. Diffusion of the excess current carriers in the crystal can be neglected (cf. [3, 4]).
4. Only electron current will be discussed (the similar relationships can be obtained also for the hole currents).
5. The trap states of uniform spatial distribution occur within the energy range (E_L, E_U). The distribution function for the density of traps has been approximated by the formula:

$$h(E) = \frac{H}{2kT_c}\exp\left(-\frac{|E-E_T|}{kT_c}\right) \qquad (1)$$

where: $h(E)$—trap density in the energy range (E, $E+\mathrm{d}E$); H—total space density of traps; E_L, E_T, E_U—energies corresponding to the lower edge, maximum and the upper edge of the trap distribution, respectively; T_c—characteristic temperature of the trap distribution. The trap band is assumed to be sufficiently wide, i.e. $E_t - E_L > 2kT_c$. The zero level of the energy scale corresponds to the lower edge of the conduction band, the positive direction of the energy axis pointing towards the top of the band.

---

*This assumption has been made on account of the relatively simple mathematical description only.

6. The Boltzmann statistics have been applied to the free carriers in the band, whereas the Fermi–Dirac statistics have been applied to the trapped ones.

The density of current (j) due to an external field applied to the crystal may be evaluated by solving the continuity equation:

$$j = u\rho_f(x)F(x) \tag{2}$$

and the Poisson's equation:

$$\frac{\mathrm{d}F(x)}{\mathrm{d}x} = -\frac{\rho_t(x)}{\epsilon} \tag{3}$$

where the functions $\rho(x)$ and $F(x)$ are defined by equations:

$$\rho(x) = en(x) \tag{4}$$

$$F(x) = -\frac{\mathrm{d}\psi(x)}{\mathrm{d}x}. \tag{5}$$

The meaning of the symbols used is as follows: u – mobility of the current carrier; $n(x)$ – particle density; $\rho_t(x)$ – total charge density; $\rho_f(x)$ – charge density of free carriers in the band; $F(x)$ – electric field intensity; $\psi(x)$ – electrostatic potential; ϵ – dielectric permittivity; x – linear variable; $x = 0$ at the injecting electrode, $x = d$ at the collecting one (d – crystal thickness); e – electron charge.

The solution of those equations depends on the particular form of the function $F(x)$. At low injection rates the crystal is free of space charge, and ohmic behaviour will be found. If the density of injected carriers exceeds that of the carriers thermally generated in the bulk, a space charge builds-up in the crystal which is dependent on the trapping. The Boltzmann statistics can be used in this case, but the so-called quasi steady-state Fermi level ($E_f(x)$) should be introduced. This quantity is defined by the equation:

$$n_f(x) = N_b \exp\left(\frac{E_f(x)}{kT}\right) \tag{6}$$

where N_b is the effective density of states in the conduction band, and $n_f(x)$ is the free carrier density in the conduction band.

In a particular case, when traps are either absent or completely filled, all injected carriers participate in the conduction process; thus $\rho_f(x) = \rho_t(x)$. The solution of the equations (2) and (3) leads to the relationship [5]:

$$j = \frac{9}{8}u\epsilon\frac{V^2}{d^3}. \tag{7}$$

When shallow traps occur in the crystal, the number of the free carriers as well as the trapped ones are mutually proportional. The general solution leads to the equation (see [1]):

$$j = \frac{9}{8}u\epsilon\Theta\frac{V^2}{d^3} \tag{8}$$

the parameter Θ being defined as follows:

$$\Theta = \frac{\rho_f(x)}{\rho_t(x)} \approx \frac{N_b}{\int_{E_t}^{E_u} h(E)\exp\left(-\frac{E}{kT}\right)\mathrm{d}E}. \tag{9}$$

Equation (8) is true for the voltage range, where the quasi steady state Fermi level lies below the bottom of the trap band. Thus the current is proportional to the square of the voltage as in the trap-free crystal, but its magnitude depends on the actual shape of the trap band. To eliminate the parameter Θ in (8), the integral in (9) should be evaluated. From equations (9) and (1) one obtains:

$$\frac{N_b}{\Theta} = \frac{H}{2kT_c}\left[\int_{E_l}^{E_T}\exp\left(-\frac{E}{kT}\right)\exp\left(\frac{E-E_T}{kT_c}\right)\mathrm{d}E + \int_{E_T}^{E_u}\exp\left(-\frac{E}{kT}\right)\exp\left(\frac{E_T-E}{kT_c}\right)\mathrm{d}E\right]. \tag{10}$$

Under the assumptions: $E_L < E_T - 2kT_c$, $T_c > T$, the approximate solution of (10) has been derived:

$$\Theta = \frac{2N_b(l-1)}{H}\exp\left(\frac{E_T-E_L}{kT_c}\right)\exp\left(\frac{E_L}{kT}\right) \qquad (11)$$

where $l = T_c/T$.

The increase in the applied voltage results in the increase of the number of injected carriers and hence in moving the quasi steady-state Fermi level towards the conduction band. At sufficiently high voltage some traps would be located below the Fermi level, i.e. would behave as deep traps. Due to the negligible possibility of the release of a carrier from these traps, they may be considered as completely and irreversibly filled. When the Fermi level is shifted sufficiently far above the lower edge of the trap band, the number of carriers captured in the deep traps exceeds the number of carriers in shallow ones, and the latter can be neglected in the discussion of the SCLC. When the condition: $E_L + kT_c < E_f(x) < E_T - kT_c$ is fulfilled, the concentration of the carriers in deep traps amounts to:

$$n_{tr}(x) = \int_{E_l}^{E_f(x)} h(E)\,\mathrm{d}E \approx \frac{H}{2}\exp\left(\frac{E_f(x)-E_T}{kT_c}\right). \qquad (12)$$

Using the equations (2), (3), (5) and (12), and assuming $F(0) = 0$, one obtains finally:

$$j = N_b u e^{1-l}\exp\left(\frac{E_T}{kT}\right) \times\left[\frac{2\epsilon}{H}\left(\frac{l}{l+1}\right)\right]^l\left(\frac{2l+1}{l+1}\right)^{l+1}\frac{V^{l+1}}{d^{2l+1}}. \qquad (13)$$

The above equation differs only by a constant factor from that derived by Muller[6] under the assumption of a different distribution of traps within the forbidden gap, and becomes identical with the equation given by Mark and Helfrich[3] when putting $E_T = 0$.

The transition voltage at which the current departs from the quadratic to the superquadratic region is given by combining the equations (8), (11) and (13):

$$V_{tr} = \frac{eHd^2}{2\epsilon}\exp\left(\frac{E_L-E_T}{kT_c}\right)\left[\frac{9}{8}(l-1)\right] \times\left(\frac{l+1}{2l+1}\right)^{l+1/l-1}\left(\frac{l+1}{l}\right)^{l/l-1}. \qquad (14)$$

Further increase in the number of injected carriers shifts the quasi steady-state Fermi level above the maximum of the trap band. If $E_f(x) > E_T + kT_c$, the concentration of trapped carriers approximates to:

$$n_{tr}(x) = \int_{E_l}^{E_f(x)} h(E)\,dE \approx H. \qquad (15)$$

In this case all traps may be considered as completely filled and the current fulfills the Mott and Gurney equation (equation (7)).

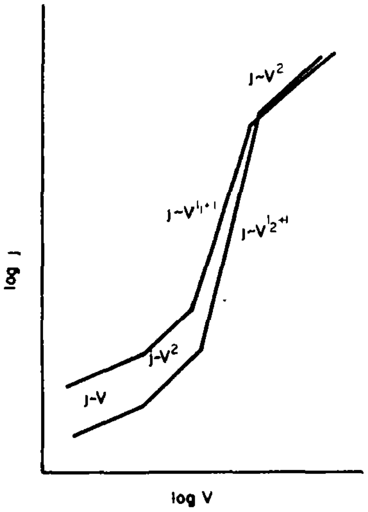

Fig. 1. Theoretical current-voltage characteristics at different temperatures ($T_1 > T_2$).

EXPERIMENTAL

Anthracene c.p. (FOCh-Gliwice) was purified by vacuum sublimation following by the repeated zone melting. The crystals were grown by slow sublimation in nitrogen atmosphere. Thin plateletts with the area of the {001} face up to 3 cm² and up to 150 μ

thick were obtained in this way. The thickness was determined by the weighing and measuring of the area. The crystals were stuck to the front wall of the measuring cell with silicone grease. The area contacting with the electrodes amounted to 7 mm^2 approximately. As the hole injecting electrodes Ce^{4+} and $Cr_2O_7^{2-}$ acidic solutions were used, the inert electrode being a Na_2SO_4 solution.

A measuring cell made of quartz or teflon was mounted in a thermostatic jacket heated by running water. The hot junction of the copper-constantan thermocouple was placed close to the crystal, without touching it however. The voltage has been applied from d.c. stabilised supply unit and the current was measured by means of a vibrating reed electrometer.

When the voltage has been applied, the current changed at first rapidly then more slowly. After some dozen (or dozens) of minutes the current was nearly constant (i.e. did not change during 2÷3 min). The results given below refer to these 'quasi steady-state' currents.

The current-voltage characteristics were determined for each crystal at several temperatures ranging from 15 to 80°C. In the low-voltage range the current is proportional to the square of the voltage, while at higher voltages it increases with 6–8th power of the voltage. This gives for the characteristic parameter of the trap distribution (kT_c) the approximate value of 0·15 eV.

According to equation (14) the transition voltage should slightly increase with temperature ($dV_{tr}/dT = 7\times10^{-2}$ V deg^{-1}). This was not found, however, in our experiments (see Fig. 2). The slight decrease of V_{tr} is probably due to the diminuation of the crystal thickness in successive runs in effect of the anode reaction.

According to equations (8) and (11) the knowledge of the temperature dependence of SCLC in the quadratic region of the characteristic makes it possible to evaluate the energy of the bottom of the trap band (E_L) if the function of u, ϵ, N_b on temperature is known. Assuming after Kepler[7] and Chojnacki[8] the approximate relationship $u \sim T^{-2}$ for holes in anthracene, and neglecting the change of ϵ, N_b and $(T_c - T)$ with temperature one obtains:

$$\log(jT^3) = A + \frac{B}{T}. \qquad (16)$$

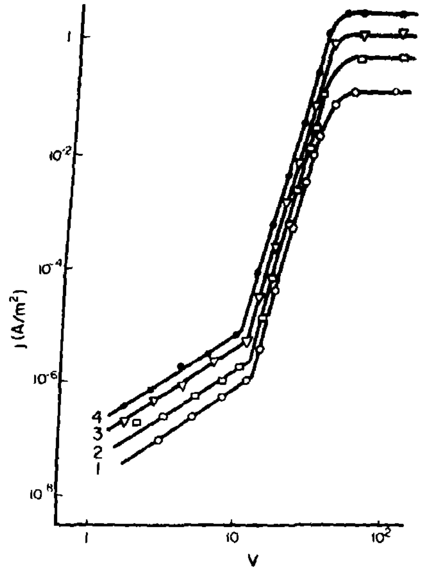

Fig. 2. Experimental current-voltage characteristics at different temperatures. Crystal thickness 26 μ. 1. T = 292°K; 2. T = 304°K; 3. T = 315°K; 4. T = 325°K.

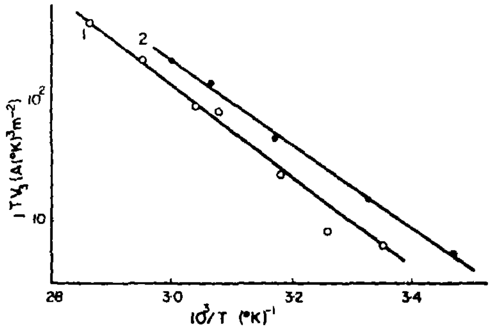

Fig. 3. Temperature dependence of SCLC in quadratic region. 1. crystal thickness 48 μ, applied voltage 15 V, 2. crystal thickness 25 μ, voltage 5 V.

From the slope B the value of E_L has been evaluated to $(-0{\cdot}76 \pm 0{\cdot}08)$ eV (mean value from 9 independent runs).

Considering the condition: $E_L < E_T - 2kT_c$ (see equations (10) and (11)) we suppose that the maximum of the trap distribution lies not deeper than at $-0{\cdot}45$ eV*. The mean value of the product $H \exp(-E_T/kT_c)$ evaluated by assuming $N_b = 4 \times 10^{27}$ m^{-3}, $\epsilon = 3 \times 10^{-11}$ F/m, $u = 8 \times 10^{-5}$ m^2/V sec, and inserting the experimental values into equations (8) and (11) amounts to 2×10^{20}m^{-3} approximately. This is the upper limit of the value of H (for $E_T \to 0$). The lower one evaluated for $E_T = -0{\cdot}45$ eV amounts to 10^{19} m^{-3} approximately.

The temperature dependence of the SCLC in the superquadratic region is, according to equation (13) much more complicated. To the first approximation the graph $\log j$ vs. $1/T$ is linear with the slope depending on the voltage, crystal thickness, and the total trap density. Assuming $-0{\cdot}45$ eV $< E_T < 0$ eV one obtains for the trap density the limiting values: $3 \times 10^{17} \div 5 \times 10^{18}$ m^{-3} for the crystal 1 and $2 \times 10^{16} \div 5 \times 10^{17}$ m^{-3} for the crystal 2. The results disagree by $1 \div 2$ orders of magnitude with the estimation based on the quadratic region.

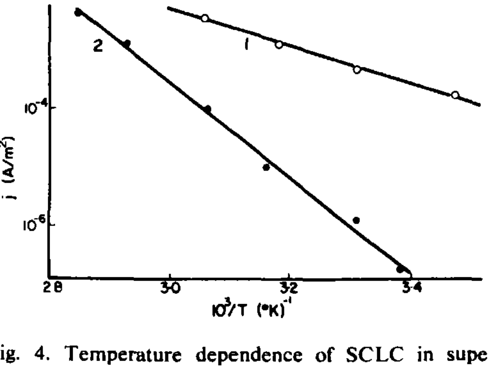

Fig. 4. Temperature dependence of SCLC in superquadratic region. 1. crystal thickness 26 μ, applied voltage 20 V, 2. crystal thickness 43 μ, voltage 160 V.

The trap densities found here are rather low as compared with the values given by most of the authors. A possible explanation for this discrepancy can be sought in assumption of the nonuniform spatial distribution of traps within the crystal. It seems reasonable to assume higher density of traps in the surface layer. After Nicolet[9] the apparent value of the trap density ignoring the effect may be too low by several orders of magnitude.

The exponential dependence on the reciprocal temperature was also found for saturation currents. It is due to the change of the injection rate with the temperature, and will be discussed elsewhere[10].

CONCLUSIONS

From the parameters which determine the shape of the trap band, i.e. T_c, E_L, E_T, E_l and H, only two former ones can be evaluated by the study of the temperature dependence of SCLCs. Contrary to the models used by Lampert[1] and Mark and Helfrich[3], only the product $H \exp(-E_T/kT_c)$ may here be determined from experimental results, and not the quantities of H and E_T separately.*

We have found in anthracene crystals the trap band having the bottom at $-0{\cdot}76$ eV approximately, and the maximum not deeper than at $-0{\cdot}45$ eV. The value of $-0{\cdot}76$ eV resembles those obtained by Kokado and Schneider[11] from thermally stimulated current (TSC) measurements. It may be shown, however, that TSC method reveals the energy of the upper limit of trap distribution, thus there are probably two sets of hole traps in anthracene: the first, relatively shallow, responsible for the shape of the current-voltage characteristics, and the other, a deeper one revealed in TSC experiments.

---

*For the hole currents the upper edge of the valence band has been chosen as the zero point of the energy scale.

*According to (10) and (11) the product $H \exp(-E_T/kT_c)$ could be evaluated from the measured current density in the quadratic region whereas from the current density in the superquadratic region (equation 13)) $Hl \exp(-E_T/kT)$, i.e. l-th power of the former expression.

REFERENCES

1. LAMPERT M. A., *Phys. Rev.* **103**, 1648 (1956).
2. ROSE A., *Phys. Rev.* **97**, 1538 (1955).
3. MARK P. and HELFRICH W., *J. appl. Phys.* **33**, 205 (1962).
4. SCHILLING R. B. and SCHACHTER K., *J. appl. Phys.* **38**, 841 (1967).
5. MOTT N. F. and GURNEY R. W., *Electronic Processes in Ionic Crystals*. Oxford University Press, Oxford (1940).
6. MULLER R. S., *Solid St. Electron.* **6**, 25 (1963).
7. KEPLER R. G., *Phys. Rev.* **119**, 1226 (1960).
8. CHOJNACKI H., *Mol. Crystals* **3**, 375 (1968).
9. NICOLET M. A., *J. appl. Phys.* **37**, 4224 (1966).
10. SWORAKOWSKI J., *Acta phys. Polon.* In press.
11. KOKADO H. and SCHNEIDER W. G., *J. Chem. Phys.* **40**, 2937 (1964).

J. Phys. Chem. Solids Pergamon Press 1969. Vol. 30, pp. 497–502. Printed in Great Britain.

PSEUDOPOTENTIAL IMPURITY THEORY AND COVALENT BONDING IN SEMICONDUCTORS*

M. JAROŠ† and P. KOSTECKÝ
Institue of Radioengineering and Electronics, Czech. Academy of Sciences, Prague 8, Czechoslovakia

(*Received* 15 *May* 1968; *in revised form* 12 *August* 1968)

Abstract – A method for constructing of the impurity potential is suggested including covalent effects. The approach presented is based on the Abarenkov–Heine model potential method. In contrast to other attempts, this method promises a quantitative estimation of the charge redistribution and polarisation effects due to the impurity potential. Special attention is paid to the impurity problem in zero-gap semiconductor. The local part of the impurity potential is given for the antimony atom as the impurity in gray tin crystal.

1. INTRODUCTION

MANY CONSIDERABLE works to describe the impurity states in insulators and semiconductors were already made. Shallow states, characterised by ionisation energy being small compared with the band gap were understood in terms of Kohn's effective mass approximation (EMA[1]; deep states within framework of Heitler–London theory. In all the following text the only shallow-like states of a donor impurity with one excess electron are the subject of our discussion. Nevertheless, the theory of Sections 2 and 3 is in principle quite general and includes the case of deep states, as well.

Using the EMA model, one can reduce the wave equation for impurity states to a hydrogenic equation for an envelope function. Hermanson and Phillips[2] have formulated the general criterion for the validity of the EMA, taking into account the form of the host crystal bands. They introduced the pseudowave equation in Wannier representation, in which apart from the hydrogenic term $1/\epsilon(r)r$ ($\epsilon(r)$ being static dielectric function) the repulsive term is introduced as an analogy to the familiar Phillips-Kleinman pseudopotential formalism. Next perturbing terms arise from the breakdown of the dielectric screening and change of the mass of the donor-contributed electron in the vicinity of the impurity atom.

Except from these 'central cell corrections', Sham[3] examined the long-range properties of the impurity potential by many-body technique. With assumptions of the Kohn's EMA model he established the change in electron mass operator in terms of the first and second order vertex parts. Using the Ward identities for perfect insulator, he found some long range terms going as $1/r^2$, as a correction to the EMA hamiltonian. In tight binding model, the impurity potential polarises the electron-ion pairs in the neighbourhood of a positive ion. The donor electron will see at large distances the Coulomb potential screened by these dipoles. Further, due to the pure exchange and correlation effects with the lattice electrons in the vicinity of the donor electron, the exchange and the correlation part of the electron impurity mass operator differs from that of the pure insulator; this change is represented by chemical potential shifted via the local change in the electrostatic potential. This change may also be expressed by adding a $\sim 1/r^2$ term to EMA hamiltonian.

Liu and Brust[4] have tried to solve the donor impurity problem in zero-gap semiconductor. They have constructed the Schrödinger equation in Wannier representation on assuming that the impurity potential does not couple different bands and two touching bands are coupled by central cell correction. The resonant energy of the impurity state can be written

---

*The work was presented in part by one of us (M.J.) in the Conference on Seminetals and Narrow Gap Semiconductors, 2–4 April 1968, University of Durham, Durham, England.

†*Present address:* Department of Theoretical Physics, University of Newcastle upon Tyne, England.

$$E_\lambda{}^{\mathrm{res}} = E_\lambda + V_{cc}|\Phi_\lambda(0)|^2 \tag{1}$$

where E_λ is the hydrogenic eigenvalue corresponding to the principal quantum number $_\lambda$ and $|\Phi\rangle$ is the respective eigenfunction. V_{cc} is the intra-c-band matric element of the impurity potential.

While the many-body method produces important results beyond the EMA, as far as the nature of the impurity problem is concerned, the only EMA(one-band and one-electron) model gives a quantitative estimation. Further, there is no way to account for the realistic host crystal valence electron distribution.* The purpose of this paper is to suggest a method which can remove the above mentioned difficulties.

Our interest is directed to the case of zero-gap semiconductor as a host material, having the gray tin as an example[7]. As we will demonstrate in our Table 1, in proof to the Heine's second order gap investigations[8], the amount of the covalent behaviour of gray tin seems to be at least the same as that of Si, against usual assumption. It is believed that it can be explained through the nonlocal potential terms[9]. Because of the fact that the donor electron states are quite sensitive to the above mentioned properties of the host crystal, the problem promises to be extremely interesting for us. Next, in zero-gap semiconductor, the impurity states disappear in valence band having the character of the resonance states. So, the many-body effects in the sense of Sham's work will apear in a new view[10].

Table 1. *Covalent contribution to the* $\langle 111\rangle$, $\langle 220\rangle$, $\langle 311\rangle$ *formfactors in Rydbergs are given for* Si, Ge *and gray tin* ($\alpha-$Sn)

	$v_G\langle 111\rangle$	$v_G\langle 220\rangle$	$v_G\langle 311\rangle$
Si	−0·013	−0·015	−0·003
Ge	−0·035	−0·032	−0·017
$\alpha-$Sn	−0·082	−0·016	−0·006

In Section 2, we present the simple method for the reformulation of the Abarenkov–Heine (A–H) model potential approach adopting the Phillips new theory of the covalent bonding in semiconductors. Both, the A–H[12] and the Phillips[13] theories are discussed carefully in the original papers and we assume the reader being acquainted with them. Nevertheless, we review briefly the basic ideas of same to make our theory easy to follow.

In Section 3 we use the results of the foregoing Section 2 to introduce the impurity potential. We have applied our theory to the calculation of the local part of the impurity potential. (Table 2). We have found a 10 per cent change in A_2 as a consequency of accounting for the covalent terms in A–H theory and for the appropriate shift of the covalent charges due to the impurity potential.

To be able to calculate nonlocal part of the impurity potential (A_0, A_l), it is necessary to follow the procedure as proposed in Section 4. There we have also discussed our theory in the sense of this section.

2. COVALENT ABARENKOV–HEINE MODEL POTENTIAL METHOD

In the sense of the OPW method, the ionic potential can be represented by some Model Potential[11]. Wave function is in this approach (w.f. of the valence electron) made orthogonal to the one-electron core states. The Model Potential is written on following A–H[12]

$$\begin{aligned} \hat{V}_M &= -\sum_l A_l(r_1E)\,\hat{P}_l \ldots r < R_M \\ \hat{V}_M &= -\frac{z}{r} \ldots r \geqslant R_M. \end{aligned} \tag{2}$$

---

*Perhaps besides of the tedious calculation in the sense of Callaway[5] or Benneman[6].

Table 2. Model potential constant A_2 *for different cases is presented*: (1) $\alpha-$Sn *in covalent model*; (2) d = 0·1 *shift included*; **no change in screening is accounted*

	$Sn_{(A-H)}$	$Sn_{(1)}$	$Sb_{(A-H)}$	$Sb:Sn_{(1)}$	$Sb:Sn_{(2)}$
A_2^*(a.u)	1·62	1·57	1·80	1·78	1·76

P_l is the projection operator separating from the operated state l-spherical harmonic part, $A_l(E,r)$ is a general function of the valence electron energy. The wave function of the electron is given by Schrödinger equation with potential (2). So, model potential is nonlocal and energy dependent. Following A–H we can understand A_l as r-independent and to use

$$A_l(E) = A_2(E); \quad l \geqslant 3. \tag{3}$$

Using the fact, that the spherical harmonics form the complete set, we have

$$\hat{V}_M = -A_2-(A_0-A_2)\hat{P}_0-(A_1-A_2)\hat{P}_1\ldots \qquad r < R_M$$

$$\hat{V}_m = -\frac{z}{r} \tag{4}$$

The local part is evidently represented by A_2, see Fig. 1.

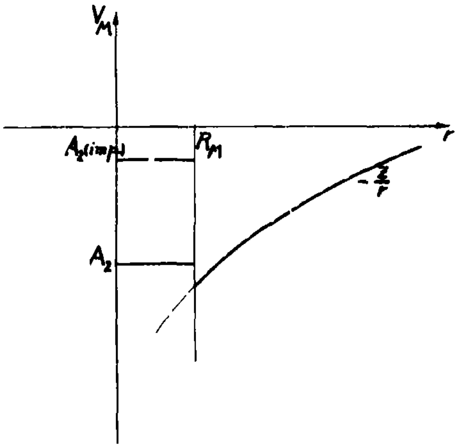

Fig. 1. Simple graphical representation of the local part of the A–H model potential. – Solid line shows the A–H ionic model potential[2]. --- Dashed line shows the hydrogenic potential - - Interupted line ($A_{2(imp)}$) shows symbolically the impurity model potential; it is obtained taking $A_{2(imp)}$ in place of the A_2 (as defined in Section 3) and putting $Z = 1$.

While (4) is the potential quite adequate for description of the isolated ion valence electron, in a solid, the valence electrons form an analogy to the electron gas which screens the ion potential (4). In linear approximation of A–H

$$V_{Screened}(\mathbf{q}) = \frac{V_{bare}(\mathbf{q})}{\epsilon(\mathbf{q})}. \tag{5}$$

Going to the q-components, atomic (bare) formfactor is

$$V(\mathbf{q}) = \langle \mathbf{k}|\hat{V}_M|\mathbf{k}+\mathbf{q}\rangle \tag{6}$$

where matrix element is calculated between plane waves normalised to the atomic volume. However, due to the nonlocal character of the (4), the equation (6) is not quite correct. We have to write

$$\langle \mathbf{k}|\hat{V}_M|\mathbf{k}+\mathbf{q}\rangle = V(\mathbf{q})+V(\mathbf{k},\mathbf{k}+\mathbf{q}). \tag{7}$$

Being restricted only to the vicinity of the Fermi sphere surface, $|\mathbf{k}| = |\mathbf{k}+\mathbf{q}| = K_F$ and the nonlocal part in (7) can be averaged over the Fermi sphere, which leads to (6). Equation (6) expresses the scattering of the free electron with Fermi impulse on the potential of (4).

The crystal potential is given as

$$V(r) = \sum_{\mathbf{G}} V_{screened}(\mathbf{q})\, S(\mathbf{G})e^{i\mathbf{G}r}$$

where $\mathbf{G}$ is the reciprocal lattice vector and $S(\mathbf{G})$ are the structure factors, introducing the lattice geometry of the solid into potential.

Now, let us write the one-electron wave function $\Phi(r)$ and wave equation in the pseudopotential representation for $\Phi(r)$ is

$$\left(-\frac{\hbar^2}{2m}\nabla^2+\hat{V}_M\right)\Phi(r) = E_F\Phi(r). \tag{9}$$

Potential V_M is that of equation (4), $V_M = V_M(E)$. The fact that the valence electron is a member of an electron gas is reflected by using $V_M(E) = V_m(E_F)$.

$$E_F = \epsilon_F - V_{\text{rest}} \tag{10}$$

where ϵ_F is the Fermi energy and V_{rest} includes the exchange, the correlation, orthogonality corrections and other electrostatic terms. Explicit formula of A–H [12] is

$$\begin{aligned} E_{F(\text{A-H})} = &- |\text{M.I.E.}| - |\text{B.E.E.}| \\ &+ \mu_c(r_s) + \mu_x(r_s) + \tfrac{3}{5}\left(\frac{\hbar^2 k_F{}^2}{2m^*}\right) - E_c \\ &- E_x + \frac{0{\cdot}6\,Ze^2}{R_A} - \mu_c(r_s) \\ &- \mu_x(r_s) - \frac{Ze^2}{R_A}\left[3 - \tfrac{3}{4}\left(\frac{R_M}{R_A}\right)^2\right]. \end{aligned} \tag{11}$$

$|\boldsymbol{\tau}|$ is the neighbour $\langle 111\rangle$ atoms distance; M.I.E. the mean of the first Z ionisation energies of the free atom; B.E.E. is the cohesive/energy of the solid per electron; $(\mu_x(r_s)_1)$ $\mu_c(r_s)$ is the total exchange and correlation potential of the free electron gas characterized by density r_s; E_x, E_c is the exchange and correlation energy of the free electron gas of density r_s; $0{\cdot}6\,Ze^2/R_A$ is the formula we have used from Kittel, *Quantum Theory of Solids* p. 112 (1964). (See also (15)).

Having defined the atomic and crystal potentials through the A–H Model Potential, we have to introduce a covalent approach; it is based on the recent study of Phillips [13].

In the sense of equation (5) the formation of the covalent bonds may be understood as local field correction; i.e. the nondiagonal part of the dielectric function tensor is neglected when accounting for the screening effects [14]. This is indicated by second term in the right part of the following equation

$$V_{\text{screened}}(\mathbf{q}) = \frac{V_{\text{bare}}(\mathbf{q})}{\epsilon(\mathbf{q},\mathbf{q})} + \sum_{\mathbf{G}} \frac{V_{\text{bare}}(\mathbf{q}+\mathbf{G})}{\epsilon(\mathbf{q},\mathbf{q}+\mathbf{G})}. \tag{12}$$

This implies that the part of the potential equivalent to the Fourier component $V_s(\mathbf{q})$ arises from the nonspherical charge density. Phillips [13] understands the formation of this part of the electron density as a consequence of the 'constructive interference' of OPW's. The deficiency in the 'atomic' valence electron density concentrates into the covalent sites, located halfway between the nearest neighbour atoms. As a first approximation Phillips supposes point charges at these sites, $2Z_b|e|$, where

$$Z_b = -\frac{1}{\epsilon(0)}. \tag{13}$$

$\epsilon(0)$ is the macroscopic dielectric constant of the material in question. Following this picture of the covalent charge distribution we write the formfactor as [13]

$$V_{\text{bare}}(\mathbf{q}) = v_a(\mathbf{q})S_a(\mathbf{q}) + v_b(\mathbf{q})S_b(\mathbf{q}). \tag{14}$$

S_a, S_b are the structure factors for system of ionic and covalent sites. As a screening function, Phillips uses the Penns one [15].

From (14), using the experimental values and $v_a(\mathbf{q})$ from the A–H tables (corrected for screening) we can estimate $v_b(\mathbf{q})$. $V(\mathbf{q})$ can be taken from the experiment as e.g. [16]. Estimated $v_b(\mathbf{q})$ have to correspond approximately to the total magnitude of the covalent charge as given in (13) [13].

We performed this rough estimation and the results are in Table 1. From the ratios of $v_b(\mathbf{q})$, $|\mathbf{q}| = \langle 111\rangle$, $\langle 220\rangle$, $\langle 311\rangle$ we can see a trend in a character of the covalent charge density shape. From the table presented it is easy to see that the point charge model for the covalent charge is probably quite adequate for Si and Ge, besides less for gray tin. The same conclusions as ours were made by Heine through his structural and second order gap investigation [8]. As far as Si is concerned, Martin's calculations [17] of the silicon lattice vibration spectra confirm the Phillips' point charge model.

Now, let us apply this consideration to the ϵ_F, V_{rest} in (10).

The total magnitude of the valence electron charge is decreased from Z to $Z(1-Z_b)$. New Madelung energy term will appear due to the system of the $-2Z_b|e|$ charges in covalent sites and $+4Z_b|e|$ in atomic sites[13]. A new term expressing the potential energy of the covalent charges tetrahedral system in the homogeneous valence electron gas in the sphere of radius R_A will appear, as well. At last, these covalent charges produce the electrostatic potential, at zero approximation r-independent. These three terms mentioned are the last ones in the following formula, respectively.

$$\begin{aligned} E_{F(\text{Covalent})} = & -|\text{M.I.E.}| - |\text{B.E.E.}| + \mu_c(r_s') \\ & + \mu_x(r_s') + \tfrac{2}{5}\left(\frac{\hbar^2 k_F'^2}{2m^*}\right) - E_c' - E_x' \\ & + \frac{0{\cdot}6Z(1-Z_b)e^2}{R_A} - \mu_c(r_s') - \mu_x(r_s') \\ & - \frac{Z(1-Z_b)e^2}{R_A}\left[3 - \tfrac{3}{4}\left(\frac{R_M}{R_A}\right)^2\right] + \tfrac{1}{2}\frac{Z_b^2 e^2 \alpha_M}{a_{\text{Lattice}}} \\ & - \frac{Z_b Z(1-Z_b)e^2}{2R_A}\left[3 - \left(\frac{|\boldsymbol{\tau}|}{2R_A}\right)^2\right] - 16\frac{Z_b e^2}{|\boldsymbol{\tau}|}. \end{aligned} \tag{15}$$

To find the model potential constants A_l, recalculated adequately to the covalent model, we use the linear approximation for the energy dependence of the A_l, following the Animalu's analysis[18]

$$A_l(E) = A_l(E_0) + (E-E_0)\left(\frac{\partial A_l}{\partial E}\right)_{E=E_0}. \tag{16}$$

$(\delta A_l/\delta E)_{E=E_F}$ are given in [18]. The numerical results for gray tin are in Table 2.

3. THE IMPURITY POTENTIAL

Let us suppose the host atom is substituted by an impurity one. To find the impurity potential, we use the energy dependence of A-constants (equation 16). So, going from the antimony crystal A–H model potential constants as given in [18] to the potential constants of the antimony as substitutional impurity in gray tin, we must recalculate A-constants according to equation (16) with $E = E_F(\alpha - Sn), E_0 = E_F(Sb)$.

In Section 2, we have defined the difference between the A–H and our covalent model. This difference is represented by some difference $E_{F(\text{A-H})} - E_{F(\text{Cov.})}$.

Next change arise from the shift of the covalent charges due to the impurity potential. Remember, that in pure gray tin the covalent charges are supposed to be at the halfway between the neighbour atoms in $\langle 111 \rangle$ directions. When antimony atom is in a tin-atom site, the covalent charge is assumed to be in a new equilibrium site which can be most simply found by comparing the point ion impurity and host atom screened potentials

$$V_{\text{impurity}}(r_1) = V_{\text{host}}(\boldsymbol{\tau} - r_1) \tag{17}$$

$\mathbf{r}_r$ is the position vector of the covalent site.

$$V_{(h,i)}(r) = \frac{1}{(2\pi)^2}\int_0^\infty \frac{\sin qr}{qr}\frac{v_{a(h,i)}(q)}{(q)} q^2 \mathrm{d}q.$$

$v_{a(h,i)}$ are the Fourier transforms of the screened point ion potentials (see Section 2 and [13]). The normalised shift d is defined as

$$d = \frac{\left|\mathbf{r}_1 - \frac{\boldsymbol{\tau}}{2}\right|}{\left|\frac{\boldsymbol{\tau}}{2}\right|}. \tag{18}$$

It means that there is an appropriate local change in E_F (through the last term in (15)), which gives a new A_2 again.

The impurity model potential (it's local part) is given by subtracting

$$A_{2(Sn)} - A_{2(Sb:Sn)} = A_{2(imp)}.$$

These constants are shown in Table 1. This local part of potential is also indicated symbolically in Fig. 1. Note that except for region inside the sphere of radius R_M, our impurity potential does not substantially differs from the hydrogenic $1/\epsilon r$ potential. The only difference is in treating the dielectric function $\epsilon(q)$.

4. DISCUSSION

Roughly speaking, the physical picture of our procedure of Sections 2 and 3 is as following: *First step*—model potential characterised by constants A_2, A_1, A_0 is dipped into homogeneous Fermi gas of density ρ; *Second step*—within an elementary cell, the Fermi gas is divided into system of covalent (point or small sphere-like) charges and homogeneous Fermi gas of new density ρ'; *Third step*—impurity atom is introduced and due to the existence of the impurity potential, the covalent charges are shifted from central position between neighbour $\langle 111 \rangle$ atoms. Using the Schrödinger equation (9) the constant A_2 is recalculated according to Animalus interpolation formula (16).

In Table 2 the constants A_2 in above mentioned approximations are shown. It detects in fact the sensitivity of the impurity potential to the local change in chemical potential. This change is achieved due to the covalency effects.

When we intend to calculation of A_0, A_1 the r-dependent terms appear in (9). The same happens when we go from the point or small sphere-like form of the covalent charge to a more general one. It is evident that r-dependent terms in potential make the matching procedure necessary for solving the equation (9) and thus (in fact repeating Animalu's procedure) we have new A–H constants in (4) and new derivative $(\partial A_n/\partial E)$. Among others, it is interesting to perform this calculation due to the uncertainty regarding the adequacy of the point-character of covalent charge distribution in gray tin; it was mentioned in some details in Section 2.

Acknowledgements—The authors are much indebted to Professor L. Liu for his critical remarks and discussions, and to Professor J. C. Phillips and Dr. V. Heine for worthy and encouraging communications. We should like to thank also to Drs. E. Šimánek and K. Žďánský for the continual interest in our work.

REFERENCES

1. KOHN W., *Solid St. Phys* **5**, 257 (1957); *Phys. Rev.* **105**, 509 (1957).
2. HERMANSON J. and PHILLIPS J. C., *Phys. Rev.* **150**, 652 (1966).
3. SHAM L. J., *Phys Rev.* **150**, 627 (1966).
4. LIU L. and BRUST D., *Phys. Rev.* **157**, 720 (1967).
5. CALLAWAY J. and HUGHES A. J., *Phys. Rev.* **156**, 860 (1967).
6. BENNEMAN K. H., *Phys. Rev.* **133A**, 1045 (1964).
7. GROVES S., and PAUL W., *Phys. Rev. Lett.* **11**, 194 (1963).
8. HEINE V., Private communications.
9. PHILLIPS J. C., Private communications.
10. JAROŠ M., and KOSTECKÝ P., To be published.
11. HARRISON W., *Pseudopotentials in the Theory of Metals*. Benjamin, New York (1966).
12. HEINE V., *et al.*, *Phil. Mag.* **9**, 451 (1964); *Phil. Mag.* **12**, 529, 1249 (1965).
13. PHILLIPS J. C., *Phys. Rev. Lett.* **19**, 415 (1967); *Phys. Rev.* **166**, 832 (1968).
14. FALK D., *Phys. Rev.* **118**, 105 (1960).
15. PENN D. R., *Phys. Rev.* **128**, 2093 (1962).
16. COHEN M. L., and BERGSTRESSER T. K., *Phys. Rev.* **141**, 789 (1966).
17. MARTIN P. C., *Phys. Rev.* To be published.
18. ANIMALU A. O. E., Technical Report No. 4. Solid State Theory Group, Cavendish Laboratory, Cambridge England (unpublished).

J. Phys. Chem. Solids Pergamon Press 1969. Vol. 30, pp. 503–508. Printed in Great Britain.

EXPERIMENTAL AND THEORETICAL STUDIES OF LOW-VOLTAGE ELECTROLUMINESCENCE OF ZnS SINGLE CRYSTALS†

W. J. BITER, INDRADEV‡ and FRED WILLIAMS
Department of Physics, University of Delaware, Newark, Delaware 19711, U.S.A.

(*Received* 27 *June* 1968; *in revised form* 5 *August* 1968)

Abstract—Blue electroluminescence of undoped ZnS single crystals has been detected at 1·6 V d.c. with a quantum efficiency of 10^{-11} photons/electron. The crystals were heat-treated in molten zinc. Previous models considered for electroluminescence with applied voltages less than the band gap, including injection and recombination via *p-n* junctions, are shown to be inadequate to explain our observations. An impact ionization-tunneling mechanism is proposed involving an n^*-n junction. Energetic electrons are injected through a blocking contact into the higher conductivity n^* region and at the n^*-n junction impact ionize an acceptor level in the n region creating a conduction electron in the n^* region. Radiative recombination then occurs in the n region between an ionized luminescent center and a second injected electron.

1. INTRODUCTION

VARIOUS authors[1–4] have reported electroluminescence (EL) in ZnS at voltages corresponding to electron energies near or below the band gap energy. Most of this work has been on thin films and crystals doped with Cl, Cu or Mn. We have obtained EL in undoped ZnS single crystals with voltages as low as 1·6 V d.c. In addition, we have obtained EL in Cu-doped samples with applied voltages as low as 2·0 V d.c.

2. MATERIAL PREPARATION

The crystals were grown by sublimation using a modification of the self-sealing tube method. The dopant was added during the growth process in the case of the ZnS:Cu crystals. Copper concentration for these crystals ranged from 10 ppm to 10^{+3} ppm. No impurities were intentionally introduced in the undoped crystals. Typical impurity concentrations for the undoped crystals were less than 10 ppm. The crystals as grown measured about 1 cm in dia. by 2 cm in length. The crystals were sliced into wafers with thicknesses varying between 0·5 and 5 mm. The wafers were heat-treated in Zn at 900°C for 10–40 hr. To insure that the wafers became totally immersed in liquid Zn, the tube was designed with a constriction in the center; the wafers were placed in one end and the Zn pellets in the other end. This tube was placed in the furnace and rotated end over end. The wafers were quenched by removing the tube from the 900°C furnace and cooling it in air or water. Both quenching media yielded similar results.

The electrical contacts were indium amalgam. Two contacts were applied, without heat-treating, to the same face of the crystal with a separation of 5 mm. The heat-treated crystals had a rough surface and the contacts were applied without polishing or etching. When polishing was attempted, EL did not appear below 15–20 V.

3. EXPERIMENTAL RESULTS

The emission was detected with a cooled RCA 7265 photomultiplier (PM) with an S-20 response. The PM output was measured

---

†Supported in part by the U.S. Army Engineers Research & Development Laboratory.

‡*Present address:* National Physics Laboratory, New Delhi, India.

with a Keithley 417 picoammeter with a current suppress feature. Voltage was applied to the crystal from a calibrated Keithley 240 power supply.

Light from the undoped ZnS crystal was detected with the PM at 1·6 V d.c. and could be seen with the dark-adapted eye at about 1·6–1·8 V. The emission from this crystal corresponds to the self-activated blue with a photon energy of 2·8 eV. The copper-doped crystal showed green emission at a threshold voltage of 2·0 V. It should be noted that due to the low light levels involved, the spectral distribution of the emission could not be determined below 5–6 V. However, the color determined by eye did not appear to change in going to lower voltages. Even though the EL was in different spectral regions for these differently doped crystals, their current-voltage characteristics, efficiencies and brightnesses were similar. This indicates that the excitation process is independent of impurities in the crystals. However, the recombination process remains dependent on the luminescent center present.

The light emission occured at the cathode and was diffuse at very low voltages. As the voltage was increased, the area of the emitting surface decreased. At voltages above about 15 V, the emission came from localized spots at the cathode. It can be concluded from both the temperature dependence and from the brightness-voltage dependence that different EL processes were dominant depending on whether the voltage was above or below about 10 V. The high-voltage characteristics probably involve impact ionization in the Schottky barrier formed at the cathode; the barrier becoming thicker at higher injection levels.

The crystàls were ohmic from 0·1 to 1 V. Above 1 V, the current rose sharply and approached a V^2 dependence at voltages greater than about 5 V. The brightness-voltage curve is shown in Fig. 1. We were unable to fit this curve with any of the commonly used EL equations for more than one or two orders of magnitude. The maximum discrepancy is at the lower voltages. The efficiency (defined by photons emitted/electron passing through the crystal) at 1·6 V was less than 10^{-11} photons/electron. The efficiency rose by about two orders of magnitude until the applied voltage reached about 6 V, where the B vs. I curve became linear.

Although measurements were made to determine photovoltages, none were found.

4. POSSIBLE MECHANISMS BASED ON INJECTION

Electroluminescence produced by injection at a p-n junction has been proposed as a possible mechanism in ZnS by some authors[1,3] and objected to by others[5].

We show that a simple injection via a p-n junction can not explain 2·8 eV light emission when the applied potential is 1·6 V or less. The following analysis applies to both a p-n homojunction of ZnS and to a p-n heterojunction, as for example Cu_2S in contact with ZnS. Since the light emission is characteristic of the ZnS (either self-activated blue or Cu Green), the injection would be positive holes into the n-type ZnS. The light emission is given by:

$$\frac{dn}{dt} = rn_n a^+$$

where n_n is the electron concentration in the n region, r is the recombination coefficient and a^+ is the ionized acceptor concentration in the n region.

In a p-n junction, the applied voltage will split the quasi-Fermi levels. Assuming the acceptor levels are in thermal equilibrium with the valence band, a^+ is given by:

$$a^+ = ae^{-(E_h - E_A)/kT}$$

where a is the concentration of acceptors in the n region, E_h is the quasi-Fermi level for holes and E_A is the energy level of the acceptor.

Putting $E_h = E_f - eV$, the light emission would be

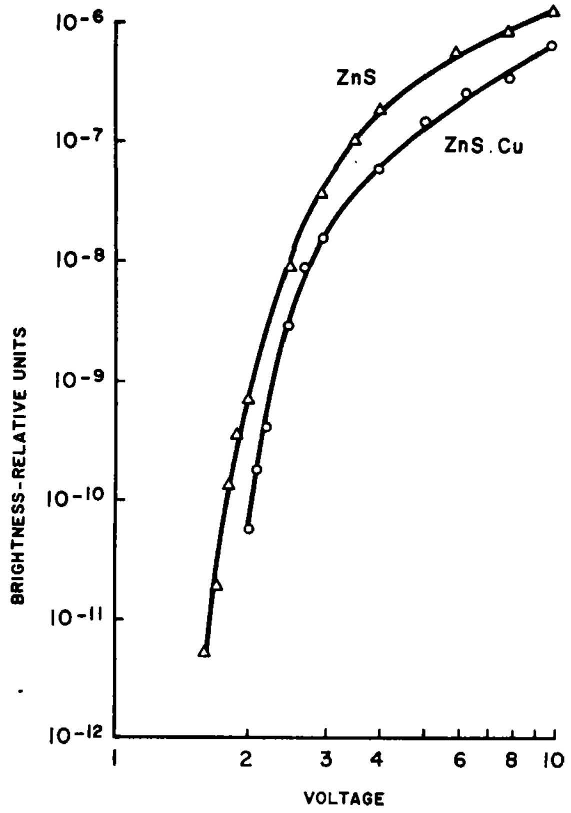

Fig. 1. Electroluminescence brightness vs. applied voltage for copper-doped and undoped ZnS crystals.

$$\frac{dn}{dt} = rN_c a e^{-(E_c-E_A)/kT} e^{eV/kT}$$

where V is the applied voltage and N_c is the density of states in the conduction band.

The acceptor energy level E_A depends on state of ionization because of lattice polarization effects. From photo-excitation measurements, the transition energy for excitation of an electron from the ionized acceptor (acceptor without a positive hole) to the conduction band edge is 3·4 eV[6]; from radiative recombination, the transition energy for capture of a conduction electron by the neutral acceptor is 2·8 eV. By considering the energy change accompanying the reversible change in state of ionization of the acceptor, including both electronic and lattice energy, it can be shown for the reasonable approximation that the lattice relaxation energies following each of the two radiative processes are the same, the average of the two values, $E_c - E_A = 3{\cdot}1$ eV, is the proper value for evaluating occupational probability. Taking r to be 10^{-13} cm^3 sec^{-1} (from Hogenstraaten[7]), $a = 10^{18}$ cm^{-3} and V equal to 1·6 V, the lowest value found experimentally, we predict an emission intensity of 10^{-2} photon cm^{-3} sec^{-1}. This is about four orders of magnitude below what was observed experimentally.

Even if the emitted light were of lower energy (e.g. Cu) the above equation would permit at most, one p-n junction in the crystal since the applied voltage appears in the exponential. If this voltage were divided between two junctions, the light intensity would decrease by many orders of magnitude. With a maximum of one p-n junction in the crystal, it becomes difficult to explain the emission always occuring at the cathode even assuming regions of low resistivity material connecting the junctions.

Attempts were made to fit the sharp rise in the I–V curve above one volt to an exponential equation of the form $I \propto e^{eV/nkT}$. This could only be done for about an order of magnitude and then gave a $n \sim 40$. The crystals also had $I \propto V^2$ at higher voltages.

In addition, formation of the second material for the case of a heterojunction would be expected at higher dopings of copper. In all cases the undoped ZnS showed a threshold voltage equal to or lower than the copper-doped crystals.

5. MECHANISM BASED ON IMPACT-TUNNELING AT AN n^*-n JUNCTION

With only 1·6 V d.c. applied to the crystal, the excitation mechanism producing the excited luminescent centers cannot involve ordinary impact ionization. In addition to a high field region, impact ionization requires a total potential drop of the order of 3 V to give the accelerated carriers sufficient energy to ionize the luminescent center.

In order to explain the observed emission of the blue light with the application of 1·6 V d.c., we propose the following. The bulk of the crystal, after heat-treatment in molten zinc is strongly conductive. However, due to the quenching, small regions are compensated and are less conductive. When one of these regions is located near the surface, an n^*-n junction is produced. With a blocking contact most of the applied potential will be across this contact. Electrons can be injected into the n^* region with kinetic energies as high as 1·6 eV above the bottom of the conduction band. Assuming these energetic electrons have approximately the same collision frequency as thermal electrons, we estimate a distance between collisions on the order of a few hundred Angstroms. Thus, with the n^* region roughly $1/10\,\mu$ wide, the injected hot electron can transverse the n^* region and, with a small but finite probability, can ionize a luminescent center in the n region by a combined impact ionization and tunneling mechanism creating a second conduction electron in the n^* region. This is shown in Fig. 2 under an applied voltage V. The injected hot electron is described by the Bloch function ψ' whose plane-wave part as modified by the n^*-n barrier is also shown in Fig. 2. Similarly, the impact ionization-tunneling transition between the effective mass function F of the luminescent center A in the n-region and the Bloch function ψ in the n^*-region are shown. Radiative recombination can occur between another injected electron which has reached the conduction band of the n region, and the ionized center, producing emission characteristic of the center.

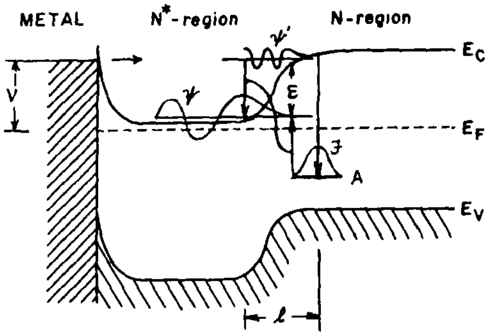

Fig. 2. Band model of impact ionization-tunneling mechanism of low voltage electroluminescence.

The maximum value for the tunneling distance l can be estimated assuming the overall electroluminescent efficiency η arises entirely from the tunneling probability which is taken as a separate factor in the impact ionization-tunneling transition probability and which is the following:

$$e^{2/\hbar \sqrt{(2m^*\epsilon)}\, l} \gtrsim \eta$$

where ϵ is the most probable barrier height for tunneling, as shown in Fig. 2, and the inequality takes care of inefficiencies in other parts of the complete mechanism. For the threshold V of 1·6 V and the photon energy of the emission maximum of 2·8 eV, ϵ must be less than 1·2 eV. With the maximum ϵ combined with the observed η of 10^{-11} photons/electron and m_e^* of 0·27[8], we find $l = 50$ Å. This is a rather abrupt junction and the associated space charge requires a density of donors of $10^{19}\,\text{cm}^{-3}$ in the n^* region. This is consistent with the work of Aven and Mead[9] who found a donor concentration in excess of $10^{18}\,\text{cm}^{-3}$ in ZnS crystals heat-treated in molten Zn.

This mechanism at lower voltages is not steady state. Every excitation process produces two electrons in the n^* region, and a bound positive hole in the n region. This will produce an increase in the required energy needed to ionize the center due to space charge effects. A rough calculation was made of the energy change assuming the stored charge to be on the surfaces of a capacitor. After 1 hr the levels shift by less than 10^{-4} eV. In addition, there is probably a considerable leakage effect in the n^* region. The formation of the n^*-n junction is apparently random, involving the heat treatment and quenching of the crystal. Unsuccessful attempts were made to determine the location of the n region by polishing.

6. DISCUSSION

Electroluminescent emission of photons with energies of about 2·8 eV under applied voltages of 1·6 V d.c. eliminated any mechanism involving only simple direct excitation of the luminescent center. Since the recombination can be identified as characteristic of ZnS (green for copper-doped crystals, blue for undoped ZnS) any injection mechanism must involve minority carrier injection into the ZnS. The assumption of a simple p-n junction to explain the observations fails to explain the emission occurring at the cathode and predicts an emission intensity at least several orders of magnitude too low.

We have proposed a two-step mechanism whereby the energy of the emitted photon originates in part from a hot electron ionizing a luminescent center by an impact-tunneling transition at an n^*-n junction and in part from a second hot electron transversing the n^* region to be radiatively captured by the ionized luminescent center in the n-region.

It can also be shown that the observed emission does not violate the laws of thermodynamics. The maximum electroluminescent efficiency can be derived from the second law of thermodynamics, and is[10]:

$$\eta = \frac{L}{W} = \frac{\text{Light out}}{\text{Work in}} = \frac{1}{1 - T/T_R}$$

where the radiation temperature T_R can be determined from

$$F = \text{flux} = \frac{8\pi\nu^2}{c^2}\frac{1}{e^{h\nu/kT_R} - 1}\cdot\Delta\nu$$

where ν is the frequency of the spectral maximum and $\Delta\nu$ is the half-width. Using the observed values of $F = 10^2$ photon/sec cm^2, $\nu = 6\times10^{14}$/sec, and $\Delta\nu = 10^{14}$/sec, yields $T_R = 640$°K and $\eta = 2·0$. With 1·6 V applied, $W = IV = 1·6$ eV.

$$\therefore L_{\text{max}} = \eta\cdot W = 3·2\,\text{eV}.$$

Experimentally, the emitted photon had an energy of 2·8 eV. In other words, from thermodynamics the emission of 2·8 eV photons at low intensity, e.g. 10^2 photons/sec cm^2, with the application of 1·6 V d.c. could occur with greater efficiencies than we observed.

Finally, it should be noted that the earlier observations of electroluminescence of zinc sulfide with applied voltages which are less than the band gap have been used as evidence for a minority carrier injection mechanism. The assumption of injection at a p-n junction is inconsistent with our experimental observations, and we have found that the impact ionization mechanism which occurs at high voltages can be modified to include concurrent tunneling and thus account for the observations at applied voltages which are approximately one-half of the band gap.

Acknowledgement—We are indebted to Professor Walter Franz for a helpful discussion of tunneling probabilities

REFERENCES

1. THORNTON W. A., *J. electrochem. Soc.* **108**, 636 (1961).
2. GILLSON J. L. and DARNELL F. J., *Phys. Rev.* **125**, 149 (1962).
3. GOLDBERG P. and NICKERSON J. W., *J. appl. Phys.* **34**, #6, 1601 (1963).
4. INDRADEV and GARLICK G. F. J., *Br. J. appl. Phys.* **18**, 1 (1967).
5. FISHER A. G., *Luminescence of Inorganic Solids* (Edited by Goldberg), p. 541. Academic Press New York (1966).
6. KODA T. and SHIONOYO S., *Phys. Rev.* **136**, A541 (1964).
7. HOOGENSTRAATEN W., *Philips Res. Rep.* **13**, 515 (1958).
8. WHEELER R. G. and MIKLOSZ J. C., *Physics of Semiconductors*, p. 873. Dunod, Paris (1964).
9. AVEN M. and MEAD C. A., *Appl. Phys. Lett.* **7**, 8 (1965).
10. WEINSTEIN M. A., *J. opt. Soc. Am* **50**, 597 (1960).

J. Phys. Chem. Solids Pergamon Press 1969. Vol. 30, pp. 509–520. Printed in Great Britain.

ELECTRODYNAMICAL PROPERTIES OF SUPERCONDUCTING CONTACTS*

G. DEUTSCHER, J. P. HURAULT* and P. A. van DALEN†
Laboratoire de Physique des Solides‡, Faculté des Sciences, 91-Orsay, France

(*Received* 26 *February* 1968; *in revised form* 19 *July* 1968)

Abstract—We have studied, experimentally and theoretically, the linear response to a small (d.c. or a.c.) magnetic field in the normal part of a normal-superconducting N/S binary layer. It has been shown that the tunneling characteristic of an N/S sandwich, measured on the N side, is sensitive to the values of the pair potential at points far away from the free surface of the N material.

Similar nonlocal effects also appear in the electromagnetic response. The greater the temperature compared to the critical temperature of N, the bigger these effects. Some experimental confirmations of these theoretical predictions have been obtained. The theory also explains: (1) why a Meissner effect has not been observed in Cu for the Pb/Cu systems, down to 1°K; (2) why, on the other hand, the r.f. absorption is much smaller in Cu coated with Pb than in normal Cu.

INTRODUCTION

WE CONSIDER a metal N backed by a superconductor S. Both materials are supposed to be 'dirty' and we assume the electrical contact between N and S to be good. At the temperature of the experiment, N is normal ($T > T_{cN}$, T_{cN} being the critical temperature of N) and S is superconducting ($T < T_{cS}$). In the normal metal, the pair potential decreases exponentially as e^{-Kx}, where K is given by[1]§.

$$\operatorname{Log}\frac{T}{T_{cN}} = \psi\left(\frac{1}{2}\right) - \psi\left(\frac{1}{2} - \frac{DK^2}{4\pi T}\right) \qquad (1)$$

D being the diffusion coefficient in N:

$$D = \tfrac{1}{3} v_F l$$

v_F being the Fermi velocity and l the mean free path.

We apply a small d.c. or a.c. magnetic field and we want to evaluate the response of the system to this perturbation. For a 'dirty' system, the relation between the resulting current $\mathbf{j}$ and the applied vector potential $\mathbf{A}$ will have the local form:

$$\mathbf{j}(\mathbf{r},\omega) = -Q(\mathbf{r},\omega)\,\mathbf{A}(\mathbf{r},\omega). \qquad (1')$$

Since Δ is small in N, we can perform expansions in powers of Δ for the evaluation of $Q(\mathbf{r},\omega)$. Δ being solution, in N, of the equation

$$\frac{d^2\Delta}{dx^2} = K^2\Delta \qquad (2)$$

we are led to a situation reminiscent of the gapless regime of ordinary dirty type II superconductors, and we might naively think that, as in this last case, $Q(\mathbf{r},\omega)$ will depend only on the value of Δ at the point $\mathbf{r}$ of interest[2].

But this is not true: Δ is not everywhere a solution of equation (2), due to the presence of the superconductor. A more careful treatment is needed then. As a result, we shall see that $Q(\mathbf{r},\omega)$ depends on the values of Δ not only around $\mathbf{r}$, but also in the superconducting metal S. We shall first treat, in Section 1, the zero frequency case ($\omega = 0$) and then in Section 2, the slightly more complicated case $\omega \neq 0$. In Section 3 we present some experimental results obtained with very low frequencies, and corresponding practically to $\omega = 0$.

---

*Partially supported by the Centre National d'Etudes Spatiales.

†On leave of absence from Philips Research Laboratories, Eindhoven, Netherlands.

‡Laboratoire associé au C.N.R.S.

§In the following, we adopt a system where $\hbar = k_B = 1$.

SECTION 1: THE STATIC RESPONSE FUNCTION

We make the following approximations (to be discussed at the end of this section): (1) The pair potential Δ is small everywhere, even in $S(T \lesssim T_{cS})$. (2) Both materials are supposed to have the same density of states at the Fermi level, and also the same diffusion coefficient D. (3) Lastly, we assume a simplified form for $\Delta(\mathbf{r})$ shown on Fig. 1: if Ox is an axis perpendicular to the interface, we take

$$\Delta(x < 0) = \text{const} = \Delta_{BCS}(T)$$

and, for $x > 0$, using relation (1)

$$\Delta(x) = \frac{1}{\alpha}\Delta_{BCS}(T)\exp(-Kx) \qquad (2')$$

where $\Delta_{BCS}(T)$ is the equilibrium value of Δ in a bulk S material at temperature T. $\alpha = V_S/V_N$, where V_S and V_N are the respective values, in S and N, of the BCS coupling constant[3].

The supercurrent resulting from the application of a small vector potential A is most easily evaluated using Green function techniques [4].

$$j(\mathbf{r}) = \frac{ie}{m}T\sum_{\omega}(\nabla_{r'} - \nabla_r)G_\omega(\mathbf{r},\mathbf{r}') - \frac{Ne^2}{m}\mathbf{A}(\mathbf{r}). \qquad (3)$$

The notations are standard. $\omega = (2n+1)\pi T$, n being an integer, N the electronic density.

Since we have assumed small values of Δ everywhere, we may expand $G_\omega(\mathbf{r},\mathbf{r}')$ in powers of Δ and evaluate $\mathbf{j}$ to the lowest order of Δ. So

$$\begin{aligned}\mathbf{j}(\mathbf{r}) = {} & \frac{ie}{m}T\sum_{\omega}(\nabla_{r'} - \nabla_r)\\ & \times\int\overline{G_\omega{}^0(\mathbf{r},\mathbf{l})\Delta(\mathbf{l})G_\omega{}^0(\mathbf{m},\mathbf{r}')}\\ & \times\overline{\Delta^+(\mathbf{m})G_\omega{}^0(\mathbf{m},\mathbf{l})}\,\mathrm{d}^3\mathbf{m}\,\mathrm{d}^3\mathbf{l}. \qquad (4)\end{aligned}$$

Here $G_\omega{}^\circ$ is the Green function of the pure normal metal and the line drawn over the integrand is associated with an average over the impurity configurations.

In order to do the calculation, it is convenient to go to the Fourier representation first without taking account of the presence of the field. So equation (4) becomes, without a magnetic field[5]:

$$\begin{aligned}\mathbf{j}(\mathbf{r}) = {} & -\frac{Ne\tau}{4m\pi T}\\ & \times\sum_n\int\frac{\mathrm{d}^3p_1}{(2\pi)^3}\frac{\mathrm{d}^3p_2}{(2\pi)^3}(\mathbf{p}_1 - \mathbf{p}_2)\Delta(\mathbf{p}_1)\Delta^+(\mathbf{p}_2)\\ & \times\frac{\mathrm{e}^{i\mathbf{p}_1\mathbf{r}}}{n+\frac{1}{2}+\dfrac{Dp_1{}^2}{4\pi T}}\frac{\mathrm{e}^{-i\mathbf{p}_2\mathbf{r}}}{n+\frac{1}{2}+\dfrac{Dp_2{}^2}{4\pi T}} \qquad (5)\end{aligned}$$

where τ is the collision time, and $\Delta(\mathbf{p})$ the Fourier transform of $\Delta(\mathbf{r})$.

It has been shown by Maki[5] that the inclusion of field effects could be realized by the replacement

$$\mathbf{p} \to \mathbf{p} \pm \frac{2e\mathbf{A}}{c}$$

the ± sign depending upon whether it operates on Δ or Δ^+. We are interested only in the lowest order term in $\mathbf{A}$. Thus we neglect terms in A^2 and, to this order, $|\Delta(\mathbf{r})|$ is not changed by the field. Furthermore, we may choose a gauge where Δ is real. Finally we get

$$\begin{aligned}\mathbf{j}(\mathbf{r}) = {} & -\frac{Ne^2\tau}{mc}\frac{\mathbf{A}}{\pi T}\\ & \times\sum_{n\geq 0}\left[\int\frac{\mathrm{d}^3p}{(2\pi)^3}\Delta(\mathbf{p})\frac{\mathrm{e}^{-i\mathbf{p}\mathbf{r}}}{n+\frac{1}{2}+\dfrac{Dp^2}{4\pi T}}\right]^2\end{aligned}$$

and since Δ depends on x only

$$\begin{aligned}\mathbf{j}(x) = {} & -\frac{Ne^2\tau}{mc}\frac{\mathbf{A}}{\pi T}\\ & \times\sum_{n\geq 0}\left[\int_{-\infty}^{+\infty}\frac{\mathrm{d}p}{2\pi}\Delta(p)\frac{\mathrm{e}^{-ipx}}{n+\frac{1}{2}+\dfrac{Dp^2}{4\pi T}}\right]^2. \qquad (6)\end{aligned}$$

We know that

$$\int_{-\infty}^{+\infty} f(q)g(q)\,\mathrm{e}^{-iqx}\frac{dq}{2\pi} = \int_{-\infty}^{+\infty} F(x')G(x-x')\,\mathrm{d}x'$$

where F and G are the respective Fourier transforms of f and g. Thus we can write

$$\int_{-\infty}^{+\infty} \frac{\mathrm{d}p}{2\pi}\Delta(p)\frac{\mathrm{e}^{-ipx}}{n+\frac{1}{2}+\dfrac{Dp^2}{4\pi T}} = \int_{-\infty}^{+\infty} \Delta(x')f_n(x-x')\,\mathrm{d}x' \quad (7)$$

with

$$f_n(u) = \frac{1}{2\pi}\int_{-\infty}^{+\infty} \frac{\mathrm{e}^{-ipu}\,\mathrm{d}p}{n+\frac{1}{2}+\dfrac{Dp^2}{4\pi T}} = \frac{2\pi T}{D}\frac{\mathrm{e}^{-q_n|u|}}{q_n} \quad (8)$$

$$q(n) = \sqrt{((n+\tfrac{1}{2})(4\pi T/D))}; \quad (n \geqslant 0).$$

Then, the final expression for $\mathbf{j}(x)$ becomes

$$\mathbf{j}(x) = -\frac{4\pi T\sigma}{D^2\;c}\mathbf{A} \times \sum_{n\geqslant 0}\left[\int_{-\infty}^{+\infty}\frac{\Delta(x')\,\mathrm{e}^{-q_n|x-x'|}}{q_n}\mathrm{d}x'\right]^2 \quad (9)$$

where σ is the normal state conductivity of the material.

If we are now interested in the penetration law of the magnetic field, it is convenient for us to introduce a local penetration depth $\lambda(x)$. Since $\operatorname{curl}\mathbf{H} = (4\pi/c)\mathbf{j}$ (assuming $\mathbf{A}$ to have nonzero components along the y axis, which allows us to choose a real value for Δ), we get

$$\frac{\mathrm{d}^2\mathbf{A}}{\mathrm{d}x^2} = \frac{1}{\lambda^2(x)}\mathbf{A}$$

$$\frac{1}{\lambda^2(x)} = \frac{16\pi^2}{D^2}T\frac{\sigma}{c^2} \times \sum_{n\geqslant 0}\left[\int_{-\infty}^{+\infty}\mathrm{d}x'\Delta(x')\frac{\mathrm{e}^{-q_n|x-x'|}}{q_n}\right]^2. \quad (10)$$

We see on formula (10) that the local penetration depth will be sensitive to the values of the pair potential not only in r, but also far from r. This is particularly true in our case where $\Delta(x.)$, for $x' < x$, is an exponentially increasing function of $|x'-x|$.

In fact, if we assume the following variation for Δ

$$\Delta(x') = \Delta(x)\,\mathrm{e}^{-K(x'-x)} \quad (11)$$

(which is reasonable for x sufficiently large), we obtain the usual formula for λ [6]:

$$\frac{1}{\lambda^2(x)} = \frac{16\pi^2}{D^2}T\frac{\sigma}{c^2}\Delta^2(x)\sum_{n\geqslant 0}\frac{4}{(q_n{}^2-K^2)^2}$$

or

$$\frac{1}{\lambda^2(x)} = \frac{4\sigma}{c^2}\frac{\Delta^2(x)}{T}\psi'\left(\tfrac{1}{2}-\frac{DK^2}{4\pi T}\right). \quad (12)$$

But, when we get closer to the interface, we must take account of the detailed shape of Δ, as depicted on Fig. 1, and some contributions to λ will come from the superconducting region. In fact, if we take account, in (10), of relation (2′), we obtain

$$\frac{1}{\lambda^2(x)} = \frac{16\pi^2}{D^2}T\frac{\sigma}{c^2}\Delta^2(x)$$

$$\sum_{n\geqslant 0}\left[\frac{2q_n}{q_n{}^2-K^2}+\mathrm{e}^{(K-q_n)x}\left(\frac{\alpha}{q_n}+\frac{1}{K-q_n}\right)\right]^2\frac{1}{q_n{}^2} \quad (13)$$

where $\alpha = V_S/V_N$.

Provided that K, as yielded by (1), be always smaller that the smallest of the q_n, i.e. q_0, the second term in the bracket of equation (13) will become negligible as one gets very far from the interface. In fact, we can consider two regions:

$-x \gg \dfrac{1}{q_0-K}$: formula (12) is valid

$-x < \dfrac{1}{q_0-K}$: formula (13) must be used.

These conclusions are similar to those of

Mauro in his study of tunneling effect [7].

Our corrections to formula (12) will be important when the region where it is significant is large. This will be the case if T is much larger than the critical temperature of the bulk normal sample T_{cN}. On the contrary, when T is of order of T_{cN}, it is correct to use formula (12) as we have already done in preceding papers [6, 8].

The case $T \gg T_{cN}$ (or, more generally, $|V_N|$ small)* is of particular interest as it is associated with the study of Meissner effect in some systems like Pb/Cu, and with the determination of the transition temperature, if it exists, of Cu or other noble metals. So let us now study the case $|V_N|$ small.

$|V_N|$ *small*

As $K \to q_0$, the leading term in the summation of equation (13) is the term $n = 0$. If we consider now the region in the proximity of the interface ($x < 1/|K-q_0|$), we can practically write

$$\frac{1}{\lambda^2(x)} = \frac{16\pi^2}{D^2} T \frac{\sigma}{c^2} \Delta^2(x) \times \sum_{n \geq 0} \frac{1}{q_n{}^2}\left[\frac{\alpha}{q_n} + \frac{1}{q_n + K}\right]^2 \qquad (14)$$

or

$$\frac{1}{\lambda^2(x)} = \frac{4\sigma}{Tc^2} \Delta^2(r) \sum_n F_n{}^2 \qquad (14')$$

with

$$F_n = \frac{2\pi T}{Dq_n}\left[\frac{\alpha}{q_n} + \frac{1}{q_n + K}\right].$$

To evaluate the summation over n, we shall make the following approximation: we replace F_n by F'_n such that

$$F'_n = \frac{2\pi T}{D} \frac{\gamma}{q_n{}^2 + K'^2}$$

γ and K'^2 being determined in such a way that $F_0 = F'_0$ and $F_1 = F'_1$. In this way we find

$$\gamma = \alpha + 0{\cdot}7$$

$$\frac{K'^2}{q_0{}^2} = \frac{0{\cdot}2}{\alpha}$$

The sum over the F'^2_n is then easily expressed in terms of digamma functions. Finally, for $x < 1/|K-q_0|$

$$\frac{1}{\lambda^2(x)} = \frac{\sigma}{c^2 T}(\alpha + 0{\cdot}5)^2 \psi'(\tfrac{1}{2}) \Delta^2(x). \qquad (15)$$

We can make the following comments about this last formula: (1). A crucial parameter is the value of the local penetration depth at the interface ($\lambda(x=0)$). It has been shown in [6] that the screening properties in N depended mainly on the value, at the interface, of the Landau–Ginzburg like parameter defined as

$$\kappa(0) = \frac{\lambda(0)}{K^{-1}}.$$

If $\kappa(0) \leq 1$, screening currents are effective in N. If $\kappa(0) > 1$, the magnetic field penetrates freely into N up to the interface. At a given temperature, since $\alpha\Delta(0) = \Delta_{BCS}(T)$, $\kappa(0)$ is proportional to $K(1 - 1/2\alpha)$. If we consider a series of materials N, the coupling constant of which increases from a small negative value to a small positive value, $1/\alpha$ decreases and κ increases. Thus the Landau–Ginzburg parameter $\kappa(0)$ increases continuously when the material becomes more repulsive. Nevertheless, provided that we are at low enough temperatures, $\kappa(0)$ may be lower than 1 and Meissner effect can be observed in such a case. Furthermore, if the

---

*When N cannot become superconducting at any temperature, i.e. if for instance the BCS coupling constant V_N is small and negative, then K is greater than q_0 and lower than q_1 and the solution of the linearized gap equation yields

$$\frac{1}{K-q_0} \sim -\frac{2\alpha}{q_0} > 0.$$

Then $1/(K-q_0) \gg 1/q_0$ and we can perform the same analysis as when V_N is small and positive: the only difference comes from the fact that α changes its sign.

N layer has a thickness of order K^{-1} and if $\kappa(0) \leq 0{\cdot}4$, one can expect the existence of a thermodynamical critical field relative to N, the breakdown field H_b[6, 9], even if N is a repulsive material. (2). For a given N material, with a critical temperature T_{cN}, and for a set of values of T such that $T > 2T_{cN}$ *and* $T > T_e^*$, $\lambda(0)$ goes $\sqrt{T}$, which is quite different from the temperature dependence predicted by [12]. (3). The ratio of $\lambda(0)$, as given by (15), to its value given by (12), is

$$\frac{2}{\alpha+0{\cdot}5}\sqrt{\left(\frac{\psi'(\frac{1}{2}-DK^2/4\pi T)}{\psi'(\frac{1}{2})}\right)}.$$

Taking account of the fact that V_N is small, and remembering (1), this ratio is roughly equal to $1/N(0)V_S$. Thus $\kappa(0)$, as given by (15), is larger than its former determination (12). For a Pb/Cu system, for instance, (12) predicted $\kappa \sim 1$ for $T \sim 1$°K, in the most favourable case. This meant that a very weak but detectable Meissner effect could be expected. On the other hand, the improved calculation (15) predicts that $\kappa(0)$ will be rather about 2·5, which explains why no screening properties have been observed in such systems†. (4).

$$\kappa(0) = \left(1-\frac{0{\cdot}5}{\alpha}\right)\frac{T}{\Delta_{\mathrm{BCS}}(T)}\frac{c}{De}\sqrt{\left(\frac{2\pi}{2N(0)\psi'(\frac{1}{2})}\right)}. \tag{16}$$

The only dependence of $\kappa(0)$ on α will be through the term $1-0{\cdot}5/\alpha$. Thus a determination of $N(0)V_N$ for weakly attractive or repulsive systems will be possible if a precision better than $0{\cdot}5/\alpha$ in the measurements is reached. Practically this represents a precision better than 10 per cent.

Finally, we would like to discuss the various approximations which have been used in these calculations. (1). We have supposed Δ to be small everywhere, which limits the validity of our estimations to the region $T > T_e$, and our results cannot be used for very low temperatures. This is particularly true for formula (15). When $|V_N|$ is small, (15) predicts that $\lambda(0) \to 0$ when $T \to 0$. In fact, in this case, λ_N must go to $\beta\lambda_S$ when $T \to 0$, λ_S being the penetration depth in the bulk superconductor. β is a coefficient which takes account of (a) the eventual lowering of Δ and S near the S/N interface; (b) the fact that the contribution to $\mathbf{j}(0)$ coming from N is very small. Thus, $\lambda(0) \geqslant 2\lambda_S$ when $T \to 0$. (2). We have assumed the same $N(0)$ and the same D in both materials. In fact, we could have used a correlation function method, as developped in [3] and [7], to evaluate $\mathbf{j}(r)$. It can then be shown that $f_n(u)$, as defined by (7), obeys diffusion type and sum rule equations. $f_n(u)$ can easily be calculated when $D_S \neq D_N$ and when $N_N(0) \neq N_S(0)$. The same result for $\lambda(x)$ is found for $x=0$ and practically the same for $x > 0$. So. even if the diffusion coefficients and the densities at the Fermi level are different in the two materials, (13) remains valid. (3). The last approximation was to assume a spatial variation for Δ as drawn on Fig. 1. Such an approximation will remain valid as long as the extrapolation length as defined in [3] (Fig. 2) is greater than $1{\cdot}5\,\xi(T)$, $\xi(T)$ being the coherence length in S*. The only modification for our formulae will be to replace $\Delta_{\mathrm{BCS}}(T)$ by the true value $\Delta(0^-)$ of the

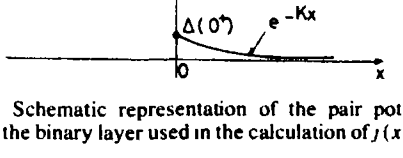

Fig. 1. Schematic representation of the pair potential inside the binary layer used in the calculation of $j(x, \omega)$.

---

*T_e is the temperature below which the expansion in powers of Δ is no more valid in S. From reference [10], T_e is such that $(\Delta_{\mathrm{BCS}}(T_e))/T_e \sim 3$.

†In the case of a Pb/Cu system, when $T = 1$°K, T is lower than T_e and we are not in the theoretical range of validity of (15). Nevertheless, as we shall see in Section 4, the $\sqrt{T}$ law for $\lambda(0)$ seems to be valid down to 1°K for the Pb/Cd system.

*This last condition is fulfilled in N is sensibly dirtier than S $(D_N \ll D_S)$.

pair potential in S, for $x = 0$. (Fig. 2(a)). If this is not the case, the variation of Δ in S can be approximated by a straight line (Fig. 2(b). This implies a slight modification of the F_n in (14) and of the coefficients γ and K'^2 which appear in the determination of the F'_n (14').

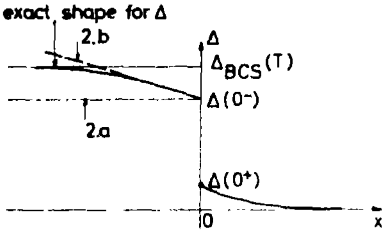

Fig. 2 Possible schematic shapes of the pair potential to be used in the calculation of $j(x,\omega)$ (2a). $D_N \neq D_S$; (2b): $D_N > D_S$

SECTION 2: THE ELECTROMAGNETIC RESPONSE AT FINITE FREQUENCIES

We make the same approximation as previously and are only interested in the case $T \gg T_{cN}$. We write

$$\mathbf{j}(r) = -Q(\mathbf{r},\omega)\,\mathbf{A}(\mathbf{r},\omega) = \frac{\sigma}{c}\,[-i\omega + 4\pi T \times I(\mathbf{r},\omega)]\,\mathbf{A}(\mathbf{r},\omega).$$

$I(\mathbf{r},\omega)$ can be obtained through an analytic continuation of the quantity $I(\mathbf{r},\omega_0)$, where $\omega_0 = 2\nu\pi T$, ν being an integer[4, 2]. $I(\mathbf{r},\omega_0)$ can be expressed in terms of the Green functions G_ω and F_ω. Assuming small values of Δ we can expand in powers of Δ. We go over the Fourier representation and perform, as previously, the averaging procedure on the impurity sites. This has already been done by Maki[11]. The result is

$$I(r,\omega_0) = \frac{1}{(2\pi T)^2}\sum_{-\infty}^{+\infty}\left\{\frac{1}{2}\,\frac{n+\frac{1}{2}}{|n+\frac{1}{2}|}\,\frac{n+\frac{1}{2}+\nu}{|n+\frac{1}{2}+\nu|}\left[\int\frac{\Delta(\mathbf{q})\mathrm{e}^{i\mathbf{q}\mathbf{r}}}{|n+\frac{1}{2}|+\dfrac{Dq^2}{4\pi T}}\,\frac{\mathrm{d}^3q}{(2\pi)^3}\right]^2 + \frac{1}{2}\,\frac{n+\frac{1}{2}}{|n+\frac{1}{2}|}\,\frac{n+\frac{1}{2}+\nu}{|n+\frac{1}{2}+\nu|}\right.$$
$$\left.\times\left[\int\frac{\Delta(\mathbf{q})\mathrm{e}^{i\mathbf{q}\mathbf{r}}}{|n+\frac{1}{2}+\nu|+\dfrac{Dq^2}{4\pi T}}\,\frac{\mathrm{d}^3q}{(2\pi)^3}\right]^2 + \int\frac{\Delta(\mathbf{q})\mathrm{e}^{i\mathbf{q}\mathbf{r}}}{|n+\frac{1}{2}|+\dfrac{Dq^2}{4\pi T}}\,\frac{\mathrm{d}^3q}{(2\pi)^3}\int\frac{\Delta(\mathbf{q}')\,\mathrm{e}^{i\mathbf{q}\mathbf{r}}}{|n+\frac{1}{2}+\nu|+\dfrac{Dq'^2}{4\pi T}}\,\frac{\mathrm{d}^3q'}{(2\pi)^3}\right\} \quad (17)$$

This expression being symmetrical in ν, we can choose $\nu > 0$. We have to consider the same integrals as in (6). Thus, as before, we sum expressions as the ones concerned in formula (13). Provided that the distance x from the interface is less than $1/|q_0 - K|$, it is sufficient to evaluate $I(x,\omega_0)$ for $x = 0$. The value of $I(x,\omega_0)$ for $x > 0$ is obtained by replacing

$$\Delta(0) \rightarrow \Delta(0)\,\mathrm{e}^{-Kx}. \quad (17')$$

Then $I(0,\omega_0)$ has the form

$$I(0,\omega_0) = \frac{(\Delta(0))^2}{(2\pi T)^2}\left[2\sum_0^\infty F_{n+\nu}^2 + \sum_0^\infty F_n F_{n+\nu} + \sum_0^{\nu-1} F_n F_{\nu-n} + \sum_n^\infty F_n F_{n-\nu}\right] \quad (18)$$

the F_n being defined as in (14').

As before, we replace F_n by $F_{n'}$. The summation in (18) can be expressed using polygamma functions and we get

$$I(0,\omega_0) = \frac{1}{2}\left(\frac{\Delta(0)}{2\pi T}\right)^2(\alpha+0\cdot7)^2\left[\psi'\left(\frac{1}{2}+\frac{\omega_0}{2\pi T}+\frac{0\cdot1}{\alpha}\right) + \left(\frac{2\pi T}{\omega_0}+\frac{2\pi T}{\omega_0+\dfrac{4\pi T}{10\alpha}}\right)\left(\psi\left(\frac{1}{2}+\frac{\omega_0}{2\pi T}+\frac{0\cdot1}{\alpha}\right) - \psi\left(\frac{1}{2}+\frac{0\cdot1}{\alpha}\right)\right)\right]. \quad (19)$$

The analytic continuation of $J(0,\omega_0)$ can be made by replacing $\omega_0 \rightarrow -i\omega$. So finally:

$$Q(0,\omega) = \frac{\sigma}{c}\Bigg\{-i\omega + \frac{(\Delta(0))^2}{2\pi T}(\alpha+0{\cdot}7)^2 \times\left[\psi'\left(\tfrac{1}{2}+\frac{0{\cdot}1}{\alpha}-\frac{i\omega}{2\pi T}\right) -\left(\frac{2\pi T}{i\omega}+\frac{2\pi T}{i\omega-(4\pi T/10\alpha)}\right) -\psi\left(\left(\tfrac{1}{2}+\frac{0{\cdot}1}{\alpha}-\frac{i\omega}{2T}\right)-\psi\left(\tfrac{1}{2}+\frac{0{\cdot}1}{\alpha}\right)\right)\right]. \quad (20)$$

Formula (20) will be valid if $\Delta_{\mathrm{BCS}}/2\pi T \ll 1$, which restricts the domain of temperature to the vicinity of the ciitical temperatue of S. (20) can be expanded in the three following cases: (a)$\omega/2\pi T < 1/5\alpha$. Then, provided that $\alpha \gg 1$

$$Q(0,\omega) = -i\omega\frac{\sigma}{c}\left[1+5\alpha\left(\frac{\Delta_{\mathrm{BCS}}}{2\pi T}\right)^2\left(1+\frac{0{\cdot}5}{\alpha}\right)^2 \times\psi'(\tfrac{1}{2})\right]+\sigma\frac{\Delta^2_{\mathrm{BCS}}}{\pi T}\left(1+\frac{0{\cdot}5}{\alpha}\right)^2\psi'(\tfrac{1}{2}) \quad (21)$$

$$(b)\,\frac{1}{5\alpha} < \frac{\omega}{2\pi T} \ll 1.$$

$$Q(0,\omega) = -i\omega\frac{\sigma}{c}\left[1+2\left(\frac{\Delta_{\mathrm{BCS}}}{2\pi T}\right)^2\left(1+\frac{0{\cdot}4}{\alpha}\right)^2\psi''(\tfrac{1}{2})\right] +3\sigma\frac{\Delta^2_{\mathrm{BCS}}}{2\pi T}\left(1+\frac{0{\cdot}5}{\alpha}\right)^2\psi'(\tfrac{1}{2}) \quad (22)$$

(c)

$$Q(0,\omega) = -i\omega\frac{\sigma}{c}\left[1-2\left(\frac{\Delta_{\mathrm{BCS}}}{\omega}\right)^2\left(1+\frac{0{\cdot}7}{\alpha}\right)^2 \left(\tfrac{1}{2}+\mathrm{Log}\,\frac{\omega}{2\pi T}-\psi\left(\tfrac{1}{2}+\frac{0{\cdot}1}{\alpha}\right)\right]-\pi\sigma\frac{\Delta^2_{\mathrm{BCS}}}{\omega} \times\left(1+\frac{0{\cdot}7}{\alpha}\right)^2. \quad (23)$$

We are interested in the surface impedance Z relative to the normal side, the thickness of which being d_N. We have to solve the Maxwell equations in N with a spatially varying $Q(x,\omega)$, as defined by (17′) and (20).

If $\delta Q(x,\omega)$ is the part of $Q(x,\omega)$ which is proportional to Δ^2, we will replace $\delta Q(x,\omega)$ by an average value $\overline{\delta Q}$ such that

$$\overline{\delta Q} = \frac{\int_{-\infty}^{d_N}\delta Q(x,\omega)A_0(x)\,\mathrm{d}x}{\int_{-\infty}^{d_N}A_0(x)\,\mathrm{d}x} \quad (24)$$

$A_0(x)$ being the vector potential in the system for $T \geq T_{cNS}$.

In order of magnitude, $\delta Q(x,\omega)$ is proportional to $\Delta^2_{\mathrm{BCS}}\ (ch^2K(x-d_N)/ch^2Kd_N)$ in N and to Δ^2_{BCS} in S. We now suppose that $2K\delta \gg 1$, δ being the skin depth in N (practically, this condition means that we are not in the Pippard, but in the London limit). Formula (24) shows that the contribution to $\overline{\delta Q}$ coming from N, $\overline{\delta Q}_N$, is essentially due to the points in the vicinity of the interface: thus, in view of the calculation of the surface impendance relative to N, we can adopt the formula

$$\delta Q(x,\omega) = \delta Q(0,\omega)\mathrm{e}^{-2Kx} \quad (25)$$

everywhere in N, even for large values of $x\ (x > 1/|K-q_0|)$.

Then, two cases are possible. (1). $D_N \sim D_s \cdot \delta Q_N$ is proportional to $\Delta^2_{\mathrm{BCS}}/2K\delta\ \mathrm{e}^{-d_N/\delta}$, as soon as $d_N > K^{-1}$, and δQ_S, the contribution to $\overline{\delta Q}$ coming from S, is proportional to $\Delta^2_{\mathrm{BCS}}\,\mathrm{e}^{-x/\delta}$.

Thus, according to our hypothesis ($2K\delta \gg 1$), it is essentially the S region which contributes to $\overline{\delta Q}$ and this remains true for arbitrarily large values of d_N.

We must note that the form we have adopted for the pair potential is not correct for $D_N \sim D_S$. Instead of being constant in S, Δ goes as $\alpha\Delta(0^+)(1-Kx)$ in S, and, in N, $\Delta = \Delta(0^+)\,\mathrm{e}^{-Kk}$. $\Delta(0^+)$ is determined using the results of reference [3]. This leads us to change the values of the F_n which appear in (18). Thus

$$F_n = \frac{2\pi T}{Dq_n}\left[\frac{\alpha}{q_n}+\frac{K}{q_n}+\frac{1}{q_n+K}\right] \quad (26)$$

$$F_n' = \frac{2\pi T}{D} \frac{\alpha + 2{\cdot}2}{q_n^2 + \frac{0{\cdot}57}{\alpha} q_0^2}. \tag{27}$$

But, concerning $\overline{\delta Q}$, our last result remains valid and

$$\frac{\overline{\delta Q}_N}{\overline{\delta Q}_S} \sim \frac{1}{2K\delta} \ll 1. \tag{28}$$

(2). $D_N \rightarrow 0$. When $D_N \rightarrow 0$, the radiofrequency field penetrates very weakly into S, $\overline{\delta Q}_S$ goes to zero and, if $d_N \leq \delta$

$$\overline{\delta Q} \rightarrow \frac{\delta Q(0, \omega)}{(3Kd_N)^2}. \tag{29}$$

Between these two extreme cases $D_N \sim D_S$ and $D_N \rightarrow 0$, we must use in (24) the exact form of $A_0(x)$.

When the ratio D_S/D_N increases, $\delta Q_N/\delta Q_S$ also increases but high values of D_S/D_N must be reached for δQ_N to be comparable to δQ_S.

But the main result is the following: $\overline{\delta Q}$ is always proportional to $\Delta^2(O^-)$, and not to $\Delta^2(O^+)$. This can explain qualitatively the results obtained by Fischer and Klein in a Pb/Cu system[12]. These authors observe, in the case $D_N \ll D_S$, an important reduction of the real part of Z, compared with the situation when the induced superconductivity in Cu has been destroyed by a magnetic field. (The thickness of the Cu layer is comparable to the skin depth in the experiment.) We also note that in their case $\delta Q_N \sim \delta Q_S$. But we stop the discussion here since the lead, in [12], is very clean and, in S, the electromagnetic wave obeys the relations of the anomalous skin depth regime [13].

Thus, the correction to the surface impedance due to the induced superconductivity by proximity effect in a normal metal will be proportional to $\Delta^2(O^-)$. This conclusion, the same as for the study of the local penetration depth, is somewhat negative: for experiments such as tunneling characteristics, surface impedance, Meissner effect, the dependence on Δ will mainly concern Δ in S, and not Δ in N. Thus the determination of $N(0)V_N$, using such experiments, will be very difficult. Further, we expect formally identical conclusions for the ultrasonic attenuation, heat conductivity or the nuclear spin relaxation time T_1.

A local dependence on Δ (in fact the value of Δ at the free surface of N) could be reached using surface impedance measurements in the anomalous regime $\delta < l$, l being the mean free path and $2K\delta < 1$. Nevertheless, for this last condition to be fulfilled, one would have to use very high frequencies ν ($\nu \sim 10^{13}$ Hz).

Finally, let us quote the results obtained for Z in the limit $D_N \rightarrow 0$ and $d_N \leq \delta$.

$$Z = R + iX. \tag{30}$$

If R_0 and X_0 are the values of R and X for $T \gtrsim Tc_{NS}$ and if we only consider the cases of practical interest $\omega \ll 2\pi T$, we get

$$\frac{\omega}{2\pi T} < \frac{1}{|5\alpha|}$$

$$R = R_0\left[1 - \frac{\bar{\Delta}^2}{2\pi T\omega}\left(1+\frac{1}{2\alpha}\right)^2 \psi'(\tfrac{1}{2}) - \frac{5\alpha}{2} \times \frac{\bar{\Delta}^2}{(2\pi T)^2}\left(1+\frac{1}{2\alpha}\right)^2 \psi'(\tfrac{1}{2})\right] \tag{31}$$

$$X = X_0\left[1 + \frac{\bar{\Delta}^2}{2\pi T\omega}\left(1+\frac{1}{2\alpha}\right)^2 \psi'(\tfrac{1}{2}) - \frac{5\alpha}{2} \times \frac{\bar{\Delta}^2}{(2\pi T)^2}\left(1+\frac{1}{2\alpha}\right)^2 \psi'(\tfrac{1}{2})\right] \tag{32}$$

$$\frac{1}{|5\alpha|} < \frac{\omega}{2\pi T} \ll 1$$

$$R = R_0\left[1 - \frac{3\bar{\Delta}^2}{4\pi T\omega}\left(1+\frac{1}{2\alpha}\right)^2 \psi'(\tfrac{1}{2}) - \frac{\bar{\Delta}^2}{(2\pi T)^2}\left(1+\frac{0{\cdot}4}{\alpha}\right)^2 \psi''(\tfrac{1}{2})\right] \tag{33}$$

$$X = X_0\left[1+\frac{3\bar{\Delta}^2}{4\pi T\omega}\left(1+\frac{1}{2\alpha}\right)^2\psi'(\tfrac{1}{2}) - \frac{\bar{\Delta}^2}{(2\pi T)^2}\left(1+\frac{0{\cdot}4}{\alpha}\right)^2\psi''(\tfrac{1}{2})\right]. \tag{34}$$

In these last formulae,

$$\bar{\Delta}^2 = \frac{\Delta(O^-)^2}{(2Kd_N)^2}. \tag{35}$$

SECTION 3: EXPERIMENTAL RESULTS IN THE ZERO FREQUENCY CASE

In a recent letter[8], experiments were reported which showed that a normal layer could display efficient screening currents well above its own critical temperature. We now present a more detailed discussion of these experiments, together with some new data.

A weak magnetic field, applied parallel to the axis of a hollow glass cylinder on which the S and N layers have been deposited, penetrates into the N layer up to a distance l from the interface. l has the following properties:

(α) At a given temperature, l increases with d_N, but goes to a finite limiting value ρ when $d_N \rightarrow \infty$.

(β) ρ is a decreasing function of H. $\rho \rightarrow \rho_0$ when $H \rightarrow 0$.

(γ) ρ_0 decreases with increasing T. In the case of the InBi/Zn system, $\rho_0 \rightarrow 0$ for $T = T_M = 3{\cdot}3°\mathrm{K}$ ($T_M \sim 4{\cdot}5 \times T_{cN}$).

Properties (α) and (β) were in agreement with theory. Moreover, the field and distance dependence of ρ agreed with the generalized Landau-Ginzburg theory[4, 5], and it was possible, with the simple set of the two parameters $\lambda(0)$ and K^{-1}, to describe correctly the variation of ρ with d_N and H. So, from this kind of experiments, we could deduce $\lambda(0)$ and K^{-1}. The values of K^{-1} were in agreement within 20 percent with theory but the experimental values of $\lambda(0)$ seemed to by systematically higher (by a factor of order 2) than the theoretical values. Later[7], it was claimed that this disagreement could be partly explained performing a more careful estimation on $\lambda(0)$ as done in the first part of this paper.

Our present aims are as follows: (1) to study a situation in which the value of T_M is not limited by T_{cS}, as seems to be the case for the InBi/Zn system; (2) to check formula (15), especially the remarkable temperature dependence of $\lambda(0)$; (3) to see if $\lambda(0)$ is a very sensitive function of T_{cN}, and of the boundary conditions at the interface.

Choice of the materials

In view of points (1) and (2), Pb is a convenient S material because of its rather high critical temperature. Further, Δ_{BCS} in Pb is practically constant below 4·2°K: thus the intrinsic temperature dependence of $\lambda(0)$ appears in a straightforward way in this temperature range.

In order to study point (3), we choose Zn and Cd as normal metals. Thus we can compare two situations where (a) the normal layer is the same (InBi/Zn and Pb/Zn); (b) the superconducting layer is the same (Pb/Zn and Pb/Cd).

Furthermore, we know that no reciprocal solubility is expected in the case of Pb/Zn and Pb/Cd.

In our experiments, the Pb layer is clean ($l \gg \xi_0$) and the Zn and Cd layers have mean free paths l_N of the order of magnitude of q_0^{-1}. Thus the normal layer cannot be considered as being really dirty. Undoubtedly, this represents a considerable disadvantage, with respect to an exact comparison with theory. Nevertheless, (i) theoretical results for the dirty case should apply at least in a semi-quantitative way to the case $l \sim q_0^{-1}$; (ii) if the normal layers were really dirty ($l \sim q_0^{-1}/10$), the screening currents would be much weaker at a given temperature ($\lambda(0) \sim 1/\sqrt{l}$ and $\kappa(0) \sim 1/l$). Thus measurements should be carried on at much lower temperatures ($T < 0{\cdot}5°\mathrm{K}$). This unfortunately was not possible at the moment in our laboratory.

(iii) It is not very convenient to have an S material much dirtier than the N one since the extrapolation length b is small then, which reduces proximity effects in N.

The experiment

We measure essentially the dynamic susceptibility $\chi(\nu)$ of our cylinder, using the Shawlow–Devlin device[13]. We recall that the cylinder is placed in a coil whose impedance is L. If $\chi(\nu)$ changes by an amount $d\chi$ due for instance to an entry of flux, a change dL, hence a change $d\nu$ of the resonance frequency of an l.c. circuit will be detected:

$$d\nu \propto dL \propto d\chi.$$

Such a variation of L is obtained for instance when we apply a static magnetic field parallel to the axis of the cylinder. In such conditions, it is shown elsewhere that

$$\Delta\nu(H) = \nu(H) - \nu(H{=}0) \propto \rho(H) - \rho(0) + H\frac{\partial\epsilon(H)}{\partial H}$$

because the flux which enters the sandwich goes as $-H\rho(H)$.

Thus we obtained $\nu(H)$ vs. H curves, an example of which is given on Fig. 3. The field was swept at a rate of about 0·5 Oe/sec and the $\nu(H)$ vs. H curve was reached by means of a digital-analog converter and an X–Y recorder. Lastly, the resonance frequency was low enough to neglect the imaginary part of $Q(\omega)$ compared to the real part.

Thus we obtained for each binary layer the following information: the screening distance ρ as a function of H and T; the temperature $T^*(d_N)$[9], below which a first-order transition can be observed at the breakdown field H_b; the temperature dependence of H_b for $T < T^*$.

About 10 samples of each S/N system were prepared, d_S being kept constant and d_N varying typically from 2000 to 20,000 Å.

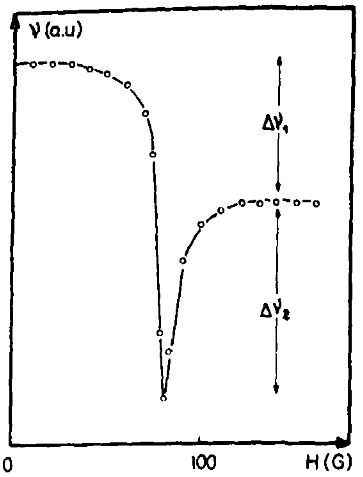

Fig 3 Example of a $\nu(H)$ plot given by the Shalow–Delvin device.

These thicknesses were determined by resistivity measurements.

The change of $\Delta\nu$ was calibrated using the determination of $\Delta\nu$ between zero applied field and the thermodynamical critical field of the S layer, the thickness d_S of the S layer being known. Most of the experiments were carried out between 1·2° and 4·2°, well above the transition temperature of Zn (0·92°K) and that of Cd (0·56°K). Some experiments were made above 4·2°K.

Methods of determining $\lambda(0)$ *and* K^{-1}

Using the above information, the lengths K^{-1} and $\lambda(0)$ can in principle be obtained by various procedures:

(a) At a given temperature, H_b is an exponentially decreasing function of d_N and can be observed if $\kappa(0) < 0{\cdot}44$[7, 5].

$$H_b = H_0 \exp(-K\, d_N).$$

The slope of the straight line $\operatorname{Log} H_b = f(d_N)$ gives K^{-1}. The intersection of this line with the H axis yields H_0 (Fig. 4):

$$H_0 = 1{\cdot}9\frac{\phi_0}{2\pi\lambda(0)K^{-1}}. \qquad (36.a)$$

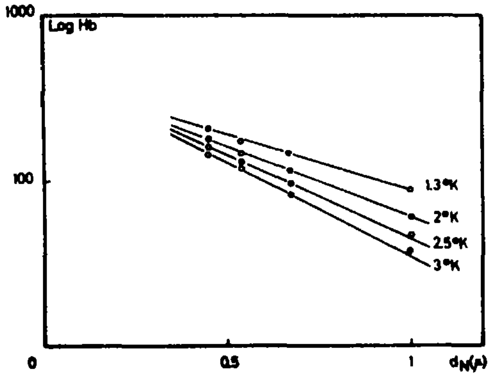

Fig. 4. Determination of K^{-1}, using the experimental values of H_b and equation (36a) in the case of a Pb/Cd binary layer.

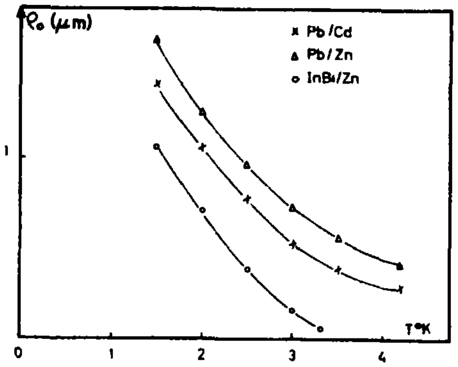

Fig. 5. The distance from the interface of the flux front, in the limit of zero applied d.c. field, ρ_0, for Pb/Cd, Pb/Zn and InBi/Zn systems.

In this way, we obtain λ(0).

(b) When $d_N \to \infty$, the $\rho(H)$ curve may be used[8] to find the values of λ(0) and K^{-1}. Nevertheless, this requires tedious calculations, so that this procedure was used only to get a confirmation of some results.

(c) As shown in reference [6], ρ_0 is a simple function of λ(0) and K^{-1} (Fig. 5):

$$\rho_0 = K^{-1}\left[\text{Log}\frac{1}{\kappa(0)} - 0{\cdot}116\right]. \qquad (36.\text{b})$$

We used (36.b) to get λ(0), the value of K^{-1} being deduced by procedure (a)†. (d) The $T^*(d_N)$ experimental curve, together with $K^{-1}(T)$, has shown to lead to another determination of λ(0). This procedure was not used here as we found it rather indirect. Moreover, the value of T^* could be very sensitive to trapped flux. In particular, the presence of trapped flux was found to result in an apparent lowering of T^*, and we are not sure that the measured values of $T^*_{\max}$ are correct ($T^*_{\max} = 2{\cdot}5$°K for the Pb/Cd system, and $T^*_{\max} = 3{\cdot}0$°K for the Pb/Zn one). We must recall here that the determination of $T^*_{\max}$ could be of interest since for $T = T^*_{\max}$, $\kappa(0) = 0{\cdot}44$.

The results

For the Pb/Zn and Pb/Cd systems, the independent determinations (a) and (c) give results in close agreement with one another. These results are shown on Figs. 6 and 7.

The observed temperature dependence of λ(0) seems to us to be a good proof of the validity of our estimations. This is particularly clear in the case of Pb/Cd, where λ is seen to vary as $\sqrt{T}$ within the experimental accuracy.

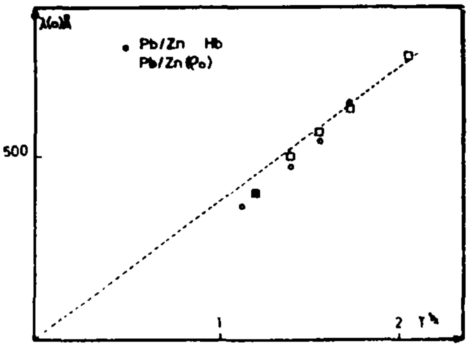

Fig. 6. The value of the penetration depth at the interface, λ(0), as a function of $\sqrt{T}$ for a Pb/Zn system. As can be seen, the $\sqrt{T}$ law for λ(0) is verified for high temperatures, but a systematic deviation from the $\sqrt{T}$ law is observed for low temperatures ($T \sim T_{cN}$).

---

† It may be emphasized that the value of λ(0) obtained in this way is relatively independent of determination (a), because ρ_0 is measured on semi-infinite layers ($d_N > 2\mu$), whereas H_b is measured on films of finite thickness ($d_N \sim K^{-1}$).

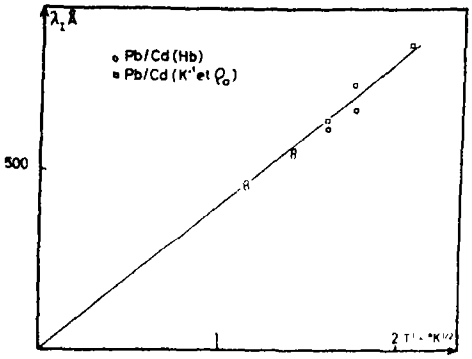

Fig. 7. $\lambda(0)$ as a function of $\sqrt{T}$ for a Pb/Cd system. The $\sqrt{T}$ law is seen to be valid for a large domain of temperature ($1°K < T < 4°K$).

In the Pb/Zn case, there seems to be a systematic deviation from formula (15) at low temperatures. In fact, in the vicinity of T_{cN} (case of Zn) the screening distance ρ_0 becomes very large and may be of the order of magnitude or greater than $1/|K-q_0|$. So the local penetration depth $\lambda(x)$ is less sensitive to the values of Δ at the interface, which results in an apparent decrease of $\lambda(x)$, which is effectively observed.

Conclusions

The study of the response to a small d.c. or a.c. magnetic field on the N part of an N/S binary layer has shown that the physical observable quantities (Meissner effect in N, surface impedance on the N side) were mainly dependent on the values of the pair potential not in N, but in the superconductor S, for N materials with very low critical temperatures. Such a result was previously obtained in the study of the tuneling characteristic on the N side of an N/S binary layer, and seems to be applicable also in the case of the ultrasonic attenuation, the heat conductivity or the nuclear spin relaxation time. Consequently, it will be necessary to perform very precise and sensitive experiments in view of determining the BCS interaction NV of materials whose critical temperature is unknown.

Acknowledgements—We would like to thank Professor P.-G. de Gennes, K. Maki, G. Fischer and R. Klein and the members of the Orsay Group for numerous stimulating discussions. One of the authors (PAVD) takes this opportunity to express his appreciation to the direction of Philips Research Laboratories for giving him the possibility to work at Service de Physique des Solides in Orsay, particularly to Professor Rathenau for his stimulating interest.

REFERENCES

1. DE GENNES P. G. and GUYON E., *Phys. Lett.* **3**, 168 (1963).
2. See for instance "Gapless Superconductivity" by MAKI K., To be published in *Superconductivity* (Edited by R. D. Parks). Marcel Dekker, New York.
3. DE GENNES P. G., *Rev. Mod. Phys.* **36**, 225 (1964).
4. See for instance ABRIKOSOV A. A., GOR'KOV L. P. and DZYALOSHINSKI I. E., *Methods of Quantum Field Theory in Statistical Physics*. Prentice-Hall, London (1963).
5. MAKI K., *Physics* **1**, 21 (1964).
6. Orsay group on superconductivity, *Proc. 1965 Sussex Univ. Symp., Quantum Fluids* (Edited by D. Brewer). North-Holland, Amsterdam (1966).
7. DE GENNES P. G. and MAURO S., *Solid State Commun.* **3**, 381 (1965).
8. DEUTSCHER G. and HURAULT J. P., *Phys. Lett.* **24A**, 102 (1967).
9. Orsay group on superconductivity, *Phys. condensed Matter* **6**, 307 (1967).
10. SILVERT W. and COOPER L. N., *Phys. Rev.* **141**, 336 (1966).
11. MAKI K., *Phys. Rev.* **141**, 331 (1966).
12. FISCHER G. and KLEIN R., Preprint.
13. ABRIKOSOV A. A., GOR'KOV L. P. and KHALATNIKOV I. M., *Sov. Phys. J.E.T.P.*

J. Phys. Chem. Solids Pergamon Press 1969. Vol. 30, pp. 521-538. Printed in Great Britain.

A MODEL FOR THE EVALUATION OF THERMODYNAMIC PROPERTIES FOR THE SOLID-SOLID AND MELTING TRANSITIONS OF MOLECULAR CRYSTALS

L. M. AMZEL and L. N. BECKA
Escuela de Quimica, Universidad Central de Venezuela, Caracas, Venezuela

(*Received* 29 *May* 1968; *in revised form* 18 *July* 1968)

Abstract—The theory of fusion of molecular crystals with orientational degrees of freedom developed by Pople and Karasz[1] is extended by taking into account the existence of more than two possible positions of minimum orientational energy in the crystal. Now the model has two parameters, D, the number of these possible positions; and, as before, ν, a measure of the relative energy barriers for the rotation of a molecule and for its diffusion to an interstitial site. The main features derived from the model, when $D > 2$, are (1) solid-solid and melting transitions are always of first order, (2) the values of ν at which solid-solid transition and fusion temperatures (T_t and T_m) coalesce increase when D increases; (3) solid-solid transition entropies increase with D and, for each D, with ν; (4) at constant ν there is a decrease of T_t and of T_m when D increases; (5) relative volume changes on melting become smaller than the relative volume changes at the solid-solid transition when $\nu > 0{\cdot}26$, this change becomes as small as 4 per cent for $D = 60$ and $\nu = 0{\cdot}5$. The quantitative predictions of the model are compared with experimental results for plastic crystals.

There is good agreement between theory and experiment. For solid-solid transitions the agreement is much better than with the calculations of Pople and Karasz, as would be expected from the fact that in the present theory D is a parameter.

INTRODUCTION

THERE is ample evidence of molecular reorientations in solids, as has been clearly established by studies of the crystal structure, thermodynamic properties, dielectric constants, nuclear magnetic resonance spectra, neutron inelastic scattering spectra, of a number of crystals. This possibility of orientational disorder was taken into account by Guthrie and McCullough[2] to interpret phase behaviour in molecular crystals exhibiting solid-solid transitions with high values of transition entropy. These authors were able to relate these values with the number of distinguishable molecular orientations in the disordered phase, and to give a reasonable description of these orientations by using steric and symmetry considerations. With this approach it is possible to predict the values of transition entropies for a number of crystals exhibiting order-disorder transitions. A theory of fusion of molecular crystals that takes into account orientational disorder, as well as positional disorder, was developed by Pople and Karasz[1], on the basis of the Lennard-Jones-Devonshire[3] theory of positional disorder as a mechanism of melting. Pople and Karasz considered that molecules may take up two orientations on any of the two sites of the two lattice model used by Lennard-Jones and Devonshire, and that there is a coupling between orientational and positional disorder. With this statistical model it is possible to make quantitative predictions about the effects of orientational disorder on the thermodynamics of melting, as well as about the thermodynamics of the solid state transitions. The only parameter of the model is the quantity ν, which is a measure of the relative energy barriers for the rotation of a molecule and for its diffusion to an interstitial site. Since in the quantitative predictions presented by Pople and Karasz there is no allowance for the fact that most molecular crystals have more than two positions of minimum orientational energy, it is clear that those predictions will not give a satisfactory agreement with the experimental values of thermodynamic properties at the solid state transition for these crystals. Nor will the model be adequate to account for the large changes of thermodynamic properties related with melting of molecular crystals that do not present solid state transitions.

Our purpose is to extend the model of Pople and Karasz by introducing as an additional parameter a number, D, which allows for the number of molecular orientations, as defined by Guthrie and McCullough. Using this model it is also possible to make quantitative predictions pertaining to the thermodynamic features of the solid state transition and of melting transition, and to construct phase diagrams. These predictions will be compared with experimental data.

FORMULATION OF THE STATISTICAL MODEL

The present statistical model is a straightforward extension of that proposed by Pople and Karasz[1], therefore we shall just give a brief description of the formulation of our model, following closely the notation of these authors.

In our model each of the N molecules can be either on the α or the β sites of one of the two interpenetrating lattices, and can take any one of D orientations on either of the sites. If the molecules are equally distributed among the α and β sites the system of N molecules is positionally disordered and corresponds to a liquid. If this is not the case and the molecules have taken all possible D orientations, there being N/D molecules in each orientation, the system corresponds to an orientationally disordered crystal. The number of pairs of molecules of neighbouring α and β sites is $N\alpha\beta$, similarly, the number of pairs having orientations i and j on neighbouring α and on neighbouring β sites are $N\alpha_i\alpha_j$ and $N\beta_i\beta_j$ respectively. In the equilibrium configuration of the completely ordered solid all molecules are on one type of site and have the same orientation. If z is the number of equivalent neighbouring β sites around an α site, and z' the number of α neighbouring sites around an α site, the energy required to move a molecule to an interstitial site is zW, and the energy to turn a molecule to another orientation is $z'W'$, when all other molecules are in the equilibrium configuration. As in the Pople and Karasz model, interaction between positional and orientational disorder is introduced by assuming that no energy is required to have two neighbouring molecules in different orientation when they are on different types of sites. The partition function of the totally ordered system is f^N, where f is the partition function of a molecule in this state and is considered to depend on volume per molecule and temperature only. All these considerations lead to a partition function of the form:

$$Z = f^N\Omega = f^N \sum_{i,j} \exp\left[-(N_{\alpha\beta} W + N_{\alpha_i\alpha_j} \times W' + N_{\beta_i\beta_j} W')/kT\right]$$

where the sum is over all orientations as well as over all arrangements of particles on α and β sites. If we call Q the quantity equal to the fraction of particles on α-sites and S_i the quantity equal to the fraction of particles with orientation i, the total Ω function may be written

$$\Omega = \sum \Omega(Q, S_1, S_2, \ldots, S_D)$$

where each term in the summation is itself a sum over all configuration in which there are NQS_1, NQS_2, ..., NQS_D in the $\alpha_1, \alpha_2, \ldots, \alpha_D$ positions, $N(1-Q)S_1$, $N(1-Q)S_2, \ldots$ $N(L-Q)S_D$ in the $\beta_1, \beta_2, \ldots, \beta_D$ positions. There are of course only $D-1$ independent values, since

$$Si = 1 - \sum_{j \neq i} Sj.$$

As usual we seek only the maximum of $\Omega(Q, S)$, and use the Bragg–Williams[4] approximation to find the values of Q, S_1, $S_2, \ldots, S_D$ that maximize the expression. Thus $\Omega(Q, S_1, S_2, \ldots, S_D) = \gamma(Q, S_1, S_2, \ldots, S_D) \exp(-E/kT)$ where $E = zWNQ(1-Q) + z'W'N(1-2Q+2Q^2)\left[\sum_{i=2} S_i(1-\sum_{j=2} S_j)\right]$ and

$$\gamma = \left\{\frac{N}{[NQ]![N(1-Q)]!}\right\}^2 \times \left\{\frac{NQ!}{NQS_1!\prod_{i=2} NQS_i}\right\} \times \left\{\frac{[N(1-Q)]!}{[N(1-Q)S_1]!\prod_{i=2} N(1-Q)S_i}\right\}$$

Using Stirling's theorem and maximizing with respect to Q, and S_i's, we see that the conditions for this expression to have a stationary value are

$$\log(S_1/(1-S_1)) - \log(D-1) = -(z'W'/kT)[1-(DS_1/(D-1))] \times (1-2Q+2Q^2) \tag{1}$$

$$\log(Q/(1-Q)) = (zW/2kT) - \{(z'W'/kT)S_1[1-(DS_1/(2D-2))](2Q-1)\} \tag{2}$$

and $S_i = (1-S_1)/(D-1)$ for $i \neq 1$.

These expressions reduce to those given by Pople and Karasz[1] when $D = 2$, as should be, since the model of these authors corresponds to a particular case of the model presented here.

At very low temperature the solution of (1) and (2) that maximizes $\log\Omega$ is $S_1 = 1$ and $Q = 1$, corresponding to the completely ordered solid with all particles on α sites and having orientation '1'. The point $Q = 1/2$ and $S_1 = 1/D$ is always a solution, and at high enough temperatures it is the only solution. At these temperatures there is thus complete positional and orientational disorder, that is, the system is an isotropic liquid. For larger values of $x = zW/kT$ the values of Q and S_1 maximizing $N^{-1}\log\Omega$ may differ from 1/2 and/or $1/D$ respectively, corresponding to order in position and/or orientation. Assuming that the ratio

$$\nu = z'W'/zW$$

is independent of temperature and volume, as is D, we can obtain the solution of expressions (1) and (2) as function of x for a series of values of ν and D. The solutions that maximize $N^{-1}\log\Omega$ are plotted in Fig. 1 for four sets of values of ν and D. When $\nu = 0{\cdot}3$ there is a temperature at which the system becomes orientationally disordered but keeps its positional order, at a higher temperature the positional order is also lost. For this value of ν it is seen that as D changes from 6 to 20 the temperature at which orientational disorder is attained is significantly lower, but the temperature at which $Q \rightarrow \frac{1}{2}$ doesn't change appreciably. For $\nu = 0{\cdot}7$ loss of positional and orientational order occur at the same value of x, and as D is increased the value of x at which this disordering takes place is lowered. The kind of behaviour exemplified above holds also for other values of ν and D. For each value of D there is a value of ν above which orientational disorder occurs at the same value of x as positional disorder. This value of ν is 0·325 when $D = 2$ and shifts to $\nu = 0{\cdot}50$ when $D = 60$. As long as ν is lower than these limiting values the Q and S_1 curves behave as curves a and a' of Fig. 1. For higher values the behaviour is similar to that of curves b and b' of Fig. 1. For values of ν near or greater than 1 (corresponding to crystals having large barriers for molecular reorientation) the Q and S curves can be interpreted as characteristic of systems with a liquid crystal phase above the melting point. For such high ν-values the positional disordering occurs at a lower x value than the orientational disordering. We shall not analyse this last case in this paper.

Evaluation of thermodynamic properties of phase transitions

We may now investigate the thermodynamics of these systems by obtaining the

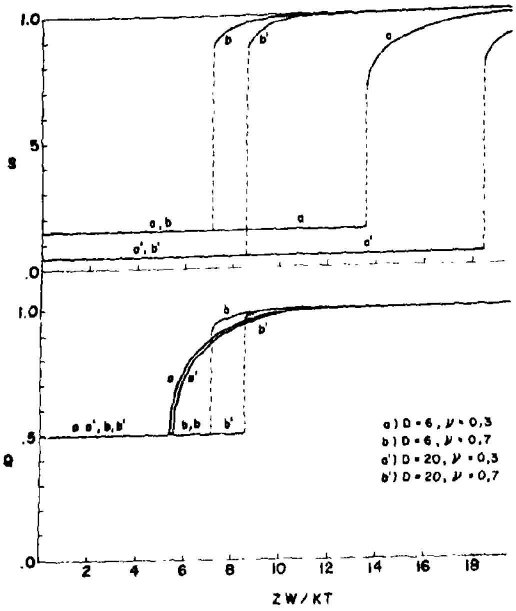

Fig. 1. Variations of positional order (Q) and orientational order (S) with zW/kT for various ν and D sets.

isotherms for sets of and D values. The isotherms are obtained by evaluating the pressure as a function of volume, temperature, ν and D. The pressure can be conveniently split in two parts[1]

$$p = p' + p''$$

where $p' = -(\partial A'/\partial v)_T$ and $p'' = -(\partial A''/\partial v)_T$. The first part gives the contribution due to the completely ordered solid, and the second gives the contribution due to disordering, that is[1]

$$A' = -NkT \log f$$

$$A'' = -kT \log \Omega\,(Q, S_1)$$

The pressure and other thermodynamic functions associated with the partition function f have been tabulated by Wentorf *et al.*[5] on the basis of a 6–12 intermolecular potential and three shell spherically smoothed cell fields. We used these tabulated values, and when necessary we extrapolated to lower temperatures. To calculate the 'Disordered' part of the thermodynamic function we specified the volume dependence of W and W'. Following Pople and Karasz[1] we take W/W' independent of volume and

$$W = W_0(v_0/v)^4$$

$$W_0/\epsilon_0 = 0{\cdot}977$$

where v_0 is the standard volume if the molecules are placed on a f.c.c. lattice with a nearest neighbouring distance of $2^{1/6} r_0$, and ϵ_0 is the energy minimum of the intermolecular potential. The pressure p'' is now given by

$$\frac{p'' v_0}{NkT} = 4\frac{v_0}{v}\frac{zW}{kT} \times \left\{Q(1-Q) + \nu S_1\left(1 - \frac{DS_1}{2D-2}\right)(1 - 2Q + 2Q^2)\right\} \tag{3}$$

using the conditions which were taken to maximize $N^{-1}\log\Omega(Q,S_1S_2,\ldots,S_n)$. This equation gives $p''v_0/NkT$ as a function of (v/v_0), kT/ϵ_0, ν and D, so that by adding to it $p'v_0/NkT$ we obtain a complete isotherm. We have looked for transitions at zero pressure, as done by Pople and Karasz.

In this way we have calculated a number of isotherms for different values of D and ν. For each set of values of D and ν there are one or two temperatures that give isotherms showing phase transitions. Figures 2(a) and (b) depict two isotherms of this type, for $D = 6$ and $\nu = 0{\cdot}3$. The two transitions are of first order type. The two phases represented by the points A and C exist in equilibrium, since the total (algebraic) sum area under the curve between these points is zero. In Fig. 2(b) the point A corresponds to the orientationally ordered solid, and the point S indicates the volume at which orientational order disappears. Figure 2(a) shows the melting isotherm, which is obtained at higher temperatures than the solid–solid transition for these values of D and ν. Now the point A corresponds to the disordered solid, C to the liquid and Q indicates the volume at which positional order disappears. In Fig. 2(c) we show a typical transition isotherm for the case where melting and orientational disorder take place at the same temperature.

The reduced transition temperatures (kT_t/ϵ_0 and kT_m/ϵ_0) corresponding to these phase transitions are shown in Fig. 3, as a function of ν and for some values of D. For each value of D there is a value of ν, ν_L, above which melting occurs at the same temperature as orientational disorder, and below which a solid–solid transition takes place at a lower

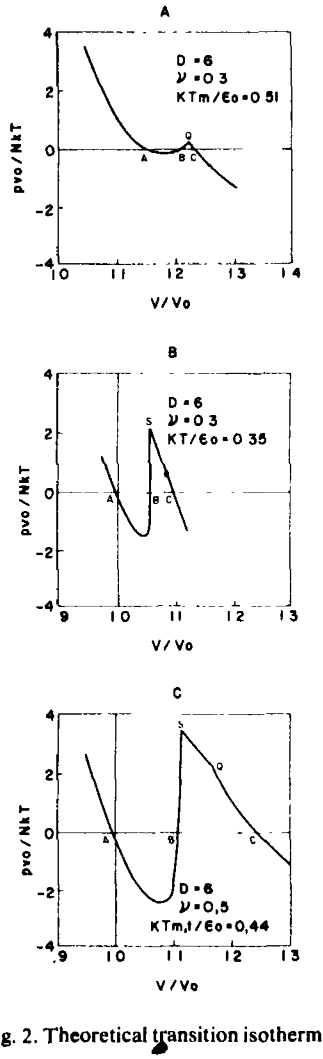

Fig. 2. Theoretical transition isotherms.

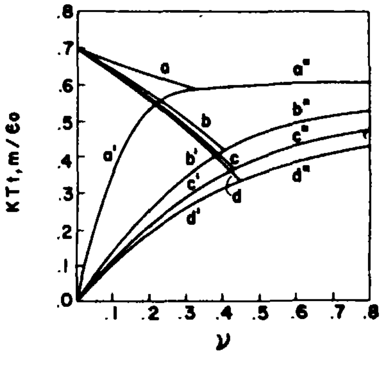

Fig. 3. Reduced temperatures of melting, kT_m/ϵ_0, and solid–solid transition, kT_t/ϵ_0, as a function of D for various ν values. Curves a, b, c and d correspond to melting curves with D values of 2, 6, 12 and 20 respectively. Curves a', b', c' and d' are the transition temperature curves for the same D values. Curves a'', b'', c'' and d'' are the corresponding curves when T_t and T_m coincide.

temperature than melting. For high values of ν, $\nu > \nu_M$, melting occurs before orientational disorder, but this case will not be discussed in this paper. All the phase transitions are of first order when $D > 2$, whereas Pople and Karasz[1] found that for $D = 2$ solid–solid transitions were of second order when ν is less than about 0·17. This difference is associated with the fact that in expression (3) the term depending on D will always give a discontinuous jump to higher pressures when S_t becomes equal to $1/D$ for $D > 2$.

From the isotherms at transition temperatures we can also obtain the relative volume changes at the transitions. These are plotted as a function of and for two values of D in Fig. 4. As long as $\nu < \nu_l$ the changes of volume on melting and for the solid–solid transition, $\Delta V_m/V_s$ and $\Delta V_t/V_t$ do not depend appreciably on D except that for larger values of D there is an asymptotic increase in ν_L allowing for smaller values of ΔV_m and larger values of ΔV_t. This allows the existence of compounds with $\Delta V_m/V_s$ as low as 4 per cent when $D = 60$ and $\nu = \nu_L$. Another interesting feature is that volume changes at the solid–solid transitions can become larger than $\Delta V_m/V_s$ for $D > 2$ and $\nu > 0·28$. When $\nu > \nu_L$ there is a strong dependence between $\Delta V/V$ and D, but $\Delta V/V$ remains practically constant for $\nu_L < \nu < \nu_M$. The changes of entropy on transitions, ΔS_t and ΔS_m, can be obtained in a similar way, and are plotted as a function of ν and for two values of Δ in Fig. 5. It is seen that ΔS_m decreases from the Lennard-Jones–Devonshire value of 1·77 R at $\nu = 0$ to values of the order of 0·8 R for $D > 20$ and ν about 0·5. The values of ΔS_t increase with D and ν. When $\nu_L < \nu < \nu_M$ the

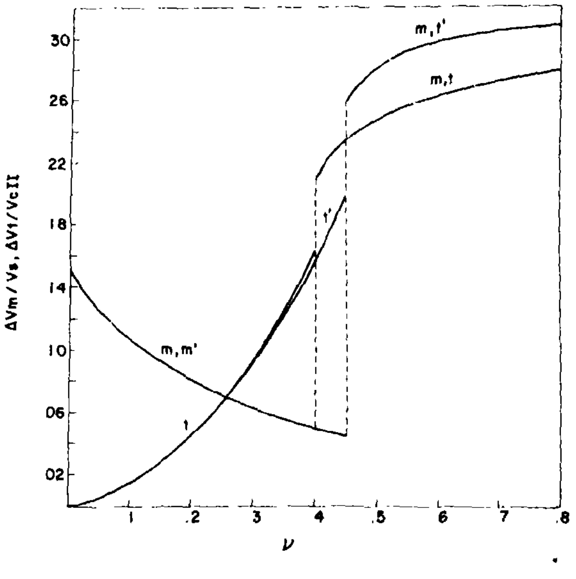

Fig 4. Relative volume change on melting, $\Delta V_m/V_s$, and for the solid–solid transition, $\Delta V_t/V_{c\text{II}}$ as a function of ν and for various D values. Curves m, t and (m,t) correspond to volume changes on melting, solid–solid transition and coincidence of the two, respectively, when $D = 6$. Curves m', t' and (m', t') correspond to the same quantities when $D = 20$.

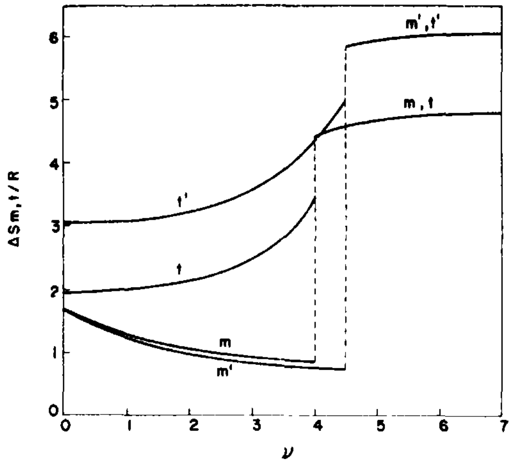

Fig. 5. Entropy of melting, ΔS_m, and of the solid–solid transition, ΔS_t, as a function of ν and for various D values. Curves t, m and (m,t) correspond to $D = 6$, giving ΔS_t, ΔS_m, and ΔS when there is no solid–solid transition, respectively. Curves t', m' and (m', t') give values for the same properties when $D = 20$.

values of ΔS depend almost exclusively on D, becoming equal to about 4·5 R for $D = 6$ and about 6 R for $D = 20$.

THEORETICAL PHASE DIAGRAMS

In order to obtain the predicted phase diagrams for the condensed system we applied the 'equal area principle'[6] to the sigmoid portions of the isotherms in order to find the equilibrium pressures for the melting and solid–solid transitions. There is a phase diagram for each set of values of D and ν. Using reduced pressure and temperature coordinates we have constructed several of these phase diagrams. Figures 6 (a–c) illustrate typical behaviour.

For $\nu = 0$ there is of course no solid–solid transition, and we obtain a two phase diagram. For $\nu > 0$ and up to ν_L we find two solid phases in equilibrium at all pressures, two such diagrams are shown in Fig. 6(a). It is seen that the shape of the two phase boundaries does not depend markedly on D, but they shift to higher values of the reduced temperature when D increases. In Fig. 6(b) we show the phase diagrams for $D = 6$, $\nu = 0·40$ and $D = 20$, $\nu = 0·45$. These two phase diagrams correspond to the cases where at zero reduced pressure there is just one phase boundary and at $P > 0$ there is again a separation between solid–solid and melting transition, the behaviour for $P > 0$ being similar to that shown in Fig. 6 (a). Keeping D constant and increasing ν the solid–liquid boundary shifts to lower reduced temperatures whilst the solid–solid phase boundary shifts to higher reduced temperatures. There is a value of ν, equal to ν_L, at which the phase boundaries coalesce at $P/P_0 = 0$. As ν continues to increase the phase diagrams show just one phase boundary up to a pressure $P_M > 0$, after which there appear again two boundaries. This kind of behaviour is exemplified in curve 6 (c). For $D = 2$, Pople and Karasz[1] found that for $\nu = 2/3$ the melting and orientational transition remain merged at all pressures; we find that the values of ν at which this behaviour occurs depends on D.

In the above discussion we have assumed that ν remains independent of pressure. With this restriction the theory does not predict the possibility of the two transitions merging at higher pressures when they occur at different temperatures at zero pressure. This case could exist if ν were to increase with pressure. That is, when the barrier to reorientation increases more than the barrier to diffusion for an increase in pressure.

COMPARISON WITH EXPERIMENTAL DATA

In order to compare theoretical predictions with experimental results we need to assign values of ν and D to each compound that is being analized. The parameter ν cannot be obtained directly from experiment nor estimated theoretically from our present knowledge of intermolecular forces. Therefore, in what follows we shall relate the thermodynamic properties of the different compounds with the ratio of transition temperature to melting temperature, T_t/T_m. Since this ratio is derived directly from experiment and is a

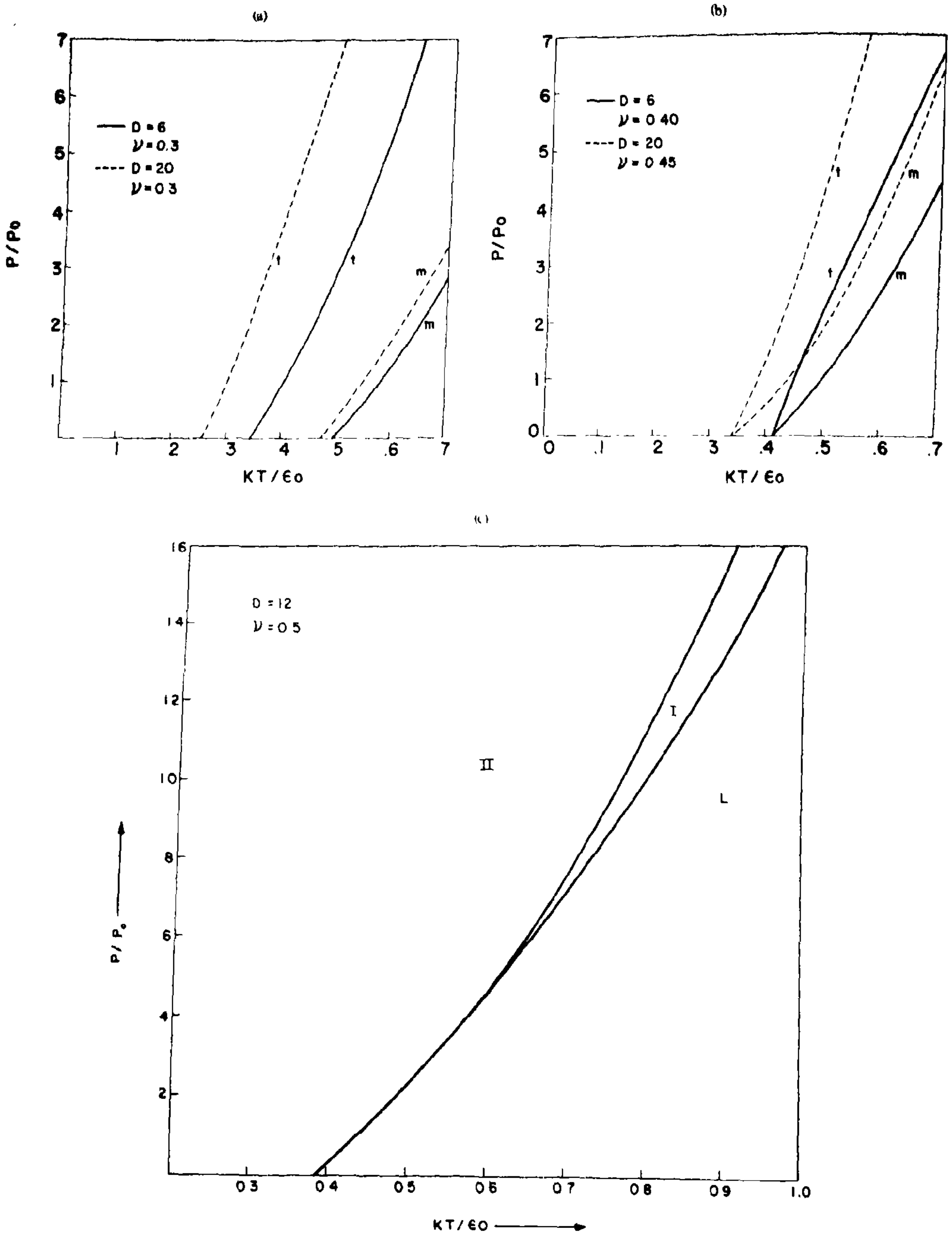

Figs. 6 (a–c). Theoretical phase diagrams for various values of ν and D.

function of ν for each value of D (the dependence was shown in Fig. 3) we have plotted theoretical values for the properties as a function of T_t/T_m and D.

For compounds having a orientationally disordered solid phase the solid–solid transition entropy, ΔS_t, is strongly dependent on D in our model. Therefore the D values can be established from these transition entropies. The D values that give good agreement between theoretical and experimental transition entropies should correspond to a reasonable number of possible distinguishable orientations in the disordered phase, as shown by Guthrie and McCullough[2]. In Fig. 7 we have shown theoretical ΔS_t curves as a function of T_t/T_m and D, together with experimental values for some plastic crystals[7]. In Table 1 theoretical ΔS_t values and the corresponding D values, compatible with steric and symmetry criteria, are given and compared with experimental data.

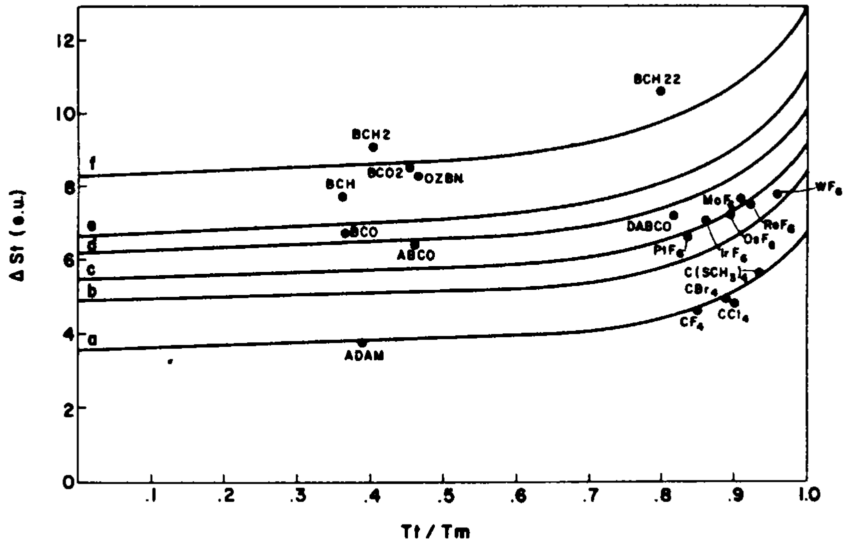

Fig. 7. Comparison of theoretical curves and experimental values of transition entropies at T_t. Theoretical curves *a*, *b*, *c*, *d*, *e* and *f* correspond to D values of 6, 12, 16, 21, 24 and 60 respectively. See also Table 1.

The values of D we have chosen for calculating thermodynamic properties at the transition have been estimated as follows: (a) CF_4, CCl_4, $C(SCH_3)_4$ and adamantane (ADAM) are molecules with T_d point group symmetry. We take $D = 6$ corresponding to the D_{2d} set of orientations, D_{2d} being the subgroup with highest symmetry compatible with the geometry of these molecules. (b) The hexafluoride molecules, MF_6, have octahedral symmetry, and can have their symmetry elements aligned with corresponding elements of the site O_h in the sets D_{4h} and C_3. There are six distinguishable orientations in set D_{4h} and eight in set C_3. we have taken $D = 6+8 = 14$ for these molecules. (c) Bicyclo[2,2,2] octane (BCO) and 1-4-Diazabicyclo[2,2,2] octane (DABCO), can be considered as having D_{3h} symmetry and with this symmetry we can take $D = 20$, as evaluated by Wen-Kuei Wong[8]. (d) 1-Azabicyclo[2,2,2] octane (ABCO), probably has C_{3v} symmetry, so that we can use $D = 16$, as evaluated by Wen-Kuei Wong[8]. (e) 3-Oxabicyclo[3,2,2] nonano (OXBN) and Bicyclo[2,2,2] octane-2 (BCO2), probably have C_{2v} symmetry and approximate D_{3h}

Table 1. Observed and calculated transition entropies (ΔS_t)

Name of compound or formula	T_t (K)	T_m (K)	T_t/T_m	D	$R \ln D$ (e.u)	ΔS(e.u) theory	ΔS(e.u) exp	References
CCl_4	225·5	250·3	0·90	6	3·52	5·23	4·79	(a)
CF_4	76·3	89·5	0·85	6	3·52	4·81	4·63	(a)
CBr_4	46·87	53·2	0·88	6	3·52	5·11	4·98	(b)
$C(SCH_3)_4$	296*						5·0	
	318	338	0·94	6	3·52	5·66	5·7	(c)
Adamantane (ADAM)	208·6	543	0·38	6	3·52	3·84	3·87	(d)
WF_6	264·7	275·2	0·96	14	5·25	7·97	7·81	(e)
ReF_6	269·8	291·7	0·93	14	5·25	7·47	7·49	(e)
OsF_6	274·5	306·4	0·90	14	5·25	7·06	7·29	(e)
IrF_6	272·0	317·1	0·86	14	5·25	6·70	7·08	(e)
PtF_6	276·5	334·8	0·83	14	5·25	6·50	6·77	(e)
MoF_6	263·6	290·6	0·91	14	5·25	7·24	7·72	(f)
1-Azabicyclo 2,2,2 octane (ABCO)	198	433	0·46	16	5·50	5·80	6·34	(g)
Bicyclo 2,2,2 octane (BCO)	164	447	0·37	20	5·95	6·30	6·66	(g)
1-4 Diazabicyclo 2,2,2 octane (DABCO)	351	433	0·81	20	5·95	7·25	7·19	(g)
Bicyclo 2,2,2 octene-2 (BCO2)	111*							
	176	389	0·44	60	8·14	8·67	8·44	(g)
3-Oxabicyclo 3,2,2 nonane (OXBN)	208	448	0·47	60	8·14	8·70	8·22	(g)
Bicyclo 2,2,1 heptane (BCH)	131	360	0·36	36	7·13	7·43	7·59	(g)
Bicyclo 2,2,1 heptene-2 (BCH2)	129	320	0·40	72	8·54	8·97	8·98	(g)
Bicyclo 2,2,1 heptadiene-2-5(BCH22)	202	254	0·80	72	8·54	10·14	10·57	(g)
3-Azabicyclo 3,2,2 nonane (AZBN)	298	467	0·64	144	9·89	10·75	11·63	(g)

*Asterisks indicate transitions to a non-plastic phase.

(a) EUCKEN A., *Ang. Chem.* **55**, 163 (1942).
(b) Quoted by STAVELEY L. A. K., *J. Phys. Chem Solids* **18**, 83 (1961)
(c) PERDOK W. G., *Helv. Chim. Acta* **30**, 1782 (1947).
(d) WESTRUM E. F., *J. Phys. Chem. Solids* **18**, 83 (1961).
(e) WESTRUM E. F., *J. Chim. Phys. et Biol.* **63**, 46 (1966).
(f) Quoted by WEINSTOCK B., *J. Phys. Chem Solids* **18**, 86 (1961).
(g) WESTRUM E. F., *Natn. Bur. Stand. Mater. Res. Symp.* (1967). To be published.

symmetry. We take $D = 60$ as proposed by Wen-Kuei Wong[8]. (f) Bicyclo[2,2,1] heptane (BCH), can be considered as having C_{2v} symmetry and approximate C_{3v} symmetry. We estimate $D = 36$, there being twelve possible orientations for the subgroup C_{2v} on a O_h type site; and twenty four additional orientations if we consider that there are eight orientations for a molecule with strictly C_{3v} symmetry and that fact that, since BCH has not true C_{3v} symmetry, rotations through 120° and 240° about the pseudo 3-fold axis results in additional distinguishable orientations. That is $D = 12 + 3 \times 8 = 36$. (g) Bicyclo[2,2,1] heptene-2, (BCH2), and Bicyclo[2,2,1] heptadiene-2-5, (BCH22), are molecules with less than C_{2v} symmetry and can be considered as having approximate C_{2v} and approximate C_{3v} symmetry. If these molecules had the same symmetry and geometry as BCH we would have used $D = 36$, but since BCH2 and BCH22 do not have a true 2-fold axis there can be twice as many distinguishable orientations. Thus, we take $D = 36 \times 2 = 72$. (h) 3-Azabicyclo[3,2,2] nonane, can also be considered as a molecule with approximate C_{2v} and C_{3v} symmetry, but can take twice as many distinguishable orientations as BCH2 and BCH22, because the nitrogen atom is not on the pseudo 2-fold axis. Thus, we take $D = 72 \times 2 = 144$.

As can be seen in Fig. 7 and in Table 1 there is very good agreement between experimental and calculated ΔS_t values. The values of transition entropies calculated with the relation used by Guthrie and McCullough [2]

$$\Delta S_t = R \ln D \qquad (4)$$

correspond to our theoretical values for $T_t/T_m = 0$, and give worse agreement with experiment than those calculated with our theory for the real values of T_t/T_m. In particular, for the hexafluoride molecules we obtain good agreement considering that $D = 14$, whereas using just the expression (4) it would be necessary to assume that $D > 24$ for molecules that have a symmetry number of 24.

Experimental values of relative volume changes at the solid–solid transition, $\Delta V_t/V_{cII}$, and theoretical values of $\Delta V_t/V_{cII}$ vs. T_t/T_m are presented in Fig. 8 and in Table 2. The agreement is also quite good, taking into account that the experimental values of $\Delta V_t/V_{cII}$ can have large errors.

Another measurable quantity is the relative volume expansion of the disordered high-temperature phase between T_t and T_m. In Fig. 9 we have shown the theoretical values for this quantity as a plot of ν vs. T_t/T_m, valid for all values of D. From this quantity and the experimental values of T_t and T_m, the value of the mean expansion coefficient between T_t and T_m can be obtained. This value for Adamantane is $3{\cdot}4 \times 10^{-4}$/°K and the approximate experimental value obtained from a X-ray diffraction study of cell expansion [9] is $4{\cdot}4 \times 10^{-4}$/°K.

Theoretical and experimental values of entropies of melting, ΔS_m, and relative volume change on melting, $\Delta V_m/V_r$ have been plotted as a function of T_t/T_m and these plots are shown in Fig. 10 and 11 respectively. In Fig. 12 we give a similar plot of entropies vs.

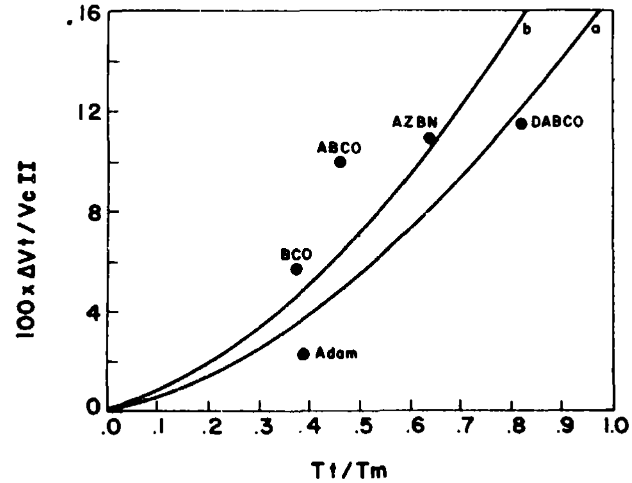

Fig. 8. Comparison of theoretical curves and experimental values of relative volume changes at T_t. Curves *a* and *b* correspond to D values of 6 and 20 respectively. See also Table 2.

Table 2. Experimental and theoretical values of $\Delta V_t/V_{cII}$

Compound	T_t/T_m	$(\Delta V_t/V_{cII}) \times 100$ exp.	theory	References
BCO	0·37	5·7	4·7	(a)
ABCO	0·46	9·0	6·3	(a)
DABCO	0·81	11·5	15·5	(a)
AZBN	0·64	10·9	11·4	(b)
ADAM	0·38	2·3	3·7	(c)

(a) BRUESCH P., *Spectrochim Acta* **22**, 861 (1966).

(b) AMZEL L. M., Dissertation, University of Buenos Aires (1966).

(c) Reference [9].

relative volume changes on melting. The experimental values of ΔS_m are, in general, higher than the theoretical predictions. The agreement for the volume changes is quite good, the theoretical values calculated for $D > 2$ being nearer to the experimental values than for $D = 2$ as calculated by Pople and Karasz[1].

COMPARISON WITH EXPERIMENTAL PHASE DIAGRAMS

Theoretical and experimental phase diagrams of ADAM[10], CCl_4[11], and CBr_4[11] are plotted in Figs. 13–15. The theoretical diagrams were constructed using D values estimated in the analysis of transition entropies and ν values that correspond to the experimental ratio T_t/T_m and the appropriate D. In order to plot the experimental data we applied the usual conversion of this data to reduced temperature, kT/ϵ_0, and pressure, $Pv_0/N\epsilon_0$, units. The experimental curves were made to coincide with the theoretical curves at $P = 0$ and the reduced volume v_0 is about 15 per cent smaller than the volume of the high temperature phase near the melting point. In spite of the fact that $d(kT/\epsilon_0)/d(Pv_0/N\epsilon_0)$ is a sensitive function of ν, we have assumed that ν is independent of pressure since otherwise the calculations would have become too complicated and dependant on another undeterminable parameter. Even with such a simple model the agreement between experiment and theory is quite good, except for the melting curve of ADAM. For the latter we believe that the experimental data is erroneous. This conclusion is based on: (a) the slope of the experimental melting curve of ADAM is of about 150 bars/deg; (b) the value of ΔS_m for ADAM, a plastic crystal, should be less than 5 e.u.; and therefore (c) the volume change on melting have to be of about 1 Å^3, implying a quite unrealistically small relative volume change of less than 1 per cent.

RELATION WITH NUCLEAR MAGNETIC RESONANCE STUDIES

Nuclear magnetic resonance studies can yield experimental values for the energies of the reorientation and of the self-diffusion barriers (E_{reor} and E_{diff}) of molecules in the solid. The ratio between these two quantities, $\Gamma = E_{\mathrm{reor}}/E_{\mathrm{diff}}$, should be related with the parameter ν of our model, and a comparison of Γ and ν would give additional evidence on the validity of the model. Smith[12] has made such a comparison between the Γ values he reports for $C(CH_3)_4$, $Si(CH_3)_4$ and $Ge(CH_3)_4$,

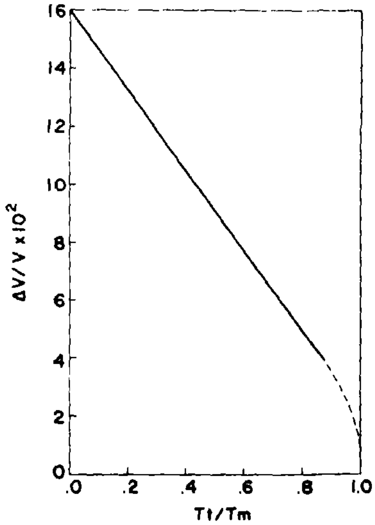

Fig. 9. Theoretical values of the relative volume change of the disordered phase form T_t to T_m.

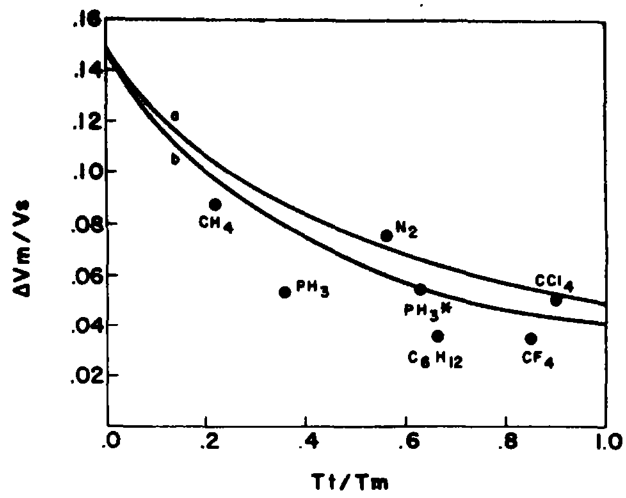

Fig. 10. Comparison of relative volume change on melting with solid transition/melting temperature ratio. Theoretical curves *a* and *b* correspond to *D* values of 6 and 20 respectively. For substances showing two solid transitions, a star denotes the upper transition.

0·17, 1·16 and 1·6 respectively, and the corresponding ν values obtained from the model of Pople and Karasz. In his analysis of the relation between the Γ and the ν values of the $X(CH_3)_4$ compounds, Smith finds a good correlation using ν values obtained from the

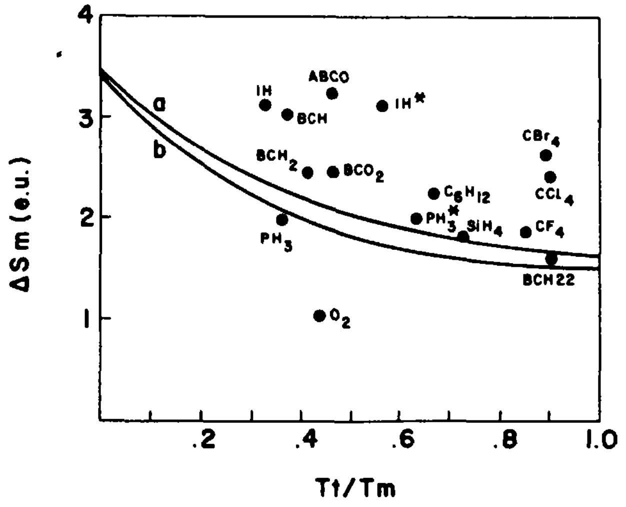

Fig. 11. Comparison of melting entropy with solid transition/melting temperature ratio. Theoretical curves *a* and *b* correspond to *D* values of 6 and 20 respectively. For substances showing two solid transitions, a star denotes the upper transition.

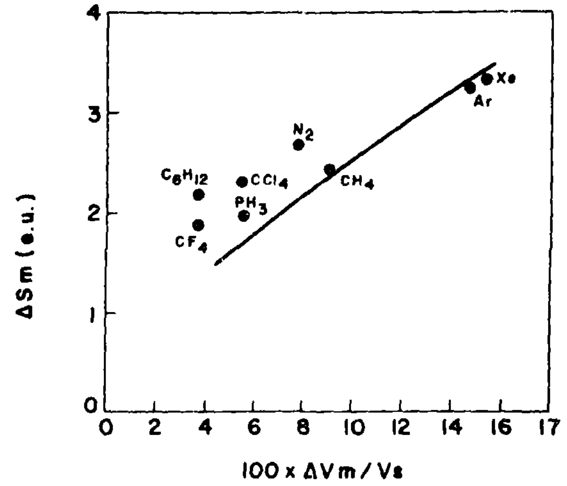

Fig. 12 Comparison of melting entropy ΔS_m with relative volume change on melting. Theoretical curve is approximately valid for D values from 6 to 150.

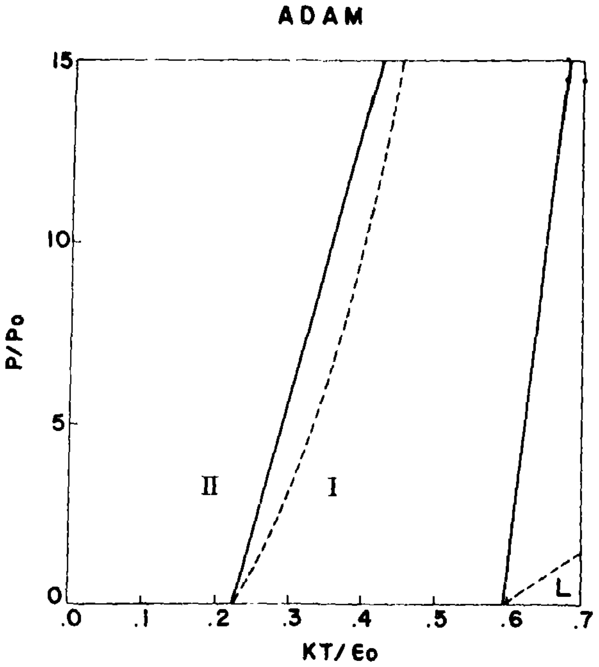

Fig. 13. Comparison of theoretical (- - -) with experimental (——) phase diagram for Adamantane. Phase II is ordered solid, I is disordered solid, and *L* is liquid.

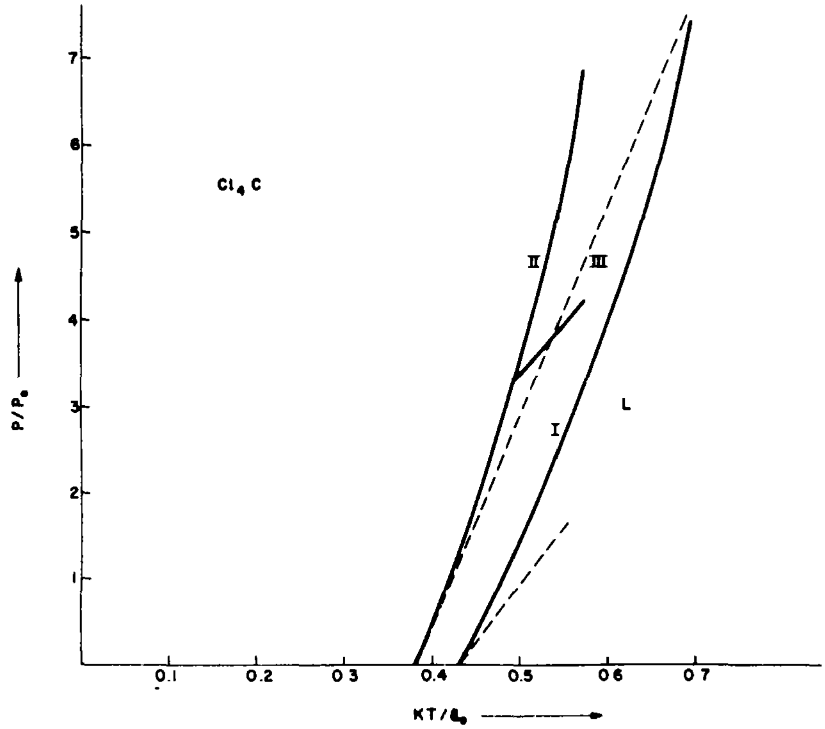

Fig. 14. Comparison of theoretical (- - -) with experimental (———) phase diagram for Br_4C. Phase II is ordered solid, I is disordered solid, III is a high pressure phase that cannot be predicted by our model, *L* is liquid.

model of Pople and Karasz. However, with that model the value of ν for $C(CH_3)_4$ is $<0{\cdot}16$, implying that the solid–solid transition is of second order, in contradiction with calorimetric studies[13] that give $\Delta S_t = 4{\cdot}4$ e.u. With our model we take $D = 6$ for $C(CH_3)_4$, since it is of T_d symmetry, and for $T_t/T_m = 0{\cdot}535$ this value of D gives ΔS_t (theoretical) $= 4{\cdot}0$ e.u. (see Fig. 7), in good agreement with the experimental value. For these values of D and T_t/T_m we obtain $\nu = 0{\cdot}25$, as can be seen in Fig. 3. For Si $(CH_3)_4$ and Ge $(CH_3)_4$ melting occurs before transition, corresponding to $\nu > 0{\cdot}42$ in our model. Values of E_{reor} in the high temperature phase (E^{I}_{reor}) have also been measured for ADAM[14] and *d*-CAMPHOR [15]; values of E_{reor} in the low temperature phase (E^{II}_{reor}) have been measured for DABCO [16], NF_3[17], and P_4[18]. For DABCO and NF_3 the value of E^{II}_{reor} corresponds to nonisotropic reorientation between undistinguishable orientations. Values of E_{diff} were measured in the high temperature phase for all the above mentioned compounds. In order to estimate an upper limit for Γ in the cases for which E^{I}_{reor} has not been measured we assume that $E^{II}_{\text{reor}} > E^{I}_{\text{reor}}$, whatever the motion involved in the measure of E^{II}_{reor}. This assumption seems reasonable considering the cell expansion on transition, and is in agreement with the measurements made for ADAM[14] and for P_4[18]. To estimate ν we take $D = 16$ for NF_3, since NF_3 has C_{3v} symmetry; for P_4 we take $D = 6$ since it has T_d symmetry; and a somewhat arbitrarily chosen value of $D = 72$ for *d*-CAMPHOR, since it might be considered to have similar symmetry to that of BCH2. For NF_3 the choice of $D = 16$ is

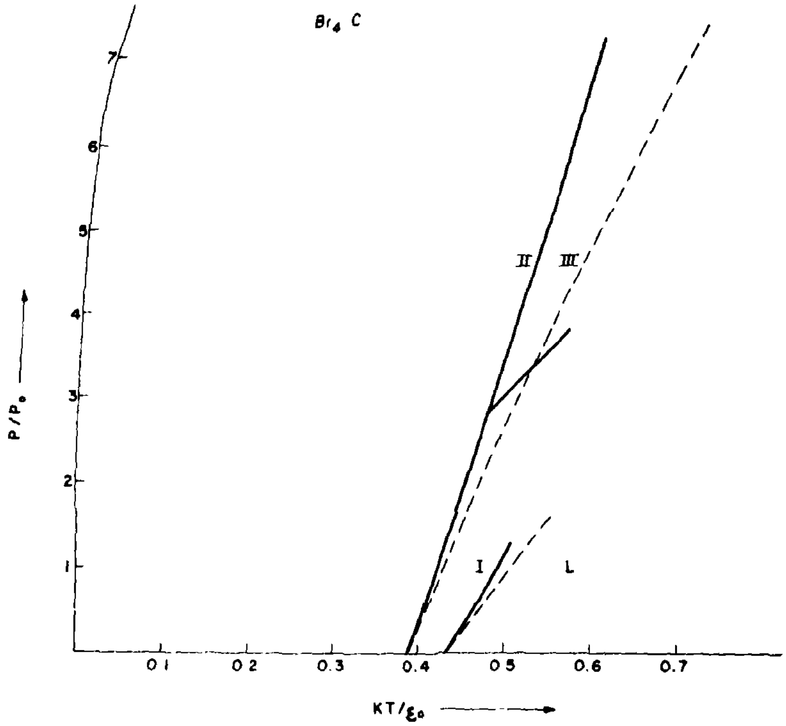

Fig. 15. Comparison of theoretical (- - -) with experimental (———) phase diagram for Br_4C. Phase II is ordered solid, I is disordered solid, III is a high pressure phase that cannot be predicted by our model, *L* is liquid.

justified further by the fact that this value of D gives $\Delta S_t = 6{\cdot}7$ e.u. in good agreement with the experimental value[19] of 6·4 e.u. Thus, for $Ge(CH_3)_4$, $Si(CH_3)_4$, DABCO, NF_3, *d*-CAMPHOR, P_4, $C(CH_3)_4$, and ADAM the correlation between the ν values (>0·42, >0·42, 0·41, 0·40, 0·30, 0·28, 0·25 and 0·19) and the corresponding Γ values (1·6, 1·2, <0·43, <0·50, 0·20, <0·33, 0·17 and 0·99) is qualitatively correct, since ν should be a monotonic function of Γ. These results are summarized in Table 3.

Darmon and Brot[20] have analysed N.M.R. data demonstrating that thermodynamics is almost insensitive to the rearrangement dynamics of the orientational disorder. By simple calculations they show that only a very small fraction of the molecules is in a state of jump between allowed orientations. In the same report these authors propose a classification that accounts for the different observable temperature relations between N.M.R. line width narrowing and transition temperature. This classification is based on the limiting assumption that in the ordered phase only thermodynamically indistinguishable orientations are allowed, and that in the high temperature phase there can also be reorientation between distinguishable reorientations. Most of the examples taken from the literature fall within the proposed classification, since few cases have been observed with a line width narrowing involving reorientation between distinguishable orientations in the low temperature phase. In relation to our model it might be noted that the following facts mentioned by Darmon and Brot are compatible with the thermodynamic

Table 3. Relation of ν with NMR studies

Compound	T_t/T_m	D	ν	E^{l}_{reor} (Kcal/mole)	E_{diff} (Kcal/mole)	Γ	Reference
$Ge(CH_3)_4$	> 1	6	> 0·42	9·8	6	1·6	[12]
$Si(CH_3)_4$	> 1	6	> 0·42	7·2	6·2	1·2	[12]
DABCO	0·81	20	0·41	< 7·0*	16·2	< 0·43	[16]
NF_3	0·85	16	0·40	< 0·98*	1·9	< 0·50	[17]
d-CAMPHOR	0·52	72	0·30	2·8	14·6	0·20	[15]
P_4	0·61	6	0·28	< 4·0*	12·1	< 0·33	[18]
$C(CH_3)_4$	0·54	6	0·25	1·0	6·0	0·17	[12]
ADAM	0·38	6	0·19	3·1	34	0·09	[14]

*This numerical value of E_{reor} has been obtained for the low temperature phase and sets a upper limit to E^{l}_{reor}. See text.

definition of our model: (a) each molecule spends most of its time in allowed orientations, (b) in the low temperature phase there is practically complete orientational order (the allowed orientation are indistinguishable), that is $S_1 \approx 1$, *c*) in the high temperature phase there is complete orientational disorder (there are D allowed distinguishable orientations with equal probability of occupation), that is $S_1 = 1/D$. The fact that most of the compounds studied so far by N.M.R. do not show in the low temperature phase a measurable reorientation rate for jumps between distinguishable orientations is not necessarily in contradiction with the fact that with our model we find that $S_1 < 1$ in the low temperature phase (as expected from the postulated cooperative establishment of the disorder). All that these N.M.R. observations tell us is that in most cases the correlation time (τ_c) for random reorientations between indistinguishable orientations, τ_c(indist), can become short enough to produce a N.M.R. line width narrowing in the low temperature phase, and that τ_c for reorientations between distinguishable orientations, τ_c(dist), becomes short enough only in the high temperature phase. Since it is reasonable to assume that in the low temperature phase the barrier to reorientation between some indistinguishable orientations is in general smaller than for reorientation between distinguishable orientations, it is to be expected that $\tau_c(\text{dist}) > \tau_c(\text{indist})$ in the low temperature phase. Finally, we think that it would be interesting to study the temperature dependence of the N.M.R. line width of a series of unsymmetric molecules to see wether a narrowing is observed in the ordered phase.. With such compounds there are no indistinguishable orientations and, in principle, there might be a line width narrowing in the low temperature phase provided the barrier to reorientation is low enough and the parameter ν is high, so that the phase transition takes place at a higher temperature than the possible line width transition. Furthermore, in the N.M.R. studies of P_4[18] and of camphor[15] the line width narrowing observed below the thermodynamic transition involves reorientations between distinguishable orientations, indicating that even to interpret N.M.R. results the extreme assumption of: "S_1 always equals 1 in the low temperature phase", is not strictly valid.

Acknowledgements—We are grateful to Professor E. F. Westrum Jr. for helpful discussions, and we thank the Director and staff of the Departamento de Computación of this University for assistance and for generous allocation of computer time.

REFERENCES

1. POPLE J. A. and KARASZ F. E., *J. Phys. Chem. Solids* **18**, 28 (1961); KARASZ F. E. and POPLE J. A., *J. Phys. Chem. Solids* **20**, 294 (1961).
2. GUTHRIE G. B. and McCULLOUGH J. P., *J. Phys. Chem. Solids* **18**, 53 (1961).
3. LENNARD-JONES S. E. and DEVONSHIRE A. F., *Proc. R. Soc.* **A168**, 3171 (1939).

4. TEMPERLEY H. N. V., *Changes of State*, p. 25., Cleaver-Hume, London (1956).
5. WENTORF R. H., BENHLER R. J., HIRSCHFELDER J. O. and CURTISS C. F., *J. chem. Phys.* **18**, 1489 (1950).
6. HILL, T. L., *An Introduction to Statistical Thermodynamics*, p. 408. Addison–Wesley, U.S.A. (1960).
7. TIMMERMANS J., *J. chem. Phys.* **35**, 331 (1938); STAVELEY L. A. K., *Ann. Rev. Phys. Chem.* **13**, 351 (1962); ASTON J. G., *Physics and Chemistry of Organic Solid State* (Edited by Fox, Labes and Weissberg), Vol. 1. Interscience, New York 1963; Vol 18, No. 1, *The Journal of Physics and Chemistry of Solids* (1961); Vol. 62, No. 1, *Journal de Chemie Physique* (1966); SMITH G W., *International Science and Technology*, 72 (1967). Plastic crystals were first studied by Professor J. Timmermans. The term 'plastic crystal' is used to name a high temperature phase of molecular crystals that has the following properties: low entropy of fusion ($\Delta S_m < 5$ e.u.), high vapour pressure, cubic or hexagonal symmetry, ease of deformation (plasticity) quasi-isotropic molecular reorientation at rates $> 10^9$ c/s, measurable autodiffusion, high entropy of transition to a low temperature solid phase (generally $\Delta S_t > 4$ e.u.). These properties are related with the fact that in this phase there is orientational disorder, and therefore an analysis of the thermodynamics of these compounds is particularly relevant to the theory presented here.
8. WONG WEN-KUEI, Ph. D. Dissertation, University of Michigan (1966).
9. MIRSKAYA K. V., *Soc. Phys. Crystallogr.* **8**, 167 (1963).
10. PISTORIUS C. W. F. T. and SNYMAN H. C., *Z. Phys. Chem.* (neue Folge) **43**, 278 (1964).
11. BRIDGMAN P. W. (Quoted by J. Timmermans), *J. Phys. Chem. Solids* **18**, 1, (1961).
12. SMITH G. W., *J. chem. Phys.* **42**, 4229 (1965).
13. ASTON J. G., KENNEDY R. M. and MESSERLY G. H., *J. Am. chem. Soc.* **63**, 2343 (1941).
14. RESING H. A., Abstracts of NBS 2nd Materials Research Symposium, Washington (1967).
15. ANDERSON J. E. and SLICHTER W. P., *J. chem. Phys.* **41**, 1922 (1964)
16. SMITH G. W., *J. chem. Phys.* **43**, 4325 (1965).
17. SMITH G. W., *J. chem. Phys.* **45**, 3483 (1966); MATKANIN G. A., SCOTT T. A. and HAIGH P. J., *J. chem. Phys.* **42**, 1646 (1965).
18. RESING H. A., *J. chem. Phys.* **37**, 2575 (1962).
19. PIERCE L. and PACE E. L., *J. chem. Phys.* **23**, 551 (1955).
20. DARMON I. and BROT C., *Mol. Cryst.* **2**, 301 (1967).

J. Phys. Chem. Solids Pergamon Press 1969. Vol. 30, pp. 539–550. Printed in Great Britain.

SOME MAGNETIC PROPERTIES OF Mn DISSOLVED IN Cu, Ag AND Au

C. M. HURD
National Research Council of Canada, Ottawa, Canada

(*Received* 16 *July* 1968)

Abstract—The atomic magnetic susceptibility of Mn dissolved in Cu, Ag and Au has been determined in the approximate range 10–300°K for α-phase polycrystalline alloys with solute concentrations ranging from 19–284 atomic ppm. The results can be well described by a Curie–Weiss law from which the mean values of the effective Bohr magneton values are $4{\cdot}93 \pm 0{\cdot}25$, $4{\cdot}73 \pm 0{\cdot}26$ and $5{\cdot}38 \pm 0{\cdot}27$ for Mn in Cu, Ag and Au respectively, and the mean values of the paramagnetic Curie temperature are respectively −14°, 0° and −7°K. The data have been fitted to an expression by Scalapino for the solute susceptibility from which have been obtained estimates of the Kondo temperature.

1. INTRODUCTION

IN THE theory of the localised magnetic moment of an isolated transition metal ion dissolved in a diamagnetic metallic host there has been much recent activity focussed upon the consequences of the spin exchange interaction between the conduction electrons of the solvent and the d electrons of the solute. It is sufficient here to consider only the general features of this theory as they relate to the results presented in Section 3; a more detailed coverage can be found in various recent reviews[1–3], although in fact many of the details of the theory are currently under active discussion by the theorists. In terms of the model due to Friedel[4] and to Anderson[5], a decoupled virtual d state localised in the conduction band of the solvent can, by exchange interaction, spin polarise the neighbouring conduction electrons of the solvent. One consequence of this interaction was discovered by Kondo[6] who showed that the scattering cross section of the exchange interaction diverges at low temperatures causing the electrical resistivity to increase logarithmically with decreasing temperature and thus providing a possible explanation of the resistance minimum phenomenon observed in certain dilute alloys. It is generally agreed from extensions to Kondo's work (see, for example, the reviews cited above) that in alloy systems exhibiting a resistance minimum phenomenon, and below a certain critical temperature T_K (commonly known as the Kondo temperature), there may be a new electronic state formed from the system consisting of the localised moment together with its neighbouring spin-polarised electrons. It has been suggested that below T_K this system should coalesce to a new quasi-bound electronic state of lower total energy than the uncompensated magnetic moment—somewhat analogous to the formation of a Cooper pair in the theory of superconductivity. Some experimental consequences of such a state have recently been reviewed[1] and there has been supporting evidence for its existence from various experiments, for example: nuclear orientation[7,8], electron transport effects[9] and magnetic susceptibility[10].

There is, however, a fundamental experimental difficulty which arises in the study of the above aspect of localised moments, and this is the problem of eliminating the effect of solute–solute interaction from the measurements. The solute state may encompass a region in space far greater than its own unit cell, either through the effect of long-range

Friedel oscillations in the density of the screening conduction electrons or from long-range effects of the exchange polarisation itself. Therefore studies of extremely dilute, randomly disordered alloys are required if the effects of solute–solute interaction are to be negligible—as they must be for the experimental results to be applicable to the theory. It will be seen from following paragraphs that most of the existing data for the magnetic properties of the systems under consideration are somewhat unsuitable for application to the theory of isolated moments because they relate to alloys of relatively high solute concentration (x) where there is empirical evidence of the effect of solute–solute interaction. Thus a study of the magnetic properties of extremely dilute alloys could be beneficial to the theory of localised moments, and indeed even if only a standard Curie–Weiss (C–W) treatment of the data is planned, it seems desirable to study only extremely dilute alloys since in those systems where both long-range and short-range solute–solute interactions coexist (as is thought to be the case for Mn dissolved in the group IB metals) the standard interpretation of the C–W law is probably only valid[11] in the limit $x = 0$.

This paper describes measurements of the total magnetic susceptibility of α-phase polycrystalline samples of the Cu–Mn, Ag–Mn and Au–Mn systems in the approximate range 6–300°K and with an Mn concentration up to 0·0284 at. %. Such alloys are extremely dilute by comparison with most of those studied previously in similar work (cf Table 1), and in an earlier paper[12] we have described the apparatus and techniques which permit a systematic and controlled study of such dilute alloys. The results of the present work are applied in Section 4 to two aspects of the theory. Firstly, the values of the effective Bohr magneton number (β) and the paramagnetic Curie temperature (θ) derived from a standard C–W treatment of the data are applied to the

Table 1. Summary of previous similar measurements

Solute Concentration Range (at. %)	Temperature Range (°K)	β	(°K)	Reference
		Cu–Mn		
0·03–11	4·2–373	4·95–5·19(a)	0 to 100	[15]
0·05–1·8	~2–300		3 to 16(a)	[16]
10–70	80–1,000	~5·0(a)	−50 to −400(a)	[17]
0·25–5·3	1·2–368	4·35–4·54	−3·4 to 20	[18]
0·81–1·8	273–473	4·52–4·83	21 to 35	[19]
1.3	93–300	4·82–4·85	0 to 11	[20]
0·02–1·8	0·1–4·2	4·66–5·16		[21]
		Ag–Mn		
7·5–19·8	20–700	4·67–5·77		[24]
4·2	4·2–373		13	[15]
0·25–5·3	1·2–368	5·65–6·03	−13 to 19	[18]
4·44–38·1	100–500	5·12–5·39	27 to 30	[22]
2–17	300–700	5·00–5·66	0·5 to 32	[23]
		Au–Mn		
9·73, 14·7	20–700	4·78–5·22		[24]
1·8	4–400	5·6	15	(b)
1·0, 2·0	6–37	5·8–6·6	2·9	[25]

(a) Estimated from the author's data.

(b) Work by Cohen *et al.* cited in reference[25].

semi-empirical form of Friedel's model[13] in the calculation of the residual resistivity of the solute for comparison with experiment, and secondly the data are fitted to Scalapino's quantum mechanical expression[14] for the solute susceptibility which derives from Anderson's model of the solute ion[5]. This fitting leads to estimates of the Kondo temperature and of the effective antiferromagnetic coupling constant between the spin of the solute ion and the conduction electrons.

2. SURVEY OF PREVIOUS SIMILAR MEASUREMENTS

Previous similar work published since 1954 is summarised in Table 1 from which it is seen that the emphasis has been upon alloys of relatively high solute concentration with particular interest in the solute–solute interaction which results in an apparent antiferromagnetic transition below room temperature in alloys for which $x \simeq 1$ at. %. Such a transition has been observed for Mn in Cu[15], Ag[15] and Au[25], while almost all the theoretical work has been directed towards the Cu–Mn system (cf. [26]). It is known that the antiferromagnetic transition temperature in such alloys is lowered by a reduction in solute concentration, and a rough extrapolation from previous work[15] suggests that for alloys as dilute as those studied here the antiferromagnetic transition (if it exists at all at such dilution) will be outside the temperature range of the measurements (i.e. < ~6°K).

It is useful to briefly summarise from the results of Table 1 what is known about the magnetic properties of Mn dissolved in the group 1 B metals. It seems well established that for sufficiently high temperatures the susceptibility of Mn in the above solvents obeys a C–W law, and in most cases the available values of β and θ show a dependence upon x. This is taken as direct empirical evidence of the influence of the solute–solute interaction in the alloys studied. Indeed there is some evidence from direct magnetisation measurements at very low temperatures[21] and from NMR results[27] of solute–solute interaction in Cu–Mn alloys with solute concentrations as low as ~ 200 ppm. It has been suggested[21,27] that this apparent solute interaction arises basically from a nonuniform distribution of the solute in the alloy[28], and the above evidence serves as a reminder that the metallurgical state of the sample is an important (and often relatively unknown) parameter in all such measurements as those reported here. The sign of θ is generally reported positive for Mn in each group 1 B solvent, although there is the evidence referred to above of an antiferromagnetic transition in each system. It is generally concluded from this information[11] that both a short-range ferromagnetic and a longer range antiferromagnetic interaction coexist in these systems at moderate solute concentrations. In α-phase Au–Mn at least, there is evidence of a ferromagnetic transition[25]. The values of β for infinite dilution for Mn in Cu, Ag and Au obtained from previous work[29] are approximately 4·9, 5·9 and 5·9 respectively. After the usual numerous assumptions, including that the angular momentum of the ion is completely quenched, that the Landé splitting factor is 2 and that there is negligible contribution to the effective solute spin from local polarisation of the conduction electrons, these values lead to the electronic configuration of Mn in Cu, Ag and Au of $3d^6 4s^1$, $3d^5 4s^2$ and $3d^5 4s^2$ respectively.

It is known from the data of Table 1 that of the 1st row transition elements Mn has the largest localised moment when dissolved in a group 1 B metal. In terms of the usual model [4,5] this implies that the split virtual d levels are more separated for Mn dissolved in a noble metal than for any other 1st row transition solute, and that the polarisation of the conduction electrons will be relatively slight[30] because of the correspondingly small s–d interaction (which must be negative since the alloy systems exhibit the resistance minimum phenomenon) resulting from the virtual d level being relatively far below the Fermi level in energy. This picture is supported by the magnitude of T_K which is generally put forward for these systems, it being smallest for Mn among the 1st row transition elements[1,7], and by the specific electrical resistance of these elements in Cu of which, it is claimed[31], Ti, V and Mn follow a form of Linde's rule. The latter behaviour is taken to indicate[31] a very small interaction between the split d levels and the electrons at the Fermi level. The usual pictorial representation of the Friedel model for the 1st row transition elements in Cu and Au due to Daniel[13] is consistent with the above remarks and is frequently adopted[31].

There is, however, some experimental evidence which can be interpreted as being inconsistent with Daniel's representation. Firstly, optical absorption measurements[32] for Cu–Mn indicate a very small (~ 0·25 eV) energy splitting between the d states, which is entirely contrary to the above evidence and to Daniel's model. Secondly, it is possible from measurements of the de Haas–van Alphen effect in very dilute alloys to obtain estimates of the number of electrons contributed by the solute to the conduction band. *If it is assumed that all the localised electrons are in* d *states*, then estimates of the number of electrons in each split d band can be made directly from the known magnetic properties of the solute. Coleridge and Templeton[33] have made such measurements for Ni, Co, Fe, Mn, and Cr in Cu, and in some of these systems (including Cu–Mn) the calculated number of electrons in each d band is not consistent with Daniel's model[13]. Although the dHvA results are interesting in their own right, it should be noted that they do not directly provide a valid criticism of Daniel's model since that model does not assume that the localised charge can exist only in d levels.

3. EXPERIMENTAL PROCEDURE AND RESULTS

The measurements were made with a Faraday apparatus which has been described elsewhere[34]. The samples were prepared from Cu, Ag and Au of 6 N grade[35] and the solute material was of 4 N grade[36]. The samples were chill cast in an apparatus and by techniques which have both previously been described in some detail[12]. Prior to measurement the Cu–Mn alloys were vacuum annealed at 500°C for 24 hr and slow-cooled to room temperature, while the Ag–Mn and Au–Mn alloys were vacuum annealed at 700°C for at least 40 hr before rapid quenching into a mixture of iced brine. The chemical analyses were carried out by the Analysis Section in this Division using the method of atomic absorption.

The alloy susceptibility measurements were made relative to the total mass susceptibility of pure Cu at 295°K as previously described[12], and the susceptibility of the alloy was determined for two values of the applied field (approximately 7 K and 20 K G) at each temperature. Significant field dependence of the susceptibility was observed only for the most concentrated alloy in each series and only at temperatures $< \sim 16$°K. For these field-dependent results the value of the total susceptibility of the alloy was obtained by the usual method of extrapolation to infinite applied field and it is given in Tables 2–4 together with the mean of field-independent determinations. The precision of any datum in Tables 2–4 is estimated to be $\pm 0{\cdot}6 \times 10^{-9}$ c.g.s. e.m.u/g at any temperature.

The atomic susceptibility of the solute (χ_A) was determined from the relation for dilute alloys

$$\chi_A = 100A(\chi - \chi^s)/x \qquad (1)$$

where the quantities have previously been defined[12]. Values of $1/\chi_A$ and their statistical weights were calculated at each temperature of measurement from (1) and the known values of χ^s for the solvent metals[12]. χ^s for Ag as a function of temperature (T)[12] can be conveniently represented by the polynomial (in units of 10^{-9} c.g.s.e.m.u./g):

$$-\chi^{s}_{\mathrm{Ag}} = 182{\cdot}59 - 0{\cdot}2486 \times 10^{-2}T - 0{\cdot}114 \times 10^{-4}T^{2}. \quad (2)$$

The weight of each datum was obtained using a precision for both χ and χ^{s} of $\pm 0{\cdot}6 \times 10^{-9}$ c.g.s. e.m.u./g at any temperature. The values of $1/\chi_A$ plotted against T are shown in Figs. 1–3; where the length of a scatter bar is inversely proportional to the calculated weight of the datum.

We would like to take this opportunity to correct an inadvertant error in a previous letter on this subject[37]. This reported an apparent anomaly in the temperature dependence of the solute susceptibility of very dilute Cu-Fe alloys in the range 6–17°K which was not observed in similar measurements of Au-Fe alloys[12]. During the course of the measurements described in the present paper it was discovered that this appparent anomaly was caused by an instrumental effect associated with the presence of an

Table 2. *Mass susceptibility of* Cu–Mn *alloys:* $-\chi \times 10^{7}$ *(c.g.s. e.m.u./g)*

Temperature (°K)	Solute concentration in atomic ppm 19	36	106	147	216
10				−2·572	
17			−0·792		−3·856
20	0·582	0·329			
28	0·656	0·416	−0·400	−0·799	−1·949
48	0·726	0·594	0·000	−0·279	−0·920
63	0·763	0·655	0·134	−0·109	−0·506
84	0·775	0·688	0·268	0·041	−0·291
103	0·794	0·715	0·379	0·196	−0·078
128	0·808	0·750	0·480	0·347	0·150
163	0·818	0·775	0·555	0·447	0·273
197	0·824	0·789	0·601	0·520	0·361
237	0·825	0·796	0·641	0·561	0·438
293	0·826	0·794	0·674	0·608	0·508

Table 3. *Mass susceptibility of* Ag–Mn *alloys:* $-\chi \times 10^{7}$ *(c.g.s.e.m.u./g)*

Temperature (°K)	Solute concentration in atomic ppm 25	50	100	213
10	1·092	—	—	−5·289
11	—	0·385	—	—
17	1·514	1·142	0·506	−1·791
28	1·611	1·420	0·910	0·010
50	—	1·598	1·289	0·670
60	1·823	1·622	1·390	0·846
83	1·751	1·661	1·470	1·047
102	1·765	1·692	1·537	1·194
129	—	1·723	1·599	1·310
162	1·781	1·740	1·640	1·420
193	1·788	1·749	1·662	1·490
227	—	1·756	—	—
233			1·690	1·533
292	1·784		1·704	1·579

Table 4. *Mass susceptibility of* Au–Mn *alloys:* $-\chi \times 10^{7}$ *(c.g.s. e.m.u./g)*

Temperature (°K)	Solute concentration in atomic ppm 106	231	284
10	−0·489		
14	0·419		−1·829
17		−0·401	
27	0·853	0·219	−0·147
48	1·070	0·665	0·486
57	1·120	0·800	0·560
84	1·195	0·951	0·797
102	1·239	1·042	0·925
128	1·279	1·120	1·020
161	1·313	1·192	1·106
195	1·330	1·229	1·170
227	1·344	1·258	1·210
292	1·362	1·295	1·248

exchange gas which interferred only with measurements upon the samples of relatively low density and at temperatures below about 17°K. Under these conditions the values of $1/\chi_A$ obtained were erroneously small. The only published data to be disregarded because of this error are those for Cu–Fe obtained [12] below ~ 15°K, together with the main thesis of our previous letter[37].

In the present and following paragraphs we shall give the values of certain parameters derived from the data in Tables 1–3, and in Section 4 these results are discussed in the light of previous data. The best values of the constants A and B in the expression

$$1/\chi_A = A + BT \tag{3}$$

were determined for each sample by the method of weighted least squares. The results are summarised in Table 5, and the best linear fit to the data is shown in Figs. 1–3. The corresponding values of θ and β calculated from the usual formulae ((4) of [12]) are also given in Table 5.

Scalapino's expression[14] for the gram atomic solute susceptibility (χ_A^{calc}) can be conveniently written as

$$1/\chi_A^{\text{calc}} = \left[\frac{3k}{\mu_B^2 N_0}\right]\left[T + \frac{T_K\tau}{\log\tau - 1}\right] \tag{4}$$

where $\tau = T/T_K$ and $\mu_B = \mu\beta$. N_0, μ, β and k are respectively Avogadro's number, the Bohr magneton, the effective Bohr magneton number of the ion, and Boltzmann's constant. In the temperature region covered by the present experimental results the factor $\tau/(\log\tau - 1)$ has the temperature dependence shown in Fig. 4. for $\tau < \sim 10$ the effect of the singularity in (4) is felt, and it is usual to therefore regard (4) as being unphysical in this region. In the following we shall refer specifically to the regions $\tau > \sim 10$ and $T < \sim 300$°K.

Table 5. Summary of experimental results

System	Solute concentration (atomic ppm)	σ^* $\left[\frac{10^6}{\text{e.m.u./g. atom}}\right]$	Approximate range of data (°K)	Paramagnetic Curie temperature (°K)	Effective Bohr magneton values
Cu–Mn	216	0·14	10–300	-7 ± 2	$4{\cdot}90 \pm 0{\cdot}24$
Cu–Mn	147	0·22	10–300	-21 ± 4	$5{\cdot}36 \pm 0{\cdot}30$
Cu–Mn	106	0·06	17–300	-18 ± 2	$5{\cdot}36 \pm 0{\cdot}24$
Cu–Mn	36	0·07	20–300	-11 ± 2	$4{\cdot}99 \pm 0{\cdot}24$
Cu–Mn	19	0·25	20–300	-13 ± 2	$5{\cdot}06 \pm 0{\cdot}25$
			Mean values =	-14 ± 3	$4{\cdot}93 \pm 0{\cdot}25$
Ag–Mn	213	0·45	10–300	-2 ± 2	$5{\cdot}02 \pm 0{\cdot}35$
Ag–Mn	100	0·05	17–300	-5 ± 2	$5{\cdot}08 \pm 0{\cdot}23$
Ag–Mn	50	0·14	11–230	3 ± 2	$4{\cdot}49 \pm 0{\cdot}26$
Ag–Mn	25	0·04	10–194	3 ± 2	$4{\cdot}34 \pm 0{\cdot}21$
			Mean values =	0 ± 2	$4{\cdot}73 \pm 0{\cdot}26$
Au–Mn	284	0·95	14–300	-8 ± 2	$5{\cdot}57 \pm 0{\cdot}27$
Au–Mn	231	0·04	17–300	-6 ± 2	$5{\cdot}31 \pm 0{\cdot}24$
Au–Mn	106	0·07	10–300	0 ± 2	$5{\cdot}27 \pm 0{\cdot}30$
			Mean values =	-7 ± 2	$5{\cdot}38 \pm 0{\cdot}27$

*Weighted standard deviation of the data from equation (3) over the temperature range of column 4.

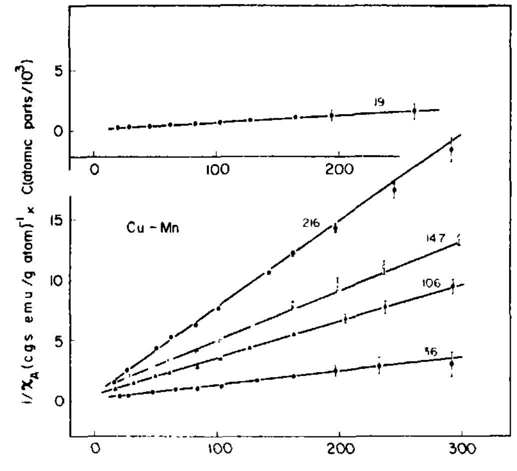

Fig. 1.

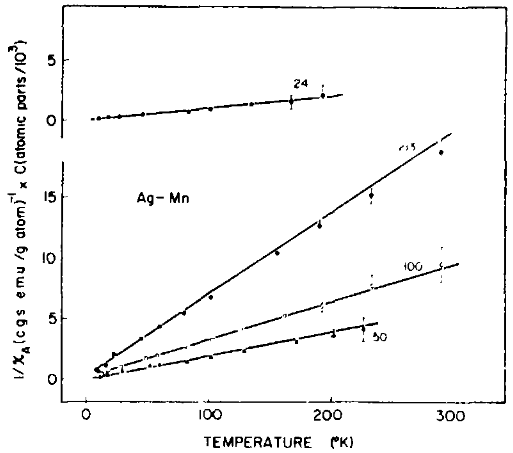

Fig. 2.

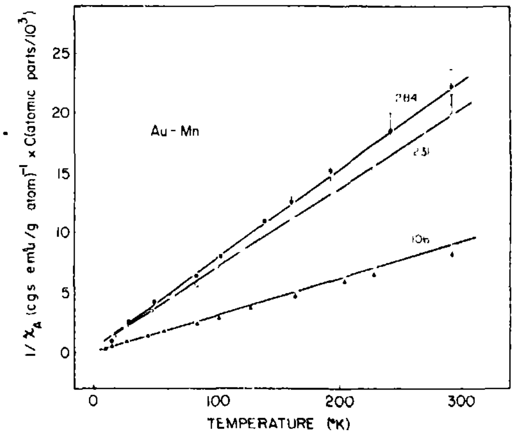

Fig. 3.

Figs. 1-3. The product of inverse atomic susceptibility of the solute and its concentration (in atomic parts per 10^3) plotted against temperature. The solute concentration is indicated in atomic ppm and some typical values of the precision of the data are shown.

Figure 4 shows that $\tau/(\log\tau - 1)$ has approximately a linear dependence upon T, becoming increasingly independent of T for increasing T_K. It follows that $1/\chi_A^{\mathrm{calc}}$ will show a linear temperature dependence, and it would be possible (in a very rough approximation) to assume $\tau/(\log\tau - 1)$ is independent of temperature for sufficiently large T_K. From a comparison of (4) with the usual C-W law, it follows that under this assumption T_K can be estimated directly from the paramagnetic Curie temperature θ by[1] $T_K = \theta/4$, or even by[38] $T_K = \theta$. It would seem from Fig. 4 that for $T_K < \sim 15°\mathrm{K}$

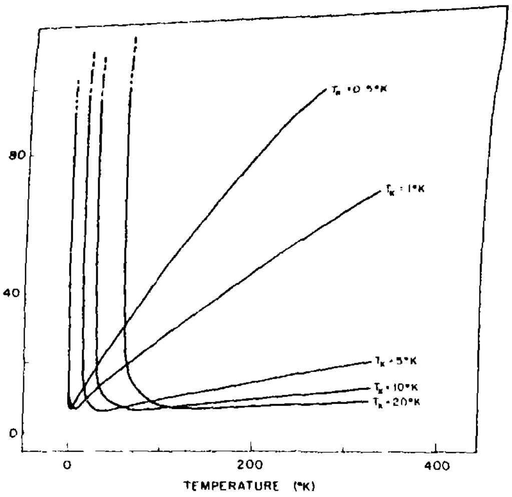

Fig. 4. Factor $\tau/(\log \tau - 1)$ from Scalapino's formula (4) plotted against temperature for different T_K; $\tau = T/T_K$.

the above method is not satisfactory because of the increasing temperature dependence of $\tau/(\log\tau - 1)$. A better estimate of T_K in (4) can be obtained by allowing T_K and β in (4) to be adjustable parameters with values chosen such that the weighted standard deviation:

$$\sigma = \left(\sum_i w_i (\chi_i^{\text{obs}} - \chi_i^{\text{calc}})^2/(N-1)\right)^{1/2} \quad (5)$$

is a minimum. In (5) χ_i^{obs} is the observed gram atomic susceptibility of the solute, and w_i and N are respectively the weight of the ith datum and the total number of data. One would expect that the optimum value of β needed to minimise σ will be the same as that resulting from the standard C–W treatment of the data since both (4) and the C–W law show an essentially linear dependence of $1/\chi_A$ upon T with a gradient of $3k/\mu_B^2 N_0$. It must be emphasised that the value of T_K so obtained is simply a fitting parameter of the experimental data to (4); whether this should be interpreted as a Kondo temperature depends upon the applicability of (4) to the alloy system in question, and upon whether there is other evidence which confirms that a quasi-bound state does exist in the system. (We have referred in Section 2 to the evidence that Mn in the 1B metals can form such a state). The results of this fitting are given in Table 6, which also includes the results for the similar data for the Cu–Fe and Au–Fe systems previously obtained[12] with the same apparatus, and are shown graphically in Fig. 5 for the cases where Mn is the solute. The solid lines in Fig. 5 are the values of $1/\chi_A^{\text{calc}}$ obtained from (4) and the T_K and β values of Table 6.

Table 6. Results of weighted least squares fit to equation (4)

Solvent	Solute	β*	T_K^*	σ	N
Cu	Fe	3·79	3·8	0·79	69
Cu	Mn	5·27	1·1	0·37	56
Au	Fe	3·80	1·0	0·70	54
Au	Mn	5·97	0·88	0·59	34
Ag	Mn	5·44	0·50	0·20	42

*Optimised values of parameters obtained by weighted least squares fit of data to (4) (T_K in °K). σ is weighted standard deviation of fit (cf (5)) in $10^6 \times$ g. atom/c.g.s. e.m.u. N is total number of data used in the fitting.

4. CONCLUSIONS

We find (Table 5) θ to be negative for Mn dissolved in Cu and Au and to be close to zero for Mn dissolved in Ag. This is in disagreement with the bulk of the previous work (Table 1), which is for more concentrated alloys and which usually reports θ as positive in each system, but more in line with what is expected from the simple C–W theory for an alloy system known to show an antiferromagnetic transition. This supports our presumption that, because of the dilution of the alloys studied, our results are more representative of systems having relatively small solute–solute interactions than those previously available. The mean value of β obtained for Mn in Cu and Au is in good agreement with the values previously obtained (Table 1) for alloys of infinite dilution, but

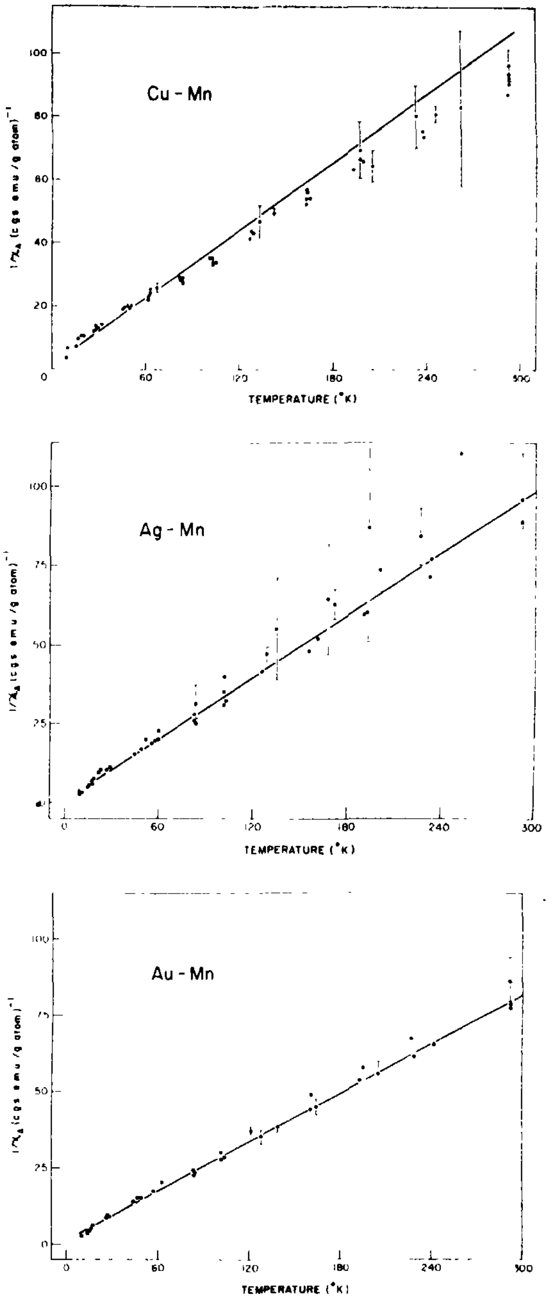

Fig. 5. Inverse atomic susceptibility v. temperature. The solid lines are the best weighted least squares fit to the data of Scalapino's expression (4). Values of the appropritate fitting parameters are given in Table 6.

this is not the case for Mn in Ag; here most previous values of β are significantly larger than that obtained here. At the present time we can offer no explanation of this fact. The β values of Table 5, taken under the assumption that the orbital momentum of the ion is completely quenched and that the Landé g factor is 2, lead to values for the number of electrons in the ion which contribute to its magnetic moment of 4·02 ± 0·25, 3·84 ± 0·25 and 4·47 ± 0·27 for Mn in Cu, Ag and Au respectively, with corresponding values of S (the resultant spin quantum number of the ion) of 2·13, 2·04 and 2·37.

It is possible from these data to make an estimate (which, in view of the approximations involved, will admittedly be very crude) of the solute structure in the solvent. We have in the above paragraph an experimental value for the difference (Z_m) in the number of electrons localised in the split d levels. We have also the estimate of this simple model[13] of the total excess charge localised about the ion (Z_l); we take $Z_l = 6$ for Mn in the noble metals, which for Mn in Cu at least is supported by experimental evidence from dHvA measurements[33]. We wish to assign an appropriate amount of charge to the s, p and d levels which is consistent with

$$\begin{aligned} n_{d\downarrow} - n_{d\uparrow} &= Z_m \\ n_{d\downarrow} + n_{d\uparrow} + n_{s,p} &= Z_l \end{aligned} \qquad (6)$$

where the subscript refers to the type of state in which the n electrons are localised. As a check upon the plausibility of the assignment we compare the calculated electrical resistance per atomic percent of solute ($\Delta\rho$) with the experimental value. We assume that the s and p states have similar relative structures in the IB metals to those of the polyvalent solutes to the right of the solvent in the periodic table[13]. From a recent simple model[39] we have the following approximate relationships for the polyvalent structures

$$\begin{aligned} 0 < n_{s,p} \leqslant 1{\cdot}1 &\text{ then } \eta_1 = \tfrac{3}{4}\eta_0 \\ 1{\cdot}1 < n_{s,p} \leqslant 2{\cdot}1 &\text{ then } \eta_1 = \tfrac{9}{10}\eta_0 \\ n_{s,p} > 2{\cdot}1 &\text{ then } \eta_1 = \eta_0 \end{aligned} \qquad (7)$$

where η is the phase shift of the usual partial wave analysis. $\Delta\rho$ is then calculated from the usual Friedel formula for split d bands [13] together with (7), and the results are presented in Table 7. The error limits are those arising solely from the experimental accuracy of Z_m given in Table 5 and do not include the effect of inaccuracy in Z_l. In the case of Mn in Au it is necessary to assign a small charge to s and p states to bring $n_\downarrow$ within acceptable limits (i.e. < 5), and this assumption also reduces $\Delta\rho$ to within the range of experimental values. The serious discrepancy between the observed and calculated $\Delta\rho$ values for Ag–Mn is accountable, at least in part, to the fact referred to earlier that we find a somewhat smaller value of β for this system than most previous workers. In view of this evidence, our results for the Ag–Mn system come under some suspicion,

Table 7. Proposed solute structures of Mn *dissolved in* 1 B *metals*

					$\Delta\rho$ ($\mu\Omega$ cm/at.%)	
Solvent	Z_l	$n_\downarrow$	$n_\uparrow$	$n_{s,p}$	Calculated	Experimental
Cu	6·0	4·91 ± 0·13	0·89 ± 0·1	0·2	2·5 ± 0·9	2·76(a)
Ag	6·0	4·92 ± 0·13	1·08 ± 0·2	0	4·68 ± 1·1	1·6(b)
Au	6·0	5·18 ± 0·14	0·71 ± 0·2	0·1	2·23 ± 0·6	2·23 – 2·37(c)

(a)Reference [31].
(b)Reference [40].
(c)Reference [25].

although at present we can offer no other reasons why they should be more suspect than the other data.

The T_K values obtained from the fitting to Scalapino's formula and given in Table 6 show qualitatively the behaviour anticipated from the remarks of Section 2 and other estimates[1], but quantitative comparison with other estimates is not encouraging; for example, T_K for Cu–Fe is fairly well established[9, 27] to be ~ 16°K, and a previous value of T_K for Cu–Mn is[7] ~ 0·06°K. In addition, for some of the systems the value of β produced by the fitting is only in order of magnitude agreement with that obtained from the standard C–W treatment.

An antiferromagnetic coupling constant (J) between the solute's spin and the conduction electrons can be defined by

$$kT_K = W \exp [1/N(O)J] \qquad (8)$$

where $N(O)$ is the unperturbed single-particle conduction electron density of states, and W is the effective bandwidth of the solvent. Table 8 shows the values of J calculated from (8) and the T_K values of Table 6 together with the assumption that $W = kT_F$, where T_F is the Fermi temperature. The values of the density of states per atom of Table 8 (column 3) were calculated directly from some recent values[41] of the electronic specific heat of the solvents.

Table 8. Calculated effective coupling constant J

Solvent	Solute	$N(0)$ (eV)$^{-1}$	$-J$ (eV)
Cu	Fe	0·29	0·34
Cu	Mn	0·29	0·29
Au	Fe	0·29	0·31
Au	Mn	0·29	0·30
Ag	Mn	0·27	0·31

Acknowledgements—I am grateful to the members of the Analysis Section of this Division who carried out the chemical analyses, to Drs. Coleridge, Karlsson and Templeton for permission to refer to unpublished work, and to Mr. F. Turner for his careful preparation of the samples.

REFERENCES

1. DAYBELL M. D. and STEYERT W. A., *Rev. mod. Phys.* **40**, 380 (1968).
2. ARROTT A., *Magnetism*, Vol. 2B. Academic Press, New York (1966).
3. JACCARINO V., *J. appl. Phys.* **39**, 1166 (1968).
4. FRIEDEL J., *Can. J. Phys.* **34**, 1190 (1956).
5. ANDERSON P. W., *Phys. Rev.* **124**, 41 (1961).
6. KONDO J., *Prog. theor. Phys.* **28**, 846 (1962); *ibid.* **32**, 37 (1964).
7. CAMPBELL I. A., COMPTON J. P., WILLIAMS I. R. and WILSON G. V. H., *Phys. Rev Lett.* **19**, 1319 (1967).
8. HOUSLEY R. M., *J. appl. Phys.* **39**, 1107 (1968).
9. DAYBELL M. D. and STEYERT W. A., *Phys. Rev.* **167**, 536 (1968).
10. DREYFUS B., SOULETIE J., THOLENCE J.L. and TOURNIER R., *J. appl. Phys.* **39**, 846 (1968).
11. SATO H., ARROTT A. and KIKUCHI R., *J. Phys. Chem. Solids* **10**, 19 (1959).
12. HURD C. M., *J. Phys. Chem. Solids* **28**, 1345 (1967).
13. DANIEL E., *J. Phys. Chem. Solids* **23**, 975 (1962).
14. SCALAPINO D. J., *Phys. Rev. Lett.* **16**, 937 (1966).
15. OWEN J., BROWNE M. E., ARP V. and KIP A. F., *J. Phys. Chem. Solids* **2**, 85 (1956).
16. SCHMITT R. W. and JACOBS I. S., *J. Phys. Chem. Solids* **3**, 324 (1957).
17. SCHEIL E. and WACHTEL E., *Z. Metallk.* **48**, 571 (1957).
18. VAN ITTERBEEK A., POLLENTIER R. and PEELAERS W., *Appl. Sci. Res.* **B7**, 329 (1959); VAN ITTERBEEK A., PEELAERS W. and STEFFENS E., *ibid.* **B8**, 337 (1960).
19. MYERS H. P. and WESTIN R., *Phil. Mag.* **8**, 669 (1963).
20. WEISS W. D., *Z. Metallk.* **58**, 909 (1967).
21. CAREAGA J. A., DREYFUS B., TOURNIER R. and WEIL L., *Proceedings of the LT10 Conference Moscow*. To be published.
22. MORRIS D. P. and WILLIAMS I., *Proc. phys. Soc.* **73**, 422 (1959).
23. HENDERSON B. and RAYNOR G. V., *J. Phys. Radium, Paris* **23**, 685 (1962).
24. KRONQVIST E. and GIANSOLDATI A., *Ark. Fys.* **7**, 343 (1954).
25. LUTES O. S. and SCHMIT J. L., *Phys. Rev.* **134**, A676 (1964).
26. VIOLET C. E. and BORG R. J., *Phys. Rev.* **149**, 540 (1966).
27. HEEGER A. J., WELSH L. B., JENSEN M. A. and GLADSTONE G., *Phys. Rev.* **172**, 302 (1968).
28. KOUVEL J. S., *J. Phys. Chem. Solids* **21**, 57 (1961).
29. VAN DEN BERG G. J., *Prog. Low Temp. Phys.* **4**, 194 (1964).
30. SOKOLOFF J. B., *Phys. Rev.* **161**, 540 (1967).

31. KIERSPE W., *Z. Metallk.* **58**, 895 (1967).
32. MYERS H. P., WALLDEN L. and KARLSSON Å., *Phil. Mag.* **18**, 725 (1968).
33. COLERIDGE P. T. and TEMPLETON I. M., Private communication.
34. HURD C. M., *Cryogenics* **6**, 264 (1966).
35. Cu supplied by Gallard-Schlesinger Chemical Mnfg Corp.; Ag and Au by Consolidated Mining and Smelting Co. Some typical spectrographic trace analyses have been made of these materials and are cited in HURD C. M. *J. Phys. Chem. Solids* **28**, 1345 (1967).
36. Mn supplied by King Products, Arlington, N.J.
37. HURD C. M., *Phys. Rev. Lett.* **18**, 1127 (1967).
38. KUME K., *J. phys. Soc. Japan* **23**, 1226 (1967).
39. HURD C. M. and GORDON E. M., *J. Phys. Chem. Solids* **29** 2205 (1968).
40. LANDOLT-BORNSTEIN, *Zahlenwerte und Functionen*, Vol. 6, Part 1 (1959).
41. MARTIN D. L., Private communication.

J. Phys. Chem. Solids Pergamon Press 1969. Vol. 30, pp. 551-564. Printed in Great Britain.

KINETICS AND MECHANISM OF THERMAL OXIDATION OF SILICON WITH SPECIAL EMPHASIS ON IMPURITY EFFECTS

A. G. REVESZ and **R. J. EVANS**
RCA Laboratories, Princeton, N.J. 08540, U.S.A.

(*Received* 18 *April* 1968; *in revised form* 11 *July* 1968)

Abstract—Thermal oxidation of silicon was investigated under a variety of conditions. The oxidation follows a combination of linear and parabolic rate lows; the rate constants obey the Arrhenius relationship. Under very clean conditions (dry 0_2, r.f. heating) the rate constants differ substantially from the values obtained by oxidation in resistance heated furnaces. In comparison with oxidation in dry O_2, oxidation in water vapor is characterized by larger pre-exponential terms and activation energies in the linear regime, but both are smaller in the parabolic regime. Sodium, that was deliberately introduced during oxidation, increased the parabolic and linear pre-exponential factors and activation energies It is proposed that oxide growth takes place via an interstitialcy diffusion mechanism in which both ionic and molecular oxygen participate. The surface reaction in the linear growth regime and the diffusion mechanism, as well as the concentration of the diffusing species in the parabolic regime, are greatly affected by sodium (or similar impurities) and water vapor in the oxidizing ambient. MOS capacitance measurements of Na-doped oxides showed that most of the sodium is inactive from the viewpoint of both surface state density and ion migration under high field at elevated temperature.

INTRODUCTION

IN THE COURSE of our studies on the properties of the Si–SiO_2 interface we have observed that the kinetics of thermal oxidation of silicon in dry oxygen is influenced by the oxidation method. Specifically, we found that the rate constants associated with oxidation by r.f. heating in a carefully cleaned gas-cooled reactor tube were considerably different from those characteristic of oxidation in resistance-heated silica or alumina tubes [1]. We thought that besides the well-known effects of water, sodium might play a role in the oxidation mechanism. The purpose of this work was to establish the oxidation kinetics under very clean conditions, that is, when impurities in the oxidation ambient had been minimized. Furthermore, we wanted to obtain more information on the role of sodium and the combined effect of sodium and water than has been already published[2]. Evaluation of these results and comparison with other works on the thermal oxidation of silicon, as well as with various transport processes in noncrystalline SiO_2, led us to a tentative model for the thermal oxidation of silicon. In this model the specific defect structure of noncrystalline SiO_2 and the role of impurities, mostly sodium and hydroxyl, are considered.

EXPERIMENTAL

Experiments on the thermal oxidation of silicon normally employ resistance-heated silica tubes. These tubes are subject to contamination from the furnace and surrounding ambient. Moreover, at high temperature, 900–1300°C, water vapor and/or hydrogen can very easily diffuse through the silica tube since the solubility and diffusion constants of these species are quite high. Indeed, Christie [3] has found appreciable amounts of water in the gas efflux from conventional fused silica furnace tubes. Nakayama and Collins[4] measured non-negligible oxidation rates when silicon was heated in dry argon in a resistance-heated silica tube, indicating the presence of 0·22 Torr. water vapor at 850°C and 0·35 Torr. at 1000°C.

In order to minimize the effect of hydrogen and/or water vapor we have performed most of our experiments in a carefully cleaned double wall silica tube with nitrogen cooling. The specimen was supported on a SiC-coated graphite pedestal and heated with an r.f. generator. This arrangement not only minimized diffusion through the reactor tube, but also other contamination effects, since the pedestal and specimen were the hottest parts of the system. The oxidation was preceded by a 10 min hydrogen treatment at 1200°C which removed the thin oxide film that forms on silicon in room ambient together with possible adsorbed impurities. The oxidation was performed in dry oxygen with an estimated water content of less than 0·1 ppm.

Two sets of experiments were performed under these conditions; one set without any doping, another one with sodium doping. The sodium was introduced by decomposing $NaNO_3$ on the pre-oxidized pedestal, thereby forming a Na_2O–SiO_2 glass layer. The sodium content of the oxide film, as determined by atomic absorption spectrometry, was of the order of 10^{20}Na atoms per cm^3. The high sodium content of these films was also revealed in their refractive index values: 1·50–1·60, whereas for fused silica the value is 1·46.

We attempted to investigate the combined effect of water vapor and sodium in the r.f. heated system but the results were not reproducible, probably due to the poor control of doping. This effect was studied with a resistance-heated alumina tube furnace used in our previous work[5]. Water vapor was introduced by bubbling helium through distilled water. Assuming saturation, the water vapor pressure was about 24 Torr. Sodium was introduced from sodium oxide kept in a boat at the oxidation temperature. Under these conditions the oxidation was under better control than in the r.f. system but the spread in the results was still large. This indicated strong impurity effects. In order to assess the effect of sodium a series of oxidation experiments were done in water vapor under identical conditions but without sodium doping. No pre-oxidation hydrogen treatment was applied for oxidation in the alumina tube furnace.

In each series the oxidation was performed at four temperatures between 900 and 1300°C. At each temperature 4 to 16 specimens were oxidized covering a wide thickness range (see Table 1). Chemically polished *p*-type (111) Si wafers of 10Ωcm resistivity were used. The oxide thickness was determined by ellipsometry using a computer evaluation method [6]. It was also measured by multiple beam interferometry[7]; the results obtained by the two methods agreed within the experimental errors. The relative errors of thickness vary from 0·9 to 2·6 per cent. The reproducibility of the oxidation under various conditions was also determined; the relative standard deviation varies from 3·3 to 5·8 per cent. Details of error and reproducibility calculations are given in the Appendix.

The properties of the Si–SiO_2 interface obtained by r.f.-oxidation with sodium doping were investigated by the MOS capacitance method[8]. For the fabrication of MOS capacitors aluminum electrodes were deposited on the oxide in high vacuum.

EVALUATION METHODS AND RESULTS

Before presenting the experimental results we will briefly outline the evaluation method. Oxidation of a metal or semiconductor is, in general, controlled by an interface reaction or transport through the oxide film. In the first case the oxidation follows a linear rate law. In the second case various growth laws can be observed, depending on temperature, oxide thickness, etc; at reasonably high temperatures and for not too thin films the parabolic rate law is the most frequently observed.

Linear-parabolic rate law

The combination of linear and parabolic rates results in the equation[9];

$$\frac{t}{x-x_0} = A + B\,(x-x_0) \qquad (1)$$

where x_0 is the thickness of oxide film present at the beginning of the oxidation (usually less than about 40 Å), and A and B are constants. The oxidation rate is given as

$$\frac{\mathrm{d}x}{\mathrm{d}t} = \frac{1}{A+2B(x-x_0)}. \qquad (2)$$

At the beginning of the oxidation, that is, for $x = x_0$

$$\frac{\mathrm{d}x}{\mathrm{d}t} = \frac{1}{A} \equiv a. \qquad (3)$$

This is the linear rate law and a is linear rate constant. This relationship is approximately valid for small thickness values, that is, for $(x-x_0) \ll A/2B$. On the other hand, for large thickness, that is, for $(x-x_0) \gg A/2B$, the following relationship holds

$$\frac{\mathrm{d}x}{\mathrm{d}t} \cong \frac{1}{2B(x-x_0)} \cong \frac{1}{2Bx}. \qquad (4)$$

This corresponds to the parabolic rate law:

$$x^2 = \frac{1}{B}t \equiv kt: \qquad (5)$$

If the oxidation was preceded by a hydrogen treatment, the initial oxide thickness, x_0, was taken as zero, otherwise as 35 Å (determined by ellipsometry).

The experimental results have been evaluated in the following way. For a given oxidation method and temperature the constants A and B of Equation (1) were determined from a set of $t/(x-x_0)$ and $(x-x_0)$ values by the method of least squares. The results are summarized in Table 1. This Table also gives error terms, correlation coefficients and significance levels. (A brief outline of the statistical method used in obtaining the least square fit is given in the Appendix.) The significance level is used to judge the fit between $t/(x-x_0)$ and $(x-x_0)$ as given by equation (1). If its value is less than or equal to 10^{-3}, 10^{-2}, and 5×10^{-2}, then the linear relationship between $t/(x-x_0)$ can be statistically qualified as highly significant, significant, and probably significant, in this order. We thus see from Table 1 that, except for two cases, equation (1) holds at least as probably significant, but in most cases as highly significant or better. The last statement is especially true for oxidation under very clean conditions (Group (1)). Introduction of sodium during oxide growth or changing the oxidizing ambient from oxygen to water vapor led to increased scatter in the measurements. This is revealed in the lower values of the correlation coefficient, and larger values of the significance level, error terms, and spread in the error terms. The larger values of significance level in Groups (2) to (5), as compared with Group (1), can be only partially attributed to the small number of measurements; contamination effects definitely contribute to larger scatter.*

In addition to our earlier work[5], various forms of linear and parabolic rate laws have been used in connection with thermal oxidation of silicon[4, 10–13].

We have assumed that the rate constants fulfill the usual Arrhenius relation, i.e.

$$a = a_0 \exp(-Q_a/kT \qquad (6)$$

and

$$k = k_0 \exp(-Q_k/kT) \qquad (7)$$

where Q_a and Q_k are the activation energies of the linear and parabolic rate constants, respectively. The pre-exponential constants and activation energies were determined by the method of least squares from the values of $\ln a$ and $\ln k$, and the corresponding $1/T$. The

---

*Our main objective was to determine the oxidation kinetics under minimum contamination, hence the largest number of measurements were performed in connection with Group (1). Oxidation with deliberate sodium and sodium-water contamination was primarily investigated in order to confirm suspected trends in a semi-quantitative sense. For this purpose a smaller number of experiments seemed to be sufficient. For a more exact evaluation of impurity effects better control of doping and a larger number of experiments would be needed.

Table 1. *Summary of experimental results*

Group	Oxidation conditions	Temperature (°C)	Thickness range. (Å)	n	r	t	Signif level	A (min/Å)	a (Å/min)	$\delta a/a$ (%)	B (min/Å^2)	k (Å^2/min)	$\delta k/k$ (%)
1	r.f. heating, dry O_2 very clean conditions	1300	160-3300	8	0·999	54·7	$< 10^{-7}$	$3{\cdot}59 \times 10^{-3}$	278·0	18·7	$9{\cdot}91 \times 10^{-6}$	$1{\cdot}01 \times 10^{5}$	3·4
		1350	300-4500	15	0·993	30·2	$< 10^{-7}$	$6{\cdot}03 \times 10^{-3}$	166·0	11·3	$1{\cdot}08 \times 10^{-5}$	$9{\cdot}25 \times 10^{4}$	3·2
		1100	55-2950	16	0·976	16·7	$< 10^{-7}$	$1{\cdot}47 \times 10^{-2}$	68·0	16·7	$3{\cdot}67 \times 10^{-5}$	$2{\cdot}72 \times 10^{4}$	14·8
		900	150-2660	12	0·997	40·5	$< 10^{-7}$	$6{\cdot}55 \times 10^{-2}$	15·2	5·5	$1{\cdot}79 \times 10^{-4}$	$5{\cdot}63 \times 10^{3}$	2·2
2	r.f. heating dry O_2, Na-doping	1250	500-4215	6	0·987	3·9	5×10^{-3}	$2{\cdot}34 \times 10^{-3}$	478·0	23·1	$5{\cdot}17 \times 10^{-6}$	$1{\cdot}94 \times 10^{5}$	3·6
		1100	210-3365	11	0·956	9·7	10^{-6}	$5{\cdot}68 \times 10^{-3}$	176·0	36·2	$1{\cdot}43 \times 10^{-5}$	$6{\cdot}95 \times 10^{4}$	8·7
		1000	140-1625	7	0·938	6·0	5×10^{-4}	$1{\cdot}53 \times 10^{-2}$	65·0	51·0	$6{\cdot}91 \times 10^{-5}$	$1{\cdot}45 \times 10^{4}$	12·8
		900	63-1365	13	0·969	13·0	10^{-7}	$3{\cdot}41 \times 10^{-2}$	29·4	17·0	$1{\cdot}14 \times 10^{-4}$	$8{\cdot}80 \times 10^{3}$	8·2
3	resistance heating, Al_2O_3 tube, dry O_2	1250	600-8800	11	0·991	22·2	10^{-7}	$1{\cdot}29 \times 10^{-3}$	775·0	17·1	$1{\cdot}07 \times 10^{-5}$	$9{\cdot}35 \times 10^{4}$	3·6
		1145	460-6464	8	0·902	5·2	10^{-3}	$6{\cdot}67 \times 10^{-3}$	150·0	11·4	$2{\cdot}09 \times 10^{-5}$	$4{\cdot}80 \times 10^{4}$	1·5
		1050	770-5500	7	0·992	17·6	5×10^{-6}	$1{\cdot}06 \times 10^{-2}$	94·0	32·3	$4{\cdot}08 \times 10^{-5}$	$2{\cdot}45 \times 10^{4}$	2·6
		900	154-4544	7	0·873	4·0	5×10^{-3}	$1{\cdot}04 \times 10^{-1}$	9·7	15·6	$1{\cdot}61 \times 10^{-4}$	$6{\cdot}22 \times 10^{4}$	4·0
4	resistance heating, Al_2O_3 tube, H_2O-He	1200	450-2100	7	0·997	29·9	$2{\cdot}5 \times 10^{-7}$	$-9{\cdot}33 \times 10^{-4}$			$2{\cdot}75 \times 10^{-5}$	$3{\cdot}64 \times 10^{4}$	3·7
		1100	300-1700	6	0·848	3·6	10^{-2}	$2{\cdot}06 \times 10^{-2}$	48·7	41·8	$3{\cdot}20 \times 10^{-5}$	$3{\cdot}12 \times 10^{4}$	26·9
		1000	180-1500	6	0·950	6·1	10^{-3}	$8{\cdot}02 \times 10^{-2}$	12·5	12·5	$5{\cdot}34 \times 10^{-5}$	$1{\cdot}88 \times 10^{4}$	1·9
		920	250-1000	3	0·866	1·7	10^{-1}	$2{\cdot}48 \times 10^{-1}$	4·0	4·0	$4{\cdot}86 \times 10^{-5}$	$2{\cdot}06 \times 10^{4}$	34·2
5	resistance heating, Al_2O_3 tube, H_2O–He, Na-doping	1200	465-3085	5	0·748	1·9	5×10^{-2}	$2{\cdot}08 \times 10^{-3}$	480·0	13·8	$2{\cdot}75 \times 10^{-7}$	$3{\cdot}64 \times 10^{6}$	48·6
		1100	1350-2000	4	0·923	3·4	$2{\cdot}5 \times 10^{-2}$	$-5{\cdot}47 \times 10^{-3}$			$4{\cdot}99 \times 10^{-6}$	$2{\cdot}00 \times 10^{5}$	26·6
		1000	450-2350	5	0·901	3·6	10^{-2}	$1{\cdot}67 \times 10^{-3}$	600·0	118·6	$4{\cdot}67 \times 10^{-6}$	$2{\cdot}14 \times 10^{5}$	26·3
		920	170-1600	5	0·940	4·7	5×10^{-3}	$2{\cdot}22 \times 10^{-2}$	45·0	16·1	$1{\cdot}96 \times 10^{-5}$	$5{\cdot}10 \times 10^{4}$	18·8

*In this Table A and B are given by equation (1), and a and k by equations (3) and (5), respectively; $\delta a/a$ and $\delta k/k$, as well as the significance level were calculated by the method described in the Appendix. The number of points, n, the correlation coefficient, r, and Student's t-value are also shown obtained values of a_0, Q_a, k_0 and Q_k are tabulated in Table 2. This Table also gives error terms, correlation coefficients and significance levels. Except for the linear rate constant in the case of oxidation in sodium-doped water vapor ambient, the Arrhenius relationships can be considered at least as significant. Because of error considerations (see Appendix) and fluctuations due to contamination effects, the kinetic parameters of Table 2 (except for r.f. oxidation in dry 0_2) and those reported in the literature must be compared cautiously.

Influence of sodium and water on the oxidation kinetics

From Table 2 the effects of sodium and/or water vapor can be assessed as follows. Sodium doping results in increased values of k_0 and Q_k, especially for oxidation in water vapor. Furthermore, sodium increases the linear rate constant for both dry oxygen and water vapor oxidations. In the first case this is a result of increased a_0 even though Q_a increases. In the case of water vapor oxidation the determination of a_0 and Q_a is somewhat uncertain. From a comparison of oxidation in oxygen and water vapor we can deduce that water vapor increases a_0 and Q_a, and decreases k_0 and Q_k.

These results can be put in their proper perspective if we compare them with other works on the oxidation of silicon and with various transport processes in noncrystalline SiO_2. In Table 3 results of some pertinent works on the oxidation of silicon are summarized. Inspection of Tables 2 and 3 shows that ever for apparently similar conditions large variations in the kinetic parameters occur. Even if we consider the fact that determinations of the constants of Table 3 may not be very accurate, these large variations cannot be attributed to errors.

Especially striking is the fact that the rate constants for oxidation in 0_2 under very clean conditions with *r.f.* heating differ considerably from those characteristic of oxidation in resistance-heated tubes. Evidently, impurity effects play an important role. Let us consider first the effect of water. A comparison of oxidation in oxygen and water vapor reveals

Table 2. Kinetical constants and other parameters as determined from the data of Table 1

	Oxidation method (as given in Table 1)				
Parameter	1	2	3	4	5
n	4	4	4	3	2
r	0·969	0·959	0·994	1·000	
Signif. level	10^{-2}	10^{-2}	$2·5 \times 10^{-3}$	$< 10^{-7}$	
a_0 (min)	$8·8 \times 10^{-5}$	$7·0 \times 10^{-4}$	$1·4 \times 10^{-1}$	$4·3 \times 10^{-1}$	
a_0 (cm s^{-1})	$1·7 \times 10^{-4}$	$1·1 \times 10^{-3}$	$1·7 \times 10^{-1}$	$8·3 \times 10^{-2}$	$4·2 \times 10^{-3}$
a_0 (max)	$3·2 \times 10^{-4}$	$1·8 \times 10^{-3}$	$2·0 \times 10^{-1}$	$1·6 \times 10^{-1}$	
Q_a (eV)	1·12	1·25	1·88	1·91	1·3
$\delta Q_a/Q_a(\%)$	6·7	4·6	1·2	3·7	
n	4	4	4	3	3
r	1·000	0·968	1·000	1·000	1·000
Signif. level	$< 10^{-7}$	10^{-2}	$< 10^{-7}$	$< 10^{-7}$	$< 10^{-7}$
k_0 (min)	$6·8 \times 10^{-10}$	$8·8 \times 10^{-10}$	$1·0 \times 10^{-9}$	$2·9 \times 10^{-12}$	$4·2 \times 10^{-4}$
k_0 (cm^2 s^{-1})	$1·2 \times 10^{-9}$	$5·9 \times 10^{-9}$	$1·1 \times 10^{-9}$	$4·3 \times 10^{-12}$	$4·4 \times 10^{-4}$
k_0 (max)	$2·0 \times 10^{-9}$	$4·0 \times 10^{-8}$	$1·2 \times 10^{-9}$	$8·2 \times 10^{-12}$	$4·7 \times 10^{-5}$
Q_k (eV)	1·20	1·32	1·22	0·54	2·29
$\delta Q_k/Qk(\%)$	5·3	1·7	1·2	8·4	0·3

that water vapor exerts a gradual influence rather than resulting in a drastically different mechanism. This gradual influence of water vapor is also indicated by the activation energies of parabolic rate constants for H_2O–O_2 mixtures as determined by Nakayama and Collins[4]; in the range of 4·6 to 150 Torr. water vapor and 0–500 Torr. oxygen partial pressures the values vary from 0·4 to 1·4 eV. The data of Table 3 confirm the above mentioned trend that a_0 and Q_a increase with increasing water content of the oxidizing ambient. This indicates that water diffuses through the tube if it is hot. The extent of this water contamination is less when double wall silica tube is used, but it is still noticeable; it can be minimized by r.f. heating, or heating by passing current through the silicon. Neglecting low pressure oxidation, the data of Tables 2 and 3 indicate that with increasing water content in the oxidizing ambient k_0 and Q_k decrease.

From the values of k_0 and Q_k characteristic of 'dry' oxygen oxidation ($p = 760$ Torr.) the following approximate order of increasing sodium contamination can be established: (1) r.f. heating; (2) resistance heating using alumina tube; (3) resistance heating using silica tube; (4) r.f. heating, sodium doping.

From this comparison of our results with those of others we conclude that the kinetics of thermal oxidation of silicon is very greatly influenced by impurities, especially sodium and water. Varying levels of such contaminations can exist in resistance-heated tubes.

Table 3. Some typical kinetical constants determined by others

Reference	Oxidation ambient	Pressure (Torr)	Temperature range, (°C)	a_0 (cm s^{-1})	Q_a (eV)	k_0 ($cm^2 s^{-1}$)	Q_k (eV)
Law[10]	O_2	5×10^{-2}	730–1030	$4\cdot7 \times 10^{-6}$(1) $3\cdot6 \times 10^{-8}$(2)	0·90(1) 0·84(2)	$6\cdot2 \times 10^{-8}$	1·57
Burkhardt and Gregor[13]	O_2	$20 < p < 400$	900–1150	$2\cdot8 \times 10^{-1}$(4)	2·10(3)	2×10^{-9}	1·35
	O_2	760	950–1100	$1\cdot5 \times 10^{-3}$(3)	1·50(4)	1×10^{-10}	1·00
Deal and Grove[11]	O_2	760	700–1200	$2\cdot4 \times 10^{-1}$(5)	2·03(5)	$3\cdot7 \times 10^{-9}$(5)	1·29(5)
Nakayama and Collins[4]	Ar–H_2O	4·6	850–1217	$8\cdot4 \times 10^{-2}$(6) 1·7(7)	1·90 2·2	$1\cdot1 \times 10^{-10}$ $2\cdot1 \times 10^{-10}$	1·09 1·16
Deal and Grove[11]	O_2–H_2O	$p_{O_2} = 415$ $p_{H_2O} = 345$(8)	920–1200	2·08(9) 1·33(10)	1·96 1·91	$5\cdot6 \times 10^{-10}$ $3\cdot7 \times 10^{-10}$	0·72 0·67
Pliskin[12]	H_2O	760	917–1202	$7\cdot8 \times 10^{2}$(11)	2·60	$5\cdot6 \times 10^{-10}$	0·70

(1) Calculated from his Fig. 1 by determining $\Delta n/t$ in the neighborhood of zero Δn.

(2) Calculated from his values of n_0 and the parabolic rate constant using $a = K_1/K_2$ at $x = 0$.

(3) Calculated from their Table 2 using $K_2 = 2x_0$ and $a = k_1/k_2$ at $x = 0$.

(4) Determined from the intercepts of x vs. $t^{1/2}$ curves in their Fig. 6.

(5) Determined from their Table 2 by the method of least squares. The values of Q_k differ somewhat from that given in the paper, 1·24 eV, probably due to their incorrect fitting of the log B vs. $1/T$ curve. The pre-exponential constants a_0 and k_0 were not given in the paper.

(8) Deal and Grove bubbled O_2 through 95°C water. The equilibrium vapor pressure is 634 Torr. Since the O_2–H_2O gas mixture flows into an open tube, the total pressure can be taken approximately 760 Torr. Hence the partial pressure of water vapor is $634/634 + 760 \times 760 = 345$ Torr. (instead of 640 Torr. as given in their paper) and that of oxygen is 415 Torr.

(9) Determined from their Table 1 by the method of least squares.

(10) Determined from their Fig. 4.

(11) Determined from his Table 2 for (111) orientation using $a = k_2/k_1$.

THEORY

From the results presented in this paper, as well as from the comparison of these results with other works, it is clear that thermal oxidation of silicon is not a simple process. Nevertheless, from the results reported in this paper and by others, and from a comparison with other transport processes in noncrystalline SiO_2 a tentative model can be constructed.

The high temperature oxidation of silicon can be generally represented by a combination of linear and parabolic rate laws. The transition from the linear to the parabolic regime extends to a few thousand Angstroms, as demonstrated in Fig. 1. This behavior of silicon is somewhat unique because generally metals that show a strong tendency towards linear oxidation are those which have a ratio of oxide to metal molecular volume either less than one or larger than about 2·5[14]. When this ratio is less than one, the oxide is not protective and, hence, transport is not the rate controlling step. If this ratio is larger than one, the oxide film has a great tendency to crack; this results in a parabolic growth followed by a linear one. The SiO_2 to Si molar volume ratio is 2·2, thus the oxide film is expected to be protective, but due to increasing stress during growth it may develop cracks. In the thickness range that we are concerned with, that is below 1 μm, this does not generally occur. However, SiO_2 films are non-crystalline and may contain structural micro-heterogeneities, especially channels[8], along which transport of diffusion species might occur preferentially. It was shown by Ing *et al.*[15] that the room temperature permeability of thermally grown SiO_2 films can be considerably higher than that of fused silica. They attributed this to the presence of channels whose diameter is less than 50 Å. Thus, it is possible that relatively fast transport through channels occurs during the transition from linear to parabolic growth.

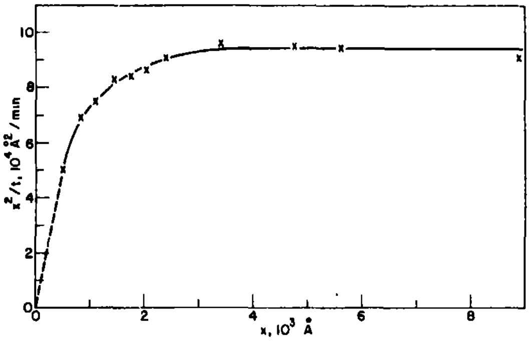

Fig. 1. Transition from linear to parabolic oxide growth. The ratio x^2/t is shown as a function of oxide thickness, x; t is the oxidation time. The slope of the curve extrapolated to zero thickness gives the linear growth rate at $x = 0$. With increasing oxide thickness x^2/t approaches a constant value characteristic of the parabolic regime of growth. The oxidation was done in dry O_2 at 1250°C in a resistance heated alumina tube.

In our discussion we shall only deal with the limiting cases, that is, linear growth in the beginning of the oxidation and parabolic growth for relatively thick oxide film.

LINEAR REGIME OF OXIDATION

In the beginning of oxidation, especially when no initial oxide is present, the process is most probably determined by an interface reaction which gives rise to a linear rate law. Since chemisorption up to a monolayer generally takes place very fast, the rate determining step is either the creation of the defect responsible for the growth at one of the two interfaces, or the oxidation reaction. As we shall discuss below, it is very probable that the migrating species is oxygen in ionic or molecular interstitial form. Thus, the possible interface reactions are

$$O_{2(\mathrm{gas})} \rightarrow O_{2(\mathrm{ads.})} \rightarrow (O_{2,i})_{SiO_2} \qquad (8)$$

at the SiO_2–O_2 interface, and

$$Si + (O_{2,i})_{SiO_2} \rightarrow SiO_2 \qquad (9)$$

at the oxide-silicon interface. (In these and the following reactions the subscript i designates interstitial and the subscript outside a parenthesis indicates location.)

In addition to the reactions already stated the following reactions take place in the presence of water vapor:

$$H_2O_{(ads.)} + \equiv Si - O - Si \equiv \rightarrow \equiv Si - OH\ HO{-}Si \equiv \qquad (10)$$

or

$$H_2O_{(ads.)} \rightarrow (H_2O_i)_{SiO_2} \qquad (11)$$

at the oxide-gas interface, and

$$Si + 2(OH)_{SiO_2} \rightarrow SiO_2 + (H_{2,i})_{SiO_2} \qquad (12)$$

or

$$Si + 2(H_2O_i)_{SiO_2} \rightarrow SiO_2 + 2(H_{2,i})_{SiO_2} \qquad (13)$$

at the oxide-silicon interface. The hydrogen (or proton) produced by these reactions may diffuse to the oxide-gas interface where it facilitates the entry of oxygen. This catalytic role of water in the oxidation of silicon was pointed out by Nakayama and Collins[4].

The linear rate constants depend on the silicon orientation. This effect was studied in detail by Pliskin[12] for atmospheric steam and by Ligenza[16] for high pressure steam oxidation. Some qualitative results are also available for oxidation in oxygen[17]. In all cases the order of increasing oxidation rates in the range 500–12000°C is as follows: (100), (110) and (111). These observations show that the rate controlling step occurs at the oxide-silicon interface. Ligenza attributed this orientation dependence to steric effects, i.e. how the directional silicon bonds can form an activated complex with the reacting water molecule. The strain energy of various Ge–O complexes formed at the germanium surface also increases in the order (100), (110), (111)[18]. From studies of interface effects we have concluded that the silicon-oxide interface has a greater tendency to order if it is formed on (100) than on (111) surface[19]. Thus, the greater the disorder at the Si–SiO_2 interface the faster the oxide grows (in the linear regime) and the larger is the density of interface states.

The large variations in a_0 and Q_a as shown in Tables 2 and 3 indicate that this interface reaction is not a simple one. As we discussed above, with increasing water content in the oxidizing ambient both a_0 and Q_a increase. The first effect is probably due to the greater ease by which reaction (10) proceeds as compared with (8). This effect is well-known from the chemistry of silicate glasses [20]. The increase in Q_a may be caused by steric factors involved in the reaction at the oxide-silicon interface. Formation of an activated complex could be easier with oxygen than with water. Since Deal and Grove [11] did not find a great difference in Q_a for oxidation in dry and wet oxygen (note, however, that a_0 is appreciably different but it was not considered), they have concluded that the surface controlled mechanism is similar for both oxidants, and that the activation energy is the energy needed to break the Si–Si bonds. This conclusion is evidently at variance with the results given in Tables 2 and 3.

The role of sodium can be explained as follows. If water vapor is the oxidizing gas then its reaction with the oxide can be greatly enhanced by the following autocatalytic process known from the corrosion of silicate glasses[21]:

$$\equiv Si{-}O^-Na^+ + H_2O \rightarrow \equiv Si{-}OH + Na^+ + OH^-, \qquad (14a)$$

$$\equiv Si{-}O{-}Si \equiv + OH^- \rightarrow \equiv Si{-}OH + \equiv Si{-}O^-, \qquad (14b)$$

$$\equiv Si{-}O^- + H_2O \rightarrow \equiv Si{-}OH + OH^-. \qquad (14c)$$

Without the presence of hydroxyl, that is, in dry oxygen, less enhancement by sodium is expected. However, even in this case the incorporation of sodium facilitates the entry of oxygen since it is known that oxygen (or, better, O^-) alone does not react easily with SiO_2[20]. Thus, the reaction can be written as

$$\equiv Si{-}O{-}Si \equiv + O^- + Na^+ \rightarrow \equiv Si{-}O^-Na^+. \qquad (15)$$

The reaction at the oxide-silicon interface:

$$\equiv Si—O^-Na^+ + Si \rightarrow \equiv Si—O—Si\equiv + Na \quad (16)$$

results in neutral sodium that might diffuse to the oxide-gas interface. There it can lead to the formation of O^- and Na^+ ions. Thus, similarly to water, relatively small amounts of sodium may have a catalytic effect on the oxidation. It is possible that sodium which can be found even in r.f.-grown oxides is responsible for this effect.*

PARABOLIC REGIME OF OXIDATION

It is a well established fact by now that thermal oxidation of silicon proceeds by diffusion of oxygen through the oxide film. This and the observed pressure dependence of the parabolic rate constant were used to argue that the main migrating species is interstitial oxygen molecule or ion [23], or hydroxyl when oxidation occurs in water vapor.† Diffusion of silicon vacancies, which would give rise to similar pressure dependence, can be neglected since the formation of these defects in the strongly covalent SiO_2 is very difficult energetically [24]. Oxygen diffusion through vacancies would lead to an approximately pressure-independent rate constant [25]. This, however, does not mean that these defects, especially oxygen vacancies in the vicinity of the oxide-silicon interface, cannot be present. Since the oxidation rate could be influenced by electric current [26], the migrating species must be, at least partially, in ionic form.

Since many details of the growth process, such as the exact influence of pressure, ionic and electronic conduction as a function of temperature, etc. are unknown at the present, we can obtain some insight only by comparing oxidation with other transport processes in noncrystalline silica. Such a comparison is based on the essential similarity between oxide films and fused silica as revealed in structural, optical, etc. properties. However, we have to keep in mind that the nature of the Si–O bond and the microheterogeneous structure of the oxide films depend on the oxidation conditions [8, 27]. Furthermore, the use of concepts, which were introduced for crystalline solids, is a priori not justified for a non-crystalline solid where the transition from inhomogeneities in the electron distribution to gross morphological defects may be gradual. Therefore, it can be expected that parameters, such as activation energy, that have well-defined values for crystalline solids, will be characterized by a range in value.

Parabolic oxidation in oxygen

As two extreme cases let us discuss now the parabolic rate constants for oxidation in oxygen and water vapor. First consider oxygen. Two types of transport processes in fused silica are pertinent to this problem: permeation and self-diffusion of oxygen. Motzfeldt [28] pointed out that the permeation and oxidation in the parabolic regime are closely related. Also, both processes depend linearly on pressure and can be influenced by an externally imposed electric current [26, 29]. It is proposed here that, similarly to self-diffusion of oxygen in fused silica [30], permeation and oxide growth take place via an interstitialcy diffusion mechanism; the total flux is the sum of molecular and ionic fluxes. The oxygen interstitial molecules are in a constant exchange process with the oxide resulting in atomic oxygen interstitials which can dissociate into negative ions and holes. Assuming that at a given temperature the concentration of holes originating from this process is much larger than the intrinsic hole concentration, and that the diffusion coefficient is much larger for holes than for ions, following Kroeger [25] the ratio of the

---

*Carlson *et al.*[22] reported 10^{16} Na atoms/cm^3 uniformly distributed in oxide grown in water-cooled silica tube by r.f. heating. The sodium content of our r.f.-grown oxides was estimated by neutron activation analysis as about 5×10^{15}/cm^3. The nature of sodium in this oxide will be subsequently discussed.

†The non-bridging oxygen or hydroxyl group in SiO_2 can be considered as a peculier form of interstitial anions. For a discussion of defects in SiO_2 see Stevels and Kats [24].

concentrations of ionic to molecular oxygen at 1000°C can be estimated as about 4×10^6. Because of this high ratio the ionic flux predominates, but it is the molecular form which reacts with silicon at the oxide-silicon interface.

This model of oxide growth, based on molecular and ionic diffusion of oxygen, does not require the presence of O_2 ions as postulated by Deal and Grove[11]. It is not very likely that these ions would be present because no paramagnetic centers have been observed in grown SiO_2 unless it was irradiated or treated in hydrogen at elevated temperature [31] even though O_2^- is known to be paramagnetic[32].

Impurities in fused silica affect the diffusion of oxygen. Thus, Sucov[33] observed that the pre-exponential term of the diffusion constant rapidly increases if other oxides, for instance, Na_2O, are incorporated into SiO_2, whereas the activation energy hardly changes. Since the activation energies were found to be very similar for various glasses, a large pre-exponential term means that at a given temperature more oxygen is participating in the diffusion process. Williams [34] found that the diffusion coefficient at 1100°C increases with increasing water content of the silica.*

The role of sodium in the parabolic regime of oxide growth can be tentatively explained in the following way. Similarly to Sucov's[33] argument, incorporation of sodium results in an increased density of nonbridging oxygen and hence in a large value of k_0. Our observation, that the activation energy, Q_k, is larger when sodium is present, indicates that the diffusion of oxygen is now hindered. It is well known from the field of glasses that the activation energy of diffusion increases with the concentration of network modifying ions [36].

Parabolic oxidation in water vapor

If water vapor is present in the oxidizing ambient then the mechanism of parabolic oxide growth becomes complicated by several factors[35, 37]: (1) Interaction between H_2O and SiO_2 leads to a large variety of reaction products, for instance, OH groups attached to Si that can be in permanent or metastable form, interstitial (dissolved) H_2O molecules in SiO_2, and interstitial H_2. Depending on temperature, impurities, pressure of water vapor, etc., the concentration of these species, as determined by various equilibria, might vary considerably. (2) With increasing temperature adsorption of H_2O on SiO_2 occurs increasingly as OH rather than H_2O. (3) The transport mechanism is very complex. One of the reasons for this is the nature of the diffusion species. The solubility of 'water' in silica varies as the square root of the water vapor-pressure indicating that water is present at hydroxyl. On the other hand, there are indications that at higher pressures the diffusing species is water molecule. The situation is further complicated by the fact that diffusion of H_2 may result from the conversion of metastable hydroxyls.

Another difficulty related to the diffusion of 'water' in silica is that the diffusion coefficient increases with increasing concentration of H_2O in SiO_2 and that the activation energy varies from 0·44 to 0·88 eV [38].

The role of impurities, that might influence the interaction between H_2O and SiO_2 as well as the transport mechanism, is not quite clear. It is known, however, that (1) the permeability of hydrogen decreases with increasing amounts of glass modifying oxides [37], (2) under the influence of an applied d.c.

---

*Jorgensen and Norton[29] considered the possibility that oxygen is transported through hydroxyl ions. But, since the diffusion constant, as calculated from the ionic current, was three orders of magnitude smaller than that determined by a direct method, they discarded this hypothesis. For the water content of the silica they used 1 per cent in their calculation. However, if a smaller value would have been taken, the diffusion coefficient would be larger. This might be very well the case considering the fact that hydroxyl in SiO_2 can exist in metastable and permanent forms[35]. It is thus not unlikely that only a fraction of the total hydroxyl participates in the diffusion (see subsequent discussion).

voltage alkali impurity atoms are replaced by protons that originate from water vapor in the ambient[39], (3) removal of 'water' from SiO_2 by electrolysis requires the presence of aluminum as a silicon-substitutional impurity[39] and (4) sodium in thermally grown SiO_2 influences the hydration of the oxide as revealed in the dielectric dissipation due to dipoles in the bulk[40].

From this discussion it is evident that a straightforward comparison between thermal oxidation of silicon in water vapor and diffusion of 'water' in noncrystalline silica cannot be made at present. This statement is substantiated by the discrepancy of the pressure-dependence of solubility of 'water' in silica and parabolic rate constant for oxidation in water vapor. The solubility is proportional to the square root of pressure, whereas the rate constant is linearly proportional to it. Also observe that the activation energy of the parabolic growth depends on the partial pressure of water vapor.*

We see from Tables 2 and 3 that with increasing water pressure Q_k decreases and k_0 increases. This is probably due to the increased density of broken Si–O–Si bridges. In the case of high pressure steam oxidation the parabolic regime disappears[16]; this may be due to the fact that the migration of water in molecular form is extremely easy compared to the rate of reaction with silicon. Apparently, sodium facilitates the incorporation of hydroxyl into the oxide leading to larger k_0, but it increases the energy barrier of the diffusion.

Nature of sodium in the oxide

It has already been indicated that sodium incorporated into the oxide during its growth is largely in the so-called bound or inactive form[1]. That is to say, it essentially does not contribute to the migration of positive charges under high field (about 10^6V/cm) at 200–300° C. This fact has been further substantiated by several observations related to the electric behavior of the $Si–SiO_2$ interface. From MOS capacitance measurements on samples produced by r.f.-oxidation with sodium-doping we have determined the effective density of surface states at zero silicon surface potential, N_0, and the density of states within the silicon forbidden band, dN/dE. The following values are typical for the as-grown condition: $N_0 = 7{\cdot}6 \times 10^{12}cm^{-2}$ and dN/dE: $2{\cdot}8 \times 10^{12}$ $(eV)^{-1}$ cm^2. After annealing in helium at 1100°C for 15 min dN/dE became virtually zero and N_0 was 8×10^{11} cm^{-2}. According to Kooi[42] high sodium content in the SiO_2 films results in high values of N_0. However, the N_0 value for the annealed specimen is only twice as large as that given by Kooi despite the fact that the Na concentration was about 10^{20} atoms/cm^3, whereas in Kooi's case it was 2×10^{16} atoms/cm^3. This means that, although sodium contamination during oxidation may contribute to the surface states, it is not primarily responsible for them.

The stability test of sodium doped oxides also demonstrated that most of the sodium is in an electrically inactive form. After applying +10V bias to the electrode on the oxide (760 Å thick) at 250°C for 5 min the $C–V$ curve became very distorted as shown by the new value of dN/dE, roughly $2{\cdot}5 \times 10^{12}$ $(eV)^{-1}$ cm^{-2}. As a matter of fact, the change in N_0 can be approximately attributed to the distortion of the $C–V$curve rather than to the appearance of a positive charge in the oxide that does not interact with the silicon space-charge region (this is often called the oxide-charge). This behavior is quite different than observed for clean oxides, where, after application of the bias, the $C–V$ curve shifts slightly (on the order of 0·1 V for 1000 Å oxide) toward more negative electrode voltages. It is also different from the behavior of those samples that were contaminated with sodium at the surface before electrode deposition; in this case the C–V curve shifted considerably toward more negative electrode voltages, but without any change in dN/dE[43]. After applying -10 V at 250°C for 5 min the C–V curve shifted in the positive direction without distortion, corresponding to a change in N_0 of 3×10^{11} cm^{-2}. This behavior is somewhat similar to that observed for MOS structures in which the SiO_2 was replaced by an alkali glass[44]. These observations demonstrate that from the standpoints of both interface states and ion migration most of the sodium incorporated into the oxide during growth is in an inactive form, but some sodium may contribute to the interface states after applying positive bias to the metal electrode.

---

*Deal and Grove[11] determined the solubility of 'water' in SiO_2 grown thermally in an $O_2–H_2O$ mixture at 1000°C. This value compared favorably with the solubility given by Moulson and Roberts[41]. However, this agreement can be only considered as fortuitous, since the solubility given by Moulson and Roberts varies with the square root of the water vapor pressure, whereas the parabolic rate constant varies linearly. Also, the similarity of the activation energies is not generally valid, since, depending on pressure and impurity content, the activation energy of parabolic growth may have a value anywhere from about 0·4 to 2·3 eV.

SUMMARY AND CONCLUSIONS

Thermal oxidation of silicon under a variety of conditions follows a combination of linear and parabolic rate laws. The linear and parabolic rate constants, that describe the oxidation for very small and very large oxide thicknesses, respectively, obey the Arrhenius relationship. Under very clean conditions the linear (a) and parabolic (k) rate constants for oxidation in dry oxygen differ substantially from those values obtained by oxidation in resistance heated furnaces. Oxidation in water vapor is characterized by larger values of a_0 and Q_a as well as by smaller values of k_0 and Q_k. Sodium doping results in increased values of K_0 and Q_k, especially in the presence of water vapor; it also leads to larger values of a_0 and Q_a for oxidation in dry oxygen, and increases the linear oxidation rate for oxidation in water vapor. A comparison of our results with those obtained by others, who generally employed resistance-heated silica tube furnaces, reveals that oxidation of silicon in these furnaces proceeds by sodium and/or water in varying degree. The oxidation kinetics is greatly affected, or even determined, by water and sodium (or similar) impurities in the oxidizing ambient.

The observations reported in this paper and by others can be tentatively explained by the following model. At the beginning of oxidation surface reaction is the rate-determining step. This gives rise to linear rate. Since a_0 is larger for water than for oxygen, the density of Si–OH groups in the oxide is probably larger than that of interstitial oxygen. In the presence of sodium the entrance of OH is facilitated through autocatalytic reactions. The increase in Q_a when water and/or sodium is present is probably due to steric hindrance in the formation of Si–O bonds at the oxide-silicon interface. The transition from linear to parabolic rate generally extends to 1000–2000 Å. This unusually large thickness range may be due to the relatively easy migration of oxygen along microheterogeneities (channels) in the oxide.

Parabolic growth in dry O_2 shows a remarkable similarity to oxygen permeation through fused silica. It is proposed here that permeation and oxide growth take place via an interstitialcy diffusion mechanism; the total flux is the sum of molecular and ionic fluxes. Incorporation of sodium results in an increased density of broken Si–O–Si bridges, hence the increase in k_0, but the presence of sodium hinders the motion of oxygen, hence the increase in Q_k. If water vapor is present, a large variety of interactions between H_2O and SiO_2 can occur leading to Si–OH, interstitial H_2 and H_2O, etc. Also, the transport mechanism is quite complex. Qualitatively, with increasing water pressure k_0 increases and Q_k decreases due to the increased density of broken Si–O–Si bridges. In the presence of sodium the incorporation of OH is easier, hence the increase in k_0; but its motion is hindered, hence the increase in Q_k.

MOS capacitance measurements of Na-doped oxides showed that most of the sodium is inactive from the viewpoint of both surface state density and ion migration at elevated temperature under high field.

Acknowledgements—R. F. Bailey analyzed the sodium content of some samples with neutron activation techniques and H. H. Whitaker performed the sodium analysis by the atomic absorption method. S. G. Ellis critically read the manuscript. The authors are indebted to them.

REFERENCES

1. REVESZ A. G., *Phys. Status Solidi* **19**, 193 (1967).
2. REVESZ A. G. and EVANS R. J. *IEEE Trans. Electr. Dev.* **14**, 789 (1967).
3. CHRISTIE G. L., U.S. Govt. Rept. No. AD 456798 (1964).
4. NAKAYAMA T. and COLLINS F. C., *J. electrochem. Soc.* **113**, 706 (1966).
5. REVESZ A. G., ZAININGER K. H. and EVANS R. J., *Appl. Phys. Lett.* **8**, 57 (1966).
6. McCRACKIN F. L., PASSAGLIA E., STROMBERG and STEINBERG H. L., *J. Res. natn. Bur. Stand.* **67A**, 363 (1963).
7. TOLANSKY S., *Surface Microtopography*. Interscience, New York (1960).
8. REVESZ A. G. and ZAININGER K. H., *RCA Rev.* **29**, 22 (1968).
9. e.g. FISCHBECK K., *Z. Elektrochem.* **39**, 316 (1933).
10. LAW J. T., *J. phys. Chem.* **61**, 1200 (1957).
11. DEAL B. E. and GROVE A. S., *J. appl. Phys.* **36**, 3770 (1965).
12. PLISKIN W. A., *IBM J. Res. Dev.* **10**, 198 (1966).
13. BURKHARDT P. J. and GREGOR L. V., *Trans Met. Soc. AIME* **236**, 299 (1966).
14. e.g. KUBASHEWSKI O. and HOPKINS B. E., *Oxidation of Metals and Alloys*. Butterworth, London (1962).
15. ING S. W., MORRISON R. E. and SANDOR J. E., *J. electrochem. Soc.* **109**, 221 (1962).
16. LIGENZA J. R., *J. phys. Chem.* **65**, 2011 (1961).
17. DEAL B. E., *J. electrochem. Soc.* **110**, 527 (1963).
18. GREEN M. and LIBERMAN A., *J. Phys. Chem. Solids* **23**, 1407 (1962).
19. REVESZ A. G., ZAININGER K. H. and EVANS R. J., *J. Phys. Chem. Solids* **28**, 197 (1967).
20. BUDD S. M., *Phys. Chem. Glass* **2**, 111 (1961).
21. CHARLES R. J., *J. appl. Phys.* **29**, 1549 (1958).
22. CARLSON H. G., HARRAP V. and OSBORNE J. F., *Fall Meeting of the Electrochemical Society*. Philadelphia (1966).
23. REVESZ A. G., *IEEE Trans. Electr Dev.* **12**, 97 (1965).
24. STEVELS J. M. and KATS A., *Philips Res. Rep.* **11**, 103 (1956).
25. KROEGER F. A., *The Chemistry of Imperfect Crystals*, Chaps. 20–22. Wiley, New York (1964).
26. JORGENSEN P. J., *J. chem. Phys.* **37**, 874 (1962).
27. REVESZ A. G., *Phys. Status Solidi*, **24**, 115 (1967).
28. MOTZFELDT K., *Acta chem. scand.* **18**, 1596 (1964).
29. JORGENSEN P. J. and NORTON F. J., *VIIth International Congress on Glass*, p. 310. Gordon and Breach, New York (1966).
30. HAUL R. and DUEMBGEN G., *Z. Elektrochem.* **66**, 636 (1962).
31. NISHI Y., *Jap. J. appl. Phys.* **5**, 333 (1966).
32. PAULING L., *The Nature of the Chemical Bond*, p. 351. Cornell University Press, Ithaca (1960).
33. SUCOV E. W., *J. Am. Ceram. Soc.* **46**, 14 (1963).
34. WILLIAMS E. L., *J. Am. Ceram. Soc.* **48**, 190 (1965).
35. LEE R. W., *J. Phys. Chem. Glass* **5**, 35 (1964).
36. DOREMUS R. H., In *Modern Aspects of the Vitreous State* (Edited by J. D. Mackewzie), Vol. 2, p. 1. Butterworths, London (1962).
37. LEE R. W. and FRY D L., *Phys. Chem. Glass* **7**. 19 (1966).
38. DRURY T., ROBERTS G. J. and ROBERTS J. P., In *Advances in Glass Technology*, p. 249. Plenum Press, New York (1962).
39. HETHERINGTON G., JACK K. H. and RAMSAY M W., *J. Phys. Chem. Glass.* **6**, 6 (1965).
40. DORDA G. and KADERKA M., *Solid State Commun.* **5**, 791 (1967).
41. MOULSON A. J. and ROBERTS J P., *Trans. Faraday Soc.* **57**, 1208 (1961).
42. KOOI E., *Philips Res. Rep.* **21**. 477 (1966).
43. SNOW E., GROVE A. S., DEAL B. E. and SAH C. T., *J. appl. Phys.* **36**, 1664 (1965).
44. KERR D. R., *IBM J. Res. Dev.* **8**, 385 (1964).
45. e.g. WILSON E. B., *An Introduction to Scientific Research*, p. 219. McGraw-Hill, New York (1952).
46. MARGENAU H. and MURPHY G. M., *The Mathematics of Physics and Chemistry*, p. 519. Van Nostrand, Princeton (1956)
47. FEDERIGHI E. T, *J. Am. statist. Ass.* **54**. 683 (1959).

APPENDIX

Errors, reproducibility and least square fit

Errors and reproducibility. The random errors of thickness were determined by repeating the ellipsometric or interferometric measurement of a given specimen 5 to 8 times. This was done for several specimens prepared under various conditions. Then the standard error, δX, was calculated. The reproducibility of the oxidation under some selected conditions was determined by oxidizing 5 to 15 specimens individually under identical conditions. For each specimen the thickness and its error were determined. The average thickness, $\bar{X}$, average error, $\delta\bar{X}$, and average relative error, $d\delta\bar{X}/\bar{x}$, have been calculated for each set. Also, the standard deviation of the sample, σ, was determined. The reproducibility is characterized by $\sigma/\delta\bar{X}$ These data are summarized in Table 4

For several sets of specimens the thickness was determined by both ellipsometry and multiple beam interferometry. Since the two methods resulted in identical values of A and B (see equation (1)) within the experimental errors and reproducibility, the possibility of systematic errors has been discarded.

Method of least squares. For determining the A and B constants of equation (1) as well as the pre-exponential factor and activation energy of the rate constants (equations (6) and (7)) we have used the method of least squares. The α intercept and β slope of the general relationship

$$z = \alpha + \beta y \qquad \text{(A-1)}$$

Table 4. Errors and reproducibility

Oxidation conditions	Thickness measurement	n	$\bar{X}$ (Å)	$\delta\bar{X}$ (Å)	$\delta X/\bar{X}$ (%)	σ (Å)	$\sigma/\delta\bar{X}$
O_2, Al_2O_3-tube 1145°C	Interferometry	7	1964	52·0	2·6	93	1·7
O_2, Al_2O_3-tube, 900°C	Interferometry	15	2074	26·3	1·2	112	5
O_2, r.f., 1250°C	Ellipsometry	6	738	8·2	1·1	23·8	3·0
O_2, r.f., 1250°C	Ellipsometry	6	1068	10·0	0·9	43·3	4·4
O_2-Na, r.f. 900°C	Ellipsometry	5	163	6·4	4·0	6·7	1

were determined by computer using well-known equations[45].

The errors of α and β, $\delta\alpha$ and $\delta\beta$, were also determined[46]. The error $\delta\alpha$ corresponds to δA in equation (1) and to $\delta \ln a_0$ or $\delta \ln k_0$ as obtained from equations (6) and (7). The error $\delta\beta$ corresponds to δB in equation (1) and to δQ_a or δQ_k in equations (6) and (7) From equation (3) the error of a, δa, can be calculated as

$$\delta a = \frac{\delta A}{A^2} \tag{A-2}$$

and from equation (5) the error of k, δk, as

$$\delta k = \frac{\delta B}{B^2}. \tag{A-3}$$

These last two error terms, in a relative form, are listed in Table 1 From the error terms $\delta \ln a_0$ and $\delta \ln k_0$ the upper and lower limits of a_0 and k_0 have been determined.

The probability that a linear relationship between z and y is due to chance rather than a physical cause was checked by calculating the significance level. The lower its value for a given set of z and y, the smaller the probability that the linear relationship, as determined by the method of least square, is due to chance. From Student's t-values and correlation coefficients the significance level was determined by using appropriate tables[47].

In the method of the least square fit, as described above, it is assumed that the precision of the y values is constant. This assumption is very often made, but usually tacitly and without sufficient justification. It is also implied in the commonly used graphical curve fitting procedure. Frequently, the relative rather than the absolute errors can be considered as constant. In such a case the equations used in determining the α intercept and β slope are somewhat different[45].

Inspection of Table 1 shows that it is a better approximation to consider the relative, rather than the absolute, errors of a and k as constant. Using a constant relative error instead of absolute one (as in the case with our computer program) the kinetic parameters have been redetermined from Group (1). These values differ considerably from the originally determined parameters (see Table 5). Since the relative errors generally vary within a group, in the strict sense individually weighted a and k values should have been used for setting up Table 11. However, since the number of points is relatively small, 3 to 4, this calculation method did not seem to us to be warranted.

Table 5. Comparison of kinetical constants obtained for r.f. oxidation in dry O_2 under very clean conditions by two evaluation methods

Evaluation method	A_0 (cm s^{-1})	Q_a (eV)	k_0 (cm^2 s^{-1})	Q_k (eV)
Absolute errors taken as constant	$1{\cdot}7 \times 10^{-4}$	1·12	$1{\cdot}2 \times 10^{-9}$	1·20
Relative errors taken as constant	$2{\cdot}8 \times 10^{-5}$	0·93	$1{\cdot}3 \times 10^{-10}$	1·02

J. Phys. Chem. Solids Pergamon Press 1969. Vol. 30, pp. 565–570. Printed in Great Britain.

INTERPRETATION OF THE RESISTIVITY TEMPERATURE DEPENDENCE OF HIGH PURITY $(ZrO_2)_{0\cdot 90}(Y_2O_3)_{0\cdot 10}$*

J. E. BAUERLE and J. HRIZO
Westinghouse Research Laboratories, Pittsburgh, Penn. 15235, U.S.A.

(*Received* 15 *January* 1968; *in revised form* 11 *July* 1968)

Abstract—The resistivity of a very stable high purity specimen of $(ZrO_2)_{0\cdot 90}(Y_2O_3)_{0\cdot 10}$ has been measured between 400° and 1000°C. It is found that the dependence of the resistivity ρ on temperature is precisely described by

$$\frac{\rho}{T} = A_1 e^{E_1/kT} + A_2 e^{E_2/kT}$$

where the A's and E's are empirically determined constants.

Two hypotheses which yield such a temperature dependence are discussed. The first involves vacancy trapping by the yttria ions. The second involves the resistance of an yttria-rich layer near the grain boundaries.

1. INTRODUCTION

IONIC CONDUCTION in zirconia-based solid electrolytes has been investigated by numerous workers[1–3]. Usually, the data are plotted as log σ (or log σT) vs. $1/T$ and a single straight line is fitted to this data. In most cases a more elaborate treatment of the data would be unjustified in view of the experimental uncertainties.

During several years' work on both zirconia–calcia[4] and zirconia–yttria we have observed a distinct curvature in the conductivity plots toward a lower activation energy at the higher temperatures. The same effect has been observed by Strickler[5] and Casselton[6]. This effect is most pronounced in specimens prepared from high purity materials and having compositions near the lower end of the cubic range of solid solution.

The purpose of this work is (1) to obtain accurate resistivity data on a *stable*†, high purity specimen of $(ZrO_2)_{0\cdot 90}(Y_2O_3)_{0\cdot 10}$, and (2) to compare the data quantitatively with some possible mechanisms for the above-mentioned curvature.

2. EXPERIMENTAL PROCEDURE

(*A*) *Specimen preparation*

The preparation of the $(ZrO_2)_{0\cdot 90}(Y_2O_3)_{0\cdot 10}$ was accomplished by a decomposition reaction. Zirconium–oxychloride and yttrium oxide powders‡ were mixed in proper proportion and heated in a covered recrystallized aluminia crucible at 1450°C for 4 hr. The resulting soft white powder was pressed into disks (1 mm thick × 12·7 mm dia.) at 100,000 psi. The final sintering was done in an arc image furnace at a temperature of at least 2000°C for 30 min. Apparent specimen densities, determined by weight and geometric dimensions, were 85 per cent of the theoretical value. Examination of a polished and etched specimen under a metallographic microscope revealed a porosity consistent with the above figure, and a mean grain size of approximately

---

*This work was supported by U.S. Naval Ship Systems Command under Contract Nobs-94295.

†We were unable to obtain highly stable resistivity measurements with $(ZrO_2)_{0\cdot 86}(CaO)_{0\cdot 14}$ due to interference from the hysteresis phenomenon[7–9] which occurs in the zirconia-calcia system.

‡Y_2O_3, 99·99 per cent; Lindsay Rare Earth Chemicals. $ZrOCl_2 \cdot xH_2O$, 99·97 per cent; Titanium Alloy Manufacturing Co.

10 μ. No traces of second phase inclusions were observed.

X-ray diffraction powder photographs (11·4 cm Debye–Scherrer camera) were obtained of the specimen material after the 1450°C reaction and also after the 2000°C sintering. Sharpness of the lines indicated complete reaction and apparent single phase cubic material at both stages of preparation. The lattice parameter, 5·143 Å is in good agreement with the values obtained by other workers[1, 3].

(*B*) *Resistivity measurements*

The high purity $(ZrO_2)_{0\cdot90}(Y_2O_3)_{0\cdot10}$, in disk form, was sliced into bars approximately 10 mm in length and 1 mm × 1 mm in cross-section. Four platinum paste electrodes were baked on the bar and 0·008 in. Pt leads attached by wrapping. The specimen was suspended by its leads in the hot zone of a furnace. Resistivities were then determined by a four terminal technique employing an electrometer for the measurement of potentials across the sample and across the current resistor. Currents employed ranged from 1 to 100 μA, and the potential across the specimen was always less than 1 V. The specimen temperature, as monitored by a Pt–Pt 10 per cent Rh thermocouple adjacent to the specimen, was constant to within ±0·2°C during a measurement. The atmosphere of the furnace was air.

Resistivity measurements were taken at 100 deg intervals from 500° to 1000°C and back down during the first day. After an overnight hold at 400°C, measurements were taken from 400° to 1000°C and back down on the second day; thus two values were obtained at 400° and at 1000°C and four values at each of the other intermediate temperatures.

3. RESULTS

The experimental results are given in Fig. 1 and Table 1. The scatter of ρ/T was approximaterly 0·5 per cent at 400°C and 1000°C, and 0·3 per cent or less at the other temperatures. The stability of this specimen may be appreciated when one notes that ρ/T varied over a range of 2000.

An expression of the form

$$\frac{\rho}{T} = A_1 e^{E_1/kT} + A_2 e^{E_2/kT} \tag{1}$$

was fitted to the data. For the sake of simplicity, the constants were chosen so that exact agreement would be obtained at the end points (400° and 1000°C) and optimum agreement elsewhere. A comparison of $(\rho/T)_{\text{exper.}}$ and $(\rho/T)_{\text{calc.}}$ is given in Table 1. The error in the fit was about the same as the experimental error, i.e. about ±0·3 per cent. For the constants, we obtained

$$\left.\begin{aligned} A_1 &= 9\cdot056 \times 10^{-6}\,\Omega\ \text{cm deg}^{-1} \\ A_2 &= 4\cdot572 \times 10^{-8}\,\Omega\ \text{cm deg}^{-1} \\ E_1 &= 0\cdot682\ \text{eV} \\ E_2 &= 1\cdot168\ \text{eV} \end{aligned}\right\} \tag{2}$$

Table 1. *Summary of resistivity data*

Temp. (°C)	Number of measurements	$(\rho/T)_{\text{exper}}$ (Ω cm)	$(\rho/T)_{\text{calc.}}$ (Ω cm)	Diff. (%)
400	2	$2\cdot666 \times 10$	$2\cdot666 \times 10$*	
500	4	$2\cdot134$	$2\cdot137$	+0·14
600	4	$3\cdot314 \times 10^{-1}$	$3\cdot309 \times 10^{-1}$	−0·15
700	4	$8\cdot218 \times 10^{-2}$	$8\cdot206 + 10^{-2}$	−0·15
800	4	$2\cdot851 \times 10^{-2}$	$2\cdot842 \times 10^{-2}$	−0·31
900	4	$1\cdot243 \times 10^{-2}$	$1\cdot247 \times 10^{-2}$	+0·30
1000	2	$6\cdot454 \times 10^{-3}$	$6\cdot454 \times 10^{-3}$*	

*Constants were chosen to give exact agreement at these values.

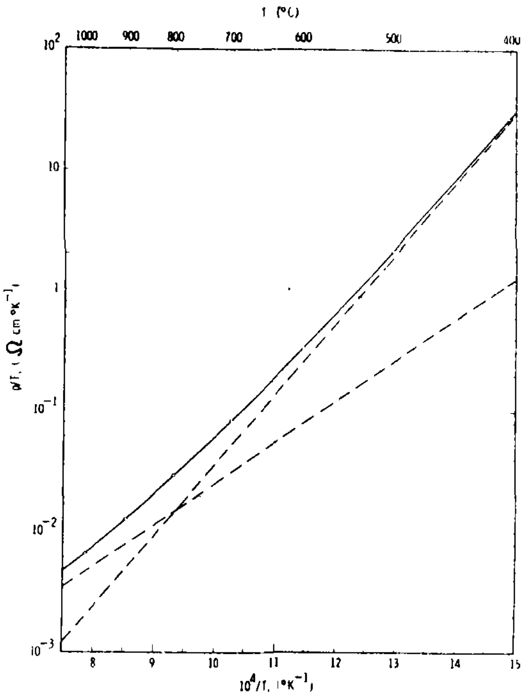

Fig. 1. Resistivity-temperature behavior for high purity $(ZrO_2)_{0.90}(Y_2O_3)_{0.10}$. Circles are experimental points; the solid line is equation (1) fitted to these points; the dotted lines are the two terms of equation (1) plotted individually.

4. DISCUSSION OF THEORY AND RESULTS

Before discussing specific mechanisms which would give rise to two terms in the expression for resistivity as in equation (1), let us consider the theory for a single phase material with non-interacting vacancies.

It has been established that in $(ZrO_2)_{0.90}(Y_2O_3)_{0.10}$, electrical conduction occurs by an oxygen ion vacancy mechanism[1, 10]. The appropriate expression for the resistivity ρ in this case can be shown to be

$$\frac{\rho}{T} = A e^{E/kT} \tag{3}$$

where

$$A = \frac{ak}{8ce^2\nu\, e^{S/k}}. \tag{4}$$

Here, T is the absolute temperature, a is the lattice parameter, k is Boltzmann's constant, c is the *fractional* concentration of vacancies in the oxygen ion sublattice, e is the electronic charge, ν is the vibration frequency of an oxygen ion adjacent to a vacancy ($\sim 10^{13}$ sec^{-1}), S is the activation entropy for vacancy motion, and E is the activation enthalpy for vacancy motion. The constant A may be calculated, subject to some uncertainty in the entropy factor $e^{S/k}$. For the alkali halides, this factor commonly lies between 1 and 10. We shall assume a value of unity for our present purposes, but will consider the effect of a larger value later in this discussion.

From equation (4) we calculate a value of $A = 7{\cdot}6\times10^{-6}\,\Omega$ cm deg^{-1} for a perfectly dense specimen of $(ZrO_2)_{0.90}(Y_2O_3)_{0.10}$, and for our specimen, which is 85 per cent of theoretical density, we have

$$A = 9{\cdot}0\times10^{-6}\,\Omega\,\text{cm deg}^{-1}. \tag{5}$$

Let us now consider two specific mechanisms which lead to expressions for ρ/T having the form of Equation (1).

(*A*) *Vacancy trapping hypothesis*

Consider a solid containing a *fractional* concentration of vacancies c_0, of vacancy traps c_t, and of free vacancies c_v. Then the concentration of trapped vacancies is $c_0 - c_v$, and the concentration of empty traps is $c_t - (c_0 - c_v)$. We may describe the trapping process by the reaction

free vacancy + empty trap ⇄ trapped vacancy. (6)

Applying the ideal mass action law, one obtains

$$\frac{c_0 - c_v}{c_v(c_t - c_0 + c_v)} = K = ze^{\zeta/kT} = ze^{-\eta/k}e^{\chi/kT} \tag{7}$$

where K is the equilibrium constant, z is the number of distinct orientations of the trap-vacancy complex, ζ is the Gibbs free energy of trapping, η is the entropy of trapping and χ is the enthalpy of trapping.

In order to simplify this expression we need an estimate of the relative concentrations of traps c_t and vacancies c_0. We can state at once that $c_t \geqslant c_0$; if the number of traps were *smaller* than the total number of vacancies, we would observe an inflection point in the $\log \rho/T$ vs. $1/T$ plot, because then only part of the vacancies could be trapped, even at the lowest temperatures. A likely candidate for the trapping center is the Y^{+3} ion; its charge and size relative to the Zr^{+4} ions should give rise to both an electrostatic and strain field which could attract oxygen ion vacancies. The concentration of Y^{+3} ions is twice that of the oxygen ion vacancies; therefore to a good approximation we can replace the factor $c_t - c_0 + c_v$ in equation (7) with its average value of $\frac{3}{2}c_0$. The fraction f of vacancies which are free is then found from equation (7) to be

$$f \cong \frac{c_v}{c_0} = (1 + \tfrac{3}{2}c_0 z e^{\eta/k} e^{\chi/kT})^{-1}. \quad (8)$$

In the simple expression for resistivity, equation (3), the effects of vacancy trapping may be taken into account by replacing A with Af^{-1}. Then we obtain

$$\frac{\rho}{T} = Af^{-1} e^{E/kT} = Ae^{E/kT} + (\tfrac{3}{2}Az\, c_0\, e^{-\eta/k}) e^{(E+\chi)/kT}. \quad (9)$$

This is identical in form with equation (1) so that we may equate coefficients:

$$\left.\begin{aligned} A &= A_1 \\ E &= E_1 \\ \chi &= E_2 - E_1 \\ \tfrac{3}{2}zc_0 e^{-\eta/k} &= A_2/A_1 \end{aligned}\right\}. \quad (10)$$

On the basis of equations (10) and (2) we arrive at the following conclusions:

(1) The activation enthalpy for vacancy motion is 0·682 eV.

(2) The trapping enthalpy between an yttria ion and an oxygen ion vacancy is 0·486 eV.

(3) The trapping entropy η/k is approximately 4·4.

(4) At 1000°C, 70 per cent of the vacancies are free, but at 400°C only about 4 per cent are free. (Calculated with equation (8)).

Some comments are appropriate here. The activation enthalpy for vacancy motion is quite low compared to values in the literature [1, 2], which are about 0·96 eV.* The trapping enthalpy appears reasonable, compared to those occurring in the alkali halides [11], at least. A more severe problem arises with the entropy value, η/k, however. In the alkali halides, for example, it is expected to be near zero [11]. Despite this disagreement, it does not seem probable that the trapping hypothesis can be ruled out on this basis alone. One might, in fact, expect deviations from our theory due to the high defect concentrations with which we are dealing.

(*B*) *Grain boundary layer hypothesis*

Consider a solid, composed of two phases differing in their resistivity and so distributed that the resistive effects are additive; for example, a bulk resistivity and a grain boundary resistivity. Then one may write

$$\rho = \alpha'\rho' + \alpha''\rho'' \quad (11)$$

where the α's represent fractional thicknesses† of the phases present, i.e. $\alpha' + a'' = 1$. If each ρ has the form of equation (3) we have

$$\frac{\rho}{T} = \alpha'A'\, e^{E'/kT} + \alpha''A''\, e^{E''/kT}. \quad (12)$$

This has the same form as equation (1) so that we may equate coefficients:

---

*When data are compared between various workers one should note whether $\sigma = Ce^{-E/kT}$ is used or $\sigma T = C'e^{-E'/kT}$. The relationship between the two is, to a good approximation, as follows:

$$C' \cong C\, e\, \tilde{T}$$
$$E' \cong E + k\tilde{T}$$

where

$$\tilde{T} = (\tilde{T}_{\text{highest}}\, \tilde{T}_{\text{lowest}})^{1/2}.$$

For the data discussed here $k\tilde{T} \cong 0{\cdot}1$ eV and $e\tilde{T} \cong 3{\cdot}1\ 10^3$ deg.

† If the grain diameter is D and the grain boundary layer thickness is d, then $\alpha' = D/(D+d)$ and $\alpha'' = d/(D+d)$.

$$\left.\begin{aligned} \alpha'A' &= A_1 \\ \alpha''A'' &= A_2 \\ E' &= E_1 \\ E'' &= E_2 \end{aligned}\right\}. \qquad (13)$$

We shall assume at this point that the vacancy concentrations in both bulk and grain boundary material are comparable so that we may use our previously calculated value of A as follows:

$$A' \sim A'' \sim A = 9{\cdot}0 \times 10^{-6}\,\Omega\,\text{cm deg}^{-1}. \qquad (14)$$

On the basis of equations (2), (13) and (14) we conclude that

$$\left.\begin{aligned} \alpha' &\sim 1, & E' &= 0{\cdot}682\,\text{eV} \\ \alpha'' &\sim 0{\cdot}005, & E'' &= 1{\cdot}168\,\text{eV} \end{aligned}\right\}. \qquad (15)$$

These values suggest that the bulk of the specimen has an activation energy for conduction of about 0·68 eV, but that a small amount of material having a higher activation energy, about 1·17 eV, is distributed throughout the specimen in thin layer form.* If it is assumed that this material is located at the grain boundaries, a rough calculation indicates that its thickness would be about 500 Å, and its volume about 1·5 per cent of the specimen.

The simple additive resistivity model employed here breaks down if the entropy factor $e^{S/k}$ in equation (4) is assumed to be appreciably larger than unity; α's which are greater than unity are then required, which, by their definition, is not possible.

We should now consider more specifically what the hypothetical grain boundary layer might be. By the assumption of equation (14), its vacancy concentration should be comparable to that of the bulk, and by experiment, it should have a higher activation energy for conduction than the bulk material. These requirements are met most simply by postulating that the outer layer of each grain is still cubic zirconia–yttria but with a higher proportion of yttria than the bulk. The apparent activation energy of this layer, 1·17 eV, corresponds roughly to $(ZrO_2)_{0\cdot85}(Y_2O_3)_{0\cdot15}$, according to the data of Dixon *et al.*[2], and is still well within the cubic range. Due to its similarity to the bulk material, its distribution as a thin layer, and the small total amount present, such a 'second phase' would be very difficult to detect by most standard techniques.

A very similar type of layer has been postulated by Jorgenson and Anderson[12] in the solid solution $(Y_2O_3)_{0\cdot9}(ThO_2)_{0\cdot1}$. From their microhardness, grain growth, and surface activity experiments, they inferred that a thoria-rich layer existed at the grain boundaries.

On the basis of our present information the two mechanisms above appear equally likely. Conductivity data on single crystal specimens would be very helpful in deciding the matter.

5. SUMMARY

(1) Between 400° and 1000°C, the resistivity of a high purity $(ZrO_2)_{0\cdot90}(Y_2O_3)_{0\cdot10}$ specimen may be described by the expression

$$\frac{\rho}{T} = A_1\,e^{E_1/kT} + A_2\,e^{E_2/kT}.$$

(2) If a vacancy trapping mechanism is assumed to explain this temperature dependence, one concludes that (a) the activation enthalpy for free vacancy motion is 0·68 eV, and (b) the yttria ions act as traps for the vacancies; the trapping enthalpy if 0·49 eV and the trapping entropy η/k is 4·4.

(3) If a grain boundary layer mechanism is assumed to explain the temperature dependence one concludes that (a) the activation enthalpy for conduction in the bulk of the grains is 0·68 eV, and (b) a grain boundary layer exists which is on the order of 500 Å in thickness and which contains a higher

---

* A thin layer-type distribution is required for the *resistivities* to be additive.

proportion of yttria than the bulk material. The activation enthalpy for conduction in this layer is about 1·17 eV.

Acknowledgements—The authors wish to thank Drs. R. J. Ruka and A. J. Panson for helpful discussions concerning this work.

REFERENCES

1. STRICKLER D. W. and CARLSON W. G., *J. Am. Ceram. Soc.* **47**, 122 (1964).
2. DIXON J. M., LaGRANGE L. D., MERTEN U., MILLER C. F. and PORTER J. T., *J. electrochem Soc.* **110**, 276 (1963).
3. LEFEVRE J., *Annls. Chim.* **8**, 117 (1963)
4. BAUERLE J. E. and HRIZO J., Westinghouse Technical Report, March (1965).
5. STRICKLER D. W., Westinghouse Report No. 64-918-273-R6 (Contains data on high purity material).
6. CASSELTON R. E. W., In *Electromotive Force Measurements in High Temperature Systems* (Edited by C. B. Alcock), pp. 151–157. Institution of Mining and Metallurgy, London (1968).
7. CARTER R. E. and ROTH W. L., *Electrochem. Soc. Extended Abstracts*, No. 154, April (1963).
8. SUBBARAO E. C. and SUTTER P. H., *J. Phys. Chem. Solids* **25**, 148 (1964).
9. TIEN T. Y. and SUBBARAO E. C., *J. chem. Phys.* **39**, 1041 (1963).
10. BRAY D. T. and MERTEN U., *J. electrochem. Soc.* **111**, 447 (1964).
11. BEAUMONT J. H. and JACOBS P. W. M., *J. chem. Phys.* **45**, 1496 (1966).
12. JORGENSON P. J. and ANDERSON R. C., *J. Am. Ceram. Soc.* **50**, 553 (1967).

J. Phys. Chem. Solids Pergamon Press 1969. Vol. 30, pp. 571–584. Printed in Great Britain.

HIGH TEMPERATURE NMR STUDIES OF BROMINE AND IODINE CHEMICAL SHIFTS IN ALKALI BROMIDES AND IODIDES AND IN THALLIUM BROMIDE*

LINSEN HSIA NGAI†
The James Franck Institute and Department of Chemistry, The University of Chicago,
Chicago, Ill. 60637, U.S.A.

(*Received* 9 *May* 1968; *in revised form* 28 *June* 1968)

Abstract—The Br-81 and I-127 chemical shifts of the alkali halides and of TlBr were studied as a function of temperature. The room temperature results are in close agreement with previous workers, and more information is deduced. A consistent explanation can be obtained by assuming Kondo-Yamashita's (K-Y) overlap model with due consideration of next-nearest-neighbor (NNN) interactions between halide ions. The possibility of a slight covalent effect in the heavy metal end of the alkali halides is discussed. The effect of covalency is manifested by TlBr, whose measurements can be successfully explained by the covalent model of Yosida-Moriya (Y-M). A correct way of averaging the effect of thermal vibronic motion on chemical shift in the K-Y overlap model is formulated, and a general formula is derived for the temperature variation of chemical shift. For the alkali halides, the thermal dilation of the lattice together with the thermal-vibration-induced enhancement of overlap account for the downfield shift with increasing temperature. The results are analyzed quantitatively, and a physically meaningful factor F has been calculated to indicate the selective degree of importance of NN interactions. As for TlBr, similar explanations for the observed results are deduced in the light of the Y-M covalent model. NNN is important to account for the difference in sign of the chemical shifts at the transition temperature from solid to molten states of TlBr as observed.

INTRODUCTION

IN THE early 1950's, Gutowsky and McGarvey[1] and Kanda[2] had undertaken the study of anion chemical shifts in some solid alkali halides. They suggested that the origin of the observed chemical shifts arises in covalent bonding between cation and anion in the crystal. In 1956, Yosida and Moriya[3] derived a theoretical model to explain the empirical chemical shift values. Their model was based on the principle that chemical shift arises from the transfer of an electron from the anion to the cation in the crystal. Mathematically, the chemical shift of an anion and cation, respectively, can be represented as follows:

$$\delta_H = -\frac{8}{3}Z\lambda\frac{1}{\Delta E'}\mu_B{}^2\left\langle\frac{1}{r^3}\right\rangle_H, \qquad (1)$$

$$\delta_M = -\frac{8}{3}|a_p|^2Z\lambda\frac{1}{\Delta E'}\mu_B{}^2\left\langle\frac{1}{r^3}\right\rangle_M,$$

where Z is the number of nearest neighbors; $Z\lambda$ is a parameter which describes the total covalent character in the molecule; $\Delta E'$ is the difference in energy between the ionic state and the charge-transferred state without bonding; μ_B is the Bohr magneton, $\langle 1/r^3\rangle_H$ is the average of $1/r^3$ over the outermost p states of the *halogen atom*; $\langle 1/r^3\rangle_M$ is the corresponding average over the outermost p states of the *metal atom*; and a_p is the fraction of p character in the mixed s–p state. However, the covalent picture has failed to agree with the observed values of the quadrupolar relaxation times. Moreover, it predicts that both the chemical shift and the reciprocal of the spin-lattice relaxation time ($1/T_1$) should be much smaller for alkali ions than those for the halogen ions with similar electronic configurations. This is because the electronic state forming the covalent bond is mainly of atomic p-type in the neighborhood of the halogen nucleus, whereas it is mainly of atomic s-type around the alkali nucleus. However, an s-electronic state makes no contribution to either the spin-lattice relaxation time or to the chemical shift. Itoh and Yamagata[4] have studied salts like RbBr and KCl but did not observe this predicted behavior. This shows the inadequacy of the covalent picture, at least for the alkali halides.

---

*A dissertation submitted in partial fulfillment of the requirements for the degree of Doctor of Philosophy, University of Chicago.

†*Present address:* Chemistry Department, Northwestern University, Evanston, Illinois 60201, U.S.A.

Kondo and Yamashita[5] have advanced another theory in which the effect of the overlapping of neighboring ions is considered. This idea is motivated by Löwdin's[6] calculation of the cohesive energy of the simple ionic crystals. The chemical shift for the metal ion δ_M, and that for the halogen ion, δ_H, that follow from the Kondo–Yamashita theory are:

$$\begin{aligned} \delta_H &= -\frac{16}{3} Z\Lambda \frac{1}{\langle\Delta E\rangle_H} \mu_B{}^2 \left\langle\frac{1}{r^3}\right\rangle_{H^-}, \\ \delta_M &= -\frac{16}{3} Z\Lambda \frac{1}{\langle\Delta E\rangle_M} \mu_B{}^2 \left\langle\frac{1}{r^3}\right\rangle_{M^+}, \end{aligned} \tag{2}$$

where Λ is the sum of the squares of the overlap integrals between outermost orbitals on a pair of nearest-neighbor (NN) ions; $\langle\Delta E\rangle_{M,H}$ is a suitable average over the excited states of an ion; $\langle 1/r^3\rangle_H$ is the average of $1/r^3$ over the outermost p-states of a *halogen ion*; $\langle 1/r^3\rangle_M$, is the corresponding average over the outermost p-states of a *metal ion*. Hereafter, equations 1 and 2 will be referred to as the Y–M and K–Y equations, respectively.

The K–Y theory can explain reasonably well the experimental results for the spin-lattice relaxation time and the chemical shift for the ionic crystals. The analysis of Das and Karplus[7] on the field gradient of KCl has also borne out the importance of overlap effect in alkali halides. However, more recent experimental results on alkali halides (for example, Yamagata[8] and Baron[9]) indicate that there are discrepancies between experiment and the original K–Y theory. Effects of overlap with next nearest neighbor (NNN) (Yamagata, and Baron) and ionic polarization effects are invoked to explain this deviation of the chemical shift and the relaxation time from the original K–Y theory, with qualitative and semiquantitative success in different cases. Hafemeister and Flygare[10] have undertaken the calculation of the pressure dependence of NMR chemical shifts assuming the K–Y model and concluded that NNN halogen–halogen interactions contribute significantly to the chemical shift. It is evident therefore, that Kondo-Yamashita's model when suitably modified with respect to NNN interaction and electrostatic interactions can account for the NMR studies of the alkali halides to a great extent. Yet it should be remarked here that despite this semiquantitative agreement, there still exist systematic discrepancies from the experimental data of previous workers. Our present work will shed light on this problem, as will be discussed in detail in the following sections.

Nuclear magnetic resonance in the thallium halides has been studied by Rowland and Bromberg[11] and later by Hafner and Nachtrieb[12] and by Saito[13]. In a thallium ion, the outermost orbitals contributing to a paramagnetic shift are the 5 p and 5 d orbitals. The K–Y equation for the chemical shift is given for a p-orbital. The corresponding expression for a d-orbital can easily be derived by using the same overlap model, as done by Saito. He observed that the experimental values deviate markedly from the prediction of the overlap model even when generalized to include the d-orbitals. Rowland and Bromberg correlated the thallium chemical shifts with electronegativities but did not develop this concept in detail. The present work on bromine-81 resonance in thallium bromide, taken together with the thallium-205 results on the same salt, will help to clarify the question of overlap and covalency in the thallium halides in both the solid and molten states.

EXPERIMENTAL METHODS

The chemical shift is measured as

$$\delta = \left(\frac{H_s - H_r}{H_r}\right)_\nu$$

where H_s and H_r are the magnetic fields for which resonance of the nuclei is observed at a particular frequency, ν, in the sample and reference, respectively. In the present experiments the reference sample used for bromine-81 resonance was a saturated aqueous solution of NaBr, and that for iodine-127 resonance was a sample of solid KI. Most of the alkali halides used were Baker Analyzed Reagent Grade. The thallium bromide and salts of rubidium bromide and cesium bromide were from the K & K Company. The salts were not further purified nor were they analyzed for impurity contents since impurity effects on chemical shifts are known to be negligible. All substances were dried in an oven over night at 180°C before they were packed tightly into the sample tubes for sealing. The sample tubes were made of Vycor tubing, 14 mm O.D. with a deep reentrant well for the thermocouple for temperature measurement. The tubes were sealed off at a constriction near the bulb which was filled with the appropriate salt. Each sample was evacuated on a vacuum line for about 20 min before sealing so as to assure complete dryness of the salt. The length of the final sealed-off sample cells was 25 mm for the bromides, and 37 mm for the iodides. The volume of the salt used was about 0·7 to 0·8 cm^3 in the solid state.

The single-coil method together with twin-T bridge arrangements were used for the detection of the absorption resonance signal. The magnetic field was scanned over a range of 50 G in a period of 10 min. At 13·99785 Mc/sec (hereafter referred to as 14 Mc/sec) the bromine-81 resonance is observed when the magnetic field was set at 12·195 kG. For iodine-127 resonance the magnetic field was 14·107 kG, while the frequency was kept constant at 12·00166 Mc/sec. Two quartz crystals at 14 Mc/sec and at 12 Mc/sec were used for the bromine and iodine measurements, respectively, so as to maintain the frequency stable to within a hundredth of a kc/s.

The furnace is made up of 30 vertical loops of 0·010 in. dia. platinum wire set into grooves which were milled into a thin-walled Lava cylinder. The cooling element is a brass water-cooled jacket of 40 mm o.d. surrounding the furnace and the rf coil (99·9 per cent pure silver wire, gauge number 20). The current to the furnace is supplied by a bank of storage batteries providing voltages varying from 12 to 96 V. It requires a current of about 3·4 A to reach a temperature of about 500°C. in the sample. The temperature of the sample was measured potentiometrically by means of a calibrated platinum–platinum + 13 per cent rhodium thermocouple, using an ice-water bath as reference junction. The experimental chemical shifts (corrected for furnace current effect) as a function of temperature are shown in Figs. 1–3.

ALKALI HALIDES

The chemical shifts as a function of temperature of the alkali halides are plotted in Figs 1 and 2. In all these cases there is a linear dependence of the chemical shift on temperature, and the negative signs of the slopes indicate that the salts become more paramagnetic with increasing temperature.

Room temperature chemical shifts of alkali halides

A careful examination of the chemical shifts at room temperature reveals the interesting fact that if the anion chemical shifts in the alkali halides are plotted as an increasing function of the *Y*-axis against the atomic numbers of the metal ions for the same halogen partners on the *X*-axis, there exists a minimum in the chemical shift of the halogen ion when the atomic number of the metal ion is increased from lithium to cesium. This minimum occurs at sodium for the bromides, and at potassium for the iodides. A plot of the metal ion versus chemical shift is shown in Fig. 4. Beyond the minimum, there appears a systematic downfield trend in the chemical shift of the halogen ion with increasing atomic number of the metal ion in the alkali halides. Such a trend can be easily accounted for as the following: Hafemeister and Flygare[14] have calculated the outer *s*- and *p*-electron overlap integrals in all the alkali halides. The K–Y equation predicts that the chemical shift is proportional to the sum of the squares of the overlap integrals. Calculation of these integrals and substituting them into the K–Y equation leads to values of the anion chemical shifts on the overlap model which are indeed larger for substances with the heavier metal partner in both the bromide and the iodide series. The

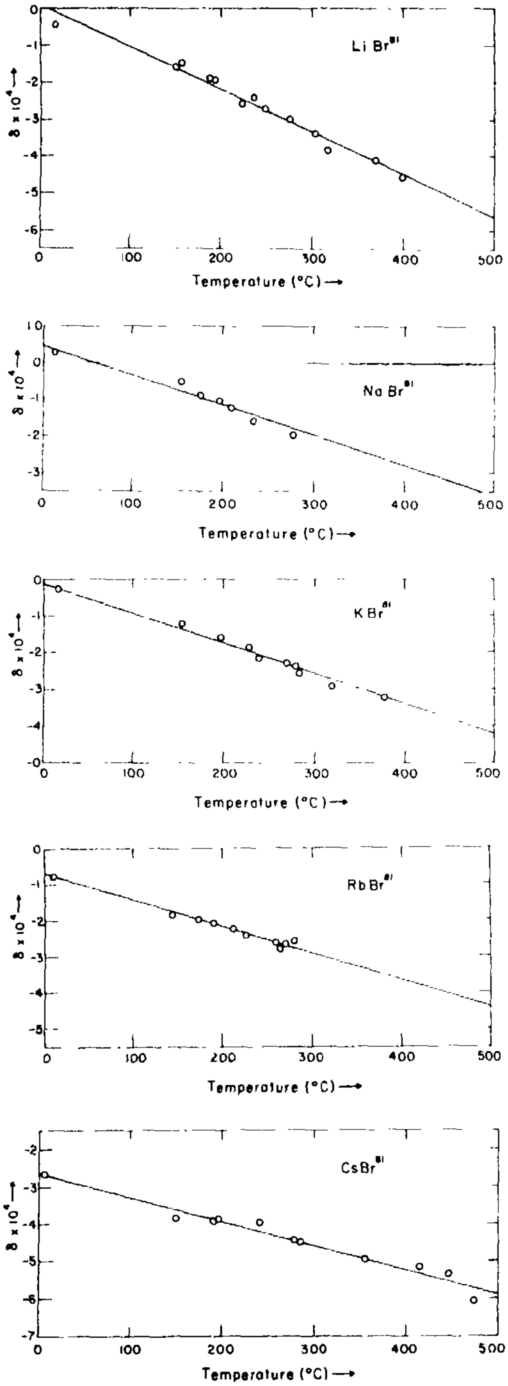

Fig. 1. Bromine-81 chemical shifts in alkali bromides.

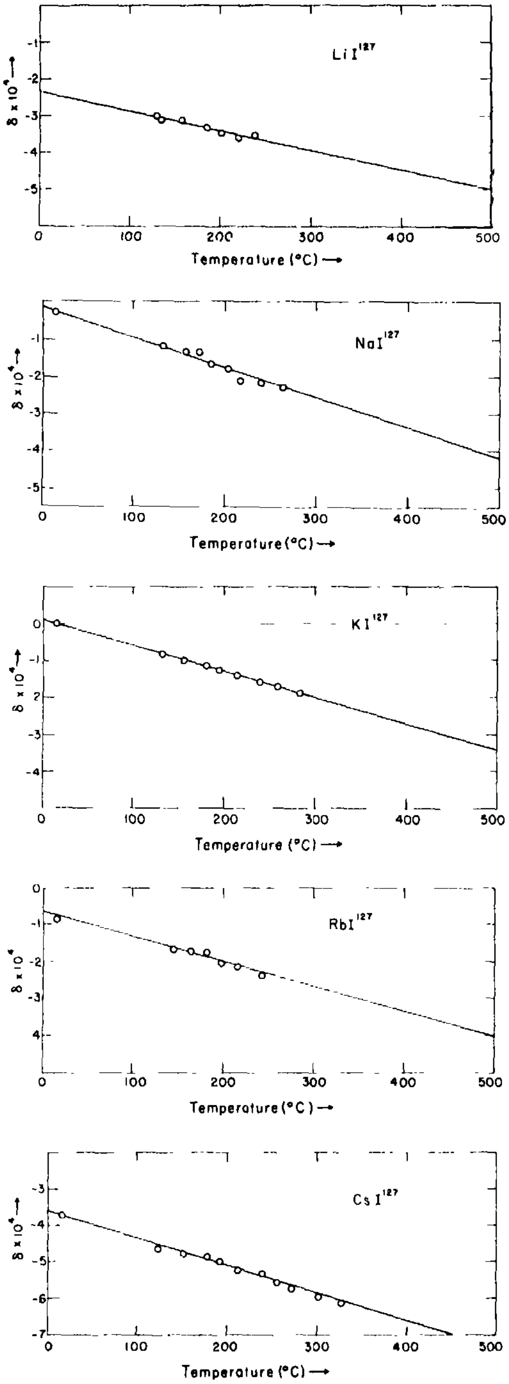

Fig. 2. Iodine-127 chemical shifts in alkali iodides.

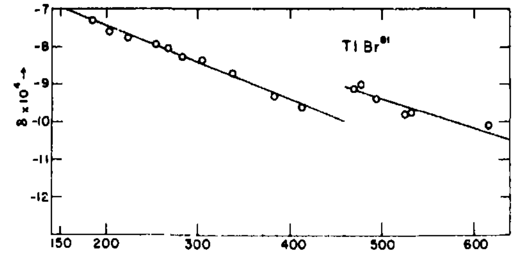

Fig. 3. Bromine-81 chemical shifts in TlBr.

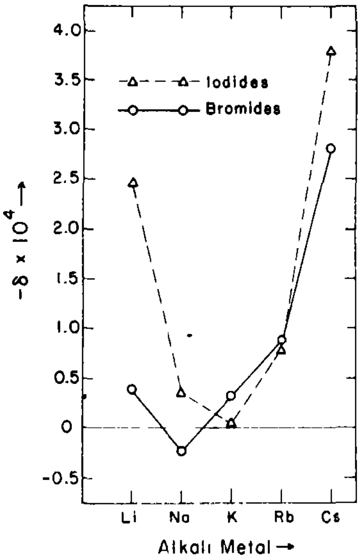

Fig. 4. Experimental results at room temperature of the chemical shifts of the halogen nuclei versus alkali metal ions.

anomalous increase in the chemical shift of LiBr, LiI, and NaI from the present experiments cannot be explained by the overlap effect in the original version of the K–Y theory, which would otherwise show the least shifts in the lighter alkali halides, contrary to the experimental results. Thus, an additional mechanism must be present to account for this anomaly. Yamagata[8] observed the same trend in his study of the anion chemical shift of the alkali halides at room temperature with respect to a dilute aqueous solution as reference. He proposed that the main contribution for such anomalies is due to the overlap effect with NNN interactions included, while rejecting the explanations of the covalent and electrostatic effects. A comparison of the present results with Yamagata's values referred to the same reference is shown in Fig. 5. The agreement is perfect.

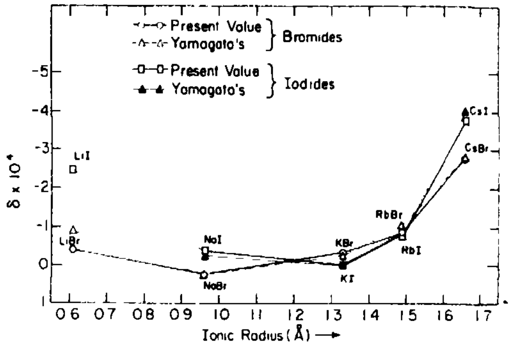

Fig. 5. Comparison of the present values of alkali bromides and iodides with Yamagata's at 25°C.

Born–Mayer formulated the overlap repulsion energy as proportional to the sum of the squares of the overlap integrals, and it has been shown classically by Born and Huang[15] that the ratio,

$$J=\frac{\text{Overlap energy of second neighbors}}{\text{Overlap energy of first neighbors}}=f(\eta),$$

depends on the radius ratio of $\eta = r_+/r_-$, as plotted in Fig. 6. The curve shows that for

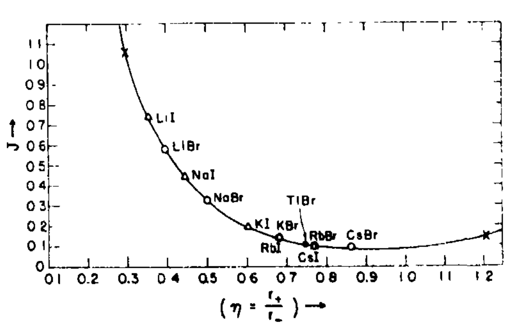

Fig. 6. J vs. η plot from Born and Huang.

salts of K, Rb and Cs the contributions due to second neighbors are much less than those due to nearest neighbors. However, in the salts of the lighter metal ions, especially those of lithium, the NNN halogen-halogen overlap effect makes an important contribution to the lattice energy. It is interesting to propose that the anomalous downfield chemical shifts of the anion resonances in LiI, LiBr and NaI, may also be due to the overlap of NNN halogen ions. The overlap of metal-metal ions, however, would not contribute much to the chemical shift because of their small sizes. This idea has been well confirmed from theoretical calculations by Hafemeister and Flygare [14]. Based on this model explanation, the anomalous downfield shift of the anion resonance in LiI should be larger than for LiBr, since η is smaller for each alkali iodide than for the corresponding bromide. This behavior is indeed observed in our experiment as can be seen in Fig. 4.

Hafemeister and Flygare[10] have calculated the theoretical chemical shifts of the alkali halides with the inclusion of NN and NNN. A plot of these theoretical chemical shifts $\delta_{solid}-\delta_{KI}$ vs. ionic radii of the alkali ions is shown in Fig. 7. Comparing this figure with that of Fig. 5, we can see that the NNN interaction contributes significantly for the light metal partner of the halogen shifts of the alkali halides. From the calculated chemical shifts of RbI and CsI with the inclusion of the NNN anions we see that such values are small when compared with that of LiI. But the experimental values of RbI and CsI are large when measured relative to solid KI as reference. Hence, with the inclusion of NNN interactions, it is not possible to explain the large experimental chemical shifts observed in RbI and CsI relative to solid KI. Thus, the NNN anion interaction cannot be the only mechanism for the complete explanation of the experimental data. We suggest here that a very slight partial covalent bonding effect must be invoked to give a satisfactory agreement of the data as represented graphically in Fig. 5, especially for the rubidium and cesium halides.* Gutowsky and McGarvey measured the chemical shift of Rb and Cs resonance in their respective halides. For each cation they observed the paramagnetic chemical shift to be larger for iodides than for bromides, and they suggested that the origin of the shift lies in covalent bonding between cation and anion in the crystal. The larger shifts in the iodides than in the bromides are also observed in the present experiments. Kanda has also argued that the origin of the field gradient in the metal halides of the low ionicity is due to the covalent bonding in the crystals.

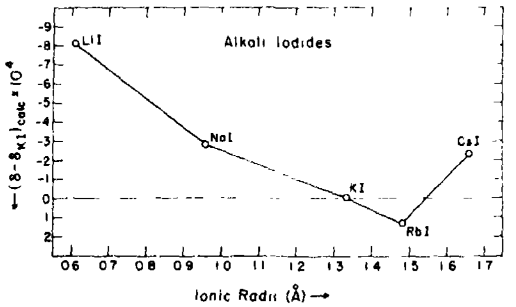

Fig. 7. Calculated chemical shifts vs. metal radii of alkali iodides.

From the iodine plot in Figure 5, we obtain the experimental ratio of $K_{expt}=(\delta_{CsI}-\delta_{KI})/(\delta_{RbI}-\delta_{KI})=5\cdot4$. We now use the overlap integral S† tabulated by Hafemeister and Flygare[14] to evaluate the chemical shifts of iodine-127 values for KI, RbI and CsI, using the Ikenberry and Das[17] modification of the K-Y theory. The result of this calculation which only includes the NN overlap contributions, yields $K_{ovlp}=(\delta_{CsI}-$

---

*We agree with Wikner *et al.*[16] that for cesium halides the chemical shift formula should be modified to include bonding d orbitals to account for the observed large shifts.

†It should be noted that all overlap calculations are merely a first order approximation, in that electron correlations and polarization are neglected. Their inclusion would increase the chemical shift calculations.

$\delta_{KI})/(\delta_{RbI}-\delta_{KI}) = 1{\cdot}9$.† The discrepancy between K_{expt} and K_{ovlp} demonstrates the fact that the NN overlapping-ion model of K-Y cannot account for the large observed downfield shifts in rubidium and cesium halides. While it is true that the Ikenberry-Das model neglects NNN interactions, and it has also been shown that they play a large role in the chemical shifts of large anions associated with small cations, the NNN overlap is expected to be of minor importance for the heavy metal alkali halides. The basis for this assertion is the Born-Huang J vs. η plot, which shows the minor contribution of NNN interactions to the lattice energy when $\eta > 0{\cdot}6$, and hence, the NNN interaction is not expected to be very sensitive when one goes from potassium to cesium. It must be recalled at this point that all the cesium halides have the CsCl structure, while all the rest of the alkali halides have the NaCl structure, with 6 NN and 12 NNN. RbI, for example, has twice as many NNN as does CsI. Inclusion of NNN overlap would decrease K_{ovlp} and increase its discrepancy with K_{expt}. Baron has also shown that a combination of overlap and covalent effects would give a better agreement between experimental results and theories. The above arguments further support. our suggestion that in addition to the modified K-Y theory with NNN included, there also exists a small but distinct partial covalent bonding in ionic crystals. We expect that this contribution of covalent bonding is negligible compared with the overlap effect in determining the chemical shifts when we consider the light metal end of the halide series, and it should increase monotonically when we go to the heavy metal side. Qualitatively the three effects of NN overlap, NNN overlap and the degree of partial covalent character have the behavior as shown in Fig. 8 when one varies the metal ion in any halide series. The chemical shift is obtained as the interplay of these three major contributions. The above discussion also applies to the bromide series.

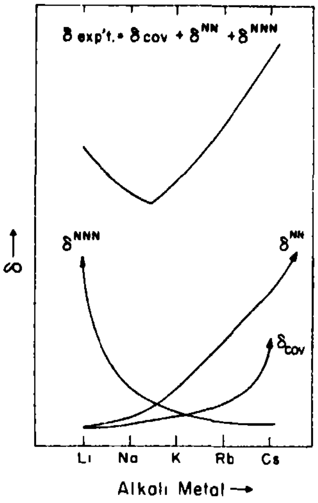

Fig. 8. A schematic plot showing the dominating effects of the chemical shifts as one goes from Li to Cs.

Temperature variation of δ for alkali halides

The discussion in the last section is restricted to the various properties related to chemical shifts of alkali halides at room temperature. It is of considerable interest to study how the chemical shift varies when the crystal lattice is perturbed. One way of altering the interionic distances in crystal lattices is by varying the temperature. This method definitely would introduce effects that do not occur in a hydrostatic pressure experiment as that performed by Baron, and it may complicate the comparison of theory and experiment. However, Baron's studies and Hafemeister and Flygare's work permit us to isolate unambiguously various effects in a temperature variation experiment and thus, furnish us with further information about the chemical shift as related to various parameters of the crystal lattice. It has been suggested by Watkins and Pound[18] and by Watkins[19] that the experimental results on the relaxation time of the crystals can be explained if they assume that the most dominant mechanism in the relaxation is the deformation of the electron shell surrounding the nucleus when the ions are displaced from the equilibrium positions by thermal vibrations. In the K–Y theory, if we neglect this deformation of ions, i.e. assume a rigid ion approximation, the concomitant overlap integrals would now be modified as a function of the interionic distance. In effect, due to thermal vibrations a non-cubic field appears at the nucleus, as is obvious from the picture that now the six NN are no longer at equal distance from that nucleus. Thus, it would be of great interest to study the thermal vibration of the chemical shift in the alkali halides.

---

†The number of nearest neighbors has been taken into consideration for the two different cubic structures.

Due to thermal vibrations, the mean overlap integrals $\langle\Lambda\rangle$ depend on the temperature through both the explicit dependence on interionic distance, r, and the amplitude of vibration, u. In general, the individual overlap integrals, S, have the functional dependence

$$S = A\,\mathrm{e}^{-r/\rho} \tag{5}$$

where A and ρ are assignable constants. The relations

$$\begin{aligned} \langle u_x^2\rangle &= \langle u_y^2\rangle = \langle u_z^2\rangle = \tfrac{1}{3}\langle u^2\rangle; \\ \langle u^2\rangle &= \frac{18}{M\omega_0^2}kT \end{aligned} \tag{6}$$

from Leibfried[20] hold for the temperature region of our interest, where M is the reduced mass; ω_D is the Debye frequency; k is the Boltzmann's constant; and T is the temperature. Equation (6) is derived in the harmonic approximation and without taking into account the many-body nature of lattice dynamics, and thus, it would not account for the actual situation when this approximation breaks down, or when the influence of NNN is very important. In particular, when discussing the alkali halides we have seen in the previous section that the NNN interactions are prominent. Thus, in the limit of light metal ions, we would not expect equation (6) to be a good approximation of a harmonic oscillator. We shall derive a general formula of the variation of the thermal vibrational induced overlap with temperature. Let Λ have the form

$$\Lambda = S^2 = A^2\,\mathrm{e}^{-2(r+x)/\rho} \tag{7}$$

where x is a displacement from the internuclear distance, r. Assuming that x is small, we can expand the exponential form in x/ρ, and by using the relations such that

$$u_x^2 = KT$$

$$\frac{\mathrm{d}r}{\mathrm{d}T} = \frac{r\alpha_{\mathrm{vol}}}{l}$$

where $K = 6k/M\omega_D^2$, and α_{vol} is the coefficient of volume expansion, we obtain:

$$\frac{\mathrm{d}\langle\Lambda\rangle}{\mathrm{d}T} = -\frac{\Lambda}{\rho}\left[\frac{2\alpha_{\mathrm{vol}}r}{3} - \frac{K}{\rho}\right]. \tag{8}$$

Equation (8) demonstrates that the thermal vibrational contribution to $\mathrm{d}\delta/\mathrm{d}T$ is opposite in sign to the dilatation effect of the crystal lattice due to expansion; it may be possible that the former can dominate the sign of the whole expression, thus explaining the downfield shift when temperature is increased, as is observed experimentally. It is clear that we do not expect that our range of temperature, which is equivalent to a maximum variation of about 1/40 eV in energy, would change the atomic parameters appreciably to account with the existing models for the downfield shift with increasing temperature. No other model thus far proposed accounts for the negative temperature coefficient of the chemical shift, and we shall take the thermal vibrational effect as the main cause for the downfield shift as temperature increases. We shall discuss our results further based on this picture. One way of analyzing the experimental results is to compute $d\delta/dT$ from equation (8) and from the Ikenberry and Das extension of the K–Y theory. The values used are tabulated in Table 1.

Ikenberry and Das[17] extended K–Y's work by inclusion of pi-bonding terms and the nonlocal terms. They expressed the NN contribution to δ for f.c.c. structure as

$$\delta_{\mathrm{NaCl}}^{\mathrm{NN}}=-\frac{16\alpha^2}{\langle\Delta E\rangle}\langle r_0{}^{-3}\rangle_p\,[|\langle S_{0i}^{\pi\pi}\rangle|^2+|\langle S_{0i}^{\sigma\sigma}\rangle|^2$$
$$+|\langle S_{0i}^{\sigma s}\rangle|^2-2\langle S_{0i}^{\sigma\sigma}\rangle\langle S_{0i}^{\pi\pi}\rangle]$$
$$+\frac{32}{\langle\Delta E\rangle}\alpha^2[\langle\cdots\rangle+\cdots] \tag{9}$$

where α is the fine structure constant. For our problem we have replaced all S by $\langle S\rangle$ as was explained above. The variation of the chemical shift with temperature has the form,

$$\frac{d\delta_{\mathrm{NaCl}}^{\mathrm{NN}}}{dT}=-\frac{16\alpha^2}{\langle\Delta E\rangle}\langle r_0{}^{-3}\rangle_p\frac{d}{dT}[|\langle S_{0i}^{\pi\pi}\rangle|^2$$
$$+|\langle S_{0i}^{\sigma\sigma}\rangle|^2+|\langle S_{0i}^{\sigma s}\rangle|^2-2\langle S_{0i}^{\sigma\sigma}\rangle\langle S_{0i}^{\pi\pi}\rangle]$$
$$+\frac{32}{\langle\Delta E\rangle}\alpha^2\frac{d}{dT}[\langle\cdots\rangle+\cdots]. \tag{10}$$

The second term on the right hand side involves the nonlocal terms, and we shall neglect it because of its smallness. It then follows from equation (8):

$$\frac{d\delta_{\mathrm{NaCl}}}{dT}=\frac{16}{\langle\Delta E\rangle}\alpha^2\langle r_0{}^{-3}\rangle_p\left[\frac{2\alpha_{\mathrm{vol}}r_{0i}}{3}\left\{\frac{|\delta_{0i}^{\pi\pi}|^2}{\rho_{\pi\pi}}\right.\right.$$
$$\left.+\frac{|S_{0i}^{\sigma\sigma}|^2}{\rho_{\sigma\sigma}}+\frac{|S_{0i}^{\sigma s}|^2}{\rho_{\sigma s}}-S_{0i}^{\sigma\sigma}S_{0i}^{\pi\pi}(\rho_{\sigma\sigma}^{-1}+\rho_{\pi\pi}^{-1})\right\}$$
$$-FK\left\{\frac{|S_{0i}^{\pi\pi}|^2}{\rho_{\pi\pi}^2}+\frac{|S_{0i}^{\sigma\sigma}|^2}{\rho_{\sigma\sigma}^2}+\frac{|S_{0i}^{\sigma s}|^2}{\rho_{\sigma s}^2}\right.$$
$$\left.\left.-\tfrac{1}{2}S_{0i}^{\sigma\sigma}S_{0i}^{\pi\pi}(\rho_{\sigma\sigma}^{-1}+\rho_{\pi\pi}^{-1})^2\right\}\right]. \tag{11}$$

Care should be exercised that the $d\delta_{\mathrm{NaCl}}^{\mathrm{NN}}/dT$ for CsCl structure is 8/6 of equation (11). We have introduced a phenomenological factor F, whose physical significance and interpretations shall be discussed in the following section. We shall also include the effect of NNN, whose contributions $(d\delta_{\mathrm{NaCl}}/dT)^{\mathrm{NNN}}$ and $(d\delta_{\mathrm{CsCl}}/dT)^{\mathrm{NNN}}$ for NaCl- and CsCl-structures have expressions which can be obtained by multiplying by factors of 2 and 6/8, which is the ratio of NNN/NN into $(d\delta_{\mathrm{NaCl}}/dT)^{\mathrm{NN}}$ and $(d\delta_{\mathrm{CsCl}}/dT)^{\mathrm{NN}}$, respectively.

The parameters and the overlap integrals are taken from Hafemeister and Flygare [10, 14] for the alkali halides, and the value of $d\delta/dT$ is calculated with both NN and NNN taken into consideration for the dilatation

Table 1. Numerical parameters of alkali halides

Compound	$1/M\times10^{-22}$ (1/g)	θ(°K)*	$K\times10^{20}$ $\left(\frac{\text{erg. sec}^2}{\text{g. deg}}\right)$	$r_0\alpha_{\mathrm{lin.}}\times10^{12}$ (cm/deg)	$\alpha_{\mathrm{vol}}\times10^4$ (deg^{-1})†
LiBr	9·43	389·0	3·05	1·29	1·40
NaBr	3·36	239·9	2·82	1·19	1·19
KBr	2·30	227·5	2·14	1·25	1·10
RbBr	1·46	114·0	5·42	1·19	1·04
CsBr	1·21	69·2	12·1	1·73	1·39
LiI	9·14	287·3	5·33	1·67	1·67
NaI	3·09	202·0	3·64	1·46	1·35
KI	2·02	193·3	2·60	1·47	1·25
RbI	1·18	100·2	5·68	1·45	1·19
CsI	0·93	54·5	15·1	1·92	1·46

*Values calculated from M. Blackman, see reference[26].
†Values from M. Tosi, see reference [27].

part. But as was discussed before, since the many-body lattice dynamics when the NNN effect is very important (thus implying the breakdown of Leibfried's approximation) is not known, we have introduced F as a phenomenological parameter to account for this. $d\delta/dT$ is then calculated numerically, and F is adjusted to fit the experimental data. The F values so obtained are listed in Table 2.

Table 2. *The phenomenological factor*

Compound	F	Compound	F
LiBr	9·99	LiI	2·37
NaBr	8·29	NaI	6·50
KBr	7·23	KI	6·34
RbBr	2·47	RbI	3·29
CsBr	0·88	CsI	1·33

As seen from the table, the F values for CsBr and CsI are close to one. Hence at least for these compounds the thermal vibrational induced overlap picture accounts well for the data. Except for LiI, there is in both the bromide and iodide series a systematic trend of decreasing values of F as we go from light to heavy metal ions. This relatively large value of F in light metal halides is expected as the NNN interaction plays a relatively more important role as compared with the heavier metal halides. Due to the arbitrary method of averaging that we adopt here and the approximations of Leibfried with a Debye spectrum to the actual lattice spectrum, the actual value of F could have been changed. It is possible that the approximation of Leibfried breaks down when applied to the system in which the detailed knowledge of the lattice modes is necessary, as for example, in the case when NNN interactions are particularly important. We believe that the quantity F has a physical meaning, and that it reflects the relative importance of NN and NNN interactions. If the trends of the chemical shifts of alkali bromides are the resultant of the competing NN alkali-bromide overlaps with the NNN bromide–bromide overlaps, then F clearly correlates strongly with a measure of the ratio of their importance, cf. J vs. η curve, Fig. 6. We expect that if experiments were performed to study the metal nucleus chemical shift variations with temperature, we would obtain a better understanding of the situation since NNN alkali–alkali overlaps are relatively less important; the F values could be compared, given that the K–Y theory adequately describes the chemical shift of the alkali halides, and the thermal vibrational effect plus the dilatation of the lattice account for its temperature variation. We would expect a much smaller range of f values. Theoretical treatment of the lattice dynamics and its influence on the chemical shift in the case of light metal, heavy halogen alkali halides would definitely be of great use, when compared with experiment, for arriving at a better physical picture. Calculations of the mean square amplitudes of the ions in alkali halides may be done in a manner similar to Flinn *et al.*[21] for copper in which they adopted an NN and NNN interaction central force model for copper and evaluated the eigenvalues and eigenvectors of the dynamical matrix.

THALLIUM BROMIDE

Thallium-205 chemical shift studies have been done on TlCl, TlBr and TlI. It would be of great interest to study the halogen chemical shifts of the thallium halides and to compare the results with the metal ion values. Unfortunately the chlorine resonance frequency occurs too low to be studied by the present probe design. No iodine-127 resonance signal of TlI could be observed in either the solid or molten states. Hence, only the TlBr system could be studied.

Figure 3 shows the experimental chemical shifts of TlBr as a function of temperature. Linear downfield shifts are observed in both the solid and molten states. But at the melting point, there is an *upfield* shift on passing from the crystalline state to the liquid state.

Hafner and Nachtrieb observed downfield shifts in both the solid and molten states, and a *downfield* shift at the melting point, just opposite in direction to the bromine case. The difference in sign of the chemical shift on fusion demonstrates that there are additional mechanisms present which contribute significantly to the chemical shift of TlBr on melting. Two important effects from the experimental results are to be discussed: (1) The temperature variation of the chemical shift, and (2) the change in the chemical shift at transition temperature of TlBr from solid state to molten phase.

Linear downfield shift in TlBr

It is tempting to explain the linear downfield shift in the solid and molten states of TlBr as temperature is increased by the same argument as that of the alkali halides. If this were so, then the formulas previously developed are similarly applicable to TlBr. The radius ratio for TlBr is 0·75, which according to Fig. 6 lies very close to RbBr, CsBr, and CsI. One would not expect the relative importance of NNN to NN interactions of TlBr to be very different from RbBr or CsBr. The measured values $(\mathrm{d}\delta/\mathrm{d}T)_{\mathrm{Tl}} = -0{\cdot}6\times10^{-6}$ (Hafner and Nachtrieb) and $(\mathrm{d}\delta/\mathrm{d}T)_{\mathrm{Br}} = -0{\cdot}98\times10^{-6}$ (present work) for the thallium and bromine nuclei, respectively. We expect the slope for the metal nucleus to be smaller than that of the halogen nucleus because NNN halide–halide contributes significantly at the halide site, while NNN alkali–alkali interactions contribute negligibly at the metal site. This expectation is indeed consistent with the measured slopes. However, we shall see immediately the K–Y overlapping-ion model is doubtful for the thallium halides which are of lower ionicity than the alkali halides. Hence, a covalent model would be more applicable to explain the experimental chemical shifts in thallium halides.

Saito has measured the room temperature chemical shifts of thallium halides and compared with the predicted values from the overlap model. The values expected from an overlap model are too small compared with the experimental value for the thallium nucleus, but large for the bromine nucleus. When K–Y's theory is applied to the ground state thallous ion, whose outermost orbitals contributing to a paramagnetic shift are the 5 *p* and 5 *d* orbitals, we find that their overlap integrals with the halogen ion are very small because in a thallous ion, all the occupied *p* and *d* orbitals in the ground state are core orbitals. On the other hand, the overlap of the outermost *p*-electron of a halogen ion with the 6 *s* orbital of its nearest thallous ion predicts a value for the halogen shift which is large compared with the experimental results. The experimental values for the shifts as measured by Saito are confirmed by Hafner and Nachtrieb's measurement for thallium-205 with $\delta = -11{\cdot}03\times10^{-4}$ which we obtained by extrapolating their values to room temperature and our present data for bromine-81 with $\delta = -5{\cdot}73\times10^{-4}$. We are thus led to conclude that an electron is partially transferred from the halogen ion to a nearest thallium ion to form a covalent bond. In a manner similar to Saito, we find the covalent character per ion for TlBr is 2·74 per cent to fit the thallium-205 chemical shift value. This degree of covalent character indicates that the bromine-81 shift would be $-5{\cdot}82\times10^{-4}$ (compared with the experimental value of $-5{\cdot}73\times10^{-4}$). Thus the model of partial covalent bonding between thallium and bromine ions with 2·74 per cent covalent character per ion can explain our present data with great success.

Due to the inadequacy of the K–Y overlap model in this case, the possibility that cause for the linear downfield shift of TlBr with increasing temperature is the thermal vibrational enhancement of overlap may be ruled out. However, we can still understand this temperature variation behavior in the covalent bonding model for TlBr. Consider the halogen atom is in a state of covalent bonding. Thermal vibration will induce a change in interionic distance and hence, alter the degree of covalency for each of the thallium neighbors of the halogen atom. This mechanism is the analogue of the thermal vibrational induced variation of the overlap integrals in the K–Y model. It also leads to the explanation of the observed downfield shift with temperature in TlBr. This mechanism can also cause an electric field gradient at the halogen nucleus that gives rise to quadrupolar relaxation as pointed out by Kanda. Quantitative analysis of the problem in this case will also involve the same problem of the lack of the correct method of thermal averaging and detailed knowledge of the lattice dynamics. Nevertheless, this should provide another testing ground for the covalent model theory if the variation of covalent character with interionic distance can be calculated.

Discontinuity at the melting point

The change in sign $\Delta\delta_T$ at the melting point of TlBr between thallium-205 and bromine-81 measurements can be explained qualitatively in the light of the covalent model of Y–M. Here we shall introduce the concept of NNN interactions. NNN effect is important in the covalent model because the degree of covalency in a molecule would be affected by the exponential tail of the wave functions of its second neighbors. An attempt is made in the following sections to use the Y–M covalent model with inclusion of NNN effects for the sign-reversal in TlBr.

TlBr has the CsCl structure in the solid state at room temperature. The exact structure of TlBr at the melting point is not known. Bernal[22] and Furukawa[23] have proposed that molten alkali halides have typical ionic liquid structure which is homogeneous and coherent in nature. Johnson, Agron and Bredig[24] from their molar volume studies of cesium halides at their melting points concluded that the coordination number decreases from eight to six on melting. Based on the above information it is reasonable to construct a model for TlBr which may undergo a structural change on fusion. Let us assume short range order exists such that in the molten state ions are regularly arranged and that we can place all the atoms into uniformly arrayed cubical cells. This simplified model of the molten TlBr has the rock salt structure. At the transition point, the radius r which is the NN distance in the melt is assumed to be the sum of the cationic and anionic radii for the molten TlBr. The shortening of the internuclear distance at melting for alkali halides has been observed (see for example, Levy and Danford[25]). Thus the assumption for $r_{\text{melt}} < r_{\text{solid}}$ is quite reasonable.

Y–M has assumed that the degree of covalency per ion pair to be proportional to the square of the overlap integral after charge transfer, and λ is proportional to the repulsive energy. In order to include the NNN effects, we can extend the overlap integrals to include second neighbors. The degree of covalency due to second neighbors can be approximated by the Born–Mayer theory. We can write down the total covalent character in a crystal as:

$$\lambda = \lambda_{\text{NN}} + \lambda_{\text{NNN}}. \qquad (12)$$

We have to note that λ_{NN} is the same for both metal and halide ions, while λ_{NNN} would be different between metal ions and halide ions because the metal–metal interaction is much smaller than the halogen–halogen interaction due to size differences. The Born repulsive energy due to NN and NNN contributions are formulated as:

$$E_B = C_{+-}AZ\,\mathrm{e}_{(r_+ + r_- - r)/\rho} + \tfrac{1}{2}C_{++}AZ'\,\mathrm{e}_{(2r_+ - kr)/\rho}$$
$$+\tfrac{1}{2}C_{--}AZ'\,\mathrm{e}^{(2r_- - kr)/\rho} \qquad (13)$$

where A is a universal constant; C_{++}, C_{+-}, C_{--} are Pauling overlap constants; Z is the number of NN; Z' is the number of NNN; r_+ and r_- are the basic radii; ρ is a repulsive parameter; and k is the distance ratio of NNN to NN. By introducing a parameter ξ such that $\xi = r_- - r_+$, we can express λ in view of the Born–Mayer theory in a more convenient form as:

$$\lambda = A'C_{+-}\,\mathrm{e}^{a(r_+ + r_- - r)}X \qquad (14)$$

where

$$X_M = 1 + \tfrac{1}{2}\frac{C_{++}}{C_{+-}}\left(\frac{Z'}{Z}\right)\mathrm{e}^{a(\xi-(k-1)r)}$$

$$X_H = 1 + \tfrac{1}{2}\frac{C_{--}}{C_{+-}}\left(\frac{Z'}{Z}\right)\mathrm{e}^{a(\xi-(k-1)r)} \qquad (15)$$

where the subscripts M and H are referred to as metal and halogen, respectively. At the melting point of TlBr, the change in chemical shift is:

$$\Delta\delta_T = \delta_{\mathrm{melt}} - \delta_{\mathrm{solid}} = \delta_m - \delta_s. \qquad (16)$$

Two cases have to be considered: (1) chemical shift of metal ion in both the solid and molten phases, and (2) chemical shift of halogen ion in the solid and molten phases. By assuming that $\Delta E'$, $\langle 1/r^3\rangle$, and $|a_p|^2$ in the Y–M equations to have the same values respectively in the solid state and in the melt, we obtain for the metal ion,

$$\Delta\delta_T = -\frac{8}{3}|a_p|^2\frac{1}{\Delta E'}\left\langle\frac{1}{r^3}\right\rangle[Z_m\lambda_m - Z_s\lambda_s]. \qquad (17)$$

By substituting the values tabulated in Table 3 into the above equation, we have for the metal ion case,

$$\Delta\delta_T = K_1[-0{\cdot}15 + 0{\cdot}169\,\mathrm{e}^{-0{\cdot}3\times 10^8\xi}]. \qquad (18)$$

By similar calculations for the halogen ion, we have

$$\Delta\delta_T = K_2[-0{\cdot}15 + 0{\cdot}101\,\mathrm{e}^{0{\cdot}3\times 10^8\xi}] \qquad (19)$$

Equations (18) and (19) describe the transition chemical shifts of thallium-205 and of bromine-81, respectively, in TlBr. The K_1 and K_2 are positive quantities such that

Table 3. Structural constants

Constants	Solid TlBr	Molten TlBr
C_{++}	1·25	1·25
C_{+-}	1·00	1·00
C_{--}	0·75	0·75
k	1·1547	1·4142
Z	8	6
Z'	6	12
r_T	3·536A	3·42A
a	$0{\cdot}3\times 10^8$ cm	$0{\cdot}3\times 10^8$ cm

$$K_1 = \frac{8}{3}|a_p|^2\frac{1}{\Delta E'}\mu_B{}^2\left\langle\frac{1}{r^3}\right\rangle\ A'C_{+-}\mathrm{e}^{a(r_+ + r_-)-10}$$

$$K_2 = \frac{8}{3}\frac{1}{\Delta E'}\mu_B{}^2\left\langle\frac{1}{r^3}\right\rangle_H A'C_{+-}\mathrm{e}^{a(r_+ + r_-)-10}.$$

The first term in equations (18) and (19) is obtained by considering contributions from NN, while the second term in both equations describes the NNN effect. The NN and NNN effects are opposite in sign. From the experimental results we see, that the downfield shift of thallium-205 at the melting point can be explained from equation (18) that NN interaction is more important than the NNN effect. In a similar manner, the upfield shift of bromine-81 at the melting point of TlBr can be explained from equation (19) that NNN effect is important.

It is now to be reemphasized about the importance of NNN interactions in the covalent model. Its significance can be recognized in view of the fact that the bromine ion is much larger than the thallium ion. And it is this NNN effect which contributes mainly to the sign flip at the melting point of TlBr. Based on the results from thallium-205 and bromine-81 experiments, more can be said about other thallium halides by considering the size factor and all other effects mentioned. Similar types of downfield shift may be predicted for $\mathrm{Tl^{205}Cl}$ and $\mathrm{Tl^{205}I}$. Less pronounced $\mathrm{TlCl^{35}}$ and more pronounced $\mathrm{TlI^{127}}$ upfield shifts at melting are predicted due to the different degrees of halogen-halogen interactions.

Acknowledgements – The author would like to thank Professors N. Nachtrieb, W Stout and O. Kleppa for their critical reading of the manuscript

This research was supported in part by the Air Force Office of Scientific Research and benefitted from the general support at the University of Chicago by the Advanced Research Projects Agency.

REFERENCES

1. GUTOWSKY H. and McGARVEY B., *J. chem. Phys.* **21**, 1423 (1953)
2. KANDA T., *J. phys. Soc. Japan* **10**, 85 (1955)
3. YOSIDA K. and MORIYA T., *J. phys. Soc. Japan* **13**, 1232 (1956).
4. ITOH J. and YAMAGATA Y., *J. phys. Soc. Japan* **14**, 225 (1959).
5. KONDO J and YAMASHITA J., *J. Phys. Chem Solids* **10**, 245 (1959)
6. LOWDIN P., *Adv. Phys.* **5**, 1 (1956).
7. DAS T. and KARPLUS M., *J. chem. Phys* **42**, 2885 (1965)
8. YAMAGATA Y., *J. phys. Soc. Japan* **19** 10 (1964).
9. BARON R., *J chem Phys.* **38**, 173 (1963).
10. HAFEMEISTER D and FLYGARE W., *J. chem Phys.* **44**, 3584 (1966).
11. ROWLAND T and BROMBERG J., *J. chem Phys.* **29**, 626 (1958).
12. HAFNER S. and NACHTRIEB N., *J. chem. Phys.* **40**, 2891 (1964).
13. SAITO Y., *J. phys. Soc. Japan* **21**, 1072 (1966).
14. HAFMEISTER D. and FLYGARE W., *J. chem. Phys.* **4** , 795 (1965).
15. BORN M. and HUANG K., *Dynamical Theory of Crystal Lattices*, p. 32. The International Series of Monographs on Physics, Oxford (1954).
16. WIKNER E., BLUMBERG W. and HAHN E., *Phys. Rev.* **118**, 631 (1960).
17. IKENBERRY D. and DAS T., *J. chem. Phys.* **43**, 2199 (1965).
18. WATKINS G. and POUND R., *Phys. Rev.* **89**, 658 (1953).
19. WATKINS G., *Thesis*. Harvard (1952).
20. LEIBFRIED G., *Handbuch der Physik* (Edited by S. Flugge), VII/1 Berlin (1955).
21. FLINN R., McMANNS G. and RAYNE J., *Phys. Rev.* **123**, 809 (1961).
22. BERNAL J., *Nature* **183**, 141 (1959).
23. FURUKAWA K., *Disc. Faraday Soc.* **32**, 53 (1961).
24. JOHNSON J., AGRON P. and BREDIG M., *J. Am. chem. Soc.* **77**, 2734 (1955).
25. LEVY H. and DANFORD M., *Molten Salt Chemistry* (Edited by Blander), p. 120. Interscience, New York (1964)
26. BLACKMAN M., *Handbuch der Physik* (Edited by S. Flugge), VII/1. Berlin (1955).
27. TOSI M., *Solid State Physics*, Vol. 16, p 44. Academic Press, New York (1964).

J. Phys. Chem. Solids Pergamon Press 1969. Vol. 30, pp. 585–588. Printed in Great Britain.

THE PREPARATION AND SEMICONDUCTING PROPERTIES OF HEXAGONAL $Zn_{3-x}Mn_xAs_2$

G. A. CASTELLION, L. A. SIEGEL and H. BURKHARD
Central Research Division, American Cyanamid Company, Stamford, Conn. 06904, U.S.A

(*Received* 13 *June* 1968)

Abstract—A new semiconducting compound, $Zn_{3-x}Mn_xAs_2$ $(2{\cdot}1 \leq x \leq 2{\cdot}5)$, has been prepared. X-ray analysis indicates that the compound has a hexagonal unit cell and contains one formula unit per unit cell. The following properties of the compound have been studied as a function of temperature: electrical resistivity, Hall coefficient and Seebeck coefficient. The width of the forbidden energy gap has been estimated by an optical method to be 0·8 eV. The values determined for the semiconducting properties of $Zn_{3-x}Mn_xAs_2$ in the range $2{\cdot}1 \leq x \leq 2{\cdot}5$ are consistent with those expected for a *p*-type semiconductor with the majority carriers moving in a broad band.

INTRODUCTION

THERE ARE few semiconducting arsenides where the number of cations per formula unit is greater than the number of arsenic atoms[1]. We report here the preparation and some of the properties of a new semiconducting compound, $Zn_{3-x}Mn_xAs_2$, where x is between 2·1 and 2·5. In this range, X-ray analysis indicates that the compound has a hexagonal unit cell, in contrast to the tetragonal cells of Zn_3As_2 and Mn_3As_2[2].

PREPARATION

The specimens studied were prepared by melting finely divided zinc, manganese, and arsenic in stoichiometric amounts, in heavy-walled cylindrical quartz crucibles. The elements were used as received from the supplier (United Mineral and Chemical Corporation), who gave the following values for purity: Zn (99·9998%), Mn (99·99%), and As (99·9995%). The inside surface of the crucible was abraded by aluminum oxide particles and then given a coating of carbon by pyrolysis of acetone. After loading the elements into the crucible, it was evacuated to a pressure of less than 1×10^{-3} Torr. and enough argon was condensed into the crucible to give, at 1000°C, a pressure of 20 atm over the melt. The crucible was sealed, placed in a vertical position, and heated until its contents were completely molten. The crucible was then lowered slowly through a steep temperature gradient and cooled to room temperature. By following this procedure, the occurrence of explosions was minimized and polycrystalline ingots free from voids could be prepared.

PROPERTIES

Ingots were made with values of x of 0·1, 0·35, 0·75, 1·0, 1·5, 2·1, 2·2 and 2·5. X-ray power-diffraction patterns were obtained for specimens of these ingots. For compositions with values of x in the range $2{\cdot}1 \leq x \leq 2{\cdot}5$, the powder patterns showed that a single phase existed with lattice parameters varying with x. For compositions with values of x in the range $0{\cdot}1 \leq x \leq 1{\cdot}5$, two or more phases were found. At $x = 1{\cdot}5$, the powder pattern of the major phase was similar to that for the single phase found in the range $2{\cdot}1 \leq x \leq 2{\cdot}5$. For the other multiphase compositions, the pattern of the major phase is similar to that of Zn_3As_2.

The lines for compositions in the range $2{\cdot}1 \leq x \leq 2{\cdot}5$ could be graphically indexed, via a Bunn chart, to fit a hexagonal cell. This was confirmed by rotation and Weissenberg patterns obtained using thin cleavage flakes. The symmetry of the Weissenberg patterns indicated also that the hexagonal unit cell belongs to the trigonal system. From the single crystal measurements, it was found that for $x = 2{\cdot}5$, $a = 4{\cdot}112$ Å and $c = 6{\cdot}54$ Å, while for $x = 2{\cdot}1$, $a = 4{\cdot}104$ Å and $c = 6{\cdot}56$ Å. The density of the $x = 2{\cdot}1$ sample is approximately 5·6 g/cm³ indicating that there is one formula unit of $Zn_{3-x}Mn_xAs_2$ per unit cell.

The quality of the single crystal patterns was poor, primarily because of fragmentation around the edges of the cleavage flakes, and the precision of the c values quoted above is accordingly low. The powder patterns were also not suitable for precise lattice parameter evaluation, since even light grinding introduced enough distortion to cause marked broadening of the back-reflection lines.

The same ingots in the range $2{\cdot}1 \leq x \leq 2{\cdot}5$ that had been analyzed by X-ray techniques were also analyzed chemically by atomic absorption spectroscopy. The results of the chemical analysis were within 1·0 at. % of the values calculated from the stoichiometric formula.

The melting point of $Zn_{0{\cdot}9}Mn_{2{\cdot}1}As_2$ was 924°C and that of $Zn_{0{\cdot}5}Mn_{2{\cdot}5}As_2$ was 916°C. A powdered sample of $Zn_{0{\cdot}5}Mn_{2{\cdot}5}As_2$ was analyzed by a differential thermal analysis procedure described previously[3]. On heating the sample above room temperature, the only transition observed was a sharp one at the melting point.

The electrical resistivity (ρ) and Hall coefficient (R_H) were determined on lamellar specimens of $Zn_{0{\cdot}5}Mn_{2{\cdot}5}As_2$, $Zn_{0{\cdot}8}Mn_{2{\cdot}2}As_2$, and $Zn_{0{\cdot}9}Mn_{2{\cdot}1}As_2$ cut from the polycrystalline ingots. In these determinations of ρ and R_H, the van der Pauw method[4] and the potential comparator circuit of Dauphinee and Mooser[5] were used. The Hall coefficient was measured at 2·75 kG and 5·50 kG and, at a given temperature, was identical for both fields. The temperature dependence of ρ and R_H for specimens of $Zn_{3-x}Mn_xAs_2$ is shown in Figs. 1(A) and 1(B). The Hall mobility (μ_H) can be defined by the equation, $\mu_H = R_H/\rho$. In Fig. 2 the Hall mobility, calculated using this equation and data from

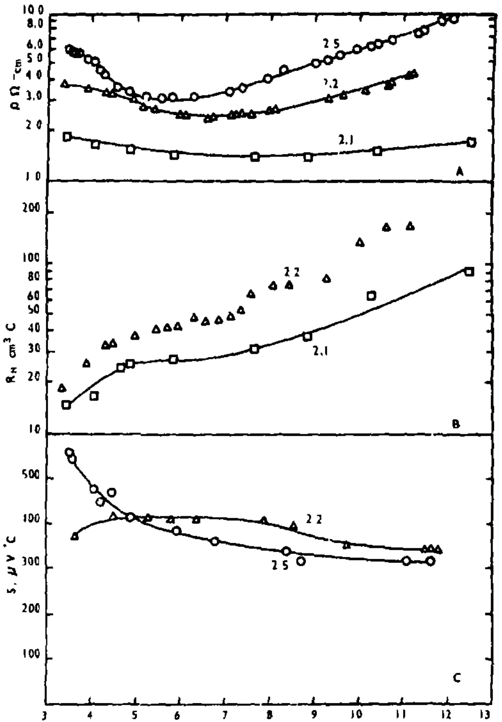

Fig. 1. (A) Electrical resistivity vs. $1/T$. (B) Hall coefficient vs. $1/T$. (C) Seebeck coefficient vs. $1/T$. The numbers correspond to the values for x in $Zn_{3-x}Mn_xAs_2$.

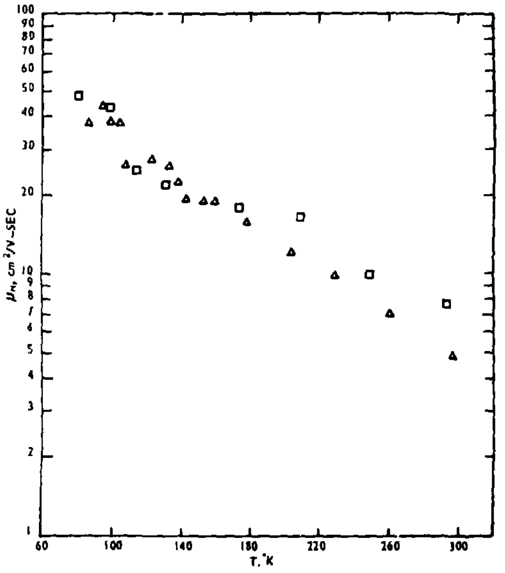

Fig. 2. Hall mobility vs. T for $Zn_{0{\cdot}9}Mn_{2{\cdot}1}As_2$ (□) and $Zn_{0{\cdot}8}Mn_{2{\cdot}2}As_2$ (△).

Figs. 1(A) and 1(B), is plotted as a function of temperature.

The variation of Seebeck coefficient (S) with temperature for $Zn_{0\cdot8}Mn_{2\cdot2}As_2$ and $Zn_{0\cdot5}Mn_{2\cdot5}As_2$ is shown in Fig. 1(C). A standard experimental arrangement[6] and bar-shaped specimens cut from the same ingots as the lamellar specimens were used. Electrical resistivities measured at the same time on the bar-shaped specimens agreed with the ρ vs. $1/T$ curves shown in Fig. 1(A). The Seebeck coefficient of $Zn_{0\cdot9}Mn_{2\cdot1}As_2$ was determined only at room temperature and was $+475\ \mu V/°C$.

It was found that a temperature of 360°K could not be exceeded during the measurement of ρ, R_H, and S without irreversible changes in these properties taking place. These changes occurred in air, in an atmosphere of nitrogen, or in vacuum. Similar irreversible changes are found to occur at these temperatures in other arsenides in which the number of cations is greater than the number of anions[3]. Heating the $Zn_{3-x}Mn_xAs_2$ specimens above 360°K appears to increase the number of acceptor levels.

Optical energy gaps were obtained for $Zn_{0\cdot5}Mn_{2\cdot5}As_2$ and $Zn_{0\cdot8}Mn_{2\cdot2}As_2$ by transmission measurements using a Cary 14 spectrophotometer. From a plot of log absorbance vs. wavelength, we estimate the width of the forbidden energy gap for $Zn_{0\cdot5}Mn_{2\cdot5}As_2$ to be 0·76 eV and that for $Zn_{0\cdot8}Mn_{2\cdot2}As_2$ to be 0·75 eV.

DISCUSSION

X-ray and chemical analyses of ingots of $Zn_{3-x}Mn_xAs_2$ show the existence of a new arsenide having a hexagonal unit cell (trigonal system) and containing one formula unit per unit cell. This structure exists in the range $2\cdot1 \leq x \leq 2\cdot5$, and its symmetry contrasts with the tetragonal cells of Zn_3As_2 and Mn_3As_2.

No attempt was made to determine the crystal structure of this material. Presumably, the structure would involve some disorder between zinc and manganese and would be consistent with the pronounced cleavage perpendicular to the c-axis.

The multiphase character we found for ingots in the composition range $0\cdot1 \leq x \leq 1\cdot5$ is in disagreement with the results of Kasaya, Komatsubara and Hirahara[7] who studied the magnetoresistance of $Zn_{3-x}Mn_xAs_2$ compositions in the range $0\cdot5 \leq x \leq 2\cdot0$. They state that compound formation according to the expected formula takes place in this range and that these compounds have essentially the same crystal structure as Zn_3As_2. No details are given in their paper as to how the structure was determined or how the compounds were prepared, and we have no explanation for the difference between our results and theirs on the structure of $Zn_{3-x}Mn_xAs_2$ compositions in this range.

Inspection of the plots of ρ, S, R_H, and μ_H vs. temperature (Figs. 1(A–C) and Fig. 2) indicates that in the range of compositions studied $Zn_{3-x}Mn_xAs_2$ behaves like a p-type semiconductor. At low temperatures the ρ vs. $1/T$ plot shows an impurity-dominated region with an approach to a linear asymptote. At higher temperatures a transition temperature range is seen in which the temperature coefficient of ρ changes sign because of the filling of the acceptor levels to saturation and the dependence of the hole mobility upon temperature.

The irreversible changes in the transport properties when the specimens are heated above 360°K confine our measurements to the impurity-dominated and transition temperature ranges. It is, therefore, not possible to extend the ρ or the R_H measurements to higher temperatures so as to obtain an estimate of the width of the forbidden energy gap for comparison with the value of $\sim 0\cdot8$ eV obtained from optical measurements.

Plots of the log of the carrier concentration (p) vs. $1/T$ in the impurity-dominated temperature range were made for $Zn_{0\cdot9}Mn_{2\cdot1}As_2$ and $Zn_{0\cdot8}Mn_{2\cdot2}As_2$ using the data given in Fig. 1(B) and the equation, $p = 1/R_H e$ where e is the electronic charge. From the slope of these plots, activation energies of 0·04 and 0·06 eV are calculated for the acceptors in $Zn_{0\cdot 9}Mn_{2\cdot 1}As_2$ and $Zn_{0\cdot 8}Mn_{2\cdot 2}As_2$ respectively. In the transition temperature range, the acceptor levels are filled to saturation at a concentration of 3×10^{17} carriers/cc for $Zn_{0\cdot 9}Mn_{2\cdot 1}As_2$ and 2×10^{17} carriers/cc for $Zn_{0\cdot 8}Mn_{2\cdot 2}As_2$.

A density of states effective mass (m^*) for the holes in $Zn_{0\cdot 8}Mn_{2\cdot 2}As_2$ was calculated from measurements of the Seebeck coefficient combined with those of the Hall coefficient. First the position of the reduced Fermi level (η) was calculated using the relationship:

$$S = \frac{k}{e}\left[\left(\frac{5}{2}+\lambda\right)-\eta\right] \qquad (1)$$

where k is Boltzman's constant and λ is the exponent of the kinetic energy (ϵ) of the carriers in the scattering law: relaxation time $\propto \epsilon^{\lambda}$. In view of the experimentally observed dependence of mobility with temperature for $Zn_{0\cdot 8}Mn_{2\cdot 2}As_2$ ($\mu \propto T^{-1\cdot 8}$), a value of λ of $-\frac{1}{2}$ which corresponds to acoustic-mode scattering of the carriers ($\mu \propto T^{-1\cdot 5}$) was assumed in making the calculation.

We can now estimate the effective mass using the carrier concentration as determined from the Hall coefficient and the relationship:

$$p = 2\left(\frac{2\pi m^* kT}{h^2}\right)^{3/2} \exp \eta \qquad (2)$$

where h is Planck's constant. The hole effective mass estimated in this manner for $Zn_{0\cdot 8}Mn_{2\cdot 2}As_2$ at 143°K is $0\cdot 4\, m_0$. The value obtained for the m* of the carriers in $Zn_{0\cdot 8}Mn_{2\cdot 2}As_2$ is comparable to those reported for the positive holes in other ternary semiconducting arsenides[1]. The mobilities measured are low for a semiconductor with this small and effective mass. It seems probable, therefore, that much higher mobilities will be observed in single crystal specimens of this arsenide.

The values determined for the semiconducting properties of $Zn_{3-x}Mn_xAs_2$ in the range $2\cdot 1 \leq x \leq 2\cdot 5$ are consistent with those expected for a p-type extrinsic semiconductor with holes moving in a fairly broad band. Measurement of the magnetic properties as a function of temperature and composition, coupled with a complete determination of the crystal structure, should permit some conclusions to be drawn as to the nature of the bonding between the various atoms in the compound and their valence.

REFERENCES

1. RODOT M., *Les Materiaux Semi-conducteurs*, Tableau VIII, p. 258. Dunod, Paris (1965).
2. ELLIOTT R. P., *Constitution of Binary Alloys, First Supplement*. McGraw-Hill, New York (1965).
3. CASTELLION G. A. and BEEGLE L. C., *J. Phys. Chem. Solids* **26**, 727 (1965).
4. VAN DER PAUW L. J., *Philips Res. Rep.* **13**, 1 (1958).
5. DAUPHINEE T. M. and MOOSER E., *Rev. scient. Instrum.* **26**, 660 (1955).
6. GOLDSMID H. J., *Thermoelectric Refrigeration*, Fig. 6-1(b), p. 134. Plenum Press, New York (1964).
7. KASAYA M., KOMATSUBARA T. and HIRAHARA E., *J. phys. Soc. Japan* **18**, 1221 (1963).

J. Phys. Chem. Solids Pergamon Press 1969. Vol. 30, pp. 589–600. Printed in Great Britain.

THE PRESSURE DERIVATIVES OF THE ELASTIC CONSTANTS OF LEAD

R. A. MILLER
Corning Glass Works, Corning, N.Y. 14830, U.S.A.

and

D. E. SCHUELE
Case Western Reserve University, Cleveland, Ohio, U.S.A.

(*Received* 10 *June* 1968)

Abstract—The pressure derivatives of the adiabatic elastic constants of lead have been measured at 296° and 195°K using an ultrasonic pulse-echo technique. The values found are:

	$\frac{dC'_{11}}{dP}$	$\frac{dC'}{dP}$	$\frac{dC_{44}}{dP}$
296°K	7·69	0·301	2·06
195°K	7·51	0·280	1·97

where the notation $C'_{11} = (C_{11}+C_{12}+2C_{44})/2$ and $C' = (C_{11}-C_{12})/2$ has been used. The low temperature limiting value of the Grüneisen parameter has been calculated and is compared with the value obtained from thermodynamic data. The ultrasonic equation of state is discussed.

INTRODUCTION

THE PURPOSE of this paper is to present the measurements of the pressure derivatives of the adiabatic elastic constants of lead and to compare the thermodynamic Grüneisen parameter with the Grüneisen parameter calculated from the pressure data. The main contribution to the pressure variation of the elastic constants is an anharmonic property of the lattice and lead is an interesting material from this standpoint since it has a relatively low Debye temperature. Also at low temperatures lead becomes superconducting and the measurements by White[13] of the thermal expansion coefficient lead to different values of the Grüneisen parameter in the normal and superconducting states.

SAMPLE PREPARATION

The crystal used in this study was one of a series grown by a modification of the Bridgman technique. They were grown under vacuum in 5/8" dia. pyrex brand test tubes which had been internally coated with aqua dag or india ink. A tight fitting graphite insert in which a nucleating tip had been machined was placed in the bottom of each test tube. These crucibles were loaded with 99·98 per cent pure lead, heated to 400°C, and then cooled at about 15 C°/hr until the samples had solidified. A gradient of 3·5 C°/in maintained along the length of the crucible during the cooling was sufficient to produce single crystals in better than 75 per cent of the attempts made.

To determine whether a boule was single, it was etched in a solution of about two parts glacial acetic acid and one part 30 per cent hydrogen peroxide which brought out blaze planes and any grain boundries present. If a boule appeared single, its two ends were removed with a fine toothed jewlers saw, the resulting specimen waxed into a lapping block, and the ends lapped flat and parallel on an etchant soaked cloth stretched across a glass plate. Then a number of back reflection Laue X-rays were taken across each of the two end faces. The orientations of the crystals shown to be single by this process were random, but the one chosen for use in this investigation grew with a [110] direction only 8° away from the axis of the boule.

Final preparation consisted of cutting an 8° wedge from this specimen with a string saw charged with a 50–50 mixture of hydrogen peroxide and acetic acid and again lapping the two ends flat and parallel. The resulting specimen was in the shape of a slightly oblique circular cylinder about 1·5 cm in dia. and 1·2379 cm long at 23°C. The acoustic surfaces were parallel to better than one part in 5000 and oriented to better than 1 deg of the desired [110] direction.

MEASUREMENTS

The ultrasonic pulse-echo system used to determine the zero pressure transit times of 10 Mc/s acoustic pulses has been described in previous papers from this laboratory [1, 2]. The room temperature transit times were found by the usual echo to echo time measurements and these results were spot checked by buffer measurements. The 195°K (Freon 11 and dry ice temperature bath) transit times were also determined by echo to echo time measurements, spot checked by buffer measurements, and were further checked by determining the difference in transit times between room temperature and 195°K while following a given cycle during the cooling process. In all cases the material used for the crystal-transducer seal or buffer-transducer and buffer-crystal seal was Nonaq stopcock grease.

The pressure system was originally developed by Daniels [3] and modified by Bartels and Schuele [4] in order to reach pressure at 195°K. The pressure fluid used throughout was a 50–50 mixture of normal pentane and isopentane. The general method used in measuring the hydrostatic pressure derivatives of the elastic constants has also been described in previous papers from this laboratory [2, 5]. Basically, at room temperature, an echo was displayed on an oscilloscope at an arrival time t_n and the data recorded was the change in the arrival time, Δt_n, of this echo and the corresponding change of resistance, ΔR_g, of a manganin coil pressure gage as the pressure was changed. Then without changing anything in the transducer-specimen system, the pressure vessel which contained the sample was placed in the temperature bath of Freon 11 and dry ice; and when the system had come to thermal equilibrium, the procedure was repeated. A typical data plot is shown in Fig. 1. The pressure range over which the measurements were made was about 3500 bars.

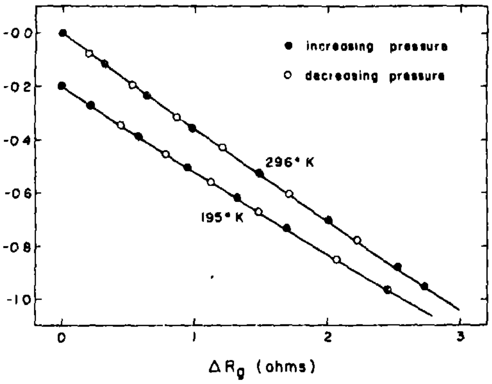

Fig. 1. Typical data plot showing the change in arrival time, Δt_n, of the 4th echo for the C'_{11} longitudinal wave in *Pb* vs. the change in resistance of the pressure gage coil, ΔR_g. Zero pressure transit times for this wave are 10·679 μsec and 10·416 μsec at 296° and 195°K. The pressure gage constant is 1·408 Kbar/Ω. The curves for the two temperatures are displaced for the sake of clarity.

RESULTS

The basic data used in the reduction of the experimental data are given in Table 1. The isothermal bulk modulus, B_T, was found from the measured adiabatic bulk modulus, B_s, and the relation

$$\frac{B_s}{B_T} = 1 + \frac{9\alpha^2 TVB_s}{C_p} \qquad (1)$$

where α is the linear coefficient of thermal expansion, T is the absolute temperature, V

Table 1. *Basic data for* Pb *used in this work. In computing the density an Avogadro's number of* $6{\cdot}02305 \times 10^{23}$ *has been used*

Data	296°K	195°K
Crystal length (cm)	1·2379	1·2343
Lattice constant$^{(a)}$ (Å)	4·9504	4·9361
Molecular weight (g mole^{-1})	207·21	207·21
X-ray density, ρ, (g cm^{-3})	11·344	11·442
Linear coefficient of thermal expansion$^{(b)}$ (10^{-6}deg^{-1})	29·1	27·6
$(\partial\alpha/\partial T)_p{}^{(b)}$ (10^{-8}deg^{-2})	~1	~2
Specific heat, $C_p{}^{(c)}$, (Cal mole^{-1}deg^{-1})	6·410	6·171
$(\partial C_p/\partial T)_p{}^{(c)}$ (10^{-3} Cal mole^{-1}deg^{-2})	2·0	2·4
Isothermal bulk modulus, B_T, (10^{11}dyn cm^{-2})	4·189	4·436

(a) *American Institute of Physics Handbook*, p. 9–7. (McGraw-Hill New York 1963).

(b) NIX F. C. and MACNAIR D., *Phys. Rev.* **61**, 74 (1941).

(c) MEADS P. F., FORSYTHE W. R. and GIAUQUE W. F., *J. Am. chem. Soc.* **63**, 1902 (1941).

is the molar volume, and C_p is the molar heat capacity.

For a cubic crystal with a [110] orientation, three independent acoustic waves can be excited. There is one longitudinal wave governed by the stiffness $C'_{11} = (C_{11}+C_{12}+2C_{44})/2$ and two transverse waves governed y the stiffnesses $C' \doteq (C_{11}-C_{12})/2$ and C_{11}. xperimental quantities are related to these nesses by

$$C_i = \rho v_i{}^2 = \rho \frac{4L^2}{t_i{}^2} \tag{2}$$

where ρ is the density of the crystal and $v_i (= 2L/t_i)$ is the velocity of a particular acoustic wave pulse traveling twice the length, L, of the crystal in the time t_i. The results of the zero pressure elastic constant measurements and the calculated adiabatic bulk modulus, $B_s = (C_{11}+2C_{12})/3$, at 296° and 195°K can be found in Table 2. These values have been corrected for the misorientation of the acoustic wave direction from [110] according to the procedure of Neighbours[6]; but for the worse case, the C' wave, the correction amounted to only 0·1 per cent for the less than one degree misorientation of the crystal. Waldorf and Alers[7] have previously determined the elastic constants of lead from 4·2° to 300°K using an ultrasonic pulse echo method. Our results differ from the interpolated values of Waldorf and Alers by 0·3 per cent or less except for the 296°K value of C' where the difference is about 1 per cent. We feel that the precision of our measurements is on the order of 0·5 per cent.

Table 2. *Adiabatic elastic stiffnesses of* Pb *in units of* 10^{11} *dyn cm*$^{-2}$

Temperature	C'_{11}	C	C'	B_s
296°K	6·096	1·4977	0·3676	4·476
195°K	6·426	1·6588	0·4165	4·629

For convenience we have included at this point in Table 3 the computed isothermal elastic stiffnesses and the adiabatic and isothermal compliances of Pb at 296° and 195°K. These constants have been obtained from the measured adiabatic stiffnesses using the usual elastic and thermodynamic relations. The auxiliary thermodynamic information which is necessary for such calculations is given in Table 1.

The expression relating pressure data such as shown in Fig. 1 to the change with pressure of the elastic constants is

$$\frac{\mathrm{d}\ln C}{\mathrm{d}P} = \frac{1}{3B_T} - 2\frac{\mathrm{d}\ln t}{\mathrm{d}P} \tag{3}$$

Table 3. Adiabatic and isothermal elastic stiffnesses, C, *and adiabatic and isothermal elastic compliances,* S, *for* Pb. *Units are* 10^{11} *dyn* cm^{-2} *for* C *and* 10^{-11} cm^2 dyn^{-1} *for* S

	C_{11}	C_{12}	C_{44}	S_{11}	S_{12}	S_{44}
296°K						
adiabatic	4·966	4·231	1·4977	0·9316	−0·4286	0·6677
isothermal	4·679	3·944	1·4977	0·9333	−0·4269	0·6677
195°K						
adiabatic	5·184	4·351	1·6588	0·8243	−0·3762	0·6028
isothermal	4·991	4·158	1·6588	0·8254	−0·3751	0·6028

which comes from taking the logarithmic derivative of equation (2) with respect to pressure. The $1/3B_T$ term is the correction for the change in the length and density of the crystal with pressure. The $\mathrm{d}\ln t/\mathrm{d}P$ term, the fractional rate of change of transit time with pressure, is derived from the slope of a Δt_n vs. ΔR_g plot such as Fig. 1. Changes in resistances are converted to changes in pressure by means of the pressure gage constant, k; i.e. $\mathrm{d}P = k\mathrm{d}R_g$. The resulting $\mathrm{d}t_n/\mathrm{d}P$ is divided by the zero pressure transit time for the echo under consideration to yield the desired $\mathrm{d}\ln t/\mathrm{d}P$. The desired pressure derivative is that measured at zero pressure. If the Δt_n vs. ΔR_g plot is linear, one simply takes the slope of the line; but if curvature is present in the data, the procedure is to either linearize the data or somehow extract what is equivalent to the initial or zero pressure value[4, 8]. Some non-linearity was present in the lead pressure data. Careful examination shows, however, that to the precision of the data, the non-linearity doesn't become apparent until the pressure exceeds about 1800 bars. We have, therefore, chosen to deal with the situation by restricting the pressure to this range where the data is essentially linear and to use the least squares slope of the restricted pressure range data. The justification and results of such a procedure can be seen in Fig. 2. Here the Δt_n vs. ΔR_g data for the 4th and 8th echo of the C'_{11} wave at 296°K are shown along with the least squares line derived from the data restricted to 1800 bars. It can be seen that the data taken at low pressures fits the least squares line quite well, but that taken at higher pressures fall systematically above the least squares line. In all cases the slopes of the least squares line

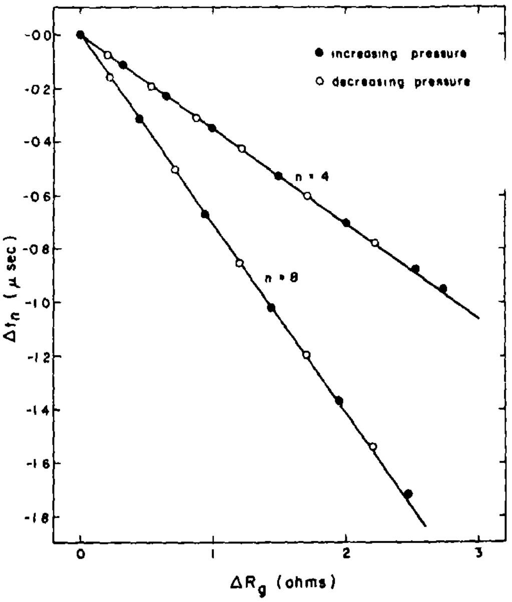

Fig. 2. The change in arrival time, Δt_n, of the 4th and 8th echo for the C'_{11} longitudinal wave in the 1·2379 cm Pb crystal vs. the changes in resistance of the pressure gage coil, ΔR_g, at 296°K. Pressure gage constant is 1·408 Kbars/Ω. The straight lines shown are the least squares fit to the data restricted to a pressure range of 1800 bars.

for data taken over the full pressure range were 1 to 2 per cent less in absolute magnitude than those for the restricted pressure range data. Slopes found by restricting the data to even smaller pressure ranges, however, were not significantly different than those found from the zero to 1800 bar data.

The results of the pressure measurements expressed in several forms are given in Table 4. The first column of numbers, the d ln $t/\mathrm{d}P$'s, have been arrived at in the manner described above, while d ln $C/\mathrm{d}P$ is calculated from d ln $t/\mathrm{d}P$ using equation (3). The third column results from the relation d ln $C/\mathrm{d}\ln r = -3B_T \,\mathrm{dln}\, C/\mathrm{d}P$, and the fourth column from $\mathrm{d}C/\mathrm{d}P = C\,\mathrm{dln}\,C/\mathrm{d}P$. No orientation corrections have been applied to the pressure data. From measurement considerations and repeatability experiments we feel that a precision in the sense of a standard deviation of about $\pm 0{\cdot}1 \times 10^{-12}$ is set on the values of dln $t/\mathrm{d}P$.

Table 4. Results of the pressure measurements for Pb *expressed in several forms. Here* t *is the acoustic wave transit time in the crystal and* r *is a crystal distance. Units of* dln t/dP *and* dln C/dP *are* 10^{-12} *cm²dyn⁻¹*

	(°K)	dln t/dP	dln C/dP	dln $C/\mathrm{dln}r$	$\mathrm{d}C/dP$
C'_{11}	296	-5·91	12·62	-15·86	7·69
	195	-5·47	11·69	-15·56	7·51
C'	296	-3·70	8·20	-10·30	0·301
	195	-2·98	6·71	-8·93	0·280
C_{44}	296	-6·47	13·73	-17·25	2·06
	195	-5·57	11·88	-15·81	1·97
B_s	296		12·36	-15·53	5·53
	195		11·77	-15·66	5·45
C_{11}	296		11·96	-15·03	5·94
	195		11·23	-14·94	5·82
C_{12}	296		12·60	-15·83	5·33
	195		12·09	-16·09	5·26

Examination of Table 4 reveals that $\mathrm{d}C/\mathrm{d}P$ decreases in going to lower temperature for all the constants, but the magnitudes of the decreases are small. The largest percentage change is for the C' wave which changes by seven percent in going from 296° to 195°K. It is in just this case, however, that even a small absolute change will lead to a rather large percentage change because of the small values of the quantities involved.

The largest changes in going from 296° to 195°K are for the quantities d ln $C/\mathrm{d}P$ and for these the changes are largest for the two shear constants, C' and C_{44}, which change by 18·2 and 13·4 percent respectively in this 101°K temperature interval. Bartels and Schuele[4] have also found that the quantity dln $C/\mathrm{d}P$ shows the greatest temperature dependence for the alkali halides NaCl and KCl. They have pointed out that since the temperature dependence of $\mathrm{d}C/\mathrm{d}P$ is small, the temperature dependence of dln $C/\mathrm{d}P$ must come chiefly from the temperature dependence of the elastic constants themselves.

The temperature dependence of the quantity dln $C/\mathrm{dln}r$ is mixed. For the two shear constants the change with temperature of this quantity is greater than for $\mathrm{d}C/\mathrm{d}P$ but less than for dln $C/\mathrm{d}P$. For the other constants listed in Table 4, however, the percentage change with temperature in dln $C/\mathrm{dln}r$ is even smaller than for $\mathrm{d}C/\mathrm{d}P$ and for the constants B_s and C_{12} is reversed in sign. This arises from the fact that the temperature dependence of $\mathrm{d}\ln C/\mathrm{d}\ln r$ is determined mainly by the temperature dependence of the ratio B_T/C.

The observed temperature coefficient at constant pressure is related to the pressure variations of the elastic constants by the thermodynamic relation

$$\left.\frac{\mathrm{d}\ln C}{\mathrm{d}T}\right)_P = \left.\frac{\mathrm{d}\ln C}{\mathrm{d}T}\right)_V + \alpha \left.\frac{\mathrm{d}\ln C}{\mathrm{d}\ln r}\right)_T \qquad (4)$$

where α is the coefficient of linear expansion and $(\mathrm{d}\ln C/\mathrm{d}\ln r)_T$ is given in Table 4. The constant volume temperature coefficient which exhibits all the explicit temperature dependence of $(\mathrm{d}\ln C/\mathrm{d}T)_P$ is of theoretical interest and can be evaluated from the above equation.

The individual terms in equation (1) are listed in Table 5 where $(\mathrm{d}\ln C/\mathrm{d}T)_P$ was obtained from the differences in the elastic constants at 296° and 195°K as given in Table 2. Since the change of the constants with temperature is linear in this temperature range[7], $(\mathrm{d}\ln C/\mathrm{d}T)_P$ differs at the two temperatures only because of the change in the elastic constants themselves. The dilatation term $(\mathrm{d}\ln C/\mathrm{d}\ln r)_T$ which is an implicit function of temperature through the temperature dependence of the volume has previously been discussed in connection with the results of Table 4.

The constant volume temperature coefficient $(\mathrm{d}\ln C/\mathrm{d}T)_V$ is negative for the shear constants and positive for the adiabatic bulk modulus, and in all cases is smaller in magnitude than $(\mathrm{d}\ln C/\mathrm{d}T)_P$. In these respects the results for Pb are similar to the metals Cu, Ag and Au[19] and to the alkali halides LiF and NaF [8] and NaCl[4]. It is interesting to note that the predominate contribution to the observed C' temperature coefficient at constant pressure arises from the constant volume temperature coefficient. Here the dilatation term is small because of the small effect of pressure on this constant.

Table 5. Constitution of the temperature coefficients of the elastic constants of Pb. *Units are* 10^{-4} *deg*$^{-1}$

		$(\mathrm{d}\ln C/\mathrm{d}T)_P$	$= (\mathrm{d}\ln C/\mathrm{d}T)_V$	$+\ \alpha(\mathrm{d}\ln C/\mathrm{d}\ln r)_T$
C	296°K	−10·6	−5·6	−5·0
	195°K	−9·6	−5·2	−4·4
C'	296°K	−13·2	−10·2	−3·0
	195°K	−11·6	−9·1	−2·5
B_s	296°K	−3·4	+1·1	−4·5
	195°K	−3·3	+1·0	−4·3

Table 6 lists the pressure derivatives of the adiabatic and isothermal elastic constants for lead at 296° and 195°K. The pressure derivative of the isothermal bulk modulus was obtained from the experimental $(\mathrm{d}B_s/\mathrm{d}P)_T$ according to the method given by Rotter and Smith[10]. Other thermodynamic quantities needed in this calculation are given in Table 1 and Table 5. The adiabatic shear constants C_{44} and C' for cubic materials are identical to the corresponding isothermal shear constants at any given temperature; and, as pointed out by Bartels and Schuele[4], these three quantities are sufficient to determine the complete set of isothermal $\mathrm{d}C/\mathrm{d}P$'s. In general the differences between the pressure derivatives of the adiabatic and isothermal constants for lead are small with the isothermal values being equal to or slightly greater than the corresponding adiabatic values.

Table 6. The pressure derivatives of the adiabatic and isothermal elastic constants of Pb

	$\mathrm{d}B/\mathrm{d}P$	$\mathrm{d}C_{11}/\mathrm{d}P$	$\mathrm{d}C_{12}/\mathrm{d}P$	$\mathrm{d}C_{44}/\mathrm{d}P$
296°K				
adiabatic	5·53	5·94	5·33	2·06
isothermal	5·72	6·12	5·52	2·06
195°K				
adiabatic	5·45	5·82	5·26	1·97
isothermal	5·61	5·98	5·42	1·97

GRÜNEISEN PARAMETERS

Introduction

The first approximation to anharmonic contributions to the lattice vibrations is usually carried out within the framework of the quasi harmonic model[11]. In this model one assumes the adiabatic approximation and expands the crystal potential in terms of the displacements of the ion cores from equilibrium keeping terms to second order in these displacements. This results in the thermal vibrations consisting of a set of harmonic oscillators whose frequencies, ω_i, are volume dependent only.

The free energy, F, of the crystal consists of four contributions: the static potential energy and the zero point energy which are volume dependent only and the vibrational energy and the conduction electron energy which are functions of both the volume and the temperature. The constant volume temperature derivative of the free energy is the negative of the entropy. One obtains the following thermodynamic relation by assuming that the entropy of the lattice vibrations and conduction electrons are additive,

$$-\frac{\partial^2 F}{\partial V \partial T} = \beta B_T = \left(\frac{\partial S_e}{\partial V}\right)_T + \left(\frac{\partial S_l}{\partial V}\right)_T$$

where S_e and S_l are respectively the electronic and vibrational contributions to the entropy and β is the volume coefficient of thermal expansion. Division of the above expression by the constant volume heat capacity per unit volume, C_V/V, yields the thermodynamic Grüneisen parameter

$$\gamma_G = \frac{\beta B_T V}{C_V} = \gamma_e \frac{C_e}{C_V} + \gamma_l \frac{C_l}{C_V}$$

where

$$\gamma_e \equiv \frac{V}{C_e}\left(\frac{\partial S_e}{\partial V}\right)_T \text{, the electronic Grüneisen parameter}$$

and

$$\gamma_l \equiv \frac{V}{C_l}\left(\frac{\partial S_l}{\partial V}\right)_T \text{ the vibrational Grüneisen parameter}$$

and C_e and C_l are the electronic and vibrational molar heat capacities and V is the molar volume.

The quasi harmonic model yields a relation for the vibrational contribution to the Grüneisen parameter in terms of the mode gammas which are defined by

$$\gamma_i = -\frac{d\ln\omega_i}{d\ln V}.$$

The contribution γ_l to the thermodynamic Grüneisen parameter is a weighted average of the γ_i, the weighting being the Einstein heat capacity of the mode.

Microscopic parameters

The sound velocity is a measure of the initial slope of the vibrational dispersion curve. Since the relationship between frequency and wave number for the low frequency modes is linear, a measure of the sound velocity with pressure or volume enables one to calculate the low frequency mode gammas. In terms of the pressure derivatives of the elastic constants this familiar relation[2] is

$$\gamma_i = -\frac{1}{6} + \frac{B_T}{2C_i}\left(\frac{\partial C_i}{\partial P}\right)_T$$

where C_i is the appropriate elastic constant for the *i*th mode. Mode gammas for the three principal directions in the crystal are listed in Table 7. In going from 296° to 195°K the mode gammas associated with the longitudinal waves show a slight change while those associated with the transverse modes exhibit a 10 to 15 per cent decrease. In magnitude this corresponds to a decrease of between 0·23 to 0·29 which is larger by about a factor of two than that shown by NaCl and KCl[4]. This may be expected since lead has a much lower Debye temperature ($\theta_D = 105$°K)[12].

Macroscopic parameters

In terms of the mode gammas, the vibrational contribution to the Grüneisen parameter

Table 7. Mode gammas for the three principle crystal directions and the average high and low temperature vibrational Grüneisen parameters for lead

Gamma	Mode	296°K	195°K	Volume extrapolation 0°K
(C'_{11})	[110] long	2·48	2·56	
(C')	[110] trans.	1·55	1·32	
(C_{44})	[110] trans.	2·71	2·42	
(C_{11})	[100] long	2·34	2·32	
(C_{44})	[100] trans.	2·71	2·42	
(C_l)	[111] long	2·51	2·45	
(C_t)	[111] trans.	2·34	2·08	
$\bar{\gamma}_L$	average low temp.	2·21	1·98	1·63
$\bar{\gamma}_H$	average high temp.	2·44		
V		18·266	18·110	17·873 (cm^3/mole)

is given by

$$\gamma_l = \frac{\sum_{i=1}^{3N} c_i \gamma_i}{\sum_{i=1}^{3N} c_i}$$

where the c_i's are the Einstein heat capacities. At high temperatures ($T \gg \theta_D$) all modes are fully excited and γ_l has a limiting value which is the arithmetic average of the mode gammas. At low temperatures, where only low frequency modes are excited, Debye theory applies and the Grüneisen parameter has a limiting value given by an average over the acoustic modes and the weighting factors become the inverse sound velocities cubed. These calculated values denoted by $\bar{\gamma}_H$ and $\bar{\gamma}_L$ given in Table 7 are the results of a computer program[4] designed to carry out these averages. The low temperature average is seen to be smaller for the 195°K data as compared to the 296°K data which is due mainly to the change of the mode gammas but also somewhat to the change in the weighting as a result of the elastic constant changes.

Thermodynamic Grüneisen parameter

The thermodynamic Grüneisen parameter has been calculated using the thermal expansion data of White[13], Channing and Weintraub[14] and Rubin *et al.*[15]; the heat capacity data of Meads *et al.*[16], Neighbours *et al.*[17] and Phillips[12]; the bulk modulus data of Waldorf and Alers[7] and the molar volume obtained from the room temperature X-ray density and the fractional length change as given by Nix and MacNair[18]. The results are shown in Fig. 3 along with the low temperature limiting values. The data used over the sensitive range from 3° to 20°K is listed in Table 8. The figure shows that the thermodynamic parameter is essentially constant at a value of 2·65 from 300° down to about 20°K. Below 10°K there is a gradual fall off with temperature. This characteristic fall off is also found in copper, silver and gold[19]. The

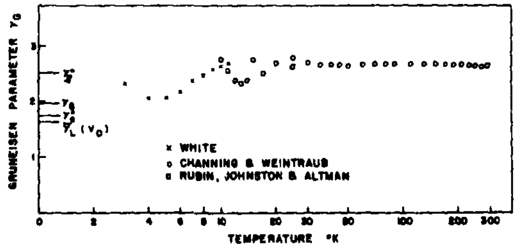

Fig. 3. The thermodynamic Grüneisen parameter γ_G vs. temperature and the limiting values corresponding to $T = 0$°K.

Table 8. *Thermodynamic Grüneisen parameter* γ_G *as a function of temperature from* 3° *to* 20°*K*

Temperature (°K)	α	C_p	γ_G
3	0·0052(a) $\times 10^{-5}(K°)^{-1}$	0·0584(c) $J/K°$ mole	2·3
4	0·011(a)	0·141(c)	2·04
5	0·024(a)	0·307(c)	2·05
6	0·048(a)	0·587(c)	2·14
7	0·090(a)	0·998(c)	2·36
8	0·144(a)	1·52(c)	2·48
9	0·212(a)	2·15(e)	2·58
10	0·288(a)	2·88(e)	2·62
	0·302(b)		2·74
11	0·380(a)	3·70(e)	2·68
	0·360(b)		2·54
12	0·420(b)	4·64(e)	2·37
13	0·490(b)	5·55(e)	2·31
14	0·572(b)	6·32(e)	2·37
15	0·663(b)	7·23(d)	2·74
17	0·850(b)	8·87(d)	2·50
20	1·137(b)	11·01(d)	2·69

The molar volume and bulk modulus at 0°K are 17·87 cm^3/mole and 4·879 × 10^{11} dyn/cm^2 respectively.

(a)White G. K., *Phil. Mag.* **7**, 271 (1962).

(b)Channing D. A. and Weintraub S., *Can. J. Phys.* **43**, 955 (1965).

(c)Neighbor J. E., Cochran J. F. and Shiffman C. A., *Phys. Rev.* **155**, 384 (1967).

(d)Meads P. F., Forsythe W. R. and Giauque W. F., *J. Am. chem. Soc.* **63**, 1902 (1941).

(e)Taken from a graph by drawing a smooth curve between the data of references (*c*) and (*d*) above.

low temperature limiting values of the lattice, γ_l^0, and electronic, γ_e^0, contributions for lead in the normal state and the limiting value γ_s in the superconducting state were calculated using the analytic form for the thermal expansion coefficient as given by White[13] for temperatures less than 4°K and the corresponding analytic form for the heat capacity as given by Phillips[12].

Comparison of thermodynamic and macroscopic Grüneisen parameters

The limiting value of the thermodynamic Grüneisen parameter for the normal state from White's data[20] is $\gamma_l^0 = 2{\cdot}51 \pm 0{\cdot}2$ for the vibrational contribution and $\gamma_e^0 = 1{\cdot}7 \pm 0{\cdot}5$ for the electronic contribution. The superconducting state has a limiting value of $\gamma_s = 1{\cdot}98$. In order to compare γ_l^0 and γ_s with $\bar{\gamma}_L$ as determined from ultrasonic measurements one needs the values of the γ_i's at 0°K and the corresponding zero pressure volume none of which have been measured. As an alternative the $\bar{\gamma}_L$ determined from data at the two temperatures has been volume extrapolated to absolute zero according to the scheme described by Bartels and Schuele[4]. This extrapolated value $\bar{\gamma}_L(V_0)$ is 1·63. Such a linear extrapolation has met with success for NaCl and KCl, however, for lead one must bear in mind that room temperature is three times the Debye temperature. The agreement between the various values at first appears quite poor. White has obtained quite different values in the normal and superconducting states and the single extrapolated value of $\bar{\gamma}_L$ determined from elasticity data lies below the corresponding thermodynamic values. In conjunction with this, however, we must note that there are no pressure data for the elastic constants in the superconducting state.

Careful examination of the thermodynamic data seems to show the need for more accurate thermal expansion data below 2°K. White has obtained the coefficients in the expression $\alpha = aT+bT^3$ for the normal state from expansivity data taken between 1·3° and 4°K. However, he states that his analysis of the data should be limited to the temperature range of the specific heat T^3 region. Since his measurements, van der Hoeven and Kessom [21] have measured the specific heat of lead between 0·4° and 4·2° and found that the T^3 region extends to only about 2°K or $\theta_D/50$. The heat capacity data of Phillips[12] also confirms that the T^3 region lies below 2°K. Thus it appears that the available expansion data does not go to low enough temperatures.

A possible consequence of fitting expansion data outside the T^3 region is too large a value of the cubic coefficient, b, and thus too large a limiting value of the lattice contribution to the thermodynamic Grüneisen parameter. We base this on the rise in the Grüneisen parameter above 4°K. Such a rise indicates that the thermal expansion rises faster than the specific heat in this temperature range. But such a rise should be due entirely to the vibrational contribution since the lattice specific heat equals the electronic specific heat at approximately 1·3° and at 4°K the electronic specific heat is only about 8 percent of the total. Thus if the T^3 region for the vibrational contribution to the thermal expansion also extends to only 2°K, then it would appear that the coefficients obtained by White are probably high. Preliminary data of Andres[22] in which the data was fit to T^3 up to 3°K gives a limiting value of $\gamma_l{}^0 = 2{\cdot}1 \pm 0{\cdot}4$ and tends to support this conclusion.

The specific heat T^3 region for the superconducting state extends to about 1·5°K [12, 21] and White's data yields a value of $\gamma_s = 1{\cdot}98$ while the data of Anores gives $\gamma_s = 1{\cdot}8 \pm 0{\cdot}3$. There is no calculated value based on elasticity data since pressure measurements in the superconducting state have not been made. However, an argument can be made for the equality of γ_s and $\gamma_l{}^0$. Alers and Waldorf[23] have measured the change in the elastic constants in going from the normal to the superconducting state with the result that they changed by only a few ppm. The Debye temperature can be calculated from the elastic constants and these measurements would indicate that θ_D(normal) $= \theta_D$ (super). This implies then that the normal state lattice specific heat in the T^3 region should equal the superconducting state specific heat in the T^3 region and Phillips[12] has found this to be the case. Now one can show that in the T^3 region the vibrational gamma is given by

$$\gamma_l = -\frac{d\ln\theta_D}{d\ln V}.$$

Thus if the vibrational heat capacities in the two states remain equal as the volume is changed then it follows that $\gamma_l{}^0 = \gamma_s$.

A favorable comparison between $\bar{\gamma}_H$ and γ_H could only be considered fortuitous because of the assumptions which go into the calculation of $\bar{\gamma}_H$. However, for the case of lead the agreement is fair with $\bar{\gamma}_H = 2{\cdot}44$ and $\gamma_H = 2{\cdot}65$. This result could imply that the high frequency mode gammas have as an average a value slightly greater value than γ_H. Recently, Lechner and Quittner[24] have measured the phonon frequency shift as a function of pressure at four points on the Brillouin zone boundary and two interior points. From their shifts they have calculated the mode gammas corresponding to their six points. Choosing those four points which lie on the zone boundary and counting the transverse modes twice, we determined a simple average of their high frequency mode gammas to be $2{\cdot}5 \pm 0{\cdot}6$. Comparison of the low frequency mode gammas in the [100] and [111] directions with corresponding high frequency mode gammas shows that the mode gammas are highly frequency dependent over a given branch.

Ultrasonic equation of state

Anderson[25] has shown that ultrasonic data taken at relatively low pressures may be used to estimate the pressure volume isotherm to pressures of the order of the bulk modulus. He assumed the bulk modulus has a linear pressure dependence which results in the Murnaghan equation of state

$$\frac{V}{V_0}=\exp\left\{-\frac{1}{B_0'}\ln\left[B_0'\frac{P}{B_0}+1\right]\right\}$$

where B_0 is the isothermal bulk modulus and B_0' its pressure derivative. In the paper by Anderson, Fig. 11 shows excellent agreement between V/V_0 as measured by Bridgman[26] and McQueen and Marsh[27] and the above expression. To obtain B_0', Anderson used an approximate relation between the Grüneisen parameter and B_0' due to Dugdale and MacDonald[28]. This expression,

$$B_0'=2\gamma+1$$

resulted in a value for B_0' of 6·30 compared to 5·72 from the present measurements. While this may seem to be quite a difference, the Murnaghan equation is fairly insensitive to change in B_0' for pressures lower than B_0. Use of Anderson's parameters, $B_0 = 416$ Kbar and $B_0' = 6{\cdot}30$, in the above expression results in a value of $V/V_0 = 0{\cdot}822$ for $P = 160$ Kbar while the parameters from the present measurements, $B_0 = 419$ Kbar and $B_0' = 5{\cdot}74$ result in a value of $V/V_0 = 0{\cdot}817$. This difference is insignificant in comparison with the experimentally determined isotherm.

It is worthwhile pointing out that because of this insensitivity one could just as well use the adiabatic pressure derivative when one is interested in the equation of state. The difference in the present measurements being 5·72 compared with 5·53. This eliminates the involved thermodynamic reduction in going from one pressure derivative to the other.

Bridgman[29] displayed the results of his pressure measurements in the form

$$\frac{V-V_0}{V_0}=-aP+bP^2.$$

The parameters a and b are related to the isothermal bulk modulus and its pressure derivative through the following relations

$$a=\frac{1}{B_T}\quad\text{and}\quad b=\frac{1}{2B_T^2}\left\{\frac{\mathrm{d}B_T}{\mathrm{d}P}+1\right\}.$$

The major discrepancy between Bridgman's work and ultrasonic data has been with the b coefficient.

For lead there is reasonable agreement, with Bridgman's value being $19{\cdot}52\times10^{-24}$ (dyn/cm^2)$^{-2}$ while the ultrasonic data gives $19{\cdot}14\times10^{-24}$ (dyn/cm^2)$^{-2}$.

REFERENCES

1. EROS S. and REITZ J. R., *J. appl Phys.* **29**, 683 (1958).
2. DANIELS W. B. and SMITH C. S., *The Physics and Chemistry of High Pressure*, p. 50. Soc. of Chem. Industry, London (1963).
3. DANIELS W. B. and HRUSCHKA A. A., *Rev. scient. Instrum.* **28**, 1058 (1957).
4. BARTELS R. A. and SCHUELE D. E., *J. Phys. Chem. Solids* **26**, 537 (1965).
5. DANIELS W. B. and SMITH C. S., *Phys. Rev.* **111**, 713 (1958).
6. NEIGHBOURS J. R., *J. acoust. Soc. Am.* **26**, 865 (1954).
7. WALDORF D. L. and ALERS G. A., *J. appl. Phys.* **33**, 3266 (1962).
8. MILLER R. A. and SMITH C. S., *J. Phys. Chem. Solids* **25**, 537 (1964).
9. NEIGHBOURS J. R. and ALERS G. A., *Phys. Rev* **111**, 707 (1958).
10. ROTTER C. A. and SMITH C. S., *J. Phys. Chem. Solids* **27**, 267 (1966).
11. LEIBFRIED G. and LUDWIG W., *Solid State Physics* (Edited by F. Seitz and D. Turnbull), Vol. 12, p. 275 Academic Press, New York (1961).
12. PHILLIPS N. E., Proceedings of the 1966 Low Temperature Calorimetry Conference, *Am. Acad. Sci. Fennicae* **210**, 69 (1966).
13. WHITE G. K., *Phil. Mag.* **7**, 271 (1962).

14. CHANNING D. A. and WEINTRAUB S., *Can. J. Phys.* **43**, 955 (1965).
15. RUBIN T., JOHNSTON H. L. and ALTMAN H. W., *J. phys. Chem.* **66**, 266 (1962).
16. MEADS P. F., FORSYTHE W. R. and GIAUQUE W. F., *J. Am. chem. Soc.* **63**, 1902 (1941).
17. NEIGHBOR J. E., COCHRAN J. F. and SHIFFMAN C. A., *Phys. Rev.* **155**, 384 (1967).
18. NIX F. C. and MACNAIR D., *Phys. Rev.* **61**, 74 (1942).
19. COLLINS J. G., *Phil. Mag.* **8**, 323 (1963).
20. WHITE G. K. and COLLINS J. G., *Progress in Low Temperature Physics* (Edited by C. J. Gorter), Vol. **4**, p. 450. North Holland, Amsterdam (1964).
21. VAN DER HOEVEN J. C. and KEESOM P. H., *Phys. Rev.* **137**, 103 (1965).
22. ANDRES K., *Cryogenics* **2**, 93 (1961).
23. ALERS G. A. and WALDORF D. L, *Phys. Rev. Lett.* **6**, 677 (1961).
24. LECHNER R. and QUITTNER G., *Phys. Rev. Lett.* **17**, 1259 (1966).
25. ANDERSON O., *J. Phys. Chem. Solids* **27**, 547 (1966).
26. BRIDGMAN P. W., *Proc. Am Acad. Arts Sci.* **76**, 1 (1945).
27. MCQUEEN R. G. and MARSH S. P., *J. appl. Phys.* **31**, 1253 (1960).
28. DUGDALE J. S. and MACDONALD, D. K. C., *Phys. Rev.* **89**, 832 (1953).
29. BRIDGMAN P. W., *Proc. Am. Acad. Arts Sci.* **70**, 285 (1935).

APPENDIX

The temperature derivatives of the C'_{11}, C' and C_{44} elastic constants from room temperature to 300°C were also determined, each on a different crystal specimen. Transducers were attached to the crystals with Eccobond 76 epoxy mix. The crystals were placed in a gradient free region of a furnace, the temperature raised in 5C° steps at about 1·5C° min, and then the system was allowed to come to thermal equilibrium at the elevated temperature. The procedure was to follow a given cycle in an echo and to record the change in transit time of this echo at each equilibrium value of the temperature. The temperature was determined by a thermocouple placed adjacent to the specimen in the furnace. The precision of these measurements was about two percent, but since the crystals used in this investigation were only oriented to within three degrees of a [110] direction, and since no orientation corrections were applied to the data, the accuracy was less. In spite of these limitations, the changes in the moduli appeared linear with temperature and the high temperature temperature derivatives were essentially those found more precisely here from 195° to 296°K and previously by Waldorf and Alers [7].

J. Phys. Chem. Solids Pergamon Press 1969. Vol. 30, pp. 601–608. Printed in Great Britain.

PROPERTIES OPTIQUES ET SPECTRE ELECTRONIQUE DU MgF_2 ET DU CaF_2 DE 10 à 48 eV

G. STEPHAN, Y. Le CALVEZ, J. C. LEMONIER et Mme S. ROBIN
Laboratoire de Spectroscopie, Faculté des Sciences, 35 Rennes, France

(*Received* 29 *April* 1968)

Résumé—On détermine la constante diélectrique complexe de monocristaux de MgF_2 et de CaF_2 à partir de mesures de pouvoirs réflecteurs sous plusieurs incidences. Les spectres obtenus montrent la présence d'excitons, de transitions interbandes et de plasmons. On met en évidence l'importance de la présence d'une bande *d* dans la bande de conduction pour le CaF_2 ainsi que les déplacements des plasmons vers le bord des bandes d'absorption principales.

INTRODUCTION

LES FLUORURES de calcium et de magnésium sont des cristaux ioniques à large bande interdite et par conséquent sont utilisés comme matériaux optiques dans l'ultraviolet lointain. Il faut atteindre une énergie de l'ordre de 10 eV environ pour que les électrons de valence commencent à être excités. L'étude du spectre d'excitation électronique entre 10 et 50 eV qui fait l'objet de cet article permet de mettre en évidence trois sortes d'excitations élémentaires des solides: les excitons, les transitions interbandes et les plasmons. La mesure du pouvoir réflecteur en fonction de l'énergie permet d'accéder à la constante diélectrique complexe $\hat{\epsilon}(\omega)$ qui décrit ces excitations. Nous avons déjà publié des résultats expérimentaux concernant le CaF_2[1] et le MgF_2[2]. Les expériences sont reprises ici de facon plus détaillée ce qui nous permet de donner une description plus complète des propriétés de ces solides.

METHODES EXPERIMENTALES ET DETERMINATION DES CONSTANTES OPTIQUES

Selon la région spectrale, nous utilisons deux appareillages différents: entre 10 et 13,6 eV, un réflectomètre[1] est placé à la fente de sortie d'un monochromateur du type 'Seya-Namioka' construit au laboratoire [3]. La source utilisée est une lampe à décharge dans l'hydrogène, sans fenêtre. Entre 12,7 et 48 eV, nous utilisons un monochromateur à incidence tangentielle[4]. La source de lumière est du type Morlais-Robin [5] dans laquelle est introduit de l'argon sous faible pression (10^{-1} mm Hg environ).

Pour chaque longueur d'onde, nous mesurons le pouvoir réflecteur de la substance étudiée aux incidences de 20, 45, 60 et 70°. Le plan d'incidence choisi est incliné à $\theta = 45°$ par rapport à la verticale pour supprimer les effets de la polarisation de la lumière émergente à la fente de sortie des monochromateurs[1, 3]. Cette lumière est partiellement polarisée linéairement: elle est équivalente[6] à celle formée de deux composantes perpendiculaires sans relation de phase entre elles, l'une verticale, l'autre horizontale d'intensités respectives I_V et I_H. Si r_s (ϕ) et r_p (ϕ) sont les pouvoirs réflecteurs pour des lumières polarisées linéairement perpendiculairement et parallèlement au plan d'incidence, ce dernier faisant un angle θ avec I_V, le pouvoir réflecteur observé est donné par

$$R(\theta, \phi) = \begin{pmatrix} r_s(\phi) & 0 \\ 0 & r_p(\phi) \end{pmatrix} \begin{pmatrix} \cos^2\theta & \sin^2\theta \\ \sin^2\theta & \cos^2\theta \end{pmatrix} \begin{pmatrix} I_H \\ I_V \end{pmatrix}$$

soit pour $\theta = 45°$;

$$R_{(45°,\phi)} = \tfrac{1}{2}(I_V + I_H)(r_s\ \phi) + r_p(\phi)).$$

Ceci correspond au pouvoir réflecteur d'une lumière naturelle d'intensité $I = I_\perp + I_{//}$, c'est-à-dire de même intensité que la lumière partiellement polarisée utilisée.

A partir des mesures de pouvoirs réflecteurs pour chaque incidence, nous déterminons les constantes optiques n et k à l'aide d'abaques et de tables établies à partir des équations de Fresnel. L'erreur commise sur les mesures dépend de la stabilité dans le temps des raies spectrales. En général, celle-ci est de 2 à 3%. Cependant, pour une dizaine de raies elle est comprise entre 5 et 7%. Il en résulte une incertitude sur les constantes optiques de 2% environ qui devient bien supérieure (10 à 20%) lorsque l'indice d'absorption k est faible (inférieur à 0,1).

A partir des constantes optiques n et k, nous déterminons la constante diélectrique complexe $\hat{\epsilon} = \epsilon_1 + i\,\epsilon_2 = (n + ik)^2$, la fonction perte d'énergie des électrons dans les solides $W = -\mathrm{Im}\,\hat{\epsilon}^{-1}$ et le coefficient d'absorption $\alpha = 4\pi k/\lambda$.

RESULTATS EXPERIMENTAUX

Les mesures ont été effectuées avec des monocristaux: le fluorure de calcium, clivé, provient des établissements Harshaw (U.S.A.), le fluorure de magnésium, poli, des établissements Sorem (France). Ce dernier cristal avait son axe optique orienté à 35° environ des faces; par suite de la biréfringence, les pouvoirs réflecteurs dépendent de l'orientation du plan d'incidence; nos mesures correspondent à un plan d'incidence orienté à 45° du plan de projection de l'axe sur les faces. Ces premières mesures de pouvoir réflecteur permettent d'obtenir les structures de ϵ_2 et $-\mathrm{Im}\,(\hat{\epsilon}^{-1})$; une étude plus détaillée de la biréfringence et des constantes optiques est actuellement en cours selon une méthode déjà utilisée pour le spath[3]. Les Fig. 1 et 2 représentent le pouvoir réflecteur du CaF_2 à l'incidence de 20° et du MgF_2 aux incidences de 20° et 70°. Cette dernière courbe en 'pic' entre 14 et 20 eV est très caractéristique de MgF_2. Ces mesures sont en accord, en ce qui concerne la position énergétique des principales discontinuités, avec nos mesures précédentes (CaF_2[1] et MgF_2[2]) et avec celles d'autres auteurs (CaF_2[7, 8] MgF_2[9]) jusqu'à 13 eV. Cependant nos nouvelles conditions expérimentales nous ont permis d'obtenir une structure plus détaillée: nous avons utilisé 130 raies spectrales environ au lieu d'une vingtaine précédemment.

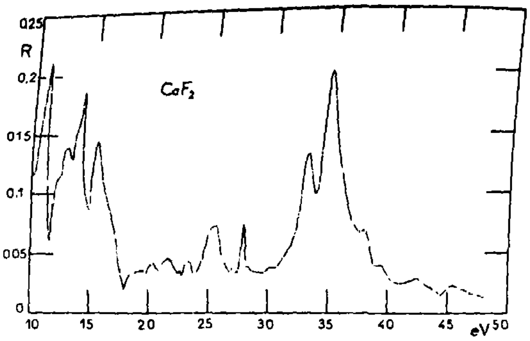

Fig. 1. Pouvoir réflecteur à l'incidence de 20° pour CaF_2.

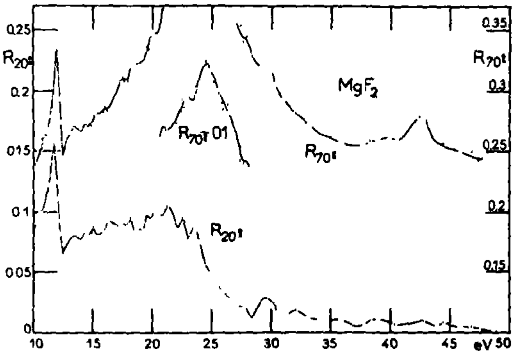

Fig. 2. Pouvoir réflectueur aux incidences de 20° ($R_{20°}$) et de 70° ($R_{70°}$) pour le MgF_2.

Les constantes diélectriques pour les 2 substances sont données Fig. 3 et 4; les coefficients d'absorption $\alpha = 4\pi k/\lambda$ Fig. 5 et 6 et les fonctions pertes Fig. 7 et 8.

DISCUSSION

Le calcul des bandes d'énergie de ces deux solides n'a pas encore été effectué. D'autre part, aucun spectre de densité d'états dans la bande de conduction n'a encore été déterminé, ni par mesures d'absorption *X*, ni par mesures photoélectriques. Il ne nous est donc pas possible d'attribuer à chaque discontinuité du spectre de ϵ_2, la transition électronique correspondante dans la zone de Brillouin comme cela a été fait pour certains isolants [10, 11]. Nous essayerons simplement d'interpréter certains groupes de transitions en nous basant d'une part sur les spectres déjà connus de KCl[12], de KF[13] et de NaCl[12] et d'autre part sur les positions

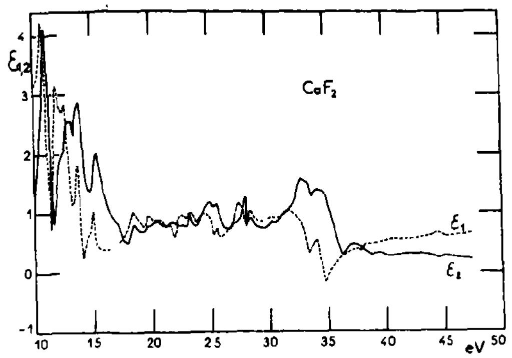

Fig. 3. Constante diélectrique du CaF_2: ϵ_1 partie réelle, ϵ_2 partie imaginaire.

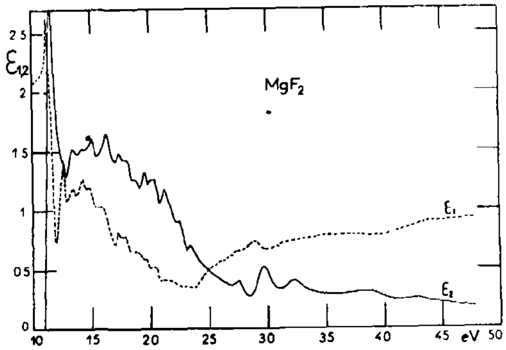

Fig. 4. Constante diélectrique du MgF_2: ϵ_1 partie réelle, ϵ_2 partie imaginaire.

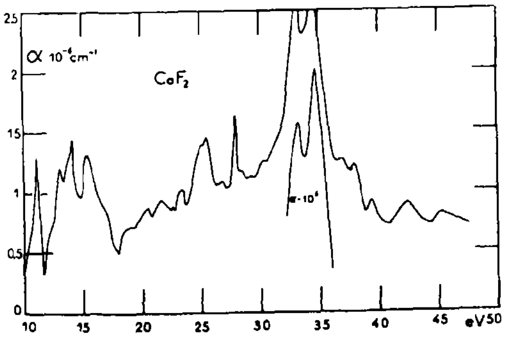

Fig. 5. Coefficient d'absorption du CaF_2: $\alpha = 4\pi k/\lambda$.

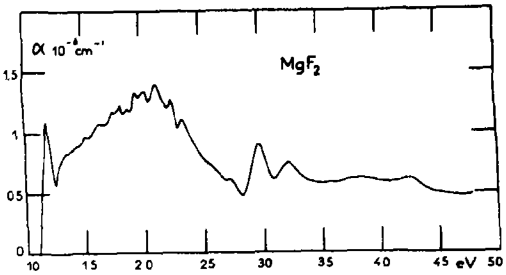

Fig. 6. Coefficient d'absorption du MgF_2: $\alpha = 4\pi k/\lambda$.

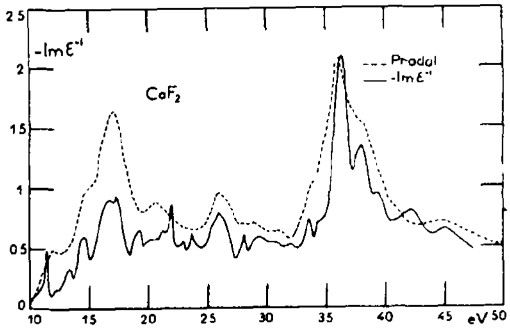

Fig. 7. Fonction perte d'énergie du CaF_2: $W = -\mathrm{Im}\,\epsilon^{-1}$, et pertes caractéristiques d'énergie des électrons[20].

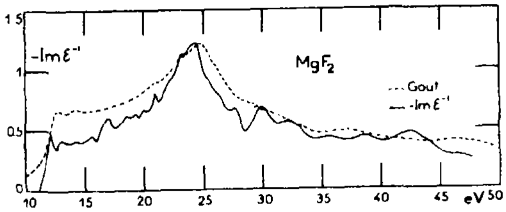

Fig. 8. Fonction perte d'énergie du MgF_2: $W = -\mathrm{Im}\,\epsilon^{-1}$, et pertes caractéristiques d'énergie des électrons[23].

énergétiques des niveaux des atomes libres déterminées par spectroscopie X[14].

(1) CaF_2

On sait que, dans les fluorures, la bande de valence est constituée par les états 2 p de l'ion fluor. Comme celui-ci est un élément léger, l'interaction spin-orbite correspond à une distance énergétigque maximum[10, 15] de 0·05 eV. C'est pourquoi, même à basse température le dédoublement des transitions correspondantes n'a pas été observé[16]. Les niveaux les plus bas de la bande de conduction sont constitués par les états 3 d du Ca^{2+}, ceux-ci ayant une énergie inférieure aux états 4 s pour l'ion du Ca^{2+} libre[17]. Le bas de la bande se trouve vraisemblablement au point Γ où il est dédoublé selon les niveaux $\Gamma_{25'}$ et Γ_{12}.

Le premier pic de réflexion à 11,1 eV (Fig. 1) est dû à un exciton parabolique Γ caractérisé par l'allure résonante de $\hat{\epsilon}(\omega)$. Si, entre 10 et 11,6 eV, on l'assimile à une seule absorption de Lorentz, la courbe de ϵ_2 nous permet alors de calculer la force d'oscillateur par molécule[18] que nous trouvons égale á 1,1. La première transition interbande est caractérisée par une discontinuité $M_0(\Gamma_{15} \rightarrow \Gamma_{25'})$ à 11,4 eV. L'énergie de liaison de l'exciton serait donc de 0,3 eV. La seconde discontinuité M_0 à 12,5 eV peut correspondre à la transition $\Gamma_{15} \rightarrow \Gamma_{12}$. La distance $\Gamma_{25'} - \Gamma_{12}$ serait donc de 1,1 eV. On remarque à 13,1 et 13,4 eV des discontinuités M_3 puis M_0 sans doute dues à des transitions états p des $F^- \rightarrow$ états s ou d de la bande de conduction en différents points de la zone de Brillouin. Le pic de réflexion à 14 eV (correspondant à une allure résonante de ϵ_1 et ϵ_2) pourrait être attribué soit à un exciton de vecteur d'onde non nul, soit à un exciton Γ. Un phénomène semblable a été discuté pour le KCl par Oyama et Miyakawa[19] et ceux-ci concluent en faveur de la dernière hypothèse. La discontinuité suivante M_0 serait alors due à la transition dipolaire $\Gamma_{15} \rightarrow \Gamma_1$ d'où il résulte une distance $\Gamma_1 - \Gamma_{25'}$ de 3 eV environ, en accord avec la distance de 2,7 eV évaluée dans l'atome deux fois ionisé[17]. A partir de 17 eV environ, on constate une baisse simultanée du pouvoir réflecteur et de α correspondant à un pic de la fonction perte. Ces caractéristiques, jointes à l'allure de la constante diélectrique conduisent à fixer à 17,3 eV l'énergie du plasmon des électrons de valence. D'autre part, cette énergie marque une coupure dans l'absorption comme dans le cas d'un gaz d'électrons libres. Ceci signifie que la force d'oscillateur des électrons de la bande de valence est donc presque entièrement épuisée et qu'au delà de l'énergie de plasma les transitions dues à ces électrons auront une faible probabilité d'où un faible pouvoir réflecteur.

Les maxima de pouvoir réflecteur à 25 et 27 eV pourraient être dûs soit à des transitions quadrupolaires états 2 s $F^- \rightarrow$ états 3 d de Ca^{2+} soit plutôt à des transitions dipolaires 2 s F^- vers des bandes à symétrie p (4 p de Ca^{2+}). On remarque à 31 eV environ le début de l'excitation des électrons 3 p du Ca^{2+} (transitions 3 p $Ca^{2+} \rightarrow \Gamma_{25'}$) puis à 34 eV la transition 3 p $Ca^{2+} \rightarrow \Gamma_1$ si on admet que la distance Γ_1, $\Gamma_{25'}$ vaut 3 eV. Le creux de réflexion pour les électrons 3 p du Ca^{2+} vers 34 eV serait donc dû à la même antirésonance que le creux de réflexion à 14,7 eV pour les électrons 2 p du F^-. Enfin, comme dans l'atome libre les niveaux 3 s du calcium sont situés à 43,7 eV[14], on peut alors penser que les pics de réflexion à partir de 45 eV sont dûs à l'excitation de ces électrons. Ceci nous conduit à proposer comme schéma de bandes au centre de la zone de Brillouin, celui donné par la Fig. 9. Enfin, le pic très important de la fonction perte, situé à 36,4 eV ne correspond à aucune absorption optique transversale: il est donc dû à une oscillation de plasma. On peut remarquer que cette résonance est quasi métallique; en effet, comme dans les métaux, ϵ_1 croît à partir de valeurs négatives, ϵ_2 est faible et $-\mathrm{Im}\,\hat{\epsilon}^{-1}$ présente un pic important. Les pertes caractéristiques d'énergie des

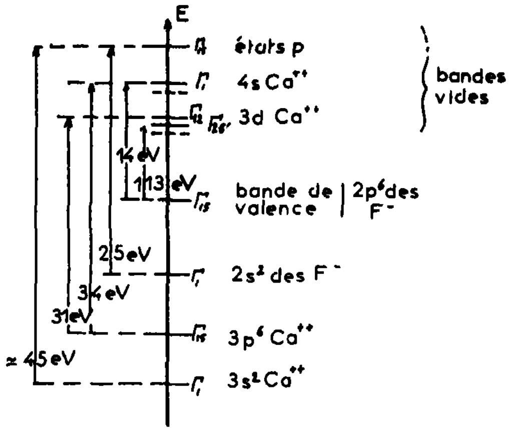

Fig. 9. Niveaux d'énergie du CaF_2 au centre de la zone de Brillouin.

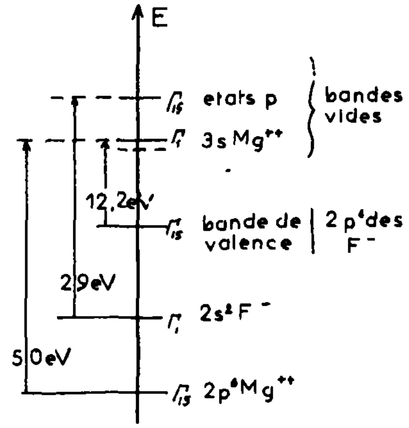

Fig. 10. Niveaux d'énergie du MgF_2 au centre de la zone de Brillouin.

électrons dans CaF_2 ont été mesurées récemment par Pradal, Gout et Lahaye[20] et leurs résultats coïncident avec la fonction perte comme le montre le tableau 1.

(2) MgF_2

Le fluorure de magnésium a une structure électronique plus simple que celle du fluorure de calcium: en particulier, on ne trouve pas de bande d au voisinage de la première bande s dans la bande de conduction, ce qui se traduit par un spectre de réflexion plus simple. Après le maximum excitonique déjà signalé [9,21]. à 11,7 eV, commencent vers 12,2 eV les transitions interbandes. Comme la bande de valence est due aux états p du F^-, son maximum se trouve au point Γ. D'autre part, la bande de conduction la plus basse est formée par les états 3 s de Mg^{2+}: le minimum est donc aussi au point Γ[22]. On peut en conclure que la largeur de la bande interdite est 12,2 eV correspondant à la première transition $\Gamma_{15} \rightarrow \Gamma_1$. Au-dessus de cette énergie on constate une absorption régulière relativement continue jusqu'à la fréquence de coupure due à l'oscillation collective située à 24,5 eV (Figs. 4 et 8). Vers 29 eV on voit un pic d'absorption relativement important que l'on peut supposer dû à l'excitation des électrons 2 s des ions fluor, excitation que nous avons située à 25 eV dans le fluorure de calcium. Ce déplacement vers les grandes énergies pour le fluorure de magnésium peut être dû à deux causes: d'abord à l'absence de 'bande d' de basse énergie dans la bande de conduction, ensuite au fait que les électrons 2 s du F^- sont plus profonds dans le MgF_2 que dans le CaF_2 puisque l'énergie de Madelung est un peu moins grande pour ce dernier corps. Les électrons 2 p du magnésium sont excités vers 50 eV environ[14]. Un diagramme des niveaux d'énergie possible pour MgF_2 est donné Fig. 10.

Enfin, nous comparons (Tableau 2) égale-

Tableau 1. Pics de perte caractéristique d'énergie des électrons[20] *et maxima de la fonction perte* – $\mathrm{Im}\,\epsilon^{-1}$ *pour le* CaF_2

Pics des pertes d'énergie en eV	11,9		15,3		17,8	20,9		26,3		29,5	31,1			34,3	36,6	38,7		40,6	45,7
Maxima de la fonction – $\mathrm{Im}\,\epsilon^{-1}$	11,3	13,3	14,6	16,5	17,3	19,3	22	26	28	29,5	31,1	32	33,3	34,3	36,4	38	39,5	42	45

Tableau 2. Pics de pertes caractéristiques d'énergie des électrons [23] *et maxima de la fonction perte* $-\mathrm{Im}\epsilon^{-1}$ *pour le* MgF_2

Pics des pértes d'énergie en eV		13		15	16,8	18,6			20,9		23	24,5	26	29	31		38,5	
Maxima de la fonction $-\mathrm{Im}\epsilon^{-1}$	12	13	14,5	15,6	16,9	18,5	19,5	20	20,8	22,5	23,2	24,5	26	30	32	36	38	42,5

ment les maximums de la fonction perte aux pertes d'énergie caractéristiques déterminées par C. Gout [23]. L'accord est bon aussi bien en ce qui concerne les positions énergétiques des maxima que pour les intensités relatives de ceux-ci. Le spectre de $-\mathrm{Im}\hat{\epsilon}^{-1}$ pour MgF_2 (Fig. 8) est essentiellement caractérisée par son allure en 'pic' entre 12 et 30 eV qui correspond à celle de la courbe $R_{70°}$ (Fig. 2). L'excitation longitudinale de plasma est responsable de ce phénomène.

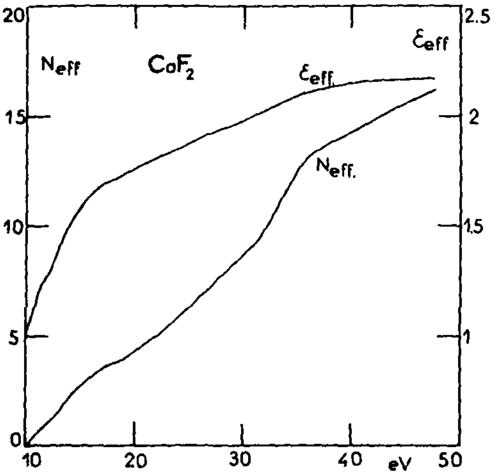

Fig. 11. Fonction ϵ_{eff} et N_{eff} pour le CaF_2.

CONCLUSIONS

La comparaison entre les spectres des deux isolants étudiés ici montre l'importance de l'introduction des bandes *d* sur les spectres électroniques: les bandes d'absorption dues aux électrons *p* sont alors dédoublées. Une conclusion identique peut être faite à partir des spectres de NaF [25, 26] et KF [13, 24]; en effet dans ce dernier cas, on observe un dédoublement à 12,5 et 20,5 eV dû à la bande 3 *d* du K^+ (cependant ici les niveaux 3 *d* sont plus élevés que les niveaux 4 *s*).

Nous avons également calculé les fonctions

$$\epsilon_{eff(\omega)} = 1 + \frac{2}{\pi}\int_0^{\omega}\frac{\epsilon_2}{\omega}\,d\omega \quad \text{et}$$

$$N_{eff}(\omega) = \frac{2m\,\epsilon_0}{\pi N e^2}\int_0^{\omega}\omega\,\epsilon_2\,d\omega$$

ϵ_{eff} représente la contribution électronique à la constante diélectrique statique et N_{eff} le nombre d'électrons participant à l'interaction électromagnétique. Ces fonctions sont représentées Figs. 11 et 12 pour CaF_2 et MgF_2 respectivement. La comparaison des deux courbes de N_{eff} montre que 3,7 et 5 électrons environ par molécule sont excités à la longueur d'onde de coupure soit à 17,3 eV pour le CaF_2 et 24,5 eV pour le MgF_2. Cette différence montre qu'une force d'oscillateur

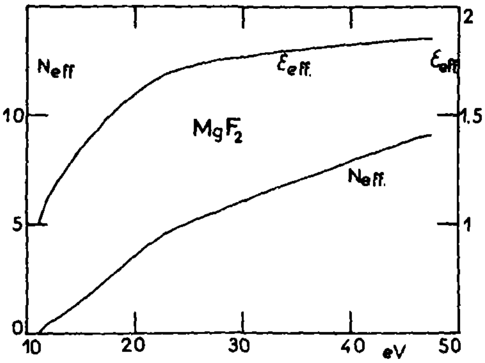

Fig. 12. Fonction ϵ_{eff} et N_{eff} pour le MgF_2.

supérieure est gardée pour les grandes énergies dans le premier cas: celle-ci est vraisemblablement utilisée lors de l'oscillation de plasma vers 36 eV. Les valeurs de N_{eff} pour MgF_2 trouvées par Arakawa *et al.*[27] sont légèrement supérieures aux nôtres; ceci semble dû à un état de surface différent des échantillons étudiés plutôt qu'à des effets d'impuretés. L'excitation des électrons 3 *p* du Ca^{2+} à 31 eV est marqué par la rapide augmentation de N_{eff} à cette énergie. Les courbes de ϵ_{eff} tendent vers une valeur limite qui devrait être égale au carré de l'indice *n* dans la région normale du spectre, soit 1,99 pour CaF_2 et 1,90 pour MgF_2. Les valeurs de palier atteintes ici sont respectivement de 2,17 et 1,86. Remarquons que pour CaF_2 la valeur est légèrement supérieure à n^2 comme cela a déjà été signalé pour d'autres substances.

Enfin, en ce qui concerne les oscillations de plasma, Horie[29] a donné certaines conditions suffisantes d'existence de ce phénomène dans les isolants et Miyakawa[30] démontre la présence d'un plasmon sur le bord des principales absorptions du côté des grandes énergies. Horie[29] pour les isolants, Wilson[31] et Pines[32] pour les métaux, montrent également que la présence des transitions interbandes peut déplacer l'énergie du plasmon par rapport à sa valeur pour des électrons libres. Les plasmons sont d'ailleurs mis en évidence par la comparaison des spectres d'absorption optique et des pertes d'énergie des électrons, les premiers donnent les absorptions transversales, les seconds les absorptions transversales et longitudinales.

Pour le CaF_2, l'énergie de plasmon en comptant les 12 électrons de valence supposés libres, serait de $h\nu = 20{,}2$ eV; expérimentalement on trouve $h\nu_{exp} = 17{,}3$ eV: ce déplacement vers les basses énergies serait dû, principalement à l'influence des bandes d'absorption situées vers 25, 30 et 35 eV. Pour MgF_2 au contraire, le plasmon est déplacé vers les grandes énergies de $h\nu = 22$ eV à $h\nu_{exp} = 24{,}5$ eV. Effectivement, dans ce cas, l'absorption est moins importante au-dessus de 25 eV et le déplacement est principalement dû aux transitions d'énergie inférieures. Comme nous l'avons déjà signalé[2], la position du plasmon peut alors être donnée par la formule de Horie $h\nu_{exp} = (\Delta^2 + (h\nu_l)^2)^{1/2}$ où Δ est la largeur de la bande interdite. La valeur obtenue de 24,8 eV est très proche de notre valeur expérimentale. Enfin on constate à 36,4 eV dans le spectre de $-\mathrm{Im}\,\hat{\epsilon}^{-1}$ de CaF_2 un important pic correspondant à une oscillation de plasma, ce qui est en accord avec la théorie de Miyakawa[30].

REFERENCES

1. STEPHAN G., LEMONNIER J. C. et Mme ROBIN S., *J. opt. Soc. Am.* **57**, 486 (1967).
2. STEPHAN G., LE CALVEZ Y., LEMONNIER J. C. et Mme ROBIN S., *C.r. hebd. Séanc. Acad. Sci., Paris* **264**, 1667 (1967).
3. LE CALVEZ Y., STEPHAN G. et Mme ROBIN S., *Optica Acta*, à paraître.
4. ROMAND J et VODAR B., *Revue Opt. théor. instrum.* **4**, 39, (1960).
5. MORLAIS M. et Mme ROBIN S., *Appl. Opt.* **6**, 409 (1967).
6. LANDAU L. et LIFCHITZ E., *Théorie du champ* (Édité par la Paix Moscou), p. 164 (1960).
7. TOUSEY R., *Phys. Rev.* **50**, 1057 (1936).
8. Mme ROBIN-KANDARE S. et ROBIN J., *C.r. hebd. Séanc. Acad. Sci.* Paris **262**, 1020 B (1966)
9. WILLIAMS M. W., MAC RAE R. A. et ARAKAWA E. T., *J. appl. Phys.* **38**, 1701 (1967).
10. PHILLIPS J. C., dans *Solid State Physics* (Édité par F. Seitz et D. Turnbull), Vol. 18, p. 55. Academic Press, New York (1966).
11. COHEN M. L., LIN P. J., ROESSLER D. M. et WALKER W. C., *Phys. Rev.* **155**, 992 (1967).
12. ROESSLER D. M. et WALKER W. C., *Phys. Rev.* **166**, 599 (1968). Nous remercions le Dr ROESSLER de nous avoir fait parvenir cet article avant publication.
13. STEPHAN G. et ROBIN S., *Solid State Commun.* **5**, 883 (1967).
14. SANDSTROM A. E., *Handb. Phys.* **30**, 78 (1957).
15. KNOX R. S. et INCHAUSPE N., *Phys. Rev.* **116**, 1093 (1964).
16. TEEGARDEN K. et BALDINI G., *Phys. Rev.* **155**, 896 (1967).
17. MOORE C. E., *Atomic Energy Levels*, Vol. 2. U.S. Department of commerce and National Bureau of Standards Circular 467 (1949).
18. SEITZ F., *Modern Theory of Solids*, Chap. XVII, Sect. 148. McGraw-Hill New York (1940).

19. OYAMA S. et MIYAKAWA T., *J. phys. Soc. Japan* **21**, 868 (1966).
20. PRADAL F., GOUT C. et Mlle LAHAYE B., *C.r. hebd. Séanc. Acad. Sci., Paris* **264**, B251 (1967).
21. Mlle FABRE., Thèse, Paris (1965).
22. PINCHERERLE L. et LEE P. M., *Proc. phys. Soc.* **78**, 1195 (1961).
23. GOUT C., Mlle LAHAYE B. et PERRIER P. *C.r. hebd. Séanc. Acad. Sci., Paris* **265**, B 1460 (1967).
24. ROESSLER M. et LEMPKA H. J., *Br. J. appl. Phys.* **17**, 1553 (1966).
25. METZGER P. H., *J. Phys. Chem. Solids* **26**, 1879 (1965).
26. STEPHAN C., Résultats non publiés.
27. ARAKAWA E. T., Rapport O.R.N.L. No. 4168, 137 (1967).
28. PHILLIPP H. R. et EHRENREICH H., *Phys. Rev.* **129**, 1550 (1963).
29. HORIE C., *Prog. theor. Phys.* **21**, 113 (1959).
30. MIYAKAWA T., *J. phys. Soc. Japan* **24**, 768 (1968).
31. WILSON C. B., *Proc. phys. Soc.* **76**, 481 (1960).
32. PINES D., *Solid St. Phys.* **1**, 367 (1955).

J. Phys. Chem. Solids Pergamon Press 1969. Vol. 30, pp. 609–626. Printed in Great Britain.

THE DENSITY OF STATES OF SOME SIMPLE EXCITATIONS IN SOLIDS

RAINER J. JELITTO
Institut für Theoretische Physik der Universität Kiel, Germany

(*Received* 4 *March* 1966)

Abstract – The density of states of the spectrum

$$E(\mathbf{k}) = E_0 - E_1 \sum_{\{\Delta\}} e^{i(\mathbf{k}\Delta)}$$

which occurs for different types of elementary excitations in solids, when only next neighbour interactions are taken into account (with $\boldsymbol{\Delta}$ being the next neighbour lattice vectors), were computed and are investigated and tabulated for the cubic space groups. Its singularities are discussed with regard to a paper of van Hove[5]. As is detailed in the paper, using the standard approximation of these functions for the calculation of thermodynamic observables proves to be justified only for very low temperatures. In order to facilitate their application for calculations in case of higher temperatures, the exact densities of states are approximated by elementary functions with a relative error of less than 1 per 1000.

THERE ARE several simple types of elementary excitations in crystalline solids, obeying even different statistics, which, when only next neighbour interactions are taken into account, have in common excitation spectra like

$$E(\mathbf{k}) = E_0 - E_1 \sum_{\{\Delta\}} e^{i(\mathbf{k}\Delta)} \tag{1}$$

where the sum extends over all next neighbour lattice vectors $\boldsymbol{\Delta}$. For instance as Bloch electrons in the tight binding approximation, being fermions, as spinwaves in the Heisenberg exchange picture, commonly treated as bosons, have energy eigenvalues of the type (1), which represents the full symmetry of the point group.

Therefore one of the most important characteristics, by which the thermodynamic properties of the crystal are determined, the density of states function, is the same for all these excitations. According to

$$g(E) = \frac{\mathrm{d}}{\mathrm{d}E} \int_{E(\mathbf{k}) \leq E} \mathrm{d}^3\mathbf{k} \tag{2}$$

this function is given by the number of eigenvalues lying between the shells of $E(\mathbf{k}) = E$ and $E(\mathbf{k}) = E + \mathrm{d}E$ in one zone of the $\mathbf{k}$-space.

In terms of the density of states the free energies for Boltzmann–, Fermi–Dirac and Bose–Einstein statistics are given by

$$F_B = -\frac{N}{\beta} \log\left(\int_{-\infty}^{+\infty} e^{-\beta E} g(E)\, \mathrm{d}E \right) \tag{3a}$$

$$F_{\binom{BE}{FD}} = \pm \frac{1}{\beta} \int_{-\infty}^{+\infty} \log\left[1 \mp e^{-\beta(E-\mu)}\right] g(E)\, \mathrm{d}E, \tag{3b,c}$$

respectively, and many thermodynamic functions more may be written as integrals of the form

$$\Phi(\beta) = \int_{-\infty}^{+\infty} f(\beta, E)\, g(E)\, \mathrm{d}E. \tag{4}$$

For cubic crystals the shape of $g(E)$ is well-known already for a very long time, at least for simple and body-centered lattices[1]. But for evaluating the partition function etc., it usually is approximated very roughly by square roots. In that way e.g. Bloch's famous

$T^{3/2}$-law for the variation of the magnetization of ferromagnets with the temperature is derived[2].

To proceed so, is as a rule fully justified whenever the excitations are treated as a gas of free independent particles. The errors involved in this method arising from physical interactions of these excitations, as in the case of ideal gases, increase considerably with the density of excitations present and this density increases exponentially with temperature. Therefore all results obtained in that way are expected to be true only in the limit of very low temperatures. In this case the exponential factor in (3) decreases very rapidly with the energy so that predominantly small energies contribute to the integral, and the approximation by roots is useful just in this limit.

These arguments are no longer valid, as soon as the interactions of the particles are taken into account in some way. Modern quantum statistics provides various methods, such as variational principles, Green's functions technics, the method of quasi-unitary transformations with the concept of quasi-particles related to it, for doing this in a more or less explicit manner. Whenever one of these tools is applied, the behaviour of the thermodynamic observables is expected to be described correctly up to higher temperatures.* But to evaluate them accurately enough the real shape of the density of states has to be taken into account instead of the approximations mentioned above. For this reason the exact evaluation of the density of states newly is of considerable interest for taking full advantage of the possibilities involved in new quantum statistical tools.

On the other hand, except for the simplest limiting cases, the thermodynamic properties may no longer be evaluated exactly but only by numerical calculations using high-speed computers.

The purpose of this paper is to give a detailed investigation of the density of states functions resulting from the spectrum (1) for the cubic space groups. Two of the three integrals in (2) may be carried out exactly leaving simple integrals, which were calculated numerically and are tabulated in this paper. In some cases there is an apparent contradiction to a general theorem given by van Hove[5] which is discussed.

For computational purposes the densities of states are approximated in terms of elementary functions, being available very fast in digital computers with an accuracy that should be sufficient for all practical calculations.

As a very simple example (having no greater physical significance) the magnetization of ferromagnets vs. temperature following from the linear spinwave theory and the exact density of states function is compared with the curve following from Bloch's $T^{3/2}$-theorem.

1. GENERAL PROPERTIES OF THE DENSITY OF STATES

For the cubic space groups the relation (1) leads to the wellknown spectra

$$E(\mathbf{k}) = E_0 - 2E_1\,(\cos k_x + \cos k_y + \cos k_z) \tag{1a}$$

for the simple cubic lattice,

$$E(\mathbf{k}) = E_0 - 4E_1(\cos(k_x/2)\cdot\cos(k_y/2) + \cos(k_x/2)\cdot\cos(k_z/2) + \cos(k_y/2)\cdot\cos(k_z/2)) \tag{1b}$$

for the face-centered lattice and

---

*The thermodynamic observables usually obey integral equations in this case, or at least transcendental equations involving integrals. As to the theory of ferromagnetism, the first attempts in this direction were made by Tjablikov[3] and Englert[4] with the result of

$$\left(\frac{M(T)}{M(0)}\right)^{1} = (2\pi)^{-1}\int_{\infty}^{+\infty} g(E)\cdot\coth\left(\frac{M(T)}{M(0)}\cdot\frac{E}{2kT}\right)\mathrm{d}E$$

for the variation of the relative specific magnetization with temperature.

$$E(\mathbf{k}) = E_0 - 8E_1 \cdot \cos(k_x/2) \cdot \cos(k_y/2) \cdot \cos(k_z/2) \qquad (1c)$$

in case of the body-centered lattice.

There is some information concerning the analytic properties of $g(E)$, which easily can be derived from the range of values and the extremal properties of the function $E(\mathbf{k})$. The formula (2) given for $g(E)$ may be transformed into the following relations:

$$g(E) = \int_S \frac{dS}{|\nabla E(\mathbf{k})|};$$

$$g(E) = \int_B \delta(E - E(\mathbf{k}))\, d^3\mathbf{k}, \qquad (2a, b)$$

where S is the surface of constant energy E, lying in one zone of the k-space. Whereas (2b) is the form, that we shall use as a starting point for the calculations of $g(E)$ in the next section, (2a) is very convenient for general considerations.

At first we notice that $g(E)$ clearly vanishes outside the range of values of $E(\mathbf{k})$, that is outside the intervals

$$E_0 - 6E_1 \leqslant E(\mathbf{k}) \leqslant E_0 + 6E_1 \qquad (5a)$$

$$E_0 - 12E_1 \leqslant E(\mathbf{k}) \leqslant E_0 + 4E_1 \qquad (5b)$$

and

$$E_0 - 8E_1 \leqslant E(\mathbf{k}) \leqslant E_0 + 8E_1 \qquad (5c)$$

for the s.c., f.c.c. and b.c.c. lattice, respectively. Furthermore according to (2a) $g(E)$ must be regular everywhere with exception of the so-called van Hove singularities arising for those values of E, for which $E(\mathbf{k})$ becomes extremal on the surface $S(E)$. These values are easily seen to be

$$\begin{aligned} E &= E_0 \pm 6E_1 \\ E &= E_0 \pm 2E_1 \end{aligned} \qquad (6a)$$

for the s.c.,

$$\begin{aligned} E &= E_0 - 12E_1 \\ E &= E_0 \\ E &= E_0 + 4E_1 \end{aligned} \qquad (6b)$$

for the f.c.c. and

$$\begin{aligned} E &= E_0 \pm 8E_1 \\ E &= E_0 \end{aligned} \qquad (6c)$$

for the b.c.c. lattice, so that the boundaries of the intervals (5) are always van Hove singularities. But there is an important topological difference between two groups of extremal values, giving rise to different types of singularities of $g(E)$. Whereas for equations (6a), the first and second equations of (6b) and the first of (6c) the function $E(\mathbf{k})$ becomes extremal in isolated points of the surfaces $S(E)$, $\nabla E(\mathbf{k})$ vanishes on one-dimensional manifolds on these surfaces for $E = E_0 + 4E_1$ in (6b) and $E = E_0$ in (6c).

2. CALCULATION OF g(E) FOR THE SIMPLE CUBIC LATTICE

After the transformation

$$\frac{E - E_0}{2E_1} \rightarrow E$$

the density of states function for the s.c. lattice is given by the integral

$$g(E) = \frac{1}{2|E_1|} \int_B \delta(E + \cos k_x + \cos k_y + \cos k_z)\, d^3\mathbf{k}, \qquad (7)$$

where the domain of integration is a cube with the sides 2π, lying symmetrically to the origin of coordinates. Henceforward we shall omit the factor $1/2|E_1|$ for simplicity.

Setting $l_i = \cos k_i$ and observing the symmetry this integral is transformed into

$$g(E) = 8 \int_{-1}^{+1} \int_{-1}^{+1} \int_{-1}^{+1} \frac{\delta(E + l_1 + l_2 + l_3)\, dl_1\, dl_2\, dl_3}{[(1 - l_1^2)(1 - l_2^2)(1 - l_3^2)]^{1/2}}. \qquad (8)$$

The integration over l_3, say, is easily performed and leads to

$$g(E) = 8 \iint_{\mathscr{L}} [(1-l_1^2) | (1-l_2^2) \{1-(E+l_1+l_2)^2\}]^{-1/2}\, \mathrm{d}l_1 \mathrm{d}l_2 \quad (9)$$

with the domain $\mathscr{L}$ given by the section of a square of the sides 2, which lies symmetrically to the origin, and the band defined by the inequality

$$|E+l_1+l_2| \leqslant 1. \quad (10)$$

There are three possibilities for this section: (a) for $|E| > 3$ it is empty, so that $g(E) = 0$ in correspondence with the relation (5a), (b) for $1 \leqslant |E| \leqslant 3$ it is a triangle and (c) for $|E| < 1$ it is a band, like that sketched in Fig. 1.

By the substitution $E \rightarrow -E$, $l_1 \rightarrow -l_1'$ and $l_2 \rightarrow -l_2'$ neither the integrand in equation (9), nor the domain of integration are modified, so that $g(E)$ is an even function and we may restrict our calculations to the range of $0 \leqslant E < 3$ henceforward.

Setting

$$I(l_1, l_2) = [(1-l_2^2)\{1-(E+l_1+l_2)^2\}]^{-1/2}, \quad (11)$$

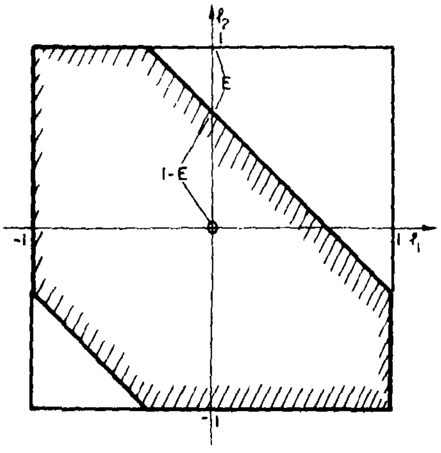

Fig. 1. Domain of integration of (9) for $|E| < 1$ (hatched).

(9) is suitably written as

$$g(E) = 8 \int_{-1}^{2-E} \mathrm{d}l_1 (1-l_1^2)^{-1/2} \int_{-1}^{(1-E)-l_1} \mathrm{d}l_2\, I(l_1, l_2) \quad (12a)$$

for $1 \leqslant E < 3$ and

$$g(E) = 8\left\{ \int_{-1}^{-E} \frac{\mathrm{d}l_1}{(1-l_1^2)^{1/2}} \int_{-1-E-l_1}^{1} \mathrm{d}l_2\, I(l_1, l_2) + \int_{-E}^{1} \frac{\mathrm{d}l_1}{(1-l_1^2)^{1/2}} \int_{-1}^{(1-E)-l_1} \mathrm{d}l_2\, I(l_1, l_2) \right\} \quad (12b)$$

for $0 \leqslant E < 1$. The integration over l_2 may be performed explicitly and leads to complete elliptic integrals[6] of the first kind, namely to $K'[(E+l_1)/2]$ in (12a) and to $K'[-(E+l_1)/2]$ and $K'[(E+l_1)/2]$, respectively, in (12b), where $K'(x)$ is the first complete elliptic integral of the complementary modul

$$K'(x) = K(x') = K(\sqrt{1-x^2}). \quad (13)$$

In this way, $g(E)$ is reduced to simple integrals*:

$$g(E) = 8 \int_{-1}^{2-E} (1-l^2)^{-1/2} K'\left(\frac{E+l}{2}\right) \mathrm{d}l \quad (14a)$$

for $+1 \leqslant E < 3$ and

$$g(E) = 8\left\{ \int_{-1}^{-E} (1-l^2)^{-1/2} K'\left(\frac{-E-l}{2}\right) \mathrm{d}l + \int_{-E}^{1} (1-l^2)^{-1/2} K'\left(\frac{E+l}{2}\right) \mathrm{d}l \right\} \quad (14b)$$

for $0 \leqslant E < 1$. These integrals must be evaluated numerically.* The function $g(E)$ is plotted in Fig. 2 and compared with its approximation by square-roots, which proves to be sufficient for very small values of E only.

---

*These formulae were obtained and evaluated formerly by T. A. Hoffmann[7] in a paper concerning A-B-type alloys.

The density of states function is continuous everywhere. The van Hove singularities show themselves as discontinuities in the slope, which becomes infinite at the points given by equation (6a). In the vicinity of these singularities $g(E)$ is approximated very well by

$$g(E) = g(E_s) + \alpha_s \sqrt{(|E-E_s|)} \qquad (15)$$

on that side, for which the *infinity* occurs. For $E_s = 3$ this is the square-root approximation by

$$g(3-\epsilon) = 4\sqrt{2}\,\pi\sqrt{\epsilon} \qquad (16)$$

mentioned above, which is easily derived by an expansion of the *cos*-functions in (7) to the second order and integration over a sphere.

3. THE DENSITY OF STATES FUNCTION FOR BODY-CENTERED LATTICES

For the sake of simplicity we now at first calculate $g(E)$ for body-centered lattices.

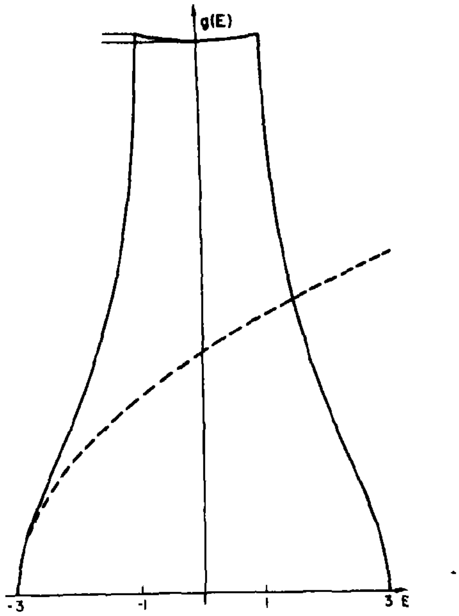

Fig. 2. The density of states for the s.c. lattice. The dashed curve is the standard approximation by square-roots (see equation (16)). The lowering of the plateau for $|E| \leq 1$ is indicated by the parallel horizontal lines.

After the transformation

$$\frac{E-E_0}{8E_1} \rightarrow E$$

we have to evaluate the integral

$$g(E) = \frac{2}{8|E_1|}\int_0^{2\pi}\int_0^{2\pi}\int_0^{2\pi} \delta(E+\cos(k_x/2) \cdot \cos(k_y/2) \cdot \cos(k_z/2))\mathrm{d}^3\mathbf{k}, \qquad (17)$$

where the domain of integration is a cube with the sides 2π†. Omitting the factor $1/8\ |E_1|$

---

*There is another very elegant representation of $g(E)$ in the case of the s.c. lattice, also starting from equation (7). By means of a Fourier-transformation and using the relation

$$J_0(x) = \frac{1}{\pi}\int_0^{\pi} e^{ix\cos t}\mathrm{d}t$$

for the Bessel-functions, $g(E)$ is found to be

$$g(E) = \frac{1}{\pi}\int_0^{\infty} \cos(Et)\ J_0^3(t)\,\mathrm{d}t$$

for all values of E. Koster and Slater [8] and Wolfram and Callaway [9] have started from this formula for computations of the density of states function. But there some problems of accuracy arise in connection with the fact, that $g(E)$ is given by an improper integral. The computations must be performed from 0 to T and it is difficult to estimate the error induced by neglecting the contribution from T to ∞. So the proper integrals (14) are more convenient for numerical calculations.

†Originally the integration has to be performed over the first Brillouin-zone. But it may be restricted at once to the part with $k_i \geq 0$ because of the symmetry of $E(\mathbf{k})$. Moreover $E(\mathbf{k})$ is invariant under the transformations $k_i \rightarrow 2\pi - k_i$, $k_j \rightarrow 2\pi - k_j$, $k_e \rightarrow k_e$ and the octant of the Brillouin-zone is reproduced by such a transformation. Therefore the domain of integration may be chosen as the cube from 0 to 2π, as is done in equation (17).

and substituting $l_i = \cos(k_i/2)$ we immediately get

$$g(E) = 16 \int_{-1}^{+1}\int_{-1}^{+1}\int_{-1}^{+1} \times \frac{\delta(E + l_1 l_2 l_3)\, dl_1 dl_2 dl_3}{[(1-l_1^2)(1-l_2^2)(1-l_3^2)]^{1/2}}. \qquad (18)$$

By virtue of the relation for δ -functions $\delta(ax) = \frac{1}{|a|}\ \delta(x)$ the integration over l_3, say, leads to the function

$$\begin{aligned} I_2(l_1, l_2, E) &= \int_{-1}^{+1} \frac{\delta(l_1 l_2 [E/l_1 l_2 + l_3])\, dl_3}{(1-l_3^2)^{1/2}} \\ &= \frac{1}{|l_1 l_2|}\int_{-1}^{+1} \frac{\delta(E/l_1 l_2 + l_3) dl_3}{(1-l_3^2)^{1/2}} \qquad (19) \\ &= \begin{cases} [(l_1 l_2)^2 - E^2]^{-1/2} & \text{for } |E/l_1 l_2| \leqslant 1 \\ 0 & \text{otherwise.} \end{cases} \end{aligned}$$

Therefore in

$$\begin{aligned} g(E) &= 16 \int_{1}^{+1}\int_{-1}^{+1} \frac{I_2(l_1, l_2, E)\, dl_1 dl_2}{[(1-l_1^2)(1-l_2^2)]^{1/2}} \\ &= 16 \int_{J} [(1-l_1^2)(1-l_2^2) \\ &\quad \times \{(l_1 l_2)^2 - E^2\}]^{-1/2} dl_1 dl_2 \qquad (20) \end{aligned}$$

the integration must be performed over the section of the square with sides 2 and the domain given by the inequality $\left|\frac{E}{l_1 l_2}\right| \leqslant 1$. This range is illustrated in Fig. 3 for a certain $|E| < 1$. For $|E| \geqslant 1$ the domain of integration vanishes and so does $g(E)$ in correspondence with equation (5c).

As in case of the s.c. lattice, $g(E)$ is an even function, because the integrand and the domain of integration are invariant under the transformation $E \rightarrow -E$. Moreover they are invariant under $l_1 \rightarrow -l_1$ and $l_2 \rightarrow -l_2$, independently, so that the integration may be restricted to one quadrant of the square.

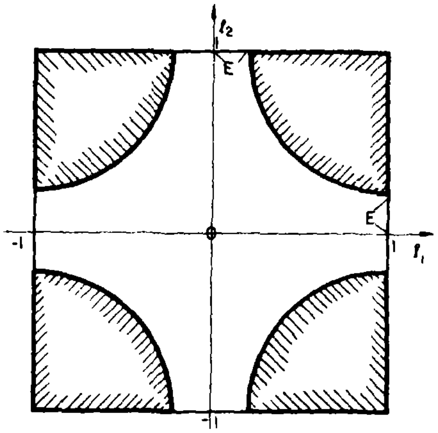

Fig. 3. Domain of integration of (20) (hatched).

This is done as

$$g(E) = 64 \int_{E}^{1} \frac{I_1(l_1, E)\, dl_1}{(1-l_1^2)^{1/2}} \qquad (21)$$

defining $I_1(l_1, E)$ by

$$I_1(l_1, E) = \int_{E/l_1}^{1} [(1-l_2)^2 \times \{(l_1 l_2)^2 - E^2\}]^{-1/2} dl_2. \qquad (22)$$

$I_1(l_1, E)$ again may be written in elliptic integrals and, taking advantage of the relation

$$K\left(\frac{1-x}{1+x}\right) = \frac{1+x}{2} K'(x) \qquad (23)$$

gives

$$I_1(l_1, E) = \frac{K'(E/l_1)}{l_1}. \qquad (24)$$

In that way we are finally left with the single integral

$$g(E) = 64 \int_{E}^{1} \frac{K'(x)\, dx}{(x^2 - E^2)^{1/2}}, \qquad (25)$$

which must be evaluated numerically.

For $E = 1-\epsilon$, $g(E)$ is approximated by

$$g(1-\epsilon) = 32\sqrt{2}\pi\sqrt{\epsilon}, \tag{26}$$

as may be evaluated directly from (17), when $E(\mathbf{k})$ is expanded in $\mathbf{k}^2$. At the point of the van Hove singularity $E = 0$ the function $g(E)$ becomes infinite. Because $K'(k)$ is a majorant to $\log(4/k)$,

$$\begin{aligned} g(0) &= 64\int_0^1 \frac{K'(k)}{k}\,\mathrm{d}k \\ &\geqslant 64\int_0^1 \frac{\log(4/k)\,\mathrm{d}k}{k} \end{aligned} \tag{27}$$

holds, and the latter integral diverges.

$g(E)$ is illustrated in Fig. 4, where also the approximation (26) is plotted.

4. g(E) FOR FACE-CENTERED LATTICES

In case of the f.c.c. lattice things are more complicated than for the other cubic lattices.

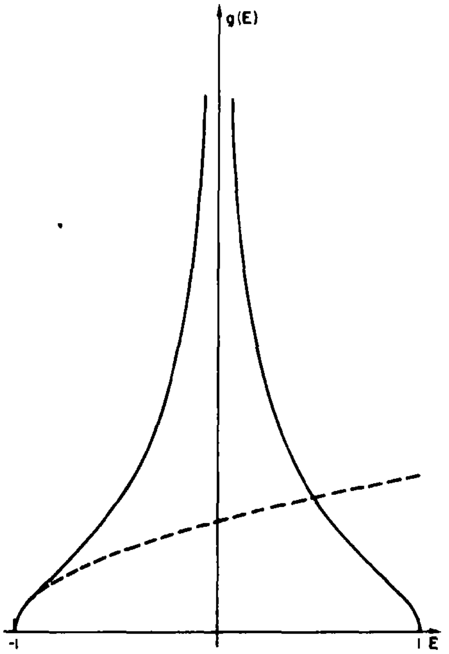

Fig. 4. The density of states for the b.c.c. lattice. The approximation (26) is plotted in dashed lines.

After the transformation

$$\frac{E-E_0}{4E_1} \rightarrow E$$

we at first get

$$g(E) = \frac{4}{4|E_1|}\int_0^{2\pi}\int_0^{2\pi}\int_0^{2\pi} \delta(E+\cos(k_x/2)\cdot\cos(k_y/2) + \cos(k_x/2)\cdot\cos(k_z/2) + \cos(k_y/2)\cdot\cos(k_z/2))\mathrm{d}^3\mathbf{k}. \tag{28}$$

The domain of integration again can be chosen to be a cube with the sides 2π*. Equation (28) is transformed into

$$g(E) = 32\int_{-1}^{+1}\int_{-1}^{+1}\int_{-1}^{+1} \times\frac{\delta(E+l_1l_2+l_1l_3+l_2l_3)\,\mathrm{d}l_1\,\mathrm{d}l_2\,\mathrm{d}l_3}{[(1-l_1^2)(1-l_2^2)(1-l_3^2)]^{1/2}} \tag{29}$$

by the substitution of $l_i = \cos(k_i/2)$: and the integration over l_3 leads to

$$I_2(l_1, l_2, E) = \int_{-1}^{+1} \frac{\delta(E+l_1l_2+l_1l_3+l_2l_3)\,\mathrm{d}l_3}{(1-l_3^2)^{1/2}}$$

$$= \begin{cases} [(l_1+l_2)^2-(E+l_1l_2)^2]^{-1/2} & \text{for } \left|\dfrac{E+l_1l_2}{l_1+l_2}\right| \leqslant 1 \\ 0 & \text{otherwise} \end{cases} \tag{30}$$

The factor $1/4|E_1|$ again is omitted from equation (29) forward. So the domain $\mathscr{L}$ of the double integral

---

*The arguments for choosing this domain are similar to those given for the b.c.c. lattice. The integrand is invariant under the transformation $k_i \rightarrow 2\pi - k_i$ in this case and the part of the Brillouin-zone with $k_i \geqslant 0$ is reproduced by it. Therefore the integral over the cube has a quarter of the value that the integral over the Brillouin-zone has.

$$g(E) = 32 \iint [(1 - l_1^2)(1 - l_2^2)\{(l_1 + l_2)^2 - (E + l_1 l_2)^2\}]^{-1/2}\, \mathrm{d}l_1 \mathrm{d}l_2, \qquad (31)$$

we are left with, is that part of the range $\left|\dfrac{E + l_1 l_2}{l_1 + l_2}\right| \leqslant 1$, lying inside the square with sides 2 symmetrical to the origin of coordinates. Again this domain vanishes in correspondence to relation (5b), i.e. for $E > 1$ and $E < -3$ and so does $g(E)$.

The borders of the domain of integration

$$l_2 = \left(\frac{E - l_1}{1 - l_1}\right), \quad l_2 = -\left(\frac{E + l_1}{1 + l_1}\right) \qquad (32)$$

are monotonely falling curves for all $E \in (-3, 1)$ and for different values of E three different types of domains must be distinguished. These types are illustrated in the Figs. 5(a–c), with the statement of the ranges of E, which they are valid for.

There is a symmetry of the integrand and the domain of integration under the transformation $l_1 \to -l_1$, $l_2 \to -l_2$, so that the integration may be restricted to the part right of the line $l_2 = -l_1$. But there is no more symmetry with respect to $E \to -E$ and therefore $g(E)$ is not a symmetrical function for the f.c.c. lattice.

Defining

$$I_1(l_1, E) = \int_{L(E)}^{1} [(1 - l_2^2)\{(l_1 + l_2)^2 - (E + l_1 l_2)^2\}]^{-1/2}\, \mathrm{d}l_2, \qquad (33)$$

where $L(E)$ is the lower boundary of the domain of integration, the density of states becomes

$$g(E) = 64 \int_{-\left(\frac{E+1}{2}\right)}^{1} \frac{I_1(l_1, E)\, \mathrm{d}l_1}{(1 - l_1^2)^{1/2}}. \qquad (34)$$

As is well known, the sequence of the zeros of the denominator is crucial for the result of integrals like (33). As these zeros are given

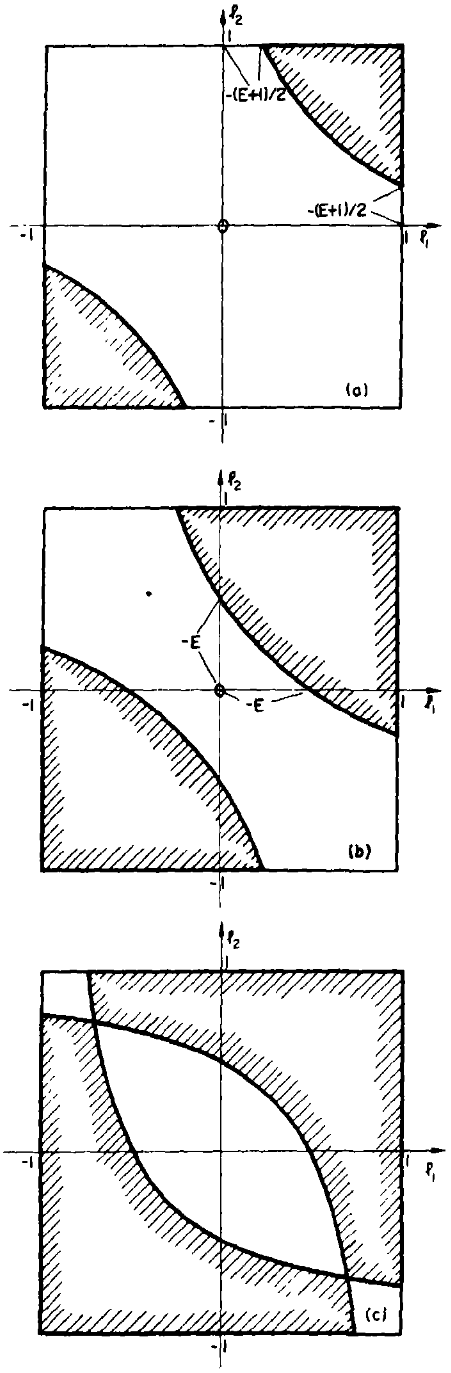

Fig. 5. Domain of integration of (31) (hatched) (a) for $-3 < E \leqslant -1$, (b) for $-1 < E \leqslant 0$, (c) for $0 < E \leqslant 1$.

by the borders of the domain of integration, i.e. $|l_2| = 1$ and the functions (32), this succession changes, whenever two of these curves intersect. So the interval $[-1, +1]$ of l_1 is divided into several parts by these points of intersection, as can be seen in the Figs. 5, and there will be different results for $I_1(l_1, E)$ in different intervals.

For $-3 \leqslant E \leqslant -1$ only one of these intervals comes into the play (see Fig. 5(a)). $I_1(l_1, E)$ is found to be

$$I_1(l_1,E) = (l_1^2-E)^{-1/2}K'\left(\frac{1-E}{2}\cdot\frac{1}{(l_1^2-E)^{1/2}}\right) \tag{35a}$$

in this case.

For $-1 < E \leqslant 0$ two regions must be distinguished (see Fig. 5(b))

$$I_1(l_1,E) = \begin{cases} \dfrac{2}{1-E}K'\left(\dfrac{2}{1-E}(l_1^2-E)^{1/2}\right) & \text{for } -\left(\dfrac{E+1}{2}\right) \leqslant l_1 \leqslant \left(\dfrac{E+1}{2}\right) \\[2ex] (l_1^2-E)^{-1/2}K'\left(\dfrac{1-E}{2}\cdot\dfrac{1}{(l_1^2-E)^{1/2}}\right) & \text{for } \dfrac{E+1}{2} < l_1 \leqslant 1 \end{cases} \tag{35b}$$

and for $0 < E \leqslant 1$ the l_1-interval must be divided into 4 parts according to Fig. 5(c), providing for $I_1(l_1, E)$ the results

$$I_1(l_1,E) = \begin{cases} \dfrac{2}{1-E}K'\left(\dfrac{2}{1-E}(l^2-E)^{1/2}\right) & \text{for } -\left(\dfrac{E+1}{2}\right) \leqslant l_1 \leqslant -\sqrt{E} \\[2ex] \left[\left(\dfrac{1+E}{2}\right)^2-l_1^2\right]^{-1/2}K\left(\dfrac{1-E}{2}\left[\left(\dfrac{1+E}{2}\right)^2-l_1^2\right]^{-1/2}\right) & \text{for } -\sqrt{E} < l_1 \leqslant \sqrt{E} \\[2ex] \dfrac{2}{1-E}K'\left(\dfrac{2}{1-E}(l_1^2-E)^{1/2}\right) & \text{for } \sqrt{E} < l_1 \leqslant \dfrac{E+1}{2} \\[2ex] (l_1^2-E)^{-1/2}K'\left(\dfrac{1-E}{2}\cdot\dfrac{1}{(l_1^2-E)^{1/2}}\right) & \text{for } \dfrac{E+1}{2} < l_1 \leqslant 1. \end{cases} \tag{35c}$$

With (34) and (35) we finally get for the density of states

$$g(E) = 64 \int\limits_{-\left(\frac{E+1}{2}\right)}^{1} \frac{K'\left[\dfrac{1-E}{2}(l_1^2-E)^{-1/2}\right]}{[(l_1^2-E)(1-l_1^2)]^{1/2}}\,\mathrm{d}l_1 \quad \text{for } -3 \leqslant E \leqslant -1, \tag{36a}$$

$$g(E) = 64\left\{\int\limits_{\left(\frac{E+1}{2}\right)}^{1} \frac{K'\left[\dfrac{1-E}{2}(l_1^2-E)^{-1/2}\right]}{[(l_1^2-E)(1-l_1^2)]^{1/2}}\mathrm{d}l_1 + \frac{4}{1-E}\int\limits_{0}^{\left(\frac{E+1}{2}\right)} \frac{K'\left[\dfrac{2}{1-E}(l_1^2-E)^{1/2}\right]}{(1-l_1^2)^{1/2}}\mathrm{d}l_1\right\} \tag{36b}$$

for $-1 < E \leqslant 0$

and

$$g(E) = 64\left\{ \int_{\left(\frac{E+1}{2}\right)}^{1} \frac{K'\left[\frac{1-E}{2}(l_1{}^2-E)^{-1/2}\right]}{[(l_1{}^2-E)(1-l_1{}^2)]^{1/2}}\mathrm{d}l_1 + \frac{4}{1-E}\int_{\sqrt{E}}^{\left(\frac{E+1}{2}\right)} \frac{K'\left[\frac{2}{1-E}(l_1{}^2-E)^{1/2}\right]}{(1-l_1{}^2)^{1/2}}\mathrm{d}l_1 \right.$$

$$\left. +2\int_0^{\sqrt{E}} \frac{K\left[\frac{1-E}{2}\left\{\left(\frac{1+E}{2}\right)^2-l_1{}^2\right\}^{-1/2}\right]}{\left[(1-l_1{}^2)\left\{\left(\frac{1+E}{2}\right)^2-l_1{}^2\right\}\right]^{1/2}}\mathrm{d}l_1\right\} \quad \text{for } 0 < E \leqslant 1. \qquad (36c)$$

In these formulae we have taken advantage of some simple symmetries of the integrands.

The integrals in equation (36) again must be computed numerically. The result is plotted in Fig. 6.

In accordance with direct calculations from equation (28) $g(E)$ begins like

$$g(E) = 16\pi\sqrt{\epsilon} \qquad (37)$$

for $E = \epsilon - 3$. For $E = -1$ (that is the point, where (36a) and (36b) interfere) there is no van Hove singularity and $g(E)$ is a smooth function in this point, but in $E = 0$ such a singularity exists. As in case of the s.c. lattice $g(E)$ is continuous in this point, but has an infinite slope. At $E = 1$ there is another van Hove singularity that one being a pole of $g(E)$. For $g(1)$ is infinite, because

$$g(1) = 128\,K(0)\int_0^1 \frac{\mathrm{d}l_1}{1-l_1{}^2} \qquad (38)$$

diverges.

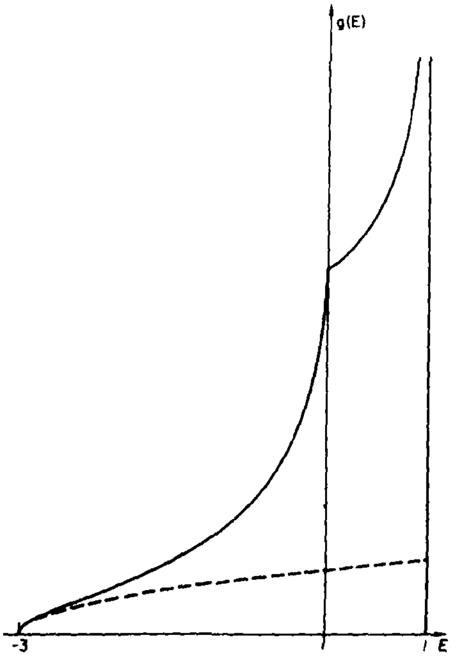

Fig. 6. The density of states for the f.c.c. lattice. The approximation (37) is plotted in dashed lines.

5. THE SINGULARITIES OF THE DENSITY OF STATES

As we have seen, there are two types of singularities, which may occur in the density of states function. The first one, realised at $E = 0$ for the b.c.c. lattice and at $E = 1$ in case of the f.c.c lattice, is a logarithmic peak. For the second type, occuring for all singular points of the s.c. lattice, for $E = \pm 1$ in the b.c.c. and for $E = -3$ and $E = 0$ for the f.c.c lattice, $g(E)$ is a continuous and finite function, but has an infinity in its slope.

It is worth mentioning that there is apparently a contradiction to a theorem of van Hove[5] or at least to *a wide-spread opinion as to its contents*. This theorem states that the density of states for three dimensional periodic lattices always should have at least four singular points with singularities only of the second type mentioned above. But for its derivation van Hove confined himself to the case of spectra, which possess zeros of $\nabla E(\mathbf{k})$ only in isolated points in the $\mathbf{k}$-space.

Indeed for singular points, where this assumption is fulfilled, his theorem holds in our calculations. But for $E = 0$ for the b.c.c. and $E = 1$ for the f.c.c. lattice we, have seen in section 1 that $\nabla E(\mathbf{k})$ vanishes on onedimensional manifolds in the **k**-space and so his condition is not met. For these values of E the function $g(E)$ may have logarithmic infinities, as van Hove remarks, and indeed, in those cases we have been concerned with it has.

6. RESULTS OF NUMERICAL CALCULATIONS AND APPROXIMATION FUNCTIONS

The formulae (14), (25) and (36) for the density of states were evaluated on a digital computer* with an accuracy of more than 1 per 10000†. Special care was taken of some characteristic points as $E = 1$ and $E = 0$ for the s.c. lattice and $E = 0$ for the f.c.c. lattice.

The results of these computations are tabulated in the second column of the Tables 1-3 for the three lattice types.

With regard to the fact that integrals like those given by equation (4) must be evaluated for obtaining thermodynamic functions, it seems desirable to give simple approximation functions for the density of states, which are very fast available in computers.

In reference to the kind of singularities that $g(E)$ and its slope possess in the critical points, such approximation functions were formulated and adapted to the density of states with a relative error of less than 1 per 1000.

This accuracy is achieved by

$$g(E) = \begin{cases} \sqrt{(3-|E|)}[(80\cdot3702 - 16\cdot3846(3-|E|) + 0\cdot78978(3-|E|)^2) \\ \quad + (-44\cdot2639 + 3\cdot66394(3-|E|) - 0\cdot17248(3-|E|)^2)\sqrt{(|E|-1)}] \quad \text{for} \quad 1 \leqslant |E| \leqslant 3 \\ 70\cdot7801 + 1\cdot0053\,E^2 \quad \text{for} \quad |E| < 1 \\ 0 \quad \text{for} \quad |E| > 3 \end{cases} \tag{39a}$$

for the s.c. lattice,

$$g(E) = \begin{cases} 2\sqrt{(1-|E|)} \cdot \ln^2\left(\dfrac{5\cdot845}{|E|}\right) \cdot \\ \quad (16\cdot6791 + 3\cdot6364|E| + 2\cdot4880 \cdot |E|^2) \quad \text{for} \quad |E| < 1 \\ 0 \quad \text{for} \quad |E| \geqslant 1 \end{cases} \tag{39b}$$

for the b.c.c. lattice and

$$g(E) = \begin{cases} 4\sqrt{(3+E)}[(-85\cdot9325 + 101\cdot103(3+E) - 16\cdot2885(3+E)^2) \\ \quad + (56\cdot8683 - 47\cdot1215(3+E) + 2\cdot9045(3+E)^2)\sqrt{E}] \quad \text{for} \quad -3 < E < 0 \\ 4[(122\cdot595 - 19\cdot4100E + 1\cdot76011E^2) + (-44\cdot8100 + 7\cdot18628E)\ln(1-E)] \\ \quad \text{for} \quad 0 \leqslant E \leqslant 1 \\ 0 \quad \text{for} \quad -3 \leqslant E, E > 1 \end{cases} \tag{39c}$$

for the f.c.c. lattice.

These functions are tabulated in the third

---

*X 1, Rechenzentrum der Universität Kiel.

†For details of the computations see the appendix.

Table 1. g(E) *for the s.c. lattice.* g(−E) = g(E)

E	$g(E)$ exact	$g(E)$ approx.	Diff.	Rel. error (× 1000)
3·0000	0	0	0	–
2·9900	+1·7816	+1·7816	−0·5058$_{10}$−05	−0·0028
2·9800	+2·5259	+2·5259	−0·1823$_{10}$−04	−0·0072
2·9700	+3·1014	+3·1014	−0·2541$_{10}$−04	−0·0082
2·9600	+3·5902	+3·5903	−0·3291$_{10}$−04	−0·0092
2·9500	+4·0242	+4·0242	−0·4937$_{10}$−04	−0·0123
2·9000	+5·7643	+5·7644	−0·9868$_{10}$−04	−0·0171
2·8500	+7·1521	+7·1523	−0·1322$_{10}$−03	−0·0185
2·8000	+8·3683	+8·3685	−0·1542$_{10}$−03	−0·0184
2·7500	+9·4825	+9·4826	−0·1546$_{10}$−03	−0·0163
2·7000	+10·5302	+10·5304	−0·1790$_{10}$−03	−0·0170
2·6500	+11·5330	+11·5331	−0·6282$_{10}$−04	−0·0054
2·6000	+12·5047	+12·5047	−0·4871$_{10}$−04	−0·0039
2·5500	+13·4554	+13·4554	−0·3028$_{10}$−04	−0·0023
2·5000	+14·3926	+14·3926	−0·2491$_{10}$−04	−0·0017
2·4500	+15·3223	+15·3223	+0·3363$_{10}$−04	+0·0022
2·4000	+16·2493	+16·2492	+0·6035$_{10}$−04	+0·0037
2·3500	+17·1778	+17·1777	+0·7866$_{10}$−04	+0·0046
2·3000	+18·1114	+18·1114	−0·8078$_{10}$−05	−0·0004
2·2500	+19·0538	+19·0537	+0·2221$_{10}$−04	+0·0012
2·2000	+20·0076	+20·0077	−0·1094$_{10}$−03	−0·0055
2·1500	+20·9764	+20·9766	−0·1769$_{10}$−03	−0·0084
2·1000	+21·9630	+21·9633	−0·3270$_{10}$−03	−0·0149
2·0500	+22·9706	+22·9710	−0·4490$_{10}$−03	−0·0195
2·0000	+24·0024	+24·0029	−0·5400$_{10}$−03	−0·0225
1·9500	+25·0617	+25·0624	−0·6718$_{10}$−03	−0·0268
1·9000	+26·1521	+26·1530	−0·8619$_{10}$−03	−0·0330
1·8500	+27·2777	+27·2787	−0·9540$_{10}$−03	−0·0350
1·8000	+28·4428	+28·4438	−0·1014$_{10}$−02	−0·0356
1·7500	+29·6524	+29·6533	−0·9437$_{10}$−03	−0·0318
1·7000	+30·9120	+30·9128	−0·8320$_{10}$−03	−0·0269
1·6500	+32·2282	+32·2287	−0·5412$_{10}$−03	−0·0168
1·6000	+33·6085	+33·6087	−0·1630$_{10}$−03	−0·0048
1·5500	+35·0621	+35·0617	+0·4342$_{10}$−03	+0·0124
1·5000	+36·6000	+36·5988	+0·1216$_{10}$−02	+0·0332
1·4500	+38·2360	+38·2337	+0·2267$_{10}$−02	+0·0593
1·4000	+39·9876	+39·9840	+0·3616$_{10}$−02	+0·0904
1·3500	+41·8777	+41·8725	+0·5234$_{10}$−02	+0·1250
1·3000	+43·9374	+43·9304	+0·6993$_{10}$−02	+0·1592
1·2500	+46·2112	+46·2024	+0·8790$_{10}$−02	+0·1902
1·2000	+48·7670	+48·7564	+0·1059$_{10}$−01	+0·2171
1·1500	+51·7176	+51·7059	+0·1165$_{10}$−01	+0·2253
1·1000	+55·2820	+55·2707	+0·1126$_{10}$−01	+0·2037
1·0500	+60·0209	+60·0136	+0·7336$_{10}$−02	+0·1222
1·0400	+61·2437	+61·2379	+0·5786$_{10}$−02	+0·0945
1·0300	+62·6382	+62·6343	+0·3872$_{10}$−02	+0·0618
1·0200	+64·3008	+64·2991	+0·1655$_{10}$−02	+0·0257
1·0100	+66·4796	+66·4807	−0·1045$_{10}$−02	−0·0157
1·0000	+71·7854	+71·7854	+0·3907$_{10}$−06	+0·0000
0·9000	+71·5866	+71·5944	−0·7793$_{10}$−02	−0·1089
0·8000	+71·4120	+71·4235	−0·1149$_{10}$−01	−0·1609
0·7000	+71·2604	+71·2727	−0·1230$_{10}$−01	−0·1726
0·6000	+71·1308	+71·1420	−0·1121$_{10}$−01	−0·1576
0·5000	+71·0223	+71·0314	−0·9125$_{10}$−02	−0·1285
0·4000	+70·9345	+70·9409	−0·6448$_{10}$−02	−0·0909
0·3000	+70·8667	+70·8706	−0·3877$_{10}$−02	−0·0547
0·2000	+70·8185	+70·8203	−0·1812$_{10}$−02	−0·0256
0·1000	+70·7897	+70·7902	−0·4530$_{10}$−03	−0·0064
0·0000	+70·7809	+70·7801	+0·8000$_{10}$−03	+0·0113

Table 2. g(E) *for the b.c.c. lattice.* g(−E) = g(E)

E	$g(E)$ exact	$g(E)$ approx.	Diff.	Rel. error (× 1000)
1·0000	0	0	0	–
0·9990	+4·4992	+4·4992	$+0{\cdot}1001_{10}-04$	+0·0022
0·9940	+11·0624	+11·0626	$-0{\cdot}2026_{10}-03$	−0·0183
0·9890	+15·0352	+15·0359	$-0{\cdot}6153_{10}-03$	−0·0409
0·9840	+18·2021	+18·2032	$-0{\cdot}1164_{10}-02$	−0·0639
0·9790	+20·9326	+20·9344	$-0{\cdot}1816_{10}-02$	−0·0867
0·9700	+25·1924	+25·1954	$-0{\cdot}3001_{10}-02$	−0·1191
0·9600	+29·3150	+29·3197	$-0{\cdot}4694_{10}-02$	−0·1601
0·9500	+33·0314	+33·0377	$-0{\cdot}6319_{10}-02$	−0·1913
0·9400	+36·4692	+36·4774	$-0{\cdot}8185_{10}-02$	−0·2244
0·9300	+39·7044	+39·7144	$-0{\cdot}1001_{10}-01$	−0·2521
0·9200	+42·7864	+42·7980	$-0{\cdot}1163_{10}-01$	−0·2718
0·9100	+45·7490	+45·7624	$-0{\cdot}1342_{10}-01$	−0·2932
0·9000	+48·6174	+48·6325	$-0{\cdot}1509_{10}-01$	−0·3104
0·8500	+62·0846	+62·1068	$-0{\cdot}2224_{10}-01$	−0·3583
0·8000	+74·9000	+74·9262	$-0{\cdot}2620_{10}-01$	−0·3499
0·7500	+87·6892	+87·7158	$-0{\cdot}2665_{10}-01$	−0·3039
0·7000	+100·8432	+100·8667	$-0{\cdot}2353_{10}-01$	−0·2333
0·6500	+114·6762	+114·6938	$-0{\cdot}1760_{10}-01$	−0·1535
0·6000	+129·4910	+129·5014	$-0{\cdot}1040_{10}-01$	−0·0803
0·5500	+145·6196	+145·6234	$-0{\cdot}3770_{10}-02$	−0·0259
0·5000	+163·4598	+163·4594	$+0{\cdot}3626_{10}-03$	+0·0022
0·4500	+183·5182	+183·5197	$-0{\cdot}1542_{10}-02$	−0·0084
0·4000	+206·4780	+206·4903	$-0{\cdot}1229_{10}-01$	−0·0595
0·3500	+233·3040	+233·3404	$-0{\cdot}3641_{10}-01$	−0·1561
0·3000	+265·4400	+265·5152	$-0{\cdot}7516_{10}-01$	−0·2831
0·2500	+305·1800	+305·3124	$-0{\cdot}1324_{10}+00$	−0·4338
0·2000	+356·5020	+356·7084	$-0{\cdot}2064_{10}+00$	−0·5789
0·1500	+427·1880	+427·4655	$-0{\cdot}2775_{10}+00$	−0·6495
0·1000	+535·6560	+535·9481	$-0{\cdot}2921_{10}+00$	−0·5454
0·0900	+565·5520	+565·8279	$-0{\cdot}2759_{10}+00$	−0·4878
0·0800	+599·8120	+600·0594	$-0{\cdot}2474_{10}+00$	−0·4124
0·0700	+639·7260	+639·9278	$-0{\cdot}2018_{10}+00$	−0·3155
0·0600	+687·2220	+687·3560	$-0{\cdot}1340_{10}+00$	−0·1950
0·0500	+745·3600	+745·3972	$-0{\cdot}3724_{10}-01$	−0·0500
0·0450	+779·9280	+779·9015	$+0{\cdot}2653_{10}-01$	+0·0340
0·0400	+819·4140	+819·3107	$+0{\cdot}1033_{10}+00$	+0·1261
0·0350	+865·2560	+865·0594	$+0{\cdot}1966_{10}+00$	+0·2272
0·0300	+919·5940	+919·2895	$+0{\cdot}3045_{10}+00$	+0·3311
0·0250	+985·8300	+985·3951	$+0{\cdot}4349_{10}+00$	+0·4412
0·0200	+1069·7920	+1069·2077	$+0{\cdot}5843_{10}+00$	+0·5461
0·0150	+1182·7460	+1181·9976	$+0{\cdot}7484_{10}+00$	+0·6328
0·0100	+1350·9420	+1350·0646	$+0{\cdot}8774_{10}+00$	+0·6495
0·0050	+1662·8480	+1662·1817	$+0{\cdot}6663_{10}+00$	+0·4007
0·0000	Infinite	Infinite	–	–

column of Tables 1–3, whereas the difference and relative error of this approximation are given in the fourth and fifth columns.

After all the accuracy of the calculations was checked by integration over the $g(E)$-functions from $-\infty$ to $+\infty$, where the exact integrals are known. The results of this test are given in Table 4.

7. THE CONTRIBUTIONS OF THE SINGULARITIES OF g(E) TO INTEGRALS, LIKE EQUATION (4)

There are no further difficulties in the numerical evaluation of integrals like

$$\Phi(\beta) = \int_{-\infty}^{+\infty} f(\beta, E) g(E) \mathrm{d}E \qquad (4)$$

for the s.c. lattice.

Table 3. g(E) for the f.c.c. lattice

E	$g(E)$ exact	$g(E)$ approx.	Diff.	Rel. error (× 1000)
−3·0000	0	0	0	–
−2·9950	+3·5588	+3·5586	+0·1258$_{10}$−03	+0·0353
−2·9900	+5·0392	+5·0388	+0·3352$_{10}$−03	+0·0665
−2·9850	+6·1794	+6·1789	+0·5388$_{10}$−03	+0·0872
−2·9800	+7·1443	+7·1435	+0·8059$_{10}$−03	+0·1128
−2·9750	+7·9976	+7·9965	+0·1101$_{10}$−02	+0·1377
−2·9700	+8·7720	+8·7706	+0·1449$_{10}$−02	+0·1652
−2·9600	+10·1546	+10·1525	+0·2127$_{10}$−02	+0·2095
−2·9500	+11·3820	+11·3791	+0·2859$_{10}$−02	+0·2512
−2·9400	+12·5000	+12·4963	+0·3643$_{10}$−02	+0·2915
−2·9300	+13·5359	+13·5314	+0·4475$_{10}$−02	+0·3306
−2·9200	+14·5074	+14·5021	+0·5277$_{10}$−02	+0·3638
−2·9100	+15·4268	+15·4206	+0·6129$_{10}$−02	+0·3973
−2·9000	+16·3029	+16·2960	+0·6945$_{10}$−02	+0·4260
−2·8000	+23·6626	+23·6486	+0·1401$_{10}$−01	+0·5921
−2·7000	+29·7641	+29·7469	+0·1717$_{10}$−01	+0·5770
−2·6000	+35·3238	+35·3082	+0·1557$_{10}$−01	+0·4408
−2·5000	+40·6228	+40·6129	+0·9867$_{10}$−02	+0·2429
−2·4000	+45·8104	+45·8100	+0·4099$_{10}$−03	+0·0089
−2·3000	+50·9836	+50·9940	−0·1041$_{10}$−01	−0·2041
−2·2000	+56·2120	+56·2336	−0·2157$_{10}$−01	−0·3838
−2·1000	+61·5528	+61·5841	−0·3128$_{10}$−01	−0·5082
−2·0000	+67·0560	+67·0946	−0·3856$_{10}$−01	−0·5750
−1·9000	+72·7708	+72·8118	−0·4099$_{10}$−01	−0·5633
−1·8000	+78·7444	+78·7832	−0·3881$_{10}$−01	−0·4928
−1·7000	+85·0284	+85·0592	−0·3083$_{10}$−01	−0·3626
−1·6000	+91·6780	+91·6954	−0·1737$_{10}$−01	−0·1895
−1·5000	+98·7552	+98·7545	+0·7318$_{10}$−03	+0·0074
−1·4000	+106·3320	+106·3091	+0·2286$_{10}$−01	+0·2150
−1·3000	+114·4912	+114·4448	+0·4638$_{10}$−01	+0·4051
−1·2000	+123·3320	+123·2635	+0·6846$_{10}$−01	+0·5551
−1·1000	+132·9760	+132·8890	+0·8696$_{10}$−01	+0·6539
−1·0000	+143·5708	+143·4737	+0·9714$_{10}$−01	+0·6766
−0·9000	+155·3040	+155·2082	+0·9579$_{10}$−01	+0·6168
−0·8000	+168·4168	+168·3366	+0·8023$_{10}$−01	+0·4764
−0·7000	+183·2260	+183·1782	+0·4779$_{10}$−01	+0·2608
−0·6000	+200·1660	+200·1651	+0·9293$_{10}$−03	+0·0046
−0·5000	+219·8508	+219·9061	−0·5527$_{10}$−01	−0·2514
−0·4000	+243·2056	+243·3109	−0·1053$_{10}$+00	−0·4329
−0·3000	+271·7380	+271·8600	−0·1220$_{10}$+00	−0·4490
−0·2000	+308·2600	+308·3227	−0·6268$_{10}$−01	−0·2033
−0·1000	+359·6044	+359·4865	+0·1179$_{10}$+00	+0·3280
−0·0900	+366·1992	+366·0575	+0·1417$_{10}$+00	+0·3868
−0·0800	+373·2152	+373·0495	+0·1657$_{10}$+00	+0·4440
−0·0700	+380·7284	+380·5395	+0·1889$_{10}$+00	+0·4960
−0·0600	+388·8440	+388·6331	+0·2109$_{10}$+00	+0·5425
−0·0500	+397·7108	+397·4808	+0·2300$_{10}$+00	+0·5783
−0·0400	+407·5560	+407·3126	+0·2434$_{10}$+00	+0·5973
−0·0300	+418·7600	+418·5127	+0·2473$_{10}$+00	+0·5905
−0·0250	+425·0800	+424·8321	+0·2479$_{10}$+00	+0·5832
−0·0200	+432·0640	+431·8255	+0·2385$_{10}$+00	+0·5519
−0·0150	+439·9840	+439·7609	+0·2231$_{10}$+00	+0·5070
−0·0100	+449·3560	+449·1588	+0·1972$_{10}$+00	+0·4389
−0·0050	+461·5080	+461·3581	+0·1499$_{10}$+00	+0·3248
−0·0000	+490·3800	+490·3782	+0·1775$_{10}$−02	+0·0036
+0·0200	+492·4400	+492·4395	+0·4651$_{10}$−03	+0·0009
+0·0400	+494·5560	+494·4557	+0·3383$_{10}$−03	+0·0007

Table 3. (*cont.*)

E	$g(E)$ exact	$g(E)$ approx.	Diff.	Rel. error (× 1000)
+0·0600	+496·7320	+496·7308	$+0{\cdot}1224_{10}-02$	+0·0025
+0·0800	+498·9680	+498·9674	$+0{\cdot}5667_{10}-03$	+0·0011
+0·1000	+501·2680	+501·2684	$--0{\cdot}3632_{10}-03$	−0·0007
+0·2000	+513·8480	+513·8470	$+0{\cdot}9899_{10}-03$	+0·0019
+0·3000	+528·5760	+528·5763	$-0{\cdot}2573_{10}-03$	−0·0005
+0·4000	+546·1400	+546·1374	$+0{\cdot}2642_{10}-02$	+0·0048
+0·5000	+567·6040	+567·5975	$+0{\cdot}6489_{10}-02$	+0·0114
+0·6000	+594·7760	+594·7632	$+0{\cdot}1282_{10}-01$	+0·0216
+0·7000	+631·0760	+631·0561	$+0{\cdot}1994_{10}-01$	+0·0316
+0·8000	+684·2520	+684·2387	$+0{\cdot}1326_{10}-01$	+0·0194
+0·9000	+779·3280	+779·3528	$-0{\cdot}2483_{10}-01$	−0·0319
+0·9250	+819·9400	+819·9932	$-0{\cdot}5324_{10}-01$	−0·0649
+0·9500	+878·0440	+878·1240	$-0{\cdot}8000_{10}-01$	−0·0911
+0·9600	+910·3720	+910·4595	$-0{\cdot}8748_{10}-01$	−0·0961
+0·9700	+952·3400	+952·4365	$+0{\cdot}9645_{10}-01$	−0·1013
+0·9750	+979·0880	+979·1822	$-0{\cdot}9422_{10}-01$	−0·0962
+0·9800	+1011·9560	+1012·0429	$-0{\cdot}8691_{10}-01$	−0·0859
+0·9850	+1054·5080	+1054·5803	$-0{\cdot}7237_{10}-01$	−0·0686
+0·9900	+1114·7600	+1114·7950	$-0{\cdot}3503_{10}-01$	−0·0314
+0·9950	+1218·2921	+1218·2296	$+0{\cdot}6257_{10}-01$	+0·0514
+1·0000	Infinite	Infinite	–	–

But for the b.c.c. and f.c.c. lattices the contribution arising from the singularities of $g(E)$ needs to be taken into account separately.

This can be easily done by developing $f(\beta,E)$ into a power series at the point E_p of the singularity and writing

$$\Phi_g{}^{\Lambda}(\beta) = \sum_{n=0}^{\infty} \frac{1}{n!} \left. \frac{\partial^n f(\beta,E)}{\partial E^n} \right|_{E=E_p} \cdot M^n(\Lambda), \tag{40}$$

where $M^n(\Lambda)$ is the n^{th} momentum of $g(E)$, defined by

$$M^n(\Lambda) = \int_{E_p-\Lambda}^{E_p+\Lambda} (E-E_p)^n g(E)\,\mathrm{d}E. \tag{41}$$

For the b.c.c. lattice $g(E)$ is symmetrical to $E = E_p$ and therefore all odd momenta vanish, but this is not true for the f.c.c. lattice. But at any rate

$$\frac{M^n(\Lambda)}{M^m(\Lambda)} \sim o(\Lambda^{n-m}) \tag{42}$$

holds. Provided that $f(\beta,E)$ is a slowly varying function at $E = E_p$, the summation may be restricted to the first few terms.

For the b.c.c. lattice the momenta are conveniently derived directly from equation (18). Integrating over E and observing symmetries one is led to

$$M^{2m}(\Lambda) = 128 \int_{\mathscr{L}} \frac{(l_1 l_2 l_3)^{2m}\,\mathrm{d}l_1\,\mathrm{d}l_2\,\mathrm{d}l_3}{[(1-l_1{}^2)(1-l_2{}^2)(1-l_3{}^2)]^{1/2}} \tag{43}$$

with $\mathscr{L}$ given by the domain where as $0 \leqslant l_i \leqslant 1$ as $l_1 l_2 l_3 \leqslant \Lambda$ hold.

The first integration is easily performed, leaving

$$\begin{aligned} M^{0}(\Lambda) = 128\Bigg[&\left(\frac{\pi}{2}\right)^2 \arcsin\Lambda + \frac{\pi}{2} \int_{\arcsin\Lambda}^{\pi/2} \arcsin\left(\frac{\Lambda}{\sin x}\right) \mathrm{d}x \\ &+ \int_{\arcsin\Lambda}^{\pi/2} \mathrm{d}x \int_{\arcsin\left(\frac{\Lambda}{\sin x}\right)}^{\pi/2} \mathrm{d}y \arcsin\left(\frac{\Lambda}{\sin x \sin y}\right)\Bigg] \end{aligned} \tag{44a}$$

and

$$\begin{aligned}M^2(\Lambda) = 64\Bigg[&\left(\frac{\pi}{4}\right)^2 (\arcsin\Lambda - \Lambda\sqrt{(1-\Lambda^2)})\\ &+\left(\frac{\pi}{2}\right)\left(\int\limits_{\arcsin\Lambda}^{\pi/2} \sin^2 x \arcsin\left(\frac{\Lambda}{\sin x}\right)\mathrm{d}x - \Lambda\int\limits_{\Lambda}^{1} x\left[\frac{1-(\Lambda/x)^2}{1-x^2}\right]^{1/2}\mathrm{d}x\right)\\ &+\left(\int\limits_{\arcsin\Lambda}^{\pi/2}\sin^2 x\,\mathrm{d}x\int\limits_{\arcsin\left(\frac{\Lambda}{\sin x}\right)}^{\pi/2}\sin^2 y\cdot\arcsin\left(\frac{\Lambda}{\sin x\cdot\sin y}\right)\mathrm{d}y\right.\\ &\left.-\Lambda\int\limits_{\Lambda}^{1}\frac{x\mathrm{d}x}{(1-x^2)^{1/2}}\int\limits_{\frac{\Lambda}{x}}^{1} y\mathrm{d}y\left[\frac{1-\left(\frac{\Lambda}{xy}\right)^2}{1-y^2}\right]^{1/2}\right)\Bigg].\end{aligned} \tag{44b}$$

These formulae were computed for $\Lambda = 10^{-2}$ with the results

$$M^0(10^{-2}) = 36{\cdot}855; \quad M^2(10^{-2}) = 1\times 10^{-3}$$

so that M^2 may be neglected for all practical purposes*. In case of f.c.c. lattices the calculation of the momenta

$$M^n(\Lambda) = \int\limits_{1-\Lambda}^{1} (E-1)^n g(E)\,\mathrm{d}E \tag{45}$$

directly from the definition of $g(E)$ in equation (29) is difficult because of the complicated topological structure of the domain of integration.

Here we have taken advantage of the fact that (45) may be calculated exactly when the density of states is replaced by its approximation function (39c); for $\Lambda \leqslant 1$ it has the result

$$\begin{aligned}M^n(\Lambda) = (-1)^n\cdot 4\,\Lambda^{n+1}\Bigg\{\Bigg[&\frac{104{\cdot}94511}{n+1}+\frac{15{\cdot}88978}{n+2}\cdot\Lambda+\frac{1{\cdot}76011}{n+3}\cdot\Lambda^2\\ &+\frac{37{\cdot}62372}{(n+1)^2}+\frac{7{\cdot}18628}{(n+2)^2}\cdot\Lambda\Bigg]-\left[\frac{37{\cdot}62372}{n+1}+\frac{7{\cdot}18628}{n+2}\Lambda\right]\ln\Lambda\Bigg\}.\end{aligned} \tag{46}$$

Table 4. Control of the numerical accuracy by integration over g(E). $G_{ex.}$ *gives the theoretical value*, $G_{num.}$ *was obtained by numerical integration over the exact functions, as tabulated in the second columns of Tables* 1–3, *and* $G_{ap.}$ *by integration over the approximation functions* (39)

	s.c.	b.c.c.	f.c.c.
G_{ex}	$(2\pi)^3 =$ 248·050	$2\cdot(2\pi)^3 =$ 496·100	$4\cdot(2\pi)^3 =$ 992·2009
$G_{num.}$	248·064	496·111	992·2010
$G_{ap.}$	248·057	496·197	992·1736

Setting $\Lambda = 10^{-2}$ we obtain

$$M^0(10^{-2}) = 12{\cdot}644; \quad M^1(10^{-2}) = -0{\cdot}0595;$$
$$M^2(10^{-2}) = 3{\cdot}9\times 10^{-4}.$$

---

*The value of $M^0(10^{-2})$ has already been used for the calculation of G_{num} and $G_{ap.}$ in Table 4.

The error coming from the approximation of the density of states may be checked by the relation

$$M^{\circ}(\Lambda) = \int_{-3}^{1} g(E)\,\mathrm{d}E - \int_{-3}^{1-\Lambda} g(E)\,\mathrm{d}E = 32\pi^3 - \int_{-3}^{1-\Lambda} g(E)\,\mathrm{d}E \qquad (47)$$

and was found to be $1{\cdot}268 \times 10^{-4}$. So the use of this approximation should yield a sufficient accuracy of the momenta.

Summarizing the results, we have

$$\Phi_s^{10^{-2}}(\beta) = \int_{E_p-10^{-2}}^{E_p+10^{-2}} f(\beta,E)g(E)\,\mathrm{d}E \qquad (48)$$

$$= \begin{cases} 36{\cdot}855 f(\beta,0) & \text{for the b.c.c. lattice} \\ 12{\cdot}644 f(\beta,1) - 0{\cdot}0595 f'(\beta,1) & \text{for the f.c.c. lattice} \end{cases}$$

as the contribution to the integral (4) arising from a surrounding of the singularities of $g(E)$.

8. AN APPLICATION TO THE LINEAR SPINWAVE THEORY

As a simple application of the density of states derived in this paper its consequences to the spontaneous magnetization due to the linear spinwave theory were studied in detail for s.c. symmetry. That means we compared the dependence of the relative magnetization on the temperature, which follows from

$$\frac{M(T)}{M(0)} = 1 - \frac{1}{(2\pi)^3} \int_{-\infty}^{+\infty} \frac{g(E-3)\,\mathrm{d}E}{\mathrm{e}^{\left(\frac{JE}{kT}\right)} - 1} \qquad (49)$$

with that given by Bloch's T-power 3/2 law.

This theorem states

$$\frac{M(T)}{M(0)} = 1 - \zeta(3/2)\frac{1}{\sqrt{2}}\frac{1}{\pi^{3/2}}\left(\frac{kT}{J}\right)^{3/2} \qquad (50)$$

and can be derived from (49) by using the approximation (16) and integration over all positive values of E.

The results of these calculations are plotted in Fig. 7. As a reference point the Curie-temperature T_C due to a paper of Rushbrooke and Wood[10] is marked on the T-axis.

There is no physical significance in this special example, because for temperatures $T \ll T_c$ Bloch's law approximates very well equation (49) and for temperatures high enough to bring forward appreciable deviations from this law, the concept of the linear spinwave theory as a whole is no longer justified. But it is demonstrated by Fig. 7, that whenever a theory is given, which is expected of being valid up to T_c, the exact

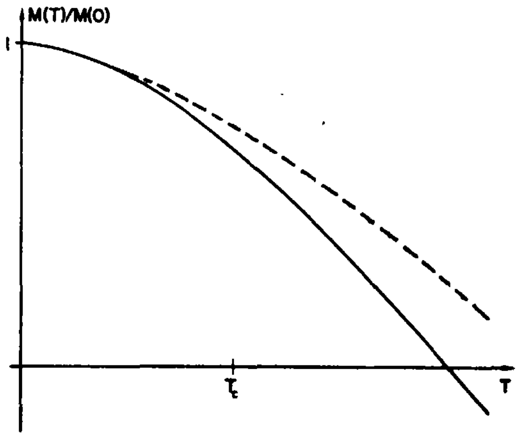

Fig. 7. Variation of the relative specific magnetization of ferromagnetic s.c. lattices with the temperature. The solid line gives this curve arising from the linear spinwave theory, when the exact density of states is taken into account, in comparison with Bloch's $T^{3/2}$ law, plotted in dashed lines. As a point of reference the Curie-temperature T_C due to Rushbrooke and Wood[10] is inscribed.

density of states should be taken into account instead of (16).

Acknowledgements—The author wishes to thank Professor Dr. H. Koppe for having given the initial stimulus to these investigations. Thanks are also due to the Rechenzentrum der Universität Kiel for having placed its equipments at our disposal.

APPENDIX: DETAILS OF THE COMPUTATIONS

Before computing the integrals (14), (25) and (36) the substitution

$$l_1 = \sin x \tag{51}$$

was performed, which eliminates the singularities of the integrands arising from the zeros of $\sqrt{(1-l_i^2)}$.

Formula (25) for the b.c.c. lattice was transformed into

$$g(E) = 64 \int_{\arcsin(E)}^{\pi/2} \frac{K'(E/\sin x)}{\sin x} \mathrm{d}x, \tag{25a}$$

in which form it is easily computed for $0 < E \leqslant 1$ because the integrand has no further singularities.

This is true also for $1 < E \leqslant 3$ in case of the s.c. lattice, where equation (14a) holds. For $0 \leqslant E \leqslant 1$ $g(E)$ is given by (14b). As $K'(x)$ has a logarithmic singularity for $x = 0$, the integrand of the first integral has one at the lower boundary of the interval of integration. For this reason the numerical integration was restricted to

$$g_n(E) = 8\left\{ \int_{\pi/2}^{\arcsin(E+\delta)} K'\left(\frac{-E-\sin x}{2}\right) \mathrm{d}x + \int_{-\arcsin(E-\delta)}^{\pi/2} K'\left(\frac{E+\sin x}{2}\right) \mathrm{d}x \right\}. \tag{52}$$

The contribution arising from the poles was estimated seperately by first approximating $K'(z(x))$ by $\ln(4/z(x))$ and then expanding $z(x)$ into a power series. For the first few terms, which contribute to the integral within the limits of accuracy, the integration can be carried out exactly. For different ranges of E different approximation formulae were used. The values of $g(0)$ and $g(1)$ were calculated separately.

The formulae (36a) and (36b), by which $g(E)$ is given for $-3 < E \leqslant 0$ in case of the f.c.c. lattice, after the transformation (51) may be computed without any further arrangements.

For $E = 0$, $g(E)$ is given by

$$g(0) = 64\left\{ \int_{\pi/6}^{\pi/2} \frac{K'\left(\frac{1}{2\sin x}\right)}{\sin x} \mathrm{d}x + 4 \int_{0}^{\pi/6} K'(2\sin x)\, \mathrm{d}x \right\}. \tag{53}$$

The second integrand becomes infinite for $x = 0$ and the contribution arising from the interval $[0, \arcsin(\delta)]$ was estimated by

$$g_s(0) = \arcsin(\delta) \cdot \ln 2 - \ln \delta \left(\delta + \frac{\delta^3}{6}\right) + \left(\delta + \frac{\delta^3}{18}\right) \tag{54}$$

in the same way, as it was done for the s.c. lattice in $0 \leqslant E \leqslant 1$. For $0 < E < 1$ singularities of the integrands occur for $l = \sqrt{E}$, that is in the second and the third integral of (36c). They were overcome by the same method as sketched above.

All programs for the computer were written in ALGOL 60. For the generation of the complete elliptic integral a procedure given by Hofsommer and Van de Riet[11], and for the integrations a procedure from the program library of the Kiel Rechenzentrum was used. The method of integration is a variant of Simpson's formula, which permits the statement of the absolute accuracy of calculation.

For the computations of the densities of states the absolute accuracy was fixed as a function of E, as to be large where $g(E)$ is small. The influence of the estimates for the contribution of the singularities could be checked by variation of δ.

REFERENCES

1. MOTT N. F. and JONES H., *The Theory of the Properties of Metals and Alloys*, p. 85. Dover, New York (1958).
2. BLOCH F., *Z. Phys.* **61**, 206 (1930)
3. TJABLIKOV S. V., *Ukr. Mat. Zh.* **11**, 287 (1959)
4. ENGLERT F., *Phys. Rev. Lett.* **5**, 102 (1960)
5. VAN HOVE L., *Phys. Rev.* **89**, 1189 (1953)
6. OBERHETTINGER F. and MAGNUS W., *Anwendungen der elliptischen Funktionen in Physik und Technik*, pp. 2–9. Springer, Berlin (1949).
7. HOFFMANN T. A., *Acta phys. hung.* **2**, 97, 107 (1952)
8. KOSTER G. F. and SLATER J. C., *Phys. Rev.* **96**, 1208 (1954)
9. WOLFRAM T. and CALLAWAY J., *Phys. Rev.* **130**, 2207 (1963)
10. RUSHBROOKE G. S. and WOOD P. J., *Mol. Phys.* **1**, 257 (1958)
11. HOFSOMMER D. J. and VAN DE RIET R. P., *Num. Math.* **5**, 291 (1963)

J. Phys. Chem. Solids Pergamon Press 1969. Vol. 30, pp. 627–641. Printed in Great Britain.

DISTRIBUTION COEFFICIENT STUDIES IN INDIUM ANTIMONIDE

U. MERTEN, K. D. VOS* and A. P. HATCHER
Gulf General Atomic Incorporated, P.O. Box 608, San Diego, Calif. 92112, U.S.A.

(*Received* 11 *April* 1968)

Abstract – Distribution coefficient measurements have been made for Ga, Zn, Cu, Cd, Se, Zn–Cu, Zn–Cd and Zn–Se between InSb and In–Sb melts. In these studies, the concentration and growth rate dependence of the distribution coefficients were examined. Gallium appears to substitute for In in a straightforward manner. A concentration of material in the facet is observed for both Cd and Se, even in the presence of Zn. Zinc does not show a facet effect either alone or in the presence of Se. The observed concentration dependence of the distribution coefficients for Zn, Zn–Cd and Zn–Se is consistent with the assumption of an elevated Fermi level at the surface of the crystal. Neither variations in the Fermi level at the surface nor the more commonly suggested adsorption and trapping on the facet appear to be adequate explanations for the facet effects observed.

INTRODUCTION

OBSERVATIONS of crystal-habit-dependent [1, 2] and concentration-dependent[3] distribution coefficients in InSb have focused attention on the chemical behavior of impurities during growth of InSb crystals. The effect of crystal habit was first pointed out by Hulme and Mullin[1], who observed that tellurium was preferentially incorporated into that part of an In–Sb crystal that was formed by growth on a {111} facet. This observation invalidates, for some impurities and under some conditions, the often-used assumption that the interface distribution coefficient has essentially its equilibrium value at the growth rates commonly employed in crystal pulling (of the order of 1 cm/hr). Furthermore, it suggests that the growth-rate dependence of the distribution coefficient may be more complicated than predicted by the usual form of the Burton–Prim–Slichter (BPS) theory[4]. The rate-limiting step, which makes the facet different from the rest of the crystal, may compete with diffusion in the melt in determining the observed growth-rate dependence.

The concentration dependence of the distribution coefficient for zinc in InSb was pointed out by Merten and Hatcher[3], who found a rapid decrease in distribution coefficient with increasing zinc concentration above ~0·1 at.% zinc in the solid. Since the zinc activity coefficient in the liquid solution has been found to be independent of concentration up to ~1 at.%[5] this behavior had to be attributed to nonideality in the solid phase.

The experiments reported here were designed to throw some further light on the behavior of these systems (1) through the examination of gallium, an impurity whose behavior should be particularly simple because of its close similarity to one element of the host substance[16] and (2) through the study of a number of additional aspects of the behavior of the impurities zinc, cadmium, selenium, and copper.

EXPERIMENTAL PROCEDURE

Ingots of InSb were pulled by the Czochralski technique from In–Sb melts containing the different doping materials. The melts were held in silica crucibles, and the crystals were grown under a hydrogen atmosphere. The rotational speed of the crystals was 30 rev/min. All of the data reported here are for single crystals grown in the ⟨111⟩ direction, using the designation of Dewald[7], except where the $\langle\bar{1}\bar{1}\bar{1}\rangle$ direction is specified or it is stated that polycrystalline ingots were accepted. Except in the growth-rate studies, all crystals were grown at 1·5 cm/hr.

---

*Present address: S. C. Johnson and Sons, Inc., Racine, Wisconsin.

Indium and antimony were obtained from the Indium Corporation of America and the United Mineral and Chemical Corporation, respectively; the elements had an advertised purity of 99·999 per cent or better. Hall measurements gave room-temperature carrier densities of 5×10^{15} to $1\times10^{16}\,\text{cm}^{-3}$ for the undoped material. The indium and antimony contents of the melt were determined by weighing; the crystals grown comprised only several percent of the total melt, so the compositional variations during growth were small.

Neutron irradiation in a TRIGA Mark I nuclear reactor was used to induce 245 day Zn^{65}, 12·9 hr Cu^{64}, 14·1 hr Ga^{72}, and 43 day Cd^{115} activities in the high-purity samples of the metals used for doping. High-specific-activity 120 day Se^{75} and 245 day Zn^{65} were purchased from Oak Ridge National Laboratory for use in low-concentration experiments. The purchased isotopes had to be recovered from aqueous solution. The selenium was isolated by adding the desired amount of inactive selenium carrier, precipitating with hydroxylamine, and filtering. The zinc was recovered by electrolyzing it into gallium, volatilizing it onto the surface of a piece of antimony in a sealed tube, and then melting the antimony to prepare a master alloy from which In–Sb–Zn mixtures of the desired composition could be prepared.

The amount of doping material in the melt and crystal was determined by counting in a 3 in., well-type NaI(Tl) scintillation crystal, using a weighed sample irradiated with the doping material as a standard. In the case of the purchased isotopes, no such standards were available, but since the amount of inactive isotopic carrier added was always large compared with the amount of the element of interest in the purchased solutions, the specific activities could be calculated readily from the known amount of carrier added and the total activity of the original sample.

The distribution coefficients reported here are defined as

$$K=\frac{C_s}{C_l} \tag{1}$$

where C_s and C_l are the concentrations of the doping material in the crystal and the melt, respectively, expressed as atom fractions.

Autoradiographs of the single crystals and melts were made on Kodak No-Screen X-ray film; the film was developed in General Electric Supermix X-ray developer. Standards containing different concentrations of radioactive material were prepared by dissolving a weighed amount of doping material in a known amount of InSb; the concentration was checked by counting. The standards, four for each crystal, were run simultaneously on the same film as the crystal and the melt. The standards were made to cover the range of concentration represented by the melt and the crystal. A Jarrell–Ash densitometer was used to measure the density of the autoradiographs. Some segregation of the tagged species in the melts and standards was observed despite rapid quenching. The densitometer appeared to average these finely divided inhomogeneities satisfactorily. It was found that the density of the film for the standards obeyed the linear portion of the Hurter and Driffield curve[8].

RESULTS

Gallium

The distribution coefficient of gallium in stoichiometric InSb was studied as a function of concentration in the range 0·01– 10 at.% gallium. The eight crystals covering this concentration range are indicated by the vertical arrow in Fig. 1. The distribution coefficient was found to be constant at 3·00 ± 0·13. Hall-effect measurements showed the extrinsic carrier densities at room temperature to be small compared with the gallium concentration.

The distribution-coefficient data obtained

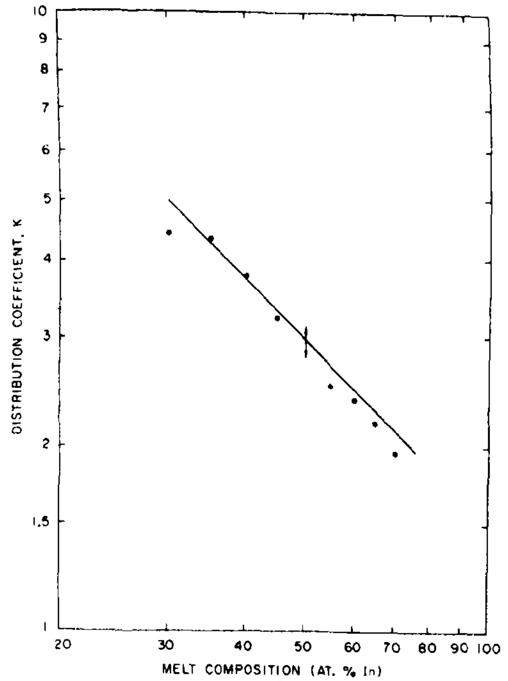

Fig. 1. Distribution coefficient for gallium in In-Sb alloys.

for gallium are presented in Fig. 1 as a function of the indium content of the melt. In all the nonstoichiometric cases, the concentration of gallium in the melt was 0·02–0·03 at.% gallium. The points obtained at 30 and 70 at.% indium are for polycrystals.

It is apparent that the distribution coefficient is markedly affected by the gross melt composition. It is generally assumed that gallium replaces indium in the crystal, and this may be represented by the chemical equation:

$$Ga_l + InSb_s = In_l + GaSb_s \qquad (2)$$

where the subscripts l and s refer to the liquid and solid solutions, respectively. If we assume the $InSb_s$ activity to be unchanged by the small addition of $GaSb_s$, the equilibrium constant is

$$K' = \frac{\{GaSb_s\}\{In_l\}}{\{Ga_l\}} \qquad (3)$$

where the braces denote activities. The measurements made on stoichiometric melts indicate that the activity coefficient of $GaSb_s$ is independent of gallium concentration in the range of interest, and if we assume that the ratio of the activity coefficients of gallium and indium in the liquid is independent of concentration, we may then replace the activities by concentrations (denoted by brackets). The equation then becomes

$$K = \frac{[GaSb_s]}{[Ga_l]} = \frac{K'}{[In_l]}. \qquad (4)$$

Using the value of k at the 50 at.% indium concentration, we obtain a value of 1·50 for K'. The solid line in Fig. 1 was drawn to agree with equation (4), using this value of K'. The line is seen to represent the data reasonably well.

On the basis of a number of simplifying assumptions, Burton, Prim and Slichter[4] have derived the following equation for the effective distribution coefficient:

$$K = \frac{k_0}{k_0 + (1-k_0)\exp-(f\delta/D)} \qquad (5)$$

where k_0 is the equilibrium distribution coefficient, f is the growth rate, δ is the thickness of the diffusion-dominated layer in the liquid, and D is the diffusion coefficient of the impurity in the liquid. For a simple comparison with experiment this equation may conveniently be rewritten as an equation for a straight line in either of two forms depending on the magnitude of the distribution coefficient:

$$\ln\left(\frac{1}{K}-1\right) = -\frac{\delta}{D}f + \ln\left(\frac{1}{k_0}-1\right);\ K < 1 \qquad (6)$$

or

$$\ln\left(1-\frac{1}{K}\right) = -\frac{\delta}{D}f + \ln\left(1-\frac{1}{k_0}\right);\ K > 1. \qquad (7)$$

A plot of $\ln[(1/K)-1)$ or $\ln[1-(1/K)]$ vs. f gives a straight line with a slope of $-(\delta/D)$

and an intercept of ln $[(1/k_0)-1]$ or ln $[1-(1/k_0)]$.

Growth-rate data are presented in Fig. 2 for single crystals of InSb grown from a melt containing 0·06–0·08 at.% Ga in the melt. Using equation (7) and the data of Fig. 2, we obtain values of 324 sec/cm and 3·57 for δ/D and k_0, respectively. Mullin[9] obtained a value of 2·4 for the distribution coefficient at a growth rate of 2 cm/hr and a rotational value of 100 rev/min. Using the BPS theory and our value of δ/D to extrapolate Mullin's result to zero growth rate, we find that the values for the distribution coefficient differ by only ~16 per cent.

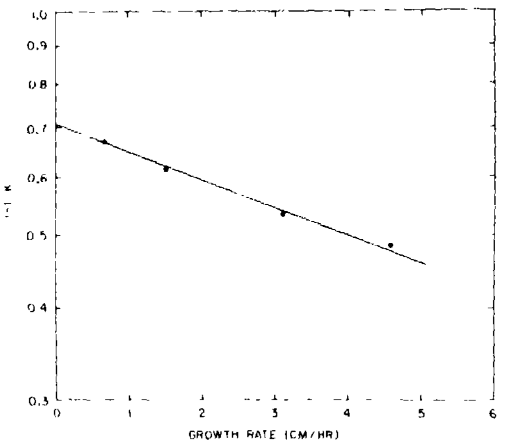

Fig. 2. Growth-rate effects for gallium in InSb.

Zinc

In our earlier report on the behavior of zinc in InSb[3], we pointed out that the growth-rate data obtained were insufficiently reproducible to permit reliable extrapolation to zero growth rate. Further investigation has shown that this problem exists only at the higher zinc concentrations. The results of growth-rate studies are presented in Fig. 3. The data have been grouped into three concentration regions, with region *A* covering the very dilute solutions, 3×10^{-4} to 3×10^{-3} at.% zinc in the solid, and region *B* covering the intermediate range, 3×10^{-3} to 7×10^{-2} at.% zinc in the solid. Within regions *A* and *B*, the low-growth-rate *K* is essentially independent of concentration[3]. The data for region *A* have been plotted separately because they presumably give the best estimates of δ/D and k_0 at infinite dilution. The data given in region *C* were obtained on a group of samples in the narrow concentration range 0·17–0·22 at.% zinc in the solid (0·10–0·15 at.% zinc in the melt). The data obtained in this region are for polycrystals, since it was generally difficult to obtain single crystals at the high zinc concentrations. In region *A* the distribution coefficients follow the BPS theory, yielding values of 242 sec/cm and 4·16 for δ/D and k_0, respectively. In region *C*, the experimental uncertainty is greater than in region *A*, but it is clear that the line has little or no slope, indicating either that δ/D is small, certainly less than 100 sec/cm, or that some new growth-rate effect has entered the picture.

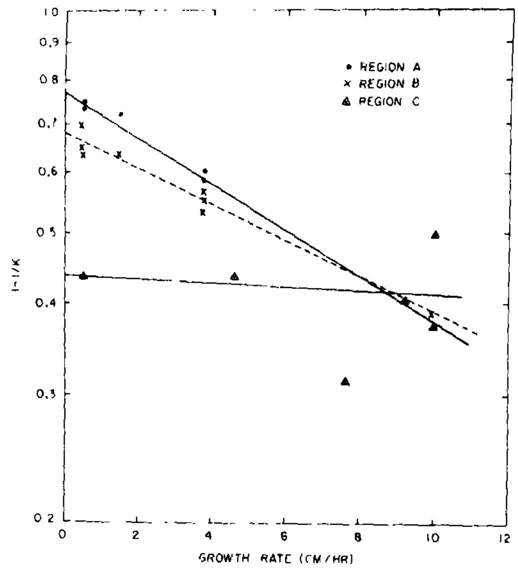

Fig. 3. Growth-rate effects for zinc in InSb.

Strauss[10] reports results of 239 sec/cm and 4·13 for δ/D and k_0, respectively. These results were obtained in the concentration range we have called region *A*. Our value of

k_0 and that obtained by Strauss are in excellent agreement. Using the BPS theory to put Strauss' rotational rate on the same basis as ours, we find that the values of δ/D also agree very well.

The autoradiographic technique was used to examine the uniformity of zinc distribution in cross sections of pulled crystals. No inhomogeneities were found, indicating that there was no significant facet effect on the distribution coefficient[11].

Copper

Results of growth-rate studies on copper distribution at a concentration of 0·03 at.% copper in the melt are given in Fig. 4. From Fig. 4 and equation (6), values of 770 sec/cm and $3{\cdot}24\times10^{-4}$ are obtained from the BPS theory for δ/D and k_0, respectively. This large value for δ/D requires the assumption that the diffusion coefficient of copper in the melt is half that of gallium.

Mullin[9] has reported a value of $6{\cdot}6\times10^{-4}$ for the distribution coefficient. Using the BPS theory to put Mullin's rotational rate on the same basis as ours, we find that the reported values for the distribution coefficient differ by ~30 per cent. In view of the difficulty of measuring the small distribution coefficient, the agreement is good.

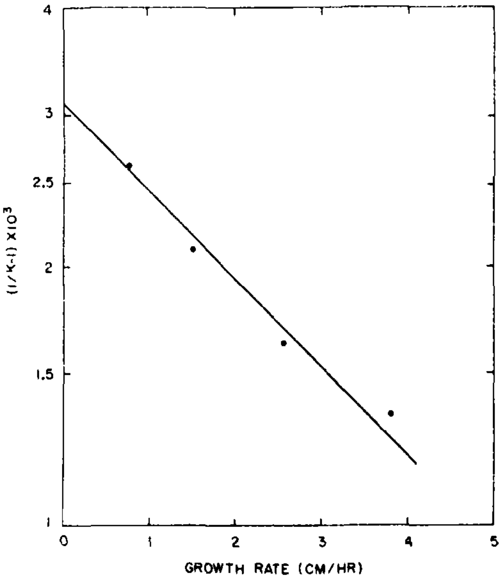

Fig. 4. Growth-rate effects for copper in InSb.

Two series of measurements were carried out on the distribution coefficient for copper (0·03–0·05 at.% copper in the melt) in the presence of zinc. In series 1, inactive zinc and tagged copper were added to the melt, the copper distribution was measured in the usual manner, and the zinc concentrations in the solid and the liquid were calculated from the known amount of zinc added initially and from the distribution coefficients previously measured in the absence of copper[3]. In series 2, both added elements were tagged, the 0·55 MeV annihilation radiation was counted shortly after the experiment, and the Cu^{64} concentration was calculated from this result after correcting for the Zn^{65} contribution as determined from the 1·1 MeV peak counted after the copper had decayed out. The zinc concentrations were calculated from the last determination.

The results of both series of experiments are displayed in Fig. 5 as a function of the zinc content of the solid. The K_{Zn} curve shown is drawn from the data of Merten and Hatcher [3]. The melt compositions obtained for the second series by counting were in good agreement with those calculated from the zinc additions made, indicating that zinc losses were small and that the method used to calculate zinc concentrations in the first series was reasonable. The zinc distribution coefficients found at high concentrations were slightly larger than those observed in the absence of copper, but not by an amount that is clearly significant. The copper distribution is clearly dependent on zinc concentration.

Cadmium

The distribution coefficients of cadmium were studied as a function of concentration in the range $1{\cdot}0\times10^{-3}$ to $1{\cdot}3\times10^{-1}$ at.% cadmium in the melt. The ten ⟨111⟩ crystals

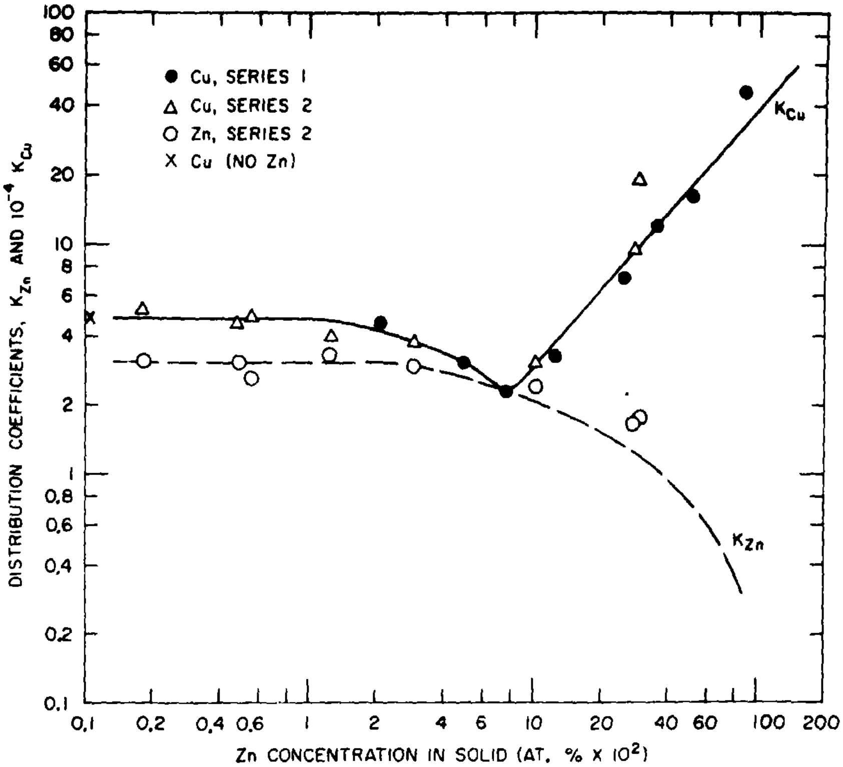

Fig. 5. Distribution coefficients for copper in the presence of zinc.

covering this concentration range gave distribution coefficients that were independent of concentration. The values obtained were: on-facet/melt, 0·73 ± 0·10; off-facet/melt, 0·33 ± 0·05; and on-facet/off-facet, 2·24 ± 0·14. Three crystals were grown in the $\langle\bar{1}\bar{1}\bar{1}\rangle$ direction from melts containing 5×10^{-3} to 9×10^{-3} at.% cadmium, and these again gave a value of 0·33 for the off-facet/melt coefficient, but gave an on-facet/melt value of 0·44 ± 0·05 and on-facet/off facet ratio of 1·33. The on-facet/melt ratio for the two crystallographic orientations differ by a factor of 1·66. Both Mullin[9] and Strauss[10] reported lower gross distribution coefficients, 0·26, before the facet effect was recognized. The on-facet/off-facet ratio has been reported as 3·3[11].

Growth-rate studies for cadmium have been made at a concentration of 0·006–0·01 at.% cadmium in the melt. These results are plotted in Fig. 6. The off-facet distribution coefficient is, within experimental error, independent of growth rate in this range. Using BPS representation, we can calculate that δ/D must be less than 100 sec/cm, a value much smaller than that found in the gallium, copper, or low-zinc-concentration cases.

The on-facet distribution coefficient increases up to ~1·5 cm/hr and then remains constant. This trend is made clear by examination of the on-facet/off-facet ratio, which is somewhat more accurately determined in these studies than the distribution coefficients. The on-facet area may logically be expected to deviate from the BPS behavior since processes other than simple solid-melt equilibrium must be important. The Trainor–Bartlett[12] theory for the facet phenomenon attributed

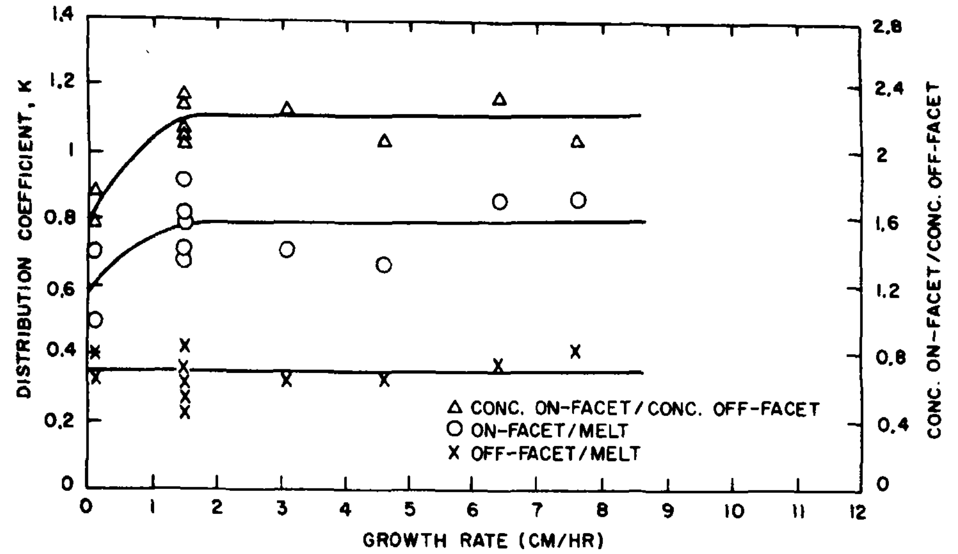

Fig. 6. Growth-rate effects for cadmium in InSb.

the high on-facet concentration to impurity trapping on the facet due to rapid sheet growth on the {111} plane. Hall[13] has proposed that solute diffusion in the solid can be important under such conditions. If the growth rate and the diffusion rate of the solute in the solid are of the right magnitude, it is possible for the solute in the solid and melt to come to equilibrium even for the on-facet region. Thus, the decrease in the on-facet distribution coefficient at growth rates below ~1·5 cm/hr may be attributed to the fact that at these slow growth rates, an appreciable portion of the impurity that is trapped on-facet can escape to the liquid before the next sheet forms.

A calculation similar to that made by Hall [13] may be made on the diffusion of cadmium in InSb at or very near the melting point. At a growth rate of 1·5 cm/hr, the crystal is apparently growing so rapidly that the diffusion coefficient in the solid is not able to compete with the growth of the crystal. If it is assumed that the diffusion is through only one atomic layer[11], a diffusion coefficient of $\leq 3 \times 10^{-11}$ cm^2/sec can be calculated. Orth and Watt[14] have reported diffusion coefficients for cadmium in InSb which extrapolate to a value of 5×10^{-13} cm^2/sec at the melting point.

With cadmium, as with copper, a series of experiments was carried out on the effect of zinc concentration on the distribution coefficient. The results are shown in Fig. 7 for a concentration of 0·02 at.% Cd in the melt. It is apparent that an interaction again occurs, becoming important this time at a zinc concentration in excess of 0·1 at.% zinc in the solid, as is the case in material doped with zinc only. It is particularly noteworthy that the on-facet and off-facet distribution coefficients change similarly. The K_{Zn} curve was again drawn from previously reported data[3].

Selenium

Results of growth-rate studies made for selenium at a concentration of 0·01 at.% selenium in the melt are presented in Fig. 8. The off-facet distribution coefficient increases with increasing growth rate, and when plotted according to equation (6) gives a value of 635 sec/cm and 0·30 for δ/D and k_0, respectively. The on-facet distribution coefficient appears

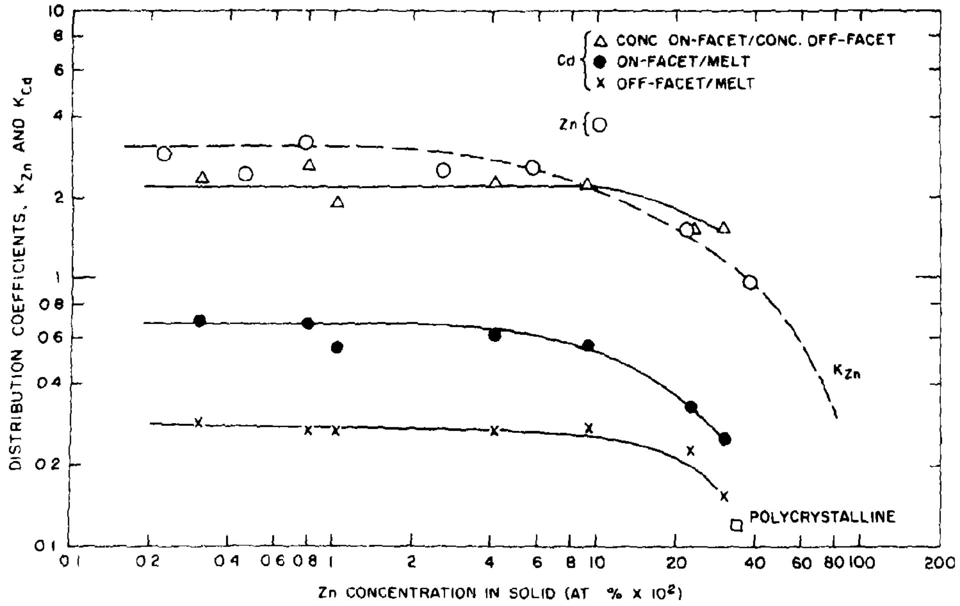

Fig. 7. Distribution coefficients for cadmium in the presence of zinc.

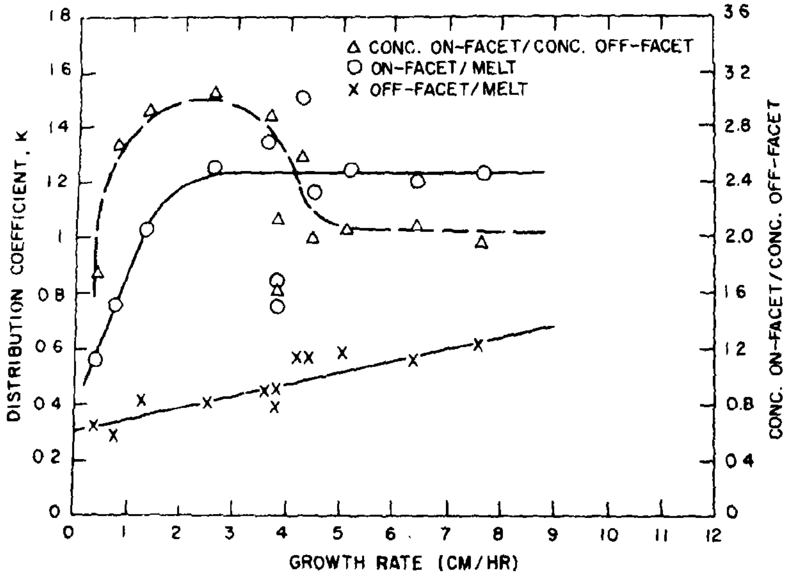

Fig. 8. Growth-rate effects for selenium in InSb.

to increase as the growth rate increases and then remain constant at ~1·23, in much the same manner as already described for cadmium. The behavior of the on-facet and off-facet distribution coefficients results in their ratio having an unusual dependence on growth rate.

An irregular distribution of an impurity in a crystal can arise from variations in the real growth rate if the distribution coefficient is growth-rate dependent. It has been reported that striations in the facet of selenium-doped crystals are related to the rotation of the crystal[15]. After cutting and polishing crystals perpendicular and parallel to the ⟨111⟩ growth direction, and then etching with a CP4 etch, we were able to observe through a microscope striations both on- and off-facet. By measuring the distance along the ⟨111⟩ axis between the striations, and knowing the growth rate, it was possible to correlate the striations with the 30 rev/min rotation. In addition to the short-period striations produced by the rotation, striations were observed that were correlated with the on-off time of the temperature controller for the furnace, 0·32 min/cycle. Striations produced by this type of temperature fluctuation have also been reported[16].

The autoradiographs did not show the striations, presumably because of the poor resolution obtainable with the γ radiation emitted by Se^{75}. The striations did, however, increase the uncertainty of the average concentration, as determined by the autoradiographs, and it is probably for this reason that the data for selenium show more scatter than is observed for other dopants.

Experiments on the effect of zinc concentration on selenium distribution were run with the selenium concentration at two different levels, 0·003 and 0·02 at.% selenium in the melt. The results are given in Fig. 9. These data were obtained by using seed crystals whose diameter was already the desired crystal diameter, and growing onto it a few millimeters of material from the doped melt. This growth was accomplished without

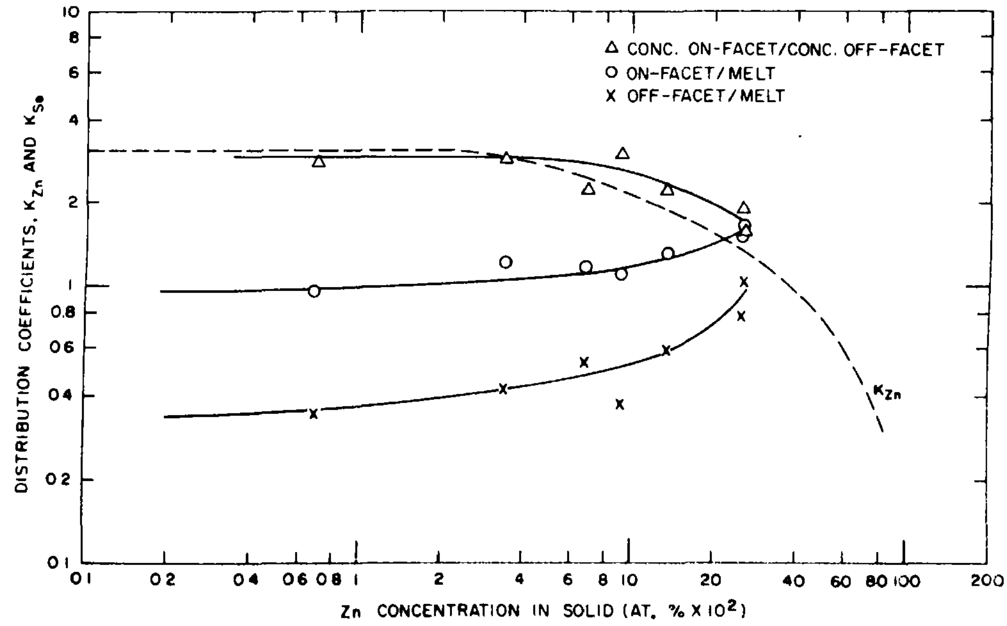

Fig. 9. Distribution coefficients for selenium in the presence of zinc.

stirring and with the furnace heater set manually at a constant level to avoid striations. It is apparent that the presence of high zinc concentrations in the melt enhances selenium solubility both on- and off-facet.

Single crystals were grown from melts that contained 0·01 at.% natural selenium and 0·03 at.% zinc tagged with Zn^{65}. These crystals were examined by the autoradiographic technique to determine if zinc showed a facet effect in the presence of selenium. No facet effect was in evidence and the distribution coefficient, as determined by counting, was similar to that reported for zinc without selenium[3].

DISCUSSION

Concentration effects

The behavior of gallium in InSb is interesting because it is a 'reference' with which we can compare the behavior of the other elements. Hall measurements have shown gallium to be electrically inactive in the In–Sb lattice; this, plus the fact that the distribution coefficient of gallium depends on the melt stoichiometry in a predictable fashion, indicates that this element simply substitutes for indium on indium sites in the lattice.

Zinc, which presumably also substitutes for indium, and gallium have similar distribution coefficients at low concentrations but are markedly different at higher concentrations. The one obvious difference between the two impurities is the acceptor character of zinc and the neutral character of gallium. It is interesting, though perhaps coincidental, that at the lowest concentrations, where Zn_s^- is the predominant species, the distribution coefficient is essentially equal to that for gallium, an atom isoelectronic with Zn^-.

In an earlier paper[3] it was pointed out that the zinc data cannot be reconciled with the known electronic properties of bulk InSb. No change in distribution coefficient is observed at the zinc concentrations ($\sim 5 \times 10^{-3}$ at.% zinc in the solid) at which the contribution of the ionized acceptor state should change, and the total change observed at higher concentration is considerably larger than one would predict. The Zn_s^- contribution to the zinc concentration in the solid is only one-third of the total at infinite dilution (as calculated from the Fermi-level data of Weiss [7]). If we assume that the uncharged zinc atoms form a Henry's law solution in the solid, then, even if the Zn_s^- contribution were negligible at the highest concentration, the ten-fold change in K_{Zn} could not be explained. It was therefore postulated that the Zn_s^- to Zn_s ratio is determined by the position of the Fermi level in the surface region and that this is considerably different from that in the bulk. If the Fermi level at the surface is raised to $\geq 0 \cdot 2$ eV above the valence band, as compared with 0·1 eV in the bulk, the ten-fold change in the zinc distribution coefficient can be explained.

The diffusion-coefficient data for zinc in InSb available at the time of our earlier publication[3] were ambiguous. Later, however, more extensive measurements were made which indicate a diffusion coefficient at the low zinc concentration of $\sim 3 \times 10^{-14}$ cm^2/sec at the melting point[11]. This diffusion is clearly too slow to permit effective equilibration between a 50 Å surface layer and the bulk at growth rates of the order of 1 cm/hr, which lends support to the surface-layer hypothesis.

Cadmium, like zinc, is presumably a substitutional acceptor impurity in InSb. Unfortunately, it was not possible to investigate the distribution coefficient for this impurity in single crystals at concentrations greater than ~0·1 at.% in the solid. No concentration dependence was observed below this concentration.

It was possible, however, to study the distribution of cadmium in the presence of varying amounts of zinc. The results, already given in Fig. 8, show that the effect of zinc concentration on cadmium distribution clearly is essentially the same as the effect on zinc distribution. This is presumably due to an acceptor-acceptor interaction between the two impurities; i.e.

$$Zn_s + Cd_s^- = Zn_s^- + Cd_s. \tag{8}$$

The curve in Fig. 7 for the on-facet data is the same as the curve obtained earlier for zinc, simply translated on the log K axis by an amount sufficient to agree with the low-zinc-concentration data. The fit of a similar curve to the off-facet data would also be reasonable, indicating that the same region of the crystal, presumably the surface region, is controlling for both impurities.

Selenium is a substitutional donor in InSb, and the fact that it shows an increased solubility in the presence of high zinc concentrations lends strong support to the general hypothesis that the interactions being observed are related to the electronic properties of the dopants. The fact that the change in selenium solubility occurs in the same concentration region in which the zinc solubility changes suggests that the surface-layer Fermi level is again controlling and that the enhanced selenium solubility results from the formation of Se^+ ions.

Copper was chosen for study because this element is reported to have a very high diffusion coefficient in InSb[18]. The results of Fig. 5 show that the addition of moderate amounts of zinc leads to a decrease in the distribution coefficient for copper, a result that can be understood as an interaction between the two acceptors,

$$Zn_s + Cu_s^- = Cu_s + Zn_s^- \tag{9}$$

which results in a decrease in Cu_s^- and therefore in the total copper concentration in the solid as the Zn_s^- concentration is increased. A very important feature of the results is the fact that the decline in distribution coefficient for copper begins at a zinc concentration that is only one-tenth of that at which the distribution coefficients for zinc and cadmium begin to decrease under similar circumstances and this is much nearer the expected intrinsic carrier density at the melting point[3]. This observation is compatible with the assumption that all three concentration dependences result from acceptor-acceptor interactions only if the copper-zinc interaction is in some way decoupled from the others, e.g. if the zinc and cadmium distributions are determined in a surface layer and the copper activity is uniform throughout the crystal because of rapid copper diffusion.

The increase in copper distribution coefficient beyond a zinc concentration of about 0·03 at.% zinc in the solid can be attributed either to a contribution from a Cu_s^+ species that becomes important as the Fermi level drops below some previously unreported copper donor level or to the formation of some kind of copper–zinc complex. If the former is the correct explanation, the Fermi-level change required to obtain the large change in occupancy of the level is so large, of the order of 0·2 eV, that one must again assume immobilization in the surface layer for the rapidly diffusing Cu. The postulation of complex formation avoids this difficulty.

Complexes that might be considered for this interstitial dopant include both types suggested by Reiss, Fuller and Morin[19] for lithium and boron in germanium, i.e. a covalently bonded Cu–Zn⁻ complex or a Cu^+–Zn^- pair. If the uncharged Zn_s concentration is assumed proportional to the Zn_l concentration, then the concentration of an uncharged binary complex should vary linearly with $[Zn_l]$; i.e.

$$Zn_l + Cu_l = CuZn_s \tag{10}$$

and

$$K'' = \frac{[CuZn_s]}{[Zn_l][Cu_l]} \tag{11}$$

so that at high zinc concentrations,

$$K \cong \frac{[CuZn_s]}{[Cu_l]} \cong K''[Zn_l]. \tag{12}$$

The concentration of a charged complex, on the other hand, would be more nearly proportional to the zinc concentration in the solid, since its formation can be represented with an equation of the form

$$Zn_i + Cu_i + e^- = Zn_s^- + Cu_i = CuZn_s^- \quad (13)$$

and Zn_s^- is the majority species for zinc in the solid. While the scatter in the data is too large to permit a definitive interpretation, it does appear that the dependence of K on zinc concentration is considerably more rapid at high concentrations than would be predicted from equation (13), while the fit to equation (12) is reasonably good.

In our earlier report[3], it was suggested that the concentration dependence observed in this work for the zinc distribution coefficient is the result of electronic interactions in a surface layer where the Fermi level is markedly elevated from its position in the remainder of the crystal. The fact that the substitutional (and presumably slowly diffusing) acceptor-impurity cadmium shows the same behavior as zinc, while the rapidly diffusing acceptor-impurity copper shows the same kind of behavior but at markedly lower concentrations, lends strong support to the earlier hypothesis that the zinc behavior is surface-controlled.

McCaldin[20] has made the suggestion that the zinc data can be explained on the basis of a discrepancy between the true conduction-electron concentration and that determined from Hall measurements. While this proposal can explain the appearance of the change in distribution coefficient at an unexpectedly high value of zinc concentration, it cannot explain the fact that the available range over which the Fermi level can change is too small to account for the effects observed. Thus, the surface-layer postulate is still to be preferred as an explanation for the zinc behavior. But McCaldin's suggestion may be the correct approach to an understanding of why the concentration at which the copper distribution decreases, while lower than that observed in the case of zinc, is still larger than would be predicted from the reported Hall carrier densities.

The Facet effect

Hulme and Mullin[11] have reviewed early work done on the facet effect. In the present work, several of the elements reported to show the effect were reexamined. Both copper and zinc have previously been reported to show a facet effect with on-facet/off-facet ratios of 1·2–1·4[11]. We have reexamined both elements, using the tracer technique and autoradiographs, but have not been able to detect a facet effect for either copper or zinc; an inhomogeneity of a few per cent would have been detectable by this means. The early determinations were made by measuring carrier densities and may be in error owing to the presence of an accidental impurity.

At least two mechanisms have been postulated for the facet effect, neither of which appears to be compatible with the results obtained here. Merten and Hatcher[3] suggested that the surface states that give rise to the high-electron-density surface layer might be nonuniformly distributed over the crystal surface and lead to a greater depression or increase in impurity solubility in one area than in another. That this is not the case is shown by the fact that zinc, the distribution of which is presumably surface-controlled, does not show a facet effect, even in the presence of selenium and under conditions of growth rate and concentration where selenium does show the effect. The difficulty with this approach is further shown by the fact that cadmium, an acceptor, has an enhanced solubility on-facet, just as do the donors selenium and tellurium. If the facet effect resulted from differences in electron activity, one would expect donors and acceptors to respond in opposite directions.

Trainor and Bartlett[12] have suggested that the facet effect results from nonequilibrium entrapment of impurity atoms adsorbed on the crystal facet. This hypothesis is very difficult to reconcile with the cadmium–zinc and selenium–zinc interactions observed in the present work. The possibility that this interaction occurs in the adsorbed layer can be ruled out, since the interaction is observed off-facet as well as on-facet and because adsorption can hardly play a major role in the behavior of zinc, which does not show a facet effect. Hence, the important interaction must occur in the solid. But an interaction in the solid of this kind cannot determine the on-facet distribution, if the distribution coefficient there is controlled by adsorption in a layer that is not in good communication with the solid phase.

The only explanation for the facet effect that appears to be formally compatible with the observed interactions and with the earlier explanation of concentration effects is the statement that the distribution coefficients, K_n and K_f for neutral cadmium, for example, are concentration-independent but different, while the surface charge densities are nearly the same everywhere. The subscripts n and f refer to the on-facet and off-facet areas, respectively. The observed distribution coefficients are

$$\left(\frac{\mathrm{Cd}_s^- + \mathrm{Cd}_s}{\mathrm{Cd}_l}\right)_n = K_n \tag{14}$$

and

$$\left(\frac{\mathrm{Cd}_s^- + \mathrm{Cd}_s}{\mathrm{Cd}_l}\right)_f = K_f. \tag{15}$$

With the assumption of uniform charge density,

$$\left(\frac{\mathrm{Cd}_s^-}{\mathrm{Cd}_s}\right)_n = \left(\frac{\mathrm{Cd}_s^-}{\mathrm{Cd}_s}\right)_f \tag{16}$$

Hence,

$$\frac{K_n}{K_f} \cong \frac{K'_n}{K'_f} \tag{17}$$

al all concentrations.

The reason K'_n and K'_f are not equal is left open by this consideration, but it is possible that that part of the crystal which is behind the facet is more disordered or has a higher vacancy concentration, and that this leads to a higher solubility for some impurities in this region. Because the distribution coefficient for Cd is orientation-dependent, if this explanation is correct, the vacancy concentration is also orientation-dependent.

Growth-rate effects

The interpretation of the growth-rate effects observed in this work has already been discussed in connection with the results obtained for each of the elements studied. Unfortunately, the number of different mechanisms which has to be invoked is large.

For those impurities that show no facet effect, gallium, copper and zinc, the results are readily accounted for on the basis of the BPS theory (except zinc at high concentrations), and under these conditions reasonable values of δ/D (329, 770 and 242 sec/cm, respectively) are obtained.

One might expect that the off-facet behavior of dopants that do show the facet effect would also follow the BPS theory in a straightforward manner, and this may in fact be the case. For selenium, a δ/D of 635 sec/cm is obtained, and this is consistent with the values obtained for the three dopants just discussed. The off-facet cadmium data can also be reconciled with the BPS theory, but only by choosing $\delta/D < 100$ sec/cm. Either the diffusion coefficient of cadmium in the melt is substantially larger than that of any of the other dopants or the growth-rate behavior of this element is complicated by some other factor.

The probable reason for the observed on-facet growth-rate behavior of cadmium and selenium has already been touched on in the discussion of cadmium, where it was shown that the solid-state diffusion constants needed to explain the observed dependence on the basis of Hall's picture[13] (and assuming adsorption to be responsible for the facet effect) are of a reasonable magnitude. Exactly similar considerations are applicable if one assumes that the distribution-coefficient enhancement on-facet is due to nonequilibrium trapping of vacancies, as suggested previously.

At high growth rates, where the escape of adsorbed impurities or nonequilibrium vacancies into the melt is no longer important, one would expect the on-facet data to follow the same BPS slope as do the off-facet data. In fact, no rate effect was seen at high growth rates, but for both cadmium and selenium the distribution coefficients were already so close to unity at a growth rate of 1·5 cm/hr as to make this observation inconclusive.

The fact that zinc ceases to obey the BPS relationships at high concentrations remains to be dealt with. A possible explanation lies in the contention of Kendall and Jones (as reported by Hulme and Mullin[11]) that the diffusion coefficient of zinc in InSb is concentration-dependent and becomes quite high in just the concentration range where the simple relationships were found to fail in the present work. At high concentrations, the diffusion rate of zinc is reported to become sufficiently high ($\sim 10^{-9}$ cm^2/sec near the melting point) so that the surface layer postulated earlier can no longer determine its chemical behavior at low growth rates. Thus, the distribution coefficient will tend to decrease with increasing growth rate as a result of liquid-state effects and tend to increase as a result of solid-state effects. The net result could be a near cancellation of the two trends.

CONCLUSIONS

These distribution-coefficient studies have shown a number of interesting features. It has generally been assumed that Ga replaces In in InSb, and this is certainly the case. The growth rate studies showed Ga to be well behaved.

It was postulated that the position of the Fermi level at the surface of the crystal determined the distribution coefficient for Zn and that the Fermi level is higher at the surface than in the bulk[3]. The results indicate that this surface layer is also important in determining the distribution coefficients for the acceptor Cd and the donor Se because these distribution coefficients change at the same point and at the same rate as does the Zn distribution coefficient. However, the distribution coefficient for Se increases instead of decreasing as does Zn and Cd; this is consistent with the formation of Se^+ ions. The fact that the distribution coefficients for the on-facet and off-facet areas for both acceptors and donors show the same shape indicates that the Fermi level at the surface is uniform. If the Fermi level were different on-facet than off-facet, these two regions would not be expected to show the same concentration dependence. For the rapidly diffusing species Cu, the surface layer is not determining, but the bulk is. The distribution coefficient for Cu decreases at a Zn concentration nearer the value calculated for the intrinsic carrier density, and, at still higher Zn concentrations, it appears that Cu and Zn form a complex.

The observation of essentially equal impurity interactions on- and off-facet indicates that the surface Fermi level is the same on-facet as off-facet, and also suggests that the same region controls the distribution coefficient in both areas; i.e. it suggests that impurity trapping on-facet in an adsorbed layer is not the correct explanation of the facet effect. It is possible that the facet effect is related to a different vacancy concentration on- and off-facet.

REFERENCES

1. HULME K. F. and MULLIN J. B., *Phil. Mag.* **4**, 1286 (1959).
2. MULLIN J. B. and HULME K. F., *J. Phys. Chem. Solids* **17**, 1 (1960); *ibid.* **19**, 352 (1961).
3. MERTEN U. and HATCHER A. P., *J. Phys. Chem. Solids* **23**, 533 (1962).
4. BURTON J. A., PRIM R. C. and SLICHTER W. P., *J. chem. Phys.* **21**, 1987 (1953).
5. NORMAN J. H., WINCHELL P. and STALEY E. G., *J. chem. Phys.* **41**, 60 (1964).
6. WOOLLEY J. C. and SMITH B. A., *Proc. phys. Soc.* **72**, 214 (1958).

7. DEWALD J. F., *J. electrochem. Soc.* **104**, 244 (1957).
8. BAKER T., *Photographic Emulsion Technique*, p. 292. American Photographic, Boston (1948).
9. MULLIN J. B., *J. electron. Control* **4**, 358 (1958).
10. STRAUSS A. J., *J. appl. Phys.* **30**, 559 (1959).
11. HULME K. F. and MULLIN J. B., *Solid-St. Electron.* **5**, 211 (1962).
12. TRAINOR A. and BARTLETT B. E., *Solid-St. Electron.* **2**, 106 (1961).
13. HALL R. N., *J. Phys. Chem.* **57**, 836 (1953).
14. ORTH R. W., and WATT L. A. K., *J. Phys. Chem. Solids* **26**, 197 (1965).
15. ALLRED W. P. and BATE R. T., *J. electrochem. Soc.* **108**, 258 (1961).
16. GATOS H. C., *et al.*, *J. appl. Phys.* **32** 2057 (1961).
17. WEISS H., *Z. Naturforsch.* **11a**, 131 (1956).
18. STOCKER H. J., *Phys. Rev.* **130**. 2160 (1963).
19. REISS H., FULLER C. S. and MORIN F. J., *Bell Syst. Tech. J.* **35**, 535 (1956).
20. McCALDIN J O., *J. appl. Phys.* **34**, 1748 (1963).

J. Phys. Chem. Solids Pergamon Press 1969. Vol. 30, pp. 643-655. Printed in Great Britain.

CALCULATION OF DISTRIBUTION FUNCTIONS BY EXPLOITING THE STABILITY OF THE STEADY STATE

H. D. REES
Royal Radar Establishment, Malvern, Worcestershire, England

(*Received* 3 *June* 1968; *in revised form* 23 *August* 1968)

Abstract—A numerical method is described for calculating distribution functions of free carriers in crystals from a knowledge of the scattering rates and applied fields. The stability of the steady state is exploited to derive an explicit expression for the distribution function without introducing any *a priori* assumptions about its form. This expression can be evaluated by a convergent iterative process. A rate of scatter leaving the free carrier wave vector unaltered is defined. This scattering process has no physical consequence, but suitable choice of its rate can make the numerical iteration straightforward. The technique is extended to accommodate scattering processes dependent on the distribution function and to analyse time dependent effects. Results are given of numerical calculations of distribution functions for free carriers in electric fields, taking into account scattering processes including polar phonon and impurity scattering.

1. INTRODUCTION

THE THEORETICAL treatment of a transport problem is frequently approached by attempting to solve the Boltzmann equation to derive the relevent distribution function. Although the Boltzmann equation describes the transport problem classically, it provides an otherwise exact description of the effects of the external fields and the scattering processes. However, except for a few elementary cases where analytic expressions for the distribution function exist, the integro-differential nature of the equation makes it difficult to solve. Often the structure of the scattering processes makes the equation so complicated that either physical approximations have to be made to simplify the equation or numerical methods have to be used to tackle it, or most usually both are necessary. A well known way of introducing the physical approximations is to assume some form for the distribution function and to adjust the parameters of the distribution function so as to satisfy the Boltzmann equation most closely. This approach has been applied to complicated problems of free carrier distributions in an electric field; for example to describe the Gunn effect in gallium arsenide where truncation of the series of a spherical harmonic expansion[1] and assuming a displaced Maxwellian distribution[2] have been utilized. However, the objection to such methods is that the consequences of the approximations are not readily assessed.

The present paper describes a method for calculating distribution functions which is not based on the Boltzmann equation. The transport problem is still described classically, but *a priori* assumptions about the form of the distribution are not made and the method is numerically straightforward. An outline of the method was described in a recent letter [3], but it is treated here in more detail.

The analysis is confined to considering distribution functions for free carriers in crystals and, as a further simplification, spatial uniformity is assumed in order that a complete description is possible in terms of momentum and time only. However, extension to spatially varying problems would not involve any change of principle, and it is likely that the technique is capable of extension to problems more general than calculating distribution function for free carriers in crystals.

The scattering of the free carriers and the accelerative effects of the fields are described in terms of a series of probability functions defined in Section 2. These probability functions are related by a recurrence relation which reflects the fact that scattering processes for any free carrier occur in sequence. A 'self' scattering rate, not altering the free carrier wave vector, is defined. It has no physical meaning, but modifies the probability functions leaving the recurrence relation unaltered in form; a result of considerable significance for numerical analysis.

The derivation of the steady state distribution function is approached by appealing firstly to the time independence and secondly to the stability of the steady state. In this context, stability describes the fact that the distribution tends to the steady state distribution after a long enough time irrespective of initial conditions. Stability is a more powerful condition than time independence, since a stable solution is necessarily time independent but the reverse is not automatically true. The stability condition leads to an explicit expression for the steady state distribution function in terms of the probability functions introduced in Section 2. This expression can be evaluated by a convergent iterative process. In Section 4 it is shown that appropriate selection of the self scattering rate can make the numerical iteration easy and can extend the technique to problems where the scattering rate depends on the distribution function itself (such as carrier-carrier scattering) and to describe time dependent effects such as the approach to equilibrium.

The iterative process has formal similarity to a method derived by Budd[4] for calculating free carrier distribution functions, which is based on the Boltzmann equation. However the present method differs in exploiting the stability of the steady state to assure iterative convergence and in incorporating the self scattering term to simplify numerical analysis. It is interesting to notice a possible connection of the present method with the Monte Carlo methods of Kurosawa [5] and of Boardman, Fawcett and Rees [6], which, although different in technique appear to appeal in a similar way to the stability of the steady state; for it would seem that the simulated flight of an electron can only be statistically reproducible if there exists a stable physical distribution.

In Section 5, some illustrative results are given of numerical calculations of distribution functions for free carriers in an electric field, including examples where there is polar phonon and impurity scattering.

2. FORMALISM FOR FORCES AND SCATTERING

The problem is to derive the distribution function for free electrons in a crystal from a knowledge of the scattering rates and of the fields, electric and magnetic, acting on the electrons. Certain simplifying assumptions about the scattering processes are made. These are that they can be treated as instantaneous and that they are not infinitely frequent. Between the scattering events each electron will of course undergo a change of momentum determined by the fields. The instantaneous nature of the scattering processes allows a function $P_n(\mathbf{k}, \mathbf{k}', t)$ to be defined as the probability that an electron initially at $\mathbf{k}$ is at $\mathbf{k}'$ a time t later having been scattered n times during the time interval. A second function $P(\mathbf{k}, \mathbf{k}', t)$ is defined by

$$P(\mathbf{k}, \mathbf{k}', t) = \sum_{n=0}^{\infty} P_n(\mathbf{k}, \mathbf{k}', t). \qquad (2.1)$$

In other words, $P(\mathbf{k}, \mathbf{k}', t)$ is the probability that an electron initially at $\mathbf{k}$ is at $\mathbf{k}'$ a time t later.

Denoting the scattering probability per unit time from $\mathbf{k}$ to $\mathbf{k}'$ by $S(\mathbf{k}, \mathbf{k}')$, the various P_n's must satisfy

$$P_{n+m+1}(\mathbf{k}, \mathbf{k}', t) = \int_0^t \mathrm{d}t' \int \mathrm{d}\mathbf{k}'' \int \mathrm{d}\mathbf{k}''' \; P_n(\mathbf{k}, \mathbf{k}'', t')\, S(\mathbf{k}'', \mathbf{k}''')\, P_m(\mathbf{k}''', \mathbf{k}', t-t') \qquad (2.2)$$

which describes the fact that the scattering events occur in sequence. The Laplace transform with respect to time of (2.2) is

$$\tilde{P}_{n+m+1}(\mathbf{k},\mathbf{k}',s) = \tilde{P}_n(\mathbf{k},\mathbf{k}'',s)\,S(\mathbf{k}'',\mathbf{k}''') \times \tilde{P}_m(\mathbf{k}''',\mathbf{k}',s). \qquad (2.3)$$

Integration over repeated k variables is understood in (2.3) and all following equations. Equation (2.3) allows the $\tilde{P}_n(\mathbf{k},\mathbf{k}',s)$ to be expressed in terms of $S(\mathbf{k},\mathbf{k}')$ and $\tilde{P}_0(\mathbf{k},\mathbf{k}',s)$, where the latter function describes the probability of zero scattering.

Now $P_0(\mathbf{k},\mathbf{k}',t)$, i.e. the probability that an electron initially at $\mathbf{k}$ is at $\mathbf{k}'$ after a time t without being scattered is given by

$$P_0(\mathbf{k},\mathbf{k}',t) = \delta(\mathbf{k}'-\mathbf{T}[\mathbf{k},t]) \times \exp\left\{-\int_0^t \lambda(\mathbf{T}[\mathbf{k},t'])\,\mathrm{d}t'\right\} \qquad (2.4)$$

where $\mathbf{T}[\mathbf{k},t]$ denotes the $\mathbf{k}$-space trajectory for an unscattered electron initially at $\mathbf{k}$, e.g. for motion in an electric field $\mathbf{F}$ alone

$$\mathbf{T}[\mathbf{k},t] = \mathbf{k} + e\mathbf{F}t/\hbar. \qquad (2.5)$$

$\lambda(\mathbf{k})$ is the scattering rate integrated over all final states i.e.

$$\lambda(\mathbf{k}) = \int \mathrm{d}\mathbf{k}' S(\mathbf{k},\mathbf{k}'). \qquad (2.6)$$

A generalisation of the equations is now made, which will be of major importance in later sections of the paper. This is to replace $S(\mathbf{k},\mathbf{k}')$ by $S'(\mathbf{k},\mathbf{k}')$ given by

$$S'(\mathbf{k},\mathbf{k}') = S(\mathbf{k},\mathbf{k}') + S(\mathbf{k})\delta(\mathbf{k}-\mathbf{k}'). \qquad (2.7)$$

The second term on the right of (2.7) describes a scattering rate leaving $\mathbf{k}$ unchanged. Since this 'self' scattering term does not describe a physical process of any consequence, $S(\mathbf{k})$ can be arbitrarily defined. However, for consistency it follows from (2.6) and (2.7) that $\lambda(\mathbf{k})$ must be replaced by $\lambda'(\mathbf{k})$ where

$$\lambda'(\mathbf{k}) = \lambda(\mathbf{k}) + S(\mathbf{k}). \qquad (2.8)$$

So λ' must replace λ in (2.4). However, having modified consistently $S(\mathbf{k},\mathbf{k}')$ and $P_0(\mathbf{k},\mathbf{k}',t)$, equations (2.1–2.3) are still formally correct, although n now counts both real and self scattering events and not just real events.

3. THE STEADY STATE DISTRIBUTION FUNCTION

There are two approaches to deriving the steady state ditribution function $f(\mathbf{k})$ within the framework of the formalism of Section 2. The first appeals to the time independence of $f(\mathbf{k})$, and is similar to the theory of Budd[4] except that the Boltzmann transport equation is not used explicitly in the present analysis. This approach allows $f(\mathbf{k})$ to be expressed as the solution of a homogeneous integral equation. The second approach appeals directly to the stability of the steady state and is more powerful in that it allows an explicit expression for $f(\mathbf{k})$ to be derived.

The time independent approach is considered first. If a time dependent distribution function is denoted by $f(\mathbf{k},t)$, it follows from the definition of $P(\mathbf{k},\mathbf{k}',t)$ of Section 2 that

$$f(\mathbf{k}',t) = f(\mathbf{k},0)P(\mathbf{k},\mathbf{k}',t) \qquad (3.1)$$

and therefore the steady state function $f(\mathbf{k})$ satisfies

$$f(\mathbf{k}') = f(\mathbf{k})P(\mathbf{k},\mathbf{k}',t) \qquad (3.2)$$

for all t. In other words, $f(\mathbf{k})$ is an eigenfunction of $P(\mathbf{k},\mathbf{k}',t)$ for all t. The Laplace transform with respect to t of (3.2) is

$$f(\mathbf{k}')/s = f(\mathbf{k})\tilde{P}(\mathbf{k},\mathbf{k}',s). \qquad (3.3)$$

Multiplying equation (3.3) by s and expanding $\tilde{P}(\mathbf{k},\mathbf{k}',s)$ using equation (2.1) gives

$$f(\mathbf{k}') = sf(\mathbf{k}) \sum_{n=0}^{\infty} \tilde{P}_n(\mathbf{k},\mathbf{k}',s). \qquad (3.4)$$

Equation (3.4) is multiplied by $S(\mathbf{k}',\mathbf{k}'')$ $\tilde{P}_0(\mathbf{k}'',\mathbf{k}''',s)$, and the recurrence relation

(2.3), with $m = 0$, is used to simplify the right-hand side, giving

$$f(\mathbf{k}')\, S'(\mathbf{k}', \mathbf{k}'')\, \tilde{P}_0(\mathbf{k}'', \mathbf{k}''', s) = sf(\mathbf{k}) \sum_{n=1}^{\infty} \tilde{P}_n(\mathbf{k}, \mathbf{k}''', s). \quad (3.5)$$

Subtraction of (3.5) from (3.4) then gives

$$f(\mathbf{k}') = f(\mathbf{k})\,[S'(\mathbf{k}, \mathbf{k}'') + s\delta(\mathbf{k} - \mathbf{k}'')]\, \tilde{P}_0(\mathbf{k}'', \mathbf{k}', s). \quad (3.6)$$

With the definition

$$P_n(\mathbf{k}, \mathbf{k}') = \tilde{P}_n(\mathbf{k}, \mathbf{k}', 0) \quad (3.7)$$

the $s = 0$ limit of (3.6) can be written as the integral equation

$$f(\mathbf{k}') = f(\mathbf{k})S'(\mathbf{k}, \mathbf{k}'')P_0(\mathbf{k}'', \mathbf{k}'). \quad (3.8)$$

The detailed form of equation (3.8) depends on the choice of the self-scattering rate. However, it is structurally the same as the integral equation for the distribution function derived by Budd[4] and also that of Chambers[7] if the time dependent distribution function is replaced by the steady state function. Although there is no simple general method for solving a homogeneous integral equation of the form of (3.8), an iterative solution may be tried, as was done by Budd, but this approach depends on the iteration converging. It will turn out that iterative convergence is a consequence of the stability of the steady state, which remark leads to the second approach to deriving $f(\mathbf{k})$.

Consider first the behaviour of $P_n(\mathbf{k}, \mathbf{k}', t)$ as n becomes large. Since the scattering processes are not infinitely frequent, it follows that by selecting n large enough $P_n(\mathbf{k}, \mathbf{k}', t)$ can be made arbitrarily small for t less than any given finite value. A formal proof of this conclusion is given in Appendix 1. Now $P_n(\mathbf{k}, \mathbf{k}')$, defined by equation (3.7), is the t integral of $P_n(\mathbf{k}, \mathbf{k}', t)$ from zero to infinity, and clearly $P_n(\mathbf{k}, \mathbf{k}')$ will depend only on the behaviour of $P_n(\mathbf{k}, \mathbf{k}', t)$ for t greater than this given value of time. The stability of the steady state means that, irrespective of its initial form, the distribution function will always settle to the steady state function after a sufficient time. Therefore, for large values of t, $P_n(\mathbf{k}, \mathbf{k}', t)$ will be independent of $\mathbf{k}$ and will vary with $\mathbf{k}'$ in the same way as the steady state distribution function $f(\mathbf{k}')$. Therefore if n is made large enough it follows that $P_n(\mathbf{k}, \mathbf{k}')$ will be independent of $\mathbf{k}$ and will vary with $\mathbf{k}'$ in the same way as $f(\mathbf{k}')$. Mathematically this conclusion can be expressed as

$$f(\mathbf{k}') = \operatorname*{limit}_{n\to\infty} g(\mathbf{k})\, P_n(\mathbf{k}, \mathbf{k}') \quad (3.9)$$

where $g(\mathbf{k})$ is arbitrary, although its normalisation will fix that of $f(\mathbf{k}')$. Hence it is seen that stability of the steady state allows an explicit form for $f(\mathbf{k}')$ to be written down.

Now although the self scattering rate $S(\mathbf{k})$ does not describe a physical process and cannot therefore affect the stability of the steady state in any physical sense, it is indicated in Appendix 2 that self scattering can be treated as real scattering only if $S(\mathbf{k})$ is not negative. Therefore (3.9) is valid only if $S(\mathbf{k})$ is positive or zero. It is assumed from now on that $S(\mathbf{k})$ is positive or zero.

Repeated use of equation (2.3) allows $P_n(\mathbf{k}, \mathbf{k}')$ to be expanded in terms of $P_0(\mathbf{k}, \mathbf{k}')$ and $S'(\mathbf{k}, \mathbf{k}')$, the expansion being indicated schematically by

$$P_n = P_0 S' P_0 \ldots S' P_0 \quad (3.10)$$

in which S' appears n times on the right of equation (3.10). When (3.10) is inserted into (3.9), the expression for $f(\mathbf{k}')$ can be written schematically as

$$f = \operatorname*{limit}_{n\to\infty} g\, P_0\, (S'P)_0)^n. \quad (3.11)$$

Since g is arbitrary, the integral gP_0 is also arbitrary. So (3.11) implies that $f(\mathbf{k}')$ is the result of a convergent iterative process, starting from an arbitrary initial function, each iteration involving integrating the product of the function first with S' and then with P_0. This is identical with saying that the iteration of equation (3.8) is convergent. However, the convergence does not automatically follow from the integral equation (3.8), but depends on the existence of the explicit solution (3.9). In Appendix 3 it is shown that equation (3.8) is equivalent to the Boltzmann equation, so the distribution function derived by iteration will necessarily satisfy the Boltzmann equation.

From the logical viewpoint, the analysis based on the time independence of $f(\mathbf{k})$ is unnecessary, but its inclusion serves to demonstrate the difference between exploiting the time independence and the stability of the steady state.

The next section will deal in more detail with the numerical iteration, but it is relevant to draw attention to the fact that although the final result of the iteration cannot depend on the self scattering rate $S(\mathbf{k})$, redefining $S(\mathbf{k})$ can, through equations (2.8) and (2.4) greatly modify the iterative process itself.

From the purely numerical viewpoint, the fact that the iteration involves only integration rather than integration and differentiation is an advantage, since errors in a function tend to be quenched by integration but accentuated by differentiation. Therefore the present method should have some numerical advantages over directly trying to solve iteratively the usual integro-differential Boltzmann equation.

4. SELECTION OF $S(\mathbf{k})$

For calculating steady state distribution functions, the selection of the self scattering rate $S(\mathbf{k})$ is relevant only to the extent that a good choice can simplify the numerical iteration. However, it will be shown later in this section that a special form of $S(\mathbf{k})$ exists such that each iteration is equivalent to a time increment of the physical system. The iterative process may then be used to evaluate the approach to equilibrium or the response to time varying fields. The problem of calculating steady state functions is discussed first, and for the purposes of illustration it will be assumed that the only field present is an electric field $\mathbf{F}$.

The first stage of each iteration involves integrating the product of the function so far developed, denoted by $g(\mathbf{k})$, with the scattering rate $S(\mathbf{k}, \mathbf{k}')$, i.e. forming

$$g'(\mathbf{k}') = \int d\mathbf{k}\, g(\mathbf{k}) \left\{S(\mathbf{k}, \mathbf{k}') + S(\mathbf{k})\, \delta(\mathbf{k} - \mathbf{k}')\right\}. \tag{4.1}$$

Now $S(\mathbf{k}, \mathbf{k}')$ will contain δ functions in the initial and final energies, and numerically there will generally be little difficulty in dealing with the first term of the integral. The self scattering component of the integral is elementary, irrespective of the precise form of $S(\mathbf{k})$.

The second stage of each iteration requires the evaluation of

$$g''(\mathbf{k}') = \int d\mathbf{k}\, g'(\mathbf{k})\, P_0(\mathbf{k}, \mathbf{k}'). \tag{4.2}$$

Using equations (2.4), (2.5) and (2.8) and, for simplicity, selecting units such that $e = \hbar = 1$, equation (4.2) becomes

$$g''(\mathbf{k}') = \int d\mathbf{k}\, g'(\mathbf{k}) \int_0^\infty dt\, \delta(\mathbf{k}' - \mathbf{k} - \mathbf{F}t) \times \exp\left\{-\int_0^t \lambda' (\mathbf{k} + \mathbf{F}t')\, dt'\right\}. \tag{4.3}$$

The $\mathbf{k}$ integration can be carried out immediately to give

$$g''(\mathbf{k}') = \int_0^\infty dt\, g' (\mathbf{k}' - \mathbf{F}t) \times \exp\left\{-\int_0^t \lambda(\mathbf{k}' - \mathbf{F}t + \mathbf{F}t')\, dt'\right\}. \tag{4.4}$$

It is immediately apparent that the difficulty of carrying out the second part of the iteration depends on the difficulty first of evaluating the exponent and then of integrating the product of the exponential with $g'(\mathbf{k}' - \mathbf{F}t)$. It is relevant to point out that $\lambda(\mathbf{k})$ is fairly easily evaluated for most physical scattering processes, but analytic integration of $\lambda(\mathbf{k})$ to give the exponent of (4.4) is possible only for certain simple processes such as optical deformation potential scattering. Analytic integration is not possible, at least in any simple way, for polar or impurity scattering. Even when the exponent has been evaluated there is still the far from easy problem of carrying out the t integration.

However, it is clear from equation (2.8) that it is possible to define $S(\mathbf{k})$ in such a way so as to make $\lambda'(\mathbf{k})$ almost anything. By careful choice of $S(\mathbf{k})$, not only can the exponent of (4.4) be made analytic, but the following t integration can be made straightforward also. This still leaves a considerable choice for the precise form of $S(\mathbf{k})$.

All the numerical results discussed in this paper were obtained with the particularly simple definition

$$S(\mathbf{k}) = \Gamma - \lambda(\mathbf{k}) \qquad (4.5)$$

where Γ is a constant larger than the largest value of $\lambda(\mathbf{k})$. With this definition of $S(\mathbf{k})$, equation (4.4) becomes

$$g''(\mathbf{k}') = \int \mathrm{d}t\, g'(\mathbf{k}' - \mathbf{F}t) \exp(-\Gamma t). \qquad (4.6)$$

In practice the evaluation of (4.6) could be made so rapid numerically that the whole second part of the iteration was quicker than the first part. However, it is not suggested that the definition (4.5) is the only useful one or necessarily the best for most purposes.

It frequently happens that the scattering rate is itself a function of the distribution function $f(\mathbf{k})$, in other words the problem is non-linear. Examples of non-linear contributions are electron–electron scattering and impurity scattering where the screening depends on the distribution function. Extension of the present iterative technique to accommodate the non-linearity may be accomplished by using at the n'th iteration a scattering rate, which may be denoted $S'(f_{n-1}, \mathbf{k}, \mathbf{k}')$, appropriate to the distribution function f_{n-1} derived after the $(n-1)$'th iteration. A non-linear part of the self scattering rate may be included, and a particularly useful form for it is one analagous to (4.5), which has the property of rendering $\lambda'(\mathbf{k})$, and hence $P_0(\mathbf{k}, \mathbf{k}')$, free of non-linear corrections. This facility for handling non-linear corrections during the iteration represents a substantial increase in the usefulness of the method.

Within the scope of the discussion of the choice of $S(\mathbf{k})$, there is the useful result that, with $S(\mathbf{k})$ defined by (4.5)

$$\lim_{\Gamma \to \infty} f_n(\mathbf{k}) = f(\mathbf{k}, n/\Gamma) \qquad (4.7)$$

where $f_n(\mathbf{k})$ is the result of n iterations starting from an initial function $f_0(\mathbf{k})$, and $f(\mathbf{k}, t)$ is the time dependent distribution function that develops from the initial function $f_0(\mathbf{k})$. One derivation of (4.7), which depends on showing that each iteration is equivalent to a time step $1/\Gamma$, is given in Appendix 4. If an infinite value of Γ was actually used the iteration would converge infinitely slowly and the numerical analysis would be pointless. However, the usefulness of equation (4.7) is that a good approximation to the time development can be obtained by using a large finite Γ. Of course, whatever value of Γ is used, the calculated steady state $f(\mathbf{k})$ is the same. This time development facility allows a description of the approach to equilibrium from any given initial function to be obtained, and also, by varying the field between iterations, to evaluate the response to time dependent fields.

5. NUMERICAL RESULTS

The objective of this section is to illustrate the type of problem for which the present numerical method is useful, rather than to analyse any one problem in detail. The results are restricted to problems where there is a single, isotropic, parabolic band. This restriction is not necessary in principle, but simplifies the analysis. However, the calculations have taken into account polar phonon, ionized impurity and carrier–carrier scattering as well as acoustic and optical deformation potential scattering. The expressions for the phonon scattering rates were taken from papers by Butcher and Fawcett[8] and by Baynham *et al.*[9]. Impurity and carrier–carrier scattering rates were evaluated using the Born approximation for an interaction potential $V(r)$ given by

$$V(r) = \pm\frac{Ze^2}{4\pi\epsilon r}\exp(-r/d) \qquad (5.1)$$

where Z is the ionic charge ($Z = 1$ for carrier–carrier scattering), ϵ is the dielectric constant and d the Debye length appropriate to free carriers at the lattice temperature. To simplify the expressions for the scattering rates, the dependence of the screening on the distribution function itself, and for carrier–carrier scattering, on the velocities of the interacting carriers, was ignored. These simplifications, together with the use of the Born approximation, emphasise the fact that the present calculations are illustrative rather than exact. For impurity scattering there is a special problem of treating the scattering of low energy carriers. Because the impurity scattering rate at very low energies is very large, a very large value of Γ would be needed to assure iterative convergence, which would in turn make the required number of iterations undesirably large. Now the effect of impurity scattering is to reduce the anisotropy of the distribution function. However, the continuity of the distribution function requires it to be nearly isotropic at low energies even in the absence of impurity scattering, and therefore impurity scattering becomes of negligible importance at very low energies. In the present calculations, impurity scattering is neglected at energies so low that the distribution function is essentially isotropic even in the absence of impurity scattering.

Purely numerical aspects of the calculations are not discussed here since they are not fundamental to the principal of the calculations.

Figures 1 and 2 relate to calculations for electrons in indium antimonide at 77°K, allowing for polar optic and deformation potential acoustic phonon scattering, but neglecting impurity and electron–electron scattering. The effective mass and scattering parameters were taken from reference[9] and are listed in Table 1. Figure 1 shows the drift velocity/field curve up to 200 V/cm. At higher fields the iteration did not converge to a stable value, reflecting the absence of a steady state due to polar breakdown. Figure 2 shows the first 4 coefficients of the surface harmonic expansion of the distribution

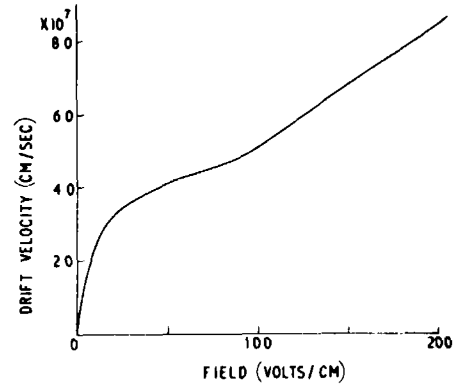

Fig. 1. Velocity/field curves for electrons in InSb at 77°K.

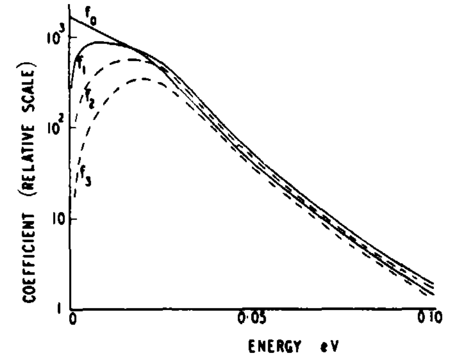

Fig. 2. Coefficients of surface harmonic expansion of electron distribution in InSb at 77°K for 75 V/cm.

Table 1. Effective mass and phonon scattering parameters used in numerical calculations

Material m^*/m_0	n-type InSb 0·012	n-type GaAs 0·066	p-type Ge 0·3
Acoustic scattering			
Ξ_u (eV)	4	7	5·7
s (cm. sec^{-1})	$5{\cdot}0\times10^5$	$5{\cdot}5\times10^5$	$5{\cdot}4\times10^5$
ρ (g. cm^{-3})	5·78	5·36	5·32
Polar scattering			
ϵ_∞	16·8	10·82	
ϵ_0	18·7	12·53	
T_{phonon} (°K)	276	410	
Optical scattering			
Ξ_0 (eV. cm^{-1})			$1{\cdot}14\times10^9$
T_{phonon} (°K)			430

function for a field of 75 V/cm. In other words, the distribution function is expanded as

$$f(\mathbf{k}) = \sum_{n=0}^{\infty} f_n(\epsilon)P_n(\cos\theta) \qquad (5.2)$$

where ϵ denotes energy and θ is the angle between $\mathbf{k}$ and $\mathbf{F}$. The normalisation of the harmonics is such that

$$\int_{-1}^{1} P_n{}^2(x)\,\mathrm{d}x = 1. \qquad (5.3)$$

The fact that the coefficients of the expansion are of comparable magnitude over a large energy range implies that the distribution is streamed rather than a perturbed thermal distribution. Although Figs. 1 and 2 should illustrate the general behaviour of the electron distribution in indium antimonide, it is to be expected that the drift velocity below breakdown and the breakdown field will be sensitive to band non-parabolicity, and therefore the parabolic band approximation is certainly an over-simplification for this particular calculation.

Figures 3 and 4 relate to calculations for electrons in gallium arsenide at 300°K. The effective mass and phonon scattering parameters used are listed in Table 1. The single valley approximation should be reasonable for fields up to 2 kV/cm since the threshold field for negative resistance is 3 kV/cm. Figure 3 shows the drift mobility/field curves for intrinsic material and for donor concentrations of 10^{15}, 3×10^{15} and $10^{16}\,\text{cm}^{-3}$. It is assumed that the donors are singly charged ions, there is no compensation and the electron concentration, determining both the screening and electron–electron scattering, is the same as the donor concentration. Impurity scattering is neglected for electron energies below 3×10^{-3} eV. It is apparent that the relative importance of the impurity scattering falls with increasing field. Figure 4 shows the first 3 terms of the harmonic expansion of the distribution function at 1·5 kV/cm for intrinsic material and $N_D = 10^{16}\,\text{cm}^{-3}$. The chief effects of the impurity scattering may be seen to be a reduction in the electron

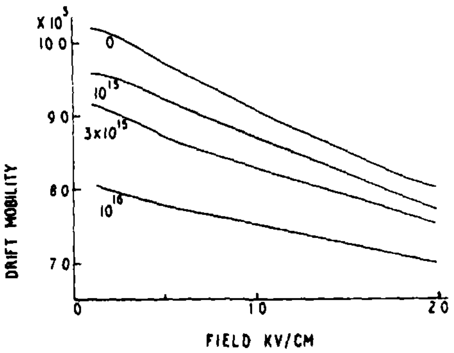

Fig. 3 Drift mobility/field curves for n GaAs at 300°K.

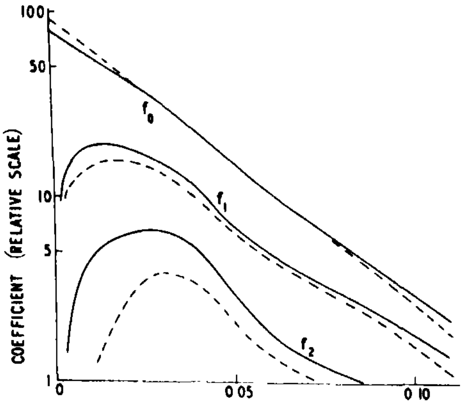

Fig. 4. Coefficients of surface harmonic expansion of electron distribution in n GaAs at 300°K for 1·5 kV/cm. Impurity scattering neglected in the computation for electron energies below 3×10^{-3} eV. Full line for intrinsic material and broken line for $n = N_D = 10^{16}\,\text{cm}^{-3}$.

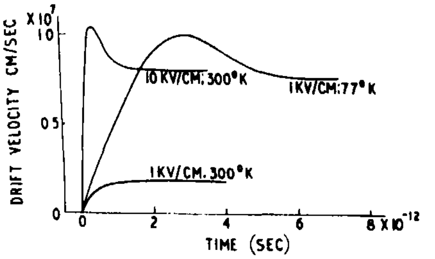

Fig. 5. Drift velocity response to field switched on at time 0 for heavy holes in p Ge.

temperature and a large reduction in the anisotropy of the distribution function at low energies. These observations are physically reasonable. What is more surprising at first sight is that dropping the electron–electron scattering from the computation makes very little difference to the distribution function. The electron–electron scattering affects the distribution function only to a few percent of the impurity scattering, too little to indicate in the figures. The probable explanation is that, without impurity or electron–electron scattering, the electrons have very roughly a displaced thermal distribution. Impurity scattering reduces the total momentum of the electron system and so has a large effect on this distribution. Electron–electron scattering only exchanges momentum between electrons (and would have no nett effect on a displaced thermal distribution) and has a smaller effect.

To illustrate the use of the present iterative technique to derive the time development of a distribution function, Figs. 5 and 6 indicate the response to an applied electric field switched on at time 0. The initial distribution is assumed to be in equilibrium with the lattice. The parameters are representative of those for p type germanium, taking into account only the heavy holes, and are listed in Table 1.

Figure 5 shows the drift velocity as a function of time for fields of 1 and 10 kV/cm at 300°K and 1 kV/cm at 77°K. Two points are worth mentioning. Firstly, the drift velocity settles down after about 10^{-12} second at 300°K but takes about 6×10^{-12} second at 77°K, reflecting the stronger phonon scattering at the higher temperature. Secondly, the drift velocity increases monotonically to the saturated value for 1 kV/cm at 300°K, but the other two response curves have a significant overswing. The explanation for this behaviour is that, in a strong enough field, the carriers are accelerated rapidly to a large drift velocity with only a small increase of thermal energy. The heating process is slower, and the drift velocity falls as the distribution heats up. Figure 6 illustrates

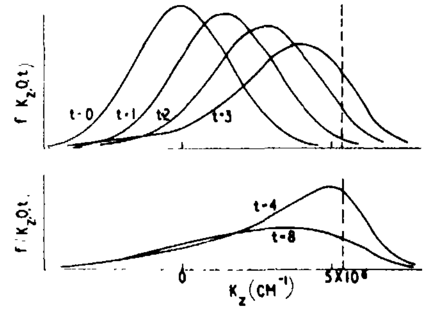

Fig. 6. Response of heavy hole distribution in p Ge at 77°K to 1 kV/cm field switched on at time 0. The lines indicate $f(k_z, k_r)$, where k_z is parallel to **F** and k_r perpendicular to field, for $k_r = 0$. The unit of time is 10^{-12} sec. The broken line marks the value of **k** above which optical phonon emission is possible.

the change of the distribution function corresponding to the 77°K, 1 kV/cm curve. The figure shows the distribution function for a zero **k**-vector perpendicular to the field, plotted as a function of k_z, the component of **k** parallel to the field, for a series of times after the field is switched on. The initial rapid displacement of the distribution (to roughly those k_z where optical phonon emission is possible) is followed by a slower broadening, illustrating the smallness of the momentum relaxation time compared with the energy relaxation time.

6. CONCLUSIONS

There are two basic principles of the present theory for the numerical calculation of distribution functions. Firstly, the stability of the steady state allows an explicit form for the steady state distribution function to be derived, which can be re-expressed as the result of a convergent iterative process. Secondly, by suitably defining a scattering rate leaving the state of a particle unaltered, the iteration can be made numerically easy. Extensions of the theory to accommodate scattering processes dependent on the distribution function and to describe time responses of the distribution function are straightforward. The numerical results given by way of illustration are confined to calculating distribution functions for free carriers in a uniform electric field where the band structure can be regarded as a single, isotropic, parabolic valley. However, the basic theory is of a more general nature and should be applicable to more general band structures, to mixed electric and magnetic fields and to spatially variable systems.

It is interesting to consider the correspondence of the present theory with those others which permit numerical calculations of distribution functions to be made without need for physical approximations. At first sight the closest similarity is with the theory of Budd[4] which uses a basically similar iterative procedure although the self scattering term is not introduced. However, there is a difference of principle in the appeal of Budd's theory to the time independence of the steady state and of the present theory to stability. The appeal to stability provides the guarantee of convergence which is essential to the general use of the iterative procedure. The Monte Carlo methods of Kurosawa[5] and of Boardman, Fawcett and Rees[6], (the latter also utilising the self scattering modification) would appear to make appeal to the stability of the steady state, for in these methods, it would seem that the simulated flight of the electron can be statistically reproducible only if there exists a stable physical distribution function. Hence, there is a similarity of principle, though not of technique, of the Monte Carlo methods and the present iterative method.

Acknowledgements—The author acknowledges valuable discussions with W. Fawcett and T. P. McLean and is indebted to J. B. Arthur who wrote some special sections of the computer programme.

Contributed by permission of the Director of R.R.E. Copyright Controller H.M.S.O.

REFERENCES

1. CONWELL E. M. and VASSELL M. O., (*Proc. Int. Conf. Phys. Semiconductors, Kyoto, 1966*) *J. phys. Soc. Japan* (Supplement) **21**, 527 (1966).
2. BUTCHER P. N. and FAWCETT W., *Phys. Lett.* **21**, 489 (1966).
3. REES H. D., *Phys. Lett.* **26A**, 416 (1968).
4. BUDD H., *Phys. Rev.* **158**, 798 (1967).
5. KUROSAWA T., (*Proc. Int. Conf. Phys. Semiconductors, Kyoto, 1966*) *J. phys. Soc. Japan* (Supplement) **21**, 424 (1966).
6. BOARDMAN A. D., FAWCETT W. and REES H. D., *Solid State Commun.* **6**, 305 (1968).
7. CHAMBERS R. G., *Proc. phys. Soc.* **A65**, 458 (1952).
8. BUTCHER P. N. and FAWCETT W. *Proc. phys. Soc.* **86**, 1205 (1965).
9. BAYNHAM A. C., BUTCHER P. N., FAWCETT W. and LOVELUCK J. M., *Proc. phys. Soc.* **92**, 783 (1967).

APPENDIX 1

It is now proved formally that, by making n large enough, $P_n(\mathbf{k},\mathbf{k}',t)$ can be made arbitrarily small for t less than any given finite time. The first step is to consider the probability density function, $D(\mathbf{k},t)$, of the time t of the first scattering of an electron with wave vector $\mathbf{k}$ at time 0. Following the notation of section 2, $D(\mathbf{k}, t)$ is given by

$$\begin{aligned} D(\mathbf{k}, t) &= \lambda'(\mathbf{T}[\mathbf{k}, t]) \exp\{-\textstyle\int_0^t \lambda'(\mathbf{T}[\mathbf{k}, t']) \, \mathrm{d}t'\} \\ &\quad \text{for } t > 0 \\ &= 0 \quad \text{for} \quad t < 0. \end{aligned} \tag{A1.1}$$

Now if the largest value of $\lambda'(\mathbf{k})$ is μ, it follows that $D(\mathbf{k}, t)$ is weighted more to large values of t than is the probability density function $D'(t)$ given by

$$\left.\begin{aligned} D'(t) &= \mu \exp(-\mu t) \quad \text{for} \quad t > 0 \\ &= 0 \text{ for } t < 0. \end{aligned}\right\} \tag{A1.2}$$

Now $D(\mathbf{k}, t)$ is the probability density function of the time between successive scatterings when the final state for the first scattering is $\mathbf{k}$. Therefore $D'(t)$ certainly underestimates the time between successive scatterings of an electron, so the time required for n successive scatterings, is certainly underestimated by the probability density given by the n-fold convolution of $D'(t)$, i.e.

$$\begin{aligned} &\frac{\mu^n t^{n-1} e^{-\mu t}}{(n-1)!} \quad \text{for} \quad t > 0 \\ &0 \quad \text{for } t < 0. \end{aligned} \tag{A1.3}$$

Therefore the probability of n scatterings occurring in a time t_0 is less than

$$\frac{\mu^n}{(n-1)!} \int_0^{t_0} t^{n-1} e^{-\mu t} \mathrm{d}t. \tag{A1.4}$$

Since (A1.4) never exceeds $(\mu t_0)^n/n!$, it follows that the probability of an electron being scattered n times in a time t_0 can be made arbitrarily small by choosing n large enough. Therefore $P_n(\mathbf{k}, \mathbf{k}', t)$ can be made arbitrarily small for $t < t_0$ by choosing n large enough.

APPENDIX 2

Unacceptability of a negative self scattering rate.

In considering the acceptability of choosing a self scattering rate, $S(\mathbf{k})$, negative for at least some $\mathbf{k}$, the difference between exploiting time independence and stability of the steady state is again demonstrated When appeal is made to time independence, the scattering processes are regarded as balancing the effects of fields. Since the self scattering does not alter the electron state, it makes no nett contribution to the rate of change of the distribution due to scattering, and so $S(\mathbf{k})$ could be arbitrarily defined.

However, when stability is exploited, the scattering processes are regarded as sequences of events which cause the electron distribution to approach the steady state. Because the distribution approaches the steady state with the advance of time, but not with backward steps in time, the scattering must be treated so as to distinguish the initial and the final states for each process. Now a positive scattering rate $S(\mathbf{k}, \mathbf{k}')$ means that, in a positive increment of time, there is a positive probability that an electron in an initial state $\mathbf{k}$ is scattered to a final state $\mathbf{k}'$. On the other hand a negative scattering rate $-S(\mathbf{k}, \mathbf{k}')$ implies that the direction of the transition is reversed. $\mathbf{k}$ and $\mathbf{k}'$ are regarded as the initial and final states, but the probability of a transition from $\mathbf{k}$ to $\mathbf{k}'$ is positive when the time increment is negative. When the scattering rate is positive, the number of scatterings of an electron increases with the advance of time, and when the rate is negative the number of scatterings increases with reversed movement in time.

Now the probability function $P_n(\mathbf{k}, \mathbf{k}', t)$ describes an average over all possible sequences of n scattering events, where n counts both real and self scattering processes. The derivation of the explicit expression for the distribution function, equation (3.9), depends on the fact that, as n becomes larger, a larger time advance is necessary for the n scatterings to occur. This must be true for every possible sequence of n scattering events; so if there is any process for which the number of scatterings increases with reversed movement in time, the derivation of equation (3.9) would be invalid. From the considerations of the previous paragraph, it follows that equation (3.9) is valid with the self scattering events counted in with the real scattering events only if $S(\mathbf{k})$ is positive or zero for all $\mathbf{k}$. If $S(\mathbf{k})$ is negative, the self scattering cannot be treated as real scattering for the purposes of the analysis leading to equation (3.9)

APPENDIX 3

Equivalence of equation (3.8) and the time independent Boltzmann equation. Consider first two functions $f(\mathbf{k})$ and $g(\mathbf{k})$ related by

$$\begin{aligned} f(\mathbf{k}') &= \int \mathrm{d}\mathbf{k} \, g(\mathbf{k}) P_0(\mathbf{k}, \mathbf{k}') \\ &= \int \mathrm{d}\mathbf{k} \int_0^\infty \mathrm{d}t \, g(\mathbf{k}) P_0(\mathbf{k}, \mathbf{k}', t). \end{aligned} \tag{A3.1}$$

The second equation derives from the first by the definition of $P_0(\mathbf{k}, \mathbf{k}')$. The basic form of $P_0(\mathbf{k}, \mathbf{k}', t)$ is that given by equation (2.4), but in order to carry out the $\mathbf{k}$ integration of (A3.1), use is made of the fact that the trajectory defined by

$$\mathbf{k}' = \mathbf{T}[\mathbf{k}, t] \tag{A3.2}$$

is also defined by

$$\mathbf{k} = \mathbf{T}^*[\mathbf{k}', t] \tag{A3.3}$$

where $\mathbf{T}^*[\mathbf{k}', t]$ is the wave vector at time $-t$ of an electron which is at $\mathbf{k}'$ at time 0. In other words, $\mathbf{T}[\mathbf{k}, t]$ describes the forward trajectory of the unscattered electron and $\mathbf{T}^*[\mathbf{k}, t]$ the backward trajectory. In terms of $\mathbf{T}^*[\mathbf{k}, t]$, $P_0(\mathbf{k}, \mathbf{k}', t)$ can be written as

$$P_0(\mathbf{k}, \mathbf{K}, t) = \delta(\mathbf{k}-\mathbf{T}^*[\mathbf{k}', t]) \exp\left\{-\int_0^t \lambda'(\mathbf{T}^*[\mathbf{k}', x]) \mathrm{d}x\right\} \tag{A3.4}$$

and consequently (A3.1) reduces to

$$f(\mathbf{k}') = \int_0^\infty \mathrm{d}t \, g(\mathbf{T}^*[\mathbf{k}' t]) \exp\left\{-\int_0^t \lambda'(\mathbf{T}^*[\mathbf{k}', x]) \mathrm{d}x\right\}. \tag{A3.5}$$

The next step is to obtain an expression for the operator usually denoted by $(\partial/\partial t)_{\text{fields}}$ in the derivation of the Boltzmann equation. This operator is denoted here by $D_{\mathbf{k}}$, where the subscript **k** *indicates that it is a purely* **k** *operator. The electric and magnetic fields will induce a* **k**-space velocity, $\dot{\mathbf{k}}$, which is in general a function of **k**. In terms of $\dot{\mathbf{k}}$, $D_{\mathbf{k}}$ can be written as

$$D_{\mathbf{k}} = -\dot{\mathbf{k}}\,.\nabla_{\mathbf{k}} \qquad (A3.6)$$

Therefore

$$D_{\mathbf{k}}\mathbf{T}^*[\mathbf{k}, t] = \underset{\delta t\to 0}{\text{limit}}\ \frac{\mathbf{T}[\mathbf{k}\text{-}\dot{\mathbf{k}}\,\delta t, t] - \mathbf{T}^*[\mathbf{k}, t]}{\delta t} \qquad (A3.7)$$

and since, from definition of $\mathbf{T}^*[\mathbf{k}, t]$, it may be seen that

$$\mathbf{T}^*[\mathbf{k} - \dot{\mathbf{k}}\delta t, t] = \mathbf{T}^*[\mathbf{k}, t + \delta t] \qquad (A3.8)$$

it follows that

$$D_{\mathbf{k}}\mathbf{T}^*[\mathbf{k}, t] = \frac{\partial}{\partial t}\mathbf{T}^*[\mathbf{k}, t]. \qquad (A3.9)$$

Now $D_{\mathbf{k}'}f(\mathbf{k}')$ may be evaluated by differentiating (A3.5) under the integral sign, but since $\mathbf{k}'$ only appears as the argument of $\mathbf{T}^*$, (A3.9) allows $D_{\mathbf{k}'}$ to be replaced under the integral sign by a time operator. $D_{\mathbf{k}'}f(\mathbf{k}')$ may be seen to be the sum of two terms, the first of which is

$$\int_0^{\infty} \mathrm{d}t\left\{\frac{\partial}{\partial t}g\,(\mathbf{T}^*[\mathbf{k}', t])\right\}\exp\left\{-\int_0^t \lambda'(\mathbf{T}^*[\mathbf{k}', x])\mathrm{d}x\right\} \qquad (A3.10)$$

and the second of which is

$$-\int_0^{\infty} \mathrm{d}t\, g(\mathbf{T}^*[\mathbf{k}', t])\exp\left\{-\int_0^t \lambda'(\mathbf{T}^*[\mathbf{k}', x]\mathrm{d}x\right\}$$
$$\times\int_0^t \frac{\partial}{\partial x}\,\lambda'(\mathbf{T}^*[\mathbf{k}', x])\mathrm{d}x. \qquad (A3.11)$$

The integral over x in (A3 11) reduces to

$$\lambda'(\mathbf{T}^*[\mathbf{k}', t]) - \lambda'(\mathbf{k}') \qquad (A3.12)$$

where use has been made of the fact that

$$\mathbf{T}^*[\mathbf{k}, 0] = \mathbf{k}. \qquad (A3.13)$$

Adding together (A3 10) and (A3.11), the terms may be regrouped to give

$$D_{\mathbf{k}'}f(\mathbf{k}') = \int_0^{\infty}\mathrm{d}t[\partial/\partial t + \lambda'(\mathbf{k}')]g\,(\mathbf{T}^*[\mathbf{k}', t])$$
$$\times\exp\left\{-\int_0^t \lambda'(\mathbf{T}^*[\mathbf{k}', x])\mathrm{d}x\right\}. \qquad (A3.14)$$

Using (A3.5), (A3.14) simplifies to

$$D_{\mathbf{k}'}f(\mathbf{k}') = -g(\mathbf{k}') + \lambda'(\mathbf{k}')f(\mathbf{k}') \qquad (A3.15)$$

or alternatively

$$g(\mathbf{k}') = [-D_{\mathbf{k}'} + \lambda'(\mathbf{k}')]f(\mathbf{k}'). \qquad (A3.16)$$

Now if $f(\mathbf{k})$ satisfies equation (3.8) and in addition

$$\int \mathrm{d}\mathbf{k} f(\mathbf{k})S'(\mathbf{k}, \mathbf{k}') = g(\mathbf{k}') \qquad (A3.17)$$

then

$$\int \mathrm{d}\mathbf{k}\, g(\mathbf{k})P_0(\mathbf{k}, \mathbf{k}') = f(\mathbf{k}'). \qquad (A3.18)$$

Now (A3.18) is the same as (A3.1), and so $g(\mathbf{k}')$ is given by (A3.16), and may be eliminated from (A3.16) and (A3.17) to give

$$\int \mathrm{d}\mathbf{k} f(\mathbf{k})S'(\mathbf{k}, \mathbf{k}) = [-D_{\mathbf{k}'} + \lambda'(\mathbf{k}')]f(\mathbf{k}'). \qquad (A3.19)$$

It will be seen that the self scattering parts of (A3.19) cancel out, leaving

$$-D_{\mathbf{k}'}f(\mathbf{k}') = \int \mathrm{d}\mathbf{k}\left[f(\mathbf{k})S(\mathbf{k}, \mathbf{k}') - f(\mathbf{k}')S(\mathbf{k}', \mathbf{k})\right] \qquad (A3.20)$$

in which $\lambda(\mathbf{k}')$ has been replaced by the integral of $S(\mathbf{k}', \mathbf{k})$. (A3.20) is the time independent Boltzmann equation, conventionally written as

$$(\partial f/\partial t)_{\text{fields}} + (\partial f/\partial t)_{\text{scattering}} = 0. \qquad (A3.21)$$

APPENDIX 4

Derivation of the time development equation (4.7).

The derivation of equation (4.7) depends on the result that each iteration is equivalent to a time increment $1/\Gamma$ for the physical system, i.e. if $f_n(\mathbf{k})$ and $f_{n+1}(\mathbf{k})$ are successive iterates and Γ is large then

$$f_{n+1}(\mathbf{k}) - f_n(\mathbf{k}) \simeq \frac{1}{\Gamma}(D_f + D_s)f_n(\mathbf{k}) \qquad (A4.1)$$

where D_f and D_s denote respectively the operators $(\partial/\partial t)_{\text{fields}}$ and $(\partial/\partial t)_{\text{scattering}}$ well known in the derivation of the Boltzmann equation. Clearly equation (4.7) is a corollary of (A4.1). The next stage is to establish (A4.1).

Now if $g(\mathbf{k})$ is defined by

$$g(\mathbf{k}') = \int \mathrm{d}\mathbf{k} f_n(\mathbf{k})S'(\mathbf{k}, \mathbf{k}') \qquad (A4.2)$$

then

$$f_{n+1}(\mathbf{k}') = \int \mathrm{d}\mathbf{k}\int_0^{\infty}\mathrm{d}t P_0(\mathbf{k}, \mathbf{k}', t)g(\mathbf{k}). \qquad (A4.3)$$

For a self scattering rate of the form (4.5), we have

$$S'(\mathbf{k}, \mathbf{k}') = S(\mathbf{k}, \mathbf{k}') + [\Gamma - \lambda(\mathbf{k})]\delta(\mathbf{k}\text{-}\mathbf{k}') \qquad (A4.4)$$

and

$$P_0(\mathbf{k}, \mathbf{k}'\, t) = \delta(\mathbf{k}' - \mathbf{T}[\mathbf{k}, t])\exp(-\Gamma t). \qquad (A4.5)$$

Now

$$D_s f_n(\mathbf{k}') = \int \mathrm{d}\mathbf{k} f_n(\mathbf{k})S(\mathbf{k}, \mathbf{k}') - \lambda(\mathbf{k}')f_n(\mathbf{k}'). \qquad (A4.6)$$

So substitution of (A4.4) into (A4.2)gives

$$g(\mathbf{k}') = (\Gamma + D_s)f_n(\mathbf{k}'). \qquad (A4.7)$$

Now when Γ is very large, $P_0(\mathbf{k}, \mathbf{k}', t)$ falls very rapidly with t, and (A4.5) may be replaced by

$$P_0(\mathbf{k}, \mathbf{k}', t) = \delta(\mathbf{k}' - \mathbf{k} - \dot{\mathbf{k}}'t)\exp(-\Gamma t) \qquad (A4.8)$$

where $\dot{\mathbf{k}}'$ is the field induced **k**-velocity of an electron with wave vector $\mathbf{k}'$. Substitution of (A4.8) into (A4.3) gives

$$f_{n+1}(\mathbf{k}') = \int_0^\infty \mathrm{d}t\, g(\mathbf{k}' - \dot{\mathbf{k}}'t)\exp(-\Gamma t). \qquad (\mathrm{A}4.9)$$

Expanding (A4.9) as a power series in $1/\Gamma$ and retaining only the first two terms gives

$$f_{n+1}(\mathbf{k}') = \frac{1}{\Gamma}[g(\mathbf{k}') - \dot{\mathbf{k}}' . \nabla_{\mathbf{k}'} g(\mathbf{k}')/\Gamma]. \qquad (\mathrm{A}4.10)$$

Now the operator-$\dot{\mathbf{k}}' . \nabla_{\mathbf{k}'}$ is the operator D_f. So (A4.10) can be rewritten as

$$f_{n+1}(\mathbf{k}') = \Gamma^{-1}(1 + D_f/\Gamma)g(\mathbf{k}'). \qquad (\mathrm{A}4.11)$$

The final step is to substitute $g(\mathbf{k}')$ from (A4.7) into (A4.11) and retain terms of order unity and $1/\Gamma$, leaving

$$f_{n+1}(\mathbf{k}') = [1 + (D_f + D_s)/\Gamma]f_n(\mathbf{k}') \qquad (\mathrm{A}4.12)$$

which establishes equation (A4.1).

J. Phys. Chem. Solids Pergamon Press 1969. Vol. 30, pp. 657–663. Printed in Great Britain.

NUCLEAR MAGNETIC RESONANCE AND RELAXATION OF THE HEUSLER ALLOY*

SHIZUKO OGAWA and JAN SMIT
Department of Materials Science, University of Southern California, Los Angeles, Calif. 90007, U.S.A.

(*Received* 1 *July* 1968; *in revised form* 23 *August* 1968)

Abstract – NMR of the Heusler alloy Cu_2MnAl has been studied for all three nuclei by using the spin echo method. The resonance frequencies at 4·2°K are 240 and 257 MHz for Cu^{63} and Cu^{65} respectively, 225 MHz for Mn^{55} and 76 MHz for Al^{27}. The hyperfine fields are −212 and −213 KG for Cu and Mn respectively, and 68·2 KG for Al, the sign of which could not be determined. The temperature variation of the Mn hyperfine field is within ½ per cent the same as that of the magnetization whereas the Cu hyperfine field decreases more with increasing T. The spin echo amplitude as a function of the applied static field shows a maximum which is caused by an increase of the relaxation times with increasing static field for resonances in both walls and domains. A discussion about the signs and the magnitudes of the hyperfine fields at the nuclei is included.

1. INTRODUCTION

THE HEUSLER alloy Cu_2MnAl is known to be a ferromagnetic compound when it is in the ordered state[1]. The magnetic moment per molecule is about 4 Bohr magnetons [2, 3]. The neutron diffraction experiment carried out by elcher *et al.*[4] shows that practically the e magnetic moment of the Heusler alloy be attributed to the Mn ions, leaving an uncertainty of 0·1 Bohr magnetons on the Cu ions. Measurements of the magnetic form factor of the Heusler alloy shows a similar result[5]. The NMR experiment carried out by Sugibuchi and Endo[6] showed that the hyperfine fields at the Cu and Mn nuclei are about the same and that both have the same temperature dependence.

In the present experiment the NMR signal of Al^{27} has been observed. The resonance frequencies of Cu and Mn showed a different temperature dependence. The resonance frequency, spin echo amplitude and relaxation times were also studied as a function of the applied static field and discussed in terms of both domain wall and domain resonance. To account for the sign and the large magnitude of the hyperfine fields at the nuclei in the Heusler alloy a nearly free electron picture in a periodic lattice is adopted.

2. EXPERIMENTAL PROCEDURE

For the measurement of NMR in the Heusler alloy the spin echo technique was used[7]. A sample was kindly supplied by Dr. J. W. Cable at Oak Ridge National Laboratory. This material was known to be about 98 per cent ordered from neutron diffraction and X-ray studies[4]. The particle size was about 200 μm. Another sample obtained from Dr. L. N. Corliss at Brookhaven National Laboratory was also used. No analysis for ordering was carried out.

The full line widths of the Mn^{55}, Cu^{63} and Cu^{65} resonances were all 2 MHz for the former sample whereas they were 4 MHz for the latter, indicating that this sample was less ordered than the first one. The sensitivity of the apparatus was low for the Al^{27} resonance as compared with that for the Mn and Cu resonances which occur at higher frequencies. For this reason 10 g of the material were used for measurement of the Al^{27} resonance while

---

*This work was supported by the Joint Services Contract No. 23-4510-1713.

2 g were sufficient for measurement of the Cu and Mn resonances.

3. TEMPERATURE DEPENDENCES OF THE RESONANCE FREQUENCIES

The NMR frequencies of Mn^{55}, Cu^{63} and Cu^{65} were measured from 4·2° to 400°K, whereas those of Al^{27} could only be observed between 4·2° and 140°K. Their values and the corresponding hyperfine fields at 4·2°, 77° and 294°K are listed in Table 1. The room temperature value for Mn^{55} is slightly higher than that reported by Sugibuchi and Endo[6], whereas those of Cu^{63} and Cu^{65} are about the same. At liquid nitrogen temperature the resonance frequency of Mn^{55} agrees with their value but our Cu^{63} and Cu^{65} data are slightly higher.

Table 1. Resonance frequency ν in MHz and hyperfine field H_{int} *in kG of the nuclei of the* Mn, Cu *and* Al *atoms in* Cu_{2MnAl}

Isotope	ν	H_{int}	ν	H_{int}	ν	H_{int}
	4·2°K		77°K		294°K	
Mn^{55}	224·8 ± 0·5	213·0	223·3 ± 0·5	211·6	204·3 ± 0·5	193·6
Cu^{63}	240·0		238·3		214·5	
		212 6		211·0		190·0
Cu^{65}	257·0		255·0		229·6	
Al^{27}	75·6	68·2	75·2	67·8		

The resonance frequencies of Mn^{55}, Cu^{63}, Cu^{65} and Al^{27} are plotted on a reduced scale (ν/ν_0) as a function of the reduced temperature (T/T_c) in Fig. 1. T_c is the Curie temperature of Cu_2MnAl which is 610°K and ν_0 is the value of the resonance frequency ν at 0°K. On the same figure the reduced value of the magnetization per gram (σ/σ_0) is plotted as measured by Endo[3]. The NMR frequency in ferromagnetic materials is roughly proportional to the magnetization. The variation of the resonance frequency of Mn^{55}, which is the only magnetic ion in the Heusler alloy, and that of the magnetization seem to coincide qualitatively though they are obtained at constant pressure. As has been pointed out by Benedek[8] in a study of pure transition metals, a comparison at constant volume shows a closer agreement of the variation of ν and σ. At 400°K ($T/T_c = 0{\cdot}6$) the fractional decrease of the resonance frequency of the Cu nuclei is 17 per cent, whereas that of Mn^{55} is 15 per cent. The reduced resonance frequency of Al^{27} for $T/T_c < 0{\cdot}2$ is also shown in Fig. 1.

4. EFFECT OF THE APPLIED STATIC MAGNETIC FIELD

Spin-echo measurements with an applied static field H were performed at room- and liquid nitrogen temperature on a nearly spherical sample. Figure 2 shows the resonance frequency of Mn^{55} at liquid nitrogen temperature as a function of H which was applied in a direction perpendicular to the r.f. field. Above 4000 G the resonance frequency decreases linearly with increasing static field at a rate $\gamma_n/2\pi = 1055$ (Oe. sec)$^{-1}$ where γ_n is the gyromagnetic ratio of the Mn^{55} nucleus. The resonances of Cu^{63} and Cu^{65} showed a similar behavior. Therefore the hyperfine fields at both the Mn and the Cu nuclei are negative. The resonance of Al^{27} could not be observed at high fields.

It has been observed by Gossard and Portis [9], and confirmed by us with our present apparatus, that the intensity of the NMR signal decreases with the application of a static magnetic field. This is to be expected [10] because of the decrease in the number of domain walls. In this regard the spin echo amplitudes of both Cu and Mn show an un-

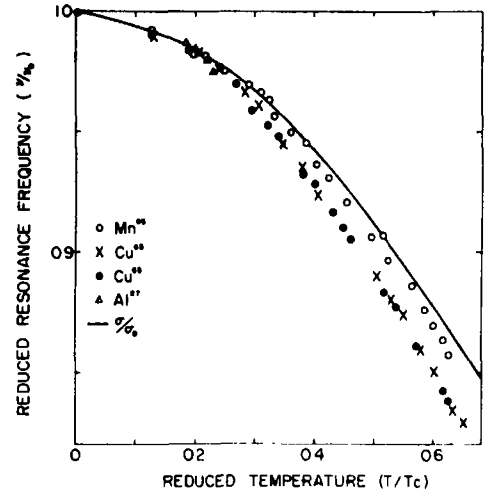

Fig. 1. NMR frequencies of Mn^{55}, Cu^{63}, Cu^{65} and Al^{27} in the Heusler alloy plotted as a function of temperature on a reduced scale. The solid line shows the reduced values of the saturation magnetization per gram taken from reference [4].

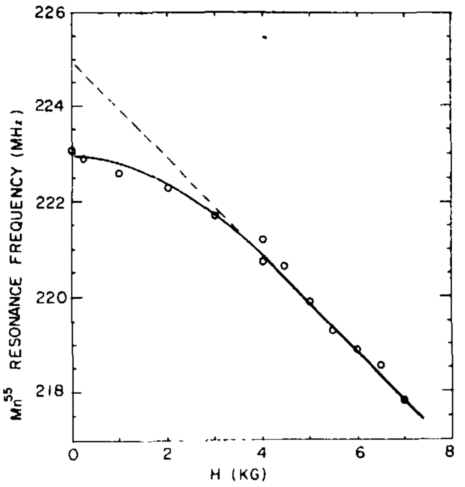

Fig. 2. NMR frequency of Mn^{55} measured with an applied static field H at liquid nitrogen temperature. The broken line has a slope equal to the gyromagnetic ratio of the Mn^{55} nucleus.

expected behavior. With increasing static field the echo amplitude increases and shows a maximum. With the r.f. field oriented parallel to the static field the spin echo amplitude showed only a small hump. The echo amplitude for the Mn^{55} resonance at liquid nitrogen temperature is shown in Fig. 3. The r.f. field amplitude b_r shown in the figures are measured at zero static field and increase by about 30 per cent for large static fields. Throughout the measurement the pulse duration t_w was fixed at a value which maximizes the spin echo at zero field. The line width is independent of H. The time interval τ between the two pulses is 30 μsec for the experiments of Fig. 3. When τ is shortened the spin echo amplitude increases and the maximum tends to disappear, as is shown in Fig. 4. Thus it appears that relaxation processes are important in determining the shapes of the curves. Therefore the relaxation times were measured.

5. MEASUREMENTS OF T_1 AND T_2

The transverse relaxation time T_2 was measured from the decay of the spin echo amplitude (Fig. 5(a)) and the longitudinal relaxation time T_1 was found from the decay of the stimulated echo (Fig. 5(b)). Both relaxations were measured for various values of the static field at room- and liquid nitrogen temperature. The r.f. field is 0·2 G. In Fig. 5 the spin echo amplitude $A(t, H)$ is plotted on a reduced scale $A(t, H)/A(0, H)$, where $A(0, H)$ is found by extrapolating $t \to 0$.

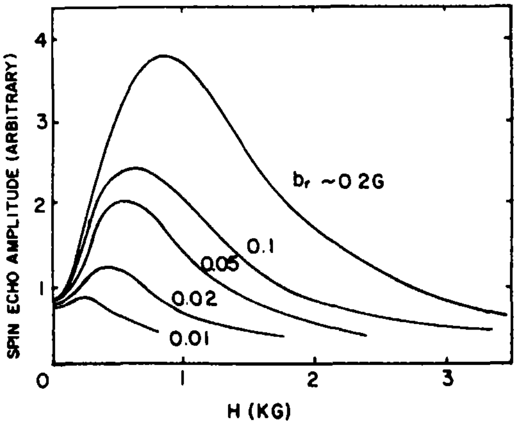

Fig. 3. Spin echo amplitude of the Mn^{55} resonance for various amplitudes of the r.f. field b_r oriented perpendicular to the static field. The pulse interval is 30 μs.

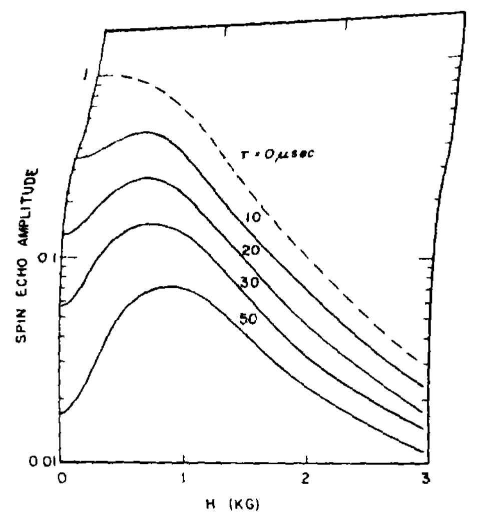

Fig. 4. Spin echo amplitude of the Mn^{55} resonance at various values of the time interval τ between the two r.f. pulses as a function of the static field oriented perpendicular to the r.f. field. The extrapolated curve for $\tau = 0$ is shown with a broken line. The spin echo amplitude A is plotted on a relative scale: $A(\tau, H)/A(0, 0)$.

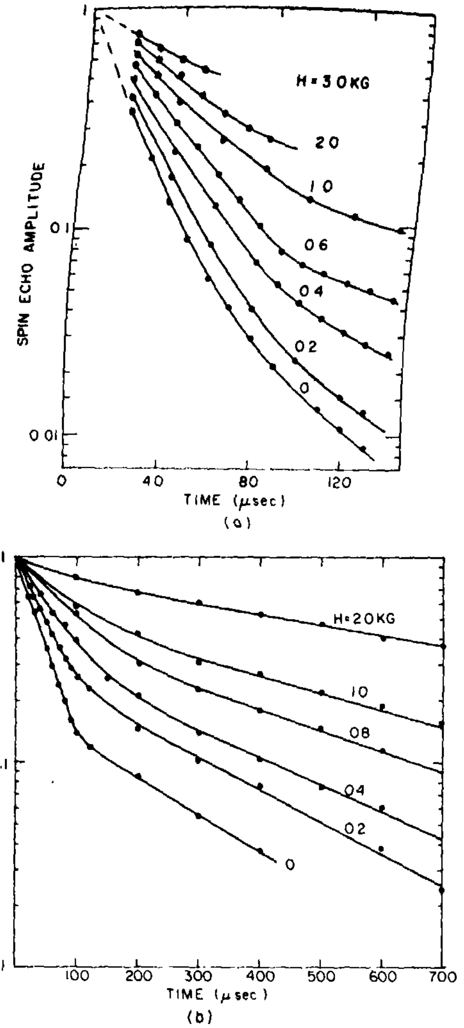

Fig. 5. Relaxation measurements for various values of the static field H, oriented perpendicular to the r.f. field at liquid nitrogen temperature. (a) Spin echo amplitude as a function of the time interval 2τ between the first pulse and the echo. (b) Stimulated echo amplitude as a function of the time interval between the two r.f. pulses and a third r.f. pulse. The spin echo amplitude A is plotted on a relative scale: $A(\tau, H)/A(0, H)$.

At zero static field the curves in Figs. 5(a, b) show two exponential decays. In Co metal the fast decay has been ascribed to the relaxation of nuclear spins inside the moving domain walls, and the slow relaxation to spins in the domains[11, 12]. Therefore apparently resonances in both walls and domains occur in the Heusler alloy.

The Heusler alloy has a small magnetocrystalline anisotropy constant $K_1 = -4 \times 10^3$ erg/cc at 77°K[13], resulting in an anisotropy field $H_a = 10$ G. The enhancement factor for domain rotations is then $H_{int}/H_a \sim 2 \times 10^4$. This value is consistent with the observed relation between b_r and t_w.

If the enhanced r.f. field is smaller than the inhomogeneous line broadening measured in gauss, spectral diffusion will occur[14]. This means that t_w should be smaller than $1/\delta\nu$, where $\delta\nu$, the line width, is 2 MHz. Thus t_w should be smaller than 0·5 μsec. At $b_r \cong 0{\cdot}2$ G, being the maximum value of the field which could be obtained, t_w was just 0·5 μ sec. This explains the dependence of the spin echo in Fig. 3 on b_r and it is possible that the echo is larger for $b_r > 0{\cdot}2$ G.

By multiplying the ordinates of one curve for a certain τ in Fig. 4 by $A(0, H)/A(\tau, H)$ obtained from Fig. 5(a), one can construct the $\tau = 0$ curve in Fig. 4, which no longer shows a maximum. The maxima in the other curves must be explained in terms of the change in relaxation times with the applied static field. For this purpose the curves of Fig. 5(a) and also of Fig. 5(b) have been decomposed into two exponential decays. The amplitudes of the two exponentials of Fig. 5(a) are plotted in Fig. 6 as a function of H. The T_1 and T_2 for these two mechanisms are given in Fig. 7. The decomposition is not unique and the assumption has been made that the two curves of Fig. 6 should be monotonic functions of H with zero slope at $H = 0$. Part (a), which decreases more strongly with increasing field than does part (b), has to be attributed to domain wall motion. Part (b) is then caused by domain rotations. As shown in Fig. 7, the relaxation of the nuclei in the walls is much more rapid than that in the domains. It should be stressed that the occurrence of the maxima in Fig. 4 is due to the increase of T_2 with the applied static field. A similar increase in T_1 has been observed in Co particles by Kaplan *et al.*[15]. The increase in T_1 and T_2 with increasing static field may be due to a reduction in eddy current damping due to the decrease in permeability.

T_1 is approximately inversely proportional to temperature as seen from Fig. 7. Such behavior is observed for transition metal ions[11, 15] in domains and is associated with the conduction electron mechanism[16]. T_2 increases by about a factor of two going from room temperature to liquid nitrogen temperature. This weak dependence of T_2 on temperature suggests that some temperature independent contributions must be included. The contribution to T_2^{-1} from the dipole–dipole interaction of the Mn nuclei is about 1/600 $(\mu\,\text{sec})^{-1}$, so that the corrected ratio is 2·5, as compared to 3·8 for the ratio of the temperatures.

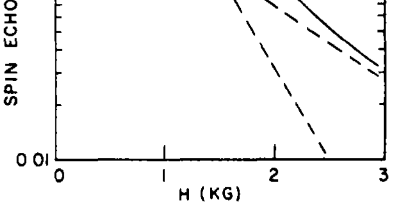

Fig. 6. Relative intensity of the fast decay component of the spin echo signal (a) and of the slow decay component (b) as a function of the static field.

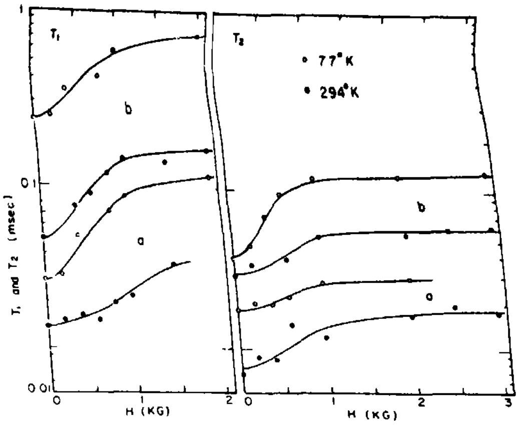

Fig. 7. Relaxation times T_1 and T_2 for the fast (a) and the slow (b) decay component of the spin echo signal as a function of the applied static field, at liquid nitrogen temperature and at room temperature.

6. DISCUSSION ON THE HYPERFINE FIELDS

It is found that the fields at the Mn, Cu and Al nuclei are about the same as those found for these atoms when dissolved into iron metal (Table 2). If Cu and Al are dissolved into Ni, Co and Fe metals, it is found that their fields are proportional to the magnetization of the host metal[17, 18]. For this reason we would expect that the values for the Heusler alloy would be much smaller than those for iron, since the ratio of their magnetizations is about 0·4. The difference might be associated with the difference in coordination of the magnetic Mn neighbors in the Heusler alloy. Figure 8

Table 2. Comparison of the hyperfine fields in kG at the Mn, Cu and Al nuclei in Cu_2MnAl with those when dissolved in metallic iron (The latter values are taken from M. KONTANI and J. ITOH *J. phys. Soc. Japan* **22**, 345 (1967))

Material	Mn	Cu	Al
Cu_2MnAl	−213	−213	±68
Fe	−225	−213	−55

shows the atomic arrangement of the ordered Heusler alloy[19].

The space lattice of Cu_2MnAl is the same as that of b.c.c. iron. For instance a Cu ion has 4 nearest Mn neighbors, as compared to 8 Fe nearest neighbors in iron. The large n_B of the Mn ion (3·6) as compared to Fe (2·2) makes up for this difference. On the other hand the next nearest neighbor numbers are 0 and 6, respectively. One could then assume that the effect of the next nearest neighbors is negligible, but this is in conflict with the Al data. The number of its Mn nearest neighbors is zero, so then the total contribution has to come from the six second nearest neighbors, because there are no third and fourth nearest neighbor Mn ions. We see that the field at the Al in the Heusler alloy exceeds that in iron, so the contribution of the second neighbors has to be quite large. In order to explain the approximately equal data for Cu in the Heusler alloy and iron in this way, one therefore has to assume that in the Heusler alloy the contributions of the second and the further neighbors accidentally cancel.

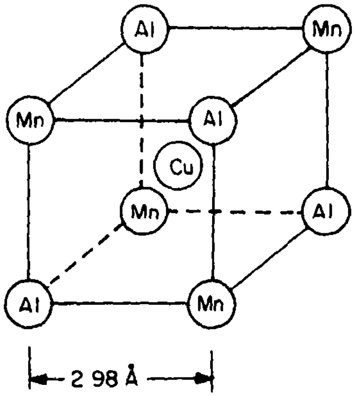

Fig. 8. The crystal structure of the Heusler alloy.

The conduction electron polarization is usually calculated with the Ruderman-Kittel theory[20]. It has been shown[21] that this theory can give reliable results when a certain parameter, proportional to Jk_F, where J is the s–d exchange interaction and k_F the Fermi wave vector, is much smaller than one. If we assume this R–K mechanism to be responsible for the Curie temperature of the Heusler alloy, we can estimate this parameter and find it to be 1·7. We assumed that $k_F = 1{\cdot}5 \times 10^8\,\mathrm{cm}^{-1}$. Since the spacial dependence of the polarization is oscillatory in nature, this inaccuracy of the final results will not only affect the amplitude but also the phase, and therefore no conclusions about either the sign or the amplitude of the effective fields can be drawn.

The validity of both local approaches may be questioned in periodic lattices such as that of Heusler alloy, especially when the summation is cut off after a few terms. We will therefore start from a periodic lattice approach with Brillouin zones, although in a very approximate way. One can easily show that the R–K theory is equivalent to it in a quadratic approximation in the periodic potential V.

That nearly free electron theory may be applied to the Heusler alloy is supported by the stability of its structure. The compounds around Cu_3Al, have a b.c.c. structure. The electron per atom ratio is 1·5 and according to Hume–Rothery[22] and Jones this is the reason for the stability of the b.c.c. structure. It is seen that the Mn–Cu–Al phase diagram [23], a whole series of compounds with an approximate Al content of 0·25, including the Heusler alloy, has this b.c.c. structure. We will therefore assume that the reason for their stability is the same. Therefore the valency of the Mn has to be +1, which corresponds to $n_B = 4$, this being close to the experimental value of 3·6.

According to Jones[22] the electronic energy is then low because the free electron Fermi sphere just touches the first Brillouin zone in the [110] directions. We may therefore expect that this [110] reflection is particularly strong. In the real lattice nearly standing electron waves occur between the successive (110) planes, with maxima at the atomic planes. The periodic potential will be different for up and down conduction electron spins due to the s–d exchange with the Mn ions. If this exchange interaction is positive, the up spins (parallel to the magnetization) have a larger energy gap than the down spins, and therefore would have larger charge density at the (110) atomic planes. These planes contain also all the Cu and Al ions, and therefore the hyperfine fields should be positive. For Cu the opposite has been observed.

There is, however, experimental evidence that the s–d exchange is negative. It has been found by Shull[24] that in iron the s-polarization is negative. Moreover the minima in the resistance of many dilute alloys like Cu; Mn could be explained quite conclusively by Kondo[25] if J is negative. The occurance of these resistance minima is quite general, so usually J seems to be negative. If we assume that this is also the case in the Heusler alloy, then the negative sign of the hyperfine follows. As to its magnitude, it can be noted that for a certain J the amount of conduction electron polarization is proportional to the density of states at the Fermi surface. Because of the Hume–Rothery condition this may be expected to be relatively high in Cu_2MnAl, and certainly much higher than in the transition metals with 0·6 conduction electrons/atom. This difference may compensate for the effect of the smaller magnetization.

Calori and Blandin[26] calculated the hyperfine fields in the Heusler alloy by considering all 7 electrons of the Mn atoms as conduction electrons, and used the Friedel sum rule for non-bound states for up and down spins separately to calculate their phase shifts. In this way the electron to atom ratio is 3, and it is not clear that it is a Hume–Rothery alloy.

REFERENCES

1. HEUSLER O., *Annls Phys.* **19**, 155 (1934).
2. OXLEY D. P., TEEBLE R. S. and WILLIAMS K. C., *J. appl. Phys.* **34**, 1362 (1963).
3. ENDO K. and OHYAMA T., *J. phys. Soc. Japan* **19**, 1494 (1964).
4. FELCHER G. P., CABLE J. W. and WILKINSON M. K., *J. Phys. Chem. Solids* **24**, 1163 (1963)
5. TAKATA H., *J. phys. Soc. Japan* **20**, 1743 (1965).
6. SUGIBUCHI K. and ENDO K., *J. Phys. Chem. Solids* **25**, 1217 (1964)
7. HAHN E. L., *Phys. Rev.* **80**, 580 (1950).
8. BENEDEK G. B. and ARMSTRONG J., *J. appl. Phys.* **32**, 106s (1960).
9. GOSSARD A. C. and PORTIS A. M., *Phys. Rev. Lett.* **3**, 164 (1959).
10. PORTIS A. M. and GOSSARD A. C., *J. appl. Phys.* **31**, 205s (1960); BENNETT L. H., *J. appl. Phys.* **37**, 1242 (1966).
11. WEGER G., *Phys. Rev.* **128**, 1505 (1963).
12. WINTER J. M., *Phys. Rev.* **124**, 452 (1961).
13. AOYAGI K. and SUGIHARA M., *J. phys. Soc. Japan* **16**, 1027 (1961).
14. MIMS W. B., NASSAU K. and MEGEE J. D., *Phys. Rev.* **123**, 2059 (1961).
15. KAPLAN N., JACCARINO V. and LEWIS R. T., *J. appl. Phys.* **39**, 500 (1968).
16. MORIYA T., *J. phys. Soc. Japan* **19**, 681 (1964).
17. ASAYAMA K., *J. phys. Soc. Japan* **18**, 1728 (1963); ASAYAMA K., KONTANI M. and ITOH J., *J. phys. Soc. Japan* **19**, 1984 (1964).
18. ROBERTS L. D. and THOMSON J. O., *Phys. Rev.* **129**, 664 (1963); GRANT R. W., KAPLAN MORTON, KELLER D. A. and SHIRLEY A. D., *Phys. Rev.* **133A**, 1062 (1964).
19. BRADLEY A. J. and ROGERS J. W., *Proc. R. Soc.* **A144**, 340 (1930).
20. RUDERMAN M. A. and KITTEL C., *Phys. Rev.* **96**, 99 (1954).
21. SMIT J., *J. appl. Phys.* **37**, 1445 (1966).
22. HUME–ROTHERY W., *J. Inst. Metals* **35**, 309 (1926); JONES H., *Proc. R. Soc.* **A144**, 255 (1934); *Proc. R. Soc.* **147**, 396 (1934).
23. BOZORTH R. M., In *Ferromagnetism*. p. 329. Van Nostrand, New York (1951).
24. SHULL C. G. and YAMADA Y., *J. phys. Soc. Japan*, Proceedings of International Conference on Magnetism and Crystallography 17, Suppl. B-III, 1, (1962).
25. KONDO J., *Prog. theor. Phys.* **32**, 37 (1964); **34**, 204 (1965).
26. CAROLI B. and BLANDIN A., *J. Phys. Chem. Solid* **27**, 503 (1966).

J. Phys. Chem. Solids Pergamon Press 1969. Vol. 30, pp. 665–667. Printed in Great Britain.

CONDUCTION ELECTRON SPIN SUSCEPTIBILITY OF METALLIC LITHIUM*†

J. E. KETTLER‡, W. L. SHANHOLTZER§ and W. E. VEHSE
Department of Physics, West Virginia University, Morgantown, West Virginia 26505, U.S.A.

(*Received* 19 *June* 1968; *in revised form* 5 *August* 1968)

Abstract – The conduction electron spin susceptibility of metallic lithium has been measured using the spin resonance technique of Schumacher and Slichter. Measured values were $2{\cdot}09 \times 10^{6}$ and $2{\cdot}18 \times 10^{-6}$ cgs volume units at 298° and 4·2°K respectively; the difference attributable to a change in the lattice parameter. The results are believed to be accurate within 5 per cent and are in agreement with previous experimental measurements and with recent calculations.

INTRODUCTION

In 1954 Schumacher and Slichter[1,2] measured χ_p^e, the paramagnetic contribution of the conduction electrons to the total static susceptibility of metallic lithium and sodium. Subsequent remeasurements of this contribution in sodium yielded results which differed by 18 per cent from the original measurements [3]; the difference attributable to a more careful analysis of the experimental data. An examination of the original data of Schumacher and Slichter suggested that comparable errors might be present in their lithium results. In view of this, we have remeasured χ_p^e for lithium at room temperature and have extended the measurements to 4·2°K.

EXPERIMENTAL PROCEDURE

The experimental technique employed to determine χ_p^e is to measure the area under a CESR absorption curve and to relate this directly to χ_p^e. The spectrometer is calibrated by measuring the nuclear susceptibility (given accurately by the Langevin–Debye formula) for the same sample, at the same frequency, changing only the value of the applied static field. The technique is described in detail elsewhere[2] with the exception that a Robinson low level spectrometer[4] was used in some of these measurements in place of the Q-meter spectrometer described in reference [4].

A problem in making these measurements is the fact that the electron resonance curves are Lorentzian in shape, so that a significant fraction of the total area is in the wings and very difficult to integrate experimentally. The difficulty is circumvented by truncating the experimental curves and, assuming the line shape is accurately known, correcting the measured areas to include that part lost in the truncation process. This correction procedure is described in detail in reference [3].

At both room temperature and 4·2°K, saturation of the nuclear resonance was a problem. Use of the low level spectrometer enables one to work at r.f. levels such that errors due to saturation should be less than 1 per cent. As a check, we have made measurements at higher levels. Since the relative area under the NMR absorption curve used for calibration may be expected to decrease as $(1+AV^2)$, where v is the voltage across the sample coil, the measured χ_p^e would increase as the square of V. Graphs of $\chi_p{}^e$ vs. V^2 were plotted and the curve extrapolated to $V = 0$ to obtain the correct value of $\chi_p{}^e$ (Figs. 1–2).

---

*This work was supported in part by the National Aeronautics and Space Administration

†Paper based in part on a dissertation submitted by J. E. Kettler to West Virginia University in partial fulfillment of the requirements for the Ph. D. degree.

‡*Present address:* Department of Physics, Belmont County Campus, Ohio University, St. Clairsville, Ohio.

§*Present address:* Department of Physics, Marshall University, Huntington, West Virginia.

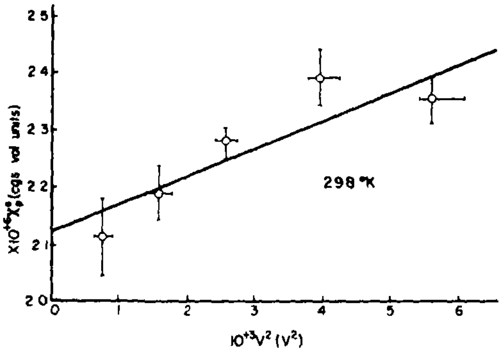

Fig. 1. A plot of the measured $\chi_p{}^e$ as a function of V^2 at 298°K. The extrapolated value of $\chi_p{}^e$ at $V = 0$ is the correct value.

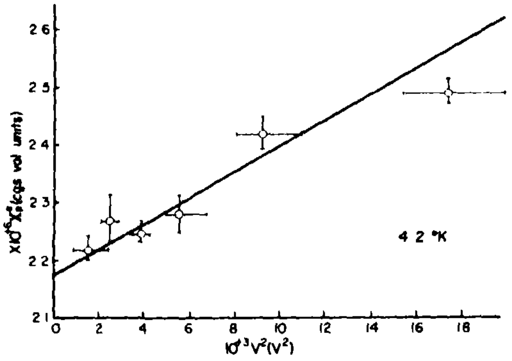

Fig. 2. A plot of the measured $\chi_p{}^e$ as a function of V^2 at 4·2°K.

Samples of lithium obtained from Fisher Scientific Company and from United Mineral and Chemical Company were prepared in an inert atmosphere by ultrasonically dispersing the molten lithium in heavy paraffin oil. Traces of oleic acid were used as an anticoagulant in order to obtain particle sizes of 2 μ dia. or less for those samples used at 4·2°K. Any samples exhibiting line shape asymmetries were rejected as containing particles large compared with the effective skin depth.

RESULTS

Five samples were used to determine $\chi_p{}^e$ at room temperature. For most of the measurements, the r.f. voltage across the sample coil was kept below the value calculated to give 1 per cent saturation of the nuclear resonance.

The electron resonance curves, described accurately by the solutions of the modified Bloch equations, were truncated in such a way that the corrections ranged from 8 to 25 per cent of the total area. The relaxation times for these samples ranged from $3 \cdot 1 \times 10^{-8}$ to $6 \cdot 9 \times 10^{-8}$ sec.

Modulation amplitudes were chosen to include what was believed to be more than 99 per cent of the area under the nuclear resonance curves. Some question arises at this point since, at room temperature, the nuclear resonance line is motionally narrowed but is not strictly a Lorentzian curve. Since the line shape is not accurately known, the correction procedure used for the electron curves cannot be applied. Errors resulting from an incomplete integration of the nuclear resonance curves might be as high as 5 per cent if the curves were Lorentzian, but are probably more like 2 per cent. The average value of $\chi_p{}^e$ for these samples in $2 \cdot 09 \times 10^{-6}$ cgs volume units.

Measurements were made on two samples at 4·2°K. Here there is no problem with the area under the nuclear resonance curves as the curves cut off sharply in the tails. The electron resonance curves are still modified Lorentzian as long as the particles are small compared with the effective skin depth. The average result of several measurements was $2 \cdot 18 \times 10^{-6}$ cgs volume units with our confidence in both these and the room temperature results about 5 per cent. The uncertainty arises chiefly from systematic errors.

Saturation curves in which $\chi_p{}^e$ is plotted as a function of V^2 are shown in Figs 1–2. The values of $\chi_p{}^e$ obtained by extrapolation, $2 \cdot 18 \times 10^{-6}$ at 4·2°K and $2 \cdot 12 \times 10^{-6}$ at

298°K, are in excellent agreement with the measurements made at low values of V at both temperatures.

DISCUSSION

When corrected for volume changes of the sample, the results at 4·2°K would yield a value of $2 \cdot 12 \times 10^{-6}$ cgs volume units at room temperature. This agrees with measurements made at that temperature within experimental accuracy, thus verifying the expected temperature independence of $\chi_p{}^e$ (when expressed in mass units) for temperatures small compared with the Fermi temperature.

Our room temperature measurements are in agreement with the original measurements of Schumacher and Slichter. It is felt that if errors did exist in their measurements of the area under the CESR curves, as was the case with sodium, compensating errors were probably made in the NMR curves. Similar compensation would not have been present in the sodium measurements.

These results are about 10 per cent higher than those reported by Hecht[5]. Both Hecht's results and those of this research are reported with an estimated uncertainty of about 5 per cent.

Recently calculations of $\chi_p{}^e$ by Shimizu[6], Silverstein[7] and Rice[8] give $2 \cdot 12 \times 10^{-6}$, $2 \cdot 08 \times 10^{-6}$ and $2 \cdot 28 \times 10^{-6}$ cgs vol units respectively in good agreement with our measurements. One can make indirect comparisons with other experimental quantities through measurements of the Knight shift and Overhauser shift and through the Korringa relations. In all of these, the agreement with experiment is satisfactory. A discussion of these comparisons is presented in reference [5].

Acknowledgements – We wish to thank Dr. N. S. Vander-Ven for providing us with one of the samples used in this measurement and Mr. R. L. Stenger, Jr. for the use of his Robinson spectrometer.

REFERENCES

1. SCHUMACHER R. T., CARVER T. R. and SLICHTER C. P., *Phys. Rev.* **95**, 1089 (1954).
2. SCHUMACHER R. T. and SLICHTER C. P., *Phys. Rev.* **101**, 158 (1956).
3. SCHUMACHER R. T. and VEHSE W. E., *J. Phys. Chem. Solids* **24**, 297 (1963).
4. ROBINSON F. N. H., *J. Sci. Instr.* **36**, 481 (1959).
5. HECHT R., *Phys. Rev.* **132**, 966 (1963).
6. SHIMIZU M., *J. phys. Soc. Japan* **15**, 2220 (1960).
7. SILVERSTEIN S. D., *Phys. Rev.* **130**, 1703 (1963).
8. RICE T. M., *Annls. Phys.* **31**, 100 (1965).

J. Phys. Chem. Solids Pergamon Press 1969. Vol. 30, pp. 669–675. Printed in Great Britain.

THERMAL ANNEALING OF NATURAL SEMICONDUCTING DIAMOND

S. M. HORSZOWSKI
Diamond Research Laboratory, Johannesburgh, South Africa

(*Received* 18 *March* 1968; *in revised form* 30 *July* 1968)

Abstract – A number of natural semiconducting diamonds were subjected to thermal annealings in the temperature range 500–2500°C. The following parameters were determined as a function of annealing:– the resistivity (ρ), the Hall mobility (μ_H) and the concentrations of acceptor levels (N_a), donor levels (N_d) and charge carriers (p). Their annealing behaviour was as follows:– N_a and μ_H remained unchanged, N_d and ρ decreased and p increased. A correlation was observed between changes in N_d, p and ρ.

The annealing data were analysed by plotting their so-called characteristic activation energy spectra. The range of activation energies over which changes could be produced varied from small values to about 9 eV. The shapes of the spectra revealed a number of distinct annealing processes. The annealing was found to be strongly specimen-dependent.

INTRODUCTION

DIAMONDS HAVE been classed into types I and II on the basis of their u.v. and i.r. absorption[1, 2]. Type I diamonds have been subdivided into Ia and Ib[3]. Similarly, type II specimens have been sub-grouped into IIa (insulators) and IIb (semiconductors)[4, 5]. The present work deals exclusively with IIb diamonds.

The Hall coefficient and the resistivity of a number of IIb specimens have been measured as a function of temperature[6]. All the specimens exhibited p-type conduction. The following parameters were determined: the effective mass of the charge carriers, the concentrations of donor and acceptor centres, the activation energy of the acceptors and the temperature dependence of the Hall mobility. A correlation was observed between the strength of an i.r. absorption peak at 0·346 eV and the concentration of unoccupied acceptor levels.

Little is known about the nature of the acceptor and the donor centres in IIb diamond. These may be due to trivalent and pentavalent impurities respectively. The present paper is an investigation into the nature of these centres as is revealed by their annealing behaviour.

EXPERIMENTAL PROCEDURE

The measurements made were those of the resistivity, the Hall coefficient and the strength of the 0·346 eV peak in the i.r. All measurements were carried out at temperatures close to ambient on IIb specimens in the form of rectangular blocks of approximate dimensions 3 × 2 × 2 mm. In electrical measurements, contacts were made by coating the appropriate specimen surfaces with electrically conducting silver paint.

The resistivity was measured by means of a specially developed pulse technique[7] whereby the contact resistance between the specimen and the measuring circuit was gradually reduced to zero by the application of progressively higher pulsed voltages across the specimen.

The Hall coefficient was measured by means of a conventional d.c. Hall effect apparatus with a potentiometric measuring circuit and a magnetic flux density of approximately 0·4 wB/m². As voltages were measured by a null method, the only effect of the specimen contact resistances was that of decreasing the sensitivity. The usual geometrical correction factor[8] was introduced to compensate for the distortion of the equipotential planes near the ends of the specimen on application of the magnetic field.

I.r. absorption measurements were carried out by means of a Unicam SP200 spectrophotometer. To minimise the effect of inhomogeneity, the beam was always passed through the same portion of a given specimen. Long-term drift in the machine was compensated for by recording the spectrum of a reference diamond within minutes of that of a given specimen. Spectra were then analysed by comparing them to that of the reference specimen.

Thermal annealings in the range 500–1200°C were carried out in a tubular electric furnace. To prevent etching, the specimens were heated in an argon atmosphere. Annealings at temperatures above 1200°C were carried out under high pressure ($\simeq$ 80,000 atm) to avoid graphitisation.

THE CHARACTERISTIC ACTIVATION ENERGY

It will be seen later that the annealing consists of a number of distinct processes. The theory of processes distributed over a spectrum of activation energies has been developed by Primak[9]. It is assumed that

$$-\mathrm{d}q/\mathrm{d}t = \phi q^n \qquad (1)$$

where q is the concentration of reactants during a variety of possible processes, t is the time, ϕ the specific reaction rate and n the order of reaction. If f is the change of property produced by the occurrence of a process and u is a property used as a measure of the concentration of processes which can still take place, equation (1) becomes

$$-\mathrm{d}u/\mathrm{d}t = \phi f(u/f)^n. \qquad (2)$$

The parameter ϕ is given by

$$\phi = A \exp\{-\epsilon/(kT)\} \qquad (3)$$

where A is the frequency factor, ϵ the activation energy, k Boltzmann's constant and T the temperature. The characteristic activation energy (c.a.e.) ϵ_0 is obtained from

$$\epsilon_0 = kT \ln(Bt) \qquad (4)$$

where B is defined by

$$B = A\,(f/u_0)^{1-n} \qquad (5)$$

where u_0 is the value of u at $t = 0$. It can be shown that[9]

$$\overline{u_0(\epsilon)} \simeq \Delta U/(\epsilon_{02} - \epsilon_{01}) \qquad (6)$$

where $\epsilon_{01}, \epsilon_{02}$ are the values of ϵ_0 corresponding to (t_1, T_1) and (t_2, T_2), $\overline{u_0(\epsilon)}$ is the mean of $u_0(\epsilon)$ in the interval $(\epsilon_{01}, \epsilon_{02})$ and ΔU is the change in the property used as a measure of the annealing. Thus an approximate c.a.e. spectrum can be obtained in the form of a histogram by plotting $\Delta U/(\epsilon_{02} - \epsilon_{01})$ as a function of $(\frac{1}{2})(\epsilon_{02} + \epsilon_{01})$, where ϵ_{01} and ϵ_{02} are found from equation (4) if B is known.

The physical significance of the c.a.e. is that the effects of t and T are described by a single parameter ϵ_0 and processes with $\epsilon = \epsilon_0$ make the maximum contribution to the annealing.

THE FREQUENCY FACTOR

It is seen that the c.a.e. spectrum can be plotted only if B is known. For this parameter to be calculated from equation (5), the frequency factor A must first be determined. As the annealing of point defects is governed by their diffusion through the lattice, A will be calculated for a number of diffusion processes.

An expression for the diffusion frequency factor is obtained by considering a particle in a potential energy field with two identical minima separated by an energy barrier[10].

The rate Γ_i at which a particle travels over the barrier is given by

$$\Gamma_i = \nu \exp\{-\Delta G/(kT)\} \quad (7)$$

where ν is the frequency of vibration at a minimum and ΔG is the free energy necessary to overcome the barrier. The temperature dependence of the diffusion coefficient D may be written as

$$\epsilon = -k\, d(\ln D)/d(1/T) \quad (8)$$

from which it can be shown that the activation energy ϵ may be identified with the increment in enthalpy ΔH. It then follows from equation (7) that

$$\Gamma_i = \nu \exp(\Delta S/k) \exp\{-\epsilon/(kT)\} \quad (9)$$

where ΔS is the increase in entropy. By comparing equations (3) and (9) it is seen that

$$A = \nu \exp(\Delta S/k). \quad (10)$$

A number of diffusion mechanisms have been considered to obtain a numerical estimate of A. These were as follows[10]: (a) Foreign solute atoms in interstitial positions: a solute atom is assumed to jump from one interstitial site into a neighbouring interstitial site. (b) Self-diffusion: three mechanisms were considered: the interchange of nearest neighbours, the rotation of rings of atoms and the migration of lattice vacancies. (c) Foreign solute atoms in substitutional positions: the solute atom is assumed to interchange with an adjacent vacancy. For all these mechanisms, the diffusion coefficient may be shown to be

$$D \simeq a^2\nu \exp(\Delta S/k) \exp\{-\epsilon/(kT)\} \quad (11)$$

where a is of the order of the inter-atomic spacing.

The temperature dependence of D is

$$D(T) = D_0 \exp\{-\epsilon/(kT)\} \quad (12)$$

and, combining equations (10), (11) and (12) it is seen that

$$A \simeq D_0/a^2. \quad (13)$$

Excluding anomalously high results, most experimental values of D_0 in a variety of materials have been found to lie in the range 10^{-1}–10^{-3} cm²/sec[11]. In the absence of data for diamond, it is assumed that $D_0 \simeq 10^{-2}$ cm²/sec. Thus, setting $a = 1{\cdot}5$ Å,

$$D_0/a^2 \simeq 4\times 10^{13}\,\text{sec.}^{-1} \quad (14)$$

The frequency factor can also be calculated from equation (10). Since the Debye frequency ν_D is the characteristic *maximum* vibrational frequency, it is assumed that $\nu \simeq \nu_D/2$, so that

$$\nu \simeq kT_D/(2h) \quad (15)$$

where h and T_D are Planck's constant and the Debye temperature. Diffusion experiments in various materials yield $\exp(\Delta S/k) \simeq 10$[11]. Using this value and setting $T_D = 1850$°K[12], it is seen that

$$\nu \exp(\Delta S/k) \simeq 2\times 10^{14}\,\text{sec}^{-1} \quad (16)$$

in reasonable agreement with equation (14). Taking the mean of the two results, $A \simeq 10^{14}\,\text{sec}^{-1}$.

As will be seen later, $n \simeq 1$, thus from equation (5), $B \simeq 10^{14}\,\text{sec}^{-1}$. It can be seen from equation (4) that if the estimate of B is in error by as much as a factor of 10^3, the corresponding error in ϵ_0 is only 20 per cent.

PARAMETER CALCULATIONS

The i.r. spectra were recorded as transmission as a function of the wave-number. The fractional transmission η was calculated and the absorption $\mu\tau$ was obtained from

$$\eta = \{(1-r)^2 \exp(-\mu\tau)\}/\{1 - r^2 \exp(-2\mu\tau)\} \quad (17)$$

where μ is the absorption coefficient, τ is the specimen thickness and r is defined by

$$r = \{(\gamma-1)/(\gamma+1)\}^2 \tag{18}$$

where γ is the refractive index. Since γ does not vary much with the wave-number in the region under investigation, it was assumed to be 2·390 throughout[13].

Graphs were plotted of the absorption as a function of the energy of the incident light, and the area α of the 0·346 eV band was measured after subtracting the background absorption. The uncompensated acceptor level concentration was determined from[6]

$$N_a - N_d \simeq (10^{22}/1{\cdot}6)(\alpha/\tau) \tag{19}$$

where N_a and N_d are the acceptor and the donor level concentrations in m^{-3} and the units of α/τ are eV/m.

The constant 1·6 is the mean of five experimental values ranging from 1·3 to 2·1. Owing to this scatter, equation (19) is somewhat inaccurate. However, the present work is concerned more with parameter changes than with absolute values.

The charge carrier (hole) concentration p was determined from the Hall coefficient R by means of

$$R = \{3\pi/(8e)\}(1/p) \tag{20}$$

where e is the electronic charge. The donor level concentration was found from[6]

$$p(p+N_d)/(N_a-N_d-p) = (2\pi mkT/h^2)^{3/2}\exp\{-\epsilon/(kT)\} \tag{21}$$

where k, h, T, m and ϵ are Boltzmann's constant, Planck's constant, the temperature, the effective mass of the holes and the activation energy for conduction. In the above equation, m and ϵ were set equal to 0·4 × the electronic mass and 0·35 eV respectively. This value of m is the best fit for a number of specimens[14]. Its uncertainty is ± 50 per cent. However, the same considerations apply as to the uncertainty in equation (19). The value $\epsilon = 0{\cdot}35$ eV is the mean of six results ranging between 0·34 and 0·36 eV[14]. $(N_a - N_d)$ and p were known from equations (19) and (20), so that N_d could be calculated. This result was substituted into equation (19) to yield the value of N_a.

The Hall mobility μ_H was found from

$$\mu_H = R/\rho \tag{22}$$

where ρ is the resistivity.

Due to the strong temperature dependence of the resistivity and of the Hall coefficient, it was necessary to reduce the experimental values of ρ and R to a common temperature. This was done by means of

$$\rho(T_2)/\rho(T_1) = \exp\{(\epsilon/k)(1/T_2 - 1/T_1)\} \tag{23}$$

$$R(T_2)/R(T_1) = (T_1/T_2)^{3/2}\exp\{(\epsilon/k)(1/T_2 - 1/T_1)\}. \tag{24}$$

EXPERIMENTAL RESULTS

Measurements were made on nine specimens. For the sake of brevity, the annealing of only two specimens will be reported, the other behaving in a similar manner.

Specimen D(vii) was subjected to a series of isochronal heatings. These consisted in heating for 10 min at each of a number of temperatures between 500 and 2500°C. The results are shown in Fig. 1. It is seen that the annealing was distributed over a wide range of temperatures. Furthermore, some temperatures contributed far more than others to the annealing process. This probably indicates the presence of a number of distinct reactions. The slight increase in N_a (Fig. 1(d)) is well within experimental error and therefore probably not significant.

A study of the 500–1100°C region was carried out by annealing the resistivity of D(viii). The results are shown in Fig. 2(a), where the dotted line is used to smooth over experimental error. A comparison with Fig. 1(c) clearly brings out the specimen dependence. Thus Fig. 1(c) shows that heating at 500°C for 10 min is enough to bring about a reduction in ρ. On the other hand it is seen from Fig. 2(a) that no change is produced by heating at 506°C for 5 hr and at 600°C for 1 hr.

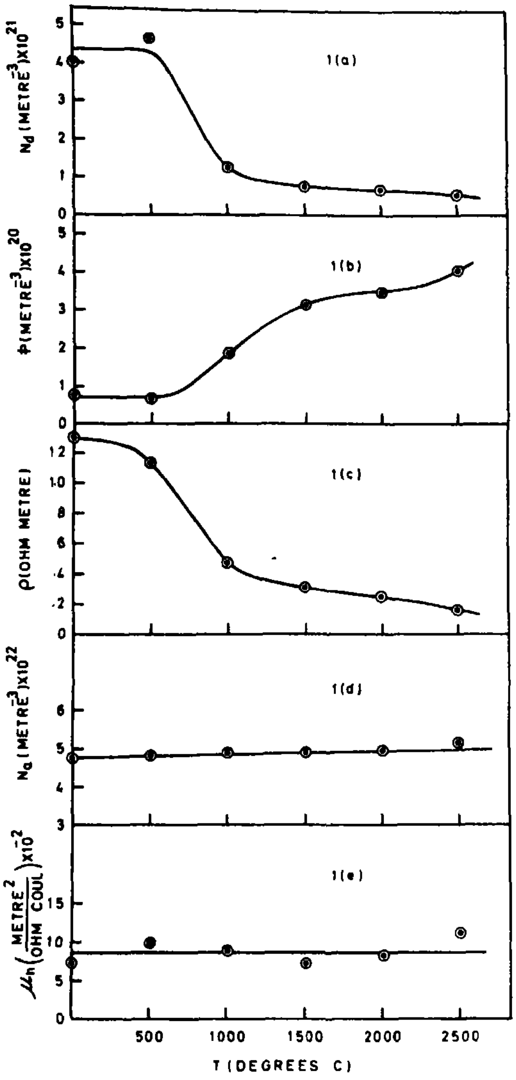

Fig. 1. Annealing of D(vii): N_d, p, ρ, N_a and μ_H as a function of the annealing temperature T.

The parameters μ_H and N_a were determined for D(viii) before treatment and also after the last heating. Both were found to remain constant. Assuming the constancy of μ_H and N_a, p and N_d were calculated at each step of annealing. The results are shown in Figs. 2(b) and 2(c). It is seen that no further annealing took place after the first hour's heating. This is additional evidence for a number of distinct reactions.

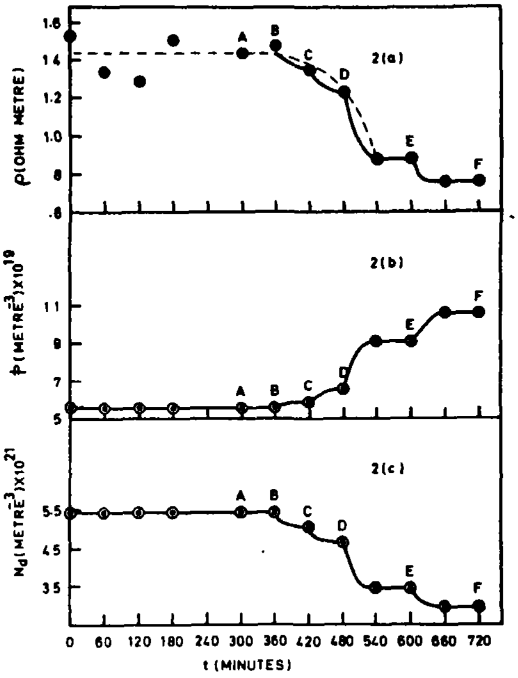

Fig. 2. Annealing of D(viii): ρ, p and N_d as a function of the cumulative time of annealing t. The annealing temperatures: up to A: 506°C, A to B: 600°C, B to C: 694°C, C to D: 864°C, D to E: 1016°C, E to F: 1061°C.

The order of reaction n was determined for the annealing of the resistivity of D(viii) at 1179°C by carrying out heatings for successive time intervals of 5, 10, 20, 40 and 80 min. It is seen from equation (1) that

$$-d\rho/dt = \phi(\rho-\rho_\infty)^n \qquad (25)$$

where ρ_∞ is the terminal value of ρ at a given temperature. The order is then simply obtained from

$$(\mathrm{d}\rho/\mathrm{d}t)_{t1}/(\mathrm{d}\rho/\mathrm{d}t)_{t2} = [\{\rho(t_1)-\rho_\infty\}/\{\rho(t_2)-\rho_\infty\}]^n \quad (26)$$

where n is the only unknown. The best fit to the results yielded $n = 0{\cdot}8 \pm 0{\cdot}2$.

A typical set of c.a.e. spectra are shown for specimen D(viii) in Fig. 3. The origin is set at $\epsilon_0 = 0$. For convenience, the ordinates are plotted as $\overline{|u_0(\epsilon)|}$ instead of $\overline{u_0(\epsilon)}$ as in equation (6), but this does not alter the shapes of the histograms. The spectra clearly show the presence of distinct reactions. They also exhibit a strong correlation between ρ, p and N_d, which is to be expected in view of the functional relation between these quantities (See Discussion).

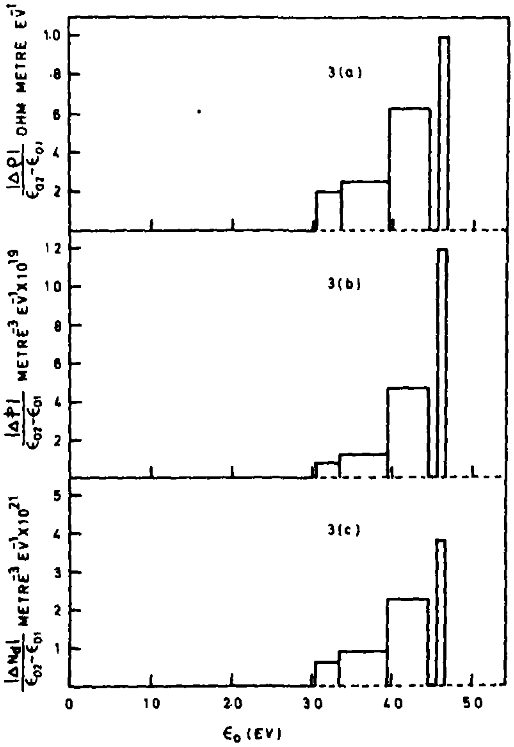

Fig. 3. Activation energy spectra of D(viii): the annealing of ρ, p and N_d is shown as a function of ϵ_0.

Measurements on the other seven specimens confirmed the following points: the annealing was specimen-dependent, it was distributed over a large range of temperatures some of which contributed more than others to the annealing process, no further change took place after the first hour's heating at any temperature, μ_H and N_a remained constant.

DISCUSSION

The observation that the acceptor level concentration remained constant suggests that the acceptor centres are firmly bonded in the lattice. This is consistent with the hypothesis that the acceptor levels are due to foreign trivalent atoms, such as aluminium or boron, in substitutional positions. Neutron activation analysis[15] gives some indication that aluminium might in fact be the impurity responsible for the acceptor centres.

The donor level concentration decreased on heating. Thus, the annealing of the donor centres is energetically easier than that of the acceptor centres.

The activation energies over which changes could be produced for temperatures up to 2500°C ranged from small values to about 9 eV. The energy for the diffusion of vacancies in diamond has been calculated to be approximately 6 eV[16]. Thus this diffusion mechanism may be responsible for some of the annealing processes observed in the present work.

The activation energies were distributed over a wide spectrum. This could be due to a variation of the following parameters over different portions of a given specimen: (i) the position of the migrating defects with respect to some crystal imperfection at which they may be anchored, (ii) the size of the clusters resulting from the conglomeration of like defects, (iii) the type and concentration of foreign elements. Moreover, the ratio of the reaction rate of any process to that of another would be expected to depend on the annealing temperature.

The calculation of the c.a.e. is subject to a number of defects: the order of reaction was determined for only one specimen, at only one temperature and for only one process (the annealing of the resistivity). These factors may affect the value of B. The values of t inserted into equation (4) may be in error due to the duration of heating being possibly greater than the time required for the annealing to come to completion at that temperature. However, due the logarithmic dependence of ϵ_0 on Bt, these inaccuracies are not likely to introduce a serious error.

An investigation into the annealing of the optical absorption produced in IIa diamond by 2 MeV electron irradiation[17] resulted in activation energies of the same order as those reported here.

The specimen dependence of the annealing is genuine, since the observed differences are too large to be accounted for by experimental error. This dependence is probably due to differences between specimens. Differences have been observed in semiconducting diamond between various portions of the same specimen[6, 18]. It should therefore not be unexpected to find variations in the nature and concentration of defects between different specimens.

The Hall mobility was found to remain constant. If annealing produces the removal of structural defects, the scattering produced by these defects would be expected to decrease, thus resulting in an increase in the mobility. Thus, if impurity scattering remains unchanged, the overall mobility, assumed to depend on the scattering produced by the perfect lattice, impurities and structural defects, would be expected to increase. It is possible that a slight increase did take place but that it was too small to be detected.

The dependence of the resistivity on the charge carrier concentration and the drift mobility μ_D is given by

$$1/\rho = pe\mu_D \qquad (27)$$

where $\mu_D = \text{constant} \times \mu_H$. Thus, if this constant does not change with annealing, it follows that the drift mobility does not vary, so that the observed decrease in the resistivity may be attributed completely to an increase in the carrier concentration. The correlation between N_d, p and ρ is readily explained by the accepted model of IIb diamond[6]. The forbidden gap contains N_a acceptor levels and a smaller number N_d of donor levels above the acceptors. Positive hole conduction occurs through the excitation of electrons from the valence band into the $(N_a - N_d)$ unoccupied acceptor levels. Thus, as N_d decreases, there is an increase in $(N_a - N_d)$, (N_a was found constant), leading to an increase in p and thus to a decrease in ρ (at constant μ_D) as indicated by equation (27).

Acknowledgements—It is a pleasure to thank Dr. F. A. Raal for frequent encouragement, Dr. P. T. Wedepohl for helpful discussions and Messrs. Industrial Distributors (1946) Limited for permission to publish this work.

REFERENCES

1. ROBERTSON R. *et al., Trans. R. Soc.* **A232**, 463 (1934).
2. ROBERTSON R. *et al., Proc. R. Soc.* **A157**, 579 (1936).
3. DYER H. B. *et al., Phil. Mag.* **11**, 763 (1965).
4. CUSTERS J. F. H., *Physica* **18**, 489 (1952).
5. CUSTERS J. F. H., *Nature* **176**, 173 (1955).
6. WEDEPOHL P. T., Ph.D. Thesis, Reading, England (1957); *Proc. phys. Soc.* **B70**, 177 (1957).
7. HORSZOWSKI S. M., *J. Scient. Instrum.* **44**, 296 (1967).
8. ISENBERG I. *et al., Rev. scient. Instrum.* **19**, 685 (1948).
9. PRIMAK W., *Phys. Rev.* **100**, 1677 (1955).
10. SHOCKLEY W. (Editor) *Imperfections in Nearly Perfect Crystals.* Wiley, N.Y. (1952).
11. SHEWMON P. G., *Diffusion in Solids.* Mc Graw-Hill, N.Y. (1963).
12. WERT C. A. and THOMSON R. M., *Physics of Solids.* Mc Graw-Hill, N.Y. (1964).
13. PETER F., *Z. Phys.* **15**, 358 (1923).
14. BERMAN R. (Editor), *Physical Properties of Diamond.* Clarendon Press, Oxford (1965). KEMMEY P. J., Ph.D. Thesis, Reading, England (1960).
15. LIGHTOWLERS E., *Diamond Conference. Bristol,* England (1963).
16. SWALIN R. A., *J. Phys. Chem. Solids* **18**, 290 (1961).
17. CLARK C. D. and PALMER D. W., *Symposium on the Reactivity of Solids.* Amsterdam (1960).
18. RAAL F. A. and MUTCH R. E., *Nature* **184**, 1857 (1959).

J. Phys. Chem. Solids Pergamon Press 1969. Vol. 30, pp. 677–685. Printed in Great Britain.

CATION SELF-DIFFUSION IN SINGLE CRYSTAL CaO

V. KUMAR
Department of Materials Sciences, University of Southern California,
Los Angeles, Calif. 90024, U.S.A.
and
Y.P. GUPTA
Materials Sciences Laboratory, Northrop Corporate Laboratories, Hawthorne, Calif. 90250, U.S.A.

(*Received* 29 *July* 1968)

Abstract—The self-diffusion coefficient of calcium in single crystals of calcium oxide has been measured in the temperature range, 1465–1760°C, using vapordeposited thin film of radioactive $Ca^{45}O$ and boundary conditions for diffusion from a plane source into a semi-infinite medium. The temperature dependence of the diffusivity can be expressed as:

$$D = (11\cdot 25 \pm 2\cdot 2) \times 10^{-5} \exp[-(64{,}300 \pm 1400)/RT].$$

In this temperature range, diffusion appears to be intrinsic. The activation energy of 64·3 kcal/mole is suggested to be the sum of energy of cation vacancy migration and one half the energy of cation vacancy formation by Schottky disorder. After a reanalysis of the raw data from a previous investigation[2] of cation self-diffusion in calcium oxide single crystals in the temperature range 1000–1400°C, an activation energy of 28·2 kcal/mole is obtained for cation vacancy migration. From the experimental results.the energy of Schottky defect formation in calcium oxide is calculated to be 3·08 eV, a value in satisfactory agreement with the theoretical estimate of Yamashita and Kurosawa.

1. INTRODUCTION

CALCIUM OXIDE is used in the electronics industry as a thermionic emitter and in the refractories industry as an additive for super-refractory oxides such as stabilized zirconia. Because of its high melting temperature it is likely to find more industrial applications with the advancement of high temperature technology. A knowledge of diffusion parameters is not only important in controlling the solid state reactions that inevitably occur in high temperature applications but it is also often required for obtaining a better insight into the defect structure of a solid.

Previous studies on diffusion in CaO and other alkaline earth oxides present an inconsistent picture. The data on electrical conductivity do not help to clarify the picture because part of the current is carried by electrons and holes and thus the Nernst–Einstein equation relating electrical conductivity to diffusion is not applicable in a simple way.

Previous work on cation self-diffusion in calcium oxide has used sintered compacts as well as single crystals. Lindner[1] studied diffusion in sintered compacts in the temperature range 900–1600°C, with no data points at temperatures between 1400° and 1600°C. Of the three different methods tried by Lindner, only the contact method gave reproducible results wherein a diffusion couple consisting of normal and radioactive pellets of sintered CaO was used. Lindner's results can be expressed as:

$$D = 0\cdot 4 \exp(-81{,}000/RT) \text{ cm}^2/\text{sec}.$$

Gupta and Weirick[2] studied cation self-diffusion in CaO single crystals in the temperature range 1000–1400°C. A sectioning and residual activity technique with boundary conditions for diffusion from a plane source into a semi-infinite medium was used. Two regions of diffusion were observed:

(i) near the surface (0–20 μ) where

$$D = (8{\cdot}75 \pm 1{\cdot}32) \times 10^{-8} \exp[(-34{,}600 \pm 950)/RT]$$

and (ii) deep in the crystal (beyond 20 μ) where

$$D = (1{\cdot}95 \pm 0{\cdot}6) \times 10^{-7} \exp[(-34{,}020 \pm 1800)/RT].$$

Over the temperature range 1000–1400°C, the near-surface diffusion was identified as being extrinsic, resulting from the effects due to impurities and possibly the diffusion anneal environment. A superposition on the extrinsic diffusion of the mass transport along the high-diffusivity paths like dislocations was postulated for regions deep inside the crystal.

Gupta and Weirick also measured the electrical conductivity of the crystals in the same temperature range. The activation energy for conduction from these experiments is between 38 and 42 kcal/mole. The results also showed that CaO is about 2 per cent ionic in this temperature range. In contrast to this, measurements by Palguev and Neuimin[3] on cells with gaseous electrodes and solid sintered CaO show it to be 50–60 per cent ionic at 1300°C. An activation energy of 84 kcal/mole for electrical conduction is obtained from another study by Shakhtin, Levintovich, Pivovar and Elisera[4] on sintered CaO in the temperature range 1300–2000°C.

Work on other alkaline earth oxides is also not enough to serve as a guideline. Redington [5] from measurements of cation self-diffusion in BaO single crystals, observed two temperature regions, one of high and the other of low activation energy with two diffusion constants: (i) near the surface and (ii) in the bulk in each temperature range. The activation energy for diffusion of Ba in BaO was observed to vary from 7 to 11·5 kcal/mole in the lower temperature region 277–1077°C and from 250 to 280 kcal/mole in the higher temperature region 1077–1277°C. Extrapolation of Redington's data to the melting point of BaO yields a value of $D_{Ba} = 10^4$ cm²/sec. Such high diffusivities are impossible in the solid state. Reported values of activation energy for cation self-diffusion in MgO range from 50 to 78 kcal/mole[6, 7].

Unfortunately, there is no reported work on diffusion in SrO. It is evident that an understanding of the nature of mass and charge transport in alkaline earth oxides will require several investigations of these oxides, particularly using single crystals.

2. EXPERIMENTAL

Calcium oxide crystals cleaved along (100) planes were received from Muscle-Shoals Electrochemical Corporation, Tuscumbia, Alabama. Spectrographic analysis* of the crystals showed that the only impurities detected were Mg (0·02 per cent), Sr (0·02 per cent) and Ba (0·001 per cent). The optically clear crystals from the lot were cut parallel to (100) planes on a precision diamond cutter into approximately cubic specimens; each edge of the cube was 5–6 mm. One face of the crystal was polished flat using 1 μ diamond dust. The crystal was washed in dilute HCl to get a clean face for deposition of radioactive Ca^{45}.

Ca^{45} received as $CaCl_2$ in HCl solution was converted chemically to oxalate using ammonium oxalate which, after heating to 900°C, decomposed to $Ca^{45}O$. The polished and cleaned face of the crystal was plated with a thin film of $Ca^{45}O$ using the vapor deposition technique. The crystal was held 2 in. above a tungsten wire basket containing the radioactive powder and heated to about 1600°C. Evaporation was done under a pressure of 10^{-5} mm of Hg. After the deposition, the unpolished faces of the crystal were ground to remove any deposited activity. The uniformity of the thin film was checked by placing the sample with the radioactive face on a no-screen X-ray film for five minutes. Under the conditions used, the film thickness was about 1500–2000 Å.

---

*Spectrographic analysis was performed by the American Spectrographic Laboratories, San Francisco, California.

A molybdenum furnace was used for diffusion anneals from 1450–1600°C. For still higher temperature anneals, a graphite tube furnace was used. All diffusion anneal experiments were carried out in dry argon atmosphere. Temperatures above 1500°C were measured with a (Pt–20%Rh)–(Pt–40%Rh) thermocouple, while for temperatures below 1500°C, a Pt–(Pt–10%Rh) thermocouple was used. A temperature variation of ± 1° in the molybdenum furnace and ± 3° in the graphite tube furnace was observed at the control temperature.

The furnace tubes used for diffusion runs in both the furnaces were 99·9 per cent alumina. Since calcium oxide forms a liquid phase with alumina around 1400°C, CaO samples were wrapped in platinum foil and then inserted in the furnace tube in an alumina boat. However, it was found that platinum reacts with calcium oxide and cannot be used beyond 1500°C. For higher temperature diffusion annealing the crystals, covered with thin MgO crystal wafers on all sides, were placed in MgO boats. Two specimens with their radioactive faces in contact were used for each anneal. This procedure was followed to prevent any observable loss of radioactivity by evaporation. At the end of a run, the specimens were pulled to a zone of about 1000°C and allowed to stay there for a few minutes before being removed from the furnace. Two to three diffusion experiments were made at each temperature.

Prior to determination of the diffusion profiles the faces perpendicular to the radioactive face were ground very slightly to remove any radioactivity due to surface migration of Ca^{45} along the sample faces. Penetration profiles were determined by removing thin sections parallel to the original face and determining the residual radioactivity in the specimen after each section was removed. Removal of thin sections was accomplished with the help of a precision lapping device similar to that used by DeBruin and Watson [8]. To ensure sectioning parallel to the original face, the specimen was mounted in the device by letting molten Wood's metal freeze around it while it was held in the desired position with the help of a bridge as shown in Fig. 1. Several undiffused samples were sectioned to check the alignment of the sample parallel to the hone. The surface activity of the undiffused samples dropped to zero within a distance of less than 1·25 μ. By adjusting the micrometer, sections as thin as 1·25 μ could be ground off as the device holding the specimen and supported on optically flat railings on either side was moved with a rotary and back-and-forth motion over a diamond hone.

By rotation, the micrometer can be brought to a position where the specimen surface just comes in contact with the hone as the device slides on the railings. Taking this as the zero position, 5 μ sections were removed. Following removal of successive

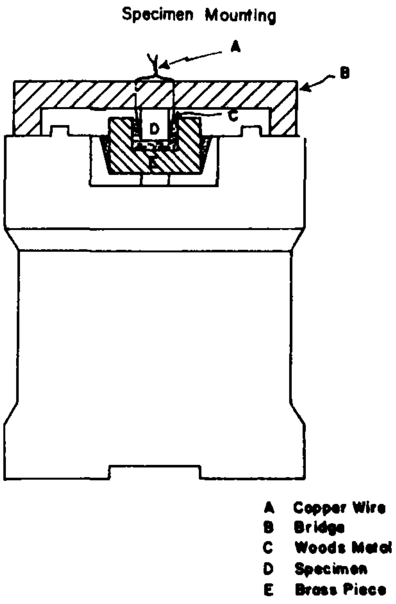

Fig. 1. Device for specimen mounting.

sections the total residual activity of the sample was determined by use of a beta well-counter. The statistical counting error was kept within 1 per cent. Prior to any sectioning an initial count was taken to calculate the fractional remaining activity after subsequent sections.

3. DATA COMPUTATION AND RESULTS

Fick's equation for unidimensional diffusion with constant diffusivity is

$$\frac{dI}{dt} = D\frac{d^2I}{dx^2} \qquad (1)$$

The boundary conditions for undirectional diffusion from a thin film on the surface of a semi-infinite homogeneous medium are:

(i) $I(x, O) = Ox > O, t = O$

and,

(ii) $\int_0^{\infty} I(x, t)dx = I_0 \text{ for } t \geq O,$

assuming no loss of activity due to evaporation. A solution[9] of equation (1) for the specified boundary conditions is:

$$I(x, t) = \frac{I_0}{(\pi Dt)^{1/2}} \exp(-x^2/4Dt)$$

where t is the diffusion anneal time.

However, experimentally it was very inconvenient to measure $I(x)$ for a predetermined value of t, because of very small penetrations and the difficulty in collecting the sectioned material. The counts from the face of the crystal, after removal of a thickness δ, represent the activity left in the specimen after taking into account the absorption by the specimen itself. This integrated intensity coming from various depths of the crystal is represented by the integral

$$I = \int_{\delta}^{\infty} I(x) \exp -\mu(x - \Delta)\, dx \qquad (2)$$

where μ is the linear absorption coefficient for β-radiation of Ca^{45} in CaO. The reported value[1] of μ for β-radiations from Ca^{45} in CaO is 430 cm^{-1}. Using an analysis due to Gruzin[10] the integrated intensity I can be used to calculate diffusivities. According to Gruzin's analysis, if δ is infinitesimal, equation (2) can be written as:

$$\ln(I - 1/\mu\frac{dI}{dx}) = -x^2/4Dt + \text{constant} \qquad (3)$$

To apply equation (3) directly δ must be $\leq 1{\cdot}5\,(Dt)^{1/2}$ to limit errors in the experimental values of D to less than 10 per cent. The section thickness ($\delta = 5\,\mu$) was kept less than $0{\cdot}25\,(Dt)^{1/2}$ in all cases by choosing proper values of time, t.

A digital computer was used to fit a smooth curve to the experimental points (I, x) and to calculate the term $(1/\mu)\,(dI/dx)$ for the respective x values. Figure 2 shows the smooth curves, I vs. x, as obtained from the computer analysis. Values of the diffusion constant D was evaluated from the slope of the plot of $\ln I^* = \ln\,[I - 1/\mu(dI/dx)]$ vs. x^2 shown in Fig. 3, since the slope $m = -\frac{1}{4}Dt$. Figure 4, a plot of $\log D$ vs. $1/T$, shows the temperature dependence of diffusivity. A

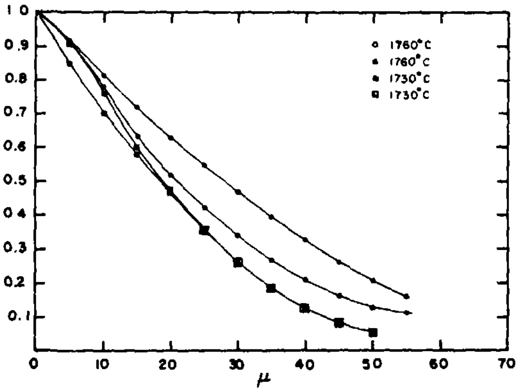

Fig. 2. Fraction of original activity remaining vs. penetration distance.

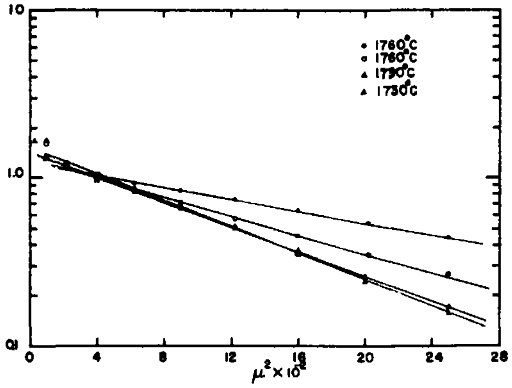

Fig. 3. Logarithm of corrected fraction remaining vs. penetration distance squared.

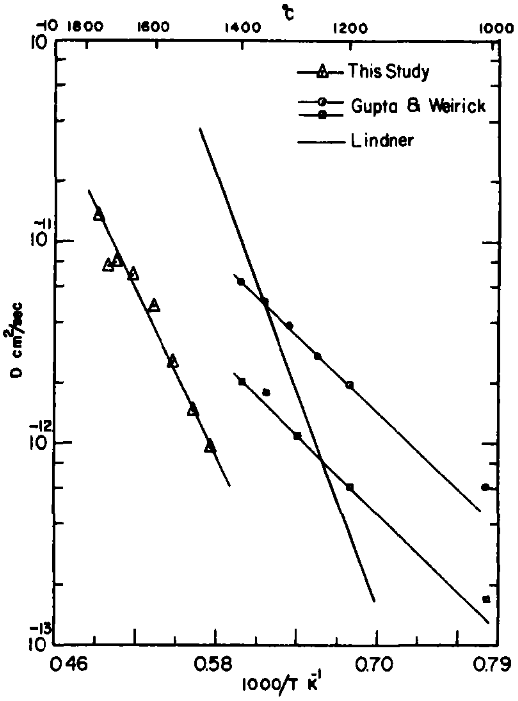

Fig. 4. Log D vs. reciprocal temperature.

least square fit of the data in Fig. 4 yields equation (4):

$$D = (11{\cdot}25 \pm 2{\cdot}2) \times 10^{-5} \exp[-(64{,}300 \pm 1400)/RT] \quad (4)$$

4. DISCUSSION

Since diffusion in a solid is very closely related to the type and concentration of mobile point defects, correlations between diffusion and other physical properties dependent on the movement of these point defects can be used to elucidate diffusion mechanisms. In ionic compounds the nature and concentration of mobile defects, and hence the diffusion mechanisms, are considerably influenced by the requirement of electrical neutrality and by the presence of a strong coulombic interaction between the diffusing ion and the lattice. Furthermore, the charge transfer by the motion of ions involved in the diffusion process can be related to the electrical conductivity through the Nernst-Einstein equation which yields

$$D_i = \sigma t_i kT / n_i Z_i^2 e^2$$

where σ is the total conductivity at the temperature T, t_i is the transference number for the species i of change $Z_i e$, and n_i is the mobile ion or defect concentration.

Studies of cation diffusion and conductivity in NaCl[11] and AgBr[12] crystals show how useful the above equation is in understanding the ionic transport in these materials. For NaCl, complete agreement is observed between the conductivity and diffusivity data in the high temperature range where mobile defects are predominantly intrinsic. Lack of agreement in the low temperature range where mobile defects are dependent only on the impurity content reveals the formation of impurity-vacancy associates. Similarly, in considering diffusion of Ag in AgBr, a need for compatibility between the conductivity and diffusivity data requires that diffusion must occur by a combination of vacancy and interstitial mechanisms.

The reliance in diffusivities calculated from the conductivity comes from the fact that in both these cases the cations are known to carry all the current. For the case of oxides of the NaCl structure this is not always true.

Transition metal oxides, for example, are well known semiconductors. The alkaline-earth oxides also exhibit nonionic conduction, especially at elevated temperatures. However, for alkaline earth oxides the band gap (MgO = 8·7 eV[13]; CaO = 7·7 eV[14]; SrO = 5·7 eV [15]; BaO = 5·0 eV[16] for intrinsic electronic conduction is so high that appreciable intrinsic conductivity in conduction and valence bands even at moderate or elevated temperatures is unlikely. The electronic transport may, however, occur through the interactions of localized electrons on impurity and/or defect sites. Whether such charge transfer transitions can contribute appreciably to conduction depends on the lifetime and mobilities of the resulting holes or electrons. Since in the alkaline earth oxides both impurities and thermal excitation can give rise to electronic carriers, it becomes ambiguous to interpret the activation energy for electrical conduction and relate it to ionic transport.

Experimental data of Shakhtin, Levintovich, Pivovar and Elisera[4] on the conductivity of CaO sintered compacts yield an activation energy of 84 kcal/mole in the temperature range 1300–2000°C. In contrast Gupta and Weirick's[3] data on single crystals give a value between 38 and 42 kcal/mole in the range 900–1400°C, where, according to these authors, CaO is about 2 per cent ionic. Since ionic character is expected to be suppressed at higher temperatures[3], it is uncertain as to what an activation energy of 84 kcal/mole really represents. Similarly, the data of Shakhtin *et al.*[4] on MgO sintered compacts yield a value of 91 kcal/mole in the temperature range 1300–2100°C. This is very high compared to Mitoff's[6] value of 50 kcal/mole for conduction in MgO single crystals, whereas the measured[7] activation energy for Mg diffusion in MgO single crystals has the intermediate value of 78·2 kcal/mole.

Since for the case of calcium oxide a correlation between diffusivity and electrical conductivity is at present partially uncertain, one has to invoke other considerations to decide between the two types of dominant defects (e.g. vacancies and interstitials) responsible for cation diffusion in CaO. Interstitial positions in the CaO lattice are the body centers of each of the smaller cubes in the CaO unit cell. A Ca^{2+} in an interstitial position is at the overlapping center of the Ca^{2+} and O^{2-} tetrahedra. In this position the Ca–O distance is 2·08 Å. Since the equilibrium Ca–O distance is 2·4 Å, the interstitial would be in a very high energy state as compared to its normal position because of strong repulsions from the four Ca ions as well as O^{2-} placed tetrahedrally about this position. Moreover, the size of the interstitial hole calculated from the reported values of the lattice parameters[17] 4·8105 Å, of CaO and ionic radii [17] 0·99 Å and 1·32 Å, for the Ca^{2+} and O^{2-} ions, respectively, is 1·85 Å. Introduction of a Ca^{2+} (ionic diameter = 1·98 Å) involves considerable distortion of the lattice and polarization of the ion. Consequently, the formation of Ca^{2+} interstitials in calcium oxide is unlikely.

In a study of Ca diffusion in CaO single crystals, Gupta and Weirick[2] suggested a vacancy mechanism for the cation diffusion in the temperature range 1000–1400°C. In this temperature range, diffusion was concluded to be extrinsic, involving only vacancy migration in the near surface region. In regions deep in the crystal, dislocation-pipe diffusion enhanced the extrinsic diffusion. In support of a vacancy mechanism for cation diffusion in CaO, two observations were made:

(i) An activation energy of 34·6 kcal/mole for diffusion of Ca in CaO in the extrinsic region is comparable to the activation energy for cation diffusion in FeO (30 kcal/mole) and CoO (34·5 kcal/mole) at fixed partial pressure of oxygen in the cation deficient range; the cation deficiency being caused by the formation of cation vacancies. A vacancy mechanism is known to operate for cation diffusion in these semiconductor oxides of the same structure as CaO.

(ii) The activation energies for cation self-diffusion in various oxides of the NaCl structure, including CaO, are well represented by a straight line on a plot of log (activation energy) vs. r/α, where r and α are, respectively, the ionic radius and the ionic electronic-polarizability of the diffusing ion. Thus, the mechanism of cation diffusion in CaO should be the same as in other oxides (FeO, CoO, MgO, NiO) of the NaCl structure.

In the absence of an unambiguous correlation between electrical conductivity and diffusivity for the case of CaO, the vacancy mechanism appears most likely to operate at higher temperatures, particularly in view of the observations made by Gupta and Weirick. Since calcium oxide is not a semiconductor like the transition metal oxides, the cation vacancy-electron hole pairs should be very difficult to form unless acceptor impurities of the right kind are present. The spectrographic analysis of the CaO crystals used for the present study does not show any other impurities except Mg (0·02 per cent), Sr (0·02 per cent), and Ba (0·001 per cent), all of which belong to the alkaline earth group. Since no hetrovalent impurities are present, the cation vacancies must be produced by thermal excitation. Thus, a Schottky defect pair is most likely to form in CaO in order to satisfy the restriction of electrical neutrality. A calculation of the energy of Schottky defect, based on the combined results of the present study and that by Gupta and Weirick[2], yields a value which is in satisfactory agreement with the theoretical estimate as shown later.

It is, however, interesting to compare the results of this study with those of Gupta and Weirick. To make the comparison more meaningful the raw data of Gupta and Weirick were reanalyzed using the same computational procedures as used in the present work. This was important since identical experimental procedures were used and the actual sectioning was done with the same device in both cases. However, the curve-fitting and slope calculations were performed manually in the previous work[2]. The results of these computations, shown in Fig. 4 along with the results of the present study, can be represented by the equations

(i) $D = 10^{-8} \exp(-28{,}200/RT)$ in the near-surface regions,

and

(ii) $D = 3{\cdot}08 \times 10^{-8} \exp(-28{,}200/RT)$ in regions deep in the crystal.

From Fig. 4 several differences can be noted between the two studies:

(i) There is only one well defined diffusion constant in this study, in contrast to the two separate diffusion constants in the study by Gupta and Weirick; one near the surface (0–20 μ) and the other deep in the crystal. According to these authors the diffusion behavior in the crystal interior is a result of the superposition on extrinsic diffusion of contributions from diffusion along dislocation pipes. An attempt to observe any real difference in the dislocation density in the two sets of crystals was unsuccessful, partly because a suitable etchant could not be developed to reveal well defined dislocation etch-pits. However, the fact that, for the same or longer annealing time but higher temperatures, the radioisotope penetrated to smaller depths in the present study, suggests that the crystals used by Gupta and Weirick had a higher dislocation density. Also, since the crystals were received from two different sources, there may have been some differences in the inherent crystal defects. It is, therefore, reasonable to consider that the diffusion constants from this study correspond to the near-surface diffusion constants obtained in the study by Gupta and Weirick.

(ii) The absolute values of the diffusivities are lower in the present study as compared to those obtained by Gupta and Weirick. Extrapolation of the results from the two studies to about 1450°C shows that diffusion constants obtained by Gupta and Weirick for the near-surface region are about three times as large as the values obtained in the present study. Since similar procedures were used for radioisotope deposition in the two studies, the observed difference cannot be due to the presence of a diffusion barrier at the initial surface in the present work. However, the crystals used by Gupta and Weirick contained 0·001 per cent Al. Trivalent impurities like Al can produce cation vacancies in the alkaline earth oxides, thereby enhancing the cation diffusion rates. A difference in the inherent crystal defects due to differences in the crystal growth procedures may also be partially responsible for the difference in the magnitude of diffusivity in the two studies.

(iii) The activation energy for diffusion obtained in the present study is more than twice the value obtained by Gupta and Weirick, who proposed extrinsic diffusion in the temperature range of their study. The extrinsic nature was attributed by these authors to (i) the lower observed activation energy for diffusion and a lower temperature range (less than 0·6 T_m where T_m is the melting point of CaO), (ii) presence of trivalent impurities like Al, and (iii) the anneal environment, $P_{O_2} = 10^{-6}$ atm., all of which tend to produce a concentration of cation vacancies that is predominantly extrinsic. Higher annealing temperatures, absence of hetrovalent impurities and the much higher activation energy suggest the diffusion to be intrinsic under the conditions of the present study.

The energy of formation of the Schottky defect in CaO can now be calculated by combining the results of this study with the previous study by Gupta and Weirick. Since the energy for vacancy migration is 1·22 eV (28·2 kcal/mole), and the activation energy for intrinsic diffusion of Ca in CaO is 2·79 eV (64·3 kcal/mole), the energy for the formation of a Schottky defect pair is calculated to be 3·08 eV, following the procedure in reference [12].

The calculated value of the energy for the formation of the Schottky defect pair is within the range of theoretical estimates of Yamashita and Kurosawa[18]. Using the interionic potentials in MgO, CaO and SrO these authors have calculated the energy for Schottky defect formation as 4–6, 3–5 and 3–5 eV, respectively. The fact that the energy of Schottky pair formation in MgO is about 1 eV greater than that for CaO appears to by supported by the work of Lindner and Parfitt on the self-diffusion of Mg in MgO single crystals in the temperature range, 1400–1600°C. The activation energy for diffusion of Mg in MgO single crystals is found to be 3·41 eV and has been presumably suggested by these authors as the activation energy for intrinsic diffusion of Mg. Since the activation energy for cation vacancy migration in oxides of the NaCl structure is about 1·3–1·5 eV (30–35 kcal/mole)[19], an energy of about 4·1 eV (93 kcal/mole) is obtained for the formation of Schottky defect pairs in MgO.

It is difficult to explain Lindner's value of 81 kcal/mole as the activation energy for cation self-diffusion in CaO. In the temperature range 900–1400°C it is unlikely that lattice diffusion should predominate over the grain boundary diffusion in CaO sintered compacts of moderate purity and 5–9 per cent porosity. Lindner did not report the chemical analysis of his compacts. Since high purity oxides have become available only recently, it is likely that Lindner's material contained hetrovalent impurities, especially the alkali oxides. It can be shown that both the activation energy for cation diffusion and the preexponential factor increase in the presence of alkali cations[2]. The diffusion constants measured by Lindner, therefore, represent a superposition of impurity effects on a combination of lattice, grain boundary, and pore surface diffusion.

The contact method may itself be responsible for a higher activation energy. There is a possibility of the existence of a diffusion barrier at the contact interface between the activated and normal compacts. Such a barrier would be quite effective at lower temperatures, thus lowering the diffusivities in this range and consequently increasing the activation energy. The diffusivities obtained by Lindner are at least an order of magnitude greater than those from the present study. This is easily attributable to grain boundary and void diffusion in sintered compacts.

5. CONCLUSIONS

In the temperature range of 1465–1760°C, the temperature variation of self-diffusion of calcium in single crystal CaO is given by the equation:

$$D = (11\cdot25 \pm 2\cdot2) \times 10^{-5} \exp[-(64{,}300 \pm 1{,}400)/RT]\ \mathrm{cm^2\,sec^{-1}}.$$

In this temperature range, cation diffusion appears to be intrinsic and occurs via a vacancy mechanism. Based on the present results between 1465–1760°C and a reanalysis of the raw data of Gupta and Weirick from 1000–1400°C on diffusion of Ca in single crystal CaO, the calculated energies for the formation of the Schottky defect pairs and for cation vacancy migration are, respectively, 3·08 and 1·22 eV.

Acknowledgements—The financial support of this research by the National Science Foundation is gratefully acknowledged.

REFERENCES

1. LINDNER R., *Acta chem. scand.* **6**, 468 (1952).
2. GUPTA Y. P. and WEIRICK L. J., *J. Phys. Chem. Solids* **28**, 811 (1967).
3. PALGUEV S. F. and NEUIMIN A. D., *Soviet Phys. solid st.* **4**, No. 4 (1962).
4. SHAKHTIN D. M., LEVINTOVICH E. V., PIVOVAR T. L. and ELISEVA G. G., *Ogneupory* **7**, 37 (1965).
5. REDINGTON R. W., *Phys. Rev.* **87**, 1066 (1952).
6. MITOFF S. P., *J. chem. Phys.* **36**, 1383 (1962).
7. LINDNER R. and PARFITT G. D., *J. chem. Phys.* **26**, 182 (1957).
8. DeBRUIN H. J. and WATSON G. M., ORNL-3526 *Self-Diffusion of Be in Unirradiated, Cold Pressed and Sintered BeO.* Oak Ridge Nat. Lab.
9. CRANK J., *The Mathematics of Diffusion*, 1st Edn. (corrected), pp. 9–11. Oxford University Press, Oxford (1957).
10. GRUZIN P. L., *Dokl. Akad. Nauk SSSR* **86**, 289 (1952).
11. MAPOTHER D., CROOKS H. N. and MAURER R., *J. chem. Phys.* **18**, 1231 (1950).
12. SHEWMON P. G., *Diffusion in Solids*, pp. 151–155. McGraw-Hill, N.Y. (1963).
13. REILING G. H. and HENSLEY E. B., *Phys. Rev.* **112**, 1106 (1958).
14. GLASSCOCK H. H., Jr. and HENSLEY E. B., *Phys. Rev.* **131**, 649 (1963).
15. ZOLLWEG R. J., *Phys. Rev.* **111**, 113 (1958).
16. PHILLIPS H. R., *Phys. Rev.* **107**, 687 (1957); APKER L., TAFT E. and DICKEY J., *Phys. Rev.* **84**, 508 (1951).
17. WYCKOFF RALPH W. G., *Crystal Structures*, Vol. 1, 2nd End, p. 86. Wiley, N.Y. (1963); *Handb. Phys. Chem.* 46th Edn. F-117 (1966).
18. YAMASHITA J. and KUROSAWA T., *J. phys. Soc. Japan* **9**, 944 (1954).
19. KINGERY W. D., Diffusion in Oxides, In *Conference on Kinetics of High Temperature Processes M.I.T.* (Edited by W. D. Kingery). p. 37. M. I. T. Press and Wiley, N.Y. (1959).

J. Phys. Chem. Solids Pergamon Press 1969. Vol. 30, pp. 687-703. Printed in Great Britain.

CANALISATION DES DEUTONS DANS LE QUARTZ†

FRANÇOIS ABEL, GEORGES AMSEL, MICHEL BRUNEAUX et EMMANUEL d'ARTEMARE
Groupe de Physique du Solide de l'Ecole Normale Supérieure, Tour 23,9 quai St-Bernard-Paris 5e

(*Received* 26 *July* 1968)

Résumé—La canalisation des deutons dans le quartz a été étudiée afin de séparer les effets des sous-réseaux oxygène et silicium. La diffusion élastique et la réaction $O^{16}(d, p)O^{17*}$ ont été observées à 900 KeV. Une technique de balayage angulaire automatique a été utilisée et un soin particulier a été accordé à la réduction de l'effet du dommage causé au cristal par le faisceau. Le taux d'extinction apparente des sections efficaces en fonction de l'angle de tir avec l'axe *c* et de la profondeur dans le cristal a été mesuré, et trouvé égal, en surface, à 96,8% pour le silicium et 89% pour l'oxygène. Les largeurs à mi-hauteur correspondantes étaient de 64' et 36'. Ces expériences montrent tout l'intérêt de l'observation, en plus de la diffusion élastique, de réactions nucléaires, ce qui est particulièrement aisé, avec des deutons, aux basses énergies. Il apparaît que la présence de rangées d'atomes de silicium a pour effet de rétrécir la courbe d'extinction et d'augmenter le rendement minimal relatifs aux rangées d'oxygène

Abstract—The channeling of deuterons in quartz was studied in order to separate the effects of the oxygen and silicon sub-lattices. The elastic scattering and the reaction $O^{16}(d, p)O^{17*}$ were observed at 900 KeV. An automatic angular scanning device was used and particular care was taken to reduce the effects on the crystal of the radiation damage induced by the beam. The extinction ratio of the yields was measured as a function of the beam angle with the *c* axis and of the depth in the crystal. It was found equal, near the surface, to 96·8 per cent for silicon and 89 per cent for oxygen. The corresponding widths at half minimum were 64' and 36'. These experiments show that, in addition to elastic scattering, nuclear reactions should also be observed; this is especially easy at low energies with deuterons. It appears that the silicon strings tend to narrow the extinction curve and to increase the minimum yield associated with the oxygen strings.

INTRODUCTION

SI LES études portant sur les phénomènes de canalisation dans les cristaux monoatomiques ont été nombreuses au cours des dernières années, celles consacrées aux cristaux diatomiques restent rares. Brice, Sattler et Dearnaley[1, 2] ont examiné GaAs, Palmer et d'Artemare[3] le quartz, mais leurs mesures n'ont pas permis de séparer les effets dus aux deux éléments constituants. L'objet du présent travail était de réaliser une telle séparation pour connaître la façon dont se combinent les effets des deux sous réseaux. Le quartz, bombardé par des deutons, permet d'atteindre aisément cet objectif. L'expérience consiste à observer l'extinction apparente de la section efficace d'interaction nucléaire pour des directions de tir voisines de l'axe de symétrie ternaire *c* du cristal. Dans le cas de la diffusion élastique, l'énergie E_s du deuton sortant à grand angle est proche de $E_s = E_d (M-2)^2/(M+2)^2$ (E_d: énergie des deutons incidents, M: masse du noyau) et l'effet du silicium est bien isolé de celui de l'oxygène par la différence d'énergie, qui est de 131 KeV pour $E_d = 900$ KeV. Un proton incident ou des noyaux cibles plus lourds fourniraient une différence bien moins grande. Lorsqu'on observe des réactions nucléaires, la séparation devient complète, celles-ci étant spécifiques. Les deutons sont de ce point de vue très efficaces, induisant aux basses énergies de nombreuses réactions avec des sections efficaces et des valeurs Q élevées. Nous avons utilisé la réaction $O^{16}(d, p)O^{17*}$ selon les techniques déjà décrites (microanalyse de l'oxygène par réactions nucléaires[4, 5]).

---

†Travail effectué dans le cadre de la Recherche Coopérative sur Programme N°69-157 du Centre National de la Recherche Scientifique.

Pour faciliter la présentation et la discussion des résultats, nous décrivons ici brièvement la structure cristalline du quartz; de nombreux détails peuvent être trouvés sur ce sujet dans la référence[6]. A la température ordinaire le quartz se présente dans la variété α qui appartient à la classe de symétrie $P32$ (tétartoédrie énantiomorphe du système hexagonal). La maille a pour paramètres: $a = 4{,}903$ Å et $c = 5{,}393$ Å et contient trois groupes SiO_2. On peut décrire simplement l'arrangement des atomes Si et O dans le quartz α en disant que des tétraèdres SiO_4, enchaînés les uns aux autres par mise en commun des atomes d'oxygène forment des hélices de pas c, axées sur l'axe de symétrie ternaire hélicoïdal, parallèle à la direction c. La Fig. 1 montre la projection de la structure du quartz α sur un plan perpendiculaire à l'axe c. Il apparaît nettement que dans cette structure il existe un large canal parallèle à l'axe ternaire. La photographie (Fig. 2) d'un modèle spatial, vu dans cette direction, illustre également la structure. Dans ce travail, seule la canalisation selon l'axe c a été étudiée; la recherche d'autres axes ou plans de canalisation, fait l'objet de travaux en cours.

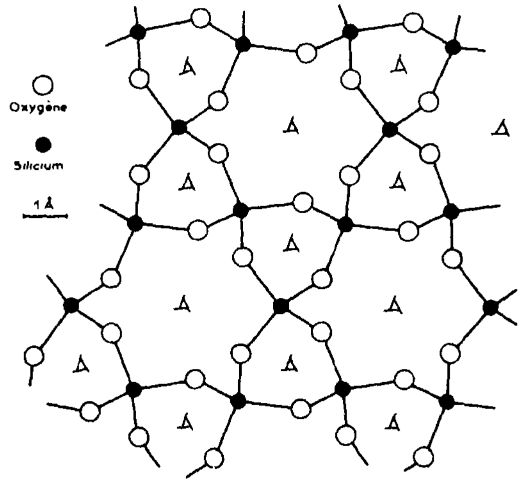

Fig. 1. Projection de la structure du quartz α sur un plan perpendiculaire à l'axe c. Le rayon des cercles représentant les atomes est à l'échelle (rayon d'écran de Thomas-Fermi).

TECHNIQUES EXPERIMENTALES

(*A*) *Préparation des échantillons*

Les échantillons sont des lames de quartz rectangulaires de 10 mm sur 20 mm, taillées perpendiculairement à l'axe c, ayant subi un polissage mécanique soigneux (poli optique), suivi d'une attaque chimique à l'acide fluorhydrique. Cette dernière élimine les défauts de surface induits par le traitement mécanique.

Une couche de carbone est déposée sur la surface étudiée, afin de la rendre conductrice, afin que l'évacuation des charges déposées par le faisceau soit assurée. Cette couche doit être assez épaisse pour éviter les claquages électriques, mais assez mince pour ne pas perturber le phénomène de canalisation. Le dépôt était effectué par évaporation sous vide à partir des pointes en contact de bâtonnets de carbone de qualité spectroscopique selon des techniques classiques. Les échantillons étaient exposés à l'évaporation par l'ouverture d'un cache pendant des temps de l'ordre de quelques secondes. La qualité de la couche de carbone déposée était estimée par une mesure de résistivité superficielle effectuée à l'air libre. L'expérience a montré qu'une résistivité de l'ordre de 1000 MΩ carré était suffisante pour éviter les claquages jusqu'à un courant de faisceau de l'ordre de 0,1 μA, le contact avec la couche étant assuré par deux plages de laque d'argent bordant la lame et séparées d'environ 15 mm. Cette résistivité évolue au cours du temps et n'est pas reliée de façon univoque à l'épaisseur de la couche, du moins pour les couches très minces envisagées ici (moins de 50 Å). L'épaisseur moyenne des couches, exprimée en masse par unité de surface, a été mesurée à l'aide de la technique de microanalyse par réactions nucléaires[4], appliquée au noyau C^{12}. Les valeurs trouvées étaient inférieures à 1 $\mu g/cm^2$. Cette quantité est du même ordre de grandeur que celle

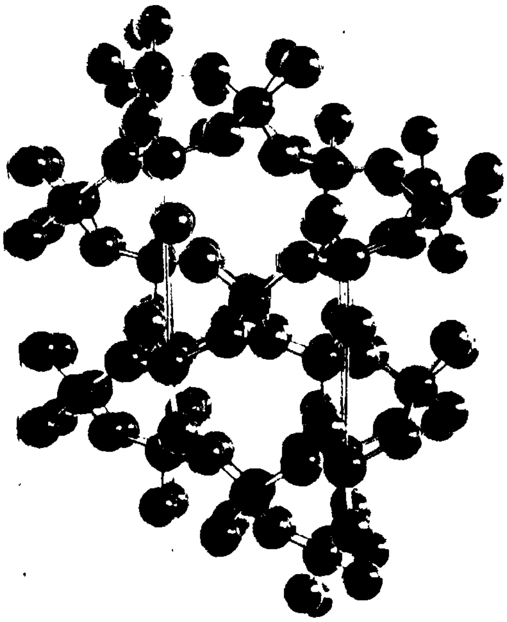

Fig. 2. Modèle du quartz α, vu dans la direction de l'axe *c* (les boules noires représentent les atomes de silicium).

déposée par le faisceau au cours de l'expérience par la contamination due au carbone provenant des gaz résiduels; elle semble assez faible pour que son effet sur les résultats puisse être négligé (voir plus bas).

(B) Appareillage experimental

(1) *Faisceau.* Le faisceau de deutons était fourni par l'accélérateur Van de Graaff de 2 MeV de l'Ecole Normale Supérieure. Sa divergence angulaire était inférieure à 1 mrad., le diamètre du point d'impact étant de 1 mm. L'énergie incidente, 900 KeV, est dans le voisinage d'un plateau des courbes d'excitation des réactions $O^{16}(d,p)O^{17*}$ [4, 5] et $O^{16}(d,d)O^{16}$ [7], ce qui améliore la précision des mesures [4, 5]. Le courant était de l'ordre de 30 nA, ce qui évitait l'échauffement et réduisait le dommage causé au cristal (voir plus bas). L'intégration du courant était effectuée à l'aide d'un intégrateur Modèle 1000 de Brookhaven Nuclear Instruments, fournissant des impulsions, qui permet de lire les doses sous forme digitale.

(2) *Détection.* L'angle d'observation, 150°, était tel que les particules sortantes n'étaient pas canalisées. Les détecteurs placés à 5 cm de la cible étaient de type Ortec à barrière de surface. Pour la réaction $O^{16}(d,p)O^{17*}$, le détecteur avait une surface de 1 cm^2 et une zone sensible de 150 μ [4]; une feuille de Mylar de 13 μ filtrait les deutons rétrodiffusés. Pour la diffusion élastique un détecteur de 25 mm^2 avec une zone sensible de 100 μ était diaphragmé à 2 mm pour limiter le taux de comptage. Un préamplificateur Ortec 109 A était utilisé; la contribution du bruit électronique à la largeur des raies mesurées était négligeable. Les détecteurs étaient reliés par leur masse à la masse de la chambre de réaction (Fig. 3). Le préamplificateur était alimenté par batteries et les signaux étaient transmis à travers un transformateur d'impulsions à haut isolement réalisé avec un tore en ferrite et bouclé sur un câble de 50 Ω terminé. Ce dispositif flottant évitait la fuite d'électrons secondaires vers le détecteur et permettait la mesure correcte des faibles courants mis en jeu dans l'expérience.

(3) *Orientation angulaire des cristaux et enregistrement des spectres.* Les spectres d'énergie des particules produites ont été enregistrés en fonction de l'angle de tir θ avec l'axe *c*. Le plan 'axe *c*—faisceau' ne correspondait à aucune direction privilégiée du quartz.

La variation de θ était obtenue au moyen d'un dispositif représenté schématiquement Fig. 3. Une vis micrométrique provoque la rotation du support de l'échantillon, l'axe passant par le point d'impact. A l'approximation des petits angles, θ varie linéairement avec le déplacement de la vis, laquelle est entraînée par un moteur pas à pas. Chaque saut du moteur provoque une variation $\Delta\theta$ de 0,1'. Ce dispositif permet de positionner l'échantillon avec une grande précision et de façon bien reproductible. L'ensemble de la chambre peut tourner autour d'un axe vertical, ce deuxième degré de liberté permettant d'aligner l'axe c avec le faisceau au début de l'expérience. Cette chambre ne permet pas de changer le point d'impact du faisceau sur l'échantillon en cours d'expérience. Comme on le verra, cela représente dans le cas du quartz un désavantage important. Une chambre plus perfectionnée de ce point de vue est en cours de réalisation.

Le dispositif décrit permet de relever les spectres en balayant les valeurs de θ, de façon entièrement automatique, l'axe des angles étant découpé en canaux de largeur $\Delta\theta$. L'intégrateur, qui fournit des impulsions en nombre proportionnel à la charge déposée, sert de pilote à l'expérience, assurant qu'à chaque largeur de canal $\Delta\theta$, correspond une charge fixe, selon les principes exposés dans la référence [8]. Les diviseurs 1 et 2 permettent de régler les doses par pas du moteur et par canal angulaire (Fig. 3). Les spectres successifs correspondant aux canaux θ_i sont stockés dans un bloc mémoire BM96 d'Intertechnique, fonctionnant en multispectre. On obtient

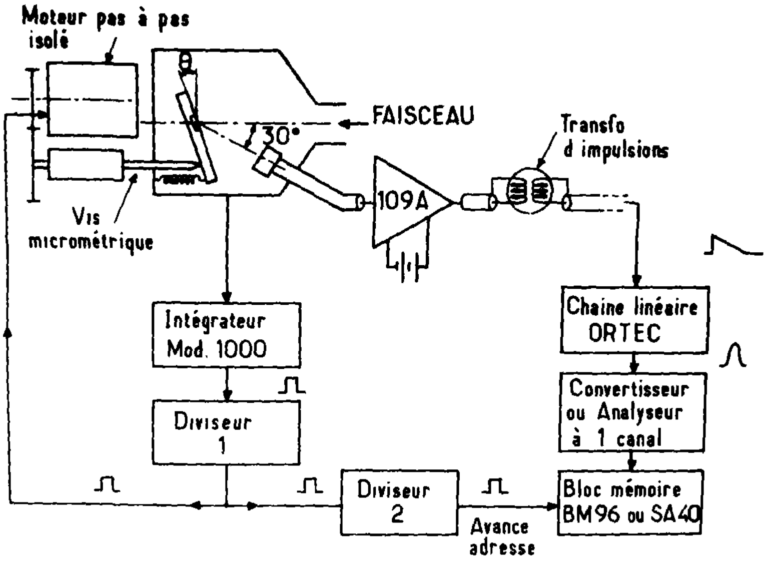

Fig. 3. Schéma de principe de l'appareillage.

ainsi une représentation bidimensionnelle du phénomène. On peut aussi choisir une bande d'énergie fixe et tracer seulement une courbe d'extinction; il suffit alors d'utiliser un analyseur monodimensionnel (de type SA40 ici). Les résultats présentés plus bas illustrent les possibilités du dispositif.

Remarquons que l'intégrateur Modèle 1000 a été modifié de façon à ramener la constante de temps à l'entrée de 1 à 0,03 sec, pour assurer une bonne corrélation temporelle entre l'entrée et la sortie. Par ailleurs, dans ce mode de fonctionnement, les indications de l'intégrateur ne sont justes qu'à un coup prés. Par conséquent, il faut régler l'intégrateur et les échelles, de telle sorte que le nombre total d'impulsions correspondant à un canal $\Delta\theta$ soit suffisamment élevé pour que cette incertitude soit négligeable. En prenant par exemple 250 coups par canal, on a une précision meilleure que 0,5% sur la dose; chaque canal est alors exploré pendant 5 sec environ.

(4) *Précautions pour éviter les dommages d'irradiation.* Les expériences préliminaires ont montré que le quartz est très sensible au faisceau et que les effets de canalisation évoluent rapidement au cours de l'irradiation. C'est pourquoi nous avons utilisé un courant aussi faible que le permettait l'accélérateur dont nous disposions, et des doses très réduites compatibles avec les statistiques. Pour minimiser les dommages, nous avons adopté une 'politique' d'irradiation soigneusement définie, imposée par le fait que le point d'impact ne pouvait être changé. La recherche de l'axe était effectuée en relevant par balayage automatique les courbes d'extinction relatives à la surface de l'échantillon (voir plus bas), avec des doses très faibles. Un alignement complet pouvait être obtenu avec une dose de 40 μCb au maximum (sur 1 mm^2). Plusieurs spectres étaient alors enregistrés à l'extinction avec 12 μCb pour chaque spectre. La comparaison des mesures successives permettait de vérifier que l'influence du dommage n'intervenait pas de facon sensible. Des spectres ont été alors enregistrés à des angles θ croissants, les spectres hors canalisation ($\theta \geqslant 2°$) étant enregistrés en dernier; les dommages éventuels n'intervenaient pas dans ce cas où la structure cristalline ne joue plus de rôle. Au cours de ces expériences, on n'a pas pu tirer pleinement parti des possibili-

tés de mesure automatique en représentation bidimensionnelle offertes par l'appareillage à cause de l'impossibilité de changer le point d'impact. De telles mesures, de courte durée, ont cependant été faites, illustrant la méthode (voir plus bas), mais présentant des statistiques trop faibles pour permettre une exploitation numérique satisfaisante. L'appareillage en construction permettra d'utiliser toutes les potentialités de cette technique de mesure.

RESULTATS EXPERIMENTAUX

Nous montrons et nous discutons ici une série de résultats bruts de l'expérience, confirmés par d'autres mesures. Leur dépouillement et leur interprétation seront examinés au chapitre suivant.

(*A*) *Diffusion élastique*

La Fig. 4 montre les spectres 'hors canalisation' ($\theta = 3°$) et 'en canalisation' ($\theta = 0°$) pour la diffusion élastique. Ce dernier spectre est la somme de 4 spectres partiels de 12 μCb sur lesquels aucune évolution due au dommage n'a été mise en évidence. La résolution en énergie, mesurée avec une cible mince d'or déposée sur aluminium est de 12,5 KeV. L'expérience a été effectuée avec une définition de 3,1 KeV par canal, mais dans la Fig. 4, les canaux ont été groupés deux à deux pour améliorer les statistiques. La séparation de l'effet du silicium de celui de l'oxygène apparaît clairement sur la figure; elle est illustrée encore par les pics provenant d'une couche mince, sans support, d'oxyde d'aluminium Al_2O_3 (les énergies maximales relatives à l'aluminium et au silicium ne diffèrent ici que de 5 KeV). On voit que l'extinction en surface (énergie maximale) est très forte, mais diminue avec la profondeur (énergies décroissantes, voir plus bas). Néanmoins, on note qu'à l'énergie maximale un petit pic apparaît sur le spectre en canalisation et que le spectre hors canalisation présente un léger soubresaut. Ce pic pourrait être attribué à la présence à la surface de l'échantillon d'une couche amorphe (et ne provoquant donc pas d'extinction) plus riche en silicium que SiO_2, SiO par exemple. Cette couche, dont l'épaisseur a été estimée à une cinquantaine d'Angström, pourrait être

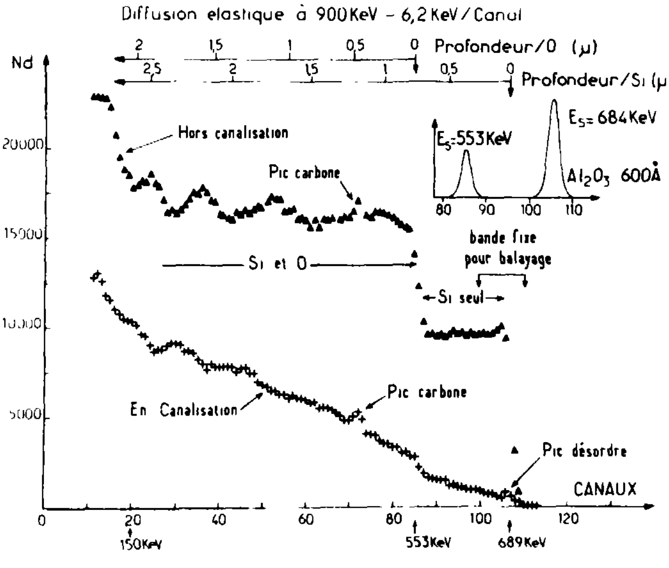

Fig. 4. Spectres hors canalisation et en canalisation pour la diffusion élastique.

un résidu insoluble de l'attaque chimique. On distingue également sur ces spectres un léger pic dû au carbone déposé sur l'échantillon. L'effet sur la canalisation de cette couche de carbone est négligeable devant celui de la couche amorphe SiO plus épaisse (en poids) et de Z plus élevé. On n'a donc pas à en tenir compte, comme nous l'avons déjà mentionné.

La Fig. 5 montre une courbe d'extinction correspondant aux coups provenant de la bande d'énergie indiquée sur la Fig. 4. Cette courbe a été relevée immédiatement après l'enregistrement des spectres en canalisation. D'autres spectres ont été ensuite enregistrés à des angles indiqués par une flèche sur la Fig. 5.

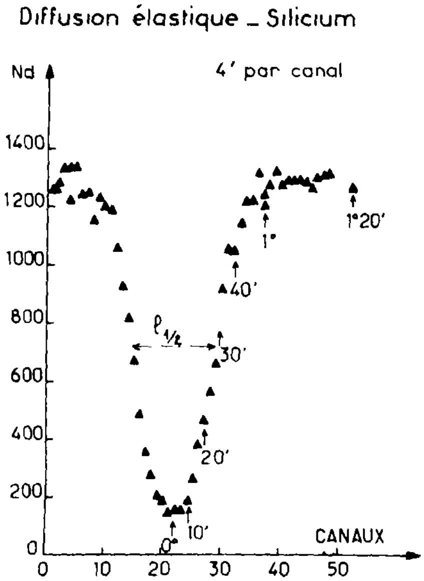

Fig. 5. Courbe d'extinction correspondant à la bande d'énergie indiquée sur la Fig. 4.

La Fig. 6 montre des résultats typiques en représentation bidimensionnelle. La 'surface d'extinction' $N = f(E, \theta)$ apparaît en perspective sur la Fig. 6(a). Sur la Fig. 6(b), plusieurs coupes de cette surface selon E et θ ont été visualisées par surbrillance. On distingue deux spectres hors canalisation, un spectre en canalisation et une courbe d'extinction relative à la surface. La Fig. 6(c) représente la projection sur le plan (E, θ) d'une coupe horizontale de cette surface, montrant le contour correspondant de la 'vallée d'extinction'. On se rend compte aisément qu'une telle 'surface d'extinction' contient toutes les données relatives au phénomène étudié.

(*B*) *Réaction* $O^{16}(d, p)O^{17*}$

La Fig. 7 montre les spectres hors canalisation ($\theta = 2°$) et en canalisation pour la réaction $O^{16}(d, p)O^{17*}$, obtenus de la même façon que dans le cas précédent. La résolution mesurée avec une cible mince d'oxyde anodique de tantale Ta_2O_5[4, 5] est de 41 KeV; le pic correspondant est également représenté sur la figure. Il est à noter que les deux courbes se rejoignent aux basses énergies indiquant qu'aux grandes profondeurs l'effet de canalisation ne se manifeste plus (voir plus bas).

La Fig. 8 montre une courbe d'extinction relative à la bande d'énergie indiquée sur la Fig. 7. Les angles auxquels des spectres ont été ensuite enregistrés sont également indiqués sur cette figure.

La Fig. 9 montre en relief des résultats typiques pour cette réaction. La Fig. 9(a) montre la surface vue dans la direction des énergies croissantes, laissant apparaître le 'col d'extinction'. La Fig. 9(b) montre quelques coupes de cette surface. La Fig. 9(c) montre la même surface vue du côté des angles croissants, la surbrillance ayant été utilisée pour dégager le spectre en canalisation et la cime de la surface.

(*C*) *Les effets du dommage par rayonnement*

A la fin de chaque cycle d'expériences, un spectre en canalisation a été enregistré. Ces spectres ont été pris après qu'une charge de faisceau de 220 μCb ait frappé le point d'impact, alors que les spectres des Fig. 4 et 7 correspondent à 40 μCb seulement. Les spectres relatifs à la diffusion élastique et

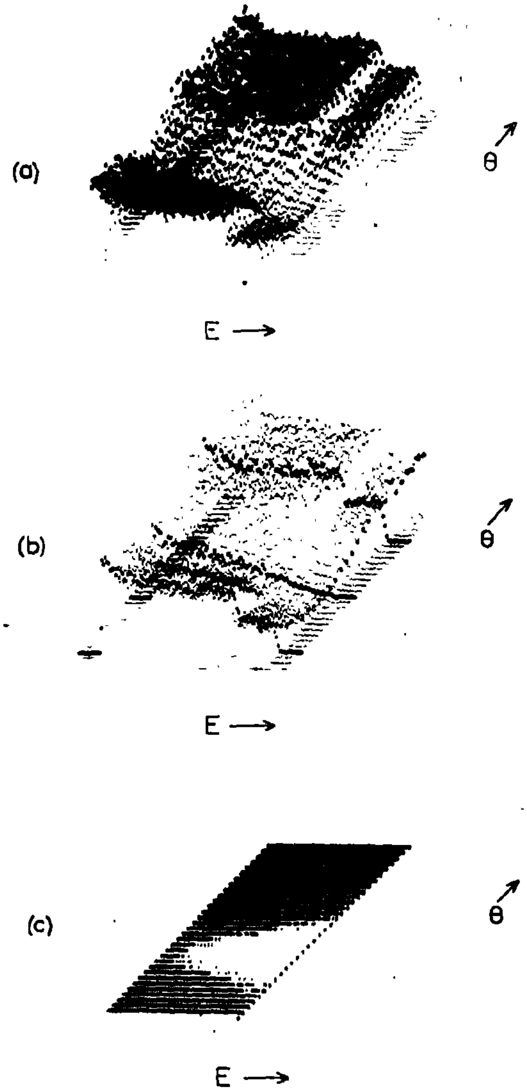

Fig. 6. Représentations bidimensionnelles de la surface d'extinction pour la diffusion élastique. Echelle: 6 keV/canal pour l'énergie E; 8'/canal pour l'angle θ.

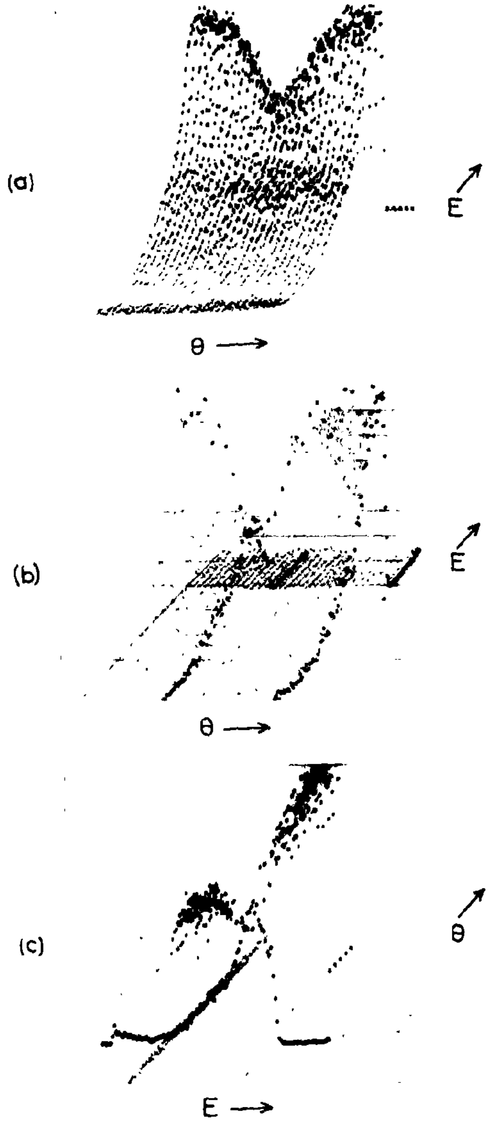

Fig. 9. Représentations bidimensionnelles de la surface d'extinction pour la réaction $0^{16}(d, p)0^{17*}$. Echelle: 13 KeV/canal pour l'énergie E, 4′/canal l'angle θ.

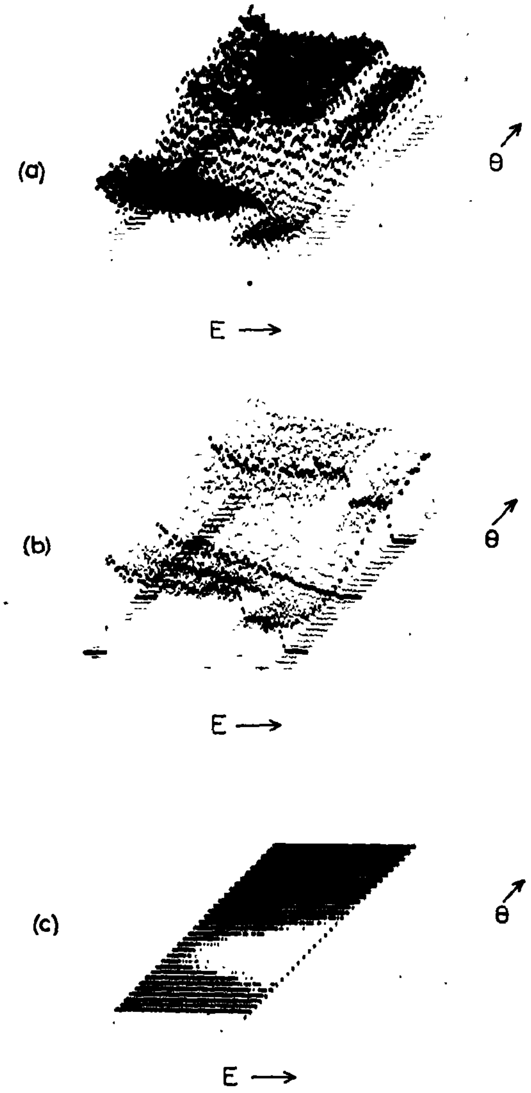

Fig. 6. Représentations bidimensionnelles de la surface d'extinction pour la diffusion élastique. Echelle: 6 keV/canal pour l'énergie E; 8'/canal pour l'angle θ.

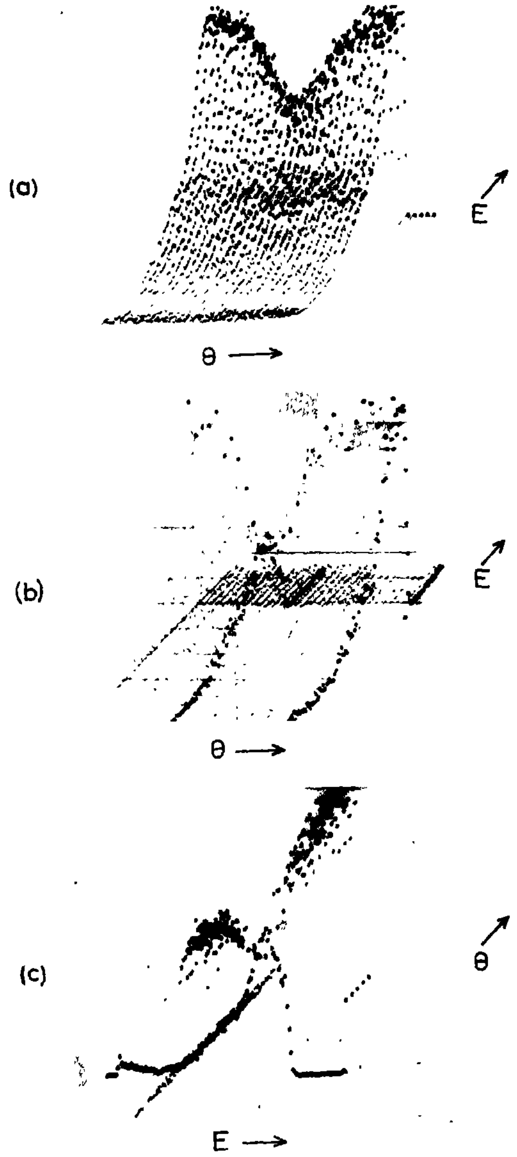

Fig. 9. Représentations bidimensionnelles de la surface d'extinction pour la réaction $0^{16}(d, p)0^{17*}$. Echelle: 13 KeV/canal pour l'énergie E, 4'/canal l'angle θ.

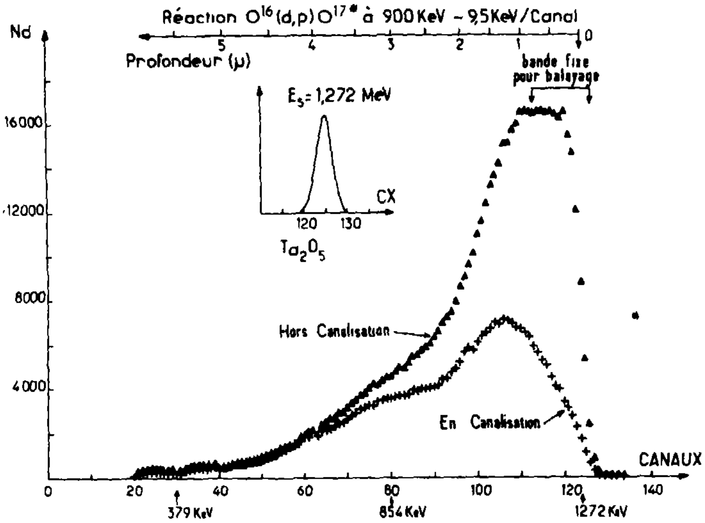

Fig. 7. Spectres hors canalisation et en canalisation pour la réaction $O^{16}(d,p)O^{17*}$.

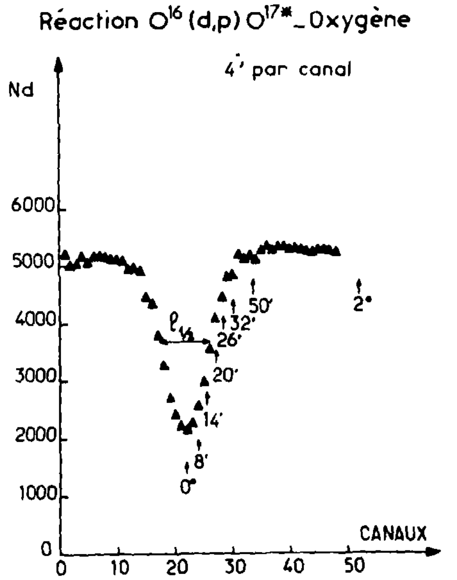

Fig. 8. Courbe d'extinction correspondant à la bande d'énergie indiquée sur la Fig. 7.

à la réaction $O^{16}(d,p)O^{17*}$ sont montrés dans la Fig. 10(a et b) comparés aux spectres des Fig. 4 et 7. Ces figures seront discutées plus loin.

INTERPRETATION DES SPECTRES

L'interprétation des spectres peut être faite ici de la même facon que lors des expériences de dosage par réaction nucléaire, où la concentration $C(x)$ d'un élément en fonction de la profondeur était recherchée[5]. La section efficace apparente peut être mise sous la forme: $\sigma_a[E(x)] = C(x)\cdot\sigma[E(x)]$, où $E(x)$ est l'énergie du deuton à la profondeur x, et σ la section efficace nucléaire. Le taux d'extinction pour $\theta = 0$ à la profondeur x vaut $\tau(x) = 1 - C(x)$. On voit que tout se passe comme si le noyau étudié avait une concentration variable avec x, égale à $C(x)$; hors canalisation, on a $C(x) \equiv 1$. Ainsi en négligeant la résolution finie du détecteur et les fluctuations de perte d'énergie, le spectre d'énergie observé $N(E_s)$ s'écrit[5]

$$N(E_s) = \left[C(x)\sigma[E(x)]\cdot\frac{\mathrm{d}x}{\mathrm{d}E_s}\right]\cdot cte \quad (1)$$

où $x = f(E_s)$, $f(E_s)$ exprimant la relation qui existe entre une énergie détectée E_s et la profondeur x à laquelle la réaction a eu lieu. Hors canalisation, $f(E_s)$ se calcule[5] à partir de la cinématique et des relations

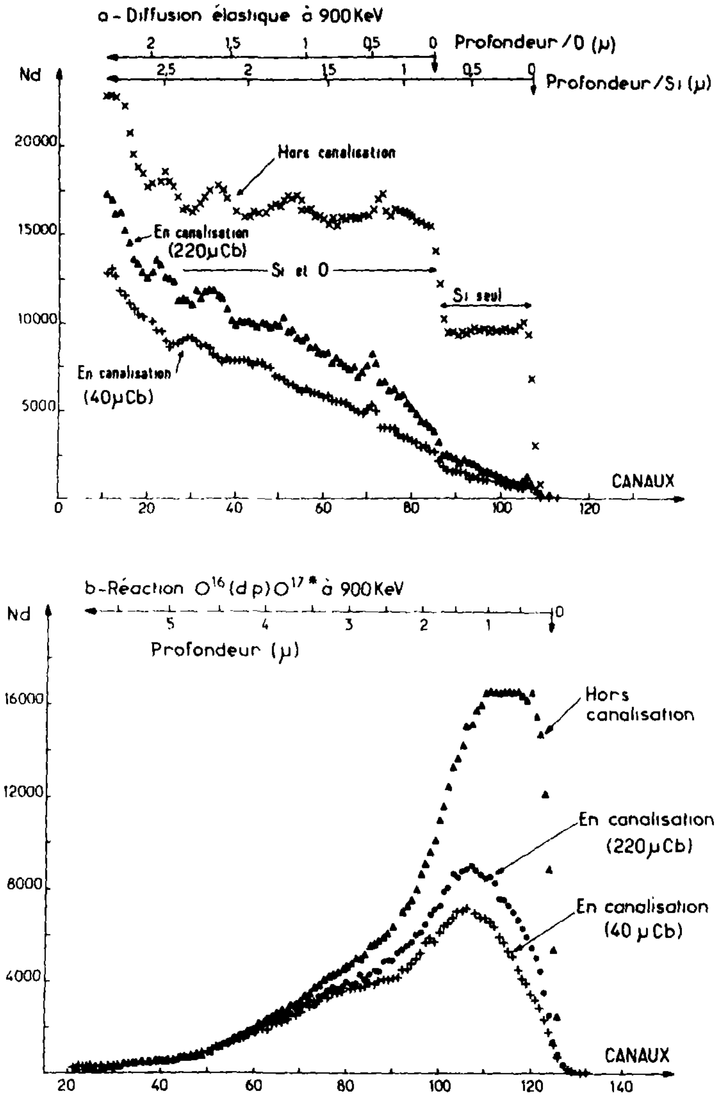

Fig. 10. Effet du dommage par rayonnement sur les spectres en canalisation.

parcours-énergie, et est sensiblement linéaire dans le domaine considéré. En canalisation, il n'y a plus de relation biunivoque entre E_s et x. En effet, avant de réagir, la particule a pu être canalisée sur une distance aléatoire $Y \leq x$, sur laquelle la perte d'énergie par unité de longueur, dE/dx, est réduite. $N(E_s)$ dépend donc ici de la forme même du spectre d'énergie des particules non canalisées à la profondeur x.

Un traitement complet de cet aspect aléatoire des pertes d'énergie, dû à l'effet de canalisation, sera exposé par ailleurs. Le calcul très simplifié qui suit, déjà évoqué dans la référence[3], permet une estimation de l'importance de cet effet.

Soient S le pouvoir d'arrêt normal et Z le pouvoir d'arrêt pour un deuton canalisé. On admettra que S est constant au voisinage de la surface. Il y a tout lieu de croire que Z dépend en particulier du paramètre d'impact de la particule incidente par rapport aux rangées atomiques, c'est à dire de la valeur de l'énergie transverse $E_\perp$[9] près de la surface. Z apparaît donc comme une variable aléatoire satisfaisant à $Z \leq S$. Plusieurs auteurs, dont Eisen[10], Appleton *et al.*[11] ont étudié le quotient $\alpha = Z/S$ et ont trouvé des valeurs voisines de 1/2 dans divers cristaux. En fait, ces valeurs représentent selon toute vraisemblance des valeurs moyennes. Dans le cas du quartz la dispersion de Z est probablement plus forte que dans le cas de cristaux monoatomiques, car, comme on le verra, les particules peuvent subir deux types de canalisation selon la valeur de $E_\perp$ (canalisation pour O et Si ou pour Si seulement).

Le deuton d'énergie incidente E_0 canalisé jusqu'à la profondeur Y, puis décanalisé et arrivant à la profondeur x, a subi une perte d'énergie égale à:

$$\Delta E_0 = YZ + (x-Y)S = xS - (S-Z)Y \quad (2)$$

Il réagit alors, soit par diffusion élastique, soit par réaction nucléaire, avec une énergie

$$E(x) = E_0 - \Delta E_0 \quad (3)$$

Il provoque l'émission d'une particule dont l'énergie peut s'écrire

$$E' = KE(x) + E'_0 \quad (4)$$

K et E'_0 étant des constantes obtenues par linéarisation de la relation cinématique.

La particule perd au retour une énergie:

$$\Delta E_s = \frac{x}{|\cos\varphi|} S' \quad (5)$$

où φ est l'angle d'observation par rapport au faisceau (l'échantillon étant quasi perpendiculaire à ce dernier) et S' le pouvoir d'arrêt normal pour la particule émise. L'énergie de la particule sortante, provenant de la profondeur x, est d'après [4]:

$$E_s(x) = KE(x) + E'_0 - \Delta E_s. \quad (6)$$

Dans le cas de la diffusion élastique $E_s(x)$ est directement enregistré et correspond aux canaux E_n sur l'analyseur. Dans le cas de la réaction $0^{16}(d,p)0^{17*}$ le Mylar interposé effectue une transformation sur $E_s(x)$ aisée à évaluer.

On a en définitive, par (2), (3), (5) et (6):

$$E_s(x) = KE_0 + E'_0 - K[xS - (S-Z)Y] - \frac{x}{|\cos\varphi|} S'. \quad (7)$$

Notant que $E(0) = E_0$, on tire de (4):

$$E_s(0) = KE_0 + E'_0 \quad (8)$$

et (7) peut s'écrire:

$$E_s(0) - E_s(x) = x\left[KS + \frac{S'}{|\cos\varphi|}\right] - KY(S-Z) \quad (9)$$

Le premier terme est la perte normale, le deuxième, Δ, représentant le défaut dû à la canalisation. Une première approximation consiste à remplacer ce terme par sa valeur moyenne $\bar{\Delta}_x$, prise sur le segment $[0, x]$

$$\bar{\Delta}_x = K\bar{Y}_x(S - \bar{Z}) \quad (10)$$

Bien entendu, $\bar{\Delta}_x$ dépend de x par $\bar{Y}_x$ ($\bar{Z}$ pouvant être supposé peu dépendant de x). Cette dépendance est liée au taux d'extinction $\tau(x)$ dans le cas d'un cristal monoatomique de façon simple, $\tau(x)$ déterminant la densité de probabilité de Y. Dans le cas d'un cristal diatomique la dépendance est certainement plus complexe (voir discussion). On obtient ainsi une nouvelle relation moyenne profondeurénergie, qui n'est pas connue *a priori*; un dépouillement rigoureux n'est donc possible que par des méthodes d'itération, avec, comme condition de départ, $\bar{Y}_x = 0$, par exemple.

Cependant, pour x grand, $\tau(x) \rightarrow 0$ et $\bar{Y}_x \rightarrow \bar{Y}_\infty$. La présence de ce terme correctif devrait conduire sur la Fig. 7 à un croisement des spectres en canalisation et hors canalisation. Ceci peut encore être exprimé en disant que les deutons canalisés sur une fraction de leur parcours atteignent une énergie donnée, donc une valeur donnée de la section efficace, à une profondeur plus grande que la normale, et la particule détectée, freinée davantage, a moins d'énergie; la courbe en canalisation devrait alors être translatée vers les basses énergies.

Comme aucun déplacement de cette sorte n'est observable sur la Fig. 7, on peut admettre ici que $\bar{Z}$ est assez voisin de S pour que $\bar{\Delta}_x$ ait une influence réduite. Cette observation nous a permis de négliger ici l'effet de la canalisation sur les pertes d'énergie dans les calculs d'interprétation et d'utiliser les mêmes échelles de profondeur pour les spectres en et hors canalisation (Fig. 4 et 7). Les calculs cidessus montrent cependant la nécessité, pour une interprétation plus rigoureuse des données, de déterminer $\bar{Y}_x$ et $\bar{Z}$ par le calcul ou, mieux, par l'expérience.

Les figures 11a et 11b montrent les valeurs calculées de τ correspondant aux Fig. 4 et 7; où on a pris:

$$\tau = 1 - \frac{N(E_s)\ \text{(en canalisation)}}{N(E_s)\ \text{(hors canalisation)}}. \quad (11)$$

Cette formule ne s'applique pas en toute rigueur si on tient compte de la résolution finie de l'instrument; l'effet de cette dernière est cependant négligeable, sauf au voisinage des discontinuités du spectre idéal[5], c'est à dire vers $x = 0$. Remarquons que la probabilité de décanalisation par unité de longueur pour une particule canalisée est:

$$\frac{1}{\tau}\frac{d\tau}{dx} = \left|\frac{d}{dx}\log\tau\right|. \quad (12)$$

En conséquence τ a été porté sur la Fig. 11 en représentation logarithmique, la pente des courbes étant proportionnelle aux probabilités de décanalisation. On voit que cette probabilité est sensiblement constante et que τ peut s'écrire sous la forme

$$\tau(x) = \tau_0 \exp\left(-\frac{x}{\lambda}\right). \quad (13)$$

La relation exponentielle a été utilisée pour déduire par extrapolation $\tau(0) = \tau_0$, c'est a dire le taux d'extinction maximale, près de la surface, qui n'est pas directement accessible à cause de la résolution finie du détecteur et de l'existence de la couche amorphe de désordre (dont l'effet est très visible sur la Fig. 11(a), vers la profondeur zéro par rapport au silicium).

Les valeurs de τ_0 et λ, ainsi que leurs erreurs statistiques, ont été déduites des résultats expérimentaux analogues à ceux de la Fig. 11, en utilisant une méthode de réduction par les moindres carrés pondérés[12], en se limitant au domaine obéissant effectivement à la loi linéaire, c'est à dire que nous n'avons pas tenu compte des points situés près de la surface. Dans le cas de la diffusion élastique, nous n'avons exploité que la partie de la courbe correspondant au silicium seul (Fig. 11(a)). Nous avons obtenu ainsi des valeurs de τ_0 et de λ, relatives à l'oxygène et au silicium, pris séparément. Les Tableaux 1 et 2 regroupent les valeurs des τ_0 et λ pour les différents angles (les valeurs des λ étant données avec les réserves faites au sujet des échelles de profondeur elles-mêmes; voir discussion). Nous donnons, à titre indicatif, les λ pour quelques valeurs de θ; lorsqu'on s'écarte de la position $\theta = 0°$, λ perd rapidement sa signification physique.

Finalement, les spectres pris à divers θ ont permis de tracer les courbes d'extinction $\tau(x, \theta)$ (Fig. 12(a) et 12(b), d'où ont été déduites les largeurs à mi-hauteur $l_{1/2}(x)$ des courbes d'extinction en fonction de θ, pour les noyaux O^{16} et Si (Fig. 13).

a-Diffusion élastique — Ed = 900 KeV - 6,2 KeV par canal

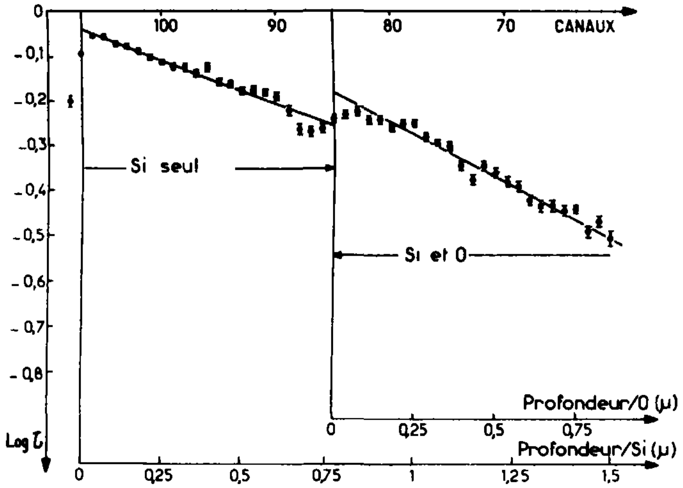

b-Réaction $O^{16}(d,p)O^{17*}$ - Ed = 900 KeV - 9,5 KeV par canal

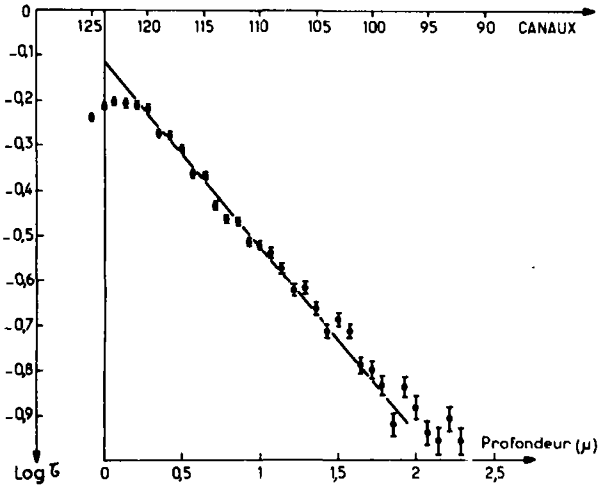

Fig. 11. Taux d'extinction en fonction de la profondeur, en canalisation.

DISCUSSION

(A) Interprétation des spectres

On peut estimer la limite supérieure de l'erreur commise sur les λ en négligeant le terme $\bar{\Delta}_x$ (formule 10) de la façon suivante. L'erreur sur λ provient de celle sur l'échelle des profondeurs adoptée, qui est déterminée par (9). L'erreur relative sur cette échelle vaut dans les hypothèses ci-dessus:

$$\epsilon = \frac{K\,\bar{Y}_x(S-\bar{Z})}{x\left[KS+\frac{S'}{|\cos\varphi|}\right]} = \frac{\bar{Y}_x}{x}\,\frac{1-\bar{Z}/S}{1+\frac{S'}{S\,K|\cos\varphi|}}. \quad (14)$$

Y ayant une distribution de type exponentiel (puisque déterminée par $\tau_0(x)$ et $\tau_{Si}(x)$), on

Tableau 1. τ_0 *et* λ *pour l'oxygène** (*réaction nucléaire*)

Dose reçue μCb	Dose μCb	θ	τ_0	λ
38	24	0°(E.C.)	0,8945 ± 0,0035	2,43 ± 0,03
62	24	0°(E.C.)	0,887 ± 0,004	2,40 ± 0.05
86	12	8'	0,851 ± 0,004	2,23 ± 0,05
110	12	14'	0,636 ± 0,006	1,69 ± 0,05
122	12	20'	0,355 ± 0,008	
134	12	26'	0,150 ± 0,008	
146	12	32'	0,080 ± 0,010	
158	12	50'	0,00 ± 0,01	
170	48	2°(H.C.)	0	
218	12	0°(E.C.)	0,759 ± 0,005	2,14 ± 0,05

*erreurs indiquées égales à l'écart quadratique moyen.

Tableau 2. τ_0 *et* λ *pour le silicium** (*diffusion élastique*)

Dose reçue μCb	Dose μCb	θ	τ_0	λ
40	24	0° (E.C.)	0,968 ± 0,002	3,90 ± 0,13
67	24	0° (E.C.)	0,967 ± 0,002	4,22 ± 0,15
94	12	10'	0,965 ± 0,002	3,28 ± 0,15
106	12	20'	0,917 ± 0,004	1,14 ± 0,03
121	12	30'	0,563 ± 0,008	0,778 ± 0.038
133	12	40'	0,246 ± 0,011	
151	12	60'	0.074 ± 0,016	
163	12	100'	0,00 ± 0,02	
175	48	3° (H.C.)	0	
223	12	0°(E.C.)	0,953 ± 0,003	2.77 ± 0,10

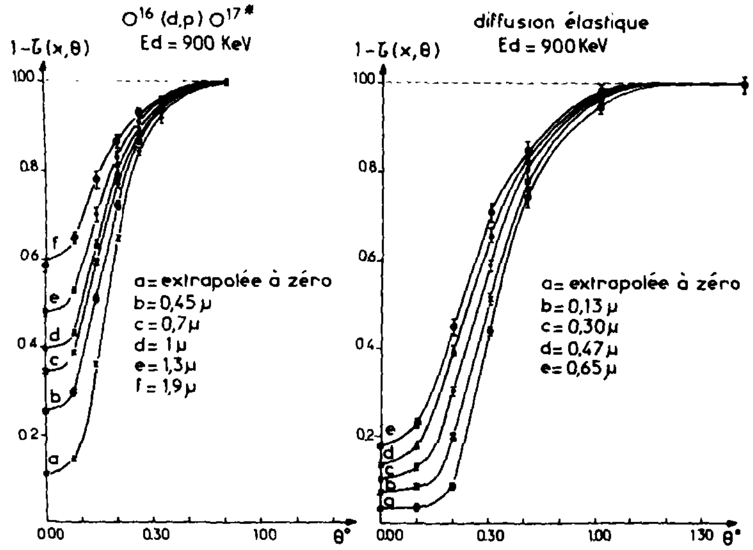

Fig. 12. Taux d'extinction en fonction de l'angle θ du faisceau avec l'axe c, pour quelques profondeurs.

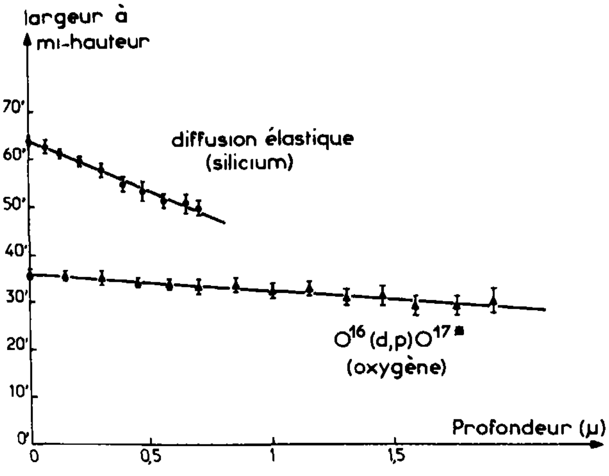

Fig 13. Largeur à mi-hauteur des courbes d'extinction en fonction de la profondeur.

peut écrire

$$\frac{\bar{Y}_x}{x} < \frac{1}{2} \qquad (15)$$

Pour déterminer l'erreur due à l'hypothèse $\bar{Z} = S$, on prendra pour $\bar{Z}$ la valeur indiquée dans les références [10] et [11], qui fournit:

$$1 - \frac{\bar{Z}}{S} \simeq \frac{1}{2}. \qquad (16)$$

L'erreur calculée ainsi représente donc une limite supérieure largement estimée. Ainsi,

$$\epsilon < \frac{1}{4v} \quad \text{avec} \quad v = 1 + \frac{S'}{SK|\cos\varphi|} \qquad (17)$$

v se calcule aisément et vaut ici 2,6 pour la diffusion élastique et 1,7 pour la réaction $O^{16}(d,p)O^{17*}$.

On a donc $\epsilon < 10\%$ pour le silicium et $\epsilon < 15\%$ pour l'oxygène. Encore faut-il remarquer que ϵ joue toujours dans le même sens et que les λ sont donc *sous-estimés* avec la marge d'erreur maximale indiquée.

Cette méthode de calcul des échelles de profondeur diffère essentiellement de celle où l'on admettrait que la particule qui réagit à la profondeur x a été canalisée sur l'intégralité de son parcours, ce qui revient à poser $Y \equiv x$. Une telle hypothèse implique que toute particule provoque une réaction nucléaire ou une diffusion à grand angle dès qu'elle est décanalisée. En fait, la probabilité pour une particule de provoquer de telles réactions est très faible, inférieure à quelques 10^{-4}. La présence de la variable aléatoire Y dans les formules (3) ou (9) implique l'existence, en position de canalisation, d'un continuum dans le spectre d'énergie des particules, à une profondeur x, de forme dépendant des $\tau(x)$, s'étendant entre deux pics, l'un relatif aux particules non canalisées dès la surface, l'autre relatif aux particules canalisées jusqu'à x. Les spectres observés par Appleton *et al.*[11] semblent confirmer ce raisonnement. Des expériences sont en cours pour étudier le comportement détaillé de Y, pour mesurer $\bar{Y}_x$ et $\bar{Z}$ et pour vérifier les calculs du type exposé ci-dessus.

(B) Largeurs à mi-hauteur

Les largeurs à mi-hauteur des courbes d'extinction près de la surface (relevées sur les courbes extrapolées de la Fig. 12) valent 64′ pour le silicium et 36′ pour l'oxygène. Les balayages automatiques des Fig. 5 et 8 fournissent les mêmes chiffres, ce qui confirme le peu d'influence du dommage par rayonnement sur ces résultats, puisque ces balayages ont été réalisés après une dose d'environ 200 μCb. La formule classique de Lindhard[9] fournit des angles critiques Ψ_1 de 43′ pour le silicium et de 33′ pour l'oxygène; le quotient $l_{1/2}/\Psi_1$ valant 1,5 et 1,1 respectivement. Le rapport de ces largeurs à mi-hauteur (1,78) est supérieur au rapport théorique (1,33, racine carré du rapport des Z).

Lorsque la particule pénètre dans le cristal, elle prend instantanément une énergie transverse[9]

$$E_\perp = E_0\psi^2 + U(\mathbf{r}) \qquad (18)$$

où Ψ est l'angle du faisceau avec l'axe c, $\mathbf{r}$ définit la position du point d'entrée de la particule dans le réseau et $U(\mathbf{r})$ le potentiel d'interaction cristallin. Comme toutes les valeurs de $\mathbf{r}$ sont également probables, $U(\mathbf{r})$ se présente comme une variable aléatoire U dont la loi $f(u)\,\mathrm{d}u$ est déterminée par la fraction de la surface du canal pour laquelle $U(\mathbf{r})$ est comprise entre u et $u+\mathrm{d}u$. $f(u)$ peut donc être déduite des équipotentielles de $U(\mathbf{r})$; on peut s'en faire une idée d'après la Fig. 14 où sont tracées quelques équipotentielles, calculées en utilisant les potentiels de corde de Molière[13] pour un réseau statique. $E_\perp$ possède donc elle-même un spectre continu, dépendant du paramètre ψ, lié au spectre de U par (18), et appelé 'facteur de transmission' par Lindhard[9]. Un choc élastique entre une particule et une rangée d'atomes est impossible si $E_\perp$ est inférieure à une certaine énergie critique qui dépend de la nature de cette rangée. On dit alors que la particule est canalisée *par rapport* à cette rangée. Dans le cas étudié ici, il existe deux types de rangées, l'une constituée entièrement d'atomes d'oxygène, l'autre de silicium (Fig. 1 et 2), les énergies critiques correspondantes étant $E_\perp^{\mathrm{O}}$ et $E_\perp^{\mathrm{Si}}$ Les valeurs de ces constantes peuvent être évaluées par la formule de Lindhard qui fournit pour une rangée isolée $E_\perp^{\mathrm{O}} = 42{,}5$ eV et $E_\perp^{\mathrm{Si}} = 74{,}5$ eV. Il apparaît clairement sur la Fig. 14 qu'une certaine fraction des particules incidentes tombant au voisinage d'une rangée d'atomes de silicium se retrouve d'emblée avec une $E_\perp$ proche de l'énergie critique pour l'oxygène $E_\perp^{\mathrm{O}}$. La courbe d'extinction pour l'oxygène déterminée par la condition tirée de (18)

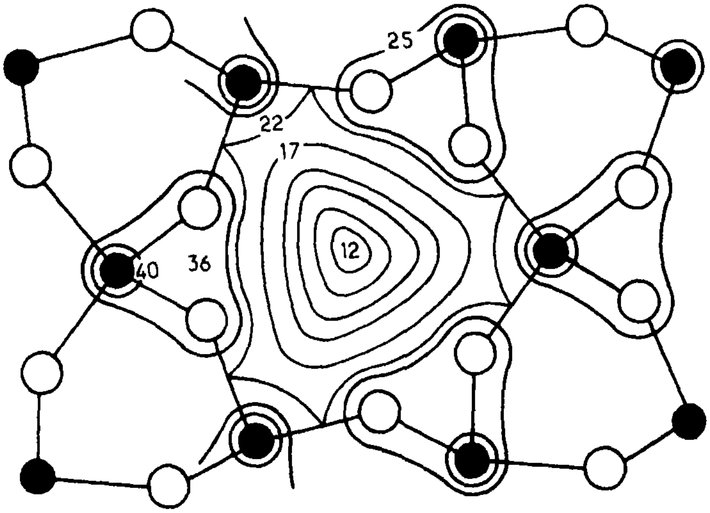

Fig. 14. Répartition du potentiel d'interaction particule-cristal dans le quartz.

$$E_0\psi^2+U \leq E_\perp^0 \qquad (19)$$

s'en trouve rétrécie, puisque pour les grandes valeurs de U même une faible variation de ψ projette des particules correspondantes dans le mode décanalisé, pour l'oxygène. Rien de tel ne se produit pour le silicium.

Ce raisonnement qui explique qualitativement la faible valeur de $l_{1/2}$ pour l'oxygène permet également d'expliquer la forme des courbes d'extinction extrapolées près de leur minimum (Fig. 12), la courbe relative au silicium étant à fond plat, ce qui n'est pas le cas pour l'oxygène.

La variation des largeurs à mi-hauteur avec la profondeur (Fig. 13) est sensiblement linéaire. Ces résultats sont analogues à ceux de Davies *et al.*[14]. On observe que $l_{1/2}$ décroît plus vite pour Si que pour O; il semble qu'aux grandes profondeurs le phénomène de décanalisation sous-jacente soit dominé par l'oxygène (voir plus bas). Une théorie détaillée du processus de décanalisation serait nécessaire pour interprêter ces résultats de facon plus approfondie.

(*C*) *Extinctions maximales*

Les Tableaux 1 et 2 fournissant les valeurs de τ_0 en canalisation: 96,8% pour le silicium et 89% pour l'oxygène. Ces valeurs extrapolées caractérisent l'extinction près de la surface, l'influence des tout premier plans cristallins et de la couche amorphe superficielle étant éliminée: elles se comparent donc directement à celles estimées par la théorie[9]. L'influence que la couche amorphe exerce par la diffusion multiple du faisceau reste néanmoins. Nous ferons ici l'hypothèse qu'elle n'intervient que peu, car la couche est très mince; une étude détaillée de l'influence de telles couches amorphes est en cours.

Les courbes d'extinction 5 et 8 fournissent des valeurs plus faibles; ceci est dû au rendement résiduel de la couche amorphe dont la contribution n'est pas éliminée ici et à l'effet de l'intégration sur une épaisseur finie du cristal. Nous utiliserons donc les valeurs extrapolées pour définir les rendements minimaux correspondants: $\chi_{Si} = 0{,}032\pm0{,}002$ et $\chi_O = 0{,}110\pm0{,}005$, les erreurs indiquées étant des erreurs statistiques. Ces valeurs doivent être comparées aux estimations théoriques[9], modifiées pour tenir compte du cas particulier d'un cristal diatomique. En considérant d'abord le réseau statique on peut écrire en effet, d'après les raisonnements du paragraphe précédent:

$$\chi_O = N\pi(2a^2+b^2) \qquad (20)$$

où N est le nombre de groupes SiO_2 par unité de surface dans un plan cristallin, a le rayon d'écran de Thomas–Fermi pour l'oxygène et b le rayon de l'équipotentielle autour d'une rangée de silicium où le potentiel est égal à l'énergie critique $E_\perp^0$. Une formule similaire est applicable au silicium. On a pour l'oxygène $a = 0{,}195$ Å et une grossière estimation de b peut être tirée de la Fig. 14, $b = 0{,}23$ Å ce qui conduit à $\chi_O = 0{,}06$. Pour le silicium l'estimation de b est plus difficile, mais ici $b < a$, et une erreur sur b est moins grave. On a: $a = 0{,}17$ Å et on prendra à titre indicatif $b = 0{,}1$ Å, ce qui conduit à $\chi_{Si} = 0{,}022$. On obtient pour χ_{exp}/χ_{calc}, 1,8 pour l'oxygène et 1,5 pour le silicium. Ces écarts peuvent être attribués d'une part aux éventuelles imperfections du cristal (y compris les dommages), d'autre part aux effets de la température. Les valeurs de l'amplitude quadratique moyenne des vibrations atomiques dans le quartz ont été données par Young et Post[15]. Ces amplitudes sont nettement plus grandes pour l'oxygène que pour le silicium et il n'est donc pas étonnant de trouver que l'écart relatif est plus grand dans le premier cas que le second. Une étude du comportement des τ_0 en fonction de la température est nécessaire pour préciser l'interprétation.

(*D*) *Décanalisation*

Lorsqu'on observe les phénomènes, non plus en surface mais en fonction de la profondeur, on aborde le problème de la décanalisation, le plus complexe du point de vue théorique. Evoquée à propos des échelles de profondeur et des largeurs à mi-hauteur, cette question est fondamentale pour l'interprétation des $\tau(x)$, de leur forme exponentielle et des λ correspondants. Là encore, en l'absence d'une théorie complète, nous *nous limiterons à une discussion qualitative. La décanalisation* est un effet de diffusion multiple dû aux perturbations des rangées atomiques causées en particulier par les vibrations thermiques. Elle peut être décrite comme un processus stochastique, plus précisément un mouvement brownien (diffusion avec migration) sur l'axe $E_\perp$. Cela signifie que le phénomène est gouverné par l'évolution du spectre de probabilité de $E_\perp$ en fonction de la profondeur x, le facteur de transmission représentant la condition initiale pour $x = 0$. Les énergies critiques $E_\perp^{O}$ et $E_\perp^{Si}$ jouent le rôle de barrières parfaitement absorbantes, le domaine compris entre $E_\perp^{O}$ et $E_\perp^{Si}$ correspondant à un changement de régime où un choc inélastique avec les rangées d'oxygène est déjà possible, tout en étant encore exclu avec les rangées de silicium. Cette description laisse prévoir que $\lambda_O < \lambda_{Si}$ puisque $E_\perp^{O} < E_\perp^{Si}$ et que le facteur de transmission défavorise la canalisation pour l'oxygène dès le départ, comme on l'a décrit plus haut. Ce raisonnement montre aussi qu'à une faible largeur à mi-hauteur est associé un faible parcours moyen λ. Expérimentalement (Tableaux 1 et 2) $\lambda_O/\lambda_{Si} = 0{,}6$. Il est à noter que, en surface, $\Gamma^{O}_{1/2}/\Gamma^{Si}_{1/2} = 0{,}56$. Ces deux valeurs sont voisines, ce qui est à remarquer; néanmoins aucune conclusion générale ne peut en être tirée, dans l'état actuel des travaux. Le fait que la loi de $\tau(x)$ soit exponentielle ne peut être expliqué par ces considérations seules; cela n'a d'ailleurs été établi que dans un domaine de profondeurs relativement limité.

Il est à remarquer que la grande amplitude des vibrations des atomes d'oxygène tend encore à augmenter leur rôle dans le processus de décanalisation. Ceci n'a pourtant pas une influence directe sur λ_O, mais joue indirectement, en déterminant l'évolution du spectre de $E_\perp$.

(*E*) *Dommages par rayonnement*

Les mesures en canalisation faites au début et à la fin de chaque cycle d'expériences donnent une idée de la façon dont agit l'irradiation sur le phénomène d'extinction. Les tableaux 1 et 2 présentent les résultats correspondants aux courbes de la Fig. 10. Il apparaît que pour une dose de 220 μCb sur 1 mm^2, soit $1{,}3.10^{17}$ deutons par cm^2, χ^O passe de 0,11 à 0,24 et χ_{Si} passe de 0,032 à 0,047. La variation relative est beaucoup plus importante pour l'oxygène que pour le silicium. Cela peut signifier qu'un nombre plus important d'atomes d'oxygène que de silicium a été déplacé en position interstitielle. Cela n'est pas étonnant car, comme le montrent les Fig. 1 et 2, les atomes de silicium sont à l'intérieur de tétraèdres SiO_4 ce qui leur assure une stabilité de position plus grande que celle de l'oxygène. Dans les mêmes conditions, λ_O passe de 2,4 μ à 2,1 μ et λ_{Si} passe de 4 μ à 2,8 μ. Cette fois ci l'effet est nettement plus fort pour le silicium, les deux λ tendant à se rapprocher. Des mesures systématiques sont nécessaires pour tenter d'interprêter ces résultats. Observons seulement que la dose intégrée n'est pas le seul paramètre puisque l'expérience a montré que le dommage pour une même dose croît avec l'intensité du courant de faisceau.

CONCLUSION

Des indications ont été obtenues sur la façon dont se combinent les effets des deux sous-réseaux oxygène et silicium. Il apparaît que la présence de rangées d'atomes de silicium a pour effet de rétrécir la courbe d'extinction et d'augmenter le rendement minimal relatifs aux rangées d'oxygène. Des expériences plus détaillées sur le quartz et portant sur d'autres oxydes cristallins devraient permettre d'approfondir et de généraliser les interprétations qui ont conduit à ces conclusions.

Remerciements—Nous tenons à exprimer nos remerciements à M. E. Girard pour sa précieuse contribution à la mise au point de l'appareillage électronique utilisé au cours de ce travail.

REFERENCES

1. BRICE D. K. et SATTLER A. R., *Bull. Am. phys. Soc.* **11**, 177 (1966).
2. SATTLER A. R. et DEARNALEY G., *Phys. Rev.* **161**, 2, 244 (1967).
3. PALMER D. W. et d'ARTEMARE E., *Phil. Mag.* **17**, 1195 (1968)
4. AMSEL G. et SAMUEL D., *Anal. Chem.* **39**, 1689 (1967)
5. AMSEL G., BÉRANGER G., DE GELAS B. et LACOMBE P., *J. appl. Phys.* **39**, 5, 2246 (1968); NADAI J. P., Thèse 3ème cycle, Paris (1967).
6. WYCKOFF R. W. G., *Crystal Structures*, Vol. 1, p.312. Interscience N.Y. (1963).
7. AMSEL G., *Annl. Phys.* **9**, 297 (1964).
8. AMSEL G. et d'ARTEMARE E., *I.E.E.E. Trans. Nucl. Sci.* **NS-14**, 189 (1966).
9. LINDHARD J., *Mat. Fys. Medd. Dan. Vid. Selsk.* **34**, N°14 (1965).
10. EISEN F. H., *Phys. Rev. Lett.* **23**, 401 (1966).
11. APPLETON B. R., ERGINSOY C. et GIBSON W. M., *Phys. Rev.* **161**, 330 (1967).
12. ROSE M. E., *Phys. Rev.* **91**, 610 (1953).
13. MOLIÈRE G., *Z. Naturf.* **2a**, 133 (1947).
14. DAVIES J. A., DENHARTOG J. et WHITTON A. J., *Phys. Rev.* **165**, 345 (1968).
15. YOUNG R. A. et POST B., *Acta crystallogr.* **15**, 337 (1962).

Note sur epreuve: Les phénomènes de décanalisation ont été récemment décrits à l'aide d'un modèle de diffusion à rapprocher de celui exposé au paragraphe (*D*) de la discussion du présent article: "A diffusion model of escape from channels" by FELDMAN L. C., APPLETON B.R. and BROWN W. L., publié dans *Proceedings of the International Conference on Solid State Physics Research with Accelerators*, September 1967, BNL 50083 (C 52), pp. 58–73 (1968). La comparaison de nos résultats avec les calculs de ces auteurs est à l'étude.

J. Phys. Chem. Solids Pergamon Press 1969. Vol. 30, pp. 705–711. Printed in Great Britain.

THE DEFECT CONTRIBUTION TO THE EXCESS ENTHALPY OF URANIUM DIOXIDE-CALCULATION OF THE FRENKEL ENERGY*

R. SZWARC

General Electric Company, Nuclear Systems Programs, Cincinnati, Ohio 45215, U.S.A.

(*Received* 20 *May* 1968; *in revised form* 15 *July* 1968)

Abstract—An equation for the enthalpy of UO_2 was derived from earlier data. It is comprised of a lattice parabolic segment to which was added an enthalpy exponential term.

$$H_T = -5601{\cdot}5 + 17{\cdot}78T + 1{\cdot}02 \times 10^{-3}T^2 + 71300\sqrt{2}\exp\frac{14{\cdot}83}{2R}\exp\frac{-71300}{2RT}.$$

This equation agrees well with the experimental data up to the melting point of UO_2. The formation energy and entropy of Frenkel pairs in UO_2 were derived from the high temperature data to be 71,300 ± 2.200 cal mole^{-1} and 14·83 ± 0·84 cal mole^{-1} deg^{-1}, respectively. The model is based upon the assumption that disordering occurs on the oxygen sublattice only and that oxygen Frenkel defects predominate.

1. INTRODUCTION

RECENTLY the enthalpy measurements of UO_2 were obtained for the first time up to and above the melting point[1]. A rapid rise in enthalpy was observed for specimens quenched from above 2300°K, higher than that predicted for a perfect lattice. A similar anomalous effect in the specific heat of silver halides was predicted by Mott and Gurney[2] and has actually been observed in AgBr[3] and AgCl[4]. Similar observations in metals [5] have also been made. In metals, in addition to excess enthalpy, excess thermal expansion has also been observed. These effects can be interpreted by postulating the formation of point defects; they occur in the temperature range where the concentration of imperfections increases markedly, and, of course, the formation of defects is a thermally activated process. Both Frenkel and Schottky defects may be expected to affect the high temperature specific heat of solids, but excess thermal expansion behavior can be explained only in terms of Schottky defects[6]. In uranium dioxide both Schottky and Frenkel defects may exist. Comparison of bulk and X-ray thermal expansion coefficients[7,8] has not provided an unambiguous identification of the defect structure; in this paper it is assumed that only oxygen Frenkel defects are present, and that the uranium sublattice is perfect. From this assumption, and the observed excess enthalpy, the energy for defect formation (Frenkel energy for the case of UO_2) may be calculated.

2. EXPERIMENTAL RESULTS

The enthalpy measurements were carried out by means of the drop calorimetric technique. Stoichiometric UO_2 specimens sealed by electron beam welding in tungsten capsules were heated in a hydrogen atmosphere and dropped into an adiabatic calorimeter. The enthalpy of a specimen was determined by the difference in heat content between a loaded and empty capsule. The specimens were prepared from 99·9 per cent pure UO_2 powder which was cold pressed into pellets and sintered for 5 hr at 1980°K in hydrogen.

---

*This paper originated from work sponsored by the Fuels and Materials Development Branch, Atomic Energy Commission, under Contract AT(40-1)-2847.

The O/U ratio as-sintered was 2·003 ± 0·003 and was found unchanged after the measurements within the error limits of the chemical analysis. A more detailed description of the experimental method and treatment of the data were published elsewhere[1].

The enthalpy data obtained are given in Table 1, where, in addition to the heat content, the mean heat capacity defined by $H_T - H_{298}/T - 298$, is noted for each drop temperature. A plot of the mean heat capacity (Fig. 1) clearly shows the anomalous enthalpy effect. Figure 2 shows the temperature dependence of the excess enthalpy. The excess is derived by fitting the low temperature enthalpy data to a parabolic equation of the form

$$H_T = a + bT + cT^2 \qquad (1)$$

and the overall data to equation (2)

$$H_T = a + bT + cT^2 + \Delta H_F \, \xi'; \qquad (2)$$

where ΔH_F is a constant and ξ' depends exponentially on T.

3. THEORETICAL CONSIDERATIONS

Uranium dioxide has a fluorite structure which is characterized by large interstitial

Table 1. Comparison of actual enthalpy with values calculated from equation (13) and mean heat capacity calculated from the actual enthalpy

Temperature (°K)	Actual enthalpy (cal/g mole)	Calculated enthalpy (cal/g mole)	Mean heat capacity (cal/mol-°K)
1174	16,660	16,775	19·02
1273	18,660	17,751	19·14
1331	19,950	19,919	19·33
1427	21,870	21,872	19·37
1503	23,440	23,439	19·57
1648	26,792	26,498	19·63
1679	27,320	27,166	19·78
1776	29,430	29,297	19·91
1869	31,480	31,408	20·05
1950	33,210	33,311	20·10
2073	36,260	36,336	20·43
2124	37,770	37,646	20·68
2235	40,740	40,624	21·00
2341	43,200	43,649	21·14
2409	45,360	45,629	21·52
2501	48,110	48,595	21·84
2526	48,820	49,413	21·85
2577	50,540	51,112	22·17
2582	51,170	51,292	22·40
2613	52,410	52,360	22·64
2640	53,460	53,307	22·82
2641	53,760	53,343	22·94
2680	55,510	54,740	23·30
2741	57,460	56,995	23·52
2774	57,830	58,250	23·36
2843	61,370	60,958	24·11
2884	63,450	62,620	24·53
2936	64,720	64,788	24·55
2976	66,740	66,501	24·92
3011	68,390	68,032	25·20
3027	68,550	68,742	25·12
3101	71,360	72,113	25·46
3107	72,140	72,392	25·68

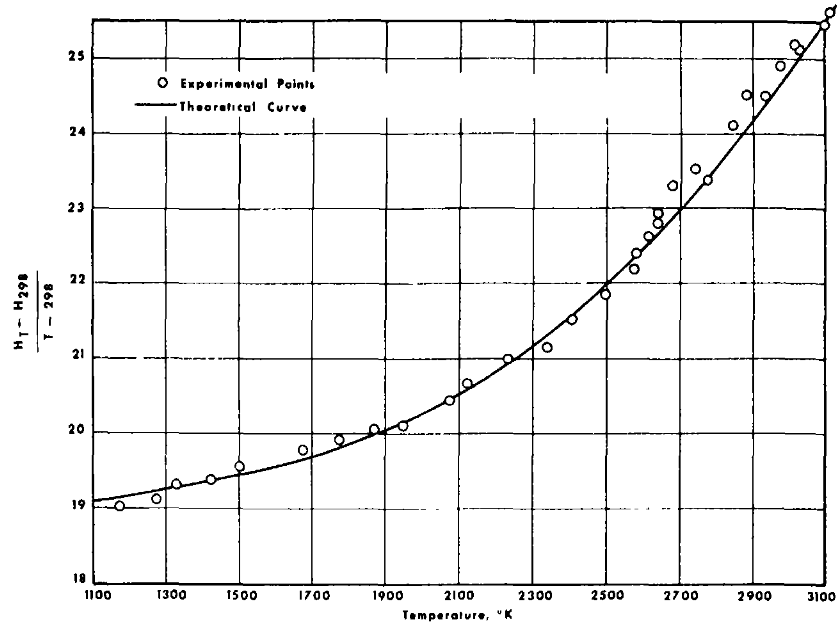

Fig. 1. Mean heat capacity for stoichiometric UO_2, cal/mole °K.

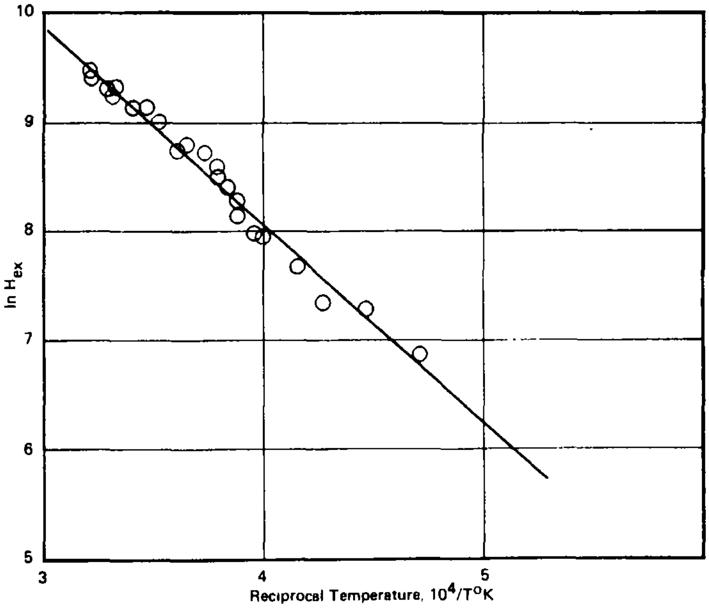

Fig. 2. Temperature dependence of the excess enthalpy. ln H_{ex} vs. reciprocal temperature.

voids. UO_2 is known to be able to pick up significant amounts of excess oxygen (up to $UO_{2.267}$ at 2083°K)[9] but also exhibits the ability to lose oxygen (down to $UO_{1.87}$ at 3000°K)[10]. The defect responsible for the nonstoichiometry of UO_2 has been fairly well established to be oxygen Frenkel defects on the oxygen sublattice. Oxygen interstitials predominate at hyperstoichiometric compositions and oxygen vacancies in the hypostoichiometric region. The evidence for this defect structure has been gathered from a variety of experimental sources; the variation of density[11] with oxygen content in nonstoichiometric UO_2, the mechanism of oxygen diffusion[12] in UO_2, which has been suggested to be the interstitialcy mechanism, magnetic studies[13], and oxygen pressure versus composition measurements[14]. In the last study cited, Kiukkola[14] tried to explain the data on the basis of the formation of oxygen interstitials, but was unable to obtain the right value for the power dependence of the oxygen partial pressure. This may be due to the fact that at large deviations from stoichiometry the simple Schottky–Wagner theory does not hold. Gerdanian and Dode [15] applied the Anderson theory[16] to the pressure-composition data of Aronson and Belle[17] and obtained good agreement only if clusters of defects randomly distributed in the lattice were assumed. Aukrust *et al.*[18] determined the defect complex to be $U^{+5}O_iU^{+5}$ from theoretical considerations and an experimental value for the partial molal entropy. Finally, from neutron diffraction studies, Willis[19] determined that in UO_2 a defect complex $(O_iV_0O_i)$ associated with two U^{+5} ions exists, rather than a simple oxygen interstitial.

The contribution of defect formation to the excess specific heat at constant pressure (C_{ex}) is proportional to the temperature derivative of the defect concentration

$$C_{ex}=\frac{\partial(n\Delta H)}{\partial T} \qquad (3A)$$

where n is the number, and ΔH the enthalpy of formation of the defects; ΔH will be assumed temperature independent. The excess enthalpy can be obtained by integration of (3A)

$$H_{ex}=\Delta H\,\Delta n. \qquad (3B)$$

We wish to calculate the formation energy of Frenkel pairs in UO_2 from the observed excess enthalpy; this enthalpy is defined as the energy required to transfer an oxygen atom from its normal lattice site to an interstitial site.

Neglecting the electronic contribution, the expression for the specific heat of a solid is given by

$$C_p=C_v+\frac{TV\alpha^2}{\chi}+\Delta H\frac{\mathrm{d}n}{\mathrm{d}T} \qquad (4A)$$

or

$$C_p=C_v+T\alpha C_v\gamma+\Delta H\frac{\mathrm{d}n}{\mathrm{d}T} \qquad (4B)$$

where C_p and C_v are the specific heats at constant pressure and constant volume respectively, α is the volume thermal expansion, χ the compressibility and γ, the Gruneisen constant defined as $\gamma=\alpha V/\chi C_v$. C_v can be considered a constant, since the measurements were made at temperatures well above the Debye temperature of UO_2 (θ_D for UO_2 is approximately equal to room temperature). The last term in (4A) and (4B) is the excess term as defined by (3A). By integrating (4B):

$$H_T=H_L+H_{ex}; \qquad (5A)$$

$$H_L=a+bT+cT^2; \qquad (5B)$$

where H_L is the lattice enthalpy, H_{ex} the excess enthalpy, a, the integration constant, $b=9R$ according to the Neumann–Kopp rule for a triatomic molecule* and $c=V\alpha^2/2\chi\cong 8{\cdot}8\times10^{-4}$ for UO_2. It is possible to express the lattice enthalpy in terms of a cubic or a quartic equation, but it turns out that these higher order terms are small and may be neglected[20].

---

*The molar heat capacity of the compound is a weighted sum of the molar heat capacities of oxygen and uranium.

The evaluation of the last term in equation (5A) i.e. the excess enthalpy H_{ex}, is accomplished from the statistical thermodynamic approach developed by Wagner and Schottky [21], which is valid for small deviations from stoichiometry. In writing the grand partition function of a UO_2 crystal, the following assumptions are made:

1. the disorder is confined to the oxygen sublattice only, the predominant defect being the oxygen Frenkel pair,
2. the enthalpy of formation per Frenkel pair is constant and,
3. the defects are distributed at random among the available sites.

$$GPF = \sum_{N_1} \frac{N!}{N_1!(N-N_1)!}\frac{(2N)!}{N_2!(2N-N_2)!} \times a_U{}^N a_O{}^{2N} \exp -\left[\frac{\Delta G_F}{RT} + \frac{N_1{}^2}{2N}\frac{\Delta G_F^*}{RT}\right] \quad (6)$$

where:

N_1 is the number of oxygen interstitials, which is also equal to the number of vacant oxygen sites for the stoichiometric crystal.
N is the number of uranium atoms, assumed fixed. Thus $2N$ is the number of normal oxygen sites.
N_2 is the number of oxygen atoms on normal sites. It is equal to $2N - N_1$.
ΔG_F is the Gibbs free energy of formation of the Frenkel pair.
ΔG_F^* is the free energy of interaction of the defects.
a_U is the uranium activity.
a_O is the oxygen activity.

By the well known methods of statistical mechanics, minimization with respect to N_1 leads to

$$\frac{x^2}{(1-x)(2-x)} = \exp -[\Delta G_F/RT + x\Delta G_F^*/RT]. \quad (7)$$

For this case the site fraction of interstitials or vacancies is $x = N_1/2N$, where $2N$ is the number of normal oxygen sites. Near stoichiometry $x \ll 1$ and, as generally $\Delta G_F^* < \Delta G_F$, the term $x\Delta G_F^*$ is small and may be neglected.† Also, we can write $\Delta G_F = \Delta H_F - T\Delta S_F$ and get an equation of the form

$$\frac{x^2}{(1-x)(2-x)} = \exp\left[\frac{\Delta S_F}{R}\right]\exp -\left[\frac{\Delta H_F}{RT}\right] \quad (8)$$

where ΔS_F and ΔH_F are the entropy and enthalpy of formation per Frenkel pair. Since x is assumed small, (8) can be simplified as

$$x^2 \cong 2\cdot \exp\frac{\Delta S_F}{R}\exp\frac{-\Delta H_F}{RT} \quad (9)$$

or

$$x \cong \sqrt{2}\exp\frac{\Delta S_F}{2R}\exp\frac{-\Delta H_F}{2RT}. \quad (10)$$

Defining

$$\xi^2 = \exp\frac{\Delta S_F}{2R}\exp\frac{-\Delta H_F}{2RT}$$

we obtain the following expression for H_{ex}

$$H_{ex} = \sqrt{2}\xi\,\Delta H_F \quad (11)$$

where ΔH_F is the Frenkel energy. The defect contribution to the excess enthalpy in UO_2 originally introduced in equation (3B) is now defined explicitly in equation (11). The complete expression for the enthalpy is given by

$$H_T = a + bT + cT^2 + \Delta H_F\,\xi\,\sqrt{2}. \quad (12)$$

---

†If ΔG_F^* were significant, the random distribution of defects assumed in equation (6) would no longer apply.

4. DISCUSSION OF THE RESULTS

The Frenkel energy was evaluated by fitting the data to an equation of the form of (12) by an iterative process of varying ΔH_F to obtain a value for the coefficient 'b' to be approximately equal to $9R$ while simultaneously rejecting equations which gave negative values of 'c'. The resulting equation is

$$H_T = -5601{\cdot}5 + 17{\cdot}78T + 1{\cdot}02 \times 10^{-3}T^2 + 71300\sqrt{2}\exp\frac{14{\cdot}83}{2R}\exp\frac{-71300}{2RT} \quad (13)$$

It should be noted that very little sacrifice in the goodness of the fit resulted in the use of equation (13) as opposed to the equation which had the minimum standard deviation but inacceptable values for the coefficients.

As a second method of computation, the excess enthalpy H_{ex} was evaluated by subtracting enthalpy values calculated from the parabolic portion of equation (13) from experimental values at the higher temperatures. If the concentration of Frenkel defects, x, is expressed by the equation

$$x \cong \sqrt{2}\exp\frac{\Delta S_F}{2R}\exp\frac{-\Delta H_F}{2RT} \quad (14)$$

where ΔS_F is the entropy term, the excess enthalpy per mole is given by

$$\ln H_{ex} = \frac{\Delta S_F}{2R}\ln(\sqrt{2}\Delta H_F) - \frac{\Delta H_F}{2RT}. \quad (15)$$

Figure 2 shows that the plot is approximately linear. The Frenkel energy and entropy were obtained from the slope and intercept of a plot of ln H_{ex} v. 1/T. A slight negative deviation from linearity may be detected at the high temperature end. However, calorimetric data are probably not sufficiently sensitive to show such variations from linearity which may be attributed to association of the defects. (The effect on the enthalpy value ΔH_F due to clustering is probably on the order of the errors associated with ΔH_F determined by the method.) The term $x\Delta G_F^*$ neglected in equation (7) would have to be included if ordering becomes a major factor. Since in the temperature range of interest the experimental error in the measured enthalpy is roughly a constant percentage of the enthalpy, the error expressed in calories per mole is approximately proportional to enthalpy. When this situation prevails, a least squares analysis is not valid unless each data pair, enthalpy and temperature, is weighted by the reciprocal of the square of the error appropriate to the pair. In the equation derived, the actual weighting factors used were proportional to the reciprocal of the square of the enthalpy, thus properly favoring the lower temperature, more accurate, data in the analysis. The data were weighted in this manner for both methods of data treatment.

The values of ΔH_F and ΔS_F obtained by a linear least squares fit of all data points in which $H_{ex} > 3\delta$, where δ is the standard deviation of equation (13), are $71{,}300 \pm 2200$ cal mole^{-1} and $14{\cdot}83 \pm 0{\cdot}84$ cal mole^{-1} deg^{-1}, respectively. The values obtained by the second method were: $\Delta H_F = 72{,}500 \pm 2{,}200$ cal mole^{-1} and $\Delta S_F = 15{\cdot}20 \pm 0{\cdot}84$ cal mole^{-1} deg^{-1}. These values for the Frenkel energy are in excellent agreement with the 71 kcal/mole estimated by Belle[22] from oxygen diffusion in UO_2 and higher than the 60 kcal/mole used by Aitken *et al.*[10]. It should be realized that the first part of equation (12) is parabolic as a consequence of the assumption that the Gruneisen constant is independent of temperature. If this were not true and the Gruneisen constant did vary with temperature, then the extrapolated lattice enthalpy at high temperature would be larger. The excess enthalpy would therefore be smaller, the Frenkel energy would be larger, and higher order terms would have to be added to equation (12). The calculated value of the Frenkel energy appears to be very sensitive to the particular parabolic equation chosen to describe the lattice contribution to the enthalpy.

No upward deviation in Fig. 2 was observed to support formation of Schottky defects at high temperature. High upward deviation in similar plots for silver halides have been observed by other workers[4, 23] and attributed to the formation of Schottky defects. No appreciable downward deviation in Fig. 2 at high temperature was observed either. Mutual interaction of defects would give rise to this effect, but it is felt that such effects are beyond the sensitivity of the calorimetric method.

In conclusion, the data can best be represented by equation (13). When the value of the coefficient 'b' in equation (12) was checked with the value obtained by a calculation using published thermal expansion data [24] and compressibility data as a function of temperature[25] for UO_2, the resulting two values agree very satisfactorily. The agreement of the value of the Frenkel energy obtained here with the previously cited earlier estimates is gratifying.

Acknowledgements—The author wishes to express his sincere appreciation to Professors D. Lazarus and R. A. Swalin and Drs. R. E. Fryxell and E. A. Aitken for many helpful discussions.

REFERENCES

1. HEIN R. A., SJODAHL L. H. and SZWARC R., *J. Nucl. Mat.* **25**, 99 (1968); The heat of fusion and enthalpy above the melting point were reported by HEIN R. A., FLAGELLA P. N. and CONWAY J. B., *J. Am. Ceram. Soc.* **51**, 291 (1968).
2. MOTT N. F. and GURNEY R. W., *Electronic Processes in Ionic Crystals*, p.48. Clarendon Press, Oxford (1940).
3. KANAZAKI H., *Phys. Rev.* **81**, 884 (1951); POCHOPSKI T. E., *J. chem. Phys.* **21**, 1539 (1953).
4. KOBYASHI K., *Phys. Rev.* **85**, 150 (1952).
5. GINNINGS D. C., DOUGLAS T. B. and BALL A. F., *J. Res. natn. Bur. Stand.* **45**, 23 (1950); HOCH M., *The Energy and Entropy of Vacancy Formation in Body-Centered Cubic Refractory Metals*, Report GE-TM 65-12-2. General Electric Company, Cincinnati, Ohio (1965); KNOMYAKOV K. G. and STRELKOV P. G. cited by UBBELOHDE A. R., *Melting and Crystal Structure*, Chap. 11. Clarendon Press, Oxford (1965).
6. LAWSON A. W., *Phys. Rev.* **78**, 185 (1950).
7. BALDOCK P. J., SPINDLER W. E. and BAKER T. W., *J. Nucl. Mat.* **18**, 305 (1966).
8. HOCH M., Personal communication.
9. ANTHONY A. M., KIYOURA R. and SATA T., *J. Nucl. Mat.* **10**, 8 (1963).
10. AITKEN E. A., BRASSFIELD H. C. and FRYXELL R. E., *Symp. Thermodynamics with Emphasis on Nuclear Materials and Atomic Transport in Solids, Vienna, Austria, July 1965*, p. 435. International Atomic Energy Agency, Vienna (1966).
11. LYNDS L., YOUNG W. A., Molic J. S. and LIBOWITZ G. G., *Adv. Chem* **39**, 58 (1963).
12. AUSKERN A. B. and BELLE J., *J. Nucl. Mat.* **3**, 267 (1961).
13. ARROTT A. and GOLDMAN J. E., *Phys. Rev.* **108**, 948 (1957).
14. KIUKKOLA K., *Acta. chem. scand.* **16**, 327 (1962).
15. GERDANIAN P. and DODE M., *C.R. hebd. Séanc. Acad. Sci., Paris* **254**, 1005 (1962).
16. ANDERSON J. S., *Proc. R. Soc.* **A185**, 69 (1946).
17. ARONSON S. and BELLE J., *J. chem. Phys.* **29**, 151 (1958).
18. AUKRUST E., FORLAND T. and HAGEMARK K., *Proc. Symp. Thermodynamics of Nuclear Materials*, p. 713. International Atomic Energy Agency, Vienna (1962).
19. WILLIS B. T. M., *Proc. Brit. Ceram. Soc.* **1**, 9 (1964)
20. FOREMAN A. J.-E., *Proc. phys Soc.* **79**, 1124 (1962).
21. WAGNER C. and SCHOTTKY W., *Z. phys. Chem.* **B11**, 163 (1931); For a review of the early work see ANDERSON J. S., *Ann. R. Chem. Soc.* **43**, 104 (1946).
22. BELLE J., AUSKERN A. B., BOSTROM W. A. and SUSKO F. S., *Proc. 4th Int. Symp. of Reactivity of Solids* (Edited by J. H. DeBoer), p. 452. Elvesier, Amsterdam (1961).
23. KURNICK S. W., *J. chem. Phys.* **20** [2], 218 (1952).
24. CONWAY J. B., FINCEL R. M. and HEIN R. A., *Trans. Am. Nucl. Soc.* **6**, 153 (1963).
25. SUNG P. and TURNBAUGH J. E., *J. Nucl. Mat.* **24**, 107 (1967).

J. Phys. Chem. Solids Pergamon Press 1969. Vol. 30, pp. 713–717. Printed in Great Britain.

THE EPR SPECTRA OF Gd^{3+} AND Eu^{2+} IN LEAD CHALCOGENIDES

G. B. BACSKAY, P. J. FENSHAM,* I. M. RITCHIE and R. N. RUFF
School of Chemistry, Melbourne University, Parkville, Victoria 3052, Australia

(*Received* 1 *July* 1968)

Abstract—The EPR spectra of Gd^{3+} and Eu^{2+} in the lead chalcogenides PbS, PbSe and PbTe have been studied at room temperature. In each case the fine structure is characteristic of cubic field splitting. The b_4 values for the europium doped samples show a steady decrease in going from PbS to PbTe, but the b_4 values for the gadolinium doped materials are approximately constant. These results are interpreted in terms of a simple electrostatic model. The Eu^{2+} ions are assumed to occupy a lattice site, and the Gd^{3+} ions an interstitial site around which distortion of the lattice has taken place.

1. INTRODUCTION

BOTH Gd^{3+} and Eu^{2+} have an f^7 electronic configuration and their ground state is $^8S_{7/2}$. The EPR spectrum of Gd^{3+} has been extensively studied in a wide range of environments, but less is known about the Eu^{2+} spectrum.

The EPR spectrum of Gd^{3+} in PbSe has already been reported[1], but since very few comparative EPR studies exist, it was felt that it might be useful to extend these spectral measurements to the closely related compounds PbS and PbTe. Moreover, by preparing the three corresponding Eu doped compounds, it would be possible to compare the Gd^{3+} and Eu^{2+} spectra in three different, but rather similar environments. Lead sulphide, selenide and telluride all have a cubic NaCl structure[2], and it is reasonably easy to obtain single crystals of sufficient quality for paramagnetic resonance measurements.

The splitting of the $^8S_{7/2}$ ground state has been the subject of some controversy for a number of years, but it is generally agreed that the action of the crystal field, together with spin-orbit coupling, can cause zero field-splitting[3–5]. For example, the Hamiltonian for a cubic crystal field may be written as,

$$\mathcal{H} = \beta S.g.H + B_4{}^0(O_4{}^0 + 5O_4{}^4) + B_6{}^0(O_6{}^0 - 21\,O_6{}^4)$$

$B_4{}^0$ and $B_6{}^0$ can be expressed as a product of matrix elements of the crystal field potential and of the spin-orbit coupling operator $L.S$. Thus the magnitudes and signs of $B_4{}^0$ and $B_6{}^0$ are expected to vary with different crystalline environments.

2. EXPERIMENTAL

Doped single crystals were obtained by adding gadolinium metal (99·9 per cent, Koch–Light Laboratories) to the lead chalcogenides in approximately 0·1 mole% proportion before crystal growth. Europium was introduced as EuO (99·9 per cent, Koch–Light Laboratories) in approximately 0·3 mole% proportion. The lead chalcogenides were prepared and the crystals grown in a manner similar to that described previously [1]. For the Eu doped crystals, in order to prevent oxidation to Eu^{3+}, it was found neces- to add a slight excess (approximately 0·5 mole%) of lead to the mixture. The EPR signals obtained from these samples were much more intense than the signals of lead deficient crystals.

The paramagnetic resonance measurements were carried out at room temperature using a Varian V4502 spectrometer operating in the X band. The crystals were always aligned with the magnetic field perpendicular to the (100) face.

---

*Faculty of Education, Monash University, Clayton, Victoria, Australia.

3. RESULTS

All spectra consisted of seven lines roughly symmetrical about the central absorption following the intensity pattern 7:15:12:16:12:15:7, typical of the fine structure due to cubic field splitting.

With the exception of Eu^{2+} in PbS, the calculation of the crystal field parameters was carried out in the way described in the previous paper[1]. The spectrum of Eu^{2+} in PbS was strongly asymmetric because the zero field splitting was very large. Consequently the crystal field parameters were calculated in the following way. A preliminary estimate of the crystal field parameters was obtained using the transitions observed above 3500 G. Using these values the energy levels and transition energies were estimated as a function of magnetic field. These values of the transition energies were successively refined by a trial and error method to bring the calculated spectrum into coincidence with the one experimentally observed. The calculations were carried out using an IBM 7044 digital computer. Thus, all the spectra were fitted to the Hamiltonian given in Section 1, and the results are summarized in Table 1.

The variation of b_4 is also depicted in Fig. 1.

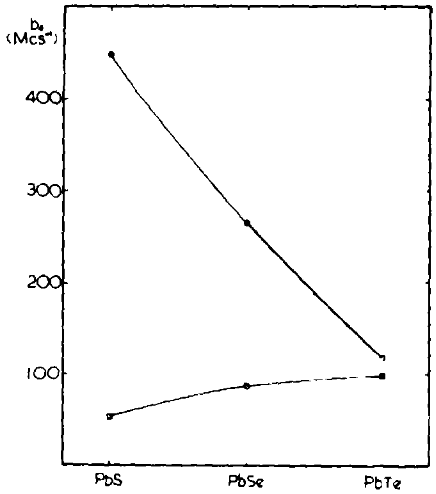

Fig. 1. The variation of b_4 in Mcs^{-1} as a function of chalcogenide. ($O = Eu^{2+}$, $\square = Gd^{3+}$)

Hyperfine splittings were observed for the Eu doped crystals, but the resolution of the spectra was insufficient to allow accurate determination of the coupling constants for any of the systems except PbSe. In this case, the values obtained agreed with those reported by Pifer[6].

4. DISCUSSION

The spectra of Gd and Eu in all three chalcogenides were characteristic of the Gd^{3+} and Eu^{2+} ions respectively, in sites of cubic symmetry. There was no evidence of spin-spin coupling and the absence of an axial field indicated that there were no compensating vacancies.

The variation of b_4 for the Gd doped and Eu doped compounds is strikingly different, as

Table 1. Spin parameters of Eu^{2+} *and* Gd^{3+} *in lead chalcogenides*
(All errors quoted are estimated maximum errors)

System	g value	$b_4 = \frac{1}{60}(B_4{}^0)\text{Mcs}^{-1}$	$b_6 = \frac{1}{1260}(B_6{}^0)\text{Mcs}^{-1}$
Eu in PbS	$1{\cdot}980 \pm 0{\cdot}005$	$\pm 448 \pm 3$	$0{\cdot}0 \pm 3$
PbSe	$1{\cdot}970 \pm 0{\cdot}005$	$\pm 266 \pm 1$	$\mp 1{\cdot}1 \pm 0{\cdot}3$
PbTe	$1{\cdot}980 \pm 0{\cdot}005$	$\pm 129{\cdot}0 \pm 0{\cdot}6$	$\mp 2{\cdot}2 \pm 0{\cdot}3$
Gd in PbS	$1{\cdot}991 \pm 0{\cdot}003$	$\pm 55{\cdot}5 \pm 0{\cdot}5$	$\mp 0{\cdot}8 \pm 0{\cdot}5$
PbSe	$1{\cdot}990 \pm 0{\cdot}002$	$-87{\cdot}3 \pm 0{\cdot}2$	$+1{\cdot}1 \pm 0{\cdot}5$
PbTe	$1{\cdot}990 \pm 0{\cdot}002$	$\pm 96{\cdot}0 \pm 0{\cdot}31$	$\mp 2{\cdot}1 \pm 0{\cdot}6$

shown by Fig. 1. In this paper, we attempt to give a simple, semiquantitative explanation of this phenomenon.

Since the electrons involved in the paramagnetism are *f* electrons, effects due to covalency involving the rare earth ion may be neglected in this treatment. This situation may be compared with the effect of covalent bonding on the *d* electrons of transition metal ions. In this latter case, the magnitude of the zero field splitting is partially dependent on the covalency. Furthermore, if it is assumed that the mechanism of perturbation is the same in all six doped compounds, and that the spin-orbit coupling is constant, the differences in splittings must be due to variations in the electrostatic crystal fields. These two assumptions seem reasonable for such closely related crystals.

The dopant atoms must occupy either lattice or interstitial sites, both of which have cubic symmetry in the NaCl type structure. A lattice site is octahedrally co-ordinated by nearest neighbour anions and the fourth order crystal field potential for it is given by [7]

$$V_4 = \frac{35q}{4a^5}[(x^4+y^4+z^4)-\tfrac{3}{5}r^4].$$

To a first approximation only the nearest neighbour anions need to be considered since the potential falls off as $1/a^5$. For a tetrahedrally co-ordinated site, the potential is given by

$$V_4 = \frac{-35q}{9a^5}[(x^4+y^4+z^4)-\tfrac{3}{5}r^4].$$

An interstitial site is, however, surrounded by a tetrahedron of anions and an equal tetrahedron of cations. Hence, unless some distortion occurs in the lattice, the fourth order potential will be zero. In a previous paper, we concluded that Gd^{3+} occupies interstitial sites in PbSe [1]. We now explore the consequences of assuming that gadolinium is similarly positioned in PbS and PbTe, together with those consequences that follow if europium occupies a lattice site in each compound. The latter case is treated first.

Eu^{2+} on a lattice site

If the perturbation is second order in the crystal field potential the following relationships will hold:-

$$\begin{aligned} &b_4(\mathrm{PbS}):b_4(\mathrm{PbSe}):b_4(\mathrm{PbTe}) \\ &= [V_4(\mathrm{PbS})]^2:[V_4(\mathrm{PbSe})]^2:[V_4(\mathrm{PbTe})]^2 \\ &= \left[\frac{q}{a^5}(\mathrm{PbS})\right]^2:\left[\frac{q}{a^5}(\mathrm{PbSe})\right]^2:\left[\frac{q}{a^5}(\mathrm{PbTe})\right]^2. \end{aligned}$$

This expression relates the crystal field parameter b_4, the charge carried by the nearest neighbour anion and the distance between that anion and the paramagnetic ion for the three compounds. Knowing the b_4 values and the appropriate interionic distances, the ratios of the charges in the three compounds can be calculated. If there is no distortion of the lattice, the value of a may be set equal to one half of the lattice constant a_0. On this basis the ratio of the charges was calculated to be equal to 1·00:0·90:0·85 for PbS, PbSe and PbTe respectively. Whether distortion will or will not take place will in part depend on the relative affinity of each anion for europium and lead. Some measure of the relative affinity can be obtained by comparing the free energies of formation of the lead and europium chalcogenides. We have been unable to locate this information. However, the standard enthalpies of formation of lead [8] and europium oxide [9] are −52 and −145·1 kcal mole^{-1} respectively. These data imply that europium may dictate its environment to a large extent. Nevertheless, appreciable distortion is unlikely to occur, since the structures of the europium chalcogenides are all NaCl type, having lattice parameters very little different from the corresponding lead compounds. For the sulphide, selenide and telluride of europium the lattice constants are 5·957, 6·191 and 6·584 Å respectively, which may be compared with the values for the lead compounds of 5·936, 6·124 and 6·454 Å[2]. The charge ratios are the same as those given above even if they are calculated on the basis of the europium chalcogenide lattice constants. The close correspondence between the lead and europium structures further strengthens the belief that Eu^{2+} will occupy lattice sites.

The values of the charge ratios calculated above imply that the amount of ionic character is rather similar in all three compounds. Although this conclusion is at variance with Suchet's[10] partial charge values (PbS, 0·6*e*; PbSe, 0·4*e*; PbTe, 0·2*e*), it is consistent with an analysis that can be made of the results of Pifer[6]. He found that the hyperfine coupling constants of manganese in the lead chalcogenides show a gradual decrease from PbS to PbTe. According to Matumura[11] there is a linear relationship between ionicity and hyperfine coupling constant*. On this basis the change in ionicity for the Mn doped compounds is small, and it seems reasonable to suppose that the same may be true for the Eu doped compounds of the present work.

It seems reasonable to us, therefore, that the variation in crystal field parameter between the compounds studied can be accounted for in terms of simple crystal field theory.

Gd^{3+} *on an interstitial site*

The gadolinium compounds, like the europium compounds, are almost certainly much more stable than those of lead. (e.g. the enthalpy of formation of Gd_2O_3 is −433·94 kcal $mole^{-1}$[13] If the gadolinium ions tend to create in their immediate vicinity structures similar to the gadolinium chalcogenides, they will be co-ordinated tetrahedrally rather than octahedrally. Gd_2S_3 has the Th_3P_4 type structure[14], which is the same as the fluorite structure with anion vacancies disposed randomly throughout the lattice. The selenide and telluride of gadolinium have the same structure as Sb_2S_3[15], in which the metal ion is 7-fold co-ordinated, although the selenide has been shown to assume the Th_3P_4 structure when selenium deficient[16].

Our assumption that the Gd^{3+} ions are present interstitially ensures that the ions are co-ordinated in a similar fashion to the way they would be in their parent compounds.

At first sight, one might expect the same trend in b_4 values for a Gd^{3+} ion in an interstitial site as for Eu^{2+} on a lattice site. The decreasing formal charges and increasing lattice constants observed in passing from lead sulphide to telluride, would serve to decrease the crystal field potential at an interstitial site, as well as at a lattice site. However it has been noted that the crystal field potential at an interstice consists of a contribution from the surrounding anions and a contribution from the surrounding cations. While the individual contributions from the anions and cations will decrease across the series PbS, PbSe and PbTe, in each compound, they will remain equal in magnitude, but opposite in sign. The net crystal field will, therefore, be zero unless some distortion in the surrounding lattice takes place. The b_4 values are not zero, but are much smaller than the values for europium. We have calculated what distortion of the lattice, as shown in Fig. 2. is necessary to obtain the b_4 values. The assumption of equal and opposite distortion for cations and anions is, of course, purely arbitrary. We assume that the ratios of the formal charges are the same as those calculated for Eu doping. At an interstitial site

$$\begin{aligned}V_4 &= V_4(\text{anions}) - V_4(\text{cations})\\ &= \frac{(-35q)}{9}\left[\frac{1}{(b-d)^5} - \frac{1}{(b+d)^5}\right]\\ &\quad\times[(x^4+y^2+z^4)-\tfrac{3}{5}r^4]\end{aligned}$$

---

*The method of computing ionicities, due to Pauling [12] and as used by Matumura[11] must be treated with caution. In addition, it would appear that Matumura's calculations are in error in that he allowed only one covalent bond for divalent compounds.

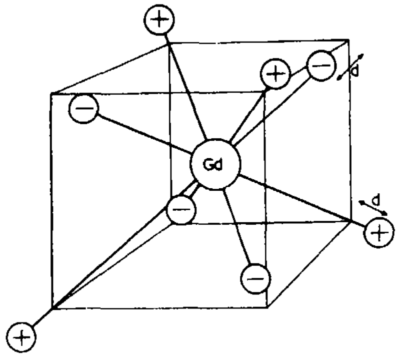

Fig. 2. Postulated distortion of lead chalcogenide lattice surrounding an interstitial gadolinium.

where d is the distance in Å through which the anions and cations have been displaced, and b is the interstice-lattice site distance.

Assuming a second order perturbation

$$\left[\frac{V_4(\text{interstitial})}{V_4(\text{lattice site})}\right]^2 = \frac{b_4(\text{Gd}^{3+})}{b_4(\text{Eu}^{2+})}.$$

The values of d obtained are 0·10, 0·17 and 0·27 Å for lead sulphide, selenide and telluride respectively, and the gadolinium chalcogenide distances will then be 2·47, 2·48 and 2·55 Å. The increasing distortion found in going from PbS to PbTe correlates with the expected decrease in the strength of the lead-chalcogen bond. The values of interionic distances calculated above are consistent with values estimated for the gadolinium chalcogenides, although the exact calculation of these distances for the latter compounds was not possible in the absence of suitable X-ray diffraction analyses.

We may conclude that the observed trends in the b_4 values, obtained from a study of the EPR spectra of Gd^{3+} and Eu^{2+} in PbS, PbSe and PbTe, can be interpreted in terms of these simple electrostatic models. According to them, the Eu^{2+} occupies a lattice site, and the Gd^{3+} occupies an interstitial site around which the anions and cations are displaced.

We do not suggest that the variation in b_4 can always be accounted for in the way we have outlined in this paper. Nevertheless, for such closely related compounds as the lead chalcogenides, it seems plausible that the perturbation mechanism is common to all three. This is consistent with our experimental results.

5. REFERENCES

1. BACSKAY G. B., FENSHAM P. M. and RITCHIE I. M., *J. Phys. Chem. Solids* **29**, 1213 (1968).
2. WYCKOFF R. W. G., *Crystal Structures*, 2nd Edn. Vol. 1, p. 86. Interscience, New York (1963).
3. LOW W., *Phys. Rev.* **109**, 265 (1958).
4. PRYCE M. H. L., *Phys. Rev.* **80**, 1107 (1950).
5. LOW W. and SHALTIEL D., *J. Phys. Chem. Solids* **6**, 315 (1955).
6. PIFER J. H., *Phys. Rev.* **157**, 272 (1967).
7. HUTCHINGS M. T., *Solid St. Phys* **16**, 227 (1964).
8. *Handbook of Chemistry and Physics* (Edited by R. C. West and S. M. Selby), p. D. 43. The Chemical Rubber Co (1967).
9. BURNETT J. L., U.S. At Energy Comm. UCRL-11850, 66 pp (1964).
10. SUCHET J. P., *The Chemical Physics of Semiconductors*, p. 119. Van Nostrand, New York (1965).
11. MATUMURA O., *J. phys. Soc. Japan* **14**, 108 (1959).
12. PAULING L., *The Nature of the Chemical Bond*, p. 69. Cornell University Press, New York (1940).
13. JUSTICE B. H. and WESTRUM E. F. Jnr., *J. phys. Chem.* **67**, 345 (1963).
14. FLAHAUT J., DOMANGE L., and PATRIE M., *Bull. Soc. Chim. Fr.* 1048 (1962).
15. FLAHAUT J., DOMANGE L., GUITTARD M. and PARDO M. P., *Bull. Soc. Chim. Fr.* 326 (1965).
16. GUITTARD M., FLAHAUT J. and DOMANGE L., *C.r. hebd. Séanc. Acad. Sci., Paris* **256**, 427 (1963).

J. Phys. Chem. Solids Pergamon Press 1969. Vol. 30, pp. 719–731. Printed in Great Britain.

HOMOGENEITY RANGES AND Te_2-PRESSURE ALONG THE THREE-PHASE CURVES FOR $Bi_2Te_3(c)$ AND A 55–58 at.% Te, PERITECTIC PHASE

R. F. BREBRICK

Lincoln Laboratory,* Massachusetts Institute of Technology, Lexington, Mass. 02173, U.S.A.

(*Received* 27 *June* 1968)

Abstract – The partial pressure of Te_2, P_2, has been determined for preannealed Bi–Te samples between 44 and 70 at.% Te and 400 and 635°C by measuring the optical density of the vapor between 7000 and 1990 Å. Values of P_2 and $10^3/T$ were obtained along the three-phase curves of the $Bi_2Te_3(c)$ phase and of a 55–58 at.% Te phase decomposing peritectically at 563 ± 2°C. The detailed liquidus line between 44 and 70 at.% and the solidus line for Bi_2Te_3 are obtained. The homogeneity range of the latter is roughly symmetrical about the ideal 60 at.% composition and is a maximum of about 0·4 at.% wide, between 460 and 520°C. Bi_2Te_3 melts congruently at 586·0°C and 59·95 at.% Te. It is shown that the antistructure model provides a nearly correct relationship between composition and carrier concentration in Bi_2Te_3. The P_2 isotherms, however, deviate from mass-action law predictions.

1. INTRODUCTION

THE SEMICONDUCTING compound Bi_2Te_3 has been the subject of numerous investigations concerning its galvano-magnetic, optical and thermal properties[1]. The only vapor pressure measurements, however, have been Knudsen-cell weight-loss measurements [2, 3] which give no indication of the variation of partial pressures along the three-phase curve. Moreover, there has been only one partially successful attempt[4], based on precision-density measurements, to check the adequacy of the antistructure model suggested [5, 6] by Hall measurements and no detailed determination of the homogeneity range. In the present investigation we have filled these gaps by determining the partial pressure of Te_2 as a function of temperature for a number of pre-annealed Bi–Te compositions between 44 and 70 at.% Te. The method used is to measure the optical density between 7000 and 1990 Å of the vapor at 755°C that is in equilibrium with a solid or liquid phase at a known, lower temperature. This method has been successfully applied to a number of tellurium [7] and selenium[8] systems.

2. EXPERIMENTAL

(A) *Synthesis of samples*

The method of preparation was extremely important since we were attempting to obtain samples which were equilibrated near 525°C and which in a few critical cases had compositions known to within about ±0·005 at.%.

Step 1 – react elements. Chunk Bi and Te, 99·999 per cent pure by the supplier's analysis, were each weighed to the nearest 0·1 mg to make a total of about 15 g. The elements were then loaded into a 10 cm long, 2·0 cm O.D. silica tube and put under vacuum. (All silica tubes used in this study, including the optical cells, were first cleaned and outgassed prior to loading as previously described[9].) The elements were outgassed 4–5 hr at 190°C until the pressure dropped below 10^{-7} Torr. The tube was then sealed. The tube and contents were heated to 700°C and held there for 30 min with occasional shaking (the highest melting point in the Bi–Te system is that of Bi_2Te_3 at 586°C), furnace-cooled to about 600°C, and quenched by rapid immersion in water. In order to minimize the formation of a condensed film of tellurium over the entire tube in the quench, the tube was immersed only slightly deeper than the height of the melt.

---

*Operated with support from the U.S. Air Force.

In order to minimize any segregation incurred by condensation of a Te-rich film around the ingot, the tube was reheated for 16 hr at 520°C in an isothermal enclosure and quenched again. This served to almost eliminate any film.

The isothermal enclosures used here and in all subsequent heat treatments were 1·2 cm wall thickness, 15 cm long cylindrical silver liners. The liners were closed with 1·2 cm thick silver caps, wrapped in a 1·2 cm thickness of insulating blanket of aluminum oxide fiber, and placed in a box furnace. A thermocouple was placed inside the cavity of one liner. These enclosures were isothermal enough that there was no sublimation away from the material during the anneals.

Step 2—anneal. The samples which were annealed, the annealing conditions used, and the optical cells are listed in Table 1. The sample numbers are given in order of increasing Te content except for those in the bottom section of the Table, which form a group among themselves. The optical cell numbers in the last column indicate the chronological order of sample preparation and optical density measurements. The samples were generally prepared by the reaction described in Step 1, which is indicated by *R* in the Origin column of Table 1. After Step 1 the tube was broken open and the material ground with an agate mortar and pestle to pass a stainless-steel standard sieve, the opening of which is listed under maximum particle size in the Table. The sample was then loaded into a second silica tube, outgassed 3–5 hr at 190°C and 10^{-7} Torr, and sealed off at about 10^{-7} Torr. The tube was placed in one of the silver

Table 1. Sample synthesis and optical cell data

Sample synthesis				Annealing step			Optical cell		
Sample	Composition (at. % Te)	Weight (g)	Origin	Max. particle size (mm)	Temp. (°C)	Time (hr)	Sample weight loaded (g)	Optical path length (mm)	Cell number
1	44·0	10	*R* (react elements)	1	525	166	5	98·2	1
2	51·0	10	*R*	1	520	188	2·3	98·8	4
3	55·0	10	*R*	1	520	182	2	98·8	5
4	58·0	10	*R*	1	525	166	5 2	101·8 98·7	2 2b
5	58·0	15	*R*	0·5	527	204	2	99·3	12
6	58·0	3	part of sample 5	0·044	524	1	1	100·5	15
7	58 0	2	part of sample 5	0·044	—	—	2	98·3	16
8	59·0	15	*R*	1	525	165	2	98·3	19
9	59·80	15	*R*	1	519	240	1·8	98·1	6
10	59·80	13·2	remainder of sample 9	0·177	526	165	1·5	99·1	17
11	59·90	15	*R*	0·5	519	161	2	97·4	8
12	59·99	15	*R*	0·5	519	163	2·3	99·9	10
13	60·07	15	*R*	0·5	519	184	2	100·3	9
14	60·2	15	*R*	1	518	188	2	48·1	7
15	60·2	13	remainder of sample 14	0·5	390	187	2	99·4	13
16	62·0	15	*R*	1	520	164	2	46·6	3
17	62·0	13	remainder of sample 16	0·5	520	166	2·5	99·0	11
18	62·0	2·3	elements put directly into optical cell, sample held 10 min 600°C, quenched				2·3	100·3	14
19	63·0	2·5	elements put directly into optical cell, sample				2·3	47·8	18
20	70·0	2·5	held 10 min 600°C, quenched				2·5	47·6	20

liners described above and annealed as indicated in the Annealing Step columns of Table 1, generally for about 6 days at 525°C. The sample was then quenched by rapid immersion in water. In 5 instances most of a sample was reannealed to form a new sample. For example, after 1·8 g of sample 9 was sealed in an optical cell, the remainder was ground to 0·177 mm maximum particle size and annealed 165 hr at 526°C to give sample 10.

Step 3 – load optical cell. Finally 1–5 g of an annealed sample was loaded into the sidearm of an optical cell and the material outgassed 3–5 hr at 190°C and 10^{-7} Torr. The optical cell was then sealed off. For the optical cells listed in the bottom section of Table 1, measurements were made only at temperatures for which the samples were completely molten. Some of the preparative steps were therefore unnecessary. The elements were loaded directly into the sidearm of an optical cell. After heating the samples to 600°C and quenching, they were ready for measurements.

The fused silica optical cells consisted of a cylindrical cell proper and a 21 cm long sidearm at right angles to the cylindrical axis[10]. The end of the sidearm was the seal-off point. The inside length of the cell proper was taken as the optical path length and is given in Table 1. Except for 2 Te-rich samples the path lengths were near 100 mm.

The loss of material for each outgassing and seal-off is estimated to be about 1–5 mg. This would change the composition by less than $3(10^{-3})$ at.% Te for samples near 60 at.% Te.

(B) *Optical density measurements*

The sample was spread over the last 2–5 cm of the sidearm and the optical cell proper put into the sample beam of a Cary 14 H double-beam spectrophotometer with the sidearm tilting downwards about 15° from the horizontal. Furnaces enclosed the entire cell so that the optical cell proper was held at 755°C while the sample could be held at any lower temperature and had the lowest temperature in the entire cell. Temperatures were measured to ±3/4°C at 6 positions along the cell proper and sidearm with an automatic potentiometric recorder. The temperature across the sample, as measured by thermocouples just outside the sidearm, did not vary by more than 2°C in any measurement. The sample temperature was taken as that obtained from a calibrated Pt; Pt, 13 per cent Rh thermocouple which was located near the middle of the sample and just outside the sidearm in a 6 mm wall thickness, 10 cm long Ag liner. The temperature of this thermocouple, which was provided with an ice junction, was measured and recorded to ±0·05°C. During the 10–20 min required to make the optical density measurements the sample temperature was constant to within 0·3°C.

At the beginning of a run, with the cell proper at 755°C and the sample near room temperature, the zero of optical density, $D \equiv \log I_0/I$, was measured as a function of wavelength. The sample temperature was raised to about 300°C, where the vapor density is still negligible, and the zero measurement repeated. The sample temperature was then increased and the optical density (D_{1995}) at 1995·5 Å, where $Te_2(g)$ absorbs most strongly in the 1990–7000 Å interval, recorded. Once D_{1995} became measurable the sample temperature was increased in 5–8°C steps. Generally the sample temperature and D_{1995} simultaneously reached a steady state about 15–25 min after the temperature had been increased. Generally each sample was allowed to remain at temperature overnight at least once. The agreement observed between the optical densities before and after this 16 hr period tends to confirm the assumption that the samples were in complete equilibrium. The u.v. spectra were obtained between 1990 and 2100 Å using the hydrogen light source of the Cary 14H, a scanning speed of 1/2 Å/sec, a 12·7 cm/min chart speed giving 2·36 Å/cm, and a 1 sec recorder-pen period. The nominal spectral band pass was 1·28 and 1·68 Å at 2100 and 2000 Å, respectively.

As D_{1995} approached 2, the highest optical density which could be measured, the spectra were measured throughout the u.v. region to 4000 Å. At the highest Te_2-pressures the optical density was measured at 7000, 6000 and 5000 Å and scanned between 4400 and 4300 Å. The scanning speed was ½ Å/sec, the chart speed was 12·7 cm/min, and the pen period was 1 sec. At 4357 Å the nominal spectral band pass was 1·7 Å. Above 4000 Å the tungsten light source of the Cary 14H was used.

Value of D were measured between about 0·01 and 2·0. The noise in the zero runs (with no vapor in the cell) was ±0·005. As can be deduced from what follows, this corresponds to an error of $\pm 10^{-6}$ atm in the partial pressure of Te_2 for a 100 mm optical path-length cell.

3. RESULTS

(A) *General*

With the exception of one wavelength interval, the normalized spectra observed were quantitatively the same as that seen with a pure Te sample, i.e. the $Te_2(g)$ spectrum[7]. About 590°C and above, additional bands are seen between 2200 and 2350 Å, the strongest being at 2231 Å. These appear to be the same as those attributed to BiTe(g)[11]. They will not be discussed further here. The spectra of Bi(g) and $Bi_2(g)$ were not seen at temperatures as high as 700°C, the highest sample temperature investigated.

The structure of the 1995·5, 2025, 2056 and 4357 Å absorption-band maxima of $Te_2(g)$ were discussed[7] in an earlier study of the vapor pressure of Te(c, l). After correction of optical densities greater than 1·0 (for what appears to be a stray light error and amounts to a 6 per cent correction at $D = 2$) these optical densities are proportional to the partial pressure of $Te_2(g)$, P_2, to within better than 3·5 per cent. The equations are

$$P_2(\mathrm{atm}) = 2{\cdot}69(10^{-2})D_{1995}/L \qquad (1)$$

$$D_{1995}:D_{2025}:D_{2056}:D_{4357} = 1{\cdot}00:0{\cdot}410:0{\cdot}317:0{\cdot}106 \qquad (2)$$

where D_λ is the optical density at wavelength λ and L is the path length in mm. In the present investigation values of D_λ above 1·0 were corrected and plots of log D_λ vs. $10^3/T$ showed that equation (2) was satisfied. The value of P_2 was generally calculated using equation (1) for sample temperatures below 590°C. At higher temperatures the largest optical density below the upper limit of measurement, $D = 2{\cdot}0$, was used in equation (2) to calculate P_2.

(B) *Pressure-temperature diagram*

The results for the 13 different compositions are shown in Fig. 1, in which P_2 is plotted on a log scale against $10^3/T$, where T is the absolute sample temperature. It is seen that the range of P_2 is between 10^{-6} and 10^{-3} atm. We shall first describe Fig. 1 qualitatively and then list the quantitative phase-diagram and thermodynamic information it contains.

The uppermost unbroken line with no data points at high temperatures gives the partial pressure of $Te_2(g)$ over pure Te(c, l)[7, 12]. This is essentially equal to the total vapor pressure of Te. The discontinuity in slope at 450°C occurs at the melting point of Te(c). The approximately parallel lines at the highest temperatures (left side of Fig. 1) give P_2 for a series of melts with compositions between 44·0 and 70·0 at.% Te. Higher temperature data extending to 700°C, which are omitted from Fig. 1, all fall along straight lines which are extensions of the lines shown. (The high temperature data will be discussed in another paper in a thermodynamic characterization of Bi–Te melts.) With decreasing temperature, these lines intersect a large, parabola-like curve. The values of P_2 for each composition then fall along one or the other leg of this curve for some characteristic range of temperatures. Except for a complication involving the low pressure leg below about 560°C and discussed shortly, the parabola-like curve is the three-phase curve for $Bi_2Te_3(c)$, where this solid phase, vapor, and a liquid phase coexist. Of particular interest is the fact that the upper or Te-rich leg of the three-phase

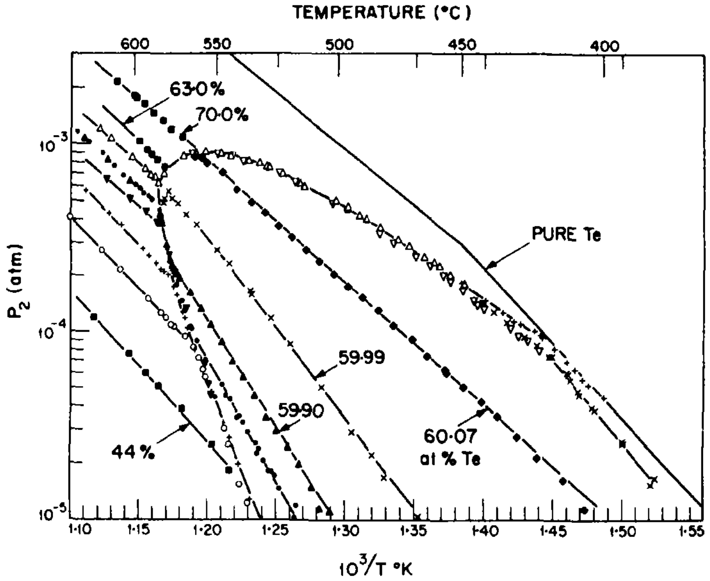

Fig. 1. Partial pressure of Te_2 as a function of $10^3/T$ where T is the absolute temperature for a number of Bi–Te compositions. The uppermost line showing a break in slope at $10^3/T = 1·383$ is the vapor pressure of pure Te(c, l). The data points for the 2 compositions represented by crosses do not overlap, nor do the data points for the 2 compositions represented as x. Hence in these cases the composition intended can be unambiguously identified remembering P_2 is larger at a given temperature, the larger the at % Te.

Symbol	○	+	▼	●	▲
at.% Te	51·0	55·0	58·0	59·80	59·90
Optical cell	4	5	2,12	6,17	8

Symbol	×	◆	▽	×	△	+	. ■
at.% Te	59·99	60·07	60·2	60·2	62·0	62·0	44,63,70
Optical cell	10	9	7	13	3	11	as labelled.

curve approaches the P_2 line of pure Te(c, l) and then coincides with it below 415·7–416·6°C. This shows that the temperature of the eutectic between Bi_2Te_3(c) and Te(c) is 416·1±0·5°C, and the value of P_2 over Bi_2Te_3-saturated Te(c) is essentially that over pure Te(c).

At temperatures approaching 586°C the slope of the three-phase curve is clearly shown to approach large values, a slope of infinity being expected at the maximum melting point of a congruently-melting compound. The curves within the three-phase curve, for samples containing 59·80, 59·90, 59·99, 60·07 and 60·20 at.% Te, are for compositions within the homogeneity range of the Bi_2Te_3(c) phase and are generally straight lines. With increasing temperature, P_2 lines for these compositions intersect the three-phase curve, coincide with it for a range of temperatures, change slope a second time and break away from the three-phase curve to form the lines in the liquid-phase region described above. The temperatures at which these sharp changes occur are solidus and liquidus temperatures respectively for the composition in question. It is seen that the 59·90 and 59·99 at.% samples bracket the congruently-melting composition, whose P_2 curve should coincide with the three-phase curve at only one point, the two discontinuities in slope coalescing to one. For the critical compositions near 60 at.% Te, the change in composition due to preferential loss of Te to the vapor phase is less than 10^{-3} at.% for $P_2 = 10^{-3}$ atm and can be neglected. The values of P_2 obtained with cells 6 and 17, both containing 59·80 at.% samples, agree. As seen in Table 1 the sample in cell 17 underwent the same annealing treatment as that in cell 6, then was reduced in maximum particle size by a factor of about 5 and annealed as long again at about the same temperature.

In order to discuss the Bi-rich three-phase curve a portion of the P_2 vs. $10^3/T$ plot is shown in Fig. 2, which is on an expanded scale and includes some points omitted from Fig. 1 for clarity. The lowest straight line is determined by the values of P_2 for the 51·0 and 55·0 at.% samples (cells 4 and 5, respectively) at values of $10^3/T$ below 1·15. The reliability of this line is supported by the fact that the liquidus temperature determined by its intersection with the line for the 44 at.% liquid is 539°C, which is the same value obtained from DTA cooling curves by Strauss[13] and is in good agreement with the value of 537°C in Hansen's summary[14]. The points clustering about the middle line were obtained with the 59·0 at.% sample (cell 19) and 3 differently annealed 58·0 at.% samples (cells 12, 15 and 16) and were taken with both increasing and decreasing temperatures in the range below 560°C. There is somewhat more scatter than usual associated with these compositions although most of the points fall on the line within the estimated experimental error of $\pm 10^{-6}$ atm. The middle line is simultaneously the Bi-rich three-phase line of the $Bi_2Te_3(c)$ phase and the Te-rich three-phase line of a peritectic phase whose homogeneity range lies between 55 and 58 at.% Te near 540°C. We point out that the upper line was obtained with two differently annealed 59·80 at.% samples and falls just inside the Bi_2Te3 homogeneity range.

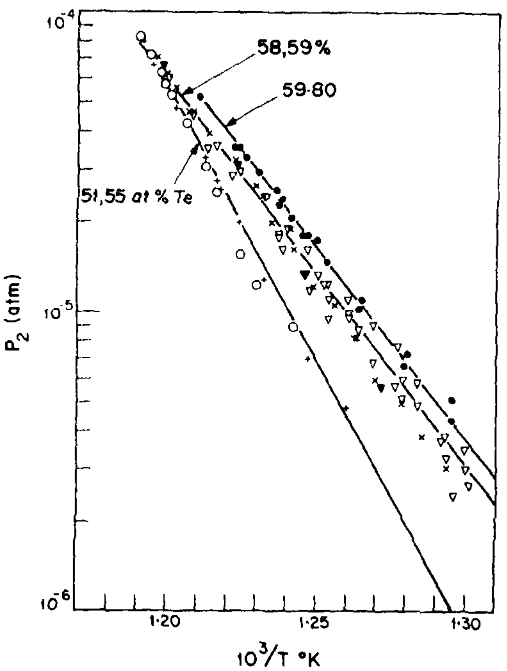

Fig. 2. Partial pressure of Te_2 as a function of $10^3/T$ for the most Bi-rich compositions. Lowest two lines form the three-phase curve for the 55–58 at. % Te peritectic phase. Uppermost line shows 59·80 at. % Te is just inside the $Bi_2Te_3(c)$ homogeneity range.

Symbol	○	+	▼	▽	×	●
at. % Te	51·0	55·0	58·0	58·0	59·0	59·80
Optical cell	4	5	12	15,16	19	6,17.

The upper limit of 58 at.% Te for the homogeneity range of the peritectic compound is supported by room temperature X-ray powder diffraction data to be discussed in another paper. These data indicate the 58 and 59 at.% Te powders are two phase, whereas there is no such indication for a 57 at.% Te powder (no optical density measurements made). Finally, although the data in Fig. 2 clearly show that the 55·0 at.% sample data coincides with the Bi-rich three-phase line of the peritectic phase and is therefore two-phase above about 540°C, X-ray powder diffraction data indicate this composition is single phase at 525°C and has a different structure than the 57·0 at.% Te sample.

The data for the various compositions are internally self-consistent with two exceptions, which are judged minor. The values of P_2 for the 59·80 at.% Te sample (6) above about 560°C do not coincide with the Bi-rich three-phase line but are about 10 per cent high. The values of P_2 for samples containing more than 60·07 at.% Te show some scatter between 575 and 586°C where the three-phase curve shows strong curvature.

(C) *Quantitative phase diagram data*

As noted above, the Te-rich leg of the $Bi_2Te_3(c)$ three-phase curve coincides within experimental error with our previously measured[7] vapor pressure of Te up to 416°C. Between 416 and 501°C the values of log P_2 fall along a straight line given by:

$$\log P_2(\text{atm}) = -4{\cdot}907(10^3)/T + 3{\cdot}050; \quad (416 \leq T \leq 501°\text{C}). \tag{3}$$

Up to 563°C the three-phase line between $Bi_2Te_3(c)$ and the 55–58 at.% Te peritectic-compound shown in Fig. 2 is given by

$$\log P_2(\text{atm}) = -12{\cdot}785(10^3)/T + 11{\cdot}113; \quad (525 \leq T \leq 563°\text{C}). \tag{4}$$

The Bi-rich leg of the three-phase line for the peritectic compound is given by:

$$\log P_2(\text{atm}) = -18{\cdot}265(10^3)/T + 17{\cdot}669; \quad (525 \leq T \leq 563°\text{C}). \tag{5}$$

A peritectic temperature of 563 ± 2°C is obtained from the simultaneous solution of equations (4) and (5) which corresponds to the intersection of the bottom and middle lines in Fig. 2. This is in agreement with the value of 562°C obtained by Glatz[15] from DTA heating curves of pre-annealed samples. A recent determination by Strauss[13] using DTA cooling curves gave 556°C. In contrast, a value of 540°C had been obtained earlier by Abrikosov *et al.*[16] from DTA heating curves on preannealed samples. This latter value now seems too low.

Values of P_2 and $10^3/T$ for the higher temperature portion of the $Bi_2Te_3(c)$ three-phase curve were read from the smoothed curve of Fig. 1 and are given in Part (*A*) of Table 2. There are some small discrepancies for the values of P_2 along the Te-rich leg between about 575 and 586°C. The higher values obtained with the 62·0 at.% Te sample (2) are taken as correct and those from the 60·2 per cent sample (7) ignored.

Solidus and liquidus temperatures for each sample were taken as those temperatures at which the P_2-lines inside the Bi_2Te_3 three-

Table 2. *Phase Diagram Data in the* Bi-Te *System*

(*A*) Partial pressure of $Te_2(g)$ along the $Bi_2Te_3(c)$ three-phase curve			(*B*) Liquidus points, estimated error ± 0·5°C		(*C*) Solidus points for Bi_2Te_3 and interpolated liquidus points		
$10^3/T$ (°K)	$10^3 \times P_2$ (atm)	$10^3 \times P_2$ (atm)	at.% Te	T°C	at.% Te (solidus)	at.% Te (liquidus)	T°C
1·165	6·40	4·70	44·0	539 ± 1		47·6	554·0
1·167	6·70	3·60	51·0	568·0		49·0	561·3
1·170	7·30	2·50	55·0	579·0	59·80	50·4	566·0
1·174	7·90	2·00	58·0	584·3		53·1	574·0
1·178	8·30	1·62	59·80	585·3	59·90	55·3	580·3
1·182	8·70	1·32	59·90	586·0		56·4	583·0
1·188	8·90	0·97	59·99	586·0		61·3	586·0
1·192	8·90	0·79	60·07	586·0	59·99	62·3	585·0
1·200	8·90	0·56	62·0	585·3		63·9	581·7
1·210	8·80	0·362	63·0	584·0		66·1	575·5
1·230	8·10	0·0148	70·0	564·0	60·07	69·0	566·6
1·250	7·20				60·20		513·0
1·290	5·10						

phase curve and the P_2-lines for the melts, respectively, intersected the Bi_2Te_3 three-phase curve. The liquidus temperatures are given in Part (*B*) of Table 2. The solidus temperatures are given in Part (*C*) of Table 2 which also lists a number of interpolated liquidus temperatures. The latter were obtained by constructing $\log P_2$-$10^3/T$ lines for various compositions at temperatures above 586°C and extrapolating these until they intersected the three-phase curve of Fig. 1. The temperatures of intersection were taken to be the liquidus temperatures. The values of $\log P_2$ for the compositions selected were interpolated from isotherms of $\log(P_2^{1/2}/X)$ vs. $(1-X)^2$, where X is the atom-fraction of Te. These isotherms are linear above 586°C.

The liquidus points given in Parts (*B*) and (*C*) of Table 2 all fall within 1° or less of a simple, smooth curve, indicating the general internal consistency of the data from the various samples. The liquidus curve is in good agreement with that given in Hansen's summary[14]. It is also in good agreement with the recent determination by Strauss[13]. Between 42 and 52 at.% Te our results agree with his to better than 1°. Between 52 and 67 per cent our results are lower by 1·0–1·5°, Strauss obtaining 587·3°C as the maximum melting point. Near 70 per cent the two sets of data agree again to better than 1°.

The values of P_2 for compositions inside the Bi_2Te_3 homogeneity range are given by equations of the form:

$$\log P_2(\text{atm}) = -10^3 A/T + B. \qquad (6)$$

The constants A and B are given in Table 3 along with the number of data points and an indication of the adequacy of the fit. It is to be noted that the values of A decrease with increasing Te-content. The partial relative enthalpy and entropy of Te in Bi_2Te_3 can be obtained directly from the constants A and B, the former decreasing with increasing Te-content.

FURTHER ANALYSIS AND DISCUSSION

(A) *Homogeneity range of* Bi_2Te_3

The isothermal dependence of $P_2^{1/2}$ upon composition using log-log scales is shown in Fig. 3. Compositions with less than 60 at.% Te are shown in the left side of the figure, where the abscissa is $100(\frac{3}{5}-X_{Te})$, increasing to the left. Compositions with more than 60 at.% Te are shown in the right side, where the abscissa is $100(X_{Te}-\frac{3}{5})$, increasing to the right. Thus the Te-content increases to the right in both halves. The abscissas for the two halves are made to coincide at $100|\frac{3}{5}-X_{Te}| = 0{\cdot}01$. The points used to construct the isotherms were interpolated from the $\log P_2 - 10^3/T$ curves of Figs. 1 and 2. In drawing the isotherms it was assumed that the value of P_2 for a 60·01 at.% Te sample would be the same as that observed for the 59·99 per cent

Table 3. *Partial Pressures of* Te_2 *inside the* $Bi_2Te_3(c)$ *homogeneity range* $\text{Log } P_2(\text{atm}) = -10^3 A/T + B$; T in °K

at.% Te	*A* (°K)	*B*	Temperature interval (°C)	Number of data points Total	Δ† ≤ 10%	Δ ≤ 5%	Δ ≤ 3%
60·07	6·5076	4·7210	395–567	31	30	29	23
59·99	10·0755	8·6294	443–538	9	–	9	7
	8·8692	7·1397	538–585	10	–	–	10
59·90	11·4942	9·8620	480–580	27	23	21	19
59·80	12·8590	11·2889	500–566	18	18	14	12

†Δ is the percentage difference between the measured value of P_2 and that calculated from the equation.

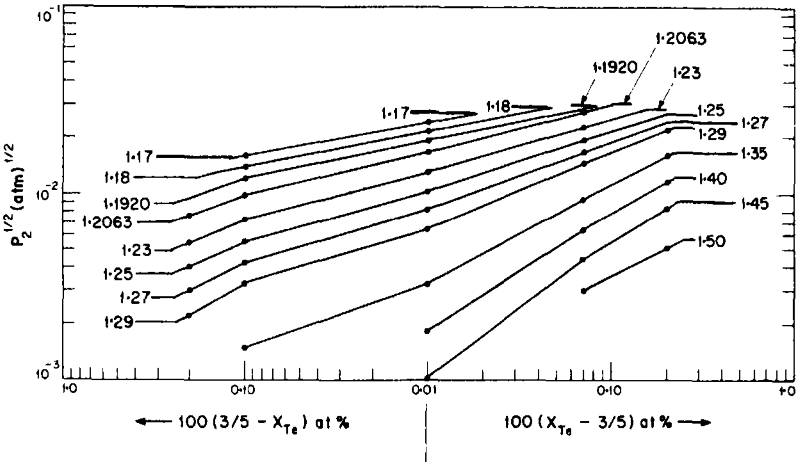

Fig. 3. Isotherms for the square root of the Te_2-pressure plotted against $\pm 100(X_{Te}-\frac{3}{5})$ where X_{Te} is the atom-fraction tellurium in the condensed phase establishing the vapor. The two abscissas, plotted on a log scale, are joined at $|100(X_{Te}-\frac{3}{5})| = 0{\cdot}01$. The numbers for each isotherm give the value of $10^3/T$.

sample. For each of the isotherms at $10^3/T =$ 1·17, 1·18 and 1·192, the straight line between 59·90 and 59·99 at.% is extrapolated to Te-rich compositions. The horizontal lines at either side of the figure with the attached values of $10^3/T$ show the values of P_2 along the three-phase curve for Bi_2Te_3. The intersections of the isotherms with the horizontal lines give interpolated values for the homogeneity limits of the Bi_2Te_3 phase. These are shown as circles in Fig. 4. The points obtained from data for the individual samples, as listed in Part (*C*) of Table 2 are shown as triangles. The agreement among the two types of points is seen to be generally satisfactory. The largest discrepancy is for the Bi-rich solidus at 565·9°C and is attributable to the fact that above 565°C the values of P_2 for the 59·80 per cent sample lie about 10 per cent above those on the Bi-rich three-phase curve adopted here.

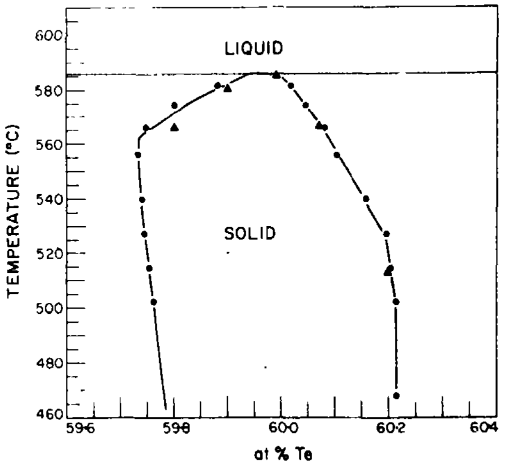

Fig. 4. Homogeneity range for the Bi_2Te_3-phase on a plot of temperature vs. at. % Te. Points shown as circles were obtained using the interpolation scheme of Fig. 3. Those shown as triangles were obtained directly from plots of log P_2 vs. $10^3/T$ for the various compositions as described in the text.

Figure 4 shows that the homogeneity range of Bi_2Te_3 encompasses compositions about 0·2 at.% on either side of stoichiometry between 460 and 520°C. The maximum melting point is estimated to be at 59·95 at.% Te. From DTA heating curves on annealed samples, Offergeld and Cakenberghe[17] obtained a value of 59·935 ± 0·015 at.%, in good agreement with ours. However, their values of 59·92 and 60·05 ± 0·05 at.% Te, for the homogeneity limits between 500 and 525°C, are significantly closer to stoichiometry than ours. They give no details of the annealing conditions used to prepare their samples.

From the variation of the room-temperature lattice parameters of samples annealed at 400°C, Glatz[15] has given the homogeneity limits at 400°C as 59·6 and 60·5 at.% Te. Within an uncertainty of 0·2 at.% these results are consistent with ours, which extend only as low as 460°C. In our opinion such an uncertainty in Glatz's results is not unreasonable, since the observed composition dependence of the parameters is not simple and the total variation is only 2 parts in about $4(10)^3$, about twice the precision of the measurements.

On the basis of lattice parameter measurements, Brown and Lewis[18] concluded that the Bi_2Te_3 phase extends some 30 at.% toward pure Bi. This conclusion is incorrect because they indexed the powder patterns on the assumption that the structure of the Bi-rich compositions is the same as for Bi_2Te_3. Stasova[19, 20] has demonstrated that this assumption is invalid for BiTe and suggested it is also invalid for other possible phases in the 50–60 at.% Te interval. We have identified two such phases from X-ray powder diffraction patterns for 55·0 and 57·0 at.% Te compositions. The indexing of these patterns is of course different from that for the Bi_2Te_3 phase. The 57·0 at.% phase is the same as the 55–58 at.% peritectic phase identified here from the partial pressure data and discussed earlier. A more extensive discussion of our x-ray results will be given in another paper. The conclusion we wish to present here is that the broad solidus field between 50 and 57 at.% Te found by Glatz[15] and Abrikosov[16] actually consists of at least 3 phases.

(B) *Correlation of composition and electrical properties through the antistructure model*

Measurements of carrier concentration indicate that Bi-rich samples of the Bi_2Te_3 phase are *p*-type, while Te-rich samples are *n*-type, the predominant point defects therefore being of the antistructure type[5, 6]. Thus excess Bi-atoms replace Te-atoms substitutionally and behave as acceptors, whereas excess Te-atoms substitute for Bi-atoms and behave as donors. The finding [5, 17] that the maximum-melting, *p*-type composition is on the Bi-rich side of 60 at.% Te, confirmed here, is consistent with this picture of the point defects.

Satterthwaite and Ure[5] measured the Hall coefficient in the plane perpendicular to the *c*-axis for the crystals first to freeze from a large volume of melt of known composition. Comparing their experimental results with ours, as listed in Table 4, makes it possible to test the adequacy of the antistructure model. The first two columns of Table 4 give respectively the melt composition and the apparent hole or electron concentration in the first-to-freeze solid as read from the smoothed curve in Fig. 1 of Satterthwaite and Ure. From our smoothed liquidus curve, constructed from the data in Parts (*B*) and (*C*) of Table 2, we find the liquidus temperature corresponding to the melt composition, and finally from Fig. 4 the corresponding solidus composition. Assuming the first-to-freeze solid in Satterthwaite and Ure's experiments was always in equilibrium with the liquid, the apparent carrier concentration in column 2 is determined by the solid composition in column 4. We have obtained only 2 solid compositions for Bi-rich material with apparent hole concentrations less than 6×10^{19} cm^{-3}. This is because the corresponding temperatures are within 0·5°C of the maximum melting point, where we do not have points to establish the solidus curve accurately. We have interpolated our results to obtain the composition corresponding to an apparent hole concentration of $6(10^{19})$ cm^{-3}. We have also listed our estimate of the maximum-melting composition.

The solid composition can be calculated from the apparent carrier concentration by using the antistructure model defined by the following assumptions. All the normal sites

Table 4. Comparison of observed composition of $Bi_2Te_3(c)$ *phase with that calculated from observed apparent carrier concentrations*

Liquid at.% Te	Satterwaite and Ure[5] p^* or n^* (cm^{-3})	T°C	Present results Solid composition at.% Te	Calc. solid composition at.% Te
50·4	–	565·5	59·980 ± ·025	–
55·3	–	580·5	59·882 ± ·012	–
59·0	6×10^{19}	585·5	(59·942)	59·899
59·95	$3{\cdot}03 \times 10^{19}$	586·0	59·95†	59·947
61·1	1×10^{19}	–	–	59·983
62·4	$1{\cdot}3 \times 10^{18}$	584·8	59·995	59·998
62·7	intrinsic	584·3	60·001	60·000
63·0	2×10^{18}n	584·0	60·002	60·002
63·9	6×10^{18}	581·70	60·016	60·007
64·4	1×10^{19}	580·3	60·020	60·011
65·3	2×10^{19}	577·8	60·031	60·022
66·0	$3{\cdot}03 \times 10^{19}$	576·0	60·037	60·033
60·0	–	566·6	60·074	–

†Estimated maximum melting composition.

and only the normal sites of the Bi_2Te_3 structure are assumed to be occupied. There are 3 N Te-sites and 2 N Bi-sites per cm^3, where N is the number of primitive cells per cm^3. From Francombe's[21] or Glatz's [15] lattice parameters, N is $5{\cdot}91(10^{21})$ cm^{-3}. If the number of Te-atoms per cm^3 occupying Bi-sites is W_{Te} and the number of Bi-atoms per cm^3 occupying Te-sites is W_{Bi}, then the atom fraction of Te is given by:

$$X_{Te} = (3N - W_{Bi} + W_{Te})/5N \qquad (7)$$

Rearranging this equation we obtain the deviation from stoichiometry as:

$$X_{Te} - \tfrac{3}{5} = (W_{Te} - W_{Bi})/5N. \qquad (8)$$

If each Te on a Bi-site is a singly-ionized donor and each Bi on a Te-site is a singly-ionized acceptor, then the difference in the concentration of conduction band electrons, n, and valence band holes, p, is

$$n - p = W_{Te} - W_{Bi}. \qquad (9)$$

The relationship of the extrinsic electron or hole concentration to the 77°K Hall coefficient in the plane perpendicular to the c-axis is given by[22]:

$$p = 0{\cdot}514/eR_H = 0{\cdot}514p^*; \quad p \gg n \qquad (10)$$

$$n = 0{\cdot}326/eR_H = 0{\cdot}326n^*; \quad n \gg p. \qquad (11)$$

Substituting equations (9) and (10) or (11) into (8) and rearranging we obtain

$$X_{Te} - \tfrac{3}{5} = 3{\cdot}38(10^{-23})(0{\cdot}326n^*); \quad n \gg p \qquad (12)$$

$$\tfrac{3}{5} - X_{Te} = 3{\cdot}38(10^{-23})(0{\cdot}514p^*); \quad p \gg n. \qquad (13)$$

The solid compositions calculated by these equations from the measured value of n^* or p^* are given in the last column of Table 4. The agreement between observed and calculated values is outside the estimated error of ±0·005 at.% for the intermediate n-type, Te-rich compositions compared. However, for the lowest and highest electron concentrations it is more than good enough to rule out the doubly-ionized antistructure model. It may be significant that for compositions where good agreement is obtained, the solidus line is fixed by the directly determined points (triangles in Fig. 4). The extrapolation used in Fig. 3 to get the Te-rich solidus points for the 3 highest temperature isotherms, though reasonable in view of the data, may be at fault. Drawing a straight line between the triangles for Te-rich compositions at 566·5 and 585°C in Fig. 4 improves the overall agreement between observed and calculated solidus compositions. Although we do not have an extensive check for the Bi-rich compositions, we note that our estimate for the maximum melting composition agrees with the calculated value.

Miller and Che-Yu[4] have observed discrepancies as large as 1 part in 10^3 between their weighing densities for Bi_2Te_3 of various compositions and the values calculated using Francombe's lattice parameters[21], Satterthwaite and Ure's[5] apparent carrier concentrations, and the antistructure model. However, some or all of these discrepancies may be due to the current uncertainty in the volume of the unit cell as a function of composition.

(C) *Partial pressure isotherms*

A fit of the isotherms shown in Fig. 3 requires further characterization of the antistructure model and hence further assumptions. Rather than list these individually here, we lump them into the assumed validity of the mass-action laws. We can then write:

$$P_{Bi}/P_2^{1/2} = pW_{Bi}K_1 \qquad (14)$$

and

$$P_{Bi}^2 P_2^{3/2} = K_2 \qquad (15)$$

corresponding to the quasi-chemical reactions

$$Bi(g) \rightarrow Bi_{Te} + h + \tfrac{1}{2}Te_2(g) \qquad (16)$$

$$\tfrac{3}{2}Te_2(g) + 2Bi(g) \rightarrow Bi_2Te_3(c) \qquad (17)$$

where Bi_{Te} is a Bi-atom on a Te site and h is a valence band hole. A statistical mechanical approach or a more careful mass action approach would lead to factors such as $(3N - W_{Te})$ and $(2N - W_{Bi})$ in equations (14) and (15) that are close to unity and can be neglected. For large enough Bi excess, $p = W_{Bi} \propto (\frac{3}{5} - X_{Te})$, and

$$P_2^{1/2} = W_{Bi}^{-4/5}(K_1K_2)^{2/5} = c_1(3/5 - X_{Te})^{-4/5}. \qquad (18)$$

Analogous equations for large enough Te excess, $n = W_{Te} \propto (X_{Te} - \frac{3}{5})$, lead to

$$P_2^{1/2} = W_{Te}^{4/5}(K_1^{1/2}K_3)^{2/5} = c_2(X_{Te} - 3/5)^{4/5}. \qquad (19)$$

The actual dependence of $P_2^{1/2}$ upon $(X_{Te} - \frac{3}{5})$, as shown in Fig. 3, is always weaker than required by equations (18) and (19). The steepest parts of the isotherms occur at the lowest temperatures where $P_2^{1/2}$ varies as $(X_{Te} - \frac{3}{5})^{-0.56}$ between 59.90 and 59.80 at.% and as $(X_{Te} - \frac{3}{5})^{0.72}$ between 60·07 and 60·20 at.%. Since the energy gap of Bi_2Te_3 at 20°C is 0·13 eV and the temperature dependence is $-9{\cdot}5(10^{-5})$ eV/°K[1], the extrapolated value of the energy gap at 500°C is 0·08 eV, i.e. slightly larger than kT. Thus even intrinsic Bi_2Te_3 is probably a degenerate semiconductor at 500°C and above. In this case the activities of electrons and holes are no longer equal to their concentrations, and mass-action equations such as equation (14) are invalid. One would then expect $P_2^{1/2}$ to depend less strongly upon $(X_{Te} - \frac{3}{5})$ than required by equations (18) and (19), as is observed. Further analysis using published expressions[24] for the chemical potentials would require a knowledge of the effective masses, as well as the energy gap, so that shift of the Fermi level with carrier concentration could be calculated.

(D) *Vaporization*

The total vapor pressure over Bi_2Te_3 between 455 and 575°C has been determined in two different investigations[2, 3] from the weight loss of a Knudsen cell. The apparent vapor pressures calculated on the assumption that the vapor species is $Bi_2Te_3(g)$ agree within 11 per cent for the two determinations. From reference [3] the equation is

$$\log P^*(\text{Torr.}) = -(10{\cdot}433 \pm 0{\cdot}468)\, 10^3/T + (10{\cdot}809 \pm 0{\cdot}026). \qquad (20)$$

The values of the total and partial pressures are related to the apparent pressure in a manner dependent upon the vapor species actually present. Boncheva-Mladenova *et al.* [2] assume the vaporization is described by the reaction:

$$Bi_2Te_3(c) \rightarrow \tfrac{1}{2}Te_2(g) + 2BiTe(g). \qquad (21)$$

For this model the total pressure, P_{tot}, and the partial pressure of $Te_2(g)$ are given by $P_{Tot} = 1{\cdot}58\, P^*$; $P_2 = P^*/5$. The values of P_2 are then 10^{-6} atm at 502°C ($10^3/T = 1{\cdot}2903$) and $6{\cdot}2(10^{-6})$ atm at 550°C ($10^3/T = 1{\cdot}2151$). According to our Fig. 1 these values are too low for the Bi_2Te_3 phase. Rather they are near values appropriate for liquid phases containing less than 44 at.% Te. The effusion product was analyzed to confirm the sublimation was congruent and equation (21) seems a reasonable description. Therefore we speculate the discrepancy is due to a lack of equilibrium in the Knudsen-cell. (The sublimation scheme of Gorbov *et al.* [3] results in values for the partial pressure of $Bi(g)$ larger than those over pure bismuth and is obviously incorrect.)

Acknowledgement—The author takes pleasure in acknowledging the capable experimental help of Mr. R. Capes.

REFERENCES

1. GOLDSMID, H. J., *Materials Used in Semiconductor Devices* (Edited by C. A. Hogarth), Chap. 7. Interscience, N.Y. (1965).
2. BONCHEVA-MLADENOVA Z., PASHINKIN A. S. and NOVOSELOVA A. V., *Izv. AN SSSR, Neor. Mat.* **2**, 1542 (1966).
3. GORBOV S. I. and KRESTOVNIKOV A. N., *Izv. AN SSSR, Neor. Mat.* **2**, 1702 (1966).
4. MILLER G. R. and LI CHE-YU, *J. Phys. Chem. Solids* **26**, 173 (1965).
5. SATTERTHWAITE C. B. and URE R. W., Jr., *Phys. Rev.* **108**, 1164 (1957).
6. HARMAN T. C., PARIS B., MILLER S. E. and GOERING H. L., *J. Phys. Chem. Solids* **2**, 181 (1957).
7. BREBRICK R. F., *J. phys. Chem.* **72**, 1032 (1968).
8. BREBRICK R. F., *J. chem. Phys.* **43**, 3031 (1965).
9. BREBRICK R. F., *J. Phys. Chem. Solids* **24**, 27 (1963).
10. BREBRICK R. F., *J. Phys. Chem. Solids* **26**, 989 (1965).
11. SHARMA C. B., *Proc. phys. Soc.* **67**, 935 (1954).
12. BROOKS L. S., *J. Am. Chem. Soc.* **74**, 227 (1952).
13. STRAUSS A. J., Personal communication.
14. HANSEN M., *Constitution of Binary Alloys*, 2nd Edn, p. 339. McGraw-Hill, N.Y. (1958).
15. GLATZ A. C., *J. electrochem. Soc.* **112**, 1204 (1965).
16. ABRIKOSOV N. Kh. and BANKINA V. F., *J. inorg. Chem. USSR* **3**, 659 (1958).
17. OFFERGELD G. and VAN CAKENBERGHE J., *J. Phys. Chem. Solids* **11**, 310 (1959).
18. BROWN A. and LEWIS B., *J. Phys. Chem. Solids* **23**, 1597 (1962).
19. STASOVA M. M. and KARPINSKII O. G., *Zh. Strukt. Khim.* **8**, 85 (1967).
20. STASOVA M. M., *Zh. Strukt. Khim.* **8**, 655 (1967).
21. FRANCOMBE M. H., *Br. J. appl. Phys.* **9**, 415 (1958)
22. DRABBLE J. R., *Proc. phys. Soc.* **72**, 380 (1958).
23. DRABBLE J. R., GROVES R. D. and WOLFE R., *Proc. phys. Soc.* **71**, 430 (1958).
24. BREBRICK R. F., *Progress in Solid State Chemistry* (Edited by H. Reiss), Vol. 3 Pergamon Press, Oxford (1966).

J. Phys. Chem. Solids Pergamon Press 1969. Vol. 30, pp. 733–737. Printed in Great Britain.

NEUTRON DIFFRACTION STUDY OF NpC*

G. H. LANDER, L. HEATON, M. H. MUELLER and K. D. ANDERSON
Argonne National Laboratory, Argonne, Ill. 60439, U.S.A.

(*Received* 3 *June* 1968; *in revised form* 27 *June* 1968)

Abstract – A neutron diffraction investigation of polycrystalline NpC has confirmed the measurements of magnetic susceptibility which suggested that the compound is antiferromagnetic between 310° and 220°K, and ferromagnetic below 220°K. Neptunium carbide has the NaCl type structure (a = 4·992 Å); the antiferromagnetic structure consists of ferromagnetic layers perpendicular to [001] coupled antiferromagnetically with the spin direction along the [001] axis. The change in ordered moment in the antiferromagnetic region below 310°K does not follow a Brillouin function. The maximum moment in the antiferromagnetic state is 1·3 ± 0·1 μ_B and the magnetic form factor for the neptunium atom has been determined at low angles. The transition to ferromagnetism is probably first order, and the initial moment at 218°K is 1·6 μ_B. The moment increases to a maximum value of 2·1 ± 0·1 μ_B at ~150°K and remains constant to 6°K.

INTRODUCTION

THE PRESENT neutron diffraction study is a part of a program in which the magnetic ordering and electronic structure of actinide intermetallic compounds are being investigated. Recent magnetic susceptibility measurements[1] indicate that NpC becomes antiferromagnetic at 310°K and ferromagnetic at 220°K. The neutron diffraction study was undertaken to determine the moments in the antiferro- and ferromagnetic states, the nature of the magnetic transition and the magnetic form factor of the neptunium atom.

EXPERIMENTAL

The compound NpC has the NaCl (Bl) type structure with $a = 4\cdot992 \pm 0\cdot002$ Å as determined by X-ray powder photographs taken at room temperature. Five grams of polycrystalline NpC was sealed in a ¼ in. vanadium tube[2]. Five grams is less than the usual amount of polycrystalline material used for neutron diffraction experiments but additional sample was unavailable. The vanadium capsule was contained in a cryostat where the sample temperature could be controlled between 4·2° and 330°K. Above 30°K the temperature was measured with a copper-constantan thermocouple that was in physical contact with the sample; below 30°K, by a germanium sensor located near the sample. Temperature stability was ±0·3°K and the absolute temperature estimated to ±0·5°K.

RESULTS

(1) *Paramagnetic region*

Neutron diffraction patterns were taken at a wavelength of 1·005 Å. Patterns in the paramagnetic region (>310°K) confirmed the NaCl-type structure of NpC and gave values for the scale factor, chemical composition and temperature factor. The results of a least-squares refinement are given in Table 1. Separate thermal parameters for Np and C could not be refined due to an insufficient number of reflections. A chemical analysis of the present sample gave $NpC_{0\cdot91}$, which is in agreement with $NpC_{0\cdot93}$ derived from the diffraction data. At lower temperatures all additional reflections could be ascribed to magnetic scattering. No evidence of structural distortion was found over the temperature range examined and although no abrupt change in lattice parameter was detected at

---

*Work performed under the auspices of the U.S. Atomic Energy Commission.

Table 1. Results from a least-squares refinement of nuclear reflections (sample temperature 320°K*)*

hkl	Integrated intensity $\times 10^{-3}$	F_{obs}	sF_{calc}
1 1 1	44·6	1·83 ± 0·05	1·91
2 0 0	406 5	7·34 ± 0·05	7·22
2 2 0	386·0	7·07 ± 0·08	7·13
3 1 1	43·1	1·95 ± 0·09	1·86
2 2 2	167·8	6·91 ± 0·08	7·03
4 0 0	98·4	6·98 ± 0·12	6 94
4 2 0	254·3	6·70 ± 0·06	6·76
3 3 1 5 1 1	29·8	1·75 ± 0·11	1·76
4 4 0	99·0	6 64 ± 0·10	6·58

Scattering lengths, $b_C = 0{\cdot}66$, $b_{Np} = 1{\cdot}055$[2, 3] $\times 10^{-12}$ cms; Scale factor, $s = 1{\cdot}095 \pm 0{\cdot}013$, Temperature factor, $B = 0{\cdot}33 \pm 0{\cdot}06 \times 10^{-16}$ Å^2, Carbon occupation $= 0{\cdot}93 \pm 0{\cdot}02$; R value $= 0{\cdot}013$.

either of the transition temperatures, some uncertainty exists because the sensitivity to such changes is relatively poor with this technique.

(2) *Antiferromagnetic region*

The antiferromagnetic structure of NpC is of the first kind in which ferromagnetic sheets perpendicular to [001] are coupled antiferromagnetically with the spin direction parallel to the [001] axis. This magnetic ordering has been reported for several uranium compounds that also have the NaCl structure, e.g., UN[4], UP[5, 6] and UAs[7, 8]. The magnetic reflections (Table 2) can all be indexed on the basis of the chemical cell and are present only if $h + k =$ even.

The ordered magnetic moment per neptunium atom (proportional to the square root of the integrated intensity) is shown in Fig. 1 as a function of temperature. The smallest magnetic moment that can be detected reliably is approximately 0·5 μ_B[2]. In the region between 280 and 310°K an accurate measurement of the magnetic moment is impossible, and the Néel temperature of 310°K is accepted from the susceptibility data[1]. There is certainly no antiferromagnetic ordering above 310°K. Because of the transition to the ferromagnetic state discussed below, it should be stressed that no evidence of any magnetic structure was found in the antiferromagnetic region, except that already described. This was established experimentally by observing the variation with temperature of a number of reflections arising from the antiferromagnetic ordering. The behavior of the (110) reflection, which has the greatest intensity, is shown in Fig. 3 and the variations in intensity of other reflections, e.g. (201), (112) and (221) are similar. The absence of any intensity at the position of the (001) reflection further indicates that the spin direction remains parallel to the [001] axis throughout the antiferromagnetic region.

Table 2. Antiferromagnetic reflections (sample temperature 221°K*)*

hkl	Integrated intensity $\times 10^{-3}$	j*	q^2†	$\mu_B f$
1 1 0	18·9	4	1	1·16 ± 0·08
2 0 1	9·5	8	$\frac{4}{5}$	1·02 ± 0·08
1 1 2	2·9	8	$\frac{1}{3}$	0·95 ± 0·12
2 2 1	4·9	8	$\frac{8}{9}$	0·92 ± 0·10
3 1 0	4·4	8	1	0·82 ± 0·10
0 2 3	< 1·5	8	$\frac{4}{13}$	
3 1 2	3·3	16	$\frac{5}{7}$	0·73 ± 0 13

*j is the multiplicity.

†q^2 the magnetic interaction vector.

The transition to an ordered antiferromagnetic state is usually a second-order phase transition, and the increase in ordered magnetic moment below the Néel temperature can be described by a Brillouin function. The Brillouin function for $J = \frac{9}{2}$ (normalized to $\mu_B = 0$ at 310°K and to $\mu_B = 1{\cdot}3$ at 230°K) is shown in Fig. 1. An extrapolation of the Brillouin function to 0°K gives 1·9 μ_B. However, at 220°K the magnetic ordering changes, but the variation in moment in the antiferromagnetic region clearly cannot be approximated by a Brillouin-type function.

The intensities of the magnetic reflections and values of $\mu_B f$ are given in Table 2. The value of μ_B per neptunium atom was ob-

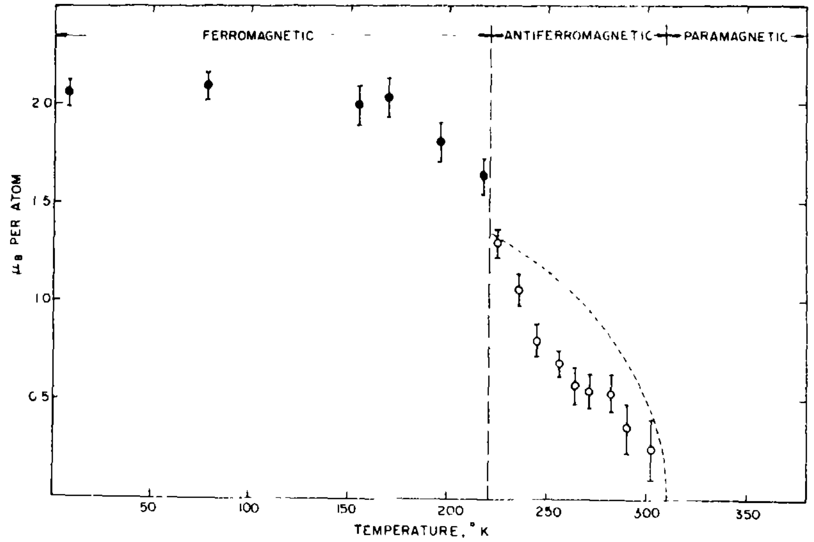

Fig. 1. Temperature variation of the ordered magnetic moment per neptunium atom in neptunium carbide The filled circles, which indicate a ferromagnetic alignment of the moments, are derived from the (111) integrated intensity. The open circles, which indicate the moments are antiferromagnetically aligned, are derived from the integrated intensity of the (110) reflection. The value of f, the magnetic form factor, has been taken as 0·90 for both reflections. The broken curve is the Brillouin function calculated for $J = \frac{9}{2}$, normalized to $\mu_B = 0$ at 310°K, and $\mu_B = 1{\cdot}3$ at 230°K.

tained by using the value of $f_{(110)}$ (0·90) given by the theoretical form factor calculated by Johnston[9] for the uranium ion in the $5f^3$ state. This form factor is drawn in Fig. 2 and is in good agreement with the experimental results.

(3) *Ferromagnetic region*

Below 220°K NpC is ferromagnetic; the transition is illustrated in Fig. 3. The figure shows the increases in the peak intensities of the (200) and (110) reflections that represent ferromagnetic and antiferromagnetic ordering, respectively. As shown in Fig. 1 the initial moment of 1·6 μ_B in the ferromagnetic state is some 26 per cent higher than the maximum moment in the antiferromagnetic state.

Neutron diffraction experiments indicate that a first-order phase transition occurs in UO_2[10], and possibly in UP. Recent results at this Laboratory show that the transition in UP occurs within a narrower temperature range that reported by Curry[6]. A criterion usually used in deciding whether a transition is first order is that the transition occurs over a very narrow temperature range. A relatively large polycrystalline sample has obvious disadvantages for defining a precise transition temperature since it is difficult to be sure that the temperature is completely uniform. Our measurements indicate that the transition takes place over a temperature range of approximately 3°K. The intensities were measured during both heating and cooling through the transition temperature. No difference could be detected which indicates no appreciable thermal hysteresis; the points in Fig. 3 are from both runs.

An accurate magnetic form factor is difficult to determine because of the superposition of nuclear and magnetic intensities in the diffraction data when the sample is ferromagnetic. Qualitatively, however, the intensities give a form factor comparable to that in the antiferromagnetic state illustrated in Fig. 2.

DISCUSSION

The transition from antiferromagnetic to ferromagnetic ordering has been observed in the rare earth metals[11] but not in the rare earth compounds with the NaCl-type structure. The antiferromagnetic structures are complicated in these elements and often

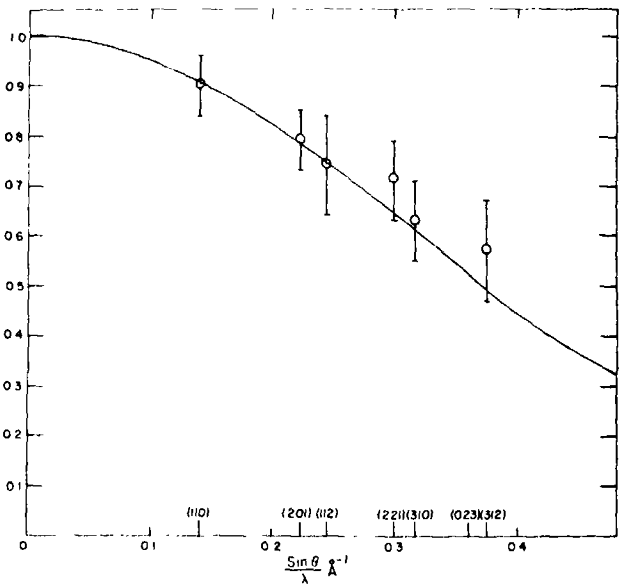

Fig. 2. Magnetic form factor at 230°K for the neptunium atom in neptunium carbide, assuming the magnetic moment is 1·29μ_B. Continuous curve from the table by Sidhu *et al.*[5] and quoted as Johnston's[4, 9] calculation for uranium in the 5f^3 configuration.

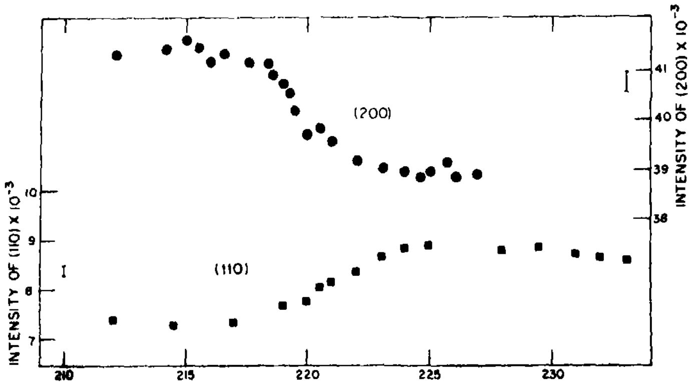

Fig. 3. Peak intensities of the (110) and (200) reflections showing the transition from the antiferro- to ferromagnetic state. The error bars represent the statistical uncertainty on any one measurement. The intensity at the (110) reflection position below 220°K is due to background scattering together with a small (0·5 per cent) λ/2 contribution from the (220) reflection.

important parameters used to describe the structures are temperature dependent. The temperature range in which the transition occurs in NpC is narrower than reported for the rare earths, and in the latter, the variations of the net magnetic moments follow Brillouin functions. A comparison of properties indicates that the transition in NpC is probably different in nature from those in the rare earths. Single crystals are required for neutron diffraction experiments to more fully understand the interesting magnetic behavior of NpC. The possibility arises that the antiferromagnetic state of NpC may be metastable and that a ferri- or ferromagnetic arrangement might be induced in the presence of an applied field.

Although the error bars on the magnetic form-factor measurements preclude any detailed analysis, the general shape supports the view that the magnetic scattering is mainly from the tightly bound f electrons rather than those in the $6d$ sub-shell. This is consistent with the results reported for uranium compounds.

Acknowledgements—The authors are indebted to Dr. D. J. Lam for helpful discussion. We are grateful to A. W. Mitchell and D. D. Zauberis for technical assistance.

REFERENCES

1. ROSS J. W. and LAM D. J., *J. appl. Phys.* **38**. 1451 (1967).
2. HEATON L., MUELLER M. H. and WILLIAMS J. M., *J. Phys. Chem. Solids* **28**, 1651 (1967).
3. COX D. E. and FRAZER B. C., *J. Phys. Chem. Solids* **28**. 1649 (1967).
4. CURRY N. A., *Proc. phys. Soc.* **86**. 1193 (1965).
5. SIDHU S. S., VOGELSANG W. and ANDERSON K. D., *J. Phys. Chem. Solids* **27**. 1197 (1966).
6. CURRY N. A., *Proc. phys. Soc.* **89**, 427 (1967).
7. TROC R., MURASIK A., ZYGMUNT A. and LECIEJEWICZ J., *Phys. Status Solidi* **23**. K123 (1967).
8. WILLIAMS J. M., HEATON L. and CAMPOS F. P., *J. Phys. Chem. Solids* **29**, 1702 (1968).
9. JOHNSTON D. F., *Proc. phys. Soc.* **88**. 37 (1966).
10. FRAZER B. C., SHIRANE G., COX D. E. and OLSEN C. E., *Phys. Rev.* **140**. A1448 (1965).
11. KOEHLER W. C., CABLE J. W., WOLLAN E. O. and WILKINSON M. K., *J. phys. Soc. Japan* **17**. Supp. BIII, 32 (1962).

J. Phys. Chem. Solids Pergamon Press 1969. Vol. 30, pp. 739–747. Printed in Great Britain.

INTERBAND FARADAY ROTATION AND VOIGT EFFECT IN Ge

YUICHIRO NISHINA

The Research Institute for Iron, Steel and Other Metals, Tohoku University, Sendai and Francis Bitter Magnet Laboratory*, Massachusetts Institute of Technology, Cambridge, Mass. 02139, U.S.A.

and

BENJAMIN LAX

Francis Bitter National Magnet Laboratory*, Massachusetts Institute of Technology, Cambridge, Mass. 02139, U.S.A.

(*Received* 6 *June* 1968)

Abstract—The interband Faraday and Voigt effect near the direct edge of Ge were measured near liquid helium temperature in the magnetic fields up to 56·7 kG applied in the [110] axis. The sample, about $4\,\mu$ thick, was backed by the glass substrate of 3 mm thick. In the low temperature the difference in the linear expansion coefficients of the sample and substrate induced a uniaxial stress equivalently in the direction perpendicular to the surface of the sample. Consequently the strain removed the four-fold degeneracy of the valence bands at Γ point, so that each of the observed Faraday singularities could be interpreted as caused by electronic transition to a non-degenerate excitonic state. An anomalous reversal in the sign of the Faraday peak was observed near the field of 45 kG, corresponding to the magneto-absorption line of the lowest photon energy. This phenomenon is due to the competitive effects of strain and magnetic field.

1. INTRODUCTION

SINCE the oscillatory behavior of the interband magneto-optical absorption was observed at room temperature in Ge[1] and InSb[2], the optical measurement in the high magnetic fields has proved to be an excellent method for determination of the electronic band parameters in semiconductors and semimetals with high precision[3]. The experiments on Ge near liquid helium temperature by Zwerdling, Lax, Roth and Button[4] revealed the effect of the Coulomb interaction between the excited electron and hole as represented by their dependence on the external magnetic fields. With the use of the steady high magnetic field in the order of 90 kG, our measurements of the interband Faraday rotation at room temperature near the direct absorption edge of Ge[5] showed the fine structures on each of the magnetic sublevels due to the spin-orbit interaction. Similar measurements by Mitchell[6] were performed to verify that the effect of the direct exciton was possibly present in the tail of the Faraday rotation just below the absorption edge. The results of our measurements were subsequently analyzed by Korovin and Kharitonov[7], who explained semi-quantitatively the origin of the fine structures observed in the oscillatory behavior of the Faraday rotation with respect to the photon energy. The theoretical formalism, however, did not explain the line shapes near the rotatory singularities because it did not take into account the effect of the Coulomb interaction in the electron-hold pair. It has been pointed out by our preliminary analysis on the low temperature data[8] that there is a distinct difference between the line shape for the excitonic transition and that for the transition between a pair of Landau levels, each belonging to a different band. The importance of the Coulomb effect in Ge has

---

*Supported by the U.S. Air Force Office of Scientific Research.

been recognized by Elliott and Loudon[9], Hasegawa and Howard[10] and by Suffczynski[11].

To substantiate the above arguments, this report presents the experimental results on the measurements of the interband Faraday and the Voigt effect near the direct absorption edge of Ge in the neighborhood of 10°K and in the magnetic fields up to 56·7 kG. Strain is another important factor of consideration in the analysis of these data[12]. Since the sample used in the present work was thin, it was backed by the glass substrate for mechanical reenforcement. At low temperatures the difference in the linear expansion coefficients of the sample and of the substrate induced the deformation in the plane parallel to the sample surface. With the superposition of hydrostatic pressure, the strain configuration may be expressed equivalently in terms of a uniaxial stress and strain in the direction perpendicular to the sample surface. This strain removed the degeneracy at the top of the valence band. Consequently the energy splitting led to the observation of the rotatory dispersion associated with an electronic transition to a nondegenerate excitonic level.

The following paper by Suzuki and Hanamura[13] gives the variational analysis on our experimental results in terms of the effective mass approximation. The results are found to be consistent with the observed fine structures in the over-all line shapes of the rotatory dispersion. Furthermore, it explains the sign reversal of the Faraday rotation in the magnetic field of about 45 kG as a consequence of the competition between the effect of the field and of the strain on mixing of the wave functions for the valence band.

2. EXPERIMENTAL ARRANGEMENTS

The principle of the technique for measuring the Faraday rotation was described briefly in the previous report[5] on our measurements at room temperature.

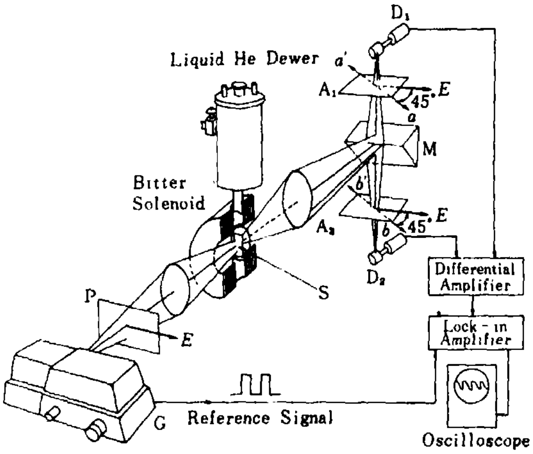

Fig. 1. Optical arrangements of the measurements of the Faraday rotation. The Voigt rotation was measured with a rotation of the Helmholtz-type Bitter solenoid by 90° around the horizontal axis, so that its 2 in. (I.D.) bore for the light propagation was exchanged with the 1 in. bore, to insert the liquid helium dewar. *aa'* and *bb'* are the polarising planes of the analyzers A_1 and A_2, respectively.

Figure 1 shows the schematic of the optical arrangments. The monochromatic radiation from the grating monochromator *G* (Perkin-Elmer Model 99G) was polarized by a sheet P (Polaroid HR 20). The monochromatic beam was chopped by a 13 c/sec chopper which generated a reference signal of square wave-form for phase-sensitive detection. The sample was placed in the center of the Bitter solenoid which could produce the maximum field of 57 kG with 10 kA d.c. Since the solenoid was made in a form of a Helmholtz pair, its field could be applied on the sample either in the Faraday configuration (perpendicular to the surface of the sample) or in the Voigt (parallel to the surface) with a 90° rotation of the solenoid about its horizontal axis. The beam of the radiation through the sample was split by the right angle mirror *M* so that two beams were focused on the PbS detectors D_1 and D_2 through the analyzers A_1 and A_2, respectively. The polarizing planes of both analyzers were set at 45 deg with respect to the plane of polarization of the incident ray, but they were set at 90 deg with respect to each other. This arrangement made an optical bridge out of a two detector system for discriminating the rotatory dispersion in the sample. In the absence of the external field, the 13 c/sec electrical signals out of D_1 and D_2 were equal, so that when they were fed into the differential amplifier Tektronix Type 122, its output was balanced out to null. When the external field caused the rotatory dispersion in the sample, the signal output of either one of the two detectors increased whereas the other decreased. The two analyzers were mechanically coupled together so that both signals could be balanced out again, if these analyzers were rotated by the angle equal to that of rotation in the plane of the polarization through the sample. Thus the rotatory dispersion of a sample could be measured by the reading of the analyzer orientation with its best accuracy of 1/180 of a degree in this optical arrangement.

The signal output of the Type 122 amplifier was amplified by a lock-in amplifier (a modification of the Princeton Applied Research JB-4) to improve the S/N ratio. Then the balancing condition was monitored with an oscilloscope (Tektronix 521) which displayed the output of the lock-in amplifier.

The ellipticity of the radiation influenced the sensitivity for the null point of the optical bridge, but not the null condition itself. To minimize the errors caused by the optical misalignment and the higher order effects of the magnetic field in the sample, the measurements were carried out in both normal and reverse direction of the magnetic field, and with the exchange in the orientations of the analyzers A_1 and A_2.

For preparation of the sample a single crystal of Ge was ground to the thickness in the order of 4 μ in the [110] plane. It was glued on the substrate of spectacle crown glass with Alymer cement[14].

The sample was cooled in the slot of a copper cold finger at the bottom of a liquid helium dewar. The cold finger had two vertical bores inside its bulk so that they could be filled with liquid helium to attain the lowest possible temperature in the sample. The temperature of the sample was measured with the resistance of the Allen-Bradly resistor[15] in mechanical contact with the lower end of the glass substrate for the sample.

3. EXPERIMENTAL RESULTS

(1) *Faraday rotation*

The Faraday rotation is caused by the difference in the indices of refraction for the circularly polarized waves of right and left senses. The rotation in the plane of the polarization per unit length in the medium of our interest is given by,*

$$\theta = \frac{\omega}{2c}(n_- - n_+) \simeq \frac{2\pi}{nc}\operatorname{Re}(\sigma_{xy}) \qquad (1)$$

where $n_+(n_-)$ is the index of refraction for the circularly polarized wave rotating clockwise (counter-clockwise) in space coordinates when looked from the source toward the direction of the propagation of the wave, i.e. the $+z$-direction. σ_{xy} is the non-diagonal component of the conductivity tensor where the external magnetic field is applied in the z-direction. ω is the angular frequency of the wave, c the speed of light and $n \simeq 1/2(n_+ + n_-)$. The sign of the observed Faraday rotation is determined here according to the above definition. It is also same as the convention taken by the following paper[13] for theoretical interpretation.

The spectra of the Faraday rotation can be analyzed more easily if they are compared with the corresponding magneto-absorption spectra. For the particular sample of our measurements, the two magneto-absorption lines, lowest in their photon energies, gave the dependence on the magnetic field as shown in Fig. 2. The non-linearities of the field dependence in absorption are quite characteristic of the Coulomb interaction between an electron-hole pair.

The Faraday spectra, corresponding to the magneto-absorption, are shown in Figs. 3(a–c) for the magnetic fields of 16·0, 39·5 and 56·7 kG, respectively. In Fig. 3(a) the lowest peak at 0·892 eV is larger in amplitude than that at 0·896 eV, whereas in Fig. 3(b) the relative heights of these two peaks are reversed in the field of 39·5 kG. In Fig. 3(c) the sign of the lowest peak is completely reversed in the field of 56·7 kG. In phenomenological theories of the interband Faraday rotation[16–20] the anomalous reversal of the sign of the rotation implies the change in the sign of the sum of the effective g-factor for electron and that for hole. Conversely, the relative magnitudes of the characteristic energy, $\hbar\omega_{\pm}$, for the transitions with $\Delta M^* \equiv M_c - M_v = +1$ and -1 are reversed since,

---

*The Gaussian unit is used.

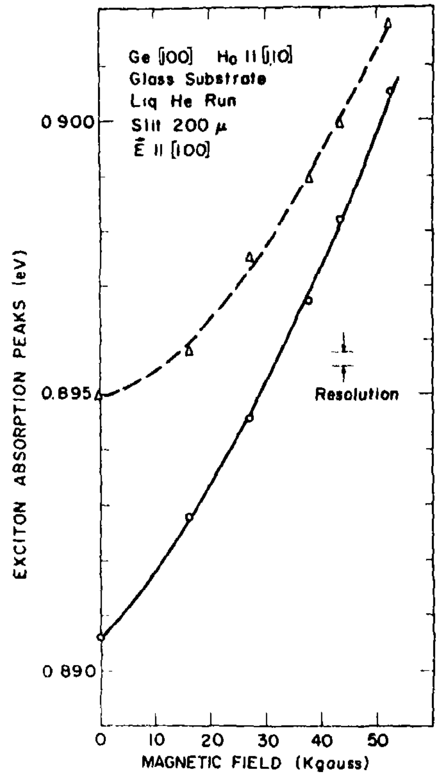

Fig. 2. The magnetic field dependence of the two absorption peaks, lowest in photon energies, in the Faraday configuration. The assignment of the two branches of absorption peak are given in Fig. 1 of the following paper [13].

$$(\omega_+ - \omega_-) \equiv 2\gamma H_0 = (g_e + g_h)\frac{\beta}{\hbar}H_0 \qquad (2)$$

where $M_c(M_v)$ is the z-component of the angular momentum in the conduction (valence), β, the Bohr magneton and $g_e(g_h)$ the effective g-factor of the electron (hole), respectively.

Comparison of the magneto-absorption with the Faraday spectra in Fig. 3(c) shows that the measurement of the latter provides more resolving power than the former, because the two peaks, neighboring close to each other with opposite sign, are represented simply by a broad absorption band without any additional information about its details. In principle, the absorption measurements for the circularly polarized waves should also resolve the fine structures. The sample, however, would have to be thinner than this

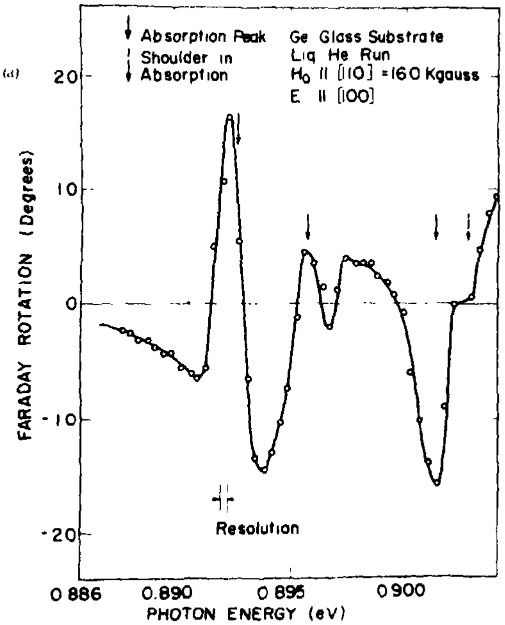

---

*This $M_{v(c)}$ corresponds to the $m_{J(S)}$ in the work of Roth *et al.*[4].

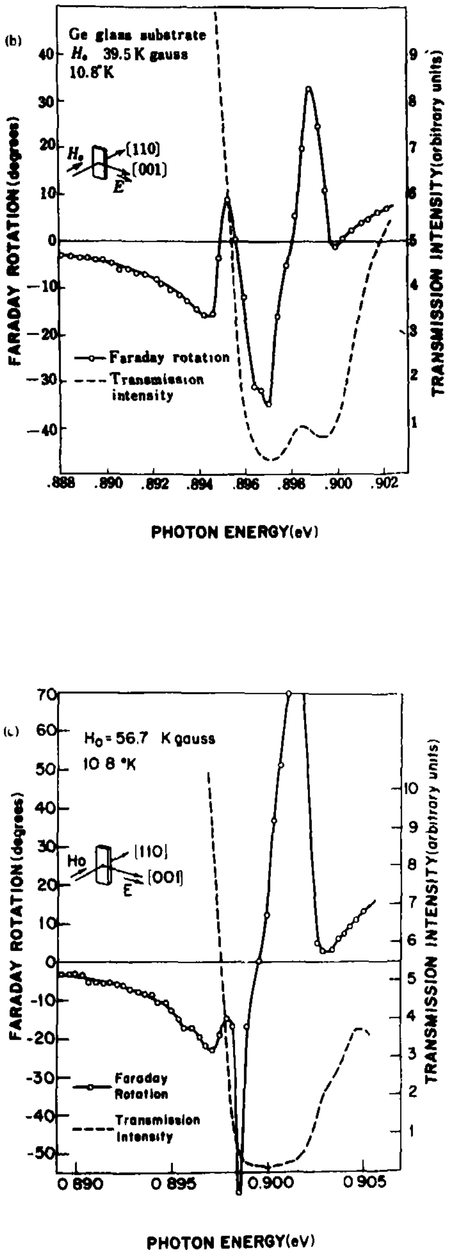

Figs. 3(a–c). The spectra of the Faraday rotation, corresponding to the magneto-absorptions of Fig. 2, at 10·8°K in the magnetic field of (a) 16·0 kG, (b) 39·5 kG and (c) 56·7 kG. The relative intensities of transmitted radiation are shown for their comparisons with the Faraday spectra.

case, and such requirement would add more to the technical difficulty.

(2) *Voigt effect*

The Voigt effect is defined by the phase difference, δ, per unit length of medium between the waves of two polarizations, one with the electric field parallel to the applied magnetic field and the other perpendicular, when they propagate in the direction perpendicular to the external field. If the field is applied in the z-direction and the light propagates in the y,

$$\delta = \frac{\omega}{c}(n_\perp - n_\parallel) \simeq \frac{2\pi}{nc}\,\mathrm{Im}(\sigma_{xx}-\sigma_{zz}) \qquad (3)$$

where $n_\perp$ ($n_\parallel$) is the index of refraction for the wave with its electric field perpendicular (parallel) to the external field. The experimental arrangement of Fig. 1, however, was more convenient for measuring the rotation of the plane of polarization of the wave incident upon sample with $\mathbf{E}_x = \mathbf{E}_z$ rather than the phase difference, δ, between the $\mathbf{E}_x$-wave and the $\mathbf{E}_z$-wave, because the rotation could be measured simply by rotating the Bitter solenoid by 90° about its horizontal axis perpendicular to the direction of the wave propagation. In a weak magnetic field region ($\sigma_{xy} \ll \sigma_{zz}$), the Voigt rotation, ϕ, is given by,

$$\phi \simeq \frac{-\pi}{nc}\,\mathrm{Re}(\sigma_{xx}-\sigma_{zz}) \qquad (4)$$

where the sign of rotation is the same as in the case of the Faraday rotation.

Figure 4 gives the magnetic field dependence of the two lowest absorption lines in the Voigt configuration. The sample used here was oriented in such a way that the field is applied in the $[\bar{1}10]$ direction (same orientation as in the Faraday measurement). The strain in this case, however, is applied in the [110] which is perpendicular to the magnetic field, whereas in the Faraday configuration they were parallel to each other along the [110]. This difference in the relative configuration of the strain and the magnetic field is the cause for the additional line splitting near the field of 10 kG[13].

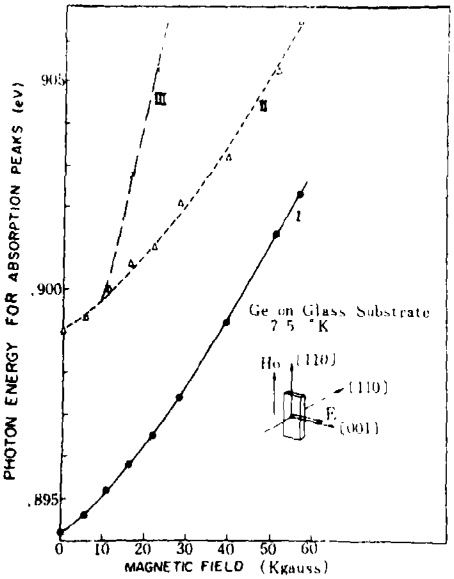

Fig. 4. The magnetic field dependence of the two absorption peaks, lowest in photon energies, in the Voigt configuration. The splitting of the higher branch into II and III near the field of 10 kG is due to the combined effect of uniaxial strain and the magnetic field. The assignments of the absorption lines I, II and III are given in Fig. 2 of the following paper[13].

The Voigt rotational spectra for the magnetic fields of 16·4, 39·2 and 56·7 kG are given in Figs. 5(a–c), respectively, together with the recordings of the magneto-transmission. In the Voigt configuration the electronic transition with $\Delta M = 0$ is allowed because of the presence of the wave with $E_z \parallel H_0$ component, in addition to the transitions expected in the Faraday configuration. The position and the strength of the absorption lines are determined by the relative magnitudes of the matrix elements for these transitions. The multiple possibilities of these transitions together with mixing of wave functions by magnetic field and strain cause considerable complications in interpreting the Voigt spectra.

4. DISCUSSIONS

As shown in Fig. 2, two absorption peaks were observed in the absence of magnetic field with the separation of 4·5 meV in the sample for the Faraday measurements. According to Kleiner and Roth[12], these two peaks are caused by the removal of four-fold degeneracy at the top of the valence bands at

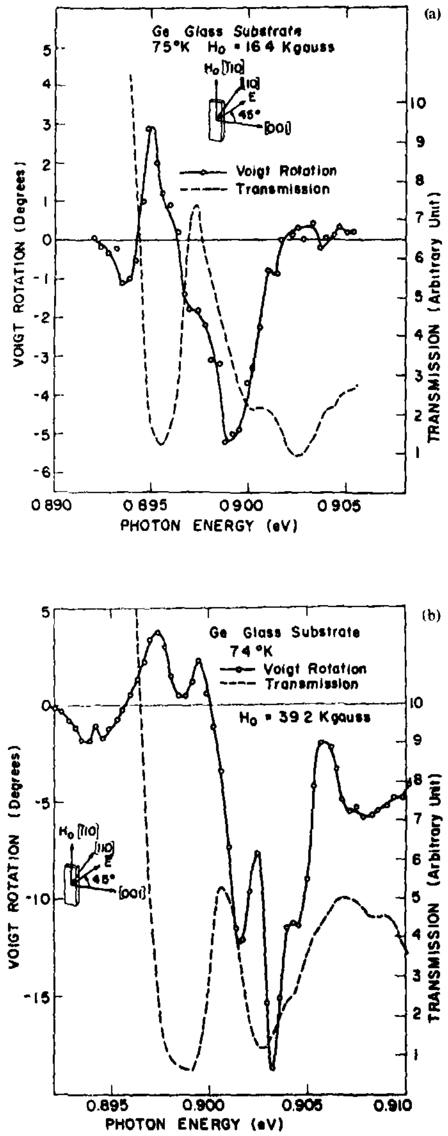

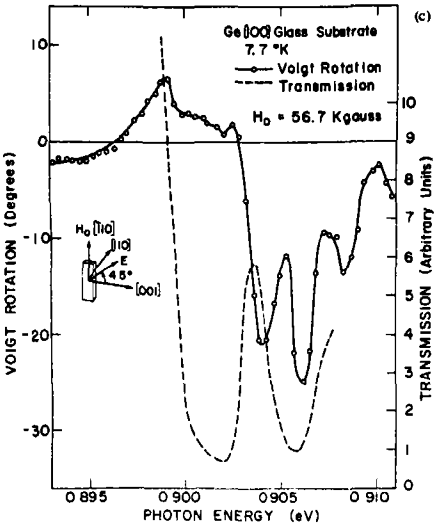

Figs. 5(a–c). The spectra of the Voigt rotation, corresponding to the magneto-absorption of Fig. 4 in the magnetic fields of (a) 16·4 kG at 7·5°K, (b) 39·2 kG at 7·4°K and (c) 56·7 kG at 7·7°K. The relative intensities of the transmitted radiation shown for their comparisons with the Voigt spectra.

$k=0$, so that it was split into two sets of bands. As will be shown in the work of Suzuki and Hanamura[13], one of the bands may be assigned approximately to $M_v = \pm\frac{1}{2}$ in the weak magnetic region in the Faraday configuration and the stress applied in the [110] direction. Hence in Fig. 3(a) the Faraday peak at 0·892 eV corresponds to the exciton absorption line for the two transitions from $M_v = \pm\frac{3}{2}$, $n=0$ in the valence band to $M_c = \pm\frac{1}{2}$, $n'=0$ in the conduction band with the selection rule $\Delta M = \mp 1$. Similarly the minor peak at 0·896 eV is for the transition from $M_v = \pm\frac{1}{2}$, $n=0$ to $M_c = \mp\frac{1}{2}$, $n'=0$.

The formula for the rotatory dispersion, θ_k, for an ideal model of exciton formation has been given by[8]*

$$\theta_k = A\left[\frac{X_k+Y_k}{(X_k+Y_k)^2+1} - \frac{X_k-Y_k}{(X_k-Y_k)^2+1}\right] \quad (5)$$

where $X_k = (\omega_k - \omega)\tau_k$, $Y_k = \gamma_k H_0 \tau_k$, ω_k the characteristic frequency for forming an exciton in its state k. γ_k is an effective gyromagnetic constant so that $2\hbar\gamma_k H_0 = \beta g_k H_0$ represents the Zeeman splitting of an excitonic state k. τ_k is a phenomenological relaxation time and A a constant determined by the transition matrix element, dielectric constant and various physical constants, all of which are assumed not to change over the photon energy range of our interest. On the other hand, the Faraday angle, θ_n, near the characteristic frequency ω_n for a transition between a pair of Landau levels is expressed by,

$$\theta_n = \frac{\omega_c}{4\pi\sqrt{\tau_n}}\left(\frac{u}{\hbar}\right)^{3/2} A \times\left[\left\{\frac{\sqrt{((X_n+Y_n)^2+1)}+X_n+Y_n}{(X_n+Y_n)^2+1}\right\}^{1/2} - \left\{\frac{\sqrt{((X_n-Y_n)^2+1)}+X_n-Y_n}{(X_n-Y_n)^2+1}\right\}^{1/2}\right] \quad (6)$$

where $\omega_n = \omega_g + (n+\frac{1}{2})\omega_c$, $X_n = (\omega_n - \omega)\tau_n$, $Y_n = \gamma_n H_0 \tau_n$ for an ideal band structure with the energy gap $\hbar\omega_g$, and the cyclotron frequency of ω_c for the reduced mass, μ, of electron and hole. The comparison of equation (5) with equation (6) shows an obvious difference as recognized in the plots of Fig. 6 for a particular case of $\gamma_n H_0 \tau_n = 1$. If Fig. 6 is compared with the spectra of Fig. 3(a), it may be understood at least qualitatively that the line shapes of afore-mentioned two peaks are associated with the exciton formation, and not with Landau level transitions.

The qualitative disagreement in the rotatory line shapes between an ideal model and the particular case of our measurement is attributed to the following possibilities.

(1) Since the valence band structures are complicated (particularly so in the presence of stress) the matrix element for the transition $\Delta M = 1$ is not equal in its magnitude to that for $\Delta M = -1$ even in the absence of the external field. This inequality causes asymmetry of

---

*In equations (5) and (6), only the terms with singularities are given and other non-singular terms are neglected, since our main interest lies in the line shapes near X_k or $X_n = 0$.

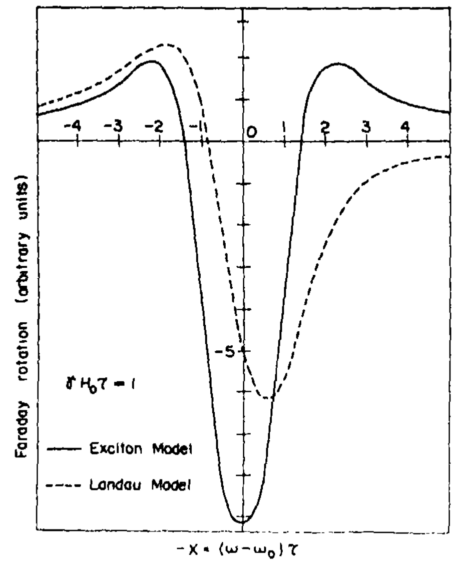

Fig. 6. The comparison of the line shape of the Faraday rotation for an exciton line in an ideal model of equation (5) with that for a Landau level transition expressed by equation (6). The particular case $\gamma_{kln}H_0\tau_{kln} = 1$ was chosen ω_0 is the angular frequency of the energy, characteristic of the absorption in the field H_0

the line shape about the photon energy for the maximum angle of rotation.

(2) Besides the singularity for each absorption line, there is a background rotation due to higher exciton levels[17]. The deep minimum in rotation at 0·894 eV in Fig. 3(a), for an example, may be explained in terms of such contribution.

(3) The electronic transitions considered so far are 'allowed' in terms of the selection rule. The intensities of the forbidden transitions have not been estimated for a particular case where the magnitude field and strain are present. A small fraction of such transition (say, in the order of 0·1 per cent in intensity compared to allowed transition) could give rise to an observable asymmetry in the line shape of the Faraday singularity [21].

Another observed phenomena of our interest here is the reversal in the sign of a Faraday singularity in the magnetic field near 45 kG. In the room temperature measurements such anomaly was never observed up to the field of 88 kG. It is caused by the competitive effects of strain and magnetic field on the relative difference in the energies for the $\Delta M = \pm 1$ transitions from the $M_v = \mp \frac{3}{2}$, $n = 0$ level to the $M_c = \mp \frac{1}{2}$, $n' = 0$ level (both in approximate assignment). Reader may refer to the work of Suzuki and Hanamura[13] for its analytical reason.

Acknowledgements – Authors would like to appreciate Drs. H. Hasegawa, M. Okazaki, E. Hanamura and K. Suzuki for their stimulating discussions regarding the interpretation of the experimental results. They are also grateful to Mr. R. E. Newcomb for the technical assistance during the course of experimental work. Ge samples were provided by Dr. S. Zwerdling.

REFERENCES

1. ZWERDLING S., KEYES R. J., FONER S., KOLM H. and LAX B., *Phys. Rev.* **104**, 1805 (1956).
2. BURSTEIN E., PICUS G. S., GEBBIE H. A. and BLATT F. J., *Phys. Rev.* **103**, 826 (1956).
3. For a review of the magneto-optical measurements, see, for an example, LAX B. and MAVROIDES J. G., *Semiconductors and Semi-metals* (Edited by R. K. Willardson and A. C. Beer), Vol. 3, Chap. 8, p. 321. Academic Press, New York (1967); A list of references up to December 1966 is given by PALIK E. D. and HENVIS B. W, *Appl. Optics* **6**, 603 (1967).
4. ZWERDLING S., LAX B., ROTH L. M. and BUTTON K. J., *Phys. Rev.* **114**, 80 (1959); ROTH L. M., LAX B. and ZWERDLING S., *Phys. Rev.* **114**, 90 (1959).
5. NISHINA Y., KOLODZIEJCZAK J. and LAX B., *Phys. Rev. Lett.* **9**, 55 (1962).
6. MITCHELL D. L. and WALLIS R. F., *Phys. Rev.* **131**, 1965 (1963).
7. KOROVIN L. I. and KHARITONOV E. V., *Fiz Tverd. Tela* **5**, 2035 (1963) [English Transl. *Soviet Phys. solid St.* **5**, 1488 (1964)]
8. NISHINA Y., KOLODZIEJCZAK J. and LAX B., *Proc. Int. Conf. Phys. Semiconductors, Paris 1964*, p. 867. Dunod, Paris (1964).
9. ELLIOTT R. J. and LOUDON R., *J. Phys. Chem. Solids* **15**, 196 (1960).
10. HASEGAWA H. and HOWARD R. E., *J. Phys. Chem. Solids* **21**, 179 (1961).
11. SUFFCZYNSKI M., *Proc. Int. Conf. Phys. Semiconductors, Paris 1964*, p. 885. Dunod, Paris (1964).
12. KLEINER W. H. and ROTH L. M., *Phys. Rev. Lett.* **2**, 334 (1959).
13. SUZUKI K. and HANAMURA E., *J. Phys. Chem. Solids* **29**, 749 (1968).

14. ZWERDLING S. Private communication.
15. WHITE G. K., *Experimental Techniques in Low-Temperature Physics*, p. 127. Oxford Press (1959).
16. KOLODZIEJCZAK J., LAX B. and NISHINA Y., *Phys. Rev.* **128**, 2655 (1962).
17. HALPERN J., LAX B. and NISHINA Y., *Phys. Rev.* **134**, A140 (1964).
18. BENNETT H. S. and STERN E. A., *Phys. Rev.* **137**, A448 (1965).
19. BOSWARVA I. M. and LIDIARD A. B., *Proc. R. Soc.* **278**, 588 (1964).
20. ROTH L. M., *Phys. Rev.* **133**, A542 (1964).
21. MURAO T. and EBINA A., *J. phys. Soc. Japan* **20**, 997 (1965).

J. Phys. Chem. Solids Pergamon Press 1969. Vol. 30, pp. 749–761. Printed in Great Britain.

EFFECTIVE MASS THEORETICAL APPROACH TO OPTICAL AND MICROWAVE PHENOMENA IN SEMICONDUCTORS – II.

THEORY OF THE FARADAY AND VOIGT EFFECTS DUE TO EXCITONS IN GERMANIUM

KATUHISA SUZUKI*
Department of Physics, University of Tokyo, Bunkyo-ku, Tokyo
and
EIICHI HANAMURA
The Institute for Solid State Physics, University of Tokyo, Roppongi, Tokyo

(*Received* 6 *June* 1968)

Abstract – The oscillatory Faraday and Voigt spectra observed by Nishina and Lax near the direct band gap of germanium have been analysed on the effective mass theory of the excitons in a strong magnetic field. The effective mass equation is solved variationally and assignment of each rotational singularity is made. The exciton binding turns out to be essential for the interpretation of the rotation spectra at room temperature as well as at low temperature. The effect of the existing strain is emphasized in the low temperature spectrum. The sign reversal of the first Faraday singularity observed at low temperatures is accounted for as an interplay between the effects of strain and magnetic field on a degenerate band.

1. INTRODUCTION

OPTICAL rotary effects involve the interaction of planepolarized electromagnetic waves with matter under the influence of a magnetic field. In the Faraday configuration light propagates along the magnetic field and normally incident on a surface of a crystal. The transmitted light generally exhibits elliptic polarization with its major axis rotated from the incident plane of polarization. In the Voigt configuration light travels perpendicularly to the magnetic field and the incident electric vector is polarized in a plane which makes 45 deg with the magnetic field. Again the transmitted light is rotated and elliptically polarized. Observation of the Faraday and Voigt spectra at various frequencies and magnetic field strengths has provided considerable information about the electronic structure of solids[1].

In a recent experiment Nishina, Kolodziejczak, and Lax have observed oscillatory Faraday and Voigt spectra near the direct band gap of germanium both at room temperature[2] and near liquid helium temperatures [3, 4]. This was the first observation of oscillatory effects in the rotatory dispersion spectra of solids and provided an analogue of the quantum oscillation in the interband magneto-optical absorption[5]. Their striking results have stimulated us to make a detailed investigation to assign each rotatory singularity. In the room-temperature Faraday spectrum several distinct rotation peaks were seen over a photon energy range of 0·1 eV near the direct band gap at 42, 60 and 88 kG. The change of the position and the magnitude of individual peaks with magnetic field is rather regular, so that the primary interest in this case is to assign the magnetic levels pertinent to each rotation peak, taking into account the complexity of the valence band of germanium. Another interest concerns the existence of an exciton effect at this temperature. A question was raised whether the observed room-temperature spectra involve the electron-hole binding or not[6]. A later experiment by Mitchell and Wallis[7] has given some indication of the existence of this. Korovin and Kharitonov[8] tried to analyse the spectra, assuming the transitions between free Landau states, but their result was not in satisfactory agreement with the experimental observation. The aforementioned question, at any rate, does not seem to have been conclusively answered on a firm ground.

---

*Present address: Bell Telephone Laboratories, Murray Hill, N.J. 07971, U.S.A.

For the low temperature Faraday spectrum, oscillatory rotation studies were limited to a photon energy range of 0·01 eV, but an entirely unexpected phenomenon was observed in which the rotational sign of the first singularity was reversed when the magnetic field intensity was raised[4]. This occurs at approximately 45 kG. An inherent difference between the room- and low-temperature experiments is the existence of a strain in the latter which is caused by the difference in the linear expansion coefficients of the thin germanium crystal and the glass substrate. Both the absorption and Voigt spectra at low temperatures show manifestly the existence of strain in the sample. The effect of exciton formation is naturally expected to bear much importance in the low-temperature spectrum.

In this paper we analyze the experiment of Nishina and co-workers in the framework of the effective-mass theory and on the assumption of exciton transitions. The analysis is particularly related to the experimental paper of Nishina and Lax[4], which hereafter will be referred to as NL. Expressions for the rotation angles in the both configurations are given first in macroscopic terms and then rewritten in the effective-mass formalism. The magnetic levels are calculated in the absence and presence of strain for the room- and low-temperature spectra, respectively. The shape of the rotation curves is studied on the knowledge of the calculated levels and on the assumption of an appropriate relaxation time.

The results of the present analysis are summarized as follows:

(1) The sign reversal in the low-temperature Faraday spectrum can be accounted for in terms of the interplay between the effects of strain and magnetic field on a degenerate band.

(2) Inclusion of the exciton binding is not less indispensable for interpreting the room-temperature spectrum than it is in the low-temperature case.

It is thus seen that two of the questions concerning the puzzling and controversial aspects of the observed spectrum can be clearly answered within the framework of the effective-mass approximation.

2. EXPRESSIONS FOR THE FARADAY AND VOIGT ANGLES

Consider a solid in a static magnetic field in the z-direction. If the system is at least three-fold symmetric* about the z-direction the dielectric constant tensor necessarily has the form[9]

$$\begin{pmatrix} \epsilon_{xx} & \epsilon_{xy} & 0 \\ -\epsilon_{xy} & \epsilon_{xx} & 0 \\ 0 & 0 & \epsilon_{zz} \end{pmatrix} \tag{2.1}$$

each component of which being in general a complex quantity.

For the Faraday configuration, assuming a plane wave of the form

$$E = E_0 \exp\left[i\omega t - \frac{i\omega}{c} N z\right] \tag{2.2}$$

where $N = n - i\kappa$ is the complex refractivity, we obtain as an eigenmode of the electric vector in the medium either the right circular polarization

---

*The [110] axis of germanium, along which a magnetic field was applied in references [2–4], has no more than a two-fold symmetry, but, in accordance with later simplifications, we neglect a small deviation of this axis from higher symmetries. From a symmetry point of view, experiments with H‖[111] or [001] are most preferable for analysis.

$$E_x = iE_y;\quad N_+^2 = \epsilon_{xx} - i\epsilon_{xy} \tag{2.3}$$

or the left circular polarization

$$E_x = -iE_y;\quad N_-^2 = \epsilon_{xx} + i\epsilon_{xy}. \tag{2.4}$$

The light plane-polarized in the y-direction at $z = 0$ is expressed by the superposition of two polarizations, each of which propagates through the medium with its characteristic complex refractivity. At $z = l$ the superposition of the two polarizations no longer forms a plane polarization but an elliptic polarization, whose major axis is rotated from the y-axis by an angle

$$\theta_F = \frac{\omega l}{2c}(n_- - n_+) \tag{2.5}$$

and the ratio of whose minor to major axis is given by

$$(a/b)_F = \tanh\frac{\omega l}{2c}(\kappa_- - \kappa_+). \tag{2.6}$$

Here a positive θ_F corresponds to a clockwise rotation to an observer looking along the magnetic field and $(a/b)_F$ is positive if the electric vector is rotating anti-clockwise at $z = l$ to the same observer. Noting from (2.3) and (2.4) that

$$\begin{aligned} N_- - N_+ &= \frac{N_-^2 - N_+^2}{N_- + N_+} \\ &= \frac{2i\epsilon_{xy}}{N_- + N_+} \\ &= \frac{i\epsilon_{xy}}{N_0} \end{aligned}$$

where N_0 refers to the complex refractivity in the absence of the field, we obtain

$$\theta_F = \frac{\omega l}{2c}\,\mathrm{Re}\,(N_- - N_+) = -\frac{\omega l}{2c}\,\mathrm{Im}\frac{\epsilon_{xy}}{N_0} \tag{2.7}$$

and

$$\tanh^{-1}(a/b)_F = \frac{\omega l}{2c}\,\mathrm{Im}\,(N_- - N_+) = \frac{\omega l}{2c}\,\mathrm{Re}\frac{\epsilon_{xy}}{N_0} \tag{2.8}$$

for the Faraday angle and ellipticity in the absorption region of the crystal*. These provide a counterpart of the formulas obtained by Boswarva, Howard and Lidiard[9] in the transparent region. A quantum-mechanical expression for the dielectric constant tensor at the radiation frequency ω is given by the Kramers-Heisenberg dispersion relation[10]

$$\begin{aligned} \epsilon_{\mu\nu} = \delta_{\mu\nu} - \frac{4\pi e^2}{\hbar\omega}\sum_n \frac{1}{\omega_{n0}}\Big[&\langle 0|\sum_j v_{j\mu}|n\rangle \\ &\times\langle n|\sum_j v_{j\nu}|0\rangle\left(\frac{1}{\omega_{n0}+\omega} + i\pi\delta(\omega_{n0}+\omega)\right) - \\ &-\langle 0|\sum_j v_{j\nu}|n\rangle\langle n|\sum_j v_{j\mu}|0\rangle \\ &\times\left(\frac{1}{\omega_{n0}-\omega} - i\pi\delta(\omega_{n0}-\omega)\right)\Big] \end{aligned} \tag{2.9}$$

where 0 and n refer to the ground and excited states, respectively, of the crystal in a magnetic field, with $\hbar\omega_{n0} = E_n - E_0$. The velocity operator for the j-th electron v_j is defined as

$$v_j = \frac{1}{m}\left(\mathbf{p}_j + \frac{e}{c}\mathbf{A}_{8j}\right) + \frac{1}{2m^2c^2}(\mathbf{s}_j \times \nabla_j V), \tag{2.10}$$

where A_{8j} is the vector potential for the static field, s_j the spin, and V the crystal potential. The summation over j extends over all the electrons in the crystal and μ, ν are the Cartesian components. In the effective mass theory of the direct excitons in germanium the wave function of the exciton state is expressed as[11]

$$|K,n\rangle = \sum_{M_c M_v} e^{i\boldsymbol{K}\boldsymbol{R}}\, U_{M_c M_v n}(r)\phi_{mc}\phi_{mv}, \tag{2.11}$$

where $\boldsymbol{R}$ and $\boldsymbol{r}$ are the central and relative coordinates of the electron-hole system. $\phi_{Mc}(M_c = \pm\frac{1}{2})$ and $\phi_{Mv}(M_v = -\frac{3}{2}, -\frac{1}{2}, \frac{1}{2}, \frac{3}{2})$ are the Bloch functions at $\boldsymbol{k} = 0$ of the conduction (Γ_2) and the valence (Γ_8) bands. $U_n(\boldsymbol{r})$ is the envelope function for the n-th quantum state in the relative motion, which is to be determined from the effective mass equation. Substitution of (2.11) and (2.9) into (2.7) leads to an exciton contribution to the Faraday rotation

---

*We can arrive at equation (1) of NL by noting $\sigma_{xy} = i\omega\epsilon_{xy}/4\pi$.

$$\theta_F = \frac{\pi e^2 l}{2nc\hbar\omega_g} \sum_{M_cM_vn} \left(|(v_-)_{M_cM_v}|^2 - |(v_+)_{M_cM_v}|^2\right) \mathrm{Re}\,\frac{|U_{M_cM_vn}(0)|^2}{\omega_{n0}-\omega+i/\tau_n}, \qquad (2.12)$$

where

$$(v_\pm)_{M_cM_v} = \frac{1}{\Omega}\int \phi^*_{M_c}(v_x \pm iv_y)\phi_{M_v}\,\mathrm{d}\tau, \qquad (2.13)$$

and we have assumed ω close to ω_g, the frequency corresponding to the band gap, and replaced the term containing the delta function by a Lorentzian term in which τ_n is an appropriate relaxation time. We have also assumed $|\kappa| \ll |n|$ and replaced N_0 by n in (2.7).

In the Voigt configuration light propagates along the x-direction, and E_y and E_z components have distinct propagation constants. Let the radiation polarized at $x=0$ in a plane bisecting the y- and z-directions be expressed by

$$E_y = E\cos\left(\omega t - \frac{\omega}{c}n_\perp x\right)e^{-\frac{\omega}{c}K_\perp x}$$

$$E_z = E\cos\left(\omega t - \frac{\omega}{c}n_\parallel x\right)e^{-\frac{\omega}{c}K_\parallel x} \qquad (2.14)$$

then at $x=l$ we observe an elliptic polarization whose major axis is rotated by θ_v[*] and whose ellipticity is given by $(a/b)_v$:

$$\tan 2\theta_v = -\frac{\sinh\chi}{\cos\delta} \qquad (2.15)$$

$$(a/b)_v = \frac{\sin\delta}{(\cosh^2\chi - \sin^2\delta)^{1/2} + \cosh\chi} \qquad (2.16)$$

with

$$\chi = \frac{\omega l}{c}(K_\perp - K_\parallel)$$

and

$$\delta = \frac{\omega l}{c}(n_\perp - n_\parallel).$$

For small χ and δ, (2.15) and (2.16) reduce to

$$\theta_v = \frac{\omega l}{2c}(K_\perp - K_\parallel) \qquad (2.17)$$

and

$$(a/b)_v = \frac{\omega l}{2c}(n_\perp - n_\parallel). \qquad (2.18)$$

The quantities $\kappa_\perp$ and $\kappa_\parallel$ are directly related to the extinction or absorption coefficient for the perpendicular and parallel polarizations, for which we have familiar quantum-mechanical expressions[12]. Thus in the effective mass approximation the exciton contribution to θ_v is given by

$$\theta_v = A\sum_{M_cM_vn}\left(|(v_y)_{M_cM_v}|^2 - |(v_2)_{M_cM_v}|^2\right)\mathrm{Im}\,\frac{|U_{M_cM_vn}(0)|^2}{\omega_{n0}-\omega+i/\tau_n} \qquad (2.19)$$

where A is a positive constant containing l and ω_g.

3. DETERMINATION OF THE EXCITON LEVELS FROM THE EFFECTIVE MASS EQUATION

In this section determination of the direct exciton states will be made, the information on which, as seen in the previous section, is a requisite for the analysis of the rotatory spectra. We restrict ourselves to the effective mass approximation[11], in which the wave function of the exciton states is represented by a linear combination of the products of the Bloch functions forming the conduction and valence band extrema. The set of coefficients of the linear combination is known as the envelope function and is determined as an eigenvector of an appropriate effective mass Hamiltonian. In our problem we are dealing with three effects, namely, the formation of Landau levels, the electron-hole Coulomb interaction, and the strain effect (at low temperatures), the characteristic energies of which are comparable or of the same order of magnitude under the experimental conditions. For an averaged reduced mass $\mu = 0{\cdot}03\,m$ and a dielectric constant $\epsilon_0 = 16$, the lowest Zeeman energy $\hbar eH/2\mu c$ is 1·9 meV at 10 kG and the exciton binding energy $\mu e^4/2\epsilon_0{}^2\hbar^2$ is 1·6 meV, while the strain splitting of the valence band is 4·4 ~ 4·8 meV in the low temperature experiments. Thus we are more or less forced to adopt a scheme which takes the three effects rather simultaneously into account.

---

[*] The sign of θ_v is so defined that a negative θ_v implies a rotation toward the direction of the magnetic field through an angle smaller than 45 deg.

The effective mass Hamiltonian for the excitons is expressed as the sum of that for the electron, that for the hole, and the interaction term, for which we adopt the Coulomb interaction. The conduction band at $k = 0$ is nondegenerate and spherical, so the effective Hamiltonian for the electron is simply

$$H_e = \frac{\alpha\hbar^2\mathbf{k}_e{}^2}{2m} + g_e\beta(H\cdot S), \qquad (3.1)$$

where $(1/\alpha)$m and $\mathbf{g}_e$ are the effective mass and the $\mathbf{g}$-factor of the conduction band, β the Bohr magneton, s the electron spin ($s = \frac{1}{2}$), and

$$\mathbf{k}_e = \frac{1}{\hbar}p_e + \frac{e}{2c\hbar}\mathbf{H}\times\mathbf{r}_e \qquad (3.2)$$

with $\mathbf{p}_e$ the momentum operator for the electron coordinate. For the hole we take the matrix Hamiltonian of Luttinger[13] for the degenerate Γ_8 valence band, viz.

$$H_h = -\frac{\hbar^2}{m}\left[\frac{\gamma_1}{2}k_h{}^2 - \gamma\left(\left(J_1{}^2 - \frac{1}{3}J^2\right)k_{hl}^2 + \text{c.p.}\right)\right.$$
$$\left. - 2\gamma(\{J_1J_2\}\{k_{h1}k_{h2}\} + \text{c.p.})\right] - 2\kappa\beta\,\mathbf{J}\cdot\mathbf{H}, \quad (3.3)$$

where γ_1, $\bar{\gamma}$, and κ are the valence band parameters (we have made the spherical approximation, i.e. $\gamma^2 = \gamma^3 = \bar{\gamma}$), J the angular momentum matrices corresponding to $J = \frac{3}{2}$, and

$$k_h = \frac{1}{\hbar}\mathbf{p}_h - \frac{e}{2c\hbar}\mathbf{H}\times\mathbf{r}_h. \qquad (3.4)$$

The curly bracket denotes the symmetric product, c.p. implies cyclically permuted terms, and the coordinate (1, 2, 3) refers to the cubic axes.

The effect of anisotropic strain on the conduction band is merely to shift the band edge, while that on the valence band is to lift, partly, the fourfold degeneracy. This effect is described by the Kleiner–Roth matrix Hamiltonian[14]

$$H_s = \tfrac{2}{3}D_u[(J_1{}^2 - \tfrac{1}{3}J^2)e_{11} + \text{c.p.}]$$
$$+ \tfrac{2}{3}D_u'[\{J_1J_2\}e_{12} + \text{c.p.}], \qquad (3.5)$$

where D_u and D_u' are the valence band deformation potentials and e_{11} etc. are the strain components.

In NL a [110] face of a thin germanium slab (4μ thick) was glued to a glass substrate, and the magnetic field was applied along [110] (perpendicular to the slab) in the Faraday configuration and along [$\bar{1}$10] (parallel to the slab) in the Voigt configuration. We hereafter take the quantization axis z along the magnetic field (either [110] or [$\bar{1}$10]) and label the rows and columns of the J matrices so that J_z has components $3/2, -1/2, 1/2, -3/2$ along its diagonal. Then the strain Hamiltonian is expressed by the matrix

$$H_s = -\begin{bmatrix} E_1 & E_2 & 0 & 0 \\ E_2 & -E_1 & 0 & 0 \\ 0 & 0 & -E_1 & E_2 \\ 0 & 0 & E_2 & E_1 \end{bmatrix} \qquad (3.6)$$

with

$$E_1 = \tfrac{2}{3}(1-\lambda)S\cdot\tfrac{1}{4}(D_u \pm 3D_{u'})$$
$$E_2 = -\tfrac{2}{3}(1-\lambda)S\cdot\tfrac{\sqrt{3}}{4}(D_u \mp D_{u'}) \qquad (3.7)$$
$$\lambda = \frac{c_{11} + 3c_{12} - 2c_{44}}{c_{11} + c_{12} + 2c_{44}} = 0{\cdot}44$$

where the upper and lower signs correspond to the Faraday and Voigt configurations, respectively. The magnitude of the strain S is determined by the condition that the strain splitting $2E_s = 2\sqrt{(E_1^2+E_2^2)}$ give the observed splitting of the absorption peaks at $H = 0$ and its sign is taken negative so that the germanium slab suffers a compressional strain along the interface.

The effective mass Hamiltonian for the exciton in a magnetic field is thus

$$H_{\text{exc.}} = H_e - H_h - \frac{e^2}{\epsilon_0|r_e - r_h|} - H_s + \hbar\omega_g, \quad (3.8)$$

in which H_h, like H_s in (3.6), is understood to be in the J_z-diagonal representation. Since the translational symmetry of the system allows separation of the central coordinate $\boldsymbol{R} = (\boldsymbol{r}_e + \boldsymbol{r}_h)/2$ in the form $e^{i\boldsymbol{K}\cdot\boldsymbol{R}}$ and, further, momentum conservation requires $\boldsymbol{K} \cong 0$ in the final state, our interest is only in the relative motion in the coordinate $\boldsymbol{r} = \boldsymbol{r}_h - \boldsymbol{r}_e$. The effective mass equation for the relative motion has been solved variationally by assuming an envelope function of the form

$$U_{M_cM_vn}(\boldsymbol{r}) = \sum_n c_{M_cM_v}\, v_n(\boldsymbol{r}), \quad (3.9)$$

where v_n is a harmonic-oscillator-like function, but having a finite radius in the z-direction also, namely

$$v_n = i^n\left(\frac{1}{(2\pi)^{3/2}\cdot 2^n\cdot n!\,a_\perp^2 a_\parallel}\right)^{1/2}\left(\frac{x^2+y^2}{a_\perp^2}\right)^{n/2} \times \exp\left(-\frac{x^2+y^2}{4a_\perp^2} - \frac{z^2}{4a_\parallel^2}\right)\left(\frac{iZ}{a_\parallel}\right)^{\nu} e^{in\phi}, \quad \begin{pmatrix} n = 0, 1, 2, \ldots, \\ \nu = 0 \text{ for even } n, 1 \text{ for odd } n \end{pmatrix}. \quad (3.10)$$

where ϕ is the azimuthal angle about z.

The (x, y) dependence of v_n has been so chosen that it coincides exactly with that of the n-th true harmonic oscillator function u_n if we set $a_\perp$ = cyclotron radius $= \sqrt{(\hbar c/eH)}$. In (3.9) and (3.10) the coefficients $c_{m_cm_vn}$ and the radii $a_\perp$ and $a_\parallel$ are the variational parameters to be determined.

Before presenting the variational solutions of the problem, we shall examine in physical terms the nature of the eigenstates in the high field limit, where the exciton binding and the strain are not of primary importance in defining individual states. An exciton transition in this case is correlated with one of the transitions from a Landau level defined by the Hamiltonian (3.3) in the valence band to that defined by (3.1) in the conduction band both at $k_z = 0$. These Landau states have true harmonic oscillator functions u_n as their envelopes[13], and the allowed transitions (interband selection rule $\Delta n = 0$) at $k_z = 0$ with lowest energies are: transitions with v_+, $\Delta M = M_c - M_v = 1$

$$\begin{aligned} &(a_+)\ |M_v = -\tfrac{3}{2}, n = 0\rangle \rightarrow |M_c = -\tfrac{1}{2}, n = 0\rangle \\ &(b_+)\ |-\tfrac{1}{2}, 0\rangle \rightarrow |\tfrac{1}{2}, 0\rangle \end{aligned} \quad (3.11)$$

transitions with $v_{-1}\, \Delta M = -1$

$$\begin{aligned} &(a_-) \quad a|\tfrac{3}{2}, 0\rangle + b|-\tfrac{1}{2}, 2\rangle \rightarrow |\tfrac{1}{2}, 0\rangle \\ &(b_-) \quad a'|\tfrac{1}{2}, 0\rangle + b'/-\tfrac{3}{2}, 2\rangle \rightarrow |-\tfrac{1}{2}, 0\rangle \end{aligned} \quad (3.12)$$

in the Faraday configuration* and transitions with v_z, $\Delta M = 0$

$$\begin{aligned} &(c_1) \quad |-\tfrac{1}{2}, 0\rangle \rightarrow |-\tfrac{1}{2}, 0\rangle, \\ &(c_2) \quad a'|\tfrac{1}{2}, 0\rangle + b'|-\tfrac{3}{2}, 2\rangle \rightarrow |\tfrac{1}{2}, 0\rangle \end{aligned} \quad (3.13)$$

transitions with v_y, $\Delta M = \pm 1$ all the four transitions listed in (3.11) and (3.12). For an extended photon energy 1 → 1 and 2 → 2 transitions are also observable.

The variationally calculated photon energies required in the transitions from the ground states are shown in Fig. 1 and 2 as functions of the magnetic field for the Faraday and Voigt configurations, respectively, including strain for the low temperature. Only states with appreciable $U(0)$ values are given in the figures.

---

*The valence band states involved in the transitions a_4, b_4, a_- and b_- are 2(0), 1(0), $1\pm(2)$ and $2\pm(2)$, respectively, in Luttinger's notation[13].

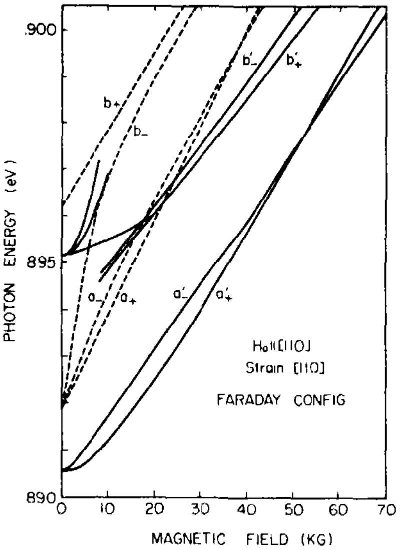

Fig. 1. Variationally calculated photon energies for the exciton transitions (primed) as functions of the magnetic field in the Faraday configuration near the liquid helium temperature. Unprimed transitions (broken curves) show the Landau transitions whose asymptotic forms are represented by (3.11) and (3.12). Both types of transitions are calculated for a strained germanium. The energy gap $h\omega_g$ has been taken 0·894 eV.

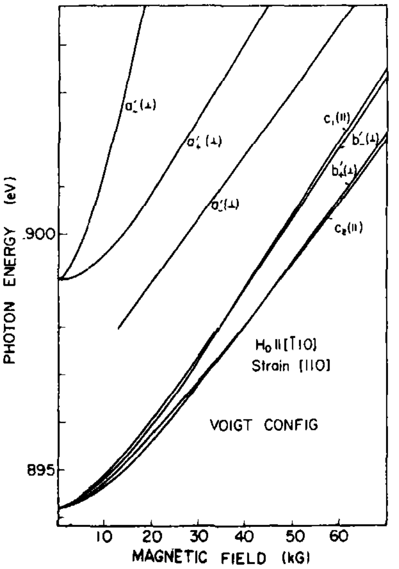

Fig. 2. Variationally calculated photon energies for the exciton transitions in the Voigt configuration near the liquid helium temperature. The energy gap has been set at 0·8978 eV.

The adopted band parameters are $\alpha = 25$[15] $\gamma_1 = 13{\cdot}08$[16], $\bar{\gamma} = 5{\cdot}45$[16] $g_c = -3{\cdot}2$[17], $\kappa = 3{\cdot}29$[18], $\epsilon_0 = 16$, $D_u = 3{\cdot}15$ eV[19], $D_{u'} = 6{\cdot}10$ eV[19], and $2E_s = 4{\cdot}4$ and 4·8 meV for the Faraday and Voigt configurations, respectively. The direct band gap is fixed at the values given in the captions to give the best fit with experiment.

In both the Faraday and Voigt configurations all the energy vs. H curves are, as expected, linear at high fields, but at small fields a bend of the curves is seen, which is characteristic of the exciton formation and has its origin in the increase of the binding energy in a magnetic field[20]. At low fields and in a strained crystal the splitting due to strain is most significant. Details of the competition will be discussed later. Some of the exciton transitions are specified in the figures according to their corresponding asymptotic Landau transitions (3.11) ~ (3.13).

It is noted in Fig. 1 that the two lowest exciton levels in the Faraday configuration cross at a magnetic field near 50 kG. This is responsible for that peculiar sign reversal of the first Faraday singularity mentioned in the introduction and will be discussed in the next section.

4. ROTATION SPECTRA

We are now at a position to calculate the exciton contribution to the Faraday and Voigt spectra near the direct band gap. We do this using the expressions (2.12) and (2.19) for the Faraday and Voigt rotation angles, respectively, in which we further make use of the selection rules on the interband matrix elements $V_{mcmv'}$

$$(v_z)_{1/2,1/2} = (v_z)_{-1/2,-1/2} \equiv V$$
$$(v_-)_{1/2,3/2} = -\sqrt{3}V, \quad (v_+)_{-1/2,-3/2} = \sqrt{3}V$$
$$(v_-)_{-1/2,1/2} = -V, \quad (v_+)_{1/2,-1/2} = V \qquad (4.1)$$
$$(v_y)_{+1/2,+3/2} = -i\frac{\sqrt{3}}{2}V,$$
$$(v_y)_{\mp 1/2,\pm 1/2} = -i\tfrac{1}{2}V,$$

all other matrix elements being zero.*

The calculated spectra are shown in Fig. 3 and 4. The relaxation time τ_n was so chosen as to reproduce the experimentally observed line shapes near the singularities. It was changed with magnetic field, but taken common to all the peaks at a fixed field. In Fig. 3 only the lowest two paris of transitions are included for the Faraday rotation at low temperatures, since all the other transitions have much higher photon energies or much smaller intensities.

We now discuss the features of the rotary spectra in connection with the level schemes in a magnetic field. Let us first make an in-

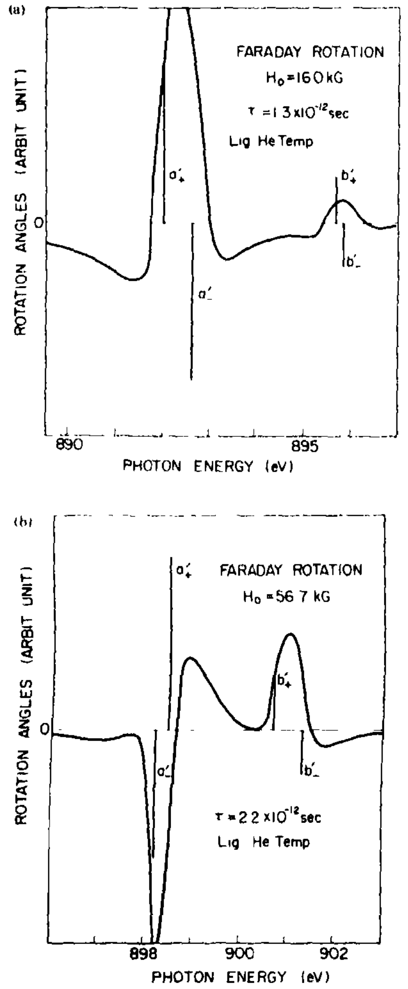

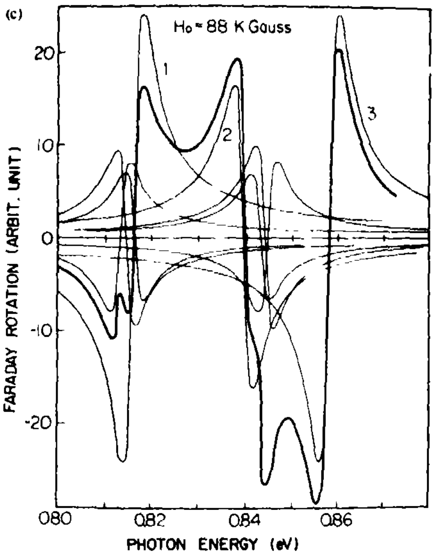

Fig. 3. Calculated Faraday rotation spectra in germanium. (a) and (b) show the low temperature spectra at low and high magnetic fields, respectively, and (c) gives the room temperature spectrum at 88 kG.

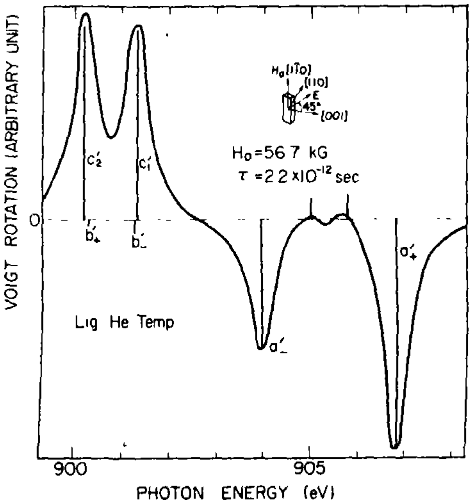

Fig. 4. Calculated Voigt rotation spectrum in germanium near the liquid helium temperature at 56·7 kG.

---

*We have discarded small corrections of the order of ω_c/ω_g throughout.

quiry into what features a faraday spectrum is expected to show when a set of electronic states are designated, without paying special attention to their detailed properties. For the sake of clarity we treat the problem for a moment in terms of Landau transitions without Coulomb effect. In the absence of a magnetic field, an electronic level is necessarily at least twofold degenerate because of the time reversal symmetry, and by a proper choice of the wave functions we can assume

$$|(n|v_+|m)|^2 = |(n'|v_-|m')|^2 \tag{4.2}$$

where the states n and n' in the conduction band and the states m and m' in the valence band are degenerate. (For example n' and m' are the Kramers conjugates of n and ln, respectively.) When a magnetic field is applied, one of the transitions, say $m \rightarrow n$, is polarized in v_+ and has a photon energy $h(\omega_0+\gamma H)$, while all the other transition $m' \rightarrow n'$ has polarization v_- and a photon energy $\hbar(\omega_0-\gamma H)$. The Faraday rotation induced by this pair of transitions is

$$C \cdot \mathrm{Re}\left[\frac{1}{\omega_0-\gamma H-\omega+i/\tau}-\frac{1}{\omega_0+\gamma H-\omega+i/\tau}\right] \tag{4.3}$$

if we assume (4.2) as a zeroth order approximation in H. This is the experession derived by Halpern, Lax and Nishina[21] and used by Nishina, Kolodziejczak and Lax[3] in the analysis of their experiment. According to (4.3), where C is a positive constant, the rotation peak due to this pair of transitions is positive if $\gamma < 0$, and negative if $\gamma > 0$. Thus a reversal of the rotational sign is understood as a reversal of the constant γ in this approximation. The rotation spectrum given by (4·3) is symmetric on the both sides of a singularity.

In a general case of exciton transistors, especially when degeneracy is involved, the transitions degenerate at $H=0$ are not split into perfectly right and perfectly left hand polarized transitions, but we can only say that one group of transitions are almost right hand polarized and the others polarized in the left. Then the relation (4.2) does not hold even in a moderate magnetic field. This fact leads to an asymmetry of the line shape.* The magnetic field dependence of the transition energies is generally complicated, but if a transition nearly polarized in the right crosses a one in the left in photon energy, a reversal of the Faraday rotational singularly takes place.

This actually happens in Fig. 1 in the lowest pair of transitions and it exactly the reason why in the calculated specta (Figs. 3(a) and 3(b)) the sign of the first rotational singularity is reversed between low and high magnetic fields. The origin of this crossing will be explained in the next section.

At room temperature where no strain exists in the sample no crossing of the levels is expected, so the Faraday spectrum changes rather regularly with magnetic field. This is in agreement with experiment.

In the Voigt configuration at low temperature the existing strain has such an action that in zero magnetic field the valence bands mainly consisting of $M_v = \pm\frac{1}{2}$ along z are raised higher in electronic energy than those mainly consisting of $M_v = \pm\frac{3}{2}$. Thus transitions involving $M_v = \pm\frac{1}{2}$, appreciably, $\kappa_{\parallel}$ which, because of the selection rules (4.1), are the only transitions contributing to , have lower energies than those involving $M_v = \pm\frac{3}{2}$, which contribute solely to $\kappa_{\perp}$. The former transitions contribute to $\kappa_{\perp}$ also, but usually not appreciably because of a partial cancellation due to mixing of more than one M_v's. This leads to a general feature of the Voigt spectrum in which positive peaks appear in lower photon energies and negative peaks in higher. In NL's experiment (See Fig. 5 of NL) in this configuration, two broad *absorption* peaks appear, of which the one appearing in a lower energy is associated with positive *rotational* peaks and the other with negative rotational peaks, in agreement with our interpretation.

---

*A further speculation or the line shape is given in NL.

5. DISCUSSION

(1) *Origin of the sign reversal in the low temperature Faraday spectrum*

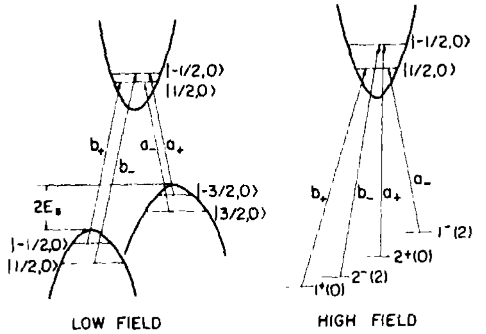

Fig. 5. Schematic representation of the lowest transitions in the Faraday configuration in a strained germanium crystal.

A direct understanding of the sign reversal is presented first, for clarity's sake, in terms of Landau transition at $k_z = 0$, and the necessary modification introduced by the inclusion of exciton effect will be discussed afterwards. As is mentioned in Section 3, the mechanism which plays a dominant role in determining a state in the valence band changes with magnetic field. Figure 5 shows schematically the situations met in low and high fields. At low fields the strain splitting of the valence band is so large that transitions are described as those from a Landau level in either of the two pairs of strain-split valence bands to a one in the conduction band. The off-diagonal component E_2 of the strain Hamiltonian (Equation (3.7) with the upper sign) is much smaller than the diagonal component E_1, since E_2 is proportional to $D_u - D'_u$, which represents a deviation from spherical symmetry. The valence band, therefore, is almost completely split into a pair of bands with $M_v = \pm\frac{3}{2}$ and a one with $M_v = \pm\frac{1}{2}$, the former lying higher in electronic energy. The lowest transitions compatible with the selection rules are those from the lowest Landau levels ($n = 0$) formed in the valence bands $M_v = \pm\frac{3}{2}$. They are explicitly

$$(a_+)\,|-\tfrac{3}{2}, 0\rangle \rightarrow |-\tfrac{1}{2}, 0\rangle \qquad (5.1)$$

at frequency

$$\omega_+ = \frac{eH}{mc}\left(\tfrac{1}{2}\alpha - \tfrac{1}{4}g_c + \tfrac{1}{2}\gamma_1 + \tfrac{1}{2}\bar{\gamma} - \tfrac{3}{2}\kappa\right) + \omega_g + \frac{E_1}{\hbar} \qquad (5.2)$$

and

$$(a_-)\,|\tfrac{3}{2}, 0\rangle \rightarrow |\tfrac{1}{2}, 0\rangle \qquad (5.3)$$

at

$$\omega_- = \frac{eH}{mc}\left(\tfrac{1}{2}\alpha + \tfrac{1}{4}g_c + \tfrac{1}{2}\gamma_1 + \tfrac{1}{2}\bar{\gamma} + \tfrac{3}{2}\kappa\right) + \omega_g + \frac{E_1}{\hbar} \qquad (5.4)$$

leading to a γ at low fields

$$\gamma_l = (\omega_+ - \omega_-)/2H = -\frac{e}{4mc}(g_c + 6\kappa)$$
$$= -4{\cdot}3\beta/\hbar. \qquad (5.5)$$

At high magnetic fields the magnetic coupling between $M_v = \frac{3}{2}$ and $-\frac{1}{2}$, and between $M_v = \frac{1}{2}$ and $-\frac{3}{2}$ exceeds the strain splitting of the $M_v = \pm\frac{3}{2}$ and $\pm\frac{1}{2}$ bands, and Landau levels are formed according to the four-ladder scheme described by Luttinger[13]. The state $|-\frac{3}{2}, 0\rangle$, however, has quantum number $n = 0$ in the 2^+ ladder and does *not* mix with any of the other bands. The state $|\frac{3}{2}, 0\rangle$, on the other hand, converges to the one designated by $1^-(2)$, which mixes considerably with the $M_v = -\frac{1}{2}$ band (corresponding to the asymptotic transition (a_-) in (3.12)). The asymptotic transition frequency is given by

$$\omega_- = \frac{eH}{mc}\left(\tfrac{1}{2}\alpha + \tfrac{1}{4}g_c + \epsilon_1^-(2)\right) + \text{const.} \qquad (5.6)$$

where

$$\epsilon_1^-(2) = \tfrac{3}{2}\gamma_1 - \bar{\gamma} + \tfrac{1}{2}\kappa - \left[(\gamma_1 - \tfrac{3}{2}\bar{\gamma} - \kappa)^2 + 6\bar{\gamma}^2\right]^{1/2}.$$

From (5.2) and (5.6) we obtain a γ at high fields,

$$\gamma_h = \frac{e}{4mc}\left(-g_c + \gamma_1 + \bar{\gamma} - 3\kappa - 2\epsilon_1^-(2)\right)$$
$$= 3{\cdot}6\beta/\hbar \qquad (5.7)$$

which is of opposite sign to γ_l. We have added in Fig. 1 the curves of photon energies calculated on the assumption of Landau transitions. These were obtained by solving H_h+H_s with the use of envelope functions $\sum_n b_{M_cM_vn}u_n$. (The u_n are true harmonic oscillator functions, to be distinguished from the v_n.) For (a_+), the photon energy $\hbar\omega_+$ is almost perfectly linear throughout the range of H, while for (a_-), $\hbar\omega_-$ has a complicated dependence of the predicted form and crosses $\hbar\omega_+$ near $H = 40$ kG. The opposite signs in (5.5) and (5.7) are essentially responsible for the reversal of the Faraday singularity.

The change of exciton transition energies is not so easily predictable in a similar way. Our numerical calculation, however, has proved the existence of a crossing in the lowest pair of exciton transitions, also. The chief modifications caused by exciton binding are (i) the crossing field appears near 50 kG. (ii) both the exciton curves $(a_{+'})$ and $(a_{-'})$ are downwards convex, instead of straight (a_+) and upwards convex (a_-).

(2) *Existence of the exciton effect*

The necessity of the exciton effect in interpreting the experimental result of Nishina and co-workers has so far not been emphasized, although early absorption experiments[22] demonstrated clearly the existence of this in the band edge spectrum at low temperatures. We shall give in this subsection reasons why our rotational peaks should be considered to involve exciton transitions at room temperature as well as at low temperatures.

Low temperature. The observed change of the absorption peak positions with H at this temperature (See Figs. 2 and 4 of NL) cannot be explained on the assumption of Landau transitions. The two broad absorption peaks, separated 4.4 m eV at $H = 0$, are most likely to correspond to the two pairs of exciton transitions $(a_{+'})$, $(a_{-'})$ and $(b_{+'})$, $(b_{-'})$, the separation within each pair being too small to be resolved by absorption. If we had assumed the corresponding Landau transitions (a_+), (a_-) and (b_+), (b_-), we would never have obtained the bending of the energy vs. H curves at low fields, which is essentially characteristic of the exciton effect. A further support of the exciton effect is rendered by the analysis of rotational line shapes where the superiority of discrete levels in fitting the experimental curves is assured. This situation is more pronounced in the room-temperature case and will be discussed in more detail in a later paragraph.

Room temperature. The room-temperature Faraday spectrum was once analysed by Korovin and Kharitonov[8] on the assumption of Landau transitions between the valence and conduction bands, thereby the exciton formation being entirely neglected. We here demonstrate that each rotational singularity is actually formed by the superposition of the Faraday rotations associated with the exciton fine structure for the complex energy bands in germanium.

Firstly, the photon energy corresponding to a particular singularity in the spectrum establishes the existence of the exciton effect. Judging from its intensity and its relative position in the spectrum, the peak denoted by 1 in Fig. 3(c) is assigned to the transition which in the high field limit converges to (a_+). With the room-temperature direct band gap not smaller than 0·803 eV*[23], calculation shows that this transition should have a photon energy not smaller than 0·821 eV at 88 kG which is 4 me V larger than the observed value. This difference is most well understood in terms of the exciton binding energy.

Secondly, line shape study shows that the observed shape of the Faraday singularities is not of continuous levels, but of discrete ones. As the electronic motion along the magnetic field is not quantized in a free

---

*Zwerdling *et al.*[23] measured the change of several absorption peaks with magnetic field. It is not clear whether the zero field energy 0·803 eV, to which all the peaks approximately converge as $H \to 0$, should involve the exciton binding energy or not, but the true band gap cannot be smaller than this value.

Landau state, the photon energy changes with k_z as

$$\omega(k_z) = \omega(0) + \frac{\hbar k_z^2}{2\mu} \tag{5.8}$$

where μ is an appropriate reduced mass, and we have to integrate rotation angles over k_z to obtain

$$\int_{-\infty}^{\infty} \frac{dk_z}{2\pi} \cdot C \cdot \mathrm{Re} \frac{1}{\omega(0) + \frac{\hbar k_z^2}{2\mu} - \gamma H - \omega + \frac{i}{\tau}}$$

$$= -\frac{C}{2}\left(\frac{2\mu}{\hbar}\right)^{1/2} \mathrm{Im}\left[\omega + \gamma H - \omega(0) - \frac{i}{\tau}\right]^{-1/2} \tag{5.9}$$

corresponding to the first term of (4.3) and a similar expression for the second term. We have tried to fit the observed line shape by properly choosing τ in (5.9), but the obtained line does not usually show any sharp oscillation. In the case of exciton transitions, on the other hand, the motion along z is quantized by the Coulomb binding and no integration is needed. We could obtain in this case a fairly good fit of the experimental curves*. With variational solutions of the secular equation, we calculated rotation curves associated with each transition and then superposed them to obtain the overall rotation. The transitions contributing to singularities are listed in Table 1.

(3) *Additional absorption peak in the Voigt configuration*

In the low-temperature absorption experiment in the Voigt configuration, NL have observed a third peak (See Fig. 4 of NL, the peak denoted by III) in addition to the two peaks which behave similarly to those in the Faraday configuration. This is resolved at fields exceeding 15 kG and the corresponding photon energy rises rapidly with field, in comparison with the two other peaks.

The appearance of this third peak can be understood in terms of the difference of the strain effect in the two configurations. For an illustrative purpose, we shall consider the mixing of the $M_v = \frac{3}{2}$ and $-\frac{1}{2}$ bands at $k_z = 0$. In the Faraday configuration the diagonal component E_1 of the strain Hamiltonian (3.6) is much larger than the off-diagonal component E_2, while in the Voigt configuration the two quantities are almost equal. The magnetic field has the same effect in the both configurations in our approximation. Thus at intermediate fields at which the strain and magnetic energies compete, the strain in the Faraday configuration, schematically speaking, acts to prevent the magnetic mixing of $|\frac{3}{2}, 0\rangle$ and $|-\frac{1}{2}, 2\rangle$, while that in the Voigt configuration acts to augment it. Actually at 25 kG, the state $|\frac{3}{2}, 0\rangle$ is almost unmixed in the Faraday configuration, but this state mixes considerably with $|-\frac{1}{2}, 2\rangle$ in the Voigt configuration, and two states result which contain $|\frac{3}{2}, 0\rangle$ appreciably, namely

$$0{\cdot}62\,|\tfrac{3}{2}, 0\rangle + 0{\cdot}69\,|-\tfrac{1}{2}, 2\rangle + \text{small contributions from other states,}$$

and

$$0{\cdot}66\,|\tfrac{3}{2}, 0\rangle - 0{\cdot}61\,|-\tfrac{1}{2}, 2\rangle + \ldots$$

The second of these induces the transition denoted by III in the intermediate field region.

Table 1. Assignment of the Faraday rotation singularities at room temperature

Singularity		1	2	3	4	5	6	7	8	9	10	11	12
Conduction	M_c	$\frac{1}{2}$	$\frac{1}{2}$	$-\frac{1}{2}$	$-\frac{1}{2}$	$-\frac{1}{2}$	$\frac{1}{2}$	$\frac{1}{2}$	$\frac{1}{2}$	$-\frac{1}{2}$	$-\frac{1}{2}$	$-\frac{1}{2}$	$\frac{1}{2}$
Band	n	0	0	0	0	0	1	1	1	0	1	2	2
Valence	M_v	$-\frac{1}{2}$	$\frac{3}{2}$	$-\frac{3}{2}$	$\frac{1}{2}$	$\frac{3}{2}$	$\frac{1}{2}$	$\frac{3}{2}$	$-\frac{1}{2}$	$\frac{1}{2}$	$-\frac{3}{2}$	$\frac{1}{2}$	$\frac{3}{2}$
Band	n	0	0	0	0	0	1	1	1	0	1	2	2
Energy deviation from band edge at 88 kG (meV)		13·2	14·4	15·9	16·3	39·4	43	44	44·7	56·7	58·0	64·5	65·4
Relative oscillator strength		1	1·17	3	0·87	2·01	0·86	1·23	1	0·1	3	0·62	1·05
Sign of Faraday rotation		+	−	+	−	−	−	−	+	−	+	−	−

---

*Compare also the discussion given in NL.

6. CONCLUSION

We have analysed the oscillatory rotation spectra in germanium observed by Nishina and co-workers. The analysis is based on the effective mass theory of the direct excitons in germanium. The transitions pertinent to the rotation were assumed to be those from the ground state of the crystal to exciton states, instead of those between the Landau states. Expressions for the rotation angles in the Faraday and Voigt configurations were derived, which include the interband velocity matrix element and the envelope function for the relative motion of the electron-hole system. The Voigt rotation in NL's experiment was interpreted as essentially the difference in the absorption coefficients of the polarizations parallel and perpendicular to the magnetic field.

The eigenstates of the exciton in a magnetic field were determined variationally, using appropriate vector wave functions. Strain energy was added in the low temperature analysis.

The existence of strain has proved to be essential in determining the feature of the low-temperature rotation spectrum. The peculiar reversal of the Faraday singularity in the experiment is explained by the competing effect of the strain and the magnetic field.

The importance of the Coulomb binding between the electron excited to the conduction band and the hole left behind was recognized in the room-temperature spectrum as well as at low temperature. We have concluded that the observed features of the spectrum at the band edge show every sign of exciton transitions.

Acknowledgements — This work was performed under the guidance of Professors T. Inui and Y. Uemura, to whom the authors express their cordial gratitude.

The authors are greatly indebted to Dr. H. Hasegawa for the original suggestion of the problem and many invaluable adivces, to Dr. Y. Nishina for the communication of his experimental data prior to publication, and to Dr. M. Okazaki for cooperation in the initial stage of the program. They profited from enlightening discussions with Drs. Y. Toyozawa and M. Inoue.

The financial support to the authors from the Sakkokai Foundation is greatly acknowledged.

REFERENCES

1. LAX B. and ZWERDLING S., *Progress in Semiconductors*, Vol. 5, p. 221. Heywood, London (1960).
2. NISHINA Y., KOLODZIEJCZAK J. and LAX B., *Phys. Rev. Lett.* **9**, 55 (1962); *Bull. Am. phys. Soc.* **7**, 535 (1962).
3. NISHINA Y., KOLODZIEJCZAK J. and LAX B., *Proc. 7th Internat'l Conf. Phys. Semiconductors*, p. 867. Dunod, Paris (1964).
4. NISHINA Y. and LAX B., *J. Phys. Chem. Solids* **29**, 739 (1968). (referred to as NL in the text.)
5. ROTH L. M., LAX B. and ZWERDLING S., *Phys. Rev.* **114**, 90 (1959).
6. NISHINA Y., Private communication.
7. MITCHELL D. L. and WALLIS R. F., *Phys. Rev.* **131**, 1965 (1963).
8. KOROVIN L. I. and KHARIFONOV E. V., *Fiz. Tverd. Tela* **5**, 2035 (1963); English transl.: *Soviet Phys. solid St.* **5**, 1488 (1964).
9. BOSWARVA I. M., HOWARD R. E. and LIDIARD A. B., *Proc. R. Soc.* **A269**, 125 (1962).
10. SEITZ F., *The Modern Theory of Solids*, Chap. V. McGraw-Hill, New York (1940); BORN M. and HUANG K., *Dynamical Theory of Crystal Lattices*, Chap. IV. Oxford University Press, London (1954).
11. ELLIOTT R. J., *Phys. Rev.* **108**, 1384 (1957); DRESSELHAUS G., *J. Phys. Chem. Solids* **1**, 14 (1956).
12. SCHIFF L. I., *Quantum Mechanics*, 2nd. Edn. Chap. X. McGraw-Hill, New York (1955).
13. LUTTINGER J. M., *Phys. Rev.* **102**, 1030 (1956).
14. KLEINER W. H. and ROTH L. M., *Phys. Rev. Lett.* **2**, 334 (1959).
15. CARDONA M., *J. Phys. Chem. Solids* **24**, 1543 (1963).
16. HENSEL J. C., Private communication (to be published).
17. Obtained from the formula of ROTH L. M., LAX B. and ZWERDLING S., *Phys. Rev.* **114**, 90 (1959).
18. STICKLER J. J., ZEIGER H. J. and HELLER G. S., *Phys. Rev.* **127**, 1077 (1962).
19. HALL J. J., *Phys. Rev.* **128**, 68 (1962).
20. YAFET Y., KEYES R. W. and ADAMS E. N., *J. Phys. Chem. Solids* **1**, 137 (1956); HASEGAWA H. and HOWARD R. E., *J. Phys. Chem. Solids* **21**, 179 (1961); ELLIOTT R. J. and LOUDON R., *J. Phys. Chem. Solids* **15**, 196 (1960).
21. HALPERN J., LAX B. and NISHINA Y., *Phys. Rev.* **134**, A140 (1964).
22. MACFARLANE G. G., MCLEAN T. P., QUARRINGTON and ROBERTS V., *Proc. phys. Soc.* **71**, 863 (1958); ZWERDLING S., LAX B., ROTH L. M. and BUTTON K., *Phys. Rev.* **114**, 80 (1959).
23. ZWERDLING S. and LAX B., *Phys. Rev.* **106**, 51 (1957); ZWERDLING S., LAX B. and ROTH L. M., *Phys. Rev.* **108**, 1402 (1957).

J. Phys. Chem. Solids Pergamon Press 1969. Vol. 30, pp. 763–773. Printed in Great Britain.

CLASSICAL EFFECTIVE SPIN HAMILTONIAN AND SYMMETRY GROUPS OF THE MULTISPIN-AXIS MODEL OF CoO

E. F. BERTAUT

Laboratoire d'Electrostatique et de Physique de Métal C.N.R.S, B.P. 319 et Centre d'Etudes Nucléaires, B.P. 269 Grenoble, France

(*Received* 17 *May* 1968)

Abstract—The multispin axis model recently proposed by van Laar for the magnetic structure of CoO reflects the tetragonal nature of the crystal structure below the Néel temperature. Starting from simple symmetry arguments we construct an effective anisotropic spin hamiltonian H_{an} of order two in the spins. The minimization of H_{an} leads directly to the multispin axis model. An essential feature of H_{an} is to show that Dzialoshinski–Moriya coupling is mainly responsible for the 90° canting invoked by the van Laar model for the spin components in the Oxyplane. This is in agreement with the large spin-orbit coupling usually observed in bivalent Co. The magnetic structure transforms according to irreducible representations of several space groups which leave H_{an} invariant. Possible Shubnikov groups are also indicated.

INTRODUCTION

It is well known that MnO, NiO, FeO undergo at the Neel temperature a small rhombohedral distortion. This fact is also reflected by their type of antiferromagnetic ordering the so-called ordering of the second kind. CoO is an exception in so far as the antiferromagnetic transition is accompanied by a tetragonal deformation[1]. However even for that case a collinear structure was proposed[2, 3] with the same MnO-type of ordering, the spins being tipped out from the tetragonal axis by an angle of about 27°4′. It was up to van Laar[4] to find a non collinear spin structure of a tetragonal type (Fig. 1) which fits the observed magnetic intensities as well as the conventional model.

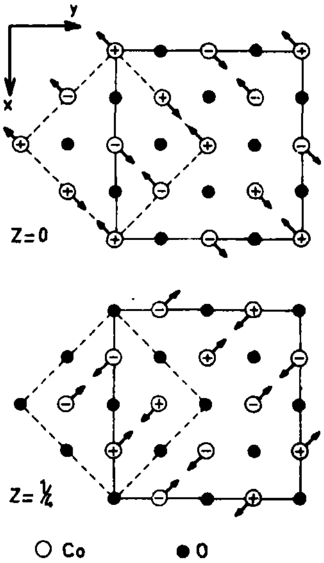

Fig. 1. The van Laar multispin-axis model. Sections $z = 0$ and $z = \frac{1}{4}$ of the magnetic unit cell $(2a, 2a, 2a)$ are represented. The arrows indicate the projections of the spins in the oxy-plane. The signs + or − indicate the direction of the spins along Oz. Sections $z = \frac{1}{2}$ and $z = \frac{3}{4}$ are obtained by reversing all the spins of sections $z = 0$ and $z = \frac{1}{4}$ respectively.

The second kind of ordering belongs to a propagation or wave-vector $\mathbf{k} = \frac{1}{2}\mathbf{b}_1 + \frac{1}{2}\mathbf{b}_2 + \frac{1}{2}\mathbf{b}_3 = [\frac{1}{2}\frac{1}{2}\frac{1}{2}]$ where the $\mathbf{b}_j$ $(j = 1, 2, 3)$ are the reciprocal vectors of the lattice vectors $\mathbf{a}_j$ $(j = 1, 2, 3)$ of the chemical cell. It is easily checked indeed that all spins are 'in phase' in (1 1 1) planes, their signs being given by [4]

$$\sigma_r = \cos 2\pi\, \mathbf{k}.\mathbf{r} = \cos \pi\, (x_1 + x_2 + x_3). \quad (1)$$

Here $\mathbf{r} = x_1\mathbf{a}_1 + x_2\mathbf{a}_2 + x_3\mathbf{a}_3$ is the position vector of the spin and x_1, x_2, x_3 are the crystallographic coordinates of $\mathbf{r}$ in the chemical cell. For instance the sign being +1 for the spin in 0,0,0 according to (1) σ_r is −1 for the spin at the point $\mathbf{r} = 1,0,0$ which means that the magnetic cell has to be doubled in the x_1 direction (and also along the x_2- and the the x_3-directions). If J_1 has the conventional meaning of an exchange integral between first neighbours related by direct and 90° super-exchange and if similarly J_2 is the exchange integral for 180° super-exchange, it must be noted that J_1 does not enter the expression of the magnetic energy or of the Neel temperature T_N in the molecular field approximation.

$$T_N = \rho \,.\, 6J_2. \tag{2}$$

The physical reason is that each spin has among its 12 first neighbours as many (six) *parallel spins in its own (111) plane as opposite* spins (six) in the two neighbouring (111) planes. Here striction effects, due to deformations, are neglected to a first approximation.

From this brief discussion we note that there is a high degeneracy in the second kind of ordering and many multi-axis spin systems [3, 5] may be indicated having the same energy. Ways to lift the degeneracy are exchange strictions and (or) anisotropic interactions between first neighbours. The van Laar model essentially retains the negative correlation of spins connected by 180° super-exchange and is still indifferent to first neighbour interactions as far as isotropic exchange is concerned.

We shall show that the van Laar model is compatible with group theory and that an effective Hamiltonian of order two in the spins can be derived which reflects the anisotropic couplings (mainly between first neighbours) present in his model and characteristic for the high spin-orbit coupling usually found in bivalent cobalt. There is a strong orbital contribution, the moment being 3,52 μ_b[4] instead of 3 μ_b for spin only.

THE SPIN HAMILTONIAN

Several steps are needed. We look first for a crystallographic space group to describe the tetragonal structure below the Neel temperature. We then find the representations $\Gamma^{(\nu)}$ of the group associated with the wave vector $\mathbf{k} = [\frac{1}{2}\frac{1}{2}\frac{1}{2}]$ and we construct the basis vectors of irreducible representations, i.e. peculiar vectors which are linear combinations of the spins. Finally with the basis vectors we form invariants and derive a spin Hamiltonian of order two which shows already the features of the intervening anisotropic coupling mecanisms.

As an essential symmetry element of the paramagnetic space group we retain a fourfold screw axis noted 4_2 and shown in Fig. 2. The crystallographic structure below T_N may thus be described by the minimum symmetry group $P4_2$. (Higher symmetries will be indicated later). According to the International Tables for Crystallography [6] we place the c-axis along the 4_2 screw axis. The coordinates of the Co-atoms, numbered from one to four and related by the 4 operations $(4_2)^j$ (with $j = 0,1,2,3$) will be

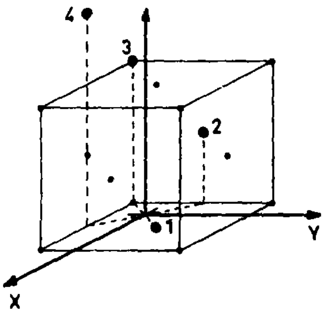

Fig. 2. Reference atoms in CoO. The Co atoms in the f.c.c. structure are represented by black circles. The reference atoms marked 1, 2, 3, 4 are related by a fourfold screw axis 4_2 chosen as the Oz axis

$$x,y,z\ (1);\quad \bar{y},x,\ z+\tfrac{1}{2}\ (2);\quad \bar{x},\bar{y},\ z+1\ (3);$$
$$y,\bar{x},\ z+\tfrac{3}{2}\ (4) \tag{3}$$

with x and y near to $\frac{1}{4}$ and $z \simeq 0$ or $\frac{1}{4}$. The oxygen locations may be described by the same positions with x_0 and y_0 near to $\frac{1}{4}$ and $z_0 \simeq \frac{1}{2}$ or $\frac{3}{4}$. Before going further let us re-examine the neutron diffraction evidence and its implications. In his fine high resolution powder diagram, van Laar[4] could resolve the doublet {311} {113} and show the magnetic reflection {113} to have a negligible intensity with respect to {311}. We prove in Appendix A-1 that the near disappearance of the intensity {113} already implies the sign sequences of four possible spin models and determines the spin angle with the z-axis to a good approximation (~ 25°). Table 1 summarizes the spin models. In spite of the surprising manifold of choices for the signs of the four reference spins, the four models noted $\mathscr{A}$, $\mathscr{B}$, $\mathscr{C}$ and $\mathscr{D}$ are closely related. For instance $\mathscr{A}$ always contains $\mathscr{D}$, $\mathscr{B}$ always contains $\mathscr{C}$ as can be proved by appropriate translations shown in Fig. 3. Furthermore the right handed model $\mathscr{A}$ always contains a lefthanded model $\mathscr{C}'$ and $\mathscr{B}'$ as shown in Figs. 3-4; vice versa $\mathscr{B}$ contains the left handed structures $\mathscr{A}'$ and $\mathscr{C}'$. We call here a structure 'right handed' *if the screw* axis 4_2 is operating counterclockwise on the atoms 1,2,3,4. The question arises if there are still other sign combinations compatible with the quasi-extinction of {113}. In fact, if we reverse in, say, model $\mathscr{B}$ all the spin components in the xy-plane, keeping fixed the z-components (still in conformity with $\sum_j s_{j\alpha} = 0$, $\alpha = x$ or y or z), we get a model $\mathscr{B}''$ which is no longer compatible with the observed intensities. This clearly demonstrates the existence of a definite anisotropic coupling between the (xy)- and the z-components of the spins. This coupling must be bilinear.

TRANSFORMATION PROPERTIES AND BASIS VECTORS

The wave-vector $\mathbf{k} = [\frac{1}{2}\frac{1}{2}\frac{1}{2}]$ has still the full point group symmetry **4**, i.e. $\mathbf{4}^j\mathbf{k} = \mathbf{k} + \mathbf{K}$ where $\mathbf{K}$ is a reciprocal lattice vector. The transformation equations of the spin vector components are

$$\mathbf{4}_2 s_{j,x} = +s_{j+1,y};\quad \mathbf{4}_2 s_{j,y} = -s_{j+1,x};\quad \mathbf{4}_2 s_{j,z} = s_{j+1,z}. \tag{4}$$

Here the first index refers to the numbering of

Table 1. *Van Laar models*

	Conditions on the spins			Signs of the spin components x, y, z			
Model	Σs_{jx}	Σs_{jy}	Σs_{jz}	s_1	s_2	s_3	s_4
$\mathscr{A}$	0	0	$\neq 0$	$-++$	$--+$	$+-+$	$+++$
$\mathscr{B}$	0	0	0	$+-+$	$---$	$-++$	$++-$
$\mathscr{C}$	$\neq 0$	0	0	$--+$	$-++$	$---$	$-+-$
$\mathscr{D}$	0	$\neq 0$	0	$+++$	$-+-$	$++-$	$-++$

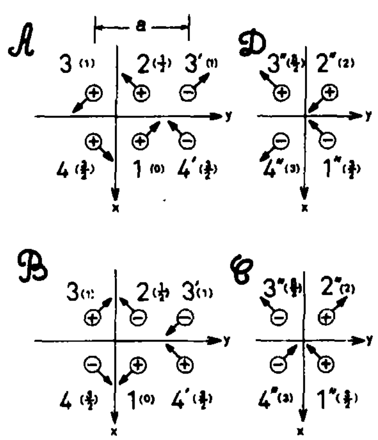

Fig. 3. Upper left corner. The $\mathscr{A}$ model. The spins are numbered 1, 2, 3, 4. Numbers in parenthesis indicate the height in the chemical cell. The signs in the circles are for the z-components. When 3 and 4 are displaced by the distance a to 3′ and 4′, the spins 1, 2, 3′, 4′ form a left handed $\mathscr{C}'$ arrangement. In the upper right corner, the atoms 4′ 3′ 2′ and 1 are relabeled 1″, 2″, 3″ and 4″ respectively and shifted vertically so as to be on a right handed screw axis. They form a $\mathscr{D}$ structure. Lower left corner: The $\mathscr{B}$ model. With the same notations, the $\mathscr{B}$-model 1, 2, 3, 4 contains a left handed $\mathscr{D}'$ model 1, 2, 3′, 4′ and a $\mathscr{C}$-model 1″, 2″, 3″, 4″.

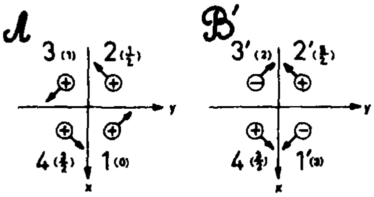

Fig. 4. If the atoms 1, 2, 3, 4 of the right-handed $\mathscr{A}$ structure are shifted vertically, one obtains a lefthanded $\mathscr{B}'$ structure 1′ 2′ 3′ 4.

the atoms and the second one to the axes. A rotation $(\mathbf{4}_2)^4$ sends point 1 in x, y, z to point 5 in $x, y, z+2$ which has the same spin as point 1. Thus the relations (4) are cyclic.

The operation $\mathbf{4}_2$ may be represented by a 12-dimensional matrix $(\mathbf{4}_2)$ acting on the 12 spin components $s_{j,\alpha}(\alpha = x,\ y,\ z)$ with $j = 1, 2, 3, 4$. The matrix $(\mathbf{4}_2)$ defined by (4) and its powers engender a representation Γ of a cyclic group of order 4. Γ is reducible and one may find the basis vectors by the reduction of Γ. However when the irreducible representations are known it is easier to construct the basis vectors $V_{jk}^{(\nu)}$ belonging to the irreducible representation $\Gamma^{(\nu)}$ by applying the projection operator formula [7]

$$V_{jk}^{(\nu)} = \sum_{g} \Gamma_{jk}^{(\nu)}(g)^{*} T_g \psi. \qquad (5)$$

Here $\Gamma^{(\nu)}(g)$ is the matrix representative of the group element g in the irreducible representation $\Gamma^{(\nu)}$. T_g is the operator associated with g and operating on a function ψ. The summation is over all group elements. For a cyclic group, all irreducible representations are one-dimensional and (5) simplifies to

$$V^{(\nu)} = \sum_{g} \chi^{(\nu)*}(g) \,.\, T_g \psi \qquad (6)$$

where $\chi^{(\nu)}(g)$ is the character of g in $\Gamma^{(\nu)}$. For the function ψ we take simply the spin components of $\mathbf{s}_1$, say successively s_{1x}, s_{1y} and s_{1z}. From the well known characters of the cyclic group of order 4 (Table 2) and from the equations (4) and (6) we find the following real vectors for $\Gamma^{(1)}$:

Table 2. Irreducible representations for $P4_2$; $\mathbf{k} = [\frac{1}{2}\frac{1}{2}\frac{1}{2}]$

	e	4_2	4_2^2	4_2^3
$\Gamma^{(1)}$	1	1	1	1
$\Gamma^{(2)}$	1	i	-1	$-i$
$\Gamma^{(3)}$	1	-1	1	-1
$\Gamma^{(4)}$	1	$-i$	-1	$+i$

$$\begin{aligned} V_1^{(1)} &= s_{1x} + s_{2y} - s_{3x} - s_{4y} = A_1 \\ V_2^{(1)} &= s_{1y} - s_{2x} - s_{3y} + s_{4x} = A_2 \\ V_3^{(1)} &= s_{1z} + s_{2z} + s_{3z} + s_{4z} = A_3 \end{aligned} \qquad (7a)$$

and for $\Gamma^{(3)}$:

$$\begin{aligned} V_1^{(3)} &= s_{1x} - s_{2y} - s_{3x} + s_{4y} = B_1 \\ V_2^{(3)} &= s_{1y} + s_{2x} - s_{3y} - s_{4x} = B_2 \\ V_3^{(3)} &= s_{1z} - s_{2z} + s_{3z} - s_{4z} = B_3. \end{aligned} \qquad (7b)$$

Consider first the vectors of (7a) and make

$$\begin{aligned} s_{1x} &= +s_{2y} = -s_{3x} = -s_{4y} \\ s_{1y} &= -s_{2x} = -s_{3y} = +s_{4y} \\ s_{1z} &= s_{2z} = s_{3z} = s_{4z}. \end{aligned} \qquad (8a)$$

This solution maximizes the vectors $V_j^{(1)}$ and corresponds to the van Laar model $\mathscr{A}$ with $A_1 = -A_2$. At the same time the solution (8a) gives zero values to the $V_j^{(3)} = B_j$ vectors. Alternatively the solution (8b) maximizes the vectors $V_j^{(3)}$, gives zero values to the $V_j^{(1)}$ vectors and represents the van Laar $\mathscr{B}$ model.

$$\begin{aligned} s_{1x} &= -s_{2y} = -s_{3x} = +s_{4y} \\ s_{1y} &= +s_{2x} = -s_{3y} = -s_{4x} \\ s_{1z} &= -s_{2z} = +s_{3z} = -s_{4z}. \end{aligned} \qquad (8b)$$

We can describe the two main structures $\mathscr{A}$ and $\mathscr{B}$ by the concise notations

$$\mathscr{A} = (-A_1, A_2, A_3) = (A_2, -A_1, A_3) \qquad (9a)$$

$$\mathscr{B} = (B_1, -B_2, B_3) = (-B_2, B_1, B_3) \qquad (9b)$$

We may now construct the most general effective anisotropic hamiltonian of order two

$$H_{an} = \tfrac{1}{2}a_1V_1^2 + \tfrac{1}{2}a_2V_2^2 + \tfrac{1}{2}a_3V_3^2 + a_{1,2}V_1V_2 + a_{2,3}V_2V_3 + a_{3,1}V_3V_1 \quad (10)$$

either with the vectors (7*a*) of $\Gamma^{(1)}$ or (7b) of $\Gamma^{(3)}$. Let us assume $a_1 = a_2 = a$ (this restriction is justified later), and evaluate in $\Gamma^{(1)}$ the invariant $a(A_1^2+A_2^2)$.

$$a(A_1^2+A_2^2) = 2a\mathbf{z}.(\mathbf{s}_1\times\mathbf{s}_2+\mathbf{s}_2\times\mathbf{s}_3+\mathbf{s}_3\times\mathbf{s}_4+\mathbf{s}_4\times\mathbf{s}_1)_{x,y} + a\sum_j (s_x^2+s_y^2)_j - 2a(\mathbf{s}_1\,.\,\mathbf{s}_3+\mathbf{s}_2\,.\,\mathbf{s}_4)_{x,y}. \quad (11)$$

Here $\mathbf{z}$ is the unit vector in the *Oz* direction and the lower indices *x*, *y* mean that the vectors are taken in the *Oxy* plane. It is clear that $A_1^2+A_2^2$ reaches its maximal value of $16\,s^2$ for $\mathbf{s}_j$ orthogonal to $\mathbf{s}_{j+1}$ and rotating in the same sense so that the 90° *canting in the Oxy-plane of the van Laar model is due to a large part to the vector products* or to *Dzialoshinski–Moriya*[8, 9] *coupling* (abreviated D–M coupling) of the type $\mathbf{D}_{jk}\,.\,(\mathbf{s}_j\times\mathbf{s}_k)$ between nearest neighbors. Thus the coefficient $2a\mathbf{z}$ in (11) plays the role of a D–M vector $\mathbf{D}_{jk}$ which is proportional to exchange (J_{jk}) and to spin orbit coupling.

Another term which may produce canting is the product A_1A_2. It can be written in dyadic notation

$$A_1A_2 = -\tfrac{1}{2}\sum_{j=1}^{4}(-1)^j\mathbf{s}_j\,.\,\boldsymbol{\phi}_1\,.\,(\mathbf{s}_j-\mathbf{s}_{j+2}).$$
$$+\tfrac{1}{2}\sum_{j=1}^{4}(-1)^j\mathbf{s}_j\,.\,\boldsymbol{\phi}_2\,.\,(\mathbf{s}_{j+1}-\mathbf{s}_{j-1}). \quad (12)$$

Here

$$\boldsymbol{\phi}_1 = \mathbf{x},\mathbf{y}+\mathbf{y},\mathbf{x}; \quad \boldsymbol{\phi}_2 = \mathbf{x},\mathbf{x}-\mathbf{y},\mathbf{y}. \quad (13)$$

The dyadics $\boldsymbol{\phi}_1$ and $\boldsymbol{\phi}_2$ have zero scalars and their matrix equivalents are symmetric and traceless, characteristic of symmetric coupling, i.e. crystal field, dipolar and pseudo-dipolar coupling, the most important terms being probably the 'one ion' terms of the form $s_{1x}s_{1y}$ coupled by $\boldsymbol{\phi}_1$.

We shall discuss later the coefficients of a_{23} and a_{31} which couple the (*xy*)- with the *z*-components after proceeding to a further reduction of the coefficients of the hamiltonian implied by observation.

Minimizing the hamiltonian under the condition $V_1^2+V_2^2+V_3^2 = C^t$, and introducing a Lagrange parameter λ we get the following set of equations

$$\begin{aligned} \lambda V_1 &= a_1V_1 + a_{12}V_2 + a_{13}V_3 \\ \lambda V_2 &= a_{12}V_1 + a_2V_2 + a_{23}V_3 \\ \lambda V_3 &= a_{13}V_1 + a_{23}V_2 + a_3V_3. \end{aligned} \quad (14)$$

For this set to be compatible with the equilibrium conditions (15) which are observed as well for model $\mathscr{A}$ as for model $\mathscr{B}$ the relations (16) between coefficients must be obeyed.

$$V_1 = -V_2 \quad (15)$$

$$a_1 = a_2 = a; \quad a_{23} = -a_{31}. \quad (16)$$

The hamiltonian can be written (17) with λ given by (18)

$$H = \tfrac{1}{2}\lambda(V_1^2+V_2^2+V_3^2) \quad (17)$$

$$\lambda = \tfrac{1}{2}(a_3+a') - \tfrac{1}{2}\left[(a_3-a')^2+8\,a_{31}^2\right]^{1/2} \quad (18)$$

Here we have abbreviated

$$a' = a - a_{12} \quad (19)$$

Resubstitution of λ (18) into the set (14) allows calculation of the magnitudes of ratios of basis vectors V_j which may be checked against experience. Another way is to rewrite the hamiltonian

$$H_{an} = \tfrac{1}{2}a(V_1^2+V_2^2) + \tfrac{1}{2}a_3V_3^2 + a_{12}V_1V_2 + a_{31}(V_1-V_2)V_3 \quad (20)$$

and to minimize it with respect to Θ and φ

when putting

$$V_1 = 4s \,.\, \sin\Theta \,.\, \cos\varphi \quad V_2 = 4s \,.\, \sin\Theta \,.\, \sin\Theta;$$
$$V_3 = 4s \,.\, \cos\Theta. \tag{21}$$

It is easily seen that if

$$a_{13} > 0; \quad a' - a_3 > 0; \quad \sqrt{2}a_{12}\tan\Theta + a_{13} > 0 \tag{22}$$

we have the following equilibrium conditions (model $\mathscr{A}$)

$$\cos\varphi = -\sin\varphi = -\sqrt{2}/2$$
$$\operatorname{tg} 2\Theta = 2\sqrt{2}a_{13}/(a' - a_3). \tag{23}$$

The value of Θ is known from experiment ($\Theta = 27{,}4°$) so that we finally get the following ratio (which is perhaps amenable to quantum mechanical calculations) for coefficients of the effective spin hamiltonian

$$a_{13}/(a' - a_3) = 0{,}501. \tag{24}$$

Finally the hamiltonian (20) may be written in the form of a two sublattice hamiltonian depending only on the components of $\mathbf{s}_1$ and $\mathbf{s}_2$ by observing that in model $\mathscr{A}$

$$s_{1\alpha} = -s_{3\alpha}; \quad s_{2\alpha} = -s_{4\alpha} \quad (\alpha = x, y)$$
$$s_{1z} = s_{3z}; \quad s_{2z} = s_{4z}.$$

When this is done, the coefficient of a_{13} is seen to have a complex nature, its principal terms being one ion anisotropy (of the form $s_{j\alpha}s_{jz}$ with $\alpha = x, y$) and anisotropic asymmetric exchange between nearest neighbors (as $s_{1z}s_{2x} - s_{1x}s_{2z}$ and so on). We note that a non zero value of a_{13} is essential to our problem although a_{13} may be small if a' and a_3 (say mainly D–M coupling and one ion anisotropy in the z-direction) are of comparable strength. We also note that no anisotropy of order four in the moments is required to explain the 'canted multispin axis' model of van Laar.

The complete hamiltonian is obtained by adding the well known isotropic part H_{is} to H_{an}

$$H_{is} = -2\Sigma_1 y_1 \mathbf{s}_i \cdot \mathbf{s}_j - 2\Sigma_2 y_2 \mathbf{s}_i \cdot \mathbf{s}_j.$$

The indices 1 and 2 refer to the first and second neighbors respectively. The first sum is zero (see introduction).

THE SYMMETRY GROUPS

We shall call symmetry groups of the hamiltonian (20) all those groups which automatically imply the symmetry relations (16) between the coefficients of the effective spin hamiltonian (10). In other words, we shall complete the 4_2 screw axis by other symmetry elements in such a way that the basis vectors of irreducible representations [10] associated with $\mathbf{k} = (\frac{1}{2}\frac{1}{2}\frac{1}{2})$ describe the CoO $\mathscr{A}$ or $\mathscr{B}$ structure (9a, 9b). The simplest method is to add one symmetry element at the time, to let it operate on the spins or better on the A_j and B_j vectors, and finally to see if and how it modifies the hamiltonian (10). We know already that

$$4_2 A_j = A_j; \quad 4_2 B_j = -B_j \quad (j = 1,2,3). \tag{25}$$

It will prove useful to introduce as 'vectors' the structure $\mathscr{A}$ and $\mathscr{B}$ themselves. Thus for instance (25) can be written

$$4_2\,\mathscr{A} = \mathscr{A}; \quad 4_2\,\mathscr{B} = -\mathscr{B} \tag{25'}$$

which expresses the fact that model $\mathscr{A}$ belongs to $\Gamma^{(1)}$ and model $\mathscr{B}$ to $\Gamma^{(3)}$ of the group $P4_2$ ($\mathbf{k} = [\frac{1}{2}\frac{1}{2}\frac{1}{2}]$). We have investigated the tetragonal space groups (C_{4h}^2, C_{4h}^4, D_4^5, C_{4v}^4, D_{4h}^{10}, D_{4h}^{12}, D_{4h}^{14}, D_{4h}^{16}) in which the CoO nuclear structure is possible with fourfold positions. We explain the procedure in some detail for $P4_2/m$, $P4_2/n$ and $P4_22$. Only the last one is a complete symmetry group as defined above. We bypass the discussion of the groups $P4_22_1$ and $P4_2m$ in which $\mathscr{A}$ and $\mathscr{B}$ belong to two-dimensional real representations. These groups which do not restrict the hamiltonian (10) are contained as subgroups in complete symmetry groups of the class D_{4h}, discussed later.

$P4_2/m - C_{4h}^2$

Add for instance a center of symmetry I in 000 (on the 4_2 axis at $00z$) and take for the Co-atoms the positions (3) with $z = 0$. One has

$$\mathbf{I}(x,y,0) = \bar{x},\bar{y},0 = \bar{x},\bar{y},1+00\bar{1}. \quad (26)$$

This relations means that I transfers the spin from point 1 to point 3 but with an additional translation $\mathbf{t} = 00\bar{1}$ which introduces a phase factor $\exp 2\pi\, i\mathbf{k}\,.\,\mathbf{t} = -1$. Recalling that spins transform as axial vectors, one finds in this way

$$\mathbf{Is}_1 = -\mathbf{s}_3;\quad \mathbf{Is}_2 = +\mathbf{s}_4;\quad \mathbf{Is}_3 = -\mathbf{s}_1;\quad \mathbf{Is}_4 = \mathbf{s}_2. \quad (27)$$

From these (and similar) relations, we derive the action of I on the A_j and B_j vectors

$$\mathbf{I}[A_1,A_2,A_3] = [B_1,B_2,-B_3];\quad \mathbf{I}[B_1,B_2,B_3] = [A_1,A_2,-A_3]. \quad (28)$$

Here we have written row vectors instead of column vectors for the sake of brevity and space. The set of equations (28) may also be written

$$\mathbf{I}[-A_1,A_2,A_3] = [-B_1,B_2,-B_3]. \quad (29)$$

We can infer from (28) and (29), recalling the definitions (9a) and (9b)

$$\mathbf{I}\mathscr{A} = -\mathscr{B};\quad \mathbf{I}\mathscr{B} = -\mathscr{A}. \quad (30)$$

Thus the matrices (31) generate a two-dimensional irreducible representation in which the structures $\mathscr{A}$ and $\mathscr{B}$ are equivalent partners

$$(\mathbf{4_2}) = \begin{bmatrix} 1 & \cdot \\ \cdot & -1 \end{bmatrix};\quad (\mathbf{I}) = \begin{bmatrix} \cdot & -1 \\ -1 & \cdot \end{bmatrix}. \quad (31)$$

Let us remark however that if the center of inversion transforms the hamiltonian $H(A_j)$ into $H(B_j)$, it does not restrict the coefficients; $P4_2/m$ is not yet a complete symmetry group (i.e. it does not imply $A_1 = -A_2$; $B_1 = -B_2$).

$P4_2/n - C_{4h}^4$

4_2 is still in $00z$, but the center of symmetry is now in $\frac{1}{4}\frac{1}{4}\frac{1}{4}$. The interesting feature of this group is that the four Co-atoms move to the parameterless positions (centers of symmetry) $4c$ [6]

$$\tfrac{1}{4}\tfrac{1}{4}\tfrac{1}{4}\,(1);\quad -\tfrac{1}{4}\tfrac{1}{4}\tfrac{3}{4}\,(2);\quad -\tfrac{1}{4},-\tfrac{1}{4},\tfrac{5}{4}\,(3);\quad \tfrac{1}{4},-\tfrac{1}{4},\tfrac{7}{4}. \quad (32)$$

The same is true for the 4 0-atoms in $\frac{1}{4}\frac{1}{4}\frac{3}{4}$ and so on. The effect of the symmetry center I on the spins can be described by

$$\mathbf{Is}_j = \mathbf{s}_j \quad\text{or}\quad \mathbf{I}V_j = V_j \quad (V = A \text{ or } B). \quad (33)$$

Thus

$$\mathbf{I}\mathscr{A} = \mathscr{A};\quad \mathbf{I}\mathscr{B} = \mathscr{B}. \quad (34)$$

No restriction is implied on the coefficients of H; $\mathscr{A}$ and $\mathscr{B}$ belong to one dimensional representations associated with $\mathbf{k} = [\frac{1}{2}\frac{1}{2}\frac{1}{2}]$ in space group $P4_2/n$. Although $P4_2/n$ is not yet a complete symmetry group, it shows already that deviations from the 'ideal' values $\frac{1}{4}\frac{1}{4}\frac{1}{4}$ are *not essential* to our problem. The positions (32) are not translationnally equivalent (by face centered translations). But they will give rise to the same diffraction pattern (indices of the same parity) as if they were on face-centered positions.

$P4_22 - D_4^5$

Let us add a twofold axis 2_x in $x00$ crossing through 4_2 in $00z$. One finds easily from the equations of transformation acting on the spin positions (3) with $x = y$ and $z = \frac{1}{4}$ ($4n$ [6]) that

$$\mathbf{2_x}[A_1,A_2,A_3] = [A_2,A_1,-A_3];\quad \mathbf{2_x}[B_1,B_2,B_3] = [-B_2,-B_1,B_3]. \quad (35)$$

The operator $\mathbf{2}_x$ acting on $H(10)$ transforms H to

$$\mathbf{2}_x H = \tfrac{1}{2}a_1A_2^2 + \tfrac{1}{2}a_2A_1^2 + \tfrac{1}{2}a_3A_3^2 + a_{12}A_2A_1 - a_{23}A_1A_3 - a_{13}A_2A_3 \quad (36)$$

so that by comparison with (10) we get immediately the restrictions (16) on the coefficients. The equations (35) may be rewritten

$$\mathbf{2}_x\mathscr{A} = -\mathscr{A}; \quad \mathbf{2}_x\mathscr{B} = \mathscr{B} \quad (37)$$

so that the models $\mathscr{A}$ and $\mathscr{B}$ belong to one dimensional representations associated with the wave-vector $\mathbf{k} = [\frac{1}{2}\frac{1}{2}\frac{1}{2}]$ in space group $P4_22$ (see Appendix B). It is easily checked that $(A_1-A_2)A_3$ and $(B_1-B_2)B_3$ are invariants. Thus $P4_22$ is the first complete symmetry group we have encountered.

Now that the procedure is clear, we only tabulate in Table 3 the results for complete symmetry groups (including the present one): $P4_22-D_4^5$, $P4_2nm-C_{4v}^4$, $P(4_2/m)\,cm-D_{4h}^{10}$, $P(4_2/m)\,nm-D_{4h}^{12}$ and $P(4_2/m)\,nm-D_{4h}^{14}$ and their irreducible representations, associated with the wave-vector $\mathbf{k} = [\frac{1}{2}\frac{1}{2}\frac{1}{2}]$ and having the structures $\mathscr{A}$ and (or) $\mathscr{B}$ as basis vectors.

The explicite relations, leading to Table 3 and showing these groups to be complete are given in Appendix C.

Note that the only complete symmetry group with parameterless positions is $P(4_2/n)\,nm-D_{4h}^{12}$.

In $P4_22-D_4^5$, $P4_2\,nm-C_{4v}^4$, and $P(4_2/n)\,nm-D_{4h}^{12}$, $\mathscr{A}$ and $\mathscr{B}$ belong to one-dimensional different representations (D_4^5 is subgroup of C_{4v}^4 which is subgroup of D_{4h}^{12}).

In $P(4_2/m)\,cm-D_{4h}^{10}$ and in $P(4_2/m)\,nm-D_{4h}^{14}$, $\mathscr{A}$ and $\mathscr{B}$ appear as equivalent partners of two-dimensional irreducible representations which is perhaps more satisfactory from the point of view of the physicist, $\mathscr{A}$ and $\mathscr{B}$ having the same energy.

Inversely one may determine the irreducible representations of D_{4h}^{14} belonging to the wave-vector $\mathbf{k} = [\frac{1}{2}\frac{1}{2}\frac{1}{2}]$ and show that basis-vectors of one of them describe the spin configuration. This is done in Appendix D for completeness.

SHUBNIKOV GROUPS

Only those magnetic structures which transform according to real one-dimensional representations of the 230 space groups[10] can be described in the formalism of Shubnikov groups. These are given in the two last columns of Table 3 in the notations of Opechowski and Guccione[12] and of Belov, Neronova and Smirnova[13]. To the $\mathbf{k} = [\frac{1}{2}\frac{1}{2}\frac{1}{2}]$ wave-vector correspond the magnetic translation lattices P_I in the O-G-notation and I_c in the B-N-S notation. They are still subgroups of each other. It would also have been possible of course to build the hamiltonian of order two with basis vectors belonging to the identity representations of the Shubnikov groups.

Table 3. *Complete symmetry groups*

Group	Generators*	Representations for $\mathscr{A}$	$\mathscr{B}$	Shubnikov Group O-G	B-N-S
$P4_222-D_4^5$	$4_2\ 2_x\ .$	$1, -1\ .$	$-1,\ 1\ .$	P_I4_222	I_c4_122
$P4_2nm-C_{4v}^4$	$4_2\ n\ \ .$	$1, -1\ .$	$-1,\ 1\ .$	$P_I4_2n'm'$	I_c4_1cd
$P4_2/nnm-D_{4h}^{12}$	$4_2\ 2_x\ \bar{1}$	$1,\ 1, -1$	$-1, -1, -1$	$P_I4_2/nn'm'$	I_c4_1/acd
$P4_2/mcm-D_{4h}^{10}$	$4_2\ 2_x\ \bar{1}$	$\begin{pmatrix}1 & .\\ . & -1\end{pmatrix}$	$\begin{pmatrix}1 & .\\ . & -1\end{pmatrix}$	$\begin{pmatrix}. & -1\\ -1 & .\end{pmatrix}$	
$P4_2/mnm-D_{4h}^{14}$	$4_2\ 2_{1x}\ \bar{1}$	$\begin{pmatrix}1 & .\\ . & -1\end{pmatrix}$	$\begin{pmatrix}. & -1\\ 1 & .\end{pmatrix}$	$\begin{pmatrix}. & 1\\ 1 & .\end{pmatrix}$	

*For the positions of the generators, see text. Representations are given in the same order as the generators.

CONCLUSION

Throughout this paper we have justified our classical spin hamiltonian by symmetry considerations only. Some quantum mechanical speculation may not be out of place. Actually Co^{2+} has an odd number of electrons and in all groups here investigated the site symmetry is low enough (orthorhombic *m m* in the groups D_{4h}^{10} and D_{4h}^{14}, monoclinic in the other ones, pseudotetragonal in any case) to expect a Kramers doublet lying lowest[14]. Thus the conditions for the existence of antisymmetric exchange in the fictitions ($\mathscr{S} = \frac{1}{2}$) spin space[15] are met.

To summarize our results, the van Laar model looks quite reasonable because it is consistent not only with diffraction dates, but also with an effective anisotropic spin hamiltonian of order two and although the answer is not unic, tetragonal symmetry groups may be found for the magnetic structure as well in the frame of representation analysis as within that of Shubnikov groups. Correspondance with Mme Hartmann-Boutron on the quantum mechanical aspects is gratefully acknowledged.

REFERENCES

1. TOMBS N. C. and ROOKSBY H. P., *Nature* **165**, 442 (1950).
2. SHULL C. G., STRAUSER W. A. and WOLLAN E. O., *Phys. Rev.* **83**, 333 (1951).
3. ROTH W. L., *Phys. Rev.* **110**, 1333 (1958).
4. van LAAR B., *Phys. Rev.* **138**, A584 (1965).
5. LI Y. Y., *Phys. Rev.* **100**, 627 (1955).
6. LONSDALE and HENRY, *International Tables for Crystallography*. Kynoch Press, Birmingham (1954).
7. KNOX R. S. and GOLD A., *Symmetry in the Solid State*. Benjamin, New York (1964).
8. DZIALOSHINSKI I. E., *J. Phys. Chem. Solids* **4**, 241 (1958).
9. MORIYA T., *Phys. Rev.* **120**, 91 (1960).
10. BERTAUT E. F., *Acta crystallogr.* **A24**, 217 (1968).
11. NAGAMIYA T., SAITO S., SHIMOMURA Y. and UCHIDA E., *J. phys. Soc. Japan* **20**, 1285 (1965).
12. OPECHOWSKI W. and GUCCIONE R., *Treatise on Magnetism* (Edited by Rado and Suhl), Chap. 3, p. 105. Academic Press, New York.
13. BELOV N. V., NERONOVA N. N. and SMIRNOVA T. S., *Kristallografiya* **2**, 315 (1957); (translation: *Soviet Phys. Cryst.* **2**, 311).
14. ELLIOTT R. J. and THORPE M. F., *J. appl. Phys.* **39**, 802 (1968).
15. LEVY P. M., *Phys. Rev. Lett.* **20**, 1366 (1968).
16. OLBRYCHSKI K., *Phys. Status Solidi* **3**, 1868 (1963).

APPENDIX A. VAN LAAR MODELS

Take ideal coordinates $\frac14\,\frac14\,\frac14$; $\bar{\frac14}\,\frac14\,\frac34$; $\bar{\frac14}\,\bar{\frac14}\,\frac54$; $\frac14\,\bar{\frac14}\,\frac34$ for our 4 Co-atoms and shift the origin to the first one, so that the sequence becomes $0\,0\,0$; $\bar{\frac12}\,0\,\frac12$; $\bar{\frac12}\,\bar{\frac12}\,1$; $0\,\bar{\frac12}\,\frac12$. In the magnetic unit cell ($2a_0$, $2a_0$, $2a_0$) we must halve these coordinates. Finally the structure factor of the spins in ($0\,0\,0$; $\bar{\frac14}\,0\,\frac14$; $\bar{\frac14}\,\bar{\frac14}\,\frac12$; $0\,\bar{\frac14}\,\frac34$) is simply

$$\mathbf{F} = \sum \mathbf{s}_j \exp(2\pi i \mathbf{h}\,.\,\mathbf{r}_j) = \mathbf{s}_1 + \mathbf{s}_2\, i^{l-h} + \mathbf{s}_3\,(-1)^l\, i^{h-k} + \mathbf{s}_4\, i^{-k-l}. \qquad \text{(A-1)}$$

It is well known that a propagation vector $[\frac12\,\frac12\,\frac12]$ implies for the magnetic cell an inner anticentring, so that $h+k+l$ must be odd and a face centering (all indices of same parity) so that finally all indices must be odd. One sees easily that for any allowed reflexion

$$|\mathbf{F}| = 2|\mathbf{s}_j|. \qquad \text{(A-2)}$$

Consider for instance model $\mathscr{B}$ where we only use the fact that

$$\sum s_{jx} = \sum s_{jy} = \sum s_{jz} = 0. \qquad \text{(A-3)}$$

One finds

$$\mathbf{F}(1\,\bar{1}\,3) = 2\mathbf{s}_1, \quad \mathbf{F}(1\,1\,3) = -2\mathbf{s}_2, \quad \mathbf{F}(\bar{1}\,1\,3) = -2\mathbf{s}_3, \quad \mathbf{F}(1\,1\,\bar{3}) = -2\mathbf{s}_4 \qquad \text{(A-4)}$$

Actually neutron diffraction intensities are proportional to $|\mathbf{F}|^2 \sin^2\alpha$ where α is the angle between the vector $\mathbf{F}$ and the diffusion vector $\mathbf{h}$. In other words, if $|\mathbf{F}|^2 \sin^2\alpha$ is very small for the $\{1\,1\,3\}$ reflexions, the quantity $\cos^2\alpha$ (A-5) must be maximal

$$\cos^2\alpha = \left|\frac{\mathbf{F}\,.\,\mathbf{h}}{|\mathbf{F}|\;|\mathbf{h}|}\right|^2. \qquad \text{(A-5)}$$

One finds explicitely

$$\begin{aligned}
\cos^2\alpha(1\,\bar{1}\,3) &= \tfrac{1}{11}(s_{1x} - s_{1y} + 3s_{1z})^2\\
\cos^2\alpha(1\,1\,3) &= \tfrac{1}{11}(s_{2x} + s_{2y} + 3s_{2z})^2;\\
\cos^2\alpha(\bar{1}\,1\,3) &= (-s_{3x} + s_{3y} + 3s_{3z})^2;\\
\cos^2\alpha(1\,1\,\bar{3}) &= \tfrac{1}{11}(s_{4x} + s_{4y} - 3s_{4z})^2.
\end{aligned} \qquad \text{(A-6)}$$

Choosing s_{1z} positive, the maximization of the $\cos^2\alpha$ with the conditions (A-3) *uniquely* determines the sign sequence of model $\mathscr{B}$ as given under Table 1. Furthermore, if u, v and Θ are the angles of spin $\mathbf{s}_1$ with the axes, we may write, assuming $|\cos u| = |\cos v|$,

$$\tfrac{1}{11}(2\cos u + 3\cos\Theta)^2 = 1 \qquad \text{(A-7)}$$

wherefrom we find with $2\cos^2 u + \cos^2\Theta = 1$

$$\Theta = 25°.$$

This result, obtained by maximizing $\cos^2\alpha$, does not depend on the exact form factor of Co and invalidates the reasoning of reference[11]. The exact value, taking into account the true intensity of {1 1 3} and of other reflexions [4] is $\Theta = 27{,}4°$.

One proceeds in the same way as above to establish the sign relations for the models $\mathscr{A}$, $\mathscr{C}$ and $\mathscr{G}$. Although van Laar has not enumerated these equivalent models, we continue to call them 'van Laar models'. They will play the role of new types of domains in the multispin axis model.

APPENDIX B

Irreducible space group representation of $P4_2{}^2$ *associated with the wave vector* $\mathbf{k} = [\frac{1}{2}\frac{1}{2}\frac{1}{2}]$

We prove the quite unexpected result that the irreducible representation are the same ones as those of group *P*42 associated with $\mathbf{k} = 0$. We apply a method due to Olbrychski[16]. Let the group generators be

$$\mathbf{2}_x = \{2\,|0\};\quad \mathbf{4}_z = \{4_z|\tau\}, \tag{B-1}$$

For $\mathbf{2}_x$ and $\mathbf{4}_z$ we use the matrix representations (B-2). τ is the translation $0\,0\,\frac{1}{2}$ along the fourfold axis We note $\mathbf{e}$ the unit matrix

$$\mathbf{2}_x = \begin{bmatrix} 1 & \cdot & \cdot \\ \cdot & -1 & \cdot \\ \cdot & \cdot & -1 \end{bmatrix};\quad \mathbf{4}_z = \begin{bmatrix} \cdot & -1 & \cdot \\ 1 & \cdot & \cdot \\ \cdot & \cdot & 1 \end{bmatrix}. \tag{B-2}$$

Straightforward algebra with the Koester–Seitz symbols shows that

$$\begin{aligned} (\mathbf{4}_z\cdot\mathbf{2}_x)^2 &= \{(\mathbf{4}_z\mathbf{2}_x)^2|(\mathbf{4}_z\mathbf{2}_x+\mathbf{e})\tau\} = \{\mathbf{e}|0\} \\ (\mathbf{2}_x\cdot\mathbf{4}_z)^2 &= \{\mathbf{e}|0\} \\ (\mathbf{4}_z)^4 &= (\mathbf{2}_x)^2 = \mathbf{e}. \end{aligned} \tag{B-3}$$

Let be M_1 and M_2 the irreducible matrix representations of $\mathbf{4}_z$ and $\mathbf{2}_x$ respectively The relations (B-3) show that

$$M_1{}^4 = M_2{}^2 = 1;\quad (M_1M_2)^2 = (M_2M_1)^2 = 1. \tag{B-4}$$

These relations are the same ones as in the group 42. (They generate four irreducible one-dimensional representations corresponding to the solution $M_1 = \pm 1$; $M_2 = \pm 1$ and one two-dimensional complex solution (corresponding to $M_1M_2 \neq M_2M_1$)) The reason is the fact that the translations $(\mathbf{4}_z\mathbf{2}_x + \mathbf{e})\tau$ and $(\mathbf{2}_x\mathbf{4}_z + \mathbf{e})\tau$ are zero.

APPENDIX C. COMPLETE SYMMETRY GROUPS

$P4_2nm$-C_{4v}^4, in full notation $P4_2(2/n)(2/m)$, has a 4_2 axis in $0\,\frac{1}{2}\,z$ and a *n* plane in $x\,0\,z$. The four Co-atoms are in 4c with $x = \frac{1}{4}$, $z = 0$.

$$\tfrac{1}{2}-x,\ \tfrac{1}{2}+x,\ z\ (1);\quad -x,\ 1-x,\ z+\tfrac{1}{2}\ (2);$$
$$-\tfrac{1}{2}+x,\ \tfrac{1}{2}-x,\ z+1\ (3);\quad x, x,\ z+\tfrac{3}{2}\ (4).$$

The relations C–1 give the hamiltonian the form (20)

$$\begin{aligned} \mathbf{n}[A_1, A_2, A_3] &= [A_2, A_1, -A_3]; \\ \mathbf{n}[B_1, B_2, B_3] &= [-B_2, -B_1, B_3] \end{aligned} \tag{C-1}$$

one has

$$\mathbf{n}\,\mathscr{A}_1 = -\mathscr{A};\quad \mathbf{n}\,\mathscr{B} = \mathscr{B}. \tag{C-2}$$

$\mathscr{A}$ and $\mathscr{B}$ belong to one dimensional representations.

$P4_2/m\,cm$-D_{4h}^{10}, in full notation $P4_2/m\,(2/c)(2/m)$, contains $P4_2cm$-C_{4v}^3, $P4_2/m$-C_{4h}^2 and also $P4_22$-$D_4{}^5$ as subgroups. Here 4_2 is in $0\,0\,z$, 2_x in $x\,0\,\frac{1}{4}$ and there is a center of symmetry *I* in 0 0 0. The four Co-atoms are in the positions (3) with $x = y = \frac{1}{4}$ and $z = 0$ (4*i*[6]). The transformation equations are found to be

$$\begin{aligned} \mathbf{2}_x[A_1, A_2, A_3] &= [-A_2, -A_1, A_3]; \\ \mathbf{2}_x[B_1, B_2, B_3] &= [B_2, B_1, -B_3] \\ \mathbf{I}[A_1, A_2, A_3] &= [B_1, B_2, -B_3], \\ \mathbf{I}[B_1, B_2, B_3] &= [A_1, A_2, -A_3]. \end{aligned} \tag{C-3}$$

so that $\mathscr{A}$ and $\mathscr{B}$ belong as equivalent partners to a two-dimensional irreducible representation generated by the three matrices

$$(\mathbf{4}_z) = \begin{pmatrix} 1 & \cdot \\ \cdot & -1 \end{pmatrix};\ (\mathbf{2}_x) = \begin{pmatrix} 1 & \cdot \\ \cdot & -1 \end{pmatrix};\ \mathbf{I} = \begin{pmatrix} \cdot & -1 \\ -1 & \cdot \end{pmatrix}. \tag{C-4}$$

$P\,4_2/n\,nm - D_{4h}^{12}$, in full notation $P\,4_2/n\,2/n\,2/m$, contains as subgroups as well $P4_22 - D_4{}^5$ as $P4_2\,nm - C_{4v}^4$; 4_2 is in $0\frac{1}{2}z$, 2_x in $x0\frac{1}{4}$ and *I* in 000. The four Co-atoms are now in parameterless positions 4 f [6]

$$\tfrac{1}{4}\tfrac{3}{4}\tfrac{1}{4}\,(1);\ -\tfrac{1}{4}\tfrac{1}{4}\tfrac{3}{4}\,(2), -\tfrac{1}{4}\tfrac{1}{4}\tfrac{5}{4}\,(3);\ \tfrac{1}{4}\tfrac{1}{4}\tfrac{7}{4}\,(4). \tag{C-6}$$

One finds for 2_x the same relations as under (35); for *I* one has simply

$$\mathbf{I}\mathbf{s}_j = -\mathbf{s}_j\,(j = 1, \ldots, 4) \tag{C-5}$$

so that finally $\mathscr{A}$ and $\mathscr{B}$ belong to real one dimensional representations (cf. Table 3).

$P4_2/m\,nm - D_{4h}^{14}$, in full notation $P\,4_2/m\,2_1/n\,2/m$, contains $P4_22_1 - D_4$ and $P4_2nm - C_{4v}^4$ as subgroups. We chose as generators 4_2 in $0\,\frac{1}{2}\,z$; 2_{1x} in $x\,\frac{1}{4}\,\frac{1}{4}$ and a symmetry center *I* in 0 0 0: the four Co-atoms are taken in 4*g* with $x = \frac{1}{4}$

$$x,\ 1-x,\ 0\,(1);\ -\tfrac{1}{2}+x,\ \tfrac{1}{2}+x,\ \tfrac{1}{2}\,(2);\ x,\ x,\ 1\,(3);$$
$$\tfrac{1}{2}-x,\ \tfrac{1}{2}-x,\ \tfrac{3}{2}\,(4).$$

One finds here

$$\begin{aligned} \mathbf{2}_{1x}[A_1, A_2, A_3] &= [B_2, B_1, B_3]; \\ \mathbf{2}_{1x}[B_1, B_2, B_3] &= [-A_2, -A_1, -A_3 \\ \mathbf{I}[A_1, A_2, A_3] &= [-B_1, -B_2, -B_3]; \\ \mathbf{I}[B_1, B_2, B_3] &= [-A_1, -A_2, A_3]. \end{aligned} \tag{C-6}$$

First of all the $\mathbf{2}_{1x}$ operation will transform the $H(A_i)$ hamiltonian into a $H(B_j)$ hamiltonian, but the last **I**-operation will bring $H(B_j)$ back to a $H'(A_j)$ hamiltonian. The comparison of $H(A_j)$ and $H'(A_j)$ yields the same restrictions on the coefficients as under (16) and leads to (20). From (C-6) we get

$$\begin{aligned} \mathbf{2}_{1x}\mathscr{A} &= \mathscr{B};\quad \mathbf{I} = \mathscr{A} = \mathscr{B} \\ \mathbf{2}_{1x}\mathscr{B} &= -\mathscr{A};\quad \mathbf{I}\mathscr{B} = \mathscr{A}. \end{aligned} \tag{C-7}$$

Thus the structures $\mathscr{A}$ and $\mathscr{B}$ belong as equivalent

Table 4. *The two-dimensional irreducible representation in* $P4_2/mnm - D_{4h}^{14}$; $\mathbf{k} = [\frac{1}{2}\frac{1}{2}\frac{1}{2}]$ *for the* $\mathscr{A}$ *and* $\mathscr{B}$*-structures**

e	M_1	M_1^2	M_1^3	M_2	M_2M_1	$M_2M_1^2$	$M_2M_1^3$
$\begin{pmatrix}1 & . \\ . & 1\end{pmatrix}$	$\begin{pmatrix}1 & . \\ . & -1\end{pmatrix}$	$\begin{pmatrix}1 & . \\ . & 1\end{pmatrix}$	$\begin{pmatrix}1 & . \\ . & -1\end{pmatrix}$	$\begin{pmatrix}1 & -1 \\ 1 & .\end{pmatrix}$	$\begin{pmatrix}. & 1 \\ 1 & .\end{pmatrix}$	$\begin{pmatrix}. & -1 \\ 1 & .\end{pmatrix}$	$\begin{pmatrix}. & 1 \\ 1 & .\end{pmatrix}$

M_3	M_3M_1	$M_3M_1^2$	$M_3M_1^3$	M_3M_2	$M_3M_2M_1$	$M_3M_2M_1^2$	$M_3M_2M_1^3$
$\begin{pmatrix}. & 1 \\ 1 & .\end{pmatrix}$	$\begin{pmatrix}. & -1 \\ 1 & .\end{pmatrix}$	$\begin{pmatrix}. & 1 \\ 1 & .\end{pmatrix}$	$\begin{pmatrix}. & -1 \\ 1 & .\end{pmatrix}$	$\begin{pmatrix}1 & . \\ . & -1\end{pmatrix}$	$\begin{pmatrix}1 & . \\ . & 1\end{pmatrix}$	$\begin{pmatrix}1 & . \\ . & -1\end{pmatrix}$	$\begin{pmatrix}1 & . \\ . & 1\end{pmatrix}$

*M_1, M_2, M_3 are the matrix representatives for the operators $\mathbf{4}_2$, $\mathbf{2}_{1x}$ and $\mathbf{I}$.

APPENDIX D.

Basis vectors in space group $P\,4_2/m\,nm - D_{4h}^{14}$; $\mathbf{k} = [\frac{1}{2}\frac{1}{2}\frac{1}{2}]$

The generators 4_2 in $0\frac{1}{2}z$, 2_{1x} in $x\frac{1}{4}\frac{1}{4}$ and I in $0\,0\,0$ are given by the symbols

$$\mathbf{4}_2 = \{\mathbf{4}_z|\boldsymbol{\tau}\};\quad \mathbf{2}_{1x} = \{\mathbf{2}_x|\boldsymbol{\tau}\};\quad \mathbf{I} = \{\bar{\mathbf{I}}|0\}. \qquad \text{(D-1)}$$

Here $\boldsymbol{\tau}$ is the translation $\boldsymbol{\tau} = \frac{1}{2}\frac{1}{2}\frac{1}{2}$ and the matrices $\mathbf{4}_x$ and $\mathbf{2}_x$ are as under (B-2). One finds here:

$$\mathbf{2}_1^2 = \{\mathbf{e}|1\,0\,0\};\quad (\mathbf{2}_1\mathbf{4}_2)^2 = \{\mathbf{e}|0\};\quad (\mathbf{4}_2\mathbf{2}_1)^2 = \{\mathbf{e}|1\,0\,\bar{1}\}$$
$$\mathbf{2}_1\mathbf{I} = \mathbf{I}\mathbf{2}_1\{\mathbf{e}|1\,1\,1\};\quad \mathbf{I}\mathbf{4}_2 = \mathbf{4}_2\mathbf{I}\{\mathbf{e}|1\,1\,1\}. \qquad \text{(D-2)}$$

Recalling that a translation $\mathbf{t}$ is represented by $\exp 2\pi i\,\mathbf{k}\,.\,\mathbf{t}$ and noting M_1, M_2, M_3 the matrix representatives of $\mathbf{4}_2$, $\mathbf{2}_1$ and $\mathbf{I}$, one finds

$$M_1^4 = 1 = M_3^2,\quad M_2^2 = -1.$$
$$(M_1M_2)^2 = (M_2M_1)^2 = 1;\quad M_jM_3 = -M_3M_j \quad (j = 1,2). \qquad \text{(D-3)}$$

The fact that M_3 anticommutes with M_1 and M_2 allows only for four two-dimensional representations ($g = 16 =$ order of the group $= 2^2+2^2+2^2+2^2$) one of which has partners to the two-dimensional representations generated by the 3 matrices of Table 3 and given in full in Table 4. Note that the matrix representing $\mathbf{2}_{1x}$ is the transpose of the transformation matrix under (C-7); see reference [7]. been already found in Appendix C. The reader may check that the matrices of Table 4 fulfill the relations (D-3). Taking into account the equations of transofmration (D-4)

$$\mathbf{2}_1 s_{1x} = s_{2x};\quad \mathbf{2}_1 s_{2x} = -s_{1x};\quad \mathbf{2}_1 s_{3x} = s_{4x};\quad \mathbf{2}_1 s_{4x} = -s_{3x} \qquad \text{(D-4)}$$

and similar equations for the y and z components with a change of signs as well as (D-5) and relation (4) of the text

$$\mathbf{I}\mathbf{s}_1 = \mathbf{s}_3;\quad \mathbf{I}\mathbf{s}_2 = \mathbf{s}_4;\quad \mathbf{I}\mathbf{s}_3 = \mathbf{s}_1;\quad \mathbf{I}\mathbf{s}_4 = -\mathbf{s}_2 \qquad \text{(D-5)}$$

we can for instance apply the projection operator relation (5) using for $\Gamma_{jk}^{(\nu)}$ the matrix elements of Table 4 and for ψ the spin component $\psi = s_{1x}$. We find

$$V_{11} = s_{1x} + s_{2y} - s_{3x} - s_{4y} - s_{4x} + s_{3y} + s_{2x} - s_{1y} = A_1 - A_2. \qquad \text{(D-6)}$$

This vector is maximal for the $\mathscr{A}$ configuration. An equivalent partner is V_{21} (D-7) which is maximal for the $\mathscr{B}$ configuration

$$V_{21} = s_{2x} + s_{1y} - s_{4x} - s_{3y} + s_{3x} - s_{4y} - s_{1x} + s_{2y} = B_2 - B_1. \qquad \text{(D-7)}$$

One finds in the same way

$$V_{12} = A_2 - A_1;\quad V_{22} = B_1 - B_2.$$

J. Phys. Chem. Solids Pergamon Press 1969. Vol. 30, pp. 775-776. Printed in Great Britain.

TECHNICAL NOTES

The dielectric constant of EuS

(*Received* 20 *August* 1968)

THE DIELECTRIC constant of f.c.c. EuS is of interest in connection with energy band calculations[1, 2].

The principal difficulty in determining the dielectric constant of EuS is the preparation of suitable samples. The EuS used here was formed by the reduction[3] of Eu_2O_3 by H_2S. The resultant powder was then purified by vapor distillation. The small crystallites (~ 10 μ) produced by this process were then pulverized and pressed into pills ½ in. in dia. and varying in thickness from 0·020 to 0·078 in. Such pills are porous, having a density about 10 per cent less than the crystallographic density[4] of 5·80 g/cm³.

The capacitance of the pills was measured with a general Radio Type 1615-A Bridge using a Type 1311A audio oscillator and Type 1232-A tuned amplifier and receiver. The quantity ϵ was calculated from the observed capacitance and the measured values of the thickness and diameter. The density ρ of the pills and hence δ were also calculated from the two latter quantities and the mass of the pills. Values of ϵ, ρ, δ and ϵ_0 are given in Table 1 for two samples taken from separately prepared batches of EuS. The values quoted in this table are average values measured on successively lapped thicknesses of the same sample. The largest source of error in ϵ and ρ is the uncertainty in the thickness which was larger for sample *A* because it was appreciably thinner than sample *B*. For this reason we have weighted the value of ϵ_0 for sample *B* in determining the dielectric constant to be 13·10 ± 0·04.

Table 1

Sample	ρ in (g/cm³)	δ	ϵ	ϵ_0
A	5·221 ± 0·060	0·900 ± 0·010	11·52 ± 0·13	13·28 ± 0·33
B	5·230 ± 0·010	0·902 ± 0·002	11·39 ± 0·03	13·10 ± 0·04

The intrinsic dielectric constant ϵ_0 of EuS may be calculated from the observed dielectric constant ϵ of the porous pills by a formula due to Böttcher[5] which states that

$$\epsilon_0 = \frac{3\epsilon\delta + 2\epsilon(\epsilon - 1)}{3\epsilon\delta - (\epsilon - 1)} \qquad (1)$$

where δ is the packing fraction of the pill.

At room temperature and above, the capacitance and loss angle of the pills are frequency dependent[6]. It was found necessary to cool the pills substantially to avoid this complication. Therefore, all measurements of ϵ were made at 80°K where the capacitance and shunt resistance are frequency independent from 500 to 500,000 Hz.

Acknowledgements — Thanks are due to Dr. M. Pollak for many helpful suggestions and to J. H Mullin for furnishing the samples. This work was supported by the U.S. Atomic Energy Commission

Department of Physics,
University of California,
Riverside,
Calif. 92507,
U.S.A.

T G. CAMPBELL
A. W. LAWSON

REFERENCES

1. PENN D. R., *Phys. Rev* **128**, 2093 (1962).
2. PHILLIPS J. C., *Phys. Rev.* **168**, 905 (1968).

3. WILD R. L. and ARCHER R. D., *Bull Am. Phys. Soc. Ser II*, 440 (1962).
4. McGUIRE T. R. and SHAFER M. W., *J. appl. Phys.* **35**, 984 (1964)
5. BÖTTCHER C. J. F. *Theory of Electric Polarisation*, p. 417. Elsevier, Amsterdam (1952).
6. MULLIN J H and LAWSON A. W., Private communication.

J. Phys. Chem Solids Vol 30, pp. 776–778.

Energy band parameters of gallium antimonide

(*Received* 2 *February* 1968; *in revised form* 19 *August* 1968)

THE PRESENT paper concerns the determination of the energy band parameters of GaSb from the magneto-absorption data obtained by Zwerdling *et al.*[1]. The calculation of energy levels in a magnetic field is carried out by using the method of Pidgeon and Brown [2], which includes the effect of the interaction between conduction and valence bands. The assumption of the spherical symmetry of the valence band has been made and exciton effect[3] has been neglected. We made a theoretical assignment in terms of only the principal allowed ($\Delta n = 0, -2$) Landau transitions.

In Figs. 1 and 2 are shown the experimental spectra obtained by Zwerdling *et al.*[1]. The theoretical transition energies and relative strengths of the allowed transitions, calculated by us, are shown in Table 1 and beneath the spectra of Figs. 1 and 2.

The following final set of parameters was obtained for a good fit of the experimental spectra:

$$P^2 = 0{\cdot}384 \text{ atomic units}; \quad \gamma_1 = 14{\cdot}5; \quad \tilde{\gamma} = 4{\cdot}5;$$

$$\kappa = 2{\cdot}7; \quad E_g = 0{\cdot}813 \text{ eV}; \quad \Delta = 0{\cdot}81 \text{ eV}$$

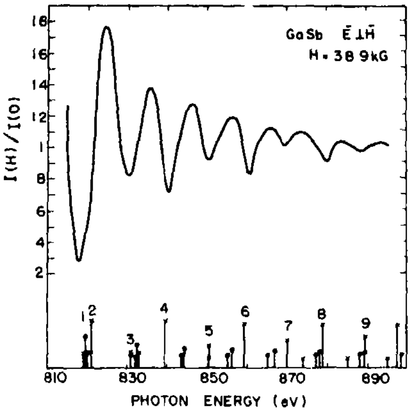

Fig. 1. Plot of the ratio of transmitted intensity with the magnetic field to that without field, $I(H)/I(O)$, against photon energy for $E \perp H$ polarization. The theoretical positions and relative strengths of the allowed transitions are shown beneath the spectrum.

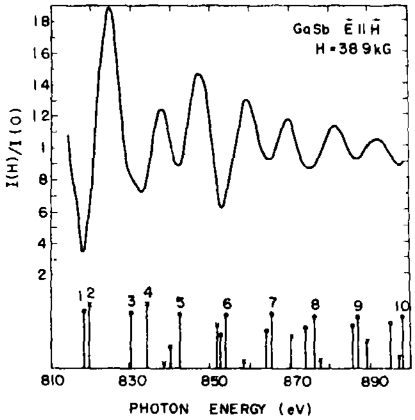

Fig. 2. Plot of the ratio of transmitted intensity with the magnetic field to that without field, $I(H)/I(O)$, against photon energy for $E \parallel H$ polarization. The theoretical positions and relative strengths of the allowed transitions are shown beneath the spectrum.

where P is the momentum matrix element defined by Kane[5]; $\gamma_1, \tilde{\gamma}$ and κ are the band parameters defined by Luttinger[6]; E_g is the energy gap; Δ is the spin-orbit splitting. This determination was made without the use of the lowest transition line of Figs 1 and 2, which was indentified as exciton transition [1, 4].

Figure 3 shows computed magnetic energy levels as a function of magnetic field H. The

Table 1. Comparison between experimental and theoretical transition energies at 38·9 kG

Polarization	Assignment†	Experiment (eV)	Theory (eV)
	$a^-(2)a^c(0)$ $b^+(0)b^c(0)$	0·8177	0·8197 0·8212
	$a^+(2)a^c(0)$	0·8303	0·8310
	$b^+(1)b^c(1)$	0·8405	0·8396
$E \perp H$	$a^+(3)a^c(1)$	0·8499	0·8505
	$b^+(2)b^c(2)$	0 8604	0·8591
	$a^+(4)a^c(2)$	0·8695	0·8700
	$b^+(3)b^c(3)$	0·8796	0·8784
	$a^+(5)a^c(3)$	0·8890	0·8893
	$b^-(2)a^c(0)$ $a^+(0)b^c(0)$	0·8187	0·8185 0·8202
	$b^-(3)a^c(1)$	(0·830)	0·8307
	$a^+(1)b^c(1)$	0·8327	0·8343
$E \parallel H$	$b^-(4)a^c(2)$	0·8421	0·8425
	$b^-(5)a^c(3)$	0·8533	0·8540
	$b^-(6)a^c(4)$	0·8653	0·8653
	$b^-(7)a^c(5)$	0·8754	0·8764
	$b^-(8\ a^c(6)$	0·8876	0·8873
	$b^-(9)a^c(7)$	0·8975	0·8979

†This notation is used by Pidgeon *et al.*[2]

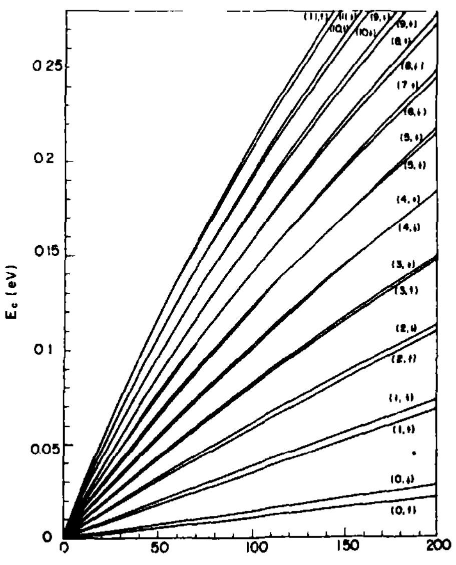

Fig. 3. Computed conduction-band energy levels for GaSb as a function of magnetic field. The numbers in brackets are the Landau quantum number n for the levels and the arrows represent spin up (↑) and spin down (↓).

number of blackets are the Landau quantum number n for the levels and the arrows represent spin up and down. Figure 4 shows

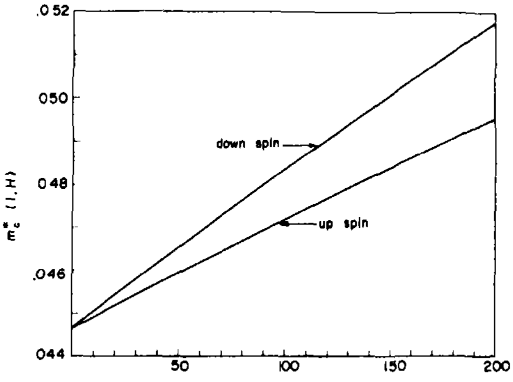

Fig. 4. Plots of the lowest Landau-level effective mass defined in equation (1) as a function of magnetic field for the conduction band of GaSb.

computed cyclotron mass for the conduction band as a function of magnetic field, which is defined as follows:

$$m_c^*(n,H) = eH/c(E_{n+1}^c - E_n^c) \qquad (1)$$

where e is the proton charge; c is the velocity of light; E_n^c is the electron energy in the n Landau level of the conduction band. Similarly Fig. 5 shows g-factor for the conduction band as a function of magnetic field, which is defined as

$$g_c^*(n,H) = 2c(E_{\uparrow,n}^c - E_{\downarrow,n}^c)/eH. \qquad (2)$$

The g-factor of the $n \geq 4$ Landau levels shows a change of sign with increasing magnetic field from zero to 200 kG. Extrapolating to low magnetic field and large n limit (classical limit) we obtain the following values for effective masses and g-factor:

$$m_c = 0{\cdot}045\, m_0$$
$$m_{lh} = 0{\cdot}041\, m_0$$
$$g_c = -6{\cdot}5.$$

Figure 6 shows that the g-factor for the conduction band depends upon the Landau quantum number n as well as the energy [7] in the conduction band.

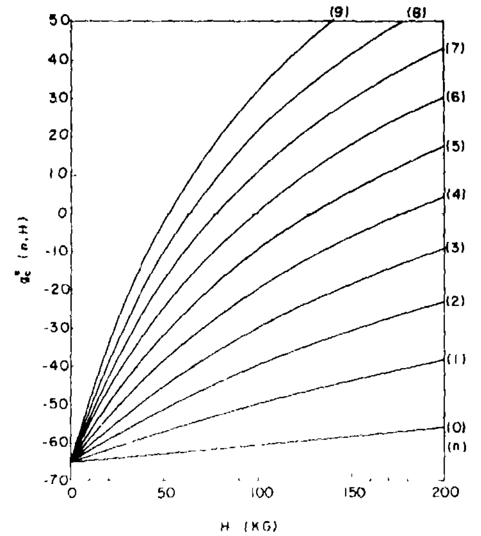

Fig. 5. Plots of the effective g-factor, defined in equation (2), as a function of magnetic field for the conduction band of GaSb. The landau quantum number are shown in brackets.

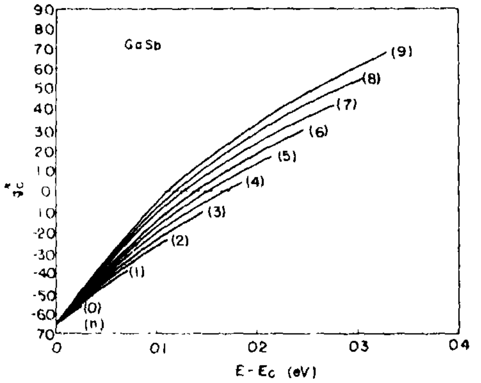

Fig. 6. Plots of the g-factor for the conduction band of GaSb vs. the electron energy in magnetic field ranged from 0 to 200 kG. Mean values of the electron energy of spin up and down are taken as the electron energy. The zero energy is taken at the bottom of the conduction band. The numbers in brackets are the Landau quantum number n for the levels in the conduction band.

It must be pointed out the fact that light hole mass is smaller than conduction electron mass in GaSb. We computed the energy band structure and the band parameters of GaSb by the $k \cdot p$ method[8]; the computed results confirm the fact.

Central Research Laboratory,
Hitachi Ltd.,
Kokubunji,
Tokyo,
Japan

E. ADACHI

REFERENCES

1. ZWERDLING S., LAX B., BUTTON K. J. and ROTH L. M., *J. Phys. Chem. Solids* **9**, 320 (1959).
2. PIDGEON C. R. and BROWN R. N., *Phys. Rev.* **146**, 575 (1966).
3. ELLIOTT R. J. and LOUDON R., *J. Phys. Chem. Solids* **15**, 196 (1960).
4. JOHNSON E. J. and FAN H. Y., *Phys. Rev.* **139**, A1991 (1965).
5. KANE E. O., *J. Phys. Chem. Solids* **1**, 249 (1957).
6. LUTTINGER J. M. and KOHN W., *Phys. Rev.* **97**, 869 (1955).
7. ZAWADZKI W., *Phys. Rev. Lett.* **4**, 190 (1963).
8. CARDONA M and POLLAK F. H., *Phys. Rev.* **142**, 530 (1966); POLLAK F. H., HIGGINBOTHAM C.W. and CARDONA M., *Proc. Int. Conf. Semiconductor Physics*, p. 20 Kyoto (1966).

J. Phys. Chem. Solids Vol. 30, pp. 778–781.

E.S.R. studies of paramagnetic centres in irradiated $Li_2SO_4 . H_2O$

(*Received* 6 *June* 1968, *in revised form* 15 *August* 1968)

SINGLE crystals of $Li_2SO_4 . H_2O$ grown from aqueous solution at room temperature and at 60°C were exposed to u.v. and X-radiation and e.s.r. spectra of these crystals were obtained at room temperature and liquid nitrogen temperature. There are two molecules in the monoclinic unit cell of this crystal with dimensions $a = 5{\cdot}43$, $b = 4{\cdot}84$, $c = 8{\cdot}14$ Å and $\beta = 107°35'$. The two crystal axes 'a' and 'b' and a third axis 'c^*' are taken as the three orthogonal axes. The crystals were irradiated with X-rays from a 30 KV, 15 ma copper target for several hours. No visible coloration could be detected in the crystal even after heavy doses. A mercury discharge tube was used as the ultraviolet source. A Varian X-band spectrometer (type V4500) was used for taking the e.s.r. spectra in each of the three orthogonal planes for every 5° rotation of the magnetic field. X-ray diffraction studies revealed that the two crystals grown at different temperatures have the same monoclinic unit cell with identical dimensions. The e.s.r. spectra of the two crystals after irradiation was, however, markedly different.

The results obtained on this investigation are compared with those obtained by Wigen and Cowen[1] and Aseltine and Kim[2] with single crystals of $Li_2SO_4 . H_2O$ irradiated and examined at liquid nitrogen temperature (in beams of 1 meV electrons). The experiments of Aseltine and Kim have been performed practically in the same way as the Wigen and Cowen experiment with regard to electron irradiation by using the same radiation facilities, time and beam intensity at liquid nitrogen temperature. The only apparent difference in the experiment seems to lie in the growth of the single crystals (Wigen and Cowen grew crystals at room temperature while Aseltine and Kim grew at 60°C). The spectra consisted of an isotropic line at free spin g-value and a hyperfine doublet in both the investigations. Though the general behaviour of the hyperfine structures with regard to angle of rotation seems to be similar, the principal values of the g and A tensors and tensor directions differ noticeably in the two investigations. The separation between the two proton hyperfine lines in the work of Aseltine and Kim is approximately two times larger than that of the corresponding separation in the Wigen and Cowen work.

A comparison of these results with those obtained by the authors in the present investigation reveal some interesting effects which apparently result from (i) different conditions of crystal growth (ii) different sources of irradiation and (iii) temperature at which the experiment is carried out.

CRYSTALS GROWN AT ROOM TEMPERATURE AND IRRADIATED WITH X-RAYS

1. *E.S.R. spectra at room temperature*

An isotropic line (Fig. 1) with a free spin 'g'-value is observed in the present investigation also, which may be due to an electron or hole trapped in a vacancy.

A pair of lines attributed to a hyperfine doublet have been observed: but the principal g-values of this doublet ($g_{\parallel} = 2{\cdot}006$,

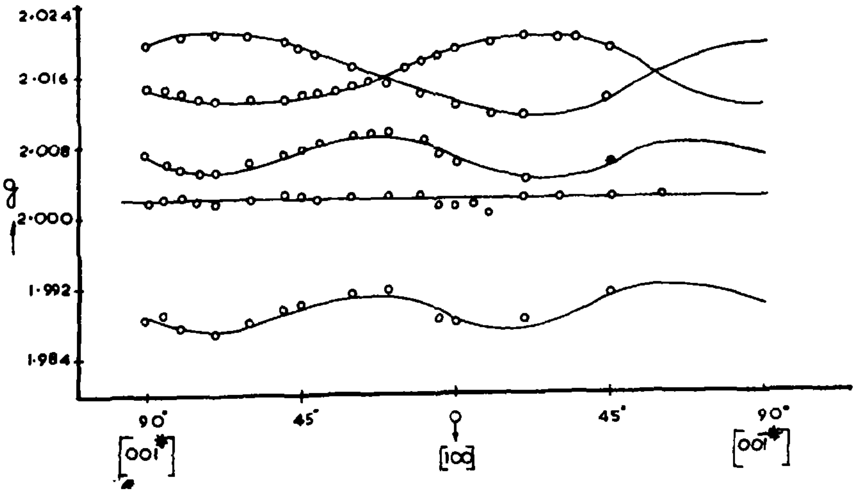

Fig. 1. Angular variation of spectral lines for magnetic field rotation about [010] axis.

$g_\perp = 1{\cdot}997$) are very much different from those obtained by either Wigen and Cowen ($g_\parallel = 2{\cdot}040$ and $g_\perp = 2{\cdot}002$) or Aseltine and Kim ($g_\parallel = 2{\cdot}064$; $g_\perp = 2{\cdot}005$). Further, these, two lines of the doublet are always on either side of the free spin line in the present investigation, while for the electron irradiated crystals, the pair was mostly on the higher g-side of the free spin line. Aseltine and Kim observed that there are two possible sites per unit cell for the paramagnetic defect responsible for the hyperfine doublet and that the two sites are equivalent with regard to the b-axis rotation. This was consistent with the fact that in their spectra only two lines were observed for rotation about 'b' axis, while for rotation about 'a' axis each of these single lines split into two lines corresponding to the inequivalence of the two sites. In the present investigation, the spectral distribution for rotation about 'a'-axis and 'b'-axis are almost identical and did not indicate the possibility of more than a single site for the paramagnetic defect. For this reason and also since the principal g-values obtained in this investigation are different from those of either Wigen and Cowen or Aseltine and Kim, the paramagnetic defect must be of a different type and not an OH radical. However, the configuration of the defect responsible for this spectrum must contain H.

Aseltine and Kim recently investigated [3] the thermal decay of the hyperfine doublet. After warming to room temperature and again returning to 77°K, the OH radical spectrum disappeared and two new types of spectra were observed one of which was again a hyperfine doublet as before but with different A and g values. The other spectrum was anisotropic and no hyperfine splitting was noticed. This suggests that the hyperfine doublet is very sensitive to temperature.

Two more anisotropic lines are observed in the present investigation whose angular variation indicated that there are two possible sites per unit cell for the paramagnetic defect responsible for this spectrum. The principal g-values are obtained as 2·0078, 2·0115 and 2·0320. There was no corresponding spectrum from the experiments of Wigen and Cowen or Aseltine and Kim. Since SO_4^- has nearly similar principal g values (2·0118, 2·0235 and 2·0462)[4] it might be SO_4^-.

2. *E.S.R. spectra at liquid nitrogen temperature*

The e.s.r. spectra of the same crystal taken at liquid nitrogen temperature is shown in Fig. 2.

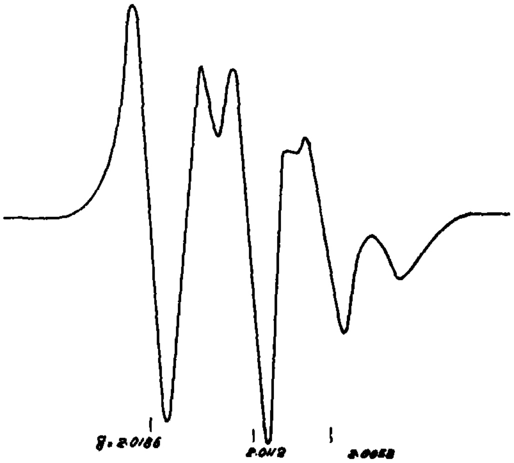

Fig. 2. E.S.R. spectrum at liquid nitrogen temperature of $Li_2SO_4H_2O$ grown and irradiated at room temperature. H makes 45° with [100] axis in ac^* plane.

An intense line centered at $g = 2{\cdot}011$ is observed with marked shoulders at low and high fields resembling the spectrum to be expected for a single radical with no magnetic nuclei and three clearly different principal g values. The three principal g values are 2·0139, 2·0112 and 2·0078. A similar feature was observed by Symons *et al.*[5] where the defect was identified as O_3^- with principal g values 2·0174, 2·0113 and 2·0025.

The hyperfine doublet observed at room temperature disappears and a single line is observed at $g = 2{\cdot}006$.

The isotropic line at free spin g value is

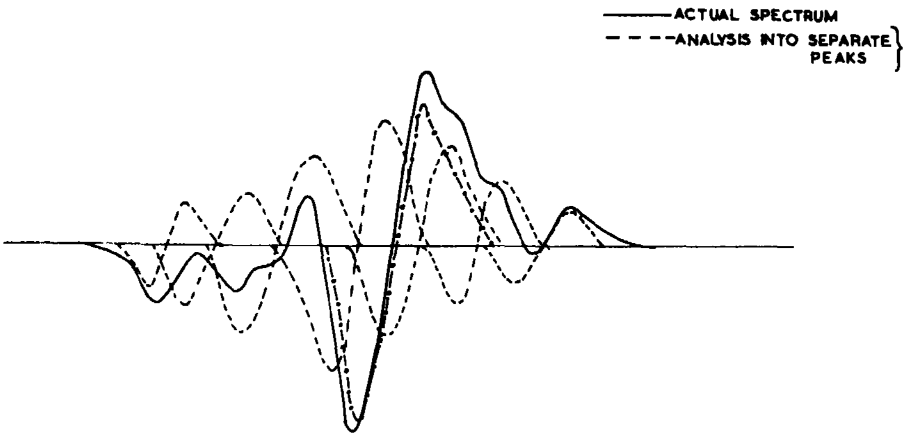

Fig. 3. E.S.R spectrum of u.v. irradiated $Li_2SO_4H_2O$ grown at 60°C. H makes 70° with [100] axis in *ac** plane.

also observed but with reduced relative intensity.

The two line group observed at room temperature is seen here as a single line with $g = 2{\cdot}018$.

All these observations are completely different from those of both Wigen and Cowen and Aseltine and Kim where the irradiation was also done at liquid nitrogen temperature.

Crystals grown at room temperature when exposed to u.v. radiation did not give any e.s.r. spectrum.

CRYSTALS GROWN AT 60°C AND IRRADIATED WITH U.V. AND X-RADIATION

The room temperature e.s.r. spectra of u.v. irradiated crystal grown at 60°C when analysed (Fig. 3) revealed a particular pattern of seven lines in all the orientations in the intensity ratio 1 : 2 : 3 : 4 : 3 : 2 : 1, with a separation of 8 G and can only to be due to hyperfine splitting with a nucleus of total spin 3. In $Li_2So_4 . H_2O$ there are two Li^+ ions and it is possible that in the process of irradiation an electron may get trapped near the Li^+ ion site and h.f.s. due to two lithium nuclei may give rise to a spectra of seven lines. In addition there was an anisotropic line with g variation from 2·004 to 2·010.

The e.s.r. spectra of these crystals when irradiated with X-rays also revealed the seven line spectrum with the same separation and intensity ratio. In addition, two distinct pairs of anisotropic lines are observed on either side of the free spin line with a separation of about 85 ± 5 G.

The authors are grateful to Professor Putcha Venkateswarlu Department of Physics, I.I.T. Kanpur for providing the facilities to work with their ESR spectrometer.

Department of Physics,
Indian Institute of Technology,
Madras – 36,
India

N. HARIHARAN
J. SOBHANADRI

REFERENCES

1. WIGEN P. E. and COWEN J. A., *J. Phys. Chem. Solids* **17**, 26 (1960).
2. ASELTINE C. L. and KIM Y. W., *J. Phys. Chem. solids* **28**, 867 (1967).
3. ASELTINE C. L. and KIM Y. W., *J. Phys. Chem. Solids* **29**, 531 (1968).
4. GROMOV V. V. and MORTON J. R., *Can. J. Chem.* **45**, 1948 (1966).
5. ATKINS P. W., BRIVATI J. A., KEEN N, SYMONS M. C. R. and TREVALION P. A., *J. chem. Soc.* 4785 (1962).

J. Phys. Chem. Solids Vol. 30, p. 782.

The electronic specific heat of h.c.p. Fe–Ru alloys*

(*Received* 24 *June* 1968)

IN OUR RECENT paper[1] on the low temperature specific heat of h.c.p. Fe–Ru alloys, we reported a monotonic increase in the electronic specific heat coefficient γ with increasing Fe concentration. Because new measurements on this alloy system by Andres *et al.*[2] apparently did not agree with our results we made additional measurements. We prepared the alloy $Fe_{59}Ru_{41}$ and measured its low temperature specific heat (see ref. 1 for the experimental technique). The new alloy has an electronic specific heat coefficient $\gamma = 21{\cdot}9 \times 10^{-4}$ cal mol^{-1}deg.$^{-2}$ Figure 1 shows the revised γ vs. Ru concentration. The additional γ value at 41 at % Ru clearly shows that γ has a pronounced peak at around 40 at % Ru. In view of this peak there is good agreement between the γ values of different authors (Fig. 1). A smooth connection to the estimated γ of h.c.p. Fe[3] is possible (Fig. 1).

It is at present not clear how to explain this rather surprising maximum. Obviously it cannot be explained in terms of paramagnon enhancement[4] of the electronic density of states. This would require ferromagnetic coupling in alloys on one side of the γ-peak[4], whereas Andres *et al.*[2] found that all h.c.p. Fe–Ru alloys up to 70 at % Fe show Pauli-type paramagnetism down to 1·4°K.

It may well be that the peak in γ is caused by formation of localized electronic states at the Fermi surface of these alloys. Friedel [5] has shown that such states may occur in dilute alloys where the charge difference between the solute and the solvent ions is large in relation to the number of carriers.

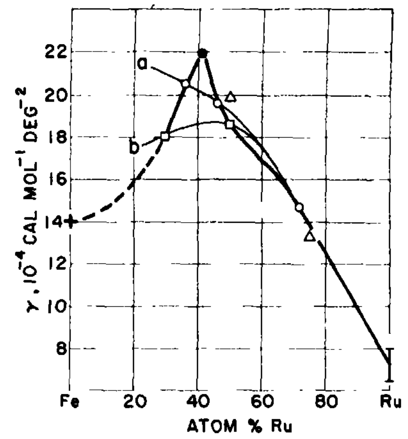

Fig. 1. γ vs. Ru-concentration: ● this work, ○ and curve *a* from reference[1], □ and curve *b* from reference[2], △ from reference[6], + estimated γ for h.c.p. Fe from reference[3].

Acknowledgements—The author would like to thank Professor P. A. Beck for helpful discussions, Dr. E. Bucher for making available his data prior to publication, and Dr. L. Kaufman for the loan of Fe-Ru alloy specimens.

Department of Metallurgy and
Materials Research Laboratory,
University of Illinois,
Urbana,
Ill. 61801, U.S.A.

H. CLAUS

REFERENCES

1. CLAUS H., *J. Phys. Chem. Solids* **28**, 2449 (1967).
2. ANDRES K., BUCHER E., MAITA J. P. and SHERWOOD R. C., To be published.
3. STEPAKOFF G. L. and KAUFMAN L., *Acta. Metall.* **16**, 13 (1968).
4. BERK N. F. and SCHRIEFFER J. R., *Phys. Rev. Lett.* **17**, 433 (1966).
5. FRIEDEL J., Ser. X del *Nuovo Cim.* Suppl. AL, VII, 287 (1958).
6. HEINIGER F., BUCHER E. and MULLER J., *Phys. condensed Matter* **5**, 243 (1966).

---

*This work was supported by the U.S. Atomic Energy Commission, Contract AT(11-1)-1198. Report No. COO-1198-550.

J. Phys. Chem. Solids Pergamon Press 1969. Vol. 30, p. 783. Printed in Great Britain.

NOTICE

AMERICAN COMMITTEE FOR CRYSTAL GROWTH TO SPONSOR MEETING

AN AMERICAN Committee for Crystal Growth has been organized to coordinate and foster activities concerned with crystal growth theory and practice in the United States. This Committee will sponsor a conference on crystal growth to be held at the National Bureau of Standards near Washington, D.C. on 11th, 12th and 13th of August 1969. This meeting will encompass all aspects of the theory and practice of crystal growth. Sessions especially devoted to impurity distribution; new results in vapor phase growth; melt and solution growth; polymers (including selenium and tellurium); and eutectics, dendrites, and morphological stability will be held. Two hundred word abstracts for fifteen minute contributed papers should be submitted to *C. S. Sahagian, Conference Secretary, Air Force Cambridge Research Laboratories, L. G. Hanscom Field, Bedford, Mass. 01730, U.S.A.*, before May 1, 1969. The subjects and speakers for invited talks will be announced at a later time. For further information write to the Conference Secretary.

J. Phys. Chem. Solids Pergamon Press 1969. Vol. 30, p. 784. Printed in Great Britain.

ERRATUM

D. L. MILLS and A. A. MARADUDIN: Some thermodynamic properties of a semi-infinite Heisenberg ferromagnet, *J. Phys. Chem. Solids* **28**, 1855 (1967).

In the calculation of the contribution to the specific heat from the presence of the free surface, we included in the function $\Delta F(\omega)$ (equation (4.3)) a contribution from poles of the summand at the surface spin wave frequencies, and from a branch cut of the summand on the real axis of the frequency plane, in the region of frequencies allowed for bulk spin waves. There is an additional contribution to ΔF from a pole at the bottom of the frequency band associated with the bulk waves of given wave vector component $\mathbf{k}_{\parallel}$ parallel to the surface. This contribution to ΔF was not included in the calculation of the magnon contribution to the surface specific heat. When it is included, the contribution to the specific heat exhibited in equation (4.51) is reduced by a factor of two.

For the simple case $J_2 = 0$, when no surface waves are present, the allowed values of k_z for the spin waves in a thin film are easily found from equation (2.10). For this situation, one may easily see that the contribution to ΔF from the pole at the bottom of the bulk band describes a correction to the bulk specific heat that has its origin in the first correction term to the expression for the specific heat obtained by replacing the discreet sum over k_z by an integral.

The results obtained in the paper for the mean spin deviation near the surface are not influenced by the pole at the bottom of the bulk band.

We are grateful to Leonard Dobrzynski for pointing out the presence of this contribution to the specific heat.

J. Phys. Chem. Solids Pergamon Press 1969. Vol. 30, pp. 785–792. Printed in Great Britain.

LOW TEMPERATURE SPECIFIC HEAT STUDY OF THE ELECTRON TRANSFER THEORY IN REFRACTORY METAL BORIDES

Y. S. TYAN and LOUIS E. TOTH
School of Mineral and Metallurgical Engineering, University of Minnesota, Minneapolis, Minn 55455, U.S.A.

and

Y. A. CHANG
Materials Department, College of Applied Science and Engineering, University of Wisconsin, Milwaukee, Wisc. 53211, U S.A.

(*Received* 12 *July* 1968: *in revised form* 1 *October* 1968)

Abstract – Low temperature heat capacities of eleven 4th, 5th and 6th group transition metal borides were measured from 1·5–18°K to test current theories about bonding and band structure of borides. The electron transfer theory helps to interpret γ values, but the experiments also suggest certain modifications to that theory.

INTRODUCTION

BORIDES ARE noted for their refractory properties, chemical stability and hardness. Many conflicting theories about bonding and band structure of borides have been proposed to explain these properties[1–11]. One of the proposed theories, the electron transfer theory, was tested by a series of low temperature heat capacity measurements. The idea of an electron transfer probably originated with Ubbelohde[1] and was later expanded upon by others[3–5, 7, 9]. This theory is based on two explicit assumptions: (1) each boron atom donates from 1 to 1·5 electrons to the *d* band of the transition metal atom and (2) the band structure of the borides is *very* similar to that existing for pure transition elements. It is not necessary to have an actual electron transfer; the presence of boron could also stabilize the *d* bands with respect to the *s* band of the transition metal atoms and promote $s \rightarrow d$ transfer[12].

Convincing evidence by Cadeville and Meyer supporting this theory was recently discussed by Friedel[12]. They show that the Slater–Pauling magnetization curve for pure elements and transition-metal alloys is displaced for Me_2B and MeB borides by about 1·5 electrons/boron atom (see Fig. 1).

The applicability of the electron transfer theory to fourth, fifth and sixth group borides has not been adequately tested. Dempsey[5] used the model to correlate electrical resistivities and melting points of borides with the transition elements. Juretschke and Steinitz[9] interpreted their Hall coefficient measurements with the model but assumed an unreasonably large electron transfer.

The approach used here to test the model first determines γ for a series of borides and then compares these values to those for the transition elements or alloys, with the appropriate electron transfer taken into account. For those borides which superconduct, an additional comparison of the "band structure" density of states is possible.

It should be emphasized that the two assumptions of the electron transfer theory are obvious simplifications. The band structure of borides will be different from that of a pure transition element, and the band structure will vary with composition and crystal

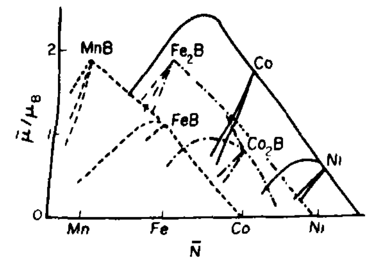

Fig. 1. Average magnetic moment per transition metal atom vs. average atomic number of transition elements $\bar{N}$. The solid curve shows the behavior for the elements and transition metal alloys and the broken curves show the behavior for the borides. The relative shift in the curves corresponds to one electron per boron atom (after reference [12]).

structure changes. An important point which emerges from the present studies is that the γ values of many borides can be interpreted as if their band structures closely resemble those of the pure transition elements.

EXPERIMENTAL AND EXPERIMENTAL RESULTS

Low temperature heat capacities were measured for eleven borides. Most samples were prepared by hot-pressing metal or metal hydride powders *(99·9%–325 mesh)* with boron powder *(99·8%)* and subsequently homogenizing them in vacuum or helium *(see Table 1). X-ray analysis was used to* check crystal structures, lattice parameters and homogeneity. Lattice parameter measurements are in excellent agreement with current literature values (see Table 1) [13–20].

Low temperature heat capacities were measured from 1·5 to 18°K (Figs. 2–4). A description of the calorimeter and measurement techniques may be found elsewhere [21]. The C_p data were fitted to the form

$$C_p = \gamma T + aT^3 + bT^5.$$

Table 1. Sample preparation techniques and lattice parameters of borides

Sample	Structure	Lattice parameter Observed	Literature	Reference	Sample preparation
Mo$_2$B	C16	$a = 5·546$ $c = 4·737$	$a = 5·543$ $c = 4·735$	[13]	Hot press + 1800°C/75 hr/vac. + 1300°C/16 hr/vac.
W$_2$B	C16	$a = 5·568$ $c = 4·745$	$a = 5·564$ $c = 4·740$	[13]	Hot press + 1700°C/66 hr/vac. + 1600°C/2 hr/vac.
Ta$_2$B*	C16	$a = 5·778$ $c = 4·864$	$a = 4·7795 \pm 5$ $c = 4·8645 \pm 3$	[14]	Arc melt + 2150°C/1 hr/vac.
MoB	B$_g$	$a = 3·103$ $c = 16·965$	$a = 3·105$ $c = 16·97$	[13]	Hot press + 1500°C/75 hr/vac. + 1300°C/16 hr/vac.
MoB$_2$	C32	$a = 3·041$ $c = 3·064$	$a = 3·04$ $b = 3·06$	[15]	Hot press + 1500°C/48 hr/vac.
WB	B$_g$	$a = 3·097$ $c = 16·96$	$a = 3·115$ $c = 16·93$	[13]	Hot press + 1500°C/48 hr/vac.
NbB†	B$_f$	$a = 3·297$ $b = 8·716$ $c = 3·164$	$a = 3·297$ $b = 8·72$ $c = 3·166$	[16]	Cold press + 1350°C/24 hr/He + 1650°C/24 hr/vac.
TiB‡	B27	$a = 6·12$ $b = 3·06$ $c = 4·56$	$a = 6·12 \pm 1$ $b = 3·06 \pm 1$ $c = 4·56 \pm 1$	[17]	Hot press + 1350°C/24 hr/He
TiB$_2$	C32	$a = 3·033$ $c = 3·229$	$a = 3·028$ $c = 3·228$	[18]	Hot press + 1350°C/24 hr/He
ZrB$_2$	C32	$a = 3·170$ $c = 3·531$	$a = 3·169$ $c = 3·530$	[19]	Hot press + 1350°C/24 hr/He
HfB$_2$	C32	$a = 3·143$ $c = 3·478$	$a = 3·141$ $c = 3·470$	[20]	Hot press + 1350°C/24/hr/He

*Contains trace of γ TaB.
†Contains trace of Nb$_3$B$_2$.
‡Contains trace of TiB$_2$.

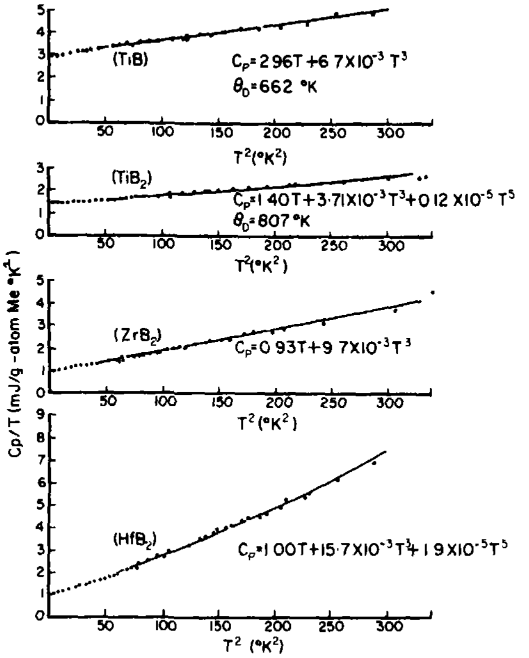

Fig. 2. Low temperature heat capacities of TiB, TiB$_2$, ZrB$_2$ and HfB$_2$.

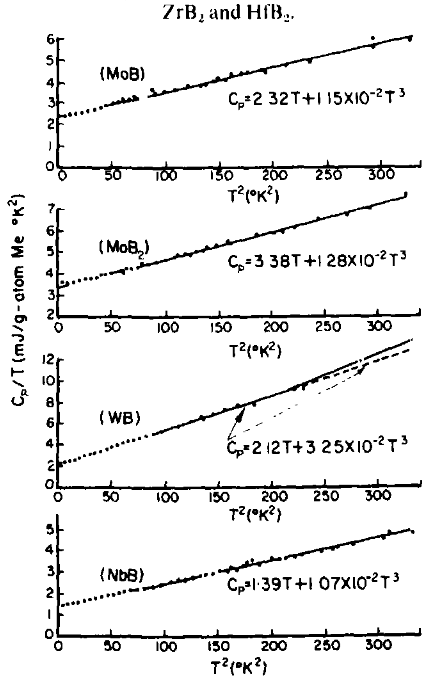

Fig. 3. Low temperature heat capacities of MoB, MoB$_2$, WB and NbB.

Table 2 lists these coefficients and θ_D. The data are given on the basis of 1 g at. of transition metal. For the compounds we define θ_D by the formula

$$\theta_D = \left(\frac{234\, N_A k}{a}\right)^{1/3}$$

where N_A is Avagadro's number. This definition of θ_D is the same as for pure elements.

DISCUSSION

(*A*) *Comparison of γ and θ_D values of borides with transition metal elements and alloys*

In analyzing the γ values, it is assumed that the electron transfer theory applies and that one electron per boron atom is transferred to the d-like bands of transition elements. Thus, the fourth group diborides should have γ values comparable to those for the sixth group elements and so on. For ease of discussion, we define 'electrons/atom ratio' to mean for borides the sum of the group number of the transition element and one electron for each boron atom in the formula, (i.e. *e*/*a* ratio for NbB = 6, for Ta$_2$B = 5·5).

As Fig. 5 shows, when account is taken of electron transfer, the γ values of TiB$_2$, ZrB$_2$, HfB$_2$, Ta$_2$B, NbB and W$_2$B are very similar to those of transition elements and alloys with the same number of electrons per atom. The solid and dashed lines in this figure are smoothed curves drawn by Heiniger *et al.*[22] through many individual γ values for transition metal elements and solid solutions plotted as a function of composition. A few of the individual γ values for the elements are shown. It is seen that the boride points lie very close to the respective curves when an electron transfer is assumed. The γ values of the transition elements and alloys are a minimum at group six (Cr, Mo, W) and rise sharply in alloys on either side of this group. It is important, therefore, to note that the γ values of the

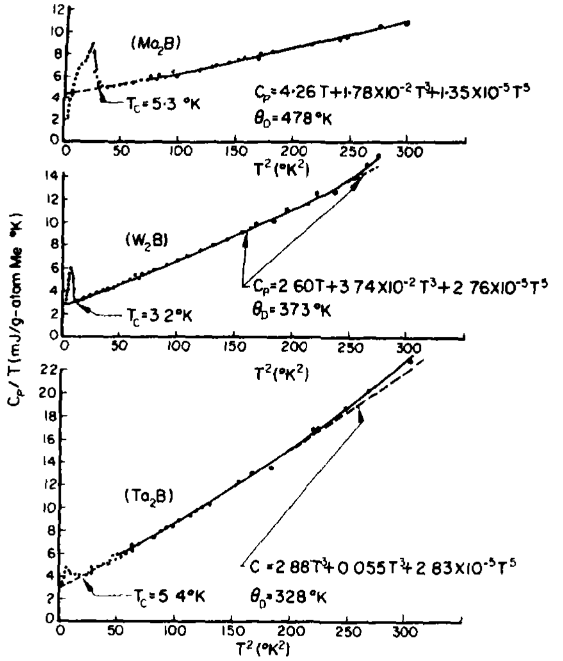

Fig 4 Low temperature heat capacities of Mo$_2$B, W$_2$B and Ta$_2$B.

Table 2. Low temperature heat capacity parameters of borides

Sample	γ (mj/gm at Me °K^2)	a (× 10^2)	b (× 10^5)	θ_D (°K)	T_c (°K)
Mo$_2$B	4·26	1·78	1·35	478	5·3
W$_2$B	2·60	3·74	2·76	373	3·2
Ta$_2$B	2·88	5·5	2·83	328	5·4
MoB	2·32	1·15		553	
MoB$_2$	3·38	1·28		534	
WB	2·12	3·25		391	
NbB	1·39	1·07		566	
TiB	2·96	0·67		662	
TiB$_2$	1·40	0·37	0·12	807	
ZrB$_2$	0·93	0·97		585	
HfB$_2$	1·00	1·57	1·9	499	

4th group diborides, NbB and Ta$_2$B are less than those of the respective parent elements, but the γ values of the borides of Mo and W are greater than those of the respective elements. Thus the γ values for the above borides with electron/atom ratios between 5·5 and 6·5 are not inconsistent with predictions of the electron transfer theory.

For TiB, the electron transfer theory predicts that its γ value should be comparable to that of V(9·9 mJ/g at.°K^2). The observed value (2·96 mJ/g at. Ti°K^2) is, however, much lower. Since TiB is the only stable 4th group monoboride and there are no metal-rich 4th group borides, it is not possible to determine whether the discrepancy for

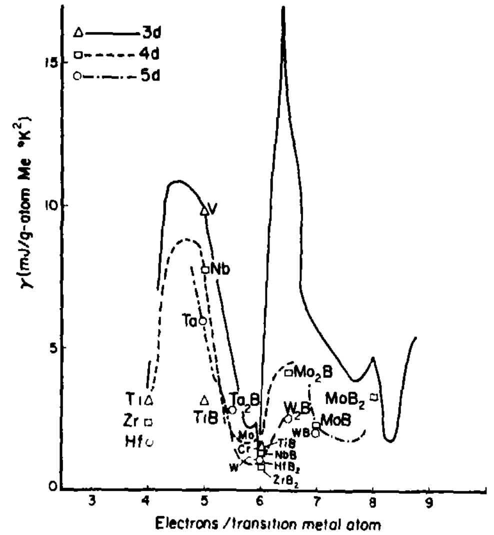

Fig. 5. Comparison of γ values for transition metal elements and alloys with those for borides assuming an electron transfer of one electron per boron atom. The solid, broken and dashed lines show the variation of γ values with electrons/atom ratio (average group number) for transition elements and alloys as experimentally determined and compiled by reference[22]. Only the individual experimental points for the elements are given and compared with the present results for the borides. For the distribution of the experimental points for the individual alloys the reader should consult reference [22]. The boride points lie close to the respective *3d*, *4d* or *5d* lines thus supporting the electron transfer theory. The only exception is TiB.

TiB is an isolated case. There is a HfB phase, but it cannot be readily prepared in pure form[23]. Thus, for electron/atom ratios less than 5·5, we cannot substantiate the assumption that the band structure, as indicated by the γ value variation with composition, is very similar to that existing for pure transition elements.

Inspection of Table 2 shows that the γ values for all the tested borides are relatively low (less than 4 mJ/g at.Me°K^2 except $Mo_2B-4{\cdot}26$). Relatively low γ values have also been observed for refractory transition metal carbides and nitrides[24–29]. These low values for carbides and nitrides have been interpreted as suggesting a strong metal–nonmetal interaction[24, 25] which splits the bonding and antibonding parts of the band structure further apart in energy than they are in the transition elements. The γ values are low because the Fermi level lies in a broad conduction band separating the bonding and anti-bonding parts. We suggest that a similar interpretation for the borides could account for the low γ value for TiB.

There is an alternate interpretation for the low γ value of TiB which allows retention of the assumption about the very close similarity of band structures of borides and transition elements. For the elements, the separation of bonding and antibonding parts occurs at about the sixth group, as indicated by heats of sublimation and melting points[5]. For the borides, this separation occurs at the fourth group diborides and the fifth group monoborides[5] or at a electron/atom ratio of 6. Since a boride could increase its cohesive energy by adding electrons to the bonding part of the band, the tendency would be for boron in compounds like TiB to donate more than one electron to fill the bonding portion. It is possible to achieve better agreement between the γ value of TiB and those of the transition elements and alloys if one assumes that boron donates 1·5 electrons to the bonding portion. Thus, the number of electrons transferred to the *d* bands may vary, depending on whether or not the bonding part of the band is filled.

It is not possible with the present experiment to choose between these two alternatives in order to account for the low γ value for TiB. Probably both factors are important. Thus the present results indicate that while the electron transfer theory can explain most of the observed γ values for borides, some modifications are indicated about the similarity of band shapes with transition metals and about a varying number of transferred electrons.

In considering these modifications, emphasis should be given to the fact that the crystal structures of the borides are not cubic, in contrast to those of most of the fourth to sixth group transition metal elements. This structural change undoubtedly alters the band shape, as does the presence of the boron atoms. Thus one would expect the band structures of the borides to differ considerably from those of the transition metals. Some evidence for this difference is probably manifest in the case of TiB. Unfortunately, no theoretical band structures have been calculated for any boride to elucidate these differences. The γ values merely reflect the density of states at the Fermi surface, and so a comparison of the entire band shape is impossible. In view of the expected differences in band structures, it is surprising that the comparison of γ values between borides and elements agrees well as it does with the prediction of the simple transfer theory. What appears most significant and unusual is that the simple electron transfer theory correctly predicts that γ values of TiB_2, ZrB_2, HfB_2 and NbB are lower than those of the other tested borides and of comparable magnitude to those of Cr, Mo and W. This agreement cannot prove the validity of the electron transfer theory; the present results are merely not inconsistent with that theory. Because of the expected differences in band structures, we conclude that the electron transfer theory is useful in predicting certain electrical, magnetic and thermo-dynamic properties of borides but that the validity of some of its basic assumptions still remain in doubt.

θ_D values for borides are relatively high. The fourth group diborides in particular have higher θ_D values than the fourth group transition metal elements. This difference is not surprising, since melting points of the fourth group diborides are much higher than those of the elements and since the two temperatures are empirically related by the well-known Lindemann formula. Dempsey [5] has noted that the melting points of fourth group diborides and fifth group monoborides are comparable to those of the sixth group elements. The same type of empirical correlation exists for θ_D values (see Table 3). The fourth group diborides and fifth group monoboride NbB have θ_D values comparable to the sixth group.

(*B*) *Comparison of 'band structure' density of states*

Several borides are superconductors. From T_c, γ and θ_D, it is possible to calculate the band structure density of states N(O) and to compare the values for borides with those for the transition elements. N(O) differs from γ and the free electron density of states $N_\gamma(N_\gamma = 3\gamma/2\pi^2k^2N_A)$ in that the enhancement of electron–phonon contributions to the heat capacity are subtracted. Therefore N(O) is a better measure of the real density of electron states than is N_γ. The difference between N(O) and N_γ is given by the expression[30]

$$\mathrm{N(O)} = N_\gamma/1+\mathrm{N(O)}V_{\mathrm{ph}}$$

where V_{ph} is the electron–phonon interaction parameter. The enhancement factor $(1+\mathrm{N(O)}V_{\mathrm{ph}})$ is significant and reduces the N_γ value by about 50 per cent. V_{ph} is obtained from T_c and θ_D measurements by[30]

$$\frac{1{\cdot}45T_c}{\theta_D} = \exp-\left\{\frac{1{\cdot}04(1+\mathrm{N(O)}V_{\mathrm{ph}})}{\mathrm{N(O)}[V_{\mathrm{ph}}-U_c(1+0{\cdot}62\mathrm{N(O)}V_{\mathrm{ph}})]}\right\}.$$

Here U_c is the screened coulomb interaction parameter and it is usually assumed that $\mathrm{N(O)}U_c = 0{\cdot}1$[30]. This latter assumption is not critical to the analysis.

For the superconducting borides, N(O) was calculated on the basis of number of states/eV transition metal atom (Table 4). Figure 6 compares the N(O) values for the borides with those of the 4*d* and 5*d* elements and alloys; an electron transfer of one electron/boron atom is again assumed[30]. The good agreement of N(O) values further

Table 3. Comparison of θ_D values for transition metal elements and several borides. The θ_D values in °K are listed directly below the element of boride

Fourth group	Fifth group (and fifth group like)		Sixth group (and sixth group like)		
Ti 425	V 399	TiB 662	Cr 630		TiB_2 807
Zr 290	Nb 277		Mo 460	NbB 566	ZrB_2 585
Hf 252	Ta 258		W 390		HfB_2 499

Table 4. Band structure density of states and electron–phonon interaction parameters for superconducting borides

Sample	N_γ (eV^{-1}(Me atom)$^{-1}$)	$N(O)V_p$	V_p (eV)	N(O) (eV^{-1}(Me atom)$^{-1}$)
Mo_2B	0·903	0·513	0·86	0·597
W_2B	0·551	0·481	1·30	0·371
Ta_2B	0·610	0·574	1·48	0·387

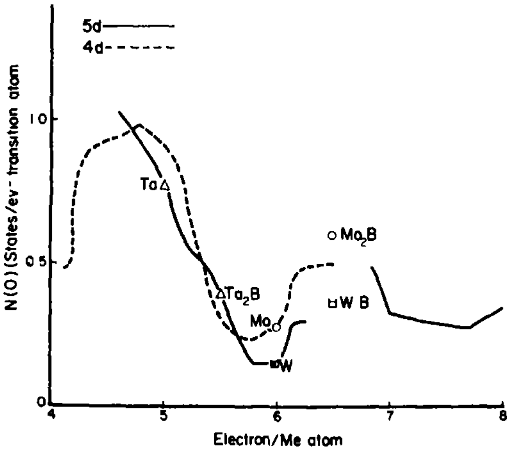

Fig. 6. Comparison of the band structure density of states of transition metal alloys with those for the superconducting borides Ta_2B, Mo_2B and W_2B. A transfer of one electron per boron atom is assumed. The solid and dashed curves were calculated by reference [30] who analyzed the γ and T_c data of specific heat measurements for a series of 3*d* and 4*d* transition elements and alloys as a function of electron/atom ratio (average group number). Individual points for Ta, Mo, W, Ta_2B, W_2B are given. The boride points, which were shifted by one electron/boron atom, lie close to the respective solid or dashed curves.

substantiates the electron transfer theory. Since only the metal-rich boride phases were superconducting, however, this test, while significant, is limited.

SUMMARY

Most of γ and N(O) values of refractory borides are consistent with predictions of the electron transfer theory with about one electron per boron atom being transferred to the *d* bands of the transition element. The low γ value for TiB suggests modifications to the transfer theory: (1) the metal boron interaction may split further apart in energy the bonding and antibonding parts of the *d* bands of the transition elements, and (2) the number of electrons transferred by boron to these *d* bands may vary, depending on the group number of the boride. Several questions are raised about the validity of the basic assumptions of the electron transfer theory.

Acknowledgements—This research was financed by a grant from the National Science Foundation. The authors are indebted to Professor R. A. Swalin and M. E.

Nicholson for suggestions in preparing the manuscript and to Dr. E. Rudy of the Aerojet Corporation Sacramento, California for use of the hot-pressing facilities.

REFERENCES

1. UBBELOHDE A. R., *Trans Faraday Soc.* **28**, 275 (1932).
2. UMANSKII Ya. S., *Ann. Sect. anal. phys.-chem., Inst., chim. gen. USSR* **16**, 127 (1943).
3. KIESSLING R , *Met. Rev* **2**, 77 (1957).
4. SAMSONOV G. V., MARKOVSKII L. Ya., ZHAGACH A F. and VALYASHKO M. G., *Boron, Its Compounds and Alloys* AEC-tr-5032 Book 1 (1962); A translation of: *Boron, ego Soedineniya i Splavy*, Akademiya Nauk Ukr. S.S.R., Kiev (1960).
5. DEMPSEY E., *Phil. Mag.* **8**, 285 (1963).
6. LIPSCOMB W N. and BRITTON D., *J chem. Phys.* **33**, 275 (1960).
7. NICHOLSON M. E., *Trans. A.I M.E.* **209**, 1 (1957)
8. LUNDQUIST N., MYERS H. P. and WESTIN R., *Phil. Mag* **7**, 1187 (1962)
9. JURETSCHKE H. J. and STEINITZ R., *J. Phys. Chem. Solids* **4**, 118 (1958).
10. JOHNSON R. W. and DAANE A H , *J. chem. Phys.* **38**, 425 (1963).
11. SILVER A. H and BRAY P J., *J chem. Phys.* **32**, 288 (1960).
12. FRIEDEL J., In *Phase Stability in Metals and Alloys* (Edited by P S. Rudman, J Stringer and R. I. Jaffee), pp. 353–354. McGraw-Hill, New York (1966) (The summary of the discussion period which includes this work was written by P. Beck).
13. KIESSLING R., *Acta chem scand* **1**, 893 (1947).
14. LEITNAKER S. N., BOWMAN N. G. and GILLES P. W., *J. electrochem. Soc.* **108**, 568 (1961).
15. RUDY E., BENESOVSKY F. and TOTH L., *Z. Metallk.* **54**, 345 (1963).
16. NOWOTNY H., BENESOVSKY F. and KIEFFER R., *Z. Metallk.* **50**, 417 (1959).
17. DECKER B. F. and KASPER J. S., *Acta crystallogr.* **7**, 77 (1954).
18. KIESSLING R., *Acta chem. scand.* **4**, 209 (1950).
19. KIESSLING R., *Acta chem. scand.* **3**, 90 (1949).
20. GLASER F. W., MOSKOWITZ D. and POST B., *J. Metals* **5**, 1119 (1953).
21. TOTH L. E., Tech. Rep. No. AFOSR 68–0265, Air Force Grant AFOSR1012–66 (1968).
22. HEINIGER F , BUCHER E. and MULLER J., *Phys. Kondens Materie* **5**, 243 (1966).
23. RUDY E. and WINDISCH St., Tech Rep. No. AFML-TR-65-2, Part I, Vol. IX (1966).
24. GEBALLE T. H., MATTHIAS B. T., REMEIKA J. P., CLOGSTON A. M., COMPTON V. B., MAITA J. P. and WILLIAMS H J., *Physics* **2**, 293 (1966).
25. TOTH L. E., ZBASNIK J., SATO Y. and GARDNER W., In *Anisotropy in Single-Crystal Refractory Compounds* (Edited by F. W. Vahldiek and S. A Mersol). Plenum Press, New York (1968).
26. COSTA P., In *Anisotropy in Single-Crystal Refractory Compounds* (Edited by F. W Vahldiek and S. A Mersol). Plenum Press, New York (1968).
27. PESSALL N., HULM J. K. and WALKER M. S., Tech. Rep. No. AFML–TR–67–168. Contract No. AF33(615)–2729 (1967)
28 TOTH L. E. and ZBASNIK J , *Acta Metall.* **16**, 1177 (1968).
29 TOTH L. E., ISHIKAWA M. and CHANG Y. A., *Acta Metall* **16**, 1183 (1968).
30. McMILLAN W. L., *Phys. Rev.* **167**, 331 (1968).

J. Phys. Chem. Solids Pergamon Press 1969. Vol. 30, pp. 793–798. Printed in Great Britain.

THERMODYNAMIC PROPERTIES OF $Fe_{1-x}O$. TRANSITIONS IN THE SINGLE PHASE REGION

B. E. F. FENDER and F. D. RILEY*
Inorganic Chemistry Laboratory, Oxford University, Oxford, England

(*Received* 29 *April* 1968; *in revised form* 18 *September* 1968)

Abstract—A detailed thermodynamic study of the $Fe_{1-x}O$ phase has been carried out in the temperature range 700°–1350°C using solid state electrochemical techniques. The results confirm the presence of three wüstite regions separated by order-disorder transitions. Partial molar enthalpies and entropies of solution of oxygen in $Fe_{1-x}O$ are reported.

INTRODUCTION

THE $Fe_{1-x}O$ system has been intensively investigated but only recently have careful studies of thermodynamic[1], structural[2] and electrical properties[3] suggested that defect ordering within the wüstite phase may be complex.

Important thermodynamic evidence that defects in $Fe_{1-x}O$ (either isolated cation vacancies and Fe^{3+} ions or Roth clusters [4]) do not have a simple random distribution over the whole composition range is provided in a series of papers by Raccah and Vallet[1, 5]. These authors propose that the $Fe_{1-x}O$ phase should be divided into three regions separated presumably by second order or higher order transitions. The present study investigates these transitions in greater detail using sensitive solid state electrochemical cell techniques. Other thermodynamic measurements include the well known gas-equilibria studies of Darken and Gurry[6], in the temperature range 1050°–1400°C, thermogravimetric studies by Swaroop and Wagner[7] (950°–1250°C) and solid state electrochemical cell studies by Barbi[8] (600°–1050°C) and Rizzo and Smith[9] (765°–965°C). In none of these investigations did the authors detect transitions within the single phase region. This point is discussed below.

EXPERIMENTAL

Thermodynamic information was obtained from the following solid state electrochemical cells:

$$Pt/Fe,\ Fe_{1-x_1}O/ZrO_2(CaO)/Fe_{1-x}O/Pt \qquad (I)$$

$$Pt/Fe,\ Fe_{1-x_1}O/ZrO_2(CaO)/Fe_{1-x_2}O,\ Fe_3O_4/Pt \qquad (II)$$

and in addition observations were made with the cell:

$$Pt/Fe,\ Fe_{1-x_1}O/ZrO_2(CaO)/Fe,\ Fe_{1-x_1})/Pt \qquad (III)$$

where $Fe_{1-x}O$ indicates the wüstite phase of variable composition and $Fe_{1-x_1}O$ and $Fe_{1-x_2}O$ are the compositions of wüstite in equilibrium with metallic iron and Fe_3O_4 respectively. The zirconia electrolyte $ZrO_2(CaO)$ contained 15 mol % CaO and was in the form of a tube supplied by the Zirconia Corporation, Ohio, U.S.A. The tube with a closed flat end effected a gas tight separation of the two oxide electrodes. The cell was housed in a molybdenum vacuum furnace capable of operating to 1450°C. In all essential details the apparatus and its method of operation were similar to that described by Fender and Hampson[10].

Oxide pellets were made by mixing iron and Fe_2O_3 powders (Johnson Matthey Co. Ltd. spectrographically standardised reagents) in correct proportions, and subsequently checked by gravimetric oxidation to Fe_2O_3 both before and after measurements in the cell. The iron powder supplied was analysed in a similar way and found to contain 1·52 per cent oxygen. Total metallic impurities were reported to be less than 8 ppm for iron and less than 5 ppm for Fe_2O_3. The Fe–Fe_2O_3 mixtures were ground under acetone, pressed at 40 tons in^{-2} and heated in vacuum for 24 hr at 850°C. Tests for silicon contamination in the heating stage showed inclusion of this element to be <2 ppm.

---

*S.R.C. Research Student.

E.m.f. measurements, to better than ±0·5 mV, were made either directly on a potentiometer (Tinsley Vernier Type 4363F) or on a high impedence voltmeter (Vibron 33B) calibrated by the potentiometer at each reading. Temperatures were measured by three Pt–Pt 13 per cent Rh thermocouples placed close to the cell. Temperature differences either in control or between individual thermocouples were never greater than ±0·5°C.

Cells (I), (II) and (III) were cycled over the full temperature range, usually 750–1350°C for a period of several days. Agreement between heating and cooling measurements or between initial and final e.m.f.s was always better than 1 mV unless the temperature was raised above 1350°C. At this temperature, but not below it, reaction between $Fe_{1-x}O$ and the electrolyte occurs and X-ray photographs of the latter show extra lines of an unidentified phase. Measurements of type (I) cells were usually carried out with a fixed composition of $Fe_{1-x}O$ but in one series of experiments the iron to oxygen ratio in wüstite was varied *in situ* by coulometric titration. Transfer of known amounts of oxygen in the cell was affected by applied voltages which gave measured currents up to 25 μA. Titrations were carried out at 1050°C for periods between 12 and 48 hr. For each new iron to oxygen ratio e.m.f.'s were recorded at a number of temperatures between 700° and 1350°C.

RESULTS

E.m.f. measurements on cells (I), (II) and (III) were recorded for overall iron contents (relative to oxygen = 1) of 0·799, 0·853, 0·870, 0·886, 0·906, 0·916, 0·930, 0·935, 0·945, 0·984 between 700° and 1350°C. In addition e.m.f. data were obtained for six compositions between 0·903 and 0·925 using the coulometric titration technique.

Figure 1 includes the e.m.f. temperature plot for $Fe_{0 \cdot 886}O$ which shows three changes in slope at about 850° (*A*), 1030° (*B*) and 1190°C (*C*).

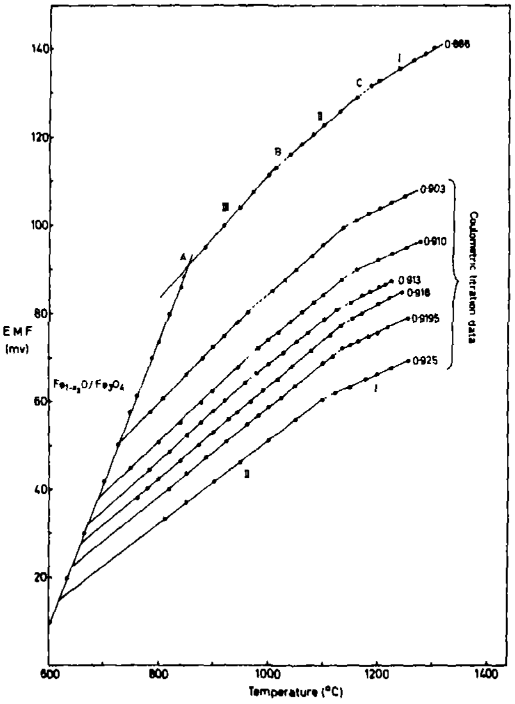

Fig. 1. Cell: $Pt/Fe/Fe_{1-x_1}O|ZrO_2.CaO|Fe_{1-x}O|Pt$.

Point *A* indicates the change from the two phase region containing $Fe_{1-x}O$ and Fe_3O_4 to the single phase wüstite, i.e. at this point there is a change from cell type (II) to type (I), Points B and C must if they fall within a thermodynamic single phase region be second (or possibly higher) order transitions though the measurements were not sufficiently sensitive to positively detect curvature near these transitions. Both transitions *B* and *C* were present at compositions between $Fe_{0\cdot916}O$ and $Fe_{0\cdot870}O$. At $Fe_{0\cdot853}O$ and between $Fe_{0\cdot913}O$ and $Fe_{0\cdot929}O$ only transition *C* was observed, and for compositions $Fe_{0\cdot935}O$ and $Fe_{0\cdot945}O$ no second order transitions were seen. Also included in Fig. 1 are the results for compositions obtained by coulometric titration.

In Fig. 2 the results at e.m.f.-temperature plots at all concentrations are summarised in a phase diagram. The limits of the $Fe_{1-x}O$ phase were (a) observed directly in e.m.f.-temperature plots, (b) obtained from intersections between extrapolated e.m.f.-temperature plots and e.m.f.-temperature plots from cells (II) and (III), (c) obtained from intersections of e.m.f.-iron composition plots and e.m.f.'s obtained from cell type (II) and type (III) (zero e.m.f.).

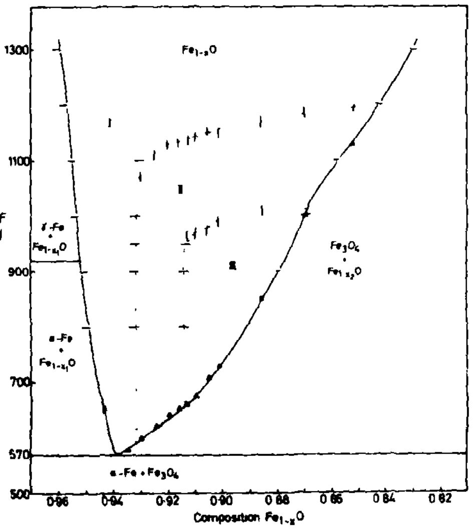

Fig. 2. | – from e.m.f.-temperature plots (constant composition)
△ – from extrapolated e.m.f.-temperature plots (constant composition)
– – from extrapolated e m.f.-composition plots (constant temperature).

Thermodynamic data were obtained from e.m.f. measurements using the standard relationship

$$\Delta G^{0}{}_{f\,Fe_{1-x_1}O} - \tfrac{1}{2}\overline{\Delta G}{}^{0}{}_{O_2} = -2FE \qquad (1)$$

where $\Delta G^{0}_{fFe_{1-x_1}O}$ is the standard free energy of formation $Fe_{1-x_1}O$ (i.e. wüstite in equilibrium with metallic iron), $\overline{\Delta G}{}^{0}{}_{O_2}$ is the standard partial molar free energy of solution of oxygen in $Fe_{1-x}O$; *E* is the measured e.m.f. from cell (I) or (II) and *F* is the Faraday. In cell (II) $\overline{\Delta G}{}^{0}{}_{O_2}$ is the partial molar free energy of solution of oxygen in $Fe_{1-x_2}O$ (i.e. wüstite in equilibrium with Fe_3O_4).

The observed e.m.f. vs. temperature plots were linear within experimental uncertainty for each wüstite region. Some plots suggested curvature near the transition and though such behaviour is to be expected for a second order transition the possibility that deviations from linearity arose from experimental error cannot be excluded. Least squares plots of E vs. T were therefore used together with equation (1) and (2) to obtain values of $\overline{\Delta G}{}^{0}{}_{O_2}$.

$$\Delta G^{0}{}_{f\,Fe_{1-x_1}O} = -62{,}580(\pm 100) + 15\cdot 25 \times (\pm 0\cdot 05)\, T(^{\circ}K). \qquad (2)$$

Equation (2) represents the averaged results of Alcock and Steele[11] and Blumenthal and Whitmore[12]. From $\overline{\Delta G}{}^{0}{}_{O_2}$ values of $\overline{\Delta H}{}^{0}{}_{\frac{1}{2}O_2}$ and $\overline{\Delta S}{}^{0}{}_{\frac{1}{2}O_2}$ were derived (Table 1) by assuming that within a particular wüstite region both these quentities do not vary with temperature. This procedure leads of course to apparent discontinuities in $\overline{\Delta H}{}^{0}{}_{\frac{1}{2}O_2}$ and $\Delta s^{0}{}_{\frac{1}{2}O_2}$ between neighbouring wüstite regions.

DISCUSSION

The phase diagram

The limits of the $Fe_{1-x}O$ phase (Fig. 2) in equilibrium with metallic iron are in reasonable agreement with those proposed by Darken and Gurry[6] and Barbi[8]. Raccah

Table 1. Partial molar enthalpies and entropies of solution of oxygen

Composition	w I		w II		w III	
$Fe_{1-x}O$ $1-x$	$-\overline{\Delta H}_{1/2O_2}$ (cal mole^{-1})	$-\overline{\Delta S}_{1/2O_2}$ (cal deg^{-1} mole^{-1})	$-\overline{\Delta H}_{1/2O_2}$ (cal mole^{-1})	$-\overline{\Delta S}_{1/2O_2}$ (cal deg^{-1} mole^{-1})	$-\overline{\Delta H}_{1/2O_2}$ (cal mole^{-1})	$-\overline{\Delta S}_{1/2O_2}$ (cal deg^{-1} mole^{-1})
0·945	64,860 ±360*	17·78 ±0·14				
0·935	64,020 ±420	18·50 ±0·15				
0·930	63,560 ±340	18·10 ±0·20	65,430 ±330	19·55 ±0·15		
0·916	63,070 ±480	18 47 ±0·16	65,320 ±370	19·93 ±0 21		
0·906	61,730 ±400	18·88 ±0·14	65,280 ±320	19·58 ±0·15	66,570 ±540	22·60 ±0·15
0·886	61,020 +460	18 85 −0·15	64,090 ±510	19·92 ±0·23	66,090 ±420	22·60 ±0·16
0·870	59,950 ±360	18·9 +0·3	62,590 ±420	19·87 ±0·19		
0·853	57,950 ±380	18·9 ±0·3	62,530 ±510	19·9 ±0·5		

*Errors do not include the uncertainty in the free energy of formation of $Fe_{1-x_1}O$ given by equation (2).

and Vallet's measurements[1] on the other hand indicate a triple point temperature at $Fe_{0\cdot 93}O$ about 40°C higher than the commonly accepted value of 570°C. At iron contents lower than $Fe_{0\cdot 93}O$ there is however good agreement with Raccah and Vallet and above 1000°C with Darken and Gurry. Agreement with Rizzo and Smith's three determinations at 765°, 865° and 965°C is also reasonably good though these authors propose limits with iron contents about 0·004 greater than the present work and that of Raccah and Vallet. The limits of the $Fe_{1-x}O$ field in equilibrium with Fe_3O_4 determined by Barbi appear to be considerably in error above 800°C.

The importance of the present results is the confirmation they provide for the three wüstite regions described by Raccah and Vallet. The boundaries of these different forms of wüstite appear to agree with those of Raccah and Vallet within experimental error but we believe that the greater precision of solid state electrochemical techniques has enabled these regions to be mapped with greater accuracy, (e.g. the standard deviation in $\Delta G^0_{O_2}$ for $Fe_{1-x_2}O$ in equilibrium with Fe_3O_4 is ±190 cals in the Raccah and Vallet results; over the same temperature range our standard deviation is ±12 cals). We could not find any evidence for two phase regions within the normal $Fe_{1-x}O$ limits even when the composition was changed by small amounts by coulometric titration (Fig. 1). We can therefore be reasonably confident that the wüstite regions are separated by second (or higher) order transitions associated with changes in the degree of ordering.

The present findings, though in broad

agreement with Raccah and Vallet, apparently disagree with other recent studies since the measurements of Barbi[8], Swaroop and Wagner[7] and Rizzo and Smith[9] failed to produce definite evidence for order-disorder transitions. Swaroop and Wagner however found some indication of defect association. All three investigations attempted in effect to detect changes in the partial molar free energy of solution of oxygen at constant temperature as a function of iron content. Deviations from a *single* linear relationship are however very small (corresponding to a maximum of about 200 cals in our studies) and changes in the slope of $\overline{\Delta G}_{O_2}$ against iron composition are not, as a result, as well defined as those in $\overline{\Delta G}_{O_2}$ (or e.m.f.)-temperature plots. For example, Fig. 1 clearly shows that the wüstite II/wüstite III boundary lies between $Fe_{0\cdot913}O$ and $Fe_{0\cdot916}O$ but this boundary is much less distinct in e.m.f.-iron content plots at different temperatures. This is the probable reason why Rizzo and Smith, who used sensitive electrochemical techniques similar to our own failed to detect any transitions. It is worth noting that Rizzo and Smith's e.m.f.'s at comparable temperatures and iron compositions agree with the present values to within 4 mV but this difference is sufficient for them to find a marked non-linearity in e.m.f.-temperature plots at constant composition. In contrast we found no evidence for non-linearity below their highest temperature (965°C).

Examination of $\overline{\Delta G^\circ}_{O_2}$ vs. $1-x$ plots (not given) shows that the slope of these plots in the wüstite II (wII) region decreases markedly with temperature. This behaviour is characteristic of a two phase system above its critical temperature[13], and extrapolation into a metastable $Fe_{1-x}O$ phase indicates that phase separation into wI and wIII would occur near 315°C. This result is in striking agreement with Manenc's preprecipitation studies [14] on quenched $Fe_{1-x}O$. At compositions between $Fe_{0\cdot947}O$ and $Fe_{0\cdot920}O$ and at temperatures below 320°C satellite X-ray diffraction peaks develop which Manenc ascribes to the formation of two phases, one a vacancy rich form of $Fe_{1-x}O$ of composition $Fe_{0\cdot920}O$ and the other a $Fe_{1-x}O$ matrix depleted of defects.

Partial molar heats and entropies of solution of oxygen

Values of $\overline{\Delta H^\circ}_{\frac{1}{2}O_2}$ and $\overline{\Delta S^\circ}_{\frac{1}{2}O_2}$ are recorded in Table 1. For wI, wII and possibly wIII $\overline{\Delta H^\circ}_{\frac{1}{2}O_2}$ decreases with increasing defect concentration. Kleman's[5] analysis of the Raccah and Vallet results suggests an opposite trend for wII and wIII. Reduction of the heat of solution of oxygen with decreasing iron content may imply that the net defect interaction is endothermic (each atom of oxygen introduced corresponds to the creation of a cation vacancy and two Fe^{3+} ions) and that ordering should be most favoured at the highest defect concentrations. This is not necessarily true, however, because the lattice parameter also changes with defect concentration. At a constant composition of $Fe_{0\cdot886}O$ we see (Table 1) that $\overline{\Delta H^\circ}_{\frac{1}{2}O_2}$ is −61,020 cals for wI, −64,090 cals for wII, and −66,090 cals for wIII while the corresponding values of $\overline{\Delta S^\circ}_{\frac{1}{2}O_2}$ are −18·85, −19·92 and −22·60 cal per deg mole, and these are the trends to be expected if defect ordering increases from wI to wII to wIII. Further support is thus provided for the view that the wüstite regions are separated by order-disorder transitions.

Detailed structural information necessary to relate the thermodynamic properties of $Fe_{1-x}O$ to particular defect models is not available. The only high temperature X-ray study reported is that of Koch[2] who in addition to a comprehensive examination of quenched $Fe_{1-x}O$ single crystals has also made a number of measurements at temperatures and compositions within the wüstite field. The quenched crystals reveal supplementary peaks which can be interpreted in terms of clusters of 4 Fe^{3+} ions on tetrahedral sites and 13 octahedral cation vacancies ordered on a single cubic superlattice with an average spacing about 2·6 × the normal $Fe_{1-x}O$ unit cell. At high temperatures coherent superlattice reflections were absent but considerable diffuse scattering was observed in the region of the strongest reflection, indicating short range ordering with a characteristic spacing similar to the superlattice. Diffraction results were obtained for $Fe_{0 \cdot 898}O$ at 800°C (from Fig. 2 this is in the wIII region), $Fe_{0 \cdot 902}O$ at 1000°C (wIII) and $Fe_{0 \cdot 872}O$ (wII), $Fe_{0 \cdot 907}O$ (wII) and $Fe_{0 \cdot 918}O$ (wI) at 1150°C. The temperatures and compositions in Koch's study were not unfortunately determined with sufficient accuracy to relate the observed scattering to particular wüstite regions with confidence, but increasing temperature and decreasing defect concentration reduced the intensity of the diffuse scattering confirming in a general way that wI, wII, wIII represent increasing degrees of order. It may also be significant that the composition of the ideal $3X$ superlattice is $Fe_{0 \cdot 917}O$ close to the observed wII/wIII boundary. The complexity of the $Fe_{1-x}O$ phase is now sufficiently well established to warrant a thorough high temperature X-ray study of this important non-stoichiometric system.

Acknowledgements—We are grateful to Pilkington Bros. Ltd., St. Helens, for the loan of a furnace and for financial support to one of us (F.D.R.).

REFERENCES

1. RACCAH P. and VALLET P., *C. r. hebd. Séanc. Acad. Sci., Paris* **253**, 2682 (1961); **254**, 1038 (1962); **254**, 2555 (1962); **255**, 1919 (1963); **256**, 136 (1963); **258**, 3679 (1964); *Mem. Sci. Rev. Met.* **62**, 1 (1965); VALLET P., *C. r. hebd. Séanc. Acad. Sci., Paris* **261**, 4396 (1966).
2. KOCH F., Ph. D. Thesis, Northwestern Univ. (1967).
3. GEIGER G. H., LEVIN R. L. and WAGNER J. B., *J. Phys. Chem. Solids* **27**, 947 (1966).
4. ROTH W. L., *Acta crystallogr.* **13**, 140 (1960).
5. KLEMAN M., *Mem. Sci. Rev. Met.* **62**, 457 (1965).
6. DARKEN L. S. and GURRY R. W., *J. Am. Chem. Soc.* **67**, 1398 (1945)
7. SWAROOP B. and WAGNER J. B., *Trans. A I.M.E.* **239**, 215 (1967).
8. RIZZO F. and SMITH J. V., *J. phys. Chem.* **72**, 485 (1968).
10. FENDER B. E. F. and HAMPSON P. J., To be published; HAMPSON P. J., D. Phil. Thesis, Oxford University (1968).
11. ALCOCK C. B. and STEELE B. C. H. *Trans. A.I.M.E.* **237**, 1359 (1965).
12. BLUMENTHAL R. N. and WHITMORE D. H., *J. Am. Ceram. Soc.* **44**, 508 (1961).
13. GIBBS T. P., *Progress in Inorganic Chemistry*, Vol. 3, p. 459. Interscience New York (1962).
14. MANENC J., BOURGEOT J. and HERAI T., *C. r. hebd. Séanc. Acad. Sci., Paris* **258**, 4263 (1964).

J. Phys. Chem. Solids Pergamon Press 1969. Vol. 30, pp. 799–804. Printed in Great Britain.

MAGNETIC PROPERTIES, CONDUCTIVITY AND IONIC ORDERING IN $Fe_{1-x}Cu_xCr_2S_4$

F. K. LOTGERING, R. P. VAN STAPELE, G.H.A.M. VAN DER STEEN and J. S. VAN WIERINGEN
Philips Research Laboratories, N.V. Philips' Gloeilampenfabrieken, Eindhoven–Netherlands

(*Received* 19 *June* 1968; *in revised form* 11 *September* 1968)

Abstract—The magnetic and electrical behaviour of $Fe_{1-x}Cu_xCr_2S_4$ recently measured by Haacke and Beegle is interpreted on the basis of a model for sulphospinels given by Lotgering and Van Stapele, with the additional assumption that the Fe^{2+} levels are situated in the energy gap between the valence and conduction band. Experimental data supporting this interpretation are given. Ionic ordering on *A*-sites in $Fe_{1/2}Cu_{1/2}Cr_2S_4$ and $In_{1/2}Cu_{1/2}Cr_2X_4$ (X = S or Se) is found by means of Mössbauer spectroscopy and X-ray diffraction.

1. INTRODUCTION

RECENTLY Haacke and Beegle[1, 2] have given a description of the electrical and magnetic properties of the mixed-crystal series between ferrimagnetic[3–5], semiconducting[3, 6] $FeCr_2S_4$ and ferromagnetic[7], metallic[6] $CuCr_2S_4$. It is a remarkable feature of this system that the Seebeck coefficient changes sign two times with increasing copper content, while at $x = \frac{1}{2}$ the mixed crystal is again a semiconductor. In this paper we present an interpretation of the observed properties using a model for the electronic structure of $CuCr_2S_4$ given by Lotgering and van Stapele[8], in which it is assumed that Cu occurs as a monovalent ion in sulphospinels. In addition to Haacke and Beegle's data, we performed experiments in order to test the model.

After a description of our model (Section 2), we will discuss the electrical (Section 3) and magnetic (Section 4) properties. In sections 5 and 6 we report the occurrence of ordering of the Me and Cu ion at the tetrahedral sites in $Me_{1/2}Cu_{1/2}Cr_2X_4$.

2. MODEL FOR $Fe_{1-x}Cu_xCr_2S_4$[8]

For materials like oxides and sulphides, the energy levels for the outer anion electrons form a broad valence band, while the metal $3d$ levels form narrow bands which may lie above or below[9] the top of the valence band. This is drawn schematically in the energy level diagrams given in Fig. 1. The energy E is plotted vs. the density of states $g(E)$ so that an area $\int g dE$ gives the number of states per molecule $Fe_{1-x}Cu_xCr_2S_4$. An occupied Me^{n+} level gives the energy of a $3d$ electron bound in the ion with valency n, and an empty Me^{n+} level denotes the presence of an ion with valency $(n+1)$.

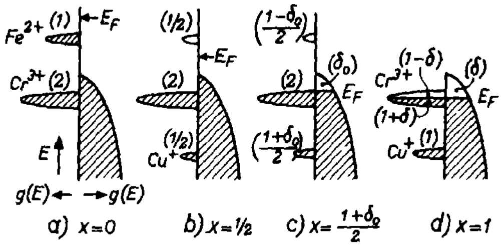

Fig. 1 Energy level schemes (see Section 2). Number of states per molecule indicated between brackets.

We assume that copper is present in the monovalent, diamagnetic state d^{10} represented by a filled Cu^+ band far below the top of the valence band, and that the Cr^{3+} level lies not far below the top of the valence band. Using these assumptions scheme 1(d) with δ holes/molecule in the valence band is found for

$CuCr_2S_4$. This model has been derived[8] from the electrical and magnetic properties of $CuCr_{2-x}Ti_xS_4$ and $CuCr_{2-x}Rh_xSe_4$.

As we will show, several properties of $Fe_{1-x}Cu_xCr_2S_4$ can be explained on the additional assumption that the Fe^{2+} level lies above the top of the valence band. Using this assumption we can draw the energy level schemes for the whole series of mixed crystals and we find Fig. 1(a–c) for $x = 0$, $\frac{1}{2}$ and $(1+\delta_0)/2$. For increasing x the Fermi level E_F drops and passes the top of the Cr^{3+} band for $x = (1+\delta_0)/2$ determined by an unknown parameter δ_0 (Fig. 1(c)).

The valencies in the mixed crystal series can be denoted by the following formulae*, in which S^- represents a hole in the valence band:

$$Fe^{2+}_{1-2x}Fe_x^{3+}Cu_x^{+}|Cr_2^{3+}|S_4^{2-} \quad \text{for} \quad 0 \leqq x \leqq \tfrac{1}{2} \tag{1}$$

$$Fe^{3+}_{1-x}Cu_x^{+}|Cr_2^{3+}|S^{2-}_{5-2x}S^{-}_{2x-1} \quad \text{for} \quad \tfrac{1}{2} \leqq x \leqq \frac{1+\delta_0}{2} \tag{2}$$

$$Fe^{3+}_{1-x}Cu_x^{+}|Cr^{3+}_{3+\delta-2x}Cr^{4+}_{2x-1-\delta}|S^{2-}_{4-\delta}S^{-}_{\delta} \quad \text{for} \quad \frac{1+\delta_0}{2} \leqq x \leqq 1. \tag{3}$$

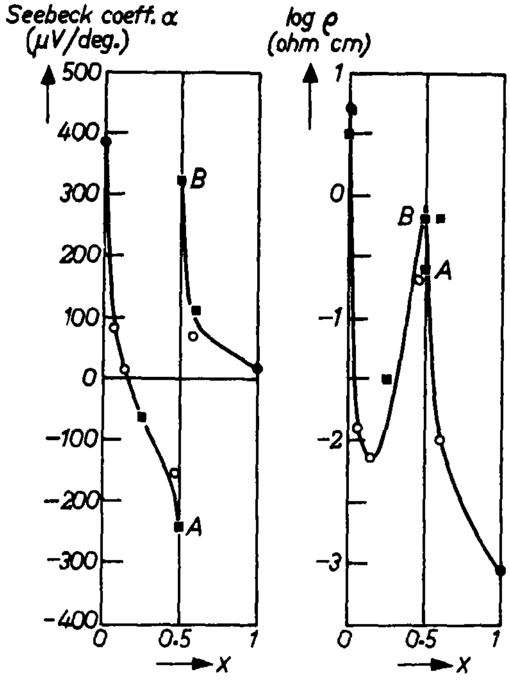

Fig. 2. $Fe_{1-x}Cu_xCr_2S_4$. Seebeck coefficient α and resistivity ρ at room temperature as functions of the composition. Open circles: after Haacke and Beegle (single crystals). Black circles: after Bouchard, Russo and Wold. Squares: own measurements. *A*: quenched from 700°C. *B* slowly cooled with annealing at 500° and 100°C.

3. ELECTRICAL PROPERTIES

We will show that our model gives a natural explanation for the change of the Seebeck coefficient α with composition as found by Haacke and Beegle[2] (Fig. 2). The shapes of the $\alpha - x$ and $\log\rho - x$ curves, and the high values of α at $x = 0$ and $x = \frac{1}{2}$ show that the latter materials are semiconductors. This is explained by the energy level schemes (a) and (b) in Fig. 1, which contain filled or empty bands. For $0 < x < \frac{1}{2}$ a mixture of Fe^{2+} and Fe^{3+} occurs according to formula (1) with an excess of Fe^{2+} for $x \ll \frac{1}{2}$ and an excess of Fe^{3+} for x slightly smaller than $x = \frac{1}{2}$. The observed change from p-type to n-type conduction for increasing x in the region $0 < x < \frac{1}{2}$ can therefore be attributed to Fe^{2+} Fe^{3+} conduction. For increasing x, holes in the valence band appear at $x = \frac{1}{2}$ with increasing concentration according to formula (2). This explains the observation of p-type conduction with a decreasing α. For sufficiently high x, holes in the valence band

---

*In a recent paper, Haacke and Nozik[18] (see also footnote in Section 6) cite these formulae and suppose that they correspond to a strictly ionic model. We should like to stress, however, that a deviation from ionic bonds is essential in our model. In the hypothetical case of a *strictly ionic crystal, the valence and conduction bands* would reduce to sharp levels below and above the metal $3d$ levels, respectively. In the actual crystal, the width of these bands is thought to arise mainly from admixing of the ligand functions and the metal $4S$ functions, i.e. a partially covalent metal-ligand bond. A broadening of the valence band to such an amount that overlap with certain $3d$ levels occurs, as essential in our model, must then be attributed to bonds with a rather strong covalent character.

(formula (3)) cause p-type metallic conduction as found in $CuCr_2S_4$.

As disucssed, α changes sign at $x=\frac{1}{2}$. We also found a different sign on a quenched and a slowly cooled samples of $Fe_{1/2}Cu_{1/2}Cr_2S_4$ (A and B in Fig. 2). This observation was made on several samples.

Remark. It can easily be seen that the electrical properties point to a position of the Fe^{2+} band in the gap between the valence and conduction bands. If, for example, it is assumed that the Fe^{2+} band lies below the top of the valence band, holes would be present in the valence band at $x=0{\cdot}5$. $Fe_{0{\cdot}5}Cu_{0{\cdot}5}Cr_2S_4$ is then expected to be a p-type metallic conductor in contradiction with the observed behaviour.

4. MAGNETIC PROPERTIES

Magnetic measurements were performed on samples with compositions $x=0$, $0{\cdot}25$, $0{\cdot}50$ and $0{\cdot}60$ (Figs. 3 and 4).

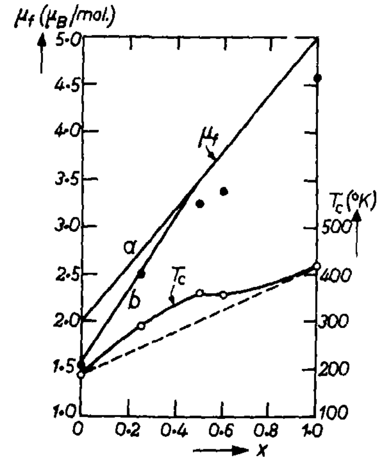

Fig. 3. $Fe_{1-x}Cu_xCr_2S_4$. Saturation moment μ_f at 4·5°K and Curie temperature T_c as functions of composition. μ_f-x curves calculated using the spin-only values (a) or using $g_{eff}=2{\cdot}2$ for Fe^{2+} (b).

The T_c-x curve found (Fig. 3) is in agreement with the curve reported by Haacke and Beegle[1]. T_c increases if magnetic Fe-ions in the ferrimagnetic compound $FeCr_2S_4$ are replaced by non-magnetic Cu ions. This unusual increase of T_c upon dilution of the magnetic ions can be attributed to the appearance of Fe^{3+} ions with a concentration proportional to the Cu content according to Formula (1), if one makes the reasonable assumption that the negative AB superexchange interaction is stronger for $AB = Fe^{3+}Cr^{3+}$ than for $AB = Fe^{2+}Cr^{3+}$. We tested this assumption by preparing the two compounds $Fe_{0{\cdot}5}Cu_{0{\cdot}5}Cr_{1{\cdot}5}\,Me_{0{\cdot}5}S_4$ with Me = Rh or Ti. Since the latter ions occur as non-magnetic Rh^{3+} or Ti^{4+} in sulphospinels[8] the expected valencies are represented by $Fe^{3+}_{0{\cdot}5}Cu^{+}_{0{\cdot}5}|Cr^{3+}_{1{\cdot}5}Rh^{3+}_{0{\cdot}5}|S_4{}^{2-}$ and $Fe^{2+}_{0{\cdot}5}Cu^{+}_{0{\cdot}5}|Cr^{3+}_{1{\cdot}5}Ti^{4+}_{0{\cdot}5}|S_4{}^{2-}$. The observed Curie temperatures are 320 and 190°K, respectively, and show that the $Fe^{3+}Cr^{3+}$ interaction is stronger than the $Fe^{2+}Cr^{3+}$ interaction.

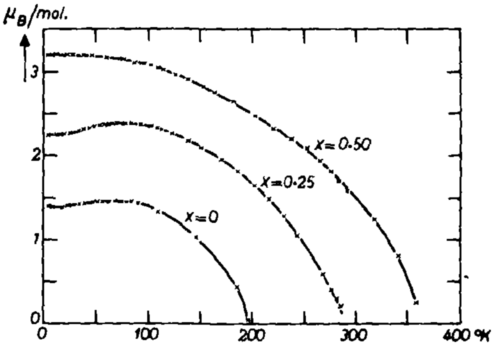

Fig. 4. $Fe_{1-x}Cu_xCr_2S_4$. Magnetization versus temperature curves measured at $H=9$ kOe for compositions indicated.

The deviation from a linear change of T_c with composition and the kink in the T_c-x curve at $x=0{\cdot}5$ (Fig. 3) point to a change in the interaction mechanism at $x=0{\cdot}5$. According to our model this can be attributed to the disappearance of the Fe^{2+} ions according to formula (1) and the appearance of holes in the valence band according to formula (2) at $x=0{\cdot}5$.

The saturation moments μ_f at 4·5°K given in Fig. 3 are not in agreement with data reported by Haacke and Beegle[1], who extrapolated their experimental curves from 77°K down to 0°K. For $x = 0$ and $0\cdot25$ the magnetization curves measured at $H = 9$ kOe show a decrease at low temperatures (Fig. 4). Since the materials were found to be not saturated completely at 4·5°K in fields up to 30 kOe and the neutrondiffraction pattern[4, 5] of $FeCr_2S_4$ shows the simple Néel configuration to occur, the anomalous shapes of the magnetization curves for $x = 0$ and $0\cdot25$ are attributed to strong anisotropy at low temperatures. A strong magnetocrystalline anisotropy at temperatures below ~ 80°K may arise from a small fraction of Fe^{2+} at octahedral sites.

The saturation moment of $FeCr_2S_4$ is considerably lower than the spin-only value of $2\mu_B$/mol. for the simple Néel configuration observed using neutron-diffraction[4, 5]. Since the Cr^{3+} moment is expected theoretically to be very close to the spin-only value (as experimentally confirmed in e.g. $ZnCr_2Se_4$[10, 11] and $CdCr_2Se_4$[11]) we attribute the saturation moment of 1·5 to 1·6 μ_B/mol. observed on $FeCr_2S_4$ to a moment of between 4·4 and 4·5 μ_B for Fe^{2+} at tetrahedral sites. This value corresponds to a g value of between 2·20 and 2·25 and is in accordance with the value $g = 2\cdot2$ for Fe^{2+} corresponding to the experimental Curie constant (3·6) of $Fe_{0\cdot3}Mg_{0\cdot7}Al_2O_4$[12]. From Fig. 3 it is seen that the measured moments for $x = 0$ and $x = 0\cdot25$ are in agreement with the values calculated using formula (1) putting $g = 2\cdot2$ for Fe^{2+} and the spin-only value for Cr^{3+} (curve (b)).

For $CuCr_2S_4$ and for the Cu-rich mixed crystals ($0\cdot5 \leqq x \leqq 1$) the observed moments are 7–12 per cent smaller than the values calculated using formula (3) in the approximation $\delta = 0$ (Fig. 3). Such deviations occur also in the system $CuTi_2S_4$–$CuCr_2S_4$ and are probably due to impurities[8].

5. IONIC ORDERING ON A-SITES IN $Me_{0\cdot5}Cu_{0\cdot5}Cr_2X_4$

According to our model, the tetrahedral sites in $Fe^{3+}_{0\cdot5}Cu^{1+}_{0\cdot5}[Cr_2]S_4$ are occupied by tri- and monovalent ions in the ratio 1 : 1, and the possibility of ionic ordering exists. Braun[13] found an ordering of Fe^{3+} and Li^{+} ions in $Fe_{0\cdot5}Li_{0\cdot5}Cr_2O_4$ with the ions of one kind surrounded by four nearest neighbours of the other kind, so that each tetrahedral site has perfect cubic symmetry. On the other hand, Flahaut *et al.*[14] investigated $Me^{III}_{0\cdot5}M^{I}_{0\cdot5}[Me^{III}_2]S_4$ with Me^{III} = Al or In and Me^{I} = Li, Cu or Ag, and did not report ionic ordering.

An ordering of Fe and Cu ions in $Fe_{0\cdot5}Cu_{0\cdot5}Cr_2S_4$ cannot be detected by means of X-ray diffraction because the difference in scattering power is too small. Here the ordering can be investigated by means of the Mössbauer effect (Section 6).

In order to be able to detect ionic ordering by means of X-ray diffraction, we prepared $In_{0\cdot5}Cu_{0\cdot5}Cr_2X_4$ with X = S or Se. The superstructure reflections (200) and (420) characteristic[15] of the ordering described were indeed found. The ordering was observed on a sample of the selenide quenched from 700°C so that the ordering temperature probably lies above the decomposition temperature (being ~ 700°C for the sulphide).

6. MÖSSBAUER SPECTROSCOPY ON $Fe_{0\cdot5}Cu_{0\cdot5}Cr_2S_4$*

Mössbauer spectra were measured on a slowly cooled sample with $x = 0\cdot5$ at temperatures between 4 and 373°K. A single six-line spectrum was found at temperatures below $T_c = 360$°K (Fig. 5) and a single line at 373°K. The internal field H_i and the isomeric shift relative to ^{57}Fe in Pd are given as functions of temperature in Fig. 6. In all spectra the quadrupole splitting was absent, the relevant parameter ϵ being smaller than

---

*During the preparation of this paper we obtained a preprint of an article on the Mössbauer effect in $Fe_{1-x}Cu_xCr_2S_4$ by G. Haacke and A. J. Nozik[18]. In this work the authors conclude that a mixture of Fe^{2+} and Fe^{3+} occurs for $0 < x < \frac{1}{2}$. The spectra reported for $Fe_{0\cdot5}Cu_{0\cdot5}Cr_2S_4$ are in good agreement with the results given in Section 6.

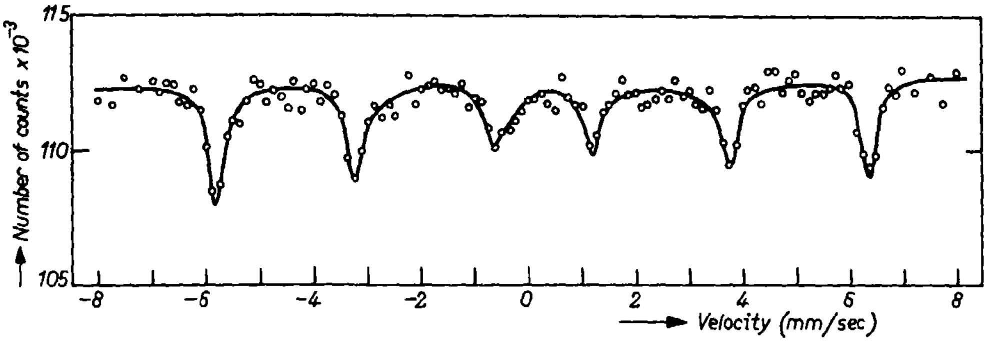

Fig. 5. Mossbauer spectrum of $Fe_{0.5}Cu_{0.5}Cr_2S_4$ at liquid helium temperature. Sample of thickness 65 mg/cm^2. Source ^{57}Co in Pd.

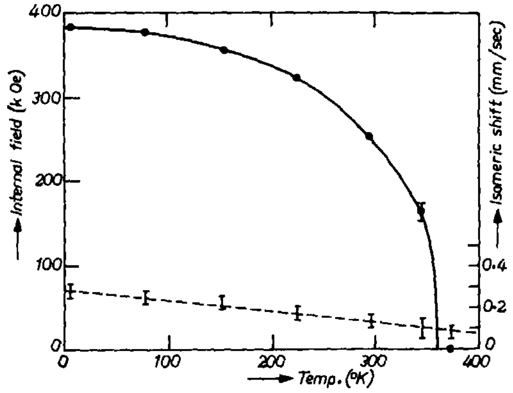

Fig. 6. Temperature dependence of internal magnetic field H_i (drawn, left-hand scale) and isomeric shift (dashed, right-hand scale) of Fe in $Fe_{0.5}Cu_{0.5}Cr_2S_4$.

0·05 mm/sec. At room temperature the spectrum was also measured with the sample in a magnetic field of 15 kOe perpendicular to the gamma beam. The six lines remained sharp and their relative intensities showed that H_i was perpendicular to the gamma beam. H_i was increased from 250 to 264 kOe, but the isomeric shift was unchanged and the quadrupole splitting remained zero.

The observations can be recapitulated as follows:

(a) there is no quadrupole splitting, irrespective of the orientation of the Fe sublattice magnetization,

(b) the change in internal field is equal to the change in external field, i.e. there are neither orbital nor dipolar contributions to H_i,

(c) the internal field is parallel to the external field.

(a) and the absence of dipolar contributions to H_i prove that the local symmetry of the iron sites is perfectly cubic. This is a strong indication for the presence of Fe^{3+} and Cu^{+} ions ordered on the A-sites as described in Section 5. Further, (a) shows also that iron is not in the divalent state because quadrupole splitting would occur at temperatures below T_c for Fe^{2+} on cubic A sites as observed and explained by Eibschütz *et al.*[16] in the case of $FeCr_2S_4$. The absence of an orbital contribution mentioned under (b) and the value of the isomeric shift, which is smaller than found in $FeCr_2S_4$[17], yield further support for the presence of Fe^{3+} ions. Since H_i for Fe^{3+} is antiparallel to the ionic moment, (c) shows that the Fe^{3+} sublattice magnetization is antiparallel to the total magnetization, in accordance with the simple Néel configuration.

Acknowledgements—The authors thank Dr. G. Haacke for sending his paper on the Mössbauer effect in $Fe_{1-x}Cu_xCr_2S_4$ prior to publication. The authors are indebted to Messrs. J. F. Fast and P. R. van Ijzendoorn for performing the magnetic measurements.

REFERENCES

1. HAACKE G. and BEEGLE L. C., *J. Phys. Chem. Solids* **28**, 1699 (1967).
2. HAACKE G. and BEEGLE L. C., *J. appl Phys.* **39**, 656 (1968).

3. LOTGERING F. K., *Philips Res. Rep.* **11**, 190 (1956).
4. BROQUETAS COLOMINAS C., BALLESTRACCI R. and ROULT G., *J. Phys.* **25**, 526 (1964).
5. SHIRANE G., COX D. E. and PICKART S. J., *J. appl. Phys.* **35**, 954 (1964).
6. BOUCHARD R. J., RUSSO P. A. and WOLD A., *Inorg. Chem.* **4**, 685 (1965).
7. LOTGERING F. K., *Proc. Int. Conf. on Magnetism, Nottingham*, p. 533 (1964).
8. LOTGERING F. K. and VAN STAPELE R. P., *J. appl. Phys.* **39**, 417 (1968).
9. ALBERS W. and HAAS C., *Phys. Lett.* **8**, 300 (1964).
10. PLUMIER R., *C. r. hebd. Séanc. Acad. Sci.*, Paris **260**, 3348 (1965).
11. LOTGERING F. K., *J. Phys. Chem. Solids* **29**, 699 (1968).
12. LOTGERING F. K., *J. Phys. Chem. Solids* **23**, 1153 (1962).
13. Cited by GORTER E. W., *Philips Res. Rep.* **9**, 403 (1954).
14. FLAHAUT J., DOMANGE J., GUITTARD M., OURMITCHI M. and KAM SU KAM J., *Bull. Soc. chim. Fr.* **2382** (1961).
15. Private communication by Dr. P. B. BRAUN.
16. EIBSCHÜTZ M., SHTRIKMAN S. and TENENBAUM Y., *Phys. Lett.* **24A**, 563 (1967).
17. HOY G. R. and CHANDRA S., *J. chem. Phys.* **47**, 961 (1967).
18. HAACKE G. and NOZIK A. J., *Solid State Commun.* **6**, 363 (1968).

J. Phys. Chem. Solids Pergamon Press 1969. Vol. 30, pp. 805-812. Printed in Great Britain.

MANGANITES SPINELLES PURS D'ELEMENTS DE TRANSITION PREPARATIONS ET STRUCTURES CRISTALLOGRAPHIQUES†

ROBERT BUHL
Laboratoire de Magnétisme et Physique du Solide, Centre National de la Recherche Scientifique, Bellevue, France

(*Received* 1 *April* 1968; *in revised form* 26 *August* 1968)

Résumé—Les conditions de préparation des différents manganites spinelles $MeMn_2O_4$ (Me = Cr, Mn, Fe, Co, Ni, Cu et Zn) et leurs zones de stabilité en phase unique sont décrites. On a étudié systématiquement l'influence des traitements thermiques sur les propriétés cristallographiques, en particulier sur le taux d'inversion déterminé par diffraction de neutrons et, sur quelques propriétés magnétiques fondamentales. On compare en conclusion nos résultats sur la variation de la distorsion Jahn-Teller coopérative en fonction de la concentration de Mn^{3+} dans les sites *B*, avec ceux d'autres auteurs.

Abstract—The conditions of preparation of several spinel manganites $MeMn_2O_4$ (Me = Cr, Mn, Fe, Co, Ni, Cu and Zn) and their stability domains as single phase are described. We have studied systematically the effect of thermal treatments upon crystallographic properties, particularly upon the inversion degree given by neutron diffraction and, upon some fundamental magnetic properties. We compare, as conclusion, our results of the variation of cooperative Jahn-Teller distorsion as a function of Mn^{3+} concentration in *B* sublattices, with some ones given by other authors.

1. INTRODUCTION

LA PRÉPARATION de la série des manganites des éléments de transition dont la formule générale est $MeMn_2O_4$ (Me étant: Cr, Mn, Fe, Co, Ni, Cu et Zn) a été entreprise dans le but d'étudier les propriétes et structures magnétiques de ces différents composés purs.

Bien que quelques équipes de chercheurs aient déjà décrit quelques propriétés de ces composés, la difficulté de préparation en phase unique de certains d'entre eux, et la grande sensibilité des propriétés aux traitements thermiques ont rendu nécessaire une définition précise de ces différents manganites dont l'étude magnétique approfondie sera publiée séparément.

2. TECHNIQUE EXPERIMENTALE

Le processus de préparation a été le même pour tous les corps. La réaction de formation a toujours été obtenue par voie sèche d'un mélange convenable des oxydes de base, fritté suivant la technique classique de fabrication des céramiques. L'oxyde de manganèse de formule MnO_x (x variant de 1,365 à 1,375 et déterminé par analyse chimique) est donc mélangé avec le second oxyde en proportion telle que le rapport atomique Mn/Me soit égal à 2. La poudre est broyée en milieu aqueux pendant environ 24 hr, elle est ensuite séchée, rebroyée à sec puis matricée en pastilles. La pression utilisée est de 5 ton/cm². Le matriçage avant le traitement thermique offre l'avantage de donner un échantillon compact, beaucoup moins sujet que la poudre à la dispersion par manipulation et à l'introduction d'impuretés, de plus très facile à tremper.

L'observation des réactions chimiques est réalisée au moyen d'une balance thermogravimétrique à atmosphère contrôlée, la température au niveau de l'échantillon peut être programmée entre l'ambiante et 1300°C. Un premier diagramme des variations de poids est effectué sur tout l'intervalle de température et permet de situer les zones de formation possible. De nouvelles expériences permettent ensuite de déterminer la véritable température de formation et de délimiter la zone de stabilité du composé pur. Les conditions de préparation sont ensuite reproduites dans un four où des échantillons, après formation, sont trempés à l'eau depuis diverses températures comprises entre les limites de stabilité. Chaque échantillon est ensuite contrôlé par diffraction X et analyse chimique. Les études cristallographiques puis magnétiques sont entreprises sur tous les échantillons ne présentant qu'une phase unique et une formule chimique stoechiométrique.

---

†Cet article recouvre une partie du travail de thése *de doctorat d'état de l'auteur.*

Les analyses chimiques donnant les proportions d'ions métalliques et le dosage de l'oxygène ont été effectuées par M. Duclos [1], les spectres de diffraction X sur poudre (Debye–Scherrer) soit par Mme Lacour[2], soit par M. Jehanno[3] avec les raies K_α du fer ou du chrome.

Les spectres de diffraction neutronique ($\lambda = 1{,}143$ Å et $\lambda = 1{,}138$ Å) sont obtenus au-dessus de la température d'ordre magnétique – généralement à la température ambiante sauf pour $FeMn_2O_4$: 120°C. Le traitement par méthode de moindres carrés sur calculateur électronique des intensités relatives et absolues des raies, permet de raffiner tous les paramètres cristallographiques difficilement ou pratiquement impossibles à déterminer par diffraction X: paramètres de l'oxygène, et répartition des ions dans les différents sites. La localisation des ions est en effet aisée par diffraction neutronique: les longueurs de diffusion du manganèse ($b = -0{,}36 \cdot 10^{-12}$ cm) et des autres éléments ($b > 0$) étant de signe opposé, les intensités des raies de diffraction sont très sensibles à toute variation du paramètre d'inversion. Ce n'est évidemment pas le cas des rayons X qui distinguent peu les éléments voisins.

Les mesures magnétiques fondamentales dont quelques résultats, utiles à la caractérisation des composés, sont mentionnés dans cet article ont été:

températures de Curie, mesurées à l'aide d'une balance de torsion, l'échantillon étant placé dans un gradient de champ et sa température pouvant varier de 20 à 900°K.

susceptibilités paramagnétiques à l'aide d'une balance de translation asservie, effectuées par M. Allain[4].

aimantations à basses températures par la technique classique d'extraction de 0 à 20 kOe ou de 0 à 80 kOe[5] en champs statiques, ou en champs pulsés jusqu'à 350 kOe[4], suivant l'importance de l'anisotropie magnétocristalline des échantillons.

3. RESULTATS

Les manganites étudiés ici appartiennent tous à la famille des spinelles cubiques ou quadratiques dont les groupes d'espace respectifs sont: $O_h^7(Fd3m)$ ou $D_{4h}^{19}(14_1/amd)$. Les atomes occupent dans la maille les positions suivantes:

	O_h^7	D_{4h}^{19}
sites oxygène	$32e$	$16h$
sites octaédriques (B)	$16d$	$8d$
sites tétraédriques (A)	$8a$	$4a$

Les paramètres desmanganites appartenant au groupe D_{4h}^{19} seront donnés dans la maille faces centrées ($a' = a\sqrt{2}$ et $c' = c$) pour faciliter la comparaison avec la maille cubique dont elle dérive. Les paramètres de l'oxygène qui sont o,x,z dans D_{4h}^{19} seront convertis de la même façon en x',x',z' (avec $x' = \sqrt{2}x$ et $z' = z$).

Le spinelle $MeMn_2O_4$ est dit 'normal' si Me occupe tous les sites tétraédriques A et, 'inverse' dans le cas où Me est en B et Mn se partage entre A et B. Le taux d'inversion ν, est défini comme étant la proportion d'ion manganèse sur les sites tétraédriques A. Le spinelle s'écrit $Me_{1-\nu}Mn_\nu[Me_\nu Mn_{2-\nu}]O_4$. ‡[ ] denote les sites B).

3.1 *Manganites de manganèse* Mn_3O_4 *et de zinc* $ZnMn_2O_4$

Mn_3O_4 est le composé le plus simple à préparer car il est la phase stable à haute température du système binaire Manganèse-Oxygène. L'oxyde dont nous disposons $MnO_{1,365}$ commence par s'oxyder en Mn_2O_3 stable entre l'ambiante et 900°C, à partir de cette température il se réduit rapidement même sous atmosphère d'oxygène et, fait place à Mn_3O_4 pur, cette réaction est irréversible et ce dernier reste stable au-dessous de 900°C. Il est inutile d'insister sur cette préparation mais, il est intéressant de noter que ce corps qu'il soit trempé de 1300°C ou bien refroidi lentement (30°/hr) jusqu'à l'ambiante possède les mêmes caractéristiques cristallographiques et magnétiques. Il cristallise dans le système quadratique $a = 8,149$ Å, $c = 9,456$ Å et $c/a = 1,16$. Les températures de Curie ($T_c = 46$°K) et les courbes d'aimantation de 0 à 20 kOe entre 4,2°K et T_c sont identiques pour les deux échantillons. Il est donc fort probable que le taux d'inversion de ce spinelle soit constant et nul quel que soit le mode de refroidissement. Le réarrangement ionique s'effectuant par transfert électronique, ce résultat est donc logique.

Comme Mn_3O_4, $ZnMn_2O_4$ se forme facilement à partir de 900°C et reste stable jusqu'à l'ambiante, les paramètres de la maille sont en accord avec ceux trouvés par Sinha *et al.* [6]; $a = 8,10$ Å, $c = 9,25$ Å et $c/a = 1,14$. De plus, la diffraction des neutrons confirme l'hypothèse très souvent donnée dans la littérature de la localisation du Zn^{2+} dans les sites A quel que soit le traitement thermique.

3.2 *Manganite de cuivre* $CuMn_2O_4$

$CuMn_2O_4$ est sans doute le composé de la série le plus difficile à former. Il nous a été impossible de l'obtenir pur en phase cubique par notre méthode, rejoignant en ceci Blasse [7] et autres [8, 9].

Par contre, il peut être préparé en phase unique tétragonale par frittage à 940°C et, trempe depuis des températures comprises entre cette dernière et 750°C. Au-dessous de 750°C, il se transforme progressivement en spinelle cubique mais avec apparition de phases parasites qu'il est impossible d'éviter quelle que soit l'atmosphère utilisée (Fig. 1).

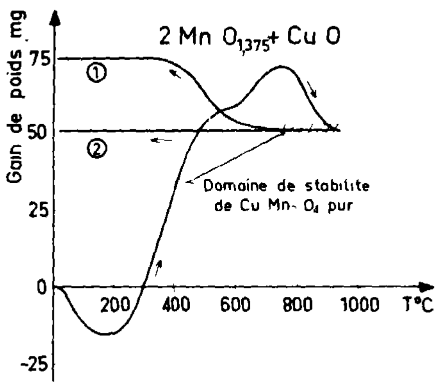

Fig. 1. Analyse thermogravimétrique de la réaction $2MnO_{1,375} + CuO$; (1) refroidissement à l'air, (2) refroidissement sous azote et sous vide.

L'existence de $CuMn_2O_4$ quadratique n'ayant jamais été signalée auparavant, nous donnons ici les paramètres de l'échantillon trempé à 940°C: $a = 8,24$ Å, $c = 8,56$ Å ($c/a = 1,03$). Les paramètres de l'oxygène déterminés par diffraction de neutrons sont: $x = y = 0,322$ et $y = 0,394$; le taux d'inversion est $\nu = 0,24 \pm 0,02$. Le facteur de véracité R calculé sur 14 intensités absolues correspondant à 30 réflexions différentes du spectre de diffraction de neutrons à la température ambiante, est de 5,7%.

La préparation de $CuMn_2O_4$ quadratique est parfaitement reproductible et l'analyse chimique en confirme la stoéchiométrie à mieux que 0,5%.

La stabilité de la phase quadratique à des températures supérieures à celle de la phase cubique est contraire à l'effet de l'agitation thermique et doit donc s'expliquer par un autre mécanisme.

La variation de l'inverse de la susceptibilité paramagnétique en fonction de la température (Fig. 2) permet de déterminer la constante de Curie moléculaire: $C_M = 4,75$ beaucoup plus proche de celle calculée pour une

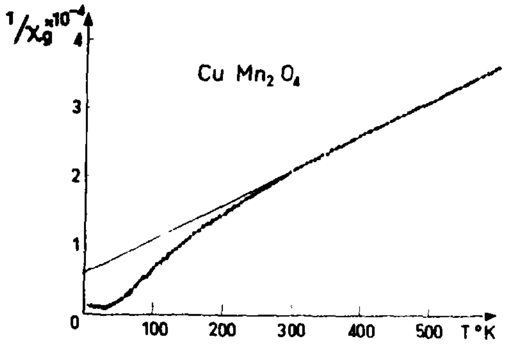

Fig. 2. Variation de l'inverse de la susceptibilité paramagnétique par gramme de $CuMn_2O_4$ en fonction de la température

configuration ionique: $Cu^+Mn^{3+}Mn^{4+}$(1)C_M = 4,88) que pour $Cu^{2+}Mn^{3+}Mn^{3+}$ ($C_M = 6{,}38$) on aboutit donc à la même conclusion que celle Sinha *et al.*[10, 11].

En tenant compte du degré d'inversion et du fait que les constantes de Curie sont voisines, on peut écrire $CuMn_2O_4$ des deux manières suivantes:

(a) $Cu^{+}_{0,76}Mn^{3+}_{0,24}[Cu^{+}_{0,24}Mn^{3+}_{0,76}Mn^{4+}]\,O_4$

(b) $Cu^{+}_{0,76}Mn^{3+}_{0,24}[Cu^{2+}_{0,24}Mn^{3+}Mn^{4+}_{0,76}]\,O_4$.

On peut remarquer que les ions Mn^{3+} dans les sites *A* sont assez dilués pour ne pas entraîner de distorsion ($c/a < 1$) appréciable. Dans les sites *B*, Cu^+ et Mn^{4+} n'entraînant pas de distorsion, la proportion de Mn^{4+} dans la formule (a) est inférieure à celle déterminée par Irani *et al.*[12] environ 60% à partir de laquelle un effet Jahn-Teller coopératif apparaît. Dans la formule (b), Mn^{3+} et Cu^{2+} ont des effets additifs et conduisent à une quadratisation qui doit être faible car leur proportion est légèrement supérieure à la valeur critique. Le rapport *c/a* observé étant de 1,03, la formule (b) est donc la plus probable conformément aux hypothèses de Blasse[7].

L'apparition de la phase cubique pour des températures inférieures à 750°C est liée à la variation du taux d'inversion: le spinelle tendant à devenir normal, la quantité d'ion Cu^{2+} dans les sites *B* diminue alors que celle de Mn^{4+} augmente, la proportion d'ions distordants (Cu^{2+} et Mn^{3+}) devient alors inférieure à la valeur critique et l'effet Jahn-Teller coopératif disparaît.

On pouvait s'attendre d'après la forme de la courbe $1/x = f(T)$ à l'apparition d'un ordre magnétique vers 20°K, il n'en est rien, à 4,2°K la diffraction neutronique ne montre aucun ordre magnétique à longue distance. Il faut noter que le manganite cubique (bien qu'il ne soit pas en phase unique pour espérer en tirer des conclusions quantitatives) devient magnétique à basses températures. Le point de Curie augmente atteignant ~115°K pour l'échantillon refroidi lentement dans l'air. Le taux d'inversion diminuant en fonction du traitement thermique de refroidissement, les sites *A* sont peu ou non magnétiques. Dans les sites *B* l'ion Cu^{2+} doit empêcher l'établissement d'un ordre à longue distance entre Mn^{3+} et Mn^{4+} quand il est en proportion suffisante comme l'a déjà constaté Blasse dans des composés semblables. D'autre part, le changement de phase tétragonale-cubique perturbe les interactions magnétiques *B*–*B* pouvant faire apparaître un ordre Mn^{3+} Mn^{4+} responsable des propriétés ferrimagnétiques.

3.3 *Manganite de nickel* $NiMn_2O_4$

L'étude détaillée de la préparation de $NiMn_2O_4$ pur suivant notre méthode a déjà été décrite[13] et comparée à celles d'autres chercheurs (par exemple[14]). Nous rappellerons simplement que sa température de formation: 940°C est assez critique, que la réaction est lente et que ses propriétés cristallographiques et magnétiques sont fortement influencées par les traitements thermiques. Les mesures de diffraction de neutrons au-dessus de la température de Curie ($115 < T_c < 165$°K suivant les échantillons) ont montré que le degré d'inversion variait entre 0,74 et 0,93 suivant le mode de refroidissement[15]. L'explication des propriétés a pu être fournie par la découverte d'une structure magnétique, à basse température, d'un type nouveau dit 'en étoile', constituée de trois sous-réseaux magnétiques dont la résultante générale n'est colinéaire à aucun d'entre eux[16, 17]. Un article détaillé écrit en collaboration avec *B*. Boucher et M. Perrin, discutant de toutes les propriétés de $NiMn_2O_4$ sera publié prochainement.

3.4 *Manganites de cobalt et de fer*

Les préparations de $CoMn_2O_4$ et $FeMn_2O_4$ sont assez semblables en effet, ils sont stables en phase unique à haute température et se décomposent partiellement par refroidissement lent. La réaction de formation de $CoMn_2O_4$ est lente et se termine à 850°C (Fig. 3) alors que celle de $FeMn_2O_4$ est très rapide et s'achève à 980°C (Fig. 4).

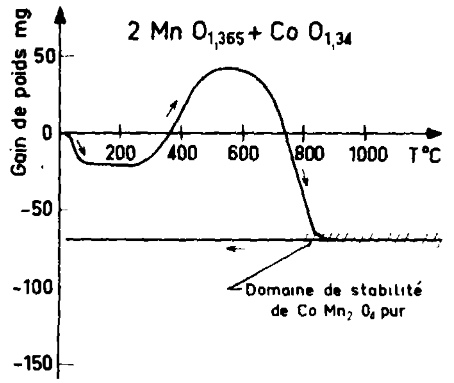

Fig. 3. Analyse thermogravimétrique de la réaction $2MnO_{1,365} + CoO_{1,34}$ dans l'air. Vitesse de chauffage 300°/hr.

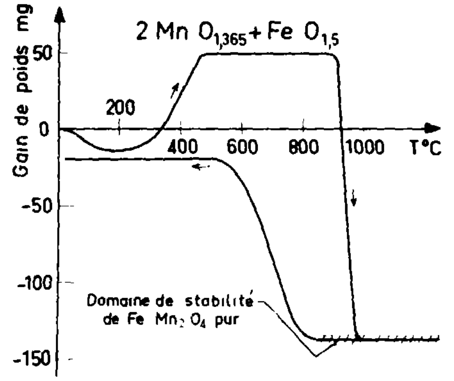

Figure 4. Analyse thermogravimétrique de la réaction $2MnO_{1,365} + FeO_{1,5}$ dans l'air. Vitesse de chauffage 300°/hr.

Bien que l'analyse thermogravimétrique ait pu laisser prévoir la stabilité du manganite de cobalt entre 1250°C et l'ambiante, il commence à apparaître des phases parasites au-dessous de 800°C, la plus importante en est le cobaltite de manganèse $MnCo_2O_4$. L'apparition de Co_2MnO_4 se traduit naturellement par de nouvelles raies sur les spectres *X* Debye–Scherrer, mais également par un nouveau point de Curie (~ 180°K) beaucoup plus élevé que celui du manganite ($T_c \sim 100$°K). Il n'est donc possible d'obtenir $CoMn_2O_4$ pur que par trempe depuis des températures comprises entre 1250°C et 800°C. Trois échantillons ont été étudiés et les résultats sont donnés dans le Tableau 1. D'après Irani *et al.*[18] $CoMn_2O_4$ est cubique entre 900° et 1250°C, cette structure n'est donc pas conservée par trempe prouvant ainsi la grande instabilité à température ambiante du spinelle non distordu. Cet état métastable n'est d'ailleurs pas conservé sur une grande gamme de température, en effet, dés 180°C apparaissent les phases parasites.

Les propriétés magnétiques de ce manganite ont pu être expliquées par une structure du type Yafet–Kittel déterminée par diffraction

Tableau 1

	(Å) a	(Å) c	c/a	$x = y$	z	ν	$R\%$	(°K) T_c
$CoMn_2O_4$ T 1250	8,168	8,958	1,097	0,320	0,386	0,39	3,7	105
T 1000	8,137	9,041	1,111	0,325	0,386	0,33	5,3	100
T 800	8,096	9,133	1,128	0,325	0,381	0,22	5,0	95

de neutrons[19]. Les valeurs expérimentales des moments des sous-réseaux correspondent à la formule ionique $Co^{2+}_{1-\nu}Mn_{\nu}{}^{3+}[Co_{\nu}{}^{2+}Mn^{3+}_{2-\nu}]O_4$.

Comme le manganite de cobalt, $FeMn_2O_4$ n'est pas stable en phase unique au-dessous de 850°C, il apparaît principalement le ferrite de manganèse Fe_2MnO_4, ce qui a pour effet d'augmenter la température de Curie d'une manière très sensible-ainsi que le moment magnétique. De même que pour $CoMn_2O_4$, l'état métastable des échantillons trempés de hautes températures est assez précaire: dès 120°C ils commencent à évoluer et à 250°C apparaissent des phases parasites.

La température de Curie d'un échantillon trempé depuis 1250° étant de 117°C, il a été nécessaire d'effectuer un traitement de stabilisation à 200°C pendant 48 hr pour ne pas avoir de spectres de diffraction de neutron en zone paramagnétique sur un corps en évolution.

Comme $CoMn_2O_4$, le manganite de fer cristallise dans le système quadratique, les résultats concernant deux échantillons sont résumés dans le Tableau 2.

Les aimantations spontanées déduites des courbes d'aimantation à, 4,2°K en champs statiques jusqu'à 80 kOE[5] et en champs pulsés[4] sont 1,65 μB/mol. et 1,55 μ_B/mol. pour les deux échantillons ci-dessus, valeurs bien inférieures à celle trouvée par Eschenfelder[20] 2,1 μ_B/mol. suggérant une certaine proportion de Fe_2MnO_4 due sans doute à sa méthode de préparation.

3.5 *Manganite de chrome* $CrMn_2O_4$

$CrMn_2O_4$, déjà signalé par Bongers[8], dernier élément de la série étudiée ici est le produit de la réaction $2MnO_{1,365} + CrO_{1,5}$ dont le diagramme thermogravimétrique est donné Fig. 5. La réaction débute vers 800° et se termine à 1000°C, le manganite pur est stable entre 1250°C et l'ambiante. Deux échantillons, l'un trempé à 1250°C, l'autre refroidi lentement, ont été étudiés. Les caractéristiques cristallographiques de ces deux corps changent très peu et en particulier l'inversion constante et égale à 1 (Tableau 3).

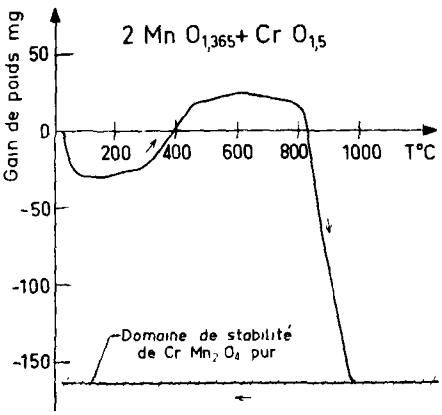

Fig. 5. Analyse thermogravimétrique de la réaction $2MnO_{1,365} + CrO_{1,5}$ dans l'air. Vitesse de chauffage 300°/hr.

Tableau 2

$FeMn_2O_4$	(Å) a	(Å) c	c/a	$x = y$	z	ν	$R\%$	(°C) T_c
Trempé à 1250°C	8,402	8,799	1,047	0,319	0,385	0,91	5,1	117
+ recuit 200°C	8,363	8.879	1,062	0,315	0,387	0,91	3,9	120

Tableau 3

$CrMn_2O_4$	(Å) a	(Å) c	c/a	$x = y$	z	ν	$R\%$	T_c°K
T 1250°	8,355	8,752	1,047	0,314	0,387	1	4,0	65
Refroidi lentement	8,343	8,760	1,050	0,314	0,387	1	4.6	65

4. CONCLUSION

La connaissance précise des degrés d'inversion des manganites purs décrits dans cet article nous permet de comparer nos résultats à ceux d'autres auteurs. Il est ainsi possible de confirmer quantitativement le rôle de l'ion Mn^{3+} ($3d^4$) occupant les sites octaédriques, dans l'apparition de l'effet Jahn–Teller coopératif déjà étudié en particulier par J. B. Goodenough[21].

La Fig. 6 montre la variation du rapport c/a en fonction de la concentration de l'ion Mn^{3+} dans les sites octaédriques pour tous les composés $MeMn_2O_4$ et leurs différents degrés d'inversion (courbe I). La courbe II tirée des traveaux de Wickham et Croft[22] est relative au système $Zn_x^{2+}Ge_{1-x}^{4+}(Co_{2-2x}^{2+}Mn_{2x}^{3+})\,O_4$. Cet exemple est particulièrement significatif car Zn^{2+} et Ge^{4+} sont connus pour leur préférence très marquée pour les sites tétraédriques, éliminant ainsi dans ce système la possibilité de migration de Co^{2+} et Mn^{3+}. Ce n'est pas a priori le cas pour $Mn_xCo_{3-x}O_4$ où les ions ne sont pas forcément localisés sur un type de site déterminé, surtout au voisinage de $CoMn_2O_4$ qui n'est pas normal (cf. 3.4). On peut remarquer que ces deux courbes sont en excellent accord. La courbe III donnée par Irani *et al.*[12] pour le système $MgMn_2O_4$–$MgAl_2O_4$ est également reproduite. Ces auteurs ont d'ailleurs étudié plusieurs systèmes du même type, c'est-à-dire le remplacement progressif de Mn^{3+} par un ion ne produisant pas d'effet Jahn-Teller mais les résultats sont très voisins entre eux. Bien qu'elles aient même allure générale, la courbe III présente un certain écart par rapport aux courbes I et II; la précision sur la détermination par rayons *X* de la localisation des ions sur les différents sites n'est pas très grande et de plus l'ion Mg^{2+} peut migrer sur les sites octaédriques (cf. Manaila[28]), ceci peut expliquer l'écart relatif entre ces courbes.

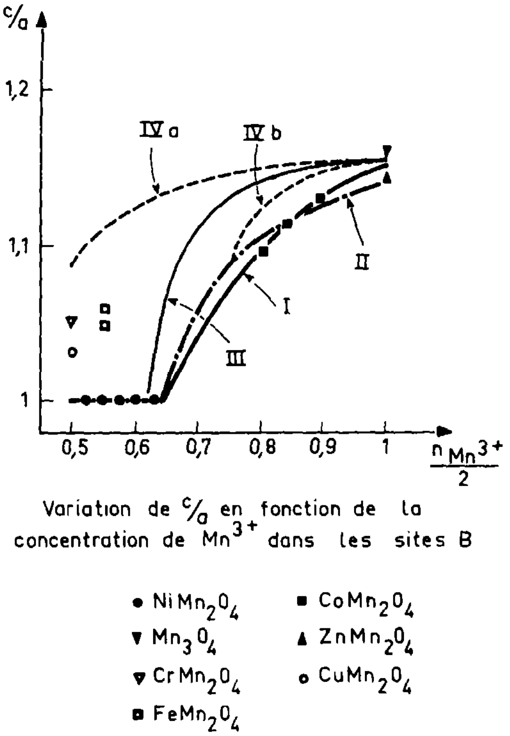

Fig. 6. Variation du rapport c/a en fonction de la concentration d'ion Mn^{3+} dans les sites *B* (*n* Mn^{3+})/2.

(I) nos résultats.
(II) système $Zn_x^{2+}Ge_{1-x}^{4+}(Co_{(2-2x)}^{2+}Mn_{2x}^{3+})\,O_4$ d'après D. G. Wickham et W. J. Croft[22].
(III) système $MgMn_2O_4$–$MgAl_2O_4$ d'après Irani.
(IV) $MgMn_2O_4$ d'après Manaila[28].

On constate bien que la transition cubique → quadratique s'effectue dans la même zone de concentration de Mn^{3+} c'est-à-dire environ 0,65. Il faut noter que les trois seuls composés qui n'obéissent pas à cette loi sont ceux pour lesquels Mn^{3+} n'est pas le seul ion distordant dans les sites B. En admettant pour $FeMn_2O_4$ la formule déterminéee par effet Mössbauer[23]:

$$Fe_{0,09}^{3+}Mn_{0,91}^{2+}[Mn_{1,09}^{3+}Fe_{0,82}^{3+}Fe_{0,09}^{2+}]\,O_4$$

et, pour $CuMn_2O_4$ (cf. 3.2):

$$Cu_{0,76}^{+}Mn_{0,24}^{3+}[Mn^{3+}Mn_{0,76}^{4+}Cu_{0,24}^{2+}]\,O_4$$

les ions Fe^{2+} et Cu^{2+} ont un effet de distorsion supplémentaire à celui de Mn^{3+}[24, 25]. Il faudrait donc tenir compte de cet effet qui est difficile à chiffrer car comme l'ont montré des travaux récents[26, 27], l'effet Jahn-Teller coopératif dépend de la nature même des ions en présence.

Pour $CrMn_2O_4$, si on admet la formule ionique $Mn^{2+}[Cr^{3+}Mn^{3+}]O_4$, Cr^{3+} dans les sites B, selon[24], ne participe pas à l'effet Jahn-Teller coopératif et il ne devrait donc pas y avoir de distorsion. La constante de Curie expérimentale $C_M = 7{,}16$ est plus faible que celle calculée pour la formule ci-dessus ($C_M = 9{,}24$), et pourrait correspondre à un état partiel de 'spin bas' pour le chrome entraînant une modification des orbitales et une participation à l'effet Jahn-Teller.

Pour terminer, nous avons reporté également Fig. 6, les courbes déduites des travaux de Manaila[28] sur la variation de c/a en fonction de l'inversion de $MgMn_2O_4$:

(a) en prenant la formule adoptée par lui (4(a))

$$Mg^{2+}_{1-\nu}Mn_\nu{}^{2+}[Mg_\nu{}^{2+}Mn_\nu{}^{4+}Mn^{3+}_{2-2\nu}]\,O_4$$

(b) en prenant une configuration ionique plus simple (4(b))

$$Mg^{2+}_{1-\nu}Mn^{3+}[Mg_\nu{}^{2+}Mn^{3+}_{2-\nu}]\,O_4.$$

Il est remarquable de constater que cette dernière est en excellent accord avec les courbes I, II et III alors que la première est en net désaccord.

Je remercie Messieurs Herpin et Mériel de m'avoir accueilli dans leur laboratoire ainsi que de leurs conseils fructueux. J'ai pu ainsi travailler en collaboration avec Messieurs Boucher et Perrin en Diffraction de Neutrons au C.E.N. Saclay, je les en remercie aussi vivement.

REFERENCES

1. M. DUCLOS, Laboratoire de Magnétisme et Physique du Solide CNRS, Bellevue.
2. M. PAULUS et Mme LACOUR, Laboratoire de Magnétisme et Physique du Solide CNRS, Bellevue.
3. M. JEHANNO SPSRM, Centre d'Etudes Nucléaires de Saclay.
4. M. ALLAIN, Centre d'Etudes Nucléaires de Saclay.
5. Mesures effectuées chez le Prof. PAUTHENET, Laboratoire d'Electrostatique et Physique du Métal, Grenoble.
6. SINHA A. P. B., SANJANA et BISWAS A. B., *Acta crystallogr.* **10**, 439 (1957).
7. BLASSE G., *J. Phys. Chem. Solids* **27**, 383 (1966).
8. BONGERS P. F., Thèse, Leiden (1957).
9. RIENACKER G et WERNER K., *Z. Anorg. Chem.* 327 (1964).
10. SINHA A P. B, SANJANA et BISWAS A. B., *J. phys. Chem.* **62** (1958).
11. JOGALEKAR P. P. et SINHA A. P. B., *Ind. J. Pure Appl. Phys.* **5**, 9 (1957).
12. IRANI K. S., SINHA A. P B. et BISWAS A. B., *J Phys. Chem. Solids* **17**, 101 (1960).
13. VILLERS G. et BUHL R., *C. r. hebd. Séanc. Acad. Sci., Paris* **260**, 3406 (1965).
14. LARSON E. G., ARNOTT R. J. et WICKHAM D. G., *J. Phys. Chem. Solids* **23**, 1771 (1962).
15. BOUCHER B, BUHL R. et PERRIN M., *C.r. hebd. Seanc. Acad. Sci., Paris*, **263**, 344 (1966).
16. BOUCHER B., BUHL R. et PERRIN M., *C.r. hebd. Séanc. Acad. Sci., Paris*, **263**, 424 (1966).
17. BOUCHER B., BUHL R. et PERRIN M., *C.r. hebd. Séanc. Acad. Sci., Paris*, **263**, 785 (1966).
18. IRANI K. S., SINHA A. P. B. et BISWAS A. B., *J. Phys. Chem. Solids* **23**, 711 (1962).
19. BOUCHER B., BUHL R. et PERRIN M., International Conference of Magnetism Boston (USA). *J. appl. Phys.* **39**, 632 (1968).
20. ESCHENFELDER A., *J. appl. Phys.* **29**, 378 (1958).
21. GOODENOUGH J. B., *J. Phys. Rad.* **20**, 155 (1959).
22. WICKHAM D. G. et CROFT W. J , *J. Phys. Chem. Solids* 7, 351 (1958).
23. TANAKA M. et MIZOGUCHI T., *J. phys. Soc. Japan* **18**, 1091 (1963).
24. DUNITZ J. D. et ORGEL L. E., *J. Phys. Chem. Solids* **3**, 20 (1957); **e**, 318 (1957).
25. KANAMORI, *J. Prog. theor. Phys.* **17**, 177 (1957).
26. KSHIRSAGAR et BISWAS A. B., *J. Phys. Chem. Solids* **28**, 1493 (1967).
27. ROBBINS M. et DARCY L , *J. Phys. Chem. Solids* **27**, 741 (1966).
28. MANAILA R., *Phys. Status Solidi* **9**, 385 (1965).

J. Phys. Chem. Solids **Pergamon Press 1969. Vol. 30, pp. 813–818. Printed in Great Britain.**

PHONON SCATTERING IN MAGNESIUM FLUORIDE*

R. A. KASHNOW† and K. A. McCARTHY
Department of Physics, Tufts University Medford, Mass. 02155, U.S.A

(*Received* 22 *July* 1968; *in revised form* 20 *August* 1968)

Abstract—The thermal conductivity of monocrystalline magnesium fluoride has been measured between 1·4 and 77°K for directions parallel to and perpendicular to the c-axis. Anisotropy in the thermal conductivity has been observed and correlated with anisotropic features of the phonon spectrum and phonon–phonon umklapp scattering using a modified Callaway model

INTRODUCTION

THE LOW TEMPERATURE thermal conductivity of a crystal can be analyzed in terms of the scattering processes which are active in the phonon gas. In most applications of the Callaway model[1] the scattering rates and the phonon spectrum are assumed to be independent of the direction of heat flow and the orientation of the crystal relative to the heat flow direction. For crystals of non-cubic crystal structure the conductivity is anisotropic and cannot be accounted for by such a model.

In this paper we report the results of measurements on magnesium fluoride crystals, which are of the tetragonal, rutile structure[2]. In our analysis we have incorporated some features of the phonon spectrum into the Callaway formalism: anisotropy in the sound velocities, as measured by Cutler, Gibson and McCarthy[3]; anisotropy in the phonon frequencies at the zone boundary, as calculated by Katiyar and Krishnan[4]. We have also allowed for anisotropy in the adjustable parameters which characterize the scattering rates, as determined by computer fit to experimental data.

EXPERIMENTAL DETAILS

The thermal conductivities of two magnesium fluoride crystals were measured in the temperature range 1·5 to 77°K. The specimens were provided by the Optovac Company, North Brookfield, Massachusetts, in the form of rectangular parallelopipeds $3{\cdot}15\times3{\cdot}20\times62{\cdot}5$ mm. One of these samples (#1) had been cut so that the c-axis was parallel to the long dimension; in sample #2 the c-axis was perpendicular to the length. Since the heat current and temperature gradient were parallel to the sample length, the conductivities of these two samples are referred to here as κ_c and κ_a, respectively.

Steady-state measurements were made in a cryostat of conventional design[5]. In the sample chamber a copper block connected to the helium bath by thin copper wires served as a variable-temperature heat sink. The block temperature was measured by a platinum resistor above 16°K and by a germanium resistor below 20°K. The bottom of the specimen was clamped to the block in a vertical position, and a manganin wire heater was attached to the top of the specimen. For temperature gradient measurements, 0·1 W carbon resistors were attached to the specimen using spring-loaded, indium-faced, copper clamps. Platinum and germanium resistances were measured by a d.c. potentiometric method; carbon resistance was

---

*Supported in part by a grant (G-7694) from the National Science Foundation.

†Presently at United States Army Natick Laboratories, Natick, Massachusetts.

measured on an a.c. Wheatstone bridge[6]. We would estimate the errors in the thermal conductivity values to be less than 10 per cent at temperatures below 40°K, and less than 20 per cent at temperatures above 40°K.

EXPERIMENTAL RESULTS

The thermal conductivity data for κ_c and κ_a are plotted in Figs. 1 and 2. The solid lines on these figures represent the theoretical fits the source of which we shall describe below. Here we point out some of the qualitative features that are common to these curves. At the lowest temperatures, κ is proportional to the cube of the temperature as expected from Casimir boundary scattering[7]. A maximum is reached at $T \sim 19°K$, beyond which unklapp scattering dominates. At the peak κ is approximately 25 W cm^{-1} °K^{-1}, and is limited by isotope and impurity scattering.

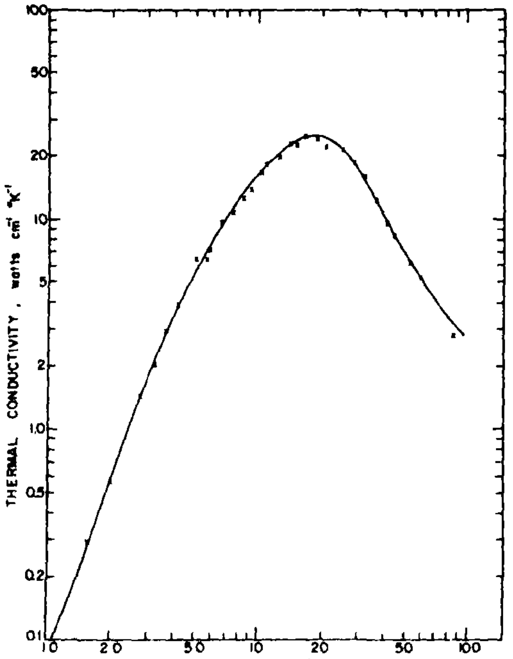

Fig. 1 The thermal conductivity κ_c of magnesium fluoride (crystal #1) The heat flow for these data is parallel to the c-axis of the sample. The solid line represents fits C-1 and C-2; the parameters for these computer fits are given in Table 2 (on this scale the fits are not distinguishable).

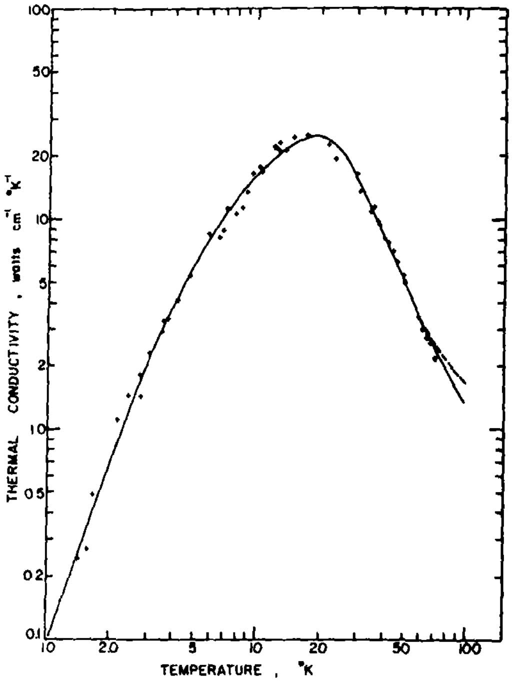

Fig. 2 The thermal conductivity κ_a of magnesium fluoride (crystal #2). The heat flow for these data is perpendicular to the c-axis of the sample. The solid line represents fit A-2; the dashed line represents the departure of fit A-1 at high temperatures The parameters for these computer fits are given in Table 2.

SOUND VELOCITIES AND DEBYE TEMPERATURES

Theoretical dispersion curves have been calculated for the (001) and (010) directions in magnesium fluoride by Katiyar and Krishnan[4]. In their calculations, which are based on the Born rigid-ion model[8], the force constants and effective ionic charges have been adjusted to agree with the Raman spectra measurements[9–11] which yield the optical phonon frequencies at $\mathbf{q} = 0$.

We are interested in two sets of quantities which may be obtained from their calculations: the sound velocities, v_p, and the maximum frequencies at the edge of the first Brillouin zone, $(\nu_p)_{\max}$, for each polarization branch p in the (001) and (010) directions. We have calculated the velocities from the slopes of the acoustic branches in the long wavelength limit; these can be compared with the velocities measured by Cutler *et al.*[3] From the maximum frequencies we have calculated a set of Debye temperatures defined by

$$\theta_p = h(\nu_p)_{\max}/\mathrm{k}. \tag{1}$$

These quantities are listed in Table 1.

Table 1. Magnesium fluoride: the sound velocities, maximum phonon frequencies at the edge of the first Brillouin zone, and the calculated Debye temperatures for the several polarization branches

Polarization branch*	Propagation direction (hkl)	Sound velocities theory 10^5 cm sec^{-1}	Sound velocities experiment 10^5 cm sec^{-1}	Max. phonon frequency 10^{13} sec^{-1}	Debye temp. (°K)
L	001	7·27	7·46	6·44	490
T	001	4·19	4·16	4·27	325
L	010	6·56	6·24	3·94	300
T_1	010	5·55	5·55	2·56	195
T_2	010	3·65	4·16	2·27	173

*Notation of Katiyar and Krishnan:

L refers to longitudinal acoustic waves, propagated along (001) and (010) directions respectively.

T refers to a transverse acoustic wave, propagated along the (001) direction.

T_1 and T_2 refer to transverse acoustic waves, propagated along the (010) directions.

The usual Debye characteristic temperature can be written as[12]

$$\theta = \frac{h}{k}(3N/4\pi V)^{1/3}\langle v\rangle \tag{2}$$

where N/V is the number of atoms per unit volume and $\langle v\rangle$ denotes an average sound velocity. In the general case of an anisotropic crystal, the average velocity is given by

$$\langle v\rangle = \left[\frac{1}{3}\sum_{p=1}^{3}\frac{1}{4\pi}\int\{v_p(\theta,\phi)\}^{-3}\,\mathrm{d}\Omega\right]^{-1/3} \tag{3}$$

where the summation is over the polarization branches and dΩ is the solid angle element in the direction associated with (θ, ϕ).

For the tetragonal symmetry of magnesium fluoride we have calculated $\langle v\rangle$ according to a formulation by Betts *et al.*[13]. The procedure is to expand the integrand in equation (3) in a series of tetragonal harmonics which can be related to the elastic constants. Using the elastic constants from reference [3], equations 3 and 2 give $\langle v\rangle = 4{\cdot}34\times10^5$ cm sec^{-1} and $\theta = 584$°K.

The lattice parameters (a equal to 4·62 Å and c equal to 3·05 Å) and the density (equal to 3·177 g cm^{-3} at 18°C) of magnesium fluoride were taken from a paper by Duncanson and Stevenson[14].

AVERAGE FITS

Usually the procedure is to fit the experimental data to the function

$$\kappa = (G'/\langle v\rangle)T^3\int_0^{\Theta/T} J_4'(x)\tau_C\,\mathrm{d}x \tag{4}$$

which is the κ_1 of the Callaway expression[1]: $G' = k^4/2\pi^2\hbar^3$ and $J_4'(x) = x^4e^x(e^x-1)^{-2}$, where $x = h\nu/kT$. τ_c^{-1} is the combined relaxation rate, equal to $\tau_N^{-1}+\tau_R^{-1}$, where the subscripts N and R denote normal and resistive processes, respectively. Since the magnesium fluoride crystals are isotopically impure, resistive scattering dominates at all temperatures. In this limit $(\tau_N^{-1} \ll \tau_R^{-1})\kappa_2$, the correction term for normal processes, may be neglected and τ_C^{-1} may be written as

$$\tau_C^{-1} = \tau_B^{-1} + \tau_P^{-1} + \tau_U^{-1}$$

where B, P and U denote boundary, point-defect and umklapp scattering, respectively. The boundary scattering rate is assumed to be frequency-independent: $\tau_B^{-1} = B$. The point-defect scattering is assumed to be Rayleigh-like: $\tau_P^{-1} = Px^4T^4$. For the umklapp scattering, we choose $\tau_U^{-1} = Ux^2T^3$ (exp $(-F/T)$). The frequency dependence (ν^2) is that suggested by Herring[15] for crystals of the appropriate symmetry; the temperature dependence is chosen to agree with experimental observations at temperatures on the order of $\Theta/10$.

In our computer programs, which are modifications of those of Aldrich[6] and Burke[16], we treat B, P, F and U as adjustable parameters. For the conductivity in each of the crystallographic directions studied (κ_C and κ_A), the computer is given a set of four experimental values of $\kappa(T)$. An association is made between each of these experimental points and one of the parameters, with B corresponding to the lowest temperature point, and so on. This association, which will be made clear below, is made because at the lowest temperatures κ is most sensitive to B, at temperatures near the peak to P and F, and at the highest temperatures to U.

In developing the fit to the data, the computer is first provided with an initial set of parameters from which it calculates κ (according to equation (4)) at each of the temperatures corresponding to the experimental points. The integration is performed by Simpson's rule, using a grid for which $dx = 0{\cdot}1$ between $x = 0{\cdot}05$ and $x = \theta/T$. At each of the four points the computer adjusts the associated parameter to minimize the deviation of the calculated κ from the experimental value. The nature of equation (4) is such that a change in one of the coefficients affects κ over a wide temperature range; the program must continue to make adjustments in one parameter after another until the entire set of parameters results in a set of κ's which agrees (within, say, 0·1 per cent) with the experimental values. When this condition is satisfied, the program generates a set of sufficient (in this case, fifty six) values of $\kappa(T)$ between 0·1 and 95·4°K so that the theoretical curve can be compared with the experimental one over the entire temperature range.

In fits C–1 and A–1, for κ_c and κ_a, respectively, we have used equation (4) with the average values of v and θ which were calculated above. These fits are shown in Figs. 1 and 2; the sets of coefficients that were required are given in Table 2. We note that the values of B are in reasonable agreement with those expected from Casimir boundary scattering. The values of P are more than three times higher than expected from a mass defect calculation of isotopes alone. A semi-quantitative analysis of the magnesium fluoride crystals revealed six elements present in concentrations of about one ppm and one element (Mn) in a concentration of 1–10 ppm. These impurities may account for the large values of P required to fit the data. A quantitative calculation cannot readily be performed, however, because the impurities cannot be treated as mass defects only.

The different values of F and U for the two crystals are significant. The anisotropy in κ at temperatures above the peak is due in large part to the intrinsic anisotropy in umklapp scattering and to a lesser extent to the anisotropy in v and Θ. Since equation (4) does not exhibit the anisotropy in v and Θ, fits C–1 and A–1 give a ratio of U_a/U_c which is slightly larger than the one given in the model below.

SEPARATION FITS

In order to express κ in a form which exhibits the anisotropy in v and Θ, we write, in place of equation (4),

Table 2. Coefficients used to fit equation (4) for the thermal conductivity of magnesium fluoride. B *is associated with boundary scattering,* P *with point-defect scattering;* U *and* F *are associated with umklapp scattering*

Coefficient	Fit C-1*	Fit A-1*	Fit C-2*	Fit A-2*
B	$3{\cdot}55\times 10^6$	$3{\cdot}12\times 10^6$	$3{\cdot}18\times 10^6$	$2{\cdot}58\times 10^6$
P	9·81	11·5	8·66	9·87
F	106	127	105	125
U	$2{\cdot}37\times 10^4$	$5{\cdot}90\times 10^4$	$2{\cdot}07\times 10^4$	$4{\cdot}13\times 10^4$

*Fit C-1 applies to the thermal conductivity data with the heat flow parallel to the c-axis, and in which average values of the velocity of sound and the Debye temperature are used; fit A-1 is for heat flow perpendicular to the c-axis, and is otherwise similar to C-1. Fits C-2 and A-2 result from using the appropriate values of velocity and the Debye temperature given in Table 1 in the form described by equation (6).

$$\kappa_i = G'\,T^3\sum_p v_{i,p}^{-1}\int_0^{\Theta i,p/T}\tau_C J_4'(x)\,\mathrm{d}x; \qquad (5)$$

here the summation is over all phonon polarization branches p in the heat flow direction $\hat{i}$. Equation (5) is actually an adaptation from Holland[17]. We have included the directional separation in v and Θ but have relaxed the polarization separation in τ_C.

For i in the (001) and (010) directions, equation (5) gives κ_c and κ_a, respectively:

$$\kappa_c = \tfrac{2}{3}G'T^3v_T^{-1}(001)\int_0^{\theta_T(001)/T}\tau_c J_4'(x)\,\mathrm{d}x$$

$$+\tfrac{1}{3}G'T^3v_L^{-1}(001)\int_0^{\theta_l(001)/T}\tau_c J_4'(x)\mathrm{d}x;$$

$$\kappa_a = \tfrac{1}{3}G'T^3v_{T_1}^{-1}(010)\int_0^{\theta_{T_1}(010)/T}\tau_c J_4'(x)\,\mathrm{d}x$$

$$+\tfrac{1}{3}G'T^3v_{T_2}^{-1}(010)\int_0^{\theta_{t_2}(010)/T}\tau_c J_4'(x)\,\mathrm{d}x$$

$$+\tfrac{1}{3}G'T^3v_L^{-1}(010)\int_0^{\theta_l(010)/T}\tau_c J_4'(x)\,\mathrm{d}x.$$

In fitting the experimental data to equation (6) we have not had to use any more adjustable parameters than for equation (4). The appropriate values of v and θ are those in Table 1. We have used the same form for the relaxation rate as in the average fit procedure. The calculated coefficients for the separation fits C-2 and A-2 are given in Table 2.

DISCUSSION

In Fig. 3 we have plotted the anisotropy ratio κ_C/κ_A as a function of temperature. To avoid scatter in the graph we have used the best theoretical fits, C-2 and A-2. The ratio is less than unity only in the boundary region. It is nearly unity in the point defect region, about the maximum in the conductivity curve. For $T \geq 25°\mathrm{K}$, κ_C/κ_A increases linearly with temperature:

$$\frac{\kappa_c}{\kappa_a} - 1 \simeq (1{\cdot}5\times 10^{-2})(T-25).$$

The extrapolated value at $T = 90°\mathrm{K}$ is $\kappa_C/\kappa_A \simeq 2$. This behavior is similar to that of manganese fluoride, as reported by Slack[18].

Recent measurements on He[4] crystals by Guyer and Hogan[19] have shown anisotropy in the umklapp region in excess of that expected from velocity anisotropy. In the case of magnesium fluoride, the anisotropy is not as severe, but a similar interpretation may be invoked. In addition to the anisotropy in v and θ, we find that $\tau_U^{-1}(010) > \tau_U^{-1}(001)$ *for all temperatures. In terms of the dispersion* curves, at a given temperature, phonons of

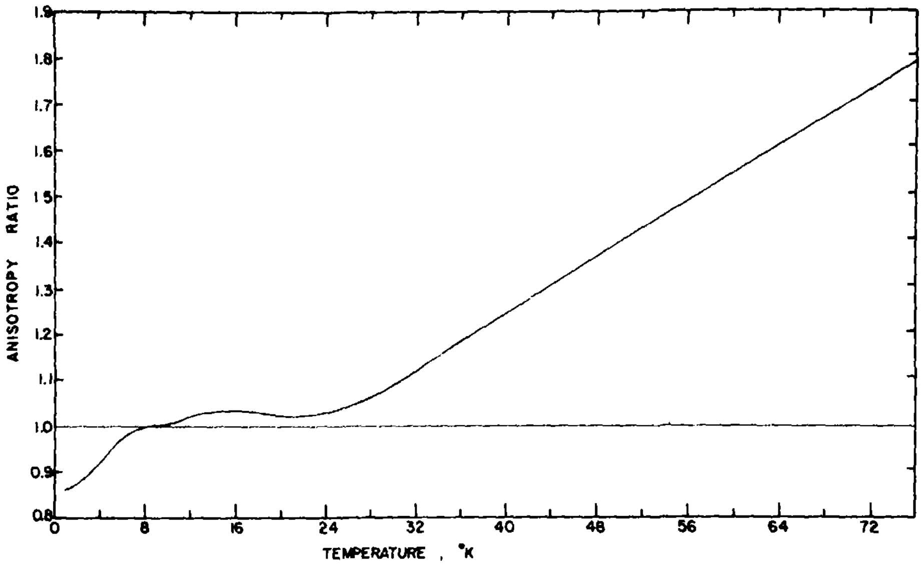

Fig. 3 The ratio of κ_t to $\kappa_{\parallel}$ as a function of temperature. The fits C–2 and A–2 were used rather than the actual data to reduce the scatter. $\kappa_t/\kappa_{\parallel}$ is less than unity only in the boundary scattering region; it is nearly unity in the point-defect region, about the thermal conductivity maximum, and above 25°K increases linearly with temperature.

higher values of **q** will be excited for the (010) direction than for the (001).

Since both the average and separation analyses result in theoretical curves which are in reasonably good agreement with experiment, we cannot prefer one over the other on this basis. In fact, the nature of the fitting procedure is such that one could obtain, through a variety of schemes, a number of theoretical curves among which the experimental data could not accurately distinguish. Since the separation analysis is more faithful to details of the phonon spectrum, however, it is likely to yield a better estimate of the anisotropy in the phonon–phonon scattering rate.

REFERENCES

1. CALLAWAY J., *Phys. Rev.* **113**, 1046 (1959).
2. SLATER J. C., *Quantum Theory of Molecules and Solids*, Vol. 2, p. 64. McGraw-Hill, New York (1965).
3. CUTLER H., GIBSON J. and MCCARTHY K. A., *Solid State Commun.* **6**, 431 (1968).
4. KATIYAR R. S. and KRISHNAN R. S., *Can. J. Phys.* **45**, 3079 (1967).
5. KASHNOW R. A., Thesis, Tufts University (1968).
6. ALDRICH R. E., Thesis, Tufts University (1967).
7. THACHER P., *Phys. Rev.* **156**, 975 (1967).
8. BORN M. and HUANG K., *Dynamical Theory of Crystal Lattices*. Oxford University Press, Oxford (1954).
9. KRISHNAN R. S. and KATIYAR R. S., *J. Phys.* **26**, 627 (1965).
10. KRISHNAN R. S. and RUSSELL J. P., *Br. J. appl. Phys.* **17**, 501 (1966).
11. PORTO S. P. S., FLEURY P. A. and DAMEN T. C., *Phys. Rev.* **154**, 522 (1967).
12. BLACKMAN M., *Rep. Prog. Phys.* **8**, 11 (1941).
13. BETTS D. D., BHATIA A. B. and HORTON G. K., *Phys. Rev.* **104**, 43 (1956).
14. DUNCANSON A. and STEVENSON R. W. H., *Proc. phys. Soc.* **72**, 1001 (1958).
15. HERRING C., *Phys. Rev.* **95**, 954 (1954).
16. BURKE W. J., Thesis, Tufts University (1965).
17. See equation (9) of HOLLAND M. G., *Phys. Rev.* **132**, 2461 (1963).
18. SLACK G. A., *Phys. Rev.* **122**, 1451 (1961).
19. GUYER R. A. and HOGAN E. M., *Solid State Commun.* **5**, 909 (1967).

J. Phys. Chem. Solids Pergamon Press 1969. Vol. 30, pp. 819–826. Printed in Great Britain.

MÖSSBAUER STUDIES OF Co_3O_4; BULK MATERIAL AND ULTRAFINE PARTICLES

WALTER KÜNDIG
University of California, Los Angeles, Calif. 90024, U.S.A.

and

M. KOBELT and H. APPEL
University of Karlsruhe, Germany

and

G. CONSTABARIS and R. H. LINDQUIST
Chevron Research Company, Richmond, California, U.S.A.

(*Received* 6 *May* 1968; *in revised form* 15 *August* 1968)

Abstract—Mössbauer spectra of bulk Co_3O_4, doped with ^{57}Co, show the two spinel sites. Above the Néel temperature, T_N, the spectra are composed of two quadrupole-split lines corresponding to Fe^{3+} at both the tetrahedral (A) sites and octahedral (B) sites. The isomeric shifts relative to Fe at the A and B sites are $(-0{\cdot}316 \pm 0{\cdot}010)$ and $(-0{\cdot}393 \pm 0{\cdot}005)$ mm/sec, respectively. A comparison with other spinels indicates a higher electronic charge density at the nucleus which is attributed to the smaller interatomic distances in Co_3O_4. Below T_N, the A site Fe^{3+} spectrum is magnetically split due to the antiferromagnetic Co^{2+} sublattice. The Fe^{3+} spectrum of the B site remains as a single somewhat broadened line that can be partially split by an external field of 6 kOe. This effect is attributed to slow relaxation of the Fe spin which results from a slight canting of the spins at the A sites. Experimentally one finds $T_N = (33{\cdot}0 \pm 1{\cdot}0)$°K, and the field at the nucleus for the A sites is (438 ± 3) kOe at 0°K. This value for Fe^{3+} in tetrahedral coordination is lower than that found in other spinels. In one sample prepared from different starting materials, some evidence was found for Fe^{2+} at the A sites.

Above T_N, the spectra of ultrafine Co_3O_4 particles, with a diameter of 100 Å, are essentially the same as those of the bulk material. Below T_N, the ultrafine particles display superparamagnetic behavior and the B site spectrum broadening is enhanced. The anisotropy constant estimated from the superparamagnetic-antiferromagnetic transition is 4×10^4 erg/cm^3.

INTRODUCTION

IN A SERIES of recent investigations[1–5] we have made a comparison of bulk and ultrafine magnetically ordered materials using the Mössbauer effect to establish some of their properties. It has been of interest to extend these measurements to Co_3O_4 because of its unusual magnetic exchange interactions. Co_3O_4 has the normal spinel structure. From a study of its magnetic susceptibility, and that of related compounds, Cossee[6] proposed that the Co^{2+} ions occupy the tetrahedral (A) sites and the Co^{3+} ions the octahedral (B) sites. Cossee based his explanation on the Co^{3+} ion having zero moment in a crystal field of octahedral symmetry. Roth [7] extended the susceptibility measurements of Cossee to liquid helium temperatures and showed that a magnetic transition occurred at a Néel temperature, T_N, of about 40°K. In addition, from an extensive neutron diffraction study, he confirmed Cossee's interpretation, established the magnetic structure of Co_3O_4 below T_N, and showed that the magnetic ordering occurred with an unusually high A–A interaction. Roth's analysis showed that below T_N the Co^{2+} ions form an antiferromagnetic sublattice having the diamond structure. The magnetic interactions in Co_3O_4 have been studied by Miyatani, Kohn, Kamimura and Iida[8, 9] by nuclear magnetic resonance.

The Co^{3+} ions are diamagnetic due to the crystal field splitting of the $3d^6$ orbitals ($\Delta \sim 27{,}000°K$) in the octahedral field. This results in a pairing of the electrons in the lower triplet t_{2g} levels leading to a diamagnetic $^1A_1$ state.

On the basis of these results, it is anticipated that the Mössbauer spectrum of ^{57}Fe in Co_3O_4 should consist of two superimposed spectra arising from the A and B sites. Further, in passing through T_N to the antiferromagnetic region, the A site spectrum should split and the B site spectrum remain unchanged. Each spectrum will, of course, depend on the charge state of the ^{57}Fe after electron capture by the parent ^{57}Co. For example, Auger processes could lead to a highly charged Fe ion, although no evidence has yet been found for such states in Mössbauer spectroscopy[5,10], so that these states must decay very rapidly to either the stable Fe^{2+} or Fe^{3+} state. Therefore, in an interpretation of the composite spectrum, one of the problems consists in establishing the valence state at each site after decay. The interpretation must be consistent with the intensity of the A site spectrum being half that of the B site.

Above T_N ultrafine particles of Co_3O_4 are expected to show the same features as the bulk material. Our interest is mainly in their behavior below T_N. For sufficiently small particles superparamagnetism will be observed, the transition from superparamagnetic behavior to antiferromagnetic behavior depending on the particle size and temperature. From Mössbauer studies of such systems information is obtained on relaxation effects and magnetic anisotropy[2] as well as stoichiometry[5].

In this paper we describe Mössbauer spectra on bulk Co_3O_4 doped with ^{57}Co measured from 7·6° to 596°K. Spectra of ultrafine particles above and below T_N are given. The data are analyzed on the basis of the above discussion.

EXPERIMENTAL

Sample preparation

Two samples of bulk Co_3O_4 were prepared by different methods. For the first, the carbonate was precipitated from a solution of cobaltous nitrate, which contained 2 mc of $^{57}Co^{2+}$, with an excess of ammonium carbonate solution. After washing, the carbonate was converted to the oxide by heating in pure flowing oxygen at 850°C for 10 hr. Most of the spectra were obtained on this sample. Only Co_3O_4 lines were present in an X-ray diffraction pattern of an identically prepared sample which contained no radiocobalt. The second sample was prepared by the decomposition of $CoCl_2 \cdot 6H_2O$, doped with $^{57}Co^{2+}$, at 800°C in oxygen for 3 hr. This sample also displayed only Co_3O_4 X-ray lines.

The ultrafine particle samples were made on a high area silica support in the manner described previously for α-Fe_2O_3[2]. The silica gel was impregnated with a solution of cobaltous nitrate which contained $^{57}Co^{2+}$. After drying at 100°C, the samples were calcined at 550°C for 2 hr in air. Two samples containing 11 and 7 per cent Co_3O_4, respectively, were made. For two duplicate nonratioactive samples, X-ray diffraction patterns showed the presence of Co_3O_4 only. Electron microscope studies of thinly sliced sections indicated the majority of particles were in clusters of 10–50 particles. The particles resolved by the microscope ranged from 60–200 Å with 100 Å particles predominating.

Apparatus

The Mössbauer spectrometer used has been described elsewhere[2]. The simple arrangement shown in Fig. 1 was used to control the sample temperature in the dewar tail during measurement. The sample, potted in wax, is mounted in the holder with good thermal contact. The holder is partially thermally insulated from the helium cold finger with a Teflon spacer. The temperature is measured with a copper-constantan thermocouple which is also used to control the temperature. The difference e.m.f. between the thermocouple and a variable bucking voltage is amplified and supplies power to the heater; the control

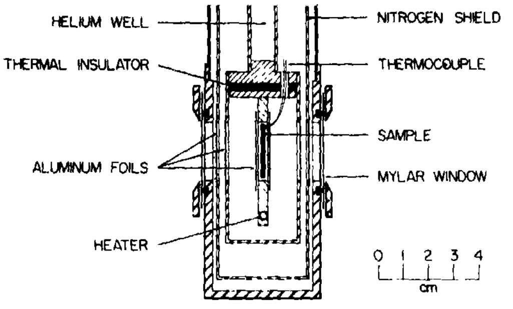

Fig. 1. Arrangement of Mössbauer source in liquid helium dewar tail.

temperature is set by the bucking voltage. This arrangement leads to a temperature stability of ±0·1°C at any point between liquid helium and room temperature with a low helium consumption rate. The absorber used was enriched $Na_4\ Fe(CN)_6 \cdot 10\ H_2O$.

Mössbauer spectra—bulk samples

Some representative spectra taken below and just above T_N for the bulk sample prepared from the carbonate are shown in Fig. 2. It is seen that T_N lies between 25° and 36°K. Below T_N, the spectra consist of an unsplit component, the rather broad center line, and a hyperfine split component.

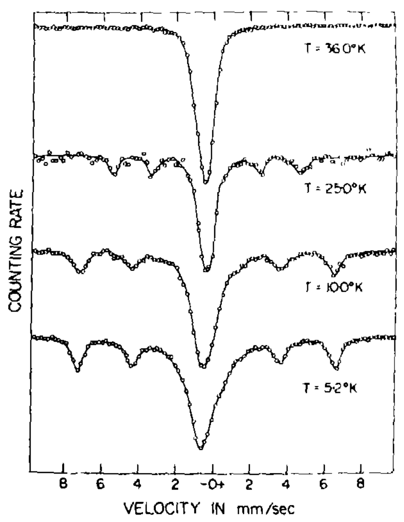

Fig. 2. Low temperature Mössbauer spectra of Co_3O_4 prepared from the carbonate.

In Fig. 3, the field at the nucleus H(O) for the hyperfine split component is plotted against the temperature for all the spectra that were taken. The temperature dependency of H(O) approximates a Brillouin function with $T_N = (33 \cdot 0 \pm 1 \cdot 0)$°K. At 0°K, the field at the nucleus is (438±3) kOe.

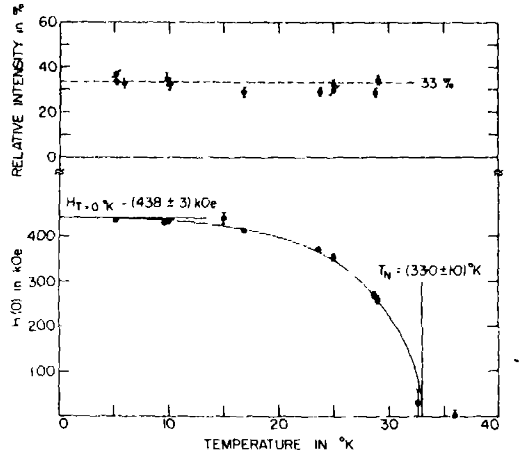

Fig. 3. Relative intensity of hyperfine split component and field at the nucleus versus temperature for bulk Co_3O_4.

Also plotted in Fig. 3 is the ratio I_r of the intensity of the hyperfine split component to the total intensity, the contribution of this component under the center line being calculated from the intensities of the outer lines and the transition probabilities. The ratio $I_r = 0 \cdot 33 \pm 0 \cdot 02$ is in agreement with the conclusions derived from magnetic susceptibility measurements[6]: the hyperfine spectrum arises from the antiferromagnetically coupled *A* sites and the center line from the diamagnetic *B* sites.

In order to ascertain the valence state of the daughter ^{57}Fe, it is necessary to establish the isomer shifts of the spectrum at each site. To make a detailed analysis, a number of spectra were measured above T_N. These spectra were computer analyzed with a least square fit program on the basis of three sets of alternative assumptions. These consisted of taking the spectra to be composed of:

(a) Two unsplit lines with the same half width arising from the *A* and *B* sites. This fit involves six adjustable parameters; the base line, two amplitudes, two line positions, and the width.
(b) Three lines of equal width (eight parameters).
(c) One quadrupole split line pair corresponding to the *B* site and a single line corresponding to the *A* site (8 parameter).
(d) As in (c) with the three lines having the same width (7 parameters).
(e) As in (c) with the three lines having equal area (7 parameters).
(f) As in (c) with the three lines having equal width and area (6 parameters).

In all cases, the line shape was taken to be Lorentzian.

The fit made with the set of assumptions in (e) gave the best representation (lowest Chi-square) of the observed spectra. This fit corresponds to the necessary condition that ⅓ of the cations are at *A* sites having cubic point symmetry and therefore no quadrupole interaction and ⅔ of the atoms are at *B* sites which has trigonal symmetry. An example of the fitting with these assumptions is shown in Fig. 4 for the room temperature spectrum. The solid line through the experimental points is the composite spectrum calculated from the best fit parameters. It shows the degree of exactness of the set of assumptions used. The quadrupole splitting obtained from the *B* site is quite reasonable. The slightly different width of the *A* and *B* site spectrum may be explained by impurities and lattice distortion and is similar to the one found in other spinels and garnets. The results of curve fitting on this basis for all the spectra above T_N are given in Table 1. Included in the table is a set of values for one spectrum below T_N. This shows that the high temperature assignments agree with those obtained from a direct measurement of the shift at the two sites.

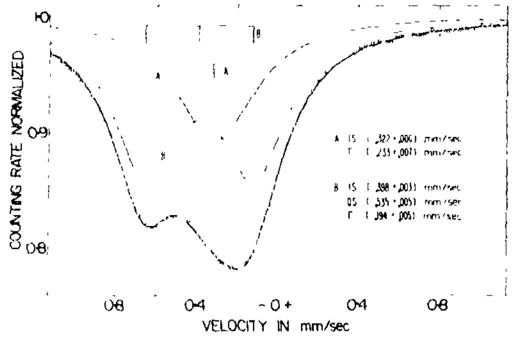

Fig 4. Least square fit of room temperature spectrum of bulk Co_3O_4 on the basis of a quadrupole split line at the *B* site and a single line at the *A* site. Γ is the half width of the Lorentzian curve.

With the isomer shifts established, the

Table 1. Quadrupole splitting and shift for the A *and* B *site of* Co_3O_4 *as a function of temperature*

	Octahedral site		Tetrahedral site
T (°K)	shift[a] (mm/sec)	Q.S. (mm/sec)	shift[a] (mm/sec)
7·6	−0·600 ± 0·050	0·7 ± 0·3[b]	−0·450 ± 0·030
80	−0·506 ± 0·005	0·550 ± 0·010	−0·439 ± 0·010
295	−0·397 ± 0·005	0·536 ± 0·010	−0·323 ± 0·010
476	−0·243 ± 0·005	0·515 ± 0·010	−0·195 ± 0·010
595	−0·184 ± 0·005	0·515 ± 0·010	−0·124 ± 0·010

[a] Relative to a $Na_4Fe(CN)_6 \cdot 10H_2O$ absorber at 295°K. To get values relative to metallic Fe add (+0·057 ± 0·001) mm/sec.

[b] The uncertainty in this value depends on the angles between the magnetic field and the electric field gradient.

valence state of the daughter ^{57}Fe at each site can be determined from a comparison of shifts measured in other oxides. Table 2 gives isomer shifts for divalent and trivalent Fe in bulk NiO, where the valence states are unequivocal[5]. Comparison of the shifts and their temperature dependency given in Table 2 with those listed in Table 1 indicates that the daughter ^{57}Fe in Co_3O_4 at both sites is trivalent. This is the case at all temperatures investigated, in contrast to ^{57}Fe in NiO in which the ratio of $Fe^{2+}:Fe^{3+}$ varies reversibly with the temperature[5].

Table 2. *Isomer shifts of* ^{57}Fe *in* NiO*

Temperature (°K)	Shift relative to $Na_4Fe(CN)_6 \cdot 10H_2O$ at 295°K in mm/sec	
	Fe^{2+}	Fe^{3+}
9	—	$-0{\cdot}53 \pm 0{\cdot}06$
78	$-1{\cdot}2 \pm 0{\cdot}10$	$-0{\cdot}53 \pm 0{\cdot}06$
296	$-1{\cdot}03 \pm 0{\cdot}06$	$-0{\cdot}40 \pm 0{\cdot}06$
433	$-1{\cdot}10 \pm 0{\cdot}08$	$-0{\cdot}29 \pm 0{\cdot}06$
537	—	$-0{\cdot}24 \pm 0{\cdot}04$

*See reference [5].

Mössbauer spectra—ultrafine particles

A room temperature spectrum of the ultrafine particle sample which contained 11 per cent Co_3O_4 is shown in Fig. 5. Here again the least square fit parameters are indicated. Comparison of Fig. 4 with Fig. 5 shows that above T_N ultrafine particle Co_3O_4 gives essentially the same Mössbauer spectrum as bulk Co_3O_4. However, below T_N, there are notable differences between the behavior of particulate and bulk material. This is demonstrated in Fig. 6 (11 per cent Co_3O_4) and Fig. 7

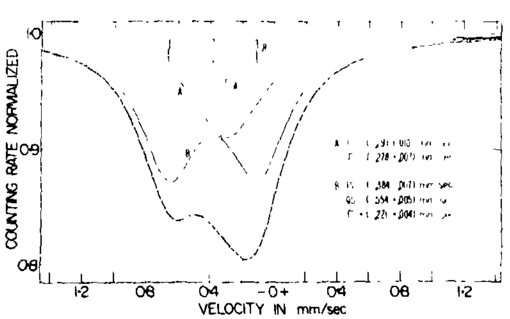

Fig. 5. Least square fit at room temperature of ultrafine particle sample with 11 per cent Co_3O_4.

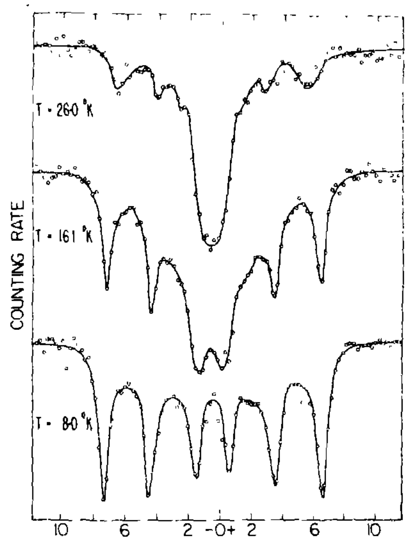

Fig. 6. Mössbauer spectra in the vicinity of T_N; ultrafine particle sample containing 11 per cent Co_3O_4.

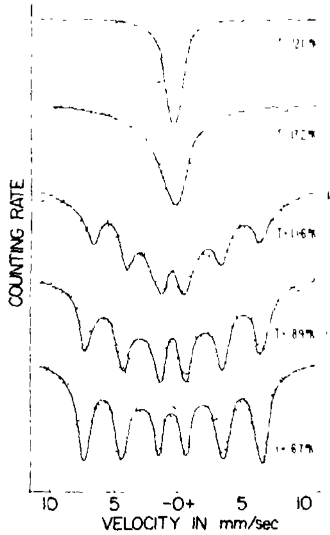

Fig. 7. Mössbauer spectra in the vicinity of T_N; ultrafine particle sample containing 7 per cent Co_3O_4.

(7 per cent Co_3O_4). First, the spectra do not split until temperatures appreciably below T_N are reached. This is a manifestation of superparamagnetic behavior in which thermal fluctuations transfer enough energy to the particle to flip the magnetization vector of the particle. If flipping occurs at a high enough rate then the nucleus experiences zero net field during the Mössbauer event. On this basis, it is evident from the spectra that the 7 per cent Co_3O_4 sample has a smaller average particle diameter than the 11 per cent sample. Second, at the lowest temperature used, the discreet center line seen with bulk Co_3O_4 is not present. In its place is a very broad center line that traverses the whole width of the spectrum. We have observed this effect previously in ultrafine NiO[5], and Ni metal[3], and have attributed it to small particle relaxation effects.

The field at the nucleus and isomer shift for the *A* sites are the same for the ultrafine particles as for the bulk. For example, at 8·0°K, the measured field is (433 ± 3) kOe; and the isomer shift is (−0·41 ± 0·05) mm/sec.

DISCUSSION

The Mössbauer spectra of Co_3O_4 clearly show the two cation sites in the spinel structure and also that the ^{57}Fe ion after decay is trivalent at both sites, at least for the sample prepared from the carbonate. The measured field at the nucleus of 438 kOe for the Fe^{3+} ion in the tetrahedral site appears to be surprisingly low. For example, in a summary of the pertinent Mössbauer and NMR data, Van Loef[12] has shown that the hyperfine fields at ferrite *A* sites are generally close to 500 kOe. At the *B* sites, the field is typically 550 kOe. The lower value of the *A* site field is attributed to a smaller FeO distance in tetrahedral than octahedral coordination. However the relative fields at the two sites also depend on the orientation of the 3 *d* orbitals with respect to the nearest neighbor O-ion. The effect of the orientation is to lead to an increased covalent transfer of O electrons to the Fe 4*s* orbitals of the tetrahedral site.

In Table 3 a comparison is made between the pertinent data for $CuFe_2O_4$[13] and Co_3O_4. From the table it is seen that the field decreases with interatomic distance. This is generally true also for the effect of the interatomic distance on the isomeric shift, but is modified by the orbital orientation effect. Thus, although the interatomic distance of the *A* and *B* site in Co_3O_4 are approximately the same, the isomeric shift at the *A* site is less, which indicates higher covalency. This leads to a lower spin density, and hence lower field at the nucleus. Therefore the Mössbauer data for Co_3O_4 agrees with the conclusions of Van Loef which were based on a study of the ferrites and garnets.

Table 3. *Comparison of Mössbauer data for* Cu $Fe_2O_4$$^{(a)}$ *and* Co_3O_4

	Cu Fe_2O_4		Co_3O_4	
Site	*A*	*B*	*A*	*B*
Interat. Dist. [Å]	1·99	2·18	1·93	1·92
IS [mm/sec]$^{(b)}$	−0·44	−0·61	−0·32	−0·39
H(O)(O°K)[kOe]	505	545	438	—

(a) See reference [13].

(b) The isomer shift is given relative to $Na_4 Fe(CN)_6 \cdot 10 H_2O$.

In Co_3O_4 the Fe^{3+} site spectrum consists of a fairly broad center line below T_N. As the temperature is reduced, the line broadens even further. This seems to be anomalous in that it appears to require some alignment of the daughter ^{57}Fe spins, notwithstanding the fact that the Fe is located in a diamagnetic sublattice. In order to examine this aspect of the results, Mössbauer spectra with and without a magnetic field were taken on the bulk Co_3O_4 sample at 7·6°K. The spectra, given in Fig. 8, show that the application of a field of 5·9 kOe does begin to split the center line. We tentatively attribute this effect to a slight canting of the Co^{2+} spins at the *A* sites. The resultant magnetization produces a field at the *B* site

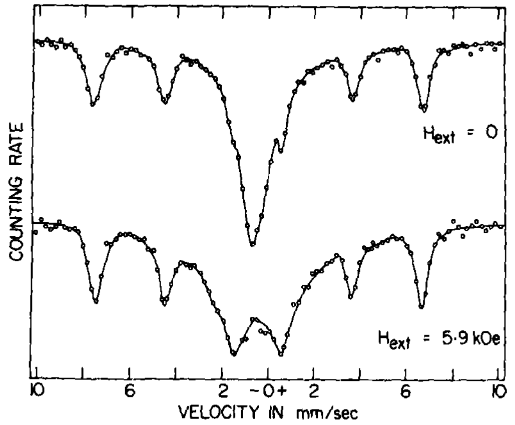

Fig. 8. Mössbauer spectra of bulk Co_3O_4 at 7·6°K with and without an applied external field.

Fe^{3+} tending to align its spin. Some support of this view is suggested by the magnetization measurements on normal Co_3O_4 below T_N given by Roth[7]. At 4·2°K, he reported a residual magnetization σ_0 of 0·041 e.m.u./g and considered that this arose from a small amount of spinel inversion. However, a slight canting of the Co^{2+} spins would also account for it. The broadening is an indication of a slow relaxation process. Using arguments described below it has been estimated that at zero field the relaxation time is 5 nsec, and at 5·9 kOe it is 10 nsec. Turning to the small particles, it then follows that the enhanced broadening of the B site center line can be attributed to a slightly larger canting of the A site spins. For the small particles, the slow transition from the single line to the hyperfine split line at the A site is due to changes in the relaxation time of the antiferromagnetic magnetization vectors. It has been shown by Néel[14] that the relaxation time τ_0 of the magnetization vectors in a small ferro- or antiferromagnetic particle may be written as $\tau_0 = (1/f)\exp(Kv/kT)$, where f is a frequency factor of the order of 10^9 Hz, K is the crystalline anisotropy constant, v the particle volume, and kT the thermal energy. The magnetic hyperfine splitting observed in a Mössbauer experiment depends on the ratio of nuclear Larmor time relative to τ_0. The formal treatment of this motional narrowing has been given by Wickman, Klein and Shirley [5]. Their calculations have been repeated here for the case of a field at the nucleus of 430 kOe and are given in Fig. 9. From a comparison of the curves in this figure to the measured spectra of Fig. 6, it is possible to estimate a kind of average relaxation time of the magnetization vector. For instance, the 16·1°K spectrum indicates that τ_0 is equal to 6 ± 2 nsec. Substitution of this value into the Néel relationship, along with an average particle size of 100 Å, leads to an anisotropy constant K of approximately 10^4 erg/cm^3. Taking ⟨100⟩ as the easy axis yields to a value of K_1 of about 4×10^4 erg/cm^3. This value is an order of magnitude less than that given by Roth[7] for bulk Co_3O_4. The estimation of K_1 from Mössbauer data depends critically on

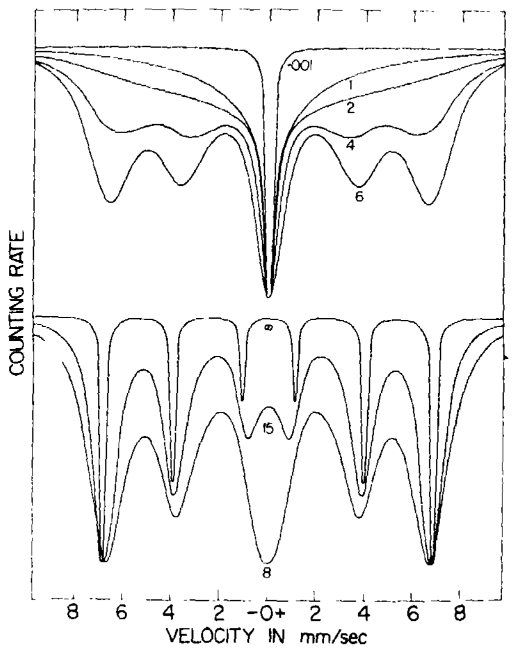

Fig. 9. Computed Mössbaüer spectra for an internal field of 430 kOe at various relaxation times τ. τ is given in nsec.

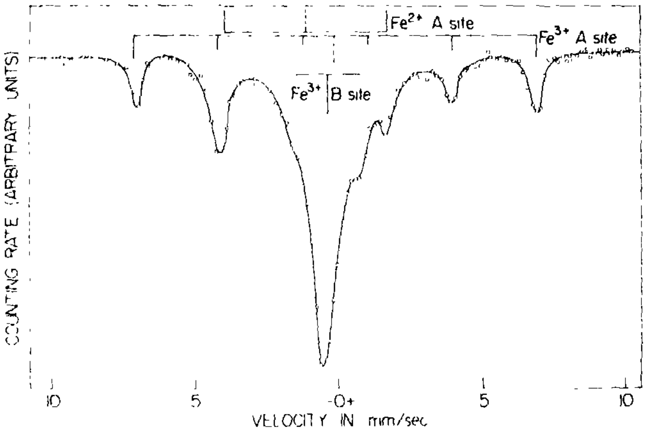

Fig. 10. Mössbauer spectrum at 5°K for bulk Co_3O_4 prepared from the chloride.

the particle volume, possible surface effects, impurities in the small particles, and the assignment of the easy axis of magnetization in the crystal. All these uncertainties may account for the discrepancy from the bulk value. The bulk value of K_1 yields a particle diameter of 50 Å, well outside the observed particle size distribution.

In the case of ^{57}Co-doped nickel oxide, we have shown that the ratio of $Fe^{2+}:Fe^{3+}$ after the decay depends on the method of sample preparation, presumably because of non-stoichiometry[5]. In this work, we have found a similar, but less marked, effect in bulk Co_3O_4. A spectrum taken at 5°K of a sample prepared by decomposition of the chloride is given in Fig. 10. The spectrum is seen to have some extra lines not present in the spectra for the sample derived from the carbonate. The decomposition of the spectrum shown in the figure indicates that this sample has a small amount of Fe^{2+} at the *A* site.

REFERENCES

1. CONSTABARIS G., LINDQUIST R. H. and KUNDIG W., *Appl. Phys. Lett.* **7**, 59 (1965).
2. KÜNDIG W., BÖMMEL H., CONSTABARIS G. and LINDQUIST R. H., *Phys. Rev.* **142**, 327 (1966).
3. LINDQUIST R. H., CONSTABARIS G., KÜNDIG W. and PORTIS A. M., *J. appl. Phys.* **39**, 1001 (1968).
4. KÜNDIG W., ANDO K. J., LINDQUIST R. H. and CONSTABARIS G., *Czech. J. Phys.* **B17**, 467 (1967).
5. ANDO K. J., KÜNDIG W., CONSTABARIS G. and LINDQUIST R. H., *J. Phys. Chem. Solids* **28**, 2291 (1967).
6. COSSEE P., *J. inorg. nucl. Chem.* **8**, 484 (1958).
7. ROTH W. L., *J. Phys. Chem. Solids* **25**, 1 (1964).
8. MIYATANI K., KOHN K., KAMIMURA H. and IIDA S., *J. phys. Soc. Japan* **21**, 464 (1966).
9. KAMIMURA H., *J. phys. Soc. Japan* **21**, 484 (1966).
10. TRIFTHAUSER W. and CRAIG P. P., *Phys. Rev.* **162**, 274 (1967).
11. KÜNDIG W., *Nucl. Inst. Meth.* **48**, 219 (1967).
12. VAN LEOF J. J., *Physica* **32**, 2102 (1966).
13. EVANS B. J., HAFNER S. and KALVIUS G. M., *Phys. Lett.* **23**, 24 (1966).
14. NÉEL L., *J. phys. Soc. Japan* **17**, Suppl. B-1, 676 (1962).
15. WICKMAN H. K., KLEIN M. P. and SHIRLEY D. A., *Phys. Rev.* **152**, 345 (1966).

J. Phys. Chem. Solids Pergamon Press 1969. Vol. 30, pp. 827–832. Printed in Great Britain.

AN H^- IMPURITY IN KBr

M. E. STRIEFLER and S. S. JASWAL
Behlen Laboratory of Physics, University of Nebraska, Lincoln, Nebr. 68508, U.S.A.

(*Received* 13 *June* 1968; *in revised form* 1 *August* 1968)

Abstract – A substitutional H^- (U center) and an interstitial H^- at the $\frac{1}{2}, \frac{1}{2}, \frac{1}{2}$ position in KBr are considered separately. The relaxations of the neighbors of the impurity are calculated The lattice vibration local mode frequencies are computed both for the unrelaxed and relaxed lattice. The computed local mode frequencies are compared with the appropriate experimental results.

1. INTRODUCTION

IN HIS INFRARED absorption studies of H^- ions in alkali halide crystals, Fritz[1] observed a band of frequencies around 1·7–1·9 times the U center frequencies in the corresponding crystals. In KBr, he attributed one of the frequencies ($14{\cdot}9\times 10^{13}$ rad./sec) to an interstitial H^- ion located at the $\frac{1}{2}, \frac{1}{2}, \frac{1}{2}$ position shown in Fig. 1 and the rest of the structure to more complicated defects. An interstitial at the $\frac{1}{2}, \frac{1}{2}, \frac{1}{2}$ position will give rise to triply degenerate local modes. Recently Gross and Bron[2] have also investigated the infrared absorption of this system and they observe three absorption peaks at the frequencies of $(14{\cdot}9, 15{\cdot}8, 16{\cdot}9)\times 10^{13}$ rad./sec. They tentatively propose this absorption to be due to the H^- ion being displaced from the $\frac{1}{2}, \frac{1}{2}, \frac{1}{2}$ position along one of the $\langle 100\rangle$ directions.

In the present work, we consider a U center in KBr and an interstitial H^- at the $\frac{1}{2}, \frac{1}{2}, \frac{1}{2}$ position in KBr separately. In each case we study theoretically the distortion of the lattice and the local mode frequencies due to the impurity. The distortion of the lattice is confined to the nearest neighbors of the U center and nearest and next-nearest neighbors of the interstitial H^-. The displacements of the neighbors, which are assumed radial with respect to the impurity, are computed by minimizing the potential energy of the imperfect crystal. The local mode frequencies for the unrelaxed and relaxed lattice are calculated in the molecular model approximation[3]. The calculated local mode frequencies are compared with the appropriate experimental results.

2. METHOD

The potential energy ϕ of the crystal is treated in the rigid ion approximation. In this case ϕ is the sum of Coulomb, short-range repulsive overlap and Van der Waals parts. The coulomb term is the electrostatic interaction between point ions. The repulsive overlap interaction between ions A and B is approximated by the Huggins–Mayer potential

$$V_{\mathrm{HM}}(r) = \lambda \exp(-r/\rho)$$

where

$$\lambda = b\{1+(Z_A/P_A)+(Z_B/P_B)\}\exp[(r_A+r_B)/\rho]$$

with b, ρ = the empirically determined parameters; $Z_{A,B}$ = the valencies of ions A and B; $P_{A,B}$ = the number of valence electrons in the outer shells of ions A and B, and $r_{A,B}$ = ionic radii of ions A and B.

The Van der Waals potential between the ions A and B is of the form[4]

$$V_{\mathrm{VW}}(r) = -(C_{AB}/r^6)-(D_{AB}/r^8)$$

where

$$C_{AB} = \frac{3h}{2}\frac{\nu_A\nu_B}{\nu_A+\nu_B}\alpha_A\alpha_B$$

$$D_{AB} = \frac{9hC_{AB}}{4e^2}\left[\frac{\nu_A\alpha_A}{P_A}+\frac{\nu_B\alpha_B}{P_B}\right]$$

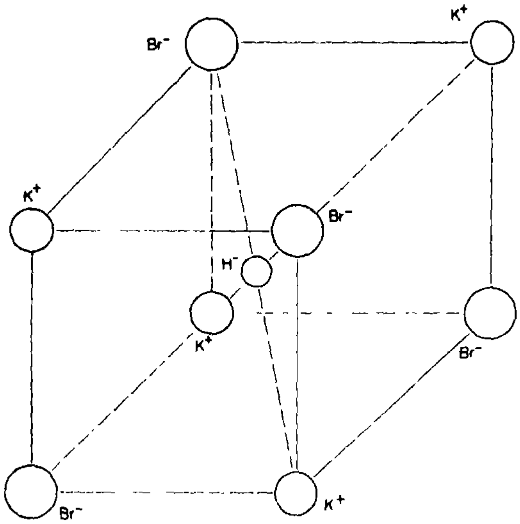

Fig. 1. An interstitial H in KBr.

with ν = the series limit frequency of the discrete spectra of the ion α = the crystal polarisability of the ion, h = Planck's constant, and e = electronic charge.

In the harmonic approximation, the potential energy of the perfect crystal is given by

$$\phi = \phi_0 + \tfrac{1}{2} \sum_{\substack{\alpha l \\ \alpha' l'}} \phi_{\alpha\alpha'}(ll') u_\alpha(l) u_{\alpha'}(l') \qquad (1)$$

where ϕ_0 is the potential energy when ions are at the equilibrium position; u_α (l) is the α-th component of the displacement of the l-th atom from its equilibrium position; and

$$\phi_{\alpha\alpha'}(ll') = \left.\frac{\partial^2 \phi}{\partial u_\alpha(l) \partial u_{\alpha'}(l')}\right|_0$$

is the coefficient evaluated at the equilibrium position in the perfect crystal.

In a lattice with a defect we take the defect as the origin of the coordinate system. If the position vector of undisplaced ion is $\mathbf{r}(l)$, the potential energy of the distorted lattice can be written as

$$\phi' = \sum_l \psi \{r(l) + u(l)\} + \phi \qquad (2)$$

where the first term on the right hand side is the change in the energy due to the defect. The equilibrium configuration of the distorted lattice is determined by minimizing ϕ' with respect to the displacements, i.e. by solving equations

$$\partial \phi' / \partial u_\alpha(l) = 0$$

or

$$\frac{\partial \psi\{r(l) + u(l)\}}{\partial u_\alpha(l)} + \sum_{\alpha' l'} \phi_{\alpha\alpha'}(ll') u_{\alpha'}(l') = 0 \qquad (3)$$

simultaneously. The number of equations is determined by the number of ions displaced from their equilibrium positions in the perfect crystal. In both the problems considered in this work, we assume that the displacements of the neighbors are radial with respect to the impurity. In this case simultaneous equations (3) can be solved analytically if one knows the interaction potential for the system.

The detail of the molecular model used to calculate the local mode frequencies are given in [3]. In this method the equations of motion for the system give the dynamical matrix whose order is determined by the number of degrees of freedom. Once again, one can form the dynamical matrix if one knows the expression for the potential energy. The matrix thus formed is diagonalised to get the local mode frequencies.

Three sets of parameters[5, 6], given in Table 1, are used in the Huggins–Mayer potential for the repulsive overlap interactions. Additional input data required are given in Table 2. The value of r_{H^-} in an alkali hydride can be determined by using the equilibrium condition in that crystal. The values of r_{H^-} used in V_{HM1} and V_{HM2} are obtained by taking the average of r_{H^-} in LiH, NaH and KH. In V_{HM3} the value of the r_{H^-} is that calculated for KH. The nearest neighbor distances in KBr [6], LiH, NaH and KH[9] are 3·298, 2·042, 2·44 and 2·854 Å respectively.

3. *U* CENTER IN KBr

We assume that the overlap repulsive and Van der Waals forces act between the nearest

Table 1. *Huggins–Mayer potentials*

	b (10^{-12} ergs/ion pair)	ρ (Å)	r_{K^+} (Å)	r_{Br^-} (Å)	r_{H^-} (Å)
V_{HM1}	1·00	0·333	1·235	1·560	1·405
V_{HM2}	0·254	0·3394	1·539	1·736	1·511
V_{HM3}	0·338	0·335	1·463	1·716	1·546

*Reference[5].
*Reference[6].

Table 2. *Additional input data**

	Li^+	Na^+	K^+	Br^-	H^-
Polarisability $\alpha(10^{-24}\,cm^3)$	0·029	0·255	1·201	4·130	1·864
Series limit frequency $\nu(10^{15}\,cps)$	13·7	8·55	5·75	2·14	2·13

*Polarisabilities of alkali and halide ions are from [7] while that of H^- ion has been calculated using the Clausius–Mossotti relation in LiH. Series limit frequencies are from [8].

and next-nearest neighbors only. By symmetry, the radial displacements of the nearest neighbors of the impurity (K^+ ions) will be the same and their value is obtained by solving equation (3) analytically. Here ψ determines the change in potential energy when a Br^- ion replaced by an H^- ion. Since the charge remains unchanged, the only changes are in the short-range repulsive and attractive terms. We subtract these contributions due to Br^- ion as included in the perfect crystal potential energy and add the corresponding interactions of the defect with its neighbors. We do not use the series expansion for the latter.

Timusk and Klein[10] have shown that the triply degenerate local mode frequency due to a U center in KBr is essentially due to the vibrations of the impurity in the field of the stationary host lattice. In this case the dynamical matrix is a diagonal 3×3 matrix whose matrix elements are determined by short-range repulsive and attractive forces only. The local mode frequencies are calculated for both the unrelaxed and relaxed lattice.

The displacements of the nearest neighbors of the impurity and the local mode frequencies for the unrelaxed and relaxed lattice are computed for three Huggins–Mayer potentials and the results are given in Table 3. In all the cases nearest neighbors of the impurity are displaced towards it. We see that V_{HM2}, a potential due to Fumi and Tosi[6], gives a local mode frequency for the relaxed lattice which is in very good agreement with the experimental value[11]. (For this potential the inward relaxation of the K^+ ions is 3·7 per cent

Table 3. U *center calculations for various Huggins–Mayer potentials*

	Displacement of a n.n. K^+ ion towards H^- (Å)	Local mode frequency (10^{13} rad./sec) Unrelaxed	Relaxed	Expt.
V_{HM1}	0·099	8·00	9·25	
V_{HM2}	0·122	7·13	8·53	8·37
V_{HM3}	0·107	8·028	9·39	

of the nearest neighbor distance). It is not surprising that the present model works so well for the U center because highly localised U center vibrations are essentially determined by the short range forces. Thus, so far as the calculations of the local mode frequency due to an H^- in KBr are concerned, the present potential with the repulsive part being given by V_{HM2} should be quite a reasonable representation of the interactions in the crystal, so long as the distances of the H^- from its nearest neighbors are of the same order as those of the U center.

4. AN INTERSTITIAL H^- IN KBr

Once again we assume that the repulsive and Van der Waals forces act between the nearest and the next-nearest neighbors. The radial displacements of the neighbors of the impurity are considered in two approximations: (a) the relaxations of the nearest neighbors only, (b) the relaxations of the nearest and next-nearest neighbors only. Equation (3) gives us two simultaneous equations in the former case and four in the latter case. In each case the simultaneous equations are solved numerically to determine the relaxed positions of the neighbors.

The computed results for the relaxations of the neighbors for the three potentials are given in Tables 4 and 5. In both the approximations K^+ ions are displaced towards the impurity while Br^- ions are displaced away from it. In (a) the cartezian component of the K^+ displacement is ~6 per cent of the nearest neighbor distance while the corresponding quantity for Br^- is ~8 per cent of the nearest neighbor distance. In (b) the nearest neighbor displacements are somewhat reduced while the largest components of second-neighbor displacements, which are of the order of the displacements themselves, are ~2 per cent of the nearest neighbor distance. Thus we can safely neglect the displacements of the further neighbors in the local mode calculations.

Here also the local mode is triply degenerate. The order of the dynamical matrix to be diagonalised is equal to the number of degrees of freedom. If we let the impurity and its eight neighbors vibrate, the 27×27 dynamical matrix is made up of Coulomb and short-range repulsive and attractive parts. However, if only the impurity ion is vibrating in the field of the static lattice, we get a 3×3 diagonal matrix which is determined by the short-range repulsive and attractive forces only. We find that the local mode frequencies in these two cases differ by less than 1 per cent. Thus the approximation that only the impurity vibrates while the rest of the ions are held fixed is even better here than in the last section and our local-mode frequency calculations are based on this approximation.

The computed values of the local mode frequency for the three potentials are given in Tables 4 and 5. The contribution of the second neighbor interactions to the local mode frequency is negligible. We note that as the crystal relaxes, the local mode frequency increases. Another interesting point is that

*Table 4. Calculations for an interstitial H^- for various Huggins–Mayer potentials in the nearest neighbor approximation**

	Displacements of nearest neighbors (Å)		Local mode frequency (10^{13} rad./sec)		
	K^+	Br^-	Unrelaxed	Relaxed	Expt.
V_{HM1}	−0·294	0·502	19·38	20·07	
V_{HM2}	−0·360	0·473	14·71	18·65	14·9†
V_{HM3}	−0·294	0·485	17·94	19·83	

*Positive displacements are away from the impurity and negative displacements are towards it.

†Reference[1].

*Table 5. Calculations for an interstitial H^- for various Huggins–Mayer potentials in the next-nearest neighbor approximation**

	Displacements (Å)				Local mode frequency (10^{13} rad./sec)		
	Nearest neighbors		Next nearest neighbors				
	K^+	Br^-	K^+	Br^-	Unrelaxed	Relaxed	Expt.
V_{HM1}	−0·260	0·464	−0·063	0·070	19·38	19·39	
V_{HM2}	−0·327	0·438	−0·053	0·063	14·71	18·02	14·9†
V_{HM3}	−0·260	0·454	−0·050	0·070	17·94	19·09	

*Positive displacements are away from the impurity and negative ones are towards it.
†Reference [1].

after relaxation the contribution of the H^--K^+ interactions to the local mode frequency is of the order of 93 per cent. Thus the accuracy of our calculated local mode frequency depends essentially on the accuracy of the H^-–K^+ interactions. We saw in the last section that V_{HM2} is a good representation of the short range interactions when the distances are of the order of perfect crystal spacings. In the present case H^-–K^+ distance is somewhat smaller than the nearest neighbor distance in KBr. Thus the short range potential may be somewhat harder than V_{HM2}. Unfortunately we are not in a position to estimate this effect quantitatively. However, we do not expect it to be very much different from V_{HM2}. Since potentials V_{HM1} and V_{HM3} are quite similar and somewhat harder than V_{HM2}, either one of them may be a better potential for the interstitial. Thus V_{HM2} determines the lower limit to the local mode frequency due to an interstitial H^- in KBr and the actual frequency is probably closer to the one given by either one of the other potentials. Comparing Tables 4 and 5 we find that the local mode frequency is somewhat lowered when we let the next-nearest neighbors of the impurity relax. As pointed out earlier the approximation (b) should be quite good for the local mode frequency. We note from Table 5 that the local mode frequency of the relaxed crystal for all the repulsive potentials are quite high as compared to the frequency that Fritz attributed to an interstitial H^- in KBr.

5. CONCLUSIONS

Our calculations for the *U* center in KBr show that repulsive potential V_{HM2} predicts the experimentally observed local mode frequency within 2 per cent after the nearest neighbors of the impurity have relaxed to their new equilibrium positions. (The relaxation of K^+ ions towards the impurity is 3·7 per cent of the nearest neighbor distance in KBr.) Such a good agreement on the basis of the present model is not surprising because the highly localised *U* center vibrations are essentially determined by the short range forces.

In the case of an interstitial H^- ion at the ½, ½, ½ position in KBr, the nearest and next-nearest neighbor Br^- ions relax away from the impurity while the corresponding K^+ ions relax towards it. Since the next-nearest neighbor relaxations are quite small, one can neglect the distortion of further neighbors for the purpose of local-mode frequency calculations. After relaxation most of the contributions to the local mode frequency come from the nearest-neighbor H^-–K^+ interactions. Thus the accuracy of the calculated frequency depends essentially on the accuracy of these interactions. Since the H^-–K^+ separation here is somewhat smaller than the nearest neighbor distance in KBr, the actual repulsive potential may be somewhat harder than V_{HM2}; perhaps it is more like the potential V_{HM1} or V_{HM3}. Thus the local mode frequency due to an interstitial H^- is either $18{\cdot}0 \times 10^{13}$ rad./sec or somewhat higher. This is about 20 per cent or more higher than the frequency that Fritz attributed to an interstitial H^- in KBr. Thus the present calculations indicate that none of the observed infrared absorption peaks may be due to a simple H^- interstitial at the $\frac{1}{2}, \frac{1}{2}, \frac{1}{2}$ position but due to more complicated defects. This conclusion is similar to that of Gross and Bron except that we do not know whether their proposed model is correct.

REFERENCES

1. FRITZ B., *J. Phys. Chem. Solids* **23**, 375 (1962).
2. GROSS U. and BRON W., *Phys. Lett.* **25A**, 312 (1967).
3. JASWAL S. S., *Phys. Rev.* **140**, A687 (1965).
4. LONDON F., *Z. Phys. Chem.* **11B**, 222 (1930).
5. BORN M. and HUANG K., *Dynamical Theory of Crystal Lattices*. Clarendon Press, Oxford (1954).
6. FUMI F. G. and TOSI M. P., *J. Phys. Chem. Solids* **25**, 31 (1964); TOSI M. P. and FUMI F. G., *J. Phys. Chem. Solids* **25**, 45 (1964).
7. KARO A. M. and HARDY J. R., *Phys. Rev.* **129**, 2024 (1963).
8. SMART C., Ph.D. Thesis, University of London (1962) Unpublished.
9. GUNN S. and GREEN L., *J. Am. chem. Soc.* **80**, 4782 (1958).
10. TIMUSK T. and KLEIN M. V., *Phys. Rev.* **141**, 664 (1966).
11. BARTH W. and FRITZ B., *Phys. Status Solidi* **19**, 515 (1967).

J. Phys. Chem. Solids Pergamon Press 1969. Vol. 30, pp. 833–844. Printed in Great Britain.

PHOTOELECTRONIC PROPERTIES OF SYNTHETIC MERCURY SULPHIDE CRYSTALS*

G. G. ROBERTS,† E. L. LIND and E. A. DAVIS‡
Research Laboratories, Xerox Corporation, Webster, N.Y. 14603, U.S.A.

(*Received* 23 *May* 1968; *in revised form* 11 *July* 1968)

Abstract – Experimental studies have been made of the photoelectronic properties of mercury sulphide crystals grown in an argon atmosphere by a slow convection technique. Peak photoconductivity for HgS ($\rho \sim 10^{12}\,\Omega$ cm) occurred at ~ 6000 Å at room temperature; the temperature coefficient of the edge being -9×10^{-4} eV/deg. Emphasis is placed on the techniques of space charge conduction and quenching of photoconductivity which have been used to determine the location of localized levels in the energy gap. Results indicate that some degree of compensation is present in HgS. Combined measurements of thermally activated ohmic and space charge limited conduction yield dominant electron and hole levels 0·62 and 1·08 eV, respectively, from the conduction band while the two band quenching spectra (characteristic of other II-VI semiconductors) show thresholds for optical quenching at 0·67 and 1·08 eV. Some results are also presented for crystals grown in the absence of any gas at 300°C but doped with the elements Ag, In and Cu.

INTRODUCTION

EXTENSIVE literature exists concerning the optical and electrical properties of several group II–VI compounds possessing either the zinc blende or wurtzite structure[1]. However, very little information is available describing the properties of single crystal mercury sulphide whose stable form at room temperature has $D_3{}^4$ symmetry. HgS is therefore the diatomic analogue of the trigonal elemental semiconductors, Se and Te. The preparation in this laboratory of thin single crystals of HgS has enabled us to investigate how this material fits into the general energy configuration picture for II–VI compounds and to determine the effect, if any, of the different crystal structure.

Trigonal mercury sulphide (αHgS) consists of parallel helical chains of alternating Hg and S atoms which spiral around axes parallel to the crystallographic, *c*-axis[2]. At approximately 280°C, the trigonal modification undergoes a polymorphic transformation to the cubic form. We have confined our investigation to αHgS; results are presented for samples grown by two different techniques.

To date the majority of the detailed measurements on HgS have been carried out on natural samples (cinnabar). The early work of Gudden and Pohl[3] has only recently been supplemented by photo-Hall measurements[4] which showed samples to be *n*-type with a mobility ~30 cm^2/Vsec, and cathodoluminescence studies[5]. Zallen, in a recent publication[6], reported on a study of electronic interband transitions in natural HgS crystals. His optical measurements revealed a pronounced dichroism at the fundamental absorption edge, interpreted as a consequence of the polarization-dependent selection rules for trigonal symmetry. The few reports on synthetic crystals of HgS that have appeared in the literature have been confined mainly to measurements on highly doped crystals ($\rho \sim 10^9\,\Omega$ cm). The impetus for these investigations appears to have stemmed from the growth of solid solutions of HgS$_x$Se$_{1-x}$ and the subsequent study of the semiconductor-semimetal transition[7]. In this paper we report the first comprehensive study of the steady state photoelectric properties of high resistivity ($\rho \sim 10^{12}\,\Omega\,\mathrm{cm}$) synthetic HgS. Some emphasis is placed on the techniques of space charge conduction and optical and thermal quenching of photoconductivity which have been used to determine the location of localized levels in the energy gap. Some results are also presented for crystals doped with elements such as silver, copper and indium.

---

*Preliminary results presented at the Boston, February, 1968, A.P.S. Meeting.

†*Present address:* Physics Department, The New University of Ulster, Coleraine, Co. Londonderry, Northern Ireland.

‡*Present address:* Department of Surface Physics, Cavendish Laboratory, Cambridge, England.

PREPARATION OF CRYSTALS

Undoped crystals of HgS were grown by a slow convection technique in an argon atmosphere. Quartz ampoules containing polycrystalline HgS prepared by reaction from the elements were sealed with argon at room temperature at a pressure of 200–400 mms Hg. The ampoule was then placed in a horizontal furnace for periods up to ten days with the charge end at 300–330°C and the crystal growth end at 270–280°C. Crystal growth thus occurred at temperatures below the polymorphic transition temperature of HgS[8]. The crystals obtained were of mm dimensions. A semi-quantitative spectrographic analysis indicated the absence of metallic impurities of concentration greater than 10 parts in 10^6.

While the argon sublimation technique was suitable for pure material, it could not be used for doping with heavy metals since the vapour pressures of the sulphides of these elements are so low relative to the vapour pressure of HgS. For HgS doped with Ag, Cu and In, these elements were sealed in heavy wall quartz ampoules with pure Hg and S under vacuum. The ampoule was placed in a vertical furnace and heated to 450°C over 8 hr and held at 450°C for 16 hr. Reaction at this point was essentially complete and the temperature measured at the bottom of the ampoule was raised rapidly to 700°C. The gradient was so arranged that the upper end of the ampoule was at approximately 300°C. Under these conditions, platelet type crystals grew in the upper part of the ampoules in 3 days. Heavy doping of the charge (0·5–1 per cent) with Cu, In and Ag, resulted in crystals with at most, a few parts per million of dopant. Thermal probe measurements indicated that conduction was *n*-type in all samples.

Bismuth, indium and nickel electrodes, all of which gave good noise free ohmic contacts, were evaporated at a pressure of about 10^{-6} Torr. The crystals were mounted on small teflon plugs which fitted conveniently into a helium exchange gas cryostat. The temperature in the cryostat could be controlled to better than 1°K between 77°–400°K. All measurements were carried out for current flow in a direction perpendicular to the crystalline *c*-axis using a sandwich type configuration. Spectral response and infra-red quenching measurements were made using a Bausch and Lomb grating monochromator and a tungsten (quartz-iodine) light source plus suitable filters (calibrated to give a constant flux of 2×10^{12} ph/cm^2/sec. using a thermopile).

UNDOPED SAMPLES

Photoconductivity

Synthetic undoped HgS, whose crystal growth is described above, has a resistivity of about $10^{12}\,\Omega\,\mathrm{cm}$, the same as that of natural samples. For this reason we concentrated our experimental study on the photoelectronic properties of these particular crystals which were grown in an argon atmosphere by a sublimation technique.

In Fig. 1 we have compared the room temperature photoconductivity and optical transmission to unpolarized light of a 0·8 mm thick HgS crystal. The dark current contribution to the conductivity was eliminated by using a.c. excitation and synchronous detection. The transmission cutoff at about 6000 Å corresponds to a room temperature band gap (E_g) of approximately 2·0 eV. In Fig. 2 the

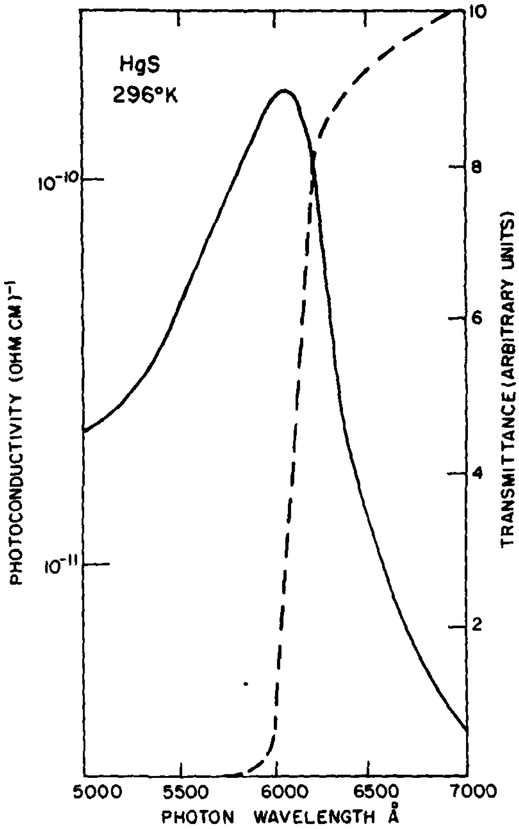

Fig. 1. Comparison of spectral response of photoconductivity (full curve) and transmittance (dotted curve) for undoped crystal of HgS at room temperature.

peak energy of photoconductivity using unpolarized light is plotted as a function of temperature. The linear variation gives $\delta E_g/\delta T = -9\times 10^{-4}$ eV/deg, which compares favourably with the value -8×10^{-4} eV/deg quoted by Dovgii and Bilen'kii[9] for unpolarized light and Zallen[6] for light polarized with $E \perp c$, and the value -9×10^{-4} eV/deg determined from a diffuse reflectivity spectral analysis by Gross and Kreingol'd[10].

Using the standard expressions for the photoconductive gain[11], G, and assuming unit quantum efficiency,

$$G = \frac{\Delta I}{\mathrm{Fe}} = \frac{\mu\tau V}{L^2} \quad (1)$$

where ΔI is the photocurrent and F is the total number of electron-hole pairs created in the photoconductor per second, we calculate $\mu\tau = 2\times 10^{-6}$ cm^2/V. Taking a mobility value of 10 cm^2/Vsec, an electron lifetime $\tau = 2\times 10^{-7}$ sec is obtained.

No structure in the photoconductivity due to impurities or higher energy transitions was observed for the undoped crystals but an interesting variation with temperature was observed below approximately 160°K. This behaviour, namely a decrease in the total photocurrent with increasing temperature, has been previously noted in HgS by Butsko [12] and is shown in the inset to Fig. 6. A suitable choice of wavelength of the incident light eliminates the possibility that the edge shift is causing the effect. It is probably associated with either a change in the $\mu\tau$ product or the variation in the surface recombination.

Space charge conduction

A well defined field of study has developed in connection with electronic currents produced by space charges injected into a wide band gap semiconductor at one or both electrodes[13, 14]. A basic requirement for such a flow of injected carriers to take place and be detected is that the contribution

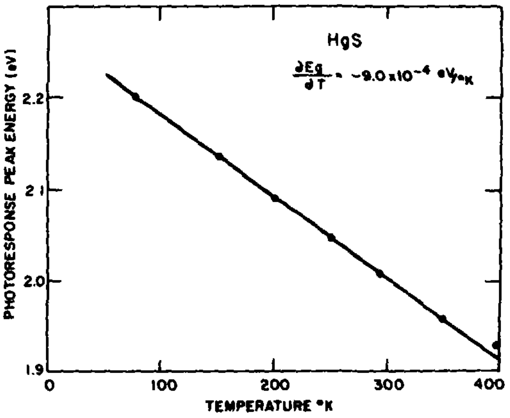

Fig. 2. Variation of HgS photoconductivity peak energy with temperature giving $\partial Eg/\partial T = -9{\cdot}0\times 10^{-4}$ eV/deg.

of thermally generated carriers be small. Another stringent condition for space charge conduction is that the electrodes furnish ohmic contacts to the material. Both these requirements are satisfied for HgS with evaporated indium electrodes and Fig. 3 presents the first report of space charge limited currents (SCLC) in this compound.

The complete treatment of current flow in a metal-semiconductor-metal system is so complex that no explicit expressions have yet been obtained relating the current and voltage. Approximations based on reasonable assumptions have necessarily been introduced and it is found that one would expect the following power relationship between current, voltage and thickness for a true space charge limited current,

$$J = \frac{9}{32\pi}\mu\kappa\frac{V^2}{L^3} \tag{2}$$

where μ is the mobility and κ the dielectric constant.

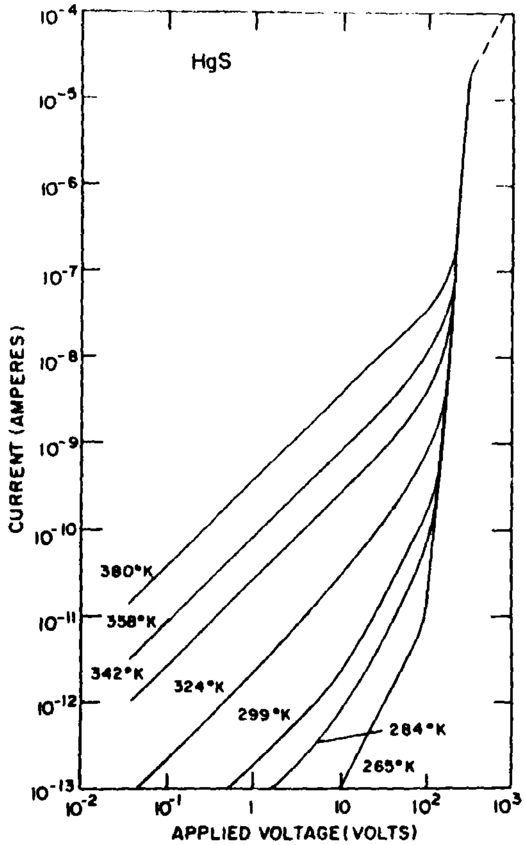

Fig. 3. Current-voltage curves at several different temperatures for undoped single crystal HgS: $L = 0{\cdot}15$ mm; electrode area $= 4{\cdot}5$ mm^2.

One general result of these theoretical investigations is that the introduction of deep trapping centres into the forbidden band usually results in a higher power dependence of current on voltage than the square law relation above. It is evident that as more and more electrons are injected into a solid, the traps will gradually fill up and eventually no further injected electrons can be trapped. The first approximate treatment of this problem was by Lampert[15] who neglected diffusion and considered a single deep trapping level together with the conduction band. By making these simplifying assumptions he was able to show that the $\log J$ vs. $\log V$ curve following a low field ohmic region should consist of three parts: a space charge current region lowered by the presence of traps, followed by an almost vertical rise through several orders of magnitude and finally a high current region showing the characteristic square law dependence of current with voltage[16, 17], which may or may not be a trap free SCLC. We see that the curves in Fig. 3 conform to this general picture (experimentally well defined square law regions tend to be obscured in this plot by the wide current and voltage range presented). Unfortunately, all the crystals of HgS available were approximately of the same thickness and therefore no systematic variation of the thickness of the material was possible to confirm the L^3 law. Although this would have been highly desirable we feel that the general features of the curves prohibit an analysis in terms of any other known effects.

The value of the critical applied potential at which the current increases rapidly, corresponds to the filling of traps and can be related to the trap density, N_m, in the solid by the expression

$$V_T = \frac{eL^2}{2\kappa} N_m. \tag{3}$$

The complete problem can be treated numerically[18] and it is thus possible to assess the accuracy of Lampert's[15] simplified expression that neglects diffusion effects. For the crystal parameters appropriate to HgS we find it is a good approximation to ignore diffusion. Equation (2) then gives a trap density $N_m = 10^{13}\,\mathrm{cm}^{-3}$ while the high field square law region may be analyzed to give $\mu = 7\,\mathrm{cm}^2/\mathrm{Vsec}$. This value for the microscopic mobility compares favourably with that obtained from transient space charge measurements made on natural samples of HgS[19]. The discrepancy with the photo Hall value[4] may be attributed to the anisotropy of HgS.

In a recent publication[20] it has been shown that the combination of measurements of SCLC and ohmic conduction can be an effective technique for locating localized levels in a wide band gap material but measurements of ohmic conduction alone are insufficient for unambiguous interpretation. Schmidlin and Roberts[20] show that a simple empirical activation energy (if it exists) for ohmic conduction in a compensated material should be interpreted as half the energy required to raise an electron from a 'dominant' hole level to a 'dominant' electron level, plus the energy required to raise an electron from the 'dominant' electron level to the conduction band (or the equivalent situation for holes). They conclude that a sufficient condition for a material to be non-extrinsic is that the activation energies for ohmic and SCL conduction be different. A transition voltage, $V_{\Omega c}$, at which the current converts from ohmic to SCL behaviour can be defined by equating the two currents. It is clear that this voltage will have a thermal activation energy equal to the difference between the activation energies for the ohmic and SCL regions. Accordingly it is equivalent to say that a temperature dependent $V_{\Omega c}$ implies a sample which is either compensated or intrinsic. Figure 4(a) shows log J vs. $10^3/T$ plots for $V = 2$ V where the current is ohmic and $V = 100$ V where the current is SCL, the respective activation energies being 0·85 and 0·62 eV. From the latter activation energy we conclude that the trap which can be filled by injected charge lies at an energy distance 0·62 eV from the conduction band. Figure 4b shows that the activation energy for the transition voltage, $V_{\Omega c}$, is approximately equal to the difference between the two individual energies shown in Fig. 4(a). The material is thus non-extrinsic and therefore the activation energy value, 0·85 eV, for the ohmic region is indicative of a compensated level at an energy depth $E_c - E_q = 2 \times 0{\cdot}85 - 0{\cdot}62 = 1{\cdot}08$ eV from the conduction band. Results presented later in this paper also indicate that the material is compensated and confirm the presence of an energy level at this position. Further application of the theory[20] yields the density of the deep trap, N_q, to be $10^{16}\,\mathrm{cm}^{-3}$ and $\mu = 10\,\mathrm{cm}^2/\mathrm{Vsec}$. The latter is consistent with the value deduced from the 'traps filled' region.

Optical quenching

The models favoured for the explanation of high photosensitivity and quenching of photoconductivity in various compounds have been summarized by Bube[21]. The sensitizing process is dependent on there existing within the material a class of centres that have a large capture cross section for a hole when occupied by an electron and a subsequent small cross section of a trapped hole for a free electron. Below temperatures at which holes are thermally freed from sensitizing centres, optical quenching, corresponding to excitation from the valence band to the sensitizing centres, can result in an

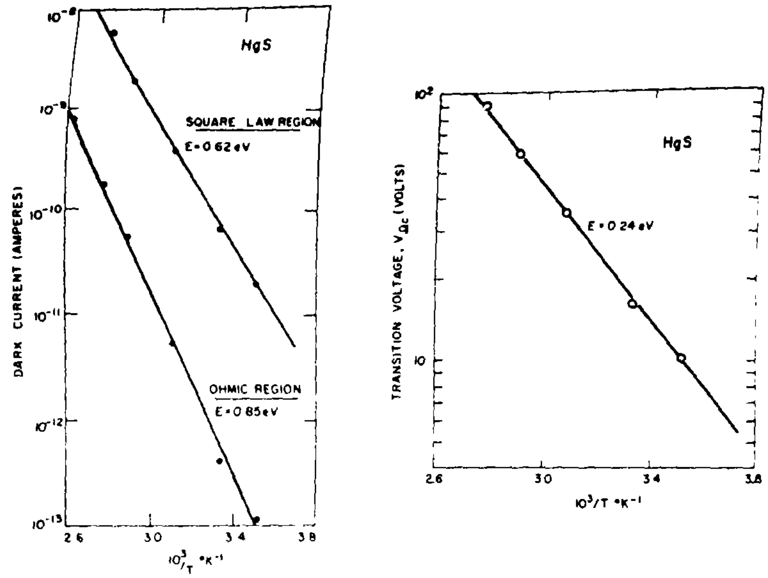

(a) (b)

Fig. 4. (a) Variation of current with temperature for $V = 2$V (ohmic region) and $V = 100$ V (square law region) for HgS crystal described in Fig. 3. (b) Variation of transition voltage, V_{tr}, with temperature for curves shown in Fig. 3.

attenuation of the photocurrent. The typical transient behaviour usually found in HgS crystals at 77°K is shown in Fig. 5. The sample is illuminated by light of wavelength near the absorption edge of the material (in our case 5660 Å) producing a certain bias photocurrent. When a second source is allowed to illuminate the sample it is seen that the dynamic current variation depends on the wavelength of the secondary radiation. For wavelengths less than about 1·5 μ, the light produces both excitation and quenching of photoconductivity while for wavelengths greater than this only quenching is found. The imbalance between excitation and quenching accounts for the initial maximum and minimum when the secondary radiation is turned on and off respectively. (A theory describing the dynamic effect of the different electron transitions induced by the quenching agent has been developed by Matossi[22].) We note that the time required to reach an equilibrium state is an order of magnitude longer than that reported for CdS[23]. Using the standard definition of percentage quenching, Q, as the ratio of the difference between the maximum current and the long time steady current, with the secondary radiation on, and the bias current, we show in Fig. 6 the quenching spectrum for HgS. A similar dynamic characteristic for HgS was reported previously by Shneider[24] but no systematic variation with temperature, intensity or wavelength was undertaken. It may be seen that, despite its different crystal structure, HgS exhibits the characteristic two band quenching spectra observed for other II–VI compounds[21]. The lower energy threshold can be fixed at 0·67 eV while the upper energy threshold is less clearly defined due to the overlap of bands but lies at approximately 1·08 eV (Lashkarev and Rybalka[25] investigated doped HgS crystals and reported the lower quenching energy for Cu doped

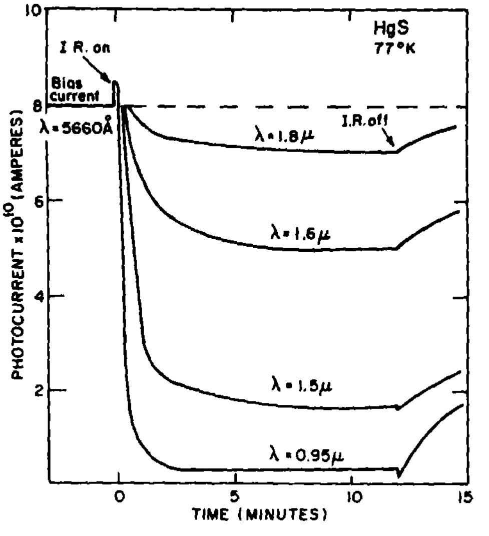

Fig. 5. Dynamic quenching curves for an HgS undoped crystal at 77°K for several secondary radiation wavelengths.

samples and the higher quenching energy for Ag doped samples). The dotted lines for high photon energies in the secondary radiation indicate a decrease in the percentage quenching due to competing excitation effects. It was thought that as two levels were participating in the quenching, an intermediate value of $\lambda = 1{\cdot}15\,\mu$, might produce two distinct slopes in a plot of log Q vs. time. However the smooth nature of the curve obtained indicated that the two centres remain in equilibrium throughout the quenching process. The variation of i.r. quenching with temperature is also shown in Fig. 6. The temperature range is necessarily limited due to the onset of thermal quenching. We note that both quenching peaks vanish simultaneously, the ratio of the peak maxima being the same for each temperature. The inset shows the temperature variation of the unquenched photocurrent, measured at an intensity which gave a conductivity at 77°K equal to that used in the quenching measurements. The quenching was also studied as a function of increasing primary light intensity. Conventional behaviour was obtained i.e., as the bias current, which is a measure of the light intensity, increased the quenching decreased.

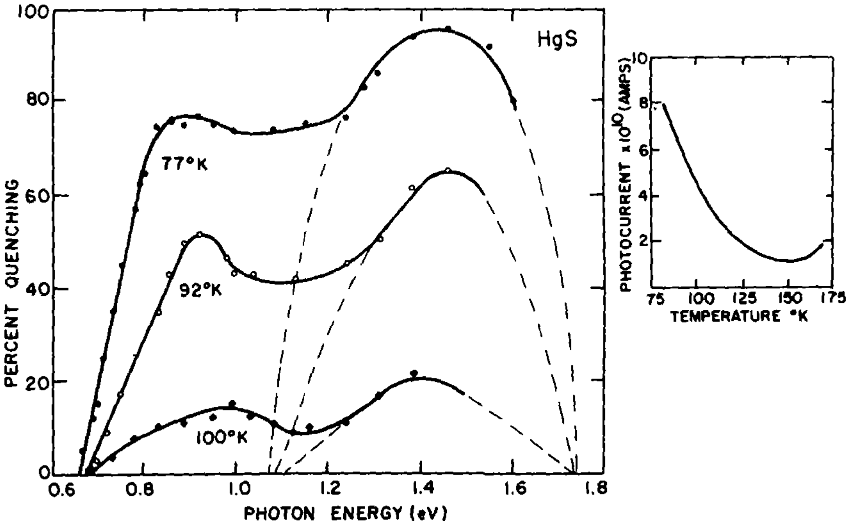

Fig. 6. Infra-red quenching spectra at three different temperatures for undoped HgS. The curve in the inset shows the temperature dependence of the photocurrent at constant primary radiation intensity.

It is instructive to compare the two quenching levels we observe with those reported in other II–VI compounds. In CdS[23], as for ZnS[26], two characteristic optical quenching levels are observed but in both cases the lower energy quenching band vanishes at lower temperatures implying a thermal step in this process. Hence the favoured interpretation of the lower energy spectrum found in these compounds is that it represents quenching from the valence band to the sensitizing centre. Two band quenching spectra have also been reported for some samples of ZnSe and CdSe. For these materials the temperature dependences of the quenching peaks suggest that the energies involved represent actual energy distances between the valence band and the sensitizing centres. However, it is generally believed that in these two compounds, the sensitization is associated with specific impurities or preparation conditions[26].

It would, of course, be desirable to see if the lower energy quenching band in HgS persists for temperatures below 77°K. However our experimental arrangement does not permit measurements to be carried out below liquid nitrogen temperature. It is interesting to note however that if one interprets the quenching spectra of HgS in the same way as those of CdS and ZnS then one arrives at almost the same two characteristic energies reported for these two materials. If this interpretation is correct, the important values for HgS are the maximum of the lower energy quenching band, 0·86 eV, and the threshold of the higher energy quenching band, 1·08 eV.

Thermal quenching

The thermal quenching experiment consists of looking at the photoconductivity as a function of temperature for different light intensities. In our case the intensity of the light was adjusted using neutral density filters in conjunction with a band pass filter in the region of the absorption edge. A typical set of curves is shown in Fig. 7. Compared to a material like CdS, the quenching in HgS is much feebler and, in order to emphasize that

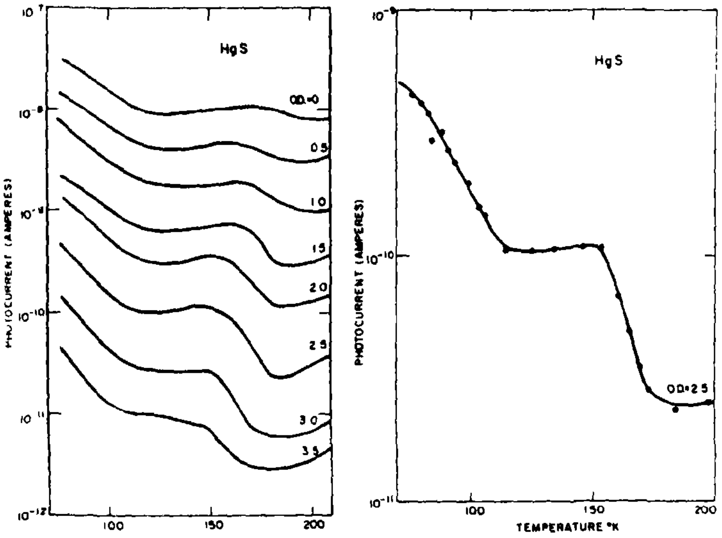

Fig. 7 (a) Photocurrent as a function of temperature for different levels of light intensity for undoped HgS crystal. (b) Photocurrent versus temperature for curve with an optical density of 2·5 in (a).

well defined break points do exist for this material, the curve for an optical density of 2·5 is redrawn in Fig. 7. Two thermal quenching regions are apparent. Following an approximate rate equation analysis by Bube[21], the energy of the lower quenching level can be determined from the first break to low sensitivity occurring near 100°K, while for the upper energy level one has the choice of looking either at the break from high sensitivity or the second break to low sensitivity as a function of temperature. The right hand curve in Fig. 8 shows that a well defined activation energy, 0·60 eV, is obtainable for the level closer to one of the bands. The left hand plots in Fig. 8 yield activation energies, 0·84 and 0·88 eV, which should of course, be equal, for the second quenching level.

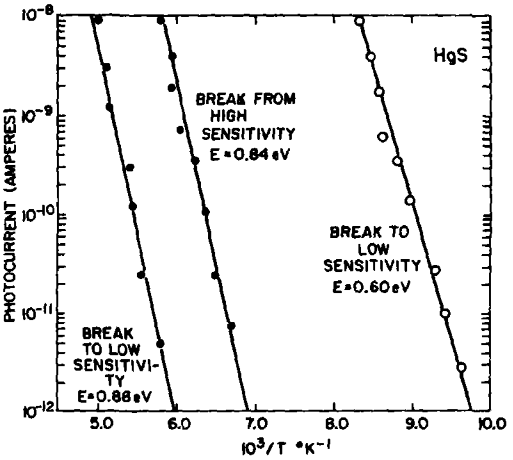

Fig. 8. The photocurrents at the break-point from high sensitivity and the two break-points to low sensitivity as a function of the temperature at which these break-points occur for the data in Fig. 7.

It would be tempting to relate the energies obtained from thermal quenching with those deduced from the optical quenching studies. However, thermal quenching associated with levels lying 0·86 and 1·08 eV above the valence band would be expected to be observed *above* room temperature. In CdS for example, for normal excitation intensities thermal quenching occurs $\sim$100°C. For HgS, the thermal quenching is complete below 200°K and this indicates that the sensitizing centres involved are different from those responsible for the optical quenching. It must therefore be construed that the attenuation of the photocurrent as the temperature is increased from 77°K is a consequence of electron traps at the approximate energy locations deduced from the rate equation analysis.

Doped samples

Some of the measurements on doped samples provide added confirmation to the conclusions arrived at earlier concerning the undoped samples. Figure 9 illustrates the dark current as a function of temperature for several different samples of HgS. For comparison, the activation energy for an undoped sample grown in an argon atmosphere is also shown in the same diagram. These results represent the average values obtained for several samples; the linearity over many decades should be emphasized. Although Ag and Cu might be expected to produce acceptor type impurities and In to produce a donor type impurity in HgS, it may be seen that there is only a slight difference in conductivity between the three types of samples. This tends to support the fact established from the space charge conduction measurements that compensation could be operative in these crystals. It appears that, in common with other II–VI compounds, there exists a difficulty in preparing low conductivity HgS without the occurrence of compensation. The doped samples have a conductivity $\sim 10^{10}\,\Omega$ cm compared to $10^{12}\,\Omega$ cm for the undoped variety.

It is worth noting that only the Ag doped samples exhibit the same activation energy as the undoped samples. One may conclude that as in the latter, the 0·83 eV activation energy relates to a trap located at about 1·08 eV. It is significant that of the three types of doped samples looked at, only the silver variety showed optical quenching (this was observed at the same energies as reported in Fig. 6). This suggests that the 1·08 eV level deduced from the log σ vs. $10^3/T$ plot is one level which contributes to the quenching. It is important to realize that in the case of the Cu and In doped samples, the observed activation energy probably corresponds to a deeper level than this but, in the absence of SCLC measurements on these crystals, the exact location cannot be determined.

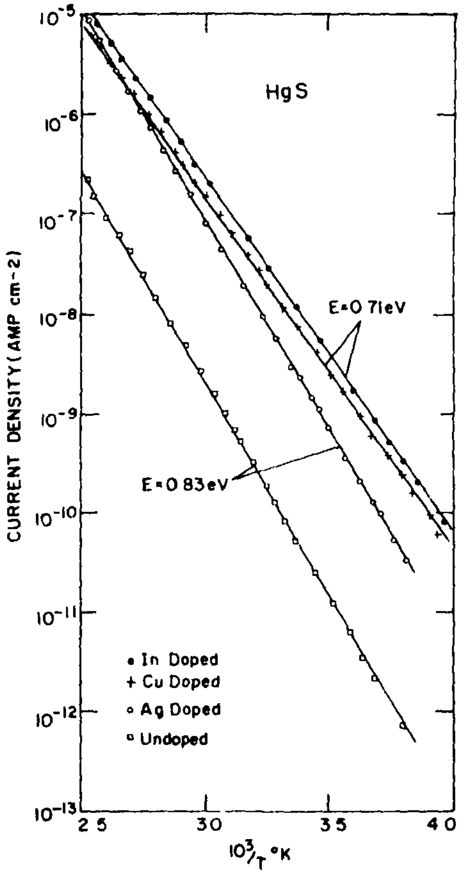

Fig. 9. Dark current density as a function of temperature for several crystals of HgS doped with the elements In, Cu and Ag (E = 1 V cm^{-1} for all samples).

Figure 10 shows a plot of the spectral response of photoconductivity at three different temperatures for a silver doped sample. The shift of the photoconductive edge with temperature was the same for all the samples investigated. The shoulder observed at energies above the photoconductivity peak is probably associated with surface recombination effects but it could conceivably be due to the first allowed direct transition. Zallen's edge-absorption spectra at 77°K indicate the onset of direct transition at 2·26 eV for $E \perp c$[6].

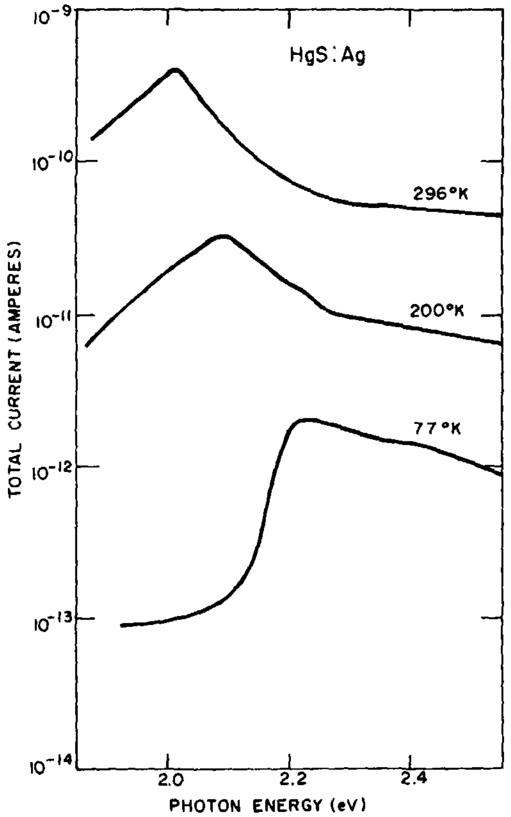

Fig. 10. Spectral response of photoconductivity at three different temperatures for a silver doped crystal of HgS.

Conclusions

The physical processes which have been used to determine the location of the localized levels in HgS have been those of space charge conduction and infra-red quenching. Some of the conclusions reached were:

(a) From SCLC flow, there exists a level, E_m, 0·62 eV from the conduction band.
(b) From an analysis of the activation energy in the ohmic region of a compensated semiconductor, $E_c - E_q = 1{\cdot}08$ eV.
(c) Optical quenching yields energy levels located at E_{q1} and E_{q2}, 1·08 and 0·22 eV, respectively above the valence band.
(d) The energy location of the photoconductivity peak varies from 2·20 eV at 77°K to 1·92 eV at 400°K.

A pair of schematic energy level diagrams illustrating these data is presented in Fig. 11.

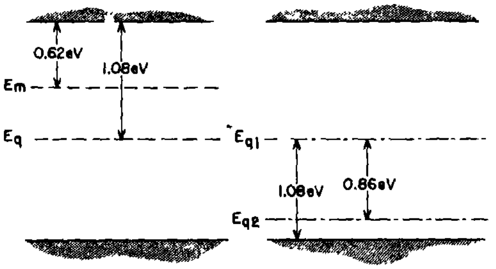

Fig 11. (a) Energy level scheme for HgS deduced from combined measurements of thermally activated ohmic and SCL conduction. (b) Energy level scheme to describe photoconductive quenching in HgS.

Two factors suggest that the level labelled E_q is in fact the sensitizing level located at approximately mid-band.

(1) In the doped HgS samples which do not exhibit a 0·85 eV slope in a log σ vs. $10^3/T$ plot, *no* optical quenching is observed at 1·08 eV.
(2) The summation of $E_q = 1{\cdot}08$ eV from the conduction band plus $E_{q1} = 1{\cdot}08$ eV from optical quenching, yields a value close to the band gap energy. (The Frank Condon principle could reduce the value of E_{q1} by a small amount).

The nature of the defects or impurities contributing to these energy levels is not known. In fact, even the atomic configurations responsible for the well documented sensitizing centres in the better known II–VI semiconductors are not, at present, well understood. However, the data presented here do indicate that the photoelectronic properties of single crystal HgS are strikingly similar to those of other II–VI compounds.

Acknowledgements—We gratefully acknowledge the valuable experimental assistance provided by F. Knier and L. Jordan. We also appreciate helpful discussions we have had with Drs. F. Schmidlin, S. Tutihasi and R. Zallen.

REFERENCES

1. AVEN M. and PRENER J. S., *Physics and Chemistry of II–VI Compounds*. North Holland, Amsterdam (1967).
2. AURIVILLIUS K. L., *Acta chem. scand.* **4**, 1413 (1950).
3. GUDDEN B. and POHL R., *Z. Phys* **B2**, 370 (1921).
4. VEROLINI C. and DIAMOND H., *J. appl. Phys.* **36**, 1891 (1965).
5. NOBLANC J. P., LOUDETTE J. and DURAFFOURG G., *Solid State Commun.* **5**, 803 (1967).
6. ZALLEN R., *II–VI Semiconducting Compounds—1967 International Conference* (Edited by D. G. Thomas), p. 877. Benjamin, New York (1967).
7. KHARAKHORIN F. F. and PETROV V. M., *Soviet Phys. Semiconductors* **1**, 112 (1967).
8. CURTIS O. L., *J. appl. Phys.* **33**, 2461 (1962)
9. DOVGII Ya. O. and BILEN'KII B. F., *Soviet Phys. solid St.* **8**, 1280 (1966).
10. GROSS E. F. and KREINGOL'D F. I., *Soviet Phys. solid St.* **4**, 210 (1963).
11. BUBE R. H., *Photoconductivity of Solids*, p. 60. Wiley, New York (1960).
12. BUTSKO N. I., *Soviet Phys. solid St* **2**, 585 (1960).
13. TREDGOLD R. H., *Space Charge Conduction in Solids*. Elsevier, Amsterdam (1966).
14. LAMPERT M. A., *Rep. Prog. Phys.* **27**, 329 (1964).
15. LAMPERT M. A., *Phys. Rev.* **103**, 1648 (1956).
16. MOTT N. F. and GURNEY R. W., *Electronic Processes in Ionic Crystals*, p. 156. Oxford University Press, Oxford (1940).
17. ROSE A., *Phys. Rev.* **97**, 1538 (1955).
18. ROBERTS G. G. and TREDGOLD R. H., *J. Phys Chem. Solids* **25**, 1349 (1964)
19. TABAK M. and ROBERTS G. G., *J. appl. Phys.* **39**, No. 10 (1968).
20. SCHMIDLIN F. W. and ROBERTS G. G., *Phys. Rev. Lett.* **20**, 1173 (1968).
21. BUBE R. H., *Photoconductivity of Solids*, Chap. 11. Wiley, New York (1960).

22. MATOSSI F., *J. electrochem. Soc.* **103**, 662 (1956).
23. BUBE R. H., *Phys. Rev.* **99**, 1105 (1955).
24. SHNEIDER A. D., *Soviet Phys. tech. Phys.* **1**, 1400 (1956).
25. LASHKAREV V. E. and RYBALKA V. V., *Ukr. fiz. Zh.* **11**, 372 (1966).
26. HEMILA S. O. and BUBE R. H., *J. appl. Phys.* **38**, 5258 (1967).

J. Phys. Chem. Solids Pergamon Press 1969. Vol. 30, pp. 845–850. Printed in Great Britain.

ON THE ENHANCEMENT OF γ-RAY COLORATION BY Mn^{2+} AND Mg^{2+} IN LITHIUM FLUORIDE

CARLO LAJ and PIERRE BERGE
Service de Physique du Solide et de Résonance Magnétique, Centre d'Etudes Nucléaires de Saclay, BP n° 2–91, Gif-sur-Yvette, France

(*Received* 25 *June* 1968)

Abstract—Experiments of γ-ray coloration with variable irradiation rates of LiF doped with Mg^{2+} and Mn^{2+} give new evidences that the vacancies created by charge compensation are converted into *F*-centers after dissociation of an impurity-vacancy complex. The results are supported by EPR and ITC parallel measurements.

1. INTRODUCTION

THE ENHANCEMENT of X-ray or γ-ray coloration by divalent impurities in alkali halides has been extensively studied by several authors. On the basis of their results on the thermal stability of the Cl_2^- molecular center in KCl and of electrostatic considerations, Crawford and Nelson[1] have suggested that a positive ion vacancy is converted into an *F*-center by X irradiation. The positive ion vacancies are present in great number in a crystal doped with divalent cation impurities to insure electrical neutrality. They can be either free or associated in an impurity-vacancy complex, according to the dissociation reaction

$$M^{2+}\boxplus \rightleftharpoons M^{2+}+\boxplus. \qquad (1)$$

The question arises whether isolated or associated vacancies are converted to anion vacancies. Crawford[2], Sibley and Russel [3], and more recently Ikeya *et al.*[4] all find evidences that isolated cation vacancies are converted to F-centers. However Hayes and Nichols[5] by ESR measurements, and Beltrami, Cappelletti and Fieschi[6] by the I.T.C. method have evidences that the bound vacancies participate to the early-stage coloration process. Therefore this question cannot be considered closed as yet.

The present paper is a report of some additional results on this subject, obtained by ESR, ionic conductivity, optical absorption and I.T.C. measurements.

2. EXPERIMENTAL TECHNIQUES

All the samples used in the present experiments were grown in a dry helium atmosphere from optical-purity powders purchased from Riedel or Johnson-Matthey [7]. Prolonged heating in vacuum was used to remove water. No treatment however was attempted to remove hydroxyl ions, which are known to exist in small amount in the powders.

The EPR experiments were performed using a Varian V-4502 spectrometer with 100 kHz modulation and the optical absorption measurements with a Cary 14 spectrophotometer. Measurements of ionic conductivity and I.T.C. were made with a Cary 31 CV vibrating reed electrometer. The lowest detectable current was about 10^{-15} A. For I.T.C. typical polarizing fields were about 15 kV cm^{-1}.

All the irradiations were made with a ^{60}Co γ-ray source.

3. EXPERIMENTAL RESULTS

It was felt that new valuable information about the early-stage coloration could be obtained by irradiating in a temperature range where the time necessary for the dissociation reaction (1) to attain thermodynamical equilibrium is longer or comparable to the time needed to obtain appreciable coloration of the samples by γ-irradiation.

The first step has then obviously been the obtention of an estimate of the time constant of equilibrium (1). This has been done in the following way.

Some lightly doped ($c = 10^{-4}$) LiF : Mg^{2+} samples were properly annealed at about 600°C and then quenched into liquid nitrogen. In these samples the $\sigma T = f(1/t)$ curve at low temperature consists of only the 'associated region'[8, 9]. The slope of the line in a semi-log plot then gives $(E/2)b + U$, where E_b is the binding energy of a complex and U the mobility activation energy for a free vacancy. In LiF $U = 0{\cdot}75$ eV as determined by ionic conductivity[8] and nuclear magnetic resonance[10], and $E_b \simeq 0{\cdot}40$ eV[9]. The slope of the line is thus $\simeq 0{\cdot}95$ eV. It is clear however that this holds for equilibrium conditions. If the sample is cooled down at a steady rate, at a sufficiently low temperature the time constant of the dissociation reaction (1) will become long enough so that some vacancies will be partially quenched in excess over thermodynamical equilibrium. The slope of the $\sigma T = f(1/T)$ curve is then expected to decrease and eventually approach 0·75 eV when the equilibrium is completely quenched

Figure 1 shows that such a break in the σT plot is effectively observed in LiF : Mg^{2+} at about −15°C for a cooling rate of 1°C sec^{-1}. From this result it was estimated that the time constant of the dissociation reaction (1) is of the order of several minutes at about −25°C. It was also assumed that for LiF : Mn^{2+} this figure should not be significantly different.

The γ-ray source having a maximum flux of $3{\cdot}3 . 10^6$ rad/hr, appreciable coloration can be obtained in a time shorter or comparable to the time constant of the equilibrium at −25°C.

Typical experiments were then conducted in the following way: six samples of LiF : Mn^{2+} or LiF : Mg^{2+} were cleaved from the same ingot, annealed at 600°C in a nitrogen atmosphere and quenched into liquid nitrogen. Three samples were irradiated in a flux of $\simeq 1{\cdot}1 . 10^6$ rad/hr, the three others in a flux of $\simeq 0{\cdot}40 . 10^6$ rad/hr for a longer time in such a way that the integrated dose was approximately the same in both cases. In each case one of the three samples was irradiated at −77°C, one at −25°C and one at +25°C. Because of the difficulty of positioning the dewar flasks around the γ-ray source, some differences in the real irradiation doses for the 6 samples were to be expected. For this reason each sample was accompanied by a pure Harshaw LiF crystal which was used as a dosimeter.

Table 1. gives a typical result obtained with an integrated dose of about 10^6 rad, in the case of LiF : Mn^{2+} ($c = 1{\cdot}4 . 10^{-4}$)

Table 1. *Optical density in* mm^{-1} *of irradiated* LiF : Mn^{2+}. *Figures in parenthesis refer to Harshaw samples*

ϕ rads/hr	T = −77°C	T = −25°C	T = +25°C
$\simeq$ 1·1	0·56 (0·54)	0·83 (0·65)	2·1 (1·03)
$\simeq$ 0·4	0·61 (0·57)	1·25 (0·65)	1·58 (0·74)

It can be seen that at −77°C the coloration is only slightly affected by the presence of Mn^{2+} in both cases. At −25°C the coloration is much more enhanced in the case of a slow irradiation rate, at +25°C the irradiation rate has no influence, coloration is enhanced much in the same way in both cases.

Parallel measurements by EPR show that the intensity of the fine structure (i.e. the dipoles) is only slightly reduced by irradiation at −77°C, while it is completely destroyed when irradiation takes place at +25°C. In this last case the EPR spectrum (Fig. 2) is composed of six hyperfine lines, with superimposed SHF structure, with an hyperfine constant $A = 90 . 10^{-4}$ cm^{-1}. This spectrum is

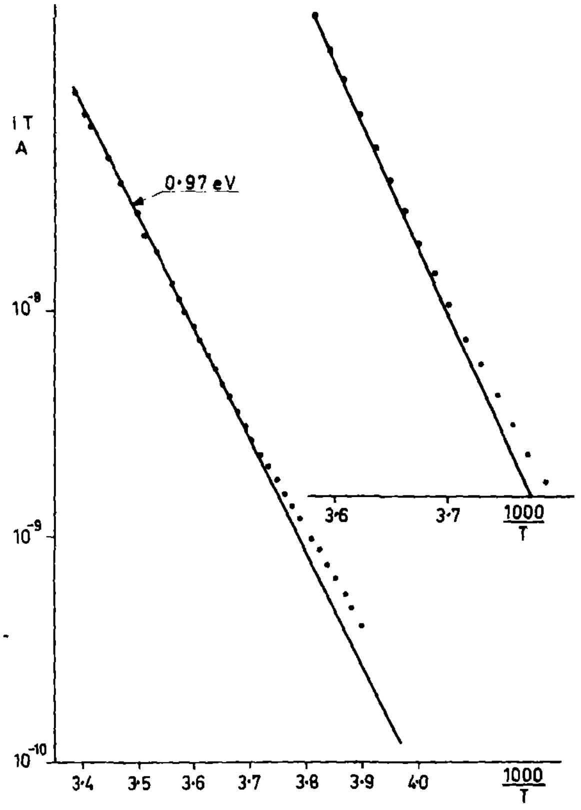

Fig. 1. Plot of the $iT = f(1/T)$ curve for LiF Mg^{2+} Applied voltage: 400V. The region of the break in the curve is given on a larger scale in the upper right hand corner.

characteristic of Mn^{2+} in a cubic field*[11]. However, the EPR spectrum shows an unexplained overall decrease of almost an order of magnitude.

At the same time the ITC technique[13] [14] was used to measure the concentration of impurity-vacancy dipoles. A typical result obtained with $LiF:Mg^{2+}$ $(c = 2{\cdot}2.10^{-4})$ is shown in Fig. 3. It can be seen that the results of ITC measurements agree fairly well with the optical absorption measurements, i.e. a much greater effect is observed at +25° than at −70°C and a marked effect depending on irradiation rate is observed at −25°C. No effect depending on irradiation rate was, on the contrary, observed at −70° or at +25°C, within the accuracy of the measurements. (≃ 10 per cent)†.

---

*Mn^{2+} in a cubic field after X irradiation, has also been observed in NaCl and KCl by Bettica *et al.*[12]. These authors however attributed this spectrum to preexisting isolated Mn^{2+}, while we think that it has been formed during irradiation.

†Because of technical problems the samples could not be irradiated in the ITC container, and had to be reheated to *RT* before the measurements. The number of dipoles and the accuracy of the measurements are then affected by the displacement of equilibrium (1).

to be taken in performing and analyzing these experiments if they are to support a suggested mechanism of conversion [4].

More sophisticated experiments are now under way to check on an eventual conversion of bound vacancies.

REFERENCES

1. CRAWFORD J. H. Jr and NELSON C. M., *Phys. Rev. Lett.* **5**, 314 (1960).
2. CRAWFORD J. H. Jr., *J. phys. Soc. Japan* **18**, Suppl. III, 329 (1963).
3. SIBLEY W. A. and RUSSEL J. R., *J. appl. Phys.* **36**, 810 (1965)
4. IKEYA M., ITOH N., OKADA T. and SUITA T., *J. phys. Soc. Japan* **21**, 1304 (1966)
5. HAYES W. and NICHOLS G. M., *Phys. Rev* **117**, 993 (1960).
6. BELTRAMI M., CAPPELLETTI R. and FIESCHI R., *Phys. Lett.* **10**, 279 (1964).
7. ADAM-BENVENISTE M., BERGE P., BLANC G., DUBOIS M. and LAJ C., *J. Phys. Appliquée* To be published.
8. ADAM-BENVENISTE M., Thesis, Paris (1967). Unpublished.
9. ADAM-BENVENISTE M., LAJ C., BERGE P. and DUBOIS M., *C. r. hebd. Seanc. Acad Sci. Paris* **264B**, 875 (1967).
10. STOIBE T. G., GURTANI T. O. and HUGGINS R. A., *Phys. Rev.* **134**, 963 (1964).
11. BERGE P., GAGO C., BLANC G., ADAM-BENVENISTE M. and DUBOIS M., *J. Phys.* **27**, 295 (1966).
12. BETTICA P., SANTUCCI S. and STEFANANI A., *Nuovo Cim.* **48**, 316 (1967).
13. BUCCI C. and FIESCHI R., *Phys. Rev. Lett.* **12**, 16 (1964); BELTRAMI M., BUCCI C. and FIESCHI R., Rendiconti LXV Riunione AEI (1964).
14. LAJ C. and BERGE P., *J Phys.* **27**, 295 (1966).

J. Phys. Chem. Solids Pergamon Press 1969. Vol. 30, pp. 851-858. Printed in Great Britain.

SIGNE ET GRANDEUR DES INTEGRALES D'ECHANGE DANS LES SOLUTIONS SOLIDES $Mn_xCr_{1-x}S$

P. BURLET* et **E. F. BERTAUT**
Centre d'Etudes Nucléaires, B.P. 269, Grenoble, France

(*Received* 10 *April* 1968)

Résumé – L'étude par diffraction neutronique des solutions solides $Mn_xCr_{1-x}S$ au-dessus de la température de Néel et l'étude de la structure magnétique de $Mg_{0,5}Cr_{0,5}S$ permettent d'évaluer les intégrales d'échange J_1 entre premiers voisins et J_2 entre seconds voisins relatives aux liaisons Mn–S–Mn, Cr–S–Cr et Mn–S–Cr. Trois types d'approximations ont été utilisés: un modèle semi-classique d'Ising, la théorie semi-classique de Stanley et Kaplan (série haute température) et l'approximation "random phase" de Lines (fonctions de Green). Le fait remarquable est le caractère fortement positif de l'intégrale d'échange J_2(Cr–S–Cr) à 180° de l'ordre de 15°K.

Abstract – The neutron diffraction study of the solid solutions $Mn_xCr_{1-x}S$ above the Neel temperature and the study of the magnetic structure of $Mg_{0.5}Cr_{0.5}S$ allow to evaluate the exchange integrals J_1 between nearest neighbourgs and J_2 between next nearest neighbourgs for the ligands Cr–S–Cr, Mn–S–Mn and Mn–S–Cr. Three types of approximation have been used: a semiclassical Ising model, the semiclassical theory of Stanley and Kaplan and the random phase approximation of Lines (green functions). The most striking fact is the strongly positive exchange integral J_2(Cr–S–Cr) at 180° which is of the order of 15°K.

DANS UNE étude antérieure[1] nous avons montré comment l'analyse de la diffusion magnétique des neutrons par une substance en état d'ordre magnétique à courte distance permet de mesurer les corrélations de spins. Nous avons alors étudié le composé $Mn_{0,33}Cr_{0,67}S$. Nous nous proposons ici d'étendre cette étude aux solutions solides $Mn_xCr_{1-x}S$ où x prend les valeurs 1; 0,66; 0,60; 0,50; 0,33. Nous chercherons comment les corrélations de spins peuvent s'exprimer théoriquement et nous en déduirons les valeurs des intégrale d'échanges relatives aux liaisons Cr–S–Cr, Cr–S–Mn, Mn–S–Mn. Enfin nous confirmerons les résultats trouvés pour la liaison Cr–S–Cr par l'étude de la structure magnétique de la solution solide $Mg_{0,5}Cr_{0,5}S$.

THEORIE

Nous avons montré[1] que l'intensité de la diffusion des neutrons par une substance en état d'ordre magnétique à courte distance est dans l'hypothèse de couplages isotropes donnée par (1):

$$I(h) = Cte\, f^2 S(S+1) \sum_i \frac{\sin hr_i}{hr_i} c_i g(r_i) \quad (1)$$

avec

$$h = \frac{4\pi \sin\theta}{\lambda}; \quad g(r_i) = \frac{S_0 S_i}{S(S+1)} \quad (2)$$

r_i est la distance entre un atome et ses ièmes voisins.

Nous avons donne dans la référénce[1] un calcul trés simplifié des g_i en fonction des J_i et de la température réduite:

$$\tau = \frac{3kT}{S(S+1)} = \frac{3kT}{X^2}. \quad (3)$$

Des calculs plus élaborés permettent d'obtenir des approximations plus exactes de la relation entre les g_i et les J_i. Stanley et Kaplan [2] ont donné l'expression (5) du développement en série de puissances de $1/kT$ de la fonction de corrélation dans l'approximation semi-classique ($S=\infty$), exacte à quelques % près selon ces auteurs

---

*Ce travail fait partie d'une thèse de Doctorat ès Sciences Physiques, enregistrée au Centre de Documentation du C.N.R.S., sous le n° A.O. 1768 "à paraître", qui sera soutenue prochainement par P. Burlet.

$$\langle S_g S_h\rangle = \frac{\text{trace}(S_g S_h \exp(-\beta\mathscr{H}))}{\text{trace}\exp(-\beta\mathscr{H})} = \sum_0^\infty \frac{(-1)^l}{l!}\beta^l \alpha_l \tag{4}$$

où α_l est donnée par (6):

$$\alpha_l = \nu_l - \sum \frac{l!}{(l-k)!k!}\alpha_k\mu_{l-k} \tag{5}$$

$$\nu_l = \langle S_g S_h \mathscr{H}^l\rangle \tag{6}$$

$$\mu_l = \langle\mathscr{H}^l\rangle. \tag{7}$$

Stanley[3] a calculé les α_l jusqu'à l'ordre 9 en utilisant la "représentation diagrammatique" de Rushbrook et Wood[4]. Le Tableau 1 rapporte les valeurs des α_l jusqu'à $l=4$ ainsi que les diagrammes correspondants dans lesquels la ligne brisée représente le produit S_gS_h et les lignes droites les facteurs $\mathscr{H}$, leur nombre égalant l'exposant de $\mathscr{H}$.

Tableau 1. Coefficients α_l et diagrammes associés (d'après Stanley[3])

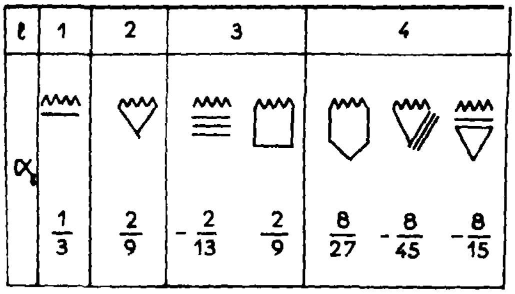

l	1	2	3		4		
α_l	$\frac{1}{3}$	$\frac{2}{9}$	$-\frac{2}{13}$	$\frac{2}{9}$	$\frac{8}{27}$	$-\frac{8}{45}$	$-\frac{8}{15}$

APPLICATION AU RÉSEAU CUBIQUE À FACES CENTRÉES (C.F.C.)

Considérons dans le réseau c.f.c., les deux seuls couplages non nuls J_1 et J_2 ainsi qu'une paire d'atomes $i^{\text{èmes}}$ voisins. Pour calculer le terme d'ordre l du développment de g_i il faut énumérer le nombre de diagrammes d'ordre l et de forme donnée j qui peuvent être construits à partir d'une ligne brisée reliant les deux spins.

Soit $n_{lj}^{(i)}$ ce nombre. Puisque nous nous limitons à J_1 et J_2 non nuls les lignes droites des diagrammes doivent joindre des premiers ou des seconds voisins. Remarquons encore que le terme $l=0$ représente l'autocorrélation des spins et ne doit pas être pris en considération dans le calcul des g_i tels qu'ils ont été définis. On peut alors écrire g_i sous la forme (8):

$$g_i = \sum_{l=1}^{\infty}\sum_j A_{jl}^{(i)}\beta^l \tag{8}$$

avec (9):

$$A_{jl}^{(i)} = \frac{(-1)^l}{l!}\alpha_l n_{jl}^{(i)} X^{2l}(-2J_1)^m(-2J_2)^p. \tag{9}$$

Ici m et p sont les nombres de lignes droites joignant respectivement des premiers et des seconds voisins dans le diagramme envisagé. Le Tableau 2 montre les différents diagrammes

Tableau 2. Diagrammes et coefficients associés dans le réseau c–f–c

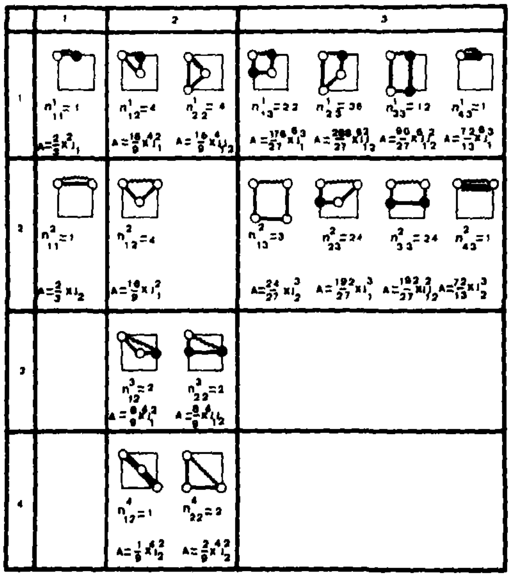

	1	2		3			
1	$n^1_{11}=1$ $A=\frac{2}{3}X^2J_1$	$n^1_{12}=4$ $A=\frac{16}{9}X^4J_1^2$	$n^1_{22}=4$ $A=\frac{16}{9}X^4J_1J_2$	$n^1_{13}=22$ $A=\frac{176}{27}X^6J_1^3$	$n^1_{23}=36$ $A=\frac{288}{27}X^6J_1^2J_2$	$n^1_{33}=12$ $A=\frac{96}{27}X^6J_1J_2^2$	$n^1_{43}=1$ $A=\frac{72}{13}X^6J_1^3$
2	$n^2_{11}=1$ $A=\frac{2}{3}XJ_2$	$n^2_{12}=4$ $A=\frac{16}{9}XJ_1^2$		$n^2_{13}=3$ $A=\frac{24}{27}XJ_2^3$	$n^2_{23}=24$ $A=\frac{192}{27}XJ_1^3$	$n^2_{33}=24$ $A=\frac{192}{27}XJ_1^2J_2$	$n^2_{43}=1$ $A=\frac{72}{13}XJ_2^3$
3		$n^3_{12}=2$ $A=\frac{8}{9}X^4J_1^2$	$n^3_{22}=2$ $A=\frac{8}{9}X^4J_1J_2$				
4		$n^4_{12}=1$ $A=\frac{1}{9}X^4J_2^2$	$n^4_{22}=2$ $A=\frac{2}{9}X^4J_2^2$				

ainsi que les n_{jl}^l et les A_{jl}^l pour $l = 1, 2, 3$. Grâce à (4) on obtient les formules (10):

$$\begin{aligned}
g_1 &= \frac{2J_1}{\tau}+\frac{16J_1(J_1+J_2)}{\tau^2}+\frac{8J_1}{\tau^3}\\
&\quad \times [21,3J_1^2+36J_1J_2+12J_2^2]+\dots\\
g_2 &= \frac{2J_2}{\tau}+\frac{16J_1^2}{\tau^2}+\frac{8}{\tau^3}\\
&\quad \times [24\,J_1^2(J_1+J_2)+2{,}3\,J_2^3]+\dots\\
g_3 &= \frac{8}{\tau^3}J_1(J_1+J_2)+\frac{8J_1}{\tau^3}\\
&\quad \times [14J_1^2+11J_2(J_1+J_2)]+\dots\\
g_4 &= \frac{4}{\tau^2}(2J_2^2+J_1^2)+\frac{48J_1}{\tau^3}(2J_1+3J_2)+\dots .
\end{aligned} \tag{10}$$

Par ailleurs Lines[5] a utilisé la méthode des fonctions de Green ("Random phase approximation") dans le cas de l'antiferromagnétisme et a appliqué ses résultats au réseau c.f.c. que noùs résumons brièvement (formules(11)):

$$\begin{aligned}
\langle S_g S_h\rangle &= 3kT\left\langle\frac{e^{iK(g-h)}}{\chi_0^{-1}+\rho}\right\rangle_K\\
(\chi_0\tau)^{-1} &= \left\langle\frac{1}{1+\chi_0\rho}\right\rangle\\
\rho &= \sum_{j-g} J_{jk}\{\exp[ik(j-g)]-1\}.
\end{aligned} \tag{11}$$

Le symbole $\langle\dots\dots\rangle_k$ représente la moyenne sur k prenant toute valeur à l'intérieur de la première zone de Brouillin du réseau réciproque. Pour des températures élevées $\langle S_g S_h\rangle$ peut être développé en série de puissance de $1/\tau$ et Lines[5] obtient les formules (12):

$$\begin{aligned}
g_1 &= \frac{2J_1}{\tau}+\frac{16J_1}{\tau^2}[J_1+J_2]+\frac{8J_1}{\tau^3}\\
&\quad \times [21J_1^2+36J_1J_2+12J_2^2]\\
g_2 &= \frac{2J_2}{\tau}+\frac{16J_1^2}{\tau^2}+\frac{8}{\tau^3}[24J_1^2(J_1+J_2)+3J_2^2]\\
g_3 &= \frac{8J_1}{\tau^2}(J_1+J_2)+\dots\\
g_4 &= \frac{4J}{\tau^2}(J_1^2+2J_2^2)+\dots .
\end{aligned} \tag{12}$$

Les formules (10) et (12) sont extrêmement semblables, il faut aller jusqu'aux termes du 3e ordre pour noter de très légères différences.

APPLICATION AUX SOLUTIONS SOLIDES $Mn_xCr_{1-x}S$

Lors de l'étude des structures magnétiques de ces composés[6] nous avons vu que les ordres antiferromagnétiques de première et de seconde espèce du réseau c.f.c. peuvent coexister dans une solution solide nucléairement désordonnée. Ceci s'explique[7] par la formation d'amas infinis d'atomes liés positivement ou négativement avec leurs seconds voisins. Le signe de cette liaison dépend de la composition statistique du second voisinage de l'atome considéré. Dans une telle substance en état d'ordre magnétique à courte distance l'intensité diffusée est la somme des intensités diffusées par chacun des deux types d'amas. Dans l'hypothèse de couplages isotropes les corrélations mesurées sont des corrélations moyennes et les valeurs des intégrales d'échange déduites de ces mesures sont aussi des valeurs moyennes.

La Fig. 1 montre les courbes $I(h)$ et $G(r)$ transformés de Fourier de $I(h)$ pour les différentes concentrations étudiées. Le Tableau 3 donne les valeurs des corrélations déduites de ces courbes.

Nous sommes en possession d'une part des valeurs numériques des fonctions de corrélations g_i et d'autre part des expressions reliant ces fonctions aux intégrales d'échange J_1 et J_2.

Dans le cas des solutions solides $Mn_xCr_{1-x}S$ nous devons modifier ces formules* pour tenir compte du fait que les liaisons Mn–S–Mn, Cr–S–Cr et Mn–S–Cr sont caractérisées

---

*Nous tenons à remercier J. Villain pour une formulation plus correcte du problème des solutions solides.

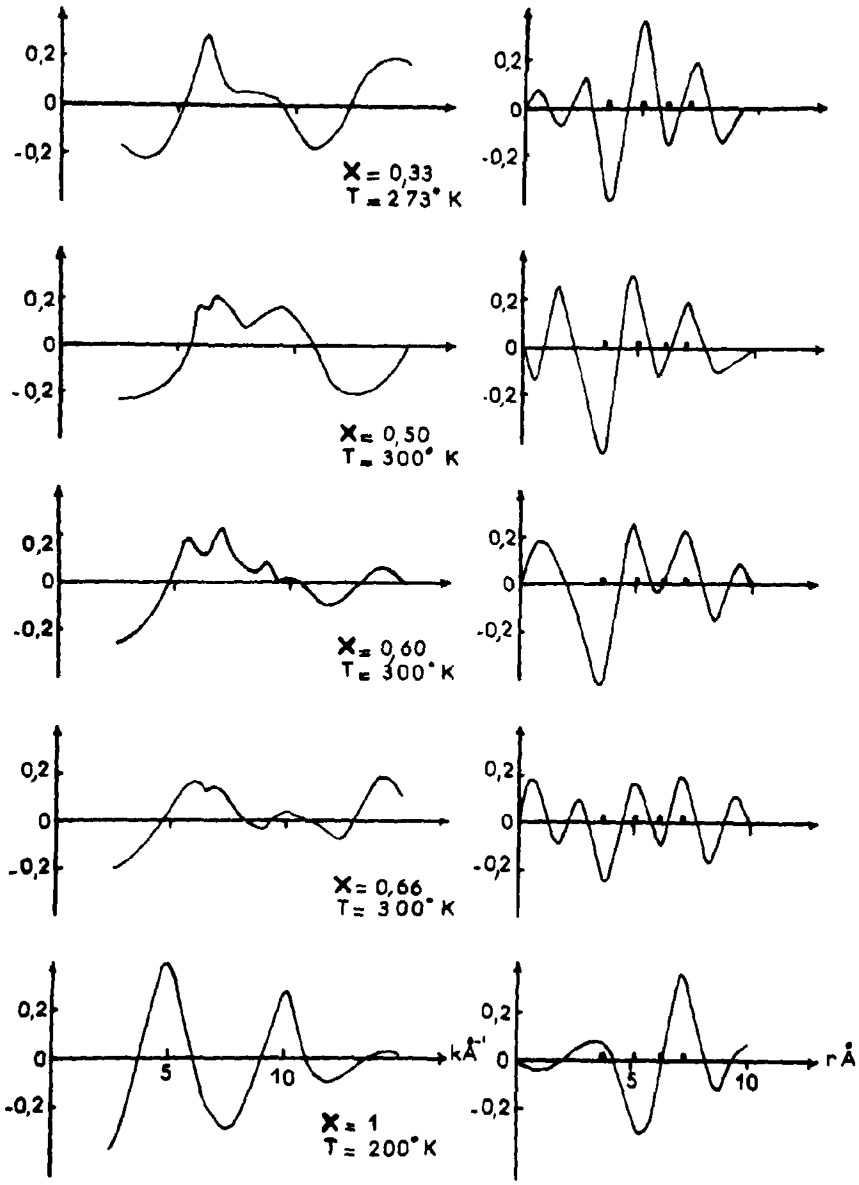

Fig. 1.

respectivement par les intégrales d'échanges J_1', J_2', J_1'', J_2'', J_1''', J_2''' et aussi de ce que les modules des spins des ions Cr^{2+} et Mn^{2+} ne sont pas identiques. La facon la plus simple d'obtenir les formules valables dans notre cas est de reprendre le calcul à partir de la méthode semi-classique de Stanley et Kaplan. Ainsi, par exemple pour les termes en T^{-1} du

Tableau 3. *Fonctions de corrélations dans les solutions solides* $Mn_xCr_{1-x}S$

x	T	g_1	g_2	g_3	g_4
1	200	−0,06	−0,19	0,02	0,05
0,66	300	−0,07	0,04	0,02	0,05
0,60	300	−0,06	0,05	−0,01	0,07
0,50	300	−0,04	0,107	0,03	0,04
0,53	273	−0,114	0,125	0,04	0,06

développement de g_1 nous devons tenir compte des diagrammes suivants: Mn$\sim\sim$Mn, Mn$\sim\sim$Cr, Cr$\sim\sim$Cr ayant les probabilités respectives x^2, $2x(1-x)$ et $(1-x)^2$. Si S' et S'' sont respectivement les spins des ions Mn^{2+} et Cr^{2+} les développements de $\overline{S_0S_1}$ et $\overline{S_0S_2}$, limités aux termes en T^{-2} s'écrivent

$$\left.\begin{aligned}\overline{S_0S_1} &= B_{1,1}^{(1)}T^{-1}+(B_{1,2}^{(1)}+B_{2,2}^{(1)})\,T^{-2}\\ \overline{S_0S_2} &= B_{11}^{(2)}T^{-1}+B_{12}^{(2)}T^{-2}\end{aligned}\right\}\quad(13)$$

avec (14):

$$B_{11}^{(1)} = \tfrac{2}{3}[J_1'x^2S'^2(S'+1)^2+2J_1'''S'(S'+1)S''(S''+1)(1-x)+J_1''S''^2(S''+1)^2(1-x)^2]$$

$$\begin{aligned}B_{12}^{(1)} = B_{12}^{(2)} = \tfrac{16}{9}\,[&x^3J_1'^2S'^3(S'+1)^3+x^2(1-x)(J_1'''^2+2J_1'J_1''')S'^2(S'+1)^2S''(S''+1)\\ &+x(1-x)^2(J_1'''^2+2J_1''J_1''')S'(S'+1)S''^2(S''+1)^2+(1-x)^3J''^2S''^3(S''+1)^3]\end{aligned}$$

$$\begin{aligned}B_{22}^{(1)} = \tfrac{16}{9}[&x^3J_1'J_2'S'^3(S'+1)^3+x^2(1-x)(J_1'J_2'''+J_1'''J_2'+J_1'''J_2''')S'^2(S'+1)^2S''(S''+1)\\ &+x(1-x)^2(J_1''J_2'''+J_1'''J_2''+J_1'''J_2''')\,S'(S'+1)S''^2(S''+1)^2+(1-x)^3J_1''J_2''S''^3(S''+1)^3]\end{aligned}$$

$$B_{11}^{(2)} = \tfrac{2}{3}[x^2J_2'S'^2(S'+1)^2+2x(1-x)\,J_2'''\,S'(S'+1)S''(S''+1)+(1-x)^2J_2''S''^2(S''+1)^2]$$

avec $S' = \frac{5}{2}$ et $S'' = 2$.

Pour un x donné on peut calculer les coefficients de ces équations. En vue de réduire le nombres des inconnues nous allons utiliser les valeurs très probables de J_1' et J_2'[9] à savoir:

$$J_2' = -3{,}5°\mathrm{K} \quad \text{et} \quad J_2' = -6{,}3°\mathrm{K}.$$

(Dans tout ce travail nous exprimons les intégrales d'échange en degrés Kelvin).

Pour déterminer les valeurs de $J_1''\,J_2''\,J_1'''$ et J_2''', nous allons utiliser les valeurs expérimentales des g_2. Ceci pour deux raisons: d'une part les fonctions g_2 sont expérimentalement plus précises que les fonctions g_1 (les erreurs de sommation finie et les erreurs sur $I(h)$ sont reportées vers l'origine de la transformé de Fourier au voisinage de laquelle est déterminée g_1), d'autre part les calculs sont facilités en remarquant que S_0S_2 ne contient pas de terme du second ordre en J_2'' et J_2''' ni de terme J_1J_2. Après élimination des termes en J_2'' et J_2''' des équations du type (13) nous aboutissons à des équations du second ordre en J_1'' et J_1''' dont la résolution graphique conduit à l'évaluation de J_1'' et J_1''' à partir de laquelle on détermine J_2'' et J_2'''. Ces résultats figurent dans le Tableau 4.

Les valeurs de g_1 calculées à l'aide de ces valeurs et de des formules (14) sont comparées dans le Tableau 5 avec l'expérience. L'écart constaté est fort compatible avec les imprécisions des mesures.

Nous remarquons les fortes valeurs positives trouvées pour J_2'' et J_2'''.

Tableau 4. *Intégrales d'échange relatives aux liaisons* Mn–Mn, Cr–Cr *et* Mn–Cr

	Mn–Mu	Cr–Cr	Mn–Cr
J_1	−3,5	−10	−1
J_2	−6,3	+14	+9

SOLUTION SOLIDE $Mg_{0.5}Cr_{0.5}S$

En vue de vérifier les résultats précédents relatifs à la liaison Cr–S–Cr nous avons préparé la solution solide $Mg_{0.5}Cr_{0.5}S$. Cette

Tableau 5. Fonctions de corrélations g_1 calculées et expérimentales

x	g_1 calculé $= S_0S_1/\bar{S}(\bar{S}+1)$	g_1 expérimental
066	$-0,050$	$-0,07$
060	$-0,055$	$-0,06$
050	$-0,062$	$-0,04$
033	$-0,095$	$-0,114$

solution solide est du type NaCl ($a = 5,15$ Å) et ne présente pas d'ordre nucléaire à longue ou courte distance mais une ségrégétion des atomes de magnésium et de chrome donnant lieu à une déformation des pics de Bragg (Fig. 3). (Remarquons que CrS a une structure intermédiaire entre CuO et PdS[10]). Des diffractogrammes neutroniques energistrés aux températures de 4,2° et 300°K montrent l'existence d'un ordre antiferromagnétique de première espèce, c'est-à-dire tel que $J_1 < 0$ et $J_2 > 0$. A 300°K cet ordre n'a pas totalement disparu, ce qui laisse supposer des valeurs très fortes des intégrales d'échanges. La structure magnétique est décrite par un empilement de plan ferromagnétique (001) dont le signe alterne selon la direction [001]. Les spins sont dirigés selon cette direction, leur grandeur observée moyenne est $S = 1,1$ ce qui donnerait pour Cr^{3+}: $S = 2,2$. Le Tableau 6 compare les valeurs observées et calculées des intensités magnétiques.

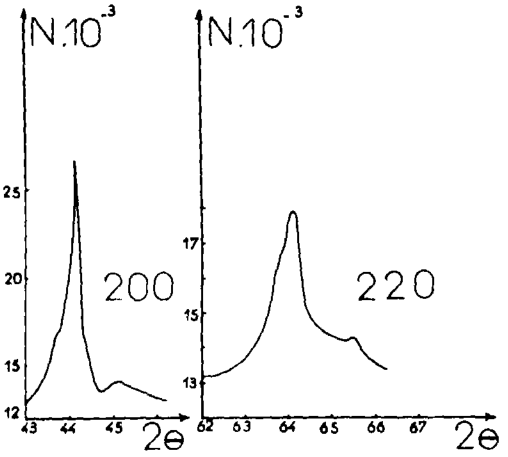

Fig. 2.

Tableau 6. Intensités magnétiques observées et calculées dans $Mg_{0.5}Cr_{0.5}S$

$h\,k\,l$	$I_{\text{observée}}$	$I_{\text{calculée}}$
0 0 1	33400	33000
1 1̄ 0	14800	13700
2 0 1	8400	6400
1 1 2	6800	5800
0 0 3 2 2 1	1100	2000
3 0 1	550	560

$I_{\text{cal}} = nL(0,539\ S\ f\ x\ 4)^2 \sin^2\alpha K$; n, multiplicite; L, facteur de Lorentz; K, facteur de normalisation déduit des intensités nucléaires; $f = f_{Cr^{2+}}$ [11].

DISCUSSION

Dans nos études précédentes nous avons toujours considéré pour interpréter les liaisons magnétiques des processus de transfert de 2 spins de l'anion vers le cation et *vice-versa*. Ceci conduisait à une valeur négative du couplage Cr–S–Cr à 180°, la partie positive étant fournie par la liaison Cr–S–Mn. Seul le mécanisme d'Anderson par transfert d'un spin de l'anion vers le cation peut expliquer la forte valeur positive trouvée ici pour la liaison Cr–S–Cr. Dans ce mécanisme le transfert a lieu entre une orbitale p_z^* de l'anion et une orbitale vide $e_{\parallel} = d_{z^2}$ du cation Cr_1 tandis que P_z est orthogonale aux 3 orbitales t_{2g} et à l'orbitale $d_{x^2-y^2}$ du cation Cr_2. De toute manière le transfert d'un spin a une probabilité plus élevée que celui de deux spins[12]. Un tel transfert pourrait expliquer aussi la forte valeur de $S(Cr^{2+})$ observée dans $Mg_{0.5}Cr_{0.5}S$.

Par ailleurs il semble y avoir contradiction entre notre étude précédente [7] et les résultats présents. Nous trouvions alors J_2(Cr–Cr)

---

*On prend l'axe Cr_1–S–Cr_2 comme axe de quantification Oz.

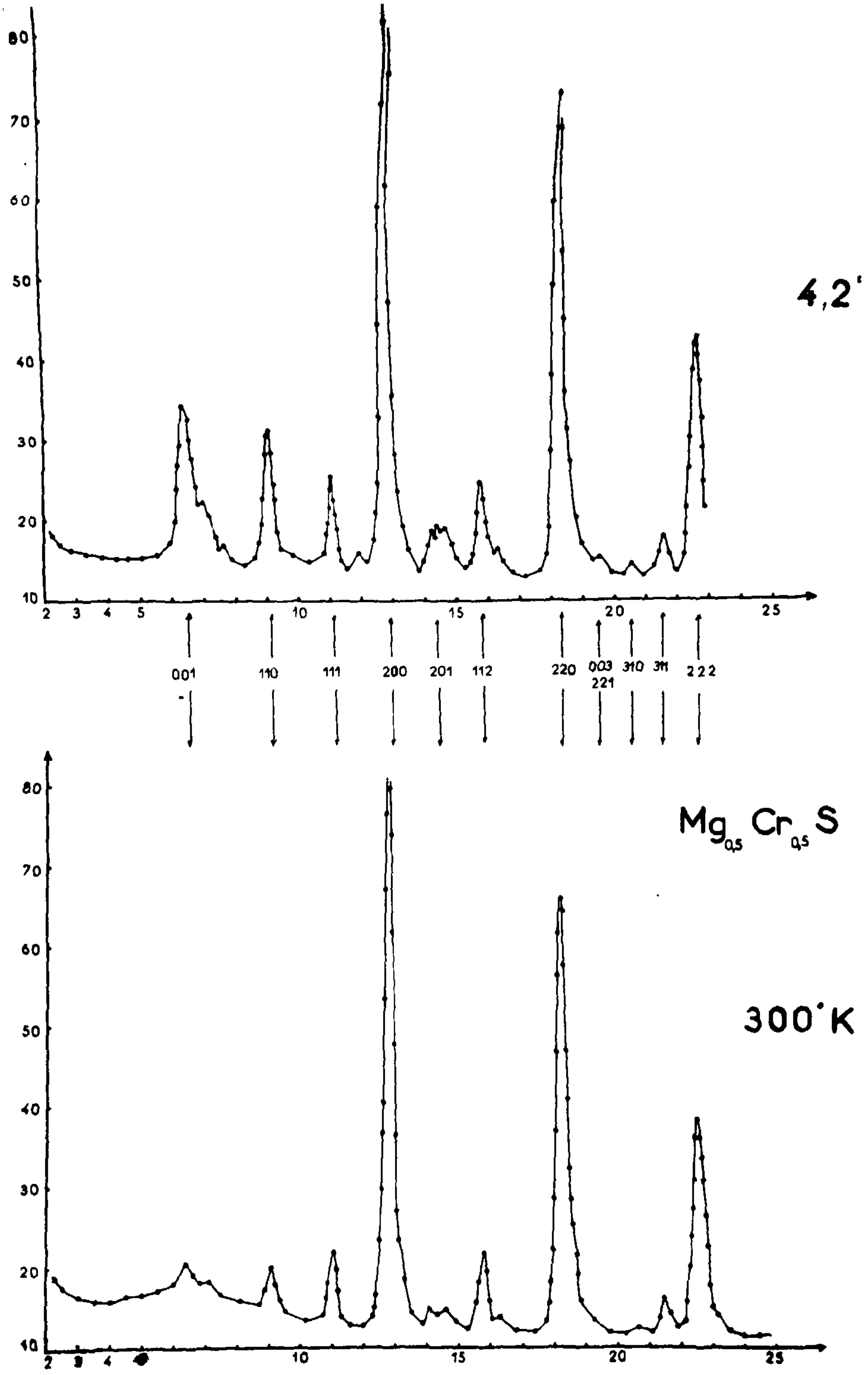
80
70
60
50
40
30
20
10
2
3
4
5
10
15
20
25
4,2°
001
110
111
200
201
112
220
003
221
310
311
222
Mg$_{0,5}$ Cr$_{0,5}$ S
300°K

Fig. 3.

légèrement négative. Si nous introduisons nos nouvelles valeurs (Tableau 4) dans le calcul de la probabilité d'amas d'atomes s'ordonnant selon l'ordre de première espèce nous obtenons les résultats représentés Fig. 4, encore en accord avec l'expérience. Notre application de la théorie des "amas infinis" [13] au problème de l'ordre magnétique des solutions solides désordonnées se vérifie donc bien.

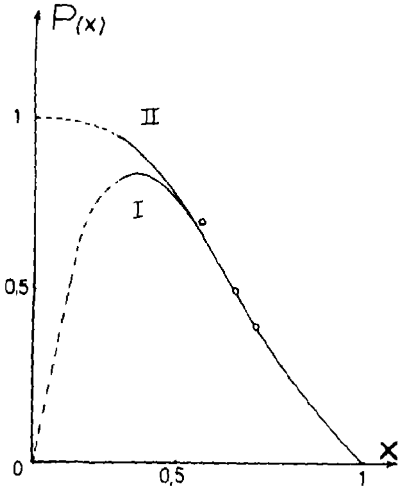

Fig. 4.

REFERENCES

1. BERTAUT E. F. et BURLET P., *Solid State Commun* **5**, 279 (1967).
2. STANLEY E. et KAPLAN J., *Phys. Rev. Lett.* **16**, 981 (1965).
3. STANLEY E., *Phys. Rev.* **158**, 537 (1967).
4. RUSHBROOK G. S. et WOOD P. J., *Mol. Phys.* **1**, 257 (1958)
5. LINES M. E., *Phys. Rev.* **139**, 1304 (1965).
6. BURLET P. et BERTAUT E. F., *C.r. hebd. Séanc. Acad. Sci. Paris* **B264**, 323 (1967).
7. BURLET P. et BERTAUT E. F., *C.r. hebd. Séanc. Acad. Sci. Paris* **B264**, 1208 (1967).
8. SMART J. S., Dans *Magnetism* (Editeé par Rado Shul), Vol. 3, Chap. 2.
9. LINES M. E. et JONES E. F., *Phys. Rev.* **141**, 525 (1966).
10. JELLINEK F., *Acta crystallogr.* **10**, 620 (1957).
11. CABLE J. W., WILKINSON M. K. et WOLLAN E. O., *Phys. Rev.* **118**, 950 (1960).
12. NAI Li HUANG, *Phys. Rev.* **154**, 487 (1967).
13. De GENNES P. G., LAFORE P. et MILLOT J. P., *J. Phys. Chem. Solids* **11**, 105 (1959).

J. Phys. Chem. Solids Pergamon Press 1969. Vol. 30, pp. 859-871. Printed in Great Britain.

HALL COEFFICIENT OF DILUTE COPPER ALLOYS

TAKESHI MATSUDA
Department of Physics, Faculty of Science, Tokyo Metropolitan University, Tokyo, Japan

(*Received* 6 *June* 1968; *in revised form* 21 *October* 1968)

Abstract—To discuss the remarkable variation of the Hall coefficient ($R_{//}$) of noble metals with temperatures near 100°K, the $R_{//}$ of copper was calculated on the basis of a simple twoband model due to the anisotropy of the relaxation time.

In order to examine how an impurity contributes to the variation, the $R_{//}$ of dilute copper alloys containing about 1 at. %. In, Ge, Sn and 0·5 ~ 5 atomic percent Al was measured over the temperature range 77°–300°K. It was found that the variation of $R_{//}$ in pure copper is reduced by a small addition of various solutes and it was discussed through the scattering mechanism.

1. INTRODUCTION

At present we have very little information about the anisotropy of the relaxation time over the Fermi surface, though there have been some experimental or theoretical investigations[1–9] with respect to anisotropies of the relaxation time of noble metals and its dilute alloys.

Now, the Hall coefficient ($R_{//}$) of noble metals[10–12] show a relatively rapid variation with temperatures below approximately 100°K, as shown in Fig. 1. This remarkable temperature-variation of the Hall coefficient cannot be caused by the non-sphericity of the Fermi surface. Ziman[1] suggested that it can be explained qualitatively by introducing the anisotropic relaxation time. Moreover, Kushibe and Yokota[13] inferred that the temperature-variation of R_H of alkali metals is caused more dominantly by anisotropies of the relaxation time. Thus the anisotropy of the relaxation time seems to reflect on the temperature-variation of R_H and it is interesting to investigate this.

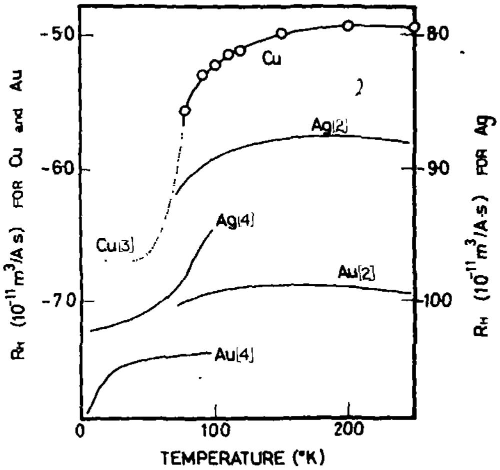

Fig. 1. Variation of the Hall coefficient of noble metals with temperature at moderately low temperatures; circular points: present work: [2] after Koster *et al.* (1963); [3] after Berlincourt (1958); [4] after Fukuroi and Ideda (1956).

In this paper, we shall actually calculate the Hall coefficient of copper as a function of the anisotropic relaxation time and use the result to explain the remarkable temperature variation successfully. It is of particular interest to examine how an impurity contributes to the variation of the Hall coefficient with temperature, from which we must be able to expect some information about the anisotropy of the impurity scattering. In order to ascertain the above expectation, the Hall coefficient of dilute binary copper alloys containing about one atomic percent Ge, In, Sn and 0·5 ~ 5 at. % Al was measured over the temperature range 77°–300°K.

2. EFFECTS OF ANISOTROPIES OF THE RELAXATION TIME UPON THE HALL COEFFICIENT

2.1 *A numerical calculation of the Hall coefficient of copper*

Ziman[3] assumed a constant relaxation time in his calculation, by the eight cone model, of the Hall coefficient of noble metals. To consider the variation of the Hall coefficient with temperature we shall modify his calculations by introducing an anisotropic relaxation time. Ziman[2] also tried from a theoretical point of view to make some estimate of the anisotropy of the relaxation time in a noble metal. To do so, he considered two extreme groups of electrons on the Fermi surface. Along these lines we shall make a simplification of the anisotropic relaxation time. We consider two groups of states: The belly states and the neck states. Let us assume that the electrons in each state have averaged relaxation times τ_B and τ_N respectively. The anisotropy we assume here, can be expressed as τ_N/τ_B.

Our notations are almost same as Ziman's [3], that is, U_{111}: $\{111\}$ component of Fourier coefficients of the lattice potential; p: the distance from the origin to midpoint of a hexagonal face (See Fig. 2).

The electron energy in unit of $(\hbar^2p^2/2m)$ is given in dimensionless form $\epsilon = x^2+y^2+2f(z)$; where $x \equiv k_x/p$; $y \equiv k_y/p$; $z \equiv k_z/p$; $2f(z) = 1+(1-z)^2-[u^2-4(1-z)^2]^{1/2}$ and $u \equiv U_{111}/(\hbar^2p^2/2m)$. The hypothetical Fermi surface is divided by the $z = z_0$ plane into two regions, i.e. the belly states and the neck states, as shown in Fig. 2. z_0 represents a value of ordinate z at which $\partial^2f(z)/\partial z^2 = 0$. z_1 denotes a value of ordinate z at which the surface terminates on the sloping sides of the cone.

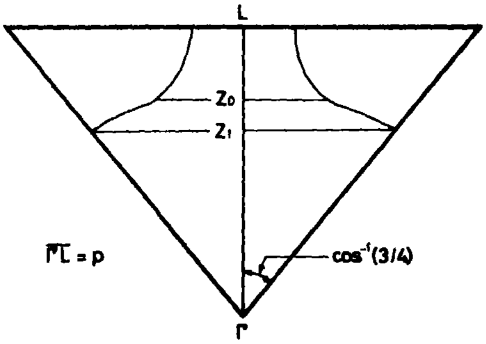

Fig. 2. A section, containing the axis of revolution (z-axis), of a cone.

The Hall coefficient is calculated from the well-known formula (for instance, equations (7.1) (7.4) in reference [3]), but as a function of τ_N/τ_B. By a trivial algebraic manipulation we obtain

$$R_H = \frac{1}{8n_0'ceN}\cdot\frac{F_1+(\tau_N/\tau_B)^2F_2}{\{F_3+(\tau_N/\tau_B)F_4\}^2}$$
$$= -0{\cdot}673\times10^{-11}\cdot\frac{F_1+(\tau_N/\tau_B)^2F_2}{\{F_3+(\tau_N/\tau_B)F_4\}^2} \quad (1)$$
$$(\mathrm{m}^3/\mathrm{C})$$

where N is the number of atoms per unit volume; c is the light velocity; e is the electronic charge; and n_0' is the number of electrons per atom contained in the inscribed sphere to $\{111\}$ planes, and

$$F_1 = I_1{}^B+4I_2{}^B+(\epsilon-2f(z_0))f'(z_0) - (\epsilon-2f(z_1))f'(z_1) \quad (2)$$

$$F_2 = I_1{}^N+4I_2{}^N+(2f(z_0)-\epsilon)f'(z_0) \quad (3)$$

$$F_3 = I_1{}^B+I_2{}^B \quad (4)$$

$$F_4 = I_1{}^N+I_2{}^N \quad (5)$$

$$I_1 = \int[\epsilon-2f(z)]\,\mathrm{d}z \quad (6)$$

$$I_2 = \int[f''(z)]^2\,\mathrm{d}z \quad (7)$$

$$I_i{}^B = I_i(z_0)-I_i(z_1) \quad (8)$$

$$I_i{}^N = I_i(1)-I_i(z_0) \quad (9)$$

z_0 is given by

$$z_0 = 1-(u/2)[2^{2/3}u^{-2/3}-1]^{1/2}. \quad (10)$$

The primes and double primes denote,

respectively, the partial and second partial derivatives of f with respect to z. When n and u are given, z_1 and ϵ are decided by solving the simultaneously equations,

$$n = (3\sqrt{3}\pi/2)\{(7/27)z_1{}^3 + [I_1]^1_{z_1}\} \quad (11)$$

and

$$\epsilon = (7/9)z_1{}^2 + 2f(z_1). \quad (12)$$

Thus we can compute R_H for various values of u and τ_N/τ_B.

In Fig. 3 we plot the Hall coefficient calculated as a function of τ_N/τ_B for various values of u. In our computation, 0·30, 0·35 and 0·40 are taken as values for u, and τ_N/τ_B are changed from 0·40 to 2·00 at intervals of 0·05. The numerical relation of u with the energy gap ($2U_{111}$) at the zone face is shown in Table 1. Our values for u are based on the following backgrounds:

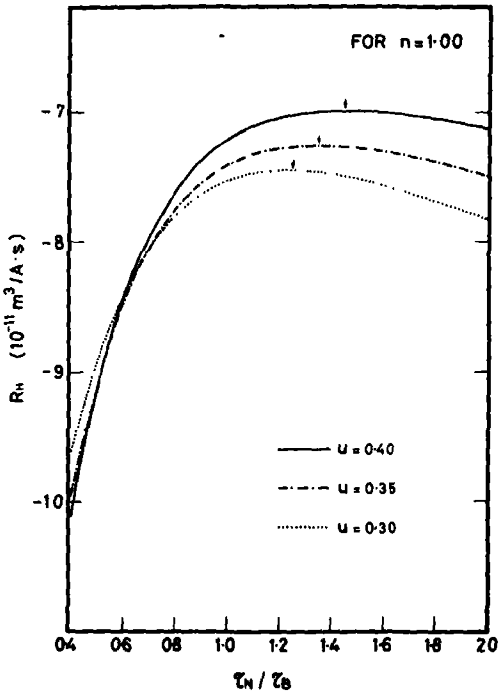

Fig. 3. The Hall coefficient calculated as a function of τ_N/τ_B, the ratio of the relaxation time on the neck states to that on the belly states, for various values of u.

Table 1. The numerical relation of u *with the energy gap at the* {111} *zone face*

u	$2U_{111}$(eV)
0·30	5·25
0·35	6·12
0·40	7·00

(1) For copper, the contact on the {111} faces at the zone occurs only when the value of $2U_{111}$ is more than approximately 5·2 eV.

(2) The calculated value of the neck radius for $u = 0{\cdot}40$ is close to the measured value due to the de Haas-van Alphen effect of Shoenberg[14].

We find in Fig. 3 that the R_H decreases rapidly with decreasing τ_N/τ_B for the range of $\tau_N/\tau_B < 1$ and has a maximum at about 1·4 in τ_N/τ_B. When we return the measured Hall coefficient of copper, it reminds us of the fact that the R_H decreases rapidly with decreasing temperature at about 100°K and has a maximum at around 200°K. It is interesting to note that the two curves (calculated and measured) are very similar to each other, although they have different abscissas. The calculated Hall coefficient shifts somewhat in absolute value from the measured one, but the difference can be winked within our approximations. Figure 4 shows the Hall coefficient calculated as a function of τ_N/τ_B for various values of n (the number of conduction electrons per atom) for the case $u = 0{\cdot}40$, provided that the theoretical values are normalized to the measured ones by fitting both maxima.

Thus, present calculations suggest that if τ_N/τ_B is a monotonic function of temperature, we may be able to explain the observed temperature dependence of the Hall coefficient in terms of τ_N/τ_B.

2.2 *The remarkable temperature variation of the Hall coefficient of copper*

It is found from preceding calculations that (1) the R_H varies considerably with varying τ_N/τ_B in the range of τ_N/τ_B less than unity,

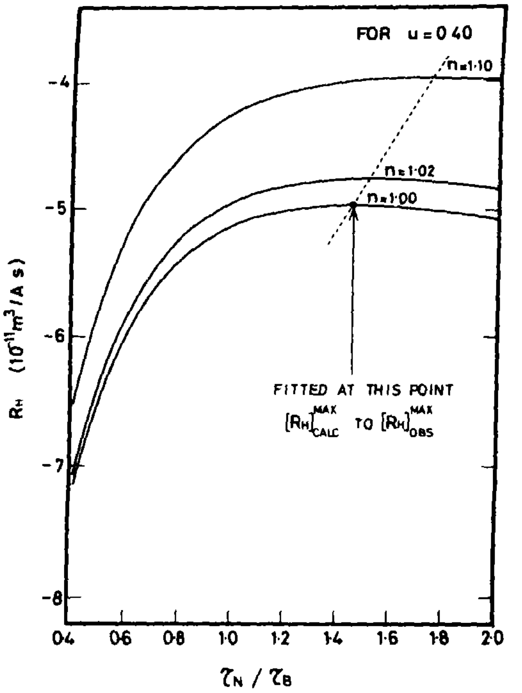

Fig. 4. The Hall coefficient calculated as a function of τ_N/τ_B for various values of n for the case $u = 0{\cdot}40$, provided that the theoretical values are normalized to the measured ones by fitting both maxima of those curves.

and (2) if, in fact, the value of τ_N/τ_b decreases effectively, from unity below around 100°K, the remarkable temperature variation of R_H observed experimentally, may be successfully explained.

Consequently, we shall consider how τ_N/τ_B depends on temperature. According to MacDonald[15], the probability of the occurance of electron-phonon U-processes at low temperature diminishes very rapidly, more or less as $\exp(-\theta^*/T)$, where θ^* is a characteristic temperature, which relates very roughly to the distortion of the Fermi surface from the ideal sphere corresponding to perfectly free electrons. Typically θ^* is assumed to be about 20°-50°K in metals. Figure 5 illustrates exp $(-\theta^*/T)$ for θ^* with 30°K as a function of temperature. It is well-known that if the Fermi surface does not touch the zone boundary there is a lower limit to the wave vector of a phonon participating in a U-process. This is easily understood on a repeated zone scheme as shown in Fig. 6. Now, let us consider two extreme groups of electrons on the Fermi surface. We assume that probabilities of occurance of electron-phonon U-process in these two bands (say α, β) can be represented by two different curves as shown in Fig. 7. When the temperature falls from T_2 to T_1, the probability P_β in band β decreases markedly more than P_α in band α. In this case, both relaxation times (say τ_α, τ_β) become longer with decreasing temperature, but the increase of τ_β is more marked.

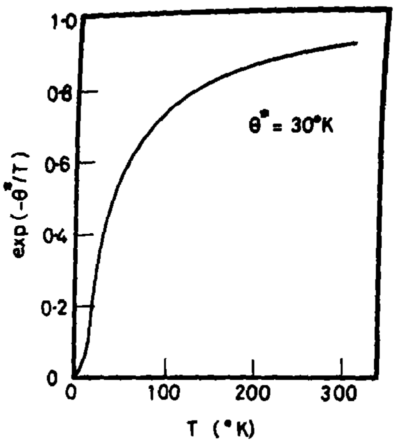

Fig. 5. $\exp(-\theta^*/T)$ for $\theta^* = 30$, plotted as a function of T.

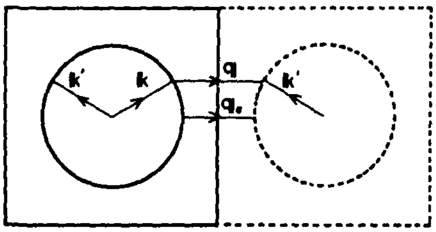

Fig. 6. The lower limit of a wave vector of a phonon participating in a U-process.

In fact, we can make the belly state and the

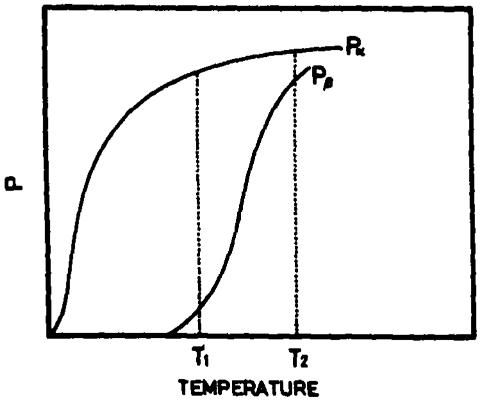

Fig. 7. Probabilities of the occurance of the electron–phonon U-process in two bands.

neck state correspond approximately to β and α respectively. For, as argued by Ziman, the U-processes on the belly states are rapidly quenched with decreasing temperature and the relaxation time τ_B, governed by N-processes, increases promptly, since at low temperatures only the long wave phonons are excited. There is no lower limit of the wave vector on the neck states, and U-processes occur down to the lowest temperature. In fact, both τ_B and τ_N become longer with decreasing temperature, although the increase of τ_B is more marked. Therefore, at low temperatures, the ratio τ_N/τ_B decreases rapidly with falling temperature. At high temperatures, where large values of the wave vector are allowed, we may expect that the scattering will be rather isotropic.

Thus the temperature variation of τ_N/τ_B is ascribed to the fact that the probability of an occurance of U-processes on two extreme groups varies differently according to temperature. This situation is reflected in the remarkable temperature variation of the Hall coefficient.

Also, it is interesting to estimate the temperature dependence† of τ_B/τ_N on the connection between the observed R_H-T curve and the calculated $R_H-\tau_N/\tau_B$ relation. The results are compared to other estimates due to Ziman [2] on a theoretical calculation, due to Häussler and Welles[16] on Azbel'-Kaner cyclotron resonance experiments, and due to Dugdale and Basinski (8) on experiments of departures from Matthiessen's rule. As seen from Fig. 8, they are in fair agreement.

The result of this calculation indicates that the remarkable variation of the R_H of pure copper with temperature may be explained through the change of the ratio, τ_N/τ_B, due to the rapid increase of τ_B. In the next section, we shall see how an impurity contributes to the variation of the Hall coefficient with temperature and how anisotropies of the impurity scattering reflect on it.

3. EFFECT OF THE IMPURITY SCATTERING ON THE HALL COEFFICIENT

3.1 *Experiments*

In order to examine the effect of impurity on the temperature variation of R_H, the R_H

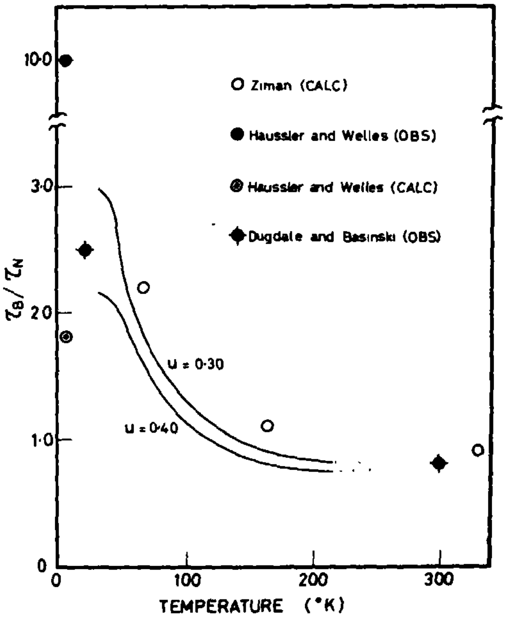

Fig. 8. Variation of τ_B/τ_N with temperature, estimated by the observed R_H-T curves and the calculated $R_H-\tau_N/\tau_B$ relations with the aid of the data observed by Berlincourt.

---

†Conforming to Ziman[2], we shall refer to τ_B/τ_N here, instead of τ_N/τ_B.

of dilute copper alloys containing about 1 at.% In, Ge, Sn and 0·5 ~ 5 at.% Al was measured over the temperature range 77°–300°K. The experimental procedure and results are summarized in Tables 2 and 3 respectively. The small Hall voltage necessitated very careful measurement. The error in the measured Hall coefficient is almost ±0·5 per cent.

Table 2. Experimental procedure

Purity of constituent metals	99·999 per cent or better
Weight of samples	30 g
Melting	by induction furnace in a high purity graphite crucible under vacuum or argon atmosphere
Weight loss after melting	negligible, 0·06 per cent at most
Heat treatment	ingots: annealing at about 650°C for 7 days specimens: annealing at about 400°C for 10 hours
Specimen size	40 × 4 × 0·3 mm
Measurement of R_H	by usual d.c. technique primary current: 1 amp. magnetic field: 1·2 × 10⁴ Oe

Table 3. Experimental data for the Hall coefficient of dilute copper alloys

Specimen	Temperature (°K)	$-R_H$ (10^{-11} m³/A·s)	Specimen	Temperature (°K)	$-R_H$ (10^{-11} m³/A·s)	Specimen	Temperature (°K)	$-R_H$ (10^{-11} m³/A·s)
Pure Cu	77	5·56	0·63 at.%Al	77	4·99	2·00 at.%Al	77	4·56
	90	5·32		93	4·97		93	4·54
	100	5·23		107	4·95		107	4·50
	110	5·15		121	4·92		119	4·52
	120	5·13		133	4·86		132	4·56
	150	5 00		161	4·90		154	4·58
	200	4·97		213	4·92		179	4·64
	250	4·97		251	4·92		200	4·65
	292	5·01		298	5·04		245	4·69
0·96 at.%In	77	4·34	1·07 at.%Al	77	4·84		299	4·76
	98	4·36		93	4·80	2·55 at.%Al	77	4·57
	119	4·43		103	4·81		94	4·56
	150	4·56		119	4·78		108	4·55
	247	4·71		135	4·76		121	4·57
	289	4·77		157	4·77		135	4·58
0·97 at.%Sn	77	4·59		205	4·82		157	4·58
	96	4·82		246	4·87		178	4·60
	120	4·89		300	4·97		197	4·61
	198	4·95	1·56 at.%Al	77	4·70		244	4·66
	246	5·03		88	4·68		299	4·68
	293	5·16		104	4·64	5·00 at.%Al	77	4·29
1·00 at.%Ge	77	5·35		117	4·62		95	4·28
	96	5·35		132	4·62		109	4·31
	117	5·33		153	4·65		121	4·31
	150	5·27		175	4·70		135	4·30
	200	5·27		202	4·73		158	4·31
	245	5·29		249	4·78		180	4·34
	290	5·52		298	4·86		202	4·33
							250	4·36
							299	4·35

Figure 9 shows the change of the temperature dependence of the Hall coefficient of copper caused by the addition of about 1 at% of various impurities. The curve of the copper-zinc systems is estimated from the measurement by Köster and Rave[17]. Figure 10 also shows the temperature variation of the R_H for dilute Cu–Al alloys.

In order to show the characteristic features more clearly, we note the deviation, ΔR_H, from a straight line obtained by extrapolating the high temperature (200° ~ 300°K) branch of the R_H. Figures 11 and 12 show ΔR_H, estimated from Figs. 9 and 10 respectively, as a function of temperature.

Figure 13 shows the R_H of alloys of present interest, plotted against the electron-atom ratio (e/a), where (i) indicates the behavior at room temperature and (ii) the behavior at liq. N_2 temperature. It should be noted that (i) and (ii) have very different features.

We find from the above results that (1) the rapid increase in $|R_H|$ at about 100°K

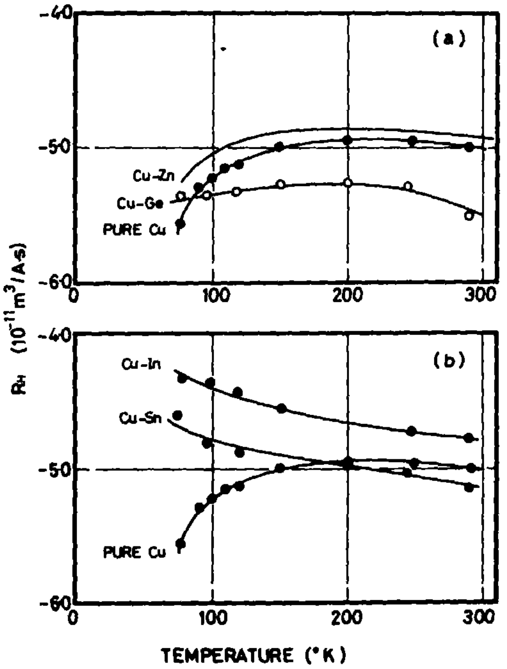

Fig. 9. Temperature dependence of the Hall coefficient of copper and its binary alloys containing about one atomic percent Zn, Ge, In and Sn. The curve for Cu–Zn is estimated from the data of Köster and Rave.

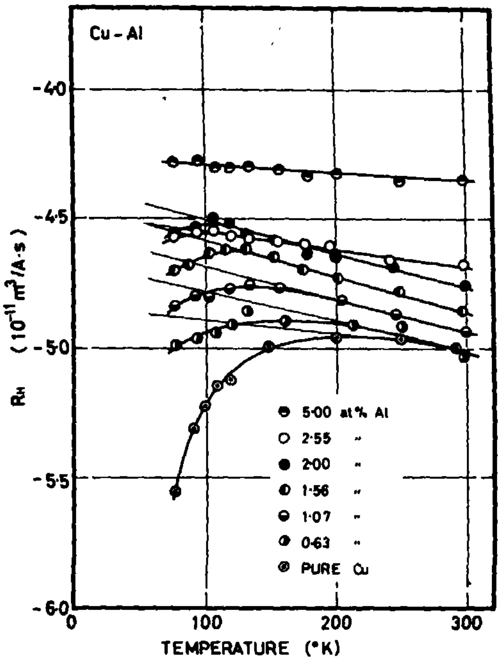

Fig. 10. Variation of the Hall coefficient of Cu–Al alloys with temperature.

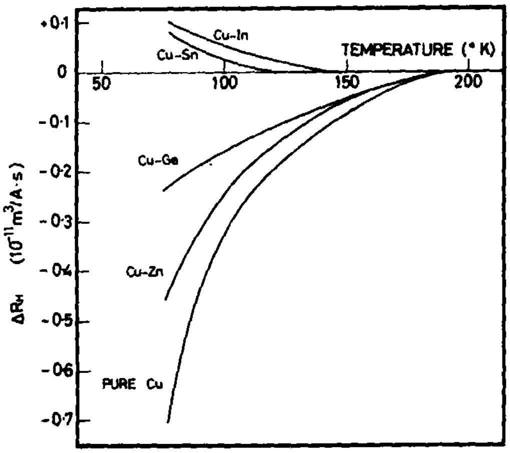

Fig. 11. Deviation, ΔR_H of the observed R_H, of various copper alloys, from a straight line obtained by extrapolating the high temperature branch (200° ~ 300°K).

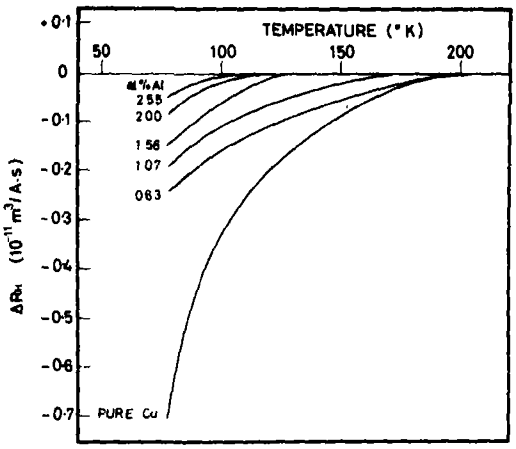

Fig. 12. Deviation, ΔR_H, of the observed R_H, of Cu–Al alloys, from a straight line obtained by extrapolating the high temperature branch (200°–300°K).

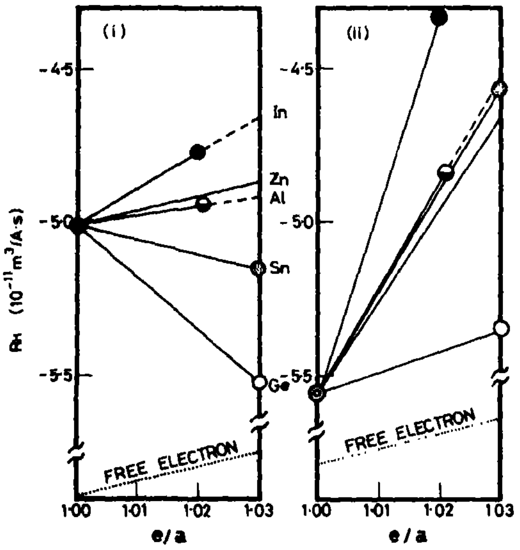

Fig. 13. The Hall coefficient of dilute copper alloys, plotted against the electron-atom ratio; (i) at room temperature (ii) at liq. N_2 temperature.

in pure copper is relieved or stopped by a small addition of various impurities, (2) the extent of reduction depends on the sort of impurity and on its concentration: For the case of alloys containing Zn and Ge as an impurity, the R_H shows a similar tendency to that of pure copper (Fig. 9(a)). For In or Sn, it shows different behavior (Fig. 9(b)). ΔR_H decreases with an increase of the solute concentration and vanishes in the case of 5 at.% of Al (Fig. 12), and (3) the *e/a*-dependences of R_H are different at different temperatures (Fig. 13).

To understand these results we must take into consideration anisotropies of impurity scattering as well as those of phonon scattering.

3.2 *Introduction of anisotropic impurity scattering*

3.2.1 *Temperature dependence of the R_H of dilute copper alloys.* As in the case of a dilute alloy, in the absence of better information it is natural to assume that

$$\tau_N^{-1} = \tau_{NP}^{-1} + \tau_{NI}^{-1}$$

and

$$\tau_B^{-1} = \tau_{BP}^{-1} + \tau_{BI}^{-1} \qquad (13)$$

where τ_{NP} and τ_{NI} denote the relaxation times for phonon scattering and for impurity scattering, respectively, on the neck states and τ_{BP}, τ_{BI} those on the belly states. τ_{NP} and τ_{BP} depend upon temperature, but τ_{NI} and τ_{BI} are almost independent of temperature. We obtain from equation (13) that

$$\tau_N(T)/\tau_B(T) = (\tau_{NP}(T)/\tau_{BP}(T))\,\frac{1+\tau_{BP}(T)/\tau_{BI}}{1+\tau_{NP}(T)/\tau_{NI}}. \qquad (14)$$

We shall define the ratio

$$A_I = \tau_{NI}/\tau_{BI} \qquad (15)$$

which denotes an anisotropy parameter for impurity scattering. We can express the impurity resistivity as

$$\rho_I = [C\tau_{BI} + C'\tau_{NI}]^{-1} \qquad (16)$$

where C and C' are constants which are almost independent of the sort of impurity.

Substituting (15) and(16) into (14) we obtain

$$\tau_N(T)/\tau_B(T) = (\tau_{NP}(T)/\tau_{BP}(T)) \times \left\{\frac{1+\rho_I(C+C'A_I)\tau_{BP}}{1+\rho_I(C/A_I+C')\tau_{NP}}\right\}. \quad (17)$$

Conveniently we express

$$\tau_N(T)/\tau_B(T) = (\tau_{NP}(T)/\tau_{BP}(T)) \cdot \Phi(T) \quad (18)$$

where

$$\Phi(T) \equiv \frac{1+\rho_I(C+C'A_I)\tau_{BP}}{1+\rho_I(C/A_I+C')\tau_{NP}}.$$

Two limiting cases can readily be considered; (a) For pure copper, $\rho_I = 0$; thus the temperature variation of τ_N/τ_B is governed only by that of τ_{NP}/τ_{BP}. (b) For high impurity concentration, $\tau_N/\tau_B \approx A_I$.

The case which is of more interest to us is an intermediate one, i.e. we are interested in dilute alloys. For pure copper we have already seen that the remarkable variation of the R_H with temperature may be ascribed to the rapid decrease of τ_{NP}/τ_{BP} due to the abrupt increase of τ_{BP} at low temperatures. For a dilute alloy it is not τ_{NP}/τ_{BP} which contributes to the temperature variation of R_H, but rather τ_N/τ_B in equation (17), namely τ_{NP}/τ_{BP} multiplied by Φ(T). For dilute alloys, the maximum impurity content being a few at.% we can almost neglect the change of τ_{NP}/τ_{BP} due to alloying. As seen from the functional forms of equations (17) and (18), Φ has a tendency to compensate for the variation of τ_{NP}/τ_{BP} with temperature. Thus it is expected that the temperature variation of R_H in dilute alloys will be smaller than that in pure copper. The extent which $\Phi(T)$ compensates for the temperature variation of τ_{NP}/τ_{BP} depends on the magnitude of the coefficient of τ_{BP} in Φ; if this is small, the extent of compensation is small. In expression (17), therefore, there are two factors that determine how R_H depends on impurity: one is the impurity resistivity ρ_I and the other is A_I.

If ρ_I and A_I are small, the extent of compensation is small, hence, the temperature variation of R_H of the alloy approaches that of pure copper. As seen from Figs. 9 or 10, the temperature variation of R_H of Cu–Zn and Cu–Ge approaches that of pure copper, and those of Cu–In and Cu–Sn do not. Let us pursue the situations of ρ_I and A_I for these various impurities.

ρ_I may be seen from the following data taken from Linde's measurements, where x denotes the solute concentration and

Solute	Zn	Ge	In	Sn	Al
$d\rho_I/dx$	0·32	3·79	1·06	2·88	1·25

$d\rho_I/dx$ is expressed in $\mu\Omega$ cm/at.%. From this fact with respect to ρ_I, we can explain, qualitatively, the experimental results (1) and (2), with a further assumption for A_I as follows; (cf. Appendix)

Impurities	Zn	Ge	In	Sn	Al
A_I	≈ 1	< 1	> 1	≈ 1	≈ 1

(I) *Zn*: As seen from equation (17), the extent of compensation may be small since ρ_I is extremely small for this alloy. Hence, the temperature variation of the R_H would approach that of pure copper.

(II) *Ge*: ρ_I is very large for this case. But, if A_I is considerably small so that the extent of compensation may be small, the temperature variation of the R_H is also comprehensible.

(III) *In*: ρ_I is not so large. But, if A_I is large so that the extent of compensation may be large, the experimental result can be understood.

Similar explanations are available for the case of other impurities. In Fig. 12 $|\Delta R_H|$ decreases with increasing of Al concentration. This would be ascribed to the increase of ρ_I with increasing of Al concentration.

Our assumption for A_I may be assured by the fact that it is able to satisfy also the result (3) as can be seen in the next.

3.2.2 *e/a dependence of the R_H.* Inspecting the data in the past it is found that there is a tendency for the curve of R_H plotted against e/a to have a 'cusp' or a 'valley' at the e/a corresponding to pure metal [18–20]. Figure 14 shows schematically this behavior of R_H. It has been explained mainly due to anisotropic impurity scattering by many authors[1, 3, 18–25]. Generally speaking, different impurities produce different shapes of the cusp (or valley). It is plausible that the steepness of the cusp (or valley) depends on the difference of the anisotropy of impurity scattering with that of phonon scattering at the temperature. If the anisotropy of impurity scattering is largely different from that of phonon scattering, it is expected that a large cusp (or valley) appears.

In Fig. 14, (A) indicates the case of the large difference, (C) the case of almost same anisotropy and (B) the intermediate case. Since the anisotropy of phonon scattering varies with temperature and that of impurity scattering is independent of temperature, the shape of the cusp (valley) is to depend on temperature.

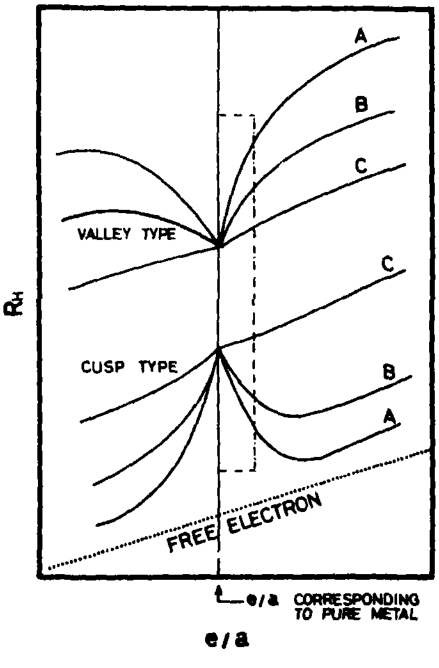

Fig. 14. Characteristic behaviors of the Hall coefficient drawn schematically against *e/a* of usual dilute alloys.

We shall express the anisotropy of phonon scattering as

$$A_P = \tau_{NP}/\tau_{BP} \tag{19}$$

in contrast to $A_I = \tau_{NI}/\tau_{BI}$. It should be remembered that

$$A_P \begin{cases} \approx 1 & \text{at room temperature,} \\ < 1 & \text{at liq. } N_2 \text{ temperature.} \end{cases}$$

Figure 13 corresponds to the part of the initial slope enclosed with broken line in Fig. 14. Thus we shall show that the result (3) can be plausibly explained if we use our assumption for A_I.

(I) *Zn (assumed $A_I \approx 1$).* In Fig. 13 (i), where $A_P \approx 1$, we can infer $A_I \approx A_P$ since the slope for Zn is close to the free electron slope. Therefore, $A_I \approx 1$. In Fig. 13 (ii), where $A_P < 1$, it is reasonable that slope for Zn is more steep than the free electron slope.

(II) *Ge (assumed $A_I < 1$).* In Fig. 13 (ii), where $A_P < 1$, we can find $A_I \approx A_P$, since the slope for Ge is near to the free electron slope. Therefore, $A_I < 1$. In Fig. 13 (i), where $A_P \approx 1$, the slope for Ge is reasonable.

(III) *In (assumed $A_I > 1$).* Figure 13 (i) tells us that $A_I > 1$ for this case. Figure 13 (ii) is also the case.

Similar explanations are available for the case of other impurities.

Thus, our assumptions for A_I are likely to satisfy both the concentration dependence at different temperatures and the temperature dependence of R_H for copper alloys. Here we must refer to the work of Barnard[25], who derived that $A_I < 1$ for all of copper and silver alloys. It is difficult to understand the present result by his suggestion, as seen from this section. The origin of this discrepancy is not so clear at the present stage, but we may say that it comes partly from the fact as follows; Barnard's estimation of A_l is made on rather uncertain assumption that effective number of free electrons are separated into two terms associated with impurity scattering and with the band structure produced by alloying.

3.3 *Au–Ag alloys*

This explanation is also applicable for the comparison between Au in Ag and Ag in Au dilute alloy systems. These elements both have the same valency and also nearly same atomic volume. Both alloys have the same $d\rho_l/dx$, 0·36 in $\mu\Omega$ cm/at.%. Hence it is expected that the effect of only A_l reflects directly on the temperature dependence of the Hall coefficient. For the case of such parent metal and such impurity, impurity scattering is well known to be predominantly s-like symmetry[2, 8]. On the neck the electrons are in p-state for Ag and rather s-like for Au according to Cohen and Heine [26]. For Au in Ag, therefore, the neck electrons would scarcely be scattered by this impurity (Au) though for Ag in Au they would not. Thus we may be able to predict about A_l of both alloys as follows:

$$A_l \begin{cases} >1 & \text{for Au in Ag,} \\ <1 & \text{for Ag in Au.} \end{cases}$$

This situation is reflected in the R_H of these alloys, which are plotted against a solute concentration measured by Köster, Hagman and Saeger (10), as shown in Fig. 15. Figure 16 shows the temperature variation of the R_H measured by them. This behavior would also confirm the above predictions about A_l, although the comparison between both alloys is inappropriate because of the different concentrations of these alloys.

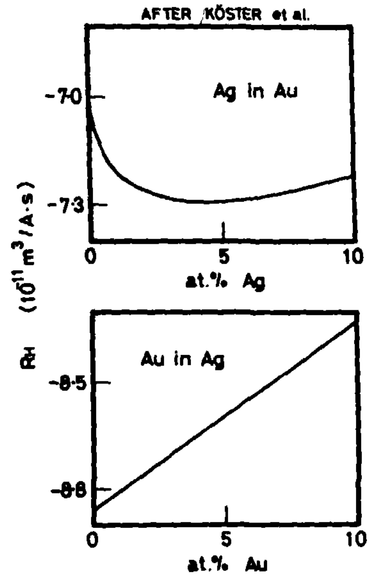

Fig. 15. The Hall coefficient of Au–Ag dilute alloys, plotted as a function of solute concentration. Data taken from Köster, Hagman and Saeger (1963).

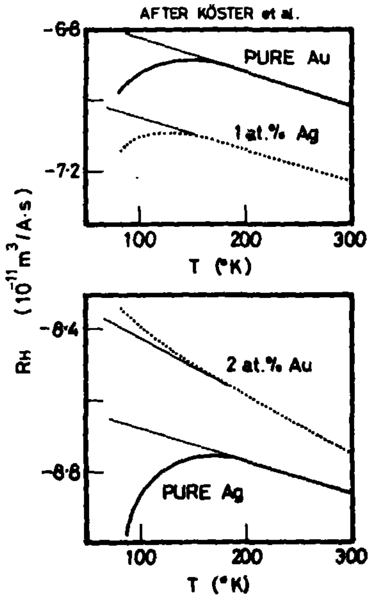

Fig. 16. Temperature variation of the Hall coefficient of Au–Ag dilute alloys. After Köster, Hagman and Saeger (1963).

4. CONCLUSION

We calculated the Hall coefficient of copper as a function of the anisotropic relaxation time. In the analysis, (1) We considered two extreme groups of electrons on the Fermi surface; the belly states and the neck states. (2) We assumed that the electrons in each state had average relaxation times (τ_B and τ_N). (3) We expressed the anisotropy of the relaxation times as τ_N/τ_B.

Obviously our division into extreme groups of electrons on the Fermi surface may be an oversimplification, but we can expect to find from this simple two-band model the qualitative effects caused by an anisotropic relaxation time. We found, as a result of a numerical calculation, that R_H varies considerably with varying τ_N/τ_B in the range of this ratio less than unity. The temperature variation of τ_N/τ_B was ascribed to the fact that the probability of the occurence of a *U*-process on two extreme groups varies differently with temperature. This situation is reflected by the remarkable temperature variation of the R_H below a temperature of about 200°K.

In order to examine how an impurity contributes to the variation of the Hall coefficient with temperature, the Hall coefficient of several dilute copper alloys containing about 0·5–5 at.% solute were measured over the temperature range 77°–300°K. We found that the remarkable temperature variation of R_H in pure copper is reduced by a small addition of various solutes and that the extent of this reduction depends on the sort of impurity and its concentration. It was stated that this reduction depends on the impurity resistivity (ρ_I) and also upon an anisotropy parameter for impurity scattering, $A_I = \tau_{NI}/\tau_{BI}$. As for this matter, however, further systematic experiments would be required.

Acknowledgements—The author wishes to express his sincere gratitude to Professor T. Sato for his continued interest and encouragement. He is also very grateful to Dr. K. Yonemitsu, Mr. K. Takano and Miss I. Shiozaki for their illuminating discussions at every stage of the present work.

REFERENCES

1. COOPER J. R. A. and RAIMES S., *Phil. Mag.* **4**, 145 (1959).
2. ZIMAN J. M., *Phys. Rev.* **121**, 1320 (1961).
3. ZIMAN J. M., *Adv. Phys.* **10**, 1 (1961).
4. DEATON B. C. and GAVENDA J. D., *Phys. Rev.* **129**, 1990 (1963).
5. KING-SMITH P. F., *Phil. Mag.* **12**, 1123 (1965).
6. HEINE V., *Phil. Mag.* **12**, 53 (1965).
7. DUGDALE J. S. and BAILYN M., *Phys. Rev.* **157**, 485 (1967).
8. DUGDALE J. S. and BASINSKI Z. S., *Phys. Rev.* **157**, 552 (1967).
9. VAN BAARLE C., *Physica* **33**, 424 (1967).
10. KÖSTER W., HAGMAN D. and SAEGER K. E., *Z. Metallk.* **54**, 619 (1963).
11. BERLINCOURT T. G., *Phys. Rev.* **112**, 381 (1958).
12. FUKUROI T. and IKEDA T., *Sci. Rep. Tohoku Univ.* **A8**, 205 (1956).
13. KUSHIBE H. and YOKOTA M., *Prog. theor. Phys.* **34**, 320 (1965).
14. SHOENBERG D., *Phil. Mag.* **5**, 105 (1960).
15. MACDONALD D. K. C., *Principles of Thermoelectricity*. Wiley, New York (1962).
16. HÄUSSLER P. and WELLES S. J., *Phys. Rev.* **152**, 675 (1966)
17. KÖSTER W. and RAVE H., *Z. Metallk.* **55**, 750 (1964).
18. YONEMITSU K., TAKANO K., HISHIYAMA Y., MATSUDA T. and SHIOZAKI I., *J. phys. Soc. Japan* **20**, 1797 (1965).
19. TAKANO K. and SATO T., *J. phys. Soc. Japan* **20**, 2013 (1965).
20. MATSUDA T. and SATO T., *J. phys. Soc. Japan* **21**, 1494 (1966).
21. TAKANO K., YONEMITSU K. and SATO T., *J. phys. Soc. Japan* **21**, 1053 (1966).
22. TAKANO K., *J. phys. Soc. Japan* **23**, 1234 (1967).
23. HURD C. M., *Phil. Mag.* **12**, 47 (1965).
24. HURD C. M., *Z. Metallk.* **58**, 194 (1967).
25. BARNARD R. D., *Phil. Mag.* **14**, 1097 (1966).
26. COHEN M. H. and HEINE V., *Adv. Phys.* **7**, 395 (1957).

APPENDIX

This assumption for A_I is likely to be justified by the following rough estimation of $|\Delta R_H|$. Using A_P given by equation (19)

$$\tau_N/\tau_B = A_P \cdot \Phi, \qquad \text{(A-1)}$$

where

$$\Phi = \frac{1 + \tau_{NP}\rho_I(C + C'A_I)/A_P}{1 + \tau_{NP}\rho_I(C/A_I + C')}. \qquad \text{(A-2)}$$

Let us estimate values of Φ at about 80°K for each alloys containing about 1 at.% impurities as a function of A_I. From the discussion in Section 2.2 we postulate that $A_P \approx 0{\cdot}6$ at 80°K. We note how τ_N/τ_B is modified by Φ in the case of alloys.

Constants C, C' are given by

$$C = \frac{Nn_Be^2}{\langle m_B\rangle} \quad \text{and} \quad C' = \frac{Nn_Ne^2}{\langle m_N\rangle}$$

where $\langle m_B \rangle$, $\langle m_N \rangle$ are average effective masses of the belly and the neck electrons respectively. n_B and n_N are numbers of belly and neck electrons per atom respectively and are given using the eight cone model as follows:

$$
\begin{aligned}
n_B &= \frac{3\sqrt{3}\pi}{2}\left[\frac{7}{27}Z_1{}^3 + \int_{Z_1}^{Z_0} (\epsilon - 2f(Z))\,\mathrm{d}Z\right] \\
n_N &= \frac{3\sqrt{3}\pi}{2}\int_{Z_0}^{1} (\epsilon - 2f(Z))\,\mathrm{d}Z.
\end{aligned}
\tag{A-3}
$$

When $u = 0{\cdot}4$ and $n(= n_B + n_N) = 1{\cdot}0$, we have $n_B = 0{\cdot}745$ and $n_N = 0{\cdot}255$. Using $\langle m_B \rangle \approx 1{\cdot}2$ and $\langle m_N \rangle \approx 0{\cdot}5$ (in electron mass unit) expected from the cyclotron mass measurement, we obtain $C = 13{\cdot}4 \times 10^{30}$ and $C' = 11 \times 10^{30}$ in c.g.s./e.s.u. unit. We shall use an appropriate value of τ_{NP} at about 80°K, perhaps $\sim 5 \times 10^{-14}$ sec. For ρ_I we can use $\mathrm{d}\rho_I/\mathrm{d}x$ from Linde's measurements. Thus Φ can be calculated for various alloys as a function of A_I. τ_N/τ_B is obtained by multiplying Φ by 0·6. Therefore, on the basis of the discussion in Section 2.2 we can roughly estimate $|\Delta R_H|$ at about 80°K as a function of A_I.

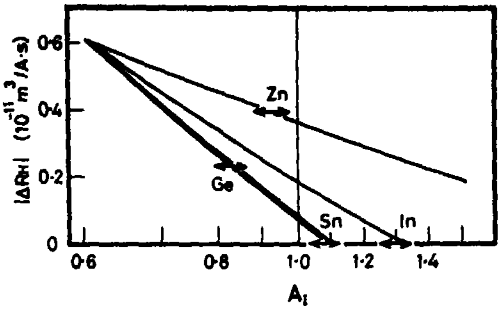

Fig. A-1. $|\Delta R_H|$ at about 80°K calculated as a function of A_I; arrows represent the range of experimental values.

The result is shown in Fig. A-1. As can be seen from the figure, we can approximately assume for A_I as follows;

$$
A_I \begin{cases} \approx 1 & \text{for Zn or Sn as impurity} \\ > 1 & \text{for In as impurity} \\ < 1 & \text{for Ge as impurity.} \end{cases}
$$

J. Phys. Chem. Solids Pergamon Press 1969. Vol. 30, pp. 873–879. Printed in Great Britain.

SUPERCONDUCTIVITY IN NIOBIUM AND NIOBIUM–TANTALUM ALLOYS

AKIRA IKUSHIMA* and **TAKAO MIZUSAKI**†
Department of Material Physics, Faculty of Engineering Science, Osaka University, Toyonaka, Osaka, Japan

(*Received* 16 *July* 1968; *in revised form* 23 *September* 1968)

Abstract—From magnetization measurements in superconducting Nb and Nb-rich Nb–Ta alloys, it was found that the discrepancies between experiment and theory in the upper critical field and two Ginzburg–Landau parameters as a function of temperature in pure Nb are directly related to the anisotropy of the superconducting energy gap, and not to its non-weak coupling nature.

Besides the above-mentioned conclusion, several electronic parameters were deduced from the measurements. The temperature coefficient of the electronic specific heat, γ, as a function of Ta concentration has a peak at several atomic per cent of Ta, whereas the superconducting transition temperature drops very rapidly from 9·23°K for pure Nb as Ta is added. An estimation of the carrier concentration in Nb showed that all carriers in the normal state probably go into the superconducting state at sufficiently low temperatures.

1. INTRODUCTION

RATHER extensive studies have been made of the magnetization behavior of the type II superconductors. One of the remarkable facts is[1–6] that the variations of the upper critical field, H_{c2}, and the two Ginzburg–Landau parameters, κ_1 and κ_2, as a function of temperature do not agree at all in pure Nb with any theoretical predictions given so far [7–10] based on the Ginzburg–Landau–Abrikosov–Gor'kov theory[11–13].

There is an experimental indication that Nb has two bands which are both in the superconducting state at sufficiently low temperatures[14]. However, it is not likely that the peculiar superconductivity characteristics of pure Nb come from its two-bands character, since the multi-band nature is very common in metals and alloys. Rather, it seems to be more reasonable to consider that it comes from the non-weak coupling nature of Nb and/or the anisotropy of the electronic structure.

Here, we would like to report an experimental result of magnetization measurements in pure Nb and several Nb-rich Nb–Ta alloys in their superconducting states, which were carried out in order to shed some light on the above-mentioned interesting problem. A brief report has already been given[15].

We chose the Nb–Ta system because it is very simple in the sense that Nb and Ta form solid solution alloys over the entire range of the composition[16], that the valence of Nb and Ta are the same, and that the lattice parameter does not change in three decimal places over the entire composition range[17]. The maximum Ta concentration in the present work was 19·7 at.%. This was determined because the electronic mean free path in that alloy was found to be short enough to correspond to the theoretical dirty limit. Recently Ogasawara[18] has made an investigation similar to this over Ta concentrations from 12·5 to 92 at.%.

**Present address:* Department of Physics and Materials Research Laboratory, University of Illinois, Urbana, Ill. 61803, U.S.A.

†*Present address:* Department of Physics, Rutgers, The State University, New Brunswick, N.J. 08903, U.S.A.

2. EXPERIMENTAL PROCEDURE

Specimen

The specimens were made from zone-refined Nb and Ta. The resistivity ratios of these starting materials were about 1100 and 600, respectively. They were melted to alloys of desired composition in an electron-beam melting furnace in a vacuum of 1×10^{-6} Torr., and then drawn into wires of about 2 mm dia. The alloy wires were then finally annealed in an ultra-high vacuum furnace with a vacuum of 1×10^{-10} Torr. just below the melting temperatures for about 1 week. The final dimension of the specimens was about 2 mm dia. and 22 mm length.

By the usual 4-points method with a d.c. potentiometer, the residual resistivities of the specimens were measured at 4·2°K while applying a magnetic field just above H_{c3} of each specimen. Table 1 lists the measured results for the residual resistivity ρ_r, the resistivity ratio Γ, and the mean free path of the electrons l_{tr}, derived from ρ_r as described in the last part of the next section.

Magnetization measurement[19]

Magnetization as a function of the magnetic field, $M(H)$, were deduced from the differential permeability. Varnish coated, thin copper wire of 0·05 mm dia. was wound around the specimen about 100 times as a pick-up coil. A magnetic field was applied in the longitudinal direction of the specimen and was increased or decreased at a constant rate. The electromotive force from the pick-up coil was amplified and fed to the Y-axis of an X–Y recorder. The X-axis of the recorder was the intensity of the magnetic field, so the recorder tracing obtained was $\mathrm{d}B/\mathrm{d}H$ vs. H, where B and H are the magnetic induction and the magnetic field in the specimen, respectively. Then, we could deduce the magnetization curve, $M(H)$, by integrating the recorder tracing.

The measurements were always made after demagnetization of the specimen by elevating the temperature above T_c.

As was already mentioned, the size of the present specimens was 22 mm length and 2 mm dia. So, by taking into account the demagnetization field, the correction of the magnetic field in the specimen was estimated to be 1·75 per cent at the lower critical field, H_{c1}, and of course was smaller than this figure at any other field strength[20].

The measured magnetization curves were found to be almost reversible: If we express the magnitude of the hysteresis as the difference of the area under the magnetization curve, $\int_0^{H_{c2}} M(H)\mathrm{d}H$, for the increasing and decreasing magnetic field, this difference was about 2 per cent in pure Nb and 5 per cent in the specimen of the largest Ta concentration.

3. EXPERIMENTAL RESULTS

Superconducting transition temperature

The transition temperature from normal to superconducting state was obtained by extrapolating the relation of H_{c1} and H_{c2} vs. temperature down to $H_{c1} = H_{c2} = 0$. Figure 1 shows the transition temperature plotted as a function of Ta concentration. The steep drop of T_c near pure Nb is remarkable.

Table 1. Specimens in this work

Specimen	No. 1	No. 2	No. 3	No. 4	No. 5	No. 6
at.% Ta	pure Nb	0·87	1·56	4·22	6·23	19·7
ρ_r($\mu\Omega$·cm)	0·016	0·219	0·373	0·843	1·29	2·56
Γ	1100	80	46	20	12	7·6
l_{tr} (10^{-4} cm)	3·78	0·27	0·16	0·070	0·046	0·023

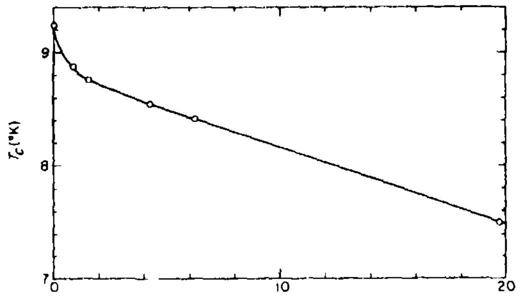

Fig. 1. Superconducting transition temperature, T_c, plotted vs. Ta concentration in the Nb–Ta system.

Critical fields and Ginzburg–Landau parameters

The lower critical field, H_{c1}, was defined in this study as the field strength at which the derivative dM/dH took on its maximum value. The thermodynamical critical field, H_c, was determined in the usual manner from $(\frac{1}{8}\pi)H_c^2 = \int_0 Hc_2 M(H)dH$.

In Fig. 2 are plotted the magnitude of three critical fields extrapolated to 0°K as a function

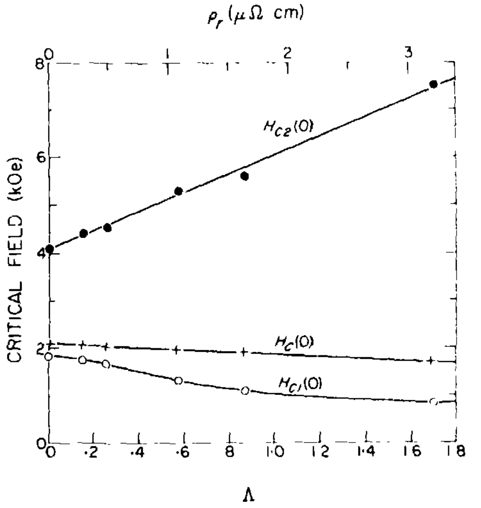

Fig. 2. Lower critical field H_{c1}, upper critical field H_{c2} and thermodynamical critical field H_c extrapolated to 0°K plotted vs. the residual resistivity ρ_r and the reduced collision frequency Λ.

of the residual resistivity and the reduced collision frequency, $\Lambda = \hbar/(2\pi k_B T_c \tau_{tr.}) = 0{\cdot}882\,\xi_0/l_{tr.}$, where $\tau_{tr.}$ is the collision time of electrons, $l_{tr.}$ is the mean free path of electrons estimated from the residual resistivity, and ξ_0 is the coherence distance in pure Nb estimated from the magnetization measurement. See Tables 1 and 2 and the last part of this section.

Figure 3 is the variation of the temperature derivative of the upper critical field at T_c, $(dH_{c2}/dT)_{T=T_c}$, as a function of Λ, together with the theoretical curve given by Helfand and Werthamer[21]. The agreement is bad for Λ less than unity.

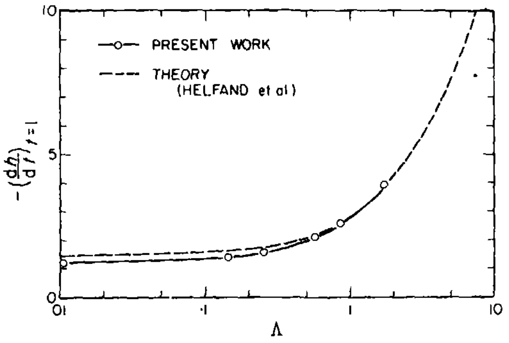

Fig. 3. Temperature derivative of the upper critical field at T_c plotted vs. Λ together with a theoretical curve given by Helfand and Werthamer[21]. Here, h is a reduced magnetic field defined in reference[21], and is proportional to H_{c2}, and $t = T/T_c$.

From the measured results, we can calculate the two Ginzburg–Landau parameters. Figures 4 and 5 are the plots of these quantities in various alloys as a function of temperature. In these figures are also shown the theoretical curves recently calculated by Eilenberger[10]. In Fig. 6, are plotted the experimental $\kappa_1(0)/\kappa_c$ and $\kappa_2(0)/\kappa_c$ vs. Λ again with the theoretical curves for the parameter $l_{tr.}/l$ in Eilenberger's treatment equals to unity, where $\kappa_c = \kappa_1(T_c) = \kappa_2(T_c)$. As is indicated here, the agreement between the experimental results and the theory is again bad for Λ smaller than unity.

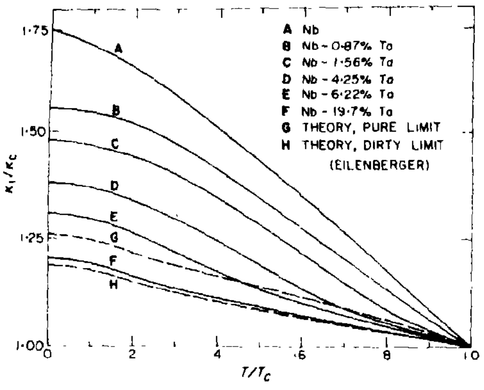

Fig. 4. κ_1 in various Nb–Ta alloys plotted vs. reduced temperature together with theoretical curves for the pure limit and the dirty limit given by Eilenberger[10].

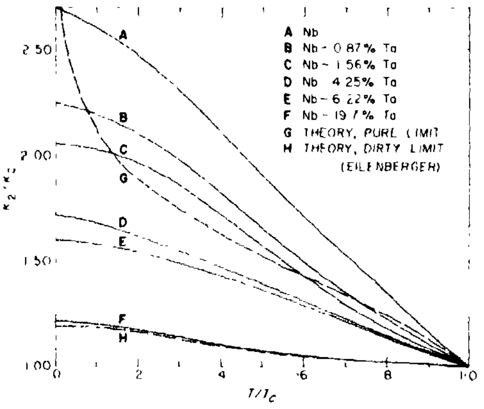

Fig. 5. κ_2 in various Nb–Ta alloys plotted vs. reduced temperature together with theoretical curves.

It should be worth noting that the anisotropy in the superconducting energy gap is smoothed out by the impurity scattering and disappears when $l \approx \xi_0$[22].

Finally, κ_c as a function of the residual resistivity or Λ obeys well the theoretical predictions. In Fig. 7, the variation of κ_c as a function of Λ is compared with Eilenberger's result, which is equivalent to the well-known Gor'kov equation[23]. From this, the magnitude of κ_c for ideally pure Nb was extrapolated to be 0·79.

Electronic parameters

Some electronic parameters can be deduced from the measured results. First of all, the temperature coefficient of the electronic specific heat, γ, is known from the expression:

$$H_c^2(T) = H_c^2(0) - (4\pi\gamma/V_m)T^2$$

where V_m is the molar volume and equals to 10·8 for any Nb–Ta alloys. γ for Nb was obtained to be $(7{\cdot}6_5 \pm 0{\cdot}2)$ mJ/mol. deg^2 which agrees with the magnitudes so far obtained [4, 14, 24, 25]. Figure 8 shows the change of γ

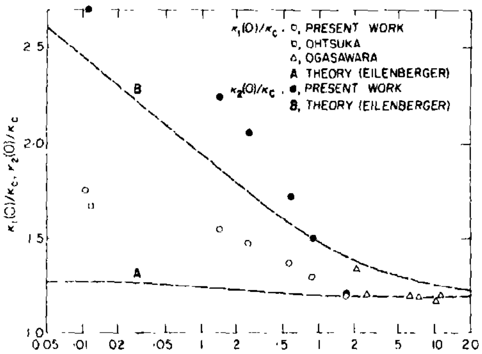

Fig. 6. $\kappa_1(0)/\kappa_c$ and $\kappa_2(0)/\kappa_c$ plotted vs. Λ together with theoretical curves given by Eilenberger[10] for the case $l_{tr}/l = 1$.

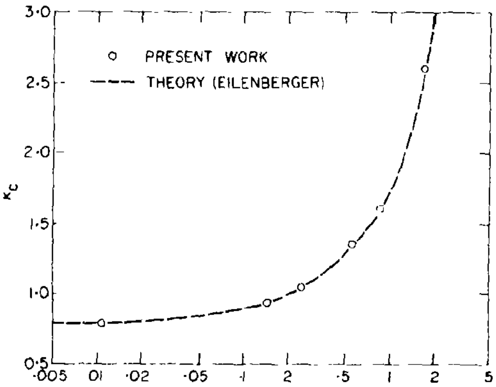

Fig. 7. κ_c plotted vs. Λ together with the theoretical curve given by Eilenberger[10].

thus obtained as a function of Ta concentration. It appears that γ has a peak at a Ta concentration of several at. per cent. The value obtained from the magnetization measurement is accompanied by a rather large experimental error. In the Nb–Ta system, γ has also been measured by a direct specific heat method in the group of the present authors and the co-workers[26], the result of which, also shown in Fig. 8, makes it safe to conclude that there exists a peak in γ vs. Ta concentration. This variation of γ should be compared with the steep drop of T_c on the Nb-rich side of the present system.

We get the superconducting energy gap at 0°K, $2\Delta(0)$, from the expression[27]:

$$\Delta^2(0) = (V_m/4\pi)\cdot[H_c^2(0)/N(E_F)]$$

where $N(E_F)$ is the density of states at the Fermi energy derived from γ, which should be magnified to some extent by the electron-phonon interaction[28].

Figure 9 gives the plots of $2\Delta(0)/k_BT_c$, T_c/θ_D (θ_D, the Debye temperature) and T_c vs. Λ[29]. The ratio, T_c/θ_D, is considered to be a good measure of the strength of the coupling in a superconductor. As is shown here, the variations of $2\Delta(0)/k_BT_c$ and T_c/θ_D are both unrelated to the discrepancies between theory and experiment in $H_{c2}(T)$, $\kappa_1(T)/\kappa_c$ and $\kappa_2(T)/\kappa_c$.

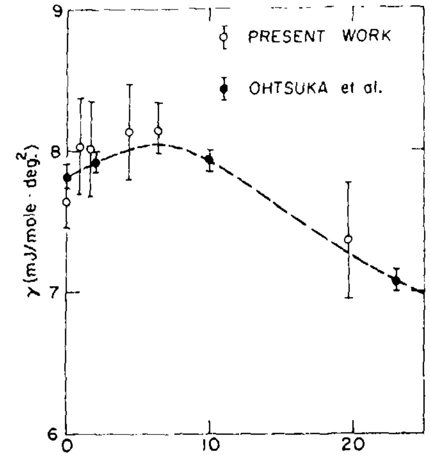

Fig. 8. Temperature coefficient of the electronic specific heat, γ, plotted vs. Ta concentration in the Nb–Ta system together with the experimental result in the specific heat measurements[26].

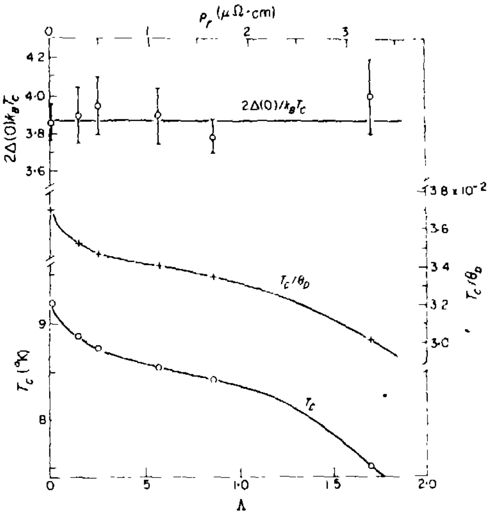

Fig. 9. $2\Delta(0)/k_BT_c$, T_c/θ_D and T_c plotted vs. Λ and the residual resistivity.

Abrikosov[31] and Tinkham[32] obtained the following expression for the upper critical field,

$$H_{c2}(t) = \frac{4\pi\lambda^2(t)H_c^2(t)}{\phi_0}\cdot\frac{1-t^2}{1+t^2}$$

where $\lambda(t)$ is the penetration depth as a function of the reduced temperature $t = T/T_c$, and ϕ_0 is the flux quantum. This yields a value of $\lambda(0)$. Using the expression for the Ginzburg–Landau parameters, $\kappa = 0{\cdot}96\,\lambda_L(0)/\xi_0$, and the BCS expression[33] for the ratio λ/λ_L as a function of ξ_0/λ_L, where λ_L is the London penetration depth, we estimate $\lambda_L(0)$ and ξ_0. Using this result, the Fermi velocity v_F is calculated from another BCS expression:

$$\xi_0 = \hbar v_F/\pi\Delta(0).$$

Since the value of $\lambda_L(0)$ depends on whether the electrons are scattered randomly or specularly at the specimen surface, ξ_0 and v_F also depend on this. It is hard to say which is more realistic, so we tentatively assume here that the scattering is specular. This assumption does not affect the matter much.

For Nb, calculated results are: $\lambda(0) = 390$ Å, $\lambda_L(0) = 370$ Å, $\xi_0 = 450$ Å and $v_F = 3{\cdot}3 \times 10^7$ cm/sec. Finally, the effective mass ratio of the electrons m^*/m_0, and the carrier concentration n in Nb are found to be $m^*/m_0 = 4{\cdot}9$ and $n = 9{\cdot}8 \times 10^{22}$ cm^{-3} (see Table 2).

Combining this value of the carrier concentration and the value of $\lambda_L(0) = 4\pi n_s(0)e^2/m^*c^2$, where $n_s(0)$ is the density of the superconducting electrons at 0°K, e is the electron charge and c is the light velocity, we find that the ratio $n_s(0)/n$ in Nb is 1·0. Therefore, almost all electrons seem to go into the superconducting state at sufficiently low temperatures.

Finally, the electron mean free path which we have been already using in this paper can be derived from what we have obtained so far. The mean free path in Nb can be calculated without any ambiguity, but that in alloys cannot be estimated without making some assumption. We assumed here that the carrier concentration is unchanged by the alloying of Ta with Nb.

4. DISCUSSION AND CONCLUSION

From the informations obtained here, we can conclude that the peculiar character which pure Nb shows in $H_{c2}(T)$, $\kappa_1(T)$ and $\kappa_2(T)$ does not come from its non-weak coupling nature, but is directly related to the anisotropy in the superconducting energy gap. Anisotropy in the superconducting energy gap of Nb has been clearly revealed, for example, by the ultrasonic experiment [34], although the anistropy shown by these ultrasonic experiments is not exactly the same thing as that which we are discussing here. It should be also worth noting that pure V has been found to show the same discrepancies between experiment and theory as discussed here, whereas the ratio T_c/θ_D in V has a typical value for the weak coupling superconductor [35].

Table 2. Summary of the results

Specimen	No 1	No. 2	No 3	No. 4	No. 5	No. 6
at.% Ta	pure Nb	0·87	1·56	4·25	6·22	19·7
l_{tr} (10^{-4} cm)	3·78	0·27	0·16	0·070	0·046	0·023
l_{tr}/ξ_0	84	6·0	3·5	1·6	1·0	0·52
ξ_0/l_{tr}	0·012	0·17	0·28	0·64	0·98	1·9
γ (mj/mol deg^2)	$7{\cdot}6_5$	$8{\cdot}0_2$	$7{\cdot}9_3$	$8{\cdot}0_1$	$8{\cdot}0_9$	$7{\cdot}3_8$
T_c (°K)	9·23	8·87	8·76	8·55	8·42	7·50
$H_{c1}(0)$ (kOe)	1·85	1·75	1·70	1·37	1·12	0·83
$H_{c2}(0)$ (kOe)	4·10	4·40	4·50	5·30	5·56	7·50
$H_c(0)$ (kOe)	$2{\cdot}0_7$	$2{\cdot}0_5$	$2{\cdot}0_4$	$1{\cdot}9_8$	$1{\cdot}8_9$	$1{\cdot}7_5$
$-(dH_{c2}/dt)_{t=1}$ (kOe)	$3{\cdot}7_1$	$4{\cdot}1_0$	$4{\cdot}6_8$	$6{\cdot}0_1$	$6{\cdot}9_2$	$9{\cdot}7_8$
κ_c	0·80	0·94	$1{\cdot}0_5$	$1{\cdot}3_6$	$1{\cdot}6_2$	2·6
$\kappa_1(0)/\kappa_c$	$1{\cdot}7_5$	$1{\cdot}5_6$	$1{\cdot}4_8$	$1{\cdot}3_8$	$1{\cdot}3_0$	1·2
$\kappa_2(0)/\kappa_c$	$2{\cdot}7_0$	$2{\cdot}2_5$	$2{\cdot}0_6$	$1{\cdot}7_2$	$1{\cdot}5_1$	1·2
$2\Delta(0)/k_BT_c$	$3{\cdot}8_6$	$3{\cdot}9_1$	$3{\cdot}9_5$	$3{\cdot}8_9$	$3{\cdot}7_5$	4·0
$\lambda(0)$ (Å)	350†	410	420	460	500	630

Pure Nb: $\lambda_L(0) = 370$ Å, $\xi_0 = 450$ Å, $v_F = 3{\cdot}3 \times 10^7$ cm/sec, $m^*/m_0 = 4{\cdot}9$, $n = 9{\cdot}8 \times 10^{22}$ cm^{-3}.

†See reference [38].

From the theoretical standpoint, Werthamer and his co-workers [36, 37] treated the present problem, concluding that the discrepancy cannot be accounted for by the strong-coupling nature of the superconductor, but can probably be explained by the anisotropy of the electronic structure. The remaining problem would then be to show how the anisotropic superconducting energy gap is related to the anisotropic electronic structure. Fermi surface studies of pure Nb or V would be most desirable in making the present discussion more quantitative.

Finally, Table 2 summarizes some numerical results obtained in this study.

Acknowledgements—The present authors would like to thank sincerely Dr. L. Tewordt, Dr. T. Ohtsuka and Dr. A. V. Granato for their valuable discussions and help. Thanks are also due to Dr. T. Asada and his co-workers of the Asada Fundamental Research Institute, Kobe Steel Co., Dr. K. Yasukochi and Dr. T. Ogasawara of the Nihon University and Mr. T. Odaka of Kobe University for their assistance during the experiment.

REFERENCES

1. CALVERLEY A. and ROSE-INNES A. C., *Proc. R. Soc.* **255**, 267 (1960).
2. OHTSUKA T., *Phys. Lett.* **17**, 194 (1965).
3. McCONVILLE T. and SERIN B., *Phys. Rev.* **140**, A1169 (1965).
4. FINNEMORE D. K., STROMBERG T. F. and SWENSON C. A., *Phys. Rev.* **149**, 231 (1966).
5. SKINNER II L. C., ROSE R. M. and WULFF J., *J. appl. Phys.* **37**, 2191 (1966).
6. OHTSUKA T. and TAKANO N., *J. phys. Soc. Japan* **23**, 983 (1967).
7. MAKI K., *Physics* **1**, 21 (1964).
8. MAKI K. and TSUZUKI T., *Phys. Rev.* **139**, A868 (1965).
9. TEWORDT L., *Z. Phys.* **184**, 319 (1965).
10. EILENBERGER G., *Phys. Rev.* **153**, 584 (1967).
11. GINZBURG V. L. and LANDAU L. D., *Zh. Eksp. Teor. Fiz.* **20**, 1064 (1950).
12. ABRIKOSOV A. A., *Soviet Phys. JETP* **5**, 1174 (1957).
13. GOR'KOV L. P., *Soviet Phys. JETP* **9**, 1364 (1959)
14. SHEN L., SENOZAN N. M. and PHILLIPS N. E., *Phys. Rev. Lett.* **14**, 1025 (1965).
15. IKUSHIMA A., MIZUSAKI T. and ODAKA T., *Phys. Lett.* **26A**, 582 (1968).
16. HANSEN M., *The Constitution of Binary Alloys*. McGraw-Hill, N.Y. (1958).
17. WILLIAMS D. E. and PECHIN W. H., *Trans. Am. Soc. Metals* **50**, 1081 (1958).
18. OGASAWARA T., Thesis. Nihon University No. NUP-B-67-8 (1967).
19. For further details, see IKUSHIMA A., FUJII M. and SUZUKI T., *J. Phys. Chem. Solids* **27**, 327 (1966)
20. BECKER R. and DÖRING W., *Ferromagnetismus*. Springer, Berlin (1939).
21. HELFAND E. and WERTHAMER N. R., *Phys. Rev.* **147**, 288 (1966).
22. ANDERSON P. W., *J. Phys. Chem. Solids* **11**, 26 (1959).
23. GOR'KOV L. P., *Soviet Phys. JETP* **10**, 998 (1960). See also, GOODMAN B. B., *Phys. Lett.* **1**, 215 (1962)
24. LEOPOLD H. A. and BOORSE H. A., *Phys. Rev.* **134**, A1322 (1964).
25. VAN DER HOEVEN B. J. C. and KEESOM P. H., *Phys. Rev.* **134**, A1322 (1964).
26. OHTSUKA T., MATSUI T. and MIZUSAKI T., To be published.
27. SCHRIEFFER J. R., *Theory of Superconductivity*. Benjamin, N.Y. (1965).
28. See, for example, McMILLAN W. L., *Phys. Rev.* **167**, 331 (1968).
29. The Debye temperature in Nb–Ta system has been measured. The present analysis is based on that result which indicates that the Debye temperature depends almost linearly on Ta concentration between 252°K for Nb and 231°K for Ta[30]. See OHTSUKA T., MATSUI T., and MIZUSAKI T., To be published.
30. KITTEL C., *Introduction to Solids State Physics*, 2nd. Edn p. 232. Wiley, N.Y. (1956).
31. ABRIKOSOV A. A., *Soviet Phys. JETP* **6**, 1172 (1957).
32. TINKHAM M., *Phys. Rev.* **129**, 2413 (1963).
33. BARDEEN J., COOPER L. N. and SCHRIEFFER J. R., *Phys. Rev.* **108**, 1175 (1957).
34. PERZ J. M. and DOBBS E. R., *Proc. R. Soc.* **A296**, 113 (1967).
35. RADEBAUGH R. and KEESOM P. H., *Phys. Rev.* **149**, 217 (1966).
36. HOHENBERG P. C. and WERTHAMER N. R., *Phys. Rev.* **153**, 493 (1967).
37. WERTHAMER N. R. and McMILLAN W. L., *Phys. Rev.* **158**, 415 (1967)
38. MAXFIELD B. W. and McLEAN W. L., *Phys. Rev.* **139**, A1515 (1965)

J. Phys. Chem. Solids Pergamon Press 1969. Vol. 30, pp. 881–887. Printed in Great Britain.

FORMATION OF POINT DEFECTS IN CALCIUM TITANATE

W. L. GEORGE* and R. E. GRACE
School of Materials Science and Metallurgical Engineering, Purdue University,
Lafayette, Ind. 47907, U.S.A.

(*Received* 13 *August* 1968, *in revised form* 19 *September* 1968)

Abstract—The electrical conductivity and Seebeck coefficient of single crystal calcium titanate were measured as a function of temperature and P_{H_2O}/P_{H_2}. The electrical conductivity was determined at temperatures from 1100° to 1300°C. The P_{H_2O}/P_{H_2} ratio extended from 2×10^{-4} to 8×10^{-2}. At 1200°C the electrical conductivity was $3{\cdot}70\ \Omega^{-1}\text{cm}^{-1}$ at $P_{H_2O}/P_{H_2} = 10^{-3}$ and $1{\cdot}75\ \Omega^{-1}\text{cm}^{-1}$ at $P_{H_2O}/P_{H_2} = 10^{-2}$; the Seebeck coefficients were -500 and $-580\ \mu V/°K$ under the same conditions. The electrical conductivity was proportional to the $-\frac{1}{3}$ power of P_{H_2O}/P_{H_2}. The sign of the Seebeck coefficient indicated the majority carriers to be electrons. The results may be described by a majority defect model consisting of doubly ionized oxygen vacancies and electrons. The standard enthalpy of formation was found to be $93{,}000 \pm 4000$ cal/mol. of oxygen vacancies.

INTRODUCTION

THE PURPOSE of this investigation was to study the defect structure of non-stoichiometric calcium titanate, $CaTiO_3$. It was desired to gain information concerning the identity and formation of the predominant point defects. Although the perovskite structure compounds derive their name from calcium titanate, this compound is slightly distorted from the cubic structure and exhibits orthorhombic symmetry[1]. This distortion tends to be reduced at high temperatures, and the lattice becomes more nearly cubic. Linz and Herrington[2] investigated some low temperature electrical and optical properties of calcium titanate. They found no observable anisotropy, and the properties investigated were quite similar to those of strontium titanate.

Walters and Grace[3] examined the electrical conductivity and Seebeck coefficient of strontium titanate in water-hydrogen atmospheres. They concluded an oxygen vacancy defect model was applicable to their results. Paladino *et al.*[4] studied oxygen self-diffusion in single crystal strontium titanate. Paladino[5] also investigated the oxidation kinetics of single crystal strontium titanate and concluded that an oxygen vacancy defect model was applicable at high temperatures.

In this study measurement of the high temperature electrical conductivity and thermoelectric power in water-hydrogen atmospheres was chosen as a means of examining the behavior of point defects in single crystal calcium titanate. The dependence of the point defect concentrations in ABO_3 compounds upon various thermodynamic variables was derived for a variety of defect models. Identification of the predominant defects was accomplished by matching the experimental data to predicted behavior based upon the thermodynamic relations.

EXPERIMENTAL

Samples of single crystal calcium titanate† of nominal dimensions $4 \times 7 \times 1$ mm were first polished with $15\,\mu$ diamond paste, then with $6\,\mu$ diamond paste, until all dimensions were uniform to within $\pm 0{\cdot}01$ mm. The samples were ultrasonically cleaned in benzene and rinsed in ethyl alcohol. Thermocouples, whose low alloy legs served as voltage probes, were inserted into two 0·4 mm dia. holes drilled into the samples with a Sheffield Cavitron. Current leads were spring-loaded by means of mullite rods against the sample ends as shown in Fig. 1.

**Present address:* Motorola Semiconductor Products Division, Phoenix, Ariz. 85008, U.S.A.

†Obtained from the National Lead Company, South Amboy, New Jersey. Their synthesis has been described by Merker[6].

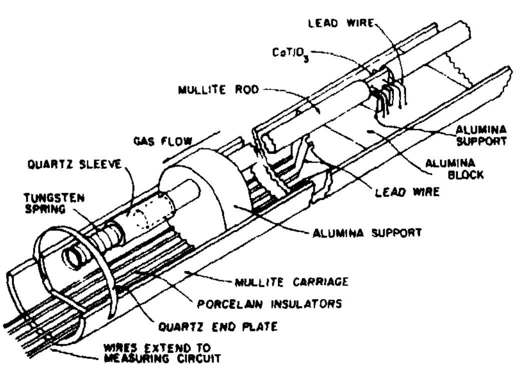

Fig. 1 Sample holder for electrical conductivity and Seebeck coefficient measurements.

Lead wire combinations used were Pt, Pt–10% Rh; Pt–6% Rh, Pt–30% Rh, and W–5% Re, W–26% Re. Results obtained from each system were the same, but the tungsten–rhenium alloys gave service of at least three weeks at temperature, whereas the Pt–Rh combinations lasted only a few days in water-hydrogen atmospheres.

The sample and holder were placed horizontally in a Kanthal tube furnace controlled to ±2°C. A gas train which allowed control of the P_{H_2O}/P_{H_2} ratio was connected to the furnace tube. Variation of the P_{H_2O}/P_{H_2} ratio was accomplished by saturating a stream of hydrogen with water at one of several prescribed temperatures and then mixing this stream with essentially dry hydrogen in a dual-flowmeter gas-proportioner. The P_{H_2O}/P_{H_2} ratio was calculated from the known dew point of the wet stream and the flow rates of wet and dry streams. To study hydrogen solubility in the crystals and to extend the range of P_{H_2O}/P_{H_2} ratios, mixtures of argon and hydrogen of nominal compositions 1% H_2–99% Ar, 10% H_2–90% Ar, and 100% H_2 were used. The total pressure in the system was typically 750 mm Hg. A range of P_{H_2O}/P_{H_2} ratios from 2×10^{-4} to 8×10^{-2} was attained, and the gas system was stable for hours with ±0·5°C variation in dew point as measured in the effluent gas with an Alnor dew point meter.

RESULTS

The electrical conductivity as a function of P_{H_2O}/P_{H_2} ratio at temperatures of 1100°, 1200° and 1300°C is shown in Fig. 2. The data represents results from eleven experiments using six single crystals. Least squares slopes of the lines are shown in Table 1.

The temperature dependence of the electrical conductivity is shown in Fig. 3 for six values of the P_{H_2O}/P_{H_2} ratio.

The Seebeck coefficient is plotted as a

Table 1. *Slopes of isotherms of* ln *electrical conductivity vs.* ln P_{H_2O}/P_{H_2}

Temperature (°C)	Slope	Standard deviation of the slope
1100	−0·325	0·002
1200	−0·329	0·006
1300	−0·326	0·004

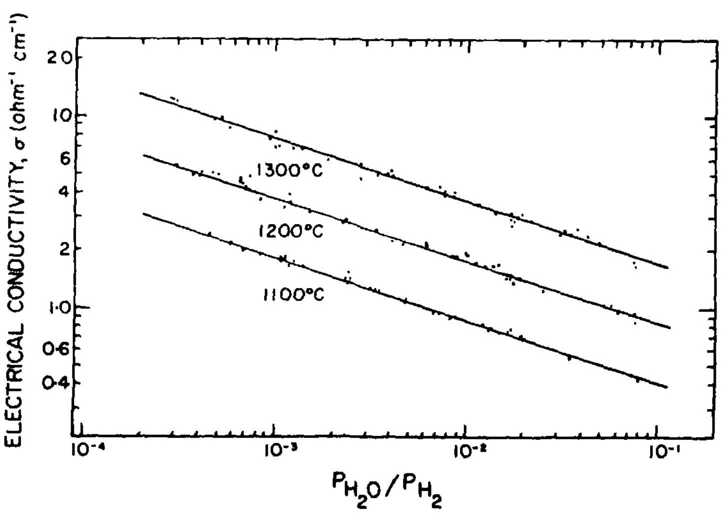

Fig. 2. P_{H_2O}/P_{H_2} dependence of the electrical conductivity.

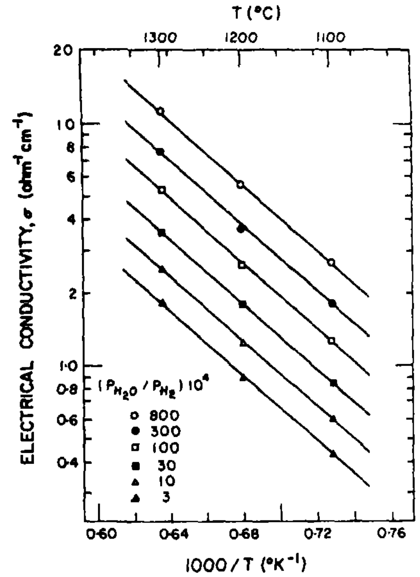

Fig. 3. Temperature dependence of the electrical conductivity.

function of P_{H_2O}/P_{H_2} ratio at a temperature of 1200°C in Fig. 4. Figure 5 shows the temperature dependence of the Seebeck coefficient for two values of P_{H_2O}/P_{H_2}. All Seebeck coefficient measurements and room temperature hot point probe measurements performed after the experiments showed the crystals to be *n*-type.

The electrical conductivity showed no dependence upon P_{H_2} in the range 7·5–750 mm Hg at fixed P_{H_2O}/P_{H_2} ratio and temperature. The solubility and/or dissociation of dissolved hydrogen are thus negligible. Also, two-probe *d–c* polarization measurements showed no observable transient in the electrical conductivity after switching the current.

DISCUSSION

In order to specify the thermodynamic state of a system the number of independent variables which must be fixed is given by the Gibbs phase rule. If the gas phase over an ABO_3 crystal consists of a water-hydrogen mixture, the number of components is four: A, B, O, H for a two phase crystal-gas equilibrium the number of independent thermodynamic variables is also four. The two most obvious variables are temperature and total pressure. In this work the other variables

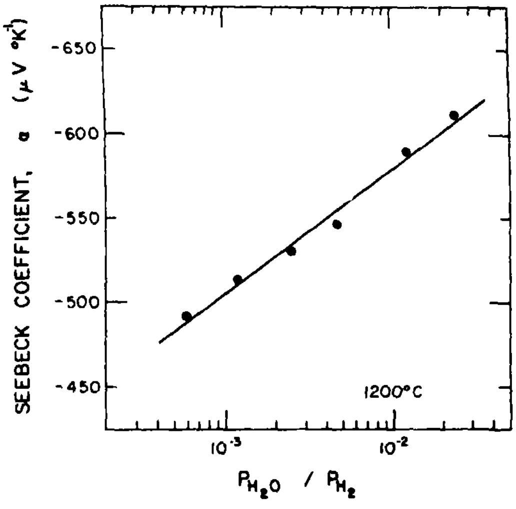

Fig. 4. P_{H_2O}/P_{H_2} dependence of the Seebeck coefficient

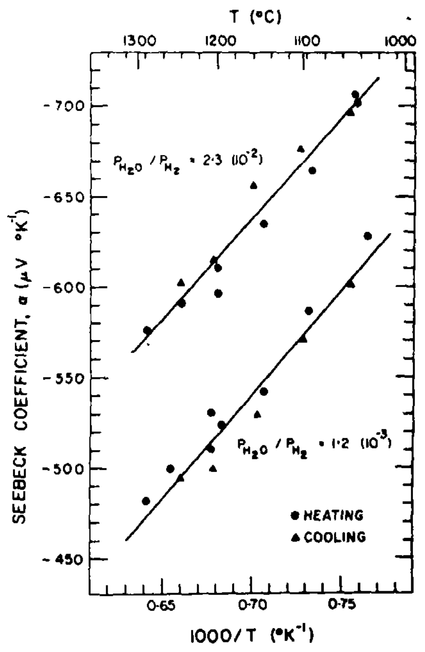

Fig. 5. Temperature dependence of the Seebeck coefficient.

are P_{H_2O}/P_{H_2}, the water-hydrogen pressure ratio, and a_A/a_B, the chemical activity ratio of two independent components.

The method of Schmalzried and Wagner [7] yields the following independent relations between fully ionized point defects* in ABO_3 crystals equilibrated with a water-hydrogen gas phase:

$$\mathrm{d}\ln(|A|'') + \mathrm{d}\ln(|B|'''') + 3\,\mathrm{d}\ln(|O|^{\cdot\cdot}) = 0 \quad (1)$$

$$\mathrm{d}\ln(A^{\cdot\cdot}) + \mathrm{d}\ln(|A|'') = 0 \quad (2)$$

$$\mathrm{d}\ln(B^{\cdot\cdot\cdot\cdot}) + \mathrm{d}\ln(|B|'''') = 0 \quad (3)$$

$$\mathrm{d}\ln(O'') + \mathrm{d}\ln(|O|^{\cdot\cdot}) = 0 \quad (4)$$

$$\mathrm{d}\ln(A^{\cdot\cdot}) + \mathrm{d}\ln(|B|'''') - \mathrm{d}\ln(A|B|'') = 0 \quad (5)$$

$$\mathrm{d}\ln(B^{\cdot\cdot\cdot\cdot}) + \mathrm{d}\ln(|A|'') - \mathrm{d}\ln(B|A|^{\cdot\cdot}) = 0 \quad (6)$$

$$\mathrm{d}\ln(e') + \mathrm{d}\ln(|e|^{\cdot}) = 0 \quad (7)$$

$$\tfrac{4}{3}\,\mathrm{d}\ln(A^{\cdot\cdot}) - \tfrac{2}{3}\,\mathrm{d}\ln(B^{\cdot\cdot\cdot\cdot}) = \mathrm{d}\ln\frac{a_A}{a_B} - \mathrm{d}\ln\frac{P_{H_2O}}{P_{H_2}} \quad (8)$$

$$\mathrm{d}\ln(|O|^{\cdot\cdot}) + 2\,\mathrm{d}\ln(e') = -\mathrm{d}\ln\frac{P_{H_2O}}{P_{H_2}}. \quad (9)$$

The tenth equation is the electroneutrality condition:

$$(e') + 2(|A|'') + 4(|B|'''') + 2(A|B|'') + 2(O'') = (|e|^{\cdot}) + 2(A^{\cdot\cdot}) + 4(B^{\cdot\cdot\cdot\cdot}) + 2(B|A|^{\cdot\cdot}) + 2(|O|^{\cdot\cdot}). \quad (10)$$

This set of ten equations has been solved for all possible combinations of positively and negatively charged defect pairs, and the results are given in the Appendix.

Since the electrical conductivity of an oxide is proportional to the concentration of mobile defects, the observed results can be compared with the logarimthic derivatives given in the Appendix. The experimental results agree with the defect model of oxygen vacancies, $|O|^{\cdot\cdot}$, charge-compensated by excess electrons, e'. The formation reaction for the majority defects is as follows:

$$H_2(g) + O|O| \rightleftarrows H_2O(g) + |O|^{\cdot\cdot} + 2e' \quad (11)$$

with the equilibrium constant:

$$K = \left[\frac{P_{H_2O}}{P_{H_2}}\right](|O|^{\cdot\cdot})(e')^2 = \exp\left[-\frac{\Delta F^\circ}{RT}\right]. \quad (12)$$

The condition of electrical neutrality, $2(|O|^{\cdot\cdot}) = (e')$, results in the following:

$$(e') = 2^{1/3}\left[\frac{P_{H_2O}}{P_{H_2}}\right]^{-1/3} \exp\left[\frac{\Delta S^\circ}{3R}\right] \exp\left[-\frac{\Delta H^\circ}{3RT}\right]. \quad (13)$$

Two probe polarization measurements indicated that the observed conductivity was predominantly electronic. Thus the electrical conductivity becomes

$$\sigma = e\mu 2^{1/3}\left[\frac{P_{H_2O}}{P_{H_2}}\right]^{-1/3} \exp\left[\frac{\Delta S^\circ}{3R}\right] \exp\left[-\frac{\Delta H^\circ}{3RT}\right]. \quad (14)$$

The partial logarithmic derivative of the electrical conductivity with the P_{H_2O}/P_{H_2} ratio is given by

$$\left[\frac{\partial \ln \sigma}{\partial \ln \dfrac{P_{H_2O}}{P_{H_2}}}\right]_T = -\tfrac{1}{3} \quad (15)$$

which is in agreement with the results shown in Fig. 2 and in Table A-2 of the Appendix for the oxygen vacancy defect model.

The partial logarithmic derivative of the electrical conductivity with respect to reciprocal temperature is

$$\left[\frac{\partial \ln \sigma}{\partial\, 1/T}\right]_{P_{H_2O}/P_{H_2}} = -\frac{\Delta H^\circ}{3R} \quad (16)$$

**The notation is as follows:* (footnote)

$A^{\cdot\cdot}$	A on an interstitial site
$\vert A\vert''$	vacancy in the A sublattice
$B^{\cdot\cdot\cdot\cdot}$	B on an interstitial site
$\vert B\vert''''$	vacancy in the B sublattice
$B\vert A\vert^{\cdot\cdot}$	B on a regular lattice site in the A sublattice
$A\vert B\vert''$	A on a regular lattice site in the B sublattice
$\vert O\vert^{\cdot}$	vacancy in the O sublattice
O''	O on an interstitial site
$(e\vert$	free electron hole
$e^{\cdot}$	free electron.

if the mobility, μ, varies slowly ($\approx T^{-3/2}$) with temperature. The slopes of Fig. 3 give a value of the standard enthalpy of formation, ΔH°, of $93{,}000 \pm 4000$ cal/mol. of oxygen vacancies. Walters and Grace[3] found a value of $86{,}500 \pm 3000$ cal/mol. for the similar term in strontium titanate.

The Seebeck coefficient given by Johnson [8] for an extrinsic, n-type semiconductor is

$$\alpha = -\frac{k}{e}[A - \ln(e') + \ln N_c] \qquad (17)$$

where α is the Seebeck coefficient, N_c is the thermally available density of states, and A is a term which depends upon the particular scattering mechanism. Substitution of equation (13) into equation (17) yields

$$\alpha = \frac{k}{e}\left[\ln\left(\frac{P_{H_2O}}{P_{H_2}}\right)^{-1/3} - \frac{\Delta H_f}{3RT} - \ln N_c + \text{const.}\right]. \qquad (18)$$

The dependence of the Seebeck coefficient upon the P_{H_2O}/P_{H_2} ratio is given by

$$\left[\frac{\partial \alpha}{\partial \ln \frac{P_{H_2O}}{P_{H_2}}}\right]_T = -\frac{k}{3e}. \qquad (19)$$

The plot given in Fig. 4 is linear with a slope of $-32{\cdot}5\ \mu$V/°K and a standard deviation of $1{\cdot}8\ \mu$V/°K. This value is in reasonable agreement with the calculated values of $-(k/3e) = -28{\cdot}89\ \mu$V/°K.

If one ignores the relatively small temperature dependence ($\approx T^{3/2}$) of N_c, the partial derivative of the Seebeck coefficient with respect to reciprocal temperature is

$$\left[\frac{\partial \alpha}{\partial\, 1/T}\right]_{P_{H_2O}/P_{H_2}} = -\frac{k}{e}\left[\frac{\Delta H^\circ}{3R}\right] \qquad (20)$$

Thus the Seebeck coefficient data permits an independent determination of ΔH° for equation (11). The slopes of Fig. 5 give an average value of the standard enthalpy of formation of 80,000 cal/mol. of oxygen vacancies with a standard deviation of 6500 cal/mol.

The difference in ΔH° as determined from electrical conductivity and Seebeck coefficient measurements may be a result of experimental uncertainties. In this case the value of $\Delta H^\circ = 93$ Kcal/mol. is to be preferred. An alternate possibility is small polaron conduction with an exponential temperature coefficient of the mobility, μ, in equation (14). The activation energy for such polaron motion may be estimated by inserting $\Delta H^\circ = 80$ Kcal/mol. into equation (14); this results in an activation energy for motion of approximately 4000 cal/mol. However, Frederikse and Hosler[9] have found dual optical mode scattering in strontium titanate in the range from 200–1000°K; because of the similarities of the compounds the mobility in calcium titanate is not likely to be activated.

Although the effective mass is not known for $CaTiO_3$, the value of $m^* = 16\, m_0$ for $SrTiO_3$[10] was used to estimate the carrier concentration from the Seebeck coefficients. Equation (17) for simple lattice scattering was used with $A = 2$ and $N_c = 2(2\pi m^* kT/h^2)^{3/2}$. At $T = 1100$°C and $P_{H_2O}/P_{H_2} = 10^{-3}$ the Seebeck coefficient is $-570\ \mu$V/°K. The carrier concentration, (e'), is approximately 10^{20} cm^{-3}. Although this estimate indicates only the order of magnitude of the electron concentration, it shows that reduction in water-hydrogen is likely to overcome compensation due to minor impurities.

CONCLUSIONS

The defect structure of calcium titanate at high temperatures may be described by majority defect pairs of oxygen vacancies and excess electrons. The experimental results which support this are summarized as follows: (1) The partial logarithmic derivative of the electrical conductivity with the P_{H_2O}/P_{H_2} ratio at constant temperature was linear with a slope of $-\frac{1}{3}$. This dependence of the electronic conductivity agreed with the predicted value for the majority carriers. (2) The Seebeck coefficient was negative in sign and was a linear function of the logarithm of the P_{H_2O}/P_{H_2}

ratio at constant temperature with a slope of $-32{\cdot}5\,\mu V/°K$ and a standard deviation of $1{\cdot}8\,\mu V/°K$. *N*-type behavior and a slope of $-28{\cdot}89\,\mu V/°K$ were predicted from the defect model of oxygen vacancies and excess electrons.

Acknowledgements—This manuscript was taken from a dissertation submitted by W. L. George to Purdue University in partial fulfillment of the requirements for the Ph.D. degree. The research was supported by the National Science Foundation through a Graduate Fellowship, by the United States Atomic Energy Commission through Contract AT(11-1)-1436, and by a Donnan Award from Purdue University. The single crystals of CaTiO₃ were a gift of the National Lead Company, South Amboy, New Jersey.

REFERENCES

1. KAY H. F. and BAILEY P. C., *Acta crystallogr.* **10**, 219 (1957).
2. LINZ A., Jr. and HERRINGTON K., *J. chem. Phys* **28**, 824 (1958).
3. WALTERS L. C. and GRACE R. E., *J. Phys. Chem Solids* **28**, 239 (1967).
4. PALADINO A. E., RUBIN L. G. and WAUGH J. S., *J. Phys. Chem Solids* **26**, 39 (1965).
5. PALADINO A. E., *J. Am. Ceram. Soc.* **48**, 476 (1965).
6. MERKER L., *J. Am. Ceram. Soc.* **45**, 366 (1962).
7. SCHMALZRIED H. and WAGNER C., *Z. phys. Chem* **31**, 198 (1962).
8. JOHNSON V. A., *Progress in Semiconductors*, Vol. 1, pp. 65–97. Heywood, London (1956).
9. FREDERIKSE H. P. R. and HOLSER W. R., *Phys. Rev.* **161**, 822 (1967).
10. FREDERIKSE H. P. R., THURBER W. R. and HOSLER W. R., *Phys. Rev.* **134**, 442 (1964).

APPENDIX

The partial logarithmic derivatives of point defect concentrations with respect to the P_{H_2O}/P_{H_2} ratio and the chemical activity ratio a_A/a_B have been calculated for the ternary oxide ABO_3 with the method of Schmalzried and Wagner[7]. Twenty-five choices of fully ionized defect pairs were considered. As Schmalzried and Wagner noted, the defect models fall readily into several classes according to the type of majority defects:

Class 1. Both majority defects are ionic.
Class 2. One majority defect is ionic; the other is electronic.
Class 3. Both majority defects are electronic.

Table A-1 gives the logarithmic derivatives for Class 1 defect models. An important contribution to transport properties may be made by minority electrons or electron holes, because the mobilities of these species are normally much larger than ionic mobilities. The logarithmic derivatives of the minority electron concentrations are thus included in Table A-1. The electron hole derivatives are equal in magnitude but opposite in sign to the electron derivatives.

Tables A-2 and A-3 give the logarithmic derivatives of defect concentrations for crystals containing electronic majority defects. In Table A-3 the logarithmic derivatives for minority ions are also included for completeness.

Table A-1. Logarithmic derivatives for class 1 defects

Defect model	Majority defects		Minority electrons	
Type of majority defects	$\left[\dfrac{\partial \ln (i')}{\partial \ln \dfrac{P_{H_2O}}{P_{H_2}}}\right]_{a_A/a_B}$	$\left[\dfrac{\partial \ln (i')}{\partial \ln \dfrac{a_A}{a_B}}\right]_{P_{H_2O}/P_{H_2}}$	$\left[\dfrac{\partial \ln (i)}{\partial \ln \dfrac{P_{H_2O}}{P_{H_2}}}\right]_{a_A/a_B}$	$\left[\dfrac{\partial \ln (e')}{\partial \ln \dfrac{a_A}{a_B}}\right]_{P_{H_2O}/P_{H_2}}$
A , |B|''''	$-\frac{1}{2}$	$\frac{1}{2}$	$-\frac{1}{2}$	0
A , A|B|''	$-\frac{3}{4}$	$\frac{3}{4}$	$-\frac{3}{8}$	$-\frac{1}{8}$
B· , A|B|''	$-\frac{1}{2}$	$\frac{1}{2}$	$-\frac{1}{4}$	$-\frac{1}{4}$
|B|'''', |O|	$-\frac{1}{6}$	$\frac{1}{6}$	$-\frac{5}{12}$	$-\frac{1}{12}$
A|B|'', |O|	$-\frac{1}{2}$	$\frac{1}{2}$	$-\frac{1}{4}$	$-\frac{1}{4}$
A , O''	$-\frac{1}{4}$	$\frac{1}{4}$	$-\frac{5}{8}$	$\frac{1}{8}$
A ·, |A|''	0	0	$-\frac{3}{4}$	$\frac{1}{4}$
B ···, |B|''''	0	0	$-\frac{1}{8}$	$-\frac{1}{8}$
A|B|'', B|A|··	0	0	0	$-\frac{1}{2}$
|O| , O''	0	0	$-\frac{1}{2}$	0
|A|'', B··	$\frac{1}{2}$	$-\frac{1}{2}$	$-\frac{1}{2}$	0
B|A|·, |B|''''	$\frac{1}{2}$	$-\frac{1}{2}$	$-\frac{1}{4}$	$-\frac{1}{4}$
B|A|··, |A|''	$\frac{3}{4}$	$-\frac{3}{4}$	$-\frac{3}{8}$	$-\frac{1}{8}$
|A|'', |O|·	$\frac{1}{4}$	$-\frac{1}{4}$	$-\frac{3}{8}$	$\frac{1}{8}$
O'', B·	$\frac{1}{6}$	$-\frac{1}{6}$	$-\frac{5}{12}$	$-\frac{1}{12}$
O'', B|A|·	$\frac{1}{2}$	$-\frac{1}{2}$	$-\frac{1}{4}$	$-\frac{1}{4}$

Table A – 2. *Logarithmic derivatives for class 2 defects*

Defect model	Majority defects	
Type of majority defects	$\left[\frac{\partial \ln (i)}{\partial \ln \frac{P_{H_2O}}{P_{H_2}}}\right]_{a_A/a_B}$	$\left[\frac{\partial \ln (i)}{\partial \ln \frac{a_A}{a_B}}\right]_{P_{H_2O}/P_{H_2}}$
$A^{\cdot\cdot}, e'$	$-\frac{1}{2}$	$\frac{1}{6}$
$\lvert B\rvert'''', \lvert e\rvert$	$\frac{3}{10}$	$\frac{1}{10}$
$A\lvert B\rvert'', \lvert e\rvert^{\cdot}$	0	$\frac{1}{3}$
$B^{\cdot\cdot}, e'$	$-\frac{3}{10}$	$-\frac{1}{10}$
$\lvert A\rvert'', \lvert e\rvert^{\cdot}$	$\frac{1}{2}$	$-\frac{1}{6}$
$B\lvert A\rvert^{\cdot}, e'$	0	$-\frac{1}{3}$
$\lvert O\rvert, e'$	$-\frac{1}{3}$	0
$O'', \lvert e\rvert^{\cdot}$	$\frac{1}{3}$	0

Table A – 3. *Logarithmic derivatives for class 3 defects*

Defect model	$\left[\frac{\partial \ln (i)}{\partial \ln \frac{P_{H_2O}}{P_{H_2}}}\right]_{a_A/a_B}$	$\left[\frac{\partial \ln (i)}{\partial \ln \frac{a_A}{a_B}}\right]_{P_{H_2O}/P_{H_2}}$
$e', \lvert e\rvert$		
Minority ions	0	0
A	$-\frac{3}{2}$	$\frac{1}{2}$
$\lvert A\rvert''$	$\frac{3}{2}$	$-\frac{1}{2}$
$B^{\cdot}$	$-\frac{3}{2}$	$-\frac{1}{2}$
$\lvert B\rvert''''$	$\frac{3}{2}$	$\frac{1}{2}$
$B\lvert A\rvert$	0	-1
$A\lvert B\rvert''$	0	1
$\lvert O\rvert^{\cdot\cdot}$	-1	0
O''	1	0

J. Phys. Chem. Solids Pergamon Press 1969. Vol. 30, pp. 889-892. Printed in Great Britain.

DIFFUSION OF POINT DEFECTS IN CALCIUM TITANATE

W. L. GEORGE* and R. E. GRACE
School of Materials Science and Metallurgical Engineering, Purdue University,
Lafayette, Ind. 47907, U.S.A.

(*Received* 13 *August* 1968; *in revised form* 19 *September* 1968)

Abstract – Single crystal samples of calcium titanate were equilibrated with water-hydrogen atmospheres of a known P_{H_2O}/P_{H_2} ratio at temperatures of 1100°, 1200° and 1300°C. After a step in the P_{H_2O}/P_{H_2} ratio over the sample, the electrical conductivity was measured continuously until a new equilibrium was attained. Diffusion coefficients were determined by analysis of the transient electrical conductivity data. The effective diffusion coefficient at 1200°C and $P_{H_2O}/P_{H_2} = 10^{-3}$ was $5{\cdot}2 \times 10^{-6}$ cm^{2}sec^{-1}; the enthalpy of motion of oxygen vacancies was 13,000 cal/mol.

THE ELECTRICAL conductivity and thermoelectric power of single crystal calcium titanate equilibrated with water-hydrogen atmospheres were presented in a previous paper[1]. It was shown that when calcium titanate is reduced in damp hydrogen at elevated temperatures, the predominant point defects are doubly ionized oxygen vacancies and excess electrons. This paper presents transient electrical conductivity measurements taken as the stoichiometry of $CaTiO_3$ crystals was varied between equilibrium states.

Since the electrical conductivity is proportional to the concentration of oxygen vacancies, it is possible to use the transient conductivity to follow the kinetics of interdiffusion. This has been done by several authors[2–4].

EXPERIMENTAL

Details of the general experimental procedure were presented in the previous paper[1]. The electrical conductivity was measured with a four probe d.c. technique. A small current (less than 10 mA) was allowed to flow through the sample by means of lead wires spring-loaded against the sample ends. The voltage drop was measured between the low alloy legs of two thermocouples embedded in the sample. First the crystal was held at a prescribed temperature and P_{H_2O}/P_{H_2} ratio until equilibrium was established and the electrical conductivity did not change with time. A new P_{H_2O}/P_{H_2} ratio was then established rapidly over the sample, and the voltage drop at constant sample current was recorded until the conductivity again became constant. The crystal could then be returned to the original equilibrium state by reestablishing the original P_{H_2O}/P_{H_2} ratio, or further excursions could be introduced before returning the crystal to its original state. The electrical conductivity was monitored continuously during all steps, and no hysteresis was observed. Experiments were performed both in water-hydrogen atmospheres and in water-hydrogen-argon atmospheres made from a 10 per cent hydrogen, 90 per cent argon mixture.

RESULTS

Figure 1 shows representative transient electrical conductivity data. The points are values of electrical conductivity calculated from the recorded voltage and current. The initial horizontal portion represents equilibrium of the sample at 1200°C with gas of $P_{H_2O}/P_{H_2} = 1{\cdot}71 \times 10^{-2}$. The P_{H_2O}/P_{H_2} ratio was changed to $1{\cdot}12 \times 10^{-2}$ and the electrical

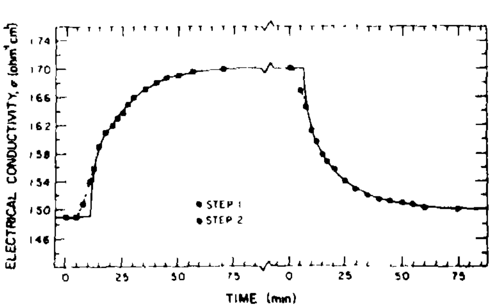

Fig. 1. Transient electrical conductivity data at 1200°C.

**Present address*: Motorola Semiconductor Products Division, Phoenix, Ariz. 85008, U.S.A.

conductivity increased to the new equilibrium value. After equilibration the original P_{H_2O}/P_{H_2} ratio was reestablished, and the electrical conductivity returned to the original value. The zero times shown in Fig. 1 are arbitrary since several minutes were required to purge the system with new gas.

The solid curves of Fig. 1 represent the solution to the diffusion problem as described below. A slab of dimensions $-a_1 < x_1 < a_1$, $-a_2 < x_2 < a_2$, $-a_3 < x_3 < a_3$ is in equilibrium with a gas of known composition. The conductivity, σ_0, is proportional to the initial uniform concentration of vacancies, C_0. At time zero, through a step function change in the composition of the gas phase, the surface concentration is changed to C_f, and the sample approaches a new equilibrium conductivity, σ_f, proportional to C_f, as time approaches ∞.

Fick's second law was solved for the above boundary conditions by Newman[5], who found that the fractional saturation is given by

$$\frac{\bar{C}(t)-C_f}{C_0-C_f} = s_1(t)\,s_2(t)\,s_3(t). \qquad (1)$$

The functions in the right hand side of equation (1) are defined by

$$s_j(t) = \frac{2}{\pi^2}\sum_{n=0}^{\infty}\left[\frac{1}{(n+\frac{1}{2})^2}\right]\exp\left[-\frac{(n+\frac{1}{2})^2\pi^2 Dt}{a_j^2}\right] \qquad (2)$$

where D is the effective diffusion coefficient and t is the time.

Campbell, Kass and O'Keeffe[6] calculated the quantity $\Sigma = (\bar{\sigma}(t)-\sigma_f)/(\sigma_0-\sigma_f)$ and compared it with $(\bar{C}(t)-C_f)/(C_0-C_f)$ as a function of Dt/a_1^2 for various shapes of samples and values of σ_0/σ_f. For long, thin samples and σ_0/σ_f ratios not very different from unity, the two quantities are substantially the same function of Dt/a_1^2. In view of the above analysis the series solutions of Newman can be used to obtain diffusion coefficients from conductivity data for appropriately chosen sample shapes. A computer program was written to calculate $(\bar{C}(t)-C_f)/(C_0-C_f)$ vs. Dt/a_1^2 from Newman's solution, then to compare the theoretical curves with experimental data to yield Dt/a_1^2 as a function of t. Figure 2 is this plot for the data of Fig. 1. The data are linear up to values of Dt/a_1^2 in excess of 0·6; scatter above this point reflects the magnified sensitivity of the expression, $(\bar{\sigma}(t)-\sigma_f)/(\sigma_0-\sigma_f)$, to small errors as equilibrium is approached.

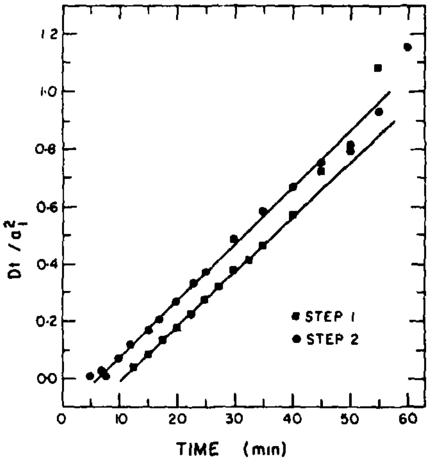

Fig. 2. Dt/a_1^2 vs. time from data in Fig. 1.

Figure 1 shows that the agreement between the measured conductivity and that calculated from Newman's solution to the diffusion equation is generally quite good. This agreement indicates that the difference between the Σ function above and the three dimensional fractional saturation is very small for the sample geometry employed. At short times there is a small difference between the measured and calculated conductivities. This arises primarily from the time required to establish new boundary conditions at the crystal/gas interface.

Figure 3 shows the dependence of the effective diffusion coefficient upon the P_{H_2O}/P_{H_2} ratio; D is a slowly varying function of the

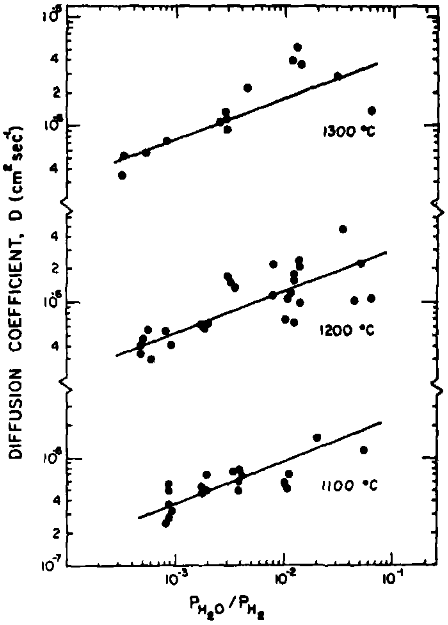

Fig. 3. P_{H_2O}/P_{H_2} dependence of the diffusion coefficient.

pressure ratio, i.e. $(P_{H_2O}/P_{H_2})^{0.4}$. There was no observable difference between steps where the original P_{H_2O}/P_{H_2} ratio was greater than the final P_{H_2O}/P_{H_2} ratio and *vice versa*. Also, steps in which the original P_{H_2O}/P_{H_2} ratio differed from the final P_{H_2O}/P_{H_2} ratio by less than a factor of two minimized errors caused by assuming a constant diffusion coefficient in the analysis. Figure 4 shows the temperature dependence of the diffusion coefficient for $P_{H_2O}/P_{H_2} = 10^{-2}$. The dashed lines show the estimated uncertainty in the diffusion coefficient arising from the standard deviation of D from the least squares 1200°C isotherm of Fig. 3. The activation energy calculated from the slope of Fig. 4 is 13,000 cal/mol.

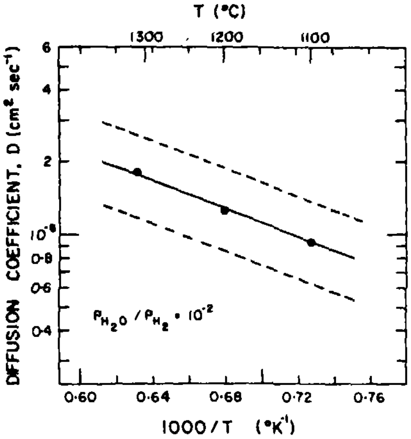

Fig. 4. Temperature dependence of the diffusion coefficient.

DISCUSSION

As shown by Wagner[7], the effective diffusion coefficient, D, reflects the ambipolar diffusion of both anion vacancies and electrons. The effective diffusion coefficient is related to the vacancy diffusion coefficient, $D_\square$, by $D = (1+z)\,D_\square$, i.e. $D = 3D_\square$ for ionized oxygen vacancies.

The dependence of $\ln D_\square$ upon reciprocal temperature is given by

$$\frac{\mathrm{d}\ln D_\square}{\mathrm{d}1/T} = -\frac{\Delta H_m}{R}. \tag{3}$$

Since the effective diffusion coefficient is proportional to the vacancy diffusion coefficient, the activation energy from Fig. 4 may be interpreted as the enthalpy of motion of oxygen vacancies, i.e. $\Delta H_m = 13{,}000$ cal/mol.

Although few experimental investigations have been made of calcium titanate, oxygen vacancy diffusion in $CaTiO_3$ may be compared to diffusion in the similar ABO_3 compound, strontium titanate. As Linz and Herrington[8] pointed out, the Ti–O bonds in $CaTiO_3$ are shorter than in $SrTiO_3$; such tighter binding should lead to a larger enthalpy of motion for oxygen vacancies in calcium titanate than in strontium titanate. Walters and Grace[4] reported an enthalpy of motion for oxygen vacancies in strontium titanate of 6000 cal/mol., which is approximately half that found for calcium titanate.

CONCLUSIONS

Transient electrical conductivity measurements were used to study interdiffusion in calcium titanate. The effective diffusion coefficient was a slowly varying function of P_{H_2O}/P_{H_2}, and the enthalpy of motion of oxygen vacancies was 13000 cal/mol.

Acknowledgements—This manuscript was taken from a dissertation submitted by W. L. George to Purdue University in partial fulfillment of the requirements for the Ph.D. degree. The research was supported by the National Science Foundation through a Graduate Fellowship, by the United States Atomic Energy Commission through Contract AT(11-1)-1436, and by a Donnan Award from Purdue University. The single crystals of $CaTiO_3$ were a gift of the National Lead Company, South Amboy, New Jersey.

REFERENCES

1. GEORGE W. L. and GRACE R. E., *J. Phys. Chem. Solids* **30**, 881 (1969).
2. THOMAS D. G. and LANDER J. J., *J. chem. Phys.* **25**, 1136 (1956).
3. PRICE J. B. and WAGNER J. B., *Z. phys. Chem.* **49**, 257 (1966).
4. WALTERS L. C. and GRACE R. E., *J. Phys. Chem. Solids* **28**, 245 (1967).
5. NEWMAN A. B., *Trans. Am. Inst. Chem. Engrs.* **27**, 310 (1931).
6. CAMPBELL R. J., KASS W. J. and O'KEEFFE M., *Natn Bur. Stand. Wash.* **296**, 173 (1968).
7. WAGNER C., *Z. phys. Chem.* **B32**, 447 (1936).
8. LINZ A., Jr. and HERRINGTON K., *J. chem. Phys.* **28**, 824 (1958).

J. Phys. Chem. Solids Pergamon Press 1969. Vol. 30, pp. 893–901. Printed in Great Britain.

MAGNETO-ACOUSTIC INVESTIGATION OF THE FERMI SURFACE AND SPIN SPLITTING OF THE LANDAU LEVELS IN *p*-TYPE AND *n*-TYPE PbTe

W. SCHILZ

Philips Zentrallaboratorium Hamburg, Hamburg 54, Vogt-Köllnstr. 30, Germany

(*Received* 14 *August* 1968; *in revised form* 17 *September* 1968)

Abstract – Quantum oscillations of the magneto-acoustic attenuation have been measured in *p*-type and *n*-type samples of lead telluride. From the periods of these oscillations, measured as a function of the angle ϕ between the direction of magnetic field and the [100] axis of the crystal, the shape of the Fermi surface has been investigated as a function of the carrier concentration. A strong non-ellipsoidal behavior was observed for both *p*-type and *n*-type material. Furthermore, spin splitting of the Landau levels was measured. The splitting was found to be around $\frac{1}{2}$ of the Landau-level spacing and decreases slightly with decreasing carrier concentration.

1. INTRODUCTION

THE SEMICONDUCTING compound PbTe has been the object of extensive investigations for over a decade. Measurements of the weak-field magnetoresistance, piezoresistance, de Haas–van Alphen and Shubnikov–de Haas effect and cyclotron resonance experiments[1] are each consistent with a multi-valley model of the Fermi surface in which the extrema of the principal conduction and valence band are located at the *L*-points of the Brillouin zone. The constant energy surface consists of four prolate ellipsoids directed along the [111] axes of the f.c.c. crystal (see Fig. 1). These experimental results are in good agreement with theoretical energy-band calculations of lead telluride[2–5]. Furthermore, nonparabolicity of both the conduction and the valence band has been reported[1a, 6–9], and spin splitting of about $\frac{1}{2}$ of the Landau-level spacing has been observed in Shubnikov–de Haas experiments [7, 10, 11]. Quantum oscillations of the magneto-acoustic absorption in PbTe were first observed by Shapira and Lax[12].

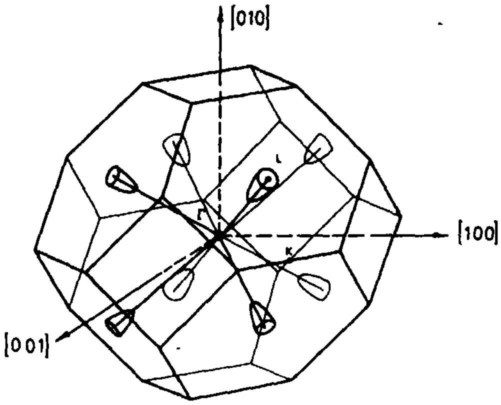

Fig. 1. Brillouin zone and Fermi surface of PbTe.

We have performed measurements of the quantum oscillations of the magneto-acoustic attenuation in various samples of *p*-type and *n*-type PbTe of different carrier concentrations. The carrier density ranged from 10^{17} cm^{-3} to 6×10^{18} cm^{-3}. In these measurements, a strong nonellipsoidal behavior of the Fermi surface of *p*-type and *n*-type PbTe was observed. The deviation from ellipsoidal shape was found to increase with increasing carrier concentration. A similar nonellipsoidal behavior of the Fermi surface of the lead compound PbSe has been observed by Shapira and Beckmann[13]. Furthermore, we have measured the amount and, partially, the anisotropy of the spin splitting of the Landau levels in *p*-type and *n*-type PbTe as a function of the carrier density. This paper is organized as follows: in Section 2 we discuss theoretically the influence of the non-ellipsoidal and the non-parabolic behavior of the Fermi surface on the periods of the quantum oscillations and the dependence of the extremal cross section of the Fermi surface on the carrier concentration. Section 3 deals with the experimental procedure and in Section 4 the experimental results are reported and discussed.

2. THEORETICAL

The theory of the acoustic quantum oscillations was developed extensively[14–18]. Sharp spikes occur in the ultrasonic attenuation as a function of the magnetic field whenever a Landau level, accompanied by a singularity in the density of states of the charge carriers, crosses the Fermi energy. Since the attenuation peaks are very narrow at low temperatures, the oscillation patterns due to the four ellipsoids of the Fermi surface of PbTe can be separated by means of the magnetic field.

For a single ellipsoid of the Fermi surface in the parabolic approximation the energy levels in the presence of a quantizing magnetic field are given by:

$$E_{n,s}(k_b) = (n+1/2)\hbar\omega_c + \frac{\hbar^2 k_b^2}{2m_0 m_b} + sg\mu_B B. \quad (1)$$

The first term describes the quantization of the cyclotron motion in the plane perpendicular to **B** with orbital quantum number $n = 0,1,2,\ldots$ where:

$\omega_c = \dfrac{eB}{m_0 m_c}$ = cyclotron frequency

m_0 = free electron mass

$m_c = (\det[\mathbf{m}]/\hat{b}\,\mathbf{m}\,\hat{b})^{1/2}$ = cyclotron mass (2)

$\mathbf{m}$ = tensor of effective mass in units of m_0

$\hat{b}$ = unit vector in the direction of **B**.

The second term in equation (1) refers to the translational motion of the charge carriers in the direction of the magnetic field, where k_b and $m_b = (\hat{b}\mathbf{m}\hat{b})$ are the wave number and effective mass parallel to **B**, respectively. The third term gives the spin splitting of the Landau levels due to an anisotropic g factor, where μ_B is the Bohr's magneton and $s = \pm\frac{1}{2}$ the spin quantum number. The anisotropy of the spin splitting can be expressed by a spin mass m_s which is related to the spin mass tensor $\mathbf{m}_s$ by:

$$m_s = (\det[\mathbf{m}_s]/\hat{b}\,\mathbf{m}_s\,\hat{b})^{1/2}. \quad (3)$$

The spin mass is related to the g-factor by:

$$g = 2/m_s. \quad (4)$$

In the ellipsoidal parabolic model (ep-model) the shape of the Fermi surface in k-space is given by:

$$\frac{\hbar^2}{2m_0}\mathbf{k}_F(\mathbf{m})^{-1}\mathbf{k}_F = E_F = \frac{\hbar^2}{2m_0 m_d}(3\pi^2 n)^{2/3} \quad (5)$$

$$m_d = (\det \mathbf{m})^{1/3} N^{2/3}$$

where E_F = Fermi energy, n = carrier concentration, m_d = density of states mass in units of m_0, $\mathbf{k}_F$ = wave vector at the Fermi surface and N = number of equivalent ellipsoids of the Fermi surface. As can be seen from equation (1) and (5), the period $\Delta(1/B)$ of the quantum oscillations is inversely proportional to the extremal cross section α of the Fermi surface:

$$\Delta(1/B) = \frac{e\hbar}{m_0 m_c E_F} \sim \frac{1}{\alpha} \quad (6)$$

since the relation between the extremal cross section α and the cyclotron mass is given by:

$$m_c = \frac{(\hbar^2/2\pi)}{m_0}|\mathrm{d}\alpha/\mathrm{d}E_F| \sim \alpha/E_F. \quad (7)$$

The extremal cross section increases proportional to $n^{2/3}$ with increasing carrier density n. The angular dependence of α in the *ep*-model for spheroids of the mass ratio $K_m = m_l/m_t$ is given by the following equation:

$$\alpha = \frac{\hbar}{2e}(3\pi^2 n/N)^{2/3} K_m^{1/6} \times [(K_m - 1)\cos^2\theta + 1]^{-1/2} \quad (8)$$

for α in units of 10^4 G and n in units of 10^{18} cm^{-3}. θ is the angle between the direction of the magnetic field and the mayor axis of the ellipsoid. In the ellipsoidal nonparabolic model (*enp*-model) the dispersion relation of equation (5) in the second order approximation reads[19]

$$(\hbar^2/2m_0)\mathbf{k}\,\mathbf{m}^{-1}\,\mathbf{k} = \gamma(E) \sim n^{2/3} \quad (9)$$

where $\gamma(E) = E(1 + E/E_g)$, E_g = energy gap to the energy band causing the non-parabolicity. In this case the mass ratio K_m is not affected by the nonparabolicity and thus is independent of the carrier density. As a consequence, the extremal cross section α increases proportional to $n^{2/3}$ as in the *ep*-model. Introducing equation (9) into equation (1) shows that the energy difference between adjacent Landau levels is no longer constant but depends on the energy. In the case of relatively low magnetic fields (i.e. if the orbital quantum number n_F of the Landau level, located at the Fermi energy, is large enough to prevent oscillations of the Fermi energy as a function of the magnetic field) the Landau level spacing, neglecting spin splitting, is given by:

$$E_{n+1} - E_n = \hbar\omega_{c,n} = (eB\hbar/m_0 m_{c,0}) \times \left[1 + \frac{4eB\hbar n}{E_g m_{c,0} m_0}\right]^{-1/2} \quad (10)$$

where $m_{c,0}$ = cyclotron mass at the bottom of the band. As can be seen from equations (5), (9) and (10), the Landau level spacing at the Fermi energy is given by:

$$\Delta E^{(F)} = \hbar\omega_c^{(F)} = (eB\hbar/m_0 m_{c,0}) \times \left[1 + \frac{4}{E_g}\gamma(E)\right]^{-1/2}$$

$$= (eB\hbar/m_0 m_{c,0})\left[1 + \frac{2\hbar^2}{E_g m_d}(3\pi^2 n)^{2/3}\right]^{-1/2}. \quad (11)$$

The square root of equation (11) is the ratio of the density of states mass at the Fermi energy to the density of states mass at the bottom of the conduction band, as has been calculated by Zhitinskay *et al.*[6] and Kolodziejczak *et al.*[19]. As can be seen from the above calculation in cyclotron-resonance experiments $\omega_c^{(F)}$ i.e. the cyclotron mass at the Fermi energy is measured ($\Delta n = 1$ transition in equation (1)), however, the period of the quantum oscillations is inversely proportional to the cyclotron mass at the bottom of the band[19]. ($\Delta n = 0$ transition in equation (1)):

$$\Delta\frac{1}{B} = \frac{e\hbar}{m_0 m_{c,0} E_F(1 + E_F/E_g)}. \quad (12)$$

The kind of nonparabolicity discussed above cannot be investigated by measurements of the quantum oscillations at constant temperature. A second kind of nonparabolicity has been observed in PbTe[7] when the dependence of the effective mass on carrier concentration is different for the transverse and longitudinal mass components. In this case, the mass ratio and thus the components of the effective mass tensor in equation (9) become a function of the carrier density and the proportionality $\alpha \sim n^{2/3}$ is violated. As can easily be seen from equation (8) α increases stronger than $n^{2/3}$ for $\theta = 0°$ and less than $n^{2/3}$ for $\theta = 90°$ when K_m decreases with increasing carrier concentration. In contrast to this, the extremal cross section of spheroids with different K_m and n = const. remains nearly constant at $\theta = 75°$, as shown in Table 1.

Table 1

	Extremal cross section		
θ	$K_m = 15$	$K_m = 10$	$K_m = 5$
0°	0·87	1·00	1·26
75°	2·42	2·50	2·50
90°	3·38	3·16	2·82

At high carrier densities, the Fermi energy becomes comparable with the energy gap in PbTe. In this range the non-ellipsoidal behavior of the Fermi surface becomes important. For simplicity, we consider only the transition from ellipsoidal to cyclindrical Fermi surface. The mass ratio of the cylinder may be given by $(l/d)^2$ where l and d are the length and diameter of the cylinder in k-space, respectively. The angular dependence of the extremal cross section of an infinite cylinder is given by:

$$\alpha^c \sim (\cos\theta)^{-1} \tag{13}$$

where θ = angle between the axis of the cylinder and the direction of the magnetic field. Assuming constant carrier concentration (i.e. constant volume of the Fermi surface) and constant K_m for ellipsoid and finite cylinder the following relations between the extremal cross sections of ellipsoid and cylinder can be deduced:

$$\alpha_0{}^c/\alpha_0{}^\epsilon = 0{\cdot}825 \quad (\theta = 0°)$$

$$\alpha_{75}{}^c/\alpha_{75}{}^\epsilon = 3{\cdot}19\, K_m{}^{-1/2}[(K_m-1)\cos^2 75°+1]^{1/2} \quad (\theta = 75°) \tag{14a}$$

$$\alpha_{75}{}^c/\alpha_0{}^c = 3{\cdot}87$$

$$\alpha_{75}{}^\epsilon/\alpha_0{}^\epsilon = K_m{}^{1/2}[(K_m-1)\cos^2 75°+1]^{-1/2}. \tag{14b}$$

These equations are valid when the Fermi surface is cylindrical up to an angle $\theta = 75°$. The indices ϵ and c refer to ellipsoid and cylinder, respectively. These relations will be necessary for the discussion of the experimental results in Section 4.

3. EXPERIMENTAL PROCEDURE

The experiments were carried out at $T = 4{\cdot}2$ and $1{\cdot}9$°K in static magnetic fields up to 56 kG and in the frequency range between 60 and 420 MHz. Ultrasonic pulses where excited and detected by Y-cut quartz transducers, attached to both sides of the sample. The amplitude of the transmitted signal was recorded as a function of the magnetic field by use of a standard sampling technique. An example of such an x–y recorder plot is given in Fig. 2. The samples could be rotated in the bore of a superconducting solenoid, thus varying the angle ϕ between the crystal axis and the direction of the magnetic field. In all experiments reported in this paper the wave vector of the transverse ultrasound was

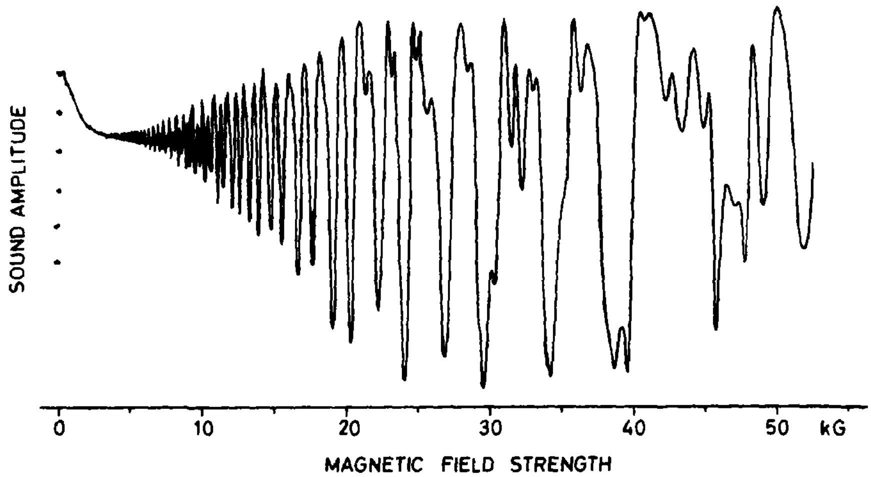

Fig. 2. Recorder plot of the quantum oscillations of the magneto-acoustic attenuation. Sample: n-type, $n = 2{\cdot}8 \times 10^{18}$ cm^{-3}, $T = 1{\cdot}9$°K, f = 140 MHz, $\phi = \sphericalangle\, \mathbf{q},\mathbf{B} = 75°$.

directed along a [100] axis with the polarization along a[110] direction of the crystal. The magnetic field was rotated in a ⟨110⟩ plane. All samples were cut from one ingot, grown by the Stockbarger method[20]. The ingot was p-type material having a carrier concentration of $2{\cdot}15\times10^{18}\,\text{cm}^{-3}$ and a carrier mobility of about $5\times10^5\,\text{cm}^2/\text{V sec}$. The sample dimensions were generally about $5\times5\times10\,\text{mm}^3$, the long axis was directed along the [100] axis of the crystal. The carrier concentration of the samples has been varied by doping and annealing in a lead rich atmosphere at temperatures up to 750°C. Thus carrier concentrations between $10^{17}\,\text{cm}^{-3}$ and $5\times10^{18}\,\text{cm}^{-3}$ for p-type and between $8\times10^{17}\,\text{cm}^{-3}$ and $6\times10^{18}\,\text{cm}^{-3}$ for n-type material have been obtained. The carrier concentration was determined with high accuracy by means of helicon resonances.

The magnetic-field dependence of the ultrasonic attenuation was measured for various directions of the magnetic field with respect to the crystal axis. Generally, the angular range $\mathbf{B}\parallel\mathbf{q}$ to $\mathbf{B}\perp\mathbf{q}$ ($\mathbf{q}$ = phonon wave vector) was investigated. From the x–y recorder plots of the quantum oscillations up to three different periods $\Delta(1/B)$ have been obtained as a function of the magnetic-field direction. The oscillation periods with light cyclotron masses could be determined with the best accuracy. Spin splitting of the Landau levels was observed in this range only. As an example, the angular dependence of the periods $\Delta(1/B)$ of a p-type sample is shown in Fig. 3.

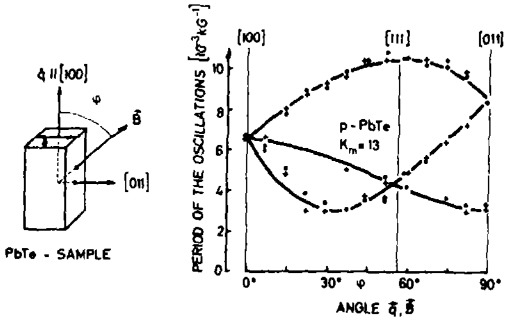

Fig. 3. Angular dependence of the period $\Delta(1/B)$ of the quantum oscillations versus $\phi = \sphericalangle\, \mathbf{q},\mathbf{B}$. (sample: p-type, $p = 2{\cdot}14\times10^{18}\,\text{cm}^{-3}$, $f = 140$ MHz, $T = 4{\cdot}2$°K) and sketch of the sample arrangement ($\mathbf{q}$: wave vector, $\hat{\mathbf{e}}$: polarization vector).

4. EXPERIMENTAL RESULTS AND DISCUSSION

(A) Shape of the Fermi surface

The results shown in Fig. 3 have been obtained with a p-type sample having a carrier concentration of $2{\cdot}14\times10^{18}\,\text{cm}^{-3}$. For this sample good agreement with the calculated angular dependence of $\Delta(1/B)$ for an ellipsoidal Fermi surface with $K_m = 13$ has been obtained (calculation: full curve in Fig. 3). In contrast to this behavior, all n-type samples and the highly doped p-type samples show a marked deviation from ellipsoidal shape. In order to demonstrate the deviations from an ellipsoidal Fermi surface, the experimentally determined extremal cross sections α are plotted as a function of the angle θ between the direction of the magnetic field and the major axis of one of the Fermi ellipsoids (i.e. a [111] direction of the crystal). By this procedure all experimental points contribute to one curve, as shown in Fig. 4.

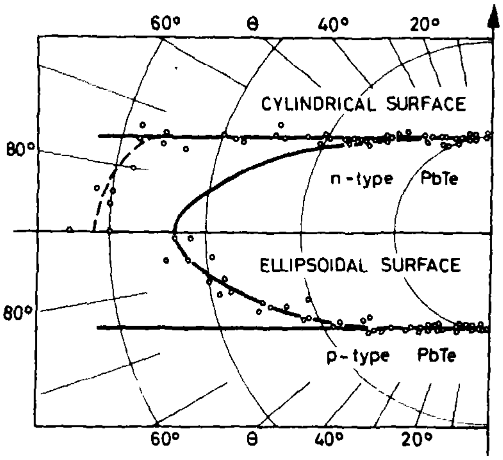

Fig. 4. Polar diagram of the angular dependence of the extremal section α. θ = angle between the magnetic field direction and the major axis of the energy surface (Carrier concentrations: p-type: $1{\cdot}80\times10^{18}\,\text{cm}^{-3}$, n-type: $2{\cdot}15\times10^{18}\,\text{cm}^{-3}$).

It can be seen from equation (13) that the angular dependence of the extremal cross section for an infinite cylinder gives a straight horizontal line in the polar diagram. In addition, the calculated angular dependence of α for an ellipsoidal Fermi surface is plotted in Fig. 4. Both theoretical curves are compared with experimental results of two samples (plotted in arbitrary units). The n-type crystal shows nearly cylindrical behavior of the Fermi surface up to angles $\theta \approx 75°$, while the p-type sample within good approximation has an ellipsoidal Fermi surface. As can be seen from the scattering of the measuring points in the vicinity of $\theta = 90°$, the experimental accuracy is very low in this region. Since the heavy cyclotron masses contribute to the quantum oscillations in this angular range, a better accuracy is to be expected from measurements at higher magnetic fields. At present, due to the inaccuracy of the results near $\theta = 90°$, the cover of the 'cylinder' cannot be determined exactly.

The experimental results for most of the samples are summarized in Fig. 5, (the curve for the p-type sample $p = 1{\cdot}7 \times 10^{17}\,\mathrm{cm}^{-3}$ was enlarged by a factor of two) showing the angular dependence of the extremal cross section α as a function of θ in a polar diagram.

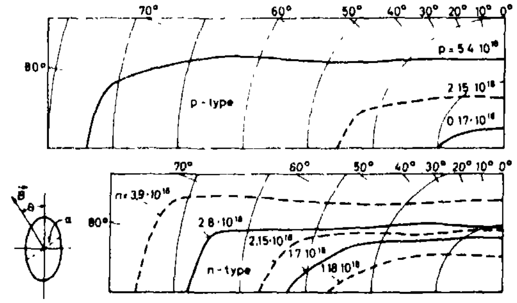

Fig. 5. Polar diagram of the extremal cross section α vs. the angle θ between B and the major axis of the energy surface (the curve $p = 0{\cdot}17 \times 10^{18}$ has been enlarged by a factor of two)

The p-type material shows a transition from exactly ellipsoidal to nearly cylindrical Fermi surface in the carrier density range between $1{\cdot}7 \times 10^{17}\,\mathrm{cm}^{-3}$ and $6{\cdot}0 \times 10^{18}\,\mathrm{cm}^{-3}$. Similar results have been obtained for n-type material (Fig. 5). Only at the lowest carrier concentration ($n = 1{\cdot}18 \times 10^{18}\,\mathrm{cm}^{-3}$) the Fermi surface can be approximated by an ellipsoid.

In order to get a more quantitative information about the shape of the Fermi surface, the extremal cross sections at $\theta = 0°$ and $\theta = 75°$ (α_0 and α_{75}) have been plotted as a function of the carrier density. The results obtained from n-type samples are shown in Fig. 6 on a double log. scale. Both experimental curves deviate from the $n^{2/3}$ law which is indicated by the straight lines. The experimental α_0 increases weaker than $n^{2/3}$ and α_{75} increases stronger than $n^{2/3}$ which is to be expected when a transition from ellipsoidal to cylindrical Fermi surface takes place. The experimentally determined ratio α_{75}/α_0 increases with increasing carrier concentration:

$$n = 10^{18}\,\mathrm{cm}^{-3}: \qquad \alpha_{75}/\alpha_0 = 2{\cdot}73;$$

$$n = 5 \times 10^{18}\,\mathrm{cm}^{-3}: \quad \alpha_{75}/\alpha_0 = 3{\cdot}93.$$

This is in good agreement with the theory (equation (14)) which gives:

for the ellipsoid: $\alpha_{75}/\alpha_0 = 2{\cdot}62$;

for the cylinder: $\alpha_{75}/\alpha_0 = 3{\cdot}9$

with a mass ratio $K_m = 12$.

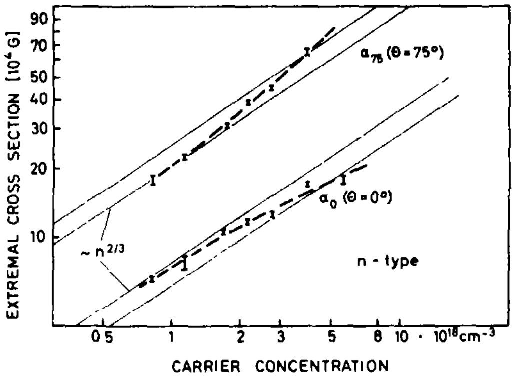

Fig. 6. Carrier concentration dependence of the extremal cross sections α_0 and α_{75} of n-type PbTe as compared with the $n^{2/3}$ law.

The results for p-type material are plotted in Fig. 7. The extremal cross sections α_0 and α_{75} increase proportional to $n^{2/3}$ in the carrier density range between $10^{17}\,\text{cm}^{-3}$ and $2\times 10^{18}\,\text{cm}^{-3}$. Ellipsoidal shape of the Fermi surface is to be expected in this range. By use of equation (14) a mass ratio $K_m = 11{\cdot}2$ can be calculated from the experimental ratio $\alpha_{75}/\alpha_0 = 2{\cdot}57$. At higher carrier concentrations the α_{75} curve shows a deviation from the $n^{2/3}$ law, however, the α_0 remains proportional to $n^{2/3}$. This may be explained by a non-parabolicity which results in a decrease of the mass ratio K_m with increasing carrier density. Non-parabolicity of this kind has been reported for PbTe and is to be expected on theoretical grounds[1] in the carrier concentration range around $3\times 10^{18}\,\text{cm}^{-3}$.

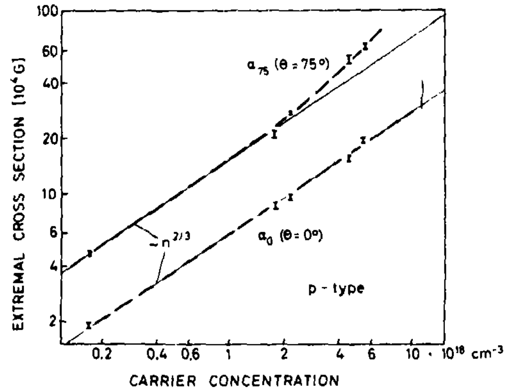

Fig. 7. Carrier concentration dependence of the extremal cross sections α_0 and α_{75} of p-type material as compared with the $n^{2/3}$ law.

It has been shown in Table 1 that the extremal cross section α_{75} is insensitive to variations of K_m. Therefore, the deviation of the α_{75} curve in Fig. 7 is due to a non-ellipsoidal behavior. A comparison of the experimental cross section ratios and the relations given in equation (14) is shown in Table 2.

These results indicate a nearly cylindrical shape of the Fermi surface in accordance with the $\alpha(\theta)$ curves in Fig. 5. Therefore, the absence of a negative deviation of the α_0 curve in Fig. 7 has to be explained by a decrease of the mass ratio K_m. As it has been shown in Section 2, the ratio $\alpha_0{}^c/\alpha_0{}^e = 0{\cdot}825$. In order to compensate this effect by a variation of K_m (since the experimental ratio $\alpha_0{}^c/\alpha_0{}^e = 1$ in Fig. 7), a mass ratio around 7 would be necessary at $p = 5\times 10^{18}\,\text{cm}^{-3}$.

Table 2. Ratios of extremal cross sections

	Calculated (equation (14))		Experimental
	$K_m = 9$	$K_m = 11{\cdot}2$	$p = 5\times 10^{18}\,\text{cm}^{-3}$
$\alpha^c_{75}/\alpha^e_{75}$	1·35	1·25	1·28
α^c_{75}/α^c_0	3·87		≈3·40

(*B*) *Spin splitting of the Landau levels*

Spin splitting of the Landau levels has been observed in the carrier density range above $10^{18}\,\text{cm}^{-3}$ and $4\times 10^{18}\,\text{cm}^{-3}$ for n- and p-type material, respectively. The spin splitting is nearly $\frac{1}{2}$ of the Landau-level spacing and thus leads to a doubling of the attenuation peaks as shown in Fig. 8. The spin splitting could be resolved in the light cyclotron mass region, i.e. along the upper curve of Fig. 3. As an example, the reciprocal cyclotron mass and spin mass, both in units of $10^{-3}\,\text{kG}^{-1}$ for an n-type sample are plotted in Fig. 9 as a function of the angle ϕ between the [100] axis of the crystal and the direction of the magnetic field. It can be seen from Fig. 9 that the cyclotron mass m_c and the spin mass m_s have nearly the same anisotropy in the angular range con-

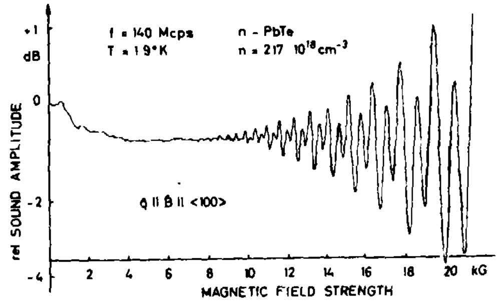

Fig. 8. Quantum oscillations of the magneto-acoustic attenuation showing the doubling of the attenuation peaks due to spin splitting.

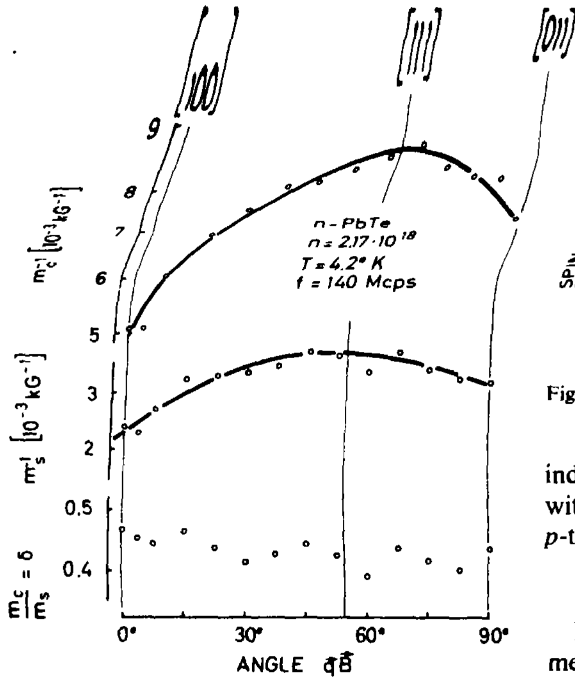

Fig. 9. Cyclotron mass m_c, spin mass m_s and relative spin splitting δ vs. the angle ϕ for an n-type PbTe sample.

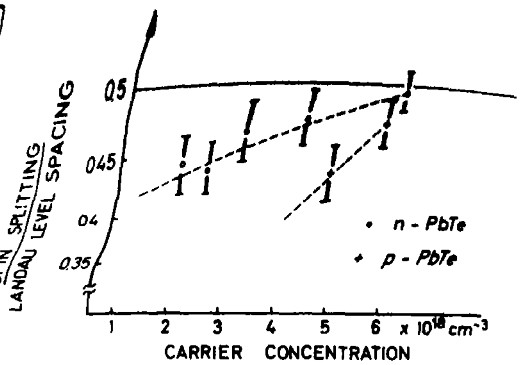

Fig. 10. Relative spin splitting δ of p-type and n-type PbTe versus carrier concentration.

sidered here. As a consequence the relative spin splitting $\delta = m_c/m_s$ can be assumed to be independent of the angle ϕ (see Fig. 9). The carrier-density dependence of δ including experimental error is plotted in Fig. 10 for both p-type and n-type material. The splitting is found to be always close to $\frac{1}{2}$ of the Landau level spacing as has been reported previously [1] but decreases with decreasing carrier density. Using effective mass parameters from literature[1b] the g-factor $g_{\parallel}$ was calculated from the experimentally determined δ and is shown in Table 3.

Table 3. *Experimental g-factors*

	p-type		n-type	
carrier con.	6×10^{18}	4×10^{18}	6×10^{18}	$1 \cdot 5 \times 10^{18}$
$\lvert g_{\parallel} \rvert$ ($\theta = 0°$)	$45 \cdot 5 \pm 2$	$36 \cdot 0 \pm 2$	$41 \cdot 5 \pm 2$	$33 \cdot 0 \pm 1 \cdot 5$

Recently, a g-factor $g_{\parallel} = |11 \cdot 6|$, ($\delta \approx 0 \cdot 13$) has been reported for p-type PbTe with a carrier concentration of $2 \cdot 85 \times 10^{18}$ cm^{-3}[11]. In connection with our results, this would indicate a strong decrease of the spin splitting with decreasing carrier concentration in p-type PbTe.

4. SUMMARY

It has been shown by magneto-acoustic measurement of the quantum oscillations that the Fermi surface of p-type and n-type PbTe is strongly non ellipsoidal. The transition from ellipsoidal to a nearly cylindrical Fermi surface was found in the carrier density range between 10^{18} cm^{-3} and 6×10^{18} cm^{-3}. In agreement with previous investigations non-parabolicity of p-type PbTe has been found resulting in a decrease of the mass anisotropy ratio K_m with increasing carrier concentration. The combination of the nonparabolic and non ellipsoidal behavior of the Fermi surface makes the exact determination of the mass anisotropy very difficult. This may explain some discrepancy about the mass anisotropy which exists in the literature between cyclotron resonance and Shubnikov–de Haas experiments. Spin splitting of the Landau levels has been observed in both p-type and n-type PbTe. The splitting was found to be around ½ of the Landau level spacing and decreases slightly with decreasing carrier density.

Acknowledgements – Stimulating discussions with K. Walther and K. H. Sarges are acknowledged. The author is indebted to J. Reher for carrying out most of the measurements.

REFERENCES

1. For a review of this work see (a) BURKE J. R., Jr., *Phys. Rev.* **160**, 636 (1967); (b) CUFF K. F., ELLETT M. R., KUGLIN C. D. and WILLIAMS L. R., *Physics of Semiconductors, Paris 1964*, p. 677. Dunod, Paris (1964).
2. LIN P. J. and KLEINMAN L., *Phys. Rev.* **142**, 478 (1966).
3. MITCHELL D. L. and WALLIS R. F., *Phys. Rev.* **151**, 581 (1966).
4. PRATT G. W., Jr. and FEMEIRA L. G., *Physics of Semiconductors, Paris 1964*, p. 69. Dunod, Paris (1964).
5. DIMMOCK J. O. and WRIGHT G. B., *Physics of Semiconductors, Paris 1964*, p. 77. Dunod, Paris (1964).
6. ZHITINSKAYA M. K., KAIDANOV V. I. and CHERNIK I. A., *Soviet Phys. solid St.* **8**, 246 (1966).
7. CUFF K. F., ELLETT M. R. and KUGLIN C. D., *Proc. Int. Conf. Physics, Exeter 1962*, p. 316.
8. STAVITSKAYA T. S., PROKOFEVA L. V., RAVICH Yu. I. and EFIMOVA B. A., *Soviet Phys. Semicond.* **1**, 952 (1968).
9. KOLOMOETS N. V., VINOGRADOVA M. N. and SYSOEVA L. M., *Soviet Phys. Semicond.* **1**, 1020 (1968).
10. ELLETT M. R., CUFF K. F. and KUGLIN C. D., *Bull. Am. Phys. Soc.* **8**, 246 (1963).
11. BURKE J. R. *et al.*, *Bull Am. Phys. Soc.* **13**, 485 (1968).
12. SHAPIRA Y. and LAX B., *Phys. Lett.* **7**, 133 (1963).
13. BECKMANN O. and SHAPIRA Y., *Phys. Lett.* **21**, 282 (1966).
14. GUREVICH V. L., SKOBOV V. G. and FIRSOV Y. A., *Soviet Phys. JETP* **13**, 552 (1961).
15. SKOBOV V. G., *Soviet Phys. JETP* **13**, 1014 (1961).
16. QUINN J. J. and RODRIGUEZ S., *Phys. Rev.* **128**, 2487 and 2494 (1962).
17. QUINN J. J., *Phys. Rev.* **135**, A181 (1964).
18. QUINN J. J., *Phys. Rev.* **137**, A889 (1965).
19. KOLODZIEJCZAK J. and ZUKOTYNSKI S., *Phys. Status Solidi* **5**, 145 (1964).
20. The crystal was kindly supplied by Hollandse Metallurgische Industrie Billiton, Arnheim, Netherlands.

Note added in proof: Due to the ambiguity in the experimental determination of the relative spin splitting δ the value $\delta' = 1-\delta$ is also a possible solution. Recent measurements of Burke have shown that the value δ' should be correct for p-type PbTe. Burke reports $\delta' = 0{\cdot}58 \pm 0{\cdot}01$ at $p = 2{\cdot}85 \times 10^{18}\,\mathrm{cm}^{-3}$ in contrast to his earlier publication[11] (Private communication). As a consequence, the $g_{\parallel}$-factors of p-PbTe in Table 3 have to be multiplied by a factor of δ'/δ.

J. Phys. Chem. Solids Pergamon Press 1969. Vol. 30, pp. 903–907. Printed in Great Britain.

STRUCTURAL AND MAGNETIC PROPERTIES OF NON-STOICHIOMETRIC PRASEODYMIUM MONOPHOSPHIDE

ENRICO FRANCESCHI and GIORGIO L. OLCESE
Istituto di Chimica Fisica, Universita' di Genova, Genova, Italy

(*Received* 5 *August* 1968; *in revised form* 13 *September* 1968)

Abstract—An investigation on the occurrence of non-stoichiometry in solid praseodymium monophosphide was carried out by evaluating the variation of the lattice constant and density with the composition. A range of solid solution by vacancies in the phosphorus sub-lattice was found between the compositions corresponding to PrP and $PrP_{0.85}$ phases. Magnetic properties and their dependence on non-stoichiometry were determined in the temperature range 4·2°–500°K; for the quasi-stoichiometric phases there is no evidence of magnetic ordering and a superconducting transition seems to occur below 7°K, while an antiferromagnetic coupling of praseodymium ions becomes possible when the interionic distances decrease by introduction of vacancies in the phosphorus sub-lattice.

INTRODUCTION

THE EXISTENCE of the NaCl structure type praseodymium monophosphide has been known since 1936[1]. Recently Mironov *et al.*[2] pointed out that this phase may exist in a non-stoichiometric state; however, a search of the literature failed to reveal any information about an exhaustive study on this subject. In the present work the extent and kind of the praseodymium monophosphide homogeneity range and the magnetic properties (between 4·2° and 500°K) of its intermediate solid solutions have been determined.

EXPERIMENTAL PROCEDURE

Praseodymium 99·9 per cent supplied by Lindsay Co., and distilled white phosphorus were used for direct synthesis of different samples near to the PrP composition.

An X-ray examination was made after each of the following three reaction steps: (1) the constituents, sealed off in evacuated silica tubes in weighed amounts, were combined at 600°–800°C until complete phosphorus disappearance; (2) the resulting powders were pressed into cylindrical tablets and then sintered at 800°–1100°C for at least 48 hr,* in tantalum crucibles under vacuum; (3) some of these sintered samples were melted in a tantalum resistance furnace under argon atmosphere (the melting point, determined by means of an optical pyrometer, appeared to be about 2400°C).

The effective composition of the samples was determined by chemical analysis. Mironov *et al.*[3] have already emphasized the difficulties of an accurate analytical determination of phosphorus. In the present work the two elements were determined on separate samples of each phase as follows: the praseodymium was precipitated as oxalate from a phosphorus free solution (obtained by dissolving the alloy with dilute hydrocloric acid in a non-oxidizing atmosphere), ignited to form oxide and weighed; the phosphorus, oxidized to orthophosphoric acid by dissolving the sample with concentrated nitric acid and $KMnO_4$, was precipitated as ammonium phosphomolybdate and titrated against standard sodium hydroxide solution.

The lattice constant determination was carried out by the powder method, using Cu K_α radiation.

The susceptibility measurements, between 500° and 77°K, were made using equipment and techniques that have been already described by Iandelli[4]. For the determination of magnetic properties at lower temperatures (77°–4·2°K), an a.c. mutual inductance bridge supplied by Cryotronics Inc., adapted for susceptibility measurements, was used.

RESULTS

X-ray diffraction and density data

The low-temperature products were black powders, very unstable under atmospheric conditions, and generally gave non-homogeneous diffraction powder patterns.

All the sintered and melted samples were more stable in air and appeared well crystallized and of bright grey color.

During the melting treatment some loss in phosphorus was always observed, and all attempts to obtain melted samples richer in P than $PrP_{0\cdot86}$ were unsuccessful.

The X-ray and analytical results (listed in Table 1) show that the lattice constant of praseodymium monophosphide decreases gradually from 5·908 to 5·875 Å as the phosphorus content decreases from 50 at.% (PrP) to 46 at.% ($PrP_{0\cdot85}$). Outside this range of compositions the lattice constant stops at the value reached, and the diffraction powder patterns exhibit some extra-lines, corresponding to free Pr metal for the samples with less than 46 at.% of phosphorus, and to a complex phase (probably PrP_2) for those containing more than 50 at.% of phosphorus.

From these results, which are plotted in Fig. 1, one deduces that praseodymium monophosphide can exist in non-stoichiometric compositions: the homogeneity range is in the metal-rich side, and its extent, which obviously depends on temperature at equilibrium conditions, lies between PrP and $PrP_{0\cdot85}$

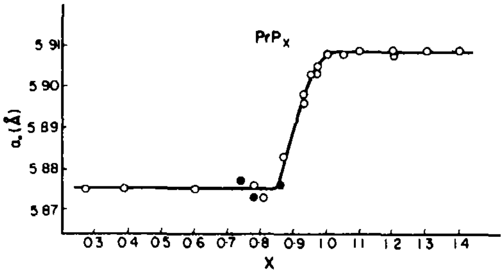

Fig. 1. Lattice spacing vs. x for PrP_x phases ○ = sintered samples; ● = melted samples.

Table 1. *Analytical and X-ray data for* PrP_x *samples*

Sample	Heat treatment	Analytical formula	Lattice spacing (Å ±0·002 Å)	Remarks
1	reaction at 600°C	$PrP_{1\cdot40}$	5·909	two phases(PrP + PrP_2?)
2	sintering at 800°C	$PrP_{1\cdot40}$	5·909	two phases(PrP + PrP_2?)
3	reaction at 760°C	$PrP_{1\cdot30}$	5·909	two phases(PrP + PrP_2?)
4	reaction at 600°C	$PrP_{1\cdot20}$	5·908	two phases(PrP + PrP_2?)
5	sintering at 800°C	$PrP_{1\cdot20}$	5·909	two phases(PrP + PrP_2?)
6	sintering at 600°C	$PrP_{1\cdot10}$	5·909	two phases(PrP + PrP_2?)
7	sintering at 600°C	$PrP_{1\cdot05}$	5·908	two phases(PrP + PrP_2?)
8	sintering at 900°C	PrP	5·908	no extra lines
9	sintering at 1100°C	$PrP_{0\cdot97}$	5·905	no extra lines
10	sintering at 1000°C	$PrP_{0\cdot97}$	5·903	no extra lines
11	sintering at 1000°C	$PrP_{0\cdot95}$	5·903	no extra lines
12	sintering at 1100°C	$PrP_{0\cdot93}$	5·898	no extra lines
13	sintering at 1100°C	$PrP_{0\cdot93}$	5·896	no extra lines
14	sintering at 1000°C	$PrP_{0\cdot87}$	5·883	no extra lines
15	melting	$PrP_{0\cdot86}$	5·876	no extra lines
16	sintering at 1100°C	$PrP_{0\cdot81}$	5·873	no extra lines
17	sintering at 1000°C	$PrP_{0\cdot78}$	5·876	two phases($PrP_{0\cdot85}$ + Pr)
18	melting	$PrP_{0\cdot78}$	5·873	two phases($PrP_{0\cdot85}$ + Pr)
19	melting	$PrP_{0\cdot74}$	5·877	two phases($PrP_{0\cdot85}$ + Pr)
20	sintering at 1000°C	$PrP_{0\cdot60}$	5·875	two phases($PrP_{0\cdot85}$ + Pr)
21	sintering at 1000°C	$PrP_{0\cdot39}$	5·875	two phases($PrP_{0\cdot85}$ + Pr)
22	sintering at 1000°C	$PrP_{0\cdot27}$	5·875	two phases($PrP_{0\cdot85}$ + Pr)

for samples quickly cooled to room temperature from about 1000°C.

In order to decide the solid solution mechanism, the densities were gravimetrically determined and calculated from lattice parameters on a basis of vacancies or substitution. As it will be seen from the data in Table 2, the experimental values are in good agreement with calculations carried out on the basis of vacancies, up to the $PrP_{0\cdot86}$ compound. The higher values found for praseodymium-richer samples are consistent with those calculated for the corresponding $Pr–PrP_{0\cdot85}$ mixtures, emphasizing that the latter phase must be near to the limit of the homogeneity range.

Table 2. Density data for PrP_x *phases*

Phase	$d^{25°C}_{obs.}$	$d^{25°C}_{calc}$ by vacancies	$d^{25°C}_{calc}$ by substitution	$d^{25°C}_{calc}$ for $PrP_{0\cdot85}$ - Pr mixture
PrP	$5{\cdot}5_2$	5·54	5·54	
$PrP_{0\cdot97}$	$5{\cdot}4_9$	5·51	5·60	
$PrP_{0\cdot95}$	$5{\cdot}4_7$	5·50	5·64	
$PrP_{0\cdot93}$	$5{\cdot}4_1$	5·49	5·69	
$PrP_{0\cdot87}$	$5{\cdot}4_2$	5·48	5·86	
$PrP_{0\cdot81}$	$5{\cdot}5_0$			5·53
$PrP_{0\cdot78}$	$5{\cdot}6_0$			5·58
$PrP_{0\cdot74}$	$5{\cdot}6_0$			5·64

Magnetic measurement data

The magnetic results for samples within the solid solution range are summarized in Table 3 and Fig. 2.

Table 3. Magnetic properties for non-stoichiometric praseodymium monophosphide in the Curie-Weiss region

Compound	μ_B	θ_p (°K)
PrP	3·31	+38
$PrP_{0\cdot97}$	3·36	+49
$PrP_{0\cdot95}$	3·27	+59
$PrP_{0\cdot87}$	3·30	+56
$PrP_{0\cdot86}$	3·22	+36

In all cases, between about 500° and 220°K, the Curie–Weiss law dependence was observed, and the effective magnetic moments deduced for praseodymium are rather less than the theoretical value for a free tripositive ion ($\mu_B = 3{\cdot}62$). The θ_p extrapolated values are positive, indicating the predominance of ferromagnetic interactions.

Below about 220°K the inverse susceptibility-temperature relationship shows a

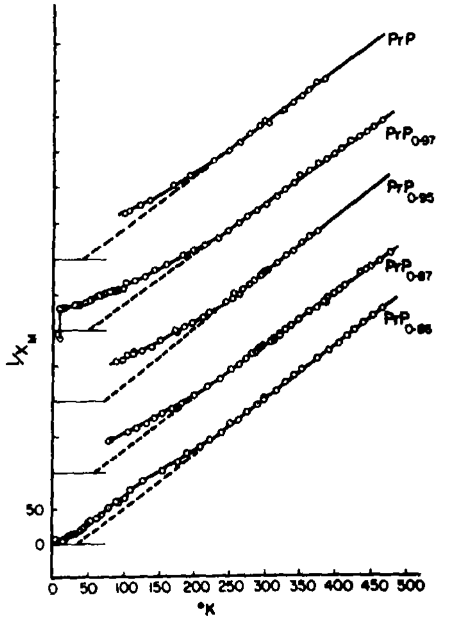

Fig. 2. Inverse susceptibility-temperature data for non-stoichiometric praseodymium monophosphide.

positive deviation from the Curie–Weiss law. The nature of this anomaly was investigated in two ways:

(a) the crystal structure of $PrP_{0 \cdot 97}$ between 300° and 77°K was investigated. The results allow us to exclude that the magnetic anomaly which occurs in that temperature range, is due to a crystallographic transformation or to a praseodymium valency change: in fact, down to 77°K the NaCl structure type is stable, and its lattice constant versus temperature behavior is linear without any singularity, as plotted in Fig. 3.

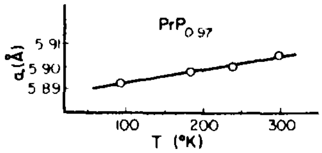

Fig. 3 Lattice spacing vs. temperature for $PrP_{0 \cdot 97}$.

(b) magnetic measurements were made, up to 4·2°K, on two phases close to both limits of the solid solution range: $PrP_{0 \cdot 97}$ and $PrP_{0 \cdot 86}$. The results, plotted in Fig. 2, show that the χ vs. T behavior from about 220° to 10°K can be interpreted as being wholly due to crystal field interaction. At very low temperatures the two phases have different properties: (1) $PrP_{0 \cdot 97}$ is paramagnetic above 7°K and below this temperature it suddenly becomes strongly diamagnetic. This seems to be a superconducting transition: a further investigation on this subject is in progress; (2) $PrP_{0 \cdot 86}$ exhibits a susceptibility peak near 10°K, that must be regarded as an antiferromagnetic ordering (the low temperature measurements were carried out at very low magnetic field, and their field dependence was not determined).

DISCUSSION

The possibility of deviation from ideal stoichiometry of praseodymium monophosphide, by vacancies in the metalloid sublattice, is like that which occurs also for some other NaCl structure type compounds of rare earths [5].

From the magnetic properties of PrP_x phases ($1 \geqslant x \geqslant 0 \cdot 85$) it can be deduced that the praseodymium electronic configuration corresponds to a valency greater than three. In fact the low moments, obtained from the Curie–Weiss dependence in the upper portion of the temperature range covered, can be interpreted in terms of further ionization of some of the 4*f* electrons. The effective valency of Pr, which appears to be independent of the P-content, is approximately 3·3. This result shows that the praseodymium monophosphide, even in the ideal stoichiometric composition, cannot be regarded as a simple ionic compound.

The high value of magnetic moment ($\mu_B = 3 \cdot 77$) reported by Tsuchida and Wallace[6] for a sample of praseodymium monophosphide does not seem to be correct because it was deduced from a linear χ vs. T interpolation outside the Curie–Weiss region.

The deviation from the Curie-Weiss law below about 220°K, due to crystal field interaction, is difficult to explain quantitatively owing to the presence of free electrons and to the field asymmetry produced by the random distribution of vacancies.

It is interesting to observe that the very low temperature properties of praseodymium monophosphide exhibit a strong dependence on the composition: for the quasi-stoichiometric phases there is no evidence of magnetic ordering; while an antiferromagnetic coupling of praseodymium ions becomes possible when the interionic distances decrease by introduction of vacancies in the phosphorus sub-lattice.

Acknowledgements—The authors thank Professor A. Iandelli for his guidance during the course of the present work. They are also indebted to Professor G. Boato and Doctors G. Gallinaro and C. Rizzuto for their assistance in carrying out the low-temperature magnetic measurements at the Institute of Physics of the University of Genoa and for their stimulating discussions. The research was supported in part by the Italian Consiglio Nazionale delle Ricerche.

REFERENCES

1. IANDELLI A. and BOTTI E., *Atti Acc. Naz. Lincei, Rend. Classe Sc. fis. mat. nat.* **24**, 459 (1936).
2. MIRONOV K. E., VASIL'EVA I. G., SINITSYNA E. D. and PROKHOROVA N. M., *Dokl. Akad. Nauk. S.S.S.R.* **176**, 841 (1967).
3. MIRONOV K. E., VASIL'EVA I. G. and SINITSYNA E. D., *Izv. Akad. Nauk. S. S. S. R. Neorg. Mat.* **2**, 1315 (1966).
4. IANDELLI A., *Atti Acc. Naz. Lincei, Rend. Classe Sc. fis. mat. nat.* **30**, 201 (1961).
5. BRUZZONE G. and OLCESE G. L., *Coll. Intern. sur les propriétés thermodynamiques, physiques et structurales des dérivés semimétalliques, Orsay 1965*, p. 387. C. N. R. S., Paris.
6. TSUCHIDA T. and WALLACE W. E., *J. chem. Phys.* **43**, 2885 (1965).

J. Phys. Chem. Solids Pergamon Press 1969. Vol. 30, pp. 909-917. Printed in Great Britain.

INTERDIFFUSION STUDIES IN THE SYSTEM MgO-Cr_2O_3*

C. GRESKOVICH† and V. S. STUBICAN
Department of Material Science, The Pennsylvania State University,
Univerisy Park, Penn. 16802, U.S.A.

(*Received* 26 *August* 1968)

Abstract—The rate of formation of single crystal $MgCr_2O_4$ from MgO single crystal and polycrystalline Cr_2O_3 in air can be described by the expression $k = 16{\cdot}3 \exp(80{,}000 \pm 9{,}000/RT)$ cm^2 sec^{-1}. The single crystal of $MgCr_2O_4$ grew by the advancement of (110) planes at the $MgCr_2O_4/Cr_2O_3$ interface.

Two different methods were used for the calculation of interdiffusion coefficients of Cr^{3+} in MgO in the temperature range 1340–1640°C. Wagner's recent analysis was applied for the calculation of interdiffusion coefficients in the MgO–Cr_2O_3 system where an intermediate spinel phase exists. A different mathematical treatment was derived for the calculation of interdiffusion coefficients at the saturation concentration of Cr_2O_3 in MgO single crystal.

The interdiffusion coefficients increased linearly with increasing mole fraction of Cr^{3+} cations and with increasing mole fraction of cation vacancies. For a concentration of one mol.% Cr_2O_3 in MgO, the interdiffusion coefficient can be expressed as $D = 5{\cdot}50 \times 10^{-3} \exp(67{,}000 \pm 2{,}000/RT)$ cm^2 sec^{-1}. The enthalpy of activation was independent of cation vacancy concentration while the entropy of activation increased with increasing vacancy concentration. The measured interdiffusion coefficients were deduced to be the intrinsic diffusion coefficients for Cr^{3+} cations in MgO. Interdiffusion coefficients were in the range of 10^{-12}–10^{-9} cm^2 sec^{-1} for the temperatures and concentrations studied.

1. INTRODUCTION

MOST INVESTIGATIONS of diffusion in oxides consisted of the determination of self-diffusion coefficients[1–4]. Relatively little work has been done on interdiffusion studies between oxides. Practically all the interdiffusion studies involved systems which exhibited complete miscibilities[5–9].

A more complicated type of interdiffusion study consists of the diffusion of a higher valent cation into a host lattice, with the accompanying formation of a new phase. The reaction of particular interest is the one between the binary oxides MgO and Cr_2O_3 to form the normal spinel $MgCr_2O_4$. Alper *et al.* [10] have shown that appreciable solubility of Cr_2O_3 in MgO exists at temperatures above 1200°C while Schmalzried[11] pointed out that the formation of $MgCr_2O_4$ from the reactants MgO and Cr_2O_3 occurs by counterdiffusion of Mg^{2+} and Cr^{3+} cations through the spinel layer. If the Cr^{3+} concentration in MgO is fairly low but not extremely low, the intrinsic disorder of MgO can be neglected and only chemical defects created by the presence of Cr^{3+} cations need be taken into consideration. In order to conform to the principle of electrical neutrality, the substitution of $2Cr^{3+}$ for $3Mg^{2+}$ cations creates one cation vacancy, similar to the solubility of Al^{3+} in MgO[12]. Obviously a concentration gradient of Cr^{3+} cations in MgO implies a corresponding gradient of cation vacancies.

The purpose of this investigation was to determine the interdiffusion coefficients of Cr^{3+} cations in MgO as a function of composition. An appropriate and convenient mathematical solution was desireable for the calculation of the interdiffusion coefficients.

---

*Contribution No. 68-4 from the College of Earth and Mineral Sciences, The Pennsylvania State University, University Park, Pa.

†This research was part of a thesis submitted by C. Greskovich in partial fulfillment of the requirements for the degree of Doctor of Philosophy in Ceramic Science, The Pennsylvania State University, December (1968).

2. EXPERIMENTAL PROCEDURES

Single crystals of MgO obtained from Norton Company were cleaved along the (100) planes. Spectrographic analysis indicated the presence of the following major impurities: $Ca = 0{\cdot}048\%$, $Fe = 0{\cdot}46\%$, $Al < 0{\cdot}01\%$ and $Ti < 0{\cdot}005\%$. Highly pure (99·999%) Cr_2O_3 powder was obtained from Spex Industries, Inc., and contained the major impurities of Mg, K and Na in the 1–3 ppm range.

The MgO crystals and sintered Cr_2O_3 pellets (1450°C for 2 days) were gound and polished as described previously[13]. MgO crystals were then annealed for 2 days at 1100°C and stored in a desiccator until used.

The diffusion couple consisted of wrapping Pt foil around a MgO crystal whose (100) plane was placed in contact with a sintered Cr_2O_3 pellet. The wrapped couple was then wedged in a stabilized zirconia holder, placed in a Pt bucket and introduced into a preheated vertical furnace with Pt–40% Rh wire as the heating element. Diffusion runs were conducted in air at 1340°C for 97 hr, 1410°C for 159 hr, 1465°C for 96 hr, 1465°C for 144 hr, 1520°C for 72 hr, and 1640°C for 48 hr. After the desired heat treatments, the diffusion couples were rapidly quenched to 400°C below the diffusion annealing temperature so that the spinel structure could not precipitate from the supersaturated MgO crystals. The diffusion couples were then slowly cooled to room temperature, mounted in the Bioplastic medium and ground and polished as described previously[13].

Diffusion couples were prepared for electron microprobe analysis by exposing a surface parallel to the diffusion direction and cutting to the central depth of the couple. An ARL electron microprobe analyzer was used to determine the diffusion profiles of chromium in $MgCr_2O_4$ and in MgO.

The thickness of the spinel layer which developed during the diffusion anneal was measured with a calibrated micrometer at 200X magnification on a Unitron metallographic microscope. At least 10 thickness measurements were used to calculate an average apparent thickness. When a sintered pellet of Cr_2O_3 was used as a reactant, the spinel boundary at the spinel/Cr_2O_3 interface was corrugated. Thus, thickness measurements were in error by approximately ±2 per cent.

Homogeneous polycrystalline standards containing 0·55, 1·4 and 2·3 mol.% Cr_2O_3 in MgO were prepared by pressing the powder mixtures into pellet forms, sealing the pellets in Pt tubing, firing the sealed tubes in an induction furnace and quenching the specimens in water at room temperature. X-ray diffraction indicated that only a crystalline solution phase existed in each of the standards. These standards were properly mounted and prepared for the electron microprobe. The general procedure was to analyze two diffusion couples and immediately afterwards run the standard compositions. In every case, all intensity measurements were made by point-count analysis for 10 sec. At least 10 analysis points were used to calculate an average intensity for the known standards. The standard calibration curve for the CrK_α intensity as a function of mol.% Cr_2O_3 in MgO was linear and essentially did not change because all diffusion couples and standards were analyzed within 4 hr on the same day.

No concentration gradient of Cr_2O_3 across the spinel $MgCr_2O_4$ could be detected with the electron microprobe technique.

3. RESULTS AND DISCUSSION

3.1 *Reaction kinetics for* $MgCr_2O_4$ *formation*

The reaction between MgO single crystals and polycrystalline Cr_2O_3 pellets resulted in the formation of the normal spinel $MgCr_2O_4$ (see Fig. 1). This photomicrograph is viewed perpendicularly to the diffusion direction. The gap at the MgO/$MgCr_2O_4$ interface occurred on fast cooling because adherence could be attained on slow cooling. At the $MgCr_2O_4$/Cr_2O_3 interface a gas gap occurred as previously found by Sockel and Schmalzried[14]. The grown spinel was single crystal with the

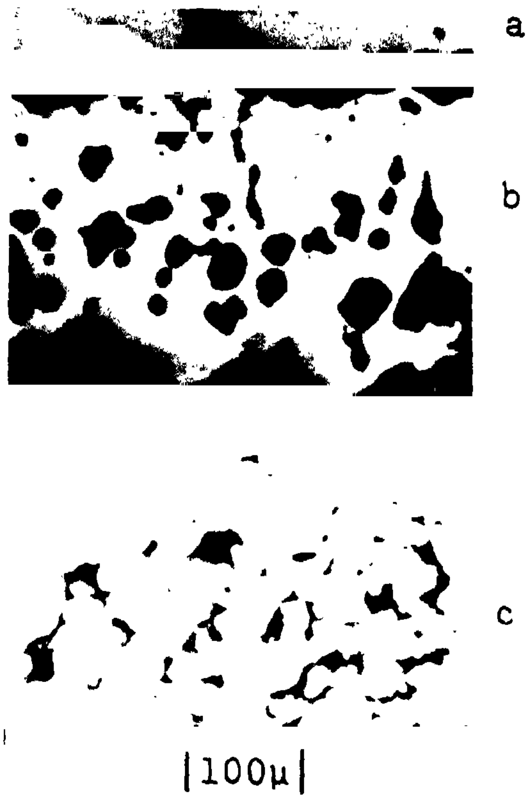

A

Fig. 1. Typical photomicrograph of the $MgCr_2O_4$ reaction layer viewed perpendicularly to the diffusion direction. The $MgCr_2O_4$ reaction layer (b) is formed from MgO single crystal (a) and polycrystalline Cr_2O_3 (c).

⟨100⟩ directions of $MgCr_2O_4$ parallel to the ⟨100⟩ directions of MgO, in accord with reference[14]. Furthermore, close examination revealed that the $MgCr_2O_4$ spinel at the $MgCr_2O_4/Cr_2O_3$ interface is corrugated with planes intersecting at approximately 90°. Since the view perpendicular to the diffusion direction was a ⟨100⟩ direction and since the diffusion direction was also a ⟨100⟩ direction, the growth of the spinel layer at the $MgCr_2O_4/Cr_2O_3$ interface may be caused by the ad-advancement of ⟨110⟩ planes.

The growth of single crystal spinel obeyed the parabolic rate law initially expressed by Tammann[15]. A plot of the spinel thickness squared versus time at 1465°C was approximately linear with a reaction rate constant $k = 1{\cdot}9 \times 10^{-9}\ cm^2\,sec^{-1}$. It appeared that the $MgCr_2O_4$ formation was diffusion-controlled in accord with Schmalzried's results[11].

The reaction rate constant varied with temperature according to the Arrhenius equation,

$$k = A\exp(-Q/RT) \qquad (1)$$

where k = reaction rate constant; A = the pre-exponential factor; Q = the experimental activation energy. A plot of ln k vs. $1/T$ is shown in Fig. 2. The graph approximated a linear relationship with an activation energy of 80 ± 9 Kcal/mole and a pre-exponential factor of 16·3 cm^2sec^{-1}.

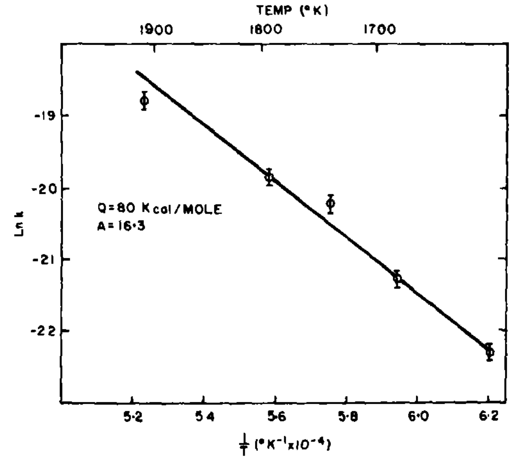

Fig. 2. Natural logarithm of the reaction rate constant as a function of reciprocal temperature for the $MgCr_2O_4$ reaction layer.

3.2 *Diffusion of Cr^{3+} cations in* MgO

The concentration-penetration data obtained from the electron microprobe for three diffusion couples are given in Figs. 3 and 4. All curves were linear with the exception of the diffusion anneal at 1640°C. The deviation from linearity in Fig. 4 is perhaps caused by vapor transport of chromium oxide to the $MgO/MgCr_2O_4$ interface and surface diffusion of Cr^{3+} cations down the interface.

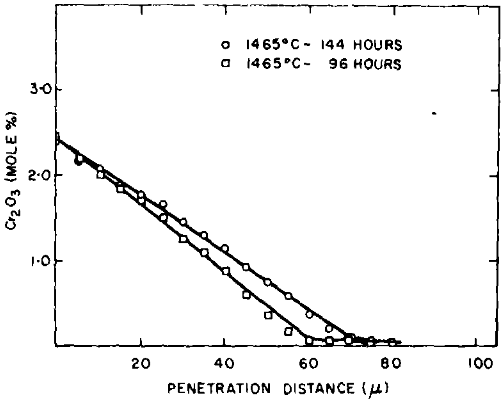

Fig. 3. Concentration of Cr_2O_3 vs. penetration distance (microns) in MgO at 1465°C for 96 and 144 hr.

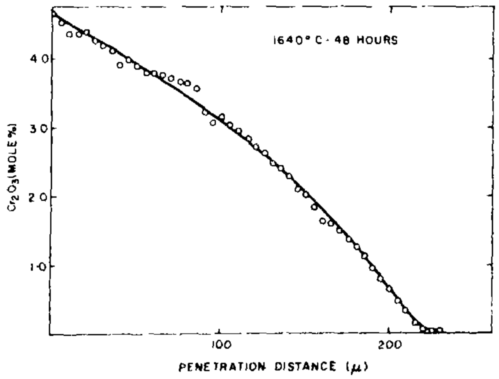

Fig. 4. Concentration of Cr_2O_3 vs. penetration distance (microns) in MgO at 1640°C for 48 hr.

Diffusion in a binary isotropic system at constant pressure and temperature can be described in terms of a single parameter D called the interdiffusion coefficient which, in general, depends on the composition as does the molar volume (V_m). Since the Boltzman [16], Matano[17] and Appel[18] treatments require knowledge of a designated reference plane ($x = 0$) without considering molar volume changes with composition, a more generalized treatment which has been recently developed by Wagner[10] will be used for the diffusion of Cr^{3+} cations in MgO.

The generalized equation is

$$D(N_2^*) = \frac{(N_2^+ - N_2^-)V_m(N_2^*)}{2t(\partial N_2/\partial x)_{x=x^*}} \times\left[(1-Y^*)\int_{-\infty}^{x^*}\frac{Y}{V_m}\,\mathrm{d}x + Y^*\int_{x^*}^{\infty}\frac{1-Y}{V_m}\,\mathrm{d}x\right] \tag{2}$$

where N_2^* = the particular mole fraction of cation 2 on the concentration profile at the particular distance x^*; $V_m(N_2^*)$ = the molar volume of cations at the particular mole fraction of interest N_2^*; t = time of diffusion anneal; $(\partial N_2/\partial x)_{x=x^*}$ = tangent to the profile curve at the particular distance x^*; $Y = (N_2 - N_2^-)/(N_2^+ - N_2^-)$ and is an auxiliary variable of composition; Y^* = a unique value for the above relation when $N_2 = N_2^*$. The evaluation of the integrals in equation (2) can be accomplished quite easily by graphical integration if the concentration profile is plotted in terms of Y/V_m.

If the diffusion couple of MgO and Cr_2O_3 is considered after a diffusion anneal, the experimentally determined shape of the concentration profile for Cr^{3+} cations is illustrated in Fig. 5. Equation (2) can be simplified because the diffusion couple consists initially of the pure components. Subsequently, if N_2^+ (mole fraction of Cr^{3+} cations in Cr_2O_3) is 1 and N_2^- (mole fraction of Cr^{3+} cations in MgO) is 0, the auxiliary variable Y equals the mole fraction N_2. Hence, the actual working equation becomes

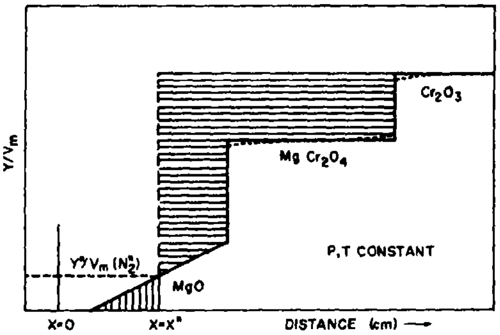

Fig. 5. Concentration (Y/V_m) of Cr^{3+} cations vs. distanc for the diffusion couple MgO/Cr_2O_3 after a diffusio anneal. Heavy dark lines represent the experimenta concentration profile while the dashed part represents th probable theoretical profile. The hatched areas are neede for the integrals in equation (3).

$$D(N_2^*) = \frac{V_m(N_2^*)}{2t(\partial N_2/\partial x)_{x=x^*}} \times\left[(1-N_2^*)\int_{-\infty}^{x^*}\frac{Y}{V_m}\,\mathrm{d}x + N_2^*\int_{x^*}^{\infty}\frac{1-Y}{V_m}\,\mathrm{d}x\right.$$

(

Since equation (3) contains only values (dx, the distance from any arbitrary referen plane can be used for the calculation of t slope and integrals.

The general procedure is to read off a co centration in mol.% Cr_2O_3 from the conce tration profile, calculate correspondi N_2 and V_m values, form the ratio $Y/$ ($Y = N_2$) and plot Y/V_m vs. penetrati distance for each diffusion couple as in F 5. The first integral in equation (3) equals t vertically hatched area while the seco integral equals the horizontally hatched area

The interdiffusion coefficients D as function of concentration are given in Fig. The D values increase linearly with concent tion of Cr^{3+} cations for all specimens exc the one annealed at 1640°C. An increase i value with an increase in Cr^{3+} concentratio expected because there is a correspond

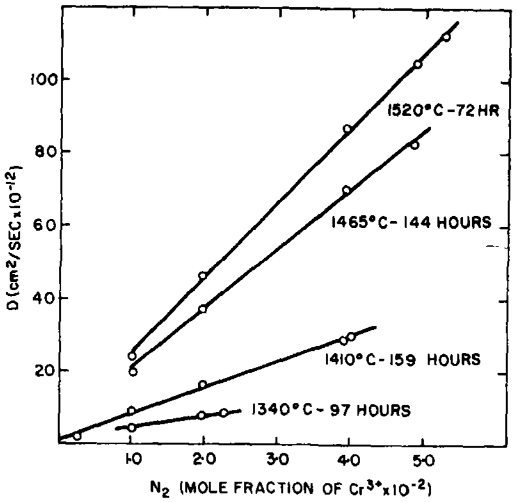

Fig. 6. The variation of the interdiffusion coefficient D with mole fraction of Cr^{3+} ions (N_2) for various specimens.

increase in cation vacancy concentration. The D value increases linearly with increasing cation vacancy concentration as shown in Fig. 7.

In order to check if thermodynamic equilibrium was established at the $MgO/MgCr_2O_4$ interface, diffusion anneals for different times were done at the same temperature. Both concentration profiles in Fig. 3 indicate that the maximum solubility of Cr_2O_3 in MgO at 1465°C was approximately 2·5 mol.%, a value in agreement with the phase diagram provided by Alper *et al.*[10]. For the diffusion couples annealed for 96 and 144 hr at 1465°C, the D values were found to be essentially the same for identical compositions.

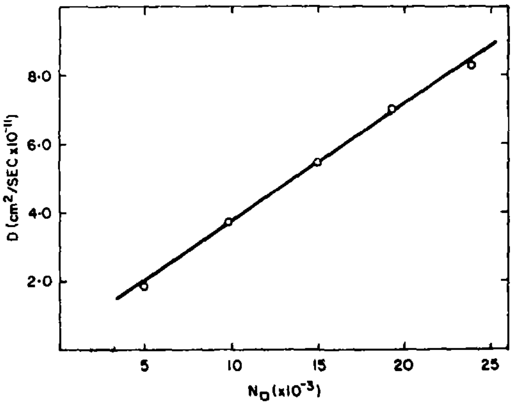

Fig. 7. The variation of interdiffusion coefficient D with mole fraction of cation vacancies for the diffusion anneal at 1465°C for 144 hr.

Empirically, the interdiffusion D can almost always be described by the Arrhenius expression for an activated process,

$$D = D_0 \exp(-\Delta H^*/RT)$$

where D_0 = pre-exponential factor; ΔH^* = the enthalpy of activation. A plot of ln D vs. $1/T$ for several mole fractions of Cr^{3+} cations is shown in Fig. 8. The curves are straight and essentially parallel to each other. The calculated value for ΔH^* is 67 ± 2Kcal/mol. and is independent of temperature and mole fraction of Cr^{3+} cations. From the foregoing information, there apparently is no change in the diffusion mechanism over the temperature range 1340–1640°C. It should be pointed out that for a high concentration of cation vacancies created by the presence of Cr^{3+} cations, ΔH^* actually equals the enthalpy of activation for motion.

A few comparisons can be made with the diffusion data. Bickelhaupt[20] found that the activation energy for the diffusion of Cr^{3+}

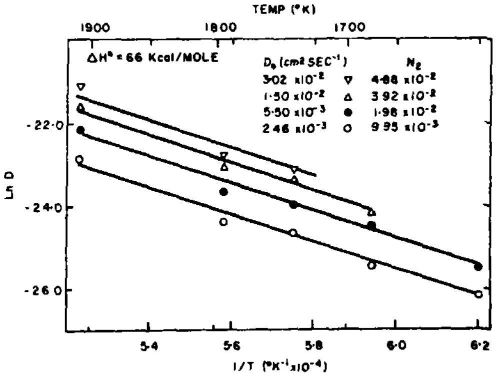

Fig. 8. Natural logarithm of the interdiffusion coefficients plotted as a function of reciprocal temperature.

ions in MgO was 59·9 Kcal/mol. For a concentration of one mol.% Cr_2O_3, the interdiffusion coefficient was expressed as $D = 2{\cdot}18 \times 10^{-3} \exp(-59{,}900/RT)$ cm^2 sec^{-1}. The interdiffusion coefficient which was found in this research for the same concentration can be expressed as $D = 5{\cdot}50 \times 10^{-3} \exp(-67{,}000 \pm 2000/RT)$ cm^2 sec^{-1}. At 1340°C the D value found in this research was nearly 3 times smaller. Probably the much higher purity of Cr_2O_3, the electron microprobe technique and the availability of Wagner's [19] analysis all contributed to lower and more reliable D values.

According to Eyring's[21] absolute rate theory for diffusion the entropy of activation (ΔS^*) was calculated by taking the jump distance as 2·97 Å and using an average value for the temperature, 1763°K. The entropy of activation increased with increasing cation vacancy concentration (see Fig. 9). Between the vacancy concentrations of $4{\cdot}95 \times 10^{-3}$ and $2{\cdot}39 \times 10^{-2}$ (mole fraction), the entropy of activation ranged from $+5{\cdot}4$ to $7{\cdot}3$ cal/deg mol.

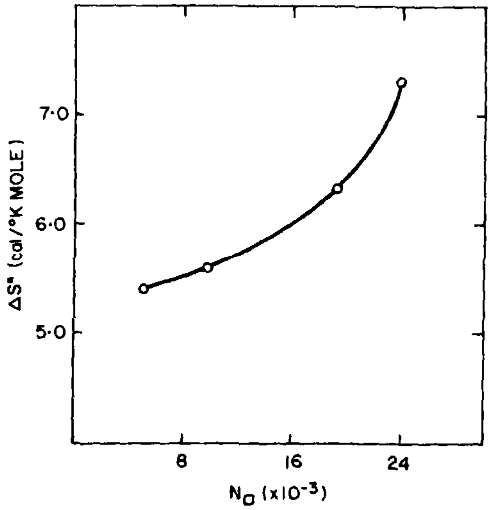

Fig. 9. Entropy of activation as a function of mole fraction of vacancies.

The D value increased linearly with increasing cation vacancy concentration as experimentally shown in Fig. 7. This suggests that ΔH^* and ΔS^* should be independent of vacancy concentration in accord with Eyring's absolute rate theory for diffusion[21]. Since ΔH^* and ΔS^* are experimentally found to be independent and dependent of the cation vacancy concentration, respectively, this implies that the quantity ΔS^* in Eyring's formulation should be a function of vacancy concentration. In the diffusion process between iron and magnesium cations[22], an increase of entropy of activation was also noted with increasing vacancy concentration.

The measured interdiffusion coefficient will be, at any Cr^{3+} concentration, determined by the slowest diffusing cation. In fact, the interdiffusion coefficient will be equal to the intrinsic diffusion coefficient of the slowest diffusing cation (ideal solution assumed). The question to be answered is which cation, Mg^{2+} or Cr^{3+}, is the rate determining cation. An answer to this question may be provided by extrapolating the curves to $N_2 = 0$ in Fig. 6. Linder and Parfitt[23] have shown that the self-diffusion coefficient of Mg^{2+} in MgO at 1520°C is about 70×10^{-12} cm^2 sec^{-1}, a value which is more than an order of magnitude higher than the corresponding extrapolated values of 5×10^{-12} cm^2 sec^{-1}. This suggests that the measured interdiffusion coefficient D is probably the intrinsic diffusion coefficient for Cr^{3+} cations. Furthermore, the interdiffusion coefficient is 46×10^{-12} cm^2 sec^{-1} for $N_2 = 1{\cdot}98 \times 10^{-2}$ (or $N_{\square} = 9{\cdot}8 \times 10^{-3}$) at 1520°C, a value which is still smaller than the self-diffusion coefficient quoted for Mg^{2+} in MgO. It appears that the measured interdiffusion coefficient is probably the intrinsic diffusion coefficient for Cr^{3+} cations in MgO.

It was further desirable to find an appropriate different method of calculating interdiffusion coefficients of Cr^{3+} cations in MgO. With the help of Professor Carl Wagner[24] the following mathematical analysis is provided which will yield an interdiffusion coefficient at the point where the MgO crystal is equilibrated with the $MgCr_2O_4$ spinel phase.

If the diffusion coefficient is assumed to be proportional to concentration, then Fick's second law for non-stationary, one-dimensional diffusion is

$$\frac{\partial c}{\partial t}=\frac{\partial}{\partial x}\left(D_0\frac{c}{c_0}\frac{\partial c}{\partial x}\right) \tag{5}$$

where $D_0=$ the diffusion coefficient for a reference concentration c_0.

Wagner[25] has found a solution of the differential equation (5) for the initial condition

$$c=0 \quad \text{at} \quad x>0, \quad t=0$$

and the boundary condition

$$c=c_0 \quad \text{at} \quad x=0, \quad t>0.$$

In view of the graph in Fig. 2 (Wagner's paper[25]), which is practically a straight line, the solution may be approximated as

$$\frac{c}{c_0}=1-\frac{1{\cdot}23\,x}{2(D_0t)^{1/2}}. \tag{6}$$

This solution is provided for the diffusion of lead chloride dissolved in silver chloride.

For the diffusion of Cr^{3+} cations into MgO with the accompanying formation of $MgCr_2O_4$ (moving boundaries), equation (6) cannot be used directly but is nevertheless helpful as is shown in what follows. The following symbols are introduced: x, distance from the boundary Cr_2O_3/MgO at $t=0$; x', distance of the boundary $MgCr_2O_4/MgO$ at $t>0$ from the boundary Cr_2O_3/MgO at $t=0$; x^+, distance x at which the concentration of Cr^{3+} tends to zero at $t>0$.

The problem now is to obtain a solution of equation (5) for the boundary condition

$$c=c' \quad \text{at} \quad x=x'$$

where c' is the saturation concentration of Cr^{3+} in MgO equilibrated with the $MgCr_2O_4$ phase and x' is given by the Wagner[26] mechanism. Further, let the diffusivity D' be for $c=c'$, which is related to D_0 by

$$D'=D(c=c')=D_0(c'/c_0) \tag{7}$$

if D is proportional to c. In view of equation (7), equation (6) may be rewritten as

$$\frac{c}{c'}\cdot\frac{c'}{c_0}=1-1{\cdot}23\left(\frac{c'}{c_0}\right)^{1/2}\frac{x}{2(D't)^{1/2}}. \tag{8}$$

Letting $c=0$ and $x=x^+$, equation (8) can be transformed to

$$\frac{c'}{c_0}=4D't/(1{\cdot}23x^+)^2. \tag{9}$$

Substituting equation (9) in equation (8) and regrouping,

$$c/c'=1{\cdot}23^2x^+(x^+-x)/4D't. \tag{10}$$

Letting $x=x'$ and $c=c'$, equation (10) transforms to

$$D'=1{\cdot}23^2x^+(x^+-x')/4t. \tag{11}$$

Hence, if x' and x^+ are observed, then D' can be calculated where D' denotes the interdiffusion coefficient at the saturation concentration of Cr_2O_3 in MgO equilibrated with $MgCr_2O_4$.

A hypothetical concentration profile of Cr^{3+} cations for the diffusion couple MgO/Cr_2O_3 is given along with the x^+ and x' designations in Fig. 10. The original concentration profile data and the $MgCr_2O_4$ thickness measurements were used for the determination of the interdiffusion coefficients D'. In order to determine the x^+ values, the concentration profiles were extrapolated to c equals zero.

The data in Table 1 compares the interdiffusion coefficients calculated according to

Table 1. Comparison of the interdiffusion coefficients calculated according to equations (11) and (3)

Temp. (°C)	Time (sec × 10^5)	Description concentration Mol.% Cr_2O_3 in MgO	Interdiffusion coefficients D' (cm²/sec)	D (cm²/sec)
1640	1·73	4·65	$1{\cdot}6 \times 10^{-9}$	$2{\cdot}0 \times 10^{-9}$
1520	2·59	2·70	$1{\cdot}2 \times 10^{-10}$	$1{\cdot}1 \times 10^{-10}$
1465	5·18	2·50	$8{\cdot}4 \times 10^{-11}$	$8{\cdot}3 \times 10^{-11}$
1465	3·46	2·44	$8{\cdot}1 \times 10^{-11}$	$8{\cdot}4 \times 10^{-11}$
1410	5·72	2·08	$3{\cdot}1 \times 10^{-11}$	$3{\cdot}0 \times 10^{-11}$
1340	3·49	1·16	$8{\cdot}2 \times 10^{-12}$	$9{\cdot}0 \times 10^{-12}$

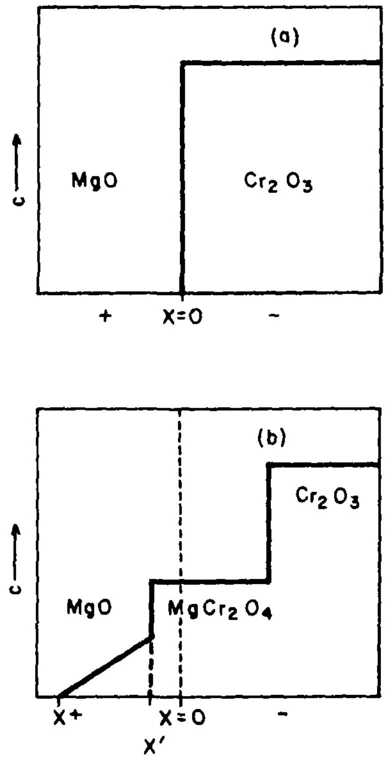

Fig. 10. A hypothetical concentration profile of Cr^{3+} cations for the diffusion couple MgO/Cr_2O_3 (a) at $t = 0$ and (b) at $t > 0$.

equation (3) and (11) at the saturation concentration of Cr_2O_3. If the same concentration and temperatures are considered, the interdiffusion coefficients D' and D are evidently in good agreement. Consequently, equations (3) and (11) are appropriate for the calculations of interdiffusion coefficients. Both equations may be applied to any diffusion-controlled system where a spinel reaction layer forms and a linear concentration gradient of one reactant in another exists. The interdiffusion coefficients D calculated according to equation (3) appear, then, to be quite acceptable as valid values for the counterdiffusion of Mg^{2+} and Cr^{3+} cations in MgO.

Acknowledgements—The authors express their thanks to Dr. W. R. Bitler for many helpful discussions on diffusion and to Professor C. Wagner for his comments on the theory of diffusion through correspondence The authors are grateful to the Bethlehem Steel Company for financial support of this investigation.

REFERENCES

1. LINDER R. and PARFITT G. D., *J. chem. Phys.* **26**, 182 (1957).
2. SUN R., *J. chem. Phys.* **28**, 290 (1958).
3. OISHI Y. and KINGERY W. D., *J. chem. Phys.* **33**, 905 (1960).
4. SHIM M. T. and MOORE W. J., *J. chem. Phys.* **26**, 802 (1957).
5. WUENSCH B. J. and VASILOS T., *J. chem. Phys.* **36**, 2917 (1962).
6. WUENSCH B. J. and VASILOS T., *Am. Ceram. Soc. Bull.* **44**, 303 (1965).
7. ZAPLATYNSKY I., *J. Am. Ceram. Soc.* **45**, 28 (1962).
8. SINCLAIR W. R. and LOOMIS T. C., In *Kinetics of High-Temperature Processes* (Edited by W. D. Kingery), p. 58. Wiley, N.Y. (1959).
9. WILSON R. P., *Acta. Poly. scand.* **60**, 3 (1967).
10. ALPER A. M., McNALLY R. N., DOMAN R. C. and KEIHN F. G., *J. Am. Ceram. Soc.* **47**, 40 (1964).
11. SCHMALZRIED H., *Z. phys. Chem.* **31**, 185 (1962).

12. STUBICAN V. S. and ROY R., *J. Phys. Chem. Solids* **26**, 1293 (1965).
13. STUBICAN V. S. and MENEZES I. *J. Am. Ceram. Soc.* **49**, 535 (1966).
14. SOCKEL H. G. and SCHMALZRIED H., *Materials Science Research* 3 (Edited by Kreigel and Palmour), Chap. III, p. 61. Plenum Press, N.Y. (1966).
15. TAMMANN G., *Z. anorg. allg. Chem.* **111**, 78 (1921).
16. BOTLZMANN L., *Annls. Phys.* **53**, 960 (1894).
17. MATANO C., *Physics* **8**, 109 (1933).
18. APPEL M., *Scripta Met.* **2**, 217 (1968).
19. WAGNER C., *Acta Metall.* In press.
20. BICKELHAUPT R. E., Ph.D. thesis, University of Illinois (1963).
21. GLASSTONE S., LAIDLER K. J. and EYRING H., *Theory of Rate Processes. Kinetics of Chemical Reactions, Viscosity, Diffusion, and Electrochemical Phenomena*, p. 524. McGraw-Hill, N.Y. (1941).
22. RIGBY E. B. and CUTLER I. B., *J. Am. Ceram. Soc.* **48**, 95 (1965).
23. LINDNER R. and PARFITT D., *J. chem. Phys.* **26**, 182 (1957).
24. WAGNER C., Private Communications (1968).
25. WAGNER C., *J. chem. Phys.* **18**, 1227 (1950).
26. KOCH E. and WAGNER C., *Z. phys. Chem.* **B34**, 317 (1936).

J. Phys. Chem. Solids Pergamon Press 1969. Vol. 30, pp. 919–921. Printed in Great Britain.

ON THE SCATTERING OF X-RAYS BY STRUCTURES CONTAINING A RANDOM DISTRIBUTION OF DEFECTS

C. R. HALL
Cavendish Laboratory, Free School Lane, Cambridge, England

(*Received* 20 *August* 1968)

Abstract – An approximation made in a recent treatment of the scattering of X-rays by defect structures (Keating 1968) is examined and shown to be incorrect. It appears that if the treatment is modified to allow such an approximation to be made then it leads to results consistent with those found by previous authors (Cochran and Kartha 1956).

1. INTRODUCTION

IN A RECENT paper (Keating[2]) the scattering of X-rays by a crystal containing a random array of defects is considered. This treatment shows that when there is a dilatation of the average crystal lattice the Bragg peaks in the diffraction pattern are displaced by a corresponding amount. The diffuse scattering is predicted to be given approximately by the square of the Fourier transform of a single defect. However in contrast with previous treatments (e.g. Cochran and Kartha[1]) the displacements to be used are those referred to the original crystal lattice and not the mean lattice, and the atomic scattering factors are not multiplied by any attenuation factor. This causes the diffuse intensity to be located about the reciprocal lattice points of the original crystal. X-ray diffraction profiles from irradiated BeO and Diamond, where the Bragg peaks are displaced and the diffuse scattering is centred about directions close to the Bragg directions of the perfect crystal are shown as evidence for the effect.

It is thought that the treatment which predicts the displacements of the Bragg peaks leads to a correct result. It is shown below that owing to an inadmissable approximation the treatment of the diffuse scattering is in error, and that if the treatment is modified so that the approximation is not made then the result is similar to that of Cochran and Kartha[1].

2. CALCULATION

For the sake of clarity only the scattering by the matrix atoms is considered in detail. The notation is that used by Keating, where atoms located initially in the perfect crystal at r_m and r_n are displaced by amounts u_{mj} and u_{nj} due to the presence of a defect at the j-th defect site. The amplitude A_M scattered by the matrix atoms is given by

$$\mathrm{A}_M = f_A \sum_m \mathrm{e}^{iK.r_m + i\sum_j' K\, u_{mj}}. \tag{1}$$

The diffuse intensity I_M scattered by the matrix atoms is then found by Keating (see equation (31)) to be:

$$\begin{aligned} I_M = f_A{}^2 \sum_m \sum_n \mathrm{e}^{iK.(r_m - r_n)} \\ \times \Big[\prod_j \{1 + p(\mathrm{e}^{iK(u_{mj} - u_{nj})} - 1)\} \\ - \prod_j \{1 + p(\mathrm{e}^{iK.(u_{mj} - u_{nj})} - 1) \\ - p(1-p)(\mathrm{e}^{iK.u_{mj}} - 1)(\mathrm{e}^{-iK.u_{nj}} - 1)\}\Big]. \quad (2) \end{aligned}$$

The products $\prod_j$ are taken over all possible defect sites, p is the probability that such a site is occupied, K is the scattering vector and f_A is the scattering factor for a matrix atom. We now use the fact that:

$$\prod_j (1+x_j) = 1+\sum_j x_j+\frac{1}{2!}\sum\sum_{j\neq k} x_j x_k + \frac{1}{3!}\sum\sum\sum_{j\neq k\neq l} x_j x_k x_l \ldots \tag{3}$$

Keating uses this expansion also, but takes only the first two terms. Including the third term as well gives:

$$\begin{aligned} I_M = f_A{}^2 \sum_m \sum_n & \mathrm{e}^{iK.(r_m-r_n)} \\ & \times \sum_j p(1-p)(\mathrm{e}^{iK.u_{mj}}-1)(\mathrm{e}^{-iK.u_{nj}}-1) \\ & \times \Big[1+\{\tfrac{1}{2}p(1-p)(\mathrm{e}^{iK.u_{mj}}-1)(\mathrm{e}^{-iK.u_{nj}}-1) \\ & - p(\mathrm{e}^{iK.(u_{mj}-u_{nj})}-1)\} \\ & + \Big\{p\sum_k (\mathrm{e}^{iK(u_{mk}-u_{nk})}-1) \\ & - \tfrac{1}{2}p(1-p)\sum_k (\mathrm{e}^{iK.u_{mk}}-1)(\mathrm{e}^{-iK.u_{nk}}-1)\Big\}\Big]. \end{aligned} \tag{4}$$

The approximation made by Keating corresponds to the neglect of all the terms within the square brackets except the first, the justification being that subsequent terms are multiplied by p and therefore can be made small compared with unity. This argument is valid for the second term in the square brackets, but not for the third, as although each term in the summation is small for this reason, there are a very large number of these terms (as many terms as there are defect sites), and their sum is not necesssarily negligible. If this term is included and the exponentials expanded then approximately:

$$\begin{aligned} I_M = f_A{}^2 \sum_m \sum_n & \mathrm{e}^{iK.(r_m-r_n)} \\ & \times \sum_j p(1-p)(\mathrm{e}^{K.u_{mj}}-1)(\mathrm{e}^{-iK.u_{nj}}-1) \\ & \times \Big[1+ipK.\sum_k (u_{mk}-u_{nk})\Big]. \end{aligned} \tag{5}$$

This is similar to the corresponding intensity obtained by Keating except for the second term in the square brackets, which he neglects. Now the sum over k of pu_{mk} is just the mean displacement of the atom originally at r_m, i.e. the displacement due to the dilatation of the mean crystal lattice. This displacement depends both upon p and upon the distance of the atom from the origin at which the original and dilated lattices coincide. For any value of p, however small, this displacement can be made large for some atoms by making the crystal large: thus this term cannot be neglected.

There are two ways in which this and subsequent terms can be taken into account. One method is to expand as in equation (3) but taking more terms, then to expand the exponentials to several terms each, and then to group and sum the resulting set of terms. It is however simpler to split the displacement u_{mj} at the outset into two parts: η_{mj}, which is that part of the displacement corresponding to the lattice dilatation caused by the defect, and ϵ_{mj}, which is the residue and depends upon the position of the defect in the crystal. Equation (1) then becomes:

$$A_M = f_A \sum_m \mathrm{e}^{iK.r'_m+iK.\Sigma\epsilon_{mj}}$$

r'_m is a vector in the dilated lattice. The treatment proceeds as before, and equation (5) becomes approximately:

$$\begin{aligned} I_M = f_A{}^2 \sum_m \sum_n & \mathrm{e}^{iK.(r'_m-r'_n)}\, p(1-p) \\ & \times \sum_j (\mathrm{e}^{iK.\epsilon_{mj}}-1)(\mathrm{e}^{-iK.\epsilon_{nj}}-1) \\ & \times \Big[1+p\sum_k iK.(\epsilon_{mk}-\epsilon_{nk}) \\ & -\frac{p}{2}\sum_k (K.(\epsilon_{mk}-\epsilon_{nk}))^2+\ldots\Big]. \end{aligned} \tag{6}$$

The second term in the square brackets is now zero, as expected. The third term is approximately

$$\frac{p}{2}\sum_{k}\{(K.\epsilon_{mk})^2+K.\epsilon_{nk})^2\}.$$

Making the usual approximation the contents of the square brackets in equation (6) can be written as a Debye–Waller factor, so that for I_M we get:

$$I_M = p(1-p)\sum_{j}\left|\sum_{m} f_A\,\mathrm{e}^{-M_m}\mathrm{e}^{iK.r_m'} \times (\mathrm{e}^{iK.\epsilon_{mj}}-1)\right|^2. \tag{7}$$

This is effectively the same equation as equation (13) of Cochran and Kartha (1956), the displacements in each case being from the mean lattice and the amplitude being attenuated by the same Debye–Waller type factor. The two equations are slightly different in that an additional factor $(1-p)$ is obtained by Keating: this factor also results from the treatment of Cochran and Kartha if it is modified to prevent two defects occupying the same site.

The other terms in equation (31) of Keating can be treated in a similar manner to give an expression for the diffuse intensity similar to his equation (32), except that the displacements are now all referred to the mean lattice and the scattering factors are multiplied by attenuation factors. The main term in that equation is therefore correctly:

$$I_D = p(1-p)\sum_{j}\Big| f_B + \sum_{m} f_A\mathrm{e}^{-M_m}\mathrm{e}^{iK.r_{mj}}(\mathrm{e}^{iK.\epsilon_{mj}}-1) + p\sum_{i} f_B\mathrm{e}^{-M_i}\mathrm{e}^{iK.r_{ij}}(\mathrm{e}^{iK.\epsilon_{ij}}-1)\Big|^2. \tag{8}$$

Being now expressed in terms of the mean lattice, this equation predicts that the diffuse intensity should be located about the displaced Bragg peak, and therefore does not explain the experimental results.

3. DISCUSSION

Thus it is still not clear what is the correct explanation for experimental observations of the type considered by Keating. The solution to this problem could lie in one of two directions.

In the first place there may be some other incorrect approximation in the treatment as it now stands. However the intensity distribution does not seem to be appreciably affected either by including more of the terms obtained by expanding quantities like $\exp(iK.\sum_k(u_{mk}-u_{nk})$, or by including in the ϵ_{mj} the displacements due to the image fields (except for when the defect lies at a distance from the surface comparable with the defect size). The treatment also makes the approximation that the displacements due to the different defects can be added: i.e. that the strain is always elastic. This is not true very close to a defect, and as the concentration of defects in the cases being considered is probably very high an appreciable proportion of the crystal is likely to be in a state of anharmonic strain. Whether or not taking this into account can change the theory sufficiently to explain the experimental results is not clear.

Alternatively it may simply be that the internal state of the irradiated material is different from what has previously been supposed. The intensity distributions shown by Keating, where there is a sharp peak with a diffuse peak nearby, is the type of distribution one might expect to get from a two phase material in which almost coherent precipitates give a sharp peak while the matrix, having a slightly different lattice constant, is highly strained causing its diffraction peak to be considerably broadened. There are of course difficulties in applying this model to the cases under consideration, but it could be that a correct detailed description of the internal state of the material would lead to a predicted diffraction pattern of the type observed. In which of these two directions the solution lies is as yet not obvious.

Acknowledgements—The Author is grateful to Drs. A. Howie and L. M. Brown for helpful discussions.

References

1. COCHRAN W. and KARTHA C., *Acta crystallogr.* **9**, 941 (1956).
2. KEATING D. T., *J. Phys. Chem. Solids* **29**, 771 (1968).

J. Phys. Chem. Solids Pergamon Press 1969. Vol. 30, pp. 923–937. Printed in Great Britain.

THE SPIN WAVE GREEN'S FUNCTION FOR A BODY-CENTERED TWO SUB-LATTICE ANTIFERROMAGNET

LAURENCE R. WALKER and B. B. CETLIN
Bell Telephone Laboratories, Incorporated, Murray Hill, N.J. 07971, U.S.A.
and
DANIEL HONE*†
Physics Department, University of California, Santa Barbara, Calif. 93106, U.S.A.

(*Received* 20 *August* 1968)

Abstract – The reciprocal lattice sum which occurs in the calculation of the spin wave Green's function appropriate to a body-centered, two sublattice antiferromagnet, having next-nearest neighbor interactions only and arbitrary local anisotropy, has been evaluated for 10 lattice points at various energies below, within and above the spin-wave band.

IN A NUMBER of dynamical problems in magnetically ordered systems, such as those connected with the interaction of elementary excitations or with the presence of impurities, one encounters the response function of the homogeneous system to a local impulse. Such a pure crystal Green's function is associated, clearly, with some specific assumption about the dynamics and it will be a functional of the dispersion relation for the elementary excitations. Spin wave theory yields one such relation and there are other, slightly more sophisticated, methods which give the same general form of dispersion. This paper is concerned with the evaluation of the reciprocal lattice sum involved in calculating the Green's function associated with a dispersion relation of the spin wave type in a definite system, a body-centered orthorhombic, two sub-lattice antiferromagnet.

We define the two simple orthorhombic sub-lattices to have identical spins at sites $\mathbf{r} = la\mathbf{i} + mb\mathbf{j} + nc\mathbf{k}$ and $\mathbf{r} = (l+\frac{1}{2})a\mathbf{i} + (m+\frac{1}{2})b\mathbf{j} + (n+\frac{1}{2})c\mathbf{k}$, respectively, where $(l, m, n) \equiv \mathbf{p}$ is a triplet of integers and $\mathbf{i}$, $\mathbf{j}$, $\mathbf{k}$ are three mutually perpendicular unit vectors. The Green's function, $G(\epsilon, \mathbf{r})$ is proportional to the function $U(\epsilon, \mathbf{r})$ [or, equally well, $U(\epsilon, \mathbf{p})$] which is a function of the energy ϵ, where this is expressed in dimensionless units.‡ and of a particular lattice displacement, $\mathbf{r}$.§ The latter is defined by

$$U(\epsilon, \mathbf{r}) = \frac{1}{N} \lim_{\eta \to 0} \sum_{\boldsymbol{\kappa}} \frac{e^{i\boldsymbol{\kappa}\cdot\mathbf{r}}}{(\epsilon + i\eta)^2 - \epsilon^2(\boldsymbol{\kappa})} \qquad (1)$$

where N is the number of sites on one sub-lattice and the $\boldsymbol{\kappa}$-summation is carried over the first Brillouin zone appropriate to the sub-lattice. $\epsilon(\boldsymbol{\kappa})$ describes the assumed dispersion relation and is taken to be [1]

$$\epsilon(\boldsymbol{\kappa}) = [(1+\alpha)^2 - \gamma^2(\boldsymbol{\kappa})]^{1/2} \qquad (2)$$

with

$$\gamma(\boldsymbol{\kappa}) = \frac{1}{8} \sum_{\boldsymbol{\delta}_i} \exp \boldsymbol{\kappa} \cdot \boldsymbol{\delta}_i. \qquad (3)$$

---

*Supported in part by the Advanced Research Projects Agency and by the National Science Foundation under Grant No. GP 6771.

†At the Department of Physics, University of Pennsylvania, Philadelphia, Pennsylvania when this work was initiated.

‡The 'energy' is more properly a frequency and as such runs from $-\infty$ to $+\infty$.

§The relationship between G and U is: $G(\epsilon, \mathbf{r}) = (1/\pi)\langle S^z\rangle(\epsilon + \alpha + 1)U(\epsilon, \mathbf{r})$ (see e.g. reference [5] equation (3.16)).

Here α is an anisotropy parameter, greater than zero, and the $\boldsymbol{\delta}_i$ are the displacements from a given site to its 8 nearest neighbors on the other sub-lattic.* The $\boldsymbol{\delta}_i$ are clearly of the form, $\frac{1}{2}(\pm a\mathbf{i} \pm b\mathbf{j} \pm c\mathbf{k})$. It is convenient to introduce the vector $\boldsymbol{\Phi} = (\phi_1, \phi_2, \phi_3)$, where

$$\phi_1 = k_1 a; \quad \phi_2 = k_2 b; \quad \phi_3 = k_3 c. \tag{4}$$

The Brillouin zone is then described by $-\pi \leqslant \phi_i \leqslant \pi, i = 1, 2, 3$. One now has

$$\gamma(\boldsymbol{\kappa}) \equiv \gamma(\boldsymbol{\Phi}) = \cos\tfrac{1}{2}\phi_1 \cos\tfrac{1}{2}\phi_2 \cos\tfrac{1}{2}\phi_3. \tag{5}$$

If N is allowed to become infinite, $U(\epsilon, \mathbf{p})$ assumes the form

$$U(\epsilon, \mathbf{p}) = \frac{1}{(2\pi)^3} \lim_{\eta \to 0^+} \int_{-\pi}^{+\pi} \mathrm{d}\phi_1 \int_{-\pi}^{+\pi} \mathrm{d}\phi_2 \int_{-\pi}^{+\pi} \mathrm{d}\phi_3 \times \frac{\exp i(\mathbf{p}\cdot\boldsymbol{\Phi})}{(\epsilon + i\eta)^2 - (1+\alpha)^2 + \cos^2\frac{1}{2}\phi_1 \cos^2\frac{1}{2}\phi_2 \cos^2\frac{1}{2}\phi_3}. \tag{6}$$

There is, in addition to $U(\epsilon, \mathbf{p})$, a second type of reciprocal lattice sum which also occurs in practice. This function, labelled $V(\epsilon, \mathbf{q})$ is defined by

$$V(\epsilon, q) = \frac{1}{(2\pi)^3} \lim_{\eta \to 0^+} \int_{-\pi}^{+\pi} \mathrm{d}\phi_1 \int_{-\pi}^{+\pi} \mathrm{d}\phi_2 \int_{-\pi}^{+\pi} \mathrm{d}\phi_3 \times \frac{\gamma(\boldsymbol{\Phi}) \exp i(\mathbf{q}\cdot\boldsymbol{\Phi})}{(\epsilon + i\eta)^2 - (1+\alpha)^2 + \cos^2\frac{1}{2}\phi_1 \cos^2\frac{1}{2}\phi_2 \cos^2\frac{1}{2}\phi_3} \tag{7}$$

where $\mathbf{q}$ is now of the form $(l' + \frac{1}{2}, m' + \frac{1}{2}, n' + \frac{1}{2})$, with l', m' and n' being integers. The functions U and V are connected by the easily verified relationships

$$V(\epsilon, \mathbf{q}) = \tfrac{1}{8} \sum_{\boldsymbol{\delta}_i} U(\epsilon, \mathbf{q} + \boldsymbol{\delta}_i) \tag{8a}$$

$$[\epsilon^2 - (1+\alpha)^2] U(\epsilon, \mathbf{p}) = \delta(\mathbf{p}) - \tfrac{1}{8} \sum_{\boldsymbol{\delta}_i} V(\epsilon, \mathbf{p} + \boldsymbol{\delta}_i) \tag{8b}$$

where δ is the (vector) Kronecker delta. The first relation may be used to derive V from other U's. By eliminating V between (8a) and (8b) one may obtain the relation between the U's:

$$[\epsilon^2 - (1+\alpha)^2] U(\epsilon, \mathbf{p}) = \delta(\mathbf{p}) - \tfrac{1}{64} \sum_{\boldsymbol{\delta}_i \boldsymbol{\delta}_j} U(\mathbf{p} + \boldsymbol{\delta}_i + \boldsymbol{\delta}_j). \tag{9}$$

This provides a useful check upon the consistency of independently calculated U's.

Certain features of the dispersion relation (2) should be kept in mind. $\epsilon(\boldsymbol{\kappa})$ has its minimum value, $(2\alpha + \alpha^2)^{1/2}$, at the center of the zone, $\boldsymbol{\kappa} = 0$, and achieves its maximum value of $1 + \alpha$ at the points where $\gamma(\kappa)$ vanishes. These occur whenever any one of $\cos\frac{1}{2}\phi_1$, $\cos\frac{1}{2}\phi_2$, $\cos\frac{1}{2}\phi_3$ is zero and, therefore, the whole surface of the Brillouin zone, consisting of the cube faces $|\phi_i| = \pi$, is a surface of constant energy. For each energy within the spin wave band, $(2\alpha + \alpha^2)^{1/2} \leqslant \epsilon \leqslant 1 + \alpha$, there is a surface in $\boldsymbol{\kappa}$-space on which $\epsilon = |\epsilon(\boldsymbol{\kappa})|$ and it follows that, since $\eta \to 0^+$, U is complex for such energies. (Note that since $\epsilon(\boldsymbol{\kappa}) = \epsilon(-\boldsymbol{\kappa})$ the numerator $e^{i\boldsymbol{\kappa}\cdot\mathbf{r}}$

---

*We are considering here only the dispersion relation arising from an interaction between such nearest neighbors on different sublattices. This has the disadvantage for practical applications that in certain cases other interactions are not, in fact, negligible; it has the advantage, as we shall see below, that the function we calculate may be used for a system with arbitrary anisotropy by a simple change of variable.

could be replaced by its real part.) Below the band, $0 < |\epsilon| < (2\alpha+\alpha^2)^{1/2}$, and above the band, $1+\alpha < |\epsilon|$, $|\epsilon|$ is never equal to $|\epsilon(\kappa)|$ and U is purely real.*

The method chosen to evaluate $U(\epsilon, \mathbf{p})$ was such as to transform away the singular denominator at the expense of introducing a four-dimensional integral. We distinguish two slightly different procedures according as ϵ^2 is less than or greater than $(1+\alpha)^2$. In the former case one first writes

$$U(\epsilon, p) = \frac{1}{(2\pi)^3} \lim_{\eta\to 0^+} \frac{1}{2[(1+\alpha)^2-(\epsilon+i\eta)^2]^{1/2}} \times \int_{-\pi}^{+\pi} d\phi_1 \int_{-\pi}^{+\pi} d\phi_2 \int_{-\pi}^{+\pi} d\phi_3 e^{i\mathbf{p}\cdot\mathbf{\Phi}} \times \left[\frac{1}{\gamma(\mathbf{\Phi}) - [(1+\alpha)^2-(\epsilon+i\eta)^2]^{1/2}} - \frac{1}{\gamma(\mathbf{\Phi}) + [(1+\alpha)^2-(\epsilon+i\eta)^2]^{1/2}}\right]. \quad (10)$$

A new variable may now be introduced which simplifies the following algebra and also will be seen to remove the parameter α from most of the formulae. We write

$$x = +[(1+\alpha)^2-\epsilon^2]^{1/2} \quad (11)$$

and find for $U(\epsilon, \mathbf{p})$ the representation

$$U(\epsilon, \mathbf{p}) = \frac{1}{(2\pi)^3}\left(-i\frac{sgn\epsilon}{2x}\right) \lim_{\eta\to 0^+} \int d^3\mathbf{\Phi} e^{i\mathbf{p}\cdot\mathbf{\Phi}} \int_0^\infty ds e^{-s\eta} e^{-isx\, sgn\epsilon} \times 2\cos s\gamma(\mathbf{\Phi}) = -i\frac{sgn\epsilon}{x}\int_0^\infty \times ds e^{-isx\,sgn\epsilon} \frac{1}{(2\pi)^3}\int d^3\mathbf{\Phi} e^{i\mathbf{p}\cdot\mathbf{\Phi}} \cos s\gamma(\mathbf{\Phi}). \quad (12)$$

We shall define

$$U(\epsilon, \mathbf{p}) = -i\frac{F(x, \mathbf{p})}{x}; \quad 0 \leqslant \epsilon \leqslant 1+\alpha$$
$$= i\frac{\tilde{F}(x, \mathbf{p})}{x}; \quad -1-\alpha \leqslant \epsilon \leqslant 0 \quad (13)$$

where the tilde denotes complex conjugation and

$$F(x, \mathbf{p}) = \int_0^\infty e^{-isx} Q(s, \mathbf{p}) ds \quad (14)$$

and

$$Q(s, \mathbf{p}) = \frac{1}{(2\pi)^3}\int_{-\pi}^{+\pi} d\phi_1 \int_{+\pi}^{+\pi} d\phi_2 \int_{-\pi}^{+\pi} \times d\phi_3 e^{i\mathbf{p}\cdot\mathbf{\Phi}} \cos s\gamma(\mathbf{\Phi}).\dagger \quad (15)$$

Proceeding in a similar way for $\epsilon^2 > (1+\alpha)^2$ and here defining

$$y = +[\epsilon^2-(1+\alpha)^2]^{1/2} \quad (16)$$

one obtains for either sign of ϵ

$$U(\epsilon, \mathbf{p}) = \frac{1}{y} H(y, \mathbf{p}) \quad (17)$$

$$H(y, \mathbf{p}) = \int_0^\infty e^{-isy} Q(s, \mathbf{p}) ds. \quad (18)$$

We remark again that U is evaluated as a function of x or y, independently of α; the dependence upon energy in a particular problem is restored by expressing x and y

---

*If we suppose that two of the integrations in (6) have been carried out over a surface of constant γ then (6) becomes

$$U(\epsilon, \mathbf{p}) = \lim_{\eta\to 0}\int_0^1 \frac{A(\gamma, \mathbf{p})d\gamma}{(\epsilon+i\eta)^2-(1+\alpha)^2+\gamma^2}.$$

Making use of this form we can derive an expression for $U(z, \mathbf{p})$ where z is now complex:

$$U(z, \mathbf{p}) = -\frac{2}{\pi}\int_{\sqrt{(2\alpha+\alpha^2)}}^{1+\alpha} \frac{\zeta \operatorname{Im} U(\zeta, \mathbf{p})}{z^2-\zeta^2} d\zeta.$$

A knowledge of $\operatorname{Im}U(\epsilon, \mathbf{p})$ within the band thus determines U everywhere.

†It should be noted that in this method of calculation, ImU or ReF is not explicitly zero for $x > 1$ as it has to be. Any departure of the computed value from zero provides a check on errors.

in terms of ϵ. However, since we frequently wish to integrate expressions containing Green's functions over ϵ, it is more convenient to transform the variables of integration to x and y.

The evaluation of $Q(s, \mathbf{p})$ is carried out by rewriting $\cos s\gamma(\Phi)$ explicitly as

$$\tfrac{1}{2}\left[\exp i\frac{s}{8}\sum_{\delta_i} \mathrm{e}^{i\Phi\delta_i}+\text{c.c.}\right]$$

and expanding each factor

$$\exp\left(\frac{is}{8}\mathrm{e}^{i\Phi\cdot\delta_i}\right)$$

in powers of s. The Φ-integrations are then carried out and the resulting terms rearranged to produce the series

$$Q(s,\mathbf{p}) = \sum_{\tau=-\infty}^{+\infty} i^{|\tau|+|l+m-\tau|+|m+n-\tau|+|n+l-\tau|} \times J_{|\tau|}\left(\frac{s}{4}\right)J_{|l+m-\tau|}\left(\frac{s}{4}\right)J_{|m+n-\tau|}\left(\frac{s}{4}\right) \times J_{|n+l-\tau|}\left(\frac{s}{4}\right) \tag{19}$$

which is real for all integral l, m, n. The J's are Bessel functions. For l, m, n small, which is the case we have considered, the orders of the four Bessel functions in each term are not appreciably different and each falls off rapidly when the order exceeds the argument. Thus the summand of (19) cuts off very sharply at this point and the number of significant terms increases more or less linearly with s. Since the Bessel functions are computed from their recursion relation all the orders needed for a given s in (19) are generated essentially simultaneously and the evaluation of the sums is quite efficient. $Q(s, \mathbf{p})$ has been calculated in the interval $0 \leqslant s \leqslant 300\,\pi$ in steps of $\pi/20$ between 0 and $10\,\pi$ and in steps of $\pi/10$ between $10\,\pi$ and $300\,\pi$.

Beyond $300\,\pi$, $Q(s,\mathbf{p})$ falls off rather slowly, behavior which is directly related to the vanishing of $\gamma(\Phi)$ over the whole zone boundary. In the Appendix it is shown that

$$Q(s,\mathbf{p}) \sim (-1)^{l+m+n}\frac{4}{\pi^2 s}\left[\ln 2s-\psi(\tfrac{1}{2}) -2\left(\sum_{r=0}^{l-1}\frac{1}{2r+1}+\sum_{r=0}^{m-1}\frac{1}{2r+1}+\sum_{r=0}^{n-1}\frac{1}{2r+1}\right)\right] \tag{20}$$

where ψ is the digamma function. The stationary behavior of $\gamma(\Phi)$ at the origin produces in $Q(s, \mathbf{p})$ at large s an oscillatory term of small amplitude. It behaves like $s^{-3/2}\mathrm{e}^{is}$ and is important in the evaluation of $F(x)$ when x is close to 1, for then the product $\mathrm{e}^{-isx}Q(s, \mathbf{p})$ is slowly varying. To sufficient accuracy we may evaluate this term by writing

$$\begin{aligned} Q_{osc}(s,\mathbf{p}) &= \tfrac{1}{2}(2\pi)^{-3}\int \mathrm{d}^3\Phi \mathrm{e}^{i\mathbf{p}\cdot\Phi}\,\mathrm{e}^{is[1-\Phi\cdot\Phi/8]} \\ &= -(1+i)(\pi s)^{-3/2}\mathrm{e}^{is}+0(s^{-5/2}). \end{aligned} \tag{21}$$

The integral contribution to $U(\epsilon, \mathbf{p})$ from $s > 300\,\pi = s_0$ which arises from the slowly decaying part of $Q(s, \mathbf{p})$ has been evaluated in two ways. For x not too small we have used the formula

$$\int_{s_0}^{\infty} \mathrm{e}^{-ixs}f(s)\mathrm{d}s = \mathrm{e}^{-ixs_0}\left[\frac{f(s_0)}{ix}+\frac{f'(s_0)}{(ix)^2} +\frac{f''(s_0)}{(ix)^3}+\dots\right] \tag{22}$$

which is valid for functions $f(s)$ which vary much more slowly than e^{-ixs}. In the present case, $f(s)$ is taken to be $s^{-1}(a+b\ln s)$, with a and b given by (20). The derivatives in (22) may be found explicitly. Equation (22) is asymptotic in character and one should not take too many terms of the series. For a very small x, we have evaluated

$$\int_{s_0}^{\infty} \mathrm{e}^{-ixs}\frac{a+b\ln s}{s}\mathrm{d}s$$

numerically after integrating by parts in such a way as to improve the convergence. The smallest x value for which F has been computed is 0·0040114, which is the first point in a 16-point Gaussian quadrature scheme covering the range $x = 0{\cdot}0035$ to $x = 0{\cdot}1$. We outline below a procedure to be used for carrying out integrals of F over the uncalculated range from $x = 0$ to $x = 0{\cdot}0035$.

$F(x, \mathbf{p})$ (and $U(x, \mathbf{p})$) are, of course, singular at $x = 0$ and it is useful to have explicit expressions for their behavior at that point. We need consider only the integral

$$\int_{s_0}^{\infty} e^{-ixs} \frac{a + b \ln s}{s} \, ds$$

where a and b are the coefficients of $1/s$ and $\ln s/s$ in (20). We write this as

$$(a - b \ln x) \int_{xs_0}^{\infty} e^{-it} \frac{dt}{t} + b \int_{xs_0}^{\infty} e^{-it} \frac{\ln t}{t} \, dt.$$

The first integral may be rewritten in the form

$$(a - b \ln x) \left[-\gamma - \ln xs_0 + \int_{0}^{xs_0} \frac{1 - \cos t}{t} \, dt - i \int_{xs_0}^{\infty} \frac{\sin t}{t} \, dt \right]$$

where γ in Euler's constant. The last two integrals now converge. The divergent part of the second integral above is, if c is some arbitrary constant $> xs_0$,

$$\int_{xs_0}^{c} \frac{\cos t}{t} \ln t \, dt = \left[\cos t \frac{(\ln t)^2}{2} \right]_{xs_0}^{c} + \int_{xs_0}^{c} \sin t \frac{(\ln t)^2}{2} \, dt$$

and the divergent part is $-\frac{1}{2}[(\ln x)^2 + 2 \ln s_0 \ln x]$. Collecting the divergent terms we are left with

$$\frac{b}{2}(\ln x)^2 + (b\gamma - a + i\pi b/2) \ln x.$$

Near $x = 1$ the contribution of Q_{osc} becomes significant integration of the first term given in (21) yields a correction to $F(x)$ of the form

$$-\frac{1+i}{\pi^{3/2}} \left\{ \frac{2}{s_0^{1/2}} e^{i(1-x)s_0} \pm 2i(2\pi)^{1/2} (|1 - x|)^{1/2} \times \left[\frac{1+i}{2} - C(t) \mp iS(t) \right] \right\} \tag{23}$$

where $t = (2s_0|1 - x|/\pi)^{1/2}$, C and S are Fresnel integrals and the upper sign is to be taken for $x < 1$, the lower for $x > 1$. It is also possible to derive explicit approximations for $U(\epsilon, p)$ near $x = 1$. The imaginary part of U goes to zero like $(1 - x^2)^{1/2}$ as $x \to 1^-$, while the real part is regular for $x \to 1^-$ and goes as $(x^2 - 1)^{1/2}$ for $x \to 1^+$. We have the results

$$\mathrm{Re}\, U(\epsilon, \mathbf{p}) = \mathrm{Re}\, U(\epsilon_1, \mathbf{p}) + \frac{2}{\pi} (x^2 - 1)^{1/2}$$

$$\text{for } x \to 1^+ \, [\text{where } \epsilon_1 \equiv \epsilon(x = 1) = (2\alpha + \alpha^2)^{1/2}] \tag{24a}$$

and, more exactly

$$\mathrm{Im}\, U(\epsilon, \mathbf{p}) = -\frac{2}{\pi} (1 - x^2)^{1/2} \{ 1 + (1 - x^2) \times [1 - \tfrac{2}{3}(l^2 + m^2 + n^2)] \} \quad \text{for} \quad x \to 1^-. \tag{24b}$$

For large $(x, y > 2)$ values of x or y another method of computation has been used, which is much faster for such cases. For $x > 1$, the original U-integral is non-singular and

$$U(\epsilon, \mathbf{p}) = \frac{1}{(2\pi)^3} \int d\Phi \frac{e^{i\mathbf{p} \cdot \boldsymbol{\varphi}}}{\gamma^2(\Phi) - x^2}. \tag{25a}$$

Similarly in the range $\epsilon^2 > (1 + \alpha)^2$

$$U(\epsilon, \mathbf{p}) = \frac{1}{(2\pi)^3} \int d\Phi \frac{e^{i\mathbf{p} \cdot \Phi}}{\gamma^2(\Phi) + y^2}. \tag{25b}$$

The denominator may be expanded in powers of z^{-2} where $z^2 = y^2$ or $-x^2$ and the Φ-integrations carried out. The resultant formula is

$$U(\epsilon,\mathbf{p})=\frac{\delta(\mathbf{p})}{z^2}+\sum_{\substack{r=\max(l,m,n)\\ r=1,\text{ if } l=m=n=0}}^{\infty}\frac{(-1)^r}{z^{2r+2}}$$

$$\frac{1}{2^{6r}}\frac{(2r!)^3}{(r-l)!(r+l)!(r-m)!(r+m)!(r+n)!(r-n)!}\tag{26}$$

We have evaluated $F(x,\mathbf{p})$ (see equation (13)) and $H(y,\mathbf{p})$ (see equation (17)) for all lattice vectors $\mathbf{p}\equiv(l,m,n)$ with $l,m,n\leqslant 2$ at the following energy values:

$3\cdot0\leqslant y\leqslant 10\cdot0$	(0·5)
$0\cdot2\leqslant y\leqslant 3\cdot0$	(0·2)
$0<y\leqslant 0\cdot2$	(0·02)
$0\cdot0035<x<0\cdot1$	at 16 points corresponding to the ordinates for 16 point Gaussian quadrature in this interval[2]
$0\cdot1<x<0\cdot2$	at 12 Gaussian ordinates
$0\cdot2<x<0\cdot9$	at 24 Gaussian ordinates
$0\cdot9<x<0\cdot99$	at 8 Gaussian ordinates
$0\cdot99<x<0\cdot999$	(0·0005)
$0\cdot999<x<0\cdot9999$	(0·0001)
$1\cdot0\leqslant x\leqslant 1\cdot02$	(0·004)
$1\cdot02\leqslant x\leqslant 1\cdot10$	(0·02)
$1\cdot10\leqslant x\leqslant 2\cdot0$	(0·10).

The results are given in Tables 1(a) and 1(b). The use of ordinates corresponding to Gaussian quadrature procedures is indicated within the spin wave band, $0\leqslant x\leqslant 1$, since one is very frequently called upon to integrate expressions containing the Green's functions over this range. The use of the variable x, in place of ϵ, while allowing one to use Green's functions evaluated at a set of x's independent of α, has possible disadvantages. It may turn out that the integration net in terms of ϵ is undesirably coarse in certain ranges. It is also true that the particular net division into four ranges for separate Gaussian routines which has been adopted here is far from optimum in some cases.

Integrals over the range from $x=0$ to $x=0\cdot0035$ require special attention because of the singular character of U at $x=0$. If one is integrating a product of U (or F) and a relatively slowly varying function of x over this range, the latter function may be removed from under the integration and we are concerned with

$$\int_0^{0\cdot0035}F(x)\,\mathrm{d}x.$$

This has been evaluated in the following manner. $F(x)$ is divided into two parts, $F_1(x)$ and $F_2(x)$. $F_1(x)$ is the part arising from the s-integral up to 300π. To evaluate $\int_0^{0\cdot0035}F_1(x)\,\mathrm{d}x$, $F_1(x)$ is written as a power series in

Table 1(a). *The real and imaginary parts of the function* $F(x,p)$ *(see equation (13)), where* $x=\sqrt{((1+\alpha)^2-\epsilon^2)}$

	000		100		110		111	
x	ReF	ImF	ReF	ImF	ReF	ImF	ReF	ImF
0·0040114	11·1985	−4·8370	−5·8503	3·5638	2·1235	−2·2906	−0·0167	1·0492
0·0061743	9·9082	−4·5625	−4·9095	3·2892	1·5325	−2·0162	0·2257	0·7916
0·0099833	8·5594	−4·2566	−3·9499	2·9832	0·9631	−1·7106	0·4080	0·5152
0·0153017	7·4391	−3·9848	−3·1756	2·7112	0·5360	−1·4393	0·4934	0·2840
0·0219375	6·5517	−3·7555	−2·5797	2·4816	0·2340	−1·2109	0·5108	0·1046
0·0296507	5·8499	−3·5639	−2·1216	2·2894	0·0225	−1·0205	0·4884	−0·0304
0·0381626	5·2904	−3·4034	−1·7660	2·1281	−0·1253	−0·8619	0·4451	−0·1298
0·0471656	4·8407	−3·2687	−1·4873	1·9926	−0·2286	−0·7295	0·3930	−0·2012
0·0563344	4·4777	−3·1559	−1·2674	1·8787	−0·3004	−0·6194	0·3392	−0·2512

Table 1(a), (*contd.*)

	000		100		110		111	
x	ReF	ImF	ReF	ImF	ReF	ImF	ReF	ImF
0·0653374	4·1844	−3·0618	−1·0935	1·7833	−0·3497	−0·5284	0·2882	−0·2851
0·0738493	3·9489	−2·9841	−0·9565	1·7044	−0·3831	−0·4539	0·2423	−0·3070
0·0815625	3·7623	−2·9211	−0·8498	1·6402	−0·4053	−0·3940	0·2031	−0·3205
0·0881983	3·6183	−2·8715	−0·7685	1·5896	−0·4196	−0·3474	0·1712	−0·3282
0·0935167	3·5120	−2·8344	−0·7093	1·5516	−0·4284	−0·3127	0·1468	−0·3323
0·0973257	3·4404	−2·8092	−0·6697	1·5256	−0·4335	−0·2893	0·1300	−0·3341
0·0994886	3·4012	−2·7952	−0·6481	1·5113	−0·4361	−0·2764	0·1207	−0·3348
0·1009220	3·3758	−2·7862	−0·6342	1·5020	−0·4376	−0·2681	0·1146	−0·3352
0·1047941	3·3094	−2·7624	−0·5980	1·4774	−0·4411	−0·2462	0·0986	−0·3356
0·1115049	3·2011	−2·7231	−0·5395	1·4369	−0·4454	−0·2105	0·0720	−0·3349
0·1206341	3·0661	−2·6734	−0·4676	1·3853	−0·4483	−0·1658	0·0383	−0·3313
0·1316084	2·9196	−2·6185	−0·3908	1·3280	−0·4479	−0·1173	0·0013	−0·3236
0·1437383	2·7743	−2·5629	−0·3163	1·2697	−0·4438	−0·0693	−0·0354	−0·3119
0·1562617	2·6396	−2·5103	−0·2485	1·2141	−0·4364	−0·0251	−0·0692	−0·2970
0·1683916	2·5213	−2·4633	−0·1902	1·1641	−0·4268	0·0134	−0·0981	−0·2807
0·1793659	2·4232	−2·4237	−0·1428	1·1216	−0·4166	0·0448	−0·1214	−0·2645
0·1884951	2·3471	−2·3926	−0·1067	1·0880	−0·4070	0·0689	−0·1388	−0·2504
0·1952059	2·2941	−2·3707	−0·0818	1·0643	−0·3996	0·0855	−0·1505	−0·2397
0·1990780	2·2645	−2·3584	−0·0681	1·0509	−0·3951	0·0947	−0·1569	−0·2334
0·2016845	2·2450	−2·3502	−0·0591	1·0420	−0·3921	0·1007	−0·1610	−0·2291
0·2088450	2·1930	−2·3284	−0·0353	1·0181	−0·3834	0·1166	−0·1717	−0·2173
0·2216039	2·1058	−2·2914	0·0040	0·9773	−0·3673	0·1426	−0·1886	−0·1958
0·2397546	1·9921	−2·2424	0·0539	0·9227	−0·3432	0·1753	−0·2081	−0·1648
0·2629993	1·8614	−2·1849	0·1090	0·8577	−0·3108	0·2106	−0·2261	−0·1250
0·2909565	1·7223	−2·1224	0·1648	0·7857	−0·2705	0·2446	−0·2388	−0·0783
0·3231672	1·5817	−2·0577	0·2177	0·7094	−0·2234	0·2742	−0·2431	−0·0270
0·3591025	1·4443	−1·9931	0·2654	0·6312	−0·1711	0·2968	−0·2370	0·0257
0·3981723	1·3133	−1·9301	0·3063	0·5527	−0·1155	0·3109	−0·2199	0·0766
0·4397351	1·1903	−1·8700	0·3397	0·4752	−0·0586	0·3156	−0·1922	0·1225
0·4831084	1·0763	−1·8134	0·3655	0·3997	−0·0025	0·3109	−0·1555	0·1606
0·5275801	0·9713	−1·7609	0·3836	0·3269	0·0508	0·2969	−0·1118	0·1889
0·5724199	0·8752	−1·7125	0·3946	0·2575	0·0997	0·2747	−0·0640	0·2063
0·6168916	0·7875	−1·6685	0·3989	0·1919	0·1428	0·2454	−0·0148	0·2122
0·6602649	0·7078	−1·6288	0·3970	0·1305	0·1789	0·2105	0·0329	0·2072
0·7018277	0·6355	−1·5934	0·3898	0·0738	0·2076	0·1718	0·0767	0·1924
0·7408975	0·5702	−1·5621	0·3780	0·0222	0·2284	0·1310	0·1146	0·1697
0·7768328	0·5117	−1·5350	0·3626	−0·0241	0·2418	0·0900	0·1453	0·1413
0·8090435	0·4597	−1·5119	0·3448	−0·0646	0·2483	0·0505	0·1681	0·1099
0·8370007	0·4144	−1·4926	0·3258	−0·0992	0·2492	0·0143	0·1834	0·0780
0·8602454	0·3762	−1·4771	0·3070	−0·1275	0·2459	−0·0172	0·1921	0·0482
0·8783961	0·3456	−1·4654	0·2902	−0·1494	0·2404	−0·0425	0·1958	0·0230
0·8911550	0·3235	−1·4573	0·2771	−0·1646	0·2348	−0·0608	0·1964	0·0042
0·8983155	0·3109	−1·4528	0·2692	−0·1731	0·2309	−0·0712	0·1959	−0·0068
0·9017869	0·3047	−1·4506	0·2651	−0·1772	0·2288	−0·0762	0·1955	−0·0122
0·9091500	0·2913	−1·4461	0·2563	−0·1859	0·2239	−0·0871	0·1940	−0·0238
0·9213510	0·2684	−1·4386	0·2404	−0·2003	0·2143	−0·1053	0·1899	−0·0438
0·9367454	0·2377	−1·4294	0·2178	−0·2183	0·1989	−0·1287	0·1810	−0·0700
0·9532546	0·2017	−1·4197	0·1892	−0·2374	0·1772	−0·1543	0·1656	−0·0996
0·9686489	0·1633	−1·4108	0·1564	−0·2551	0·1498	−0·1787	0·1434	−0·1284
0·9808500	0·1264	−1·4039	0·1232	−0·2691	0·1200	−0·1983	0·1169	−0·1521
0·9882130	0·0986	−1·3998	0·0971	−0·2775	0·0955	−0·2102	0·0940	−0·1668
0·9900	0·0907	−1·3988	0·0895	−0·2795	0·0883	−0·2132	0·0871	−0·1704
0·9905	0·0884	−1·3985	0·0873	−0·2801	0·0862	−0·2140	0·0851	−0·1715
0·9910	0·0860	−1·3982	0·0850	−0·2807	0·0839	−0·2148	0·0829	−0·1725
0·9915	0·0835	−1·3979	0·0826	−0·2812	0·0817	−0·2156	0·0807	−0·1735
0·9920	0·0810	−1·3977	0·0802	−0·2818	0·0793	−0·2164	0·0784	−0·1745
0·9925	0·0784	−1·3974	0·0776	−0·2824	0·0768	−0·2173	0·0761	−0·1755

Table 1(a). (*contd.*)

	000		100		110		111	
x	ReF	ImF	ReF	ImF	ReF	ImF	ReF	ImF
0·9930	0·0757	−1·3971	0·0750	−0·2830	0·0743	−0·2181	0·0736	−0·1765
0·9935	0·0729	−1·3968	0·0723	−0·2835	0·0717	−0·2189	0·0710	−0·1776
0·9940	0·0700	−1·3966	0·0695	−0·2841	0·0689	−0·2197	0·0684	−0·1786
0·9945	0·0670	−1·3963	0·0666	−0·2847	0·0661	−0·2205	0·0656	−0·1796
0·9950	0·0639	−1·3960	0·0635	−0·2852	0·0630	−0·2214	0·0626	−0·1806
0·9955	0·0606	−1·3957	0·0602	−0·2858	0·0599	−0·2222	0·0595	−0·1816
0·9960	0·0571	−1·3954	0·0568	−0·2863	0·0565	−0·2230	0·0562	−0·1827
0·9965	0·0534	−1·3952	0·0532	−0·2869	0·0529	−0·2238	0·0527	−0·1837
0·9970	0·0494	−1·3949	0·0492	−0·2875	0·0490	−0·2247	0·0489	−0·1847
0·9975	0·0451	−1·3946	0·0450	−0·2881	0·0448	−0·2255	0·0447	−0·1858
0·9980	0·0403	−1·3943	0·0402	−0·2886	0·0401	−0·2263	0·0400	−0·1868
0·9985	0·0349	−1·3941	0·0348	−0·2892	0·0348	−0·2271	0·0347	−0·1878
0·9990	0·0285	−1·3938	0·0285	−0·2898	0·0284	−0·2280	0·0284	−0·1889
0·9991	0·0270	−1·3937	0·0270	−0·2899	0·0270	−0·2281	0·0269	−0·1891
0·9992	0·0255	−1·3937	0·0255	−0·2900	0·0254	−0·2283	0·0254	−0·1893
0·9993	0·0238	−1·3936	0·0238	−0·2901	0·0238	−0·2285	0·0237	−0·1895
0·9994	0·0221	−1·3936	0·0220	−0·2902	0·0220	−0·2286	0·0220	−0·1897
0·9995	0·0201	−1·3935	0·0201	−0·2903	0·0201	−0·2288	0·0201	−0·1899
0·9996	0·0180	−1·3935	0·0180	−0·2904	0·0180	−0·2289	0·0180	−0·1901
0·9997	0·0156	−1·3934	0·0156	−0·2906	0·0156	−0·2291	0·0156	−0·1903
0·9998	0·0127	−1·3934	0·0127	−0·2907	0·0127	−0·2293	0·0127	−0·1905
0·9999	0·0090	−1·3933	0·0090	−0·2908	0·0090	−0·2294	0·0090	−0·1907
1·000	0	−1·3932	0	−0·2909	0	−0·2296	0	−0·1909
1·004	0	−1·3343	0	−0·2383	0	−0·1789	0	−0·1416
1·008	0	−1·3088	0	−0·2190	0	−0·1611	0	−0·1251
1·012	0	−1·2889	0	−0·2052	0	−0·1487	0	−0·1137
1·016	0	−1·2720	0	−0·1940	0	−0·1389	0	−0·1049
1·020	0	−1·2569	0	−0·1847	0	−0·1308	0	−0·0978
1·040	0	−1·1969	0	−0·1517	0	−0·1033	0	−0·0742
1·060	0	−1·1502	0	−0·1301	0	−0·0861	0	−0·0601
1·080	0	−1·1108	0	−0·1141	0	−0·0739	0	−0·0503
1·100	0	−1·0762	0	−0·1015	0	−0·0646	0	−0·0431
1·2	0	−0·9439	0	−0·0637	0	−0·0382	0	−0·0238
1·3	0	−0·8487	0	−0·0445	0	−0·0256	0	−0·0153
1·4	0	−0·7742	0	−0·0328	0	−0·0185	0	−0·0107
1·5	0	−0·7132	0	−0·0252	0	−0·0139	0	−0·0079
1·6	0	−0·6622	0	−0·0198	0	−0·0108	0	−0·0060
1·7	0	−0·6184	0	−0·0160	0	−0·0086	0	−0·0047
1·8	0	−0·5806	0	−0·0130	0	−0·0070	0	−0·0038
1·9	0	−0·5471	0	−0·0109	0	−0·0057	0	−0·0031
2·0	0	−0·5178	0	−0·0091	0	−0·0048	0	−0·0026

	200		210		211		220	
x	ReF	ImF	ReF	ImF	ReF	ImF	ReF	ImF
0·0040114	4·4277	−3·1393	−1·2419	1·8665	−0·3268	−0·6559	0·5415	−1·4432
0·0061743	3·6033	−2·8646	−0·7679	1·5924	−0·4547	−0·4145	0·1855	−1·1704
0·0099833	2·7734	−2·5584	−0·3294	1·2876	−0·5118	−0·1658	−0·1201	−0·8686
0·0153017	2·1140	−2·2859	−0·0197	1·0180	−0·4903	0·0285	−0·3095	−0·6049
0·0219375	1·6149	−2·0555	0·1822	0·7923	−0·4233	0·1646	−0·4076	−0·3888
0·0296507	1·2375	−1·8622	0·3085	0·6060	−0·3374	0·2524	−0·4450	−0·2160
0·0381626	0·9496	−1·6995	0·3837	0·4528	−0·2482	0·3032	−0·4442	−0·0802
0·0471656	0·7275	−1·5622	0·4249	0·3272	−0·1649	0·3273	−0·4211	0·0248
0·0563344	0·5552	−1·4463	0·4436	0·2249	−0·0916	0·3328	−0·3860	0·1043
0·0653374	0·4211	−1·3489	0·4480	0·1423	−0·0300	0·3264	−0·3460	0·1630

Table 1(a). (*contd.*)

	200		210		211		220	
x	ReF	ImF	ReF	ImF	ReF	ImF	ReF	ImF
0·0738493	0·3171	−1·2678	0·4438	0·0765	0·0199	0·3132	−0·3061	0·2051
0·0815625	0·2372	−1·2016	0·4352	0·0251	0·0589	0·2972	−0·2695	0·2344
0·0881983	0·1772	−1·1491	0·4251	−0·0139	0·0882	0·2813	−0·2383	0·2540
0·0935167	0·1340	−1·1096	0·4156	−0·0422	0·1091	0·2674	−0·2136	0·2665
0·0973257	0·1054	−1·0826	0·4082	−0·0610	0·1228	0·2570	−0·1962	0·2740
0·0994886	0·0899	−1·0676	0·4038	−0·0711	0·1301	0·2510	−0·1865	0·2776
0·1009220	0·0799	−1·0579	0·4008	−0·0777	0·1348	0·2470	−0·1801	0·2799
0·1047941	0·0542	−1·0322	0·3925	−0·0946	0·1467	0·2359	−0·1630	0·2852
0·1115049	0·0130	−0·9897	0·3773	−0·1215	0·1651	0·2163	−0·1342	0·2919
0·1206341	−0·0368	−0·9354	0·3554	−0·1538	0·1859	0·1892	−0·0968	0·2966
0·1316084	−0·0885	−0·8747	0·3279	−0·1868	0·2052	0·1564	−0·0547	0·2967
0·1437383	−0·1374	−0·8126	0·2967	−0·2169	0·2203	0·1207	−0·0122	0·2910
0·1562617	−0·1802	−0·7532	0·2640	−0·2420	0·2300	0·0850	0·0274	0·2799
0·1683916	−0·2155	−0·6994	0·2325	−0·2614	0·2344	0·0519	0·0616	0·2652
0·1793659	−0·2430	−0·6536	0·2042	−0·2752	0·2347	0·0235	0·0890	0·2493
0·1884951	−0·2632	−0·6172	0·1811	−0·2843	0·2328	0·0011	0·1094	0·2346
0·1952059	−0·2765	−0·5915	0·1643	−0·2898	0·2302	−0·0147	0·1230	0·2230
0·1990780	−0·2837	−0·5770	0·1548	−0·2925	0·2283	−0·0234	0·1303	0·2161
0·2016845	−0·2883	−0·5673	0·1484	−0·2941	0·2268	−0·0292	0·1350	0·2114
0·2088450	−0·3003	−0·5414	0·1311	−0·2978	0·2222	−0·0446	0·1471	0·1981
0·2216039	−0·3188	−0·4971	0·1010	−0·3021	0·2119	−0·0701	0·1655	0·1735
0·2397546	−0·3400	−0·4378	0·0603	−0·3035	0·1935	−0·1021	0·1854	0·1373
0·2629993	−0·3594	−0·3674	0·0118	−0·2982	0·1650	−0·1358	0·2008	0·0906
0·2909565	−0·3732	−0·2900	−0·0405	−0·2835	0·1260	−0·1658	0·2060	0·0362
0·3231672	−0·3785	−0·2093	−0·0924	−0·2576	0·0779	−0·1870	0·1970	−0·0210
0·3591025	−0·3736	−0·1290	−0·1395	−0·2203	0·0239	−0·1953	0·1718	−0·0750
0·3981723	−0·3575	−0·0520	−0·1777	−0·1730	−0·0312	−0·1884	0·1315	−0·1193
0·4397351	−0·3305	0·0189	−0·2040	−0·1183	−0·0822	−0·1660	0·0799	−0·1485
0·4831084	−0·2934	0·0811	−0·2162	−0·0598	−0·1240	−0·1298	0·0226	−0·1590
0·5275801	−0·2478	0·1328	−0·2136	−0·0013	−0·1527	−0·0836	−0·0333	−0·1499
0·5724199	−0·1960	0·1724	−0·1968	0·0530	−0·1658	−0·0319	−0·0811	−0·1230
0·6168916	−0·1405	0·1992	−0·1676	0·0994	−0·1628	0·0198	−0·1154	−0·0827
0·6602649	−0·0841	0·2129	−0·1290	0·1352	−0·1449	0·0665	−0·1328	−0·0350
0·7018277	−0·0296	0·2143	−0·0846	0·1587	−0·1150	0·1043	−0·1327	0·0135
0·7408975	0·0203	0·2046	−0·0383	0·1694	−0·0773	0·1303	−0·1170	0·0567
0·7768328	0·0636	0·1861	0·0062	0·1682	−0·0363	0·1437	−0·0896	0·0902
0·8090435	0·0988	0·1615	0·0458	0·1573	0·0037	0·1453	−0·0558	0·1116
0·8370007	0·1255	0·1337	0·0784	0·1396	0·0391	0·1375	−0·0208	0·1210
0·8602454	0·1439	0·1059	0·1030	0·1187	0·0676	0·1238	0·0108	0·1208
0·8783961	0·1552	0·0813	0·1197	0·0983	0·0883	0·1081	0·0360	0·1146
0·8911550	0·1611	0·0623	0·1298	0·0817	0·1016	0·0943	0·0534	0·1067
0·8983155	0·1637	0·0511	0·1347	0·0715	0·1083	0·0855	0·0628	0·1009
0·9017869	0·1646	0·0456	0·1368	0·0664	0·1114	0·0809	0·0673	0·0977
0·9091500	0·1662	0·0334	0·1408	0·0551	0·1175	0·0707	0·0765	0·0901
0·9213510	0·1669	0·0122	0·1457	0·0348	0·1259	0·0518	0·0904	0·0750
0·9367454	0·1640	−0·0162	0·1479	0·0067	0·1327	0·0247	0·1048	0·0510
0·9532546	0·1544	−0·0491	0·1437	−0·0269	0·1335	−0·0089	0·1141	0·0188
0·9686489	0·1371	−0·0817	0·1309	−0·0613	0·1249	−0·0445	0·1135	−0·0176
0·9808500	0·1138	−0·1091	0·1108	−0·0909	0·1078	−0·0757	0·1020	−0·0513
0·9882130	0·0925	−0·1263	0·0910	−0·1096	0·0895	−0·0959	0·0866	−0·0738
0·9900	0·0859	−0·1306	0·0848	−0·1143	0·0836	−0·1009	0·0813	−0·0795
0·9905	0·0840	−0·1317	0·0829	−0·1156	0·0818	−0·1024	0·0797	−0·0811
0·9910	0·0819	−0·1329	0·0809	−0·1170	0·0799	−0·1038	0·0780	−0·0827
0·9915	0·0798	−0·1341	0·0789	−0·1183	0·0780	−0·1052	0·0762	−0·0843
0·9920	0·0776	−0·1353	0·0768	−0·1196	0·0759	−0·1067	0·0743	−0·0860

Table 1(a). *(contd.)*

	200		210		211		220	
x	ReF	ImF	ReF	ImF	ReF	ImF	ReF	ImF
0·9925	0·0753	−0·1365	0·0745	−0·1210	0·0738	−0·1081	0·0723	−0·0876
0·9930	0·0729	−0·1377	0·0722	−0·1223	0·0715	−0·1096	0·0702	−0·0893
0·9935	0·0704	−0·1389	0·0698	−0·1236	0·0692	−0·1110	0·0680	−0·0909
0·9940	0·0678	−0·1401	0·0673	−0·1250	0·0667	−0·1125	0·0656	−0·0926
0·9945	0·0651	−0·1414	0·0646	−0·1263	0·0641	−0·1139	0·0632	−0·0942
0·9950	0·0622	−0·1426	0·0618	−0·1276	0·0614	−0·1154	0·0605	−0·0959
0·9955	0·0592	−0·1438	0·0588	−0·1290	0·0584	−0·1169	0·0577	−0·0976
0·9960	0·0559	−0·1450	0·0556	−0·1303	0·0553	−0·1183	0·0547	−0·0993
0·9965	0·0524	−0·1462	0·0522	−0·1317	0·0519	−0·1198	0·0515	−0·1010
0·9970	0·0487	−0·1474	0·0485	−0·1331	0·0483	−0·1213	0·0479	−0·1027
0·9975	0·0445	−0·1487	0·0444	−0·1344	0·0442	−0·1228	0·0439	−0·1045
0·9980	0·0399	−0·1499	0·0398	−0·1358	0·0397	−0·1243	0·0395	−0·1062
0·9985	0·0346	−0·1511	0·0346	−0·1372	0·0345	−0·1259	0·0343	−0·1080
0·9990	0·0283	−0·1524	0·0283	−0·1386	0·0282	−0·1274	0·0281	−0·1097
0·9991	0·0269	−0·1526	0·0268	−0·1388	0·0268	−0·1277	0·0267	−0·1101
0·9992	0·0253	−0·1529	0·0253	−0·1391	0·0253	−0·1280	0·0252	−0·1104
0·9993	0·0237	−0·1531	0·0237	−0·1394	0·0237	−0·1283	0·0236	−0·1107
0·9994	0·0220	−0·1533	0·0219	−0·1397	0·0219	−0·1285	0·0219	−0·1111
0·9995	0·0201	−0·1536	0·0200	−0·1399	0·0200	−0·1288	0·0200	−0·1114
0·9996	0·0179	−0·1538	0·0179	−0·1402	0·0179	−0·1291	0·0179	−0·1118
0·9997	0·0155	−0·1541	0·0155	−0·1405	0·0155	−0·1294	0·0155	−0·1121
0·9998	0·0127	−0·1543	0·0127	−0·1407	0·0127	−0·1297	0·0126	−0·1124
0·9999	0·0090	−0·1545	0·0090	−0·1410	0·0089	−0·1300	0·0089	−0·1128
1·000	0	−0·1548	0	−0·1413	0	−0·1304	0	−0·1132
1·004	0	−0·1068	0	−0·0942	0	−0·0841	0	−0·0683
1·008	0	−0·0914	0	−0·0795	0	−0·0700	0	−0·0554
1·012	0	−0·0810	0	−0·0698	0	−0·0609	0	−0·0472
1·016	0	−0·0732	0	−0·0625	0	−0·0541	0	−0·0412
1·020	0	−0·0668	0	−0·0567	0	−0·0487	0	−0·0366
1·040	0	−0·0468	0	−0·0387	0	−0·0323	0	−0·0229
1·060	0	−0·0355	0	−0·0288	0	−0·0236	0	−0·0160
1·080	0	−0·0281	0	−0·0224	0	−0·0181	0	−0·0119
1·100	0	−0·0228	0	−0·0180	0	−0·0144	0	−0·0091
1·2	0	−0·0101	0	−0·0076	0	−0·0058	0	−0·0033
1·3	0	−0·0054	0	−0·0040	0	−0·0030	0	−0·0016
1·4	0	−0·0032	0	−0·0023	0	−0·0017	0	−0·0009
1·5	0	−0·0020	0	−0·0015	0	−0·0011	0	−0·0005
1·6	0	−0·0014	0	−0·0010	0	−0·0007	0	−0·0003
1·7	0	−0·0009	0	−0·0007	0	−0·0005	0	−0·0002
1·8	0	−0·0007	0	−0·0005	0	−0·0003	0	−0·0002
1·9	0	−0·0004	0	−0·0004	0	−0·0002	0	−0·0001
2·0	0	−0·0004	0	−0·0002	0	−0·0002	0	−0·0001

	221		222	
x	ReF	ImF	ReF	ImF
0·0040114	0·4948	0·2921	−0·4963	0·0182
0·0061743	0·5125	0·0807	−0·4162	0·1772
0·0099833	0·4540	−0·1180	−0·2669	0·2937
0·0153017	0·3418	−0·2490	−0·1022	0·3294
0·0219375	0·2137	−0·3145	0·0383	0·3006
0·0296507	0·0933	−0·3307	0·1388	0·2345
0·0381626	−0·0084	−0·3140	0·1986	0·1536
0·0471656	−0·0876	−0·2777	0·2241	0·0733

Table 1(a). (*contd.*)

	221		222	
x	ReF	ImF	ReF	ImF
0·0563344	−0·1451	−0·2321	0·2246	0·0026
0·0653374	−0·1841	−0·1846	0·2090	−0·0545
0·0738493	−0·2083	−0·1398	0·1852	−0·0974
0·0815625	−0·2217	−0·1005	0·1590	−0·1277
0·0881983	−0·2280	−0·0684	0·1344	−0·1478
0·0935167	−0·2300	−0·0439	0·1140	−0·1602
0·0973257	−0·2299	−0·0271	0·0992	−0·1673
0·0994886	−0·2295	−0·0179	0·0908	−0·1707
0·1009220	−0·2290	−0·0118	0·0853	−0·1727
0·1047941	−0·2269	0·0039	0·0704	−0·1771
0·1115049	−0·2212	0·0296	0·0450	−0·1818
0·1206341	−0·2099	0·0611	0·0122	−0·1827
0·1316084	−0·1920	0·0938	−0·0242	−0·1768
0·1437383	−0·1683	0·1237	−0·0593	−0·1632
0·1562617	−0·1410	0·1479	−0·0896	−0·1435
0·1683916	−0·1130	0·1653	−0·1129	−0·1205
0·1793659	−0·0871	0·1765	−0·1290	−0·0976
0·1884951	−0·0657	0·1827	−0 1389	−0·0777
0·1952059	−0·0500	0·1856	−0·1442	−0·0629
0·1990780	−0·0411	0·1866	−0·1466	−0·0543
0·2016845	−0·0352	0·1871	−0·1479	−0·0485
0·2088450	−0·0191	0·1875	−0·1503	−0·0328
0·2216039	0·0083	0·1850	−0·1507	−0·0055
0·2397546	0·0440	0·1753	−0·1437	0·0305
0·2629993	0·0833	0·1545	−0·1241	0·0697
0·2909565	0·1195	0·1205	−0·0897	0·1044
0·3231672	0·1458	0·0744	−0·0423	0·1259
0·3591025	0·1563	0·0204	0·0116	0·1277
0·3981723	0·1477	−0·0348	0·0621	0·1073
0·4397351	0·1200	−0·0834	0·0993	0·0674
0·4831084	0·0771	−0·1181	0·1153	0·0159
0·5275801	0·0252	−0·1339	0·1071	−0·0364
0·5724199	−0·0274	−0·1292	0·0772	−0·0786
0·6168916	−0·0729	−0·1056	0·0330	−0·1024
0·6602649	−0·1050	−0·0680	−0·0156	−0·1042
0·7018277	−0·1200	−0·0229	−0·0583	−0·0852
0·7408975	−0·1176	0·0222	−0·0875	−0·0515
0·7768328	−0·1004	0·0612	−0·0994	−0·0112
0·8090435	−0·0731	0·0898	−0·0948	0·0277
0·8370007	−0·0414	0·1065	−0·0780	0·0590
0·8602454	−0·0107	0·1126	−0·0549	0·0799
0·8783961	0·0150	0·1112	−0·0318	0·0909
0·8911550	0·0334	0·1065	−0·0134	0·0950
0·8983155	0·0437	0·1024	−0·0024	0·0956
0·9017869	0·0485	0·1000	0·0030	0·0955
0·9091500	0·0587	0·0940	0·0148	0·0942
0·9213510	0·0747	0·0811	0·0344	0·0885
0·9367454	0·0921	0·0594	0·0583	0·0744
0·9532546	0·1050	0·0286	0·0800	0·0492
0·9686489	0·1079	−0·0077	0·0923	0·0150
0·9808500	0·0991	−0·0421	0·0909	−0·0203
0·9882130	0·0852	−0·0654	0·0810	−0·0456
0·9900	0·0802	−0·0714	0·0769	−0·0522
0·9905	0·0786	−0·0731	0·0755	−0·0541
0·9910	0·0770	−0·0748	0·0741	−0·0560
0·9915	0·0753	−0·0765	0·0726	−0·0579
0·9920	0·0734	−0·0782	0·0710	−0·0598

Table 1(a). *(Contd.)*

	221		222	
x	ReF	ImF	ReF	ImF
0·9925	0·0715	−0·0799	0·0693	−0·0611
0·9930	0·0695	−0·0817	0·0675	−0·0637
0·9935	0·0674	−0·0834	0·0655	−0·0657
0·9940	0·0651	−0·0851	0·0635	−0·0676
0·9945	0·0627	−0·0869	0·0613	−0·0696
0·9950	0·0601	−0·0887	0·0589	−0·0716
0·9955	0·0574	−0·0904	0·0563	−0·0736
0·9960	0·0544	−0·0922	0·0536	−0·0757
0·9965	0·0512	−0·0940	0·0505	−0·0778
0·9970	0·0477	−0·0959	0·0471	−0·0799
0·9975	0·0438	−0·0977	0·0434	−0·0820
0·9980	0·0394	−0·0996	0·0391	−0·0841
0·9985	0·0343	−0·1014	0·0341	−0·0862
0·9990	0·0281	−0·1033	0·0280	−0·0884
0·9991	0·0267	−0·1036	0·0266	−0·0888
0·9992	0·0252	−0·1040	0·0251	−0·0892
0·9993	0·0236	−0·1044	0·0235	−0·0896
0·9994	0·0218	−0·1047	0·0218	−0·0900
0·9995	0·0199	−0·1051	0·0199	−0·0905
0·9996	0·0178	−0·1055	0·0178	−0·0909
0·9997	0·0155	−0·1058	0·0154	−0·0913
0·9998	0·0126	−0·1062	0·0126	−0·0917
0·9999	0·0089	−0·1065	0·0089	−0·0921
1·000	0	−0·1070	0	−0·0926
1·004	0	−0·0627	0	−0·0501
1·008	0	−0·0503	0	−0·0388
1·012	0	−0·0424	0	−0·0319
1·016	0	−0·0368	0	−0·0271
1·020	0	−0·0324	0	−0·0234
1·040	0	−0·0198	0	−0·0133
1·060	0	−0·0136	0	−0·0087
1·080	0	−0·0099	0	−0·0060
1·100	0	−0·0076	0	−0·0044
1·2	0	−0·0026	0	−0·0013
1·3	0	−0·0012	0	−0·0006
1·4	0	−0·0007	0	−0·0003
1·5	0	−0·0004	0	−0·0002
1·6	0	−0·0002	0	−0·0001
1·7	0	−0·0001	0	−0·0001
1·8	0	−0·0001	0	−0·0000
1·9	0	−0·0001	0	−0·0000
2·0	0	−0·0001	0	−0·0000

Table 1(b). *The function* $H(y, \mathbf{p})$ *(see equation (17)), where* $y = \sqrt{(\epsilon^2 - (1+\alpha)^2)}$

	H						
y	000	100	110	111	200	210	211
0·02	7·2742	−3·2292	0·8006	0·1483	2·2424	−0·3457	−0·1874
0·04	5·6881	−2·2068	0·3321	0·1830	1·4097	−0·0518	−0·1373
0·06	4·8504	−1·7000	0·1436	0·1590	1·0149	0·0427	−0·0890
0·08	4·2964	−1·3816	0·0462	0·1299	0·7767	0·0794	−0·0547
0·10	3·8896	−1·1583	−0·0098	0·1037	0·6158	0·0930	−0·0311
0·12	3·5723	−0·9914	−0·0437	0·0817	0·5000	0·0961	−0·0149

Table 1(b). *(Contd.)*

	H						
y	000	100	110	111	200	210	211
0·14	3·3145	−0·8612	−0·0646	0·0635	0·4129	0·0939	−0·0038
0·16	3·0989	−0·7566	−0·0775	0·0486	0·3454	0·0892	0·0037
0·18	2·9148	−0·6706	−0·0850	0·0364	0·2919	0·0833	0·0088
0·20	2·7550	−0·5986	−0·0891	0·0265	0·2487	0·0771	0·0121
0·40	1·8184	−0·2414	−0·0703	−0·0111	0·0656	0·0303	0·0124
0·60	1·3674	−0·1204	−0·0438	−0·0129	0·0224	0·0120	0·0061
0·80	1·0938	−0·0674	−0·0273	−0·0099	0·0090	0·0052	0·0029
1·00	0·9092	−0·0409	−0·0176	−0·0071	0·0040	0·0024	0·0014
1·20	0·7763	−0·0263	−0·0118	−0·0051	0·0020	0·0012	0·0007
1·40	0·6764	−0·0178	−0·0082	−0·0037	0·0010	0·0007	0·0004
1·60	0·5986	−0·0126	−0·0059	−0·0027	0·0006	0·0004	0·0002
1·80	0·5365	−0·0092	−0·0043	−0·0020	0·0003	0·0002	
2·00	0·4858	−0·0069	−0·0033	−0·0015	0·0002		
2·20	0·4437	−0·0053	−0·0025	−0·0012			
2·40	0·4082	−0·0041	−0·0020	−0·0010			
2·60	0·3779	−0·0033	−0·0016	−0·0008			
2·80	0·3517	−0·0027	−0·0013	−0·0006			
3·00	0·3289	−0·0022	−0·0011	−0·0005			
3·50	0·2829	−0·0014	−0·0007	−0·0003			
4·00	0·2481	−0·0009	−0·0005	−0·0002			
4·50	0·2209	−0·0007	−0·0003	−0·0002			
5·00	0·1990	−0·0005	−0·0002				
5·50	0·1811	−0·0004	−0·0002				
6·00	0·1661	−0·0003					
6·50	0·1534	−0·0002					
7·00	0·1425	−0·0002					
7·50	0·1330						
8·00	0·1248						
8·50	0·1174						
9·00	0·1109						
9·50	0·1051						
10·00	0·0999						

	H		
y	220	221	222
0·02	0·0577	0·1447	−0·0678
0·04	−0·0809	0·0611	0·0002
0·06	−0·1009	0·0188	0·0180
0·08	−0·0956	−0·0023	0·0207
0·10	−0·0839	−0·0125	0·0185
0·12	−0·0714	−0·0169	0·0151
0·14	−0·0599	−0·0183	0·0117
0·16	−0·0499	−0·0180	0·0087
0·18	−0·0413	−0·0169	0·0063
0·20	−0·0341	−0·0154	0·0044
0·40	−0·0044	−0·0034	−0·0007
0·60	−0·0001	−0·0004	−0·0004
0·80	0·0004	0·0001	−0·0001
1·00	0·0003	0·0001	
1·20	0·0002	0·0001	

x up to x^4 and integrated term by term. The coefficients involve the integrals, $\int_0^\infty s^n Q(s,\mathbf{p})\,\mathrm{d}s$, for $n = 0$–4 and these have been evaluated. $F_2(x)$, which comes from the integral from s_0 to ∞ is evaluated in the following manner.

$$\int_0^\delta F_2(x)\,\mathrm{d}x = \int_{s_0}^\infty \mathrm{d}sQ(s)\int_0^\delta \mathrm{e}^{-ixs}\,\mathrm{d}x$$
$$= \int_{s_0}^\infty \mathrm{d}sQ(s)\frac{1-\mathrm{e}^{ix\delta}}{is}\,\mathrm{d}s$$

$Q(s)$ is now replaced by the large s approximation $a + b\ln s/s$ and the remaining integrals are evaluated numerically. The final values of $\int_0^{0\cdot 0035} F(x)\,\mathrm{d}x$ are listed in Table 2.

Table 2. The integral $\int_0^{0\cdot 0035}$

p	$R(p)$	$I(p)$
0, 0, 0	0·05358	−0·01821
1, 0, 0	−0·03153	0·01402
1, 1, 0	0·01515	−0·00984
1, 1, 1	−0·00445	0·00570
2, 0, 0	0·02544	−0·01263
2, 1, 0	−0·01095	0·00844
2, 1, 1	0·00214	−0·00435
2, 2, 0	0·00739	−0·00705
2, 2, 1	−0·00045	0·00305
2, 2, 2	−0·00061	−0·00183

Recently Tonegawa[4] has calculated values of the spin wave Green's function for four lattice sites in the absence of anisotropy. He has also evaluated the function for several cases relevant to the specific antiferromagnet, $\mathrm{MnF_2}$. Here exchange between nearest neighbors on the same sublattice is important and the dispersion relation therefore more involved than the one used here[6].

REFERENCES

1. *Magnetism* (Edited by G. T. Rado and H. Suhl), Vol. 1, p. 327. Academic Press, New York (1963).
2. *Handbook of Mathematical Functions* (Edited by M. Abramovitz and J. A. Stegun). Nat. Bur. of Standards, Applied Mathematics series 55, Washington, D.C. (1964).
3. *Tables of Integral Transforms* (Edited by A. Erdelyi), Vol. 2, p. 32. McGraw-Hill, New York (1954).
4. TONEGAWA T., Doctorate Thesis, Osaka University (1968).
5. *Localized Excitations In Solids* (Edited by R. F. Wallis), p. 341. Plenum Press, New York (1968).
6. TANABE Y., GONDAIRA K-I and MURATA H., *J. phys. Soc. Japan* **25**, 1562 (1968).

APPENDIX

We are interested in the form of $Q(x,\mathbf{p})$ for large s, which has been shown above to determine the singular behavior of F at $x = 0$. We write the argument of the cosine in equation (15) as $(s/2)\cos\frac{1}{2}\varphi_x\cos\frac{1}{2}\varphi_y(\mathrm{e}^{i\varphi_z/2}+\mathrm{e}^{-i\varphi_z/2})$, expand the cosine in powers of $\mathrm{e}^{i\varphi_z/2}$ and integrate over φ_z. This yields the form

$$Q(s,\mathbf{p}) = \frac{(-1)^n}{(2\pi)^2}\int_{-\pi}^{+\pi}\int_{-\pi}^{+\pi}\mathrm{e}^{-i[l\varphi_x+m\varphi_y]}$$
$$\times J_{2n}[s\cos\tfrac{1}{2}\varphi_x\cos\tfrac{1}{2}\varphi_y]\,\mathrm{d}\varphi_x\mathrm{d}\varphi_y$$
$$= \frac{4}{\pi^2}(-1)^n\int_0^{\pi/2}\int_0^{\pi/2}\cos(2l\theta_x+2m\theta_y)$$
$$\times J_{2n}[s\cos\theta_x\cos\theta_y]\,\mathrm{d}\theta_x\,\mathrm{d}\theta_y. \qquad \text{(A-1)}$$

We write

$$\cos\theta_x\cos\theta_y = r$$
$$\sin\theta_x\sin\theta_y = t \qquad \text{(A-2)}$$

from which one has

$$\mathrm{d}\theta_x\,\mathrm{d}\theta_y = \frac{\mathrm{d}r\,\mathrm{d}t}{[1-(r+t)^2]^{1/2}[1-(r-t)^2]^{1/2}}. \qquad \text{(A-3)}$$

If one integrates with constant r, t increases from 0 to $1-r$ and then decreases to 0 again. Introduce Ψ by the relation

$$t = (1-r)\sin\Psi. \qquad \text{(A-4)}$$

Then

$$\mathrm{d}\theta_x\,\mathrm{d}\theta_y = \frac{\mathrm{d}r\mathrm{d}\Psi}{[(1+r)^2-(1-r)^2\sin^2\Psi]^{1/2}}.$$

The Ψ-integration will be written as $\left[\int_0^{\pi/2}+\int_{\pi/2}^0\right]$ and $Q(s,\mathbf{p})$ is now given by

$$Q(s,\mathbf{p}) = (-1)^n\frac{4}{\pi^2}\int_0^1\mathrm{d}rJ_{2n}(sr)\left[\int_0^{\pi/2}+\int_{\pi/2}^0\right]$$
$$\times\frac{\cos(2l\theta_x+2m\theta_y)\,\mathrm{d}\Psi}{[(1+r)^2-(1-r)^2\sin^2\Psi]^{1/2}}$$
$$= (-1)^n\frac{4}{\pi^2}\int_0^s\mathrm{d}uJ_{2n}(u)\frac{1}{1+u/s}$$
$$\times\left[\int_0^{\pi/2}+\int_{\pi/2}^0\right]\frac{\cos(2l\theta_x+2m\theta_y)\,\mathrm{d}\Psi}{\left[1-\left(\frac{1-u/s}{1+u/s}\right)^2\sin^2\Psi\right]^{1/2}}.$$
$$\text{(A-5)}$$

The numerator of the last term is decomposed as $(-1)^{l+m} + [\cos(2l\theta_x + 2m\theta_y) - (-1)^{l+m}]$ and the two resulting integrals treated separately. Now choose ζ to go to infinity more slowly than $s^{1/2}$; then, in the range $0 < \Psi < \pi/2 - \zeta(u/s)^{1/2}$, the denominator in (A5) is of the form $\cos\Psi + 0(1/s)$. The first Ψ-integral of (A5) may now be written

$$2(-1)^{l+m}\Bigg\{\int_0^{\pi/2-\zeta(u/s)^{1/2}} \frac{d\Psi}{\cos\Psi} + \int_{\pi/2-\zeta(u/s)^{1/2}}^{\pi/2} \frac{d\psi}{\left[\cos^2\Psi + \dfrac{4u/s}{(1+u/s)^2}\sin^2\Psi\right]^{1/2}}\Bigg].$$

Under the radical, $\cos\Psi \sim (u/s)^{1/2}$ and to this order the above integral is

$$2(-1)^{l+m}\left[-\ln\tan\frac{\zeta}{2}\left(\frac{u}{s}\right)^{1/2} + \sinh^{-1}\frac{\zeta}{2}\right] \rightarrow (-1)^{l+m} \times [\ln s - \log u + 2\ln 2] \qquad \text{(A-6)}$$

as $\zeta \rightarrow \infty$.

In the second Ψ-integral it is easily shown that in the range $0 < \Psi < \pi/2$, θ_x is essentially $\pi/2$ and $\theta_y \sim \Psi$ for large s, whereas in the descending range $\pi/2$ to 0, $\theta_y \sim \pi/2$ and $\theta_x \sim \Psi$. Since the numerator goes to zero for large s in the range $\pi/2 - \zeta(u/s)^{1/2}$ to $\pi/2$, the approximation $\cos\Psi$ may be made for the denominator for all Ψ. The integral now becomes

$$(-1)^l \int_0^{\pi/2} \frac{\cos 2m\Psi - (-1)^m}{\cos\Psi}\,d\Psi + (-1)^m \int_0^{\pi/2} \frac{\cos 2l\Psi - (-1)^l}{\cos\Psi}\,d\Psi = -2(-1)^{l+m}\left\{\sum_{r=0}^{m-1}\frac{1}{2r+1} + \sum_{r=0}^{l-1}\frac{1}{2r+1}\right\}.$$

In the integrals over u it is consistent with the previous approximations to take the upper limit as infinite. Then using the results

$$\int_0^\infty J_{2n}(u)\,du = 1 \qquad \text{(A-7)}$$

and [3]

$$\int_0^\infty J_{2n}(u)\ln u\,du = \Psi(n+\tfrac{1}{2}) + \ln 2 \qquad \text{(A-8)}$$

one finally obtains

$$Q(s,\mathbf{p}) = (-1)^{l+m+n}\frac{4}{\pi^2 s}\Bigg\{\ln s + \ln 2 - \Psi(n+\tfrac{1}{2}) - 2 \times \sum_{r=0}^{m-1}\frac{1}{2r+1} - 2\sum_{r=0}^{l-1}\frac{1}{2r+1}\Bigg]$$

which may be rewritten in the form given in the text.

J. Phys. Chem. Solids Pergamon Press 1969. Vol. 30, pp. 939–945. Printed in Great Britain.

FERRIMAGNETIC STRUCTURE OF Mn_2Co_2C

N. S. SATYA MURTHY, R. J. BEGUM, C. S. SOMANATHAN,
B. S. SRINIVASAN and M. R. L. N. MURTHY
Bhabha Atomic Research Centre, Trombay, Bombay-74, India

(*Received* 20 *August* 1968)

Abstract—The carbide Mn_2Co_2C has been found to be ferrimagnetic with a Neel temperature of 535°C by means of neutron diffraction. It has a cubic unit cell with an Mn atom at the cube corner and the carbon atom at the body centre. The face centre sites are taken up by the other Mn and the two Co atoms in a statistical manner. The Mn moments are aligned anti-parallel to each other while the two Co moments are parallel to the corner Mn moment. The most reasonable values for the moments are: $4\cdot0\,\mu_B$ for the corner Mn atom, $3\cdot36\,\mu_B$ for the face centre Mn and $1\cdot25\,\mu_B$ for each Co atom. The smaller moments of the face centre atoms arise from the influence of the carbon atom. Polarised neutrons were used to choose a structure having cubic symmetry over one of tetragonal symmetry.

INTRODUCTION

SEVERAL COMPOUNDS having the composition $(M, M')_4X$ where one or both of the atoms M and M' belong to the $3d$ transition group and X is either nitrogen or carbon have been studied extensively[1–7] on account of their interesting magnetic properties. Fe_4N[4] is ferromagnetic with a large magnetic moment of about 9 μ_B/unit cell, while most manganese compounds exhibit ferrimagnetic properties as in the case of Mn_4N[6, 7], which has a net magnetic moment of $1\cdot2\,\mu_B$/unit cell. The crystal structure is usually cubic in which the metal atoms form a f.c.c. lattice and the carbon or the nitrogen atom goes to the body centre. The corner metal atom has the normal magnetic moment but the face centre atoms always have different magnetic moments. This difference has been attributed to the bonding interaction between the face centre metal atoms and the non-metal atom, both nigrogen and carbon being regarded as electron donors. But careful X-ray scattering factor measurements by Elliott[8] and by Kuriyama *et al.*[9] indicate that the valence state of nitrogen in Mn_4N and $(Fe, Ni)_4N$ is such that it is more likely to behave as an 'acceptor' of electrons rather than as a 'donor'. The present study was undertaken with a view to a further understanding of the role of the non-magnetic atom in the atomic and magnetic ordering processes in these compounds.

Mn_2Co_2C is a particularly interesting compound in that the binary f.c.c. alloy Mn–Co[10] is highly disordered and non-magnetic at room temperature and shows a tendency for antiferromagnetic ordering only at very low temperatures when carefully annealed. But X-ray and magnetisation studies by Holtzman [5, 11] show that Mn_2Co_2C is an ordered magnetic compound. According to him it is ferrimagnetic with a net magnetic moment of $3\cdot14\,\mu_B$/unit cell at liquid nitrogen temperature and a transition temperature higher than 600°C.

Polarised neutrons can be used to advantage in the study of ferrimagnetic structures to fix the directions of the individual moments with respect to the net magnetisation. The large intensity variations for the two states of neutron polarisation for the same reflections not only provide a clue to the correct relative spin arrangement but enable a more accurate determination of the individual moment values. As in the earlier neutron diffraction study of Mn_4N by Takei *et al.*[6] polarised neutrons have been used in the present case to resolve the structure in favour of a cubic model rather than one of tetragonal symmetry suggested by Holtzman.

EXPERIMENTAL DETAILS

Fifty atomic per cent each of spectroscopically pure Mn flakes and Co chips were melted in an arc furnace under a pressure of 1 μ. The alloy buttons so formed (about 100 g) were repeatedly melted to ensure the formation of a homogeneous alloy. They were crushed into powder and intimately mixed with carbon of electrolytic purity (taken slightly in excess of the required 20 at.% to ensure complete carbonisation) and melted in an induction furnace at a temperature of 1400°C to allow carbon to dissolve in the molten alloy. The resulting mass was cooled slowly in the furnace. The hard brittle product was powdered to 100 mesh particles. The material was found to be strongly magnetic. The unreacted carbon was removed by magnetic separation. An X-ray examination using Cu Kα radiation revealed the presence of a single phase with a cubic unit cell of $a_0 = 3{\cdot}786$ Å, agreeing very well with Holtzman's value of 3·79 Å.

Thin walled flat aluminium cassettes were used for taking the diffraction patterns of the sample at room temperature and at liquid nitrogen temperature with unpolarised neutrons. The sample was enclosed in vanadium tubes with vanadium end plugs for the high temperature data. With a magnetic field applied parallel to the scattering vector the variation of the (100) and (110) reflection intensities was studied. A field of 4·5 kOe was found to saturate the sample. Figure 1 shows the diffraction patterns at room temperature and at 600°C. The pattern at nitrogen temperature gave relative intensities which were substantially the same as those at the room temperature showing that the magnetic moments at room temperature are not very much different from their saturation values. The nearly complete disappearance of (110) reflection at 600°C indicates that it is almost purely magnetic in origin. The temperature dependence of this peak as well as that of (100) was followed which lead to a transition temperature of 535°C.

For measurements on the polarised neutron spectrometer the sample was pressed into

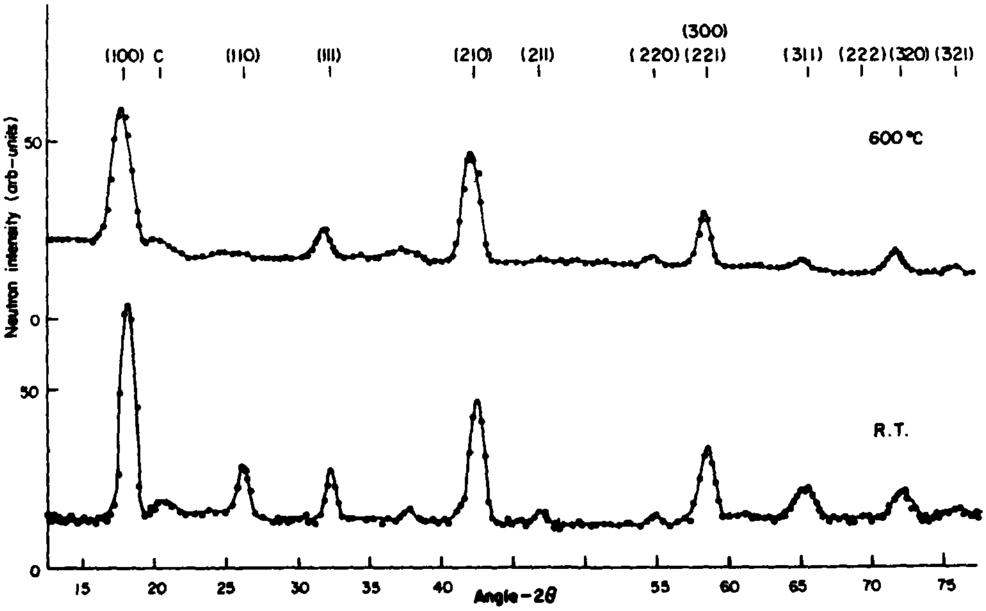

Fig. 1. Unpolarised Neutron diffraction patterns of Mn_2Co_2C at room temperature and at 600°C. $\lambda = 1{\cdot}25$ Å. C refers to a peak due to free carbon present in the sample.

pellets 16 mm in dia. and 3 mm thick using a pressure of 1 kbar. The magnetic field on the sample was 6 kOe applied at right angles to the scattering vector. Patterns were taken for both the neutron spin states, parallel and antiparallel to the direction of magnetisation of the sample. The ratio, R, of the intensites with the two neutron spin states is given by

$$R = \frac{\Sigma j[N^2 + M^2 - 2PDNM(2\mathrm{F} - 1)]}{\Sigma j[N^2 + M^2 + 2\,PDNM]}$$

where the summation is over the number of reflections occuring at a particular Bragg angle. Here j is the multiplicity of $\{hkl\}$ reflections, P is the polarisation of the incident neutron beam, D is the polarisation transmission through the sample and F is the flipping efficiency of the r.f. field used to reverse the neutron spin. N and M refer respectively to the nuclear and magnetic structures factors. It should be noted that R values will show significant departure from unity only for high values of PD and hence D should be fairly large. In order to bring out the striking differences in the diffraction patterns for the two neutron spin states, the behaviour of (100) and (110) reflections with respect to the neutron polarisation is shown in Fig. 2. Also shown for comparison are the patterns with unpolarised neutrons at room temperature ($F^2 \propto N^2 + \frac{2}{3}M^2$), at a temperature beyond T_N($F^2 \propto N^2$) and with an applied field along the scattering vector ($F^2 \propto N^2$). It can be seen that the intensities are strongly dependent on the neutron polarisation and depending on the signs of their structure factors, different reflections behave differently with respect to the neutron polarisation, so that there are, in effect, two additional sets of diffraction data for the same material. In the present case, while the (100) reflection has a higher intensity with r.f. on than with r.f. off, the opposite is the case with the (110) reflection. This is due to the fact that N and M have opposite signs for (100) whereas they are of the the same sign for the (110) reflection. It should also be noted that the coherence between N and M enables accurate estimate of the nuclear component of the (110) reflection which was barely measurable in the high temperature unpolarised neutron diffraction pattern.

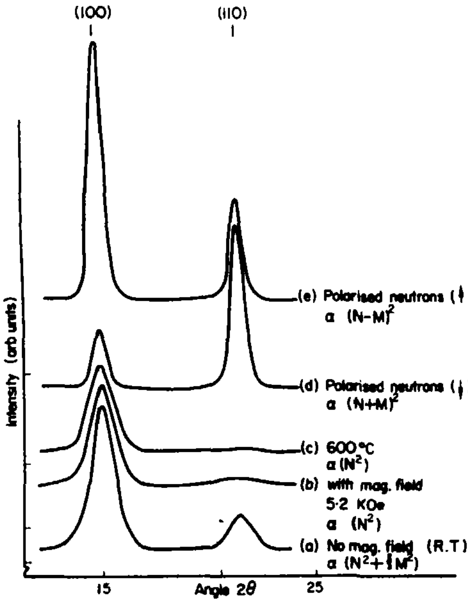

Fig. 2. The diffraction patterns of the first two peaks of Mn_2Co_2C under various conditions: (a), (b) and (c) show patterns taken with unpolarised neutrons; (a) at room temperature, (b) at room temperature with a saturating magnetic field applied parallel to the scattering vector and (c) at 600°C, above T_N. Polarised neutron patterns are (d) with the incident neutron spin antiparallel to the direction of net magnetisation of the sample and (e) with the neutron spin parallel to the magnetisation.

RESULTS

The data were analysed in terms of various possible models. Holtzman suggested that Mn atoms occupy (000) and ($\frac{1}{2}\frac{1}{2}0$) sites while Co atoms take up ($\frac{1}{2}0\frac{1}{2}$) and ($0\frac{1}{2}\frac{1}{2}$) positions, giving a structure of tetragonal symmetry. Although no experimental evidence of any crystallographic distortion was found to support a tetragonal unit cell, the observed intensities were compared with the ones calculated on the basis of Holtzman's model (Model I). Table 1 lists the observed and calculated

Table 1. *Comparison of the observed and calculated intensities of* Mn_2Co_2C

hkl	Obs.	600°C Calc.		Obs.	R.T. Calc.		
		Model I	Model II		Model IA	Model IIA	Model IIB
1 0 0	100·00	100·00	100·00	100·00	100·00	100·00	100·00
1 1 0	small	25·63	4·71	25·34	33·93	23·58	24·20
1 1 1	22·22	20·34	26·53	27·88	14·92	28·21	25·50
2 0 0	7·41	2·73	3·55	7·80	3·17	6·15	4·78
2 1 0	70·38	64·84	64·74	61·01	46·10	61·88	63·01
2 1 1	—	—	—	5·85	13·62	4·93	5·38
2 2 0	7·41	2·22	2·89	3·90	2·21	4·20	3·57
2 2 1 3 0 0	37·04	57·05	36·69	39·57	30·02	42·20	42·74
3 1 1	11·11	11·08	19·44	22·03	10·38	19·72	19·21
3 2 0	22·22	16·74	16·73	23·39	17·22	24·91	25·16
3 2 1	—	—	—	3·90	32·64	2·36	2·41
	Agreement factor (on F^2)	13·8%	9·6%	$B_{600°C} = 1{\cdot}94 \times 10^{-16}\,cm^2$ $B_{r.t.} = 0{\cdot}62 \times 10^{-16}\,cm^2$			

intensities. It is seen that several of the intensities show agreement with Model I, the disagreement in the case of high temperature data being only for two reflections, namely (110) and (221,300). Model II corresponds to a structure with cubic symmetry in which the corner site is occupied by an Mn atom and the face centres are taken up statistically by the other Mn and the two Co atoms. To analyse the room temperature data, the following set of moment values were chosen:

$$\mu_{Mn_I} = 4{\cdot}00\,\mu_B$$
$$\mu_{Mn_{II}} = -3{\cdot}36\,\mu_B$$
$$\mu_{Co} = 1{\cdot}25\,\mu_B$$

where Mn_I stands for the corner manganese atom and Mn_{II} for the face centre atom. These values were based on a straight forward reduction of the magnetic moments of the face centre atoms due to bonding interaction with the carbon atom at the body centre. The moments were assumed to be directed along any of the three cubic axes while for the tetragonal case the *c*-axis was assumed to be the direction of the moments. Any ferromagnetic alignment of spins can be ruled out as it requires all the moments to have unrealistically small values. The fact that the (110) intensity is almost entirely magnetic in origin and that (111) and (200) have low magnetic contributions bears this out. The calculated intensities are shown in the columns IA and IIA. The agreement of the room temperature data with Model II is definitely better, but it should be noted that only weak and outer reflections like (211), (311) and (321) are crucial for choosing between the two models. There is also the possibility that the compound is not fully stoichiometric and the amount of carbon deficiency can be adjusted to give a better agreement of the experimental data with Model I. Polarised neutron intensity ratios were examined for several reflections in order to choose between the two structures. Table 2 gives a comparison of the observed *R* values with the ones calculated on the two models

Table 2. *Polarised neutron ratios*, R, *for* Mn_2Co_2C. P = 0·95, D = 0·76, F = 0·95

hkl	Obs.	Calculated Model IA	Model IIA	Model IIB
1 0 0	5·65	1·37	5·51	5·47
1 1 0	0·52	0·29	0·42	0·42
1 1 1	3·25	5·18	5·16	4·09
2 1 0	3·02	1·18	2·52	2·66

for the (100), (110), (111) and (210) reflections. The experimental values of *P*, *D* and *F* are also shown in the table. A single crystal of Co–Fe was used as an analyser to measure *D*. There is now a striking difference between the values based on the two models for the more prominent reflections and the experimental data clearly favours the cubic model. Also from the signs of the structure factors it can be concluded that the magnetic moment of the face centre Mn atom is directed opposite to the net magnetisation while those of Co atoms are along the net magnetisation. No other spin configuration will be compatible with the observed data. The magnetic structure of the carbide as deduced above is shown in Fig. 3.

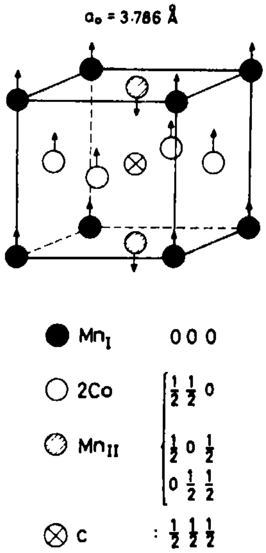
$a_0 = 3{\cdot}786$ Å
● Mn_I 0 0 0
○ 2Co $\frac{1}{2}\frac{1}{2}0$
Mn_{II} $\frac{1}{2}0\frac{1}{2}$
$0\frac{1}{2}\frac{1}{2}$
⊗ C : $\frac{1}{2}\frac{1}{2}\frac{1}{2}$

Fig. 3. The unit cell of Mn_2Co_2C with the arrows indicating magnetic moment directions.

It should be noted that the magnetic structure factors for the cubic case are of two kinds: $(p_{\mathrm{Mn}_1} + 3p_{\mathrm{M}})$ or $(p_{\mathrm{Mn}_1} - p_{\mathrm{M}})$, where p_{Mn_2} refers to the magnetic scattering amplitude of the Mn_1 atom and $p_{\mathrm{M}} = \frac{1}{3}(2p_{\mathrm{Co}} - p_{\mathrm{Mn}_{\mathrm{II}}})$ is the composite magnetic scattering amplitude of the f.c. sites. In the case of Mn_4N, however, the situation is simpler in view of all the face centre atoms being of one kind. So any other set of magnetic moment values which would give almost the same numbers for the above two expressions cannot be distinguished by neutron diffraction techniques from the set A mentioned earlier. Curiously enough, this happens to be the case with the following set of moment values which were suggested by Takei *et al.*[7] (THS) for Mn_4C on the basis of extrapolation of their data on carbon substituted Mn_4N compounds:

$$\mu_{\mathrm{Mn}_{\mathrm{I}}} = 3{\cdot}85\,\mu_B$$
$$\mu_{\mathrm{Mn}_{\mathrm{II}}} = -1{\cdot}23\,\mu_B$$
$$\mu_{\mathrm{Co}} = 0{\cdot}26\,\mu_B.$$

The intensities calculated on this set of moment values are also shown in Table 1 as Model IIB.

DISCUSSION

The fact that the binary MnCo alloy shows very little tendency for magnetic ordering while the carbide with the same proportion of metal atoms is highly ordered indicates that carbon plays an important role in stabilising the structure. This is a consequence of the difference in the carbide forming habits of Mn and Co. Cobalt being known to have a greater affinity for carbon is accommodated at the two face centre sites which are closer to carbon, while the remaining site is occupied by Mn. The other Mn atom is relegated to the corner site which is too far from the body-centre site to have any appreciable interaction with carbon. MnCo has a cell constant of 3·615 Å. A saturation magnetisation study by Crangle[12] of Mn–Co alloys in the composition range 18 at.% Mn indicates than on increasing the Mn content there is a reduction in the magnetisation per atom suggesting an antiparallel alignment of Mn and Co spins. This can be seen qualitatively to be due to an overlap of Mn and Co 3*d* orbitals. The Mn–Co distance in the alloy is 2·55 Å which is smaller than the sum of their radii, namely, 1·35 Å for Mn and 1·22 Å for Co (according to recent self consistent Hartree–Fock calculations). In the case of the carbide there is an expansion of the unit cell to accommodate the carbon atom at the body centre and the significant interatomic distances are:

$$\begin{aligned} \mathrm{Mn_I - Mn_{II}}\ \text{or}\ \mathrm{Co} &= 2{\cdot}677\ \text{Å} \\ \mathrm{C - Mn_{II}}\ \text{or}\ \mathrm{Co} &= 1{\cdot}893\ \text{Å} \\ \mathrm{Mn_I - C} &= 3{\cdot}279\ \text{Å}. \end{aligned}$$

There is now no overlap between the Mn and Co atoms and hence a ferromagnetic interaction is expected between them, while between the Mn atoms an antiferromagnetic interaction persists as the $\mathrm{Mn_I - Mn_{II}}$ distance is still smaller than twice the Mn radius. Any superexchange interaction among the face centre atoms via the carbon orbitals is weak because of the unfavourable, 90° angle. Thus the magnetic structure is brought about by direct exchange interactions among the metal atoms.

Although the two cubic models IIA and IIB cannot be distinguished by means of neutron diffraction, set A is preferable as these moment values can be explained in a sample way, without any *ad hoc* assumptions. The carbon $2p$ electrons can be assumed to spend some of their time in the neighbourhood of the f.c.c. atoms, thereby decreasing their effective magnetic moment values. In fact, it may be thought of that the two p electrons of carbon spend a third of their time near each face centre atom and this would result in an increase of 0·67 in the effective electron concentration of each atom. Thus the Mn moment is reduced by 0·64 from its normal value of 4·0 μ_B while each Co moment is reduced by 0·48 μ_B from the normal Co moment of 1·73 μ_B. The smaller reduction in the Co moment may be due to its larger bonding interaction with carbon. Set B necessitates the assumption of a definite number of electrons being donated by the carbon atom to the face centre atoms. THS[7] studied the carbon substituted Mn_4N system, $Mn_4N_{1-x}C_x$ as well as partially filled compounds like $Mn_4N_{0{\cdot}92}$ and extrapolated their results to the case of the hypothetical carbide Mn_4C. They assumed that in $(M, M')_4X$ compounds, the magnetic moment of the corner Mn atom remains essentially constant, while the face centre atoms lose 3 μ_B when X is nitrogen and 2 μ_B when it is a carbon atom. This was supported by their experimental results on Mn_4N, $Mn_4N_{0{\cdot}92}$, Mn_3AlC[2], $Mn_4N_{0{\cdot}75}C_{0{\cdot}25}$ etc. But this argument failed to explain their observed magnetic moment values in the case of $Mn_4N_{0{\cdot}8}$. According to THS, this change in the face centre moments arises because of a reversal in the relative positions of the two d sub-bands, so that Hund's Rule operates on one sub-band when the number of nitrogen vacancies is small (< 20 per cent) and on the other sub-band for larger number of vacancies. In the latter situation, THS suggested that even the corner moment is affected. This assumption is *ad hoc* and need not be expected to be followed by carbides as well. Moreover, it may be pointed out that in Fe_4N [4] the face centre moments have also been explained without recourse to any such assumptions. The present interpretation of the moments is analogous to the situation in Fe_4N.

The study of compounds such as the present one undoubtedly leads to a better understanding of magnetism in covalent compounds and of the role of non magnetic atoms in magnetic structures. It would be worthwhile to investigate carbides and nitrides for other concentrations of Mn and Co.

Acknowledgements—We are grateful to Dr. P. K. Iyengar for his keen interest in the work. We thank Mr. M. G. Natera and Mr. S. I. Youssef for assistance with the calculations.

REFERENCES

1. WIENER G. W. and BERGER J. A., *J. Metals* **7**, 360 (1955).
2. BUTTERS R. G. and MYERS H. P., *Phil. Mag.* **46**, 895 (1955).
3. BROCKHOUSE B. N. and MYERS H. P., *Can. J. Phys.* **35**, 313 (1957).
4. FRAZER B. C., *Phys. Rev.* **112**, 751 (1958).
5. HOLTZMAN A. H. and CONARD II G. P., *J. appl. Phys.* **30**, 103S (1959).

6. TAKEI W. J., SHIRANE G. and FRAZER B. C., *Phys. Rev.* **119**, 122 (1960).
7. TAKEI W. J., HEIKES R. R. and SHIRANE G., *Phys. Rev.* **125**, 1893 (1962).
8. ELLIOTT N., *Phys. Rev.* **129**, 1120 (1963).
9. KURIYAMA M., HOSOYA S. and SUZUKI T., *Phys. Rev.* **130**, 898 (1963).
10. SIDHU S. S., SATYA MURTHY N. S., CAMPOS F. P. and ZAUBERIS D. D., *Pittsburgh Diffraction Conf. (1961)*. Unpublished.
11. HOLTZMAN A. H., Ph.D. Thesis, Lehigh University (1958).
12. CRANGLE J., *Phil. Mag.* 7, 589 (1957).

J. Phys. Chem. Solids Pergamon Press 1969. Vol. 30, pp. 947–957. Printed in Great Britain.

ELECTROTRANSPORT AND DIFFUSION IN MOLYBDENUM–TUNGSTEN AND IRON–NICKEL ALLOYS OVER WIDE RANGES OF TEMPERATURES

I. N. FRANTSEVICH, D. F. KALINOVICH, I. I. KOVENSKII and M. D. SMOLIN
Institute for Problems of Material Science, Academy of Science, Kiev, Ukraine, U.S.S.R.

(*Received* 11 *January* 1965; *in revised form* 20 *August* 1968)

Abstract – In this work the results of investigations of electrotransport and diffusion of components of 11 Mo–W alloys and of the alloys of Fe with 2 and 4 at.% of Ni over wide temperature ranges are set forth. Experiments were carried out on the basis of techniques elaborated by the authors, using the tracers Mo^{99}, W^{185}, Fe^{55} and Ni^{63}. Using the experimental data obtained, a row of parameters which characterize the condition of ions and current carriers and their interaction in the investigated alloys were estimated by the authors in the approximation of two bands model.

INVESTIGATION of ions electrotransport in metals and alloys offers a great practical and theoretical interest.

On the one hand, as the electrotransport process represents a directed quickened diffusional movement of ions of alloys components, this phenomenon may be used for a row of practical purposes, for example, for separation of isotopes, for refinement of metals and semi-conductors, for activation of processes, of chemical-heat treatment etc.

On the other hand, as the ions migration during an electrotransport process is conditioned by their interaction with the electric field and current carriers, the electrotransport effect measured from an experiment is connected directly with parameters which characterize the condition of ions and current carriers and their interaction in metals and alloys. A practical possibility that ensues from this is that of determination of those very important parameters by the electrotransport experimental data.

In this paper are presented the results of investigation of electrotransport of the components of 11 alloys Mo–W and of the alloys of iron with 2 and 4 at.% of nickel over wide temperature ranges.

1. THE EXPERIMENTAL TECHNIQUES

The basic parameter of electrotransport is the value of the effective charge of a migrating ion Z^*. The latter is fixed by a value of a partial electrotransport velocity v, of a diffusion coefficient D and of a specific electrical resistivity ρ. In this work all those quantities were determined experimentally. The techniques of determination of v and D on the one specimen in one experiment by the same points on the same experimental curves are described in details in [1] and [2]. As to determination of ρ, see [3]. In general outline the technique of determination of the values v and D is as follows.

In the initial moment the tracer of the element under investigation is distributed along a specimen which represents a section of wire:

$$\left.\begin{aligned} &C = C_0 \text{ by } |x| \leqslant l,\ R \leqslant r \leqslant R+\Delta R,\\ &C = 0 \text{ for the rest of } x \text{ and } r,\\ &\left.\frac{\partial c}{\partial r}\right|_{r=R+\Delta R} = 0. \end{aligned}\right\} \quad (1)$$

These conditions correspond to a layer of tracer of the width ΔR and the length $2l$ which is put on a specimen electrolytically. The graphs of such distribution of radioactivity must represent Π-formed curves.

The values v and D by a temperature T are determined after the heating of specimens with the help of direct current by a displacement of tracer atoms with respect to the initial Π-formed zone, this displacement being the result of electrotransport and diffusion processes which by such heating are taking place simultaneously.

The solution of Fick's equation for the experimental conditions aforesaid leads to an expression for the distribution of concentration of migrating substance along a specimen after its heating during the time t as follows:

$$C(x,t)=\frac{C_0}{2}\operatorname{erfc}\frac{x-l}{2\sqrt{(Dt)}}. \qquad (2)$$

The calculation of diffusion coefficients D by experimental curves is carried out in the following way. The ratio $\operatorname{erfc}\lambda y/\operatorname{erfc} y$ (here $\lambda=x_1-l/x_2-l$, $y=x_2-l/2\sqrt{Dt}$) is figured up and brought into tables. Then the ratio

$$\frac{C(x_1,t)}{C(x_2,t)}=\frac{\operatorname{erfc}\dfrac{x_1-l}{2\sqrt{(Dt)}}}{\operatorname{erfc}\dfrac{x_2-l}{2\sqrt{(Dt)}}} \qquad (3)$$

is determined, the latter being equal to the ratio of radioactivities in the points x_1 and x_2 of the curves. Using the values of $c(x_1,t)/c(x_2,t)$, with the help of tables y is determined and D is computed.

The values of D may be as well calculated by the ratio of integral radioactivities in ranges (x_1,∞) and (x_2,∞). In this case the ratio $i\operatorname{erfc}\lambda y/i\operatorname{erfc} y$ must be brought into tables.

By heating of specimens with direct current one deals with a simultaneous migration of atoms in two processes namely those of electrotransport and diffusion. This leads to a displacement of diffusion curves towards the anode or the cathode for a distance v^*t, v^* being the velocity of the tracer migration.

In a general case $v^*\neq v$ as electrotransport of components is accompanied by general transport of the alloy substance. The latter displays itself in a shift of the lattice planes towards the anode or the cathode. A similar phenomenon takes place by diffusion in nonhomogeneous alloys if the partial diffusion coefficients of components differ from one another (Kirkendall effect). That is why the value of the partial electrotransport velocity v must be calculated by the formula as follows [4]:

$$v=v^*+W \qquad (4)$$

where W stands for the velocity of general transport in an alloy.

The value of v^* may be determined by the displacement of the ends of the radioactive zone as well as by the displacement of any pair of points which lay on the same horizontal line. This value may be besides calculated by the displacement of the symmetry axis of the diffusion curves. The value of the velocity W may be determined by the displacement of some inertial mark, for instance, of microhardness mark, which is put in the zone of transport.

The use of tracers for investigation of diffusion and electrotransport allows to obtain the most precise values of D and v. It permits in the same time to accomplish a control of results and conditions of experiments. The essence of such control consists in as follows:

(1) The conditions (1) show that an initial radioactive zone must be strictly Π-formed. Specimens with the zone appreciably different are not used.

(2) The value of the displacement of tracers in the processes of diffusion and electrotransport are determined with respect to several marks of reading.

(3) The integral radioactivities of the initial Π-formed zone and of active zones after heatings must be equal by their values.

(4) The equation (2) shows that by $x=\pm l$ the radioactivity distribution curves for any D and t must pass through the point $C_0/2$ which corresponds to the radioactivity $A_0/2$. If after

several heatings of one specimen the curves will not cross in this point perverted data will be obtained.

(5) All curves as well as the initial Π-formed one must have symmetry axes.

(6) The radioactivity distribution curve, which is obtained after heating with direct current, being shifted on the distance v^*t in the direction opposite to that of electrotransport must take the same position as in the result of diffusion only (by the same duration of heating). It means that this curve must be symmetrical with respect to Π-formed one and must cross with it in the points $A_0/2$.

(7) In the two-components system[4]

$$W = v_1\gamma_1 + v_2\gamma_2. \qquad (5)$$

Here γ_1 and γ_2, v_1 and v_2 represent atomic portions and partial velocities of electrotransport of the components. A value of W may be determined as well directly by a shift of an inertial mark. The values of W obtained by the data of those two independent experiments must coincide.

(8) The control of experimental data may be as well accomplished in a way of comparison of a large number of results of repeated measurements of D and v.

2. THE EXPERIMENTAL DATA

Investigation of diffusion and electrotransport of both components of the alloys of molybdenum with 0·1; 15; 20; 25; 35; 50; 65; 75; 80; 85 and 99·9 at.% of tungsten as well as in the alloys of iron with 2 and 4 at.% of nickel over wide temperature ranges was carried out with the help of tracers Mo^{99}, W^{185}, Fe^{55} and Ni^{63}. Measurements of specific resitivities were accomplished too in the same alloys.

Since value of the electrotransport velocity depends on the current density the values of partial and general electrotransport numbers are presented in Tables 1 and 2. Using the values of these quantities one can calculate v and W for any current density.

Table 1. The partial and general electrotransport numbers in Mo–W alloys

Temperature (°C)	U_w $\left(\frac{g\text{-ion}}{\text{Faraday}}\right)$	U_{Mo} $\left(\frac{g\text{-ion}}{\text{Faraday}}\right)$	U $\left(\frac{g\text{-ion}}{\text{Faraday}}\right)$
1	2	3	4
	Mo–0·1 at.% W alloy		
1800	$3\cdot15\times10^{-11}$	$-2\cdot75\times10^{-8}$	$-2\cdot75\times10^{-8}$
1900	$7\cdot94\times10^{-11}$	$-5\cdot16\times10^{-8}$	$-5\cdot15\times10^{-8}$
2000	$1\cdot07\times10^{-10}$	$-1\cdot65\times10^{-7}$	$-1\cdot65\times10^{-7}$
2100	$2\cdot42\times10^{-10}$	$-6\cdot37\times10^{-7}$	$-6\cdot37\times10^{-7}$
2200	$3\cdot90\times10^{-10}$	$-1\cdot56\times10^{-6}$	$-1\cdot56\times10^{-6}$
2300	$6\cdot23\times10^{-10}$	$-3\cdot12\times10^{-6}$	$-3\cdot12\times10^{-6}$
2400	$1\cdot34\times10^{-9}$	$-5\cdot21\times10^{-6}$	$-5\cdot21\times10^{-6}$
	Mo–15 at.% W alloy		
1400	$1\cdot56\times10^{-8}$		$1\cdot44\times10^{-8}$
1500	$3\cdot66\times10^{-8}$		$2\cdot81\times10^{-8}$
1600	$7\cdot46\times10^{-8}$	$-1\cdot37\times10^{-8}$	$6\cdot09\times10^{-8}$
1700	$2\cdot69\times10^{-7}$	$-4\cdot06\times10^{-8}$	$2\cdot28\times10^{-7}$
1800	$5\cdot38\times10^{-7}$	$-1\cdot24\times10^{-7}$	$4\cdot14\times10^{-7}$
1900	$1\cdot24\times10^{-6}$	$-3\cdot15\times10^{-7}$	$9\cdot25\times10^{-7}$
2000	$2\cdot30\times10^{-6}$	$-1\cdot09\times10^{-6}$	$1\cdot21\times10^{-6}$
2100	$3\cdot96\times10^{-6}$	$-2\cdot45\times10^{-6}$	$1\cdot51\times10^{-6}$
2200	$7\cdot71\times10^{-6}$	$-6\cdot11\times10^{-6}$	$1\cdot60\times10^{-6}$
2300	$1\cdot24\times10^{-5}$	$-1\cdot05\times10^{-5}$	$1\cdot90\times10^{-6}$
2400	$2\cdot78\times10^{-5}$	$-1\cdot96\times10^{-5}$	$8\cdot20\times10^{-6}$
	Mo–20 at % W alloy		
1400	$1\cdot44\times10^{-8}$		$8\cdot12\times10^{-9}$
1500	$3\cdot56\times10^{-8}$		$2\cdot11\times10^{-8}$
1600	$8\cdot20\times10^{-8}$	$-1\cdot80\times10^{-8}$	$6\cdot40\times10^{-8}$
1700	$2\cdot53\times10^{-7}$	$-6\cdot79\times10^{-8}$	$1\cdot85\times10^{-7}$
1800	$5\cdot23\times10^{-7}$	$-1\cdot82\times10^{-7}$	$3\cdot41\times10^{-7}$
1900	$1\cdot31\times10^{-6}$	$-4\cdot52\times10^{-7}$	$8\cdot58\times10^{-7}$
2000	$2\cdot55\times10^{-6}$	$-1\cdot41\times10^{-6}$	$1\cdot14\times10^{-6}$
2100	$4\cdot59\times10^{-6}$	$-3\cdot07\times10^{-6}$	$1\cdot52\times10^{-6}$
2200	$8\cdot84\times10^{-6}$	$-6\cdot99\times10^{-6}$	$1\cdot85\times10^{-6}$
2300	$1\cdot29\times10^{-5}$	$-1\cdot06\times10^{-5}$	$2\cdot30\times10^{-6}$
2400	$2\cdot09\times10^{-5}$	$-1\cdot78\times10^{-5}$	$3\cdot10\times10^{-6}$
	Mo–25 at.% W alloy		
1400	$9\cdot62\times10^{-9}$		$3\cdot24\times10^{-9}$
1500	$1\cdot83\times10^{-8}$		$7\cdot99\times10^{-9}$
1600	$6\cdot23\times10^{-8}$	$-1\cdot94\times10^{-8}$	$4\cdot29\times10^{-8}$
1700	$1\cdot27\times10^{-7}$	$-7\cdot99\times10^{-8}$	$4\cdot71\times10^{-8}$
1800	$3\cdot16\times10^{-7}$	$-1\cdot97\times10^{-7}$	$1\cdot19\times10^{-7}$
1900	$8\cdot94\times10^{-7}$	$-5\cdot32\times10^{-7}$	$3\cdot62\times10^{-7}$
2000	$1\cdot92\times10^{-6}$	$-1\cdot39\times10^{-6}$	$5\cdot30\times10^{-7}$
2100	$3\cdot66\times10^{-6}$	$-2\cdot90\times10^{-6}$	$7\cdot60\times10^{-7}$
2200	$7\cdot75\times10^{-6}$	$-6\cdot46\times10^{-6}$	$1\cdot29\times10^{-6}$
2300	$1\cdot30\times10^{-5}$	$-9\cdot38\times10^{-6}$	$3\cdot62\times10^{-6}$
2400	$2\cdot37\times10^{-5}$	$-1\cdot62\times10^{-5}$	$7\cdot50\times10^{-6}$

Table 1. (*cont.*)

Temperature (°C)	U_W $\left(\frac{g\text{-ion}}{\text{Faraday}}\right)$	U_{Mo} $\left(\frac{g\text{-ion}}{\text{Faraday}}\right)$	U $\left(\frac{g\text{-ion}}{\text{Faraday}}\right)$
1	2	3	4
	Mo – 35 at.% W alloy		
1500	$9{\cdot}40\times10^{-9}$		$3{\cdot}25\times10^{-9}$
1600	$2{\cdot}30\times10^{-8}$	$-1{\cdot}77\times10^{-8}$	$5{\cdot}30\times10^{-9}$
1700	$7{\cdot}14\times10^{-8}$	$-4{\cdot}52\times10^{-8}$	$2{\cdot}62\times10^{-8}$
1800	$1{\cdot}82\times10^{-7}$	$-1{\cdot}17\times10^{-7}$	$6{\cdot}50\times10^{-8}$
1900	$6{\cdot}27\times10^{-7}$	$-4{\cdot}11\times10^{-7}$	$2{\cdot}16\times10^{-7}$
2000	$1{\cdot}52\times10^{-6}$	$-1{\cdot}22\times10^{-6}$	$3{\cdot}00\times10^{-7}$
2100	$2{\cdot}15\times10^{-6}$	$-1{\cdot}79\times10^{-6}$	$3{\cdot}60\times10^{-7}$
2200	$4{\cdot}97\times10^{-6}$	$-4{\cdot}43\times10^{-6}$	$5{\cdot}40\times10^{-7}$
2300	$6{\cdot}63\times10^{-6}$	$-5{\cdot}72\times10^{-6}$	$9{\cdot}10\times10^{-7}$
2400	$1{\cdot}40\times10^{-5}$	$-1{\cdot}25\times10^{-5}$	$1{\cdot}50\times10^{-6}$
	Mo – 50 at.% W alloy		
1700	$7{\cdot}84\times10^{-9}$	$-1{\cdot}80\times10^{-8}$	$-1{\cdot}02\times10^{-8}$
1800	$3{\cdot}10\times10^{-8}$	$-5{\cdot}22\times10^{-8}$	$-2{\cdot}12\times10^{-8}$
1900	$7{\cdot}30\times10^{-8}$	$-9{\cdot}89\times10^{-8}$	$-2{\cdot}59\times10^{-8}$
2000	$2{\cdot}80\times10^{-7}$	$-3{\cdot}51\times10^{-7}$	$-7{\cdot}10\times10^{-8}$
2100	$5{\cdot}19\times10^{-7}$	$-6{\cdot}75\times10^{-7}$	$-1{\cdot}56\times10^{-7}$
2200	$1{\cdot}30\times10^{-6}$	$-1{\cdot}33\times10^{-6}$	$-3{\cdot}00\times10^{-8}$
2300	$2{\cdot}43\times10^{-6}$	$-1{\cdot}82\times10^{-6}$	$6{\cdot}10\times10^{-7}$
2400	$5{\cdot}42\times10^{-6}$	$-4{\cdot}06\times10^{-6}$	$1{\cdot}36\times10^{-6}$
2500	$8{\cdot}24\times10^{-6}$	$-4{\cdot}97\times10^{-6}$	$3{\cdot}27\times10^{-6}$
	Mo – 65 at.% W alloy		
1800	$1{\cdot}64\times10^{-8}$	$-1{\cdot}95\times10^{-8}$	$-3{\cdot}10\times10^{-9}$
1900	$3{\cdot}16\times10^{-8}$	$-3{\cdot}94\times10^{-8}$	$-7{\cdot}80\times10^{-9}$
2000	$9{\cdot}69\times10^{-8}$	$-1{\cdot}11\times10^{-7}$	$-1{\cdot}41\times10^{-8}$
2100	$2{\cdot}13\times10^{-7}$	$-2{\cdot}46\times10^{-7}$	$-3{\cdot}30\times10^{-8}$
2200	$4{\cdot}65\times10^{-7}$	$-4{\cdot}65\times10^{-7}$	0
2300	$1{\cdot}27\times10^{-6}$	$-7{\cdot}61\times10^{-7}$	$5{\cdot}09\times10^{-7}$
2400	$3{\cdot}01\times10^{-6}$	$-1{\cdot}73\times10^{-6}$	$1{\cdot}28\times10^{-6}$
2500	$5{\cdot}82\times10^{-6}$	$-2{\cdot}66\times10^{-6}$	$3{\cdot}16\times10^{-6}$
2600	$9{\cdot}12\times10^{-6}$	$-3{\cdot}63\times10^{-6}$	$5{\cdot}49\times10^{-6}$
	Mo – 75 at.% W alloy		
1800		$-6{\cdot}19\times10^{-9}$	$-1{\cdot}93\times10^{-9}$
1900		$-1{\cdot}18\times10^{-8}$	$-2{\cdot}96\times10^{-9}$
2000	$1{\cdot}07\times10^{-8}$	$-1{\cdot}73\times10^{-8}$	$-6{\cdot}60\times10^{-9}$
2100	$2{\cdot}04\times10^{-8}$	$-3{\cdot}82\times10^{-8}$	$-1{\cdot}78\times10^{-8}$
2200	$3{\cdot}60\times10^{-8}$	$-6{\cdot}41\times10^{-8}$	$-2{\cdot}81\times10^{-8}$
2300	$1{\cdot}03\times10^{-7}$	$-1{\cdot}67\times10^{-7}$	$-6{\cdot}40\times10^{-8}$
2400	$2{\cdot}44\times10^{-7}$	$-3{\cdot}52\times10^{-7}$	$-1{\cdot}08\times10^{-7}$
2500	$5{\cdot}55\times10^{-7}$	$-7{\cdot}13\times10^{-7}$	$-1{\cdot}58\times10^{-7}$
2600	$1{\cdot}09\times10^{-6}$	$-1{\cdot}25\times10^{-6}$	$-1{\cdot}60\times10^{-7}$
2700	$1{\cdot}98\times10^{-6}$	$-2{\cdot}21\times10^{-6}$	$-2{\cdot}30\times10^{-7}$
2800	$3{\cdot}31\times10^{-6}$	$-3{\cdot}71\times10^{-6}$	$-4{\cdot}00\times10^{-7}$
	Mo – 80 at.% W alloy		
1800		$-6{\cdot}49\times10^{-9}$	$-2{\cdot}85\times10^{-9}$
1900		$-9{\cdot}46\times10^{-9}$	$-5{\cdot}64\times10^{-9}$
2000	$8{\cdot}88\times10^{-9}$	$-1{\cdot}95\times10^{-8}$	$-1{\cdot}06\times10^{-8}$
2100	$1{\cdot}50\times10^{-8}$	$-3{\cdot}68\times10^{-8}$	$-2{\cdot}18\times10^{-8}$
2200	$3{\cdot}62\times10^{-8}$	$-8{\cdot}69\times10^{-8}$	$-5{\cdot}07\times10^{-8}$
2300	$8{\cdot}85\times10^{-8}$	$-1{\cdot}50\times10^{-7}$	$-6{\cdot}15\times10^{-8}$
2400	$2{\cdot}11\times10^{-7}$	$-3{\cdot}19\times10^{-7}$	$-1{\cdot}08\times10^{-7}$
2500	$4{\cdot}18\times10^{-7}$	$-6{\cdot}29\times10^{-7}$	$-2{\cdot}11\times10^{-7}$
2600	$6{\cdot}42\times10^{-7}$	$-9{\cdot}16\times10^{-7}$	$-2{\cdot}74\times10^{-7}$
2700	$1{\cdot}24\times10^{-6}$	$-1{\cdot}67\times10^{-6}$	$-4{\cdot}30\times10^{-7}$
2800	$2{\cdot}18\times10^{-6}$	$-3{\cdot}13\times10^{-6}$	$-9{\cdot}50\times10^{-7}$
	Mo – 85 at.% W alloy		
1800		$-5{\cdot}97\times10^{-9}$	$-3{\cdot}71\times10^{-9}$
1900		$-9{\cdot}86\times10^{-9}$	$-8{\cdot}79\times10^{-9}$
2000	$6{\cdot}48\times10^{-9}$	$-1{\cdot}95\times10^{-8}$	$-1{\cdot}30\times10^{-8}$
2100	$1{\cdot}28\times10^{-8}$	$-3{\cdot}22\times10^{-8}$	$-1{\cdot}94\times10^{-8}$
2200	$4{\cdot}02\times10^{-8}$	$-6{\cdot}78\times10^{-8}$	$-2{\cdot}76\times10^{-8}$
2300	$7{\cdot}12\times10^{-8}$	$-1{\cdot}33\times10^{-7}$	$-6{\cdot}18\times10^{-8}$
2400	$2{\cdot}13\times10^{-7}$	$-3{\cdot}08\times10^{-7}$	$-9{\cdot}50\times10^{-8}$
2500	$3{\cdot}12\times10^{-7}$	$-4{\cdot}63\times10^{-7}$	$-1{\cdot}51\times10^{-7}$
2600	$6{\cdot}91\times10^{-7}$	$-8{\cdot}77\times10^{-7}$	$-1{\cdot}86\times10^{-7}$
2700	$1{\cdot}24\times10^{-6}$	$-1{\cdot}49\times10^{-6}$	$-2{\cdot}50\times10^{-7}$
2800	$2{\cdot}05\times10^{-6}$	$-2{\cdot}41\times10^{-6}$	$-3{\cdot}60\times10^{-7}$
	Mo – 99·9 at.% W alloy		
2200	$8{\cdot}27\times10^{-9}$	$-3{\cdot}06\times10^{-11}$	$8{\cdot}24\times10^{-9}$
2300	$1{\cdot}26\times10^{-8}$	$-6{\cdot}81\times10^{-11}$	$1{\cdot}25\times10^{-8}$
2400	$2{\cdot}36\times10^{-8}$	$-1{\cdot}10\times10^{-10}$	$2{\cdot}35\times10^{-8}$
2500	$1{\cdot}11\times10^{-7}$	$-1{\cdot}77\times10^{-10}$	$1{\cdot}11\times10^{-7}$
2600	$1{\cdot}81\times10^{-7}$	$-2{\cdot}46\times10^{-10}$	$1{\cdot}81\times10^{-7}$
2700	$2{\cdot}67\times10^{-7}$	$-4{\cdot}52\times10^{-10}$	$2{\cdot}67\times10^{-7}$
2800	$6{\cdot}85\times10^{-7}$	$-7{\cdot}68\times10^{-10}$	$6{\cdot}84\times10^{-7}$

The values of partial electrotransport numbers were calculated by the formula[5]:

$$U = \frac{vq\gamma F}{VI} \tag{6}$$

where q is the cross-section area of a specimen; γ, atomic portion of a respective component; F, Faraday's number; V, atomic volume of an alloy; I, current strength.

The general electrotransport numbers U were computed as the algebraical sums of partial ones. In the cases when by some temperature electrotransport of only one component of an alloy was investigated the general electrotransport number was calculated by the velocity of the neutral mark.

Table 2. The partial and general electrotransport numbers in Fe–Ni *alloys*

Temperature (°C)	U_{Ni} $\left(\frac{g\text{-ion}}{\text{Faraday}}\right)$	U_{Fe} $\left(\frac{g\text{-ion}}{\text{Faraday}}\right)$	U_1 $\left(\frac{g\text{-ion}}{\text{Faraday}}\right)$
	Fe – 2 at.% Ni alloy		
1000	$1{\cdot}83\times10^{-10}$	$1{\cdot}16\times10^{-8}$	$1{\cdot}18\times10^{-8}$
1050	$3{\cdot}44\times10^{-10}$	$2{\cdot}29\times10^{-8}$	$2{\cdot}32\times10^{-8}$
1100	$6{\cdot}09\times10^{-10}$	$5{\cdot}21\times10^{-8}$	$5{\cdot}27\times10^{-8}$
1150	$1{\cdot}20\times10^{-9}$	$8{\cdot}00\times10^{-8}$	$8{\cdot}12\times10^{-8}$
1200	$1{\cdot}88\times10^{-9}$	$1{\cdot}57\times10^{-7}$	$1{\cdot}59\times10^{-7}$
1250	$3{\cdot}16\times10^{-9}$	$3{\cdot}04\times10^{-7}$	$3{\cdot}07\times10^{-7}$
1300	$3{\cdot}80\times10^{-9}$	$5{\cdot}77\times10^{-7}$	$5{\cdot}81\times10^{-7}$
1350	$6{\cdot}47\times10^{-9}$	$7{\cdot}75\times10^{-7}$	$7{\cdot}81\times10^{-7}$
1400	$6{\cdot}48\times10^{-9}$	$1{\cdot}10\times10^{-6}$	$1{\cdot}10\times10^{-6}$
	Fe – 4 at.% Ni alloy		
1000	$5{\cdot}09\times10^{-10}$	$1{\cdot}39\times10^{-8}$	$1{\cdot}44\times10^{-8}$
1050	$7{\cdot}37\times10^{-10}$	$3{\cdot}28\times10^{-8}$	$3{\cdot}35\times10^{-8}$
1100	$1{\cdot}15\times10^{-9}$	$5{\cdot}11\times10^{-8}$	$5{\cdot}22\times10^{-8}$
1150	$1{\cdot}46\times10^{-9}$	$1{\cdot}22\times10^{-7}$	$1{\cdot}23\times10^{-7}$
1200	$2{\cdot}45\times10^{-9}$	$2{\cdot}08\times10^{-7}$	$2{\cdot}10\times10^{-7}$
1250	$1{\cdot}58\times10^{-9}$	$3{\cdot}27\times10^{-7}$	$3{\cdot}29\times10^{-7}$
1300	0	$5{\cdot}87\times10^{-7}$	$5{\cdot}87\times10^{-7}$
1350	$-4{\cdot}46\times10^{-9}$	$8{\cdot}53\times10^{-7}$	$8{\cdot}49\times10^{-7}$
1400	$-1{\cdot}44\times10^{-8}$	$1{\cdot}74\times10^{-6}$	$1{\cdot}74\times10^{-6}$

The signs '+' and '–' in the tables mean the transport towards the cathode and anodé respectively. Etching off of thin surface layers of specimens and repeated measurements of activity distribution along them have shown the absence of preferable surface transport.

The analysis of the experimental values of the diffusion coefficients in all the alloys investigated here has shown that in spite of very large values of temperature ranges of experiments the temperature dependance of D in all the cases is very well described by the usual exponential law $D = D_0 \exp[-E/RT]$.

The computed values of pre-exponential factors D_0 and activation energies of diffusion E are presented in Tables 3 and 4.

The elaborated by the authors of this paper techniques of measurements of v, D and ρ allow to determine these quantities with errors $\pm(8–12)\%$, $\pm(14–21)\%$ and $\pm(2–4)\%$ respectively. The subsequent increase of precision was achieved with the help of statistical treatment of a large number of measurements of v, D and ρ. The values of v and ρ were averaged by 24 experimental points and the values of D by 48 ones. When taking it into account, one can see that $\Delta v/v = \pm(2{\cdot}7–4{\cdot}2)\%$; $\Delta D/D = \pm(3{\cdot}4–5{\cdot}1)\%$; $\Delta\rho/\rho = \pm(0{\cdot}7–1{\cdot}4)\%$ with the trustworthiness 0·9. If the latter is limited to 0·7, the errors are equal to $\pm(1{\cdot}6–2{\cdot}4)\%$; $\pm(2–3)\%$ and $\pm(0{\cdot}4–0{\cdot}8)\%$ respectively.

Durations of experiments were chosen so that the values Dt were not less than $2{\cdot}7\times10^{-4}$ cm^2 and the values of displacements of tracers

Table 3. The temperature parameters of diffusion of components of Mo–W *alloys*

Concentration of W in the alloy in at.%	Diffusing element Tungsten D_0(cm^2/sec)	 E(cal/mol.)	 Molybdenum D_0(cm^2/sec)	 E(cal/mol.)
0·1	$8{\cdot}5\times10^{-3}$	71,000	$1{\cdot}42\times10^2$	112,000
15	1·4	73,000	$2{\cdot}65\times10^2$	106,000
20	1·7	74,600	$1{\cdot}46\times10^2$	102,000
25	2·2	77,000	47	95,000
35	6·9	85,000	28	92,000
50	14	95,000	12	88,000
65	16	102,000	1·3	86,000
75	20	116,000	0·2	84,500
80	22	119,000	0·11	82,000
85	25	122,000	$8{\cdot}0\times10^{-2}$	80,000
99·9	24	130,000	$2{\cdot}5\times10^{-3}$	78,000

Table 4. The temperature parameters of diffusion of components of Fe–Ni *alloys*

Concentration of Ni in the alloy in at. %	Diffusing element	D_0 (cm²/sec)	E (cal/mole)
2	Ni	1·1	59,000
	Fe	2·5	61,000
4	Ni	1·4	58,000
	Fe	2·9	59,000

zone, not less than 0·3 mm. In the cases when it turned out to be not possible, the amount of experiments was increased so that the errors were in the limites aforesaid.

Since this paper is devoted to investigation of electrotransport and diffusion, the values of ρ are not presented in order that the tables were not overloaded.

3. THE CALCULATION OF EFFECTIVE CHARGES

A value of an effective charge Z^* of an ion which is migrating during the electrotransport process may be determined by experimental data using known Einstein's correlation[6]:

$$Z^*eD = BkTf; \quad \left(B = \frac{v}{I\rho}q\right), \tag{7}$$

where B is mobility of ions in the electric field of intensity of 1^{v}/cm by an absolute temperature T; k is Boltzmann's constant; e is the elementary charge; f is the correlating factor [7].

All quantities in equation (7) except from f are to be determined in experiment. The quantity f according to equation (7) depends on the lattice type and is equal to 0·78 for f.c.c. and 0·72 for b.c.c. cell. It was shown however, for example, in the paper[8] that it is valid only for pure metals and dilute solutions. In non-dilute alloys the correlating factor f in general must be replaced by a complex quantity which can change considerably as a function of composition and temperature. As the theory of this problem is not yet finally elaborated the calculation of Z^* in general is not possible at this time in non-dilute alloys.

The difficulty above as to determination of f may be overcome in a row of cases in the way of successive selection of values of f and of comparison of values of Z^* calculated using the formers with other quantities which are to be determined in experiment and which do not depend on f but are connected with Z^* by some correlations.

In this work the connection between parameters of temperature dependances of Z^* and ρ was used for this purpose. It was established that if the values of f are equal to 0·72 for Mo–W alloys and 0·78 for Fe–Ni ones, takes place quite satisfactory agreement between parameters of $Z^*(T)$ and $\rho(T)$ which are determined by independent experimental measurements.

It ensues from this that in the alloys investigated here the correlating factor f differs apparently very little from that for metals and dilute alloys.

The values of Z^* are presented in Tables 5 and 6. Taking into account the experimental errors in determination of quantities which enter in equation (7) (except from f), $\Delta Z^*/Z^* = \pm(5\text{–}8)\%$.

4. THE TREATMENT OF EXPERIMENTAL DATA ON THE BASIS OF TWO BANDS MODEL

As it was already said above, the data obtained in investigations of electrotransport in metals and alloys may be used for estimations of parameters which characterize the condition of ions and current carriers and their interaction in metallic alloys. Such estimations may be done proceeding from considerations as follow below.

The theory of electrotransport worked up in approximation of two bands model leads to the expression for the quantity Z^* as follows [9–10]:

$$Z^* = z - n_-\sigma_-l_- + n_+\sigma_+l_+ \tag{8}$$

where z is the real charge of an ion of a metal or of a component of a metal alloy; n_-, σ_-, l_-;

Table 5. The effective charges of components of Mo–W *alloys*

Temp	Concentration of W in the alloy in at.%																					
	0·1		15		20		25		35		50		65		75		80		85		99·9	
(°C)	Z_W^*	Z_{Mo}^*	Z_W^*	Z_{Mo}^*	Z_W^*	Z_{Mo}^*	Z_W^*	Z_{Mo}^*	Z_W^*	Z_{Mo}^*	Z_W^*	Z_{Mo}^*	Z_W^*	Z_{Mo}^*	Z_W^*	Z_{Mo}^*	Z_W^*	Z_{Mo}^*	Z_W^*	Z_{Mo}^*	Z_W^*	Z_{Mo}^*
1400			25·2		22·3		16·9															
1500			22·8		21·0		16·7		12·3													
1600			21·9	−13·0	17·9	−10·8	16·2	−8·8	11·3	−6·2												
1700			20·1	−12·6	18·0	−10·0	15·6	−8·2	10·3	−5·5	6·0	−2·3										
1800	18·9	−14·7	19·1	−11·6	17·6	−9·3	14·2	−7·7	10·1	−5·1	6·1	−2·1	9·8	−6·2		−10·8		−14·2		−18·6		
1900	17·8	−13·1	17·9	−10·6	17·3	−9·5	13·4	−7·0	9·9	−4·7	6·0	−1·9	9·0	−5·5		−10·3		−13·6		−17·6		
2000	17·1	−12·9	17·3	−10·2	15·1	−8·3	12·4	−7·1	9·0	−4·9	5·3	−1·8	9·1	−5·6	9·4	−10·2	10·4	−13·5	11·0	−17·2		
2100	15·6	−12·1	16·1	−9·8	14·2	−7·9	12·3	−6·5	8·2	−4·3	5·4	−1·7	8·6	−5·4	9·6	−9·3	10·0	−12·4	10·4	−16·5		
2200	15·3	−11·9	15·5	−9·7	14·3	−7·6	11·5	−6·4	7·9	−3·8	5·2	−1·7	8·2	−5·4	9·0	−9·3	9·3	−12·4	10·5	−15·7	10·3	−19·9
2300	15·1	−11·7	15·2	−8·7	13·3	−7·1	10·3	−6·0	8·0	−3·7	5·1	−1·5	8·3	−5·3	8·8	−9·1	9·6	−11·7	10·0	−15·6	9·7	−18·0
2400	13·6	−10·2	15·0	−8·6	12·7	−7·0	9·8	−5·1	7·4	−3·8	5·0	−1·4	8·0	−5·1	8·6	−9·2	9·2	−11·5	9·9	−15·2	9·5	−17·7
2500											4·8	−1·1	7·9	−5·3	8·5	−8·5	8·8	−11·5	9·3	−14·2	9·5	−17·5
2600													7·3	−4·6	8·3	−8·7	8·8	−11·2	9·2	−14·4	9·3	−17·3
2700															8·0	−8·5	8·7	−11·1	9·2	−14·2	9·4	−17·1
2800															7·3	−7·7	7·9	−10·1	8·4	−13·0	8·1	−15·7

Table 6. The effective charges of components of Fe–Ni *alloys*

Temperature (°C)	Concentration of Ni in the alloy in at. % 2		4	
	Z^*_{Ni}	Z^*_{Fe}	Z^*_{Ni}	Z^*_{Fe}
1000	4·6	6·2	2·0	4·2
1050	3·8	5·2	1·5	3·6
1100	3·2	5·0	1·1	3·1
1150	2·6	4·3	0·7	3·0
1200	1·8	4·0	0·45	2·6
1250	1·5	3·5	0·2	2·3
1300	1·2	3·4	0	2·4
1350	0·9	3·0	−0·15	2·1
1400	0·6	2·9	−0·3	2·0

n_+, σ_+, l_+ are the concentration, the scattering section and the free race length of conductivity electrons and holes respectively.

A similar expression for Z^* was obtained as well in the paper[11] but with an additional factor ½ introduced since only a fraction of the electron-atom interactions during a jump takes place when the atom is actually near the saddle point. In the way of calculations it was shown by the authors of this paper that as concerns the alloys investigated here the conformity of the theory with the experiment is better assuming that this factor is equal to 1.

To eliminate the quantities of free race lengths l_- and l_+ from equation (8) one can use an expression for specific conductivities λ_- and λ_+ also deduced in the approximation of two bands model[12]:

$$\lambda_\pm = \left(\frac{8\bar{n}}{3}\right)^{1/3}\frac{e^2}{h}\, l_\pm n^{2/3}, \tag{9}$$

where h is Plank's constant.

Then putting (9) and (8) one obtains:

$$Z^* = z - \frac{h}{\left(\frac{8\bar{n}}{3}\right)^{1/3} e^2}\left(n_-{}^{1/3}\sigma_-\lambda_- - n_+{}^{1/3}\sigma_+\lambda_+\right). \tag{10}$$

By temperatures which are far enough from the melting point the values of z, n_-, n_+, σ_- and σ_+ do not depend on temperature and may be considered as practically constant. It means that in the approximation above the temperature dependence of Z^* is fixed by temperature dependencies of the quantities $\lambda_- = 1/\rho_-$ and $\lambda_+ = 1/\rho_+$.

In the approximation of two bands model the question of temperature dependence of specific electrical resistivity was considered providing that in conductivity of metals current carriers of both signs take part. This consideration leads to results as follow.

In a particular case when the ratio of mobilities of current carriers $u_-/u_+ = \text{const}$ over the whole temperature range of experiments specific resistivities ρ_- and ρ_+ as well as general specific resistivity of a metal or alloy ρ depend on the temperature linearly:

$$\left.\begin{aligned} \rho_- &= \rho_{0-} + \alpha_- T \\ \rho_+ &= \rho_{0+} + \alpha_+ T \\ \rho &= \rho_0 + \alpha T \end{aligned}\right\}. \tag{11}$$

The temperature parameters ρ_{0-} and α_-; ρ_{0+} and α_+ are connected here with one another by correlations as follow:

$$\frac{1}{\alpha} = \frac{1}{\alpha_-} + \frac{1}{\alpha_+}; \quad \frac{\rho_{0-}}{\alpha_-} = \frac{\rho_0}{\alpha}; \quad \frac{\rho_{0+}}{\alpha_+} = \frac{\rho_0}{\alpha}. \tag{12}$$

In a general case when the ratio u_-/u_+ changes with temperature, i.e. $u_-/u_+(T) \neq \text{const}$, ρ_- and ρ_+ are connected with T by linear dependances but temperature dependance of ρ is described by an equation of hyperbola:

$$T^2 - AT\rho + BT - C\rho + D = 0 \tag{13}$$

where

$$A = \frac{1}{\alpha_-} + \frac{1}{\alpha_+}; \quad B = \frac{\rho_{0-}}{\alpha_-} + \frac{\rho_{0+}}{\alpha_+};$$

$$C = \frac{\rho_{0-}}{\alpha_-} \cdot \frac{1}{\alpha_+} + \frac{\rho_{0+}}{\alpha_+} \cdot \frac{1}{\alpha_-}; \quad D = \frac{\rho_{0-}}{\alpha_-} \cdot \frac{\rho_{0+}}{\alpha_+} \quad . \quad (14)$$

The transformation of equation (10) when taking into account the expressions (11–14) leads to the results as follow.

In a general case when $u_-/u_+(T) \neq$ const the temperature dependence of Z^* is described by the equation

$$T^2Z^* - zT^2 + ETZ^* - FT + KZ^* - L = 0 \quad (15)$$

where

$$E = \frac{\rho_{0-}}{\alpha_-} + \frac{\rho_{0+}}{\alpha_+}; K = \frac{\rho_{0-}}{\alpha_-} \cdot \quad \frac{\rho_{0+}}{\alpha_+};$$

$$F = \left(\frac{\rho_{0-}}{\alpha_-} + \frac{\rho_{0+}}{\alpha_+}\right) z - \frac{h}{(8\bar{n}/3)^{1/3}e^2}$$

$$\left(n_-{}^{1/3}\sigma_- \cdot \frac{1}{\alpha_-} - n_+{}^{1/3}\sigma_+ \cdot \frac{1}{\alpha_+}\right); \quad (16)$$

$$L = \frac{\rho_{0-}}{\alpha_-} \cdot \frac{\rho_{0+}}{\alpha_+} z - \frac{h}{(8\bar{n}/3)^{1/3}e^2}$$

$$\left(n_-{}^{1/3}\sigma_- \cdot \frac{\rho_{0+}}{\alpha_+} \cdot \frac{1}{\alpha_-} - n_+{}^{1/3}\sigma_+ \cdot \frac{\rho_{0-}}{\alpha_-} \cdot \frac{1}{\alpha_+}\right) \quad .$$

In a particular case when $u_-/u_+ =$ const over the whole range of T of experiments the temperature dependence of Z^* is as follows:

$$Z^* = z + k \frac{1}{T + \rho_0/\alpha} \quad (17)$$

where

$$k = \frac{h}{(8\bar{n}/3)^{1/3}e^2}\left[n_+{}^{1/3}\sigma_+\left(\frac{1}{\alpha} - \frac{1}{\alpha_-}\right)\right.$$

$$\left. - n_-{}^{1/3}\sigma_- \cdot \frac{1}{\alpha_-}\right]. \quad (18)$$

The values of A, B, C and D; z, E, F, K and L; z and k in equations (13), (15) and (17) respectively may be determined if the values of ρ and Z^* are determined from experiment for large enough number of temperature points. To calculate the concentration of conductivity electrons n_- one can use the formula

$$n_- = C_1 z_1 + C_2 z_2, \quad (19)$$

where z_1 and z_2; C_1 and C_2 are the charges and the atomic portions of the alloy components.

Besides of this one can approximately take that

$$\frac{\sigma_1}{\sigma_2} = \frac{z_1{}^2}{z_2{}^2} \quad (20)$$

where indexes 1 and 2 mean different compositions of an alloy. Equation (20) may be used as well for calculations.

The analysis of the values of effective charges of the components of the Mo–W and Fe–Ni alloys, which are presented in the tables 5, 6 leads to results as follow.

In all the Mo–W alloys investigated the dependences

$$Z^* = f\left(\frac{1}{T + \rho_0/\alpha}\right)$$

for the ions of both components are described by the linear equations (17) with good enough precision. In the same time by linear equations are described in all those alloys as well the functions $\rho = f(T)$. It indicates an accordance between dependences which are determined by independent experimental data. It ensues from this that as far as two bands model of metals is concerned the temperature dependences of electrotransport of both components, of Mo–W alloys correspond to the temperature dependences of their specific resistivities (see (11) and (17)).

Using equations (12) and (17–20), the values of the quantities $n_-, n_+, \rho_{0-}, \alpha_-, \rho_{0+}, \alpha_+$ as well as those of z, k, σ_- and σ_+ were estimated. In these calculations the values of Hall-coefficients R_H were used, the latters being taken from [13]. It was taken into account that by $u_-/u_+(T) =$ const

$$R_H = -\frac{\alpha^2}{e}\left[\frac{1}{\alpha_-{}^2}\frac{1}{n_-} - \left(\frac{1}{\alpha} - \frac{1}{\alpha_-}\right)^2\frac{1}{n_+}\right] [12, 14].$$

The results obtained are presented in Tables 7 and 8.

The temperature dependences of Z^*_{Ni} and Z^*_{Fe} for Fe–Ni alloys are well described by the equation (15). For these alloys the hyperbolical temperature dependences of specific resistivities take place. It ensues from this that the curves $Z^*(T)$ and $\rho(T)$ are in accordance with one another in the approximation of two bands model of metals. One can see from equations (13–16) that in this case the equalities of coefficients $D=K$, $B=E$ must be realized, the latters being calculated by independent experimental data. Their values are presented in Table 9, which shows that the curves $\rho(T)$, $Z^*_{Ni}(T)$ and $Z^*_{Fe}(T)$ correspond to one another well enough.

Using equations (14–16, 19, 20), the values of n_-, n_+, ρ_{0-}, α_-, ρ_{0+}, α_+ as well as those of z, σ_- and σ_+ were calculated. They are presented in the Tables 10, 11.

The values of ρ_{0-} and ρ_{0+} given in the Table 10 refer to 850°C for the alloy with 2 at.% of Ni and to 800°C for the alloy with 4 at.% of Ni. Their extrapolation to absolute zero has no physical sense for by temperature values above the α–γ transformation occurs and the curves $\rho = f(T)$ have bend points.

The errors of the values given in Tables 7, 8, 10, 11 are as follow:

Table 7. The physical characteristics of Mo–W *alloys*

Concentration of *W* in the alloy in at. %	$R_H \times 10^5$ (cm³/C)	$n_- \times 10^{-22}$ (1/cm³)	$n_+ \times 10^{-22}$ (1/cm³)	α_- ($\mu\Omega \cdot$ cm/grades)	α_+ ($\mu\Omega \cdot$ cm/grades)	ρ_{0-} ($\mu\Omega \cdot$ cm)	ρ_{0+} ($\mu\Omega \cdot$ cm)
0·1	11·8	14·1	2·3	0·100	0·048	0·09	0·04
15	10·6	9·5	2·5	0·103	0·049	0·41	0·20
20	10·2	8·8	3·0	0·121	0·046	2·06	0·79
25	9·8	7·5	3·3	0·129	0·046	4·01	1·43
35	9·0	5·1	3·6	0·139	0·046	6·25	2·08
50	7·8	9·8	4·3	0·143	0·047	8·29	2·74
65	8·0	3·6	3·4	0·124	0·048	6·31	2·47
75	8·15	5·9	3·4	0·117	0·049	4·32	1·81
80	8·2	7·5	3·3	0·110	0·049	3·09	1·38
85	8·3	9·4	3·2	0·105	0·050	1·15	0·55
99·9	8·5	13·9	3·1	0·099	0·049	0·27	0·13

Table 8. The physical characteristics of components of Mo–W *alloys*

Concentration of W in the alloy in at. %	Tungsten				Molybdenum			
	$k \times 10^4$ (el. units × grades)	z (electronic units)	$\sigma_- \times 10^{16}$ (cm²)	$\sigma_+ \times 10^{15}$ (cm²)	$k \times 10^4$ (el. units × grades)	z (electronic units)	$\sigma_- \times 10^{15}$ (cm²)	$\sigma_+ \times 10^{16}$ (cm²)
0·1	4·60	−3·3	7·9	6·7	−3·42	2·2	5·8	5·7
15	4·70	−3·3	7·9	6·7	−2·86	2·2	5·8	5·7
20	4·20	−2·9	6·1	5·2	−2·47	2·3	6·4	6·2
25	3·49	−2·6	4·9	4·2	−2·11	2·3	6·4	6·2
35	2·60	−2·2	3·5	3·0	−1·60	2·3	6·4	6·2
50	0·97	1·4	1·3	1·1	−0·75	1·4	2·4	2·3
65	1·64	1·9	2·4	2·0	−0·84	−2·0	3·3	3·2
75	1·77	2·0	2·6	2·2	−1·73	−2·5	5·1	5·0
80	1·90	2·1	2·9	2·4	−2·41	−2·7	6·0	5·8
85	2·01	2·2	3·2	2·7	−3·25	−2·9	6·9	6·7
99·9	1·98	2·2	3·2	2·7	−4·05	−2·9	6·9	6·7

Table 9. *The values of coefficients* B *and* E. D *and* K

Alloy	$B\times10^{-3}$ (grades)	$E_{Ni}\times10^{-3}$ (grades)	$E_{Fe}\times10^{-3}$ (grades)	$D\times10^{-6}$ (grades^{2})	$K_{Ni}\times10^{-6}$ (grades^{2})	$K_{Fe}\times10^{-6}$ (grades^{2})
Fe–2 at.% Ni	1·73	1·57	1·85	−2·34	−2·13	−2·51
Fe–4 at.% Ni	2·89	3·21	2·71	−3·47	−3·81	−3·25

Table 10. *The physical characteristics of* Fe–Ni *alloys*

Alloy	$n_-\times10^{-23}$ (1/cm^3)	$n_+\times10^{-23}$ (1/cm^3)	α_- ($\mu\Omega\cdot$cm/grades)	α_+ ($\mu\Omega\cdot$cm/grades)	ρ_0 ($\mu\Omega\cdot$cm)	ρ_{0+} ($\mu\Omega\cdot$cm)
Fe–2 at.% Ni	1·2	3·7	0·040	1·5	150	340
Fe–4 at.% Ni	1·0	3·0	0·033	1·7	160	280

Table 11. *The physical characteristics of components of* Fe–Ni *alloys*

Alloy	Nickel z (electronic units)	$\sigma_-\times10^{16}$ (cm^2)	$\sigma_+\times10^{15}$ (cm^2)	Iron z (electronic units)	$\sigma_-\times10^{16}$ (cm^2)	$\sigma_+\times10^{15}$ (cm^2)
Fe–2 at.% Ni	−2·0	4·0	5·1	1·4	5·3	4·2
Fe–4 at.% Ni	−1·6	2·6	3·3	1·2	3·9	3·1

$$\frac{\Delta R_H}{R_H}=\pm(1\text{–}3)\%;\quad \frac{\Delta z}{z}=\pm(10\text{–}20)\%;$$

$$\frac{\Delta k}{k}=\pm(3\text{–}8)\%;\quad \frac{\Delta n_-}{n_-}=\pm(15\text{–}30)\%$$

and ±(20–40)% for the rest of parameters.

The results obtained show that even in such complicated objects as Mo–W and Fe–Ni alloys, which consist of transition metals, a quite satisfactory quantitative accordance of two bands model with experimental data for Z^* takes place.

Acknowledgement—This work was carried out in the Institute for Problems of Material Science, Academy of Science of the Ukrainian, S.S.R.

REFERENCES

1. KALINOVICH D. F., KOVENSKII I. I. and SMOLIN M. D., *Fis. Metall.* **13**, 930 (1962).
2. KALINOVICH D. F., KOVENSKII I. I. and SMOLIN M. D., *Porosh. Metal.* **11**, 55 (1966).
3. KALINOVICH D. F., KOVENSKII I. I. and SMOLIN M. D., *Zav. Lab.* **7**, 823 (1965)
4. KALINOVICH D. F., KOVENSKII I. I. and SMOLIN M. D., *Fiz. Tverd. Tela* **3**, 3367 (1961).
5. FELLER H.-G., HEUMANN Th. and WEVER H., *Z. Naturf.* **13a**, 152 (1958).
6. EINSTEIN A., *Annls. Phys.* **17**, 549 (1905).
7. COMPAAN K. and HAVEN G., *Trans. Faraday Soc.* **52**, 786 (1956).
8. MANNING J. R., *Phys. Rev.* **139**, A2027 (1965).
9. FIKS V. B., *Fiz. Tverd. Tela* **1**, 16 (1959).
10. GLINCHUK M. D., *Ukr fiz. Zh.* **4**, 684 (1959).
11. HUNTINGTON H. B. and GRONE A. R., *J. Phys. Chem. Solids* **20**, 76 (1961).
12. SONDHEIMER E. H. and WILSON A. H., *Proc. R. Soc.* **A190**, 435 (1947).
13. GRUM-GRZYMAILO N. V., *Khimicheskaja svjaz v metallicheskich splavakh.* Moskva (1960).
14. SMOLIN M. D., *Dokl. Akad. Nauk USSR* **12**, 1586 (1965)

J. Phys. Chem. Solids Pergamon Press 1969. Vol. 30, pp, 959–961. Printed in Great Britain

OPTICAL CONDUCTIVITY IN ALKALI METALS

H. BÜTTNER and E. GERLACH
Battelle-Institut e.V., Frankfurt/Main, Germany

(*Received* 29 *May* 1968; *in revised form* 14 *August* 1968)

Abstract – It is shown that the Mayer–Naby peak in the optical conductivity of alkali metals possibly arises from transitions from the Fermi sea to the Brillouin zone boundaries.

1. INTRODUCTION

DESPITE A large number of attempts to explain the Mayer–Naby peak[1, 2] in the optical conductivity of alkali metals, no satisfactory solution to the problem has been obtained as yet. An extensive critical analysis of the subject was given in [1]. In a more recent paper, Nettel[2] followed a suggestion by Mayer[1] and Ferrell[1] and studied phonon-aided optical absorption (for Na).

We considered the general problem from a similar point of view using simple perturbation theory and taking electron phonon interaction explicitly into account. It is shown that the band gap parameter $E_g = 2V$ is the crucial quantity determining the various processes of optical absorption.

We find that in the framework of the nearly free electron approximation phonon-assisted transitions to the *zone boundary* yield a transition rate which is of *lower* order in the band gap parameter than those to other regions and is also of lower order than the direct interband[3] transition. (The ordinary Drude transition is negligible in the Mayer–Naby frequency range[1]). We derive a formula which shows that the resulting absorption peak has the correct position on the frequency scale and the correct magnitude and fulfills most requirements to explain the experiments. Nettel[2] also considers transitions to the zone boundaries, but does not give a detailed discussion of this point.

2. THEORY

We consider a system of nearly free electrons in a weak periodic potential whose wave functions are modified by the phonon scattering operator H_s. In first order we have

$$|n,\mathbf{k}+\mathbf{K}) = |n,\mathbf{k}+\mathbf{K}\rangle + \sum_{n',\mathbf{K},\mathbf{K}'} \frac{|n',\mathbf{k}'+\mathbf{K}')\langle n',\mathbf{k}'+\mathbf{K}'|H_s|n,\mathbf{k}+\mathbf{K})}{E(n,\mathbf{k}+\mathbf{K})-E(n',\mathbf{k}'+\mathbf{K}')} \tag{1}$$

where $|n,\mathbf{k}+\mathbf{k}>$ is the wave function of the non-interacting electron phonon system of energy $E = E_{\mathrm{el}}+E_{\mathrm{phon}}$; **k** lies in the reduced zone; **K** is a reciprocal lattice vector of b.c.c. structures.

Now, transitions due to an electromagnetic interaction

$$H_0 = \hbar e/\mathrm{im}\mathbf{A}\cdot\nabla \tag{2}$$

from the Fermi sea to unoccupied states in the lower and upper band are given by the following matrix element:

$$\begin{aligned}(n,\mathbf{k}|H_0|n',\mathbf{k}'+\mathbf{K}') &= \theta(k_F-k)\,\theta(|\mathbf{k}'+\mathbf{K}'|-k_F)\\ &\times\sum_{\mathbf{K}_1}\theta(|\mathbf{k}+\mathbf{K}_1|-k_F)\,\frac{\langle\mathbf{k}|H_0|\mathbf{k}+\mathbf{K}\rangle\langle n,\mathbf{k}+\mathbf{K}_1|H_s|n',\mathbf{k}'+\mathbf{K}'\rangle}{E_{el}(\mathbf{k})-E_{el}(\mathbf{k}'+\mathbf{K}_1)}\\ &+\sum_{\mathbf{K}_1}\theta(|\mathbf{k}'+\mathbf{K}_1|-k_F)\,\frac{\langle\mathbf{k}'+\mathbf{K}_1|H_0|\mathbf{k}'+\mathbf{K}'\rangle\langle n',\mathbf{k}'+\mathbf{K}_1|H_s|n,\mathbf{k}\rangle^*}{E_{el}(\mathbf{k})-E_{el}(\mathbf{k}'+\mathbf{K}_1)}.\end{aligned} \tag{3}$$

Here we have neglected the small contributions from the phonon energies in the denominators.

First we consider the electron phonon matrix element using the deformation potential approximation

$$\langle n, \mathbf{k}+\mathbf{K}_1|H_g|n', \mathbf{k}'+\mathbf{K}'\rangle = il(\hbar_q/2MNc_s)^{1/2}\{(n+1)^{1/2}\delta_{n,n'-1}+n^{1/2}\delta_{n,n'+1}\} \quad (4)$$

where l is an energy constant of about 27 eV [4] (atomic unit), q is the phonon wave vector, M the ionic mass, N the ionic density, c_s the longitudinal velocity of sound and n the Bose distribution for a given T (whereas the pure electron system is assumed to be at $T = 0$, if the Fermi level is well below the band edge). For $T \gg \theta_D$ (Debye-temperature) equation (4) can be approximated by

$$il(k_BT/2MNc_s^2)^{1/2}\{\delta_{n,n'-1}+\delta_{n,n'+1}\}. \quad (5)$$

The electron photon matrix element was studied by a number of authors [3] in the context of direct interband transitions to states not too close to the boundaries and was found to be proportional to V (first Fourier coefficient of the lattice potential). In addition, in our problem virtual optical transitions close to the zone boundary have to be considered, whose matrix elements turn out to be independent of V. The nearly free electron wave functions in the vicinity of the band edge can easily be obtained from a degenerate perturbation treatment which yields.

$$|\mathbf{K}/2\rangle^{\pm} = (2L^3)^{1/2} [\exp(i\mathbf{K}\cdot\mathbf{r}/2 \pm \exp(-i\mathbf{K}\cdot\mathbf{r}/2)] \quad (6)$$

corresponding to the eigenvalues

$$E_{el}^{\pm}(\mathbf{K}/2) = (\hbar\mathbf{K}/2)^2/2m \pm V. \quad (7)$$

Hence with equations (2) and (6), the virtual optical transition at the zone boundary gives the following matrix element:

$$^{-}(\mathbf{K}/2|\mathbf{H}_0|\mathbf{K}/2\rangle^{+} = (e\hbar/2m)\ \mathbf{K}\cdot\mathbf{A} \quad (8)$$

which does not depend on V.

Now we neglect the ordinary Drude term [1] and all contributions proportional to V (indirect transitions not too close to the zone boundaries and direct transitions).

Inserting (5) and (8) into (3) we obtain two contributions, $\sigma^{\pm} = 2\hbar W^{\pm}/\omega|\mathbf{A}|^2$, to the optic conductivity arising from transitions of rate $W^{\pm}$ to the upper and lower band, respectively

$$\sigma^{\pm} = \frac{4\pi}{\omega|\mathbf{A}|^2}\left[2\frac{l^2k_BT}{2MNc_s^2}\right]\left[\frac{1}{2}\left(\frac{e\hbar|\mathbf{A}|}{2m}\right)^2\right] \times \sum_{\mathbf{k},\mathbf{k}',\mathbf{K}'} \frac{(\mathbf{K}'\cdot\mathbf{A})^2 Q(k_F-k)}{\left(\frac{\hbar^2k^2}{2m}-\frac{\hbar^2}{2m}\left(\frac{\mathbf{K}'}{2}\right)^2 \pm V\right)^2}\ \delta\left(\hbar\omega-\frac{\hbar^2}{2m}\left(\frac{\mathbf{K}'}{2}\right)^2+\frac{\hbar^2k^2}{2m}\mp V\right). \quad (9)$$

The factor 2 arises from phonon emission and absorption, the factor ½ from time averaging the electromagnetic field. The **k**′ summation is carried out by putting **k**′ equal to **K**′/2 and multiplying by the volume of a narrow wave vector shell at the zone boundary. From the breakdown of the non-degenerate perturbation theory, the width of the shell is estimated to be $mV/\hbar K$. In the lowest-order approximation a constant gap width is assumed to exist all over the zone boundary, which we take to be spherical. The constant gap approximation corresponds to a reasonable simplification of Ham's [5] results (except for Na). This is reconfirmed later from the good agreement of our curves with the experimental ones. For a more accurate treatment detailed knowledge of the band structure of the zone boundary would be required, but this is expected to lead only to minor corrections.

We consider only transitions between the conduction and the *first* excited band. This implies that **K**′ and **k**′ are not independent so that only $\frac{1}{12}$ of the shell has to be considered. Summation over **K**′ gives a factor $32\,(|\mathbf{A}|\pi/a)^2$ (a = lattice constant).

Carrying out the **k**-summation we finally obtain

$$\sigma^{\pm} = \frac{1}{6}\frac{e^2 l^2 k_B T m^{1/2} E_g}{\hbar^2 N M a^3 c_s^2}\frac{(E_{el}^{\pm}-\hbar\omega)^{1/2}}{(\hbar\omega)^3} \times \theta(\hbar\omega - E_{el}^{\pm} + E_F). \quad (10)$$

The optical conductivity $\sigma = \sigma^+ + \sigma^-$ calculated for Na and K gives the order of $10^{14}\,\mathrm{sec}^{-1}$ in agreement with the experiments. However, it should be emphasized that there is some uncertainty in the sound velocity, the band edges, the interaction parameter l, and also in the shell width. In Fig. 1 an example is given for the ω-dependence of σ (normalized to $10^{14}\,\mathrm{sec}^{-1}$), which still has to be superimposed and smeared out by the ordinary Drude and the direct interband term.

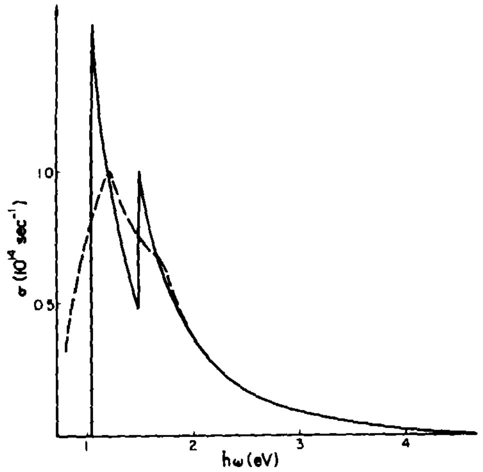

Fig. 1. Calculated optical conductivity in the Mayer–Naby frequency range (broken line: averaged by 0·4 eV intervals).

3. CONCLUSIONS

We have shown that the Mayer–Naby peak can be explained by simple indirect transitions from the Fermi sea to the zone boundaries. We find the calculated peak for all alkali metals to have the correct position on the frequency scale and to be of the order of $10^{14}\,\mathrm{sec}^{-1}$ as required to explain the Mayer–Naby experiments. The curves in Fig. 1 show an asymmetry in the same sense as the experimental ones, the steepest descent being on the low energy side. The fact that our peak for Na is more pronounced than the experimental one may be due to the constant gap approximation, which in this case is not as well justified as for the other alkali metals. Further, the temperature dependence of (10) is in agreement with experimental results obtained for Na; it does not explain the behavior of K and Cs. The interference dip[1] at the threshold of the Mayer–Naby peak is expected to appear if the $|V|^2$-contributions and the Drude term are taken into account. It can be shown that there is no interference between the Drude term and our approximation.

Since we used only small portions of the detailed band structure which are uncritical in transitions to the liquid state, no major deviations are to be expected in this case, in agreement with the experiments (see [2]).

After completion of the present work new experimental data on Na and K were published by Neville V. Smith[6], which do not exhibit the Mayer–Naby peak. As suggested by the author this discrepancy may be explained by the fact, that the experiments were performed on evaporated films rather than on bulk material.

REFERENCES

1. ABELÈS F., (Editor) *Optical properties and electronic structure of metals and alloys*. North Holland, Amsterdam (1966).
2. NETTEL S. J., *Phys. Rev.* **150**, 421 (1966); see also PHILLIPS J. C., *Solid St. Phys.* **18**, 55 (1966).
3. BUTCHER P. N., *Proc. phys. Soc* **A64**, 765 (1951); HOPFIELD J. J., *Phys. Rev.* **139**, A 419 (1965); OVERHAUSER A. W., *Phys. Rev.* **156**, 844 (1967); APPELBAUM J. A., *Phys. Rev.* **144**, 453 (1966); ANIMALU A. O. E., *Phys. Rev.* **163**, 557; 562 (1967).
4. KITTEL C., *Quantum Theory of Solids*. Wiley, New York (1963).
5. HAM F. S., *Phys. Rev.* **128**, 82 (1962).
6. SMITH N. V., *Phys. Rev. Lett.* **21**, 96 (1968).

J. Phys. Chem. Solids Pergamon Press 1969. Vol. 30, pp. 963–977. Printed in Great Britain.

PARAMAGNETIC COPPER CENTERS IN ZnS*

W. C. HOLTON, M. DE WIT and R. K. WATTS
Texas Instruments Incorporated, Dallas, Texas 75222, U. S. A.
and
T. L. ESTLE†
Physics Department, Rice University, Houston, Texas 77001, U.S.A.
and
J. SCHNEIDER
Physikalisches Institut, Universität Freiburg, Freiburg i. Br., Germany

(*Received* 19 *August* 1968)

Abstract—The results of studies by electron paramagnetic resonance of Cu-doped ZnS crystals are presented and discussed along with similar results of other impurities having the d^9 electron configuration in additional crystals. There are ten copper centers in ZnS, and altogether properties of twenty-three related centers are tabulated. The observations are grouped into five classes, each having rather similar characteristics. Plausible models for a few centers are discussed.

1. INTRODUCTION

THE ROLE of impurities in the luminescence of doped ZnS crystals has been investigated for many years[1]. Recently electron paramagnetic resonance (EPR) has been successfully applied to assist in understanding the self-activated luminescence in halogen and group III doped ZnS crystals[2]. With this work for a stimulus, EPR studies have been conducted in an attempt to elucidate the role of copper impurities in the luminescence of Cu-doped ZnS crystals[3]. The results of the paramagnetic resonance part of this study are presented here. Ten distinct EPR spectra involving copper have been observed in ZnS, seven of which are photosensitive. Identification and characterization of the imperfections producing these EPR spectra and the association of each with a specific luminescence emission has not been accomplished because of the large number of EPR and luminescence spectra and because of the number of potentially applicable theoretical considerations. The infrared luminescent copper center has not been observed by the paramagnetic resonance technique, but the Zeeman effect in the absorption spectrum has been studied[4].

2. EXPERIMENT

The ZnS crystals used in this study are microscopic rotational twins with the twin axis and growth direction being $\langle 111\rangle_H$. They are prepared in either a vapor transport method or a chemical transport reaction with HCl[5]. Intermediate regions of the crystal may have the hexagonal rather than cubic crystal structure with the *c*-axis coincident with $\langle 111\rangle_W$. Individual doped samples have been prepared mainly by the diffusion of copper from an evaporated metallic layer. The diffusions are done at a variety of temperatures for various lengths of time with the sample in a sealed quartz tube which may also contain a sulfur, helium, or other appropriate atmosphere. No definite prescription for the preparation of each center is known. The most common center is Cu–H, which appears in

---

*This research sponsored in part by the Air Force Office of Scientific Research Contract No. F44620-67-C-0073.

†This work was performed while this author was at Texas Instruments Incorporated.

both halogen-transported ZnS crystals and in halogen-free ones. Diffusions in the presence of $CuCl_2$, CuS, S, H_2 and $Cu(NO_3)_2$ were successfully used in producing this center. The strongest EPR signal was obtained in a halogen-free crystal, which showed the Cu-red luminescence. This crystal was embedded in a mixture of ZnS and 10^{-4} CuS and fired in flowing H_2S at 1100°C for 1 hr, which is the technique used for preparation of the red luminescence in ZnS powders[6].

A portion of the paramagnetic resonance spectrum of the Cu–H center with the $\langle 111 \rangle_W$ crystal axis along the magnetic field (H_0) is shown in Fig. 1. For this spectrum, obtained in the usual manner with a 10 GHz superheterodyne EPR spectrometer, the sample is mounted with a $(1\bar{1}0)$ cleavage surface against the end of a quartz rod which protrudes axially into an erect right circular cylindrical TE_{011} mode microwave cavity which is immersed in liquid helium. In this way the dependence of

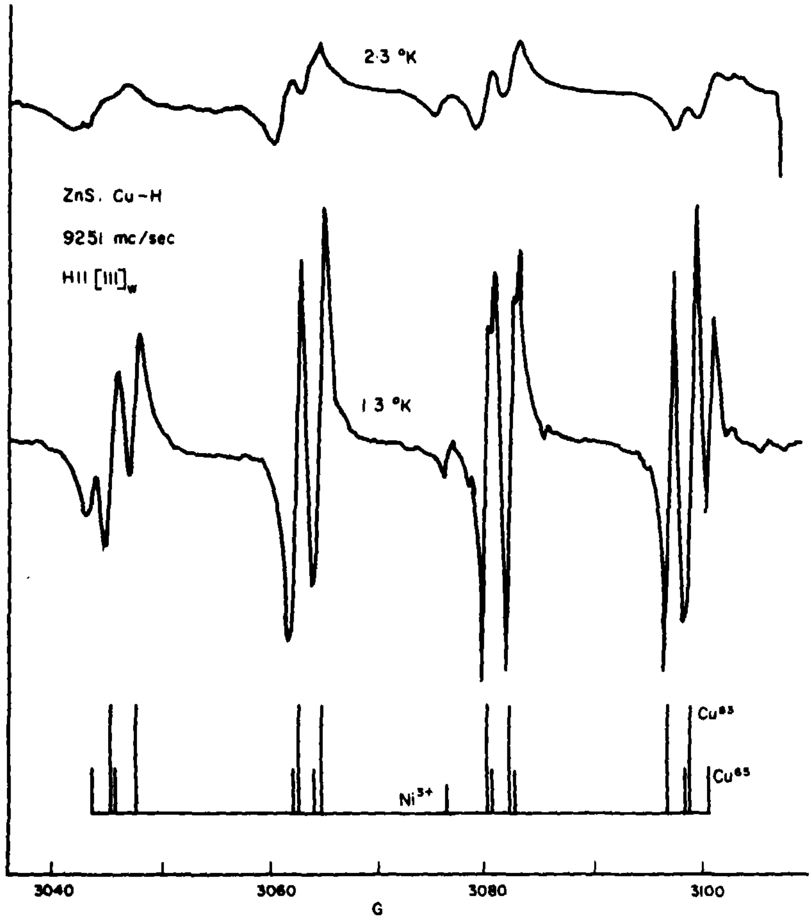

Fig. 1. EPR spectra of the Cu–H center at low temperatures. Only that portion of the spectrum near $g_{\parallel}$ is shown. The spectra of the centers having $g_{\parallel}$ along the remaining $\langle 111 \rangle$ directions not along **H** (these $\langle 111 \rangle$ axes are 70·5° to **H** for this orientation) consist of four broad non-descript lines similar to the corresponding lines of Cu–N (see Fig. 3).

the spectra on sample orientation in the magnetic field is obtained with the field in the $(1\bar{1}0)$ plane, by magnet rotation about a vertical axis. That portion of the spectrum near $g_{\parallel}$ is shown in Fig. 1. For this same orientation, i.e. $\langle 111\rangle_w \| H_0$ those centers having their symmetry axes along the $\langle 111\rangle$ crystal axes not parallel to H_0 are 70·5° to H_0; however, additional unknown spectra and broadening of the spectral lines obscure this spectral region. For this reason this region is not shown. In order to determine $g_{\perp}$ the orientation dependence of the spectrum is observed as a function of θ for $\theta = 0°$ to $\theta \simeq 50°$, where θ is the angle between the $\langle 111\rangle_W$ crystal axis and H_0 in the $(1\bar{1}0)$ plane; and a cosine law is assumed to extrapolate the results to $\theta = 90°$. As shown by the line drawing below the spectrum in Fig. 1, the Cu^{63} and Cu^{65} isotope hyperfine structure occurs in the proper intensity and splitting ratios, positively identifying the presence of copper. In addition, there is an unexplainable doubling of every line in the spectrum, which is even more evident in samples prepared using isotopically enriched Cu^{63}. This doubling occurs at all *orientations up to* $\theta \sim 30°$, *at which point the* breadth of the lines obscures any doubling which may exist. As the sample temperature is raised from 1·3 K the spectral lines first broaden, as shown in Fig. 1 for $T = 2{\cdot}3°K$, and then disappear. By 4·2°K the spectrum is no longer observable and does not reappear at any higher temperature. Another striking feature of the spectrum is the asymmetrical broadening of the lines. In the Cu–H case, where $g_{\perp} < g_{\parallel}$, the lowest field line of the entire spectrum is broadest. Quantitatively this asymmetric broadening is not explained by motional or mosaic effects, although qualitatively these effects produce the observed features[7].

The Cu–M spectrum, see Fig. 2, appears in two samples, which also show the Cu–H center. The starting crystals were halogen-free and the Cu metal was evaporated onto the crystal. In one case, in which the diffusion was done with $CuCl_2$ powder in the ampoule at 600°C for 48 hr, the Cu–M center is observed in the dark. When the diffusion was done in a sulphur atmosphere without $CuCl_2$, the Cu–M center is present in the dark, but increased in intensity under 365 nm illumination. Besides Cu–H in these samples, the latter also showed Cu–N. Like the Cu–H spectra, the Cu–M spectra also have the proper intensity and splitting ratios for the two copper isotopes. For crystal orientations other than those very close to $g_{\parallel}$, i.e. $\langle 111\rangle \| H_0$, the spectra rapidly broaden and disappear. For this reason no value is given for $g_{\perp}$ in Table 1, except that $g_{\perp} < g_{\parallel}$. The Cu–M center is only observed with the crystal at 1·3°K.

The Cu–N and Cu–O spectra, see Figs. 3 and 4, frequently appear in the same crystal. The preparation of these samples is as described for Cu–M, except that a halogen-transported starting crystal is used. In the Cu–N spectrum in Fig. 3, the parallel spectrum appears at the left side of the figure. The two isotopes of Cu are resolved and the spectrum is asymmetric but not doubled as Cu–H is. *Again the lowest field line is broadest. The* ratios of the intensities and of the hyperfine splittings for the parallel spectrum are in the ratio of the relative abundance and the magnetic moments of the naturally occurring copper. The right-hand part of the figure shows four broad lines corresponding to centers with their axes 70·5° from the magnetic field direction. At 4·2°K the spectrum has broadened beyond detection. The Cu–O spectrum in the region of $g_{\parallel}$ is shown in Fig. 4. The asymmetry in the width and intensity of the four copper hyperfine components is greater here than for any other copper center. The breadth of the lines in the region of $g_{\perp}$ prevent an accurate determination of $g_{\perp}$.

The Cu–L spectrum was observed in one halogen-free crystal on which Li has been evaporated and then fired in a sulfur atmosphere at 1100°C for 16 hr. The spectrum is shown in Fig. 5 for H_0 along the *c*-axis. The

Table 1. *Paramagnetic copper centers in* ZnS

Class	Center	Symmetry axis	g-factor(a)	Cu^{63} h.f.s. (10^{-4} cm^{-1})(a)	Photo-sensitive	References
III	Cu–H	⟨111⟩	2·1505(‖) 1·99(⊥)	17·3(‖) ~ 14(⊥)	Yes	(b)
I	Cu–M	⟨111⟩	2·30(‖) (⊥) < (‖)	46(‖)	Yes	(b)
I	Cu–N	⟨111⟩	2·3064 ± 8(‖) 1·845 ± 2(⊥)	124 ± 1(‖) ~0(⊥)	Yes	(b)
I	Cu–O	⟨111⟩	2·2743(‖) <2·0(⊥)	97·2(‖)	Yes	(b)
I	Cu–L	*C*	2·17(‖) (⊥) < (‖)	57·2(‖) (⊥) < (‖)	?	(b)
VI	Cu–IR	Cubic	0·71			(c)
IV	Cu–R	Monoclinic	$g_1 = 2{\cdot}002$ $g_2 = 2{\cdot}035$ $g_3 = 2{\cdot}027$	$A_1 \leqslant 0{\cdot}5$ $A_2 \leqslant 0{\cdot}5$ $A_3 = 1{\cdot}2$	Yes	(b)
II	Cu–S	⟨111⟩	2·0013(‖) 2·1290(⊥)	66·39(‖) 71·31(⊥)	No	(b)
V	$(Cu_{Zn}V_S)^0$	⟨111⟩	2·0061(‖) 2·0026(⊥)	~0·8	Yes	(d)
Fe–X	$(Fe_{Zn}Cu_{Zn})^0$	Monoclinic in cubic ZnS	$g_1 = 1{\cdot}26$ $g_2 < 0{\cdot}6$ $g_3 = 9{\cdot}66$		No	(e, f)
Fe–X	$(Fe_{Zn}Cu_{Zn})^0$	Monoclinic in cubic ZnS	$g_1 = 4{\cdot}35$ $g_2 = 4{\cdot}53$ $g_3 = 4{\cdot}06$		No	(e, f)
Fe–X	$(Fe_{Zn}Cu_{Zn})^0$	Monoclinic in hexagonal ZnS	$g_1 = 8{\cdot}03$ $g_2 = 3{\cdot}58$		No	(f)

(a) Reference [16].
(b) This work.
(c) Reference [4].
(d) Reference [15].
(e) Reference [17]. The spectra near $g = 4$ are more prominent with the sample ~77°K.
(f) Reference [9]. See reference [9] for orientation of symmetry axes.

entire spectrum is seen in this case, since the symmetry axis of the center is the c-axis of the hexagonal part of the crystal. Again, broadening of the lines away from $g_\parallel$ prevents a determination of $g_\perp$ except that $g_\perp < g_\parallel$. Note the opposite asymmetry in the hyperfine components, shown by the line drawing in the figure, to that observed in several other Cu centers. Two additional lines are present whose origin is not understood, although it is suspected these lines belong to the Cu–L spectrum.

All of our samples containing these Cu centers frequently show the EPR spectra of Mn^{2+}, Fe^{+}, Fe^{3+}, Cr^{+}[8] and Fe–Cu associates[9]. The Cu centers can be generated, or if already present in the dark, can be enhanced by illuminating the sample at low temperature with 365 nm light. Radiation at 580 nm can act as both a generator of Cu–H or can quench this center depending on sample preparation. Many of the samples are quite dark after firing, and absorption spectra have only been obtained for a few of them in which case the Cu infrared absorption at 1·44 μ is observed [10]. The Zeeman effect of this single line has been measured in pure cubic halogen-transported crystals[4] prepared by a Cu diffusion from an evaporated metal layer in a sulfur atmosphere at 530°C. In no sample is the paramagnetic resonance seen which corresponds to the same center, i.e. Cu($3d^9$) in T_d sym-

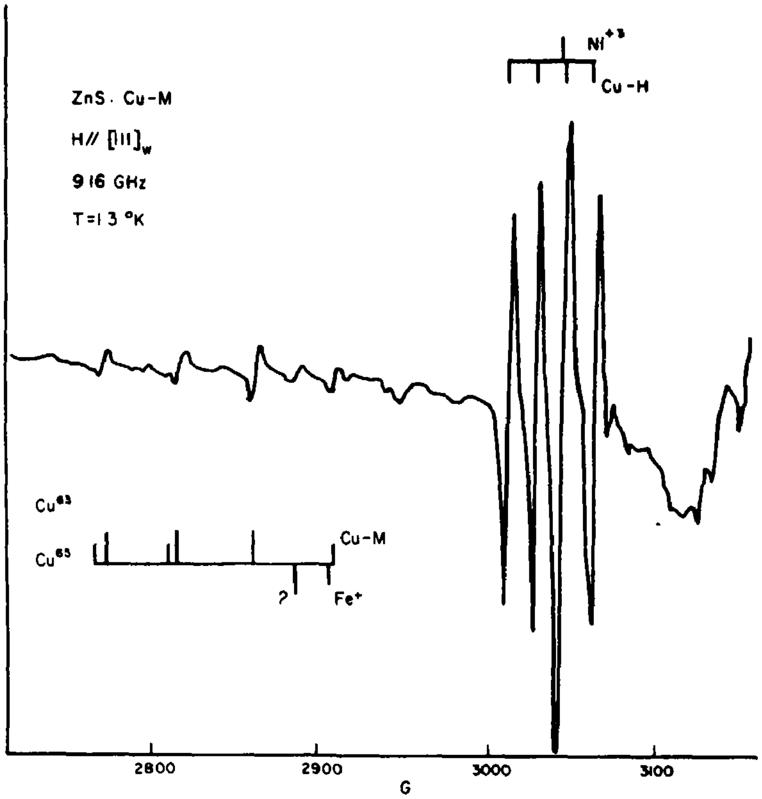

Fig. 2. EPR spectrum of the Cu-M center showing its relation to Cu-H. Again only the spectra in the region of $g_{\parallel}$ are shown.

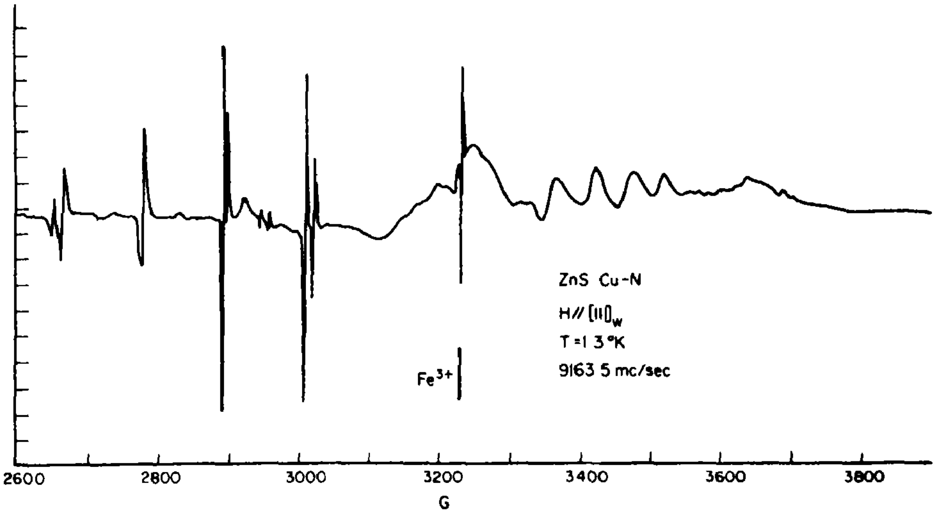

Fig. 3. EPR spectrum of the Cu-N center.

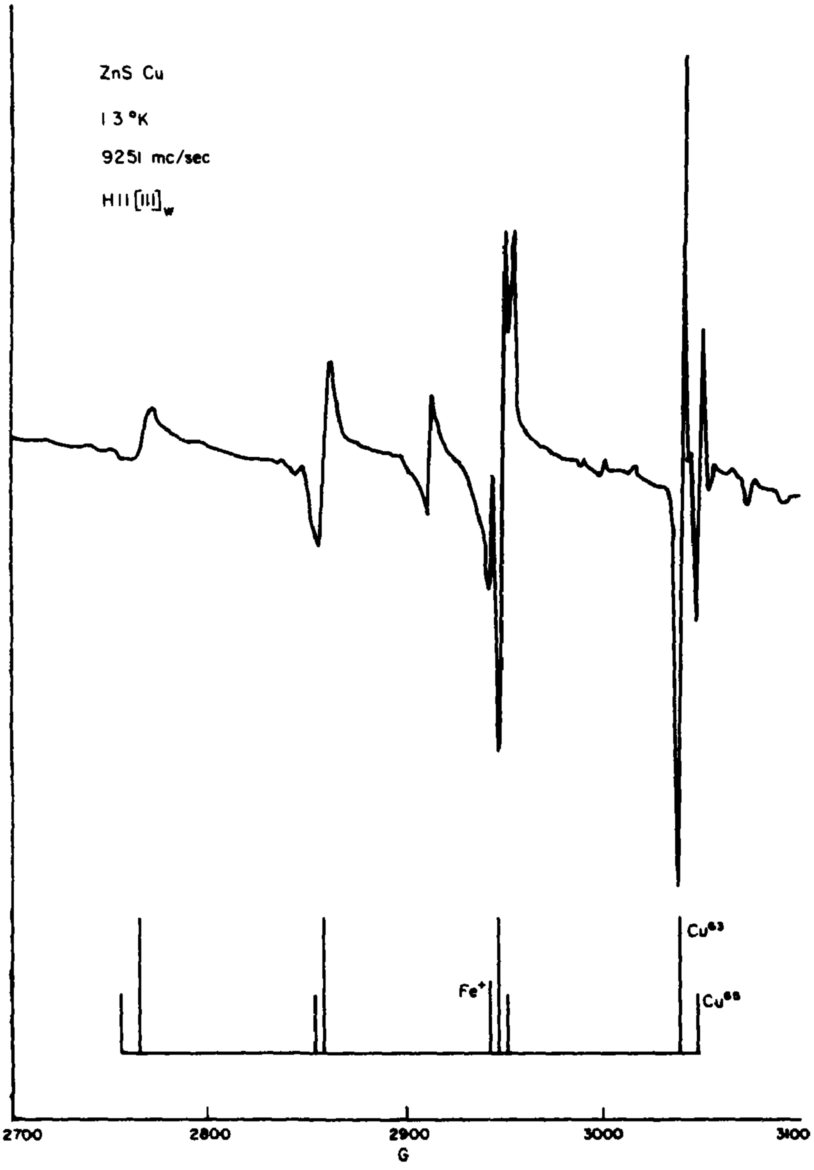

Fig. 4. EPR spectrum of the Cu–O center. The properties of this center are quite similar to those of Cu–N.

metry, as that producing the 1·4 μ absorption.

The samples all luminesce. The samples that show the Cu–H EPR spectrum, some of which also show Cu–N and Cu–M spectra, have a strong luminescence band at 2·65 eV with a half width of 0·25 eV. There is also a weak secondary band in the region 2·2–2·3 eV of comparable width. Two exceptions were found, one with a band at 2·35 eV and half width 0·4 eV and one with three bands at 2·0, 2·42 and 2·7 eV. On the other hand, the samples which do not show the Cu–H EPR spectrum and also do not show the Cu–M spectrum have two bands a strong one at 2·78 and 0·25 eV half width and a weaker one at 2·41 and 0·25 eV half width. Again there is an exception, one of the six samples has the same emission as the Cu–H samples. These results were obtained at 77°K with 365 nm excitation and a quartz prism analyzer with a cooled S-20 photomultiplier detector and have not been corrected for the nonlinear response of either the detector or the analyzing monochromator.

The Cu–R center has been seen in only one crystal which was neutron-irradiated, annealed, and the Cu^{65} isotope produced by radioactive decay of the activated Zn at room temperature over a period of months. Those crystals have the absorption spectrum near 1·4 μ[10]. The EPR spectrum is shown in Fig. 6, the upper spectrum was obtained with $\mathbf{H} \parallel [111]_W$ and the lower spectrum with **H** at 15° to $[111]_W$ in the $(1\bar{1}0)$ plane. Corresponding lines in the two spectra are marked in the figure. Perfect alignment of the crystal was not achieved, consequently the four-line hyperfine structure appears as five and seven line patterns. This results from centers made slightly nonequivalent, but which would have been equivalent if **H** were in the $(1\bar{1}0)$ plane. The anisotropic dependence of the spectra on crystal orientation in the magnetic field correspond to a center of monoclinic symmetry with a $(1\bar{1}0)$ symmetry plane. The four line hyperfine structure resulting from Cu^{65} indicates the presence of copper. Although not likely, a Ga impurity center is possible since naturally occurring Ga has two isotopes with $I = \frac{3}{2}$ and one Ga isotope is also formed by radioactive decay of zinc following neutron capture. Unfortunately, sufficient resolution is not obtained completely to eliminate this possibility. The Cu–S spectrum has been observed in a crystal, kindly supplied by Professor S. Shionoya, which exhibits the Cu-red luminescence[11]. This crystal was grown from the luminescent powder at high pressure. The complete EPR spectra are shown in Fig. 7 with $\mathbf{H} \parallel \langle 111 \rangle_W$ upper spectrum, and $\mathbf{H}_\perp \langle 111 \rangle_W$ in a $(1\bar{1}0)$ plane, lower spectrum. Hyperfine quartets, which display resolved Cu^{63} and Cu^{65} hyperfine splitting, are delineated by the line drawings. The spectral shapes are distorted by passage effects. The angular variation of the spectra are shown in Fig. 8. The ZnS crystal was rotationally twinned about the $\langle 111 \rangle_W$ axis, the orientation of the magnetic field being measured from $\langle 111 \rangle_W$ in a $(1\bar{1}0)$ plane common to both twins. The angular dependence is characteristic of a center with C_{3V} symmetry having a $\langle 111 \rangle$ symmetry axis for both the *g*-tensor and the hyperfine tensor. The quadrupole splitting of the Cu^{63} is determined to be, $Q_{Cu^{63}} = 8 \cdot 31 \times 10^{-4}\ \mathrm{cm}^{-1}$.

3. RESULTS

The results are summarized in three tables which contain a list of all paramagnetic centers involving copper observed in the II–VI semiconducting compounds, as well as some closely related centers involving other impurities. More than one of these centers are often observed in the same crystal, as are other unrelated centers. To observe most of the listed centers it is necessary to irradiate the crystal at low temperatures with light of the proper wavelength. There may be other defects present, some of which involve copper, but which are not observed by EPR for various reasons. Thus it is quite possible that a given luminescence process is associated with a defect unobserved by EPR or involves

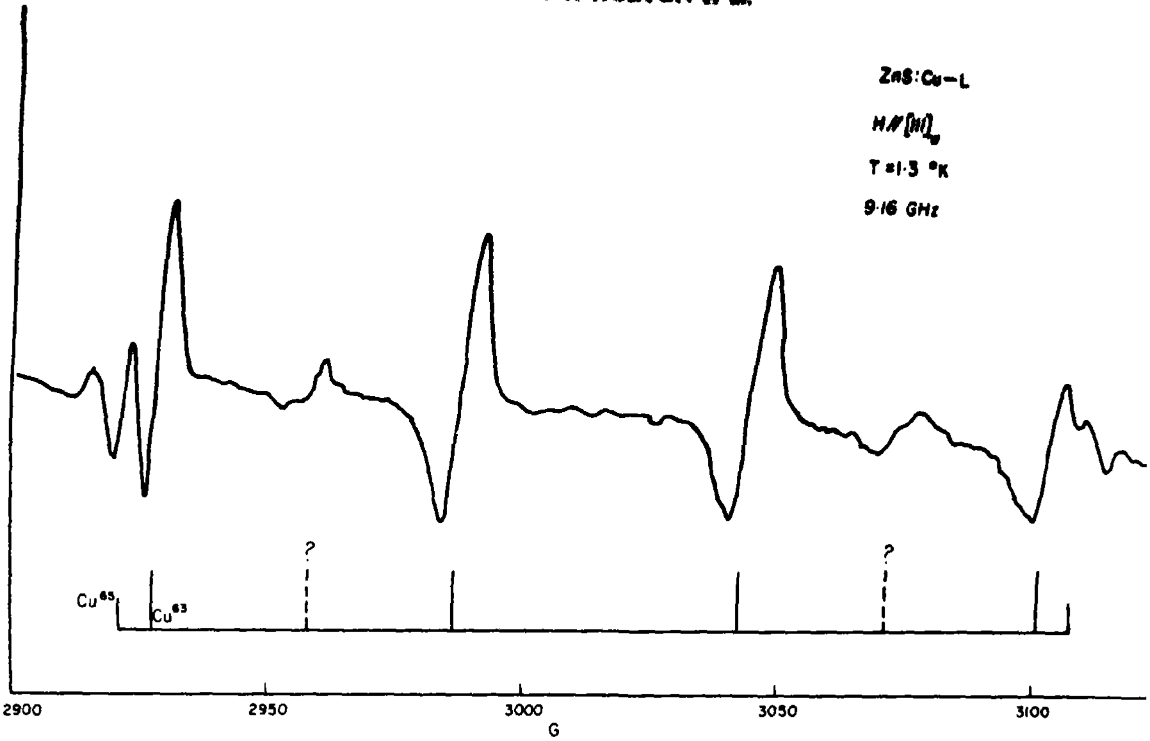

Fig. 5. EPR spectrum of the Cu–L center.

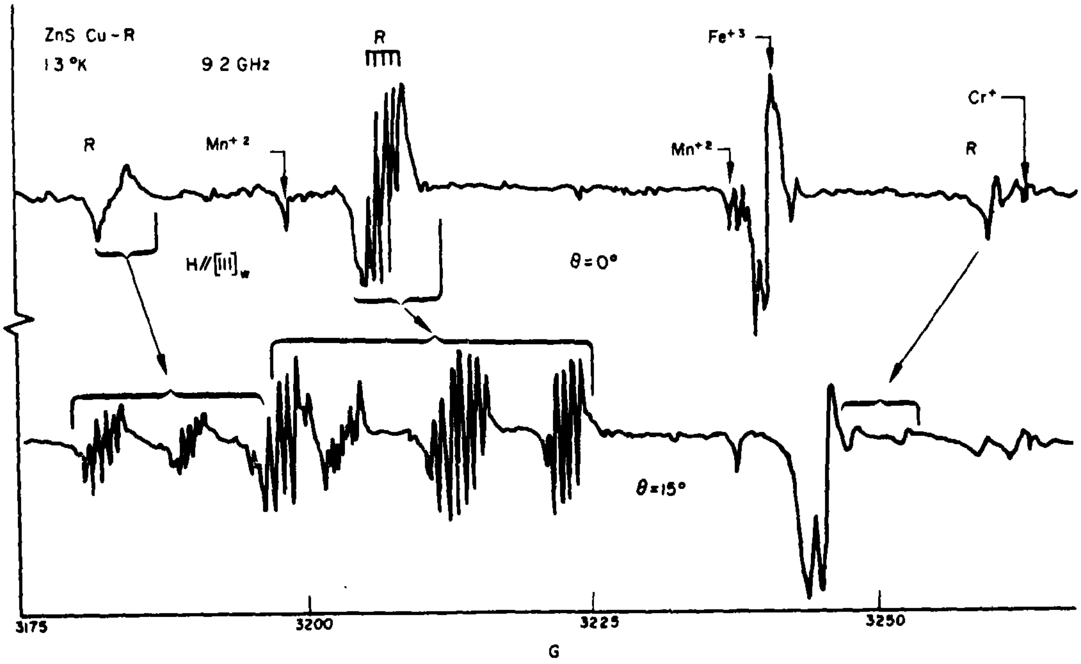

Fig. 6. EPR spectra of the monoclinic Cu–R center (see text for explaination).

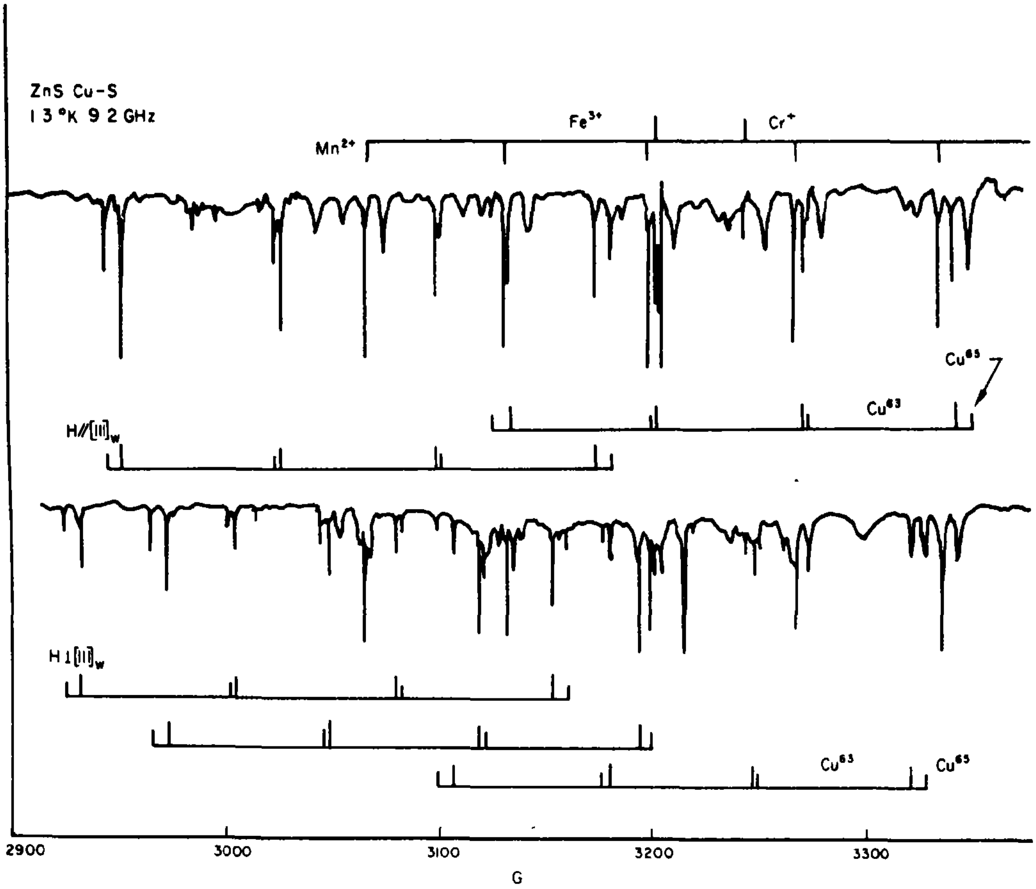

Fig. 7. EPR spectra of the Cu–S center.

primarily a diamagnetic charge state of an observed center.

Table 1 lists the ten copper centers in zinc sulfide which have been observed by EPR and one observed only by optical absorption and emission. Two of these centers are nearest associates of substitional Cu^{+} and Fe^{3+}, are iron-like in their properties and probably play no role in luminescence. These and other associates with iron have been discussed previously[9] but are included here for purposes of comparison. The general features of Table 1 are:

(1) All but one of the copper centers in zinc sulfide have g factors near $g = 2$, the free spin value.

(2) No center having cubic symmetry has been observed in EPR; one has been identified by an optical Zeeman experiment.

(3) The majority of noncubic centers have a ⟨111⟩ symmetry axis. Fe–Cu associates and Cu–R, which are monoclinic, are the only exceptions.

(4) The majority are photosensitive, Cu–S and Fe–Cu associates being the only exceptions.

(5) No EPR spectrum can definitely be

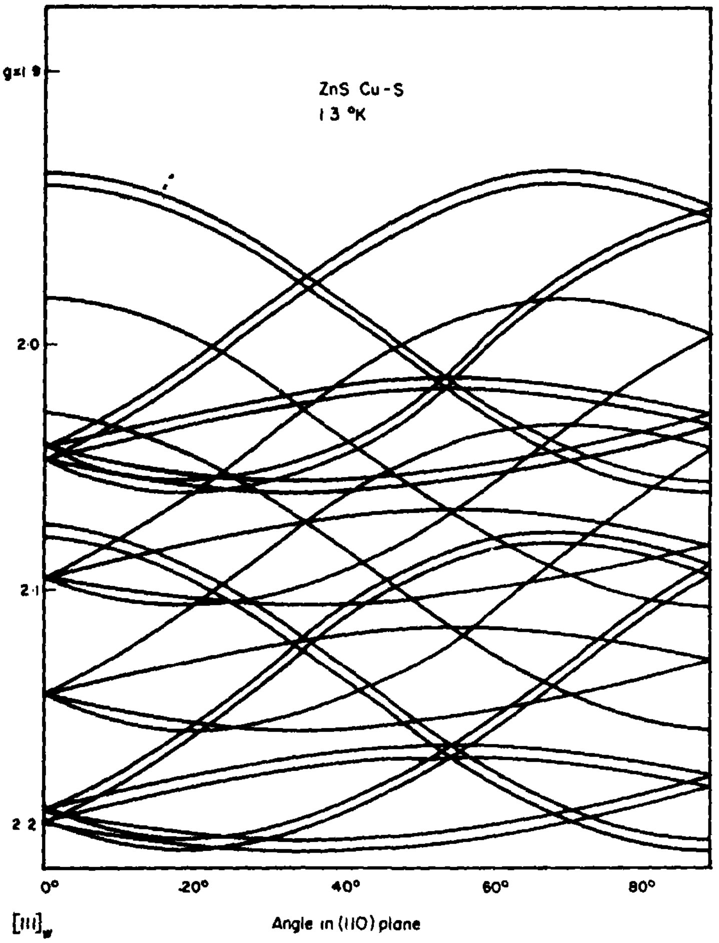

Fig. 8. The 9·14 GHz angular variation of the Cu–S spectrum.

> explained with the usual crystal field theory of Cu($3d^9$) in nearly octahedral or tetrahedral environments.

The nine centers, excluding the iron-copper associates, have been empirically grouped into six classes [3] in order to simplify comparisons and discussions. Each class, indicated by the first column of each Table, contains centers having rather similar characteristics. Each class may consist of isomorphic or fairly similar imperfections. Classes I and II have fairly large copper hyperfine interactions and therefore most likely correspond to centers with the spin localized primarily on the copper impurity. These values are all smaller than the calculated one for Cu($3d^9$) in T_d symmetry which is 500×10^{-4} cm^{-1} when the free ion values for the parameters are used. Classes IV and V correspond to very small copper hyperfine interactions and hence the spin is probably not localized on the copper. Class III is intermediate between the two extremes and might correspond to the spin on the copper or nearby, but with a fairly strong interaction. The iron-copper associates, for which the copper is at a second nearest-neighbor site from the iron where the spin is primarily localized, have a copper hyperfine interaction[9] between that of Class III and Class IV or V. Other features of the classification include the following:

(1) Class IV is the only one with lower than C_{3v} symmetry. It has C_s symmetry.
(2) Classes II and IV are the only ones with $g_{\parallel} < g_{\perp}$ and $A < B$ (Class IV is considered approximately axial for purposes of this comparison).
(3) Class II is the only one to have shown no photosensitivity.
(4) In Class III the EPR lines have additional structure.
(5) For Classes I and III the line intensities are asymmetric, the spectra are poor in the perpendicular direction and seem to be quickly broadened as the temperature is raised above 1·3°K.
(6) Class VI, see Table 2, has drastically modified g factors.

Table 2 shows the results for copper centers in other II–VI compounds. A full discussion of these centers appears in the cited references. Table 3 gives the results for other impurities which are thought to produce centers isomorphic with the copper centers. A seventh class is now utilized to include those centers having $g_{\parallel}$ near 4.

4. DISCUSSION

The theoretical considerations which are potentially relevant to this problem are complex. Most of the physically reasonable simple models for copper centers which have the spin localized primarily on the copper, involve the copper possessing a $3d^9$ configuration, i.e. one hole in an otherwise complete $3d$ shell. The d orbitals in a cubic or nearly cubic environment will split into a doubly degenerate e state, and a triply degenerate t_2 state. For substitutional copper, coordinated with a tetrahedron of anions, the t_2 level is higher and will lack one electron of being completely filled. This leads to a three-fold orbital degeneracy and a two-fold spin degeneracy in cubic symmetry. This degeneracy can be reduced either by lowering the symmetry or by the spin-orbit interaction (which is large in

Table 2. Paramagnetic copper centers in other II–VI *compounds*

Class	Crystal	Center	Symmetry axis	g-factor(a)	Cu^{63} h.f.s. (10^{-4} cm^{-1})(a)	Reference
I	CdS	Cu–A	C	2·240 ± 5(∥) 1·75(⊥)	99 ± 5(∥) 28(⊥)(c)	(b)
II	CdS	Cu–B	C	1·93(∥) 2·14(⊥)	21(∥)	(b)
VI	BeO	Cu	C	1·712(∥) 2·378(⊥)	52·4(∥) 108(⊥)	(d)
VI	ZnO	Cu	C	0·7383(∥) 1·5237(⊥)	198 ± 3(∥) 224 ± 1(⊥)	(e)
Fe–X	ZnSe	Fe–Cu		$g_1 = 2·99$ $g_2 = 8·29$ $g_3 = 1·52$		(f)
Fe–X	ZnTe	Fe–Cu		$g_1 = 5·30$ $g_2 = 7·29$ $g_3 = 2·02$		(f)

(a) Reference [16].
(b) Reference [18].
(c) This work, this number is tentative since the complete spectrum was not obtained.
(d) de WIT M. and REINBERG A. R., *Phys. Rev.* **163**, 261 (1967).
(e) de WIT M. and ESTLE T. L., *Bull. Am. Phys. Soc.* **8**, 24 (1963) and reference [13].
(f) Reference [9]. Also see reference [9] for orientation of center symmetry axes.

Table 3. *Related paramagnetic centers in* II–VI *compounds*

Class	Crystal	Center	Symmetry	g-factor[a]	Impurity h.f.s. (10^{-4} cm^{-1})[a]	Reference
V	ZnS	$(\mathrm{Ag_{Zn}V_S})^0$	⟨111⟩	2·0072(‖) 2·0024(⊥)	 0·1(⊥)	[b]
V	ZnS	$(\mathrm{Au_{Zn}V_S})^0$				[b]
VI	ZnS	Ni$^+$	Cubic	1·40	80 ± 4	[c]
VI	CdS	Ag–A	*C*	1·226(‖) 1·509(⊥)		[d]
VII	ZnS	Ni–E	⟨111⟩	4·185(‖) 0·0(⊥)	203 ± 5(‖) 0 ± 20(⊥)	[c]
VII	ZnS(hex)	Ni–D	⟨111⟩ ≠*c*-axis	4·000(‖) 1·172(⊥)	182 ± 2(‖) 0 ± 12(⊥)	[c]
Fe–X	ZnS	$(\mathrm{Fe_{Zn}Ag_{Zn}})^0$	Monoclinic	$g_1 = 3{\cdot}99$ $g_2 = 7{\cdot}48$ $g_3 < 1{\cdot}7$		[e,f]
Fe–X	ZnS	$(\mathrm{Fe_{Zn}Ag_{Zn}})^0$	Monoclinic	$g_1 = 2{\cdot}27$ $g_2 = 1{\cdot}33$ $g_3 = 5{\cdot}85$		[e,f]

[a] Reference[16].
[b] Reference[15].
[c] Reference[14].
[d] Reference[18]
[e] Reference[17]
[f] Reference[9].

Cu^{2+}). Lower symmetry can arise from defect association or the Jahn–Teller effect[12]. Even for certain defect associates further energy reduction may occur via the Jahn–Teller effect. Finally the states resulting from the Jahn–Teller effect may interact strongly, leading to a dynamic Jahn–Teller effect, or they may interact weakly, yielding the static Jahn–Teller effect[12]. If the copper is interstitial at the appropriate interstice, it will be octahedrally coordinated. The role of the e and t_2 orbitals may be exchanged. Similar considerations then follow as in the previous case of e lower. All of these possibilities, plus those for a spin external to the copper, must be examined for all plausible models and compared to the observed spectra.

In spite of the theoretical and experimental complexities, some conclusions can be drawn, and some rather plausible explanations can be suggested. The first explanation concerns the case of isolated substitutional Cu^{2+}. Isolated copper in zinc oxide has been identified[13]. The characteristic EPR spectrum observed is interpreted with the help of optical absorption data. The isolated Cu interpretation is given strong experimental support by the observation of a nickel center in zinc sulfide[14] with a similar characteristically small g factor which, however, is isotropic. The latter is attributed to isolated nickel substituting for zinc with a single net negative charge, i.e. a Ni$^+$ ion. The theoretical treatment of Dietz *et al.*[13] attributes the small g factors to a reduction of the orbital contribution to the magnetic moment. The orbital reduction occurs because covalency effects reduce the wave function density on the copper. One might, therefore, expect to observe one isotropic spectrum and possibly some anisotropic spectra in copper-doped zinc sulfide arising from the presence of Cu^{2+} isolated or associated and all having characteristically small g factors. No such paramagnetic resonance spectra have yet been observed. However, the copper infrared spectrum has been interpreted by Broser *et al.*[10] as caused by substitutional Cu^{2+}. Recently the g factor of this absorption has been measured in an optical Zeeman experiment and is also found to be small[14]. The reason for the absence of an EPR spectrum in these same samples is not understood. The interpretation of the Class VI centers in terms of the crystal field model and covalency effects is not too satisfying. Large reductions of the orbital part of the magnetic moment are needed to explain the EPR data and as a consequence of using covalency effects to obtain these reductions, a large delocalization of the Cu $3d$ electrons is implied. A physically more plausible interpretation may be possible with the dynamic Jahn–Teller effect which also gives rise to large reduction factors but not to delocalization of the electron density onto the ligands [12].

It is possible to adjust the parameters characterizing the delocalization and the axial crystalline field so as to obtain a rough fit to the g factors of most of the observed EPR spectra, but the h.f.s. is difficult to fit. One way this may be done is by assuming a very strong axial field which splits an orbital singlet level below the orbital doublet, such as could occur for Cu^{2+} associated with other defects or impurities. However, the associated imperfection would have to be negatively charged to cause the singlet to be lowest, which would require the copper to be donor-like with respect to these associates. This does not seem to be a particularly attractive feature. The observed g factors are all fairly nondescript, being close to the value 2·0023 for a free electron spin. Hence, there is nothing which would lead one to believe that the Cu^{2+} delocalization theory could explain the bulk of the results. If a dynamic Jahn–Teller effect is involved in addition to association with donor impurities, it might be possible to explain the majority of the centers. No detailed calculations of this sort have yet been made.

The Cu–R center of Class IV which was observed after neutron irradiation, is one of only two centers for which it definitely appears that the spin is not on the copper. The most striking characteristic of the Cu–R spectrum is its great similarity, both qualitatively and quantitatively, to the spectra observed for the paramagnetic charge state of the self-activated luminescence centers[2]. Thus the most tempting model to postulate is the one in Fig. 9. This model is isomorphic with the paramagnetic charge state of the group III self-activated luminescence centers, i.e. a Cu^{3+} ion at the nearest zinc site to a zinc vacancy with a hole trapped on the sulfur ion adjacent to the vacancy but as far from the Cu^{3+} as possible.

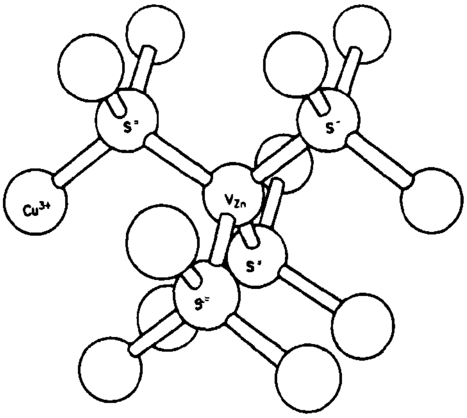

Fig. 9. Possible model of the defect producing the Cu–R spectrum. This center is isomorphic with the paramagnetic charge state of the group III self-activated luminescence center. The hole is trapped on the sulfur adjacent to the zinc vacancy which is farthest from the Cu^{3+}.

There are two other distinctive copper centers in zinc sulfide, Cu–S of Class II and the center in Class V observed by Dieleman *et al.*[15] both of which have been seen in samples showing the copper-red luminescence. Dieleman *et al.*[15] made their observations on copper-red luminescent powders and, at least for the analogous silver center, in single crystals as well. By a careful combination of optical and EPR experiments they obtained strong evidence that the observed defect was responsible for the copper-red luminescence. They identify the defect as

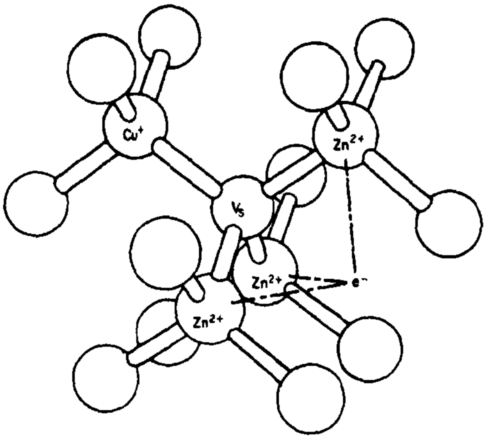

Fig. 10. The probable model for the center observed by Dieleman *et al.* (see reference [15]) which causes the copper-red luminescence. This center is the antimorph of the self activated luminescence center. The extra electron most likely occupies an orbital localized primarily on the three zincs adjacent to the sulfur vacancy.

$(Cu_{Zn}V_S)^0$, shown in Fig. 10 with the extra electron quite probably primarily on the three zinc sites nearest the vacancy. This is the antimorph of the self-activated luminescence center but an unexpectedly small Zn hyperfine structure is observed.

In an examination of a ZnS crystal supplied by Professor S. Shionoya which is doped with copper and aluminum and which shows the copper-green luminescence[19], no copper EPR signals were observed, although a strong photosensitive EPR signal from the aluminum self-activated luminescence center[2] was present.

We have presented the accumulated experimental information on copper electron paramagnetic resonance in zinc sulfide together with some other pertinent data, a rough classification, and a few speculative comments. It is quite apparent that further research is necessary before achieving an understanding of this problem.

Acknowledgements—We wish to acknowledge Drs. A. Räuber and A. R. Reinberg for stimulating discussions during the course of this research, and Dr. Räuber and Mr. Stinedurf for the preparation of many of the samples. We thank Professor S. Shionoya for this interest in our research and for giving us two samples on which he had made luminescence measurements.

REFERENCES

1. For an excellent review see *Physics and Chemistry of II-VI Compounds* (Edited by M. Aven and J. S. Prener), Chap. 4 by S. Shionoya. Wiley, New York (1966).
2. SCHNEIDER J., *II-VI Semiconducting Compounds, 1967 International Conference* (Edited by D. G. Thomas), p. 40, and references therein. Benjamin, New York (1967).
3. A preliminary report of this research was presented at the *International Conference on Luminescence, Budapest, Hungary, 1966.* Proceedings to be published; HOLTON W. C., de WIT M., ESTLE T. L., SCHNEIDER J. and DISCHLER B., *Bull Am. Phys. Soc.* **10**, 330 (1965).
4. de WIT M., *Bull Am. Phys. Soc.* **13**, 405 (1968); *Phys. Rev.* In press (1969).
5. *Physics and Chemistry of II-VI Compounds* (Edited by M. Aven and J. S. Prener), Chap. 2 by M. R. Lorenz and references therein. Wiley, New York (1967).
6. APPLE E. F. and PRENER J. S., *J. Phys. Chem. Solids* **13**, 81 (1960).
7. McCONNELL H. M., *J. chem. Phys.* **25**, 709 (1956).
8. *Physics and Chemistry of II-VI Compounds* (Edited by M. Aven and J. S. Prener), Chap. 6 by R. S. Title. Wiley, New York (1967).
9. HOLTON W. C., de WIT M., ESTLE T. L., DISCHLER B. and SCHNEIDER J., *Phys. Rev.* **169**, 359 (1968).
10. BROSER I. and MAIER H., *Proc. Int. Conf. Physics of Semiconductors, Kyoto, 1966* In *J. phys. Soc. Japan* **21** supp. 254 (1966); BROSER I., MAIER H. and SCHULZ H. J., *Phys. Rev.* **140**, A2135 (1965).
11. SHIONOYA S., URABE K., KODA T., ERA K. and FUJIWARA H., *J. Phys. Chem. Solids* **27**, 865 (1966).
12. HAM F. S., *Phys. Rev.* **138**, A1727 (1965).
13. DIETZ R. E., KAMIMURA H., STURGE M. D. and YARIV A., *Phys. Rev.* **132**, 1559 (1963).
14. de WIT M., ESTLE T. L., HOLTON W. C. and SCHNEIDER J., *Bull. Am. Phys. Soc.* **9**, 249 (1964); WATTS R. K., de WIT M., HOLTON W. C., To be published.
15. DIELEMAN J., deBRUIN S. H., Van DOORN C. Z. and HAANSTRA J. H., *Philips Res Rep.* **19**, 311 (1964).
16. The g factors are designated (‖) or (⊥) meaning the value of $(h\nu/\beta H)$ along or perpendicular to the symmetry axis, where ν is the microwave frequency (in this case ≈ 10 GHz), H is the magnetic field of the average of the hyperfine pattern, and h and β have the usual meaning. The hyperfine structure (‖) or

(⊥) is measured along the respective symmetry directions.

17. Both the ground state and first excited state of this center have been observed. The ground state *g* factors are given first and the excited state values in the following table entry.

18. MORIGAKI K., *II-VI Semiconducting Compounds, 1967 International Conference* (Edited by D. G. Thomas) p. 1348. Benjamin, New York (1967).
19. SHIONOYA S., KOBAYASHI Y. and KODA T., *J. phys. Soc. Japan* **20**, 2046 (1965).

J. Phys. Chem. Solids Pergamon Press 1969. Vol. 30, pp. 979–991. Printed in Great Britain.

TRANSIENT PROCESSES IN SPIN-WAVE SYSTEMS WITH MAGNETIC DIPOLE RADIATION – I. THEORY*†

H. LE GALL
Laboratoire du Magnétisme et de Physique du Solide, C.N.R.S., 92, Bellevue, France
and
B. DESORMIÈRE and E. MILOT
C.F.T.H., B.P. 10, 92, Bagneux, France

(*Received* 19 *July* 1967; *in revised form* 8 *August* 1968)

Abstract – The transient evolution of the spin-wave populations is studied in detail under perpendicular pumping, in the linear case and in the non-linear case with three-magnon processes. Calculations are derived taking into account of the variation with time of the dipolar radiation of the uniform magnons which produce reverse magnon → photon transitions. We define the transient growth of the uniform and parametric states on the second quantization basis of the ferromagnetic system, and the electromagnetic field, in the case where coincidence condition is satisfied. From the expressions of the field radiation and the transient power absorbed by the ferromagnetic crystal, we discuss the validity of the theory, showing the importance of the dipolar radiation of the uniform magnons.

1. INTRODUCTION

A SYSTEM OF spin-waves has an anharmonic evolution when the number of quasi-particles called magnons becomes important. This has been first experimentally realized by Damon[1] and Bloembergen and Wang[2] exciting the uniform mode under perpendicular pumping at high power level. From the theoretical analysis of Akhiezer[3] which shows that the dipolar energy of the ferromagnetic crystals can induce interactions between spin-waves, Suhl has explained the non-linear behaviour of the uniform resonance; this author attributes the origin of the subsidiary resonance and the saturation of the main resonance respectively to the three-magnon and four-magnon transitions[4]. The investigation of Suhl has been restricted to the stationary state.

In the present paper, we study the transient growth of the uniform and parametric magnons after an electromagnetic pulse is applied to a ferromagnetic crystal with perpendicular pumping. The calculations are derived on the second quantization of the ferromagnetic system and the electromagnetic field in the linear and non-linear cases. The non-linear case concerns only the first-order processes assuming that the condition of coincidence is satisfied (three-magnon non-linear processes at resonance). In the present theory, we have introduced the dipolar radiation which becomes important for crystals having large filling factor and low relaxation rate like YiG and lithium ferrite. We show that the dipolar radiation induces reverse magnon → photon processes with transition probabilities so high in some cases that the crystal becomes a mirror for the incident electromagnetic field: all the photons absorbed by the magnons are re-radiated. In what follows we have analyzed the transient evolution of uniform and parametric magnons as a function of the dipolar radiation rate in the linear and non-linear cases.

The paper is divided into six sections. Section 2 is devoted to the determination of the effective photon–magnon Hamiltonian which includes the magnetic dipolar radiation

---

*A detailed comparison of experimental data with the present theory will be published in a further paper, henceforth referred to as II.

†This work was supported in part by the Direction des Recherches et Moyens d'Essais, Paris.

of the magnons. For this, the expression of the electromagnetic field radiated by the magnetic system is derived for a spherical sample placed in a non-resonant wave-guide structure.

In Section 3, the Hamiltonian which induces the magnon–magnon transitions is defined with the second quantization method of Holstein and Primakoff[5].

The general theory of the three-magnon non-linear excitation is stated in Section 4. For this, the evolution of the creation and annihilation operators in the Heisenberg representation is first defined for the uniform and parametric magnons in the linear and non-linear cases. This method is similar to the one carried out recently by Savchenko and Tarasenko[6]. These authors have treated the general case of non-linear excitation of quasti-particles, studying the evolution of the non-equilibrium density matrix of the magnetic system. This work is concerned mainly with the determination of the stationary amplitude of the parametric excitations. Then, in order to experimentally verify this theoretical data, we derive the expression of the transient power absorbed and radiated by the ferromagnetic crystal.

In the Section 5, we analyze the influence of the magnetic dipolar radiation on the non-linear critical threshold of the parametric spin-waves and on the linear and non-linear evolution of the magnon system.

Finally, Section 6 is concerned with a summary and conclusions.

2. EFFECTIVE PHOTON–MAGNON HAMILTONIAN

We consider a ferromagnetic insulator where all the magnetic moments are defined by the spin of the electrons which are localized at each unit cell of the lattice. The magnetic dipolar interaction between the electromagnetic field and the spins is given by:

$$\begin{aligned} H_{m-p} &= -g\mu_B \sum_i \boldsymbol{h}(\mathbf{r}_i)\mathbf{S}_i \\ &= -\tfrac{1}{2}g\mu_B \sum_i (h_i^+S_i^- + h_i^-S_i^+) \end{aligned} \qquad (1)$$

where g, μ_B, $\boldsymbol{h}$ and S_i are respectively the Landé factor, the Bohr magneton, the magnetic field operator and the spin operator at the position r_i. The summation runs over all the unit cells i of the crystal.

In the second quantization notation[7], the electromagnetic field components are defined from the vector potential $A(\mathbf{r}, t)$:

$$\mathbf{A}(\mathbf{r}, t) = \sum_q \left(\frac{2\pi\hbar\omega_q}{V_1 k_q^2}\right)^{1/2} \mathbf{e}_q \left[q\mathrm{e}^{-i(\mathbf{k}_q\mathbf{r}-\omega t)} - q^+\mathrm{e}^{i(\mathbf{k}_q\mathbf{r}-\omega t)}\right] \qquad (2)$$

by:

$$\begin{aligned} \mathbf{e}(\mathbf{r}, t) &= -c^{-1}\,\mathrm{d}\mathbf{A}(\mathbf{r}, t)/dt \\ \mathbf{h}(\mathbf{r}, t) &= \mathbf{curl.\,A} \end{aligned} \qquad (3)$$

where $2\pi\hbar$ is the Planck constant, c is the light velocity and V_1 is the volume which determines, for n_q incident photons, an electromagnetic energy density $n_q\hbar\omega_q/V_1$. $\mathbf{k}_q(|\mathbf{k}_q| = \omega_q/c)$ and $\mathbf{e}_q$ are the propagation and polarization vectors of the radiation and q^+ and q are the creation and annihilation operators for the photons. The only non-vanishing matrix elements of these operators are:

$$\begin{aligned} \langle n_q+1|q^+|n_q\rangle &= (n_q+1)^{1/2}\,\mathrm{e}^{-i\omega_q t} \\ \langle n_q-1|q|n_q\rangle &= (n_q)^{1/2}\,\mathrm{e}^{i\omega_q t} \\ \langle n_q|q^+q|n_q\rangle &= n_q. \end{aligned} \qquad (4)$$

Assuming that the radiation is monochromatic ($\omega_q \equiv \omega$) and polarized along the oz direction, and is propagating along the oy direction, the magnetic field operator becomes:

$$\mathbf{h}_x = (\mathbf{q}_0 \times \mathbf{e}_q)(h^+\,\mathrm{e}^{i\omega_q t} + h^-\,\mathrm{e}^{-i\omega_q t}) \qquad (5)$$

with:

$$\left.\begin{aligned} h^+ &= i\left(\frac{2\pi\hbar\omega_q}{V_1}\right)^{1/2} q\,\mathrm{e}^{-ik_q y} \\ h^- &= -i\left(\frac{2\pi\hbar\omega_q}{V_1}\right)^{1/2} q^+\,\mathrm{e}^{ik_q y} \\ q_0 &= q/|q|. \end{aligned}\right\} \qquad (6)$$

Under perpendicular pumping, the spin-photon interaction is a linear process and the photon–magnon Hamiltonian[1] is defined from the spin operators related to the magnon operators by the following harmonic transformations[5]:

$$\left.\begin{aligned} S_i^+ &= S_i^x + iS_i^y = (2S/N)^{1/2} \sum_k a_{\mathbf{k}} e^{i\mathbf{k}\mathbf{r}_i} \\ S_i^- &= S_i^x - iS_i^y = (2S/N)^{1/2} \sum_k a_{\mathbf{k}}^+ e^{-i\mathbf{k}\mathbf{r}_i} \end{aligned}\right\} \quad (7)$$

where $a_{\mathbf{k}}^+$ and $a_{\mathbf{k}}$ are the magnon creation and annihilation operators which must satisfy:

$$[a_{\mathbf{k}}(t), a_{\mathbf{k}'}^+(t)] = \Delta(\mathbf{k}-\mathbf{k}').$$

S is the magnitude of the spin vector, and N is the number of unit cells in the crystal of volume V. The spin-waves are characterized with their propagation vector $\mathbf{k}$ which takes one of the N values evenly spaced in the Brillouin zone.

$$H_{m-p} = -\tfrac{1}{2} g \mu_B (2NS)^{1/2} \Big(h^+ \sum_k a_{\mathbf{k}}^+ \sum_i e^{-i\mathbf{k}\mathbf{r}_i} + \text{herm. conj.}\Big) \quad (8)$$

or:

$$H_{m-p} = -iA(qa_0^+ - q^+ a_0) \quad (9)$$

with:

$$A = q\mu_B (2\pi\hbar\omega NS/2V_1)^{1/2} \quad (10)$$

The expression (9), which defines the spin-photon coupling, is incorrect in most of real cases for two reasons: first, it does not include the microwave structure which contains the crystal, and second, it neglects the dipolar radiation of the uniform magnons. Indeed, as supported by experiments, this radiation, which produces reverse magnon → photon transitions and so decreases the effective number of photons absorbed by the sample, becomes very large when the magnetization $\mathbf{M}_0$ is high and when the relaxation rate η_0 of the uniform mode is low.

Hence, we have to consider this phenomenon in the ultra-pure single-crystals as Yttrium Iron Garnet (YIG), lithium ferrite or cal Van Big, where the line width is about or less than 1 Oe.

Determination of the radiated field

Accurate experiments on transient processes in ferromagnetic samples are now easy to perform using microwave square wave pulses with rise time less than ten nanoseconds produced by a diode modulator. In order to avoid the rise time of the microwaves cavities ($\tau \sim 0{\cdot}5\,\mu$sec) which can perturb measurements, we take a non-resonant structure, putting the sample at the center of a wave-guide at a distance l from an adjustable short-circuit. We shall derive the expression of the magnetic field radiated by the crystal from the study of L. K. Anderson[8] who has applied the theory of discontinuities in wave guides, made by N. Marcuvitz and J. Schwinger[9], to the case of a ferromagnetic sample. With this theory, assuming excited only a propagation mode, the magnetic field $\mathbf{H}$ of a progressive wave is written as:

$$\mathbf{H} = I\mathbf{V}_p \quad (11)$$

where I is similar to a current and characterizes the maximal amplitude of the wave and its variation along the direction of propagation (oy direction in our case). $\mathbf{V}_p$ is the eigenvector of the mode and describes the magnetic field distribution in a transverse plane of the guide. Assuming only the TE_{10} mode is excited here (see Fig. 1 for definition of axis), we have:

$$I = \left(\frac{ab}{2}\right)^{1/2} h_0 e^{i(\omega t - k_g y)} \quad (12)$$

$$\begin{aligned} V_{px} &= \left(\frac{2}{ab}\right)^{1/2} \sin(\pi x/a), \\ V_{py} &= -i\left(\frac{2}{ab}\right)^{1/2} \frac{\lambda_g}{2a} \cos(\pi x/a), \\ V_{pz} &= 0 \end{aligned} \quad (13)$$

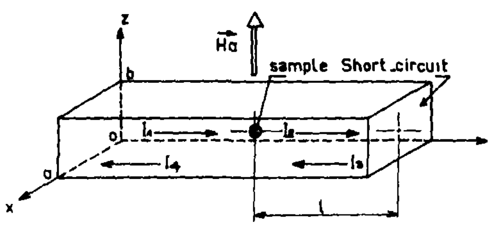

Fig. 1. Microwave set-up.

where a and b are the transverse dimensions of the guide, h_0 is the maximal amplitude of the microwave field, $\lambda_g = 2\pi/|k_g|$ and λ are the wave lengths in the guide and the vacuum. With this representation one can show[8] that the dipolar radiation is equivalent to the introduction of a current source i_d:

$$i_d = -iKm_y V_{py} \qquad (14)$$

and of a voltage source v_d:

$$v_d = iZ_g K m_x V_{px} \qquad (15)$$

placed in the equivalent circuit as indicated in Fig. 2. m_x and m_y are the components of the transverse magnetization m_t, $K = 2\pi V/\mu_0\lambda_g$ and $Z_g = (\mu_0/\epsilon_0)^{1/2}\lambda_g/\lambda$ is the characteristic impedance of the TE_{10} mode. The Maxwell equations and the conventional boundary conditions give the following relations for the waves scattered by the crystal:

$$\left.\begin{aligned} I_2 &= -\tfrac{1}{2}(i_d + v_d/Z_g) + I_1 \\ I_4 &= -\tfrac{1}{2}(-i_d + v_d/Z_g) + I_3 \end{aligned}\right\}. \qquad (16)$$

If $\mathbf{V}'_p$ is the eigen-vector of a wave propagating in the $-\mathbf{oy}$ direction, the microwave field near the sample becomes[8]:

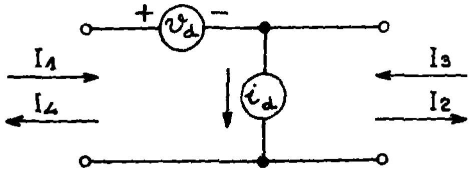

Fig. 2. Equivalent sources of the magnetic dipolar radiation.

$$\mathbf{H} = \left(\frac{I_1 + I_2}{2}\right)\mathbf{V}_p + \left(\frac{I_3 + I_4}{2}\right)\mathbf{V}'_p \qquad (17)$$

with

$$V'_{p_x} = V_{p_x} \quad \text{and} \quad V'_{p_y} = -V_{p_y}. \qquad (18)$$

Then the magnetic field which effectively interacts with the crystal can be defined from the hypothesis of our problem which are: – the incident wave amplitude (I_1 or $\mathbf{h}_{inc} = I_1\mathbf{V}_p$); – the coefficient of reflection Γ which characterizes in the plane of the sample, the impedance which limits the wave guide:

$$I_3 = -\Gamma I_2 \qquad (19)$$

the magnetization components.

From these remarks, we obtain:

$$H_x = (1-\Gamma)hinc_x + i\frac{K}{2}[(\Gamma - 1)V_{p_x}^2 m_x - \Gamma V_{p_x}V_{p_y}m_y] \qquad (20)$$

$$H_y = (1+\Gamma)hinc_y + i\frac{K}{2}[-\Gamma V_{p_x}V_{p_y}m_x + (1+\Gamma)V_{p_y}^2 m_y]. \qquad (21)$$

The first term in H_x and H_y is the field at the site of the sample when the microwave magnetization is zero. The second term defines the dipolar radiation of the ferromagnetic system. We note that the relation between the components of the effective field and those of the magnetization is generally tensorial. Now, we adopt the following restrictions: the wave-guide is limited by a short-circuit having the coefficient of reflection $\Gamma = -\exp(-2ik_g l)$ in the crystal plane; the only principal propagation mode TE_{10} is excited; the sample is punctual with respect to the wave length and is situated at the center of the guide ($x = a/2$, $z = b/2$); the polarization of the uniform mode is circular.

With these hypothesis the components of the r.f. field are reduced to:

$$H_x = (1-\Gamma)\left(hinc_x - i\frac{K}{ab}m_x\right)$$
$$H_y = 0. \qquad (22)$$

If we take the origin of the oy axis in the short-circuit plane, the position of the sample is $oy = -l$, and then:

$$H_x(-l,t) = 2\cos k_g l \times \left(hinc_x - i\frac{K}{ab}\mathrm{e}^{-ik_g l}m_x\right). \qquad (23)$$

Figure 3 shows the phase-shifts between H_x, m_x and h_{inc} with the Fresnel representation. We note the phase-shift of $-\pi/2$ of m_x with respect to H_x, since the system is at the resonance. Then, the linear component of the effective magnetic field is:

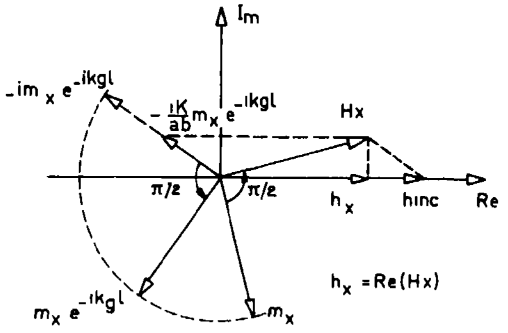

Fig. 3. Determination of the phase-shift produced by the dipolar radiation between the incident field hinc and the effective field h_x.

$$h_x(-l,t) = \mathscr{R}\mathrm{e}(H_x) = h_1^+\mathrm{e}^{i\omega t} + h_1^-\mathrm{e}^{-i\omega t} \qquad (24)$$

with:

$$h_1^+ = \cos k_g l\left(h^+inc_x - i\frac{K}{ab}\mathrm{e}^{-ik_g l}m_0^+\right). \qquad (25)$$

Indeed, by definition, we have:

$$m_0^\pm = m_x(t) \pm im_y(t) \qquad (26)$$

or

$$m_0^\pm = \left(\frac{m_x \pm im_y}{2}\right)\mathrm{e}^{i\omega_0 t} + \left(\frac{m_x^* \pm im_y^*}{2}\right)\mathrm{e}^{-i\omega_0 t} \qquad (27)$$

where ω_0 is the pulsation of uniform magnons. The expression (27) shows that the components $m^\pm$ have generally an elliptic polarization due to the factor $\exp(-i\omega_0 t)$. But, near the resonance this polarization is quasi-circular, which implies that:

$$m_x = m_0^+\mathrm{e}^{-i\omega_0 t}. \qquad (28)$$

From the second quantization of the magnetic system [eq. (7)], we deduce for the uniform magnons:

$$\left.\begin{aligned} m_0^+ &= (2g\mu_B M_0/V)^{1/2}a_0 \\ m_0^- &= (2g\mu_B M_0/V)^{1/2}a_0^+ \end{aligned}\right\} \qquad (29)$$

where M_0 is the crystal magnetization. Then, from equations (6) and (29), the magnetic field operator (24) is defined in terms of $h_1^\pm$ by:

$$\left.\begin{aligned} h_1^+ &= i(\alpha_1 q - \beta_1 a_0) \\ h_1^- &= -i(\alpha_1^* q^+ - \beta_1^* a_0^+) \end{aligned}\right\} \qquad (30)$$

with:

$$\alpha_1 = 2\cos k_g l\left(\frac{2\pi\hbar\omega}{V_1}\right)^{1/2} \qquad (31)$$

$$\beta_1 = \frac{\beta_0\eta_0}{g\gamma}\left(\frac{2g\mu_B}{M_0 V}\right)^{1/2}\mathrm{e}^{-ik_g l}\cos k_g l \qquad (32)$$

where η_0 and β_0 are respectively the relaxation rate and the coupling coefficient of uniform magnons with the explicit expressions:

$$\left.\begin{aligned} \eta_0 &= g\gamma\Delta H_0/2 \\ \beta_0 &= \frac{4\pi V}{ab\lambda_g}\cdot\frac{4\pi M_0}{\Delta H_0}. \end{aligned}\right\} \qquad (33)$$

$\gamma = \mathrm{e}/2mc$ is the gyromagnetic factor. Finally, from equations (1), (7) and (30), we obtain the effective Hamiltonian which described the photon–magnon transitions:

$$H_{m-p} = -i[(\alpha q - \beta a_0)a_0{}^+ - a_0(\alpha q^+ - \beta^* a_0{}^+)] \quad (34)$$

with:

$$\left.\begin{aligned} \alpha &= (2g\mu_B M_0 V 2\pi\hbar\omega/V_1)^{1/2}\cos k_y l \\ &= \text{direct processes coefficient} \\ \beta &= \hbar\beta_0\eta_0 e^{-ik_y l}\cos k_y l \\ &= \text{reverse processes coefficient} \end{aligned}\right\}. \quad (35)$$

The first term, in the relation (34), is the conventional Hamiltonian which represents the direct photon-magnon transitions. The second term in equation (34) is the Hamiltonian which defines the reverse magnon–photon transitions due to the dipolar radiation of the uniform mode. These reverse processes, which are equivalent to an additional damping of the uniform mode, increase with the filling factor and the magnetization of the crystal (factor β) and with the population of the uniform magnons. We shall see later the importance of this dipolar radiation during the exponential growth of the spin-waves in crystals having very low relaxation rate. If the reverse transitions are neglected and the short-circuit suppressed, Hamiltonian (34) is reduced to equation (9) derived above.

3. HAMILTONIAN OF THE MAGNON–MAGNON INTERACTIONS

The quantum theory of the magnon–magnon interactions based on the second quantization method of Holstein and Primakoff[5] has been developed by several authors[10–12]. The Hamiltonian which describes the behaviour of the spin system in an undeformed lattice is:

$$H_m = \int_V \mathrm{d}v\left[\frac{1}{2}A_{ik}\left(\frac{\partial\mathbf{M}}{\partial x_i}\frac{\partial\mathbf{M}}{\partial x_k}\right) - \frac{1}{2}B(\mathbf{Mn})^2 - \frac{H^2}{8\pi}\right]. \quad (36)$$

In what follows, the magnon–phonon and electron–phonon interactions are neglected. A_{ik} is the tensor of exchange constants, $\mathbf{M}$ is the *magnetic moment density*, B is the anisotropic constant and $\mathbf{n}$ is a unit vector directed along the easy axis of magnetization. Let $\mathbf{H} = \mathbf{H}_i + \mathbf{h}_d$ and $\mathbf{M} = \mathbf{M}_0 + \mathbf{m}$, where $\mathbf{H}_i$ and $\mathbf{M}_0$ are the internal d.c. magnetic field and the magnetization at the equilibrium; $\mathbf{h}_d$ and $\mathbf{m}$ are small deviations from $\mathbf{H}_i$ and $\mathbf{M}_0$ corresponding to the dipolar energy of the magnons (Fig. 4). We take the z axis parallel to $\mathbf{M}_0$.

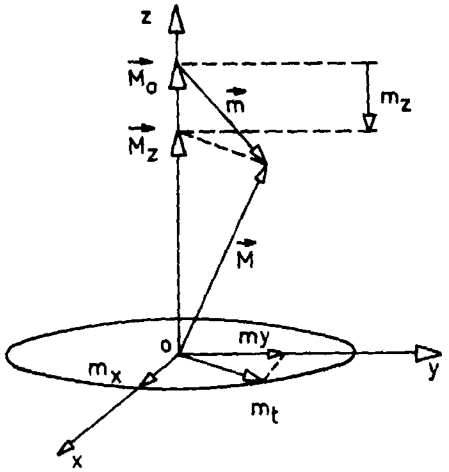

Fig. 4. Definition of the steady-state and dynamical components of the magnetization.

If we consider states near saturation, we can, as Holstein and Primakoff[5], expand the total Hamiltonian of the crystal in terms of the creation and destruction operators $c_{\mathbf{k}}{}^+$ and $c_{\mathbf{k}}$ for the magnons:

$$\begin{aligned} H = \sum_k \hbar\omega_k c_{\mathbf{k}}^+ c_{\mathbf{k}} + \sum_{k\neq 0}\hbar(f_k c_0{}^+ c_{\mathbf{k}} c_{\mathbf{k}} \\ + f_k^* c_0 c_{\mathbf{k}}^+ c_{\mathbf{k}}^+) - i[(\alpha q - \beta c_0)c_0{}^+ \\ - c_0(\alpha q^+ - \beta^* c_0{}^+)] \end{aligned} \quad (37)$$

with

$$f_k = \pi g\gamma\left(\frac{2g\mu_B M_0}{V}\right)^{1/2} \times \left(\frac{\omega_i + Dk^2 + \omega_k}{4\omega_k}\right)\sin 2\theta_k e^{-i\phi_{\mathbf{k}}}$$

$$\omega_i = g\gamma H_i$$

$$\omega_k = g\gamma[(H_i + Dk^2)(H_i + Dk^2 + 4\pi M_0 \times \sin^2\theta_k)]^{1/2}$$

$$D = g\gamma M_0 A_{ex}$$

k, θ_k and ϕ_k are the magnitude and polar and azimuthal angles of the propagation vector **k**, the angles being measured from the z axis (direction of H_i) and the x axis, respectively. To obtain the Hamiltonian (37), we have considered the case of a cubic crystal ($A_{ik} \rightarrow A_{ex}$). The new dynamical variables $c_{\mathbf{k}}^+$ and $c_{\mathbf{k}}$ are related to the magnon operators $a_{\mathbf{k}}^+$ and $a_{\mathbf{k}}$ by the linear transformation of Bogoliubov and Tyablikov[10-13] which diagonalize the quadratic part of the crystal Hamiltonian. The operators c_k^+ and c_k satisfy the following commutation relations:

$$[c_{\mathbf{k}_1}, c_{\mathbf{k}_2}^+] = \Delta(\mathbf{k}_1 - \mathbf{k}_2).$$

The transformation of Bogoliubov and Tyadlikov is a simple identity for the effective photon-magnon Hamiltonian. f_k is a coupling parameter of the parametric state k with the uniform mode. In equation (37), we have retained only third-order terms which are important for three-magnon non-linear transitions. We have, for instance, neglected four-magnon terms which determine second-order processes, since their critical threshold is much higher than that for first-order processes. In addition, we have not taken into account the two-magnon and three-magnon terms which contribute to the linear relaxation of the uniform mode and spinwaves respectively. The linear damping of those modes will be introduced later on with the complex frequencies $\omega_k + i\eta_k$. It can be shown that this is mathematically equivalent to assuming that their line shapes are Lorentzian. Third-order terms in equation (37) are of two kinds. The first term $c_0^+ c_{\mathbf{k}} c_{-\mathbf{k}}$ (splitting transitions) is the direct process in which a $k = 0$ magnon is absorbed and two magnons ($\pm\mathbf{k}$) are created. The second term $c_0^+ c_{\mathbf{k}} c_{-\mathbf{k}}$ (fusion transition) is the reverse process where two magnons with same energy and opposite momentum are destroyed and a uniform magnon is created. The amplitude $\langle c_0^+ c_0 \rangle$ of the uniform mode remains constant with the transfer of the energy from this mode to the parametric states. This property is the basis of the coincidence microwave limiters[14]. Every photon absorbed by the crystal above the critical threshold is immediately converted into two $k \neq 0$ magnons. The population of the parametric magnons can reach very high values since under these conditions, the probabilities of the direct processes exceed the probabilities of relaxation. When the excitation is suppressed, the reverse terms $c_0^+ c_{\mathbf{k}} c_{-\mathbf{k}}$ play an important role. Indeed, the magnetic energy stored in the parametric magnon system vanishes in part in fusion with thermal magnons (linear relaxation) and in part by radiation of photons via the uniform mode. This reverse process is the origin of the radiation peak observed for a short time when the electromagnetic field is switched off.

4. GENERAL THEORY OF THE TRANSIENT PROCESSES IN SPIN-WAVE SYSTEMS

Since the second-order Hamiltonian of the crystal is diagonalized in terms of the dynamical variables $c_{\mathbf{k}}$, we can write:

$$c_0 = b_0 e^{i\omega t}; \quad c_{\mathbf{k}} = b_{\mathbf{k}} e^{i\omega_{\mathbf{k}} t} \tag{38}$$

The evolution of the operator $c(t)$ is described by:

$$i\hbar\dot{c} = [H, c]. \tag{39}$$

By use of equations (37-39), the equation of evolution of the uniform mode without radiation is:

$$\dot{b}_0 = i(\Omega_0 - \omega)b_0 + \hbar^{-1}\alpha q$$

with:

$$\Omega_0 = \omega_0 + i\eta_0.$$

We can introduce a frequency shift and an additional damping due to the dipolar radiation by changing in the last equation of motion, the simplified field operator (equation

(6)) by the complete expression (30), then we have:

$$\dot{b}_0 = [i(\omega_L - \omega) - \eta_L]b_0 + \hbar^{-1}\alpha q \quad (40)$$

with:

$$\omega_L = \omega_0 + \tfrac{1}{2}\beta_0\eta_0 \sin 2k_g l \quad (41)$$

$$\eta_L = \eta_0(1 + \beta_0 \cos^2 k_g l). \quad (42)$$

Then, the crystal radiation produces a frequency-shift of the resonance and a supplementary damping of the uniform magnons which vary with the distance l from the short-circuit to the sample. In the linear state, the equation (40) gives the evolution of b_0:

$$b_0 = b_0{}^0 e^{i\delta\Omega t} + i\frac{\alpha q}{\hbar\delta\Omega}(1 - e^{i\delta\Omega t}) \quad (43)$$

with:

$$\delta\Omega = \omega_L - \omega + i\eta_L.$$

At resonance ($\omega = \omega_L$), this equation is reduced to:

$$b_0 = b_0{}^0 e^{-\eta_L t} + \frac{\alpha q}{\hbar\eta_L}(1 - e^{-\eta_L t}). \quad (44)$$

This linear solution is obtained, neglecting third-order terms in equation (37). So, in the linear state b_0 increases from the thermal level $b_0{}^0$ to the stationary values $b_0{}^m = \alpha q/\hbar\eta_L$ with a time constant $\eta_L{}^{-1}$.

We now assume that the condition of coincidence in which the three-magnon non-linear processes arise exactly at resonance is realized. Thus, the energy of the first excited parametric states is equal to half the energy of the photons ($\omega = \omega_L = 2\omega_k$). With these conditions, the transient non-linear behaviour of c_0 and $c_{\mathbf{k}}$ will be determined by equations (45–47) and their hermitian conjugated equations for the quantum dynamical variables $c_0{}^+$ and $c_{\mathbf{k}}{}^+$:

$$\dot{b}_0 = -\eta_L b_0 + i\sum_{k\neq 0} f_k b_{\mathbf{k}} b_{-\mathbf{k}} + \alpha\hbar^{-1}q \quad (45)$$

$$\dot{b}_{\mathbf{k}} = -\eta_k b_{\mathbf{k}} + if_k^* b_0 b^+_{-\mathbf{k}} \quad (46)$$

$$\dot{b}_{-\mathbf{k}} = -\eta_k b_- + if_k^* b_0 b^+_{\mathbf{k}}. \quad (47)$$

Transient anharmonic evolution of the uniform and parametric magnons

In order to analyze the *transient evolution* of the modes b_0, $b_{\mathbf{k}}$ and $b_{-\mathbf{k}}$ (equations (45–47)), the method we have described earlier[15] to study the evolution of a spin-wave system without magnetic dipolar radiation, is used. First-order processes arise when b_0, during its transient growth, exceeds a critical value $b_0{}^{\text{crit}}$ above which the interaction term $f_k^* b_0 b_{-\mathbf{k}}$ in equation (46) becomes greater than the damping term $-\eta_k b_{\mathbf{k}}$. The transient growth of $b_{\mathbf{k}}$ determines the decrease of b_0 (equation (45)) until the threshold value $b_0{}^{\text{crit}}$, which defines the stationary state, is reached. In what follows, we analyze the theoretical evolution of the uniform mode as a function of the time at the beginning of the spin-wave growth. We suppose, which is supported by experiments, that the uniform mode reaches its linear stationary amplitude before the reaction of the spin-waves becomes too important. In addition, it is assumed that the stationary value $b_0{}^m$ is constant at the beginning of the parametric excitation of the magnons (i.e. $b_0{}^m \gg b_{\mathbf{k}}$). Then the equation (46) gives the time dependence of $b_{\mathbf{k}}$:

$$b_{\mathbf{k}} = e^{-\eta_k t}(b_{\mathbf{k}}^0 \cosh \rho_k t + if_k^* \rho_k{}^{-1} b_0{}^m b^{0+}_{-\mathbf{k}} \sinh \rho_k t) \quad (48)$$

where ρ_k is the excitation rate of the parametric magnons defined by:

$$\rho_k = |f_k|(\langle b_0{}^{m+} b_0{}^m \rangle)^{1/2} = \frac{|f_k|\alpha n_q{}^{1/2}}{\hbar\eta_L}.$$

Now, the transient evolution of the uniform mode with three-magnon non-linear processes is obtained using in equation (45) $b_{\mathbf{k}}$ defined by equation (48). Then the general analytic expression of b_0 is:

$$b_0 = b_0{}^m\left[1 - \sum_{k\neq 0} \frac{\hbar|f_k|n_k{}^0\eta_L}{2\alpha n_q{}^{1/2}}\left(\frac{e^{2(\rho_k-\eta_k)t} - e^{-\eta_L t}}{\eta_L + 2\rho_k - 2\eta_k} - \frac{e^{-2(\rho_k+\eta_k)t} - e^{-\eta_L t}}{\eta_L - 2\rho_k - 2\eta_k}\right)\right] \quad (49)$$

when $\rho_k > \eta_k$ and $t > \eta_L{}^{-1}$, the excitation of the parametric magnons gives an exponential decrease of the uniform mode from its maximum linear value $b_0^m = \alpha q/\hbar\eta_L$:

$$c_0 \simeq b_0^m\Big[1-\sum_{k\neq 0} F_k e^{2(\rho_k-\eta_k)t}\Big]e^{i\omega t} \quad (50)$$

with:

$$F_k = \frac{\hbar|f_k|n_k^0\eta_L}{2\alpha n_q^{1/2}(\eta_L+2\rho_k-2\eta_k)}.$$

The condition $\rho_k = \eta_k$ determines the excitation threshold of the parametric modes.

Transient power absorbed by the ferromagnetic crystal

When the excitation rate of the parametric modes is greater than their relaxation rate, the uniform mode evolution with three-magnon transitions is described by equation (50). Then, the behaviour of the sample is defined by the imaginary part of the non-linear susceptibility $\chi''_{nL}(t)$ which is related to the power Pa absorbed per unit volume by:

$$P_a = \tfrac{1}{2}\omega\chi''_{nL}h^2inc. \quad (51)$$

The power absorbed by the sample is:

$$P_a = \frac{1}{2}\left\langle\frac{dm_0^+}{dt}\cdot h_1^- + \frac{dm_0^-}{dt}\cdot h_1^+\right\rangle \text{ time average} \quad (52)$$

With equations (29) and (30), we have:

$$P_a = \hbar\omega[\alpha'(b_0q^+ + b_0^+q) - (\beta'+\beta'^*)b_0^+b_0] \quad (53)$$

with

$$\alpha' = \alpha/\hbar; \quad \beta' = \beta/\hbar.$$

The first two terms of this expression give the number of incident photons which are coupled to the uniform magnons per unit time, and the last two terms define the number of photons re-emitted by dipolar radiation. From equations (50) and (53), we obtain the power absorbed by the crystal at the beginning of the parametric spin-waves excitation:

$$P_a = 2\alpha'^2\eta_L^{-1}n_q\hbar\omega\Big[\Big(1-\sum_k U_k(t)\Big) - \beta_l(1+\beta_l)^{-1}\Big(1-\sum_k U_k(t)\Big)^2\Big] \quad (54)$$

with:

$$U_k(t) = F_k \exp 2(\rho_k-\eta_k)t$$

$$\beta_l = \beta_0 \cos^2 k_g l \quad (= \text{coupling coefficient}).$$

The incident power *Pinc* is determined from the incident field $hinc_x$ and the characteristic impedance Z_g by:

$$Pinc = \frac{ab}{4}Z_g h^2inc_x. \quad (55)$$

In addition, the electromagnetic energy density is defined by:

$$\frac{h^2inc_x}{8\pi} \simeq \frac{n_q\hbar\omega}{V_1} \quad (56)$$

Then, the final expression of the absorbed power can be written as:

$$\frac{P_a}{Pinc} = \frac{4\beta_l}{(1+\beta_l)^2}\Big[1-(1-\beta_l)\sum_k U_k(t) - \beta_l\Big(\sum_k U_k(t)\Big)^2\Big]. \quad (57)$$

5. DISCUSSION

Threshold of the three-magnon processes

We have seen in the precedent section that the three-magnon processes arise when b_0, during its transient growth from the thermal value b_0^0 to the stationary level $\alpha q/\hbar\eta_L$, exceeds a critical value b_0^{crit} above which the interaction term in equation (46) becomes greater than the damping term. So, the condition:

$$\frac{\alpha q}{\hbar\eta_L} < b_0^{\text{crit}}$$

defines the linear evolution of the uniform mode. In this case, the uniform magnon population n_0 which is proportional to the incident photons n_q has the following value in the stationary state:

$$n_0 = \left(\frac{\alpha}{\hbar\eta_L}\right)^2 n_q \gg n_0^0 \quad (58)$$

where n_0^0 is the thermal value of n_0 given by the Bose–Einstein statistics. The critical number n_q^{crit} of photons at the threshold is deduced directly from the transient solution (50) by:

$$\rho_k \geqslant \eta_k$$

or:

$$n_q^{\text{crit}} = \min_k \left(\frac{\hbar \eta_L \eta_k}{\alpha |f_k|} \right)^2 \tag{59}$$

where $\min_k$ implies that the condition (59) is minimized with respect to k and θ_k. This indicates what pair of magnons first becomes unstable. The equivalent critical field is defined immediately from equations (56) and (59). Finally, from equations (58) and (59), we deduce the stationary population of the uniform magnons when the three-magnon transitions exist:

$$n_0 = \left(\frac{\eta_k}{|f_k|} \right)^2 \tag{60}$$

Now, n_0 is independent of the external excitation. Above the threshold, every created uniform magnon is directly converted into a pair of parametric magnons ($\pm \mathbf{k}$). Equation (59) shows that the threshold now depends on the uniform magnon radiation and of their coupling to the measurement structure by the factors η_L and α. Then the critical field increases proportionally to the radiation factor $\beta_0 \eta_0$ and, for a given microwave structure, to the sample volume.

Transient harmonic processes

If $n_q < n_q^{\text{crit}}$, the evolution of the magnetic system is defined by the linear solution (44) where the uniform mode amplitude increases exponentially with time from the thermal value b_0^0 to the maximal value b_0^m, with a time constant η_L^{-1}. The general expression of the radiation field h_r is obtained from equation (30):

$$h_r = -i(\beta_1 c_0 - \beta_1^* c_0^+). \tag{61}$$

Taking into account the solution (44), the dipolar radiation of the crystal becomes:

$$h_r = -i \left(\frac{2\pi\hbar\omega}{V_1} \right)^{1/2} (q - q^+) \frac{2\beta_l}{1+\beta_l} (1 - e^{-\eta_L t}). \tag{62}$$

The minus sign before this expression indicates that h_r is radiated by the sample, the factor 2 is produced by the short-circuit, and the quantity:

$$y = \frac{\beta_l}{1+\beta_l} \tag{63}$$

which is the 'radiation rate', gives the proportion of the incident field reflected by the uniform magnons. Then, the effective field in the crystal is:

$$h_x(-l, t) = 2i \left(\frac{2\pi\hbar\omega}{V_1} \right)^{1/2} (q - q^+)(1 - y)(1 - e^{-\eta_L t}) \tag{64}$$

The dipolar radiation is maximum when $l = n(\lambda/2)$ and vanishes when $l = m(\lambda/4)$, n and m being integers. Figure 5 shows the evolution of the effective and radiated field as a function of the time. The radiation field amplitude increases with the sample volume and η_0^{-1}. For this, it is instructive to compare the radiation rate of YIG spheres vs. their diameter d and relaxation rate as shown in Fig. 6, where we have considered a maximum coupling ($l = \lambda g/2$) and an excitation fre-

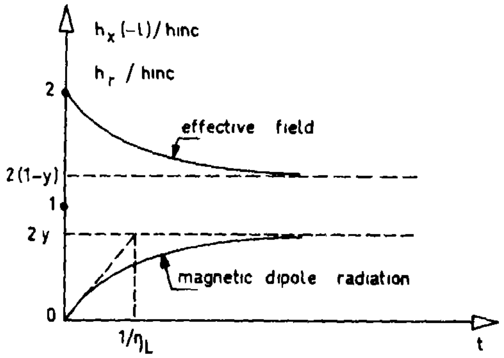

Fig. 5. Time evolution of the effective and magnetic dipolar radiation fields in the ferromagnetic crystal.

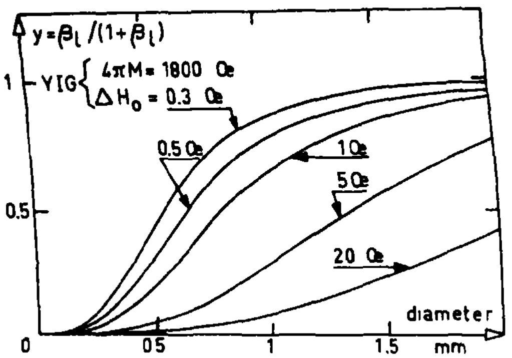

Fig. 6. Evolution of the radiation rate of a YIG sphere versus the sample diameter for some values of the uniform mode line-width. The frequency of the excitation is 10 GHz.

quency of 10 GHz ($a \simeq 1$ cm, $b = 2{\cdot}2$ cm, $\lambda = 3$ cm). So, the dipolar radiation rate of a YIG sphere having a line-width less than 1 Oe is important when the diameters are greater than a few tenth of millimeters and becomes greater than 90 per cent with $d > 2$ mm. In the same way, the radiation of a polycristalline sample with a diameter less than 1 mm vanishes because of its large line-width. In this case, the ferromagnetic relaxation does not allow the uniform magnons to convert their energy into the electro-magnetic radiation. For those reasons, we must take into account this phenomenon in the relaxation rate and critical threshold measurements of the low line-width crystals[16].

The experimentally observed parameter is the microwave absorbed power. If the electromagnetic excitation is applied at the resonance at the time $t = 0$, the transient evolution of this absorption is deduced in linear state from equations (44) and (53):

$$\frac{P_a}{P_{inc}} = \frac{4\beta_l}{(1+\beta_l)^2}\left(1 - e^{-\eta_L t} + \beta_l e^{-\eta_L t} - \beta_l e^{-2\eta_L t}\right). \tag{65}$$

If now the excitation is suddenly suppressed after a time $t = t_c$, where the stationary absorption is reached, the evolutions of the uniform mode, the magnetic field and the radiated power P_r are given from equation (40) by:

$$b_0(t > t_c) = \frac{\alpha q}{\hbar\eta_L} e^{-\eta_L(t-t_c)} \tag{66}$$

$$h_x(-l, t > t_c) = 2i\left(\frac{2\pi\hbar\omega}{V_1}\right)^{1/2}(q - q^+) \times (1-y)e^{-\eta_L(t-t_c)} \tag{67}$$

$$\frac{P_r(t > t_c)}{Pinc} = -\frac{4\beta_l^2}{(1+\beta_l)^2} e^{-2\eta_L(t-t_c)}. \tag{68}$$

So, the intrinsic relaxation rate of the uniform magnons can be defined from the measurements of the exponential decrease of the radiated power for some value of β_l, as shown by Desormiere and Milot[16].

The magnetic dipolar radiation gives important modification in the transient evolution of Pa as shown in Fig. 7 for some value of β_l. If $\beta_l > 1$, Pa reaches a stationary level lower than $Pinc$ after an overshoot due to the third term of equation (65). This is produced in this case by the important delay of the dipolar radiation with respect to the uniform magnons excitation. If $\beta_l = 1$, the whole incident power is absorbed in stationary state: the magnetic system is at the critical coupling. In the stationary state, when $\beta_l \neq 1$, Pa is lower than $Pinc$ because of the low coupling of the magnons with the photons if $\beta_l < 1$, and

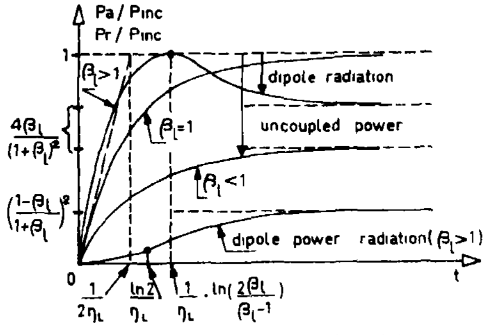

Fig. 7. Transient harmonic time evolution of the powers absorbed and re-radiated by the ferromagnetic sample for different values of the coupling parameter β_l

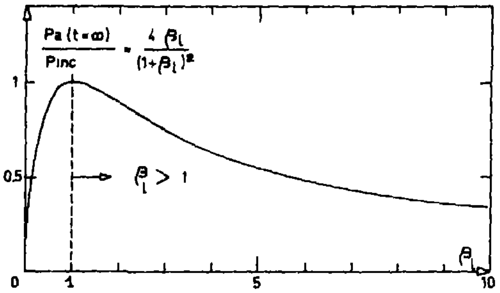

Fig. 8. Steady-state power un-coupled to ($\beta_l < 1$) or re-radiated ($\beta_l > 1$) by the sample vs. the coupling parameter β_l.

because of the dipolar radiation if $\beta_l > 1$ (see Fig. 8).

Finally, if the magnetic system is not at resonance ($\omega \neq \omega_L$), we must change $-\eta_L$ by $i\delta\Omega$ defined above, in the expressions of b_0, h_x, h_r, Pa and P_r. Then, we obtain a modulation of those last quantities with the angular frequency $\omega - \omega_L$.

Transient anharmonic processes

If $n_q > n_q^{\text{crit}}$, three-magnon processes rise and the power absorbed by the magnetic system is derived from transient evolution of the uniform mode described by equation (50). As in the linear case, the evolution of this power is greatly modified by the radiation and the coupling of the sample with the microwave field (factor β_l in equation 57). The growth of the spin-wave populations decreases the amplitude c_0 of the uniform magnons (equation (50)). The radiated field follows a similar evolution from equation (61) which gives:

$$h_r = -i\left(\frac{2\pi\hbar\omega}{V_1}\right)^{1/2} \frac{2\beta_l}{1+\beta_l}(q-q^+) \left[1 - \sum_{k\neq 0} U_k(t)\right]. \quad (69)$$

When $\beta_l < 1$, equation (57) shows that the rise of the parametric magnons produces an exponential decrease of the absorbed power as seen in Fig. 9. At the critical coupling ($\beta_l = 1$), the situation is quite similar to the last one; only the diminution of Pa with time is slower in this case, since:

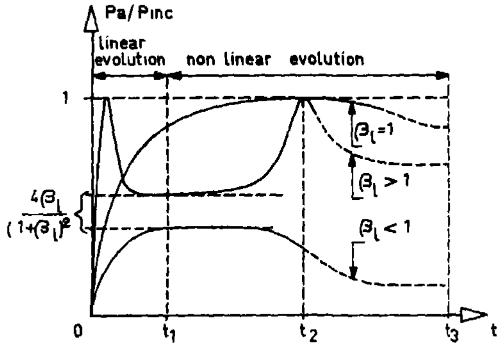

Fig. 9. Transient anharmonic time evolution of the power effectively absorbed by the ferromagnetic sample for different values of the coupling parameter β_l. The solid curves are defined by the present theory and the broken curves are deduced from experiments

$$\frac{Pa}{Pinc} = \frac{4\beta_l}{1+\beta_l}\left[1 - \beta_l\Big(\sum_{k\neq 0} U_k(t)\Big)^2\right]. \quad (70)$$

If $\beta_l > 1$, the evolution of Pa is very different from the last two cases. Indeed, in a first time, $t_2 - t_1$ (see Fig. 9), the diminution of c_0, due to the parametric magnon creation, gives larger modification on the radiated power (term $\beta' c_0^+ c_0$ in equation (53)) than on the power absorbed by the uniform mode (term $\alpha' c_0^+ q$ in equation (53)). The radiated power evolution during the spin-wave growth is defined by the factor $\beta' c_0^+ c_0$ which is proportional to:

$$1 + (\beta_l - 1)\sum_{k\neq 0} U_k(t) - \beta_l\Big(\sum_{k\neq 0} U_k(t)\Big)^2.$$

This factor gives to Pa a second maximum at time t_c before the non-linear stationary level is reached after the time t_3 (see Fig. 9). When $\beta_l > 1$, we note that, contrary to the case $\beta_l < 1$, the non-linear stationary absorption is higher than the linear stationary level because of the large diminution of the dipolar radiation in this case.

6. CONCLUSION

In this study we have analyzed the transient linear and non-linear evolution of the uniform and parametric magnons in ferromagnetic crystals submitted to a perpendicular pumping. We have shown that the dipolar radiation of the magnetic system modifies greatly the growth and the steady-state population of the uniform and parametric modes by the creation of reverse magnon-photon transitions. This radiation is negligible in polycristalline samples but becomes very important in low line-width samples, as the YIG, where a quasi-complete re-radiation of the incident power is observed in certain cases. The expressions of the radiated electromagnetic field and the power effectively absorbed by the crystal have been derived as a function of the coupling factor.

In the non-linear case, the power absorption is defined by discrete summation over the states k. If this summation is replaced by an integration, we can evaluate the transient power as performed recently by Joseph and Schlömann[17] for the parallel pumping case. But that implies tedious calculations with a great number of simplifying assumptions and finally the use of numerical calculations. The above analytical expressions have the advantage of describing well physically the transient processes with dipolar radiation at the beginning of the spin-wave growth. The full description of the parametric and uniform modes up to the beginning of non-linear steady-state has been studied with a computer making certain hypothesis. Those latter theoretical results will be described and experimentally compared with in a further paper.

Acknowledgements – The authors would like to thank Dr. R. Vautier and Professor J. Friedel for helpful comments and their interest in the work and Dr. J. P. Sage for interesting discussions of various points.

REFERENCES

1. DAMON R. W., *Rev. mod. Phys.* **25**, 239 (1953).
2. BLOEMBERGEN N. and WANG S., *Phys. Rev.* **93**, 72 (1954).
3. AKHIEZER A. I., *J. Phys.* **10**, 217 (1946).
4. SUHL H., *J. Phys. Chem. Solids* **1**, 209 (1957).
5. HOLSTEIN T. and PRIMAKOFF H., *Phys. Rev.* **58**, 1098 (1940).
6. SAVCHENKO M. A. and TARASENKO V. V., *JETP* **51**, 482 (1966); *Soviet Phys. JETP* **24**, 325 (1967).
7. HEITLER W., *The Quantum Theory of Radiation*. Oxford University, Oxford (1954).
8. ANDERSON L. K., M.L. Report No. 880 Stanford University (Feb. 1962). Unpublished.
9. MARCUVITZ N and SCHWINGER J., *J. appl. Phys.* **22**, 806 (1951).
10. AKHIEZER A. I., BARYAKHTAR V. G. and PELETMINSKII S. V., *JETP* **36**, (1959); *Soviet Phys JETP* **9**, 146 (1959).
11. KAGANOV M. I. and TSUKERNIK V. M., *JETP* **37**, 823 (1959), *Soviet Phys. JETP* **10**, 587 (1960).
12. WHITE R. M and SPARKS M., *Phys. Rev* **130**, 632 (1963).
13. BOGOLIUBOV N. N. and TYABLIKOV S. V., *JETP* **19**, 256 (1948).
14. See for example, LAX B. and BUTTON K., *Microwave ferrites and ferrimagnetics*. McGraw-Hill, N.Y. (1962)
15. LE GALL H., MILOT E. and DESORMIÈRE B., *Solid State Commun.* **5**, 637 (1967).
16. DESORMIÈRE B. and MILOT E., *Phys. Lett.* **24-A**, 202 (1967).
17. JOSEPH R. T. and SCHLÖMANN E., *J. appl. Phys.* **38**, 1915 (1967).

J. Phys. Chem. Solids Pergamon Press 1969. Vol. 30, pp. 993–1001. Printed in Great Britain.

THE EFFECT OF METAL VACANCIES ON THE OXIDATION KINETICS OF METALS

M. J. MINDEL*† and S. R. POLLACK

School of Metallurgy and Materials Science University of Pennsylvania, Philadelphia, Penn. 19104
U.S.A.

(*Received* 24 *July* 1968)

Abstract – When transport through a strongly adherent oxide film on a metal is via cations, vacancies are generated in the metal at the metal-oxide interface. If the concentration of vacancies at the metal-oxide interface rises above the equilibrium concentration, the reverse reaction at that interface (i.e. metal ions going from the oxide into the metal) will be enhanced. This will have the effect of reducing the oxidation rate thereby altering the oxidation kinetics. Rate equations are calculated for a variety of limiting cases. For the cases where no internal vacancy sinks are present in the metal the thickness of the metal being oxidized enters the rate equations as a parameter.

INTRODUCTION

DURING THE oxidation of a metal, oxide is created at the oxide-gas interface whenever ionic transport through the oxide is via cations. Only diffusion takes place at the metal-oxide interface. At the metal-oxide interface diffusion takes place so that for every metal ion entering the oxide a vacancy is created in the metal. On the whole, effects of these vacancies have been ignored; indeed in most cases discussion[1, 2] has taken the form of qualitative arguments as to why such effects would be minimal. While the effects of these vacancies on oxide morphology and on mechanical properties will not be discussed in this paper, we will consider the effect of these vacancies upon oxidation kinetics in some detail.

Vermilyea[2] has suggested that these vacancies are actually not created at all. Instead, jogs in ledges on the metal surface move so as to eliminate lattice sites caused by the flux of metal atoms away from the surface. This mechanism is certainly what happens during vaporization of solids or during chemical etching, but in the case of oxidation of a metal, where a solid–solid interface exists, such a mechanism would involve severing bonds across the interface. Depending upon the magnitude of the interatomic forces across the interface it is entirely possible for either the jog mechanism or the vacancy mechanism to be operative. The former would be more probable for weak forces, while the latter would be more probable when the forces are strong.

Experimentally the generation of vacancies during oxidation has been confirmed by observation of the growth of vacancy loops in metal foils oxidizing in the electron microscope[3, 4]. The authors[5, 6] have utilized this generation of vacancies and the mathematics of the next section to explain the dependence of oxidation kinetics of titanium thin films upon the initial thickness of the metal. Furthermore the literature abounds[1] with photomicrographs showing the presence of voids near the surface of oxidized metal samples. We believe these were most likely caused by the precipitation of vacancies generated during oxidation. The effect of vacancies has been qualitatively utilized by Hancock and Fletcher[7] to explain the thickness dependence of the oxidation of nickel sheet at high temperatures.

---

*Submitted in partial fulfillment of the requirement for the Ph.D. degree of Metallurgy and Materials Science, University of Pennsylvania.

†*Present address:* Bell Telephone Laboratories, Allentown, Pa.

THEORY

1. *Diffusional control*

Upon considering the mobilities of ions and electrons in oxides, halides, or sulphides, Wagner[8] derived the following equation for the rate of formation of the tarnishing layer on a metal. For the case of diffusional control:

$$\frac{X\Omega\,\mathrm{d}X}{\mathrm{d}t}=\frac{300}{96500N_Ae}\int_{\mu'_m}^{\mu''_m}\frac{1}{z_1}(t_1+t_2)t_3\,\eta\,\mathrm{d}\mu_m \tag{1}$$

where X is the instantaneous thickness of the reaction product, N_A is Avogadro's number, e is the charge of the electron in e.s.u., z_1 is the charge on the cation, μ_m is the chemical potential of the cations, μ''_m and μ'_m are the chemical potentials which are characteristic of equilibria between reaction product and metal and between reaction product and non-metal respectively, η is the electrical conductivity, Ω is the volume of oxide per cation and t_1, t_2 and t_3 are the transference numbers for cations, anions and electrons respectively.

In the following paragraphs it will be shown that the limit μ''_m explicitly contains the concentration of metal vacancies at the metal-oxide interface, and since in certain limits the concentration of vacancies will depend upon the thickness of the reaction product, μ''_m contains implicitly the thickness of the reaction product. (Hereafter the reaction product will be referred to as oxide.)

Consider the case of an oxide in which the transport takes place via cation interstitials, and look at the reaction at the metal-oxide phase boundary. The forward reaction consists of removing a metal atom from the metal surface and placing it in an interstitial site at the oxide surface. The flux J_f associated with this is given by

$$J_f=N_m(1-\alpha C_v)\,\nu\,T_fg_f(1-\Omega\,C''_i) \tag{2}$$

where N_m is the number of lattice sites per unit area of surface on the metal, α is the volume per atom in the metal, C_v is the value of vacancy concentration the metal at the interface, ν is an average vibrational frequency for surface atoms in the metal, T_f is the probability of overcoming the activation barrier to the reaction per vibration, g_f is the number of cation interstitial sites in the oxide about an atom on the metal surface, and C''_i is the value of the interstitial concentration at the metal-oxide interface.

In a similar manner the flux in the reverse direction is given by:

$$J_r=N_i\Omega C''_i\nu_0T_rg_r\alpha C_v \tag{3}$$

where N_i is the number of interstitial sites per unit area of oxide surface, ν_0 is a vibrational frequency characteristic of interstitials at the interface, T_r is the probability of passing over the activation barrier per vibration in the reverse direction, and g_r is the number of lattice on the metal surface to which an interstitial on the oxide surface can jump. In equations (2) and (3) terms can be collected such that the fluxes are given by the product of the number of attempts to overcome the activation barrier, the probability of getting the necessary thermal energy to overcome it, and the probability of finding a vacant site.

Since the assumption of diffusional control requires that both J_f and J_r be much greater than the diffusional flux, (which is J_f-J_r) they may be equated. Since αC_v and $\Omega C''_i$ will generally be much less than unity and since ν, N, T and g can reasonably be expected to be independent of concentrations

$$C''_iC_v=1/K \tag{4}$$

where

$$K=\frac{N_i}{N_m}\frac{\nu_0}{\nu}\frac{T_r}{T_f}\frac{g_r}{g_f}\frac{\alpha\Omega}{1}. \tag{5}$$

In the same manner one can consider the case of diffusion via cation vacancies; in that case the forward flux of atoms is

$$\mathbf{J}_f = N_m(1-\alpha C_v)\,\nu\,\mathbf{T}_f g_f\,\Omega\,C''_\square \qquad (6)$$

where $\mathbf{T}_f$ and g_f are defined similarly to the corresponding quantities in the preceding paragraphs and $C''_\square$ is the value of the cation vacancy concentration in the oxide at the metal-oxide interface. The reverse flux is

$$\mathbf{J}_r = N_c(1-\Omega C''_\square)\,\nu\,\mathbf{T}_r\mathbf{g}_r\alpha C_v. \qquad (7)$$

Where N_c is the number of normal cation sites per unit area in the oxide at the oxide-metal interface ν is a vibrational frequency for cations at the metal-oxide interface, and $\mathbf{T}_r$ and $\mathbf{g}_r$ are analogous to the T's and g's preceeding. Again the fluxes may be equated under the assumption of diffusional control and $\Omega C''_\square$ and αC_v can be considered much less than unity giving

$$C''_\square = \mathbf{K}C_v \qquad (8)$$

where

$$\mathbf{K} = \frac{N_c}{N_m}\frac{\nu}{\nu}\frac{\mathbf{T}_r}{\mathbf{T}_f}\frac{\mathbf{g}_r}{\mathbf{g}_f}\frac{\alpha}{\Omega}. \qquad (9)$$

After the formation of the initial oxide layer, one vacancy will be produced in the metal for each cation taken into the oxide. This is necessary if the forward and reverse reactions are to be truly the inverse of each other. If no large sinks (such as voids) are present in the metal, the increase in the total number of vacancies will be proportional to the thickness of the oxide scale. If one assumes that diffusion of vacancies in the metal takes place sufficiently rapidly to homogenize the vacancy concentration (a reasonably good assumption for thin films due to di-vacancy formation[9]) then for a plate with initial thickness w,

$$C_v - C_v{}^0 = \frac{2X}{w\Omega}$$

where $C_v{}^0$ is the initial concentration of vacancies in the metal. Since C_v will be much greater than $C_v{}^0$ for any appreciable amount of oxidation

$$C_v = \frac{2X}{w\Omega}. \qquad (10)$$

If the cation interstitial (vacancy) concentration in the oxide is small, if the transference number of electrons is nearly unity, and if the Einstein relationship between the mobility and the diffusivity holds, equation (1) has been shown by Wagner[10] to reduce to

$$\frac{X\mathrm{d}X}{\mathrm{d}t} = \frac{z_1}{\Omega}\int_{a'_m}^{a''_m}\left(D_1^* + \frac{z_2}{z_1}D_2^*\right)\mathrm{d}\ln a_m \qquad (11)$$

where $RT\,1na_m = \mu_m$, D_1^* and D_2^* are the self diffusion coefficients for cations and anions respectively and a_m is the activity of the metal in the oxide. Since we are considering pure cationic diffusion, $D_1^* \gg D_2^*$. Also

$$D_1^* = D_iC_i\text{(cation interstitial diffusion)} \qquad (12a)$$

$$D_1^* = D_\square C_\square\text{(cation vacancy diffusion)} \qquad (12b)$$

where C is the concentration of the *defect* (interstitial or vacancy) that is moving and D is its diffusivity. In addition, for an oxide containing excess interstitials

$$a_m = \gamma_i C_i \qquad (13)$$

where γ_i is the activity coefficient for interstitials, in the oxide and C_i is the interstitial concentration in the oxide. Similarly

$$a_m = 1 - \gamma_\square C_\square \qquad (14)$$

for an oxide containing excess cation vacancies, where $\gamma_\square$ is the activity coefficient for cation vacancies in the oxide and $C_\square$ is the cation vacancy concentration in the oxide. Differentiating equations (13) and (14) and substituting these along with equation (12) into equation (11) gives

$$\frac{X\mathrm{d}X}{\mathrm{d}t} = \frac{z_1}{\Omega}\int_{\gamma_i C'_i}^{\gamma_i C''_i}\frac{D_i}{\gamma_i}\mathrm{d}(\gamma_i C_i) \qquad (15)$$

for the interstitial diffusion and

$$\frac{X\mathrm{d}X}{\mathrm{d}t}=\frac{z_1}{\Omega}\int_{\gamma_\Box C''_\Box}^{\gamma_\Box C'_\Box}\frac{D_\Box}{\gamma_\Box}\,\mathrm{d}(\gamma_\Box C_\Box) \qquad (16)$$

for cation diffusion.

Under the assumption of small concentrations of defects (Henry's Law limit), the γ's are explicitly constants and the D's are independent of composition. Thus D/γ can be taken outside of the integrals in equations (15) and (17) whereupon integration gives

$$\frac{X\mathrm{d}X}{\mathrm{d}t}=\frac{z_1}{\Omega}D_i(C''_i-C'_i) \qquad (17)$$

and

$$\frac{X\mathrm{d}X}{\mathrm{d}t}=\frac{z_1}{\Omega}D_\Box(C'_\Box-C''_\Box) \qquad (18)$$

for interstitial and vacancy diffusion respectively. C''_i and $C''_\Box$ are given by equations (4) and (8) respectively; thus

$$\frac{X\mathrm{d}X}{\mathrm{d}t}=\frac{z_1D_i}{\Omega}\left(\frac{1}{KC_v}-C'_i\right) \qquad (19)$$

and

$$\frac{X\mathrm{d}X}{\mathrm{d}t}=\frac{z_1D_\Box}{\Omega}(C'_\Box-\mathbf{K}C_v). \qquad (20)$$

It should be noted at this point that equations (19) and (20) are quite general in that they do not involve any assumptions concerning the distribution of vacancies in the metal. C_v, the concentration of vacancies in the metal at the metal-oxide interface, may be given by complicated expressions derived from models of the diffusion of the vacancies to the interior of the sample or to sinks. In general, solution of these equations will involve numerical solution of coupled partial differential equations. In the following we will make simplifying assumptions which will lead to analytic solutions.

If vacancies do not precipitate out of solution in the metal, and if they are uniformly distributed in the metal, then C_v is given by equation (10) which can be combined with equations (19) and (20) to give

$$\frac{X\mathrm{d}X}{\mathrm{d}t}=\frac{z_1}{\Omega}D_i\left(\frac{w\Omega}{X2K}-C'_i\right) \qquad (21)$$

$$\frac{X\mathrm{d}X}{\mathrm{d}t}=\frac{z_1}{\Omega}D_\Box\left(C'_\Box-\frac{2\mathbf{K}X}{w\Omega}\right) \qquad (22)$$

for cation interstitial diffusion and for cation vacancy diffusion controlled reactions respectively. If the vacancies can precipitate, and their transport is rapid compared to their rate of generation the term C_v will be constant and equations (19) and (20) will reduce to the conventional parabolic rate equations as derived by Wagner[8].

For sufficiently small values of X/w equations (21) and (22) will be dominated by the first terms inside of the parentheses on the right. Thus in this limit the rate laws reduce to

$$\frac{\mathrm{d}(X)^3}{\mathrm{d}t}=\frac{3z_1D_iw}{2K} \qquad (23)$$

$$\frac{\mathrm{d}(X)^2}{\mathrm{d}t}=2\frac{z_1}{\Omega}D_\Box C'_\Box. \qquad (24)$$

Thus for cation interstitial diffusion control one can obtain a cubic rate law whose rate constant depends linearly upon the initial thickness of the metal. Of course the assumptions of Henry's Law, the Einstein relationship, uniform distribution of vacancies, and no vacancy precipitation are implicit in equations (23) and (24). For small oxide thickness, the first term in the brackets of equations (21) and (22) dominates. As the oxide continues to thicken the two terms become comparable and eventually add to zero. At this thickness the growth stops. This is reflected in the full solutions of equations (21) and (22).

$$\exp\left[\frac{C_iz_1D_it}{\Omega q^2}\right]=\frac{\mathrm{e}^{-X/q}\mathrm{e}^{-(X)^2/2q^2}}{1-\dfrac{X}{q}} \qquad (25)$$

where

$$q = \frac{\Omega w}{2C'K} \tag{26}$$

for interstitial diffusion. For vacancy diffusion

$$\exp\left[\frac{z_1 C'_\square D_\square t}{\Omega}\right] = \frac{e^{-X/a}}{1 - \frac{X}{a}} \tag{27}$$

where

$$a = \frac{C'_\square \Omega w}{2K}. \tag{28}$$

Equations (25) and (27) are plotted in Fig. 1 and can be seen to asymptote to q and a respectively. These asymptotic limits depend linearly upon the initial thickness of the metal and *implicitly contain a pressure dependence in the C's*. Physically these limits describe the conditions at which the defect concentrations at the oxide-metal interface become equal to those at the oxide-gas interface.

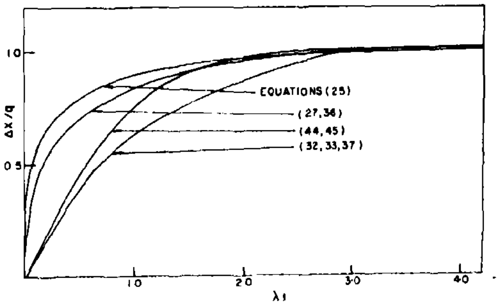

Fig. 1. Normalized curves of equations (25, 27, 32, 33, 36, 37, 44 and 45).

2. *Surface control*

In the above analysis the growth of the oxide was limited by defect diffusion in the oxide. We now consider the case where the reaction rate is limited by the reaction at two interfaces: namely the metal-oxide and the oxide-gas interfaces.

(a) *Metal-oxide interface*. The forward and reverse reaction rates are still given by equations (2) and (3) for cation interstitials and by equations (6) and (7) for the case of cation vacancies. However the rate of growth of the oxide is now determined by their difference, i.e.

$$\frac{dX}{dt} = \Omega(J_f - J_r). \tag{29}$$

Using the same approximation as before one obtains for the case of cation interstitial diffusion

$$\frac{dX}{dt} = \Omega N_m \nu T_f g_f (C_i - C_r K) \tag{30}$$

while for the case of cation vacancy diffusion one obtains

$$\frac{dX}{dt} = \Omega N_m \nu \mathbf{T}_f \mathbf{g}_f C'_\square \left(1 - \frac{\mathbf{K} C_r}{C'_\square}\right) \tag{31}$$

where all quantities are as defined in the previous section. In equations (30) and (31) the oxide is assumed to be wholly in equilibrium with the gas and therefore C' is appropriate rather than C''. If the vacancies in the metal are assumed to remain in solution, C_r is given by equation (10) which together with equations (30) and (31) result in

$$\frac{1}{1 - \frac{X}{q}} = \exp\left[\frac{2N_i \nu_0 T_r g_r \alpha \Omega C'_i t}{w}\right] \tag{32}$$

and

$$\frac{1}{1 - \frac{X}{a}} = \exp\left[\frac{2N_r \boldsymbol{\nu} \mathbf{T}_r \mathbf{g}_r \alpha \Omega t}{w}\right] \tag{33}$$

for cation interstitials and cation vacancies respectively, and where q and a are defined by equations (26) and (28). These functions have been put into the same form as that of equations (25) and (27). Rearranging terms in equations (32) and (33) results in the more convenient form.

$$X = q\left(1-\exp\left[-\frac{2N_i\nu_0T_rg_r\,\alpha\Omega C_i't}{w}\right]\right)$$

$$X = a\left(1-\exp\left[-\frac{2N_c\nu\mathrm{T}_r\mathrm{g}_r\,\alpha\Omega t}{w}\right]\right).$$

(b) *Oxide-gas interface.* We consider now the case in which the rate controlling reaction is the *incorporation* of oxygen into the oxide at the oxide-gas interface. In this case the oxide is assumed to be in equilibrium with the metal and we further assume that linear rate theory is applicable. Therefore in the case of cation interstitials the forward reaction rate will be proportional to C_i''.

As long as C_i'' is small compared to N_i, the number of interstitial sites per unit area, the reverse reaction rate can be considered constant and characterized by C_i'. In this case C_i' has precisely the same meaning it had previously; namely the concentration of metal interstitials in the oxide when the oxide is in equilibrium with the gas at the oxidizing pressure. Under these conditions

$$\frac{\mathrm{d}X}{\mathrm{d}t} = \Omega K^*(C_i''-C_i') \tag{34}$$

where K^* is the reaction rate constant for the reaction at the oxide-gas interface.

For the case of cation vacancies, the forward rate can be considered constant and is proportional to $C_\square'$ and the reverse rate can be considered proportional to $C_\square''$. Thus

$$\frac{\mathrm{d}X}{\mathrm{d}t} = \Omega \mathrm{K}^*(C_\square'-C_\square''). \tag{35}$$

When the vacancies in the metal remain in solution, we can substitute of equation (12) into equations (34) and (35) and upon integration give

$$\exp\frac{[\Omega K^*C_i't]}{q} = \frac{\mathrm{e}^{-X/q}}{1-\dfrac{X}{q}} \tag{36}$$

for interstitial diffusion where q is defined as before, and

$$\exp\left[\frac{\Omega K^*C_\square't}{a}\right] = \frac{1}{1-\dfrac{X}{a}} \tag{37}$$

for diffusion of cation vacancies where a is also as defined as before.

3. *Diffusion in high electric fields*

For the case of high electric fields equation (1) is no longer applicable since the mean drift velocity of the ions is not a linear function of the electric field and therefore the Einstein relation is no longer valid. Under conditions of very high field, Cabrera and Mott[11] have derived the following expression for the mean drift velocity of ions

$$u = 2\nu c \exp(-U/kT) \sinh(z_1cF/2kT) \tag{38}$$

where ν is a vibrational frequency for the defect in the oxide, c is the distance traveled per jump, U is the activation energy for a jump in the absence of any field, F is the electric field at that point, and all other quantities are as previously defined. If one considers that the oxide at the metal-oxide interface is in equilibrium with the metal and has the number of defects appropriate to this; and similarly this oxide is equilibrated with the gas at the oxide-gas interface, the concentration of defects will vary continuously through the oxide. If we assume that the oxide is an extrinsic, non-degenerate semiconductor, and the defects are either donors or acceptors, the value of Fermi energy in the oxide relative to the top of the valance band will vary with their concentration in a calculable manner. For example, if the defects are all donors and the effective mass of the electrons can be considered constant, the Fermi energy relative to the top of the valance band will be given by [12].

$$E_f = E_g + kT\ln(C_d/2(2\pi m_e kT/h^2)^{3/2}) \tag{39}$$

where E_g is the energy gap, k is Boltzmann's constant, T is the absolute temperature, C_d is the concentration of donors, m_e is the effective mass of the electrons and h is Planck's constant. A similar relationship can be derived for holes and acceptors. Using the continuing assumption that the electrons are considerably more mobile than the defects, the Fermi level must be constant throughout the oxide, hence a potential varying as, but opposite to, E_f must be set up in the oxide. Taking the potential at the metal-oxide interface as ground, then from equation (39) the potential as a function position is:

$$V(x) = kT \ln (C(x)/C''). \tag{40}$$

For this one dimensional problem $F = -\mathrm{d}V/\mathrm{d}x$, hence,

$$u(x) = 2\nu c \exp(-U/kT) \sinh\left(-\frac{z_1 c}{2} \times \frac{\mathrm{d} \ln C(x)}{\mathrm{d}x}\right). \tag{41}$$

Since the divergence of the current must be zero for the case of simple diffusion

$$\frac{\mathrm{d}(C(x)u(x))}{\mathrm{d}x} = 0. \tag{42}$$

Equations (41) and (42) define $C(x)$ by a second order differential equation. The boundary conditions are $C(0) = C''$ and $C(X) = C'$. This differential equation cannot readily be solved, but if one takes the limit of very high fields and replaces sinh by exp/2 one can then solve the resulting differential equation to obtain:

$$\ln\left(\frac{C(x)}{C''}\right) + \frac{1}{e^{\frac{2X}{z_1 C}} - 1} \ln\left(\frac{C'}{C''}\right) = \frac{e^{2x/z_1 C}}{e^{\frac{2X}{z_1 C}} - 1} \ln\left(\frac{C'}{C''}\right). \tag{43}$$

If one substitutes this into equation (41), in the limit that $e^{2X/z_1 c} \gg 1$, the rate laws derived for cationic interstitial, and cationic vacancy control are, for the cases where the vacancies are retained in the metal,

$$X = q \tanh (D_i C_i \Omega t) \tag{44}$$

and

$$X = a \tanh (D_{\square} C'_{\square} \Omega t) \tag{45}$$

respectively where the diffusion coefficients include νc and $\exp[-U/kT]$ and all other quantities are as previously defined. This rate law is also shown in Fig. 1.

DISCUSSION

There are some assumptions implicitly contained in these equations. It was assumed that the oxide started at zero thickness and grew in thickness evenly. Experimental work by the authors[5, 6] and others[13] has shown that the normal sequence of oxidation events on a clean metal surface is first the formation of discrete nuclei followed by their lateral growth and coalescence finally followed by gradual thickening. Only after the coalescence of the oxide and the elimination of free surface are vacancies which are generated confined to the surface. Thus the kinetics of the earliest stages of oxidation are controlled by this lateral growth rather than thickening.

A further point is that the thickness of oxide, X, which is used in calculating the number of vacancies should differ from the true thickness of the oxide by the thickness of the layer at the time it coalesces. This would also tend to cause the oxidation kinetics to deviate from the derived rate laws for short times, and finally the assumption that the vacancies are homogeneously distributed would probably be strictly true only for very thin specimens.

Figures 2 and 3 are from the authors[5] work on the oxidation of titanium thin films. Figure 2 shows oxidation kinetics for films of different thickness under the same oxidizing

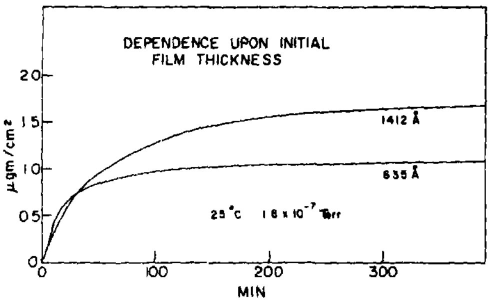

Fig. 2. Oxidation kinetics of titanium thin films of different average thickness which were prepared and oxidized under identical conditions[5].

conditions and in Fig. 3 the asymptotic oxygen take up of the films is plotted as a function of the product of the titanium film thickness by the oxygen pressure to the 1/9 power. An examination of equation (26) shows that this product should be proportional to q the asymptotic thickness. The intercept of the line at the zero of the ordinate, W_0 should correspond to the mass of the oxide at the time when it coalesces. This value for the mass of the oxide at coalescence is in quite good agreement with the value obtained from the initial kinetics.

For thicker samples diffusion of vacancies away from a saturated surface layer might become wholly or in part rate determining. One sign of this would be enhanced oxidation in the vicinity of grain boundaries since they are easier paths for the diffusion for vacancies.

The point to note is that the vacancies, as long as they remain in solution, oppose further oxidation; or in the electrochemical sense they passivate the metal. Hence anything which would promote the precipitation of vacancies either at internal voids or at the surface would enhance oxidation or corrosion. For example, Fiegna and Weisgerber[14] deposited noble metal films on zirconium under conditions where they formed isolated islands. They found that this enhanced the oxidation of zirconium in oxygen and in water vapor at 450°C. We suggest that since no protecting oxide is present on the noble metal islands vacancies probably travel to the zirconium noble metal interface and then either move along the interface and get eliminated at the zirconium-noble metal-oxide triple boundary or diffuse through the noble metal to the free surface. Hence one would expect oxidation to be enhanced under these circumstances.

Now consider the case where, after some oxidation and its concomitant generation of

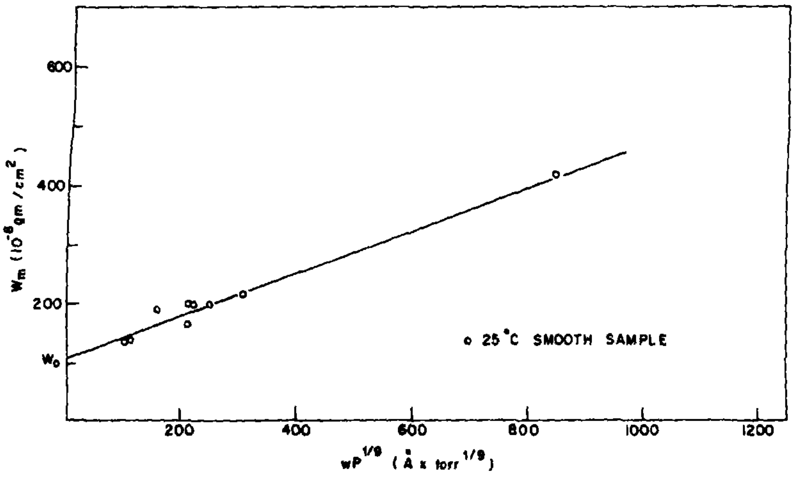

Fig. 3. Asymptotic oxygen take up shown as a function of the product of initial film thickness by the one-ninth power of the oxygen pressure[5].

vacancies, for some reason vacancies can condense to form a small pit at the surface. The area around this pit would have a lower vacancy concentration and in line with the considerations of the previous paragraphs will be active with respect to the rest of the sample. Also the gradient in vacancy concentration will tend to move more and more vacancies to the pit which would tend to enlarge it. Thus if transport through the oxide layer on an oxidizing or corroding metal sample is via cations the sample is inherently unstable with respect to the formation of pits or voids. Furthermore, if a tensile stress is present the pits or voids will grow in such a manner as to present the maximum cross-section perpendicular to the tensile axis (the analysis showing this is exactly the same as the Griffith analysis[15]). Therefore, under conditions of cationic transport through the oxide, and in the presence of a tensile stress, a metal sample would be unstable with respect to the *initiation of cracks*. This could play a significant role in stress corrosion cracking.

Finally we should like to make some comment about 'rate laws'. First of all it can be seen that similar rate laws can be derived for a variety of circumstances. Thus the fitting of an experimental curve to a particular rate law is not sufficient to delineate a particular mechanism. Although rate laws derived in this paper seem rather complex, at short times they resemble the usual simple empirical laws to which people routinely fit data. For example equation (25) will, for short times, appear to follow a cubic rate law, equations (27) and (38) a parabolic rate law, and equations (32), (33) and (39) will appear to follow logarithmic rate laws. However at longer times (greater ratios of $X/q(X/a)$) these curves will break away from the simple empirical laws as can be seen by the example in Fig. 2. When such 'breaks' are seen in experimental data they are usually explained by a change of rate determining mechanism; this may not always be the case.

Acknowledgements—This work was supported by the National Science Foundation and the Advanced Research Projects Agency.

REFERENCES

1. HAUFFE K., *Oxidation of Metals.*
2. VERMILYEA D. A., *Acta Metall.* **5**, 492 (1957).
3. DOBSON P. S. and SMALLMAN R. E., *Proc. R. Soc.* **A293**, 423 (1966).
4. KRITZINGER S., DOBSON P. S. and SMALLMAN R. E., *Phil. Mag.* **140**, 217 (1967).
5. MINDEL M. J. and POLLACK S. R., To be published in *Proceedings of the International Conference on Titanium.* May (1968).
6. MINDEL M. J., Doctoral dissertation, Univ. of Penna. (1968).
7. HANCOCK P. and FLETCHER R., *Journees Internationales De Etude Sur L'Oxydation Des Metaux.* Brussels (1965).
8. WAGNER C. *Z. phys. Chem.* **B21**, 25 (1933).
9. PICKERING H. W. and WAGNER C., *J. electrochem. Soc.* **104**, 698 (1967).
10. WAGNER C., *Atom Movements.* ASM (1949).
11. CABRERA N. and MOTT N. F., *Rep. Prog. Phys.* **12**, 1163 (1948–49).
12. See for example KITTEL C., *Introduction to Solid State Physics*, 2nd Edn. Wiley, New York (1956).
13. RHODIN T. N., ORR W. H. and WALTON D., *Processus de Nucleation dans les Reactions des gaz sur les Metaux et Problemes Connexes* Paris (1963).
14. FIEGNA A. and WEISGERBER P., *J. electrochem. Soc.* **119**, 369 (1968).
15. GRIFFITH A. A., *Phil. Trans. R. Soc.* **A221**, 163 (1920).

J. Phys. Chem. Solids Pergamon Press 1969. Vol. 30, pp. 1003–1007. Printed in Great Britain

CATION DIFFUSION IN FLUORITE SINGLE CRYSTALS*

M. BAKER and **A. TAYLOR**
Department of Materials Science and Engineering, Cornell University, Ithaca, N.Y. 14850, U.S.A.

(*Received* 3 *April* 1968)

Abstract—Tracer diffusion of strontium in CaF_2, SrF_2 and BaF_2 can be represented by the following equations

$$D_{CaF_2} = 1{\cdot}72 \times 10^5 \exp(-4{\cdot}37/kT)\,(1000°–1200°C)$$

$$D_{SrF_2} = 1{\cdot}09 \times 10^4 \exp(-4{\cdot}30/kT)\,(1000°–1200°C)$$

$$D_{BaF_2} = 4{\cdot}45 \times 10^3 \exp(-3{\cdot}75/kT)\,(1000°–1200°C)$$

Diffusion is probably due to some Schottky disorder in this range. The large values of Q and D_0 could be explained in terms of excess impurity-induced anion vacancies and/or cation diffusion by means of associated vacancy pairs.

1. INTRODUCTION

THE PROPERTIES of lattice defects in fluorite crystals have been investigated by several techniques. Ionic conductivity[1, 2] measurements up to 0·8 of the melting temperatures show that the predominant disorder is a Frenkel type disorder on the anion sublattice. The disorder above these temperatures has not been established experimentally. The properties of fluorine vacancies and fluorine interstitials have been studied in crystals doped with aliovalent ions using E.S.R.[3–7], N.M.R.[8, 9], dielectric[10] and anelastic[11] relaxation, and conductivity measurements. In contrast, little work has been done on cation lattice defects[12, 13]. In order to study cation defects in fluorite crystals we have measured the diffusion of strontium 89 in single crystals of CaF_2, SrF_2 and BaF_2.

2. EXPERIMENTAL PROCEDURE

Single crystal rods (½ in. dia. and 1 in. long) of optical grade CaF_2, SrF_2, BaF_2 were purchased from the Harshaw Chemical Company. Disks at least ¼ in. thick were cleaved from the rod and were then ground flat and parallel to within 10 μ, using standard metallographic grinding through grade 600 emergy paper. A final surface polish was obtained with 3 μ garnet powder. Strontium 89, purchased from Isotopes Development Center, Oak Ridge National Laboratory, was evaporated as SrF_2 onto the disks which were then sealed off in the quartz tube with graphite liners under a vacuum of 5×10^{-6} Torr. The specimens were annealed in a platinum wound furnace controlled by a platinum–platinum + 10 per cent rhodium thermocouple to within ± 2°C of the annealing temperature. After the anneal, the sides of the disk were ground down to eliminate any surface diffusion effects. The penetration profile was obtained by grinding off 2–35 μ slices with emery paper mounted on glass slides. The thickness of the slice was determined by weighing it and by direct measurement with a 0·0001 in. dial gage. The error in the thickness of the slice was 1 percent. The activity of the slice was measured in a fixed geometry by an anthracene scintillation detector connected to a Hewlett-Packard 5210 L scaler timer.

---

*This work is supported by the Advanced Research Projects Agency through the Materials Science Center at Cornell University.

At least 10,000 counts were taken on each slice.

3. RESULTS AND DISCUSSION

The penetration curves were analyzed using the standard thin film solution for bulk diffusion in one dimension,

$$C(x, t) = \frac{C_0}{\sqrt{\pi D t}} \exp(-x^2/4Dt) \qquad (1)$$

where $C(xt)$ is the concentration at a distance x below the surface after an isothermal anneal for time t, C_0 is the initial surface concentration, D the diffusivity at the annealing temperature. D's were determined from the slopes of the plot of log-activity vs. x^2 which were linear in the temperature range 1300°–1500°K. Figure 1, shows some typical penetration curves for Sr^{89} in CaF$_2$, and SrF$_2$ crystals.

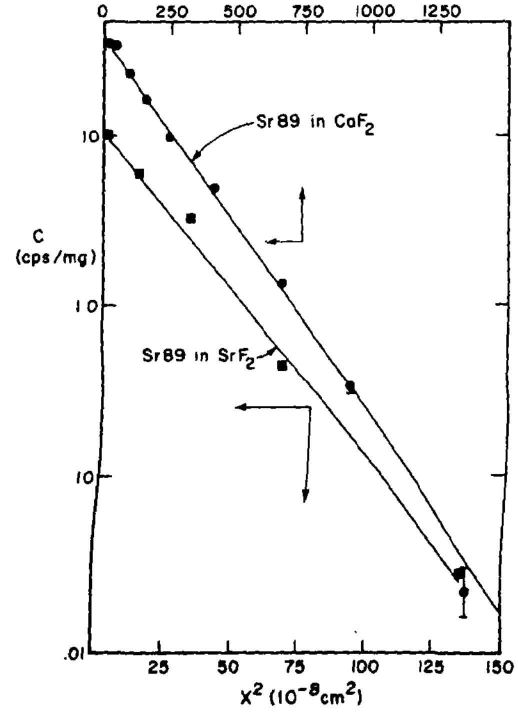

Fig. 1. Penetration profiles of Sr^{89} in CaF$_2$ and SrF$_2$ crystals at 1393°K for 2·04 × 10^4/sec.

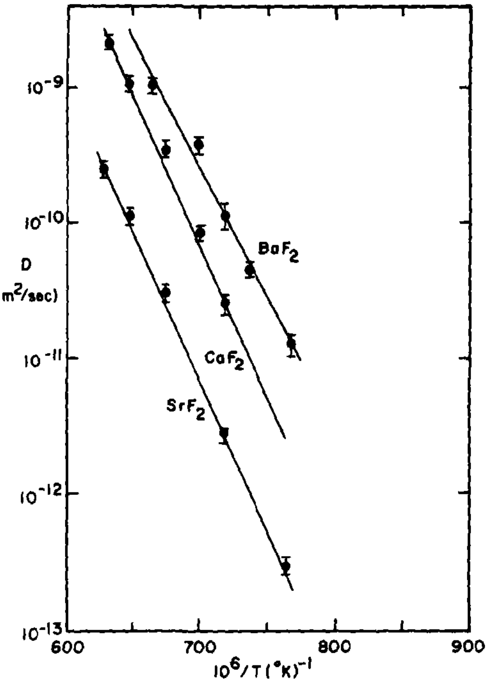

Fig. 2. Arrenhius plot of the diffusion coefficient for Sr^{89} in CaF$_2$, SrF$_2$ and BaF$_2$ crystals.

An Arrhenius plot of the data, shown in Fig. 2, indicates that in this temperature range the diffusivity is governed by a single activation energy Q. The experimental values of Q and D_0, the diffusivities at infinite temperature, are listed in Table 1 together with defect formation energies available in the literature.

The activation energies for diffusion are considerably larger than the 1·7 eV obtained by Short and Roy[12] for Ca^{2+} diffusion in polycrystalline CaF$_2$, but they are comparable to Matzke's[13] value for Ca^{2+} diffusion in single crystals of CaF$_2$.

As might be expected from size factor considerations, the energies for diffusion increase with decreasing lattice parameter of the host crystals. The values of D_0 show a similar systematic trend; however, the values of D_0 are at least two orders of magnitude higher than is normally found for intrinsic diffusion.

Table 1

	CaF_2	SrF_2	BaF_2
Q Exptl	$4{\cdot}37 \pm 0{\cdot}3$ eV	$4{\cdot}30 \pm 0{\cdot}3$ eV	$3{\cdot}75 \pm 0{\cdot}3$ eV
D_0 Exptl	$1{\cdot}72 \times 10^{5}\ \mathrm{cm^2/sec}$	$1{\cdot}09 \times 10^{4}\ \mathrm{cm^2/sec}$	$4{\cdot}45 \times 10^{3}\ \mathrm{cm^2/sec}$
W_s Calculated[19, 14]	$5{\cdot}1 \pm 0{\cdot}7$ eV	$5{\cdot}30 \pm 0{\cdot}7$ eV	$5{\cdot}2 \pm 0{\cdot}7$ eV
W_f Calculated[14]	$2{\cdot}7$ eV	$2{\cdot}5$ eV	$2{\cdot}3$ eV
W_f Exptl	$2{\cdot}8 \pm 0{\cdot}2$ eV[2]	$2{\cdot}4 \pm 0{\cdot}2$ eV[15]	$1{\cdot}9 \pm 0{\cdot}1$ eV[1]
U_M (equation (5))	$2{\cdot}1 \pm 1{\cdot}2$ eV	$1{\cdot}4 \pm 1{\cdot}2$ eV	$0{\cdot}45 \pm 1{\cdot}1$ eV

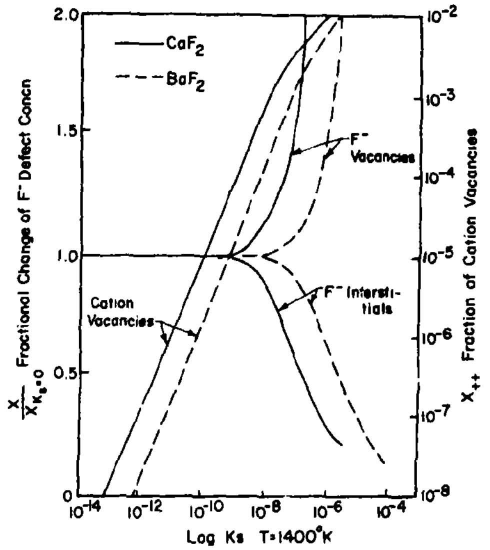

Fig. 3. Showing the influence of Schottky minor disorder on the concentration of lattice defects at high temperatures for various of K_s. Solid line CaF_2 Broken line BaF_2.

On the basis of the diffusion energies alone the results appear consistent with an intrinsic diffusion governed by free cation Schottky vacancies. The activation energy Q will be the sum of a motion energy plus a contribution from the formation energy of the intrinsic defects. The concentration of cation defects may be obtained from the expressions for the equilibria for anion Frenkel disorder and for Schottky disorder, equations (2) and (3) respectively,

$$X_{\boxminus}^{2} X_{\boxed{++}} = K_s \tag{2}$$

$$X_{\boxminus} X_{\ominus} = K_f \tag{3}$$

and the charge neutrality condition

$$2X_{\boxminus} - 2X_{\boxed{++}} - X_{\ominus} = 0. \tag{4}$$

Here X represents the fraction of defects and $\boxed{++}$, $\boxminus$, $\ominus$ represent vacancies and interstitials respectively and K the equilibrium constant.

From results in the current literature one must conclude that $K_f \gg K_s$ in the solid crystal. The values for K_f in CaF_2 and BaF_2 are available in the literature. For SrF_2 a value of $K_f \simeq 10^4 \exp(-2{\cdot}5/kT)$ may be obtained from recent conductivity measurements at intermediate temperatures. The value of K_s has been estimated using the formation energy of $5{\cdot}3 \pm 0{\cdot}7$ eV calculated by Franklin[14] and an arbitrary upper limit value for the entropy of formation factor $\exp(S_f/k) = 10^5$, where S_f is the formation entropy.

When $K_f \gg K_s$ the concentration of anion vacancies is hardly affected by the Schottky disorder as is shown in Fig. 3. We may use a simplified expression for the fraction of intrinsic cation vacancies namely

$$X_{++} = \frac{K_s}{K_f} = A \exp\left(-\frac{W_s - W_f}{kT}\right) \tag{5}$$

where A is an entropy factor ≈ 10, and W_s and W_f are the appropriate defect formation energies. By setting Q equal to the sum of $(W_s - W_f + U_M)$, where U_M is the cation motion energy we obtain the values listed in Table 1. Whilst the values of U obtained for CaF_2 and SrF_2 are reasonable, little significance can be given to U_M for BaF_2. It is the difference between a large calculated value of W_s and an experimental value of W_f which is considerably smaller than W_f calculated using similar assumptions to those for W_s.

The present magnitudes of D_0 are not readily explicable on the basis of the usual arguments which show

$$D_0 \approx a^2 \nu A \exp \frac{S_M}{k}$$

unless very large values are taken both for the entropy of formation of a Schottky trio and for the entropy of motion S_M. Such large values of S_M could be justified as due to the displacement of many ions surrounding the diffusion cation.

Small values of D_0 are usually considered characteristic of extrinsic behavior where the concentration of cation vacancies is fixed by aliovalent cation impurities. In any case the concentration of these cation vacancies would be approximately equal to the total trivalent cation impurity concentration which is less than 10 ppm in the present crystals. However, it is interesting to conjecture that if the anion vacancy concentration were pegged at some value $X'_{\boxminus} \approx 10^{-3}$ because of aliovalent anions, then from equation (2) we see that the concentration of cation vacancies is governed by the energy W_s while

$$D_0 \approx \frac{a^2 \nu}{X'^2_{\boxminus}} \exp \frac{\Delta S_M + \Delta S_f}{k}.$$

D_0 would then take on much larger values because of the $X'^2_{\boxminus}$ term in the denominator. A vacancy pair model for the diffusion under the condition of this type of extrinsic behavior gives a reasonable explanation for the values of Q and D_0 compatible with the energies calculated by Franklin. The equilibrium concentration of cation–anion vacancy pairs X_p is approximately given by

$$X_p = X'_{\boxminus} X_{\boxplus\boxplus} \exp + \frac{E_a}{kT} \tag{6}$$

where E_a is an association energy of the pair formation. Thus

$$Q = (W_s - E_a + U_M) \approx 5\,\mathrm{eV}$$

and

$$D_0 \approx \frac{a^2 \nu}{X'_{\boxminus}} \exp \frac{\Delta S_M + \Delta S_f - S_a}{k} \approx 10^5.$$

At present no verification of the mechanism has been attempted.

Considerable assistance in the interpretation of this data would come from reliable conductivity measurements in these fluorites at higher temperatures. Since both the F^- vacancy and F^- interstitial motion energy are known, the influence of the minor Schottky disorder might be detectable in the Arrenhius plots of the conductivity of CaF_2, although probably not for BaF_2.

This is demonstrated in the concentration of these defects shown in Fig. 3.

Departures from linearity in the conductivity $\ln \sigma \; Tv \; 1/T_2$ curves at higher temperatures have been observed by Rossing but these measurements were taken over too limited a temperature range to permit a quantitative interpretation of the slope. We hope that further work along the lines proposed will help to pin down the mechanism of diffusion.

REFERENCES

1. BARSIS E. and TAYLOR A., *J. chem. Phys.* **45**, 1154 (1966).
2. ROSSING B., Thesis, Lattice Disorder in CaF_2 M.I.T. (1966).
3. BERULAVA B. G., SANADZE T. I. and KHAKHAWASHVILI O. G., *Soviet Phys. JETP* **21**, 288 (1965).
4. BLEANEY B., LLEWELLYN P. M. and JONES D. A., *Proc. phys. Soc.* **B69**, 858 (1956).
5. SIERRO J., *Phys. Lett.* **4**, 178 (1963).
6. RAMON V. and YANIV A., *Phys. Lett.* **9**, 17 (1964).
7. HAYES W. and TWIDELL J. W., *J. chem. Phys.* **35**, 1521 (1961).
8. LYSIAK R. and MAHENDROO P., *J. chem. Phys.* **44**, 4025 (1966).
9. MILLER J. and MAHENDROO P., *Phys. Lett.* **23**, 535 (1966).
10. CHEN J. and MCDONOUGH M., *Bull. Am. Phys. Soc.* **647** (1964).
11. SOUTHGATE P. D., *J. Phys. Chem. Solids* **27**, 1623 (1966).
12. SHORT J. and ROY R., *J. phys. Chem.* **68**, 3877 (1964).

13. MATZKE H. and LINDNER R., *Z. Naturf.* **19**, 1178 (1964).
14. FRANKLIN A. D., *Born Model Calculation of Point Defect Formation Energies in Alkaline Earth Fluorides*. Proceedings of British Ceramic Society, No. 9 (1967).
15. FIELDER W. L., NASA Report TND-3816.

J. Phys. Chem. Solids Pergamon Press 1969. Vol. 30, pp. 1009–1012. Printed in Great Britain.

TECHNICAL NOTES

Ferromagnetic resonance linewidth and relaxation in the system $Mn_xFe_{3-x}O_{4+\gamma}$

(*Received* 21 *May* 1968; *in revised form* 27 *September* 1968)

FERROMAGNETIC relaxations in the system $Mn_xFe_{3-x}O_{4+\gamma}$ ($x \approx 1$) was examined by Heeger *et al.*[1, 2] and Clarke[3]. All the authors have found two peaks in linewidth as a function of temperature, one at ≈20° and the other at ≈250°K. The high temperature effect was definitely attributed to the presence of Fe^{2+} and it is believed that it is due to slow-relaxing mechanism[2, 3]. The details of loss mechanism in manganese ferrite are, however, still in doubt, as the authors[1–3] differ both in experimental data and in their interpretation. The study of Iida[4, 5] seems to indicate that the origin of the loss is connected most probably with 'electron hopping'. The frequency viaration found by Clarke is, however, not consistent with this model. The purpose of this contribution is to extend the new experimental data for $x < 1$ and to help thus to the solution of this problem.

Single crystals $Mn_xFe_{3-x}O_{4+\gamma}$ was prepared both by the Bridgman's method ($x = 0{\cdot}95$, 0·98 and 1·013) and by the Verneuil's method ($x = 0{\cdot}71$, 0·73, 0·78 and 1·45). More details about the preparation of the crystals and their quality are published elsewhere[6]. Note also that the quality of all the crystals were quite good from point of view of ferromagnetic resonance measurements, for example the $\Delta H(111)$ and $H_{res}(111)$ were the same for all [111] directions. In the Table 1 their chemical analysis are given. A polished sphere with diameter about 0·3 mm made of single crystals were fixed on a sample rod in such a way that the magnetic applied field was parallel to a (110) plane.

Usual technique using TE_{102} reflection cavity and a 'square law detector' was employed the proper function of the latter being carefully checked during the measurements. The frequency of the klystron was stabilised to the frequency of the microwave cavity by means of the frequency discriminator. In this case the real part of the permeability was not efficient. The measurements were performed at frequency 9·2 GHz in temperature range from 80° up to 300°K.

Figure 1 shows the full linewidths ΔH temperature for the different compositions. It is obvious that with increasing contents of Fe^{2+} ions the positions of the peaks in ΔH are shifted towards the lower temperatures and their magnitudes are increased. For the composition $x = 0{\cdot}95$ our measurements agree with those by Clarke[3]. Note that Clarke's crystals were prepared by Verneuil's method, whereas our one was by Bridgman's method.

The slow-relaxing theory gives rise to the linewidth ΔH and to a downward shift S in

Table 1. *Summary of main results for the system* $Mn_xFe_{3-x}O_{4+\gamma}$

x	γ	E (meV)	τ_∞ (10^{-12} sec)	F (10^4 erg/cm^3)	G (10^4 erg/cm^3)
0·71	0·040	35	1·8	16	32
0·78	0·067	40	2·5	12·7	24
0·95	0·010	70	1	6·45	11·2
0·98	—	80	1	4·3	7·5

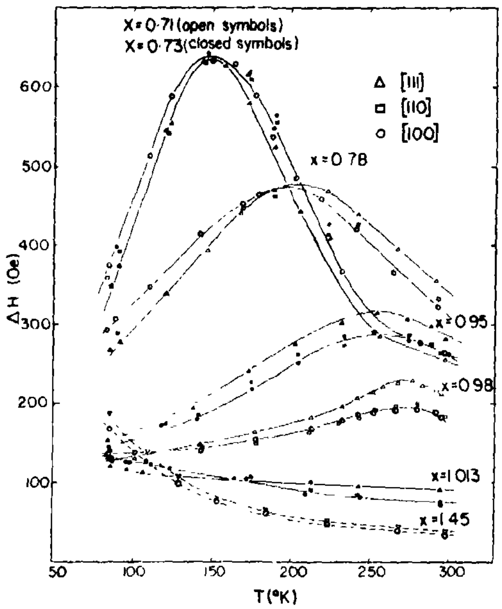

Fig. 1. Temperature dependence of the linewidth of $Mn_xFe_{3-x}O_{4+\gamma}$ in principal directions in a (110) plane at 9·2 GHz.

the resonance magnetic field. For the system of low laying pair of energy levels with energy splitting δ the expressions reduce to[3]

$$\Delta H = \frac{C}{MkT} f(\theta, \phi)\,\mathrm{sech}^2(\delta/2kT)\,\omega\tau/[1+(\omega\tau)^2] \quad (1)$$

$$S = \frac{\omega}{\gamma_t} - \frac{\omega}{\gamma_{\mathrm{eff}}} = \tfrac{1}{2}\Delta H\omega\tau \quad (2)$$

C is the concentration of the ions responsible for relaxation, $f(\theta, \phi)$ is a function of anisotropy in δ, γ_t and γ_{eff} represents the true and measured gyromagnetic ratios. In equation (1) both the term $1/kT\ \mathrm{sech}^2(\delta/2kT)$ and $\omega\tau/[1+(\omega\tau)^2]$ gives the maxima in temperature dependence.

Clarke[3] supposed $\omega\tau \ll 1$ and explained the temperature maximum by the first term and used for $\delta = g\beta H_{ex} - D$. According to this interpretation we obtain $\delta = 270\,\mathrm{cm}^{-1}$ from temperature of the maximum (for $x = 0{\cdot}95$), in very good agreement with Clarke's results. Our experimental results, as a whole, however, cannot be sufficiently explained in this way, according to the following two reasons.

(1) The values δ very rapidly fall with decreasing x. If we persist in Clarke's interpretation, it is possible to explain this decrease either by lowering $g\beta H_{\mathrm{ex}}$ or by raising D with decreasing x. The first possibility is contradictory both to the experimental fact of the raising of Curie temperature with increasing constants of Fe^{2+} ions[7] and to the conclusions of Slonczewski[8]. Hence it remains to admit for $x = 0{\cdot}71$ ($\delta = 150\,\mathrm{cm}^{-1}$) the raising of D to unreasonably high value $D \approx 200\,\mathrm{cm}^{-1}$ (e.g. Slonczewski[8] reports for the value $|D| \approx 10\,\mathrm{cm}^{-1}$).

(2) Were the maximum ΔH due to the term $1/kT\ \mathrm{sech}^2(\delta/2kT)$ a maximum should also appear in the dependence g_{eff} vs. T (equations (1) and (2)). The observed increase of g_{eff} towards lower temperatures at $x \approx 0{\cdot}7-0{\cdot}8$ (Fig. 2), however, when interpreted in terms of a dynamic shift, fits better to the frequency factor $(\omega\tau)^2/[1+(\omega\tau)^2]$. This conclusion is supported by the presence of a point of inflection on each curve, which nearly coincides with the position of the respective peak of ΔH in Fig. 1. (The values g_{eff} agree well with those obtained at room temperature by Funatogawa *et al.*[9].)

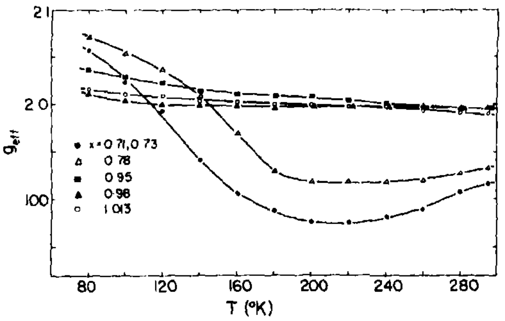

Fig. 2. A plot of effective g-factor, that was evaluated from resonance magnetic fields for the main crystallographic directions.

Thus we attempt an explanation of ΔH and g_{eff} by means of the frequency factors in (1) and (2) respectively.

We rewrite equation (1) into the form

$$\Delta H = \frac{A}{MT}\frac{\omega\tau}{1+(\omega\tau)^2}. \tag{3}$$

The value A will be regarded as independent of temperature in the closed vicinity of the peak in ΔH. Now if we compare the curves $MT\Delta H$ vs. T with the term $\omega\tau/[1+(\omega\tau)^2]$ we may calculate the relaxation times τ at each temperature. The resulting values thus obtained are plotted in the logarithmic scale vs. T^{-1} in Fig. 3. They seem to fulfil the linear dependence described by the relation

$$\tau = \tau_\infty \exp{(E/kT)}. \tag{4}$$

This dependence, which is typical for the 'hopping mechanism' leads us to the interpretation of the temperature peaks in terms of this loss mechanism (we suppose the hopping of electrons occurs between Fe^{2+} and Fe^{3+} ions). This conclusion is supported by quantitative comparison of our values E and τ_∞ in Table 1 (determined from the slopes of the lines in Fig. 3) with those obtained from measurements of conductivity[10–12] and $tg\delta$[13–15, 5]. The $tg\delta$ measurements in the system $Mn_xFe_{3-x}O_{4+\gamma}$ ($x < 1$) observed at frequency $\omega \approx 10^6\,\text{sec}^{-1}$ in temperature region 20–30°K are also explained by means of the loss mechanism connected with the hopping of electrons[14, 15]. Our experimental points lies near the extrapolated line, according to the relation (4), using the values E and τ_∞ from[14]. This agreement would be better, if we admit a slight temperature dependence of activation energy[16].

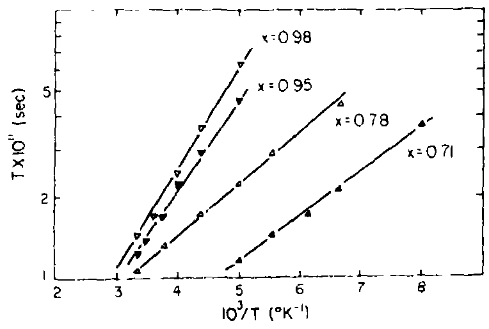

Fig. 3. Semilog plot of τ vs. $1/T$. Relaxation times are derived from Fig. 1 by comparing with equation (3) (relating to the direction [111]).

Furthermore, the results following from our measurements are very similar to the recent measurements of Iida[4, 5] who observed the peaks of dielectric losses at the frequency 9·3 GHz in manganese ferrites with $x < 1$. This process is very probably connected with the hopping of electrons. Their peaks occur roughly at the same temperature and frequency as in our case.

The original Clogstŏn's model was developed for the 'hopping mechanism'. Its phenomenological version was given by Teale[17]. It is possible to determine the induced anisotropy constant F and G (Table 1) in terms of this phenomenological description from the angular dependence of ΔH (which is very slight in our case). In the microscopic description the local anisotropy energy of Fe^{2+} ion is equal to $W\cos^2\nu$, where ν is the angle of the Fe^{2+} spin with the local symmetry axis. The microscopic anisotropy constant W can be determined from values F and G on the basis of Clogston's[18] and Slonczenski's[19] theory using the model of distribution of cations and their valencies according to Šimša [20]. The value $W \approx 1$ meV thus obtained is in reasonable agreement with $W \approx 0{\cdot}6$ meV for silicon doped garnet[21].

Unfortunately we have not measured the frequency variation and thus we cannot fully confront our results with Clarke's conclusions. Clarke states that the position of the peak does not depend on frequency, which is not consistent with the present model. Let us note, however, that certain shift ($\approx$30 deg) of the peak towards higher temperatures for higher frequency is visible, if Clarke's results are plotted in the form $MT\Delta H$ vs. T. Thus model proposed in this paper would be supported. Nevertheless, the larger ΔH at higher frequency remains in the framework of our model unexplained.

Acknowledgements – It is pleasure to thank the staff of workers of the Institute of Solid State Physics, ČSAV for the help at preparation of the samples to measurements, Ing. J. Dušek for lending his apparatus and especially to Dr. S. Krupička for his suggestions, valuable advices and discussions.

Institute of Solid State Physics,
Czechoslovak Academy of Sciences,
Prague

Z. SMETANA*

REFERENCES

1. HEEGER A. J., BLOCKER III T. G. and GHOSH S. K., *Phys. Rev.* **134**, A399 (1964).
2. HEEGER A. J., Preprint of the *Conference on the Magnetism and Magnetic Materials in Washington* (1966).
3. CLARKE B. H., *J. Phys. Chem. Solids* **27**, 353 (1966).
4. MIZUSHIMA K. and IIDA S., *J. phys. Soc. Japan* **22**, 1300 (1967).
5. IIDA S., MIZUSHIMA K., YAMADA N. and IIZUKA T., *J appl. Phys.* **39**, 818 (1968).
6. VICHR M., *Symposium on Crystal Growth, Moscow* (1966). To be published in Rost Kristallov.
7. GERBER R., ŠIMŠA Z. and VICHR M., *Czech. J. Phys.* **B16**, 913 (1966).
8. SLONCZEWSKI J. C., *J. appl. Phys.* **32**, 253 S (1961).
9. FUNATOGAWA Z., MIYATA N. and USAMI S., *J. phys. Soc. Japan* **14**, 1583 (1959).
10. ZÁVĚTA K., *Czech. J. Phys.* **9**, 748 (1959).
11. MIYATA N., *J. phys. Soc. Japan* **16**, 206 (1961).
12. LOTGERING F. K., *J. Phys. Chem. Solids* **25**, 95 (1964).
13. BROESE VAN GROENOU A., *J. Phys. Chem. Solids* **28**, 325 (1967).
14. ZÁVETA K., ZOUNOVÁ F. and TRINKLER E., *Czech. J. Phys.* **B18**, 1314 (1968).
15. KRUPIČKA S. and ZÁVĚTA K., *J. appl. Phys.* **39**, 930 (1968).
16. ZÁVĚTA K., *Czech. J. Phys.* **B18**, 810 (1968)..
17. TEALE R. W., *Proc. phys. Soc.* **92**, 411 (1967).
18. CLOGSTON A. M., *Bell System tech. J.* **34**, 739 (1955).
19. SLONCZEWSKI J. C., *Magnetism* (Edited by G. T. Rado and H. Suhl), vol. 1. Academic Press, N.Y. (1963).
20. ŠIMŠA Z., *Czech. J. Phys.* **B15**, 435 (1965).
21. HUNT R. P., *J. appl. Phys.* **37**, 1330 (1966).

**Present address:* Faculty of Mathematics and Physics, Charles University, Prague, Ke Karlovu 5

J. Phys. Chem. Solids Vol. 30, pp. 1012–1015.

Effect of impurities on the growth of *F* and *M* bands in KCl

(*Received* 13 *September* 1968)

SINGLE CRYSTALS of highly pure KCl (background divalent cation impurities ~1 ppm) were grown in the laboratory by the Kyropoulos method[1], and are designated as H crystals. Crystals doped with Ca, Cd, Mn and Pb, grown from the melt, are designated by their respective chemical symbols. Known amounts of each impurity in the form of chlorides (E. Merck's Grade) was added to the weighed amount of highly pure KCl powder prior to crystal growth. Blocks of approximate size 1 cm^3 were cleaved from the central portion of the large crystals. The blocks thus obtained were quenched from 650°C after having been kept at that temperature for 2 hr. The concentration of each impurity in these blocks was estimated by the methods described earlier[2]. The quenched blocks were cleaved into slices of dimensions $10 \times 10 \times 0{\cdot}5$ mm. The slices were X-irradiated through their broad faces at room temperature with a Philips PW 1009 X-ray Diffraction Unit, using a Mo target and operating at 35 kV and 10 mA. A thin KCl filter (0·3 mm thick) was used to cut off the effect of soft X-rays. For uniform coloration the slices were X-irradiated from both the sides for half of the time from each side[3]. The dose rate at the crystal position was measured by a *r*-meter type MR-125 (Atomic Energy Establishment, Trombay make) and was in the range of ~300 rev/hr. Care was taken to avoid the crystals from exposure to stray light during the X-irradiation and the subsequent optical absorption measurements. The method used to measure the optical absorption of the X-irradiated crystals has been described earlier[1].

To compare the effect of the nature and the concentration of the impurities on the growth

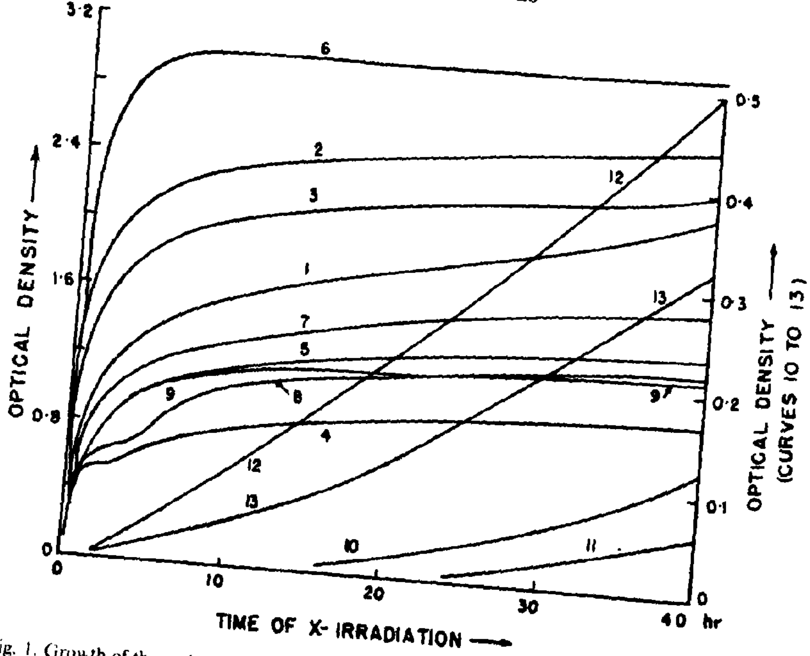

Fig. 1. Growth of the optical density at the peaks of F (curves 1–9) and M (curves 10–13) bands as a function of the time of X-irradiation at room temperature in highly pure and doped KCl crystals. Curves 1 and 10 are for H crystals. Curves 2–5 are for crystals Ca1, Cd1, Mn1 and Pb1 (containing 50 ppm of respective impurity) whereas curves 6–9 are for crystals Ca2, Cd2, Mn2 and Pb2 (containing 100 ppm of the respective impurity), respectively. Curves 11–13 are for crystals Ca1, Mn1 and Pb1, respectively.

of F and M bands, several crystals containing different concentrations of these impurities were studied. Typical results obtained with the H and the doped crystals containing 50 and 100 ppm of each of these impurities (and represented by numerals 1 and 2, respectively, as suffixes with the chemical symbols) are reported here.

Curves 1–9 in Fig. 1 show the growth of optical density at the F band peak (OD_F) at room temperature (RT) with the time of X-irradiation. Curve 1 is for the H crystal. Curves 2–5 are for crystals Ca1, Cd1, Mn1 and Pb1 whereas curves 6–9 are for crystals Ca2, Cd2, Mn2 and Pb2, respectively. Comparing curve 1 (for the H crystal) with curves 2 and 6 (for crystals Ca1 and Ca2, respectively) it is seen that under identical conditions of X-irradiation there is a large increase in the OD_F in Ca doped crystals. It is observed from curves 2 and 6 that on doping KCl with Ca the growth of the first stage F centers is enhanced whereas that of the second stage F centers is suppressed. It is further seen from these curves (and from those obtained for other concentrations of Ca, not shown in the figure) that the enhancement in the growth of the first stage F centers and the suppression in that of the second stage F centers increase with the increase of the concentration of Ca. This observation is in agreement with the results reported earlier by Jain and Mehendru[1]. The growth of OD_F in Cd1 and Cd2 crystals (curves 3 and 7, respectively) when compared with that for the H crystals (curve 1) shows that for small concentrations of Cd (e.g. crystal Cd1), the OD_F is larger in the Cd doped crystals. With the increase of the concentration of Cd impurity (e.g. crystal Cd2), OD_F is suppressed as compared with that in H crystals, X-irradiated under identical conditions. It is also seen from curve 3 that for small concentrations of Cd in KCl the first stage *F* centers are enhanced whereas the second stage *F* centers are suppressed. For concentrations of Cd > 50 ppm (typical results of which are shown for crystal Cd2, curve 7) both the first as well as the second stage *F* centers are suppressed. This observation is qualitatively in agreement with the results obtained by Jain *et al.*[4]. For Mn doped crystals (curves 4 and 8) and for Pb doped crystals (curves 5 and 9), *the magnitude of* OD_F *is always less* than that for an H crystal (curve 1) under identical conditions of X-irradiation. It is seen from curves 4 and 8 that the suppression in OD_F in Mn doped crystals decreases with the increase of the concentration of Mn impurity. It was observed that the magnitude of OD_F even for the highest* concentration of Mn (~200 ppm) was smaller than that for an H crystal, X-irradiated under identical conditions. The result that OD_F increases with the increase of Mn concentration has also been confirmed by thermoluminescence[5] and by EPR (result not reported here). It is also seen from curves 4 and 8 that the presence of Mn in KCl crystals suppresses the growth of both the first and the second stage *F* centers. However, the suppression in both the stages of *F* centers decreases with the increase of Mn concentration. It is further observed from the growth curves 4 and 8 that for times of X-irradiation lying between 2 to 5 hours, there occurs a small depression in the OD_F. This depression was found to increase with the increase in the concentration of Mn. From the present investigations no plausible explanation can be given for this depression in OD_F.

As is seen from curves 5 and 9 for the Pb1 and Pb2 crystals, respectively, the magnitude of OD_F is smaller than that for an H crystal, X-irradiated under identical conditions. It is further observed from these curves that with the increase of Pb concentration, there is no suppression caused in the first stage *F* centers whereas the growth of second stage *F* centers is suppressed The observation that the second stage *F* centers are suppressed with the increasing Pb content is in agreement with the results reported by Sibley *et al.*[6].

Curves 10–13 in Fig. 1 show the growth of the optical density OD_M at the *M* band peak in H, Ca1, Mn1 and Pb1 crystals, respectively, at *RT*. It is seen from curve 10 that in H crystals the *M* band appears only after about *15 hr of X-irradiation and continues increasing* thereafter gradually upto 40 hr of X-irradiation. In Ca1 crystals no *M* band is observed upto ~25 hr of X-irradiation (curve 11). Moreover, the growth of OD_M in Ca1 crystals beyond 25 hr of X-irradiation (curve 11) is comparatively smaller than that in the H crystals (curve 10) under identical conditions of X-irradiation. From the growth of OD_M in Mn1 and Pb1 crystals shown by curves 12 and 13, respectively, it is seen that the *M* band in these crystals appears in much shorter time of X-irradiation as compared with the H crystals. For example, a sizeable *M* band appears in these crystals in ~5 hr of X-irradiation. The OD_M in these crystals is greater by a factor of ~3 as compared with that observed in H crystals for time of X-irradiation > 15 hr. No *M* band was observed in Cdl crystals even upto 40 hr of X-irradiation.

The results of the growth of OD_M in Ca2, Cd2, Mn2 and Pb2 crystals were, in general, similar to those obtained with crystals Ca1, Cd1, Mn1 and Pb1. The *M* band in Ca2 crystals could be observed only after ~32 hr of X-irradiation and the magnitude of OD_M in these crystals was always smaller than in crystal Ca1 X-irradiated under similar conditions. The magnitude of OD_M in Mn2 and Pb2 crystals was larger than that obtained with crystals Mn1 and Pb1, respectively, when X-irradiated under identical conditions.

---

*Since the crystals containing > 200 ppm of Mn were translucent or even opaque hence no optical absorption measurements could be made with them.

The increase in the growth of OD_F in crystals containing Ca has already been reported by several workers[1, 7]. Although this enhancement in OD_F in Ca doped crystals has been attributed to the overlapping of Z_1 and F bands[8] but the recent ESR results[9] have shown that the increase in OD_F in Ca doped crystals is due to the F centers alone indicating thereby that the mechanism of Crawford and Nelson[11] is perhaps responsible for the increase in OD_F. The growth of OD_F in crystals Cd1 (curve 3) is similar to the growth observed in crystals doped with Ca and can be explained in a similar manner. The decrease in the growth of OD_F in crystals Cd2 (curve 7) could be due to the presence of higher aggregates of Cd which perhaps give rise to deep electron traps[4].

In the case of Pb1 and Pb2 crystals, the growth of OD_F is similar to that obtained for Cd2 crystal suggesting thereby that the suppression caused in OD_F due to the presence of Pb may also be due to the presence of deep electron traps. However, in the case of crystals doped with Mn, the results of the growth of OD_F are rather different. For smaller concentrations of Mn the suppression caused in OD_F is more (curve 4) than for higher concentration (curve 8). This is rather a very interesting result and further work is necessary to understand this anamolous behaviour of the growth of OD_F in Mn doped crystals.

The value of S in the relation[7] $\alpha_M = S\alpha_F^2$ where α_F and α_M are the absorption coefficients at the peaks of the F and M bands, respectively, is very small for crystals containing Ca. This result is similar to those reported by the earlier authors[6, 7]. However, in the case of Mn and Pb doped KCl crystals the magnitude of S is enhanced and is greater by at least an order of magnitude than that observed in H crystals under identical conditions of X-irradiation. Jain and Parashar [11] have also obtained a similar increase in the value of S in the Co doped KCl crystals. Several observations made with crystals containing different concentrations of Mn and X-irradiated under identical conditions (results not reported here) show that the value of S in these crystals remains almost the same. Further investigations are necessary to understand this non-dependence of S on the concentration of Mn in KCl crystals.

National Physical Laboratory,
New Delhi-12,
India

P. C. MEHENDRU
G D. SOOTHA

REFERENCES

1. JAIN S. C and MEHENDRU P. C., *Phys. Rev* **140**, A957 (1965).
2. JAIN S. C. and DAHAKE S. L., *Ind. J. Pure Appl. Phys.* **2**, 71 (1964).
3. WALKER C. T., *Phys. Rev.* **132**, 1963 (1963)
4. JAIN S. C., SOOTHA G D. and JAIN R. K., *Proc. phys. Soc.* **1**, 1220 (1968).
5. MEHENDRU P C and MITRA VED., *Ind. J. Pure Phys.* **6**, 350 (1968).
6. SIBLEY W. A., SONDER E. and BUTLER C. T., *Phys. Rev.* **136**, A537 (1964).
7. COMPTON W. D. and RABIN H., *Solid St. Phys.* **16**, 121 (1964).
8. JAIN S. C. and PARASHAR D. C., *Phys. Lett.* **4**, 36 (1963).
9. JAIN S. C., JAIN V. K. and SOOTHA G. D. To be published.
10. CRAWFORD J. H. and NELSON C. M., *Phys. Rev. Lett.* **5**, 314 (1960).
11. JAIN S. C. and PARASHAR D C., Unpublished work.

J. Phys. Chem. Solids Vol. 30, pp. 1015–1019.

The role of poison and undersaturation of the solvent in the etching mechanism

(*Received 8 August 1968*)

INTRODUCTION

SEVERAL etchants are mentioned in the literature[1] for revealing the dislocations in alkali halide crystals. Every etchant primarily contains a solvent whose function is to dissolve the crystal by nucleating kinks at the defect sites and a poison which retards the motion of steps across the crystal surface by inhibiting the kinks. The requirements that have to be fulfilled by the solvent and the poison to get good etch pits were subject of intensive research by several workers. Moran[2], Vermilyea[3] and Kostin *et al.* [4] suggested that the solubility of the crystal in the solvent must be low in order to produce satisfactory etch pits. On the contrary Gilman *et al.*[5] and Rozhanski *et al.*[6] suggested that the radius of the cation of the poison should not differ much from the radius of the cation of the lattice in order to get distinct etch pits. The recent results of Thyagarajan and Urusovskaya[7] however showed that neither the radius of the cation nor valency to be a determining factor in the selective etching of CsI crystals. Hari Babu and Bansigir[8, 9] obtained well defined etch pits on NaCl crystals at different undersaturations of the solvent (ethyl alcohol) using the same poison $CdCl_2$.

From the aforesaid it follows that most of the workers tried to find the requirements of the solvent and the poison independently in order to get well defined etch pits. In this paper an attempt has therefore been made to know more about the interdependance of the poison and undersaturation of the solvent. This has been achieved by studying the etching behaviour of different poisons at various undersaturations of the solvent in NaCl crystals.

EXPERIMENTAL

NaCl crystals used in the present investigation were grown in air by the Kyropoulos technique. After the growth, the crystals were annealed for sufficiently long time and brought to the room temperature slowly. Freshly cleaved samples were etched in 10 cc of etchants and after etching they were rinsed in ethyl alcohol (99·5 per cent). The rinsed samples were immediately blotted with fine filter papers. Ethyl alcohol containing 0·5 per cent water is taken as the standard solution and it is termed as *A*. To the solution *A* distilled water is added and alcohols having 2·5, 5 and 10 per cent water are prepared and termed as *B*, *C* and *D* respectively.

EXPERIMENTAL RESULTS

(*a*) *Effect of undersaturation of the solvent*

Rozhanski *et al.*[6] added Fe^{3+} ions and Cu^{2+} ions to acetic acid in order to inhibit the motion of steps across the surface of NaCl crystals and thereby wanted to obtain well defined etch pits. But these ions were not able to inhibit the motion of steps. However, Ca^{2+}, Hg^{2+} and Pb^{2+} ions reduced the step motion to a small extent and Cd^{2+} and Bi^{2+} ions reduced the step motion to a large extent. Kostin *et al.*[4] tried the above poisons in ethyl alcohol and in the case of some poisons like Hg^{2+} and Bi^{3+}, slightly different results were obtained. Kostin *et al.*[4] obtained good etch pits using Hg^{2+} ions and only satisfactory etch pits with Bi^{3+} ions.

In order to see why the same poisons behave differently in different solvents, the behaviour of several poisons in solutions *A*, *B*, *C* and *D* were investigated. The results obtained with $CdCl_2$, $CuCl_2 4H_2O$ and $CaCl_2$ are presented below through the photomicrographs.

The photomicrographs obtained on the matching surfaces one obtained by etching for 1 hr in solution *A* having 1 mg/cc $CdCl_2$ and the other obtained by etching for 10 min in solution *D* having 1 mg/cc $CdCl_2$ are shown in Figs. 1(a) and 1(b) respectively. To both the solutions *A* and *D* the same amount of poison is added and the photomicrographs show that the etch pits obtained due to solutions *A* and *D* are well defined. The etching behaviour or the effectiveness of the poison $CdCl_2$ in producing etch pits can be regarded as good, because, it is able to produce well defined etch pits both at low and high undersaturations of the solvent.

The etch pits obtained on the matching surfaces one etched for 45 min in solution *A*

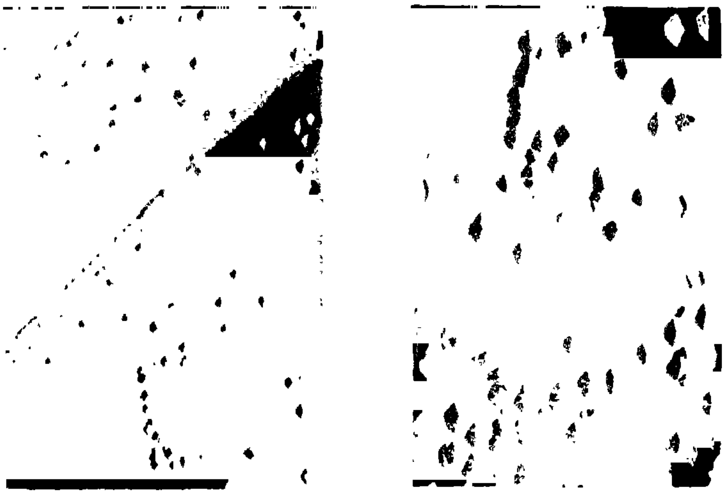

(a) (b)

Fig. 1. The photomicrographs are obtained on the matching surfaces: (a) etched for 1 hr in solution *A* having 1 mg/cc $CdCl_2$ and (b) etched for 10 min in solution *D* having 1 mg/cc $CdCl_2$. The definition of etch pits in both the photomicrographs is good. Magnification: 88 ×.

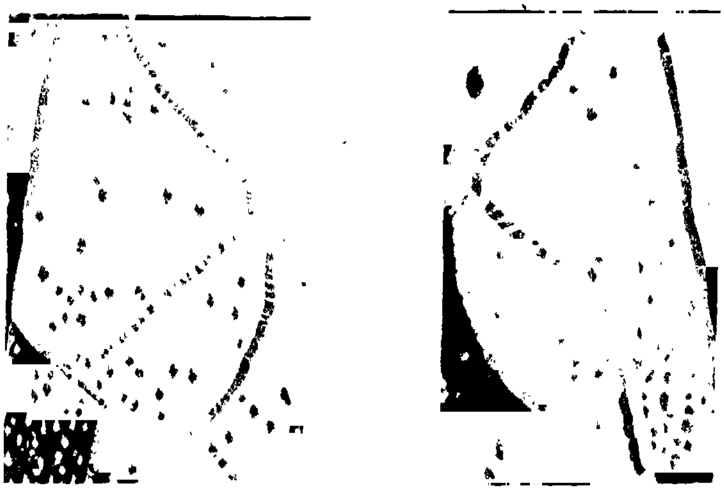

(a) (b)

Fig. 2. The photomicrographs are obtained on the matching surfaces: (a) etched for 45 min in solution *A* having 2 mg/cc $CuCl_2 4H_2O$ and (b) etched for 15 min in solution *D* having 30 mg/cc $CuCl_2 4H_2O$. The definition of the etch pits in the photomicrographs (a) is good and that shown in (b) is fair. Magnification: 88 ×.

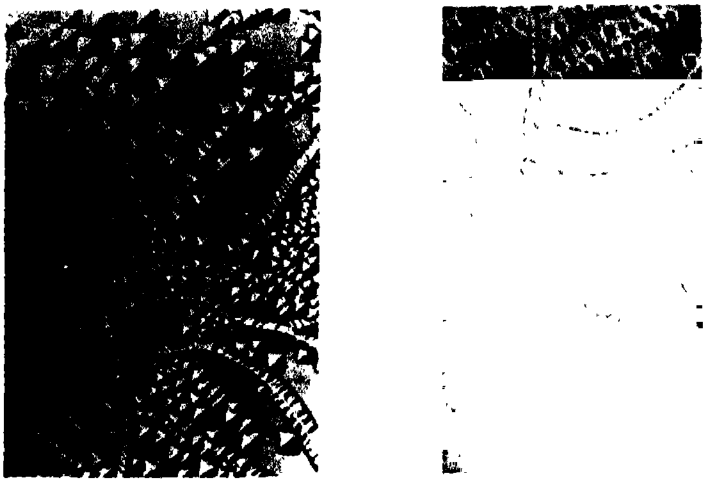
(a) (b)

Fig. 3. The photomicrographs are obtained on the matching surfaces: (a) etched for 30 min in solution *A* having 2 mg/cc $CaCl_2$ and (b) etched for 10 min in solution *C* having 20 mg/cc $CaCl_2$. The definition of etch pits shown in (a) is good and that shown in (b) is poor. Magnification: 88 ×.

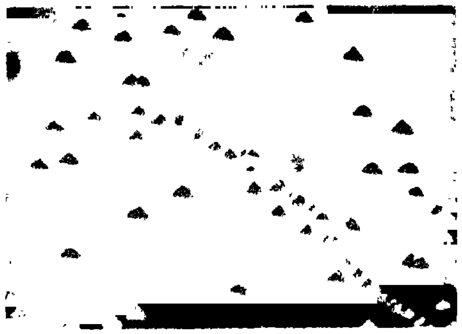
Fig. 4. Etch pits are due to an etchant consisting of solution *A* and $HgCl_2$. The definition of the pits is good. Magnification: 88 ×.

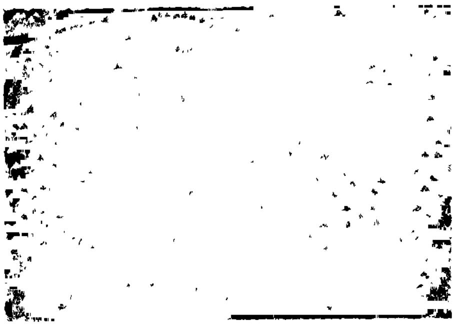
Fig. 5. Etch pits due to an etchant consisting of solution *A* and $Pb(C_2H_3O_2)_2$. The definition of the pits is good. Magnification: 88 ×.

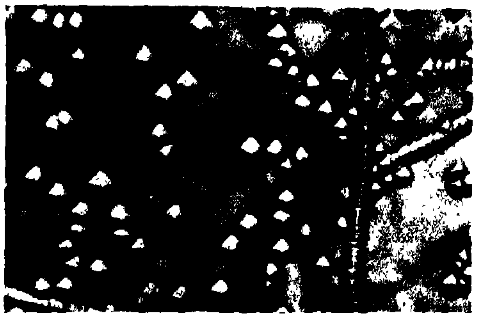

Fig. 6. Etch pits due to an etchant consisting of solution *A* and $BiCl_3$. The definition of the etch pits is good. Magnification: 88 ×.

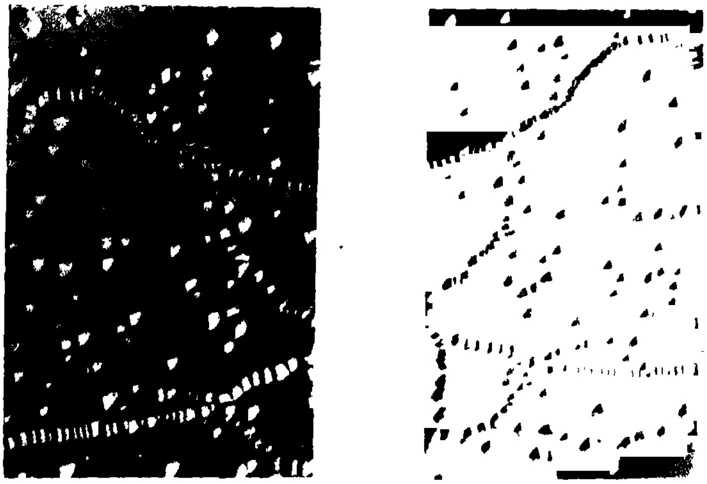

(a) (b)

Fig. 7. The photomicrographs are obtained on the matching surfaces: (a) etched for 30 min in solution *B* having 2 mg/cc $FeCl_3$ and (b) etched for 30 min in solution *B* having 2 mg/cc NH_4Cl. The definition of the etch pits in both the photomicrographs is good. Magnification: 88 ×.

Table 1

				Etching behaviour			
S. no.	Salt added (poison)	Cation	Ionic radius Å*	Solution *A*	Solution *B*	Solution *C*	Solution *D*
1.	Ammonium chloride	NH_4^+	1·48	Good	Good	Fair	Poor
2.	Mercurous chloride	Hg^+	0·965	No pits	No pits	No pits	No pits
3.	Lithium chloride	Li^+	0·64	No pits	No pits	No pits	No pits
4.	Cadmium chloride	Cd^{2+}	0·945	Good	Good	Good	Good
5.	Cadmium bromide	Cd^{2+}	0·945	Good	Good	Good	Good
6.	Cadmium iodide	Cd^{2+}	0·945	Good	Good	Good	Good
7.	Cadmium nitrate	Cd^{2+}	0·945	Good	Good	Good	Good
8.	Cadmium oxide	Cd^{2+}	0·945	Good	Fair	Fair	Poor
9.	Cadmium carbonate	Cd^{2+}	0·945	Good	Fair	Fair	Poor
10	Calcium chloride	Ca^{2+}	1·06	Good	Fair	Poor	No pits
11.	Stannous chloride	Sn^{2+}	0·71	Good	Good	Fair	Poor
12.	Manganese chloride	Mn^{2+}	0·91	Good	Good	Fair	Poor
13.	Lead acetate	Pb^{2+}	0·84	Good	Good	Fair	Poor
14.	Cupric chloride	Cu^{2+}	0·96	Good	Good	Good	Fair
15.	Mercuric chloride	Hg^{2+}	1·12	Good	Good	Fair	Poor
16.	Barium chloride	Ba^{2+}	1·43	Fair	Poor	No pits	No pits
17.	Bismuth trichloride	Bi^{3+}	1·20	Good	Good	Fair	Poor
18.	Ferric chloride	Fe^{3+}	0·67	Good	Good	Good	Fair

*PAULING L., *The Nature of the Chemical Bond*. Cornell University Press, New York (1960).

having 2 mg/cc $CuCl_24H_2O$ and the other etched for 15 min in solution *D* having 30 mg/cc $CuCl_24H_2O$ are shown in Figs. 2(a) and 2(b) respectively. The results show that at higher undersaturations of the solvent the amount of poison $CuCl_24H_2O$ needed to obtain etch pits is enormous. The photomicrographs also show that the etch pits obtained at lower undersaturation of the solvent are more distinct compared to those obtained at high undersaturation of the solvent. If the etching behaviour of the Cu^{2+} ion in solution *A* is regarded as good then its behaviour in solution *D* can be regarded as fair.

Figures 3(a) and 3(b) represent the photomicrographs obtained on the matching surfaces one etched for 30 min in solution *A* having 2 mg/cc $CaCl_2$ and the other etched for 10 min in solution *C* having 20 mg/cc $CaCl_2$. The pits shown in Fig. 3(b) are not clear. If the pits shown in Fig. 3(a) are regarded as good then those shown in Fig. 3(b) can be said to be poor. These results show that the etching behaviour of $CaCl_2$ poison becomes poor at higher undersaturation of the solvent.

In a similar manner several other poisons having different ionic radii and valency have been studied in solutions *A*, *B*, *C* and *D*. The etching behaviour of these poisons in the above solutions are given in Table 1. The results presented in Table 1 show that most of the poisons which produce good etch pits when they are present in solution *A* produce no etch pits or etch pits with poor definition when they are present in solution *D*. These results therefore suggest that the etching behaviour of the poison or its effectiveness to produce etch pits is not independent but is dependent on the undersaturation of the solvent. The fact that the Cd^{2+} ions produce good etch pits even at higher undersaturation of the solvent compared to other poisons also suggests the importance of the poison. In other words two factors namely the degree of undersaturation of the solvent and also the nature of the poison seem to be important factors in the etching mechanism.

(*b*) *Ionic radius*

Kostin *et al.*[4], Gilman *et al.*[5] and Thyagarajan and Urusovskaya[7] studied the effect of the ionic radius of the cation of the poison on the etching behaviour and as pointed out, they expressed different views. The results of the present investigation on the ionic radius are presented below.

The results presented in Table 1 for NaCl crystals show that the etching behaviour of a poison does not depend upon the radius of its cation. The etch pits obtained with $HgCl_2$, $Pb(C_2H_3O_2)_2$ and $BiCl_3$ in solution *A* are shown in Figs. 4–6. From the photomicrographs one can see that the pits obtained by the above mentioned poisons are good. However, the ionic radii of the above poisons does not differ by more than 25 per cent from that of Na^+.

The photomicrographs obtained on the matching surfaces, one by etching for 30 min in solution *B* containing 2 mg/cc $FeCl_3$ and the other by etching for 30 min in solution *B* having 2 mg/cc NH_4Cl are shown in Figs. 7(a) and 7(b) respectively. The quality of the etch pits obtained with either of the poisons is good. The ionic radius of Fe^{3+} is 0·67 *A* and it is less than that of Na^+ (0·98 *A*) by more than 30 per cent. The ionic radius of NH_4^+ is 1·48 *A* and it is approximately 50 per cent more than that of Na^+. Both Fe^{3+} and NH_4^+ which have nearly 0·8 *A* difference in ionic radii produce good etch pits. These results therefore show that the etch pit formation does not seem to depend very much on the ionic radius of the cation.

(*c*) *Valency*

The results presented in Table 1 show that the valency of the cation of the poison has no influence on its etching behaviour. The monovalent NH_4^+, the divalent (Cd^{2+}, Hg^{2+} and Pb^{2+}) and the trivalent (Bi^{3+} and Fe^{3+}) cations produce equally good etch pits in solution *A* or in solution *B*.

DISCUSSION

The results of these investigations therefore suggest that neither the size of the cation nor its valency are the responsible factors in producing good etch pits. The undersaturation of the solvent and the nature of the poison seem to be the determining factors. However, one important point worth discussing is the etching behaviour of the poison at different undersaturations of the solvent. From Figs. 2 and 3 we see that the etch pits produced at higher undersaturations are not as good as those produced at lower undersaturations. The increase in undersaturation of the solvent increases the kink nucleation rate and to inhibit these kinks which are produced at a greater rate, the poison concentration has to be increased. But in the case of $CaCl_2$ even increase in the poison concentration from 2 mg/cc to 20 mg/cc in solution *C* has resulted in poor etch pits.

Gilman *et al.*[5], Ives and Baskin[8] and Ives[9] pointed out the important role played by the complexes in the formation of etch pits. In the case of $CaCl_2$ and other poisons which produce good etch pits at lower undersaturation of the solvent (solution *A*) compared to those produced at higher undersaturations (solution *B*, *C* or *D*), the stability of the complexes produced at the kink site with respect to those present in the solvent layer close to the crystal surface may be different at different undersaturations. This may be the reason why good etch pits are not formed at higher undersaturations of the solvent. These suggestions regarding the stability of the complexes have to be confirmed by experiments.

SUMMARY

1. Most of the poisons investigated produce good etch pits at lower undersaturations of the solvent compared to those obtained at higher undersaturations.

2. The ionic radius of the cation of the poison seem to have no effect on the etching behaviour of the poison.

3. The formation of the etch pits does not depend upon the valency of the cation of the poison.

4. The stability of the complexes formed at the kind site and those formed in the solvent layer very close to the crystal surface seem to play very important role in the formation of etch pits.

Department of Physics,
Osmania University,
Hyderabad-7,
India

V. HARI BABU
K. G. BANSIGIR

REFERENCES

1. AMELINCKX S., *The direct observation of dislocations*, p. 40. Academic Press, New York (1964).
2. MORAN P. R., *J. appl. Phys.* **29**, 1768 (1958).
3. VERMILYEA D., *Acta Metall.* **6**, 381 (1958).
4. KOSTIN N. F., LUBENETS S. V. and ALEXANDROV K. S. *Kristallografiya* **6**, 737 (1961); Eng. Transl. *Soviet Phys. Crystallogr.* **6**, 588 (1962).
5. GILMAN J. J., JOHNSTON W. G. and SEARS G. W., *J. appl. Phys.* **29**, 741 (1958).
6. ROZHANSKI V. N., PARVOVA E. V., STEPANOVA V. M. and PREDVODITELOV A. A., *Kristallografiya* **6**, 704 (1961); Eng. Transl. *Soviet Phys. Crystallogr.* **6**, 564 (1962).
7. THYGARAJAN R. and URUSOVSKAYA A. A., *J. Phys. Chem. Solids* **28**, 1251 (1967).
8. HARI BABU V. and BANSIGIR K. G., *J. appl. Phys.* **38**, 908 (1967).
9. HARI BABU V. and BANSIGIR K. G., *J. phys. Soc. Japan* **23**, 860 (1967).

J. Phys. Chem. Solids Vol. 30, pp. 1019–1021

Some comments on the Lindemann melting formula

(*Received* 19 *June* 1968)

RECENTLY there has been interest in the properties of rare gas solids along their melting lines. High pressure measurements in argon by Crawford and Daniels[12] and by van Witzenburg and Stryland[13] have provided data to test the validity of Lindemann's[4] law of melting which states that a substance melts when the mean amplitude of the nuclear oscillations reach a critical value, roughly 10 per cent of the nearest neighbor distance. The mean square displacement, $\langle u^2\rangle$, in the quasi-harmonic approximation is defined by

$$\langle u^2\rangle = \frac{1}{MN}\sum_{qj}\left\{\frac{1}{2}+\frac{1}{e^{\hbar\omega_{qj}/kT}-1}\right\}\frac{\hbar}{\omega_{qj}} \quad (1)$$

where M is the nuclear mass, N is the number of atoms, and ω_{qj} are the quasi-harmonic phonon frequencies corresponding to the wave vector q and polarization j. In the quasi-harmonic approximation, at high temperatures, Lindemann's law is commonly expressed as follows

$$T_m = CM\Theta^2 v_m^{2/3} \quad (2)$$

where T_m is the melting temperature, M is the molecular weight, v_m is the specific melting volume, Θ is the specific melting volume, Θ is the Debye temperature appropriate to the inverse second moment of the frequency distribution and C is a constant. It is proportional to the relative mean square amplitude

$$\left(C = \frac{2^{1/3}k}{9\hbar^2 N_0^{5/3}}\frac{\langle u^2\rangle}{R^2}\right)N_0$$

N_0 is Avogadro's number and R is the nearest neighbor distance). Recent tests of the law in rare gas solids[2, 5] have made use of equation (2) because no direct measurements of the mean square displacements were available. In addition, the Debye Θ appropriate to the second moment instead of the inverse second moment has been used.

In this note we present a calculation of the root mean square displacement as a fraction of the nearest neighbor distance along the melting line of argon. Argon is considered in detail because the experimental data in this case is the most reliable. An (m–6) Mie–Lennard–Jones pair potential was used with nearest neighbor interactions only. The effects of anharmonicity were taken into account by using the frequency shift method[6–8]. The frequency shifts used in equation (2) were those obtained by Feldman and Horton[9]. This model has had some success in accounting for thermal and elastic properties of rare gas crystals[10]. We calculate $\langle u^2 \rangle$ for the (12–6) and (13–6) Mie–Lennard–Jones potentials.

The relative root mean square amplitudes for argon along its melting line are shown in Fig. 1. Experimental volumes were obtained from Crawford and Daniels[1, 2], van Witzenburg and Stryland[3], and Peterson *et al.*[11].

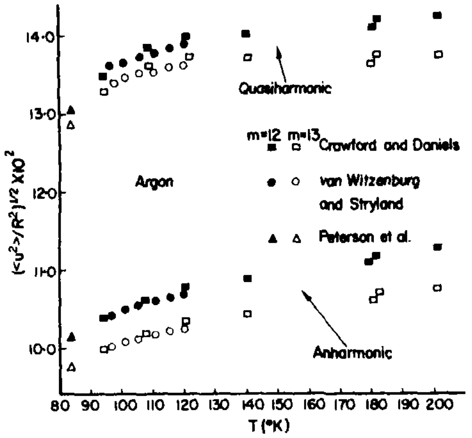

Fig. 1. Root mean square amplitudes as a fraction of nearest neighbor distance for argon along the melting line.

Quasi-harmonic and anharmonic results are shown and in both cases the values of the root mean square amplitudes increase mildly with temperature. The effect of including anharmonicity is appreciable.

Table 1. *Relative root mean square amplitudes for neon, argon, krypton, and xenon at their triple point*

Substance	T^*_m	$(\langle u^2 \rangle / R^2)^{1/2} \times 10^2$			
		Quasi-harmonic		Anharmonic	
	(°K)	$m = 12$	$m = 13$	$m = 12$	$m = 13$
Neon	24·6	15·6	15·5	10·9	10·5
Argon	83·8	13·0	12·8	10·1	9·7
Krypton	115·8	12·7	12·6	10·0	9·6
Xenon	161·4	12·5	12·2	9·9	9·5

*Obtained from POLLACK G. L., *Rev. mod. Phys.* 36, 748 (1964).

The relative root mean square amplitudes for neon, argon, krypton and xenon at their triple point are shown in Table 1. Domb[5] had earlier verified Lindemann's law in a rough fashion whereas we find that it is, in fact, obeyed to 10 per cent for neon, argon, krypton and xenon, and xenon, and better than 3 per cent for argon, krypton and xenon. As expected the root mean square amplitude increases slightly with decreasing mass. Along the melting line for argon our results show that Lindemann's law is obeyed to 10 percent for the temperature range considered. Crawford [2], who computed C in equation (2) by calculating the second moment in the Einstein approximation, found a similar variation in the value of C. His revised values of C are also in good agreement with ours.

Although our results show that Lindemann's law is rather well obeyed for the class of substances considered, at this time there seems to be no understanding of the connection between the Lindemann hypothesis and melting.

An experimental investigation of the Debye–Waller factor along the melting line would be extremely interesting.

Acknowledgements—It is a pleasure to thank Dr. G. K. Horton and Dr. M. L. Klein for suggesting this work and for helpful discussions and guidance. I wish to thank Drs. W. B. Daniels and R. K. Crawford for an enjoyable visit to their laboratory and thanks to Dr. Crawford for lending me a copy of his thesis before publication of results. I gratefully acknowledge financial support from AFOSR grant no. 68- 1372.

Physics Department, VICTOR V. GOLDMAN
Rutgers, The State University,
New Brunswick,
N.J. 08903, U.S.A.

REFERENCES

1. CRAWFORD R. K. and DANIELS W. J., *Phys. Rev. Lett.* **21**, 367 (1968).
2. CRAWFORD R. K., Ph.D. thesis, Princeton University (1968).
3. VAN WITZENBURG W. and STRYLAND J. C. *Can. J. Phys.* **46**, 811 (1968).
4. LINDEMANN F. A., *Phys. Z.* **11**, 609 (1910).
5. DOMB C., *Nuovo Cim. Suppl.*, series 10, **9**, 9 (1958).
6. BARRON T. H. K., In *Lattice Dynamics*, p. 247. Pergamon Press, Oxford (1965).
7. FELDMAN J. L., HORTON G. K. and LURIE J. B., *J. Phys. Chem. Solids* **26**, 1507 (1965).
8. COWLEY E. R. and COWLEY R. A., *Proc. R. Soc.* **A292**, 209 (1966).
9. FELDMAN J. L. and HORTON G. K., *Proc. phys. Soc.* **92**, 227 (1967).
10. HORTON G. K., *Am. J. Phys.* **36**, 93 (1968).
    PETERSON O. G., BATCHELDER D. N. and SIMMONS R. O., *Phys. Rev.* **150**, 703 (1966).

J. Phys. Chem. Solids Vol. 30, pp. 1021–1023.

F centers growth and thermoluminescence in Mn doped KCl crystals

(*Received* 12 *June* 1968)

THE METHODS used for growing highly pure and Mn doped KCl single crystals, X-irradiation, optical absorption and thermoluminescence have been described earlier[1, 2]. Letters H and D, respectively, denote the crystals grown from spectroscopically pure KCl (divalent impurity $\leqslant 1$ ppm) and Mn doped in spectroscopically pure KCl materials. *D*1, *D*2 and *D*3, respectively, denote crystals containing 50, 100 and 200 ppm of Mn.

In Fig. 1 are shown the curves for the growth of the optical density under the *F* band (peaking at 560 nm), at room temperature, with the time of X-irradiation. Curve 1 is for a slice cleaved from an *H* crystal whereas curves 2–4, respectively, are for slices cleaved from crystals *D*1, *D*2 and *D*3. From the shape of the growth curves 2–4, it is seen that in Mn doped crystals also (as in *H* crystals[1, 3]) the *F* centers grow in two stages. It is further seen from these curves that the first or fast stage *F* centers saturate in about 4 hr whereas the slow or second stage of *F* centers continue increasing even upto 30 hr of X-irradiation. These observations that the growth of first stage *F* centers saturates in about 4 hr and that the second stage *F* centers continue increasing even upto 30 hr of X-irradiation are qualitatively similar to those obtained with *H* crystals[1, 3]. It is also seen from curves 2–4 in Fig. 1 (for *D* crystals) that there occurs a slight bend in the growth curves when the time of X-irradiation lies between 2 and 4 hr. No such behaviour is observed for *H* crystals (curve 1, Fig. 1). There is no plausible explanation for this behaviour in the *D* crystals presently. Further work may perhaps throw some light.

From several thermoluminescence experiments performed on X-irradiatively coloured *D* crystals for various lengths of time it was observed that *F* centers bleach in two stages, giving rise to the two thermoluminescence peaks at 135 and 190°C besides the usual impurity peak[1] at 80°C. Growth of the areas under the various thermoluminescence peaks, with the time of X-irradiation, in *D* crystals have shown that the areas under the 80° and 135°C peaks saturate in $\leqslant 30$ min and ~ 3 hr, respectively, whereas that under the 190°C peak continues increasing with the time of X-irradiation upto ~ 30 hr. The observation that the area under the thermoluminescence peak at 80°C saturates in $\leqslant 30$ min indicates that the centers responsible for this peak, as in the case of 135°C peak, are limited in number. In Fig. 2 are shown the results of thermoluminescence obtained after 6 hr of X-irradiation, i.e. beyond the time of saturation of the growth of first stage *F* centers. Curves 1–4 in Fig. 2 are the thermoluminescence results obtained with slices cleaved from crystals *H*, *D*1, *D*2 and *D*3, respectively. It is seen from curves 2–4 that the areas under the 135°C thermoluminescence peak are 600, 810 and 1020 small squares[1], respectively. However, the

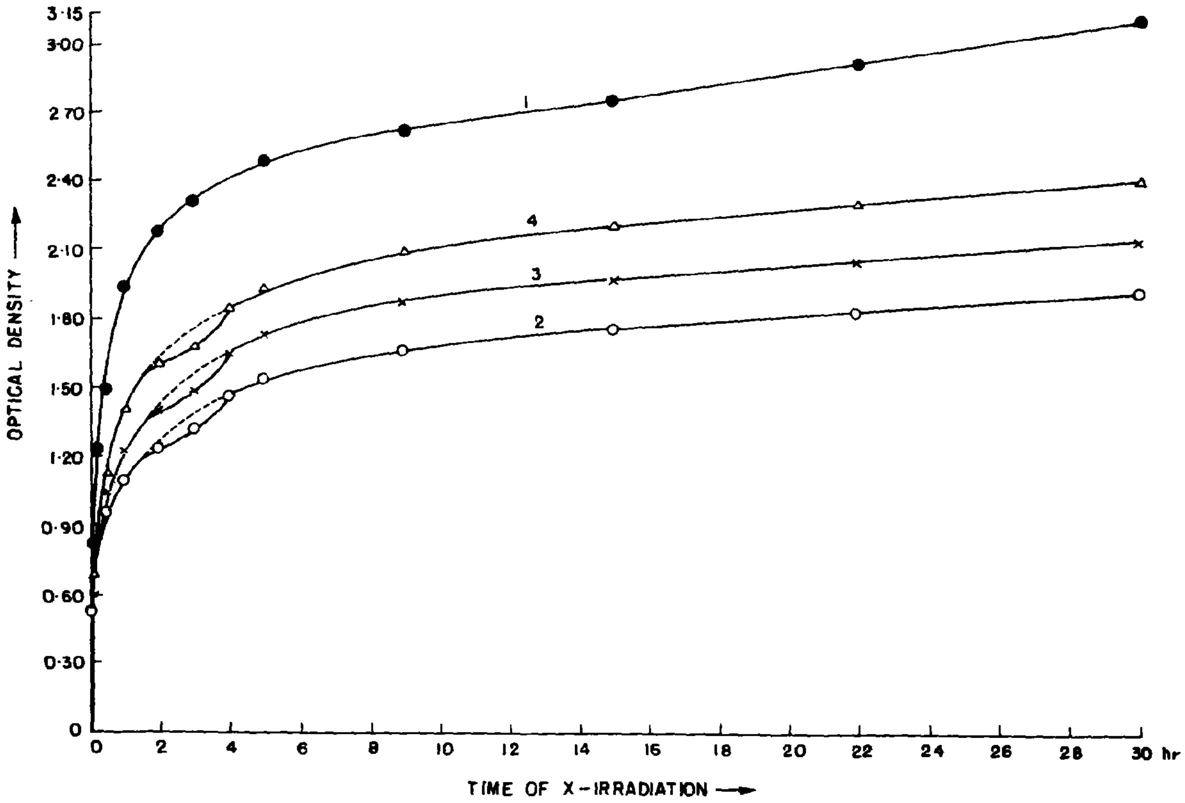

Fig. 1. Growth of the optical density under the peak of the *F* band (560 nm) as a function of the time of X-irradiation in pure and Mn doped KCl crystals. Curves 1–4 are for identical slices cleaved from crystals *H*, *D*1, *D*2 and *D*3, respectively.

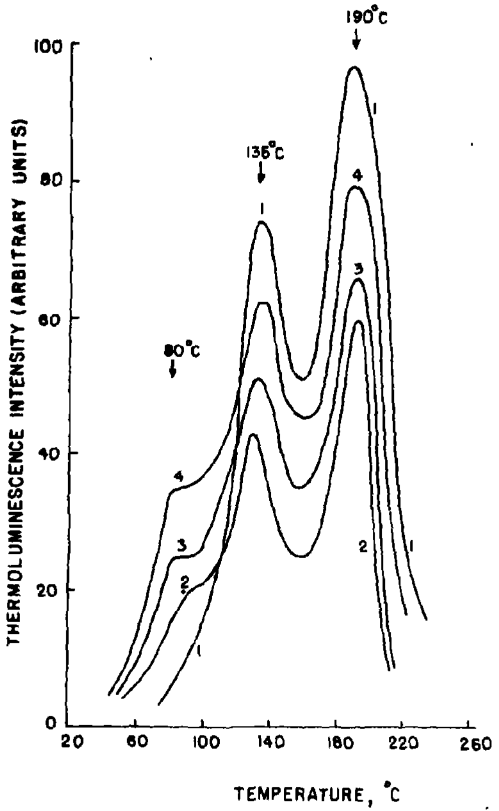

Fig. 2. Plot of thermoluminescence as a function of temperature. Curves 1–4 are for identical slices from crystals H, $D1$, $D2$ and $D3$, respectively. The slices were X-irradiated for 8 hr, with Mo target working at 35 kV and 10 mA, prior to heating at 40°C/min for thermoluminescence.

saturation area under this peak for an H crystal is 1180 small squares. Thus the saturation areas under the fast or first stage F centers peak at 135°C enhance with the increase in the concentration of Mn but even for $D3$ crystals (which contained the maximum concentration of Mn), the first stage F centers concentration is less than that for an H crystal.

Both these observations, namely, that the first stage F centers' growth is suppressed in D crystals as compared with that observed in H crystals and that the increasing concentration of Mn enhances the first stage F centers' growth, are rather inconsistent with the results reported earlier[1, 4–6] for other divalent cation impurities in alkali halides. Further work is necessary to understand these interesting observations.

It is also seen from curves 2–4 in Fig. 2 that the area under the 190°C thermoluminescence peak increases with the increase of Mn concentration and as in the case of 135°C thermoluminescence peak, the area under the 190°C peak for $D3$ crystals is less than that obtained for an H crystal (curve 1), X-irradiated under similar conditions and for the same length of time.

From the slope of the growth curves for the second stage F centers, the values of the parameter[1, 3] a for curves 2–4 in Fig. 1 are 0·70, 0·75 and 0·80 O.D. hr^{-1}, respectively, whereas the value of a for an H crystal under identical conditions is 1·5 (curve 1, Fig. 1). Thus the magnitude of a is almost twice for H crystals than for Mn doped crystals. The result that the rate of generation of anion vacancies in D crystals is suppressed by the presence of Mn in KCl as compared with that in H crystals, is in agreement with the results reported earlier[1, 5, 6] but the observation that the magnitude of a increases with the increase of the concentration of Mn is rather inconsistent with those reported earlier for other divalent cation impurities[1, 5, 6].

Acknowledgements—The authors are grateful to Dr S. C. Jain for helpful discussions. They also wish to thank Dr. A. R. Verma for constant encouragement.

National Physical Laboratory,
New Delhi-12,
India

P. C MEHENDRU
V. MITRA

REFERENCES

1. JAIN S. C. and MEHENDRU P. C., *Phys. Rev.* **140**, A957 (1965).
2. MEHENDRU P. C. and MITRA V., *Ind. J. Pure Appl. Phys.* 6, 350 (1968).
3. MITCHELL P. V., WIEGAND D. A. and SMOLUCHOWSKI R., *Phys. Rev.* **121**, 484 (1961).
4. SCHULMAN J. H. and COMPTON W. D., *Color Centers in Solids*, Pergamon Press, Oxford (1962).
5. SIBLEY W. A., SONDER E. and BUTLER C. T., *Phys. Rev.* **136**, A537 (1964).
6. SIBLEY W. A. and RUSSEL J. R., *J. appl. Phys.* **36**, 810 (1965).